ISSN 0031–8949
(ISSN 0281–1847)
ISBN 91-89621-21-2

12th X-ray Absorption Fine Structure International Conference (XAFS12)

Malmö/Lund, Sweden,
June 22–27, 2003

Editors: N. Mårtensson
D. Arvanitis
O. Karis

Physica Scripta

Vol. **T115** 2005

www.physica.org

Recognized by the European Physical Society

Author Index

The Author Index is arranged alphabetically by author, by subject area.

Click here to go to the Author Index

Click below to go to the Subject area:

Invited and Plenary
Theory and Fundamental Aspects
Materials
Magnetism
Catalysis and Nano
Biology
Environmental
Instrumentation
Emerging Techniques
Related Phenomena

Physica Scripta

Published jointly by

The Royal Danish Academy of Sciences and Letters in cooperation with the Danish Physical Society
The Delegation of the Finnish Academies of Science and Letters in cooperation with the Finnish Physical Societies
The Icelandic Scientific Society in cooperation with the Icelandic Physical Society
The Norwegian Academy of Science and Letters in cooperation with the Norwegian Physical Society
The Royal Swedish Academy of Sciences in cooperation with the Swedish Physical Society

Editorial Office
Physica Scripta
The Royal Swedish Academy of Sciences
Box 50005, SE-104 05 Stockholm, Swedish
email: physica@kva.se
web: www.physica.org

Production Editor
Katarina Lundin
Telephone: +46 8673 9528
email: kat@physica.kva.se

Scientific Editors
Managing Editor:
Prof. Roger Wäppling
Department of Physics, University of Uppsala
Box 530, SE-751 21 Uppsala, Sweden
Facsimile: +46 1851 2227
email: roger.wappling@fysik.uu.se

Technical Editor:
Dr Agneta Seidel
Department of Physics, University of Uppsala
Box 530, SE-751 21 Uppsala, Sweden
email: agnetas@physica.kva.se

Subscriptions
The Royal Swedish Academy of Sciences
PO Box 168, Didcot D.O., Oxford, OX11 7WD, United Kingdom

Subscription enquiries
May be made to the above address or by email to subscriptions@physica.org

Subscription Rates
Subscription to Physica Scripta for 2005 (includes Topical Issues) at **Sterling Pounds 995** for EEC countries: Austria, Belgium, Cyprus, Czech Republic, Denmark, Estonia, Finland, France, Germany, Greece, Hungary, Italy, Ireland, Latvia, Lithuania, Luxembourg, Malta, Netherlands, Poland, Portugal, Slovakia, Slovenia, Spain, Sweden, United Kingdom along with Iceland and Norway. Payment for all other countries can only be accepted at **US$1638**. Payment by credit card will be converted at the prevailing rate for Sterling pounds. Further details are available from **subscriptions@physica.org**. Topical Issues are supplied in CD format. Printed versions of Topical Issues are available at an additional charge.

Back numbers and single issues
Can be ordered separately. Price information on request to the above address or by email to subscriptions@physica.org

Manuscripts
Shall be submitted electronically to submissions@physica.org
Please see Instructions to Authors or consult http://www.physica.org. Enquiries as to the status of submitted manuscripts should be made to physica@kva.se

Offprints
The corresponding author will receive a .pdf file upon completion of publication

Typeset by J. W. Arrowsmith Ltd and Printed in Great Britain by Marston Book Services Ltd, Didcot, Oxon.

Physica Scripta, Vol. T115, 2005

Contents

Committees 16

Foreword 17

Lars Hedin and the Quest for a Theory of Excited States. *J. J. Rehr* 19

Invited and plenary

Nonspherical Potential, Vibronic and Local Field Effects in X-Ray Absorption. *A. L. Ankudinov and J. J. Rehr* 24

Advances in the Theoretical Analysis of the XANES (X-ray Absorption Near Edge Structure) Energy Region for Quantitative Structural Use. *M. Benfatto, S. Della Longa and P. D'Angelo* 28

Modeling Core-Hole Screening in Core-Excitation Spectroscopies. *E. L. Shirley, J. A. Soininen and J. J. Rehr* 31

Relativistic Keldysh Green's Function Approach to XAFS Theory. *T. Fujikawa* 35

New Insights for Materials Science Characterisation Using Different Complementary Techniques Combined with X-ray Absorption Spectroscopy. *V. Briois, S. Belin, F. Villain, F. Bouamrane, H. Lucas, R. Lescouëzec, M. Julve, M. Verdaguer, M. S. Tokumoto, C. V. Santilli, S. H. Pulcinelli, X. Carrier, J. M. Krafft, C. Jubin and M. Che* 38

Lattice Dynamics Information Obtained from EXAFS Measurements on Ta. *H. H. Rossner, E. Holub-Krappe, M. Fieber-Erdmann and H. J. Krappe* 45

X-ray Magnetic Dichroism: The Technique of Choice to Study Magnetism Element Specifically. *K. Baberschke* 49

Magneto-Electric Interactions Probed by X-ray Optical Activity. *J. Goulon, A. Rogalev, F. Wilhelm, N. Jaouen, C. Goulon-Ginet, P. Carra, I. Marri and Ch. Brouder* 54

Time-Resolved Energy-Dispersive XAFS for *In-situ* Characterization of Nano-Structures and Catalysts. *Y. Iwasawa, A. Suzuki and M. Nomura* 59

Evolution of Catalyst Structure under Reaction Conditions from Time-resolved *in situ* XAS Investigations. *T. Ressler, J. Wienold and O. Timpe* 66

In Situ Monitoring of Oxide-Supported Platinum-Group Metal Catalysts by Energy Dispersive EXAFS. *A. J. Dent, S. Diaz-Moreno, J. Evans, S. G. Fiddy, B. Jyoti and M. A. Newton* 72

In-situ Al K-edge Spectroscopy on Zeolites: Instrumentation, Data-interpretation and Catalytic Consequences. *J. A. van Bokhoven* 76

Environmental Interfaces, Heavy Metals, Microbes, and Plants: Applications of XAFS Spectroscopy and Related Synchrotron Radiation Methods to Environmental Science. *G. E. Brown, Jr., J. G. Catalano, A. S. Templeton, T. P. Trainor, F. Farges, B. C. Bostick, T. Kendelewicz, C. S. Doyle, A. M. Spormann, K. Revill, G. Morin, F. Juillot and G. Calas* 80

Energy-Dispersed Near-Edge X-Ray Absorption Fine Structure: a New Technique to Study Dynamic Surface Processes. *H. Kondoh, K. Amemiya, I. Nakai, M. Nagasaka, A. Nambu, T. Shimada, T. Yokoyama and T. Ohta* 88

Capturing Excited State Molecular Structures in Disordered Media with 100 ps Time Resolution by Laser Pump X-ray Probe XAFS. *L. X. Chen, G. B. Shaw, T. Liu, G. Jennings and K. Attenkofer* 93

Capacitance XAFS Method: A New Site-Selective and Microscopic X-Ray Absorption Spectroscopy. *M. Ishii, A. Nakao and T. Uchihashi* 97

Picosecond Time-Resolved X-Ray Absorption Spectroscopy of Solvated Organometallic Complexes. *W. Gawelda, C. Bressler, M. Saes, M. Kaiser, A. N. Tarnovsky, D. Grolimund, S. L. Johnson, R. Abela and M. Chergui* 102

Sub-Nanosecond Time Resolved XAFS of Laser Excited Thin Ge Films. *E. A. Stern, D. L. Brewe, K. M. Beck, S. M. Heald and Y. Feng* 1044

This page contains the contents of this issue. Full contents are contained on the CD and in the online version at www.physica.org. The following pages contain these additional contents.

Theory and fundamental aspects

Local Structure of Spin-Crossover Complex Studied by X-Ray Absorption Spectroscopy: Nature of Photo-Induced Phase. *H. Oyanagi, T. Tayagaki and K. Tanaka* 107

Size- and Site-Dependence of XMCD Spectra of Iron Clusters from *ab-initio* Calculations. *O. Šipr and H. Ebert* 110

XMCD Study on Electronic and Magnetic States of Rare-Earth 5d Electrons in Laves Compounds, RFe$_2$ (R = Rare-Earth). *A. Fujiwara, K. Asakura, I. Harada, H. Ogasawara and A. Kotani* 113

Structure of New Heterometallic Complexes in Hexane on Modelling the Recovery of Ruthenium From Radioactive Solutions. *S. B. Erenburg, N. V. Bausk, L. N. Mazalov, R. S. Shulman, T. V. Us and V. G. Torgov* 115

Strong Electron Correlation in Ca 2p, Sr 3d and Ba 4d Core Hole States Investigated by Means of Photoelectron Spectroscopy and MCDF Calculations. *J. Nikkinen, H. Aksela, S. Heinäsmäki, E. Kukk, N. Berrah and S. Aksela* 119

Theoretical Study of X-ray Photoemission, X-ray Absorption and Resonant X-ray Emission Spectroscopy of Mn Films on Ag. *M. Taguchi, P. Küger, J. C. Parlebas and A. Kotani* 122

Conjugate Shake Processes upon 2p-Photoabsorption of Atomic Sulphur. *A. G. Kochur and D. Petrini*. . . 125

Oxygen 1s NEXAFS Spectra of theV_2O_5(010) Surface: Theoretical Studies Using *ab initio* DFT Cluster Models. *C. Kolczewski and K. Hermann*. 128

XANES Calculation with an Efficient ''Non Muffin-Tin'' Method: Application to the Angular Dependence of the Al K-Edge in Corundum. *D. Cabaret, E. Gaudry, M. Taillefumier, P. Sainctavit and F. Mauri* 131

Self-Consistent Non-Local Optical Potential for XANES. *K. Hatada, M. Benfatto and C. R. Natoli* 134

Ab Initio R-Matrix/MQDT Method for Near-Edge X-ray Absorption Fine Structure. *M. Hiyama and N. Kosugi* 136

Temperature Dependence of Local Structure of Ge Impurity in Si (001)Thin Film Probed by Multiple-Scattering XAFS. *S. Wei, Z. Sun, H. Oyanagi, W. Zhong and D. Chen* 140

EXAFS and Local Thermal Expansion. *P. Fornasini, S. a Beccara, G. Dalba, R. Grisenti, J. Purans, A. Sanson, F. Rocca and D. Diop* 143

Multi-Channel Multiple Scattering Theory for XAFS. Application to $L_{2,3}$ Edges of Ca. *P. Krüger and C. R. Natoli*. 146

XANES and EXAFS Modelling of Configurational Disorder in Silver Borate Glasses. *G. Dalba, P. Fornasini, A. Kuzmin, F. Monti, A. Sanson, O. Sipr and F. Rocca* 149

A Quantitative Structural Investigation of the XANES Spectra of Potassium Ferrocyanide (III) at the Iron K-Edge. *K. Hayakawa, K. Hatada, C. R. Natoli, P. D'Angelo, S. D. Longa and M. Benfatto* 152

The Mean Square Variation of Multiple Scattering Path Length by Molecular Dynamics Simulation. *N. Binsted, A. B. Edwards, J. Evans and M. T. Weller* 155

Using Bond Valence Sums as Restraints in XAFS Analysis. *M. Newville* 159

X-ray Spectra and Electron Densities of States of the Complicated Semiconductors $TlAsS_2$, Tl_3AsS_3, Tl_3AsS_4 and Tl_3PS_4. *A. A. Lavrentyev, B. V. Gabrelian, I. Ya. Nikiforov, J. J. Rehr and A. L. Ankudinov* 162

Sodium K Edge XANES Calculation in 'NaCl' Type Structures. *R. J. Prado and A. M. Flank* 165

The Fourier-Transform Analysis of Ti K-XANES in Metamicts and Glasses. *L. Bugaev, F. Farges, E. Rusakova, A. Sokolenko,Ya. Latokha and L. Avakyan* 168

Aluminium K-edge XANES Study of Mica Preiswerkite. *Z. Wu, A. Marcelli, G. Cibin, A. Mottana and G. D. Ventura* 172

Initial Results of the One-Dimensional XAFS Debye-Waller Models for Active Sites of Cu Histidine and Cystein Metalloproteins. *N. Dimakis and G. Bunker* 175

Similarities and Differences Between XANES Spectra at Analogous Edges of Ternary Semiconductors $CuGaSe_2$, $ZnGeAs_2$ and $CuFeS_2$. *O. Šipr, J. Drahokoupil, P. Machek and A. Šimůnek* 179

Localized Nature of Valence-Hole States in $Ca_{2+x}Y_{2-x}Cu_5O_{10}$ Shown by O 1s XAS. *K. Okada* 182

Real Space Approach to Thermal Factor in EXAFS for Asymmetric Double-Well Potential. *K. Nitta, T. Miyanaga and T. Fujikawa*. 185

Selective Detection of Deep Level Centers by X-ray Absorption Fine Structure Questioned. *J. Bollmann, S. Knack, J. Weber, V. Koteski, H.-E. Mahnke and E. Welter* 188

Ab Initio Calculation of the Cr K Edge in α-Al_2O_3:Cr^{3+}. *E. Gaudry, D. Cabaret, Ph. Sainctavit, Ch. Brouder, F. Mauri, A. Rogalev and J. Goulon* 191

Overlapping XAFS L Spectra of 3d Metals: A New Application of the Regularization Method. *Yu. Babanov, S. Kiryanov, A. Sidorenko, L. Romashev, D. Vyalikh, S. Molodtsov, G. Guentherodt, U. Ruediger, Yu. Dedkov, M. Fonine, K. Baberschke, H. Wende and Y. U. Idzerda* 194

Thickness Inhomogeneity Effect in EXAFS Spectroscopy. *A. V. Ryazhkin, Yu. A. Babanov, T. Miyanaga, E. D. Crozier, R. A. Gordon, T. Reich and H. Funke* 197

Improvement of Double-Shell *R*-Space Resolution by the EXAFS Regularization Method. *D.-S. Yang and J. M. Lee* 200

Improved Self-Absorption Correction for Fluorescence Measurements of Extended X-Ray Absorption Fine-Structure. *C. H. Booth and F. Bridges* 202

REX2000: Yet Another XAFS Analysis Package. *T. Taguchi, T. Ozawa and H. Yashiro* 205

Final-State Rule vs the Bethe-Salpeter Equation for Deep-Core X-ray Absorption Spectra. *J. J. Rehr, J. A. Soininen and E. L. Shirley* 207

Nonlinear Energy Dependence of the Forbidden Energy Band in the Solid Solutions $Cu_xAg_{1-x}B^{III}C_2^{VI}$. *A. A. Lavrentyev, B. V. Gabrelian, I. Ya. Nikiforov, J. J. Rehr and A. L. Ankudinov* 212

Fe Coordination Environment in Fe(II)- and Fe(III)-Silicate Glasses via the Fourier-Transform Analysis of Fe K-XANES. *L. Bugaev, F. Farges, E. Rusakova, A. Sokolenko, Ya. Latokha and L. Avakyan* 215

Atomic Absorption Background in EXAFS of Rb in Inter-Alkaline Alloys. *A. Kodre, I. Arčon, J. P. Gomilšek and A. Mihelič* 218

Continuous Cauchy Wavelet Transform of XAFS Spectra. *M. Muñoz, F. Farges and P. Argoul* 221

A Study of the Pre-Edge X-Ray Absorption Fine Structures in Ni Monoxide. *S. J. Li, Z. Y. Wu, T. D. Hu, Y. N. Xie, J. Zhang, T. Liu, C. R. Natoli, E. Paris and A. Marcelli* 223

3D Molecular Graphical user Interface Add-On for Analysis Program for EXAFS: A New Prospect. *N. Dimakis and G. Bunker* 226

Lifetime dependency of the VUV-excited resonant photoemission spectra of ionic molecules. *M. Huttula, E. Kukk, H. Aksela, R. Sankari and S. Aksela* 229

Wavelet Analysis of Extended X-Ray Absorption Fine Structure Data. *H. Funke, M. Chukalina and A. Rossberg* 232

Cs L-Edge EXAFS Atomic Absorption Background. *I. Arčon, A. Kodre, J. P. Gomilšek, M. Hribar and A. Mihelič* 235

Efficient Determination of Optimal Regularization Parameter for Inverse Problem in EXAFS Spectroscopy. *M. Kunicke, I. Yu. Kamensky, Yu. A. Babanov and H. Funke* 237

Simultaneous Fitting with Constraints for EXAFS Study of Anharmonic Vibrational System. *D.-S. Yang, H.-M. Park and I. Nakai* 240

Multi-pole Representation of the Dielectric Matrix. *J. A. Soininen, J. J. Rehr and E. L. Shirley* 243

Calculation of Grazing Incidence EXAFS: Fresnel Theory Versus DWBA. *P. Keil, D. Lützenkirchen-Hecht and R. Frahm* 246

Local Structures of GaAs Semiconductor in High Shells Studied by Multiple-Scattering Extended X-ray Absorption Fine Structure. *Z. Sun and S. Wei* 249

Thermal-Motion-Induced Resonant Reflections at the Ge K-edge: Calculation of the Intensity Dependence on Atomic Displacements. *E. N. Ovchinnikova, A. P. Oreshko, Y. Joly, A. Kirfel, B. P. Tolochko and V. E. Dmitrienko* 252

Materials

DAFS and XAFS Investigation of Structural Short-Range Order of Decagonal Al-Co-Ni. *A. Kupsch, D. C. Meyer, P. Gille and P. Paufler* 255

Near-edge Absorption Spectroscopy of Interplanetary Dust Particles. *S. Brennan, K. Luening, P. Pianetta, J. Bradley, G. Graham, A. Westphal, C. Snead and G. Dominguez* 261

Correlations in the Vibrations of Atoms in Complex Unit Cells. *F. Bridges and D. Cao* 264

Thermal Vibration of the Rutile-Type Difluorides of First-Row Transition Metals. *K.-i. Murai, A. Yoshiasa, T. Yamanaka and I. Nakabayashi* 267

EXAFS and XRD Study of Local Dynamics in Cu_2O and Ag_2O. *A. Sanson, G. Dalba, P. Fornasini, R. Grisenti, F. Rocca, G. Artioli, M. Dapiaggi and W. Tiano* 271

XAFS Analysis of Layered $Li_xNi_{0.5}Mn_{0.5}O_2$ ($0 < x \leq 2$) Electrodes for Lithium Batteries. *A. J. Kropf, C. S. Johnson, J. T. Vaughey and M. M. Thackeray* 274

X-Ray Studies of Pd/Ag Membranes for Hydrogen Separation. *L. C. Witjens, J. H. Bitter, A. J. van Dillen, F. M. F. de Groot, D. C. Koningsberger and K. P. de Jong* 278

Combined XAFS/Powder Diffraction Analysis of Randomly Substituted Cation Sites in Crystalline Oxides. *N. Binsted, M. Stange, H. Fjellvåg and M. T. Weller* 281

Local Structure Analyses of Contamination Metals on the Silicon Wafer After LSI Processes Using XAFS Technique. *H. Hashimoto, J. Tsuji, H. Yokoi, S. Murakami and Y. Hanada* 285

Evidence by XAS of Tin Oxide Coating Layered Double Hydroxides. *M. Intissar, V. Briois, J.-P. Besse and F. Leroux* 288

Densification of Mn-Doped Tin Oxide Films by Conventional Heating and Microwave Heating Treatment. *A. P. Rizzato, C. V. Santilli, S. H. Pulcinelli, D. Stuerga, D. Chaumont and V. Briois* 291

Short Range Structure of Lanthanum Chloride/Oxychloride Determined by EXAFS. *H. Matsuura, S. Watanabe, T. Kanuma, H. Akatsuka, T. Honma, N. Umesaki, A. Kajinami, A. K. Adya and R. Fujita* 294

Short Range Structure of Lead-Lithium Fluoride Obtained by XAFS Analysis. *S. Watanabe, R. Toyoyoshi, T. Sakamoto, Y. Okamoto, Y. Iwadate, H. Akatsuka and H. Matsuura* 297

XAFS and Spectroscopic Characterization for the Structure and Electronic Structure of Ce-DMDPhPDA Complexes in Methanol. *T. Yaita, H. Shiwaku, S. Suzuki, Y. Okamoto, A. Shimada, Z. Assefa and R. G. Haire* 302

Structural Analysis of Co-Extracted Heptavalent, Technetium and Rhenium Complexes by EXAFS. *S. Suzuki, T. Yaita, Y. Okamoto, H. Shiwaku and H. Motohashi* 306

C K-Edge NEXAFS of 6H-SiC and 3C-SiC Systems. *M. Pedio, A. Giglia, N. Mahne, S. Nannarone, S. Giovannini, C. Cepek, F. Boscherini, R. Carboni, M. Benfatto and S. D. Longa* 308

Zinc Oxynitride Powders Examined by X-ray Absorption Near Edge Spectroscopy. *T. Moriga, T. Sakamoto, R. Saki, K.-i. Murai, I. Nakabayashi and J. B. Metson* 312

Local Structure of Six-Coordinated Silicon in Li_2O-SiO_2-P_2O_5 Glasses by Transmission XAFS Experiments. *K. Handa , J. Ide, K. Yamamoto, N. Kurosawa, K. Ozutsumi, T. Harami, K. Kojima and N. Umesaki* 314

A XANES Study at the Na and Al K-edge of Soda-Lime Aluminosilicate Glasses and Crystals. *D. R. Neuville, L. Cormier, A.-M. Flank and P. Lagarde* 316

XAFS Study of BI*ME*VOX Ionic Conductors for *ME* = Mg, Si, Zr, Zn. *A. Twaróg, R. Bacewicz, A. Kozanecka, W. Wróbel, F. Krok and I. Abrahams* 318

Behavior of Sodium Deposited on SiO_2 at High Coverages. *R. J. Prado, P. Lagarde, A.-M. Flank and J. Jupille* 320

Unoccupied Electronic States of MgS, CaS, FeS: X-Ray Absorption Fine Structure Theoretical Analysis. *A. V. Soldatov, A. N. Kravtsova, M. E. Fleet and X. Liu* 323

Characterization by XAS of NiO Thin Films Prepared by Pulsed LASER Deposition. *J. Moscovici, I. Bouessay, A. Rougier and A. Michalowicz* 326

EXAFS Study of SnO_2 Xerogel Doped with Sb and PTCDA. *J. P. Gomilšek, U. L. Štangar, A. Š. Vuk, G. Bratina, I. Arčon and A. Kodre* 329

XANES Study of Tribofilms Generated from Belt-Drive Continuously Variable Transmission Fluids. *Y. Iwanami, H. Wada and M. Nomura* 332

Near Edge X-Ray Absorption Spectroscopy: a Novel Approach for Determining Conduction Band Edge States in Transition Metal Oxide Gate Dielectrics. *G. Lucovsky, Y. Zhang, J. L. Whitten, D. G. Schlom and J. L. Freeouf* 335

Determination of the Short-Range Structure of $ZnCl_2$ in its Liquid, Vitreous and Crystalline Phases by XAS, at High Pressure and High Temperature. *C. Fillaux, B. Couzinet, C. Dreyfus, J. P. Itié and A. Polian* 339

X-ray Absorption Studies of Borosilicate Glasses Containing Dissolved Actinides or Surrogates. *C. Lopez, X. Deschanels, C. D. Auwer, J.-N. Cachia, S. Peuget and J.-M. Bart* 342

Characterization of Lithium Battery Materials During their Functioning in Using Dispersive XAS. *G. Ouvrard, N. Bourgeon, D. Guyomard, F. Baudelet and S. Belin* 346

EXAFS Study on Disorder in Microstructure of Amorphous Mesoporous Titania with Large Surface Areas. *H. Yoshitake, T. Sugihara and T. Tatsumi* 349

Combining EXAFS and X-Ray Powder Diffraction to Solve Structures Containing Heavy Atoms. *C. Hennig, T. Reich, W. Kraus, G. Reck, F. Prokert and N. Schell* 352

Lattice Location of N in $In_xGa_{1-x}As_{1-y}N_y$ Dilute Nitrogen Alloys. *G. Ciatto, F. Boscherini, F. D'Acapito, D. De Salvador, D. Batchelor, R. Carboni, L. Grenouillet, H. Mariette and S. Mobilio* 356

XAFS Study of Local Structure Change in Perovskite Titanates. *K. Sato, T. Miyanaga, S. Ikeda and D. Diop* 359

XAFS Study of Cu(II), Ni(II) and Co(II) β-Aminovinylketone Complexes. *V. G. Vlasenko, A. I. Uraev and A. D. Garnovskii* 362

Determination of Tm Charge State in PbTe(Tm) by XANES Method. *A. I. Lebedev, I. A. Sluchinskaya, S. G. Nikitenko and S. G. Dorofeev* 365

Lattice Relaxation around Arsenic and Selenium in CdTe. *V. Koteski, H. Haas, E. H.-Krappe, N. Ivanovic and H.-E. Mahnke* 369

XAFS Study of A-site-Deficient $La_{0.63}Ti_{0.92}Nb_{0.08}O_3$ Perovskite. *A. Yoshiasa, M. Okube, H. Okudera, A. Nakatsuka, M. Yashima, A. Sakai, M. Mori and R. Ali* 372

XAFS Study of the Perovskite-Type Proton Conductor $SrZr_{0.9}Yb_{0.1}O_{3-\delta}$. *M. Okube, A. Yoshiasa, M. Yashima, K. Ohuchi, T. Ishimura, C. Numako and K. Koto* 375

XANES Study of Lanthanum-Doped Lead Titanate Ceramics. *P. P. Neves, V. R. Mastelaro, A. Michalowicz, J. A. Eiras, L. P. Lopes, A. C. Doriguetto and Y. P. Mascarenhas* 378

Pressure Induced Phase Transitions in Amorphous Ge. *E. Principi, F. Decremps, A. Di Cicco, F. Datchi, S. De Panfilis, A. Filipponi and A. Polian* 381

Local Order Around Er^{3+} Ions in thin Silicon Oxide Layers Grown in Si by MBE. *F. d'Acapito, S. Mobilio, A. Terrasi, S. Scalese, G. Franzó and F. Priolo* 384

The Structural Role of Ag in Galena (PbS). A XANES Study. *G. Giuli, E. Paris, Z. Wu, S. De Panfilis, G. Pratesi and C. Cipriani* 387

Reflection mode XAFS at the Ti K-edge of Lithium Intercalated TiO_2 Electrodes. *D. Lützenkirchen-Hecht, M. Wagemaker, A. A. van Well and R. Frahm* 390

Linearly Polarized Carbon K-edge X-ray Absorption Spectroscopic Study of Heavily *p*-Doped Polyacetylene Film with Preferred Orientation. *M. G. Kim, H. J. Lee, B. H. Kim, J. S. Kim and Y. W. Park* 393

Cs 3d Absorption and Resonant Photoemission Study of Caesium Halogenides. *R. Ruus, K. Kooser, E. Nõmmiste, A. Saar, I. Martinson and A. Kikas* 396

In-situ XAFS Studies on Local Structures of Molten InSb Compounds. *S. Wei, K. Lu, C. Li, W. Zhong, W. Yan, T. Uruga, W. Chen, X. Niu, Z. Wu, D. Chen and Z. Sun* 399

XAFS Study on Cathode Materials for Li-ion Batteries using X-ray Microbeam. *T. Nonaka, C. Okuda, H. Nakano, Y. Ukyo and Y. Seno* 402

Tin and Niobium in Dry and Fluid-Rich (H_2O, F) Silicate Glasses. *P. C. Piilonen, F. Farges, R. L. Linnen and G. E. Brown Jr.* 405

XANES Study on Solid Electrolyte Interface of Li Ion Battery. *T. Akai, H. Ota, H. Namita, S. Yamaguchi and M. Nomura* 408

Comparison of Photo-Degradation of Polyimide Film by UV Irradiation in Air and in Vacuum . *T. Tanaka, K. K. Bando, N. Matsubayashi, M. Imamura and H. Shimada* 412

Structure Determination by EXAFS of Nb-Peroxo-Citrato Complexes in Aqueous Solution-Gel Systems. *M. K. Van Bael, I. Arčon, K. Van Werde, D. Nelis, J. Mullens and L. C. Van Poucke* 415

Debye-Waller Factor Study of Co, Cu and CoCu Granular Alloy. *J. C. Cezar, N. P. Abreu and H. C. N. Tolentino* 418

Microstructures of Mechanically Alloyed $Fe_{60}Ni_{40}$ Studied by XAFS and XRD. *S. Yin, Z. Xie, J. Zhang, Q. Bian, W. Yan, Z. Jiang and S. Wei* 421

Multiple Scattering Analysis of O K-Edge NEXAFS in Iron Oxides. *S. Giovannini, F. Boscherini, R. Carboni, L. Signorini, L. Pasquini, N. Mahne, A. Giglia, M. Pedio, S. Nannarone, M. Benfatto and S. Della Longa* 424

Local Structure in $LaMnO_3$ Across the Jahn-Teller Transition. *Raquel. A. Souza, Aline Y. Ramos, Helio C. N. Tolentino and E. Granado* 428

Fluorescence EXAFS Analysis of Nanoscale Zinc-Blende MnAs Dots Grown on GaAs(001) by Molecular Beam Epitaxy. *H. Ofuchi, J. Okabayashi, M. Mizuguchi, M. Yamada, K. Ono, Y. Takeda, M. Oshima and H. Akinaga* 431

Soft X-ray XAFS Experiments of SiO_2-P_2O_5 Sol-Gel Film. *J. Ide, K. Handa, H. Takakura, K. Ozutsumi and N. Umesaki* 433

XAFS Study on Silica Glasses Irradiated by High-Energy Particles. *T. Yoshida, T. Tanabe and H. Yoshida* 435

Quantum Dots Microstructure and Energy Spectrum Peculiarities. *S. B. Erenburg, N. V. Bausk, L. N. Mazalov, A. I. Nikiforov and A. I. Yakimov* 439

Orbital Ordering in $Pr_{0.5}Sr_{0.5}MnO_3$: Pr K-Edge XAFS Study. *K. R. Priolkar, V. D. Kulkarni, P. R. Sarode, R. Kumashiro and S. Emura* 442

An Investigation of Valence State and Structural Geometry of Polyvalent Fe and Ti Ions in Sodium Borosilicate Glasses by X-Ray Absorption Spectroscopy. *X. C. Yang, M. Dubiel, D. Ehrt and A. Schütz* 445

Zr K-Edge EXAFS Study of PZT Thin Film Formation From Sols. *I. Arčon, B. Malič, M. Kosec and A. Kodre* . 448

EXAFS and XRD Characterization of Iron Thin Films Prepared by Sputtering at Very Low Temperatures. *F. Jiménez-Villacorta, A. Muñoz-Martín, M. Vila, C. Prieto and A. Traverse* 450

EXAFS Characterization of Nickel Clusters in Ni/Si_3N_4 Sputtered Thin Films. *M. Vila, F. Jiménez-Villacorta, C. Prieto and A. Traverse* 454

Local Structure of $Sr_2FeMo_xW_{1-x}O_6$ Double Perovskites Studied by EXAFS. *F. Bardelli, C. Meneghini, S. Mobilio, S. Ray and D. D. Sarma* 457

Local Structure of Ag Nano-Clusters Deposited on Silicon Wafer by Total Conversion Electron Yield XAFS. *Y. Suzuki, T. Miyanaga, K. Kita, T. Uruga and I. Watanabe* 459

EXAFS Study of $PbPb_{1/3}Ta_{2/3}O_3$ Perovskite. *V. G. Vlasenko, I. V. Pirog, I. P. Raevskii, O. N. Razumovskaya, S. I. Raevskaya and L. A. Shilkina* 462

Changes in the Local Structure of Nanocrystalline Electrochromic Films of Hydrated Nickel Vanadium Oxide upon Ozone-Induced Coloration. *E. Avendaño, A. Kuzmin, J. Purans, A. Azens, G. A. Niklasson and C. G. Granqvist* 464

Application of a Metal Ion-Implantation for the Preparation of Visible-Light Sensitive Zeolite Photocatalyst: V Ion-Implanted Ti-Containing HMS Mesoporous Molecular Sieves. *H. Yamashita, Y. Kanazawa, K. Kida and M. Anpo* 467

XAS Study of A_2FeMoO_6 Double Perovskite. *J. Herrero-Martín, J. García, G. Subías, J. Blasco and M. C. Sánchez* 471

Confined Lead Nano-Granules Investigated with X-ray Absorption Spectroscopy. *A. Witkowska, J. Rybicki, A. Trapananti, E. Principi and A. Di Cicco* 474

Structural Analysis of Manganese Borate Glasses by XAFS Measurement. *A. Kajinami, S. Deki and K. Handa* 477

Chemical State Analysis of 0.2 mass% Mo in Steel by XAFS. *M. Nagoshi, T. Kawano, K. Sato, M. Funakawa, T. Shiozaki and K. Kobayashi* 480

Ce 2p3d Resonant Inelastic X-ray Scattering in Ce–Ni Intermetallic Compounds. *J.-M. Mariot, L. Journel, R. Delaunay, J.-P. Rueff, G. Schmerber, J.-P. Kappler, N. Jaouen, F. Wilhelm, A. Rogalev, C. F. Hague and G. Krill* 483

XANES Study of Titanium Environment in $BaO\text{-}B_2O_3\text{-}TiO_2$ System. *V. R. Mastelaro, C. A. C. Feitosa, L. J. Q. Maia, A. C. Hernandes, A. Ibanez and A. Michalowicz* 486

Mineralogy of Greigite Fe_3S_4. *I. Letard, Ph. Sainctavit, N. Menguy, J.-P. Valet, A. Isambert, M. Dekkers and A. Gloter* 489

Evolution of an Iron Film on GaAs(001)-4 $\times$ 6. *R. A. Gordon, P. S. Budnik, D. T. Jiang and E. D. Crozier* . . 492

Structure of the Magnetic Trilayer System Fe/Pd/Fe Epitaxially Grown on GaAs(001)-4 $\times$ 6. *P. S. Budnik, R. A. Gordon and E. D. Crozier* 495

Valence State of Ru at the Mn sites in $Pr_{0.5}Sr_{0.5}MnO_3$. *J. S. Kim, B. H. Kim, D. C. Kim, M. G. Kim, A. Maignan, B. Raveau and Y. W. Park* 498

Soft X-ray Absorption Spectra of Amorphous Carbon. *Y. Muramatsu, E. M. Gullikson and R. C. C. Perera* . 501

Glancing Angle Fluorescence XAFS Study on Metal Oxide Thin Films Obtained by Oxygen Gas Cluster Ion Beam Assisted Deposition Techniques. *H. Kageyama, T. Asanuma, T. Takeuchi, K. Kadono, J. Matsuo, T. Seki, T. Kitagawa, N. Toyoda, Y. Shimizugawa and T. Uruga* 504

Pseudo Jahn-Teller Effect Observed in $Eu@C_{60}$. *S. Emura, K. Shirai and Y. Kubozono* 507

The Hybridized M3d-F2p Character of Low-Energy Unoccupied Electron States in 3d Metal Fluorides Observed by F 1s Absorption. *A. S. Vinogradov, S. I. Fedoseenko, S. A. Krasnikov, A. B. Preobrajenski, V. N. Sivkov, D. V. Vyalikh, S. L. Molodtsov, V. K. Adamchuk, C. Laubschat and G. Kaindl* 510

Investigation of Structural and Electronic Properties in Ru Perovskite Oxides by XAFS Measurements. *M. Mizumaki, K. Yoshii, Y. Hinatsu, Y. Doi and T. Uruga* 513

Correlation Between Local Structure and Ionic Conductivity of Potassium-Doped Siloxane Poly(propyleneoxyde) Ormolytes. *J. Chaker, K. Dahmouche, V. Briois, C. V. Santilli, S. H. Pulcinelli and P. Judeinstein* 516

Solvation Structure of Bromobenzene Molecule Doped in Supercritical Xenon Studied with Fluorescent XAFS Measurement. *Z. Jin, K. Nakagawa, M. Tanaka, I. Shimoyama, F. Kaneko and T. Murata* 520

XAFS Observations of Initial Growth of (0001) ZnO on {1120} Sapphire Substrates. *P. Fons, K. Nakahara, A. Yamada, K. Matsubara, K. Iwata, H. Takasu and S. Niki* 523

Ge Coordination States in SiO_2-GeO_2 Glasses at High Pressure, Inferred from *in situ* XAFS at the Ge K-Edge. *O. Majérus, L. Cormier, J.-P. Itié and G. Calas* 525

Measurement of Luminescence from Silica Glasses: an Optical X-Ray Absorption Fine Structures Study at Si K-Edge. *T. Yoshida, T. Tanabe, S. Takahara and H. Yoshida* 528

Sodium Adsorption on the TiO_2(110) Surface: an XAFS Structural Study. *R. J. Prado, P. Lagarde, A.-M. Flank, J. Jupille and S. Bourgeois* 531

XANES Studies of Thallium Compounds and Valence States and Local Environment of Thallium in Some of its Superconducting Cuprates. *A. Agarwal and A. N. Vishnoi* 534

High-Pressure EXAFS and XRD Investigation of Unit Cell Parameters of SnO. *H. Giefers, F. Porsch and G. Wortmann* 538

Mn on the Surface of ZnO(0001) – a Resonant Photoemisson Study. *E. Guziewicz, K. Kopalko, J. Sadowski, M. Guziewicz, Z. Golacki, J. Kanski and L. Ilver* 541

X-ray Excited Optical Luminescence Studies of PPh_3AuCl: Site-Specificity at the C and P K-Edges and the Au $M_{5,4}$-Edges. *P.-S. G. Kim, Y. F. Hu, R. J. Puddephatt and T. K. Sham* 545

The P(1s) and P(2p) XAFS Spectra of Elemental Phosphorus, Theory and Experiment. *A. Jürgensen* . . . 548

XANES, EXAFS and RMN Contributions to Follow the Structural Evolution Induced by Alkali-Silica Reaction in SiO_2 Aggregate. *L. Khouchaf, J. Verstraete, R. J. Prado and M. H. Tuilier* 552

EXAFS Study of Pressure-Induced Phase Transition in $SrWO_4$. *A. Kuzmin, R. Kalendarev, J. Purans, J. P. Itié, F. Baudelet, A. Congeduti and P. Munsch* 556

Electrochemical Lithium Intercalation into Transition Metal Oxides. *U. Haake, D. Lützenkirchen-Hecht and R. Frahm* 559

Local Structures of Liquid Semi-Metal Sb Studied by *in-situ* XAFS. *W. Yan, C. Li, S. Wei, Z. Wu, X. Niu, W. Chen, K. Lu and T. Uruga* 562

In situ X-ray Absorption Spectroscopic Study of Oxide Film on Fe Alloy. *J. S. Kim, C. H. Chang and K. Y. Kim* 564

XAFS Analyses of Zinc Compound in Corrosion Product for Magnesium Alloy of Super Plastic Processing. *T. Honma, H. Mori, K. Higashi, H. Okado, K. Maehara, I. Hirosawa and N. Umesaki* 567

X-ray Absorption Studies of Al-Mn System. *L. K. Mehta, S. K. Joshi and A. P. Deshpande* 570

X-Ray K-Absorption Studies of Cobalt (II) Imidazoles. *S. K. Joshi and B. D. Shrivastava* 573

XAFS Study on $Li_{1-x}Ni_{0.5}Mn_{0.5}O_2$ Cathode Materials for Li-Ion Battteries. *Y. Arachi, H. Kobayashi, S. Emura, Y. Nakata, M. Tanaka and T. Asai* 577

Magnetism

Magnetic moment in the Top Pt Layer of Co/Pt Bilayers. *M. Suzuki, H. Miyagawa, N. Kawamura, H. Muraoka, Y. Inaba, T. Shimatsu, Y. Sonobe, Y. Isohama, N. Nakamura, N. Ishimatsu and H. Maruyama* . 580

CO Induced Spin Reorientation Transition of Co/Pd(111) Studied by XMCD and XPS. *D. Matsumura, T.Yokoyama, K. Amemiya, S. Kitagawa and T. Ohta* 583

Limitations of Integral XMCD Sum-Rules for the Early 3d Elements. *A. Scherz, H. Wende, C. Sorg, K. Baberschke, J. Minár, D. Benea and H. Ebert* 586

Local Structure in Strained Manganite thin Films. *N. M. Souza-Neto, A. Y. Ramos, H. C. N. Tolentino, E. Favre-Nicolin and L. Ranno* 589

Ga Magnetic Polarization in Mn_3GaC under High Pressure Probed by Ga *K*-Edge XMCD. *N. Kawamura, N. Ishimatsu, M. Isshiki, Y. Komatsu and H. Maruyama* 591

Jahn-Teller Dynamic Distortions in $LaMnO_3$ Determined by EXAFS. *J. García, G. Subías, M. C. Sánchez and J. Blasco* 594

XAFS Study of Epitaxial $Co_xTi_{1-x}O_{2-x}$ Anatase. *S. M. Heald, S. A. Chambers and T. Droubay* 597

Temperature Dependence of Magnetic EXAFS for Rare Earth Elements. *H. Wende, A. Scherz, C. Sorg, Z. Li, P. Poulopoulos, K. Baberschke, A. L. Ankudinov, J. J. Rehr, F. Wilhelm, N. Jaouen, A. Rogalev, D. L. Schlagel and T. A. Lograsso* 600

X-Ray Resonant Scattering in Fe_3O_4, $MnFe_2O_4$ and $CoFe_2O_4$ Ferrites. *G. Subías, J. Garcia, M. G. Proietti, J. Blasco, H. Renevier, J. L. Hodeau and M. C. Sánchez* 603

Atomic Structure and the Magnetic Properties of Zr-Doped Sm_2Co_{17}. *B. Ravel and K. Gallagher* 606

Theoretical Analysis of Spin-Dependent Mn K-Edge X-Ray Absorption of MnP. *G. Smolentsev and A. V. Soldatov* 609

Direct Observation of the Fe Substitution Effect on the MCD Spectra of the Dysprosium Iron Garnet Family. *A. Agui, M. Mizumaki, T. Matsushita, N. Kawamura and T. Nakatani* 611

Fluorescence EXAFS Study on Local Structures around Mn and Fe Atoms Doped in ZnO. *H. Ofuchi, Z. W. Jin, T. Fukumura, M. Kawasaki, Y. Matsumoto, T. Hasegawa, H. Fujioka, M. Oshima and H. Koinuma* . 614

Temperature Dependence of X-Ray Magnetic Circular Dichroism in Rare Earth Iron Garnets (Rare Earth = Gd, Dy and Sm). *H. Miyagawa, N. Kawamura and M. Suzuki* 616

X-ray Absorption Fine-Structure Determination of Interfacial Polarization in $SrTiO_3$ Thin Films Grown on Si(001). *J. C. Woicik, F. S. Aguirre-Tostada, A. Herrera-Gomez, R. Droopad, Z. Yu, D. Schlom, E. Karapetrova, P. Zschack and P. Pianetta* 620

XAS Characterization of Growth Parameter Effects for Pulsed Laser Deposited $CoxTi_{1-x}O_{2-\delta}$ Films. *A. Lussier, J. Dvorak, Y. U. Idzerda, S. R. Shinde, S. B. Ogale and T. Venkatesan* 623

XMCD Investigation of Spin Disorder in γ-Fe_2O_3 Nanoparticles at the Fe $L_{2,3}$ Edges. *S. Brice-Profeta, M.-A. Arrio, E. Tronc, I. Letard, Ch. Cartier dit Moulin and Ph. Sainctavit* 626

A Universal Relationship Between Magnetization and the Local Structure in $La_{1-x}Ca_xMnO_3$; a Probe of the Magnetization Process. *L. Downward, F. Bridges, S. Bushart, J. Neumeier and L. Zhou* 629

Mn K-Edge Magnetic EXAFS for Ni-Mn Alloys. *T. Miyanaga, T. Okazaki, R. Maruko, S. Nagamatsu, T. Fujikawa and Y. Sakisaka* 632

XMCD Signals of the High Spin Molecules Fe_8. *I. Letard, Ph. Sainctavit, D. Gatteschi, Ch. Cartier dit Moulin, G. Champion and J.-P. Kappler* 635

Co/Cu/Ni Trilayers Near Their CurieTemperature Studied by XMCD. *C. Sorg, A. Scherz, H. Wende, T. Gleitsmann, Z. Li, S. Rüttinger, Ch. Litwinski and K. Baberschke* 638

XAS Study of $LaMn_{1-x}Ga_xO_3$ Series. *M. C. Sánchez, G. Subías, J. García and J. Blasco* 641

Analysis for Fe-*M* (*M* = Si, Al, Sn) Alloys by Multiple Scattering X-Ray Magnetic Circular Dichroism of Fe K-Edge. *K. Okamoto, S. Nagamatsu, E. V. Voronina, T. Miyanaga and T. Fujikawa* 645

Evolution of Ni Local Structure in $NdNiO_3$ Perovskite Across the Metal-InsulatorTransition. *C. Piamonteze, H. C. N. Tolentino, A. Y. Ramos, N. E. Massa, J. A. Alonso, M. J. Martínez-Lopes and M. T. Casais* 648

Information in Magnetic EXAFS. *A. L. Ankudinov, J. J. Rehr, H. Wende and K. Baberschke* 651

Resonant Photoemission Study of $La_{1-x}Sr_xMnO_3$ Single Crystals. *L. L. Lev, M. B. Tsetlin, M. Leandersson, H. Nylen, I. Lindau, M. N. Mikheeva and A. M. Balbashev* 654

XAFS and XRD Studies on Structures of $Nd_9Fe_{85-x}Mn_xB_6$ Nanocomposites. *S. Yin, S. Wei, G. Xie, Q. Bian, J. Zhang, O. Chen and H. Yang* 658

Catalysis and nano

Temperature Dependence of the Growth of Cerium Oxide Nanoparticles investigated by SAXS and XANES. *J. Zhang, Z. Y. Wu, L. X. Rong and B. Z. Dong* 661

Study on the Thermal Degradation of CeO_2-ZrO_2 Solid Solution by XAFS and XRD. *Y. Nagai, T. Yamamoto, T. Tanaka, T. Nonaka and A. Suda* 664

Study of the Probe Molecule Adsorption on Co-Mo Sulfide Model Catalysts by Means of XANES and FT-IR. *T. Kubota, M. Kawano and Y. Okamoto* 667

In-situ X-ray Absorption Spectroscopy Investigations During the Conditioning Procedure of PtRu Colloid Catalysts. *H. Modrow, G. Köhl, J. Hormes, H. Bönnemann, U. Endruschat and R. Mörtel* 671

Monolayer Dispersive Supported CuO/γ-Al_2O_3 Catalysts Studied by XAFS. *D. Chen, X. Zhang, Y. Hu, Y. Chen, S. Zou and S. Wei* 675

In situ Study of the Crystallisation of Nano-Sized Zinc and Cobalt Aluminate Spinel Catalysts from Ion-Exchanged Zeolite Precursors. *A. M. Beale, G. Sankar, D. G. Nicholson and W. van Beek* 678

Structure of Dioxygen Binding Xerogels Incorporating Cyclams Complexed with $CuCl_2$ Salts. *C. Goulon-Ginet, J. Goulon, A. Rogalev, F. Wilhelm, N. Jaouen, G. Dubois, S. Brandès, G. David, R. Guilard, R. Corriu, D. Cabaret and Y. Joly* 681

EXAFS Study of Electrolytic Nanosolution Confined in Interstitial Nanospaces of Single-Wall Carbon Nanohorn Colloids. *T. Ohkubo, Y. Hattori, H. Kanoh, T. Konishi, H. Sakai, M. Abe, D. Kasuya, M. Yudasaka, S. Iijima, T. Fujikawa and K. Kaneko* 685

EXAFS Characterization of the Local Structure of Fe in Fe-ZSM-5: an Experimental and Theoretical Study. *S. H. Choi, B. R. Wood, J. A. Ryder and A. T. Bell* 688

XAFS Study on the Visible-Light Sensitive Cr-Containing Zeolite Photocatalyst: Mesoporous Cr-HMS Molecular Sieves. *H. Yamashita, K. Yoshizawa, K. Kida, S. Ohshiro and M. Anpo* 691

Annealing Temperature Dependence of C_{60} on Silicon Surfaces: Bond Evolution and Fragmentation as Detected by NEXAFS. *M. Pedio, F. Borgatti, A. Giglia, N. Mahne, S. Nannarone, S. Giovannini, C. Cepek, E. Magnano, G. Bertoni, E. Spiller, M. Sancrotti, L. Giovanelli, L. Floreano, R. Gotter and A. Morgante* 695

EXAFS and XANES Study of Two Novel Pd Doped Sn/SnO_x Nanomaterials. *D. Grandjean, R. E. Benfield, C. Nayral, L. Erades, K. Soulantica, A. Maisonnat and B. Chaudret* 699

Cd and Se Atomic Environments During the Growth of CdSe Nanoparticles in Glass. *T. M. Hayes, P. D. Persans, A. Filin, C. Peng and W. Huang* 703

Ni K- and Au L_3-edge XAFS of $[Au_6Ni_{32}(CO)_{44}]^{6-}$ and a Study of its Transformations in Acetonitrile Solutions. *O. A. Belyakova, Y. Kubozono, S. Kashino and Yu. L. Slovokhotov* 705

Investigation of Size Effects in Magnetoelectric $BiFeO_3$. *S. Chattopadhyay, S. D. Kelly, V. R. Palkar, L. Fan and C. U. Segre* 709

Nucleation and Growth of Copper Nanoparticles on Silicon Surfaces. *A. Singh, K. Luening, S. Brennan, T. Homma, N. Kubo and P. Pianetta* 714

Electronic Characterization of the Single-Wall Carbon Nanotubes: a XANES Study. *Z. Y. Wu, I. Davoli, M. L. Terranova, S. Orlanducci, V. Sessa, M. Abbas, K. Ibrahim, J. Zhong and S. Botti* 717

Structural Stability of Giant Polyoxomolybdate Molecules as Probed by EXAFS. *A. I. Frenkel, S. C. Frankel and T. Liu* 721

In Situ XAFS study on Mo Oxide Catalysts by Molten Salt Preparation. *N. Matsubayashi, K. Sato, M. Imamura, H. Shimada, P. Afanasiev and C. Geantet* 724

XAS and XRD Studies on the Structural Changes of Ni-Raney Catalyst after a Hydrogenation Process. *N. Watanabe, A. Y. Ramos, J. A. M. Ferreira and H. C. N. Tolentino* 727

Investigation of Stress State of Silver Nanoparticles in Silicate Glasses by Means of EXAFS. *M. Dubiel, X. C. Yang and S. Brunsch* 729

Local Structures of Nanocomposite $Co\text{-}C_{60}$ and $Co\text{-}SiO_2$ Thin Films Studied by Fluorescence XAFS. *B. Sheng, D. Chen, J. Fan, W. Liu, X. Zhang, Y. Jiang, W. Yan and S. Wei* 733

EXAFS Study of Fe(3+) Interaction with ZrO_2 and TiO_2 Oxides. *V. V. Kriventsov, D. I. Kochubey, G. Colón, M. C. Hidalgo, J. A. Navio, M. V. Tsodikov and Yu. V. Maksimov* 736

EXAFS Study of Nb Doped $Sr(Co/Fe)O_{3-x}$ Perovskites. *V. V. Kriventsov, D. I. Kochubey, Z. R. Ismagilov, O. Yu. Podyacheva and A. P. Nemudry* 740

Estimating Crystallite Size in Polydispersed Samples using EXAFS. *S. Calvin, C. J. Riedel, E. E. Carpenter, S. A. Morrison, R. M. Stroud and V. G. Harris* 744

XAFS and XRD Studies of $PdO\text{-}CeO_2$ Catalysts on $\chi\text{-}Al_2O_3$. *W. B. Li, Y. Murakami, M. Orihara, S. Tanaka, K. Kanaoka, K.-i. Murai, T. Moriga, E. Kanezaki and I. Nakabayashi* 749

XAS Investigation of Iron Substitution in Triclinic FeAPO-34. *I. Arčon, A. Ristić, N. Novak Tušar, A. Kodre and V. Kaučič* 753

Multiple Scattering Approach to Au L_3-edge XANES of $spr\text{-}Au/Al_2O_3$ Catalyst. *S.-i. Nagamatsu, N. Ichikuni, S. Shimazu, T. Fujikawa, K. Fukuda and T. Uematsu* 756

XANES Study of Carbon Nanotubes Grown without Catalyst. *M. I. Abbas, Z. Y. Wu, K. Ibrahim, S. Botti, R. Ciardi and A. Marcelli* 759

XAFS Study on Active Iron Sites in MCM-41 as a Catalyst for Liquid Phase Oxidation. *T. Shishido, Q. Zhang, Y. Wang, T. Tanaka and K. Takehira* 762

In-Situ XAFS Study of Ag Clusters in Zeolite 4A. *Y. Suzuki, T. Miyanaga, H. Hoshino, N. Matsumoto, and T. Ainai* 765

X-ray Absorption Spectroscopy on Heterogeneous Catalysts at the new XAS Beamline at ANKA. *J.-D. Grunwaldt, S. Hannemann, J. Göttlicher, S. Mangold, M. A. Denecke and A. Baiker* 769

In-Situ X-Ray Absorption Near Edge Structure (Xanes) Spectroscopy of PtRu Colloid Catalysts at Operating Temperature. *B. Brendebach, S. Bucher, J. Hormes, H. Bönnemann, K. S. Nagabhushana, R. Brinkmann and H. Modrow* 773

EXAFS Studies of Bimetallic Ag-Pt and Ag-Pd Nanorods. *D. Lahiri, B. A. Bunker, C. M. Doudna, M. F. Bertino, F. Blum, A. Tokuhiro and J. Terry* 776

An XAFS Study on the Polymer Protected CuPd Bimetallic Nanoparticles – A Novel Heterobond-Philic Structure. *K. Asakura, C. R. Bian, S. Suzuki, W.-J. Chun, N. Watari, S. Ohnishi, P. Lu and N. Toshima* 781

Local Structures of Ultra-Thin Pt Films Probed by Grazing Incidence Fluorescence XAFS. *Z. Xie, I. Kojima, Y. Xie, B. He, D. Chen, T. Liu, T. Hu, X. Zhang and S. Wei* 784

Mo K-edge EXAFS Analysis of Mo/USY Zeolite – Effects of Extra-Framework Aluminum on the Location and Dispersion of Mo Sulfide Catalysts. *K. Sato, N. Matsubayashi, M. Imamura, K. K. Bando and H. Shimada* 787

Characterization of Size Dependent Structural and Electronic Properties of CTAB-Stabilized Cobalt Nanoparticles by X-ray Absorption Spectroscopy. *H. Modrow, N. Palina, Ch. S. S. R. Kumar, E. E. Doomes, M. Aghasyan, V. Palshin, R. Tittsworth, J. C. Jiang and J. Hormes* 790

XAS *In Situ* Cell for Measurements of Mn and Fe Promoted Sulfated Zirconia Catalysts. *R. E. Jentoft, A. H. P. Hahn, F. C. Jentoft and T. Ressler* 794

The Structure of a VO_x/TiO_2 (anatase) Powder Catalyst under Reduction and Oxidation at 623 K. *G. Silversmit, J. A. van Bokhoven, H. Poelman, A. van der Eerden, G. B. Marin, M.-F. Reyniers and Roger De Gryse* 798

XAFS Study on the Local Atomic Structures of Cerium-Oxide Nanoparticles with Surface Coatings. *Z. Wu, J. Zhang, X. Chen, Z. Chen, M. Sun, Z. Wu and L. Guo* 802

Preparation of Mesoporous Silica Supported Nb Catalysts and *in-situ* XAFS Characterization During Carburization Process. *N. Ichikuni, H. Hachiya, K. K. Bando, S. Shimazu and T. Uematsu* 807

XAS Studies on Incorporation of Mn and Co into Silicalite-1. *I. Arčon, N. Novak Tušar, A. Ristić, A. Kodre and V. Kaučič* 810

Quantitative Determination of Platinum Oxidation State by XANES Analysis. *H. Yoshida, S. Nonoyama, Y. Yazawa and T. Hattori* 813

Spontaneous Dispersion of PdO and Generation of Metal Pd cluster in Zeolites Studied by Means of *in situ* DXAFS. *K. Okumura, R. Yoshimoto, S. Yokota, K. Kato, H. Tanida, T. Uruga and M. Niwa* 816

X-ray Absorption Spectroscopy on Cu/ZnO Catalysts Selected by High-Throughput Experimentation Techniques. *J.-D. Grunwaldt, C. Kiener, F. Schüth and A. Baiker* 819

In Situ X-Ray Absorption Fine Structure Studies on the Structure of Ni_2P Supported on SiO_2. *T. Kawai, S. Sato, W.-J. Chun, K. Asakura, K.-K. Bando, T. Matsui, Y. Yoshimura, T. Kubota, Y. Okamoto, Y.-K. Lee and T. S. Oyama* 822

Structural Analysis of Photo-Chemically Anchored Molybdenum Oxide Catalysts by EXAFS. *H. Murayama, N. Ichikuni, K. K. Bando, S. Shimazu and T. Uematsu* 825

In-Situ XAFS Analysis of Dynamic Structural Change of Pd-Pt Nano-Particles Supported on Catalyst Surface Under Sulfidation Conditions. *K. K. Bando, T. Matsui, Y. Ichihashi, K. Sato, T. Tanaka, M. Imamura, N. Matsubayashi and Y. Yoshimura* 828

Monitoring of fast Transformations in Solid State Chemistry and Heterogeneous Catalysis by QEXAFS in the Second Scale. *D. Lützenkirchen-Hecht, J.-D. Grunwaldt, M. Richwin, B. Griesebock, A. Baiker and R. Frahm* 831

XAFS Study on the Local Structure of Zirconium Containing Mesoporous Silicas, Zr-MCM-41 and Their Catalytic Properties. *A. Yamaguchi, M. Yokoyama, A. Suzuki, Y. Iwasawa, H. Sakai, M. Yuasa and M. Abe* 834

Structure and Magnetism of Ni Clusters in AlO_x: Importance of XAS in the Synthesis Optimization. *E. Fonda, D. Babonneau, F. Pailloux, S. R. Teixeira and A. Traverse* 837

Effects of Boron and Phosphorous on Nano-Amorphous Ni-B and Ni-P Alloys Studied by X-ray Spectroscopy. *S. Wei, Z. Jiang, Z. Wei, X. Zhang and S. Zou* 841

Biology

The Manganese Complex of Oxygenic Photosynthesis: Conversion of Five-Coordinated Mn(III) to Six-Coordinated Mn(IV) in the S_2-S_3 Transition is Implied by XANES Simulations. *H. Dau, P. Liebisch and M. Haumann* 844

The Location of Calcium in the Manganese Complex of Oxygenic Photosynthesis Studied by X-Ray Absorption Spectroscopy at the Ca K-Edge. *C. Müller, P. Liebisch, M. Barra, H. Dau and M. Haumann* 847

NEXAFS Study of Amino Acid Analogues Assembled on Gold. *R. M. Petoral Jr. and K. Uvdal* 851

An XAS Study of the Cation Binding Sites in the Purple Membrane of *Halobacterium Salinarum*. *F. Sepulcre, M. Grazia Proietti, M. Benfatto, S. D. Longa, J. García and E. Padrós* 855

Simulation of XANES Spectra for Protein-Bound Metal Centers: Analysis of Linear Dichroism Data. *P. Liebisch, M. Haumann and H. Dau* 859

Investigation of the Local Structure of Fe(II) Bleomycin and Peplomycins using Theoretical Analysis of XANES. *G. Smolentsev, A. V. Soldatov, E. Wasinger, E. Solomon, K. Hodgson and B. Hedman* 862

An Enhanced Electronic State in ZnTPP Induced by Interaction with Solvation: A Multiple-Scattering Calculation of X-ray Absorption Near-Edge Spectra. *T. Liu and L. X. Chen* 864

Biological XAFS at the BioCAT Undulator Beamline 18ID at the APS. *R. A. Barrea, R. Fischetti, S. Stepanov, G. Rosenbaum, E. Kondrashkina, G. B. Bunker, E. Black, K. Zhang, D. Gore, R. Heurich, M. Vukonich, C. Karanfil, A. J. Kropf, S. Wang and T. C. Irving* 867

Methodological Study Using XAS of an Arsenic-Based Antileukemia Treatment. *E. Curis, I. Nicolis, S. Bohic, A. Somogyi, A. Simionovici and S. Bénazeth* 870

First Observation of Natural Circular Dichroism for Biomolecules in Soft X-ray Region Studied with a Polarizing Undulator. *M. Tanaka, K. Nakagawa, A. Agui, K. Fujii and A. Yokoya* 873

Environmental

Polarization Dependent Grazing Incidence (GI) XAFS Measurements of Uranyl Cation Sorption onto Mineral Surfaces. *M. A. Denecke, D. Bosbach, K. Dardenne, P. Lindqvist-Reis, J. Rothe and R. Z. Yin* . . . 877

Tridimensional Imaging of Local Structure by X-Ray Absorption Spectroscopy. *A. Di Cicco, A. Trapananti and A. Filipponi* 882

Archeological Applications of XAFS: Prehistorical Paintings and Medieval Glasses. *F. Farges, E. Chalmin, C. Vignaud, I. Pallot-Frossard, J. Susini, J. Bargar, G. E. Brown Jr and M. Menu* 885

EXAFS, XANES, and *In-Situ* SR-XRD Characterization of Biogenic Manganese Oxides Produced in Sea Water. *J. R. Bargar, S. M. Webb and B. M. Tebo* 888

Investigating Actinide Molecular Adducts from Absorption Edge Spectroscopy. *C. D. Auwer, S. D. Conradson, P. Guilbaud, P. Moisy, J. Mustre de Leon and E. Simoni* 891

Combined XANES and EXAFS Study on the Bonding of Methyl Mercury to Thiol Groups in Soil and Aquatic Organic Matter. *U. Skyllberg, J. Qian and W. Frech* 894

XAFS Study on the Trace Amounts of Ytterbium Ions Incorporated in Calcium Carbonate Crystal. *H. Tsuno, H. Kagi, Y. Takahashi, T. Akagi and M. Nomura* 897

A Preliminary Study on the Speciation of Inorganic and Organic Tin Compounds Using XAFS. *N. Sakakibara, Y. Takahashi, Y. Yamaguchi and M. Nomura* 901

Hydration Effect on Structural Parameter of Chromium Loaded in Silica. *Y.-L. Wei, H.-C. Wang, Y.-W. Yang and J.-F. Lee* 905

Effect of Water on XAS Spectrum of $Cu(NO_3)_2$ Reference. *N. Cheng, Y.-L. Wei, Y.-W. Yang and J.-F. Lee* . . 907

Effect of Thermal Stabilization on Lead Speciation in Silica Leached with H_2SO_4/HNO_3. *M.-J. Hu, Y.-L. Wei, H.-C. Huang, Y.-W. Yang and J.-F. Lee* 909

Linking Monte-Carlo Simulation and Target Transformation Factor Analysis:A Novel Tool for the EXAFS Analysis of Mixtures. *A. Rossberg and A. Scheinost* 912

Ca-UO_2-CO_3 Complexation – Implications for Bioremediation of U(VI). *S. D. Kelly, K. M. Kemner, S. C. Brooks, J. K. Fredrickson, S. L. Carroll, D. W. Kennedy, J. M. Zachara, A. E. Plymale and S. Fendorf* . . 915

Iron and Manganese Minerals from South African Ironstone Deposits. *A. Roy, G. R. Byerly, D. R. Lowe, M. W. Walsh and C. Bianchetti* 918

In Situ Speciation of Nickel in Hydrous Melts Exposed to Extreme Conditions. *M. Muñoz, H. Bureau, V. Malavergne, B. Ménez, M. Wilke, C. Schmidt, A. Simionovici, A. Somogyi and F. Farges* 921

Reverse Monte Carlo Simulations of EXAFS Spectra: Application to the Sorption of Gold on Iron Oxy-Hydroxides. *M. Winterer and F. Farges* 923

XAFS Study of Local Structure with Picometer Accuracy: $Th_{1-x}U_xO_2$ and $Th_{1-x}Pu_xO_2$ Solid Solutions. *J. Purans, G. Heisbourg, N. Dacheux, Ph. Moisy and S. Hubert* 925

XAFS and Molecular Dynamics Study of Natural Minerals, Analogues of Ceramics for NuclearWaste Storage. *M. Harfouche, F. Farges, J. P. Crocombette and A. M. Flank* 928

XAFS Studies on Vitrified Industrial Waste. *F. Pinakidou, M. Katsikini, E. C. Paloura, P. Kavouras, Ph. Komninou, Th. Karakostas and A. Erko* 931

Monitoring Trace Amounts of Lead and Arsenic Adsorption by X-ray Absorption Fine Structure Combined with Fluorescence Spectrometry. *Y. Izumi, F. Kiyotaki, T. Minato, D. Masih and Y. Seida* 933

Determination of the Ce(IV)/Ce(III) Ratio by XANES in Soil Horizons and its Comparison with the Degree of Ce Anomaly. *Y. Takahashi, K.Yuita, N. Kihou, H. Shimizu and M. Nomura* 936

XRF and XAFS Analysis of Electrophoretically Isolated Nondenatured Proteins. *K. M. Kemner, S. D. Kelly, E. J. O'Loughlin, T. Khare, L. A. Moe, B. G. Fox, M. I. Donnelly, Y. Londer, M. Schiffer and C. S. Giometti* 940

Direct Speciation of Lead, Zinc and Antimony in Fly Ash from WasteTreatment Facilities by XAFS spectroscopy. *M. Takaoka, T. Yamamoto, T. Tanaka, N. Takeda, K. Oshita and T. Uruga* 943

Chemical States of Trace Heavy Metals in Sewage Sludge by XAFS Spectroscopy. *M. Nagoshi, T. Kawano, S. Fujiwara, T. Miura, S. Udagawa, K. Nakahara, M. Takaoka and T. Uruga* 946

Determination of Uranyl Incorporation into Biogenic Manganese Oxides Using X-ray Absorption Spectroscopy and Scattering. *S. M. Webb, J. R. Bargar and B. M. Tebo* 949

Determination of Chemical Speciation by XAFS. *F. Tannazi and G. Bunker* 953

Iron in Silicate Glasses: a Systematic Analysis of Pre-Edge, XANES and EXAFS Features. *F. Farges, S. Rossano, Y. Lefrère, M. Wilke and G. E. Brown Jr.* 957

Instrumentation

Copper and Silver Alloys under Extreme Conditions. *A. Trapananti, A. Di Cicco, E. Principi, S. De Panfilis and A. Filipponi* 960

In Situ Investigations of Thin Film Formation by Reactive Sputtering. *K. Bruder, P. Keil, D. Lützenkirchen-Hecht and R. Frahm* 963

The Electronic Structures of Crystalline and Aqueous Solutions of NaBr and $NaBrO_3$ Using *In-situ* Na K and Br L edge X-ray Absorption Spectroscopy. *S. Matsuo, P. Nachimuthu, D. W. Lindle, R. C. C. Perera and H. Wakita* 966

FAME: A New Beamline for X-Ray Absorption Investigations of Very-Diluted Systems of Environmental, Material and Biological Interests. *O. Proux, X. Biquard, E. Lahera, J.-J. Menthonnex, A. Prat, O. Ulrich, Y. Soldo, P. Trévisson, G. Kapoujyan, G. Perroux, P. Taunier, D. Grand, P. Jeantet, M. Deleglise, J-P. Roux and J.-L. Hazemann* 970

Recent Advances and New Applications of Time-Resolved X-ray Absorption Spectroscopy. *R. Frahm, M. Richwin and D. Lützenkirchen-Hecht* 974

The Dispersive X-ray Absorption Spectroscopy beamline at LNLS. *H. C. N. Tolentino, J. C. Cezar, N. Watanabe, C. Piamonteze, N. M. Souza-Neto, E. Tamura, A. Y. Ramos and R. Neueschwander* 977

SAMBA a New Beamline at SOLEIL for X-Ray Absorption Spectroscopy in the 4–40 keV Energy Range. *S. Belin, V. Briois, A. Traverse, M. Idir, T. Moreno and M. Ribbens* 980

X-Ray Absorption and De-Excitation Processes of Krypton Clusters Studied by the XAFS-PEPICO Synchronous Measurements. *K. Nagaya, A. Mori, H. Murakami, M. Yao, Y. Ohmasa, H. Kajikawa, K. Kobayashi, Y. Kajihara, A. Chiba, Y. Nishikawa, M. Ishii, Y. Fujii and E. Hayata* 984

Self-Absorption Correction Strategy for Fluorescence-Yield Soft X-ray Near Edge Spectra. *R. Carboni, S. Giovannini, G. Antonioli and F. Boscherini* 986

XANES Mn K Edge in $NaNbO_3$ Based Ceramics Doped with Mn and Bi Ions. *A. Wolska, A. Molak, K. Lawniczak-Jablonska, J. Kachniarz, E. Piskorska, I. Demchenko, I. Gruszka and D. W. Lindle* 989

XAFS at Ritsumeikan SR Center. *K. Handa, K. Ozutsumi and K. Kojima* 992

Sub-Millimeter Synchrotron X-ray Focusing by Crystal Bender. *Y. Yoneda, N. Matsumoto, Y. Furukawa and T. Ishikawa* 995

A Bent Silicon Crystal in the Laue Geometry to Resolve Actinide X-Ray Fluorescence for X-Ray Absorption Spectroscopy. *A. J. Kropf, J. A. Fortner, R. J. Finch, J. C. Cunnane and C. Karanfil* 998

The INE-Beamline for Actinide Research at ANKA. *M. A. Denecke, J. Rothe, K. Dardenne, H. Blank and J. Hormes* 1001

Ge Pixel Array Detector for high Throughput X-Ray Absorption Spectroscopy: Performance and Unconventional Applications. *H. Oyanagi, C. Fonne, D. Gutknecht, P. Dressler, R. Henck, M.-O. Lampert, S. Ogawa, K. Kasai, A. Fukano and S. Mohamed* 1004

ATHENA and ARTEMIS: Interactive Graphical Data Analysis using IFEFFIT. *B. Ravel and M. Newville* . . . 1007

SIXPack: a Graphical User Interface for XAS Analysis Using IFEFFIT. *S. M. Webb* 1011

Determination of Chemical Valence States in Dilute Samples Using a Combination of Fluorescence Ion Chamber and PIN Photon Diode. *Y. N. Xie, J. Zhang, J. Liu, T. Liu, T. D. Hu and Z. Y. Wu* 1015

Customization of an In-House XAFS Spectrometer for Sulfur Measurement. *T. Taguchi, K. Shinoda and K. Tohji* 1017

Emerging techniques

The Electronic and Optical Properties of Dendrimer-capped CdS Quantum Dots: A UV-vis and X-ray spectroscopy study. *P. Zhang and T. K. Sham* 1019

Chemical Phase Separation in Zr Silicate Alloys: an *EXAFS Study Distinguishing Between Phase Separation with, and without XRD Detectable Crystallization. G. B. Rayner, G. Lucovsky and D. Kang* . . . 1022

Tomographic X-Ray Absorption Spectroscopy. *C. G. Schroer, M. Kuhlmann, T. F. Günzler, B. Lengeler, M. Richwin, B. Griesebock, D. Lützenkirchen-Hecht, R. Frahm, A. Mashayekhi, D. R. Haeffner, E. Ziegler, J.-D. Grunwaldt, and A. Baiker* 1026

Implementing Sub-ns Time Resolution into Magnetic X-Ray Microscopies. *A. Puzic, H. Stoll, P. Fischer, B. v. Waeyenberge, J. Raabe, G. Denbeaux, T. Haug, D. Weiss and G. Schütz* 1029

A Study of Transition Metal K Absorption Pre-Edges by Resonant Inelastic X-Ray Scattering (RIXS). *P. Glatzel, U. Bergmann, F. M. F. de Groot, B. M. Weckhuysen and S. P. Cramer* 1032

Direct Observation of Magnetic Depth Profile with a Depth-Resolved X-Ray Magnetic Dichroism Technique. *K. Amemiya, S. Kitagawa, T. Yokoyama, D. Matsumura, H. Abe, H. Watanabe and T. Ohta* 1035

Quantitative Zinc Speciation in Soil with XAFS Spectroscopy: Evaluation of Iterative Transformation Factor Analysis. *A. C. Scheinost, A. Rossberg, M. Marcus, S. Pfister and R. Kretzschmar* 1038

X-Ray Natural Linear Dichroism (XNLD) Applied to the Determination of Relaxations Around Transition Metal Impurities in α-Al_2O_3. *E. Gaudry, A. Kiratisin, Ph. Sainctavit, Ch. Brouder, F. Mauri, A. Ramos, A. Rogalev and J. Goulon* 1041

Sub-Nanosecond Time Resolved XAFS of Laser Excited Thin Ge Films. *E. A. Stern, D. L. Brewe, K. M. Beck, S. M. Heald and Y. Feng* 1044

An X-ray Microspectroscopy Study of Hemochromatosis Liver and Diabetic Mice Kidney Tissues: Preliminary Observations. *T. K. Sham, P.-S. G. Kim, H. Ngo, S. Chakrabati and P. C. Adams* 1047

Light-Modulated XAFS Spectroscopy for Photo-Induced Structural Changes. *K. Okamoto, K. Kohdate, K. Nagai, J. Miyawaki, H. Kondoh, T. Yokoyama, A. Nojima and T. Ohta* 1050

Anomalous Fine Structure in X-Ray Resonant Diffuse Scattering from Multilayers. *A. Michel, M. Jaouen, A. Debelle, G. Abadias, C. Jaouen and M. Gailhanou* 1053

Cadmium under High Pressure and High Temperature Conditions. *M. Minicucci, A. Trapananti, A. Di Cicco, S. De Panfilis and G. Aquilanti* 1056

Radial Distribution Function in Ionic Compounds at High Temperature and Pressure. *E. Principi, M. Minicucci, S. De Panfilis and A. Di Cicco* 1059

Real and Imaginary Parts of the Anisotropic Atomic Factor near the Fe K-Edge: Comparison Between two Theories and Experiment for Pyrite. *J. Kokubun, K. Ishida, D. Cabaret, R. V. Vedrinskii, V. L. Kraizman, A. A. Novakovich, E. V. Krivitskii and V. E. Dmitrienko* 1062

Related phenomena

Evidence for Two Mechanisms of Temperature-Dependent ''Forbidden'' Resonant Diffraction in ZnO. *S. P. Collins, D. Laundy, V. E. Dmitrienko, D. Mannix and P. Thompson* 1065

Melting of the Ge(111) Surface Probed by EELS. *A. Di Cicco, B. Giovenali, R. Bernardini and E. Principi* . . 1068

Strong Participator Channels in the Non-Radiative Resonant Decay of B 1s Excitation in B_2O_3. *A. B. Preobrajenski, A. S. Vinogradov, E. Kleimenov, A. Knop-Gericke, S. A. Krasnikov, R. Szargan and N. Mårtensson* 1071

Electronic Structure of FeF_2 and FeF_3 Studied by X-ray Absorption and Fluorescence Spectroscopy. *S. A. Krasnikov, A. S. Vinogradov, A. B. Preobrajenski, L. K. Gridneva, S. L. Molodtsov, C. Laubschat and R. Szargan* 1074

Sulfur K-Edge X-Ray Absorption Spectra for Dimethyl Sulfoxide in the Solvated Thallium(III), Indium(III), Gallium(III) and Aluminum(III) Ions. *E. Damian, F. Jalilehvand, A. Molla-Abbassi, L. G. M. Pettersson and M. Sandström* 1077

Analysis of Ti Kα'' Spectra in X-ray Emission Spectroscopy. *N. Shigeoka, H. Oohashi, T. Tochio,Y. Ito, T. Mukoyama, A. M. Vlaicu, H. Yoshikawa and S. Fukushima* 1080

[K + L] Double-Electron Transition in Fe. *N. Shigeoka, H. Oohashi, T. Tochio, Y. Ito, T. Mukoyama, A. M. Vlaicu, H. Yoshikawa and S. Fukushima* 1084

Reversed Monte Carlo Simulation to XAFS Spectra of Liquid GeO_2 Polymorphs. *Z. Wu, K. Lu, C. Li, W. Wang, X. Niu, T. Uruga and M. Nomura* 1088

Keldysh's Green Function Approach to the Radiation Field Screening in MARPE and XAFS. *H. Arai and T. Fujikawa* 1091

Lifetime-Broadening-Removed XANES Spectroscopy by High-Resolution Resonant Inelastic X-Ray Scattering. *H. Hayashi, R. Takeda, Y. Udagawa, T. Nakamura, H. Miyagawa, H. Shoji, S. Nanao and N. Kawamura* 1094

A Multi-Crystal Spectrometer with a Two-Dimensional Position-Sensitive Detector for X-ray Fluorescence Spectroscopy. *H. Hayashi, M. Kawata, R. Takeda and Y. Udagawa* 1097

ELNES Analysis for Silicon, Silicon Oxide and Their Interface. *H. Matsumoto, S.-i. Nagamatsu, M. Nakazawa and T. Fujikawa* 1099

Committees

Organizing committee

N. Mårtensson (Chair), MAX-lab
I. Lindau (Co-chair), Univ. Lund and Stanford
D. Arvanitis (Secr.), Univ. Uppsala
O. Karis, Univ. Uppsala
J. Hunter Dunn, MAX-lab
S. Werin, MAX-lab

Program committee

I. Lindau (Chair), Univ. Lund and Stanford
B. Clausen (Co-Chair), Haldor Topsøe A/S
D. Chandersis, LURE
D. Arvanitis, Univ. Uppsala
H. Bertagnolli, Univ. Stuttgart
N. Mårtensson, MAX-lab
J. Nordgren, Univ. Uppsala
M. Sandström, Univ. Stockholm
O. Karis, Univ. Uppsala
C.-O. Almbladh, Univ. Lund

International Advisory Committee

K. Baberschke, Germany
N. Greaves, UK
D. C. Koningsberger, Netherlands
N. Kosugi, Japan
G. Krill, France
S. Mobilio, Italy
T. Ohta, Japan
H. Oyanagi, Japan
A. Pavlychev, Russia
J. Penner-Hahn, USA
J. J. Rehr, USA
D. D. Sarma, India
D. Sayers, USA
T. K. Sham, Canada
H. Tolentino, Brazil
F. van der Veen, Switzerland
G. Wortmann, Germany

FOREWORD

Dear participants and other readers of the 12th X-ray Absorption Fine Structure International Conference (XAFS12) proceedings volume. What you are holding in your hands, or reading off your computer screen if you are accessing the electronic version of the proceedings, is the result of a long process. It was initiated in Ako, Japan, already in the summer of 2000 at XAFS11. At that time, Sweden and the Swedish national synchrotron facility, MAX-lab, were chosen to organize the next event in the series of International conferences on X-ray Absorption Fine Structure. After a process of preparations we opened the conference site on the web for electronic submission of abstracts about 6 months before the realization of the event in June 2003. On the way the world had experienced September 11 and a dramatic slowdown in world economics. Given the circumstances at that point we felt uncertain about the possibilities to have a meeting that would reach the size of previous XAFS events. Instead we expected to break the trend of increasing number of participants as documented at previous conferences. Fortunately, we were proven to be wrong.

XAFS-12 was held in late June, 2003 in Malmö, Sweden. More than 450 participants from 30 countries attended the event. The conference accommodated seven plenary lectures, three parallel oral sessions and three poster sessions resulting in some 650 invited and contributed presentations. A breakdown by nation of the submitted contributions is given in Fig. 1.

Among the plenary events the "Lars Hedin Memorial Session" including the lecture of J. J. Rehr (Seattle, USA) highlighted the importance of the longstanding efforts and successes of the late Lars Hedin and his coworkers at the Department of Theoretical Physics, Lund University, for the theoretical description of excited states. Professor Lars Hedin was a member of the XAFS12 organizing committee before he prematurely passed away.

A wide range of topics and areas were covered at the conference, including XAFS applications to materials science, catalysis and nano-science, biology, chemistry, environmental science, and magnetism. The latest developments in theoretical advances related to XAFS, instrumentation, and novel applications of XAFS were presented. Special sessions were also devoted to related phenomena and emerging techniques. More than 350 papers were eventually submitted to the XAFS-12 proceedings. The number of contributed papers was far greater than expected. A summary of how the contributed papers were divided into categories is given in Fig. 2. As one might expect, the largest body is found in the rather generic materials category.

It is our view that the XAFS proceedings have a high value for the community and serves as a good indicator of the present trends and developments. It is our opinion that the volume you are accessing is still another convincing example of the power of XAFS based tools using modern light sources. Amongst the contribution you will find many fascinating examples for future trends for the XAFS technique.

Finally, the organizers of XAFS-12 want to gratefully acknowledge the support from the main conference sponsors: the Royal Swedish Academy of Sciences through its Nobel Institute for Physics, the Swedish Foundation for Strategic Research, the Crafoord Foundation, the University of Lund, the Swedish Research Council, the City of Malmö and the Region of Skåne.

We thank all of you for your commitment to this conference and we look forward to another successful gathering of the XAFS-community during the 13th conference in Stanford, California in 2006.

Ingolf Lindau, Nils Mårtensson, Dimitri Arvanitis, Olof "Charlie" Karis

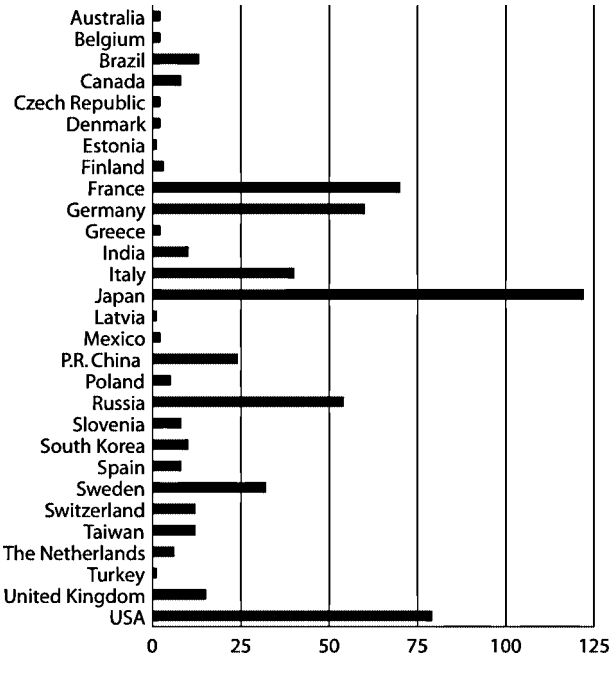

Fig. 1. The number of submitted contributions to the XAFS-12 conference presented by country of origin. The countries are ordered alphabetically from top to bottom.

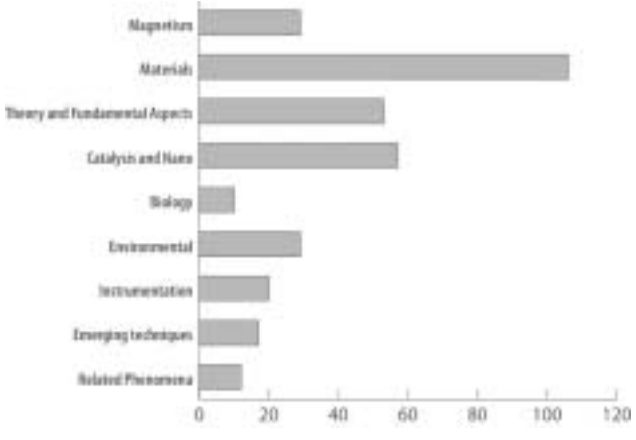

Fig. 2. More than 350 papers were submitted to the XAFS-12 proceedings. Here we give the number of contributions by main category.

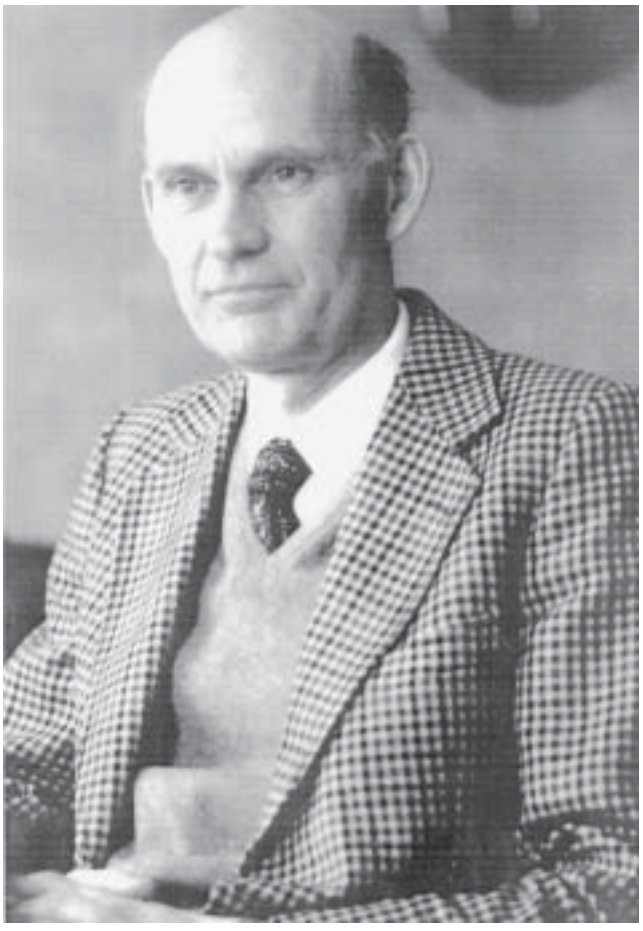

LARS HEDIN

Physica Scripta. Vol. T115, 19–23, 2005

Lars Hedin and the Quest for a Theory of Excited States

J. J. Rehr

Dept. of Physics, Box 351560, University of Washington, Seattle, Washington 98195, USA

Received June 26, 2003; accepted October 14, 2003

PACS number: 7870Dm.

Abstract

The theory of excited electronic states is central to a quantitative understanding of the interaction between light and matter and hence to calculations of various X-ray and optical spectra. Although ground state properties are well described by density functional theory (DFT), that theory is inappropriate for excited states, for which a fully quantitative theory has yet to be developed. No one has contributed more to than Lars Hedin to the quest for such a theory. Here we briefly review a number of his key contributions. One of the most influential is the "GW" approximation for the self-energy of an excited electron. Another is the "blue-electron" approximation for photon and electron spectroscopies. A third, which is relevant to the topics of this conference, is a many-body theory of X-ray spectra based on the "quasi-boson" approximation. This approach is a generalization of the GW approximation which takes into account both extrinsic and intrinsic losses as well as the interference between them, and simplifies the treatment of losses and the core-hole interaction. What makes Hedin's theories stand out is their mathematical elegance and physical robustness, based on ideas conceived before their full implementation was practical. With today's advances in computational power, however, the impact of Lars' work is becoming ever more widely appreciated.

1. Introduction

Lars Hedin [1930–2002] was a key figure in the development of modern theories of excited states. Such developments are crucial to a quantitative understanding of photon and electron spectroscopies. Indeed much of our current computational framework for excited state calculations in condensed matter is derived from Lars' work. To paraphrase Carl-Olof Almbladh and Ulf von Barth, his colleagues at Lund, Hedin's strength as a researcher was marked by his extraordinary ability to see the practical physics in otherwise very complicated theories. Hedin's idea was to try to simplify the basic physics of many-electron systems to a level suitable for computer calculations, and later for comparisons with experiments. A few of Lars' early works are as valid and influential today as they were then. With today's improvements in computers and algorithms, Hedin's GW approximation has become the dominant method for calculating excitation properties in semiconductors and metals.

In this tribute to Lars, I will discuss a few of his major contributions along with some of the history behind them. These include, for example, the "Hedin Equations," the GW approximation for the electron self-energy, the "blue-electron" approximation, and the quasi-boson treatment of electronic excitations. I will focus particularly on Lars' contributions in the field of X-ray spectroscopy. Besides being a central topic of this conference and a personal favorite of my own, it is a topic on which I have had the good fortune to collaborate with Lars since the mid 1990's.

Many of Hedin's ground breaking developments appeared so rapidly in the 1960's that one wonders how he did it and what were the sources that inspired him. Lars provides some of the answers both in his early work [1], and in an unpublished festschrift for Stig Lundqvist [2], a distinguished Swedish condensed matter physicist with whom Lars worked closely at that time. The 1950's and 1960's was a period when the ideas of quantum field theory were beginning to revolutionize condensed matter physics. Feynman diagrams flourished in theoretical papers, explaining everything from electron-scattering to superconductivity in fancy pictographs. But there was a problem. As Lars put it: "Although we now have a wealth of beautiful general theorems, fairly little has been done toward manageable and reliable approximation schemes especially for interacting electrons" [1].

Lars' foray into many-body theory apparently began about 1960. He had gone to Uppsala to do graduate research, first in the quantum chemistry group of Per-Olov Löwdin, one of the world's leading theoretical quantum chemists. Lars also began interacting with Stig Lundqvist and eventually became Stig's first Ph. D. student. Together Lars and Stig gave a seminar series on "Introduction to the field theoretical approach to the many body problem." As Lars remarked, "Stig who was very much the senior and mature physicist did most of the reading of the papers and wrote drafts for our seminars, while I struggled to get the algebra right and tried to understand what it was all about."

2. 1969 Review of Many-body Theory

Like many others, I first learned of Lars' works from his comprehensive 1969 Review article with Stig Lundqvist, "Effects of Electron-electron and Electron-Phonon Interactions on the One-Electron States of Solids" [3]. Part of the article grew from an "intensive collaboration" between Lars, Stig, and their graduate student Bengt Lundqvist, "working out properties" of what John Wilkins termed the "Swedish Electron Gas." This appellation reflects the notable advances by Swedish scientists on the theory of the homogeneous electron gas, which has long been a prototype many-body system. Wilkins was a condensed matter theorist at Cornell, where I did my own graduate work. But he traveled back and forth to Scandinavia regularly to collaborate with Bengt and others and always knew what was going on there. Besides the new physics, the 1969 Review constitutes a superb overview of the concepts used in many-body theories of solids, including Green's function theory, elementary excitations, quasi-particles, etc. It is a model of clarity, and was a godsend to us neophytes trying to make sense of field-theoretical techniques.

Interestingly, much of the final manuscript was completed in less than a month! As Lars described the effort: "This was when solid state physics was still very much in the shadow of nuclear physics in Sweden, and Stig started spending a lot of time on meetings in Stockholm successfully promoting support for solid state physics. At the same time he vigorously pushed our joint efforts on understanding many-body physics and writing the review. I always found it difficult to meet deadlines however much pushed, and when we had dragged delivering our review to [the Solid State Physics editor] Henry Ehrenreich for several years he gave us an ultimatum, 'Deliver by January 1st or the deal is off'. I had agreed with Stig to write a first preliminary sketch. In early December I started on this in earnest and poor Stig read, rewrote,

wrote new drafts and rewrote again in between shuffling back and forth to Stockholm and Nobel activities. We got the article in by January 1, and perhaps it benefited by being written in such a concentrated effort."

3. The Swedish Electron Gas vs Density Functional Theory

The "Swedish electron gas" refers to a Green's function treatment of a uniform system of electrons [1]. The central quantity in the theory is the one-particle Green's function or propagator $G(1,1') = -\mathrm{i}\langle N|T[\psi(1)\psi^\dagger(1')]|N\rangle$, which is the amplitude that an electron added at the 5 dimensional space-spin-time point $1 \equiv \boldsymbol{r}, s, t$ in an interacting N particle system propagates to the point $1'$. Despite its formidable nature one of Hedin's achievements was to tame the approach into a calculable form (i.e., the GW approximation) as benign looking as the Schrödinger equation. In frequency (or energy $E = \hbar\omega$) space, which is convenient for treating spectra, the Green's function is $G(\omega)$ is formally the solution to

$$[\omega - h - \Sigma(\omega)]G(\omega) = 1. \tag{1}$$

Here the one-particle Hamiltonian h includes the kinetic energy $p^2/2m$, the external potential of the nuclei $V_{\rm ext}$, and the Coulomb (or Hartree) potential $V_{\rm Coul} = \int \mathrm{d}^3 r v(\boldsymbol{r} - \boldsymbol{r}')n(\boldsymbol{r}')$, from the average electron charge density $n(\boldsymbol{r})$, and $\Sigma(E)$ is the "self-energy" of an electron due to its interaction with the rest of the system. Thus the homogeneous equation

$$[\omega - h - \Sigma(\omega)]\psi = 0, \tag{2}$$

has the form of a one-particle Schrödinger equation with a self-energy, as first discussed by Schwinger in 1951. Its eigenstates ψ_k and (complex) eigenvalues ω_k have the interpretation of Landau "quasiparticle states" and their energies, respectively. The Green's function approach can be viewed as a mapping of the many-body problem onto a one-particle problem with an effective Hamiltonian $h + \Sigma(\omega)$. All the many-body effects of exchange and correlation are contained in the self-energy $\Sigma(\omega)$.

It is interesting to compare these results with Density Functional Theory (DFT), which was developed by Walter Kohn and collaborators also in the mid 1960's [4]. DFT provided a powerful alternative approach to the problem of many interacting electrons based on a beautiful variational theorem that relates ground state properties of a system to functionals of the electron density. The approach maps the many body problem onto a system of non-interacting electrons with precisely the same density. Thus all ground state properties can be described in terms of eigenstates of a one-particle Schrödinger equation,

$$[\omega - h - V_{\rm xc}]\psi = 0, \tag{3}$$

where h is the above Hartree Hamiltonian, and $V_{\rm xc}([n(\boldsymbol{r})])$ is the exchange-correlation density functional which includes all the many-body effects. I was fortunate to have been one of Walter's postdocs in the mid-1970's, and have always appreciated both the power and simplicity of the method. Lars did too and contributed significantly to the development of DFT. For example, Ulf von Barth and Lars developed the local spin density (LSD) generalization [5]. Although formally exact, the fundamental difficulty with DFT is, as Walter put it, "God only knows what the exact exchange-correlation potential $V_{\rm xc}[n]$ is." Never mind. A variety of approximations exist, which are adequate for ground state properties. Indeed the DFT revolutionized calculations of condensed systems, as recognized by the 1998 Nobel Prize in Chemistry. It's practical advantage (compared e.g., to the Green's function approach) is that the DFT yields a standard one-electron eigenvalue problem which is computationally efficient.

4. The Hedin Equations

The Green's function approach clearly hinges on a suitable approximation for the self-energy $\Sigma(\omega)$, and Lars set out to derive a systematic scheme for its determination. In particular, Lars' treatment is based on an expansion, not in the long range Coulomb potential $v(\boldsymbol{r}, \boldsymbol{r}') = 1/|\boldsymbol{r} - \boldsymbol{r}'|$, but rather on the screened potential W (see below) which leads to more rapid convergence. His solution can be described compactly in a set of four coupled integral equations now referred to as the "Hedin Equations." Since they may be viewed as matrix multiplications over the space-spin-time coordinates, I will drop the indices for notational simplicity except when needed for clarity, i.e.,

$$\Sigma = \mathrm{i}GW\Gamma, \quad W = v + WPv,$$
$$P = -\mathrm{i}GG\Gamma, \quad \Gamma = 1 + \frac{\delta\Sigma}{\delta G}GG\Gamma. \tag{4}$$

The quantities involved are the self-energy $\Sigma(12)$, the screened coulomb interaction $W(12)$, the polarizability (or density response function) $P(12) = \delta n(1)/\delta V(2)$, and the "vertex function" $\Gamma(123)$. These equations are derived in Hedin's *tour de force* paper "New Method for Calculating the One-Particle Green's Function with Application to the Electron-Gas Problem" [1]. In his characteristically non-aggressive style, Lars states that "The results ... are well known to the 'Green's-function people.' The present derivation, however, utilizes only the Schrödinger equation. It constitutes a 'low-brow' version of those parts of the 'high-brow' Green's function theory that we need here." Though their derivation is still not trivial, Hedin does give hints on how to carry out the functional derivatives. The recent review of GW theory by Aryasetiawan and Gunnarsson [6] also gives a clear derivation.

Although the compact structure of the Hedin equations is appealing, a full solution remains a formidable challenge. To simplify the equations, Lars proceeds systematically. To zeroth order in W, $\Sigma = 0$ and the vertex $\Gamma = 1$, and hence to leading order in the screened interaction W one arrives at Lars' famous GW approximation:

$$\Sigma = \mathrm{i}GW, \quad W = v + WPv, \quad P = -\mathrm{i}GG. \tag{5}$$

The physical interpretation of the terms is as follows. The polarizability P is directly related to the dielectric matrix $\epsilon = 1 - Pv$, so that $W = \epsilon^{-1}v$ is the screened coulomb interaction, which is non-local in space and time. Therefore $\Sigma = \mathrm{i}GW$ can be interpreted as a dynamically screened exchange and correlation potential. When the screening becomes negligible, e.g., high densities, $\Sigma = \mathrm{i}Gv \equiv V_{\rm x}$ which is just the non-local Fock exchange. The equations were evaluated in great detail for the uniform electron gas in a beautiful series of papers by Bengt Lundqvist e.g., [7]. Additional terms in the expansions have also been studied, e.g., in studies of the optical potential in atomic scattering with Takashi Fujikawa [8]. For reviews of various aspects of GW theory and its applications, see e.g., Ref. [9] and especially the review by Hedin [10] which focuses on the physical ideas, extensions to spectroscopies, and also generalizations for strongly correlated systems.

Though not universal the GW approximation explicitly incorporates the dielectric response of a given material and

provides a constructive theory. One of the major successes of the GW approach is in the study of excited states. GW calculations, e.g., in Ref. [11, 12], yield band gaps in excellent agreement with experiment in a wide range of materials while the DFT gives substantial errors. Thus the energy dependence of the self-energy shows up clearly in experiment, especially in X-ray spectra. The failure of DFT to predict accurate excitation energies is not surprising since, as Kohn emphasized, the DFT eigenvalues cannot be interpreted as excitation energies. However, Hedin showed that the DFT orbitals are robust – i.e., they possess "orbital stability" [13]. Thus with a given $\Sigma(\omega)$ they can be used to determine the self-energy corrections to the excitation energies $\langle k|\Sigma(\omega_k) - V_{\rm xc}|k\rangle$.

5. Blue Electron Theory

Now I would like to turn to some related aspects of GW theory, and in particular the case of excitation spectra with large energies, as in photoemission. This is a subject on which Lars has contributed extensively, as discussed, e.g., in another big review written with Carl-Olof Ambladh [14]. Through discussions with Stig Lundqvist, Lars developed a way of looking at high energy excited states using *blue electron theory* [2]. As Lars put it: "By a blue electron I understand an electron which to some degree is regarded as distinguishable from the other electrons in the medium, among which its moves. This is clearly in violation of the Pauli principle, but I will try to explore where this idea can lead."

An example of such a blue electron is the ejected electron in photoemission with high kinetic energy compared to the electrons in a solid. When the energy is about 50 eV or higher, the exchange coupling with the solid becomes negligible. In this limit the violation of the Pauli principle is small and one can factor the excited state of the system and the photoelectron, i.e., $|N\rangle \approx |N-1;s\rangle|k\rangle$, where $|N-1;s\rangle$ refers to a particular excited state labeled by s of the "passive" electrons in the system and $|k\rangle$ is the blue electron state. This approach was extensively developed for photoemission, in particular by Witold Bardyszewski and Lars [15]. Another application is the many body theory of XAFS. Since these applications have many common features I will only discuss the latter here.

6. XAFS and the Quasi-boson Approximation

Dramatic progress has been made in the theory of X-ray absorption fine structure (XAFS) over the past few decades [16], and Lars' contributions have played an important role more than once. Inelastic losses are critical to a quantitative theory, since experiment reveals a substantial reduction in XAFS amplitudes compared with ground state calculations.

An important development in X-ray absorption theory was the introduction of a local density approximation for the GW self energy [17]. This is based on a single plasmon-pole approximation of the dielectric function, as discussed in detail by Bengt Lundqvist [7]. Since the GW approximation requires an integral over the dielectric function, its precise form is not crucial. This plasmon-pole self energy is accurate at high energies, and has proved to be adequate for most EXAFS calculations [16]. The imaginary part of the self energy is related to the mean free path $\lambda = k/|\mathrm{Im}\,\Sigma|$ and characterizes the "extrinsic losses," where k is the photoelectron wave number. Moreover, the real part of Σ accounts reasonably well for the observed shifts in peak positions. Another source of amplitude reduction is the "intrinsic loss," from the shake-up and shake-off processes, which give rise to the many-body amplitude reduction factor S_0^2 in the EXAFS formula [18].

However there are problems with these treatments. First they give too much loss. Second, since the excitations caused by extrinsic and intrinsic losses are indistinguishable, *interference* is also possible. Indeed, for photoemission spectroscopy, it had been shown (see e.g., [15, 19]) that the interference is strong near excitation thresholds, where the losses strongly cancel due to the opposite signs of the coupling between the photoelectron and the core-hole to excited states. Physically this reflects the dipole-like behavior or the photoelectron/core-hole pair at low energies, and hence is likely responsible for the surprising weakness of multi-electron excitations in the observed spectra at low energies.

In a remarkable three page paper presented at the 1989 International XAFS Conference in Seattle, Hedin suggested how one might calculate the interference terms [20]. The method uses a generalization of GW theory that incorporates blue electron ideas [21]. Hedin's interest in XAFS was influenced in part by discussions with Giancarlo Strinati who had been working on the Bethe-Salpeter Equation, i.e., the two-particle Green's function approach, and had also done some of first GW calculations [12]. Since Hedin's approach provides an example which incorporates several of his theories, I will summarize the method in some detail below.

From Fermi's Golden rule, the *many-body* formula for X-ray absorption can be expressed in terms of an effective one-particle Green's function as

$$\mu(\omega) = -\mathrm{Im}\,\langle k|d^\dagger G_{\rm eff}(\omega)d|k\rangle,$$

$$G_{\rm eff}(\omega) = \langle\Psi|(\omega - H - h' - V_{\rm es} - V_{\rm sc} + \mathrm{i}\delta)^{-1}|\Psi\rangle, \qquad (6)$$

where d is the dipole operator, H is the Hamiltonian for the solid including all electrons but the (blue) photoelectron, h' is the one-electron Hamiltonian for the photoelectron in the presence of the core-hole, and $V_{\rm es}$ and $V_{\rm sc}$ are the interactions between the photoelectron and the solid, and the solid and the core-hole, respectively. The expectation value $\langle\Psi|\ldots|\Psi\rangle$ integrates over all electron coordinates in the solid. Thus $G_{\rm eff}(\omega)$ is an effective propagator with only the photoelectron coordinates. This propagator takes into account the core-hole interaction, and hence is not equivalent to the usual one-particle Green's function.

Lars often uses limiting cases to check a theoretical formalism. Thus when the interaction $V_{\rm es}$ with the photoelectron is negligible (e.g., at high energies), one can insert a complete set of eigenstates of $H' = H + V_{\rm sc}$ with excitation energies ω_n in Eq. (6) to get an expression as a sum over intrinsic losses,

$$\mu(\omega) = \sum_n |S_n|^2 \mu^{(1)}(\omega - \omega_n),$$

$$G_{\rm eff}(\omega) = \sum_n |S_n|^2 G(\omega - \omega_n), \qquad (7)$$

where $S_n = \langle\Psi|\Psi'_n\rangle$ is a many-body overlap integral, and $\mu^{(1)} = \Sigma_k|\langle c|d|k\rangle|^2\delta(\omega - \epsilon_k)$ is the one-particle Golden rule formula for the X-ray absorption cross-section. Eq. (7) is equivalent to the theory based on the *sudden approximation* with only intrinsic losses [18]. The second limiting case is when the core-hole-solid interaction $V_{\rm sc} = 0$. Then the result for $G_{\rm eff}$ is essentially the GW approximation $G_{\rm eff}(\omega) = [\omega - h' - \Sigma(\omega)]^{-1}$ with only extrinsic losses but including the core-hole interaction.

The treatment of the interference effects is carried out using a "quasi-boson" approximation [7, 15]. The essence of the model is that the dominant excitations of the solid, i.e., plasmons,

electron hole pairs, etc., are bosons. Often only a few such bosons dominate, e.g., plasmons in the case of simple metals. In general the excitations can be represented quantum mechanically by boson (oscillator) operators a_n with energies ω_n and labeled by an index n. Their interactions are represented by terms linear in the boson operators, with coupling constants V^n known as *fluctuation potentials* [19]. For plasmons for example, the fluctuation potentials are simply plane waves and n refers to the plasmon wave number $\boldsymbol{q}$, i.e., $V^q = (2\pi\omega_p^2/q^2\omega_q)^{1/2}\exp(\mathrm{i}\boldsymbol{q}\cdot\boldsymbol{r})$. This method has the promise to simplify considerably self-energy calculations since both W and Σ can be represented in terms of fluctuation potentials, e.g., $\Sigma(\omega) \approx \Sigma_n V^n G(\omega-\omega_n)V^n$, and the V_n can be calculated within the random phase approximation (RPA). Thus the quasi-boson model Hamiltonian is

$$H = \sum_n \omega_n a_n^\dagger a_n, \quad h' = \sum_{k>k_F} \epsilon_k c_k^\dagger c_k,$$
$$V_{\mathrm{sc}} = -\sum_n V_{cc}^n (a_n^\dagger + a_n), \quad V_{\mathrm{es}} = \sum_{nkk'} [V_{kk'}^n a_n^\dagger + (V_{kk'}^n)^* a_n] c_k^\dagger c_{k'}. \tag{8}$$

As in all such a shifted oscillator models, the ground states of H and H', with and without a core hole respectively, are simply related by a canonical transformation $|\Psi\rangle = \mathrm{e}^{-S}|\Psi'\rangle$, $S = a/2 - \Sigma_n (V_{cc}^n/\omega_n) a_n'^\dagger$, and the dimensionless strength $a = \Sigma_n (V_{cc}^n/\omega_n)^2$, where a_n' belongs to $H' = \Sigma_n \omega_n a_n'^\dagger a_n'$. Expanding Eq. (6) to second order in V^n, corresponding to the ways of exciting of a single boson n, then gives

$$G_{\mathrm{eff}}(\omega) = \mathrm{e}^{-a}\Bigg[G(\omega) + \sum_n \left(\frac{V_{cc}^n}{\omega_n}\right)^2 G(\omega-\omega_n) - 2\sum_n \frac{V_{cc}^n}{\omega_n} G(\omega-\omega_n) V^n G(\omega)\Bigg]. \tag{9}$$

This key result for $G_{\mathrm{eff}}(\omega)$ gives an expression for the XAS as an expansion in final state one-particle Green's functions. The theory is essentially a generalization of GW theory and makes use of essentially the same ingredients. The first term $G(\omega) \equiv [\omega - h' - \Sigma(\omega) + i\gamma]^{-1}$ is the damped Green's function calculated *in the presence of a core hole*, and yields the standard theory of XAS given by the *final state rule* [22] with only extrinsic losses. The second term accounts for the intrinsic losses, $S_n = V_{\mathrm{cc}}^n/\omega_n$ being the many-body overlap integral. The third term comes in with a minus sign and accounts for the interference.

The results can be interpreted in terms of the spectral function $A_{\mathrm{eff}} = -(1/\pi)\mathrm{Im}\, G_{\mathrm{eff}}$, which describes the energy distribution of the photoelectron. For the plasmon-pole model, for example, this consists of a asymmetrical quasi-particle peak and a broad satellite separated by the plasmon energy ω_p. The effect of the interference terms is to increase the strength of the quasi-particle peak at $\omega = E_k$, and to decrease the strength of the satellites. Remarkably the satellite strength cancels completely at the excitation thresholds! This can be seen by looking at the residues of the poles of $G(\omega-\omega_n)G(\omega)$. Thus, in addition to the intrinsic amplitude $V_{\mathrm{cc}}^n/\omega_n$ the amplitude of the satellite excitations has a competing contribution of opposite sign from the extrinsic losses,

$$S_n(\omega) = G(\omega)V^n - \frac{V_{\mathrm{cc}}^n}{\omega_n}, \tag{10}$$

which vanishes at the plasmon excitation threshold $\boldsymbol{q} = 0$. Precisely the same *cancellation theorem* applies in photoemission [15]. This also explains why the quasi-particle approximation is accurate at low energies and satellite excitations can be neglected, consistent with the *adiabatic approximation*. Thus Lar's model naturally explains the transition from the the sudden to adiabatic limits.

I had spent the spring of 1995 in Lund working on this model, but it took several more years to develop the theory to a semi-quantitative level [23]. A key result, using Eq. (9) and Eq. (6), is many-body expression for the XAS as a convolution of the final state one-electron spectrum $\mu^{(1)}$ [defined below Eq. (7)] with an asymmetric, energy dependent spectral function $A_{\mathrm{eff}}(\omega,\omega')$,

$$\mu(\omega) = \int \mathrm{d}\omega'\, A_{\mathrm{eff}}(\omega,\omega')\mu^{(1)}(\omega-\omega'). \tag{11}$$

This may be viewed as an energy dependent broadening of $\mu^{(1)}$ by the spectral function A_{eff}, i.e., $\mu(\omega) = \langle\mu^{(1)}(\omega)\rangle$. As discussed above, the amplitudes of the quasi-particle peak and the satellite contributions are energy dependent: in the adiabatic limit, the satellite contribution is small and the quasi-particle amplitude tends toward unity, while at high energies (compared to ω_p) the interference becomes small and the theory crosses over to the sudden limit dominated by intrinsic losses. Eq. (11) implies that XAFS spectrum $\chi = \langle\chi^{(1)}\rangle$ is similarly broadened, since it is linear in μ. The effect of such broadening is a decreased and phase shifted XAFS amplitude,yielding the energy dependent amplitude reduction factor $S_0^2(\omega)$, in reasonable agreement with experiment [23].

The last topic I worked on with Lars, just after midsummer 2002, dealt with the comparison between the two-particle Bethe-Salpeter equation and the one-particle final state rule (FSR), for treating core-hole interaction effects in deep-core X-ray spectra. Despite their apparent differences, Lars had suggested that the methods are rather similar. Recent work in collaboration with Eric Shirley and Aleksi Soininen has corroborated Lars' suggestion [24]. The main difference is that the FSR treats screening of the core-hole self-consistently while BSE uses linear response, but these differences often have little effect numerically. Moreover, the use of the quasi-boson approach to calculate satellite excitations suggests how both the FSR and the BSE can be improved, leading to a more complete many-body treatment of X-ray spectra.

Acknowledgments

This paper is dedicated to Lars Hedin whose works and encouragement have been an inspiration. We also thank Bob Albers, Alexei Ankudinov, Carl-Olof Almbladh, Witold Bardyszewski, Chuck Fadley, Takashi Fujikawa, Eric Shirley, Giancarlo Strinati, and John Wilkins for comments and suggestions, and especially Hillevi Hedin for her gracious hospitality all these years. This work was supported in part by US DOE Grant DE-FG03-97ER45623 and facilitated by the DOE CMSN.

References

1. Hedin, L., Phys. Rev. **139**, A796 (1965).
2. Hedin, L., Correlation Effects in Atoms and Solids, paper presented at the Symposium on Frontiers in Condensed Matter Physics in honor of Stig Lundqvist, 1990 (unpublished).
3. Hedin, L. and Lundqvist, S., "Solid State Physics", (F. Seitz, D. Turnbull and H. Ehrenreich, eds.), **23**, 1 (1969).
4. Hohenberg, P. and Kohn, W., Phys. Rev. B **136**, 864 (1964); Kohn, W. and Sham, L. J., Phys. Rev. A **140**, 1133 (1965).
5. von Barth, U. and Hedin, L., J. Phys C **5**, 1629 (1972).
6. Aryasetiawan, F. and Gunnarsson, O., Rep. Prog. Phys. **61**, 237 (1998).
7. Lundqvist, B. I., Phys. Kondens. Materie **6**, 193 (1967), and references therein.

8. Fujikawa, T. and Hedin, L., Phys. Rev. B**40**, 11507 (1989).
9. Aulbur, W. G., Jönsson, L. and Wilkins, J. W., Solid State Phys. **54**, 1 (1999).
10. Hedin, L., J. Phys. Cond. Mat. **11**, R489 (1999).
11. Strinati, G., Mattausch, H. J. and Hanke, W., Phys. Rev. Lett. **45**, 290 (1980).
12. Hybertsen, M. S. and Louie, S. G., Phys. Rev. B**34**, 5390 (1986).
13. Hedin, L., Int. J. Quantum Chem. **56**, 445 (1995).
14. Almbladh, C.-O. and Hedin, L. in: "Handbook on Synchrotron Radiation", (ed. E. E. Koch) **1b**, p. 607 (North Holland, 1983).
15. Bardyszewski, W. and Hedin, L., Physica Scripta **32**, 439 (1985).
16. Rehr, J. J. and Albers, R. C., Rev. Mod. Phys. **72**, 721 (2000).
17. Lee, P. A. and Beni, G., Phys. Rev. B **15**, 2862 (1977).
18. Rehr, J. J., Stern, E. A., Martin, R. L. and Davidson, E. R., Phys. Rev. B**17**, 560 (1978).
19. Hedin, L., Michiels, J. and Inglesfield, J., Phys. Rev. B**58**, 15565 (1998).
20. Hedin, L., Physica B **158** 344 (1989).
21. de Physique, J., Colloque C9 **48**, C9-1103 (1987).
22. von Barth, U. and Grossmann, G., Phys. Rev. B **25**, 5150 (1982).
23. Campbell, L., Hedin, L., Rehr, J. J. and Bardyszewski, W., Phys. Rev. B **65**, 064107 (2002).
24. Rehr, J. J., Shirley, E. L. and Soininen, A. J., this conference.

Physica Scripta. Vol. T115, 24–27, 2005

Nonspherical Potential, Vibronic and Local Field Effects in X-Ray Absorption

A. L. Ankudinov and J. J. Rehr

Dept. of Physics, Box 351560, University of Washington, Seattle, Washington 98195, USA

Received June 26, 2003; accepted October 14, 2003

PACS numbers: 78.70.Dm, 78.20.Bh, 71.15.Qe

Abstract

The theory of X-ray absorption near edge structure (XANES) is complicated due to the difficulty of treating chemical, many-body, and core-hole effects. To address these problems we introduce a full potential, real space Green's function approach for calculations of both local electronic structure and X-ray spectra. Our approach includes inelastic losses as well as screened core-hole and local field effects. The latter are due to the screening of the X-ray electric field. The approach is illustrated in calculations for periodic solids and for small molecules. Calculations for the K-edge absorption of Si crystals show significant improvements in the XANES compared with that calculated with spherical, muffin-tin potentials. However, for systems of high symmetry like the S K-edge in the SF_6 molecule, we find that the non-spherical corrections are small. Instead, local atomic displacements are responsible for additional XANES peaks. Local field effects are shown to be important at the diamond K-edge, which effectively counteract the core-hole interaction.

1. Introduction

An X-ray photon is absorbed in matter by promoting one of the core electrons into an unoccupied photoelectron state of a molecule or solid. Thus if the resulting core-hole and photoelectron did not interact, the X-ray would serve as a direct probe of the energy position of the unoccupied states. However, several many body effects contribute to X-ray absorption: self-energy, core-hole interaction, local field effects, and multi-electron excitations. Their relative importance varies depending on material, edge and energy with respect to a given edge.

Neverless, the dominant features of the absorption spectrum can usually be calculated using the *standard model* [1] developed for EXAFS calculations. The model uses 1) overlapping self-consistent muffin-tin potentials constructed from the spherically symmetric density around each atom; 2) the final state rule to account for the core-hole interaction, i.e., the potentials are calculated in the presence of a static, fully screened core-hole; and 3) a local Hedin-Lundqvist self-energy is used to account for energy level shifts and inelastic losses during propagation of the photoelectron. This standard theory is usually so successful that it can been used even for a quantitative analysis of XANES for structure determinations [2].

In this paper we demonstrate that several effects not fully included in this standard model can sometimes play an important role, and therefore should be included in XANES calculations. For example, we find that non-spherical charge densities and potentials in a full potential calculation resolves the double peak structure at the K-edge white line of crystalline Si. The complicated structure at the S K-edge of the SF_6 molecule can be explained if one accounts for the vibrational motion of the molecule (i.e., the vibronic interactions). Local field effects are shown to be important for the diamond K-edge calculation, where they counteracts the transfer of oscillator strength to the edge region due to the core-hole interaction.

2. Full Potential Multiple scattering approach

Originally multiple scattering theory was developed for the muffin-tin potential. It's generalization for the "full potential" was suggested by Lloyd and Smith [3] in 1972, and independently by Williams and Morgan in 1974 [4]. The full potential multiple scattering theory for XANES calculations was first suggested by Natoli [5] to account for the effects of non-spherical potentials. Later Foulis *et al.* [6] demonstrated that both full potential and self-consistency are essential to understand the spectral features at the Cl K-edge of the Cl_2 molecule.

Our implementation of the full potential multiple scattering theory (MST) mostly follows the above cited references. However, we have introduced several modifications. First, instead of non-overlapping cell potentials, which have jumps at the Voronoi polyhedra boundaries, we use the overlapping "fuzzy" Voronoi polyhedron construction suggested by Becke [7]. One defines cell functions $w_n(\vec{r})$ which smoothly go from 1 inside Voronoi cell to 0 outside, so that the sum over all cell functions $\Sigma_n w_n(\vec{r}) = 1$ for all spacial points. Using these cell functions we separate total potential into the cell potentials:

$$V_n(\vec{r}) = w_n(\vec{r}) V_{tot}(\vec{r}). \tag{1}$$

Thus potential changes smoothly across the boundary, which results in fewer spherical harmonics being needed in calculations. In the second step we find regular and irregular solutions of the Schrödinger equation in each cell,

$$(H - E)\Psi_L(\vec{r}) = 0, \qquad (H - E)H_L(\vec{r}) = 0. \tag{2}$$

Due to the non-spherical potential these are expressed as a sum over all angular momenta e.g., $\Psi_L(\vec{r}) = \sum_{L'} \Psi_{LL'}(r) Y_{L'}(\hat{r})$. They are normalized so that at large distances ($r \to \infty$)

$$\Psi_{nL}(\vec{r}) \to j_L(\vec{r}) + \sum_{L'} h_{L'}(\vec{r}) t_{nL',nL}, \tag{3}$$

$$H_{nL}(\vec{r}) \to h_L(\vec{r}), \tag{4}$$

where for convenience we have defined $j_L(\vec{r}) = i^l j_l(kr) Y_{lm}(\hat{r})$, $h_L(\vec{r}) = i^l h_l(kr) Y_{lm}(\hat{r})$, and $\bar{j}_L(\vec{r}) = i^{-l} j_l(kr) Y^*_{lm}(\hat{r})$. Notice that for complex wavevector k, $\bar{j}_L(\vec{r}) \neq j_L(\vec{r})^*$. Thus the t-matrix is found from normalization of the regular solution, and unlike the spherically symmetric case, t has off diagonal matrix elements.

Thus the full multiple scattering (FMS) part of calculations, which is the most time consuming part of the FEFF8 XAS code, [1] remains practically the same for full potential calculations,

$$G^{FMS}_{iL,jL'} = G^0 (I - TG^0)^{-1}, \tag{5}$$

where we have suppressed the matrix indices for $T_{iL,iL'} = t^i_{LL'}$ and the free propagator $G^0_{iL,jL'}$. Finally, one can calculate the total Green's function as a sum over central atom and scattering parts,

$$G^c(\vec{r},\vec{r}',E) = -2k\sum_L H_{cL}(r_<)\bar{\Psi}_{cL}(r_>), \tag{6}$$

$$G^{sc}(\vec{r},\vec{r}',E) = -2k\sum_{L,L'} \Psi_{cL}(\vec{r})G^{FMS}_{cL,cL'}\bar{\Psi}_{cL'}(\vec{r}\,'), \tag{7}$$

where $\bar{\Psi}$ is also a Solution of Schrödinger equation but normalized differently at large distances: $\bar{\Psi}_L \to \bar{j}_L(\vec{r}) + \sum_{L'} t_{LL'}\bar{h}_{L'}(\vec{r})$.

However, the above *standard* MST expression for the Green's function is not useful at large distances since there the regular solution grows exponentially, spurriously leading to exponential growth of electron density for molecules or for spacial points above the surface of a solid. Traditionally this problem has been avoided by using empty cells and neglecting the leakage of charge of "filled" and empty cells. In this paper, however, we do not use empty cells, but still limit the use of the standard expression to within small spheres around each nucleus. For the region outside we use electron density approximated by the alternative, well-behaved expression,

$$G^c - G^0 = -2k[\bar{\Phi}_L H_L + \bar{j}_L(H_L - h_L)], \tag{8}$$

$$G^{sc}(\vec{r},\vec{r}',E) = -2k\sum_{iL,jL'} \Phi_{iL}(\vec{r})G^{FMS}_{iL,jL'}\bar{\Phi}_{jL'}(\vec{r}\,'), \tag{9}$$

where $\Phi_{iL} = \Psi_{iL} - j_L$ and $\bar{\Phi}_{iL} = \bar{\Psi}_{iL} - \bar{j}_L$ exponentially decay at high distances for energies below interstitial level or when the energy has a nonzero imaginary part. This is important for calculations of the total charge density using MST, especially for molecules. However for X-ray absorption from deep core hole levels, the standard expression does not have a problem at large distances due to the finite core-hole dimension. The standard expression is also much easier to use for calculations, due to the absence of the site off-diagonal matrix elements of G^{FMS}.

Knowledge of the Green's function then allows us to calculate various physical quantities. The density of states and electron densities are determined by its imaginary part, and are needed in self-consistent calculations. The X-ray absorption is given by

$$\mu(\omega) \propto \sum_{iLL'} M_{iL}[\delta_{LL'} + \mathrm{Im}\, G^{FMS}_{iL,iL'}]\bar{M}_{iL'}, \tag{10}$$

where the dipole matrix elements coupling with the X-ray field to the initial state i and final Ψ_L are $M_{iL} = \langle i|\vec{\epsilon}\cdot\vec{r}|\Psi_L\rangle$ and $\bar{M}_{iL} = \langle\bar{\Psi}_L|\vec{\epsilon}\cdot\vec{r}|i\rangle$.

We demonstrate the importance of the full potential in the XANES for Si crystals (Fig. 1). The full potential code (solid) clearly reproduces the double peak structure of the white line in the experimental data [11] (dots), while muffin-tin code FEFF8 (dashes) gives primarily a single peak of about the same width. Thus the double peak structure can be understood as the additional splitting of the unoccupied bands due to the non-spherical, and hence anisotropic part of potential due to the strong directional bonds in Si.

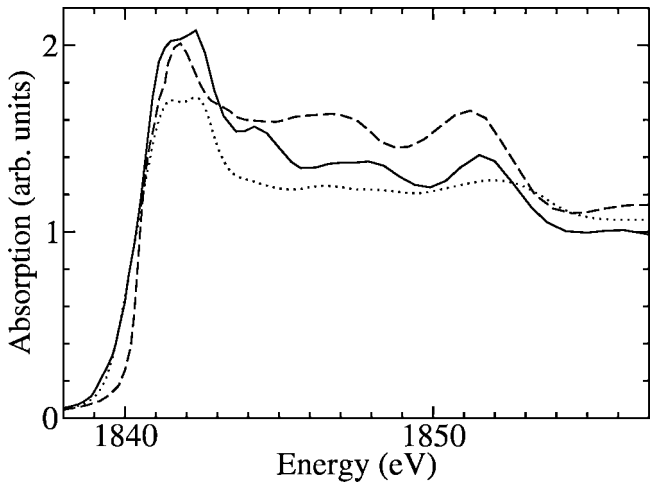

Fig. 1. K-edge absorption of Si crystal. The full potential (solid) calculations with 329 atom clusters reproduce the double peak structure of the white line in experimental data (dots). In contrast, muffin-tin calculations (dashes) with 849 atom clusters have a single dominant peak.

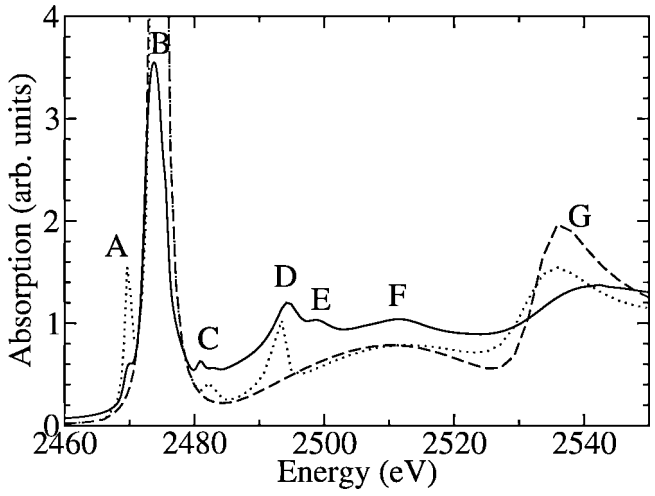

Fig. 2. S K-edge absorption of SF_6 molecule. Full potential calculations for S in the center of octahedron (dashes) and for S shifted by (0.1,0.1,0.1)Å (dashes) versus experiment (solid). This shift is reasonable to describe vibronic coupling in SF_6.

3. Vibronic coupling

Next we want to demonstrate the applicability of our full potential code to molecules. We chose the K-edge of SF_6 molecule as an example, since surprisingly the standard MST calculation lacks many of the peaks observed in experiment. Thus in the work of Tyson *et al.* [12] only 3 XANES peaks out of 7 (B, F and G on Fig. 2) are reproduced by MST calculations. This is even more surprising since the L_2 and L_3 edges of SF_6 are well reproduced [13]. However, we found that even our full potential code gives only 3 peaks for the perfect octahedron structure. Thus we found that to explain the experimental data at S K-edge, it is important to consider vibronic coupling effects. Since in the ground state, this molecule is a perfect octahedron, some transitions are forbidden by the dipole approximation. However, atomic displacements continually break the symmetry, and in actual calculations one has to average calculated XANES over various distorted atomic configurations. Fujikawa [14] has suggested a general treatment of vibrations for X-ray absorption calculations. In general it requires one to know the vibrational Hamiltonian for the excited state. If we neglect the difference of vibrations in ground and excited states, the X-ray absorption is given as an average over possible initial atomic displacements,

$$\mu(\omega) = \langle\mu(\omega,\vec{Q})\rangle, \tag{11}$$

where $\vec{Q}$ describes the displacement of an atom (or atoms) from its equilibrium position. One obtains the same expression assuming the atoms don't move significantly during the transition. If one

expands $\mu(\omega, \vec{\boldsymbol{Q}})$ in powers of Q, assuming small dependence of X-ray absorption on atomic positions we obtain to leading order,

$$\mu(\omega) = \mu(\omega, Q) + \frac{\delta^2 \mu(\omega, \vec{\boldsymbol{Q}})}{\delta Q_i \, \delta Q_j} \langle Q_i Q_j \rangle, \tag{12}$$

where the first order terms cancel since $\langle Q_i \rangle = 0$. Thus the leading correction to the absorption at the equilibrium position is connected with the Debye-Waller factors. Thus for SF_6 the typical displacement is about 0.05 Ångström [12].

In Fig. 2 we also show calculations performed for configurations where the S atom is displaced by (0.1,0.1,0.1) Å from its equilibrium position at the origin. We simply used the amplitude which is consistent with measured Debye-Waller factor for this molecule. As one can see this shift reproduces 6 peaks out of 7 in the correct positions, and even gives reasonable agreement with experiment [12] in their intensities. The intensity of 3 additional peaks (A,C,D) scales as a square of the distortion amplitude. This still did not produce peak E, which may be due to a different type of distortion or possibly to some other source like multi-electron excitations. Even though we do not perform an average over all possible displacements, it is clear from Fig. 2 that some ensenble averaging may be important more generally, and may have significant effect on calculated XANES spectrum. Indeed, this should be essential for structural XANES analysis, since the assumption of perfect octahedral equilibrium positions, even with thermal or structural Debye Waller factors $\exp(-2k^2\sigma^2)$ fails to account the observed XANES.

This calculation clearly demonstrates that especially for symmetric equilibrium positions, atomic motion may lead to additional peaks due to vibronic coupling to states for which dipole transitions are forbidden for the equilibrium geometry. Such coupling can be reproduced by averaging XANES using quantum molecular-dynamics simulations. Even simple shifts of the order of typical Debye-Waller factors may reveal some forbidden transitions. However, appropriate averaging may be necessary to get the right intensities. These findings are consistent with an earlier interpretation of the spectral features in SF_6 K-edge XANES as a vibronically induced coupling, by Zimkina and Vinogradov [15]. Here we are able to support such an interpretation quantitatively.

4. Local Field Effects and Core-hole interaction

Local field effects were used by Zangwill and Soven to describe the screening of X-ray field within an absorbing atom. This effect arises since the external electric field of the X-ray polarizes the electron cloud around the nuclei, which creates an induced screening electric field and hence modifies the transition matrix elements. From another point of view, the local fields can be shown to arise from the non-local exchange term in the photoelectron-hole interaction.

Local fields must be distinguished from the core-hole interaction which can lead to excitons in dielectrics and edge singularities in metals. However, these two effects are directly connected to the direct and exchange terms in the interaction kernel in time dependent density functional theory (TDDFT).

The TDDFT [16, 18, 19] provides an efficient formalism to include simultaneously local field effects and the core-hole interaction in calculations of response functions. The TDDFT was originally introduced for atoms within the local density approximation (LDA), an approach also referred to as the TDLDA [16]. It has since been extended to many other systems [17, 19]. Moreover, the TDDFT equations are similar to the Bethe-Salpeter equation (BSE) [20, 21, 22, 23, 24], which provides a systematic many-body framework for treating local field effects. The main difference between the TDDFT and the BSE lies in the structure of the exchange-correlation kernel $f_{xc}(\omega)$ in the TDDFT and the screened core-hole interaction in the BSE. In addition the single-particle states in the BSE are taken to be quasiparticle states which account for self-energy effects.

Within all of these approaches, the XAS (or cross-section) $\mu(\omega)$ can be expressed as an integral over the *non-interacting* response function $\chi_0(\vec{r}, \vec{r}\,', \omega)$ and the screened X-ray field $\phi(\vec{r}, \omega)$,

$$\mu(\omega) = -\frac{4\pi\omega}{c} \int \mathrm{d}\vec{r} \, \mathrm{d}\vec{r}\,' \phi^*(\vec{r}, \omega)[\mathrm{Im}\, \chi_0(\vec{r}, \vec{r}\,', \omega)]\phi(\vec{r}\,', \omega),$$

$$\chi_0(\vec{r}, \vec{r}\,', \omega) = \sum_{ij} (f_i - f_j) \frac{\psi_i^*(\vec{r})\psi_i(\vec{r}\,')\psi_j^*(\vec{r}\,')\psi_j(\vec{r})}{\omega + E_i - E_j + \mathrm{i}0^+}. \tag{13}$$

Here f_i are Fermi occupation numbers (1 or 0), and the sums run over all one-electron eigenstates $\psi_i(\vec{r})$ of the ground state Hamiltonian.

Remarkably it has been proved that Eq. (13) is equivalent to an analogous expression with ϕ replaced by the external X-ray field ϕ^{ext} and χ_0 by the full response function $\chi = [1 - \chi^0 K]^{-1}\chi^0(\omega)$ [16]. However, the form in Eq. (13) has the advantage of putting all screening effects into the effective transition operator $\phi(\omega)$. The field $\phi(\omega)$ consists of the external X-ray field coupling the electrons $\phi^{ext} \equiv \hat{\boldsymbol{\epsilon}} \cdot \vec{r}$ (in the dipole approximation) plus an induced local field. In matrix form this is given by

$$\phi(\omega) = \epsilon^{-1}(\omega)\phi^{ext}(\omega), \qquad \epsilon(\omega) = 1 - K(\omega)\chi^0(\omega). \tag{14}$$

The kernel $K(\vec{r}, \vec{r}\,', \omega)$ characterizes the particle-hole interaction and contains direct and exchange parts, i.e., $K(\vec{r}, \vec{r}\,', \omega) = V(\vec{r}, \vec{r}\,') + f_{xc}(\vec{r}, \vec{r}\,', \omega)$ where $V = 1/|\vec{r} - \vec{r}\,'|$ is the bare Coulomb interaction, which accounts for the local field effects. The $f_{xc}(\vec{r}, \vec{r}\,', \omega)$ represents the screened core-hole interaction, which is approximated by a local function. Thus within TDLDA $f_{xc}^0(\vec{r}, \vec{r}\,') = \delta(\vec{r} - \vec{r}\,')\delta v_{xc}[\rho(\vec{r})]/\delta\rho$ avoids the non-locality of BSE and is obtained from the ground-state LDA exchange-correlation potential $v_{xc}[\rho]$. This often works well at low energies, e.g., for optical spectra. For the X-rays one in general needs a dynamic model [25].

The TDLDA approach fits well with the the RSMS formalism used in FEFF8 [25]. Carrying out the integrations over χ_0, Eq. (13) becomes

$$\sigma(\omega) = \frac{4\pi e^2 \omega}{c} \sum_{v,LL'} \tilde{M}_{vL}(\omega)[\delta_{L,L'}(E) + G_{LL'}^{FMS}]\tilde{M}_{vL'}(\omega), \tag{15}$$

where $E = \omega + E_v - E_F$ is the photoelectron energy and E_v the energy of the occupied (or valence states). The screening of both the X-ray field and the photoelectron-core hole interaction are included implicitly in the renormalized dipole matrix elements $\tilde{M}_{vL}(\omega) = \langle R_L|\phi|v\rangle$. Here $R_L(\vec{r}, E)$ are normalized scattering states calculated with the absorbing atom ground state potential, and $G_{LL'}^{FMS}(E)$ contains the fine structure due to scattering by the environment [1]. The calculation of renormalized matrix elements within a local screening approximation is achieved by a small matrix inversion [25]. Note that by replacing ϕ with ϕ^{ext} in Eq. (5), the screened matrix elements $\tilde{M}_{vL}$ become bare dipole matrix elements $M_{vL} = \langle R_L|\hat{\boldsymbol{\epsilon}} \cdot \vec{r}\,|i\rangle$, and one recovers the independent electron formula, equivalent to Fermi's Golden Rule. Since the strength of the XAS is a measure of the screening response, the

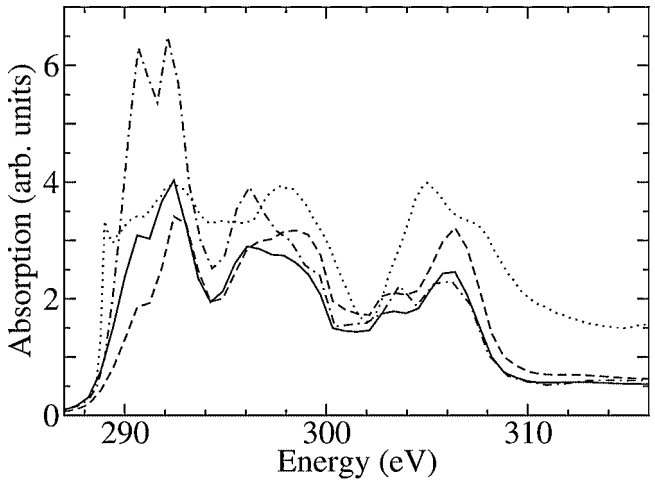

Fig. 3. K-edge absorption of diamond. Experiment (dots) is compared to calculations with the initial, ground state potential without a core-hole (dashes), with the fully relaxed core-hole potential (dash-dots), and with the adiabatic TDLDA kernel (solid).

independent-electron approximation should become increasingly valid away from the edge region. Several kernels were compared for the transition metals L_3/L_2 branching ratio [25]. However, for the diamond K-edge calculations the adiabatic TDLDA kernel is appropriate since there is only one edge.

In Fig. 3 we show calculations for the K-edge of diamond with the TDLDA approach (solid) that includes both the core-hole interaction and local field effects. It is compared to experiment [26] (dots) and a calculation with the final state rule (dash-dots), that includes core-hole interaction and neglects local field effect, and for the initial, ground state potential (dashes) which neglects both core-hole and local field effects. As one can see the ratios of the first 3 peak intensities differ significantly among the calculations. If one takes into account that the experimental data has a roughly linear background, the TDLDA calculation seems to be the best to reproduce the relative intensity of the peaks. All of our calculations miss the excitonic peak right at the edge (which may require bigger clusters), but the consequent double peak structure again is best described by TDLDA calculations. This suggests that local field effects are important in this case and have an amplitude comparable to that of the core-hole interaction. Both final state rule (Fig. 3) and BSE calculations [21] overestimate the strength of the white line suggesting that the white line sensitive both to the screening of the core-hole interaction and the local fields. Notice that core-hole effects tends to bring oscillator strength closer to the edge, while the local field effect tends to move it away from the edge. In practice, there are cases where either of the effects dominates, which means that simultaneous treatment of both is essential.

5. Conclusions

The *standard* theory of X-ray absorption originally developed for the EXAFS region, is usually accurate even for XANES calculations [1]. This theory makes use of spherically symmetric densities and potentials, a fully screened core-hole potential, and inelastic losses and energy shifts based on the Hedin-Lundqvist self-energy approximation. However, this standard theory sometimes breaks down for XANES calculations, as illustrated by several examples. Non spherical corrections are needed to resolve the Si K-edge double peak white line, which illustrates the sensitivity of XANES calculations to the details of the potential construction beyond the spherical approximation. Vibronic coupling or average over possible initial atomic displacements needs to be included for the SF_6 K-edge absorption calculation and hence in other cases where local distortions are important. And finally, local field effects and the screening of the core-hole interaction are important and may change relative intensities of the peaks in XANES significantly, especially for energies below 1 keV, as demonstrated by diamond K-edge calculations. Thus extensions of the standard XANES theory are generally needed for reliable structural XANES analysis. Our examples show that such a theory should include non-spherical potentials, vibronic, local field, and core-hole interaction effects.

Acknowledgments

This work is supported in part by DOE grant 98ER45623 and the DOE CMSN.

References

1. Ankudinov, A. L., Ravel, B., Rehr, J. J. and Conradson, S. D., Phys. Rev. B **58**, 7565 (1998).
2. Della Longa, S., *et al.*, Phys. Rev. Lett. **87**, 155501 (2001).
3. Lloyd, P. and Smith, P. V., Adv. Phys., **21**, 69 (1972).
4. Williams, A. R. and van W. Morgan, J., J. Phys. C **7**, 37 (1974).
5. Natoli, C. R., Benfatto, M. and Doniach, S., Phys. Rev. A **34**, 4682 (1986).
6. Foulis, D. L., *et al.*, Phys. Rev. A **41**, 6922 (1990).
7. Becke, A. D., J. Chem. Phys. **88**, 2547 (1988).
8. Zeller, R., J. Phys. C **20**, 2347 (1987).
9. Dederichs, P. H., Drittler, B. and Zeller, R., "Applications of Multiple Scattering Theory to Material Science," (ed. W. H. Butler *et al.*), Material Science Research Society symposium proc., v. 253., p. 185 (1992).
10. Wang, X., Zhang, X.-G., Butler, W. H., Harmon, B. N. and Stocks, G. M., in "Applications of Multiple Scattering Theory to Material Science," (ed. W. H. Butler *et al.*), Material Science Research Society symposium proc. v. 253., p. 185, (1992).
11. Hitchcock, A. P., *et al.*, Surface Sci. **291**, 349 (1993); Flank, A. M., private communication.
12. Tyson, T. A., Hodgson, K., Natoli, C. R. and Benfatto, M., Phys. Rev. B **46**, 5997 (1992).
13. Vedrinskii, R. V., *et al.*, Izv. Akad. Nauk SSSR, Ser. Fizicheskaya, **38**, 8 (1974).
14. Fujikawa, T., J. Phys. Soc. Jap. **65**, 87 (1995).
15. Zimkina, T. M. and Vinogradov, A. S., J. Phys. (Paris) C **4**, 3 (1971).
16. Zangwill, A. and Soven, P., Phys. Rev. A **21**, 1561 (1980); Zangwill, A. and Liberman, J., Phys. B: At. Mol. Phys. **17**, L253 (1984).
17. Schwitalla, J. and Ebert, H., Phys. Rev. Lett. **80**, 4586 (1998).
18. Gross, E. K. U. and Kohn, W., Adv. Quantum Chem. **21**, 255 (1990).
19. See for example, Bertsch, G. F., Iwata, J.-I., Rubio, A. and Yabana, K., Phys. Rev. B **62**, 7998 (2000); Vasiliev, I., Ögut, S. and Chelikowsky, J., Phys. Rev. Lett. **82**, 1919 (1999).
20. Rohlfing, M. and Louie, S. G., Phys. Rev. B **62**, 4927 (2000).
21. Soininen, J. A. and Shirley, E. L., Phys. Rev. B **64**, 165112 (2001).
22. Strinati, G., Phys. Rev. B **29**, 5718 (1984).
23. Hanke, W. and Sham, L. J., Phys. Rev. B **21**, 4656 (1980).
24. Reining, L., Olevano, V., Rubio, A. and Onida, G., Phys. Rev. Lett. **88**, 066404 (2002); Onida, G., Reining, L. and Rubio, A., Rev. Mod. Phys. **74**, 601 (2002).
25. Ankudinov, A. L., Nesvizhskii, A. I. and Rehr, J. J., Phys. Rev. B **67**, 115120 (2003).
26. Jaouen, M. and Hug, G., private communication.

Physica Scripta. Vol. T115, 28–30, 2005

Advances in the Theoretical Analysis of the XANES (X-ray Absorption Near Edge Structure) Energy Region for Quantitative Structural Use

M. Benfatto[a], S. Della Longa[b,a] and P. D'Angelo[c]

[a]Laboratori Nazionali di Frascati dell'INFN - C.P.13 - 00044 Frascati, Italy
[b]Universita' dell'Aquila - via Vetoio, loc. Coppito II - 67100 l'Aquila, Italy
[c]Dipartimento di Chimica, Universita' di Roma "La Sapienza", Piazzale A. Moro 5, 00185 Rome, Italy

Received June 26, 2003; accepted June 28, 2004

PACS numbers: 78.70. Dm, 71.20.Nr

Abstract

X-Ray Absorption Near Edge Structure (XANES) spectroscopy is a powerful method to study the local structure around an absorbing site of various types of matter. Analysis of the spectrum can give both electronic and structural information on the site around the absorbing atom. In this paper we present some recent theoretical advances that allow a complete quantitative analysis of the XANES energy region in term of structural parameters. Some examples will be presented in details with a complete discussion of the strengths and limitations of the method when applied to real systems.

1. Introduction

X-ray absorption spectroscopy (XAS) is one of the most powerful methods to obtain structural and electronic information on the local environment of an excited atom. During the past ten years, much theoretical and computational effort has been made that has led to the development of *ab-initio* methods for XAS calculations in arbitrary systems [1]. In the high-energy region (typically from 50–100 eV above the rising edge) several approximations can be made to reduce the complicate many-body photo-absorption process in that of a photoelectron scattering in an effective potential. This allows a quantitative analysis of the extended X-ray-absorption fine-structure (EXAFS) region of the XAS spectra. The EXAFS technique has found many applications ranging from chemistry to molecular biology, including liquid and solid-state problems in condensed-matter physics.

The situation is different concerning the low-energy part of the X-ray absorption cross section extending up to around 50–100 eV above the threshold, the so called XANES (X-ray absorption near-edge structure) region. This part is very sensitive to the geometrical details of the absorbing site (overall symmetry, distances and bond angles), so that, in principle, an almost complete recovery of the geometrical structure within 6–7 Å from the absorbing site can be achieved from the experimental data with atomic resolution. However, the quantitative analysis of the full XAS spectrum, including the edge, is a complex many-body problem that requires an adequate treatment and the need for heavy time-consuming algorithms to calculate the absorbing cross section including all multiple-scattering (MS) contributions of any order, the so-called full MS approach. Due to these difficulties, the analysis of the pre-edge and first part of the XAS spectra (up to 50–100 eV) has been exploited so far only on qualitative ground, by comparison with model compounds or as an aid for EXAFS studies or more advanced investigations, such as the ones based on the analysis of contributions related to correlation functions of orders higher than two [2].

Recently some of us have proposed [3] and applied to several systems [4, 5] a new method, called MXAN, to perform a quantitative analysis of the XANES energy range, i.e. from the edge up to 200 eV. In this paper we present details of the method and some results obtained for some test cases with the aim to validate the method and define its potentiality and limitation.

2. The MXAN procedure

The method is based on the comparison between experimental data and many theoretical calculations performed by varying selected structural parameters starting from a plausible ansatz for the structure, i.e. from a well defined initial geometrical configuration around the absorber. The calculation of XANES spectra related to the hundreds of different geometrical configurations needed to obtain the best fit of the experimental data is done in a reasonable time and the optimization in the space of parameters is achieved by the minimization of the square residual function in the parameter space.

The calculations are performed within the so-called full MS approach, i.e. the inverse of the scattering path operator is computed exactly, avoiding any "*a-priori*" selection of the relevant MS paths. The MXAN procedure uses the set of programs developed by the Frascati theory group [1, 5]; in particular VGEN, a generator of muffin-tin potentials, and the CONTINUUM code for the full MS cross section calculation. The optimization in the space of the parameters is achieved using the MINUIT routines of the CERN library by minimizing the square residual function

$$S^2 = n\frac{\sum_{i=1}^{m} w_i[(y_i^{\mathrm{th}} - y_i^{\mathrm{exp}})\varepsilon_i^{-1}]^2}{\sum_{i=1}^{m} w_i} \qquad (1)$$

where n is the number of independent parameters, m the number of data points, y_i^{th} and y_i^{exp} the theoretical and experimental values of absorption, ε_i the individual errors in the experimental data set, and w_i is a statistical weight. For w_i = constant = 1, the square residual function S^2 becomes the statistical χ^2 function. A typical fit involves an experimental energy range of about 150–200 eV from the rising edge and the application to several test cases shows that the best-fit solution is independent from the minimization strategy and from the starting conditions.

The MXAN method is based on the muffin-tin (MT) approximation for the shape of the potential and the use of the concept of complex optical potential, based on the local density approximation of the self-energy of the excited photoelectron. The MT radii are chosen according to the Norman criterion with some percentage of overlapping and the potential is recalculated at each step of the minimization procedure keeping fix the overlapping factor. The effects of the non-MT corrections will be discussed in some details later in this paper, but evidence exists that their

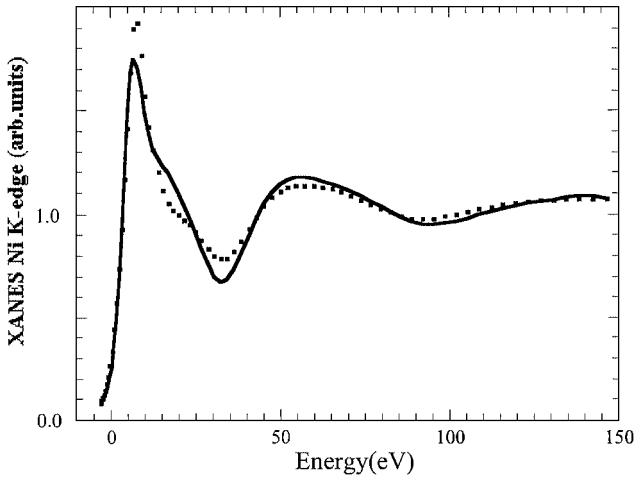

Fig. 1. Comparison between the experimental data (dotted line) and the best-fit calculation (solid line) of the Ni K-edge spectrum of the Ni^{2+} aqua ion. In this case the full complex HL potential has been used.

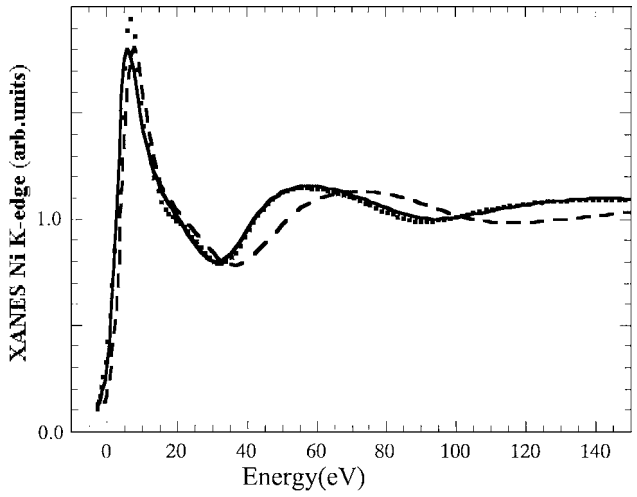

Fig. 2. Comparison between the experimental (dotted line) and best-fit calculation (solid line) of the Ni K-edge XANES spectrum of Ni^{2+} aqua ion. The dashed line corresponds to the calculation associated to the starting structure.

relevance is confined within the first 20–30 eV from the edge [6, 7] with very weak influence on the structural determination due to the relatively large energy range used in the fit. In this way the geometrical arrangements restrain the numerical results of the fitting procedure.

The self-energy is calculated in the framework of the Hedin-Lundqvist (HL) scheme [1]. The use of the full complex HL potential introduces a relevant over damping at low energies in the case of covalent molecular systems as shown in Fig. 1 where we report a comparison between the experimental data related to Ni^{2+} ion in water and the calculation, at the best fit condition, obtained by using the full complex HL potential. H atoms are included in the calculation. In this case the best-fit structure corresponds to an octahedron with an oxygen-metal distance of 2.04(2) Å in good agreement with the more recent EXAFS results.

Note that we obtain the correct geometry despite the presence of relevant discrepancies between experimental data and the best-fit calculation in the first 40 eV. For the experimental details see references [8].

In order to have a full access to the structural information contained in the low-energy part of the XANES spectrum, we have developed a phenomenological approach to calculate the inelastic losses based on the convolution of the theoretical spectrum, calculated by using only the real part of the HL potential, with a suitable Lorentzian function having an energy dependent width of the form $\Gamma_{tot}(E) = \Gamma_c + \Gamma_{mfp}(E)$. The constant part Γ_c includes the core hole lifetime and the experimental resolution, while the energy dependent term represents all the intrinsic and extrinsic inelastic processes. The $\Gamma_{mfp}(E)$ function is zero below an onset energy E_s (which in extended systems corresponds to the plasmon excitation energy) and begins to increase from a value A_s following the universal functional form of the mean free path in solids. Both the onset energy E_s and the jump A_s are introduced in the $\Gamma_{tot}(E)$ function via an arctangent functional form to avoid discontinuities and to simulate the electron-hole pair excitations. Their numerical values are derived at each step of computation (i.e. for each geometrical configuration) on the basis of a Monte Carlo fit, similarly to the procedure used in optimisation by simulated annealing [9].

Using this procedure the agreement between the experimental data and the best fit theoretical curves becomes good in the whole energy range, small discrepancies remaining in the intensity of the resonance at 15 eV as shown in Fig. 2. The best fit corresponds to an octahedral symmetry with an oxygen-metal distance of 2.03 ± 0.03 Å in good agreement with the value obtained by the GNXAS analysis using the EXAFS energy region [5, 8]. The dashed line corresponds to the calculation associated with the starting putative structure that is an elongated octahedron.

Applications of this approach to different systems produce the same type of agreement between experimental data and best-fit calculations confirming the reliability of our phenomenological approach to the inelastic losses treatment in the XANES spectroscopy. To clarify this important point we report in Fig. 3 the behavior of the $\Gamma_{tot}(E)$ function for Ni^{2+} ion in water from the edge up to 80 eV. This function, starting from the value $\Gamma_c = 1.70$ eV, which is in good agreement with the core-hole lifetime ($\Gamma_{c-h} = 1.44$ eV) plus the experimental resolution, increases smoothly up to the value E_s that is the onset of the plasmon-like excitations for the considered charge density. Hereby after it follows the universal form with the size increased by the A_s value.

This phenomenological approach can be justified on the basis of a multi-channel multiple scattering theory [10]. In the sudden

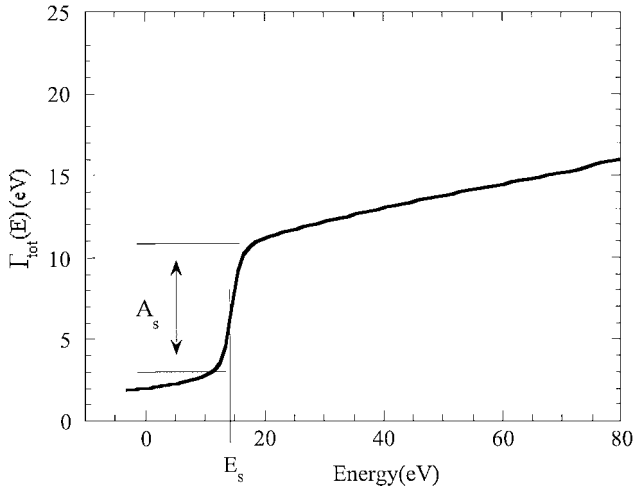

Fig. 3. Behaviour of the energy dependent width $\Gamma_c(E)$ of the Lorentzian function used in the convolution procedure to account for the inelastic losses. It refers to Ni^{2+} in water and the parameters T_c, E_s and A_s are derived on the basis of simulated annealing Monte Carlo search.

limit, the net absorption is given by a sum over all the possible excited states of the (N-1)-electron system [1, 10]. By assuming that the channels coming from the excitation of the N-1 electrons are near in energy, the total absorption is given by a convolution of the one-particle spectrum, calculated with the full-relaxed potential, with a spectral function $A(\omega)$ representing the weight of the other excited states. Hence the total XAS cross-section can be written as

$$\mu = \sum_n \mu_n \xrightarrow[\Delta E \to 0]{} \int \mu(\omega - \omega')A(\omega')\mathrm{d}\omega' \tag{2}$$

where the "ansatz" is made that the spectral function $A(\omega)$ is well approximated by a Lorentzian function with the energy dependent width $\Gamma_{\mathrm{mfp}}(E)$ previously defined. Moreover, it is possible to demonstrate that in the case of dominance of only one electronic channel (the elastic one), the corresponding Green's function G_0 obeys a Dyson-like equation with a suitable complex optical potential $\Sigma^{\mathrm{opt}}(r, r'; E)$ that, with some approximation (locality, homogeneous systems...) is equivalent to a "real" calculation convoluted by a Lorentzian function of suitable energy dependent width [10]. Therefore the $\Gamma_{\mathrm{tot}}(E)$ function is characterized by parameters which have a clear physical meaning and they are not free to assume any value, but are varied in a well defined interval. Obviously, when contributions from one or more of these excited states become relevant, they must be considered explicitly in the calculations.

We also note that the shape of the $\Gamma_{\mathrm{mfp}}(E)$ function is similar to the inverse lifetime of the quasiparticles Γ_{k} derived in the GW_0 scheme, without the sharp onset at the plasmon excitation energy to account for the interference between the intrinsic and extrinsic inelastic losses [11].

Note that the MXAN method introduces as a total four non-structural parameters. Applications to several test cases indicate that their influence on the structural reconstruction is weak and it reduces to an increase of a few percent of the error in the structural parameters determination [12].

The use of the MXAN procedure to the analysis of potassium ferrocyanide (III) in water allowed us to shed light on the relevance of non-MT corrections on the quantitative structural determination. Due to its high symmetry and to the shortness of the cyanide bond length this molecular system has often been used as a test case for any XANES calculations, but a good reconstruction of the experimental data has never been achieved. A thorough analysis of the Fe K-edge XANES is presented in a paper in these proceedings [13], here we just want to stress that the non-MT corrections are small even in this case and do not affect the structural determination. In fact we observe that it is possible to write a MS theory, which does not use the MT approximation for the shape of the potential, having the same formal structure of the usual MS theory by adding some suitable quantities to the scattering matrix and propagators [14].

In this way the total photo-absorption cross section is proportional to

$$\sigma_t \approx \mathrm{Im}(T + H)^{-1} \tag{3}$$

where $T = (T_{\mathrm{a}})^{-1} + \Delta T$ and $H = H_{MT} + \Delta H$. Here $(T_{\mathrm{a}})^{-1}$ and H_{MT} are the usual MS quantities calculated within the MT approximation. The corrections are proportional to the interstitial volume. Indicating $\Delta = \Delta T + \Delta H$ we can expand the total cross section σ_{t} in series using Δ as a parameter:

$$\sigma_t \approx \mathrm{Im}\left\{ \sum_{n=0} (-1)^n [T_a^{-1} + H_{MT})^{-1}\Delta]^n (T_a^{-1} + H_{MT})^{-1} \right\}. \tag{4}$$

In this way σ_{t} becomes:

$$\sigma_t \approx \sigma_{MT} + corr(E; V_{\mathrm{int}}). \tag{5}$$

In other words the total non-MT cross section can be written as the sum of the cross section calculated in the MT approximation and corrections that decrease with the energy and depend on the potential in the interstitial volume. For these reasons the corrections are usually small for molecular systems with high symmetry. In fact a full potential calculation does not improve dramatically the agreement between theory and the potassium ferrocyanide experimental data [13].

3. Conclusions

In conclusion, we have presented a new method for a quantitative analysis of XANES spectra based on a fitting procedure in the framework of full multiple scattering calculations. In this way we achieve a full access to the whole XANES energy range allowing complete structural determination of the local geometry around the absorber. The MXAN method has been proven to provide reliable structural results confirming the validity of the application of the full MS scheme in the framework of the MT approximation. The results of the present investigation represent a step forward in understanding the role that the XANES technique can play in providing quantitative structural information on chemical systems.

References

1. Tyson, T. A., Hodgson, K. O., Natoli, C. R. and Benfatto, M., Phys. Rev. B **46**, 5997 (1992); Rehr, J. J. and Albers, R. C., Rev. Mod. Phys. **72**, 621 (2000); Natoli, C. R. and Benfatto, M., J. Phys. (France) Colloq. **47**, C8:11–23 (1986).
2. Filipponi, A. and Di Cicco, A., Phys. Rev. B **52**, 15135 (1995).
3. Benfatto, M. and Della Longa, S., J. Synchrotron Rad. **8**, 1087 (2001).
4. Della Longa, S., Arcovito, A., Girasole, M., Hazemann, J. L. and Benfatto, M., Phys. Rev. Lett. **87**, 155501 (2001).
5. D'Angelo, P., Benfatto, M., Della Longa, S. and Pavel, N. V., Phys. Rev. B **66**, 064209 (2002).
6. Cabaret, D., Joly, Y., Renevier, H. and Natoli, C. R., J. Synchrotron Rad. **6**, 258 (1999).
7. Joly, Y., Phys. Rev. B **63**, 125120 (2001).
8. D'Angelo, P. *et al*., J. Am. Chem. Soc. **124**, 1958 (2002).
9. Kirkpatrick, S., Gelatt Jr, C. D. and Vecchi, M. P., Science **220**, 671 (1983).
10. Natoli, C. R., Benfatto, M., Brouder, C., Ruiz Lopez, M. F. and Foulis, D. L., Phys. Rev. B **42**, 1944 (1990); Natoli, C. R., Benfatto, M., Della Longa, S. and Hatada, K., J. Synchrotron Rad. **10**, 26 (2003).
11. Holm, B. and von Barth, U., Phys. Rev. B **57**, 2108 (1998) and reference therein.
12. Benfatto, M., Della Longa, S. and D'Angelo, P., Proc. "X-Ray and Inner-Shell Processes: 19th International Conference on X-Ray and Inner-Shell Processes" (edited by A. Bianconi, A. Marcelli and N. L. Saini) p. 362 AIP (2003).
13. Hayakawa, K. *et al*., Physica Scripta, these proceedings (2003).
14. Natoli, C. R., Benfatto, M. and Doniach, S., Phys. Rev. A **34**, 4682 (1986).

Physica Scripta. Vol. T115, 31–34, 2005

Modeling Core-Hole Screening in Core-Excitation Spectroscopies

E. L. Shirley[1], J. A. Soininen[1,2] and J. J. Rehr[2]

[1]Optical Technology Division, National Institute of Standards and Technology, 100 Bureau Dr., Mail Stop 8441, Gaithersburg, MD 20899-8441, USA
[2]Department of Physics, Box 351560, University of Washington, Seattle, WA 98195, USA

Received June 26, 2003; accepted July 1, 2004

PACS numbers: 71.15.Qe, 71.15.−m, 78.70.Dm

Abstract

We consider screening of the core-hole potential experienced by the ejected electron in core-excitation processes. This potential affects near-edge structure strongly, but it appears difficult to consistently obtain reliable screened core-hole potentials without substantial computation. Screening effects have both atomic and solid-state (or molecular/cluster) contributions. We emphasize aspects that must be true of "correct" screening models, in an attempt to circumvent the need to carry out full-scale random-phase approximation (RPA) or self-consistent-field calculations of the screening. We present and discuss three spectra computed with RPA and model screened potentials, suggesting ideas to be considered in future work developing screening models.

1. Introduction

Core-excitation spectra provide information about structural properties and electronic states of molecules, clusters, and solids. Depending on the probe [e.g., X-ray absorption (XAS), inelastic X-ray scattering (IXS), or inelastic electron scattering (EELS)], a core-excitation spectrum provides information about unoccupied electron states in the form of a partial density of states (PDOS). This is weighted by matrix elements, perturbed by the final-state core-hole potential and complicated by vibrational and many-body effects on spectra.

High-resolution near-edge spectra are highly detailed and informative, but are also most strongly affected by core-hole effects. These effects have been treated in multiple-scattering work [1]–[2], supercell calculations [3], and the Bethe-Salpeter equation [4]. Because the core-hole effects influence near-edge spectral features so strongly, it is important to calculate the screened core-hole potential experienced by the excited electron accurately, and reliable means to do so appear to require substantial calculations.

Here we consider aspects of models for core-hole screening. We review salient aspects of traditional or "orbital-based" screening calculations, such as the random-phase approximation (RPA), which are based on self-consistent field calculations and perturbation theory. We then propose two screening models that are "density-based," which require only the total electron density as input and so are computationally much more efficient. This is an especially important consideration in complex systems, where orbital-based calculations tend to scale more poorly with system size. We present results obtained using three screening models (RPA and two density-based models) for F, O and Mg 1s edges in solid LiF and MgO. We show theoretical screening effects and concomitant absorption spectra, so one can estimate how a screening model affects a spectrum. We discuss the results and provide some possible suggestions intended to aid development of efficient yet accurate screening models in future work.

2. Orbital-based (numerical) screening calculations

Most practical numerical calculations of electronic structure begin with self-consistent-field (SCF) calculations, where one-electron orbitals solve a Schrödinger-like equation. We shall refer to all such calculations as being *orbital-based*. These calculations are usually numerically intensive because of the need to use supercells or sum over large numbers of virtual electron states. As an key example, in density-functional theory, one has (in Hartree atomic units)

$$\left[-\tfrac{1}{2}\nabla^2 + V_{\rm ext} + V_{\rm H} + V_{\rm xc}\right]\psi_i(\mathbf{r}) = \epsilon_i\psi_i(\mathbf{r}), \tag{1}$$

where the potential has contributions $V_{\rm ext}$, accounting for atomic nuclei or pseudopotentials, $V_{\rm H}$, which is the Hartree potential, and $V_{\rm xc}$, which is the "exchange-correlation potential" that approximately describes exchange and correlation effects. We have

$$V_{\rm H}(\mathbf{r}) + V_{\rm xc}(\mathbf{r}) = \int {\rm d}^3\mathbf{r}'\,\frac{n(\mathbf{r}')}{|\mathbf{r}-\mathbf{r}'|} + \frac{\delta E_{\rm xc}}{\delta n(\mathbf{r})}, \tag{2}$$

where n is the total electron density because of occupied electron levels, given by

$$n(\mathbf{r}) = \sum_i^{\rm occ.} |\psi_i(\mathbf{r})|^2\,. \tag{3}$$

$E_{\rm xc}$ is the total exchange-correlation energy. The eigenvalues $\{\epsilon_i\}$ qualitatively mimic electron-level energies in atoms, molecules and solids.

Core-hole screening in SCF calculations can be determined by computing $V_{\rm H} + V_{\rm xc}$ when a core level on the "central site" is occupied and unoccupied and subtracting the difference. This can be difficult in an extended systems because of system size, but one can also calculate the same screening effects perturbatively in linear-response theory. The perturbed density is given by

$$\begin{aligned}\Delta n(\mathbf{r}) &= \int {\rm d}^3\mathbf{r}'\chi^0(\mathbf{r},\mathbf{r}';\omega=0)\Delta V_{\rm tot}(\mathbf{r}') \\ &= \int {\rm d}^3\mathbf{r}'\chi(\mathbf{r},\mathbf{r}';\omega=0)\Delta V_{\rm C}(\mathbf{r}').\end{aligned} \tag{4}$$

$\Delta V_{\rm C}$ is the unscreened potential of a core hole. Here, the *irreducible* polarization function $\chi^0(\mathbf{r},\mathbf{r}';\omega=0) = \delta n(\mathbf{r})/\delta V_{\rm tot}(\mathbf{r}')$ describes the induced change in density because of the change in the total potential,

$$\Delta V_{\rm tot}(\mathbf{r}) = \Delta V_{\rm C}(\mathbf{r}) + \Delta V_{\rm H}(\mathbf{r}) + \Delta V_{\rm xc}(\mathbf{r}). \tag{5}$$

The function χ^0 may be computed in one step, because it involves perturbation of the one-electron Schrödinger equation for independent electrons, suggesting that it is easier to model than the *reducible* polarization, $\chi(\mathbf{r},\mathbf{r}';\omega=0) = \delta n(\mathbf{r})/\delta V_{\rm C}(\mathbf{r}')$. The density is perturbed by a potential to which it contributes,

according to the integral equation,

$$\chi(\mathbf{r},\mathbf{r}';\omega) = \chi^0(\mathbf{r},\mathbf{r}';\omega) + \int \mathrm{d}^3\mathbf{r}'' \times \int \mathrm{d}^3\mathbf{r}''' \chi^0(\mathbf{r},\mathbf{r}'';\omega)\frac{\delta V_{\mathrm{tot}}(\mathbf{r}'')}{\delta n(\mathbf{r}''')}\chi(\mathbf{r}''',\mathbf{r}';\omega). \quad (6)$$

One can consider the response to a static potential, ΔV_{C}, by setting angular frequency $\omega = 0$, and this equation ignores ω-dependence of the kernel, $\delta V_{\mathrm{tot}}(\mathbf{r}'')/\delta n(\mathbf{r}''')$. Omitting exchange-correlation contributions to the kernel yields the time-dependent Hartree or random-phase approximation (RPA). Including these contributions yields a time-dependent density-functional-theory (TDDFT) calculation. In practice, these calculations give similar results for core-hole screening (as physics is dominated by the Hartree-potential effects in atomic core regions), and similar results are found in supercell SCF calculations [3].

3. Interplay of core and valence screening

The ejected electron involved in a core excitation basically witnesses the average screened potential of the core hole. Screening is done by core electrons localized on the central site and valence electrons with extended wave functions. One can consider screening by these two categories of electrons in turn. A deep core hole causes other core electrons to "contract" toward the atomic nucleus. This contraction is weakly affected by valence electrons and an atom's environment. We may rewrite Eq. (4) as

$$\Delta n(\mathbf{r}) = \int \mathrm{d}^3\mathbf{r}'\chi(\mathbf{r},\mathbf{r}';\omega=0)\Delta V_{\mathrm{C}}(\mathbf{r}') \approx \int \mathrm{d}^3\mathbf{r}'\chi_{\mathrm{V}}(\mathbf{r},\mathbf{r}';\omega=0)\Delta W_{\mathrm{C}}(\mathbf{r}'), \quad (7)$$

where χ_{V} is the polarizability if only the valence electrons are permitted to relax, and ΔW_{C} is ΔV_{C} screened by core electrons. ΔW_{C} can be obtained in atomic-structure calculations.

4. Density-based (model) screening calculations

Orbital-based screening calculations can scale poorly with system size. Moreover, short-range screening of a core hole, say on the scale of one or two atomic radii, should depend mostly on the central site's local enviroment, but most of the effort expended in an orbital-based calculation may be devoted to more remote regions of one's system. Density-based screening models may help address these issues. Just as for orbital-based screening calculations, density-based screening calculations can focus on computing χ or χ^0, which are related by Eq. 6. Any viable model for χ or χ^0 should obey all known constraints such as sum rules, some of which are cited here. First, χ or χ^0 should assume the "correct" value in the "homogeneous limit," which is the uniform electron gas in metallic systems, and which has reasonable counterparts in insulators, such as the Levine-Louie model dielectric function [5]. (This points to a shortcoming for such dielectric functions, because an insulator must intrinsically be a non-uniform system on the atomic scale, must possess an intrinsically non-metallic one-electron density matrix $\rho_1(\mathbf{r},\mathbf{r}')$, etc. It appears difficult to ascertain all of the ramifications of this for model dielectric functions, and how these ramifications may best be addressed. Perhaps the zero-moment sum rule for Im χ^0 may be of use:

$$\frac{1}{\pi}\int_0^\infty \mathrm{d}\omega\,\mathrm{Im}\,\chi^0_{\mathrm{L}}(\mathbf{r},\mathbf{r}';\omega) = \tfrac{1}{2}|\rho_1(\mathbf{r},\mathbf{r}')|^2 - \langle n(\mathbf{r})\rangle\delta^3(\mathbf{r}-\mathbf{r}'). \quad (8)$$

Here χ^0_{L} denotes the Lindhard polarizability or its analogue in a real material, and this sum-rule is easily derived using completeness.)

Kramers-Kronig relations and the f-sum rule are well know results, giving

$$\mathrm{Re}\left\{\begin{array}{c}\chi\\ \chi^0\end{array}\right\}(\mathbf{r},\mathbf{r}';\omega=0) = \frac{2}{\pi}\int_0^\infty \frac{\mathrm{d}\omega}{\omega}\,\mathrm{Im}\left\{\begin{array}{c}\chi\\ \chi^0\end{array}\right\}(\mathbf{r},\mathbf{r}';\omega) \quad (9)$$

and

$$\int_0^\infty \mathrm{d}\omega\,\omega\int \mathrm{d}^3\mathbf{r}\int \mathrm{d}^3\mathbf{r}'\,\mathrm{Im}\left\{\begin{array}{c}\chi\\ \chi^0\end{array}\right\}(\mathbf{r},\mathbf{r}';\omega)f(\mathbf{r},\mathbf{r}') = -\frac{\pi}{2}\int \mathrm{d}^3\mathbf{r}\,n(\mathbf{r})\left[(\nabla_{\mathbf{r}}\cdot\nabla_{\mathbf{r}'})\,f(\mathbf{r},\mathbf{r}')\right]_{\mathbf{r}'=\mathbf{r}}. \quad (10)$$

Here, $f(\mathbf{r},\mathbf{r}')$ can be any well-behaved function, and in reciprocal space we have the simplified formula in a periodic crystal,

$$\int_0^\infty \mathrm{d}\omega\,\omega\mathrm{Im}\left\{\begin{array}{c}\chi\\ \chi^0\end{array}\right\}(\mathbf{G}+\mathbf{q},\mathbf{G}'+\mathbf{q};\omega) = -\frac{\pi}{2}\tilde{n}(\mathbf{G}-\mathbf{G}')(\mathbf{G}+\mathbf{q})\cdot(\mathbf{G}'+\mathbf{q}). \quad (11)$$

(Note that the "Im" is restricted as defined by Zhang *et al.* [6].) There are also related constraints for certain limits, i.e.,

$$\lim_{\mathbf{Q}\to\infty}\chi^0(\mathbf{Q},\mathbf{Q};\omega=0) = \lim_{\mathbf{Q}\to\infty}\chi(\mathbf{Q},\mathbf{Q};\omega=0) \sim -\frac{4\tilde{n}(0)}{Q^2} \quad (12)$$

and

$$\lim_{\mathbf{r}\to\mathbf{r}'}\chi^0(\mathbf{r},\mathbf{r}';\omega) \sim -\frac{n(\mathbf{r})}{\pi\,|\mathbf{r}-\mathbf{r}'|}. \quad (13)$$

Other constraints can be found as well, such as through relating the ω^0, ω^1 and ω^{-1} moments of $\mathrm{Im}\chi^0(\mathbf{r},\mathbf{r}';\omega)$ using the Cauchy-Schwarz inequality. More stringent constraints and/or bounds on the polarizability would also be of use to the authors and others, if such properties could be stipulated.

However, we have found that satisfying these constraints – other than the one involving $\rho_1(\mathbf{r},\mathbf{r}')$, which might prove to be a paradigmatic challenge for screening models – is not sufficient to ensure that a screening model leads to accurate core-excitation spectra. Instead, we present two bulk models that have proved most successful in our work.

Our models are inspired by the Levine-Louie (LL) dielectric function [5], which describes screening in a homogeneous insulating system, obeying Eqs. (9–13) for that case. Having the correct value of $\epsilon(q\to 0;\omega=0)$, this model exhibits reasonable behavior of $\epsilon^{-1}(q,\omega=0)$ for intermediate q, though its results differ from RPA results for $\epsilon^{-1}(\mathbf{Q},\mathbf{Q};\omega=0)$ in real materials. The RPA results include local-field effects and concomitant effects of non-plane-wave character of Bloch functions. Incorporating these effects better into a model dielectric function is desirable.

Hybertsen and Louie introduced local-field effects in the LL model [7], but in a way that appears to have potential to violate Eq. (11). We note the following way to include local-field effects into the polarizability and dielectric response. Defining $B^0(q,\omega) = \chi^0_{\mathrm{LL}}(q,\omega)/q^2$ and $B(q,\omega) = \chi_{\mathrm{LL}}(q,\omega)/q^2$, with real-space counterparts $\tilde{B}^0(r)$ and $\tilde{B}(r)$, one may introduce the

model polarizability,

$$\left\{\begin{matrix}\chi_M\\ \chi_M^0\end{matrix}\right\}(\mathbf{r},\mathbf{r}';\omega) = -\nabla\cdot\nabla'\left(\frac{n(\mathbf{r})+n(\mathbf{r}')}{2\bar{n}}\right)\left\{\begin{matrix}\tilde{B}\\ \tilde{B}^0\end{matrix}\right\}(|\mathbf{r}-\mathbf{r}'|,\omega). \tag{14}$$

Noting

$$\int_0^\infty \mathrm{d}\omega\,\omega\,\mathrm{Im}\left\{\begin{matrix}B\\ B^0\end{matrix}\right\}(q,\omega) = -\frac{\pi\bar{n}}{2} \tag{15}$$

for all q, inserting the above formula into Eq. (10) and integration by parts ensures fully satisfying Eqs. (10–11). Here $\bar{n}$ is the average valence electron density in a bulk system.

Use of χ_M allows direct evaluation of $\epsilon^{-1}(\mathbf{Q},\mathbf{Q}';\omega)$, and its form allows computation of the dynamical part of a GW self-energy to be an $O(N_\mathrm{G}\log_2 N_\mathrm{G})$ rather than $O(N_\mathrm{G}^2)$ process. Use of χ_M^0 requires evaluation and inversion of $\epsilon(\mathbf{Q},\mathbf{Q}';\omega)$. In principle, this can give more accurate results, although the χ_M^0 that is used should yield the correct macroscopic dielectric properties only *after* local-field effects are included by inverting ϵ, suggesting that our present χ_M^0 may tend to underestimate screening effects. In a different context, if something analogous to χ_M^0 were similarly constructed and used when it involved averaging of the mesoscopic polarizability on a superatomic length scale that was smaller than all other critical dimensions in one's system, it could lead to correct treatment of polarizabilities and screening in cases of objects with a variety of shapes, surfaces, image-charge effects, etc.

5. Screened potentials and concomitant spectra

Figures 1–3 illustrate core-hole screening effects and near-edge spectra for F, O and Mg 1s edges in LiF and MgO. Theoretical results were obtained as in Ref. [4], with self-energy effects computed according to Ref. [8]. The plane-wave cutoffs used for band-structure and self-energy or screening calculations were as found in Ref. [9], ensuring that peak positions in spectra are converged to better than 0.1 eV, and peak amplitudes to with a few percent. Brillouin-zone sampling in Bethe-Salpeter calculations (see Ref. [4]) employed 4096 **k**-points in the full Brillouin zone on a regular grid, shifted according to Ref. [10]. Tests using denser grids indicated that spectral features could change by at most a few percent of the largest spectral features. The self-energy effects shift and Lorentz-broaden spectral features. Additional broadening was also included to match the measured width of the lowest-energy spectra feature, with data taken from Refs. [11] and [12]. The energy scale for each edge was shifted to align this feature using RPA screening with its experimental counterpart.

Three types of screening were considered: orbital-based RPA screening, and density-based model screening involving χ and χ^0 as discussed above. ΔW_C and associated valence screening effects are shown in the lower panel of each figure. In the F(1s) and O(1s) cases, the χ and χ^0 models respectively overestimate and underestimate screening effects at the nucleus, whereas both screening models underestimate screening effects at intermediate distances (around 1 a_0 to 2 a_0), and achieve the correct behavior of $(1-1/\epsilon_\infty)/r$ at long-range. This leads to gross exaggeration of core-hole effects at both near-edges by the χ^0 model, as compared to a more accurate description of core-hole effects by the χ model, slightly underestimating them in LiF, and slightly overestimating them in MgO. Note that the results for MgO and LiF are quite analogous, as both anions assume noble-gas configurations in

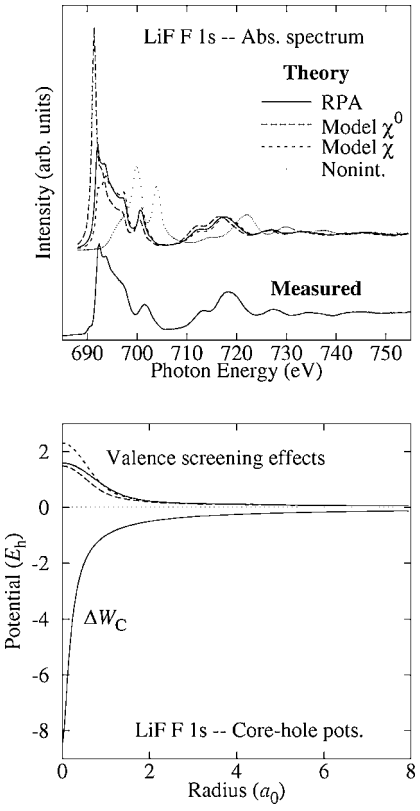

Fig. 1. Contributions to the core-hole potential (lower panel) and absorption spectra (upper panel) for the F 1s edge in LiF. In the lower panel, ΔW_C is the core-screened core-hole potential. Valence screening effects are shown as computed three ways according to the legend in the upper panel. Atomic units are used, with the energy unit being the Hartree energy, $E_\mathrm{h} \approx 27.2114\,\mathrm{eV}$. In the upper panel, corresponding theoretical absorption spectra are shown using the same legend, and a theoretical spectrum that omits core-hole effects is shown to illustrate the total magnitude of core-hole effects (labeled "Nonint."). A measured spectrum cited in the text is shown for comparison.

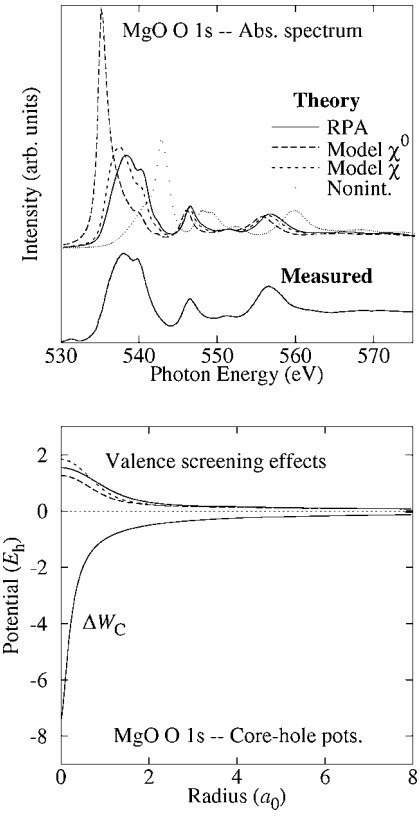

Fig. 2. Same as for Fig. 1, but for the O 1s edge in MgO.

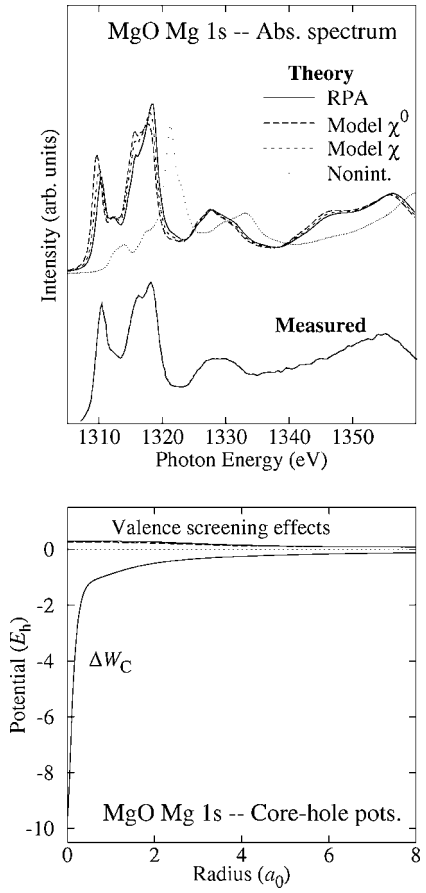

Fig. 3. Same as for Fig. 1, but for the Mg 1s edge in MgO.

these rocksalt-structure solids. Meanwhile, valence screening effects are very modest in the case of a Mg 1s hole in MgO, which is not surprising in view of the nominal Mg^{2+} configuration. Core-hole effects appear similar for all types of screening, with RPA results underestimating the effects the most. In all three cases, note that the qualitative change in spectral features because of core-hole effects vastly improves agreement with experiment, with the best overall agreement achieved with RPA screening.

6. Discussion

The vastly different spectra found in Figs. 1–2 are disconcerting in view of the modest difference in valence screening effects compared to the absolute size of the total core-hole potential. In diamond, screening effects are about 80%, so that they must be treated exceptionally well to obtain an accurate total screening potential. Often, differences between results found using χ and χ^0 models and RPA results in solids are borne out in atomic calculations. Thus, atomic calculations might help improve density-based screening models in a corrective sense, if issues such as identifying appropriate reference configurations and boundary conditions are resolved. Also, the spherically symmetrical component of screening effects can be only weakly affected by non-spherical site symmetry, suggesting simplifications to explore. As mainly short-range screening effects are treated poorly in density-based screening models, the models may be helpful for long-range screening, whereas atomic-like calculations that exploit simplifications afforded by spherical symmetry may be most helpful for correcting χ or χ^0 model results at short distances. These possibilities are currently being investigated.

Acknowledgments

This work was supported in part by U.S. Department of Energy (DOE) Grants DE-FG03-97ER45623 and DE-FG03-98ER45718, and was facilitated by the DOE Computational Materials Science Network (CMSN).

References

1. Rehr, J. J. and Albers, R. C., Rev. Mod. Phys. **72**, 621 (2000).
2. Ankudinov, A. L., Ravel, B., Rehr, J. J. and Conradson, S. D., Phys. Rev. B **58**, 7565 (1998).
3. Taillefumier, M., Cabaret, D., Flank, A. M. and Mauri, F., Phys. Rev. B **66**, 195107 (2002).
4. Soininen, J. A. and Shirley, E. L., Phys. Rev. B **64**, 165112 (2001), and references therein.
5. Levine, Z. H. and Louie, S. G., Phys. Rev. B **25**, 6310 (1982).
6. Zhang, S. B., Tománek, D., Cohen, M. L., Louie, S. G. and Hybertsen, M. S., Phys. Rev. B **40**, 3162 (1989).
7. Hybertsen, M. S. and Louie, S. G., Phys. Rev. B **37**, 2733 (1988).
8. Soininen, J. A., Rehr, J. J. and Shirley, E. L., J. Phys.: Condens. Matter **15**, 2573 (2003).
9. Shirley, E. L., Phys. Rev. B **58**, 9579 (1998).
10. Benedict, L. X., Bohn, R. B. and Shirley, E. L., Phys. Rev. B **57**, R9385 (1998).
11. Hudson, E. A. *et al.*, Phys. Rev. B **49**, 3701 (1994).
12. Lindner, T., Sauer, H., Engel, W. and Kambe, K., Phys. Rev. B **33**, 22 (1986).

Physica Scripta. Vol. T115, 35–37, 2005

Relativistic Keldysh Green's Function Approach to XAFS Theory

Takashi Fujikawa*

Graduate School for Science, Chiba University, Yayoi-cho 1-33, Inage-ku, Chiba, 263-8522, Japan

Received June 26, 2003; accepted October 16, 2003

PACS numbers: 79.60.i, 68.35.p, 78.20.Ci, 78.70.Dm

Abstract

A many-body relativistic XAFS theory has been developed on the basis of quantum electrodynamic Keldysh Green's function approach. To obtain photon absorption rate we calculate the time derivative of the projected photon Green's function whose self-energy includes relativistic electron Green's functions. For retarded and advanced electron Green's functions we can apply a useful expansion in terms of correlated quasi-nonrelativistic Green's functions.

1. Introduction

Many-body XAFS theory has been developed on the basis of many-body scattering theory [1–3] and Keldysh Green's function theory [4, 5] in the framework of non-relativistic theory. As is well known, the influence of relativistic effects increases with atomic number Z. So far several relativistic XAFS theoretical approaches have been proposed, however all of them are in one-electron theoretical framework. Here we discuss a many-body relativistic XAFS theory based on quantum electrodynamic Keldysh Green's function approach [6]. As a simple application we obtain a sound theoretical background for the current relativistic one-electron XMCD theory written in terms of many-body optical potential. The present approach also provides us a tool to analyse XAFS spectra irradiated by high intensity X-rays by applying renormalization of photon Green's functions.

2. Relativistic Keldysh Green's Functions

We now define the nonequilibrium photon Green's function $D^{\mu\nu}$ by use of the functional derivative with respect to external current j_ν^{ext}

$$\frac{4\pi}{c}D^{\mu\nu}(1,2)=\frac{\delta\langle A^\mu(1)\rangle}{\delta j_\nu^{ext}(2)} \tag{1}$$

which satisfies the equation [6]

$$\Box D^{\mu\nu}(1,2)-\partial^\mu\partial_\lambda D^{\lambda\nu}(1,2)-\int_c \mathrm{d}3\Pi^\mu{}_\lambda(1,3)D^{\lambda\nu}(3,2) = \delta_c(1-2)\delta^{\mu\nu}, \tag{2}$$

where $\int_c$ means the time integration on the closed path and delta function δ_c on the closed path is defined as

$$\delta_c(t_1-t_2)=\delta(t_1-t_2)\ t_1,t_2\ on-leg = -\delta(t_1-t_2)\ t_1,t_2\ on+leg. \tag{3}$$

The functional derivative in eq. (1) yields a useful expression of the photon Green's funciton

$$D^{\mu\nu}(1,2)=\frac{\mathrm{i}p_2}{4\pi}\langle T_c[\delta A^\mu(1)\delta A^\nu(2)]\rangle \tag{4}$$

where p_1 is 1 when t_1 is on + leg (from ∞ to $-\infty$), and -1 when on − leg (from $-\infty$ to ∞), T_c is the path-ordering operator on the Keldysh contour and $\delta A^\mu(1)=A^\mu(1)-\langle A^\mu(1)\rangle$. Here we define the photon selfenergy

$$\Pi^\mu{}_\nu(1,2)=\frac{4\pi}{c}\frac{\delta\langle j^\mu(1)\rangle}{\delta\langle A^\nu(2)\rangle}. \tag{5}$$

We also define the one-electron Green's function

$$\mathrm{i}G(1,2)=\langle T_c[\psi(1)\bar\psi(2)]\rangle,\qquad \bar\psi(2)=\psi^\dagger(2)\gamma^0 \tag{6}$$

which satisfies the Dyson equation

$$\left\{c\gamma_\mu\left(p^\mu+\frac{1}{c}\langle A^\mu(1)\rangle\right)-c^2\right\}G(1,2)-\int_c \mathrm{d}3\Sigma(1,3)G(3,2) = \delta_c(1-2). \tag{7}$$

Two different self energies Π and Σ are closely related in terms of the vertex function Γ_ν defined by

$$\Sigma(1,2)=cp_1\gamma_\mu\int_c \mathrm{d}3\,\mathrm{d}4G(1,3)\Gamma_\nu(32,4)D^{\nu\mu}(4,1^+),$$

$$\Pi^\mu{}_\nu(1,2)=c\,\mathrm{tr}\left[\gamma^\mu\int_c \mathrm{d}3\,\mathrm{d}4G(1,3)\Gamma_\nu(32,4)G(4,1^+)\right],$$

$$\Gamma_\nu(34,2)=-\frac{4\pi\mathrm{i}}{c}\frac{\delta G^{-1}(3,4)}{\delta\langle A^\nu(2)\rangle}. \tag{8}$$

Useful approximations can be obtained from a closed set of intergro-differential equations, Hedin's equations. For this purpose the vertex function Γ_ν is written by use of Σ

$$\Gamma_\nu(12,3)=-\frac{4\pi\mathrm{i}}{c}\left[\gamma_\nu\delta_c(1-2)\delta_c(1-3)-\frac{\delta\Sigma(1,2)}{\delta\langle A^\nu(3)\rangle}\right]. \tag{9}$$

The first order approximation for the electron and the photon selfenergies are given by

$$\Sigma^{(1)}(1,2)=-4\pi p_1\mathrm{i}\gamma_\mu G(1,2)\gamma_\nu D^{\nu\mu}(2,1^+) = \Sigma_l^{(1)}(1,2)-4\pi p_1\mathrm{i}\gamma_i G(1,2)\gamma_j D^{ji}(2,1^+), \tag{10}$$

$$\Pi^{\mu(1)}{}_\nu(1,2)=-4\mathrm{i}\pi\,\mathrm{tr}[\gamma^\mu G(1,2)\gamma_\nu G(2,1^+)]. \tag{11}$$

The longitudinal part of $\Sigma^{(1)}(1,2)$ is just a "GW" term

$$\Sigma_l^{(1)}(1,2)=\mathrm{i}p_1\gamma_0 G_l(1,2)\gamma_0 W(2,1^+), \tag{12}$$

where G_l is the longitudinal Green's function defined by eq. (14) and the transverse part $\Sigma_t^{(1)}(1,2)$ (the second term of eq. (10)) can contribute to electron-photon interaction. In the approximation $\Sigma^{(1)}=\Sigma_l^{(1)}+\Sigma_t^{(1)}$, we have neglected the transverse-longitudinal coupling terms such as D^{0i}, which should be small enough in the Coulomb gauge [6]. Up to the first order skeleton selfenergy, the electron Green's function G can be writtenin the matrix notation

*Electronic address: tfujikawa@faculty.chiba-u.jp

($\Sigma_l^{(1)}$ and $\Sigma_t^{(1)}$ are abbreviated as Σ_l and Σ_t)

$$G = G_0 + G_l\Sigma_t G_l + G_l\Sigma_t G_l\Sigma_t G_l + \cdots \tag{13}$$

where G_l is longitudinal electron Green's function

$$G_l = G_0 + G_0\Sigma_l G_l. \tag{14}$$

In the QED approach one-electron Green's function $G_l(1,2)$ can be assumed to be only dependent on the time difference $t_1 - t_2$, and we can define the spectral representation of $G_l(1,2)$. As the advanced g^a and the retarded Green's function g^r satisfy the closed Dyson equations on the contour from $-\infty$ to ∞, these Green's functions have simple expression in the energy space by use of the Hartree potential V_H as a 4×4 matrix

$$g_l(\varepsilon) = \begin{pmatrix} \varepsilon - V_H - \Sigma_{11} & -c\sigma\cdot\boldsymbol{p} - \Sigma_{12} \\ -c\sigma\cdot\boldsymbol{p} - \Sigma_{21} & \varepsilon + 2c^2 - V_H - \Sigma_{22} \end{pmatrix}^{-1} \tag{15}$$

where $\Sigma_{ij} = \Sigma_{ij}(\varepsilon)$ is the 2×2 (i, j) submatrix of the longitudinal selfenergy $\Sigma_l(\varepsilon)$. After some algebra we can rewrite the relativistic Green's function g_l in terms of the quasi-nonrelativistic one-electron Green's function g_{11},

$$g_l(\varepsilon) = (1 - X)^{-1} \begin{pmatrix} g_{11} & g_{11}Q \\ Qg_{11} & Qg_{11}Q + 1/2c^2 \end{pmatrix} \tag{16}$$

where

$$X = \begin{pmatrix} g_{11}Q\Sigma_{21} & X_{12} \\ X_{21} & X_{22} \end{pmatrix}, \qquad Q = \sigma\cdot\boldsymbol{p}/2c,$$

$$\begin{aligned} X_{12} &= g_{11}\{\Sigma_{12} - Q(\varepsilon - \Sigma_{22})\}, \\ X_{21} &= \left(Qg_{11} + \frac{1}{2c^2}\right)\Sigma_{21}, \\ X_{22} &= Qg_{11}\Sigma_{12} - \left(Qg_{11}Q + \frac{1}{2c^2}\right)(\varepsilon - \Sigma_{22}). \end{aligned} \tag{17}$$

The quasi-nonrelativistic one-electron Green's function g_{11} satisfies the Dyson equation for the selfenergy Σ_{11}

$$g_{11} = g_{11}^0 + g_{11}^0\Sigma_{11}g_{11}. \tag{18}$$

Up to the relativistic order g_{11}/c^2, $g_l(\varepsilon)$ is given by

$$g_l(\varepsilon) = \begin{pmatrix} g_{11} + \delta g_{11} & g_{11}Q \\ Qg_{11} & Qg_{11}Q + 1/(2c^2) \end{pmatrix}, \tag{19}$$

$$\delta g_{11}(\varepsilon) = g_{11}Q\Sigma_{21}g_{11} + g_{11}\Sigma_{12}Qg_{11} + g_{11}Q(\Sigma_{22} - \varepsilon)Qg_{11}. \tag{20}$$

In the relativistic "GW" approximation for $\Sigma_l^{(1)}$ shown by eq. (12), each of submatrix $\Sigma_l^{(1)}(\varepsilon)_{ij}$ is given with aid of the approximation (19),

$$\begin{aligned} \Sigma_{11}(1,2) &= \mathrm{i}\{g_{11}(1,2) + \delta g_{11}(1,2)\}W(2,1^+), \\ \Sigma_{12}(1,2) &= \mathrm{i}g_{11}(1,2)QW(2,1^+), \\ \Sigma_{21}(1,2) &= \mathrm{i}Qg_{11}(1,2)W(2,1^+), \\ \Sigma_{22}(1,2) &= \left\{Qg_{11}(1,2)Q + \frac{1}{2c^2}\right\}W(2,1^+). \end{aligned} \tag{21}$$

We notice that Σ_{11} has finite contribution even in the nonrelativistic limit $c \to \infty$, whereas other selfenergies have no contribution in that limit. We see that Σ_{12}, Σ_{21} are in the order of Σ_{11}/c, Σ_{22} is in the order of Σ_{11}/c^2.

3. Relativistic Many-Body XAFS Theory

To obtain the photoabsorption rate of the photon state $(\boldsymbol{k}, \alpha)$ is obtained by

$$w(\boldsymbol{k}\alpha) = -\frac{\mathrm{d}}{\mathrm{d}t}\langle n_{\boldsymbol{k}\alpha}(t)\rangle|_{t=0}. \tag{22}$$

We should note that $w(\boldsymbol{k}\alpha)$ has contribution from absorption, emission and scattering and so on. In the Heisenberg operator $n_{\boldsymbol{k}\alpha}(t) = a^\dagger_{\boldsymbol{k}\alpha}(t)a_{\boldsymbol{k}\alpha}(t)$, the time t in $a^\dagger_{\boldsymbol{k}\alpha}(t)$ has to be on $+$ leg, whereas that in $a_{\boldsymbol{k}\alpha}(t)$ on $-$ leg to keep the order of the operators. First we should represent $\langle n_{\boldsymbol{k}\alpha}(t)\rangle$ in terms of transverse photon Green's function $D^{>ij}$. By use of the polarization vector $\mathrm{e}^i(\boldsymbol{k}\alpha)$ and plane wave $\phi_{\boldsymbol{k}}(\boldsymbol{r}) = \exp(\mathrm{i}\boldsymbol{k}\cdot\boldsymbol{r})/\sqrt{V}$, we can obtain

$$\begin{aligned} &\mathrm{i}\mathrm{e}^i(\boldsymbol{k}\alpha)^*\mathrm{e}^j(\boldsymbol{k}\alpha)\int \phi^*_{\boldsymbol{k}}(\boldsymbol{r}_1)D^{>ij}(1,2)\phi_{\boldsymbol{k}}(\boldsymbol{r}_2)\,\mathrm{d}\boldsymbol{r}_1\,\mathrm{d}\boldsymbol{r}_2 \\ &= \frac{c^2}{2\omega_k}\langle a_{-\boldsymbol{k}\alpha}(t_1)a^\dagger_{-\boldsymbol{k}\alpha}(t_2) + a^\dagger_{\boldsymbol{k}\alpha}(t_1)a_{\boldsymbol{k}\alpha}(t_2) \\ &\quad + a^\dagger_{\boldsymbol{k}\alpha}(t_1)a^\dagger_{-\boldsymbol{k}\alpha}(t_2) + a_{-\boldsymbol{k}\alpha}(t_1)a_{\boldsymbol{k}\alpha}(t_2)\rangle \end{aligned} \tag{23}$$

which contains $\langle n_{\boldsymbol{k}\alpha}(t_1)\rangle$ in the limit $t_2 \to t_1$.

The next job is to systematically calculate $D^>$ starting from the Dyson equation $D = D^0 + D^0\Pi D^0 + D^0\Pi D\Pi D^0$. Of course the free photon Green's function never contribute to the photoabsorption processes. The greater part of the second term of the above Dyson equation is given by use of the Langreth rule [7],

$$(D^0\Pi D^0)^> = D^{0>}\Pi^a D^{0a} + D^{0r}\Pi^> D^{0a} + D^{0r}\Pi^r D^{0>} \tag{24}$$

where for the matrix product AB we do not use time integration on Keldysh contour but from $-\infty$ to ∞

$$(AB)(1,2) = \int_{-\infty}^{\infty}\mathrm{d}t_3\,\mathrm{d}x_3 A(1,3)B(3,2).$$

To obtain the photoabsorption rate we calculate the time derivative of eq. (24) which yields the following formula by using infinitly small positive η to take causality into account

$$\begin{aligned} &\frac{\mathrm{d}}{\mathrm{d}t}\int_{t,t'\to 0} D^0(t - t_1)\Pi(t_1 - t_2)D^0(t_2 - t')\mathrm{e}^{\eta(t+t')}\mathrm{d}t_1\,\mathrm{d}t_2 \\ &= 2\eta\int\frac{\mathrm{d}\varepsilon}{2\pi}D^0(\varepsilon)\Pi(\varepsilon)D^0(\varepsilon). \end{aligned} \tag{25}$$

From now on we focus our attention to the lowest order contribution in regard to D^0, that is, the term $D^0\Pi D^0$, which gives golden rule expressions. Substituting explicit formulas of free photon Green's functions into eq. (25), we obtain the photon absorption rate neglecting other contributions

$$\begin{aligned} &\frac{\mathrm{d}}{\mathrm{d}t}\langle n_{\boldsymbol{k}\alpha}(t)\rangle \\ &\approx 2\eta\int\frac{\mathrm{d}\varepsilon}{2\pi}\mathrm{e}^i(\boldsymbol{k}\alpha)^*\mathrm{e}^j(\boldsymbol{k}\alpha)\langle\phi_{\boldsymbol{k}}|(D^0\Pi D^0)^>(\varepsilon)|\phi_{\boldsymbol{k}}\rangle \\ &\approx \frac{\mathrm{i}c^2}{2\omega_k^2}\langle d_i(-\boldsymbol{k}\alpha)|(\Pi^r - \Pi^a - \Pi^>)_{ij}(\omega_k)|d_j(-\boldsymbol{k}\alpha)\rangle\langle\eta_{\boldsymbol{k}\alpha}\rangle \end{aligned} \tag{26}$$

where we define

$$d_i(\boldsymbol{k}\alpha;\boldsymbol{r}) = \exp(\mathrm{i}\boldsymbol{k}\cdot\boldsymbol{r})\mathrm{e}^i(\boldsymbol{k}\alpha)/\sqrt{V}.$$

From the first line to the second, we pick up all terms contributing to the photoabsorption. We thus obtain a fundamental relativistic formula for the X-ray absorption rate of the photonstate $(\boldsymbol{k}\alpha)$

neglecting unimportant factor,

$$I(\boldsymbol{k}\alpha) = -\mathrm{Im}[\langle d_i(\boldsymbol{k}\alpha)|\Pi^{>}_{ij}(\omega_k)|d_j(\boldsymbol{k}\alpha)\rangle]\langle n_{\boldsymbol{k}\alpha}\rangle. \quad (27)$$

To closely compare this with the one-electron theory, we further introduce GW approximation for Π as shown by eq. (11) where G's are approximated by the longitudinal part g_l. For g_l (g^a_l or g^r_l) we can use the expansion in terms of quasi-nonrelativistic Green's function g_{11} as shown by eq. (16), which yields

$$\begin{aligned} I(\boldsymbol{k}\alpha) = -\mathrm{Im}\sum_p |S_p|^2(&\langle\varphi_c|\Delta^* g^{>}_{11}(\varepsilon_p+\omega_k)\Delta|\varphi_c\rangle \\ &+\langle\varphi_c|\Delta^*\delta g^{>}_{11}(\varepsilon_p+\omega_k)\Delta|\varphi_c\rangle \\ &+\langle\varphi_c|\Delta^* g^{>}_{11}(\varepsilon_p+\omega_k)Q\Delta|\chi_c\rangle \\ &+\langle\chi_c|\Delta^* Q g^{>}_{11}(\varepsilon_p+\omega_k)\Delta|\varphi_c\rangle + \cdots)\langle n_{\boldsymbol{k}\alpha}\rangle. \end{aligned} \quad (28)$$

where $|\varphi_c\rangle$ and $|\chi_c\rangle$ are the large and small components of the core function c. The first term of eq. (28) has finite contribution even in the nonrelativistic limit ($c \to \infty$), whereas the other terms vanish in that limit. In the energy region well above the Fermi energy, $I(\boldsymbol{k}\alpha)$ is written in terms of scattering Green's function g_{sc} under the influence of the optical potential. This formula can be compared with that derived within relativistic one-electron theoretical framework [8].

4. Concluding Remarks

In this work a relativistic QED theory for XAFS analyses is discussed on the basis of Keldysh Green's functions, which goes beyond relativistic one-electron theory. In the same way we can discuss resonant and loss effects in XAFS. Because of restricted space, detailed discussion on these effects cannot be shown here.

References

1. Almbladh, C.-O. and Hedin, L., "Handbook on Synchrotron Radiation" (ed. E. E. Koch), (North-Holland, 1983) Vol. 1b, p. 607.
2. Hedin, L., Physica B**158**, 344 (1989).
3. Campbell, L., Hedin, L., Rehr, J. J. and Bardyszewski, W., Phys. Rev. B**65**, 064107 (2002).
4. Fujikawa, T., J. Phys. Soc. Jpn. **62**, 2155 (1999).
5. Fujikawa, T., J. Synchrotron Rad. **8**, 76 (2001).
6. Bezzerides, B. and DuBois, D. F., Ann. Phys. **70**, 10 (1972).
7. Langreth, D. C., "Linear and Non-linear Transport in Solids" (ed. J. Devreese and V. E. van Doren), (Plenum, 1976) p. 3.
8. Fujikawa, T. and Nagamatsu, S., J. Elect. Spect. **129**, 55 (2003).

Physica Scripta. Vol. T115, 38–44, 2005

New Insights for Materials Science Characterisation Using Different Complementary Techniques Combined with X-ray Absorption Spectroscopy

V. Briois[1], S. Belin[1], F. Villain[1,2], F. Bouamrane[1], H. Lucas[3], R. Lescouëzec[4], M. Julve[4], M. Verdaguer[2], M. S. Tokumoto[5], C. V. Santilli[5], S. H. Pulcinelli[5], X. Carrier[6], J. M. Krafft[6], C. Jubin[6] and M. Che[6]

[1]LURE, Centre Universitaire Paris-Sud, BP 34, 91898 Orsay Cedex, France
[2]LCIM2, Bât. F. Case 42, UPMC, 4 place Jussieu, 75252 Paris Cedex 05, France
[3]Kaiser Optical Systems, 5 allée du Moulin Berger, 69130 Ecully, France
[4]DQI/ICM, Facultad de Quimica de la Universitat de Valencia, 46100 Burjassot, Valencia, Spain
[5]Institut de Chimie, UNESP, CP 355, 14800-900 Araraquara, Brazil
[6]LRS, Tour 54, UPMC, 4 place Jussieu, 75252 Paris Cedex 05, France

Received June 26, 2003; accepted February 6, 2004

Abstract

The combination of X-ray absorption spectroscopy (XAS) with UV-Vis and Raman spectroscopies or with Differential Scanning Calorimetry (DSC) has been recently carried out on the D44 beamline of DCI-LURE. The different set-ups used to perform such combinations are described and examples of combined investigations belonging to different field of materials science (coordination chemistry, sol-gel and catalysis) are presented.

1. Introduction

The use of complementary techniques in Materials Science is a well-established prerequisite for accessing a deeper structural description of a given material. The recent emergence of a combination of techniques using synchrotron radiation facilities appears as a significant progress for the understanding of materials processing. Indeed this approach which offers a simultaneous access to different kinds of information for the same material has great advantages with respect to separate experiments in order to eliminate errors due to differences in sample environment, thermal history, ageing, temperature, sample preparation. Even more important is the possibility to resolve ambiguities in the understanding of materials processing by allowing an accurate determination of the order of occurrence of the chemical and physical events by the different techniques.

The community using synchrotron radiation scattering techniques was pioneer in the development of such approach with the combination of Small or Wide Angle X-ray Scattering (SAXS/WAXS) or X-ray Diffraction (XRD) with Differential Scanning Calorimetry (DSC) [1–5], SAXS or WAXS with Raman spectroscopy [3, 6, 7] and SAXS with Fourier Transform-Infrared spectroscopy (FT-IR) [8]. Besides the combination of X-ray Absorption Spectroscopy (XAS) with X- Ray Diffraction (XRD) for which a lot of concrete combined studies are published [9–11], examples of combination of XAS with conventional physico-chemical characterisation techniques like DSC [12, 13] or FT-IR [14] are rather scarce. One of the possible reasons may be the non-triviality to design versatile cells with windows, substrate materials and sample conditioning suitable for the two techniques in a large range of X-ray energy and experimental conditions (temperature, controlled atmosphere . . .). Namely, a problem to overcome when performing simultaneous experiments with XAS is that of the difference in optimum sample thickness for the two techniques. For example, several orders of magnitude for optimum thickness exist for performing FT-IR and XAS or SAXS experiments in the transmission mode [8, 14]. This problem forces the experimentalist to adapt the detection mode of techniques, e.g. to use the attenuated total reflection method for the FT-IR experiment [8, 14]. Furthermore, whereas scattering techniques can adapt the photon energy for minimising absorption from cell windows and from the sample itself, this possibility is not available for the combination with XAS for which the X-ray energy is determined by the threshold energy of the element of interest.

Another complication arising for measuring complementary data simultaneously to XAS data comes from the difficulty of setting the apparatuses around the same sample. However, the advent of innovative designs for the extra instruments has recently helped solving this technical limitation. The main innovation for spectroscopic techniques is the use of intense sources, of efficient optical fibres and high-sensitive detector systems allowing a miniaturisation of the spectrometer, which is not at the expense of the data quality (resolution and detection limit). Such development will be extensively illustrated in this paper with the combination of XAS with UV-Vis and with Raman spectroscopies. To the best of our knowledge, these spectroscopies have never been combined with XAS. UV-Vis spectroscopy uses ultraviolet and visible electromagnetic radiation to energetically promote valence electrons in a molecule to an excited energy state. Besides characteristic bands used as fingerprints of chromophores in a molecule, this technique is also powerful to provide electronic information such as oxidation state or optical band gap. Raman scattering measurements, like infrared absorption, are used to obtain information about the structure and properties of molecules from their vibrational transitions. This technique is very well suited for the combination with XAS because both have a lot of common specificities. Namely, both can be used for many types of samples (liquid, solid or gas) under operating conditions and in time-resolved measurements.

Finally we have also developed a DSC set-up allowing combination with XAS in transmission mode. DSC is a technique determining the variation in the heat flow given out or taken by a sample when it undergoes a change of structure or chemical composition under temperature change in a controlled atmosphere. Therefore thermally induced processes can be accurately followed. The device described herein allows to work in a larger temperature range and in a wider energy range than devices previously combined with XAS [12, 13]. An example of combined DSC and XAS study will be presented.

2. Combined processing techniques

XAS experiments were performed at the DCI source at LURE, on the D44 beamline. Examples of combination presented herein were carried out in transmission mode using ionisation chambers filled with suitable gases. Fe, Co and Zn K edge data were recorded using a Si(111) double crystal monochromator whereas Mo K-edge measurements were done using a Ge(400) monochromator. The beam size on the sample was adjusted to ≈5 mm horizontally and 1 mm vertically. The monochromator allows step by step acquisitions ranging between 6 to 20 minutes depending on the energy range, energy step and data acquisition time (typically 1 or 2 s).

We describe in the following the different technical solutions used to perform the combined experiments presented in Section 3. The versatility of some of them has been tested on several systems and will be mentioned.

The differential scanning calorimeter used was a commercial Setaram DSC 111 apparatus based on the Calvet heat-flux principle. This apparatus is a performant laboratory DSC instrument characterised by a high sensitivity (5–10 μW). The sample of interest and an inert reference are each positioned at the centre of two horizontal juxtaposed alumina tubes (internal diameter ≈7 mm) inserted into the silver calorimetric block. The temperature difference arising from thermal activity is balanced by two independent compensatory heaters surrounding the samples. Due to the specific design of this apparatus, a quantitative measurement of the change in enthalpy is possible. Two kapton windows seal both extremities of alumina tubes in order to work under controlled atmosphere. The available operating temperatures are between −120 °C and 830 °C with heating rates from 0.01 to 30 °C min^{-1}. A photon beam (lateral size ≈4–5 mm) passes through the tube containing the sample of interest. The sample is pressed as a pellet (≈6 mm diameter) inside a platinum tube and sandwiched in a vertical arrangement by two coaxial Pt tubes. The sample so-inserted in the Pt-tube is set at the centre of the alumina tube. On one hand, the Pt tube ensures a good thermal conduction towards the sample. On the other hand, its length (≈26 mm) is sufficient to avoid contamination of the alumina tube by direct contact at the melting temperature of the sample.

The UV-Vis-near IR spectrophotometer is a commercial Varian Cary 50 dual beam apparatus working in the 190–1100 nm wavelength range with approximately 1.5 nm fixed spectral bandwidth. Scan rates up to 400 nm/s are available making this apparatus powerful for time-resolved experiments. The pulsed Xenon lamp source is narrow and very intense and the Si diode detectors are unaffected by room light. These specifications make this apparatus suitable to be fitted with a fibre optic coupler allowing a flexible arrangement for combined measurements with XAS. The reduction of transmittance of 2 m length fibre optic probes (Hellma) compared to the direct beam is about 41% in the 220–1100 nm range. At this time, the UV-Vis set-up is only equipped for solution analysis in transmission for both techniques but it could be upgraded for solid characterisation by means of diffuse reflectance accessory. The main problems to solve for characterising simultaneously liquid media by XAS and UV-Vis are the windows and the thickness of the cell. On one hand, the use of commercial cuvettes made of quartz suprasyl or fused silica, well adapted for UV-Vis, must be thrown out for XAS measurements below 15 keV and replaced by plastic like polystyrene (PS) or polymethylmethacrylate (PMMA) cuvettes. On the other hand, the suitable thickness is extremely dependent on the system of interest, *i.e.* concentration and solvent. So it is well known that for a given thickness, organic and aqueous media do not absorb the same amount of X-ray photons at a given energy. Then versatile technical solutions must be based on cells with variable optical path as the cell [15] developed by Graseby Specac Co working with controlled optical path up to 6 mm and using thin Mylar, polypropylene or polyethylene windows (between 10 to 50 μm). For example this cell is very well suited for combinations at energies ranging from the Cr-K (5989 eV) to the Zr-K (17998 eV) edges.

The Raman spectrometer is a commercial modular Raman spectrometer (Model HL5R of Kaiser Optical Systems, Inc.). It incorporates a small but high-powered near IR laser diode working at 785 nm, a high sensitive Charge Coupled Device (CCD) detector providing fast and simultaneous full spectral collection of Raman data from 100 to 3450 cm^{-1}, holographic Notch filters. The average resolution is 2 cm^{-1}. The use of excitation light in the near-IR region allows minimising possible strong fluorescence originating from the sample which could cover the weak Raman signal. The laser beam is incident on the sample through a laser probe made of a probehead and of a single optical fibre for the excitation by the laser and of another one for the collection of the scattered Raman signals. Both fibres are packed in a common sheath of 10 m length. The probehead can be equipped with non-contact or immersion optics with different fixed focal lengths. The choice of the optics depends on the studied system and on the geometry of the cell. On one hand, the Raman scattering signal arising from windows (liquid cell or windows of controlled atmosphere chambers) can be minimised by adjusting the focus point of the optics away from the optical window. On the other hand, for studying solutions, immersible optics can be used with long focal length for transparent media and short focal length for opaque solutions or turbid media. This flexibility for the focal length of the Raman optics makes appreciably easy the design of the sample environment to study systems under constraints. Therefore, a lot of systems were recently investigated by combined XAS and Raman spectroscopies. Among them we can mention the study of ionic conduction into $K(CF_3SO_3)$-doped polyelectrolytes at the potassium K-edge (3609 eV) [16], the study of the thermally induced electron transfer of an Prussian Blue analogue $Na_{1.5}Co_4[Fe(CN)_6]_{3.2}.13H_2O$ [17] at the iron and cobalt K-edges (7112 and 7709 eV, respectively) and the study of hydrolysis-condensation of $SnCl_4.5H_2O$ in ethanolic medium at the tin K-edge (29200 eV) [18]. In this paper, we present results obtained on Mo-based heterogeneous catalysts. Solids are prepared as self-supporting pellets where possible, or by diluting the powder prior to pelletizing, in γ alumina that is suitable for both techniques (low absorption for XAS and very weak Raman signal with limited fluorescence). The sample thickness was adapted to the XAS constraints.

3. Experimental results

3.1. *Combined XAS and DSC measurements on the dehydration study of a cyanide-bridged Fe(III) and Co(II) ferromagnetic chain (Coll. Laboratories 2 and 4)*

The combination of XAS and DSC measurements was performed to study the thermal dehydration of the cyanide-bridged iron(III)–cobalt(II) double zigzag ferromagnetic chain, $[Fe^{III}(bpy)(CN)_4]_2[Co^{II}(H_2O)_2].4H_2O$, where bpy is the 2,2′-bipyridine. The occurrence of slow relaxation of the magnetisation

when the applied magnetic field is set to zero allows to classify this system among the few first «linear nano-magnets» [19]. But unexplained occurrence of two rates of relaxation has been observed. Two hypotheses were proposed to account for this phenomenon, both based on a mixture of species: the fully hydrated chain mixed either with a dehydrated form of the initial molecule or with a species implying photoinduced electron transfer. Indeed the single crystal XRD structure of the fully hydrated chain [19] shows that two kinds of water molecules are involved in the structure: two are linked to the cobalt ion and four are hydration water molecules linked through van der Waals forces and hydrogen bonds to the two coordinated water molecules. The metal atoms are six-coordinate: two nitrogen atoms from bpy and four cyanide carbon atoms around Fe and four cyanide nitrogen atoms and two water molecules around Co. No similar XRD data were available in the operating conditions of measurement of relaxation rates using a SQUID (Superconducting quantum-interference device). Nevertheless it was evidenced by XAS that structural changes [20] occur by submitting the fully hydrated chain to primary vacuum as that encountered in SQUID apparatus, but, no change in the oxidation state of the two metallic ions occurs. This first set of results binds us to study carefully the thermal dehydration processes of the system by a combined DSC-XAS study.

Figure 1 shows a DSC curve recorded under nitrogen atmosphere at a heating rate of 5 °C min^{-1} on a pellet of sample (≈8 mg of product) suitable for the combination of XAS. Two intense endothermic peaks well defined over about 30 °C and centred at ≈66 °C and 168°C were observed in agreement with thermogravimetry analysis (TGA). Figure 2 shows XANES spectra recorded at the Co K edge during isothermal processes performed with the DSC apparatus between RT and 180 °C. The conditions (duration and temperature) of isothermal treatment chosen as a function of DSC data are indicated in Figure 1. XANES data at both edges were collected at each isothermal treatment temperature whereas EXAFS data were only recorded at RT, 66 °C and 168 °C. First, we observe during isothermal treatments at different temperatures between RT and 180 °C a continuous decrease of the intensity of the white line with a concomitant increase of the intensity of the preedge indicating

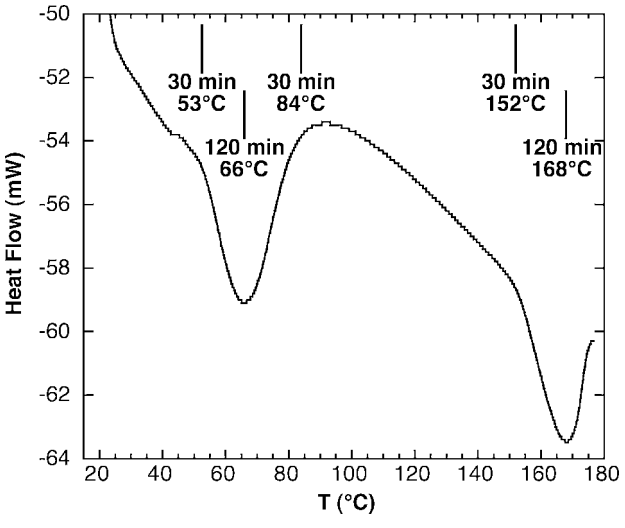

Fig. 1. DSC scan for the $[Fe^{III}(bpy)(CN)_4]_2[Co^{II}(H_2O)_2].4H_2O$ sample obtained at a heating rate of 5 °C min^{-1} under N_2 atmosphere. The temperatures of the isothermal EXAFS and XANES measurements at the Fe and Co K edges are indicated by vertical bars. Isothermal treatments were done either for 30 or 120 min.

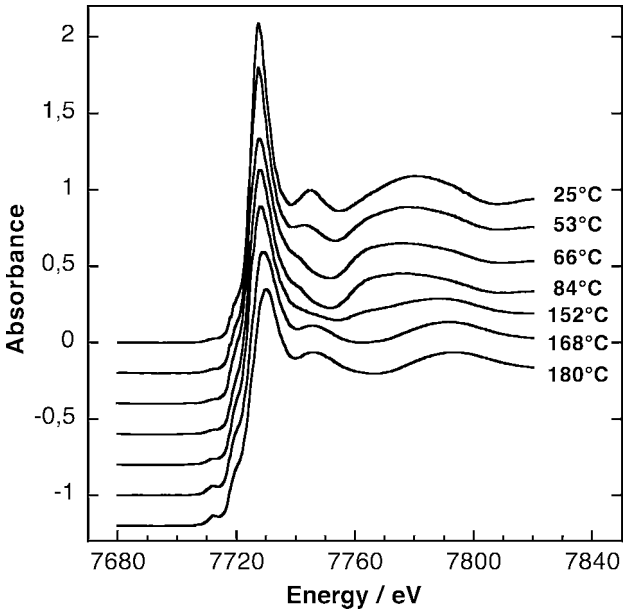

Fig. 2. XANES spectra recorded at the Co K edge during the isothermal heating of the $[Fe^{III}(bpy)(CN)_4]_2[Co^{II}(H_2O)_2].4H_2O$ sample from RT to 180 °C under N_2 atmosphere.

a change of the regular octahedral symmetry of the fully hydrated chain towards a more distorted one at higher temperatures. Second, the intensity of the resonance at ≈7745 eV decreases after the first endothermic event and increases again after the second one. Finally a non monotonous shift of the position of the first EXAFS oscillation has been evidenced: first a shift at lower energy from RT to 84 °C followed by a shift at higher energy from 84 °C to 180 °C. The structural changes were solved by FeFF7 calculations done to simulate the Co and Fe K-edges EXAFS spectra recorded in the same set of experiments [20]. The first endothermic peak is associated to the loss of the four hydration molecules affecting the overall structure around Co, with in particular a change of the Co-NC-Fe angle from 167° (RT XRD data) to 140° (FeFF7 simulations for 84 °C data). The second endothermic event is related to the loss of the two coordinated-water molecules leading to a tetra-coordinated symmetry for Co and a decrease of the Co-N distances (from 2.11 Å in the RT-XRD structure to 2.04 Å in the FeFF7 simulations for 180 °C data) as suggested by XANES measurements. Furthermore the Co-NC-Fe angular arrangement, which is well known to be strongly affected by multiple scattering events due to its quasi-linearity, undergoes again a change from 140° to 167° (FeFF7 simulations for 180 °C data) explaining the overall non monotonous change observed in resonances above the white line energy (Fig. 2).

Finally the comparison of the XANES spectra recorded during the dehydration processes of the $[Fe^{III}(bpy)(CN)_4]_2[Co^{II}(H_2O)_2].4H_2O$ chain with the XANES spectrum of the pumped sample under primary vacuum allows to conclude that the change in the magnetisation relaxation of the chain is assigned to structural changes around Co due to the departure of hydration water molecules.

In this study, DSC curve and XAS data were not recorded simultaneously for two reasons: the compulsory DSC heating rate and the limiting step by step scanning mode of the D44 experiment which obliges, at the moment, to record the XAS data during isothermal treatment. But no technical limitations for the DSC111 Setaram apparatus hinder its use on a time-resolved or dispersive XAS experiment, as done recently on the dispersive D11 beamline at LURE for studying phase transitions in lead

carboxylate liquid crystals [21]. Nevertheless, DSC and XAS measurements were performed in sequence, strictly under the same conditions: same pellet as in DSC, same oven geometry and same reference temperature, which is essential for the accuracy of the correlation between thermodynamic and structural changes.

3.2. *Combined in-situ XAS/UV-Vis measurements to study the formation of ZnO nanoparticles (Coll. Laboratory 5)*

During the past years considerable interest has been paid to the preparation of II-VI semiconductor nanometer-sized colloids by sol-gel routes [22]. Indeed these materials present a phenomenon of quantum confinement by excitons as primary particles are smaller than 7 nm offering potential applications in many technologies, such as solar energy conversion or optoelectronic devices. The control of the particles formation, and in this case of the nanoparticle size, is of prime importance on the optimisation of the properties of the final materials. Generally speaking, this task can be achieved by XAS investigation of the structure of precursors involved in the hydrolysis-condensation processes, and of the different building blocks during the solid-state growth. Nevertheless, our expertise in this field shows also that the use of XAS alone often does not allow to unravel the mechanisms of hydrolysis-condensation of cations and must be combined to complementary techniques, as reported for Ce [23], Cr and Zn [24] and Ga [25] cations.

For quantum dot colloids, UV-Vis spectroscopy is routinely used to determine their particle sizes [22] because the presence of exciton levels in the 250 to 500 nm wavelength range. In this context, we have developed at LURE a methodology to follow the kinetics of formation of II-VI semiconductor colloidal suspensions by combining XAS and UV-Vis. This approach is illustrated for ZnO nanoparticles preparation.

The colloid synthesis follows the previously reported procedure [26] based on the preparation in ethanolic medium of $Zn_4O(CH_3COO)_6$ precursors [27] from zinc acetate solution and subsequent hydrolysis-condensation induced by LiOH addition and thermal activation at moderate temperature (between 20 and 70 °C). XAS and UV-Vis spectra were recorded simultaneously on the same precursor solution heated at 60 °C by using a thermostated cell with optical path adjusted at 6 mm [15], and equipped with polypropylene windows of 10 µm thickness. Besides the determination of local order around Zn and of the particle sizes during the colloidal formation, the motivation of the combined investigation was also to clarify the occurrence of a Zn-based hydroxy double salt phase, $Zn_5(OH)_8(OCOCH_3)_2.2H_2O$ (labelled hereafter Zn-HDS) observed as final solid mixed with ZnO and zinc acetate phases [26]. In particular, we had interest to determine if the formation of the Zn-HDS phase was concomitant to the ZnO formation or arose from the reaction of ZnO with zinc acetate during ageing of the colloidal suspension before extraction of solids.

Figure 3 displays optical UV absorption spectra recorded during heating of solution whereas Figure 4 shows the corresponding Zn-K edge EXAFS spectra. The formation of ZnO colloidal particles is evidenced in UV-Vis by the presence of a pronounced HOMO-LUMO transition at ≈331 nm. For comparison, ZnO bulk crystals have an absorption band edge at 388 nm whereas 3 nm colloidal particles present an excitonic transition peak at ≈320 nm. In this example, the particle size determined by UV-Vis spectroscopy is around 4 nm. We note an increase of the intensity of the excitonic peaks but no shift of the

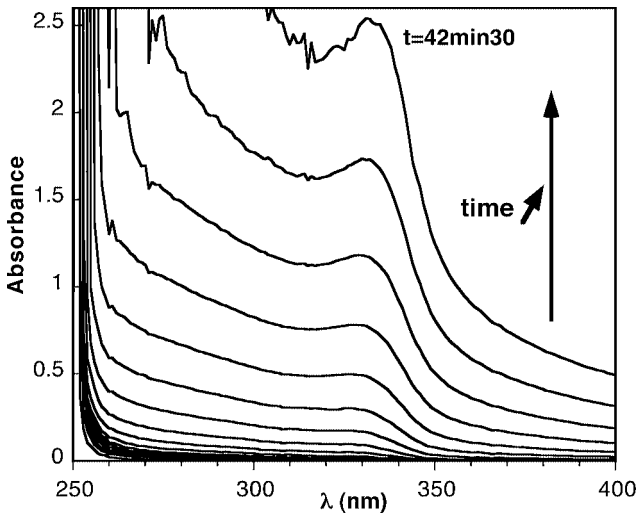

Fig. 3. Temporal evolution of the optical absorption spectra recorded during the formation of ZnO quantum dots by heating of a precursor solution at 60 °C in presence of LiOH. One UV-Vis spectrum was recorded every 2 min 30.

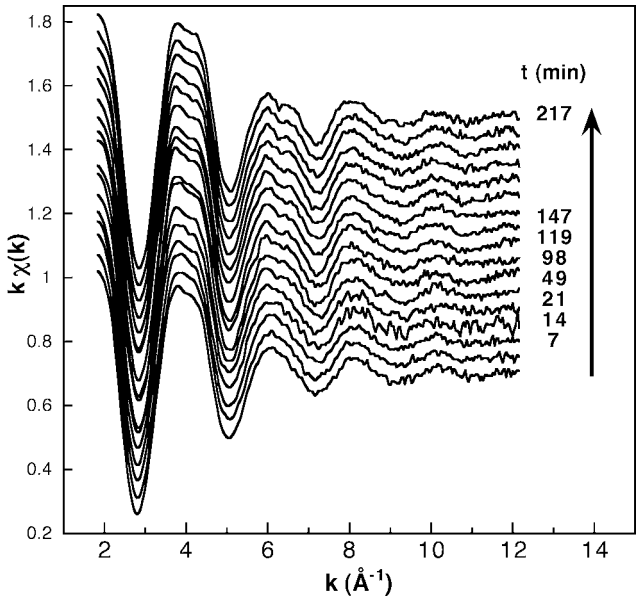

Fig. 4. Temporal evolution of the Zn-K edge EXAFS spectra recorded simultaneously with the UV-Vis spectra presented in Fig. 3. The data acquisition time for one EXAFS spectrum was 7 min.

absorption onset to longer wavelength indicating that the nearly monodisperse size of particles is constant at the early stage of ZnO formation. The observed change of EXAFS spectra is also associated to the formation of ZnO colloidal particles in solution. At the end of the process (at 217 min), the EXAFS spectrum presents features in phase with the characteristic oscillations measured on ZnO bulk crystals but with damped intensities. The damping of EXAFS oscillations is not only due to the nanocrystalline size of ZnO particles but also to the fact that the solution is a mixture of different species, here ZnO and precursors. It is noteworthy that due to the mixture of species, EXAFS appears less sensitive than UV-Vis to evidence the formation of ZnO nanoparticles. Indeed, the splitting of the first and second EXAFS oscillations characteristic of the ZnO formation is only obvious after 98 min of heating, whereas the excitonic UV peak is defined after 20 min. Nevertheless, XAS is also powerful to reveal that the formation of Zn-HDS is not concomitant to the formation of ZnO particles for 217 min of heating at 60 °C.

The complementarity of information available by both techniques is well illustrated with this study. The difference in sensitivity can be useful for unravelling complex kinetic formation pathway, but also for interpreting deeply XAS data. Indeed, structural parameters related to ZnO colloids can be constrained from the particle size available by UV-Vis, making the EXAFS analysis procedure more reliable and accurate in the determination of structural parameters related to a mixture of species.

3.3. *Combined in-situ XAS/Raman measurements: rehydration of a calcined Mo/Al_2O_3-SiO_2 supported catalyst (Coll. Laboratory 6)*

In situ studies of heterogeneous catalyst preparation, activation and reactivity has tremendously benefit from the advent of combined experiments such as XRD and (quick)EXAFS [9–11]. Hence, it is currently recognised that most of the effort on catalyst characterisation has to be directed toward the combination of spectroscopic techniques [28] since information available from synchronised spectroscopic measurements may lead to the establishment of structure-reactivity relationships essential for improving the molecular engineering of new catalytic materials. In this communication, we show the first *in situ* molecular-scale characterisation of heterogeneous catalysts by simultaneously combining EXAFS with Raman spectroscopy.

We have investigated the room-temperature hydration of a calcined 5 wt% Mo/ASA supported catalyst (ASA stands for an amorphous silica alumina containing 25 wt% Al_2O_3 and 75 wt% SiO_2) which is a potential candidate for the hydro-desulfurisation of petroleum feedstocks. The catalyst was prepared by impregnation of ammonium heptamolybdate and calcination at 500 °C (more details on the sample preparation will be given elsewhere [29]). This study is aimed at showing that drastic changes in Mo speciation can occur when exposing the catalyst to water vapour after calcination. It will be shown that these changes can be related to the dissolution of the oxide support [30]. The sample-holder containing a self-supported pellet of the catalyst was put into a rectangular aluminium cell in which a stream of water-saturated oxygen gas was allowed to flow at room temperature. A geometry similar to conventional fluorescence XAS experiment was adopted for Raman signal detection. The sample-holder orientation was set to 45° with respect to incident X-rays in order to allow the simultaneous recording of the Raman signal from the direction perpendicular to the X-rays. The Raman probehead was located outside the sample cell at ≈7.5 cm from the sample and the window through which the Raman signal was collected was a thin polypropylene foil (20 µm). Laser and X-rays impinged the sample at the same position. Each Raman spectrum corresponds to an integration time of 10 s. In order to compare Mo-K edge EXAFS and Raman spectra in the same temporal frame, 200 Raman spectra were averaged while 4 EXAFS spectra were recorded.

Figure 5 displays selected Raman spectra and Figure 6 shows the corresponding Fourier Transforms (FT). The time nomenclature given in these figures corresponds to the duration of the hydration step. The spectrum recorded at "0 h" corresponds to the sample before flowing water-saturated oxygen through the cell whereas spectra recorded at "*n* h" are related to samples that were submitted to *n* hours of hydration. The Raman (liquid-state) and EXAFS (solid-state) spectra of the aluminomolybdate ion $[Al(OH)_6Mo_6O_{18}]^{3-}$ (labelled hereafter $AlMo_6$) are given for comparison. The Raman spectrum of the "0 h" sample

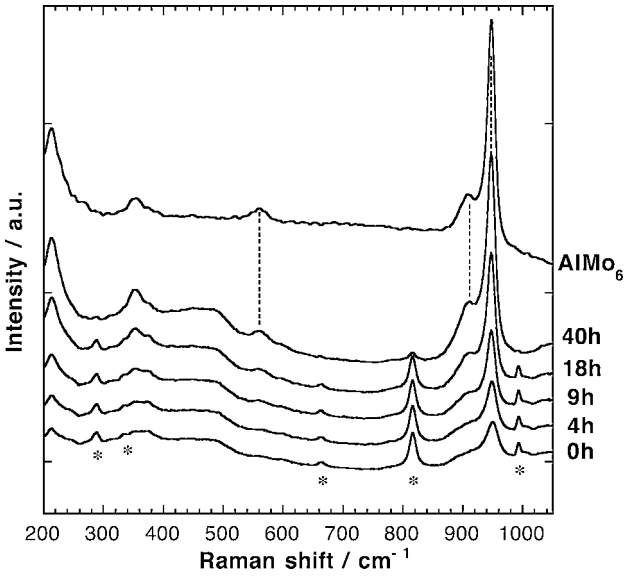

Fig. 5. Temporal evolution of the Raman spectra recorded during the RT-rehydration of a calcined Mo/Al_2O_3-SiO_2 supported catalyst. The Raman spectrum of the aluminomolybdate ion (liquid state), labelled $AlMo_6$, is presented for comparison. Stars indicate the position of characteristic bands of MoO_3.

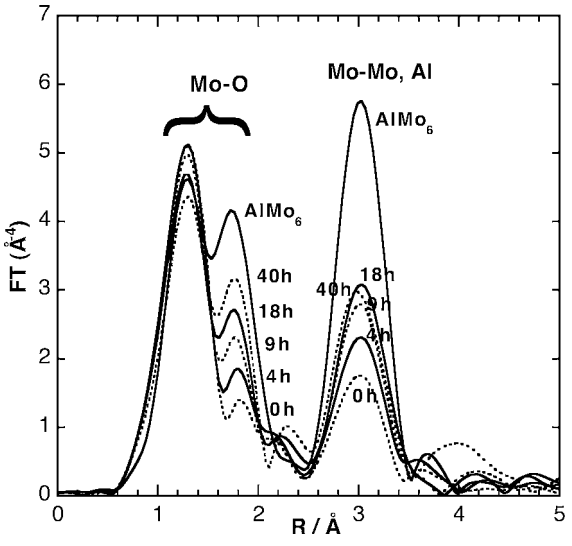

Fig. 6. Temporal evolution of the FT of the Mo K-edge EXAFS spectra recorded simultaneously with the Raman spectra shown in Fig. 5. The FT of the EXAFS signal for $AlMo_6$ entities (solid state) is also reported.

exhibits the characteristic lines of MoO_3 at 817 and 995 cm^{-1} together with a broad band centred at ≈950 cm^{-1} characteristic of surface isopolymolybdic entities [31]. Note that the relative band intensities for MoO_3 and the isopolymolybdic species does not reflect the relative amount of each phase. Indeed, MoO_3 is a strong Raman scatterer and the bands that are related to MoO_3 correspond to a small amount of oxide. Raman spectra obtained after exposure to moisture show *i*) a sharpening and increase of the band at about 950 cm^{-1} and *ii*) the appearance of a shoulder at 910 cm^{-1} along with a weak band at about 560 cm^{-1}. All of these bands are clear spectroscopic signatures for the formation of $AlMO_6$ entities (see the liquid-state Raman spectrum of $AlMO_6$) and ref. [31]. Hence, Raman results clearly evidence that exposing the calcined sample "0 h" to prolonged moisture leads to an almost total disappearance of the MoO_3 phase and initial isopolymolybdic entities whereas the formation of $AlMO_6$ entities becomes evident. At the same time, EXAFS data show a change of the first and

second coordination sphere around Mo that can be related to the above structural changes since the "40 h" spectrum can be satisfactorily fitted with $AlMo_6$ crystallographic data. As a matter of fact this study reveals for the first time that despite the dominant presence of silica in the ASA oxide support, silicomolybdic acid is not formed by exposing the sample to extensive moisture at RT as reported before for Mo/SiO_2 catalyst [32]. It is noteworthy again that XAS or Raman results alone would be very difficult to interpret. On one hand, the mixture of MoO_3 and isopolymolybdic entities in the "0 h" sample can not be revealed by XAS alone due to the very low amount of MoO_3 in the mixture. On the other hand, although the "40 h" sample can be satisfactorily reproduced by FeFF7 simulations based on the $AlMo_6$ crystallographic structure, the addition of a Mo-Al contribution to simulate the second intense peak of the FT could be considered, without the support of Raman results, as a fitting trick since a rather satisfactory fit is already achieved by considering Mo-Mo contributions only. More quantitative analysis of this combined XAS-Raman study will be given in a forthcoming paper [29].

This study shows again the benefit that XAS can get when combined with complementary techniques, in particular with vibrational spectroscopies. That leads a lot of teams to vigorously work on the design of suitable cells for such combination [28]. As an example, effort was devoted recently to design a common cell usable for XAS and synchrotron-based far-IR and for conventional mid-IR in laboratory [33]. Unfortunately, one has to change the windows for using the cell in separate experiments. This can be a drawback for catalyst characterisation, as already mentioned in the introduction. As regards vibrational spectroscopy, it is worth noting some advantages of the Raman technique as compared to IR spectroscopy. First, as shown herein, the Raman signal is not affected by absorption of Al_2O_3 and SiO_2 oxide supports contrary to IR for which strong IR absorption is observed below $\approx 1000\,cm^{-1}$. Furthermore, the Raman signal arising from alumina and silica is very weak. Second, in contrast to IR spectroscopy, Raman spectroscopy can provide information from aqueous solution during materials processing because water gives a very weak Raman signal in the metal-oxide vibration range. Finally the design of cells for simultaneous *in situ* characterisation suitable for XAS and Raman spectroscopies is easier than for combination of XAS and IR. Indeed we have to optimise the cell for XAS constrains only since Raman signal can be recorded on the same sample through a glass or plastic window. All these advantages make Raman spectroscopy a promising technique for combination with XAS.

4. Conclusion and perspectives

We have successfully developed a new experimental approach for studying materials processing based on the simultaneous combination of XAS with techniques routinely applied in materials science, such as DSC, UV-Vis or Raman spectroscopies. The potential of such an approach has been demonstrated with different examples. Besides the access to complementary information, we can summarise the advantages of such combination: *i*) elimination of artefacts introduced by the use of separate experiments (sample history and environment, ageing, temperature control...), *ii*) increase of the accuracy in the time correlation between different physical and chemical events and *iii*) improvement of the reliability of XAS analysis. All the combined techniques are based on robust and versatile devices which are laboratory equipment.

Whereas the combination with spectroscopic methods (UV-Vis, Raman) presented above are a totally innovative approach, the combination of XAS with DSC has already been reported in the past [12, 13]. However we have carefully considered the main directions mentioned as further development by these pioneering reports for offering to the materials science community an improved XAS-DSC set-up. In particular, the temperature range of −60 °C–375 °C accessible in [12, 13] has been extended from −120 °C to 830 °C offering new possibilities for the study of solid-state reactions. On the other hand, the geometry of the device allows the use of kapton windows for the crossing of X-rays allowing to work at lower energy than Br K-edge (13474 eV). So combined DSC- XAS measurements between RT and 550 °C on glassy systems [34] at the Fe (7112 eV) and Ni (8333 eV) K edges have been recently carried out using this set-up. Similar experiments on hydrocalumite intercalated with oxochromium entities [35] will soon be carried out at the Cr K-edge (5989 eV).

The improvement to the UV-Vis/XAS combined set-up could be directed towards the possibility of studying solid systems and not only liquid media as now. The design of an *in situ* cell allowing to study materials at high temperatures with both Raman and XAS is a prerequisite for further developing the combination of spectroscopic techniques.

In fact the main weakness of previous combinations was not related to the use of complementary techniques but to the performance of the D44 beamline and DCI source (acquisition time, photons flux available at the sample position and beam size). The advent of third generation synchrotron radiation sources with high brilliance will clearly offer new possibilities for such combined experiments. As a matter of fact, all the combined apparatuses which are suitable for time-resolved experiments presented above will be installed on the future SAMBA (acronym for "Spectroscopies Applied to Materials Based on the Absorption") beamline dedicated to X-ray absorption spectroscopy at SOLEIL. The SAMBA beamline is fully described in a contributed paper of this conference [36] and will offer the possibility to record high-quality Quick-EXAFS data in few seconds.

Finally the advent of microfocus beamlines dedicated to XAS should also gain great benefit from the developments in MicroRaman spectroscopy. Indeed the size of the laser spot being of the same order of magnitude as a microfocused X-ray beam, both techniques could be combined in order to obtain complementary information about the heterogeneity of samples. The field of applications of such combination is very large from environmental science to materials science. Such a combination will soon be tested on the LUCIA beamline (acronym for "Line for Ultimate Characterisation by Imagery and Absorption") which will be first built at the SLS before being installed at SOLEIL.

Acknowledgement

F. Alves is strongly acknowledged for technical assistance for adapting the combined techniques on the D44 beamline. E. Fonda and A. M. Flank are sincerely acknowledged for logistic support during Raman/XAS combinations.

References

1. Chung, H. and Caffrey, M., Biophys. J. **63**, 438 (1992).
2. Bras, W., *et al*., J. Appl. Cryst. 28, **26** (1995).
3. Bras, W. and Ryan, A. J., J. Molecul. Struc. **383**, 309 (1996).
4. Keller, G., *et al*., J. Thermal Analysis **51**, 783 (1998).
5. Jenkins, P. J. and Donald, A. M., Carbohyds. Res. **308**, 133 (1998).

6. Everall, H., Owen, H. and Slater, J., J. Appl. Spectrosc. **49**, 610 (1995).
7. Tashiro, K., *et al*., Polym. Sci. Polym. Phys. Ed. **40**, 495 (2002).
8. Bras, W., *et al*., Science **267**, 996 (1995).
9. Thomas, J. M. and Greaves, G. N., Science **265**, 1675 (1994).
10. Clausen, B. S., Catalysis Today **39**, 293 (1998) and references herein.
11. Meneau, F., *et al*., Nucl. Instr. Meth. Phys. Res. B **199**, 499 (2003) and references herein.
12. Epple, M., *et al*., Chem. Commun. **15**, 1755 (1996).
13. Tröger, L., Hilbrandt, N. and Epple, M., Synchrotron Rad. News **10**, 11 (1997).
14. Wilkin, O. M. and Young, N. A., J. Synchrotron Rad. **6**, 204 (1999).
15. Villain, F., Briois, V., Castro, I., Helary, C. and Verdaguer, M., Anal. Chem. **65**, 2545 (1993).
16. Chaker, J., *et al*., J. Sol-Gel Sci. Techno. **26**, 1075 (2003).
17. Bleuzen A., *et al*., J. Am. Chem. Soc. **122**, 6648 (2000).
18. Broussous, L., Santilli, C. V., Pulcinelli, S. H. and Craievich, A. F., J. Phys. Chem. B **106**, 2855 (2002).
19. Lescouëzec, R., *et al*., Angew. Chem. **115**, 1521 (2003).
20. Lescouëzec, R., PhD Thesis, Universitat de valencia and Université Pierre et Marie Curie, Paris VI (2002); Villain, F., Cartier dit Moulin, C., Verdaguer, M., Lescouëzec, R. and Julve, M., VIIIth Int. Conf. Molecule-based Magnets, ICMM'2002, Valencia (Spain) 5–10 October 2002, contribution A107.
21. Belin, S., François, M., Steinmetz, J. and Baudelet, F., unpublished results.
22. Spanhel, L. and Anderson, M. A., J. Am. Chem. Soc. **113**, 2826 (1991); Murray, C. B., Kagan, C. R. and Bawendi, M. G., Science **270**, 1335 (1995).
23. Briois, V., *et al.*, J. Mater. Sci. **28**, 5019 (1993).
24. Roussel, H., *et al*., Chem. Mater. **13**, 329 (2001).
25. Michot, L. J., Montargès-Pelletier, A., Lartiges, B. S., d'Espinose de la Caillerie, J. B. and Briois, V., J. Am. Chem. Soc. **122**, 6048 (2000).
26. Tokumoto, M. S., Pulcinelli, S. H., Santilli, C. V. and Briois, V., J. Phys. Chem. B **107**, 568 (2003).
27. Tokumoto, M. S., Briois, V., Santilli, C. V. and Pulcinelli, S. H., J. Sol-Gel Sci. Techno. **26**, 547 (2003).
28. Weckhuysen, B. M., Chem. Commun. **2**, 97 (2002).
29. Jubin, C., *et al*., in preparation.
30. Carrier, X., Lambert, J. F. and Che, M., J. Am. Chem. Soc. **119**, 10137 (1997).
31. Carrier, X., Lambert, J. F., Kuba, S., Knözinger, H. and Che, M., J. Mol. Struct. **656**, 231 (2003).
32. Rocchiccioli-Deltcheff, C., Amirouche, M., Che, M., Tatibouët, J. M. and Fournier, M., J. Catal. **125**, 292 (1990).
33. Lamberti, C., *et al*., Nucl. Instr. Meth. Phys. Res. B **200**, 196 (2003).
34. Neuville, D., Cormier, L. and Belin, S., in preparation.
35. Rousselot, I., *et al*., J. Solid State Chem. **167**, 137 (2002).
36. Belin, S., *et al*., Physica Scripta, this conference.

Physica Scripta. Vol. T115, 45–48, 2005

Lattice Dynamics Information Obtained from EXAFS Measurements on Ta

H. H. Rossner[1*], E. Holub-Krappe[1], M. Fieber-Erdmann[2] and H. J. Krappe[1]

[1]Hahn-Meitner-Institut Berlin, Glienicker Strasse 100, D-14109 Berlin, Germany
[2]BMBF-Leitprojekt Proteinstrukturfabrik, c/o Bessy GmbH, Albert-Einstein-Strasse-15, D-12489 Berlin, Germany

Received June 26, 2003; accepted February 6, 2004

PACS numbers: 61.10.Ht, 63.22.+m

Abstract

Extended X-ray absorption fine structure (EXAFS) data were measured at three temperatures (20 K, 80 K and 300 K) above the L_3-edge of polycrystalline α-tantalum. The data analysis is based on a recently developed Bayesian approach and uses the FEFF8 code results. Besides the temperature dependence of the lattice constant we obtain a separation of the Debye-Waller parameters into structural and thermal contributions. The latter are well described by a force-field model with two force parameters. *A posteriori* errors and cross correlations between the model parameters are calculated, taking the errors of the input EXAFS function as well as systematic uncertainties of the model into account. Lattice-dynamical observables determined independently are compared with the results of our force-field model using the parameters from the fit of our EXAFS data.

1. Introduction

EXAFS measurements have been performed on a commercially available tantalum foil at 20 K, 80 K, and 300 K. In order to analyze the absorption functions $\mu(k_l)$, measured at wave numbers k_l, $l = 1,\ldots,L$, in terms of a set of model parameters $\boldsymbol{x} = \{x_n\}$ we use a Bayesian approach [1]. The objective of this approach is (I) to determine the subspace **R** of the total model-parameter space **Q** in which the data determine the result of the fit, (II) to find a natural scaling of the model parameters, which makes their errors comparable and error cross-correlations meaningful, and (III) to obtain most probable *a posteriori* values for the model parameters and their errors and error correlations. The method requires the repeated solution of the direct problem of calculating $\boldsymbol{\chi}(\boldsymbol{k})$ from given model parameters $\boldsymbol{x}$. For the electronic part of the direct problem we use the FEFF8 code [2] results and for the lattice-dynamical part the iterative procedure introduced by Poiarkova and Rehr [3] and presented in detail by Krappe and Rossner [1].

For the solution of the inverse problem of inferring model parameters **x** together with their uncertainties from given EXAFS data $\boldsymbol{\mu}(k_l)$, we apply Bayes' theorem. It requires to specify (I) the overall efficiency $A(k)$ to normalize the measured absorption coefficient to the atomic background absorption coefficient computed by FEFF, (II) *a priori* values for the model parameters, (III) errors for the experimental input $\mu(k_l)$, and (IV) an estimate of the uncertainties connected with the truncation of the infinite multiple-scattering series for $\boldsymbol{\chi}(k_l)$ and the muffin-tin and local-density approximations in FEFF, and with the restriction of the electron and lattice dynamics to finite clusters surrounding the absorbing atom.

With the ansatz

$$\sigma_j^2 = (\sigma_j^{therm})^2 + (\sigma_j^{struct})^2 \tag{1}$$

for the Debye-Waller (DW) parameters and assuming that the structural contributions σ_j^{struct} do not change with temperature, a consistent set of force-field parameters can be determined to account for the thermal contribution to the DW parameters σ_j^{therm}.

2. Experimental setup

We used a tantalum foil of 5 µm thickness from Goodfellow Corporation with 99.9% Ta. No heat treatment in vacuum was performed on the sample. EXAFS measurements were carried out at beam line E4 of HASYLAB at DESY, using a Si(111) double crystal monochromator. To reduce the higher harmonic content of the beam, the monochromator was detuned to approximately 50% of the maximal transmitted X-ray intensity. The width of the vertical slit was opened up to 1 mm resulting in an estimated energy resolution of ≈2 eV. All data were taken in transmission mode and collected around the L_3-edge of Ta (9.61–10.85 keV). Energy calibration was accomplished by assigning the position of the first inflection point of the tantalum absorption-spectrum to 9.881 keV. We used nitrogen gas at atmospheric pressure in the ion chambers before and behind the sample. For each of the three measurements at 20 K, 80 K, and 300 K three scans were collected to improve statistics.

3. Data analysis

The fitting procedure of Ref. [1] has been extended to include a correction $\Delta\mu_0(k)$ to the embedded-atom absorption-coefficient $\mu_0^{\mathrm{FEFF}}(k)$. Similar to Klementev [5] the correction term is expressed as cubic-spline function with N_p support points k_p. In addition, a k dependent overall efficiency $A(k) = \bar{\mu}(k)/\bar{\mu}_0^{FEFF}(k)$ of the experimental set-up is introduced, where $\bar{\mu}$ is the measured absorption coefficient $\mu(k)$ after preedge-background subtraction and after averaging in k to remove the EXAFS wiggles, and $\bar{\mu}_0^{FEFF}$ is the similarly averaged μ_0 from FEFF. We then represent $\mu(k)$ by

$$\mu(k) = A(k)(\mu_0^{FEFF}(k) + \Delta\mu_0(k))(\chi(k) + 1). \tag{2}$$

A thorough discussion of this procedure is given in a forthcoming paper [4]. The set of model parameters x_n consists of the amplitudes $\Delta\mu_0(k_\mathrm{p})$ at the support points k_p, the many-body correction to the scattering amplitude, ${S_0}^2$, the reference energy E_0 in the expression $k^2 = 2m\hbar^{-2}(h\nu - E_0)$, the lattice constant a, assuming that the half-path lengths R_j are related to the lattice constant by the geometry of the ideal bcc lattice, the multiplicity number of the first shell, N_1, the (projected) DW parameters of the single and multiple-scattering paths, considered in the multiple-scattering series, σ_j^2, $j = 1,\ldots,J$, and the third cumulant of the first single-scattering path, $C_{3,1}$. Alternatively, instead of fitting the total DW

*e-mail: rossner@hmi.de

parameters of all scattering paths we use a force-field model to express the thermal contribution to the $\sigma^2{}_j$ in terms of nearest and next-nearest neighbor central-force constants $\kappa_s, s = 1, 2$. The following bootstrap procedure is used to separate the thermal from the structural contribution to $\sigma^2{}_j$: We start with the 300 K data and determine spring constants $\kappa_1{}^{(1)}$ and $\kappa_2{}^{(1)}$, assuming that

$$\sigma_j^2 = (\sigma_j^{therm}(T = 300\,\mathrm{K};\ \kappa_1{}^{(1)}, \kappa_2{}^{(1)}))^2. \tag{3}$$

We then determine $\sigma^2{}_j$ from the 20 K data and define

$$(\sigma_j^{struct})^2 = \sigma_j^2 - (\sigma_j^{therm}(T = 20\,\mathrm{K}; \kappa_s{}^{(1)}))^2. \tag{4}$$

New spring constants $\kappa_s{}^{(2)}$ are determined by fitting

$$(\sigma_j^{therrm}(T = 300\,\mathrm{K}; \kappa_s{}^{(2)}))^2 = \sigma_j^2 - (\sigma_j^{struct})^2 \tag{5}$$

to the 300 K data and the cycle is repeated. Convergence is typically achieved after 3–5 cycles.

In our fitting procedure we use a cluster size of $I = 10$ shells ($R_{\max} = 9$ Å) in FEFF and $I = 19$ shells ($R_{\max} = 12$ Å) in the lattice-dynamics calculation. As *a priori* values for the model parameters we use $\Delta\mu_0(k_p) = 0, k_p = 1, \ldots, 14, S_0{}^{(0)} = 1$, $E_0{}^{(0)} = 9884$ eV (the peak position of the white line); the $R_j{}^{(0)}$ are calculated from a lattice constant $a = 3.30$ Å, assuming an ideal bcc structure; from the same assumption the $N_j{}^{(0)}$ were derived; the $(\sigma_j{}^{(0)})^2$ are obtained from the Debye model with a Debye temperature of 240 K, and all third cumulants were set to $C_{3,j} = 0$. In FEFF8 the option of a self-consistent potential was used with a cluster of 65 atoms within a sphere radius of 7 Å, a Hedin-Lundqvist exchange correlation potential with a constant imaginary part of 0.75 eV, a maximum number of 6 legs in multiple-scattering paths, a 4% cutoff of the mean amplitude relative to the largest path amplitude, and a radial grid parameter of 0.01 for atomic background computations. The normalized absorption functions for Ta at 20 K, 80 K, and 300 K are shown in Fig. 1. The experimental data are represented by dots with error bars and the final fits are shown by solid lines. All experimental data points to the left of the dotted line at 3.2 Å are disregarded because the multiple-scattering series converges too poorly for the chosen cluster size in this range of k-values. Truncation and model errors are determined as in Ref. [1].

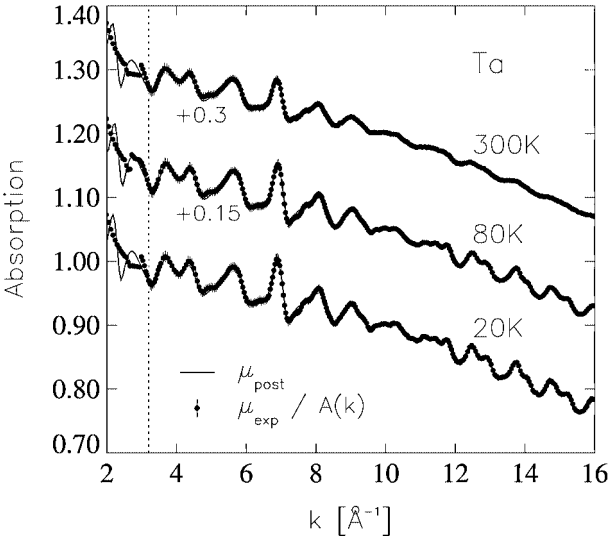

Fig. 1. The absorption coefficients $\mu(k)$ of the experimental data for Ta at 20 K, 80 K, and 300 K after preedge-background subtraction and normalization to μ_0^{FEFF} (dots with error bars) and the corresponding *a posteriori* values (solid line).

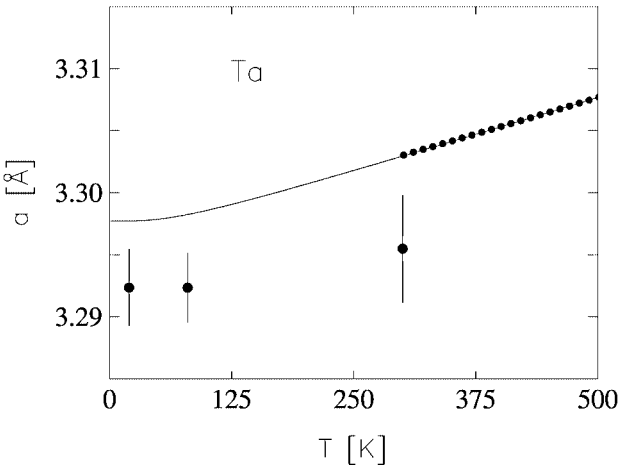

Fig. 2. Temperature dependence of the lattice constant a, extracted from the fits (solid points with error bars), results of Ref. [5] (small dots), and extension of these results to lower temperatures (line).

4. Discussion of results

The lattice constants obtained from the fit for the three temperatures are shown in Fig. 2. There seem to be no measurements of the lattice constant of Ta below room temperature. We have therefore extrapolated the measured lattice constants and thermal expansion coefficients from Amonenko *et al.* [6] at 500 K to lower temperatures using the temperature-integrated form of the Grüneisen formula [7] with the assumption that the Debye model is valid with a Debye temperature of 248 K and that the temperature dependence of the compression modulus can be neglected in the extrapolated temperature range. The extrapolation is also shown in Fig. 2 for a rough comparison with our data which are, as usual, about one order of magnitude less accurate than the X-ray diffraction data of Amonenko *et al.* [6]. Still larger uncertainties are due to the fact that neither for our probe nor for the one of Amonenko *et al.* were the degree of oxidation and the gas load of the lattice accurately determined.

More interesting is the result on the lattice dynamics. A consistent description of the DW parameters at all three temperatures is obtained with a temperature-independent contribution $\sigma_j^{\mathrm{struct}}$ and a thermal part $\sigma_j^{\mathrm{therm}}$ derived from a force-field model with only nearest and next-nearest neighbor central-force constants κ_1 and κ_2. A fit of the same quality is obtained with a Debye model for $\sigma_j^{\mathrm{therm}}$, using a Debye temperature of 248 K. The contributions to the DW parameters are shown in Fig. 3 for all 72 scattering paths. We find that even at 20 K the $\sigma^2{}_j$ depends primarily on the vibrational structure. The 'melting' of the EXAFS oscillations for long path lengths is shown by the first 10 path numbers which represent single scattering paths plotted with increasing paths lengths. The figure further demonstrates the sensitivity of $\sigma^2{}_j$ to displacement-displacement correlations which are absent in the unprojected DW parameter measured in diffraction experiments [8]. Especially $\sigma^2{}_{65}$ of the multiple-scattering path number 65, where all scattering centers are aligned and follow the sequence A-B-C-B-A-B-A, is more than twice as high as $\sigma^2{}_{66}$ with a sequence A-B-C-D-C-B-A for the aligned atoms.

A two-parameter force-field model can of course not describe the whole phonon dispersion-relations, in particular in the elastic limit. We calculated the unprojected densities of phonon states ρ_0 for a 19-shell cluster with 411 atoms and a 28-shell cluster with 749 atoms by a recursion method in analogy to the one used for the

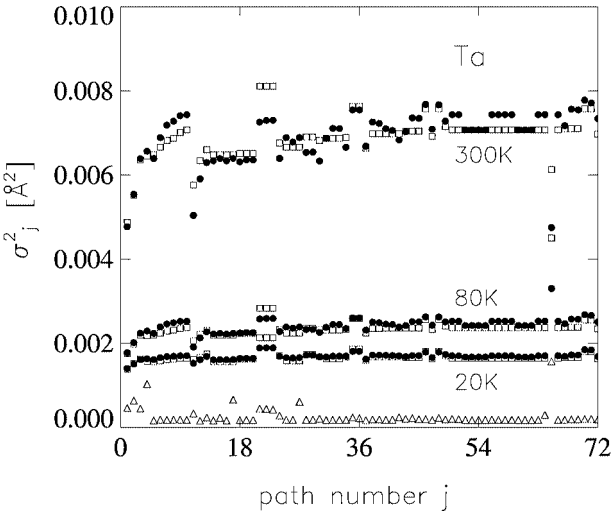

Fig. 3. Thermal DW parameters for 20 K, 80 K, and 300 K (open and filles circles) and structural DW parameters (open triangles) for all scattering paths. The thermal DW parameters derived from a force-field model are represented by filled circles and those derived from a Debye model ($\Theta_{\mathrm{Debye}} = 248$ K) are shown by open circles. Path numbers 1–10 represent single scattering paths, path numbers 11–72 number multiple scattering paths.

projected level densities and described in the appendix. The result for the 28-shell cluster is shown in Fig. 4 in comparison with the state density in the Debye model, and in a Born-von Karman model [9, 10] using the same 28-shell cluster. In this model 19 parameters were fitted to reproduce the measured phonon-dispersion curves. The unprojected DW exponent 2W divided by the recoil frequency ν_R of the free ion is shown as function of the temperature in Fig. 5. for two cluster sizes in our force-field model and for the Born-von Karman parameters [10] in the infinite lattice. The figure indicates that with increasing cluster size $2W/\nu_R$ decreases towards the values of the infinite lattice result. Projected DW parameters are less influenced by the low-frequency properties of the projected state density ρ_R because the latter vanishes much faster for $\nu \to 0$. This is seen analytically in the Debye model, where $\rho_0(\nu)$ vanishes as ν^2, but $\rho_{\mathrm{R}}(\nu)$ as ν^4 for

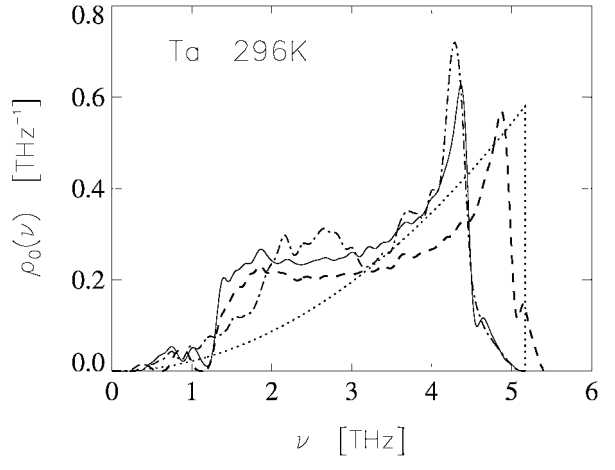

Fig. 4. Comparison of unprojected densities of phonon states for a cluster with 749 atoms using Woods' parametrization of the dynamical matrix and calculating its eigenvalues by a standard library routine (dashed dotted line), using Woods' parametrization and our recursion method (solid line), using our two spring constants in combination with the recursion method (dashed line), and using the Debye model (dotted line).

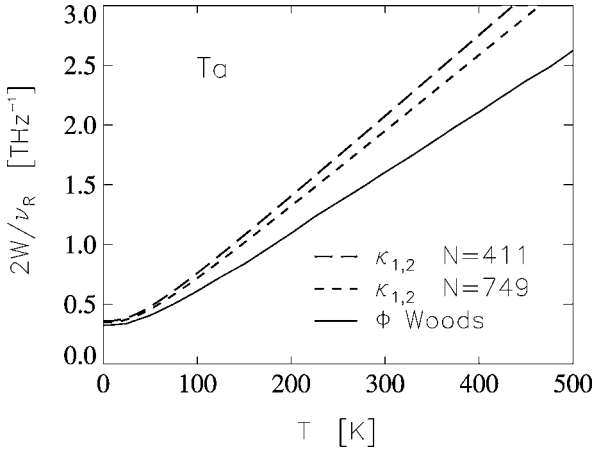

Fig. 5. The unprojected DW exponent 2W divided by the recoil frequency ν_{R} of the free ion plotted as function of the temperature for the Born-von Karman parameters in an infinite lattice [9] (solid line) and for our force-field model using two cluster sizes of 411 atoms (long dashed line) and 749 atoms (short dashed line).

small ν. For force-field models this effect is shown in Fig. 6 and also seen in the numerical results of Sevillano *et al.* [8].

The fitted values of the parameters including the corrections $\Delta\mu_0(k_l)$ to the FEFF results for $\mu_0(k)$ are shown in table I together with their *a posteriori* errors. The corrections $\Delta\mu_0(k_l)$ are zero within one standard deviation of the *a posteriori* errors. Also the unharmonicity parameter $C_{3;1}$ vanishes within these limits.

5. Conclusions

The introduction of an energy-dependent overall detection efficiency enables us to determine empirical corrections to the embedded-atom absorption-coefficient from FEFF in a simultaneous fit with the lattice constant, the structural contribution to the DW parameter and a pair of spring constants describing the essential features of the lattice dynamics in a cluster surrounding the absorbing atom. A bootstrap procedure was used to separate the thermal from the structural contribution to the total DW parameters. The thermal contribution has been described by a force-field model with only two central force

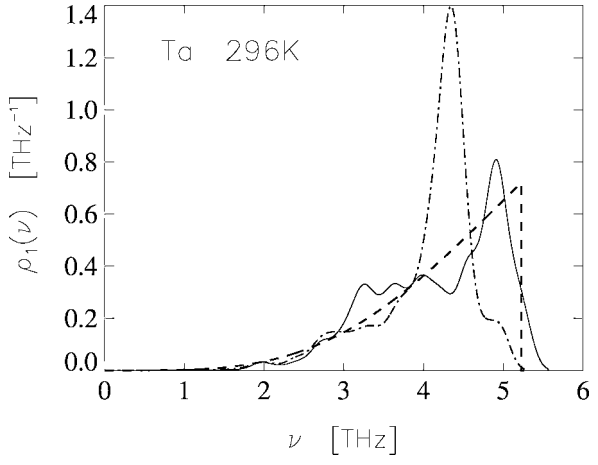

Fig. 6. Comparison of densities of phonon states projected onto the first single scattering path for a cluster with 749 atoms using our recursion method in combination with Woods' parametrization [8] (dashed dotted line) as well as our two spring constants (solid line). The Debye model results are represented by the dashed line.

Table I. *A posteriori fit parameters with their uncertainties for Ta measured at temperatures of 20 K, 80 K, and 300 K.*

T [K]	20	80	300
$S_0{}^2$	1 ± 0.02	1 ± 0.03	1 ± 0.03
E_0 [eV]	9882.7 ± 0.1	9883.4 ± 0.2	9882.6 ± 0.1
R_1 [Å]	2.851 ± 0.003	2.851 ± 0.002	2.854 ± 0.004
κ_1 [N/m]	44.5 ± 1	44.5 ± 1	44.5 ± 1
κ_2 [N/m]	25.5 ± 1	25.5 ± 1	25.5 ± 1
$C_{3,1}$ [Å^3]	−1E-5 ± 3E-5	0 ± 2E-5	1E-5 ± 3E-5
N_1	8 ± 0.08	8 ± 0.07	8 ± 0.05
$\Delta\mu_0$ ($k = 0.5$ Å)	3.1E-6 ± 1.3E-3	1.2E-5 ± 1.2E-3	6.2E-6 ± 1.2E-3
$\Delta\mu_0$ ($k = 3.2$ Å)	2.3E-4 ± 1.2E-3	−3.6E-4 ± 1.1E-3	−3.2E-6 ± 1.1E-3
$\Delta\mu_0$ ($k = 4.3$ Å)	1.8E-3 ± 1.1E-3	8.0E-4 ± 9.8E-4	1.6E-3 ± 9.5E-4
$\Delta\mu_0$ ($k = 5.4$ Å)	1.3E-3 ± 9.7E-4	1.4E-3 ± 9.2E-4	1.3E-3 ± 8.9E-4
$\Delta\mu_0$ ($k = 6.4$ Å)	−1.4E-3 ± 8.9E-4	−1.1E-3 ± 8.5E-4	−1.2E-3 ± 8.1E-4
$\Delta\mu_0$ ($k = 7.5$ Å)	−1.4E-3 ± 8.1E-4	−8.0E-4 ± 7.8E-4	−1.4E-3 ± 7.4E-4
$\Delta\mu_0$ ($k = 8.5$ Å)	−1.9E-4 ± 8.0E-4	−7.3E-4 ± 7.7E-4	−5.3E-4 ± 7.3E-4
$\Delta\mu_0$ ($k = 9.6$ Å)	−5.8E-4 ± 7.8E-4	−2.4E-4 ± 7.5E-4	2.3E-4 ± 7.1E-4
$\Delta\mu_0$ ($k = 10.7$ Å)	−1.3E-4 ± 7.1E-4	−8.1E-4 ± 6.8E-4	−2.8E-4 ± 6.4E-4
$\Delta\mu_0$ ($k = 11.7$ Å)	1.4E-3 ± 6.4E-4	1.1E-3 ± 6.2E-4	1.1E-3 ± 5.8E-4
$\Delta\mu_0$ ($k = 12.8$ Å)	7.9E-4 ± 6.8E-4	4.6E-4 ± 6.5E-4	3.3E-4 ± 6.2E-4
$\Delta\mu_0$ ($k = 13.8$ Å)	4.3E-4 ± 6.1E-4	1.3E-3 ± 5.9E-4	3.6E-4 ± 5.6E-4
$\Delta\mu_0$ ($k = 14.9$ Å)	4.1E-4 ± 5.5E-4	4.4E-4 ± 5.3E-4	1.4E-4 ± 5.0E-4
$\Delta\mu_0$ ($k = 15.9$ Å)	−1.7E-4 ± 8.0E-4	8.8E-5 ± 7.6E-4	3.0E-4 ± 7.0E-4

constants and the projected and unprojected densities of phonon states were compared with results of a 19-parameter Born-von Karman model, fitted to neutron diffraction data. We find good agreement of the projected state densities from EXAFS and neutron diffraction data, and still rather fair agreement for the unprojected quantities when the finite cluster size probed in EXAFS is taken into account.

Acknowledgment

The general support by the HASYLAB group is gratefully acknowledged.

Appendix I: Calculation of unprojected Debye-Waller parameters in a force-field model

In the following we show that a variant of the iteration method proposed by Poiarkova and Rehr [3] to evaluate the projected phonon level-density and the projected Debye-Waller parameters can be used to obtain also the total level density. Following our presentation of the iteration method in Section II of Ref. [1] one has to substitute the projected density of states $\rho_j(\omega)$ in Eq. (5) of Ref. [1] by the total density of vibrational states

$$\rho_0(\omega)\,\mathrm{d}\omega = \sum_\gamma \delta(\omega - \omega_\gamma)\,\mathrm{d}\omega = -\frac{1}{\pi}\mathrm{Im}\,tr\left(\frac{1}{z - \Phi + \mathrm{i}\varepsilon}\right)\mathrm{d}z =: \omega_0(z) \tag{6}$$

with $z = \omega^2$. Calling the determinant of the matrix $(z\delta_{vv'} - \langle v|\Phi|v'\rangle)$ again D_{-1} and $A_{vv'}$ its cofactors, we find

$$\mathrm{tr}\left(\frac{1}{z - \Phi}\right) = \frac{1}{D_{-1}}\sum_v A_{vv} = \frac{1}{D_{-1}}\partial_z D_{-1}. \tag{7}$$

As in Ref. [1] we introduce the determinants D_v of the tridiagonal matrices obtained from $(z\delta_{vv'} - \langle v|\Phi|v'\rangle)$ by removing rows and columns 0 to v and find the recursion relation

$$D_v = (z - a_{v+1})D_{v+1} - b_{v+2}^2 D_{v+2}, \tag{8}$$

with $v = -1, 0, \ldots$, or

$$D_{v+1}/D_v = \frac{1}{z - a_{v+1} - b_{v+2}^2 D_{v+2}/D_{v+1}}. \tag{9}$$

The basis states $|v\rangle$ are generated by the dynamical matrix Φ with the Lanczos algorithm, starting with a vector $|0\rangle$. It should be stressed that Φ has to be symmetrized when used in this context.

The convergence of the recursion (9) implies that D_{-1} is a minimal solution of the recursion (8) according to a theorem by Pincherle [11, 12]. To obtain an approximation to the minimal solution, we use Miller's algorithm in a version proposed by Gautschi [12]. Defining

$$r_v = \frac{D_{v+1}(z)}{D_v(z)}, \quad v = -1, 0, \ldots, N, \tag{10}$$

Eq. (9) becomes

$$r_v = (z - a_{v+1} - b_{v+2}^2 r_{v+1})^{-1}, \quad v = N-1, N-2, \ldots, -1, \tag{11}$$

which is solved backwards, starting with $D_{N+1} = 0$, $D_N = z - a_N$, $b_{N+1}^2 = 0$, and $r_N = 0$. In terms of the set of ratios r_v an approximation to $D_{-1}(z)$ is given by

$$D_{-1} = (z - a_N)\left(\prod_{v=-1}^{N-1} r_v\right)^{-1}. \tag{12}$$

The zeros of D_{-1} may be called z_v, $v = 0, \ldots, N_0$. The state density $\omega_0(z)$ is then given by $\sum_{v=0}^{N_0}\delta(z - z_v)$, the weight factors w_v being all equal to 1 in this case. In principle any start vector $|0\rangle$ could be used in the Lanczos algorithm, e.g. the vector $\{1, 0, \ldots, 0\}$.

As discussed already by Haydock and Te [13] the convergence of the iteration method is much faster for the projected level density and the projected DW parameters than for the unprojected density. In fact we found that N had to be of the order of the number of degrees of freedom in the cluster to get acceptable results. The method is therefore suitable to calculate the phonon level-density of finite clusters of up to a few Å size, where calculations in Fourier space are not suitable.

References

1. Krappe, H. J. and Rossner, H. H., Phys. Rev. B **66**, 184303 (2002).
2. Zabinsky, S. I., Rehr, J. J., Ankudinov, A., Albers, R. and Eller, M. J., Phys. Rev. B **52**, 2995 (1995); Ankudinov, A. L., PhD thesis, Univ. of Washington (1996).
3. Poiarkova, A. V. and Rehr, J. J., J. Synchrotron Rad. **8**, 313 (2001).
4. Klementev, K. V., J. Phys. D: Appl. Phys. **34**, 209 (2001).
5. Krappe, H. J. and Rossner, H. H., Phys. Rev. B **70**, 104102 (2004).
6. Amonenko, V. M., Vasyutinskiy, B. M., Kartmazov, G. N., Smirnov, Yu. N. and Finkel, V. A., Fiz. metal. metalloved. **15**, 444 (1963) [Phys. Metals Metallogr. **15**, 102 (1963)].
7. Kittel, C., "Introduction to Solid State Physics" (4th ed., John Wiley, New York 1968), p. 183.
8. Sevillano, E., Meuth, H. and Rehr, J. J., Phys. Rev. B **20**, 4908 (1979).
9. Woods, A. D. B., Phys. Rev. **136**, A781 (1964).
10. Schober, H. R. and Dederichs, P. H., "Landolt-Börnstein: Numerical Data and Functional Relationships in Science and Technology" (edited by K.-H. Hellwege, Springer) (Berlin, 1981), Group III, Vol. 13a.
11. Pincherle, S., Giorn. Mat. Battaglini **32**, 209 (1894).
12. Gautschi, W., SIAM Rev. **9**, 24 (1967).
13. Haydock, R. and Te, R. L., Phys. Rev. B **49**, 10845 (1994).

Physica Scripta. Vol. T115, 49–53, 2005

X-ray Magnetic Dichroism: The Technique of Choice to Study Magnetism Element Specifically

Klaus Baberschke*

Institut für Experimentalphysik, Freie Universität Berlin, Arnimallee 14, D-14195 Berlin-Dahlem, Germany

Received June 26, 2003; accepted October 20, 2003

PACS numbers: 78.70.Dm, 75.70.−i

Abstract

X-ray Magnetic Circular Dichroism became mature and is used in a large variety of applications. Taking advantage of the element-specificity of XAS, a variety of important problems was addressed: e.g. magnetism and magnetic profiles at interfaces of nanostructures, induced magnetism at chemisorbed molecules, enhanced 2D spin-fluctuations in coupled ultrathin ferromagnet films, the revival of orbital magnetic moments and its relative alignment to the spin moment, limitations for the applicability of the integral XMCD sum rules, separation of dipolar (E1) and quadrupolar (E2) contributions in the XMCD. An equally important progress in the fundamental understanding is the symbiosis of theory and advanced experiments. In all examples given the combination of both was very successful. Theory can 'switch on and off' various effects, i.e. L_3-L_2 edges, dipol-quadrupolar effects, layer selective magnetic moments, multiple vs. single scattering. This serves for a better understanding of magnetism on an atomic scale.

1. Introduction

In 1988 at the XAFS V conference Gisela Schütz and coworkers reported their first results on X-ray magnetic circular dichroism (XMCD). They pointed out that X-ray absorption spectroscopy (XAS) is the most appropriate technique to study selectively almost every element in the periodic table. They demonstrated that by taking the difference spectra between right and left circular polarization ($\mu^+ - \mu^-$) one was sensitive to study *spin densities* [1]. This opened a complete new field to study magnetic materials. Clearly, Mössbauer effect and nuclear magnetic resonance are also element-specific, for example the spin-polarization/induced magnetism at Cu in the vicinity of Mn in MnCu alloys has been detected by NMR long time ago – the so-called RKKY-oscillations. However, it is obvious that the XAS via the various K-, L-, M-edges is not only sensitive to most of the elements but also probes different parts of the electron density (s-, p-, d-shells). Years later at XAFS IX in 1996 Jo Stoehr pointed out that these new discoveries would have a major impact on information technology and material science [2]. He also demonstrated that by employing the so-called *integral sum-rules* XMCD is able to probe separately the orbital and the spin magnetism, μ_L and μ_S [3]. Again, μ_L and μ_S have been determined long time ago since the early days of Charles Kittel by measuring the g-factor in ferromagnets via magnetic resonance and yielding $\mu_L/\mu_S = (g-2)/2$ [4]. However, one has to admit that by virtue of XMCD the field of atomic magnetism in solids has been re-activated and makes enormous progress in experiment as well as in theory.

The research grew enormously and spread out addressing almost all fields in material science nowadays. Only few examples can be mentioned here: ferromagnetic ultrathin multilayers exchange coupled via nonmagnetic spacers like Co/Cu/Ni form in- and out-of-plane magnetic domains which were recently studied by element-specific and magnetic microscopy [5]. The magnetic coupling between ferro- and antiferromagnetic films and its exchange bias field like at Co/NiO interfaces are enormously important for storage media. Recently, it has been shown that at such an interface one will not have an intact Co metal and NiO interface but rather oxygen interdiffuses into Co leading to metallic Ni areas at the interface [6]. Molecules like CO on ferromagnetic Ni surface are hybridized and see a spin-polarization resulting in a magnetic moment at the oxygen atom [7]. For small clusters of few atoms of Fe, Co, or Ni almost the full orbital moments survive. (They are not quenched like in solids.) This was shown twice by groups from Lausanne: years back for the gas phase [8], and recently for clusters on surfaces [9].

In this work we will not review the full variety of technological applications but focus on another aspect of this highly active research field, namely the fact that new external parameters in magnetic nanostructures can be used to manipulate the magnetism and serve for a better understanding of fundamentals. It seems to be an accidental coincidence that in the same period of time when the XMCD grew up also the theory made progress in *ab initio* calculations. Clearly, magnetism is only a relativistic correction in total energy calculations. Out of a $\approx$ eV total energy per particle only a few μeV are of magnetic origin. In some cases it may therefore not be sufficient to treat spin-orbit coupling as a perturbative part of the Hamiltonian adding small corrections. It may be rather important to treat the system fully relativisticly.

In the real structure and experiment there are two important 'knobs' to manipulate the magnetism: (*i*) Via the *finite size effect* one can shift the Curie temperature T_C of ferromagnets from its bulk value almost down to zero. E.g., just by varying the thickness of a Co film and a Ni film one can move $T_C^{Co} < T_C^{Ni}$. Such a manipulation is impossible in bulk systems. (*ii*) Special growth recipes for nanostructures enable to prepare crystallographic structures not available in the bulk, e.g. pseudomorphic growth of Ni/Cu(100) produces tetragonal Ni or Co/Cu(111) trigonal Co. Both are not available in bulk structures. However, these small perturbation from cubic fcc or bcc structures are very important for reactivation of orbital magnetism. Changes of the crystallographic structure by ≈ 0.05 Å change the magnetic anisotropy energy (MAE) by 10^2–10^3 [10]. Selected examples for prototype studies in experiment and theory are: In Sec. 2 we discuss the effects of spin-fluctuations in two-dimensional (2D) nanostructures by virtue of element-specific magnetization profiles for Ni and Co exchange coupled films. Sec. 3 gives examples of combined theory and experiment to study the layer-resolved magnetic profile at interfaces of ferromagnets/nonmagnetic metals. In Sec. 4 we disentangle the XMCD at L edges of Rare Earths with assistance of theory to separate dipolar and quadrupolar contributions. Most of the experimental analysis of XMCD spectra take the intensity of the XMCD signal as a measure of the magnetization, i.e. the area

*Corresponding author: Electronic address: bab@physik.fu-berlin.de; URL: http://www.physik.fu-berlin.de/~ag-baberschke/index.html

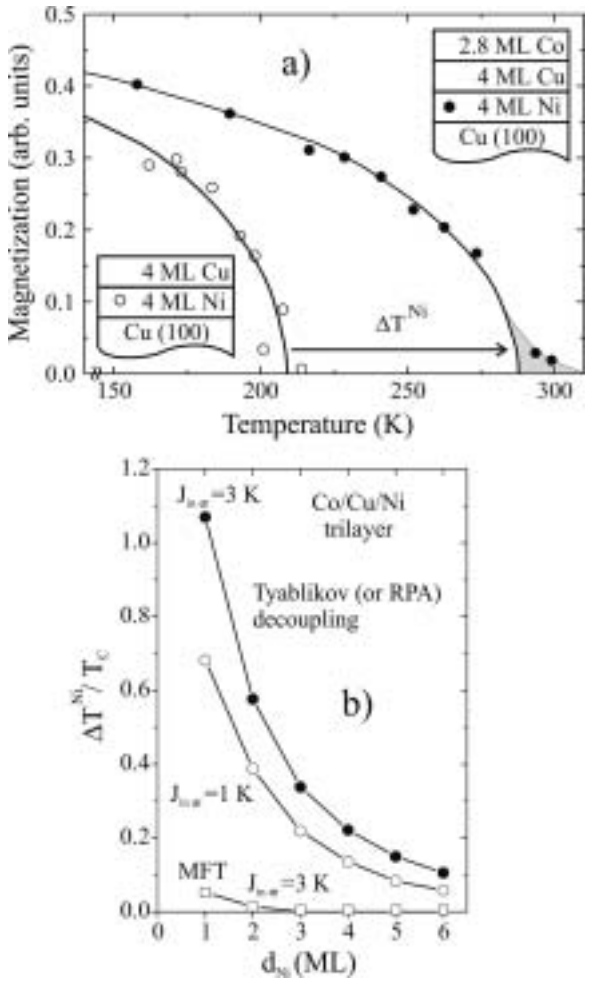

Fig. 1. (a) $M^{Ni}(T)$ measured at the Ni L_3 edge XMCD before and after evaporating a second ferromagnetic film (Co) on top. A small DC magnetic field was applied to avoid domain formation close to T_C, for details see [12]. (b) Shift of T_C^{Ni} calculated in mean field approximation and RPA [17]. It is obvious that the shift is the larger the stronger J_{inter} and the thinner the Ni layer is.

under the $(\mu^+ - \mu^-)$ spectrum. It is obvious that a spectroscopy delivers much more information: the line width of the resonance, the line shape, the asymmetry etc. For a full interpretation of experimental XMCD spectra it would be most advisable that the theory calculates the full X-ray absorption cross-section $\mu(E)$ as a function of energy. Examples are given in Sec. 5.

2. Enhanced Spin-Fluctuations in 2D Nanostructures

In Fig. 1 we show the temperature-dependent magnetization of an ultrathin Ni film (4 atomic layers) before and after the evaporation of a second ferromagnetic film (2.8 ML Co). The Co and Ni films are separated by a nonmagnetic spacer film of 4 ML Cu. XMCD is the technique of choice to measure the Ni and Co magnetizations separately. Here we show only the Ni magnetization, Co has a much higher magnetization and higher Curie temperature. At XAFS XI we have shown that by reducing the Co thickness one can even achieve that the Co film orders at a lower temperature than the Ni film [11]. The details of the current experiments are discussed in [12]. The exchange coupling of the Co and Ni film is described in an itinerant model as the interlayer exchange coupling (IEC), depending on the spin-dependent band structure for each layer. Experiments are usually analyzed in a local Heisenberg model where the coupling between two ferromagnets is defined as the difference in the free energy between parallel and antiparallel alignment $\Delta E \approx J_{inter}\vec{M}_1 \cdot \vec{M}_2$. Typical values for such a coupling (depending on d_{Cu}) correspond to 1 K $\triangleq$ 100 μeV $\triangleq$ 2.5 kG. XMCD and other techniques like ferromagnetic resonance have determined the coupling constant J_{inter} in a quantitative way [13]. It is also clear that the difference in the free energy between ferromagnetic and antiferromagnetic alignment depends on the temperature, details have been discussed elsewhere [14]. Here we focus exclusively on the effect of the Co exchange coupling on the Ni magnetization as shown in Fig. 1a). At first glance one might argue that Co produces an exchange field in the order of a few kG and that this exchange field leads to a so-called field induced magnetization ($M^{Co}(T)$ is not shown in Fig. 1a). A static field corresponding to $\langle S_z^{Co}\rangle$ would enhance $M^{Ni}(T)$ and T_C only by 2–5 K. Surprisingly, we observe in Fig. 1a) a shift $\Delta T^{Ni} \approx 80$ K. A shift of 80 K out of 210 K (≈40%) has never been observed in bulk materials [15]. It can be interpreted as follows: P. Jensen has calculated ΔT^{Ni} in a Heisenberg model to lowest order (mean field approximation). We see in Fig. 1b) that for $J_{inter} = 3$ K the shift is only a few percent. If he includes higher order approximation in the calculation (RPA), the higher spin correlations $\langle S^2\rangle$ result in a dramatic increase ΔT^{Ni}. In other words, for a 2D ferromagnet like 4 ML Ni higher order spin-fluctuations are very dramatic. Their effect is influenced very much by the Co exchange coupling and produces such a high shift in T_C. W. Nolting and coworkers have addressed the same experimental finding using an itinerant electron model with single Hubbard band. They find similar results. If they treat the itinerant model to lowest order (Stoner model) they fail to calculate the correct T_C and its shift. If they include higher order correlation they are able to explain the experiments fairly well [16].

In conclusion, for a complete description of the magnetization for nanostructures and two-dimensional films it is insufficient to treat only in a static manner spin-up and spin-down bands (Stoner model). Spin-fluctuation and higher order electron–electron correlations are very important and influence the magnetization close to T_C dramatically.

3. Layer Resolved Magnetic Profiles

Interfaces of 3d ferromagnets and 4d and 5d nonmagnetic metals are of technological importance. In the early days XMCD of 3d-4d and 3d-5d alloys were investigated by several groups. However, in principle one should speculate that an interface of these elements might not have the same electronic and magnetic band structure as in an alloy because the nearest neighbor coordination is well ordered at an interface and random in an alloy. Experiments do have the handicap that interfaces are never mathematically flat. The minimum are steps of one atomic layer. The theory might assume a perfect flat interface but the real crystallographic structure may not be treated correctly (layer relaxation, tetragonal distortion, etc). Only recently, with the new high power synchrotron facilities in the soft and the hard X-ray regime it has become possible to measure XMCD for single atomic layers more or less free of noise. One example is the layer resolved magnetic moment profile of Ni_n/Pt_m multilayers [18]. Induced magnetic moments at the Pt interface of 2 ML Pt only were recorded free of noise in the energy range of 11–13 keV at the ESRF beamline ID 12. By varying the number n of the Ni layers and m of Pt layers, the authors were able to construct layer resolved profiles of the Ni magnetic moment and the induced Pt moments. Pt carries a large magnetic moment only at the interface.

Already the second and third layer contribute very little to the Pt magnetization. The XMCD at the Ni L edges shows that the magnetic moment of the Ni atoms reduces at the interface, but remains magnetic. This is in contrast to earlier publications where it was believed that there are dead layers at such an interface. The Ebert group calculated the magnetic profile for these Pt/Ni multilayer. The results are in fair agreement. Differences between theory and experiment may be attributed to details of the local structure in the real specimen [18].

Another interesting case is the interface of Fe/W. An induced magnetization was also recorded at the W interface [19]. Even the smaller XMCD signal at the L_2 edge was intense. This enables us to apply the integral sum rules [3] and separate the orbital and spin moment and their relative alignment. The integral sum rules account only for the area under the L_3 and L_2 XMCD signal and they are derived assuming an atomic picture and λLS coupling. Both can be questioned for an element with $Z = 74$ and in a metallic state. Nevertheless, this commonly used procedure demonstrates the principal power and capability of XMCD analysis and interpretation. It follows straight forward from the sum rules that if the integral over the $L_3 + L_2$ XMCD (which determines the orbital moment) changes the sign as a function of energy, μ_S and μ_L are antiparallel aligned, if it does not change its sign they are parallel aligned. The experiment shows unambiguously that the integral does not change the sign, and consequently in Ref. [19] it is concluded $\mu_S || \mu_L$. This is in a way surprising because W is located at the beginning of the 5d series and following simple atomic Hund's rules one expects an antiparallel alignment of spin and orbital moment. Strictly speaking the Hund's rules are for single atom physics and small λLS coupling. However, it is surprising that these rules mostly hold also in solid state physics even up to heavy elements as uranium. Further experiments and theory are needed to get a better insight, but this example shows the full potential of a detailed analysis of orbital and spin magnetic moments in a large variety of nanostructures. For a detailed discussion see [20].

Although Ti and V, the early 3d metals, are nonmagnetic they show an induced magnetic moment if they get in contact with the ferromagnetic 3d elements. Recent progress in the gap-scan technique of the undulator beamline UE56/1-PGM at BESSY II did allow to measure the XMCD signal even of 1 ML V (or Ti) interface layer sandwiched between Fe films. These spectra are free of noise and also free of oxygen contamination so that a full V-XMCD signal from 510 eV up to 540 eV is recorded with a very detailed fine structure [20, 21]. In Fig. 2 we show spectra for the early and the late 3d elements. Also Cr was sandwiched between Fe to gain a net magnetization. It is obvious that the XMCD spectra (dashed lines) of Ti, V, and Cr show a detailed fine structure reflecting details of the spin-resolved DOS. We will come back to this in Sec. 5.

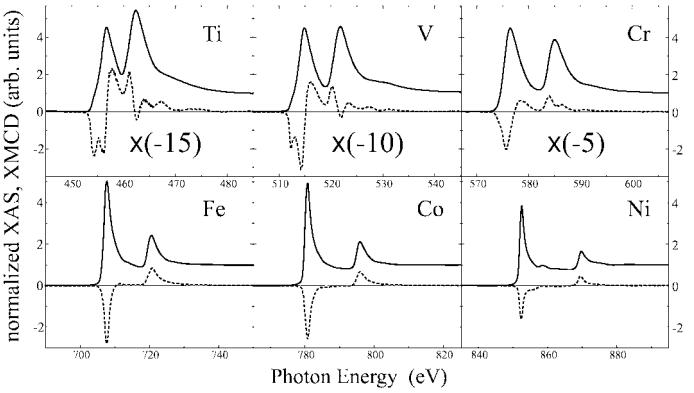

Fig. 2. Normalized XAS and XMDC spectra of the early 3d transition metals (TM's) in the upper panel versus the late 3d TM's, i.e. the ferromagnetic Fe, Co and Ni, in the lower panel. The XMCD spectra of the early TM's have been obtained from Fe/TM/Fe(110) trilayers. For clearer presentation of the systematics we have changed the sign of these XMCD spectra. (Please note the negative enlargement factors for Ti, V, and Cr).

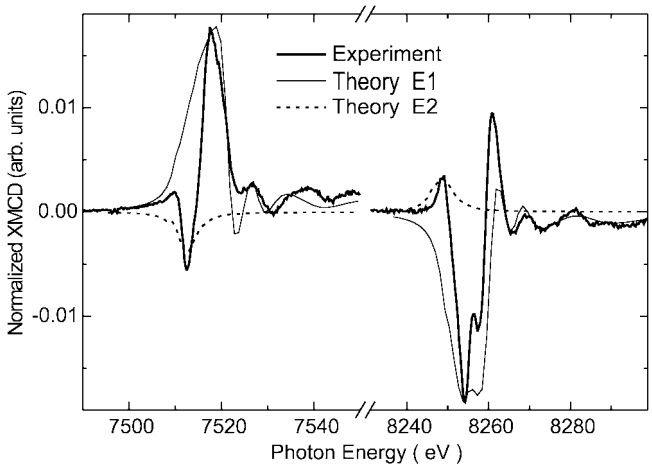

Fig. 3. Experimental and calculated XMCD signal for the L_3 and L_2 edges of Tb metal. Using FEFF8.2 the calculated cross section was separated into quadrupolar and dipolar contributions. The quadrupolar part (dashed) contributes only at the pre-edge with a single peak, the dipolar part (thin solid line) shows all the essential features including the EXAFS oscillations at the high energy side [24].

4. Disentanglement of E1 and E2 Contributions to XMCD

Usually, the near edge structure of the L_3 and L_2 absorption spectra – XANES and spin resolved XMCD – is discussed in terms of transitions from initial $p_{3/2}$ and $p_{1/2}$ states to final d states. It is clear that there are also transition probabilities to final *s* states which are usually assumed to be small. For heavy elements in reality it is even more complicated. Besides the dipole transitions E1 there exists also a finite probability for quadrupolar transitions E2. For example for the Rare Earth elements this would lead to final f states which mostly carry the magnetic information. This allows to determine in one experiment a shell-selective measurement of the magnetism in the 4f and in the 5d shell at the same time. In a real experiment both effects are superimposed and this may lead to a questionable interpretation if, for example, the area under the XMCD signal is taken as a measure of the magnetization. One way to disentangle this is to measure the different angular dependencies of E1 and E2 transitions. This was used in the early experiments by the french groups [22, 23]. In our days, using third generation synchrotron facilities and elliptical undulator beamlines as the ID 12 at the ESRF, it is possible to record experimental XMCD spectra of Rare Earth elements at the $L_{3,2}$ edges free of noise with a variety of spectral fine structures. An example is given in Fig. 3 taken from a Tb single crystal. The solid line shows oscillatory plus and minus intensities at the L_3 and L_2 edges as well as small oscillatory EXAFS wiggles. For such a spectrum it would be nice to separate in one experimental spectral recording the E2 from the E1 intensities. This is the great advantage of theory. Here one can calculate only the transition probability for E1, E2 only, and E1 + E2. Similar to the separation of single and multiple scattering in theoretical calculations, we are now able to switch on/off the various types of multipole transitions. This has been performed with the help of the UW

theory group and the most advanced FEFF version (FEFF8.2). Fig. 3 shows very nicely that the dipolar E1 simulation repeats the experimental spectra at the L_3 and L_2 edge including the small oscillatory feature at the high energy side. The theory explains also the double peak at the L_2 edge (main negative peak). It is caused by a spin-resolved fine structure in the final d states. The same is present at the positive peak of the L_3 edge but the splitting is smaller and it is neither resolved in theory nor in experiment [24]. The quadrupolar intensity appears at the L_3 edge, at lower energies as it is expected from a simple atomic picture: $2p \rightarrow 4f$ transitions have lower energy than $2p \rightarrow 5d$ transitions. This example demonstrates that the hand in hand work of advanced theory and experiments serves for a better understanding of the XMCD fine structure and consequently of fine details of the 4f and 5d magnetism.

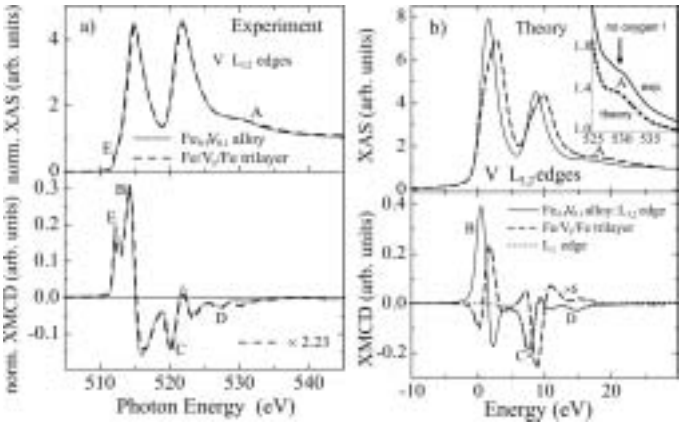

Fig. 4. Induced magnetism in vanadium at an Fe/V/Fe interface. (a) Experimental XAS and XMCD signals and (b) corresponding calculated $\mu(E)$ and $\mu^+(E) - \mu^-(E)$. The experiments show a detailed XMCD fine structure which is very much reproduced by the theoretical calculation (b – lower part). Note that in theory one is able to calculate only the L_2 signal (dotted line). The deviations in the XAS spectra between theory and experiment (branching ratio) is due to the fact that the theory did not take into account core hole correlation effects [25].

5. XMCD Beyond Sum Rules

The analysis of XMCD spectra at the L_3 and L_2 edges made an enormous progress by the so-called *sum rules*. In an atomic localized picture the integral sum rules relate the area under the L_3 XMCD and L_2 XMCD to the orbital and the spin moments. Numerous experimental groups have used these rules to determine separately μ_S and μ_L or even more sophisticated to investigate the anisotropy of the orbital moment $\Delta\mu_L$. This anisotropy of the non-spherical charge distribution is the main origin for the intrinsic magnetic anisotropy energy. (In an itinerant picture it corresponds to the difference in the band energy.) The community is well aware that these integral sum rules have certain limitations: Where does the L_3 edge stop and the L_2 edge start? Is there a dichroic response not originating from the $2p \rightarrow 3d$ transition but rather from some 4s polarization (diffuse magnetism)? How much does the core hole at the L_3 edge influence the L_2 edge (branching ratio)? As one can see in Fig. 3, there is a very detailed fine structure of the spin-dependent 5d band. Giving all credit to the pioneering success of the application of sum rules, we advocate very strongly to calculate and analyze the full spin-dependent spectral distribution. We know from other spectroscopy techniques that in addition to the integral intensity the line width and the line shape, i.e. the full spectral function of $\Delta\mu(E)$, include more specific information. One example is given for the induced vanadium magnetism at an Fe/V interface [25]. Already the integrated XANES spectrum of V $L_{3,2}$ edges at 515 eV – 525 eV shows interesting features. If one scans to higher photon energy up to 540 eV crossing the K edge of oxygen (532 eV) a small bump is seen in the experiment. At first glance one assumes that this stems from some oxygen contamination. Only the theory with the full band structure calculation could clarify that this is due to a van Hove singularity at the N point of the bcc Brillouin zone [25]. In the same work the dichroic spectrum was measured and calculated. Since the spin-orbit splitting between L_3 and L_2 decreases towards the early 3d elements, it is almost impossible in the experiment to separate the contributions of the two edges. Again, only the theory allows to calculate separately the XMCD L_2 edge only and compare it with experimental spectra. This path of analysis has been extended to other early 3d elements (Ti, Cr) [21]. We mention another approach to go beyond the sum rules: In [26] a multipole moment analysis is advertised to take care of the spectral changes. Expansion to first, second, third moment take care of the center of gravity, the width and asymmetry of the spectra. Such an approach is well known in the EXAFS commuity with cumulant expansion taking into account all details of the pair distribution function. Another step beyond simple application of sum rules is to take care of the dynamic screening of the core hole. In XAS the relative intensity of L_3 and L_2 signal change dramatically, e.g. the theory in Fig. 4 did not take into consideration core hole effects and therefore the experimental branching ratio differs very much from Fig. 4b). On the other hand the spin-resolved electronic structure as seen in XMCD shows rather detailed spectral features and seems to be much more sensitive to small changes in the local structure. Core hole effects have been addressed again recently in Refs. [27] and [28]. In conclusion, it seems that we have just opened the door to enter the field of XMCD spectroscopy and that many important details need to be discovered and clarified.

6. Conclusion and Future

The research in magnetism using circular and linear polarized synchrotron radiation in the soft and hard X-ray regime is very vital. With the advanced experimental possibilities new questions are addressed but also long standing problems to interpret magnetism have been reactivated. In the early days magnetism was usually discussed and interpreted in the language of thermodynamics calculating the free energy and its derivatives. Nowadays it is possible in theory as well as in experiment to discuss magnetism on an atomic scale. Magnetism is only a relativistic correction in electrodynamics. Depending on the observable neither s nor ℓ but only j is a good quantum number. These advanced theoretical treatments have become possible very recently and have an important impact on the interpretation and analysis of XMCD experiments. First attempts are made to calculate the full absorption cross section $\mu(E)$ also spin-dependendly and compare the results with experimental spectra. Experiments at the advanced light sources with much higher flux and brilliance yield spectra free of noise with detailed fine structure even for small induced magnetism in nonmagnetic materials. Undulator beamlines with a gap-scan technique provide a constant high degree of polarization over a large energy range which is important for recording $(\mu^+ - \mu^-)$ spectra. Having brilliant experimental spectra, it seems to us insufficient to analyze only the integral intensity. It will become much more advisable to analyze in detail the fine structure as it is usually done

in other spectroscopical techniques. Element specific magnetic microscopy and time-resolution down to femtoseconds open new experimental and theoretical possibilities.

Further work needs to be done to incorporate in the analysis the full spin and energy dependence of transition matrix elements in XAS and XMCD [29]. The well known core hole effects in the absorption spectra need to be included in the analysis. Finally, one needs to compare the magnetic quantities determined by XMD with other well established magnetization measurements. It is still an open question why magnetic anisotropy energy and/or the anisotropy of the orbital moments $\Delta\mu_L$ in recently published results are in most cases by more than an order of magnitude larger than taken from standard magnetic measurements.

Acknowledgments

This work has been performed in collaboration with C. Sorg, A. Scherz and H. Wende. We thank in particular C. Sorg for preparation of this manuscript. Ongoing discussions with the theory groups of K. H. Bennemann, H. Ebert, O. Eriksson, J. J. Rehr, D. L. Mills, W. Nolting, P. Weinberger, and R. Wu are acknowledged. The work is supported by BMBF (05KS1 KEB4) and DFG, Sfb 290.

References

1. Schütz, G. *et al*., Physica B **158**, 284 (1989).
2. Stoehr, J. and Nakajima, R., J. Phys. IV France, **7**, Colloque **C2**, C2-47 (1997).
3. Thole, B.T. *et al*., Phys. Rev. Lett. **68**, 1943 (1992).
   Ebert, H., Rep. Prog. Phys. **59**, 1665 (1996).
4. Kittel, Ch., Phys. Rev. **73**, 155 (1947).
5. Kuch, W. *et al*., Phys. Rev. B **67**, 214403 (2003).
6. Regan, T. J. *et al*., Phys. Rev. B **64**, 214422 (2001).
7. Yokoyama, T. *et al*., Phys. Rev. B **62**, 14191 (2000).
8. Billas, I. M. L., Chatelain, A. and de Heer, W. A., Science **265**, 1682 (1994).
9. Gambardella, P. *et al*., Science 300, 1130 (2003). See also Carbone, C., this conference, Physica Scripta (2003).
10. Baberschke, K., "Lecture Notes in Physics" (Springer **580**, 27 2001).
11. Scherz, A., Wilhelm, F., Poulopoulos, P., Wende, H. and Baberschke, K., J. Synchrotron Rad. **8**, 472 (2001).
12. Sorg, C. *et al*., this conference, Physica Scripta (2003).
13. Lindner, J. and Baberschke, K., J. Phys.: Condens. Matter **15**, S465 (2003).
14. Lindner, J. *et al*., Phys. Rev. Lett. **88**, 167206 (2002).
15. Poulopoulos, P. and Baberschke, K., Lecture Notes in Physics (Springer **580**, 283 2001).
16. Wu, J. H., Herrmann, T., Potthoff, M. and Nolting, W., J. Phys: Cond. Mat. **12**, 2847 (2000).
17. Jensen, P. J. *et al*., Phys. Rev. B **60**, R14994 (1999).
18. Wilhelm, F. *et al*., Phys. Rev. Lett. **85**, 413 (2000).
19. Wilhelm, F. *et al*., Phys. Rev. Lett. **87**, 207202 (2001).
20. Wende *et al*., H., J. Phys.: Condens. Matter **15**, S547 (2003).
21. Scherz, A. *et al*., this conference, Physica Scripta (2003).
22. Bartolome, F. *et al*., Phys. Rev. Lett. **79**, 3775 (1997).
23. Giorgetti, Ch., Dartyge, E., Baudelet, F. and Brouder, Ch., Appl. Phys. A, **73**, 703 (2001).
24. Wende, H., J. Appl. Phys. **91**, 7361 (2002).
25. Scherz, A. *et al*. Phys. Rev. B **66**, 184401 (2002).
26. van der Laan, G., J. Electr. Spectr. Rel. Phenom. **101–103**, 859 (1999).
27. Ankudinov, A. L., Nesvizhskii, A. I. and Rehr, J. J., Phys. Rev. B **67**, 115120 (2003).
28. Schwitalla, J. and Ebert, H., Phys. Rev. Lett. **80**, 4586 (1998).
29. Ankudinov, A. L., Rehr, J. J., Wende, H., Scherz, A. and Baberschke, K., Europhys. Lett. **66**, 44A (2004).

Physica Scripta. Vol. T115, 54–58, 2005

Magneto-Electric Interactions Probed by X-ray Optical Activity

J. Goulon[1], A. Rogalev[1], F. Wilhelm[1], N. Jaouen[1], C. Goulon-Ginet[1,2], P. Carra[1], I. Marri[1] and Ch. Brouder[3]

[1]European Synchrotron Radiation Facility, BP 220, F-38043 Grenoble Cedex, France
[2]Université Joseph Fourier, Faculté de Pharmacie, F-38706 La Tronche, France
[3]Laboratoire de Minéralogie-Cristallographic, UMR 7590, Université Pierre et Marie Curie, case 115, 4 place Jussieu F-75252 Paris Cedex 05, France

Received June 26, 2003; accepted June 23, 2004

PACS number: 7870

Abstract

X-ray Optical Activity (XOA) is caused mainly by *E1E2* interference terms in systems with *odd* space Parity (P). Extra emphasis is put below on *nonreciprocal* XOA effects in Magneto-Electric (ME) solids in which both Parity and Time-reversal (Θ) symmetries are broken whereas the magnetic structure remains invariant in the product $P\Theta$. Two types of dichroism related to non-reciprocal XOA have been observed experimentally: (*i*) The X-ray Magnetochiral dichroism (XMχD) detected in the antiferromagnetic (AFM) phase of Cr_2O_3 is associated with the (unpolarized) Stokes component S_0; (*ii*) A *non-reciprocal* X-ray Magnetic Linear Dichroism (XMLD) was also observed in the low temperature AFM phase a $(V_{1-x}Cr_x)_2O_3$ single crystal and is associated with the Stokes components S_1 or S_2. Edge selective XOA sum rules were derived recently which give a unique access to a whole family of spherical ME operators mixing orbitals of different parities in what is assumed to be the ground state. It is proved that the *orbital anapole* moment $\Omega_0^{(1)}$ is primarily responsible for the XMχD signal measured both with a single crystal or a powdered sample of Cr_2O_3. It is suggested that the non-reciprocal XOA in both Cr_2O_3 and $(V_{1-x}Cr_x)_2$ O_3 is due to partially unquenched angular moments that had a different quantization axis from the spins.

1. Introduction

Unlike magneto-optical effects such as Faraday Rotation or Magnetic Circular Dichroism which refer to pure electric dipole ($E1E1$) or pure electric quadrupole ($E2E2$) transitions, Optical Activity (OA) is associated with transition probabilities mixing multipole moments of opposite parity (*e.g.* $E1M1$ or $E1E2$). The Curie principle states that OA can be observed only in *parity non-conserving systems*. OA related properties which are *even* with respect to the time-reversal operator Θ are commonly called "*natural*"; those which are *odd* with respect to Θ are referred to as "*non-reciprocal*". We have shown elsewhere [1] how to transpose for X-rays the theories of OA at optical wavelengths. Following Buckingham [2] and Barron [3], we found most convenient to introduce a complex *gyration tensor*: $\zeta_{\alpha\beta\gamma} = \zeta'_{\alpha\beta\gamma} - i\zeta''_{\alpha\beta\gamma}$. Since in deep core level spectroscopies, magnetic dipole transitions ($M1$) are very weak [4], it seems legitimate to neglect hereafter the $E1M1$ terms. Under such conditions, one is left with:

$$\zeta'_{\alpha\beta\gamma} = \mathrm{Im}\{E1_\alpha E2_{\beta\gamma}\} + \mathrm{Im}\{E1_\beta E2_{\alpha\gamma}\},$$
$$\zeta''_{\alpha\beta\gamma} = \mathrm{Re}\{E1_\alpha E2_{\beta\gamma}\} - \mathrm{Re}\{E1_\beta E2_{\alpha\gamma}\}. \quad (1)$$

The imaginary part (ζ'') is antisymmetric with respect to inter change of the α,β subscripts but also time-reversal *even*: it is therefore responsible for *natural* XOA. In contrast, the real part (ζ') is symmetrical but also time-reversal *odd* [3]: it is responsible for the *non-reciprocal* effects considered in this paper.

Every Stokes component S_j is associated with a well identified dichroism related to XOA [5, 6, 7, 8, 9, 10, 11, 12]:

- The X-ray magnetochiral dichroism:

  $XM_\chi D(S_0) \propto [\zeta'_{\beta\beta\gamma} + \zeta'_{\alpha\alpha\gamma}]$.
- The non-reciprocal X-ray magnetic linear dichroism:

  $XMLD(S_1) \propto [\zeta'_{\beta\beta\gamma} - \zeta'_{\alpha\alpha\gamma}]$.
- The non-reciprocal, *Jones* X-ray linear dichroism:

  $XMLD(S_2) \propto 2\zeta'_{\alpha\beta\gamma}$.
- The X-ray natural circular dichroism:

  $XNCD(S_3) \propto 2\zeta''_{\alpha\beta\gamma}$.

In the present paper, extra emphasis is put on the detection and the interpretation of non-reciprocal dichroisms measured in Magneto-Electric (ME) materials. ME solids appear as good candidates for detecting non-reciprocal OA effects because, as pointed out by Dzyaloshinskii [14], the ME tensor is *odd* with respect to both parity (P) and time-reversal (Θ) but it is left invariant in the product $P\Theta$. We will review in section 2 the experimental configuration used for such experiments. The cases of two antiferromagnetic crystals, *i.e.* chromium sesquioxide (Cr_2O_3) and a chromium doped vanadium sesquioxide $(V_{1-x}Cr_x)_2O_3$, were retained in order to illustrate the corresponding non-reciprocal dichroisms.

In section 3, we wish to draw attention onto the edge-selective XOA sum rules which were derived recently by Carra *et al.* [15]. There sum rules give access to a whole family of four spherical operators which mix orbitals of different parities in what is assumed to be the true ground state. In particular, it will be shown that XMχD spectra give a unique access to the projection of the *orbital anapole* moment $\boldsymbol{\Omega}_0^{(1)}$ along the direction of the wavevector $\boldsymbol{k}$. Finally, we will discuss briefly the physical implications of this result.

2. Non-reciprocal XOA: experimental evidence

2.1. *Experimental configuration*

The experiments reported below were carried out at the ESRF beamline ID 12 [16, 17]. The concept of the beamline is sketched in figure 1. Three helical undulators are available to cover the energy range 2–15 keV. They were optimized to deliver intense beams of circularly polarized X-ray photons with the capability to flip rapidly the polarization from left (L) to right (R). All spectra are systematically recorded in the total fluorescence yield mode using low noise PNN$^+$ photodiodes as detectors. The backscattering geometry makes it possible: (*i*) to set the optical

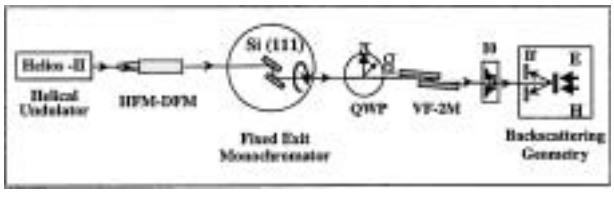

Fig. 1. ESRF beamline ID12 block diagram. Abbreviations: HFM-DFM = horizontally focusing and deflecting mirrors; QWP = quarter-wave plate; VF-2M = vertically focusing double mirror; I0 = photodiode intensity monitor.

axis of the crystal colinear with the wavevector $\boldsymbol{k}$ of the incident X-ray photons; (*ii*) to rotate the crystal around the direction of $\boldsymbol{k}$. The sample was inserted inside a cryomagnet so that both a magnetic field ($\boldsymbol{H}$) and an electric field ($\boldsymbol{E}$) parallel to $\boldsymbol{k}$ can be applied simultaneously for ME annealing. Using circularly polarized X-ray photons, two types of differential fluorescence signals (F) can be measured:

$$XNCD = F(I_0^L) - F(I_0^R)$$
$$XM\chi D = [F(I_0^L, H\uparrow) + F(I_0^R, H\uparrow)] - [F(I_0^L, H\downarrow) + F(I_0^R, H\downarrow)]. \quad (2)$$

The first one is the X-ray Natural Circular Dichroism, and the second, that is characteristic of an *unpolarized beam* is the non-reciprocal X-ray magnetochiral dichroism which we are looking for. Inserting a diamond quarter-wave plate (QWP) downstream with respect to the monochromator allows us to record two non-reciprocal linear dichroisms:

$$XMLD(S_1) = [F(I_0^{90^\circ}, H\uparrow) - F(I_0^{0^\circ}, H\uparrow)],$$
$$XMLD(S_2) = [F(I_0^{135^\circ}, H\uparrow) - F(I_0^{45^\circ}, H\uparrow)]. \quad (3)$$

The non-reciprocal character of these dichroisms implies that their sign should change whenever the direction of the magnetic field is inverted: this makes a fundamental difference with the time-reversal *even* X-ray magneto-optical linear dichroism first observed by Van der Laan *et al*. [18] in the soft X-ray range.

2.2. *Magnetochiral dichroism in eskolaite*

The generic example of ME solids is chromium sesquioxide (Cr_2O_3) also known in mineralogy as *eskolaite*. Below the Néel temperature ($T_N \approx 310$ K), the spin moments at the Cr sites order in either one of the two AFM domains shown in figure 2 and which

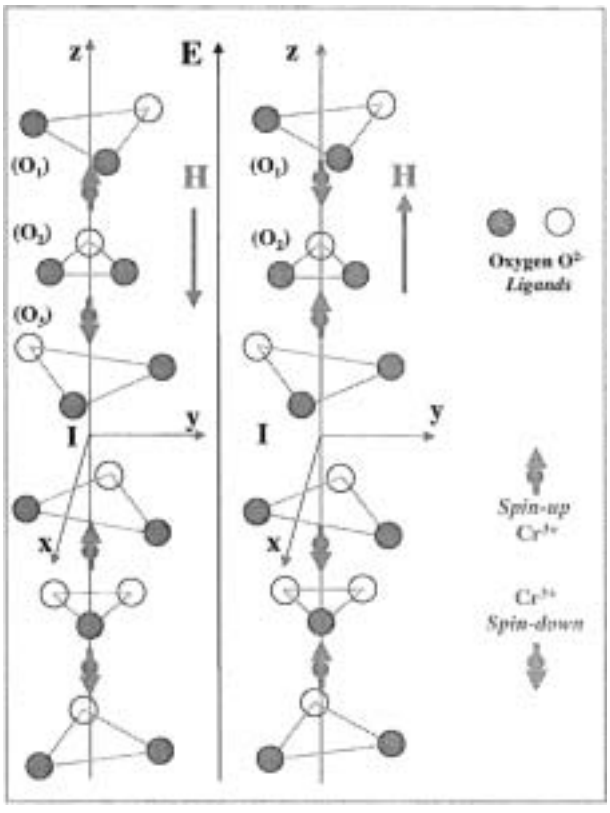

Fig. 2. Schematic representation of the two 180° antiferromagnetic domains of Cr_2O_3 grown by magnetoelectric annealing with antiparallel and parallel electric and magnetic fields.

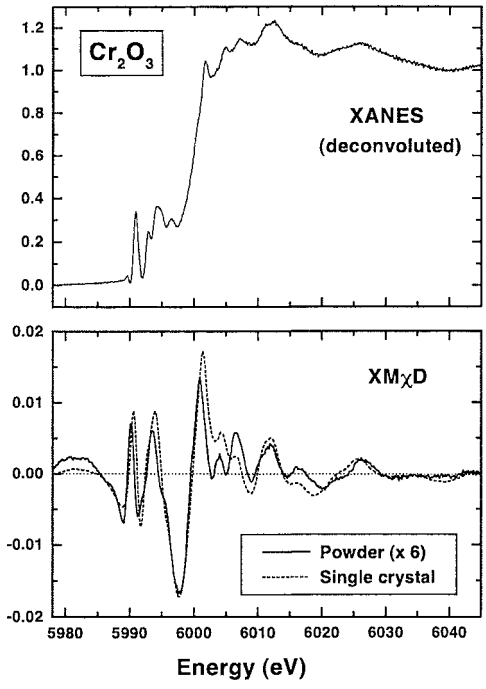

Fig. 3. Cr K-edge XMχD spectra of Cr_2O_3 recorded with either a single crystal ($\boldsymbol{c} \,||\, \boldsymbol{k}$) or with a powdered sample. The differential signal refers to the 180° domains of Fig. 2. The upper trace is the deconvoluted XANES spectrum.

transform into each other by time reversal symmetry. As far as one considers **only** the spin moments, the *space-time* group $\bar{3}'m'$ is well known to be ME [19] and one would easily check that, for each domain, the metal sites are left invariant in the product $P\Theta$ [14]. Recall, however, that no ME susceptibility nor any XMχD signal can be measured in equidomain states: ME *annealing* is required to create a remanent ME state with a net excess of one ME domain with respect to the other. This can be achieved by heating first the crystal in its paramagnetic state far above T_N: a modest electric field $\boldsymbol{E}$ (5 kV.cm^{-1}) plus a weak magnetic field $\boldsymbol{H}$ ($\pm$0.5 T) are then applied along the c axis before cooling the crystal slowly down below T_N [20]. Depending on whether $\boldsymbol{E}$ and $\boldsymbol{H}$ are parallel or antiparallel, the ME free energy is different and a single domain of well defined sign will grow [21].

The Cr K-edge XMχD spectra displayed in figure 3 were obtained by growing successively the two ME domains of figure 2 using either parallel or antiparallel $\boldsymbol{E}$, $\boldsymbol{H}$ fields in the annealing process. This first experiment [7] has been reproduced several times using different azimuthal orientations of the Cr_2O_3 (001) single crystal. We also proved that it was feasible to investigate with a focused beam the XMχD response to multiple domain inversions using only one single scan but our experimental configuration was not suitable to determine the size of the macroscopic ME domains. However, we perfectly succeeded in recording the magnetochiral dichroism using a powdered sample of chromium sesquioxide: as illustrated by figure 3, the XMχD spectra recorded with a single crystal or the powdered sample only differ by a 1 : 6 scaling factor.

2.3. *Non-reciprocal XMLD in* $(V_{1-x}Cr_x)_2O_3$

The magnetic structure of chromium doped vanadium sesquioxides $(V_{1-x}Cr_x)_2O_3$ in their low temperature antiferromagnetic *insulating* (AFI) phase is more controversial. The starting point of our work is a neutron diffraction study carried out on pure V_2O_3 (also known in mineralogy as the karelianite). Word *et al*. [22, 23]

confirmed the distorted, centrosymmetric $I2/a$ symmetry of the AFI phase and established that the vanadium atoms should carry a magnetic moment of *ca.* $1.2\,\mu_B$ tilted away from the trigonal **c** axis by 71° and perpendicular to the a axis. The observation of a forbidden reflection for $\ell = 6h + 3$ led them to conclude that the space-time group was not $2/m \otimes \Theta$ but rather a low symmetry group A2. They tentatively explained the symmetry reduction by a small magnetic contribution of the oxygen lattice. Interestingly, it was first considered by Moon, in an earlier paper [24], that *orbital moments* could result in a reduction of symmetry. Yethiraj [25] again admitted that a reduction of the magnetic symmetry could perfectly well be envisaged. The important point here is that the group A2 is inherently ME and should be compatible with the observation of non-reciprocal XMLD. A difficulty arises from the fact that the group A2 is not a subgroup of $2/m \otimes \Theta$ but Carra *et al.* [15] pointed out that the subgroup $2/m'$ would as well be compatible with the X-ray diffraction data: it can be shown that this group would have strictly the same generic ME tensor as the magnetic group A2 [5, 19].

The V K-edge non-reciprocal XMLD spectra [8] reproduced in figure 4 seem to support nicely the interpretation first proposed by Word *et al.* [22, 23]. For our experiments, we used a chromium doped crystal ($x = 0.028$) which is not prone to self-destruction at the phase transition ($T_N = 181$ K). It was realized recently that our crystal was miscut so that the c axis was tilted away from $\boldsymbol{k}$ by *ca.* 10°. Unfortunately, the orientations of the crystallographic axes **a** and **b** were unspecified in this first experiment so that we ignore whether we measured XMLD (S_1) or XMLD (S_2). Anyhow, let us note that the non-reciprocal XMLD signal measured in $(V_{1-x}Cr_x)_2O_3$ and the non-reciprocal XMχD signal in Cr_2O_3 are nearly of the same order of magnitude. One should not confuse the *non-reciprocal* dichroisms of figure 4 with a *reciprocal* XMLD signal of the van der Laan type. Recall that the reciprocal XMLD is expected to be very small at a K-edge: recently we have shown that, in the case of a ferrimagnetic YIG single crystal, it was only of the order of $2.5 \cdot 10^{-4}$ at the iron K-edge.

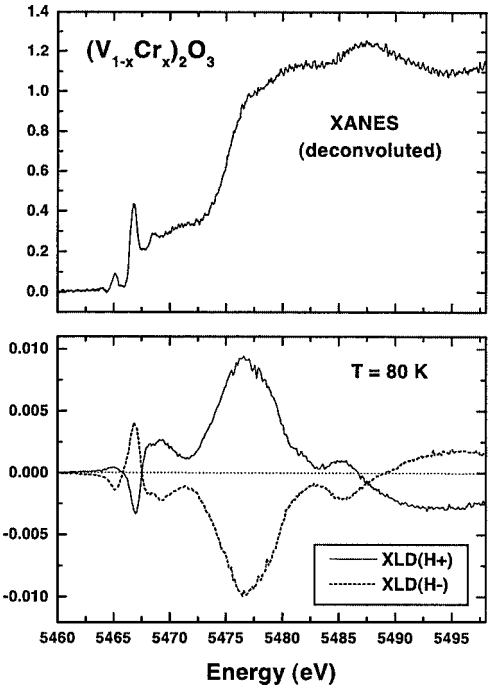

Fig. 4. V K-edge non-reciprocal XMLD spectra recorded with a single crystal of $(V_{1-x}Cr_x)_2O_3$ in the low temperature, antiferromagnetic, insulating phase. The differential signal refers to domains grown under the conditions of time-reversality. The upper trace is again the deconvoluted XANES spectrum.

Recently, Di Matteo and Jansen [26] reported that they failed to measure any ME susceptibility with the same crystal. We already argued elsewhere [5] that the use of a *static* field method was highly questionable to measure a ME susceptibility in a crystal exhibiting high conductivity losses: this might well explain the reported negative result. In contrast, apart from the ME annealing that can be achieved in several ways, XOA measurements are intrinsically insensitive to conductivity losses. Furthermore, it should be emphasized that ME susceptibility measurements and XOA do not probe the same properties of matter: non-reciprocal XOA probes only the *orbital* contribution to the total ME tensor, whereas all ME susceptibility measurements reported so far refer to *only* the spin part of the ME tensor. In the case of Cr_2O_3, our XMχD spectra tend precisely to show that the orbital contribution is much too small to be detected by macroscopic ME susceptibility measurements [5].

3. XOA Sum-Rules: first application

3.1. *Effective operators of XOA*

In 1992, Thole *et al.* [27] established a useful sum rule for X-ray magnetic circular dichroism (XMCD): it states that the integrated dichroic signal should be proportional to $\langle L_z \rangle$, *i.e.* to the ground state expectation value of the projection along the quantification axis of the angular momentum operator acting on the electronic shell accepting the excited photoelectron. In 1998, Natoli *et al.* [13] established a similar sum rule for XNCD:

$$\Sigma_{E1E2} = \int_{\Delta E} \frac{\sigma_{E1E2}(E)}{E^2}\,\mathrm{d}E \propto \langle \psi_g | \mathbf{N}^{(2)}(\ell, \ell') | \psi_g \rangle \tag{4}$$

where σ_{E1E2} denotes the X-ray absorption cross section due to the $E1E2$ interference terms in a finite energy range ΔE which should include, whenever this is relevant, the two partners (j_+, j_-) of a spin-orbit split edge. On the right handside, ℓ still refers to the final angular momentum of the electric dipole ($E1$) transition whereas ℓ' refers to the electric quadrupole transition ($E2$) and should satisfy the selection rule: $\ell' = \ell_c \pm 0, 2$, excluding $\ell' = \ell_c = 0$. Obviously, ℓ and ℓ' have opposite parity and the operator $\mathbf{N}^{(2)}(\ell, \ell')$ probes the mixing of atomic orbitals of the corresponding parity. The problem with eqn. (4) was that no clear physical meaning was given to the rank-2, spherical tensor $\mathbf{N}^{(2)}$.

Regarding eqn. (4), there is a serious limitation underlined by Di Matteo and Natoli [28]. Due to the core hole perturbation, $|\psi_g\rangle$ is merely a *pseudo* ground state. If we expand $|\psi_g\rangle$ in terms of *stationary* states $|\Psi_n\rangle$, the quantity which is obtained is actually:

$$\langle \psi_g | \mathbf{O}^{(q)} | \psi_g \rangle = \sum_{n,n'} \alpha_n^* \alpha_{n'} \langle \Psi_n | \mathbf{O}^{(b)} | \Psi_{n'} \rangle \tag{5}$$

where $\mathbf{O}^{(b)}$ is the pertinent parity mixing effective operator. As yet, there is no proof that the sum over all configurations will cancel the effects of the core hole and restore the property of a *true* ground state. Note that cross terms ($n \neq n'$) could contribute as well: typically, in the case of *XMCD* where $\mathbf{O}^{(1)} = L_z$, the matrix elements on the right handside of eqn. (5) are those of the Van Vleck paramagnetism.

In order to extend eq. (4) to all $E1E2$ dichroisms, it is most convenient to rewrite Σ_{E1E2} as:

$$\Sigma_{E1E2} = \sum_{b=1}^{3} \sum_{\beta=-b}^{b} \sum_{\theta=\pm 1} (-1)^{\beta} \mathbf{T}_{\beta}^{(b,\theta)} \boldsymbol{\Sigma}_{-\beta}^{(b,\theta)} \tag{6}$$

where $\boldsymbol{\Sigma}^{(b,\theta)}_{-\beta}$ are rank-b spherical tensors which characterize parity non conserving systems, whereas the spherical tensors $\mathbf{T}^{(b,\theta)}_{\beta} = [\hat{\epsilon}^*, [\hat{\epsilon}, \hat{k}]^{(2)}]^{(b)}_{\beta}$ characterize the polarization states of the X-ray photons and are split into their time-reversal even ($\theta = 1$) or time-reversal odd ($\theta = -1$) parts.

Carra *et al*. [15] established that all operators $\boldsymbol{\Sigma}^{(b,\theta)}$ can be built from the triad of mutually orthogonal vector operators:

1. $\boldsymbol{n} = \boldsymbol{r}/r$ which is a time-reversal *even*, polar vector typically associated with the electric dipole moment.
2. $\boldsymbol{L}$ which is the time-reversal *odd*, axial vector of the orbital angular momentum.
3. $\boldsymbol{\Omega} = [(\boldsymbol{n} \times \boldsymbol{L}) - (\boldsymbol{L} \times \boldsymbol{n})]/2$ which is a *toroidal* vector that is odd with respect to both P and Θ.

Clearly $\boldsymbol{\Omega}$ is to be identified with the *orbital anapole* moment as defined in textbooks [29]. Up to four spherical operators are required for a full description of XOA:

- The projection of the *orbital anapole* moment $\boldsymbol{\Omega}^{(1,-1)}_0$ along the direction of the wavevector $\boldsymbol{k}$ appears in the XMχD sum rule.
- The Θ-odd *pseudodeviator* $\boldsymbol{W}^{(2,-1)} = [\boldsymbol{L}, \boldsymbol{n}]^{(2,-1)}$ appears in the non-reciprocal XMLD sum-rules.
- The Θ-even *pseudodeviator* $\mathbf{N}^{(2,+1)} = [\boldsymbol{L}, \boldsymbol{\Omega}]^{(2,+1)}$ appears in the XNCD sum rule.
- The Θ-odd *septor* $\boldsymbol{\Gamma}^{(3,-1)} = [[\boldsymbol{L}, \boldsymbol{L}]^{(2)}, \boldsymbol{\Omega}^{(1)}]^{(3,-1)}$ will contribute as higher order terms to all non-reciprocal XOA sum rules.

3.2. *Orbital Anapole moment in eskolaite*

In the simplest case of magnetochiral dichroism XMχD (S_0), the sum rule reads:

$$\Sigma_{E1E2} = \frac{-2\pi^2\alpha}{\hbar c}(2\ell_c + 1)\sum_{\ell,\ell'} R^{(1)}_{\ell} R^{(2)}_{\ell'} \times \{\tfrac{2}{5} a^{(1,-1)}(\ell_c, \ell, \ell')\langle \Omega^{(1,-1)}_0(\ell, \ell')\rangle - \tfrac{16}{\sqrt{10}} b^{(3,-1)}(\ell_c, \ell, \ell')\langle \boldsymbol{\Gamma}^{(3,-1)}_0(\ell, \ell')\rangle\} \quad (7)$$

where $a^{(1,-1)}$ and $b^{(3,-1)}$ are basically numerical factors that are tabulated elsewhere [5, 15]. In eqn. (7), $R^{(1)}_{\ell}$ and $R^{(2)}_{\ell'}$ are the radial dipole and quadrupole integrals which need to be calculated numerically: this was done in the case of Cr_2O_3 using the FDMNES code (MSW option) of Y. Joly [30].

Recently, Di Matteo and Natoli [31] claimed that the largest contribution should come from the (octupolar) septor term $\boldsymbol{\Gamma}^{(3,-1)}_0$. This is however contradicted by our experiment carried on the powdered sample and illustrated with figure 3. Recall that the nucleation of ME domains of opposite timereversality in a powder depends critically on the orientation of each cristallite: one may use precisely this angular dependence in order to check whether the relevant spherical operator $\mathbf{O}^{(b)}$ will average out as a vector or as a higher order septor [5]. Typically, in a powder: $\langle \mathbf{O}^{(b)}_{\beta}\rangle_{powder} = \delta_{\beta,0}\langle \mathbf{O}^{(b)}_0\rangle_{crystal} I_{(b)}$ where $I_{(b)}$ is an integral taken over all orientations of a cristallite. This integral has already been calculated analytically by O'Dell [32] for a rank-2 tensor ($b = 2$): we simply extended the same calculation for $b = 1, 3$. This led us to predict that the XMχD signal in the powdered sample should be reduced by the factor $I_{(1)} \approx 0.18$ if the effective operator is $\boldsymbol{\Omega}^{(1,-1)}_0$, whereas it should become hardly measurable if the effective operator was $\boldsymbol{\Gamma}^{(3,-1)}_0$ since $I_{(3)} \leq 0.05$. This is nicely supporting our interpretation that the XMχD sum rule may give us – at least – a raw estimation of the expectation value of the orbital anapole moment in Cr_2O_3 : $\langle \boldsymbol{\Omega}^{(1,-1)}_0\rangle \approx 0.03$ a.u. This is a rather small value compared to known spin anapoles [5].

4. Discussion

It is a prerequisite to detect XOA that at least one of the four spherical effective operators discussed in the previous section should be an irreducible representation of the space-time group of the crystal. We have indicated elsewhere which dichroic effect could be measured for every ME group [5]. A problem arises precisely in the case of Cr_2O_3 since the universally cited magnetic group compatible with neutron diffraction, *i.e*. $\bar{3}'m'$, does not admit $\boldsymbol{\Omega}^{(1,-1)}_0$ nor $\boldsymbol{\Gamma}^{(3,-1)}_0$ as irreducible representations. The detection of a XMχD signal thus implies that the magnetic symmetry should be lower than in figure 2.

Di Matteo and Natoli [31] suggested that the presence of a weak magnetic field ($\boldsymbol{H} = \pm 0.5\,\mathrm{T}$) during the experiment could have induced some metamagnetic transition. This seems unlikely since recent experiments have confirmed the absence of any detectable spin-flop domain below the critical field of 5.8 T. On the other hand the ferromagnetic group $3m'$ resulting from a metamagnetic transition would still be incompatible with the detection of a magnetochiral dichroism [5].

It is our view that two alternative interpretations deserve attention:

- The reduction of symmetry could be due to some partially unquenched angular momentum that had a different quantization axis from the spins [33].
- The deep core hole could induce some mixing of the true ground state with low-lying excited states, as in the Van Vleck paramagnetism.

Let us stress that the two ME domains illustrated by figure 2 take only into consideration the spin configuration: the magnetic group $\bar{3}'m'$ implicitly assumes that there is no orbital magnetism. Recall that Shirane *et al*. [34] admitted that neutron diffraction data could not disprove models with canting angles less than 3 degrees: this implies that orbital moments as large as 0.13 μ_B may not be seen. The existence of orbital magnetism in Cr_2O_3 has however been suspected since it was reported by Foner [35] that the parallel magnetic susceptibility of Cr_2O_3 did not drop to zero below 4 K: this was interpreted by Siverstein and Jacob [36] as resulting from a large (orbital) Van Vleck Paramagnetism.

Unrestricted Hartree-Fock calculations reported recently by Dovesi *et al*. [37] revealed that covalency effects were particularly important in eskolaite. These calculations also produced clear evidence of a local spin polarization of the oxygens around the chromium sites. Given that spin-orbit coupling should lower the ligand field symmetry, it seems pertectly realistic to expect a component of an orbital magnetic moment perpendicular to the **c** axis thus inducing a small canting of the total magnetic moments. Dovesi *et al*. explicitly noted that the magnetic symmetry should be reduced below the Néel temperature: interestingly, the group $3m$ which they proposed admits the anapole as irreducible representation. Unfortunately, the ME tensor of this group would have no diagonal elements: this is in contradiction with the known ME (spin) properties of Cr_2O_3. This led us to suggest that the only magnetic group that would reconcile our XMχD spectra with the ME (spin) properties of Cr_2O_3 is $\bar{3}'$: it would combine the off-diagonal elements of the ME tensor of the group $3m$ with the diagonal elements of the ME tensor of the group $\bar{3}'m'$ [5].

Similar considerations could be transposed to the case of V_2O_3 which also exhibits a strong Van Vleck paramagnetism [38]. Particularly relevant is a model proposed by Tanaka [39] according to which each V atom has an *orbital* magnetic moment of $\approx 0.7\,\mu_B$ slightly tilted away from the antiferromagnetic spin lattice, with the practical consequences that the $2/m \otimes \Theta$ symmetry should be broken and that the low temperature phase should become *orbitally* Magneto-Electric [15].

Acknowledgments

Stimulating discussions with E. Katz are gratefully acknowledged. This work was supported by the INTAS grant 01-822. This is also IPGP contribution number 1921#.

References

1. Goulon, J., *et al*., Eur. Phys. J. B **12**, 373 (1999).
2. Buckingham, A. D., Adv. Chem. Phys. **12**, 107 (1968).
3. Barron, L. D., "Molecular Light Scattering and Optical Activity," (Cambridge University Press, 1982).
4. Cooper, J. W., Phys. Rev. A **47**, 1841 (1993).
5. Goulon, J., *et al*., J. Exp. Theor. Phys. **97**, 1 (2003).
6. Goulon, J., *et al*., J. Phys.: Condens. Matter **15**, S633 (2003).
7. Goulon, J., *et al*., Phys. Rev. Lett. **88**, 237401-1 (2002).
8. Goulon, J., *et al*., Phys. Rev. Lett. **85**, 4385 (2000).
9. Goulon, J., *et al*., J. Chem. Phys. **108**, 6394 (1998).
10. Alagna, L., *et al*., Phys. Rev. Lett. **80**, 4799 (1998).
11. Stewart, B., *et al*., J. Am. Chem. Soc. **121**, 10233 (1999).
12. Goulon, J., *et al*., J. Synchrotron Rad. **7**, 182 (2000).
13. Natoli, C. R., *et al*., Eur. Phys. J. B **4**, 1 (1998).
14. Dzyaloshinskii, I. E., Soviet Phys. JETP **10**, 628 (1960).
15. Carra, P., Jerez, A. and Marri, I., Phys. Rev. B **67**, 045111 (2003).
16. Goulon, J., *et al*., J. Synchrotron Radiat. **5**, 232 (1998).
17. Rogalev, A., Goulon, J., Goulon Ginet, C. and Malgrange, C., Magnetism and Synchrotron Radiation, Lecture Notes in Physics, **Vol. 565**, (Beaurepaire, E. *et al.* editors), 60 (2001).
18. Van der Laan, G., *et al*., Phys. Rev. B **34**, 6529 (1986).
19. Rivera, J. P., Ferroelectrics **161**, 165 (1994).
20. Astrov, D. N., Sov. Phys. JETP **13**, 729 (1961).
21. Brown, P. J., Forsyth, J. B. and Tasset, F., J. Phys.: Condens. Matter **10**, 663 (1998).
22. Yelon, W. B., Werner, S. A. and Word, R. E., J. Appl. Phys. **52**, 2237 (1980).
23. Word, R. E., Werner, S. A., Yelon, W. B., Honig, J. M. and Shivashankar, S., Phys. Rev. B **23**, 3533 (1981).
24. Moon, R. M., Phys. Rev. Lett. **25**, 527 (1970).
25. Yethiraj, M., J. Sol. St. Chem. **8**, 53 (1990).
26. Di Matteo, S. and Jansen, A. G. M., Phys. Rev. B **66**, 100402R (2002).
27. Thole, B. T., Carra, P., Sette, F. and Van der Laan, G., Phys. Rev. Lett. **68**, 1943 (1992).
28. Di Matteo, S. and Natoli, C. R., J. Synchrotron Rad. **9**, 9 (2002).
29. Khriplovich, I. B., "Parity Non-conservation in Atomic Phenomena," (Gordon and Breach Science Publ., New York, 1991).
30. Joly, Y., Phys. Rev. B **63**, 125120 (2001).
31. Di Matteo, S. and Natoli, C. R., Phys. Rev. B **66**, 212413 (2002).
32. O'Dell, T. H., Phil. Mag. **13**, 921 (1966).
33. Platkhy, V. P., Solid State Commun. **79**, 313 (1991).
34. Corliss, L. M., Hastings, J. M., Nathans, R. and Shirane, G., J. Appl. Phys. **36**, 1099 (1965).
35. Foner, S., Phys. Rev. **130**, 183 (1963).
36. Silverstein, S. D. and Jacob, I. S., Phys. Rev. Lett. **12**, 670 (1964).
37. Catti, M., Sandrone, G., Valerio, G. and Dovesi, R., J. Phys. Chem. Solids **57**, 1735 (1996).
38. Greenwood, M., Mires, R. W. and Smith, A. R., J. Chem. Phys. Lett. **54**, 1417 (1971).
39. Tanaka, A., J. Phys. Soc. Jpn **71**, 1091 (2002).

Physica Scripta. Vol. T115, 59–65, 2005

Time-Resolved Energy-Dispersive XAFS for *In-situ* Characterization of Nano-Structures and Catalysts

Yasuhiro Iwasawa[1*], Akane Suzuki[1] and Masaharu Nomura[2]

[1]Department of Chemistry, Graduate School of Science, The University of Tokyo, Hongo, Bunkyo-ku, Tokyo, 113-0033, Japan
[2]Photon Factory, Institute of Materials Structure Science, KEK, Ibaraki 305-0801, Japan

Received June 26, 2003; accepted November 14, 2003

PACS numbers: 61.10 Ht, 68.36.−p, 68.35. Fx, 68.43. Hn, 82.33 Hk

Abstract

This paper reviews our recent study on the improvement of time-resolved energy-dispersive X-ray absorption fine structure (DXAFS) and its application to *in situ* dynamic characterization for structural changes in nano-structures and catalysts, also presenting new data. The issue addressed in this paper is relevant to deeper understanding of catalytic intermediate structures, elementary steps, and reaction mechanisms.

1. Introduction

Molecular-level to nano-scale chemical design of active structures on robust oxide surfaces and crystalline porous supports with the aid of *in-situ* analysis by modern physical techniques as well as chemistry of definite precursors is crucial to create new nano-structures and efficient catalysts [1–4]. It may also be prerequisite for fulfillment of the precise design to understand the dynamic change of active structures *in situ* during preparation and reaction processes of nano-structures and catalytic materials.

Local structures of non-crystalline dispersed metal species have been extensively studied by X-ray Absorption Fine Structure (XAFS) because it does not require long range order of the metal species [1, 5–9]. Perhaps the most important attribute for XAFS to be applied to characterization of supported catalysts is *in situ* investigation of the working catalyst because X-rays are not interfered by the reaction gases present in the catalytic systems. However, it takes about ten to several ten minutes to measure an Extended X-ray Absorption Fine Structure (EXAFS) spectrum for dispersed metal species by conventional XAFS technique. So the conventional technique cannot monitor time-dependent structures during dynamic chemical processes.

Recently time-resolved energy-dispersive XAFS (DXAFS) has been much improved and applied to studies on dynamic structural changes of metal sites during chemical processes and catalytic reactions [10–31]. The aim of this paper is to find the time scale and sequence of bond rearrangements in supported nano-structures and catalysts, such as bond formation-breaking and bond elongation-shortening, which may be relevant to the mechanism, efficiency, and stability for the catalysis, by time-resolved energy-dispersive XAFS (DXAFS). Two examples $[Ru_6C]/MgO$ (time resolution of 1 s) and $[Rh]_x/Al_2O_3$ (time resolution of 100 ms) are discussed.

2. Experimental

DXAFS is a technique to measure a whole range of X-ray absorption spectra using a bent crystal and a position sensitive detector (1024 ch. photodiode arrays) as shown in Fig. 1. While it is necessary in conventional XAFS technique to mechanically rotate a monochromator to monochromatize white X-rays stemming from a synchrotron storage ring (Fig. 1(a)), there is no mechanical motion for monochromatizing X-rays in the DXAFS technique as shown in Fig. 1(b) and (c). When a sample is placed at the focusing point, the sample can absorb X-rays of the whole energy range simultaneously, so EXAFS spectra for dispersed nano-structures and catalysts can be measured in a time period shorter than 1 s. By using the DXAFS technique (Bragg case) the structural changes in the temperature programmed reduction of Cu/ZSM-5 and the temperature programmed decarbonylation of $Mo(CO)_6/YZ$ by DXAFS have been analyzed [21–24, 31].

DXAFS measurements were carried out on BL-9C at KEK-PF with a Si(311) polychromator [24]. DXAFS setups using three-point bent and four-point bent Si crystals are shown in Fig. 1(b) and (c). The source-to-crystal distance, the crystal-to-focus distance, the radius of curvature of the Si crystal, and the Bragg angle at the center of the crystal are 30 m, 0.385 nm, 4.5 m and 9.9 degrees, respectively for the three-point bending system, and 30 m, 0.35 m, 2.1 m and 9.4 degrees, respectively for the four-point bending system. The two systems were used for $[Ru_6C]/MgO$ and $[Rh]_x/Al_2O_3$, respectively. At first the three-point bent crystal system was also applied to the $[Rh]_x/Al_2O_3$ catalyst, but the DXAFS quality was not good enough for analysis. Therefore a four-point supporting crystal bender was recently developed for a Si(311) bent-crystal polychromator (Bragg-type) to achieve elliptical optics for focusing the incident X-rays at the sample. The energy calibration at each sensing element of the PDA was performed by comparison with an XAFS spectrum of a Ru foil or Rh foil recorded using a Si(311) channel-cut monochromator. The quality of the DXAFS data in the Bragg case was high enough in the analysis though there may be asymmetric reflectivity at the Ru and Rh K-edges [32]. The *in-situ* DXAFS cell was made of stainless steel and had two slit windows with capton films to measure the incident and transmitted X-rays.

EXAFS data were analyzed by the UWXAFS package [33]. After background subtraction using AUTOBK [34], k^3-weighted EXAFS functions were Fourier transformed into *R*-space and fitted in *R*-space. Backscattering amplitudes and phase shifts were calculated by the FEFF8.0 code [35]. The energy resolution of spectrometers (5 eV for Ru and 4 eV for Rh) was taken into account to calculate the parameters by using the EXCHANGE flag of an input file in the FEFF8.0 code. To analyze DXAFS data, Debye-Waller factors calculated from conventional EXAFS data measured at several temperatures were used.

*Corresponding author: E-mail: iwasawa@chem.s.u-tokyo.ac.jp

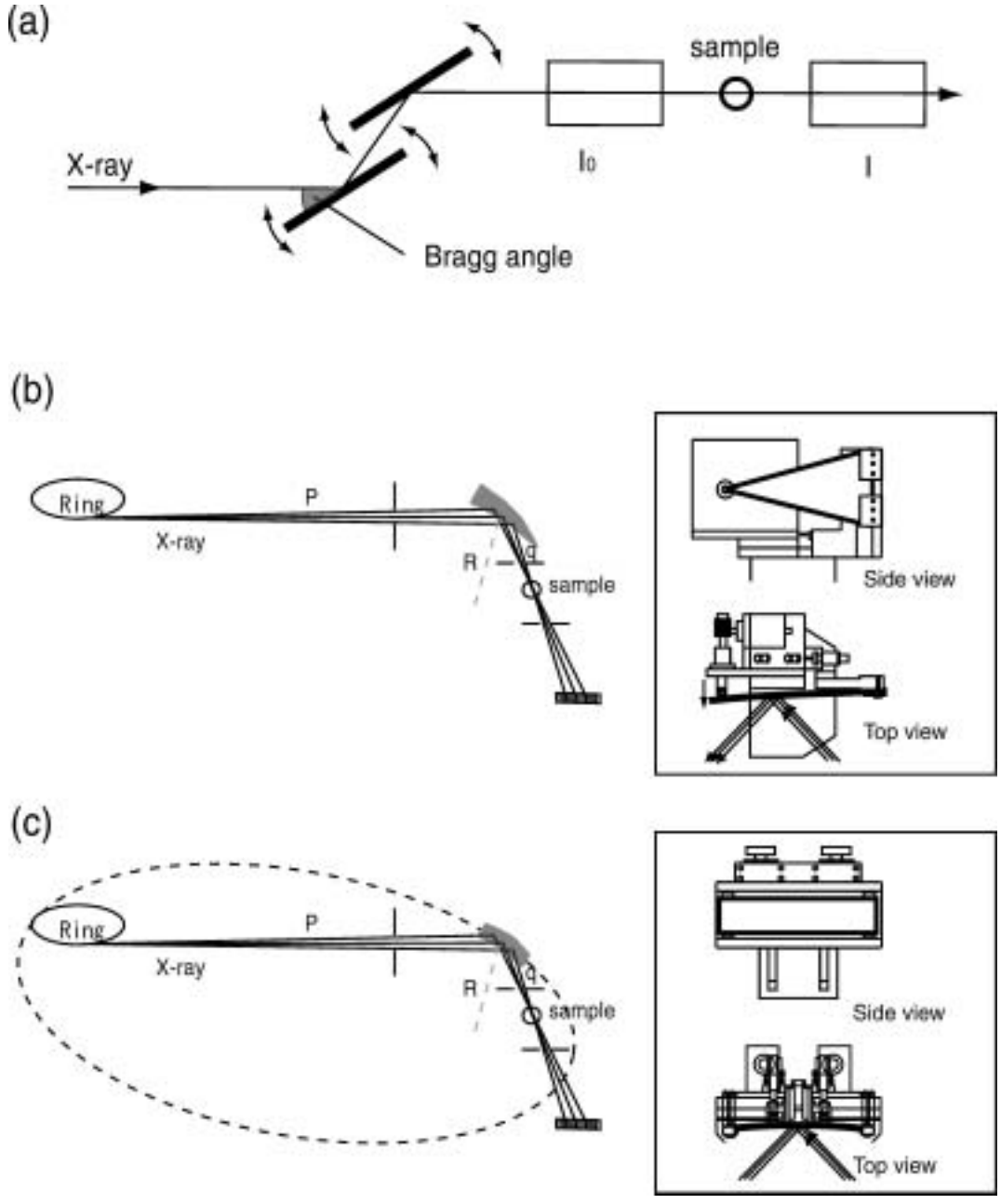

Fig. 1. The set-up of a conventional XAFS(a) and energy-dispersive XAFS (DXAFS) (b: three-point bent crystal; c: four-point bent crystal).

3. Results and Discussion

3.1. *Structural kinetics of [Ru_6C]/MgO*

We reported the specific catalysis of [Ru_6C] clusters on MgO for CO conversion to oxygenated compounds such as methanol, dimethyl ether and formaldehyde as main products [36, 37]. This is in contrast to the catalysis of supported Ru particles, which produce methane as the main product under identical reaction conditions. We also observed a structural change of the cluster framework; namely when the [Ru_6C]/MgO species with Ru-Ru bond at 0.265 nm was exposed to CO/H_2 reaction gas at 523 K, the cluster framework expanded to the framework with the Ru-Ru bond at 0.271 nm, adsorbing 11 CO molecules per cluster. At low CO pressure carbonylated [$Ru_6C(CO)_{11}$]/MgO was transformed back to the original shrunk [Ru_6C] framework, desorbing CO, under which reaction conditions the reaction rate for the oxygenate synthesis was much lower than that on the expanded framework. The information on how and when the cluster structure changes upon CO adsorption/desorption will provide knowledge and understanding, at the molecular-level detail, of the origin of key factors and structural dynamics for catalysis. The following is the first study on the kinetics of reversible structural change in cluster framework at surfaces [31].

[Ru_6C]/MgO catalyst was prepared by supporting [$Ru_6C(CO)_{16}Me]^-$ cluster on MgO, followed by evacuation at 623 K as shown in Fig. 2 [36, 37]. The Ru loading was 4.0 wt%. Figure 3 shows a series of DXAFS oscillations (a) and associated Fourier transformed functions (b) at the Ru K-edge during the carbonylation of [Ru_6C]/MgO under CO/H_2 at 523 K. Each spectrum was measured with a time-resolution of 1 s. The structural parameters, coordination numbers (*CN*s) and bond distances (*Rs*), determined by curve-fitting in R space were plotted against the CO/H_2 exposure time at 423, 473, and 523 K in Fig. 4. The *CN*s of Ru-C-(O) and Ru-(C)-O for the carbonyl ligands were set to be the same value in the curve fitting analysis. The detailed analysis will be described in a separate paper [31, 38].

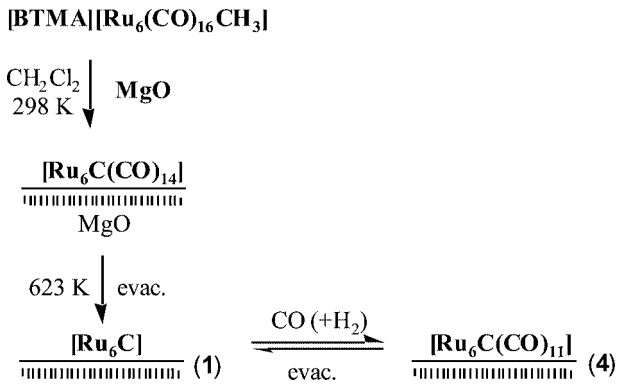

Fig. 2. Preparation steps for the $[Ru_6C]$/MgO catalyst and the reversible transformations between $[Ru_6C]$ (**1**) and $[Ru_6C(CO)_{11}]$ (**2**) on MgO.

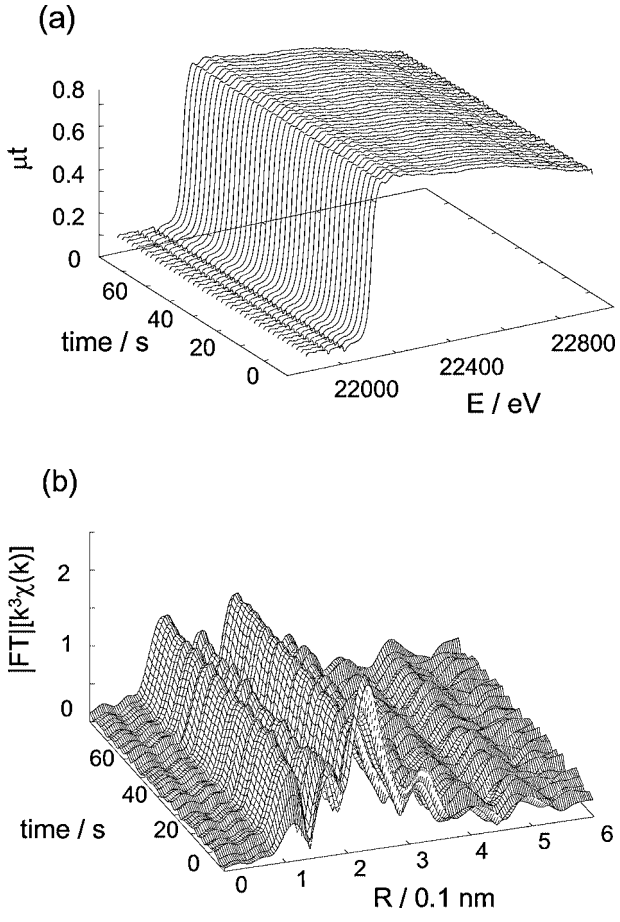

Fig. 3. (a) A series of DXAFS oscillations at Ru K-edge and (b) a series of their associated Fourier transformed functions during the carbonylation of $[Ru_6C]$/MgO under CO/H_2 at 523 K.

CN of Ru-CO increased from 0 to 0.7 for the first 2.1 s at 423 K, where *R* of Ru-Ru changed little. *CN* of Ru-CO increased to about half of the value at saturation after 4.2 s, but *R* of Ru-Ru did hardly change. After 4.2 s *R* rapidly increased to 0.269 nm and the bond expansion was completed in 10.4 s at 423 K. The rates of the carbonylation and the bond expansion were promoted by an increase in temperature. There was break at 4.2 s in the slope of the increase in *CN*, followed by a gentle slope over 35 s. It is obvious that the increase in *R* has a time lag from the CO adsorption. Both CN and R values increased further over 30 s. Thus it is reasonable that we postulate the existence of two intermediate structures $[Ru_6C(CO)_6]$ with Ru-Ru

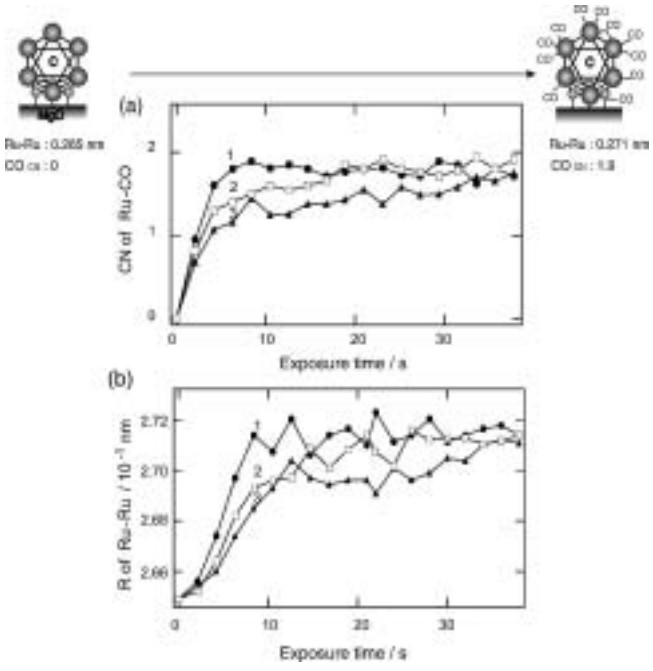

Fig. 4. The coordination numbers (*CN*s) of Ru-CO (a) and the bond distances (Rs) of Ru-Ru (b) as a function of the CO-exposure time in the carbonylation processes at 423 K (filled triangle), 473 K (open square), 523 K (filled circle).

distances of 0.265 nm and 0.269 nm during the CO adsorption on $[Ru_6C]$/MgO [31, 38]. The number of carbonyls per cluster was also estimated by CO adsorption experiments and FTIR spectra [38]. In the first step, six CO molecules adsorb on a $[Ru_6C]$ cluster and in the second step, following the CO adsorption, the cluster framework expands from 0.265 to 0.269 nm. After the formation of the second intermediate $[Ru_6C(CO)_6]$ with a Ru-Ru distance of 0.269 nm, CO molecules further adsorb on the cluster, and eventually the final cluster structure $[Ru_6C(CO)_{11}]$ with 11 CO ligands and Ru-Ru of 0.271 nm is formed. The rates of the structural transformations increased by increasing temperature, indicating thermally activated processes, by which the activation energies were calculated.

Figure 5 shows a series of DXAFS oscillations (a) and associated Fourier transformed functions (b) at the Ru K-edge during the decarbonylation of the carbonylated $[Ru_6C(CO)_{11}]$/MgO under vacuum at 573 K. Each spectrum was measured with a time-resolution of 2 s. The structural parameters determined by curve-fitting in *R* space were plotted against the evacuation time at 623 K and 573 K in Fig. 6. The error bars for *R* for Ru-Ru and *CN* for Ru-CO were ± 0.001 nm and ± 0.2–0.3, respectively. The decarbonylation process was slower than the carbonylation process. At 573 K, *R* changed slightly from 0.271 to 0.269 nm in 4 min, while *CN* of Ru-CO decreased to about half of the original value. *R* remained constant during 13 min, whereas *CN* decreased to zero after 11 min. After the complete CO desorption *R* of Ru-Ru decreased from 0.269 nm to 0.265 nm at 16 min. The stepwise feature of the decarbonylation was also observed at 623 K in Fig. 6. It is reasonable to postulate the existence of two intermediate structures $[Ru_6C(CO)_6]$ and $[Ru_6C]$ with Ru-Ru of 0.269 nm during the CO desorption from $[Ru_6C(CO)_{11}]$/MgO [31, 38]. The number of carbonyls per cluster in the slow decarbonylation process was confirmed by FTIR [38]. Consequently, in the first step the $[Ru_6C(CO)_{11}]$ cluster is partially decarbonylated and simultaneously the framework slightly shrinks. In the second step the CO completely desorbs, whereas the Ru-Ru bond length does

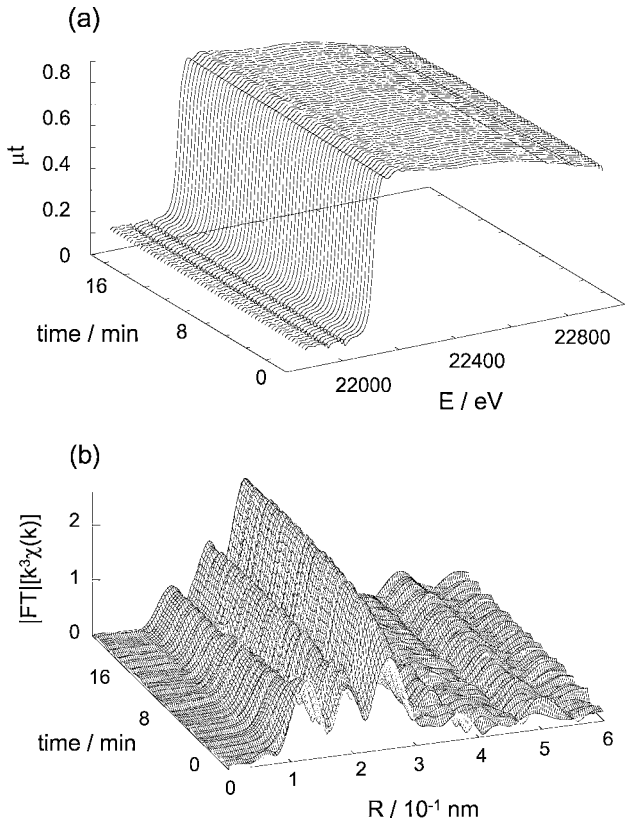

Fig. 5. (a) A series of DXAFS oscillations at Ru K-edge and (b) a series of their associated Fourier transformed functions during the decarbonylation of $[Ru_6C(CO)_{11}]$/MgO under vacuum at 573 K.

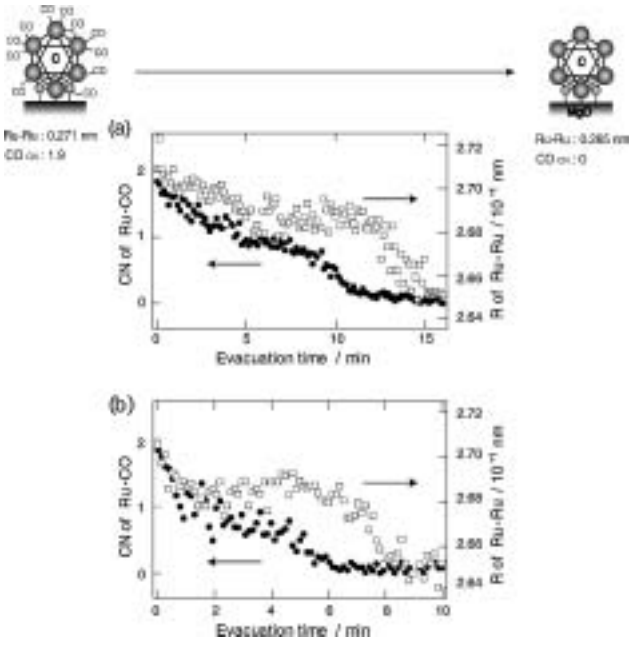

Fig. 6. The coordination numbers (CNs) of Ru-CO (filled circle) and the bond distances (Rs) of Ru-Ru (open square) during the decarbonylation processes at 573 K (a) and 623 K (b).

not change. After completion of the CO desorption, the cluster framework shrinks from 0.269 to 0.265 nm.

The structural changes in the carbonylation and decarbonylation processes are illustrated in Fig. 7, where the energy profile involving the activation energies for each step are also shown. The activation energy for the step from $[Ru_6C]$ (**1**)

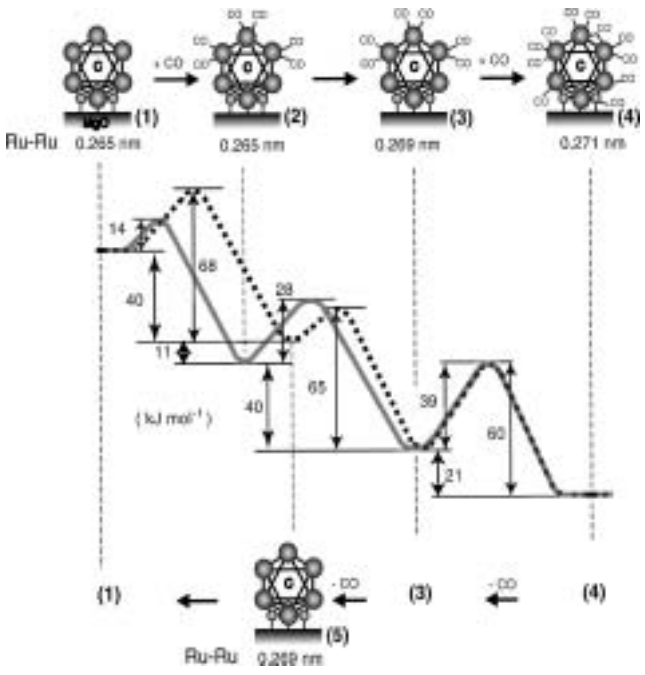

Fig. 7. The structural changes in the carbonylation and decarbonylation processes and the energy profile for the structural changes involving the activation energies.

(Ru-Ru : 0.265 nm) to $[Ru_6C(CO)_6]$ (**2**) (0.265 nm) was determined to be 14 kJ mol^{-1} by using the rates of the increase in *CN* of Ru-CO, while the activation energy for the step from $[Ru_6C(CO)_6]$ (**2**) (0.265 nm) to $[Ru_6C(CO)_6]$ (**3**) (0.269 nm) was determined to be 28 kJ mol^{-1} by using the rates of the increase in *R* of the Ru-Ru bond. The activation energy for the step from $[Ru_6C(CO)_6]$ (**3**) (0.269 nm) to $[Ru_6C(CO)_{11}]$ (**4**) (0.271 nm) was obtained by using the rates of the increases in *CN* and the *R*, independently. The values determined from *CN* and *R* were 41 and 38 kJ mol^{-1}, respectively, which agreed well with each other. The activation energies for the decarbonylation processes were also determined by the DXAFS analysis. The activation energy for the step from $[Ru_6C(CO)_{11}]$ (**4**) (0.271 nm) to $[Ru_6C(CO)_6]$ (**3**) (0.269 nm) was determined to be 59 and 62 kJ mol^{-1} from the rates of the decreases in *CN* of Ru-CO and *R* of Ru-Ru bond, respectively. The values agree with each other, indicating the validity of the values. The activation energy for the step from $[Ru_6C(CO)_6]$ (**3**) (0.269 nm) to $[Ru_6C]$ (**5**) (0.269 nm) was determined to be 65 kJ mol^{-1} from *CN*. The activation energy for the step from $[Ru_6C]$ (**5**) (0.269 nm) to $[Ru_6C]$ (**1**) (0.265 nm) was determined to be 68 kJ mol^{-1} from *R*. This sort of information on the kinetics of structural change in the cluster framework at the surface as the catalytically active site was obtained by the time-resolved DXAFS technique for the first time, which may open a new area of kinetics of active structures at catalyst surfaces [31, 38].

3.2. *Structural kinetics of* $[Rh]_x/Al_2O_3$

We have succeeded in observing the CO-induced disintegration process of Rh clusters on Al_2O_3 surface by DXAFS every 100 ms. The details of the time-resolved DXAFS study will be reported in a separate paper [39], but the results are summarized here. Previous static studies on a similar surface phenomena have been performed by IR [40–42], XAFS [43, 44], and STM [44, 45], which revealed the structural modification of highly dispersed Rh nanoparticles/Al_2O_3 catalysts leading to the formation of isolated $Rh(CO)_2$ species by CO adsorption.

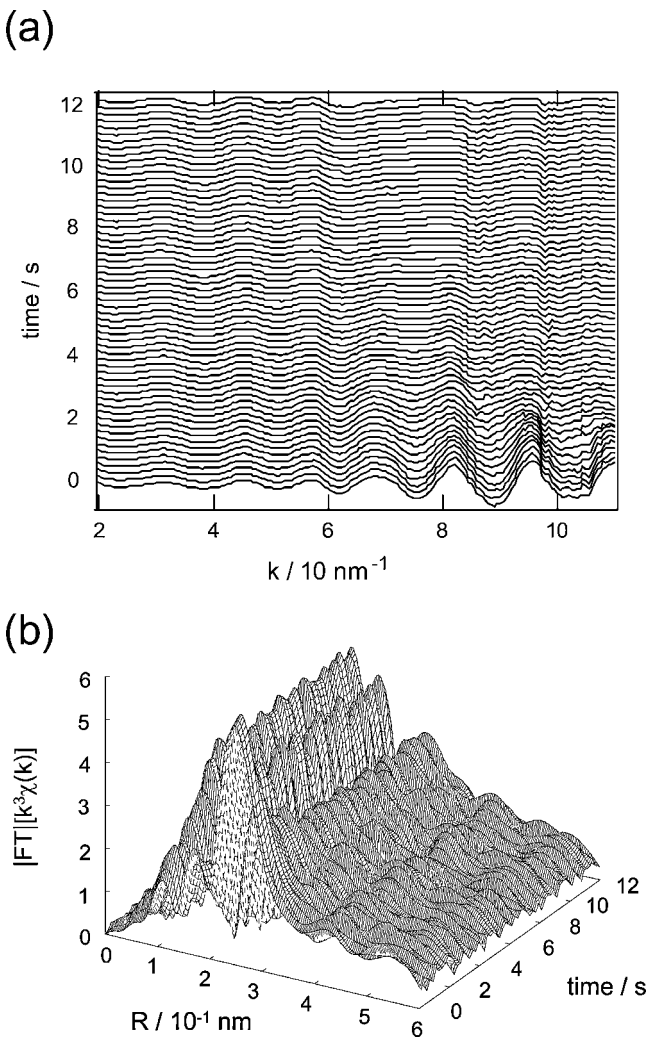

Fig. 8. A series of k^3-weighted DXAFS oscillations (a) and a series of their associated Fourier transformed functions (b) for Rh/Al_2O_3 at the Rh K-edge during the CO adsorption process at 298 K measured by DXAFS every 100 ms.

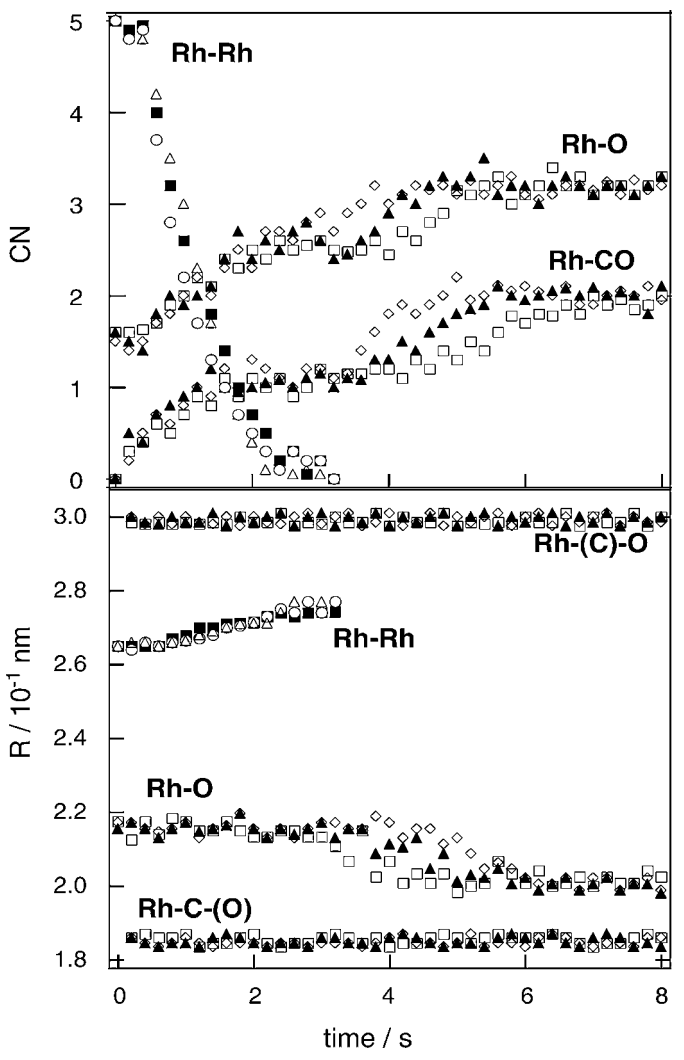

Fig. 9. The values of coordination numbers (*CN*) and bond distances (*R*) determined by the curve fitting as a function of CO exposure time at 298, 333, and 353 K. 298 K: Rh-Rh (filled sqaure); Rh-CO (open square); Rh-O (open square). 333 K: Rh-Rh (open triangle); Rh-CO (filled triange); Rh-O (filled triangle). 353 K: Rh-Rh (open circle); Rh-CO (open diamond); Rh-O (open diamond).

There were two isosbestic points at 23.234 keV and 23.239 keV in the serial XANES spectra at the Rh K-edge during the CO adsorption process of the Rh/Al_2O_3 catalyst under 26.7 kPa of CO at 298 K, indicating the existence of two intermediates in the process [39]. The k^3-weighted EXAFS oscillations at the Rh K-edge during the CO adsorption process and associated Fourier transformed functions are shown in Fig. 8. The amplitude of EXAFS oscillations did not change significantly at 0–600 ms, but a remarkable decrease in the amplitude in the higher k range was observed from 600 ms till 3000 ms (Fig. 8(a)). This corresponds to the first isosbestic point in the XNAES. A change in the EXAFS oscillations after 3 s corresponds to the second isosbestic point, which indicates that another structural change occurs as a sequential process during the period of 3–6 s (Fig. 8(a)).

At $t = 0$ two distinct peaks in the FT at 0.174 and 0.248 nm (phase-shift uncorrected) due to Rh-O and Rh-Rh, respectively, were observed as shown in Fig. 8(b). By the CO admission a FT peak due to Rh-C-(O) bond appeared at 0.123 nm (phase-shift uncorrected) within the first 200 ms, while the FT peaks for Rh-O and Rh-Rh remained unchanged over 600 ms. A drastic change in the FT occurred at 800–3000 ms, where the Rh-Rh peak completely dumped. The *CN* and *R* values determined by the curve fitting in R space were plotted as a function of CO exposure time at 298, 333, and 353 K in Fig. 9. There were no changes in the Rh-Rh and Rh-O bonds at 0–600 ms, but *CN* for Rh-CO increased from 0 to 0.7 at 600 ms. After 600 ms, the *CN* of Rh-Rh bond decreased monotonously during the period of 800-3000 ms, accompanied with elongation of *R* of Rh-Rh and an increase of *CN* for Rh-O from 1.6 to 2.5 at 3000 ms. The *CN* values for Rh-O and Rh-CO were almost constant at 2000–3000 ms, indicating the existence of a semistable structural state for CO-adsorbed Rh clusters on Al_2O_3. After 3000 ms the *CN*s increased from 2.5 to 3.2 and from 1.2 to 1.9, respectively as shown in Fig. 9, where *R* of Rh-O also decreased from 0.213 to 0.200 nm. The rate of changes at this step increased with increasing temperature. The details of structural parameters will be reported in a separate paper [39]. The change in the *CN* values for Rh-CO determined by DXAFS analysis was in excellent accordance with the result of volumetric measurements [39].

Thus the time-resolved DXAFS analysis evidences the existence of three elementary steps for the surface disintegration of Rh clusters (**6**) involving two intermediate states ((**7**) and (**8**)) as depicted in Fig. 10 [39]. At $t = 0$ Rh atoms in the cluster interact with the surface oxygen atoms of Al_2O_3 at a distance of 0.213 nm. *CN* and *R* of Rh-Rh were 5.0 and 0.265 nm, respectively, and they were in good agreement with those (4.9 and 0.264 nm) determined

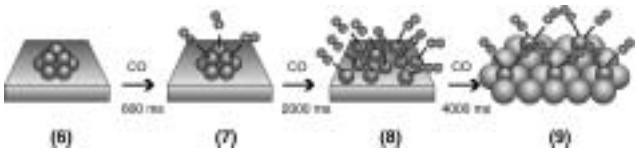

Fig. 10. An illustrative mechanism and time scales of three elementary steps at 298 K for the disintegration of Rh clusters on Al_2O_3 during CO adsorption by time-resolved DXAFS.

by conventional XAFS. These structural parameters assume that the Rh cluster (**6**) consists of 7 atoms in the first layer and 3 atoms in the second layer as shown in Fig. 10, which shows a *CN* of 5.4 for the Rh-Rh bond. The *CN* value of 1.6 for Rh-O indicates that each Rh atom in the lower layer interacts with two O atoms of the Al_2O_3 surface. At the first step of the dynamic disintegration processes (0–600 ms) CO rapidly adsorbs on the Rh cluster to show the *CN* of 0.7 for Rh-CO, which indicates that one CO molecule adsorbs on each Rh atom of the second layer of the cluster (**7**). At this stage no Rh-Rh bond breaking occurs. At the second step after 600 ms the Rh-Rh bonds become weaker by further CO adsorption and the Rh clusters are completely disintegrated at 3000 ms, where the ratio of adsorbed CO to Rh is one. The [Rh-CO] (**8**) can migrate across the Al_2O_3 surface to react with OH groups. The fragmentation of the Rh cluster permits the adsorption of further CO molecules on the Rh atoms at the third step (3000–6000 ms) to form [$Rh(CO)_2$] (**9**) which interacts with three surface O atoms as shown in Fig. 10. The Rh atoms more strongly interact with the surface because of a decrease in the Rh-O distance from 0.213 to 0.200 nm (Fig. 9). These processes proceed consecutively as evidenced by the existence of the isosbestic points and by the time profile of *CN*. The [Rh-CO] species and the [$Rh(CO)_2$] species were also confirmed by *in-situ* FT-IR, which exhibits a peak at 2060 cm^{-1} for terminal CO on Rh atom and two peaks around 2095 and 2023 cm^{-1} for Rh discarbonyl species [39]. After the 1.5 s CO exposure, the peak intensity at 2060 cm^{-1} increased at first, followed by the development of peaks at 2095 and 2023 cm^{-1} (4.5 s). Only these two bands were observed at 10.5 s. The formation of Rh dicarbonyl species (**9**) is in accordance with the previous reports [1–3].

The rates of the first and second steps in Fig. 10 were independent of temperature under the present conditions. On the contrary, the rate of the third step depended on temperature. The activation energies were calculated to be 15 ± 2, 17 ± 2, and 19 ± 2 kJ mol^{-1}, respectively for the changes in the CN of Rh–CO, the *CN* of Rh–O, and the *R* of Rh–O, which are in good agreement with each other. By CO adsorption the Rh-Rh bond distance increased from 0.26 nm for the incipient Rh clusters (**6**) to 0.27 nm for the $[Rh\text{-}CO]_{10}$ species, while the Rh cluster framework was disintegrated during the Rh-Rh elongation. Thus the [Rh-CO] species (**8**) are dispatched from the cluster and move on the surface without any significant energy barrier. The slowest step in the cluster disintegration with an energy barrier of 17 kJ mol^{-1} is the formation of [$Rh(CO)_2$] monomers (**9**) which occur concertedly with the bond rearrangement (change in *CN* and *R* of Rh-O) at the interface.

4. Conclusion

We have shown the time scale and bond sequence in the dynamic structural changes of Ru-carbido clusters on MgO and Rh clusters on γ-Al_2O_3, which both proceed through two intermediate states detected by means of *in-situ* time-resolved DXAFS every 1 s or 100 ms. The present time-resolved structural analysis provides crucial structural aspects to grasp the mechanism for dynamic surface processes and catalysis and contributes to a new area of structural dynamics of metal clusters and nanoparticles dispersed at surfaces.

Further improvements in the synchrotron source and detection systems will make it possible to measure the change of active structures with much shorter life time in catalytic reaction processes by time-resolved DXAFS. The trends of XAFS relevant to future progress in the study of nano-structures and heterogeneous catalysts may be μs-ns time-resolved XAFS observation, and besides space-resolved XAFS, more precise 3D-structure characterization, characterization of each metal site with different chemical states, more routinely reliable structural analysis, and more accurate theoretical analysis.

Acknowledgement

This study was supported by a Grant-in-aid for The 21st Century COE Program for Frontiers in Fundamental Chemistry from the Ministry of Education, Culture, Sports, Science and Technology.

References

1. Iwasawa, Y., Adv. Catal. **35**, 187 (1987).
2. Iwasawa, Y., Stud. Surf. Sci. Catal. (Proc. 11th Int. Congr. Catal. Baltimore) **101**, 21 (1996).
3. Iwasawa, Y., Acc. Chem. Res. **30**, 103 (1997).
4. Iwasawa, Y., Catal. Today **18**, 21 (1993).
5. Koningsberger, D. C. and Prins, R. ed., "X-Ray Absorption: Principles, Applications, Techniques of EXAFS, SEXAFS and XANES", (Wiley, New York, 1988).
6. Teo, B. K., "EXAFS; Basic Princoples and Data Analysis", (Springer, Berlin, 1986).
7. Bart, J. C. J. and Vlaic, G., Adv. Catal. **35**, 1 (1987).
8. Topsøe, H., Stud. Suf. Sci. Catal. (Proc. 12th Int. Congr. Catal. Granada), **130**, 1 (2000).
9. Iwasawa, Y. ed., "X-Ray Absorption Fine Structure for Catalysts and Surfaces", (World Scientific, Singapore, 1996).
10. Matsushita, T. and Phizackerley, R. P., Jpn. J. Appl. Phys. **20**, 2223 (1981).
11. Flank, A. M., Fontaine, A., Jucha, A., Lemonnier, M. and Williams, C., J. Phys. Lett. **43**, L315 (1982).
12. Flank, A. M., *et al.*, Nucl. Instrum. Meth. **208**, 651 (1983).
13. Dartyge, E., Fontaine, A., Jucha, A. and Sayers, D., "EXAFS and Near Edge Structure III", (Springer-Verlag, Berlin, 1984).
14. Bazin, D., Dexpert, H., Lagarde, P. and Bournonville, P., J. Catal. **110**, 209 (1988).
15. Fontaine, A., *et al.*, Topics in Current Chem. **151**, 179 (1989).
16. Couves, J. W., *et al.*, Nature **354**, 465 (1991).
17. Sanker, G., *et al.*, J. Phys. Chem. **96**, 7485 (1992).
18. Ressler, T., Hagelstein, M., Hatje, U. and Metz, W., J. Phys. Chem. B **101**, 6680 (1997).
19. Hilbrandt, N., Frahm, R. and Martin, M., J. Phys. IV **7**, 727 (1997).
20. Fiddy, S. G., *et al.*, J. Chem. Soc., Chem. Commun. 851 (1999).
21. Yamaguchi, A., *et al.*, Catal. Lett. **68**, 139 (2000).
22. Yamaguchi, A., *et al.*, Catal. Lett. **71**, 203 (2001).
23. Yamaguchi, A., *et al.*, Bull. Chem. Soc. Jpn. **74**, 801 (2001).
24. Yamaguchi, A., *et al.*, J. Phys. Chem. B **106**, 2415 (2002).
25. Newton, M. A., *et al.*, J. Phys. Chem. A **105**, 5965 (2001).
26. Fiddy, S. G., *et al.*, Chem. Commun. 445 (2001).
27. Newton, M. A., Dent, A. J., Diaz-Moreno, S., Fiddy, S. G. and Evans, J., Angew. Chem. Int. Ed. **41**, 2587 (2002).
28. Dent, A. J., Top. Catal. **18**, 27 (2002).
29. Carlo, L., *et al.*, Angew. Chem. Int. Ed. **41**, 2247 (2002).
30. Meneau, F., *et al.*, Faraday Discuss. **122**, 203 (2003).
31. Iwasawa, Y., J. Catal. **216**, 165 (2003).

32. Hagelstein, M., Ferraro, C., Hatje, U., Ressler, T. and Metz, W., J. Synchrotron Rad. **2**, 174 (1995).
33. Stern, E. A., Newville, M., Ravel, B., Yacoby, Y. and Haskel, D., Physica B **208**, 117 (1995).
34. Newville, M., Livins, P., Yacoby, Y., Stern, E. A. and Rehr, J. J., Phys. Rev. B **47**, 14126 (1993).
35. Ankudinov, A. L., Ravel, B., Rehr, J. J. and Conradson, S. D., Phys. Rev. B **58**, 7565 (1998).
36. Izumi, Y., Chihara, T., Yamazaki, H. and Iwasawa, Y., J. Phys. Chem. **98**, 594 (1994).
37. Izumi, Y. and Iwasawa, Y., Chemtech **24**, 20 (1994).
38. Suzuki, A., *et al.*, J. Phys. Chem. B **108**, 5609 (2004).
39. Suzuki, A., *et al*., Angew. Chem. Int. Ed. **42**, 4795 (2003).
40. Yang, A. C. and Garland, C. W., J. Phys. Chem. **61**, 1504 (1957).
41. Cabanagh, R. R. and Yates, Jr, J. T., J. Chem. Phys. **74**, 1 (1981).
42. Basu, P., Panayotov, D. and Yates, Jr, J. T., J. Am. Chem. Soc. **110**, 2074 (1988).
43. van't Blik, H. D. J., van Zon, J. B. A. D., Huizunga, T., Koningsberger, D. C. and Prins, R., J. Am. Chem. Soc. **107**, 3140 (1985).
44. Berko, A., Menesi, G. and Solymosi, F., J. Phys. Chem. **100**, 17732 (1996).
45. Berko, A. and Solymosi, F., J. Catal. **183**, 91 (1999).

Physica Scripta. Vol. T115, 66–71, 2005

Evolution of Catalyst Structure under Reaction Conditions from Time-resolved *in situ* XAS Investigations

Thorsten Ressler*, Julia Wienold and Olaf Timpe

Department of Inorganic Chemistry, Fritz-Haber-Institut of the MPG, Faradayweg 4-6, 14195 Berlin, Germany

Received June 26, 2003; accepted November 4, 2003

PACS number: 6110ht

Abstract

Time-resolved X-ray absorption spectroscopy (TR-XAS) possesses excellent capabilities to reveal *quantitative phase composition and average valence* together with the evolution of the *local structure* of a system under dynamic reaction conditions. The work discussed here focused on time-resolved *in situ* XAS investigations aiming, first, at understanding structural evolution under dynamic conditions and, second, at revealing properties of the system studied not available from investigations under stationary conditions. In order to demonstrate the potential of TR-XAS in heterogeneous catalysis, TR-XAS investigations combined with mass spectrometry of the structural evolution of Keggin type heteropolyoxomolybdates (HPOM) during thermal treatment in propene and in propene and oxygen in the temperature range from 300 K to 773 K are presented. It is concluded, that the undistorted Keggin ion in the as-prepared HPOM has to be regarded as a precursor of the active catalyst, while the formation of lacunary Keggin ions is a prerequisite for catalytic activity.

1. Introduction

X-ray absorption spectroscopy (XAS) is a powerful technique that can provide element specific short-range structural information in heterogeneous catalysis. Moreover, XAS studies in catalysis can be performed in situ under reaction conditions with pressures and temperatures larger than 1 bar and 293 K, respectively. Several recent publications have reviewed parts of the literature related to time-resolved XAS (TR-XAS) [1–5]. The majority of studies that used time-resolved XAS in heterogeneous catalysis, focused on both structure-reactivity relationships from investigating the catalyst under reaction conditions and sevolution of the catalyst structure under preparation conditions [6–13, 14]. Time-resolved energy-dispersive XAS (TR-DXAS) has been used to elucidate reaction intermediates [15–20] and for a kinetic analysis of the reactions proceeding in bulk catalysts [21, 22] and on supported catalysts [23–26] TR-XAS investigations employing the Quick-EXAFS mode were performed of both bulk metal and metal oxide catalysts, [27, 28] sulfidation catalysts [29–32], and supported catalysts [33–37].

The work discussed in this paper focused on *in situ* XAS investigations aiming, first, at understanding structural evolution under dynamic conditions and, second, at revealing properties of the system studied not available from investigations under stationary conditions. In order to demonstrate the capabilities of TR-XAS investigations in heterogeneous catalysis, combined *in situ* time-resolved XAS/mass spectrometry studies on the evolution of the structure of various heteropolyoxomolybdates (i.e. $H_3[PMo_{12}O_{40}]$*$13H_2O$ denoted as HPOM, $Cs_2H[PMo_{12}O40]$ denoted as Cs_2-HPOM, $Cs_3[PMo_{12}O_{40}]$ denoted as Cs3-HPOM, and $Cs_2H_2[PVMo_{11}O_{40}]$ denoted as Cs_2-V-HPOM) during thermal treatment in 10% propene in helium (reducing conditions), and 10% propene and 10% oxygen in helium (catalytic partial oxidation conditions) are presented. In addition, some specific details about the TR-XAS experimental set-up and the data analysis procedure employed is provided. The latter is intended to illustrate the characteristic requirements of time-resolved XAS investigations compared to conventional *in situ* XAS studies.

Heteropolyoxomolybdates (HPOM) composed of Keggin ions (Figure 1) constitute highly active heterogeneous catalysts for partial oxidation of alkenes and alkanes (e.g. methacrolein to methacrylic acid) [38, 39]). Hence, the structure and the catalytic properties of the material have been extensively studied in the past. It has been suggested that the active phase of the HPOM under reaction conditions may correspond to the intact and undistorted Keggin structure of the HPOM [40, 41, 42, 43]. Other authors have observed, that the Keggin ions may not be particularly stable during thermal treatment and under catalytic conditions, resulting in partial reduction of the HPOM under reaction conditions, [44, 45] a considerable inhomogeneity of HPOM, [46, 47, 48, 49, 50, 51] and migration of molybdenum addenda ions [51, 52, 53, 54, 55, 56] or vanadium addenda substituents [51, 53, 57, 58, 59, 60, 61] from the Keggin anion onto interstitial sites in the HPOM structure. Apparently, reliable structure-reactivity relationships for HPOM needed for a rational improvement of the catalytic properties of the material are lacking. Open questions remain such as (*i*) what is the thermal and chemical stability of intact or partially decomposed Keggin ions and (*ii*) is the onset of the structural instability of the Keggin ion correlated to the catalytic activity of the material?

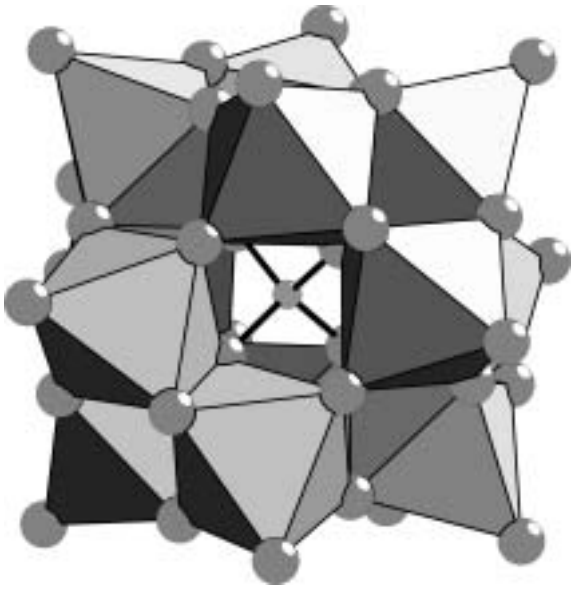

Fig. 1. Schematic structural representation of the Keggin anion in heteropolyoxomolybdates.

*Corresponding author, E-mail: Ressler@fhi-berlin.mpg.de

2. Experimental

2.1. *Sample preparation*

The heteropolyoxomolybdates $H_3[PMo_{12}O_{40}]^*13H_2O$, $Cs_2H[PMo_{12}O_{40}]$, and $Cs_3[PMo_{12}O_{40}]$ were prepared according to the method described by Tsigdinos *et al*. [62] Phase purity was verified by XRD.

2.2. *Instrumentation for TR-XAS in Catalysis*

The majority of XAS beamlines operating in the hard X-ray regime (>2.5 keV) are dedicated to transmission and fluorescence EXAFS using a double crystal monochromator. In order to obtain a reliable data quality in the step-scanning mode, a total measuring time of at least several minutes is required. Using the QEXAFS (Quick-EXAFS) [63, 64] technique, the measuring time is reduced to several tens of seconds. Evidently, QEXAFS offers a superior versatility as experiments can be performed in different detection modes (transmission, fluorescence, electron yield, etc.) on a large variety of systems (solid, liquid, or diluted samples, enhanced surface sensitivity, etc.). Conversely, with the energy-dispersive XAFS set-up (DXAS [65]), an entire absorption spectrum is collected at once, without requiring any movement of the spectrometer components. However, the energy range available for EXAFS analysis is restricted by the monochromator angle used and DXAS studies are restricted to the transmission mode. The *in situ* transmission XAS experiments reported here were performed at the Mo K edge (19.999 keV) at beamline X1 at the *Hamburg Synchrotron Radiation Laboratory*, HASYLAB. Because the objective of the investigations presented was a detailed analysis of the structural evolution of the heterogeneous catalysts employed, a conventional Si (311) double monochromator set-up was chosen.

2.3. *In situ cell for TR-XAS studies in Catalysis*

A variety of flow-through cells or batch reactors can be used for *in situ* X-ray absorption studies in the energy range from 2.5 keV to 30 keV. The *in situ* XAS experiments described here were conducted in a flow-reactor [35] on 5 mm self-supporting pellets at atmospheric pressure in flowing reactants (~30 ml/min, temperature range from 300 K to 773 K at 5 K/min). The heteropolyoxomolybates were mixed with boron nitride (7 mg HPA, 30 mg BN) and pressed with a force of 1 ton into a 5 mm in diameter pellet resulting in an edge jump at the Mo K-edge of $\Delta\mu_x \sim 1.5$. The twofold advantage of the set-up employed is the very small volume and the fact that the reactor can be used with both the DXAS set-up and the QEXAFS set-up. Hence, by using the same experimental cell, time-resolved DXAS data under rapidly changing conditions can be obtained (time-resolution better than 1 s) as well as high quality EXAFS data in the conventional scanning mode or the QEXAFS mode (time-resolution of ~1 min). Temperature and reactant mass flow can be controlled with an *Eurotherm* PID temperature controller and *Bronkhorst* mass flow controllers, respectively. The product composition at the *in situ* cell gas outlet is continuously monitored using a mass spectrometer in a mass scan mode (QMS200 from *Pfeiffer*) which is crucial for *in situ* studies in heterogeneous catalysis when bulk structural changes are to be correlated to catalytic performance.

2.4. *Analysis of TR-XAS data in catalysis*

X-ray absorption fine structure (XAFS) analysis was performed using the software package WinXAS v2.3 [67]. Background subtraction and normalization were carried out by fitting linear polynomials to the pre-edge and the post-edge region of an absorption spectrum, respectively. A quantitative phase analysis of mixtures is particularly desirable for studies in heterogeneous catalysis where one frequently has to deal with more than one phase present under reaction conditions. Principle component analysis (PCA) permits a quantitative determination of the number of primary components in a set of experimental XANES spectra [68, 69]. Recently, this approach has been successfully extended to the analysis of EXAFS data measured for various phase mixtures [70, 71].

The extended X-ray absorption fine structure (EXAFS) $\chi(k)$ was extracted by using cubic splines to obtain a smooth atomic background, $\mu_0(k)$. The radial distribution function FT($\chi(k)$) was calculated by Fourier transforming the k^3-weighted experimental $\chi(k)$ function, multiplied by a Bessel window, into the R space. EXAFS data analysis was performed using theoretical backscattering phases and amplitudes calculated with the *ab-initio* multiple-scattering code FEFF7 [72]. Single scattering and multiple scattering paths in the Keggin ion model structure were calculated up to 6.0 Å with a lower limit of 2.0% in amplitude with respect to the strongest backscattering path. EXAFS refinements were performed in R space to magnitude and imaginary part of a Fourier transformed k^3-weighted experimental $\chi(k)$ using the standard EXAFS formula (k range from 3.4 to 15.1 $Å^{-1}$, R range 0.7 to 4.1 Å) [73]. Structural parameters that are determined by a least-squares EXAFS refinement of a Keggin model structure to the experimental spectra are (*i*) one E_0 shift, (*ii*) Debye-Waller factors for single-scattering paths, (*iii*) distances of single-scattering paths, (*iv*) one third cumulant for the Mo–O distances in the first coordination shell and one third cumulant for all remaining scattering paths. Coordination numbers (CN) and S_0^2 were kept invariant in the refinement.

3. Results and Discussion

3.1. *Structural evolution during thermal treatment in propene*

An experimental Mo K edge $\chi(k)$ of Cs_2-HPOM at 300 K is shown in Figure 2. The sufficient signal to noise ratio up to

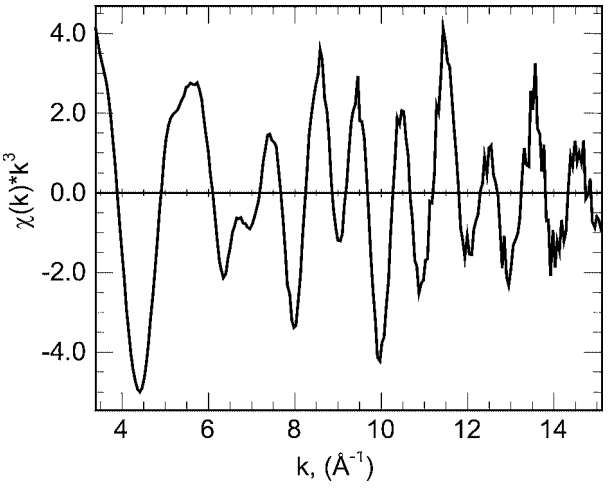

Fig. 2. Experimental Mo K edge $\chi(k)$ of $Cs_2H[PMo_{12}O_{40}]$ measured at 300 K.

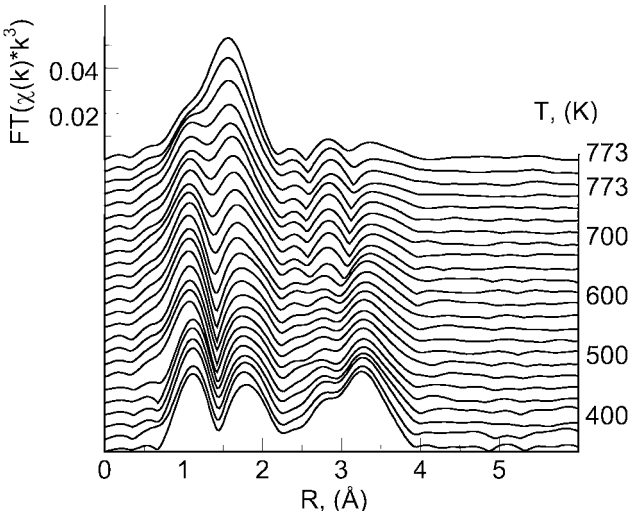

Fig. 3. Evolution of Fourier transformed Mo K edge $\chi(k)$ measured during treatment of $H_3[PMo_{12}O_{40}]$ in 10% propene in helium in the temperature range from 300 K to 770 K.

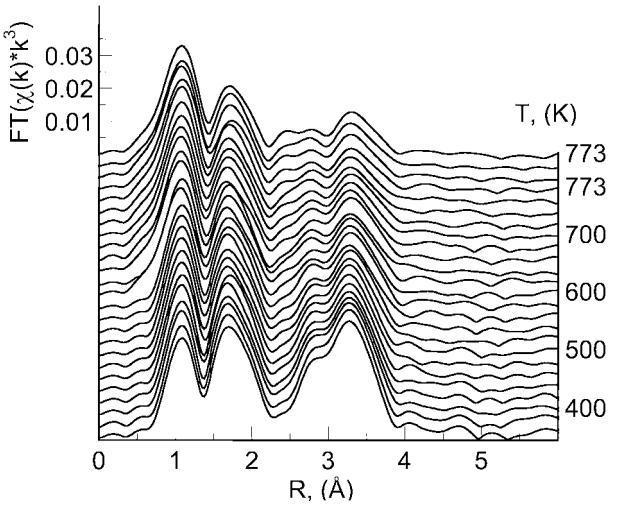

Fig. 4. Evolution of Fourier transformed Mo K edge $\chi(k)$ measured during treatment of $Cs_2H[PMo_{12}O_{40}]$ in 10% propene and 10% oxygen in helium in the temperature range from 300 K to 770 K.

$\sim$15 Å^{-1} enables a reliable structural analysis of changes in the local structure of the Keggin ion under reaction conditions. The evolution of the Fourier transformed Mo K edge $\chi(k)$ during thermal treatment of HPOM in 10% propene in the temperature range from 300 K to 773 K is depicted in Figure 3. Significant changes in the local structure of the Keggin anion in both materials can be seen at temperatures above $\sim$600 K. The Mo K edge spectrum measured at 773 K can be assigned to that of the cubic HPOM observed by *in situ* XRD. Conversely, no significant changes in the local structure were detected during thermal treatment of Cs_3-HPOM in propene or hydrogen. *In situ* XRD experiments performed during the thermal treatment of HPOM in propene revealed the formation of a HPOM consisting of a cubic arrangement of Keggin anions with a certain amount of the molybdenum ions migrated onto sites between the Keggin anions [74].

In order to elucidate the evolution of the short-range order structure of the heteropolyoxomolybdates studied under reducing and partial oxidation reaction conditions, a detailed XAFS analysis of the Mo K edge $\chi(k)$ measured was performed. From Figure 6, a good agreement between the experimental

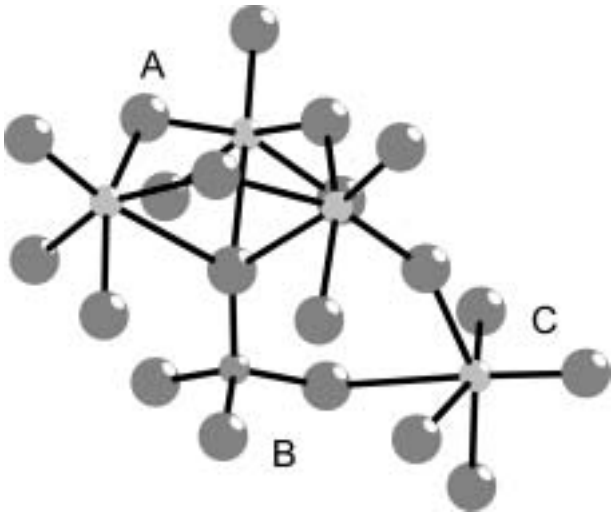

Fig. 5. Experimental (Exp.) and theoretical (Fit) Mo K edge $\chi(k)$ of $H_3[PMo_{12}O_{40}]$ *$13H_2O$ (HPOM) and $Mo_zH_{3-x}[PMo_{12-z}O_{40-x/2}]$ (Mo-HPOM) (measured *in situ* during treatment of HPA in 10% propene at 773 K). Selected individual single-scattering paths in cubic "Mo-HPOM" are shown.

Fourier transformed $\chi(k)$ of HPOM and a XAFS refinement using theoretical phases and amplitudes calculated for the Keggin ion in the structure of $K_2H[PMo_{12}O_{40}]^*H_2O$ (*P*n-3m, [ICSD 209]) can be seen. Very similar results of the corresponding XAFS refinements were obtained for Cs_2-HPOM, Cs_2-V-HPOM, and Cs_3-HPOM. Figure 5 shows a schematic representation of a part

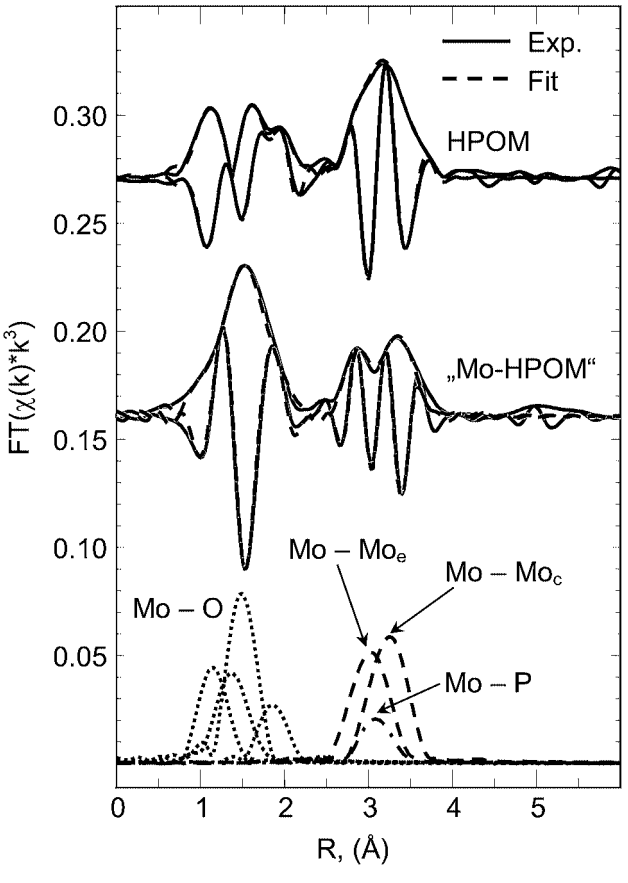

Fig. 6. Schematic structural representation of a section of the Keggin anion. Shown is a "triad" consisting of three edge-sharing MoO_6 units connected to the central PO_4 tetrahedron and connected via corner-sharing to one MoO_6 unit of one of the neighboring "triades".

of the Keggin structure. The Keggin ion consists of four "triades", each built up by three edge-sharing MoO_6 units (A in Figure 5). The three MoO_6 units share one common oxygen atom that is connected to the central heteroatom in the Keggin ion (B in Figure 5). The four triads in the Keggin anion are linked together by common corners of the corresponding MoO_6 units (C in Figure 5). The individual shells that can be clearly distinguished in the FT($\chi(k)$) of the heteropolyoxomolybdates correspond to the Mo–O distances within the MoO_6 units (from 1.69 Å to 2.43 Å), the Mo–Mo distances within the triads (3.41 Å, edge-sharing), and the Mo–Mo distances between the triads (3.71 Å, corner-sharing). Additionally, Figure 6 displays the experimental Fourier transformed $\chi(k)$ of the cubic HPOM obtained from the treatment of HPOM in propene (Figure 3) and a XAFS refinement using the same phases and amplitudes as described above. A good agreement between the experimental spectrum of the cubic HPOM and the theoretical XAFS calculations was achieved using the Mo–O and Mo–Mo distances and the respective coordination numbers in the Keggin ion as start parameters. The Mo–O, Mo–P, and Mo–Mo distances in the Keggin anion of HPOM and the cubic HPOM obtained from the XAFS analysis indicate, that treatment of HPOM, Cs_2-HPOM, and Cs_2-V-HPOM in propene results in slightly modified Keggin anions with elongated Mo–O and Mo–Mo distances.

In Figure 7 the evolution of selected Mo–O and Mo–Mo distances in the Keggin anion of Cs_2-HPOM, Cs_2-V-HPOM, and Cs_3-HPOM during treatment in 10% propene in the temperature range from 300 K to 773 K is depicted. At temperatures above ~573 K an increase in the Mo–O and Mo–Mo distances in Cs_2-HPOM and Cs_2-V-HPOM can be noticed, being the strongest for the Mo-Mo distance between edge-sharing octahedra in the Keggin anion (within the "triades"). Eventually, at 773 K the treatment results in the formation of the characteristic local structure of the Keggin ion of the cubic HPOM structure (Figure 5). Interestingly, the presence of vanadium as an addenda substituent in the Keggin ion shows no significant effect on the structural evolution of Cs_2-V-HPOM compared to that of Cs_2-HPOM.

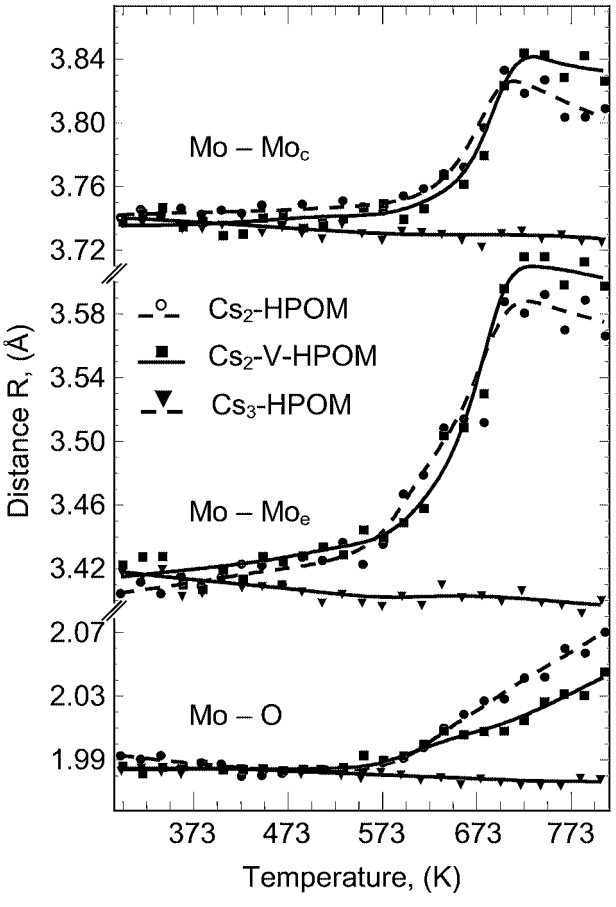

Fig. 7. Evolution of selected Mo–O and Mo–Mo distances in the Keggin structure of $Cs_2H[PMo_{12}O_{40}]$, $Cs_2H_2[PVMo_{11}O_{40}]$, and $Cs_3[PMo_{12}O_{40}]$ during treatment in 10% propene in helium in the temperature range from 300 K to 773 K.

The changes in the Fourier transformed Mo K edge $\chi(k)$ of HPOM (Figure 3) indicate significant alterations of the local structure under reducing conditions. The FT($\chi(k)$) of the cubic HPOM and Cs_2-HPOM with Mo on interstitial sites indicate a remarkable degree of order in the partially reduced and decomposed Keggin ions. Hence, it must be concluded that most Keggin ions undergo a structural transition into a stable modification of the Keggin ions. The local structure of the HPOM probed by XAFS corresponds to the local arrangement of edge and corner-sharing MoO_6 units in the Keggin anion (Figure 6). Both the structure of the original HPOM and the structure of the cubic HPOM obtained after treatment in a reducing atmosphere can be simulated by theoretical XAFS calculations based on the structure of the Keggin anion (Figure 5). For the former the Mo–O and Mo–Mo distances obtained from the XAFS refinement agree well with those obtained from single crystal structure analysis, whereas for the latter a significant lengthening of the Mo–O and Mo–Mo distances in the Keggin anion is obtained.

From Figure 7 it can be seen, that the onset of the structural changes in the Keggin anion of Cs_2-HPOM is at about 573 K. In comparison, no significant structural changes were observed in Cs_3-HPOM over the temperature range studied (Figure 7). The same holds for the evolution of the average Mo valence of the Keggin anion, where no changes were observed during treatment of Cs_3-HPOM in propene or hydrogen. The average Mo valence was obtained from comparing the Mo K edge position of the heteropolyoxomolybdates to that of various molybdenum oxide reference compounds [75]. Conversely, a partial reduction of the molybdenum in Cs_2-HPOM was detected at temperatures above 573 K which coincides with the local structural changes observed at this temperature. The average Mo valence of ~5.4 of the resulting cubic HPOM at 773 K is in good agreement with thermogravimetric measurements of the treatment of HPOM in propene that showed a loss of about four oxygen atoms per Keggin ion in the temperature range from 573 K to 773 K (Mo average valence of 5.33) [76].

3.2. *Structural evolution during activation in propene and oxygen*

The evolution of Fourier transformed Mo K edge $\chi(k)$ during thermal treatment of Cs_2-HPOM in 10% propene and 10% oxygen in helium in the temperature range from 300 K to 773 K shows minor changes to the FT($\chi(k)$), mostly attributable to the increasing reaction temperature (Figure 4). Figure 8 illustrates the corresponding evolution of selected Mo–O and Mo–Mo distances in the Keggin anion of Cs_2-HPOM and Cs_2-V-HPOM. At temperatures above ~573 K an increase in the Mo–O and Mo–Mo distances in Cs_2-HPOM and Cs_2-V-HPOM can be noticed. The onset of the structural changes in the Keggin ion in Cs_2-HPOM and Cs_2-V-HPOM are correlated to the onset of catalytic activity of the materials as can be seen from the increasing

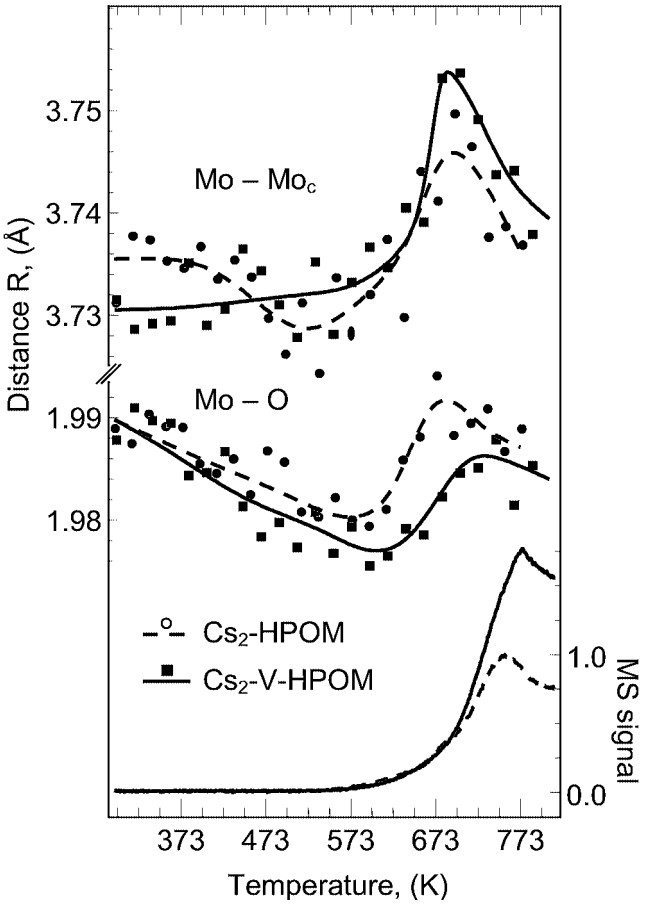

Fig. 8. Evolution of selected Mo–O and Mo–Mo distances in the Keggin structure of $Cs_2H[PMo_{12}O_{40}]$ and $Cs_2H_2[PVMo_{11}O_{40}]$ during treatment in 10% propene and 10% oxygen in helium in the temperature range from 300 K to 773 K together with the acrolein concentration in the gas phase measured by MS.

concentration of the partial oxidation product acrolein in the gas phase. It can be seen from Figure 7 and Figure 8 that the onset temperature and the relative amplitude of the lengthening of the Mo–O and Mo–Mo distances in the Keggin anion of Cs_2-HPOM and Cs_2-V-HPOM under catalytic reaction conditions coincide with the formation of the cubic HPOM during the treatment of Cs_2-HPOM and Cs_2-V-HPOM in propene (Figure 7).

During activation of HPOM in propene and oxygen, the evolution of the local structure of Cs_2-HPOM in the temperature range from 300 K to ~700 K indicates, that the structural characteristics of the Keggin anion are mostly preserved (Figure 4). This is in agreement with the structural evolution of Cs_2-HPOM during thermal treatment in propene. The local structural changes observed in the Keggin ion of Cs_2-HPOM during treatment in propene and oxygen, that coincide with the onset of catalytic activity, are in good agreement with those observed during treatment in propene. Both onset temperature and changes in the Mo–O and Mo–Mo distances during treatment in propene and oxygen indicate that similar to the treatment of Cs_2-HPOM in propene, in both Cs_2-V-HPOM and Cs_2-HPOM a partial decomposition of the Keggin ion (i.e. migration of Mo cations and modified short-range coordination) takes place during activation in propene and oxygen at temperatures above ~573 K.

3.3. *Structure-activity relationships in heteropolyoxomolybdates*

Elucidating relationships between the structure of a heterogeneous catalyst and its reactivity requires a detailed knowledge about the structure of the catalyst under reaction conditions ("in situ"). The *in situ* TR-XAS results presented indicate, that for heteropolyoxomolybdates under reaction conditions, 'structure' does not refer to the undisturbed Keggin structure of the initial material but rather to the electronically and geometrically distorted structure of lacunary partially reduced Keggion ions. It seems, that a certain instability of the structure of the heteropolyoxomolybdates is inevitable in order to obtain an active catalyst under reaction conditions (inactive Cs_3-HPOM compared to active Cs_2-HPOM). Moreover, the correlation between the structural changes described and the onset of catalytic activity indicates, that the original Keggin structure is the precursor for the structure of the partially reduced active catalyst. Time-resolved in situ XAS under dynamic reaction conditions (i.e. increasing reaction temperature) has proven very valuable to elucidate the subtle structural changes that occur in Keggin ions during activation in propene. The slightly altered structure of the HPOM under reaction conditions would have been difficult to unambiguously identify from measurements under stationary conditions. Therefore, the evolution of the local structure of HPOM under reaction conditions as monitored by *in situ* XAS revealed new insights into the correlation of the structure of this heterogeneous catalyst and its catalytic behavior, complementary to structural changes in HPOM as previously reported in the literature (for instance from XRD, Raman, or IR measurements).

4. Concluding remarks

The examples presented clearly demonstrate the potential of TR-XAS investigations to extend the suitability of XAS for *in situ* studies in heterogeneous catalysis to investigations under dynamic conditions. XAS experiments under stationary conditions may reveal the structure of a working catalyst, however, correlations between the structure of the catalyst and its catalytic properties can more readily be elucidated from monitoring the structural response of the catalyst to changing reaction conditions (i.e. temperature, gas phase, etc.). Although the experiments shown demonstrate the structural details that can be obtained from TR-XAS studies, the structural information obtained becomes much more reliable when corroborated by results from complementary techniques (in the case presented for instance *in situ* XRD, TG/DTA, IR, etc.). When used complementary with other techniques, the capability of TR-XAS to reveal *quantitative phase composition and average valence* together with the evolution of the local structure of a system under dynamic (reaction) conditions, combined with a time-resolution of 100 ms is a very powerful tool for structural and kinetic studies in heterogeneous catalysis.

Acknowledgement

We are grateful to R. E. Jentoft and F. Girgsdies for participating in the XAS measurements, to HASYLAB for providing beamtime for this work, and to Prof. R. Schlögl for continuous support.

References

1. Dent, A. J., Top. Catal. **18**, 27 (2002).
2. Ressler, T., Wienold, J., Jentoft, R. E., Neisius, T. and Gunter, M. M., Top. Catal. **18**, 45 (2002).
3. Grunwaldt, J. D. and Clausen, B. S., Top. Catal. **18**, 37 (2002).
4. Newton, M. A., Dent, A. J. and Evans, J., Chem. Soc. Rev. **31**, 83 (2002).
5. Shido, T. and Prins, R., Curr. Opin. Solid State Mat. Sci. **3**, 330 (1998).

6. Shido, T., *et al*., Top. Catal. **18**, 53 (2002).
7. Yamaguchi, A., *et al*., J. Phys. Chem. B **106**, 2415 (2002).
8. Fiddy, S. G., *et al*., J., Phys. Chem. Chem. Phys. **4**, 827 (2002).
9. Yamaguchi, A., *et al*., Catal. Lett. **68**, 139 (2000).
10. Hatje, U., Ressler, T., Petersen, S. and Forster, H., J. Phys. IV **4**, 141 (1994).
11. Sankar, G., *et al*., J. Phys. Chem. **97**, 9550 (1993).
12. Thomas, J. M., *et al*., Angew. Chemie Intl. Ed. **33**, 1871 (1993).
13. Couves, J. W., Catlow, C. R. A., Greaves, G. N. and Thomas, J. M., J. Phys. Chem. **96**, 7485 (1992).
14. Cimini, F. and Prins, R., J. Phys. Chem. B **101**, 5277 (1997).
15. Lamberti, C., *et al*., Angew. Chem.-Int. Edit. **41**, 2341 (2002).
16. Bottger, I., *et al*., Chem.-Eur. J. **6**, 1870 (2000).
17. Ressler, T., *et al*., J. Catal. **191**, 75 (2000).
18. Hagelstein, M., Hatje, U., Forster, H., Ressler, T. and Metz, W., Studies Surf. Sci. Catal. **84**, 1217 (1994).
19. Sankar, G., *et al*., J. Phys. Chem. **96**, 7485 (1992).
20. Ressler, T., Hagelstein, M., Hatje, U. and Metz, W., J. Phys. Chem. B **101**, 34, 6680 (1997).
21. Ressler, T., Wienold, J., Jentoft, R. E. and Girgsdies, F., Eur. J. Inorg. Chem. **2**, 301 (2003).
22. Ressler, T., Jentoft, R. E., Wienold, J. and Neisius, T., J. Catal. **210**, 67 (2002).
23. Evans, J. and Newton, M. A., J. Mol. Catal. A – Chem. **182**, 351 (2002)
24. Evans, J., *et al*., J. Chem. Soc.-Dalton Trans. **10**, 2207 (2002).
25. Newton, M. A., *et al*., J. Chem. Phys. B **106**, 4214 (2002).
26. Newton, M. A., *et al*., J. Chem. Phys. A **105**, 5965 (2001).
27. Gunter, M. M., Ressler, T., Jentoft, R. E. and Bems, B., J. Catal. **203**, 133 (2001).
28. Reitz, T. L., *et al*., J. Catal. **199**, 193 (2001).
29. Sun, M. Y., Burgi, T., Cattaneo, R., van Langeveld, D. and Prins, R., J. Catal. **201**, 258 (2001).
30. Geantet, C., *et al*., Catal. Lett. **73**, 95 (2001).
31. Cattaneo, R., Rota, F. and Prins, R., J. Catal. **199**, 318 (2001).
32. Cattaneo, R., Weber, T., Shido, T. and Prins, R., J. Catal. **191**, 225 (2000).
33. Oudenhuijzen, M. K., Kooyman, P. J., Tappel, B. van Bokhoven, J. A. and Koningsberger, D. C., J. Catal. **205**, 135 (2002).
34. Grunwaldt, J. D., Kappen, P., Basini, L. and Clausen, B. S., Catal. Lett. **78**, 13 (2002).
35. Grunwaldt, J. D., Molenbroek, A. M., Topsoe, N. Y., Topsoe, H. and Clausen, B. S., J. Catal. **194**, 452 (2000).
36. Ovesen, C. V., *et al*., J. Catal. **168**, 133 (1997).
37. Clausen, B. S., Grabaek, L., Steffensen, G., Hansen, P. L. and Topsoe, H., Catal. Lett. **20**, 23 (1993).
38. Okuhara, T., Mizuno, N. and Misono, M., Adv. Catal. **41**, 443 (2001).
39. Brown, G. M., Noe-Spirlet, M.-R., Busing, W. R. and Levy, H. A., Acta Cryst. **B33**, 1038 (1977).
40. Mizuno, N., Suh, D.-J., Han, W. and Kudo, T., J. Mol. Catal. A **114**, 309 (1996).
41. Mizuno, N., Tateishi, M. and Iwamoto, M., Appl. Catal. A: General **118**, L1 (1994).
42. Mizuno, N., Tateishi, M. and Iwamoto, M., Appl. Catal. A: General **128**, L165 (1995).
43. Staroverova, N., Kutyrev, M. Yu. and Khvtisiashvili, L. G., Kin. Kata. **27**, 596 (1985).
44. Watzenberger, O., Emig, G. and Lynch, D. T., J. Catal. **124**, 247 (1990).
45. Lee, K. E., *et al*., Appl. Catal. A: General **214**, 125 (2001).
46. Black, J. B., *et al*., J. Catal. **106**, 1 (1987).
47. Staroverova, I. N., Kutyrev, M. Yu. and Stakheev, M. Yu., Kin. Katal. **33**, 127 (1992).
48. Langpape, M., Millet, J. M. M., Ozkan, U. S. and Boudeulle, M., J. Catal. **181**, 80 (1999).
49. Black, J. B., Scott, J. D. Serwicka, E. M. and Goodenough, J. B., J. Catal. **106**, 16 (1987).
50. Berndt, S., *et al*., Ber. Bunsenges. Phys. Chem. **102**, 763 (1998).
51. Mestl, G., *et al*., Appl. Catal. A: General **210**, 13 (2001).
52. Cavani, F., Etienne, E., Mezzogori, R., Pigamo, A. and Trifiro, F., Catal. Lett. **75**, 99 (2001).
53. Cavani, F., Mezzogori, R., Pigamo, A., Trifiro, F. and Etienne, E., Catal. Today **71**, 97 (2001).
54. Marosi, L., Cox, G., Tenten, A. and Hibst, H., J. Catal. **194**, 140 (2000).
55. Bayer, R., Marchal, C., Liu, F. X., Teze, A. and Herve, G., J. Mol. Catal. A: Chem. **110**, 65 (1996).
56. Albonetti, S., *et al*., J. Catal. **146**, 491 (1994).
57. Marchal-Roch, C., Laronze, N., Guilou, N., Teze, A. and Herve, G., Appl. Catal. A **199**, 33 (2000).
58. Marchal-Roch, C., Bayer, R., Moisan, J. F., Teze, A. and Herve, G., Topics Catal. **3**, 407 (1996).
59. Ilkenhans, T., Herzog, B., Braun, T. and Schlögl, R., J. Catal. **153**, 275 (1995).
60. Marchal-Roch, C. and Millet, J.-M. M., C. R. Acad. Sci. **C4**, 321 (2001).
61. Centi, G., *et al*., J. Chem. Soc. Faraday Trans. **86**, 2775 (1990).
62. Tsigdinos, G. A., Topics Current Chem. **76**, 1 (1987).
63. Frahm, R., Nucl. Instrum. Meth. **A270**, 578 (1988).
64. Frahm, R., Rev. Sci. Instrum. **60**, 2515 (1989).
65. Hagelstein, M., San Miguel, A., Fontaine, A. and Goulon, J., J. de Physique IV **7**, C2-303 (1997).
66. Designed by Hagelstein, M., *et al*., ESRF, in a collaborative effort with the Fritz-Haber-Institut, Berlin, Germany.
67. Ressler, T., J. Synch. Rad. **5**, 118 (1998).
68. Malinowski, E. R. and Howery, D. G., "Factor Analysis in Chemistry", (John Wiley and Sons, New York, 1980).
69. Ressler, T., Wong, J., Roos, J. and Smith, I. L., Environ. Science & Techn. **34**, 950 (2000).
70. Frenkel, A. I., Kleifeld, O., Wasserman, S. R. and Sagi, I., J. Chem. Phys. **116**, 9449 (2002).
71. Ressler, T., Wienold, J., Jentoft, R. E., Timpe, O. and Neisius, T., Solid State Commun. **119**, 169 (2001).
72. Rehr, J. J., Booth, C. H., Bridges, F. and Zabinsky, S. I., Phys. Rev. B **49**, 12347 (1994).
73. Ressler, T., Brock, S. L., Wong, J. and Suib, S. L., J. Phys. Chem. B **103**, 6407 (1999).
74. Wienold, J., Timpe, O. and Ressler, T., Chem. A Eur. J. **9**, 6007 (2003).
75. Ressler, T., Jentoft, R. E., Wienold, J. and Neisius, T., J. Catal. **210**, 67 (2002)
76. Jentoft, F., *et al*., Appl. Catal. A, **256**, 291 (2003).

Physica Scripta. Vol. T115, 72–75, 2005

In Situ Monitoring of Oxide-Supported Platinum-Group Metal Catalysts by Energy Dispersive EXAFS

Andrew J Dent[2], Sofia Diaz-Moreno[3], John Evans*[1,2], Steven G Fiddy[3], Bhrat Jyoti[1] and Mark A Newton*[1]

[1]Department of Chemistry, University of Southampton, Southampton, SO17 1BJ, UK
[2]Diamond Light Source, Rutherford Appleton Laboratory, Chilton, Oxon, OX11 0QX, UK
[3]ESRF, BP 220, F-38043 Grenoble cedex, France

Received June 26, 2003; accepted November 4, 2003

Abstract

Energy dispersive EXAFS (EDE), using a Laue monochromator on ID24 of the ESRF, and multiple ion monitoring mass spectrometry have been used to monitor the structure and function of alumina-supported rhodium and palladium catalysts within a microreactor. Metallic 5%-Rh/Al_2O_3 was preformed *in situ* by hydrogen reduction, and shown to react rapidly with NO at room temperature yielding an oxidised phase. In order for this material to catalyse the reduction of NO by H_2 (to N_2), it was shown that the metallic phase must be reformed. The "light-off" temperature at which the metallic phase was formed and catalysis commenced varied with NO : H_2 stoichiometry, this temperature lowering in more reducing conditions. N_2O formation was concomitant with the conversion from the oxidised to the metallic phase.

The EDE configuration allowed the simultaneous monitoring of structure at both the rhodium and palladium K-edges. Incorporation of a 20% palladium mole fraction into 5%-Rh-Pd/Al_2O_3 protected rhodium from oxidation and also reduced the light-off temperature, and this is reflected in low coordination number values for the composite Pd to Rh/Pd shell. This favours palladium being preferentially on the surface of the nanoparticles. At higher temperatures there are changes in coordination numbers than imply a redistribution of metal sites under catalytic conditions. Future plans to include infrared spectroscopy as a third simultaneous technique will be outlined.

1. Introduction

Many platinum group metal heterogeneous catalysts consist of a dispersion of small metal particles chemisorbed onto a low-ordered surface of an often disordered support, such as a metal oxide. It is thus not surprising unravelling these complexities to create an atomic-level understanding of catalytic processes has proven to be tantalisingly difficult. Elegant surface science approaches to this problem have included imaging of reaction fronts at the atomic scale by scanning tunnelling microscopy (STM) on single-crystal metal surfaces [1]. This is certainly an excellent approach to modelling catalysts with very large metal particle sizes, but the possibility of more complicated chemistry when metal particles are interacting with their supports is also evident. Again, surface science approaches can be employed based upon single crystal oxides [2]. So, for example, platinum group metals may be introduced onto the surface of a single-crystal rutile surface by metal vapour deposition (MVD) [3] and metalorganometallic chemical vapour deposition (MOCVD) [4]. In such cases, deriving a surface of sufficient order and stability to achieve a diffraction analysis from the overlayer has proven difficult. However, STM has been employed to probe the arrangement of $Rh(CO)_2$ units on a rutile (110) surface and to monitor the aggregation of these mononuclear centres into metal particles [5]. The nature of the oxide surface plane of rutile has been found to have a significant effect upon the initially observed rhodium site after MOCVD of $[RhCl(CO)_2]_2$ also on subsequent particle growth patterns [6].

This support-surface dependence on the properties of adsorbed metal particles makes it therefore important to be able to identify the nature of these particles on catalysts themselves, since, they provide a variety of local surface morphologies. X-ray absorption spectroscopy (XAS) has proven to be a very effective technique for such studies [7, 8, 9, 10]. An important feature of XAS has been the capability of probing structure under ambient, reactive gases and this allowed the technique to settle a long-standing dichotomy on the structure of the heterogeneous catalyst Rh/Al_2O_3 that had resulted from the divergence of surface environment in TEM and IR spectroscopy studies that used CO as a probe molecule. Here analysis of the extended X-ray absorption fine structure (EXAFS) revealed the corrosive nature of the chemisorption of CO on small rhodium particles, affording mononuclear $Rh^I(CO)_2$ sites [11].

Such spectra were recorded by scanning XAS as structural studies, and thus require that the nature of the sample is invariant during the acquisition period. In practice this means that any reaction that might be studied *in situ* should proceed over a time period that is considerably longer than the acquisition period. In order to monitor changing systems, there are four approaches that may be adopted [12]:

i) quenching of the reaction,
ii) a rapid-scanning, quick EXAFS approach (QEXAFS),
iii) a parallel measurement, energy dispersive or dynamic EXAFS approach (EDE or DEXAFS),
iv) a time-drive spectral reconstruction method.

Each of these is appropriate to different circumstances. Quenching is essential when rapid acquisition cannot provide viable data. It suffers from the possibility of sample reaction during the cooling period, unless the cooling is sufficiently rapid, but recently a rapid freeze quench method (2 ms) has been applied to metalloenzyme studies [13]. The QEXAFS approach has been developed to a very high degree using a piezo mechanism [14], providing repetition rates of EXAFS data of $\sim$10 Hz. Since this is a scanning technique, again the reactions studied should be of the order of 1–2 Hz to ensure that the recorded spectra are representative of the same species throughout the energy range. The last method involving a single X-ray energy was used to provide a kinetic study of a zinc metalloenzyme site [13], and, as in FTIR spectroscopy, probably, with microchannel flow reactors as an alternative, provides the best means of studying extremely rapid reactions ($<$1 μs) by XAS.

2. Energy Dispersive EXAFS (EDE) experimental techniques

In this paper we describe our application of the energy dispersive method to *in situ* catalytic studies. The potential advantages

*email: je@soton.ac.uk; john.evans@diamond.ac.uk; M.A.Newton@soton.ac.uk

of this technique have been established for 20 years [15, 16]. Since then there have been some seminal applications, such as monitoring reactions under stopped flow conditions [17], and heterogeneous catalysts [18]. However, the uptake of the method has been restricted due to stringent requirements on beam stability, focus characteristics and X-ray detector [12]. The incorporation of feedback systems into the electron beam has proven to achieve a significant improvement in beam stability, and the focal characteristics have also been improved by use of 4-point bender mechanisms [19, 20]. Differing solutions to detectors were adopted, with photodiode arrays [21] and a masked CCD camera [22], respectively, adopted on Station 9.3 at the SRS and ID24 at the ESRF. In the experiments described in this paper that were performed of Beamline ID24, each exposure time is of the order of 1–3 ms. Normally data from ∼10 strips of the CCD are collected and accumulated. The readout time is ∼300 ms, and this limits the repetition rate of these experiments to multiples ∼3 Hz, depending upon the number of acquisitions collected for each sample (typically 1–10). This matches the gas pulse width attained with this sampling arrangement. The monochromator used was an asymmetric cut Si(111) crystal used in a Laue geometry to avoid the loss of energy resolution intrinsic to attempting to record spectra at the Rh and Pd K-edges using a Bragg monochromator, due to the broad reflectivity curves at these energies [19].

The catalysis cell is based upon quartz microreactors in containing a bed of powdered sample catalyst. Pressed discs were eschewed to avoid their known problems of confined cavities, surface reconstruction and restricted diffusion [23]. The experimental arrangement as set up on ID24 is shown in Fig. 1. This allows for the microreactor, an I_0 sample and a calibration foil to be incorporated. The use of this cell for *in situ* studies of metal particle formation was on the reduction of $Pt(acac)_2$ on the mesoporous silica H_1-SiO_2 [22] on Station 9.3 of the SRS. The interesting capability of EDE to monitor two elements simultaneously was then demonstrated as the steps in the formation of Pt-Ge/H_1-SiO_2 were investigated using the Pt L_{III} and Ge K-edges [24]. The co-monitoring of the gas phase composition by mass spectrometry and metal structure by EDE was performed on the reaction of $RhCl(CO)_2/Al_2O_3$ with NO using the Rh K edge on ID24 [25]. This showed that different steps in the reaction sequence could be monitored kinetically using the two different monitoring techniques. In situ monitoring of solid state reactions (*e.g.* reduction of MoO_3 [26]) and catalysis (*e.g.* CO oxidation by Pd/C [27] and oxychlorination catalysis by Cu/Al_2O_3 [28]) have also been reported from experiments performed with alternative, pressed disc reactors. Our studies have focussed upon reactions related to the three-way automotive catalysts [29], which contain Rh, Pd and Pt supported on oxides [30].

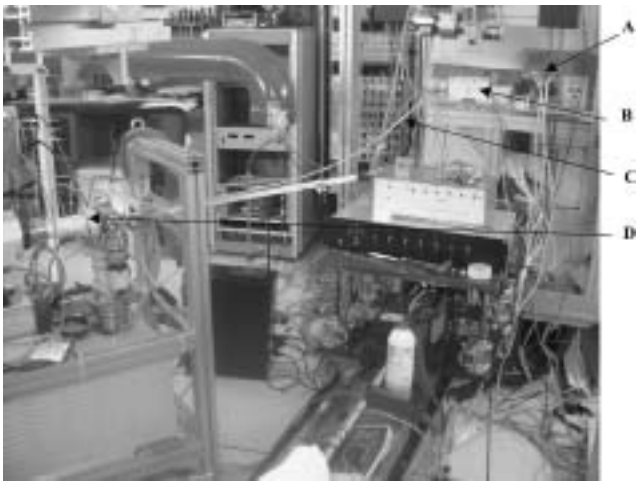

Fig. 1. Equipment used for *in situ* microreactor studies of ID24 at the ESRF. This shows the mass flow controllers (A), the reactor cell in its furnace (B), the capillary lead (C) and the mass spectrometer (D).

3. In Situ EDE characterisation of Rh/Al_2O_3 catalysts for the reduction of NO by H_2

Once loaded into the reactor, the 5% Rh/Al_2O_3 samples (prepared after deposition from aqueous rhodium trichloride, drying, calcinations and reduction by hydrogen) displayed Rh K-edge EXAFS curves unlike those of a fcc structure, indicating that oxidation had transpired in storage and loading (Fig. 2a). Exposure to 4% H_2/He evidently effects reduction to metallic rhodium (Fig. 2b), which may be readily re-oxidised on exposure to 4% O_2/He (Fig. 2c).

Such *in situ* reduced samples of Rh/Al_2O_3 are very rapidly oxidised on exposure to 4% NO/He at 313 K [31], with a similar oxidised rhodium material being formed. This exothermic oxidation is accompanied by the liberation of N_2, and N_2O, both of which require there to have been dissociative chemisorption of the nitric oxide. The NO oxidised rhodium species is rather resistant to reduction by hydrogen. When heated under 4% H_2/He, desorption of molecular NO occurs above room temperature. Reduction of the rhodium to a metallic form, as evidenced by the rise Rh-Rh coordination number, occurs once the temperature reached ∼400 K, at which point the evolution of NO is complete. This reduction is accompanied by evolution of N_2O, and at slightly higher temperatures N_2 is evolved. The temperature required for reduction is considerably higher than that for O_2 treated catalysts, which are readily reduced at room temperature, suggesting that the NO coordination may be stabilising the oxidised rhodium

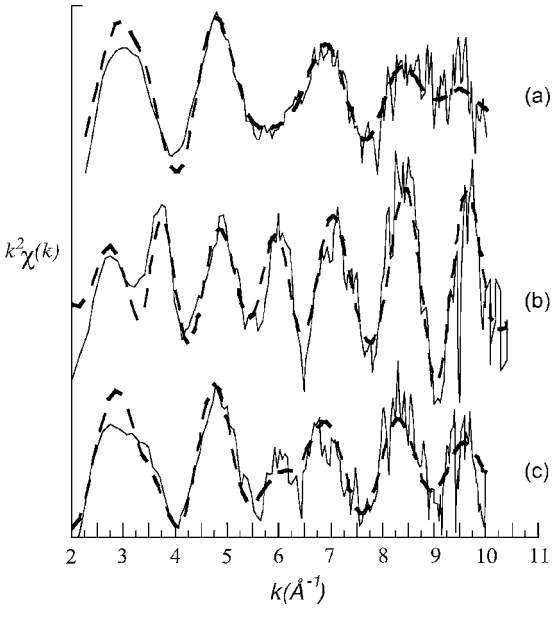

Fig. 2. k^2 weighted EDE derived from (a) a fresh 4 wt% air-exposed Rh/Al_2O_3 under a flow of He; (b) a 5 wt% Rh/Al_2O_3 after subsequent *in situ* reduction to 373 K in 10 ml min^{-1} 4% H_2/He; (c) from the 5 wt% Rh/Al_2O_3 used in (b) after subsequent exposure to 10 mlmin^{-1} 4% O_2/He at 373 K. Solid lines = experiment; dashed line = theory.

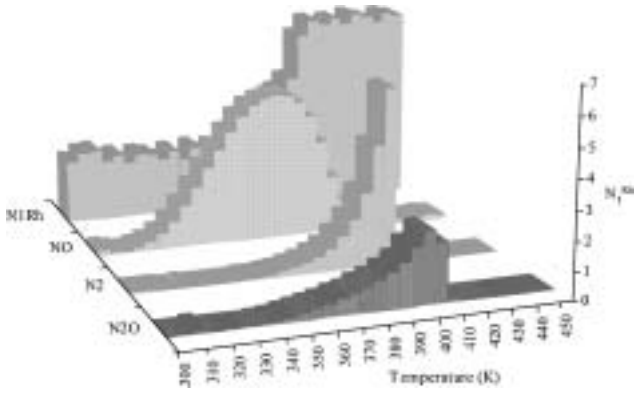

Fig. 3. Variation in the Rh-Rh co-ordination number (grey) and relative mass spectrum intensities for NO (dotted), N_2 (hatched) and N_2O (lined) of a 5 wt% Rh sample previously oxidised by 4% NO/He and then exposed to 4% H_2/He with a 10 K/min temperature ramp.

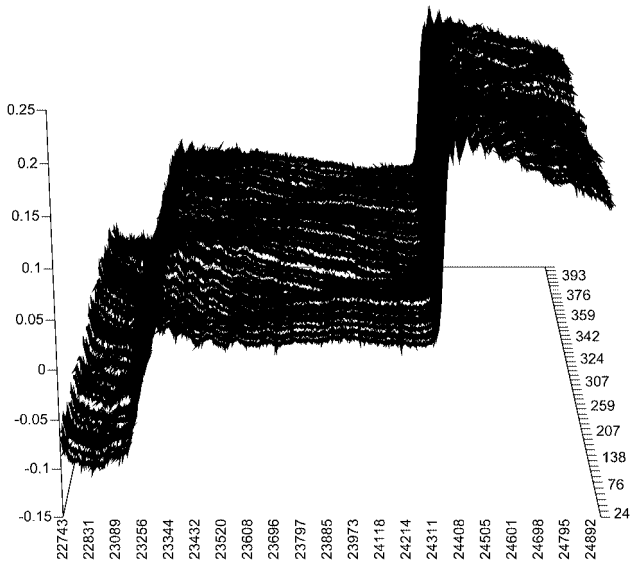

Fig. 4. Plots of the Rh and Pd K-edge XAS of (3% Rh-2% Pd)/Al_2O_3 prepared by co-impregation. Under a 10 ml/min flow of 5% H_2/NO (3 : 2) in He.

species. This provides a background to probing structural changes that occur accompanying the catalytic reduction of NO by H_2 [32]. This demonstrates that metallic rhodium is essential for effecting efficient reduction of NO to N_2. This requires at least a 50% fraction of H_2 in the NO/H_2 proportions. The light-off temperature, at which the efficiency of the catalytic process rises rapidly with temperature decreases with higher H_2/NO ratios, and this is mirrored by the rise in Rh-Rh coordination number to a value of ∼8, which corresponds to a mean particle size of 70–150 atoms [33]. Under the most oxidising (leanest) conditions, the Rh-Rh coordination number remains at ∼2 and only a small proportion of NO is converted to N_2O. See fig. 3.

The EDE/MS experiments with sampling rates of 0.3–3 Hz allow the catalytic process to be investigated over a wide range of experimental conditions with a fine toothcomb. They demonstrate an intimate relationship between the catalytic activity and selectivity and the nature of the dominant phase of the supported rhodium. At the catalytic temperatures studied (>400 K), it is clear that the potential rate of dissociative chemisorption of NO and oxidative fragmentation of the rhodium particles is fast (≪1 s), and so sufficient hydrogen is required to remove the N and O (as N_2 and H_2O respectively) to avoid this.

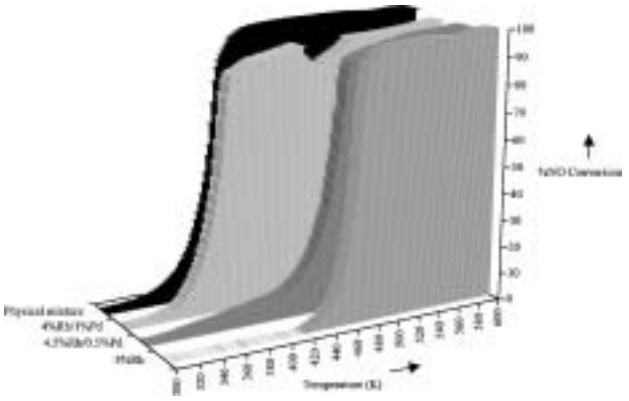

Fig. 5. Plot of NO conversion for a series of 5% (Rh-Pd)/Al_2O_3 catalysts under 5% H_2/NO (3 : 2) in He.

4. In Situ EDE characterisation of Rh-Pd/Al_2O_3 catalysts for the reduction of NO by H_2

The degree of bending of the monochromator affords an energy span over ∼2500 eV, quite sufficient to monitor both the Rh and the Pd K-edges simultaneously and provide a digital resolution of 2 eV [12]. Both of these are key elements in formulations of automotive exhaust catalysts [29, 30]. So a series of catalysts were prepared based upon a 5 wt% (Rh, Pd)/Al_2O_3 synthesised in differing ways: co-impregnation of Pd and Rh (CI), sequential impregnation of Rh and then Pd (SI) and also a physical mixture of 5% Rh/Al_2O_3 and 5% Pd/Al_2O_3.

The raw, calibrated double-edge X-ray absorption spectra of a 3% Rh-2% Pd/Al_2O_3 sample are shown in Figure 4, the sample being under a flow of H_2-NO (3 : 2)/He and undergoing a temperature ramp. It may be seen that there are some variations in the background, probably due to optical instabilities, but these do not prevent the data from being treated with standard background subtraction [34] and spherical wave analysis analysis methods [35]. The NO conversion for a series of four catalysts is presented in Figure 5. Incorporation of 10% Pd into the Rh-Pd phase has relatively little effect, apart from an increase in activity at lower temperatures. As the proportion is increased to 20%, the "light-off" temperature, at which convertion starts to rise rapidly is markedly reduced, and this behaviour is similar to that observed for a physical mixture of 5%Rh/Al_2O_3 and 5%Pd/Al_2O_3 (1 : 1). Figure 6 shows the refined Rh-Rh/Pd coordination number (first shell) from the EDE data. As discussed above, the increase in Rh-Rh coordination number for the Rh/Al_2O_3 sample parallels the onset of catalytic activity showing the importance of creating metallic clusters for the onset of catalysis (forming N_2 with high selectivity). It was also observed previously that this could not be achieved under oxidising conditions (excess of NO over H_2). It is interesting therefore that once a proportion of 20% Pd is achieved that the rhodium centres maintain there metallic environment over the entire temperature range studies, suggesting that palladium is stabilising the rhodium from oxidation. By comparing the results from the Pd edge, it appears that small alloy particles are present. From a catalytic point of view, however, this stabilisation is accompanied by a loss in selectivity for N_2 formation, with the proportion of N_2O substantially increased, as is observed for Pd/Al_2O_3 alone. Nevertheless, these results do provide considerable insight into the strong dependence of catalyst structure on the ambient conditions.

At the Rh edge, not surprisingly the behaviour of the physical mixture of the two alumina supported catalysts is essentially as found for Rh/Al_2O_3 on its own.

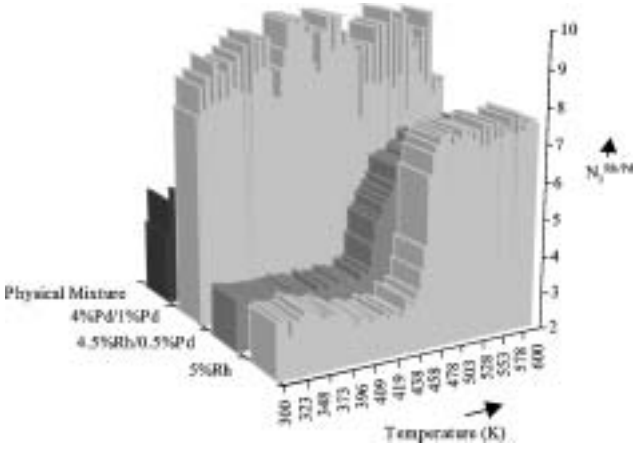

Fig. 6. Plot of the first shell Rh-Pd coordination number from analysis of the Rh K-edge EXAFS data during NO reduction for a series of 5% (Rh-Pd)/Al_2O_3 catalysts under 5% H_2/NO (3:2) in He.

5. Future possibilities

These experiments do not represent any limit on the time resolution that is currently attainable under practical conditions. Stopped flow experiments, with mixing times of ∼1 ms or below, now closely match the normally attainable rate of acquisition for single scans [36, 37]. In order to improve the time resolution of these catalysis experiments and to gain more information about the surface species, two developments are in progress: incorporating a modulated gas composition flow programme and to combine diffuse reflectance Fourier transform infra red spectroscopy (DRIFTS) as a third simultaneous technique.

Detector developments are also important for enhancing acquisition and repetition rates, and considerable progress has been made with the silicon microstrip detector, XSTRIP [38], which offers a repetition rate of 10 s of microseconds. Then very rapid system perturbations may be introduced to try to identify in transients in catalysis.

Acknowledgements

We wish to thank the staff of the ESRF for enabling these experiments and providing access. The technical skills of John James, Melanie Hill, Sebastian Pasternak, and Ralph Wiegel, are gratefully acknowledged, as is the beamline stewardship of Dr Sakura Pascarelli (ID 24). This work was funded under the "Catalysis and Chemical Processes initiative of the EPSRC" and through Long Term Projects for allocation of beamtime by the ESRF. We would like to thank the ESPRC (MAN) and ICI (SGF) for postdoctoral funding and EPSRC for a project studentship (BJ). The technical skills of John James, Melanie Hill, Sebastian Pasternak, and Ralph Wiegel are Gratefully acknowledged.

References

1. Ertl, G., J. Mol. Catal. A–Chemical **182**, 5 (2002).
2. Henrich, V. E. and Cox, P. A., "The Surface Science of Metal Oxides," (Cambridge University Press, Cambridge, 1994)
3. Evans, J., Hayden, B. E. and Lu, G., Surf. Sci. **360**, 61 (1996).
4. Evans, J., Hayden, B. E., Mosselmans, F. and Murray, A., Surf. Sci. **301**, 61 (1994).
5. Newton, M. A., Bennett, R. A., Smith, R. D., Bowker, M. and Evans, J., Chem. Commun. 1677 (2000).
6. Bennett, R. A., Newton, M. A., Smith, R. D., Bowker, M. and Evans, J., Surf. Sci. **487**, 223 (2001); Bennett, R. A., Newton, M. A., Smith, R. D., Evans, J. and Bowker, M., Mater. Sci. Technol. **18**, 710 (2002).
7. Sinfelt, J. H., "Bimetallic Catalysts: Discoveries, Concepts and Applications," (John Wiley, New York, 1983).
8. Koningsberger, D. C. and Prins, R. eds "X-ray Absorption: Principles, Applications, Techniques of EXAFS, SEXAFS and XANES," (John Wiley, New York, 1988).
9. Grunwaldt, J. D. and Clausen, B. S., Topics Catal. **18**, 37 (2002).
10. Gunter, M. M. *et al.*, Catal. Lett. **71**, 37 (2001).
11. Van't Blik, H. F. J., van Zon, J. B. A. D., Huizinga, T., Koningsberger, D. C. and Prins, R., J. Phys. Chem. **87**, 2264 (1983); Van't Blik, H. F. J., van Zon, J. B. A. D., Huizinga, T., Koningsberger, D. C. and Prins, R., J. Am. Chem. Soc. **107**, 3139 (1985).
12. Newton, M. A., Dent, A. J. and Evans, J., Chem. Soc. Rev. **31**, 83 (2002).
13. Kleifeld, O., Frenkel, A., Martin, J. M. L. and Sagi, I., Nature Struct. Biol. **10**, 98 (2003).
14. Richwin, M., Zaeper, R., Lutzenkirchen-Hecht, D. and Frahm, R., Rev. Sci. Instrum. **73**, 1668 (2002).
15. Dartyge, E., Fontaine, A., Jucha, A. and Sayers, D., in Hodgson, K. O., Hedman, B. and Penner-Hahn, J. E., "EXAFS and Near Edge Structure III," (Springer-Verlag, Berlin, 1984), p 473.
16. Matsushita, T., Oyanagi, H., Saigo, S., Kihara, H. and Kaminaga, U. in Hodgson, K. O., Hedman, B. and Penner-Hahn, J. E., "EXAFS and Near Edge Structure III," (Springer-Verlag, Berlin, 1984), p 476.
17. Yoshida, N. *et al.*, Chem. Commun. 354 (1990).
18. Couves, J. W. *et al.*, Nature **354**, 465 (1991).
19. Hagelstein, M., Ferraro, C., Hatje, U., Ressler, T. and Metz, W., J. Synchrotron Radiat. **2**, 174 (1998); San Miguel, A., Hagelstein, M., Bornel, J. C., Marot, G. and Renier, M., J. Synchrotron Radiat. **5**, 1396 (1998).
20. Dent, A. *et al.*, J. Synchrotron Radiat. **6**, 381 (1999).
21. Bogg, D. *et al.*, Nucl. Instr. Meth. **A392**, 461 (1997).
22. Hagelstein, M., San Miguel, A., Fontaine, A. and Goulon, J., J. Physique IV **7**, 303 (1997).
23. Fiddy, S. G. *et al.*, J. Chem. Soc. Chem. Commun. 851 (1999).
24. Fiddy, S. G. *et al.*, Chem. Commun. 445 (2001); Fiddy, S. G. *et al.*, Phys. Chem. Chem. Phys. **4**, 827 (2002).
25. Newton, M. A. *et al.*, J. Phys. Chem. A **105**, 5965 (2001).
26. Ressler, T., Wienold, J., Jentoft, R. E. and Neisius, T., J. Catal. **210**, 67 (2002).
27. Ressler, T., Hagelstein, M., Hatje, U. and Metz, W., J. Phys. Chem. B **101**, 6680 (1997).
28. Lamberti, C. *et al.*, Angew. Chem. Int. Edn. **41**, 2341 (2002).
29. Bowker, M. and Joyner, R. W. in Thompson, D., " Insights into Speciality Inorganic Chemicals," (Royal Society of Chemistry, Cambridge, 1995), p 145.
30. Twigg, M. V., Platinum Metals Rev. **45**, 71 (2001); *ibid* **47**, 15 (2003).
31. Campbell, T. *et al.*, Chem. Commun. 304 (2002).
32. Newton, M. A., Dent, A. J., Diaz-Moreno, S., Fiddy, S. G. and Evans, J., Angew. Chem. Int. Edn. **41**, 2587 (2002).
33. Jentys, A., Phys. Chem. Chem. Phys. **1**, 4059 (1999).
34. Binsted, N., PAXAS Program for the analysis of X-ray absorption spectra (University of Southampton, 1990).
35. Binsted, N., EXCURV98 (CCLRC Daresbury Laboratory, 1998)
36. Diaz Moreno, S. in Billinge, S. J. L. and Thorpe, M., "From Semiconductors to Proteins: Beyond the Average Structure," (Plenum, New York, 2002), p 203.
37. Abdul Rahman, M. B. B. *et al.*, Disc. Faraday Soc. **122**, 211 (2003).
38. Iles, G. *et al.*, J. Synchrotron Radiat. **7**, 221 (2000); O'Malley, R. *et al.*, Electrochem. Commun. **5**, 15 (2003); Anderson, C. *et al.*, http://detserv1.dl.ac.uk/xstrip/

Physica Scripta. Vol. T115, 76–79, 2005

In-situ Al K-edge Spectroscopy on Zeolites: Instrumentation, Data-interpretation and Catalytic Consequences

Jeroen A. van Bokhoven[1]

Institute for Chemical and Bioengineering, Swiss Federal Institute of Technology (ETH), 8093 Zurich, Switzerland

Received June 26, 2003; accepted November 4, 2003

Abstract

Zeolites are used for a wide variety of reactions, such as cracking and isomerization of alkanes, and for the production of fine-chemicals. Although these catalytic systems are extensively studied, very often structure – activity relations are lacking. Relevant techniques that determine the catalyst structure under catalytic conditions are limited. In many reactions, the aluminum atom is associated with catalytic activity, making an experimental tool that detects the aluminum coordination in a controlled atmosphere extremely valuable. Conventional methods often fail in providing such data.

Developments in instrumentation and data-interpretation enable measurements in controlled gas-atmosphere at elevated temperature at the Al K edge. A thorough theoretical interpretation of the XANES spectra using FEFF8 enables assignment of different aluminum coordinations in the samples. The measurements on zeolitic samples have shown that the aluminum coordination is a subtle function of the precise measurement conditions, which has consequences for interpretation of catalytic data. Moreover, measurements at extreme high temperature show the appearance of unique spectral features that can be attributed to a unique aluminum coordination previously not observed using *ex-situ* techniques.

1. Introduction

Alumina-silicates and zeolites are active in a wide variety of Brønsted and Lewis acid catalyzed reactions. Commercial applications are found in the petrochemical and refining industry [1]. Moreover, they are active in the production of fine-chemicals and intermediates [2] and new applications continue being reported. A unique feature of zeolites is, besides their high activity, the selectivity imposed by the limited sizes of the micropores in the crystals.

Zeolites are built of alumina and silica tetrahedra, forming a three-dimensional crystalline network with pores and cages with sizes in the range of 2–14 Å (vide infra), which equals the size of small molecules [3]. The structure of a zeolite determines its activity and the aluminum atom is responsible for Brønsted and Lewis acid-catalyzed reactions. For this reason, many studies are concerned with the determination of the aluminum coordination in zeolites [4, 5, 6]. The crystal structures of zeolites are well known, however, an active structure is obtained after one or more activation steps that generally consist of steaming and acid or base leaching. Dealumination and stabilization of the framework occurs, thereby partly destroying the crystalline framework and forming framework and non-framework species. An additional complication during the determination of structure/activity relationships is that the catalytic conditions differ from those used in a typical characterization method like ^{27}Al MAS NMR. In principle, X-ray absorption fine-structure spectroscopy at the Al K edge enables these measurements.

This article describes the developments that enable *in-situ* XAS spectroscopy on samples with adsorption edges of energies between $1 < E < 3$ keV. Instrumentation has been developed and implemented at station 3.4 of the SRS Daresbury (UK). Theoretical interpretation of experimental spectra using the FEFF8 code was performed, and fingerprinting of the Al K edge spectra enables the determination of different aluminum coordinations from the spectra. The range of conditions that can be achieved in the developed instrumentation has opened up the possibilities of studying a wide range of edges in the low energy range ($E > 1$ keV) in *in-situ* conditions up to 1000 K in vacuum and 675 K at 1.5 bars pressure. Application to zeolitic systems has provided vital information on the structure of these catalysts in catalytic relevant conditions and during treatment of the material.

2. Experimental

2.1. *Samples*

Zeolitic samples were obtained from Linde and checked for crystallinity with ^{27}Al MAS NMR, X-ray diffraction, and nitrogen physisorption.

NaY (LZ-Y54) was converted into NH_4Y via threefold ion exchange with 1 M NH_4NO_3. Steamed zeolite Y, H-USY, was obtained by calcination of LZ-Y84 at 725 K for 4 h using a ramp of 1 K/min. ^{27}Al MAS NMR showed 100% tetrahedrally coordinated aluminum in NH_4Y zeolite.

2.2. *XAS measurements*

Al K edge XAS measurements have been performed at the SRS, Daresbury (UK), Station 3.4. The synchrotron was operating at 2.0 GeV with an average current of 120 mA. A double crystal scanning monochromator mounted with YB_{66} crystals was used. Measurements were performed in the ILEXAFS set-up [7, 8] that enables treatment of the sample during measurement. The intensity of the incoming photon beam (I_0) is measured by the total electron yield signal of a fine copper or gold mesh. The X-ray energy is calibrated using an aluminum foil, setting the energy at the first maximum of the first derivative to 1560 eV.

2.3. *FEFF8 calculations*

Interpretation of the XANES spectra is performed using the *ab-initio* self-consistent field full multiple scattering code, Feff8 [9, 10]. The output of a calculation includes the X-ray absorption spectrum and the density of states. It is known that multiple scattering within a radius of 15 Å affects the shape of the spectra [11, 12]. A cluster ($HAlSi_{28}O_{78}$) of about 20 Å in diameter was taken from the crystallographic structure of zeolite Y. The aluminum atom is positioned in the center of the cluster. The structure of a three-coordinate aluminum is unknown. Therefore, the structure of three-coordinate aluminum is mimicked by distorting the tetrahedrally coordinated aluminum into threefold coordination [13].

[1] j.a.vanbokhoven@tech.chem.ethz.ch

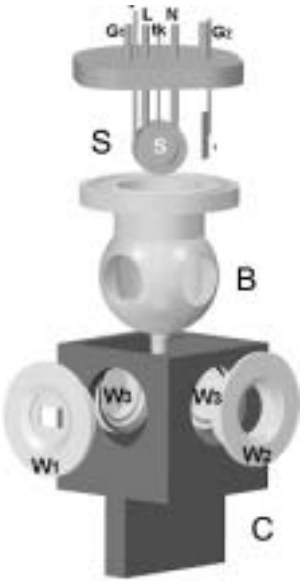

Fig. 1. In-situ cell for measurement of edges of energies $1 < E < 3$ keV; maximum achievable temperature is 1000 K, maximum pressure is 1.5 bar. S is the sample-holder; B is the reaction chamber; and Wx are the window holders.

3. Instrumentation

Figure 1 shows the cell for *in-situ* low-energy X-ray absorption fine-structure (ILEXAFS) spectroscopy [7]. The sample holder (S) is connected to a flange that fits vacuum tight onto a hollow sphere (A). The flange has several gas and electric feedthroughs that enable gas-flow through the sphere and the transport of electric signals: electron yield signal, heating wire, and thermocouple. Two openings in the sphere at an angle of 90 degrees enable the initial X-ray radiation to irradiate the sample and the produced fluorescence radiation to exit the sphere. The sphere fits into a cube (B) onto which window-holders (Wx) are attached that seal the hollow sphere vacuum tight. The entrance window is a supported 7 µm thick beryllium window of 8 × 12 mm. The exit window is spherical with a diameter of 22 mm and thickness of 13 µm. This window holder is integrated in a gas proportional counter fluorescence detector, ensuring a large solid angle for the fluorescence radiation. The *in-situ* cell is mounted in a large vacuum vessel (not shown) onto a (x, y, z) manipulator at beamline 3.4 of the SRS Darebsury (UK). The vacuum vessel has several connectors for feedthrough of gasses and electric signals, in addition to view ports. Specially shielded electrical feedthroughs are used for the measured signals. In the vacuum vessel, a fine metal mesh can be positioned in the initial X-ray beam for measuring the I_{zero} signal.

4. Data-analysis

XAS spectra of compounds with a well-known structure are simulated with the full multiple scattering code FEFF8. Figure 2 shows the large agreement between experimental (left) and theoretical spectra (right) of tetrahedrally and octahedrally coordinated aluminum. All characteristic experimental features are reproduced by theory. The spectrum of a tetrahedrally coordinated aluminum atom is that of a zeolite NH_4Y. The spectrum of an octahedrally coordinated aluminum is that of an aluminum in corund, a crystalline alumina (α-Al_2O_3). Based on these spectra and a large number of spectra from the literature, typical features for different aluminum coordinations

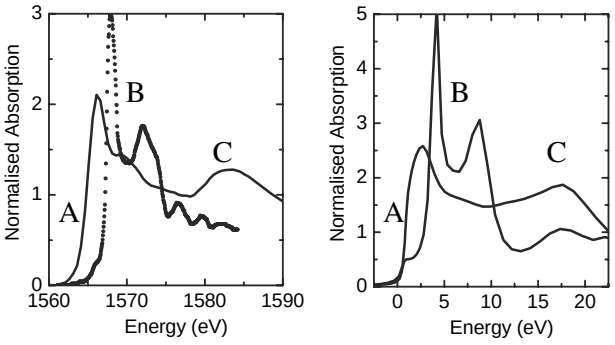

Fig. 2. There is a large agreement between the experimental (left) and theoretical spectra (right). The dotted line represents the data points of the octahedrally coordinated aluminum. FEFF8 reproduces the characteristic features for tetrahedrally and octahedrally coordinated aluminum: A. different energy of the edge; B. characteristic shape of the whiteline, and C. characteristic multiple scattering peaks.

are distinguished as summarized in detail in ref [14]. In the figure, typical characteristic features are emphasized.

From full multiple scattering calculations and symmetry considerations using Extended Huckel theory, the orbital origin of the spectral features has been determined [11, 12]. The spectral region up to about 15 eV above the absorption edge is determined by long-range scattering up to a radius of 15 Å, which originates from hybridization of d-orbitals with the p DOS. The little pre-edge feature that is typically visible in spectra of an octahedrally coordinated aluminum is a non-localized p orbital that contains s and d character. Hybridization of p and d orbitals is allowed when the geometry deviates from an ideal octahedron. Multiple scattering in the first coordination shell of a tetrahedrally coordinated aluminum causes a broad peak at about 20 eV above the adsorption edge. The exact energy position is sensitive to the aluminum oxygen bond length. Other coordinations have comparable peaks at different energies.

The edge position in a spectrum of a tetrahedrally coordinated aluminum is about 2 eV lower than for an octahedrally coordinated aluminum, because of the allowed p,d hybridization in the tetrahedral coordination. Based on symmetry arguments, the core-hole in an octahedral coordination is more shielded, because of the allowed mixing of the aluminum p orbitals with the oxygen p orbitals near the valence band maximum.

5. Zeolite structure in *in-situ* conditions

Figure 3a shows the cages that are typical of the structure of Y zeolite. Figure 3b shows the atomic network in this zeolite, with the tetrahedrally coordinated silicon or aluminum atoms. Due to the lower charge on an aluminum atom compared to silicon, there is a negative charge on the framework for each aluminum atom. Extra-framework cations in the pores or cages of the structure compensated this charge. When protons compensate the charge, a bridging hydroxyl causes Brønsted acidity (figure 3c).

Figure 4 shows the influence of water on the aluminum coordinations in acidic zeolites. Figure 4a shows the room temperature spectrum of H-Y, which is obtained after heating NH_4-Y in the in-situ cell to 675 K in vacuum. The spectrum shows the typical characteristics of tetrahedrally coordinated aluminum. Spectral changes occur under a flow of helium containing 40 mbar water. The differences can be attributed to the presence of a small amount of octahedrally coordinated aluminum [15], covering 8% of the total aluminum content. These measurement conditions

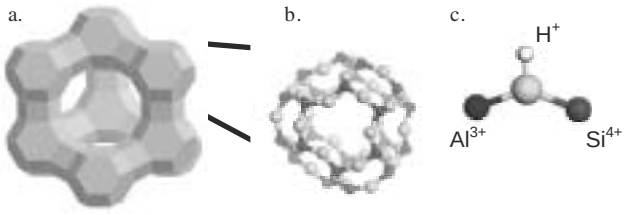

Fig. 3. Schematic view of the pore wall in zeolite Y showing the 12 Å opening; b. atomic connection of the tetrahedrally coordinated Si and Al atoms bridged by oxygen atoms; and c. schematic view of the bridging Brønsted acid hydroxyl group in zeolites.

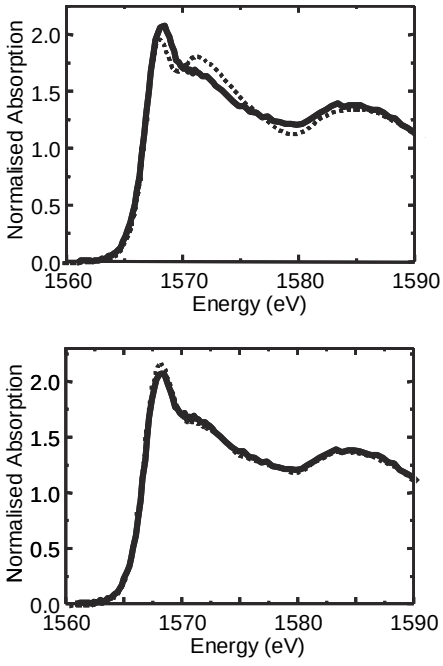

Fig. 4. The spectrum of H-Y zeolite under different measurement conditions: (top) solid line: dry conditions at room temperature; dotted line: wet conditions at room temperature; (bottom) solid line: dry conditions at room temperature; dotted line: wet conditions at 395 K.

resemble those of a typical ^{27}Al MAS NMR experiment, which also showed the presence of about 10% octahedral aluminum [16]. In the spectrum of the same sample measured at a temperature of 395 K (Figure 4 bottom), the characteristics of the octahedral coordination are no longer visible and the octahedral aluminum has converted into tetrahedral. These measurements indicate that the zeolitic aluminum coordination is a subtle function of the temperature and water content present in the pores of the zeolite. Spectra of zeolites Beta (not shown) and H-Mordenite that are taken under identical conditions showed an identical behavior. This indicates that in acidic zeolites a transformation of framework tetrahedral aluminum into octahedral and back occurs easily.

The effect of steaming on the aluminum coordination and its sensitivity to the presence of water and temperature is shown in Figure 5. It shows the spectrum of ultra-stable Y, which is a commercial sample of a steamed zeolite Y measured at room temperature in the presence and absence of water. The large intensity in the range of 5–15 eV above the absorption edge is indicative of the presence of a large amount of octahedrally coordinated aluminum in the sample that is measured in wet environment. When measuring the sample in vacuum, part of the octahedrally coordinated aluminum is transformed into tetrahedral, visible in Figure 5 by a loss of intensity at 5–15 eV

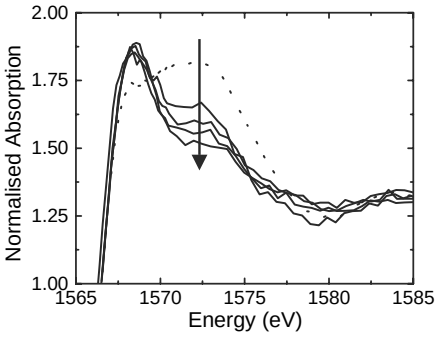

Fig. 5. Al K edge XAS spectra of steamed Y zeolite. The dotted line represents the room temperature spectrum under a flow of wet helium. The solid lines represent spectra taken in vacuum. The temperature increase from room temperature, via 375 K, 475 K, to 675 K.

above the absorption edge and an increase in intensity of the tetrahedral whiteline. Up to 600 K, a transformation of octahedral aluminum into tetrahedral occurs. This differs from the non-steamed sample that showed no octahedrally coordinated aluminum at temperatures higher than 395 K. This indicates that during steaming a different silica-alumina phase is formed in which the octahedrally coordinated aluminum is stabilized.

The spectra of H-USY measured at temperatures higher than 675 K (Figure 6) show a small pre-edge feature at 1565 eV, which is still present after cooling the sample down to room temperature (not shown). Such pre-edge features have been observed for the acidic zeolites that have been measured: Mordenite, Beta and Y. Increasing the temperature enhances the intensity of the pre-edge feature. Full multiple scattering calculations with the FEFF8 code on several large clusters with various aluminum coordinations indicate that a pre-edge feature is indicative of the presence of a non-bonding p orbital. Figure 7 shows the p DOS of a three-coordinated aluminum in a zeolitic structure. A different local geometry of the threefold coordinated aluminum shows small variations in the pre-edge intensity. Also the DOS of a square planar and a square pyramidal coordinated aluminum atom shows a pre-edge feature. However, based on chemical arguments [13], these coordinations are highly unlikely in a zeolitic structure. It is more likely that a partial dehydroxylation of the bridging hydroxyl group occurs, creating a threefold coordinated aluminum. Previously, it was shown that the presence

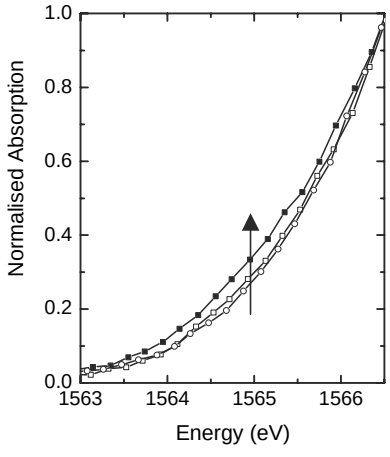

Fig. 6. Pre-edge region of H-USY measured in vacuum at room temperature (◯), 675 K (□), and 975 K (■). At $T > 675$ K, a small pre-edge feature appears. This pre-edge feature is stable after cooling the sample to room temperature, however, disappears after the adsorption of water.

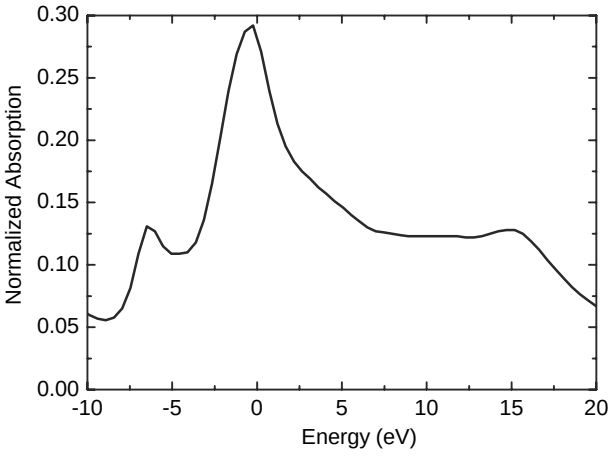

Fig. 7. p DOS of a three-coordinated aluminum, showing a pre-edge feature, which arises from a non-bonding p-orbital. Three-coordinate aluminum is embedded in a large cluster of about 20 Å radius cut from the crystalline structure of Y zeolite. The exact position of the Fermi level determines the intensity of the pre-edge in the X-ray absorption spectrum.

of traces of water annihilates the pre-edge feature, and thus the three-coordinate aluminum. In the meantime, octahedrally coordinated aluminum is created.

6. Aluminum coordinations in zeolites

ILEXAFS measurements on zeolites at the Al K edge provide detailed information about the aluminum coordination chemistry in zeolites. Part of the framework tetrahedral aluminum shows Lewis acid character by coordinating to the Lewis base water. The aluminum coordination thereby changes to octahedral. This process is reversible as function of temperature. It is likely that this process is accompanied by hydrolysis of part of the aluminum oxygen bonds [17]. The ability of framework tetrahedral aluminum to transform into an octahedral has been associated with activity in Lewis acid catalyzed reactions [18, 19, 20]. The Al K edge XAS measurements during controlled conditions provide unique detail on the stability of octahedrally coordinated aluminum in zeolites. Activation of a zeolite by steaming shows a significant amount of octahedrally coordinated aluminum that is transformed into tetrahedral by heating to temperatures above 600 K. It is likely that a non-framework silica alumina phase is formed that stabilizes the octahedrally coordinated aluminum. The formation of a unique aluminum coordination occurs at temperatures higher than 675 K. The exact structure remains to be resolved, however, its coordination is likely threefold. At such high temperatures, dehydroxylation of the framework occurs, which lowers the aluminum coordination to threefold. Low-coordinated aluminum sites are energetically unfavorable and therefore strongly attract water molecules or any other Lewis basic molecule. This process is accompanied by the formation of octahedrally coordinated aluminum, suggesting that these processes are linked. Low-coordinated aluminum, like the threefold coordination observed here, is often associated with Lewis catalytic activity, however, the precise mechanism remains unclear. The Al K edge XAS measurements indicate that traces of water are sufficient to coordinate to the threefold coordinated aluminum. Only the harsh conditions during heat treatment above 675 K may restore the three-coordinate aluminum. During typical reaction conditions in a Lewis catalyzed reaction, traces of water are often present, thus a direct catalytic role of the three-coordinate aluminum is not expected. The role of the three-coordinate aluminum on catalytic activity for this type of reactions may however be indirect via the formation of octahedrally coordinated aluminum. This remains topic of further research.

7. Conclusions

Developments in the fields of instrumentation, data-analysis and theoretical interpretation enable the performance and interpretation of *in-situ* measurements on zeolite catalysts at the Al K edge. The ILEXAFS set-up can be used for measuring X-ray absorption edges in the range of $1 < E < 3$ keV. This covers the K edges of sodium until chlorine and the L edges of the second row of the d block elements. The temperature range that can be achieved is $77 < T < 1000$ K. The fragile windows can withstand a total pressure difference of 1.5 bar at a maximum temperature of 675 K. Structural information on zeolites that is relevant for catalysis has been obtained in ILEXAFS and unique structural changes in zeolitic catalysts are observed under well-defined measurement conditions.

Acknowledgments

Many people have been involved in this work. I would like to explicitly thank the following people for their contributions to this work: Professor D. C. Koningsberger (Utrecht University), A. M. J. van der Eerden (Utrecht University), Dr J. T. Miller (BP), Dr A. D. Smith (SRS Daresbury), and Professor D. E. Ramaker (George Washington University). The SRS in Daresbury (UK) is acknowledged for providing the beamtime under allocation numbers 38108 and 37410.

References

1. Sie, T., in "Introduction to Zeolite Science and Practice", (Eds. Van Bekkum, Jacobs, P. A., Flanigen, E. M. and Jansen, J. C.), (Elsevier, Amsterdam 2001).
2. Hölderich, W. F. and van Bekkum, H., Stud. Surf. Sci. Catal. **58**, 631 (1991).
3. Baerlocher, Ch., Meier, W. M. and Olson, D. H., "Atlas of Zeolite Framework Types", Fifth Revised Edition, (Elsevier, Amsterdam, 2001).
4. Bourgeat-Lami, E., *et al.*, Appl. Catal. **72**, 139 (1991).
5. Kirisci, I., *et al.*, J. Phys. Chem. **98**, 4627 (1994).
6. Woolery, G. L., Huehl, G. H., Timken, H. C., Chester, A. W. and Vartuli, J. C., Zeolites **19**, 288 (1997).
7. van der Eerden, A. M. J., van Bokhoven, J. A., Smith, A. D. and Koningsberger, D. C., Rev. Sci. Instrum. **71**, 3260 (2000).
8. Van Bokhoven, J. A., van der Eerden, A. M. J., Smith, A. D. and Koningsberger, D. C., J. Synchrotron Rad. **6**, 201 (1999).
9. Ankudinov, A. L., Ravel, B., Rehr, J. J. and Conradson, S. D., Phys. Rev. **B58**, 7565 (1998).
10. Mustre de Leon, J., Rehr, J. J., Zabinski, S. I. and Albers, R. C., Phys. Rev. **B44**, 4146 (1991).
11. Cabaret, D., Sainctavit, P., Ildefonse, Ph. and Flank, A.-M., J. Phys.: Condens. Matter **8**, 3691 (1996).
12. van Bokhoven, J. A., Sambe, H., Ramaker, D. E. and Koningsberger, D. C., J. Phys.: Condens. Matter **13**, 10247 (2001).
13. van Bokhoven, J. A., van der Eerden, A. M. J. and Koningsberger, D. C., J. Am. Chem. Soc. **125**, 7435 (2003).
14. van Bokhoven, J. A., Sambe, H., Ramaker, D. E., and Koningsberger, D. C., J. Phys. Chem. B **103**, 7557 (1999).
15. van Bokhoven, J. A., van der Eerden, A. M. J. and Koningsberger, D. C., Stud. Surf. Sci. Catal. **142**, 1885 (2002).
16. Omegna, A., van Bokhoven, J. A. and Prins, R., J. Phys. Chem. B **107**, 8854 (2003).
17. Wouters, B. H., Chen, T.-H. and Grobet, P. J., J. Am. Chem. Soc. **120**, 11419 (1998).
18. Woolery, G. L., Kuehl, G. H., Timken, H. C., Chester, A. W. and Vartuli, J. C., Zeolites **19**, 288 (1997).
19. Kunkeler, P. J., *et al.*, J. Catal. **180**, 234 (1998).
20. Haouas, M., Kogelbauer, A. and Prins, R., Catal. Lett. **70**, 61 (2000).

Physica Scripta. Vol. T115, 80–87, 2005

Environmental Interfaces, Heavy Metals, Microbes, and Plants: Applications of XAFS Spectroscopy and Related Synchrotron Radiation Methods to Environmental Science

Gordon E. Brown, Jr.[1,2*], Jeffrey G. Catalano[2], Alexis S. Templeton[2,3], Thomas P. Trainor[2,4], Francois Farges[2,5], Benjamin C. Bostick[2,6], Tom Kendelewicz[2], Colin S. Doyle[2], Alfred M. Spormann[7], Kristin Revill[2], Guillaume Morin[8], Farid Juillot[8] and Georges Calas[8]

[1]Stanford Synchrotron Radiation Laboratory, SLAC, MS 99, 2575 Sand Hill Road, Menlo Park, CA 94025, USA
[2]Dept. of Geological & Environmental Sciences, Stanford University, Stanford, CA 94305-2115, USA
[3]Marine Biology Research Division, Scripps Institution of Oceanography, University of California, San Diego, La Jolla, CA 92093, USA
[4]Consortium for Advanced Radiation Sources, University of Chicago, 5640 South Ellis Avenue, Chicago, IL 60637, USA
[5]Laboratoire des géomatériaux, Université de Marne-la-Vallée, FRE CNRS 2455 "G_2I", 77454 Marne la Vallée cedex 2, France
[6]Dept. of Earth Sciences, Dartmouth College, 6105 Fairchild Hall, Hanover, NH 03755, USA
[7]Dept. of Civil and Environmental Engineering, Stanford University, Stanford, CA 94305, USA
[8]Laboratoire de Minéralogie-Cristallographie, Universités de Paris 6 et 7, IPGP and UMR CNRS 7590, 2 place Jussieu, 75252 Paris cedex 05, France

Received June 26, 2003; accepted November 4, 2003

PACS number: 61.10.Ht

Abstract

During the past decade, applications of synchrotron radiation (SR) methods to environmental science have grown significantly, resulting in a new interdisciplinary field known as *molecular environmental science*, which focuses on the molecular-level speciation of environmental pollutants and the fundamental chemical and biological processes determining their behavior in complex systems. Here we review some recent applications of XAFS spectroscopy and related SR methods, including micro-XANES and X-ray Standing Wave (XSW) spectroscopy, micro-XRD, X-ray fluorescence micro-tomography, and photoemission spectroscopy to heavy metals and actinides in model systems and more complex environmental samples. Examples include XAFS studies of heavy metals and actinides at environmental interfaces, combined XAFS and XSW studies of heavy metal interactions with microbial biofilm-coated metal oxide surfaces, and combined XANES and photoemission studies of microbial interactions with metal sulfide surfaces.

1. Introduction

Since X-ray absorption fine structure (XAFS) spectroscopy was introduced over 30 years ago as an element-specific local structural probe [1, 2], it has become the technique of choice for determining the local coordination environment of specific elements in solids (both amorphous and crystalline) and liquids at low concentrations, where X-ray and neutron diffraction methods are relatively insensitive. Because of this attribute and the ability to examine samples under *in situ* conditions with minimal preparation, XAFS spectroscopy has become the most important method for determining the speciation of environmental pollutants such as zinc, lead, and arsenic, which are often present in complex, multi-phase, natural samples at concentrations ranging from greater than a weight percent to less than a ppm in a variety of chemical forms, including those in which such elements are sorbed at solid/aqueous solution interfaces [3, 4]. Applications of XAFS and micro-XAFS spectroscopy and other SR methods (micro-synchrotron X-ray fluorescence (μ-SXRF), X-ray standing wave (XSW) spectroscopy, photoemission spectroscopy (PES), and micro-X-ray diffraction (μ-XRD), X-ray fluorescence micro-tomography, scanning transmission X-ray microscopy (STXM), transmission X-ray microscopy (TXM)) to complex environmental samples has led to the development of a new field referred to as *molecular environmental science* (MES) [5–7]. MES is concerned with determining the speciation of environmental pollutants and with understanding the chemical and biological processes that affect their speciation, transformation, sequestration, transport, toxicity, and potential bioavailability. The term *speciation*, as used here, refers to (1) the identity of the element (or elements), (2) its (their) oxidation state, (3) its (their) physical state (*i.e.*, phase association; presence in a liquid, gas, or solid phase (amorphous or crystalline), colloidal particle, animal or plant cell, or biofilm; presence as a surface coating or thin film on a solid, as a sorption complex (monomeric or polymeric) on a solid, colloidal particle, or an organic substance; etc.), (4) its stoichiometry, and (5) its detailed molecular structure. Knowledge of the molecular-level speciation of pollutants is essential for predicting their environmental properties, *i.e.*, their stability, mobility, toxicity, and potential bioavailability to humans and other organisms [5, 8], as well as for designing effective remediation strategies (*e.g.*, [9, 10]).

Because of the complexity of environmental samples, which often contain dissolved and solid phases, including amorphous materials (natural organic matter), as well as biological components (plant matter, fungi, microorganisms), it is essential to conduct SR-based studies of simplified model systems in parallel with studies of natural samples in order to gain a more fundamental understanding of the chemical and biological processes that control the behavior and toxicity of environmental pollutants. This need has led to numerous studies of adsorption processes at environmental interfaces, including interfaces between minerals and microbial biofilm coatings, as well as plant-root/water and microbe/water interfaces [4]. To date, XAFS studies of environmental samples have focused mainly on inorganic pollutants, particularly heavy metals such as Cr, Ni, Zn, Cd, Hg, and Pb, metalloids such as As and Se, and actinides such as U, Pu, and Np. Such elements have relatively high K- or L-edge energies, thus can be studied at low concentrations (currently $\leq$50 ppm with insertion device beam lines on 3rd-generation SR sources) even in strongly absorbing matrices, assuming that spectral interferences are minimal

*e-mail: gordon@pangea.stanford.edu

or can be resolved using solid-state detectors or wavelength dispersive spectrometers. Nonetheless, XAFS studies of organic pollutants and natural organic matter (NOM) are becoming more common using UHV soft X-ray XAFS methods (*e.g.*, [11–13]). Soft X-ray μ-XANES studies by Myneni, in particular, are beginning to reveal the types and distribution of the dominant carbon-containing functional groups in NOM [12]. In addition, soft X-ray XANES spectroscopy methods have been used to characterize sulfur in S-containing coals by Huffman, Huggins, and co-workers [14], Bancroft and co-workers [15], and Fendorf *et al.* [16].

In this paper, we present examples of recent MES research that has utilized XAFS spectroscopy and related methods, such as PES and XSW spectroscopy, to address fundamental issues involving chemical processes at environmental interfaces and in biota. We also present several examples of more applied XAFS and μ-XAFS studies that address the question of speciation of heavy metal, metalloid, and actinide ions in environmental samples. A more comprehensive review of recent SR-based studies of environmental samples can be found in [4].

We begin with a brief discussion of some of the major issues that must be considered in molecular-level studies of complex environmental samples and in simplified model systems designed to mimic natural systems in order to highlight the utility of XAFS spectroscopy and other SR-based methods in such studies.

2. Major Issues in Molecular Environmental Science Addressable by SR Methods

2.1. *Environmental materials are complex, requiring parallel studies of real and model systems and the use of complementary characterization methods*

This issue can be addressed using bulk XAFS, μ-XAFS, and μ-SXRF methods in an element-specific fashion, which is a major advantage over phase-specific methods when the pollutant element of interest is at low concentrations, as is often the case, or is associated with amorphous materials. A given element in different phases often has a XANES or EXAFS spectral signature that makes it possible to identify the phase in which a particular element is located, even when the phase is at a concentration far below that needed for identification by X-ray diffraction ($\approx$1 percent by volume). Linear combination fitting of XANES (*e.g.*, [17, 18]) or EXAFS spectra (*e.g.*, [19, 20]) can be used in cases where the spectra of an element in different phases are unique. μ-XRD is becoming an important complement to XAFS and μ-SXRF to definitively identify crystalline phases and determine the spatial distribution and association of specific pollutant elements with different solids (*e.g.*, [21]). The use of bulk XAFS methods is still essential in such studies, however, because it provides a more statistically significant sample volume in which to identify and quantify the different chemical species of a particular element than μ-XAFS methods. Non-SR-based methods can also provide important information on the speciation of pollutants in environmental samples. For example, the use of analytical transmission electron microscopy can provide important information, complementary to XAFS spectroscopy, on the identification of nanoparticles containing the element of interest (*e.g.*, [22]). In addition, indirect macroscopic methods such as sequential chemical extractions, combined with XAFS spectroscopy, are often essential for distinguishing among different phases with different solubilities that have similar EXAFS signatures for a given element (*e.g.*, [20, 23]).

2.2. *Water and atmospheric or soil gases are ubiquitous in environmental systems*

Because of the presence of water and hydrous phases (*e.g.*, hydrous metal oxides, microbial organisms, plant roots) in environmental samples and the fact that introducing such samples into UHV systems for SEM, TEM, or XPS studies can result in their desiccation, and thus potential changes in speciation, it is desirable to study environmental samples with a minimum of sample preparation under conditions that closely mimic those in a particular environmental setting. Hard X-ray XAFS spectroscopy can be used under such conditions, thus can provide unique information about the speciation of heavy metal and metalloid pollutants under appropriate conditions. It is also possible to carry out soft X-ray XAFS spectroscopy studies of elements like oxygen [24] and carbon [12] in the presence of water using differentially pumped vacuum chambers and photon in-photon out methods.

2.3. *The nature of the solid/water interface and of sorbed species must be known*

Most chemical reactions important in controlling the speciation, transformation, and distribution of pollutant species in the environment occur at interfaces, particularly those involving solids and aqueous solutions [6, 25]. Surface complexation models of various levels of sophistication have been developed [26, 27], based on the Gouy-Chapman-Stern-Graham model of the solid/water interface [28]. Such models allow prediction of the partitioning of solute species from aqueous solutions to solid surfaces under different solution conditions and may be parameterized through fitting macroscopic uptake data. This approach, although very useful, cannot provide a molecular-scale description of the electrical double layer (EDL) or of sorbed species at the solid surface. Instead, direct molecular-level probes are needed to map out the spatial distribution of solute species in the EDL and to identify the types of surface complexes they form as a function of solution conditions. XAFS spectroscopy (see [29] for review), in combination with X-ray reflectivity (*e.g.*, [30]) and X-ray standing wave measurements (*e.g.*, [31, 32]), is capable of providing this type of information.

2.4. *Nanoscale environmental materials play a major role in interfacial chemical reactions*

There is growing recognition that nanoparticles of earth and environmental materials play major roles in environmental processes [33]. This is true because such nanoparticles collectively have immense surface areas and therefore are often a significant, if not dominant, fraction of the reactive surface area available for complexing dissolved species. There is also growing evidence that the structure and properties of nanoparticles change as particle size decreases [34–36]. For example, TiO_2 nanoparticles exhibit differences in photocatalytic reduction of redox-sensitive metals like Cu(II) and Hg(II) in the presence and absence of surface adsorbers like alanine, thiolactic acid, and ascorbic acid relative to bulk TiO_2 [37–40]. These differences are attributed to different surface structures of nanoparticulate *vs*. bulk TiO_2. Using EXAFS spectroscopy, Chen *et al.* [37, 38] found shorter Ti-O bonds and increasing disorder around Ti with decreasing size of TiO_2 nanoparticles. The unique surface chemistry exhibited by nanoparticulate TiO_2 was attributed to

the increasing number of coordinatively unsaturated surface Ti sites with decreasing nanoparticle size. In a similar EXAFS study of nanoparticulate α-Fe_2O_3, surface Fe sites were found to be undercoordinated relative to Fe in the bulk structure and are restructured to octahedral sites when the nanoparticles are reacted with enediol ligands [41].

Nanoparticles play an important role in the transport of heavy metal and organic contaminants in the environment. For example, Kersting *et al.* [42] concluded that colloid-facilitated transport of Pu is responsible for its subsurface movement from the Nevada Test Site in the United States to a site 1.3 km south over a relatively short time period (≈40 years), based on the unique $^{240}Pu/^{239}Pu$ isotope ratios of the samples. EXAFS spectroscopy and μ-SXRF are now shedding light on how Pu and other actinide ions sorb on colloidal mineral particles and undergo redox transformations in some cases [43, 44].

2.5. *Inorganic and organic ligands and coatings can have a major impact on the sorption behavior of metal ions*

There are a number of common natural inorganic ligands (*e.g.*, SO_4^{2-}, PO_4^{3-}, CO_3^{2-}, Cl^-) and organic ligands (*e.g.*, oxalate, citrate, humic materials) that can enhance or inhibit the sorption of metal ions from aqueous solutions onto mineral surfaces. For example, sulfate enhances the sorption of Pb(II) on goethite surfaces over the pH range 5 to 7 due to the reduction of the positive surface charge of goethite at these pH values and the formation of a stable ternary Pb(II)/SO_4^{2-}/goethite surface complex [45]. In contrast, chloride ligands inhibit the sorption of Hg(II) on goethite at similar pH values because of the formation of a stable Hg(II)-chloride aqueous complex [46]. Organic ligands can have similar effects. For example, citrate [47] and malonic acid [48] can enhance the sorption of U(VI) and Pb(II), respectively, onto goethite through the formation of ternary surface complexes, as revealed by EXAFS and FTIR spectroscopy. Combined *in situ* XAFS and ATR-FTIR spectroscopy studies are beginning to reveal some of the molecular-level details of ternary surface complexes involving metal ions, organic (or inorganic) molecules, and mineral surfaces (*e.g.*, [49–51]).

2.6. *Biota can have a major effect on the speciation and sequestration of contaminant and pollutant species*

Many microorganisms and plants can sequester toxic chemical species and transform them into less toxic forms. EXAFS spectroscopy studies of microorganism-metal interactions are beginning to reveal the types of cell-wall functional groups to which metal ions bind [52–61]. For example, in an EXAFS study of the sorption products of Cd(II) and U(VI) on *Bacillus subtilis*, Kelly *et al.* [58] found that U(VI) binds to phosphoryl groups and that Cd(II) binds to carboxyl groups at low pH.

The transformations and sequestration of metal ions in hyperaccumulating plants has also been studied in several systems using XAFS and μ-XAFS spectroscopy (*e.g.*, [62–66]) and X-ray fluorescence μ-tomography [66]. For example, several groups have found that aqueous Cr(VI) is accumulated in and rapidly reduced to Cr(III) in aquatic ferns [62, 63]. In one of the first X-ray fluorescence μ-tomography studies (coupled with XAFS), Hansel *et al.* [66] showed that Pb and As are associated with iron plaque (in the form of ferrihydrite, goethite, and siderite) on plant roots of *Phalaris arundinacea*, a common aquatic plant from a mine waste impacted wetland in the Coeur d'Alene Basin of northern Idaho, U.S.A. Mn and Zn occur as isolated nodules of mixed-metal carbonate (rhodochrosite/hydrozincite) on the root surface. In most cases, the molecular-scale mechanisms of metal transformations or hyperaccumulation by bacteria or plants are unknown.

3. XAFS Studies of Metal Ion Adsorption at Solid/Aqueous Solution Interfaces

Most chemical reactions involving environmental materials take place at interfaces, most importantly solid/aqueous solution interfaces [6, 25]. Although not inherently surface (or interface) sensitive, when the element of interest occurs dominantly at a surface (or interface), XAFS spectroscopy is often capable of providing unique information about the structure and composition of an adsorbate, as well as its mode of attachment to a solid surface (*i.e.*, inner-sphere vs. outer-sphere, mononuclear vs. multinuclear, and (if inner-sphere) monodentate vs. bidentate or tridentate). Because of this capability, XAFS studies have now been carried out on over 200 metal ion/mineral sorption systems (see [4] for a recent review). Here we review the results of two such studies, one on Zn(II) sorption on alumina [67] and one on Au(III) sorption on Fe(III)- and Al-oxyhydroxides [68, 69].

The products of sorption reactions of Zn(II) with high surface area alumina (Linde-A) were characterized by XAFS spectroscopy as a function of Zn sorption density ($\Gamma = 0.2$ to $3.3\,\mu mole/m^2$) at pH values of 7.0 to 8.2 by Trainor *et al.* [67] (see Fig. 1). Over equilibration times of 15–111 hrs and at low Zn sorption densities ($\Gamma = 0.2$ to $1.1\,\mu mole/m^2$), we found that Zn(II) forms dominantly inner-sphere bidentate surface complexes with AlO_6 polyhedra. At higher sorption densities

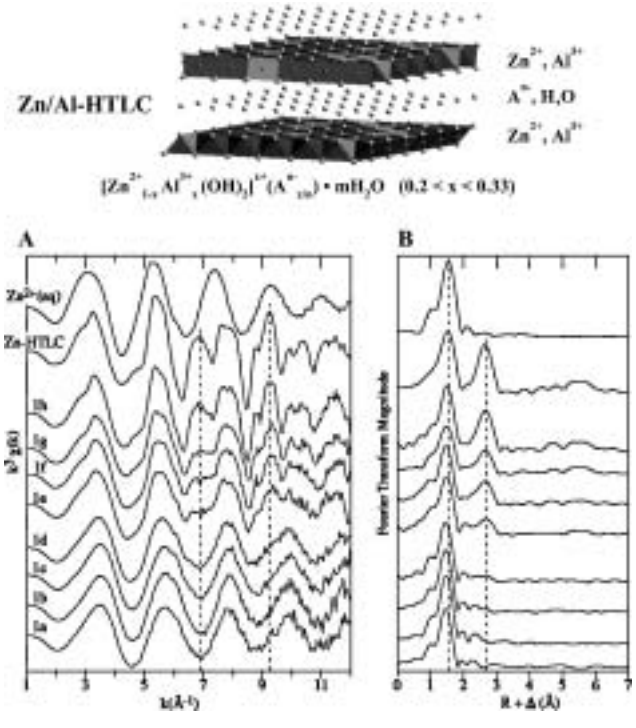

Fig. 1. Zn K-edge EXAFS spectra (k^3 weighted) (A) and corresponding Fourier transforms (B) of Zn sorbed onto high surface area alumina at the following surface coverages (Γ = μmoles m^{-2}): 0.2 (1a), 0.3 (1b), 0.8 (1c), 1.1 (1d), 1.7 (1e), 1.6 (1f), 1.5 (1g), and 3.3 (1h), compared with Zn-hydrotalcite (Zn-HTLC) and Zn^{2+} in a 10 mM $Zn(NO_3)_2$ aqueous solution (Zn^{2+}(aq)) (after [67]). The structure and composition of Zn/Al-hydrotalcite (Zn/Al-HTLC) are shown.

($\Gamma = 1.5$ to $3.5\,\mu mole/m^2$), we found evidence for the formation of a mixed-metal Zn(II)-Al(III)-hydroxide co-precipitate with a hydrotalcite-type local structure. These conclusions are based on an analysis of first- and second-neighbor interatomic distances derived from EXAFS spectra collected under ambient conditions on wet samples. At low Γ the sorption mechanism involves a transformation from six-coordinated Zn-hexaaquo solution complexes (with an average Zn-O distance of 2.07 Å) to four-coordinated surface complexes (with an average Zn-O distance of 1.97 Å) as described by reaction (1):

$$\equiv Al(OH_a)(OH_b) + Zn(H_2O)_6{}^{2+} \rightarrow \equiv Al(OH_{a'})(OH_{b'})Zn(OH_{c'})(OH_{d'}) + 2H_2O + zH^+ \quad (1)$$

where $\equiv Al(OH_a)(OH_b)$ represents edge-sharing sites of $Al(O,OH,OH_2)_6$ octahedra to which $Zn(O,OH,OH_2)_4$ bonds in a bidentate fashion. The proton release consistent with this reaction ($z = a\text{-}a' + b\text{-}b' + 4\text{-}c'\text{-}d'$), and with Pauling bond valence analysis falls in the range of 0 to 2 $H^+/Zn(II)$ when hydrolysis of the adsorbed Zn(II) complex is neglected. This interpretation suggests that proton release is likely a strong function of the coordination chemistry of the surface hydroxyl groups. At higher Γ (1.5 to $3.5\,\mu mole/m^2$), a high amplitude, second-shell feature in the Fourier transform of the EXAFS spectra (Fig. 1B) indicates the formation of a three-dimensional mixed-metal co-precipitate, with a hydrotalcite-like local structure. Al(III) is provided by dissolution of the alumina substrate. Nitrate anions presumably satisfy the positive layer charge of the Al(III)-Zn(II)-hydroxide layers in which the Zn/Al ratio falls in the range of 1 : 1 to 2 : 1. Our results for the higher Γ-value sorption samples suggest that Zn-hydrotalcite-like phases (Zn-HTLC) may be a significant sink for Zn(II) in natural or catalytic systems containing appreciable dissolved aluminum. In section 6, we show evidence for the presence of Zn-HTLC phases in Zn-contaminated soils from northern France.

Another recent example of XAFS applied to sorption reactions at solid/aqueous interfaces involves the study of gold sorption products on powdered ferrihydrite, goethite, and boehmite samples [68, 69]. The samples were prepared by reacting Au(III)-chloride solutions ($[Au] = 3.10^{-3}$–4.10^{-5} M; $[Cl] = 0.02$–0.60 M) with these sorbents at pH values of 4 to 9 and Au sorption densities ranging from 0.046 to $1.53\,\mu mol/m^2$. The speciation of gold was determined using Au-L_{III} XAFS spectroscopy. Several effects observed in the Au L_{III}-edge XAFS spectra, including X-ray beam-induced photo-reduction, multi-electronic excitations, disorder effects, and multiple scattering, would complicate interpretation of the spectra if not accounted for. A combination of methods (spectral deconvolution, principal component analysis, spectral inversion, and wavelet analysis (see [70]) (see Fig. 2) was used to identify and quantify these effects, to characterize the nature of mixed ligands around gold, and to distinguish between multiple-scattering features and features due to next-nearest neighbors in the XAFS spectra.

Analysis of the Au-L_{III} XAFS spectra showed that Au(III) is present as square-planar $Au(III)(O,Cl)_4$ complexes in the aqueous solutions and on the surfaces of the Al/Fe-(oxy)hydroxide sorption samples with dominantly O ligands at pH > 6 and mixed O/Cl ligands at lower pH values [69]. The EXAFS-derived Au-O and Au-Cl distances are 2.00(2) and 2.28(2) Å, respectively, and the magnitudes of the Debye-Waller factors and third cumulants from anharmonic analyses indicate very little thermal or positional disorder around Au(III) in the sorption samples. Iron second neighbors are present around Au in the Au(III)/ferrihydrite and Au(III)/goethite sorption samples, with Au-Fe distances of 3.1(1) and 3.3(1) Å. In boehmite, two sets of Au-Al distances were detected at 3.0(1) and 3.2(1) Å. A reverse Monte Carlo study of the XAFS data suggests the presence of a continuum of edge-shared AuO_4-FeO_6 distances, which cannot be described correctly by a classical model in which only a mean distance is derived. These results indicate that $Au(III)(O,Cl)_4$ units are bonded as inner-sphere, bidentate binuclear and monodentate (corner-shared) complexes with $Fe(O,OH)_6$ and $Al(O,OH)_6$ octahedra on the Fe(III)-(oxy)hydroxide and boehmite surfaces, respectively. No Au second neighbors were detected in any of the sorption samples, except for natural goethite, indicating that gold atoms don't form clusters on the synthetic sorbents under the conditions investigated.

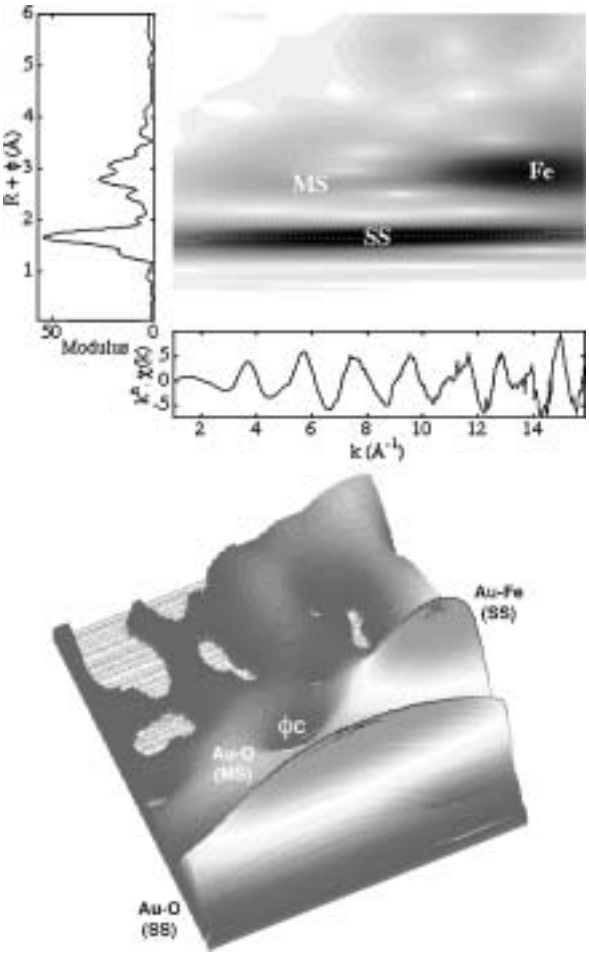

Fig. 2. (a) top: Wavelet Transform (WT) plot for Au(III) sorbed at the goethite/water interface (pH 7.9), with the momentum vector (k) plotted along the abscissa and the direct space distance ($R + \phi$) plotted along the ordinate. (b) bottom: reconstructed surface of the WT, using false gray levels for the WT magnitude. Three types of contributions around Au(III) consist of (1) harmonic Au-O pair correlations, (2) single and multiple-scattering Au-O features, and (3) Au-Fe next nearest neighbor contributions (important to k values of 15.5 Å). The modeled edge for the first neighbors (dotted line) is essentially horizontal, indicating a harmonic Au-O shell of neighbors (from [69]).

4. Effects of Microbial Biofilm Coatings on Metal Ion Adsorption at Metal Oxide/Aqueous Solution Interfaces

Long-period X-ray standing wave (XSW) techniques provide a direct approach for studying the partitioning of metal ions between a single crystal surface and a microbial biofilm coating

[52, 53, 61]. In a long-period XSW experiment, the crystal is used as a reflecting mirror substrate. The interference of the (grazing) incident and specular reflected beams generates a standing wave in the direction normal to the surface. The position and spacing of the standing wave antinodes are determined by the angle of X-ray incidence. As the standing wave intensity field above the mirror substrate is varied by adjusting the X-ray incident angle, a characteristic fluorescent yield (FY) profile is generated from metal ions residing at and above the reflecting surface (*e.g.*, [32]). The FY profiles generated can be analyzed to provide quantitative information on the distribution function of each metal species above the solid-solution interface, thus yield unique information on the relative affinity of each metal species for reactive sites present within the biofilm *vs.* the underlying solid surface.

In a detailed XSW-FY study of heavy metal interactions with biofilm-coated mineral surfaces, Templeton *et al.* [53] measured the Pb L_{III}-edge FY from *Burkholderia cepacia*-coated α-Al_2O_3 (0001) and (1-102) and α-Fe_2O_3(0001) surfaces that had been exposed for 2 hr. to aqueous solutions containing various Pb concentrations (ranging from 1 μM to 60 μM) at pH 6 and an ionic strength of 0.005 M. At a Pb concentration of 1 μM, the FY intensity for the α-Al_2O_3 (1-102) and α-Fe_2O_3 (0001) surfaces peaks at the critical angles of the two substrates (≈160 mdeg and 185 mdeg, respectively, at 14 keV), indicating that Pb(II) is located primarily at the corundum or hematite surfaces at this concentration (Fig. 3). With increasing Pb concentration, the FY peaks show a doublet, with a peak in intensity at the critical angle as well as increasing intensity at ≈60 mdeg for the α-Al_2O_3 (1-102)-coated surface and at about 85 mdeg for the α-Fe_2O_3 (0001) surface. The growing intensity at the lower incidence angles indicates that Pb(II) is also binding to sites in the *B. cepacia* biofilm coating, which increases with increasing Pb concentration. At all Pb concentrations studied, the FY-data indicate that Pb(II) binds primarily to functional groups in the biofilm on the α-Al_2O_3 (0001) sample (Fig. 3).

The results of this study show that Pb(II) binds initially to reactive sites on the α-Al_2O_3 (1-102) and α-Fe_2O_3 (0001) surfaces even with a biofilm coating that covers essentially the entire mineral surface, as shown by SEM and confocal microscopy studies. The order of reactivity of these biofilm-coated surfaces for Pb(II) [α-Fe_2O_3 (0001) > α-Al_2O_3 (1-102) ≫ α-Al_2O_3 (0001)] is the same as that observed in uptake and EXAFS studies of Pb(II) sorption on biofilm-free alumina and hematite surfaces [71–74]. This XSW study also shows that the *B. cepacia* biofilm does not block all reactive sites on the alumina and hematite surfaces and that sites on the α-Al_2O_3 (1-102) and α-Fe_2O_3 (0001) surfaces "outcompete" functional groups in the biofilm (including the exopolysaccharide exhudate) at low Pb concentrations. Although these findings should not be generalized to the interaction of aqueous metal ions with all NOM- or biofilm-coated mineral surfaces, they do raise questions about the generalization that NOM or biofilm coatings change the adsorption characteristics of mineral surfaces (*cf.*, [75–77]), and they are also inconsistent with the suggestion that NOM blocks reactive sites on mineral surfaces (*cf.*, [78]).

When the XSW approach is coupled with grazing-incidence (GI) XAFS and μ-XAFS spectroscopy, it is also possible to determine the speciation of each metal(loid) at separate locations within the sample (*i.e.*, at the mineral surface and within the biofilm matrix). This can be accomplished by taking GI-XAFS data at an incident angle corresponding to the critical angle of the substrate, which is sensitive primarily to the metal(loid) sorbed

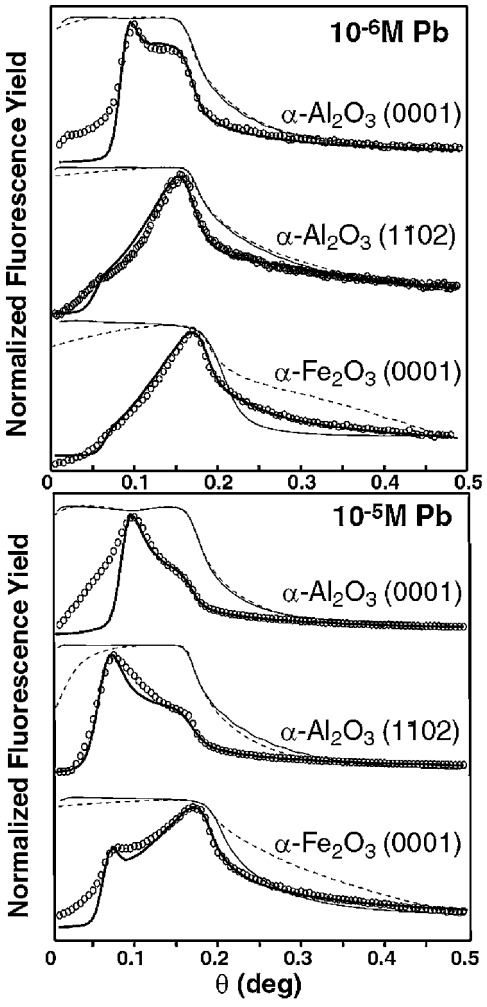

Fig. 3. Measured (dashed) and modeled (light line) reflectivity (log I_0/I_1) profiles and Pb La FY profiles (circles) with model fits (heavy line) for the α-Al_2O_3 (0001), α-Al_2O_3 (1-102), and α-Fe_2O_3 (0001) surfaces at 10^{-6} M and 10^{-5} M [Pb]. Data were taken on SSRL beam station 6-2 (from [53] with permission).

at the mineral surface, and, in separate measurements, at an incident angle corresponding to the lower angle FY peak, which is sensitive primarily to the metal(loid) sorbed in the biofilm. The results of these types of experiments for the Pb(II)-*B. cepacia*-alumina and Pb(II)-*B. cepacia*-hematite systems indicate major differences in the local coordination environment of Pb(II) at these two interfaces [79–82]. This type of spatially resolved speciation information has also been extended to redox processes within biofilms. A combined XSW and GI-XANES study of the reaction of selenate and selenite with *B. cepacia*-coated α-Al_2O_3 (1-102) surfaces has provided unique information about the partitioning behavior of Se(VI), Se(IV), and Se(0) between the biofilms and alumina surfaces. In particular, the angle-dependent Se K-edge XANES measurements show that microbially-induced reduction of selenate leads to a strong vertical segregation of selenium species at the interface, where Se(IV) preferentially binds to the alumina surface whereas Se(VI) and Se(0) accumulate within the overlying biofilms [82].

5. Pyrite Oxidation – A Major Cause of Acid Mine Drainage

The oxidation of pyrite is one of the major causes of acid mine drainage [83], yet the mechanism of this oxidation reaction is not completely understood at a molecular level. A number of studies

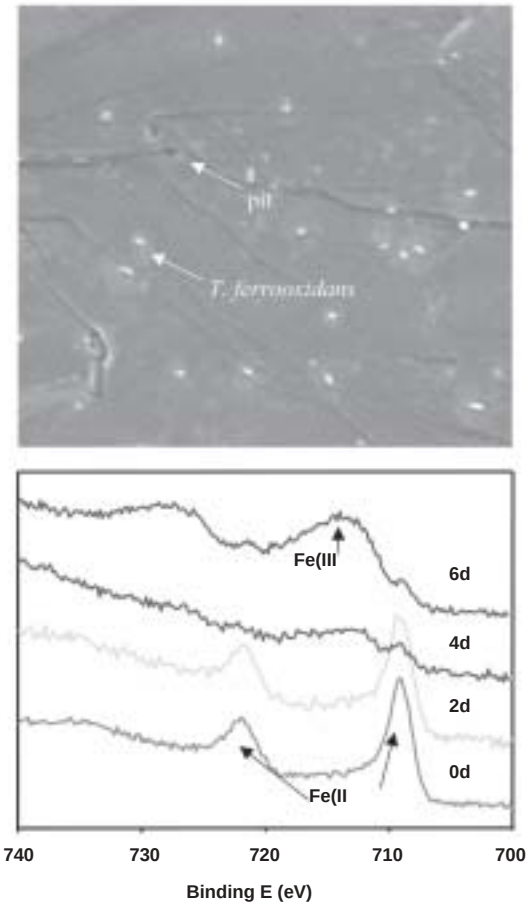

Fig. 4. Top: SEM image of pyrite fracture surface in air showing *Thiobacillus ferroxidans*, after six days of exposure to the bacteria. Halos of oxidized Fe species (identified by Fe 2p photoemission spectra) are visible around the bacteria on a pyrite fracture surface. Bottom: Fe 2p photoemission spectra of Fe of pyrite fracture surfaces after 0 days, 2 days, 4 days, and 6 days of exposure to *T. ferroxidans* (from [84]).

have suggested that various acidophililc, chemolithoautotrophic bacteria (*e.g.*, *Thiobacillus* sp.) catalyze part of this multi-step reaction, resulting in oxidation rates that are one to five orders of magnitude faster than abiotic oxidation rates [83]. We have recently investigated this reaction on natural pyrites before and after exposure to various inorganic oxidants (O_2, As(V), Cr(VI), water, peroxide solutions) and *Thiobacillus ferrooxidans* using ultra-high vacuum SR methods, including O K-edge, S K-edge, and Fe L-edge XANES spectroscopy and S 2p and Fe 2p photoemission spectroscopy [84–86]. Figure 4 shows an SEM image of the pyrite surface after 6 days exposure to *T. ferrooxidans* in air [84]. Small light-colored haloes are visible around each bacterium, suggesting the build-up of some type of reaction product. Fe 2p photoemission spectra (Fig. 4) clearly show that oxidation of iron from Fe(II) to Fe(III) has occurred during this exposure. In abiotic systems following exposure to molecular oxygen, air, water, or peroxide solutions, defective pyrite surfaces (*i.e.*, those with monosulfide groups) show oxidation of both sulfur and iron, resulting in the formation of ferric sulfate coatings, as revealed by O K-edge, Fe L-edge, and S K-edge XANES spectra taken in total electron yield [85] (see Fe L-edge and O K-edge XANES spectra in Fig. 5). However, the build-up of oxidation products at the pyrite surface only proceeds when the oxidant is sufficiently concentrated to facilitate rapid surface oxidation.

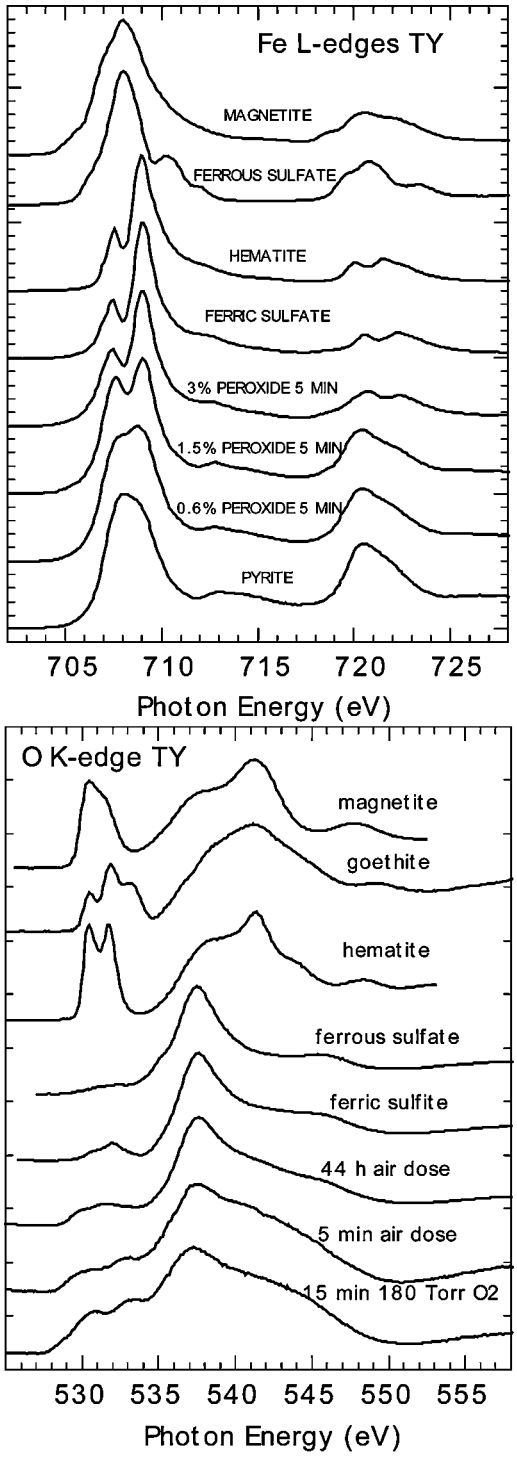

Fig. 5. Fe L_{III}-edge and O K-edge XANES spectra of a fracture surface of pyrite before and after exposure to various inorganic oxidants (O_2, air, and peroxide solutions) compared with XANES spectra of several Fe-containing model compounds (from [85]).

6. XAFS Studies of Metal Speciation in Contaminated Environmental Samples

One of the growing uses of XAFS and μ-XAFS spectroscopy is determination of the major metal and metalloid species present in complex environmental samples (see [4] for recent review). Such contaminants are typically at such low concentrations that conventional XRD (assuming they are in crystalline forms) and spectroscopic methods are of little use in determining their speciation. Here we focus on two recent studies – one on the speciation of zinc in smelter-impacted soils in northern

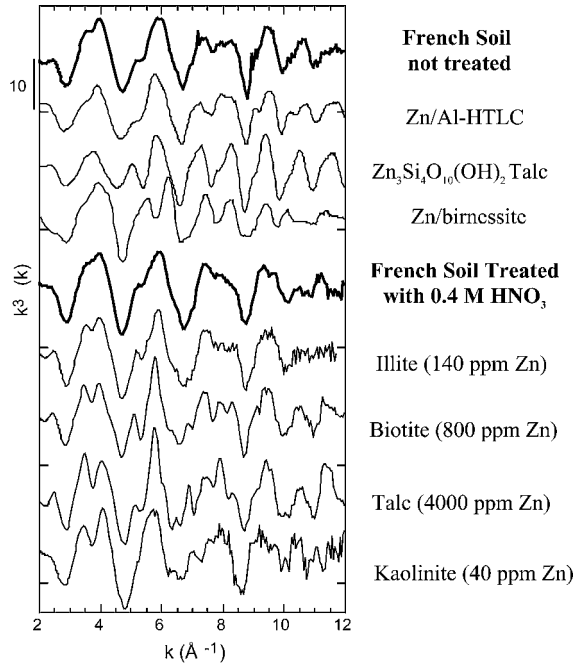

Fig. 6. Zn K-edge EXAFS spectra (background-subtracted and k^3-weighted) of a Zn-contaminated French soil (600 ppm Zn) before and after treatment with 0.4 M HNO_3, compared with EXAFS spectra of various Zn-containing model compounds (after [23]).

France and one on the speciation of uranium in vadose zone sediments beneath high-level waste tanks at the Hanford, WA (USA). In the case of the Zn-contaminated soils from northern France, the study by Juillot *et al.* [23] used a combination of EXAFS spectroscopy, μ-SXRF, XRD, and selective chemical extractions to show that Zn is present as sphalerite (and wurtzite) and Zn(II)-bearing magnetite in the dense soil fraction, whereas it is associated with soil organic matter and present as Zn(II)/Al(III)-hydrotalcite (Zn/Al-HTLC), Zn(II)-bearing phyllosilicate, and Zn(II)-bearing magnetite-franklinite solid solution in the clay fraction (see Figs. 6 and 7). A study by Manceau *et al.* [87] of Zn-contaminated soils from the same locality concluded that Zn is present in the high-temperature phases franklinite ($ZnFeO_4$), willemite (Zn_2SiO_4), hemimorphite ($Zn_4Si_2O_7(OH)_2 \cdot H_2O$), and Zn-containing magnetite-franklinite solid solution based on EXAFS (both powder and polarized) and powder XRD analysis. They also concluded that zinc released during the weathering of these phases is present in the clay soil fraction as "neoformed" Zn(II)-phyllosilicate, Zn(II) incorporated in Fe-(oxyhydr)oxides, and Zn(II) sorbed onto birnessite.

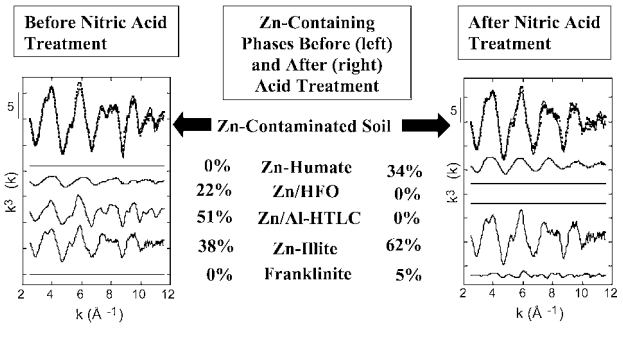

Fig. 7. Results of linear combination fitting of Zn K-edge EXAFS spectra of a Zn-contaminated French soil, showing fit components and the estimated percentages of each component present in the soil before and after nitric acid treatment (after [23]).

The differences in Zn(II) phase association determined in these two studies of smelter-contaminated soils show that in complex phase assemblages, EXAFS data alone may not be sufficient to uniquely identify the types of phases with which a contaminant is associated. In these cases, other complementary methods, such as selective chemical extraction, μ-XRD, and TEM, are needed in combination with EXAFS spectroscopy. For example, EXAFS spectra of these Zn-contaminated soils taken before and after nitric acid treatment are consistent with the presence of a significant amount of Zn/Al-HTLC, in addition to less acid soluble phases such as Zn-containing illite and Zn adsorbed to humic material (Fig. 7) [23].

A recent XAFS study by Catalano *et al.* [88] of uranium speciation in vadose zone sediments beneath the high-level waste tank BX-102 at the Hanford Site in Washington State, USA, where seven to eight metric tons of uranium have been spilled, revealed the dominant U species present. The U L_{III}-edge XANES data clearly show that uranium is in the uranyl form. The corresponding EXAFS spectra of all samples studied are very similar to those of the uranophane group minerals (see Fig. 8 and Table I). However, it was not possible using EXAFS spectroscopy alone to uniquely determine which member or members of this mineral group were present, as the minerals from this group have nearly identical EXAFS spectra. Micro-XRD data taken at the Advanced Photon Source (BL-ID-20) on μm-sized crystals in quartz veins clearly showed that the dominant phase is sodium boltwoodite, which should be less soluble than uranophane in Na-rich Hanford Tank leachates.

7. Conclusions

Synchrotron-based XAFS spectroscopy and related SR methods are contributing a great deal to our understanding of chemical processes that affect the environment, including the speciation of metal and metalloid pollutants, the types of sorption products they form at aqueous solution/solid interfaces, their redox transformations, and their interactions with microbial

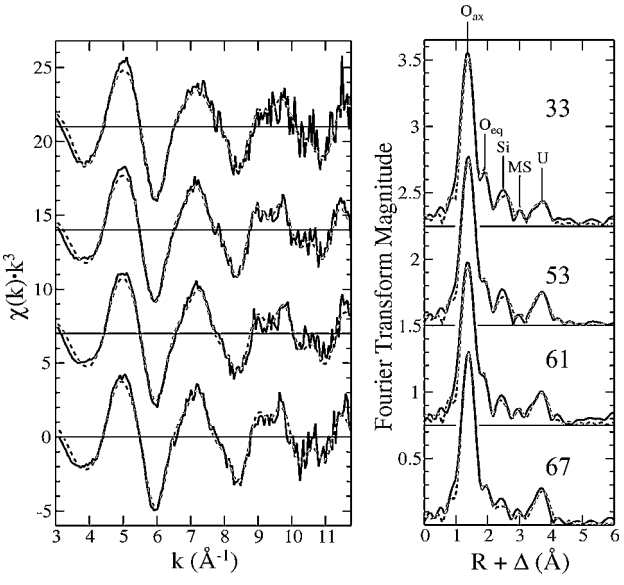

Fig. 8. U L_{III}-edge EXAFS spectra (k^3-weighted) and Fourier transforms for four U-contaminated samples from a borehole drilled beneath Hanford HLW Tank BX-102, showing fits to the data (dotted lines) (from [88]).

Table I. *EXAFS fit results for Borehole 102 sample 61A compared with fit results for boltwoodite [$(K,Na)_2(UO_2)_2(SiO_3OH)_2 \cdot 3H_2O$)] and uranophane [$Ca(UO_2)_2(SiO_3OH)_2 \cdot 5H_2O$], two members of the uranophane group (from [88]).*

Sample	U=O_{ax}	U-O_{eq1}	U-O_{eq2}	U-Si	U-U
61A	2–1.81 Å	2.9–2.29 Å	1.8–2.46 Å	0.9–3.17 Å	1.8–3.94 Å
Boltwoodite	2–1.81 Å	3–2.30 Å	2–2.45 Å	1–3.15 Å	2–3.95 Å
Uranophane	2–1.81 Å	3–2.28 Å	2–2.46 Å	1–3.16 Å	2–3.93 Å

cells, microbial biofilms, natural organic matter, and plants. Micro-XAFS methods are contributing unique insights about the association of heavy metal and metalloid pollutants with environmental materials. With the increasing availability of high brightness synchrotron X-ray sources, it is likely that information on molecular-level speciation of environmental pollutants will be increasingly utilized in making decisions about environmental remediation.

Acknowledgments

We thank the U.S. National Science Foundation (CRAEMS Grant CHE-0089215, GEB), the U.S. Department of Energy (DOE-BES Grant DE-FG03-93ER14347-A008, GEB), and the French CNRS (GC, GM, FJ, FF) for financial support of the research reported here. We also thank the staffs of SSRL, APS, LURE, and ESRF, where the data used in our studies were collected. SSRL is supported by the U.S. Department of Energy (Office of Basic Energy Science) and the U.S. National Institutes of Health.

References

1. Lytle, F. W., Adv. X-ray Anal. **9**, 398 (1966).
2. Sayers, D. E., Stern, E. A. and Lytle, F. W., Phys. Rev. Lett. **27**, 1204 (1971).
3. Brown, G. E., Jr., Parks, G. A. and Chisholm-Brause, C. J., Chimia **43**, 248 (1989).
4. Brown, G. E., Jr. and Sturchio, N. C., Rev. Mineral. Geochem. **49**, 1 (2002).
5. Brown, G. E., Jr., Foster, A. L. and Ostergren, J. D., Proc. Nat. Acad. Sci. U.S.A. **96**, 3388 (1999).
6. Brown, G. E., Jr. *et al.*, Chem. Rev. **99**, 77 (1999).
7. O'Day, P. A., Rev. Geophys. **37**, 249 (1999).
8. Stern, R. H., Environ. Health (World Health Org., Copenhagen) **26**, 3 (1987).
9. Fuller, C. C. *et al.*, Environ. Sci. Technol. **36**, 158 (2002).
10. Neu, M. P. *et al.*, Book of Abstracts, 218th American Chem. Soc. Nat. Mtg., New Orleans, LA (1999).
11. Cody, G. D. *et al.*, Energy Fuels **9**, 75 (1995).
12. Myneni, S. C. B., Rev. Mineral. Geochem. **49**, 485 (2002).
13. Myneni, S. C. B., Science **295**, 1039 (2002).
14. Huffman, G. P. *et al.*, Energy Fuels **3**, 200 (1989).
15. Kasrai, M. *et al.*, Internat. J. Coal Geol. **32**, 107 (1996).
16. Morra, M. J., Fendorf, S. E., Brown, P. D., Geochim. Cosmochim. Acta **61**, 683 (1997).
17. Pickering, I. J., Brown, G. E., Jr. and Tokunaga, T. K., Environ. Sci. Technol. **29**, 2456 (1995).
18. Foster, A. L. *et al.*, American Mineral. **83**, 553 (1998).
19. Manceau, A. *et al.*, Environ. Sci. Technol. **30**, 1540 (1996).
20. Ostergren, J. D. *et al.*, Environ. Sci. Technol. **33**, 1627 (1999).
21. Manceau, A. *et al.*, American Mineral. **87**, 1494 (2002).
22. Shaw, S. *et al.*, Environ Sci. Technol. (2003, submitted).
23. Juillot, F. *et al.*, American Mineral. **88**, 509 (2003).
24. Myneni, S. C. B. *et al.*, J. Phys. Condensed Matter **14**, L213 (2002).
25. Stumm. W., Werhli. B. and Wieland. E., Croatica Chemica Acta **60**, 429 (1987).
26. Davis, J. A. and Kent, D. B., Rev. Mineral. **23**, 177 (1990).
27. Hiemstra, T. and Van Riemsdijk, W. H., J. Colloid Interface Sci. **179**, 488 (1996).
28. Hunter, R. J., "Foundations of Colloid Science, Vol. 1" (Oxford University Press, Oxford, UK, 1987).
29. Brown, G. E., Jr. and Parks, G. A., Internat. Geol. Rev. **43**, 963 (2001).
30. Fenter, P. A., Rev. Mineral. Geochem. **49**, 149 (2002).
31. Fenter, P. A. *et al.*, J. Colloid Interface Sci. **225**, 154 (2000).
32. Trainor, T. P. *et al.*, Langmuir **18**, 5782 (2002).
33. Banfield, J. F. and Zhang, H., Rev. Mineral. Geochem. **44**, 1 (2001).
34. Gleiter, H., Adv. Materials (Weinheim, Germany) **4**, 474 (1992).
35. Siegel, R. W., Scientific American **275**, 74 (1996).
36. McHale, J. M. *et al.*, Science **277**, 788 (1997).
37. Chen, L. X. *et al.*, J. Phys. Chem. B **101**, 10688 (1997).
38. Chen, L. X. *et al.*, Nucl. Instrum. Meth. B **133**, 8 (1997).
39. Chen, L. X. *et al.*, J. Synchrotron. Rad. **6**, 445 (1999).
40. Rajh, T. *et al.*, J. Phys. Chem. B **103**, 3515 (1999).
41. Chen, L. X. *et al.*, J. Phys. Chem. B **106**, 8539 (2002).
42. Kersting, A. B. *et al.*, Nature **397**, 56 (1999).
43. Kaplan, D. I. *et al.*, Environ. Sci. Technol. **28**, 1186 (1994).
44. Allen, P. G. *et al.*, Abstracts of Papers, 222nd American Chem. Soc. Nat. Mtg., Chicago, IL, GEOC-042 (2001).
45. Ostergren, J. D. *et al.*, J. Colloid Interface Sci. **225**, 483 (2000).
46. Kim, C. S., Rytuba, J. J. and Brown, G. E., Jr., J. Colloid Interface Sci. (2003, in press).
47. Redden, G. D., Bargar, J. R. and Bencheikh-Latmani, R., J. Colloid Interface Sci. **244**, 211 (2001).
48. Lenhart, J. J., Bargar, J. R. and Davis, J. A., J. Colloid Interface Sci. **234**, 448 (2001).
49. Bargar, J. R., Persson, P. and Brown, G. E., Jr., Geochim. Cosmochim. Acta **63**, 2957 (1999).
50. Bargar, J. R., Reitmeyer, R. and Davis, J. A., Environ. Sci. Technol. **33**, 2481 (1999).
51. Fitts, J. P. *et al.*, J. Colloid Interface Sci. **220**, 133(1999).
52. Templeton, A. S. *et al.*, J. Synchrotron Rad. **6**, 642 (1999).
53. Templeton, A. S. *et al.*, Proc. Nat. Acad. Sci. U.S.A. **98**, 11897 (2001).
54. Hennig, C. *et al.*, Radiochim. Acta **89**, 625 (2001).
55. Kelly, S. D. *et al.*, J. Synchrotron Rad. **8**, 946 (2001).
56. Webb, S. M. *et al.*, J. Synchrotron Rad. **8**, 943 (2001).
57. Panak, P. J. *et al.*, Radiochim. Acta **90**, 315 (2002).
58. Kelly, S. D. *et al.*, Geochim. Cosmochim. Acta **66**, 3855 (2002).
59. Templeton, A. S. *et al.*, Environ. Sci. Technol. **37**, 300 (2003).
60. Templeton, A. S., Spormann, A. M. and Brown, G. E., Jr., Environ. Sci. Technol. **37**, 2166 (2003).
61. Templeton, A. S. *et al.*, Geochim. Cosmochim. Acta **67** (2003, in press).
62. Hunter, D. B. *et al.*, J. Phys. IV **7** (Colloque C2, X-Ray Absorption Fine Structure, Vol. 2), 767 (1997).
63. Lytle, C. M. *et al.*, Environ. Sci. Technol. **32**, 3087 (1998).
64. Pickering, I. J. *et al.*, Proc. Nat. Acad. Sci. USA **97**, 10717 (2000).
65. Pickering, I. J. *et al.*, Plant Physiol. **131**, 1460 (2003).
66. Hansel, C. M. *et al.*, Environ. Sci. Technol. **35**, 3863 (2001).
67. Trainor, T. P., Brown, G. E., Jr. and Parks, G. A., J. Colloid. Interface Sci. **231**, 359 (2000).
68. Berrodier, I. *et al.*, J. Synchrotron Rad. **6**, 651 (1999).
69. Berrodier, I. *et al.*, Geochim. Cosmochim Acta (2003, submitted).
70. Munoz, M., Argoul, P. and Farges, F., American Mineral. **88**, 694 (2003).
71. Bargar, J. R. *et al.*, Geochim. Cosmochim. Acta **60**, 3541 (1996).
72. Bargar, J. R. *et al.*, J. Colloid Interface Sci. **85**, 473 (1997).
73. Bargar, J. R., Brown, G. E., Jr. and Parks, G. A., Geochim. Cosmochim. Acta **61**, 2617 (1997).
74. Bargar, J. R., Brown, G. E., Jr. and Parks, G. A., Geochim. Cosmochim. Acta **61**, 2639 (1997).
75. Neihof, R. A. and Loeb, G. I., Limnol. Oceanogr. **17**, 7 (1972).
76. Neihof, R. A. and Loeb, G. I., J. Marine Res. **32**, 5 (1974).
77. Mayer, L. M., Chem. Geol. **114**, 347 (1994).
78. Davis, J. A., Geochim. Cosmochim. Acta **48**, 679 (1984).
79. Templeton, A. S., Spormann, A. M. and Brown, G. E., Jr., Environ. Sci. Technol. **37**, 2166 (2003).
80. Templeton, A. S. *et al.*, Environ. Sci. Technol. **37**, 300 (2003).
81. Templeton, A. S., Ph.D. Thesis, Stanford University, Stanford, CA (2002).
82. Templeton, A. S. *et al.*, Geochim. Cosmochim. Acta **67** (2003, in press).
83. Nordstrom, D. K. and Alpers, C. N., In: "The Environmental Geochemistry of Mineral Deposits," Rev. Econom. Geol. **6A**, 133 (1999).
84. Bostick, B. C. *et al.* (2003, in preparation).
85. Kendelewicz, T. *et al.* (2003, in preparation).
86. Andersson, K. *et al.* (2003, in preparation).
87. Manceau, A. *et al.*, Am. J. Sci. **300**, 289 (2000).
88. Catalano, J. G. *et al.*, Abstracts of Papers, 225th American Chem. Soc. Nat. Mtg., New Orleans, LA, (2003).

Physica Scripta. Vol. T115, 88–92, 2005

Energy-Dispersed Near-Edge X-Ray Absorption Fine Structure: a New Technique to Study Dynamic Surface Processes

H. Kondoh[1], K. Amemiya[1], I. Nakai[1], M. Nagasaka[1], A. Nambu[1], T. Shimada[1], T. Yokoyama[2] and T. Ohta[1]

[1]Department of Chemistry, School of Science, the University of Tokyo, Tokyo, 113-0033, Japan
[2]Institute for Molecular Science, Okazaki, 444-8585, Japan

Received June 26, 2003; accepted October 21, 2003

PACS numbers: 61.10.Ht, 68.47.De, 82.65.+r

Abstract

We have recently developed a new type of near-edge X-ray absorption fine structure (NEXAFS) technique, "dispersive-NEXAFS" by using energy-dispersed X-rays and a position-sensitive electron-energy analyzer. With this technique a NEXAFS spectrum is taken in a one-shot manner without scanning photon energy resulting in a typical data acquisition time of several tens seconds. This enables to monitor the dynamic surface processes such as film growth and surface reaction. As examples of such applications, we present kinetics studies of catalytic oxidation reactions on the platinum (111) surfaces. Future possible improvements of this technique are also addressed.

1. Introduction

Studies of dynamic molecular processes on solid surfaces have attracted much interest for the fundamental understanding of the phenomena such as surface diffusion, surface chemical reaction and molecular self-assembly formation on substrates, which are closely related to the development of actual systems like catalysts and sensors. A number of time-resolved surface science techniques have been developed in this decade. Fast scanning tunneling microscopy (STM) has successfully provided microscopic information on dynamic surface processes such as diffusion of adsorbates and reaction between adsorbates [1–3]. Vibrational spectroscopies have also contributed to kinetics study on catalytic surface reactions [4, 5]. Furthermore, recent time-resolved experiments using short-pulse lasers have revealed (sub) picosecond reaction dynamics of adsorbates [6, 7].

As for X-ray spectroscopies, combined use of high-flux X-rays from an undulator and the multi-channel electron detection system has enabled X-ray photoelectron spectroscopy (XPS) to apply real time monitoring of surface processes for submonolayer adsorbates in several tens seconds [8–10]. On the other hand, for X-ray absorption fine structure (XAFS) spectroscopy, "energy dispersive XAFS" has been developed by using a curved crystal and a position-sensitive X-ray detector [11]. However, it is a transmission type not applicable to solid surfaces. For surface XAFS, we have to exploit a new method for the study of dynamic phenomena.

Near edge X-ray absorption fine structure (NEXAFS) is a kind of XAFS spectroscopy in the near edge region, mostly applied for the study of surface adsorbates. This is similar to XPS and contains additional information about geometric and electronic structures such as molecular orientation and unoccupied local density of states.

We have recently developed a new version of the NEXAFS technique by combining energy-dispersed X-rays with a position-sensitive electron energy analyzer [12, 13]. With this technique we can measure a NEXAFS spectrum within several tens seconds without scanning the monochromator. Here we present a couple of the applications on dynamic surface processes to demonstrate the potential of this novel technique.

2. Energy Dispersive NEXAFS technique

The energy-dispersive NEXAFS technique has been developed at a soft X-ray bending-magnet beamline BL-7A at the Photon Factory of High Energy Accelerator Research Organization (KEK-PF, Tsukuba). At this beamline, varied-line-spacing gratings are used with a Hettrick-type mount and energy-dispersed X-rays can be obtained by simply opening the exit slit. The energy width of the dispersed X-rays is approximately 12 eV at the sample position around the C K edge with a 150-l/mm grating and 20 eV for the O K edge with a 300-l/mm grating. By combining the energy dispersed X-rays with a position sensitive electron analyzer (GAMMADATA-SCIENTA SES-2002), the energy-dispersive NEXAFS spectra are measured, with which dynamic surface processes can be directly monitored as schematically illustrated in Fig. 1. X-ray absorption-induced Auger electrons are emitted from each position on the sample. Since the Auger electrons are collected on a two-dimensional (2D) detector with distinguishing where they are emitted along the spatially-resolved direction (in our case a horizontal axis), raw data are acquired at once in the form of a 2D image with axes of kinetic-energy vs. position on the sample, that is, photon energy. Integrating the electron counts for a particular Auger-electron energy region and plotting them as a function of photon energy, we can obtain an Auger-electron-yield NEXAFS spectrum in the one-shot manner. By continuous acquisition of the dispersive-NEXAFS spectra, the surface processes are monitored every several tens seconds.

As a typical example of such a monitoring, we present a series of C K-edge dispersive NEXAFS spectra taken during

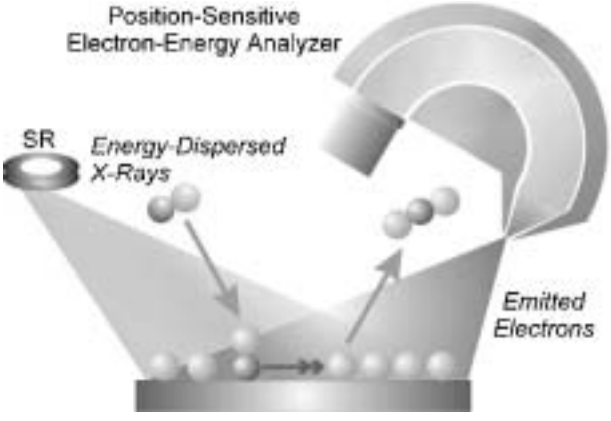

Fig. 1. Schematic illustration for the monitoring of a dynamic surface process with the dispersive-NEXAFS method. The substrate surface is irradiated by energy-dispersed X-rays from the synchrotron ring (SR) and electrons emitted from the surface are analyzed by a position-sensitive electron-energy analyzer with a spatial resolution along one direction on the surface which is parallel to the X-ray energy-dispersed direction.

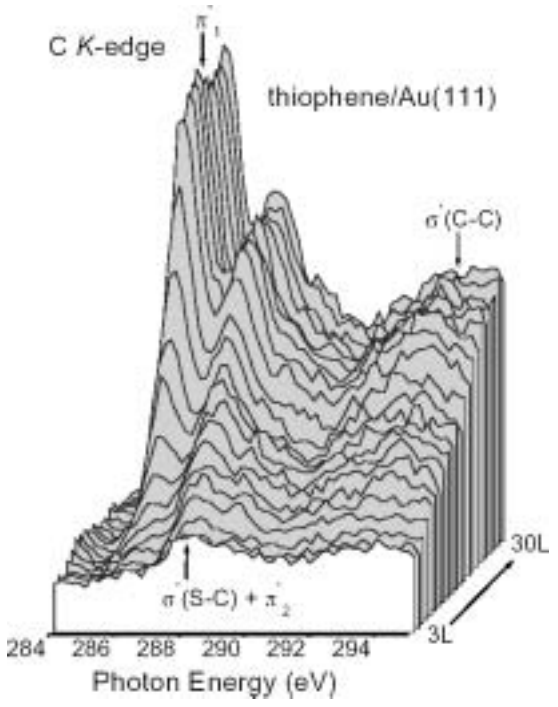

Fig. 2. Time-evolution of C K-edge dispersive-NEXAFS spectra for film growth of thiophene on a Au(111) surface at 140 K under an ambient thiophene pressure of 3×10^{-9} Torr. The accumulation time for each spectrum was 30 s.

thiophene (C_4H_4S) exposure onto a Au(111) surface in Fig. 2. The spectra were taken at the normal-incidence geometry and the accumulation time was 30 s for each spectrum. They were divided by the spectrum from the clean surface taken just before exposure to thiophene to cancel out the effect of inhomogeneous sensitivity of the 2D detector. Two prominent peaks are observed at around 286 and 288 eV, which are assigned to the C1s $\rightarrow \pi_1^*$ and $\sigma^*(C\text{-}S) + \pi_2^*$ transitions, respectively. The ratio between the two peaks changes as exposure increases; the π_1^* resonance is not found at the initial stage, but later it starts to grow and overtakes the $\sigma^*(C\text{-}S) + \pi_2^*$ with increasing exposure. This is because thiophene adsorbs with its molecular plane parallel to the surface until a flat-lying monolayer completes, and then gradually stands up as exposure increases. This adsorption behavior is consistent with results of conventional static NEXAFS measurements [14]. However, it is more clearly seen in the dispersive spectra that the change from the flat-lying configuration to the standing-up one is not like a sudden phase transition but a gradual transformation.

3. Application to dynamic surface processes

3.1. *Catalytic CO oxidation reaction on a Pt(111) surface*

The CO oxidation reaction on oxygen-precovered Pt(111) surfaces ($O_{ad} + CO_{ad} \rightarrow CO_2 \uparrow$) has been considered to be a prototypical example for the site-specific reaction, which shows significant deviations from simple collision theory for a homogeneous mixture of adsorbates. Two distinct models for the active sites in this reaction have been proposed; peripheral sites of 2D islands of oxygen [15] and interior sites of the islands [16]. Atomically-resolved scanning tunneling microscopy (STM) observations supported the former island-perimeter model [2]. Subsequent Monte-Carlo simulations assuming an attractive interaction between adsorbed oxygen atoms [17] successfully reproduced the formation of the oxygen 2D islands and the reaction kinetics obtained from the STM study. From the comparison between the STM and the simulated results, the perimeter-specific reaction was explained in terms of relative destabilization of the peripheral oxygen atoms due to lower coordination numbers of surrounding oxygen atoms compared with the interior oxygen atoms, which decreases the activation-energy barrier resulting in higher reaction probability [17]. This explanation, however, fails to rationalize the presence of "induction period" before the commencement of the oxidation reaction proposed by the STM observations [2], because at the initial stage not a negligible amount of isolated oxygen atoms are diffusing between the 2D islands which should be more reactive due to absence of surrounding oxygen atoms. Although STM provides quite rich information on distribution of adsorbates and their local electronic structures, motions and chemical reactions, it is a drawback that fast diffusing species are often invisible. To elucidate the mechanism of the CO oxidation reaction on the O-precovered Pt(111) surfaces, we have conducted real-time monitoring of this reaction with the dispersive-NEXAFS.

The oxygen-precovered Pt(111) surfaces were exposed to CO at constant surface temperatures to proceed the reaction. By continuous acquisition of the dispersive-NEXAFS spectra for the reacting surfaces, the progress of the reaction was monitored every 37 s. Figure 3 shows a data set of O K-edge dispersive-NEXAFS spectra for the CO oxidation reaction on an oxygen-precovered Pt(111) surface at 240 K under an ambient CO pressure of 1×10^{-8} Torr, which is almost the same experimental condition as used in the STM study [2]. Atomic oxygen and CO give peaks at 530 and 534 eV, respectively, the latter of which increases with time at the expense of the former peak. Time-evolution of both O and CO coverages for the O/Pt(111) surface is shown

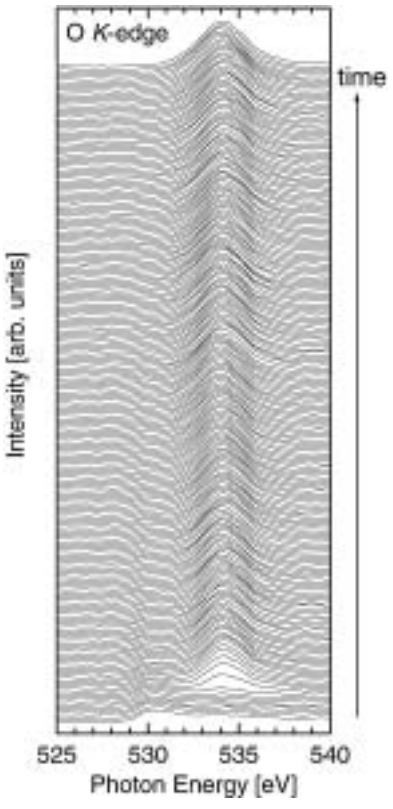

Fig. 3. A data set of O K-edge dispersive-NEXAFS spectra taken for an O-precovered ($\theta_O = 0.13$ ML) Pt(111) surface at 240 K under an ambient CO pressure of 1.0×10^{-8} Torr. The accumulation time was 30 s for each spectrum.

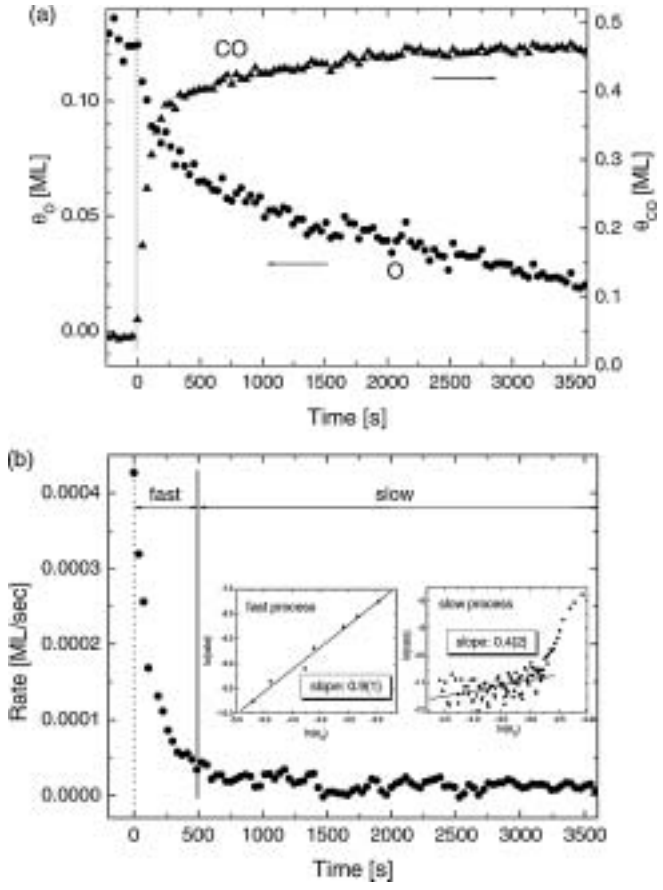

Fig. 4. (a) Coverage change of O (circles) and CO (triangles) as a function of time during the CO oxidation reaction on a O-precovered Pt(111) surface at 240 K. CO exposure was started at $t = 0$ s with an ambient CO pressure of 1.0×10^{-8} Torr. There is no induction period observed at the beginning of CO exposure. (b) Time-dependence of reaction rate. Initially quite a fast process is observed until 500 s, which is followed by a slow process. As shown in the Inset, the former process obeys almost the first-order kinetics with respect to the oxygen coverage, while the latter process exhibits approximately the 1/2nd-order kinetics.

in Fig. 4(a). Contrary to the previous STM results, no induction period is seen at all. The reaction proceeds at the maximum rate at the beginning of CO exposure, which is more evident from the rate vs. time plot shown in Fig. 4(b). The reaction rate rapidly decreases initially and reaches an almost constant rate at around 300 s. Thus, the reaction can be divided into two processes; that is, the initial fast process ($t = 0$–300 s) and the following slow process ($t > 300$ s). In the insets of Fig. 4(b) are depicted results of analyses of reaction order for the two processes. From the slope of the ln$v$ vs. lnθ_O plot the former process can be regarded as the first-order reaction with respect to the oxygen coverage θ_O, while the latter slow process is the 1/2-order reaction. Thus, two distinct processes with different reaction orders operate sequentially. The latter process corresponds to the previously reported perimeter-specific reaction process [17], since the rate of the perimeter-specific reaction should be proportional to the square-root of the oxygen coverage. The former process was newly found by the present in-situ monitoring. The first-order kinetics seen for this process suggests that the reactive species is isolated oxygen or interior oxygen of the islands.

In order to judge which oxygen species contributes to the this process, we have conducted a similar experiment for a O/Pt(111) surface with a different average size of the oxygen islands formed by pre-annealing at 350 K (not shown). The pre-annealed surface exhibited more sharp and intense p(2 × 2) LEED spots indicating a larger average size of the oxygen islands. Compared to the results for the non-annealed surface, the first process is obviously shortened and a smaller amount of oxygen is consumed in this process. The significant suppression of the first process by the pre-annealing indicates that this process is not associated with the interior oxygen but with the isolated oxygen, because such annealing causes an increase in the island size and a reduction of the isolated oxygen. It was confirmed that the reaction order keeps unchanged for the annealed surface.

To get more information about difference between the two processes, activation energies were obtained from temperature dependence of the rate constant. The activation energy for the first process was estimated to be 0.22 ± 0.03 eV, while for the second process 0.32 ± 0.01 eV. The first process exhibits the lower activation energy by 0.1 eV with respect to that for the second process. If the transition states of the both processes are the same, the difference in activation energy is associated with the difference in the initial adsorption energy. Since the interatomic interaction between the oxygen adatoms is known to be attractive [17], the adsorption energy of an oxygen atom is stabilized by coordination of surrounding oxygen atoms, meaning that the difference in effective coordination number causes a difference in adsorption energy. The effective coordination numbers for the island-perimeter atoms is obviously higher than that for the isolated atoms, which results in the lower adsorption energy for the island-perimeter atoms. Thus, the observed difference in the activation energy can be attributed to the difference in coordination number between the isolated atoms and the island-perimeter atoms.

From all the results mentioned above, we conclude that the initial fast process corresponds to the reaction of isolated oxygen atoms whereas the following slow process is the island-perimeter reaction. This reaction mechanism was confirmed by kinetic Monte-Carlo simulations that take accounts of the adsorbate-adsorbate interactions [18]. The former process was found for the first time with the present dispersive-NEXAFS monitoring. The isolated oxygen atoms are diffusing so fast that they might be invisible in the STM observation.

3.2. *Water formation reaction on a Pt(111) surface*

The water formation reaction on Pt(111) is a model reaction for a fuel cell. Adsorbed hydrogen is oxidized by pre-adsorbed oxygen to give H_2O. Although this reaction seems rather simple, interesting findings have been reported for this reaction [3]: First, this reaction is auto-catalytic in the presence of H_2O. Secondly domains of intermediate OH are traveling on the surface during the reaction, which was evidenced by previous STM observations [3, 19]. However, drawbacks in the STM observations are that not all surface species are visible and it provides only information of a limited area. We conducted dispersive-NEXAFS experiments for this reaction to get information on behavior of O, OH, and H_2O on a macroscopic scale, particularly focusing on quantitative detection of the intermediate OH coverage during the reaction [20].

Figure 5 shows oxygen K-edge dispersive-NEXAFS spectra taken for an oxygen-precovered Pt(111) surface with exposing to H_2. The experimental conditions were similar to those used in the STM observation. The oxygen peak decreases with H_2 exposure and instead a broad peak, which comes from both OH and H_2O, grows. Each spectrum was curve-fitted by summation of standard spectra of the three species to estimate the coverages. Coverage

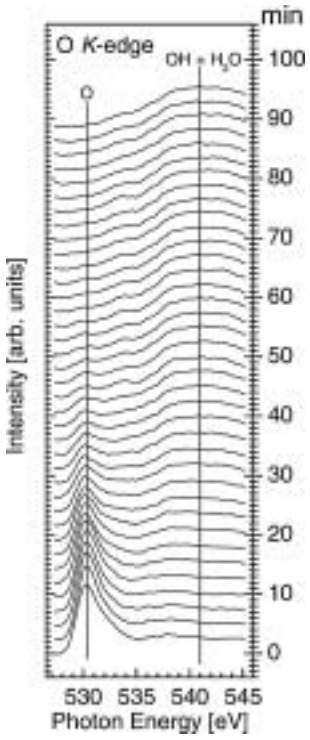

Fig. 5. A data set of O K-edge dispersive-NEXAFS spectra taken for an O-precovered ($\theta_O = 0.25$ ML) Pt(111) surface at 130 K under an ambient H_2 pressure of 5.0×10^{-9} Torr. The accumulation time was 30 s for each spectrum.

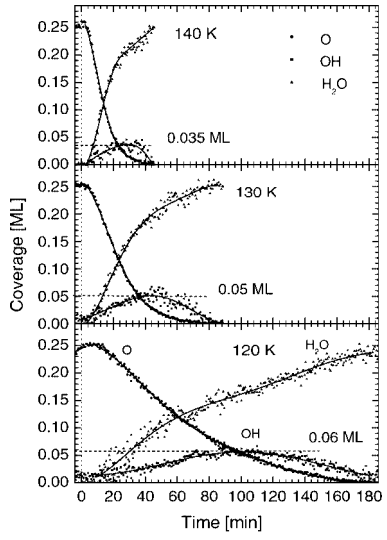

Fig. 6. (a) Coverage changes of O (circles), OH (squares) and H_2O (triangles) as a function of time during the hydrogen oxidation reaction on a O-precovered Pt(111) surface at 140 K (top), 130 K (middle) and 120 K (bottom). H_2 exposure was started at $t = 0$ s with an ambient H_2 pressure of 5.0×10^{-9} Torr.

changes of O, OH and H_2O thus obtained at different temperatures are shown in Fig. 6. The OH coverage gradually increases with time and after passing through a maximum decreases to zero. The total coverage of O, OH, H_2O always keeps constant, indicating that this analysis appears self-consistent. This is the first case that the time-evolution of all the surface species including the reaction intermediate is quantitatively estimated at several temperatures. It is interesting to note that the maximum coverage of OH increases with decreasing temperature.

In order to understand this trend, we performed simulations based on the reaction diffusion model. The elementary steps of the water formation reaction are described as follows:

$$O + H \xrightarrow{k_1} OH, \tag{1}$$

$$OH + H \xrightarrow{k_2} H_2O, \tag{2}$$

$$O + 2H_2O \xrightarrow{k_3} 3OH + H. \tag{3}$$

Since k_1 is very small, the first step can be neglected. The cycle of the second and the third step acts as an autocatalytic cycle which yields one H_2O molecule per cycle. This cycle is driven by diffusion of H_2O to a reaction front. Based on these elementary steps, rate equations are numerically solved using a grid with an assumed initial configuration where a certain number of H_2O nuclei are randomly distributed on the oxygen-saturated surface. A small amount of H_2O molecules are inevitably adsorbed from residual gas [3]. To conduct this simulation, we needed a couple of kinetic parameter values, the rate constants k_2, k_3 and the diffusion coefficient of H_2O D. k_2 and k_3 were estimated by separate dispersive-NEXAFS experiments to be $k_2 = 1.2 \times 10^{-4}$, 4.1×10^{-4} and 1.1×10^{-3} [$ML^{-1}s^{-1}$] and $k_3 = 3.5 \times 10^{-3}$, 1.1×10^{-2} and 3.1×10^{-2} [$ML^{-1}s^{-1}$] at 120, 130 and 140 K, respectively [20], and as for D we referred to the previous STM study [3]. From reaction diffusion simulations using these kinetic parameters, we obtained coverage changes of O, OH and H_2O as a function of time. Simulated results at different temperatures with a fixed number of H_2O nuclei showed no apparent temperature dependence except for differences in overall reaction time (not shown). On the other hand, nucleus-number dependence at a fixed temperature is significant; the higher nucleus number causes the higher OH maximum coverage as shown in Fig. 7. Considering these simulated results, we interpret the temperature dependence of the OH maximum coverage by the difference in initial nucleus density that depends on surface temperature. At the lower temperature the larger number of the H_2O nuclei are

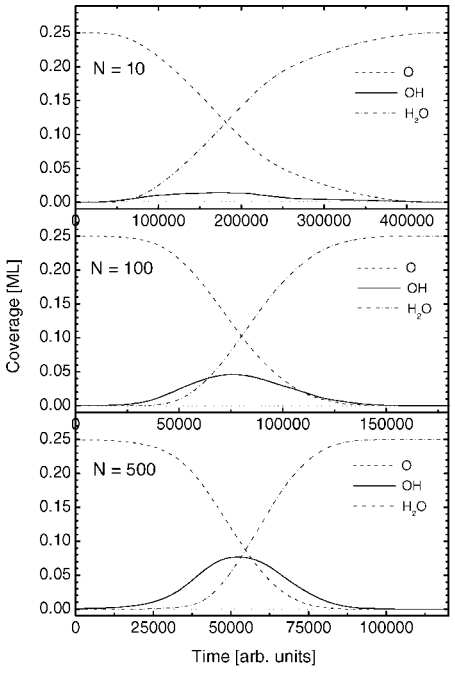

Fig. 7. Simulated coverage changes of O (circles), OH (squares) and H_2O (triangles) as a function of time based on the reaction diffusion model. The temperature was fixed at 130 K, while the number of the initial H_2O nuclei (N) was assumed to be 10 (top), 100 (middle) and 500 (bottom).

formed due to a limited diffusion of H_2O. It is emphasized here that the combination of the dispersive-NEXAFS and the kinetic simulations is a powerful tool to study the mechanism of the surface non-linear reactions as described above.

4. Future improvements

Finally, we discuss future possible improvements of the dispersive-NEXAFS technique. It is necessary for the fast XPS to use the undulator beamline, while the present dispersive-NEXAFS is set up at the bending magnet beamline with a similar performance. If we use a tapered undulator as a light source of the dispersive NEXAFS, we can expect two orders of magnitude higher intensity. Another possible improvement is to optimize the electron analyzer system. The present system uses a commercial electron analyzer which has a high energy resolution, but a small acceptance angle ($\pm 5^\circ$). In fact, we do not need any high energy resolution but need a large acceptance angle. By using an electron energy analyzer fully optimized to this technique, the detection efficiency will be improved by two orders of magnitude. Combined improvement of the photon flux and the detection efficiency will lead to a milli-second order acquisition of a NEXAFS spectrum.

Furthermore, if the improved technique is combined with a chopped X-ray or a gated-ICCD camera and applied to repeatable fast surface phenomena triggered by an arrival of a pulsed molecular beam or other external stimuli such as pulsed light and pulsed electric field, time-resolved NEXAFS experiments will be able to be performed with a microsecond-order resolution. Such a time-resolved NEXAFS technique will provide information on dynamics of surface species such as a transient reaction intermediate, an adsorption precursor and a photosensitive organic molecule adsorbed on a substrate.

Acknowledgments

The authors acknowledge staffs of the Photon Factory for technical and financial support. We are grateful for the financial support of the Grant-in-Aid for Scientific Research (No. 14204069) and for the 21st Century COE Program from the Ministry of Education, Culture, Sports, Science and Technology. The present work has been performed under the approval of the Photon Factory Program Advisory Committee (PF PAC No. 01S2-003).

References

1. Briner, B. G., Doering, M., Rust, H.-P. and Bradshaw, A. M., Science **278**, 257 (1997).
2. Wintterlin, J., Völkening, S., Janssens, T. V. W., Zambelli, T. and Ertl, G., Science **278**, 1931 (1997).
3. Sachs, C., Hildebrand, M., Völkening, S., Wintterlin, J. and Ertl, G., Science **293**, 1635 (2001).
4. Germer, T. A. and Ho, W., Chem. Phys. Lett. **163**, 449 (1989).
5. Tripa, C. E. and Yates, Jr., J. T., Nature **398**, 591 (1999).
6. Bonn, M. *et al*., Science **285**, 1042 (1999).
7. Noguchi, H. *et al*., Surf. Sci. **528**, 183 (2003).
8. Baraldi, A. *et al*., J. Electron Spectrosc. Relat. Phenom. **76**, 145 (1995).
9. Cobden, P. D. *et al*., Surf. Sci. **416**, 264 (1998).
10. Vattuone, L. *et al*., Phys. Rev. **B 66**, 085403 (2002).
11. Matsushita, T. and Phizackerley, R. P., Jpn. J. Appl. Phys. **20**, 2223 (1981).
12. Amemiya, K. *et al*., Jpn. J. Appl. Phys. **40**, L718–L720 (2001).
13. Amemiya, K., Kondoh, H., Yokoyama, T. and Ohta, T., J. Electron. Spectrosc. Relat. Phenom. **124**, 151 (2002).
14. Nambu, A., Kondoh, H., Nakai, I., Amemiya, K. and Ohta, T., Surf. Sci. **530**, 101 (2003).
15. Gland, J. L. and Kollin, E. B., J. Chem. Phys. **78**, 963 (1983).
16. Xu, M., Liu, J. and Zaera, F., J. Chem. Phys. **104**, 8825 (1996).
17. Völkening, S. and Wintterlin, J., J. Chem. Phys. **114**, 6382 (2000).
18. Nakai, I., Kondoh, H., Amemiya, K., Nagasaka, M., Nambu, A., Shimada, T. and Ohta, T., J. Chem. Phys. **121**, 5035 (2004).
19. Völkening, S., Bedürftig, K., Jacobi, K., Wintterlin, J. and Ertl, G., Phys. Rev. Lett. **83**, 2672 (1999).
20. Nagasaka, M., Kondoh, H., Amemiya, K., Nambu, A., Nakai, I., Shimada, T. and Ohta, T., J. Chem. Phys. **119**, 9233 (2003).

Physica Scripta. Vol. T115, 93–96, 2005

Capturing Excited State Molecular Structures in Disordered Media with 100 ps Time Resolution by Laser Pump X-ray Probe XAFS

L. X. Chen[1]*, G. B. Shaw[1], T. Liu[1], G. Jennings[2] and K. Attenkofer[2]

Chemistry Division[1] and Advanced Photon Source[2], Argonne National Laboratory Argonne, Illinois 60439, U.S.A.

Received June 26, 2003; accepted November 4, 2003

PACS number: 78.47.+p

Abstract

The timing structure and the high photon flux of X-ray pulses from the Advanced Photon Source permit pump-probe techniques widely used in ultrafast laser spectroscopy to be extended into the X-ray regime. The intrinsic time resolution of the experiments is determined by the FWHM of the single pulses from the synchrotron at 70–100 ps. The challenges and the solutions in such experiments will be discussed. Using laser pulse pump, X-ray pulse probe XAFS, several excited state molecular structures in solutions were studied. We will mainly describe molecular structures of the photoexcited metal-to-ligand-charge-transfer state of $[Cu^{I}(dmp)_2]^+$, where dmp is 2,9-dimethyl-1,10-phenanthroline, in toluene and acetonitrile. The experimental results indicated that the copper ion in the thermally equilibrated MLCT state in both solvents had the same oxidation state as the corresponding Cu(II) complex in the ground state and was found to be penta-coordinate with an average nearest neighbor Cu-N distances 0.04 Å longer in toluene and 0.04 Å shorter in acetonitrile than that of the ground state $[Cu^{I}(dmp)_2]^+$. The results further revealed that what distinguishes the MLCT state structures in non-coordinating and coordinating solvents is not the "exciplex" formation, but the strength of the interactions between the solvent and the Cu(II)* species at the MLCT state. In addition, future direction of time-resolved XAFS will be discussed.

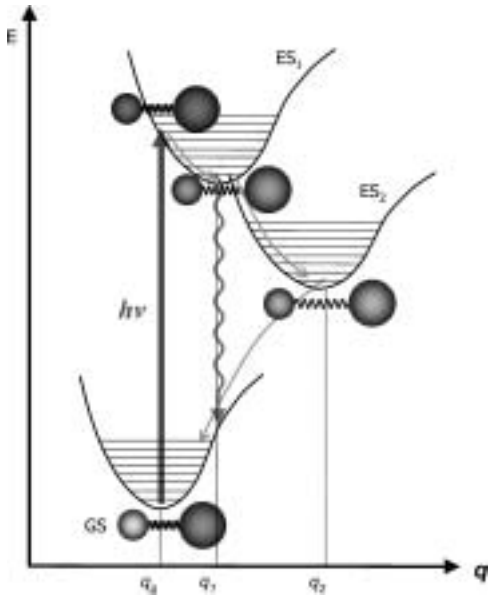

Fig. 1. Interactions between light and molecule. The potential energy E vs. reaction coordinates as the reaction proceeds from excited state 1 (ES_1) to excited state 2 (ES_2). The pump-probe XAFS with 100-ps resolution will capture the thermally equilibrated excited states with the coordinates at the bottom of the potential wells.

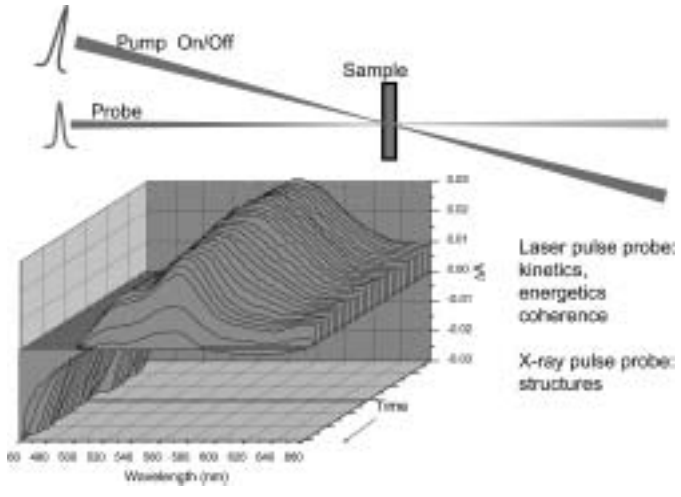

Fig. 2. Illustration of the pump-probe approach. Using laser pulse as a probe, the kinetics, energetics and coherence of the excited state molecules can be obtained. Using X-ray pulse as the probe, we can obtain the direct structural information of the excited state molecules.

Photoexcited molecules are key ingredients for photochemical processes that are important to natural and artificial photosynthesis, photocatalysis, molecular photonics, and devices [1]. In these processes, the excited state molecules are reactants generated by light and are either transformed into products or are vehicles for converting light energy into other forms of energy. The fundamental aspect of the reaction can be understood by the interactions between molecules and light. When a molecule absorbs a photon with energy ranging from ultra-violet to near infrared, its valence electron density is redistributed, and its nuclei experience a new field while retaining the same configuration as the ground state (Fig. 1) [2]. However, within femtoseconds (fs) to a few picoseconds (ps) of the excitation, nuclei of the excited molecule will rapidly adjust themselves to accommodate the new field via structural relaxation to a configuration corresponding to that at the bottom of the potential well in Fig. 1, which differs from the ground state and retains this thermally equilibrated configuration for ps to ms. The pump-probe approach is most commonly used in ultrafast laser spectroscopy, where a laser pulse creates the excited state molecules and another laser pulse probes the optical absorption change due to the pump laser pulse as a function of time delay between the pump and the probe (Fig. 2) [3]. Such an approach allows us to obtain the kinetics, energetics and coherence of the excited states. However, the excited state structures remain elusive, which severely hinders advances in photochemistry.

The Advanced Photon Source (APS) at Argonne provides unprecedented photon flux in each X-ray pulse and timing structures of X-ray pulses [4], which enable the transient structure of the excited state molecules to be probed with an intrinsic time resolution only limited by the pulse duration of the pump or the probe pulse, whichever is longer. In most of the cases, that is the limit of the X-ray pulse duration of ∼30–100 ps. Although it is still too slow for following actual atomic movements from

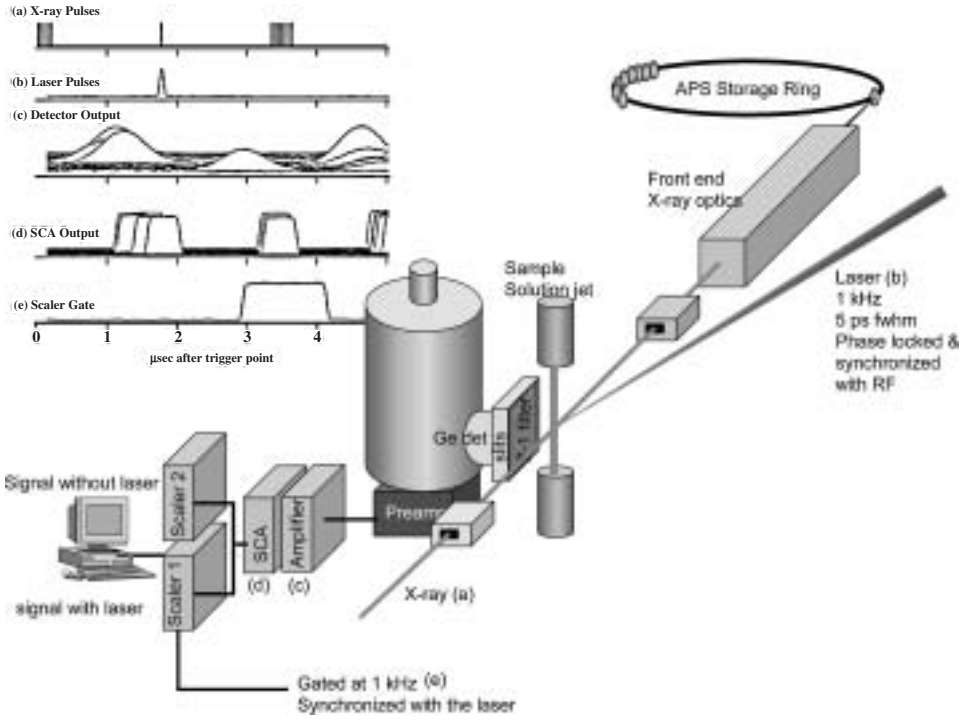

Fig. 3. Illustration of the experimental setup for the pump-probe XAFS. The signals shown in the upper left are marked at corresponding points with the same letter.

the initial Franck-Condon state to the structural relaxed excited state, 100-ps resolution is sufficient for capturing the thermally equilibrated excited state structures with lifetimes from hundreds of ps to ms. Currently, limited information on these excited state structures is available. Because most photochemical reactions take place in disordered media, our studies has been focused on X-ray absorption spectroscopy [5, 6].

Challenges were encountered by the pump-probe XANES and XAFS measurements due to the mismatches in 1) repetition rates of the laser pump and the X-ray probe pulses, 2) the absorption coefficients for optical and X-ray photons, 3) sample concentration preference by XAFS and photochemistry, as well as 4) response times of detectors and the intrinsic time resolution provided by 100-ps X-ray pulses [7]. In addition, the partial conversion of the ground state to the excited state in almost all cases imposes difficulties in extracting an excited state spectrum as indicated by Equation (1),

$$\mu(E,t) = \left[1 - \sum_j f_{es_j}(0)\mathrm{e}^{-k_j t}\right]\mu_{gs}(E) + \sum_j f_{es_j}(0)\mathrm{e}^{-k_j t}\mu_{es_j}(E) \tag{1}$$

where $\mu(E,t)$ is the total X-ray absorption signal, E and t are X-ray photon energy and time, respectively. The subscripts *es* and *gs* stand for the excited and the ground states, and j is the index for the excited states. f_{esj} is the fraction of the jth excited state, and k_j is the decay time constant for the jth excited state. Assuming there is only one excited state and the time of the measurement is zero from the pump, Equation 1 can be further simplified as below,

$$\mu(E) = [1 - f_{es}(0)]\mu_{gs}(E) + f_{es}(0)\mu_{es}(E)$$

where $f_{es}(0)$ is the fraction of the excited state at zero delay between the pump and probe pulses. Therefore, the excited state molecular structure at the optimal concentration can be probed.

In spite of experimental challenges mentioned above, pump-probe XAFS experiments have been carried out at the beamline 11ID-D under the hybrid timing operation mode (Fig. 3), where a single electron bunch or bunch cluster is separated in time from the rest of the electron bunches in the storage ring to satisfy time domain studies and other studies concerning the average X-ray photon flux only. In the first pump-probe XAFS, the structure of a photodissociation intermediate of nickeltetraphenylporphyrin (NiTPP) with two axial piperidine ligands was captured in solution within its lifetime of 28 ns by a sextuplet X-ray pulse cluster with a 14 ns time resolution at 1 mM concentration. The results indicated that the recombination of the ligands was concerted within the time resolution of the experiment and about 30% of the molecules underwent photodissociation. The structure of the photodissociation intermediate had a structure resembled that of the ground state NiTPP without the axial ligands [8].

Following the initial success, we expanded our interests to the real photoexcited state molecules other than reaction intermediates. The metal-to-ligand-charge-transfer (MLCT) states of metal complexes are essential for many photochemical reactions, where the electron is depleted from the metal center and transferred to the ligands upon absorbing light by the molecule. Such an intra-molecular electron transfer creates transient change in the oxidation state of the metal. Consequently, such an electron movement could induce nuclear rearrangement in the MLCT state. Pump-probe XAFS measurements with 100-ps time resolution obtained by using single X-ray pulses from the APS during the hybrid fill operation were conducted to investigate structural origins of the MLCT excited state behavior of $[Cu^{I}(dmp)_2]^+$ (dmp = 2,9-dimethyl-1,10-phenanthroline), which is strongly solvent dependent [9, 10]. Absorption of a visible photon promotes an electron from Cu^{I} to one of the ligands, achieving an intra-molecular charge separation with a Cu^{II*} center coordinated to one reduced and one neutral dmp ligand. The initial Franck- Condon MLCT state has an identical pseudo-tetrahedral

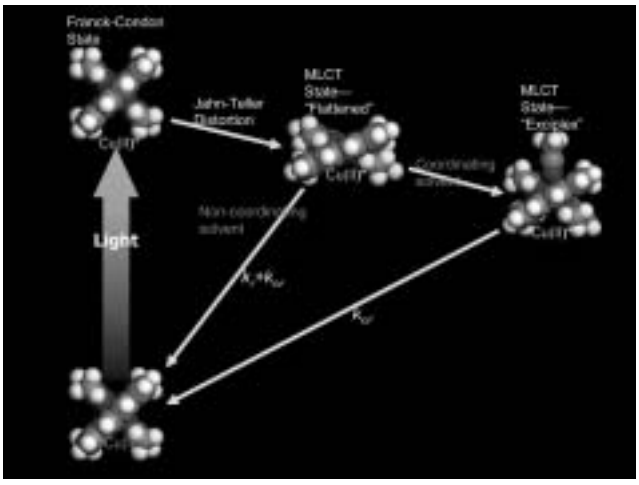

Fig. 4. Previously accepted photoexcitation pathway for $Cu^{I}(dmp)_2{}^{+}$, where only a coordinating solvent molecule would form "exciplex" that causes quenching of room temperature luminescence and shortened lifetime for the MLCT state, but a non-coordinating solvent molecule would not form the complex with copper resulting in a much longer lifetime of the MLCT state and room temperature luminescence.

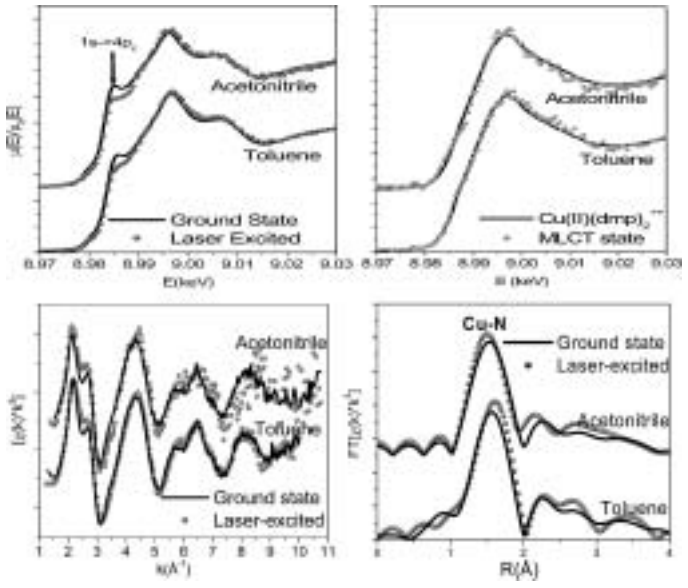

Fig. 5. XANES and XAFS of $Cu^{I}(dmp)_2{}^{+}$ in coordinating solvent acetonitrile and non-coordinating solvent toluene, with and without laser excitation.

coordination geometry as the ground state, but the Cu^{II*} center with a d^9 electronic configuration is susceptible to a Jahn-Teller distortion resulting in a MLCT state with flattened tetrahedral coordination (Fig. 4). In non-coordinating solvents, such as toluene, the MLCT state is luminescent at room temperature and has lifetimes up to 100 ns. In contrast, the MLCT state is almost non-luminescent and has lifetimes as short as 1–2 ns at room temperature in strongly coordinating solvents, such as acetonitrile. The large "Stokes-like" shift observed between the absorption and emission is consistent with significant structural changes in the MLCT state that either returns to the ground state via a radiative decay pathway in non-coordinating solvents, or forms a penta-coordinate complex with a strongly coordinating solvent molecule, resulting in the "exciplex" quenching.

Transient optical spectra with fs time resolution were also measured in a coordinating solvent acetonitrile and in a non-coordinating solvent toluene respectively, revealing three time constants in the excited state dynamics in each solvent. The first two fast time constants of 500–700 fs and 10–20 ps are similar in both solvents, but the third time constants are 1.7 ns in acetonitrile and 100 ns in toluene, about 60-fold difference! The optical transient absorption data suggest that the sub-ps time constant is due to the formation of the triplet state via the inter- system crossing and the 10 ps time constant is due to the structural flattening of the tetrahedral coordination in the excited state. Because these two time scales are beyond reach of the current X-ray probe with single pulses, the pump-probe XAFS was carried out to investigate the structures of the thermally equilibrated MLCT state with 1.7 and 100 ns lifetimes, respectively.

Laser pulses at 527 nm were used to excite the copper complex, and differences between the XANES spectra of the ground state and the laser excited $[Cu^{I}(dmp)_2]^{+}$ in acetonitrile and in toluene are clearly visible in Fig. 5. The shoulder feature at 8.985 keV was reduced upon laser excitation, accompanied by a slight increase of the peak intensity at 8.996 keV. After subtracting the 80% remaining ground state spectrum respectively from the laser illuminated sample spectra in both solutions, the MLCT state XANES spectra were extracted in both solvents. In both cases, the shoulder feature for the ground state $[Cu^{I}(dmp)_2]^{+}$ is missing in the MLCT state, and the transition edge is shifted by about 3 eV to the same edge energy as the ground state $[Cu^{II}(dmp)_2]^{2+}$ obtained via *in situ* electrolysis of $[Cu^{I}(dmp)_2]^{+}$ in acetonitrile. The shoulder feature at 8.985 keV is due to the $1s \rightarrow 4p_z$ transition that is pronounced in $[Cu^{I}(dmp)_2]^{+}$ and missing from $[Cu^{II}(dmp)_2]^{2+}$. This is a typical observation for transformation from 4- to 5- or 6-coordinate geometry.

The copper coordination number and the Cu-to-ligand bond lengths for the MLCT state of $[Cu^{I}(dmp)_2]^{+}$ were extracted from the XAFS data. Interestingly, the Cu-N peak shifts to a shorter distance in acetonitrile, but to a longer distance in toluene, compared to the average Cu-N distance at 2.07 Å for the ground state. The average Cu-N distance for the laser-excited sample in acetonitrile fits distances of 2.07 and 2.03 Å, whereas that in toluene fits distances of 2.06 and 2.11 Å, while keeping the relative ratio of the two distances to 4:1. Clearly, the first Cu-N distance is from the ground state, and the second, the MLCT state. The results of the experiment demonstrated: 1) light excitation generated a formally Cu^{II*} center, 2) the inner-sphere reorganization changed the coordination number of the MLCT state from four to five in presumed non-coordinating toluene, and 3) the average Cu-ligand bond distances lengthened in the MLCT state in toluene, but shortened in acetonitrile.

The XANES spectra provided strong evidence for the penta-coordinate Cu^{II*} in both acetonitrile and toluene. These results are in accordance with the fact that Cu^{II*} in the MLCT excited state is formally a 17 electron d^9 system prone to the addition of a fifth ligand. It is well-known that MLCT excited states in general follow the energy gap law that the non-radiative rate constant increases exponentially with decreasing energy separation between the ground state and the excited state. The formation of the "exciplex" stabilizes the MLCT state, reducing the energy gap between the ground state and the MLCT state. As the energy gap becomes small enough due to the strong interaction of the Cu center with the ligand, the non-radiative decay dominates the relaxation pathway and no emission is detected (*e.g.*, as in the acetonitrile solution case). However, the above statements are unable to explain the solvent dependency of the MLCT state behaviors.

The XANES results for $[Cu^{I}(dmp)_2]^+$ in both toluene and acetonitrile solutions support the formation of a penta-coordinated Cu^{II*} center in the MLCT state based on the attenuation of the shoulder feature in the transition K-edge of copper in the spectra. However, a broad range of the Cu-to-ligand bond distances for the fifth ligand could smooth the transition edge as seen in previous studies. The respective elongation and the shortening of the average Cu-N bond distance for the MLCT state of the $[Cu^{I}(dmp)_2]^+$ in toluene and in acetonitrile signal the difference in the interactions of the copper with the fifth ligand. Such variation was also seen by a broad range of the MLCT state lifetimes in various Lewis base solvents with different electron donating capabilities. The variation of the MLCT state structure in different solvents confirmed that the origin of distinctly different excited state behavior is due to formation of MLCT state-solvent complexes with different electronic interactions. When the interaction is strong, the MLCT state lifetime is shortened significantly and the luminescence is quenched, which has been characterized by the "exciplex" formation in previous literature. Therefore, the pump-probe XAFS measurements in the time domain provide new insights into the fundamental aspects of structural factors that may influence photoinduced electron and energy transfer processes.

Acknowledgement

This work was supported by the Division of Chemical Sciences and Materials Science, Office of Basic Energy Sciences, Department of Energy under contract W-31-109-ENG-38. We thank Professor Gerald J. Meyer for his insightful discussions and the help from BESSRC beamline staff is greatly appreciated.

References

1. P. F. Barbara, T. J. Meyer and M. A. Ratner J. Phys. Chem., 100 (1996) 13148.
2. P. W. Atkins, Quanta, Oxford University Press, Oxford, (1991) 133.
3. A. H. Zewail Angew. Chem., Int. Ed., 39 (2000) 2586.
4. G. K. Shenoy, P. J. Viccaro and D. M. Mills, Characteristics of the 7-GeV Advanced Photon Source, Argonne National Laboratory, (1988).
5. D. E. Sayers, E. A. Stern and F. Lytle Phys. Rev. Lett., 27 (1971) 1204.
6. E. A. Stern, D. E. Sayers and F. W. Lytle Phys. Rev. B, 11 (1975) 4836.
7. L. X. Chen, G. B. Shaw, I. Novozhilovad, T. Liu, G. Jennings, K. Attenkofer, G. J. Meyer and P. Coppens J. Am. Chem. Soc., 125 (2003) 7022.
8. L. X. Chen, W. J. H. Jager, G. Jennings, D. J. Gosztola, A. Munkholm and J. P. Hessler Science (Washington, DC, U. S.), 292 (2001) 262.
9. L. X. Chen, G. Jenings, T. Liu, D. J. Gosztola, J. P. Hessler, D. V. Scaltrito and G. J. Meyer J. Am. Chem. Soc., 124 (2002) 10861.
10. L. X. Chen, G. B. Shaw, I. Novozhilova, L. Tao, G. Jenings, K. Attenkofer, G. J. Meyer and P. Coppens J. Am. Chem. Soc. 125 (2003) 7022.

Physica Scripta. Vol. T115, 97–101, 2005

Capacitance XAFS Method: A New Site-Selective and Microscopic X-Ray Absorption Spectroscopy

Masashi Ishii*,[1,2], Aiko Nakao[3] and Takayuki Uchihashi[4]

[1]JASRI (Japan Synchrotron Radiation Research Institute), SPring-8, Mikaduki, Sayo-gun, Hyogo 679-5198, Japan
[2]RIKEN (The Institute of Physical and Chemical Research) Harima Institute, Mikaduki, Sayo, Hyogo 679-5148, Japan
[3]RIKEN (The Institute of Physical and Chemical Research), Hirosawa, Wako, Saitama 351-0198, Japan
[4]SFI Laboratory, Trinity College, Dublin 2, Ireland

Received June 26, 2003; accepted November 4, 2003

PACS numbers: 78.70 Dm; 84.37 +q; 07.79 Lh; 68.37 Ps; 61.10 Ht

Abstract

For local structure and electronic state analyses of electron trapping centers, we developed a site-selective X-ray absorption fine structure (XAFS) measurement, i.e., the capacitance XAFS method. The concept of the capacitance XAFS measurement is based on the fact that the X-ray absorption of trapping centers, not the bulk, can be evaluated from the capacitance change due to X-ray induced photoemission of a localized electron. With this method, micro spectroscopy can be achieved by scanning probe detection of the capacitance. Moreover, trapping centers with a specific eigen-energy can be selectively observed by controlling the sample bias voltage. We tested these advantages in detail for two typical metal and semiconductor systems. (1) The capacitance XAFS spectrum of Cu indicated two-dimensional (2D) electronic states at a hetero interface between native oxide (Cu_2O) and bulk Cu; the Cu 4pπ states of the electron trap were confined into a 2D plane. (2) The capacitance XAFS spectrum of GaAs depends on the sample bias voltage and on selectively indicated electronic states of surface trapping center due to Ga oxide, which captures electrons at a positive bias voltage.

1. Introduction

X-ray absorption fine structure (XAFS) measurement [1, 2] has already been established as an experimental technique for analyzing local structures and electronic states. One advantage of this method is that local information of a specific atom can be obtained even when the atom is incorporated into a compound, because XAFS oscillation appears around the inner-shell absorption-edge energy intrinsic to individual atoms. However, the fact that local information is derived from macroscopic absorption implies the structural homogeneity of the sample. When the sample is heterogeneous with various local structures dependent on their chemical environments, only rarely can the spectrum be deconvoluted into spectra of common structures, so a significant analysis is generally impossible. However, heterogeneous systems are not only common but also of interest to current material science. For instance, defect, hetero interfaces or nanometer-scale quantum structures provide optical luminescence at industrially profitable wavelengths and a high electron mobility applicable to active devices in a central processing unit [3–5]. Therefore, many efforts have been made to fabricate well-defined heterogeneous structures with nanometer-scale precision [6]. Obviously, the applicability of the XAFS measurement method to nanotechnology is restricted if the sample needs to be homogeneous.

High spatial resolution measurements are one candidate for evaluating heterogeneous systems. However, generally speaking, the X-ray beam size and the emittance are large, and focusing on a nanometer-scale object is not easy because of the high transmittance and low refractive index of the X-ray [7]. Though precise focusing optics represented by a Fresnel zone plate have been developed for X-ray microscopy [8], they are not suitable for spectroscopy accompanied with photon energy scanning.

Recently, we proposed a new XAFS measurement method, called capacitance XAFS [9, 10]. Since in this method X-ray absorption is evaluated by a capacitance change caused by X-ray induced photoemission of a localized electron, it can achieve a site-selective XAFS analysis of the specific atoms with the localized electron. Considering that the target characteristics of the heterogeneous system are obtained by confining electrons in a nanometer-scale region, the capacitance XAFS measurement method has the potential for selectively observing optically and electronically active sites in heterogeneous systems [11, 12].

Moreover, we can take microspectroscopic measurements by using the capacitance XAFS method with a metal scanning probe as the electrode facing a sample becomes a local capacitor. The observation area can be conceptually narrowed down to the probe size rather than the X-ray beam size; the focusing optics is not necessary.

In this report, we discuss two experimental results of capacitance XAFS measurements of a nanometer-scale thickness native oxide layer (1) on a metal (Cu_2O/Cu) and (2) on semiconductor (GaO/GaAs). Though the basic idea for the measurements is the same in both systems, the photoemission process of the localized electron depends on their valence states. We propose electron transition models for the site selectivity in metal and semiconductor systems, and we discuss the chemical properties of the trapping centers obtained by the site selectivity.

2. Capacitance XAFS measurement of a Cu_2O/Cu system

2.1. *Experiments*

Figure 1(a) shows the schematic diagram of an experimental apparatus for the capacitance XAFS measurement of metals. A sample is mounted in an insulator cell, and it is also electrically isolated by a polymer film (poly vinylidene chloride) and a glass plate each on the front and the rear surfaces. A capacitor was formed by placing grounded Al foil parallel to a metal electrode on a capacitance detector. A synchrotron radiation (SR) beam was irradiated into the sample surface through the Al foil and the poly vinylidene chloride film. The films were 15 and 10 μm thick, respectively; any attenuation of the SR beam by these layers is negligible. The incidence angle of the SR beam was normal to the sample surface ($\theta = 90^\circ$), and the electric and magnetic fields were polarized in the sample surface plane. The experimental

*e-mail: ishiim@spring8.or.jp

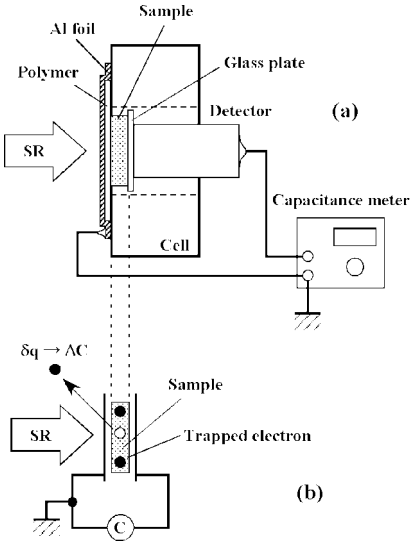

Fig. 1. (a) Schematic diagram of experimental apparatus for a capacitance XAFS measurement of metals. (b) Equivalent circuit of (a).

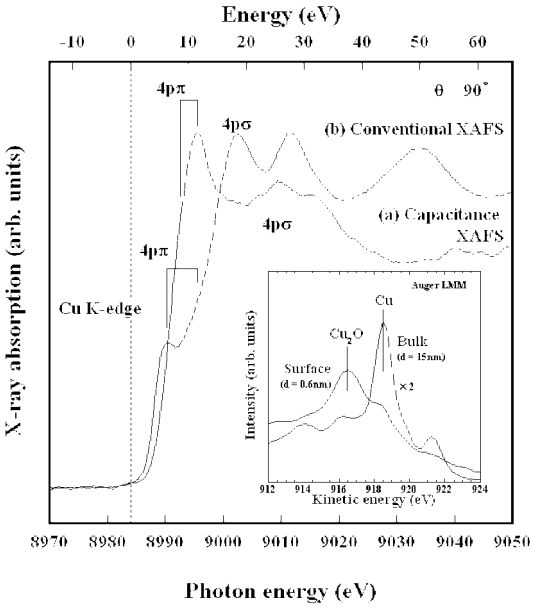

Fig. 2. Capacitance XAFS spectrum of Cu sheet at K-edge (8984 eV) and XAFS spectrum of reference Cu foil measured by using the conventional transmission XAFS method. The inset shows a Cu Auger *LMM* transition peak at the bulk and the surface of the Cu sheet.

setup including the sample made up an electric circuit, which can be equivalently expressed by Fig. 1(b). The sample can be considered as an insertion in the capacitor. Therefore, the electric charge on the sample can be detected by a capacitance meter. In this study, a 500 µm thick polycrystalline Cu sheet was used as the sample. The X-ray induced photoemission of the electron from a trapping center, δq, resulted in a capacitance variation, ΔC. The trapping center is not specified in this figure. However, considering that free charge compensates δq in the Cu bulk, ΔC with respect to the X-ray photon energy indicates the XAFS spectrum of the trapping center. The detailed electron transition process dependent on the sites in the sample is discussed in sections 2.2 and 2.3.

The capacitance XAFS experiments were performed at SPring-8 BL10XU High-Brilliance XAFS Experimental Station [13, 14] in Hyogo Prefecture, in Japan. In this beamline, a high-intensity and quasi-monochromatized SR beam can be obtained from an in-vacuum undulator [15] set in a storage ring. A Si (111) double crystal was used to monochromatize the SR beam. The undulator gap was controlled synchronized with the Bragg angle of the monochromator to maintain the high-intensity SR beam over the wide photon energy range for the XAFS measurements. A rhodium-coated double-mirror positioned after the monochromator eliminated the higher-order X-rays such as third harmonics. The X-ray incidence angle to the double-mirror was fixed at 3 mrad.

2.2. *Results*

Figure 2(a) shows the capacitance XAFS spectrum of the Cu sheet at Cu K-edge (8984 eV). As a reference, an XAFS spectrum of Cu foil evaluated by a conventional transmission XAFS method is also indicated in Fig. 2(b). The spectroscopic structure at the edge energy is mainly caused by resonant electron excitations from the Cu 1s inner-shell to Cu 4p unoccupied states, and it thereby reflects the chemical bonding states such as 4pπ and 4pσ. As shown in this figure, the capacitance XAFS spectrum is obviously different from a conventional one. The absorption edge is shifted to a higher energy side by approximately 2 eV in the capacitance XAFS spectrum. Moreover, resonant peaks related to 4pπ in the capacitance XAFS spectrum are significantly enhanced, while another resonance produced by 4pσ is relatively suppressed. These results strongly suggest that the spectrum (a) shows electronic states of a specific site different from the Cu bulk, because the reference spectrum (b) indicated a Cu bulk site.

We used X-ray photoelectron spectroscopy (XPS) employing ESCALAB 250 produced by VG for a more detailed characterization of the sample. Al Kα (1453.6 eV) was used for sample surface excitation. The depth profile of the chemical composition was measured by in-situ Ar ion sputtering during the XPS measurement. The inset of Fig. 2 is the XPS spectra of the sample Cu sheet. We found that the Cu Auger *LMM* transition peak depends on the depth from the sample surface. An intense peak at a kinetic energy of approximately 919 eV is obtained at depth $d = 15$ nm, which originates from the Cu bulk. However, another peak at approximately 917 eV indicating that Cu_2O is dominant at the sample surface ($d = 0.6$ nm). These results indicate that Cu_2O covers the sample surface as a native oxide. CuO, which can be identified by a Cu $2p_{3/2}$ XPS peak, was not found in our sample. The thickness of the surface Cu_2O is estimated to be approximately 3 nm from a detailed depth-profile measurement. This result provides another possibility that the capacitance XAFS spectrum in Fig. 2(a) corresponds to Cu_2O. However, the capacitance XAFS spectrum indicated by Fig. 2(a) is also different from the previously reported Cu_2O XAFS spectrum [16], which has a sharp pre-edge peak of 4pπ and strong absorption of 4pσ at approximately 20 eV above the K-edge energy.

The capacitance XAFS spectrum that is not a result of either bulk Cu or surface Cu_2O is considered to indicate the local electronic state of the Cu/Cu_2O interface. The electron trapping center is formed at this Cu/Cu_2O hetero interface because an electron lone pair is produced. In this two dimensional (2D) trapping center, the strong σ-bond in the vertical direction cannot be formed by discontinuous atomic arrangement. Consequently, Cu $4p_z$ orbital tends to be confined into the 2D plane, and the π-bond, not the σ-bond, becomes dominant. Confining $4p_z$ should also enhance the degeneracy with the $4p_x$ and $4p_y$ orbitals in the plane, yielding the intense 4pπ peak as shown in Fig. 2(a).

Moreover, the absorption edge shift of by approximately 2 eV to the higher energy in the capacitance XAFS spectrum indicates an increase in the ionic number of Cu. We know that though the absorption edge energy of Cu^0 and $Cu^{1+}{}_2O$ is almost the same, that of $Cu^{2+}O$ is abruptly shifted to higher energy [16]. It is consistent with the 2D trapping center model, because a CuO-like structure is expected to form at the Cu/Cu_2O hetero interface. Therefore, we can conclude that the capacitance XAFS spectrum shows the CuO-like structure as the origin of the trapping center.

Note that the Cu atom is included in all areas, i.e., the Cu bulk, the CuO-like trapping center, and the Cu_2O native oxide. The conventional XAFS measurement using a normal X-ray incidence gives local information of the dominant absorption area, i.e., the Cu bulk. The capacitance XAFS method can only observe a specific site, the Cu-O like trapping center with a sub-atomic layer thickness. The electron transition process in the capacitance XAFS measurement of this CuO-like trapping center at the Cu/Cu_2O interface is as follows.

2.3. *Electron transition model*

Figure 3 shows a band diagram of the sample and the expected electron transition process of the Cu sheet sample under X-ray irradiation. This figure simultaneously indicates the valence and inner-shell states at the front side of the sample to discuss the electron transition process of the 2D electron trapping center at the Cu/Cu_2O interface. In this experiment, the Fermi energy E_F of the Al electrode and the Cu sample was not equal because the sample was electrically isolated. The isolation is indicated by a space between the Al electrode and the sample, which corresponds to the poly vinylidene chloride insulator film in the actual system. The Cu_2O native oxide is a semiconductor, and it is connected to the Cu bulk. The band pinning of thin Cu_2O is superior to the floated E_F of the Cu bulk, resulting in band bending in the Cu bulk.

At the Cu bulk site [Fig. 3(b)], (1) a core-hall produced by the X-ray excitation is immediately occupied by the relaxation of a free electron in the conduction band (2). In this case, the electronic state rapidly returns to the initial state because the conduction band is filled sufficiently with free electrons (3). Therefore, there is no effective X-ray induced photoemission of the localized electron ($\delta q = 0$) resulting in no ΔC. This is the reason why the capacitance XAFS spectrum does not indicate the XAFS spectrum of the Cu bulk as shown in Fig. 2.

As discussed in 2.2, the CuO-like structure is considered to form an electron trapping level and capture electrons at the Cu/Cu_2O hetero interface [Fig. 3(a)]. If the inner-shell excitation of the trapping center atom ($1'$) and the following electron relaxation from the trapping level ($2'$) produce an unoccupied level, this transition induces δq, i.e., Δc. Consequently, ΔC with respect to the X-ray photon energy selectively indicates the XAFS spectrum of the trapping center. Obviously, a lifetime of unoccupied trapping level after the relaxation ($2'$) in Fig. 3(a) is crucial for the ΔC observation. If this level is immediately occupied by a free electron from Cu as well as (3) in Fig. 3(b) ΔC cannot be observed. The electrically floating sample can locally produce an unoccupied level with a longer lifetime. In fact, when the potential in the sample is fixed by a bias voltage applied to the sample, the capacitance XAFS spectrum cannot be obtained. The isolation of the trapping center from the free electrons is realized by a band bending in this figure. However, the free electron can easily fill the trapping level under the fixed bias condition that the band in the Cu bulk is flattened. Though this band bending model is only a speculation, a similar theory can explain a site-selection of a trapping center with a specific eigen-energy in semiconductors as discussed below.

3. Capacitance XAFS measurement of a GaO/GaAs system

3.1. *Experiments*

Figure 4(a) shows the schematic diagram of an experimental apparatus for capacitance XAFS measurements of semiconductors. In the developed system, a scanning capacitance microscopy (SCM) with an Au coated Si microprobe was used for detecting the capacitance in a random area. This combination of XAFS and SCM techniques aims at concluding micro spectroscopy and is called the SCM-XAFS method [17]. A piezoelectric scanning stage with an Al sample holder was used to

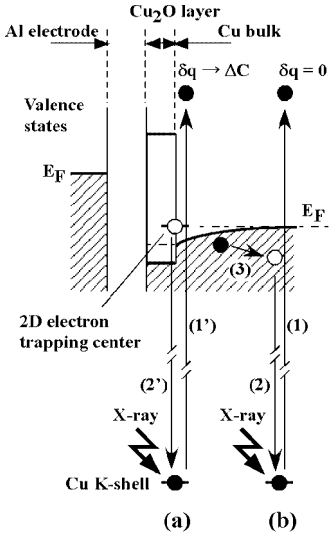

Fig. 3. Band diagram of the Cu sheet and electron transition models at (a) CuO-like trapping center and at (b) Cu bulk site.

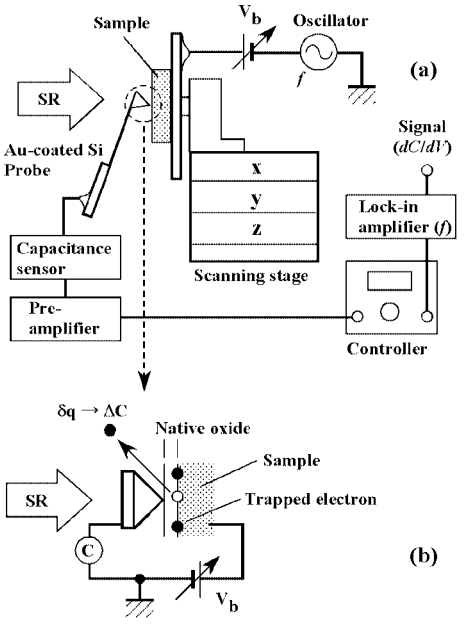

Fig. 4. (a) Schematic setup for SCM-XAFS measurement of a semiconductor. (b) Microscopic MOS capacitor formation by point contact of an Au probe to the semiconductor.

control the position. A semiconductor was attached to the sample holder with conductive silver paste. A voltage variable DC power supply and an AC oscillator were serially connected to the sample holder. So a modulated bias voltage can be applied to the sample. The point contact of the Au microprobe with the semiconductor locally formed a metal-oxide-semiconductor (MOS) capacitor due to a native oxide on the sample surface, as shown in Fig. 4(b). The capacitance of the MOS capacitor was measured by a capacitance sensor, which was a videodisc capacitance pickup circuit developed by RCA [18]. The electronic property of this microscopic MOS capacitor can be evaluated by regarding the capacitance–bias voltage (C-V) characteristics. We can analyze the trapping centers based on the C-V characteristics, as discussed in 3.2. For the capacitance XAFS measurements, we adopted a lock-in amplifier technique using the sample bias modulation for sensitive signal detection. The modulation frequency was fixed at 131 Hz.

The semiconductor sample used in this study was Sn-doped n-type GaAs grown by liquid phase epitaxy. The GaAs surface was covered by a few nanometers thick native oxide layer [19] as well as a Cu_2O/Cu sample, and the electron trapping centers were considered to form at the interface between the GaAs and the native oxide. The SR beam was irradiated into the trapping center under the SCM microprobe and induced the photoemission of localized electrons, δq, resulting in ΔC of the MOS capacitor. The incidence angle of the SR beam was fixed at 45°. The SCM-XAFS experiments were also performed at SPring-8 BL10XU. The X-ray source and the optics of this beamline were the same as those described in section 2.1.

3.2. *Results*

Figure 5 indicates the SCM-XAFS spectra at Ga K-edge (10375 eV). In this experiment, bias voltage V_b was varied from -0.4 to $+0.4$ V. These spectra are normalized by edge jump. As shown in the figure, in the positive V_b region the intensity of a resonant absorption peak at ∼10378 eV gradually increased with increasing V_b. However, the intensity was almost constant in the negative V_b region. This unique dependence on V_b suggests the site of the trapping center with a specific eigen-energy can be selected by controlling V_b. The sharp resonant peak at the absorption edge can be identified as a "white line" produced by Ga oxide. Moreover, an XPS analysis of this GaAs sample found a thin GaO surface layer as a native oxide containing Ga. Therefore, we can conclude that the SCM-XAFS spectra in the positive V_b region indicates a specific trapping center caused by Ga oxide at the GaO/GaAs interface.

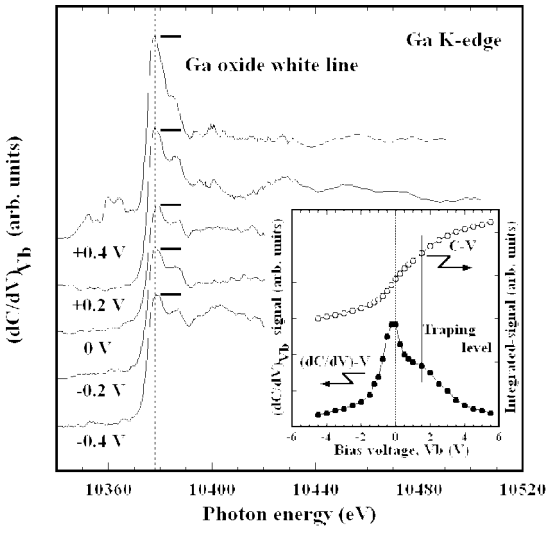

Fig. 5. SCM-XAFS spectra. Inset indicates C-V and $\mathrm{d}C/\mathrm{d}V$ V characteristics of the MOS capacitor.

The C-V characteristics of this GaAs sample measured by SCM is shown in the inset of Fig. 5 (open circles). A sigmoid property typical of MOS capacitors was obtained. However, the $\mathrm{d}C/\mathrm{d}V$-V curve (closed circles) for a more detailed analysis of the C-V characteristics is not symmetrical; it has a broad peak in the $V_b > 0$ region. This finding means that some trapping center in the sample captures electrons, and the electron emission from the trapping center can be detected by ΔC in the $V_b > 0$ region. Note that this V_b region corresponds to that for the selective observation of the Ga oxide trapping center in the capacitance XAFS measurement discussed above. Hence, the trapping center found in the C-V characteristics is caused by the Ga oxide trapping center, and its local electronic states and structure are selectively obtained by the capacitance XAFS measurement under the $V_b > 0$ condition because the X-ray-induced photoemission of the localized electron can be precisely detected.

Though the XPS analyses obtain the chemical information on the sample surface, they cannot clarify the electric characteristics of the surface species. On the other hand, though the electric properties of the microscopic MOS capacitor can be analyzed by regarding the C-V characteristics, the chemical information of the trapping centers cannot be obtained in the electric measurements. In general, microscopic chemical and electric properties have been independently analyzed. In nano structures, the microscopic chemistry at atomic level determines the electronic characteristics of the device, so these properties need to correlate. Based on selecting the sites by controlling V_b, the SCM-XAFS method is a powerful tool for this purpose.

Though the SCM-XAFS spectra in Fig. 5 conceptually indicate a potential for concluding micro spectroscopy, an experimental evaluation of spatial resolution is necessary. Unfortunately, various unpredictable factors such as the moisture between the probe and the substrate and vibration in the experimental station, obstruct an accurate evaluation of the spatial resolution at that time. However, selective observations of the trapping centers at hetero interfaces indicate the spatial resolution of the atomic level in vertical direction. Therefore, an isolated trapping center on the sample surface should be distinguished from other sites by applying site selectivity, and site selectivity should equivalently improve the spatial resolution.

3.3. *Electron transition model*

Figure 6 shows an electron transition model in the SCM-XAFS method. The band diagram of the microscopic MOS structure is illustrated in Fig. 6(a). The E_F of the Au probe equals to that of the GaAs sample without the bias ($V_b = 0$), while the bias forms an E_F step of eV_b as shown in this figure. Therefore, the absolute energy level of the Au probe and the GaAs sample is determined by E_F and V_b, which is different from the electrically floated Cu_2O/Cu system in Fig. 3. In this diagram, a trapping level in the GaAs band gap is assumed at the interface of GaO/GaAs. The X-ray absorption of the trapping center excites the inner-shell electron (1). Following that, the localized electron from the trapping center is relaxed into the core hole (2). This sequential process corresponds to the photoemission of δq and is detected

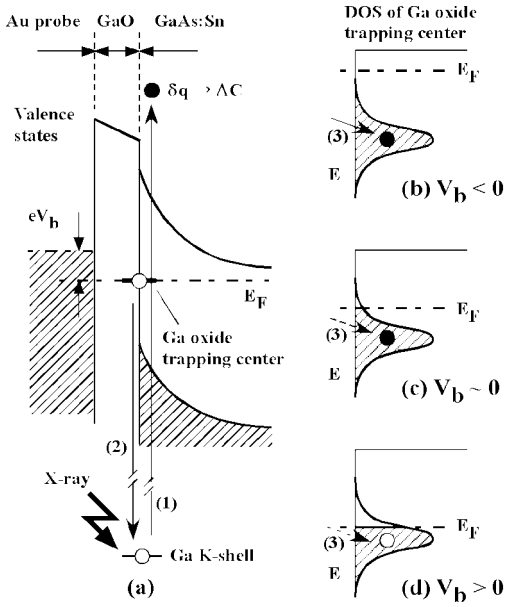

Fig. 6. (a) Band diagram of microscopic MOS capacitor and electron transition model under X-ray irradiation. Electron filling model at various V_b; (b) $V_b < 0$, (c) $V_b \sim 0$, and (d) $V_b > 0$.

by ΔC. Though this electron transition process is similar to that in Fig. 3(a), electric isolation of the trapping level in the GaAs band gap can realizes an unoccupied state with a relatively long lifetime under specific V_b conditions. By taking the variable lifetime into account, the capacitance XAFS spectrum dependent on V_b can be explained as follows. Figures 6(b)–(d) are schematic density of stats (DOS) diagrams of the trapping center. Under the condition of $V_b < 0$, E_F of the semiconductor is considered to be higher than the trapping level of Ga oxide as shown in Fig. 6(b). In this case, the trapping level is immediately filled by free electrons (3). As discussed in the Cu_2O/Cu system, this short lifetime immediately restores the electronic state to the initial state resulting in no effective ΔC [Fig. 3(b)]. However, E_F begins to cross the trapping level when V_b is approximately 0 [Fig. 6(c)]. The lifetime increases too much because the electron transition (3) is suppressed. Accordingly, a ΔC corresponding to the X-ray absorption of the trapping center can be observed. The ΔC increases with increasing V_b [Fig. 6(d)]. Finally, when the E_F becomes equal to the trapping level with the maximum DOS, the ΔC is expected to become the strongest. This is the reason why the Ga oxide trapping center is selectively observed in the $V_b > 0$ region in Fig. 5. Obviously, this model demonstrates site selectivity of a trapping center with a specific eigen-energy by controlling V_b. Moreover, as illustrated in Figs. 6(b)–(d), it also indicates a possibility of new capacitance spectroscopy of the valence states using a resonant inner-shell absorption, such as double resonance capacitance spectroscopy (DORCAS) [20] because the dependency of ΔC on V_b reflects the DOS of the trapping center.

4. Conclusion

We propose a new site-selective and microscopic X-ray absorption fine structure (XAFS) technique called capacitance XAFS method. In this technique a XAFS spectrum can be obtained by regarding the capacitance change with respect to the X-ray photon energy. An electron trapping center can be selectively analyzed because the X-ray induced photoemission of localized electrons is detected by the capacitance. This basic idea was experimentally demonstrated in both a metal and a semiconductor system. We proposed an electron transition model for each system; the inner-shell absorption of the trapping center and the following relaxation of the localized electron into the core-hall produced an unoccupied valence level with a relatively long lifetime. In the semiconductor system, the lifetime can be controlled by applying a bias voltage to the sample. When the Fermi energy is sufficiently higher than the trapping level, the unoccupied level is immediately filled by free electrons resulting in a short lifetime. The short lifetime cannot produce the capacitance XAFS spectrum. Based on this lifetime control, a trapping center with a specific eigen-energy can be selectively observed. Moreover, detecting the capacitance by scanning the microprobe indicated a potential for concluding micro spectroscopy with this method.

Acknowledgement

This work was supported by a Grant-in-aid for Young Scientists (A) (No. 15681004) from the Ministry of Education, Sports, Science and Technology (MEXT). The synchrotron radiation experiments were performed at SPring-8 with the approval of JASRI (Proposal No. 2001B0503-NX-np and 2002B0586-NX-np). The authors would like to thank T. Kudo and T. Kobayashi for their technical assistance.

References

1. Lytle, F. W., Sayers, D. E. and Stern, E. A., Phys. Rev. **B 11**, 4825 (1975).
2. Teo, B.-K. and Lee, P. A., J. Am. Chem. Soc. **101**, 2815 (1979).
3. Armitage, R. *et al.*, Appl. Phys. Lett. **82**, 3457 (2003).
4. Mehandru, R. *et al*., Appl. Phys. Lett. **82**, 2530 (2003).
5. Leifer, K., Hartmann, A., Ducommun, Y. and Kapon, E., Appl. Phys. Lett. **77**, 3923 (2000).
6. Ozasa, K. *et al*., Appl. Phys. Lett. **71**, 797 (1997).
7. Windt, D. L. *et al*., Appl. Opt. **42**, 2415 (2003).
8. Weitkamp, T. *et al*., AIP Conference Proceedings **507**, 424 (2000).
9. Ishii, M., Yoshino, Y., Takarabe, K. and Shimomura, O., Appl. Phys. Lett. **74**, 2672 (1999).
10. Ishii, M., Phys. Rev. **B 65**, 085310 (2002).
11. Ishii, M., Ozasa, K. and Aoyagi, Y., Microelec. Eng. **67–68**, 955 (2003).
12. Ishii, M., Jpn. J. Appl. Phys. **40**, 7129 (2001).
13. Oyanagi, H. *et al*., J. Synchrotron Rad. **7**, 89 (2000).
14. Tanida, H. and Ishii, M., Nucl. Instr. Meth. Phys. Res. **A467–468**, 1564 (2001).
15. Kitamura, H., Rev. Sci. Instrum. **66**, 2007 (1995).
16. Kosugi, N., J. Jpn. Soc. Synchrotron Rad. Res. **2**, 1 (1989) (in Japanese).
17. Ishii, M., Jpn. J. Appl. Phys. **41**, 4415 (2002).
18. Palmer, R. C., Denlinger, E. J. and Kawamoto, H., RCA Rev. **43**, 194 (1982).
19. Wada, S., Kashihara, F., Harada, A. and Ikoma, H., Jpn. J. Appl. Phys. **37**, L427 (1998).
20. Ishii, M., Nucl. Instr. Meth. Phys. Res. **B199**, 205 (2003).

Physica Scripta. Vol. T115, 102–106, 2005

Picosecond Time-Resolved X-Ray Absorption Spectroscopy of Solvated Organometallic Complexes

W. Gawelda[1], C. Bressler[1,*], M. Saes[1,2], M. Kaiser[1], A. N. Tarnovsky[1], D. Grolimund[2], S. L. Johnson[2], R. Abela[2] and M. Chergui[1]

[1]Laboratoire de Spectroscopie ultrarapide, ISIC-FSB-BSP, Ecole Polytechnique Fédérale de Lausanne, CH-1015 Lausanne, Switzerland
[2]Swiss Light Source, Paul-Scherrer Institut PSI, CH-5232 Villigen, Switzerland

Received June 26, 2003; accepted February 10, 2004

PACS numbers: 78.47.+p, 78.70.Dm, 61.10.Ht, 82.20.−w, 82.50.kx

Abstract

We describe an experimental setup, which measures transient chemical changes of photoexcited solutes in disordered systems via time-resolved X-ray Absorption Spectroscopy (XAS) with picosecond temporal resolution. The setup combines a femtosecond amplified laser with picosecond X-ray pulses at beamline 5.3.1 at the *Advanced Light Source* in Berkeley, USA. New results on time-resolved XAS used for probing both the electronic and the geometric modifications of a photoexcited tris-(2,2′-bipyridine) ruthenium (II), $[Ru^{II}(bpy)_3]^{2+}$ in water solution are presented.

1. Introduction

With the advent of time-resolved optical spectroscopy and the rapid development of femtosecond lasers, it has become possible to monitor the transient chemical changes occurring during an ongoing chemical reaction on fundamental timescales, which range from femtoseconds for molecular vibrational motions up to nanoseconds and microseconds for slower diffusion-controlled processes. In addition, since all chemical reactions take place on the atomic level, the complete study of transient chemical structures requires both ultrafast temporal resolution and atomic-level spatial resolution, usually in the picometer range. Femtosecond laser spectroscopy provides the necessary time-resolution to observe fully the photoinduced time evolution of a chemical system under investigation however it is less sensitive in detecting transient molecular structures.

On the other hand, there are many well-established structure-sensitive experimental techniques, such as Electron Diffraction, X-ray Absorption Spectroscopy (XAS) and X-ray or Neutron Diffraction, which are useful in determining the structures of complex many-body systems with atomic-level spatial resolution. Therefore, combining the advantages of ultrahigh atomic-level resolution and ultrafast temporal resolution of these techniques, one could visualize nuclear and electronic motions during the chemical reaction and capture the transient molecular structures. Among these structural tools, XAS offers distinct advantages, when applied to chemical and biological systems in the condensed phase. It is element specific and allows the measurement of the local electronic structure of an atom of interest in a disordered medium, such as a liquid, by X-ray Absorption Near Edge Structure (XANES) and the local geometric structure, including nearest neighbor distribution and relevant bond distances, by Extended X-ray Absorption Fine Structure (EXAFS).

Ultrafast Time-Resolved X-Ray Absorption Spectroscopy is a novel experimental technique which has not found wide-spread use yet. Although this scheme was originally proposed many years ago [1–3], up to now, only a few time-resolved XAS measurements were carried out successfully, both in liquid [4–9] and gas phase systems [2] with nanosecond or longer temporal resolution. Only recently, Chen *et al.* [10] carried out a sub-nanosecond measurement of structural dynamics of an excited Copper (I) Diimine complex using both XANES and EXAFS and we reported on picosecond time-resolved XANES studies of a Ruthenium (II) tris-bipyridine complex in water solution reaching the sub-100 picosecond pulse-limited time resolution [11].

In our laser-pump X-ray-probe experiment, a femtosecond laser pulse starts a chemical reaction and a delayed X-ray pulse probes the photoinduced changes in a system. In full analogy to a laser-only experiment, by scanning the time delay between pump and probe pulse one can observe the time evolution of the transient chemical species. Synchrotrons are currently the brightest and the most stable pulsed X-ray sources. Moreover, they produce radiation that can be tuned over an extremely broad range up to the hard X-ray regime, e.g. hundreds of keV, however, the delivered X-ray pulse widths are usually limited to the tens of ps range, except for recent breakthrough experiments carried out by Schoenlein *et al.*, where a successful experimental scheme providing femtosecond synchrotron pulses was realized [12].

The feasibility of time resolved XAS depends on the number of available X-ray photons per data point. This depends on the X-ray pulse intensity and on the repetition rate of the measurement, which is typically in the 1 kHz range, when using femtosecond amplified lasers. On the other hand, synchrotrons operate at much higher repetition rate of usually 100–500 MHz, which means that after synchronization of both sources we reduce the available X-ray photon flux by more than 5 orders of magnitude. Therefore, these experiments require a very sensitive detection scheme given that the X-ray pulse intensity at 3rd generation X-ray beamlines is rather weak, i.e. 10^4–10^6 photons/pulse. Furthermore, there are other experimental challenges imposed by the nature of the experiment itself and a careful optimization of the sample geometry is required. The details on both sample and detection scheme optimization can be found elsewhere [13].

2. Experimental Setup

The experiments are carried out at bend magnet beamline 5.3.1 of the *Advanced Light Source* in Berkeley, USA, which operates between 2.5 and 12 keV. We use a special filling pattern of the storage ring called *camshaft mode* (Fig. 1). It consists of a close-packed multibunch train followed by a 100 ns empty section, in which a ten-fold more intense single electron bunch is placed, whose radiation we use in the pump-probe measurement. The beamline provides a hard X-ray photon flux of about

*E-mail: Christian.Bressler@epfl.ch

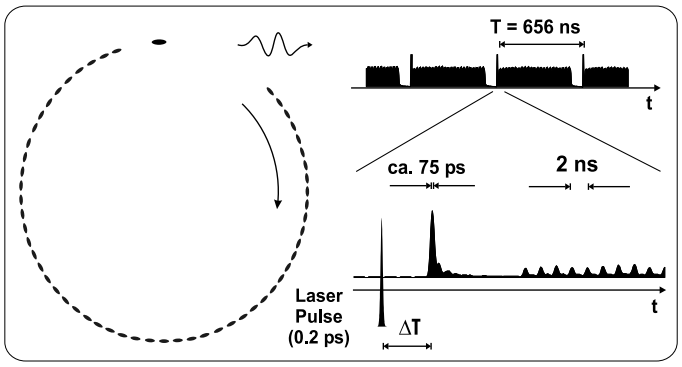

Fig. 1. The ALS storage ring filling pattern (left). The single electron bunch, so called *camshaft pulse*, is placed in a 100 ns empty section and thus is well separated from the 600 ns long multibunch. The X-ray radiation resulting from this bunch provides us with 60–80 ps single X-ray pulses at 1.52 MHz repetition rate used in our experiments (top right). The 200 fs laser pulse at 1 kHz repetition rate is synchronized to one of these camshaft pulses with fixed time delay (bottom right).

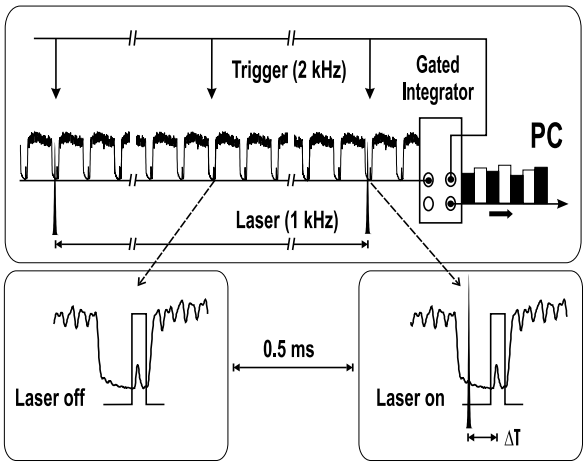

Fig. 2. Data acquisition scheme for recording time-resolved XAS. The X-ray pulses are recorded with a sensitive and suitably fast X-ray detector, i.e. avalanche photodiode, at 2 kHz repetition rate, which permits us to record *in situ* the unexcited and photoexcited sample on a shot-to-shot basis. The measured single X-ray pulse intensities are then fed into the gated integrator. The pair-wise subtraction of adjacent pumped (black) and unpumped (white) intensities yields the transient difference XAS spectra. The PC sorts the recorded data and controls both the X-ray monochromator and the laser-X-ray time delay settings.

10^{12} photons/s (corresponding to ca. 10^4 photons/single X-ray pulse) with a spectral resolution of $3 \cdot 10^{-4}$ bandwidth around 3 keV energy range. The bend magnet radiation is imaged 1 : 1 via a grazing incidence Pt-coated mirror (5 mrad deflection) into the experimental X-ray hutch. A Ge (111) double monochromator with fixed output height selects X-ray photon energies between 2–12 keV. An X-ray chopper in front of the monochromator is set to 2 kHz repetition rate reducing the heat load on the first monochromator crystal. The experimental chamber is filled with atmospheric He gas in order to minimize transmission losses for radiation below 7 keV.

The laser source is a Ti: sapphire based amplified femtosecond laser system, which delivers 1.8 mJ, 200 fs, 800 nm laser pulses at a repetition rate of 1 kHz. Both sources, i.e. the laser and the storage ring, require stable and precise synchronization. The key factor in the synchronization scheme is locking of the laser oscillator frequency to the radio frequency (RF) of the storage ring with a stable phase. The oscillator timing is the most important step in this process, because its temporal precision defines the relative jitter between laser and X-ray pulses. Once the complete synchronization between laser pump pulses and camshaft probe pulses is properly set, the relative time delay between them can be kept fixed in order to scan the energy spectra at a given time instant after the photoexcitation or alternatively we can scan the time delay electronically (at a fixed X-ray energy) to record the temporal evolution of the transient X-ray absorption. The sample consists of a free-flowing liquid jet with a thickness of 100 μm. The amplified femtosecond laser pulses provide the photoexcitation source and they can be delivered at the fundamental wavelength of 800 nm, or frequency-doubled and trippled, namely 400 nm and 266 nm respectively. The amplified and frequency-doubled Ti: Sapphire laser at 1 kHz can currently deliver up to 550 μJ pulse energy at 400 nm.

The laser is focused on the sample down to ca. 300 μm diameter with its beam size being slightly larger than the X-ray focal size, which is 250 × 90 μm. The flow speed of the jet is adjusted in a way that we can always provide a fresh sample solution at the site where the photoexciting laser pulse arrives, i.e. the jet flow speed of 5 m/s ensures that after 60 μs the sample will move out of the probe focus. Spatial and temporal overlaps are secured in two steps. Initially, we align both X-ray and laser beams through a 50 mm pinhole at the sample position. Then we monitor at the sample position both pulses individually with a fast photodiode. This allows us to set the timing with a precision around 100 ps by comparing the rise times of both signals. After this procedure, we place the sample within both beams and measure a photoinduced signal to fine tune both spatial and temporal overlap.

The transmitted X-ray pulse train is detected using an avalanche photodiode (APD) as an X-ray detector, which resolves the single X-ray pulse intensities and camshaft pulses can be resolved and detected yielding the output signal of about 10 ns (FWHM), as shown in Fig. 2. The APD signal is amplified by a fast pre-amplifier and subsequently plugged into a gated integrator. The gate of the integrator is set to this 10 ns width for an optimum signal-to-noise ratio. The single X-ray pulse intensities are then recorded at twice the laser repetition rate, i.e. 2 kHz, which means that we acquire simultaneously transmitted camshaft pulse intensities originating from laser-pumped and unpumped species. Later on, the subtraction of adjacent pairs of X-ray pulse intensities yields the transient difference XAS in transmission mode. Using the described data acquisition strategy cancels out any noise contributions and electronics drifts at frequencies lower than 1 kHz for a given pump-probe difference signal. Moreover, this difference detection scheme reduces our susceptibility towards gradual sample deterioration due to extended exposure to radiation, since we always measure the unexcited sample every 0.5 ms before probing the photoinduced changes and thus long-term changes in the sample do not contribute to our difference signal. One interesting prospect of our detection scheme is that we can envision studying of non-cyclic photochemical reactions without contaminating our pump-probe spectra with the overall change in XAS due to sample degradation.

With the above-described detection strategy, we are able to record high precision and quality XAS spectra. In fact, careful noise analysis shows that our current sensitivity has reached 90% of the shot-noise limit of the X-ray source. It is illustrated in Fig. 3a, which shows the pulse height distribution of 10^4 recorded single X-ray pulse intensities. From this distribution, we can

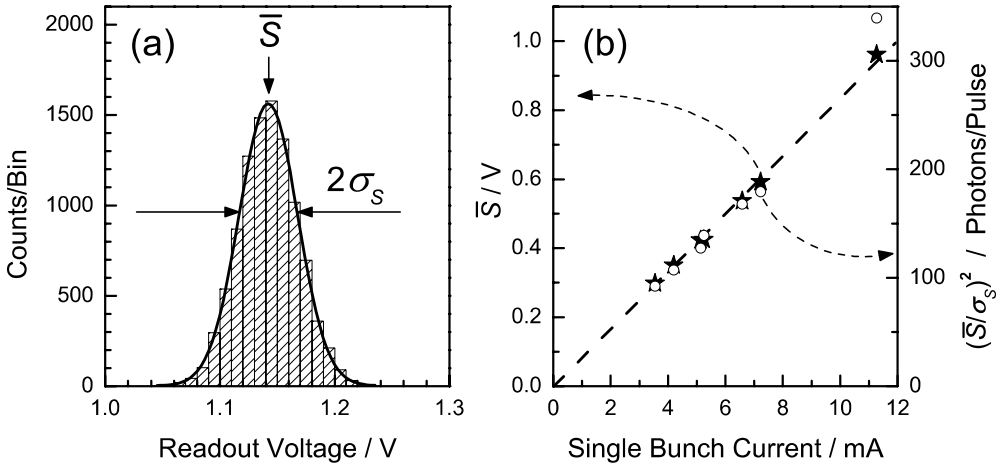

Fig. 3. a) Pulse height distribution of 10^4 recorded single X-ray pulses at a fixed energy without laser. In our data acquisition scheme we record the averaged value $\bar{S}$ together with its standard deviation σ_S for a given number of single X-ray pulses. b) On the left ordinate (stars), the averaged readout voltage is plotted as a function of stored current in the single electron pulse. The right ordinate (circles) corresponds to the effective number of recorded photons, according to relation (1), plotted as a function of the same value of the single bunch current. We find the linear response of the utilized detection scheme and very good agreement between measured pulse height distribution and the effective number of single X-ray pulse photons.

estimate an effective number of monochromatic X-ray photons per pulse, via the equation:

$$N = \left(\frac{N}{\Delta N}\right)^2 = \left(\frac{N}{\sqrt{N}}\right)^2 \geq \left(\frac{\bar{S}}{\sigma_S}\right)^2 \qquad (1)$$

with N being the average number of photons per pulse, $\Delta N = N^{1/2}$ being the standard deviation or shot noise distribution of the X-ray source, $\bar{S}$ denotes the averaged measured signal height (in Volts), and σ_S the measured standard deviation (in Volts) of the pulse height distribution. Of course, this relation holds only if σ_S contains no other contributions, e.g., electronic noise. On the other hand, using Eq. (1) we can estimate the number of photons per X-ray pulse and compare it to the calculated value for the beamline (at the given X-ray energy) where the experiment is carried out.

The beamline is specified to deliver ca. 1×10^{12} photons/(s $\times$ 0.1% bandwidth) at 2.8 keV for 400 mA of stored current. At this beam current value, the camshaft current amounts to 10 mA, which corresponds to 1.65×10^4 camshaft photons/pulse and 0.1% bandwidth. Due to the fact that we only use 0.03% of the available bandwidth, the corresponding number of X-ray photons on the sample scales down to ca. 5000 photons/pulse. Taking into account the transmission through the sample (10%) and through Be filters (70%), we obtain a value of 350 photons per pulse incident on the X-ray detector at 10 mA of camshaft current, and this is very close to the value measured via the pulse height distribution of single recorded X-ray pulses (Fig. 3b).

3. Results and discussion

With the above-described experimental setup, we have investigated the photoexcited Metal-to-Ligand Charge Transfer (MLCT) reaction of aqueous tris-(2,2′-bipyridine) ruthenium (II), $[Ru^{II}(bpy)_3]^{2+}$. Its excited state properties have been extensively studied with optical spectroscopy [14–18], nevertheless, still little is known about its excited state structure, which can be investigated via time-resolved XAS. The photoexcitation cycle (which is completed on a sub-microsecond time scale) is displayed in Fig. 4. Light absorption by $[Ru^{II}(bpy)_3]^{2+}$ results in the formation of a Franck-Condon MLCT singlet excited state, ^{1}(MLCT), which undergoes sub-picosecond intersystem

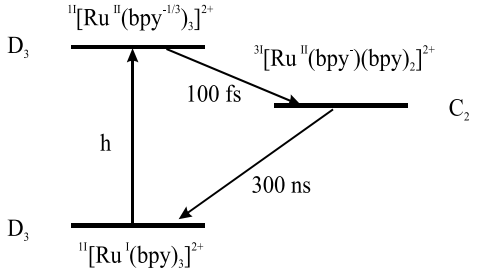

Fig. 4. Photoexcitation cycle of the solvated reactant species in its singlet ground state leads to formation of an intermediate triplet excited state of $[Ru^{III}(bpy^-)(bpy)_2]^{2+}$, which radiatively returns to the initial reactant state after ca. 300 ns.

crossing to a long-lived triplet excited state, ^{3}(MLCT) [17], with near-unity quantum yield. In the process, the D_3 symmetry of ground state $[Ru^{II}(bpy)_3]^{2+}$ is reduced to C_2 symmetry of $[Ru^{III}(bpy^-)(bpy)_2]^{2+}$ in the ^{3}(MLCT) state. This reaction involves a change of oxidation state of the Ru central atom, which can be probed by monitoring the XANES region around the ruthenium L_3-edge. Indeed, oxidation states of (ground state) Ru^{II} and (photoexcited) Ru^{III} complexes exhibit clear differences in their L-edge XANES [19–21]. This can be seen in Fig. 5a around the Ru L_3 edge. A pre edge absorption feature at 2841.0 eV (denoted B in Fig. 5a) characterizes the bivalent compounds due to the $2p_{3/2} \rightarrow 4d_{3/2}$ (e_g) transition [19], next to the weaker $2p_{3/2} \rightarrow 5s_{1/2}$ transition around 2851 eV (feature C) [20]. Removal of the weakest bound electron from the fully occupied $4d_{5/2}$ (t_{2g}) level generates a trivalent ruthenium compound [19], opening up additional absorption due to the allowed $2p_{3/2} \rightarrow 4d_{5/2}(t_{2g})$ (feature A') in addition to an oxidation state induced shift [19]. Thus we observe the appearance of the A'/B' doublet structure in the trivalent L_3 XANES together with the energetic $B \rightarrow B'$ and $C \rightarrow C'$ shift (Fig. 5a), resulting from the change of oxidation state of the Ru central atom and formation of ^{3}(MLCT) (see Fig. 4).

The recorded transient difference absorption spectrum is shown on Fig. 5b. It is plotted as a function of the X-ray probe energy E, recorded 50 ps after laser excitation (data points with error bars) for a sample containing 80 mmol/l solution of

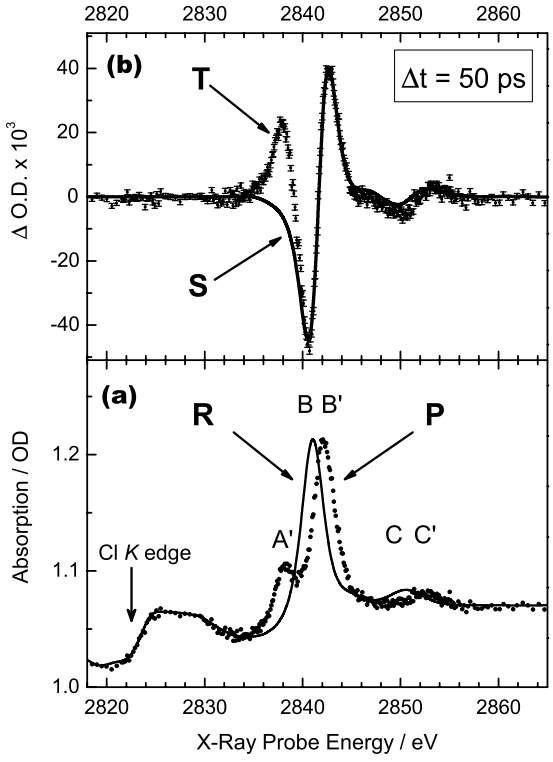

Fig. 5. (a): Static L_3-edge X-ray absorption spectrum of ground state $[Ru(bpy)_3]^{2+}$ (black trace, measured 0.5 ms before the laser strikes the sample), and excited state absorption spectrum (red dots) generated from the transient data curve T in (b) via Eq. (2). (b): Transient X-ray absorption spectrum of photoexcited aqueous $[Ru(bpy)_3]^{2+}$ measured 50 ps after laser excitation.

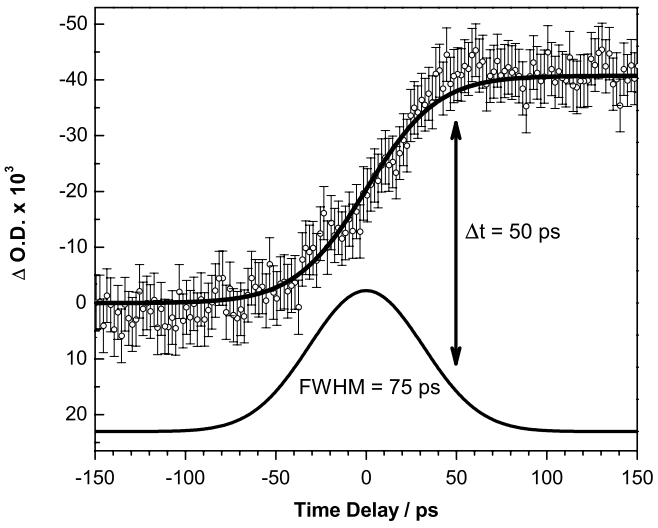

Fig. 6. Time delay scan between laser and X-ray pulses around time zero of photoexcited aqueous $[Ru(bpy)_3]^{2+}$. Cross-correlation signal recorded between the 200 fs laser pulse and the 70–80 ps long X-ray pulse can be fitted with a Gaussian error function, which derivative is a Gaussian with a FWHM around 70–80 ps, which corresponds to the single X-ray pulse width.

$[Ru^{II}(bpy)_3]^{2+}$ in H_2O. This transient contains all the electronic changes from the reactant state absorption spectrum, $R(E)$, to the product state absorption spectrum, $P(E,t)$, at the time t after photoexcitation can be expressed by the following relation:

$$T(E,t) = f(t) \cdot [P(E,t) - R(E)], \tag{2}$$

with $f(t)$ being the fraction of excited state species at time t. Therefore, one can directly access the XANES spectrum of the product state from the measured transient signal and the reactant state XAS, provided that the $f(t)$ value is known. Alternatively, one can derive $f(t)$, if the exact shape of the product state XAS, $P(E,t)$ is given. From laser-only measurements we know that the photoexcitation yield of the sample is ca. 10%, but here we have treated the data differently: Assuming no change in oscillator strength for the B feature, we have constructed the product state spectrum $P(E, \Delta t = 50\,\text{ps})$ via Eq. (2) by adjusting $f(t)$, until features B and B' have equal amplitudes. This yields a value of $f = 10.4\%$ in close agreement with our prediction from the optical-only measurements. It contains an energetic shift of all features by 1.2 eV together with the photoinduced appearance of the A' feature, as expected. The A'-B' splitting (4 eV) and the B'/A' intensity ratio (ca. 2.3) is indeed close to the values observed for $[Ru^{III}(NH_3)_6]^{3+}$ complex, which has the same valency and a similar coordination symmetry (O_h versus D_3) as the bipyridine complex. Assuming no change in oscillator strength for the B feature in the ground and photoexcited states seems plausible, since the $4d_{3/2}$ (e_g) level should remain empty in both cases. In addition, the peak intensities of the B feature of ground state $[Ru^{II}(bpy)_3]^{2+}$ and $[Ru^{III}(NH_3)_6]^{3+}$, as compared in Ref. [11], are indeed very similar.

Our experimental setup allows us also to vary the delay time between laser and X-ray pulses. As it is presented in Fig. 6, we scanned the time delay in 2 ps steps with the X-ray energy set near the maximum of feature B (ca. 2840 eV) thus allowing us to observe the appearance of the photoinduced bleach signal. Once the electron has been excited to the triplet MLCT state (in ca. 300 fs, [17]) we can observe the induced oxidation state change of the Ru central atom, and therefore the time evolution of this transient signal is entirely governed by the cross-correlation time of the laser and the X-ray pulses. Cross-correlation signal recorded between the 200 fs laser pulse and the 70–80 ps long X-ray pulse can be fitted with a Gaussian error function, which derivative is a Gaussian with a FWHM around 70–80 ps, which corresponds to the actual single X-ray pulse width provided by the ALS (depending on the stored charge in the single electron bunch). It should be stressed that our current temporal resolution is X-ray pulse-limited and our setup is prepared to be directly implemented into femtosecond-resolved XAS measurements given that ultrashort X-ray pulses could be provided. With this precise timing measurement, we can then set a fixed time delay with better than 10 ps accuracy. While this method serves as a convenient analog of conventional laser cross-correlation measurement for setting the correct time delay between the pulses, our setup can be exploited for measurements of kinetic traces out to several hundred of microseconds in a few picosecond steps.

In order to verify the limits of our experimental setup, we carried out a solute concentration dependence study. In fact, the 80 mmol/l sample concentration used to collect the data in Fig. 5 is rather high for typical photochemical studies, and gives rise to additional processes occurring on nanosecond time scales. Therefore, we decreased the concentration and repeated the measurement of its transient absorption. The results are shown in Fig. 7 for different concentrations down to 1 mmol/l and using an increased laser focus thus reducing the laser intensity (and the photoexcitation yield) in the overlap volume. The spectra represent single scans with 2 s accumulation time per data point except for the 1 mmol/l sample, which utilized 40 s. The corresponding error bars of the 1 mmol/l spectrum are ca. a factor

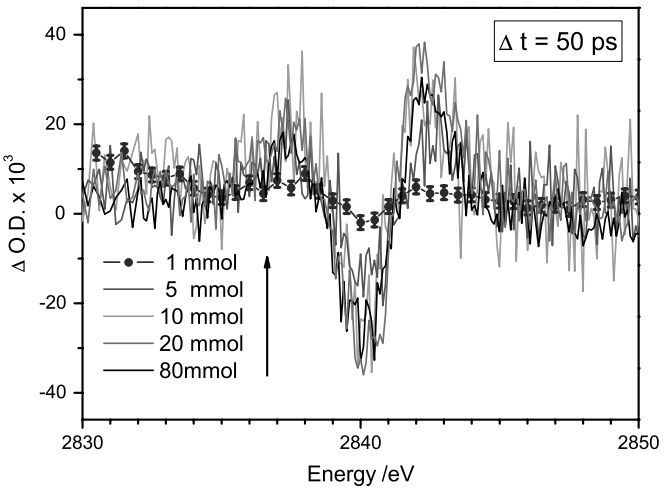

Fig. 7. Solute concentration dependence of the photoinduced aqueous $[Ru(bpy)_3]^{2+}$. All data, except for 1mM trace (solid line with open circles), were recorded at the same experimental conditions (laser intensity, data accumulation time, etc.). The arrow indicates the decreasing concentration of the sample. The lowest concentration sample was recorded at 20 times larger data accumulation time in order to improve the signal-to-noise ratio. All data were collected during single energy scan around Ru L_3-edge (feature B) and measured 50 ps after laser excitation.

of 4.5 smaller than those of the other samples, which we expect from a shot-noise limited detection scheme. These measurements prove that we are capable of descending into significantly lower concentration regions without dramatic loss of signal-to-noise ratio. These results are very promising because one can envision the study of samples for which large concentrations are impossible to prepare.

Moreover, decreasing sample concentration rules out several unwanted effects, such as proximity effects of closely-packed excited species that can influence the ongoing photochemical reaction. In addition, biologically relevant samples are usually investigated in solutions with up to 1 mmol/l concentration, and hence we can imagine such studies in the near future. Furthermore, it should be remarked that these results were obtained in transmission mode. Another possible near-future extension of our technique could be the application of X-ray fluorescence spectroscopy, which is in principle background-free, and could bring another improvement in signal-to-noise ratio.

4. Conclusion

Time-Resolved X-ray Absorption Spectroscopy is a new technique, which permits the investigation of photoinduced processes on various chemical systems on time scales down to the cross-correlation time between the laser and the X-ray pulses. We have successfully applied this technique to investigate the photoinduced charge transfer reaction of aqueous $[Ru^{II}(bpy)_3]^{2+}$ in both X-ray absorption energy and in time. This result demonstrates the utility of current pulsed X-ray sources for future ultrafast XAS studies. Furthermore, we showed the high sensitivity of our technique, which allows measurements of very weak transient XAS signals with X-ray pulse-limited temporal resolution (currently in 60–80 ps range). With only ca. 10^6 photons per data point (corresponding roughly to 1 second accumulation time per data point in the range 3–10 keV), we have achieved a signal-to-noise ratio of ca. 20 for measuring the 10% amount of transient species via time-resolved XANES with sensitivity nearly corresponding to the shot-noise limit of the source.

Particularly promising are the prospects of carrying out time-resolved structural studies via EXAFS. The modified transient structure of the MLCT species has never been directly observed in experiment. Time-resolved EXAFS exploiting our new technique are feasible and could yield the individual Ru-ligand distances of the intermediate species for the first time. Our future work will focus on exploiting this structural tool to study nuclear rearrangements with picosecond temporal resolution.

Acknowledgments

This work is funded by the Swiss National Science Foundation via contracts no. 2000-059146.99 and 620-66145.01, by the Swiss Light Source (SLS), and by the Advanced Light Source (ALS). We would like to thank R. W. Falcone from UC Berkeley for fruitful discussions and Drs P. A. Heimann, R. W. Schoenlein, M. Hertlein, A. Belkacem and A. Lindenberg from the ALS for their assistance during the measurements.

References

1. Bergsma, J. P., *et al.*, J. Chem. Phys. **84**, 6151 (1986).
2. Ráksi, F., *et al.*, J. Chem. Phys. **104**, 6066 (1996).
3. Brown, F. L., Wilson, K. R. and Cao, J., J. Chem. Phys. **111**, 6238 (1999).
4. Mills, D. M., Lewis, A., Harootian, A. and Smith, B., Science **223**, 811 (1984).
5. Thiel, D. J., Livins, P., Stern E. A. and Lewis, A., Nature **362**, 40 (1993).
6. Clozza, A., Castellano, A. C., Longa, S. D., Giovannelli, A. and Bianconi, A., Rev. Sci. Instrum. **60**, 2519 (1989).
7. Chance, M. R., *et al.*, Rev. Sci. Instrum. **64**, 2035 (1993).
8. Wang, H., *et al.*, J. Am. Chem. Soc. **119**, 4921 (1997).
9. Chen, L. X., *et al.*, Science **292**, 262 (2001).
10. Chen, L. X., *et al.*, J. Am. Chem. Soc. **125**, 7022 (2003).
11. Saes, M., *et al.*, Phys. Rev. Lett. **90**, 047403 (2003).
12. Schoenlein, R. W., *et al.*, Science **287**, 223 (2000).
13. Bressler, C., *et al.*, J. Chem. Phys. **116**, 2954 (2002).
14. Vlček, A., Coord. Chem. Rev. **200–202**, 933 (2000).
15. Gray, H. B. and Winkler, J., "Electron Transfer in Metalloproteins in Electron Transfer in Chemistry", (Edited by V. Balzani) (Wiley-CH, Weinheim, 2001), vol. III, p. 3.
16. Damrauer, N. H., *et al.*, Science **275**, 54 (1997).
17. Yeh, A. T., Shank, C. V. and McCusker, J. K., Science **289**, 935 (2000).
18. Juris, A., *et al.*, Coord. Chem. Rev. **84**, 85 (1988).
19. de Groot, F. M. F., J. Chem. Phys. **101**, 6570 (1994).
20. Sham, T. K., J. Chem. Phys. **83**, 3222 (1985).
21. Sigiura, C., Kitamura, M. and Muramatsu, S., J. Chem. Phys. **84**, 4824 (1986).

Physica Scripta. Vol. T115, 107–109, 2005

Local Structure of Spin-Crossover Complex Studied by X-Ray Absorption Spectroscopy: Nature of Photo-Induced Phase

Hiroyuki Oyanagi*[1], Takeshi Tayagaki[2] and Koichiro Tanaka[3]

[1]National Institute of Advanced Industrial Science and Technology, 1-1-1 Umezono, Tsukuba, Ibaraki 305-8568, Japan
[2]Department of Physics, Graduate School of Science, Kyoto University, Kyoto 606-8502, Japan

Received June 26, 2003; accepted November 10, 2003

PACS numbers: 61.10.Lx, 64.60.My, 78.90.+t

Abstract

In-situ x-ray absorption spectroscopy (XAS) was used to probe the local structure of photo-induced phase of Fe(II) spin-crossover complex. High-quality XAS data under photo-excitation were obtained *for fine powder specimen* using a novel pixel array detector (PAD). It was demonstrated that the technique can x-ray probe opaque specimen with high sensitivity (requiring less than 10^{-3} g) which is irradiated with visible photons. We find that the nearly octahedral ligand coordination (O_h) of FeN_6 cluster undergoes a significant expansion upon the diamagnetic (S = 0) ↔ paramagnetic (S = 2) transformation induced by laser light (532 nm), at much lower temperature than the critical temperature of thermally induced phase transition. Indication of symmetry breaking was observed in the distorted ligand molecules, in contrast to the relaxed undistorted structure in the thermally induced high spin phase.

1. Introduction

Recently, photo-induced phase transition attracts much attention as a novel means of nanotechnology where multistability of a ground state gives rise to a variety of nanoscale modifications of local structure with modified macroscopic properties [1]. Photo-irradiation stimulates a cooperative phase transition between a ground state and a metastable state which may not be the same phase with that of thermally excited phase transition. Photo-induced phase transitions such as ionic-neutral phase transitions in organic charge transfer (CT) crystals [2], magnetic phase transitions in spin crossover complexes [3, 4]. and photo-induced charge, spin and orbital order/disorder transitions in perovskite manganites [5.6] form rich class of multistable ground state materials where photo-stimulation eventually results in a global phase transition with pronounced changes in macroscopic physical properties. $[Fe(II)(2\text{-pic})_3]Cl_2EtOH$ (2-pic = 2-aminomethyl-pyridine), hereafter abbreviated as Fe-pic, is a typical spin-crossover complex which shows a thermally induced first-order phase transition from a low-spin (LS, S = 0) to a high spin (HS, S = 2) state.

It was shown that photo-induced magnetic transitions [7, 8] have nonlinear characteristics such as threshold light intensity, incubation period and phase separation [9]. The photo-induced phase transition is understood in terms of trapping of metastable spin state *i.e.*, light-induced excited spin state trapping (LIESST) [10]. It was pointed out that a structural relaxation in an excited state may proceed with symmetric and non-symmetric normal coordinates and therefore symmetry breaking could be observed. The excited state trapped by a metastable state may also relax to another "*false*" ground state which may not be the same with the original one. Thus the nature of photo-induced phase is still unclear. Tayagaki *et al.* recently investigated the symmetry of photo-induced phase by Raman spectroscopy and observed broken symmetry in the photo-induced phase which is distinguished from thermally induced phase [11]. The information on the local structure is essential to understand the nature of photo-induced high spin (PIHS) phase, *i.e.*, symmetry breaking. Here, we report the *in-situ* XAS study of $[Fe(II)(2\text{-pic})_3]Cl_2EtOH$ under light irradiation at low temperature.

2. Experimental

High brilliance photon sources (insertion devices) and grazing-incidence geometry have solved thickness mismatch problem [12]. Using high brilliance x-ray beam and grazing incidence fluorescence excitation geometry, an efficient optical excitation and x-ray absorption data collection with a good statistics became feasible. In our experimental set-up, fine particles mounted on a closed cycle helium cryostat rotate on a high precision goniometer (Huber 420) so that the incidence angle is controlled with a minimum step of 10^{-4} degree. The fluorescence x-ray yield is measured with a germanium pixel array detector (PAD) details of which are described elsewhere [13]. Each pixel (4.7 mm × 4.7 mm) can independently count upto 100 kcps, providing a total count rate of 10 MHz. Grazing-incidence geometry requires high brilliance x-ray beam. The wiggler x-radiation from MPW #13 of Photon Factory was used as an x-ray source. The energy and maximum positron current are 2.5 GeV and 400–500 mA, respectively. A directly water-cooled silicon (111) double-crystal monochromator [14] was used that covers the energy range between 4 keV and 25 keV. The energy resolution of XAS measurements was better than 2 eV at 9 keV, calibrated from the near-edge features of copper metal at 9.8 keV. A 100 mW CW laser (532 nm) was used as a light source.

3. Results and discussion

The Fe K-edge x-ray near-edge absorption structure (XANES) spectra and the difference spectra taking the low temperature low spin (LTLS) phase as a standard are shown in Fig. 1a. Energy shift of features B and C to higher energy upon laser light (532 nm) illumination is due to the S = 0 → S = 2 spin transformation. Photo-induced spin conversion induces stretching of R_{Fe-N} on going from a low spin state (strong ligand field) to a high spin state (weak ligand field). Thermally induced first order S = 0 → S = 2 phase transition occurs at 120 K. Fig. 1b shows the variation of difference spectra (measured at a and b) as photo-illumination is repeated. It is clear that photo-induced spin conversion between S = 0 and S = 2 states (5.1 K) are reproducible and bi-directional.

*e-mail: h.oyanagi@aist.go.jp

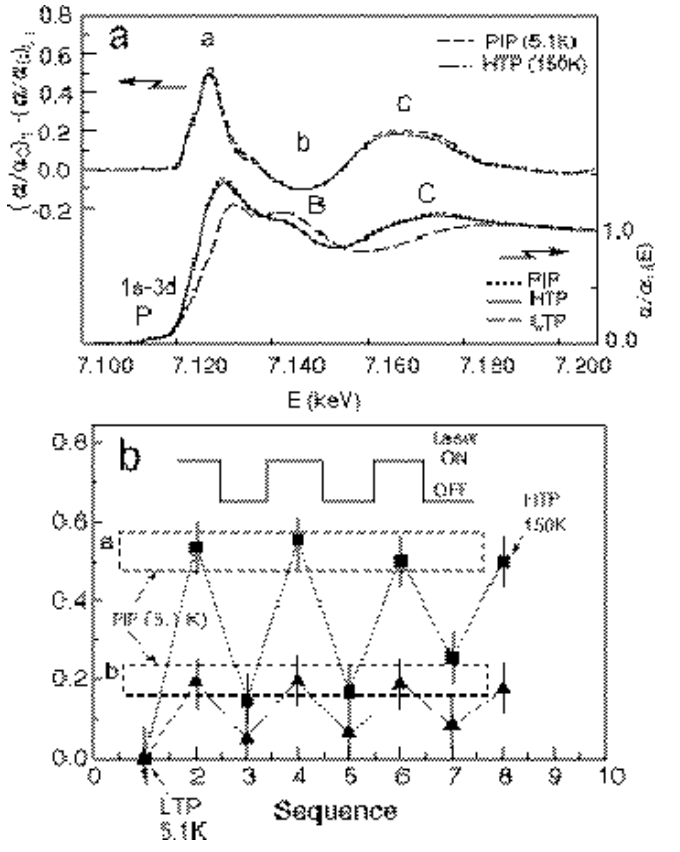

Fig. 1. **a**, Normalized Fe K-edge XANES $(\alpha/\alpha_0)_T$ and difference spectra for [Fe(2-pic)$_3$]Cl$_2$EtOH. The solid line, dashed line and dotted line indicate the spectra for high-temperature high-spin (HTHS), photo-induced high-spin (PIHS) phase and low-temperature low-spin (LTLS) phase. **b**, Variation of difference features (a, b) as laser light illumination (532 nm) is repeated at 5.1 K. The last data points are taken after S = 0 → S = 2 spin transformation took place.

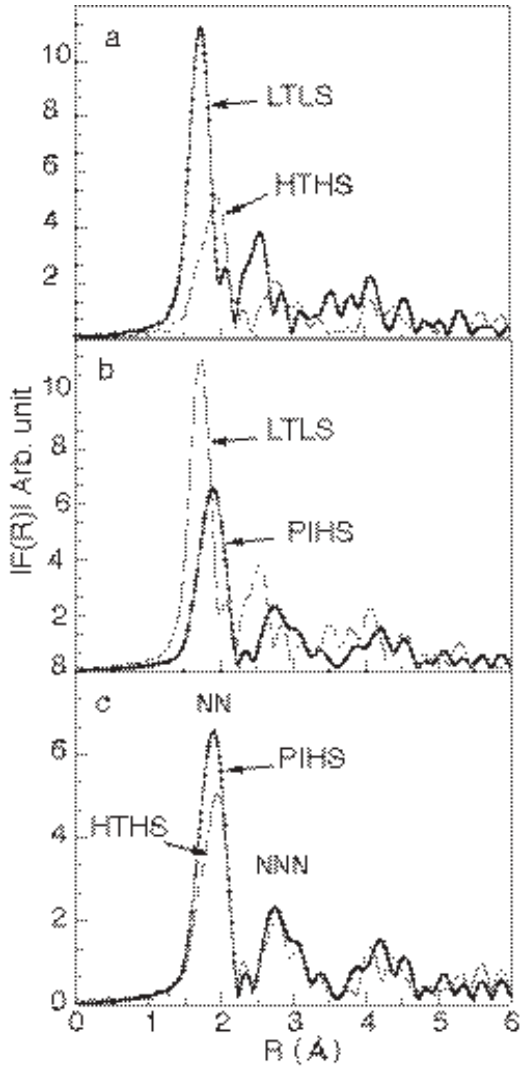

Fig. 2. **a**, Magnitude of Fourier transform (FT) of the Fe K-EXAFS oscillations times k^3 for [Fe(II)(2-pic)$_3$]Cl$_2$EtOH. FT magnitudes for HTHS and LTLS phases. **b**, FT magnitudes for PIHS and LTLS phases. **c**, FT magnitudes for PIHS and HTHS phases.

It is also indicated that the photo-induced high spin (PIHS) phase shows very similar spectral pattern to the high temperature high spin (HTHS) phase. The local structure around Fe ions was studied by Fourier transform (FT) of the Fe K-EXAFS oscillations multiplied by k^3. Figure 2 shows the FT magnitude plots for (a) LTLS and HTHS, (b) PIHS and LTLS, and (c) PIHS and HTHS phases, respectively. Prominent peaks around 1.5–1.7 Å are due to the nearest neighbor (NN) nitrogen atoms. Correcting the phase shift for the Fe-N contributions using FEFF code [15], the $R_{Fe\text{-}N}$ (LTLS) and $R_{Fe\text{-}N}$ (HTHS) values are determined as 2.01 ± 0.01 Å and 2.20 ± 0.01 Å, respectively. $\Delta R_{Fe\text{-}N} \sim 0.20$ Å is in agreement with crystallographic data of Mikami *et al.* [16]. The monoclinic space group $P2_1/c$ is unchanged upon the thermally phase transition [16].

Early studies of photo-induced phase transitions indicated that the photo-excited states are trapped by the metastable HS state at much lower temperatures than 120 K. Recently, dynamics of photo-induced spin transition showed nonlinear characteristics such as the threshold light intensity, incubation period and phase separation [9]. Although nonlinear properties are explained by a simple two-step model with a symmetrical lattice vibration mode with a long-range interaction, the recent Raman experiment raised a puzzling question [11]. Tayagaki *et al.* showed symmetry breaking in the PIHS phase from Raman lines which can not be ascribed to symmetric vibrational modes. The local structure information is needed to quantitatively understand the symmetry of PIHS [17].

As shown in Fig. 2c, the FT magnitudes of PIHS is quite similar to that of HTHS. Difference between the photo- and thermally induced HS phases is only seen in the next-nearest neighbor (NNN) peaks due to Fe-C distances. In contrast, the nearest Fe-N peak is almost the same for the two phases except thermal broadening in the high temperature phase. Change of the radial distribution could be interpreted as accompanied with distortions of FeN_6 octahedron. For instance, in Q_3 mode Jahn-Teller distortion, the in-plane bonds are shortened while the apical bond increases, giving rise to two different bond distances. We note that the split NN peak reported in our earlier works is due to the multidomain, *i.e.*, coexistence of HTHS and LTLS phases. In this work, as temperature of sample was carefully controlled, the single phase PIHS was formed that shows a single FT peak.

Symmetry breaking during photo-induced spin conversion is still an open question. In Fig. 3, the local structure (FeN_6 octahedron and coordinated ligands) of Fe-pic is schematically illustrated. The EXAFS results show that the octahedron expands by *ca.* 0.2 Å, maintaining the nearly octahedral (O_h) geometry. Thus the XANES and EXAFS results indicate that the local structure of PIHS is essentially unchanged from that of thermally

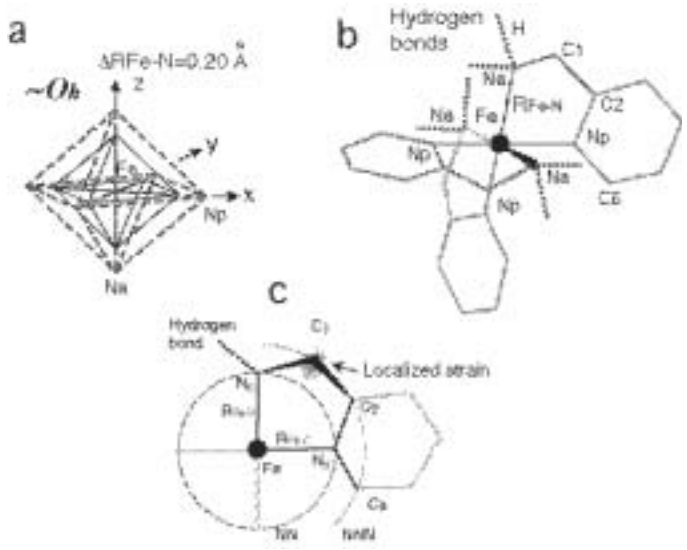

Fig. 3. **a**, Schematic local structure of FeN_6 octahedron in [Fe(II)(2-pic)$_3$]Cl_2EtOH. Upon the photo-induced spin conversion, the Fe-N distance expands by *ca.* 0.2 Å upon illumination while maintaining nearly octahedral geometry. **b**, Schematic crystal structure taken from ref. [16]. **c**, The next-nearest neighbor coordination. In the photo-induced phase, local strains are expected to persist around N_a-C_1 bonds, which can not relax since the photo-induced spin conversion takes place at low temperature where thermal fluctuation and hydrogen bond disorder are absent.

induced HS phase with respect to the NN atoms. Three ligand molecules in a unit cell are linked by hydrogen bonds and compressive strain caused by local expansion propagates *via* a long-range intermolecular interaction. The LS→HS conversion in one molecule is associated with the local expansion of FeN_6 cluster by more than 30% *local* volume change which gives a compressive strain to the nearest neighbor three molecules. As the Fe-C (NNN) distances expand roughly by the same amount, the FeN_6 deformation leads to isotropic expansion of ligand molecules. The PIHS phase is formed at low temperature where thermal relaxations can not take place. As illustrated in Fig. 3c, the local strain may give rise to bond bending distortions observed as inversion symmetry breaking. A subtle change in the next-nearest neighbor Fe-C peak between the PIHS and HTHS phases (Fig. 2c) indicate distortions of ligand molecules. Such local distortions would introduce inhomogeneous character in the strain distribution. The origin of non-linear phase transition could be due to inhomogeneous strain distribution which hampers cooperativity of phase transition [18].

4. Conclusions

Local structures of photo-induced high spin phases of spin-crossover complex [Fe(II)(2-pic)$_3$]Cl_2EtOH were studied by *in-situ* x-ray absorption spectroscopy. Fe K-edge XANES and EXAFS results showed that *the variation of nearest-neighbor local structure upon photo-induced* $S = 0 \rightarrow S = 2$ *spin transition is essentially an expansion of octahedral coordination* (O_h) *without lowering symmetry*. The nearest neighbor Fe-N distance ($R_{\text{Fe-N}}$) increases by *ca.* 0.20 Å on going from LS to HS state, resulting in an increase of *10Dq* by 60%. Symmetry of the nearest neighbor FeN_6 octahedron in the photo-induced phase is unchanged on spin conversion by laser light illumination. Perfect spin conversion and bi-directional transformation were confirmed. Slight distortions of ligand molecules were indicated in the next-nearest neighbor radial functions, which may be interpreted as *inversion symmetry breaking* observed in Raman spectra.

References

1. Photoinduced Phase Transitions by Nasu, K., Phase Transition vol. **74**, (2001), Gordon and Breach Publishers, Malasia.
2. Koshihara, S., Tokura, Y., Mitani, T., Saito, G. and Koda, T., Phys. Rev. **B42**, 6853 (1990).
3. Gutlich, P., Hauser, A. and Spiering, H., Angew. Chem. **33**, 2024 (1994).
4. Renovitch, G.A., Baker Jr., W.A., J. Am. Chem. Soc. **89**, 6377 (1967).
5. Kiryukhin, V., Casa, D., Hill, J. P., Keimer, B., Vigliante, A., Tomioka, Y. and Tokura, Y., Nature (London) **386**, 813 (1997).
6. Miyano, K., Tanaka, T., Tomioka, Y. and Tokura, Y., Phys. Rev. Lett. **78**, 4257 (1997).
7. Keneman, S. A., Appl. Phys. Lett. **19**, 205 (1971).
8. Berkes, J. S., Ing, S. W. and Hillegas, W. J., J. Appl. Phys. **42**, 4908 (1971).
9. Ogawa, Y., Koshihara, S., Koshino, K., Ogawa, T., Urano, C. and Takagi, H., Phys. Rev. Lett. **84**, 3181 (2000).
10. Hauser, A., J. Chem. Phys. **94**, 2741 (1991); Decurtins, S., Gütlich, P., Hasselbach, K. M., Hauser, A. and Spiering, H., Inorg. Chem. Cryst. **24**, 2174 (1985).
11. Tayagaki, T. and Tanaka, K., Phys. Rev. Lett. 86 (2001).
12. Oyanagi, H., Kolobov, A. and Tanaka, K., J. Synchrotron Rad. **5**, 1001 (1998).
13. Oyanagi, H., Fonne, C., Gutknecht, D., Dressler, P., Henck, R., Lampert, M-O., Ogawa, S., Kasai, K., Fukano, A. and Mohamed, S., this conference.
14. Oyanagi, H., Haga, K. and Kuwahara, Y., Rev. Sci. Instrum. **67**, 350 (1996).
15. Rehr, J. J., Zabrinsky, S. I. and Albers, R. C., Phys. Rev. Lett. **69**, 3397 (1992).
16. Mikami, M., Konno, M. and Saito, Y., Acta Cryst. **36**, 275 (1980).
17. Oyanagi, H., Tayagaki, T. and Tanaka, K., Proc. 19th International Conference on X-ray and Inner-Shell Processes, Rome, Jun. 24–28, 2002, X-ray and Inner-Shell Processes, ed. by A. Bianconi, A. Marcelli and N. L. Saini, AIP Conference Proceedings vol. 652, 439 (2002).
18. Oyanagi, H., Tayagaki, T. and Tanaka, K., unpublished.

Physica Scripta. Vol. T115, 110–112, 2005

Size- and Site-Dependence of XMCD Spectra of Iron Clusters from *ab-initio* Calculations

O. Šipr[1,*] and H. Ebert[2]

[1]Institute of Physics, Academy of Sciences of the Czech Republic, Cukrovarnická 10, 162 53 Prague, Czech Republic
[2]Universität München, Department Chemie, Butenandtstr. 5-13, D-81377 München, Germany

Received June 26, 2003; accepted November 4, 2003

PACS numbers: 75.50.Tt, 78.70.Dm

Abstract

Magnetic structure and $L_{2,3}$ edge X-ray magnetic circular dichroism (XMCD) spectra of free spherical iron clusters containing 9–89 atoms are calculated employing the *ab-initio* fully-relativistic spin-polarized multiple-scattering method. The average spin m_{spin} and orbital m_{orb} magnetic moments as well as their ratio m_{orb}/m_{spin} are larger in clusters than in the bulk, with the ratio m_{orb}/m_{spin} approaching the bulk values more rapidly than either m_{spin} or m_{orb}. Theoretical XMCD spectra of free clusters differ from their bulk counterpart mainly through smaller widths and sharper maxima of the main peaks. A small yet distinct feature just above the main L_3 edge peak appears for all the investigated clusters and could thus serve as a marker of clusterization.

1. Introduction

Transition metal clusters ought to have larger magnetic moments than bulk systems because they contain a high portion of surface atoms, which have larger spin magnetic moments m_{spin} and, especially, orbital magnetic moment m_{orb} than bulk atoms. X-ray magnetic circular dichroism (XMCD), defined as a difference of the absorption rate for left- and right-circularly polarized X-rays in magnetic targets, offers the possibility to study angular-momentum selected spin and orbital contributions to the total magnetic moment separately. Several experimental studies were performed on supported iron clusters [1, 2, 3]. These studies suggest an essential enhancement of m_{orb} as well as of the ratio m_{orb}/m_{spin} with respect to the bulk, while m_{spin} remains the same as in the bulk or even decreases. In our study we want to concentrate on *free* iron clusters with the aim to investigate theoretically the effect of clusterization on XMCD, relying on ab-initio calculations.

2. Theory

We investigate free spherical iron clusters with their geometry taken as if they were cut from a bcc Fe crystal. Our theoretical framework is based on the local density approximation. The magnetic structure and $L_{2,3}$ edge XMCD spectra were calculated employing the fully-relativistic spin-polarized multiple-scattering technique in the atomic sphere approximation, as implemented in the SPRKKR code [4]. The scattering potential was obtained from self-consistent multiple scattering calculations for molecular clusters using an amended XASCF code [5, 6]. The Vosko, Wilk and Nusair parametrization of the exchange-correlation potential was used. In order to account for the spilling of the electron charge into the vaccum, each cluster was surrounded by empty spheres. Further technical details can be found in Ref. [7].

The helicity of the incoming photons is assumed to be either parallel or antiparallel with the cluster magnetization, which coincides with the [100] direction in the parental crystal. All theoretical spectra were convoluted by Lorentzian curves of the same widths which account both for core hole lifetimes [8] as well as for (energy-dependent) photoelectron lifetime [9].

3. Results and discussion

We explored clusters ranging from 9 to 89 atoms, i.e., comprising from one to seven coordination shells. The details of their magnetic structure will be published elsewhere [10]. Generally, atoms close to the cluster surface have larger m_{spin} and m_{orb} than inner atoms. The average m_{spin} and m_{orb} per atom and the m_{orb}/m_{spin} ratio are summarized in Tab. I. We present the average number of holes in the 3d band, too, as this quantity is often used in analyzing XMCD spectra via sum rules. It can be seen from Tab. I that neither m_{spin} or m_{orb} approach their bulk values even for the largest of the investigated clusters. This is not surprising as Stern-Gerlach type experiments actually demonstrated that the total magnetic moment converges to the bulk value only for clusters containing several hundreds of atoms [11]. However, Tab. I reveals that the m_{orb}/m_{spin} *ratio* approaches the bulk value much more quickly than m_{spin} or m_{orb} separately. This finding is in contrast with some experimental studies which suggest that the m_{orb}/m_{spin} ratio is about twice as high for supported iron clusters than for the bulk Fe crystal [1, 2, 3]. The resolution of this discrepancy might be that the supported clusters investigated in those studies were in fact more flat than spherical, containing thus a much larger portion of surface and edge atoms with larger m_{orb}.

The theoretical Fe $L_{2,3}$ edge XMCD spectra shown in Fig. 1 were obtained by superposing calculated XMCD signals from

Table I. *Average moments m_{spin} and m_{orb} per atom (in μ_B), the ratio m_{orb}/m_{spin} and the number n_h of holes in the d band of spherical iron clusters of N atoms.*

N	m_{spin}	m_{orb}	m_{orb}/m_{spin}	n_h
9	2.85	0.209	0.073	2.89
15	2.54	0.070	0.028	3.02
27	2.81	0.123	0.044	3.16
51	2.58	0.076	0.030	3.20
59	2.68	0.062	0.023	3.27
65	2.62	0.071	0.027	3.30
89	2.71	0.069	0.025	3.32
bulk	2.30	0.055	0.023	3.44

*e-mail: sipr@fzu.cz

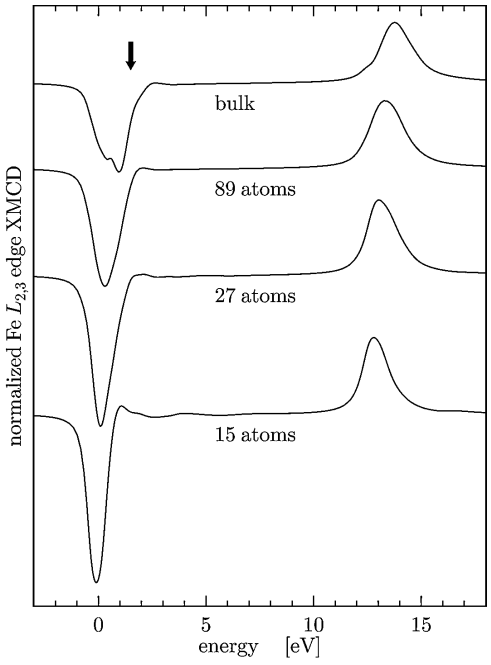

Fig. 1. Fe $L_{2,3}$ edge XMCD spectra of bulk iron crystal and of free clusters containing 15, 27 and 89 atoms.

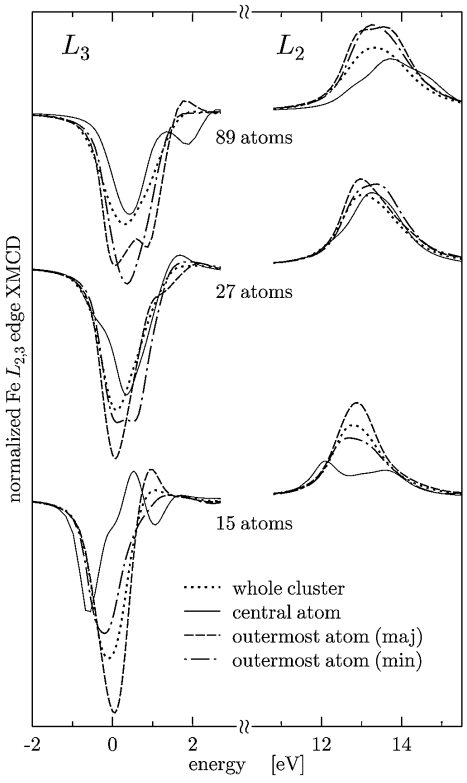

Fig. 2. Fe $L_{2,3}$ edge XMCD spectra of the central atoms, of the outermost atoms and combined spectra of the whole clusters for three cluster sizes. Spectra of inequivalent atoms belonging to the same coordination shell are distinguished by line types (dashed lines for atoms of the majority group, dash-dotted lines for atoms of the minority group).

all atoms in the given cluster and were normalized per one atom. The splitting of the L_3 negative peak at 0.5 eV in the bulk spectrum has not been observed in the experiment [12]. It seems that this discrepancy is of a many-body origin. This splitting, namely, appears even in spectra obtained via full-potential calculations [13, 14] but it disappears if a relaxed core hole is included [13].

Generally, XMCD spectra of clusters are characterized by narrowing and deepening of the main L_3 and L_2 peaks in comparison with the bulk. This systematic trend is more apparent at the L_3 edge than at the L_2 edge. There is also a systematic albeit minor change in the shapes of the main L_3 and L_2 features: in clusters, these peaks appear to be tilted towards the low-energy side.

All cluster spectra exhibit a small positive peak just after the main L_3 minimum (marked by an arrow in Fig. 1). Its intensity increases with decreasing cluster size. This feature actually may have been observed in the $L_{2,3}$ edge XMCD spectrum of supported clusters containing $N \approx 475$ atoms, as presented in Fig. 1(b) of the work [2]; unfortunately the scale of that plot does not allow to see clearly whether this was a real effect or not.

Theoretical XMCD spectra of iron crystal surface [13] or multilayers [15] display a distinct fine structure. Such fine structure cannot be seen in the spectra of clusters due to a mutual cancellation of the oscillatory contributions arising from different sites. To demonstrate this, we present in Fig. 2 spectra of the central atoms, of the outermost atoms and combined spectra of the whole clusters for three cluster sizes. (Note that there are in fact two symmetry inequivalent atomic sites in each outermost shell as indicated by the line types, because the magnetization decreases the symmetry of the cluster.) One can see that spectra of individual atoms indeed may contain quite a lot of fine structure. There is, however, no unique pattern connecting the site-dependence of XMCD spectra for clusters of different sizes. In particular, the distinct splitting of the main XMCD peaks into two components appears at some atoms of some clusters but not as a general rule.

4. Conclusions

The ratio m_{orb}/m_{spin} between orbital and spin magnetic moments of free spherical iron clusters converges towards its bulk value with increasing cluster size more quickly than m_{spin} and m_{orb} separately. The Fe $L_{2,3}$ edge XMCD spectra of free clusters distinguish themselves from the bulk spectrum mainly through smaller widths and sharper maxima of the L_3 and L_2 peaks. Most of the fine structure which is present in spectra of individual atoms is mutually cancelled when the total spectra of the clusters are formed. The notable exception is a small positive peak just above the main L_3 feature which appears for all clusters and increases in intensity when the cluster size is decreased.

Acknowledgement

This work was supported by the project A1010317 of the Academy of Sciences of the Czech Republic and by the Research Training Network "Computational Magnetoelectronics" of the European Commission (Contract RTN1-1999-00145).

References

1. Edmonds, K. W. *et al*., Phys. Rev. B **60**, 472 (1999).
2. Edmonds, K. W. *et al*., J. Mag. Mag. Mat. **231**, 113 (2001).
3. Ohresser, P., Ghiringhelli, G., Tjernberg, O. and Brookes, N. B., Phys. Rev. B **62**, 5803 (2000).
4. Ebert, H.: in "Electronic structure and physical properties of solids" (Edited by H. Dreyssé) (Springer, Berlin 2000), vol. 535, p. 191.
5. Cook, M. and Case, D. A., Computer code XASCF, Quantum Chemistry Program Exchange, Indiana University, Bloomington, (1980).
6. Šipr, O. and Šimůnek, A., J. Phys.: Condens. Matter **13**, 8519 (2001).

7. Šipr, O. and Ebert, H., Czech. J. Phys. **53**, 55 (2003).
8. Al Shamma, F., Abbate, M. and Fuggle, J. C.: in "Unoccupied Electron States" (Edited by J. C. Fuggle and J. E. Inglesfield) (Springer, Berlin 1992), p. 347.
9. Müller, J. E., Jepsen, O. and Wilkins, J. W., Solid State Commun. **42**, 365 (1982).
10. Šipr, O., Košuth, M. and Ebert, H., J. Mag. Mag. Mat. **272–276**, 713 (2004).
11. Billas, I. M. L., Becker, J. A., Châtelain, A. and Heer, W. A. de, Phys. Rev. Lett. **71**, 4067 (1993).
12. Chen, C. T. *et al*., Phys. Rev. Lett. **75**, 152 (1995).
13. Wu, R., Wang, D. and Freeman, A. J., Phys. Rev. Lett. **71**, 3581 (1993).
14. Huhne, T. and Ebert, H., Solid State Commun. **109**, 577 (1999).
15. Guo, G. Y., Ebert, H., Temmerman, W. M. and Durham, P. J., Phys. Rev. B **50**, 3861 (1994).

Physica Scripta. Vol. T115, 113–114, 2005

XMCD Study on Electronic and Magnetic States of Rare-Earth 5d Electrons in Laves Compounds, RFe$_2$ (R = Rare-Earth)

A. Fujiwara[a], K. Asakura[a], I. Harada[a], H. Ogasawara[b] and A. Kotani[b]

[a]Department of Physics, Faculty of Science, Okayama University, Okayama 700-8530, Japan
[b]Institute for Solid State Physics, University of Tokyo, Kashiwa 277-8581, Japan

Received June 26, 2003; accepted January 19, 2004

PACS numbers: 61.10.Ht; 71.20.Eh; 75.50.Gg

Abstract

X-ray magnetic circular dichroism (XMCD) at the rare-earth (RE) $L_{2,3}$ absorption edges of RFe$_2$ (R = RE) in the Laves phase has been investigated based on the tight-binding model with the intra-atomic exchange interaction between 5d and 4f electrons. We find that the magnetic polarization of 5d electrons, being essential for these XMCD, is dominated by the intra-atomic exchange interaction and by the hybridization with spin-polarized Fe 3d states. These contributions as well as the quadrupole one compete, resulting in a variety of XMCD spectra, as observed in experiments.

Intermetallic compounds RFe$_2$ (R = rare-earth (RE)) in the Laves phase have been studied intensively for the purpose of industrial applications as permanent magnets. They exhibit quite interesting magnetic properties, which are the manifestation of subtle interactions between RE 4f moments and Fe 3d moments. In order to understand the physics of these properties based on a microscopic point of view, it is quite important to obtain information on RE 5d electrons, which mediate the exchange process between them.

Recently, with the aid of circular polarized X-rays of good quality generated at the third-generation synchrotron facilities, a lot of data have been accumulated on X-ray absorption spectra (XAS) and their magnetic circular dichroism (XMCD) at the RE $L_{2,3}$ edges, since they must provide information on the 5d electrons separately from other shells. It was, however, not so straightforward to obtain the information [1]: even the sign of XMCD intensities could not be predicted by a naive theory. After many challenges, we have come to the conclusion that a novel role of the intra-atomic exchange interaction between the RE 5d and 4f states should solve the main discrepancy in XMCD [2, 3]. For a quantitative comparison, we need also to consider the effect of the Fe spin [4].

It is the purpose of this paper to reveal theoretically how we can get the detailed information on the RE 5d electrons in RFe$_2$ by reproducing quantitatively XMCD spectra at the $L_{2,3}$ edges. To this end, we simulate XMCD spectra based on a more elaborate model, in which the band nature of the RE 5d states and the Fe 3d states is treated by the tight-binding model and the intra-atomic exchange interaction between the 4f and 5d states is described by the mean-field coming from the atomic 4f electrons in the Hund's-rule ground state [2]. It will be shown that the XMCD spectra consist of the two contributions, one is from the RE 4f moments and the other is from the Fe 3d moments. As a typical example, we choose XMCD at the Sm L_3 edge since it shows the interesting spectra [5].

The tight-binding method [6] takes into account naturally the characteristics of the lattice structure and the hybridization effect. The parameters in tight-binding model are determined as follows: Firstly the integrals for LuFe$_2$ are determined according to the table in Ref. [7] and then those for other compounds are scaled by the lattice constant for each material so as to satisfy the Pettifor rule. We assume that the Fe 3d states are in magnetic state, the exchange splitting of which is fixed to 1.1 eV and that the RE 5d states are in the exchange-field of the RE 4f electrons. To distinguish the role of the 4f exchange field, we also consider RAl$_2$, where the Fe 3d states are replaced by the nonmagnetic Al 3p states while, to highlight the role of the spin-polarized Fe 3d states, LuFe$_2$ is discussed as a reference material.

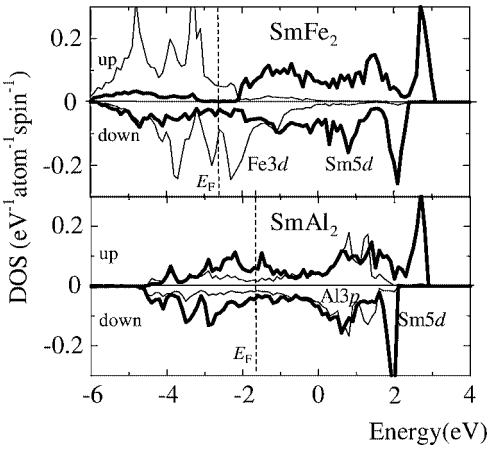

Fig. 1. Density of states for SmFe$_2$ and SmAl$_2$.

The calculated density of states for SmFe$_2$ and for SmAl$_2$ are shown in Fig. 1. We mention the following: 1) DOS of the 5d band shows the characteristic peaks of the Laves phase and 2) in addition to the polarization due to the 4f exchange field over all energy region, DOS in SmFe$_2$ is strongly distorted around the Fermi energy due to the mixing with the spin-polarized Fe 3d states, resulting in an antiferromagnetic 5d moment to the Fe moment. Thus, the tight-binding model manifests a delicate energy dependence of the spin polarization in the RE 5d states, which directly affects XMCD spectra. On the other hand, in SmAl$_2$, the 5d band is polarized only by the 4f exchange field and is not so affected by the Al 3p states, because of the relative energy position and the symmetry of the states.

The calculated XMCD spectra for SmFe$_2$ and SmAl$_2$ are compared with the experimental ones in Fig. 2, where the quadrupole contribution calculated based on the atomic model [9] is added so as to fit the experimental data. In the calculation, we have phenomenologically introduced the enhancement of dipolar matrix elements due to the intra-atomic exchange interaction, in the same manner as in Ref. [2]. Also we have used the Lorentzian with the width of 2 eV HWHM for simulating the lifetime broadening. The XMCD spectrum of SmFe$_2$ has three

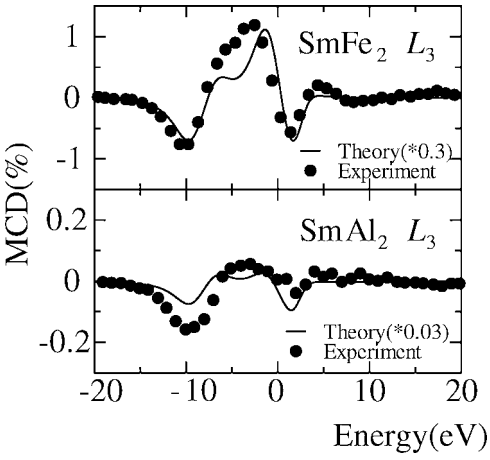

Fig. 2. XMCD spectra of $SmFe_2$ and $SmAl_2$ compared with the experimental results [8].

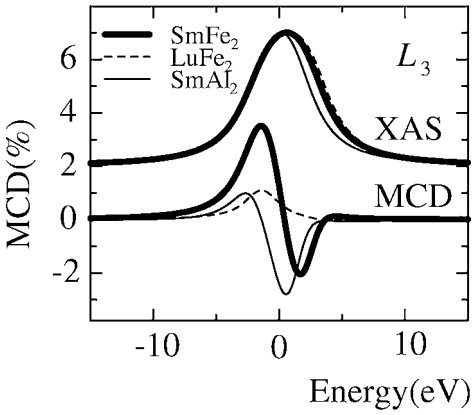

Fig. 3. Comparison of the calculated results for $SmFe_2$, $LuFe_2$ and $SmAl_2$.

distinct peaks, two negative and one positive. Roughly speaking, the lowest negative peak is due to the quadrupole transition, the middle positive peak is dominated by the hybridization effect with the spin-polarized Fe 3d states in addition to the effect from the 4f exchange field, and the highest negative peak comes from the combined effect of the 4f exchange field and the peak in DOS at high energies, which is one of the characteristics of the Laves phase. In the case of $SmAl_2$, we find only a minor positive peak in the middle, which is the consequence of the weak polarization of the 5d band in this energy region. The calculations thus reproduce the experimental XMCD spectra well on the spectral shape and the sign, although its magnitude is scaled down by the reduction factor denoted in Fig. 2 for each case. At the L_2 edge, we can similarly reproduce the XMCD spectra for both compounds based on the same model. Since the different contributions compete with each other in each compound, we have a variety of XMCD spectra at the RE $L_{2,3}$ edges, as observed in experiments [5]. Thus, we can say that, from these spectra, we can draw the detailed information on the energy dependence of the polarization in the 5d band.

To confirm the scenario, we discuss the limiting cases in Fig. 3 only for the dipole contribution. In $LuFe_2$, the XMCD spectra appear near the Fermi energy compared to XAS, while those in $SmAl_2$ spread over the vacant 5d band. These are reasonable since XMCD in the former is the consequence of the hybridization between the Fe 3d and the Lu 5d states and that in the latter is dominated by the exchange field due to the Sm 4f electrons. In $SmFe_2$, both the contributions are effective: the middle positive peak is considerably strong compared with that of $SmAl_2$, pointing out the importance of the hybridization with the Fe 3d states in this energy region.

In conclusion, we have investigated the XMCD spectra at the RE $L_{2,3}$ edges for RFe_2 in the Laves phase and expounded the basic origin of the fine structures in XMCD, which depend on the detailed polarization of the RE 5d states. It is, however, noted that the intensities calculated have been scaled down to match those observed. Furthermore, we need different reduction factors for different compounds. Although we believe that the above explanation should be still valid, we should fix a main reason for the discrepancy in the near future. The following reasons are conceivable: finite-temperature effects, widths coming from experimental resolutions, degrees of the X-ray polarization and of the saturation moment, and details of the energy bands and of the 4f states. Improvements and extensions of the present theory in these directions are now in progress.

Acknowledgments

The authors thank Prof. H. Maruyama, Prof. J. Chaboy, Dr. T. Nakamura and Dr. M. Mizumaki for fruitful discussions and for showing them the data of RAl_2 prior to publication.

References

1. Baudelet, F. *et al*., J. Elctron Spectrosc. Relat. Phenom. **62**, 153 (1993).
2. Matsuyama, H., Harada, I. and Kotani, A., J. Phys. Soc. Jpn. **66**, 337 (1997).
3. van Veenendaal, M., Goedkoop, J. B. and Thole, B. T., Phys. Rev. Lett. **78**, 1162 (1997).
4. Fukui, K. *et al*., Phys. Rev. B**64**, 104405 (2001).
5. Dartyge, E. *et al*., J. Alloys Compounds B**275–277**, 526 (1998).
6. See, for example, Yamada, H. *et al*., J. Phys. F: Met. Phys. **14**, 1943 (1984).
7. Andersen, O. K. and Jepsen, O., Physica **91B**, 317 (1977).
8. Mizumaki, M. *et al*., unpublished.
9. Fukui, K., Ph.D. thesis, Okayama Univ., (2000).

Physica Scripta. Vol. T115, 115–118, 2005

Structure of New Heterometallic Complexes in Hexane on Modelling the Recovery of Ruthenium From Radioactive Solutions

S. B. Erenburg*, N. V. Bausk, L. N. Mazalov, R. S. Shulman, T. V. Us and V. G. Torgov

Institute of Inorganic Chemistry SB RAS, Lavrentiev ave. 3, Novosibirsk 630090, Russia

Received June 26, 2003; accepted November 7, 2003

PACS numbers: 61.10.Ht, 61.20.Qg

Abstract

The analysis of EXAFS and XANES spectra of aqueous solutions and hexane extracts shows the interaction between hydrated (or solvated by $(Oct)_3PO$ molecules) Cu^{2+} cations and the complex anion $[Ru(NO_2)_4(NO)(OH)]^{2-}$. This interaction is accompanied by the increase of the interatomic distances Ru−O from 1.96 to 1.99 Å in the first coordination sphere of Ru atoms. The average interatomic Ru−Cu distances of the resulting heterometallic complexes have been estimated as 3.4 Å. The bond between Ru- and Cu- fragments of heterometallic complexes in their extracts with $(Oct)_3PO$ in hexane is most probably carried out *via* oxygen atoms of OH and NO fragments of NO_2 group of complex anion.

1. Introduction

The recovery of platinum group metals (Pd, Rh, Ru) from high level radioactive solutions is operable to eliminate the destabilizing action of these metals in the vitrification of wastes and proposes a new source of platinum metal. Nevertheless, technological processes of extraction and separation of platinum metals from high-level radioactive wastes (HLW) have not been developed up to now.

An effective extraction of nitro-nitrozo-hydroxo Ru anions by trialkylphosphine oxide to hexane has been revealed recently in the presence of transition metal cations with the participation of this report authors. This phenomenon can be explained by a formation of heterometallic complexes in organic solvent. A similar hypothesis for the formation of bimetallic complexes with Ru and Cu atoms in an aqua solvent was proposed earlier [1]. The goal of the present work is to study the local environment geometry of Ru in nitro-nitrozo-hydroxo Ru anions and a structure of Cu atoms environment in cations both existing in aqua solutions and hexane extracts.

EXAFS (extended X-ray absorption fine structure) and XANES (X-ray absorption near-edge structure) spectroscopy which are capable of studying the local environment of atoms and characterizing noncrystalline objects without long-range order provide a unique possibility to solve such problems [2]. In recent years, these methods were successfully employed, in particular by the authors of this paper, to determine the structure of different coordination compounds in solutions [3, 4].

2. Experimental

2.1. *Experimental and processing procedure*

EXAFS and XANES spectra were measured using synchrotron radiation of the VEPP-3 storage ring at the Budker Institute of Nuclear Physics in Novosibirsk. The electron-beam energy was 2 GeV, with a stored current of between 50 and 100 mA. The RuK and CuK absorption spectra were measured in the transmission mode using Ar/He and Xe ionization chambers as monitoring and final detectors, respectively. A channel-cut Si(111) single crystal was used as a monochromator.

The obtained data were processed with the EXCURV-92 package [5]. The phase and amplitude characteristics were calculated in the X_α approximation. To analyze the local surroundings of Ru and Cu atoms, Fourier-filtered data were fitted with k^2 weighing in the range of photoelectron wave vectors from 3 to 12 $Å^{-1}$. In the fitting procedure, the error of the determined interatomic distances was 0.01 Å in all cases. Structural models have been proposed to heterometallic complexes of several types that have been supposed in extracts of Ru containing anions and Cu containing cations. Various models of the local surroundings of Ru and Cu atoms are checked during the fitting procedure to examine the possibly formation of heterometallic complexes of several types in aqua solution and hexane extracts.

2.2. *Samples under study*

Sample 1 – the individual complex $Na_2[RuNO(NO_2)_4OH]\cdot 2H_2O$. Sample 2 – 0.5 Mol/l aqueous solution of Sample 1. Sample 3 – 0.5 Mol/l aqueous solutions of $Cu(NO_3)_2$. Samples 4, 5 – aqueous solutions containing: 0.5 Mol/l of the complex $Na_2[RuNO(NO_2)_4OH]\cdot 2H_2O$ and M (Mol/l) of $Cu(NO_3)_2$ (M = 0.5: Sample 4; M = 2.5: Sample 5), Samples 6, 7 – the extracts in hexane: extract of composition 0.12 Mol/l $Cu(NO_3)_2$ and 0.25 Mol/l extractant L (Sample 6), extract of composition 0.068 Mol/l of copper and 0.068 Mol/l of ruthenium complexes and 0.25 Mol/l extractant L (Sample 7). The extractant L = $(Oct)_3PO$ = TOPO.

2.3. *Experimental results*

Figs. 1 and 2 show CuK XANES spectra and their first derivatives for Samples 3, 4, 7 and 6, 7, respectively. The spectrum of copper nitrate solution in water (Sample 3) does practically not differ from the spectrum of the aqueous solution of copper nitrate in the presence of the complex of ruthenium (Sample 4). The coincidence of all features in the spectra of these compounds indicates the closeness of the electronic states of copper atoms and their local atomic environments (of the bond lengths and symmetries) [2]. The spectrum of the extracted species in the organic phase (Sample 7) shows substantial differences from the spectra in the aqueous phase (Samples 3 and 4): the main maximum decreases in intensity and broadens. Comparison of the derivatives of the absorption coefficients indicates that there are also differences in the fine structure both in the pre-edge region and below the edge. Such changes in the spectra indicate that there are distortions of the local symmetry of the copper atom

*E-mail: simon@che.nsk.su

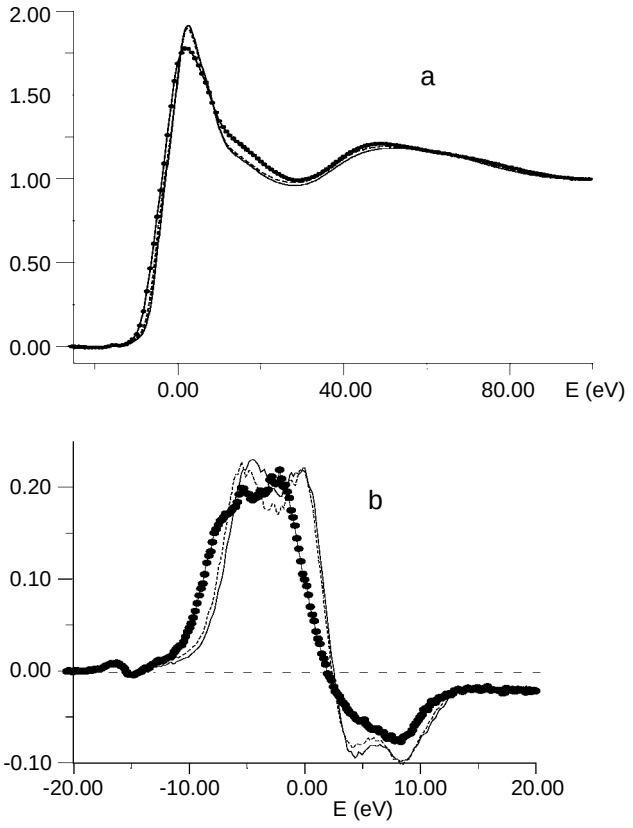

Fig. 1. CuK XANES spectra (a) and their first derivatives (b): solid lines – aqueous solutions of $Cu(NO_3)_2$ (Sample 3); dashed lines – aqueous solutions of $Cu(NO_3)_2$ with $Na_2[Ru(NO_2)_4(NO)(OH)]*2H_2O$ (Sample 4); circles – extract containing copper, ruthenium and *L* (Sample 7).

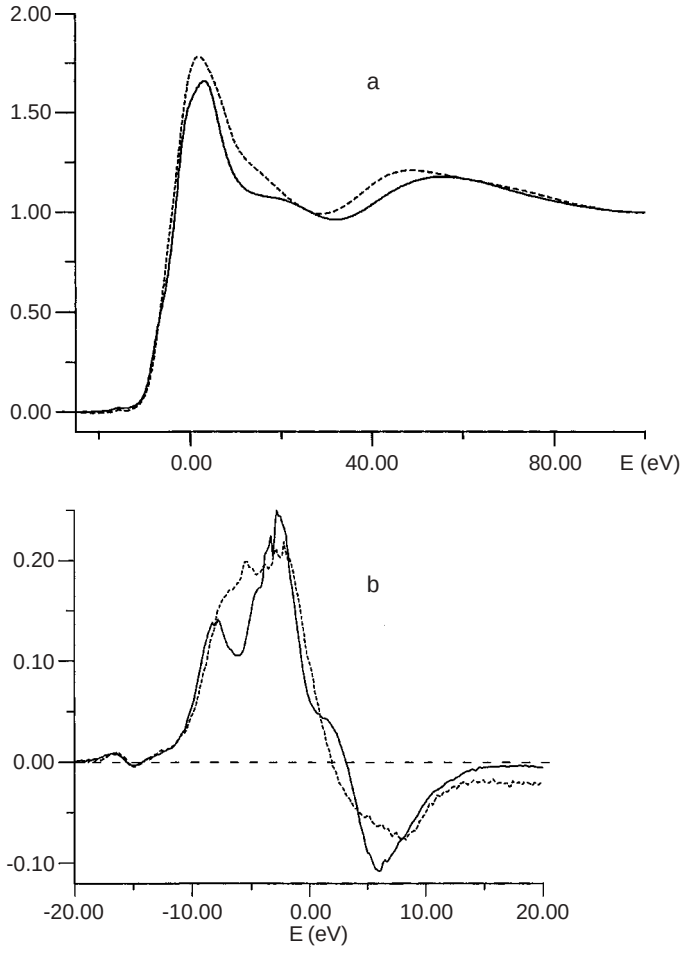

Fig. 2. CuK XANES spectra (a) and their first derivatives (b): solid lines – solutions of $Cu(NO_3)_2$ with $(Oct)_3PO$ in hexane (Sample 6); dashed lines – extract containing copper, ruthenium and $(Oct)_3PO$ (Sample 7).

environment in the organic phase. The shape of the CuK XANES spectrum of the solution of copper nitrate with trioctylphosphine oxide in hexane (Sample 6) is substantially different from that of the heterometallic complex in hexane (Sample 7) (Fig. 2) suggesting substantial differences in geometry and symmetry between the local environments of copper atoms in these samples.

3. Model calculations and discussion

First, a fitting of the RuK EXAFS data for the solid complex (Sample 1) with the known structure [6] was made. The fitting model was made to include atoms of four NO_2 groups and also atoms of the NO group and the oxygen of the OH group taking into account multiple scattering effects and photoelectron focussing. The accuracy of the interatomic distances did not exceed 0.01 Å in any of the fitting procedures.

3.1. *Environment of Ru in "mixed" Ru/Cu^{2+} complexes*

The results of the fitting of the RuK EXAFS data are shown in Table I with fixed Debye-Waller factors determined for the solid compound since their variation in the procedure did not lead to any changes in interatomic distances. Thus, the first coordination sphere of Ru in solutions also includes 4 equatorial NO_2 groups and axial nitrosyl N=O and OH groups. The Ru−O distances to the OH group oxygen in the aqueous solution of the complex with added copper nitrate (Samples 4, 5) and in the extract (Sample 7) increase equally by 0.03 Å relative to the aqueous solution of the ruthenium complex while the Ru−N distances are unchanged within the determination error. The obtained data indicate that there are coordination of copper ions to the ruthenium complex via the oxygen of the hydroxyl group linked to the ruthenium atom.

Table I. *Fitting results of the $k^2\chi(k)$ RuK EXAFS data. R(Ru−N_1), R(Ru−N_2) and R(Ru−O) – interatomic distances between Ru atoms and nitrogen atoms of NO_2, NO groups and oxygen atoms of OH groups, respectively.*

Compound	Solvent	R_1(Å) (Ru−N_1)	R_2(Å) (Ru−N_2)	R_3(Å) (Ru−O)	F_{EXAFS}
1 - (Ru)	Solid comp.	2.09	1.76	1.96	2.1
2 - (Ru)	H_2O	2.11	1.79	1.96	3.1
4 - (Ru + $Cu(NO_3)_2$	H_2O	2.11	1.79	1.99	2.6
7 - (Ru + Cu + TOPO)	C_6H_{14}	2.10	1.77	1.99	2.2

3.2. *Environment of Cu in "mixed" Ru/Cu^{2+} complexes*

Coordination numbers, interatomic distances and Debye-Waller factors presented in Table II have been determined by the computation of the CuK EXAFS data using structural models of various environments of the metal atoms.

It has been found that in $Cu(NO_3)_2$ aqueous solutions the metal atoms are only four-fold coordinated by the oxygen atoms. It has been established that in hexane extract of Cu nitrate with TOPO obtained with and without Ru the metals atoms are four-fold coordinated by oxygen atoms. In this case two additional oxygen atoms can be introduced into the fitting model that

Table II. *Fitting results obtained by $k^2\chi(k)$ CuK EXAFS data computation. Interatomic distances R(Å), Debye-Waller factors σ^2(Å^2) and goodnes of fit index F_{EXAFS} were extracted using EXURV92 package procedure [5].*

Compound	Solvent	Model	R_1(Å) (Cu−O$_1$)	R_2(Å) (Cu−O$_2$)	σ^2(Å^2) (Cu−O$_1$)	σ^2(Å^2) (Cu−O$_2$)	F_{EXAFS}
3 - $Cu(NO_3)_2$	H_2O	4O	1.94		0.005		1.2
4, 5 - Ru + $Cu(NO_3)_2$	H_2O	4O	1.94		0.005		2.4
6 - Cu + TOPO	C_6H_{14}	4O	1.94		0.005		2.0
6 - Cu + TOPO	C_6H_{14}	$4O_1 + 2O_2$	1.94	1.98	0.005	0.049	0.8
7 - Ru + Cu + TOPO	C_6H_{14}	4O	1.92		0.006		1.7
7 - Ru + Cu + TOPO	C_6H_{14}	$4O_1 + 2O_2$	1.92	2.05	0.006	0.045	1.5

results in sufficiently better fit indices. According to the fitting results greater Cu−O interatomic distances and substantially larger Debye-Waller factors for two additional oxygen atoms are found (Table II), which can indicate dynamical instability of them or even cast doubt on their existence.

In the present case it is possible to determine only average interatomic distances Cu−O for four oxygen atoms and two oxygen atoms as far as the fitting procedure gives quite large correlation coefficients of independent parameters when the model with four or six separate shells is used. The CuK XANES data analysis allows us to characterize qualitatively the variations in the local environment around metal atoms in solutions. Unfortunately, for the reason mentioned above EXAFS data computations did not add quantitative information about the Cu first coordination sphere except average interatomic distances Cu−O and coordination numbers of oxygen atoms. It is believed that the Cu first coordination sphere for Sample 3 contains four oxygen atoms of OH groups of aqua solution, for Samples 4, 5 – three atoms of water OH groups and 1 oxygen atom of OH group of the ruthenium complex (formation of Ru/Cu complex). It is suggested that Cu nearest environment for Sample 6 consist of four (or four + two) oxygen atoms from NO_3 and TOPO groups. Early in analysis it was supposed that the Cu nearest environment for Sample 7 consist of oxygen atoms from bridging OH group in addition to three (or three + two) oxygen atoms from TOPO and water OH groups. This supposition was thereafter changed. As can be seen from Fig. 3 a pronounced maximum located around 3 Å appears on the Fourier transform magnitude of the CuK EXAFS data for a heterometallic Ru/Cu complex in extract in comparison with organic Cu containing an extract without Ru. Clearly defined experimental maxima in the curves of Cu radial distribution functions give an indication of Ru atom existence at the rigidly fixed distance. This fact is direct evidence of rigid chemical binding in these binuclear complexes. The interatomic Cu−Ru distance is estimated by the value 3.4 ± 0.05 Å. The measured intensive Ru−Cu signal which corresponds to the Ru occurrence at the fixed interatomic distances in extracts allows us to propose the existence of a sufficiently rigid chemical bond between Ru- and Cu- fragments of the heterometallic complex. Such rigid binding can be provided only by double chemical bonding by two ligands of Ru fragment, especially as the Ru−Cu interatomic distance is shorter (3.4 Å) that the sum of the Ru−O and Cu−O distances (>3.9 Å) for the reason of Ru−O−Cu line bend in this case.

This means that most probably Cu is linked with Ru *via* two bridging groups, OH and NO_2. So, it is chemical bonding Ru−Cu *via* oxygen atom of OH (look above) and NO fragment of an NO_2 group. This assumption is consistent with conclusions of [7] concerning structure of "mixed" Ru/Cu^{2+} complexes in extracts obtained by IR and electron spectroscopy.

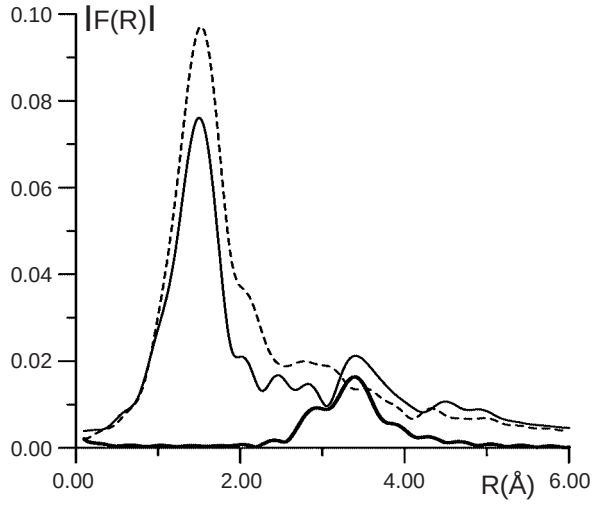

Fig. 3. Fourier transform magnitudes of $k^2\chi(k)$ CuK EXAFS data: solid line – solution of $Ru(NO_2)_4(NO)(OH)]^{2-} + CuL_n^{2+}$ in hexane (Sample 7); dashed – solution of $Cu(NO_3)_2 + 2L$ in hexane (sample 6); thick solid – model function of Cu−Ru atomic pair separated by 3.4 Å.

4. Conclusion

Structural models have been proposed to heterometallic complexes of several types that have been supposed in aqua solution and extracts of Ru containing anions and Cu containing cations. Formation of these complexes are accompanied by Ru−O distance increase while the Ru−N distances are unchanged within the determination error. Clearly defined experimental maxima in the curves of Cu radial distribution functions give an indication of Ru atom existence at the rigidly fixed distance and are direct evidence of rigid chemical bond between Ru- and Cu-fragments of heterometallic complex. The obtained data indicate that double coordination of solvated Cu^{2+} cation to the ruthenium complex could take place through the oxygens of a hydroxyl group and a nitro group both linked to the ruthenium atom.

Acknowledgement

Financial support from the Russian Foundation of Basic Research (grant 03-03-32354) is greatly appreciated.

References

1. Emelianov, V. A., Belyaev, A. V. and Fedotov, M. A., Russian J. Inorg. Chem. **45**, 728 (2000).
2. Koninsberger, D. C. and Prins, R., "X-ray Absorption: Principles, Applications, Techniques of EXAFS, SEXAFS and XANES" (New York, Wiley, 1988), p. 710.
3. Erenburg, S. B., Bausk, N. V., Zemskova, S. M. and Mazalov, L. N., J. Synchrotron Rad. **6**, 582 (1999).
4. Erenburg, S. B., *et al*., Inorg. Reaction Mechanisms **2**, 1 (2000).
5. Binsted, N., Campbell, J. W., Gurman, S. J. and Stephenson, P. C., "SERC Daresbury Lab. Rep." (1991).
6. Blake, A. J., Gould, R. O., Jonson, B. F. G. and Parisini, E., Acta Cryst. **C48**, 982 (1992).
7. Torgov, V., *et al*., J. Mol. Struct. **611**, 131 (2002).

Physica Scripta. Vol. T115, 119–121, 2005

Strong Electron Correlation in Ca 2p, Sr 3d and Ba 4d Core Hole States Investigated by Means of Photoelectron Spectroscopy and MCDF Calculations

J. Nikkinen[1,*], H. Aksela[1], S. Heinäsmäki[1], E. Kukk[1], N. Berrah[2] and S. Aksela[1]

[1]Department of Physical Sciences, University of Oulu, P.O. BOX 3000, 90014 University of Oulu, Finland
[2]Department of Physics, Western Michigan University, Kalamazoo, Michigan 49008-5151, USA

Received June 26, 2003; accepted November 4, 2003

PACS numbers: 32.80Hd, 32.80.Fb

Abstract

Many-electron (correlation) effects play a dominant role in inner-shell ionization processes in free alkaline earth metal atoms. In this work calcium 2p, strontium 3d and barium 4d photoionization processes have been investigated with emphasis on the correlation effects. Inorder to understand the details of the spectra, a series of *ab initio* calculations based on multiconfiguration Dirac–Fock method have been performed. Theoretical predictions are comapred with high-resolution synchrotron radiation induced electron spectra and the capability of the multiconfigurational computations in reproducing the experiment is discussed.

1. Introduction

Inner-shell photoionization studies of Ca, Sr and Ba atoms have proven fruitful in studying electron correlation [1–6]. In ground states they behave like closed-shell atoms and can be quite accurately described within the single configuration approximation. According to this approximation, the (Ca $2p^{-1}$, Sr $3d^{-1}$, and Ba $4d^{-1}$) photoelectron spectra (PES) should consist of just two peaks due to the spin-orbit splitting. However, strong correlation effects influence the core ionized states as a consequence of the collapse of the empty d (Ca 3d, Sr 4d, Ba 5d) and f (Ba 4f) orbitals. Large changes in the corresponding effective potentials contribute to drastic differences in the shapes and the locations between the ground and the excited states' radial wave functions. This leads to the near energy degeneracy of several electron configurations and mixing of configurations has to be included for a more accurate description of the photoionization processes. The Ba 4d photoionization was already studied in Ref. [6] and by combining the PES and Auger electron studies it was possible to deduct how the numerical simulations should be done to correclty reproduce the experiment.

In the present work the photoionization processes are described within the multiconfiguration Dirac–Fock (MCDF) calculations. The high-resolution synchrotron radiation induced gas phase Ca 2p and Sr 3d PES have been recorded in addition to the Ba 4d PES presented recently in [6]. This has enabled us to resolve the fine structure created by correlated core hole states. Our starting point is the previous study of Ba [6] which is used as a reference for Ca and Sr.

2. Experiment

The measurements of Ca, Sr and Ba vapours were carried out at three different synchrotron radiation laboratories; The Ca 2p PES was recorded at beamline U49-1/SGA at BESSY II storage ring in Berlin, Germany [7], the Sr 3d PES at beamline 10.0.1 at ALS in Berkely, USA [8], and the Ba 4d PES at beamline I411 at MAX II storage ring in Lund, Sweden [9]. The measurements were carried out using resistively heated ovens producing atomic beams of the sample, intersecting the photon beam in the interaction region. The spectra were induced using the photon energies of 400 eV (Ca), 255 eV (Sr) and 138 eV (Ba). The ejected photoelectrons were recorded with rotatable SES-100 (Ca, Ba) and SES-200 (Sr) hemispherical electron analyzers at the emission angle of 54.7° (Sr, Ba) and 0° (Ca) relative to the polarization axis of the linearly polarized light. To check the photoionization angular distribution effects for Ca, this measurement was repeated at beamline I411 at the MAX II storage ring, at an emission angle of 54.7°. No differences in relative intensities were obtained. The main parts of the resulting PES are shown in Figs. 1 (Ca), 2 (Sr), and 3 (Ba), where the binding energies have been calibrated using the well

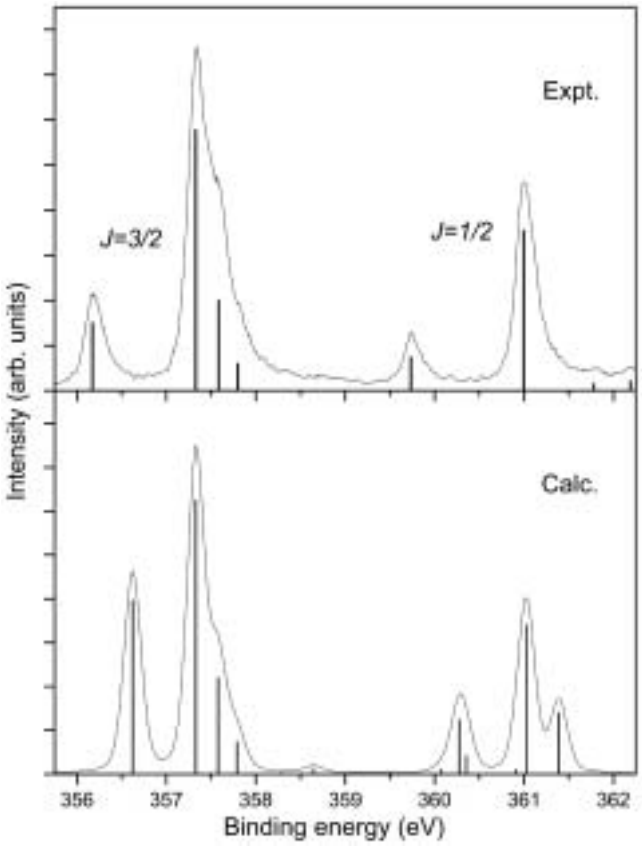

Fig. 1. Experimental (Expt.) and calculated (Calc.) Ca 2p PES.

*Electronic address: juha.nikkinen@oulu.fi

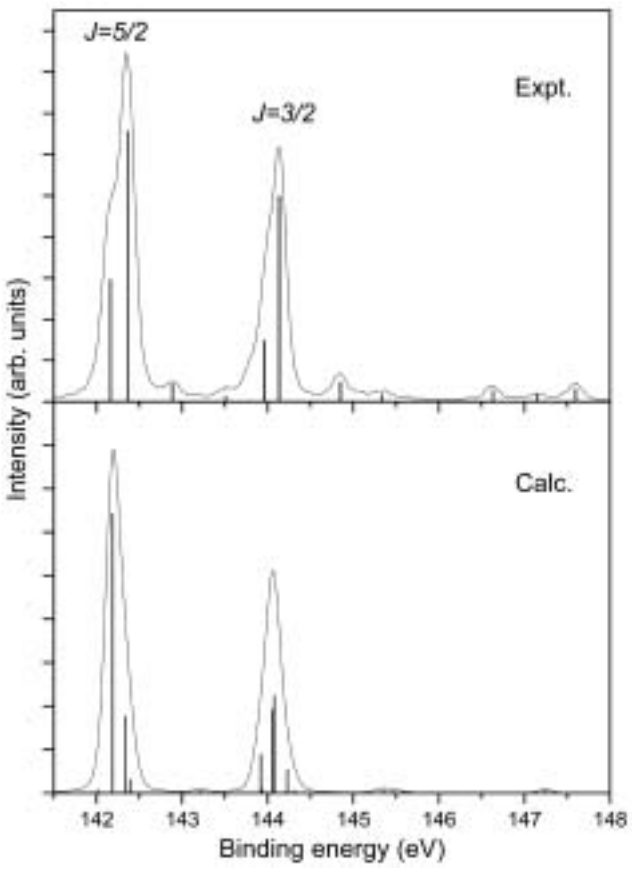

Fig. 2. Experimental (Expt.) and calculated (Calc.) Sr 3d PES.

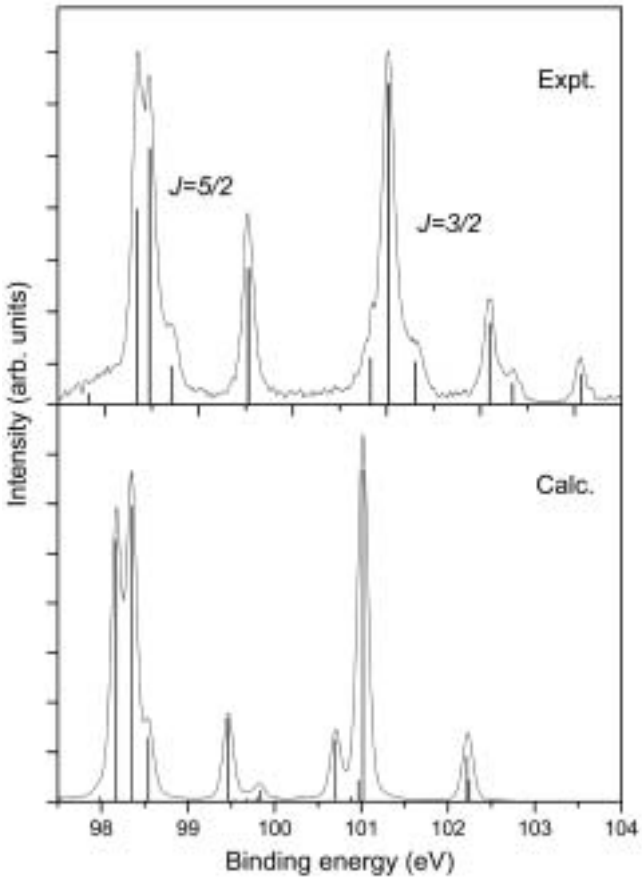

Fig. 3. Experimental (Expt.) and calculated (Calc.) Ba 4d PES.

known rare-gas photoelectron lines. The higher binding energy side of the spectra is shown in Ref. [2] for Ca and in Ref. [5] for Ba.

3. Theory

In MCDF method the atomic state functions (ASFs) are represented by the expansion

$$\Psi_\gamma(PJM) = \sum_r c_{\gamma r} \Phi_r(PJM), \tag{1}$$

where the configuration state functions (CSFs) $\Phi_r(PJM)$ are jj coupled antisymmetrized products of single-electron orbitals classified by the total angular momentum (JM) and parity (P).

In photoionization from an inner-filled subshell, induced by linearly polarized light of randomly oriented atoms, the number of emitted photoelectrons at the so-called magic angle of 54.7° is proportional to the total relative photoionization cross section. If both the ground and core hole state CSFs are constructed using the same set of orthogonal orbitals, the total relative photoionization cross section from the subshell $(n_\alpha l_\alpha j_\alpha)$, integrated over all directions of the photoelectrons, can be expressed as [3]

$$Q_\beta(J_\beta) = \frac{1}{3} Q'_\beta(J_\beta) \sum_{l,j} \int |\langle n_\alpha l_\alpha j_\alpha || r^{(1)} || \epsilon l j \rangle|^2 \, \mathrm{d}\epsilon, \tag{2}$$

where β labels the core hole states. In Eq. (2) the dipole approximation has been applied and the continuum orbitals have been evaluated in an average jj potential of the core hole states by keeping the bound orbitals fixed. The first term is the relative partial photoionization cross section,

$$Q'_\beta(J_\beta) = (2j_\alpha + 1) \left| \sum_\nu \sum_\alpha c_{\beta\nu} c_{i\alpha} \delta_{X_\nu Y_\alpha} \right|^2 \tag{3}$$

with X_ν referring to the configuration associated with $\Phi_\nu(J_\beta)$ and Y_α referring to the same parent configuration after coupling the $n_\alpha j_\alpha$ orbital from $\Phi_\alpha(J_i)$.

4. Results and Discussion

In the present work, the correlation effects were included by generating the ASFs using the GRASP92 package [10] based on the MCDF method. Calculations were performed for the ground and core hole states and the relative PES intensities were obtrained from Eq. (3). The atomic orbitals were constructed from variational calculation of the average energy of all ASFs included.

The effect of correlation in the ground states was found to be negligible in all cases. The core hole state calculations were based on results obtained for Ba in [6]. The strong dependence of calculations on the average energy of all ASFs involved was reduced by performing the calculations in two steps. First, smaller configuration sets were used to find good approximations for inner-shell orbitals,

Ca $2p^{-1}$: $1s^2 2s^2 2p^{-1} 3s^2 3p^6 (3d, 4s)^2$,
Sr $3d^{-1}$: $[Ar] 3d^{-1} 4s^2 4p^6 (4d, 5s, 5p)^2$,
Ba $4d^{-1}$: $[Kr] 4d^{-1} 5s^2 5p^6 (4f, 5d, 6s, 6p)^2$.

In the second step the core orbitals and the s-orbitals, Ca 4s, Sr 5s, and Ba 6s were frozen from the first calculations. To redistribute the intensity among the larger set of states the configuration sets were expanded to

Ca $2p^{-1}$: $1s^2 2s^2 2p^{-1} 3s^2 3p^6 (3d, 4s, 4p, 4d, 5s, 5p)^2$,
Sr $3d^{-1}$: $[Ar] 3d^{-1} 4s^2 4p^6 (4d, 5s, 5p, 5d, 6s, 6p)^2$,
Ba $4d^{-1}$: $[Kr] 4d^{-1} 5s^2 5p^6 (4f, 5d, 6s, 6p, 6d, 7s, 7p)^2$.

The results of these second step calculations are shown in Figs. 1 (Ca), 2 (Sr), and 3 (Ba). For visual comparison with the experiment the spectra are plotted using the line widths obtained from experimental results with calculated relative line intensities which are shown as vertical bars. This kind of calculation procedure seems to work very well for elements involving strong orbital relaxation as was pointed out already for Ba [6]. If we compare the results for Ba (Fig. 3) with those of Ca (Fig. 1) we can conclude that also the Ca spectrum is fairly well reproduced. There are slight deviations in the relative intensities when compared to experiment, but the main $J = 3/2$ and $J = 1/2$ structures and even the minor components of the spectra are predicted quite well. Also the energy splitting between the main structures agrees well with experiment, only the minor structures are slightly too close to the main structures. Inspection of Fig. 2 shows, however, that this type of calculation reproduces the Sr spectrum somewhat worse. There are significant deviations in the relative intensities within the $J = 5/2$ main structure but the $J = 3/2$ structure and the energy splitting is well reproduced. In total the effect of correlation is not as strong in Sr as in Ca and Ba.

Configuration set used for Ca in the first calculation differs a bit from the set used for Ba; the first correlation orbitals of p and f type (4p and 4f) were not included for Ca. This was because the CSFs produced via inclusion of these orbitals were not so strongly involved into the main structure components; they mainly affected to the average energy of the system by drawing it apart from the main structure. The effect of the 4p orbital was tested by including it to the configuration set used in the first step and repeating the similar second step calculation as discussed above. The comparison of this calculation with the experiment was worse than the one presented in Fig. 1. The 4f orbital was also neglected for Sr from the first configuration set. Instead, the first p type correlation orbital (5p) was included. The effect of neglecting the 5p orbital from the first step was tested and no significant changes were noticed. No notable improvements were obtained by further expanding or reducing the configuration sets in both steps of the procedures.

5. Conclusions

In conclusion, high-resolution experimental photoionization studies combined with extensive MCDF calculations have allowed us to resolve and to understand the fine structure in Ca 2p, Sr 3d and Ba 4d PES. Those effects arise as a consequence of strong electron correlation induced by a collapse of the empty d and f orbitals in the photoionization process; the collapsing orbitals make several configurations nearly degenerate in energy, and to describe this, the electron correlation has to be taken correctly into account in the calculations. Multiconfigurational Dirac–Fock calculations presented here reproduced the experimental results quite well, but due to the sensitivity of the calculations to the configuration sets used and to the average energy of the states, some uncertainties still remain. Note, however, that in the MCDF method the orbitals remain automatically orthogonal, which is not the case in the configuration interaction (CI) method used e.g. in the Cowan's code [11]. The correlation will also affect the partial Auger rates as shown for Ba [6] and similar studies of Ca and Sr Auger electron spectra are in progress to further test the computational methods.

Acknowledgments

We are grateful to the staff of the MAX, BESSY and ALS synchrotron laboratories for help during the measurements. Financial support from the National Graduate School in Materials Physics, the European Commuity – Access to Research Infrastructure Action of the Improving Human Potential Programme and the Research Council for the Natural Sciences of the Finnish Academy and the Department of Energy, office of Science, BES are acknowledged.

References

1. Weber, W. *et al*., J. Electron Spectrosc. Relat. Phenom. **47**, 105 (1988).
2. Wernet, Ph. *et al*., J. Phys. B **31**, 289 (1998).
3. Mäntykenttä, A., Aksela, H., Aksela, S., Tulkki, J. and Åberg, T., Phys. Rev. A **47**, 4865 (1993).
4. Matila, T. and Aksela, H., J. Phys. B **33**, 653 (2000).
5. Snell, G., Martins, M., Kukk, E., Cheng, W. T. and Berrah, N., Phys. Rev. A **63**, 062715 (2001).
6. Nikkinen, J. *et al*., Phys. Rev. A **66**, 064703 (2002).
7. Senf, F. *et al*., Nucl. Instrum. Meth. **467**, 474 (2001).
8. Berrah, N. *et al*., J. Electron Spectrosc. Relat. Phenom. **101**, 1 (1999).
9. Bassler, M. *et al*., J. Electron Spectrosc. Relat. Phenom. **101**, 953 (1999).
10. Parpia, F. A., Froese Fisher, C. and Grant, I. P., Comput. Phys. Commun. **94**, 249 (1996).
11. Cowan, R. D., "The Theory of Atomic Structure and Spectra" (University of California Press, Berkeley 1981).

Physica Scripta. Vol. T115, 122–124, 2005

Theoretical Study of X-ray Photoemission, X-ray Absorption and Resonant X-ray Emission Spectroscopy of Mn Films on Ag

M. Taguchi[1], P. Küger[2], J. C. Parlebas[3] and A. Kotani[1,4]

[1]RIKEN/SPring-8, 1-1-1, Mikazuki-cho, Sayo-gun, Hyogo 679-5148, Japan
[2]European Synchrotron Radiation Facility, B. P. 220, 38043 Grenoble, France
[3]IPCMS-GEMME, CNRS, 23, rue du Loess, Strasbourg F-67037, France
[4]Photon Factory, IMSS, High Energy Accelerator Research Organization, Tsukuba, Ibaraki 305-0801, Japan

Received June 26, 2003; accepted December 12, 2003

PACS numbers: 79.60.Dp, 73.61.At, 75.70.Ak

Abstract

We report a theoretical study of core-level X-ray photoemission (XPS), X-ray absorption (XAS) and resonant X-ray emission spectra (RXES) at Mn $L_{2,3}$ edge in Mn thin films on Ag(001). By combining band structure, atomic multiplet and impurity Anderson model calculation, we construct a realistic impurity model that includes full intra-atomic multiplet interaction and inter-atomic coupling to the Mn 3d and Ag-4d bands. The model is applied to various Mn/Ag thin films and related structures. The different systems were modeled by varying only one parameter, the hybridization strength. Good agreement with experiment is obtained. The main conclusion from the impurity model calculations is that the satellite structure observed in the thin films is due to final state charge transfer process, mainly from the Mn-3d states of the neighboring atom. Moreover we predict that the RXES spectra have a satellite structure which is highly sensitive to the local atomic structure around the Mn atoms through its strong dependence on the hybridization of the Mn 3d orbitals.

1. Introduction

Ultrathin transition metal films have attracted much experimental and theoretical interest over the past decade because of their importance for the understanding of interfacial and low dimensional magnetism. For instance, 3d transition metal monolayers (ML) adsorbed on nonmagnetic substrates might be considered as ideal systems for the study of spontaneous two dimensional itinerant magnetism. Low-index noble metal surfaces, such as Cu(100), Ag(100) and Au(100), have often been used as substrate. In the ML range, various artificial structures could be stabilized on these surfaces: adsorbed and embedded MLs [e.g., Mn/Ag(100) and Ag/Mn/Ag(100) (Ref. [1])].

In search of the correlation between structure and magnetism, the Mn/Ag(001) system has been a particular focus [2, 3, 4, 5, 6]. Various new thin film structures of Mn on Ag(001), such as "ideal" adsorbed ML (Mn/Ag) and "buried" ML (Ag/Mn/Ag), were grown and extensively studied by P. Schieffer *et al.* [1, 7, 8, 9]. The Mn 2p XPS of the 0–2 ML films show a pronounced satellite structure. The satellites are located at about 4 and 5 eV higher binding energy than the $2p_{3/2}$ and $2p_{1/2}$ main lines, respectively. Upon decreasing the film coverage their intensity increases continuously and even exceeds that of the "main" lines in the sub-ML regime.

In this context it is also instructive to recall some older experiments on Mn impurities in Ag host. In 1980, Höchst *et al.* [10] measured the Mn 2p XPS in $Mn_x\,Ag_{1-x}$ alloys as a function of x. In the dilute limit $x \to 0$, the spectrum shows a two-peak structure with very broad, but simple $2p_{3/2}$ and $2p_{1/2}$ lines. For a critical concentration range ($0.1 < x < 0.2$) a four-peak satellite structure develops, which is similar to the one in Mn/Ag thin film. Höchst *et al.* attributed the satellites to a chemical shift between Mn atoms with different local environments in the alloy. Whether this interpretation is correct can only be answered on the basis of a microscopic model which would require precise knowledge of the local structure around the Mn atoms. Such information is unfortunately not available. In the theoretical analysis in this paper, we will therefore consider only the dilute limit ($x \to 0$). In this case it is quite certain that all the Mn atoms are surrounded only by Ag atoms which occupy perfect fcc lattice sites.

The situation is more favorable in the case of the thin film systems where precise structural data have been available. For instance, in an adsorbed Mn ML system on Ag(001), which can be grown with high structural quality, all Mn atoms are structurally equivalent. Consequently, chemical shifts cannot occur [8] and the satellite structures must be an intrinsic effect, due to electron correlation [11, 8]. Pursuing this idea, we present here a theoretical study of the core-level XPS, XAS, RXES spectra of Mn thin films on Ag(001) by combining band structure, atomic multiplet and impurity model calculations. In the present work, three possible Mn/Ag(001) thin films and four related systems are considered: (a) an adsorbed Mn ML on Ag(001), (b) a "buried" one (i.e. Ag/Mn/Ag(001)), (c) an adsorbed bilayer Mn/Mn/Ag(001), (d) a free standing Mn ML, (e) bulk body-centered-tetragonal (bct) Mn, (f) Mn impurity in Ag, and (g) a single Mn atom on Ag(001).

The paper is organized as follows: The model and the formalism used in this analysis are given in Sec. 2. The results are summarized and discussed in Sec. 3.

2. Method of calculation

Here we shall give a brief description of the model. We take into account the Mn 3d orbitals of a central Mn atom (core hole site) together with appropriate linear combinations of Mn 3d orbitals on neighboring sites and Ag 4d orbitals of the Ag substrate. We make the following approximations: (*i*) We assume, mainly for simplicity, always an antiferromagnetic (AFM) order where the spins of all neighboring Mn atoms are antiparallel to that of the central Mn atom. The real magnetic structure might be more complex, since several different AFM orders are competing for the ground state. The details of the AFM order have, however, only a small effect on the core level spectra treated here. (*ii*) From the results of *ab initio* calculations [12], we infer the ground state electronic structure in the atomic limit: The central Mn atom has a $3d^5$ configuration and, on the neighboring sites, the Ag 4d band is filled (both spins), while the Mn 3d band is filled for

locally majority spin (denote ↑) and empty for locally minority spin (denote ↓). The spin of the central Mn atom is aligned antiferromagnetically to the Mn bands. (*iii*) For simplicity, we assume a cubic point symmetry throughout. While this is the exact symmetry only for system (f) (Mn impurity in Ag), we believe that it is a good approximation for all systems and that the effect of lower symmetry is small for the spectra considered here.

The ground state is represented as a linear combination of basis states from the manifold of the following eight configurations: $3d^5$, $3d^{5+n}\ \underline{(\mathrm{Ag})}^n$, $3d^{5+n}\underline{(\mathrm{Mn}\uparrow)}^n$, $3d^4(\mathrm{Mn}\downarrow)$, $3d^6\underline{(\mathrm{Mn}\uparrow)}$, $3d^7\underline{(\mathrm{Mn}\uparrow)}(\mathrm{Ag})$, $(n = 1, 2)$. $\underline{\mathrm{Ag}}$ and $\underline{\mathrm{Mn}\uparrow}$ denote holes in the Ag band and in the Mn band with (locally) majority spin, respectively. Mn↓ represents an electron in the Mn band with (locally) minority spin.

The Hamiltonian is given by

$$
\begin{aligned}
H = &\sum_{\Gamma,\sigma} \varepsilon_{3d}(\Gamma) d^\dagger_{\Gamma\sigma} d_{\Gamma\sigma} + \sum_{m,\sigma} \varepsilon_{2p} p^\dagger_{m\sigma} p_{m\sigma} \\
&+ U_{dd} \sum_{(\Gamma,\sigma)\neq(\Gamma',\sigma')} d^\dagger_{\Gamma\sigma} d_{\Gamma\sigma} d^\dagger_{\Gamma'\sigma'} d_{\Gamma'\sigma'} \\
&- U_{dc} \sum_{\Gamma,m,\sigma,\sigma'} d^\dagger_{\Gamma\sigma} d_{\Gamma\sigma} (1 - p^\dagger_{m\sigma'} p_{m\sigma'}) + H_{\mathrm{multiplet}} \\
&+ \sum_{X,k,\sigma} \varepsilon_X(k) a^\dagger_{Xk\sigma} a_{Xk\sigma} \\
&+ \sum_{X,k,\Gamma,\sigma} \frac{V_X(\Gamma)}{\sqrt{N}} (d^\dagger_{\Gamma\sigma} a_{Xk\sigma} + a^\dagger_{Xk\sigma} d_{\Gamma\sigma}). \qquad (1)
\end{aligned}
$$

The first five terms of the total Hamiltonian H are the atomic part describing the central Mn atom. The sixth term represents the X band (X = Mn↑, Mn↓ and Ag) and the last term describes the hybridization between the atomic Mn 3d state and the X band. The $\varepsilon_{3d}(\Gamma)$, ε_{2p}, and $\varepsilon_X(k)$ represent the energies of Mn 3d, Mn 2p, and X band states, respectively, with the irreducible representation Γ ($= e_g, t_{2g}$) of the O_h symmetry. The indices m and σ are the orbital and spin states. $V_X(\Gamma)$, U_{dd}, and U_{dc} are the hybridization between the central Mn 3d and X band states, the Coulomb interaction between Mn 3d states, that between Mn 3d and 2p core-hole states, respectively. The term $H_{\mathrm{multiplet}}$ describes the intra-atomic multiplet coupling between Mn 3d states and that between Mn 3d and 2p states. The spin-orbit interactions for Mn 3d and 2p states are also included. The Slater integrals and the spin-orbit coupling constant are calculated by Cowan's Hartree-Fock program [13] and then the Slater integrals are rescaled by 80%, as usual. We assume rectangular bands X of width $W(X)$, and we approximate them by N discrete levels $\varepsilon_X(k) = \varepsilon_X + \frac{W(X)}{N}(k - \frac{N+1}{2})$, $(k = 1, \ldots, N)$. For the hybridization, we use the empirical relation: $V_X(e_g) = -2V_X(t_{2g})$. The charge transfer energy Δ is defined as $\Delta \equiv \varepsilon_{3d} + 5U_{dd}$.

3. Results

Here we calculated the Mn 2p XPS, 2p XAS and 2p → 3d → 2p RXES with excitation at L_3 and L_2 for various Mn/Ag thin films and related structures. The model parameters are summarized in Table I. Most of those values are estimated from the previous *ab initio* calculations [12]. Among them, the important parameters are Δ, V_{Mn}, U_{dc} and U_{dd}. Δ and V_{Mn} control mainly the ground state properties. The relative intensity between the main line and the satellite of XPS is sensitive to V_{Mn}, while their energy separation is affected by Δ and U_{dc}. The XPS spectra are rather insensitive to U_{dd}, but the analysis of XAS is crucial in determining whether the value of U_{dd} is around 1.0 eV or 3.0 eV.

Table I. *Parameter values (in eV) used in the calculations.*

System independent impurity model parameters

Δ	U_{dd}	U_{dc}	$\varepsilon_{Mn\uparrow}$	$\varepsilon_{Mn\downarrow}$	ε_{Ag}	N	$10Dq$
−3.012	3.0	4.123	−2.5	0.5	−5.0	4	0.5

System dependent impurity model parameters

system	W(Ag)	$V_{Ag}(e_g)$	W(Mn)	$V_{Mn}(e_g)$
impurity in Ag	3	0.866	0	0
1 Mn atom/Ag	3	0.5	0	0
free Mn ML	0	0	1	0.8
Mn/Ag	3	0.5	1	0.8
Ag/Mn/Ag	3	0.707	1	0.8
Mn/Mn/Ag(S)	0	0	2	1.25
Mn/Mn/Ag(I)	3	0.707	2	1.25
Mn bct	0	0	3	2.0

The calculated Mn 2p XPS is shown in Fig. 1(a). The dashed line represents the back ground contribution which is given with an adjustable constant C, by $B(E_B) = C\int_{-\infty}^{E_B} F(E'_B)\mathrm{d}E'_B$, where $F(E_B)$ represents the 2p XPS spectrum. The core hole lifetime broadening Γ is taken to be 0.5 eV, and the Gaussian broadening to be $\sigma = 0.5$ eV. The calculated 2p XPS spectra reproduce well the experiments in the whole range of structures from Mn impurities in Ag and to Mn/Ag [8, 10]. For comparison, we also calculated the spectra of a free ML and that of a single Mn atom on Ag. The satellite intensity decreases slightly from Mn/Ag to Ag/Mn/Ag and more strongly from Mn/Ag to Mn/Mn/Ag.

Since the Ag 4d-band lies 2.5 eV below the Mn 3d↑ band, the $3d^6\underline{\mathrm{Ag}}$ configurations contribute much less to the ground state than $3d^6\ \underline{\mathrm{Mn}\uparrow}$. As for the final states, the $2p^53d^6\underline{\mathrm{Ag}}$ states have energies around the $2p^53d^5$ ones, whereas the $2p^53d^6\ \underline{\mathrm{Mn}\uparrow}$ states lie clearly below them. As a consequence, the satellites are due to poorly screened $2p^53d^5$ final states with some Ag-screened $2p^53d^6\ \underline{\mathrm{Ag}}$ contribution, whereas the main lines are due to Mn-screened $2p^53d^6\ \underline{\mathrm{Mn}\uparrow}$ states.

Figure 1(b) shows calculated Mn 2p XAS spectra where we use the same parameter values as those of 2p XPS. The experiment is also shown by closed symbol only for Mn/Ag system. The calculation for Mn/Ag is in good agreement with the experiment. All systems have very similar spectrum shape. This is because the charge transfer effect is suppressed due to the screening of the core hole potential by the 3d electron photoexcited from the core level. Unfortunately, to the author's knowledge, there is only one experiment of Mn 2p XAS for Mn/Ag(001) systems [14] so that the comparison with experiment is only limited to this system.

We also calculate the 2p → 3d → 2p RXES. For simplicity we neglect the polarization of the incident photon. The calculations at L_3 and L_2 excitations are shown in the left and right panel in Fig. 1(c), respectively. At L_3 excitation, the elastic peak have a strong intensity and the spectrum have similar shape for all systems. For L_2 excitation, the intensity of the inelastic peak increases and is larger than that of the elastic peak for all systems. Moreover, while the XAS spectra at L_2 region does not change very much, the RXES spectra with the L_2 excitation strongly depend on the systems.

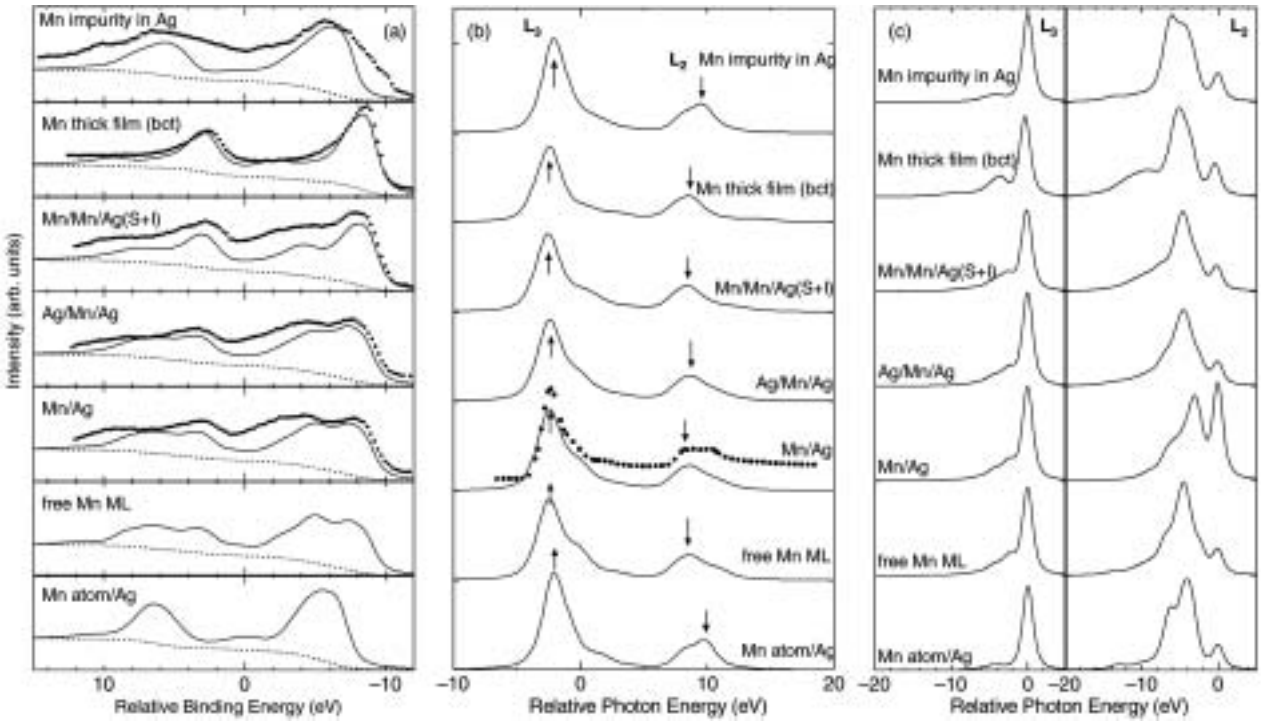

Fig. 1. Calculated XPS, XAS, and RXES spectra at Mn $L_{2,3}$ edge for various Mn-Ag structures with experimental spectra (closed symbol). (a): Mn 2p XPS spectra. The dashed line represents the calculated background spectra. (b): Mn 2p XAS. (c): 2p → 3d → 2p RXES at the photon energies marked by the vertical arrows in the $L_{2,3}$ XAS in (b).

In summary, we have presented 2p XPS, XAS and RXES spectra of various Mn/Ag thin film and related structures. The results are interpreted using the realistic impurity model that includes full atomic multiplet interaction and coupling to the Mn 3d and Ag 4d bands. Good agreement between the experimental results and the model calculations is achieved in 2p XPS. Using the same parameter values, we could also reproduce the experimental 2p XAS spectrum of the Mn/Ag(001) system. Moreover, we predict theoretically that the RXES lineshape is very sensitive to the hybridization of the Mn 3d orbitals and thus to the local atomic structure.

Acknowledgements

Financial support by the CNRS through the PICS program is greatly acknowledged.

References

1. Schieffer, P. *et al.*, Surf. Sci. **400**, 95 (1998).
2. Newstead, D. A. *et al.*, J. Phys. C **21**, 3777 (1988).
3. Jonker, B. T., Krebs, J. J. and Prinz, G. A., Phys. Rev. B **39**, 1399 (1989).
4. Egelhoff, W. F. *et al.*, J. Vac. Sci. Technol. A **8**, 1582 (1990).
5. Ortega, J. E. and Himpsel, F. J., Phys. Rev. B **47**, 16441 (1993).
6. Schieffer, P., Surf. Sci. **352–354**, 823 (1996).
7. Schieffer, P. *et al.*, Phys. Rev. B **57**, 1141 (1998).
8. Schieffer, P. *et al.*, J. Electron Spectrosc. Relat. Phenom. **104**, 127 (1999).
9. Schieffer, P. *et al.*, Phys. Rev. B **62**, 2944 (2000).
10. Höchst, H., Steiner, P. and Hüfner, S. Z., Phys. B-Cond. Matter **38**, 201 (1980).
11. Rader, O. *et al.*, Europhys. Lett. **39**, 429 (1997).
12. Krüger, P., Physica B **318**, 310 (2002).
13. Cowan, R. D., " The Theory of Atomic Structure and Spectra" (University of California Press, Berkeley, 1981).
14. Schieffer, P. *et al.*, J. Synchrotron Rad. **6**, 784 (1999).

Physica Scripta. Vol. T115, 125–127, 2005

Conjugate Shake Processes upon 2p-Photoabsorption of Atomic Sulphur

A. G. Kochur[1] and D. Petrini[2]

Rostov State University of Transport Communication, Noarodnogo Opolcheniya 2, Rostovna-Donu, 344038 Russia

Received June 26, 2003; accepted January 13, 2004

PACS numbers: 32.80.Fb, 31.25.Jf, 31.15.Md

Abstract

The probabilities of non-monopole processes of additional electron excitation/ejection (conjugate shake up/off processes) upon 2p-photoionization of atomic sulphur are calculated in the frame of first-order perturbation theory for the wavefunctions. Both conjugate shake up and conjugate shake off processes are important on a comparatively wide energy scale, and they may cause noticeable discontinuities in atomic photoabsorption.

1. Introduction

It is known that additional excitations/ionizations above inner-shell thresholds cause discontinuities in atomic photoabsorption which may cause difficulties in obtaining the normalized EXAFS (see [1] and references therein). The appearance of a more or less pronounced step at the threshold of additional excitation or ionization and the change of the slope of the atomic photabsortion spectrum above this threshold lead to appearance of non-structural low-frequency oscillations in normalized EXAFS if one approximates the atomic photoabsorption with a smooth function of the photoelectron energy. These non-structural oscillations lead to the appearance of the meddling low-R peaks in the Fourier transforms of EXAFS. This situation may become embarrassing when the structural signal is weak as, say, in amorphous samples [2] or when an absorbing atom is surrounded by light ligands with low back-scattering amplitudes.

The effect of additional monopole excitations on EXAFS treatment was studied theoretically in [3–5]. Monopole (shake) excitations are those additional excitations where an electron is either shaken up into a bound excited state or shaken off into continuum without change of its orbital momentum quantum number.

There exists another mechanism of additional non-monopole electron excitation due to dipole excitations of electrons in the final state of photoabsorption [6-10]. Those processes were called conjugate shake (CS) processes. Close-coupling calculations for sodium [7] and R-matrix calculations for boron [8], magnesium [9] and aluminum [10] showed that the conjugate shake up (CSU) processes for valence electrons may be important during photoionization having probabilities of up to about 20%. No theoretical study on conjugate shake off (CSO) processes has not yet been performed.

In this work we calculate the relative probabilities of both CSU and CSO processes upon 2p-photoionization of atomic sulphur in the frame of the first order perturbation theory for the wavefunctions.

Table I. *Conjugate shake processes and respective correlations in the 2p-photo-absorption final state.*

Process	Correlation*
CSU3p → 3d	$2p^5 3s^2 3p^4 \varepsilon_1 d - 2p^5 3s^2 3p^3 d\varepsilon_2 p^{**}$
	$\varepsilon_2 f$
CSU 3p → 4s	$2p^5 3s^2 3p^4 \varepsilon_1 d - 2p^5 3s^2 3p^3 4s\varepsilon_2 f^{**}$
	$\varepsilon_2 p$
CSO 3p	$2p^5 3s^2 3p^4 \varepsilon_1 d - 2p^5 3s^2 3p^3 \varepsilon_2 p\varepsilon_3 d^{**}$
	$\varepsilon_2 s\varepsilon_3 f$
	$\varepsilon_2 d\varepsilon_3 f$
	$\varepsilon_2 s\varepsilon_3 p$
CSU 3s → 3p	$2p^5 3s^2 3p^4 \varepsilon_1 d - 2p^5 3s^1 3p^5 \varepsilon_2 p^{**}$
	$\varepsilon_2 f$
CSO 3s	$2p^5 3s^2 3p^4 \varepsilon_1 d - 2p^5 3s^1 3p^4 \varepsilon_2 s\varepsilon_3 d^{**}$
	$\varepsilon_2 f\varepsilon_3 f$
	$\varepsilon_2 d\varepsilon_3 d$
	$\varepsilon_2 p\varepsilon_3 f$
	$\varepsilon_2 p\varepsilon_3 p$

* $1s^2 2s^2$ are omitted in the configuration notations.
** Correlation giving the principal contribution to CS probability.

2. Method of Calculation

We calculate the probabilities of additional conjugate shake up and shake off excitations due to the dipole correlations in the final state of the 2p-photoabsorption. The conjugate shake processes and respective final-state correlations are listed in Table I.

Let us denote by $|1\rangle = |2p^5 3s^2 3p^4 \varepsilon_1 d\rangle$ the wavefunction of the 2p single photoabsorption final state. Here $\varepsilon_1 d$ is the photoelectron continuous spectrum wavefunction with the energy

$$\varepsilon_1 = \varepsilon_{\rm ph} - IP_{\rm 2p}$$

where $\varepsilon_{\rm ph}$ is the exciting photon energy and $IP_{\rm 2p}$ is the ionization potential of the 2p subshell. $|2\rangle$ will stand for the wavefunction of an excited state interacting with $|1\rangle$, for example, $|2\rangle = |2p^5 3s^2 3p^3 3d\varepsilon_2 p\rangle$, see Table I. Then the corrected wavefunction of the 2p photoabsorption final state is

$$|\Psi(\varepsilon_1)\rangle = C_1|1\rangle + \int C_2|2\rangle d\varepsilon_2. \quad (1)$$

If the continuous spectrum orbitals $\varepsilon_1 d$ and $\varepsilon_2 p$ are normalized in the energy scale and for the determination of C_2 the first order perturbation theory is used, then for comparatively small interaction between $|1\rangle$ and $|2\rangle$ one has the following integral contribution from correlation states $|2\rangle$ to $|\Psi(\varepsilon_1)\rangle$ [11]:

$$P(\rm CS) = 1 - C_1^2 = \pi^2 \langle 1|V|2\rangle^2. \quad (2)$$

Here $\langle 1|V|2\rangle$ is the electrostatic interaction integral calculated upon the condition that the energies of the continua $|1\rangle$ and $|2\rangle$

[1] E-mail: agk@jeo.ru
[2] Permanent address: Observatoire de la Côte d'Azur, CNRS Laboratoire Cassini, BP 4229, 06304 Nice Cedex 4, France; e-mail: petrini@obs-nice.fr

are equal. The expression (2) gives the probability to discover the system in a state with additionally excited electron, i.e. the probability of the conjugate shake process, in the above example the conjugate 3p → 3d shake up process (CSU3p → 3d).

When $|2\rangle$ contains two continuous spectrum electrons as in the CSO processes, for example $|2p^5 3s^2 3p^3 \varepsilon_2 p \varepsilon_3 d\rangle$, then to obtain the CSO probabilities an additional integration of (2) over ε_3 is needed.

To construct the many-electron wavefunctions $|1\rangle$ and $|2\rangle$ we use the Hartree-Fock-Pauli orbitals of the configuration $|1\rangle$, whereas in $|2\rangle$ the excited electron functions are obtained in the field of respective two-hole cores. Excited channels with the orbital momenta up to 3 were included in the calculation.

3. Results and Discussion

Calculated probabilities of conjugate shake up and shake off excitations from 3p and 3s subshells of the sulphur atom upon 2p-photoionization are presented in Figure 1 and Figure 2. Each CSU or CSO excitation for the same additionally excited electron have either two or several contributing types of correlation states, see Table I.

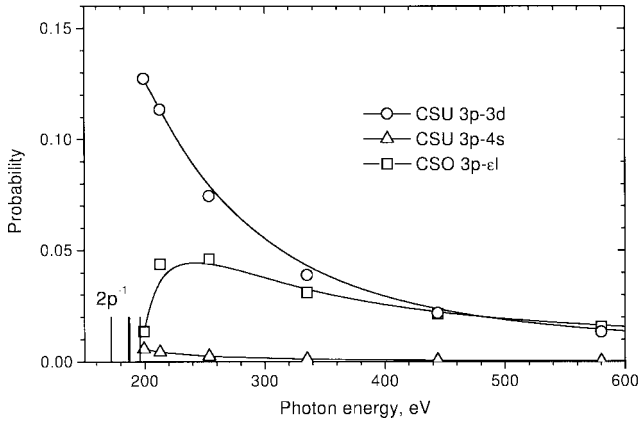

Fig. 1. Probabilities of the conjugate shake up and shake off excitations from the 3p subshell upon 2p-photoionization of atomic sulphur. Calculated values are shown with symbols, lines are the results of B-spline approximations of the calculated data. Circles, CSU3p → 3d; triangles, CSU3p → 4s; squares, CSO3p. Vertical bars show the positions of the 2p-threshold and the CS thresholds.

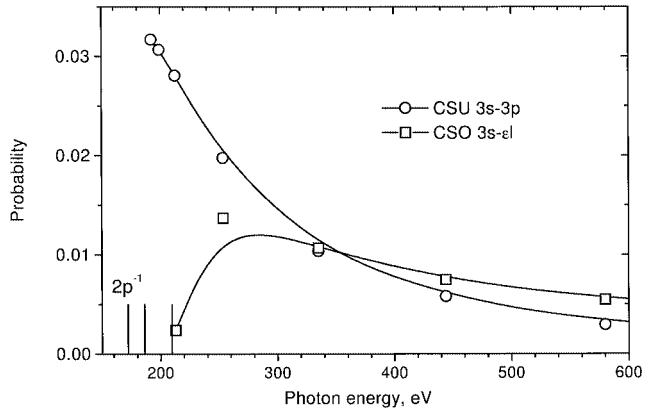

Fig. 2. Probabilities of the conjugate shake up and shake off excitations from the 3s subshell upon 2p-photoionization of atomic sulphur. Calculated values are shown with symbols, lines are the results of B-spline approximations of the calculated data. Circles, CSU3s → 3p; squares, CSO3s. Vertical bars show the positions of the 2p-threshold and the CS thresholds.

Consider first the CSU processes. Of these, the most probable is the CSU 3p → 3d process having at its threshold the probability of about 15% (Figure 1, circles). This value compares well with the CSU probabilities for Mg and A1 obtained in [9, 10] in the *R*-matrix approach. The CSU 3s → 3p process (circles in Figure 2) has lower probability of about 3% near its threshold. This is what one would have expected considering the number of 3p and 3s electrons in $|1\rangle$ and the number of accessible free bound states. The maximum value of the CSU3p → 4s probability (Figure 1, triangles) is less than 1%. We did not discover any other noticeable CSU processes.

The probabilities of all the three CSU processes discussed above behave in the same way with respect to the exciting photon energy. They have maximal values near thresholds and then decrease rapidly with the growth of energy. This behavior is in line with earlier theoretical predictions [7–10].

The probabilities of the CSO 3p → εl and 3s → εl processes are shown in Figures 1 and 2 with squares. One can see that the probabilities of these processes are significant, too. The integral relative contribution of CSO to total CS probability on the energy interval of 190 to 850 eV is 42% for 3p excitations and 48% for 3s excitations. The energy dependence of the CSO probabilities is notably different from that of the CSU processes. One can see from Figures 1 and 2 that the CSO probabilities are very small at their thresholds, then they grow rapidly reaching maximal values and then descend. The slope of the descent of the CSO probabilities is lower than that for the CSU. Resultantly, the relative importance of the CSU and CSO processes changes with the exciting photon energy. While the CSU processes dominate at small photon energies, at higher energies the CSO processes become more probable than the CSU ones. For the CSO from the 3p subshell it happens above 480eV (310 eV above the 2p-threshold), and for the CSO from the 3s subshell – above 356 eV (184 eV above the 2p-threshold).

The calculations showed that both for the CSU and CSO processes there always exists a correlation state that gives the principal contribution to the CS process probability. Those correlation states are marked in Table I. In the case of the CSU processes the principal correlation gives about 75% of the total probability. As for the CSO processes, the dominant correlations here are more pronounced giving up to 98% of the total CSO probability.

It should be noted that both "diagram" final state $|1\rangle$ and correlation states $|2\rangle$ are reached by the dipole transitions from the ground state, and the calculations of the shape of the photoabsorption cross section must deal with this fact. Although the cross sections were not calculated in this work, one can still suppose that since the probabilities of the CS processes are great and they are sharply dependent on the photon energies this may cause significant additional features in atomic XANES.

4. Conclusions

The probabilities of conjugate shake up and conjugate shake off processes upon 2p photoionization of atomic sulphur in the first-order perturbation theory for the wavefunctions. The most prominent are the CSU3p → 3d and CSU3s → 3p. The CSO processes are comparable with CSU comprising on a wide energy interval 42% (3p-excitations) and 48% (3s-excitations) of the total CS probability. In the near edge region the CSU processes dominate while due to rapid decrease of the CSU probabilities with energy the CSO processes become more probable at photon energies 200 to 300 eV above threshold. Great probabilities of

the CS processes and their sharp dependences on exciting photon energies may cause additional features in atomic XANES.

Acknowledgements

This work was partly supported by a fundamental research grant from Russian Ministry of Railroad Transport (project 19.10.00/2002).

References

1. Preseren, R., Kodre, A., Arcon, I. and Borowski, M., J. Synchrotron Rad. **8**, 279 (2001).
2. Frahm, R., Haensel, R. and Rabe, P., J. Phys. F: Met. Phys. **11**, 1029 (1984).
3. Kochur, A. G., Nadolinsky, A. M. and Demekhin, V. F., J Phys. Colloque. **C8**, C8-83 (1986).
4. Kochur, A. G., Nadolinsky, A. M. and Sukhorukov, V. L., Opt. i Spektroskopiya (USSR) **69**, 464(1990).
5. Kochur, A. G., Nadolinsky, A. M. and Demekhin, V. F., Izvestiya Vuzov (USSR) **33**, 105 (1990).
6. Sukhorukov, V. L., Hopersky, A. N., Petrov, I. D., Yavna, V. A. and Demekhin, V. F., J. Phys. (Paris) **48**, 45 (1987).
7. De Araujo, F. X. and Petrini, D., J. Phys. B: At. Mol. Opt. Phys. **21**, L117 (1988).
8. Badnell, N. R., Petrini, D. and Stoika, S. J., J. Phys. B: At. Mol. Opt. Phys. **30**, L665 (1997).
9. Kochur, A. G., Petrini, D. and da Silva, E. P., Aston. Astrophys. **365**, 248 (2001).
10. Kochur, A. G., Petrini, D. and da Silva, E. P., Astron. Astrophys. **393**, 1081 (2002).
11. Demekhin, V. F. and Demekhina, N. V., Studied in Russia (electronic journal) **91**, 1258 (2000), http://zhurnal.ape.relarn.ru/articles/2000/091.pdf

Physica Scripta. Vol. T115, 128–130, 2005

Oxygen 1s NEXAFS Spectra of the V_2O_5(010) Surface: Theoretical Studies Using *ab initio* DFT Cluster Models

C. Kolczewski[1] and K. Hermann[2]

Fritz-Haber-Institut der Max-Planck-Gesellschaft, Faradayweg 4-6, 14195 Berlin, Germany

Received June 26, 2003; accepted November 4, 2003

PACS numbers: 82.65.Jv, 61.10.Ht, 82.80.Pv, 71.15.Mb, 73.20.At

Abstract

The (010) surface of vanadium pentoxide, V_2O_5, contains 1-, 2-, and 3-fold coordinated oxygen centers which can participate as active sites in specific surface reactions. In the present work we use *ab initio* density functional theory (DFT) together with cluster models to calculate 1s core excitation spectra of the different oxygen centers. Excitation energies and intensities are characterized by details of local V-O binding where the data depend strongly on coordination. As a result, strong coordination dependence of the angle-resolved NEXAFS spectra of different oxygen centers is found. The differences can also be seen in the total spectrum obtained from a superposition of the atom specific spectra. A comparison of our theoretical spectra with experimental NEXAFS data yields good agreement and allows an assignment of the experimental peaks to the differently coordinated oxygen centers.

1. Introduction

Vanadium pentoxide V_2O_5 is member of a large vanadium oxide family, e.g. VO, VO_2, V_2O_3 [1], where the oxidation state of vanadium runs from +2 to +5. This causes a variety of geometric and electronic properties and makes vanadium oxides interesting for scientific studies as well as industrial applications [2–4]. For example, V_2O_5 is used as a component in catalysts for the reduction of NO_x with ammonia [5, 6] or for the selective oxidation of hydrocarbons [7].

V_2O_5 forms an orthorhombic layer-type crystal [1] where the layers extend perpendicular to the (010) direction with VO_5 pyramids sticking out at both sides of the layers. These layers possess three differently coordinated oxygen centers: singly coordinated vanadyl, O(1), twofold coordinated bridging, O(2), and threefold coordinated oxygen, O(3). The oxygen centers, if placed at the (010) surface, are expected to react differently with respect to adsorption of small molecules [8, 9]. However, it is quite difficult to discriminate between them in the experiment. For example, XPS studies on O 1s ionization of V_2O_5 [10] show only one broad structureless peak.

In the present work we have performed *ab initio* DFT cluster calculations of angle-resolved NEXAFS spectra for different oxygen centers in V_2O_5 which allow us to distinguish between the three oxygen species in the NEXAFS experiment.

2. Computational Methods

Density functional theory (DFT) cluster calculations are performed to evaluate the electronic structure of vanadium pentoxide. The theoretical NEXAFS spectra are calculated by the transition state approach [11, 12] in combination with a double-basis-set technique [13]. A detailed description of the method can be found elsewhere [14]. Here the orbitals of the cluster are determined using a double zeta or better quality basis set with a half-occupied core orbital at the ionization center. The orbitals of the excited electron states are obtained by diagonalizing the Kohn-Sham matrix built from the initial density with an additional diffuse basis set (150–400 functions) centered at the excited atom in order to account for states above ionization threshold. The resulting orbital transition energies and (dipole) oscillator strengths provide a good representation of the theoretical NEXAFS spectrum. In Slater's transition state approach electronic core hole relaxation is not fully accounted for. Therefore, we calculate the relaxation shifts of the ionization potentials at the three oxygen centers and shift all transition energies according to the corrected relaxation (by 1.8 eV). The theoretical spectrum is generated from the discrete transitions by gaussian convolution with varying broadening. For the region below ionization threshold a broadening of 1.0 eV is used, within 10 eV above the broadening is increased linearly to 4.5 eV and kept fixed at this value for higher energies. The angle-resolved spectra are computed from the x, y, and z components of the dipole transition matrix elements (m_x, m_y, m_z) using appropriate angle projection [15]. All DFT calculations are performed using the StoBe cluster program [16, 17] with gradient corrected RPBE exchange and correlation functionals [18, 19].

All angle-resolved NEXAFS spectra are obtained for the $V_{10}O_{31}H_{12}$ cluster used previously [20], see inset of Fig. 1. This cluster represents a section of the orthorhombic V_2O_5 bulk and provides also a good model for the V_2O_5(010) surface [21, 22]. The hydrogen atoms are added to the cluster to saturate dangling bonds of peripheral oxygen atoms.

3. Results and Discussion

NEXAFS spectra are calculated for each of the three differently coordinated oxygen centers. For the sake of briefness we will describe only results of the singly coordinated vanadyl oxygen in greater detail. The corresponding spectrum is shown in Fig. 1, bottom panel, and combined with partial density of states (PDOS) of the 2p orbitals of the excited oxygen O(1), middle panel, and of the 3d orbitals of nearest neighbor vanadium, top panel. Obviously, the shape of the NEXAFS spectrum is almost identical to that of the O 2p PDOS, whereas it is different from that of the V 3d PDOS. Therefore, the former seems to determine the shape of the NEXAFS spectrum although the O 2p PDOS is much smaller in size compared with the V 3d PDOS. This is obvious from the different scales in Fig. 1. The reason for this behavior becomes clear after a closer look at the formula for the calculation of the

[1]Email: kolczew@fhi-berlin.mpg.de
[2]Email: hermann@fhi-berlin.mpg.de

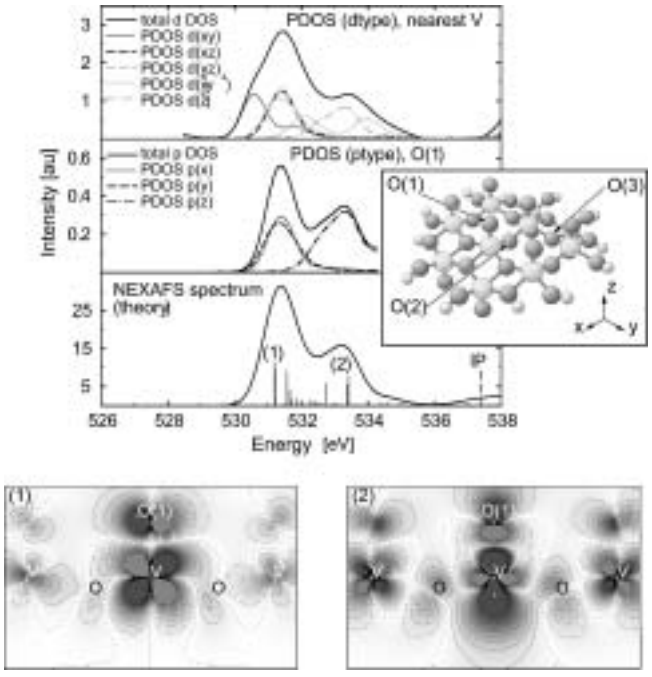

Fig. 1. Theoretical O 1s excitation results for the O(1) center of $V_{10}O_{31}H_{12}$ (the cluster is sketched in the inset). The three panels show the 3d PDOS of vanadium neighbors (top), the 2p PDOS of O(1) (middle), and the computed O(1) 1s NEXAFS spectrum (bottom). The shaded contour plots below the panels refer to final state orbitals of characteristic high intensity transitions in the spectrum. The plotting planes extend along the yz plane through O(1) and its V neighbors.

energy dependent and direction-averaged intensity $I(E)$ in the NEXAFS spectrum

$$I(E) = \text{const.} \cdot \left(\iint \varphi(\text{O 1s}) \cdot \boldsymbol{e} \cdot \boldsymbol{r} \cdot \varphi^*(\text{final})\, \mathrm{d}r^3\, \mathrm{d}\Omega \right)^2 . \qquad (1)$$

The peak intensity in the spectrum scales with the dipole matrix element of the O 1s orbital and the final state orbital. Hence, a transition appears in the spectrum only if the final state orbital has sizeable p contributions at the excited oxygen center.

The double-peak spectrum below ionization threshold, see Fig. 1, can be understood from simple geometric considerations. The bond of the oxygen O(1) with its V neighbor is aligned along the z direction. Thus O $2p_x$ and $2p_y$ orbitals are affected only weakly by nearby V 3d orbitals building weakly antibonding orbital combinations, explaining the low-energy peak. In contrast, the oxygen $2p_z$ orbital points directly towards the V $3d_z{}^2$ orbital and, thus, forms a more strongly antibonding combination, explaining the high-energy peak. The orbital plots corresponding to the two most prominent transitions in the spectra are also included in Fig. 1 and substantiate the different antibonding behavior.

The spectra of the two- and threefold coordinated oxygen centers can be explained as before. Again, the shape of the NEXFAS spectrum is almost identical to that of the O 2p PDOS exhibiting a double-peak structure. However, the assignment of the low and high-energy peaks is different. The doubly coordinated bridging oxygen O(2) $2p_y$ orbital forms weakly antibonding orbital combinations with V 3d orbitals and transitions to these orbitals appear in the low-energy peak of the double-peak spectrum. In contrast, the O(2) $2p_x$ orbital is pointing directly towards corresponding V 3d orbitals and builds strongly antibonding orbital combinations, refering to the high-energy peak. For threefold coordinated oxygen O(3) the low-energy absorption peak does not appear due to the binding geometry and only strongly antibonding orbital combinations contribute to the high-energy peak.

The theoretical NEXAFS spectra for the different oxygen centers are superimposed (using the correct stoichiometry) to yield the total spectrum to be compared with experiment. Further, angle-resolved spectra for given X-ray polarization (polar angle θ, azimuthal angle φ) are evaluated according to:

$$I(E, \boldsymbol{e}) = \text{const.} \cdot (m_x e_x + m_y e_y + m_z e_z)^2 \qquad (2)$$

where

$$\boldsymbol{e} = (e_x, e_y, e_z) = (\sin\theta\cos\varphi, \sin\theta\sin\varphi, \cos\theta). \qquad (3)$$

Fig. 2 shows a series of angle-resolved spectra for xz (Fig. 2a) and yz (Fig. 2b) polarized X-ray beams. In both cases the angular dependence is quite strong. For $\theta = 0^\circ$ the polarization vector is perpendicular to the xy plane. Thus, transitions into orbitals with O $2p_z$ character contribute. These transitions lie for all three oxygen centers in the high-energy part of the spectrum. With increasing angle θ the high-energy part looses intensity whereas the low-energy part gains. For $\theta = 90^\circ$ the polarization vector is parallel to the xy plane and transitions into orbitals with O $2p_x$ ($2p_y$) character are visible for the xz (yz) polarized beam. For xz polarization transitions into orbitals with $2p_x$ character contribute to the low-energy peak in the case of singly coordinated vanadyl oxygen, whereas for two- and threefold coordinated oxygen these transitions refer to the high-energy peak. Thus, excitations at the singly coordinated vanadyl oxygen can be clearly assigned. For yz polarization transitions into orbitals with $2p_y$ character contribute to the low-energy peak for singly and doubly coordinated oxygen,

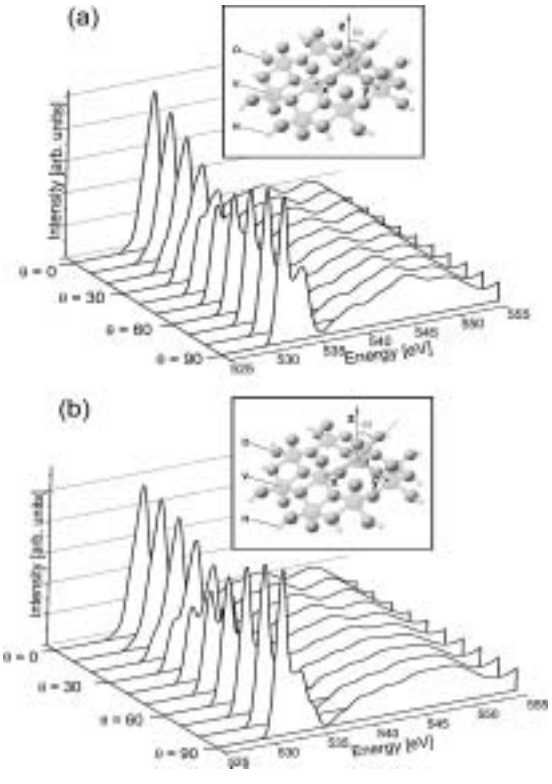

Fig. 2. Theoretical angle resolved O 1s NEXAFS spectra for different X-ray beam polarization of the V_2O_5(010) surface. The spectra refer to a superposition of all oxygen centers and polarization along (a) the xz plane, (b) the yz plane. In both cases the polar angle θ, defined in the inset, varies between 0° and 90° in steps of 10°.

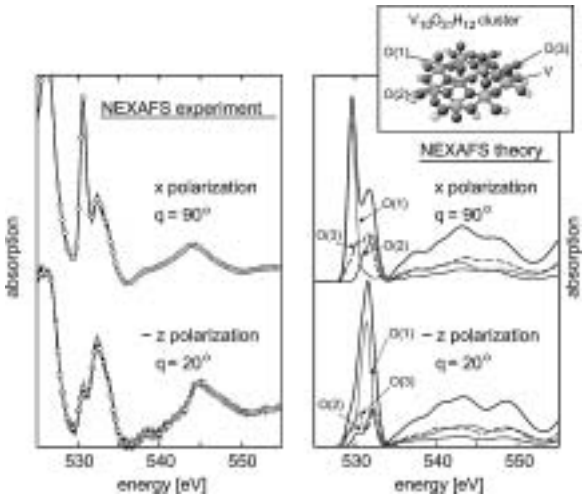

Fig. 3. Comparison of theoretical O 1s core level excitation spectra of the V_2O_5(010) surface with experimental spectra from NEXAFS studies [23] for two different polar angles with *xz* polarization. The contributions of the differently coordinated oxygen centers to the theoretical spectrum are shown in dotted (O(1)), solid (O(2)) and dashed lines (O(3)), respectively. All theoretical spectra are shifted by 1.8 eV to correct for the relaxed ionization potential.

whereas for threefold coordinated oxygen these transitions appear in the high-energy peak. Therefore, excitations at the threefold coordinated oxygen can also be clearly assigned.

A comparison of theoretical spectra with NEXAFS experiments [23] is shown in Fig. 3. The experiments refer to two different angles of incidence of the X-ray beam. For normal incidence (*x* polarization) the agreement between theory and experiment is almost perfect. Both the energetic positions and intensity ratios of the double-peak near 530 eV match extremely well. Further, the broad resonance in the continuum part of the spectrum about 540 eV is reproduced correctly by theory. It may be assigned to transitions into resonances with O 3p character. For grazing incidence ($\sim z$ polarization) the agreement is somewhat worse. While the energetic peak positions match quite well, the measured intensity ratio of the double-peak is reproduced only qualitatively by theory. This may be explained by different adjustment of the polarization angle θ in the experiment. This angle could be influenced by Fresnel diffraction effects such that the effective angle of incidence may be different from that of the primary beam. In fact, a comparison of the experimental spectrum with a theoretical angle-resolved spectrum for $\theta = 35^\circ$ yields much better agreement. Unfortunately, a complete series of angle-resolved NEXAFS spectra, which allows detailed comparison of the angle dependence, does not exist so far.

4. Conclusion

In this work we present angle-resolved NEXAFS spectra for 1s core excitation at the differently coordinated oxygen centers of V_2O_5. In contrast to the angle-integrated spectra published recently [20] a clear assignment of the peaks to specific oxygen centers is possible with the angle-resolved spectra. This may be used in adsorption experiments at the V_2O_5(010) surface where oxygen appears with the three different coordinations discussed above and participates in the adsorption as an active site. Thus, adsorption induced changes in the NEXAFS spectrum may indicate specific oxygen centers where adsorption happens. So far, experiments along these lines have not been published. However, we do hope that the present study can stimulate corresponding measurements.

References

1. Hermann, K. and Witko, M., "The Chemical Physics of Solids Surfaces". (Edited by D. P. Woodruff) (Elsevier Science, Amsterdam, 2001), vol. 9 (Oxide Surfaces), p. 136.
2. Rao, C. N. R. and Raven, B., "Transition Metal Oxides" (VCH Publishers, New York - Weinheim - Cambridge, 1995).
3. Henrich, V. E. and Cox, P. A., "The Surface Science of Metal Oxides" (University Press, Cambridge, 1994).
4. Delmon, B. and Yates, J. T. (eds), "Transition Metal Oxides: Surface Chemistry and Catalysis", ("Studies in Surface Sciences and Catalysis", edited by H. K. Kung) (Elsevier, Amsterdam 1989), vol. 45.
5. Choi, J. H., Kim, S. K. and Bak, Y. C., Korean J. Chem. Engineering **18**, 719 (2001).
6. Forzatti, P., Appl. Catalysis A-General **222**, 221 (2001).
7. Mamedov, E. A. and Corberan, V. C., Appl. Catalysis A-General **127**, 1 (1995).
8. Tepper, B. *et al.*, Surface Sci. **496**, 64 (2002).
9. Ranea, V. A. *et al.*, Surface Sci. **463**, 115 (2000).
10. Zhang, Z. M. and Henrich, V. E., Surface Sci. **321**, 133 (1994).
11. Slater, J. C., "Advances in Quantum Chemistry", (Edited by P. O. Loewdin) (Academic, New York, 1972), vol. 6, p. 1.
12. Slater, J. C. and Johnson, K. H., Phys. Rev. B **5**, 844 (1972).
13. Ågren, H., Carravetta, V., Vahtras, O. and Pettersson, L. G. M., Theor. Chem. Accounts **97**, 14 (1997).
14. Triguero, L., Pettersson, L. G. M. and Ågren, H., Phys. Rev. B **58**, 8097 (1998).
15. Kolczewski, C. and Hermann, K., Surface Sci. **552**, 98 (2004).
16. Casida, M. E. *et al.*, deMon-KS version 4.0, (deMon Software, 1997).
17. The program package StoBe is a modified version of the DFT-LCGTO program package DeMon, originally developed by A. St.-Amant and D. Salahub (University of Montreal), with extensions by L. G. M. Pettersson and K. Hermann.
18. Hammer, B., Hansen, L. B. and Nørskov, J. K., Phys. Rev. B **59**, 7413 (1999).
19. Perdew, J. P., Burke, K. and Ernzerhof, M., Phys. Rev. Lett. **77**, 3865 (1996).
20. Kolczewski, C. and Hermann, K., J. Chem. Phys. **118**, 7599 (2003).
21. Eyert, V. and Hock, K. H., Phys. Rev. B **57**, 12727 (1998).
22. Chakrabarti, A. *et al.*, Phys. Rev. B **59**, 10583 (1999).
23. Richter, B. and Kuhlenbeck, H., private communication.

Physica Scripta. Vol. T115, 131–133, 2005

XANES Calculation with an Efficient "Non Muffin-Tin" Method: Application to the Angular Dependence of the Al K-Edge in Corundum

Delphine Cabaret, Emilie Gaudry, Mathieu Taillefumier, Philippe Sainctavit and Francesco Mauri

Laboratoire de Minéralogie-Cristallographie, UMR CNRS 7590, Université Pierre et Marie Curie, case 115, 4 place Jussieu F-75252 Paris Cedex 05, France

Received June 26, 2003; accepted November 4, 2003

PACS numbers: 78.70.DM and 71.15.Mb

Abstract

We present a reciprocal-space "non muffin-tin" scheme for calculating X-ray Absorption Near-Edge Structure (XANES). The method uses pseudopotentials and reconstructs *all electron* wave functions within the Projector Augmented Wave framework. The method incorporates a recursive method to compute absorption cross section as a continued fraction. The continued fraction formulation of absorption is advantageous in that it permits the treatment of core-hole-electron interaction through large supercells (hundreds of atoms). This opens new fields of applications like surfaces, molecules, small aggregates or amorphous materials, for which large supercells are required. The method is applied to the natural linear dichroism at the Al K-edge in corundum (α-Al_2O_3). Details about the convergence process of the calculation are given. The influence of the core-hole effects is emphasized and comparison with "muffin-tin" multiple scattering calculation is made.

1. Introduction

As compared to multiple scattering cluster methods, reciprocal space approaches are not commonly used for the calculation of X-ray Near-Edge Absorption Structure (XANES). Indeed the periodicity of the system has limited the treatment of the core-hole effects, as well as the calculation of complicated materials. In order to take into account the core-hole-electron interaction, one has to build a supercell, i.e. a multiple cell where only one of the atoms is excited (with only one 1s electron for the K-edge). This supercell has to be large enough so that the excited potential does not interact with the excited potential of neighboring supercells. This requires a supercell that typically contains around one hundred of atoms. Here we present a method that overtakes this drawback by using a recursive technique. Our scheme uses pseupotentials and plane wave basis sets for the wave function expansion. Such an *ab initio* method has also the crucial advantage to be full potential and self-consistent.

Our method was successfully applied to the C K-edge in diamond and to the Si and O K-edge in α-quartz [1]. We have also calculated the Ti K-pre-edge in rutile, and confirmed the analysis given in Ref. [2]. Here we show an application to the X-ray Natural Linear Dichroism (XNLD) at the Al K-edge in corundum. Two other applications can be found in these proceedings: the case of the Cr K-edge in ruby [3] and the anisotropy of the anomalous atomic factor of Fe in pyrite [4].

2. Theory

2.1. *Derivation of the absorption cross section*

In a single-electron approach, the X-ray absorption cross section $\sigma(\omega)$ is given by the Fermi Golden rule as

$$\sigma(\omega) = 4\pi^2\alpha\hbar\omega \sum_f |\langle\psi_f|\mathcal{O}|\psi_i\rangle|^2 \delta(E_f - E_i - \hbar\omega), \tag{1}$$

where α is the fine structure constant, $\hbar\omega$ is the photon energy, $\mathcal{O}$ is a transition operator coupling the initial state $|\psi_i\rangle$ with energy E_i and the final states $|\psi_f\rangle$ with energy E_f. In the case of K-edges (or L_1-edges), the difficulty of the absorption cross section calculation concerns the determination of the final *all electron* wave function, $|\psi_f\rangle$. Our scheme uses pseudopotentials in a plane wave basis set and the *all electron* $|\psi_f\rangle$ is not directly computed. So let us see how Eq. (1) can be rewritten within the pseudopotential formalism using the Projector Augmented Wave (PAW) method [5].

The PAW formalism permits the reconstruction of the *all electron* wave function from the corresponding pseudo-wave function by using a linear operator $\mathcal{T}$, which differs from unity by a sum of local atom-centered terms:

$$\mathcal{T} = \mathbf{1} + \sum_{\boldsymbol{R},n} [|\phi_{\boldsymbol{R},n}\rangle - |\tilde{\phi}_{\boldsymbol{R},n}\rangle]\langle\tilde{p}_{\boldsymbol{R},n}|. \tag{2}$$

The local atom-centered contributions act only within spherical core regions (called $\Omega_{\boldsymbol{R}}$) centered on each atomic site $\boldsymbol{R}$. $|\phi_{\boldsymbol{R},n}\rangle$ and $|\tilde{\phi}_{\boldsymbol{R},n}\rangle$ are *all electron* and pseudo partial waves, respectively, which coincide outside $\Omega_{\boldsymbol{R}}$. A natural choice for $|\phi_{\boldsymbol{R},n}\rangle$ is the solutions of the radial Schrödinger equation for the isolated atom. The vectors $\langle\tilde{p}_{\boldsymbol{R},n}|$, called projector functions [5], are chosen arbitrarily provided they satisfy the two following conditions: (*i*) they are equal to zero outside $\Omega_{\boldsymbol{R}}$; (*ii*) $\langle\tilde{p}_{\boldsymbol{R},n}|\tilde{\phi}_{\boldsymbol{R}',n'}\rangle = \delta_{\boldsymbol{R}\boldsymbol{R}'}\delta_{nn'}$. The index n refers to the (ℓ, m) quantum numbers and to an additional number j used if there is more than one projector per angular momentum channel. It is important to notice that the $|\phi_{\boldsymbol{R},n}\rangle$ funtions and the $|\tilde{\phi}_{\boldsymbol{R},n}\rangle$ functions form a complete basis for any physical non core *all electron* and pseudo wave functions within $\Omega_{\boldsymbol{R}}$, respectively.

Now we substitute $|\psi_f\rangle = \mathcal{T}|\tilde{\psi}_f\rangle$ in Eq. (1) and replace $\mathcal{T}$ by its definition (Eq. 2). Using the fact that the initial wave function $|\psi_i\rangle$ is localized on $\boldsymbol{R}_0$, i.e. $|\psi_i\rangle$ is zero outside $\Omega_{\boldsymbol{R}_0}$, the sum over $\boldsymbol{R}$ is restricted to only one site: the absorbing atom site, $\boldsymbol{R}_0$. It is then rather easy to show [1] that the absorption cross section can be written as:

$$\sigma(\omega) = 4\pi^2\alpha\hbar\omega \sum_f |\langle\tilde{\psi}_f|\tilde{\varphi}_{\boldsymbol{R}_0}\rangle|^2 \delta(E_f - E_i - \hbar\omega), \tag{3}$$

with $|\tilde{\varphi}_{\boldsymbol{R}0}\rangle = \sum_n |\tilde{p}_{\boldsymbol{R}_0,n}\rangle\langle\phi_{\boldsymbol{R}_0,n}|\mathcal{O}|\psi_i\rangle$. In a reciprocal space approach, the index f refers to two indices: the number of empty bands and the number of $\boldsymbol{k}$-points that mesh the irreducible Brillouin zone (BZ) of the reciprocal space. The calculation of XANES from Eq. (3) requires the computation of many empty states, which is computationally expensive. The size of the supercell is then drastically limited [6].

To avoid this drawback, we use the recursion method of Haydock, Heine and Kelly [7], that contains a powerful algorithm to transform a Hermitian matrix into a tridiagonal form. We rewrite Eq. (3) within the Green function formalism

$$\sigma(\omega) = -4\pi\alpha\hbar\omega\Im[\langle\tilde{\varphi}_{\boldsymbol{R}_0}|(E - \tilde{H} + \mathrm{i}\gamma)^{-1}|\tilde{\varphi}_{\boldsymbol{R}_0}\rangle], \tag{4}$$

where $E = Ei + \hbar\omega$. The pseudo-Hamiltonian $\tilde{H} = \mathcal{T}^{\dagger} H \mathcal{T}$ is Hermitian in the plane wave basis set. The recursion method sets up a new basis (Lanczos basis) in which $\tilde{H}$ has a symmetric tridiagonal representation. The Lanczos basis is built by the repeated action of $\tilde{H}$ onto the normalized vector $|\tilde{\varphi}_{\boldsymbol{R}_0}\rangle / \sqrt{\langle\tilde{\varphi}_{\boldsymbol{R}_0}|\tilde{\varphi}_{\boldsymbol{R}_0}\rangle}$, through a three term recurrence relation [7], that is definitely less expensive than the calculation of empty states as in Eq. (3). The recursion method allows to rewrite the matrix elements $\langle\tilde{\varphi}_{\boldsymbol{R}_0}|(\tilde{H} - E - \mathrm{i}\gamma)^{-1}|\tilde{\varphi}_{\boldsymbol{R}_0}\rangle$ as a continued fraction, leading to the following expression for the cross section:

$$\sigma(\omega) = 4\pi\alpha\hbar\omega \times \Im\mathrm{m} \cfrac{\langle\tilde{\varphi}_{\boldsymbol{R}_0}|\tilde{\varphi}_{\boldsymbol{R}_0}\rangle}{a_0 - E - \mathrm{i}\gamma - \cfrac{b_1^2}{a_1 - E - \mathrm{i}\gamma - \cfrac{b_2^2}{a_2 - E - \mathrm{i}\gamma - \cfrac{b_3^2}{\ddots}}}} \tag{5}$$

$\{a_i\}$ and $\{b_i\}$ correspond to the diagonal and subdiagonal real matrix elements of the Hamiltonian tridiagonal representation, respectively. Further details about our framework can be found in Ref. [1].

2.2. *Computational details*

The formalism presented above has been implemented in an *ab initio* total energy code based on the density functional theory (DFT), called `paratec` [8]. The calculation of the absorption cross section comprises two steps: (*i*) the calculation of the self-consistent charge density of the supercell including a 1s core-hole on the absorbing atom, (*ii*) the calculation of the XANES spectrum (Eq. (5)). All the reciprocal space integrations are performed using a Monkhorst-Pack $\boldsymbol{k}$-point grid [9].

(*i*) The charge density calculation can be done either in the local density approximation (LDA) [10] or in the generalized gradient approximation (GGA) [11], and can include spin polarization. The basic ingredients of the code are the pseudopotentials. The code uses norm-conserving Troullier-Martins [12] pseudopotentials with a single component for each (ℓ, m). The pseudopotential of the excited atom is generated with only one 1s electron. The energy cut-off of the plane wave basis set and the number of $\boldsymbol{k}$-points in the BZ are two *convergence-parameters* of the calculation.

(*ii*) The second step of the calculation comprises the evaluation of the $|\tilde{\varphi}_{\boldsymbol{R}_0}\rangle$ function and the evaluation of the $\{a_i\}$ and $\{b_i\}$ coefficients obtained within the construction of the Lanczos basis. For K-edges, $|\tilde{\varphi}_{\boldsymbol{R}_0}\rangle$ is given by: $|\tilde{\varphi}_{\boldsymbol{R}_0}\rangle = \sum_{m,j} |\tilde{p}_{\boldsymbol{R}_0,\ell,m,j}\rangle\langle\phi_{R_0,\ell,m,j}|\mathcal{O}|\psi^{1s}_{\boldsymbol{R}_0}\rangle$ where $\ell = 1$ and $\mathcal{O} = \hat{\varepsilon}\cdot\boldsymbol{r}$ in the case of electric dipole (E1) transitions. $\ell = 2$ and $\mathcal{O} = \hat{\varepsilon}\cdot\boldsymbol{r}\hat{\boldsymbol{k}}\cdot\boldsymbol{r}$ in the case of electric quadrupole (E2) transitions, $\ell = 2$ and $\mathcal{O} = \frac{1}{2}(\hat{\varepsilon}\cdot\boldsymbol{r})$ and $(\boldsymbol{k}\cdot\boldsymbol{r})$, where $\hat{\varepsilon}$ and k are the direction of the polarisation vector and the wave-vector of the incident photon beam, respectively. The partial wave $|\psi^{1s}_{\boldsymbol{R}_0}\rangle$ is the 1s core wave function, solution of the Schrödinger equation for the isolated absorbing atom (non excited). The partial waves $|\phi_{\boldsymbol{R}_0,\ell,m,j}\rangle$ are ℓ valence wave functions, obtained by solving the Schrödinger equation for the isolated excited atom (with one 1s electron). The corresponding Blöchl's projectors are generated as in Ref. [13]. The dimension of the Lanczos basis and, again, the number of $\boldsymbol{k}$-points contitute two other *convergence-parameters* of the calculation. It should be noted that the number of computed Lanczos vectors strongly depends on the value of the broadening parameter γ (Eq. (5)).

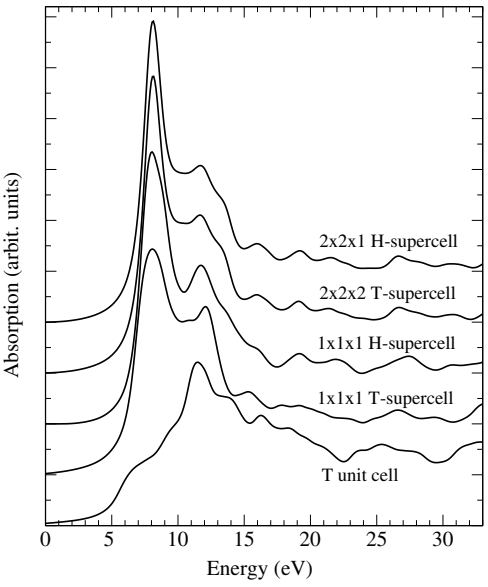

Fig. 1. Al K-XANES calculated spectra for different sizes of cell. From the bottom to the top: 10 atom trigonal (T) unit cell (ground state calculation), 10 atom trigonal $1 \times 1 \times 1$ supercell, 30 atom hexagonal (H) $1 \times 1 \times 1$ supercell, 80 atom trigonal $2 \times 2 \times 2$ supercell and 120 atom hexagonal $2 \times 2 \times 1$ supercell.

To summarize, the XANES calculation converges when increasing the size of the supercell. Increasing the energy cutoff of the plane wave expansion, adding vectors in the Lanczos basis, and adding $\boldsymbol{k}$-points in the irreducible Brillouin zone do not provoke any visible change onto the calculated spectrum.

3. Results and discussion

Corundum crystallizes in the trigonal system (space group $R\bar{3}c$), with two Al_2O_3 entities per unit cell. The structure can also be described by a triple hexagonal cell ($a = 4.759$ Å, $c = 12.991$ Å), where the [001] axis is a three-fold symmetry axis (C_3) [14]. Trigonal and hexagonal supercells were built in order to study the supercell size convergence, so demonstrating the spacial extent of the core-hole relaxation. The corresponding calculated spectra (E1 transitions) are displayed in Fig. 1. The pseudopotentials for Al (excited or in ground state) were built with 1s, 2s, 2p as core states and with 3s, 3p, 3d as valence states (core radius: 1.06 Å). The pseudopotential for O was generated with 1s as core state and with 2s and 2p as valence states (core radius: 0.77 Å). The calculations were performed in the LDA considering an energy cut-off of 64 Ry. One Blöchl's projector ($j = 1$) was used. We indicate in Table I the numbers of $\boldsymbol{k}$-points and of Lanczos vectors that were required to get convergence for each kind of cell.

Table I. *Convergence-parameters for the calculated spectra of Fig. 1. $n^{\rho}_{\boldsymbol{k}}$ (resp. $n^{\sigma}_{\boldsymbol{k}}$) is the number of $\boldsymbol{k}$-points for the charge density, ρ (resp. the cross section, σ). n_{vec} is the number of Lanczos vectors required for $\gamma = 0.3$ eV.*

Cell name	Cell dimension	$n^{\rho}_{\boldsymbol{k}}$	$n^{\sigma}_{\boldsymbol{k}}$	n_{vec}
$2 \times 2 \times 1$ H supercell	$a = 9.518$ Å, $c = 12.991$ Å	1	8	~ 1400
$2 \times 2 \times 2$ T supercell	$a = 10.257$ Å	1	11	~ 1200
$1 \times 1 \times 1$ H supercell	$a = 4.759$ Å, $c = 12.991$ Å	8	32	~ 1300
$1 \times 1 \times 1$ T supercell	$a = 5.128$ Å	6	38	~ 700
T unit cell	$a = 5.128$ Å	6	38	~ 700

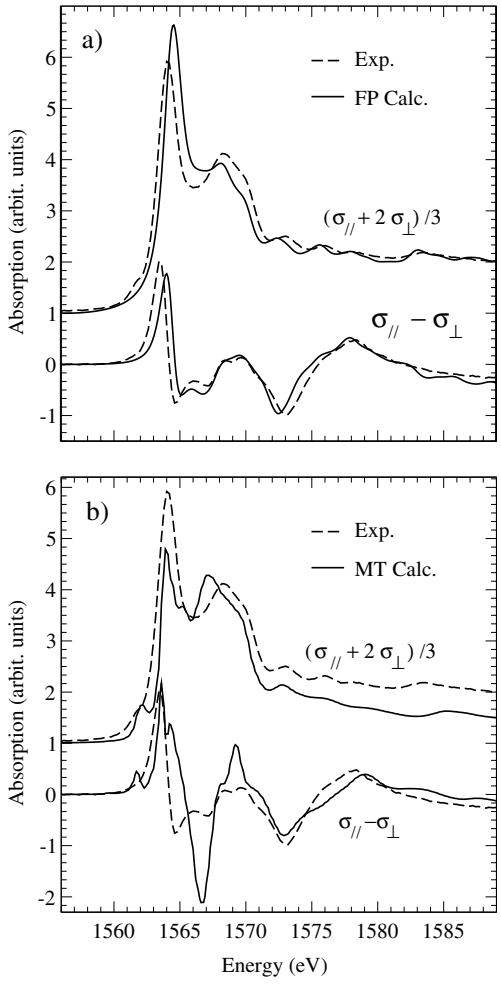

Fig. 2. Experimental Al K-XANES ($\sigma_{\rm iso}$) and corresponding XNLD signal in corundum, compared with full potential (FP) calculation (a) and "muffin-tin" (MT) calculation (b).

The spectra presented in Fig. 1 are calculated with a final broadening parameter $\gamma = 0.7$ eV. One can see that the supercell size convergence was reached for the 80 atom $2 \times 2 \times 2$ trigonal supercell, since the two upper curves are rigorously identical. The lower curve, which is a ground state calculation (no core-hole), differs strongly from the others, showing the importance of the core-hole effects at the Al K-edge in corundum.

Comparison between the converged calculation and polarization dependent experiments is presented in Fig. 2a. Experimental XANES and XNLD spectra were recorded on the SU22 beam line of the Super-ACO storage ring of LURE (Orsay). The beam line was equipped with a double α-quartz $(10\bar{1}0)$ crystal monochromator. The sample was a single crystal disk (3 mm width, 15 mm diameter), cut such as the C_3 axis is in the plane of the face. Absorption was measured in the total electron yield mode for two orientations of the sample: for the C_3 axis parallel and perpendicular to $\hat{\varepsilon}$ ($\sigma_{||}$ and $\sigma_{\perp}$, respectively). Fig. 2a diplays the isotropic spectrum given by $(\sigma_{||} + 2\sigma_{\perp})/3$ and the XNLD spectrum $(\sigma_{||} - \sigma_{\perp})$. Calculations and experiments are in good agreement.

We present in Fig. 2b calculations performed within the full multiple scattering theory, using non self-consistent "muffin-tin" (MT) potential (`continuum` code [15]). The MT calculated spectrum was obtained for a 164 atom cluster (radius 7.85 Å), by using the $Z + 1$ approximation to model the core-hole effects. All the details of this calculation are given in Ref. [16]. The agreement between calculation and experiment is not so bad, although it is definitely less convincing than the full potential (FP) calculation. To obtain such an agreement, we had to play with the MT parameters, like the MT potential level and the overlap between the MT spheres. However these parameters have no real physical meaning. As compared with usual MT multiple scattering approaches, the FP approach is a parameter-free method.

Now let us (focus our attention on the pre-edge feature located at 1561.8 eV. This peak is reproduced by the MT calculation, suggesting that it could be related to medium range order, since it appears only in large cluster calculations [16]. However the FP calculation does not at all reproduce this feature. Its presence in MT calculation is then clearly an artefact. Complementary calculation is needed to clarify the origin of the pre-edge.

4. Conclusion

We have presented an efficient *ab initio* reciprocal space scheme to calculate XANES at the K or L_1 edge. Up to now this framework has been applied to crystalline materials. Thanks to the recursive method incorporated in the method, new fields of application, like biological molecules, surfaces and amorphous systems, are also possible.

Acknowledgements

We are grateful to the Institut du Développement et des Ressources en Informatique Scientifique (IDRIS) in Orsay, that supported most of the computing time of this work.

References

1. Taillefumier, M., Cabaret, D., Flank, A.-M. and Mauri, F., Phys. Rev. B **66**, 195107 (2002).
2. Joly, Y., Cabaret, D., Renevier, H. and Natoli, C. R., Phys. Rev. Lett. **82**, 2398 (1999).
3. Gaudry, E. *et al*., these proceedings.
4. Kokubun, J. *et al*., these proceedings.
5. Blöchl, P. E., Phys. Rev. B **24**, 17953 (1994).
6. Pickard, Ch., Ph.D Thesis, Univ. of Cambridge (1997).
7. Haydock, R., Heine, V. and Kelly, M. J., J. Phys. C: Solid State Phys. **5**, 2845 (1972), J. Phys. C: Solid State Phys. **8**, 2591 (1975).
8. Pfrommer, B., Raczkowski, D., Canning, A. and Louie, S. G., "PARAllel Total Energy Code", Lawrence Berkeley National Laboratory (with contributions from Mauri, F., Cote, M., Yoon, Y., Pickard, Ch. and Haynes, P.). For more information see www.nersc. gov/projects/paratec
9. Monkhorst, H. J. and Pack, J. D., Phys. Rev. B **13**, 5188 (1976).
10. Ceperley, D. M. and Alder, B. J., Phys. Rev. Lett. **45**, 566 (1980).
11. Wang, Y. and Perdew, J. P., Phys. Rev. B **44**, 13298 (1991). Perdew, J. P., Burke, K. and Ernzerhof, M., Phys. Rev. Lett. **77**, 3865 (1996).
12. Troullier, N. and Martins, J. L., Phys. Rev. B **43**, 1993 (1991).
13. Pickard, Ch. J. and Mauri, F., Phys. Rev. B **63**, 245101 (2001).
14. Newnham, R. E. and de Haan, Y. M., Z. Kristallogr. **117**, 235 (1962).
15. Natoli, C. R., Misemer, D. K. and Doniach, S., Phys. Rev. A **22**, 1104 (1980).
16. Cabaret, D., Sainctavit, Ph., Ildefonse, Ph. and Flank, A.-M., J. Phys.: Condens. Matter **8**, 3691 (1996).

Physica Scripta. Vol. T115, 134–135, 2005

Self-Consistent Non-Local Optical Potential for XANES

Keisuke Hatada, Maurizio Benfatto and Calogero R. Natoli

Laboratori Nazionali di Frascati, INFN, CP13,00044 Frascati, Italy

Received June 26, 2003; accepted November 4, 2003

Abstract

We have studied the performance of the non local optical potential as developed by Fujikawa, Hatada and Hedin [Phys. Rev. B **62**, 5387 (2000)] along the lines of the *GW* approximation for the photoelectron self-energy, in the case of the absorption spectrum of nickel hydrate ($Ni(OH_2)_6$). Comparison with the local Hedin-Lundqvist potential [J. Phys. C **4**, 2064 (1971)] shows a substantial improvement especially in the low energy region of the spectrum.

1. Introduction

Recently a method for utilising the near edge part of the absorption spectrum (XANES) for structural analysis has been proposed by Benfatto and Della Longa [3]. In this method hundreds of theoretical signals obtained by fully inverting the multiple scattering matrix are compared with the experimental data, until a best fit is obtained in the parameter space of the atomic positions. Very good results are obtained if in the course of the fitting procedure the optical potential used to generate the theoretical signal is taken as the real part of the local Hedin-Lundqvist (H-L) potential, whereas for the imaginary part, describing the damping of the excited photoelectron, a suitably parametrised functional form is fitted together with the structural parameters. Indeed the use of the imaginary part of the H-L potential usually leads to fits with bad *R*-factors. This is an indication that the fault might lie in the single plasmon pole approximation applied also to core electron densities, as usually done in the H-L potential. Following the theory for the optical potential based on the *GW* approximation for core electrons as developed by Fujikawa, Hatada and Hedin [1], we have studied the performance of this potential in a significant test case, namely a transition metal ions in water solution. The results of this investigation are hereby presented.

2. Theory

For sake of clarity we briefly describe the *GW* approximation to the photoelectron self-energy, referring the reader to the more complete treatment of this problem by Hedin and Lundqvist [4]. In this approximation the electron self-energy $\Sigma(\boldsymbol{r}, \boldsymbol{r}'; \omega)$ is expanded in terms of the screened Coulomb interaction $W = \epsilon^{-1}V$, where V is the bare Coulomb interaction and $\epsilon = 1 - VP$ is the dielectric response function of the system, while P is the polarization propagator. This expansion has a better convergence rate than that based on the bare Coulomb potential, so that one approximates the true $\Sigma(\boldsymbol{r}, \boldsymbol{r}'; \omega)$ by the first term of this expansion, namely $\Sigma_{GW}(\boldsymbol{r}, \boldsymbol{r}'; \omega) = GW$, where G is the electron propagator.

By splitting both the polarization and the electron propagator into a core and a valence part, so that $G = G^c + G^v$ and $P = P^c + P^v$, where the index c runs over the core states while v runs over both occupied and unoccupied valence states, and noting that the core polarization is substantially smaller than the valence one, Hedin and Lundqvist [4] obtained the following expression for Σ_{GW}:

$$\begin{aligned}\Sigma_{GW} &= GW \\ &= G^c W + G^v W^v P^c W^v + G^v W^v + \cdots \\ &= V^c_{ex} + \Sigma^c_{pol} + \Sigma^v + \cdots . \end{aligned} \tag{1}$$

Here the first term V^c_{ex} is the bare Hartree-Fock exchange potential from the core electrons, the second term Σ^c_{pol} is the screened polarization potential from the core and the last term Σ^v is the self-energy of the valence electrons. This latter, when calculated *via* the plasmon pole approximation for the electron wave function [4], can be safely approximated by an H-L local potential referred only to the valence density. This potential is amenable to an analytical form, which can be found for example in ref. [5].

For the second term (screened polarization potential) Fujikawa, Hatada and Hedin developed the method to calculate it. Using the Random Phase Approximation (RPA) to calculate the polarisation propagator they obtained the following expression:

$$[G^v W^v P^c W^v](\boldsymbol{r}, \boldsymbol{r}'; \omega) = \sum_l^{core} \int_{\varepsilon_F}^{\infty} \mathrm{d}\varepsilon_k G^v(\boldsymbol{r}, \boldsymbol{r}'; \omega - \omega_{kl})$$

$$\times \mathrm{Im}\langle c_l | W^v(\boldsymbol{r}; \omega_{kl}) G(\varepsilon_k) W^{v*}(\boldsymbol{r}'; \omega_{kl}) | c_l \rangle . \tag{2}$$

Here $\omega_{kl} = \varepsilon_k - \varepsilon_l$ is the energy gap between an empty valence level ε_k and a core level ε_l, whereas $W^v(\boldsymbol{r}; \omega)$ is the energy-dependent screened Coulomb interaction. Fig. 1 gives a diagrammatic expression for this quantity.

Following the conclusions of the paper by B. Holm and U. von Barth [6] we make a non-self-consistent approximation in the actual calculation of the self-energy, meaning that we calculate the electron propagator G_0 from the solution of the Dyson equation with $\Sigma = V^c_{ex} + \Sigma^v$, the polarization function from $P_0 = -iG_0G_0$ and the screened interaction from $W_0 = VW_0P_0V$, without performing the self-consistent loop. This approach seems to give better results for excitation energies than the complete

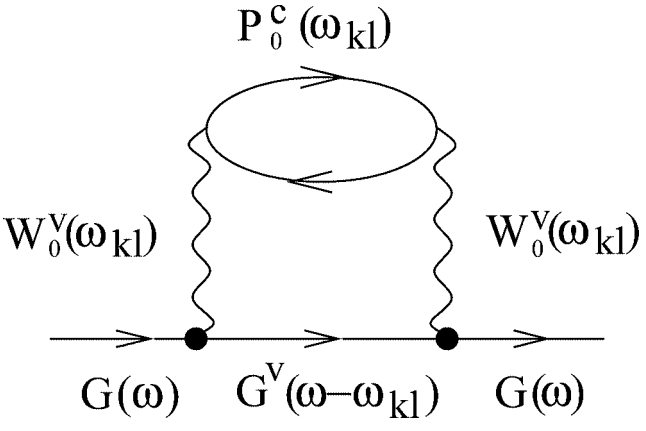

Fig. 1. Diagrammatic representation for Σ^c_{pol} $(\boldsymbol{r}, \boldsymbol{r}'; \omega) = [G^v W^v P^c W^v]$ $(\boldsymbol{r}, \boldsymbol{r}'; \omega)$.

self-consistent approach. For example in this latter the feature in Σ corresponding to the one plasmon excitation is lost. For a recent review on this problem, see also W. G. Aulbur *et al.* [7].

Moreover, following Fujikawa *et al.* [1] one can also neglect the energy dependence of the screening, so that $W^v(\boldsymbol{r};0)$ reduces to the static potential $e^{-q_{\rm TF}r}/r$, where q_{TF} is the Thomas-Fermi screening length. Finally, near the edge region, the core polarisation does not depend strongly on the photoelectron kinetic energy, so that in Eq. (2) we can put $\omega_{kl} = \varepsilon_k - \varepsilon_l = \varepsilon_{\rm F} - \varepsilon_l$, where $\varepsilon_{\rm F}$ is the Fermi energy. In this approximation the second factor in Eq. (2) can be calculated by closure giving:

$$[G^v W^v P^c W^v](\boldsymbol{r},\boldsymbol{r}';\omega) = \sum_l^{core} G^v(\boldsymbol{r},\boldsymbol{r}';\omega-\varepsilon_{\rm F}+\varepsilon_l)A_l(\boldsymbol{r},\boldsymbol{r}') \quad (3)$$

where

$$A_l(\boldsymbol{r},\boldsymbol{r}') = \sum_k^{unocc} W^v_{kl}(\boldsymbol{r};0)W^{v*}_{kl}(\boldsymbol{r}';0)$$

$$= \int W^v(\boldsymbol{r}-\boldsymbol{r}_1;0)W^v(\boldsymbol{r}'-\boldsymbol{r}_2;0)$$

$$\times[\delta(\boldsymbol{r}_1-\boldsymbol{r}_2)-\rho^{tot}(\boldsymbol{r}_1,\boldsymbol{r}_2)]\rho^c_l(\boldsymbol{r}_2,\boldsymbol{r}_1)\,d\boldsymbol{r}_1\,d\boldsymbol{r}_2.$$

Here $\rho^{tot}(\boldsymbol{r}_1,\boldsymbol{r}_2)$ is the density matrix relative the total density of the system, whereas $\rho^c_l(\boldsymbol{r}_2,\boldsymbol{r}_1)$ is the one relative to the density of the l core state. A further approximation is to use only the atomic part of the Green's function in Eq. (3), neglecting for the moment the scattering part, which is left to future developments.

Notice that this valence Green function does not take an imaginary part (therefore producing no damping) for all photoelectron energies ω below the first core excitation (in the case of $Ni(OH_2)_6$ system discussed below, this is the $3p$ core excitation of Ni, around 100 eV from the edge).

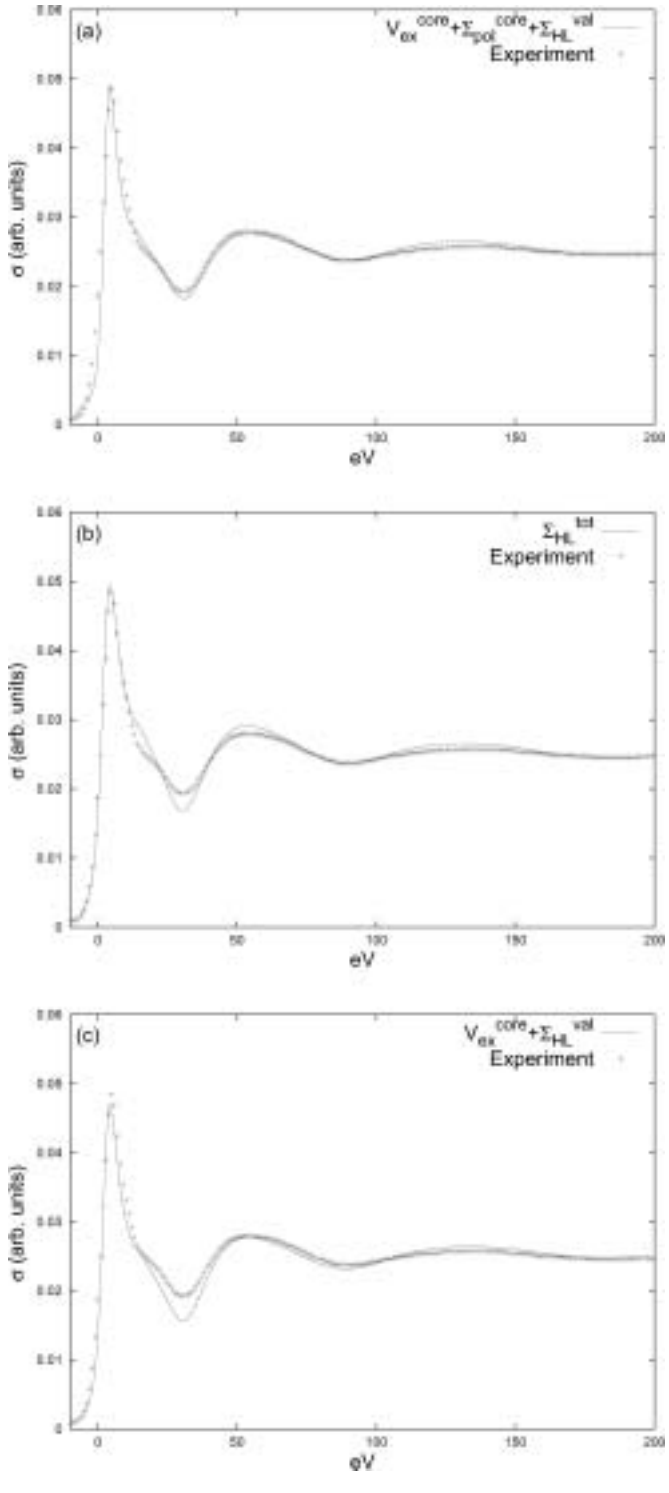

Fig. 2. Absorption cross section for $Ni(OH_2)_6$ at the Ni K-edge calculated for three types of optical potential, compared with the experimental data: the *GW* self-energy discussed in the present paper (panel (a)), the total H-L potential (panel (b)) and the *GW* self-energy less the core polarization potential (panel (c)).

3. Conclusions

We tested our new optical potential by calculating the absorption spectrum in a significant model system, namely the Ni K-edge of $Ni(OH_2)_6$ (Ni in water solution). Hydrogen atoms were included since they affect significantly the near edge structure. The geometrical and muffin-tin parameters were taken from an EXAFS analysis of the compound [8]. Fig. 2 shows the results for three different kinds of optical potential, namely: the *GW* self-energy discussed above (panel (a)), the total H-L potential (panel (b)) and the *GW* self-energy less the core polarization potential, *ie* $V^c_{ex} + \Sigma^v$ in Eq. (1). The calculated spectra were further convoluted with a Lorentzian function with a core hole width of 1.44 eV (full width half maximum of the Ni K-edge [9]).

In the comparison with experimental data the *ab initio* theoretical simulations were normalized to coincide with the experimental absorption spectrum at around 200 eV above the rising edge. This comparison shows that the best agreement is obtained with the *GW* potential, confirming in this particular case the validity of the *GW* model. Further investigation is planned in other model compounds.

Acknowledgment

We acknowledge useful discussions with Dr. K. Hayakawa.

References

1. Fujikawa, T., Hatada, K. and Hedin, L., Phys. Rev. B **62**, 5387 (2000).
2. Hedin, L. and Lundqvist, B., J. Phys. C **4**, 2064 (1971).
3. Benfatto, M. and Della Longa, S., J. Synchrotron. Rad. **8**, 1087 (2001).
4. Hedin, L. and Lundqvist, S., in "Solid State Physics," (edited by F. Seitz, D. Turnbull and H. Ehrenreich), (Academic Press, New York, 1969), Vol. 23 p. 1–181.
5. Natoli, C. R., Benfatto, M., Della Longa, S. and Hatada, K., J. Synchrotron. Rad. **10**, 26 (2003).
6. Holm, B. and von Barth, U., Phys. Rev. B **57**, 2108 (1998).
7. Aulbur, W., Jönsson, L. and Wilkins, J. W., in "Solid State Physics," (edited by F. Seitz, D. Turnbull and H. Ehrenreich), (Academic Press, New York, 2000), Vol. 54 p. 1–217.
8. D'Angelo, P. *et al*., J. Am. Chem. Soc. **124**, 1958 (2002).
9. Krause, M. O. and Oliver, J. H., J. Phys. Chem. Ref. Data **3**, 1979.

Physica Scripta. Vol. T115, 136–139, 2005

Ab Initio R-Matrix/MQDT Method for Near-Edge X-ray Absorption Fine Structure

Miyabi Hiyama and Nobuhiro Kosugi

Institute for Molecular Science, Myodaiji, Okazaki 444-8585, Japan

Received June 26, 2003; accepted November 4, 2003

PACS number: 33.20.Rm

Abstract

We have investigated the feasibility of an *ab initio* polyatomic R-matrix/MQDT (multichannel quantum defect theory) method using Gaussian type basis functions for bound and continuum states to analyze the near edge feature of molecules. Test molecules here are N_2, C_2H_2, and NO. The R-matrix/MQDT method is revealed to be indispensable for the Rydberg states with higher quantum numbers and continuum states, none of which can be described by using Gaussian type functions in the outer region from an appropriate boundary. The close-coupling calculation augmented with the correlation term, which is carried out for the inner region, is powerful to describe the valence states and the interchannel coupling in several core-ionized states.

1. Introduction

Near-edge X-ray absorption fine structure (NEXAFS or XANES) is characterized in two energy regions: below and above the ionization thresholds or photoabsorption edges ($E_{\rm th}$). Main features in NEXAFS arise from bound-state and continuum resonances. To calculate the NEXAFS feature, there are mainly two theoretical approaches: one is multiple-scattering (MS) [1] and the other is molecular orbital (MO)-like approaches. The latter includes density-functional-theory (DFT) and L^2 static-exchange (STEX) methods [2, 3]. The MO-like approach is based on the method to calculate bound states, and therefore has some deficiencies in description of the continuum. On the other hand, the MS approach flexibly describes the continuum as multiple scattering states of a photoelectron, but needs artificial $E_{\rm th}$ shift to get bound-state resonances as multiple scattering states. Furthermore, the coupled-channel, or multichannel, MS approach is developed to treat several $E_{\rm th}$ cases accompanying shakeup and shakedown excitations [4].

In recent sophisticated experiments, higher-lying Rydberg states near $E_{\rm th}$, vibrational fine structures, and multiple excitations have been resolved in the inner-shell spectroscopy of small molecules (for example, refs. [5, 6]). From a theoretical point of view, we have to treat channel couplings involving not only open channels but also closed channels such as multiply excited states. The previous multichannel MS approach [4] is not appropriate for this kind of multiple excitation problems. More accurate scattering approaches are necessary to explain such highly-resolved NEXAFS features.

The ionized states are regarded as $N-1$ electron correlated bound states Ψ_j^{N-1}, namely, target states in terms of scattering, coupled with a continuum electron η_k. The multiply excited states are N electron correlated bound states Ψ_i^N. In the region far from the ion core, the continuum electron gives only long-range electrostatic and polarization interactions; on the other hand, short-range interactions such as electron correlation and exchange are also important in the coupled Ψ_j^{N-1} with η_k and the correlated bound states Ψ_i^N. In solving molecular ionization and excitation problems, the R-matrix approach is one of the most promising approaches, which is an *ab initio* approach on an equal level with the complex Kohn and Schwinger variational methods [7]. In the R-matrix method [8], electron configuration space is divided into two parts, the inner and outer regions. The inner region is defined by the R-matrix radius R_0, which is large enough that any $N-1$ electron correlated target function Ψ_j^{N-1} is completely enveloped by the sphere $r < R_0$. In the inner region, η_k is determined in the close coupling with Ψ_j^{N-1}, which is augmented with Ψ_i^N. In the outer region ($r > R_0$), the continuum and the higher Rydberg orbitals are described in an appropriate asymptotic form, e.g. Coulomb function in the case of electron-cation scattering or photoionization/photoexcitation.

In the present work, we investigate feasibility of the polyatomic R-matrix/MQDT method (R-matrix method combined with multi channel quantum defect theory) [9] in the inner-shell excitation, where we can use Gaussian type basis functions in the inner region. For the inner part, the R-matrix code including *ab initio* configuration interaction approaches developed by Tennyson's group [12] has been used in the R-matrix/MQDT method. The R-matrix/MQDT has be successful to get diabatic potential energy curves of the Rydberg series converging to some excited ion cores by improvement on the outer part of the R-matrix method [9]. Thus, the polyatomic R-matrix/MQDT method is a promising one in the calculation of NEXAFS of polyatomic systems. In the present work, we show R-matrix/MQDT results for some simple molecules: Rydberg states in N_2, Rydberg and valence states in C_2H_2, and shape resonances of NO radical. One of the purposes of the present work is improvement of *ab initio* CI part in R-matrix/MQDT. The close-coupling calculation code for the inner region is incorporated into the *ab initio* SCF-CI code GSCF3 [10, 11] for the inner-shell excitation and ionization, which has been developed by one of the present authors (NK). In the present stage of GSCF3 implementation the Gaussian integrals including the tail integration over the $r > R_0$ region were taken from the UK molecular R-matrix codes [12]. The outer-region and MQDT codes have been developed by the other author (MH). The R-matrix radius R_0 chosen is 10 a.u.

2. Theoretical background

2.1. *R-matrix method*

In the R-matrix method, the N electron total wavefunction $\Psi^N(E)$ in the inner region is expanded by energy-dependent expansion coefficients $A_P(E)$ and energy-independent basis functions Ψ_P^N,

e-mail: miyabi@ims.ac.jp, kosugi@ims.ac.jp

$$\Psi^N(E) = \sum_P A_P(E)\Psi_P{}^N. \quad (1)$$

In the case of photoionization and photoexcitation, transition dipole matrix elements $D(E)$ from the ground state $\Psi_G{}^N$ are obtained as follows:

$$D(E) = \langle \Psi^N(E)|T|\Psi_G{}^N\rangle = \sum_P A_P(E)\langle \Psi_P{}^N|T|\Psi_G{}^N\rangle. \quad (2)$$

The correlated N electron basis function $\Psi_P{}^N$ is described by the following "close coupling plus correlation (CCPC)" form:

$$^S|\Psi_P{}^N\rangle = \sum_{jk} c_{jk}\,{}^S|\Psi_j{}^{N-1},\ \eta_k\rangle + \sum_{jt} c_{jt}\,{}^S|\Psi_j{}^{N-1},\ \varphi_t\rangle + \sum_i c_i\,{}^S|\Psi_i{}^N\rangle. \quad (3)$$

In the R-matrix method, the CCPC equation is defined only in the inner region. $^S|\Psi_j{}^{N-1}, \eta_k\rangle$ indicates an antisymmetrized spin and symmetry (denoted by S) adapted product of the corresponding $N-1$ electron correlated state function and the one electron continuum function for open channels. $^S|\Psi_j{}^{N-1}, \varphi_t\rangle$ is a similar product for closed channels; φ_t is one of square-integrable (L^2) diffuse functions which are not used in either $\Psi_j{}^{N-1}$ or $\Psi_i{}^N$. The third term $\Psi_i{}^N$ describes the N electron correlation in multiply valence excited states and intruder and dissociative states, which have different electron correlation and orbital relaxation effects from those of the ionized state $\Psi_j{}^{N-1}$. At each scattering energy E, the R-matrix is computed on the boundary ($r = R_0$), and various properties are obtained by using the R-matrix.

In the case of core excitation, the third term $\Psi_i{}^N$ involves core-to-valence excited states. The second term involves core-to-Rydberg excited states with an ion core $\Psi_j{}^{N-1}$. In the R-matrix method, the CCPC equation is solved only in the inner region ($r < R_0$). Therefore, we have to evaluate contributions to the Hamiltonian matrix in solving eq. (3) from outside the R-matrix sphere ($r > R_0$), and subtract them from the all-space Hamiltonian matrix ($r < R_0$ and $r > R_0$) [13, 14]. In the polyatomic R-matrix calculation, Gaussian type basis functions (GTF's) are used [15] to describe both the target orbitals and continuum (Coulomb) functions [16].

2.2. *Quantum chemical approach*

The $N-1$ and N electron eigensolutions $\Psi_j{}^{N-1}$ and $\Psi_i{}^N$ are obtained by standard *ab initio* CI calculations over configuration state functions (CSF's) or Slater determinants, $\Phi_r{}^{N-1}$ and $\Phi_s{}^N$ expanded by the L^2 basis functions:

$$\Psi_j{}^{N-1} = \sum_r d_{jr}\Phi_r{}^{N-1}, \qquad \Psi_i{}^N = \sum_s d_{is}\Phi_s{}^N, \quad (4)$$

where well-balanced treatment of the $N-1$ and N electron systems within the framework of the same one electron basis set (molecular orbital set) is essential to get reliable excitation and ionization energies to avoid underestimation and overestimation ("over correlation" [17]).

Decoupling by eq. (4) gives a compact description for the bound-state contributions in the close coupling eq. (3). The "contracted CI" approach removes the need for redundant re-diagonalization of the large-scale CI Hamiltonian matrix [18]. The contracted CI approach is achieved by the one-to-one correspondence between the Slater determinants expanding the $N-1$ and N electron systems to satisfy the phase matching. Tennyson [18] has resolved all phase ambiguities by using the orbital ordering convention in ALCHEMY [19]. A similar correct treatment of the phase matching has been developed to evaluate the monopole matrix element between the ground and ionized states [20]. Previous methods such as the prototype CI method [19, 21] and the dummy orbital method [22, 23] sometimes cause serious phase mismatch [18], depending on the orbital ordering convention in the CSF generation of the $N-1$ and N electron systems.

The continuum functions η_k are orthogonalized to the orbital functions used in the second and third terms *for convenience*. However, the orthogonality constraint for the continuum functions leads to physically incorrect results, especially when many virtual orbitals are used in CI expansions (4). $\Psi_i{}^N$ and $\Psi_j{}^{N-1}$ in eq. (3) should allow for relaxation of the orthogonalized continuum orbitals as well as polarization of the target states. The orbital relaxation and polarization effects can be incorporated in eq. (3) as long as enough numbers of $\Psi_i{}^N$ and $\Psi_j{}^{N-1}$ are included in eq. (3) or original CI expansions eq. (4) are optimized directly in eq. (3). However, in case it is impractical from a computational point of view, it is better to add some effective electron configurations for orbital relaxation and polarization to $\Psi_i{}^N$ and $\Psi_j{}^{N-1}$ in eq. (3). These additional configurations are not eigensolutions and are unphysical "pseudo" states [24].

In the CCPC equation (3), the second term can generally be incorporated into the third term within the same L^2 manifold. Furthermore, it is also possible to incorporate the second term ($< E_{\rm th}$) into the first term ($> E_{\rm th}$); that is, the static exchange (STEX) method for both the bound and continuum state as follows:

$$|\Psi_P{}^N\rangle = \sum_j \left| \Psi_j{}^{N-1}, \left(\sum_k c_{jk}\eta_k + \sum_t c_{jt}\varphi_t \right) \right\rangle. \quad (5)$$

The widely-used STEX method corresponds to single excitation CI to the virtual orbital space for both continuum and bound-state excitation, keeping a specified Hartree-Fock description of the ion core or fixing a hole in a specified orbital; that is the Hartree-Fock (HF) based STEX approach. It may be called SC-SRSTEX (single-channel single-reference STEX), which is also obtained with the hole or V^{N-1} potential method to improve the virtual molecular orbitals [25]. On the other hand, eq. (5) may be generally called MC-MRSTEX (muliti-channel multi-reference STEX); however, it is not so easy to take into account the orthogonality relaxing through mixing with the virtual orbitals used in the correlated CI description for the target state $\Psi_j{}^{N-1}$ [26].

2.3. *MQDT method*

The STEX approach based on the GTF expansion is ill-behaved for Rydberg states with higher principal quantum numbers due to linear dependence of diffuse basis functions. Furthermore, in the R-matrix method, the higher-lying Rydberg states are not defined within the inner region ($r < R_0$), but only the lowest s, p, and d states (and sometimes the second lowest s state as well) are defined. For the higher-lying Rydberg states we need another approach. In the present work we use the R-matrix/MQDT approach to evaluate quantum defects. The asymptotic formula of the wave function $\Psi^N(E)$ in eq. (1) is represented by the linear combination with Coulomb functions. At the R matrix radius, $\Psi^N(E)$ is written by

$$\Psi^N(E) = f - g\,K, \quad (6)$$

where f and g are the regular and irregular Coulomb functions, respectively. The K matrix in eq. (6) is related to the R matrix as follows:

$$K = (g - R\mathrm{d}g/\mathrm{d}r)^{-1}(f - R\mathrm{d}f/\mathrm{d}r). \quad (7)$$

In the R-matrix/MQDT method, the K matrix can be obtained at any energy, because both positive and negative Coulomb functions [27] are used in f and g in eq. (7). The MQDT method is based on a single target state [28]; on the other hand, the R-matrix/MQDT method can take into account interaction among multiple target states through the R matrix.

3. Results and Discussion

3.1. *Rydberg states in the 1s ionization of N_2 and C_2H_2*

Relatively large core-valence exchange interaction between the adjacent atoms results in observable $1s\sigma_g$-σ_u splittings in N_2 and C_2H_2 [29]. Rydberg transitions from the Σ_g ground state have two symmetries, Σ_u and Π_u. Thus, there are four channels; $1s\sigma_g \rightarrow n\sigma_u(\Sigma_u)$, $n\pi_u(\Pi_u)$ and $1s\sigma_u \rightarrow n\sigma_g(\Sigma_u)$, $n\pi_g(\Pi_u)$. N_2 has $\pi^*(1\pi_g{}^*)$ and $\sigma^*(3\sigma_u{}^*)$ valance orbitals. C_2H_2 has $\pi^*(1\pi_g{}^*)$ and $\sigma^*(3\sigma_u{}^*, 4\sigma_g{}^*, 4\sigma_u{}^*)$ valance orbitals. The lowest 1s excited states are the $1s\sigma_u \rightarrow 1\pi_g{}^*$ excitations, which are observed below the Rydberg states. It is generally known that the term value of the lowest Rydberg state with s character is around 4 eV. In N_2 and C_2H_2 the term values of the $1s \rightarrow \pi^*$ excitations are 8.9 eV and 5.4 eV. On the other hand, in C_2H_2, the term values of the lowest $3\sigma_u$ excited state is predicted to be 3.2 eV [30].

Diffuse functions used for the STEX calculation of the Rydberg states are taken from ref. [31] (n_s and n_d = 2.0, 2.5, 3.0, 3.5, 4.0; n_p = 2.0, 2.5, 3.0, 3.5, 4.0, 4.5) and augmented with one s and two d functions (ζ_s = 0.06, ζ_d = 1.335, 0.288). The core and valence basis functions (721/52/1*) for C and N and (42) for H are taken from the (73/7/1*) and (6) contracted Gaussian-type functions of Huzinaga *et al.* [32]. In the R-matrix calculation the continuum functions were taken from ref. [16]. The valence CI in the close-coupling calculation was based on the CAS (complete active space)-type description in the $3\sigma_g$, 2-$3\sigma_u$, $1\pi_u$, and $1\pi_g$ orbital manifold for N_2 and in the 3-4σ_g, 2-4σ_u, $1\pi_u$, and $1\pi_g$ orbital manifold for C_2H_2.

In the case of N_2, some orthogonalization procedures are compared. First of all, the unoccupied valence orbitals $3\sigma_u{}^*$ and $1\pi_g{}^*$ are optimized within the SRSTEX method using the relaxed Hartree-Fock occupied orbitals with no diffuse function. The other unoccupied orbitals are called virtual orbitals. The diffuse functions to describe Rydberg states should be orthogonal to the occupied and unoccupied orbitals (and virtual orbitals if they are used in the CCPC calculation). Some orthogonalization methods are compared in table I, which shows the term value for the Rydberg state. In STEX (1), the $n\mathrm{d}\pi_g$ Rydberg states are unphysical ones, and the $1\pi_g{}^*$ state was not obtained within the orbital manifold orthogonalized to all the diffuse functions. The $n\mathrm{d}\pi_g$ Rydberg states are correctly obtained after orthogonalization to the $1\pi_g{}^*$ orbital in STEX (2) and (3). On the other hand, the $np\sigma_u{}^*$ Rydberg states are correctly obtained in STEX (1) and (2), but are unphysical for orthogonalization to the $3\sigma_u{}^*$ orbital in STEX (3). The present results indicate that diffuse functions describing the Rydberg state should be orthogonalized to unoccupied valence orbitals corresponding to bound state resonances below the Rydberg region, but should not be orthogonalized to either unoccupied valence orbitals corresponding to continuum resonances or virtual orbitals.

Table I shows that the R-matrix/MQDT method is applicable to higher-lying Rydberg states than 5s, 5p and 4d. The STEX method is not applicable because of linear dependence in diffuse Gaussian-type functions. The CCPC calculation (eq. (3)) in the inner region ($r < R_0$) was found not to be applicable to higher-lying Rydberg states than 5s, 4p and 3d. The same behavior was found in C_2H_2 (Table II). As discussed in ref. [30], the lowest 1s-$3\sigma_u{}^*$ excited state is observed near the 1s-3s Rydberg state. The STEX calculation fails in its prediction, but the CCPC calculation predicts correctly the $3\sigma_u{}^*$ excited state and the $np\sigma_u$ Rydberg series.

Table I. *Term values in eV obtained with the STEX and R-matrix/MQDT methods for N 1s-Rydberg excitation in N_2.*

	STEX(1)	STEX(2)	STEX(3)	STEX(4)	Exp. [33]	R/MQDT
$1\pi_g{}^*$(V)		8.094	8.094	7.997	~8.9	7.457
$3s\sigma_g$	3.446	3.446	3.446	3.444	3.695	3.764
$4s\sigma_g$	1.618	1.618	1.618	1.617	1.507	1.666
$5s\sigma_g$	0.895	0.895	0.895	0.896	0.853	0.894
$6s\sigma_g$					0.562	0.547
$7s\sigma_g$					0.403	0.378
$8s\sigma_g$						0.277
$3d\sigma_g$	1.434	1.434	1.434	1.437		1.655
$4d\sigma_g$	0.799	0.799	0.799	0.800		0.737
$5d\sigma_g$						0.464
$6d\sigma_g$						0.339
$3d\pi_g$	2.020	1.456	1.456	1.444	1.51	1.471
$4d\pi_g$	1.117	0.799	0.799	0.793	0.86	0.657
$5d\pi_g$					0.556	0.436
$6d\pi_g$					0.407	0.312
$3p\sigma_u$	2.424	2.424	1.764	2.442	2.604	2.767
$4p\sigma_u$	1.172	1.172	0.931	1.181	1.283	1.177
$5p\sigma_u$	0.695	0.695	0.566	0.699		0.678
$6p\sigma_u$						0.449
$7p\sigma_u$						0.320
$3p\pi_u$	2.602	2.602	2.602	2.592	2.803	2.912
$4p\pi_u$	1.241	1.241	1.241	1.238	1.314	1.080
$5p\pi_u$	0.728	0.728	0.728	0.727	0.776	0.659
$6p\pi_u$					0.504	0.440
$7p\pi_u$					0.377	0.315

(1) The STEX calculation using only the diffuse functions orthogonalized to only the occupied orbitals 1-$3\sigma_g$, 1–$2\sigma_u$ and $1\pi_u$.
(2) The STEX calculation using only the diffuse functions orthogonalized to all the occupied orbitals and the unoccupied valence orbital $1\pi_g$.
(3) The STEX calculation using only the diffuse functions orthogonalized to all the occupied orbitals and the unoccupied valence orbitals $3\sigma_u$ and $1\pi_g$.
(4) The fully-relaxed STEX calculation using the core, valence, and virtual orbitals and additional diffuse orbitals.

3.2. *Exchange splitting in $N1s \rightarrow \sigma^*$ shape resonances of NO*

NO has the $X^2\Pi$ ground state with one more electron than N_2 and CO, but has similar π^* and σ^* valence orbitals. The $1s \rightarrow \pi^*$ excitation results in two π^* electrons and three different electronic states coupled with the 1s electron [35]. On the other hand, the $1s \rightarrow \sigma^*$ excitation results in one σ^* and one π^* electron and two dipole-allowed $^2\Pi$ states coupled with the 1s electron. The $^2\Pi$ $1s \rightarrow \sigma^*$ excited states are characterized by the singlet and triplet couplings between two of the three open-shell electrons and the doublet coupling with the remaining electron. In the N 1s excitation, the σ^* and π^* electrons have a possibility of strong coupling with the triplet and singlet spins as discussed in [36]. The N $1s \rightarrow \sigma^*$ excited states of NO are the continuum, shape resonances located above the two ionization thresholds, which correspond to triplet (T) and singlet (S) target states through coupling of the 1s and π^* electrons. Therefore, the σ^* electron in each continuum resonance is auto-ionized to both the T- and

Table II. *Term values in eV obtained with the STEX and R-matrix/MQDT methods for the C 1s-Rydberg and valence (V) excitation in C_2H_2.*

	STEX	Exp. [34]	R-matrix/ MQDT
$1\pi_g^*$(V)	4.165	~5.5	4.476
$3\sigma_u^*$(V)		~3.2	3.228
$3s\sigma_g$	3.054	3.40	3.504
$4s\sigma_g$	1.383	1.53	1.416
$5s\sigma_g$	0.791	0.90	0.952
$6s\sigma_g$			0.612
$7s\sigma_g$			0.429
$8s\sigma_g$			0.313
$3d\sigma_g$	1.851		1.228
$4d\sigma_g$	0.896		0.759
$5d\sigma_g$			0.509
$6d\sigma_g$			0.364
$3d\pi_g$	1.372	1.51	1.320
$4d\pi_g$	0.748	0.60	0.635
$5d\pi_g$		0.43	0.426
$6d\pi_g$		0.31	0.307
$3p\sigma_u$	2.671	2.31	2.380
$4p\sigma_u$	1.248	1.22	1.186
$5p\sigma_u$	0.730	0.74	0.678
$6p\sigma_u$		0.44	0.448
$7p\sigma_u$			0.319
$3p\pi_u$	2.227	2.39	2.513
$4p\pi_u$	1.119	1.15	1.238
$5p\pi_u$	0.672	0.67	0.702
$6p\pi_u$		0.43	0.461
$7p\pi_u$		0.31	0.328

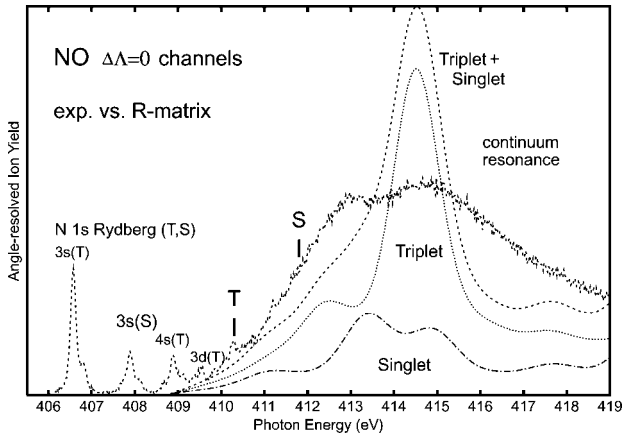

Fig. 1. R-matrix results for the $^2\Pi \leftarrow X\ ^2\Pi$ excitation (parallel transition, $\Delta\Lambda = 0$) in the NO N 1s region in comparison with 0° ion yield spectra (parallel to the linear polarization plane of the incident photon) [37] . Ionization channels to the triplet and singlet target states are decomposed.

S-target states. In terms of the R-matrix method, the σ^* continuum electron has exchange interaction with the π^* and 1s electrons in the inner region, but does not have exchange interaction with either π^* or 1s electron in the outer region. Figure 1 shows that the R-matrix results for the $^2\Pi \leftarrow X\ ^2\Pi$ excitation in the NO N 1s continuum region. The CI space and basis set were the same as in N_2. Ionization channels to the triplet and singlet target states are decomposed. This shows that the lower-energy continuum resonance (σ^* shape resonance) has more singlet target contribution and the higher-energy continuum resonance has more triplet target contribution. Thus, the R-matrix/MQDT approach is proved to be applicable to coupled-channel continuum resonances in the mutiple-target system such as singlet and triplet ionizations in NO.

Acknowledgements

The authors would like to thank Prof. J. Tennyson for fruitful discussion of the molecular R-matrix algorithm. M.H. is also grateful to Prof. M. S. Child for encouraging her to establish the R-matrix/MQDT approach during a stay in his group. M.H. and N.K. acknowledge financial support by the Grant-in-Aid for JSPS fellowship 1304814 and for Scientific Research (B) 15350017, respectively, from the Ministry of Education, Culture, Sports, Science and Technology.

References

1. Rehr, J. J. and Ankudinov, A. L., J. Synchrotron Rad. **8**, 61 (2001).
2. Triguero, L., Pettersson, L. and Ågren, H., Phys. Rev. B **58**, 8097 (1998).
3. Ågren, H., Carravetta, V., Vahtras, O. and Pettersson, L., Theoret. Chem. Acc. **97**, 14 (1997).
4. Natoli, C. R. and Benfatto, M., in "Core-Level Spectroscopy in Condensed Systems", (ed. J. Kanamori and A. Kotani), (Berlin, Springer, 1988) p. 184.
5. Shigemasa, E., Gejo, T., Nagasono, T., Hatsui, T. and Kosugi, N., Phys. Rev. A **66**, 022508 (2002).
6. Feifel, R. *et al.*, Phys. Rev. A **67**, 032504 (2002).
7. Huo, W. M. and Gianturco, F. A. (eds), "Computational Methods for Electron-Molecule Collisions", (New York, Plenum, 1995).
8. Burke, P. G. and Berrington, K. A., "Atomic and Molecular Processes: an R-Matrix Approach", (Bristol, IOP Publishing, 1993).
9. Hiyama, M. and Child, M. S., J. Phys. B **35**, 1337 (2002).
10. Kosugi, N. and Kuroda, H., Chem. Phys. Lett. **74**, 490 (1980).
11. Kosugi, N., Theoret. Chim. Acta **72**, 149 (1987).
12. Morgan, L. A., Tennyson, J. and Gillan, C. J., Comput. Phys. Commun. **114**, 120 (1998).
13. Nestmann, B. M., Nesbet, R. K. and Peyerimhoff, S. D., J. Phys. B **24**, 5133 (1991).
14. Morgan, L. A., Gillan, C. J., Tennyson, J. and Chen, X., J. Phys. B. **30**, 4087 (1997).
15. Nestmann, B. M. and Peyerimhoff, S. D., J. Phys. B **23**, L773 (1990).
16. Faure, A., Gorfinkiel, J. D., Morgan, L. A. and Tennyson, J., Comput. Phys. Commun. **144**, 224 (2002).
17. Tennyson, J., J. Phys. B **29**, 6185 (1996).
18. Tennyson, J., Comput. Phys. Comm. **100**, 26 (1997).
19. Liu, B. and Yoshimine, M., J. Chem. Phys. **74**, 612 (1981).
20. Kosugi, N. and Kuroda, H., Chem. Phys. Lett. **87**, 365 (1982).
21. Morgan, L. A. and Tennyson, J., J. Phys. B **26**, 2429 (1993).
22. Orel, A. E., Rescigno, T. N. and Lengsfield III, B. H., Phys. Rev. A **44**, 4328 (1991).
23. Tennyson, J., J. Phys. B **29**, 1817 (1996).
24. Bartschat, K., Hudson, E. T., Scott, M. P., Burke, P. G. and Burke, V. M., J. Phys. B **29**, 115 (1996).
25. Iwata, S., Kosugi, N. and Nomura, O., Jpn. J. App. Phys. **17S2**, 109 (1978).
26. Hiyama, M. and Kosugi, N., unpublished work.
27. Hiyama, M. and Child, M. S., J. Phys. B **34**, 3935 (2001).
28. Greene, C. H. and Jungen, Ch., Adv. Atom. Mol. Phys. **21**, 51 (1985).
29. Kosugi, N., J. Electron Spectrosc. **137–140**, 335 (2004).
30. Adachi, J., Kosugi, N., Shigemasa, E. and Yagishita, A., Chem. Phys. Lett. **309**, 427 (1999).
31. Kaufmann, K., Nager, Ch. and Jungen, M., Chem. Phys. **95**, 385 (1985).
32. Huzinaga, S. *et al.*, "Gaussian Basis Sets for Molecular Calculations", (Elsevier, Amsterdam, 1984).
33. Masuda, S., Gejo, T., Hatsui, T., Shigemasa, E. and Kosugi, N., unpublished.
34. Masuda, S., Gejo, T., Hiyama, M. and Kosugi, N., J. Electron Spectrosc, to be published (in press).
35. Kosugi, N., Adachi, J., Shigemasa, E. and Yagishita, A., J. Chem. Phys. **97**, 8842 (1992).
36. Kosugi, N., Chem. Phys. **289**, 117 (2003).
37. Gejo, T., Shigemasa, E. and Kosugi, N., unpublished.

Physica Scripta. Vol. T115, 140–142, 2005

Temperature Dependence of Local Structure of Ge Impurity in Si (001) Thin Film Probed by Multiple-Scattering XAFS

Shiqiang Wei[1*], Zhihu Sun[1], Hiroyuki Oyanagi[2], Wenjie Zhong[1] and Dongliang Chen[1]

[1]National Synchrotron Radiation Laboratory, University of Science and Technology of China, Hefei 230029, P. R. China
[2]Photonics Research Institute, National Institute of Advanced Industrial Science and Technology, AIST Tsukuba Central 2, 1-1-1 Umezono, Tsukuba 305-8568, Japan

Received June 26, 2003; accepted November 5, 2003

PACS numbers: 61.10.Ht, 61.72.Tt, 68.55.Ln

Abstract

The local structure of dilute Ge impurity in Si thin film has been studied by grazing incidence fluorescence XAFS in the temperature region of 20 ∼ 300 K. Multiple-scattering XAFS (MS-XAFS) data analysis is used to fit the local structures around Ge atoms from the first to third coordination shells for the $Ge_{0.006}Si_{0.994}$ thin film. The results indicate that the bond length $R_{Ge\text{-}Si}$ of the first, secong and third Ge-Si shell is 2.38, 3.83 and 4.49 Å for the $Ge_{0.006}Si_{0.994}$ thin film, respectively. The $R_{Ge\text{-}Si}$ of the first Ge-Si shell in the $Ge_{0.006}Si_{0.994}$ thin film is 0.03 Å larger than that of the first Si-Si shell in Si crystal, and the $R_{Ge\text{-}Si}$ of the second and third Ge-Si shells in the $Ge_{0.006}Si_{0.994}$ thin film are almost equal to those of the corresponding Si-Si shells in Si crystal. These results imply that the local lattice deformation exists in the first nearest neighbor around Ge atoms and the lattice distortion relieves in the second and third Ge-Si shells for the $Ge_{0.006}Si_{0.994}$ thin film. Furthermore, the results show that the Debye-Waller factor ${\sigma_1}^2$ of the first Ge-Si shell of the $Ge_{0.006}Si_{0.994}$ thin film increases slightly from 0.0018 to 0.0020 Å^2 in the temperature region between 20 and 100 K, and rises strongly to 0.0040 Å^2 at 300 K. The bond angles $\theta_{Ge\text{-}Si\text{-}Si}$ at all temperatures are about 108.1°, which is close to the value of tetragonal network of 109.47°. The bond angle variation $\Delta\theta_{Ge\text{-}Si\text{-}Si}$ is about ±3.4°, ±3.5° and ±5.0° at the temperatures of 20, 100 and 300 K, respectively, indicating a weak tetragonal distortion around the Ge atoms in the $Ge_{0.006}$ $Si_{0.994}$ thin film.

1. Introduction

For the last decade, the crystalline Ge-Si alloys and hetero-structural Ge-Si superlattices have attracted increasing attention, due to their significantly improved electronic properties with relatively simple incorporation into existing Si technology [1]. The 4.2% mismatch for the lattice constants between Ge and Si crystals leads to significant strain during the epitaxial growth of Ge-Si thin films. This changes the band structures and electronic properties relative to that of pure Ge and Si [2], creating the potential for band gap engineering in Ge-Si device technology.

Understanding the structural parameters of Ge-Si thin films is favorable to calculate the band structures of these Ge-Si quantum systems [3]. So far, a lot of XAFS studies have been done to determine the local structures in Ge-Si system [4–6], however, they have paid attention to only the local structure of the first shell around the Ge atoms, but not the local structures of their higher shells. In order to well determine the tetragonal distortion of the unit cell in a Si thin film doped by Ge atoms, the local structures for the first three shells of Ge atoms can be expected to provide an opportunity to investigate the lattice distortion around Ge atoms in the Si host matrix [7]. Moreover, the structural information of high shells is useful to determine both bond length and bond angle accommodation of strain [8]. More recently, Pascarrelli *et al.* [9], Tormen *et al.* [10], and we [11] have used the multiple-scattering (MS) XAFS to study the local structures of the high shells for III-V semiconductors with the zinc-blende structure.

In this paper, MS-XAFS analysis is performed to study the local structures of the first three shells around Ge atoms for the $Ge_{0.006}Si_{0.0994}$ thin film in the temperature range of 20 and 300 K. We aim to investigate the tetragonal distortion and the strained distribution in the Si thin film induced by the dilute Ge impurity. The temperature dependence for the local structure of Ge impurity in Si(001) thin film is also presented.

2. Experiment

The $Ge_{0.006}Si_{0.0994}$ thin film sample was prepared by molecular beam epitaxy (MBE), which was described elsewhere [12]. Boron-doped Si (001) substrate (10 Ωcm) was chemically cleaned by the Shiraki method prior to the insertion to the vacuum. The 2 μm-thick heteroepitaxial $Si_{1-x}Ge_x(x = 0.006)$ thin film was deposited on the substrate of Si (001) at 673 K in a MBE growth chamber with a base pressure 1×10^{-10} Torr.

XAFS measurements were performed at BL-13B of the Photon Factory of National Laboratory for High Energy Physics (PF, KEK). The electron beam energy was 2.5 GeV and the maximum stored current was 400 mA. The Ge K-edge XAFS spectra of the $Ge_{0.006}Si_{0.0994}$ thin film were recorded at the temperatures of 20, 100 and 300 K in a fluorescence mode with a grazing incidence geometry. The detailed experiment procedure can be found elsewhere [4]. XAFS data were analyzed by USTC-XAFS2.0 software package compiled by Zhong and Wei according to the standard procedures [13].

3. Results and Discussions

Figure 1 shows the normalized Ge K-edge EXAFS function $\chi(k)$ of the $Ge_{0.006}Si_{0.0994}$ thin film measured in the temperatures of 20, 100 and 300 K. It can be observed that the oscillation intensity of $Ge_{0.006}Si_{0.0994}$ thin film is higher at the low k region with the maximum at about $k = 4$ Å^{-1}, then it damps very fast with the k increase. This characteristic indicates that the Ge atoms in the $Ge_{0.006}Si_{0.0994}$ thin film are predominantly surrounded by the light element Si, which has been confirmed by our previous work [4].

The solid lines in Figure 2 show the radial structural functions (RSF) of the $Ge_{0.006}Si_{0.0994}$ thin film obtained from Fourier transforming their $k^2\chi(k)$ spectra. Three peaks located at about 2.0, 3.4 and 4.1 Å are related to the first, second and third coordination shells of Ge atoms, respectively. For the $Ge_{0.006}Si_{0.0994}$ thin film measured at 300 K, the peak intensity of the first shell of Ge atoms decreases to about 80% of that measured at 20 K while the peak magnitudes of the higher shells decrease to about 50% of those measured at 20 K.

*Correspondent: Shiqiang Wei, E-mail: sqwei@ustc.edu.cn

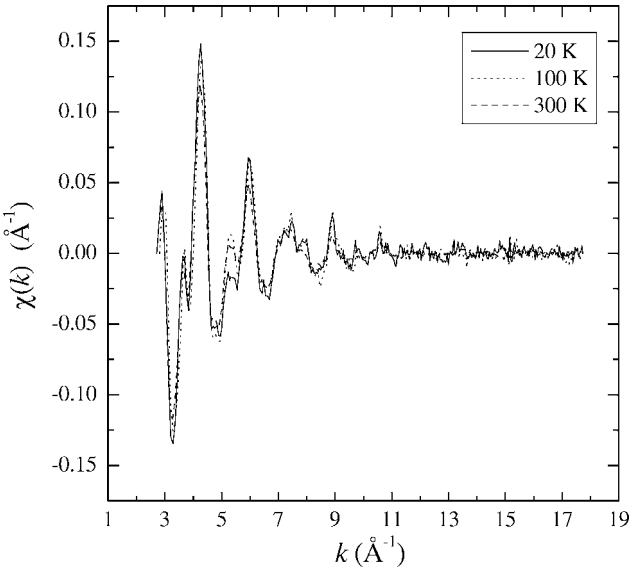

Fig. 1. Ge K-edge $\chi(k)$ EXAFS oscillation function for $Ge_{0.006}Si_{0.994}$ thin film recorded at 20, 100 and 300 K.

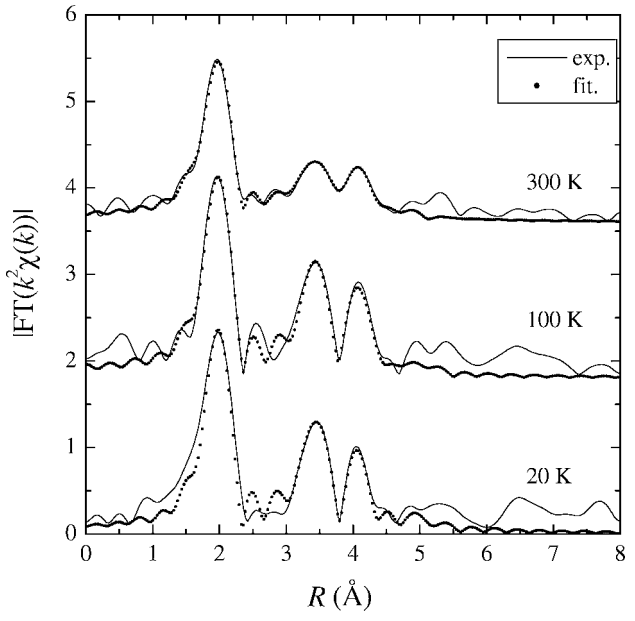

Fig. 2. The radial structural function by fourier transforming $k^2\chi(k)$ for $Ge_{0.006}Si_{0.994}$ thin film recorded at 20, 100 and 300 K: experimental (solid line) and fitting (dotted line).

For quantitative analysis, the least-squares curve fit including the multiple-scattering contributions was performed in *R*-range of [1.0, 4.8] Å using the FEFFIT code [14]. The theoretical magnitudes and phase-shifts of all the single-scattering (SS) and MS paths in the first three shells were calculated by FEFF7 [15]. In the fitting procedure, the coordination numbers were fixed to 4, 12 and 12 for the first, second and third shells, respectively. The most important MS path is the triangular double-scattering path Ge → Si_1 → Si_2 → Ge(DS2), which interferes destructively with the SS2 path of the second coordination shell [11]. The fitting results are shown in Figure 2 as dotted lines, and the structural parameters are summatized in Table I.

Seen from table I, the bond length $R_{Ge\text{-}Si}$ of the first shell in the $Ge_{0.006}Si_{0.0994}$ thin film is larger than that (2.35 Å) in c-Si by 0.03 Å, indicating the compressive strain in the first nearest neighbor around Ge atoms. However, its bond lengths $R_{Ge\text{-}Si}$ of

Table I. *The structural parameters of the first three shells of the $Ge_{0.006}Si_{0.994}$ thin film at different temperatures.*

Sample	Path	R (Å)	σ^2 (10^{-3} Å^2)	ΔE_0 (eV)
	SS1	2.38 ± 0.01	1.8 ± 0.9	9.4 ± 1.7
$Ge_{0.006}Si_{0.994}$	SS2	3.83 ± 0.03	3.7 ± 1.5	6.8 ± 3.0
(20 K)	SS3	4.49 ± 0.05	4.6 ± 4.3	6.8 ± 3.0
	DS2	4.31 ± 0.05	3.5 ± 1.6	6.8 ± 3.0
	SS1	2.38 ± 0.01	2.0 ± 0.6	9.2 ± 1.2
$Ge_{0.006}Si_{0.994}$	SS2	3.82 ± 0.02	4.0 ± 1.0	8.7 ± 2.9
(100 K)	SS3	4.49 ± 0.02	4.9 ± 1.8	8.7 ± 2.9
	DS2	4.30 ± 0.02	4.1 ± 2.0	8.7 ± 2.9
	SS1	2.39 ± 0.01	4.0 ± 0.5	8.3 ± 0.8
$Ge_{0.006}Si_{0.994}$	SS2	3.84 ± 0.02	9.6 ± 1.1	7.8 ± 2.0
(300 K)	SS3	4.49 ± 0.02	10.8 ± 1.7	7.8 ± 2.0
	DS2	4.30 ± 0.02	9.2 ± 2.0	7.8 ± 2.0
	1	2.352		
Si	2	3.840		
	3	4.503		

the second and third shells are almost equal to the corresponding interatomic distances in c-Si within the uncertainties. This shows that the shift of the nearest Si atoms toward the [111] direction can hardly affect their positions of the more distant Si atoms, despite of the second shell bonds bend. Therefore, the tetragonal distortion in the $Ge_{0.006}Si_{0.0994}$ thin film is limited to the first nearest neighbor atoms and the strain caused by the doping of Ge atoms is completely relieved in more distant atoms.

The temperature dependence of the Debye-Waller factors is plotted in Figure 3. It can be observed that in the temperature range from 20 to 100 K, the Debye-Waller factors in the first three Ge-Si shells show a slight increase with temperatures, *i.e.,* from 0.0018, 0.0037 and 0.0040 Å^2 at 20 K to 0.0020, 0.0040 and 0.0049 Å^2 at 100 K for σ_1^2, σ_2^2 and σ_3^2, respectively. However, when the temperature rises to 300 K, σ_1^2 (or σ_2^2 and σ_3^2) sharply increases to 0.0040 Å^2 (or 0.0096 and 0.0108 Å^2). These results indicate that at temperature lower than 100 K, the Debye-Waller factors in the first three Ge-Si shells are very weakly dependent on

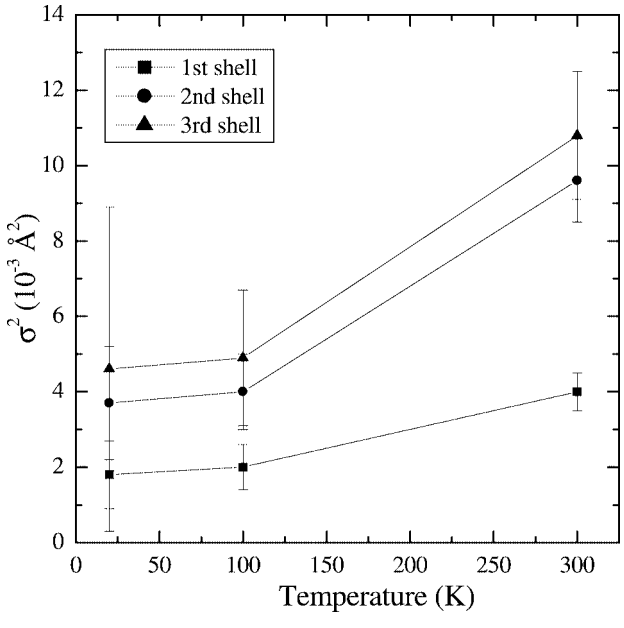

Fig. 3. The temperatures dependence of the Debye-Waller factors of the first three shells for $Ge_{0.006}Si_{0.994}$ thin film.

temperature. This means that even at temperature as high as 100 K, the zero-point contributions [16] to the Debye-Waller factors of the $Ge_{0.006}Si_{0.0994}$ thin film play the dominant role, implying that the characteristic temperature such as Debye temperature and Einstain temperature of the Ge-Si covalent bond is higher than 100 K. As the temperature increases to 300 K, the contributions of thermal motion to the Debye-Waller factors are much larger, which results in the rapid increase of the Debye-Waller factors with temperature.

An important parameter for characterizing the tetragonal distortion is the bond angle. Knowledge of the Ge-Si bond lengths of the first and second shells in the $Ge_{0.006}Si_{0.0994}$ thin film allows to determine the bond angle $\theta_{\text{Ge-Si-Si}}$ from a simple trigonometric consideration. Due to the identical bond lengths at different temperatures of 20, 100 and 300 K, their bond angles $\theta_{\text{Ge-Si-Si}}$ are all about 108.1°, close to the value expected for a tetragonal network of 109.47°. This small deviation shows a weak tetragonal distortion around Ge atoms in the unit cell of the $Ge_{0.006}Si_{0.0994}$ thin film. Moreover, the bond angle distribution is also important to understand the distortion of the tetrahedron. Following Baker *et al.*'s consideration [17], the standard variation $\Delta\theta_{\text{Ge-Si-Si}}$ can be calculated by using the Debye-Waller factors of the first, second shell Ge-Si bonds and the nearest Si-Si bond. The Debye-Waller factors of the nearest Si-Si bond in crystalline Si were theoretically calculated by Benfatto *et al.* [18] to be 0.0026 and 0.0034 $Å^2$ at 80 K and 300 K, respectively. We can determine the values of $\Delta\theta_{\text{Ge-Si-Si}}$ to be $\pm 3.4°, \pm 3.5°$ and $\pm 5.0°$ at the temperatures of 20, 100 and 300 K, respectively. The values of bond angle variation agree with that ($\pm 5°$) in crystalline GaAs at 300 K [17], indicating the weak bond angle disorder in the $Ge_{0.006}Si_{0.0994}$ thin film. Combining the bond angle variation with the result of the bond lengths, we can further confirm that the strain accumulated by the doping of Ge atoms to the Si matrix is limited to the nearest neighbors of Ge, and is easily relieved for the more distant neighbors.

Acknowledgements

This work was supported by knowledge innovation of Chinese Academy of Sciences and National Science Foundation of China (Grant No. 10174068 and 10375059).

References

1. Pearsall, T. P., Mater. Sci. Eng. B **9**, 225 (1991).
2. Ma, Q. M., Wang, K. L. and Schulman, J. N., Phys. Rev. B **47**, 1936 (1993).
3. Wong, K. B., Jaros, M., Morrison, I. and Hagon, J. P., Phys. Rev. Lett. **60**, 2221 (1988).
4. Wei, S. Q., *et al.*, J. Appl. Phys. **82**, 4810 (1997).
5. Ridgway, M. C., *et al.*, Phys. Rev. B **60**, 10831(1999).
6. Wei, S. Q., Oyanagi, H., Sakamoto, K., Takeda, Y. and Pearsall, T. P., Phys. Rev. B **62**, 1883 (2000).
7. Woicik, J. C., *et al.*, Phys. Rev. B **57**, 14592(1998).
8. Aubry, J. C., Tyliszczak, T. and Hitchcock, A. P., Phys. Rev. B **59**, 12872 (1999).
9. Parscarelli, S., Boscherini, F., Lamberti, C. and Mobilio, S., Phys. Rev. B **56**, 1936 (1997).
10. Tormen, M., *et al.*, Phys. Rev. B **63**, 115326 (2001).
11. Sun, Z. H. and Wei, S. Q., "Multiple-scattering extended X-ray absorption fine structure studies on local structures of Ga-P (As, Sb) semiconductors," submitted to Phys. Rev. B.
12. Oyanagi, H., *et al.*, Rev. Sci. Instrum. **66**, 5477 (1995).
13. Zhong, W. J. and Wei, S. Q., J. Univ. Sci. Technol. China **31**, 228 (2001).
14. Stern, E. A., Newville, M., Ravel, B., Yakoby, Y. and Haskel, D., Physica B **208&209**, 117 (1995).
15. Mustre de Leon, J., Rehr, J. J., Zabinsky, S. I. and Albers, R. C., Phys. Rev. B **44**, 4146 (1991).
16. Hung, N. V. and Rehr, J. J., Phys. Rev. B **56**, 43 (1997).
17. Baker, S. H., *et al.*, J. Phys.: Condens. Matter **5**, 519 (1993).
18. Benfatto, M., Natoli, C. R. and Filipponi, A., Phys. Rev. B **40**, 9626 (1989).

Physica Scripta. Vol. T115, 143–145, 2005

EXAFS and Local Thermal Expansion

P. Fornasini[1], S. a Beccara[1], G. Dalba[1], R. Grisenti[1], J. Purans[1], A. Sanson[1], F. Rocca[2] and D. Diop[3]

[1]Istituto Nazionale per la Fisica della Materia and Dipartimento di Fisica, dell'Università di Trento, I-38050 Povo (Trento), Italy
[2]Istituto di Fotonica e Nanotecnologie del CNR, Sezione di Trento, I-38050 Povo (Trento), Italy
[3]Faculté des Sciences et Techniques, Université Cheikh Anta Diop, Dakar, Senegal

Received June 26, 2003; accepted November 5, 2003

PACS numbers: 61.10.Ht, 65.40.−b

Abstract

EXAFS measures the thermal variation of average interatomic distances, while Bragg diffraction and dilatometric techniques measure the variation of distances between average atomic positions. The difference not only gives information on vibrational motion perpendicular to the bond direction, but can be exploited to study the local behaviour in systems affected by negative thermal expansion. Recent results on copper, germanium and Ag_2O are presented and critically compared.

1. Introduction

The expression *thermal expansion* literally refers to the increase of geometrical dimension which is observed in most substances when their temperature is raised. Many solids however exhibit anomalous behaviours [1]. A weak *negative* thermal expansion (NTE) is observed in some tetrahedrally coordinated crystals, like silicon, in a limited temperature range. Framework structures can exhibit NTE over large temperature intervals (the lattice parameter of ZrW_2O_3 regularly contracts from 0.3 to 1050 K [2]).

Well established techniques are available for accurate macroscopic measurements and a rigorous thermodynamic description of thermal expansion is possible [3, 4]. On the contrary, the microscopic interpretation is in many cases uncertain, owing to the lack of suitable experimental techniques and the limitations of theoretical approaches. For a two-atomic system, the interaction potential is typically characterised by a steep repulsive part and a smoother attractive part; the positive thermal expansion is easily explained in terms of the potential asymmetry. This simple picture cannot be trivially extended to many-atomic systems like crystals, where the potential is defined in a many-dimensional configurational space. From the microscopic point of view, interesting clues on the vibrational origin of thermal expansion and its anomalies have been proposed on the basis of simple central force mechanisms [4]. The anharmonicity of the effective pair potential induces positive thermal expansion, via a *bond-strecting* effect like in two-atomic systems. Geometrical *tension effects*, connected to vibrational motion perpendicular to the bond direction, induce a negative contribution to the thermal expansion (variation of the *distance between average atomic positions*). Further complications can be introduced by non-central forces. In framework structures, different behaviours can be expected depending on the length scale considered, from the nearest-neighbours distance variations up to the macroscopic thermal expansion.

EXAFS, by measuring the interatomic distance between selected atomic species and their first few neighbours shells, is an appealing tool for studying the microscopic mechanisms of thermal expansion. Actually, EXAFS measures the *average path-lengths between instantaneous atomic positions*, giving complementary information with respect to macroscopic dilatometry or Bragg-diffraction. Moreover, the widespread approach to EXAFS analysis based on the single scattering approximation leads to a description of thermal disorder in terms of distance distributions and corresponding effective pair potentials, which is specular to the approach to thermal expansion based on central force mechanisms. The possibility of getting from EXAFS information on atomic vibrations perpendicular to the bond direction can also help in understanding the effects of non-central forces.

Obtaining accurate information on thermal expansion from EXAFS requires a good understanding of the connection of one-dimensional distance distributions and corresponding effective pair potentials with the structural and dynamical properties of three-dimensional systems. To this purpose, a thorough study of reference systems with known structure is important.

In this paper, after a short updated account on some aspects of the cumulant analysis method relevant for thermal expansion studies, strengths and limitations of EXAFS as a probe of local thermal expansion will be illustrated by the results recently obtained on reference systems copper and germanium and on a framework structure affected by negative thermal expansion, Ag_2O.

2. Theory

Thermal disorder spreads atomic positions into three-dimensional probability distributions. In many cases, in particular when only the first coordination shell is considered within the single scattering approximation, the EXAFS analysis can be based on a one-dimensional distribution of interatomic distances, and, for moderate disorder, can be further simplified by a parametrisation in terms of cumulants [5, 6].

Let C_i^* be the cumulants of the one-dimensional distribution of distances $\rho(r, T)$ and R_0 the inter-atomic distance for an ideal classical state of absolute rest. The instantaneous relative displacement $\Delta\vec{u}$ due to thermal motion can be decomposed into its projections $\Delta u_\parallel$ and $\Delta u_\perp$ along the average bond direction and in the perpendicular plane, respectively. The instantaneous bond distance is, to first approximation [6],

$$r \simeq R_0 + \Delta u_\parallel + \Delta u_\perp^2/2R_0. \tag{1}$$

In quasi-harmonic approximation, the parallel relative displacement in Eq. (1) can be decomposed as

$$\Delta u_\parallel = b + (\Delta u_\parallel)_\mathrm{h}, \tag{2}$$

where b is the thermal expansion due to anharmonicity, while $(\Delta u_\parallel)_\mathrm{h}$ is a harmonic contribution.

Let us now consider canonical averages. To clarify the relation between the first EXAFS cumulant $C_1^* = \langle r \rangle$ and the crystallographic distance R_c measured by Bragg diffraction, we will focus the attention on two limiting cases. For a purely

translational relative motion, the three-dimensional harmonic distribution of relative distances is an ellipsoid, so that $\langle \Delta u_{\parallel} \rangle_h = 0$, and

$$C_1^* \simeq R_0 + b + \langle \Delta u_{\perp}^2 \rangle / 2R_0; \qquad R_c = R_0 + b. \tag{3}$$

For a purely *librational* relative motion, the ellipsoid is curved along a spherical surface, so that $\langle \Delta u_{\parallel} \rangle_h \simeq -\langle \Delta u_{\perp}^2 \rangle / 2R_0$, and

$$C_1^* = R_0 + b; \qquad R_c \simeq R_0 + b - \langle \Delta u_{\perp}^2 \rangle / 2R_0. \tag{4}$$

Both b and $\langle \Delta u_{\perp}^2 \rangle$ have finite values at zero kelvin, due to the zero point motion. Relative translational motion describes the behaviour of crystals with simple, highly symmetrical structures. Relative librational motion characterizes the dynamics of rigid units in molecular crystals and framework structures [7]. In any case, the average distance measured by EXAFS is larger than the crystallographic distance:

$$C_1^* \simeq R_c + \langle \Delta u_{\perp}^2 \rangle / 2R_0. \tag{5}$$

The third cumulant measures the asymmetry of $\rho(r, T)$. Frenkel and Rehr [8] have shown, through a perturbative quantum approach, that the contribution to thermal expansion due to the asymmetry of the EXAFS effective pair potential is

$$a = -3k_3 C_2^* / k_0, \tag{6}$$

where the force constants k_0 and k_3 can be obtained by fitting suitable models to the temperature dependence of the 2nd and 3rd EXAFS cumulants. If the EXAFS effective pair potential were temperature independent, then the quantity a, defined in Eq. (6), would correspond to the quantity b of Eq. (2). From the third cumulant one could then obtain the crystallographic thermal expansion via Eq. (3) in the case of a purely translational motion; for a purely librational motion, according to Eq. (4), the 1st and 3rd cumulant would carry the same information.

EXAFS is directly sensitive to an *effective* distribution of distances. The difference between cumulants C_i^* and C_i of the real and effective distributions, respectively, is relevant for the first one,

$$C_1^* \simeq C_1 + (2C_2/C_1)(1 + C_1/\lambda) \tag{7}$$

where λ is the photoelectron mean free path [6]. In the following we will always quote the first cumulants of the *real* distributions.

3. Local thermal expansion in Cu and Ge

Figures 1 and 2 refer to the first coordination shells in copper [9] and germanium [10], respectively. In both figures, the continuous line represents the crystallographic expansion δR_c, calculated from the macroscopic thermal expansion coefficient [11]. The full circles show the temperature dependence δC_1^* of the first cumulant, obtained from an EXAFS analysis based on the ratio method, taking as reference the spectra at the lowest temperature. The difference between δC_1^* and δR_c, according to Eq. (5), depends on the increases with temperature of $\langle \Delta u_{\perp}^2 \rangle$. By a suitable procedure [10] it was possible to recover the absolute values of the perpendicular Mean Square Relative Displacement and calculate the ratio $\gamma = \langle \Delta u_{\perp}^2 \rangle / \langle \Delta u_{\parallel}^2 \rangle$, which at high temperature was about 2.7 and 6 for copper and germanium, respectively.

The diamonds in Figs. 1 and 2 represent the thermal variation δa of the quantity defined in Eq. (6) and calculated from the experimental values of the 2nd and 3rd cumulants. Relative δa values have been plotted instead of absolute values a to get rid of the zero-point thermal expansion [10]. The good correspondence

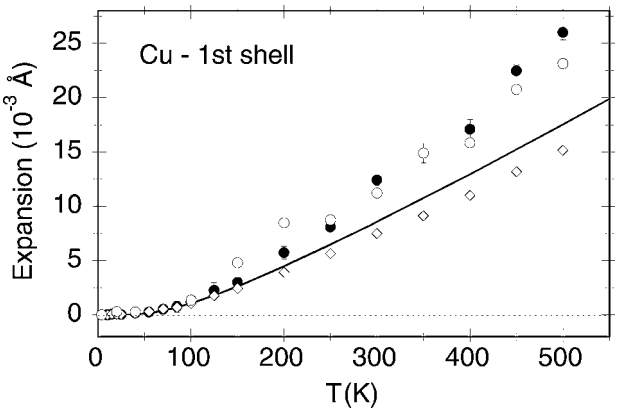

Fig. 1. Thermal expansion for the 1st shell of copper: crystallographic distance (continuous line), 1st EXAFS cumulant for $\lambda = 9$ Å (full circles), contribution of effective potential asymmetry calculated from the 3rd cumulant according to [8] (diamonds), and results from Path Integral Monte Carlo simulations [9] (open circles).

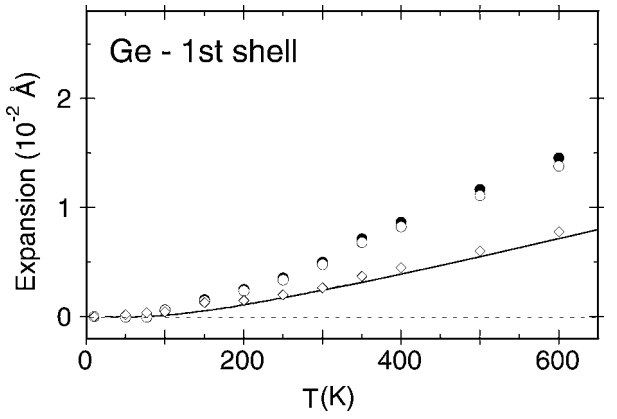

Fig. 2. Thermal expansion for the 1st shell of Germanium: crystallographic distance (continuous line), 1st EXAFS cumulants for $\lambda = 6$ Å (full circles) and $\lambda = 12$ Å (open circles), and contribution of effective potential asymmetry calculated from the 3rd cumulant according to [8] (diamonds).

between δR_c and δa found for germanium suggested that $\delta a \simeq \delta b$, so that the third cumulant could be utilised for measuring the crystallographic thermal expansion, at least for the first shell of simple crystals [10]. The non negligible disagreement found for copper shows instead that the quantity a, depending on the asymmetry of the EXAFS effective pair potential, cannot be identified with the quantity b of Eqs. (3) and (4) even for very simple crystals. The discrepancy between a and b can be explained by a temperature dependence of the effective pair potential; in view of the regular T^2 dependence of the 3rd cumulant, it is reasonable to assume that the shape of the effective potential is constant, and the temperature variation consists in a rigid shift.

The soundness of the correspondence between the coefficients C_i^* obtained from EXAFS analysis and the cumulants of the distribution of distances has been checked by a comparison with independent calculations, in order to exclude relevant artifacts of the data analysis. For germanium, the values $\langle \Delta u_{\parallel}^2 \rangle$, $\langle \Delta u_{\perp}^2 \rangle$ and the 3rd cumulant have been well reproduced by D. Strauch and coworkers through *ab initio* dynamical calculations [12]. For copper, a Path Integral Monte Carlo (PIMC) simulation was done [9], based on a many-body potential of the tight-binding family, previously used for Molecular Dynamics simulations [13]. The results of PIMC calculations are in good agreement with EXAFS results: first and third cumulants are shown in Figs. 1 and 3, respectively.

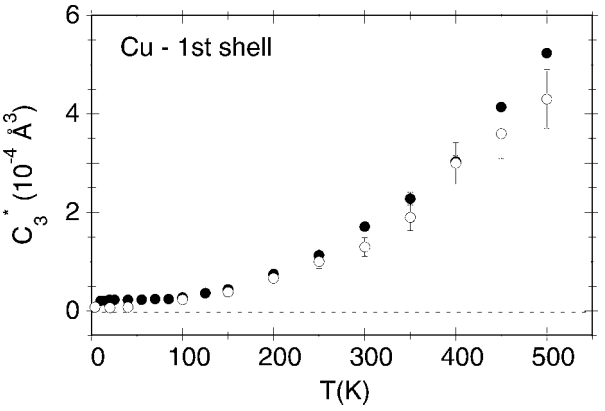

Fig. 3. 3rd cumulant for the Cu 1st shell from EXAFS (full circles) and Path Integral Monte Carlo simulations [9] (open circles).

4. Ag_2O and negative thermal expansion

The potential of EXAFS for studying systems affected by negative thermal expansion has been evidenced by a recent work on silver oxide Ag_2O [14].

Ag_2O shares with Cu_2O the *cuprite* structure. Each Ag atom is linearly coordinated to two O atoms, and each O atom is tetrahedrally coordinated to four Ag atoms. The structure can be alternatively described as a framework of two interpenetrating networks of corner-sharing Ag_4O tetrahedra. A contraction of the lattice parameter has been measured in Ag_2O in the temperature interval from 10 to 470 K by Artioli and coworkers by means of X-ray diffraction [15, 16]. EXAFS measurements were done from 7 to 500 K: the main results concerning thermal expansion are summarized in Fig. 4. The EXAFS sensitivity to local structure allows to distinguish a positive thermal expansion for the 1st-shell Ag-O distance from a negative thermal expansion of the 2nd-shell Ag-Ag distance.

The 1st-shell behaviour is consistent with the rather rigid nearest-neighbour bond with oxygen found in other framework structures affected by lattice parameter NTE [17]. The twelve Ag atoms of the 2nd-shell can be grouped into two sets: six atoms are connected to the central atom via the 1st-shell oxygen atoms and belong to the same network, the remaining six atoms belong to the other network. It is reasonable to assume that the most relevant contribution to the 2nd-shell NTE comes from the average approaching of atoms belonging to different networks, consistently with the presence of empty sites in the intermediate space.

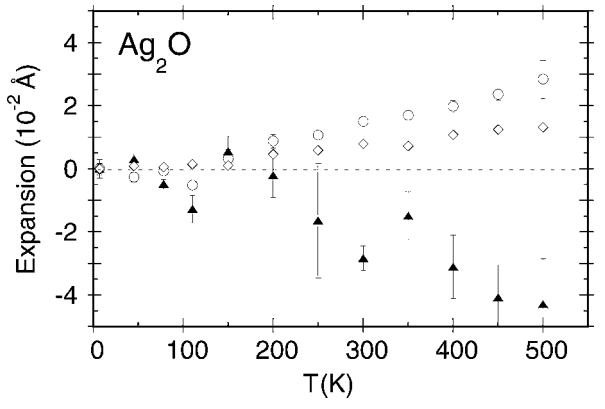

Fig. 4. Thermal expansion measured by EXAFS in Ag_2O: 1st-shell Ag–O (open circles) and 2nd-shell Ag–Ag (triangles). The diamonds are the contribution of effective potential asymmetry calculated from the 3rd cumulant according to [8].

A direct comparison of the 1st-shell EXAFS expansion δC_1^* with the crystallographic expansion δR_c was not be done in this case due to the presence of two very different atomic species and the rather complex framework structure.

An alternative procedure was attempted in Ref. [14] starting from the δa values (diamonds in Fig. 4). Assuming $\delta a \simeq \delta b$, say neglecting possible shifts of the effective pair potential, the discrepancy between δC_1^* and δa was attributed to a deviation of the motion of Ag_4O tetrahedra from a pure libration (Eq. (4)). The difference $\delta C_1^* - \delta a$ was then used to calculate the values $\langle \Delta u_\perp^2 \rangle_{\rm tr}$, where "tr" indicates a purely translational contribution. The ratio $\gamma = \langle \Delta u_\perp^2 \rangle_{\rm tr} / \langle \Delta u_\parallel^2 \rangle$ was about 9 at high temperatures.

This γ value, suggesting that the Ag-O bond is much looser with respect to bending than to strecthing, was quantitatively consistent with the high value found for the ratio between the parallel MSRD $\langle \Delta u_\parallel^2 \rangle$ of 2nd and 1st shell. The assumption $\delta a \simeq \delta b$ seem thus in this case reasonable. The main physical consequence of the difference between δC_1^* and δa is, according to Eq. (4), that the Ag_4O tetrahedra cannot be considered undistorted, as assumed by the "Rigid Unit Mode" (RUM) models which are often used to explain NTE in framework structures [18].

5. Conclusions

EXAFS measurements on Copper and Germanium have shown that the comparison between 1st cumulant and crystallographic thermal expansion gives original information on the atomic vibrations perpendicular to the bond. No general direct connection seems instead possible betwen 3rd cumulant and thermal expansion. The correctness of EXAFS cumulants obtained by the ratio mehtod was supported by independent calculations.

Measurements on Ag_2O have evidenced the peculiar ability of EXAFS to give original information on the local behaviour of systems affected by negative thermal expansion.

References

1. White, G. K., Contemp. Phys. **34**, 193 (1993).
2. Mary, T. A., Evans, J. S. O., Vogt, T. and Sleight, A. W., Science **272**, 90 (1996).
3. Ho, C. Y., editor, "Thermal expansion of solids", CINDAS Data Series on Material Properties, Vol. I-4, (ASM-International, 1998).
4. Barron, T. H. K., "Generalized theory of thermal expansion of solids", in Ref. [3].
5. Bunker, G., Nucl. Instrum. Meth. Phys. Res. **207**, 437 (1983).
6. Fornasini, P., Monti, F. and Sanson, A., J. Synchrotron Rad. **8**, 1214 (2001).
7. Willis, B. T. M. and Pryor, A. W., "Thermal vibrations in crystallography", (Cambridge University Press, Cambridge, 1975).
8. Frenkel, A. I. and Rehr, J. J., Phys. Rev. B **48**, 585 (1993).
9. a Beccara, S., Dalba, G., Fornasini, P., Grisenti, R., Pederiva, F., Sanson, A., Diop, D. and Rocca, F., Phys. Rev. B **68**, 140301 (2003).
10. Dalba, G., Fornasini, P., Grisenti, R. and Purans, J., Phys. Rev. Lett. **82**, 4240 (1999).
11. Touloukian, Y. S., Kirby, R. K., Taylor, R. K. and Desai, P. D., "Thermophysical properties of matter", vol. 13, (Plenum, New York, 1977).
12. Birner, G., Strauch, D. and Pavone, P., private commun. (2001).
13. Edwards, A. B., Tildesley, D. J. and Binsted, N., Mol. Phys. **91**, 357 (1997).
14. a Beccara, S., *et al.*, Phys. Rev. Lett. **89**, 25503 (2002).
15. Tiano, W., Dapiaggi, M. and Artioli, G., J. Appl. Crystallog. **36**, 1461 (2003).
16. Sanson, A., *et al.*, Physica Scripta, submitted (this issue).
17. Tucker, M. G., Dove, M. T. and Keen, D. A., J. Phys. Condens. Matter **12**, L425 (2000).
18. Heine, V., Welche, P. R. L. and Dove, M. T., J. Am. Ceram. Soc. **82**, 1793 (1999).

Physica Scripta. Vol. T115, 146–148, 2005

Multi-Channel Multiple Scattering Theory for XAFS. Application to $L_{2,3}$ Edges of Ca

P. Krüger[1*] and C. R. Natoli[2]

[1]European Synchrotron Radiation Facility, B.P.220, F-38043 Grenoble, France
[2]INFN Laboratori Nazionali di Frascati, Casella Postale 13, I-00044 Frascati, Italy

Received June 26, 2003; accepted November 4, 2003

PACS numbers: 71.15.Qe, 78.70.Dm

Abstract

We present a multi-channel extension of the multiple scattering method for X-ray absorption fine structure (XAFS) spectroscopy that allows to take account of atomic multiplet-like electron correlation effects in condensed systems, on the basis of *ab initio* electron structure calculations. The formalism is outlined and an application to near-edge XAFS at the $L_{2,3}$ edges of Ca metal is presented. In this system, the experimentally observed branching ratio deviates strongly from that obtained from the standard (one-electron) approach to XAFS. This is due to that fact that one-electron theory neglects the multiplet coupling between the photo-electron and the 2p core-hole. Within the multi-channel method, this correlation effect can easily be taken into account and the calculated spectrum agrees well with experiment.

1. Introduction

Multiple scattering (MS) theory provides an accurate and flexible scheme for the calculation of unoccupied electronic states which are probed by various synchrotron experiments such as X-ray absorption spectroscopy and resonant X-ray scattering. The standard theory relies on the single-particle picture, that is, it neglects electron correlation effects. This is a great shortcoming, since core-level X-ray spectra are often strongly modified by electron correlation, in particular by the Coulomb and exchange interaction of the valence electrons with the core hole. In transition metal and rare earth systems, this interaction can give rise to pronounced atomic multiplet and satellite structures in the spectra, which can only be accounted for in a many-electron calculation. A generalisation of MS theory to many-electron wave functions was developed by Natoli *et al*. [1] and is known as "multi-channel" MS theory. Using this approach together with the eigen-channel R-matrix method [2, 3], we have developed a new computational scheme that allows to take into account certain atomic multiplet effects, namely those that are due to the interaction between the photo-electron and electrons/holes in sufficiently localised orbitals. Sufficiently localised means that the wave function is negligible small beyond the atomic radius. This applies exactly to inner-core shells and well to the 4f-shell in rare earths. In this paper, we apply the method to $L_{2,3}$ near-edge XAFS of metallic Ca. A detailed description of the theory will be published elsewhere [4]. The $L_{2,3}$-edge spectrum of Ca is an interesting test case for the new method, because the L_2 and L_3 absorption channels are strongly coupled through the photo-electron–core-hole Coulomb interaction. This leads to a branching ratio of about 1 : 1, far from the statistical ratio (2 : 1) which is obtained in single-particle theory [5, 6].

2. Formalism

In the X-ray absorption process at the $L_{2,3}$ edges, an electron is excited from the 2p core-level to a continuum state above the Fermi level. We consider the six electron wave function made of the 2p core electrons, one of which becomes the photo-electron in the final state. All other electrons are not considered explicitly; they are assumed to contribute only to the mean-field potential. The initial state Ψ_g with energy E_g is simply given by the closed shell configuration $(2p^6, {}^1S_0)$. Final states have energy $E = E_g + \hbar\omega$ and a $(2p^5\epsilon^1)$ configuration, where ϵ denotes a (one-electron) state in the continuum above the Fermi energy. The crucial point is that we take into account multiplet effects through a configuration interaction ansatz for the final state wave function, which is developed as

$$\Psi = \mathcal{A} \sum_{\alpha} \tilde{\Phi}_{\alpha}(X)\phi_{\alpha}(x). \tag{1}$$

Here $\tilde{\Phi}_{\alpha}$ is one of the six $(2p^5)$ states, labelled by $\alpha = (j_c, \mu_c)$ $(j_c = 1/2, 3/2, \mu_c = -j_c \ldots j_c)$; X collects all core-electron coordinates. The $(2p^5)$ multiplet energies are $E_{\alpha} = E_g - \epsilon_c(j_c)$, where $\epsilon_c(j_c)$ are the spin-orbit split $2p(j_c)$ levels. For each $\tilde{\Phi}_{\alpha}$, there is a component ϕ_{α} of the photo-electron wave function. The (radial, angular, and spin) coordinate of the photo-electron is denoted $x = (r, \hat{x}, \sigma)$. Finally, $\mathcal{A}$ denotes the antisymmetrization operator.

For correlated N-electron wavefunctions such as Ψ, where all electrons but one occupy localized orbitals, we have derived a multi-channel multiple scattering method for XAFS in close formal analogy to the standard single-electron method [4]. The total photoabsorption cross section is given by [1, 4]

$$\sigma(\omega) \propto \omega \mathrm{Im} \left\{ \sum_{\Gamma\Gamma'} M^*_{\Gamma} \tau^{00}_{\Gamma\Gamma'} M_{\Gamma'} \right\}. \tag{2}$$

Here $\Gamma = \alpha lms$ is the set of all quantum numbers of Ψ, with lm being the orbital and s the spin quantum numbers of the photo-electron. $M_{\Gamma} = \langle \Psi^{\mathrm{in}}_{\Gamma} | D | g \rangle$ are the transition matrix elements; we consider only dipolar transition and use the length approximation. $\Psi^{\mathrm{in}}_{\Gamma}$ is the inside solution that matches smoothly onto the outside solution

$$\Psi^{\mathrm{out}}_{\Gamma} = \sum_{\Gamma'} \Phi_{\Gamma'}(X\hat{x}\sigma) Z_{\Gamma'\Gamma}(r)/r. \tag{3}$$

Here, "inside" and "outside" refer to the atomic sphere of the absorber, i.e. $r < r_0$ and $r > r_0$, respectively, r_0 being the muffin-tin radius. We have introduced $\Phi_{\Gamma} \equiv \tilde{\Phi}_{\alpha}(X) Y_{lm}(\hat{x}) \delta(s, \sigma)$. The amplitude of the radial photoelectron wave function is given by

$$Z_{\Gamma\Gamma'}(r)/r = j_l(k_{\alpha} r)[t^{-1}]_{\Gamma\Gamma'} - \mathrm{i} k_{\alpha} h^+_l(k_{\alpha} r) \delta_{\Gamma\Gamma'}. \tag{4}$$

*Present address: LRRS, UMR 5613 Université de Bourgogne-CNRS, B.P. 47870 F-21078 Dijon, France.

Here, $h_l^+ = j_l + \mathrm{i}n_l$ and j_l, n_l are the usual spherical Bessel and Neumann functions. k_α is the wave number of the photo-electron, given by $k_\alpha^2 + V_0 = \epsilon_\alpha = E - E_\alpha$, where V_0 is the interstitial potential. $t_{\Gamma\Gamma'}$ is the multi-channel atomic T-matrix of the absorber (at site $i = 0$). In Eq. (2), $\tau^{ij}_{\Gamma\Gamma'}$ is the multi-channel scattering path operator connecting sites i and j. It is calculated for a finite cluster by inversion of the τ^{-1} matrix, whose elements are given by

$$[\tau^{-1}]^{ij}_{\Gamma\Gamma'} = \delta_{ij}[t^{-1}]^i_{\Gamma\Gamma'} - \delta_{\alpha\alpha'}k_\alpha H^{ij}_{lm,l'm'}(k_\alpha)\delta_{ss'}. \quad (5)$$

Here, t^i is the atomic scattering matrix of atom i, and $H^{ij}_{lm,l'm'}$ are the real space KKR structure factors (for a definition, see Ref. [1] appendix A). Apart from the absorber, we treat all atoms in the standard one-electron muffin-tin approximation, which implies $t^i_{\Gamma\Gamma'} = t^i_l(k_\alpha)\delta_{\Gamma\Gamma'}$, for all $i \neq 0$. These T-matrices, as well as the structure factors $H^{ij}_{lm,l'm'}$, are single channel quantities and can thus be calculated using standard multiple scattering techniques [7]. For the spectra shown below we have used a symmetric fcc cluster up to the tenth neighbor shell (177 atoms) and selfconsistent linear-muffin-tin-orbital (LMTO) potentials [8] with (space-filling) Wigner-Seitz spheres for the computation of the t^i_l's. We have developed a partitioning technique for an efficient inversion of the multichannel scattering path operator in real space (for details see Ref. [4]).

The remaining problem is the calculation of the multichannel T-matrix of the absorber and the inner solutions $\Psi^{\mathrm{in}}_\Gamma$. This is done using the eigenchannel R-matrix method [2, 3]. As reaction volume, we use the (absorber's) muffin-tin sphere with radius r_0. As Hamiltonian we take $H = H_0 + V$, where H_0 is the (LMTO-LDA) mean-field hamiltonian and V is the photo-electron–core-hole Coulomb interaction. As a basis of N-electron trial wave functions we use the functions

$$\Psi_{\Gamma v} \equiv \mathcal{A}\{\Phi_\Gamma(X\hat{x}\sigma)P_v(r)/r\}. \quad (6)$$

Here, P_v are solutions of the radial Schrödinger equation for angular momentum l with the self-consistent LMTO potential. Note that this is the same differential equation as the one used for the calculation of the single-channel T-matrices t^i_l, but now we fix the boundary conditions at the muffin-tin radius instead of the single-particle energy ϵ. Since $2\mathrm{p} \rightarrow \epsilon\mathrm{s}$ transitions have negligeable intensity in the near-edge region, we here include only $l = 2$, i.e. d-waves in the basis. We use closed-type orbitals with boundary conditions $P_v\ (r_0) = 0$, and open-type orbitals with boundary conditions $\mathrm{d}P_v/\mathrm{d}r(r_0) = 0$. Convergence of the spectra was achieved with five closed-type orbitals (with zero to four nodes in $0 < r < r_0$) and one open-type orbital (with zero nodes). The Coulomb interaction V can be expressed in terms of (generalized) Slater-integrals $F^k_{vv'} \equiv (2\mathrm{p}, v\mathrm{d}|r^k/r^{k+1}|2\mathrm{p}, v'\mathrm{d})$ and $G^k_{vv'} \equiv (2\mathrm{p}, v\mathrm{d}|r^k/r^{k+1}|v'\mathrm{d}, 2\mathrm{p})$ [9]. The detailed calculation of matrix elements will be presented elsewhere [4]. The monopole part of the photo-electron–core-hole interaction (related to integrals $F^0_{vv'}$) is drastically reduced by metallic screening [5]. Solid state screening is a many-body effect that is not included in the (local) correlation effects we are dealing with in the present approach. Therefore have treated solid state screening in an empirical way.

3. Results

In Fig. 1 we show the absorption spectra as obtained in standard multiple scattering theory and using the ground state LMTO potential. As a check of the new method, we also show

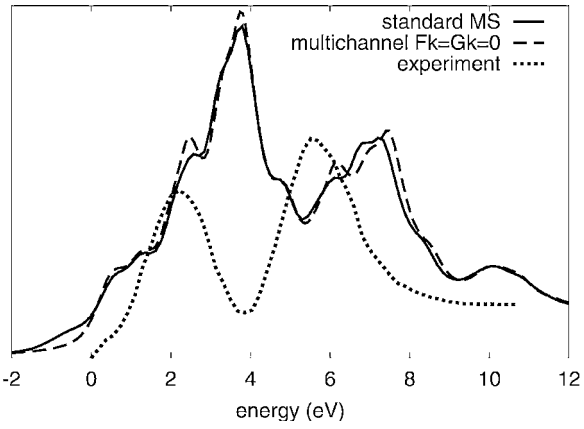

Fig. 1. Ca $L_{2,3}$-edge absorption spectra calculated using standard multiple scattering method (standard MS) and using multichannel method in non-interacting limit (multi-channel $Fk = Gk = 0$).

the spectrum calculated with the multichannel method in the non-interacting limit (i.e. putting the photo-electron–core-hole interaction to zero.) The agreement is perfect within numerical error due to broadening (we use a Lorentzian broadening of 0.5 eV FWHM), which shows that the R-matrix method with the present choice of basis functions gives the same results as direct integration. The $L_3 : L_2$ branching ratio is about 3 : 2 rather than 2 : 1 (statistical value), and thus slightly better than the density of states approximation for $L_{2,3}$-XAFS [5]. Nonetheless, the spectrum is (still) in strong disagreement with the experimental one (taken from Ref. [5]) both as far as branching ratio and line shape is concerned.

The spectra in Fig. 2 have been obtained using the multichannel method and including the photo-electron–core-hole interaction. Spectra (a) and (b) differ with respect to the mean-field potential used for the calculation of the P_v and the treatment of the monopole terms $F^0_{vv'}$. For spectrum (a), we have used the LMTO ground state potential and considered the limit $F^0_{vv'} = 0$, i.e. we simply disregarded the monopole terms. The branching ratio is about 1 : 1 in good agreement with experiment. This shows that it is mainly the multiplet coupling described by F^2, G^1 and G^3, that is responsible for the deviation of the branching ratio from statistical, as already found by Zaanen *et al.* [5] who used model calculations. As far as peak positions and fine structure are concerned, however, spectrum (a) does not improve over the one-electron spectra in Fig. 1. Let us also note that spectrum (a) is almost identical to the

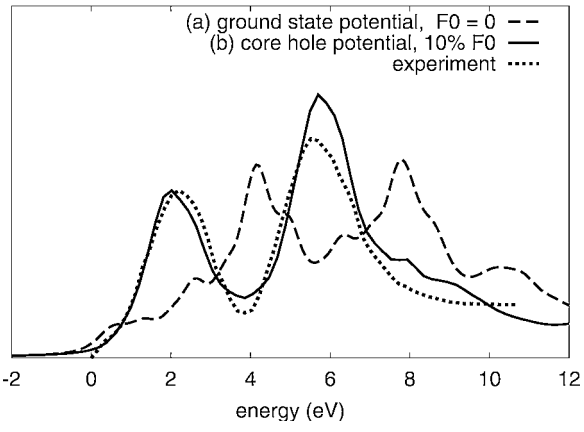

Fig. 2. Ca $L_{2,3}$-edge absorption spectra calculated using multichannel method including electron-hole interaction (see text for details).

one obtained by Schwitalla/Ebert within time-dependent density functional theory [6].

In order to treat the monopole term of the Coulomb interaction including screening, we used a statically screened potential instead of the ground state potential for the calculation of the trial orbitals $P_v(r)$ and levels ϵ_v. This potential was obtained from self-consistent supercell LMTO calculations with a 2p-core hole on the absorber atom. However, the use of the screened potential alone (with $F^0 = 0$) did not improve the spectra. In order to get agreement with experiment, we had to use screened potentials together with non-zero, but strongly rescaled F^0 terms. Specifically, we used $\alpha F^0_{vv'}$, where $F^0_{vv'}$ are the calculated integrals and α is an empirical scaling factor, which we set to 0.1. The corresponding spectrum (b) agrees well with experiment with the small remaining problem that the branching ratio is now slightly "over-corrected". The present treatment of the monopole part of the Coulomb interaction is somewhat unsatisfactory, because it involves an ajustable parameter (α). We are currently seeking for a better solution to this problem.

The main conclusions from the present work are the following. We have presented a multi-channel extention of the multiple scattering method for XAFS that allows the inclusion of multiplet effects between the photo-electron and sufficiently localized orbitals, in particular the core-hole. We have applied the new method successfully to the branching ratio problem in the $L_{2,3}$ near-edge spectrum of metallic Ca. In our method, the multiplet coupling described by Slater integrals F^k, G^k, $k > 0$ can be taken into account without ajustable parameters. In order to account for the strongly screened monopole part of the Coulomb interaction we used statically screened potentials and rescaled the F^0 integrals by an empirical factor α.

References

1. Natoli, C. R., Benfatto, M., Brouder, C., López, M. F. R. and Foulis, D. L., Phys. Rev. B **42**, 1944 (1990).
2. Hamacher, P. and Hinze, J., J. Phys. B **22**, 3397 (1989).
3. Aymar, M., Greene, C. H. and Luc-Koenig, E., Rev. Mod. Phys. **68**, 1015 (1996).
4. Krüger, P. and Natoli, C. R., to be published.
5. Zaanen, J., Sawatzky, G. A., Fink, J., Speier, W. and Fuggle, J. C., Phys. Rev. B **32**, 4905 (1985).
6. Schwitalla, J. and Ebert, H., Phys. Rev. Lett. **80**, 4586 (1998).
7. Natoli, C. R., Misemer, D. R., Doniach, S. and Kutzler, F. W., Phys. Rev. A **22**, 1104 (1980).
8. Andersen, O. K. and Jepsen, O., Phys. Rev. Lett. **53**, 2571 (1984).
9. Condon, E. U. and Shortley, G. H., "The Theory of Atomic Spectra", (Cambridge University Press, Cambridge, England, 1951).

Physica Scripta. Vol. T115, 149–151, 2005

XANES and EXAFS Modelling of Configurational Disorder in Silver Borate Glasses

G. Dalba[1], P. Fornasini[1], A. Kuzmin[2], F. Monti[3], A. Sanson[1], O. Sipr[4] and F. Rocca[5]

[1]INFM and Dipartimento di Fisica, Università di Trento, Via Sommarive 14, 38050 Povo (Trento), Italy
[2]Institute of Solid State Physics, University of Latvia, Kengaraga street 8, 1063 Riga, Latvia
[3]Dipartimento di Informatica, Università di Verona, Strada le Grazie 15, 37134 Verona, Italy
[4]Institute of Physics, Academy of Sciences of the Czech Republic, Cukrovarnická 10, 16253 Prague, Czech Republic
[5]CNR-IFN, Istituto di Fotonica e Nanotecnologie del Consiglio Nazionale delle Ricerche – Sezione "CeFSA" di Trento, I-38050 Povo (Trento), Italy

Received June 26, 2003; accepted November 4, 2003

PACS numbers: 61.43.Fs, 61.10.Ht, 78.70.Dm

Abstract

The sensitivity of X-ray absorption spectroscopy (XAS) to the local structure around a selected atomic species (symmetry, distances and angles) is commonly exploited to quantitatively describe systems where all the configurations around the absorbing atoms may be approximated by the mean one. However, in many cases of disordered systems a simple description of the local structure with single-configuration models cannot be reconciled with experimental spectra.

In this paper the necessity to analyse the XAS spectra by considering a multiplicity of atomic structural configurations is demonstrated in the case of silver borate glasses.

The local coordination around Ag cations in ($Ag_2O.nB_2O_3$) glasses has been studied by comparing the XAS experimental spectra at the Ag K edge with theoretical XANES and EXAFS spectra obtained by a configurational average of model structures.

In order to provide a reasonable agreement with experiment, these models have to take into account that there are many geometrically distinct Ag neighbourhoods present in the system, and that the measured XANES and EXAFS signals are in fact averages over spectra originated at all the non-equivalent photoabsorbing sites (multi-configuration approach).

1. Introduction

The sensitivity of X-ray absorption spectroscopy (XAS) to the local structure of the absorbing site (symmetry, distances and angles) is generally exploited to quantitatively describe systems characterised by single or few atomic configurations.

However, the use of routine best-fitting procedures to fit experimental spectra can give rise to unreliable results, when applied to systems where several atomic configurations around the absorbing species are present, as in the case of some glasses.

In this paper we present a study about the structural configurations of the Ag cation in borate glasses $Ag_2O{\cdot}nB_2O_3$. Silver borate glasses constitute a widely studied class of materials, especially when mixed with AgI to form fast ion conducting glasses, which can be used as solid electrolytes [1].

The local coordination of silver cations has been studied by various spectroscopic and structural techniques both in binary $Ag_2O{\cdot}nB_2O_3$ and ternary (i.e., with AgI) glasses [2–4]. The first X-ray absorption spectroscopy (XAS) experiments on binary glasses identified a mean Ag-O distance of about 2.3 Å, and suggested a structural model where silver is bridging between two oxygen atoms in a quasi linear configuration, like in c-Ag_2O [5, 6]. However most recent calculations, based on reverse Monte Carlo (RMC) analysis of neutron scattering data, show evidence of a broader distribution, with the presence of different local sites around Ag cations, having a higher average coordination number [7].

In particular, the pair correlation functions $G_{ij}(r)$ for $Ag_2O{\cdot}nB_2O_3$ simulated by Swenson *et al.* [8] by RMC show that the first peak of the partial $G_{AgO}(r)$ is relatively sharp and symmetrical around 2.4 Å. The corresponding coordination number is estimated to be about 3.3, in good agreement with the experimental value of 3.7 ± 0.5 previously determined by neutron diffraction [8]. On the contrary, both $G_{AgB}(r)$ and $G_{AgAg}(r)$ show a very broad peak, extending from about 2.5 Å and reaching its maximum value at about 3.1 Å [7].

Since the presence of static disorder reduces the XANES and EXAFS signals in a different way, we undertook in a previous work [9] a comparative analysis of XAS spectra calculated for the near edge region. As a first step, all the known crystalline sites for Ag in borate crystals were simulated and compared with experimental XANES spectra by increasing the number of nearest neighbours and the static disorder. Both XANES and EXAFS signals could not be reproduced by any of these sites [10]. As a second step, some simple geometrical structures were built, in order to evaluate the number and kind of nearest neighbours necessary to reproduce at least the general shape of XANES. The best agreement was reached with a configuration of 8 atoms, distributed within a radial distance of about ∼3 Å, that were displaced angularly and/or radially starting from a cubic model. From the previous [9] XANES simulations, we concluded that the most plausible model for the local coordination of Ag in borate glasses is characterised by a first shell Ag-O_4 at a distance $R = 2.2$–2.3 Å, the remaining atoms being distributed randomly at longer distances. We also verified that the substitution of some next nearest neighbours oxygen atoms with boron slightly improves the agreement with experimental spectra. In any case, the agreement was only qualitative but it gave a clear indication that a single-configuration model is not able to reproduce the experimental spectra.

In the followings, we will present some examples about the use of a multi-configuration approach.

2. Experimental and Theoretical Details

X-ray absorption spectra were measured at the Ag K-edge using the synchrotron radiation from the ESRF storage ring (Grenoble, France) at the GILDA BM08 beamline. A transmission scheme with a Si(311) crystal monochromator and two ion chambers filled with argon gas was used. Three sets of measurements were performed: (*i*) crystalline c-Ag_2O at 77 K; (*ii*) glasses g-$Ag_2O{\cdot}4B_2O_3$ and g-$Ag_2O{\cdot}2B_2O_3$ in a range of temperatures

from 77 to 450 K; (*iii*) a set of glasses g-$Ag_2O{\cdot}nB_2O_3$ with $n = 2,3,4,6,8$ at $T = 77$ K.

The obtained X-ray absorption spectra were analysed using two methods.

1) The XANES part was simulated by real-space full-multiple-scattering calculations [11] for a set of trial structures. We used the *rsms* code, which is an amended descendant of the *icxanes* code [12] and is maintained by O. Sipr [13]. In order to put into evidence the net effect of structural changes, the same scattering potential was chosen for all the trial structures. We resorted to a non-self consistent potential constructed along the Mattheiss prescription for a silver orthoborate crystal. We checked that the particular choice of the potential is not crucial for the aim of our study. Since no significant core-hole effect has been observed, we used a potential which neglects the core-hole.

2) The EXAFS signals were extracted in a conventional way using the EDA software package [14] and analysed as described below. To determine structural parameters from the EXAFS spectra of glasses, one needs to know the amplitude and phase shift functions for required atom pairs. In this work we have used theoretical *ab initio* model within FEFF8 formalism [15], which was tested using reference c-Ag_2O compound with well known structure. The calculated c-Ag_2O EXAFS signal was in excellent agreement with the experimental, confirming the good accuracy of the theoretical amplitude and phase shift functions for Ag-O and Ag-Ag atom pairs.

The EXAFS signals of glasses were extracted on the same energy scale as for the reference c-Ag_2O compound. Their Fourier transforms consist of a broad asymmetric single-peak and do not show any evidence of the contribution from outer coordination shells. This allows to perform the analysis of the first peak using the original EXAFS spectra without employing the Fourier filtering procedure.

The EXAFS signals were best fitted using two techniques, which allow to reproduce the atomic structure up to ~3.2 Å. The first one is a model-independent approach, implemented by the EDARDF code [16]. It allows to reconstruct the total radial distribution function (RDF) without any assumption on its shape. As an example, the RDFs obtained for the glasses at 77 K are shown in Fig. 1.

The second one is a conventional Gaussian multi-shell best-fit, starting from results obtained by using the EDARDF code. In particular, up to three shells were used to reproduce the EXAFS signal, with a maximum number of nine fitting parameters, three (N, R, σ^2) for each shell.

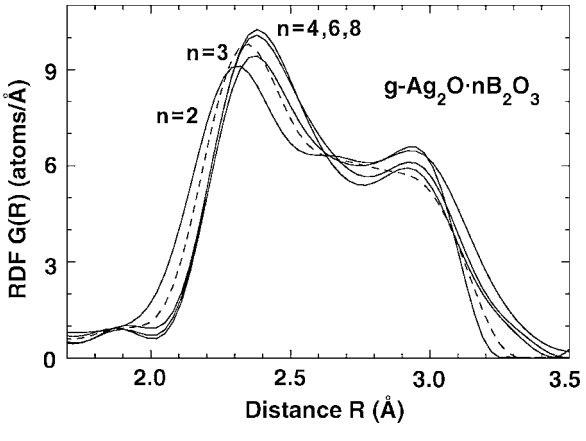

Fig. 1. RDFs in g-$Ag_2O{\cdot}nB_2O_3$ glasses at 77 K, as obtained by EDARDF code.

3. Results and discussion

3.1. *General conclusions from EXAFS analysis*

The RDF around silver ions in silver borate glasses has complex asymmetric shape. As a first approximation, based on the chemical composition of these glasses and general rules of glass network formation, the RDF can be decomposed into two parts: (*i*) the nearest oxygen atoms, which form the first coordination shell of silver ions, and (*ii*) the outer neighbours, presumably oxygens and borons which form the glass network. The oxygen atoms in the first shell show a broad but well defined distribution peaked at ~2.3 Å. At the same time, the group of more distant neighbours has a wide distribution, extending from 2.4 to 3.2 Å. Such a shape of the RDF significantly complicates the analysis, since it cannot be easily approximated by a simple analytical function. Another problem is related to the composition of the outer neighbours. The expected intermixture of oxygen and boron atoms and the similarity of their scattering amplitude and phase shift functions do not allow to separate unambiguously these two contributions. In fact, we have analysed two extreme models: in the first one, all atoms in the outer group were assumed to be oxygens and, in the second one, all atoms were assumed to be borons. The obtained results show that an exchange of oxygen atoms with borons slightly affects the values of structural parameters (N, R, σ^2), but does not substantially change the asymmetric shape of the RDF.

The approximation of the total RDF with three Gaussian functions allows to conclude that there are about 4 oxygen atoms in the first coordination shell of silver and about 4–5 oxygen/boron atoms in the next outer shells.

3.2. *Multi-configuration analysis*

On the basis of the EXAFS results, we have studied the evolution of the simulated XANES spectra, by varying in a systematic way the "1 + 8 atoms cubic cluster" previously identified: atoms were grouped into two shells, allowing different parameters (radial distances and angles, coordination numbers, type of atoms) to be independently varied. Finally, for each set of variable parameters, a mean XANES spectrum was generated by averaging over many configurations obtained from a particular distribution of possible clusters. The choice of shape of the distribution of allowed parameters is one of the crucial points of the procedure. As an illustration of our procedure, we investigate in Fig. 2 the effect of a gradually introduced randomization of the test models geometry. The top curve corresponds to a semi-ordered model with Ag at the cube centre and eight neighbouring atoms located along the cube diagonals: four oxygens form the first shell at $R = 2.3$ Å, four borons form the second shell with R covering equidistantly the 2.5–3.0 Å interval and a partial disorder is introduced via distributing these neighbouring atoms among the cube corners in all possible ways. Then we introduced angular randomization of the second-shell atoms (i.e. their angular coordinates are uniformly distributed over the full space angle) and on top of that also a radial randomization (radial distances of second-shell atoms are uniformly distributed in the interval 2.5–3.0 Å). The remaining theoretical curves describe models with additionally imposed randomization of the first-shell atoms: either only in angular coordinates (fourth curve from the top in Fig. 2) or both in angular and radial coordinates (fifth curve from the top). In the last case, the radial distances of the first shell atoms uniformly deviate from their middle value of 2.3 Å by at most 0.2 Å. A complete description of our constructing the structural models is under publication [10].

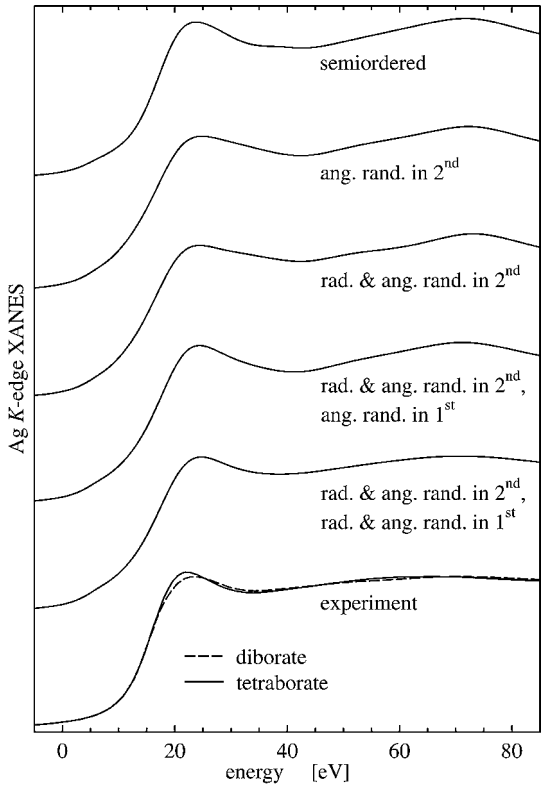

Fig. 2. Configurationally averaged XANES spectra obtained by gradually introducing the randomization in the structure of test models, as described in the text.

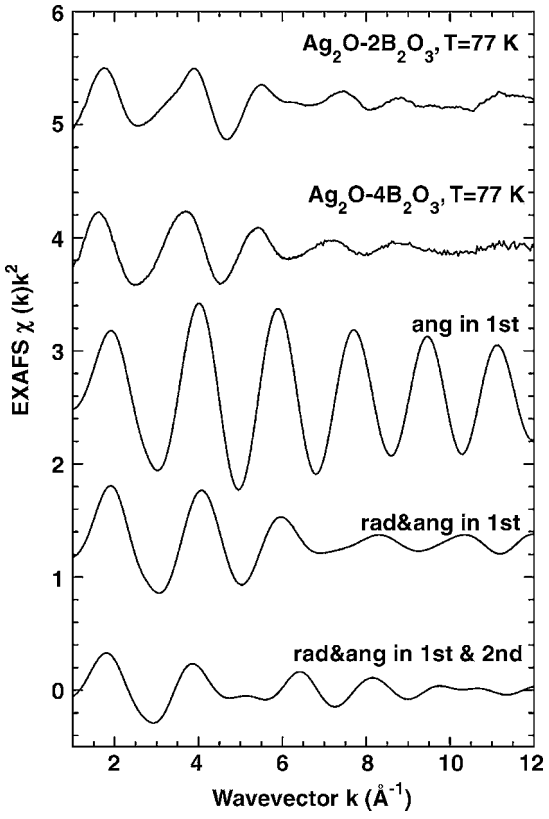

Fig. 3. Comparison of experimental EXAFS with calculations for structural models obtained by gradually introducing randomization, as described in the text.

In this way, a much better agreement with XANES experimental spectra has been obtained, but it is still difficult to identify the *good* model, if any. We have thus developed a new software code, able to calculate and average not only XANES, but also EXAFS spectra from each set of *randomly* generated clusters. Preliminary results are very promising, as shown in Fig. 3, where theoretical EXAFS curves for models explored in Fig. 2 are presented (third from the top curve represent a model with angular randomization applied for the first-shell atoms, below is the curve for a model with both angular and radial randomization of the first shell atoms and bottom curve corresponds to both angular and radial randomization in both the first and the second shells). It is quite clear (as expected) that EXAFS is much more sensitive to details of the distribution of radial distances, while XANES is more able to appreciate the influence of angular parameters, which change the multiple scattering contributions.

A first result of the comparison between XANES and EXAFS is the identification of the "wrong" distributions of generated clusters. Moreover, a careful analysis of the trends of the obtained spectra allows us to check the actual influence of each parameter on the configurationally-averaged spectra and to identify for each parameter the most probable value.

We should remember, however, that for silver borate glasses (and in general for systems where a description in terms of single-configuration is not realistic) the obtained values do not describe the local structure of Ag ions, but only a *mean* situation. In fact, the experimental spectrum is due to the superposition of several absorption spectra, corresponding to silver atoms in a quite different configuration. Work is in progress to go beyond the limits of the *random* generation of possible local clusters, aiming to build a bestfit procedure able to manage with more physical constraints for the identification of local sites of Ag ions in borate glasses.

Acknowledgements

The authors would like to thank Mrs. C. Armellini for the preparation and characterisation of glasses. This work was supported by the CNR-AV CR Common Research Project "Local order in nanosize and disordered systems" and by project AVOZ-010-914 of the Grant Agency of the Czech Republic.

The authors are grateful to the staff of the "GILDA" beamline for assistance during the experiments. Measurements have been partially supported by European Synchrotron Radiation Facility (ESRF, France) (Project HS-1254) and Istituto Nazionale per la Fisica della Materia (INFM, Italy) (Project BM08-01-225).

References

1. Minami, T., J. Non-Cryst. Solids **73**, 273 (1975).
2. Varsamis, C. P., Kamitsos, E. I. and Chryssikos, G. D., Phys. Rev. B **60**, 3885 (1999).
3. Swenson, J., Börjesson, L. and Howells, W. S., J. Phys: Condens. Matter **11**, 9275 (1999).
4. Cervinka, L., Bergerová, J., Dalmaso, A. and Rocca, F., J. Non-Cryst. Solids **232–234**, 627 (1998).
5. Dalba, G. *et al*., S., J. Non-Cryst. Solids **91**, 153 (1987).
6. Rocca, F., Dalba, G., Fornasini, P. and Monti, F., in "Proc. Second. Int. Conf. Borate Glasses, Crystals and Melts", Abington, 1996, (edited by A. C. Wright, S. A. Feller, and A. C. Hannon), (Society of Glass Technology, Sheffield, 1997), p. 295.
7. Swenson, J., Borjesson, L., McGreevy, R. L. and Howells, W. S., Phys. Rev. B **55**, 11236 (1997).
8. Swenson, J., Borjesson, L. and Howells, W. S., Phys. Rev. B **52**, 9310 (1995).
9. Sipr, O., Dalba, G. and Rocca, F., Phys. Chem. Glasses **44**, 252 (2003).
10. Sipr, O., Dalba, G. and Rocca, F., Phys. Rev. B **69**, 134201 (2004).
11. Vvedensky, D. D., "Unoccupied Electron States", (Edited by J. C. Fuggle and J. E. Inglesfield), (Springer, Berlin, 1992), p. 139.
12. Vvedensky, D. D., Saldin, D. K. and Pendry, J. B., Comput. Phys. Commun. **40**, 421 (1986).
13. Sipr, O., Rocca, F. and Dalba, G., J. Synchrotron Rad. **6**, 770 (1999).
14. Kuzmin, A., Physica B **208/209**, 175 (1995).
15. Ankudinov, A. L., Ravel, B., Rehr, J. J. and Conradson, S. D., Phys. Rev. B **58**, 7565 (1998).
16. Kuzmin, A., J. Physique IV (France) **7**, C2-213 (1997).

Physica Scripta. Vol. T115, 152–154, 2005

A Quantitative Structural Investigation of the XANES Spectra of Potassium Ferrocyanide (III) at the Iron K-Edge

Kuniko Hayakawa[1,2], Keisuke Hatada[1], Calogero R. Natoli[1], Paola D'Angelo[3], Stefano Della Longa[4,5] and Maurizio Benfatto[1]

[1]Laboratori Nazionali di Frascati, INFN, CP13,00044 Frascati, Italy
[2]Dipartimento di Biologia, Universita "Padova", Via Ugo Bassi 58b, 35121 Padova, Italy
[3]Dipartimento di Chimica, Universita "la Sapienza", Piazzale A. Maro, Maro 5, 00185 Roma, Italy
[4]Dipartimento di Medicina Sperimentale, Universita "L'Aquila", Via Vetoio 67100 L'Aquila, Italy
[5]INFM, Un. Roma 1, Pza A. Moro, 00185 Roma, Italy

Received June 26, 2003; accepted January 15, 2004

Abstract

In this paper we present a detailed quantitative analysis of the iron K-edge XANES data of potassium ferrocyanide in water solution. The right structural determination as been obtained from the XANES data by using the MXAN procedure to fit the experimental data despite the presence of small discrepancies between experimental data and best-fit calculations at low energy. The origin of such discrepancies is also discussed in terms of non muffin-tin corrections and the role of the right charge density of the cluster.

1. Introduction

In this paper we present a detailed quantitative structural analysis of the XANES spectrum (from the edge up to 150 eV) of potassium ferrocyanide (III) in water at the iron K-edge. The structural results are compared with a previous EXAFS analysis performed by the GNXAS package [1]. The XANES energy region has been fitted with the help of the MXAN procedure [2], using the Fe-C and C-N distances and the Fe-C-N angles as parameters in the fitting procedure. The structural determination fully agrees with the one obtained by EXAFS analysis despite the presence of small discrepancies between the experimental data and the fitted theoretical spectrum in the low energy region (within the first 50–60 eV), confirming the dominance of the geometrical structure in the determination of the XANES shape. We discuss the origin of such discrepancies both in terms of the need of the self-consistent field calculation of the potential, using the formal valency of the atomic species, and possible correction to the muffin-tin approximation of the shape of the potential. This work has been motivated by the need to test potential applications of the MXAN procedure to systems of biological interest.

2. Theory

Recently, a new method to perform a quantitative analysis of the XANES energy range, i.e. from the edge up to 200 eV, was proposed in the literature. The method, called MXAN [2], is based on a comparison between experimental data and many theoretical calculations performed by varying selected structural parameters starting from a putative structure, i.e. from a well defined initial geometrical configuration around the absorber. The calculation of XANES spectra related to the hundreds of different geometrical configurations needed to obtain the best fit of the experimental data is done in a reasonable time and the optimization in the space of parameters is achieved by minimization of the square residual function in parameter space. The calculations are performed in the energy space without involving any Fourier transform algorithm. The MXAN method is based on the muffin-tin approximation for the shape of the potential and the use of the concept of complex optical potential, based on the local density approximation of the self-energy of the excited photoelectron. The real part is calculated by the Hedin-Lundqvist potential using the whole charge density. Inelastic processes are taken into account by a convolution with a broadening Lorentzian function having an energy dependent width of the form $\Gamma(E) = \Gamma_c + \Gamma_{mfp}(E)$. The constant part Γ_c includes the core hole lifetime and the experimental resolution, while the energy dependent term represents all the intrinsic and extrinsic inelastic processes. The $\Gamma_{mfp}(E)$ function is zero below an onset energy E_s (which in extended systems corresponds to the plasmon excitation energy) and begins to increase from a value A_s following the universal functional form of the mean free path in solids. Both the onset energy E_s and the jump A_s are introduced in the $\Gamma_{mfp}(E)$ function via an arctangent functional form to avoid discontinuities and to simulate the electron-hole pair excitations. Their numerical values are derived at each step of computation (i.e. for each geometrical configuration) on the basis of a Monte Carlo fit [3]. The full potential calculations are based on the Finite Difference Method (FDM) which does not require any approximation for the shape of the potential. This method essentially writes the Schrodinger equation on a three-dimensional grid obtaining a large system of linear equations connecting the values of the wave function on all the grid points. We have used the program FDMNES developed by Y. Joly and we refer to reference [4] for details. The potential has been calculated on the basis of $Z + 1$ approximation for the final state.

3. Results and Discussion

In Fig. 1 we report the comparison between the experimental data and the calculation at the best fit conditions.

The Fe K-edge X-ray absorption spectrum of a 0.5 M $K_3Fe(CN)_6$ water solution was recorded at the ESRF (Grenoble, France), beam-line BM29. The data were recorded in transmission mode using a Si(311) double-crystal monochromator, detuned to 50% of the rocking curve full width at half maximum, for harmonic rejection. Data points were collected for 1 s each and several spectra were recorded and averaged. The solutions were kept in cells with Kapton film windows and Teflon spacers of 1 mm.

The best-fit conditions correspond to an octahedral geometry with Fe-C and C-N distances of 1.93 Å and 1.147 Å respectively. These values are in good agreement with those obtained by EXAFS analysis of solid $K_3Fe(CN)_6$, within the statistical error bar that is about 2% of the bond length. It is important to stress

that in water solution the Fe(III) ion forms a very stable complex where the short-range environment of the iron ion is equal to the crystalline phase one. In aqueous solution the water molecules do not contribute to the XAS spectra as they give rise to a far and disordered hydration shell. This is confirmed by Fourier Transform of the EXAFS spectrum which does not show the presence of any peak above 3.5 Å. For the sake of brevity the EXAFS analysis will be presented elsewhere.

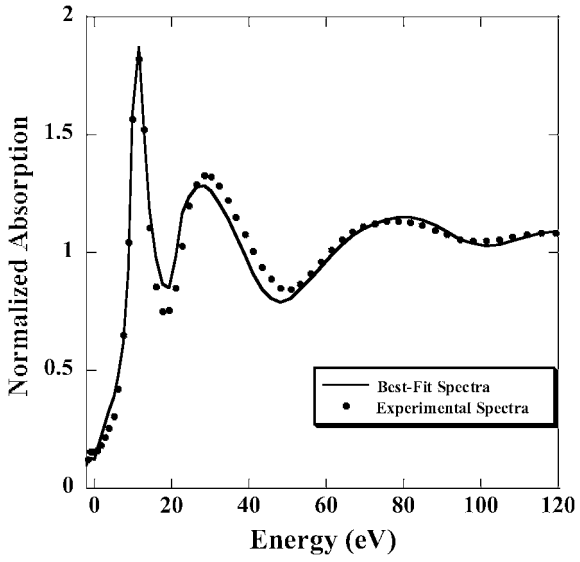

Fig. 1. Comparison between the experimental Fe K-edge data of $Fe(CN)_6$ (dotted line) and the best-fit calculation performed by the MXAN procedure (solid line).

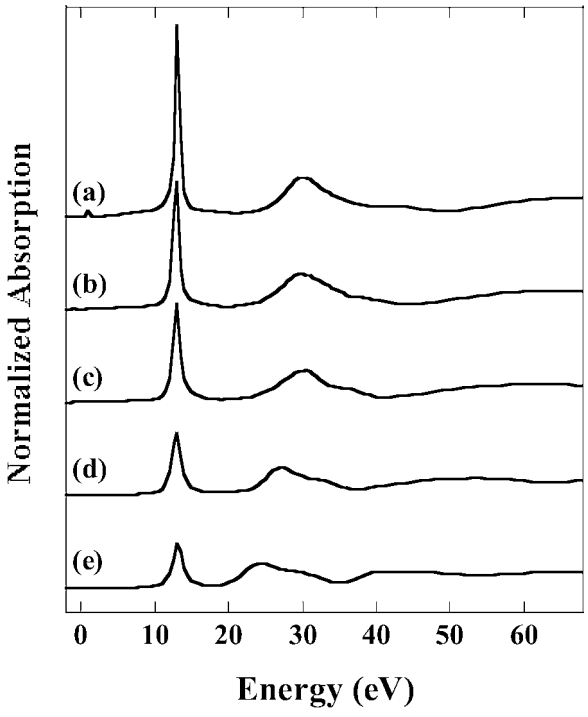

Fig. 2. The effect of electronic structure on non-muffin-tin potential using FDM program. The electronic structure of (a) is Fe: $3d^64s^2$, C: $2s^12p^3$, N: $2s^22p^3$ (cluster-charge = 0), (b) Fe: $3d^{6.5}4s^2$, C: $2s^12p^3$, N: $2s^22p^3$ (cluster-charge = −0.5), (c) Fe: $3d^74s^2$, C: $2s^12p^3$, N: $2s^22p^3$ (cluster-charge = −1), (d) Fe: $3d^84s^2$, C: $2s^12p^3$, N: $2s^22p^3$ (cluster-charge = −2) and (e) Fe: $3d^94s^2$, C: $2s^12p^3$, N: $2s^22p^3$ (cluster-charge = −3).

The used electronic structure is the typical one of the neutral atoms case, i.e. Fe: $3d^64s^2$, C: $2s^12p^3$ and N: $2s^22p^3$, with a total cluster charge equal to zero. The agreement between experimental data and the best fit calculation is rather good in the whole energy range. Small discrepancies appear in the energy range between 15 and 40 eV although they do not affect the structural reconstruction.

To understand the origin of such discrepancies, which are larger than in other systems, we have used the FDMNES program to check in details the influence of the non-muffin-tin corrections to the calculation. The geometrical structure is the same as the one obtained by MXAN at the best fit condition. In Fig. 2 we report a set of raw FDM calculations without damping. They refer to different electronic structures (see the figure caption for details). As expected the influence of changing the electronic structure is essentially confined in the low energy range and it appears rather strong in the energy range 10 eV to 40 eV.

In Fig. 3 we compare the experimental data with three fits starting from the raw calculations shown in Fig. 2 and using as fitting parameters the quantities that define the Lorentzian broadening functions. In this way we can apply our

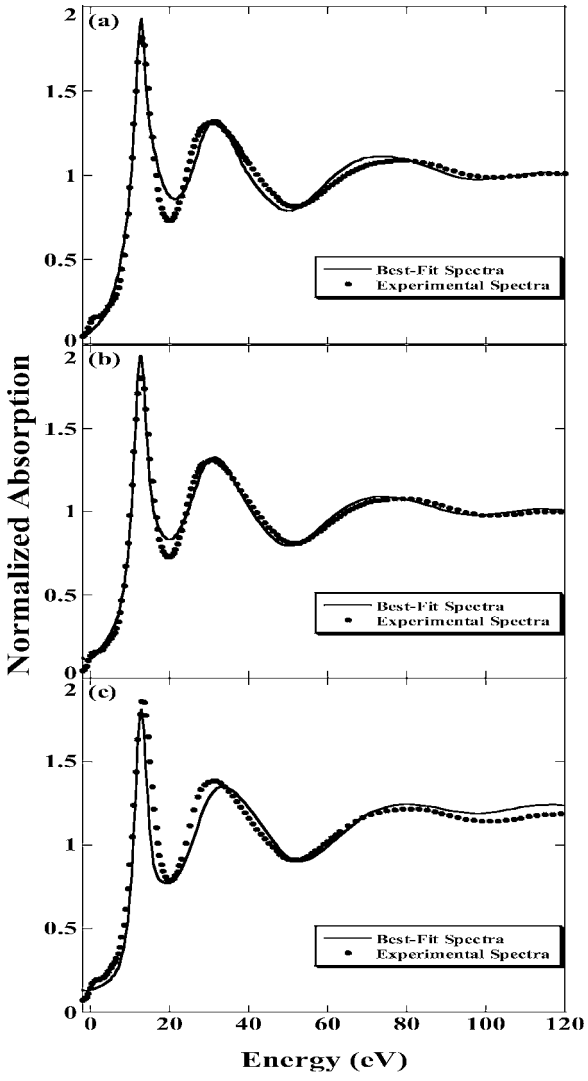

Fig. 3. Comparison between the best fit theoretical XANES spectra (solid line) performed by the MXAN procedure to non-muffin-tin potential (FDM program) and the experimental data (dotted line). The electronic structure of (a) is Fe: $3d^64s^2$, C: $2s^12p^3$, N: $2s^22p^3$ (cluster-charge = 0), (b) Fe: $3d^{6.5}4s^2$, C: $2s^12p^3$, N: $2s^22p^3$ (cluster-charge = −0.5) and (c) Fe: $3d^84s^2$, C: $2s^12p^3$, N: $2s^22p^3$ (cluster-charge = −2).

phenomenological damping method also to the FDM calculations quantifying both the non-muffin-tin corrections and the changes of charge density. Details of the calculations are in the figure caption. Panel (a) of Fig. 3 refers to the same charge density of the MXAN calculation. The agreement between the experiments and theory is better than in Fig. 1 (the error function decreases by about 20%) but the improvement is not dramatic, confirming the goodness of the muffin-tin approximation for the calculation of the absorbing cross-section in most of the systems. On the other hand changes in the electronic configuration produce strong changes in the theoretical calculations (see panels (b) and (c) of Fig. 3). In particular the calculation shown in panel (b) produces a decrease of the error function of about 50%, going from 20.4 to 11.3, indicating the need of a good charge density. Small changes in the charge distribution (from case (a) to case (b)) generate larger differences than the one produced going from muffin-tin to non muffin-tin calculations. The small discrepancies still present can be due to the use of a potential that is not self-consistent.

4. Conclusion

We performed a quantitative analysis of XANES data of potassium ferrocyanide (III) at the iron K-edge. We have demonstrated that the MXAN procedure can obtain a good structural reconstruction even in the presence of small discrepancies between experimental data and the best fit calculation. The importance of the muffin-tin approximation for the shape of the potential is discussed as well, showing that the muffin-tin approximation is good enough for structural determination. The importance of the correct charge density in theoretical calculations to construct the optical potential has also been emphasized.

References

1. Westre, T. E. *et al*., J. Am. Chem. Soc. **117**, 1566 (1995).
2. Benfatto, M. and Della Longa, S., J. Synchrotron. Rad. **8**, 1087 (2001).
3. Della Longa, S., Arcovito, A., Girasole, M., Hazemann, J. L. and Benfatto, M., Phys. Rev. Lett. **87**, 155501 (2001).
4. Joly, Y., Phys. Rev. B **63**, 125120 (2001).

Physica Scripta. Vol. T115, 155–158, 2005

The Mean Square Variation of Multiple Scattering Path Length by Molecular Dynamics Simulation

N. Binsted, A. B. Edwards*, J. Evans and M. T. Weller

Dept. of Chemistry, University of Southampton, SO17 1BJ, UK
*Dstl Land Systems Department, Dstl Fort Halstead, Sevenoaks, Kent TN14 7BP, UK

Received June 26, 2003; accepted January 7, 2004

PACS numbers: 61.10Ht, 02.70Ns

Abstract

Approximations in the treatment of Debye-Waller factors in multiple scattering calculations are one of the principal remaining uncertainties in XAFS calculations. The amplitude of each path varies as a function of the mean square variation in path length. This quantity depends on the many-body correlations involving atoms in the path, as well as the mean square displacement of individual atoms. The correlations normal as well as parallel to interatomic vectors are required, and the effects of anharmonicity must be taken into account. Although difficult to calculate accurately, these quantities can be extracted directly from molecular dynamics (MD) simulations. Here we present temperature dependent results for copper, using a semi-empirical potential based on a tight-binding model, from which the cumulants of the variation in path length as well as the correlation functions are derived. XAFS calculations based on extracted parameters are compared with those calculated directly from the MD atomic coordinates, and with results using Debye model and lattice dynamic calculations.

1. The XAFS Debye-Waller factor

The XAFS Debye-Waller factor arises from a configurational average over all possible atomic positions:

$$\iiint \mathrm{d}x_1\mathrm{d}y_1\mathrm{d}z_1 \ldots \iiint \mathrm{d}x_n\mathrm{d}y_n\mathrm{d}z_n\ \chi(k,\underline{r_1}\ldots\underline{r_n}) \times g(\underline{r_1}\ldots\underline{r_n}). \tag{1}$$

If the many-body distribution functions are replaced by products of pair distribution functions then it is given by:

$$\iiint \mathrm{d}x_1\mathrm{d}y_1\mathrm{d}z_1 \ldots \iiint \mathrm{d}x_n\mathrm{d}y_n\mathrm{d}z_n \chi(k,\underline{r_1}\ldots\underline{r_n}) \times g_{x01}\ldots\times g_{zn0}. \tag{2}$$

A further simplification arises from treating each leg of a scattering path individually, in one dimension. An approximate solution to this problem was devised by Tranquada and Ingalls [1] who approximated the interesting bit of the XAFS function, the angular momentum sum over the Hankel functions, by its asymptotic limit (plane wave approximation):

$$\int_0^\infty \mathrm{d}r\, g(r)\frac{1}{r^2}\exp^{2\mathrm{i}kr} = \frac{1}{r_0^2}\exp^{2\mathrm{i}kr'}\,\mathrm{e}^{-1/2\acute{o}_p^2k^2+1/24\acute{e}_{p4}k^4}, \tag{3}$$

$$r' = r_0 - \frac{\sigma_p^2}{2r_0} - 1/12\kappa_{p3}k^2. \tag{4}$$

Here $2r_0 = 2\langle \boldsymbol{r}\rangle$ (1st cumulant), σ_p^2 is the mean square variation in path length (2nd cumulant), and κ_{p3} and κ_{p4} the 3rd and 4th cumulants of the path, respectively. For single scattering, σ_p is given by:

$$\sigma_p^2 = 4\sigma_{ab}^2, \tag{5}$$

$$\sigma_{ab}^2 = (\langle u_a^2\rangle + \langle u_b^2\rangle)(1 - C_{ab}), \tag{6}$$

where u_i^2 is the mean square displacement of the ith individual atom, and the C_{ab} the correlations between their atomic motions.

For multiple scattering paths of order n (i.e. including atoms a to n), where legs of the path involve angles α, σ_p^2 can be given by

$$\langle u_a^2\rangle(1 - Ce_a)\cos^2(\acute{a}_a/2) + \cdots + \langle u_n^2\rangle(1 - Ce_n)\cos^2(\acute{a}_n/2), \tag{7}$$

$$Ce_a = \frac{C_{ab}\cos^2(\alpha_b/2) + C_{ac}\cos^2(\alpha_c/2)\cdots + C_{az}\cos^2(\alpha_z/2)}{\cos^2(\alpha_b/2) + \cos^2(\alpha_c/2)\cdots + \cos^2(\alpha_z/2)}. \tag{8}$$

This is the basis of the functions used to describe the mean square variation in path length in the programs EXCURVE [2] and P [3]. In EXCURVE and for the simplest disorder option in P, only the shell-dependent Debye-Waller terms are used in the calculation, rather than the individual atomic displacements and the correlation terms, so a further simplification is used:

$$\sigma_p^2 = \sum_a 1/2\sigma_{0a}^2\cos^2(\alpha_a/2). \tag{9}$$

There are some exceptions to the use of this rule, most notably when legs are used twice in the same paths (e.g. 0-*a*-0-*a*-0). Because the motion of the photoelectron is fast compared to the atomic motion, the same change in leg length applies equally to both parts of the total multiple scattering path. Thus for the case where n legs are shared:

$$\sigma_{p'}^2 = n^2\sigma_p^2, \tag{10}$$

where σ_p^2 is calculated as above.

In this paper we will discuss both cumulants of the path and cumulants of an individual distance. These can be readily interconverted by employing the relationship:

$$\kappa_{pn} = 2^n\kappa_{dn}. \tag{11}$$

The nth cumulant is in units of Å^n in each case. We note also that the EXCURVE and P parameters A and B are $2\sigma^2$ and $\kappa_3 \times 1000$, respectively, where σ^2 and κ_3 are cumulants for the distance not the path. Thus far we have ignored any three dimensional effects, but P (and some versions of EXCURVE) have the following two options:

- r_0 above may be increased to reflect motion normal to the bond, using the assumption that both $\langle u^2\rangle$ and the inter-atomic correlation are isotropic (single scattering only).
- For near-colinear bonds, the effective bond angle is reduced, according to the effect of the Debye-Waller terms on each atom in the path.

Both EXCURVE and P restrict the use of higher cumulants to single scattering paths.

The number of approximations is clearly very large. Previously, some of the approximations involved in the single scattering paths have been evaluated. For example, by using numerical integrals,

use of the plane wave approximation and truncation of the Taylor series involved in the use of Tranquada and Ingalls equation can be avoided. Where XAFS Debye-Waller terms are quite small, these effects are also small. Moreover, when the product of the wavevector and interatomic distance kr is small, and spherical wave effects tend to be large, $k^2\sigma^2$ tends to be small. In a previous MD paper [4] the difference between r_{ab} and r_0 was evaluated, the importance of higher cumulants described, and the anharmonic oscillator model (which can be used to calculate third cumulants) was tested. However, for the generalised case there is no easy way of evaluating the effect of thermal disorder on the multiple scattering paths.

Here we attempt to provide further tests of our assumptions, using lattice dynamics calculations and derivations of the multiple scattering cumulants from MD studies to gain insight into the nature of thermal motion as it effects XAFS.

2. Lattice dynamics

The displacement-displacement correlation function for face centred cubic (FCC) copper, using the 300 K crystallographic lattice parameter of 3.615 Å was calculated in the harmonic approximation from [5]:

$$\langle u_\alpha(i)u_\beta(j)\rangle = 1/(Nm_i^{1/2}m_j^{1/2})\sum_{k,v}\langle Q(k,v)Q(-k,v)\rangle \times e_\alpha(i,k,v)e_\beta(j,-k,v),$$

$$\langle |Q(k,v)|^2\rangle = E(k,v)/\omega^2(k,v). \quad (12)$$

The displacements u of atoms i, j of mass m are calculated from the N eigenvectors e and eigenvalues (frequencies) ω^2 of the mass-weighted dynamic matrix. Q are the normal mode amplitudes associated with wavevector k for which the vibrational energy is E. A sum over 10^6 equally spaced points in the Brillouin zone for the single longitudinal and two transverse modes v was used. The dynamic matrix was calculated using the force-constants of the 6-shell model of Sinha [6] who determined their numerical value by fitting room-temperature inelastic neutron scattering data. Displacements were calculated for the first 10 shells around Cu. For the case $i = j$, the displacement matrix is diagonal, with non-zero terms equal to the isotropic mean square displacement $\langle u^2\rangle$ of an individual atom. In the uncorrelated case, the XAFS Debye-Waller term σ^2_∞ is $2\langle u^2\rangle$. The phonon frequency distribution spectrum was in good agreement with previous results [6]. Table I shows the displacements in terms of the crystal lattice coordinates, together with the bond-parallel and bond-normal (averaged over two directions) values. The effective correlation for each component ($1 - \sigma/\sigma_\infty$, where σ^2_∞ is $2\langle u^2\rangle$) is also displayed.

The results for the bond-parallel component are very similar to those derived from Debye theory using the experimental Debye temperature of 317 K. The near isotropy of the interatomic correlation in bond-normal and bond-parallel directions justifies the optional three-dimensional correction available in P. The off diagonal terms are very weak – the largest being the $0x$-$4y$ correlation, which will tend to accentuate the departure of the 0-1-4 angle from 180 degrees. Atoms remain correlated to at least the 10th shell.

3. Molecular dynamics

MD simulations were performed as in our previous paper [4], using the semi-empirical tight-binding potential used initially by Rosato *et al*. [7]. The previous paper also describes the method for extracting the cumulants from the moments of the atomic distributions within an anharmonic oscillator model. The same approach is used here, but in this work we extend the analysis to the multiple scattering paths, which are the principal subject of this paper. However, for reasons of compatibility with the program P (which was used to calculate an EXAFS spectrum from actual simulation coordinates) we have increased the system size to 2916 atoms.

Table I. *The displacement-displacement correlation function for Cu, and derived XAFS Debye-Waller terms parallel and normal to the bond direction. The first three columns contain a 3 × 3 matrix of mean square relative displacements in terms of the lattice coordinates x, y, z. Columns four and five contain the components of the mean square relative displacements parallel and normal to the bond direction respectively (above), and the associated value of the correlation between the two atoms defined by equation (6) (below).*

$\sigma_x^2X^2$	$\sigma_y^2X^2$	$\sigma_z^2X^2$	$\sigma_{\|\|}{}^2X^2$ $(1-\sigma_{\|\|}{}^2/\sigma_\infty)$	$\sigma\perp^2X^2$ $(1-\sigma\perp^2/\sigma_\infty)$
Shell 1 (110)	12 × 2.556X			
.0096	−.0015	.0000	.0088	.0104
−.0015	.0096	.0000		
.0000	.0000	.0104	.37	.25
Shell 2 (200)	6 × 3.615X			
.0116	.0000	.0000	.0116	.0114
.0000	.0114	.0000		
.0000	.0000	.0114	.16	.17
Shell 3 (211)	24 × 4.427X			
.0114	−.0005	−.0005	.0108	.0120
−.0005	.0117	−.0003		
−.0005	−.0003	.0017	.22	.13
Shell 4 (220)	12 × 5.112X			
.0116	−.0008	.0000	.0111	.0121
−.0008	.0116	.0000		
.0000	.0000	.0121	.20	.12
.....				
Shell 10 (411)	12 × 7.669X			
.0127	−.0002	−.0002	.0127	.0127
−.0002	.0127	−.0002		
−.0002	−.0002	.0127	.08	.08

The cumulants for some representative single and multiple scattering paths calculated according to [4] are listed in Table II. Statistics are presented for copper simulated at 100 K and 300 K to demonstrate the temperature dependence of the cumulants. Table II also includes the values calculated by EXCURVE given the same single scattering Debye-Waller factors. The 100 K data is almost entirely harmonic. At both temperatures the 0-1-4-1-0, 0-1-4-0 and 0-4-0 paths have remarkably similar cumulants, and the motion of the intermediate atom has surprisingly little effect. For this reason, the EXCURVE derived values for the MS paths are remarkably good. The main exception is for the collinear 0-1-0-1′-0 path, which should be identical to 0-1-4-1-0 (it is irrelevant where the central atom is in the path). However, EXCURVE estimates one of these from the first shell and one from the fourth shell single scattering values, so introduces a difference in their values. Figure 1 is a distribution of scattering angles at 100 K and 300 K for the 0-1-4-1-0 path extracted from the MD simulation. Clearly, although often assumed to be colinear, the probability of the scattering angle actually being 180 degrees is very small. The displacement of the maxima of the

Table II. *Cumulants of the scattering path length from the 100 K and 300 K MD simulation (columns 1 and 2 respectively) and equivalent MS mean square path length variation calculated by EXCURVE from the first shell cumulants alone (column 3).*

Path 0-1-0-1-0	MD simulation at 100 K	MD simulation at 300 K	EXCURVE calculation at 300 K
κ_1	10.1908	10.2320	
κ_2	0.0401	0.1281	.1282
κ_3	0.0011	0.0111	
κ_4	0.0000	0.0012	
Path 0-1-0			
κ_1	5.0964	5.1160	
κ_2	0.0100	0.0320	.0320
κ_3	0.0001	.0014	
Path 0-2-0			
κ_1	7.2042	7.2295	
κ_2	0.0150	0.0486	.0486
κ_3	0.0000	−0.0002	
Path 0-3-0			
κ_1	9.8226	8.8519	
κ_2	0.0136	0.0437	.0437
κ_3	0.0000	0.0004	
Path 0-4-0			
κ_1	10.1870	10.2198	
κ_2	0.0136	0.0435	.0435
κ_3	0.0001	0.0007	
Path 0-1-0-1′-0			
κ_1	10.1908	10.2320	
κ_2	0.0137	0.0435	.0320
κ_3	0.0001	0.0007	
Path 0-1-4-1-0			
κ_1	10.1908	10.2320	
κ_2	0.0137	0.0435	.0435
κ_3	0.0001	0.0007	
Path 0-1-4-0			
κ_1	10.1890	10.2259	
κ_2	0.0136	0.0434	.0435
κ_3	0.0001	0.0007	
Path 0-1-1′-0			
κ_1	10.1890	10.2259	
κ_2	0.0136	0.0434	.0435
κ_3	0.0001	0.0007	

distribution to smaller scattering angle and a general broadening and growing asymmetry in the distributions at higher temperature is the inevitable consequence of the greater vibrational amplitude of the atoms. The peak in the angle distribution (e.g. 176° at 300 K) is very close to that calculated by the 3D correction in EXCURVE, justifying its use.

4. Calculated XAFS spectra

A number of XAFS calculations were performed using a cluster size limited to a radius of 5.5 Å. Spectra were calculated initially using (a) Debye-model parameters, (b) scattering path parameters derived from Molecular Dynamics and Lattice Dynamics methods, and (c) by using refined parameters. In addition, a spectrum was calculated directly from the 2916 atomic coordinates at a single moment in the MD simulation, by means of an average of spectra calculated for each atom individually. In each case we used the 300 K crystallographic lattice parameter of 3.615 Å, an energy zero (EF) of −11 eV, an effective core-width + resolution term (CW) of 2 eV, and the high-energy limit of the single-electron transition ratio (AFAC) of 0.95. These values were estimated from the calculation which used Debye model parameters.

The statistically optimum fit (which is compared to the experimental spectrum in Figure 2, used κ_{p3} values from the MD calculation, first shell κ_{p2} values from lattice dynamics, while the second cumulants for shells 2–4 were refined. This was very close to the best refined fit, yet required only three refined parameters. It serves as a baseline for discussion of the other fits. The calculated third cumulants improved the fit index R_{exafs} [3] by about 4%, a noticeable amount. Its inclusion is therefore important, although it is not normally possible to refine values because of correlation with other parameters, except perhaps where a series of temperature dependent spectra are available. MD is therefore very useful in either obtaining third cumulants, or testing the models used in their calculation. The accuracy required is not as great as for the second cumulants, for which inaccuracies inherent in the MD method may preclude direct use of values derived from the simulation.

The refined values of the second cumulants were, in terms of $2\sigma^2_{ab}$, .002 to .004 Å^2 higher than those calculated from the lattice dynamics values. We explain the discrepancy by our neglect of higher cumulants in the multiple scattering component of our calculation, and to a lesser extent due to the errors in estimating the mean square variations in path lengths for scattering paths within the first shell, a consequence of the simplistic algorithm used by EXCURVE as discussed above. The fit using actual MD

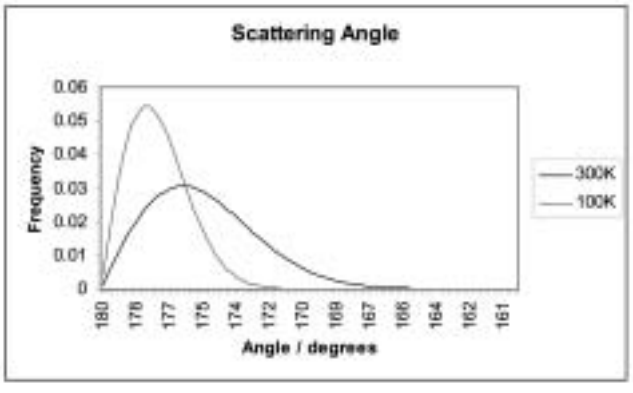

Fig. 1. Scattering angle in degrees for the 0-4-0 path at 100 K and 300 K extracted from the MD simulation.

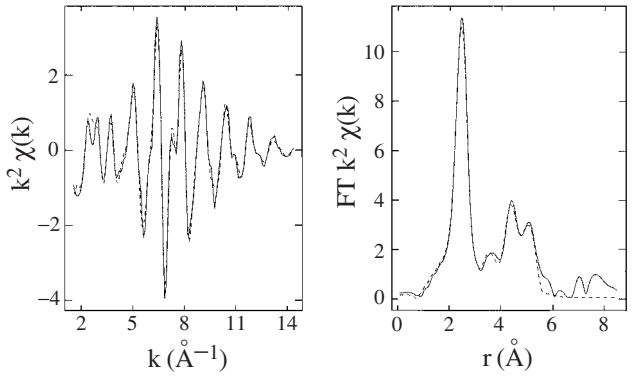

Fig. 2. EXAFS and Fourier transform for Cu at 300 K calculated using MD 3rd cumulants for all shells, 1st shell second cumulant from lattice dynamics, and refined second cumulants for other shells. Experimental data are presented as a solid line and the calculated spectrum as a dashed line.

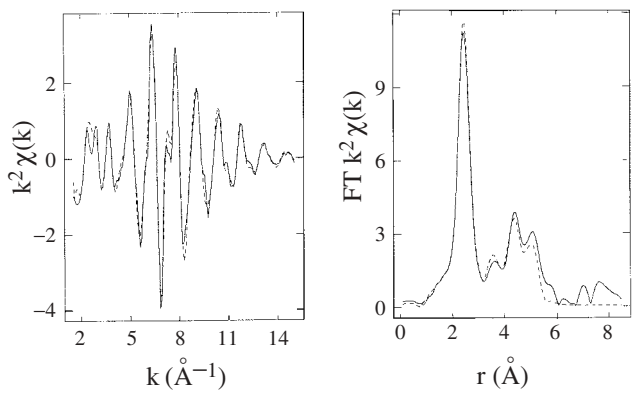

Fig. 3. EXAFS and Fourier transform for Cu at 300 K calculated directly from MD coordinates Experimental data are presented as a solid line and the calculated spectrum as a dashed line.

coordinates (figure 3) is considerably worse. The discrepancy in the first shell is to be expected, given the overall lower value of MD second cumulants compared with those obtained by lattice dynamics, Debye theory and by refining the values. More surprising is the reduction in amplitude for higher shells. This is the opposite of what we would expect, given the apparent success of the EXCURVE algorithm in estimating the second cumulants for most multiple scattering paths. We have no adequate explanation for this at present, but note that our choice of values for CW and AFAC will effect our results, and the values that were used may mask other errors used in the previous calculations.

We commented previously that the small correction due to motion normal to the bond, which can optionally be included when using P or recent versions of EXCURVE, appeared to be justified by our results. However, when used, it makes the fit slightly poorer rather than slightly better. Again, we have no explanation for this at present.

5. Conclusions

Overall we find our results to justify the unsophisticated approximations made in the calculation of multiple scattering pathlengths. The main improvement we would wish to make is to include higher cumulants in the MS paths. The close relationship between higher cumulants for the single shell and multiple scattering paths revealed by MD suggest this may be possible without introducing more variables. The third cumulants for the 1st and 4th shells may be calculated from the anharmonic oscillator model given the thermal expansion corefficient, but for the other shells it cannot. As we do not regard it as practicable to refine higher cumulant parameters, we need to develop models allowing these terms to be calculated for different lattice types. So far we have restricted out attention to a lattice with a single atom. Where optical modes contribute, estimating r_0 and the multiple scattering mean square variation in pathlength may be more complex, as different atom types can be strongly anti-correlated. Lattice dynamic calculations will be invaluable in studying these effects further.

References

1. Tranquada, J. M. and Ingalls, R., Phys. Rev. B. **28**, 3520 (1983).
2. Gurman, S. J., Binsted, N. and Ross, I., J. Phys. C. **17**, 143 (1984); J. Phys. C. **19**, 1845 (1986); Binsted, N., EXAFS analysis program EXCURVE (1982).
3. Binsted, N., Pack, M. J., Weller, M. T. and Evans, J., J. Am. Chem. Soc. **118**, 10200 (1996).
4. Edwards, A. B., Tildesley, D. J. and Binsted, N., Mol. Phys. **91**, 357 (1997).
5. Maradudin, A. A., Montroll, E. W. and Weiss, G. H., Theory of lattice dynamics in the harmonic approximation: Solid state physics, advances in research and applications, supplement 3 (Academic Press, 1963).
6. Sinha, S. K., Phys. Rev. **143**, 422 (1966).
7. Rosato, V., Guillope, M. and Legrande, B., Phil. Mag. A **59**, 321 (1989).

Physica Scripta. Vol. T115, 159–161, 2005

Using Bond Valence Sums as Restraints in XAFS Analysis

M. Newville

Consortium for Advanced Radiation Sources, The University of Chicago, Chicago, IL 60637, USA

Received June 26, 2003; revised version July 21, 2003; accepted November 4, 2003

Abstract

The Bond Valence model gives a simple, accurate relationship between the bond distance, co-ordination number, and formal valence of ions in many systems. This empirical model thus gives complementary information to EXAFS and XANES, and has been used as an independent check of XAFS results by many workers. More generally, the Bond Valence represents *prior knowledge* of the system that can be used to constrain the XAFS analysis itself. Since Bond Valence sums are not perfectly satisfied, their use as exact constraints in XAFS analysis may not be warranted and they are probably best suited as *restraints* – inexact conditions placed on the analysis that act as additional data or prior knowledge of the system. The practical use of Bond Valence sums as constraints and restraints in EXAFS analysis is demonstrated for iron oxides, and the use of Bond Valence sums as prior knowledge that can be applied to a wide-range of XAFS analyses is discussed.

1. Introduction

X-ray absorption fine-structure (XAFS) spectroscopy is ideally suited for studying the formal valence state, near-neighbor bond length, coordination number, and near-neighbor species of selected atoms. Unfortunately, determining all of these quantities independently from real experimental XAFS data is not always easy. Because of this, XAFS results are often scrutinized for "chemical plausibility" by comparing to results from other chemical and structural measurements.

An important approach to assessing the chemical plausibility is the Bond Valence Model [1]. This model gives an empirical description of chemical bonding and charge balance at an atomic scale, and relates the formal valence of an ion to the near-neighbor distances and co-ordination numbers. Originally applied by Brown and Altermatt [1, 2] to assess the quality of the data in the crystallographic literature for inorganic crystals, this model has been widely used in crystal chemistry to relate bond lengths, coordination numbers and formal charges of ions.

Recently, there has been growing interest in the formal use of Bayesian analysis for XAFS, in which prior information about the system can be statistically accounted for in XAFS analysis [3, 4]. In addition, the successful combination of EXAFS and diffraction analysis [5, 6] and more recently the combined analysis of EXAFS and XANES [7–9] have shown that information from other measurements can, in fact, be included in XAFS analysis. In this work, I will argue that the Bond Valence Model represents another form of prior knowledge that can be used in the XAFS analysis for a wide range of systems.

2. The Bond Valence Model

The Bond Valence Model begins with a simple description of chemical bonds at an atomic scale, using "bond" for neighboring cation-anion pairs (a view quite suitable for XAFS), derived from Pauling's 2nd rule of electrostatic valence [10]. *The total strength of the valency bonds which reach an ion from all neighboring atoms is equal to the charge of the ion*. The model parameterizes charge balance for interatomic bonds with a relationship between formal valence, bond distance, and coordination number, and writes the valence of a cation i as

$$V_i = \sum_j s_{ij} \tag{1}$$

where the sum is over neighboring atoms j, with the bond between atoms i and j having a *bond valence* s_{ij}. The bond valence is commonly parameterized [1, 2, 11] as

$$s_{ij} = \exp[(R'_{ij} - R_{ij})/b] \tag{2}$$

where R_{ij} is the distance between atoms i and j and R'_{ij} and b are parameters to be determined empirically. Brown and Altermatt found that b could be set to the universal value 0.37 ($\approx 1/e$), and tabulated R'_{ij} for many cation-anion pairs, so that good agreement could be found for formal valence states of very many atomic sites in the crystallographic literature.

Bond Valence sums from Eqs. (1) and (2) have been applied successfully to XAFS data by several workers [12–18] to verify the reliability of results from XAFS analysis. In general, the agreement between XAFS results and Bond Valence sums are quite good for the species measured by XAFS and can also be used to predict the valence of the anions bonded to the metal sites probed by XAFS.

3. Use of Bond Valence Sums in XAFS Analysis

The agreement of Bond Valence sums with crystallographic and XAFS data suggests that this model could be included directly in XAFS analysis as prior knowledge of the system. As a first possibility, Eqs. (1) and (2) could fully constrain R, N, and valence V. For a system with one near-neighbor pair, this can be done by setting the near-neighbor distance to

$$R_{ij} = R'_{ij} + 0.37 \log(N_{ij}/V_i) \tag{3}$$

which eliminates one of the parameters in the analysis. With this model, the parameters R and N, which are normally uncorrelated in XAFS analysis, become fully correlated with one another and with valence.

As an example use of Eq. (3) consider FeO, with regular rock-salt structure. Knowing the formal valence of Fe is $V = +2$, the Fe-O coordination number and distance can be linked, reducing the number of parameters in the fit. This leads to results shown in Fig. 1 and Table I. For this fit to the first 2 paths of FeO (Fe-O and Fe-Fe), $S_0^2 = 0.75$, $N_{\mathrm{Fe-Fe}} = 12$, and the parameters E_0, $N_{\mathrm{Fe-o}}$, $R_{\mathrm{Fe-Fe}}$, $\sigma^2_{\mathrm{Fe-O}}$, and $\sigma^2_{\mathrm{Fe-Fe}}$ were adjusted in the fit. $R_{\mathrm{Fe-O}}$ was tied to the value of $N_{\mathrm{Fe-O}}$ and $V = +2$ with Eq. (3), and parameter $R'_{\mathrm{Fe-O}} = 1.734$. The analysis was done using IFEFFIT [19] with calculations from FEFF [20]. The results show that Bond Valence sum can be used in XAFS analysis to constrain R and N for absorbing atoms with known valence state and simple coordination environment.

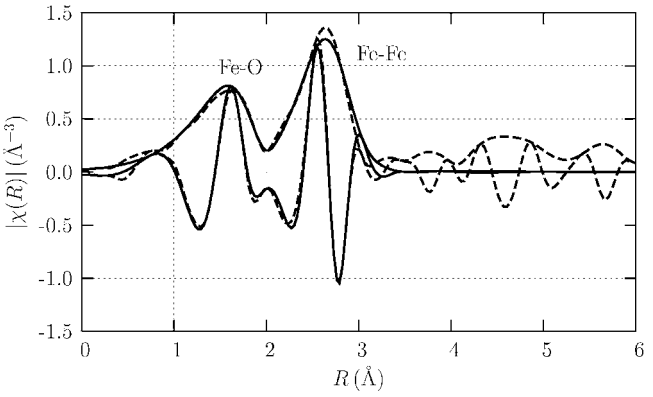

Fig. 1. Fit to FeO using a Bond Valence sum to fully constrain N and R for the Fe-O bond according to Eq. 3, with results shown in Table I. Shown are both $|\chi(R)|$ and Re$[\chi(R)]$ for data (dashed) and best-fit (solid). Bond Valence sums can be used to link the R and N parameters for simple fits.

Table I. *Fit results for FeO, using Eq. (3) to constrain R and N for the first Fe-O distance. Data were fitted in R-space, between* $R =$ *[1.1, 3.1]Å, with Fourier transform done with* $k =$ *[2.5, 14.0]Å^{-1}, a Hanning window with* $dk = 3.0$Å^{-1}, *and* k-weight $= 2$.

Parameter	Value	Parameter	Value
E_0	0.44 (0.73)	S_0^2	0.75 (fixed)
$N_{\mathrm{Fe-O}}$	5.5 (0.2)	$N_{\mathrm{Fe-Fe}}$	12.0 (fixed)
$R_{\mathrm{Fe-O}}$	2.11 (derived)	$R_{\mathrm{Fe-Fe}}$	3.05 (0.01)
$\sigma^2_{\mathrm{Fe-O}}$	0.014 (0.002)	$\sigma^2_{\mathrm{Fe-Fe}}$	0.014 (0.001)
$\mathcal{R}$	0.013	χ^2	356.0

4. Restraints in EXAFS Data Modeling

The Bond-Valence Model is simple and powerful, but it is not exact. The sums given by Eq. (1) are typically accurate to about 10%. Thus, their use as rigid constraints as for the FeO example above will not be appropriate in many cases, especially for systems with multiple sites for the absorbing atom and mixed first-shells. Still, the Bond Valence sums provide information about the relation between R, N, and valence V that may be used in XAFS analysis, even if not as the exact condition of Eq. (3).

For inexact conditions such as the Bond Valence sum, for which imposing a constraint on the analysis may be unwarranted, using a *restraint* may be more appropriate. Whereas a constraint is an exact mathematical relationship between variables in the fitting model, a restraint is a statistical preference for a particular value that includes some uncertainty. Restraints for EXAFS analysis are discussed by Binsted, *et al.* [21], and have been part of the EXCURVE analysis tools for some time, though seem to be used only to restrain bond distances and angles. As far as I know, inexact restraints are not available in other XAFS analysis methods.

A restraint adds another term, λ, to the least-squares minimization problem in the analysis, so that χ^2 becomes

$$\chi^2 \sim \frac{1}{N-P}\sum_i^N \left[\frac{\chi_i^{\mathrm{data}} - \chi_i^{\mathrm{model}}(\boldsymbol{x})}{\epsilon_i}\right]^2 + \lambda(\boldsymbol{x},\boldsymbol{b}) \qquad (4)$$

where the sum is done over N data points, χ_i^{data} and χ_i^{model} are the data and model XAFS, $\boldsymbol{x}$ is the set of p fitted variables (typically R, N, $E_0, \ldots$), and ϵ_i is the estimated uncertainty in the data. In general, the restraint $\lambda(\boldsymbol{x}, \boldsymbol{b})$ can depend on the fitted variables $\boldsymbol{x}$ and other physical parameters $\boldsymbol{b}$.

A useful form for the restraint is

$$\lambda(\boldsymbol{x},\boldsymbol{b}) = \left[\frac{V_0 - V(\boldsymbol{x},\boldsymbol{b})}{\delta V}\right]^2 \qquad (5)$$

which conveniently makes the restraint look like just another term in the χ^2 sum. V_0 represents another "measurement" for the system which can be modeled in terms of the parameters of the fit as $V(\boldsymbol{x},\boldsymbol{b})$ with uncertainty δV. This general form allows us to impose a variety of restraints on the fit based external measurements or *prior knowledge* of the system even if this knowledge is, like our measured EXAFS data, imperfect.

For the Bond Valence model, V_0 would be the formal valence, $V(\boldsymbol{x}, \boldsymbol{b})$ would be the sum from Eq. (1). In a sense, this makes the experimentally determined valence another data point in the EXAFS fit modeled with the Bond Valence sum. δV represents our confidence in both V_0 and in the Bond Valence model itself. Thus, as $\delta V \to 0$, the free parameters $\boldsymbol{x}$ will be forced to make $V(\boldsymbol{x}, \boldsymbol{b}) = V_0$, as if the Bond Valence sum was imposed as a constraint. On the other hand, as $\delta V \to \infty$, $V(\boldsymbol{x}, \boldsymbol{b})$, is determined solely the data alone, as if there was no prior knowledge of the valence. Of the parameters $\boldsymbol{x}$ that are consistent with the data, a finite δV causes the fit to chose those that bring $V(\boldsymbol{x}, \boldsymbol{b})$ closest to V_0.

5. Application of Bond Valence Restraints

As an example application of using Bond Valence sums as restraints, consider hematite Fe_2O_3. This structure has 2 distinct Fe-O near-neighbors, and the limited information in the first shell (for data to $k \approx 14.0$ Å^{-1}) can make getting unambiguous results for R and N for both oxygen sub-shells difficult.

To use the Bond Valence sum, two different distances go into Eq. (1), along with the parameter $R'_{\mathrm{Fe-O}} = 1.759$ for Fe(III)[2,11]. V_0 is set to $+3$, and δV is set to 0.1. As with the analysis of FeO, S_0^2 is set to 0.75, while E_0 is adjusted in the fit. Two oxygen distances $R_{\mathrm{Fe-O_1}}$, and $R_{\mathrm{Fe-O_2}}$ are adjusted in the fit, along with $N_{\mathrm{Fe-O_1}}$. To cut down on the number of free parameters, $N_{\mathrm{Fe-O_2}}$ is constrained to equal to $N_{\mathrm{Fe-O_1}}$, and a single σ^2 is used for the Fe-O near-neighbors. To account for the overlap from the Fe second shell, a crude model of this shell is made with one N, R, and σ^2 varied in the fit.

The results of this restrained fit are shown in Fig. 2 and Table II. The coordination numbers for the first shell come out remarkably

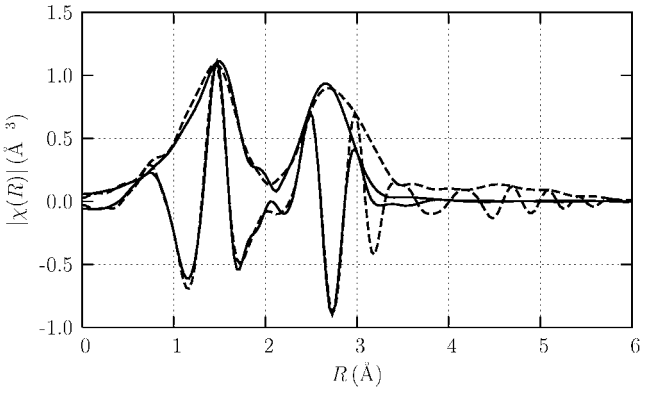

Fig. 2. Fit to Fe_2O_3 using Bond Valence sums as a restraint for the split first Fe-O shell. Results for this fit are shown in Table I. Shown are both $|\chi(R)|$ and Re$[\chi(R)]$ for data (dashed) and best-fit (solid).

Table II. *Fit results for Fe_2O_3, restraining R, N, and V for the first Fe-O distances. Data were fitted in R-space, between R = [1.1, 2.9]Å, with Fourier transform done with k = [3.0, 13.5]Å^{-1}, a Hanning window with dk = 2.0 Å^{-1}, and k-weight = 2. Best-fit values and estimated uncertainties are given for fitted parameters.*

Parameter	Value	Parameter	Value
E_0	0.7 (2.0)	S_0^2	0.75 (fixed)
$N_{\mathrm{Fe-O_1}}$	3.0 (0.4)	$N_{\mathrm{Fe-O_2}}$	3.0 (0.4)
$R_{\mathrm{Fe-O_1}}$	1.94 (0.03)	$R_{\mathrm{Fe-O_2}}$	2.07 (0.08)
$R_{\mathrm{Fe-Fe}}$	3.03 (0.05)	$N_{\mathrm{Fe-Fe}}$	6.1 (3.0)
$\sigma^2_{\mathrm{Fe-O}}$	0.005 (0.002)	$\sigma^2_{\mathrm{Fe-Fe}}$	0.015 (0.007)
V	3.17 (derived)		
$\mathcal{R}$	0.017	χ^2	223.4

well, though the uncertainties in these and all other parameters are high because the number of fitted parameters for the first shell (6) is close to amount of information available in this shell [22]. The shorter Fe-O distance is very close to its expected value, while the longer Fe-O distance of ≈2.07 Å is a bit shorter than expected and consequently the calculated valence of 3.17 is a bit higher than expected. Still, the resulting valence for Fe is within the acceptable uncertainty for Bond Valence sums, and the imposed uncertainty of $\delta V = 0.1$ for the restraint. Since this fit is near the limit of information available, the use of even this weak restraint on the Bond Valence sum improves the confidence in the validity of the results.

6. Conclusions

As has been shown by several workers, Bond Valence sums can be used to assess the validity of XAFS results. Here, Bond Valence sums have also been shown to be a viable way to constrain *R* and *N* for simple systems for which the formal valence *V* is known. More generally, Bond Valence sums provide *prior knowledge* that can be imposed to restrain the analysis of XAFS data for a wide range of systems.

Acknowledgments

I thank T. Trainor and J. O. Cross for many helpful discussions.

References

1. Altermatt, D. and Brown, I. D., Acta Cryst. A **41**, 240 (1985).
2. Brown, I. D. and Altermatt, D., Acta Cryst. A **41**, 244 (1985).
3. Krappe, H. J. and Rossner, H. H., Phys. Rev. B **61**, 6596 (2000).
4. Klementev, K. V., J. Synch. Rad. **8**, 270 (2001).
5. Binsted, N., Pack, M., Weller, M. T. and Evans, J., J. Am. Chem. Soc. **118**, 10200 (1996).
6. Binsted, N., Stange, M., Owens, C., Fjellväg, N. and Weller, M. T., J. Synch. Rad. **8**, 305 (2001).
7. D'Angelo, P., Benfatto, M., Longa, S. D. and Pavel, N. V., Phys. Rev. B **66**, 064209 (2002).
8. Benfatto, M., Longa, S. D. and Natoli, C. R., J. Synch. Rad. **10**, 51 (2003).
9. Natoli, C. R., Benfatto, M., Longa, S. D. and Hatada, K., J. Synch. Rad. **10**, 26 (2003).
10. Pauling, L., J. Am. Chem. Soc. **51**, 1010 (1929).
11. Brese, N. E. and O'Keefe, M., Acta Cryst. A **47**, 192 (1991).
12. Calas, G. *et al*., Nucl. Instrum. Meth. B **97**, 155 (1995).
13. Garner, C. D., Collison, D. and Pidcock, E., Philos. Trans. R. Soc. London A **354**, 325 (1996).
14. Farges, F. *et al*., Geochim. Cosmichim. Acta **60**, 3039 (1996).
15. Bargar, J. R., Brown, J. G. E. and Parks, G. A., Geochim. Cosmichim. Acta **61**, 2617 (1997).
16. Xia, K., Bleam, W. and Helmke, P. A., Geochim. Cosmichim. Acta **61**, 2223 (1997).
17. Farges, F., Neuville, D. and Brown, J. G. E., Am. Miner. **84**, 1562 (1999).
18. Davis, M. I. *et al*., Inorg. Chem. **38**, 3676 (1999).
19. Newville, M., J. Synch. Rad. **8**, 322 (2001).
20. Zabinsky, S. I. *et al*., Phys. Rev. B **52**, 2995 (1995).
21. Binsted, N., Strange, R. W. and Hasnain, S. S., Biochemistry **31**, 12117 (1992).
22. Stern, E. A., Phys. Rev. B **48**, 9825 (1993).

Physica Scripta. Vol. T115, 162–164, 2005

X-ray Spectra and Electron Densities of States of the Complicated Semiconductors $TlAsS_2$, Tl_3AsS_3, Tl_3AsS_4 and Tl_3PS_4

A. A. Lavrentyev[1], B. V. Gabrelian[1], I. Ya. Nikiforov[1], J. J. Rehr[2] and A. L. Ankudinov[2]

[1]Department of Physics, Don State Technical University, Gagarin Sq.1, Rostov-on-Don, Russia
[2]Department of Physics, University of Washington, Seatle, WA 98195-1560, USA

Received June 26, 2003; revised July 10, 2003; accepted November 4, 2003

PACS number: 7120−b

Abstract

The complicated as to their composition and crystal structure semiconductors $TlAsS_2$, Tl_3AsS_3, Tl_3AsS_4, called briefly TAS, and Tl_3PS_4 represent a class of compounds promising in the devices of quantum electronics. The electron energy structure of these compounds is investigated both experimentally with X-ray spectroscopy and theoretically by calculations of the local partial electron densities of states (LDOS) and X-ray K-absorption spectra of S and P using FEFF8 code. All theoretical K-absorption spectra and LDOS were calculated *ab initio* without any adjusting parameters according to the scheme: the self-consistent mt-potentials obtained for the clusters of about 35 atoms were then used in the calculations of the absorption spectra and LDOS for clusters of 87 atoms in the full multiple scattering approximation. The comparison of the calculated K-absorption spectra of S and P of sulfides investigated with their experimental analogues shows that in all cases the theoretical curve reflects good enough the energy positions of all features of the experimental curve. The results of the calculations of LDOS and the experimental emission K- and $L_{2,3}$-spectra of S and P gave the possibility to determine the energy positions of the electron occupied states of all elements in the semiconductors TAS and Tl_3PS_4 and to get the information about the hybridization of the electron states in the valence band. The compounds Tl_3AsS_3 and Tl_3AsS_4 have the same crystal structure, this leads to the likeness of their K-absorption spectrum of S and the electron energy structure of their valence bands.

1. Introduction

The complicated TAS semiconductors: $TlAsS_2$, Tl_3AsS_3, Tl_3AsSe_3, Tl_3AsS_4 and Tl_3PS_4 are widely applied in quantum electronics due to their particular physical properties [1–3]. The crystal structure of lorandite $TlAsS_2$ belongs to monoclinic system, its space group $P2_1/c - C_{2h}^5$, the parameters of the crystal lattice: $\mathbf{a} = 6.101$ Å, $\mathbf{b} = 11.30$ Å, $\mathbf{c} = 12.28$ Å, $\boldsymbol{\beta} = 104°5'$. The number of formula units in the elementary cell is equal to 4 [1]. The first atomic shell of sulfur atom in the bridge contains two atoms of As and two atoms of Ga where as every side atoms of S is surrounded by tetrahedron of one As atom and three atoms of Tl. These tetrahedra are slightly distorted. The atoms of Tl are in the centres of distorted tetrahedra of S atoms. With the inter-atomic distances Tl–S in the range 2.96–3.93 Å.

The compound Tl_3AsS_3 belongs to the space group R3m with the lattice parameters: $\mathbf{a} = 9.667$ Å, $\mathbf{c} = 7.061$ Å [1]. Its hexagonal elementary cell contains 3 formula units. This structure is formed by trigonal pyramids $[AsS_3]$ flattened a bit along axe Z. The compound Tl_3AsSe_3 isoelectronic to Tl_3AsS_3 has the lattice parameters: $\mathbf{a} = 9.870$ Å and $\mathbf{c} = 7.094$ Å. In the elementary cell of Tl_3AsS_3 and Tl_3AsSe_3 there are 21 atoms. The compounds Tl_3AsS_4 and Tl_3PS_4 crystallize into structural type K_3PS_4 [1] with the space group Pnma $- D_{2h}^{16}$. The number atoms in the elementary sell is 32. The lattice parameters (in Å) of these compounds are: $\mathbf{a} = 8.70$, $\mathbf{b} = 10.72$, $\mathbf{c} = 9.00$ for Tl_3PS_4 and $\mathbf{a} = 8.86$ (8.877), $\mathbf{b} = 10.85$ (10.877), $\mathbf{c} = 9.18$ (9.084) for Tl_3AsS_4. It is difficult to apply the traditional solid state methods (OPW, APW, KKR and of the kind) to these compounds with such a complicated structure. The code FEFF8 based on the multiple scattering theory has the advantage in this case. This method described in detail [4] was used for these compounds. In this method the crystal self-consistent mt-potentials were calculated in the approximation of full multiple scattering for clusters with about 35 atoms. Using these potentials LDOS and X-ray K-absorption spectra of sulfur and phosphorus were calculated for clusters of 87 atoms in the full multiple scattering approximation. In addition the significant paths of single scattering for the clusters of 1000 atoms were taken into account.

2. Experiment

The X-ray fluorescence bands of P and S and their K-absorption spectra were studied with the vacuum X-ray spectrograph DRS-2 with Johann's scheme of X-ray focusing and the resolution 0.2 eV. As the dispersive element the quartz crystal cut along the planes $(10\bar{1}0)$ curved to the radius 50 cm was used. The reference lines were Bi$M\alpha_1$- and Bi$M\beta$-lines with the energies 2422.5 and 2525.6 eV correspondingly [5]. Every spectrum is the average of 3 photo-films measured along 5 paths. The intensities were determined at 250 equidistant points.

The primary $L_{2,3}$-emission bands of S and P were obtained with X-ray spectrometer RSM-500 with concave spherical grating (radius of curvature = 2 m) with 600 scratches per mm. The spherical mirrors suppressed the short-wave-lengths part of the spectrum up to 52 Å, when $L_{2,3}$-emission band of S was studied, and up to 82 Å for $L_{2,3}$-emission band of P. In the first case the radius of the mirror was 1369 mm and for the second case −700 mm.

The spectra of S and P were superimposed to the common energy scale by the Kα_1-lines of P and S. X-ray spectra were corrected (deconvoluted) to take into account the inner level width and the width of the spectrometer window to determine accurately the energy position of the valence band top E_v which was chosen as energy zero. In Fig. 1–4 nevertheless uncorrected forms of X-ray spectra are presented to exclude any connections between the features of the experimental curves with deconvolution procedure.

3. Results and discussion

The calculated LDOS and X-ray K-absorption spectra of P and S for Tl_3PS_4 are compared in Fig. 1 with experimental X-ray emission and absorption spectra. The analysis of these data shows that the upper part of the valence band is formed of p-states of S and p-states of P are shifted to the higher binding energies by about 3.5 eV. The lower part of the valence band consists of s-states of S and P. There is a correspondence between positions of LDOS maxima from one side and peaks and other features of experimental emission bands. The good accordance between theory and experiment one can see also for K-absorption edges of P and S. The calculations gave us possibility to know the charge transfer: the found charges of ions are: +0.180 for

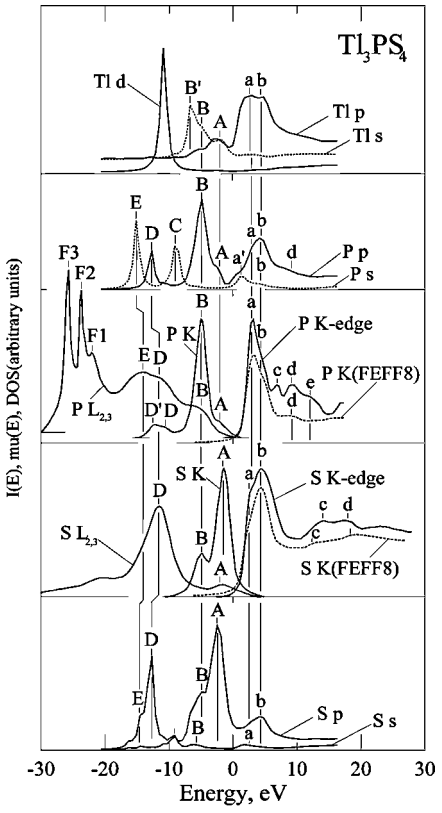

Fig. 1. The calculated local partial densities of electron states of Tl_3PS_4, depicted in the common relative energy scale with the X-ray emission and absorption spectra of sulfur and phosphorus. Energy zero is chosen at the top of the valence band.

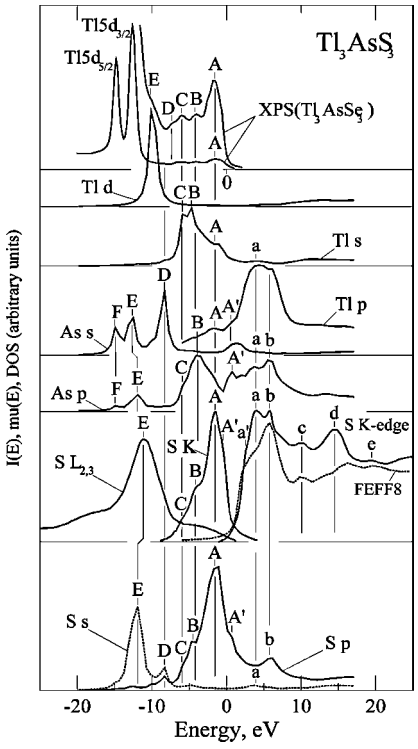

Fig. 3. The calculated densities of electron states for Tl_3AsS_3, shown in the common relative energy scale with the experimental X-ray emission and absorption spectra and the XPS-spectrum of Tl_3AsSe_3 [8]. The energy zero was chosen at the top of the valence band.

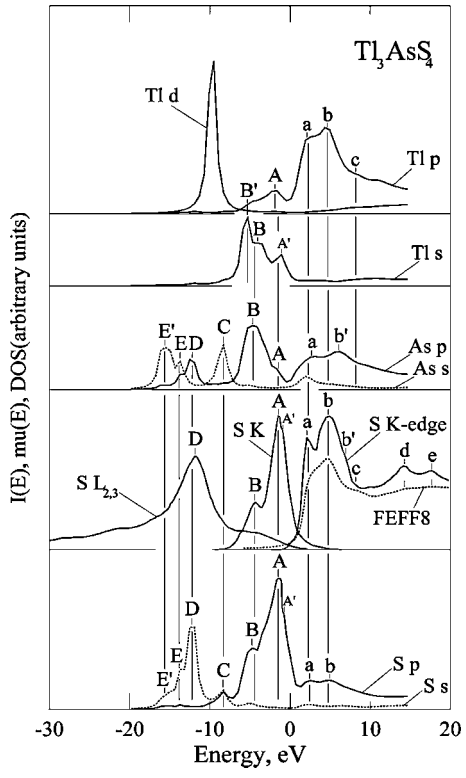

Fig. 2. The calculated local partial densities of electron states in Tl_3AsS_4, shown in the common relative energy scale with the X-ray emission and absorption spectra of sulfur. Energy zero corresponds to the top of the valence band.

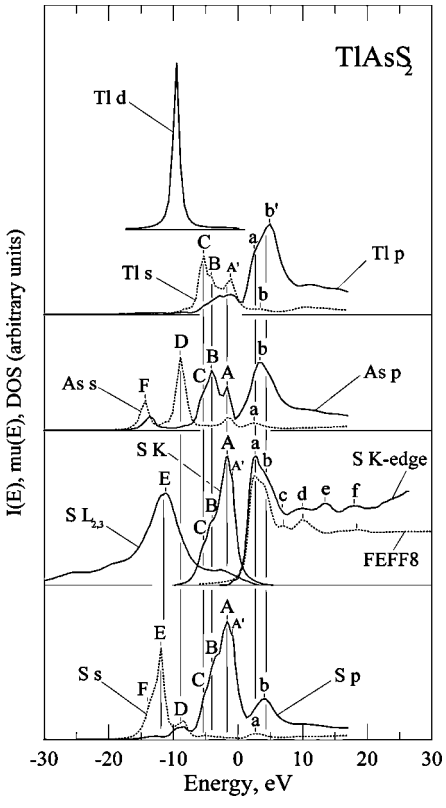

Fig. 4. The calculated local partial densities of electron states in $TlAsS_2$, presented in the common relative energy scale with the X-ray emission and absorption spectra of sulfur. Zero of the energy scale corresponding to the top of the valence band.

Tl, +0.393 for P, and −0.233 for S. It is quite understandable account electronegativity of these elements [6]. The energy correspondence of some maxima of K-emission bands and LDOS for p-states of S and P tells us about the existence of covalent bond between them, but with the ionic contribution to the chemical bonding.

The form of LDOS and of the X-ray spectra of isoelectronic compounds, which belong to the same crystallographic type, are

alike. The comparison of the X-ray K- and L-emission spectra of S in Tl_3PS_4 (Fig. 1) and Tl_3AsS_4 (Fig. 2), which do not contain the noble metals, confirms this rule [7]. The change of crystallographic structure in the row Tl_3AsS_4 - Tl_3AsS_3 - $TlAsS_2$ leads to the transformation of the X-ray spectra form (Fig. 2–4). The significant change of K-emission spectrum of sulfur occurs because of various surroundings of S atom in these compounds. These distinctions of SK-bands in TAS compounds are due to the difference of chemical interactions of atoms As-S and Tl-S in these compounds. The main structural elements of these TAS compounds are [1] the pyramids [AsS_3] and [TlS_3]. We suppose that three p-electrons of As form the strong covalent bonds with the nearest three S atoms due to the overlapping of their p-orbital. In trigonal pyramids [TlS_3] of the compounds $TlAsS_2$ and Tl_3AsS_3 [1] the chemical bond Tl–S arises, apparently, because of the overlapping p-orbital of S with the hybridized sp-orbitals of Tl. The chemical bond Tl–S has the significant ionic contribution because the inter-atomic distance Tl–S is greater than the sum of the tetrahedral covalent radii of Tl and S.

The crystallographic structure of Tl_3AsS_4 differs from ones of $TlAsS_2$ and Tl_3AsS_3 by existence coordination tetrahedra [AsS_4] and [TlS_4] instead of trigonal pyramids of $TlAsS_2$ and Tl_3AsS_3 [1]. Probably one p-electron of As transits from As to S providing the additional bond Tl-S so that every atom of Tl form 4 hybridized bonds with the 4 S atoms in the distorted tetrahedron [TlS_3]. Such an approach gives us the possibility to explain the hump **C** on the SK-emission band as due to the admixture of p-states of S to sp-states of Tl. Because of greater ionicity of the chemical bond Tl-S in Tl_3AsS_4 the hump **C** has greater binding energy (about 6.5 eV from E_v) comparing to $TlAsS_2$ and Tl_3AsS_3 where this binding energy is equal to 6.0 eV from E_v. The remaining four valence electrons of As form in Tl_3AsS_4 four sp^3 hybridized orbitals directed to S atoms. The formation of such sp^3-hybridization was discussed in [8]. The binding energy of sp^3-states of As corresponds to the feature **B** of SK-emission band in Tl_3AsS_4 (4.0 eV from E_v). The chemical bond As-S in Tl_3AsS_4 has covalent-ionic character of the same type as P-S bond in Tl_3PS_4.

From the analysis of Fig. 3, where the X-ray SK-emission band in Tl_3AsS_3, the XPS-spectrum of the isoelectronic and isostructural Tl_3AsSe_3 and calculated LDOS are shown, it follows that in the upper part of the valence band of this compound there are p-states of S mainly. The hump **B** of the SK-emission band corresponds by energy to the p-states of As and s- and p-states of Tl.

At the bottom of the valence band of all compounds investigated s-states of S are localized (Fig. 1–4). These states nearly do not take part in the chemical bonding. Only small, nearly negligible admixture of s-states of S to the valence states in the upper part of the valence band one can notice for all compounds in question.

Summarizing the results of comparison of calculated LDOS with experimental data we can affirm the correspondence of energy positions of all features of the theoretical and experimental curves. It includes the experimental and calculated using the FEFF8 code K-absorption spectra of S and P. To obtain the adequate theoretical K-absorption edges the self-consistent mt-potentials were calculated for the clusters of 35 atoms, then after the full multiple scattering calculations the contributions of single scattering paths in the clusters of about 1000 atoms were taking into account. Unfortunately the compounds investigated in the present work have rather low symmetry. That is why we had to take into account the great number of scattering centres to reproduce the main features of K-absorption spectra of sulfur and phosphorus. Here the approximation of full multiple scattering was necessary.

In the calculated LDOS there is the noticeable density of electron states in the energy gap region. That is connected firstly with the cluster method of the calculations and secondly with the smearing of LDOS curves due to the inner level width and the spectrometer window, we carried out to simplify the comparison of the theoretical curves with the experimental ones.

References

1. Bercha, D. M., Voroshilov, Yu. V., Slivka, V. Yu. and Turyanitsa, I. D., "The complicated chalcogenides and chalcohalogenides" (Vysha Shkola, Lvov 1983), p. 181 (In Russian).
2. Voroshilov, Yu. V. and Slivka, V. Yu., "Unoxide Materials for Electronic Technique" (Vysha Shkola, Lvov 1989), p. 200 (In Russian).
3. Lazarev, V. B., Kish, Z. Z., Peresh, E. Yu. and Semrad, E. E., "The complicated chalcogenides in systems A^I-B^{III}-C^{VI}" (Metallurgia, Moscow 1993), p. 240 (In Russian).
4. Ankudinov, A. L., Ravel, B., Rehr, J. J. and Conradson, S. D., Phys. Rev. B **58**, 7565 (1998).
5. Blokhin, M. A. and Shweitser, I. G., "The reference book on X-ray spectroscopy" (Nauka, Moscow 1982), p. 376 (In Russian).
6. Dei, K. and Selbin, D., "The theoretical unorganic chemistry" (Khimiya, Moscow 1976), p. 568 (In Russian).
7. Lotz, W. J., Opt. Soc. Am. **60**, 206 (1970).
8. Ewbank, M. D., Kovalczyk, S. P., Kraut, E. A. and Harrison, W. A., Phys. Rev. B **24**, 7565 (1981).

Physica Scripta. Vol. T115, 165–167, 2005

Sodium K Edge XANES Calculation in 'NaCl' Type Structures

R. J. Prado[1,2,a] and A. M. Flank[1,b]

[1]LURE – Centre Universitaire Paris-Sud, Bât. 209D, B.P. 34, 91898, Orsay CEDEX, France
[2]Instituto de Física da USP, C.P. 66318, CEP 05315-970, São Paulo – SP, Brazil

Received June 26, 2003; accepted November 4, 2003

PACS numbers: 71.20.−b, 71.20.Dg, 78.70.Dm, 61.10.Ht

Abstract

Sodium K edge XANES calculations were performed for sodium halides, using the last version of the *ab-initio* FEFF code, and compared with the experimental data. Several FEFF parameters were varied during calculations, aiming to investigate their influence on the theoretical results. The origin of the differences between the experimental data of the series are analyzed and discussed, supported by the theoretical calculation.

1. Introduction

Up to now, several different analysis of the XANES structure in alkali-halides have been performed by mean of multiple-scattering analysis [1–12]. The study of these highly symmetric materials is important to improve the degree of comprehension of the XANES spectra, as well as to test the reliability of the theoretical codes available today, for which one of the crucial problems is the construction of the muffin-tin (MT) potential of a system.

In this work, we analyze the Na K-edge XANES spectra of four sodium halides with the 'rock salt' structure, by means of full-multiple scattering (FMS) calculations, aiming to identify the physical origin of their differences.

2. Experimental

The experimental XANES spectra were recorded at the sodium K-edge (1070.8 eV) using the SA32 beam-line of the Super-ACO ring at LURE, Orsay, France. The experiments were performed from 1060 to 1135 eV, using a 0.2 eV step and total electron yield (TEY) detection mode. The beam was monochromatized by a double-crystal monochromator, equipped with two Beryl (10 $\bar{1}$ 0) single crystals, and calibrated on a NaCl sample (1075.6 eV at the inflexion point) before each data collection.

3. Results

3.1. *Experimental*

Figure 1 shows the experimental XANES spectra of NaX (X = F, Cl, Br and I), in agreement with previously published data [6, 11]. A progressive shift of the experimental Na-K threshold position is observed: the absorption edge energy of NaI is found 0.7 eV lower than that of NaF.

For the sake of clarity, the different features present in all the spectra are identified by a letter (A-E). Their energy position are shifted to higher values as we go to lighter anions and shorter interatomic distances. As well the relative amplitudes of the oscillations vary with the backscattering halide atom. But beyond these differences the XANES spectra of NaI, NaBr and NaCl are very similar while the NaF one is peculiar (weakness of feature A, strong amplitude of peak B, intensity inversion of E oscillations).

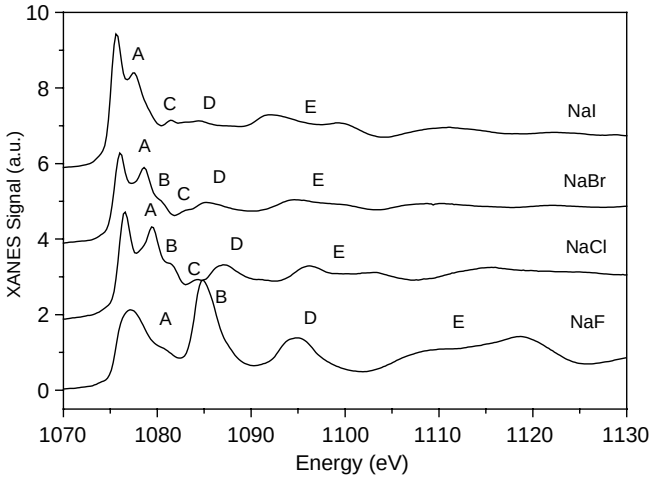

Fig. 1. Experimental data.

3.2. *Calculation*

The crystallographic 'NaCl' structure is face-centered cubic. The lattice parameters are 6.47 Å for NaI, 5.97 Å for NaBr, 5.64 Å for NaCl and 4.62 Å for NaF.

The *ab-initio* FEFF8 code [13–15] was used in this work to generate multiple-scattering simulations, and several calculation parameters of the code were varied, aiming to analyze their influence on the theoretical spectra. However, only the FMS and SCF (self-consistent field) atomic potential calculation routines are crucial to obtain a good XANES simulation, and the other instructions have only a minor importance for the final results.

After some tests, and in agreement with other works [16], the Hedin-Lundqvist exchange potential was chosen, and used in all calculations presented here.

For the calculation of the SCF muffin-tin atomic potential a 33 atoms cluster (4 shells) gives reasonable results, which can be slightly improved by increasing the size of the cluster. But the code is unable to reproduce the experimental 0.7 eV shift of the Na K-edge energy along the series.

The quality of the results very near the threshold (white-line intensity and relative energy position of the edge) was improved by using a trick as it can be seen in figure 2: the best simulation of the XANES is obtained doing the "$Z + 1$ approximation", by using Mg as the central atom in place of Na. The theoretical data for NaCl, NaBr and NaI in figure 3 were generated using this $Z + 1$ approach. This approach is no more correct for calculating

[a]e-mail: rjprado@lure.u-psud.fr
[b]e-mail: anne-marie.flank@lure.u-psud.fr

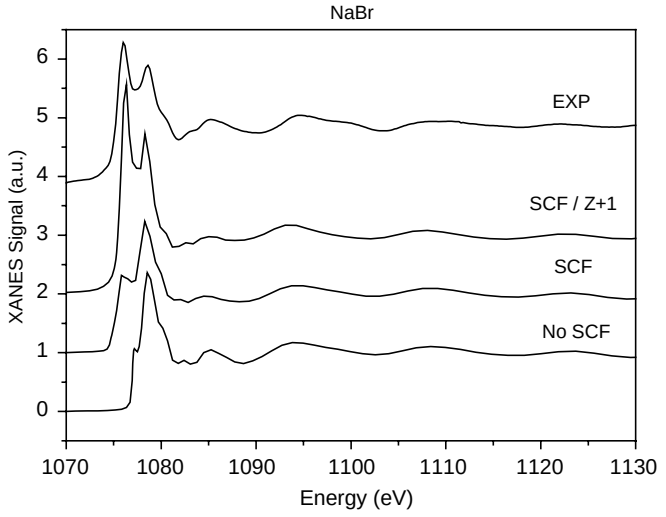

Fig. 2. FMS calculation of the XANES spectra for a NaBr cluster having 250 atoms.

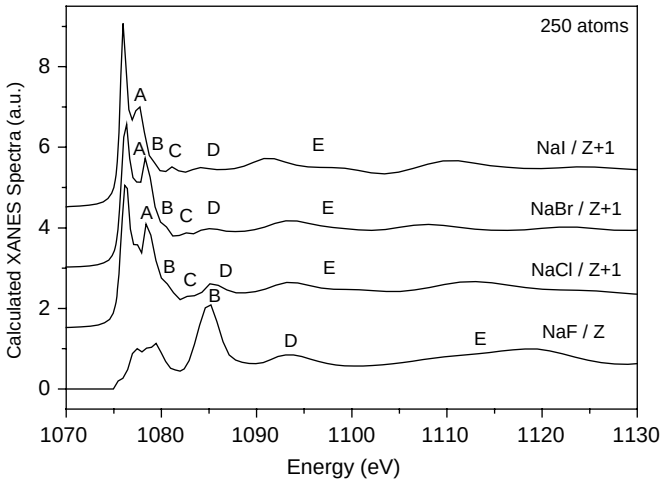

Fig. 3. Theoretical XANES spectra for the series. For sake of clarity the spectra have been shifted to their experimental positions.

the NaF spectrum, as it generates a too sharp and intense white line when compared to the experimental spectrum.

In figure 3 the NaF and NaCl spectra were shifted to their correct experimental positions in order to make easy the comparison with experimental data (figure 1). However, the spectra of NaBr and NaI were shifted of the same quantity used for NaCl, in order to keep the calculated edge's shift and show the good agreement with experience.

The FMS algorithms [14] implemented in FEFF8 code were tested for all materials analyzed here. During our tests, the different algorithms generated equivalent results for each calculation, however some were faster: the Lower-Upper decomposition (default option) was the slowest algorithm, and the Van der Vorst algorithm the fastest one (more or less three times faster than the default option for all simulations).

The main oscillatory structure of the XANES spectra is reproduced with a five-shells cluster (57 atoms). However, for NaI, the energy range around 1080–1085 eV is better reproduced when considering an eight-shells (123 atoms) cluster, while for NaF, the simulation of the threshold region is improved for clusters with more than 200 atoms. Figure 4 shows the evolution of the theoretical XANES spectra as a function of the FMS cluster's size for NaF.

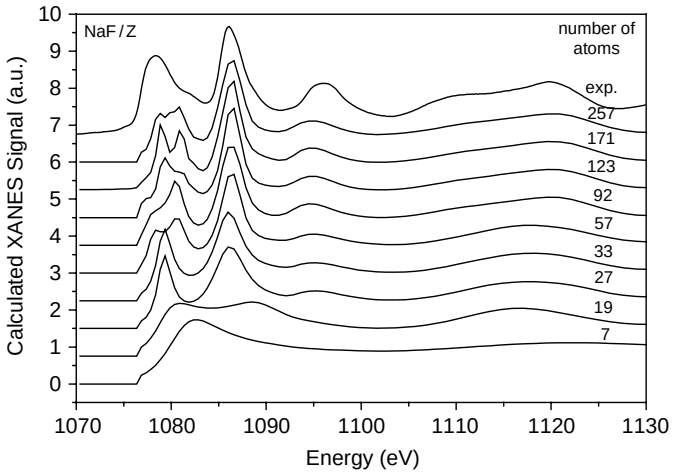

Fig. 4. Theoretical XANES spectra for different sizes of clusters.

Finally all the calculations presented here were done with an lmax = 3 for the limit of the angular momentum bases for both the self-consistent potential and the full multiple scattering calculations. This is necessary to better reproduce the oscillations above the feature E.

4. Discussion

In a first approximation, the evolution of the experimental data, (energy shifts of the maxima A, B and C) can be explained by the change of the lattice parameter (see figure 5), according to the $1/R^2$ Natoli's rule [17], therefore their origin is structural.

While a good simulation of the data was already obtained with the FEFF5 code [12], taking into account the contributions up to seventh-order MS and a very large cluster (18-shell), we show here that to reproduce all the structures including the one very near the edge, a full-multiple scattering calculation is necessary.

The calculated XANES spectra are in good agreement with the experimental ones, and the experimental differences among these last ones are fully reproduced by theory (see figures 1 and 3). However, theoretical data seem broadened, in comparison with the experimental ones, while the multiple scattering (MS) approximation based on the path expansion formalism gives always the correct amplitudes for the oscillations.

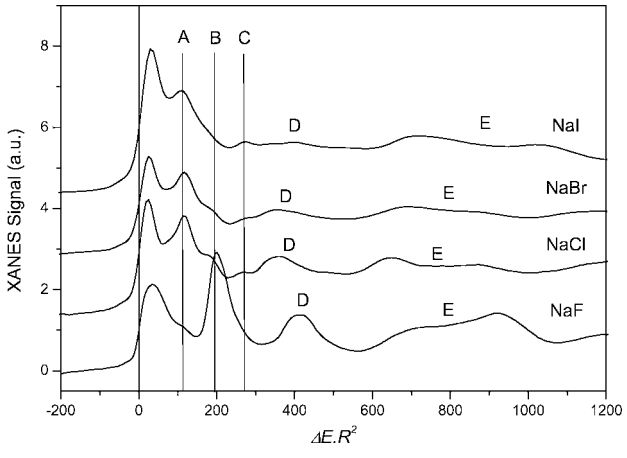

Fig. 5. Verification of the Natoli's rule for features A, B and C.

Furthermore, without considering the $Z + 1$ (Mg) absorber atom approximation, FEFF8 is unable to reproduce the experimental shift of the edge for the series, neither the relative intensity of the white-lines for NaCl, NaBr and NaI.

Another parameter, always discussed in papers dealing with simulation is the size of the cluster necessary to reproduce correctly all the features of the spectra. In the case of sodium halides, FEFF8.2 gives a satisfactory general result for a cluster of 5 shells (57 atoms), but the structure C only appears in the calculation for a cluster of 123 atoms for NaI and 251 atoms for NaCl and NaBr.

However, in a previous work [16], a cluster of only 133 atoms was necessary to reproduce feature C in the calculated NaCl spectrum. Consequently, it seems that the excessive broadness of the XANES spectra generated by FEFF, using the chosen calculation parameters, is responsible for the absence of the C feature in NaBr and NaCl for a cluster of 133 atoms.

The scattering properties of the surrounding atoms affects the structure of XANES in alkali halides, but this effect is predominant when the Na-X bond changes from ionic to a more covalent character, as it is the case for NaF, while NaCl, NaBr and NaI are purely ionic compounds [18]. This is striking, because F is more electronegative than the other halides (therefore, the common sense tell us that NaF should be more ionic than others sodium halides), however one has to point out that this covalent character of NaF is related to the very small size and/or larger chemical hardness of F atom, which places this compound apart of the series.

5. Conclusion

This work shows the importance of the FMS routine to simulate the XANES spectra of alkali-halides.

In a general way, the quality of the XANES spectra generated by FEFF is good, reproducing almost all the features of the experimental data, as well as some subtle behaviors of the series. However, these goals were obtained when considering the $Z + 1$ (Mg) absorber atom, which still remain physically understood. Moreover, theoretical data seem too much broadened, hiding small features in the theoretical spectra.

Acknowledgments

The authors are grateful to M. Henry, G. Hug, M. Jaouen and V. Briois for fruitful discussions and suggestions. Thanks are also due to CAPES (Brazilian financing agency), for the post-doc support of R. J. Prado, and for the SuperACO machine staff for providing beam.

References

1. Sipr, O., Machek, P., Simunek, A., Vackar, J. and Horak, J., Phys. Rev. B **56**, 13151 (1997).
2. Bugaev, L. A. and Vedrinskii, R. V., Phys. Stat. Sol. (b) **132**, 459 (1985).
3. Soldatov, A. V., Stekhin, I. E. and Ingalls, R., J. Phys.: Condens. Matter **8**, 7829 (1996).
4. Soldatov, A. V., Ivanchenko, T. S., Stekhin, I. E., Bianconi, A. and Ingalls, R., Phys. Stat. Sol. (b) **184**, 237 (1994).
5. Freund, J., Ingalls, R. and Crozier, E. D., Phys. Rev. B **43**, 9894 (1991).
6. Soldatov, A. V., Ivanchenko, T. S., Stekhin, I. E. and Bianconi, A., J. Phys.: Condens. Matter **5**, 7521 (1993).
7. Murata, T., Matsukawa, T. and Naoé, S. I., Physica B **158**, 610 (1989).
8. Stekhin, I. E., Soldatov, A. V. and Ingalls, R., Physica B **208&209**, 286 (1995).
9. Teodorescu, C. M., El Afif, A., Esteva, J. M. and Karnatak, R. C., Phys. Rev. B **63**, 233106 (2001).
10. Yalovega, G. *et al*., Chem. Phys. Lett. **356**, 23 (2002).
11. Kikas, A., Nommiste, E., Ruus, R., Saar, A. and Martinson, I., Surf. Rev. Lett. **9**, 1303 (2002).
12. Hudson, E. *et al*., Phys. Rev. B **49**, 3071 (1994).
13. Ankudinov, A. L., Ravel, B., Rehr, J. J. and Conradson, S. D., Phys. Rev. B **58**, 7565 (1998).
14. Rehr, J. J. and Albers, R. C., Rev. Mod. Phys. **72**, 621 (2000).
15. Ankudinov, A. L., Bouldin, C. E., Rehr, J. J., Sims, J. and Hung, H., Phys. Rev. B **65**, 104107 (2002).
16. Gunnella, R., Benfatto, M., Marcelli, A. and Natoli, C. R., Solid State Commun. **76**, 109 (1990).
17. Natoli, C. R., in " EXAFS and Near Edge Structure", (edited by A. Bianconi), (Springer, New York, 1983), p. 43.
18. Henry, M., Chem. Phys. Chem. **3**, 561 (2002).

Physica Scripta. Vol. T115, 168–171, 2005

The Fourier-Transform Analysis of Ti K-XANES in Metamicts and Glasses

L. Bugaev[1,*], F. Farges[2], E. Rusakova[1], A. Sokolenko[1], Ya. Latokha[1] and L. Avakyan[1]

[1]Department of Physics, Rostov State University, Zorge str., 5, Rostov-on-Don, 344090, Russia
[2]Laboratoire des Geomateriaux. Universite de Marne la Vallee, FRE CNRS 2455, France, and Dept. of Environmental Sciences, Stanford University, Stanford, CA 94305-2115, USA

Received June 26, 2003; revised version December 6, 2003; accepted December 8, 2003

PACS number: 61.10.Ht

Abstract

The structural parameters of Ti coordination environment in glassy titanite ($CaTiSiO_5$), natisite (Na_2TiSiO_5) and radiation damaged $CaTiSiO_5$ are determined by the method proposed earlier, based on the Fourier-transform analysis of Ti K-XANES over the short k-range of photoelectrons wave numbers. The accuracy of the determined parameters is tested for the model crystals $CaTiSiO_5$, Na_2TiSiO_5. The modelling of the extracted contribution into Ti-XANES, arising from the oxygen-polyhedron around the ionised Ti atom in amorphous titanites and natisite, performed via the single-shell fit and the two-shells fit, returns not only the averaged structural parameters, but also reveals the main groups of the Ti-O distances for this polyhedron.

1. Introduction

The Ti atoms in amorphous oxide-type compounds are often coordinated by the oxygen-polyhedron (considered as the first shell with N_1 atoms), which is characterized by a more or less complex radial distribution of Ti-O distances (R_1). Such coordination environment can be modelled into a number of sub-shells, so containing $N_{1,j}$ atoms ($N_1 = \Sigma_j N_{1,j}$, j is the sub-shell's number), located at $R_{1,j}$ – distance. For example, the available structural information for crystalline titanites [1] suggests that the Ti-O distances of the oxygen-octahedron around Ti are distributed by $\sim$0.2 Å under the diffused second and more distant shells and this local disorder increases in amorphous materials [2, 3]. In this case, the X-ray absorption spectroscopy (XAS) provides important structural information of Ti local environment [4–6]. However, the application of XAS to a wide number of these objects, which are either glassy or radiation-damaged ("metamict"), is often limited by the analysis of near edge structure (XANES), since XANES is much faster to collect than the EXAFS, often unobserved for these compounds. In addition, the XANES is richer in structural information (pre-edge and edge-crest features). At the same time, the most current approaches of the XANES analysis are based on indirect and qualitative information on the studied structure estimated by comparing "unknowns" with models. As a consequence, more quantitative tools are needed to analyse the high-resolution XANES spectra available nowadays.

In this paper, we use the method proposed in [3, 7] to determine the Ti-O distances and coordination numbers for Ti in amorphous (glassy and radiation-damaged) $CaTiSiO_5$ (titanite) and in glassy Na_2TiSiO_5 (natisite). This method, originally developed for crystalline minerals and glasses with low-Z atoms (Z < 20), is based on the Fourier-transform (FT) analysis of XANES within the short range of the photoelectron's wave numbers (k), followed by a model of the contribution related to the first neighbours.

2. The accuracy of structural parameters determined for model compounds via the FT of Ti K-XANES

The XANES calculations for the model crystalline titanite $CaTiSiO_5$ performed by the Full Multiple-Scattering (MS) approach using the FEFF8.2 package [8] and by the Low-angle scattering approach [9, 10], reveal the significant effect of the medium range order-MRO (the single-scattering from the second and more distant shells) and MS-terms on the main edge crest features of Fig. 12 in [2]. At the same time, the dominant role of the first shell's term in the Ti K-XANES formation at the higher energies ($E > 5010$ eV) was revealed. This result permits to conclude that the effect of the MRO-term in the studied crystalline compounds (which can decrease the accuracy of the determined R_1, N_1 in contrast to the MS-term [3, 7]) can be minimized by the choosing adequately the corresponding k-interval for the FT ($k = 0.2625 * (E - E_{MT})^{1/2}$, where E_{MT} is the interstitial potential for the compound studied). This conclusion is justified also by the values of structural parameters, which are obtained for the model crystals $CaTiSiO_5$, Na_2TiSiO_5 in agreement with the diffraction data, using the FT of the Ti-XANES. Moreover, the comparison of XANES formation in the model crystal and in its glass-equivalents [3] reveals that even when the MRO-term is not negligible for the crystal, the affect of the MRO-term on the first shell's peak in FT is necessarily negligible for the glasses, due to the diffusion of atoms for the second and more distant shells. Therefore, for crystalline and amorphous $CaTiSiO_5$ and Na_2TiSiO_5 the FT was applied to the $\chi(k)$ over the k-range: 3.9–5.8 Å^{-1}. This range excludes the main edge crest features (at $k < 3.9$ Å^{-1}) and the small value of k_{max} makes it even more pertinent for disordered compounds. The $\chi(k)$ was extracted from the experimental Ti K-XANES by the equation:

$$\chi(k) = \sigma^{exper}(k)/\sigma_{at}(k) - 1 \quad (1)$$

and the factorised "atomic" part of the absorption cross-section $\sigma_{at}(\varepsilon)$, obtained from the experimental Ti-XANES by the procedure proposed in [3]. The FT of the extracted $\chi(k)$ and the R-space fit (0.3–2.5 Å) of the first oxygen shell's peak were performed by FEFFIT [11]. The photoelectron phase shifts and scattering amplitudes were calculated using Hartree-Fock (HF) MT-potential model [12], which provides the values of E_{MT} for the compounds studied. The photoelectron extrinsic losses, core hole width and experimental energy resolution were accounted by $\exp(-0.2625(\Gamma_{exper} + \Gamma_h + \Gamma_{el})2R/k)$, where Γ_{exper} is the energy parameter (eV) for the experimental resolution, Γ_h and Γ_{el} are the energy widths of the core hole and the excited electron states respectively. This exponential can also be rewritten as $\exp(-2R/\lambda_{eff})$ with the effective mean free path length λ_{eff} for

*e-mail: bugaev@rsu.ru

Table I. *Structural parameters used to calculate χ for crystalline titanite and their values returned via FT of χ over the k-range 3.9–5.8 Å^{-1} and fit.*

		N_1(oxygen's number around Ti)		R_1(Ti-O distance), Å	
χ	Fit	used for χ calculation	FT, fit	used for χ calculation	FT, fit
$\chi_{1.1}$	Single-shell	2	1.99	1.89	1.892
$\chi_{1.2}$	Single-shell	4	3.99	2.02	2.016
$\chi_1 =$	Single-shell	6	6.00	1.98	1.985
$\chi_{1,1} + \chi_{1,2}$	Two-shell	$N_{1.1} = 2$	not	$R_{1,1} = 1.89$	1.893
		$N_{1.2} = 4$	varied	$R_{1,2} = 2.02$	2.022

the photoelectron: $1/\lambda_{\text{eff}} = 0.2625(\Gamma_{\text{exper}} + \Gamma_{\text{h}})/k + 1/\lambda_{\text{el}}$. The Γ_{h} and the electron mean free path length $\lambda_{\text{el}}(k) = k/(0.2625\Gamma_{\text{el}})$ for Ti-compounds were taken from [13].

The analysis of the accuracy of R_1 and N_1 values, determined via FT of XANES over the short k-interval ~2.5 Å^{-1} performed in [3], revealed that the R_1 and N_1 are determined with inaccuracy to ≤1% and ≤3–5% respectively. However, in the studied compounds the oxygen-polyhedron around Ti is often characterised by a number of Ti-O distances and hence, can be considered as a number of corresponding sub-shells. Therefore, to confirm the accuracy of R_1 and N_1 determination in the studied compounds, the FT was preliminary applied over the k-range 3.9–5.8 Å^{-1} to: *i*) the two theoretical χ-functions $\chi_{1,1}$ and $\chi_{1,2}$, which model the split of the O_6-octahedron around Ti in the reference crystal $CaTiSiO_5$ [1] ($\chi_{1,1}$-contribution of 2 oxygens at $R_{\text{Ti-O}} =$ 1.89 Å; $\chi_{1,2}$ – contribution of 4 oxygens at $R_{\text{Ti-O}} = 2.02$ Å) and to *ii*) the available references – $CaTiSiO_5$, Na_2TiSiO_5 crystals. The values of structural parameters for $CaTiSiO_5$-crystal, used for the calculated χ, are compared in Table I with their values returnedvia the FT of theoretical χ over the k-range 3.9–5.8 Å^{-1}. As can be seen, the structural parameters returned by i) the single-shell fit with three variables N_1, R_1, σ^2 or ii) the two-shell fit for the model with fixed $N_{1,1}$, $N_{1,2}$ and three variables $R_{1,1}$, $R_{1,2}$ (Ti-O distances for $\chi_{1,1}$, $\chi_{1,2}$ respectively) and σ^2, are in agreement with the values of corresponding parameters used for the direct calculations of these χ-functions.

For the crystalline titanite, the magnitude $|F(R)|$ for the FT of $\chi(k)$, extracted from the experimental Ti-XANES, is compared in Fig. 1a with the results of the single-shell model with the three variables N_1, R_1, σ^2. The obtained value of the DW-parameter σ^2 can be tested accurately by the known value of $N_1 = 6$ for the oxygen-octahedron around Ti. At the same time, the single-shell fit of the Ti-O contribution in the three amorphous titanites is performed first (next section) with the two variables N_1, R_1 using the value of σ^2 for crystalline $CaTiSiO_5$. The use of the same σ^2 for both the crystalline and the amorphous titanites can be validated if the values of structural parameters for the amorphous titanites (determined using two variables N_1, R_1, and the fixed σ^2) remain stable as compared to these with the three variables N_1, R_1, and σ^2.

The used scheme of HF MT-potential generation [12] applied to the crystalline titanite and natisite, provides a constant value of $E_{MT} = 4953$ eV and therefore the parameter E_{MT} – the beginning for the k-scale was not varied. The structural parameters for the first oxygen-shell around Ti in the model crystal $CaTiSiO_5$, determined via the single-shell fit: $N_1 = 6.1$, $R_1 = 1.99$ Å, $\sigma^2 = 0.005$ Å^2 are in agreement with the available structural information [1] (see Table II).

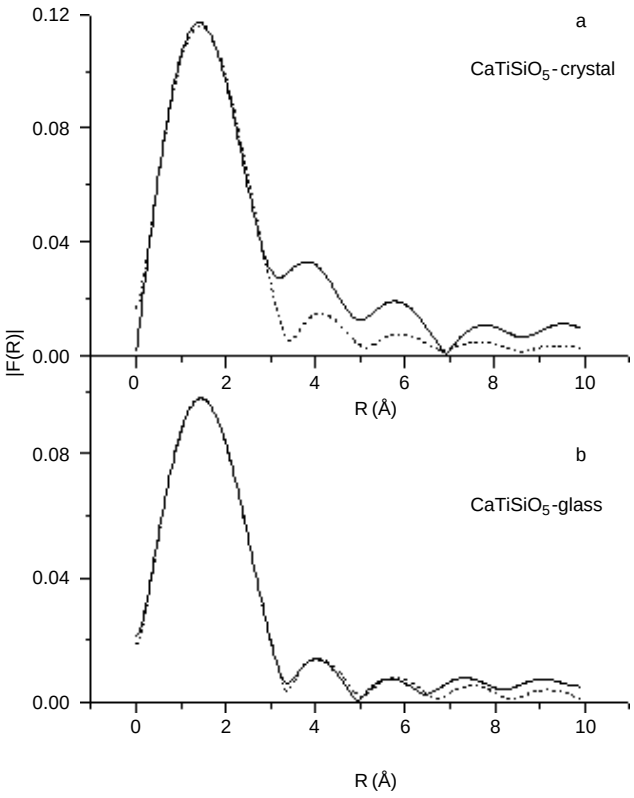

Fig. 1. $|F(R)|$ for crystalline (a) and glassy (b) $CaTiSiO_5$: solid curves – the FT of the $\chi(k)$ extracted from the Ti K-XANES and dashed curves – the results of the single-shell fit.

Table II. *Structural parameters for Ti coordination in various polymorphs of $CaTiSiO_5$ determined via the single-shell fit (the diffraction data for crystalline $CaTiSiO_5$ are in brackets).*

Samples	N_1	R_1 (Ti−O), Å
$CaTiSiO_5$ – crystalline	6.1 (6.0)	1.99 (1.98)
$CaTiSiO_5$ – glass	4.9	1.95
Egansville (metamict)	5.75	1.98
Ontario (metamict)	5.57	1.97

The number of varied parameters does not exceed the possible number of independent variables (3 or 4), found according to [11] for the chosen k-range. In this case, the effect on the determined R_1 and N_1 from the uncertainties in the used values of other parameters, traditionally varied for EXAFS and fixed in the performed XANES-analysis, can be estimated via the model simulations. According to them: *i*) the variations of Γ up to ±0.5 eV around the used value $\Gamma = 3$ eV does not destroy the above accuracy of R_1 and N_1 determination. However, the Γ variations by ±1.5 eV result in the increase of inaccuracy for N_1 up to ~10% under approximately unchanged accuracy for R_1; *ii*) the compulsory shifts of the obtained E_{MT} (or E_0) by ±2.5 eV shows the increase of errors in R_1 and N_1 determination up to 3–4% and 10% respectively. Besides, it is revealed that the HF scattering amplitudes calculated by $R_{\text{Ti-O}} = 1.9$ Å (averaged Ti-O distance for the studied titanites) provide the R_1 and N_1 determination with the above inaccuracies of ≤1% and ≤3–5% respectively for compounds with $R_{\text{Ti-O}} = 1.9 \pm 0.2$ Å. In conclusion, it must be noted that effect of the used data uncertainties and the

validity of the whole amount of the fixed parameters used within the XANES-analysis, is tested by the values of structural parameters determined for the reference crystals $CaTiSiO_5$, Na_2TiSiO_5 and is justified for the amorphous compounds of Sec.3 by the agreement of the obtained structural information with NMR-results.

3. Ti–coordination in glassy and radiation-damaged $CaTiSiO_5$ and in glassy Na_2 $TiSiO_5$

The method was applied to one glassy and two radiation-damaged titanites ($CaTiSiO_5$) and one glassy natisite (Na_2TiSiO_5) to reveal the structural changes in the environment of Ti related to two types of amorphization (temperature and radiation induced). The radiation-damaged titanites are named as "Egansville" and "Ontario". The single-shell fit of the Ti-O contribution for the above samples is performed first with a fixed value of σ^2 (taken as for the crystalline titanite) = 0.005 Å^2. The comparison of the experimental $\sigma(E)$ for the studied compounds of $CaTiSiO_5$ (figure 12 in [2]) shows the coincidence within ~1 eV in the energy position of their main near–edge peaks, suggesting the use of the same value of E_{MT} for all titanites. We use also the same values for $S_0{}^2 = 0.8$ and $\Lambda_{eff}(k)$ as for the model crystalline titanite. For the glassy titanite, the $|F(R)|$ for the FT of the $\chi(k)$, extracted from the experimental Ti K-XANES, is compared in Fig. 1b with the result of the single-shell fit. The obtained structural parameters for glassy $CaTiSiO_5$, Egansville and Ontario are presented in Table II, with the results for the model crystal $CaTiSiO_5$. Note that the fit with the three variables N_1, R_1, σ^2 gives approximately the same σ^2 value, as for the models with the two variables N_1, R_1. For the glass, $N_1 = 4.9 \pm 0.2$ [3], suggesting that the Ti–atom in glassy $CaTiSiO_5$ is coordinated by five oxygens, located at the average Ti−O distance of $R_1 = 1.95$ Å.

The single-shell models can be used as a basis for more thorough analysis of the first neighbours environment around Ti in titanites, performed via the fit, based on the two-shell model ($j = 1, 2$ is the shell's number): first shell corresponds to $\chi_{1,1}$-contribution of $N_{1,1}$ atoms located at $R_{1,1}$ and the second – to $\chi_{1,2}$-contribution of $N_{1,2}$ atoms at $R_{1,2}$. Its application permits to examine for the main groups of Ti−O pairs, while the number of variables is prevented to increase significantly. For amorphous samples the obtained $R_{1,1}$ and $R_{1,2}$ (which correspond to the best fit model with the fixed $N_{1,1}$ and $N_{1,2}$) reflect the asymmetry of the first shell's peak in the experimental $|F(R)|$, if the anharmonic effects for the studied compounds are much smaller than the static disorder. According to this approach, the oxygen–polyhedron with five atoms around Ti in glassy $CaTiSiO_5$ can be splitted into the two shells as: $1 + 4$ atoms (Model 1), $4 + 1$ (Model 2), $2 + 3$ (Model 3) or $3 + 2$ (Model 4). The results for the models 1,2 give the same distribution of distances: one Ti−O pair at $R_{1,1} = 1.85$ Å and four Ti−O pairs at $R_{1,2} = 1.97$ Å with $\sigma^2 = 0.0022$ Å^2. This σ^2 value is in agreement with its counterpart obtained for the model crystal (~0.0025 Å^2) via the two-shell fit. In parallel, the fit for the Models 3,4 return negative (non-physical) σ^2 values. Thus these models were treated as inadequate ones.

According to crystal structure information [14], the Ti-atom in crystalline natisite is coordinated by five oxygens: one at the short Ti-O distance $R_{1,1} = 1.695$ Å and the four others at $R_{1,2} = 1.99$ Å. The FT of the sum $\chi_{1,1} + \chi_{1,2}$ of the corresponding theoretical χ-functions and the fit of the corresponding Ti-O peak in $|F(R)|$ reveal that when the difference in $R_{1,1}$ and $R_{1,2}$ exceeds ~0.25 Å, then a single-shell fit doesn't provide the sufficient accuracy for the averaged values of structural parameters. However, in this case, the fit based on the two-shells model returns not only the accurate $R_{1,1}$ and $R_{1,2}$ values but permits to identify the actual split model ($1 + 4$) among other possibilities (e.g., $2 + 3$, $2 + 4$, $1 + 5$ etc.). The last result permits also to obtain the total N_1 value via the two-shell models for the oxygen-polyhedron around Ti in amorphous compounds, where this parameter can not be determined accurately via the single-shell fit. Thus, for the glassy natisite, the best fit is obtained for the model $N_{1,1} = 1$, $N_{1,2} = 4$ with the values of variables: $R_{1,1} = 1.70$ Å, $R_{1,2} = 1.94$ Å, $\sigma^2 = 0.0025$ Å^2.

4. Summary and conclusions

The obtained results can be summarized as follows:

(*i*) the sufficient accuracy for the Ti-O distances and the number of nearest oxygens for Ti-environment in the model crystalline titanite and natisite is obtained applying the FT to χ over the k-range: 3.9–5.8 Å^{-1}. This range corresponds to the Ti-XANES energies region >5010 eV (after the first main edge crest features) and is formed dominantly by the scattering contribution of the oxygen-polyhedron around the absorbing Ti-atom. The validity and the accuracy of this FT-procedure increase for amorphous compounds;

(*ii*) the R_1, N_1 for Ti-coordination environment in glassy titanite and in two modifications of radiation-damaged $CaTiSiO_5$ are determined via the single-shell fit of the oxygen-polyhedron's contribution into $|F(R)|$ using the two variables R_1, N_1 and the σ^2 value obtained for the model crystal $CaTiSiO_5$. The stability of the obtained R_1, N_1 values, as well as the used σ^2 value, is confirmed via the fit with the three variables R_1, N_1, σ^2. The values of R_1 and N_1 for radiation-damaged $CaTiSiO_5$ appear to be intermediate between the corresponding values for crystalline $CaTiSiO_5$ and its amorphous equivalent – titanite glass;

(*iii*) if the difference in Ti-O distances for the oxygen-polyhedron around Ti exceeds ~0.25 Å (the presence of the short titanyl-bonds), then the single-shell fit of such polyhedron's contribution into $|F(R)|$ does not provide the sufficient accuracy for the determined averaged values of R_1, N_1. In this case, the application of the two-shell fit with three variables $R_{1,1}$, $R_{1,2}$, σ^2 performed for the alternative models of the split of the oxygen-polyhedron into two shells ($N_1 = N_{1,1} + N_{1,2}$), permits to reveal an adequate split-model (tested for the model crystal Na_2TiSiO_5). This model gives that the Ti in glassy Na_2TiSiO_5 is coordinated by one oxygen at Ti-O distance $R_{1,1} = 1.70$ Å and 4 oxygens at $R_{1,1} = 1.94$ Å. For amorphous compound the revealed split-model reflects the asymmetry of the oxygen-polyhedron's peak in $|F(R)|$ and hence, can be validated if the anharmonicity effects are negligible.

Acknowledgment

The work is supported by RFBR Grant No 03-02-17325.

References

1. Taylor, M. and Brown, Jr. G. E., Amer. Mineral **61**, 435 (1976).
2. Farges, F., Brown, Jr. G. E. and Rehr, J., Phys. Rev. B **56**, 1809 (1997).

3. Bugaev, L., Sokolenko, A. and Flank, A., Phys. Rev. B **65**, 024105 (2002).
4. Farges, F., Brown, Jr. G. E., Navrotsky, A., Gan, H. and Rehr, J. J., Geochim. Cosmoch. Acta **60**, 3029 (1996).
5. Farges, F. and Brown, Jr. G. E., Geoch. Cosmoch. Acta **61**, 1863 (1997).
6. Farges, F., Amer. Mineral. **82**, 45 (1997).
7. Bugaev, L., Ildefonse, Ph., Flank, A., Sokolenko, A. and Dmitrienko, H., J. Phys. C **12**, 1119 (2000).
8. Ankudinov, A., Ravel, B. and Rehr, J. J., Phys. Rev. B **58**, 7565 (1998).
9. Vedrinskii, R., Bugaev, L. and Levin, I., Phys. St. Sol. b **150**, 307 (1988).
10. Bugaev, L., Ildefonse, Ph., Flank, A., Sokolenko, A. and Dmitrienko, H., J. Phys. C **10**, 5463 (1998).
11. Newville, M. *et al*., Physica B **208& 209**, 154 (1995).
12. Bugaev, L., Vedrinskii, R. and Levin, I., J. Phys. C. **3**, 8967 (1991).
13. Muller, J., Jepsen, O. and Wilkins, J., Sol. St. Commun. **42**, **5**, 365 (1982).
14. Nyman, H., O'Keeffe, M. and Bovin, J., Acta Cryst. B **34**, 905 (1978).

Physica Scripta. Vol. T115, 172–174, 2005

Aluminium K-edge XANES Study of Mica Preiswerkite

Ziyu Wu[1,2,*], A. Marcelli[2], G. Cibin[2], A. Mottana[2,3] and G. Della Ventura[2,3]

[1]Beijing Synchrotron Radiation Facility, Institute of High Energy Physics, Chinese Academy of Sciences, P.O. Box 918, Beijing 100039, P.R. China
[2]Laboratori Nazionali di Frascati, Istituto Nazionale di Fisica Nucleare, Via Enrico Fermi 40, 00044 Frascati, Italy
[3]Dipartimento di Scienze Geologiche, Universita' Roma Tre, Largo Murialdo 1, 00146 Roma, Italy

Received June 26, 2003; accepted January 15, 2004

PACS numbers: 78.70.DM; 91.60.−X; 61.10.Ht

Abstract

We present the Al K-edge XANES spectrum of synthetic mica with mixed fourfold coordinated and sixfold coordinated Al (preiswerkite). Experimental analysis and multiple scattering simulations of XANES spectra demonstrate that octahedral contributions may overlap the tetrahedral ones so that the lower energy structures in mixed coordination compounds may be associated to Al octahedral site. This unexpected behavior can be explained as due to a large local distortion of the Al octahedral site.

1. Introduction

Micas are abundant and structurally significant minerals on Earth characterized by a layered structure composed by sheets of tetrahedra and octahedra cornered by O or OH. These sheets alternate with ones centered by very large alkali and alkaline-earth atoms that are loosely coordinating only tetrahedral oxygen. Aluminium, one of the most significant constituents, may occur either in the tetrahedra or in the octahedra only, or in both these coordination polyhedra simultaneously. The line shape of the XANES spectra at the Al K edge is dominated by the first coordination sphere around the absorber, i.e., by the surrounding four and/or six O atoms, respectively. In the experimental XANES spectra recorded on micas with Al in mixed coordination, the main edge consists of two or three peaks [1, 2]. Usually these peaks are assigned to either the tetrahedral (T) or octahedral (O) sites, respectively, in terms of ligand electronegativity. However, without a careful and accurate theoretical analysis a clear interpretation is impossible or misleading because: (1) many investigations utilize the average K-edge position, neglecting possible variations in the coordination polyhedron bonding distances (i.e., large distortion that indeed may affect the edge features) and, (2) the edge position also depends on the chemical environment, such as the next-near neighbor O-H units and even higher-shell cations. As a matter of fact, recent investigations carried out on the atomic structure of model compounds, sometimes exhibit a significant disagreement [3, 4].

In order to determine a reliable relationship between type of first coordination shell and energy position of the relevant edge feature we analyzed the spectroscopic properties by comparison with a detailed full multiple scattering (MS) analysis, a strategy proved successful in the interpretation of many systems [5–9]. In this paper we present experimental data and *ab initio* full MS calculations of the XANES spectra at the Al K edge for preiswerkite (Pwk), a system having Al in both, i.e., T + O coordinations. The Al K-edge spectrum had been previously interpreted according to the ligand electronegativity model by the fingerprinting method, i.e., by comparison with the spectra of model compounds albite (CN = 4) and grossular (CN = 6) [1]. Results were satisfactory in the case of the micas with one type Al only, but certainly not clear in the case where both Al types were mixed. The resulting data presented in this manuscript suggest in fact a new kind of relationships i.e., the lower energy structure in the Al K-edge XANES spectrum of mixed-coordination compound may be attributed to the octahedral sites, or it originates mainly from the octahedral contribution. This may be due to a reduced ligand field strength owing to a rather large polyhedral distortion. This behavior is supported also by the recent analysis of the XAS spectra of Fe^{2+} and Ti^{4+} bearing compounds [10, 11].

2. Experimental and theoretical details

The preiswerkite system is a synthetic material whose preparation procedure is described in Ref. [1]. XAFS experiment was carried out at SSRL (Stanford, CA, USA), with the SPEAR storage ring operating at energy 3 GeV and injection current 100 mA, at beam line SB03-3, which is equipped with the JUMBO monochromator of the double-crystal type consisting of two plates of a single YB_{66} crystal cut along the (400) plane, with resolution less than 0.55 eV. Spectrum was recorded in the total electron yield mode by scanning the Al K edge from 1540 to 1690 eV in steps of 0.3 eV, and was corrected for background contribution from lower energy absorption edges by linear fitting of the baseline, and normalized in energy to +60 eV from the first inflection of the edge i.e., at the uppermost energy value for XANES [12]. Pwk contains one Al in the octahedral sheet and two Al in the tetrahedral sheet [13] and clearly exhibits three structures at the edge with fairly similar intensities (see Figure 1).

The Al XANES spectra have been computed using full MS theory [9]. In the muffin-tin model and one-electron approximation, the local density potentials for the Al clusters have been constructed according to Mattheiss prescription [14] by superposition of neutral atomic charge densities using the Clementi-Roetti basis set tables [15]. For the exchange-correlation part of the potential, for practical reasons, we used the energy-independent X_α potential with α equal to 0.60 for the excited Al atom. The calculated spectra have been further convoluted with a Lorentzian shaped function with a full width $\Gamma_h = 0.42$ eV [16] to account for the core hole lifetime and $\Gamma_{exp} = 0.55$ eV for the experimental resolution. We have chosen the muffin-tin radii according to Norman's criterion [17] and allowed a 10% overlap between contiguous spheres to simulate the atomic bond. The z axis in all our calculations is along the c axis of the compound.

*Corresponding author: Email: wuzy@ihep.ac.cn

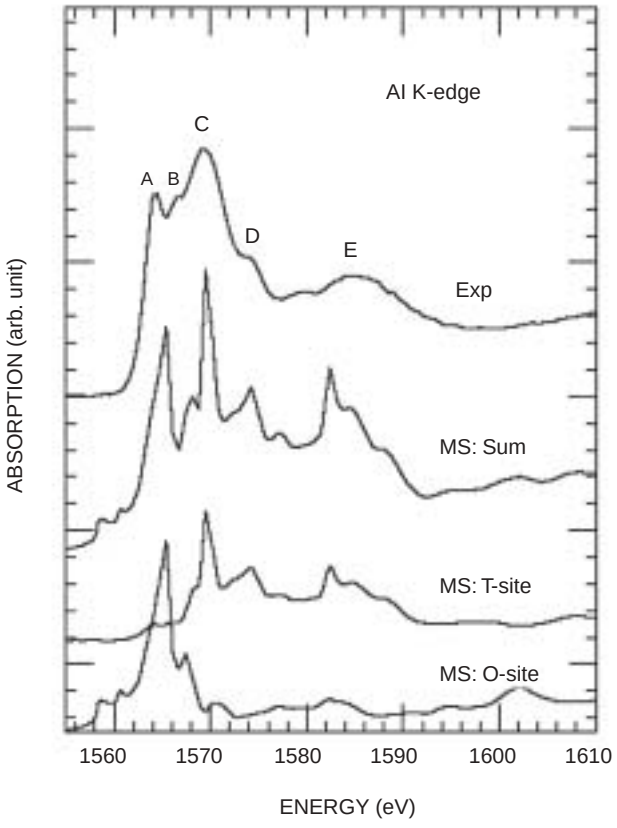

Fig. 1. Comparison of experimental spectrum of preiswerkite (top curve) with MS theoretical Al K-edge spectra for the two different sites (O and T) and the sum (total curve).

3. Discussion

Bond length vs. edge-peak position behavior is shown in Fig. 2(a) and 2(b) where a series of SCF-MS calculated spectra by using simplified cluster models (e.g., tetrahedra and octahedra) are plotted as a function of the bond distances. A clear shift of the edge towards lower energies with increasing Al-O bond length is observed. The observed shift is estimated ca. 20.4 eV/Å for fourfold-coordinated Al over the range 1.70–1.80 Å and ca. 13.6 eV/Å for six-fold-coordinated Al over the range 1.90–2.00 Å. These rates are similar to those experimentally observed for both Ti K-edge [11] and Si K-edge structures [18].

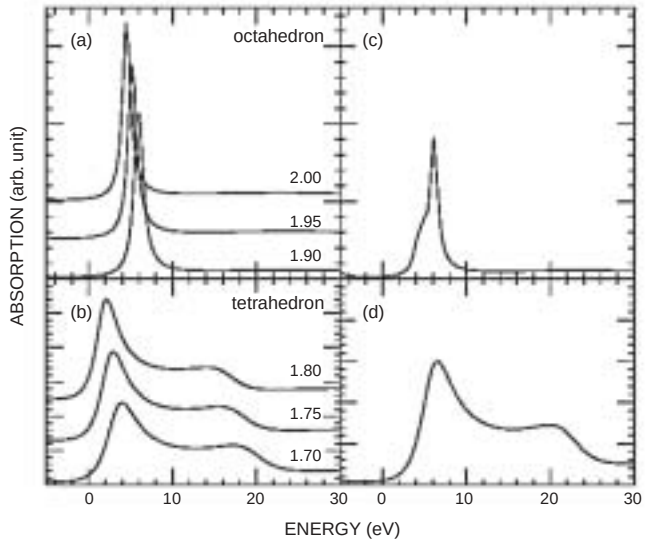

Fig. 2. On the left panels: Al K edge simplified self-consistent model calculations for different bond distances (given in Ångstrom) for: (a) octahedral clusters and (b) tetrahedral clusters. On the right panels: (c) real sixfold cluster SCF-calculations in Pwk and (d) real fourfold cluster SCF-calculations in Pwk.

In Fig. 2(c) and 2(d) we present similar SCF-potential calculations taking into account the distortions observed in the real crystal structures of Pwk. These results clearly show that the main peak of the octahedral cluster is at lower energy with respect to the tetrahedral one. The observed "anomalous chemical shift" is mainly due to the larger distortion around the photoabsorber. On the contrary, the results obtained in the ideal model case exhibit a net shift of ca. 2.2 eV (with the fourfold coordinated site contribution being followed by the sixfold coordinated site contribution). These Al K-edge calculations address the role of the structural distortion in determining the details of the transition features in compounds with mixed coordination.

In comparison to the experimental data, Fig. 1 shows also the calculated Al XANES spectra of this mica having Al in two coordination states (one octahedral $^{[6]}$Al and two tetrahedral $^{[4]}$Al) [13]. We first calculated the convergent 91-atom cluster for each site, then we combined them in the proportion 1 $^{[6]}$Al + 2 $^{[4]}$Al. Peak A originates from the O-site contribution, peak B from a superposition of contributions from both sites, while C is dominated by the T-site contribution. This result is not surprising if one notices that, according to the crystal structure determination, the Al-O bond lengths are about 2.02 Å and 1.69 Å for octahedral and tetrahedral sites, respectively. The large octahedral bond distance shifts the edge position towards lower energy (see Fig. 2), whereas the opposite occurs for Al clusters having a short tetrahedral length. Furthermore the large distortion of the tetrahedral site shifts the peak position toward higher energy by more than 2.0 eV [6]. As a matter of fact, MS calculations indicate that all features are determined by the superposition of contributions from both sites. However, although peaks A and B are mainly, but not only of octahedral origin, C is essentially due to the tetrahedral contribution. Another strong evidence of the above assignments is associated to the energy region at about 20 eV from the edge where the spectral feature E, typical of the tetrahedral Al XANES spectrum, occurs in contrast to the octahedral shape that is substantially flat in this energy range [1].

In this system we carried out a further test, albeit preliminary, on the possible effects induced by O-H bonds onto the $^{[6]}$Al spectrum. This test is actually important because of the special configuration of the Al coordination polyhedron in micas: it consists of four O anions in common with the tetrahedral sheet plus two OH located at the center of the O hexagonal network. Because the formation of the O-H bond reduces the total electronegativity of the Al-O bonds on two opposite directions, it should lead to an edge shift towards lower energies, as shown in Fig. 3. Here we present the calculations for a simplified small cluster that contains only a first-coordination oxygen shell with one O anion linked to hydrogen. Theoretical data in Fig. 3 shows that formation of the O-H bond shifts the edge position towards low energy (ca. 1.0 eV), and decreases the intensity of the main edge with a concomitant formation of new states near the Fermi level. Data support our previous assignment in agreement with other data available in literature [19–21]. Actually, the increase of the bond length, the O-H bond formation and a large site distortion are mechanisms competitive with the increasing of coordination numbers.

In conclusion, a detailed experimental and theoretical investigation of the Al K-edge XANES has been performed on preiswerkite, a mica that contains Al in the different coordinations,

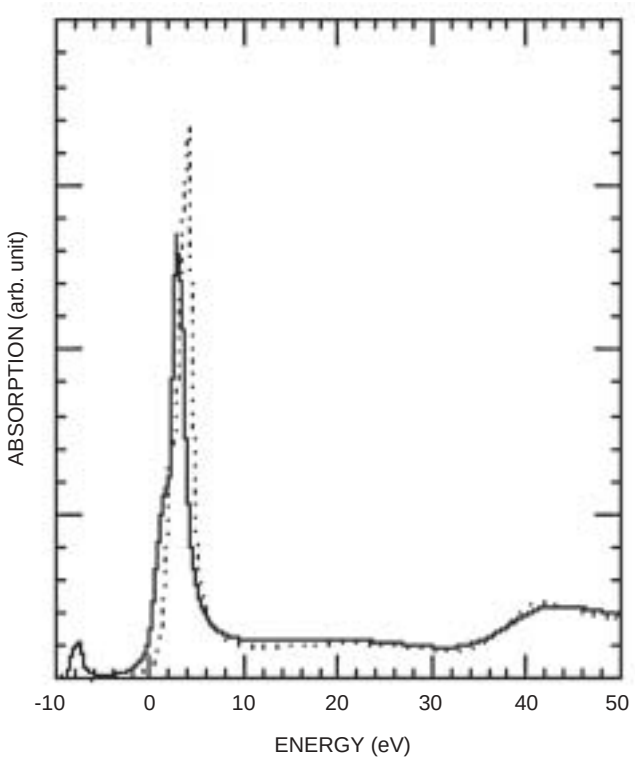

Fig. 3. Comparison of MS calculations at the Al K-edge of preiswerkite for the smallest Al cluster (Al + 6 oxygens) with (solid curve) and without (dot curve) hydrogens.

our analysis clearly demonstrates that the coordination is not the only parameter that affects the edge position. Bond length, OH formation and, most important, the site distortion have to be considered. The observed anomalous chemical shift contribution to the Al K-edge peak also indicates that a simple fingerprinting technique based on the extrapolation of the results of the four-fold and six-fold structures in the spectra of model compounds is reliable only if supported by a theoretical analysis. This is particularly significant in the analysis of compounds relevant in mineralogy and geochemistry, where Al may occur in different coordination sites and with different bond lengths, distortions and chemical environments.

Acknowledgments

The authors thank the entire SSRL staff for the experimental assistance during experimental runs. A special thanks is devoted to J.-L. Robert for providing the synthetic micas. Financial support was provided by MURST, Italy (Project *Crystal-chemical, kinetic and thermodynamic aspects of minerals*). One of us (ZYW) thanks the *100-Talent Research Program* of Chinese Academy of Sciences and the *Outstanding Youth Fund* (10125523) of the National Natural Science Foundation of China.

References

1. Mottana, A. *et al.*, Am. Mineral. **82**, 497 (1997). Mottana, A., Marcelli, A., Cibin, G. and Dyar, M. D., Rev. Mineral. Geochem. **46**, 371 (2002).
2. Li, D., Bancroft, G. M., Fleet, M. E., Feng, X. H. and Pan, Y., Am. Mineral. **80**, 432 (1995).
3. Ildefonse, Ph. *et al.*, Phys. Chem. Minerals **25**, 112 (1998).
4. Poe, B., Seifert, F., Sharp, T. and Wu, Z. Y., Phys. Chem. Minerals **24**, 477 (1997).
5. Proceedings of the XAFS XI Conference (Ako, Japan, 2000) in: J. Synchrotron Rad. **8**, (2001), and references therein. Mottana, A., in: X-Ray and Inner-Shell Processes: 19th International Conference on X-ray and Inner-Shell Processes. Bianconi, A., Marcelli, A. and Saini, N. L., eds. (American Institute of Physics CP 652. New York, 2003).
6. Wu, Z. Y. *et al.*, Phys. Rev. **B 60**, 9216 (1999).
7. Wu, Z. Y. *et al.*, Appl. Phys. Lett. **79**, 1918 (2001).
8. Rehr, J. J. and Ankudinov, A. L., J. Synchrotron Rad. **10**, 43 (2003).
9. Natoli, C. R., Benfatto, M., Della Longa, S. and Hatada, K., J. Synchrotron Rad. **10**, 26 (2003).
10. Waychunas, G. A., Apted, M. J. and Brown, G. E. Jr., Phys. Chem. Minerals **10**, 1 (1983).
11. Waychunas, G. A., Am. Mineral. **72**, 89 (1987).
12. Bianconi, A., in "X-ray Absorption: Principles, Applications, Techniques of EXAFS, SEXAFS, XANES," (D. C. Konigsberger and R. Prins, eds.), (Wiley, New York, 1988).
13. Oberti, R., Ungaretti, L., Tlili, A., Smith, D. C. and Robert, J. L., Am. Mineral. **78**, 1290 (1993).
14. Mattheiss, L., Phys. Rev. **A 134**, 970 (1964).
15. Clementi, E. and Roetti, C., At. Data Nucl. Data Tables **14**, 177 (1974).
16. Fuggle, J. C. and Inglesfield, J. E., "Unoccupied Electronic States," Topics in Applied Physics (Berlin: Springer, 1992); appendix B, p347.
17. Norman, J. G., Mol. Phys. **81**, 1191 (1974).
18. Sharp, T. *et al.*, Phys. Chem. Minerals **23**, 17 (1996).
19. Benfatto, M., Solera, J. A., Chaboy, J., Proietti, M. G. and Garcia, J., Phys. Rev. **B 56**, 2447 (1997).
20. Ruckman, M. W. *et al.*, Phys. Rev. **B 57**, 3881 (1998).
21. van Aken, P. A., Wu, Z. Y., Langenhorst, F. and Seifert, F., Phys. Rev. **B 60**, 3815 (1999).

Physica Scripta. Vol. T115, 175–178, 2005

Initial Results of the One-Dimensional XAFS Debye-Waller Models for Active Sites of Cu Histidine and Cystein Metalloproteins

N. Dimakis*[1,2] and G. Bunker[1]

[1]Illinois Institute of Technology, Chicago, IL 60616, USA
[2]Biophysics Collaborative Access Team, Argonne National Laboratory, Argonne, IL 60439, USA

Received June 26, 2003; revised December 4, 2003; accepted December 18, 2003

PACS number: 61.10Ht

Abstract

The mean square variation of the half-scattering path length in X-ray absorption fine structure Debye-Waller factors has been expressed as a function of the first shell radial distance and an angle (where applicable) for Zn^{+2} active sites of metalloproteins enabling direct and accurate calculation of the single and multiple scattering Debye-Waller factors at arbitrary temperatures. The local character of the filled d-orbital Zn^{+2} element does not obstruct us from extending this technique to other metals with unfilled d-orbital. In this report we present initial results based on one-dimensional radial models applicable to the d^9 Cu(I) and Cu(II) histidine/imidazole and cystein complexes. Results from these new models are compared with large reference structures of homogeneous and heterogeneous Cu metal ligation built and optimized by non-local Density Functional Theory.

1. Introduction

The X-ray Absorption Fine Structure (XAFS [1, 2]) Debye-Waller factor (DWF) is an exponential term of the form $e^{-2k^2\sigma_j^2}$ that reduces the amplitude of the XAFS $\chi(k)$ spectra and accounts for the structural and thermal disorder of a given sample. The temperature-dependent parameter σ_j^2 is the mean square variation of the half-length of the j-th single (SS) or multiple (MS) scattering path, and is directly related to the phonon normal mode spectrum of the sample (eigenfrequencies and eigenvectors). Evidently, the influence of the DWF parameter in the XAFS spectra is more important at higher photoelectron wavenumber $\boldsymbol{k}$ value. Depending on the sample geometry the actual number of all SS and MS DWF parameters can be on the order of several hundred in a low symmetry structure. Since experimental data can only fit a limited number of parameters (about $2\Delta k\Delta R/\pi \cong 20$–$30$ [3], where Δk and ΔR are the $\boldsymbol{k}$- and $\boldsymbol{R}$-range data ranges) the DWF parameters must be known from an alternative source to fit the experimental data without any unjustified assumptions. Considerable progress has been reported for DWF calculations using self-consistent (SCF) [4, 5, 6, 7] and force-field model (FFM) methods [8, 9, 10] to calculate the phonon normal mode spectrum. These models are alternatives to the single parameter Einstein and correlated Debye model that are insufficient to describe either single or multiple scattering paths in systems with heterogeneous bond strengths.

SCF Density Functional Theory (DFT) [11, 12, 13] methods are preferred over FFM models due to their reliability and accuracy. However calculations on the large active site structures are not always possible or feasible. Poor SCF energy and geometry convergence, high CPU demand (execution times for DFT scale as N^3 where N is the number of atomic basis sets used) and saddle points on the conformational potential energy surface lead us to investigate alternative mechanisms for the DWF calculations.

Active sites of metalloproteins consist of a central metal atom that binds to amino-acid residues from the protein. Although metal-residue distance may vary depending on many factors like ligand-coordination number and possible hydrogen bonding between residues, internal residue structure remains fairly rigid. Thus the mean square variation of a half scattering SS/MS path σ_j^2 could be expressed as a direct function of the radial distance separating the metal from the residue itself (first shell distance) at a given sample temperature. In some cases an angle can be also used as a parameter for formations involving cysteines and carboxylate amino acids. Expressing the σ_j^2 as a function of a the first shell radial distance (and angle where applicable) allows experimentalists to use temperature-dependent functions in fitting procedures to analyze XAFS spectra without the need to perform complex and time-consuming DFT calculations. Initial results for Zn^{+2} and histidine ligands using an imidazole ring have been reported [7, 14] and provided accuracy sufficient for use with XAFS data analysis.

The localized character of the filled d-orbital for Zn metalloproteins is not an impediment for extending this technique to other metals with unfilled d-orbital. Selecting the closest element to Zn, we describe two similar one dimensional models (first shell metal-ligand distance variation) that are applicable to Cu-histidine and Cu-cysteine structures (Fig. 1). Similarities and apparent differences between Cu(I) and Cu(II)-histidine and cystein models are discussed and modeled-calculated DWFs are compared with DFT optimized structures which have the advantage over experimental XAFS spectra of allowing direct path-by-path DWF comparison rather than an computing average DWF over a particular shell. DFT calculated normal mode frequencies of optimized structures under non-local functionals are in most cases within 95–98% of the corresponding experimentally reported infrared or Raman normal mode frequency [15].

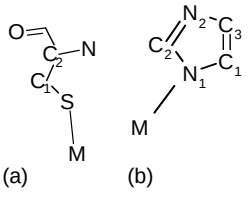

Fig. 1. (a) Cu-cysteine and (b) Cu-histidine models. Another sulfur/nitrogen atom that directly binds to the metal and opposite to the residue is not shown here.

*e-mail: dimakis@biocat2.phys.iit.edu

2. Computational Method

A small cluster that consists of the Cu metal, the amino acid residue[1] and another atom that binds directly to the metal and opposite to the residue (Fig. 1) is geometrically optimized using the non-local B88-LYP [16, 17, 18, 19] functional of the DFT method with double zeta (DZV) [20] basis set specifically optimized for DFT. The phonon normal mode eigenfrequencies and eigenvectors are calculated from the DFT optimized modeled cluster and are inputted to a program made by the authors that evaluates all possible SS and MS DWFs at any arbitrary temperature. High spin configuration was used in all clusters as it corresponds to the ground state energy of the particular cluster formation. Once the first "equilibrium" metal-ligand cluster is obtained, the first shell Cu–$N^{(1)}$/S interatomic distance(s) is perturbed and the procedure is repeated. For these subsequent clusters in addition to the Cu metal, the following residue atoms are kept "frozen" during geometry optimization: 1) $N^{(1)}$, $C^{(1)}$, and $C^{(2)}$ for Cu-histidine, and 2) S, and $C^{(1)}$ atoms for Cu cysteine model. All model clusters converge to an energy minimum and not to a saddle energy point, i.e. no negative frequencies appear in the phonon normal mode spectrum.

In general σ_j^2 are expressed as a mixture of polynomial and exponential expressions over ΔR. Similar to Zn^{+2} models, it was identified that for Cu(II)-imidazole and Cu-cystein models σ_j^2 is expressed as [14]

$$\sigma_j^2(\Delta R, T) = \sum_{i=1}^{2} C_{ij}(T)\Delta R^i + e^{A(T)+B_j(T)\Delta R} \quad (1)$$

and for Cu(I)-imidazole

$$\sigma_j^2(\Delta R, T) = \sum_{i=1}^{2} C'_{ij}(T)\Delta R^i \quad (2)$$

where A, B and C' are temperature dependent coefficients that can be approximated as a third order polynomial over temperature, $\Delta R = R - R_0$ is changes of the perturbed radial distance with respect to the equilibrium position R_0, and $C'_{0j} \equiv \sigma_j^2(R_0, T)$ are a distance-independent parameters.

The exponential growth of the σ_j^2 where applicable, dictates that amino acid residues will be non-XAFS detectable when Cu-residue distance exceeds a "cut-off" value. Figures 2 and 3 indicate that for Cu(II)-histidine and Cu(II)-cysteine formations the metal-residue distance cut-off value is approximately 2.3 Å and 2.45 Å respectively. No exponential behavior appears for the Cu(I)-histidine case for $R_{Cu\text{-}N(1)}$ values up to 2.2 Å, whereas for Cu(I)-cysteines σ_j^2 exponential growth does not rise as rapid as in the corresponding Cu(II) case. For the Cu(I)-histidine model the equilibrium distance Cu(I)–$N^{(1)}$ is detected at 1.931 approximately 0.07 Å shorter than the corresponding Cu(II)–imidazole structures. It is difficult to identify a common model for DWFs of Cu(I) and Cu(II)-histidine formations. However for Cu-cystein models shifting the value $\Delta R_{Cu\text{-}S}$ of the Cu(II)-cysteine by about −0.055 Å, σ_j^2 of the SS Cu–S shell for either Cu(I) or Cu(II) cysteine models coincide (fig. 4). Therefore in contrast with the Cu-histidine case, a single model is adequate to describe either Cu ion bound to cysteine amino acids.

[1]Metal-Histidine structures can be sufficiently mimicked by metal-imidazole rings.

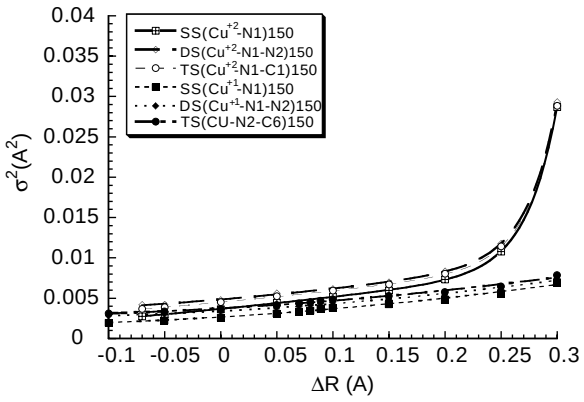

Fig. 2. Various DFT calculated σ^2 for single and multiple-scattering paths of the Cu(I)- and Cu(II)-imidazole model vs. linearly translated ΔR for the first radial shell Cu–$N^{(1)}$. R_0 is 1.995, and 1.930 Å for Cu(II) and Cu(I) respectively.

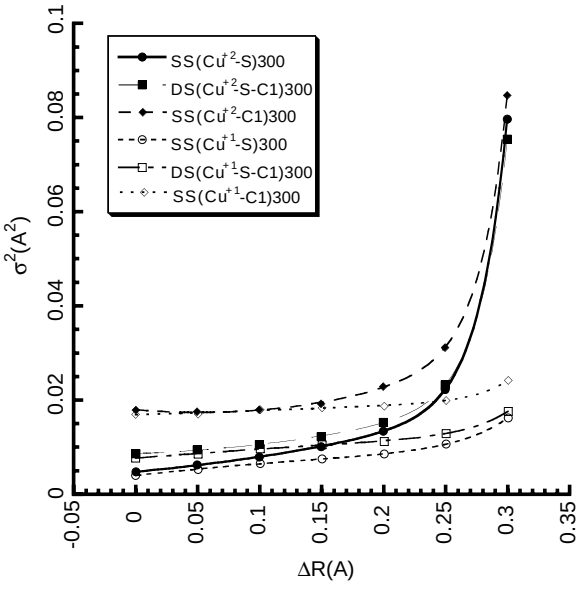

Fig. 3. Various DFT calculated σ^2 for single and multiple-scattering paths of the Cu(I)- and Cu(II)-cystein models vs. linearly translated ΔR for the first radial shell Cu-S. R_0 is 2.20 Å for either Cu(II) or Cu(I) metal.

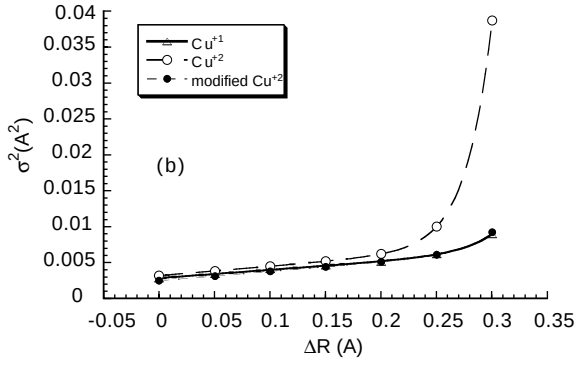

Fig. 4. DFT calculated σ^2 for the single-scattering path of the Cu-S for Cu-cystein model. Shifting the $R_{Cu(II)\text{-}S}$ by additional 0.055 Å Cu(I) and Cu(II) models coincide.

3. Results and Discussion

3.1. *Cu histidine models-homogeneous ligation*

DFT Cu–imidazole optimized structures with different imidazole-coordination number have been built, optimized and their phonon normal mode spectrum was used to calculate the corresponding

DWFs at 150 °K. For large DFT-optimized bio-structures, saddle points might appear in the energy spectrum. This is because there are multiple structural conformations with very small SCF energy differences e.g. the imidazole ring rotations about the metal-$N^{(1)}$ axis. Depending on the size of the negative eigenfrequency and the particular mode of the saddle point, its presence might affect the DWFs of the structure. The Cu(II) imidazole model is tested using Cu(II) with coordinated to three imidazole rings and also for symmetry reasons to a spare NH_2 group. One negative frequency at $-25.42\,\mathrm{cm}^{-1}$ appear in the normal mode spectrum. This frequency corresponds to carbon and nitrogen stretching modes perpendicular to the plane of the imidazole ring and thus do not affect the σ_j^2 themselves that are related to the planar imidazole modes. The Cu(I) coordinated to two imidazole rings was used as a test structure for Cu(I) model. No saddle points were observed for the later structure.

Similarly to the Zn^{+2} case, imidazole ring deformations might occur and are caused by different metal-residue and residue-residue interactions between reference and modeled metal-residue structures. For the Cu(II) complex it has been observed that $N^{(1)}$–$N^{(2)}$ and $N^{(1)}$–$C^{(3)}$ interatomic distances are overestimated from our model by about 0.07 Å and 0.03 Å respectively. These deformations will affect σ_j^2 SS Cu–$N^{(2)}$, Cu–$C^{(3)}$, double (DS)- and triple (TS)-scattering Cu–$N^{(1)}$–$N^{(2)}$, Cu–$N^{(1)}$–$C^{(3)}$ paths. Due to the almost collinear geometry of the absorbing metal with $N^{(1)}$ and $N^{(2)}/C^{(3)}$ atoms, the DS/TS of these scattering paths are very important in terms of their contribution in the amplitude of the XAFS spectrum. It has been found that adding these "extra" distances into the ΔR value compensates for these deformations and improved the accuracy of the modeled DWFs for the affected paths. No significant imidazole deformation was observed for the Cu(I) case when compared with its corresponding reference structure. The average Cu–$N^{(1)}$ first shell interatomic distance for the three-imidazole and two imidazole structures was observed at 1.995 Å and 1.883 Å respectively. The NH_2 group in the Cu(II) case was also 1.88 Å away from the Cu(II) central atom. For this SS Cu–$N^{(1)}$ path at 150 °K our models give 3.39×10^{-3} Å^2 and 2.27×10^{-3} Å^2 for Cu(II) and Cu(I) respectively vs. $3.23 \pm 0.15 \times 10^{-3}$ Å^2 and 2.24×10^{-3} Å^2 of the corresponding reference structures. For the SS Cu–$C^{(1,2)2}$ the average model-calculated σ_j^2 for both paths is 5.65×10^{-3} Å^2 and 5.10×10^{-3} Å^2 for Cu(II) and Cu(I) respectively vs. $5.89 \pm 0.8 \times 10^{-3}$ Å^2 and $4.68 \pm 0.25 \times 10^{-3}$ Å^2 of the corresponding reference structures. These short photoelectron paths range correspond to the bending $N^{(1)}$–Cu–$C^{(1,2)}$ mode. For the DS/TS Cu–$N^{(1)}$–$N^{(2)}$ similar accuracy is obtained for either case. For example for the Cu(I) case model-calculated σ_j^2 value is 3.07×10^{-3} Å^2 vs. 3.23×10^{-3} Å^2 for the reference structure. Using atom positions from the reference structures as inputs to FEFF [21] program together with DWFs from models/references XAFS $\chi(k)$ spectra are generated and their corresponding Fourier transform are shown in fig. 5. An excellent agreement between modeled and referenced spectra is obtained.

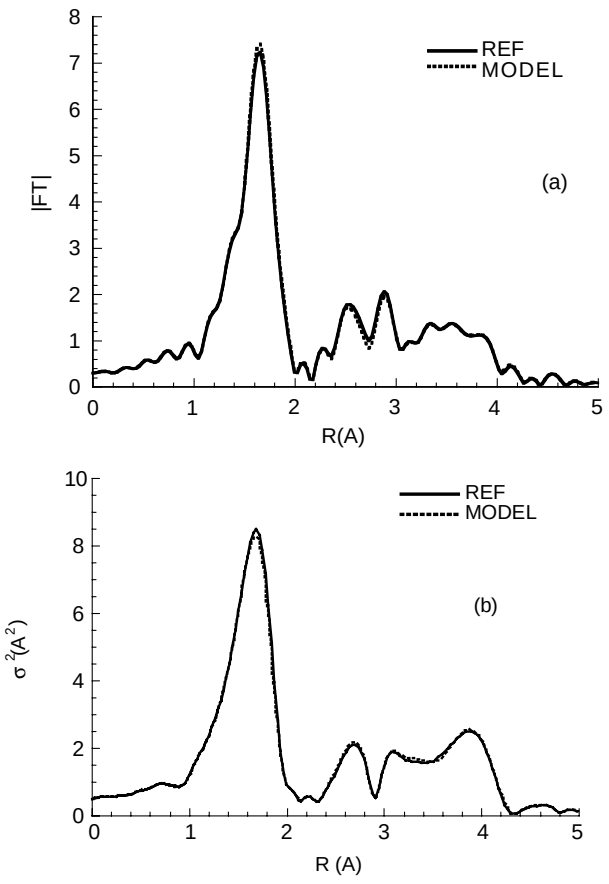

Fig. 5. Fourier Transform of calculated DWFs vs. corresponding reference structures for a) Cu^{+1} and b) Cu^{+2}-histidine formations at 150 °K.

3.2. *Cu cysteine models-heterogeneous ligation*

The Cu-cysteine model is tested using the DFT optimized Cu-Cys/His structures that serves as references for the Cu-cysteine model. Although no saddle points appear in the phonon normal mode spectrum of the Cu(II)-Cys/His reference structure, its first normal mode frequency of $0.142\,\mathrm{cm}^{-1}$ that corresponds to a translational mode of the whole molecule will not be included in the DWF calculations. However, for corresponding Cu(I) reference structure one saddle point at $-23.04\,\mathrm{cm}^{-1}$ does appear in the phonon spectrum. This corresponds to a mixture of the following modes: 1) stretching modes perpendicular to the imidazole ring, 2) stretching modes perpendicular to the plane defined by Cu(I), S and $C^{(1)}$ atoms, and 3) bending modes of the alpha carbon cysteine tail. This mode is omitted and does not affect the DWF calculations.

Interatomic distances Cu(II)–$N^{(1)}$ and Cu(II)–S of the first two shells, were detected at 1.913 Å and 2.145 Å, whereas the corresponding distances for Cu(I) were observed at 1.908 Å and 2.138 Å respectively. The "short" Cu–S bond length arises because the two ligands are on the opposite sides of the metal and their electrostatic interaction is minimal. The one-dimensional Cu-cysteine model is adequate to be used here since angle variation $\Delta\Theta$ between model and reference structures is not more than 0.3°. The first two shells can be resolved by XAFS since their corresponding interatomic distances differ by more than 0.2 Å. At 150 °K, the σ_j^2 for the SS Cu–S path of the reference structure was predicted at 2.36×10^{-3} Å^2 for either Cu ion. For the σ_j^2 of the same path and temperature our model gives 2.55×10^{-3} Å^2 and 2.22×10^{-3} Å^2 for Cu(II) and Cu(I) ions respectively. Similarly for the SS Cu–$N^{(1)}$ path and Cu(II) ion our model gave 2.62×10^{-3} Å^2 vs. 2.68×10^{-3} Å^2 for the reference structure whereas the corresponding values for the Cu(I) ion are 2.49×10^{-3} Å^2 and 2.57×10^{-3} Å^2 respectively. The Fourier transform of FEFF [22]-generated XAFS spectra using atomic positions from the

[2]Since XAFS cannot distinguish $C^{(1)}$ from $C^{(2)}$ atom, these paths are treated as a single paths with the DWF to be the average of the two.

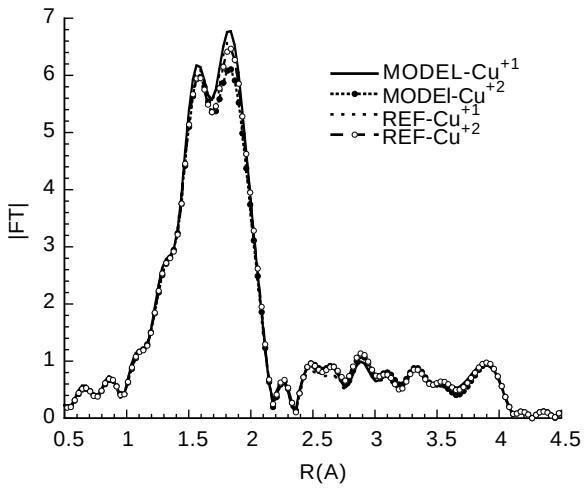

Fig. 6. Fourier Transform of calculated DWFs vs. reference for Cu-Cys/His structure at 150 °K.

reference structures are shown in fig. 6 with the corresponding DWFs being inputted from either reference or modeled compounds.

The small variation of second peak in fig. 6 between experimental and Cu(II)-modeled structures is not only due different σ_j^2 for SS Cu–S path but also due to variations on the σ_j^2 of the DS Cu(II)–S–$C^{(1)}$ path. The modeled σ_j^2 for the DS Cu(II)–S–$C^{(1)}$ path is detected at 5.4×10^{-3} Å^2 vs. 4.4×10^{-3} Å^2 for the corresponding value for the Cu(II)-Cys/His case. Similar to Zn^{+2}, for Cu-cysteine case better agreement is expected at larger metal-cysteine distances [14]. Corrections due to the imidazole ring reformation as discussed previously were also included.

4. Conclusions

- Analytical expressions that describe SS and MS σ_j^2 for Cu(I) and Cu(II) histidine and cysteine structures have been derived using the non-local DFT method for small metal-ligand structures. A single model can be used for either Cu(I) or Cu(II) bound to a cysteine amino acid residue. However although it is possible to use a single model for either Cu(I) and Cu(II) imidazole DWF calculations, two distinct models are preferred. Generalization of these models to an arbitrary temperature is underway.
- Cu-cysteine and Cu-histidine models were used to analyze active sites with heterogeneous ligation like the Cu-Cys/His structure. Similarly to the homogenous case the accuracy is sufficient for XAFS data analysis.

References

1. Stern, E. A., in "X-Ray Absorption", (edited by Koningsberger, D. C. and Prins, R.) (Willey, New York, 1988), Chap. 1.
2. Lee, P. A. and Pendry, J. B., Phys. Rev. B **11**, 2795 (1975).
3. Stern, E. A., Phys. Rev. B **48**, 9825 (1993).
4. Dimakis, N. and Bunker, G., Phys. Rev. B **58**, 2467 (1998).
5. Dimakis, N. and Bunker, G., J. Synchr. Rad. **6**, 266 (1999).
6. Dimakis, N. and Bunker, G., J. Synchr. Rad. **8**, 297 (2001).
7. Dimakis, N. and Bunker, G., Phys. Rev. B **65**, 201103 (2002).
8. Loeffen, P. W. and Pettifer, R. F., Phys. Rev. Lett. **76**, 636 (1996).
9. Loeffen, P. W., Pettifer, R. F. and Tomkinson, J., Chem. Phys. **208**, 403 (1996).
10. Poiarkova, A. V. and Rehr, J. J., Phys. Rev. B **59**, 948 (1999).
11. Hohenberg, P. and Kohn, W., Phys. Rev. B **136**, 864 (1964).
12. Kohn, W. and Sham, L. J., Phys. Rev. A **140**, 1133 (1965).
13. Parr, R. G. and Yang, W., "Density Functional Theory of Atoms and Molecules", (Oxford U. P., New York, 1989).
14. Dimakis, N. and Bunker, G., Phys. Rev. B. (2004) in print.
15. Scott, A. P. and Radom, L., J. Phys. Chem. **100**, 16502 (1996).
16. Becke, A. D., J. Chem. Phys. **84**, 4524 (1986).
17. Becke, A. D., Phys. Rev. A **38**, 3098 (1988).
18. Becke, A. D., J. Chem. Phys. **88**, 2547 (1988).
19. Lee, C., Yang, W. and Parr, R. G., Phys. Rev. B **37**, 785 (1988).
20. Godbout, N., Salahub, D. R., Andzelm, J. and Wimmer, E., Can. J. Chem. **70**, 560 (1992).
21. Ankudinov, A. L., Ravel, B., Rehr, J. J. and Conradson, S. D., Phys. Rev. B **58**, 7565 (1998).
22. Ankudinov, A. L., Ravel, B., Rehr, J. J. and Conradson, S. D., Phys. Rev. B **58**, 7565 (1998).

Physica Scripta. Vol. T115, 179–181, 2005

Similarities and Differences Between XANES Spectra at Analogous Edges of Ternary Semiconductors $CuGaSe_2$, $ZnGeAs_2$ and $CuFeS_2$

O. Šipr*, J. Drahokoupil, P. Machek and A. Šimůnek

Institute of Physics, Academy of Sciences of the Czech Republic, Cukrovarnická 10, 162 53 Prague, Czech Republic

Received June 26, 2003; revised June 30, 2003; accepted November 4, 2003

PACS number: 78.70.Dm

Abstract

K edge XANES spectra of $CuGaSe_2$, $ZnGeAs_2$ and $CuFeS_2$ are studied both experimentally and theoretically. While spectra of $CuGaSe_2$ and $ZnGeAs_2$ are remarkably similar, spectra of $CuFeS_2$ differ significantly, especially in the pre-edge region. Full-potential band structure calculations without any core hole give essentially the same results as real-space multiple-scattering calculations for a muffin-tin potential with a core hole included; the notable exception is the Cu edge in $CuGaSe_2$, where non-muffin-tin effects possibly occur. The distinct pre-peak visible at all three spectra of $CuFeS_2$ arises from transitions to delocalized multiple-scattering resonances which are confined almost exclusively to the Fe sites.

1. Introduction

Ternary semiconductors of the I-III-VI_2 and II-IV-V_2 types share the same chalcopyrite structure. Their electronic properties were extensively studied in the past, both due to fundamental reasons (they offer an opportunity to study systematic variations of their properties with chemical composition) as well as due to their technological relevance. Among the techniques which probe the low-lying unoccupied states, X-ray absorption near-edge structure (XANES) spectroscopy holds a unique position as it offers a local view from a chemically specific site. Earlier XANES studies suggested that while spectra at analogous K edges of I-III-VI_2 compounds are quite similar to each other, the spectra of the "archetypal" chalcopyrite $CuFeS_2$ exhibit remarkable differences, especially in the pre-edge region. To our knowledge, no XANES spectra of the II-IV-V_2 compounds have been published so far.

When interpreting XANES spectra, it is often assumed that the pre-edge region corresponds to semi-bound states. In accord with this reasoning and with the results of band-structure calculations, the pre-peak in $CuFeS_2$ has been interpreted as transitions to states arising from the Fe 3d band hybridized with the S and/or Cu states [1, 2, 3]. On the other hand, McKeown [4] suggested that the pre-peaks at the Cu and Fe K edge spectra may be caused by interference effects of the photoelectron wave function from the crystal structure. It is the purpose of this paper to compare experimental and theoretical XANES spectra of $CuFeS_2$ with analogous spectra of a I-III-VI_2 compound $CuGaSe_2$ and of a II-IV-V_2 compound $ZnGeAs_2$, to identify their similarities and differences and to present a comprehensive interpretation of the pre-edge region in the XANES of $CuFeS_2$.

2. Experimental and theoretical methods

The spectra of $CuGaSe_2$ and $ZnGeAs_2$ polycrystalline samples were measured using a two-crystal spectrometer and an X-ray spectrometry tube. The energy resolution varied from 0.36 eV for the Cu edge to 0.52 eV for the Se edge. The spectra were collected in a transmission mode, each measured data point represents an average of repeated measurements. The measured spectra were deconvoluted by the apparatus smearing function. The Cu and Fe K edge spectra of polycrystalline $CuFeS_2$ were measured using synchrotron radiation at HASYLAB, Hamburg. Both edges were recorded in the transmission mode at the Al beamline with a two-crystal monochromator. The energy resolution of the monochromator was about 1 eV at 7 keV. The S K edge of $CuFeS_2$ was digitized from the work [2].

Theoretical spectra were obtained within the local density approximation framework, in a twofold way: via an all-electron full-potential band-structure calculation based on a pseudopotential technique and via a real-space multiple-scattering (RSMS) method involving a self-consistent muffn-tin potential. In the latter case, we investigated both the situation without a core hole (ground state) and with a relaxed and screened core hole. More details of our application of the pseudopotential formalism can be found in Ref. [5, 6], our implementation of the RSMS formalism was described in Ref. [6, 7].

In order to facilitate the interpretation of the pre-edge region in $CuFeS_2$, wave function probability densities associated with the excited photoelectron were calculated in the RSMS formalism [8]. In that way, one can gain a well-defined picture of the spatial distribution of the photoelectrons which participate in the formation of specific XANES features.

3. Results and discussion

Our results are summarized in Figs. 1–3. The energy ranges in these figures were set using the $kR = \text{const}$ prescription, where $k = \sqrt{(2E)}$ is the photoelectron wave vector and R is a typical interatomic distance in the given compound. The horizontal alignment of the theoretical spectra at different edges of the same compound was provided by the calculation itself, the block-wise alignment of the band-structure and the RSMS calculations as well as of the experimental spectra was performed by hand. The zero of the energy scale was set to the bottom of the conduction band of the pseudopotential calculation.

$CuGaSe_2$ and $ZnGeAs_2$ spectra are quite similar to each other while $CuFeS_2$ spectra visibly differ. The resemblance of $CuGaSe_2$ and $ZnGeAs_2$ on the one hand and uniqueness of $CuFeS_2$ on the other hand gets reflected in our theoretical spectra as well. The similarity of $CuGaSe_2$ and $ZnGeAs_2$ spectra evokes the similarity of spectra of their binary isoelectronic analogues ZnSe and GaAs [9, 10]. As previous works already showed that spectra of various compounds of the I-III-VI_2 group look quite similar to each other [2, 11, 12], it is reasonable to assume that corresponding spectra

*e-mail: sipr@fzu.cz

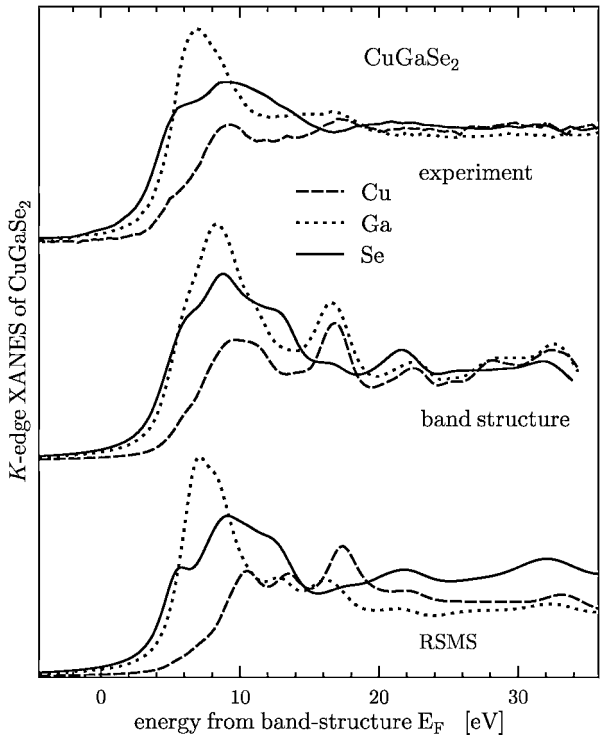

Fig. 1. K edge XANES spectra of Cu (dashed line), Ga (dotted line) and Se (full line) in $CuGaSe_2$, as provided by the experiment (uppermost panel), by the band structure calculation (middle panel) and by the RSMS calculation (lowermost panel).

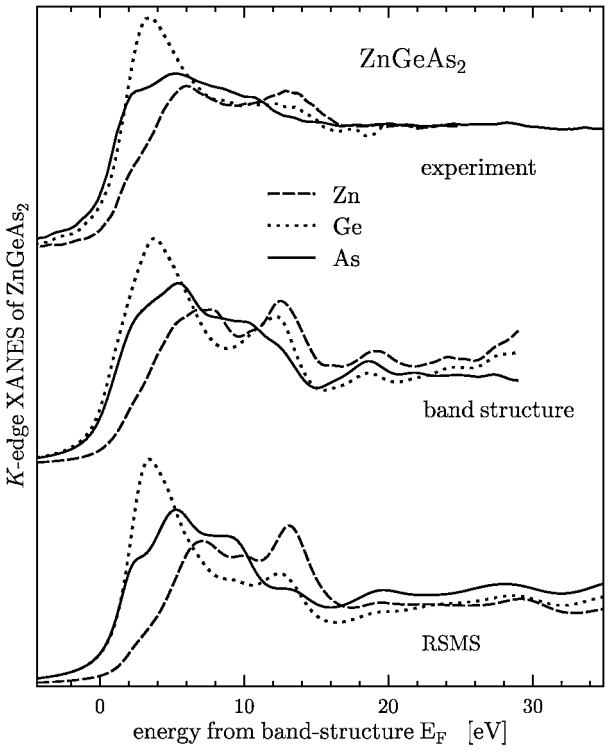

Fig. 2. Experimental and theoretical Zn, Ge and As K edge XANES spectra of $ZnGeAs_2$.

the II-IV-V_2 compounds will be similar as well. The $CuFeS_2$ case then stands out quite prominently.

The RSMS curves presented here have been obtained for a potential which accounts for the core hole. The ground state potential gives rise to spectra which are quite similar to those

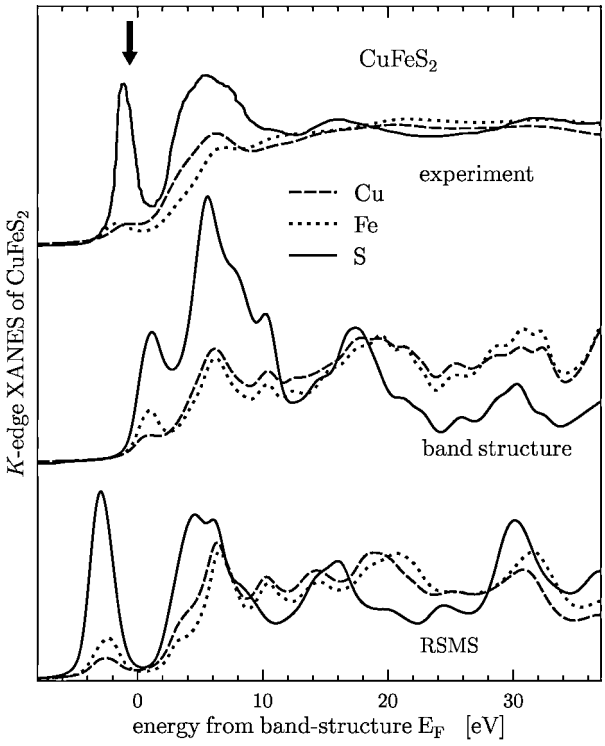

Fig. 3. Experimental and theoretical Cu, Fe and S K edge XANES spectra of $CuFeS_2$. The pre-peak is marked by an arrow.

shown here, just their peak heights at the low energy side are typically about 10% smaller. Therefore, we do not show them here for brevity. The results of the band structure calculation and of the RSMS calculation generally agree. Interestingly, the RSMS calculation does not correctly reproduce the Cu edge of $CuGaSe_2$ – the intensity of the first maximum at $E \approx 10\,\text{eV}$ in Fig. 1 is too low, being on par with the middle peak at $E \approx 13\,\text{eV}$ which itself is hardly distinguishable in the experiment. Our band-structure calculation seems to describe the Cu spectrum of $CuGaSe_2$ better. As suggested earlier [11], this difference may be a manifestation of the muffin-tin approximation, which was imposed on the RSMS calculation but not on the pseudopotential band-structure calculation.

Let us now concentrate on $CuFeS_2$ and its distinctiveness. The largest difference between $CuFeS_2$ and $CuGaSe_2$ or $ZnGeAs_2$ spectra occurs in the pre-edge region; there are no pre-peaks in the $CuGaSe_2$ or $ZnGeAs_2$ spectra, in contrast to $CuFeS_2$, where a well-defined pre-peak appears at each of the three edges (Fig. 3). The reproduction of this pre-peak by the theory is not perfect, nevertheless, it is good enough to substantiate a theory-based investigation of the mechanism of its formation. The differences between $CuFeS_2$ and $CuGaSe_2$ or $ZnGeAs_2$ spectra occur in the main peaks region as well, however, they are not so marked as at the pre-peak.

The relative roles of individual atomic sites in the formation of a particular spectral peak can be quantitatively assessed by comparing the wave function probability densities (WFPD) around those sites [8]. By performing this analysis for all the three edges, we found that the excited photoelectron is located *almost exclusively* on Fe atoms at the pre-peak energy; the calculated WFPD around the Fe sites is by three orders of magnitude higher than around any of the Cu or S sites. This is remarkably different from the main peak region, where the photoelectron WFPD is more-or-less uniformly spread among all the sites of the cluster,

as one would expect for a truly multiple-scattering resonance (we do not plot the corresponding curves here for brevity). The strong dominance of Fe sites in the WFPD distribution at the pre-edge energy is consistent with the interpretation of the pre-peak as transition to unoccupied Fe 3*d* states hybridized with Cu and/or S states [1, 2, 3]; however, these states are located on many Fe atoms simultaneously, not just a single one, and hence they correspond to a resonance which arises from multiple scattering by the Fe atoms. In this respect, it represents a crystal structure interference effect as well [4]. So both views on the origin of the pre-peak in the XANES of $CuFeS_2$ can be related and reconciled within the WFPD concept.

4. Conclusions

Analogous K edge XANES spectra of compounds of the I-III-VI_2 type ($CuGaSe_2$) and of the II-IV-V_2 type ($ZnGeAs_2$) are quite similar to each other while spectra of $CuFeS_2$ differ. The spectra can be reasonably well reproduced by one-electron calculations. Full-potential band structure calculations without any core hole give essentially the same picture as RSMS calculations for a muffin-tin potential with a core hole included; the notable exception is the Cu edge in $CuGaSe_2$, where significant non-muffin-tin effects possibly occur. The distinctiveness of $CuFeS_2$ spectra is caused by the presence of Fe atoms. Pre-peak in the XANES of $CuFeS_2$ arises from transitions to delocalized multiple-scattering resonances which are confined almost exclusively to the Fe sites.

Acknowledgement

This work was supported by the project 202/02/0841 of the Grant Agency of the Czech Republic.

References

1. Petiau, J., Sainctavit, Ph. and Calas, G., Mater. Sci. Eng. B **1**, 237 (1988).
2. Sainctavit, Ph., Petiau, J., Flank, A. M., Ringeissen, J. and Lewonczuk, S., Physica B **158**, 623 (1989).
3. Li, D. *et al.*, Phys. Chem. Minerals **20**, 489 (1994).
4. McKeown, D. A., Phys. Rev. B **45**, 2648 (1992).
5. Vackář, J., Hyt'ha, M. and Šimůnek, A., Phys. Rev. B **58**, 12712 (1998).
6. Šipr, O. and Šimůnek, A., J. Phys.: Condens. Matter **13**, 8519 (2001).
7. Bocharov, S., Kirchner, Th., Dräger, G., Šipr, O. and Šimůnek, A., Phys. Rev. B **63**, 045104 (2001).
8. Šipr, O., Phys. Rev. B **65**, 205115 (2002).
9. Drahokoupil, J., Klokočníková, H. and Šimůnek, A., J. Phys. C **9**, 2667 (1976).
10. Matsuura, T., Fujikawa, T. and Ōyanagi, H., J. Phys. Soc. Jpn. **53**, 2837 (1984).
11. Šipr, O., Machek, P., Šimůnek, A., Vackář, J. and Horák, J., Phys. Rev. B **56**, 13151 (1997).
12. Bacewicz, R., Wolska, A., Lawniczak-Jablonska, K. and Sainctavit, Ph., J. Phys.: Condens. Matter **12**, 7371 (2000).

Physica Scripta. Vol. T115, 182–184, 2005

Localized Nature of Valence-Hole States in $Ca_{2+x}Y_{2-x}Cu_5O_{10}$ Shown by O 1s XAS

Kozo Okada

The Graduate School of Natural Science and Technology, Okayama University, 3-1-1, Tsushima-naka, Okayama, 700-8530, Japan

Received June 26, 2003; accepted November 19, 2003

PACS numbers: 78.70.Dm, 74.72.Bk, 79.60.−i

Abstract

The hole doping effects on the O 1s X-ray absorption spectrum (XAS) of a quasi-one-dimensional charge-transfer insulator, $Ca_{2+x}Y_{2-x}Cu_5O_{10}$, are discussed on the basis of numerically-exact diagonalization calculations applied to finite-size cluster models. The angle-resolved photoemission and inverse one are also calculated to understand the characteristic features in the XAS. The role of "edge-share"-type crystal structure, as well as that of electron correlation, is emphasized to understand the localized nature of the electronic states. The *dp* model Hamiltonian used in the O 1s XAS calculation can be mapped onto a single-band Hubbard model with the intra-atomic Coulomb repulsion, U, and the first and second neighbor hoppings, t_1 and t_2 ($t_1 \approx t_2$).

Core-level X-ray absorption (XA) spectroscopy provides element-selective information on the unoccupied part of the electronic states in solids. In the case of cuprates, the XA spectra from the O 1s and Cu 2p core states are often used to discuss the electronic states near the Fermi energy. In contrast to the Cu 2p X-ray absorption spectrum (XAS), the O 1s XAS is almost free from the core-hole effects. This enables us to discuss the electronic state of the ground state by means of the O 1s XAS more easily.

As is well known, the O 1s XAS in $La_{2-x}Sr_xCuO_4$ consists of two peaks separated by 1.5–2 eV [1]. The higher and lower energy peaks correspond to the absorption to the upper Hubbard band (UHB) and the Zhang-Rice singlet (ZRS) band [2], respectively. In a CuO_4 model description, as shown later, they are assigned to the d^{10} and d^9 final states, respectively. The similar double-peak feature was seen in a recent experiment for $Ca_{2+x}Y_{2-x}Cu_5O_{10}$ reported by Nakamura *et al.* [3, 4]. However, the details of hole doping dependence of the O 1s XAS spectrum differs for $Ca_{2+x}Y_{2-x}Cu_5O_{10}$ and $La_{2-x}Sr_xCuO_4$. In the case of $Ca_{2+x}Y_{2-x}Cu_5O_{10}$, the UHB and ZRS peaks can be well identified as separate ones even in the nominally 40% hole doping regime. In other words, the localized nature of the valence band hole states is remarkable even in such a heavy doping regime. In the present study, we discuss the electronic state of this compound, calculating the hole doping dependence of the O 1s XAS. To understand the origin of such characteristic O 1s XAS features, we also calculate the dispersion curves of the Cu3d-O2p valence and conduction bands and derive an effective Hubbard model.

In the present study, we use an edge-share-type Cu_6O_{12} cluster model with the periodic boundary condition along the chain direction, which is illustrated in Fig. 1. The x axis is along the chain direction (= the a axis in $Ca_2Y_2Cu_5O_{10}$). The Hamiltonian, H_{pd}, is a conventional *dp* Hamiltonian and consists of one-body energy parts of Cu $3d_{xy}$ and O $2p_{x,y}$, nearest O-O and Cu-O hopping terms and an on-site Coulomb repulsion term for Cu 3d holes [5]. Since the average O 2p hole number per site is small in the following calculations, the effects of on-site Coulomb interactions at O sites

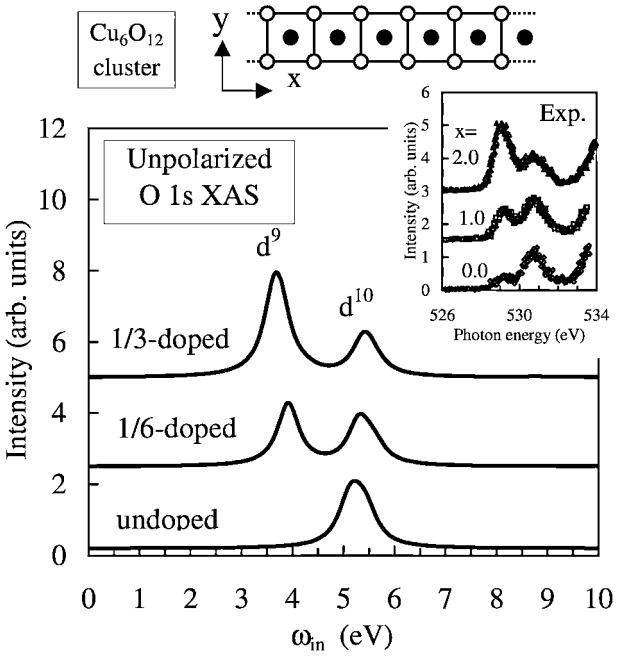

Fig. 1. Hole doping dependence of O 1s XAS. The cluster used in the calculation is also illustrated, where the open and closed circles represent the O and Cu ions, respectively. The inset shows the experiment for $Ca_{2+x}Y_{2-x}Cu_5O_{10}$ reported by Nakamura *et al.* [3].

are neglected for simplicity. The numerical values for the relevant parameters are as follows [4]. The Slater-Koster parameter for Cu $3d_{xy}$ and O $2p_{x,y}$ is taken as $(pd\sigma) = -1.5$ eV. For simplicity, the Cu-O-Cu bond angle is assumed to be 90 degrees, though it is 96 degrees in $Ca_2Y_2Cu_5O_{10}$ [6, 7]. The on-site Coulomb repulsion between Cu 3d holes (U_{dd}) is 8 eV. The CT energy between Cu $3d_{xy}$ and O $2p_{x,y}$ is taken as 3.5 eV. These numerical values are close to those estimated by Mizuno *et al.* [8].

For instance, the angle-resolved inverse photoemission spectrum (IPES) for $O2p_{\mu\sigma}$ with spin σ and orbital symmetry μ (= x, y) is given by

$$I^{\mathrm{IPES}}_{\mu,\sigma}(\varepsilon - \omega_{\mathrm{out}}, k) = \sum_f |\langle f|T^{\mathrm{IPES}}_{\mu,\sigma}(k)|g\rangle|^2 \delta(\varepsilon - \omega_{\mathrm{out}} - E_f + E_g) \quad (1)$$

for incident electron wave number k and energy ε and outgoing photon energy ω_{out}. The transition operator is given by

$$T^{\mathrm{IPES}}_{\mu,\sigma}(k) = \sum_j e^{ikr_j} p^\dagger_{j\mu\sigma}, \quad (2)$$

where $p^\dagger_{j\mu\sigma}$ creates an $O2p_{\mu\sigma}$ electron at the j-th O site. Since the core-hole potential effect is neglected for simplicity in the present

study, the O 1s XAS is equivalent to the angle-integrated IPES. The unpolarized O 1s XAS for incident energy $\omega_{\rm in}$ is given by

$$I^{\rm XAS}(\omega_{\rm in}) = \sum_{\mu,\sigma,k} I^{\rm IPES}_{\mu,\sigma}(\omega_{\rm in}, k). \quad (3)$$

In the following calculations, we adopt the Lanczos method to diagonalize H_{pd} in order to treat the electron correlation as exactly as possible. The obtained line spectra are convoluted with Lorentzian and Gaussian functions of an appropriate width, Γ. For the O 1s XAS, Γ is taken at 0.5 eV. For the photoemission and inverse photoemission, Γ is taken at 0.2 eV.

In the present study, a $(Cu_6O_{12})^{12-}$ cluster is called an "undoped system", while $(Cu_6O_{12})^{11-}$ is "1/6-doped" and so on. In the undoped case, the formal electron configuration of Cu ions is d^9 and that of O ions is p^6. However, owing to strong pd hybridization between Cu 3d and O 2p orbitals, the actual O 2p electron configuration deviates from p^6. Using this unoccupied part of O 2p states, the O 1s XAS process occurs, resulting in a sharp XAS peak. This O 1s XAS is also understood on the basis of a configuration-interaction (CI) picture. In the case of the undoped CuO_4 cluster, the ground state is described by a linear combination of d^9 and $d^{10}\underline{L}$ electron configurations, where $\underline{L}$ denotes a ligand (O 2p) hole [9]. The O 1s XAS process occurs using that $d^{10}\underline{L}$ weight contained in the ground state. The resulting XAS final state is purely d^{10}. In the calculated result shown in Fig. 1, the width of the d^{10} peak for the undoped case is about 1 eV, which is somewhat narrower than the experiment shown in the inset [3]. Since the lifetime of the O 1s core hole is assumed to be 0.5 eV in the present calculations, the intrinsic width of the d^{10} band in the theory is about 0.5 eV. With hole doping, the intensity of the d^{10} peak decreases and a new peak denoted as "d^9" grows up about 1.5 eV below the d^{10} peak instead.

In a CI picture, the ground state of "100%"-doped CuO_4, which is often called the ZRS state, is described by a linear combination of d^8, $d^9\underline{L}$ and $d^{10}\underline{L}^2$. For the ZRS-type initial state, there are two XAS final states, d^9 and $d^{10}\underline{L}$. According to numerical calculations (not shown here), the XAS intensity for d^9 is very high, while that to $d^{10}\underline{L}$ is negligible owing to phase matching between the initial- and final-state wave functions. In an approximation that regards the present doped six-plaquette cluster as the statistical average of undoped and 100%-doped isolated plaquettes, the lower energy peak (d^9) is interpreted as the XAS at the doped plaquettes, while the higher energy peak (d^{10}) the XAS at the undoped plaquettes. This simple statistical average approximation explains the doping dependence of the d^9 peak intensity relative to the d^{10} one shown in Fig. 1.

To understand the details of the O 1s XAS, we show the angle-resolved PES and IPES for the undoped system in Fig. 2, where the Cu $3d_{xy}$ and O $2p_{x,y}$ components are plotted separately for each k. Each k-integrated spectrum is the sum for $k/\pi = n/6\,(n = 0 - 5)$. In Fig. 2, the convolution width is 0.2 eV. If the convolution width is increased up to 0.5 eV, the sum of O $2p_{x,y}$ IPES coincides with the undoped case of the O 1s XAS shown in Fig. 1. As seen in Fig. 2, the intensity of the Cu 3d IPES is large over the Brillouin zone, which is contrast to the corner-share-type one-dimensional cuprates [10]. The band width seen in the present IPES is only about 0.5 eV. These show the localized nature of Cu 3d state. The origin of this small band width is in the fact that the Cu-O-Cu bond angle is 90 degrees. The coupling between Cu 3d orbitals occurs via the Cu-O-O-Cu path [11]. This make the effective Cu 3d band width small. Instead, owing to this small band width, the electron correlation effect is likely to be emphasized. For instance,

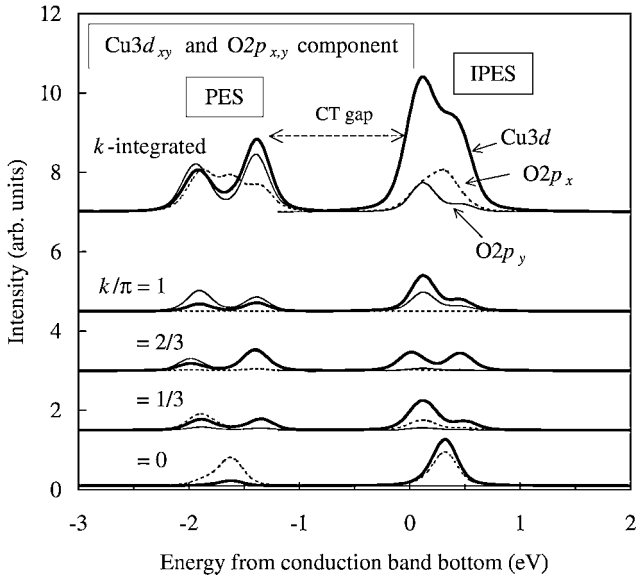

Fig. 2. The O $2p_x$ (dotted), O $2p_y$ (thin) and Cu $3d_{xy}$ (thick) components of the angle-resolved PES and IPES for the undoped case are plotted for each k point, together with the k-integrated spectra.

all the Cu 3d IPES intensity at $k/\pi = 2/3$ must be caused by the electron correlation, since there is no IPES intensity at this k point in the limit of vanishing U_{dd}. One may regard that the split IPES peaks at $k/\pi = 1/3, 2/3, 1$ represent dispersive *real* and *shadow* bands [12]. On the other hand, owing to the pd hybridization, the O $2p_x$ and $2p_y$ IPES is strong at $k/\pi = 0$ and 1, respectively. At $k/\pi = 2/3$, the O 2p contribution is very small. As a result, the O 2p component of the k-integrated IPES appears to be somewhat narrower than the Cu 3d component.

We show the angle-resolved IPES for the 1/3-doped case in Fig. 3. Upon hole doping, the Fermi energy shifts to the lower energy band below the CT energy gap. For each k point, the IPES consists of two peaks separated by the CT gap, which correspond to the d^9 and d^{10} peaks in the XAS. In contrast to the undoped case, there is no shadow band. It seems to be reasonable, since the antiferromagnetic spin fluctuations must be suppressed in the doped system.

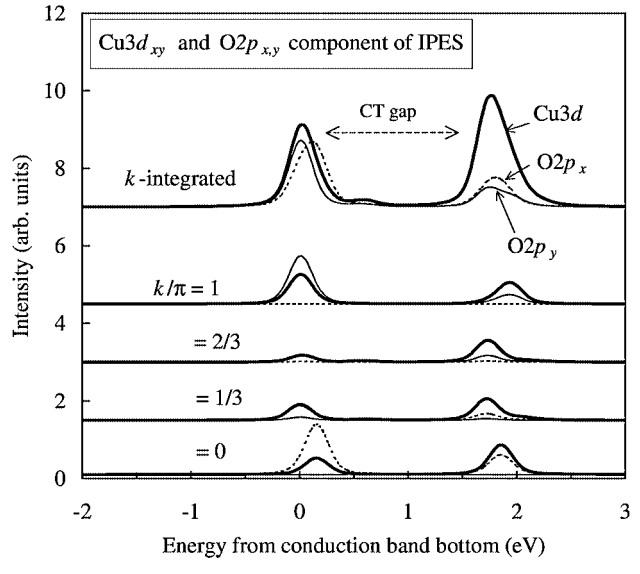

Fig. 3. The O $2p_x$ (dotted), O $2p_y$ (thin) and Cu $3d_{xy}$ (thick) components of the angle-resolved IPES for the 1/3-doped case are plotted for each k point, together with the k-integrated spectra.

To understand the angle-resolved spectra more in detail, we need to increase the cluster size. For this reason, we derive an effective single-band Hubbard Hamiltonian. The mapping procedure from the original *dp* Hamiltonian starts with an undoped CuO_4 plaquette. We define an effective d state by the ground state wave-function of the plaquette. Using this wave-function, we are able to calculate the effective hopping strength between the neighboring effective d states (t_1) and that between the next-neighbor pair (t_2) in larger clusters. With the present parameter values listed above, both t_1 and t_2 are estimated to be about 0.1 eV. The width of the corresponding tight-binding band (W) is about 0.6 eV. On the other hand, the effective Coulomb repulsion strength (U) is estimated to be about 1.8 eV to reproduce the insulating energy gap seen in the original pd model shown in Fig. 2. Thus U/W is about 3, which indicates the importance of electron correlation. Similarly, the mapping to a single band Hubbard model can be performed for the corner-share-type cuprates where the Cu-O-Cu bond angle is 180 degrees. With the parameter values used in the present study, t_1, t_2 and U are estimated to be about 0.35eV, zero and 2 eV, respectively [13]. In this case, U/W is 1.43, which is considerably smaller than that for the edge-share system. It is to be noted that the importance of t_2 in edge-share-type cuprates was suggested on the basis of theoretical calculations for Cu 2p core level photoemission [11].

In summary, we have discussed the O 1s XAS of edge-share-type cuprates. In this type of crystal structure, the effective hopping strength between Cu sites is very small. This is the reason why the localized nature of Cu 3d is emphasized. It is represented by the Cu 3d IPES component over the Brillouin zone. On the other hand, the k dispersion is small, since the effective hopping strength between Cu sites is small. These characteristic features are in contrast to the corner-share-type cuprates. The O $2p_{x,y}$ IPES component is strong only around $k/\pi = 0, 1$. As a result, the total width of k-integrated O $2p_{x,y}$ IPES is narrower than that of k-integrated Cu $3d_{xy}$ IPES. Even upon hole doping, the localized nature seen in the IPES remains unchanged. These characteristic features are consistent with the recent experiment.

We have also derived an effective single-band Hubbard model, which reproduces the band dispersion of the original *dp* Hamiltonian. A characteristic of the present system is that the hopping strength between the nearest neighbor sites is almost the same as that between the next-neighbor pairs.

Acknowledgments

The present author thanks Professor N. Yamada and Dr. J. Nakamura for useful discussions and for providing their experimental data before publication. This work was partially supported by a Grant-in-Aid for Scientific Research from the Ministry of Education, Science, Sports and Culture.

References

1. Chen, C. T. *et al.*, Phys. Rev. Lett. **68**, 2543 (1992).
2. Zhang, F. C. and Rice, T. M., Phys. Rev. B **37**, 3759 (1988).
3. Nakamura, J. *et al.*, read at the 13th International Conference on Vacuum Ultraviolet Radiation Physics (Trieste, Italy, 2001) We142.
4. Okada, K. and Kotani, A., J. Phys. Soc. Jpn. **72**, 797 (2003).
5. Okada, K. and Kotani, A., Phys. Rev. B **65**, 144530 (2002).
6. Hayashi, A., Batlogg, B. and Cava, R. J., Phys. Rev. B **58**, 2678 (1998).
7. Fong, H. F., Keimer, B., Lynn, J. W., Hayashi, A. and Cava, R. J., Phys. Rev. B **59**, 6873 (1999).
8. Mizuno, Y. *et al.*, Phys. Rev. B **57**, 5326 (1998).
9. van der Laan, G., Westra, C., Haas, C. and Sawatzky, G. A., Phys. Rev. B **23**, 4369 (1981).
10. Kim, C. *et al.*, Phys. Rev. B **56**, 15589 (1997).
11. Okada, K. and Kotani, A., J. Electron Spectrosc. Relat. Phenom. **88–91**, 255 (1998).
12. Kampf, A. P. and Schrieffer, J. R., Phys. Rev. B **42**, 7967 (1990).
13. Okada, K., (unpublished).

Physica Scripta. Vol. T115, 185–187, 2005

Real Space Approach to Thermal Factor in EXAFS for Asymmetric Double-Well Potential

K. Nitta[1], T. Miyanaga[1*] and T. Fujikawa[2]

[1]Department of Materials Science and Technology, Faculty of Science and Technology, Hirosaki University, Hirosaki, Aomori 036-8561, Japan
[2]Graduate School of Science, Chiba University, Yayoi-cho 1-33, Inage, Chiba 263-8522, Japan

Received June 26, 2003; accepted November 4, 2003

PACS numbers: 02.40.−k, 12.39. Dc, 14.80.Hv

Abstract

This paper describes a Path Integral approach to the thermal factor in EXAFS applied to one-dimensional systems with asymmetric double-well potentials, which is considered to be one of the models for chemical reactions, structual phase transitions and surfaces within of the clusters. For these systems quantum-tunneling effect plays an important role in both amplitude and phase of the EXAFS thermal factor. Classical approximation is not valid in the low temperature region, on the other hand cumulant expansion breaks at high temperature. We find an oscillating behavior in the phase of the thermal damping function, which is a specific feature for the case of asymmetric double-well potential.

1. Introduction

Theoretical approaches to the EXAFS thermal factor have been developed beyond harmonic approximation and classical approximation [1, 2]. The perturbation approaches are useful to describe weak anharmonicity in the analyses of temperature effects in EXAFS and they have provided interesting information based on cumulant expansion [3, 4, 5]. On the other hand, real space approaches have been widely used classical mechanically to relate the EXAFS Debye-Waller factors to interatomic potential [6]. Recently path integral technique is applied to EXAFS thermal factor for strongly anharmonic systems such as quartic and symmetric double-well [7], Morse potential [8] and some real systems [9]. This approach can be applied to strongly anharmonic systems, where the cumulant analyses break. In this paper we apply the path integral approach to the EXAFS thermal factors with asymmetric double-well potential which plays an important role for structral phase transition, chemical reactions and so on [10].

2. Theory

Let consider diatomic systems in a resorvir at temperature T whose relative vibrational motion is descrived by the Hamiltonian,

$$H = \frac{p^2}{2\mu} + V(q), \tag{1}$$

where μ is the reduced mass and q is the instantaneous interatomic distance. When we deal with statistical average of an operator A, we should calculate the trace $\langle A\rangle = \frac{1}{z}\mathrm{Tr}(A\rho)$ where ρ is the density operator defined by $\rho = \exp(-\beta H)$, $\beta = 1/k_B T$ and $Z = \exp(-\beta F) = \mathrm{Tr}(\rho)$ is the partition function for the system. The trace can be calculated by applying Feynman's path integral techniques, however, instead of summing over all paths in just one step, one can classify the paths into two groups as proposed by Feynman [11, 12]. The final expression for the average of a local operator A can be represented in terms of the probability density $P(q)$ just like in classical statistical mechanics

$$\langle A\rangle = \int A(q)P(q)\,\mathrm{d}q. \tag{2}$$

This expression, however, includes important quantum effects, and the probability is represented by

$$P(q) = \frac{1}{Z}\sqrt{\frac{\mu}{2\pi\beta}}\exp[-\beta V_L(q)], \tag{3}$$

where the local effective potential $V_L(q)$ is defined by

$$\exp[-\beta V_L] = \int \mathrm{d}q' \exp[-V_e(q+q')] \times \frac{1}{\sqrt{2\pi\alpha(q+q')}}\exp[-q'^2/2\alpha(q+q')]. \tag{4}$$

Now we used the self-consistent requirement [7, 12] to obtain the effective potential $V_e(q)$ and $\alpha(q)$. In the EXAFS analyses the operator A should be $\exp(2\mathrm{i}k\Delta q)$, where k is the wave vector of an ejected photoelectron, $k = |k|$ and Δ_q is the projected relative displacement, which is simply given by $\Delta q = q - q_0$ (q_0 is the equilibrium interatomic distance, in this case q_0 = 0) in one-dimensional cases. So what we should calculate to study EXAFS thermal factor is

$$G(k) = \langle\exp(2\mathrm{i}k\Delta q)\rangle = \int_{-\infty}^{\infty}\exp(2\mathrm{i}k\Delta q)P(q)\,\mathrm{d}q \tag{5}$$

in the plane wave approximation. When all the integrals in the cumulant and also the cumulant expansion converge, the thermal damping function $G(k)$ can be written,

$$G(k) = \exp\left\{-2k^2\langle q^2\rangle_c + \frac{2}{3}k^4\langle q^4\rangle_c - \cdots\right\} \times \exp\left\{\left[\mathrm{i}\left\{k\langle q\rangle_c - \frac{4}{3}k^3\langle q^3\rangle_c + \cdots\right\}\right]\right\}. \tag{6}$$

3. Result and Discussion

We now consider a strongly anharmonic system with asymmetric double-well potential

$$V(q)/\varepsilon = (q^2 - \sigma^2)^2 + \frac{q^3}{3} - q. \tag{7}$$

In the following applications we shall use the unit, $\sigma = \mu = 1$ for simplicity. (See Fig. 1.) The asymmetric potential $V(q)$ is also shown for reference. The two minima of $V(q)$ appear at $q = \pm 1$. Figure 1 shows the quantum and classical probability density $P(q)$ for the asymmetric double-well potential described by eq. (7). The

*e-mail: takaf@cc.hirosaki-u.ac.jp

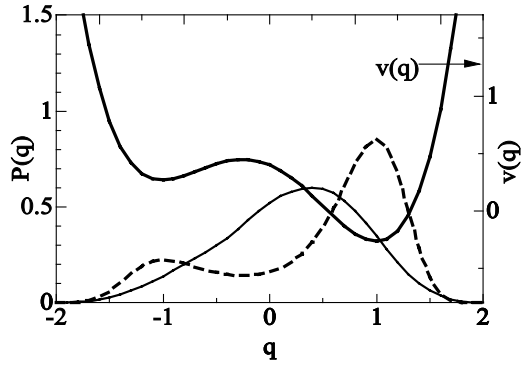

Fig. 1. An example of the quantum (solid line) and the classical (dashed line) probability density $P(q)$ for asymmetric double-well potential. The potential $V(q)$ is also presented (thick solid line).

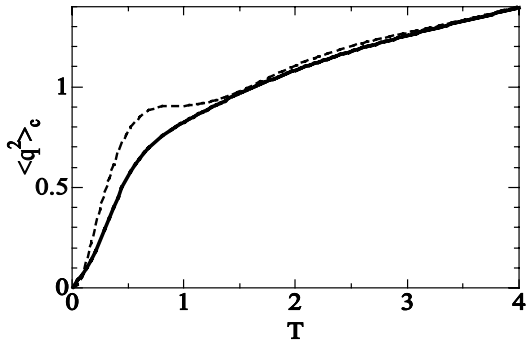

Fig. 2. The temperature dependence of the quantum (solid line) and the classical (dashed line) second order cumulant $\langle q^2\rangle_c$ for the asymmetric double-well potential. T is reduced temperature.

main peak position of the probability density is found at $q = 1$ in the classical case, on the other hand the peaks are shifted to the potential barrier in the quantum case because of the quantum tunneling effect. Figure 2 shows the second order cumulant $\langle q^2\rangle_c$ as a function of reduced temperature T calculated by use of the quantum (solid line) and the classical (dashed line) probability density $P(q)$. A classical particle in asymmetric double well potential is frozen at the lower bottom of the potential well at low temperature, so $\langle q\rangle = 1$ at $T = 0$. In the present asymmetric double-well potential, $\langle q^2\rangle_c = 0$ at $T = 0$, whereas $\langle q^2\rangle_c = 1$ for symmetric double-well potential [7]. In the quantum case, $\langle q^2\rangle_c$ for an asymmetric double-well potential shows similar behavior to that for quartic and symmetric double-well potentials [7].

Figure 3 shows the third order cumulant $\langle q^3\rangle_c$ as a function of reduced temperature T calculated by use of the quantum (solid line) and the classical (dashed line) probability density. The classical approximation gives good result at high temperature, on the other hand at low temperature that gives a poor result because of the quantum tunneling effect.

Figure 4 shows the amplitude $|G(k)|$ and phase ϕ in the thermal damping function at low temperature ($T = 0.016$) and Fig. 5 shows the same functions at high temperature ($T = 2$). They correspond to 8 K and 1000 K using the same parameter as for the symmetric double-well potential [7]. Although the symmetric double-well potential provides a real thermal factor as shown by eq. (5) because of the parity of $P(q)$, the asymmetric double-well potential gives complicated k-dependence of $|G(k)|$ and ϕ as shown in Fig. 4 and 5. The photoelectron wave number k is scaled for the case of potential minimum $\sigma = \pm 0.1$ Å. For the amplitude of the damping function $|G(k)|$, the

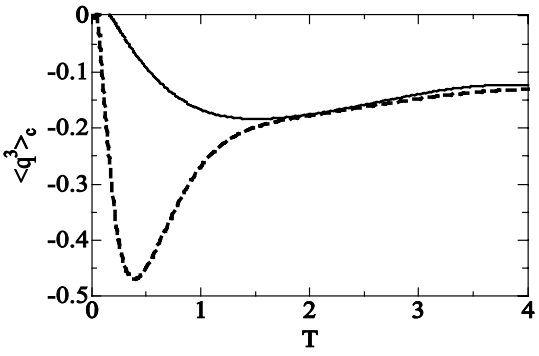

Fig. 3. The temperature dependence of the quantum (solid line) and the classical (dashed line) third order cumulant $\langle q^2\rangle_c$ for the asymmetric double-well potential. T is reduced temperature.

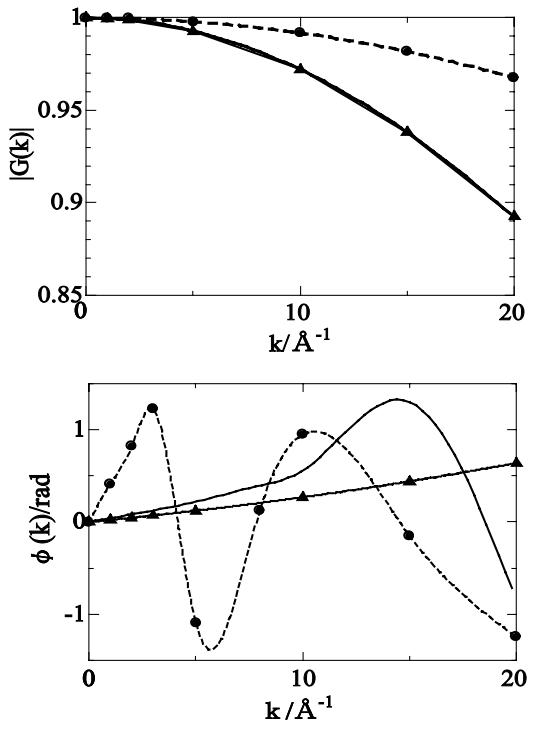

Fig. 4. The amplitude $|G(k)|$ and phase part ϕ in thermal damping function of EXAFS for the quantum (solid line) and the classical (dashed line with circle) probability density at $T = 0.016$ (this reduced temperature corresponds to 8 K using the same parameter as for the symmetric double-well potential). The cumulant expansion up to forth order (solid line with triangle) is also presented.

cumulant expansion provides much better result close to the self-consistent calculations obtained from eq. (5) than the classical approximation at lower temperature (Fig. 4). On the other hand, the result of the classical approximation is better than the cumulant expansion at higher temperature (Fig. 5).

For the phase function ϕ, the cumulant expansion is considerably good only at $k < 10$ Å^{-1} but it is poor at $k > 10$ Å^{-1} at lower temperature (Fig. 4). The classical approximation oscillates and gives poor results. At higher temperature (Fig. 5), the phase function in the classical and the self-consistent calculation show similar oscillations. This oscillation in the phase is characteristic for asymmetric double-well potentials due to the reflection of the photoelectron by two potential barriers. The cumulant expansion cannot predict such oscillating behavior any more.

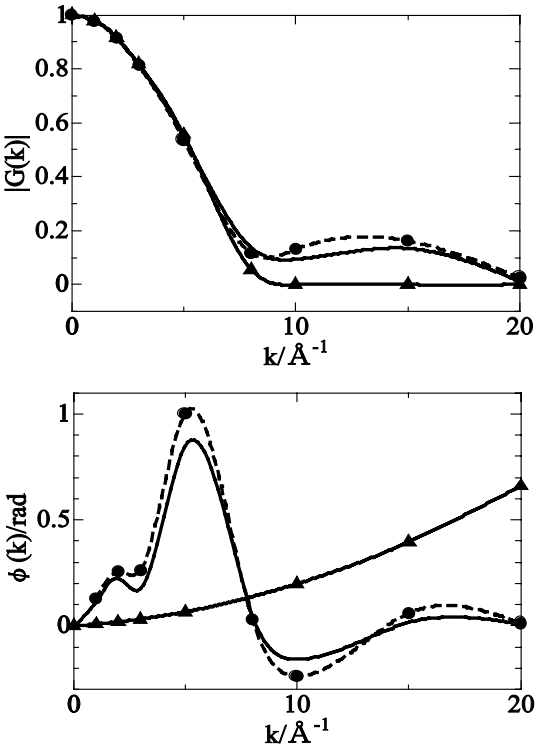

Fig. 5. The amplitude $|G(k)|$ and phase part ϕ in thermal damping function of EXAFS for the quantum (solid line) and the classical (dashed line with circle) probability density at $T = 2$ (this reduced temperature corresponds to 1000 K using the same parameter as for the symmetric double-well potential). The cumulant expansion up to forth order (solid line with triangle) is also presented.

4. Conclusion

The real space method based on finite temperature path integral theory has been applied to EXAFS thermal factor for strongly anharmonic systems as asymmetric double-well potentials. We can study the applicability of the cumulant expansion and the classical approximation in EXAFS analyses. First, the probability density $P(q)$ was calculated using a path integral approach for asymmetric double-well potentials. From the probability density, the second order cumulant $\langle q^2 \rangle_c$ and the third order cumulant $\langle q^3 \rangle_c$ were evaluated as a function of temperature. We also discuss a new feature observed in the phase oscillating of the EXAFS thermal factor for the present asymmetric double-well potential.

References

1. Beni, G. and Platzman, P. M., Phys. Rev. B **14**, 1514 (1976).
2. Tranquada, J. M. and Ingalls, R., Phys. Rev. B **28**, 3520 (1983).
3. Fujikawa, T. and Miyanaga, T. J., Phys. Soc. Jpn. **62**, 4108 (1993).
4. Fujikawa, T. and Miyanaga, T. J., Phys. Soc. Jpn. **63**, 1036 (1994).
5. Fujikawa, T. and Miynaga, T. J., Phys. Soc. Jpn. **63**, 3683 (1994).
6. Yokoyama, T., Satsukawa, T. and Ohta, T., Jpn. J. Appl. Phys. **28**, 1905 (1989).
7. Fujikawa, T., Miyanaga, T. and Suzuki, T. J., Phys. Soc. Jpn. **66**, 2897 (1997).
8. Miyanaga, T. and Fujikawa, T., J. Phys. Soc. Jpn. **67**, 2930 (1998).
9. Yokoyama, T., Phys. Rev., B **57**, 3423 (1998).
10. Freeman, D. L. and Doll, J. D., Ann. Rev. Phys. Chem. **47** (1996)
11. Feynman, R. P., "Statistical Mechanics", (Benjamin, Reading, Massachusetts, 1972).
12. Cuccoli, A., Giachetti, R., Tognetti, V., Vaia, R. and Verrucchi, P., J. Phys. Condens, Matter. **7**, 7891 (1995).

Physica Scripta. Vol. T115, 188–190, 2005

Selective Detection of Deep Level Centers by X-ray Absorption Fine Structure Questioned

J. Bollmann[(a)], S. Knack[(a)], J. Weber[(a)], V. Koteski[(b)], H.-E. Mahnke[(b)] and E. Welter[(c)]

[(a)]Technische Universität Dresden, D-01062 Dresden, Germany
[(b)]Hahn-Meitner-Institut Berlin GmbH, D-14109 Berlin, Germany
[(c)]Hamburger Elektronen Synchrotron (HASYLAB) at Deutsches Elektronen Synchrotron (DESY), D-22607 Hamburg, Germany

Received June 26, 2003; accepted November 4, 2003

PACS number: 78.70.Dm, 61.72.Ji, 61.10.Ht, 71.55.Eq

Abstract

A new scheme of capacitance-detection for the X-ray absorption fine structure (XAFS) was reported recently [M. Ishii, Phys. Rev. B **65**, 085310 (2002)]. The absorption of X-rays leads to oscillations in the steady state capacitance of a Schottky barrier diode which were interpreted as a "site-selective" detection of deep level centers. We have performed XAFS at the K-edge of gallium and arsenic on GaAs and AlGaAs Schottky-diodes containing DX and EL2 defect centers. For the detection, different techniques were applied: the photocurrent under short circuit conditions, the steady state impedance, and X-ray induced capacitance transients were measured. The results are compared with conventionally detected XAFS spectra (absorption, fluorescence). No evidence for a site-selectivity of the capacitance EXAFS is found in our studies. Based on a detailed analysis of the different detection techniques we strongly question the proposed "site-selectivity".

1. Introduction

The method of X-ray absorption fine structure (XAFS) analysis is ideally suited to determine the properties of point defects in semiconductors [1, 2]. The major limit of this technique is the incapability to separate signals from the same atoms located at different lattice sites. Point defects in semiconductors in concentrations lower than $10^{15}\,\mathrm{cm}^{-3}$ crucially determine material properties and their attributes are of eminent interest in device processing. The X-ray absorption on such highly diluted systems is hidden in the absorption background from elastic scattering and from photoionization of other elements and of higher atomic shells. Techniques, sensitive to defect specific properties, are used in routine studies of semiconductors [3]. Most prominent method is the Deep Level Transient Spectroscopy (DLTS) [4], which analyses thermally stimulated changes of deep level charge state. As a thermal spectroscopy the spectral resolution is limited, but their sensitivity is extremely high [4].

2. Experimental

Our experiments are based on (*i*) thin layers (5 µm) of $Al_xGa_{1-x}As$ ($x = 0.3$) grown by molecular beam epitaxy on highly conductive GaAs substrates doped with Se and on (*ii*) (100)-oriented, virtually gradient free (VGF) grown, n-type bulk GaAs from MCP Wafer Technology Ltd., which was nominally undoped. The free electron concentration is $1.3 \times 10^{17}\,\mathrm{cm}^{-3}$ in the epitaxial layers and is $2.5 \times 10^{16}\,\mathrm{cm}^{-3}$ in the bulk GaAs samples. The XAFS measurements were performed at HASYLAB, DESY, Hamburg using a double crystal Si(111) monochromator with a flux of up to 10^{10} photons $\mathrm{s}^{-1}\,\mathrm{mm}^{-2}$.

3. Principles of site-selectivity

One major limit of EXAFS technique is the incapability to separate signals from the same atoms located at different lattice sites. 'Site-selective' means to sort out just one lattice position of an atom from others by measuring the specific response of that configuration stimulated by the X-ray absorption at that atom. This can be, for example, a change in charge state of deep level center or an excitonic-like emission of photons.

Site-selectivity could be achieved by inner shell excitation of a defect atom and the de-excitation which results in the loss of an electron already trapped at the defect level. In a space charge region the density of fixed charges will change by this process and a junction capacitance response is observable.

There are different possibilities for the photon absorption:

(*i*) The X-ray photons interact directly with the defect by exciting the trapped electron to the conduction band.
(*ii*) The X-ray photons excite the K-shell electron to leave the defect and the trapped electron is consumed in the relaxation of the core hole (Fig. 1(a)).
(*iii*) The relaxation of the core hole occurs via Auger processes and the K-shell energy is transferred to electron hole pairs and subsequently an excess hole from the valenc band is captured by the defect with no distinction which atom (bulk or defect constituent) was primarily excited (Fig. 1(b)).

The relaxation times for processes (*i*) and (*ii*) are proportional to the absorption cross-section of the K-shell; whereas the process (*iii*) is proportional to amount of excess carriers from the photocurrent. The time constants of these two processes can be computed easily and have to be compared with the observed capacitance transients.

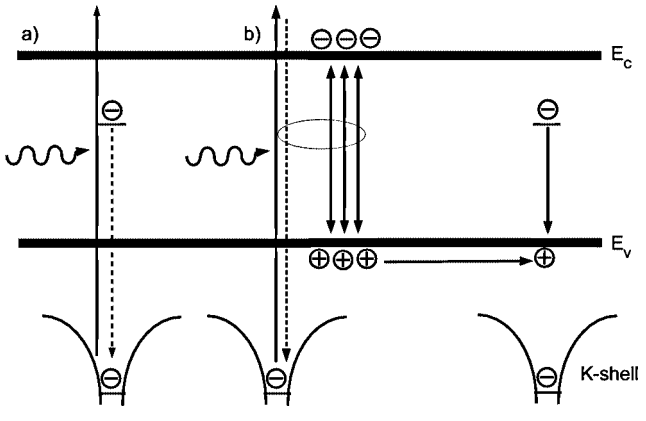

Fig. 1. Change of defect level occupation by bulk absorption of X-ray absorption: a) a site selective, direct absorption at the defect and successive capture of the devect electron, b) bulk absorption and subsequent generation of diffusing electron-hole pairs, subsequent recombination of minority carrier with the defect electron.

4. Results

4.1. *X-ray induced photocurrent*

The detection of X-ray absorption oscillations by induced currents in space charge structures is a rarely realized technique. Early reports on measurements of XAFS spectra on GaAs diodes show that the fluorescence signal and the photocurrent contain the same information if appropriate corrections are applied [5]. Furthermore, XAFS detection by X-ray stimulated photoconduction of bulk crystals was reported [6]. The relaxation of core holes inside the sample creates electron-hole pairs. The photocurrent generated directly in the space-charge region is negligible here, because the penetration depth of X-rays is much larger than the space-charge width of the junction (less than 1 μm). Therefore the dominant part of the photocurrent originates from minority charge carriers generated in bulk which diffuse with a diffusion lengths of some ten microns to the edge of the depletion region and and drift throughout that layer to the metal electrode.

4.2. *Changes in the steady-state capacitance due to X-ray irradiation*

Capacitance and photocurrent signals are within experimental error identical and show the expected energy of the Ga(K)-edge as well as a fine structure due to Ga atoms on undisturbed lattice sites in an almost perfect Al_xGa_{1-x} As crystal (Fig. 2).

The X-ray irradiation not only induces a photocurrent, but also leads to changes in the diode steady state capacitance. By phase-sensitive measurements of the alternating currents at small applied alternating bias one estimates the parameters of the overall sample as an electrical network with an imaginary and a real part. Such data are easily interpreted, if the sample is a passive two pole network dominated by its imaginary part. Under irradiation the Schottky barrier diode becomes an active two pole network with a more complex behavior. The photo current j_{photo} has now to be added to the network as a current source parallel to the capacitance and the total current density j_{total} is given by:

$$j_{total} = j_{diode} - j_{photo}.$$

Taking into account the dependence of j_{diode} on the (internal) voltage U over the depletion layer one obtains for the open circuit photo voltage U_{open}, i.e. $j_{total} \equiv 0$

$$U_{open} = U_T \ln(j_{photo}/j_0 + 1). \quad (1)$$

The saturation current j_0 contains all material and junction specific parameters as e.g. Schottky barrier height or band gap energy for pn-junctions. From current voltage measurements j_0 can be estimated experimentally and with (1) the actual voltage over the depletion layer in dependence on the photo current is obtained. That means, independent of the operation mode of the diode (open or short circuit conditions) the capacitance increases with increasing photocurrent because of the decreasing depletion width. For the relative change of capacitance by a relative variation of bias at the depletion layer one obtains:

$$\Delta C/C_0 = 0.5\left(1 - \frac{1}{1 + \Delta U/U_0}\right). \quad (2)$$

For our Schottky diodes j_0 was $10^{-9}\,\mathrm{A\,cm^{-2}}$ and j_{photo} under X-ray illumination was about $10^{-7}\,\mathrm{A\,cm^{-2}}$. From that a potential change of 50 mV can be expected, which would result in a capacitance change of up to one percent as observed in experiment.

From the above discussion we conclude, that the photocurrent is responsible for the changes in the steady state capacitance. Therefore, the capacitance-EXAFS spectrum can not contain additional or other information that what is obtained by the X-ray induced photo current.

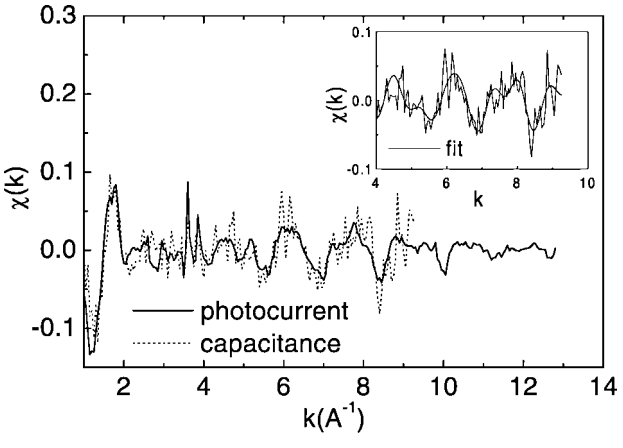

Fig. 2. EXAFS spectra $\chi(k)$, measured as steady-state capacitance and as photocurrent of a Schottky barrier diode on n-type $Al_xGa_{1-x}As$:Se ($x = 0.3$). The original energy spectra were taken near the Ga absorption K-edge ($V = 0$ V, $f = 5$ MHz). The insert shows an enhanced fraction of the capacitance signal together with a fit with the parameters according to the photocurrent signal.

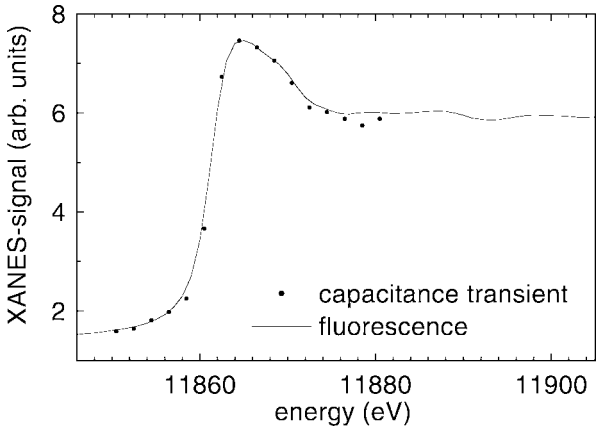

Fig. 3. Comparison of X-ray induced capacitance time constants with the fluorescence spectrum at the K-edge of As in bulk GaAS.

4.3. *X-ray induced capacitance transients*

A new way to measure XAFS oscillations arises from the detection of the time constant from capacitance transients as a function of X-ray energy (Fig. 3) [7]. The photon absorption at the defect is described by an optical cross section σ under the local photon flux ϕ at the defect which is simply related to a transition time constant τ by:

$$\tau = (\sigma \times \phi)^{-1}.$$

The absorption cross section of arsenic at the K-edge is $\mu = 2 \times 10^{-20}\,\mathrm{cm^2}$. The time constant for the trap ionization by 'site-selective' X-ray absorption (process (a)) can be estimated at HASYLAB to be

$$\tau = (\mu \times \phi)^{-1} \approx 5 \times 10^5\,\mathrm{s};$$

far beyond any experimental relevance.

The time constant of process (b) is related to the minority capture coefficient c_p from Shockley-Read-Hall statistics and is

given by:

$$\tau = \frac{q v_{drift}}{c_p j_{photo}}$$

with q denoting the elementary charge unit, v_{drift} the drift velocity inside the depletion layer, and j_{photo} the photocurrent density. With the measured photocurrent density $j \approx 1 \times 10^{-7}\,\mathrm{A\,cm^{-2}}$ and the capture coefficient for hole capture $c_p = 5.5 \times 10^{-8}\,\mathrm{cm^3\,s^{-1}}$ [3] one gets:

$\tau \approx 300\,\mathrm{s}$.

Thus, from the occurrence, amplitude or direction of a transient itself one can not deduce the underlying physical process. Only a calculation of the expected time constants according to the experimental conditions and the given specific defect parameters can clarify what physical process dominates.

5. Conclusions

Our measurements have shown that the trap ionization takes place significantly faster and can only be explained by hole capture from the photocurrent and not by direct 'site-selective' absorption processes. Thus, the capacitance EXAFS gives the same information as the measurement of the photocurrent – which is the absorption fine structure of the bulk material and not of the defects. From our analyses we find no evidence for a site-selectivity of capacitance EXAFS.

Acknowledgments

We acknowledge the stimulating discussions with R. Sielemann which initiated this study. A. W. R. Leitch, University of Port Elizabeth, SA supplied the AlGaAs samples and P. Gladkov prepared the contacts to the GaAs samples. Valuable and numerous discussions with D. Meyer on the EXAFS technique are acknowledged. The work was funded by the BMBF under contract 05KK10DA/2.

References

1. Stern, E. A., Phys. Rev. B **10**, 3027 (1974).
2. Aksenov, V. L., Kuzmin, A. Y., Purans, J. and Tyutyunnikov, S. I., Phys. Particles Nuc. **32**, 675 (2001).
3. Schroder, D. K., "Semiconductor Material and Device Characterization," (John Wiley & Sons, New York 1990).
4. Lang, D. V., Appl. Phys. **45**, 3023 (1974).
5. Boehme, R. F., Cargill III, G. S., Weber, W. and Jackson, T., J. Appl. Phys. **58**, 811 (1985).
6. Hu, T. D., *et al*., Phys. Rev. B **50**, 2216 (1994).
7. Bollmann, J., *et al*., Phys. Rev. B **68**, 125206 (2003).

Physica Scripta. Vol. T115, 191–193, 2005

Ab Initio Calculation of the Cr K Edge in α-Al_2O_3:Cr^{3+}

E. Gaudry[1], D. Cabaret[1], Ph. Sainctavit[1], Ch. Brouder[1], F. Mauri[1], A. Rogalev[2] and J. Goulon[2]

[1]Laboratoire de Minéralogie-Cristallographie, UMR 7590, Université Pierre et Marie Curie, case 115, 4 place Jussieu F-75252 Paris Cedex 05, France
[2]European Synchrotron Radiation Facility, BP 220, F-38043 Grenoble Cedex, France

Received June 26, 2003; accepted November 4, 2003

PACS numbers: 6110Ht, 7115Dx, 7870Dm

Abstract

The red color of ruby (α-Al_2O_3:Cr^{3+}) is assigned to transitions between 3d states of the chromium ion. A precise description of the structural and electronic environment of the Cr^{3+} ion in its slightly distorted octahedral site (C_3 symmetry) is needed to understand the cause of the color. We have analysed the Cr K-edge in α-Al_2O_3:Cr^{3+} with a reciprocal space approach that allows the computation of self-consistent spin polarized charge density for large unit cells, beyond the traditional "muffin-tin" approximation. Structural and electronic information is deduced from the calculation.

1. Introduction

The beautiful red color of ruby (α-Al_2O_3:Cr^{3+}) results from chromium impurities, that substitute for aluminum atoms in the structure. To understand the cause of the color, it is necessary to have a precise description of the local environment around the coloring atom. The positions of UV-VIS absorption bands indeed depend on the chemical bonding between the coloring atom and its nearest neighbors [1, 2, 3]. X-ray absorption spectroscopy is a powerful structural and electronic probe of matter. However, structural determination by Extended X-ray Absorption Fine Structure (EXAFS) is difficult in that case due to the low chromium concentration [4]. The XANES signal (X-ray Absorption Near Edge Structure), including the pre-edge, presents larger features, and contains structural and electronic information up to the medium range order. However, its interpretation is not straightforward and requires sophisticated simulation tools. In this paper, we show what kind of information it is possible to extract from the analysis of the angular dependence of the XANES spectrum at the Cr K-edge of α-Al_2O_3:Cr^{3+}, using a recently developed full potential scheme [5].

The crystal structure of α-Al_2O_3 belongs to the space group $R\bar{3}2/c$ or D^6_{3d} [6]. Therefore, in the electric dipole approximation, the absorption cross section of such a material depends on the angle θ between the C_3 axis and the polarization of X-rays [7]. The ionic radius of chromium atoms is larger than the ionic radius of aluminum atoms ($r_{Cr^{3+}} = 0.615$ Å and $r_{Al^{3+}} = 0.535$ Å in an octahedral site [8]). A modification of the chromium site in α-Al_2O_3:Cr^{3+} compared with the one of aluminum in α-Al_2O_3 is expected.

This article is divided into three parts. In the first part, we recall the main aspects of the calculation method. In the second part, we detail the structural information extracted from the XANES analysis. Electronic information is also given from the analysis of pre-edge features. In the third part, the results are discussed.

2. Calculation of the Cr K-edge XANES spectrum

Since the calculation method is detailed in a recent article [5] and in these proceedings [9], we just recall the main aspects of this reciprocal-space non "muffin-tin" approach. The scheme is implemented in an *ab initio* code [10] based on the Density Functional Theory (DFT) within the Local Density Approximation (LDA) that computes the spin polarized charge density self-consistently. The absorption cross section is computed in the electric dipole (E1) and quadrupole (E2) approximation. It is then possible to calculate the XANES signal on large supercells, and to take into account the 1*s* core hole effect on the absorption atom. In fig. 1, the calculation is compared to the experimental spectrum registered on the ID12A beam line (European Synchrotron Radiation Facility). The spectrum has been recorded on a single crystal and a reliable method has been applied to remove diffraction peaks [4]. The experimental layout is described in the following. All measurements have been made with the direction of the $\hat{k}$ X-ray wave vector ($[10\bar{1}]$ in the rhombohedral lattice) perpendicular to the surface of the sample, where the C_3 axis ([111]) and the polarization vector lie.

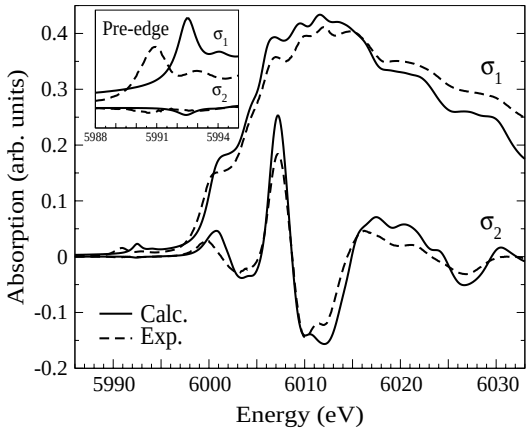

Fig. 1. Calculated (bold line) and experimental (dashed line) σ_1 and σ_2 spectra at the Cr K-edge in α-Al_2O_3-Cr^{3+}.

When $\theta = 0$ (resp. $\pi/2$), the absorption cross section measured is $\sigma_\parallel$ (resp. $\sigma_\perp$). In the electric dipole approximation, the angular mean $\sigma_1 = \frac{2\sigma_\perp + \sigma_\parallel}{3}$ is the isotropic absorption cross section, while $\sigma_2 = \sigma_\parallel - \sigma_\perp$ is the dichroic cross section.

The calculation is carried out on a rhombohedral $2 \times 2 \times 2$ supercell, resulting from an *ab initio* Car Parrinello energy minimization [11], and containing 1 chromium atom, 31 aluminum atoms and 48 oxygen atoms [4]. The calculation is carried out in two steps. First, charge density is computed using Troullier Martins potentials [12]. The electronic configuration of the chromium atom is $1s^1 2s^2 2p^6 3s^2 3p^6 3d^3$. The 1s, 2s, 2p are core states and the core radii of 3s, 3p, and 3d valence states are 0.53 Å, 0.90 Å, and 0.90 Å respectively. The charge density is computed on one *k*-point, with a 64 Ryd energy cut-off. The

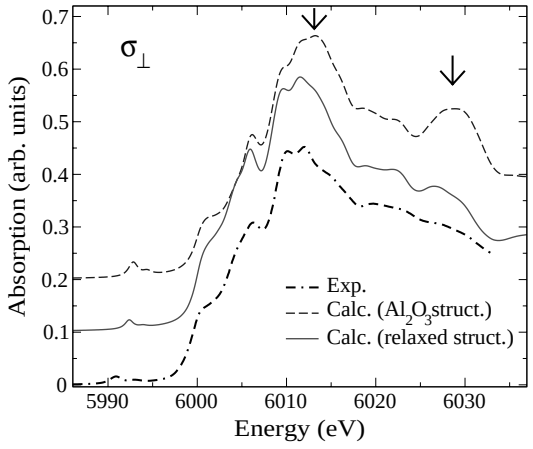

Fig. 2. Comparison of the SCF FP calculation on two different structural models. In the unrelaxed structure, the chromium atom substitutes exactly for an aluminum atom. The relaxed structure is given by an *ab initio* Car Parrinello code.

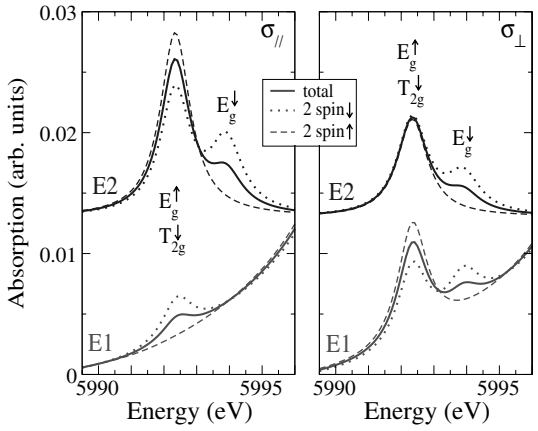

Fig. 3. Zoom on the pre-edge features of $\sigma_{\parallel}$ (left) and $\sigma_{\perp}$ (right) absorption cross sections in Al_2O_3:Cr^{3+}. The full lines are the calculated spectrum in the electric dipole (E1) and electric quadrupole (E2) approximation. The dotted lines are the spin down component and the dashed line are the spin up component of the signals.

XANES calculation is made in a second step. The cross section is computed on a 32 k-point grid.

3. XANES interpretation

3.1. *Structural information*

The XANES $\sigma_{\perp}$ cross section has been calculated on two different structural models (fig. 2). In the first one, atoms have the same position as in α-Al_2O_3 but one aluminum atom has been replaced by one chromium atom. The second structural model is given by an *ab initio* energy minimization [4]. The two calculated spectra reproduce the experimental spectrum reasonably well. However, the two features around 6010 eV on the experimental spectrum are not given by the calculation performed on the non relaxed structure. Moreover, this computed signal displays a large feature around 6030 eV, that does not appear in the experiment. The calculated spectrum obtained with the relaxed stucture is in good agreement with the experiment, it is then validated.

3.2. *Electronic information*

The pre-edge features contain useful information on the electronic structure around the probed atom. The electronic configuration of the absorbing atom in its ground state is [Ar]$3d^3$. It lies in a slightly distorted octahedral site. The asymmetry of the site can be evaluated by the parameter $2\frac{d_{Cr-O_1}-d_{Cr-O_2}}{d_{Cr-O_1}+d_{Cr-O_2}}$, whose value is 2.5%. The pre-edge features are made from a sum of electric quadrupole $1s \rightarrow 3d$ transitions, and of electric dipole $1s \rightarrow p$ transitions. Since the chromium site is not centrosymmetric, the p states are present at the pre-edge through 3d – p hybridization. The electric dipole and electric quadrupole contributions to the absorption cross section in the pre-edge region are represented in fig. 3. The contributions of spin up and spin down are detailed. The interpretation of the features is possible through group theory in the monoelectronic approach, using the character tables of the C_3, C_{3v} and O_h symmetry groups from [3]. The irreducible representations (irrep) of transitions, given by $\Gamma_f \otimes \Gamma_{\mathcal{O}} \otimes \Gamma_i$ depends on the symmetries $\Gamma_{\mathcal{O}}$ of the transition operator $\mathcal{O}$ and on the ones (Γ_f) of the final state (p or d) since the initial state (Γ_i) is totally symmetric. Allowed transitions belongs to the totally symmetric irrep. Although the symmetry of the Cr site in α-Al_2O_3 is C_3, it is allowed to treat it as if it is C_{3v} because there is no spin orbit coupling in the calculation. It is interesting to know what becomes the C_{3v} irrep in O_h symmetry. The p orbitals ($t_{1u}(O_h)$ irrep) are split into two irreps, that are $A_1(C_{3v})$ for the $p_{\parallel C_3}$ states and $E(C_{3v})$ for the $p_{\perp C_3}$ states. Concerning d states, the $e_g(O_h)$ irrep becomes $E(C_{3v})$ and the $t_{2g}(O_h)$ irrep is split into $A_1(C_{3v})$ and $E(C_{3v})$.

According to the experimental layout described before, the wave vector $\hat{k}$ stays perpendicular to the C_3 axis. In the case of pure electric quadrupole transitions ($1s \rightarrow 3d$), $\mathcal{O} = \hat{\varepsilon}{\cdot}r\hat{k}{\cdot}r$ belongs to the $E(C_{3v})$ irrep, for all angles θ between the C_3 axis and the X-ray polarization $\hat{\varepsilon}$ ($\hat{k} \perp C_3$ axis). Permitted transitions happen toward states belonging to the $E(C_{3v})$ irrep. These states are the corresponding $e_g(O_h)$ and $t_{2g}(O_h)$ in O_h symmetry. Since the $t_{2g}^{\uparrow}(O_h)$ are full, the transition toward $e_g^{\uparrow}(O_h)$ is the single transition permitted for spin up states. For spin down states, transitions toward $t_{2g}^{\downarrow}(O_h)$ and $e_g^{\downarrow}(O_h)$ are permitted. In the case of electric dipole transitions ($1s \rightarrow p$), the irrep of $\mathcal{O} = \hat{\varepsilon} \cdot r$ depends on the angle θ. If $\hat{\varepsilon}$ is parallel to the C_3 axis, then $\mathcal{O}_{\parallel} = \hat{\varepsilon}_{\parallel} \cdot r$ belongs to $A_1(C_{3v})$. The transition toward $A_1(C_{3v})$ is the single permitted transition. It corresponds to the $p_{\parallel C_3}$ states. These states cannot hybridize with $E(C_{3v})$ states, because they have not the same symmetry. There is no $p_{\parallel C_3}$-$e_g(O_h)$ hybridization. Given that $t_{2g}^{\uparrow}(O_h)$ states are full, no transition is allowed for spin up states. One transition toward $t_{2g}^{\downarrow}(O_h)$ is allowed for spin down states. If $\hat{\varepsilon}$ is perpendicular to the C_3 axis, then $\mathcal{O}_{\perp} = \hat{\varepsilon}_{\perp} \cdot r$ belongs to $E(C_{3v})$. The transition toward $E(C_{3v})$ symmetry states are the single permitted transitions. It corresponds to the $p_{\perp C_3}$ states in C_3 symmetry. Hybridization with both $e_g(O_h)$ and $t_{2g}(O_h)$ states are possible. For spin up states, the transitions occurs toward $e_g^{\uparrow}(O_h)$ and for spin down states, the transitions are toward both $e_g^{\downarrow}(O_h)$ and $t_{2g}^{\downarrow}(O_h)$ states.

From the calculation, we deduce that the $e_g^{\uparrow}(O_h)$ states lie about at the same energy as the $t_{2g}^{\downarrow}(O_h)$ states. Moreover, it is possible to deduce the energy difference between the $e_g^{\downarrow}(O_h)$ and the $t_{2g}^{\downarrow}(O_h)$ states by the energy difference of the first two features, which are 1.4 eV (resp. 2.0 eV) for the calculated (resp. experimental) spectrum. The difference between these two values may be linked to the DFT approach.

4. Discussion

Our main goal is to show that it is possible to extract precise information from XANES, thanks to an efficient self consistent (SCF) full potential (FP) code.

From fig. 1, the SCF FP calculation is in good agreement with the experimental spectrum. The calculation reproduces well the positions and the intensities of the features. A good adequacy between the calculated and the experimental spectrum is needed to succeed in extracting information from XANES spectra. It is obtained only by both a full potential and a self consistent approach. Indeed, a comparison on the shape of the potential used has been made between two SCF calculations in the electric dipole approximation: the above FP SCF method and a SCF "muffin-tin" calculation. The SCF "muffin-tin" calculation was made in real space on a system containing 102 atoms, within the full multiple scattering approach using the `feff8` code [13]. We have also analyzed the influence of the self consistency on two FP calculations in the electric dipole approximation. The FP non-SCF calculation is made in real space on a system containing 102 atoms, within the finite difference full potential approach (`fdmnes` code) [14]. The electronic density is described by the superposition of the neutral atoms. In the case of a SCF non-FP or FP non-SCF calculation, the shape of the calculated spectrum is not so good. In particular, for such calculations, the differences between the spectra calculated with the relaxed or the unrelaxed structure are as large as the differences between the calculated and the experimental spectra. The validation of any structural model is then impossible with FP non-SCF or SCF non-FP methods. It should be noticed that in the case of Al_2O_3:Cr^{3+}, the two structural models are very close, since they are different only by the positions of the neighboring atoms of the chromium atom. The Cr-O and Cr-Al distances deduced from the validation of the relaxed structure by the SCF FP method have already been discussed in [4].

The presence of the 1s core hole is needed to obtain a good agreement between the calculation and the experimental spectrum. In particular, the positions of the pre and near edge features are shifted towards lower energies due to the presence of the 1s core hole. But even with the 1s core hole, the positions of the calculated pre and near edge features are displaced with respect to experiment. This may be due to the approximations that are made in the DFT-LDA calculation. Excited states are usually rather badly described by DFT calculations. Multielectronic interactions are not taken into account by the effective potential. Localized states like the core hole or the Cr 3d orbitals are present in the calculation within the LDA approximation.

Pre-edge features measure the density of localized empty states (3d and hybridized p – 3d states). They contain information on the electronic structure of Al_2O_3:Cr^{3+}, particularly on 3d orbitals, that are involved in the absorption process that causes the color. From the calculation, it is possible to separate the contributions from each spin, and from electric dipole and electric quadrupole transitions. The pre-edge is composed of a large contribution of electric quadrupole transitions, compared to electric dipole ones. In fact, the chromium site is not centrosymmetric, but the asymmetry from a pure octahedral site is small (2.5%). Electric dipole transitions are then rather weak, corresponding to a weak p-d mixing.

The crystal field extracted from XANES should be compared carefully with results from other spectroscopies, because it has not the same signification in all cases. The value from XANES is 2.0 eV, while it is 1.8 eV from X-ray magnetic circular dichroism ($2p^63d^3 \rightarrow 2p^53d^4$ transitions) [15], and 2.23 eV from UV-VIS spectroscopy (d-d transitions) [16].

5. Conclusion

We have calculated the Cr K-edge XANES spectrum though an efficient calculation scheme. The XANES structural interpretation offers an alternative to the EXAFS analysis and the electronic structure interpretation provides useful information to clarify the origin of color in ruby. Such a kind of XANES interpretation will be applied to the study of other impurities in α-Al_2O_3, particularly in blue sapphires (α-Al_2O_3:Fe-Ti), to show the role of charge transfer in the cause of the color.

Acknowledgments

We are grateful to the Institut du Développement et des Ressources en Informatique Scientifique (IDRIS) in ORSAY, that supported most of the computing time of this work. This is IPGP contribution number 2912.

References

1. Nassau, K., "The Physics and Chemistry of Color." (Wiley Interscience, 1983).
2. Solomon, E. I. and Lever, A. B. P., "Inorganic electronic structure and spectroscopy." (Wiley, 1999).
3. Lever, A. B. P., "Inorganic Electronic Spectroscopy" (Elsevier, 1984).
4. Gaudry, E. *et al*., Phys. Rev. B **67**, 94108 (2003).
5. Taillefumier, M., Cabaret, D., Flank, A.-M. and Mauri, F., Phys. Rev. B **66**, 195107 (2002).
6. Pearson, W. B., Structure Reports, volume 27, International Union of Crystallography, (1962).
7. Brouder, Ch., J. Phys.: Condens. Matter **2**, 701 (1990).
8. Shannon, R. D., Acta. Cryst. **A32**, 751 (1976).
9. Cabaret, D., Gaudry, E., Taillefumier, M. and Mauri, F., these proceedings, XAFS12 (2003).
10. Pfrommer, B., Raczkowski, D., Canning, A. and Louie, S. G., "PARAllel Total Energy Code", Lawrence Berkeley National Laboratory (with contributions from F. Mauri, M. Cote, Y. Yoon, Ch. Pickard and P. Haynes). For more information see www.nersc.gov/projects/paratec
11. Car, R. and Parrinello, M., Phys. Rev. Lett. **55**, 2471 (1985).
12. Troullier, N. and Martins, J. L., Phys. Rev. B **43**, 1993 (1991).
13. Ankudinov, A. L., Ravel, B., Rehr, J. J. and Conradson, S. D., Phys. Rev. B **58**, 7565 (1998).
14. Joly, Y., Cabaret, D., Renevier, H. and Natoli, C. R., Phys. Rev. Lett. **82**, 2398 (1999).
15. Gaudry, E. *et al*., in preparation.
16. Reinen, D., Structure and bonding **6**, 30 (1969).

Physica Scripta. Vol. T115, 194–196, 2005

Overlapping XAFS L Spectra of 3d Metals: A New Application of the Regularization Method

Yu. Babanov[1,2], S. Kiryanov[1], A. Sidorenko[1], L. Romashev[1], D. Vyalikh[3,4], S. Molodtsov[3,5], G. Guentherodt[6], U. Ruediger[6], Yu. Dedkov[6], M. Fonine[6], K. Baberschke[4], H. Wende[4] and Y. U. Idzerda[7]

[1]Institute of Metal Physics, RAS, GSP-170, 620219, Ekaterinburg, Russia
[2]Udmurt State University, Izhevsk, Russia
[3]Russian–German Laboratory at BESSY II, 12489 Berlin, Germany
[4]Freie Universität Berlin, 14195 Berlin, Germany
[5]Technische Universität Dresden, 01062 Dresden, Germany
[6]Physikalisches Institut RWTH, Aachen D-52056, Germany
[7]Montana State University, Bozeman, MT 59717-3840, USA

Received June 26, 2003; accepted November 14, 2003

PACS 6110Ht

Abstract

L XAFS spectra of polycrystalline Fe and Cr films are investigated by EXAFS and TEY (Total Electron Yield) techniques. A new method of obtaining local structure information from overlapping *L* XAFS spectra for 3d metals is proposed. Tikhonov regularization method of solving ill-posed problem is used. In contrast to the conventional methods (Fourier transformation and fitting procedures) this method does not demand any model assumption and any special procedure of deconvolution of L_1 –, L_2 –, L_3 – contributions. The parameters obtained from *L* XAFS spectra of polycrystalline Fe and Cr films (interatomic distance and coordination number for the first and the second coordination shells) agree with the expected crystallographic values. Up to now the regularization method was applied only to nonoverlapping XAFS spectra.

1. Introduction

If the photon energy is high enough to excite an electron from an atomic core to the continuum, an edge-jump is found in the X-ray absorption coefficient. The excitation thresholds K, L_1, L_2, L_3 correspond to the transition of $1s_{1/2} \rightarrow \varepsilon p, 2s_{1/2} \rightarrow \varepsilon p, 2p_{1/2} \rightarrow \varepsilon s, \varepsilon d, 2p_{3/2} \rightarrow \varepsilon s, \varepsilon d$. The special feature of *L* spectra of 3d metals is overlapping. Fig. 1 shows model *L* spectra (total one and separate contributions) for pure Fe calculated by FEFF8 [1].

We propose a new method of obtaining local structure information from the overlapping *L* XAFS spectra for 3d metals using Tikhonov's method of solving ill-posed problem [2]. Up to now this method was applied to nonoverlapping EXAFS spectra [3, 4]. Recently a special procedure of deconvolution L_2 –, L_3 – contributions [5] was used for obtaining local structure information.

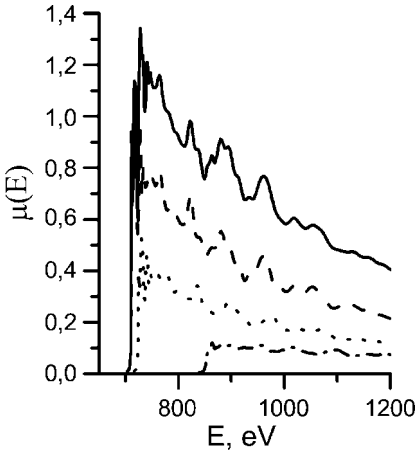

Fig. 1. FEFF8 simulation of *L* spectra (the total one (solid line) and the separate contributions: L_3 (dash line), L_2 (dot line) and L_1 (dash dot line)) for pure Fe.

2. Mathematical algorithm

For one component systems the atomic distribution is described by the pair correlation function (PCF) $g(r)$ which may be written as

$$g(r) = \frac{1}{4\pi\rho_0} \sum_l \frac{N_l}{r_l^2 \sigma_l \sqrt{2\pi}} \exp\left(-\frac{(r-r_l)^2}{2\sigma_l^2}\right). \quad (1)$$

Here ρ_0 is atomic density, N_l is coordination number for the l shell, σ_l is Debye–Waller factor for the l shell, r_l is position of the l shell. The normalized oscillating part of the EXAFS signal $\chi(k)$ for the K – spectrum is described as

$$\chi(k) = 4\pi\rho_0 \int_0^\infty R(k) \frac{f(k,r)}{k} \exp\left(\frac{-2r}{\lambda(k)}\right) \times \sin(2kr + 2\delta(k) + \varphi(k,r)) g(r) \mathrm{d}r. \quad (2)$$

Here $R(k)$ is reduction factor, $f(k,r)$ is a backscattering amplitude module, $\lambda(k)$ is the mean free path of a photoelectron, $\delta(k)$ is central atom phase shift and $\varphi(k,r)$ is a backscattering phase. All values are calculated by FEFF8 [1].

Using the dispersion laws for L_3, L_2, L_1 spectra one may conclude that *L* spectra have the same *E* space but different *k* spaces (namely, k_1, k_2, k_3). The laws for connection of k_1, k_2, k_3 spaces is found as:

$$k_2 = f(k_3) = \sqrt{k_3^2 + (E_3 - E_2)/a},$$
$$k_1 = h(k_3) = \sqrt{k_3^2 + (E_3 - E_1)/a}, \quad (3)$$

where E_3, E_2, E_1 are energies of L_3, L_2, L_1 edges, $a = \hbar^2 k^2/(2m) = 3.81$. Now the equation for the sum of L_1, L_2, L_3 EXAFS spectra in unified k_3 space may be written as [6]:

$$\chi_{sum}(k_3) = W_{L3}\chi_{L3}(k_3) + W_{L2}\chi_{L2}(k_2 = f(k_3)) + W_{L1}\chi_{L1}(k_1 = h(k_3)), \quad (4)$$

where W_{L3}, W_{L2}, W_{L1} are weight coefficients used to account the contributions of each edge and calculated by FEFF8 [1].

For *L* spectra the radial matrix elements are given by M_{01} for $l = 1 \rightarrow l = 0$ transitions and M_{21} for $l = 1 \rightarrow l = 2$ transitions. As shown in [7] for elements with $Z \geq 20$ the ratio M_{01}/M_{21}

is nearly independent of k, and the $p \to s$ contributions are practically unobservable, as $p \to d$ transitions are favored by a factor of 50. This means that all M_{01} contributions in the integral equation can be neglected and hence the L spectra can be analyzed in the same way as is done for the K spectra.

The integral equation for overlapping L spectra has the form:

$$\chi(k_3) = 4\pi\rho_0 \int_0^\infty \mathrm{d}r\ g(r) \times \left\{ W_{l1} \frac{f_1(k_1,r)}{k_1} \exp\left(\frac{-2r}{\lambda_1(k_1)}\right) \sin(2k_1 r + 2\delta_1(k_1) + \varphi_1(k_1,r)) + W_{l2} \frac{f_2(k_2,r)}{k_2} \exp\left(\frac{-2r}{\lambda_2(k_2)}\right) \sin(2k_2 r + 2\delta_2(k_2) + \varphi_2(k_2,r)) + W_{l3} \frac{f_3(k_3,r)}{k_3} \exp\left(\frac{-2r}{\lambda_3(k_3)}\right) \sin(2k_3 r + 2\delta_3(k_3) + \varphi_3(k_3,r)) \right\}. \quad (5)$$

If we compare Eq. (2) for Kspectra and Eq. (5) for L spectra we can see that in the last case we have the integral Fredholm equation with more complex kernel than in the first one. For L spectra it is possible to use the regularization method without any modification. Details of solving the EXAFS ill-posed problem may be found in [2–4]. For multicomponent systems the theory is easy to generalize. It is possible to apply this approach not only for overlapping L spectra but also for overlapping K-L spectra (for example, in the oxides Fe_3O_4, Cr_2O_3).

3. Experimental details

Two different techniques of experiment were used in this article – EXAFS in transmission mode and Total Electron Yield (TEY) technique.

TEY experiments were performed at room temperature using the facility of the RGBL beamline of BESSY II. The samples were polycrystalline Fe and Cr films. Fe film of thickness ∼300 Å was evaporated under UHV conditions onto W(110) substrate and the measurements were performed immediately after deposition. Cr film of thickness ∼300–400 Å was evaporated under UHV conditions onto MgO(100) substrate at the Institute of Metal Physics, RAS.

The low temperature (70 K) EXAFS measurements were carried out in transmission mode at the U4B beamline of the National Synchrotron Light Source (NSLS) located at Brookhaven National Laboratory (BNL, USA). The sample was polycrystalline Fe film. This film with thickness of 500 Å was evaporated under UHV conditions onto ∼1 μm thick semitransparent parylene $(C_8H_8)_n$ substrate (100). To prevent the film from oxidising an additional Al cap layer was deposited on the film.

For obtaining $\chi(k)$ functions for Fe and Cr films from raw experimental data we use the conventional procedure [8]. We normalise the experimental spectrum on sum of L_3, L_2, L_1 edge jumps, but we do not remove L_1 edge jump from the experimental $\chi(k)$ because the value of this jump in comparing with the common jump is approximately 0.1 (see Fig. 1). It validates by the fact that there is no jump at $k \sim 6\,\text{Å}^{-1}$ in the experimental spectra in contrast with the model simulation at the temperature 70 K (Fig. 2).

4. Discussion

Fig. 2 shows experimental $\chi(k)$ functions for Fe and Cr films obtained from TEY measurements and for Fe film obtained from EXAFS measurements in transmission mode. The extraction of the $\chi(k)$ functions from raw data was used [3, 4]. TEY $\chi(k)$ functions were rather noisy due to low statistics so these curves were smoothed. All curves are compared with the model functions calculated by FEFF8 [1].

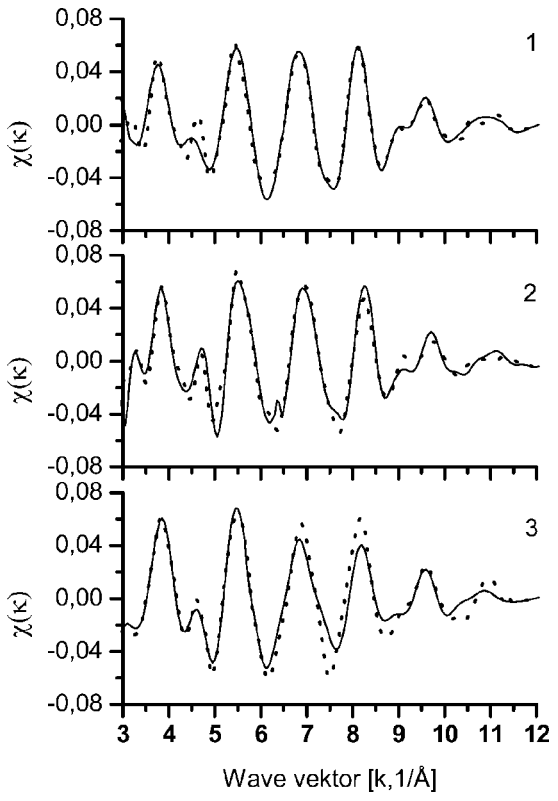

Fig. 2. Experimental EXAFS and TEY $\chi(k)$ spectra (dot line) in comparison with simulated functions by FEFF8 (solid lines) (1 – TEY spectra of Fe at 300 K, 2 – EXAFS spectra of Fe at 70 K, 3 – TEY spectra of Cr at 300 K).

Applying the regularization method described [2–4], one can find the solutions which are shown on Fig. 3. The obtained results

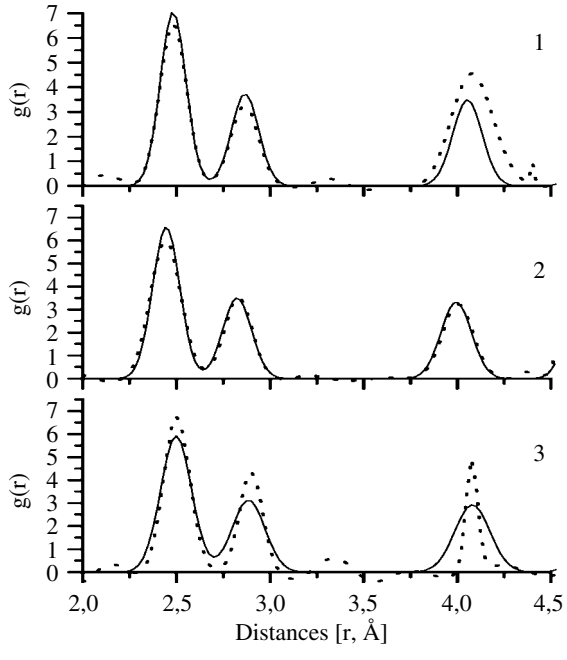

Fig. 3. Model PCF (solid line) and obtained (dot line) solution (1 – Fe at 300 K, 2 – Fe at 70 K, 3 – Cr at 300 K).

Table I. *Comparison of the model and experimental values obtained for the first and second shells of crystalline Fe and Cr (interatomic distance r and nearest neighbors coordination number N).*

		1st coordination shell		2nd coordination shell	
Edge	Type of experiment	r, Å	N, at.	r, Å	N, at.
Fe	Model 300 K	2.483	8.00	2.867	6.00
	TEY	2.482	7.87	2.865	5.38
	Model 70 K	2.446	8.00	2.824	6.00
	EXAFS	2.443	8.12	2.832	5.84
Cr	Model 300 K	2.499	8.00	2.885	6.00
	TEY	2.501	7.85	2.899	5.90

are compared with model PCF functions calculated on the basis of the well known crystallographic data.

The following main characteristics of the peaks for the function $g(r)$ have been selected: interatomic distance r and the nearest neighbors' coordination number N. These values were estimated according to the Gauss functions approximating the peaks of the solution and presented in Table I.

As it can be seen the main characteristics of the first and the second shells for crystalline Fe and Cr correspond to the crystallographic table values. There is a very high resolution in real space r with comparing the Fourier transformation. On the curve of Fourier transformation it is impossible to distinguish the first and the second shells of BCC lattice.

It is necessary to note that during the solution of the inverse problem (2) the contribution of photoelectron multiple scattering on the nearest neighbours were not accounted. It seems than simultaneous solving of three L spectra made the problem more stable.

5. Conclusion

The proposed new method of obtaining local structure information from overlapping XAFS spectra for 3d metals shows its efficiency. In contrast to the conventional methods (Fourier transformation and fitting procedures) this method does not demand any model assumption and any special procedure of deconvolution of L_1 –, L_2 –, L_3 – contributions and has a high resolution in real space r. Obtained parameters – interatomic distance, coordination number for the first and the second coordination shells agree well with the expected crystallographic values.

References

1. Ankudinov, A., Ravel, B., Rehr, J. J. and Conradson, S., Phys. Rev. **B58**, 7565 (1998).
2. Tikhonov, A. N. and Arsenin, V. Ya., "Solution of Ill-Posed Problems" (John Willey and Sons, Inc., New York, 1981).
3. Babanov, Yu. A., Vasin, V. V., Ershov, N. V. and Ageev, A. L., Phys. Stat. Sol. B **105**, 747 (1981).
4. Babanov, Yu. A., *et al*., J. Non-Cryst. Sol. **79**, 1 (1986).
5. Wende, H., *et al*., J. Appl. Phys. **83**, 7028 (1998).
6. Lemke, L., *et al*., J. Phys. Condens. Matter **10**, 1917 (1998).
7. Teo, B. K., "EXAFS: Basic Principles and Data Analysis" (Springer-Verlag, Berlin, 1986).
8. Newville, M., Livins, P., Yacoby, Y., Stern, E. A. and Rehr, J. J., Phys. Rev. B **47**, 14126 (1993).

Physica Scripta. Vol. T115, 197–199, 2005

Thickness Inhomogeneity Effect in EXAFS Spectroscopy

A. V. Ryazhkin[1], Yu. A. Babanov[1,2], T. Miyanaga[3], E. D. Crozier[4], R. A. Gordon[4], T. Reich[5] and H. Funke[6]

[1]Institute of the Metal Physics Ural Branch of RAS. S. Kovalevskaya st. 18 GSP 170, 620219, Ekaterinburg, Russia
[2]Udmurt State University, Ichevsk, Russia
[3]Department of Materials Science and Technology, Faculty of Science, Hirosaki University, 3 Bunkyo-cho, Hirosaki, Aomori 036-8561, Japan
[4]Department of Physics, Simon Fraser University, Burnaby, B.C. V5A 1S6, Canada
[5]Johannes Gutenberg-Universität Mainz, Institut für Kernchemie, Fritz-Strassmann-Weg 2, 55128 Mainz, Germany
[6]Forschungszentrum Rossendorf e. V., Institute of Radiochemistry, PO Box 510119, D-01314 Dresden, Germany

Received June 26, 2003; accepted November 4, 2003

PACS number: 6110Ht

Abstract

In many cases X-ray absorption spectra measured in transmission mode are degraded by an inhomogeneity in thickness of the samples. As a result, the EXAFS amplitude is decreased and information about the coordination numbers is distorted. To avoid this influence, it is necessary to prepare a homogeneous sample. But, for powder samples, thick inhomogeneous foils, and sputtered films this is not possible. Absorption spectra on these samples should be corrected for the thickness inhomogeneity effect.

To correct an absorption spectrum it is necessary to know the sample thickness distribution function. We propose a method of solving an integral equation for a distribution function as an inverse problem. We use and compare the experimental pre-edge absorption behaviour with the theoretical Victoreen function. We apply the Tikhonov regularization algorithm to determine the distribution function. Model calculations are carried out to check the reproducibility of the calculations. This method is applied to preliminary procession of X-ray absorption spectra for high quality foils of crystalline Cu, crystalline Cu powder samples, and an inhomogeneous foil of ordered $Ni_{50}Mn_{50}$ alloy. We estimate the thickness inhomogeneity effect on the coordination numbers in the cases before and after correcting the spectra.

1. Introduction

The thickness effect, which is caused by leakage of radiation accompanying the absorption process, has been discussed earlier [1–11]. The samples for experiment in transmission mode need to be uniform [8], but it is difficult to prepare an uniform sample from powders, for example. For inhomogeneous samples, the EXAFS amplitude is decreased.

An integral equation for the sample thickness distribution function was written by L. Ottaviano *et al*. [9]. They proposed a sample preparation technique, suitable for X-ray absorption measurements of liquid and supercooled metals and determined experimentally the size distribution of metal droplets by means of an optical microscope. This distribution was described within the framework of a log-normal model of thickness distribution. A special procedure for correcting the raw data due to the inhomogeneity of the thickness was applied. Bausk *et al*. [10] proposed to correct the XAFS amplitude by constructing a correcting function using pre-edge data without restoring the thickness distribution.

In a previous paper [11] the idea to correct XAFS amplitude using pre-edge data [10] was adopted and a simple model describing the influence of thickness inhomogeneity on the edge step, the amplitude of EXAFS oscillations and the asymptotic behavior of absorption spectra was proposed. The asymptotic behavior was used in order to find some parameters of the model and to reconstruct the true absorption coefficient.

In the present paper we propose to solve an integral equation for the sample thickness distribution function. The problem is reduced to a system of linear equations by the regularization method. We present the sample thickness distribution functions and the correction of the effects related to the thickness inhomogeneity for crystalline Cu foils, powder samples of Cu and a thick inhomogeneous foil of $Ni_{50}Mn_{50}$.

2. A short description of the mathematical algorithm

A sample inhomogeneity can be characterized by the thickness distribution function $\alpha(x)$ [9, 10]. For discrete thickness it equals the ratio of sample area with thickness x_i to full area of sample, or $\alpha_i = S_i/S$, where $S = \Sigma S_i$.

For X-ray absorption we have an integral equation [9]:

$$e^{-\mu'(E)} = \int e^{-\mu(E)x}\alpha(x)\,dx, \tag{1}$$

where $\mu'(E)$ is the measured absorption of the sample and $\mu(E)$ is the true absorption of the sample.

Rewrite this equation in symbolic form:

$$U = A\alpha. \tag{2}$$

In discrete approximation eq. (1) represents a system of linear algebraic equations.

To solve the problem (1), we use the pre-edge asymptotic behavior of X-ray absorption. The slope of this curve is very weak. That is why the matrix A is ill conditioned and the problem is unstable. We replace the exact equation (2) in discrete form by the approximated one and obtain the so called Tikhonov solution using the regularization method [11]:

$$\alpha = (A + B)^{-1}U. \tag{3}$$

The average thickness $\langle x\rangle$ is defined as

$$\langle x\rangle = \int x\alpha(x)\,dx. \tag{4}$$

From the obtained $\alpha(x)$ and $\langle x\rangle$, we find the reconstructed spectrum for a homogeneous sample with thickness $\langle x\rangle$ using the iterative procedure:

$$\mu_l(E)\langle x\rangle = \mu'(E) + \ln\int e^{-\mu_{l-1}(E)(x-\langle x\rangle)}\alpha(x)\,dx \tag{5}$$

where l is the iteration number, $\mu'(E)$ is the initial experimental spectrum. At $l = 1$ we use an atomic absorption function $\mu_V(E)$ [12] as $\mu_{l=1}(E)$. Less than 10 iterations are required. Details of the mathematical algorithm will be published elsewhere.

3. Experimental details and results of spectra correction

To be able to evaluate the results of our method, we choose: two crystalline Cu foils with different thickness; two Cu powder samples; and a crystalline inhomogeneous foil $Ni_{50}Mn_{50}$.

3.1. *Crystalline Cu foils*

The first sample of crystalline Cu was prepared by EXAFS Materials Company (Danville, USA) with thickness 7 μm. The Cu K-edge of the X-ray absorption spectrum was collected in transmission mode at room temperature. The measurements were performed at the Rossendorf Beamline (ROBL) at the European Synchrotron Radiation Facility (ESRF) using a Si(111) double-crystal monochromator in fixed-exit mode [13]. In addition, a blank run of the Cu K-edge spectrum was made in order to determine the apparatus function by measuring the absorption spectrum without any sample. These measurements should be performed before and after measurement of the Cu spectrum without changing amplification. If the apparatus function is changed, it is necessary to repeat the measurements. This procedure was realized for all samples studies in this paper. The blank run is important because we use pre-edge asymptotic behavior for determination of the sample thickness distribution function. Fig. 1 shows the absorption Cu spectra before and after removing the apparatus function.

The second sample of crystalline Cu was prepared by polishing the foil to a nominal thickness of 5 μm. The Cu K-edge X-ray absorption spectrum was collected in transmission mode at room temperature at the PNC-CAT beamline, 20-BM at the Advanced Photon Source (APS) using a Si(111) double-crystal monochromator in fixed-exit mode [14].

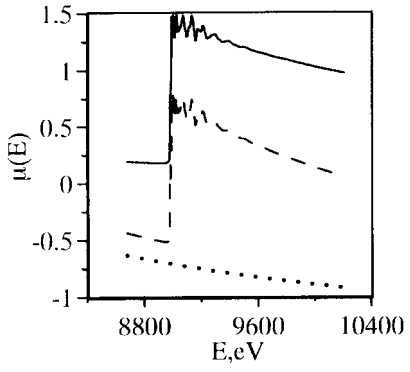

Fig. 1. Absorption data for Cu foil. Dotted line – blank run, dashed line – raw absorption spectra, solid line – absorption spectra after blank run removed.

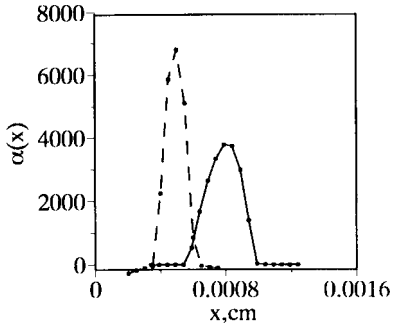

Fig. 2. Thickness distribution functions for homogeneous Cu foils. Solid line – distribution function for first foil sample ($\langle x\rangle = 7.2$ μm), dashed line – for second foil sample ($\langle x\rangle = 5.2$ μm).

Table I. *Coordination numbers for homogeneous Cu foils.*

	First foil sample		Second foil sample	
Model	Before correction	After correction	Before correction	After correction
12.00	11.97	12.01	11.96	12.05

The distribution function for both crystalline Cu foils (Fig. 2) have narrow symmetric peaks with the average thickness 7.2 μm (the first sample) and 5.2 μm (the second one). With these functions we have reconstructed the true signal, obtained the EXAFS spectrum and compared it with the initial EXAFS spectrum (before correction). We did not find any thickness effect and consider these samples to be good.

The first coordination numbers are listed in Table I. We conclude: the thickness inhomogeneity effect does not distort the EXAFS–spectra for homogeneous foils.

3.2. *Crystalline Cu powder samples*

The Cu particle size was 3.25–4.5 μm. The powder was spread onto Kapton tape in inert gas in a glove box and oxidation was minimized by covering with another layer of Kapton. The number of layers of Cu/Kapton was changed to produce the jumps 0.5 (1 layer) and 1.0 (3 layers).

The Cu K-edge X-ray absorption spectrum was collected in transmission mode at room temperature at the PNC-CAT beamline 20-BM at the APS.

The most interesting feature of these spectra before correction is the $\chi(E)$ function of 1 layer of Cu particles is almost identical to that for 3 layers. Significant differences occur only in the 10 eV interval above the first inflection point in $\mu'(E)$. We find this surprising because the effective sample thicknesses differ by a factor of 3.

Naively, one would have expected the effect of pinholes to cause a much greater distortion for 1 layer than for 3 layers. The thickness distributions $\alpha(x)$ obtained (Fig. 3) confirm that increasing the number of layers reduces the fraction of sample with thickness approaching zero. But the 3-layer sample is not homogeneous and has a wide asymmetric distribution function.

Fig. 4 shows EXAFS spectra for the first powder sample before (solid line) and after (dashed line) correction for the thickness inhomogeneity effect.

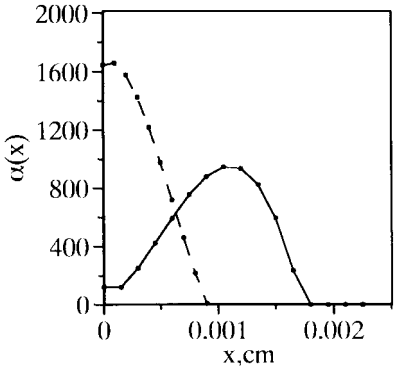

Fig. 3. Thickness distribution functions from Cu powder samples. Dashed line is the distribution function for 1 layer ($\langle x\rangle = 3.0$ μm) and the solid line is for 3 layers ($\langle x\rangle = 9.8$ μm).

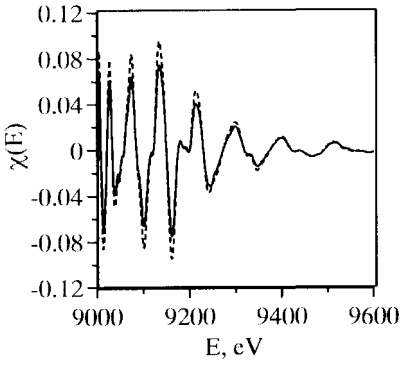

Fig. 4. EXAFS spectra from the first powder sample before (solid line) and after (dash line) correction on the thickness inhomogeneity effect.

Table II. *Coordination numbers for inhomogeneous Cu powder samples.*

	First power sample		Second power sample	
Model	Before correction	After correction	Before correction	After correction
12.00	8.86	12.05	8.75	12.01

Coordination numbers from EXAFS–spectra before and after correction are presented in Table II.

3.3. *Thick foils of $Ni_{50}Mn_{50}$ alloys*

The foil of the ordered $Ni_{0.50}Mn_{0.50}$ sample was prepared from a massive piece by polishing to a nominal thickness of 20 μm. The Ni and Mn K-edge absorption spectra of ordered $Ni_{0.50}Mn_{0.50}$ alloy were recorded in transmission mode at the PNC-CAT beamline 20-ID, APS [14]. A Si(111) double crystal monochromator was used (65% tune at 200 eV above each K-edge absorption edge). The storage ring was operated at 7.0 GeV and ring current was 65–100 mA.

We determined the thickness distribution function using only the Mn pre-edge. In this case the fluorescence effect is absent and the distribution function obtained for the Mn edge can be used for the Ni edge. The thick foil of the ordered $Ni_{50}Mn_{50}$ has a very asymmetric distribution with a small amount of pinholds (Fig. 5). The average thickness calculated for the sample of ordered $Ni_{50}Mn_{50}$ alloy is $\langle x \rangle = 23.1$ μm.

Coordination numbers for $Ni_{50}Mn_{50}$ alloy before and after correction are presented in Table III.

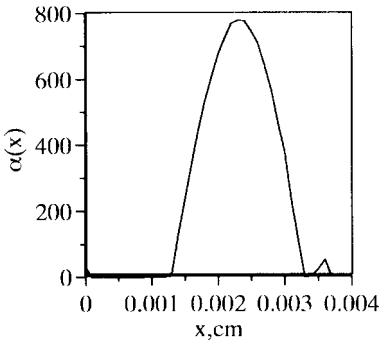

Fig. 5. Thickness distribution function for $Ni_{50}Mn_{50}$ alloy.

Table III. *Coordination numbers for first shell of $Ni_{50}Mn_{50}$ ordered alloy with and without the correction for the thickness inhomogeneity effect.*

	Ni–Ni	Ni–Mn	Mn–Ni	Mn–Mn
Before correction	0.17	7.06	6.98	−0.14
After correction	−0.14	8.16	8.16	−0.17
Model	0.00	8.00	8.00	0.00

Acknowledgements

Experiments performed at the PNC-CAT beamlines, APS are supported by a major facilities access grant from the Natural Sciences and Engineering Research Council Canada, the United States Department of Energy, Basic Energy Sciences. Offices of Science under Contract numbers W-31-109-Eng-38 (APS) and DE-FG03-97ER45628 (PNC-CAT).

References

1. Rose, M. E. and Shapiro, M. M., Phys. Rev. B **74**, 1853 (1948).
2. Parrat, L. G., Hempsted, C. F. and Jossem, E. I., Phys. Rev. **105**, 1228 (1957).
3. Heald, S. M. and Stern, E. A., Phys. Rev. B **16**, 5549 (1977).
4. Stern, E. A., Heald, S. M. and Bunker, B. A., Phys. Rev. Lett. **42**, 1372 (1979).
5. Rabe, P., Tolkiehn, G. and Werner, A., Nucl. Instrum. Meth. **171**, 329 (1980).
6. Stern, E. A. and Kim, K., Phys. Rev. B **23**, 3781 (1981).
7. Lu, K. Q. and Stern, E. A., Nucl. Instrum. Meth. **212**, 475 (1983).
8. Goulon, J., Goulon-Ginet, C., Cortes, R. and Dubois, J. M., J. Physique **43**, 539 (1982).
9. Ottaviano, L., Filipponi, A. and Di Cicco, A., Phys. Rev. B **49**, 11749 (1994).
10. Bausk, N. V., Erenburg, S. B. and Mazalov, L. N., J. Synchrot. Rad. **6**, 268 (1999).
11. Ryazhkin, A. V., Babanov, Yu. A. and Miyanaga, T., J. Synchrot. Rad. **8**(2), 291 (2001).
12. 'X-ray data booklet'. (editors A. C. Thompson and D. Vaughan), (LBNI., Univ. of Califoria. Second edition, January 2001).
13. Matz, W., Schell, N. *et al*., J. Synchrot. Rad. **6**, 1067 (1999).
14. Heald, S.M. *et al*., J. Synchrotron Radiation **6**, 347 (1999).

Physica Scripta. Vol. T115, 200–201, 2005

Improvement of Double-Shell *R*-Space Resolution by the EXAFS Regularization Method

Dong-Seok Yang[1,*] and Jay Min Lee[2]

[1]School of Science Education, Chungbuk National University, 361-763, Korea
[2]Beamline Research Division, Pohang Accelerator Laboratory, POSTECH, 790-784, Korea

Received June 26, 2003; accepted November 10, 2003

PACS number: 61.10.Ht

Abstract

We propose the chemical matched EXAFS regularization method through the numerical analysis of Mn K-edge EXAFS data for $La_{1-x}Ca_xMnO_3$ specimens. A relatively narrow k-space window ($k_{max} - k_{min} = 6\,Å^{-1}$) has been used to compute the Mn-O pair distribution function in the specific r-space range of 1.8–2.2 Å. Results show that the resolution in r-space is greatly improved in the pair distribution functions of the Mn-O bond. EXAFS data of specimens with double shell pair distributions were hardly analyzed by the conventional method because they are not resolved in the Fourier transform. A preliminary test of the EXAFS regularization method shows that this is very effective method to study the double shell distribution due to the Jahn Teller effect. The test was performed on $La_{1-x}Ca_xMnO_3$ at $x = 0.2$ and 0.3.

1. Introduction

Extended X-ray absorption fine structure (EXAFS) analysis [1] gives useful information on the local structure of solid atoms. However, the method fails to analyze the double-shell configuration in which the distribution of the first and the second nearest neighbor atoms are partially overlapped.

Recently, this situation appears in a practical application of the analysis of colossal magnetic resistance (CMR) materials. Mn ions in $La_{1-x}Ca_xMnO_3$ have three different bond distances, $R = 1.91$, 1.97 and 2.12 Å. It has been reported that manganese-oxide perovskites (e.g. La-A-MnO_3 where A = Ca, Sr, Pr, etc.) have the strong electron-lattice coupling effect and their structural features are known as the Jahn Teller distortion of Mn^{3+} ion [2, 3]. The conventional EXAFS has hardly explained this phenomenon.

As one method to overcome the limitation of the conventional EXAFS, a regularization method has been proposed. The regularization method uses matrix inversion instead of Fourier transform to extract r-space information such as the pair distribution function. Therefore, the method is free from the requirements of the large k- and r-space window in Fourier and inverse Fourier transforms, respectively. The details of this method are described in next section.

2. EXAFS regularization method

In previous work [4], simulation has shown that the regularization method is more flexible and useful to seek the r-space information directly from the pair distribution function (PDF). The EXAFS equation can be expressed by:

$$\chi(k) = \frac{NS_0^2(k)}{k} \int_0^\infty \frac{g(r)}{r^2} F(k,r)\, \mathrm{e}^{-2r/\lambda(k)} \sin(2kr + \varphi(k,r))\, \mathrm{d}r \tag{1}$$

where $g(r)$ is the pair distribution function, N is the coordination number, k is the photoelectron wave vector, $S_0^2(k)$ is the many-electron overlap factor, $\lambda(k)$ is the mean free path, r is the interatomic distance, $F(k,r)$ is the effective backscattering amplitude, and $\varphi(k,r)$ is the phase shift due to the atomic potentials.

Spectrum $\chi(k)$ is obtained from experimental data of $\mu(E)$, by specifying E_0 position and applying the proper background subtraction. The first-shell filtered spectrum $\chi_1(k)$ is extracted properly by the procedure of the Fourier and inverse Fourier transform of $\chi(k)$.

The EXAFS inversion problem implies how accurately $g(r)$ can be computed from $\chi_1(k)$. In a linear system, we can define the χ-vector as $\chi = \mathrm{A}^* g$, where A is an $(m \times n)$ matrix, and g is a column vector, i.e. PDF. More specifically, A is an r-to-k transformation matrix defined with chemical matching to the Mn-O shell in terms of r-dependent functions computed by theoretical FEFF code. Here, the solution for g is obtained by solving the "ill-posed" mathematical problem.

The resultant g in vector form can be determined by the following algebraic equation:

$$\left(\sum_m A^*_{mn} A_{mn} + \tau(\alpha + 2\gamma S^n) I + \beta \sum_m B^{mn} \right) g^n = \sum_m A^*_{mn} \chi^m \tag{2}$$

where $\tau = \Delta r / \Delta k$. Δr and Δk are the step sizes in the vectorized g^n and χ^m, respectively. S^n and B^{mn}-matrices are described in previous works [4, 5]. In this regularization method, the optimal values of the regularization parameter α, the smoothness parameter β and the positivity parameter γ are obtained by minimizing $\|\chi - A^* g\|^2$, and simultaneously $g(r)$ is rendered as smooth as possible.

In this study, both the chemical matched EXAFS regularization method and the improvement of r-space resolution are pursued. We selected the Mn-O bond configurations for $La_{1-x}Ca_xMnO_3$ specimens to make a comparison test between the data analysis result and the structural interpretation related to materials essence.

To test the r-space resolution for Mn-O distances, $\chi(k)$-spectra were confined in a relatively narrow k-range window, $[k_{min}, k_{max}]$, where $k_{max} - k_{min} = 6\,Å^{-1}$. In a general EXAFS fitting procedure, the number of independent variables is given by $N_{idp} = 1 + 2(k_{max} - k_{min})(R_{max} - R_{min})/\pi$. To investigate the closely spaced double-shell distances in 1.8–2.2 Å in PDF (apparently, 1–2 Å in FT), the general fitting algorithm requires that $N_{inp} > 6$. Moreover, the summation and the separation of the typical Gauss distribution are only applicable with a relatively small

*e-mail: dsyang@chungbuk.ac.kr

Debye-Waller factor and its cumulant expansion terms. Hence, unless the effective k-range is extended, the PDF interpretation is hardly solved by the general EXAFS fitting procedures such as FEFFIT or other kinds.

3. Results and Discussion

The EXAFS regularization program is coded with a fixed number of data points and a fixed data interval (Δk) in this work. The window size of the k-region selection was not adjustable, but the window positioning from the $k_{\min}$-position (the significant limit in the lower k region) was selectable. In our preliminary test with the specimens $La_{1-x}Ca_xMnO_3$ ($x = 0.2$ and 0.3), we gave an arbitrary variation in choosing an $k_{\min}$-position around 3.9 Å, which is the significant knot position of $\chi_1(k)$, filtered Mn-O spectrum by FT and inverse FT with parameters; $k_1 = 2.9\,\text{Å}^{-1}$, $k_2 = 12.0\,\text{Å}^{-1}$, $dk_1 = dk_2 = 0.6\,\text{Å}^{-1}$ (for the Hanning window), $k$weight = 3 for FT, and $r_1 = 0.95$ Å, $r_2 = 1.90$ Å, $dr_1 = dr_2 = 0.1$ Å for inverse FT. When the $k_{\min}$-position is chosen at a typical knot (3.9 Å), the computed PDF represents a relatively stable feature, but not irregularly valued into a negative background level. It is also necessary to tune the E_0-position between the experimental data and the theoretical FEFF calculation. Though our experience of combined k_1 and E_0 adjustment, we specify the best minimum condition, namely the typical regularization condition, by choosing $k_{\min} = 3.9\,\text{Å}^{-1}$ and $E_0 = 6548$ eV. ($E_0 = 6539$ eV was calibrated using Mn metal foil.) Thus, the k-range selection is $[3.9 \sim 9.9]\ \text{Å}^{-1}$. This typical regularization condition is useful for finding realistic PDF representations, corresponding to the typical window function with the starting $k_{\min}$-position as a knot-point reference.

By choosing this typical regularization condition, the PDF results are plotted in Fig. 1, illustrating the PDF characteristics on the two different specimens; (a) $La_{0.7}Ca_{0.3}MnO_3$ and (b) $La_{0.8}Ca_{0.2}MnO_3$, respectively. As demonstrated in Fig. 1, our typical regularization condition is very convincing because the derivative PDF feature with respect to the $k_{\min}$-variable illustrates the remarkably minimum variation characters at the k_1-knot.

First of all, it should be pointed out that the regularization method improves the r-space resolution significantly. The first-shell |FT| peak regime which is not displayed in this figure is broadly covering [1.0, 2.0] in k-space, and each peak is not separated. On the other hand, in part (b) of Fig. 1, the typical PDF (solid line) is an obvious feature to observe that there are at least two separable shells which are even merged or distributed in crossover resolution. In contrast, in part (a) of Fig. 1, the typical PDF (solid line) also represents the asymmetric PDF caused by two different merged shells. In both cases, Mn-O distances are attributed to the static or dynamic broadening of shell distributions due to the Jahn Teller effect [2, 3].

In summary, our preliminary test evaluating the chemical matched EXAFS regularization method and its application to the Mn-O bond characteristics associated with the Jahn Teller effect was successful enough to highlight that the r-space resolution can be improved significantly.

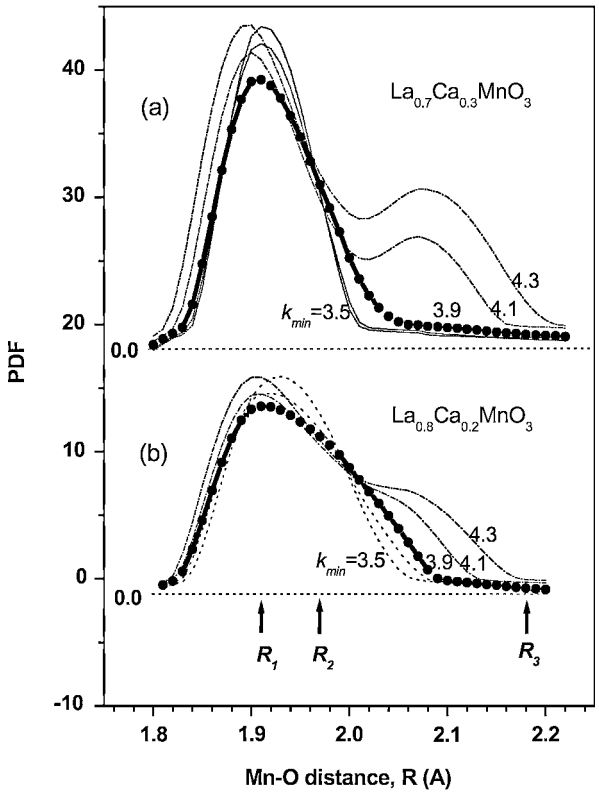

Fig. 1. Mn-O pair distribution function computed by the chemical matched regularization method. Comparisons are made for two specimens: (a) $La_{0.7}Ca_{0.3}MnO_3$ and (b) $La_{0.8}Ca_{0.2}MnO_3$. The typical regularization condition is given with k-range windowing from $k_{\min} = 3.9$ (at a knot-point reference). The $k_{\min}$-dependent variations are shown with dotted-line PDF curves, denoted by $k_{\min}$-value individually. Two regularized PDF plots with a shift of base line indicate a good r-space resolution for the case of double-shell crossover feature. The PDF as a function of r-space is compared with arrow-marked Mn-O distances, $R_1 = 1.91$ Å, $R_2 = 1.97$ Å and $R_3 = 2.18$ Å, as computed from the crystalline group *pbnm* of $LaMnO_3$.

Acknowledgments

Authors thank Dr. Alexander Ulyanov and Dr. Tae Young Koo who provided the samples and valuable discussions on $La_{0.7}Ca_{0.3}MnO_3$ and $La_{0.8}Ca_{0.2}MnO_3$, respectively. This work was partially supported by the Korean Research Foundation Grant (KRF-2001-005-D20010). Measurements at PLS were supported through the "X-ray-particle-beam Nano-characterization program" by the MOST and POSTECH foundation.

References

1. Sayers, D. E., Stern, E. A. and Lytle, F. W., Phys. Rev. Lett. **27**, 1204 (1971).
2. Lanzara, A. *et al.*, Phys. Rev. Lett. **81**, 878 (1998).
3. Song, J. H., Park, J. H., Lee, K.-B., Lee, J. M. and Jeong, Y. H., Phys. Rev. B **66**, 020407(R) (2002).
4. Yang, D. S. and Bunker, G., Phys. Rev. B **54**, 3169 (1996).
5. Babanov, Yu. A., Vasin, V. V., Ageev, A. L. and Ershov, N. V., Phys. Stat. Solidi B **105**, 747 (1981).

Physica Scripta. Vol. T115, 202–204, 2005

Improved Self-Absorption Correction for Fluorescence Measurements of Extended X-Ray Absorption Fine-Structure

C. H. Booth[1,*] and F. Bridges[2]

[1]Chemical Sciences Division, Lawrence Berkeley National Laboratory, Berkeley, California 94720, USA
[2]Physics Department, University of California, Santa Cruz, California 95064, USA

Received June 26, 2003; accepted November 4, 2003

PACS number: 61.10.Ht

Abstract

Extended X-ray absorption fine-structure (EXAFS) data collected in the fluorescence mode are susceptible to an apparent amplitude reduction due to the self-absorption of the fluorescing photon by the sample before it reaches a detector. Previous treatments have made the simplifying assumption that the effect of the EXAFS on the correction term is negligible, and that the samples are in the thick limit. We present a nearly exact treatment that can be applied for any sample thickness or concentration, and retains the EXAFS oscillations in the correction term.

Under ideal circumstances, such as a very dilute sample, the photoelectric part of the X-ray absorption coefficient, μ, is proportional to the number of fluorescence photons escaping the sample. However, in extended X-ray absorption fine-structure spectroscopy (EXAFS), the mean absorption depth changes with the energy of the incident photon, E, which changes the probability that the fluorescence photon will be reabsorbed by the sample. This self-absorption causes a reduction in the measured EXAFS oscillations, χ_{exp}, from the true χ, and hence needs to be included in any subsequent analysis.

Previous treatments [1–3] to correct for the self-absorption effect account for the change in depth due to the absorption edge and due to the smooth decrease in μ that follows, for instance, a Victoreen formula, and have been shown to be quite effective in certain limits. These treatments typically make two important assumptions. First, the so-called "thick limit" is used to eliminate the dependence on the actual sample thickness, limiting the applicability to thick, concentrated samples, such as single crystals. One exception is the work of Tan, Budnick and Heald [2], which makes a number of other assumptions to estimate the correction to the amplitude reduction factor, ${S_0}^2$, and to the Debye-Waller factors, σ^2's, rather than correcting the data in a model-independent way. A second assumption is that, in order to make the correction factor analytical, at one point in the calculation, the true absorption coefficients for the absorbing species and the whole sample are replaced with their average values; in other words, the modulating effect of χ on the correction factor is taken as very small. Below, we present a treatment that, with only one assumption that is nearly exact for all cases we have measured, corrects fluorescence EXAFS data directly in k-space for any concentration or thickness. This correction is demonstrated for a copper foil that is about one absorption-length thick, and is therefore not in the thick limit.

Figure 1 shows the geometry used in this calculation. The fluorescence yield at the point of absorption is proportional to the X-ray intensity I at that point and the fluorescence efficiency. The intensity I at a depth y is

$$I = I_0 \mathrm{e}^{-\mu(E)y}.$$

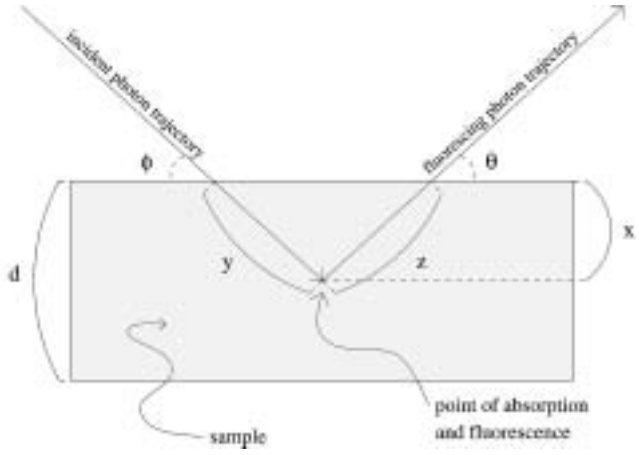

Fig. 1. Geometry used in calculating self-absorption correction in EXAFS.

The fluorescence photon then has to escape. The fluorescence flux from this point in the sample is then

$$I_f = I_0 \mathrm{e}^{-\mu(E)y} \mathrm{e}^{-\mu(E_f)z} \epsilon_a(E) \mu_a(E),$$

where $\mu_a(E)$ is the absorption due to the given core excitation of the absorbing atom, $\mu(E)$ is the total absorption, $\epsilon_a(E)$ is the fluorescence efficiency per unit solid angle, E is the incident beam energy, E_f is the energy of the fluorescing photon, and we're assuming that all the measured fluorescence is coming from the desired process (eg. Cu K_α, any other counts can be subtracted off).This equation is only true at a particular y and z, so we must integrate

$$\mathrm{d}I_f = I_0 \epsilon_a \mu_a \mathrm{e}^{-(\mu_T y + \mu_f z)} \, \mathrm{d}y.$$

Here the energy dependences are implicit and we have used $\mu_T = \mu(E)$ and $\mu_f = \mu(E_f)$. The variables z and y are dependent via $y \sin\phi = z \sin\theta = x$. Changing variables, we obtain

$$\mathrm{d}I_f = I_0 \epsilon_a \mu_a \frac{1}{\sin\phi} \mathrm{e}^{-(\frac{\mu_T}{\sin\phi} + \frac{\mu_f}{\sin\theta})x} \, \mathrm{d}x,$$

$$I_f = I_0 \epsilon_a \mu_a \frac{1}{\sin\phi} \int_0^d \mathrm{e}^{-(\frac{\mu_T}{\sin\phi} + \frac{\mu_f}{\sin\theta})x} \, \mathrm{d}x,$$

$$I_f = \frac{I_0 \epsilon_a \mu_a}{\mu_T + g\mu_f} \left[1 - \mathrm{e}^{-(\frac{\mu_T}{\sin\phi} + \frac{\mu_f}{\sin\theta})d}\right], \tag{1}$$

where $g \equiv \sin\phi / \sin\theta$. Eq. (1) describes the fluorescence in the direction given by θ. At this point one should integrate over the detector's solid angle. Ignoring this integral can affect the final obtained correction [4], especially for glancing-emergent

*Electronic address: chbooth@lbl.gov

angle experiments. However, for detector geometries where $\phi + \theta = 90^\circ$, we find the maximum error in g is on the order of $\sim$7% even for $\Delta\theta \approx 5^\circ$ at $\theta = 10^\circ$. For more severe geometries, the solid angle should considered, but for the following, we ignore this correction.

In EXAFS measurements, we want

$$\chi = \frac{\mu_a - \bar{\mu}_a}{\bar{\mu}_a},$$

but what we actually obtain experimentally is

$$\chi_{exp} = \frac{I_f - \bar{I}_f}{\bar{I}_f},$$

where $\bar{I}_f$ is the spline function fit to the data to simulate the "embedded atom" background fluorescence (roughly I_f without the EXAFS oscillations). Now make the following substitutions:

$$\mu_T = \bar{\mu}_T + \chi\bar{\mu}_a,$$

$$\mu_a = (\chi + 1)\bar{\mu}_a,$$

$$\mu_T - \bar{\mu}_T = \mu_a - \bar{\mu}_a.$$

These equations and Eq. (1) are then plugged into χ_{exp}:

$$1 + \chi_{exp} = \frac{\mu_a(\bar{\mu}_T + g\mu_f)[1 - \mathrm{e}^{-(\frac{\mu_T}{\sin\phi} + \frac{\mu_f}{\sin\theta})d}]}{\bar{\mu}_a(\mu_T + g\mu_f)[1 - \mathrm{e}^{-(\frac{\bar{\mu}_T}{\sin\phi} + \frac{\mu_f}{\sin\theta})d}]}.$$

Dividing by $1 + \chi$ and defining $\alpha \equiv \bar{\mu}_T + g\mu_f$, we get:

$$\frac{1 + \chi_{exp}}{1 + \chi} = \frac{[1 - \mathrm{e}^{-(\bar{\mu}_T + \chi\bar{\mu}_a + g\mu_f)\frac{d}{\sin\phi}}]\alpha}{(\alpha + \chi\bar{\mu}_a)[1 - \mathrm{e}^{-\frac{\alpha d}{\sin\phi}}]}.$$

Now χ_{exp} can be written in terms of the actual χ:

$$\chi_{exp} = \left[\frac{1 - \mathrm{e}^{-(\alpha + \chi\bar{\mu}_a)\frac{d}{\sin\phi}}}{1 - \mathrm{e}^{-\frac{\alpha d}{\sin\phi}}}\right]\left[\frac{\alpha(\chi + 1)}{\alpha + \chi\bar{\mu}_a}\right] - 1. \quad (2)$$

At this point in the calculation, the relation between χ and χ_{exp} is exact. However, we need χ in terms of χ_{exp}, and Eq. (2) is for χ_{exp} in terms of χ. In order to invert Eq. (2), we make a simple approximation. Assuming that

$$\frac{\chi\bar{\mu}_a d}{\sin\phi} \ll 1$$

we can say

$$1 - \mathrm{e}^{-(\alpha + \chi\bar{\mu}_a)\frac{d}{\sin\phi}} \sim 1 - \mathrm{e}^{-\frac{\alpha d}{\sin\phi}}\left(1 - \frac{\chi\bar{\mu}_a d}{\sin\phi}\right). \quad (3)$$

This approximation gets worse with large χ and $\bar{\mu}_a$. It also has a maximum for both ϕ and d, because of the $\mathrm{e}^{-(\alpha d)/(\sin\phi)}$ term. Plugging in some typical numbers from the Cu K-edge of $YBa_2Cu_3O_7$ ($\phi = 10^\circ$, $\bar{\mu}_T = 1284\,\mathrm{cm}^{-1}$, $\mu_F = 1115\,\mathrm{cm}^{-1}$, $\bar{\mu}_a = 462\,\mathrm{cm}^{-1}$ and $\chi = 0.5$) the maximum error is $\sim$0.7% at a thickness of $\sim$1.9 μm. Such a high value of χ does not actually occur in YBCO. Indeed, such a high χ is rare. In any case, various combinations of the above parameters can conspire to produce errors above 1%, so the approximation should be monitored when making the corrections outlined below.

With the above approximation, and defining the following quantities:

$$\beta = \frac{\bar{\mu}_a d\alpha}{\sin\phi}\mathrm{e}^{-\frac{\alpha d}{\sin\phi}}, \quad \gamma = 1 - \mathrm{e}^{-\frac{\alpha d}{\sin\phi}},$$

Eq. (2) is reduced to a quadratic equation in χ and we can finally write the full correction formula:

$$\chi = \frac{-[\gamma(\alpha - \bar{\mu}_a(\chi_{exp} + 1)) + \beta] + \sqrt{[\gamma(\alpha - \bar{\mu}_a(\chi_{exp} + 1)) + \beta]^2 + 4\alpha\beta\gamma\chi_{exp}}}{2\beta}, \quad (4)$$

where the sign of the square root was determined by taking the thick or thin limits. In the thick limit ($d \to \infty$), Eq. (4) gives:

$$\chi = \frac{\chi_{exp}}{1 - \frac{\bar{\mu}}{\alpha}\chi_{exp} - \frac{\bar{\mu}_a}{\alpha}},$$

which is the same as that calculated in Ref. [3] without the χ_{exp} term in the denominator. In the thin limit, it can be shown that Eq. (4) reduces to $\chi = \chi_{exp}$ as expected.

We performed an experiment on a copper foil to demonstrate the correction. Cu K-edge data were collected both in the transmission mode and in the fluorescence mode using a 32-element Canberra germanium detector on beam line 11-2 at the Stanford Synchrotron Radiation Laboratory (SSRL). The transmission data were checked for pinhole effects (found to be negligible) and the fluroscence data were corrected for dead time. The sample thickness was estimated to be 4.6 μm from the absorption step at the edge, and was oriented such that $\phi = 49.4 \pm 0.5^\circ$. The thickness is about 25% of the estimated thick-limit thickness. The data were reduced to k-space using the RSXAP analysis program REDUCE [5–7], which incorporate these corrections. Figure 2 shows the correction factor (χ/χ_{exp}) for these data. The error in the approximation in Eq. (3) exceeds 2% only below $\sim$1.6 Å^{-1}. The total correction in the thick limit is much larger (about 3 times the displayed correction). As shown in Fig. 3, the corrected fluorescence data in k-space are remarkably similar to the transmission data, despite the large magnitude of the correction.

Although only a copper foil is reported as an example, we have successfully applied this correction to a wide range of oxides and intermetallics, including single crystals and thin films [8–12]. The ability to correct for intermediate film thicknesses is, in fact, crucial for studying films thinner than $\sim$20 μm thick.

In summary, we have provided an improved self-absorption correction for EXAFS data that operates at any sample thickness

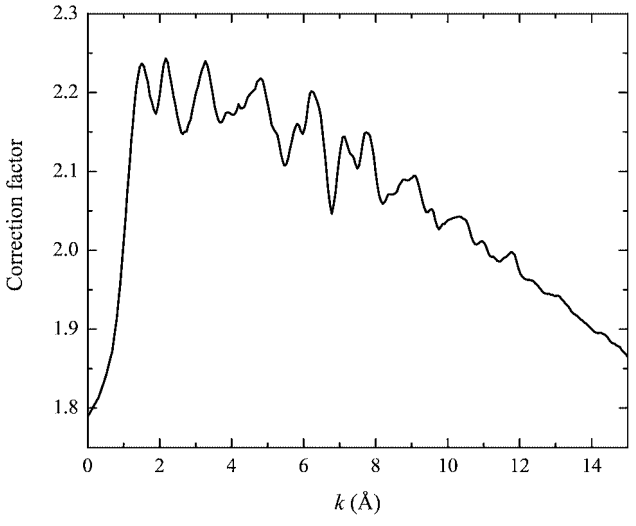

Fig. 2. Correction term χ/χ_{exp} given by Eq. (4) for Cu K-edge absorption data from a 4.6 μm-thick copper foil at $\phi = 49.4^\circ$.

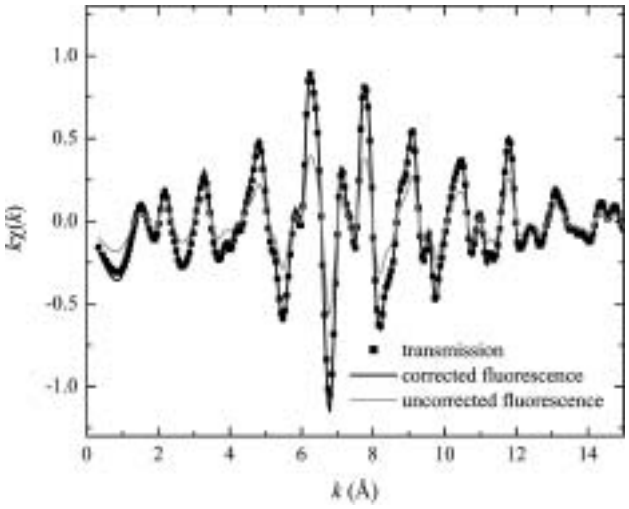

Fig. 3. Corrected EXAFS data in k-space for the copper foil data, compared to transmission data and uncorrected fluorescence data. Note that the corrected data are difficult to discern on top of the transmission data.

or concentration. Our example of a pure copper foil demonstrates both the accuracy of the correction and that, for concentrated samples, the correction can be surprisingly large. Moreover, for well-ordered materials, χ can have a surprisingly large effect.

Acknowledgments

The work of CHB was supported by the Director, Office of Science, Office of Basic Energy Sciences (OBES), Chemical Sciences, Geosciences and Biosciences Division, U.S. Department of Energy (DOE) under Contract No. AC03-76SF00098. The work of FB was supported in part by National Science Foundation grant DMR 0301971. EXAFS data were collected at SSRL, a national user facility operated by Stanford University on behalf of the DOE/OBES.

References

1. Goulon, J., Goulon-Ginet, C., Cortes, R. and Dubois, J. M., J. Physique **43**, 539 (1982).
2. Tan, Z., Budnick, J. I. and Heald, S. M., Rev. Sci. Instrum. **60**, 1021 (1989).
3. Tröger, L. *et al.*, Phys. Rev. B **46**, 3283 (1992).
4. Brewe, D. L., Pease, D. M. and Budnick, J. I., Phys. Rev. B **50**, 9025 (1994).
5. Hayes, T. M. and Boyce, J. B., in "Solid State Physics," (edited by H. Ehrenreich, F. Seitz and D. Turnbull), (Academic, New York, 1982), vol. 37, p. 173.
6. Li, G. G., Bridges, F. and Booth, C. H., Phys. Rev. B **52**, 6332 (1995).
7. http://lise.lbl.gov/RSXAP/.
8. Booth, C. H. *et al.*, Phys. Rev. B **54**, 9542 (1996).
9. Ren, J. Z. *et al.*, J. Appl. Phys. **83**, 7613 (1998).
10. Mannella, N. *et al.*, Phys. Rev. Lett. **92**, 166401 (2004).
11. Booth, C. H., Shlyk, L., Nenkov, K., Huber, J. G. and De Long, L. E., Phys. Rev. B **69**, 104430 (2004).
12. Cao, D., Bridges, F., Worledge, D. C., Booth, C. H. and Geballe, T., Phys. Rev. B **61**, 11373 (2000).

Physica Scripta. Vol. T115, 205–206, 2005

REX2000: Yet Another XAFS Analysis Package

T. Taguchi[1,*], T. Ozawa[1] and H. Yashiro[2]

[1]XRD-division, Rigaku Corporation, 3-9-12 Matsubara-cho, Akishima-shi, Tokyo 196-8666, Japan
[2]Application Laboratory, Rigaku Corporation, 3-9-12 Matsubara-cho, Akishima-shi, Tokyo 196-8666, Japan

Received June 26, 2003; accepted January 30, 2004

Abstract

Today a lot of XAFS analysis software is available either free of charge, licensed or commercially. The list of the programs can be found on web sites (IXS web site display 35 programs and ESRF web site displays 23) and there are many XAFS analysis softwares not on such lists yet. We describe recent progress of the latest version of the REX2000 XAFS analysis package. The REX2000 run on MS-Windows family operating system, and is an entirely new package with user-friendly interface and simple operation. The package provides many classic DATA reduction methods for EXAFS and XANES. All the parameters needed for DATA analysis can be set on graphics windows as well as numerical input. The package also has FEFF interface for multiple scattering capability.

1. Introduction

The original version of Rigaku EXAFS analysis package (REX) was established in 1990. It ran on NEC's 16 bits personal computer PC-9800 series. The MS-DOS for PC-9800 is the Japan localized version. Neither the hardware nor the software were compatible with regular MS-DOS (or IBM-DOS). Therefore the program was modified shortly after the initial release so that it runs on IBM PC/AT compatible machines. The program was developed with collaboration of Prof. Kuroda's group (The University of Tokyo) and the data reduction algorithm was referred to their mainframe program EXAFS1 [1], but the source code was independent.

This program had been modified since then and eventually transferred to the Microsoft Windows platform in 2000. The windows version REX is named REX2000 and has presently been distributed in more than 80 sets.

2. EXAFS DATA reduction

REX2000 consists of 8 programs. They are named: "EXAFS", "Reference", "RATIO", "FEFF", "XANES", "Simulation", "multi-plot" and "DATA Editorial". The "EXAFS" program carries out ordinary EXAFS data reduction [2, 3, 4]. Several ways of data processing are provided in each step. For instance, linear to 6th order polynominal functions as well as ordinary Victoreen extrapolation (with and without constant) can be used for background subtraction. The EXAFS oscillation extraction method advocated by Cook and Sayers [5] is well implemented and successfully extracts the fine structure for most cases with default parameter sets (Fig. 1). The range or node point can be set either by clicking mouse pointer on the plotted data or by input energy values in the parameter window. After extracting the EXAFS oscillation, fast Fourier transformation is applied and the pair distribution function is obtained. Then non-linear least square curve fitting is performed to minimize the sum of the residuals, Δ;

$$\Delta = \sum (k^n \chi_{obs}(k) - k^n \chi_{calc}(k) / k^n \chi_{obs}(k))^2. \quad (1)$$

Up to 10 shells can be fitted at the same time. All the parameters and method used for the data reduction can be saved in a file and used for other data reductions to minimize uncertainty. The "Reference" program extracts the empirical backscattering amplitude and phase shift out of reference sample data for which the crystallographic structure is already known. Then those parameters are used for the fit and sometimes gives a more accurate result than using theoretical parameters.

FEFF [6, 7] developed by Professor Rehr's group is a program calculating XAFS spectra considering ab initio multiple scattering effects and is widely used in many XAFS analysis software. Although REX2000 employs theoretical tables calculated by McKale *et al*. [8] as default parameters for backscattering amplitude and phase shift, FEFF tables [9] can be alternatively used. Furthermore the parameters calculated by FEFF software can be used for a curve fit. There are two ways doing that. One is using chi.dat (one of output files of FEFF code) as measured data. The chi.dat is treated as reference data and empirical parameters are extracted in the same manner as the standard sample. The other way is using FEFFnnnn.dat. FEFFnnnn.dat is intermediate products of a FEFF calculation and it contains both backscattering amplitude and phase shift of a specific path. REX2000 can extract and use those parameters for a curve fit. One of the minor problems using FEFF stand-alone would be its interface. Because FEFF is FORTRAN program running on command line, it does not have a graphical user interface. REX2000 provides a graphical user interface for FEFF version 6, 7 and 8. The REX2000's FEFF dialog makes it easy for users to select many options just by clicking on a button. Making a model structure is another troublesome process for a FEFF calculation. A wizard style program to make crystallographic structure is available. An input file for atoms [10] can also obtained easily from the metal data file (CRYSTMET) according to the collaboration with the Tosh Information Systems Inc [11].

3. XANES analysis

The DATA reduction procedure for EXAFS is well established and standardized, but the DATA reduction of XANES spectra is not standardized yet because of the complexity of the phenomenon. REX2000 provides two DATA reduction tools, which are fairly popular for XANES analysis. One is spectrum fit and the other is peak deconvolution. An XANES spectrum of a mixture can be expressed as a linear sum of standard XANES spectra, the tools for background subtraction, normalization and linear least square fit of summed spectrum are provided. The most common numerical approach for quantitive analysis of XANES is to deconvolute the spectrum into Lorentzian functions and an arctangent function, which is the contribution of the continuum state [12]. REX2000 offers the tools for the deconvolution.

*e-mail: takey@rigaku.co.jp

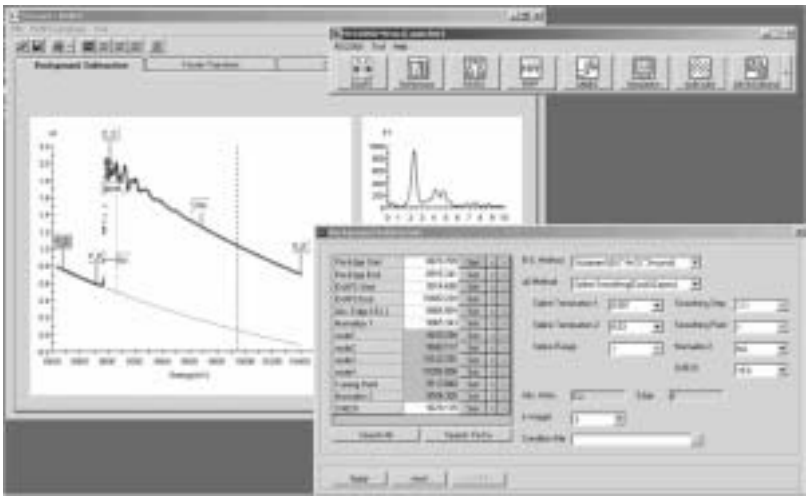

Fig. 1. EXAFS data reduction window.

4. Extra features

DATA conversion function is separated from the main program in order to cope with many different DATA format. The most recently added feature is multi-element Solid State Detector (SSD) DATA conversion with dead time correction. A nineteen-element SSD system for fluorescent XAFS experiments has been installed in the Photon Factory [13]. Although it is a powerful tool for characterization of very thin film and diluted system, summing up the output signals out of many elements is troublesome task. Moreover the output signals from the 19 elements are not always all usable. For instance, in the case of total reflection fluorescence XAFS, some elements are physically in a shadow region and only output background noise, and some elements might contain undesired diffraction peak(s). Summing up such signals spoils the DATA and can lead to incorrect conclusion. The REX2000 data conversion procedure for 19 elements SSD provides a visual interface to select the useful output, apply dead time correction if necessary and sum them up.

A procedure of error estimation for XAFS data analysis has been discussed for a long time, but no definite way of obtaining errors is established. Then we follow the recommendation of IXS Standards and Criteria Committee [14]. We assume the uncertainty of the j-th independent parameter P_j as

$$\mathrm{d}P_j = \sqrt{C_{jj}} \tag{2}$$

where C_{jj} is the j-th diagonal element of the covariance matrix used for the fit.

5. Conclusions

The latest version of REX2000 offers many useful features for XAFS analysis. Its intuitive interface helps simple analysis for a novice and a lot of options makes complicated analyses possible for an experienced user.

Acknowledgements

We would like to thank Professor Kuroda for his initial guidance and Professor Asakura for his advice for the recent improvements of this software.

References

1. Kosugi, N. and Kuroda, H., Program EXAFS 1, Research Center for Spectrochemistry, the University of Tokyo, (1985).
2. Iwasawa, Y. ed., "X-ray Absorption Fine Structure for Catalysts and Surfaces", (World Scientific, 1996), 33–58.
3. Teo, B. K., EXAFS: Basic Principles and Data Analysis, (Springer Verlag, New York, 1986).
4. Konigsberger, D. C. and Prins, R., "X-ray Absorption: Principles, Applications, Techniques of EXAFS, SEXAFS and XANES, Chemical Analysis", 92, (John Wiley & Sons, 1988), 211–252.
5. Cook, J. W. and Sayers, D. E., J. Appl. Phys. **52**, 5024 (1981).
6. Ankudinov, A. L. and Rehr, J. J., Phys. Rev. **B56**, R1712 (1997).
7. Ankudinov, A. L., Ravel, B., Rehr, J. J. and Conradson, S. D., Phys. Rev. **B58**, 7565 (1998).
8. McKale, A. D., Veal, B. W., Pailikas, A. P., Chan, C. K. and Knapp, G. S., J. Am. Chem. Soc. **110**, 3764 (1988).
9. Rehr, J. J., Mustre de Leon, J., Zabinsky, S. I. and Albers, R. C., J. Am. Chem. Soc. **113**, 5135 (1991).
10. Ravel, B., J. Synchrotron Rad. **8**, 314 (2001).
11. Taguchi, T. and White, Acta Cryst. **B58**, 358 (2002).
12. Stohr, J., "NEXAFS Spectroscopy", (Springer, 1992), 222–238.
13. Nomura, M., "Design and performance of a multi-element SSD for fluorescent XAFS", KEK Report **98-4**, (1998).
14. "Error Reporting Recommendations: A Report of the Standards and Criteria Committee", on IXS web site, (2000).

Physica Scripta. Vol. T115, 207–211, 2005

Final-State Rule vs the Bethe-Salpeter Equation for Deep-Core X-ray Absorption Spectra*

J. J. Rehr,[1] J. A. Soininen[1,2] and E. L. Shirley[2]

[1]Department of Physics, Box 351560, University of Washington, Seattle, WA 98195, USA
[2]Optical Technology Division, Physics Laboratory, National Institute of Standards Technology, Gaithersburg, MD 20899-8441, USA

Received June 26, 2003; revised July 30, 2003; accepted November 4, 2003

Abstract

The independent-electron approximation together with the final-state rule provides a well established method for calculating X-ray absorption spectra that takes into account both core-hole effects and inelastic losses. Recently a Bethe-Salpeter Equation approach based on Hedin's GW approximation that explicitly treats particle-hole excitations has been applied to the same problem. We discuss here the formal relationships between these approaches for deep-core X-ray spectra and show that they are similar, apart from differences in their practical implementations. Their similarity is illustrated with results from both theoretical approaches and compared with experiment. This comparison also suggests ways to improve both approaches.

1. Introduction

The question of how to treat the core-hole effects in X-ray absorption spectra (XAS) has long been unsettled. Within the independent-electron approximation, the core hole is often treated within the "final-state rule," (FSR) i.e., the one-electron Golden rule with final-state potentials calculated in the presence of a fully relaxed core hole. This approach provides a well established and efficient method for calculating X-ray absorption spectra and also includes electron damping effects by virtue of a complex electron self-energy [1]. More detailed treatments of the core-hole interaction require approximations that go beyond the independent-electron approximation. For example, a two-particle Bethe-Salpeter Equation (BSE) approach has recently been applied to XAS [2]. This approach explicitly treats particle-hole excitations and includes a self-energy based on Hedin's GW approximation (*GWA*) [3]. Simpler approximations have also been proposed. For example, one-electron methods that treat the core hole with various *ad hoc* approximations include the "$Z + 1$" [4], and "transition state" [5] approaches. Also, approximate methods that go beyond the independent electron model include time-dependent density-functional theory (TDDFT) [6–8]. In this paper, we discuss the formal relationships between these various approaches for calculations of deep core XAS. We show that the BSE for deep-core XAS and FSR are closely similar, apart from differences in their practical implementations. Their similarities help explain the numerical agreement often observed in calculations. Their formal differences rest largely in the treatments of local-field effects and exchange. These differences help explain why the effect of the core-hole varies from case to case, and also suggest how these approaches can be improved. Results from these theoretical approaches are compared with experimental near-edge spectra to illustrate these findings. We also discuss how additional many-body effects such as intrinsic losses and edge singularities can be included.

2. Final-State Rule

The final-state rule (FSR) was introduced by von Barth and Grossmann [9] for model, many-body treatments of XAS. The rule states that the X-ray absorption spectra $\mu'(\omega)$ is given to a good approximation by a one-electron Fermi Golden rule expression

$$\mu'(\omega) \sim \sum_f \left|\langle \psi'_f \,|d|\, \psi_i\rangle\right|^2 \delta_\Gamma(E_f - E_i - \hbar\omega), \tag{1}$$

where ψ'_f denotes a *final state* wave function calculated self-consistently in the presence of a static core hole with wave function ψ_i, and δ_Γ is a Lorentzian of with a width Γ determined by the core-hole lifetime. Here and elsewhere we use a prime to denote quantities calculated in the presence of a core hole. The matrix element involves the dipole-transition operator $d = \hat{\boldsymbol{\epsilon}} \cdot \vec{\boldsymbol{r}}$ coupling the electrons to the X-ray field.

Because of its computational efficiency, the FSR approach is often used in practical calculations [1, 10], and typically leads to good agreement with experiment for deep core-hole XAS. The FSR can be understood heuristically from the ΔSCF approximation in which the many-body final and initial states of the system are taken to be Slater determinants and non-orthogonality effects are ignored. Nevertheless, the validity of the FSR and other one-electron approaches has remained questionable, because many-body effects beyond the one-electron approximation are neglected. Indeed "failures" of the rule have sometimes been observed where core-hole effects are significantly suppressed [7].

Recently, however, the final-state rule has emerged as the leading term in a "quasi-boson model" for XAS [11]. This formulation encompasses a many-body treatment of X-ray absorption in terms of convolution of $\mu'(\omega)$ and an energy-dependent spectral function $A(\omega, \omega')$,

$$\mu(\omega) = \int \mathrm{d}\omega' A(\omega, \omega')\mu'(\omega). \tag{2}$$

The spectral function also includes satellite terms which account for inelastic intrinsic losses (e.g., multi-electron excitations) and interference effects beyond the quasiparticle approximation. The quasi-boson model also explains how edge-singularities can be incorporated in the theory [11]. The above convolution shows that the main effect of the satellite excitations is an additional broadening, which has been shown to be small near threshold.

Within the FSR a precise statement of the final state rule is given by a quasiparticle model that incorporates the core hole. That is, the the final states $|\psi'_f\rangle$ are scattering states which satisfy the Dyson equation,

$$h'\psi'_f = E_f\psi'_f, \tag{3}$$

$$h' = \frac{p^2}{2m} + V'_C + \Sigma'(E_f). \tag{4}$$

Here h' denotes the lossy quasiparticle final-state Hamiltonian for an excited state with energy E_f and a core-hole in state ψ_i.

V_C' is the final-state Coulomb potential, and $\Sigma'(E_f)$ is the complex self-energy operator, which is also primed in Eq. (4) to remind one that the self-energy should be evaluated in the core-excited state. In practice, the self-energy operator $\Sigma(E) \approx iGW$ is usually calculated within the GWA, where $G(E)$ is the one-particle Green's function and $W(\omega) = \epsilon^{-1}(\omega)v$ is the screened Coulomb interaction, $\epsilon^{-1}(\omega)$ being the inverse dielectric matrix, and $v = 1/|\vec{r} - \vec{r}'|$, the Coulomb interaction. Also, although the self-energy is formally a non-local operator, local-density approximations are often used in practice [12].

Thus calculations of X-ray absorption spectra within the FSR require the one-particle excited-state electronic structure and a final-state Coulomb potential $V_C' = V_C + \Delta V_C$. We have used V_C to represent the total Coulomb potential in the ground state, i.e., it has contributions from the ions as well as the electrons, and ΔV_C is the change in the Coulomb potential due to the core-hole, including screening by relaxation of the electrons.

Note that the quasiparticle Hamiltonian is non-Hermitian; this implies the existence of inelastic mean free paths $\lambda \approx p/|\mathrm{Im}\Sigma'(E)|$ which are typically between 5 Å and 20 Å. Moreover, there are systematic shifts in the spectral peak positions which affect the E-vs-p dispersion relation, $E_p = p^2/2m + |\mathrm{Re}\Sigma'(E_p)|$ and, concomitantly, the excitation spectra.

3. Bethe-Salpeter Equation

Another many-body approach for calculating XAS which explicitly treats particle-hole excitations is the Bethe-Salpeter equation (BSE). A practical approximation to the BSE based on the GWA has been derived from many-body perturbation theory [13], and has been implemented in various ways [2, 14, 15]. An important ingredient in the BSE is the quasiparticle approximation, with a self-energy based on GWA. In this approach the intrinsic and extrinsic losses are approximated by quasiparticle lifetimes, and dynamic interference effects and inelastic satellite excitations are ignored, an approximation which is reasonable close to an absorption edge. Here we follow the treatment of Soininen and Shirley [2] and adapt the discussion specifically for deep core-hole states. In their approach, the particle-hole basis states are represented as

$$\Phi(\vec{r},\vec{r}') = \sum_{ki} C_{ki}\phi_k(\vec{r})\frac{1}{N^{1/2}}\sum_{\vec{R}}\chi^*_{i,\vec{R}}(\vec{r}') \times \exp[-\mathrm{i}(\vec{k}-\vec{q})\cdot\vec{R}], \quad (5)$$

where e.g., in crystals, $k \equiv n\vec{k}$ denotes a band index and Bloch wave number of the final state, and i denotes the quantum numbers of the initial core level. Here $\phi_k(\vec{r})$ is a Bloch function and $\chi_{i,\vec{R}}(\vec{r}')$ is a core-level wave function in the unit cell associated with lattice vector $\vec{R}$. These quasiparticle states are, in principle, eigenfunctions of the GW Hamiltonian,

$$h = \frac{p^2}{2m} + V_C + \Sigma(E), \quad (6)$$

but ground-state wave functions can provide a good approximation in practice, and the excitation energies are corrected for self-energy effects. The electron and hole coordinates are respectively denoted by $\vec{r}$ and $\vec{r}'$. The vector $\vec{q}$ is the momentum of the excitation. This is the incident photon momentum in XAS, but modest revisions of the approaches discussed here allow one to study inelastic electron and X-ray scattering. N is the number of unit cells in the crystal, and the electron and hole wave functions in each pair state are properly normalized when integrated over the entire crystal. The excitation energies E_λ are the solutions of a coupled, electron-hole equation of motion,

$$H_{\mathrm{eff}}\Phi_\lambda = E_\lambda\Phi_\lambda, \quad (7)$$

$$H_{\mathrm{eff}} = \hat{H}_0 + \hat{V}_D + \hat{V}_X. \quad (8)$$

Here $\hat{H}_0$ denotes the Hamiltonian for the single-particle terms. The operator $\hat{V}_D$ accounts for the direct, screened electron-core hole attraction involving the screened Coulomb interaction $W(\omega)$. Usually the static limit $W(\omega = 0)$ is used in practice [2]. The corresponding exchange term $\hat{V}_X$ is unscreened. Instead of solving the eigenvalue problem of Eq. (7) it is usually easier to calculate the spectra in a continued fraction form as done for example in Ref. [2, 16]. There the matrix elements of H_{eff} are taken to be

$$\langle ki|H_{\mathrm{eff}}|k'i'\rangle = (E_k - E_i)\delta_{kk'}\delta_{ii'} + \langle k|V_D(i) + V_X(i)|k'\rangle\delta_{ii'}, \quad (9)$$

where $E_k = \epsilon_k + \Sigma(E_k)$ denotes the GWA quasiparticle energies.

Clearly static screening of a core-hole reduces its effect. Also the exchange term has an opposite sign from the direct term giving a further reduction. For these reasons the net effect of the core-hole can be substantially reduced. This explains why sometimes transition-state (i.e., calculations with 1/2 a core hole) or even "initial-state rule" (i.e., with the ground state Hamiltonian of the initial state with no hole) calculations are reasonable, especially in cases with strong screening.

The BSE is usually more computationally demanding than the FSR, due to the need for a much larger particle-hole basis and also a calculation of the inverse dielectric matrix ϵ^{-1}. However, the above formulation of the BSE is efficient for calculations in crystals with band-structure techniques, because a super-cell approach is not needed. Single-particle wave functions can be calculated to high accuracy, and self-energy effects can be included, including real shifts in band energies and lifetime damping effects.

The TDDFT approach for XAS is similar in several respects to the BSE [15]. For example, within TDDFT the term $\hat{V}_X$ is similar to that in the BSE. However, instead of $\hat{V}_D$, the analogous term in the TDDFT is the exchange-correlation kernel $f_{xc}(\omega)$, which in the local-density approximation is density-dependent and derived from the ground state exchange-correlation potential. Also the, particle-hole basis states are taken to be eigenstates of the ground-state density-functional Hamiltonian. For these reasons, the treatments of the screened core-hole interaction and inelastic losses are obscured in the TDDFT approach with local kernels.

4. Deep Core Level XAS

Let us now consider the XAS from a deep core level i that is static and structureless, e.g., in a K-shell of a sufficiently heavy atom. In the BSE with the approximations discussed above, the Golden rule for XAS can be expressed as a particle-hole resolvent,

$$\mu(\omega) = -\frac{1}{\pi}\mathrm{Im}\left\langle 0\left| d^\dagger \frac{1}{\omega - H_{\mathrm{eff}} + \mathrm{i}\Gamma} d\right| 0\right\rangle, \quad (10)$$

where d is the dipole operator, and where we have included the core-hole lifetime Γ. For a sufficiently deep core level, this yields

$$\mu(\omega) = -\frac{1}{\pi}\mathrm{Im}\sum_{kk'}\langle i\,|d^\dagger|\,k\rangle\left\langle ki\left|\frac{1}{\omega - H_{\mathrm{eff}} + \mathrm{i}\Gamma}\right|k'i\right\rangle\langle k'|d|i\rangle,$$

$$\approx -\frac{1}{\pi}\mathrm{Im}\sum_{kk'}M^*_{ik}\left\langle k\left|\frac{1}{\omega - h'_{\mathrm{eff}} + E_i + \mathrm{i}\Gamma}\right|k'\right\rangle M_{ik'}, \quad (11)$$

where $M_{ik'} = \langle k'|d|i\rangle$ is a one-particle matrix element, and h'_{eff} is an effective single-particle Hamiltonian derived from the BSE for a given core hole level i,

$$h'_{\mathrm{eff}} = h + V_D(i) + V_X(i). \quad (12)$$

Clearly h'_{eff} is analogous to the quasiparticle final state Hamiltonian h' in the FSR. In particular, the first term h is the quasiparticle Hamiltonian of Eq. (6) for single-particle excitations with $E = \omega + E_i$.

In the treatment of Soininen and Shirley the direct interaction $V_D(i)$ is calculated by static linear response, giving rise to the real-space potential,

$$V_D(\vec{r}) = \int \mathrm{d}^3r' W(\vec{r},\vec{r}';\omega = 0)$$

$$\times\ \frac{1}{N}\sum_{\vec{R}}|\chi^*_{i,\vec{R}}(\vec{r}')|^2\exp[-\mathrm{i}(\vec{k}-\vec{q})\cdot\vec{R}]$$

$$\equiv V_i(\vec{r}) + V_{\mathrm{ind}}(\vec{r}), \quad (13)$$

where $V_i(\vec{r})$ is the bare core-hole potential, and the induced potential from the valence electrons that screen the core hole is

$$V_{\mathrm{ind}}(\vec{r}) = \int \mathrm{d}^3r'[\epsilon^{-1}(\vec{r},\vec{r}';\omega = 0) - \delta(\vec{r}-\vec{r}')]V_i(\vec{r}'). \quad (14)$$

This is a good approximation, since the valence-electron screening is well described by linear response [2]. The corresponding exchange term involves the *unscreened* Coulomb matrix element

$$\langle k|V_X(i)|k'\rangle = \langle ki|v|ik'\rangle. \quad (15)$$

What above are (for simplicity) written as matrix elements of $V_D(i)$ and $V_X(i)$ between Bloch states are actually two-particle matrix elements between pair states in which the electron and core hole carry a net total crystal momentum of $\vec{q}$. Such a matrix element is equivalent to N times the matrix element for a Bloch wave scattered from a core-hole potential in each unit cell scaled by a factor of $1/N$. The factor $1/N$ arises because of normalization of the Bloch sum of atomic core-state wave functions in each pair state. The factor of N accounts for coherent summation over all units cells when computing the two-particle matrix element. This assumes that core-level wave functions on different sites are non-overlapping, which should be a very good approximation. Consequently, the effective matrix elements can be expressed as

$$\langle k|V_D(i)|k'\rangle = \int \mathrm{d}^3r\phi^*_k(\vec{r})V_D(i,\vec{\mathbf{0}};\vec{r})\phi_{k'}(\vec{r}),$$

$$\langle k|V_X(i)|k'\rangle = \int \mathrm{d}^3r\mathrm{d}^3r'\phi^*_k(\vec{r})V_X(i,\vec{\mathbf{0}};\vec{r},\vec{r}')\phi_{k'}(\vec{r}'). \quad (16)$$

Here $V_D(i,\vec{R} = \vec{\mathbf{0}};\vec{r})$ is the screened potential of a hole in core level i in the unit cell of the crystal associated with the origin $\vec{R} = \vec{\mathbf{0}}$. Choosing this cell eliminates the need to consider complex phases related to the core-hole crystal momentum in each pair state. Correspondingly, $V_X(i,\vec{R} = \vec{\mathbf{0}};\vec{r},\vec{r}')$ is the "Fock" exchange term for this potential. Finally, we note that we are only considering matrix elements that are diagonal in i.

5. Final-State Rule vs Bethe-Salpeter Equation

We now compare the FSR and BSE term by term, and find that they can be put in near one-to-one correspondence. The effective Hamiltonian h' for the quasiparticle (photoelectron) state in the FSR has three terms,

$$h' = \frac{p^2}{2m} + V'_C + \Sigma'$$

$$\equiv h + [V'_C - V_C] + \left[\Sigma' - \Sigma\right]. \quad (17)$$

Here h is the quasiparticle Hamiltonian of Eq. (6).

The screened core-hole potential appears in $V_D(i)$ in the BSE and analogously in $[V'_C - V_C]$ in the FSR. Within the FSR the bare core-hole potential is always accompanied by an induced screening potential in response to the core hole which is generated by the SCF loop,

$$V'_C(\vec{r}) - V_C(\vec{r}) \equiv V_i(\vec{r}) + \Delta V_{\mathrm{scf}}(\vec{r}). \quad (18)$$

Hence, these seemingly different expressions for the direct screened core-hole interaction are quantitatively similar,

$$\Delta V_{\mathrm{scf}}(\vec{r}) \approx V_{\mathrm{ind}}(\vec{r}). \quad (19)$$

This near equivalence largely explains the typical close numerical similarity in the results of the two methods for the Mg K edge of MgO (Fig. 1) and the O K edge of MgO (Fig. 2), both of which agree reasonably well with experiment.

The biggest formal differences between the BSE for deep core levels and the FSR lie in the treatments of the exchange term $V_X(i)$ in the BSE, and correspondingly the difference in self-energies $\Sigma' - \Sigma$ in the FSR. These terms are analogous physically, because the self-energy can be viewed as a dynamically screened exchange interaction, i.e.,

$$\Sigma(\omega) = \mathrm{i}G[v + (\epsilon^{-1}(\omega) - 1)v] = V_{ex} + \Sigma_C(\omega), \quad (20)$$

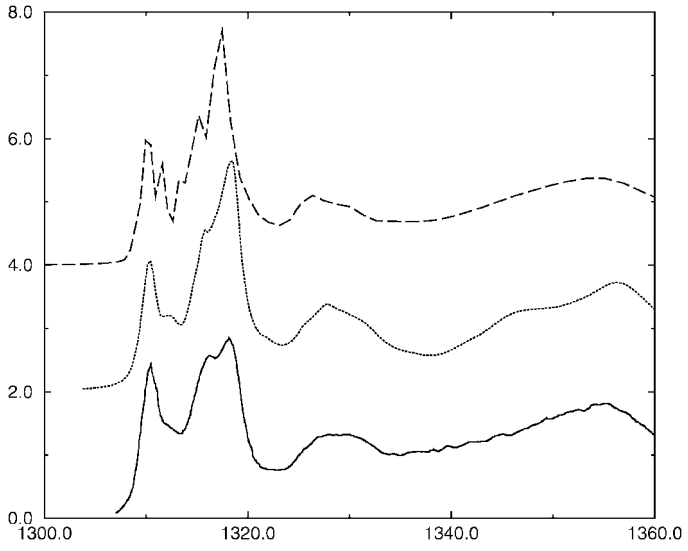

Fig. 1. Comparison of final-state rule (dashes) and Bethe-Salpeter equation (dots) calculations of XAS vs energy E in eV with experiment (solid) for the Mg K edge for MgO. The theoretical curves are shifted vertically for clarity.

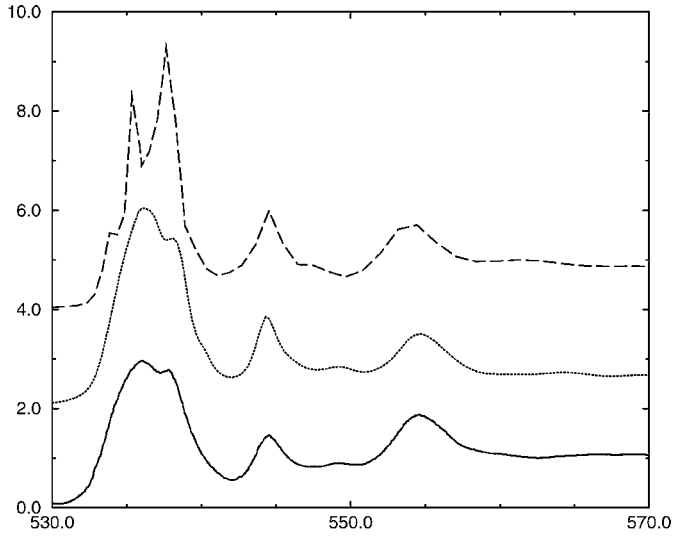

Fig. 2. Comparison of final-state rule (dashes) and Bethe-Salpeter equation (dots) calculations of XAS vs energy E in eV with experiment (solid) for the O K edge for MgO. The theoretical curves are shifted vertically for clarity.

where $V_{\rm ex}$ is the unscreened Fock exchange interaction

$$V_{\rm ex}(\vec{\boldsymbol{r}},\vec{\boldsymbol{r}}') = \sum_n^{occ} \frac{\langle\vec{\boldsymbol{r}}|n\rangle\langle n|\vec{\boldsymbol{r}}'\rangle}{|\vec{\boldsymbol{r}}-\vec{\boldsymbol{r}}'|}, \tag{21}$$

and $\Sigma_C(\omega)$ is the dynamic part of the self-energy. Now we can express the difference between the initial- and final-state self-energy operators as

$$\Sigma' - \Sigma = V_X(i) + \Delta V_{ex} + \Delta\Sigma_C, \tag{22}$$

where ΔV_{ex} represent the change in the exchange-operator due to the relaxation of the occupied states (excluding the core state) and $\Delta\Sigma_C$ is the change in Σ_C. If these last two terms can be neglected, the FSR and BSE approaches are rather similar. In particular, this is a good approximation below typical plasmon energies, where the quasiparticle corrections are small.

6. Discussion and Conclusions

We have shown that the BSE and FSR approaches for calculations of deep core XAS are formally similar. In particular they both incorporate GWA self-energies and their treatments of the screened core-hole are comparable. Apart from their formal similarities, however, these approaches differ in their practical implementations. For example, in the BSE approach described above, Σ and $V_X(i)$ are treated as non-local operators, while in typical applications of the FSR [10], the self-energy Σ (or Σ') is approximated using plasmon-pole, electron-gas self-energy models within a local-density approximation [12].

The difference in the treatment of the locality of the exchange operator V_X turns out to be crucial. It appears that the non-local treatment of V_X used in the BSE is generally preferable to the local exchange approximation used in the FSR. In particular, the non-local form naturally includes "local-field effects," namely the screening of the X-ray field which is particularly important for soft X-ray edges. This screening may be described formally by the random-phase approximation (RPA) bubble diagrams [6, 17]. Indeed, if the screened-core-hole interaction $\hat{V}_D$ were neglected, the BSE would be equivalent to the RPA. Screening by electrons other than resonantly excited core electrons would necessarily need to be included as well for a complete treatment. However, such screening is weak and has a weak energy dependence. However, in many cases the local-field corrections are small, especially for very deep-core XAS. For such cases, the present comparisons show that the FSR and BSE are expected to give similar results, consistent with numerical calculations.

Thus, we suggest that it may be preferable in calculations of deep core XAS to replace the FSR Hamiltonian h' with its deep-core BSE counterpart $h'_{\rm eff}$. This approach requires some additional computational effort to incorporate the non-local exchange matrix elements of $V_X(i)$. However, this can be facilitated with iterative techniques, a local-basis approach [7], and/or the use of atomic-structure calculations [2]. The most time-consuming part of this approach is still the calculation of the inverse dielectric matrix. However, this calculation can be avoided by calculating the screening of the core hole within the SCF loop using Eq. (18). The resulting FSR-like one-particle theory is defined self-consistently by the Hamiltonian

$$\begin{aligned} h'_{\rm scf} &= \frac{p^2}{2m} + V'_C + \Sigma(\omega) + V_X(i) \\ &= h + V_X(i) + \Delta V_{\rm scf}, \end{aligned} \tag{23}$$

and is thus simpler than the BSE for deep core levels. Moreover, since the quasi-particle corrections are small at low photoelectron energies (below the plasmon onset) one could use the ground state LDA (or Hartree-Fock) band energies (or Green's functions) in that regime.

The above approach can also be generalized to treat XAS from several nearly degenerate deep core levels, e.g., L-shell XAS. This leads to a coupled set of equations that mix the various levels i, similar to that discussed in Ref. [7]. For this case, the screening response to the core hole $\Delta V_{\rm scf}$ can also be calculated using the SCF loop instead of linear response.

On the other hand, all FSR-like theories are explicitly level dependent, and become impractical for valence band excitations. Moreover, an explicit calculation of the dielectric matrix makes it possible additionally to study the effects of energy dependence of V_D (i.e. dynamic screening of the core-hole), which has been argued to be important in some cases [7]. Finally, the inclusion of satellite inelastic losses interference terms can be included in the theory via a convolution, adapting the treatment of Ref. [11].

Acknowledgments

We respectfully acknowledge our indebtedness to Lars Hedin for discussions that led to this work. We also thank A. Ankudinov, G. Bertsch, S. Pantelides and L. Reining for useful comments. This work was supported in part by DOE grant DE-FG03-97ER45623 and NIST and was facilitated by the DOE Computational Materials Science Network.

References

1. Rehr, J. J. and Albers, R. C., Rev. Mod. Phys. **72**, 621 (2000).
2. Soininen, J. A. and Shirley, E. L., Phys. Rev. B **64**, 165112 (2001), and references therein.
3. Hedin, L. and Lundqvist, S., in "Solid State Physics," (edited by H. Ehrenreich, F. Seitz and D. Turnbull), (Academic, New York, 1969), Vol. 23, p. 1; L. Hedin, J. Phys. Cond. Mat. **11**, R489 (1999).
4. See, for example, Bukzko, R., Duscher, G., Pennycock, S. J. and Pantelides, S. T., Phys. Rev. Lett. **85**, 2168 (2000).
5. Slater, J. C., "Quantum Theory of Molecules and Solids," (McGraw Hill, NY, 1974).
6. Zangwill, A. and Soven, P., Phys. Rev. A **21** 1561, (1980); A. Zangwill and Liberman, J., Phys. B: At. Mol. Phys. **17**, L253 (1984).
7. Ankudinov, A. L., Nesvizhaskii, A. I. and Rehr, J. J., Phys. Rev. B. **67**, 115120 (2003).
8. Schwitalla, J. and Ebert, H., Phys. Rev. Lett. **80**, 4586 (1998).

9. von Barth, U. and Grossmann, G., Phys. Rev. B **25**, 5150 (1982).
10. Ankudinov, A. L., Ravel, B., Rehr, J. J. and Conradson, S. D., Phys. Rev. B **58**, 7565 (1998).
11. Campbell, L., Hedin, L., Rehr, J. J. and Bardyszewski, W., Phys. Rev. B **65**, 064107 (2002).
12. Lundqvist, B. I., Phys. Kondens. Mater. **6**, 193 (1967).
13. Strinati, G., Phys. Rev. B **29**, 5718 (1984).
14. Rohlfing, M. and Louie, S. G., Phys. Rev. B **62**, 4927 (2000).
15. Reining, L., Olevano, V., Rubio, A. and Onida, G., Phys. Rev. Lett. **88**, 066404 (2002).
16. Shirley, E. L., Phys. Rev. Lett. **80**, 794 (1998).
17. Crljen, Z. and Wendin, G., Phys. Rev. A **35**, 1555 (1987).

Physica Scripta. Vol. T115, 212–214, 2005

Nonlinear Energy Dependence of the Forbidden Energy Band in the Solid Solutions $Cu_xAg_{1-x}B^{III}C_2^{VI}$

A. A. Lavrentyev[1], B. V. Gabrelian[1], I. Ya. Nikiforov[1], J. J. Rehr[2] and A. L. Ankudinov[2]

[1]Department of Physics, Don State Technical University, Gagarin Sq.1, Rostov-on-Don, Russia
[2]Department of Physics, University of Washington, Seatle, WA 98195-1560, USA

Received June 26, 2003; revised July 10, 2003; accepted November 10, 2003

PACS number: 7120−b

Abstract

The solid solutions $Cu_xAg_{1-x}GaS_2$ and $Cu_xAg_{1-x}InSe_2$ for $x = 0.5$ and their terminal compounds ($x = 0$; 1) have been investigated both theoretically and experimentally using X-ray emission and absorption spectroscopy. These solid solutions are advanced materials for the transformation of solar energy. The electron structure of these solutions and compounds was investigated using FEFF8 code. The calculated local densities of electron states and X-ray absorption spectra were compared with our experimental X-ray spectra and photoelectron curves taken from the literature. The good correspondence of the theory to the experiment guarantees the assumed interpretation of the results for the solid solutions $Cu_xAg_{1-x}GaS_2$ and $Cu_xAg_{1-x}InSe_2$. It was found that in these solid solutions "pushing apart" of d-states of Cu and Ag takes place, which can be explained by the splitting of p-states of the atoms C^{VI} and d-states of A^I-atom (Cu and Ag). Our calculations have proved and explained the nonlinear dependence of the energy gap E_g on x.

1. Introduction

The solid solutions $Cu_xAg_{1-x}GaS_2$ and $Cu_xAg_{1-x}InSe_2$ and their marginal compounds have interesting optical properties and nonlinear dependence of the energy gap E_g on x [1, 2]. It was shown [3, 4], that the doping of $CuInSe_2$ can change the type of conductivity of it. The compound $CuInSe_2$ can be used as sun-battery cell [5].

The electron energy structure (EES) of $CuInSe_2$ and the defect structure $CuIn_3Se_5$ have been investigated in the work of J. Jaffe and A. Zunger [6] and recently [7–9]. In work of Japanese authors [9] the LOPW-method was applied to calculate EES of $CuInSe_2$. It was shown that the great value of E_g in $CuIn_3Se_5$ was caused by p-d hybridization and by d-d mixing.

The compounds $CuGaS_2$ and $AgGaS_2$ and their solid solutions crystallize into the chalcopyrite structure with the space group I42d (D_{2d}^{12}) [10]. The solid solutions $Cu_xAg_{1-x}InS_2$ [1] and $Cu_xAg_{1-x}InSe_2$ [2] have the same crystalline structure. The lattice of chalcopyrite can be presented in the first approximation as a supersphalerite structure, which for $CuGaS_2$ can be derived from close-packed fcc lattice of sulfur atoms, the tetrahedral interatomic emptinesses being occupied by atoms of copper and gallium such that in the first atomic shell of sulfur atom there are two atoms of copper and two atoms of gallium. The tetragonal elementary cell of chalcopyrite is characterized by the parameters: $\boldsymbol{a}$ along axes X and Y and $\boldsymbol{c} \approx 2\boldsymbol{a}$ along axis Z. In contrast to sphalerite lattice the face-centred cation sublattice of chalcopyrite consists of two types of atoms, that results in the distortion of the tetrahedral surrounding of every anion (S or Se). This distortion is described by two parameters: by the difference between $\boldsymbol{c}$ and $2\boldsymbol{a}$ and by the parameter $\boldsymbol{u}$, which shows the shift of a cation along the space diagonal.

In the present work theoretical EES and X-ray absorption spectra of the solid solutions $Cu_{0.5}Ag_{0.5}GaS_2$ and $Cu_{0.5}Ag_{0.5}InSe_2$ and their marginal compounds were investigated using FEFF8 code. The calculated local partial electron densities of states (LPDOS) and X-ray absorption edges for the compounds were compared with X-ray emission and absorption spectra studied earlier [11] and taken from the literature [12–14]. One of the main purposes of this work was to prove theoretically the results of experiments [1, 2], a nonlinear dependence of the energy gap E_g on the concentration x of these solid solutions.

2. Method of calculations

The experimental values of the lattice parameters for compounds $CuGaS_2$, $AgGaS_2$ $CuInSe_2$ and $AgInSe_2$ were taken from review [15]. The crystallographic parameters for the solid solutions were determined according to Vegard's law as the averages of ones for the margin compounds.

To calculate EES and theoretical forms of X-ray absorption spectra the *ab initio* full multiple scattering method realized in FEFF8 code [16] was used. The self-consistent densities of electron states, electron density in real space and Fermi energy E_F were calculated. The calculations of the theoretical form of X-ray absorption edges were carried out taking into account the screened core hole and the broadening effect due to the X-ray spectrometer window width and to the core hole life-time. The LPDOS for every type of atom in the system were determined by calculations using the retarded Green function by integration in complex plane for a cluster centred at this type of atom. At the first stage of the calculations the self-consistent mt-potentials for a clusters of about 35 atoms were obtained. After that the full multiple scattering calculations were fulfilled, taking into account 87 atoms as centres of scattering and then all significant pathes were considered for 1000 atoms. To achieve the self-consistency for Fermi energy up to some-hundredths of eV less than 11 iterations were enough.

3. Results and discussion

The results of the calculations of LPDOS and X-ray absorption spectra are shown in figures 1–5. The superposition of the experimental and theoretical curves for the compounds were made the standard way [11]. The energy zero corresponds to the top of the valence band, which was found by the SK-emission band corrected (by deconvolution), taking into account the width of the K-level of sulfur and the spectrometer window width. As for the solid solutions, the superimposition of the LPDOS and the experiment curves were carried out in the following way: the energy positions of the peaks B and C of the corresponding XPS bands of the margin compounds $CuGaS_2$ and $AgGaS_2$ were put in coincidence with the maxima of Cu 3d-states and Ag 4d-states of the solid solution $Cu_{0.5}Ag_{0.5}GaS_2$ (Fig. 1). It reflects the fact

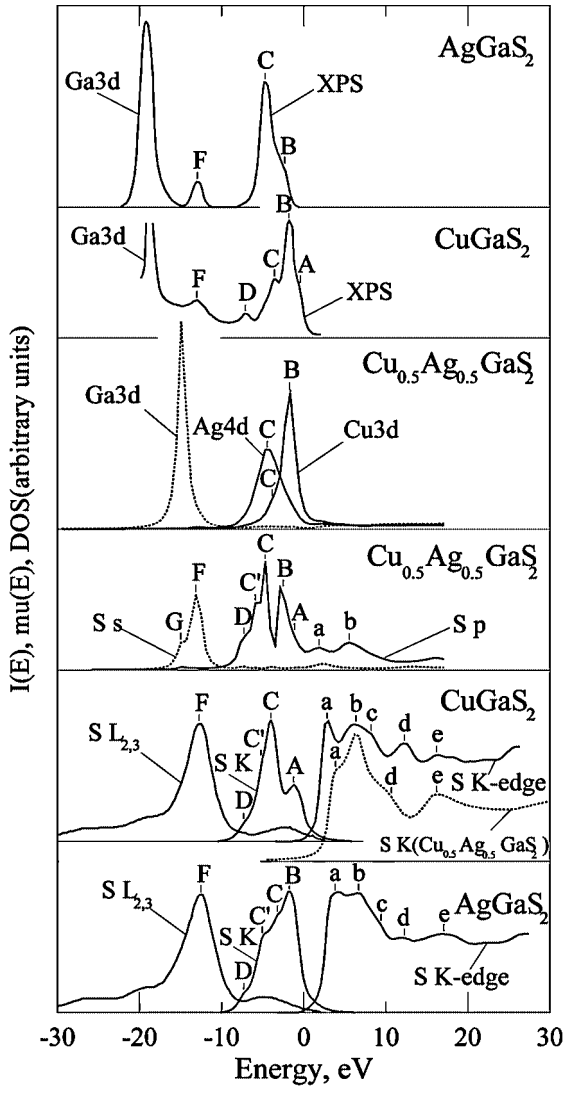

Fig. 1. The calculated densities of electron states in the solid solution $Cu_{0.5}Ag_{0.5}GaS_2$ in comparison with X-ray spectra of emission and absorption in the compounds $CuGaS_2$ and $AgGaS_2$, and also with XPS-spectra for $CuGaS_2$ and $AgGaS_2$ from the literature [12, 13]. The zero of the energy scale corresponds to the top of the valence band.

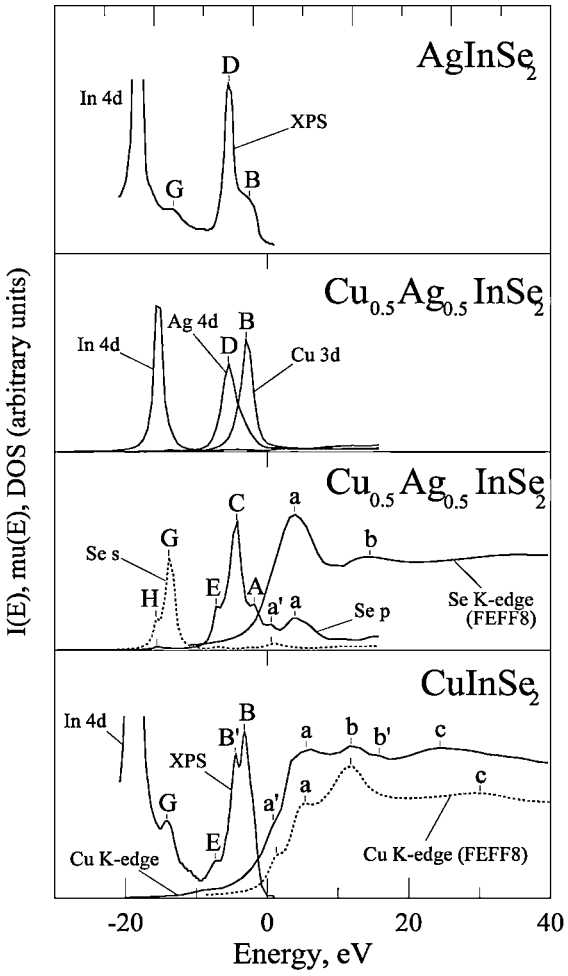

Fig. 2. The calculated density of electron states, X-ray K-absorption spectrum of Se in the solid solution $Cu_{0.5}Ag_{0.5}InSe_2$, and K-absorption edge of Cu in $CuInSe_2$ compared with taken from the literature: XPS-spectra in the compounds $CuInSe_2$ and $AgInSe_2$ [12] and K-abosrption spectrum of Cu in $CuInSe_2$ [14]. The energy zero corresponds to the top of the valence band.

that XPS bands of such metals represent the energy distribution of d-electrons mainly, because their cross-sections are greater than ones for s- and p-electrons. One can see in Fig. 1 the good correspondence of theory and experiment. The only exception is the energy position of 3d-states of Ga, their energy is about 3 eV less than for the XPS-spectrum.

In Fig. 2 the experimental XPS-spectra [12] for the compounds $AgInSe_2$ and $CuInSe_2$ and the X-ray CuK-absorption spectrum of $CuInSe_2$ are shown in comparison with the calculated LPDOS for s- and p-electrons of Se and d-electrons of Cu, Ag, and In in the solid solution $Cu_{0.5}Ag_{0.5}InSe_2$. Further, the form of the SeK-absorption edge was calculated for this solution and the theoretical CuK-absorption edge was obtained.

To be sure that our calculations are adequate we have compared (Fig. 3) the calculated LPDOS for $CuInSe_2$ with the experimental XPS spectrum [12] and X-ray emission $SeM_{4,5}$-spectrum. One can see, that the energy positions of all maxima of Cu d-states and Se p-states nearly coincide with the energy positions of the corresponding features of the experimental curves. It was found that 4p-states of Se are splitted in two subbands A and C, which is proven by the $SeM_{4,5}$-spectrum. The hybridizing interaction

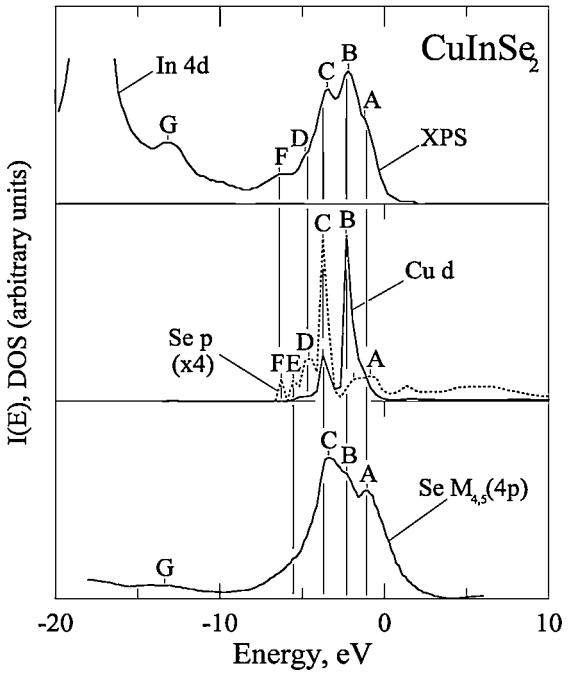

Fig. 3. The calculated densities of electron d-states of Cu and p-states of Se in $CuInSe_2$ compared with X-ray emission spectrum of Se $M_{4,5}$ and XPS-spectrum [12]. Zero energy is chosen at the top of the valence band.

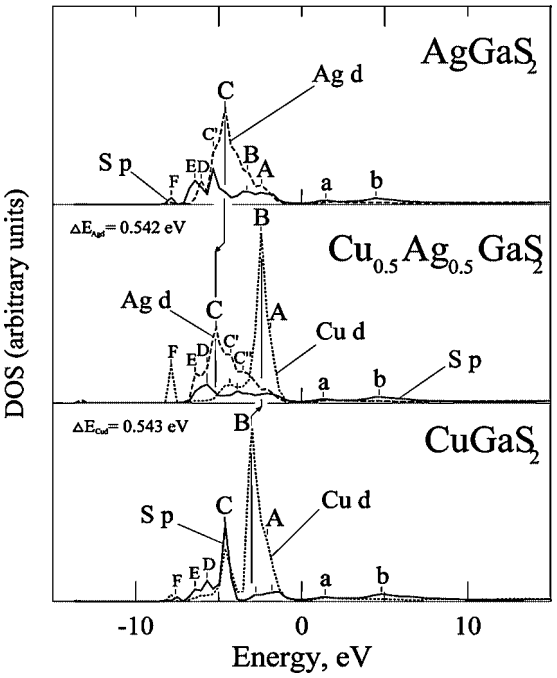

Fig. 4. Calculated electron densities of p-states of S (bold curves) and d-states of the noble metals (dashed curve for Ag and dotted curve for Cu) in compounds $AgGaS_2$ and $CuGaS_2$ and in the solid solution $Cu_{0.5}Ag_{0.5}GaS_2$ superposed by Fermi level.

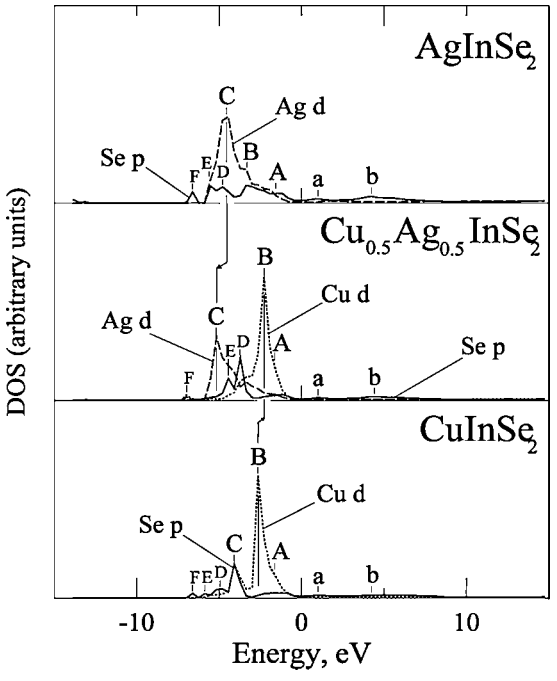

Fig. 5. Calculated electron densities of p-states of Se (bold curves) and d-states of the noble metals (dashed curve of Ag and dotted curve for Cu) in compounds $AgInSe_2$ and the solid solution $Cu_{0.5}Ag_{0.5}InSe_2$, superposed by the Fermi level.

brings a splitting of d-states of copper to subbands B and C also. These maxima of the theoretical curve correspond to peaks B and C of the XPS spectrum [12]. For such compounds one always observe in the upper part of the valence band a so-called d-s,p, resonance [17, 18], that leads to decreasing forbidden energy band width E_g. For $CuInSe_2$ it is the interaction of the p-states of Se with d-states of Cu, that results in the evident splitting of the p-band of Se to two maxima. From our previous investigations [11, 19] it follows, that the bottom of the conduction band in the compounds $A^IB^{III}C_2^{VI}$ form s-states of the metal B^{III} (Ga, In), which also decrease E_g compared to their isoelectronal analogues $A^{II}B^{VI}$.

For the solid solutions $Cu_{0.5}Ag_{0.5}GaS_2$ (Fig. 4) and $Cu_{0.5}Ag_{0.5}InSe_2$ (Fig. 5) the calculations of PLDOS show, that the d-states of the noble metals Cu and Ag are "pushed apart" comparing to the marginal compounds with increased energy distance between them by about 0.9 eV. This "pushing apart" of d-states of Cu and Ag and the energy positions of s-states of Ga and In atoms at the bottom of the conduction band can lead to a nonlinear change of E_g in the solid solutions. Following I. V. Bodnar *et al.* [2], we also suppose that the dependence $E_g(x)$ can be described by the formula $E_g(x) = ax^2 + bx + c$. The coefficient 'a' characterizes the non- linearity of this dependence. For the solution $Cu_xAg_{1-x}InS_2$ we found for this coefficient the value 0.088 eV. The empirical estimation [2] of 'a' for $T = 77$ K is 0.102 eV. However one has take into account that our calculations were carried out for $T = 0$ K. For the solution $Cu_xAg_{1-x}InSe_2$ we obtained $a = 0.18$ eV, that is twice that for the previous solution. So our theoretical investigation has proved the nonlinear dependence of $E_g(x)$ in correspondence with the experimental data.

Acknowledgments

The authors are grateful to Domashevskaya, E. P. and Terekhov, V. A. which gave us the Se$M_{4,5}$-emission band data, studied by them.

References

1. Bodnar, I. V., Yasyukevich, L. V., Korzoun, B. V. and Karoza, A. G., J. Mater. Sci. **33**, 183 (1998).
2. Bodnar, I. V. and Sergeev-Nekrasov, C. L., J. Unorganic Chem. **44**, 1012 (1999) (In Russian).
3. Wei, S. H., Zhang, S. B. and Zunger, A., Appl. Phys. Lett. **72**, 3199 (1998).
4. Wei, S. H., Zhang, S. B. and Zunger, A., J. Appl. Phys. **85**, 7214 (1999).
5. Kohiki, S., Nishitani, M., Negami, T. and Wada, T., Phys. Rev. B **45**, 9163 (1992).
6. Jaffe, J. E. and Zunger, A., Phys. Rev. B **28**, 5822 (1983).
7. Zhang, S. B., Wei, S. H. and Zunger, A., Phys. Rev. B **57**, 9642 (1998).
8. Rodrigez, J. A., Quiroga, L., Camacho, A. and Baquero, R., Phys. Rev. B **59**, 1555 (1999).
9. Masakatsu, S., Takeshi, U., Takahiro, W., Takeshi, H. and Yoshio, N., Jap. J. Appl. Phys. Pt 2, **36**, L.1139 (1997).
10. Bodnar, I. V., Opt. Spectrosc. **85**, 220 (1998) (In Russian).
11. Lavrentyev, A. A., Nikiforov, I. Ya., Kolpachev, A. B. and Gabrelian, B. V., Solid State Physics (S.-Peterbourg) **38**, 2347 (1996) (In Russian).
12. Rife, J. C., Dexter, R. N., Brindenbaygh, P. M. and Veal, B. W., Phys. Rev. B **16**, 4491 (1977).
13. Luciano, M. J. and Vesely, C. J., Appl. Phys. Lett. **23**, 60 (1973).
14. Toyoda, T. *et al*., J. Cryst. Growth **99**, 762 (1990).
15. Jaffe, J. E. and Zunger, A., Phys. Rev. B **29**, 1882 (1984).
16. Ankudinov, A. L., Ravel, B., Rehr, J. J. and Conradson, S. D., Phys. Rev. B **58**, 7565 (1998).
17. Brudnii, V. N. *et al*., Izv. Vuzov, Fizika **41**, 26 (1998) (In Russian).
18. Domashevskaya, E. P. and Terekhov, V. A., Phys. stat. sol. (b) **105**, 121 (1981).
19. Lavrentyev, A. A., Gabrelian, B. V. and Nikiforov, I. Ya., J. Sructural Chemistry **41**, 515 (2000) (In Russian).

Physica Scripta. Vol. T115, 215–217, 2005

Fe Coordination Environment in Fe(II)- and Fe(III)-Silicate Glasses via the Fourier-Transform Analysis of Fe K-XANES

L. Bugaev[1*], F. Farges[2], E. Rusakova[1], A. Sokolenko[1], Ya. Latokha[1] and L. Avakyan[1]

[1]Department of Physics, Rostov State University, Zorge str.,5, Rostov-on-Don, 344090, Russia
[2]Laboratoire des Geomateriaux. Universite de Marne la Vallee, FRE CNRS 2455, France, and Dept. of Environmental Sciences, Stanford University, Stanford, CA 94305-2115, USA

Received June 26, 2003; revised July 12, 2003; accepted November 4, 2003

PACS number: 61.10.Ht

Abstract

The Fe-O distances (R_1) and the number of nearest oxygen atoms (N_1), which coordinate Fe in Fe(II) and Fe(III) containing silicate glasses are determined by the method based on the Fourier-transform analysis of XANES performed for the short k-range and the subsequent fit of the extracted first shell's contribution. The scattering amplitudes for Fe-O pair, used for the fit, are calculated by the HF MT-potential with the neutral electronic configurations of atoms. The validity of this model for the different redox states of Fe in glasses and the accuracy of the determined R_1 and N_1 are analyzed applying the method to the Fe K-XANES of the references – Fe(II) and Fe(III) aqueous sulfate solutions. The modeling of the contribution of the Fe nearest oxygens to the Fe K-XANES of Fe(II)- and Fe(III)-rich silicate glasses, as well as in the series of glasses with the mixture of Fe(II) and Fe(III) states, performed through a single-shell fit and a subsequent two-shell fit, provides structural parameters for the oxygen-polyhedron around the ionized Fe^{2+} and Fe^{3+}-atoms and gives access to the estimates for the Fe^{2+}/Fe^{3+} ratio changes among all samples studied.

1. Introduction

The application of X-ray absorption spectroscopy (XAS) to determine the coordination environment of Fe in Fe-bearing silicate glasses, that suffered reduction or weathering, can provide important structural information, including 2D/3D micro mapping of Fe-O distances and Fe-coordination numbers, in addition to redox mapping. However, for a large number of these amorphous compounds, the application of XAS is often limited by the analysis of XANES. The very high resolution and poly-dimensional (2D mapping and 3D-tomography) XANES studies are benefiting highly from the recent development of micro-absorption methods on third generation sources. At the same time, the most current approaches of XANES analysis are based on indirect and qualitative information on the studied local structure estimated by comparing "unknowns" with model compounds. In this paper, the method proposed in [1, 2] is used to quantitatively determine Fe-O distances and coordination numbers for Fe in Fe(II)- and Fe(III)-bearing silicate glasses. This method, originally developed for crystalline minerals and glasses with low-Z atoms ($Z < 20$), is based on the Fourier-transform (FT) analysis of XANES within the short range of the photoelectron's wave numbers ($k = 0.2625^*(E - E_{MT})^{1/2}$, where E_{MT} is the interstitial potential for the compound studied), followed by a model of the contribution related to the first neighbours.

2. Determination of structural parameters for Fe coordination environment in the references Fe(II)- and Fe(III)-aqueous sulfate solutions

Analysis of the accuracy of metal-oxygen distances (R_1) and the number of nearest oxygen-atoms (N_1) of the first shell around the absorbing atom, determined by FT of XANES over the short k-interval $\sim 2.5\,\text{Å}^{-1}$ was performed in [1] for crystalline minerals and glasses consisting of low-Z atoms. To confirm the accuracy of R_1 and N_1 determination in the studied Fe-containing amorphous compounds, the method (including the accuracy of the scattering amplitudes and phase shifts calculated for the Fe-O pair) was validated using two Fe(II)- and Fe(III)-sulfate aqueous solutions (0.2 M), with pre-edge typical of regular 6-coordinated Fe(II,III) environments and with no medium-range order (MRO) contribution [3]. As was shown in [1, 2], the MRO-contribution can decrease (in contrast to the multiple-scattering (MS) term the accuracy of structural parameters obtained via FT and fit performed over the short k-interval. The XANES-simulations for the model crystals and their glass equivalents [1, 4, 5] reveal that for the studied crystalline compounds the first main edge crest features in their XANES are often strongly affected by the MRO- and MS-terms. At the same time, these simulations for glasses reveal that the fine structure at higher energies, after the first main edge crest features in XANES, is formed dominantly by the oxygen-polyhedron around the absorbing atom, due to the increasing diffusion for the second and more distant shells. According to this result the effect of the MRO-term in the studied Fe-containing silicate glasses can be minimized by the choosing adequately the corresponding k-interval for the FT. Therefore, for the Fe(II)- and Fe(III)-silicate glasses, as well as for the used references Fe(II) and Fe(III)-aqueous sulfate solutions, the FT was applied to the $\chi(k)$ over the short range of the wave numbers k: 3.9–5.8 Å^{-1}. This k-range excludes the main edge crest features (at $k < 3.9\,\text{Å}^{-1}$) and the small value of k_{max} makes it even more pertinent for disordered compounds. The $\chi(k)$ was extracted from the experimental Fe K-XANES spectra by the equation:

$$\chi(k) = \sigma^{exper}(k)/\sigma_{at}(k) - 1 \quad (1)$$

and the factorised "atomic" part of the absorption cross-section σ_{at}, obtained from the experimental Fe-XANES by the procedure proposed in [1]. The photoelectron phase shifts and scattering amplitudes were calculated by Hartree-Fock (HF) MT-potential [6], generated using the electronic configurations: $Fe(1s^1 2s^2 \ldots 3d^7 4s^2)$ – for the absorbing atom and $O(1s^2 2s^2 2p^4)$ – for the neighboring oxygens, which provides the value of $E_{MT} = 7092.7$ eV for the compounds studied. The photoelectron extrinsic

*e-mail: bugaev@rnd.runnet.ru

losses, core hole width and experimental energy resolution were accounted for by $\exp(-0.2625(\Gamma_{\text{exper}} + \Gamma_{\text{h}} + \Gamma_{\text{el}})2R/k)$, where Γ_{exper} is the energy parameter (eV) for the experimental resolution, Γ_{h} and Γ_{el} are the energy widths of the core hole and the excited electron states respectively. This exponential can also be rewritten as $\exp(-2R/\lambda_{\text{eff}})$ with the effective mean free path λ_{eff} for the photoelectron, given by:

$$1/\lambda_{\text{eff}} = 0.2625\ (\Gamma_{\text{exper}} + \Gamma_{\text{h}})/k + 1/\lambda_{\text{el}}. \quad (2)$$

The Γ_{h} and the photoelectron mean free path length $\lambda_{\text{el}}(k) = k/(0.2625\,\Gamma_{\text{el}})$ for Fe containing compounds were taken from [7]. The FT of the $\chi(k)$ extracted from the experimental Fe K-XANES and the three-parameters (N_1, R_1, σ^2) fit in R-space (0.3–2.5 Å) of the first oxygen shell's peak in $|F(R)|$ were performed under the constant reduction factor $S_0{}^2 = 0.8$, using FEFFIT [8].

The agreement between the determined structural parameters for Fe-environment in Fe(II)-solution with the available structural information [3] appears to be similar to that for the crystalline minerals consisting of low-Z atoms [1]. This accuracy suggests that the fit for the $\chi(k)$, extracted by the $E_{\text{MT}} = 7092.7$ eV of the used HF MT-potential, can be performed without any additional energy shift (i.e. under the parameter $E_0 = 0$ eV for the FEFFIT model). This conclusion justifies the adequacy of the HF MT-potential based on the neutral electronic configurations of atoms for the FT-analysis of the Fe(II)-rich compounds.

However, the same comparison for the model Fe(III)-sulfate solution reveals that to obtain sufficient accuracy for the Fe-O distance by the same scattering amplitudes and phase shifts as for the Fe^{2+} state and by the E_{MT} of the used HF MT-potential, the energy shift $E_0 = 2$ eV is needed for the FEFFIT model. The last conclusion is justified by the results on the scattering phase shifts parameterization [9], which showed that for the different charge states of atom, the logarithmic derivatives of the photoelectron wave functions at the MT-radius (used for the phase shifts calculation) are only shifted in the energy scale, without the change of their shapes.

3. Fe-coordination environment in Fe(II)- and Fe(III)-silicate glasses

The results of the FT-analysis for the reference solutions permit us to apply the method to a set of silicate glasses of float composition (molar composition $\sim Ca_1Na_1Al_1Si_4O_{11}$) doped with 1 wt.% Fe, quenched from their respective melts equilibrated at different oxygen fugacities and characterized using Fe K pre-edge information at the Fe K-edge [10]. Two end-members were isolated from that series, which contains more than 99 atom% of iron, as Fe(II) and Fe(III) respectively [10]. In Fig. 1, the FT for the experimental Fe K-XANES in Fe(II)-rich glass and in Fe(III)-rich glass are compared with the corresponding single-shell models, performed with $S_0{}^2 = 0.8$ and $\Lambda_{\text{eff}}(k)$ obtained by (2). The determined structural parameters of the models for the Fe(II)-rich glass are: $N_1 = 5.1$, $R_1 = 2.0$ Å and for the Fe(III)-rich glass: $N_1 = 4.5$, $R_1 = 1.92$ Å, under approximately the same $\sigma^2 = 0.005$ Å^2 as for the Ti-containing glasses [5].

The Fe(II)- and Fe(III)-rich silicate glasses were treated as the boundary samples for the series of eight silicate glasses (named further as Sample1, Sample2, ..., Sample8) which contain the mixture of Fe^{2+} and Fe^{3+} states with the concentration (C) of Fe^{2+}, decreased along this row. The analysis of the asymmetry of the first shell's peak (nearest oxygens contribution) in $|F(R)|$ performed via the two-shell fit gives access to the estimate for the

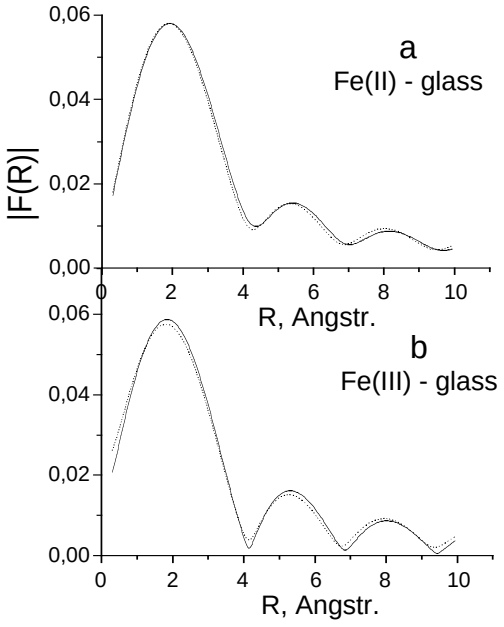

Fig. 1. $|F(R)|$ for Fe(II)-bearing (a) and Fe(III)-bearing (b) silicate glasses: solid curves – the FT of the $\chi(k)$ extracted from the Fe K-XANES and dashed curves – the results of the single-shell fit.

change of the ratio Fe^{2+}/Fe^{3+} among all the samples studied, in assumption that the anharmonicity effects in atomic motion are negligible. For this purpose, the possible concentrations of the two mixed Fe-states with different oxygen-coordinations can be estimated by the two-shells fit. This fit is based on the assumption that each shell (which contains $N_{1,j}$ atoms at $R_{1,j}$ distance, $j = 1, 2$ is the shell's number) represents the different type of oxygen-coordination environment of corresponding Fe-state. In this case, the fitting function $\chi(k)$ can be constructed by FEFFIT as follows:

$$\chi(k) = C\chi_{1,1}(k) + (1 - C)\chi_{1,2}(k) \quad (3)$$

where $\chi_{1,1}(k)$ – is the contribution of the first shell – oxygen polyhedron for Fe^{2+} environment, with $N_{1,1} = 5.1$ atoms at $R_{1,1} = 2.0$ Å (as was determined for the Fe(II)-rich glass); C – the concentration of the Fe^{2+}-states; $\chi_{1,2}(k)$ – is the contribution of the second shell – oxygen polyhedron for Fe^{3+} environment with $N_{1,2} = 4.5$ atoms at $R_{1,1} = 1.92$ Å (as was determined for the Fe(III)-rich glass). Then, a two-shell fit was performed considering the fixed $N_{1,1}$, $R_{1,1}$ and $N_{1,2}$, $R_{1,2}$, but with a "single-shell" value of $\sigma^2 = 0.005$ Å^2 (as for Fe(II), Fe(III)-rich glasses) and with the concentration C allowed to vary. According to the results for the used references Fe(II)- and Fe(III)-aqueous sulfate solutions, the fit was performed by the same set of HF scattering amplitudes and phase shifts both for the $\chi_{1,1}(k)$ and $\chi_{1,2}(k)$ using, however, the constant energy shift $E_0 = 2$ eV for $\chi_{1,2}(k)$ within the FEFFIT model. This scheme of the two-shell fit was tested for the boundary Fe(II)- and Fe(III)-rich glasses. The results of the fit for the other eight silicate glasses (Samples 1–8) give the values of concentrations C for Fe^{2+} in them. These C values are presented in Table I in comparison with the corresponding concentrations obtained via the chemical method (using ferrous ortophenantroline after glass dissolution under inert atmosphere). As can be seen, the values of concentrations for Fe^{2+} determined by Fe K-XANES correlate reasonably with the chemically obtained C values and show the nonmonotonous decrease of the Fe^{2+}/Fe^{3+} ratio along the studied row of glasses, from Fe(II)- to Fe(III)-rich silicate glass.

Table I. *Concentrations of Fe^{2+} in the series of glasses with the mixture of Fe^{2+} and Fe^{3+} states, obtained by Fe K-XANES and by the chemical method.*

Glasses with the mixture of Fe^{2+}, Fe^{3+} states	Concentration C (%) of Fe^{2+}	
	Fe K-XANES	Chem. method
Sample1	96.0	96
Sample2	71.0	69
Sample3	60.8	62
Sample4	45.4	45
Sample5	33.0	27
Sample6	21.9	26
Sample7	18.5	22
Sample8	9.0	9

For the Fe-bearing glasses, the obtained structural information is in agreement with pre-edge, Mössbauer, optical properties and molecular dynamics studies on these glasses [10] as well as circular dichroism experiments in similar glasses [11]. From these models, one can now use a similar approach for 2D/3D micro mapping of Fe-O distances and/or Fe-coordination number in glass samples.

Acknowledgment

The work is supported by RFBR Grant №03-02-17325.

References

1. Bugaev, L., Sokolenko, A. and Flank, A., Phys. Rev. B **65**, 024105 (2002).
2. Bugaev, L., Ildefonse, Ph., Flank, A., Sokolenko, A. and Dmitrienko, H., J. Phys. C **12**, 1119 (2000).
3. Pokrovski, G., Schott, J., Farges, F. and Hazemann, J.-L., Geochim. Cosmochim. Acta (2003) (in press).
4. Bugaev, L., Ildefonse, Ph., Flank, A., Sokolenko, A. and Dmitrienko, H., J. Phys. C **10**, 5463 (1998).
5. Bugaev, L., Farges, F., Rusakova, E., Sokolenko, A., Latokha, Ya. and Avakyan, L., Physica Scripta (this issue) (2004).
6. Bugaev, L., Vedrinskii, R. and Levin, I., J. Phys. C **3**, 8967 (1991).
7. Muller, J., Jepsen, O. and Wilkins, J., Sol. St. Commun. **42**, 365 (1982).
8. Newville, M. *et al.*, Physica B **208&209**, 154 (1995).
9. Vedrnskii, R. and Bugaev, L., Fizika., Izv.vuzov **23**, 74 (1980).
10. Farges, F., Lefrere, Y., Rossano, S., Berthereau, A., Calas, G. and Brown, Jr. G. E., J. Non-Crystalline Solids **344**, 176 (2004).
11. Brown, Jr. G. E., Farges, F. and Calas, G., Rev. Mineral. **32**, 317 (1995).

Physica Scripta. Vol. T115, 218–220, 2005

Atomic Absorption Background in EXAFS of Rb in Inter-Alkaline Alloys

A. Kodre[1,2,*], I. Arčon[3,2], J. Padežnik Gomilšek[4] and A. Mihelič[2]

[1]Faculty of Mathematics and Physics, Jadranska 19, SI-1000 Ljubljana, Slovenia
[2]J. Stefan Institute, Jamova 39, SI-1000 Ljubljana, Slovenia
[3]Nova Gorica Polytechnic, Vipavska 13, SI-5000 Nova Gorica, Slovenia
[4]Faculty of Mechanical Engineering, Smetanova 17, SI-2000 Maribor, Slovenia

Received June 26, 2003; revised October 13, 2003; accepted November 14, 2003

PACS numbers: 61.10.Ht, 61.43.−j, 78.70.Dm

Abstract

In the room-temperature EXAFS spectrum of Rb in the Rb/K alloy, the sharp spectral features due to double photoexcitation are plainly visible from 40 eV above the K edge. The weak and short structural signal is attributed to the strong thermal disorder. A unique atomic absorption background of the Rb atoms in the solid alloy is extracted and compared to the pure atomic absorption, measured on the monatomic Rb vapor, as a direct test of the practical transferability of experimentally determined atomic absorption backgrounds.

1. Introduction

It is well known in X-ray absorption spectrometry that the EXAFS region above an absorption edge hosts, beside the structural signal, also one or more groups of small sharp features, the multielectron excitations [1–3]. These, together with their extended tails, comprise the so-called atomic absorption background (AAB), characteristic of the target atom but only weakly depending on its environment. In the standard EXAFS analysis, the AAB is approximated by a spline background, constructed from the Fourier components of the absorption signal with periods below the range of possible neighbor distances. This may be adequate for samples with a strong structural signal. For weakly ordered or amorphous substances, however, the structural signal and AAB may be of comparable amplitude with widely overlapping harmonic components so that Fourier separation is not feasible and the analysis can only proceed with a directly determined AAB, exploiting its transferability for a given atomic species [4, 5].

The scarce data on the directly determined AAB come either from experiments on monatomic elemental samples or from the reverse analysis where the structural signal can be removed from the absorption spectrum with sufficient accuracy. The first and the only exact approach provided AABs of alkaline metals [6–9] and Zn [10], Cd [11] and Hg [12], if the data on noble gases could be momentarily put aside for the evident lack of interest from EXAFS practitioners. The second approach is more generally applicable, its early examples may be found in comparative studies using reference standards [3, 13–15].

Absorption spectra of inter-alkaline alloys open another path to AAB, seemingly related to both approaches. The Cs L edge absorption of a Cs/Na alloy at room temperature shows virtually no structural signal [16, 17]. Its atomic character is suggested after comparison with the purely atomic absorption of the adjacent noble gas Xe [18]. In the same way, the Rb K-edge absorption measured on a thin layer of the Rb/K or Rb/Na alloy is almost EXAFS-free, surprisingly similar to the absorption spectrum of the monatomic Rb vapor [6, 8]. In the present study, the absorption of the Rb/K alloy with atomic ratio 1 : 6 is measured at several temperature points between 80 K and room temperature with the aim to establish the temperature dependence of the crystalline order, i.e. to decide whether the absence of the structural signal is caused merely by the thermal disorder or by formation of a specific highly disordered phase.

2. Experiment

The alloys of Rb and Cs with the lighter homologues K and Na in different mixing ratios were prepared by melting together and homogenizing appropriate amounts of the constituent elements under the bath of paraffine oil. A speck of the solid alloy was placed between kapton foils with a drop of the oil, squeezed between carbon platelets in a special container and inserted into the cryostat. The absorption measurement was performed at the BM29 beamline of the European Synchrotron Radiation Facility (ESRF), Grenoble, with a two-crystal Si(311) monochromator with a resolution of ∼0.5 eV at the Rb K edge (15200 eV). The high flux of monochromatic beam and remote vision system of the station with a TV camera and a fluorescent screen was crucial for the success of the experiment, allowing to choose a small patch of homogeneous transmission on the sample.

3. Results and discussion

In view of the weak structural signal of the alloy, the standard spline construction of the absorption background is precluded. Instead, the available AAB, measured on Rb vapor [6, 8], is applied. A similar procedure has been used before for Br and Rb compounds [5] and in the extraction of AAB of 4p elements [15]:

- the data in the pre-edge region are modeled by a sum of a linear function and an arctan profile of the edge: after subtraction of the linear part, the K-shell Rb contribution remains (Fig. 1),
- the K-shell absorption is normalized by a Victoreen fit of the above-edge region beyond 500 eV (i.e. beyond the last visible MPE feature),
- a similarly prepared absorption spectrum of the Rb vapor (cf. insert in Fig. 1) is subtracted, whereby the non-structural contributions are removed,
- the remaining structural signal is transformed into $\chi(k)$ by conversion from E-space to k-space.

In a FEFF model [19, 20] potassium and rubidium are placed as closest neighbors at respective contact distances ($R_{\text{Rb-K}} = 4.72$ Å, $R_{\text{Rb-Rb}} = 4.96$ Å) [21]. The perfect agreement of the model and experiment is shown in Fig. 2 for the 80 K spectrum

*E-mail: alojz.kodre@fmf.uni-lj.si

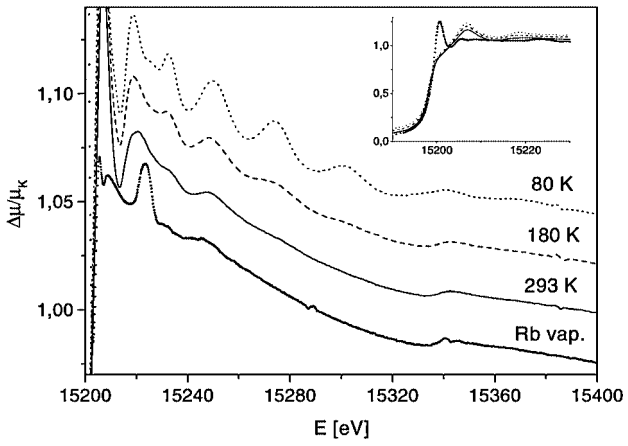

Fig. 1. Normalized K-shell photoabsorption cross-section of Rb in Rb/K = 1 : 6 alloy for three different temperatures, and of Rb vapor. Insert: corresponding K edge profiles to illustrate the procedure of AAB removal. A vertical displacement of 0.03 per spectrum is added for clarity.

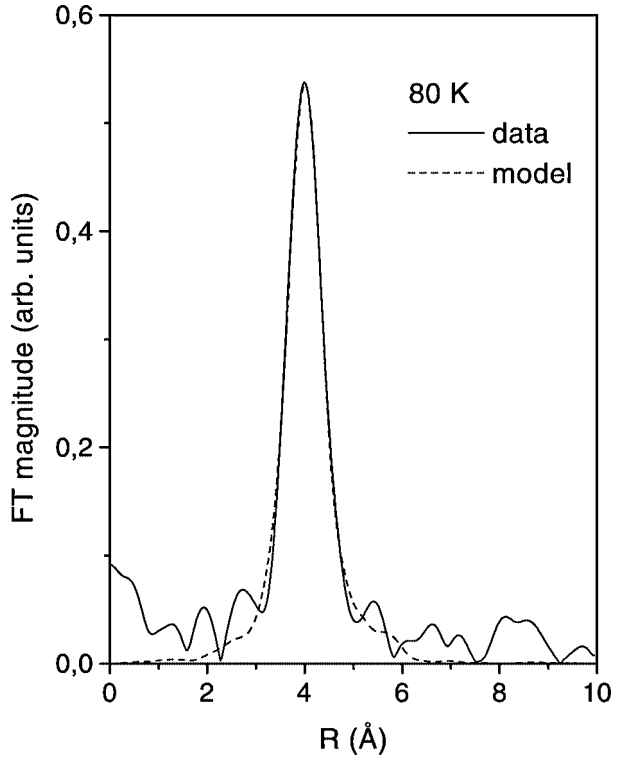

Fig. 2. Fourier transforms of Rb/K EXAFS data and the model (k^3 weight, 1.5 .. 10 Å^{-1}).

where both neighbor shells are well defined, with $N_K = 7.4 \pm 0.7$ and $N_{Rb} = 2.0 \pm 0.5$. In all other spectra, only the potassium shell is statistically significant: with increasing temperature the EXAFS signal wanes and the weakly populated second shell is drowned in noise. For that reason, a single-shell model is applied to all spectra (Table I). Neglecting the second shell, though, has an unwanted side effect: its vestiges shift the first-neighbor distance (r_1) upwards. Since the second-shell signal wanes with temperature faster than the first-shell signal, r_1 spuriously shows a slight decrease with temperature.

The parameters of the model show a good consistency: the number of neighbors is steady within the error bars, and the Debye-Waller factor grows steadily (practically linearly) with temperature, as expected. It is worth noting that $\sigma^2 = 0.03$ Å^2 at

Table I. *Parameters of the single-shell model of Rb neighborhood in the Rb/K alloy: shell radius correction ($R_1 = 4.72$ Å), the number of K atom neighbors and the Debye-Waller factor. Parameter errors (in parentheses) are given in units of the last decimal place. The N_1 value at 293 K is fixed to stabilize the fit.*

Best fit parameters	Rb/K sample temp. (K)				
	80	130	180	250	293
ΔR_1 (Å)	−0.108(4)	−0.124(4)	−0.131(5)	−0.138(5)	−0.149(6)
N_1	7.5(4)	7.7(5)	8.1(7)	7.2(7)	[8]
σ_1^2 (Å^2)	0.032(3)	0.050(4)	0.069(5)	0.077(5)	0.094(8)

the low-temperature end means a strong suppression of the signal and that value triples within the observed temperature range. The dramatic decrease of the structural signal is thus a purely kinetic effect: no order-disorder phase transition is involved. The large σ^2 value usually affects the accuracy of the other shell parameters: if only one or two oscillations are evident before the interference pattern is suppressed by the thermal motion, the amplitude and phase of the Fourier component cannot be determined with good precision. In the Rb/K alloy, however, the large interatomic distance means a short period of the EXAFS oscillation. Even if the 80 K signal vanishes by ∼100 eV above the edge, it completes ∼6 cycles and its parameters can be read with sufficient precision.

With the calculated structural signals the atomic absorption background can now be reconstructed. The k-space model signal of FEFFIT [19] is transformed back to the energy space and subtracted from the respective Rb K-shell contribution spectrum of Fig. 1. What remains is the atomic absorption background – but this time specifically the background of the metallic Rb in the alloy. Except for the 80 K spectrum, where the AAB still shows some vestiges of the higher harmonics of the structural signal, the resulting AABs are identical. In Fig. 3, this AAB is compared to the K-edge absorption of the Rb vapor. The difference is minute – the linewidth of the MPE features in the Rb/K AAB is somewhat larger. The [1s4p] peak at 26 eV above the edge is slightly broader and the miniature edges of the 4s and 3d coexcitations at 50 and 130 eV, respectively, are more extended. The additional width can be attributed to the band structure of available final states in the conducting alloy.

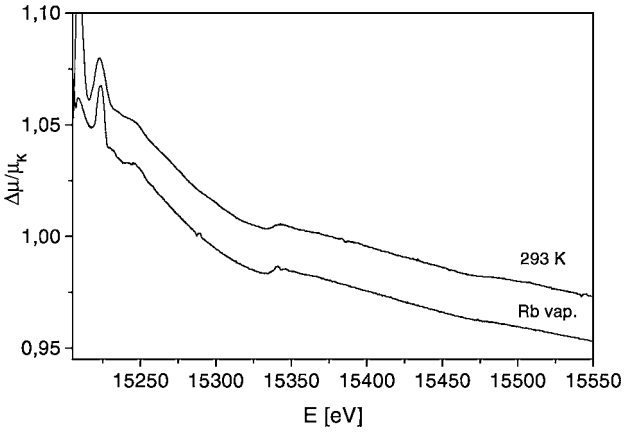

Fig. 3. The comparison of the Rb AAB extracted from the Rb/K alloy spectrum at room temperature, and the atomic absorption on Rb vapor. The signals are vertically displaced by 0.02 for clarity. The artifact on the Rb vapor spectrum at ∼15290 eV is a monochromator glitch.

4. Conclusion

The temperature dependence of the Debye-Waller factor shows that the EXAFS signal in the Rb/K alloy is suppressed by the thermal disorder and no specific disordered phase needs to be invoked.

The comparison of the recovered AAB and the Rb vapor absorption exhibits only minute differences in the linewidth and thus proves the transferability of the AABs for the purpose of practical EXAFS analysis.

Acknowledegements

The work was supported by Slovenian Ministry of Education, Science and Sport. We acknowledge the European Synchrotron Radiation Facility for provision of synchrotron beamtime (experiment No. CH-1298 and HE-1522) and we would like to thank M. Borowski for assistance in using beamline BM29.

References

1. Prešeren, R., Kodre, A., Arčon, I. and Borowski, M., J. Synch. Radiat. **8**, 279 (2001) (and references therein).
2. Kodre, A., Prešeren, R., Arčon, I., Padežnik Gomilšek, J. and Borowski, M., J. Synch. Radiation **8**, 282 (2001) (and references therein).
3. D'Angelo, P. and Pavel, N. V., Phys. Rev. B **64**, 233112 (2001).
4. Kodre, A., Arčon, I. and Frahm, R., J. Phys. IV France 7 **C2**, 195 (1997).
5. Kodre, A., Padežnik Gomilšek, J., Arčon, I. and Prešeren, R., J. Synch. Radiat. **6**, 306 (1999).
6. Prešeren, R., Arčon, I., Mozetič, M., Kodre, A. and Pregelj, A., Nucl. Instrum. Meth. Phys. Res. B **111**, 161 (1996).
7. Padežnik Gomilšek, J., Kodre, A., Arčon, I. and Prešeren, R., Phys. Rev. A **64**, 22508 (2001).
8. Kodre, A., Arčon, I., Padežnik Gomilšek, J., Prešeren, R. and Frahm, R., J. Phys. B **35**, 3497 (2002).
9. Padežnik Gomilšek, J., Kodre, A., Arčon, I. and Hribar, M., Phys. Rev. A **68**, 042505 (2003).
10. Mihelič, A., Kodre, A., Arčon, I., Padežnik Gomilšek, J. and Borowski, M., Nucl. Instrum. Meth. Phys. Res. B **196**, 194 (2002).
11. Kodre, A., Padežnik Gomilšek, J., Mihelič, A. and Arčon, I., Radiat. Phys. Chem., in print.
12. Filipponi, A., Ottaviano, L. and Tyson, T. A., Phys. Rev. A **48**, 2098 (1993).
13. Di Cicco, A., Filipponi, A., Itie, J. P. and Polian, A., Phys. Rev. B **54**, 9086 (1996).
14. Li, G., Bridges, F. and Brown, G. S., Phys. Rev. Lett. **68**, 1609 (1992).
15. Padežnik Gomilšek, J., Kodre, A., Arčon, I., Loireau-Lozac'h, A. M. and Bénazeth, S., Phys. Rev. A **59**, 3078 (1999).
16. Arčon, I., Kodre, A., Padežnik Gomilšek, J., Mihelič, A. and Hribar, M., in Hamburger Synchrotronstrahlungslabor HASYLAB am Deutschen Elektronen-Synchrotron DESY: Jahresbericht 2002 (Hamburger Synchrotronstrahlugslabor HASYLAB at Deutsches Elektronen-Synchrotron DESY, Hamburg 2002) p. 737.
17. Arčon, I., Kodre, A., Padežnik Gomilšek, J., Hribar, M. and Mihelič, A. in this issue of Physica Scripta.
18. Arčon, I., Kodre, A., Štuhec, M., Glavič-Cindro, D. and Drube, W., Phys. Rev. A **51**, 147 (1995).
19. Stern, E. A., Newville, M., Ravel, B., Yacoby, Y. and Haskel, D., Physica B **117**, 208 (1995).
20. Rehr, J. J., Albers, R. C. and Zabinsky, S. I., Phys. Rev. Lett. **69**, 3397 (1992).
21. Greenwood, N. N. and Earnshaw, A., "Chemistry of the elements" (Butterworth Heinemann, University Press, Cambridge 1984).

Physica Scripta. Vol. T115, 221–222, 2005

Continuous Cauchy Wavelet Transform of XAFS Spectra

M. Muñoz[1], F. Farges[1,2*] and P. Argoul[3]

[1]Laboratoire des Géomatériaux, Université de Marne-La-Vallée, CNRS FRE 2455, 77454 Marne-La-Vallée cedex 2, France
[2]Department of Geological and Environmental Sciences, Stanford University, CA 94305-2115, USA
[3]Laboratoire Analyse des Matériaux et Identification, Unité Mixte ENPC-LCPC, 77455 Marne-La-Vallée cedex 2, France

Received June 26, 2003; revised July 20, 2003; accepted November 4, 2003

PACS numbers: 61.10.Ht, 02.30.Nw, 07.05.Kf

Abstract

The continuous Cauchy wavelet transform (CCWT) is applied to the analysis of XAFS spectra. Thanks to that method, XANES and EXAFS signals can be visualized in three-dimensions: the wavevector (k), the interatomic distance uncorrected for phase-shifts (R') and the CCWT modulus (corresponding to the continuous decomposition of the amplitude terms). Applied to EXAFS spectra, the CCWT analysis provides straightforward qualitative information related to the k-range of each "R'-EXAFS" contribution. Such information is particularly useful to perform next nearest-neighbors identification, despite the presence of spectral artifacts such as multiple-scattering features, multi-electronic excitations or noise. When applied to XANES spectra, the CCWT analysis helps highly to measure the "spectral limit" between XANES and EXAFS regions, as well as the energy range required to model properly next-nearest neighbors. To further illustrate the potential of CCWT analyses applied to XAFS spectra, we present examples related to: (1) a XANES spectrum collected at the Ti K-edge for titanite ($CaTiSiO_5$); (2) an experimental Au L_{III}-edge EXAFS spectrum for gold sorbed on goethite (FeO(OH)).

1. Introduction

X-ray absorption fine structure (XAFS) spectroscopy (including XANES and EXAFS regions) is a powerful tool for investigating the short-, and medium range environment around a selected absorbing atom in structurally complex materials like ceramics, glasses and solutions. However, the experimental signals can often be complex to analyze due to the overlapping of several contributions such as single-scattering (SS), multiple-scattering (MS), multi-electronic excitations and various constructive and destructive interferences among next-nearest neighbor contributions. Usually, Fourier transform (FT) methods are used to obtain a frequency decomposition of the normalized EXAFS signal. FT analyses only provide a one-dimensional decomposition in the R'-space (interatomic distances uncorrected for phase-shifts) of the data processed in k-space (wavevector). Alternatively, we present here a continuous wavelet transform approach [1], providing a two-dimensional representation of the analyzed signal (e.g., a "time-frequency" correlation). More particularly, we use the continuous Cauchy wavelet transform (CCWT), which was recently proven to be successful for analyzing EXAFS signals in a two-dimensional (k, R')-space [2]; the third dimension (i.e., the CCWT modulus) representing the amplitude terms to within a wavelet-defined constant. Details on the theory of the method and the choice of the Cauchy "mother-wavelet" are explained in [2] and [3]. In this study, we present new applications of the CCWT theory.

2. Application to XANES and EXAFS spectra for complex materials

Figure 1 shows a CCWT modulus (2D and 3D), calculated between 0.2 and 6.0 Å, for the Ti K-edge XANES spectrum of crystalline titanite ($CaTiSiO_5$; data from [4]). The XANES spectrum was previously converted into k-space, and normalized using cubic splines, like for an EXAFS spectrum. Thanks to the (k, R') decomposition, the CCWT modulus clearly distinguish the "XANES" region (coming essentially from first-neighbors MS events near 3.5 Å), from the "EXAFS" region (where the SS events from distant neighbors dominate, e.g., near 1.5 Å). Note that the FT analysis only provides an average magnitude between both regions and underestimates drastically the signal in the "XANES" region. This example shows the particular interest of a (k, R')

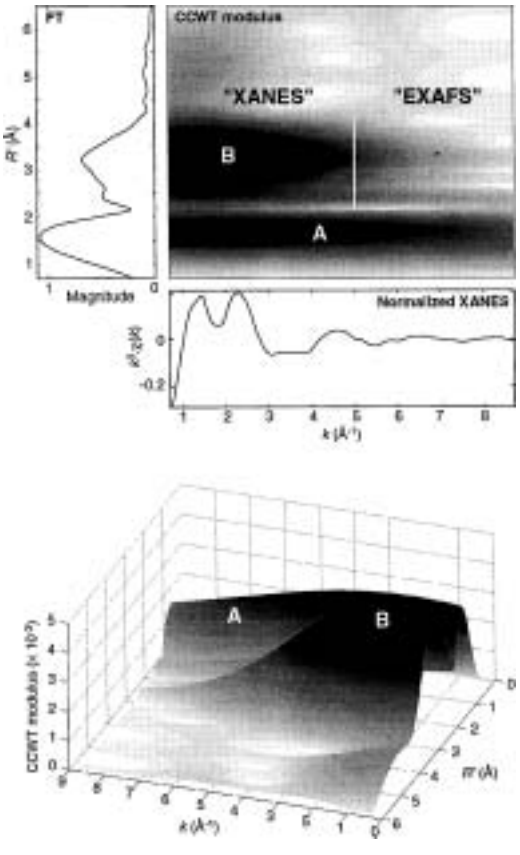

Fig. 1. CCWT analysis for a Ti K-edge XANES spectrum of titanite, (up) 2D modulus; (down) 3D modulus. Note that on the FT magnitude, the intensity of "B" is averaged over the k-range 0–9 $Å^{-1}$, whereas its intensity is higher than "A" (i.e., first neighbors contribution) in the low k-region (see "XANES" on the CCWT modulus).

*e-mail: farges@univ-mlv.fr

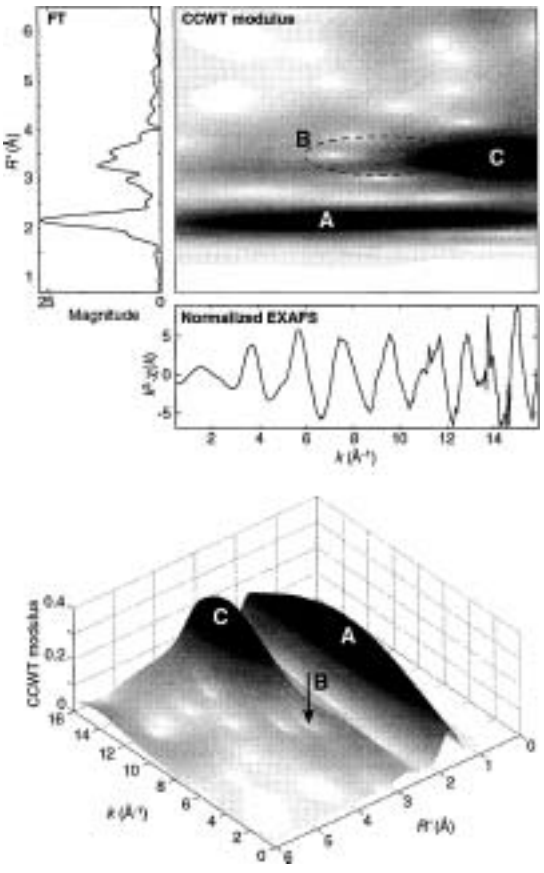

Fig. 2. CCWT analysis for a Au L_{III}-edge EXAFS spectrum of gold sorbed on goethite, (up) 2D modulus; (down) 3D modulus. Note the destructive interference "B" between the MS from the oxygen first neighbors, and the SS from the iron second neighbors. Note also that collecting data up to 16 $Å^{-1}$ is required to model robustly the Au-Fe pairs.

representation, as compared to a direct space representation (R') provided by conventional FT analyses.

Figure 2 shows the analysis (2D and 3D CCWT modulus) of an experimental Au L_{III}-edge k^3-weighted EXAFS spectrum, collected for gold sorbed on a goethite (FeOOH); data from [5]. The CCWT modulus, calculated between 0.2 and 6.0 Å, shows a second neighbors contribution (ridge C) occurring for high k-values, which suggests the presence of "heavy" atoms (i.e., high atomic number) in that coordination shell [2]. However, based on other evidence (see [5] for details), Au atoms cannot be located in the next-nearest environment around gold. Consequently, the CCWT modulus highlights an important destructive interaction (see region B) between, at least, two EXAFS contributions. Based on a detailed analysis of the EXAFS spectrum [5], the first contribution is related to "Au–O" MS events, whereas the other one is related to Au–Fe SS events. Also, the CCWT analysis shows the importance, in that specific case, to collect data up to 16 $Å^{-1}$ in order to get significant contributions from the distant Fe atoms.

3. Conclusions

The continuous Cauchy wavelet analysis is a useful tool to better understand the various contributions that compose an XANES and EXAFS spectrum. The code requires only a minimum number of pre-defined parameters (Cauchy order and number of steps, usually both set to 200). Its simplicity of use makes it quite powerful, especially for non-expert users. Our code can be freely downloaded from http://www.univ-mlv.fr/~farges/wav/. This code is a script that runs under Matlab, which was positively tested in Windows and MacOS platforms (both 9 and X).

References

1. Chui, C. K., "An Introduction to Wavelets" (Academic Press, London 1992), p. 264.
2. Muñoz, M., Argoul, P. and Farges, F., Am. Mineral. **88**, 694 (2003).
3. Argoul, P. and Le, T.-P., Mech. Syst. Signal Process. **17**, 243 (2003).
4. Farges, F., Am. Mineral. **82**, 44 (1997).
5. Berrodier, I. *et al*., Geochim. Cosmochim. Acta (2003), submitted.

Physica Scripta. Vol. T115, 223–225, 2005

A Study of the Pre-Edge X-Ray Absorption Fine Structures in Ni Monoxide

S. J. Li[1], Z. Y. Wu[1,2,*], T. D. Hu[1], Y. N. Xie[1], J. Zhang[1], T. Liu[1], C. R. Natoli[2], E. Paris[3] and A. Marcelli[2]

[1]Beijing Synchrotron Radiation Facility, Institute of High Energy Physics, Chinese Academy of Sciences, P.O. Box 918, 100039 Beijing, China
[2]Laboratori Nazionali di Frascati, Istituto Nazionale di Fisica Nucleare, Via Enrico Fermi 40, I-00044 Frascati, Italy
[3]Dipartimento di Scienze della Terra and INFM, Universita' di Camerino, I-62032 Camerino, Italy

Received June 26, 2003; accepted November 4, 2003

PACS numbers: 78.70.Dm, 72.80.Ga, 71.70.Ch

Abstract

Pre-edge features in the Ni K-edge X-ray absorption near-edge structure (XANES) spectrum of Ni monoxide (NiO) in octahedral coordination, were investigated. By comparing experimental data with dipolar and quadrupolar cross-section calculations in the framework of the full multiple-scattering theory we assign the first pre-edge peak to a direct quadrupolar transitions from the 1s core state to the 3d molecular orbitals of the central atom (due to the more effective attraction of the core hole). The intensity of quadrupolar transition is almost equal to the dipolar pre-edge structure, at higher energy, due to the hybridization between the p-orbitals of the central atom with the higher-shell metal octahedral orbitals, that reflects the density of states derived by the medium range order of the system.

1. Introduction

X-ray absorption fine structure (XAFS) is a unique probe to determine local atomic structure as well electronic information in many systems, e.g., in biology, chemistry, geophysics, metallurgy, or materials science [1, 2]. Over the past three decades this technique has made great progress by providing high precision information. In fact, the success of the XAFS technique must be attributed, in large part to the advance of the theory, which allows a reliable quantitative structural information. So far systematical theoretical analyses of X-ray absorption spectroscopies in 3d TM compounds have not been conclusive and most of the interpretations and general understanding of the X-ray-absorption near edge structure (XANES), in particular at the pre-edge, remains an open and controversial problem [3–9].

It is well known that various properties of these transition-metal oxides are correlated to the geometrical structure around the transition-metal sites [10, 11]. Therefore a quantitative understanding of the transition features in the spectra is a prerequisite to a full investigation of the atomic environment around the photoabsorber as well as the electronic structure of metal-ligand atoms. In this work we present a detailed theoretical analysis of experimental XANES data at the K edge of the Ni for the NiO system.

2. Experiment and Calculation

XANES spectrum at the Ni K edge was measured in transmission mode using a Si(111) double crystal monochromator at the X-ray absorption station (beam line 4W1B) of the Beijing Synchrotron Radiation Facility (BSRF). The storage ring was working at the typical energy of 2.2 GeV with an electron current of about 100 mA. To suppress higher harmonics, a detuning of 30% was performed between the monochromator crystals. The spectrum was stored at steps of 0.5 eV and at the energy resolution of ∼1.5 eV. NiO samples of fine powders were achieved spreading powders on two pieces of a Kapton tape.

The calculations were carried out using the one-electron full multiple-scattering theory [12–14] and the Mattheiss prescription [15] to construct the cluster electronic density and the Coulomb part of the potential (by superposition of neutral atomic charge densities obtained from the Clementi-Roetti tables [16]), and the screened $Z + 1$ approximation (final state rule) [17] for simulating the charge relaxation around the core hole. The energy-dependent real Hedin-Lundqvist exchange potentials was used, followed by a Lorentzian convolution (∼2.9 eV consistent with the core hole life time and the experimental resolution) to account for inelastic losses of the photoelectron in the final state and the core hole width. We have chosen the muffin-tin radii allowing a 10% overlap between contiguous spheres to simulate the atomic bonds [18, 19].

3. Results and Discussion

Nickel K-edge experimental XANES spectrum of NiO is shown in Fig. 1 (upper curve). It displays several main features labeled (A1, A2, B and C) in good agreement with other published work

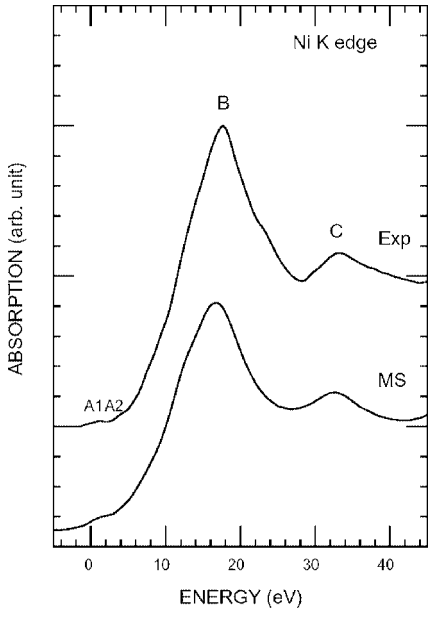

Fig. 1. The experimental and the multiple-scattering calculation of the XANES spectra at the Ni K edge of the NiO system.

*Corresponding author: E-mail: wuzy@ihep.ac.cn and/or wuziyu@lnf.infn.it

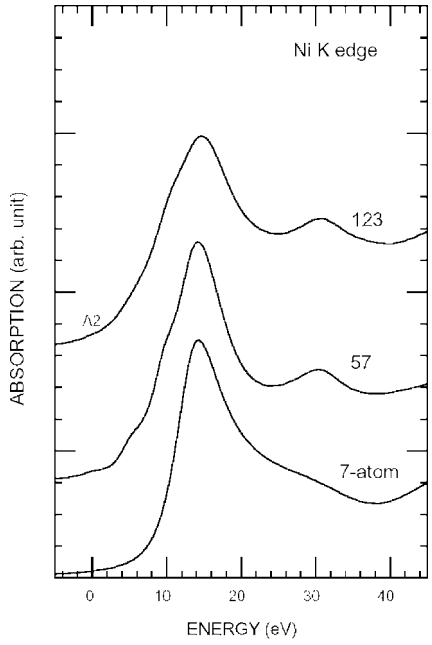

Fig. 2. Theoretical dipolar XANES spectra at the Ni K edge in NiO, as a function of the cluster size (7, 57 and 123 atoms).

[20]. Actually, we may divide the spectrum in three regions:

(I) the first region (labeled A) named the "pre-edge" region. For NiO, in this region two components (not resolved very well), A_1 and A_2 of approximately equal intensity, separated by about 1.3 eV appear;
(II) the second region, around the maximum of the cross section, that presents a strong feature labeled B;
(III) the third region, that extends up to about 20 eV from the edge contains the broad peak labeled C.

The comparison in Fig. 1 reveals a good agreement between the calculated (bottom curve) and experimental Ni K-edge XANES spectra for the NiO. The calculation takes into account all multiple-scattering paths in a rather big cluster (123 atoms) but do not allow us to assign a particular shell of neighbors to each feature. To clarify this point, we have to perform MS calculations adding consecutive Ni and O shells around the emitter atom.

NiO has a cubic structure with a lattice constant $a_0 = 4.16$ Å [21]. The coordinating oxygen octahedron around the nickel atom is perfect with a bond length of Ni-O of 2.08 Å. In Fig. 2, we present computations of the Ni K-edge XANES spectra for NiO by using a fully relaxed final state potential obtained within the $Z + 1$ approximation [17] for different cluster sizes (7, 57, and 123 atoms) up to the convergence. The last one contains all atoms within 7 Å from the photoabsorber (i.e., the Ni) taken as the center of the cluster. For a minimal cluster composed just of a Ni as the central atom (emitter) and six nearest neighbors (O atoms), the calculated absorption spectrum shows the main peak B and a broad peak C which correspond to transition to the Ni p-like final states. In MS calculations, from the point of view of the scattering, the second shell (six oxygen atoms) is necessary to reproduce the quite strong peak B as well as the broad peak C. So, these features arise from scattering within the first oxygen atomic shell. This behavior is the demonstration of the relatively strong backscattering of the O^{2+} ions [22].

Increasing the cluster, up to the fourth shell of Ni and oxygen atoms, the pre-peak A_2 appears. The reason for this is rather clear. Higher coordination neighbors (the next-nearest Ni shell plus surrounding oxygen atoms) are necessary to construct the appropriately hybridized 3d-like molecular orbitals around each Ni atom in the cluster which are made up of 3d metal orbitals and 2p oxygen orbitals. The 57-atom cluster in fact already includes enough oxygen around Ni to form octahedra whose orbitals mix with the 4p states of the central atom. Furthermore, these neighboring octahedra strongly interact with each other and cause molecular orbitals to overlap, forming extended energy bands and modifying their energy position.

All features observed in the experimental spectrum, except the pre-edge A_1, are reasonably well reproduced in the last large cluster calculation (123 atoms), not only in term of relative intensities but also in energy separations. This points out that a 123-atom cluster is sufficient to describe bulk properties and that the pre-peak is, at the same time, very sensitive to the "medium-range" order of the solid. They might therefore be used to extract information on this range. Furthermore, the peak A_2 comes from dipole transition based on theoretical MS simulation of absorption cross sections.

Since in transition-metal compounds the empty 3d-derived states normally lie at lower energies than the empty 4p-like states, significant quadrupole transitions are mostly to occur mainly in the pre-edge region. In order to shed light on the type of transition involved and identify the origin of spectral feature A_1, we present theoretical simulation, based on one-electron full multiple scattering theory, the unpolarized quadrupole absorption cross sections based on the following equations:

$$\sigma^{Q}(\omega) = 4\pi^2(\alpha\hbar\omega)^3 \frac{1}{240} \frac{2l_0+1}{2l+1} \sum_{lm} \mathrm{Im}\tau^{00}_{lm,lm}(M^q_{l_0 l})^2(l_0 020 \mid l0)^2.$$

As usual in MS theory, $\tau^{00}_{lm,lm}$ is the scattering path operator calculated at the photoabsorbing site for angular momentum lm, the imaginary part of which is proportional to the site and lm projected density of state of the system, $M^q_{l_0 l}$ is the radial matrix element of the quadrupole operator between the core state and the l component of the final state wavefunction, l_0 is the angular momentum of the initial core state and $(l_0 0 l_t 0 \mid l0)$ is a Clebsh-Gordan coefficient. We use atomic units (au) for lengths and Rydberg units for energy so that the cross section is expressed in $(\mathrm{au})^2$.

In Fig. 3 the contribution of the quadrupole allowed absorption is presented by the solid line (bottom curves) and compared with the dipole allowed absorption dot line (bottom curves), before the convolution, for the 123-atom cluster. As can be recognized, the quadrupolar spectrum is almost featureless except for a pronounced pre-edge peak A_1 lying at the lower energy about 1.3 eV than the dipole allowed pre-edge structure A_2, with the similar intensity. The agreement between the experiment and theoretical simulations is much better by taking into account both contributions of dipole and quadrupole as shown in Fig. 3, curves (b) and (c), indicating that the first prepeak in the Ni K-edge XANES spectrum of NiO is a purely quadrupole one.

4. Conclusion

In conclusion, we have studied experimentally and theoretically for the first time the pre-edge features in the X-ray absorption spectrum of NiO at the Ni K edge in octahedral coordination. By comparison of the dipolar and quadrupolar cross sections calculated in the framework of ab initio full MS theory we claim that the lowest feature in energy is purely quadrupolar in

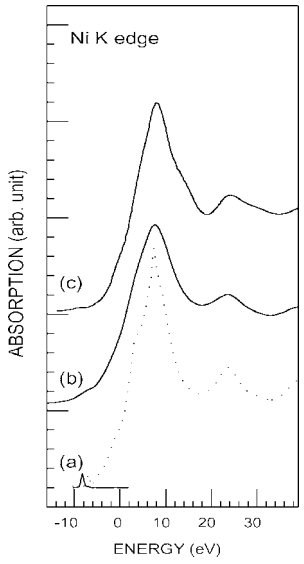

Fig. 3. The curves (a) are the multiple scattering quadrupolar (solid line) and dipolar (dot line) calculations of the XANES spectra of the Ni K edge in NiO, using a 123-atom cluster. Curve (b) is the convoluted sum of the dipolar and quadrupolar contributions while the experimental data are curve (c).

character followed by dipolar transition due to the medium range order of the system (a mixing of p orbitals of absorbing atom with 3d orbitals of higher-neighbouring metal octahedra). A good agreement between experimental data and theoretical ones has been achieved indicating that a purely quadrupole nature of the preedge was established in a positive way.

We stress here that the comparison is precise and may be extended to other 3d TM compounds and more complex systems.

Acknowledgement

We would like to thank C. R. Natoli for useful discussions. Z. Y. W. acknowledges the financial support of the Key Important Project (10490190) and of the *Outstanding Youth Fund* (10125523) of the National Natural Science Foundation of China.

References

1. Garcia, J., Blasco, J., Proietti, M. G. and Benfatto, M., Phys. Rev. **B 52**, 15823 (1995).
2. Rehr, J. J. and Albers, R. C., Rev. Mod. Phys. **72**, 621 (2000).
3. Antonangeli, F., Piacentini, M., Girlanda, R., Martino, G. and Giuliano, E. S., Phys. Rev. **B 32**, 6644 (1985).
4. Grunes, L. A., Phys. Rev. **B 27**, 2111 (1983).
5. Uozumi, T., *et al*., Europhys. Lett. **18**, 85 (1992).
6. Heumann, D., Hofmann, D. and Drager, G., Physica **B 208** & **209**, 305 (1995).
7. Maruyama, H., Harada, I., Kobayashi, K. and Yamazaki, H., Physica **B 208** & **209**, 760 (1995).
8. Brouder, C., Kappler, J. P. and Beaurepaire, E., 2nd European Conference on Progress in X-ray Synchrotron Radiation Research, (edited by A. Balerna, E. Bernieri and S. Mobilio), (Bologna: SIF 1990), Vol. **25** p19.
9. Lytle, F. W., Greegor, R. B. and Panson, A. J., Phys. Rev. **B 37**, 1550 (1988).
10. Sarma, D. D., *et al*., Phys. Rev. Lett. **75**, 1126 (1995).
11. Satpathy, S., Popović, Zoran S. and Vukajlovic, Filip R., Phys. Rev. Lett. **76**, 960 (1996).
12. Durham, P. J., in "X-ray Absorption: Principles, Applications, Techniques of EXAFS, SEXAFS, XANES", (edited by R. Prinz and D. Koningsberger), (Wiley, New York, 1988) and references therein.
13. Lee, P. A. and Pendry, J. B., Phys. Rev. **B 11**, 2795 (1975).
14. Tyson, T. A., Hodgson, K. O., Natoli, C. R. and Benfatto, M., Phys. Rev. **B 46**, 5997 (1992) and references therein.
15. Mattheiss, L., Phys. Rev. **A 134**, 970 (1964).
16. Clementi, E. and Roetti, C., At. Data Nucl. Data Tables **14**, 177 (1974).
17. Lee, P. A. and Beni, G., Phys. Rev. **B 15**, 2862 (1977).
18. Norman, J. G., Mol. Phys. **81**, 1191 (1974).
19. Joly, Y., Phys. Rev. **B 63**, 125120 and references therein (2001).
20. Lytle, F. W., Greegor, R. B. and Panson, A. J., Phys. Rev. **B 37**, 1550 (1988).
21. Wyckoff, R. W. G., "Crystal Structures", 2nd ed. (Interscience, New York, 1963).
22. Wu, Z. Y., *et al.*, Phys. Rev. Lett. **77**, 2101 (1996); Wu, Z. Y., *et al.*, Phys. Rev. **B 55**, 2570 (1997); Wu, Z. Y., Ouvrard, G., Gressier, P. and Natoli, C. R., Phys. Rev. **B 55**, 10383 (1997).

Physica Scripta. Vol. T115, 226–228, 2005

3D Molecular Graphical user Interface Add-On for Analysis Program for EXAFS: A New Prospect

N. Dimakis*[1,2] and G. Bunker[1]

[1]Illinois Institute of Technology, Chicago, IL 60616, USA
[2]Biophysics Collaborative Access Team, Argonne National Laboratory, Argonne, IL 60439, USA

Received June 26, 2003; accepted November 4, 2003

PACS number: 61.10Ht

Abstract

This report describes an effort to include three-dimensional interactive molecular graphics into the main APEX program, a free, open source, cross platform data analysis package for X-Ray Absorption Fine Structure (XAFS) data analysis. The latest version of APEX (2.7.3) based on a native TCL/TK tab-notebook style graphical user interface includes among others, user-friendly interactive two-dimensional graphics under BLT, an extension of TCL/TK with advanced printing capabilities; generic format conversion from ASCII to University of Washington binary-type files; new TCL routines for data handling; XMU corrections and multiple scattering fitting. Based on Virtual Rendering System (VRS), the 3-D version reads and displays molecular structures for various file formats allowing object rotation, translation and atoms selection for determining interatomic distances and angles. The most important feature of 3D APEX is the interaction with the FEFF program: scattering paths are displayed, selected and are used to generate appropriate $\chi(k)$ XAFS spectra. 3D APEX is the only program that offers three-dimensional graphics and in its current form is suitable for routine data analysis and training. At this time the 3D APEX add-on is only available for Windows PC. Addition of more advanced methods of data analysis are planned.

1. Introduction

The first version of Analysis Program for EXAFS (APEX) [1, 2] provided one of the first open-source cross platform graphical user interface (GUI) interfaces to EXAFS analysis programs. Early APEX versions included standard methods based on University of Washington (UW/NRL) Fortran codes for XAFS data reduction and analysis. Subsequently support for automated background subtraction and multiple scattering fitting via AUTOBK [3] and FEFFIT [4] programs was added, and two-dimensional (2D) interactive graphics was dramatically improved. Here we report additional enhancements including three-dimensional (3D) interactive graphics for simplifying manipulation of FEFF multiple scattering path files.

The main GUI for APEX 1.0/2.0 versions was written in TCL/TK [5, 6] programming language, which runs on a wide variety of the operating systems like Linux, Silicon Graphics IRIX version 6.5 and above, Apple operating systems MacOS9, MacOSX, and PC compatibles under Windows 98 and above. The 2D interactive graphics was written in BLT [7], an extension of TCL/TK that is available on all of the above mentioned platforms except the obsolete Mac OS 9.

APEX development was based on the perceived need for a cross platform XAFS data analysis package that runs without emulation on different operating systems, was easy for novices, but also useful for experts. Starting with a proven code base (UW/NRL), incrementally removing its limitations, and adding more advanced features has led to a well acceptable package. Recently we have improved the functionality of the main APEX GUI card using a native TCL tab-notebook style GUI. Writing code on native TCL ensures cross-platform compatibility and easy access to bug-fixing problems. The reading and writing to and from UW binary platform-dependent files, and most of the old UW FORTRAN based utilities are now written under native TCL, thus improving integration of the executables with the GUI cards. Improvements to the base code include adding advanced printing capabilities based on the interactive BLT graphics, adding contextual balloon style help, generating unique symbolic keys for input/output UW files using TCL, adding an XMU correction program and calculating X-Ray absorption and scattering cross sections directly from a graphical periodic table. The main APEX code (version 2.7.3) runs under Linux, IRIX and WinPC. Porting the main package to Mac OS X is underway.

During APEX development other excellent cross-platform packages like ATHENA [8] also have been developed. Between the various packages the basic needs we perceived have been addressed. We therefore we decided to add newer, more advanced capabilities to the APEX package: the inclusion of 3-D interactive graphics that could interact with the FEFF [9] program.

This 3-D OPENGL library-type window is using the Interactive Virtual Rendering System (VRS, iVRS [10]), a cross-platform C++ type application programming interface (API) that can be called as an external package from TCL/TK and provides full access to all 3D features of the VRS system. Using iVRS, complex interactive scenes can be rendered and integrated with the TK toolkit. The 3D-APEX reads and displays molecular structures in various formats allowing the user to rotate, and zoom the structure but also to determine graphically interatomic distances and angles. If a FEFF input file is read together with the corresponding scattering paths file, these paths are interactively displayed and can be selected for further analysis.

Current limitations of the main APEX program is that the Random Data File format (RDF) UW file format upon which it is based are platform dependent e.g. a Linux UW file will not be directly usable in a WinPC type environment unless its is first converted to ASCII. A new cross-platform standard file format (e.g. Hierarchical Data Format (HDF) or XML) is required for future use in APEX, and this is planned. 3D-APEX is currently available for WinPC, and ports to Linux, Mac OS X, IRIX, and other Unix derivatives are planned. Official versions of APEX 2.7.3 and 3D-APEX are available at the APEX [11], Bio-CAT [12] home pages and mirror sites.

2. Discussion

The 3D-APEX window is incorporated into the main APEX package and directly linked under APEX FEFF card. For WinPC

*e-mail: dimakis@biocat2.phys.iit.edu

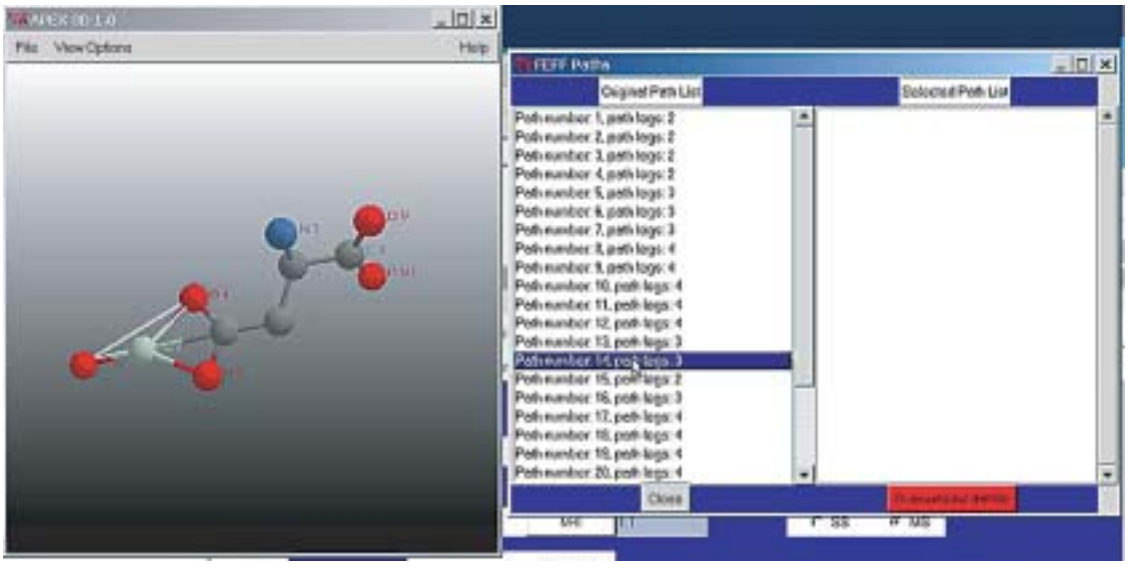

Fig. 1. Screenshot of 3D APEX window displaying Zn-Aspartic acid structure using *feff.inp* file format. The listbox on the right can be used to select FEFF generated scattering paths and overwrite the FEFF *list.dat* file for $\chi(k)$ calculation.

versions a new button appears on the FEFF card prompting the user to launch the 3D-window. A *feff.inp* file that either has been loaded into APEX or created from the package itself is read and its corresponding molecular structure is displayed. Atoms appear as colored solid spheres and these colors are defined in the periodic table card. The user can display atoms and bonds (default value) or atoms only. Although 3D-APEX has no particular information about the corresponding molecular orbitals of the displayed structure, interatomic bonds are drawn based on interatomic distance and covalent radius. The user can also define and remove labels i.e. select atoms and display their corresponding interatomic distance/angle in the main window. Background color is user selectable and subsequent versions of the 3D window will also permit user-selectable atom colors.

The most important feature of the 3D-APEX is its ability to read and display FEFF single- and multiple-scattering paths for a given molecular structure. Paths are read from FEFF *paths.dat* file and entered in a TK listbox. Selecting a particular path from the paths listbox will automatically render it in the 3D-window (Fig. 1) with its "legs" to appear as grayed cylinders. The program ensures that paths "legs" will not overlap with the interatomic bonds if the later are also present in the display. After visualizing a particular path the user may choose to keep it by copying it into another adjacent listbox. Selected copied paths in the later listbox will be used for to generate $\chi(k)$ XAFS spectra by writing out the corresponding FEFF *list.dat* file. The 3D-window also offers printing capabilities: *any* rendered graphics in the 3D canvas window can be exported into JPEG file type format (Fig. 2) for either printing or used elsewhere.

Besides the 3D graphics this latest APEX 2.7.3 offers much more than just incremental improvements. A screenshot of the BLT graphics with the printing dialog is shown in Fig. 3. The small canvas picture in the printing dialog is a direct copy of the main graphics canvas: the user may scale the graphics by resizing the small picture, print it in grayscale/color and landscape/normal page formats. Two dimensional graphics can also be exported as either GIF, PostScript or PDF file formats with the help of ghostscript program that is included in APEX package.

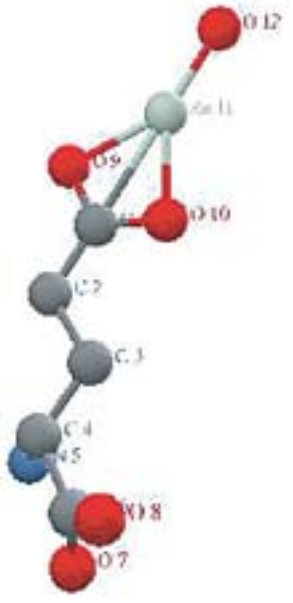

Fig. 2. Zn-Glutamic Acid structure as exported in JPEG format by 3D-APEX. The structure was in xyz-format.

Many users rarely read help manuals. Whenever they encounter a difficulty they try to experiment before they think about reading the help manual. Therefore we have included an interactive balloon type help system in addition to the local and internet help that previous APEX versions offered. Positioning the mouse over a label a balloon help text appears dialog box provide brief description about a label or a menu.

Future plans on the 3D-APEX include adding stereo capabilities, allowing the user to drag-and-drop atoms and include pre-built libraries of organic structures like amino acid residues. For the main package, designing a new type of RDF file (possibly XML or HDF) that will replace the platform specific UW format files, bundling FEFF6, incorporating the new interactive IFEFFIT, add extensions to RDF reconstruction by regularization, and adding automatic edge-energy selection are some of the near future improvements. FEFF7 and higher versions are separately

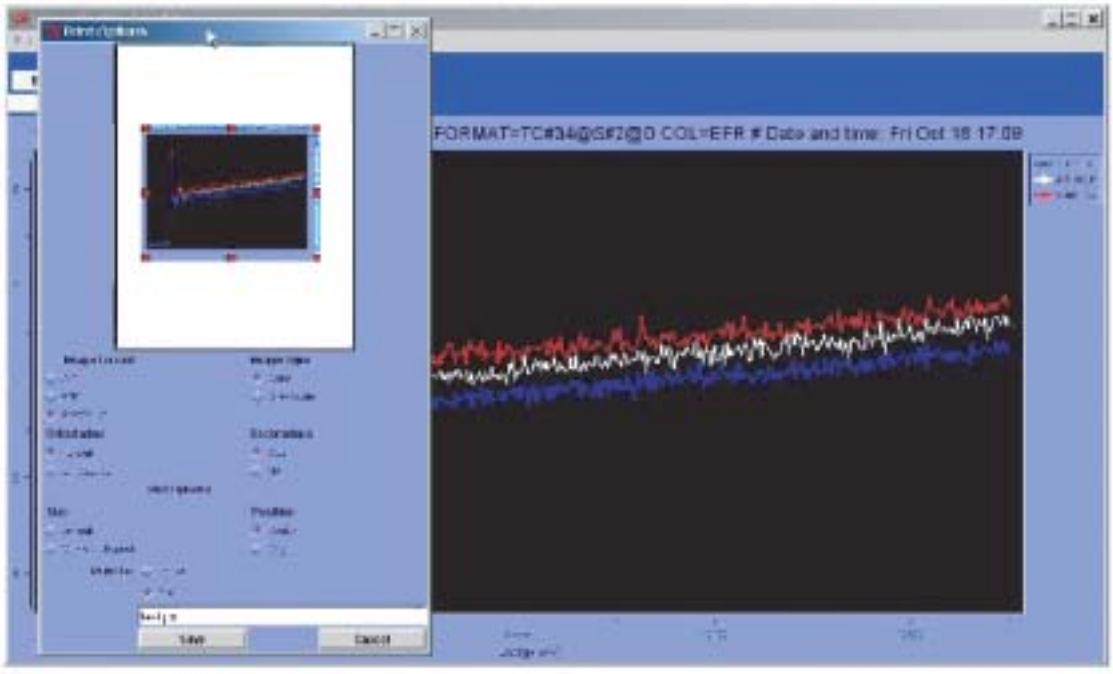

Fig. 3. Advanced Printing option for the BLT interactive graphics. The file output can be scaled, plotted in color/grayscale and exported in PostScript, GIF, and PDF file formats.

licensed and are not part of the APEX package, and must be obtained from the FEFF project.

3. Conclusion

The 3D version of APEX is an open-source XAFS data analysis package that offers support for multiple complementary algorithms for data reduction and analysis (UW/NRL, AUTOBK/FEFFIT), a friendly graphical user interface, advanced presentation-quality plotting and printing capabilities, direct interaction with FEFF, display of 3D molecular structures from FEFF path files, and graphically selection of single and multiple scattering paths for generating $\chi(k)$ XAFS. Our near-future tasks are to port these 3D capabilities into other operating systems like Linux, Mac OSX and IRIX. More advanced and automated data analysis routines in a cross-platform native TCL language are underway.

References

1. Dimakis, N. and Bunker, G., J. of Synchrotron. Radiat. **6**, 274 (1999).
2. Dimakis, N. and Bunker, G., J. of Synchrotron. Radiat. **8**, 317 (2001).
3. Newville, M., Livins, P., Yacoby, Y., Stern, E. A. and Rehr, J. J., Phys. Rev. **B47**, 14126 (1993).
4. Newville, M., Ravel, B., Haskel, D. and Stern, E. A., Physica B **208 & 209**, 154 (1995).
5. Ousterhout, J., "TCL and TK", (Addison-Wesley 1994).
6. Welch B., "Practical Programming in TCL and TK", (Prentice-Hall 1997).
7. BLT, http://www.tcltk.com/blt
8. ATHENA, http://feff.phys.washington.edu/~ravel/software/exafs/aboutathena.html
9. Ankudinov, A. L., Ravel, B., Rehr, J. J. and Cnradson, S. D., Phys. Rev. **B58**, 7565 (1998).
10. VRS and iVRS, http://www.vrs3d.org
11. APEX Home Page, http://ixs.csrri.iit.edu/ñdimakis.
12. Biophysics Collaborative Access Team, http://www.bio.aps.anl.gov/

Physica Scripta. Vol. T115, 229–231, 2005

Lifetime dependency of the VUV-excited resonant photoemission spectra of ionic molecules

M. Huttula, E. Kukk, H. Aksela, R. Sankari and S. Aksela

Department of Physical Sciences, University of Oulu, P.O. BOX 3000, 90014 University of Oulu, Finland

Received June 26, 2003; revised July 11, 2003; accepted November 4, 2003

PACS numbers: 33.60.Cv, 33.80.−b

Abstract

Electronic decay of synchrotron-radiation-excited VUV-resonances in the KCl and CsCl molecules is studied. Despite the similarity of the two compounds, qualitatively different resonant modifications of the valence electron spectra are observed and are investigated by modelling nuclear dynamics including the lifetime vibrational interference. The modelling predicts a much shorter lifetime of the resonances in KCl than in CsCl, which is confirmed by ion yield measurements as due to the opening of a spectator-type decay channel in KCl.

1. Introduction

Alkali halide molecules have a strongly ionic bond, where one outer shell electron from the alkali atom is transferred to the halide side. With the absence of shared electrons, the electronic transitions in alkali halides are typically studied as transitions in either the alkali$^+$ or halide$^-$ ion. Studying the products of the subsequent molecular dissociation allows one to identify the electronic transition channels. Previously, dissociation following the VUV-excitations in KCl and CsCl has been studied in Refs. [1] and [2], where the existence of inter-ionic electronic decay channels was found.

In the present work, the electron emission spectra at the VUV-resonances in KCl and CsCl are compared. At the resonances, the valence photoelectron spectra can be enhanced by an autoionization channel. This contribution can strongly modify the observed lineshapes, being a sensitive indicator of the lifetime of the excited state [2]. Our aim is to study the crucial role of the lifetime in decay and to arrive at a consistent interpretation of the absorption, electronic decay and dissociation processes, particularly taking into account the fact that very different fragmentation patterns were observed for these molecules [1, 2].

2. Experimental

The experiments were performed on the bending magnet beamline BL52 [3] at the MAX–I storage ring in Lund, Sweden. The synchrotron radiation is monochromatized by a normal incidence monochromator and focused to the experiment with a toroidal refocusing mirror. Photon energy calibration was done measuring simultaneously the Ar 3p photolines with the first and second order radiation from the monochromator. The experimental set-up consists of a Scienta SES-100 electron energy analyzer mounted in the same vacuum system with a Wiley-McLaren type of ion TOF spectrometer [4]. A resistively heated oven was used to produce molecular vapour of the solid KCl and CsCl. The temperatures needed to generate the 10^{-2} mbar vapour pressure inside the stainless steel crucible were in the range of 800–900 K for both of the molecules. All electron spectra were measured at the magic angle (54.7°) relative to the electric field vector of the linearly polarized light. The binding energy calibration of the measurements was obtained from the simultaneous measurement of Ar 3p photolines [5] and the studied valence photoelectron spectrum. In the ion yield measurements the fluctuations and the photon energy dependency of the incident photon flux were accounted for using the GaAsP photodiode mounted behind the interaction volume.

3. Results and Discussion

3.1. *Photoabsorption*

The photon energy range of the total ion yield (TIY) spectra of Fig. 1 represents photoabsorption by the outermost shells of the alkali and halide ions. In the TIY spectrum of CsCl [Fig. 1(a)], a resonant structure appears between 12 and 18 eV and in the TIY spectrum of KCl [Fig. 1(b)], four resonances appear at 18–24 eV. Assuming a fully ionic bond, these resonances are assigned to the Rydberg excitations in the metal end of the molecule, i.e. $3p \rightarrow nd$ in K^+ [1] and $5p \rightarrow nd$ in Cs^+ [2].

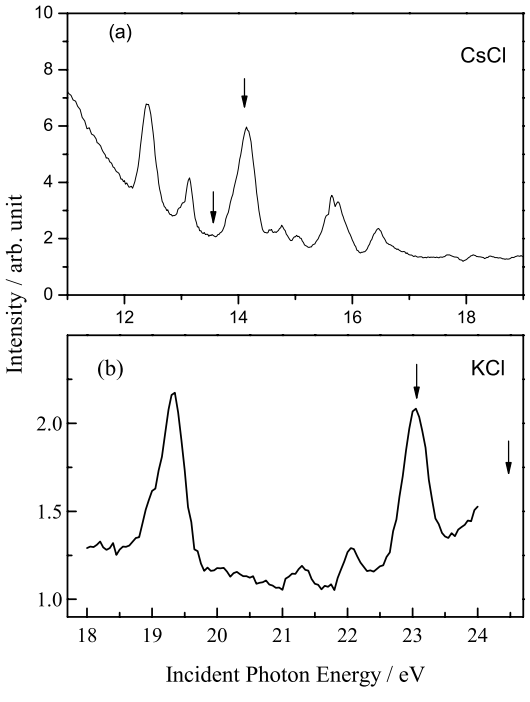

Fig. 1. Total ion yield (TIY) spectra of CsCl [2] and KCl [2]. The arrows refer to the photon energies of the photoelectron spectra of Fig. 2.

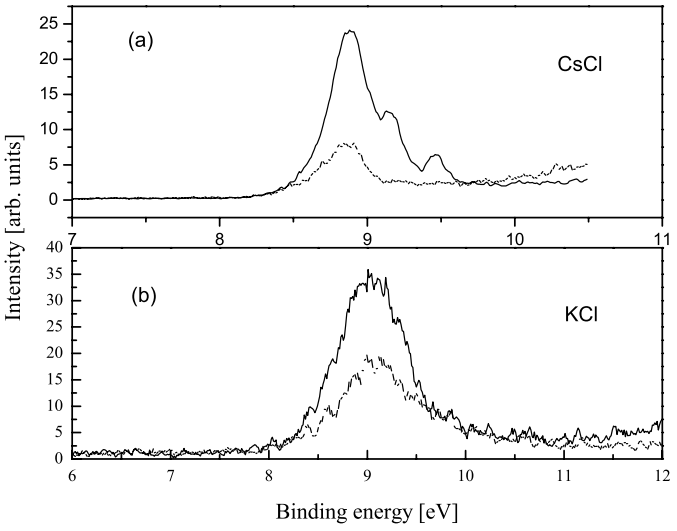

Fig. 2. Valence photoelectron spectra of the CsCl and KCl molecules. (a) CsCl, measured at a resonant [2] (14.2 eV, solid) and nonresonant photon energy (13.5 eV, dashed); (b) KCl, measured at a resonant (23.0 eV, solid) and nonresonant (24.5, dashed) energy.

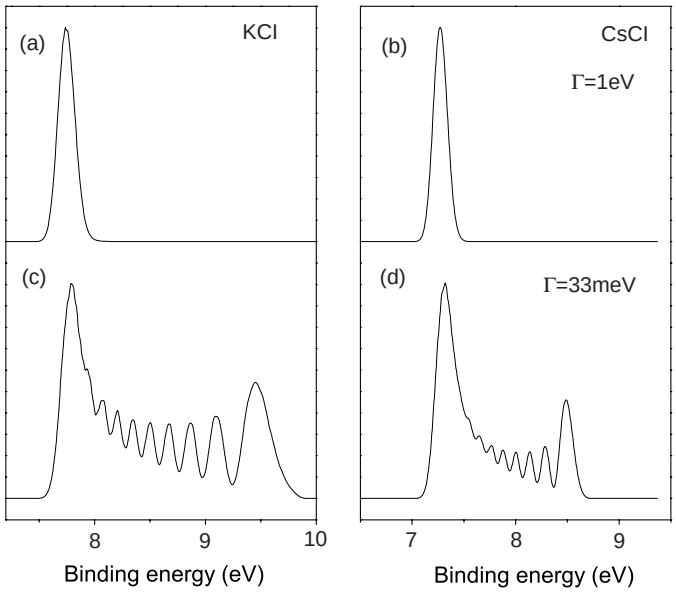

Fig. 3. The modelled electron decay spectra of KCl and CsCl. The upper spectra correspond the case where the electronic decay is fast compared to the nuclear motion; the lower spectra present the case where the timescales are similar.

3.2. *Electron spectra*

In order to study the nature of the decay of the excited states in the KCl and CsCl molecules, the valence photoelectron spectra corresponding the photoionization of the $3p$ orbital in Cl^- in our ionic model were measured at a resonant and, for reference, at a non-resonant photon energy (Fig. 2). Comparing the resonant and non-resonant spectra of KCl, about twofold intensity enhancement is seen, but the lineshape remains unaffected. The spectra of CsCl would be expected to behave similarly, since both molecules are ionically bonded and the resonances have a similar Rydberg character, but as seen in Fig. 2, remarkable differences occur. The nonresonant spectrum of CsCl [Fig. 2(a)] consists of a single peak with a width of 0.4 eV (FWHM), similarly to KCl. However, in the spectrum measured at a resonance, a clear triple-peak structure is seen in addition to the intensity enhancement by a factor of 3.6. The intensity increase at resonant photon energy in both of the molecules shows that the decay includes the inter-ionic participator-type Auger transition (autoionization) channel $A^*Cl(A^+mp^5nd, Cl^-3p^6) \rightarrow ACl^+(A^+mp^6, Cl^0 3p^5) + e^-$, where $A = K(m = 3)$ or $A = Cs$ $(m = 5)$. The final state of the autoionization is the same as for direct Cl $3p$ photoionization, after which the KCl (CsCl) molecule consists of Cl^0 and K^+ (Cs^+).

3.3. *Modelling*

The electronic decay in molecules is affected by the vibrational motion. In order to study its influence on the electron spectra, the electronic decay and nuclear relaxation processes were modelled. The modelling for CsCl is described in detail in Ref. [2] and the same procedure was followed for KCl. Briefly, the potential energy curves (PECs), vibrational wavefunctions and energy levels were calculated and the electronic transitions between the PECs were examined. The PECs for CsCl (Ref. [2]) and KCl have similar properties – the ionic state is dissociative or very weakly bound due to the lack of Coulomb attraction between the Cl^0 and Cs^+, but the excited state is more strongly bound, having a shorter equilibrium distance than the ground state.

If the nuclear wavepacket has sufficient time to evolve after photoabsorption, the excited state can be properly represented by time-independent vibrational eigenfunctions. Then, since relatively high vibrational levels are excited, the probability density has two main maxima at the classical turning points (CTPs) and the electronic decay spectra shows two main peaks at the binding energies of the final ionic states, corresponding to the vertical transitions from the excited state at the CTPs. However, if the lifetime is comparable or much shorter than the vibrational period, the time-independent eigenfunctions and Franck-Condon factors alone are unsufficient to describe the system, but interference terms must be included [6–8], modifying the electron emission lineshape.

By comparing the simulations (Fig. 3) to the experimental valence photoelectron spectra (Fig. 2), it can be concluded that in KCl the period of vibrational motion is much longer than the electronic lifetime of the excited state, while in CsCl they are comparable.

KCl: Since the period of the vibrational motion is much longer than the electronic lifetime, electronic decay only happens at the outer CTP of the excited state. The transitions at the inner CTP are completely suppressed by the interference terms and the resulting electron spectrum (a) in Fig. 3 is identical in shape with the nonresonant photoelectron spectrum, as observed [Fig. 2(b)]. The resonance only enhances the photoionization cross-section.

CsCl: In this case, the wavepacket has a significant probability to reach the inner CTP. The interference suppression of the second peak is therefore incomplete and it appears in the spectrum (d), corresponding to the new structures seen in the experiment [Fig. 2(a)]. Although the agreement between the modelling and experiment is only qualitative (the reasons are discussed in Ref. [2]), it is the appearance of any significant new structure as such that indicates a considerably longer excited state lifetime.

The model thus predicts that in addition to the decay by autoionization, which is present in both of the studied molecules, in KCl there must exist an additional, faster decay channel following the resonant exitation, shortening the lifetime.

3.4. *Partial yields*

In order to search for the differences in the decay channels that could account for the predicted large differences in the resonant state lifetimes between KCl and CsCl molecules, partial ion yields

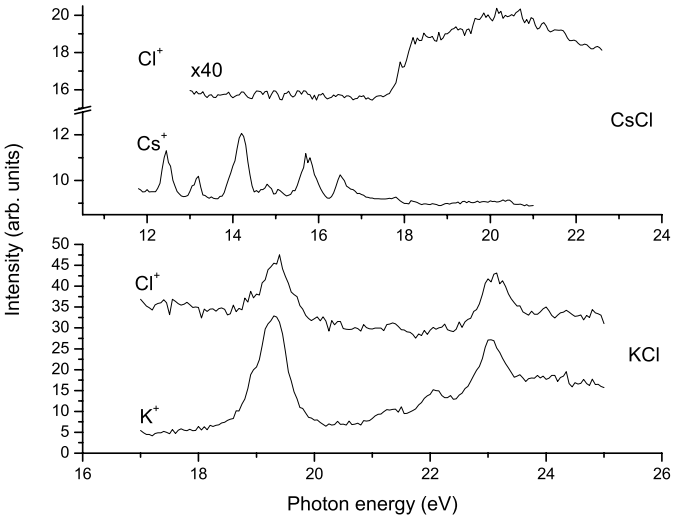

Fig. 4. The partial ion yield spectra of CsCl [2] and KCl [1].

in the energy regions of the resonances were studied. Figure 4 presents the partial yields of the $K^+(Cs^+)$ and Cl^+ of KCl (CsCl). It can be seen that in KCl the yield of both fragments follow the absorbtion pattern, but in CsCl only the amount of Cs^+ ions resonates, following the TIY-spectrum [Fig. 1(a)]. The autoionization process that contributes to the valence electron spectra produces only the metal ions. Positive chlorine ions can only be produced if the excited electron remains as a spectator electron while the vacancy is filled by a Cl^- $(3p)$ electrons and another one is emitted. So the two decay channels for KCl are autoionization $[K^*Cl(K^+3p^5nd,\ Cl^-3p^6) \rightarrow KCl^+(K^+3p^6,\ Cl^03p^5) + e^-]$ and spectator decay $[K^*Cl(K^+3p^5nd,\ Cl^-3p^6) \rightarrow KCl^+(K^03p^6nd, Cl^+3p^4) + e^-]$, whereas in CsCl only autoionization $[Cs^*Cl(Cs^+5p^5nd, Cl^-3p^6) \rightarrow CsCl^+(Cs^+5p^6, Cl^03p^5) + e^-]$ takes place. The spectator-type transition is usually very rapid, which explains the differences in the resonant state lifetimes. The absence of the spectator transitions in CsCl can be explained by taking into account that the binding energy of the electron experiencing the initial excitation in K^+ is larger than in the Cs^+ [2] and the energy released by filling the vacancy is sufficient to eject the other Cl^- $3p$ electron only in the former case.

4. Conclusions

The electronic decay of the VUV-excited resonaces, studied using electron spectroscopy, exhibits a very different character in molecular KCl and CsCl. Both cases were modelled including the lifetime intererence effects and the lifetime of the excited state in KCl was predicted to be much shorter than in CsCl. This conclusion was verified by studying the partial ion yield spectra, where in addition to the inter-ionic participator transition in both of the studied molecules, spectator Auger transitions appear only in KCl. The model was thus found to correctly predict the lifetime of the excited state based on the structure of the electon emission spectra. The lifetime dependency and lineshape modifications appear to be exceptionally strong in alkali halides and likely in other ionic compounds also.

Acknowledgments

This work has been financially supported by the Vilho, Yrjö and Kalle Väisälä Foundation, the Research Council of the Academy of Finland and the EU – Access to Research Infrastructure action of the Improving Human Potential Programme. We are gratefull to V. Kisand, E. Nõmmiste and V. Pennanen for their help in acquiring the data. The kind assistance of the MAX-lab staff is also akcnowledged.

References

1. Pennanen, V., Huttula, M., Aksela, H., Nõmmiste, E. and Aksela, S., J. Electron Spectrosc. Relat. Phenom. **114–116**, 169 (2000).
2. Kisand, V., *et al.*, J. Phys. B. **36**, 3909 (2003).
3. Sorensen, S. L., *et al.*, Nucl. Instr. and Meth. in Phys. Res. A **297**, 296 (1990).
4. Huttula, M., Harkoma, M., Nõmmiste, E. and Aksela, S., Nucl. Instrum. Methods A, **467**, 1514 (2001).
5. Moore, C. E., "Atomic energy levels, Vol. 1", (US Government Printing Office, Washington DC, 1971).
6. Kukk, E., *et al.*, J. Chem. Phys. **111**, 9642 (1999).
7. Kukk, E., Snell, G., Bozek, J. D., Cheng, W.-T. and Berrah, N., Phys. Rev. A **63**, 062702 (2001).
8. Cesar, A. and Ågren, H., Phys. Rev. A **45**, 2833 (1992).

Physica Scripta. Vol. T115, 232–234, 2005

Wavelet Analysis of Extended X-Ray Absorption Fine Structure Data

H. Funke[1,2*], M. Chukalina[3] and A. Rossberg[1,2]

[1]Research Center Rossendorf, Institute of Radiochemistry, POB 510119, 01314 Dresden, Germany
[2]European Synchrotron Radiation Facility, CRG-ROBL(BM20), POB 220, Grenoble Cedex, France
[3]Institute of Microelectronics Technology RAS, 142432 Chernogolovka, Moscow District, Russia

Received June 26, 2003; revised December 4, 2003; accepted December 9, 2003

PACS numbers: 61.10.Ht, 02.30.Uu

Abstract

Extended X-ray absorption fine structure data evaluation usually begins with the Fourier transform of the spectrum. We suggest the wavelet transform as a complement to the Fourier transform. While the Fourier transform analyzes the distances to the backscattering atoms, wavelet transform additionally reveals the wavenumber dependence of the scattering. Thus wavelet analysis can differentiate between heavier and lighter backscattering atoms, even if they are almost equidistant from the central atom. First the method of operation and the advantage of the wavelet analysis will be demonstrated by simple models. Then it is applied to the interpretation of extended X-ray absorption fine structure spectra concerning the complexation of Uranium(VI) with the carboxylic groups acetic-, formic-, and glycolic acid. The wavelet transform analysis suggests clearly for the system Uranium-formic acid both, U-U and U-C-C, structural elements. In contrast to the clear separation of different scattering paths by wavelet transform, Fourier transform analysis was not able to resolve the two different backscattering processes.

1. Introduction

Since the pioneering works of Stern, Lytle and Sayers [1–4] to the theory and data evaluation of extended X-ray absorption fine structure (EXAFS) spectra the data analysis begins with the discussion of the Fourier transform (FT) of the (k^3-weighted) EXAFS spectra. This first qualitative approximation to the determination of the searched physical parameters enables us to estimate how many co-ordination shells at which distances are entered by the EXAFS spectrum.

The theoretical basis for the quantitative analysis of the spectrum is the EXAFS equation:

$$\chi(k) = S_0^2 \sum_{i=1}^{n} \frac{N_i}{R_i^2} \frac{F_i(k,R)}{k} \mathrm{e}^{\frac{-2R_i}{\lambda}} \mathrm{e}^{-2\sigma_i^2 k^2} \sin(2kR_i + \Psi), \qquad (1)$$

where $\chi(k)$ is the measured EXAFS spectrum, k is the electron wave vector, $S_0^2(k)$ is the amplitude reduction factor, N_i is the number of atoms in the i-th coordination sphere, R_i is the average radial distance to the i-th coordination sphere, $F_i(k,R)$ is the backscattering amplitude, $\lambda(k)$ is the mean free path, σ_i^2 is the Debye Waller factor, and $\Psi(k,R)$ is the sum of the phases of the central- and backscattering atoms.

Usually, the amplitudes, phases and mean free paths were calculated by the FEFF8 code [5]. Several possible fitting programs like e.g. EXAFSPAC [6] exist for the data processing and the determining of the radial distances, coordination numbers and Debye Waller factors.

A complete summary of the standard EXAFS theory and data evaluation one finds by Teo [7].

Complementing the conventional Fourier transform analysis, the wavelet transform (WT) is able to extract more information from the k-dependence of the absorption signals. While the FT analyzes the distances of the backscattering atoms, WT reveals additionally at which energies, that is, at which wavenumbers k, the backscattering takes place. Thus wavelet analysis can differentiate between heavier and lighter backscattering atoms, even if they are at the same distance from the central atom.

Originally, wavelets were used for image and data compression, and wavelet data analysis forms a powerful tool for the evaluation of various complex time-frequency signals, see e.g. the textbooks [8–10]. The essential advantage of the WT is the fact that the time-frequency window is flexible and does in fact adapt in such way that there is always about the same number of periods of the frequency analyzed in the time window.

The disadvantage of the Fourier transformation is the following property. If the signal changes on one time moment, changes the Fourier transformation everywhere. However, if one use not infinitely expanded periodic oscillations, but located wave trains (wavelets) for the integral transformation, then one may analyze the frequencies in each place by dilatation and translation of the wavelets. Wavelets are a wide and flexible class (the function class l^2) of window functions $\psi(t)$ with zero mean:

$$\int_{-\infty}^{+\infty} \psi(t)\,\mathrm{d}t = 0. \qquad (2)$$

In the following the Morlet-wavelet [11] is chosen. First of all its structure is "similar" to an EXAFS signal. That is, the wavelet consists of a slowly varying amplitude term and a fast oscillating phase term. Secondly the formal mathematical description of the wavelet analysis should be in this introductory article in analogy to the Fourier analysis. The Morlet wavelet is obtained by taking a complex sine wave, and by localizing it with a Gaussian (bell-shaped) envelope (see figure 1).

The WT is a window operation like a windowed FT. The kernel of the WT is obtained by translation (parameter b) and scaling (parameter a) of the chosen basis "mother" wavelet. The WT of a

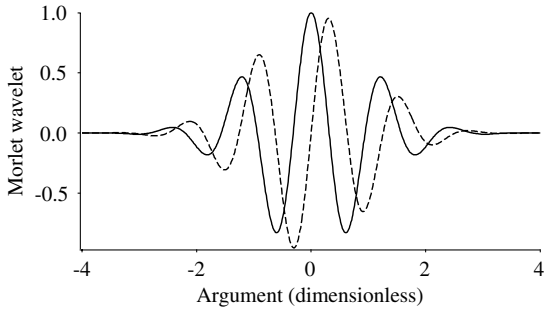

Fig. 1. Real- (full line) and imaginary (dashed line) part of the Morlet wavelet.

*e-mail: funke@esrf.fr

signal $f(t)$ according to the wavelet $\psi(t)$ is defined as:

$$W_f^{\psi}(a,b) = \frac{1}{\sqrt{a}} \int_{-\infty}^{+\infty} f(t)\psi^*\left(\frac{t-b}{a}\right) \mathrm{d}t. \quad (3)$$

Like the FT, the WT is a mathematical complete transformation [12] of a signal. Hence, its inverse transformation recovers again the primary EXAFS signal without any loss of information. It is marked that a repeated application of the FT, using narrow window functions centered at k_i, $i = 1, \ldots, n$ results in similar contour plots as the WT, shown below.

The transition of data analysis methods based on wavelets from the time-frequency to the wavenumber (k)-distance (R) regime in the EXAFS evaluation procedure is simply done by the relations: $t \to k$ and $2\pi\omega \to 2r$. So, the expression of the WT of the k^3 weighted EXAFS data takes the form:

$$W_f^{\psi}(r,k) = \sqrt{2r} \int_{-\infty}^{+\infty} \chi(k')k'^3\psi^*(2r(k'-k))\,\mathrm{d}k', \quad (4)$$

where $\chi(k')$ is the EXAFS signal, $\psi(2r(k'-k))$ is the wavelet, k is the wavenumber, and r corresponds to the interatomic distance uncorrected by phase shifts R which is the abscissa of the FT of the EXAFS data.

In the following two model calculations are presented to demonstrate the method of operation. Then the application of the wavelet analysis is described to a special difficult environmental problem of uranium complexation on humic substances.

First ideas to the present work were published in the reports [13]. Recently, Muñoz *et al*. employed WT for EXAFS studies using the continuous Cauchy wavelet [14].

2. Model calculations

Two model signals built from two simple sine functions, the second one with doubled amplitude, each with Gaussian envelopes, are used to demonstrate the possibilities of the WT to resolve the distance (r) and wavenumber (k) dependency of a signal. In figure 2 at the top at left the signals with separated centers of the Gaussian envelopes at $k = 3.75\,\text{Å}^{-1}$ and $k = 11.25\,\text{Å}^{-1}$ and at right the same signals with coinciding centers at $k = 7.5\,\text{Å}^{-1}$ are plotted. Both "absorption" signals generate the same modul of the Fourier transform, shown in the middle. The lower graphics show the magnitudes of the wavelet transforms of both signals in form of two-dimensional contour plots. In contrast to the FT, their WT show both the distances, which also follows from the FT, and the position of the centers of the two components of the signal in the k-space. The WT shows evidently the full information about the wavenumber (k)- and Distance (r) behavior of the two model spectra.

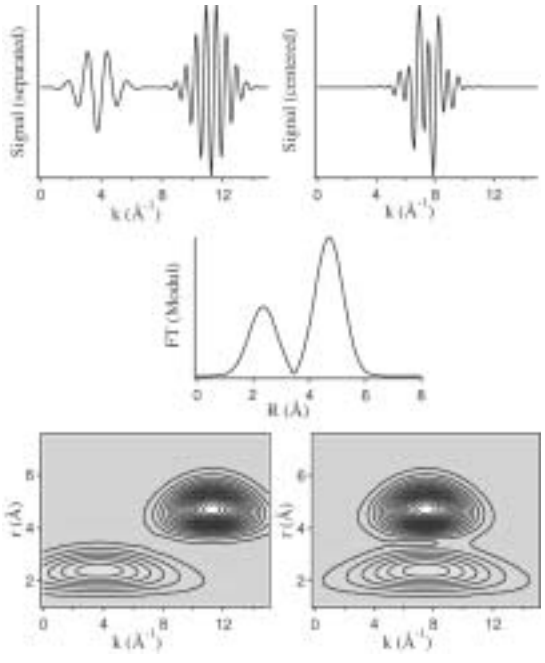

Fig. 2. Two model signals (top), their common FT modulus (middle), and the WT magnitudes of the two signals on top as a function of r and k (bottom).

3. Experimental

Three aqueous solutions were prepared at room temperature.

U-Acet: [U(VI)] = 0.025 mol/L, [acetic acid] = 0.5 mol/L, pH = 4.5.

U-Form: [U(VI)] = 0.053 mol/L, [formic acid] = 1.0 mol/L, pH = 4.5.

U-Glyc: [U(VI)] = 0.02 mol/L, [glycolic acid] = 0.25 mol/L, pH = 8.

U L_{III}-edge EXAFS spectra were measured at ROBL/ESRF. The spectra were processed following standard procedures using EXAFSPAK [6] and FEFF8 [5].

Results: U-Form: the FT of the EXAFS shows a broad peak between $R = 3.1 \ldots 4.0$ Å, which cannot be analyzed and separated using conventional FT-filtering technique. In order to find a correct approach for the structure determination of U-Form, the WT of the three spectra within the range $r = 3.2 \ldots 4.1$ are compared. See fig. 3. Thereby the spectra U-Acet and U-Glyc are used as references: spectrum U-Acet is dominated by the multiscattering at C atoms [15], while spectrum U-Glyc shows pure U-U backscattering [16].

The plot of U-Form shows two separated peaks. This means that WT is able to detect a light and a heavy scatterer at very similar distances ($\Delta r = 0.1$ Å). The extinction in the center of the WT of U-Form is a consequence of the interference of the similar backscattering waves from uranium and multi-scattering waves from carbon. Therefore, the WT analysis suggests both U- O_{ax}-U and U-O_{eq}-C structural elements, which may be interpreted as the formation of polynuclear U(VI)/formic acid complexes.

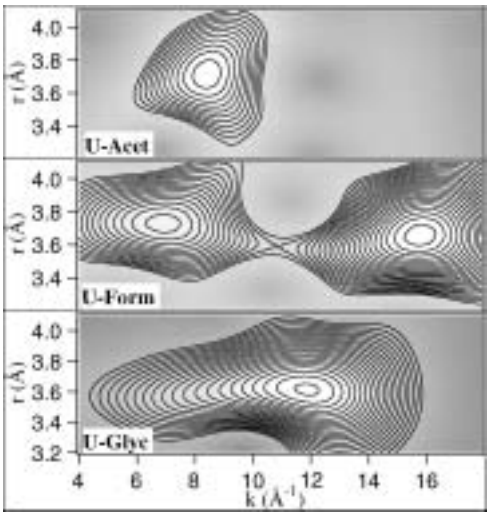

Fig. 3. The WT of the spectra U-Acet, U-Form and U-Glyc within the range $r = 3.2 - 4.1$ Å.

This example shows that the combined application of WT and FT analysis is able to provide both short-range distances and identity of neighboring atoms with unprecedented precision, and therefore may significantly improve the elucidation of complex structures.

4. Conclusions

The presented model- and real examples show that the combined application of WT and FT analysis is able to provide both short-range distances and identity of neighboring atoms with unprecedented precision.

Continuative works will be directed towards more quantitative results of the EXAFS wavelet analysis. Always important remains the question about the most suitable mother wavelet.

Acknowledgments

The authors wish to acknowledge our colleagues R. Der (University of Leipzig), T. Reich (University of Mainz), A. Scheinost (ESRF/ROBL), and C. Hennig (ESRF/ROBL) for many helpful discussions. The work of Dr. M. Chukalina was partly financially supported by the Research Center Rossendorf.

References

1. Sayers, D. E. and Stern, E. A., Phys. Rev. Lett. **27**, 1204 (1971).
2. Stern, E. A., Phys. Rev. B **10**, 3027 (1974).
3. Lytle, F. W., Sayers, D. E. and Stern, E. A., Phys. Rev. B **11**, 4825 (1975).
4. Stern, E. A., Sayers, D. E. and Lytle, F. W., Phys. Rev. B **10**, 4836 (1975).
5. Ankudinov, A. L., Ravel, B., Rehr, J. J. and Conradson, S. D., Phys. Rev. B **58**, 7565 (1998).
6. George, G. N. and Pickering, I. J., Stanford Synchrotron Radiation Laboratory, (1995).
7. Teo, B. K., "EXAFS: Basic Principles and Data Analysis", (Springer, Berlin Heidelberg New York Tokyo, 1986).
8. Mallat, S., "A Wavelet Tour of Signal Processing", (Academic Press, San Diego, London, 2001).
9. Louis, A. K., Maas, P. and Rieder, A., "Wavelets: Theory and Applications", (Wiley, New York, 1997).
10. Daubechies, I., "Ten Lectures on Wavelets", (SIAM Publishers, Philadelphia, 1992).
11. Grossmann, A., Holschneider, M., Kronland-Martinet, R. and Morlet, J., in "Adv. Electronics and Electron Phys.", Suppl. 19, proceedings of the conference Inverse Problems: an Interdisciplinary Study, (edited by P. C. Sabatier), (Montpellier, 1986).
12. Grossmann, A. and Morlet, J., SIAM J. Math. Anal. **15**, 723 (1984).
13. Funke, H. and Chukalina, M., Research Center Rossendorf, Reports No. 343, 45 (2002); 373, 43 (2003).
14. Muñoz, M., Argoul, P. and Farges, F., Am. Mineral. **88**, 694 (2003).
15. Rossberg, A., Ph.D. thesis, Technical University Dresden, (2002).
16. Moll, H. *et al*., Radiochimica Acta **90**, 1 (2002).

Physica Scripta. Vol. T115, 235–236, 2005

Cs L-Edge EXAFS Atomic Absorption Background

I. Arčon[1,2,*], A. Kodre[2,3], J. Padežnik Gomilšek[4], M. Hribar[2] and A. Mihelič[2]

[1]Nova Gorica Polytechnic, Vipavska 13, SI-5001 Nova Gorica, Slovenia
[2]J. Stefan Institute, Jamova 39, SI-1001 Ljubljana, Slovenia
[3]Faculty of Mathematics and Physics, Jadranska 19, SI-1000 Ljubljana, Slovenia
[4]Faculty of Mechanical Engineering, Smetanova 17, SI-2000 Maribor, Slovenia

Received June 26, 2003; revised October 14, 2003; accepted November 4, 2003

PACS numbers: 32.30.Rj, 61.10.Ht

Abstract

X-ray absorption coefficient of Cs in the energy region of L edges has been measured on a 1 : 9 alloy of Cs and Na at room temperature. The absorption spectrum is virtually free of the structural signal. EXAFS oscillations are visible only in a ∼70 eV wide interval immediately above the edges. The short range of the signal is attributed to a strong disorder of the alloy introduced by the complete miscibility of the constituents and the large difference of their metal radii. The spectral regions above three L-edges exhibit the same pattern of sharp multielectron photoexcitation features involving electrons from outer subshells 6s to 4p as in the adjacent element xenon. The segment above the L_3 edge can be used as the atomic absorption background for the standard EXAFS structural analysis of Cs compounds.

1. Introduction

X-ray atomic absorption can be measured either directly on a monatomic gas sample [1–5] of an element or derived from an X-ray absorption spectrum of a compound sample after removal of the structural signal [6–10]. The tiny sharp features on the smooth energy dependence of the photoabsorption cross section are fingerprints of multielectron photoexcitations (MPE). These weak processes arise from the inter-electron interactions in the target atom.

The atomic absorption spectrum is a very good approximation to the atomic absorption background (AAB) in the XAFS structural analysis of a substance containing the target element. Since the structural signal and MPE occupy the same spectral region above a major absorption edge, their interference, if unrecognized, impedes the interpretation of the structural signal leading to errors in the structure parameters determined in the XAFS analysis [8, 9].

For Cs, only the most prominent resonant MPE feature has been extracted from the L-edge EXAFS spectra of amorphous materials containing Cs [11–13]. Complete atomic Cs L-edge absorption has not been determined: apparently, an experimentally demanding and costly heat-pipe cell [4] would be required. In a substitute experiment we measured Cs absorption on a thin layer of Cs/Na alloy expecting to remove the weak EXAFS signal numerically. Surprisingly, the experiment showed that the strong disorder in the alloy produces a practically pure Cs atomic absorption spectrum almost without an EXAFS component.

To assess the purity of the measured AAB a comparison with older absorption data on gaseous Xe [2] can be used. Recent studies in K-edge absorption of noble-gas/alkali-metal neighbor pairs Ar/K and Kr/Rb [4, 5] have proven that the MPE features in a pair differ only in details while following the same overall pattern.

2. Experiment

Cs/Na alloy with a concentration ratio of 1 : 9 was prepared. A small amount of the alloy was placed, together with a drop of paraffin oil to prevent oxidation, into a small lucite container between two kapton foils and squeezed into a thin layer. The container and the oil kept the metal perfectly stable for several hours of the experiment: no sign of oxidation was observed after demounting. The stability of the sample was confirmed also by the perfect reproducibility of the scans that were recorded in sequence at each of the L subshell edges.

The absorption experiment was performed at the E4 station of the DORIS ring at HASYLAB synchrotron facility, DESY (Hamburg, Germany). The beamline provides a focused beam from Au-coated mirror and a Si(111) double-crystal monochromator with 0.8 eV resolution at the Cs L_3-edge. Harmonics are effectively eliminated by a plane Au coated mirror and by detuning the monochromator crystal using a stabilization feedback control. Exact energy calibration was established with a simultaneous measurement on a Ti metal foil ($E_K = 4966$ eV) between the second and the third ionization cell.

3. Results

A compound picture of the L edges (Fig. 1) is obtained as a superposition of three scans per subshell region. Each of the edges is preceded by a resonance due to the excitation of the 2p or 2s electron to the unoccupied bound states just below the continuum.

The spectra above each of the edges are remarkably flat, almost without oscillatory EXAFS signal characteristic of solid

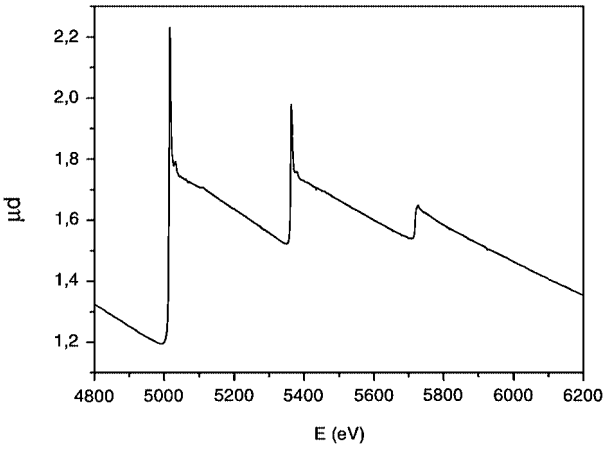

Fig. 1. The L-edge absorption spectrum of Cs measured on a thin layer of the Na/Cs alloy.

*E-mail: iztok.arcon@p-ng.si

samples. A slight convexity of the spectrum above the L_3 and L_2 edge, observed already in the L absorption spectra of some heavy elements, has been explained as a consequence of subshell polarization [14].

The strongest of the sharp MPE features are just barely visible in the spectrum. To expose the details, the average trend of each subshell region is removed from the relative cross section (Fig. 2). Several groups of MPE can be clearly discerned above each absorption edge. The groups can be identified by their energy as multiple excitations involving electrons in consecutively deeper subshells from 6s to 4p, in complete analogy with the MPE groups in the neighboring Xe [2], shown below. Hartree-Fock estimates [15] of the threshold energies of the corresponding double excitations are indicated by arrows.

Even at this level of magnification the oscillatory structural signal is visible only close to the edge. The amplitude of EXAFS oscillations is smaller than the MPE features and vanishes in the noise level about 70 eV above each edge. A more definite estimate of the EXAFS amplitude and range can be obtained from the comparison with the absorption spectrum of the cooled sample (Fig. 3). It shows that only the first two periods of the structural signal are retained in the room-temperature spectrum, further oscillations being suppressed by the Debye-Waller factor.

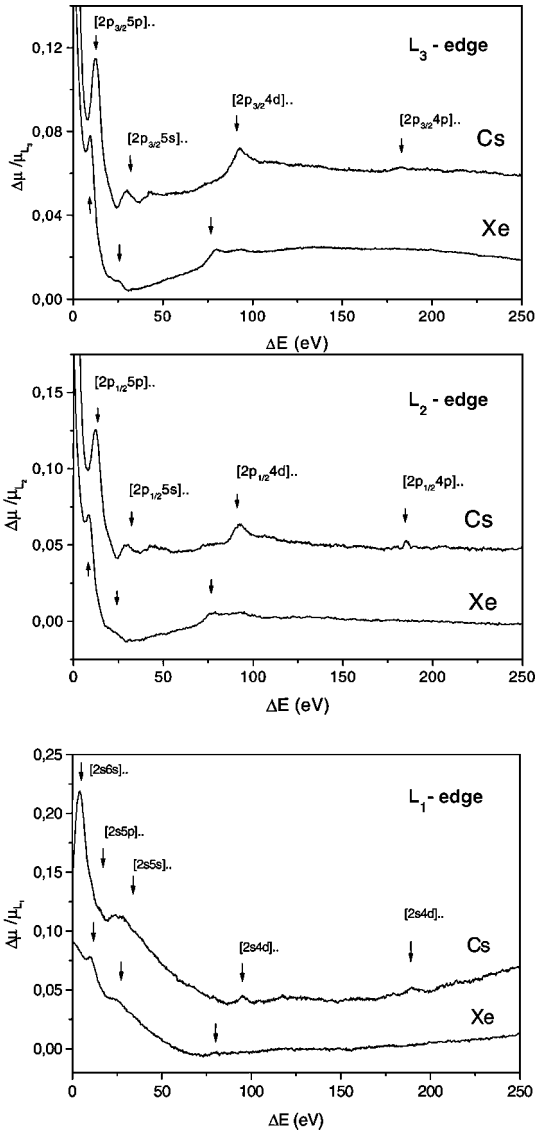

Fig. 2. The comparison of the absorption in the L subshell regions of Cs and Xe after removal of the average trend to enhance the detail. Theoretical estimates of the energy of double excited states are shown by arrows. For each subshell, the origin of the energy scale is shifted to the respective ionization threshold.

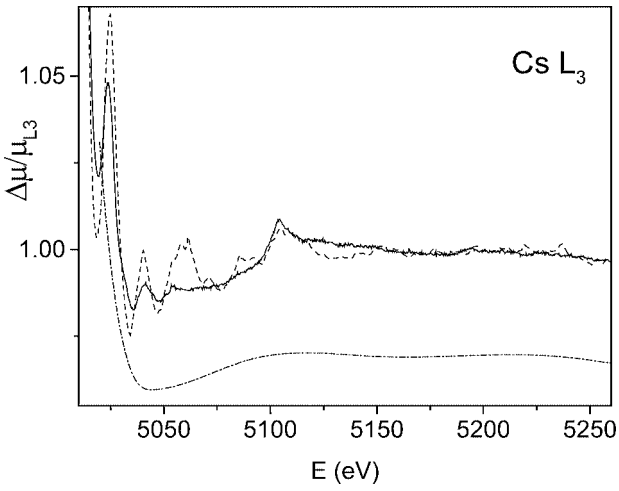

Fig. 3. The comparison of Cs/Na alloy L_3 absorption spectra at room temperature (solid line) and at liquid nitrogen temperature (dashed line). Note the contraction of the structural signal so that the atomic absorption is clearly exposed in the room-temperature spectrum from 70 eV above the edge on. Below, a standard spline background of the liquid-nitrogen spectrum is shown, shifted for −0.03 for clarity.

Incidentally, the comparison in Fig. 3 also illustrates the importance of using the proper AAB in the analysis of a weak structural signal. The XAFS and MPE are so intimately intertwined even in the low-temperature spectrum that the separation by the standard approach of the spline background constructed from the lowermost Fourier components cannot be reliable. The AAB extracted from the room-temperature spectrum, on the other hand, reproduces fully also the sharp non-structural features of the signal, as e.g. the [2p4d] edge and resonance at 5105 eV.

Acknowledgments

Support by the Ministry of Education, Science and Sport of the Republic of Slovenia, Internationales Buero BMBF (Germany) and the IHP-Contract HPRI-CT-1999-00040 of the European Commision is acknowledged. K. V. Klementiev of HASYLAB provided expert advice on beamline operation.

References

1. Schaphorst, S. J. *et al*., Phys. Rev. A **47**, 1953 (1993).
2. Arčon, I., Kodre, A., Štuhec, M., Glavič-Cindro, D. and Drube, W., Phys. Rev. A **51**, 147 (1995).
3. Prešeren, R., Arčon, I., Mozetič, M., Kodre, A. and Pregelj, A., Nucl. Instrum. Methods Phys. Res. B **111**, 161 (1996).
4. Padežnik Gomilšek, J., Kodre, A., Arčon, I. and Prešeren, R., Phys. Rev. A **64**, 22508 (2001).
5. Kodre, A., Arčon, I., Padežnik Gomilšek, J., Prešeren, R. and Frahm, R., J. Phys. B: At. Mol. Opt. Phys. **35**, 3497 (2002).
6. Li, G., Bridges, F. and Brown, G. S., Phys. Rev. Lett. **68**, 1609 (1992).
7. Filipponi, A. and Di Cicco, A., Phys. Rev. A **52**, 1072 (1995).
8. D'Angelo, P., Di Cicco, A., Filipponi, A. and Pavel, N. V., Phys. Rev. A **47**, 2055 (1993).
9. Kodre, A., Arčon, I. and Frahm, R., J. Phys. IV France 7 **C2**, 195 (1997).
10. Prešeren, R., Kodre, A., Arčon, I., Padežnik Gomilšek, J. and Borowski, M., J. Synch. Rad. **8**, 279 (2001).
11. Kodre, A., Arčon, I., Hribar, M., Štuhec, M., Villain, F. and Parent, P., J. de Physique C-9 **4**, 397 (1994).
12. Kodre, A. *et al*., Physica B **208&209**, 379 (1995).
13. Solera, J. A., Garcia, J. and Proietti, M. G., Phys. Rev. B **51**, 2678 (1995-I).
14. Jitschin, W., Werner, U., Materlik, G. and Doolen, G. D., Phys. Rev. A **35**, 5038 (1987).
15. Froese-Fischer, C., Comput. Phys. Commun. **43**, 355 (1987).

Physica Scripta. Vol. T115, 237–239, 2005

Efficient Determination of Optimal Regularization Parameter for Inverse Problem in EXAFS Spectroscopy

M. Kunicke[1], I. Yu. Kamensky[2], Yu. A. Babanov[2,3,*] and H. Funke[1]

[1]Forschungszentrum Rossendorf e.V., PO Box 510119, D-01314 Dresden, Germany
[2]Institute of Metal Physics, RAS, GSP–170, 620219, Ekaterinburg, Russia
[3]Udmurt State University, Izhevsk, Russia

Received June 26, 2003; accepted November 4, 2003

PACS 6110Ht

Abstract

This paper presents a method for choosing the optimal regularization parameter in EXAFS analysis based on the L-curve-criterion without any external parameter. The L-curve is a log-log plot of the norm of regularized solution versus the norm of the corresponding residual norm. The optimal regularization parameter is chosen as a maximum of the L-curve curvature. We apply this method in two experimental cases: crystalline Cu with well-known structure and aqua-ion Cm^{+3} with unknown structure. The optimal regularization parameter leads to a stable solution with a good convergence of the iterative process.

1. Introduction

The regularization method was suggested to EXAFS data analysis nearly two decades ago [1]. This method of numerical solution of Fredholm integral equation of the first kind which describes the EXAFS signal has been shown to be an attractive method of obtaining the structure information. After discrete approximation of the integral equation, the problem reduces to solving an ill-posed linear algebraic equation system which solution is very sensitive to the measuring error. The regularization algorithm allows to lower the influence of the measuring error and to get a stable solution. However, the choice of the regularization parameter is a difficult problem. Up to now, in EXAFS spectroscopy an external parameter – the experimental error in measuring EXAFS data – is used [2].

The EXAFS integral equation in single scattering approximation for one-component system is written as in [1]:

$$\chi(k) = \frac{4\pi\rho_0}{k} R(k) \int_0^\infty f(k,r) g(r) \exp\left\{-\frac{2r}{\lambda(k)}\right\} \times \sin(2kr + 2\delta(k) + \varphi(k,r))\,\mathrm{d}r, \quad (1)$$

where $\chi(k)$ is the normalized oscillating part of the X-ray absorption spectrum, ρ_0 is the atomic density of the material, $f(k,r)$ is the backscattering amplitude of the neighboring atom, $\delta(k)$ is the phase shift on the central atom, $\varphi(k,r)$ is the phase shift on the neighboring atom, $\lambda(k)$ is the mean free path of the photoelectron. $g(r)$ is the pair correlation function (PCF). The functions $R(k)$, $f(k,r)$, $\varphi(k,r)$, $\delta(k)$, $\lambda(k)$ are obtained from curved wave approximation using FEFF8 [3].

Let us rewrite eq. (1) in a symbolic form:

$$u = Ag. \quad (2)$$

Here u is the transformed experimental data, A is the integral operator.

As a regular approximate solution, we take the function g which minimizes in space L_2 the Tikhonov functional [4]:

$$\min M[g_\alpha] = \min\{\|(Ag - u)\|^2 + \alpha\|Lg\|^2\},\ g(r) \in L_2[a,b] \quad (3)$$

Here α is the regularization parameter and $L = I$, where I is the identity operator. The smoothness of solution $g(r)$ is taking into account when we add the second term in the functional (3). $[a,b]$ is the interval in r-space, where the unknown function $g(r)$ is obtained.

After discrete approximation of the integral operator $\boldsymbol{A}$ and the function $g(r)$, the Tikhonov solution [4] is obtained as a result of numerical calculation:

$$g_\alpha = (A^*A + \alpha L^*L)^{-1} A^* u. \quad (4)$$

The next step is an iterative procedure:

$$g_\alpha^m = (A^*A + \alpha L^*L)^{-1}(A^*u + \alpha L^* L g_\alpha^{m-1}), \quad (5)$$

where m is the number of the iteration. In our case, we obtain the solution $g^{\mathrm{m}}(r)$ from (5) and also $g^0(r)$ from (4) as a sum of peaks with lateral oscillations. During the iterative process we consider that the nearest peaks of the previous solution $g^{\mathrm{m}-1}(r)$ (in the case of experimental data for crystalline Cu we choose three peaks) can be described and replaced by the Gaussian functions [5]. After substitution $g^{\mathrm{m}-1}(r)$ in a new form to the right part of (5) we solve this equation and obtain a new solution $g^{\mathrm{m}}(r)$. This assumption is valid if we know that our sample has a crystalline form. Thus, *a priori* physical information is introduced in the algorithm to obtain a reliable solution.

2. The optimal choice of the regularization parameter using the L-curve criterion

The numerical treatment of the inverse problem arising in the EXAFS data analysis has a free parameter – the regularization parameter α. The regularized solution to an inverse problem depends essentially on the value of this parameter. A high value of the regularization parameter damps the regularized solution, on the other hand a small one leads to oscillating artifacts in the solution. So the art of solving inverse problems in the EXAFS data analysis by regularization consists in determining the optimal regularization parameter for the examined probe and the current experimental data. The L-curve-criterion gives a practical way to find the optimal value α_{opt} of the regularization parameter.

Fig. 1 shows for experimental data of crystalline Cu the L-curve which is the parametric representation of $\log(\|g_\alpha\|)$ as function of $\log(\|Ag_\alpha - u\|)$, where $\|g_\alpha\|$ is the norm of the regularized solution and $\|Ag_\alpha - u\|$ is the norm of the residual of reconstructed function obtained using the regularized solution and the transformed experimental data $u(k)$. The regularized solution itself is a function of the regularization parameter α. The L-curve shows a shape like the capital letter "L" what gave the name. The

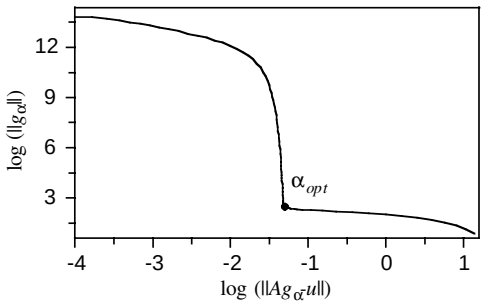

Fig. 1. The L-curve for experimental data of crystalline Cu.

L-curve-criterion means: a value α_{opt} of the regularization parameter α corresponding to the corner of the L-curve is an optimal one. Details can be found in [6, 7].

There is an empirical explanation of the L-curve-criterion. On the L-curve plot the right bottom area of the L-curve corresponds to the higher values of α, and the left upper area – the small values. As α decreases the norm of the residual function decreases much faster than the norm of the regularized solution increases as long as the values of $\alpha > \alpha_{\rm opt}$. A region of α values follows where the norm of the regularized solution starts to increase dramatically. This means a value $\alpha = \alpha_{\rm opt}$ corresponding to the corner of the L-curve gives an optimum in the effort to minimize simultaneously the norm of the residual of the solution and the norm of the solution.

To make the L-curve for an inverse problem, a set of regularized solutions g_α depending on α is needed. On the other hand the set of linear algebraic equations describing the inverse problem in EXAFS data analysis is numerically very close to singular. To deal with such sets of equations needs very powerful technique namely the Singular Value Decomposition (SVD) [8]. If the discrete matrix of the inverse problem is decomposed into $A = UWV^*$, with $UU^* = I$, $VV^* = I$ and $W = [\mathrm{diag}(\omega_j)]$ then the Tikhonov solution of the problem (4) and the iterative equation (5) can be rewritten as

$$g_\alpha = V(WW + \alpha I)^{-1} WU^* u, \tag{6}$$

$$g_\alpha^{\rm m} = V(WW + \alpha I)^{-1}(WU^* u + \alpha V^* g_\alpha^{\rm m-1}). \tag{7}$$

This formulation shows:

1. The numerical calculations of the inverse problem are shifted into the SVD. (There are good implementations of SVD in several numerical libraries, for example, in the IMSL.)
2. The regularized solution g_α is a simple function of the regularization parameter α.

That means we have an available way to calculate that value of g_α for which the curvature of the L-curve has a maximum (the corner in the L-curve). The L-curve criterion gives an optimal value of the regularization parameter.

The described optimal regularization method is implemented in the Program ALPHA of EXAFS data analysis for one-component system.

3. Experimental aspects and results

To be able to evaluate the results of our method, we choose, on the one hand, a well-defined reference – a crystalline foil Cu; on the other hand, a trivalent actinide (curium) in aqueous solution.

3.1. *Crystalline foil Cu*

The sample of crystalline Cu was prepared by EXAFS Materials Company (Danville, USA) with thickness 7 µm. The Cu K-edge of X-ray absorption spectrum was collected in transmission mode at a room temperature of sample. The measurements were performed at the Rossendorf Beamline (ROBL) at the European Synchrotron Radiation Facility (ESRF) using a Si(111) double-crystal monochromator in fixed-exit mode [9]. Harmonic suppression better than 8×10^{-4} was achieved by two Pt coated mirrors with a cut-off energy. The photon energy was calibrated using the K-edge energy of Zn foil at 9.6 keV. In addition, the background absorption of the Cu K-edge spectrum was determined by measuring the absorption spectrum without any sample. These measurements were performed before and after measurement of the K Cu spectrum without any changing amplification.

We present on Fig. 2 the PCF Cu-Cu for crystalline Cu. The model function was calculated using the table structure information and the temperature Debye $\theta_{\rm D} = 315$ K. For the known crystal structure, it is possible to calculate the multiple scattering (MS) contribution by FEFF 8 and eliminate it from the experimental input data $\chi(k)$. We obtain new 'experimental' data that should contain only SS contribution, which is described by equation (1). If we compare the Tikhonov solution of the inverse problem (6) obtained using the optimal value of regularization parameter $\alpha_{\rm opt} = 8 \times 10^{-5}$ and the model function, we note that this solution is still far from the exact solution. In this case it is necessary to perform the iterative procedure according (7). At optimal value $\alpha_{\rm opt}$ the solution is converged quickly (Fig. 3) to the stable one.

The following main characteristics of the first peak for the function $g^{\rm m}(r)$ are selected: the interatomic distance, the nearest neighbors coordination number and Debye-Waller (DW) factor. We estimated these values according to the Gauss function

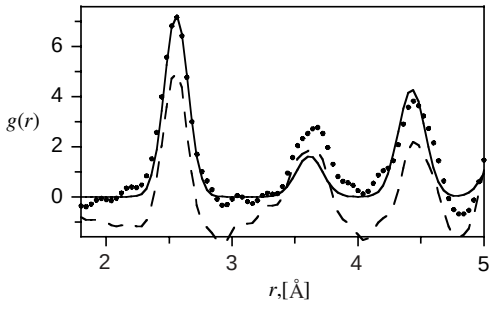

Fig. 2. Pair correlation function Cu-Cu for crystalline Cu: a) model function (solid line); b) Tikhonov solution (dashed line); c) solution after 50 iteration (dotted line).

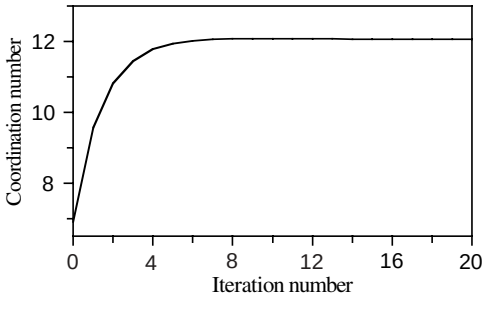

Fig. 3. Convergence of iteration procedure at solving the inverse problem for the first coordination number of crystalline Cu (experimental data).

Table I. *The interatomic distance R, the nearest neighbors coordination number N and Debye-Waller (DW) factor σ^2, obtained from experimental EXAFS data for crystalline Cu.*

	R [Å]	N	$\sigma^2 \cdot 10^3$ [Å^2]
Model	2.55	12	9
Experiment	2.55	12.06	9.5

describing the peak of the solution. In Table I we compare the final stable characteristics of the first peak with the model values and find an excellent agreement.

3.2. *Cm^{3+} in aqueous solution*

Besides plutonium, the long-lived isotope curium plays a crucial role for long-term performance assessment of nuclear waste repositories. In order to predict the mobilization and retardation of this nuclide, it is necessary to know the structures of the inorganic and organic actinide species that are involved in the process of migration. Thereby, the characterization of the Cm^{3+} aqua-ion forms the base for further investigations.

In the literature only few measurements can be found of co-ordination numbers of trivalent actinides in aqueous solutions [10–13].

In order to determine a reliable reference value for the co-ordination number of Cm^{3+} aqua ion, the samples used in our EXAFS measurements were prepared in non-complexing 1.0 M perchloric acid. High actinide concentrations (1×10^{-3} mol/L) were used in order to achieve low-noise EXAFS spectra, which enable a precise determination of bond lengths and co-ordination numbers of the Cm^{3+} aqua ion.

The experiments were performed at the Rossendorf beamline (ROBL) at the ESRF in Grenoble as described above. The radiochemistry experimental station at ROBL has been designed to perform XAFS spectroscopy of solid and liquid non-sealed radioactive samples [14]. EXAFS spectra were collected in transmission mode at the curium L_{III}-edge at 18970 eV ($E_0 = 18990$ eV). Nb metal foils were measured and the first inflection point of the X-ray absorption spectra (Nb K-edge at 18986 eV) was used for energy calibration. We used two methods of obtaining structural information from the same experimental data: 1) a regularization method; 2) EXAFS data fit by using the EXAFSPAK program package with an additional free parameter S_0 [15]. Parameters for the backscattering phase and amplitude, the mean free path, and the reduction factor were calculated using the FEFF8 code [3]. Fig. 4 shows the solution obtained by the regularization method at optimal regularization parameter $\alpha_{opt} = 6.3 \times 10^{-6}$ and $S_0 = 1.0$. Fig. 5 demonstrates the comparison the input experimental data and $\chi(k)$ obtained from solution (Fig. 4). The structural parameters obtained from EXAFS data by both methods are collocated in Table II. It is necessary to note that we don't use any model for obtaining the result by the regularization method.

Table II. *The interatomic distance R, the nearest neighbors coordination number N and Debye-Waller (DW) factor σ^2, obtained from experimental EXAFS data for Cm^{+3} aqua-ion.*

	R [Å]	N	$\sigma^2 \cdot 10^3$ [Å^2]
UV/V [10]		9	
EXAFSPAK ($S_0{}^2 = 0.9$)	2.46	9.3(0.3)	7.5
EXAFSPAK ($S_0{}^2 = 1.0$)	2.46	8.4(0.3)	7.5
Regularization	2.45	9.2	8

So, it was shown that using the L-curve criterion makes the regularization method in EXAFS spectroscopy a very perspective one for a wide range of materials.

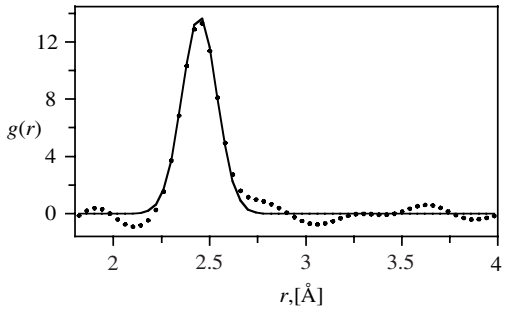

Fig. 4. The solution (dotted line) obtained by the regularization method and approximated by the Gauss function (solid line).

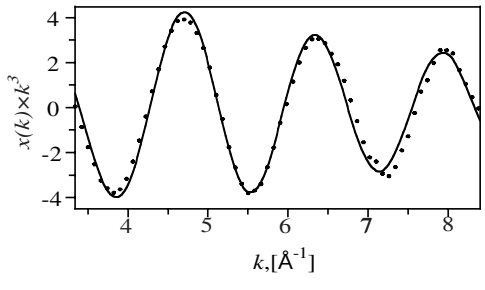

Fig. 5. Comparison the input experimental (dotted line) data and $\chi(k)$ obtained from solution (solid line).

Acknowledgement

The authors would like to thank Professor Tobias Reich for fruitful discussion and interest for this work.

References

1. Babanov, Yu. A., Vasin, V. V., Ageev, A. L. and Ershov, N. V., Phys. Stat. Sol. (b) **105**, 747 (1981).
2. Khelashvili, G. and Bunker, G., J. Synchrotron Rad. **6**, 271 (1999).
3. Ankudinov, A., Ravel, B., Rehr, J. J. and Conradson, S., Phys. Rev. **B58**, 7565 (1998).
4. Tikhonov, A. N., Arsenin, V. Ya., "Solution of Ill-Posed Problems", (John Willey and Sons Inc., New York 1981).
5. Deev, A. N. and Babanov, Yu. A., Phys. Metals Metallogr. **95**, 5 (2003).
6. Hansen, P. C., "Rank-deficient and Discrete Ill-Posed Problems", (SIAM, Philadelphia 1998), p. 80; ISBN: 0-89871-403-6.
7. Hansen, P. C., "The L-curve and its use in the numerical treatment of inverse problems; in Computational Inverse Problems in Electrocardiology", (Edited by P. R. Johnston) (WIT Press, Southampton 2001), p. 119–142; ISBN: 1-85312-614-4.
8. Press W. H., *et al*., "Numerical Recipes in Fortran 77: the art of scientific computing", (Cambridge, University Press 1999), p. 51–63.
9. Matz, W., *et al*., J. Synchr. Rad. **6**, 1067 (1999).
10. Carnall, W. T., J. Less-Common Met. **156**, 221 (1989).
11. Beitz, J. V., Radiochim. Acta **52/53**, 35 (1991).
12. Kimura, T. and Choppin, G. R. J., Alloys Comp. **213/214**, 313 (1994).
13. Allen, P. G., *et al*., Inorg. Chem. **39**, 595 (2000).
14. Reich, T., *et al*., Radiochim. Acta **88**, 633 (2000).
15. George, G. N. and Pickering, I. J., Stanford Synchrotron Radiation Laboratory, (1995).

Physica Scripta. Vol. T115, 240–242, 2005

Simultaneous Fitting with Constraints for EXAFS Study of Anharmonic Vibrational System

Dong-Seok Yang[1], Hyun-Min Park[2] and Ikuo Nakai[3]

[1]Physics Division, School of Science Education, Chungbuk National University, 361-763, Korea
[3]Materials Evaluation Center, Korea Research Institute of Standard and Science, Taejon, 305-600, Korea
[2]Department of Electrical and Electronic Engineering, Tottori University, Tottori 680-8552, Japan

Received June 26, 2003; accepted January 28, 2004

PACS number: 61.10.ht

Abstract

The anharmonic vibration of ions in solids has been measured frequently by the EXAFS technique in recent years. However, the analysis of the anharmonicity in EXAFS is still complicated. In this article, we show a new method of simultaneous fitting with constraints (SFC) which is simple and useful for the analysis of anharmonicity. As an example, copper EXAFS spectra measured at 300 K, 500 K and 700 K were analyzed by this method. Also, we propose a useful EXAFS expression for anharmonic systems. We found the physical meaning of the parameters s and δ used in the EXAFS expression for anharmonic systems.

1. Introduction

It is well known that the spectra of the extended X-ray absorption fine structure (EXAFS) change significantly with temperature [1, 2]. This phenomenon is related to the anharmonic vibration of atoms in solids. Sevillano *et al*. studied the variation of the Debye-Waller factor due to thermal vibrations [3]. In recent years, the anharmonicity of a pure metal has been discussed extensively [4]. Several methods of measuring the anharmonicity have been developed in the extended X-ray absorption fine structure (EXAFS) fields [5–10]. Amongst those methods, the cumulant method [6] is widely used to analyze the anharmonic vibration. However, the cumulant method requires very careful treatment because all cumulants and the average interatomic distance are covariant with temperatures. This article demonstrates a useful method, the simultaneous fit with constraints (SFC), to measure the anharmonicity with EXAFS techniques. This method is based on the model of effective anharmonic pair potential [7]. In this method, the effective anharmonic pair potential is obtained directly from the fitting and the thermal expansion coefficient, cumulants, and parameters of the pair distribution functions are obtained from the effective anharmonic pair potential.

2. Experiments

The XAFS measurement was carried out at the BL01B1 station of the 8 GeV storage ring in SPring-8. A couple of Si(311) crystals monochromatized the synchrotron radiation beam from a bending magnet. The photon beam was focused in the vertical direction. A Rh coated mirror was used to eliminate the higher harmonics. We measured XAFS spectra near the Cu K (8.979 keV) edge in the transmission mode using a couple of ionization chambers. The energy of the photons from the monochromator was calibrated with that of a prepeak of a 5 μm thick Cu foil with a purity of 5 N (8.97800 keV). The specimens were heated up to 900 K in an electric furnace.

3. SFC Method

The parameters of the effective anharmonic pair potential [7] can be obtained by fitting simultaneously several filtered EXAFS spectra measured at different temperatures to an anharmonic EXAFS expression with constraints. The anharmonic EXAFS expression and the constraints are explained below. This method can be applied to most anharmonic systems except for highly anharmonic vibrational systems.

An anharmonic EXAFS expression was obtained from simplification of the EXAFS equation for disordered system derived in other work [9]. The simplified equation is

$$\chi(k) = \frac{NS_0^2(k)F(k)}{kR^2} e^{-\frac{2R}{\lambda(k)}} A_c(k) \sin\{2kR + \varphi(k) + \varphi_c(k)\} \qquad (1)$$

where N is the coordination number in the first shell, R is the average bond distance, $S_0^2(k)$ is a correction factor due to multiple processes, $\lambda(k)$ is the mean free path, $F(k)$ is the backscattering amplitude and $\varphi(k)$ is the phase shift of the photoelectrons. Here, $A_c(k)$ and $\varphi_c(k)$ is the amplitude and phase corrections, respectively, due to the anharmonic vibration.

The amplitude and phase corrections are simplified from the completed expression [9]

$$A_c(k) = [1 + (2k\delta)^2]^{-\frac{s+1}{2}}, \qquad (2)$$

$$\varphi_c(k) = (s+1)[tan^{-1}(2k\delta) - (2k\delta)] \qquad (3)$$

where s and δ are the parameters of the pair distribution function [9].

From the relationship between pair distribution and the effective anharmonic pair potential as shown in the next section, we can express the distribution parameters, s and δ as a function of parameters for the Morse potential,

$$s = \frac{8}{9}\left(\frac{D}{k_B T}\right), \qquad (4)$$

$$\delta = \frac{3}{4}\sigma\left(\frac{k_B T}{D}\right). \qquad (5)$$

In the fitting process, we put constraints that the values of N, D and σ are not changed for several different EXAFS spectra obtained at different temperatures because they are independent of temperature.

4. Results and Discussion

It is interesting to know the relationship between the pair distribution and the effective anharmonic pair potential. The

pair distribution function can be obtained from the Boltzmann probability distribution function because the average bonding distance can be obtained from both distributions,

$$\langle r\rangle = \int rg(r)\,\mathrm{d}r = \int rf_B(r)4\pi r^2\,\mathrm{d}r \tag{6}$$

where $g(r)$ is the pair distribution function and $f_B(r)$ is the Boltzmann probability distribution function which is given by

$$f_B(r) = f_0 \mathrm{e}^{-\frac{V(r)}{k_B T}} \tag{7}$$

where f_0 is the normalization constant given by $f_0 = [\int \mathrm{e}^{-\frac{V(r)}{k_B T}} 4\pi r^2\,\mathrm{d}r]^{-1}$. A model of pair distribution function for disordered or anharmonic systems [9] has been proposed as

$$g(r) = g_N(r_m, s, \delta)\frac{1}{\Gamma(s+1)}\frac{1}{\delta}\left(\frac{r-r_m}{\delta}\right)^s \mathrm{e}^{-\frac{r-r_m}{\delta}} r^2 \tag{8}$$

where r_m is the minimum distance in the distribution.

Using the Morse potential as the effective anharmonic pair potential and expanding it near the equilibrium position, we obtain the following form of effective anharmonic pair potential,

$$V(r) = \frac{D}{\sigma^2}(r-r_0)^2 - \frac{D}{\sigma^3}(r-r_0)^3 \tag{9}$$

where D and σ are the dissociation energy and the potential width, respectively, and r_0 is the equilibrium distance.

From Eq. (6) and (8), we obtain

$$g_N(r_m, s, \delta)\frac{1}{\Gamma(s+1)}\frac{1}{\delta}\left(\frac{r-r_m}{\delta}\right)^s \mathrm{e}^{-\frac{r-r_m}{\delta}} = 4\pi f_0 \mathrm{e}^{-\frac{V(r)}{k_B T}}. \tag{10}$$

Expanding the logarithm of Eq. (10) about r_0 ($r_0 = r_m + s\delta$) we obtain Eqs. (4) and (5).

Here we should point out that the parameter s in Eq. (4) is given by the ratio of dissociation energy and thermal energy. The parameter δ represents thermal expansion. This is not the linear thermal expansion but the local thermal expansion of bonding distance. δ in Eq. (5) also can be expressed by [10]

$$\delta = \langle r\rangle - r_0. \tag{11}$$

The local thermal expansion coefficient α can be defined by

$$\alpha = \frac{\delta}{\langle r\rangle T}. \tag{12}$$

It has been verified that the expression for the local thermal expansion coefficient is equivalent to the expression obtained in other work [10].

Usually anharmonic vibration of ions in solids appears at high temperatures. The anharmonic vibration causes the reduction of amplitude and the shift in phase of EXAFS spectra significantly. We expect that the anharmonicity can be readily measured by EXAFS technique. The EXAFS spectra of pure copper film were measured at 300 K, 500 K and 700 K and analyzed using the SFC method for a test.

Fig. 1 shows EXAFS spectra of copper measured at the temperatures indicated. As shown in Fig. 1, the amplitude decreased and the phase increased as temperature increased. We expect that this is an anharmonic vibrational effect because there is only temperature change and there is no local structural variation.

Fig. 2 is a Fourier transform of EXAFS spectra measured above. As shown in Fig. 2, the magnitude decreases drastically as the temperature increases. Also, the higher shells are reduced significantly losing the long range order due to the anharmonic vibration.

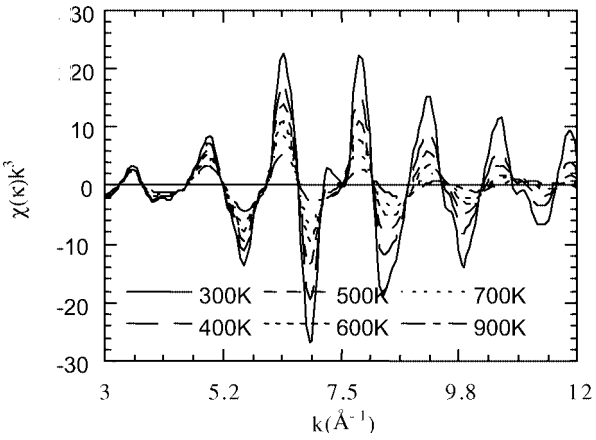

Fig. 1. EXAFS spectra for copper foil at various temperatures.

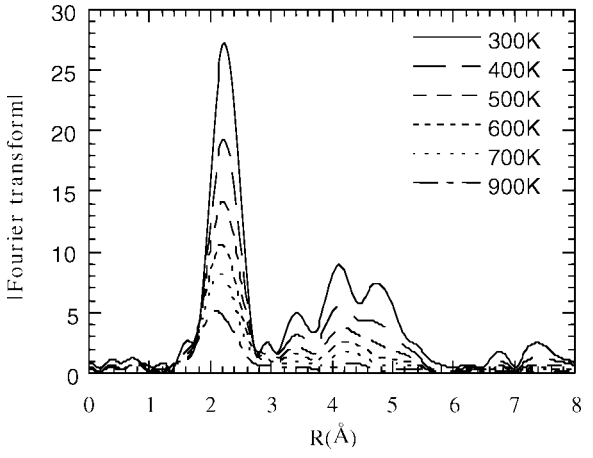

Fig. 2. Fourier transform of the EXAFS spectra for copper foil.

Table I. *Energy shift and local structural parameters at each temperature. The cumulants, C_2 and C_3 are calculated by the relationship between the cumulants and the potential parameters [10].*

Temp. (K)	ΔE (eV)	R (Å)	$C_2 \times 10^{-2}$ (Å)^2	$C_3 \times 10^{-3}$ (Å)^3
300	6.1 ± 0.2	2.55 ± 0.01	0.85 ± 0.05	0.23 ± 0.05
500	6.6 ± 0.2	2.56 ± 0.01	1.47 ± 0.05	0.68 ± 0.05
700	7.1 ± 0.2	2.57 ± 0.01	2.09 ± 0.05	1.35 ± 0.05

The first shell (first peak) in the Fourier transform was filtered by the back transform. The filtered spectra were fitted using the SFC method. From the fitting, we obtained the anharmonic vibrational parameters and the effective anharmonic pair potential.

The average bond distance and cumulants obtained by SFC method are summarized in Table I. The dissociation energy, the potential width and the local thermal expansion coefficient were

$$D = 1.28\,\mathrm{eV}, \tag{13}$$

$$\sigma = 0.92\,\text{Å}, \tag{14}$$

$$\alpha = 1.80 \times 10^{-5}/\mathrm{K}, \tag{15}$$

respectively.

The bond distances in Table I are similar to the reference values [4, 12]. The second cumulants were consistent with values obtained in other work [4]. The thermal expansion coefficient obtained for copper is also consistent with the referenced value [11]. The energy shift shown in Table I increases slightly and systematically as the temperature increases. This shows that there is some additional kinetic energy of photoelectrons at high temperatures. Unfortunately, we do not have other measurements and theoretical considerations for the energy shift, the dissociation energy or the potential width.

As shown in the above analysis, the SFC method gives consistent results on the local structural parameters with other work and we expect that this method will be useful for the analysis of anharmonicity.

5. Conclusion

We propose that the SFC EXAFS method can be used to analyze anharmonicity effectively. The method gives consistent results with other works from analysis of EXAFS spectra of pure copper measured at high temperatures.

Also, we point out that the anharmonic EXAFS expression is very useful for the analysis of anharmonicity. We found the physical meaning of the parameters s and δ used in the anharmonic EXAFS equation. It is shown that s is determined by the ratio of dissociation and thermal energy and δ is the parameter of the local thermal expansion.

Acknowledgement

This work has been partly supported by the Korea Ministry of Science and Technology (MOST) through the NRL program. The synchrotron radiation experiments were performed at the SPring-8 with the approval of Japan Synchrotron Radiation Research Institute (JASRI) (Proposal No. 2001B0135-NX-np).

References

1. Stern, E. A., LiVings, P. and Zhe Zhang, Phys. Rev. B **43**, 8850 (1991).
2. Dalba, G., Fornasini, P., Grisenti, R. and Purans, J., Phys. Rev. Lett. **82**, 4240 (1999).
3. Sevillano, E., Meuth, H. and Rehr, J. J., Phys. Rev. B **20**, 4908 (1979).
4. Edwards, A. B., Tildesley, D. J. and Binsted, N., Mol. Phys. **91**, 357 (1997).
5. Tranquada, J. M. and Ingalls, R., Phys. Rev. B **28**, 3520 (1983).
6. Bunker, G., Nuc. Inst. Meth. **207**, 473 (1983).
7. Frenkel, A. I. and Rehr, J. J., Phys. Rev. **48**, 585 (1993).
8. Cicco, A. D. *et al.*, J. Phys.: Condens. Matter **14**, 3365 (2002).
9. Yang, D. S., Fazzini, D. R., Morrison, T. I., Troger, L. and Bunker, G., J. Non-Cryst. Sol. **210**, 275 (1997).
10. Yang, D. S. and Joo, S. K., Solid State Commun. **105**, 595 (1998).
11. Brandes, E. A. and Brook, G. B., "Smithells Metals Reference Book", Seventh edition, (McGraw-Hill, New York 1983).
12. Cullity, B. D., "Elements of X-ray diffraction", 2nd edition, (Addison-Wesley publishing Co. Massachusetts 1978), 506–507.

Physica Scripta. Vol. T115, 243–245, 2005

Multi-pole Representation of the Dielectric Matrix

J. A. Soininen[1,2,*], J. J. Rehr[1] and Eric L. Shirley[2]

[1]Division of X-ray Physics, Department of Physical Sciences, University of Helsinki, FIN-00014 Finland
[2]Optical Technology Division, Physics Laboratory, National Institute of Standards and Technology, Gaithersburg, Maryland 20899, USA

Received June 26, 2003; accepted July 1, 2004

PACS numbers: 71.10.−w, 71.20.−b, 71.45.Gm, 71.15.−m

Abstract

A good approximation for the electron self-energy or the electron quasiparticle properties is needed for an accurate calculation of X-ray absorption spectra. The *GW* approximation (GWA) has been found to be relatively reliable in predicting the quasiparticle energies and lifetimes in a large variety of systems. For solids, a part of a GWA calculation is the calculation of the inverse of the dielectric matrix ε^{-1}. We introduce an iterative method for calculating an accurate multi-pole approximation for ε^{-1} and we apply it in *GW* calculations. Results for quasiparticle properties are presented for LiF and Si. For LiF we use these results to calculate the inelastic X-ray scattering spectra for energy loss close to the F K-edge. Other uses for this representation of ε^{-1} will also be discussed.

For an accurate calculation of X-ray absorption or X-ray Raman scattering (XRS) a number of important effects have to be considered. Excitation transition matrix elements have to be calculated accurately, the interaction between the photoelectron and the core hole created in the excitation process has to be treated, and the energy shifts and lifetime broadening due to the interaction of the photoelectron and the core hole with the surrounding electrons has to be included. In this article we concentrate on the photoelectron self-energy effects. Examples of how other parts of the calculation can be approached are given, for example, in Refs. [1, 2].

The GW-approximation (*GWA*) proposed by Hedin [3, 4] is often used for electron self-energy and quasiparticle calculations in solids. The basis of the GWA and its properties has been given detailed treatment in a number of recent review articles [5, 6, 7]. In X-ray absorption or XRS calculations, additional problems are caused by the presence of the core-hole. Core-excited calculations are often done by solving the photoelectron Green's function in the presence of the core-hole, as is the case when one is using the *final-state* rule (FSR). This is comparable to an impurity problem, and is still a quite demanding problem to be approached with standard *GWA* methods. This is probably part of the reason why, even to this day, a simplified plasmon-pole, electron-gas self-energy model within a local-density approximation [8] is often used in FSR calculations. An alternative approach to core excited states is to use the *Bethe-Salpeter* equation (BSE) approach of Ref. [1]. In the BSE, the final-state photoelectron Green's function is calculated in a crystal without a core-hole. In this case, the electron self-energy can be calculated relatively easily using standard *GWA* methods. Within *GWA*, the self-energy is approximated by

$$\Sigma(\mathbf{r},\mathbf{r}',\omega) = \mathrm{i}\int \frac{\mathrm{d}\omega'}{2\pi}\mathrm{e}^{\mathrm{i}\delta\omega'}\mathbf{G}(\mathbf{r},\mathbf{r}',\omega+\omega')\mathbf{W}(\mathbf{r},\mathbf{r}',\omega'), \tag{1}$$

where $\mathbf{W}$ is the screened interaction and $\mathbf{G}$ is the Green's function. We use a non-self-consistent GWA and calculate the band states needed for $\mathbf{W}$ and $\mathbf{G}$ using the local-density approximation (LDA). The random phase approximation (RPA) is used for the dielectric matrix in $\mathbf{W} = \boldsymbol{\varepsilon}^{-1}\mathbf{v}$, where $\boldsymbol{\varepsilon}^{-1}$ is the inverse of the dielectric matrix and $\mathbf{v}$ is the unscreened Coulomb potential. The inverse of the dielectric matrix is related to the polarizability $\boldsymbol{\chi}$ of the system by $\boldsymbol{\varepsilon}^{-1} = 1 + \mathbf{v}\boldsymbol{\chi}$.

The current approach is based on expressing the polarizability in the electron-hole basis [9]. Additionally, the current work uses a pseudopotential approach, and all the relevant functions (wave functions, Coulomb potential, and polarizability) are expressed in a plane-wave basis. As explained in Ref. [10], the causal $\boldsymbol{\chi}$ can be expressed in matrix form:

$$\boldsymbol{\chi}(\mathbf{q},\omega) = \boldsymbol{\Psi}^{\dagger}\frac{1}{z^2 - \mathbf{H}_{RPA}}\boldsymbol{\Psi}, \tag{2}$$

where $z = \omega + \mathrm{i}\delta$. Each column of the matrix $\boldsymbol{\Psi}$ corresponds to the total electron-hole pair wave function created using

$$P^{\dagger}_{\mathbf{G}}(\mathbf{q}) = \sum_{j\mathbf{k}}^{occ}\sum_{j'\mathbf{k}+\mathbf{q}}^{unocc}\langle\phi_{j'\mathbf{k}+\mathbf{q}}|\mathrm{e}^{\mathrm{i}(\mathbf{q}+\mathbf{G})\cdot\mathbf{r}}|\phi_{j\mathbf{k}}\rangle\Delta^{\mathbf{q}}_{jj'\mathbf{k}}a^{\dagger}_{j'\mathbf{k}+\mathbf{q}}a_{j\mathbf{k}},$$

where we have $\Delta^{\mathbf{q}}_{jj'\mathbf{k}} = \sqrt{2(E^{LDA}_{j'\mathbf{k}+\mathbf{q}} - E^{LDA}_{j\mathbf{k}})}$, and $\{E^{LDA}_{j\mathbf{k}}\}$ are LDA band energies. The matrix $\mathbf{H}_{RPA}$ can be expressed as $\mathbf{H}_{RPA} = \mathbf{H}_{1e} + \mathbf{V}_{local}$, where the "single-particle" part is diagonal in the particle-hole basis $H_{1e}|jj'\mathbf{k}\rangle_{\mathbf{q}} = (E_{j'\mathbf{k}+\mathbf{q}} - E_{j\mathbf{k}})^2|jj'\mathbf{k}\rangle_{\mathbf{q}}$ [9] and the local-field operator is $\mathbf{V}_{local} = \boldsymbol{\Psi}\,\mathbf{V}\boldsymbol{\Psi}^{\dagger}$.

The order of the matrix $\mathbf{H}_{RPA}$ is $\sim 10^4$ to 10^5 and direct inversion of the matrix in Eq. (2) would be a considerable computational task. However, here we will briefly outline how an approximation to Eq. (2) can be obtained using an iterative Band Lanczos algorithm [11, 12]. At the beginning of the iteration process an orthogonalized set of vectors $\{\mathbf{v_i}\}_{i=1,n}$ are obtained from $\boldsymbol{\Psi}$ by decomposing it in the form $\boldsymbol{\Psi} = \mathbf{VR}$. We find $\mathbf{R}$ and $\mathbf{V}$ using canonical orthogonalization [13]. At each iteration step a new vector $\mathbf{v}_{i+n}$ is generated

$$T_{i+n,i}\mathbf{v}_{i+n} = \mathbf{H}_{RPA}\mathbf{v}_i - \sum_{j=i-n}^{i+n-1}T_{j,i}\mathbf{v}_j, \tag{3}$$

where coefficients $T_{j,i} = \mathbf{v}_j^{\dagger}\mathbf{H}_{RPA}\mathbf{v}_i$ are chosen so that each new vector is orthogonal to previous Lanczos vectors and is normalized. After some finite number (I) of iterations, the matrix $\mathbf{T}$ and the generated set of vectors give an approximation for the full matrix $\mathbf{H}^{(I)}_{RPA} = \mathbf{V}^{(I)}\mathbf{T}\mathbf{V}^{(I)\dagger}$. Using decomposition of $\mathbf{T}$ in terms of its eigenvalues $\{\Omega_i\}$ and eigenvectors $\{\mathbf{X_i}\}$, we can approximate Eq. (2) as

$$\boldsymbol{\chi}(\mathbf{q},\omega) = \mathbf{S}^{\dagger}\frac{1}{z^2 - \Omega(\mathbf{q})}\mathbf{S}. \tag{4}$$

We have used $\mathbf{S} = \mathbf{X}^{\dagger}\mathbf{R}$, where only the first n components of the eigenvectors $\{\mathbf{X}_i\}$ are included in the product. Using this multi-pole approximation for $\boldsymbol{\chi}$ we can avoid a numerical calculation of

*email address: aleksi.soininen@helsinki.fi

the energy integral in Eq. (1). The fact that an arbitrary number of iterations can be chosen means that the number of poles used in the calculation can be determined on a case-by-case basis. Further information on this method and its application to *GWA* calculations can be found in Ref. [10].

The quasiparticle energy $E_{n\mathbf{k}}$ can be expressed with the help of the LDA band energy $E_{n\mathbf{k}}^{LDA}$ and the matrix elements of the self-energy as $E_{n\mathbf{k}} = E_{n\mathbf{k}}^{LDA} + \langle\psi_{n\mathbf{k}}|\Sigma(E_{n\mathbf{k}}) - V_{xc}^{LDA}|\psi_{n\mathbf{k}}\rangle$, where the LDA exchange-correlation potential V_{xc}^{LDA} is used. In X-ray absorption or XRS calculations one would, in principle, need the quasiparticle corrections $\Delta_{n\mathbf{k}} = E_{n\mathbf{k}} - E_{n\mathbf{k}}^{LDA}$ for all the **k**-points and bands used in the calculation. This number is usually quite large (typically at least 4000 **k**-points, and up to about 80 bands) and explicit calculation of $\Delta_{n\mathbf{k}}$ for each band state would be difficult. Instead we form an LDA-energy dependent quasiparticle correction averaged over the **k**-points and bands:

$$\Delta E(\omega) = \frac{1}{N_{n\mathbf{k}}} \sum_{n\mathbf{k}} (E_{n\mathbf{k}} - E_{n\mathbf{k}}^{LDA}) \mathrm{e}^{\frac{-(\omega - E_{n\mathbf{k}}^{LDA})^2}{2\sigma^2}}, \tag{5}$$

where $N_{n\mathbf{k}} = \sum_{n\mathbf{k}} \exp(-(\omega - E_{n\mathbf{k}}^{LDA})^2/2\sigma^2)$ and Gaussian broadening (controlled by the width σ) is used in the averaging. This is done using a smaller number of **k**-points (on the order of 10^2). The $\Delta E(\omega)$ is calculated separately for the conduction and valence states in order to correctly describe the near band-gap region. In Fig. 1 we show $\Delta E(\omega)$ for silicon obtain using the iterative method discussed here. We compare the results for $\mathrm{Re}\,\Delta E(\omega)$ and $\mathrm{Im}\,\Delta E(\omega)$ calculated with different numbers of poles (I). The Gaussian broadening of the poles was increased so that for $I \approx 3200$, $I \approx 1600$, and $I \approx 800$ the full width at half maximum (FWHM) of the poles was 1.0 eV, 2.0 eV and 4.0 eV respectively. It easy to see that, with respect to the number of poles, the $\Delta E(\omega)$ for the conduction band states converges faster. This is especially relevant for core-excited-state calculations, because only the conduction bands are needed. For the specified Gaussian widths and number of poles, $\mathrm{Im}\Delta E(\omega)$ is finite when ω is close to the conduction band edge, i.e., the electron-hole continuum contribution to **W** is accounted for. When comparing with other approaches it is worth noting that even the highest number of poles (3200) is less than one pole per reciprocal-lattice vector pair (approximately 80 reciprocal-lattice vectors were used in $\boldsymbol{\chi}$).

In the approach introduced in Ref. [1] the dynamic structure factor for energy transfers in the vicinity of the core binding energy is approximated by

$$I(\eta, \omega) = -\frac{1}{\pi} \mathrm{Im} \langle I | \hat{\mathbf{P}}_\eta^\dagger \frac{1}{\omega - \hat{H}_{eff} + \mathrm{i}\gamma(\omega)} \hat{\mathbf{P}}_\eta | I \rangle. \tag{6}$$

Here the operator $\hat{\mathbf{P}}_\eta$ couples a solid with the probe, i.e., the dipole field in the case of X-ray absorption and the longitudinal field in the case of XRS. The parameter $\gamma(\omega)$ introduces lifetime broadening to the spectra. The initial state ($|I\rangle$) of the electron system is assumed to be the ground state expressed in a single Slater-determinant form. We approximate the full many-body final-state Hamiltonian with an effective Hamiltonian $\hat{H}_{eff} = \hat{H}_0 + \hat{V}_{e-h}$, where $\hat{H}_0$ is a single-particle part and $\hat{V}_{e-h}$ accounts for the interaction between the particle and the hole. In this paper we will concentrate on $\hat{H}_0$; details on how $\hat{V}_{e-h}$ is approximated can be found in Ref. [1]. When expressed in the core hole-electron basis $|n'\mathbf{k}'\alpha'\rangle$ of Ref. [1], the operator $\hat{H}_0$ is diagonal: $\langle n\mathbf{k}\alpha|\hat{H}_0|n'\mathbf{k}'\alpha'\rangle = (E_{n\mathbf{k}} - E_\alpha)\delta_{nn'}\delta_{\mathbf{k}\mathbf{k}'}\delta_{\alpha\alpha'}$. The core-hole energy ($E_\alpha$) is assumed to be a constant and $E_{n\mathbf{k}}$ is the photoelectron quasiparticle energy.

Using $\Delta E(\omega)$ we can approximate the quasiparticle energies needed in the matrix elements of $\hat{H}_0$ with $E_{n\mathbf{k}} \approx \mathrm{Re}\,E_{n\mathbf{k}} = E_{n\mathbf{k}}^{LDA} + \mathrm{Re}\,\Delta E(E_{n\mathbf{k}}^{LDA})$. The lifetime broadening parameter in Eq. (6) is approximated in this work by $\gamma(\omega) = \Gamma_{hole} + \mathrm{Im}\,\Delta E(\omega)$, where Γ_{hole} is the core hole lifetime parameter and $\mathrm{Im}\,\Delta E(\omega)$ is used to approximate the effect of the photoelectron lifetime. In Fig. 2 we present a calculated XRS spectrum for the F K edge in LiF and compare it with experiment [14]. In the upper panel we show the result obtained without the quasiparticle correction (i.e., $E_{n\mathbf{k}} = E_{n\mathbf{k}}^{LDA}$ and $\gamma(\omega) = \Gamma_{hole}$) and the result when the quasiparticle corrections are included. In the lower panel $\Delta E(\omega)$ is shown. The quasiparticle correction has only a small effect close to the edge. For higher energies, both the imaginary and the real parts of $\Delta E(\omega)$ have a visible effect on the spectrum. The quasiparticle damping reduces the oscillations in the spectrum when $\omega > 10$ eV, and the experimental result is more closely

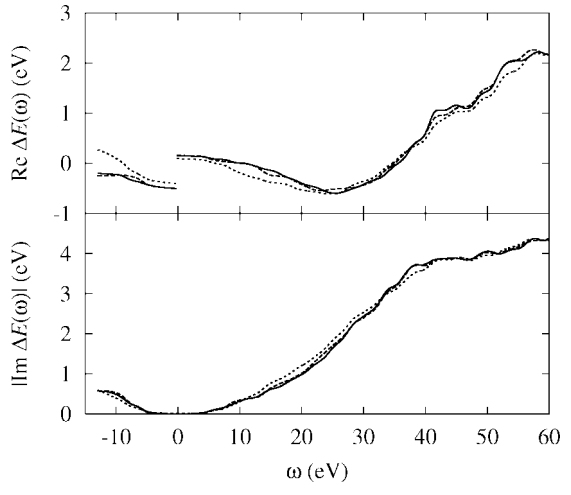

Fig. 1. The quasiparticle correction $\Delta E(\omega)$ for Si as a function of number of poles I. The upper panel shows the real part of $\Delta E(\omega)$, and the lower, the imaginary part of $\Delta E(\omega)$, in eV. The solid line gives the result for $I \approx 3200$, the dashed line for $I \approx 1600$, and the dotted line for $I \approx 800$. All of the results were obtained with $\sigma = 1.0$ eV in Eq. (5) and the pole widths are specified in the text. The horizontal axis is the LDA energy with respect to the conduction band minimum.

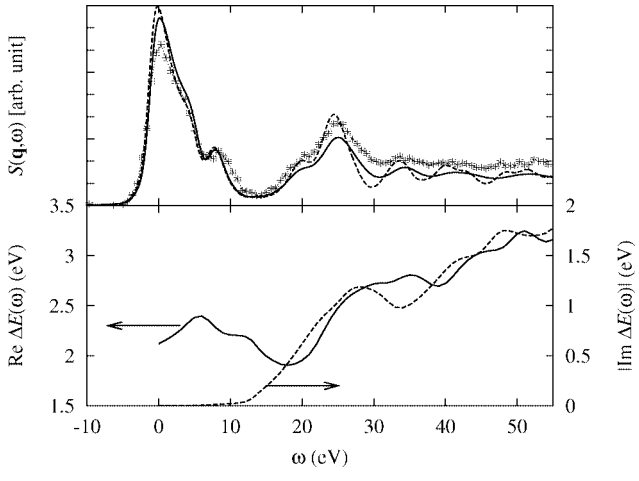

Fig. 2. The upper panel shows the comparison of the theoretical results without (dashed line) and with (solid line) the quasiparticle correction compared to experimental (line with error bars) XRS result [14]. The momentum transfer was 1.44 a.u. The experimental result was shifted in the energy scale and the zero of energy is at the conduction band minimum. In the lower panel $\mathrm{Re}\,\Delta E(\omega)$ (solid line) and $\mathrm{Im}\,\Delta E(\omega)$ (dashed line) are shown. As indicated by the arrows in the figure the vertical axis of $\mathrm{Re}\,\Delta E(\omega)$ is on the left, and of $\mathrm{Im}\,\Delta E(\omega)$ on the right.

modeled by the calculation when this effect is included. Also, the positions of the spectral features are more accurately modeled by the method including the quasiparticle shifts Re $\Delta E(\omega)$.

Besides being useful in *GWA* calculations, there are a number of ways that the pole structure of the screened interaction could be used. For example, when considering core-excited states the cross-section can be expressed as $I(\eta,\omega) = -\mathrm{Im}\langle I|\hat{\mathbf{P}}_\eta^\dagger \Pi(\omega)\hat{\mathbf{P}}_\eta|I\rangle/\pi$, where $\Pi(\omega)$ is the two-particle (core hole-electron) propagator in the particle-hole basis. In Ref. [1] the electron-hole interaction was approximated by sum of energy-independent screened interaction (V_d) and bare "exchange" (V_x) interaction terms. Using the same approximations as in Ref. [1], but including the energy dependence of the screened interaction, the inverse of the two-particle propagator is $\Pi(\omega)^{-1} = \omega - H_0 - V_x - V_d(\omega)$. The energy dependent direct interaction can be expressed as

$$(\mathbf{V}_d(\omega))_{\alpha n\mathbf{k},\alpha n'\mathbf{k}'} = \sum_p \mathbf{w}_p(\alpha n\mathbf{k}, \alpha n'\mathbf{k}') \times \left\{ \frac{1}{\omega - \omega_p - (E_{n'\mathbf{k}'} - E_\alpha)} + \frac{1}{\omega - \omega_p - (E_{n\mathbf{k}} - E_\alpha)} \right\}, \quad (7)$$

where the summation is over the poles ω_p of $\mathbf{W}$ and $\mathbf{w}_p(\alpha n\mathbf{k}, \alpha n'\mathbf{k}')$ is the matrix elements of $\mathbf{W}$ in the core hole-electron basis. Additionally, as discussed in Ref. [6], the pole structure of the screened interaction, i.e., fluctuation potentials, has several other uses in core spectroscopies.

We have reviewed a recently developed iterative scheme for calculating the pole structure of the screened interaction. The method was applied to a calculation of quasiparticle corrections needed in XRS or X-ray absorption calculations. By varying the number of poles and the width of these poles in the case of silicon, it was found that the resulting quasiparticle correction converged first for the conduction band states. The way to include these corrections into XRS or XAS calculation was discussed and results were shown for LiF. Even though these corrections are not as important at the F K-edge of LiF as they are in some other situations, it was found that they gave a clear improvement when the calculations were compared to experiment. Finally, a possible additional use for the screened interaction was suggested.

Acknowledgments

J. A. Soininen was supported in part by the U. S. Department of Energy through Grant number DE-FG03-97ER45623 and by the National Institute of Standards and Technology, through the DOE Computational Materials Science Network (CMSN). We express our gratitude to K. Hämäläinen and S. Galambosi for providing the experimental data for LiF.

References

1. Soininen, J. A. and Shirley, E. L., Phys. Rev. B **64**, 165112 (2001), and references therein.
2. Rehr, J. J. and Albers, R. C., Rev. Mod. Phys. **72**, 621 (2000).
3. Hedin, L., Phys. Rev. **139**, 796 (1965). The name of the *GW* approximation arises from the fact that the electron self-energy involves the product of the electron Green's function, *G*, and the dynamically screened Coulomb interaction, *W*.
4. Hedin, L. and Lundqvist, S., in "Solid State Physics", (edited by F. Seitz, D. D. Turnbull and H. Ehrenreich), (Academic, New York, 1969), Vol. 23, p. 1.
5. Aryasetiawan, F. and Gunnarsson, O., Rep. Prog. Phys. **61**, 237 (1998).
6. Hedin, L., J. Phys: Condens. Matter **11**, R489 (1999).
7. Aulbur, W. G., Jönsson, L. and Wilkins, J. W., in "Solid State Physics", (edited by H. Ehrenreich and F. Spaepen), (Academic, New York, 2000), Vol. 54, p. 1.
8. Lundqvist, B. I., Phys. Kondens. Materie **6**, 193 (1967).
9. Here the meaning of the particle-hole basis is similar to the one used in Benedict, L. X., Shirley, E. L. and Bohn, R. B., Phys. Rev. Lett. **80**, 4514 (1998).
10. Soininen, J. A., Shirley, E. L. and Rehr, J. J., J. Phys: Condens. Matter **15**, 2573 (2003).
11. Cullum, J. K. and Willoughby, R. A., "Lanczos Algorithms for Large Symmetric Eigenvalue Computations", (Birkhäuser, Boston, 1985), vol. 1.
12. Meyer, H.-D. and Pal, S., J. Chem. Phys. **91**, 6195.
13. Szabo, A. and Ostlund, N. S., "Modern Quantum Chemistry: Introduction to Advanced Electronic Structure Theory", (Macmillan Publishing Co., Inc., New York, 1982).
14. Hämäläinen, K. *et al.*, Phys. Rev. B **65**, 155111 (2002).

Physica Scripta. Vol. T115, 246–248, 2005

Calculation of Grazing Incidence EXAFS: Fresnel Theory Versus DWBA

P. Keil, D. Lützenkirchen-Hecht* and R. Frahm

Institut für Materialwissenschaften und Fachbereich Physik, Bergische Universität Wuppertal, Gaußstr. 20, 42097 Wuppertal, Germany

Received June 26, 2003; accepted June 28, 2004

PACS numbers: 61.10.Ht, 61.10.Kw

Abstract

The Fresnel theory with its numerous extensions is a well established method for the calculation of grazing incidence X-ray reflectivities for single surfaces and (multi-)layered systems. However, lateral surface correlations – which are always present e.g. for polycrystalline thin films – cannot be included in these calculations. Furthermore the application of the Fresnel theory is restricted to investigations of specular reflectivities, i.e. off specular reflectivities cannot be calculated. These limitations can be overcome by the application of the distorted-wave Born approximation (DWBA). Simulations of grazing incidence reflection mode EXAFS spectra will be presented and the results obtained using different calculation procedures such as the Fresnel theory, the Névot-Croce model and the DWBA are compared. Furthermore, we will also prove the existence of a fine structure similar to EXAFS which can be observed in the region of diffusely scattered intensities. We will show that this new EXAFS technique is surface sensitive even for grazing angles above the critical angle of total reflection.

1. Introduction

It is well known that X-ray specular reflectivity spectra recorded in the vicinity of an absorption edge exhibit a fine structure similar to EXAFS oscillations. However, in comparison to transmission EXAFS, both the real part δ and imaginary part β of the complex refractive index $n = 1 - \delta - i\beta$ contribute to the reflectivity fine structure. Nevertheless short range order structural information can be extracted from reflection mode EXAFS using the Fresnel theory for smooth surfaces and thin films [1–4].

Real surfaces/interfaces are generally afflicted with a variety of surface inhomogemities such as surface roughness and lateral correlations. In recent years the understanding of the scattering from a single rough surface and from rough multilayer interfaces has advanced rather far. The treatment of roughness is a very important part of the models describing the scattered intensities. If only vertical roughness features are considered only one single roughness parameter is required for each surface/interface. Normally the rms-roughness σ is used as a roughness parameter and in this case the X-ray reflectivity has been formulated a long time ago by extending the Fresnel theory [5–7]. But the application of the Fresnel theory is restricted to calculations of specular reflectivities and cannot explain off-specular reflectivities. This can be overcome by a complete description of the roughness and therefore lateral roughness features have to be taken into account as well. Thus two more parameters, namely the lateral correlation length ξ and the Hurst parameter h, are needed to characterize a surface/interface. To take this into account, the distorted-wave Born approximation (DWBA) [5, 8] provides an extremely useful basis for calculating the X-ray scattering of surfaces and layered systems.

For grazing incidence scattering experiments at a fixed photon energy the influence of these roughness-parameters on the scattered intensities are widely known and differences between the two mentioned cases have been discussed [9]. Nevertheless such a discussion for reflection mode EXAFS and the consequences on the extracted fine structure are still missing. Therefore it is of fundamental interest to see in which way rough surfaces influence the fine structure extracted from reflection mode EXAFS measurements.

2. Data preparation and simulation

We have chosen a gold sample as model system. The real part of the refraction index δ was calculated from an absorption measurement of a gold reference sample by means of a Kramers-Kronig transform. Thereafter the reflected intensities are calculated for different sets of roughness parameters and grazing angles θ according to the Fresnel theory for smooth surfaces, the Névot-Croce model [7] and the DWBA [5, 8]. For these calculations, a 50 mm long, semi-infinite, homogeneous and isotropic gold sample was assumed. The incident X-ray beam is collimated vertically by a 120 μm slit and the acceptance angle of the detector is equal to 0.03°.

3. Reflectivity simulation results

Reflection mode spectra calculated using the DWBA are presented in Fig. 1 for glancing angles θ below, in the vicinity and above the critical angle of reflection ($\theta_c = 0.32°$ at 11919 eV) and different values of σ. These spectra are compared to those determined by the Fresnel theory. The chosen lateral correlation length $\xi = 50$ nm and Hurst parameter $h = 0.7$ are typical values reported for sputtered gold films on glass substrates [see e.g. 10, 11]. In comparison to the spectra calculated with the Fresnel-formula, one can see a reduced absolute reflectivity for larger values of σ, as expected. In order to extract the fine structure data we use the method presented by Borthen *et al.* in [4]. In this case the X-ray reflectivity R above the absorption edge can be split into a smooth part R_0 and an oscillatory part ΔR with $R = R_0 + \Delta R$. The reflectivity fine structure χ_R is given by: $\chi_R = \Delta R(E)/R_0(E)$.

In Fig. 2 the magnitude of the Fourier-transform of the k^3-weighted fine structure data extracted from the spectra presented in Fig. 1 are compared to each other. In comparison to the spectra calculated with the Fresnel-formula, one can see significant changes in the magnitudes of the peaks in the Fourier-transformed data, especially for larger values of σ.

The lateral correlation length ξ and the Hurst parameter h have only a minor influence on specularly reflected intensities. As already discussed for grazing incidence scattering experiments at fixed photon energies, the influence of these parameters is less than two orders of magnitude on the intensity of the specularly reflected intensities (see e.g. [9]). Therefore their influence on the extracted fine structure can be neglected. Thus it is interesting to see if a simple roughness model using only one roughness parameter can describe the roughness effects. A comparison between the magnitude of the Fourier-transforms of the k^3-weighted fine

*e-mail: dirklh@uni-wuppertal.de

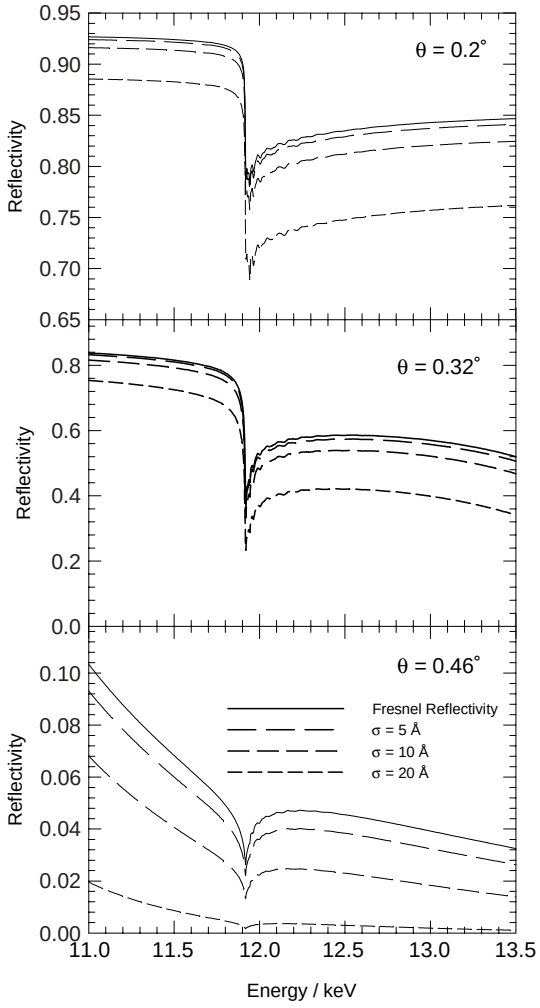

Fig. 1. DWBA and Fresnel reflectivity simulated reflection mode spectra for different grazing angles θ (as indicated) and in the case of the DWBA different values of σ (as indicated). For the simulation $\xi = 50\,\text{nm}$ and $h = 0.7$ was chosen.

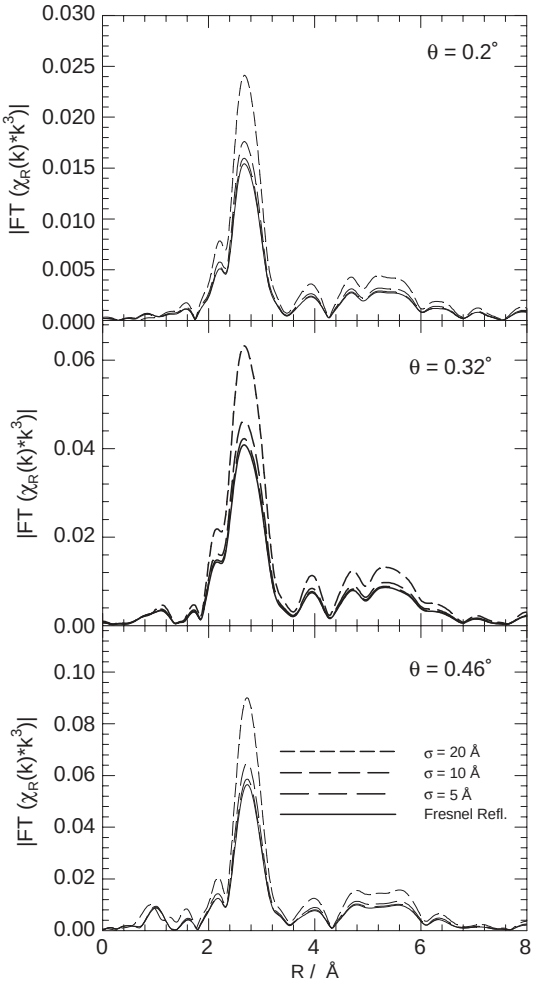

Fig. 2. Magnitudes of the Fourier-transforms of the k^3-weighted reflectivity fine structure data shown in Fig. 1 (grazing angle θ and rms-roughness σ as indicated).

structure data extracted form spectra calculated via DWBA and the Névot-Croce roughness model are presented in Fig. 3. As one can see, almost no difference between the two models can be detected in the Fourier-transforms of the k^3-weighted fine structure data.

4. Reflection mode XAFS under non-specular conditions

As mentioned above scattered intensities can also be investigated under non-specular conditions. Therefore it is of fundamental interest to see if the diffuse scattered intensities recorded in the vincinity of an absorption edge exhibit fine structure features similar to EXAFS or reflection mode EXAFS.

As an example we investigated the structure of a thin Cu-film on a float glass substrate which was prepared by magnetron sputtering. The experiments were performed at the X-ray undulator beamline BW1 [12] using a Si(111) double crystal monochromator and N_2- and Ar-filled ionization chambers as detectors for incoming and scattered intensities. The incident X-ray beam was collimated vertically by a 120 µm slit. For the in-plane non-specular X-ray reflectivity measurements a slit in front of the second ionization chamber limited the acceptance angle of this detector to approximately 0.01°. The region of interest was the so called Yoneda wing [13] which has its maximum at the position of the critical angle of total reflection. In Fig. 4 the reflection mode spectra under non-specular conditions are presented. Obviously,

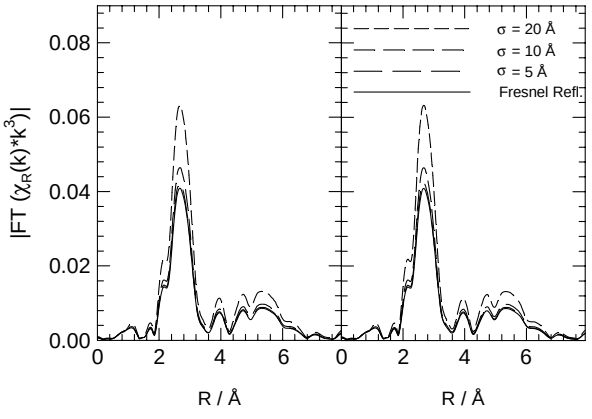

Fig. 3. A comparison between the magnitude of the Fourier-transforms from the structure data extracted form spectra calculated via DWBA (left side) and the Névot-Croce roughness model (right side). The grazing angle of the X-rays is $\theta = 0.32°$. For the DWBA calculation $\xi = 50\,\text{nm}$ and $h = 0.7$ are used.

one can see EXAFS oscillations in the spectra of the diffusely scattered X-rays.

For the further data processing we used the same method to extract the fine structure out of the non-specular spectra as described in section 3 above. In Fig. 5 the normalized magnitudes of the Fourier-transforms of the non-specular reflectivity XAFS mode as well as specular reflection mode XAFS spectra are compared to those of reference spectra obtained from a Cu metal

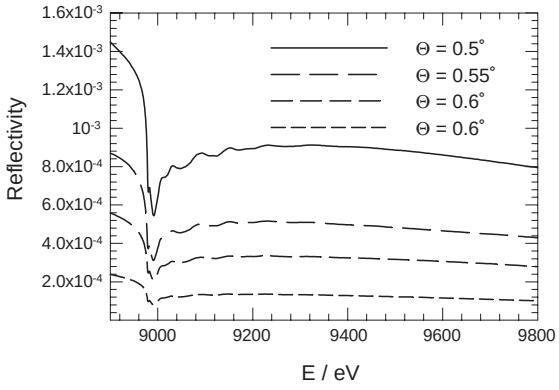

Fig. 4. Reflection mode XAFS under non-specular conditions of a sputtered Cu-film at the K-edge for several grazing angles θ as indicated. The detection angle is $\theta_d = 0.29^\circ$, which is the position of the Yoneda-wing.

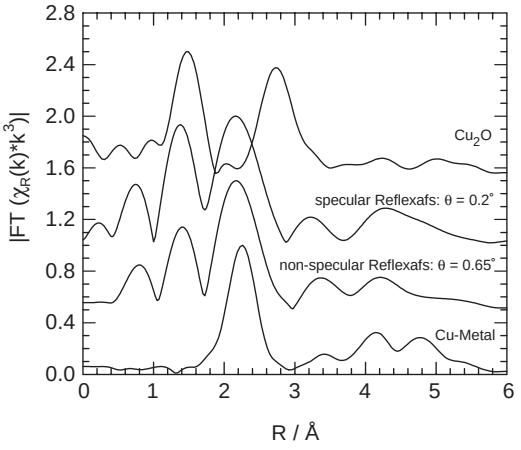

Fig. 5. Normalized magnitudes of the Fourier-transforms of the k^3-weighted fine structure function of the spectra presented in Fig. 4 and of reference compounds (Cu and Cu_2O). All curves are vertically displaced by 0.5.

foil and polycrystalline Cu_2O. Comparison shows that the Fourier-transforms derived from both types of reflection mode XAFS of the sputtered Cu-film contains characteristics of bulk Cu as well as of Cu_2O. It is well known that a thin oxide film of about 10 nm thickness is formed under ambient conditions. Thus, the peak at about 1.5 Å radial distance in the Fourier-transform of the specular reflection mode EXAFS (total information depth is about 10 nm for $\theta < \theta_c$) corresponds to the first Cu-O neighbour interaction. In the non-specular case, however the penetration depth of the X-rays amounts to about 100 nm. Therefore it is rather surprising that this Cu-O coordination is visible in the Fourier-transform of the non-specular spectra with a similar magnitude. This could be an indication that this type of EXAFS mode is still extremely sensitive to the surface structure of the sample.

5. Conclusions

Our calculations have shown that the lateral correlation length and the Hurst parameter only have an minor influence on the X-ray absorption fine structure extracted from reflection mode EXAFS spectra. Thus, it seems to be acceptable to use the Névot-Croce theory for the reflection mode EXAFS data simulation, because this approach is easier to compute. Both theoretical approaches clearly show that the surface roughness has a dramatic influence on the reflectivity fine structure, thus extreme care has to be applied when analyzing reflection mode EXAFS data in terms of coordination numbers and Debye-Waller factors.

Furthermore the existence of fine structure oscillations in the region of diffusely scattered X-rays has been successfully demonstrated. The structure of these oscillations are comparable to those known in reflection mode XAFS. We found strong evidence that this new type of reflection mode XAFS is still surface sensitive even for glancing angles much larger than the critical angle of total reflection, for which the X-ray penetration depth is in the order of about 100 nm.

Acknowledgment

This project was funded by the MWF Nordrhein-Westfalen. Additional support by HASYLAB is gratefully acknowledged.

References

1. Heald, S. M., Chen, H. and Tranquada, J. M., Phys. Rev. B **38**, 1016 (1988).
2. Heald, S. M., Rev. Sci. Inst. **63**, 873 (1991).
3. Bothen, P. and Strehblow, H.-H., Physica B **208&209**, 421 (1995).
4. Bothen, P. and Strehblow, H.-H., Phys. Rev. B **52**, 3017 (1995).
5. Sinha, S. K., Sirota, E. B., Garoff, S. and Stanley, H. B., Phys. Rev. B **38**, 2297 (1988).
6. Parratt, L. G., Phys. Rev. **95**, 359 (1954).
7. Névot, L. and Croce, P., Revue de Physique Appliqueé **15**, 761 (1980).
8. Holý, V. and Baumbach, T., Phys. Rev. B **49**, 10668 (1994).
9. De Boer, D. K. G., Phys. Rev. B **51**, 5297 (1995).
10. Schug, C., Lamparter, P. and Steeb, S., Physica B **248**, 62 (1998).
11. Lützenkirchen-Hecht, D. and Frahm, R., Physica B **283**, 108 (2000).
12. Frahm, R., Weigelt, J., Meyer, G. and Materlik, G., Rev. Sci. Instrum. **66**, 1677 (1995).
13. Yoneda, Y., Phys. Rev. **113**, 2010 (1963).

Physica Scripta. Vol. T115, 249–251, 2005

Local Structures of GaAs Semiconductor in High Shells Studied by Multiple-Scattering Extended X-ray Absorption Fine Structure

Zhihu Sun and Shiqiang Wei*

National Synchrotron Radiation Laboratory, University of Science and Technology of China, Hefei Anhui 230029, P. R. China

Received June 26, 2003; accepted November 4, 2003

PACS numbers: 61.10.Ht, 61.66.Fn, 78.70.Dm

Abstract

Multiple-scattering extended X-ray absorption fine structure (MS-EXAFS) was used to investigate the local structures around Ga atoms from the first to third coordination shells for GaAs crystals. The results revealed that among all the 7 multiple scattering paths in the first three coordination shells of Ga atoms, the dominant one is the scattering pathway of $Ga_0 \rightarrow As_1 \rightarrow Ga_2 \rightarrow Ga_0$ (DS2). The DS2 path is almost out of phase with the single scattering path (SS2) of the second shell, and destructively interferes with the SS2 path. The amplitude ratio of DS2 to SS2 is about 25%. We provide a simple and feasible MS-EXAFS analysis method for investigating the local structure of the first three shells of III-V semiconductors with the zinc-blende structure.

1. Introduction

In the last five years, the nano-structures such as quantum dots, wires and wells composed of IV-IV and III-V semiconductors, *i.e.*, GeSi and Ge quantum dots and wells [1, 2], Ga(In)As quantum dots [3, 4] and wires [5] have attracted much research interest. This is attributed to their tunable optical and optoelectronic performances that make them promising candidates for fabricating laser and light-emitting diode devices [6]. Since the electronic and optical properties of these nano-structures are determined by their atomic structures, it is essential to understand the atomic structure parameters of these III-V semiconductor quantum systems [7]. In fact, it is easy to obtain structural information of the first shell of the nano-structure semiconductors by extended X-ray absorption fine structure (EXAFS). For example, we have studied the local structure of $(Ge_4Si_4)_5$ quantum wells [2] and Ge quantum dots [8] using grazing-fluorescence XAFS. In order to completely determine the tetragonal distortions of these semiconductors, it is necessary to obtain the structural information of the second and third coordination shells. However, it is complicated to analyze the XAFS signals in the higher shells owing to the overlap of the second and third single scattering (SS) paths, as well as the multiple-scattering (MS) paths [9].

The FEFFIT code [10] that considers the multiple-scattering contributions, allows accurate analysis of EXAFS data for structural information beyond the first coordination shells. In this work, a simple MS-EXAFS data analysis method is proposed to study the local structure of III-V GaAs semiconductor in the higher shells. We aim to find the key-factor in analyzing the XAFS data of zinc-blende structure in high shells. In our subsequent work, we will use the proposed structural analysis method to study the high shell local structures of III-V quantum dots.

2. Experiment

Crystalline GaAs sample for XAFS measurement was prepared as follows. Fine powder with sizes of about 20 μm prepared from single crystal, was homogenously mixed with BN powder. Then, the mixed powder was pressed into tablets with diameter of 10 mm and thickness of 0.5 mm. The ratio of GaAs to BN powder was optimized by making the absorption jump $\Delta\mu x \approx 1$ at the GaK-edge.

XAFS measurements of crystalline GaAs powder were performed at the beamline U7C of the National Synchrotron Radiation Laboratory (NSRL, Hefei). The storage ring of NSRL was operated at 0.8 GeV with a maximum current of 160 mA. Fixed-exit Si(111) flat double crystals were used as monochromators. The X-ray harmonics were minimized by detuning the two flat Si(111) crystal monochromators to about 70% of the maximum incident light intensity. Ionization chambers filled with Ar/N_2 mixed gases were used to collect the XAFS spectra. The XAFS spectra were recorded in transmission mode at room temperature. XAFS data were analyzed by USTC-XAFS2.0 software package compiled by Zhong and Wei [11] according to the standard procedures.

3. Results and Discussion

The XAFS spectra were fitted in R space by the FEFFIT code [10]. The theoretical magnitudes and phase-shifts of all the single-scattering (SS) and MS paths in the first three shells were calculated by FEFF7 [12]. By selecting those paths whose amplitude have weights greater than 3% of the largest one, we obtained 10 pronounced scattering paths for GaAs, including 3 SS paths, 5 double-scattering (DS) paths and 2 triple-scattering (TS) paths. For fitting the structural parameters, the coordination numbers were fixed to the nominal composition of crystalline GaAs. In order to decrease the number of independent parameters, the parameter R was assumed to relate to changes in the lattice constant due to thermal expansion. Moreover, as a reasonable approximation, the Debye-Waller factors were set as equal for the corresponding DS and TS paths with the same half path lengths. The third cumulant $\sigma^{(3)}$ was also included in the fits for taking into account the possible asymmetry of distance distributions.

Figure 1 shows the radial structural function (RSF) of GaAs obtained from Fourier transform of the $k^2\chi(k)$ as open circles. The peaks related to the first three shells are well separated. The intensities of the second peak ($R = 3.58$ Å) and the third peak ($R = 4.38$ Å) drop to about 25% and 15% of that of the first peak ($R = 2.15$ Å). The dark solid line shown in Fig. 1 is the curve-fitting result in the R-range [1.5, 5.0] Å by using all the 10

*correspondent. Email: sqwei@ustc.edu.cn

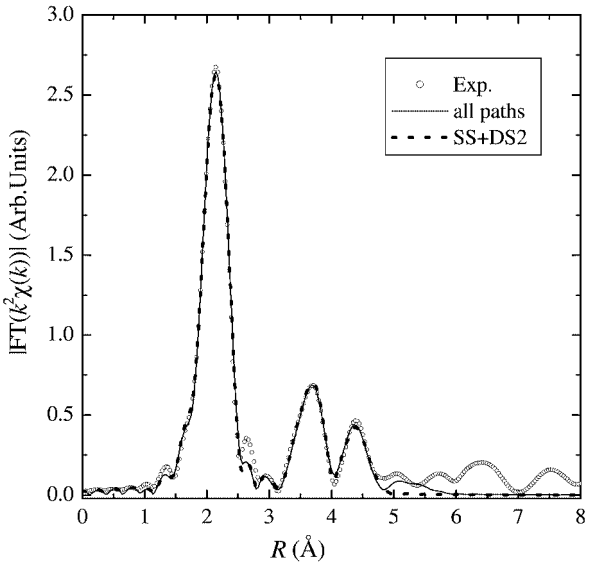

Fig. 1. The radial structural function by Fourier transforming $k^2\chi(k)$ for GaAs: experimental (open circle), fit using all 10 paths (solid line) and fit using SS + DS2 (dark dash line).

Table I. *Path parameters obtained from multiple-scattering fit by using all the 10 paths for GaAs. The parameters in parenthesis are obtained by using only 4 paths: SS1, SS2, SS3 and DS2. In the fitting procedure, the degeneracies of the paths are fixed.*

Path	R (Å)	$\sigma^2(10^{-3}$ Å$^2)$	$\sigma^{(3)}(10^{-4}$ Å$^3)$	ΔE_0 (eV)
SS1	2.458 ± 0.010	4.5 ± 0.1	1.0 ± 0.9	3.4 ± 1.5
	(2.447 ± 0.011)	(4.5 ± 0.2)	(0.8 ± 1.0)	(4.4 ± 1.5)
SS2	4.014 ± 0.016	11.8 ± 0.9	0.0 ± 2.8	4.0 ± 1.3
	(3.996 ± 0.020)	(11.4 ± 0.6)	(0.9 ± 4.0)	(4.8 ± 1.8)
SS3	4.707 ± 0.019	13.2 ± 1.0	0.6 ± 4.0	4.0 ± 1.3
	(4.687 ± 0.025)	(13.6 ± 1.6)	(1.1 ± 5.0)	(4.5 ± 2.3)
DS1	4.465 ± 0.018	10.8 ± 5.2	0.6 ± 4.0	7.7 ± 2.4
DS2	4.465 ± 0.018	10.8 ± 5.2	0.6 ± 4.0	7.7 ± 2.4
	(4.445 ± 0.022)	(11.2 ± 5.6)	(1.1 ± 5.0)	(6.4 ± 2.6)
DS3	5.589 ± 0.023	10.6 ± 10.1	0.6 ± 4.0	7.7 ± 2.4
DS4	5.589 ± 0.023	10.6 ± 10.1	0.6 ± 4.0	7.7 ± 2.4
DS5	5.589 ± 0.023	10.6 ± 10.1	0.6 ± 4.0	4.0 ± 1.3
TS1	4.916 ± 0.020	9.0 ± 0.2	0.6 ± 4.0	7.7 ± 2.4
TS1	4.916 ± 0.020	9.0 ± 0.2	0.6 ± 4.0	7.7 ± 2.4

scattering paths. One can see that the quality of the fits is pretty good. The uncertainties of these fitting parameters are the square root of the diagonal elements of the correlation matrix. The path parameters of all the SS and MS paths are presented in Table I, from which we can see that the radial distances are accurately determined. The typical uncertainty is within 0.01 Å for the first shell, and within 0.03 Å for higher shells.

In general, the RSF peaks in higher shells may originate from two types of scattering paths. One is SS path from higher shell, and the other is MS path. In order to clearly show their contributions to the EXAFS signal of GaAs, the oscillation curves of various scattering paths are shown in Fig. 2, which shows two remarkable features. The first one is that the stronger XAFS signals are the three SS paths (SS1, SS2 and SS3) and one MS path (the triangular double-scattering path DS2, $Ga_0 \rightarrow As_1 \rightarrow Ga_2 \rightarrow Ga_0$). DS2 contributes with a peak at the location of the second shell peak of SS2 and has an oscillation magnitude as high as 25% of that of SS2. The second and most noteworthy feature is the opposition

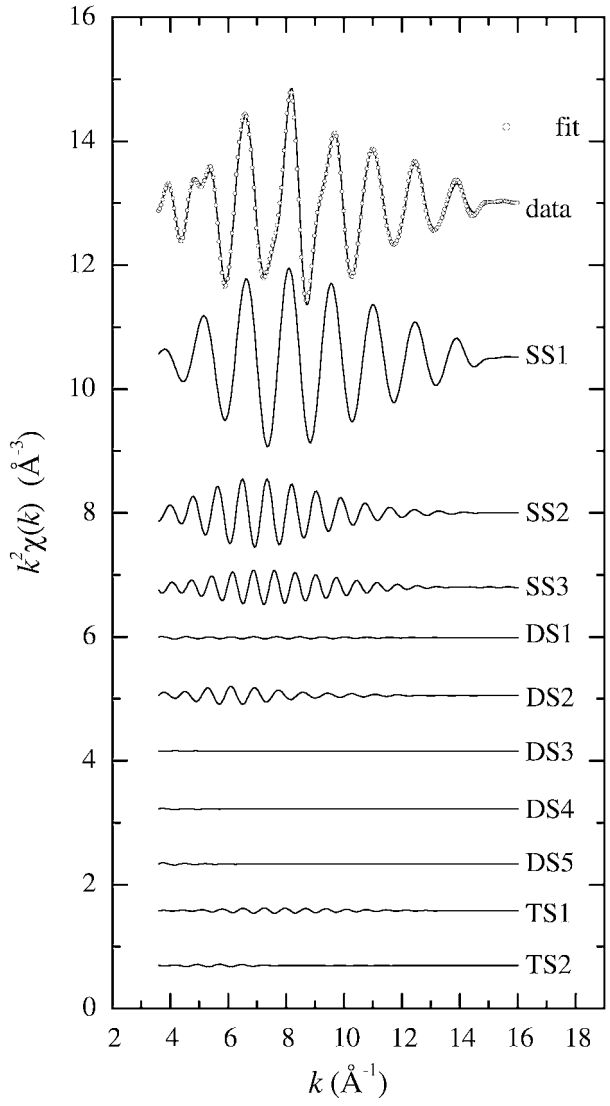

Fig. 2. Contributions of the scattering paths to the total EXAFS oscillation function $k^2\chi(k)$ for GaAs.

of phase between the oscillations of DS2 and SS2, as clearly shown in Fig. 2. Hence, the destructive interference between DS2 and SS2 paths strongly damps the intensity of the second peak, indicating that DS2 plays an important role in accurately determining the structural parameters of the second shell. If the contribution of DS2 is ignored, it would result in a larger Debye-waller factor ${\sigma_2}^2$ of the second coordination shell fitted by SS approximation than the real value. The importance of nonlinear MS process and its interference with higher shell EXAFS signals were also observed for other systems, such as metal Cu [12], and CrO_4 tetrahedron [13].

Since the other MS paths except DS2 contribute very weak signals to the EXAFS spectrum, one can expect that the features of experimental data can be well reproduced by considering only the SS paths and DS2. This result is demonstrated in Fig. 1, where the dark dash line shows the fitting result by using only these 4 paths. Furthermore, in Table I it is obvious that the structural parameters from 4 paths presented in Table I in parenthesis are almost the same as those from considering all the 10 scattering paths.

Previously Dalba *et al.* [14] investigated the MS effects of GaAs using the fast spherical approximation [15]. They calculated the dependence of the MS contribution on the bonding angle

of Ga_0-As_1-Ga_2, which corresponds to the DS2 path in this work. By comparing the amplitude of the DS2 path with that of the SS2 path, they claimed that MS effects of the second and third shells could be neglected for crystalline compounds with open structures of diamond and zinc-blende structures [14]. However, it can be easily found that Dalba *et al.*'s SS results for higher shells of GaAs ($\sigma_2{}^2 = 0.015\,\text{Å}^2$, $\sigma_3{}^2 = 0.019\,\text{Å}^2$) [14] are much larger than ours ($\sigma_2{}^2 = 0.0118\,\text{Å}^2$, $\sigma_3{}^2 = 0.0132\,\text{Å}^2$) by MS analysis.

It is interesting to note that DS1 and DS2 have the same path length, scattering atom types and Debye-Waller factors, but the amplitude peak of DS2 is significantly larger than that of DS1. The reason can be explained by Rehr's theory [12]. For a scattering path Γ, the XAFS amplitude χ_Γ can be recast in terms of the standard formula, but with an effective scattering amplitude f_{eff}:

$$\chi_\Gamma = NS_0^2 \text{Im}\left(\frac{f_{\text{eff}}}{kR^2} e^{2ikR+2i\delta_l} e^{-2k^2\sigma^2}\right), \quad (1)$$

where N is the path degeneracy, R is half the total path length, and the other parameters have their corresponding meaning as in the standard formula [7]. From Eq. (1), the intensity difference between DS1 and DS2 can be attributed to two reasons. One is that the degeneracy of DS2 is twice that of DS1. The other stems from the greatly larger effective scattering amplitude of DS2 than that of DS1, which is caused by the difference in the angle θ between the outgoing and incoming paths.

Acknowledgement

This work is supported by the Natural Science Foundation of China (Grant No. 10174068 and 10375059) and a key-program of the Chinese Academy of Science.

References

1. Koch, R., Wedler, G., Schulz, J. J. and Wassermann, B., Phys. Rev. Lett. **87**, 136104 (2001).
2. Wei, S. Q., Oyanagi, H., Sakamoto, K., Takeda, Y. and Pearsall, T. P., Phys. Rev. B **62**, 1883 (2000).
3. da Silva, M. J., *et al*., Appl. Phys. Lett. **82**, 2646 (2003).
4. Le Ru, E. C., Howe, P., Jones, T. S. and Murray, R., Phys. Rev. B **67**, 165303 (2003).
5. Weman, H., *et al*., Appl. Phys. Lett. **81**, 2839 (2001).
6. Arakawa, Y. and Sakaki, H., Appl. Phys. Lett. **40**, 939 (1982).
7. Sayers, D. E. and Bunker, B. A., in "X-ray Absorption: Principles, Applications, Techniques of EXAFS, SEXAFS and XANES", (edited by Koningsberger, D. C. and Prins, R.), (Wiley, New York, 1988), Chap. 6.
8. Kolobov, A., *et al*., Phys. Rev. B **66**, 075319 (2002).
9. Aubry, J. C., Tyliszczak, T. and Hitchcock, A. P., Phys. Rev. B **59**, 12872 (1999).
10. Stern, E. A., Newville, M., Ravel, B., Yakoby, Y. and Haskel, D., Physica B **208&209**, 117 (1995).
11. Zhong, W. J. and Wei, S. Q., J. University of Sci. Technol. China **31**, 228 (2001).
12. Rehr, J. J., Zabinsky, S. I. and Albers, R. C., Phys. Rev. Lett. **69**, 3397 (1992).
13. Pandya, K. I., Phys. Rev. B **50**, 15509 (1994).
14. Dalba, G., Diop, D., Fornasini, P. and Rocca, F., J. Phys.: Condens. Matter **6**, 3599 (1994).
15. Dalba, G., Diop, D., Fornasini, P., Kuzmin, A. and Rocca, F., J. Phys.: Condens. Matter **5**, 1643 (1993).

Physica Scripta. Vol. T115, 252–254, 2005

Thermal-Motion-Induced Resonant Reflections at the Ge K-edge: Calculation of the Intensity Dependence on Atomic Displacements

E. N. Ovchinnikova[1], A. P. Oreshko[1], Y. Joly[2], A. Kirfel[3], B. P. Tolochko[4] and V. E. Dmitrienko[5*]

[1]Moscow State University, Physics Department, 119992, Moscow, Russia
[2]Laboratoire de Cristallographie, CNRS, BP166, F-38042 Grenoble Cedex, France
[3]Mineralogisch-Petrologisches Institut der Universität Bonn, D-53115 Bonn, Germany
[4]Institute of Solid State Chemistry and Mechanochemistry, 630128 Novosibirsk, Russia
[5]Institute of Crystallography, 119333, Moscow, Russia

Received June 26, 2003; revised November 27, 2003; accepted January 28, 2004

PACS numbers: 61.10.Nz, 61.50.Ah, 74.25.Kc, 61.10.−i, 63.20.−e, 71.90.+q

Abstract

In the Ge-structure, the forbidden Bragg reflections $hk0$ ($h + k = 4n + 2$) can be excited at the Ge K-edge due to both dipole-quadrupole scattering and dipole-dipole scattering of thermally vibrating atoms. The dipole-dipole contribution is referred to as TMI (Thermal Motion Induced) and is caused by the dependence of the atomic tensor form factors on the relative atomic displacements. This effect explains the strong increase of the 600 forbidden reflection intensity with temperature observed in experiments. In the present paper, both the dipole-quadrupole and the TMI contributions to the structure factor of the 600 reflection are calculated using the FDMNES code. Two models are considered, one assuming only displacements of the scattering atom, the other assuming all atoms in a supercell randomly displaced. Both approaches reveal a strong dependence of the dipole-dipole contribution to the tensor atomic factor on the atomic displacements and thus give a qualitative explanation of the temperature behavior of the forbidden reflection 600 observed in Ge.

1. Introduction

In the last years, resonant X-ray diffraction has become a method to study details of structural, magnetic and electronic properties of solids [1]. The "forbidden" Bragg reflections, which occur due to the polarization properties of resonant scattering, are of special interest because for these reflections, the non-resonant contributions vanish. Reflections of this type were first theoretically predicted for dipole-dipole resonant scattering in non-magnetic crystals [2, 3, 4] and later experimentally confirmed [5]. Up to now, the "forbidden" reflections have been observed in many single crystals, e.g. in $NaBrO_3$ [5], Cu_2O [6], TiO_2, MnF_2 [7], $LiHSeO_3$ [8], $Ba(BrO_3)_2.H_2O$ [9], $(Ba_{1-x}Sr_x)_2Zn_2Fe_{12}O_{22}$ [10], Fe_3O_4 [11, 12, 13], FeS_2 [14, 15], $HoFe_2$ [16] and $La_{0.5}Sr_{1.5}MnO_4$ [17].

When the dipole approximation fails to account for forbidden reflection intensities, higher order terms can be responsible for their appearance. For example, the quadrupole-quadrupole contribution causes forbidden reflections in Fe_2O_3 [18] and a mixed dipole-quadrupole contribution might be partly responsible for the forbidden reflections in Ge [19, 20]. The latter also contributes to the gyrotropic properties of crystals, for example, to optical activity and natural circular dichroism [21, 22, 23, 24].

Phenomenological considerations allow for finding sets of forbidden reflections as well as describing the polarization properties of resonant scattering. However, numerical calculations are needed for quantitative comparison between theory and experiment. The calculation of resonant X-ray scattering spectra is similar to XANES calculations for which different approaches have been developed [25, 26, 27, 28]. In the present paper, we use the FDMNES code [27] to calculate the energy dependent intensities of the forbidden reflections in Ge, which have already been theoretically studied and measured with respect to their energy spectra and azimuthal, thermal and polarization dependencies [20, 29, 30, 31, 32]. There are two main mechanisms, which can explain their existence: dipole-quadrupole resonant scattering [20] and a dipole-dipole contribution when the atomic displacements owing to thermal vibrations (TMI-contribution) are taken into account [33, 34]. Only the second contribution can explain the intensity growth with temperature. Recently, similar forbidden reflections have also been observed in ZnO [35]. In the present paper, the FDMNES program is used for studying the dipole-quadrupole and TMI contributions as well as the thermal dependence of the forbidden reflections in Ge.

2. The atomic resonant scattering factor and forbidden reflections in Ge

The tensor atomic form factor, which describes resonant scattering near an absorption edge can be represented as:

$$f_{ij}(E) = f_{ij}^{dd} + \mathrm{i} f_{ijk}^{dq} k_k + \mathrm{i} f_{jik}^{dq*} k'_k + f_{ijkl}^{qq} k_k k'_l, \tag{1}$$

where dd, dq, qq denote the dipole-dipole, dipole-quadrupole and quadrupole-quadrupole contributions, respectively, and k and k' are the incident and scattered wave vectors [36].

In a single-electron approach, the X-ray atomic form factor near the absorption edge takes the form [36]:

$$f_{ij} = -m_e\omega^2 \sum_f \frac{\langle g|O|f\rangle\langle f|O|g\rangle}{E_f - E_g - \hbar\omega + \mathrm{i}\Gamma/2}, \tag{2}$$

where $\hbar\omega$ is the photon energy, O is a transition operator coupling the initial state $|g\rangle$ of energy E_g with an intermediate state $|f\rangle$ of energy E_f.

For $00l$ ($l = 4n + 2$) reflections in Ge, the structure factor equals:

$$F(00l, l = 4n + 2) = 4(f_1 - f_2), \tag{3}$$

where f_1 and f_2 are the tensor form factors associated with the Ge atoms in the sites 000 and $\frac{1}{4}\frac{1}{4}\frac{1}{4}$. These atoms (1) and (2) are connected by inversion. Since both site symmetries are $\bar{4}3m$, the tensor $f_{ij}^{dd} \sim \delta_{ij}$, $f_1^{dd} = f_2^{dd}$ and hence, these terms are not giving rise to forbidden reflections near absorption edges. The dq term, however, yields $F_{ij}(\boldsymbol{H}) = 8\mathrm{i} f_{ijk} H_k$, where f_{ijk} is the symmetric

*dmitrien@ns.crys.ras.ru

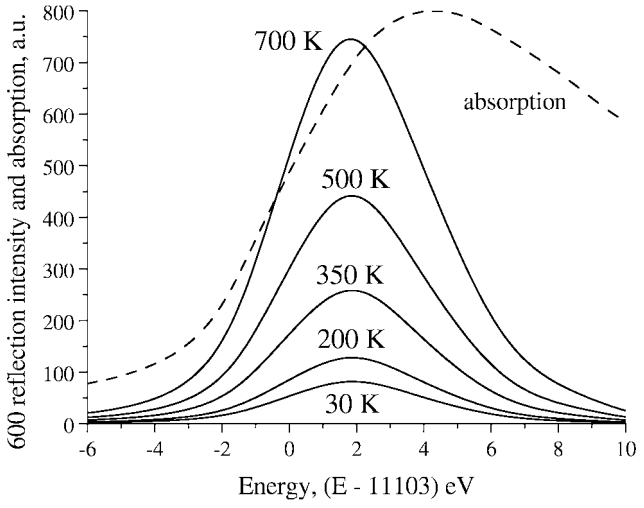

Fig. 1. Energy dependencies of the 600 forbidden reflection intensities in Ge calculated for a supercell with all atoms randomly displaced.

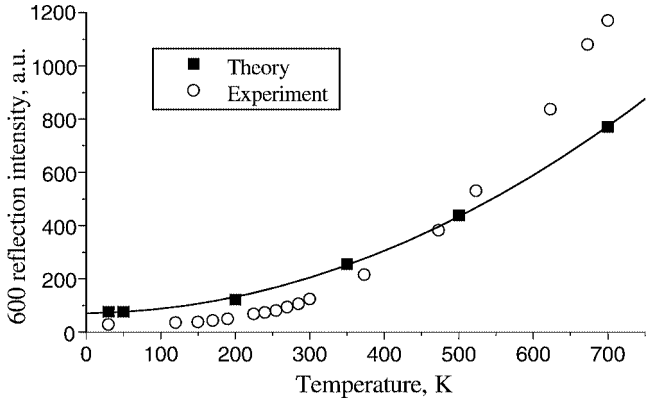

Fig. 2. Temperature dependence of the 600 integral intensity; theoretical points are fitted by a quadratic parabola.

part of a third rank tensor, which contains only one independent component $f_{xyz} = f_{yzx} = f_{zxy}$, $\boldsymbol{H} = k' - k$.

Owing to thermal motions the Ge atoms are displaced from their equilibrium sites with cubic symmetry into sites with non-cubic symmetry. Then, in accordance with the adiabatic approximation, the electrons follow the atomic displacements and since the typical time of the scattering process ($\sim 10^{-17}$ s) is much less than that of an atomic thermal vibration ($\sim 10^{-13}$ s), the scattering reflects the actual atomic configuration at the time it takes place. Generally, this configuration is characterized by atoms in sites with non-cubic symmetry and therefore, the scattering by each atom is described by an anisotropic tensor factor. It was shown in [33] that this anisotropy causes the appearance of "forbidden" $0kl$ reflections with $k + l = 4n + 2$, even in the *dd* approximation.

3. Calculation of the TMI contribution to the forbidden Bragg reflection 600 in Ge

In order to obtain the intensity of a forbidden Bragg reflection in Ge, one has to consider both the dipole-dipole TMI and the dipole-quadrupole contribution. The FDMNES program allows for calculating the tensors f_{ij}^{dd} and f_{ijk}^{dq} for any energy value within the XANES region. For optimizing the calculation time, the symmetry relations were included into the initial version of the program. But since these symmetry relations are violated by the thermal vibrations, all the Ge atoms in the unit cell become independent scatterers. This prevents performing DAFS calculations, which involve crystallographically equivalent scatterers. Hence, we have mixed analytical and numerical calculations, which means that for the scattering, the explicit theoretical expression for the scattering factor F($\boldsymbol{H}$) was applied, while the tensor atomic form factors were numerically calculated with the FDMNES program.

The first theoretical prediction of the TMI contribution [33] has used the following approximation: the tensor atomic form factor depends only on the thermal displacement $\boldsymbol{u}$ of the scattering atom. Then, for small $\boldsymbol{u}$, the *dd* term is a linear function of $\boldsymbol{u}$ resulting in a structure factor:

$$F(\boldsymbol{H})_{ij}^{dd,TMI} = 8\pi \mathrm{i} \Delta f_{ij}^{dd} H_k u_k, \tag{4}$$

where Δf_{ij}^{dd} is the correction of f_{ij}^{dd} owing to the resonant scattering atom's displacement from its equilibrium site. The product $\Delta f_{ij}^{dd} u_k$ transforms as a symmetric third-rank tensor, which possesses only one independent parameter in the cubic $\bar{4}3m$ group.

With that approximation we have calculated the TMI dipole-dipole contribution as:

$$f^{dd} = f_{ijk} T_{ijk} = \tfrac{1}{3}(f_{xy}^{dd} u_z + f_{zx}^{dd} u_y + f_{yz}^{dd} u_x), \tag{5}$$

where the different tensor components f_{ij}^{dd} were calculated using the FDMNES code. The dipole-quadrupole contribution was simulated by the invariant:

$$f^{dq} = \tfrac{1}{6}(f_{xyz}^{dq} + f_{yzx}^{dq} + f_{xzy}^{dq} + f_{zxy}^{dq} + f_{yxz}^{dq} + f_{zyx}^{dq}). \tag{6}$$

For these calculations, the random displacements of the atom in the (000) site were simulated by confining the vectors of the atomic displacements to the surface of the sphere, whose radius is defined by the mean square displacement $\sqrt{\langle u^2 \rangle}$ at a given temperature. According to the Einstein model, which is a sufficiently good approximation in the case of Ge, the mean square amplitude of vibrations was calculated using:

$$\langle u^2 \rangle = u_0^2 \coth \frac{\hbar \Omega}{2 k_B T}. \tag{7}$$

Here, $u_0 = 0.071$ Å is the zero temperature vibration amplitude, and $\Omega = 5.5 \times 10^{13}\,\mathrm{s}^{-1}$ [37].

Assuming the sphere radius to be $\sqrt{\langle u^2 \rangle}$, randomly selected spherical angles θ and ϕ were used to calculate the energy spectra associated with both invariants. Then, for each mean square displacement, the invariants were averaged over 10 random sets of angles, and finally, using the FDMPOST program, the resulting curves were convoluted with the line shape as defined by the line width Γ (Γ was varied from 1.4 eV at Fermi level to 5.7 eV at 50 eV). The obtained dependence of the forbidden reflection 600 intensity on the temperature, i.e. the atomic displacement, gives a satisfactory description of the 600 behavior. The dipole-dipole contribution rapidly increases with temperature, whereas changes of the dipole-quadrupole term are negligible.

However, these first calculations were made assuming only one atom displaced. As a consequence, the atomic potentials are more symmetric than in reality, when all atoms are displaced. Considering [30], wherein it was shown that the relative displacements of the atoms are crucial for the description of the discussed effect, the next step of our calculations took into account displacements of all atoms in the crystal.

To this purpose we used a $2 \times 2 \times 2$ Ge supercell and every atom in this supercell was displaced in such a way, that its

randomly oriented displacement-vector ended on a sphere with radius $\sqrt{\langle u^2 \rangle}$. When all supercell atoms are simultaneously displaced, the environment of a "resonant" atom is not cubic at all, hence a calculation of an invariant as in (5) does not give a good result. "DAFS" calculations are also not feasible, because all the scatterers in the cell are inequivalent. Thus, we have again used the semi-analytical approach supposing that

$$F(600)^{dd,TMI} = 8\mathrm{i} f_{ij}^{dd} \sin(\boldsymbol{Hu}), \tag{8}$$

At the azimuthal angle $\phi = 0$, only the non-diagonal terms of the second rank tensor provide a contribution to the scattering amplitude. Here, $f_{\pi\sigma}$ reaches a maximum equal to:

$$f_{\pi\sigma} = f_{xy} \cos\theta_B - f_{yz} \sin\theta_B, \tag{9}$$

where θ_B is the Bragg angle. $f_{\sigma\sigma}(\phi = 0) = f_{yy}$ vanishes for the dipole-quadrupole scattering, but not so for the TMI mechanism. However, since it is less than $f_{\pi\sigma}$, we neglect it. Hence for $\phi = 0$, one obtains: $f_{ij}^{dd} \sin(\boldsymbol{Hu})$, which coincides with the imaginary part of the "signal total" for a single atom, as given by the program FDMNES. Inserting this term into (8) allowed for calculating the scattering factor of the 600 reflection. This procedure was carried out for 3 different sets of randomly displaced supercell atoms, followed by averaging and convoluting, again taking into account $\Gamma(E)$. The results are depicted in Fig. 1. They clearly show that the dipole-dipole TMI contribution to the forbidden 600 reflection significantly grows with temperature. Similar calculations carried out for the dipole-quadrupole term revealed that in contrast to the TMI-effect the dipole-quadrupole contribution slightly decreases as the temperature is raised. The temperature dependence of the integrated 600 intensity is shown in Fig. 2. The curve is a qualitatively satisfactory description of the experimentally observed thermal dependence of the 600 reflection intensity reported in [29, 30].

Thus, the calculations of the 600 forbidden reflection intensity with the help of the FDMNES program have shown a strong dependence of the dipole-dipole atomic form factor on the atomic displacements, which leads to a qualitative description of the phenomenon. For a more quantitative comparison with the experimental data, one should: 1) calculate the scattering factor of every displaced atom in a supercell for improving the statistics; 2) take into account correlations between atomic displacements as well as dispersion of the displacement values; 3) depending on the displacements consider contributions from the diagonal terms. It seems, however, that all these measures will only give corrections to the calculated scattering factors without essentially changing the results.

4. Conclusion

Resonant X-ray diffraction provides a unique method to study the influence of atomic thermal vibrations on the electronic states of a crystal. For the cubic Ge-structure, numerical calculations of the energy spectra of the forbidden 600 reflection have demonstrated the influence of the relative displacements of all atoms on the dipole-dipole resonant tensor atomic form factor. The results derived are in good agreement with the experimental data reported before by different experimental groups. The developed method of calculation can also be applied to other crystals, for which forbidden reflection intensities growing with temperature were observed, e.g. ZnO.

Acknowledgements

The work is supported by the grant INTAS 01-0822.

References

1. Hodeau, J. L., *et al*., Chem. Rev. **101**, 1843 (2001).
2. Templeton, D. H. and Templeton, L. K., Acta Cryst. **A36**, 237 (1980).
3. Dmitrienko, V. E., Acta Cryst. **A39**, 29 (1983).
4. Dmitrienko, V. E., Acta Cryst. **A40**, 89 (1984).
5. Templeton, D. H. and Templeton, L. K., Acta Cryst. **A41**, 133 (1985).
6. Eichorn, K., Kirfel, A. and Fisher, K. Z. Naturforshung. **43a**, 391 (1988).
7. Kirfel, A., Petcov, A. and Eichhorn, K., Acta Cryst. **47**, 180 (1991).
8. Kirfel, A. and Petcov, A., Acta Cryst. **A48**, 247 (1992).
9. Templeton, D. H. and Templeton, L. K., Acta Cryst. **A48**, 746 (1992).
10. Tsuji, E., *et al*., J. Phys. Soc. Japan **65**, 610 (1996).
11. Kirfel, A., Lippmann, T. and Morgenroth, W., HASYLAB Jahresbercht 371–372 (1995).
12. Hagiwara, K., Kanazawa, M., Horie, K., Kokubun, J. and Ishida, K., J. Phys. Soc. Japan **68**, 1592 (1999).
13. García, J., *et al*., Phys. Rev. Lett. **85**, 578 (2000).
14. Nagano, T., *et al*., J. Phys. Soc. Japan **65**, 3060 (1996).
15. Templeton, D. H. and Templeton, L. K., Acta Cryst. **A53**, 352 (1997).
16. Collins, S. P., Laundy, D. and Stunault, A., J. Phys.: Cond. Mat. **13**, 1891 (2001).
17. Murakami, Y., *et al*., Phys. Rev. Lett. **80**, 1932 (1998).
18. Finkelstein, K. D., Shen, Q. and Shastri, S., Phys. Rev. Lett. **69**, 1612 (1992).
19. Templeton, D. H. and Templeton, L. K., Phys. Rev. B. **49**, 14850 (1994).
20. Templeton, D. H., in "Resonant Anomalous X-ray Scattering," (Eds. Materlik, G., Sparks C. J. and Fisher, K.) (Amsterdam, Elsevier, 1994). P. 1–7.
21. Siddons, D. P., Hart, M., Amemiya, Y. and Hastings, J. B., Phys. Rev. Lett. **64**, 1967 (1990).
22. Alagna, L., *et al*., Phys. Rev. Lett. **80**, 4799 (1998).
23. Natoli, C. R., Brouder, C., Sainctavit, P., Goulon-Ginet, C. and Rogalev, A., Eur. Phys. J. **B4**, 1 (1998).
24. Goulon, J., Goulon-Ginet, C., Rogalev, A. and Gotte, V., J. Chem. Phys. **108**, 6394 (1998).
25. Vedrinskii, R. V., Kraizman, V. I., Novakovich, A. A. and Machavariani, V. Sh., J. Phys.: Cond. Mat. **5**, 8643 (1993).
26. Rehr, J. J. and Alberts, R. C., Rev. Mod. Phys. **72**, 621 (2000).
27. Joly, Y., Phys. Rev. **B63**, 125120-1 (2001).
28. Taillefumier, M., Cabaret, D., Flank, A.-M. and Mauri, F., Phys. Rev. **B66**, 195107 (2002).
29. Kokubun, J., Kanazawa, M., Ishida, K. and Dmitrienko, V. E., Phys. Rev. **B64**, 073203 (2001).
30. Kirfel, A., Grybos, J. and Dmitrienko, V. E., Phys. Rev. **B66**, 165202 (2002).
31. Lee, T. L., *et al*., Phys. Rev. **B64**, 201316(R) (2001).
32. Detlefs, C., Physica **B345**, 45 (2004).
33. Dmitrienko, V. E., Ovchinnikova, E. N. and Ishida, K., JETP Lett. **69**, 938 (1999).
34. Dmitrienko, V. E. and Ovchinnikova, E. N., Acta Cryst. **A56**, 340 (2000).
35. Collins, S. P., Laundy, D., Dmitrienko, V. E., Mannix, D. and Thompson, P., Phys. Rev. **B68**, 064110 (2003), and Physica Scripta, paperTIT8060.
36. Blume, M., in "Resonant Anomalous X-ray scattering," (Eds. Materlik, G., Sparks, C. J. and Fisher, K.) (Amterdam, Elsevier, 1994) p 654.
37. Reissland, J. A., "The Physics of Phonons," (John Wiley and Sons Ltd. London-New York-Sidney-Toronto, 1973).

Physica Scripta. Vol. T115, 255–260, 2005

DAFS and XAFS Investigation of Structural Short-Range Order of Decagonal Al-Co-Ni

A. Kupsch[1*], D. C. Meyer[1], P. Gille[2] and P. Paufler[1]

[1]Technische Universität Dresden, Institut für Strukturphysik, D-01062 Dresden, Germany
[2]Ludwig-Maximilians-Universität München, Dept. für Geo- und Umweltwissenschaften, Theresienstr. 41, D-80333 München, Germany

Received June 26, 2003; revised July 11, 2003; accepted November 4, 2003

PACS numbers: 61.10.Ht, 61.10.Nz, 61.44.Br

Abstract

Due to the lack of long-range periodic order in quasicrystals there are restrictions concerning a straightforward structure analysis on base of X-ray diffraction data. Computed reflection intensities in X-ray diffraction patterns, which are strongly affected by the shape and occupation of hypothetical atomic surfaces, need to be compared with experimental data. The interatomic short-range correlations as to be determined by means of DAFS and XAFS have to be in agreement with these structural models. The use of linearly polarised X-rays allows for orientation sensitive determination of otherwise averaged short-range order information. Additionally wave vector-selectivity of DAFS can yield short-range order information sensitive to sites occupied by atomic species within the coherently scattering structural units.

Structural models of decagonal Al-Co-Ni were applied to compute theoretical DAFS and XAFS functions. Calculation of both, energy-dependent structure factors and pair distribution functions obtained within a hypothetical cluster of app. 81 000 atoms as the basis of computation of DAFS are outlined.

Co-K and Ni-K DAFS and XAFS measurements at 3 independent reflections of a decagonal $Al_{70}Co_{9.5}Ni_{20.5}$ single crystal were performed and the experimental data were subjected to quantitative evaluation. The reflections used involved wave vectors parallel and perpendicular to the periodic direction and in a third inclined direction. In agreement with our simulations DAFS of individual reflections and thereby corresponding short-range orders exhibited no differences within the error limits. The same was found for the case of polarized Co-K and Ni-K XAFS results.

1. Introduction

To our knowledge up to now there is no DAFS analysis of quasicrystalline phases in the literature. One advantage of DAFS compared to XAFS is its site selectivity. DAFS provides a XAFS-like radial distribution around the absorbing species, which is convoluted by their crystallographic weights. In a pioneer work Sorensen *et al*. [1] stated: "Standard crystallography cannot fully solve the structure of quasicrystals because the necessary diffraction information is distributed throughout reciprocal space in infinitely many weak Bragg peaks. This provides the motivation for pursuing further structural information with DAFS. Will all the DAFS intensities be the same, or will they look different?"

Several XAFS studies of the decagonal Al-Co-Ni phase are known from the literature [2, 3]. Both measured XAFS at the K absorption edges of Co and Ni. Braun *et al*. [2] exploited the Li/Steurer model [4], which was modified by Deus [5]. This model does not differentiate between Co and Ni atoms but unifies them in average as transition metals (TM). Comparable results were obtained from a powdered sample and quasicrystalline thin film layer at both absorption edges. This verified the radial distribution in 3 subshells (2.46 Å, 2.54 Å and 2.88 Å) as derived from the Li/Steurer model for interatomic distances $R < 3$ Å and the random distribution of Co and Ni on TM sites. Zaharko *et al*. [3] performed polarization dependent XAFS at single crystals. Electric field vector $\vec{E}$ was aligned parallel and perpendicular to periodic direction $\vec{c}$. In the Co environment the authors' fit results exhibit 3 shells of Al atoms at well separated distances (2.42 Å, 3.9 Å and 4.8 Å), exclusively. Whereas the distances did not vary depending on polarization, the higher shell's occupancy is found larger for $\vec{E} \perp \vec{c}$. In the neighbourhood of Ni atoms both, Al and TM, are found. For the case $\vec{E} \perp \vec{c}$ two distances $R_{\mathrm{Ni-Al}}$ (2.46 Å and 4.9 Å) were found to match the results in Co environment, whereas additional intermediate shells of TM at 2.65 Å and 3.6 Å were indicated. For the case $\vec{E} || \vec{c}$ the first Al and TM shells with comparable occupancies are observed again, but only one Al site at 4.0 Å is detected in the higher R range.

2. Samples

A specimen of composition $Al_{70}Co_{9.5}Ni_{20.5}$ was studied by means of DAFS and XAFS, simultaneously. This composition is at the Ni-rich edge of the narrow existence region of the decagonal phase and occurs in type I superstructure at temperatures below 620 °C [6].

The initial sample was grown from the melt by the Czochralski method as described in [7] and exhibited a size of a few cm^3, typically. As outlined below both DAFS and fluorescence XAFS analysis require careful correction for absorption and extinction effects. Hence it was convenient to prepare individual samples which were characterized by flat surfaces whose normals point in the direction of scattering vectors of strong reflections in diffraction experiments.

The initial sample was cut by means of a tungsten wire (50 µm in diameter) saw and subdivided into three samples of [00001], [00-1-11] and [10000] orientation.

The composition was confirmed by Electron Probe Micro-analysis (EPMA) within error limits of 1 at %. The mass density, ρ, was checked using a precision device based hydrostatic buoyancy in M-dodecan ($C_{12}H_{26}$) and was determined to be $\rho = 4.16 \pm 0.01$ g/cm^3.

As obtained by Laue diffraction the specimen of the subsets consisted of at least two large individual grains with relative misorientation of app. $\sim 0.3^\circ$ (angles enclosed by the normals of corresponding planes of same indexation).

3. Experimental

DAFS/XAFS experiments were carried out at the bending magnet beamline CEMO at HASYLAB/DESY. A Si(111) double crystal monochromator was used. The incident monochromatic radiation was limited by (0.2×2.62) mm^2 entrance slits and monitored with an ionization chamber.

*e-mail: andreas.kupsch@physik.tu-dresden.de

Samples were mounted to an Eulerian cradle, which allowed to adjust each of the angles (diffraction angle θ, side-ward tilting χ and the detector position 2θ) with an accuracy of 0.001°.

The measurements were carried out in the energy range 7600–9000 eV with a step width of 3 eV and effective measuring time of 15 s per step. Reflection intensities were recorded with a thermoelectrically cooled Si PIN diode. To suppress background radiation and to enhance angular resolution its entrance was narrowed by $(1.0 \times 1.09)\,\mathrm{mm}^2$ slits. Simultaneously we recorded the Co-K and Ni-K fluorescence radiation. We used an energy resolving semiconductor detector (KEVEX), which was fixed on a side-ward position about 40 mm away from the sample (grazing angle of exit). The detector entrance window was narrowed by a lead shield, resulting in an effective angle of exit of app. 7°. The use of an energy-resolving detector proved essential, since for the correct evaluation of XAFS data from the Ni-K edge (8333 eV) the fluorescence Ni-Kα and Ni-Kβ fluorescence lines have to be reliably separated from the according Co lines.

The reflections observed were rather sharp with a full width of half maximum of about 0.001°. By rocking the sample rotation at constant detector position we observed at least 4 individual crystallites, tilted by app. 0.05°.

Preliminary Bragg angle adjustment of the specimens was performed using the sample goniometer (rotation θ, tilting χ). The rough energy dependence of θ was programmed according to a second order polynomial which had been determined beforehand with the aid of a diffraction pre-experiment. Because of the rather sharp single crystal reflection, the accuracy of the θ-setting ($\Delta\theta = 0.001°$) by the sample goniometer proved insufficient for preserving the Bragg angle when changing the energy. For DAFS measurements with high-quality crystals of small mosaic spread an accuracy of θ-setting of about 0.0001° is necessary. We achieved this by adding a tuneable piezoelectric tilting table. This is described in detail by Meyer *et al*. [8].

4. Structural model

Our calculations are based on the structure model of Li *et al*. (Li/Steurer model for short) [4], which had been developed for the atomic structure of decagonal Al-Co-Cu. The refinement of Li/Steurer model by Deus [5], which was applied to the very similar Al-Co-Ni system, avoided too short interatomic distances and improved the *R*-value of structure refinement by changing the shape of the atomic surfaces.

The Deus model contains 4 hyperatoms in the 5-dimensional unit cell. The atomic surfaces are polygonal domains in 2-dimensional perpendicular (or internal) space, whose shape is of five-fold symmetry.

Hyperatoms (HA) 1 and 2 are placed at $z = 1/4$ along the periodic direction and on the body diagonal of the remaining four dimensions. HA 3 and 4, which are copies of HA 1 and 2 rotated by $\pi/5$, are placed at $z = 3/4$ along the periodic direction and on the body diagonal again.

5. EXAFS/Pair distributions

From the structural model we have calculated a 3-dimensional cluster of 140 Å in diameter, which contained app. 81 000 atoms. This huge cluster was used to derive the co-ordination numbers of the transition metals (TM) by evaluating the neighbourhood of each single TM atom. Thus we obtain a discrete spectrum of 3.22 Al at 2.45 Å, 4.88 Al and 1.12 TM at 2.55 Å, 1.41 Al and 0.35 TM at 2.88 Å, where the first and the last distance arise from pair correlations within a quasiperiodic plane, whereas the 2.55 Å distance counts for pairs in adjacent planes. If the sum of the first three distances is considered as the first shell the resulting number of app. 11 atoms is a reasonable value. A second shell is located between 4 and 5.5 Å, a third between 6.2 and 6.7 Å. At higher distances we state a dense distribution, which cannot be subdivided in shells from this simple point of view.

Since our experiment is performed with linear polarized radiation, $\vec{\boldsymbol{p}} = p\vec{\boldsymbol{e}}_p$, and single crystals of well defined orientation we make use of the effective co-ordination number $N^* = 3\sum_j \langle \vec{\boldsymbol{e}}_j, \vec{\boldsymbol{e}}_p \rangle^2$, where $\vec{\boldsymbol{e}}_j$ denotes the unit vectors of atomic sites $\vec{\boldsymbol{r}}_j$.

The reflection positions considered were adjusted by uniaxial rotation around a vector within the quasiperiodic plane parallel to the polarization vector, thus not affecting the effective co-ordination number. Therefore we expect identical XAFS spectra for the reflections selected. Since N^* proves insensitive to rotations around the periodic direction $\vec{\boldsymbol{e}}_p$||[10000] can be taken as the general case. We obtain 4.84 Al at 2.45 Å, 2.59 Al and 0.57 TM at 2.55 Å, 2.08 Al and 0.56 TM at 2.88 Å, i.e. the "in plane" correlations are emphasized.

As an example the measured XAFS, its simulation and the fit parameters recorded simultaneously with the 10000 DAFS are shown in Fig. 1 and Table I.

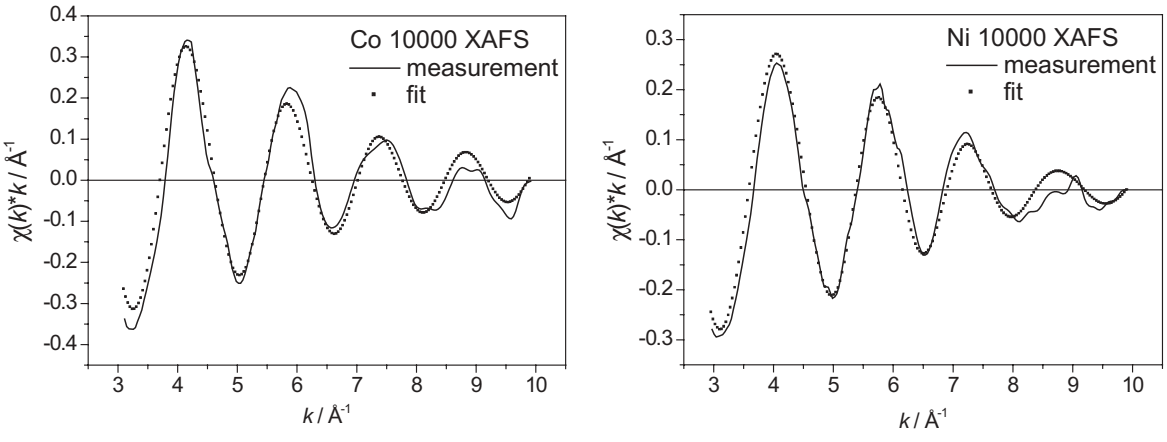

Fig. 1. Measured and fitted XAFS spectra at the Co-K (left) and Ni-K absorption edge (right).

Table I. *Fit parameters obtained from fluorescence XAFS when the 10000 reflection is excited.*

	Co-K XAFS				Ni-K XAFS			
	N^*	R/Å	σ^2/Å^2	ΔE/eV	N^*	R/Å	σ^2/Å^2	ΔE/eV
Al	5.1±0.5	2.45±0.02	0.005±0.001	4.2±1.0	4.8±0.5	2.45±0.02	0.006±0.001	2.9±1.0
Al	2.4	2.55	0.005	3.3	2.4	2.55	0.006	2.3
TM	0.5	2.55	0.005	0	0.5	2.55	0.005	0
Al	2.1	2.91	0.011	−0.5	2.1	2.90	0.005	−0.2
TM	0.7	2.92	0.006	−0.1	0.6	2.88	0.004	0

6. Structure factor of decagonal AlCoNi

The structure factor of quasicrystals is given by Yamamoto [9] as

$$F(\vec{\boldsymbol{Q}}) = \sum_j f_j(\vec{\boldsymbol{Q}}_\parallel)\exp[-B(Q_\parallel)^2/4]\exp[2\pi \mathrm{i}\,\vec{\boldsymbol{Q}}\vec{\boldsymbol{r}}_j]G_j(\vec{\boldsymbol{Q}}_\perp) \quad (1)$$

by summing over all hyperatoms j in the high-dimensional unit cell, where $G_j(\vec{\boldsymbol{Q}}_\perp)$ represents the Fourier transform (FT) of the atomic surface Δ of hyperatom j in perpendicular space:

$$G_j(\vec{\boldsymbol{Q}}_\perp) = \int_\Delta \mathrm{d}V_\perp \exp[2\pi \mathrm{i}\vec{\boldsymbol{r}}_\perp \vec{\boldsymbol{Q}}_\perp]. \quad (2)$$

In case of polygonal shaped atomic surfaces $G_j(\vec{\boldsymbol{Q}}_\perp)$ can be calculated analytically by decomposition in triangles since the Fourier transformation is linear. Following Yamamoto's [9] description its FT then is given by

$$G(\vec{\boldsymbol{Q}}_\perp) = |\vec{\boldsymbol{e}}_1 \times \vec{\boldsymbol{e}}_2| \frac{q_1[\exp(\mathrm{i}q_2) - 1] - q_2[\exp(\mathrm{i}q_1) - 1]}{q_1 q_2 (q_1 - q_2)}, \quad (3)$$

where $\vec{\boldsymbol{e}}_1$ and $\vec{\boldsymbol{e}}_2$ are two edge vectors defining a triangle and $q_i = 2\pi\vec{\boldsymbol{e}}_i\vec{\boldsymbol{Q}}_\perp$.

The FTs prove real valued and radial symmetric, leaving us with the dependence on the magnitude $Q_\perp$, only, and no differences between HA1/HA3 and HA2/HA4, respectively. Fig. 2 depicts the FT's radial dependencies for the three different occupation domains of HA1 and HA2.

Up to this point we have introduced all auxiliary tools to derive the structure factor numerically. To keep the notation short we neglect the Debye-Waller term in equation (2), which is not due to changes within one DAFS scan at constant temperature (here: room temperature), since the Bragg condition keeps the momentum transfer $\vec{\boldsymbol{Q}}_\parallel$ constant.

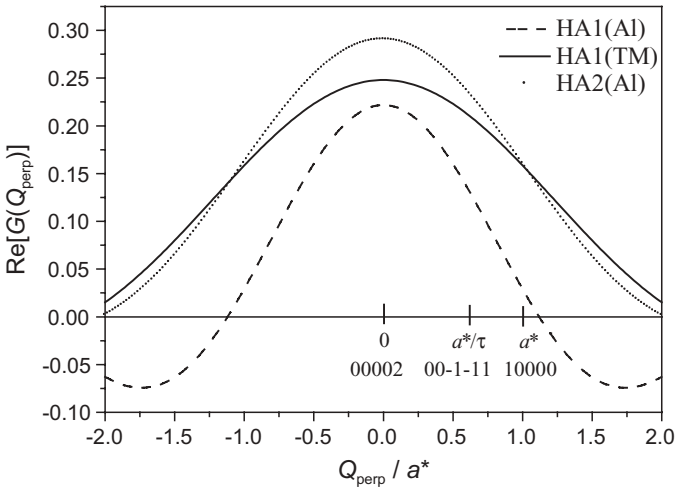

Fig. 2. Radial dependence of the Fourier transforms of the occurring occupation domains on $Q_\perp$.

Introducing the smooth resonant terms of the atomic scattering amplitude we get

$$\begin{aligned} F_s(\vec{\boldsymbol{Q}}, E) &= \sum_j (f_0 + f' + \mathrm{i}f'')_j \exp[2\pi \mathrm{i}\,\vec{\boldsymbol{Q}}\vec{\boldsymbol{r}}_j]G_j \\ &= \sum_j G_j\{[(f_0 + f')_j \cos(2\pi\vec{\boldsymbol{Q}}\vec{\boldsymbol{r}}_j) - (f'')_j \sin(2\pi\vec{\boldsymbol{Q}}\vec{\boldsymbol{r}}_j)] \\ &\quad + \mathrm{i}[(f_0 + f')_j \sin(2\pi\vec{\boldsymbol{Q}}\vec{\boldsymbol{r}}_j) + (f'')_j \cos(2\pi\vec{\boldsymbol{Q}}\vec{\boldsymbol{r}}_j)]\} \end{aligned} \quad (4)$$

The term "TM" unifies the Co and Ni atoms contained. However, we have to regard their relative contributions to atomic scattering amplitude, when introducing the oscillatory terms, which can arise from one species, only. We simply weigh f_{TM} with respect to the nominal composition: $f_{\mathrm{TM}} = c_{\mathrm{Co}}/(c_{\mathrm{Co}} + c_{\mathrm{Ni}})f_{\mathrm{Co}} + c_{\mathrm{Ni}}/(c_{\mathrm{Co}} + c_{\mathrm{Ni}})f_{\mathrm{Ni}} = w_{\mathrm{Co}}f_{\mathrm{Co}} + w_{\mathrm{Ni}}f_{\mathrm{Ni}}$, with $w_{\mathrm{Co}} = 0.317$, $w_{\mathrm{Ni}} = 0.683$.

For example $F_s(10000)$ then reads:

$$\begin{aligned} F_s(10000) &= 2(f_0 + f' + \mathrm{i}f'')_{\mathrm{Al}}[-\cos(\pi/5)G_{1\mathrm{Al}} \\ &\quad + \cos(2\pi/5)G_{2\mathrm{Al}}] \\ &\quad -2w_{\mathrm{Co}}(f_0 + f' + \mathrm{i}f'')_{\mathrm{Co}}\cos(\pi/5)G_{1\mathrm{TM}} \\ &\quad -2w_{\mathrm{Ni}}(f_0 + f' + \mathrm{i}f'')_{\mathrm{Ni}}\cos(\pi/5)G_{1\mathrm{TM}} \end{aligned} \quad (5)$$

or in compact style

$$\begin{aligned} F_s &= (f_0 + f' + \mathrm{i}f'')_{\mathrm{Al}}G_{\mathrm{Al}} + (f_0 + f' + \mathrm{i}f'')_{\mathrm{Co}}G_{\mathrm{Co}} \\ &\quad + (f_0 + f' + \mathrm{i}f'')_{\mathrm{Ni}}G_{\mathrm{Ni}}. \end{aligned} \quad (6)$$

Table II summarizes the coefficients G_j for the different reflections considered. As to be shown below, the coefficients of the absorbing species play the role of crystallographic weights.

We now introduce the oscillating contributions of the atomic scattering amplitude to the structure factor. To distinct between smooth and oscillating parts the index s is applied on all smooth terms derived above. We isolate the oscillating contributions f'_{os} and f''_{os} to the atomic scattering amplitude of the resonantly

Table II. *Coefficients G_j of the atomic species at three reflections as introduced in equ. (6).*

	G_{Al}	G_{Co}	G_{Ni}
10000	0.0521574	−0.0812844	−0.1751334
00-1-11	−0.5256615	−0.1269637	−0.2735526
00002	−1.0248092	−0.1572341	−0.3387725

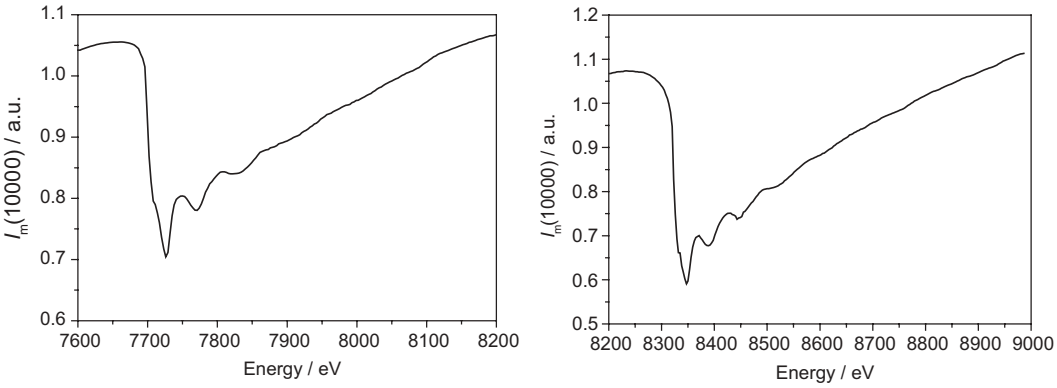

Fig. 3. Measured DAFS intensities of the 10000 reflection at the Co-K edge (left) and the Ni-K edge (right). Normalised to primary intensity and corrected for an empirical device function.

scattering species l:

$$F_{os}(\vec{\boldsymbol{Q}},E) = \sum_j (f_0 + f_s'' + \mathrm{i}f_s'')_j \exp[2\pi\mathrm{i}\,\vec{\boldsymbol{Q}}\vec{\boldsymbol{r}}_j]G_j + \sum_l (f_{os}' + \mathrm{i}f_{os}'')_l \exp[2\pi\mathrm{i}\,\vec{\boldsymbol{Q}}\vec{\boldsymbol{r}}_l]G_l = F_s + \sum_l (f_{os}' + \mathrm{i}f_{os}'')_l \exp[2\pi\mathrm{i}\,\vec{\boldsymbol{Q}}\vec{\boldsymbol{r}}_l]G_l. \quad (7)$$

To be consistent with the DAFS literature (e.g. [1]) we introduce the so-called crystallographic weights $\alpha_m(\vec{\boldsymbol{Q}})$. They are given by the sum over all the occurrences in the unit cell of each equivalent site k, producing one weight for each inequivalent site m. In conventional crystallography the crystallographic weights are defined by

$$\alpha_m(\vec{\boldsymbol{Q}}) = \sum_k \exp(2\pi\mathrm{i}\,\vec{\boldsymbol{Q}}\vec{\boldsymbol{r}}_k). \quad (8)$$

Regarding the expression obtained in equ. (7) in the case of quasicrystals we insert the Fourier transform of the atomic surface $G_k(\vec{\boldsymbol{Q}}_\perp)$ at sites k into the crystallographic weights:

$$\alpha_m(\vec{\boldsymbol{Q}}) = \sum_k G_k(\vec{\boldsymbol{Q}}) = \sum_k w_k G_k(\vec{\boldsymbol{Q}}_\perp)\exp(2\pi\mathrm{i}\,\vec{\boldsymbol{Q}}\vec{\boldsymbol{r}}_k) \quad (9)$$

as introduced in equ. (6).

This is the crucial difference between DAFS on conventional, 3-dimensional periodic crystals and on quasicrystals: the contribution of the resonantly scattering atomic species is not only defined by their crystallographic sites but is essentially determined by the size and shape of the atomic surfaces.

With that compact notation the scattered intensity reads as in the DAFS theory on conventional crystals:

$$I = |F_s|^2 + 2\mathrm{Re}(F_s)\sum_m [(f_{os}')_m \mathrm{Re}(\alpha_m) - (f_{os}'')_m \mathrm{Im}(\alpha_m)] + 2\mathrm{Im}(F_s)\sum_m [(f_{os}')_m \mathrm{Im}(\alpha_m) + (f_{os}'')_m \mathrm{Re}(\alpha_m)], \quad (10)$$

where, in our case, the terms $\mathrm{Im}(\alpha_m)$ can be neglected, since the sum in equ. (9) results in real values for the selected reflections derived by the given structural model.

Summarising the numerical results in the energy dependent reflection intensities, e.g. in the vicinity of Co-K edge, are of the general form

$$|F_{os}(\vec{\boldsymbol{Q}})|^2 = |F_s|^2 + 2\mathrm{Re}(F_s)(f_{os}')_{Co}G_{Co} + 2\mathrm{Im}(F_s)(f_{os}'')_{Co}G_{Co}. \quad (11)$$

7. DAFS measurements and data evaluation

The as-measured DAFS intensities are depicted in Fig. 3 for the 10000 reflection as an example. They are subject to the well-known corrections which are usually applied to diffraction data.

Careful handling of the absorption correction $A(Q,E)$ is of outstanding importance for evaluation of the oscillating diffracted intensities. The absorption of the radiation on its pathway within the sample produces, analogously to XAFS, an additional fine structure of the intensity detected.

Since the standard absorption as given by Sorensen *et al.* [1] did not work properly, we applied the modified absorption correction developed by Meyer *et al.* [10], which takes into account secondary extinction effects, which come into being in case of extended single crystals of small mosaic spread or highly textured polycrystals. In the limit of an infinitely extended crystal the absorption correction reads as:

$$A(Q,E) = \frac{\sin(\theta)}{2\mu(E)}\left[1 - \frac{m|F(Q,E)|^2\sin(\theta)}{2\mu(E)}\right], \quad (12)$$

where m is a proportionality factor, which is a measure for the impact of the extinction effects.

With that successfully applied absorption correction we finally find the measured DAFS normalised to the square of smooth structure factor F_s, as depicted in Fig. 4 at the example of 10000 reflection at both absorption edges.

The calculation of theoretical DAFS intensities as performed in the following is based on the oscillating fine structure easily obtained by XAFS. This way was chosen since we have stated great influences of absorption correction on further handling of experimental DAFS data. As we will outline below by that strategy a verification of validity of the structure model by DAFS is possible in the present case.

As mentioned above we recorded the fluorescence XAFS signal simultaneously to DAFS intensities. Extracted functions $\chi(E)$ probed to be nearly identical for the different reflections. Having in mind that $\chi(E)$ as obtained from XAFS corresponds to the imaginary part of the complex-valued fine structure function $\tilde{\chi}(E) = \chi'(E) + \mathrm{i}\chi''(E)$ we obtain $f_{os}''(E) = f_s''(E)\chi''(E)$. Since f_{os}'' is connected with f_{os}' by causality we subjected it to Kramers-Kronig transformation to get f_{os}'. Both are shown in Fig. 5. Having derived f_{os}' and f_{os}'' we now take advantage of the structural assumptions and insert them into equ. (11). The resulting contributions to the DAFS intensity are shown in Fig. 6.

Eye inspection of Fig. 7 indicates that there is a good correspondence of calculated and absorption corrected measured

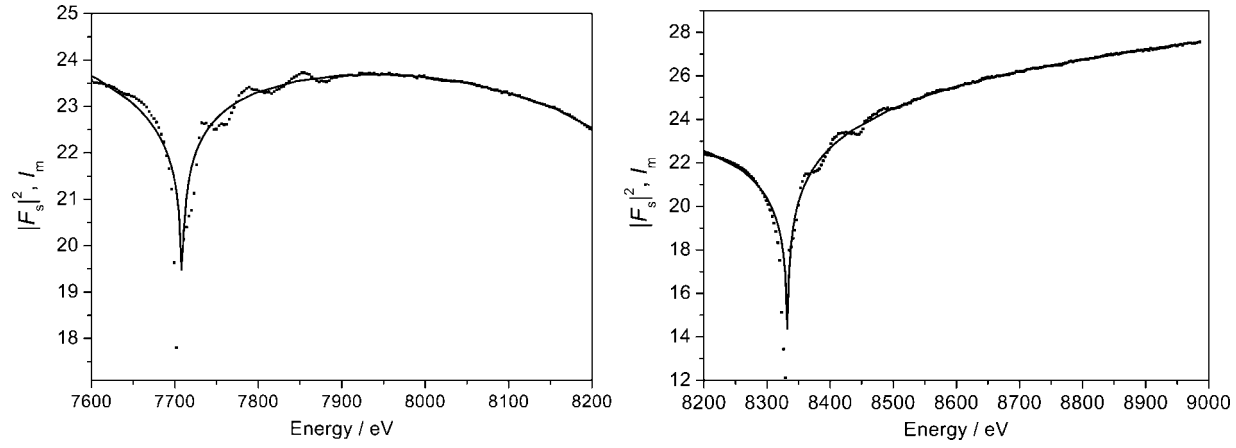

Fig. 4. Measured DAFS 10000 intensities corrected for absorption and normalised to theoretical smooth intensities $I_s(E)$ at the Co-K (left) and the Ni-K (right) absorption edges.

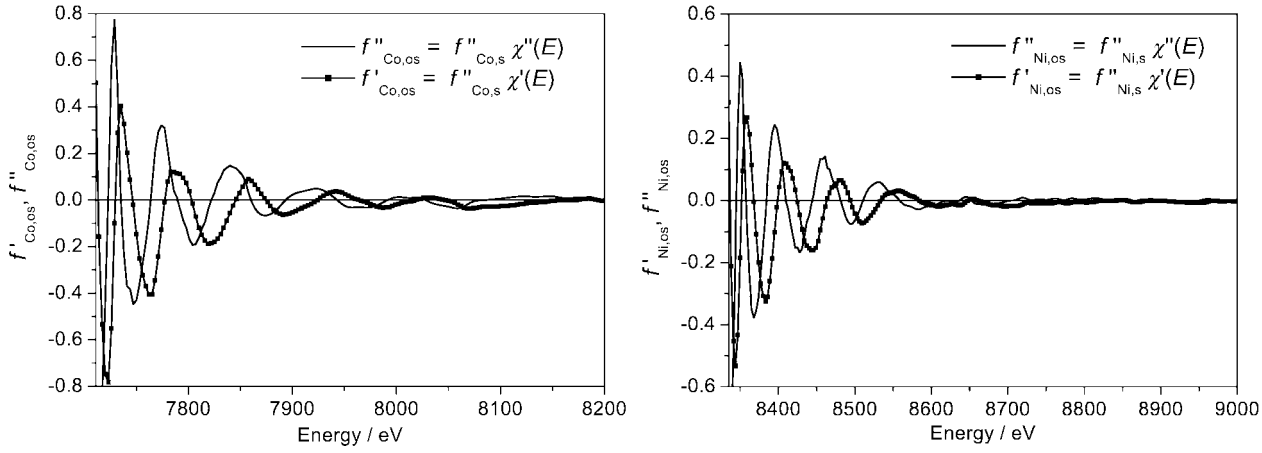

Fig. 5. Comparison of real and imaginary parts, $f'_{os}(E)$ and $f''_{os}(E)$, as obtained from Kramers-Kronig transformation and fluorescence XAFS, respectively. Note the phase difference at both edges.

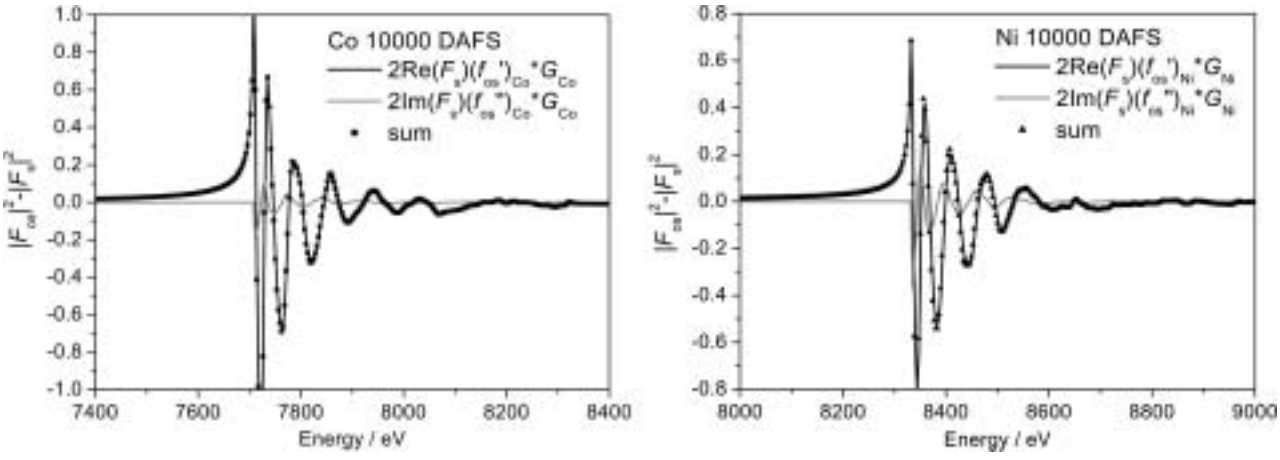

Fig. 6. Oscillating contributions to $|F_{os}(E)|^2$. Since $|\mathrm{Re}(F_s)| \approx A\ |\mathrm{Im}(F_s)|$ ($A \approx 12$ at the Co edge (left), $A \approx 5$ at the Ni edge (right)) the sum is clearly dominated by $f'_{os}(E)$.

10000 DAFS at both the Co and Ni-K absorption edge. Whereas this holds at the Ni edge for all three reflections, the computed and experimental 00-1-11 and 00002 DAFS oscillations at the Co edge differ in phase and amplitude (not shown here). These problems are attributed to the real structure of the specimen to be obtained from experiments providing more information necessary for appropriate absorption correction.

8. Conclusions

For the first time we have extended the standard approach of kinematical quantitative DAFS analysis to quasicrystalline (here: decagonal) structures. The main extension is the additional consideration of FT of the atomic surfaces (perpendicular space) to the DAFS crystallographic weights. The DAFS calculated

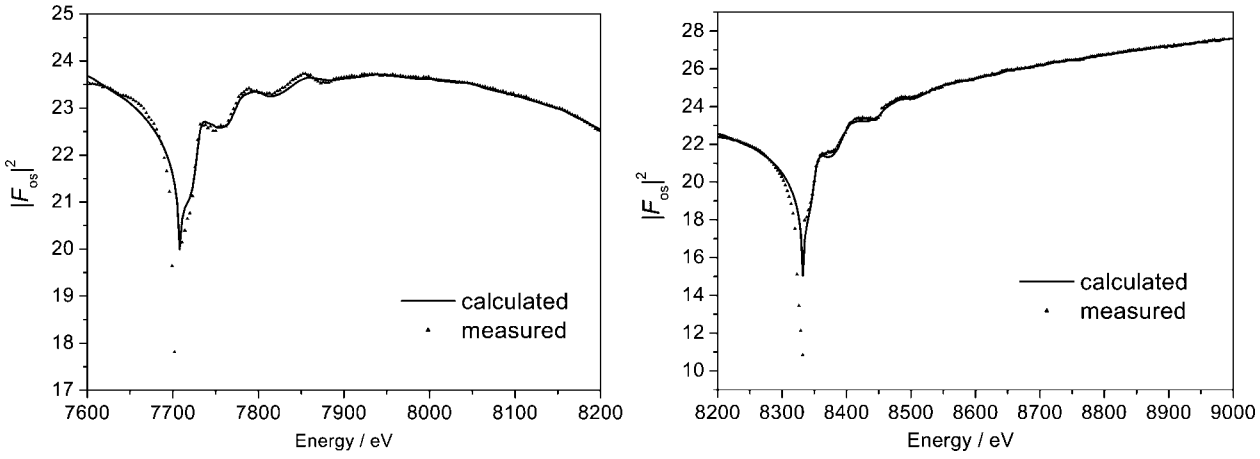

Fig. 7. Comparison of measured 10000 DAFS intensity with calculated intensity at the Co-K (left) and the Ni-K absorption edge (right).

according to the structural assumptions of the model fits the experimental data. The sum of relative deviations in the whole measuring is less than 10%.

The agreement of XAFS results with the modified Li/Steurer model of structure of decagonal Al-Co-Ni and the matching of computed and measured DAFS intensities indicate the validity of both the structural assumptions and the quantitative DAFS approach.

Acknowledgment

The authors like to thank K. Richter for the assistance with the synchrotron measurements, T. Leisegang for the determination of mass density, and T. Stephan (all Tu Dresden) for the EPMA measurements. We are particularly indebted to Prof. R. Frahm (Univ. Wuppertal) for stimulation of starting DAFS activities in our group. Financial support of the Deutsche Forschungsgemeinschaft (DFG) and the Fonds der Chemischen Industrie is gratefully acknowledged.

References

1. Sorensen, L. B. *et al*., "Resonant Anomalous X-ray Scattering" (Edited by G. Materlik, C. J. Sparks and K. Fischer) (Amsterdam: Elsevier, 1994), pp. 389–420.
2. Braun, S., Meyer, D. C., Paufler, P. and Grushko, B., J. Alloys Compd. **287**, 12 (1999).
3. Zaharko, O., Meneghini, C., Cervellino A. and Fischer, E., Eur. Phys. J. B. **19**, 207 (2001).
4. Li, X. Z. *et al*., Z. Krist. **210**, 509 (1995).
5. Deus, C., Diploma thesis, TU Dresden (1996).
6. Ritsch, S. *et al*., Phil. Mag. Lett. **78**, 67 (1998).
7. Gille, P., Dreier, P., Gräber, M. and Scholpp, T., J. Crystal Growth **207**, 95 (1999).
8. Meyer, D. C., Richter, K., Seidel, A., Weigelt, J. and Frahm, R., J. Synchr. **5**, 1275 (1998).
9. Yamamoto, A., Acta Cryst. A **52**, 509 (1996).
10. Meyer, D. C., Kupsch, A. and Paufler, P., J. Synchr. Rad. **10**, 144 (2003).

Physica Scripta. Vol. T115, 261–263, 2005

Near-edge Absorption Spectroscopy of Interplanetary Dust Particles

S. Brennan[1*], K. Luening[1], P. Pianetta[1], J. Bradley[2], G. Graham[2], A. Westphal[3], C. Snead[3] and G. Dominguez[3]

[1]Stanford Synchrotron Radiation Laboratory, Stanford Linear Accelerator Center, Menlo Park, CA 94025, USA
[2]Institute for Geophysics and Planetary Physics, Lawrence Livermore National Laboratory, Livermore, CA 94550
[3]Space Sciences Laboratory, University of California at Berkeley, Berkeley, CA 94720

Received June 26, 2003; accepted November 4, 2003

PACS numbers: 78.70.Dm, 96.50.Dj

Abstract

Interplanetary Dust Particles (IDPs) are derived from primitive Solar System bodies like asteroids and comets. Studies of IDPs provide a window onto the origins of the solar system and presolar interstellar environments. We are using Total Reflection X-ray Fluorescence (TXRF) techniques developed for the measurement of the cleanliness of silicon wafer surfaces to analyze these particles with high detection sensitivity. In addition to elemental analysis of the particles, we have collected X-ray Absorption Near-Edge spectra in a grazing incidence geometry at the Fe and Ni absorption edges for particles placed on a silicon wafer substrate. We find that the iron is dominated by Fe_2O_3.

1. Introduction

Small dust grains in the plane of the ecliptic within the inner solar system give rise to the Zodiacal light, first reported by Cassini in 1693. Astronomical observations reveal the presence of similar dust systems around both young and evolved stars. Dust grains in the solar system are referred to as interplanetary dust particles (IDPs) and are described as asteroidal and cometary. Asteroidal IDPs exhibit evidence of compaction and aqueous alteration but cometary IDPs exhibit little if any evidence of parent body processing. They are likely well-preserved remnants of the original interstellar particulate matter from which the solar system formed. Understanding the nature of IDPs not only helps us understand the origins of our solar system but also aids in the understanding of astronomical observations of other solar systems [1, 2].

IDPs are collected in the stratosphere at ∼20 km altitude using NASA ER2 aircraft. Although all IDPs are frictionally pulse heated for ∼1 second as they decelerate from cosmic velocities at ∼90 km altitude, many of them survive with minimal alteration because they are high porosity, low density objects. Recently particles have been collected by hypervelocity capture in aerogel on board the Soviet Mir Space Station. Some of these particles also appear relatively intact and they have not been exposed to the upper atmosphere.

Once collected, the particles can be assayed by a wide variety of techniques, including isotopic abundance, elemental analysis and morphology. The thermal history of an IDP can be assessed by several techniques. Obvious changes in morphology can indicate complete melting of the particle during re-entry. On a more subtle level, the oxidation state of the iron in the IDP can sometimes be an indication of the thermal history of the particle, taken in aggregate with information on the other minerals present in the IDP. From the X-ray Absorption Near-Edge Structure (XANES), information on the unoccupied density of states can be obtained and the oxidation state of the element of interest can be determined [3]. By measuring the XANES in fluorescence yield in a grazing incidence geometry, trace levels of impurities can be analyzed non-destructively. In cases where there are several different oxidation states, a decomposition of the near-edge structure into suitable reference materials can resolve significant components. There are several synchrotron-based groups who are currently working with IDPs or have done so in the past [4, 5]. In a recent experiment using soft X-rays microspectroscopy of IDPs at the carbon edge has been performed [6].

For several years a program has been active at the Stanford Synchrotron Radiation Laboratory (SSRL) to determine the cleanliness of silicon wafer surfaces by employing Total Reflection X-ray Fluorescence Spectroscopy (TXRF) [7]. This program has been a collaboration between SSRL and members of the Sematech consortium. During this process we have developed state-of-the-art techniques for detecting transition metal contaminants on silicon surfaces.

2. Experimental

TXRF and XANES measurements were performed on BL 6-2 at the Stanford Synchrotron Radiation Laboratory (SSRL), sourced by a 54-pole wiggler. A toroidal mirror and Si(111) double crystal monochromator deliver roughly 10^{11} photons/s through a 0.5 mm wide by 2 mm tall aperture. If multilayers are installed in the monochromator the flux through the pinhole is increased by two orders of magnitude, resulting in a minimum detection limit of 8×10^7 atoms/cm^2 for transition metals. This corresponds to a sensitivity to 1 femtogram of impurities. To preclude unintentional contamination of the surfaces the TXRF instrument is housed in a class 1 clean room and includes a wafer-handling robot for transferring samples into the vacuum chamber. The energy resolution of the double crystal monochromator was 1 eV at 8.9 keV. A detailed description of the beam line setup can be found elsewhere [8]. Three samples were analyzed; one dust grain collected by a NASA ER2 aircraft, one grain of Orgueil meteorite (a type CI carbonaceous chondrite), and the third an IDP collected using hypervelocity capture into aerogel on the Mir space station [9, 10]. Typical particle size is 15–20 μm diameter, although the particles are far from spherical. All three particles were mounted on 10 cm square (100) silicon wafer surfaces, the first two using static electricity for adhesion, the third, because it is still incased in a sliver of aerogel to enable easier handling of the IDP, was attached to the substrate. For standard measurements of wafer cleanliness involving atomically dispersed impurities the wafer surface is illuminated at a grazing angle of incidence of 1.7 mrad, which is below the critical angle of total external reflection for silicon, resulting in the highest detection sensitivities. However, for the analysis of particles a

*Electronic address: sean.brennan@stanford.edu

zero angle of incidence is preferable, essentially eliminating the background signal from the silicon substrate on which the particle rests. In order to convert the measured fluorescence signal observed at zero angle to an elemental concentration, a similar spectrum is collected under standard conditions and compared to the spectrum from a calibration standard containing 1×10^{11} atoms/cm^2 of Fe, Ni and Zn atoms mono-dispersed on the surface.

From these measurements the concentration of elements within the particle can be determined to a few percent. Since the apparatus is designed for the study of transition metal contaminants on silicon, a 25 μm teflon filter is routinely installed in front of the detector window to reduce the intensity of the Si Kα fluorescence. Only 0.2% of those photons are transmitted through the filter, whereas 87% of the Fe Kα photons are transmitted. For the IDP measurements this also reduces the measured signal from other elements of interest such as Al, Mg, and S. In future measurements that filter will be removed. For the XANES measurements the incidence angle on the substrate was zero. Data were collected from 7060 eV to 7210 eV, with 2 eV steps in the pre-edge, 0.5 eV steps at the edge, and 1 eV steps above the edge. Because beam passes over the sample Fe foil transmission data was collected simultaneously. Reference spectra from oxides and sulphides could also be collected in transmission mode. Data have been normalized at 7200 eV. Ni edge XANES were collected from 8300 to 8410 eV, with otherwise identical conditions to the Fe edge data.

3. Analysis

Prior to performing XANES measurements on the samples, fluorescence spectra were collected under two sets of conditions: 11.2 keV and 1.7 mrad angle of incidence (our standard conditions) and at 14 keV (to excite Br atoms expected to be present in the IDP) and zero incidence angle. Figure 1 shows a TXRF spectrum of an IDP collected by a NASA ER2 aircraft. The spectrum was taken with an excitation energy of 14 keV. The spectrum is dominated by the Fe Kα and Kβ peaks, whereas the Cr, Mn and Ni fluorescence lines show a significantly smaller contribution. The Fe peak is due to 400 picograms (pg) of atoms

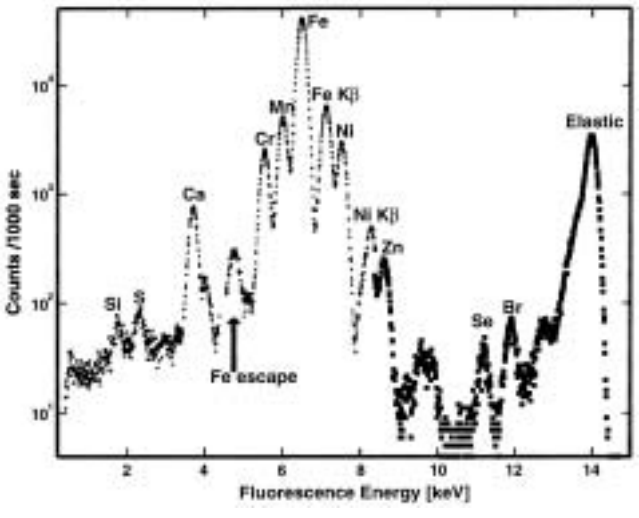

Fig. 1. Fluorescent spectrum from 20 μm meteorite with incident photon energy of 14 keV. The IDP was collected by an ER-2. Counts per 1000 s plotted on a log scale. The Fe Kα peak is the strongest.

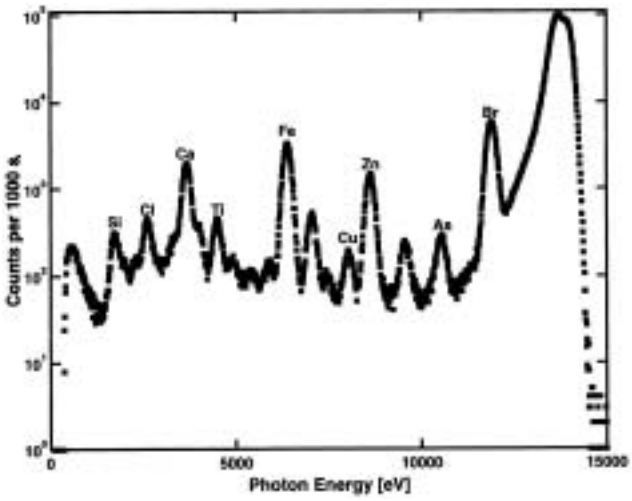

Fig. 2. Fluorescence spectrum from meteorite embedded in aerogel in which it was collected by hypervelocity capture. The high elastic peak and background is due to the aerogel matrix. Some of the observed elements (*e.g.* Br) are also present in aerogel far from the IDP.

and the Ni peak is due to 20 pg, or roughly 2% of the iron concentration. The Br peak results from only 0.1 pg of material. Although the S peak is quite weak, due to the teflon absorption and a significantly smaller fluorescence yield, it comes from 400 pg of material as well. Error bars on the S peak are much larger than for the Fe, where the error is roughly 5%.

The IDP embedded in aerogel posed a special challenge because the scattered signal from the aerogel is larger than the fluorescence from the IDP. This higher scattering contributes to a ten-fold increase in background, as is seen in Figure 2. Due to our excitation geometry the entire aerogel sliver is illuminated. The elemental constituents of this IDP are clearly different from those of the first IDP, with little Ni, strong Zn and Ca, and very strong Fe and Br. The Br raises questions because it is also observed in spectra taken from sections of the aerogel keystone where no IDP is present, suggesting either contamination during fabrication of the aerogel or during processing of the keystone. The iron signal in Figure 2 corresponds to 40 pg of material. The Br peak, although more intense, is due to 20 pg of Br atoms because the absorption cross-section is higher. The Si peak corresponds to 50 ng of material, due to the aerogel in the beam. Again, the apparent weakness of that peak is due to the teflon absorber in front of the detector window.

The Fe concentration from the sample of Orgueil meteorite was determined from the fluorescence spectrum to be 40 pg. Other significant elemental components were Ca (30 pg), K (3 pg) and Ti (3 pg). Mn, Cr and Ni were all found to be less than 1 pg. This particle was examined using Fe K-edge XANES and the results are presented in Figure 3 together with the absorption spectra of an Fe foil, Fe_2O_3, Fe_3O_4 and FeS_2. Comparing the XANES with reference spectra using a non-linear least-squares routine, the data were found to fit those from a pure Fe_2O_3 reference. Often, significant amounts of pyrite (FeS_2) are found in IDPs. However, the FeS_2 bulk XANES pattern is not consistent with the Orgueil data, nor with any of the IDPs in this study. The Fe-edge XANES from the other two IDPs are very similar, but are better fit by a combination of 20% Fe_3O_4 and 80% Fe_2O_3. All three samples have a very sharp leading edge after the pre-edge feature typically due to a 1s-3d transition [11].

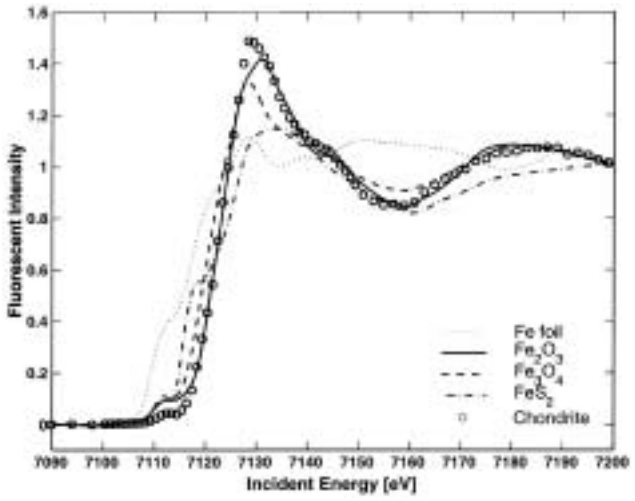

Fig. 3. XANES spectra from Fe edge of Orgueil meteorite as well as spectra from a Fe foil, FeO, Fe_2O_3, Fe_3O_4.

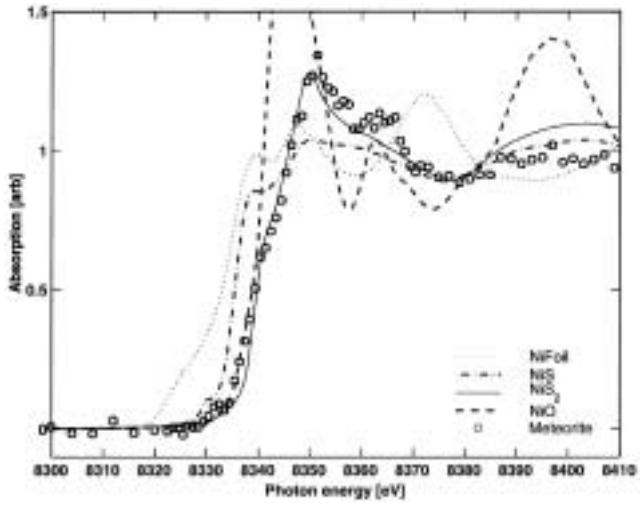

Fig. 4. XANES spectra from Ni edge of meteorite as well as spectra from a Ni foil, NiS, NiS_2, and NiO. The IDP was collected by an ER-2. While the meteorite data are noisy, the similarity to the NiS_2 spectrum is striking.

An attempt was made to measure the XANES at the Ni-edge for an IDP collected using the NASA ER2 plane. The fluorescence spectrum for this IDP is shown in Figure 1. Figure 4 shows the data as well as XANES from standards such as Ni metal, NiO, NiS and NiS_2. The quality of the data is worse than that from the Fe-edge, due to the lower concentration. However, it is sufficient to rule out both the Ni metal and oxide samples, and the data seem to fit the NiS_2 spectrum better than the NiS spectrum. Due to the poor data quality, however, no attempt was made to fit the data to a weighted sum of the two. We are confident that increases in beam intensity made possible by the SPEAR3 upgrade will enable us to do XANES from this concentration routinely.

4. Conclusions

We have performed both X-ray fluorescence and X-ray absorption near-edge spectra on interplanetary dust particles of typically 20 μm size in a grazing incidence geometry. These initial measurements were performed on a system designed for the measurement of surface contaminants on silicon wafers. As such, the instrument is currently not optimized for certain aspects of the measurements, such as quantitative analysis of low-Z elements (*e.g.* Mg, Al, Si) but in other aspects the system is very-well suited to the requirements of such an analysis, since it features a clean sample environment as well as low background and parasitic signals. The dominant element observed in the XRF spectra is iron, with a concentration in one case of roughly 400 pg by weight, but we have identified components with as little as 0.1 pg of material. This is possible due to the extremely low background we have achieved by placing the IDP on a silicon wafer and using a zero degree angle of incidence to the wafer. We find that the Fe-edge XANES for all three particles studied are well-characterized by either Fe_2O_3 or a combination of Fe_2O_3 and Fe_3O_4. The Ni-edge XANES for the ER2 particle is better characterized by NiS_2 than by NiO or Ni metal. It is clear that more reference spectra will be needed to exclude other, more exotic oxidation states. The installation of a microfocusing beam line at SSRL and the new SPEAR3 accelerator will enable us to map out the concentrations of elements within the heterogeneous particles as well as microspectroscopy. A focused beam will also significantly reduce the scatter from the aerogel in embedded samples.

References

1. "Interplanetary Dust", (Grun, E., Gustafson, Bo, S., Dermott, Stan and Fechtig, Hugo, eds.) (Springer-Verlag, Berlin, 2001) and "Analysis of Interplanetary Dust", (Zolensky, M. E., Wilson, T. L., Rietmeijer, F. J. M. and Flynn, G. J., eds.) AIP Conference Proceedings **310**, (AIP Press, New York, 1994).
2. DiSanti, M. A., *et al.*, Nature **399**, 662 (1999).
3. Stohr, J., "NEXAFS Spectroscopy," (Springer-Verlag, Berlin 1992).
4. Borg, J., *et al*., Planetary Space Sci. **50**, 1055 (2002).
5. Flynn, G. J., *et al*., Astron. Soc. Pacific Conf. Series **104**, 291 (1996).
6. Jacobsen, C., Wirick, S., Flynn, G. and Zimba, C., J. Microscopy **197**, 173 (2000).
7. Madden, M. C., Wherry, D. C., Pianetta, P. and Brennan, S., Mater. Res. Soc. Symposium Proc. **307**, 125 (1993).
8. Pianetta, P., *et al*., Thin Solid Films **373**, 222 (2000).
9. Sanford, S. A., Fund. Cosmic Phys. **12**, 1 (1987).
10. Warren, J. L. and Zolensky, M. E., in "Analysis of Interplanetary Dust", (Zolensky, M. E., Wilson, T. L., Rietmeijer, F. J. M. and Flynn, G. J., eds.) AIP Conference Proceedings **310**, pp 245–253 (AIP Press, New York, 1994).
11. Westre, T. E., *et al*., J. Am. Chem. Soc. **119**, 6297 (1997).

Physica Scripta. Vol. T115, 264–266, 2005

Correlations in the Vibrations of Atoms in Complex Unit Cells

Frank Bridges[1] and D. Cao[2]

[1]Physics Dept., University of California, Santa Cruz, CA 95064, USA
[2]MS-K764, Los Alamos National Laboratory, Los Alamos, NM 87545, USA

Received June 26, 2003; accepted November 4, 2003

PACS number: 61.10.Ht

Abstract

Correlations in the atomic motions can significantly change the interpretation of thermal effects in structural data. Including correlations of the stretching of the Zr-O bond with transverse O vibrations in the W-O-Zr linkage, in ZrW_2O_8, can explain the apparent discrepancy between a small σ^2_{W-Zr} in EXAFS data and a large O thermal parameter U^2. This work also shows that in some cases a small value of σ^2 does not always mean that the vibration frequency is high.

The presence of correlated atomic motions in crystalline structures is well known in the EXAFS community. Perhaps the best known example is the very narrow width (small σ) for the nearest neighbor pair distribution function when long wavelength acoustic phonons dominate the atomic vibrations. On a scale of a few unit cells, all the atoms locally are moving in the same direction, the stretch of the nearest neighbor bond length is small, and $\sigma^2 \ll U_A^2 + U_B^2$, where U_A^2 and U_B^2 are the diffraction thermal parameters for the two atoms. In this case, the displacements of the nearest neighbors are said to be positively correlated. Conversely if short wavelength optical phonons dominated, the displacements of the nearest neighbors would be in opposite directions (negatively correlated), and the bond length would have a large vibration amplitude. The very large value of σ^2 observed in that case would produce a low amplitude peak in the Fourier transformed XAFS data. For simple systems, the acoustic phonons usually dominate for $T < 300$ K, and the local atomic displacements are positively correlated.

For systems with more complex, open unit cells, new degrees of freedom exist. In particular, there are many optical modes; if some of them have low frequencies, they can dominate the vibration spectra. For ZrW_2O_8 which we consider here, the cubic unit cell (space group $P2_13$) is quite complex. This material is formed of corner-joined WO_4 tetrahedra and ZrO_6 octahedra, and has a number of unusual features:- a negative thermal expansion from 15–1000 K [1, 2], a large contribution to the specific heat at low T which has been modeled by two Einstein modes at 38 and 67 K [3], and two low energy peaks in the phonon density of states obtained in neutron scattering experiments at similar energies [4]. The unusual negative thermal expansion in ZrW_2O_8 has been attributed to these low energy vibration modes; EXAFS experiments suggest that these modes involve the massive WO_4 and ZrO_6 units. [5] Thus for the lowest optical modes these polyhedra units appear to vibrate as "large atoms", although some stretch of a unit is required. These motions involve highly correlated displacements of the polyhedral clusters and are not direct extensions of modes observed in simple systems.

The EXAFS data for the ZrW_2O_8 system have been presented previously [5] – here we focus on the correlations that must be present to understand the apparently conflicting results from EXAFS and diffraction. In Fig. 1 we show part of the crystal structure (a cut-away of the cubic unit cell, viewed perpendicular to a ⟨111⟩ axis) to show the local environment about the WO_4 tetrahedra. One corner of each tetrahedron, aligned along a ⟨111⟩ axis, is not connected to any other unit and is therefore unconstrained. The tetrahedra can move into empty space along this ⟨111⟩ axis with little cost in energy. The other three corners, in a plane perpendicular to the ⟨111⟩ axis, are linked to ZrO_6 octahedra. The EXAFS data show that the amplitude of the W-O peak (W L_{III} edge data) changes only a few percent up to 300 K; consequently, the W-O bonds are very rigid. For ZrO_6 however, there is a small broadening of the Zr-O pair distribution function – the Zr-O bond is not completely rigid up to 300 K in contrast to the assumptions in the rigid unit model (RUM) [6]; small distortions of this bond allow vibrations of the polyhedral units.

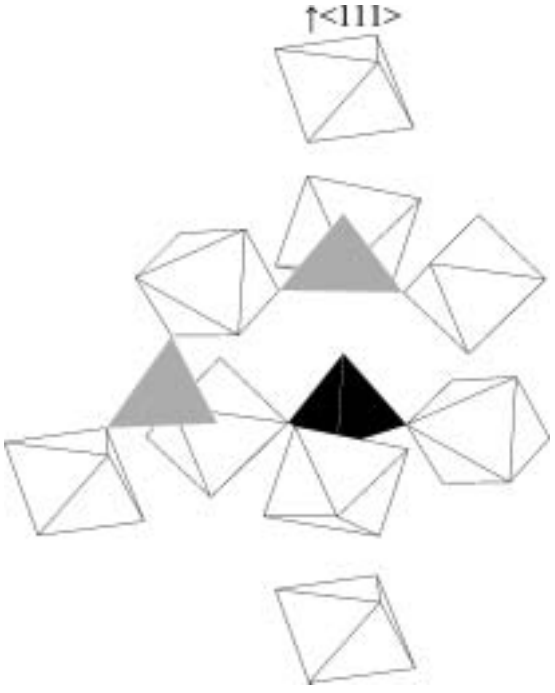

Fig. 1. A cut-away section of the cubic unit cell to show the local structure about the W(1)O_4 (gray) and W(2)O_4 (black) tetrahedra. Each tetrahedron is corner-connected to three ZrO_6 octahedra; the forth vertex, oriented along a ⟨111⟩ axis (vertical), is unconstrained. A third W(1)O_4 (gray) tetrahedron aligned along another ⟨111⟩ axis is also shown.

More surprising is the weak T-dependence of the W-Zr (or Zr-W) peak which includes multiple scattering path contributions. There is essentially no temperature change up to ∼125 K and only a small change up to 300 K that is comparable to the net change for the Zr-O peak. The T-dependences of σ^2 for the Zr-O and the W-Zr (or Zr-W) peaks are very similar.

Diffraction measurements show a large U^2 parameter for the different O atoms and smaller but significant U^2 parameters for the heavy metals, U_W^2 and U_{Zr}^2 [1, 7, 8]. The interpretation of the

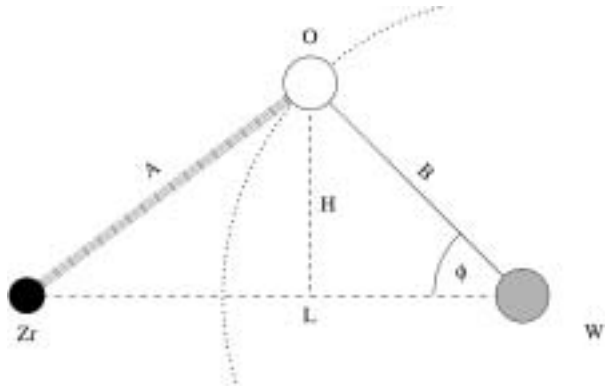

Fig. 2. The geometry of the Zr-O-W linkage; the angle ϕ is exaggerated to show the different distances. The W-O bond length B is rigid and the O would move on the dotted arc about the W atom. Between Zr and O there is a stiff spring (but the bond is not rigid).

diffraction data focused on the transverse vibrations of the O in the W-O-Zr linkage, and ignored stretching of the Zr-O bond and translations of the WO_4 tetrahedra as a rigid unit. (At least part of the O motion must correspond to the latter.) Under the assumption of rigid rotating units and uncorrelated displacements, a transverse O vibration would lead to a contraction of the Zr-W distance consistent with the observed macroscopic contraction. However it would also lead to a very large σ^2 for W-Zr or Zr-W which is not observed in the EXAFS data. If one includes the Zr-O bond stretching vibrations in the W-O-Zr linkage, but still assumes that the stretching vibration and the transverse O vibrations are uncorrelated, then the EXAFS data would imply that the transverse O vibration amplitude must be small, in conflict with the diffraction U^2 parameters. However, when correlations are included a significant transverse O vibration is possible with still only a weak temperature dependence for σ^2_{W-Zr}.

The W-O-Zr linkage is shown in Fig. 2; it is the important connection between a tetrahedron and an octahedron. The W-O bond B is taken to be rigid based on the EXAFS data, while the Zr-O bond A stretches as the W/Zr polyhedra units undergo thermal vibrations, a combination of translations and rotations. The O atom must move on an arc (to keep B rigid) and its motion is not completely transverse but includes a small component parallel to the Zr-W distance. This suggests a coupling between the rotations of the O about W and stretching of the spring A. Note that even if A were an ideal spring, the motions would not be harmonic. In the limit of no vibrations of the Zr-W distance (like the ends of a guitar string) the Zr-O bond would stretch completely in phase with the O transverse motion. For various assumptions about the stretching of A and the degree of correlation with the transverse O vibration, we need to consider the changes in the length L ($\Delta L = L - L_0$; L_0 is the length at low T) and the variance of the thermal fluctuations, $(\Delta L)^2$.

We initially allow the possibility that the motions involve two different modes – i.e. that the stretch of the Zr-O may arise from acoustic phonons while the transverse O motions might arise from low frequency optical modes. The time dependence of A and H are modeled as sinusoidal vibrations about the static values, A_0 and H_0.

$$\begin{aligned} A &= A_0 + A_1(t), \\ H &= H_0 + H_1(t), \\ A_1(t) &= a_1 \cos(\omega_A t), \\ H_1(t) &= h_1 \cos((\omega_H t + \theta). \end{aligned} \tag{1}$$

Here a_1 and h_1 are the vibration amplitudes and ω_A and ω_H are the frequencies for the stretching and transverse motions. The total Zr-W distance, L, is given by:

$$L = \sqrt{A^2 - H^2} + \sqrt{B^2 - H^2}. \tag{2}$$

To simplify the final results we will set $B = A_0$. Substituting for A and H, expanding the square roots to second order, and keeping terms up $A_1^2(t)$, $H_1^2(t)$ and $A_1(t)H_1(t)$, then

$$\begin{aligned} L = L_0 &+ \frac{1}{L_0}[2A_0A_1(t) + A_1^2(t) - 4H_0H_1(t) - 2H_1^2(t)] \\ &- \frac{1}{L_0^3}[4A_0^2A_1^2(t) + 8H_0^2H_1^2(t) - 8A_0H_0A_1(t)H_1(t)] \end{aligned} \tag{3}$$

where $L_0 = 2\sqrt{A_0^2 - H_0^2}$. Next we need to calculate the average length change $\langle \Delta L \rangle = \langle L - L_o \rangle$ and its variance, $\sigma^2_{thermal} = \langle (\Delta L)^2 \rangle$. To calculate these averages, we integrate each term over time, e.g. for $A_1^2(t)$:

$$\langle A_1(t)A_1(t) \rangle = \int A_1(t)A_1(t)\,\mathrm{d}t. \tag{4}$$

Using Eqn. (1) in this integral then:

$$\begin{aligned} &\langle A_1(t) \rangle = \langle H_1(t) \rangle = 0, \\ &\langle A_1^2(t) \rangle = a_1^2/2; \qquad \langle H_1^2(t) \rangle = h_1^2/2. \end{aligned} \tag{5}$$

The average of $A_1(t)H_1(t)$ depends on ω_A and ω_H; if $\omega_A \neq \omega_H$, then $\langle A_1(t)H_1(t) \rangle = 0$; for $\omega_A = \omega_H = \omega$,

$$\begin{aligned} \langle A_1(t)H_1(t) \rangle &= \frac{1}{T}\int_0^T h_1 a_1 \cos(\omega t)\cos(\omega t + \theta)\,\mathrm{d}t \\ &= \frac{h_1 a_1 \Phi}{2}, \end{aligned} \tag{6}$$

where $\Phi = \cos\theta$ is called the correlation parameter and can vary from -1 to 1. After averaging and simplification

$$\langle \Delta L \rangle = -\frac{1}{L_0(A_0^2 - H_0^2)}[A_0^2h_1^2 + H_0^2a_1^2/2 - A_0H_0a_1h_1\Phi]. \tag{7}$$

For $a_1 = 0$ (i.e. Zr-O is rigid), $\langle \Delta L \rangle \sim -h_1^2/L_0$ as used earlier [7]. For $a_1 \neq 0$ and Φ positive, $\langle \Delta L \rangle$ is reduced but for the relevant parameters the reduction is not large. In contrast the correlations have a very large impact on $\sigma^2_{thermal}(\Phi)$:

$$\sigma^2_{thermal}(\Phi) = \frac{2}{L_0^2}[A_0^2a_1^2 + 4H_0^2h_1^2 - 4A_0H_0a_1h_1\Phi]. \tag{8}$$

When A_1 and H_1 are uncorrelated ($\Phi = 0$) then

$$\sigma^2_{thermal}(0) = \frac{A_0^2}{2(A_0^2 - H_0^2)}\left[a_1^2 + 4\frac{H_0^2}{A_0^2}h_1^2\right]. \tag{9}$$

This is the typical results for two uncorrelated mechanisms; the contributions to the broadening add up in quadrature. For positively correlated motions, $\sigma^2_{thermal}$ is reduced because of the minus sign (Eqn. (8)). When $\Phi = 1$, Eqn. (8) simplifies to:

$$\sigma^2_{thermal}(1) = \frac{A_0^2}{2(A_0^2 - H_0^2)}\left[a_1 - 2\frac{H_0}{A_0}h_1\right]^2. \tag{10}$$

In this case, correlations effects are very large because $\sigma^2_{thermal}$ depends on the difference, $a_1 - 2H_0h_1/A_0$.

Using σ^2_{Zr-O} and U^2_O from diffraction to estimate the vibration peak amplitudes ($a_1 \sim 0.08$ Å, $h_1 = 0.21$ Å), $H_0 = 0.4$ Å for W(1)-O-Zr, and $A_0 \sim 2$ Å, then for $\Phi = 0$ $\sigma^2_{thermal}(0) \sim 7.0 \times 10^{-3}$ Å^2, while for $\Phi = 1$, $\sigma^2_{thermal}(1) \sim 8.3 \times 10^{-6}$ Å^2. For

negatively correlated displacements $\sigma^2_{thermal}$ can be very large, > 0.01 Å^2. Consequently, $\sigma^2_{thermal}(\Phi)$ can have a wide range of values depending on the value of Φ.

In this simplified discussion we have not accounted for any static distortions or zero-point motions and have not considered the multiple scattering contributions for W(2)-O-Zr. We have also used the maximum value of h_1 obtained in diffraction experiments, which assumed that the oxygen thermal parameter U^2_O arises solely from O transverse motion. This overestimates h_1, as part of the O displacement must correspond to translations of the WO_4 (and ZrO_6) units – i.e. rotations/translations of the W-O-Zr linkage. Unfortunately in Eqn. (8) h_1 and Φ are coupled and cannot be uniquely determined.

This work shows that in some cases it is crucial to recognize that atomic motions can be highly correlated and may involved quite large clusters of atoms. Although the O thermal parameters (U^2_O) from diffraction cannot be uniquely decomposed into two components – one corresponding to an O transverse motion and the other a translation of the WO_4 unit, including correlations in the atomic displacements essentially removes the discrepancies between the small value of σ^2_{W-Zr} and the relatively large values of U^2_O. The calculation also shows that in some cases, a small value of σ^2 does not necessarily mean that the thermal vibration causing the broadening has a high frequency. For the W-O-Zr linkage the Zr-O bond stretches slightly to accommodate the low frequency motions of the WO_4 and ZrO_6 units; the small stretch of the Zr-O bond is a *byproduct* of a low frequency mode and is not directly a measure of the Zr-O spring constant, κ (i.e. $\sigma^2 \sim kT/\kappa$ at high T) as is often assumed.

Acknowledgments

This work was supported by NSF grant DMR0071863 and was conducted under the auspices of the U.S. Department of Energy (DOE), Office of Basic Energy Sciences (OBES). The experiments were performed at SSRL, a national user facility operated by Stanford University on behalf of the DOE/OBES.

References

1. Mary, T. A., Evans, J. S. O., Vogt, T. and Sleight, A. W., Science **272**, 90 (1996).
2. David, W. I. F., Evans, J. S. O. and Sleight, A. W., Europhys. Lett. **46**, 661 (1999).
3. Ramirez, A. P. and Kowach, G. R., Phys. Rev. Lett. **80**, 4903 (1998).
4. Ernst, G., Broholm, C., Kowach, G. R. and Ramirez, A. P., Nature **396**, 147 (1998).
5. Cao, D., Bridges, F., Kowach, G. R. and Ramirez, A. P., Phys. Rev. Lett. **89**, 215902 (2002); Phys. Rev. B **68**, 180511 (2003).
6. Pryde, A. K. A. *et al*., J. Phys. Condens. Matter **8**, 10973 (1996).
7. Evans, J. S. O., David, W. I. F. and Sleight, A. W., Acta Cryst. **B55**, 333 (1999).
8. Evans, J. S. O., Mary, T. A., Vogt, T., Subramanian, M. A. and Sleight, A. W., Chem. Mater. **8**, 2809 (1996).

Physica Scripta. Vol. T115, 267–270, 2005

Thermal Vibration of the Rutile-Type Difluorides of First-Row Transition Metals

Kei-ichiro Murai[1], Akira Yoshiasa[2], Takamitsu Yamanaka[2] and Ichiro Nakabayashi[1]

[1]Faculty of Engineering, Tokushima University, Tokushima 770-8506, Japan
[2]Graduate School of Science, Osaka University, Toyonaka 560-0043, Japan

Received June 26, 2003; accepted January 15, 2004

PACS numbers: 61.10.Ht

Abstract

The rutile-type structure is found in many dioxides. The rutile samples in this study, difluorides of the first-row transition-metals, MF_2 (M = Mn, Fe, Co, Ni), are important materials from the view point of electronic and magnetic properties. Although almost rutile-type difluorides have the positive thermal expansion coefficient, FeF_2 has a negative thermal expansion coefficient along the c axis in the high temperature region. In this study, we could obtain a detailed information about the thermal vibration of atoms by the analysis of EXAFS Debye-Waller factors. We discuss on the atomic momentum in the local structure of the difluorides. The EXAFS Debye-Waller factor is sensitive to short-range correlation of mutual atomic motions.

The displacement correlation functions (DCF) for each neighbor atom were determined by using both the mean square relative displacement (MSRD) and the mean square displacement (MSD) by X-ray diffraction. It was proved that DCF/MSD in the second-nearest neighbor atoms of FeF_2 is small, compared with other difluorides. This result suggests that in FeF_2, the correlation between second-nearest neighbor atoms (Fe-Fe) is weak. Furthermore, we could estimate the force constant between absorbing and scattering atoms from the temperature dependence of EXAFS Debye-Waller factor. The value of the force constant suggests that in FeF_6 octahedron in FeF_2, two apical bonds are stronger than four equatorial bonds.

1. Introduction

There are many compounds with composition AB_2, having the rutile-type structure, such as TiO_2 from which the name derived. They are mostly dioxides or difluorides. The rutile-type structure was first described by Vegard [1] and has been studied, for various materials, repeatedly and with increasing accuracy over the years. The rutile type tetragonal unit cell (space group $P4_2/mnm$) contains two cations at (0, 0, 0) and (1/2, 1/2, 1/2), and four anions at $(1 \pm u, 1 \pm u, 0)$ and $(1/2 \pm u, 1/2 \mp u, 1/2)$. The rutile structure has edge-sharing octahedra which form chains along c-axis. The distance between the second-nearest neighbor cations is equal to the c edge distance. Some fluorides composed of first-row transition metals with the rutile-type structure have been investigated. Although almost difluorides have the positive thermal expansion coefficient, FeF_2 has been a negative thermal expansion coefficient along the c-axis in the high temperature region [2]. The negative coefficients of expansion in the cases of calcite and graphite have been explained by the Poisson contraction arising from the large thermal expansion coefficient in a perpendicular direction [3, 4, 5]. Such an explanation is not applicable in the case of FeF_2 which does not have a large coefficient of expansion along the other direction. In spite of the interesting thermal behavior, we have found only very few theoretical papers. In this study, we try to give an explanation of that behavior with the EXAFS technique from the viewpoint of the thermal vibrations of local structure.

EXAFS spectroscopy is a useful method for local structural investigation around a particular kind of atom in materials and provides important information on the interatomic distance and the thermal vibration of local structure. The EXAFS spectra are specific to a given cation and provide averaged data over time and positional information. EXAFS analysis provides an effective pair potential with temperature-independent shape from the Debye-Waller factor [6, 7]. The Debye-Waller factor determined by EXAFS means the mean-square relative displacement (MSRD) of the backscattering atoms with respect to the absorbing atom. The MSRD contains contributions from the mean-square displacement (MSD) of both absorbing and backscattering atoms and the displacement correlation function (DCF). The MSD of each atom from the crystallographically equivalent position is determined by diffraction methods. The MSRD is sensitive to the short-range correlation of vibrational motion of the pair of atoms considered [8, 9].

$$\begin{aligned} &MSRD_{AB} = MSD_A + MSD_B - 2DCF_{AB}, \\ &MSD_i = \langle (\boldsymbol{R}_{AB} \cdot \delta \boldsymbol{u}_i)^2 \rangle, \\ &DCF = \langle (\bar{\boldsymbol{R}}_{AB} \cdot \delta \boldsymbol{u}_A) \cdot (\bar{\boldsymbol{R}}_{AB} \cdot \delta \boldsymbol{u}_B) \rangle, \\ &\delta \boldsymbol{u}_i = \boldsymbol{u}_i - \langle \boldsymbol{u}_i \rangle, \quad i = \mathrm{A}, \mathrm{B} \end{aligned} \tag{1}$$

with $\langle\ \rangle$ being the thermal average where $\boldsymbol{u}_i$ is the displacement of atom i = A or B and

$$\bar{\boldsymbol{R}}_{AB} = \boldsymbol{R}_{AB}/|\boldsymbol{R}_{AB}| \text{ [10]}. \tag{2}$$

In this study, we have attempted to determine the local structure and MSRD in order to evaluate the DCF for each backscattering atom. The coefficients of the effective pair potentials between the absorbing atom and backscattering atom were determined from the Debye-Waller factors. The results of analysis for FeF_2 were compared with those for MnF_2, CoF_2 and NiF_2. We discussed the thermal vibration of FeF_2 in view of local structure.

2. Experimental and Analysis

The well-ground powder samples ($\sim 0.1\,\mu$m) of MF_2 (M = Mn Fe, Co and Ni) were mixed with boron nitride in an agate mortar and pressed into pellets of 1.0 mm in thickness and 10.0 mm in diameter. The samples had edge-jumps with 1 ($\Delta\mu d$), where μ and d are the linear absorption coefficient and the thickness of the samples, respectively. The EXAFS absorption spectra near the K-edge of the cations were measured in a transmission mode in the temperature range from 20 K to 700 K at BL-7C of the Photon Factory in High-Energy Accelerator Research Organization (KEK), Tsukuba. The positron storage ring current and energy were approximately 300 mA and 2.5 GeV, respectively. The synchrotron radiation was monochromatized by a Si (111) double crystal monochromator. Ionization chambers were applied as incident and transmission beam intensity detectors. N_2 gas was used for the incident detector and N_2 (85%) + Ar (15%) or N_2

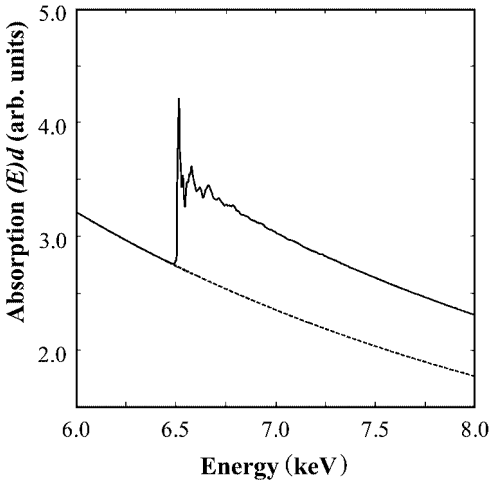

Fig. 1. X-ray absorption $\mu(E)d$ near the Mn K-edge of MnF_2 at 20 K (solid line) with Victoreen function fitted (dashed line).

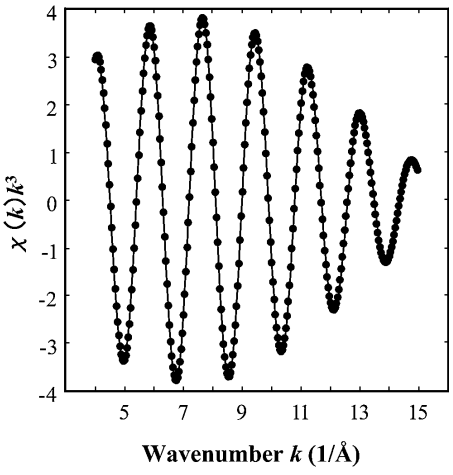

Fig. 2. Fourier-filtered EXAFS spectra (dotted curve) and least-squares fit (solid curve) for the first-nearest Mn-F distance in MnF_2 at 20 K.

(75%) + Ar (25%) gasses were employed for the transmission detector to achieve optimum signal-to-noise ratio. Mirrors were used to eliminate higher harmonics in the measurement of spectra near the Mn K-edge. On the other hand, in the measurement of spectra near Fe, Co and Ni K-edges, the 60% detuning of the monochromator was carried out in order to eliminate them. The photon energy E was calibrated with a Cu foil by assigning 8.9788 keV to the pre-edge peak of the absorption. Figure 1 shows the X-ray absorption $\mu(E)d$ near the Mn K-edge of MnF_2 at 20 K. The fitted Victoreen function is also shown in the figure.

The EXAFS interference function, $\chi(k)$, was extracted from the measured absorption spectra using standard procedures [11], where k denotes the wave number of a photoelectron: $k = [2m(E - E_0)/\hbar^2]^{1/2}$. $\chi(k)$ was normalized using MacMaster coefficients according to the EXAFS workshop report [12]. The programs *XAFS93* and *MBF93* [11] were employed for the data analysis to determine local structure parameters. The EXAFS formula is based on single-scattering theory and expressed by the cumulant expansion [9, 13]:

$$\chi(k) = \sum_j \frac{N_j}{kR_j^2} |f_j(k,\pi)| \exp\left(-2\sigma_j^{(2)}k^2 + \frac{2}{3}\sigma_j^{(4)}k^4\right) \exp\left(-\frac{2R_j}{\lambda_j}\right) \times \sin\left[2kR_j - \frac{2k}{R_j}\left(1 + \frac{2R_j}{\lambda_j}\right)\sigma_j^{(2)} - \frac{4}{3}\sigma_j^{(3)}k^3 + \Psi_j(k)\right], \quad (3)$$

where N_j is the coordination number in the jth shell at distance R_j from the absorbing atom, $|f_j(k,\pi)|$ is the back-scattering amplitude of photoelectrons, and $\Psi_j(k)$ is the total phase shift function [14]. The quantities $\sigma_j^{(n)}$ are the nth cumulants. The mean free path λ_j of the photoelectron was taken to depend on the wave number k with the relationship $\lambda_j = k/\eta_j$. In this study, because we take a harmonic vibration model, the quantities $\sigma_j^{(3)}$ and $\sigma_j^{(4)}$ must be zero. A Fourier-filtered EXAFS function of the peak in real space was compared with a theoretical EXAFS function. In the parameter fitting, the theoretical EXAFS function was filtered in the same way as the observed one in order to eliminate truncation effects through the Fourier transformation. The k range of the data used was 4–15 $Å^{-1}$ and 4–12 $Å^{-1}$ in the high and low temperature region, respectively. A double-shell fitting was carried out for the nearest neighbor distance in FeF_2, because FeF_2 is characterized by four longer coplanar Fe-F bonds over 0.1 Å than two axial bonds in FeF_6 octahedron. The coordination number in FeF_2 was fixed at the crystallographic values as $N_1 = 2$ and 4 corresponding to axial and coplanar bonds, respectively. A single-shell fitting was carried out for first-, second- and third-nearest neighbor distances in each material except for the first-nearest neighbor distance, Fe-F, in FeF_2: the number of neighboring atoms was fixed at the crystallographic value as $N_j = 6$, 2 and 8 in the first-, second- and third-nearest neighbor atoms, respectively. The equal deformation of observed and calculated EXAFS functions improves the accuracy of the parameter fitting. The determined values of the distance and $\sigma_j^{(2)}$ between the absorbing and backscattering atoms are listed in Table I. The reliability of converged parameters by least-square procedure,

$$R = \sum_s |k_s^3\chi(k_s)_{\exp} - k_s^3\chi(k_s)_{calc}|/|k_s^3\chi(k_s)_{\exp}|, \quad (4)$$

between the experimental and calculated EXAFS functions are also listed in Table I. The quality of fit between $k^3\chi_{\exp}$ and $k^3\chi_{\text{calc}}$ is shown in Figure 2.

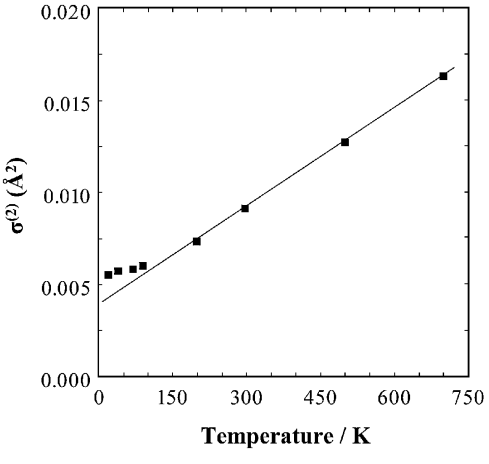

Fig. 3. Temperature dependency of Debye-Waller factor $\sigma^{(2)}$ of the second-nearest neighbor atoms in FeF_2. The straight shows the gradient of $\sigma^{(2)}$.

Table I. *Local structure parameters obtained from the fits of the M(M = Mn, Fe, Co, Ni) K-edge EXAFS spectra. R_{AB} is interatomic distance between absorbing and backscattering atoms $\sigma^{(2)}$ is the Debye-Waller factor. R is the reliability parameter.*

		First-nearest neighbor			Second-nearest neighbor			Third-nearest neighbor		
	T (K)	R_{AB} (Å)	$\sigma^{(2)}$ (Å^2)	R (%)	R_{AB} (Å)	$\sigma^{(2)}$ (Å^2)	R (%)	R_{AB} (Å)	$\sigma^{(2)}$ (Å^2)	R (%)
MnF_2	20 K	2.115(1)	0.0056(2)	2.12	3.299(2)	0.0074(3)	3.90	3.821(1)	0.0074(1)	2.85
	40 K	2.115(1)	0.0056(2)	2.12	3.299(2)	0.0074(3)	3.90	3.821(1)	0.0076(1)	3.00
	60 K	2.115(1)	0.0056(2)	2.22	3.300(3)	0.0074(3)	4.03	3.821(1)	0.0077(1)	3.77
	89 K	2.116(1)	0.0056(2)	2.18	3.300(3)	0.0076(3)	4.26	3.822(1)	0.0082(2)	4.26
	200 K	2.118(2)	0.0067(2)	2.12	3.305(3)	0.0091(4)	6.24	3.822(2)	0.0112(2)	3.91
	297 K	2.119(2)	0.0072(2)	2.29	3.310(4)	0.0102(5)	4.19	3.824(3)	0.0138(4)	4.19
	500 K	2.121(3)	0.0107(3)	1.89	3.320(6)	0.0144(8)	1.89	3.828(6)	0.0203(9)	3.43
	697 K	2.124(5)	0.0132(5)	4.48	3.329(4)	0.0193(16)	2.08	3.834(8)	0.0285(12)	4.18
FeF_2	20 (2-fold)	1.999(5)	0.0032(11)	0.16	3.303(2)	0.0055(3)	4.58	3.707(1)	0.0076(1)	1.69
	(4-fold)	2.113(3)	0.0042(7)							
	40 K	1.999(6)	0.0032(12)	0.51	3.304(2)	0.0057(3)	4.92	3.707(1)	0.0076(1)	1.21
		2.113(3)	0.0043(8)							
	70 K	2.001(5)	0.0032(11)	0.38	3.305(3)	0.0058(3)	5.18	3.707(1)	0.0079(1)	0.69
		2.114(3)	0.0045(7)							
	90 K	2.001(5)	0.0033(10)	0.63	3.304(3)	0.0060(3)	5.43	3.706(1)	0.0081(1)	1.03
		2.114(3)	0.0043(7)							
	199 K	2.003(7)	0.0039(13)	0.70	3.308(3)	0.0073(4)	5.74	3.708(2)	0.0101(2)	0.55
		2.114(4)	0.0054(10)							
	297 K	2.005(8)	0.0050(17)	0.85	3.308(4)	0.0091(5)	6.75	3.710(3)	0.0125(3)	1.49
		2.114(4)	0.0066(13)							
	500 K	2.008(8)	0.0086(23)	0.12	3.306(6)	0.0127(8)	6.58	3.714(5)	0.0179(7)	2.48
		2.120(6)	0.0152(11)							
	700 K	2.012(10)	0.0122(19)	0.50	3.304(5)	0.0163(10)	5.60	3.716(9)	0.0298(10)	0.40
CoF_2	20 K	2.000(3)	0.0033(2)	5.4	3.170(3)	0.0040(2)	2.76	3.678(1)	0.0061(2)	2.46
	65 K	2.001(3)	0.0036(2)	4.27	3.172(3)	0.0041(2)	3.01	3.680(1)	0.0068(2)	1.04
	90 K	2.002(4)	0.0040(2)	1.67	3.179(4)	0.0063(2)	2.65	3.681(2)	0.0115(3)	1.23
	297 K	2.004(4)	0.0043(2)	0.67	3.188(4)	0.0077(3)	3.38	3.683(4)	0.0141(3)	2.46
	500 K	2.006(5)	0.0062(2)	0.15	3.194(7)	0.0100(4)	4.17	3.685(7)	0.0157(4)	1.47
	700 K	2.007(10)	0.0110(2)	1.3	3.200(9)	0.0112(4)	4.05	3.687(9)	0.0177(4)	1.09
NiF_2	20 K	2.044(3)	0.0042(2)	0.2	3.074(3)	0.0028(2)	3.62	3.628(1)	0.0056(2)	1.44
	90 K	2.046(3)	0.0044(2)	2.2	3.075(4)	0.0031(2)	3.38	3.629(1)	0.0059(2)	1.48
	297 K	2.049(4)	0.0064(2)	1.5	3.076(4)	0.0032(2)	3.92	3.629(1)	0.0064(2)	2.35
	500 K	2.052(4)	0.0079(2)	1.9	3.084(5)	0.0049(2)	3.27	3.632(2)	0.0087(2)	2.66
	600 K	2.054(6)	0.0099(2)	0.7	3.090(6)	0.0074(4)	3.85	3.638(6)	0.0129(4)	2.55
	700 K	2.056(7)	0.0110(2)	2.0	3.097(9)	0.0097(5)	3.39	3.646(8)	0.0174(8)	3.24

3. Results and Discussion

3.1. *Interatomic distances and force constants*

Interatomic distances between first-, second- and third-nearest neighbor atoms determined by EXAFS analysis are shown in Table I. The errors are considered on the basis of the theory in EXAFS workshop report [12]. The results at room temperature are quite in agreement with the results derived by diffraction methods [15, 16]. In FeF_2, the distance of the second-nearest neighbor atoms, Fe-Fe, contracts as the temperature rises in the high temperature region. The coefficient of contraction is consistent with that of negative thermal expansion by diffraction experiments [1]. That is to say, the negative thermal expansion along the *c*-axis in FeF_2 is induced by the local contraction of the second-neighbor atoms distances.

Fig. 3 shows the temperature dependence of the Debye-Waller-type factor, $\sigma_j^{(2)}$ of the second-nearest neighbor atoms in FeF_2. The values of $\sigma_j^{(2)}$ do not follow a straight line in the low temperature region because of zero-point vibration. The variable $\sigma_j^{(2)}$ includes the effects of static and dynamic disorders. The static disorder is the configurational disorder, while the dynamic disorder arises from the thermal vibration of atoms. In addition, there is a correlation in calculation between $\sigma_j^{(2)}$ and the mean free path length, λ, of the photoelectron. If it is assumed that a harmonic approximation is applied up to 700 K, a straight line with the same gradient passes through the origin and the deviation of the absolute values is attributed to the static disorder and to the correlation between $\sigma_j^{(2)}$ and λ. The contribution of the thermal vibration (the straight line in Fig. 3), $\sigma_{thermal}^{(2)}$, can be extracted from $\sigma_j^{(2)}$. The same deviation from the values estimated under the assumption of classical statistic dynamics is observed in other studies [6]. We can evaluate the harmonic effective interatomic potential,

$$V(u) = \alpha u^2/2, \tag{5}$$

from the contribution to the thermal vibration ($\sigma_{thermal}^{(2)}$), where u is the deviation of the distances between the absorbing atom and backscattering atoms from the location of the potential minimum. The variable $\sigma_{thermal}$ is related to the potential coefficient,

$$\alpha = k_B T/\sigma_{thermal}^{(2)}, \tag{6}$$

where k_B is the Boltzman constant. The potential coefficient, namely the force constants, α, derived from the gradient for the experimental $\sigma_j^{(2)}$ in Figure 3, are essentially temperature independent and are listed in Table II. The longer the distances between atoms, the smaller are the values of α for the most

Table II. *Gradient of $\sigma^{(2)}$ and force constant obtained from gradient of $\sigma^{(2)}$.*

	MnF_2			FeF_2				CoF_2			NiF_2		
	nearest neighbor	second-nearest neighbor	third-nearest neighbor	nearest neighbor 2-fold	nearest neighbor 4-fold	second-nearest neighbor	third-nearest neighbor	nearest neighbor	second-nearest neighbor	third-nearest neighbor	nearest neighbor	second-nearest neighbor	third-nearest neighbor
$\sigma^{(2)}/T(\times10^{-5}$ Å^2/K)	1.55(8)	1.79(12)	2.62(10)	1.07(5)	1.15(3)	1.79(8)	2.59(7)	1.16(15)	0.99(4)	1.55(8)	1.10(8)	1.20(7)	2.08(10)
α (eV/Å^2)	5.55(13)	4.81(18)	3.29(14)	8.09(40)	7.49(29)	4.82(21)	3.33(10)	7.46(25)	8.73(36)	5.56(27)	7.83(83)	7.21(43)	4.15(20)

Table III. *DCF and the ratio of the DCF to MSD at room temperature. $DCF/MSD = 2DCF/(MSD_A + MSD_B)$.*

	MnF_2	FeF_2 2-fold	FeF_2 4-fold	NiF_2
nearest neighbor				
DCF	9.65(6)	8.44(9)	8.34(9)	6.73(8)
DCF/MSD	0.827(11)	0.840(21)	0.830(20)	0.835(14)
second-nearest neighbor				
DCF	6.76(6)	4.44(5)		4.03(8)
DCF/MSD	0.745(9)	0.601(7)		0.734(10)
third-nearest neighbor				
DCF	5.18(6)	3.38(4)		2.72(10)
DCF/MSD	0.469(9)	0.471(7)		0.469(13)

part in each material. In FeF_2, the values of α of axial bonds in FeF_6 octahedron are larger over 3 eV/Å^2 than that between the second-nearest neighbor atoms, while in other materials, the values of α between first- and second-nearest neighbor atoms are relatively close. This might be caused by the influence on 3d electrons which participate in the combination of atoms in FeF_2. These results mean that Fe-F bonds in FeF_6 octahedron are much stronger than the interaction between the second-nearest neighbor atoms (Fe-Fe). This case is quite peculiar compared with other rutile-type fluorides.

3.2. *The displacement correlation function (DCF)*

Eq. (1) is useful as we wish to discuss separately the role played by the MSD and by the DCF. It is significant to see the ratio of the DCF to MSD given by $2DCF/(MSD_A + MSD_B)$. Those at room temperature are shown in Table III. We referred to the previous study for the values of MSD [17, 18]. There are no useful MSD data for CoF_2. The magnitudes of the DCF terms to the MSD in three materials are almost equal within 1.3% and 0.2% between the first- and third-nearest neighbor atoms, respectively. On the other hand, the magnitudes of the DCF terms to the MSD between the second-nearest neighbor atoms in FeF_2 is over 13% smaller than those in the other two fluorides. These results show that the correlation between the second-nearest neighbor atoms in FeF_2 is smaller than that in the other two fluorides.

3.3. *Negative thermal expansion and thermal vibration of FeF_2*

The above results suggest the following structural thermal vibration model. A FeF_6 octahedron whose six Fe-F bonds have large force constants has the largest vibrational mode, which is perpendicular to the *c*-axis, and the vibration of each octahedron shifts the half phase for the neighboring share edged octahedral shown in Figure 4. The second-nearest neighbor Fe atoms vibrate with half phase shift to each other. This mode is reasonable to the results that the correlation with the second-nearest neighbor atoms is small. If the thermal vibrational mode of this model increases among all thermal vibrational modes, the second-nearest neighbor distance (the length of the *c*-axis) decreases. In the high temperature region, this mode contributes largely to the thermal vibrations in FeF_2, while in the low temperature region, the contribution of this mode is small.

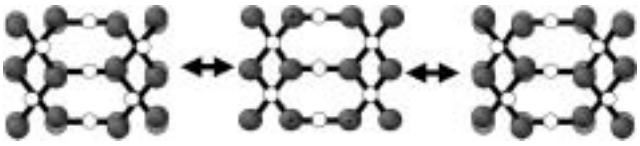

Fig. 4. Thermal vibration model of FeF_2 on the (110) plane. ● and ○ shows fluorine atom and iron atom, respectively.

References

1. Vegard, L., Philos. Mag. **32**, 505 (1916).
2. Rao, K. V. K., Naidu, S. V. N. and Iyengar, L., Curr. Sci. **35**, 280 (1966).
3. Rao, K. V. K., Naidu, S. V. N. and Murthy, K. S. N., J. Phys. Chem. Solids **29**, 245 (1968).
4. Nelson, J. B. and Riley, D. P., Proc. Phys. Soc. **57**, 477 (1945).
5. Rao, K. V. K. and Iyengar, L., Acta Cryst. **A25**, 302 (1969).
6. Yokoyama, T., Satsukawa, T. and Ohta, T., Jpn. J. Appl. Phys. **28**, 1905 (1989).
7. Yoshiasa, A., Kamishima, O., Nakatsuka, A., Ishii, T. and Maeda, H., J. Phys. IV France 7, Colloq. **C2**, 1173 (1997).
8. Beni, G. and Platzman, P. M., Phys. Rev. **B14**, 1514 (1976).
9. Ishii, T., J. Phys: Condes. Matter **4**, 8029 (1992).
10. Yoshiasa, A., Nakatsuka, A. and Ohkawa, M., Mineralogical J. **19**, 21 (1997).
11. Maeda, H., J. Phys. Soc. Jpn. **56**, 2777 (1987).
12. Lytle, F. W., Sayers, D. E. and Stern, E. A., Physica **B158**, 701 (1989).
13. Tranquada, J. M. and Ingalls, R., Phys. Rev. **B28**, 3520 (1983).
14. McKale, A. G., Veal, B. W., Paulikas, A. P., Chan, S. K. and Knapp, G. S., J. Am. Chem. Soc. **110**, 3763 (1988).
15. Stout, J. W. and Reed, S. A., J. Am. Chem. Soc. **5**, 5279 (1954).
16. Haefner, K., Thesis, Univ. of Chicago, USA (1964).
17. Jauch, W., Schneider, J. R. and Dachs, H., Solid State Commun. **48**, 907 (1983).
18. Jauch, W., Palner, A. and Schultz, A. J., Acta Cryst. **B49**, 984 (1993).

Physica Scripta. Vol. T115, 271–273, 2005

EXAFS and XRD Study of Local Dynamics in Cu_2O and Ag_2O

A. Sanson[1*], G. Dalba[1], P. Fornasini[1], R. Grisenti[1], F. Rocca[2], G. Artioli[3], M. Dapiaggi[3] and W. Tiano[3]

[1]Istituto Nazionale per la Fisica della Materia and Dipartimento di Fisica dell'Università di Trento Via Sommarive 14, I-38050 Povo (Trento), Italy
[2]Istituto di Fotonica e Nanotecnologie del CNR, Sezione di Trento, I-38050 Povo (Trento), Italy
[3]Dipartimento di Scienze della Terra, Università di Milano, Via Botticelli 23, I-20133 Milano, Italy

Received June 26, 2003; revised July 11, 2003; accepted November 4, 2003

Abstract

Copper and silver oxide share the rather unusual cuprite structure, formed by two interpenetrating networks of corner-sharing M_4O tetrahedra (M = Cu, Ag). Negative thermal expansion of the cell parameter has been observed from 5 to about 200 K for Cu_2O and up to 470 K for Ag_2O by powder diffraction. In the case of Ag_2O, it has been shown by EXAFS that the lattice contraction is accompanied by an expansion of the Ag-O distance and that the deformation of the Ag_4O tetrahedral is not negligible. In this work we present a comparison between EXAFS and XRD results for both compounds. The comparison between local and lattice thermal expansions, measured by EXAFS and XRD, respectively, and the differences found between the two compounds, allow to gain original insight on the mechanism of negative thermal expansion in framework structures.

1. Introduction

Thermal expansion is a relevant property for a wide variety of technological applications, as micromechanics, electronic devices, biomedical materials and so on [1]. In recent years, particular attention has been focused on solids exhibiting a negative thermal expansion (NTE) over a large temperature range, which could be employed to produce composite materials with specifically tailored thermal expansion properties.

NTE has been frequently observed over a large temperature range in framework structures [2] as ZrW_2O_8, where the lattice parameter contracts from 0.3 to 1050 K [3]. Framework structures are formed by networks of corner-sharing tetrahedral and/or octahedral structural units. The cuprite structure (Ag_2O and Cu_2O, space group Pn3m) can be described as a framework of two networks of corner-sharing M_4O tetrahedra (M = Ag, Cu), in which each M atom is linearly coordinated to two O atom, and each O atoms is tetrahedrally coordinated to four M atoms.

In framework structures the net thermal expansion is often attributed to the competition between two contributions: a positive contribution due to the potential anharmonicity, and a negative contribution of geometrical origin attributed to the network folding induced by low frequency rigid unit modes (RUM) [4]. Explaining NTE in terms of local structure and dynamics is a basic problem, and to this aim it is important to directly measure the thermal expansion of the nearest-neighbours distance and the degree of rigidity of the corner-sharing basic units. Owing to its selectivity of atomic species, insensitivity to long range order and sensitivity to correlation of atomic motion, EXAFS is particularly suited to study the thermal properties within a few coordination shells of a selected atomic species. Temperature dependent measurements and a data analysis based on the cumulant expansion method [5, 6] (when applicable) allow to effectively distinguish anharmonicity and geometrical effects [7]. Let us consider the instantaneous thermal displacements of absorber and back-scatterer atoms, $\bar{u}_0$ and $\bar{u}_j$ respectively. EXAFS is sensitive to the mean square relative displacement $\langle \Delta u^2 \rangle = \langle (\bar{u}_j - \bar{u}_0)^2 \rangle$, which is conveniently decomposed into its projections parallel and perpendicular to the bond direction, $\langle \Delta u_{||}^2 \rangle$ and $\langle \Delta u_{\perp}^2 \rangle$ respectively. The first EXAFS cumulant C_1^* is the average value of the distribution of the interatomic distances; it is always larger than the distance R between the centres of probability distribution functions measured by diffraction (XRD), owing to the effect of thermal vibrations perpendicular to the bond direction; quantitatively $C_1^* \cong R + \langle \Delta u_{\perp}^2 \rangle / 2R$ [8]. The second EXAFS cumulant C_2^* is the variance of the distribution of distances, and corresponds to a very good approximation to the mean square relative displacement *parallel* to the bond direction: $C_2^* \cong \langle \Delta u_{||}^2 \rangle$.

A direct comparison between EXAFS and XRD measurements not only gives original information about the correlation of atomic motion [9, 10], but also allows to obtain fundamental inputs to understand the connection between the bond length thermal expansion and the macroscopic thermal expansion, particularly in the case of NTE in framework structures. In this paper the experimental results obtained through a joint EXAFS-XRD work on the cuprite structures will be reported.

2. XRD measurements and results

High-resolution X-ray powder diffraction measurements on Cu_2O and Ag_2O have been performed with synchrotron radiation in the temperature range from 5 K to room temperature at the BM16 beam line (now transferred to ID31) of ESRF in Grenoble. The wavelength used was 0.3545 Å, calibrated against standard silicon SRM 640B (also used as a standard for line position). The temperature control was achieved by a closed-cycle helium cryostat. The angular range was between 5° and 28° 2ϑ, corresponding to $\sin\vartheta/\lambda$ between 0.12 and 0.68 $Å^{-1}$; in order to correctly estimate the goniometer zero, the lattice parameter for SRM 640B silicon, calculated from the thermal expansion taken from Swenson [11], was kept fixed. The structural refinements were performed with the Rietveld method, using the GSAS code [12].

High temperature data (from room temperature to 630 K for Cu_2O and to 470 K for Ag_2O) were collected in argon flux with a Philips X'pert ϑ-ϑ laboratory diffractometer equipped with a hot chamber (AHT PAP1600) [13], and carefully calibrated for sample position and temperature. The CuKα wavelength was used. The refinement method was the same as for the synchrotron data.

The relative thermal expansion $\Delta a/a$ of the lattice parameter a is shown in Figure 1 for both crystals: Cu_2O exhibits NTE up to about 200 K; between 200 and 300 K the lattice expansion is roughly zero; for temperature higher than 300 K the thermal expansion becomes positive but very small. This behaviour is in good agreement with the results found by Schäfer and Kirfel with

*e-mail: sanson@science.unitn.it

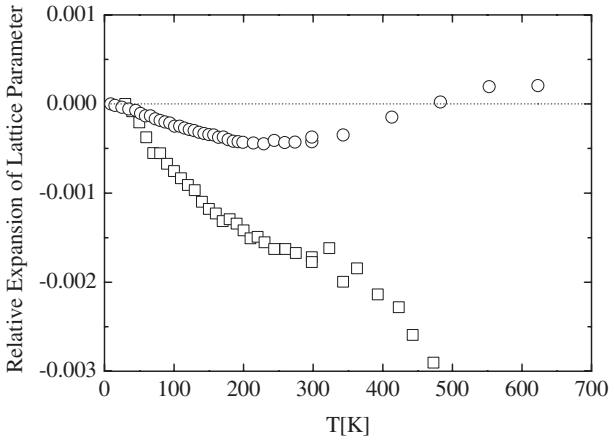

Fig. 1. Relative expansion of lattice parameter for Cu_2O (circles) and Ag_2O (square).

neutron powder diffraction [14]. In the case of Ag_2O, a stronger NTE is present on the whole temperature range considered. This result for Ag_2O is in contrast with previous measurements performed with laboratory diffractometers, which gave positive thermal expansion [15, 16].

3. EXAFS measurements and results

EXAFS data for Cu_2O were collected at the K-edge of copper in the temperature range from 25 to 410 K at the beamline BM29 of ESRF; an independent measurement run was performed at the beamline BM08 (Gilda) in the temperature range from 4 to 300 K. EXAFS measurements at the silver K-edge in Ag_2O were performed at the beamline BM08 of ESRF in the temperature range from 7 to 500 K. All the samples were prepared by depositing Cu_2O or Ag_2O powders on polytetrafluoroethylene membranes, the thickness being chosen so as to have an edge jump $\Delta\mu x \cong 1$. EXAFS was measured in transmission mode, using silicon monochromators with (311) and (111) Bragg-reflecting faces at the BM08 and BM29 beam lines, respectively.

The EXAFS signals were extracted from the experimental spectra after a careful alignment of the energy axes according to well established procedures [17]. The Fourier transforms of the EXAFS signals at low and room temperature are shown in Figure 2 for both compounds. The first peaks between about 1 and 2 Å corresponds to the first coordination shell (two oxygen atoms, at 1.85 Å for Cu_2O and at 2.04 Å for Ag_2O). The first-shell EXAFS contributions at different temperatures were singled out by Fourier back-transform and analysed by the ratio method [5, 6], using the lowest temperature spectra as reference.

The second peak between about 2 and 3.5 ÷ ·4 Å in Fig. 2 contains, in addition to the single scattering contribution from the second shell (12 Cu at 3.02 Å for Cu_2O and 12 Ag at 3.34 Å for Ag_2O), also the single scattering contribution from the third shell (6 O at 3.54 Å for Cu_2O and 6 O at 3.91 Å for Ag_2O), together with the contribution from multiple scattering (MS) paths. To estimate the relative importance of the different contributions on the analysis of the second peak, a simulation with FEFF code [18] was performed: this procedure allowed to reliably single out the structural parameters of the 2nd shell by the ratio method.

The temperature dependence of the first EXAFS cumulants in Cu_2O and Ag_2O is shown in Figure 3 for the first shell, and in Figure 4 for the second shell. (The first cumulants have been calculated using a fixed photoelectron mean free path value $\lambda = 8$ Å [6]). The second EXAFS cumulants (parallel MSRD) for the first and the second shell of both compounds are shown in

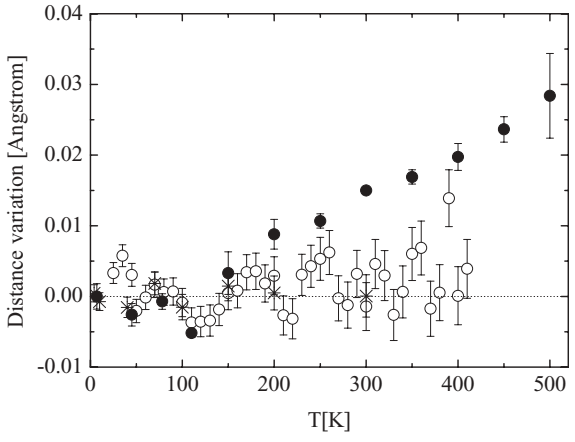

Fig. 3. Temperature dependence of the first shell distance Cu-O (open circles measures performed at BM29, stars at BM08) and of the first shell distance Ag-O (full circles).

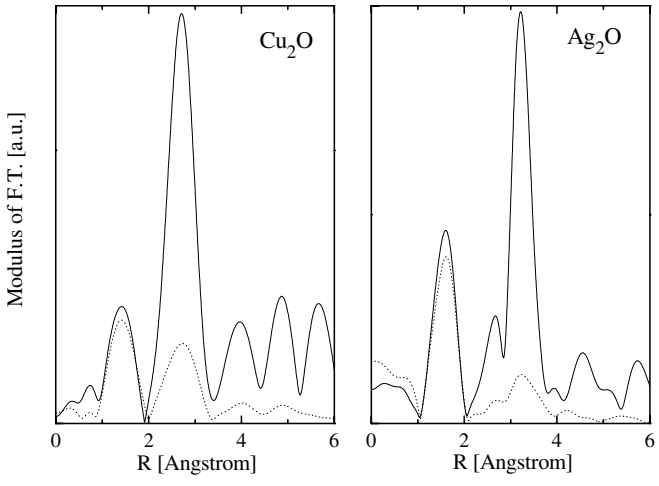

Fig. 2. Fourier Transforms for Cu_2O at 25 and 300 K (left) and for Ag_2O at 7 and 300 K (right).

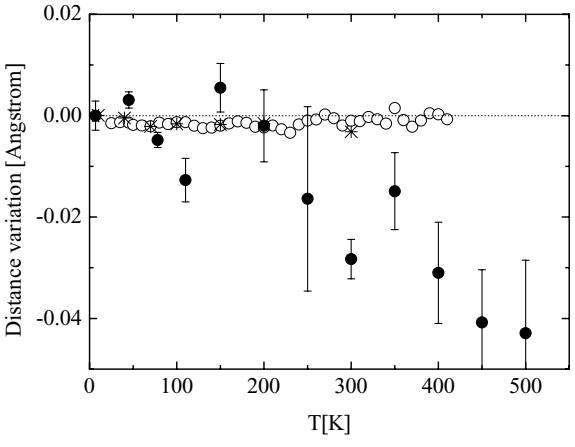

Fig. 4. Temperature dependence of the second shell distance Cu-Cu (open circles measures performed at BM29, stars at BM08) and of the second shell distance Ag-Ag (full circles).

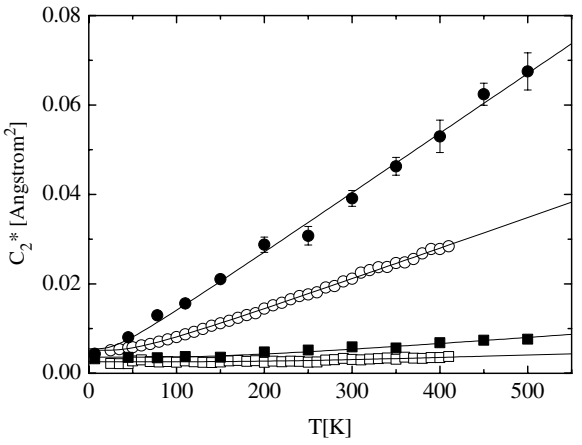

Fig. 5. Parallel MSRD for the first (open squares) and second (open circles) shell in Cu_2O, for the first (full squares) and second (full circles) in Ag_2O. Lines are the corresponding Einstein model fits.

Figure 5: the lines are the corresponding best-fitting correlated Einstein models [8].

The ratio between the intensities of the 2nd and 1st peak in the Fourier transforms is larger in Cu_2O than in Ag_2O (Fig. 2); the effect of temperature is however much stronger for the 2nd shell in Ag_2O than in Cu_2O. For these reasons, the analysis of EXAFS data were particularly difficult for the 1st shell of Cu_2O and the 2nd shell of Ag_2O. In the case of Cu_2O, a further difficulty was represented by the closeness of the peaks. These considerations in part justify the scattering of data, particularly for the Cu-O and Ag-Ag distances.

4. Discussion

The NTE of the lattice parameter measured by XRD is much larger in Ag_2O than in Cu_2O (Fig. 1). This result is qualitatively reproduced by EXAFS, where the second distance Ag- Ag exhibits a strong contraction with the temperature, while the Cu-Cu distance variation is only slightly negative or zero (Fig. 4). Of the 12 M atoms of the 2nd shell, 6 belong to the same network of connected tetrahedra as the absorbing atom (type A), while the other 6 are between different networks (type B). EXAFS measures the average behaviour, weighted by the respective Debye-Waller factor [19]. The 1st-shell results (Fig. 3) emphasize the peculiarity of EXAFS with respect to XRD, but also again show a difference between Ag_2O and Cu_2O. The Ag-O bond length exhibits a strong increment with the temperature, while the Cu-O bond length expansion is only slightly positive or zero.

The EXAFS results for Ag_2O enlighten the competition between anharmonicity of the interaction potential (increment of Ag-O distance) and geometric effects (decrease of Ag-Ag distance, probably stronger for type B pairs) in determining the lattice NTE. In the case of Cu_2O this effect is by far weaker. Some clues on the local origin of NTE, as well as on the difference between the two compounds, can be obtained by looking at dynamical properties.

The MSRD Einstein frequency allows us to estimate an effective bond-stretching force constant [8]. The obtained ratio between M-O and M-M force constant is very similar for both compounds (Fig. 5): 9.8 ± 0.2 for Cu_2O and 9.1 ± 0.2 for Ag_2O. The high value of the ratios is related to the intense transverse thermal motion of the metallic atom with respect to the O-M-O direction, and should be directly connected with the origin of NTE [20]. The absolute MSRD values are however quite different (Fig. 5), Cu_2O exhibiting a by far less intense vibrational motion than Ag_2O. It is possible that the weaker dynamics observed in MSRD explains the weaker difference between 1st and 2nd shell thermal expansion measured by EXAFS in Cu_2O with respect to Ag_2O. The different shapes of the lattice thermal expansion curves (Fig. 1) could instead require, to be explained, interactions within a longer range than observable by EXAFS.

In the case of Ag_2O, a sophisticated comparative analysis of 1st and 3rd cumulants of the 1st shell allowed to deduce the lack of rigidity of the tetrahedral units, and consequently the inadequacy of a RUM model [7] in explaining NTE. The same analysis cannot be made for Cu_2O, owing to lower signal to noise ratio in the temperature dependence of cumulants. Nevertheless, the high value of the MSRD of Cu-Cu distance suggests that tetrahedral units are probably not rigid also in Cu_2O.

5. Conclusions

A combined EXAFS-XRD temperature dependent study on Cu_2O and Ag_2O has been reported. Both compound exhibit lattice NTE, although with different intensities and within different temperature intervals. EXAFS allows to distinguish a remarkably different behaviour between 1st and 2nd shells in Ag_2O (positive and negative expansion, respectively). The difference is by far less evident in Cu_2O. These results open new perspectives for getting original experimental information on the connection between local dynamics and NTE, and stimulate the development of suitable theoretical models.

Acknowledgements

The authors are grateful to the technical staffs of the BM08, BM16 and BM29 beamlines at ESRF for assistance in XRD and EXAFS measurements.

References

1. Roy, R., Agrawal, D. K. and McKinstry, H. A., Ann. Rev. Mater. Sci. **19**, 59 (1989).
2. Evans, J. S. O., J. Chem. Soc. Dalton Trans. **19**, 3317 (1999).
3. Mary, T. A., Evans, J. S. O., Vogt, T. and Sleight, A. W., Science **272**, 90 (1996).
4. Heine, V., Welche, P. R. L. and Dove, M. T., J. Am. Ceram. Soc. **82**, 1793 (1999).
5. Bunker, G., Nucl. Instr. and Meth. **207**, 437 (1983).
6. Fornasini, P., Monti, F. and Sanson, A., J. Synchrotron Rad. **8**, 1214 (2001).
7. Beccara, S. a *et al*., Phys. Rev. Lett. **89**, 25503 (2002).
8. Fornasini, P., J. Phys.: Condens. Matter **13**, 7859 (2001).
9. Dalba, G. and Fornasini, P., J. Synchrotron Rad. **4**, 243 (1997).
10. Dapiaggi, M., Tiano, W., Artioli, G., Sanson, A. and Fornasini, P., Nucl. Instr. Meth. B **200**, 231 (2003).
11. Swenson, C. A., J. Phys. Chem. Ref. Data **12**, 179 (1983).
12. Larson, A. C. and Von Dreele, R. B., Report LAR 86-748, Los Alamos National Laboratory (1999).
13. Dapiaggi, M., Artioli, G. and Petras, L., Rigaku J. **19**, 1 (2002).
14. Schäfer, W. and Kirfel, A., Appl. Phys. A, Matter. Sci. Process., in press
15. Suzuki, T., J. Phys. Soc. Japan **15**, 2018 (1960).
16. Srivastava S. P. *et al*., J. Phys. Soc. Japan **43**, 1463 (1977).
17. Dalba, G., Fornasini, P. and Rocca, F., Phys. Rev. B **47**, 8502 (1993).
18. Rehr, J., Zabinsky, S. and Albers, R., Phys. Rev. Lett. **69**, 3397 (1992).
19. Sanson, A. and Fornasini, P., work in progress.
20. Li, J., Yokochi, A., Amos, T. G. and Sleight, A. W., Chem. Mater. **14**, 2602 (2002).

Physica Scripta. Vol. T115, 274–277, 2005

XAFS Analysis of Layered $Li_xNi_{0.5}Mn_{0.5}O_2$ ($0 < x \leq 2$) Electrodes for Lithium Batteries

A. J. Kropf†, C. S. Johnson, J. T. Vaughey and M. M. Thackeray

Argonne National Laboratory, Argonne, IL USA

Received June 26, 2003; accepted in revised form November 4, 2003

PACS numbers: 61.10.Ht, 82.47.−a

Abstract

X-ray absorption fine-structure spectroscopy was used to ascertain the individual metal oxidation states involved during the electrochemical insertion and extraction of lithium with layered $Li_xNi_{0.5}Mn_{0.5}O_2$ electrodes in lithium cells. These results, along with electrochemical cycling data, suggest that the $Li_xNi_{0.5}Mn_{0.5}O_2$ ($0 < x \leq 2$) electrodes operate predominantly via two-electron redox couples, Ni^{4+}/Ni^{2+} and Mn^{4+}/Mn^{2+}, between 4.5 and 2.0 V ($0 < x \leq 1$) and below 1.07 V ($1 < x \leq 2$) versus metallic Li, respectively. In the upper voltage region, the Ni-O bond changes by nearly 0.14 Å, while the Mn-O bond remains at nearly a fixed length. In the low-voltage region, the $LiNi_{0.5}Mn_{0.5}O_2$ electrode undergoes a two-phase reaction with Li to form a dilithium compound, $Li_2Ni_{0.5}Mn_{0.5}O_2$; during this reaction, charge transfer occurs at the Mn metal center.

1. Introduction

Layered transition metal oxides ($LiMO_2$; M = transition metal ion) such as lithium cobalt oxide ($LiCoO_2$), lithium nickel oxide ($LiNiO_2$), or lithium nickel-cobalt oxides ($LiNi_{1-y}Co_yO_2$), are commonly used as cathodes in commercial Li-ion batteries. These materials have a layered structure with trigonal symmetry, R-3m. Metal-oxygen octahedra form a hexagonal array, while lithium is located between the metal oxide layers. During discharge of the battery, lithium ions are electrochemically inserted between the metal-oxide layers with a concomitant reduction at the metal center; the reverse process occurs on charging the battery. In most $LiMO_2$ electrodes, the transition-metal undergoes a reversible one-electron transfer process, shuttling back and forth from a trivalent state at full discharge to a tetravalent state at full charge. Recent developments have shown that it is possible to synthesize $LiMO_2$ compounds with Mn and Ni, such as $LiNi_{0.5}Mn_{0.5}O_2$ and $LiCo_{0.33}Ni_{0.33}Mn_{0.33}O_2$ in which the charge is distributed unequally between the transition metal ions [1–4]. Moreover, it has been recently discovered that $LiNi_{0.5}Mn_{0.5}O_2$ can accommodate an additional lithium ion to form a $Li_2Ni_{0.5}Mn_{0.5}O_2$ compound without destroying the layered $Ni_{0.5}Mn_{0.5}O_2$ framework structure [5, 6]. The aim of this work has been to study, by *in situ* X-ray absorption spectroscopy (XAS), the structural transformations and charge transfer processes that occur when lithium is inserted into, and extracted from an $Li_xNi_{0.5}Mn_{0.5}O_2$ electrode over a wide range of x ($0 < x \leq 2$). Other groups have reported XAFS data on this material [7–9]. However, the analysis has typically been limited to a qualitative evaluation. A quantitative discussion of the results can highlight some important characteristics of the material.

2. Experiment

The sample preparation is described in detail elsewhere [5]. Analysis of the metal composition by ICP-AES showed the as-synthesized material to be $Li_{0.906}Ni_{0.506}Mn_{0.494}O_2$, assuming complete oxidation [5]. The sample will be identified as $LiNi_{0.5}Mn_{0.5}O_2$ for clarity.

The battery cell was assembled in a polypropylene bag with lithium counter electrodes on either side of the metal oxide cathode. The cell construction is described in more detail in [10]. While in the beam, the bag cell was pressed between two 0.32 mm thick beryllium foils to ensure intimate contact between the electrodes and the separators as well as maintain a constant cell thickness during the experiment. During the measurements at high-potential, the cell current was 0.18 mA/cm^2, and the charge rate was approximately C/4. The second battery cell, for the low-potential studies, was heated to 50 °C to improve the reaction kinetics and increase the speed of the discharge to faster than a C/2 rate.

X-ray absorption fine-structure spectroscopy (XAFS) measurements were performed on the insertion device beamline of the Materials Research Collaborative Access Team (MRCAT) at the Advanced Photon Source (APS), Argonne National Laboratory. A cryogenic double-crystal Si(111) monochromator was used to select the X-ray energy and an uncoated ULE glass mirror was used to remove the higher-order harmonic content from the beam. The monochromator was continuously scanned using a bin size of 0.35 eV and time per data point of 0.06 s for the X-ray absorption near-edge structure (XANES). Extended X-ray absorption fine-structure (EXAFS) and XANES spectra for both the Mn and Ni K edges were collected at a repetition rate of about 10 minutes. Transmission XAFS measurements of Mn or Ni foils accompanied every measurement to provide energy calibration and place all data from either the Mn or Ni data sets on the same energy scale to within 0.05 eV. The first inflection points of the normalized absorption spectra were set to 6538.0 eV and 8333.0 eV, for Mn and Ni, respectively. Given this reference energy, the accuracy of the edge energies reported is within ±0.20 eV.

3. Data Analysis

The data were fit to scattering paths calculated with self-consistent fields using *feff* (version 8.2) [11]. The *feffit* code [12] was used to fit the data between $k = 2.5$–14 Å^{-1} ($k = 2.5$–11.5 Å^{-1} for Mn) and $R = 1.23$–3.19 Å. Eight variables ($2E_0$'s, $2R$'s, $2\sigma^2$'s, and $2N$'s) and three single-scattering paths (M-O, M-Mn, M-Ni, where M indicates Mn or Ni) were used in the fit. Identical values were used for all the M-M paths in an individual fit. Equal numbers of Mn and Ni were assumed for the second shell, although this precise distribution would require an unusual arrangement of the metal atoms. Nonetheless, the backscattering amplitudes and phases are sufficiently similar for this approximation to be useful. The residual error was typically about 1.5%. When the individual coordination numbers and

†email: kropf@cmt.anl.gov

distances were allowed to vary, we observed a preponderance of Ni around Mn and visa versa, as expected for most arrangements of the metal centers. In this case, we did observe an intermediate Mn-Ni distance. The XANES data were fit by both principle component analysis and a linear combination of spectra.

4. Results and Discussion

Figure 1 shows several examples of the $\chi(k)$ data for the Mn and the Ni edges. The Mn data range was limited by a very small Fe impurity in the sample. It is immediately clear that the Ni spectra are changing far more than the Mn spectra between 3.60 V and 4.60 V. Figure 2 shows the Ni-O and Mn-O bond lengths as a function of the scan number. The data were collected over the initial charge and a subsequent discharge and charge cycle. The cell potential (vs. lithium) is shown at several points on the plot. For the purposes of this fit, one Ni-O bond length was assumed. Between 3.60 V, the open circuit voltage (OCV), and 4.60 V, the Ni-O bond length decreased by nearly 0.14 Å, while the Mn-O bond length decreased by only 0.01 Å. The striking difference between the Mn and the Ni bond lengths is clear evidence that the Ni is the primary actor in the redox reaction, while the Mn is merely a bystander at higher potential. If one compares the Ni-O bond length ($R_{\text{Ni-O}}$) from this electrode with that from $LiNi_{0.8}Co_{0.2}O_2$ from [10] (1.89 Å to 1.93 Å), it is clear that the change in $R_{\text{Ni-O}}$ is much greater for $Li_xNi_{0.5}Mn_{0.5}O_2$. This corroborates the supposition that Ni is in a lower +2 oxidation state.

As $R_{\text{Ni-O}}$ changes from longer to shorter distance with Li extraction, the Debye-Waller factor increases from 0.007(1) $Å^2$ up to 0.012(1) $Å^2$ (scan 17) and then decreases to 0.005(1) $Å^2$ from 3.60 V to 4.60 V during the initial charge. At the extremes, when the Ni oxidation state is closest to +4 or +2, the Debye-Waller factor is at its lowest. If $R_{\text{Ni-O}}$ truly had a length characteristic of only the +2 and the +4 states, the Debye-Waller factor would increase to at least 0.023 $Å^2$, due to the separation of at least 0.14 Å between the two lengths. Since σ^2 does not exhibit this behavior, it leads to the interpretation that the Ni atoms have a global average oxidation state that changes smoothly, as suggested by the near-edge spectra, rather than individual Ni atoms snapping from +2 to +4.

Fig. 3 shows that less lithium is stored in the electrode during the first discharge than was removed during the first charge. This is consistent with the metal-oxygen distances from Fig. 2; at the end of the first discharge, the Ni-O distance does not recover to the initial distance of 2.04 Å, but only reaches 2.01 Å.

Figure 4 shows representative near-edge spectra from the initial charge. The near edge structure, being sensitive to the oxidation state provides an independent probe of the electrochemical reaction. The Mn edge spectra change shape somewhat during the initial charge, but do not shift in energy, indicating that the Mn oxidation state is relatively constant. On the other hand, the

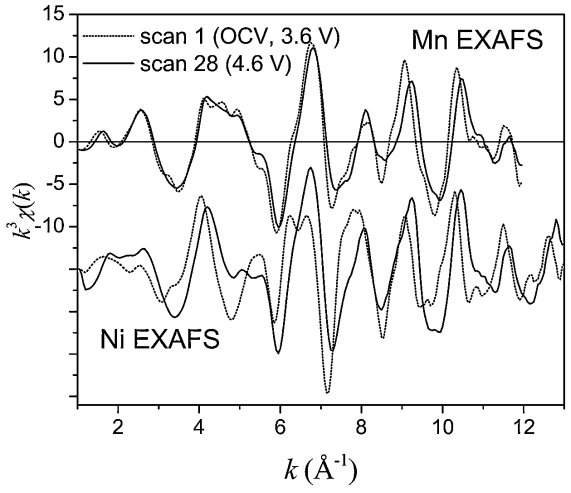

Fig. 1. $k^2\chi(k)$ data for the Mn (upper pair) and Ni (lower pair) edges.

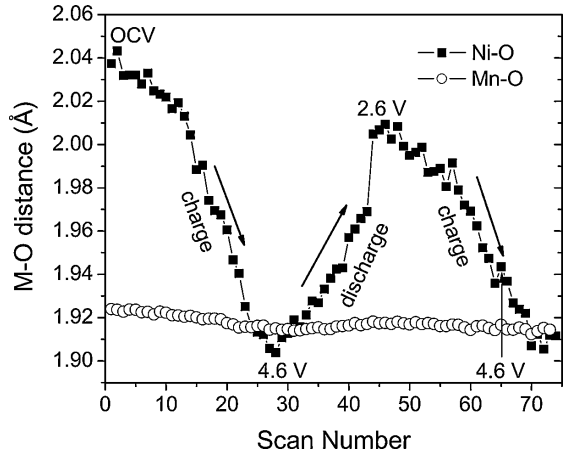

Fig. 2. Ni-O and Mn-O first shell bond length.

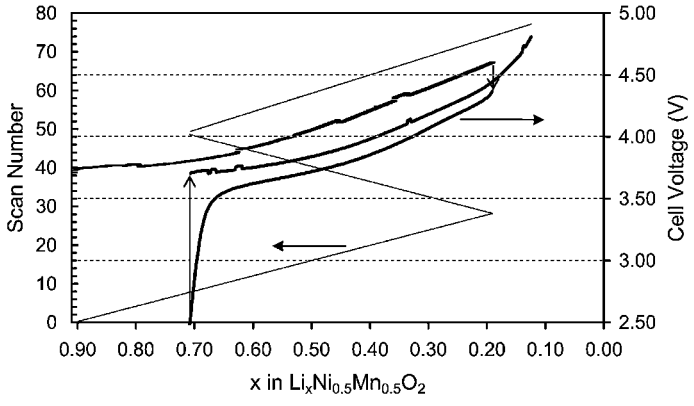

Fig. 3. Scan number (fine line) and cell voltage (thick line) vs. lithium content for the $Li_xNi_{0.5}Mn_{0.5}O_2$ electrode.

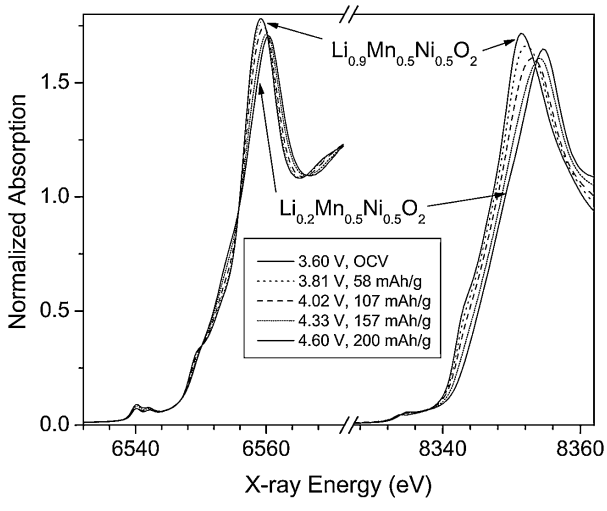

Fig. 4. Selected Mn (left) and Ni (right) XANES from initial charge.

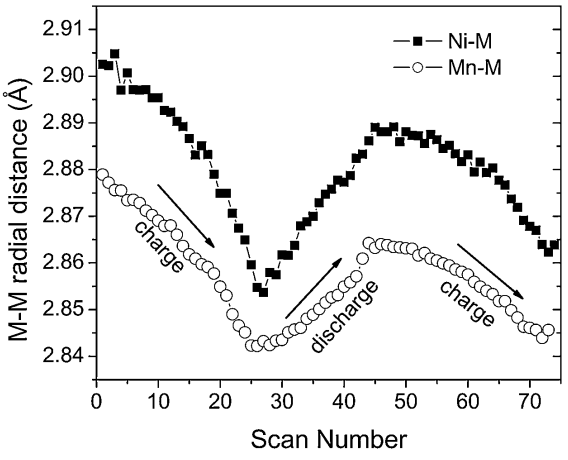

Fig. 5. Average Mn-*M* and Ni-*M* 2nd shell bond lengths. The metal-metal distance has been modeled by a single length. The relatively constant Debye-Waller factor of about 0.005 Å^2 indicates this is a reasonable choice.

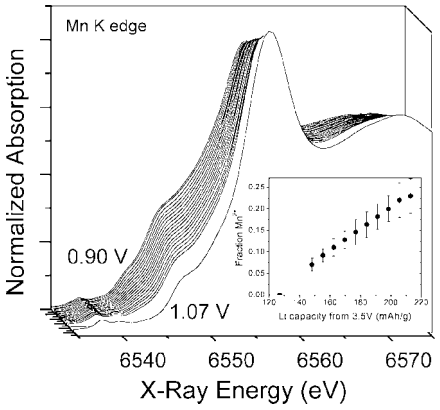

Fig. 6. Mn K edge XANES at low potential with the fraction of Mn^{2+} below 1.07 V (inset).

Ni edge ($\mu x = 0.5$) shifts to higher energy, from 8343.07 eV (at OCV, 3.60 V) to 8345.45 eV (at 4.60 V), as the lithium is removed. If one assumes a Mn^{4+} oxidation state and a fully oxidized sample (O^{2-}), one can calculate the expected Ni oxidation state from the measured composition. The initial average Ni oxidation state should be +2.21, while at the end of the first charge the oxidation state should be +3.61. By comparing the measured Ni XANES to Ni(II)O (8342.26 eV) and $LiNi(III)O_2$ (8344.67), we can estimate the Ni oxidation state to be +2.34 at the beginning of the measurement and +3.32 at the end. The as-prepared powder had an edge position of 8342.90 eV, only 0.17 eV lower than the electrode in the cell at the beginning of the measurement. Over the charge/discharge cycle, the Ni spectra behave similarly to other electrodes with similar structure, such as $LiNiO_2$ and $LiNi_{0.8}Co_{0.2}O_2$ reported in the literature [10, 13, 14].

Figure 5 shows the average metal-metal second shell bond lengths, reflecting the intralayer lattice parameter. Both the Mn-metal and the Ni-metal bond lengths decrease by about 0.04 Å, although the Ni-metal distance shrinks by a slightly larger amount. Since $R_{M\text{-}M}$ is changing by a similar amount for both Mn and Ni, while the Mn-O distance remains more or less constant, we conclude that the Mn and Ni are intimately mixed in the cathode and not phase-segregated; i.e., the Ni octahedra share edges with Mn octahedra.

If the Mn is not participating in the redox chemistry of the cell at high-potential, the Ni must cycle between Ni^{4+} and Ni^{2+}, possibly by a 2-electron process, to account for the capacity of the battery in the high-voltage region. Since the Ni edge shifts smoothly, this could indicate a global average oxidation state change, rather than a local change at individual Ni atoms.

Measurements of a second cell (with Li_2TiO_3 added) at low potential showed that the redox-active metal changes from Ni to Mn at around 1.07 V. This value could be somewhat lower than the actual potential due to the fast discharge rate. Figure 6 shows the Mn near-edge structure at low-potential. In contrast to the Ni, for which the edge position shifts smoothly from higher to lower energy with increasing lithium content, the Mn XANES spectra exhibit behavior that looks more as if the Mn is changing directly from 4+ to 2+; Mn^{2+}-like features increase as the cell potential decreases. This is consistent with a reaction that involves larger structural changes. Inset into Fig. 6 is a plot of the Mn^{2+} fraction as a function of cell potential. The Mn edge spectrum taken at 0.90 V was fit by a linear combination of the Mn^{4+} (from this cell) and a Li_2MnO_2 standard. By the end of the discharge, 23±4% of the Mn has converted to Mn^{2+}, or $Li_2Mn_{0.5}Ni_{0.5}O_2$.

The Ni edge position at 1.07 V is 8342.54, while at the end of the run, the Ni K edge energy was 8342.47 eV, a very small shift, and only 0.60 eV lower than the open circuit voltage at the beginning of the run. The Ni edge position is within 0.21 eV of the Ni(II)O standard.

5. Conclusions

Layered $LiMO_2$ compounds that contain manganese and nickel are attractive insertion electrodes for lithium-ion cells that operate at a high potential. Those that can accommodate an additional lithium within their structures, such as $LiMn_{0.5}Ni_{0.5}O_2$, hold promise for providing systems that remain stable over a very wide compositional range because the two-electron transfer processes, Ni^{4+}-Ni^{2+} and Mn^{4+}-Mn^{2+}, which occur during charge and discharge bypass the Jahn-Teller active ions Ni^{3+} and Mn^{3+} that can lead to more severe structural distortions and instabilities. Li_2MO_2 compounds are attractive because they can provide a source of excess lithium to compensate for the capacity that is typically lost at the negative electrodes of high-voltage lithium-ion cells during the first charge.

Acknowledgments

Support for this work from the U.S. Department of Energy (US-DOE), Basic Energy Sciences, Division of Chemical Sciences, under Contract No. W-31-109-Eng-38, is gratefully acknowledged. Use of the Advanced Photon Source was supported by the US-DOE, Basic Energy Sciences, Office of Science, under Contract No. W-31-109-Eng-38. Work performed at MRCAT is supported, in part, by funding from the Department of Energy under grant number DEFG0200ER45811.

The submitted manuscript has been created by the University of Chicago as Operator of Argonne National Laboratory (Argonne) under Contract No. W-31-109-ENG-38 with the U.S. Department of Energy. The U.S. Government retains for itself, and others acting on its behalf, a paid-up, nonexclusive, irrevocable worldwide license in said article to reproduce, prepare derivative works, distribute copies to the public, and perform publicly and display publicly, by or on behalf of the Government.

References

1. Lu, Z., MacNeil, D. D. and Dahn, J. R., Electrochem. Solid State Lett. **4**, A200 (2001).
2. Rossen, R., Jones, C. D. W. and Dahn, J. R., Solid State Ionics **57**, 311 (1992).

3. Yoshio, M. *et al.*, J. Power Sources **74**, 46 (1998).
4. Ohzuku, T. and Makimura, Y., Chem. Lett. **8**, 744 (2001).
5. Johnson, C. S. *et al.*, Electrochem. Commun. **4**, 492 (2002).
6. Johnson, C. S. *et al.*, Chem. Mater. **15**, 2313 (2003).
7. Yoon, W.-S. *et al.*, Electrochem. Solid State Lett. **5**, A263 (2002).
8. Kobayashi, H. *et al.*, J. Mater. Chem. **13**, 590 (2003).
9. Nakano, H., Nonaka, T., Okuda, C. and Ukyo, Y., J. Ceramic Soc. Japan **111**, 33 (2003).
10. Johnson, C. S. and Kropf, A. J., Electrochim. Acta. **47**, 3187 (2002).
11. Ankudinov, A. L., Ravel, B., Rehr, J. J. and Conradson, S. D., Phys. Rev. B **58**, 7565 (1998).
12. Newville, M. *et al.*, Physica B **208&209**, 154 (1995).
13. Pickering, I. J., George, G. N., Lewandowski, J. T. and Jacobson, A. J., J. Am. Chem. Soc. **115**, 4137 (1993).
14. Nakai, I. and Nakagome, T., Electrochem. Solid State Lett. **1**, 259 (1998).

Physica Scripta. Vol. T115, 278–280, 2005

X-Ray Studies of Pd/Ag Membranes for Hydrogen Separation

Laurens C. Witjens, J. H. Bitter, A. J. van Dillen, F. M. F. de Groot, D. C. Koningsberger and K. P. de Jong[1]

Inorganic Chemistry and Catalysis, Debye Institute, Utrecht University, P.O. Box 80083, 3508 TB Utrecht, The Netherlands

Received June 26, 2003; revised July 10, 2003; accepted November 4, 2003

PACS numbers: 61.10.Ht, 61.10.Nz

Abstract

The homogeneity of typical electrolessly plated Pd/Ag membranes for H_2 separation was investigated with XAFS and XPS depth profiling. Next the crucial mixing of the separate Pd and Ag layers, obtained after the two sequential plating steps, was followed in situ with XRD. The results show that some low temperature alloying procedures found in the field are insufficient for obtaining a well-mixed Pd/Ag alloy membrane.

Finally the Pd/Ag-H XANES was determined for the first time. In contrast to the Pd-H and Pd/Ag systems, shifts in electron density from the Ag or H atoms to the Pd could not satisfactorily explain the observed XANES. Not only is the intensity of the whiteline higher than expected, the shape and the intensity of the anti-bonding Pd 4d H 1s feature have also significantly changed. Local geometry is expected to account for these deviations.

1. Introduction

Thin $Pd_{77}Ag_{23}$ films on inert, porous supports such as α-Al_2O_3, Vycor glass or porous stainless steel are very important membrane materials [1–3]. Applications vary from separating H_2 from gas streams to use as a membrane reactor in hydrogenation or dehydrogenation reactions.

Electroless plating is the most suited technique for large scale production of these membranes. A typical electroless plating solution contains a metal salt, a strong reducing agent (here hydrazine), buffer reagents (here ammonia), water and a complexing agent (here Na_2EDTA). With electroless plating, in contrast to the electroplating technique, it is possible to deposit a metal film on a non-conducting support material such as Al_2O_3.

A Pd/Ag mixture is obtained by consecutively depositing a Pd and an Ag layer followed by a heat treatment to attain alloying. However there is no consensus on the required alloying treatment; temperatures vary from 450–900 °C, treatments last from a few hours to dozens of hours and finally both inert and H_2 atmospheres are used by different researchers [3–6].

Inadequate mixing is expected [4, 5] to seriously limit the performance and lifetime of the membranes. Therefore the homogeneity of the Ag distribution in typical electrolessly plated samples is studied in this paper with K-edge XAFS and XPS depth profiling. Furthermore the alloying of the Pd and Ag layers is studied *in situ* using XRD.

Finally the Pd/Ag-H system is studied as well; with L_3-edge XANES to learn more about the fundamentals of this system.

2. Experimental Section

The following samples were obtained with electroless plating: pure Pd on α-Al_2O_3, pure Ag on α-Al_2O_3 and samples with both a Pd (first) and an Ag layer (second) on α-Al_2O_3 (intended Ag content 23 at%). One of the Pd/Ag samples was alloyed at 500 °C under 5% H_2/He for 150 hours, the others were alloyed during the *in situ* XRD experiments described below. Visual inspection with SEM confirmed that the samples were several μm thick as intended.

A 750 nm $Pd_{80}Ag_{20}$ sample on a Si wafer (with 20 nm Ti adhesion layer) obtained with bi-sputtering, *i.e.*, the simultaneous sputtering of two pure targets to produce a binary alloy, was received from the MESA$^+$ institute of the University Twente.

Pd and Ag K-edge XAFS measurements were performed with the electrolessly plated samples at the X1 beamline of the HASYLAB facility in Hamburg, Germany. All measurements occurred in transmission mode. The samples were first measured in vacuum at 77 K. This was followed by one hour of exposure to H_2 (100 ml min^{-1} flow) at room temperature, after which the cells were closed, cooled to 77 K and the samples were measured again.

The XDAP 2.2.2 program was used for the data analysis. For each measurement at least two scans were averaged. In the subsequent procedure the pre-edge and background were subtracted, as described in [7], before fitting the data. The fit parameters can be found in Table I and II.

At the E4 beamline of the HASYLAB facility the L_3 XANES of pure, electrolessly plated, Pd and of the Pd/Ag bi-sputtered sample in vacuum and H_2 atmosphere (1.5 bar) were determined. The measurements were performed at room temperature using a fluorescence detector. At least two scans were averaged for each measurement. The pre-edges and backgrounds were subtracted and the measurements were normalised at 50 eV beyond the edge. Some saturation was visible when comparing the results to the literature [8]. A numerical compensation was determined for Pd and Pd/Ag under vacuum, which was also applied to the hydrogen measurements.

XPS depth profiling of the Pd/Ag samples were performed in our laboratory. In regular steps the metal layer was removed by sputtering with Ar^+ ions until the support material was detected. Unfortunately it is not possible to determine the amount of material removed with sputtering with our XPS set-up. Therefore, total thicknesses of the samples had earlier been determined with Rutherford backscattering with 2 MeV protons. Since the masses of the isotopes of Pd and Ag are too similar the two elements cannot be distinguished from one another with RBS. However the densities of the elements are also very similar so that there are no problems in determining the total thicknesses of the metal (alloy) layers. With the total thicknesses the rate of removal during XPS depth profiling could be calculated.

Co K-edge XRD ($\lambda = 1.78897$ Å) was used to study the alloying of the Pd and Ag domains *in situ* at temperatures from 400–600 °C in He. After the heat treatments the average Ag content was determined. For this purpose, a lattice constant vs. Ag content diagram was constructed using literature data [9, 10].

[1] email: k.p.dejong@chem.uu.nl

Table I. *Pd K-edge measurements, k^3 weighing, k range 2.5–15.69, fit range 2.0–3.0Å.*

Pd membrane			
Measurement	r (Å) (± 0.01)	ΔS^2	E_0
Vac, 77 K	**2.74**	0.0020	−0.17
H_2, 77 K	**2.86**	0.0031	−2.10
Pd/Ag membrane			
Measurement	r (Å)	ΔS^2	E_0
Vac, 77 K	**2.77**	0.0039	−0.12
H_2, 77 K	**2.85**	0.0011	−3.52

Table II. *Ag K-edge measurements, k^3 weighing, k range 2.5–11.74, fit range 2.0–3.0Å.*

Ag membrane			
Measurement	r (Å) (± 0.01)	ΔS^2	E_0
Vac, 77 K	**2.88**	−0.0001	−0.93
H_2, 77 K	**2.87**	0.0038	0.18
Pd/Ag membrane			
Measurement	r (Å)	ΔS^2	E_0
Vac, 77 K	**2.81**	0.0022	2.27
H_2, 77 K	**2.83**	0.0009	1.85

3. Results

3.1. *Homogeneity of the Pd/Ag mixtures*

In Table I the Pd K-edge and in Table II the Ag K-edge fit results are shown. Fits were carried out with the coordination number (N-cor) fixed at 12 (typical for the fcc structure).

The behaviour of the pure Pd and pure Ag membrane on exposure to H_2 was as expected: the Ag membrane showed no significant change and the Pd-Pd distance changed from 2.74 to 2.86 Å. The Pd-Pd distance in bulk Pd at 25 °C is 2.7511 Å [11]. The lattice constant of bulk β-$PdH_{0.6}$ at 25 °C is 4.025 Å [12], which corresponds to a Pd-Pd distance of 2.8461 Å. The Ag-Ag distance in bulk Ag at 25 °C is 2.8894 Å [11].

Also in case of the Pd/Ag sample the change in distance between the average Pd atom and its closest neigbours (Pd or Ag) on exposure to hydrogen corresponds with the literature values. However, the most interesting results are the Ag edge measurements of this sample.

The XAFS results suggest that on exposure to hydrogen a small change in distance to the nearest neighbour occurs, 2.81 to 2.83 Å, which can only be explained by the assumption that the average Ag atom has a relatively large number of Pd neighbours. Yet complete dissolution of atomic Ag in a true alloy of Pd and Ag is not achieved, seeing the large difference between the average Pd-X and Ag-X (X = Pd or Ag) distances. Either the Ag atoms are present in small clusters in a Pd sea or the metal layer consists mainly of Pd/Ag clusters (with different Ag contents).

The XPS depth profile of the Pd/Ag electrolessly plated sample showed an inhomogeneous Ag distribution; from 40 at% at the surface to 15 at% in the bulk and the bottom. Both microscopicly and macroscopicly the alloying is clearly incomplete.

In contrast; the Ag content of the bi-sputtered sample was very constant at 20 at% although the surface showed a small Ag enrichment (25 at%). This sample proves that a properly mixed Pd/Ag system can be synthesized. It is important to note that the result corresponds with the thermodynamic equilibrium [13, 14] and is therefore the most homogeneous Ag distribution obtainable.

With our XRD setup the alloying could be studied *in situ*. The reflections of the Pd and Ag domains present in the unmixed

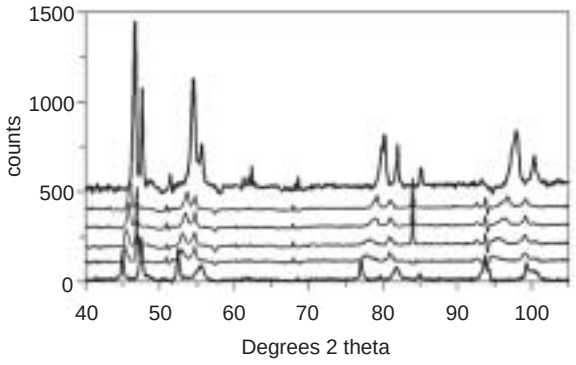

Fig. 1. From bottom to top: $t = 0$ (RT), $t = 3$ hours (375 °C), $t = 4$ hours (first measurement at 400 °C), $t = 18$ hours (400 °C), $t = 57$ hours (last measurement at 400 °C), $t = 60$ hours (RT).

electrolessly plated samples are nicely separated, as shown in figure 1. Beyond about 400 °C these reflections started to disappear and new Pd/Ag alloy reflections appeared. However even after 54 hours at 400 °C the reflections of the separate Pd and Ag domains were not completely removed.

Shorter periods of time (<20 hours) at 500 and 600 °C did completely remove these reflections. Yet the XPS depth profile of the sample alloyed at 500 °C (for a total time of 30 hours) showed that the thermodynamic equilibrium had not yet been reached and the sample was still quite inhomogeneous; the Ag content varied from 38 at% at the surface to 18 at% at the alumina support. Obtaining an Ag profile as homogeneous as the bi-sputtered sample requires a more intense treatment.

3.2. *The Pd/Ag-H XANES*

Figure 2a shows that the addition of Ag to Pd gives a lower white line, which is in agreement with results in the literature [8]. This

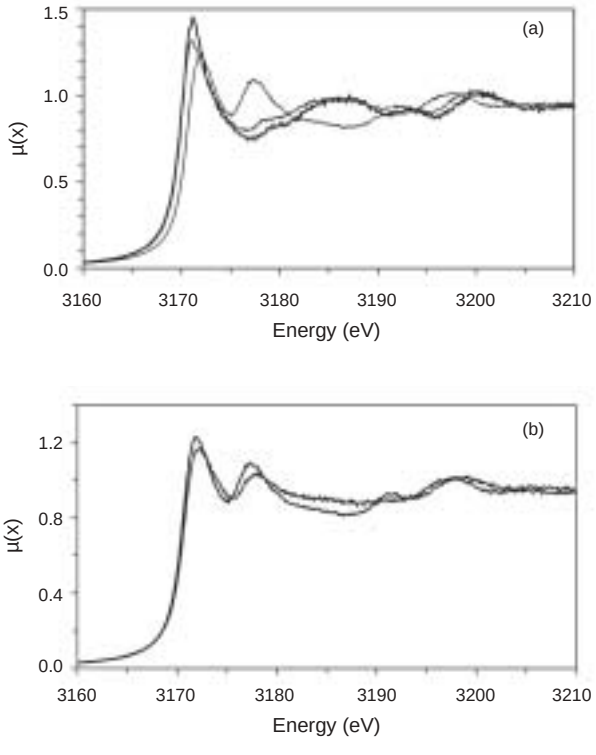

Fig. 2. (a) Pd in vacuum (black), Pd/Ag in vacuum (grey) and Pd in H_2 (thinner line). (b) Pd in H_2 (black) and Pd/Ag in H_2 (grey).

can be attributed to a decrease of the number of 4d holes in Pd, *i.e.*, to a shift of electron density from the Ag to the Pd metal. The peak at approximately 3200 eV is shifted to lower energy for Pd/Ag, indicating an increase in the lattice constant, in full agreement with the EXAFS analysis. In addition, figure 2a shows that dissolving hydrogen in Pd causes a decrease in whiteline intensity, a blue shift and a new peak at +7 eV from the whiteline [15]. This new feature is attributed to the unfilled Pd4d-H1s anti-bonding orbital and the decrease of the white line is expected because part of the empty Pd 4d states are now part of this anti-bonding orbital.

As far as we are aware of, the XANES of the Pd/Ag-H system has not yet been reported. Figure 2b, indicates that the Pd/Ag-H system is not a simple combination of the separate effects of Ag and H described above. Not only is the intensity of the whiteline higher then expected, the shape and the intensity of the hydrogen feature have also significantly changed. In our opinion these changes are a reflection of differences in the local geometry between Pd-H and Pd/Ag-H. Several effects can cause the more intense white line and broader anti-bonding state of Pd/Ag-H, for example: (1) a displacement of the H atoms from their normal octahedral position because of a preference for Pd atoms, (2) (some) clustering of Ag atoms within the Pd sea, (3) local deviations from the bulk lattice constants resulting in a range of slightly different storage sites for hydrogen atoms. The averaged local geometry obtained with XAFS cannot settle this discussion yet. At this time FEFF 8.0 calculations are performed to check whether changes in local geometry can explain our observations in more detail.

4. Conclusions

Alloying of Pd and Ag starts at low temperatures (400 °C), nevertheless achieving total bulk mixing is more problematic. Some low temperature alloying procedures found in the field most likely have resulted in inhomogeneous Ag distributions.

For the first time the Pd/Ag-H XANES was determined. The current model of electron density shift cannot completely explain the observed differences in the XANES of Pd-H and Pd/Ag-H. It is expected that local geometry has a strong influence as well, which is currently being researched with FEFF 8.0 calculations.

Acknowledgements

We acknowledge support from NWO/CW, the Dutch Ministries of VROM and Economic Affairs, ECN, the MESA$^+$ Institute of Twente University, the Surfaces, Interfaces and Devices group of Utrecht University and Shell Global Solutions. This work was supported by the IHP-Contract HPRI-CT-1999-00040/2001-00140 of the European Commission.

References

1. Shu, J., Adnot, A., Grandjean, B. P. A. and Kaliaguine, S., Thin Sol. Films **286**, 72 (1996).
2. Paglieri, S. N. and Way, J. D., Sep. Pur. Meth. **31**, 1 (2002).
3. Cheng, Y. S. and Yeung, K. L., J. Mem. Sci. **158**, 127 (1999).
4. Dittmeyer, R., Höllein, V. and Daub, K., J. Mol. Catal. A **173**, 135 (2001).
5. Uemiya, S., Matsuda, T. and Kikuchi, E., J. Mem. Sci. **56**, 315 (1991).
6. Keuler, J. N. *et al.*, Nucl. Instr. Meth. Phys. Res. B **158**, 678 (1999).
7. Koningsberger, D. C., Mojet, B. L., van Dorssen, G. E. and Ramaker, D. E., Top. Catal. **10**, 143 (2000).
8. Coulthard, I. and Sham, T. K., Phys. Rev. Lett. **77**, 4824 (1996).
9. Axelrod, S. D. and Makrides, A. C., J. Phys. Chem. **68**, 2154 (1964).
10. Hellwege, K.-H., "Landolt - Börnstein, Numerical Data and Functional Relationships in Science and Technology," (Springer-Verlag, Berlin, 1971).
11. Weast, R. C., Astle, M. J. and Beyer, W. H., "Handbook of Physics and Chemistry," 64th ed. (CRC Press, Boca Raton, 1983–1984).
12. Jamieson, H. C., Weatherly, G. C. and Manchester, F. D., J. Less-Common Metals **50**, 85 (1976).
13. Karakaya, I. and Thompson, W. T., "Binary Alloy Phase Diagrams," 2nd ed. (T. B. Massalski, 1991), Vol. 3, p. 55.
14. Gijzeman, O. L., J. Surf. Sci. **150**, 1 (1985).
15. Soldatov, A. V., Longa, S. D. and Biancconi, A., Solid State Commun. **85**, 863 (1993).

Physica Scripta. Vol. T115, 281–284, 2005

Combined XAFS/Powder Diffraction Analysis of Randomly Substituted Cation Sites in Crystalline Oxides

N. Binsted, M. Stange[1], H. Fjellvåg[2] and M. T. Weller

Dept. of Chemistry, University of Southampton, SO17 1BJ, UK
[1]IFE, P.O. Box 40, N-2027 Kjeller, Norway, Dept. of Chemistry
[2]University of Oslo, N-0315 Oslo, Norway

Received June 26, 2003; accepted November 27, 2003

PACS numbers: 61.10.Ht, 61.12.Ld, 61.43.Bn

Abstract

When complex metal oxides show locally ordered substitution of cations amongst crystallographic sites, a single-model description of the structure is relatively straightforward. Distinct local and long-range space groups, element specific cation sites, and local distortions of the oxygen lattice may be employed to give a reasonable description of the structure. Averaging over possible orientations of the local cell may be performed to simulate the effect of domain structure or stacking faults where a dual space group description is inappropriate. Full multiple scattering calculations, over multiple edges, may be performed using these models, allowing all the XAFS data to be analysed within a cluster of 5 Å or more, and information on cation-cation correlations may thus be obtained. When substitution is more or less random, such approaches are less helpful. In order to extend the range of compounds which can be studied using the combined XAFS/Powder Diffraction (PD) method, a Reverse Monte-Carlo method has been developed, which includes multiple scattering XAFS contributions, and allows crystallographic symmetry to be superimposed on the finite model. Various restraints can be applied, for example, to minimise the difference between the structure and the starting model, to maximise the symmetry of a particular site, or to minimize unreasonable departure from bond valence sums. The necessity for such a method and an example of its application is given by reference to the disordered 8–8–20 perovskite derivative $La_8Ni_4Co_4O_{20}$.

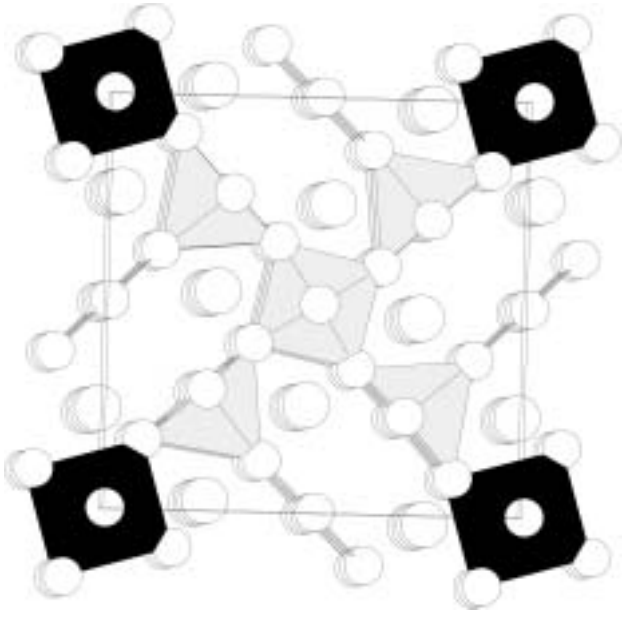

Fig. 1. The structure of $La_8Ni_4Co_4O_{20}$ in the $P4/mbm$ model.

1. Introduction

1.1. *8–8–20 perovskite derivatives*

The 8–8–20 perovskite derivatives are formed when topotactic reduction of fully oxygenated precursors gives rise to an ordered superstructure of oxygen vacancies, where omission of alternate rows of oxygen produces a combination of square planar (4-fold), square pyramidal (5-fold) and octahedral (6-fold) sites rather than the solely octahedral B sites of the parent compound (see Fig. 1). At least three different cations (including both A or B sites) must be present in order for the structure to be stable. These compounds have been extensively studied by powder neutron diffraction and XAFS methods [1–3], in order to unravel the complex local structure resulting from the lack of, partial, local, or complete ordering of their cation sites. XAFS was immediately able to identify those sites which were largely ordered, and those which were not, and indicated significant local distortions of the structure around cation sites in all the compounds studied, in comparison with the accepted structure. This structure was initially described from $La_{6.4}Sr_{1.6}Cu_8O_{20}$, as tetragonal, $P4/mbm$. Our conclusion, from having studied the systems $La_8Ni_4Co_4O_{20}$, $La_8Ni_{6.4}Mn_{1.6}O_{20}$, $La_{6.4}Ca_{1.6}Cu_6Ni_2O_{20}$ and $La_{6.4}Ca_{1.6}Cu_6CoO_{20}$ is that many of the distortions revealed by the XAFS/neutron PD refinement, and the weak additional reflections observed in some PD patterns, can be explained if a doubling of the c-axis is assumed, and an orthorhombic space group of $Pbnm$ (or $Pnma$ etc.) is used. This new cell is $2\sqrt{2} \times 2\sqrt{2} \times 2$ in terms of the basic perovskite cell. We believe this is the true space group for all the compounds we have studied, and it will therefore be used as the starting point of the analysis. However, it does not explain all the features of the XAFS spectra. Additional distortions, which are probably not ordered throughout the cell, are found in all the compounds. We note that the true stoichiometry of the cell is therefore 16–16–40.

1.2. $La_8Ni_4Co_4O_{20}$

The method described here was developed initially to resolve problems encountered in a previous analysis of compounds such as $La_8Ni_4Co_4O_{20}$ [1, 3]. Although a subsequent refinement in $Pnma$ was more successful than in the tetragonal space group used originally, a number of problems remain. The fit to the Co K-edge is actually rather good, due to a near perfect fit to bonded oxygen shells. There are significant discrepancies in the fit, however, for non-nearest neighbours. The Ni K-edge data has similar discrepancies, and in addition has a very poor fit to the first shell, for which the model produces a shell that is at too long a distance, and different in profile. The fit to the PND is also about 2% worse, in terms of the commonly used measure of fit (R_{wp}), than to the end-member or similar compounds. A number of procedures were attempted in order to improve the model, and accommodate local distortions in the lattice: The Ni/Co (5-fold) site, which is in a general position, was allowed to assume a different coordinate depending on its occupancy, nearest-neighbour dependency of the oxygen coordinate was

accommodated, by adding a neighbour dependent translation vector to the bridging oxygen coordinate, so Co−O−Co, Ni−O−Co and Ni−O−Ni can differ in terms of bond distances and angles, and the use of a dual *Pnma*/*P*1 space group, allowed the local structure seen by XAFS to be independent of bulk symmetry. None of these approaches were successful. In addition, the structure was analysed by refining the shell coordinates in order to fit the XAFS data. Although more successful in fitting the spectra, it was not possible to derive a useful model of the structure using this approach.

2. Method

2.1. *Reverse Monte-Carlo method*

The most obvious approach to solving such a structure is the Reverse Monte-Carlo (RMC) approach [4–10]. With this method, the starting model for crystalline materials is a supercell of the crystal lattice, presumed to have periodic boundary conditions. A fitting function χ^2 is calculated, utilising the sum of squares of residuals from the fits to experimental data, together with those for any restraints that are to be applied to the solution. Random changes are made to the coordinates of the model, which are accepted with probability $P(\Delta\chi^2) >= 0$ if $\Delta\chi^2$ is +ve or 1 if $\Delta\chi^2$ is −ve. The procedure is then repeated until convergence to a minimum has been achieved. A number of obstacles to using the method for cases such as $La_8Ni_4Co_4O_{20}$ exist however. These are the complexity of the crystal structure, and the fact that multiple scattering (MS), which dominates the non-nearest neighbour structure, must be included in order to derive information on metal-metal distributions and metal-oxygen-metal bond angles. This makes the calculation intrinsically more time consuming. As the neutron data that is available is not amenable to whole-profile fitting, Bragg peaks only are required. However, a small supercell behaves essentially like a *P*1 cell. It may give rise to all possible reflections, and all supercell reflections. These only disappear for very large system sizes (10 s of thousands of atoms). Smoothing of supercell reflections is possible, but is not an ideal solution. XAFS however, requires only an average over a few tens of each atom type to reproduce the data. The procedure has therefore been modified in a number of ways to allow the XAFS of systems involving randomly substituted sites to be analysed using the RMC method. In particular, when the powder pattern is calculated, the space group symmetry is applied to each atom, and the occupancy reduced by a factor equal to the multiplicity of the general position. This is equivalent to generating an extended cell, containing all symmetrically unique orientations of the supercell. Multiple scattering is included, at least approximately, in the XAFS calculations. Some changes have also been made to improve convergence for crystalline materials. The need for this can be illustrated using a combined fit to Cu metal. It is very easy to fit the first shell of Cu. It is simply necessary to add a random vector $\boldsymbol{V} = 2\sigma\boldsymbol{R}(\boldsymbol{r}_i, 0\text{–}1)$ where σ^2 is the mean square variation in first shell distance, $\boldsymbol{R}(\boldsymbol{r}_i, 0\text{–}1)$ a random vector between 0 and 1, of dimension N (number of atoms), which modifies each box coordinate $\boldsymbol{r}_i$. It is subsequently very hard to achieve further convergence for the outer shells, and for the powder diffraction profile, although an increase in the higher cumulants of the first shell is soon observed. The solution adopted here is to move atoms as clusters rather than individually. Normally a cluster is the bonded coordination sphere, or 13 atoms in Cu. This allows the expected gradual increase in the 2nd cumulant to develop, allowing a good fit to both XAFS and PD data. In general, convergence may be quite dependent on step size, so the step size may be varied, if necessary for each atom type individually. The refinement procedure for $La_8Ni_4Co_4O_{20}$ involved stages which moved all the atoms, the cluster, or individual atoms as required.

2.2. *Analysis of $La_8Ni_4Co_4O_{20}$*

Room temperature powder neutron diffraction data and the XAFS spectra above the La L_{III}, Ni K and Co K edges were refined using the MS RMC method, using the program P [11]. Details of sample preparation and data collection have been previously described [1, 3]. The starting configuration was a box of 27 unit cells, 1996 atoms in total, refined using a conventional XAFS/PD analysis. The B sites were randomly occupied by Co and Ni cations. A minimum cut-off distance of 1.7 Å was used as a constraint, with any step generating shorter distances being rejected. Three refinements were performed, using increasing weightings of a constraint which minimised departure from the original structure. Results are presented for the third, which appeared to show the greatest degree of convergence. The cluster size used for XAFS calculations was 5.5 Å. Multiple scattering was limited to paths involving only two different scattering atoms, in which the first was always oxygen. For M−O−M′−M paths, scattering angles were always obtuse at the oxygen atom, with angles greater than about 130° being included. For M−O−O−M paths, scattering angles were acute at each scattering atom. The final result, however, involved a complete MS calculation for the 5.5 Å cluster. Minimising the discrepancy between the two calculations is one of the most difficult aspects of the technique, and is the subject of ongoing development. The program is able to derive a great deal of information from the atomic coordinates, *via* the moments of different distributions. As the initial configuration is 'remembered', the cumulants of the atomic positions, modulo $\boldsymbol{r} = (a, b, c)$, can be displayed. The second cumulant is therefore equivalent to the anisotropic displacement factor for the atom. The cumulants of the individual paths may be classified by atom type, by crystallographic site, and in the latter case, sub-divided according to the character of the next-nearest neighbour. This may yield individual bond distances and mean-square variation in path length, in the very restricted case that an interatomic distance obeys a strict geometric rule, in which thermally averaged distances are strictly a function of their first few neighbour atom types. Evaluating these relationships remains a long term goal of this method. As we cannot yet confidently equate distances derived from the refinement with chemical bond distances, no attempt has been made to estimate errors in the distances.

3. Results

Refinement produced fits (see Fig. 2) which had none of the obvious problems of those derived from the starting values, with a good fit to both the Co and Ni K edges. The fit to the La L_{III} edge is less satisfactory, in part due to the exclusion of 3-scatterer MS paths during the course of the refinement, but also because the presence of two-electron channels causes perturbations in the background, reducing the quality of fit even for model compounds. For the powder diffraction data, R_{wp} (in %) is reduced by 1. Given the large number of distinct metal-metal distances, and the similarity of the scattering factors for Ni and Co, it would not be expected that a refinement, using minimal restraints, could yield a unique solution, where all distances and angles are chemically

realistic. Rather, these initial weakly constrained refinements were intended to demonstrate the feasibility of the method, and provide insights into the mechanism by which randomly substituted cations are incorporated into the structure. The results of the refinement are shown in Table I. The positions of the oxygen atoms originally in special positions x, 1/4, z in *Pnma*, remain so, with mean y values very close to 0.25. Similarly, Co atoms in positions 0, 0, 0 (6 fold), and 0, 0, 1/2 (4 fold), stay close to these positions. Ni atoms show larger off-site movements, and this appears to be a critical factor in explaining the structure. Both Co and Ni in the 5-fold sites show large movements, probably because the initial position was a compromise between XAFS and neutron diffraction data. The overall bond valence sums of 2.003 fo Ni^{2+}, 2.241 for Co^{2+} and 2.860 for La^{3+}, are within or close to acceptable values. For La, Co and some of the oxygen atoms the second cumulants of the positions are on average similar to the expected thermal contribution to disorder. For some Ni coordinates, and other oxygen coordinates, however, they are clearly larger. This is especially true of the O atoms (O11) which link the square pyramidal sites along the *b*-axis (i.e., the *c*-axis of the tetragonal model). This could be due to a genuinely random distribution, or the presence of two or three alternate neighbour-dependent sites. As it is not yet clear whether such detailed information can be trusted or how error bars can be obtained, no attempt has been made to pursue the analysis for the 5-fold sites, except to note that for Ni, axial elongation makes the site closer to square planar than for Co. For the bonds linking the square planar and octahedral sites along the *b*-axis most of the distances appear plausible, and reveal for example that Co−Co distances are longer than Ni−Ni distances, as well as the expected result that mean Ni−O distances are shorter than Co−O distances.

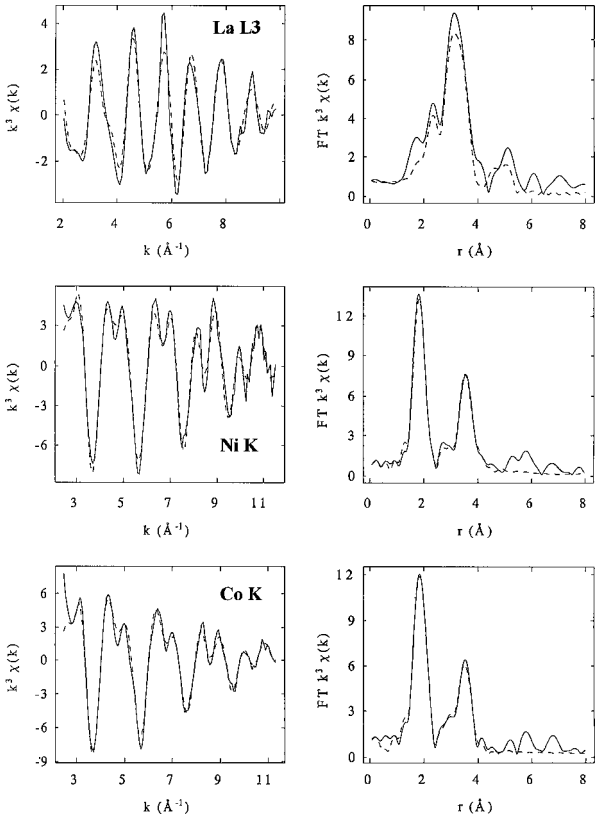

Fig. 2. Fit to the La L_{III}, Ni K and Co K edges of $La_8Ni_4Co_4O_{20}$ using the multiple scattering reverse Monte-Carlo method.

Table I. *Results of the multiple scattering reverse Monte-Carlo refinement of $La_8Ni_4Co_4O_{20}$. Coordinates in terms of the original cell, second cumulants, multiplicities (N), and coordinates of the starting model (in brackets).*

Atom	x	y	z	x^2	y^2	z^2	N
LA1	0.5172	0.2497	0.7340	0.0072	0.0038	0.0049	4.00
	(0.5176)	(0.2500)	(0.7320)				
LA2	0.7424	0.2498	0.4727	0.0073	0.0019	0.0039	4.00
	(0.7480)	(0.2500)	(0.4785)				
LA3	0.4667	0.2502	0.2599	0.0045	0.0023	0.0023	4.00
	(0.4664)	(0.2500)	(0.2643)				
LA4	0.2548	0.2503	0.5195	0.0054	0.0048	0.0082	4.00
	(0.2554)	(0.2500)	(0.5234)				
NI [4]	0.0023	0.0007	0.5020	0.0124	0.0034	0.0097	1.96
	(0.0000)	(0.0000)	(0.5000)				
NI [6]	0.0024	0.0004	0.0005	0.0065	0.0042	0.0026	2.04
	(0.0000)	(0.0000)	(0.0000)				
NI [5]	0.2773	0.5093	0.7759	0.0133	0.0088	0.0069	3.96
	(0.2776)	(0.5129)	(0.7749)				
O8	0.0194	0.2499	0.0093	0.0131	0.0016	0.0049	4.00
	(−0.0041)	(0.2500)	(−0.0044)				
O9	0.2641	0.2494	0.7796	0.0177	0.0129	0.0044	4.00
	(0.2664)	(0.2500)	(0.7841)				
O10	0.4824	0.2497	0.0183	0.0216	0.0008	0.0094	4.00
	(0.4882)	(0.2500)	(0.0235)				
O11	0.3176	0.2491	0.7734	0.0499	0.0183	0.0313	4.00
	(0.3171)	(0.2500)	(0.7738)				
O12	0.1612	0.0069	0.9071	0.0155	0.0228	0.0045	8.00
	(0.1489)	(0.0058)	(0.9090)				
O13	0.4005	0.5309	0.6566	0.0070	0.0090	0.0150	8.00
	(0.4048)	(0.5262)	(0.6484)				
O14	0.1290	0.4847	0.6200	0.0178	0.0087	0.0133	8.00
	(0.1312)	(0.4876)	(0.6155)				
CO [4]	0.0005	0.0006	0.5010	0.0062	0.0012	0.0077	2.04
	(0.0000)	(0.0000)	(0.5000)				
CO [6]	0.0007	0.0001	0.0001	0.0046	0.0017	0.0030	1.96
	(0.0000)	(0.0000)	(0.0000)				
CO [5]	0.2775	0.5087	0.7766	0.0095	0.0021	0.0079	4.04
	(0.2776)	(0.5129)	(0.7749)				

Table II. *Representative geometric information from the MS RMC refinement of $La_8Ni_4Co_4O_{20}$. Mean interatomic distances and angles for linkages between square planar sites, and for linkages between octahedral sites. Unless otherwise stated, figures are for the near collinear bonds in the direction of the b-axis.*

Ni[4]−O/Å	1.9451	Co[4]−O/Å	1.9554	(mean of 4 bonded distances per atom)			
Ni[4]−Ni[4]/Å	3.8855	Ni[4]−Co[4]/Å	3.8911	Co[4]−Co[4]/Å	3.9306		
Ni[4]−O−Ni[4]/°	171	Ni[4]−O−Co[4]/°	171	Co[4]−O−Co[4]/°	172		
(Ni[4])−O−Ni[4]/Å	1.9695	(Co[4])−O−Ni[4]/Å	1.9773	(Ni[4])−O−Co[4]/Å	1.9662	(Co[4])−O−Co[4]/Å	1.9852
Ni[6]−O/Å	2.0084	Co[6]−O/Å	2.0077	(mean of 6 bonded distances per atom)			
Ni[6]−Ni[6]/Å	3.8674	Ni[6]−Co[6]/Å	3.8916	Co[6]−Co[6]/Å	3.9003		
Ni[6]−O−Ni[6]/°	173	Ni[6]−O−Co[6]/°	173	Co[6]−O−Co[6]/°	173		
(Ni[6])−O−Ni[6]/Å	1.9695	(Co[6])−O−Ni[6]/Å	1.9598	(Ni[6])−O−Co[6]/Å	1.9675	(Co[6])−O−Co[6]/Å	1.9683

Selected values are given in Table II. Bond angles appear to be highly conserved throughout the structure.

4. Conclusions

$La_8Ni_4Co_4O_{20}$, synthesised directly from its fully oxygenated precursor, forms an ordered Pmna structure in which the three types of B site are randomly occupied by Ni or Co. (Occupancies $50+/-5\%$ of each atom). Although the initial fit to the XAFS and powder data was poor, a Multiple Scattering RMC approach has shown the feasibility of this model. A number of new features, which improve the RMC method as applied to complex crystalline materials, have been described. For the 4- and 6-fold sites, Co occupies special positions in the lattice. Ni however, occupies off centre positions in at least one of these sites.

Oxygen in special positions in *Pnma* remains in special positions during the RMC refinement, but other oxygen coordinates vary according to the nature of the neighbouring atoms. A more detailed description of this process will require the use of additional restraints, in order to test simple physical models. An example would be that the M-O Debye-Waller terms, for a specific M′-O-M-O-M″ linkage, would be restrained using values derived from end-member compounds.

Acknowledgements

We acknowledge financial support from the EPSRC, UK and the Research Council of Norway.

References

1. Stange, M., PhD Thesis, "Local and Average Structure in Selected Perovskite-like Oxides", (University of Oslo, 2001).
2. Binsted, N., Stange, M., Owens, C., Fjellvåg, H. and Weller, M. T., J. Synch. Rad. **8**, 305 (2001).
3. Binsted, N., Stange, M., Fjellvåg, H. and Weller, M. T., "Physics in Local Lattice Distortions", (American Institute for Physics, 2001), 470.
4. McGreevy, R. L., J. Phys. Condens. Matter **13**, R877 (2001).
5. Mellergård, A., McGreevy, R. L. and Eriksson, S. G., J. Phys. Condens. Matter **12**, 4975 (2000).
6. Wicks, J. D. and McGreevy, R. L., J. Non-Cryst. Solids **192**, 23 (1995).
7. McGreevy, R. L., Nucl. Instr. Methods Phys. Res. A. **354**, 1 (1995).
8. Zetterström, P. and McGreevy, R. L., Physica B. **276**, 187 (2000).
9. Swenson, J., McGreevy, R. L., Börjesson, L. and Wicks, J. D., Solid State Ionics, **105**, 55 (1998).
10. Winterer, M., Delaplane, R. and McGreevy, R. L., J. Appl. Cryst. **35**, 434 (2002).
11. Binsted, N., Pack, M. J., Weller, M. T. and Evans, J., J. Am. Chem. Soc. **118**, 10200 (1996).

Physica Scripta. Vol. T115, 285–287, 2005

Local Structure Analyses of Contamination Metals on the Silicon Wafer After LSI Processes Using XAFS Technique

H. Hashimoto[1,*], J. Tsuji[1], H. Yokoi[2], S. Murakami[2] and Y. Hanada[2]

[1]Toray Research Center, Inc., Shiga, Japan
[2]Tokyo Electron AT Ltd., Yamanashi, Japan

Received June 26, 2003; revised October 24, 2003; accepted November 4, 2003

Abstract

It is well known that metallic contamination on the silicon wafer, suffered during VLSI fabrication processes such as thin film depositions and etching, brings about lowering device performance. Determination of the chemical or structural properties of contamination metals is necessary in order to specify and remove the cause of contamination. However, the measurements are extremely difficult, because the contamination metals have very low concentrations. Grazing incidence XAFS by the X-ray fluorescence yield method is useful for the purpose. We applied the technique for the investigation of iron and copper contaminations on silicon wafers after fabrication processes.

The silicon wafers contaminated intentionally in the process chamber were used as samples. The contamination level of iron and copper was of the order of 10^{11}–10^{13} atoms/cm^2. The measurements were performed at the beamline 12C of the Photon Factory in KEK. The incident angles from the silicon surfaces were about 1 degree. A Lytle type ionization chamber was used in order to detect X-ray fluorescence photons in large solid angles. Good quality spectra were obtained. It was found from the analysis of the spectra that iron is mainly binding to fluorine and copper is binding to chlorine. The results were very useful for process improvements.

1. Introduction

It is well known that metallic contamination on a silicon wafer, suffered during VLSI fabrication processes such as thin film depositions and etching, brings about lowering device performance. Conventionally, using ICP-MS or X-ray fluorescence techniques, the quantitative analyses of trace elements for silicon wafers treated through some semiconductor process are conducted, and the obtained data are used for improvements of fabrication instruments and process sequences.

However, with growing and diversifying the ULSI fabrication process, a great number of experiments, such as quantitative analyses after process treatments, become required for reducing metallic contaminations. If the determination of the chemical bonding of each contamination metal is possible, we can identify process steps or conditions for occurring metallic impurities, and improve components and materials of the fabrication system and consequently reduce metallic contaminations. Because of low concentrations of metals on the silicon wafer, XAFS is the only technique for chemical state or structural analysis.

We have determined the local structures around residual iron and copper elements treated through the titanium nitride film deposition process with XAFS analysis using the fluorescence yield method.

2. Experimental

2.1. *Sample preparation*

The silicon wafers were set into the TiN film deposition chamber after cleaning. The samples were treated according to the conditions shown in Table I. Three kinds of samples, suffering different contaminations, were prepared. The contamination levels of iron and copper of the prepared samples were found to be of the order of 1×10^{11}–10^{13} atoms/cm^2 using the total reflection X-ray fluorescence method.

Table I. *Condition of sample preparation.*

Wafer temperature	580 degree	
Deposition stepping time	30 s	
Pressure in process	40 Pa	
Gas flow condition*	$TiCl_4$	30 sccm
	NH_3	400 sccm
	N_2	350 sccm
Dry cleaning condition	ClF_3	200 sccm
	N_2	1300 sccm

*For preparation of XAFS samples $TiCl_4$ gas was NOT flowed.

2.2. *Measurements*

X-ray Absorption spectra for Fe-K and Cu-K absorption edge were obtained at the beamline 12C of the Photon Factory [1]. Fluorescence yield mode was used because of the very low concentration, and the X-ray beam was incident on the sample at grazing angle in order to cut down diffraction lines from the silicon substrate. Lytle type detector was used. One of the obtained spectra is shown in Fig. 1. It is found that the quality of these spectra is very good even if the contamination level is of the order of 1×10^{11} atoms/cm^2.

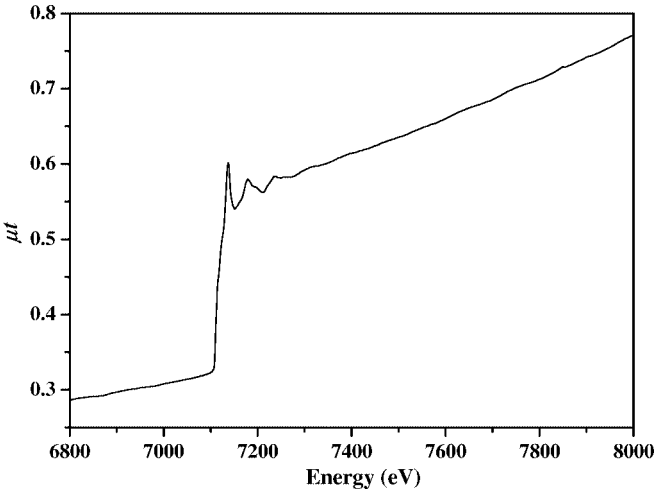

Fig. 1. Fe-K EXAFS spectrum of a sample.

*e-mail: Hideki_Hashimoto@trc.toray.co.jp

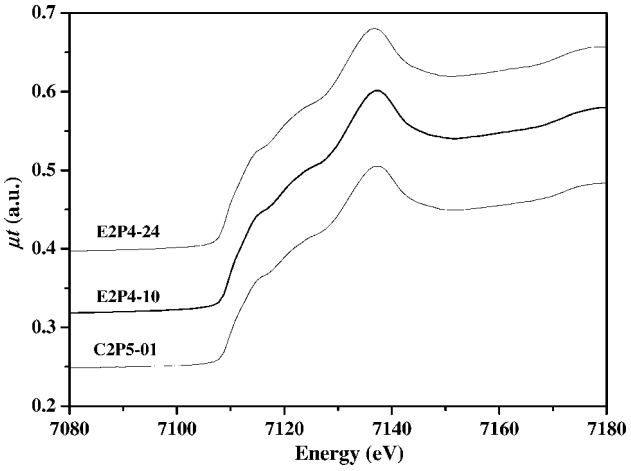

Fig. 2. Fe-K XANES spectra of various samples with different contamination levels.

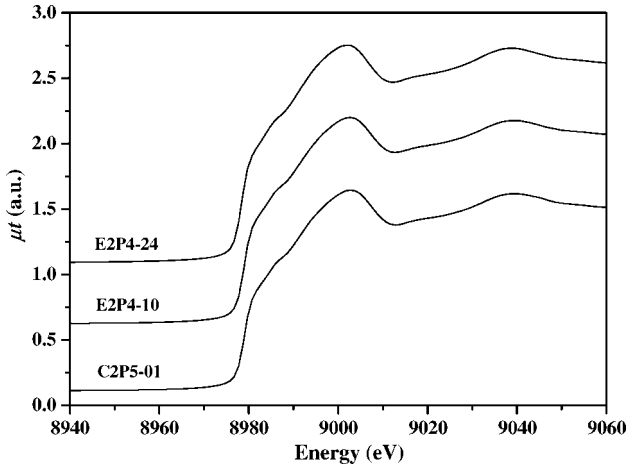

Fig. 3. Cu-K XANES spectra of various samples with different contamination levels.

3. Results and discussion

3.1. *Experimental results*

Fe-K XANES spectra and Cu-K XANES spectra of the samples with various contamination levels are shown in Fig. 2 and Fig. 3. For all contamination levels, no differences in the Fe or Cu-K XANES spectra are found.

The chemical structures of Fe contaminations turned out to be neither metal nor oxide from the features of the XANES spectra. In the case of Cu contaminations, the same results were derived from XANES.

3.2. *Curve fitting results and discussion*

Figure 4 shows the results of Fourier transform for Fe, and Table II the structure parameters and each error range obtained by curve

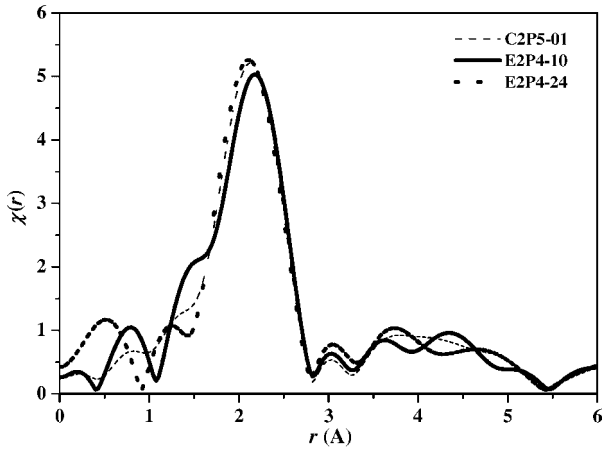

Fig. 4. Results of Fourier transform and curve fitting for Fe.

fitting. Fourier transform was carried out for the k^3-weighted spectrum in the range of $k = 2$ to $9\,\mathrm{A}^{-1}$. Table II indicates the coordination number of Fe-Cl of each sample as 5.4 to 5.9, and the distance between Fe and Cl is about 2.48 A. In contrast the coordination number of Fe-F is only 0.3. The same results are derived from every contamination level. In consequence, it was found that almost all Fe atoms on the silicon wafer bond with Cl atoms regardless of Fe concentration. It is inferred that the Cl atoms are originated in ClF_3 dry etching gas.

The results of Fourier transform for Cu are shown in Fig. 5, and the structure parameters and each error range obtained by curve fitting are shown in Table III. In Table III, the coordination number of Cu-Cl is about 0.6 while that of Cu-F is about 5.4, and the distance between Cu and F is about 2.60 A. These results do not change with the contamination level as well as in the case of Fe. It turns out that Cu atoms combine with F atoms in contrast to Fe contaminations.

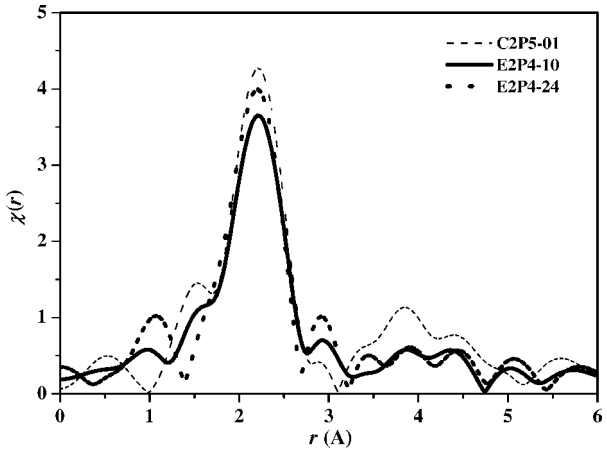

Fig. 5. Results of Fourier transform and curve fitting for Cu.

Table II. *Structure parameters of Fe obtained as the result of the curve fitting.*

	C2P5-01		E2P4-10		E2P4-24	
	n	*r* (Å)	*n*	*r* (Å)	*n*	*r* (Å)
Fe-Cl	5.7 ± 0.06	2.48 ± 0.01	5.4 ± 0.1	2.48 ± 0.02	5.9 ± 0.1	2.46 ± 0.02
Fe-F	0.3 ± 0.1	1.95 ± 0.01	0.3 ± 0.1	1.94 ± 0.02	0.2 ± 0.1	1.98 ± 0.01

*Each error range is obtained from curve fitting.

Table III. *Structure parameters of Fe obtained as a result of the curve fitting.*

	C2P5-01		E2P4-10		E2P4-24	
	n	*r* (Å)	*n*	*r* (Å)	*n*	*r* (Å)
Cu-Cl	0.5 ± 0.1	2.55 ± 0.09	0.6 ± 0.3	2.54 ± 0.06	0.7 ± 0.3	2.54 ± 0.05
Cu-F	5.5 ± 0.2	2.60 ± 0.03	5.4 ± 0.15	2.60 ± 0.07	5.3 ± 0.2	2.60 ± 0.07

*Each error range is obtained from curve fitting.

The contamination metals on the silicon wafer proved to form compounds bonded with atoms dissolved from ClF_3 dry etching gas. ClF_3 dissociate into Cl and F atoms or ions, and Cl atoms bond with Fe atoms. On the other hand F atoms combine with Cu atoms. In spite of richness of ClF_3 gas in the chamber, Cl and F atoms bond selectively. The reasons of the selectivity were not made clear in the present work.

4. Conclusion

In order to investigate the chemical bonding state of the metallic contamination on the silicon wafer, Fe and Cu-K EXAFS spectra were measured. The EXAFS spectra were clearly obtained even though the contamination level of the copper or iron was of the order of 1×10^{11} atoms/cm^2. No differences in the points in each spectrum for different contamination levels were detected. From results of the Fourier transform and curve fitting, it was proved that Fe-Cl and Cu-F are the main chemical states in the contamination. However, the reason for that selectivity of bonding was not identified.

Reference

1. Nomura, M. and Koyama, A., KEK Report **95-15**, 21 (1996).

Physica Scripta. Vol. T115, 288–290, 2005

Evidence by XAS of Tin Oxide Coating Layered Double Hydroxides

Mourad Intissar[a], Valérie Briois[b], Jean-Pierre Besse[a] and Fabrice Leroux[a]

[a]Laboratoire des Matériaux Inorganiques, UMR 6002-CNRS, Université Blaise Pascal, 24 av. des Landais, 63177 Aubiére cedex, France
[b]LURE, Centre Universitaire Paris Sud, Bât 209D, BP 34, 91898 Orsay cedex, France

Received June 26, 2003; revised October 31, 2003; accepted February 6, 2004

Abstract

XAS provides clear evidences that the tetravalent cations are not incorporated within Layered Double Hydroxide (LDH) sheets. The cations are segregated, presenting a local order close to that of SnO_2 rutile. However, the nature of the LDH influences slightly the local order probably due to some surface effect microtexture. Variation of the cell parameters for the LDH materials are explained by a substitution of Al cations by divalent cations M(II).

1. Introduction

The Layered Double Hydroxide (LDH) structure is referred to as the natural hydrotalcite, and described with the ideal formula, $[M^{II}_{x}M_{1-x}{}^{III}(OH)_2]_{intra}[A^{m-}_{x/m}\cdot nH_2O]_{inter}$, where M^{II} and M^{III} are metal cations, A the anions and *intra* and *inter* denote the intralayer domain and the interlayer space, respectively. The structure consists of brucite-like layers constituted of edge-sharing $M(OH)_6$ octahedra [1]. Partial M^{II} to M^{III} substitution induces a positive charge for the layers, balanced with the presence of the interlayered anions.

Some authors have reported the possibility to incorporate tetravalent cations into LDH-type layers, M(IV) = Zr and Sn over a large composition range [2], and claimed that up to 30% of Al could be isomorphously substituted by Sn(IV) to form a new MgAlSn ternary LDH. However, no detailed structural local picture has been supplied to ascertain the substitution process so far. In the present study, the question whether Sn^{4+} is incorporated into two LDHs, MgAlSn and CoAlSn, is investigated by XAS spectroscopy at Co and Sn K-edge.

2. Experimental

2.1. *Preparation of the samples*

$SnCl_4.5H_2O$ (Acros), $Mg(NO_3)_2.6H_2O$ (Acros, 99%), $Co(NO_3)_2.6H_2O$ (Aldrich, 99%), $Al(NO_3)_3.9H_2O$ (Acros, 99%), NaOH (Acros, 97%), $Na_2CO_3.10H_2O$ (Acros, 99%) were used as received.

All the hydrotalcite-like materials were prepared by the co-precipitation method according to Miyata [3]. Experimentally, 250 ml solution of the salts $M^{II}(3\cdot10^{-2}\,M)$ Al $(4(0.25-y)\cdot10^{-2}\,M)$ and M^{IV} $(4y\cdot10^{-2}\,M)$ of desired cation ratio was added dropwise to a solution of mixed NaOH (2 M) and Na_2CO_3 (0.3 M), as described by Velu *et al.* [2]. The pH is kept constant during the addition, pH of 10 ± 0.1 for the system $Mg_{0.75}Al_{0.25-y}Sn_y$ and 9 ± 0.1 for $Co_{0.75}Al_{0.25-y}Sn_y$. The slurry is aged overnight, centrifuged, and then washed several times with distilled water and finally dried at room temperature.

2.2. *Techniques of Characterization*

Powder X-ray diffraction profiles (PXRD) were obtained with a Siemens D500 X-ray diffractometer with a diffracted beam monochromator Cu K_α source.

2.3. *X-ray absorption spectroscopy*

2.3.1. *Co and Sn K-edges.* XAS studies were performed at LURE (Orsay, France) using X-ray synchrotron radiation emitted by the DCI storage ring at the D44 beam line. Data were collected at 77 K in transmission mode at Co and Sn K-edges (7708.9 and 29200.0 eV, respectively) using a double-crystal monochromator Si (111) and Ge (400), respectively. The energy was scanned in 2 (or 4) eV-steps from 100 eV below to 900 eV above each K-edge, and three spectra were recorded for each sample. An accumulation time of 2 s was used per point.

Extraction and analysis of EXAFS data was performed following standard procedures [4]. The $\chi(k)$ signal was fitted by using the classical single scattering approximation: $\chi(k) = S_0{}^2\Sigma A_i(k)\sin[2k\cdot r_i+\phi_i(k)]$, with $A_i(k)$ amplitude equal to $(N_i/k\cdot r_i{}^2)F_i(k)\exp(-2k^2\sigma_i{}^2)\exp(-2r_i/\Gamma)$, where r_i is the interatomic distance, ϕ_i the total phase shift of the ith shell, N_i the effective coordination number, σ_i the Debye-Waller factor, $F_i(k)$ the backscattering amplitude and Γ the mean-free path. To estimate the relative part of the cations contributing to the metal-metal correlation, the number of backscattering atoms was free to move during the refinement. This guarantees all possible cation ratios for the second shell. Phase and amplitude were taken from Mac Kale files and the validity for the refinements was tested against different reference compounds SnO_2, Co_2SnO_4, Mg_2SnO_4, $CoAl_2O_4$, $Co(OH)_2$. All results were similar using phase and amplitude extracted from FEFF 8 for MAC.

3. Results and discussion

Two hypotheses are possible: the cations Sn^{IV} are incorporated into the LDH sheets or they are segregated and form a coating. In the first case, the LDH composition is a function of the cations Sn^{IV} content, y in $M^{II}{}_{0.75}Al_{0.25-y}Sn^{IV}{}_y(OH)_2(CO_3)_{(y+0.25)/2}\cdot nH_2O$, in the second, it involves merely a change in the cation ratio M^{II}-Al^{III}, and the composition is a function of x, Al^{III} content and the formula becomes $M^{II}{}_{1-x}Al_x(OH)_2(CO_3)_{x/2}\cdot nH_2O$.

The ratio between cations are close to the expected values, indicating that the reaction was complete. The X-ray patterns for the two LDH systems are displayed in Figure 1. Diffraction peaks are typical of the layered double hydroxide structure, and the reflections were indexed in a hexagonal lattice with a R-3m rhombohedral symmetry, commonly used for the description of the LDH structure. For all the studied systems, the apparent incorporation of tetravalent cations induces a decrease in crystallinity, as the diffraction lines become wider, (110) and (113) are lumped together.

Concerning the local order, we surmise that cations Sn(IV) located inside LDH sheets must fulfil at least two conditions:

- no short Sn-Sn correlation. This would imply the presence of a segregation between LDH and Sn-based entities.
- Sn-M(II) correlation at a distance of ***a***, as expected for LDH.

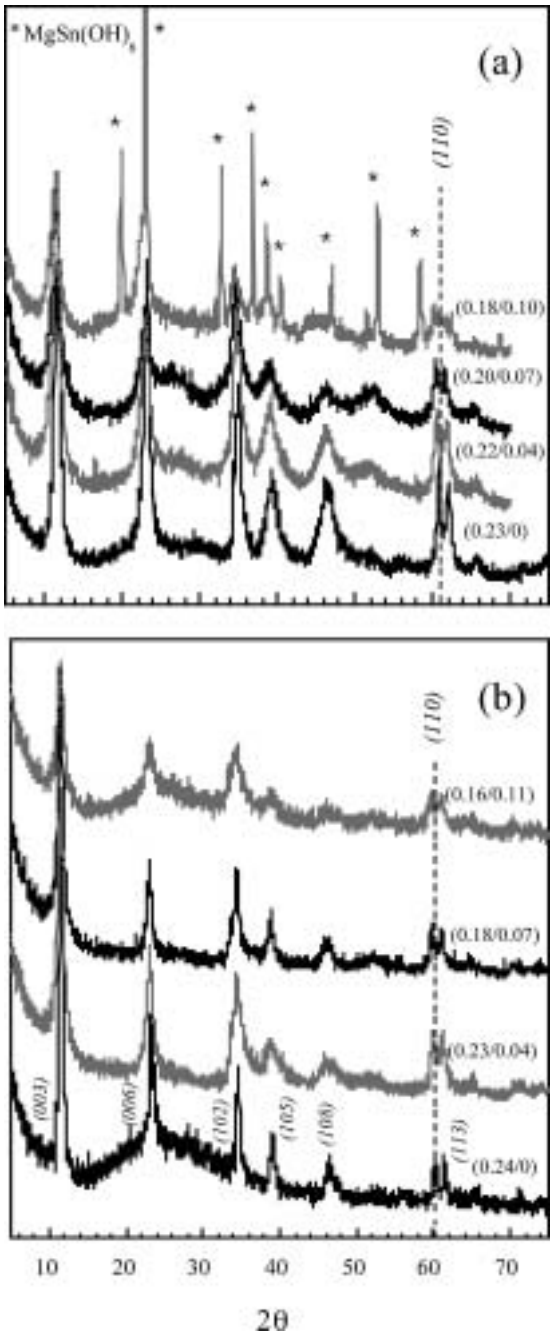

Fig. 1. X-ray patterns of the synthesized LDH materials of cation composition a) MgAlSn, and b) CoAlSn. Given the two hypotheses for the substitution, M^{II}-M^{III} ($M^{II}{}_{1-x}Al_x$) or M^{III}–M^{IV} ($Al_{1-y}M^{IV}{}_y$), the values of (x, y) are reported.

The features of the FT moduli at Co K-edge are characteristic of a LDH phase (Figure 2), namely the peak P1 represents the contribution Co-O, the contributions at longer distances arisen from multiple scattering effects and are attributed to metallic neighbors, P2 at a distance of $\boldsymbol{a}$, P3 of $\boldsymbol{a}\sqrt{3}$, and P4 of $2\boldsymbol{a}$. The latter is largely enhanced by the so- called focusing effect due to three atoms lying linearly to each other [5]. The observation of P4 implies the presence of flat inorganic sheets [6], inversely their absence would have been explained by the presence of corrugated layers. Rather small offsets in the linearity are enough to detune and lose the P4 amplification. The result of the refinements is displayed in Table I.

At the Sn K-edge, the structural local picture is different and the two contributions P3 and P4 are not observed (Figure 3).

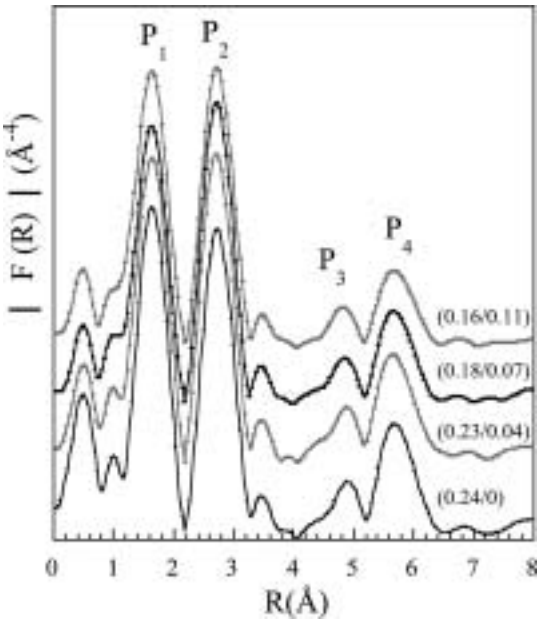

Fig. 2. Moduli of the Fourier transform for CoAlSn LDH system at Co K-edge. The distances are not corrected for phase shifts.

Table I. *XAS fit results.*

Compound	Correlation	N	R (Å)	σ (10^{-2} Å)	ρ^a (%)
SnO_2^b	Sn-O	6	2.05	6.4	
	Sn-Sn	2	3.18	7.3	
	Sn-Sn	8	3.71	5.6	9
		System MgAlSn			
(0.22/0.04)[c]	Sn-O	6.0	2.07	5.5	3.5
	Sn-Sn	2.0	3.18	8.8	
	Sn-Sn	2.5	3.74	15	
(0.20/0.075)	Sn-O	5.8	2.07	5.5	
	Sn-Sn	2.0	3.18	8.6	
	Sn-Sn	3.0	3.74	14.3	5.5
		System CoAlSn			
(0.24/0.0)	Co-O	6.0	2.06	6.4	
	Co-Co	4.3	3.10	7.5	
	Co-Al	3.0	3.03	8.6	4
(0.23/0.037)	Co-O	6.0	2.06	6.4	
	Co-Co	4.3	3.11	7.5	
	Co-Al	3.0	3.03	8.6	2
(0.18/0.072)	Co-O	5.9	2.06	7.8	
	Co-Co	4.5	3.11	8.1	
	Co-Al	2.4	3.04	9.1	1.5
(0.23/0.037)	Sn-O	6.2	2.07	6.0	
	Sn-Sn	1.0	3.20	9.1	
	Sn-Sn	2.8	3.73	7.8	9
(0.18/0.072)	Sn-O	6.5	2.07	6.3	
	Sn-Sn	1.0	3.20	8.0	
	Sn-Sn	2.35	3.73	7.5	9

[a] The residual ρ factor is defined as $\rho = [\Sigma(k^3\chi_{exp}(k) - k^3\chi_{theo}(k))^2 / \Sigma(k^3\chi_{exp}(k))^2]^{1/2}$. The commonly accepted fitting accuracy is about 0.02 Å for the distance and 15 to 20% for the number of neighbors.

[b] From structural data. SnO_2 crystallizes in space group P42/m n m (136) with tetragonal symmetry, lattice parameters $\boldsymbol{a} = 4.736$, $\boldsymbol{c} = 3.185$ Å. Distance in SnO_2: Sn-O = 2.045 (2), 2.058 (4) Å, and Sn-Sn = 3.185 (2) and 3.708 (8) Å.

[c] Given the two hypotheses for the substitution, M^{II}–M^{III} ($M^{II}{}_{1-x}Al_x$) or M^{III}–M^{IV} ($Al_{1-y}M^{IV}_y$), the values of (x, y) are reported.

Consequently, it suggests that there is no Sn-surrounding atom lying linearly to each other, and this whatever the values of y. For P2, a double structure is observed with two distinct Sn-Sn refined distances (Table I). The contributions look like those encountered

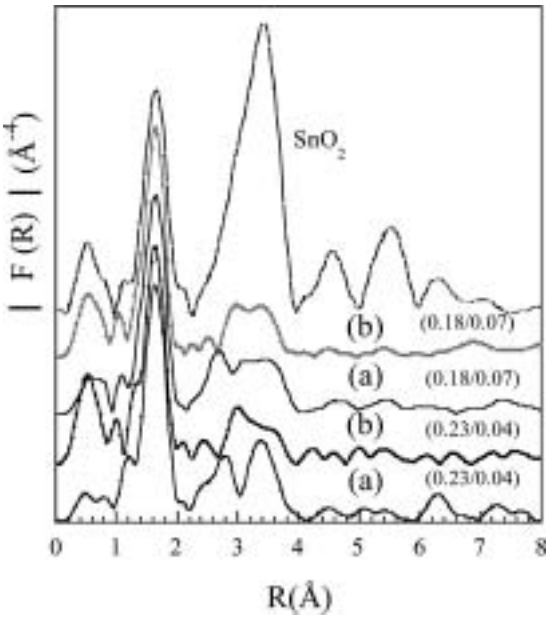

Fig. 3. Moduli of the Fourier transform at Sn K edge for (a) CoAlSn, and (b) MgAlSn LDH system. The distances are not corrected for phase shifts.

for hydrogels or xerogels of SnO_2 rutile-type samples [7]. This added to the fact that there is no Sn-Co correlation at a distance of ***a*** evidences strongly that Sn atoms are not located into LDH sheets, thus dismissing the hypothesis of Al substitution by Sn cations.

Indeed, the EXAFS fit results provide unambiguous evidence that Sn(IV) substitution does not occur. The local structures around Sn resemble the one present in tin-hydrogels [7], with Sn-Sn correlation, which cannot be explained by the LDH structure (Table I). The different acido-basic properties and reducibility of the mixed oxides formed upon calcination were recently studied [8].

Using the same method as for LDH, an amorphous precipitate "SnO_2" is obtained in absence of divalent and trivalent cation

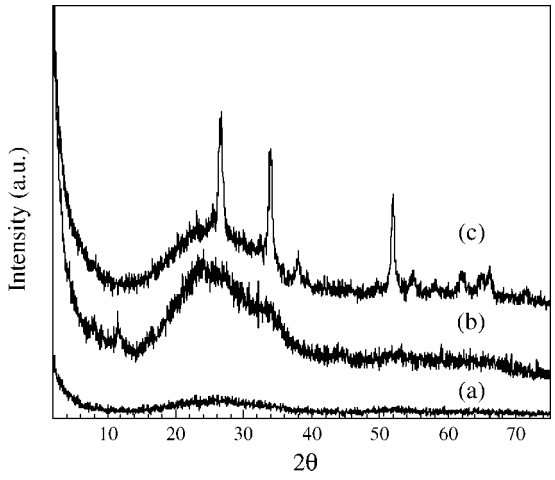

Fig. 4. XRD of SnO_2-type sample at (a) 25, (b) 800 and (c) 1000 °C.

source. It crystallizes into cassiterite-type (PDF file-41-1445) at 1000 °C (Fig. 4).

All these results were supported by additional information supplied by Mg K-edge study and ^{119}Sn Mössbauer.

References

1. De Roy, A., Forano, C., El Malki, K. and Besse, J.-P., "Synthesis of Microporous Materials", (Occelli., Robson, H., Eds), (Van Nostrand, Reinhold, **2**, 108, 1992).
2. Velu, S., *et al*., Chem. Mater. **11**, 2163 (1999); Velu, S., *et al*., Chem. Mater. **12**, 719 (2000).
3. Miyata, S., Clays Clay Miner. **28**, 50 (1980).
4. Michalowicz, A., Round Midnight, EXAFS Signal Treatment and Refinement Programs, LURE, Orsay, France. Programs available on LURE Web site: http://www.LURE.fr
5. Alberding, N. and Crozier, E. D., Phys. Rev. B **27**, 3374 (1983).
6. Roussel, H., *et al*., J. Phys. Chem. B **104**, 5915 (2000).
7. Briois, V., Santilli, C. V., Pulcinelli, S. H. and Brito, G. E. S., J. Non-Cryst. Solids **191**, 17 (1995).
8. Tichit, D., Das, N., Coq, B. and Durand, R., Chem. Mater. **14**, 1530 (2002).

Physica Scripta. Vol. T115, 291–293, 2005

Densification of Mn-Doped Tin Oxide Films by Conventional Heating and Microwave Heating Treatment

A. P. Rizzato[1,2,3], C. V. Santilli[1], S. H. Pulcinelli[1], D. Stuerga[2], D. Chaumont[2] and V. Briois[3]

[1]Instituto de Química/UNESP, C. P. 355 CEP 14800-900 Araraquara-SP, Brazil
[2]LRRS, Université de Bourgogne, BP 138, 21004 Dijon Cedex, France
[3]LURE, Centre Universitaire Paris-Sud, Bât 209D, BP 34, 91898 Orsay Cedex, France

Received June 26, 2003; revised November 3, 2003; accepted February 6, 2004

Abstract

Mn(II) doped SnO_2 thin films used for shielding fluoride glasses against corrosion were investigated by X-ray absorption spectroscopy (EXAFS and XANES) at the Sn and Mn K-edges. The effect of firing treatment on the densification of the films was studied. It has been evidenced a partial change of Mn valence from 2.3 to 2.6 upon heating which is attributed to a change of ratios of two Mn sites: grafted divalent Mn ions at the surface of SnO_2 nanocrystallites and trivalent Mn ions embedded into a substitutional solid solution with Sn.

1. Introduction

Tin oxide films present numerous applications like gas sensors [1, 2], basic components in optoelectronic devices [2] or nano and ultrafiltration membranes [3]. Moreover, SnO_2 thin films prepared by sol-gel dip coating have recently been used for shielding fluoride glasses against corrosion [4]. Nevertheless, the high porosity (≈40%) of the films so-prepared limits its use as barriers against corrosion for a long period of time ($t > 50$ h). New preparative routes involving Mn(II) doping used as densifying agent [5] and Tiron® capping molecules recently reported as crystallite growth controller [6] are under study in this paper. The sintering process of SnO_2 coatings must be achieved at low temperatures due to the melting temperature of fluoride glasses (around 350 °C). Then it was achieved either by conventional heating between 120 and 530 °C or microwave-assisted treatment [7]. The poor crystallinity of the films obtained below 530 °C, as well as the low doping concentration of manganese (1 mol %) prevents the use of X-ray diffraction (XRD) for the structural analysis. Indeed X-ray Absorption Spectroscopy appears as a powerful tool to obtain structural information on the films allowing us to rationalize the effect of the firing treatment.

2. Experimental

2.1. *Film deposition and microwave treatment*

A transparent and stable colloidal suspension was prepared from the hydrolysis of $SnCl_4.5H_2O$ in presence of 1% mol $MnCl_2.4H_2O$ and 10% mol of Tiron®using the procedures previously described [4, 6]. Doped SnO_2:Mn films deposited onto cleaned Corning 7059 glass slides were prepared from this colloidal suspension by dip-coating method. The samples were either heated for 30 min at 120, 450 and 530 °C, or heated under high microwave power [7]. For microwave treatment (250 W for 45 s), the heat conduction was improved by locating the sample between two alumina susceptors. The temperature of the sample during the microwave irradiation was not measured, but it was estimated to be near the softening temperature of glass slides (550 °C). The melting of the glass slides was observed for longer time irradiation (55 s).

2.2. *XAS measurements and data analysis*

XAS measurements were carried out at LURE (Orsay, France) on the D44 station installed on the DCI storage ring (1.85 GeV and 300 mA). Sn K edge EXAFS spectra (29200 eV) were recorded in transmission mode at room temperature using a Ge(400) double crystal monochromator and ionisation chambers filled with krypton. Due to the thickness (≈0.5 μm) of the films, several slides were stacked to obtain a typical edge jump of 0.1. The EXAFS spectrum was recorded over 1200 eV with 4 eV energy step. Mn K edge XANES and EXAFS spectra were recorded in fluorescence mode using a solid-state 7-elements detector. XANES (resp. EXAFS) data were measured by using a Si(111) (resp. Ge(111)) double crystal monochromator detuned by 40% to suppress the harmonics. XANES spectra were recorded over 120 eV with 0.3 eV energy step whereas EXAFS data were obtained over 550 eV with 2 eV energy step. At both edges, the data acquisition time was typically around 5 s and several spectra (between 8 to 20) were added for each sample to improve the signal to noise ratio. For energy calibration of XANES data a metallic Mn foil was measured between each sample.

Standard methods were used to obtain normalized EXAFS $\chi(k)$ spectra as those already described for Sn K edge data [6]. The program ROUND MIDNIGHT [8] was used to fit the weighted $k^n\chi(k)$ spectra, with input from crystallographically known reference samples used to extract experimental phase and amplitude functions or to validate theoretical FeFF6 [9] phase and amplitude functions. For the XANES data analysis, the pre-edge absorption background was subtracted from the rough data using a linear function and the spectra were normalized far from the edge (≈6630 eV). The energy threshold of the Mn metal foil was determined from the first inflection point in the spectrum and set to the tabulated absorption edge energy equal to 6539 eV.

3. Results

Fast Fourier transforms (FFT) of the Sn-K edge EXAFS spectra for the films are shown in Figure 1. FFTs of films isothermally heated at 120 and 450 °C and of the film treated by microwave present a shape similar to the one of the crystalline SnO_2 reference but with a clear reduction of intensity for the contribution labelled B. This evidences the presence of nanocrystallites with the incipient cassiterite structure [1, 6]. The structural parameters determined by a least-square fitting procedure (Figure 1) are in agreement with this conclusion. The local order around Sn is characterized by a first coordination shell of 6.2 ± 0.3 oxygen atoms at 2.07 ± 0.01 Å and tin second neighbours located at 3.18 ± 0.02 and at 3.71 ± 0.02 Å as in the SnO_2 structure. From the mean number of tin second neighbours and according to the

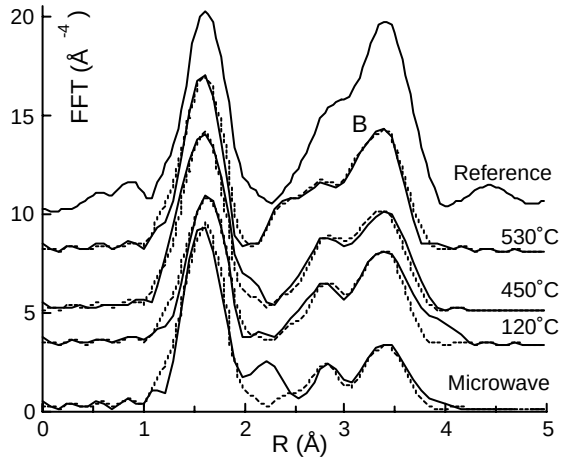

Fig. 1. Fast Fourier transforms (solid line) of the Sn-K edge $k^3\chi(k)$ EXAFS spectra of a crystalline SnO_2 reference and of the different SnO_2 : Mn films, using a Kaiser apodization window from 3.2 to 14.3 Å^{-1} with $\tau = 3$ and best fits (dashed line). The Sn-Sn coordination numbers at 3.18 and 3.71 Å are 1.6 and 5.0 for the film treated by microwave, 1.8 and 5.8 for films heated at 120 °C, 2.0 and 5.8 for those heated at 450 °C and 2.0 and 7.1 for those heated at 530 °C.

theoretical correlation published elsewhere [10] the crystallite size is determined around 4 ± 1.5 nm for the films heated below 530 °C and around 2.5 ± 0.5 nm for the film treated under microwave. For the film heated at 530 °C, the determination of the crystallite size from the EXAFS results is not yet enough accurate. The crystallite size equal to 7 ± 1 nm is determined from XRD, using the Sherrer formula. Note that the FFT of the film heated at 530 °C displays an additional pronounced shoulder on the left side of the B contribution. This shoulder has been successfully simulated by adding in the fitting procedure a Sn-Sn contribution at 2.86 Å like the one encountered for α-Sn metal.

FFTs corresponding to the Mn K-edge EXAFS spectra of the films are shown in Figure 2. The local atomic structure for Mn in the films heated at 450 and 530 °C is clearly different from that for the films treated under microwave or at 120 °C. In particular, a shift at shorter distances of the maximum of the first peak correlated to the Mn-O contribution is evidenced upon heating. The structural parameters obtained from the least-square fitting procedure dealing with the first

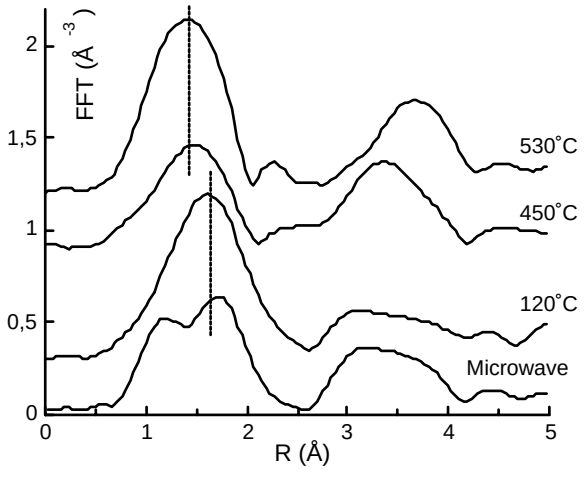

Fig. 2. Fast Fourier transforms of the Mn-K edge $k^2\chi(k)$ EXAFS spectra of the different SnO_2:Mn films, using a Kaiser apodization window from 2.7 to 10.3 Å^{-1} with $\tau = 3$. Dashed lines are a guide for eyes.

Table I. *EXAFS fit results at the Mn-K edge. The residual ρ factor is defined as* $\rho = [\Sigma(k^3\chi_{exp}(k) - k^3\chi_{theo}(k))^2 / \Sigma(k^3\chi_{exp}(k))^2]^{1/2}$. *The commonly accepted fitting accuracy is of about 0.02 Å for the distance and 15 to 20% for the number of neighbors.*

Films treated	N	R (Å)	σ (Å)	ρ (%)
By Microwave	2.9	2.16	0.06	1.8
	2.6	2.00	0.09	
At 120 °C	3.6	2.13	0.09	1.1
	1.7	1.95	0.19	
At 450 °C	1.2	2.14	0.04	1.9
	2.5	1.96	0.03	
At 530 °C	3.3	2.11	0.01	2.2
	3.2	1.93	0.01	

oxygen coordination shell are gathered in Table I. The best fits are obtained by using a two shell fitting procedure with a first Mn-O distance at 1.96 ± 0.03 Å and a second one at 2.13 ± 0.03 Å. The shortening of distances compared to the Mn-O distance found for divalent manganese (typically around 2.20 Å) suggests a change of manganese oxidation degree. This is clearly confirmed by the Mn K-edge XANES results presented in Figure 3. Everything else being equal, and by comparison with reference compounds, the rising edge position can be qualitatively used for the determination of the manganese oxidation state [11]. On one hand, the rising edges of the films treated at 120 °C (6546.1 eV) and by microwave (6546.0 eV) are almost superimposable and are in between those of Mn(II) (MnO: 6544.7 eV) and Mn(III) (Mn_2O_3: 6548.7 eV) references evidencing an intermediary average manganese valence for these films. On the other hand, the rising edge of the film treated at 530 °C (6547.1 eV) is shifted one eV above the position observed

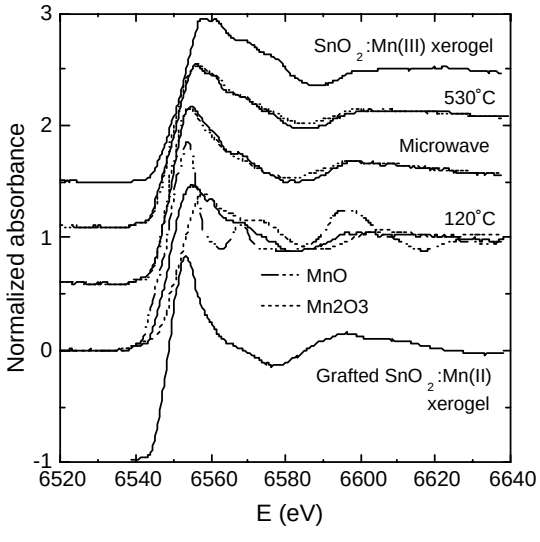

Fig. 3. Mn K-edge XANES spectra of different SnO_2:Mn films compared to divalent (MnO) and trivalent (Mn_2O_3) manganese references. The dashed line superimposed to the SnO_2:Mn film treated at 530 °C or by microwave has been obtained from the linear combination of the SnO_2 xerogel grafted by Mn(II) (site 1 at 2.13 Å) and the SnO_2:Mn(III) xerogel (site 2 at 1.96 Å), shown at the bottom and top of the figure, respectively. The ratios (site 1 : site 2) are 65% : 35% for the film treated by microwave, 55% : 45% for the film heated at 120 °C (the combination is not shown) and 38% : 62% for the film heated at 530 °C.

for the other films evidencing the increase of oxidation state upon heating at high temperature. Using a correlation between the edge energy and the Mn valence similar to the one established by Ressler *et al.* [11], the change of average Mn valence state is from ≈2.3 at 120 °C to ≈2.6 at 530 °C. In fact, the EXAFS results suggest the presence of Mn in two different sites. The site corresponding to a Mn-O distance of 1.96 Å is characteristic of trivalent manganese and is encountered alone for SnO_2 xerogels doped by Mn [12] whereas the site at longer distance is found for SnO_2 xerogels modified by Tiron® and grafted at pH = 7 by Mn(II) ions. As a matter of fact, the XANES spectra of the SnO_2:Mn films can be satisfactorily reproduced by a linear combination of the XANES spectra of the SnO_2:Mn(III) and SnO_2:Mn(II) grafted xerogels displayed in Figure 3. Note that the ratios used for the linear combinations and indicated in the caption of Figure 3 are in good agreement with the average manganese valence determined from the above correlation.

4. Discussion

Two sintering additives were introduced in the traditional route [4] to improve the densification of films and so reduce the microporosity of the SnO_2 coating. As evidenced by the EXAFS results at the Sn K edge, Tiron® grafting acts over the crystallite growth since the mean number of tin atoms as second neighbours is almost invariant when the films are heated from 120 °C to 450 °C. This effect, already reported for SnO_2 xerogels [13] and ultrafiltration membranes [6] modified by Tiron®, is ascribed to the capping coordination of Tiron® molecules at the surface of the SnO_2 crystallites. When Tiron® is burnt (i.e. above 450 °C), the crystallite growth control exercised by Tiron® disappears and the mean number of tin atoms as second nearest neighbours (3.18 and 3.71 Å) clearly increases.

Second, it is well known that suitable additives lead to the densification of the SnO_2-based ceramics during sintering. Recently we have proposed from EXAFS results [14] that the formation of a non-homogeneous solid solution between Cu(II) ions and $SnO_2$was mainly responsible for the low temperature densification (<900 °C) of Cu-doped SnO_2 xerogels. Due to the application of the coatings, we are interested in reducing the densification temperature. For MnO-doped SnO_2 xerogels [5], it has been reported faintly smaller densification temperature than those for copper doping and it is proposed that this behaviour is associated to the change of oxidation state of manganese. Indeed we have verified herein that a change of the average manganese valence from 2.3 to 2.6 occurs by heating the films from 120 to 530 °C due to a change of the proportion of sites in which manganese atoms are at the divalent and trivalent states. The oxidation of initial divalent manganese is concomitantly accompanied by a shortening of Mn-O distances from 2.13 to 1.96 Å. We propose that this process is a driving force for the bodies densification by leading to the formation of a stable substitutional solid solution Mn(III):SnO_2. Indeed for steric hindrance, the substitution of tin atom by divalent manganese is not possible (d(Mn(II)-O) = 2.13 Å and d(Sn(IV)-O) = 2.06 Å) but the decrease of ionic radius of manganese at the trivalent state is clearly a more favourable situation for stabilizing the solid solution. The formation of a substitutional solid solution has been clearly evidenced for the SnO_2:Mn(III) xerogels [12] by comparison with *ab initio* EXAFS calculations, as those already reported for Cu-doped SnO_2 xerogels [14]. Thus, the Mn-doping may have a double role in the sintering aid: *i*) the formation of Mn(III) substitutional solid solution increase the oxygen vacancy concentration improving the lattice diffusion and densifying transport mechanism; *ii*) the presence of the grafted like Mn(II) at the grain interface can act as a solute drag decreasing the grain boundary mobility. In both cases, it contributes to improve the densification of the films. Furthermore, the Sn-Sn contribution at 2.86 Å indicates the presence of a secondary phase in films fired at 530 °C that was tentatively attributed to metallic tin. The low oxygen partial pressure caused by combustion of Tiron® and reduction of Mn(II) can explain the reduction of Sn(IV)$O_2$to metallic tin. The presence of metallic tin favours liquid phase sintering explaining the fast densification rate and the amorphous-like phase observed by several research groups [5, 15].

Doped SnO_2:Mn films sintered by microwave treatment have a similar structure to those obtained from low temperature heating (120 °C), with a higher proportion of divalent manganese compared to the films heated at 450 °C. This feature can be explained by the very fast heating and short time period of firing, that reduces diffusion limited phenomena like grain growth and the Mn(II) oxidation.

5. Conclusion

A partial change of the average Mn valence degree from 2.3 to 2.6 upon conventional heating above 120 °C occurs which favours the formation of a stable substitutional solid solution Mn(III):SnO_2 in which Mn cations are surrounded by oxygen atoms at 1.96 Å. It contributes to increase the oxygen vacancy concentration improving the lattice diffusion and the densifying sintering. Both Tiron® and Mn(II) grafting are responsible for grain growth inhibition and increase of the thermal stability of the nanostructure against coarsening.

Acknowledgement

This work has been financially supported by FAPESP (Brazil), CNRS (France) and a CAPES/COFECUB program. We thank the LURE storage ring staff for providing the synchrotron radiation.

References

1. Serrini, P., Briois, V., Horrillo, M. C., Traverse, A. and Manes, L., Thin Sol. Films **304**, 113 (1997).
2. Blunden, S. J., Cusack, P. A. and Hill, R., "The industrial use of tin chemicals", (Royal Soc. Chem. London, 1985), Chap. 9 and 10.
3. Santos, L. R. B., Larbot, A., Santilli, C. V. and Pulcinelli, S. H., J. Sol-Gel Sci. Techno. **13**, 805 (1998).
4. Rizzato, A. P., Santilli, C. V., Pulcinelli, S. H. and Messaddeq, Y., J. Non-Cryst. Solids **256&257**, 154 (1999).
5. Gouvea, D., Smith, A. and Bonnet, J. P., Eur. J. Sol. State Inorg. Chem. **33**, 343 (1996).
6. Santos, L. R. B. *et al.*, J. Sol-Gel Sci. Techno. **26**, 171 (2003).
7. Calmels, A., Stuerga, D., Lepage, P. and Pribetich, P., Microw. Opt. Technol. Lett. **21**, 477 (1999).
8. Michalowicz, A., "EXAFS pour le Mac, Logiciels pour la Chimie", (Société Française de Chimie 1991), p 102.
9. Zabinsky, S. I., Rehr, J. J., Ankudinov, A., Albers, R. C. and Eller, M. J., Phys. Rev. B **52**, 2995 (1995).
10. Briois, V., Pulcinelli, S. H. and Santilli, C. V., J. Mater. Sci. Lett. **20**, 555 (2001).
11. Ressler, T., Brock, S., Wong, J. and Suib, S., J. Phys. Chem. B **103**, 6407 (1999).
12. Rizzato, A. P., Briois, V., Santilli, C. V. and Pulcinelli, S. H., in preparation.
13. Belin, S. *et al.*, Colloids Surf. A **216**, 195 (2003).
14. Santilli, C. V., Pulcinelli, S. H., Brito, G. E. S. and Briois, V., J. Phys. Chem. **103**, 2660 (1999).
15. Varela, L. A. *et al.*, Ceram. Int. **25**, 253 (1999).

Physica Scripta. Vol. T115, 294–296, 2005

Short Range Structure of Lanthanum Chloride/Oxychloride Determined by EXAFS

H. Matsuura[1*], S. Watanabe[1], T. Kanuma[1], H. Akatsuka[1], T. Honma[2], N. Umesaki[2], A. Kajinami[3], A. K. Adya[4] and R. Fujita[5]

[1]Research Laboratory for Nuclear Reactors, Tokyo Institute of Technology, 2-12-1, Meguro-ku, Tokyo, 152-8550, Japan
[2]Japan Synchrotron Radiation Research Institute, Japan/SPring-8, Mikazuki, Hyogo, 679-5198, Japan
[3]Department of Science and Engineering Chemistry, Faculty of Engineering, Kobe University, Rokko-dai, Nada-ku, Kobe 657-8501, Japan
[4]School of Contemporary Sciences, University of Abertay Dundee, Bell Street, Dundee DD1 1HG, UK
[5]Power & Industrial Systems R&D Center, Toshiba Corporation, 4-1, Ukishima-cho, Kawasaki-ku, Kawasaki 210-0862, Japan

Received June 26, 2003; revised April 27, 2004; accepted April 28, 2004

PACS number: 61.10.Ht

Abstract

Transmission XAFS measurements were performed on lanthanum chloride ($LaCl_3$) and $LaCl_3$-Li_2O mixture at various temperatures using La-K X-ray absorption edge. A distinct phase shift in the EXAFS oscillations was observed in going from the solid phase to the molten phase in $LaCl_3$. The results of curve fitting to the predominant peak in the structure function of $LaCl_3$ in real space, corresponding to the La^{3+}-Cl^- 1st coordination shell, reveal that both the inter-ionic distance and coordination number of chloride ions around a lanthanum ion decreased with increase in temperature to above its melting point. The short-range structure of $LaCl_3$-Li_2O ($x_{Li_2O} = 5$ mol%) mixture appears to be almost similar to that observed in pure $LaCl_3$.

1. Introduction

During the course of development of pyrochemical reprocessing of oxide nuclear fuels, several key issues need to be addressed in the uranium-plutonium co-electrodeposition process, *e.g.*, decrease of electric current efficiency due to circular current induced by either of the following redox reactions: Ce^{3+}/Ce^{4+} or Fe^{2+}/Fe^{3+}, noble metals contamination caused by their co-electrodeposition with (U, Pu)O_2, and possible composition variations in the electrodeposited material, *etc*. Additionally, and more importantly, the behaviour of rare-earth cations in molten chlorides in the presence of oxide anions is still unknown, and is bound to play a crucial role in the realization of this process. It is already reported that lanthanum chloride reacts with oxygen from either air or moisture to make compounds of oxychloride at *ca.* 620 K. Once oxychlorides are formed, they are very stable even above the melting point of pure lanthanum chloride (*ca.* 1100 K), and they will either float or precipitate in the melt bath. With the above point in view, we performed structural analysis of XAFS data on lanthanum oxychloride to elucidate the short-range distance environment around the lanthanum cation. As the first in a series of measurements planned to address the above issues, we chose the lanthanum compound, $LaCl_3$, among the several rare-earth compounds that generally exist in the fission products. The reason being that we expect $LaCl_3$ to behave most simply in its molten state in the presence of coexisting oxide anions as revealed by the E-pO^{2-} diagrams [1].

2. Experimental

2.1. *XAFS measurements*

X-ray Absorption spectra at the La K-edge (38.92 keV) were collected at various temperatures on BL19B2 and BL38B1 beam lines of SPring-8, Japan, using Si (311) double crystal monochromator. The energy range of the measurements was 38.6–40.4 keV, and stepped scan measurements were performed with an energy resolution of 1 eV. The SPring-8 storage ring was operated at 8 GeV and 100 mA. The intensities of the incident (I_0) and transmitted (I) X-rays were detected by using ionisation chambers filled with Kr + Ar (1 : 3) and Kr, respectively. For energy calibration, La K-edge of LaF_3 was used.

Chemicals of oxychloride (x $Li_2O = 5$ mol%) were prepared by adding Li_2O (Soekawa, 4N) to molten anhydrous $LaCl_3$ (AAPL Japan, 4N) in a glassy carbon cell kept in a dried argon atmosphere. The chemicals were grinded into a few micrometer particles, mixed with BN matrix powder (Goodfellow, 2N5) homogeneously (weight ratio; 1 : 2), and then pressed into pellets under 10 ton weight. The sample pellets disks were *ca.* 1 mm in thickness and 12 mm in diameter. The sample pellets were installed into a sample holder made of boron nitride fitted inside an electric furnace originally constructed by Rigaku Corporation [2]. The temperature was elevated from room temperature (RT) to a value (1173 K or 1223 K) above the melting point (*ca.* 1100 K) of pure $LaCl_3$. Sample environment of inert Ar atmosphere was maintained throughout the experiment by purging dried Ar gas continuously through the hermetically sealed furnace.

2.2. *XAFS data analysis*

XAFS data analysis was carried out using WinXAS Ver. 2.3 [3] software with the following procedure. Background subtraction and normalisation were performed by fitting the modified Victoreen equation to the pre-edge region and linear polynomial to the post-edge region, respectively. La K absorption threshold was decided from the first root in the second derivative of the near-edge region. XAFS oscillation, $\chi(k)$, was obtained by removing the atomic background smoothly using cubic spline method. The structure function $\mathrm{FT}|\chi(k) \cdot k^3|$ was obtained by Fourier transforming the k^3 weighted $\chi(k)$ function multiplied by a Bessel window function. The range of wave numbers used in the Fourier transformation was $2 < k < 12\,\mathrm{A}^{-1}$ for the solids, and $2 < k < 8\,\mathrm{A}^{-1}$ for the liquid melts. The curve fitting, including the 3rd and 4th cumulants, was done by nonlinear least square fits on the predominant La^{3+}-Cl^- 1st neighbour correlation peak in R-space using backscattering factors evaluated by FEFF 8.0 [4] code. The fitting and theoretical calculations were performed by assuming reasonable symmetric structures *e.g.*, hexahedron, octahedron and tetrahedron. Thus, the most reasonable coordination number of chloride ions around lanthanum ion was chosen by consideration of the inter-ionic distance and the sum of effective ionic radii [5].

*e-mail hmatsuur@nr.titech.ac.jp

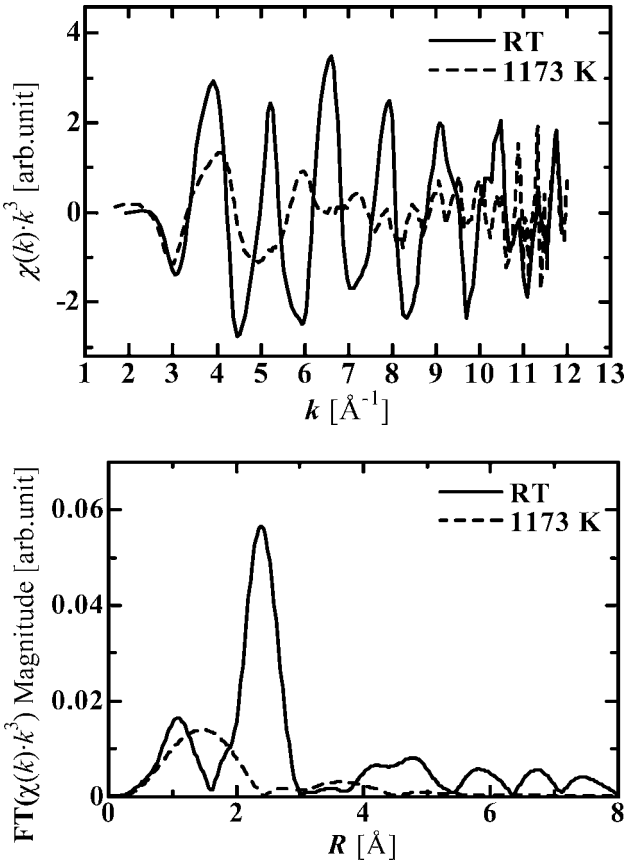

Fig. 1. (a) XAFS oscillations of $LaCl_3$ in solid phase at room temperature (RT) and in liquid phase at 1173 K collected on beamline BL19B2. (b) Structure functions of $LaCl_3$ in solid phase at RT and in liquid phase at 1173 K collected on beamline BL19B2.

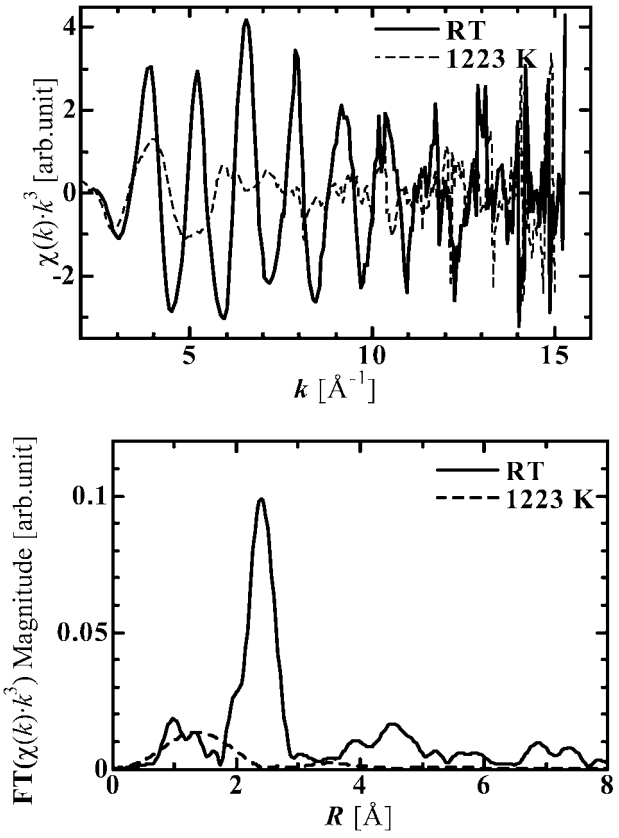

Fig. 2. (a) XAFS oscillations of $LaCl_3$ in solid phase at RT and in liquid phase at 1223 K collected on beamline BL38B1. (b) Structure functions of $LaCl_3$ in solid phase at RT and in liquid phase at 1223 K collected on beamline BL38B1.

3. Results and discussion

The extracted XAFS oscillations and their Fourier transformed structure functions of pure $LaCl_3$ in both the solid and liquid phases measured at BL19B2 and BL38B1 are depicted in Fig. 1(a, b) and Fig. 2(a, b), respectively. A comparison between the two spectra obtained on different beamlines reveals that the quality of the spectra on BL38B1 is much better than that on BL19B2. This may probably be due to some technical problems in the piezo monochromator optimization system that existed during the course of our measurements on BL19B2. Nevertheless, for our purpose of characterisation of lanthanum oxychlorides, it is not a serious problem requiring further discussion.

Similar to the observation in [6], the phase shift in the EXAFS spectra on melting $LaCl_3$ is observed, and the predominant peak corresponding to La–Cl 1st coordination shell is shifted to shorter distance upon melting. Table I shows the structural parameters obtained from the curve fitting procedure (see Section 2.2) applied to the first coordination shell. These values show a typical tendency of decreasing interionic (La^{3+}-Cl^-) distances and coordination numbers, $\bar{n}^{Cl}_{La}$, of chloride ions around a lanthanum cation on increasing the temperature. This trend is

Table I. *Structural parameters of $LaCl_3$ and $LaCl_3$-Li_2O ($x_{Li_2O} = 5$ mol%) at room temperature (RT) and at high temperatures corresponding to the solid and liquid phases, respectively, of $LaCl_3$.*

Beam Line*	Pure/ Mixture¶	T(K)	${S_0}^2$	$\bar{n}^{Cl}_{La}$	R(Å)	DWF	E_0	C_3	C_4	Residual
38B1	Pure	RT	0.90	9.00	2.93	0.009	0.916	–	–	7.35
38B1	Pure	1223	0.84	4.97	2.46	0.026	−17.48	4E-4	3E-5	7.34
38B1	Mixture	RT	0.98	9.00	2.93	0.009	−0.87	–	–	7.64
19B2	Pure	RT	0.87	9.00	2.95	0.010	2.439	–	–	6.60
19B2	Pure	1173	0.87	5.24	2.48	0.026	−15.48	9E-5	2E-6	8.97
19B2	Mixture	RT	1.00	9.08	2.95	0.012	4.258	–	–	4.64
19B2	Mixture	1173	0.93	5.09	2.48	0.028	−15.97	9E-5	−2E-6	8.49

*Beamlines on SPring-8, Japan; ¶Pure = $LaCl_3$, Mixture = $LaCl_3$-Li_2O ($x_{Li_2O} = 5$ mol%); DWF = Debye-Waller factor; $\bar{n}^{Cl}_{La}$ = Coordination number of chloride ions around a lanthanum ion; R/(Å) = Nearest-neighbour interionic distance; ${S_0}^2$ = intrinsic loss factor; E_0 = Absorption energy shifts; C_3 and C_4 are the 3rd and 4th cumulant coefficients used in the curve fitting (see Section 2.2). Residual is defined in the WinXAS manual, pp. 9.

already known from diffraction studies. However, the extent of decrease in the distance on melting is found to be much larger than that previously reported by Okamoto *et al*. [6]. The major difference between the present measurements and those reported previously [6] is in the sample confinement. While we used pellets made by mixing $LaCl_3$ in BN matrix, Okamoto *et al*. used quartz cells to contain $LaCl_3$. Although BN is not expected to react at all with lanthanum chloride, it is probable that at the high operating temperatures the sample may get oxidized by quartz/silica. The above results simply highlight the already well-accepted view that special concern should be focused on each step of the entire experimental procedure. While even the most advanced experimental techniques cannot rectify the problems generated by complicated sample preparation, the step between the points at which the analytical materials are transferred from the pure sample matrix to a form suitable for analysis is often overlooked. The sample confinement is another issue where the effects of the container material or the dilution matrix (BN or graphite powder) material used to prepare the pellets, as in the present measurements, should be addressed. Other steps, such as the sample environment, the design and construction of the furnace, the temperature control, and the whole suite of XAFS experimental procedures also need attention. To address one of our main concerns on the sample catching up the moisture even during quick transportation of the pelleted samples from the sealed polyethylene bags to the furnace in an open environment, the procedure that we adopted in the present measurements has already been revised for future studies.

Figure 3 shows a comparison between the structure factors of pure $LaCl_3$ and $LaCl_3$-Li_2O ($x_{Li_2O} = 5$ mol%) mixture obtained in this study. The structural parameters obtained by curve fitting to the 1st coordination shell of $LaCl_3$-Li_2O ($x_{Li_2O} = 5$ mol%) are also listed in Table I. It is difficult to find a recognisable difference (see Fig. 3) between the two radial structure factors at 1173 K. This observation may also imply that some problems probably existed in either the sample quality itself or the measurement procedure adopted. For a detailed quantitative discussion of the effect of the oxide ion on the structure of molten rare-earth chlorides, further similar experiments by varying the oxide ion concentrations, using the hydrated samples, revising the sample environment, i.e. the cell and furnace constructions, would be required. Some successful modifications to the above procedures have already been made, and further work is in progress.

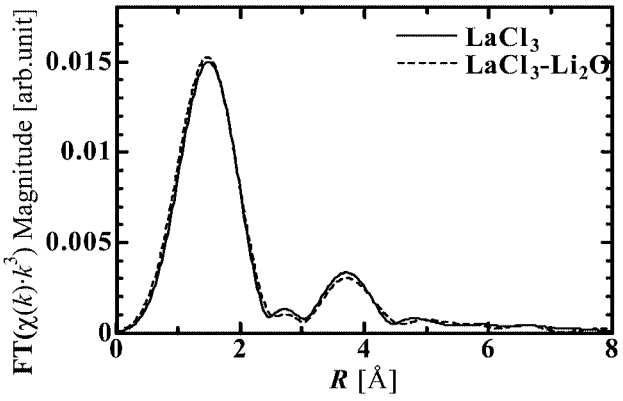

Fig. 3. Comparison between the structure functions of pure $LaCl_3$ and $LaCl_3$–Li_2O mixture ($x_{Li_2O} = 5$ mol%) at 1173 K.

4. Conclusions

XAFS measurements on $LaCl_3$ and $LaCl_3$–Li_2O ($x_{Li_2O} = 5$ mol%) were carried out over a wide temperature range from RT to above the melting point of $LaCl_3$. The structural parameters in the solid phase of pure $LaCl_3$ are in fairly good agreement with the crystallographic data. The values of the inter-ionic, La^{3+}-Cl^-, distance and the coordination number, $\bar{n}_{La}^{Cl}$, in the liquid phase are found to be lower than those in the solid phase. Further improvement and modification of the sample preparation and XAFS measurement procedures is necessary to obtain proper short-range structural parameters of rare-earth oxychlorides.

Acknowledgements

We fully acknowledge the technical assistance received from Dr. M. Matsuzaki of Tokyo Institute of Technology. XAFS spectra were collected at SPring-8, Japan, under the proposal No. 2002B0837-RI-np.

References

1. Katayama, Y., Hagiwara, R. and Ito, Y., J. Electrochem. Soc. **142**, 2174 (1995).
2. Ablanov, M., Matsuura, H. and Takagi, R., Electrochemistry **67**, 839 (1999).
3. Ressler, T., J. Phys. **IV 7** C2 (1997).
4. Zabinsky, S. I., Rehr, J. J., Aukudinov, A., Albers, R. C. and Eller, M. J., Phys. Rev. B **52**, 2995 (1995).
5. Shannon, R. D., Acta Cryst. **A32**, 751 (1976).
6. Okamoto, Y., Shiwaku, H., Yaita, T., Narita, H. and Tanida, H., J. Mol. Structure **641**, 71 (2002).

Physica Scripta. Vol. T115, 297–301, 2005

Short Range Structure of Lead-Lithium Fluoride Obtained by XAFS Analysis

S. Watanabe[1*], R. Toyoyoshi[1], T. Sakamoto[1], Y. Okamoto[2], Y. Iwadate[3], H. Akatsuka[1] and H. Matsuura[1]

[1]Research Laboratory for Nuclear Reactors, Tokyo Tech., 2-12-1, Meguro-ku, Tokyo, 152-8550, Japan
[2]Department of Material Science, JAERI, Tokai - mura, Naka - gun, Ibaraki, 319-1195, Japan
[3]Graduate School of Science and Technology, Chiba University, 1-33, Inage-ku, Chiba, 263-8522, Japan

Received June 26, 2003; revised October 14, 2003; accepted November 4, 2003

PACS number: 61.10.Ht

Abstract

Transmission XAFS measurements were performed on PbF_2 and LiF-PbF_2 at various temperatures using Pb-L_{III} X-ray absorption edge. Distinct phase shift of EXAFS oscillations was observed at the temperature range of superionic conductance phase transition in PbF_2. From the results of curve fitting to the predominant peak of PbF_2 in real space which is considered to be Pb^{2+}-F^- correlation, we can reveal that both inter-ionic distance and coordination number decreases with increasing temperature from β phase to liquid phase through the superionic conductance phase. Structural change in LiF-PbF_2 shows the same tendency with that of pure PbF_2.

1. Introduction

There are 2 phase transitions in lead fluoride under its melting point. At 589 K, $\alpha \rightarrow \beta$ phase transition occurs firstly. This phase transition is irreversible if temperature is controlled, however $\beta \rightarrow \alpha$ phase transition occurs under high pressure [1]. Lead fluoride in α phase is asymmetric orthorhombic crystal and that in β phase is symmetric cubic crystal. Then PbF_2 crystal at higher temperature than 710 K is known as 'superionic conductor', since its electric conductivity is comparable with that in the liquid phase even below the melting point. Some authors reported that fluoride ions in the superionic conductance phase move like in liquid phase [2]. According to those reports, increase of structural disorder on first neighboring Pb^{2+}-F^- correlation can be observed by XAFS measurements before and after superionic conductance phase transition. Additionally, structural parameters of Pb^{2+}-Pb^{2+} correlation are considered to be unchanged in this temperature range. Various studies have been performed on superionic conductance phase of PbF_2 and mixtures [3, 4], however clear structural variations of pure PbF_2 crystal in superionic conductance phase transition have not been investigated yet.

Incidentally, we have proposed LiF-PbF_2 system as a candidate of blanket material for fusion reactors using D-T reaction, and evaluated various properties of this system, e.g. eutectic composition (PbF_2:60 mol%, 850 K) [5], suitable material for the container [6], chemical form of tritium recovered from the molten salt when thermal neutrons were irradiated [7] and tritium inventory [8], etc. Since some other properties, such as electrical and thermal conductivity, viscosity and mobility of ions, depends on the local structure of molten salt, structural information will be necessary to apply to fusion blanket. Therefore structural information of molten PbF_2 is required as fundamental information to analyze molten LiF-PbF_2 structure.

With these objectives, we have investigated temperature dependence on short range structure of PbF_2 and LiF-PbF_2 by Pb-L_{III} XAFS measurements at various temperatures in the temperature range from room temperature to above their melting point.

2. Experimental

2.1. *XAFS measurements*

X-ray Absorption spectra of Pb L_{III}-edge (13.04 keV) were collected at various temperatures in BL10B beam line of Photon Factory at High Energy Accelerator Research Organization (KEK-PF), Japan, using Si (3 1 1) channel-cut monochromator. The energy range of the measurements was 12.54–14.14 keV, and stepped scan measurements were performed with 1 eV energy resolution. The PF storage ring was operated at 2.5 GeV with 200–400 mA. The intensities of the incident (I_0) and transmitted (I) X-rays were measured by using ionization chambers filled with Ar + N_2 (1 : 1) and Ar, respectively. For energy calibration, Pb L_{III}-edge of PbF_2 was used.

Powders of PbF_2 (Soekawa Chemical Co., 5N, m.p. = 1128 K) and LiF (Wako, superpure quality)-PbF_2 with eutectic composition were mixed with BN matrix powder (Good Fellow, 2N5) homogeneously (weight ratio; 1 : 9) at dried Ar atmosphere, and then they are pressed into pellets. The size of the sample pellet disks are ca. 1 mm thickness and 12 mm diameter. Sample pellets were installed into a sample holder made by glassy carbon in an electric furnace equipped at PF. Sample temperature was controlled as follows.

PbF_2
(*i*) RT → 1174 K (liquid phase) → RT.
(*ii*) RT → 792 K (superionic conductance phase) → RT → 1178 K (liquid phase) → RT.

LiF-PbF_2
RT → 905 K (liquid phase) → RT

Sample environment was kept at Ar atmosphere throughout the experiment.

2.2. *XAFS data analysis*

XAFS data analysis was carried out using WinXAS Ver. 2.3 [9] software package in the following procedure. Background subtraction and normalization were performed by fitting the Victoreen equation to the pre-edge region and a linear polynomial to the post edge region, respectively. Pb L_{III} absorption threshold was decided from the first root in the second derivative of

*e-mail 03d31067@nr.titech.ac.jp

the near edge region. XAFS oscillation $\chi(k)$ was obtained by removing the smooth atomic background using cubic spline method. The structural function $\mathrm{FT}|\chi(k)\cdot k^3|$ was obtained by Fourier transforming the k^3 weighted $\chi(k)$ function multiplied by a Bessel window function. Since double-electron excitation channel associated with a [2p4f] excitation and triple-electron excitation [$2p4f^2$] were indicated at about 180 eV and 410 eV above the L_{III} threshold energy [10], respectively, the range of wave numbers used in Fourier transformation was $2 < k < 7.5$ Å^{-1} to avoid these multi-electron excitation effects. Fitting including 3rd and 4th cumulants was done by nonlinear least square fits on predominant Pb^{2+}-F^- correlation peak in *R*-space using backscattering factors calculated by FEFF8.0 [11] code. Fitting and theoretical calculations were performed assuming reasonable symmetric structure e.g. hexahedron, octahedron and tetrahedron. Therefore the most reasonable coordination number of fluoride ions around the lead ion was chosen by consideration of inter-ionic distance and a sum of effective ionic radii [12]. As α-PbF2 is not suitable for this fitting procedure since its structure is asymmetric, curve fittings were performed without α-phase.

3. Results and Discussions

3.1. PbF_2

XAFS oscillations extracted and their Fourier transformed magnitudes are shown in Fig. 1(a), 2(a) and 1(b), 2(b), respectively. Spectra at 676 K in fig. 1 and at 300 K in fig. 2 show typical ones of β-PbF_2 and α-PbF_2, respectively.

Main issues are:

1) Phase shifts of XAFS oscillations in heating process.
   These phase shifts are considered to indicate superionic conductance phase transition since similar phase shifts in XAFS oscillations of $SrCl_2$, which is a superionic conductor, have been reported [13]. At the same time as for the phase shifts, the intensity of the peaks correspond to the 2nd coordination shell in *R*-space decrease suddenly. As those peaks are considered to be Pb^{2+}-Pb^{2+} contributions, they should not have changed suddenly as mentioned above.
2) Phase shifts of XAFS oscillations in cooling process.
   In temperature control (*i*), we could observe distinct phase shifts of XAFS oscillations in the cooling process. However, in temperature control (*ii*), the phase of oscillation did not change while the temperature was dropped from 792 K to 313 K although this phase shift was observed again as the temperature was elevated above the melting point. Since the phase of oscillation after the phase shift in a cooling process is regarded as the same as that before heating, those phase shifts may indicate the reverse of the phase shift observed in heating process.
3) Structural change from solid to liquid phase.
   There is little difference in XAFS oscillations and structural functions before and after the melting point. However, we would observe structural disorder in melting by evaluating the structural parameters.

Next, we will discuss issues of the structural parameters obtained by curve fitting to the predominant peak in *R*-space. Table I–II show the structural parameters obtained by curve fitting. Here $r_{\mathrm{Pb\text{-}F}}$ is inter-ionic distance, $N_{\mathrm{Pb\text{-}F}}$ is coordination number of F^- ions around the Pb^{2+} ion and DW is the Debye-Waller factor. C_3 and C_4 are 3rd and 4th cumulants, respectively. The residual is defined by the following equation

$$\text{Residual} = \sum_{i=1}^{N} \left|k^3\chi_{\mathrm{exp}}(k) - k^3\chi_{\mathrm{cal}}(k)\right| \Big/ \sum_{i=1}^{N} \left|k^3\chi_{\mathrm{exp}}(k)\right|.$$

Here letters 'exp' and 'cal' correspond to experimental and calculation, respectively.

1) The phase shift of XAFS oscillations in heating process definitely indicates the superionic conductance phase transition

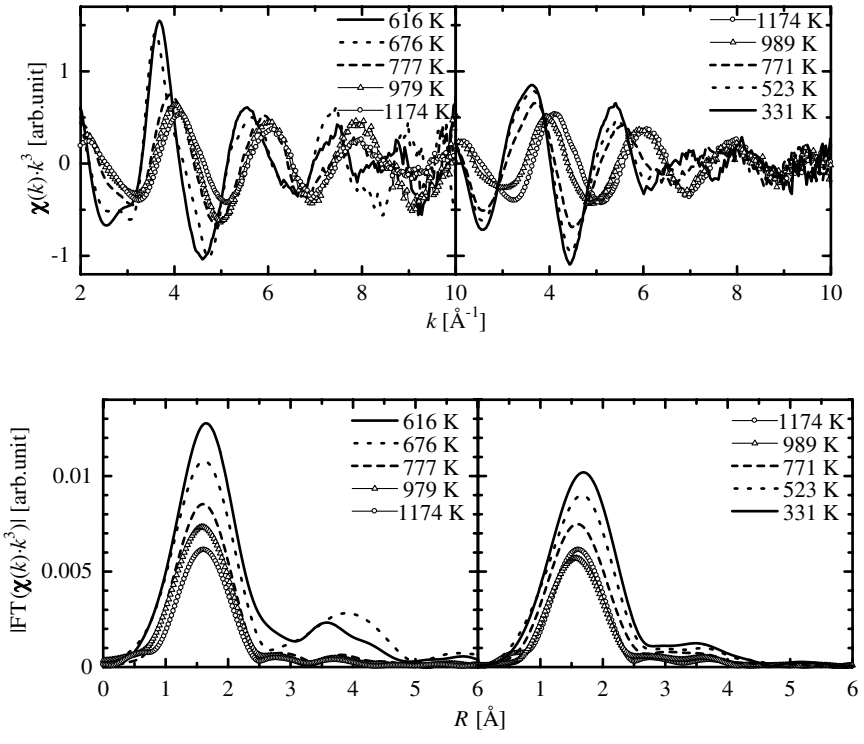

Fig. 1. (a) XAFS oscillations of PbF_2 (*i*) (right: RT → 1174 K, left: 1174 K → RT). (b) Structural functions of PbF_2 (*i*).

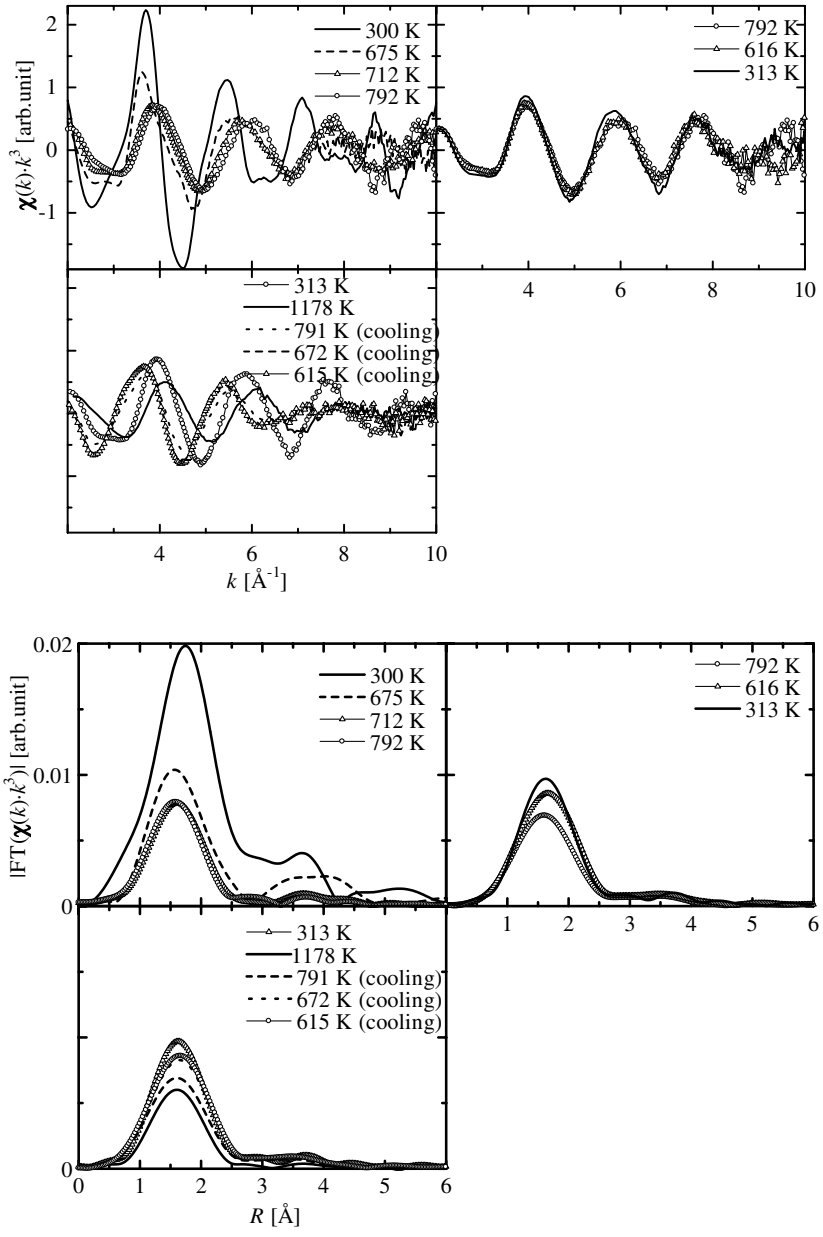

Fig. 2. (a) XAFS oscillations of PbF_2 (*ii*) (right: RT → 792 K → RT, left: RT → 1178 K → RT). (b) Structural functions of PbF_2 (*ii*).

Table I. *Structural parameters of PbF_2 (i).*

T (K)	$r_{Pb\text{-}F}$	$N_{Pb\text{-}F}$ (fix)	DW	C_3	C_4	Residual
616	2.58	8	5.70E-05	8.65E-03	−2.02E-03	1.17
676	2.49	8	7.88E-03	6.10E-03	−1.27E-03	3.18
777	2.43	8	1.06E-02	5.81E-03	−2.51E-04	1.36
881	2.40	8	1.04E-02	4.47E-03	−7.47E-05	3.26
979	2.33	6	9.61E-03	3.31E-03	−1.03E-04	3.53
1082	2.28	4	1.32E-02	1.87E-03	−2.89E-05	2.39
1174	2.26	4	2.86E-02	1.43E-03	7.77E-04	0.78
989	2.43	8	9.66E-03	6.36E-03	−1.48E-04	1.43
771	2.53	8	1.21E-02	7.23E-03	−8.73E-03	1.71
523	2.53	8	9.99E-03	5.70E-03	−1.38E-03	5.54
426	2.54	8	6.23E-03	5.34E-03	−1.72E-03	2.48
311	2.54	8	4.16E-05	5.09E-03	−1.75E-03	2.96

Table II. *Structural parameters of PbF_2 (ii).*

T (K)	$r_{Pb\text{-}F}$ (Å)	$N_{Pb\text{-}F}$ (fix)	DW (Å^2)	C_3 (Å^3)	C_4 (Å^4)	Residual
675	2.57	8	3.71E-05	9.55E-03	−1.56E-03	4.81
712	2.41	8	7.63E-03	4.37E-03	−4.72E-04	1.65
792	2.41	8	1.02E-02	6.02E-03	−1.43E-04	1.82
681	2.41	8	1.01E-02	5.01E-03	−2.91E-04	2.47
616	2.40	8	1.03E-02	5.07E-03	−3.52E-04	4.01
567	2.40	8	1.04E-02	5.27E-03	−4.79E-04	4.37
515	2.40	8	1.00E-02	5.44E-03	−3.94E-04	4.87
313	2.41	8	9.47E-03	4.66E-03	−1.46E-04	1.17
1178	2.27	4	1.98E-02	2.03E-03	3.79E-04	1.67
791	2.51	8	1.57E-02	6.18E-03	−7.07E-04	2.16
672	2.50	8	1.40E-02	4.64E-03	−9.68E-04	2.38
615	2.55	8	1.13E-02	6.20E-03	−1.10E-03	1.39

since the Debye-Waller factor increases abruptly. Additionally, the inter-ionic distance decreased suddenly which is considered to be owing to the effect of columbic interaction between Pb^{2+} and mobile F^-. Therefore decrease of intensity of the peak at 2nd coordination shell may be one of the properties of PbF_2 at superionic conductance phase. However, we can not discuss further since we did not use large enough k region for Fourier transformation to discuss the 2nd coordination shell. Other

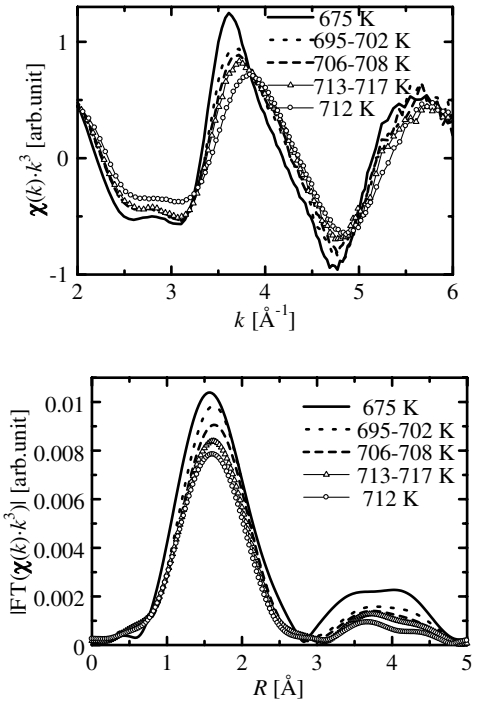

Fig. 3. (a) XAFS oscillation of PbF2 at 676 → 712 K. (b) Structural functions of PbF2 at 676 → 712 K.

Table III. *Structural parameters of PbF_2 (ii) at 676–712 K.*

T (K)	$r_{Pb\text{-}F}$ (Å)	$N_{Pb\text{-}F}$ (fix)	DW (Å^2)	C_3 (Å^3)	C_4 (Å^4)	Residual
675	2.57	8	3.71E-05	9.55E-03	−1.56E-03	4.81
684–695	2.48	8	1.89E-03	7.11E-03	−1.03E-03	3.21
695–702	2.47	8	2.63E-03	5.68E-03	−7.70E-04	4.24
702–706	2.46	8	2.06E-03	5.53E-03	−9.45E-04	3.34
706–708	2.45	8	2.63E-03	4.79E-03	−8.85E-04	4.49
708–713	2.45	8	3.51E-03	4.52E-03	−8.34E-04	3.54
713–717	2.43	8	5.34E-03	4.75E-03	−8.82E-04	3.82
717–718	2.42	8	6.06E-03	4.23E-03	−7.97E-04	2.62
712	2.41	8	7.63E-03	4.37E-03	−4.72E-04	1.65

experiments which can reveal long range structure (e.g. neutron diffraction or Pb K-edge XAFS in which multi-electron excitation channel has not been reported yet) will be necessary to investigate the temperature dependence of Pb^{2+}-Pb^{2+} correlation.

In order to evaluate detail local structural changes in the temperature range close to 710 K, we collected XAFS signals when temperature was controlled from 675 K to 712 K in experimental condition (*ii*). Fig. 3 shows the XAFS oscillations and structural functions, and Table III shows the structural parameters obtained from curve fitting. In these results, signals and parameters are arranged according to time evolution while temperature was controlled. Thus, temperature of each signal means only identification and numbers at left hand and right hand show the temperature at start and end of the measurement, respectively. These figures show both XAFS oscillations and structural functions changing continuously from 675 K to 712 K, and structural parameters also change continuously. Therefore these results reveal that the superionic conductance phase transition is a recognizable structural phase transition.

2) Judging only from the variation of structural parameters shown in the Tables, the structure of PbF_2 which has been cooled down is considered to depend on the temperature from which cooling was started. When PbF_2 is cooled down from liquid state, its structure becomes that of β-phase at room temperature. On the other hand, when it is cooled from superionic conductance state, its structure does not change during the cooling process. In this case, PbF_2 at room temperature may form a structure similar to the superionic conductance state.

In order to evaluate the state of PbF_2 which is cooled down from various temperatures, powder XRD measurements at room temperature have been performed on α-PbF_2, PbO, PbF_2 which have undergone some heat treatments. On the samples except for PbO, laboratory XAFS measurements have also been performed at room temperature. Powder diffraction patterns were collected by a NaI scintillation counter using an Cu-Kα line ($\lambda = 1.54046$ Å). Laboratory XAFS measurements have been carried out by using an XAFS spectrometer (Rigaku Corp.) with rotating molybdenum target and Ge(4 0 0) monochromator crystal. Some samples of PbF_2 were obtained by following heat treatments on α-PbF_2 in a globe box filled with dried Ar.

1) RT → 650 K (β-phase: keep 1 h) → RT.
2) RT → 800 K (superionic conductance phase: keep 1 h) → RT.
3) RT → 1200 K (liquid phase: keep 1 h) → RT.

According to our previous XAFS measurements, structures of samples PbF_2 2) and 3) are predicted to be superionic conductance phase and β-phase, respectively. Sample PbF_2-1) is β-phase crystal.

Figure 4 shows the diffraction pattern and XAFS oscillation of each sample. Opposite to previous results, all heat treated PbF_2 show the same diffraction pattern and XAFS oscillations. Diffraction patterns and XAFS oscillations of PbF_2 1), 2) and 3) are different from those of α-phase, and we can recognize by diffraction patterns that the lead ion was not oxidized, thus samples PbF_2 1), 2) and 3) are apparently in β-PbF_2 and the phase shift observed in the cooling process was not reproduced in these heat treatments. Since this phase shift was reproduced when temperature was elevated again to above the melting point, PbF_2

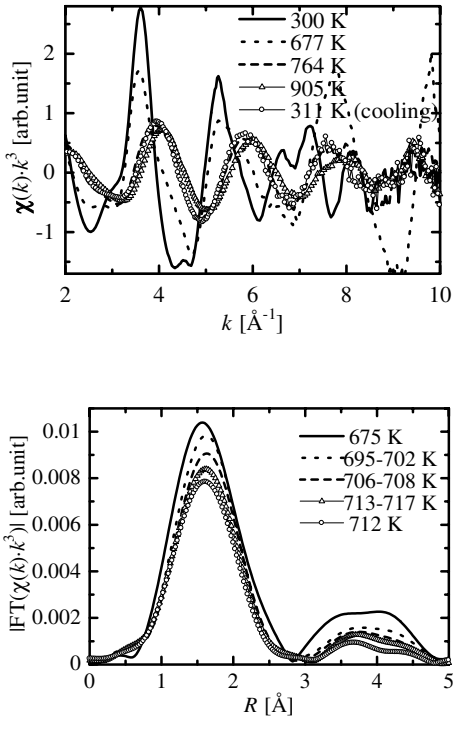

Fig. 4. (a) XAFS oscillations of LiF-PbF_2. (b) Structural functions of LiF-PbF_2.

Table IV. *Structural parameters of LiF-PbF_2.*

T (K)	$r_{Pb\text{-}F}$ (Å)	$N_{Pb\text{-}F}$ (fix)	DW (Å^2)	C_3 (Å^3)	C_4 (Å^4)	Residual
300	2.55	8	1.88E-03	3.60E-03	−1.30E-03	3.20
378	2.53	8	3.99E-03	3.42E-03	−1.55E-03	2.31
460	2.51	8	8.54E-03	3.87E-03	−1.83E-03	5.75
578	2.50	8	1.00E-02	4.53E-03	−1.33E-03	4.61
677	2.51	8	1.37E-02	5.04E-03	−4.83E-04	2.87
764	2.40	8	1.67E-02	4.41E-03	2.09E-04	1.82
905	2.33	6	2.48E-02	2.92E-03	4.90E-04	2.69
313	2.44	8	3.54E-03	5.14E-03	−5.17E-04	1.75

should not have changed chemically at high temperature. Then possible factors which lead to phase shift observed in cooling process are suggested to be cooling speed or mechanism of recrystallize process, and additional experiments will be required to confirm these possibilities. As the similar irreversible or temperature history dependent properties under its melting point are reported on another superionic conductor, LaF_3 [14], the irreversible property observed in this study may be one of the properties of superionic conductors.

3) After the superionic conductance phase transition, both inter-ionic distance and coordination number decrease with increasing temperature until above the melting point. As a jump of the Debye-Waller factor was recognized from 1082 K to 1174 K, the structural phase at 1174 K is definitely liquid. The structural parameters in liquid phase are considered to be reasonable since 4 coordinated structure is proposed for molten KF_{1-x}-PbF_{2x} system ($0.2 \leq x \leq 0.8$) [15] by Raman spectroscopy. Hence, superionic conductance phase is considered to have mean properties between solid and liquid phase, and those properties include electric conductance changing continuously from β-phase to liquid phase.

4. LiF-PbF_2

Figure 4(a), (b) show XAFS oscillations and structural functions of LiF-PbF_2, and Table IV shows the structural parameters obtained from curve fitting. As electron scattering by lithium ions is considered to be negligible and the first neighboring specie around a Pb^{2+} is considered to be F^-, the curve fitting procedure used on this system is the same as that used for pure PbF_2.

Phase shift of XAFS oscillations which corresponds to superionic conductance phase transition and decrease of 2nd coordination peaks were observed in this system again. Additionally, structural parameters are also similar with those of pure PbF_2 at comparable temperature even in the liquid phase of LiF-PbF_2. Therefore the effect of additive lithium ions on the local structure of this system is conjectured to be little since PbF_2 share more than 50% in this composition.

5. Conclusions

XAFS measurements on PbF_2 and eutectic LiF-PbF_2 were performed in a wide temperature range form RT to above their melting point. Structural parameters at liquid state of these systems are firstly revealed by this study. Temperature dependence of structural parameters is also investigated, and structural property of superionic conductance states of PbF_2 and LiF-PbF_2 are revealed. Additionally, the possibility that the structure of PbF_2 depends on temperature history was suggested.

Acknowledgements

We would like to thank Prof. M. Nomura, Dr. A. Koyama, Dr. Usami of KEK and Mr. M. Matsuzaki of Tokyo Tech. for their technical assist. This study is financially supported by Grants-in-Aid for Scientific Research from JSPS (Encouragement for Young Scientists (A) 13740376).

References

1. Ehm, L. *et al.*, J. Phys. Chem. Solid **64**, 919 (2003).
2. Kosacki, I., Appl. Phys. **A49**, 413 (1989).
3. Kosacki, I. and Dynowska, E., J. Crys. Growth **50**, 575 (1980).
4. Kosacki, I., Eddrief, M., Julien, C. and Balkanski, M., Mater., Sci. Eng. B **15**, 67 (1992).
5. Saito, N., Kawamura, K., Tanaka, H. and Takagi, R., DENKI KAGAKU **54**, 864 (1986).
6. Kawamura, K., Tanaka, H., Saito, N. and Takagi, R., DENKIKAGAKU **55**, 684 (1987).
7. Kawamura, K., Li, G. G., Takagi, R. and Horiuchi, N., KENKI KAGAKU **59**, 438 (1991).
8. Ablanov, M., Matsuura, H. and Takagi, R., J. Nucl. Mater. **258–263**, 500 (1998).
9. Ressler, T., J. Phys. IV **7**, C2-C269 (1997).
10. Cicco, A. D. and Filipponi, A., Phys. Rev. B **49**, 49 (1994).
11. Zabinsky, S. I., Rehr, J. J., Aukudinov, A., Albers, R. C. and Eller, M. J., Phys. Rev. B **52**, 2995 (1995).
12. Shannon, R. D., Acta Cryst. **A32**, 751 (1976).
13. Okamoto, Y., Yaita, T., Motohashi, H., Kobayashi, K. and Usami, N., Photon Factory Activity Report, B **141**, (2001).
14. Sinitsyn, V. V., Lips, O., Privalov, A. F., Fujara, F. and Murin, I. V., J. Phys. Chem. Solids **64**, 1201 (2003).
15. Papatheodorou, G. N., Proc. 6th international symposium on molten salt chemistry and technology, 28 (2001).

Physica Scripta. Vol. T115, 302–305, 2005

XAFS and Spectroscopic Characterization for the Structure and Electronic Structure of Ce-DMDPhPDA Complexes in Methanol

T. Yaita[1,2,3*], H. Shiwaku[2], S. Suzuki[1], Y. Okamoto[1,2], A. Shimada[1], Z. Assefa[3] and R. G. Haire[3]

[1]Department of Materials Science, Japan Atomic Energy Research Institute, Tokai-mura, Nakagun, Ibaraki 319-1195, Japan
[2]Research Center for Synchrotron Radiation, Japan Atomic Energy Research Institute, Koto, Mikazuki-cho, Sayo-gun, Hyogo 679-5148, Japan
[3]Oak Ridge National Laboratory, P.O. Box 2008, Oak Ridge, TN 37831-6375, USA

Received June 26, 2003; accepted October 16, 2003

Abstract

The structural parameters and the electronic structure of the complex between cerium(III) and *N*,*N*′-dimethyl-*N*,*N*′-diphenylpyridine-2,6-carboxyamide (DMD PhPDA) were studied by XAFS, and both luminescence and excitation spectroscopes. We investigated the fundamental aspects of this material as the ligand is promising for the separation of trivalent actinides and lanthanides. The Ce-K XAFS spectra were measured at the SPring-8 synchrotron facility in Japan. It was determined that the bond distances between the carbonyl oxygen and cerium, and between the pyridyl nitrogen and cerium were about 2.49 and 2.67 Å, respectively. The angle between the Ce-N bond and the p_z axis of the lone pair of the pyridyl nitrogen is 180° for the solution state, suggesting covalent interaction between cerium and the nitrogen of the DMDPhPDA ligand. Emission from this system is severely quenched, and red-shifts, and supports the presence of a strong inner sphere complexation between cerium and the nitrogen atom of the pyridyl group. From the XANES spectrum, the oxidation state of cerium was determined to be trivalent.

1. Introduction

In efforts to minimize radioactive waste associated with the production of electricity via nuclear energy, research is focusing on the treatment of long half-life nuclides from the viewpoint of their geological disposal. Methods for the separation of actinide(III) from lanthanide(III) species are important for several fundamental technologies and establishing accelerator driven transmutation systems for the longer lived actinides Am and Cm. This arises as there are large quantities of lanthanides with relatively high neutron cross-sections that accompany the actinides in high level radioactive wastes.

The separation of the trivalent actinides and lanthanides is difficult given their similar chemical behaviors. From recent studies, it has been found that the required separation can be accomplished using neutral soft-donor extractants [1–4]. These separation techniques are based on the more effective and preferential complexation of actinides versus lanthanides by the soft ligands (i.e., ligands that lead to covalent bonding with the metal ion). We focus here on the *N*,*N*′-dimethyl-*N*,*N*′-diphenylpyridine-2,6-carboxyamide (DMDPhPDA) compound is a promising ligand for these separation. The structural and electronic studies conducted by XAFS, luminescence, and excitation spectroscopy are reported.

2. Experimental

2.1. *Material and synthesis*

The DMDPhPDA ligand which structure shown below was synthesized as described in reference [5]. Based on liquid chromatography analysis its purity >99.5%.

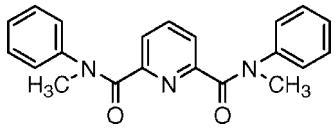

Scheme 1. Structure of *N*,*N*′-dimethyl-*N*,*N*′-diphenylpyridine-2,6-carboxyamide (DMDPhPDA).

2.2. *Sample preparation*

Hydrated cerium chlorides ($CeCl_3 \cdot 6H_2O$) were dissolved in the methanol solutions which contained DMDPhPDA at concentrations to provide the mole ratios, M : DMDPhPDA = 1 : 0, 1 : 2, 1 : 3, 1 : 4. The concentrations of the cerium was 0.05 mol/L for the samples. The methanol-solvent solution for dissolving the cerium salt was about 100 wt % MeOH. In addition, aqueous solutions of cerium ion were prepared for comparison with these methanol solutions.

2.3. *EXAFS measurements and Data analyses*

The EXAFS spectra of the Ce solutions at the K and L_{III}-edge (Ce-K edge) were measured in both the transmission and fluorescence modes at the BL11XU of SPring-8 synchrotron radiation facility, Japan. Monocromatic synchrotron radiation was obtained with a double crystal diamond (111) device.

The solutions for analysis were sealed in a polyethylene cells having a one cm path length. The data reduction and curve fitting were carried out by the WinXAS software version 2.3 [6]. The theoretical phases and amplitude were calculated by FEFF8 [7].

2.4. *Spectroscopic Studies*

The emission and excitation studies were conducted on Instrument SA's optical system, which consist of a monochromator (model 1000M) equipped with CCD, PMT and IR detectors. A 400 W xenon lamp was the light source. For absorption studies, samples were placed on quartz slides under a microscope objective and analyzed with the light from a xenon lamp delivered via a fiber optic setup. The transmitted light, collected with a second fiber, was directed into the monochromator. Emission spectra were collected at 90° from "in house" made cuvette having a diameter of 0.6 cm. Spectramax for windows software was used for data acquisition, while Grams 32 (Galactic Industries) software for data analyses.

3. Results and Discussion

3.1. *Structural studies of Ce-DMDPhPDA complexes*

Figure 1 shows the radial structural functions (RSF) of EXAFS data for cerium-DMDPhPDA complexes in methanol solutions. The data corresponding to cerium chloride in aqueous solution

*e-mail: yaita@mummy.tokai.jaeri.go.jp

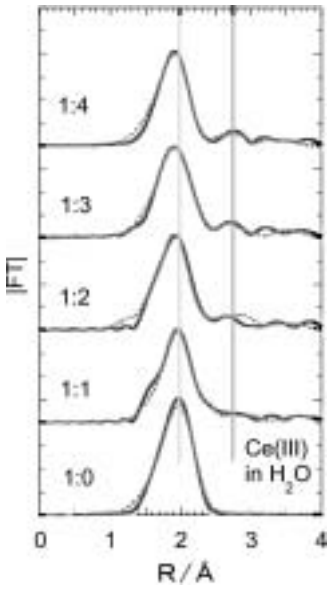

Fig. 1. The radial structural functions of Ce-DMDPhPDA in methanol. *The ratios in this figure denote Ce : DMDPhPDA(M/M). **The solid and the dotted lines mean the raw and fitting results, respectively. ***The maximum k values of the EXAFS oscillation for Fourier Transformation were taken at least 15 $Å^{-1}$.

Table I. *The Fitting results of Ce-DMDPhPDA in methanol.*

Sample	N	R/Å	σ^2/Å^2	$S_0{}^2$
1 : 0 (in H_2O)	10	2.51	0.001	1.1
	8	2.50	0.005	
1 : 1	1	2.65	0.005	1.3
	4	3.40	0.005	
	7.4	2.50	0.008	
1 : 2	1.6	2.67	0.005	1.0
	5	3.40	0.005	
	7.2	2.49	0.008	
1 : 3	1.8	2.68	0.008	1.4
	6	3.39	0.008	
	7	2.49	0.005	
1 : 4	2	2.68	0.006	1.2
	8	3.40	0.005	

is also shown in the figure for comparison. It has been reported that only water coordinates to lanthanides in this concentration range [8]. The RSF of the Ce-DMDPhPDA samples consist mainly of peaks at 2.0 and 2.7 Å. The largest peaks at 2.0 Å (in RSF) are assigned to the interaction between cerium and oxygen of the water and/or the DMDPhPDA, and the nitrogen of the DMDPhPDA molecule. This peak's position gradually shifts to lower R (Å) values with increased ratios of DMDPhPDA in the solution, suggesting interactions between cerium and the ligand.

Figure 2 shows the relationship between the bond distances and the fitting quality (Residual %) for the 1 : 4 mole ratio of the Ce : DMDPhPDA system. The first peaks of the complex systems consist of two interactions. Furthermore, the combination of the bond distances at 2.49 Å and 2.68 Å are most probable, based on the fitting quality, and are attributed to the oxygens of water, and DMDPhPDA and the nitrogen of DMDPhPDA, respectively. The small second peaks at 2.7 Å (in RSF) for the complexes are assigned to the carbon of the DMDPhPDA. The bond distances obtained by the fits are listed in Table 1.

On the basis of these results, a complex structure for the 1 : 4 complex is given in Figure 3. The crystal structure of La-DMDPhPDA complex [15] is also shown for comparison. The two oxygens of the DMDPhPDA ligand are the nearest neighbors of the Ce atom, and are located symmetrically at a distance of 2.49 Å on the axis consisting of the central nitrogen atom (Scheme 1). The angle consisting of the Ce-N bond and the p_z axis of the lone pair of the pyridyl nitrogen is probably linear in the solution, since the bond distance between Ce and 4 carbons of DMDPhPDA are almost same. However, it typical bends to 150° in the solid crystal [15]. The bend angle is important for characterizing the

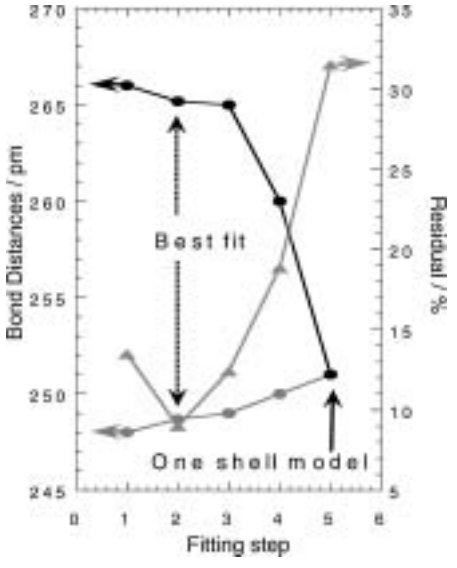

Fig. 2. The comparison between bond distance and fitting quality (residual %) *The residuals denote $\{\sum |y_{exp}(i) - y_{theo}(i)| / \sum |y_{exp}(i)|\} \times 100$ (%) where y means experimental theoretical data points.

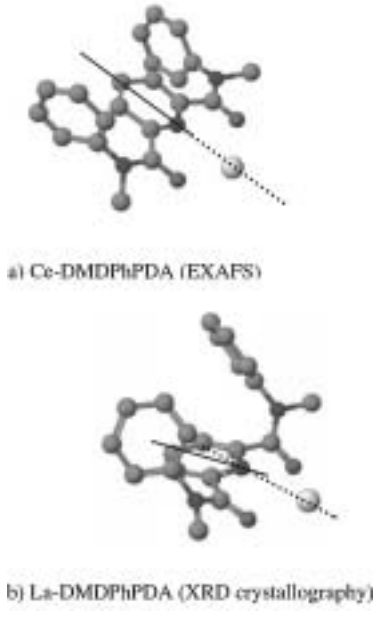

Fig. 3. The proposed coordination structure of Ce-DMDPhPDA in methanol *(a) Cluster of Ce-DMDPhPDA in methanol. This model was used for the calculation of theoretical parameter of back scattering and phase shift. (b) Cluster of La-DMDPhPDA (Solid state). This cluster is cut from $La(NO_3)_3(DMDPhPDA)_2$ complex [15].

chemical bond between the metal and ligand, as the coincidence of lobe direction of the lone electron pair of the donor atom and the bond angle has been experimentally regarded to be a measure of covalency [9, 10]. From the data, the chemical bond between the nitrogen of pyridyl group and cerium in solution appears slightly covalent. This occurs because the lobe of the lone pair of pyridyl nitrogen is about 180° degree toward the pyridine ring [11]. In the primary coordination sphere of the solid lanthanum complex, the two oxygens of the DMDPhPDA ligand coordinate to the metal asymmetrically, while in the Ce complex in the solution state, the oxygens coordinate symmetrically to the cerium.

3.2. *Photoluminescence and XANES Studies*

Cerium(III) luminescence results from 5d→4f transitions, and involves the lowest ^{2}D excited state and the two spin-orbit components of the ground term, $^2F_{7/2}$ and $^2F_{5/2}$. The accessibility and environmental sensitivity of the ^{2}D electronic state makes luminescence a useful technique to probe Ce(III) interactions with organic ligands. Except for the difference in pyridyl and the ether groups, the ligands DMDPhPDA and DMDPhDGA have similar structural motifs, and their coordination mode with lanthanide ions should be similar. However, as described below, the cerium complexes show distinctly different luminescence behavior.

In Figure 4a and b are shown the emission and excitation spectra of Ce-DMDPhPDA and DMDPhDGA systems, respectively. The Ce-DMDPhDGA system emits strongly at 370 nm (Fig. 4a) with a full width at half-maximum (FWHM) of 59 nm. In contrast, under identical experimental conditions the emission from the Ce-DMDPhPDA system is hardly detectable as it's emission intensity decreases by more than fifty-fold. Additionally, the center of mass for the emission band of the latter system is slightly red-shifted (∼376 nm) compared to the former species. The red-shifting exhibited in the emission band of the Ce-DMDPhPDA system is typical of covalent interaction between the ligand and the metal ion leading to an increase in the extent of splitting the cerium 5d levels. A larger splitting of the 5d levels reduces the energy gap between the lowest emitting state and the ground 4f level [12]. In this regard the optical property is consistent with the conclusion inferred from the bend angle analysis. The excitation spectrum for the Ce-DMDPhDGA system (fig. 4b) also shows a strong peak at 315 nm, as compared to the weak band at ∼308 nm from the Ce-DMDPhPDA system. The blue-shift (∼720 cm^{-1}) observed ffrom the Ce-DMDPhPDA system is as expected since the larger splitting of the 5d level raises the energy position of the higher excited levels, while simultaneously lowering the position of the lowest emitting level. Hence, red-shift in emission and blue shift in the excitation bands signifies the larger 5d splitting caused by the more covalent interaction between cerium and the DMDPhPDA ligand, compared to the DMDPhDGA ligand.

The quenching of the emission from the Ce-DMDPhPDA system was initially thought to indicate partial oxidation of cerium to the tetravalent state, as Ce(IV) is known [13] to be a non-luminescent species. In addition, the Ce-DMDPhPDA solution has a distinctively yellow-orange color, which was thought to provide an additional evidence for the partial oxidation. This postulate was tested by conducting the Ce-K XANES analyses. The XANES spectra of several cerium compounds and complexes

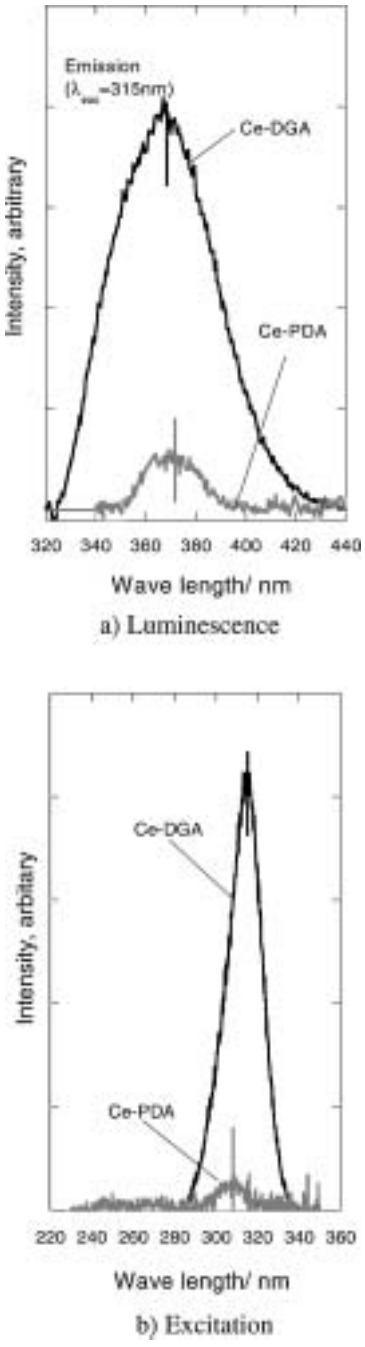

Fig. 4. The (a) luminescence and (b)excitation spectra of Ce-DMDPhPDA and –DMDPhDGA in methanol.

having different valence of cerium are shown in Figure 5. With the the Ce(IV) compounds, shift to higher energies by 7 ∼ 9 eV are observed as compared to the Ce(III) compounds. This comparison clearly indicates that the valence state of cerium in the DMDPhPDA complex is trivalent, as is the DMDPhDGA system. Hence, the quenching of emission from the former species is attributable to a strong interaction between cerium and the nitrogen of the pyridyl group of the ligand. An enhanced inner-sphere complexation with this ligand appears to affect the emission, as has been noted previously in several other chelating ligands [14].

4. Summary and Conclusions

The structural parameters of Ce-DMDPhPDA in methanol-aqueous mixtures were determined by using Ce-K EXAFS

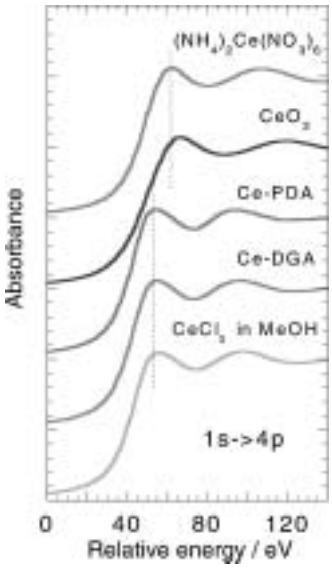

Fig. 5. The Ce-K XANES spectra of several Ce compounds. *PDA : DMDPhPDA; DGA : DMDPhDGA. (*The ratios in this figure denote Ce : DMDPhPDA(M/M).

studies. The bend angle between the Ce-N bond and the p_z axis of the lone pair of the pyridyl nitrogen for the solutions of the Ce-DMDPhPDA complex were found to be 180 degrees, which probably suggests a covalent bond property between the nitrogen and cerium. The luminescence and excitation spectra arising from the 4f-5d transition showed significant quenching, and red-shifts indicating a strong interaction between cerium and the nitrogen of the pyridyl group of the DMDPhPDA ligand. From the XANES data, the oxidation state of Ce was determined as trivalent in both the Ce-DMDPhPDA and Ce-DMDPhDGA complexes.

References

1. Kolarik, Z. and Mullich, U., Solv. Extr. Ion Exch. **15**, 361 (1997).
2. Cordier, P. Y., Hill, C., Baron, P., Madic, C., Hudson, M. J. and Liljenzin, J.-O., J. Alloys Compounds **271**, 738 (1998).
3. Jensen, M. P., Morss, L. R., Beitz, J. V. and Ensor, D. D., J. Alloys Compounds **303–304**, 137 (2000).
4. Zhu, Y., Song, C. and Jiao, R., Proceedings of Global '95, p. 571 (1995).
5. Shimada, A., Yaita, T., Narita, H., Tachimori, S. and Okuno, K., Solv. Extr. Ion Exch. **22** (2), 147–161 (2004).
6. Ressler, T., J. Synch. Rad. **5**, 118 (1998).
7. Zabinsky, S. I., Rehr, J. J., Aukudinov, A., Albers, R. C. and Eller, M. J., Phys. Rev. B **52**, 2995 (1995).
8. Yaita, T., Narita, H., Suzuki, S. *et al.*, Structural study of lanthanides(III) in aqueous nitrate and chloride solutions by EXAFS, J. Radioanal. Nucl. Chem. **239** (2), 371 (1999).
9. Benjamin P. Hay, Omoshile Clement, Giovanni Sandrone and David A. Dixon, Inorg. Chem. **37**, 5887 (1998).
10. Hancock, R. D., Prog. Inorg. Chem. **123**, 1 (1989).
11. Doblar, M., Hirata, M. and Tachimori, S., PCCP **5**, 2499 (2003).
12. Tanaka, K., Hirao, K., Tanaka, H. and Soga, N., Jpn. J. Appl. Phys. **35**, 2170 (1996); Tanaka, K., Ohyagi, T., Hirao, K. and Soga, N., Bull. Chem. Soc. Jpn. **66**, 1121 (1993).
13. Ishii, Y., Arai, K., Namikawa, H., Tanaka, M., Negishi, A. and Handa, T., J. Am. Ceram. Soc. **70**, 72 (1987).
14. Rand, E. R., Smuckler, M. B., Go, E., Bradley, M. S. and Bruno, J. W., Inorg. Chim. Acta. **233**, 71 (1995); Frey, S. T. and Horrocks, Jr. W. D., Inorg. Chem. **30**, 1073 (1991); Lis, S., J. Alloys Comp. **341**, 45 (2002).
15. Shimada, "Development of Extractat for Trivalent Actinide and Clarification of its Extraction mechanism", Doctoral dissertation, p. 77 (2004).

Physica Scripta. Vol. T115, 306–307, 2005

Structural Analysis of Co-Extracted Heptavalent Technetium and Rhenium Complexes by EXAFS

S. Suzuki[1*], T. Yaita[1], Y. Okamoto[1], H. Shiwaku[2] and H. Motohashi[3]

[1]Dept. of Materials Science, Japan Atomic Energy Research Institute, Ibaraki, 319-1195, Japan
[2]Synchrotron Radiation Research Center, Japan Atomic Energy Research Institute, SPring-8, Hyogo, 679-5143, Japan
[3]SPring-8 Service, Mikazuki-cho, Sayo-gun, Hyogo, 679-5143, Japan

Received June 26, 2003; revised September 5, 2003; accepted November 4, 2003

Abstract

The structural parameters of technetium(VII)-uranium(VI)-tri-butyl phosphate (TBP) were determined by EXAFS to elucidate the mechanism of co-extraction of technetium in the presence of uranium(VI). Sample solutions were prepared by solvent extraction methods. The bond distance between uranium and oxygen of TcO_4^- is 2.97 Å; the that of U-Tc is also observed at about 3.5 Å, suggesting that a TcO_4^- molecule exchanges with nitrate ion in the $UO_2(NO_3)_2(TBP)_2$ complex. However, the interaction of zirconium-rhenium of $Zr(NO_3)_x(ReO_4)_{4-x}(TBP)_2$ complex could not be observed. Although the rhenium also co-extracted like technetium by TBP in the presence of U(VI) and Zr(IV), this result indicates that ReO_4^- interact with Zr through water.

1. Introduction

On the behavior of technetium in the nuclear fuel re-processing, there are many reports [1–5]. In the nitric acid solution in the process, Tc exists as per-technetate ion. The pertechnetate ion is a comparatively large tetrahedral structure which consists of four oxygen, while the effective charge is comparatively smaller than that of the other anion [6]. Therefore, it is extracted in ion pair as a pertechnetic acid by TBP easily. Furthermore, the per-technetate ion is co-extracted with counter ions such as UO_2^{2+}, Pu^{4+} and Zr^{4+} with TBP [4, 5, 7]. Due to the difference this solvation, $UO_2(TcO_4)_2$ is extracted twice better on the distribution ratio of uranium than $UO_2(NO_3)_2$ by 30% TBP-n-dodecane [5]. However, there is little reported about structural analysis of these co-extracted complexes. In this study, a structural analysis of the co-extracted complexes were performed about Tc-complexes: $UO_2(NO_3)(TcO_4^-)_{2-x}(TBP)_2$ and Re-complex: $Zr(NO_3)_x(ReO_4)_{4-x}(TBP)_2$.

2. Experimental

2.1. *Sample Preparation*

The technetium samples were made as follows. 1 ml of n-dodecane as an organic solvent containing 30% tri-butyl phosphate was shaken with the same volume of nitric acid containing 40 mM of UO_2^{2+} with about 0.7 M of TcO_4^-. After centrifugation, 0.45 ml of the organic solution was separated to use as a sample.

The rhenium-zirconium sample was also made by the solvent extraction method. 1 ml of the organic solvent containing 30 % tri-butyl phosphate in n-dodecane was shaken with the same volume of 5.0 M of nitric acid containing 0.2 M of Zr^{4+} with 0.2 M ReO_4^-. After centrifugation, 0.7 ml of the organic solution was separated to use as a sample.

2.2. *Sample measurements*

0.45 ml of Tc-U-ligand complex solution was enclosed in a polyethylene tube. 0.7 ml of Re and Mn complex samples were enclosed in a polyethylene bag with 1 mm thickness adjusted by a Teflon spacer in the measurement.

EXAFS measurement were carried out at the beam line BL27B of the Photon Factory (2.5 GeV) of the high-energy accelerator research organization (KEK) in transmission mode under the condition of beam current 250–380 mA. The absorption edges were 17.16 keV for U(L_{III}), 21.05 keV for Tc(K), 10.53 keV for Re(L_{III}) and 6.54 keV for Mn(K).

The extraction of EXAFS oscillation from the absorption spectra were carried out by WinXAS V.2.3. [8]. A linear function was used for pre-edge extrapolation. Atomic absorption was modeled using cubic spline function. Normalization was achieved using the victoreen method. The Fourier transform [$k^3\chi(k)$] was calculated with Gaussian windows function in the range of 2.50–11.4 $Å^{-1}$ for Tc complexes, 2.65–14.1 $Å^{-1}$ for U complexes, 2.70–13.7 $Å^{-1}$ for Re complexes and 2.7–14.0 $Å^{-1}$ for Mn complexes. Back-Fourier transforms were performed in the ranges 0.5–4.0 Å for Tc complexes, 0.4–4.1 Å for U complexes, 0.8–1.9 Å for Re complexes and 0.77–2.0 Å for Mn complexes.

The theoretical parameters for curve fittings of the EXAFS spectra were calculated using FEFF7 [9].

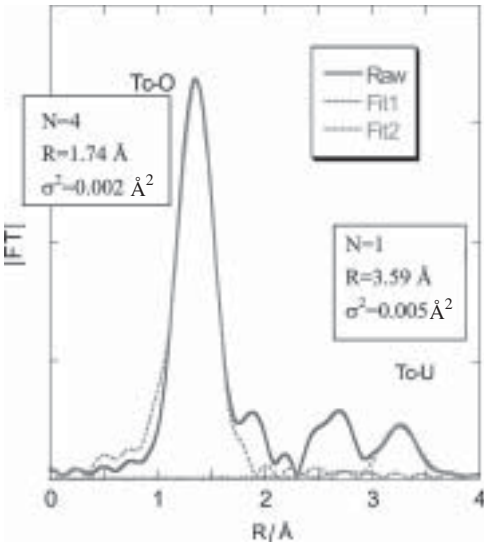

Fig. 1. The radial structural function and the curve fitting of Tc K-EXAFS spectra on the basis of UO_2-TcO_4-NO_3-TBP model. * The N, R, σ^2 present the coordination number, bond distance, and Debye-Waller factor, respectively. **The phase shifts were not corrected.

*suzuki@mummy.tokai.jaeri.go.jp

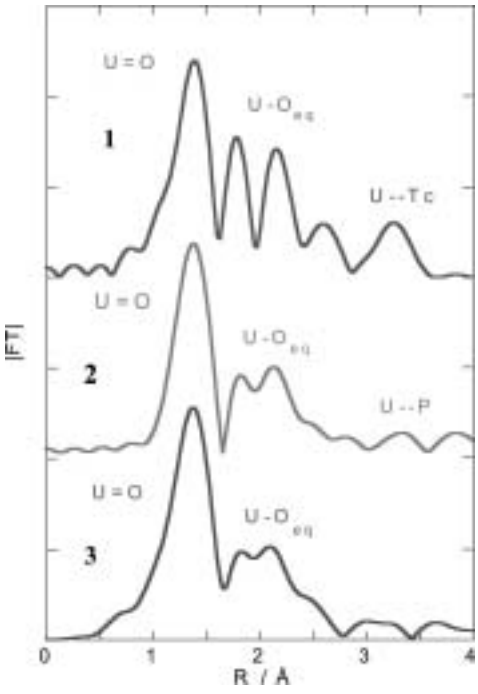

Fig. 2. Comparison of radial structural functions of Tc-ligand complexes. 1: $UO_2(NO_3)(TcO_4)(TBP)_2$, 2: $UO_2(NO_3)_2(TBP)_2$, 3: $UO_2(NO_3)_2(H_2O)_2$ *The phase shifts were not corrected.

3. Results and Discussion

The radial structural functions of Tc-K XAFS for Tc-U-TBP complex in dodecane prepared by the solvent extraction method are shown in Fig. 1. The first peak in the sample is attributed to the four oxygen atoms of the TcO_4^- ion. The bond distance of Tc-O, i.e. about 1.74 Å, agrees well with the previous data [10]. Generally, technetium is further extracted in the presence of U(VI) ion in the solvent extraction with TBP. Therefore, technetium is regarded to behave as a counter ion in the extraction of uranium. Accordingly, the peaks around 3.2 Å (in RSF) can be attributed to the Tc-U interaction. The curve fitting for the UO_2-TcO_4-NO_3-TBP complexes of Tc-K EXAFS is also shown in Fig. 1. The bond distance of Tc-O and Tc-U are about 1.74 Å and 3.59 Å, respectively. These structural analysis data suggest that TcO_4^- ion coordinates to uranium with bidentate fashion instead of a nitrate ion in the Tc co-extraction system. The comparison of radial structural functions of U-L_{III} XAFS for $UO_2(TcO_4)(NO_3)\cdot 2TBP$, $UO_2(NO_3)_2\cdot 2TBP$ and $UO_2(NO_3)_2\cdot 2H_2O$ are shown in Fig. 2. The U-O(-Tc) and U-Tc of $UO_2(TcO_4)(NO_3)\cdot 2TBP$ are also confirmed, and significant evidence of TcO_4^- for direct coordination to UO_2^{2+}. The distance U-Tc is 3.60 Å, which agrees well with the Tc-K XAFS result. The curve fitting results of U-L_{III} EXAFS spectra for $UO_2(TcO_4)\cdot(NO_3)2TBP$ are listed in Table I. The interaction of uranium are mainly 5, U=O_{axial}, U-O_{eq1} (O = P), U-O_{eq2} (O_2-NO), U-O_{eq3} (O-Tc), and U-Tc. The bond distance of U-O_{eq3}: 2.97 Å is longer than for U-O_{eq2}: 2.51 Å and U-O_{eq1}: 2.31 Å. Therefore, TcO_4^- would show weaker interaction than the other oxygens. For clarification of these results, we need to do experiments.

Table I. *Curve fitting results on the basis of $UO_2(TcO_4)(NO_3)(TBP)_2$ model. *Value in parenthesis denote the parameters of $UO_2(NO_3)_2(TBP)_2$ at the same position.*

	r/Å	N	σ^2/ Å^2
U=O_{ax}	1.77(1.76)*	2	0.002
U-O_{eq1}	2.31(2.38)*	2	0.005
U-O_{eq2}	2.51(2.51)*	2	0.006
U-O_{eq3}	2.97	2	0.008
U-Tc	3.60	1	0.006

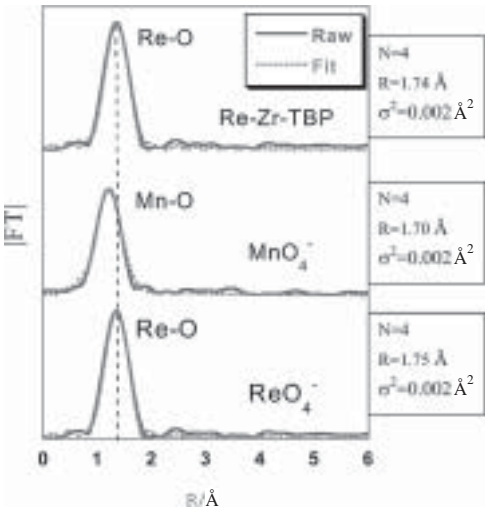

Fig. 3. Comparison of radial structural functions and curve fittings of ReO_4^- MnO_4^- in aqueous solution (3M HNO_3) and the extracted Re-Zr-TBP complex in dodecane. *N, R, σ^2 present the coordination number, bond distance, and Debye-Waller factor, respectively. **The phase shifts were not corrected.

The radial structural functions of ReO_4^-, and MnO_4^- in solution are shown in Fig. 3. The bond distance of Mn-O is about 1.70 Å, and slightly shorter than that of Re-O (1.75 Å). The radial structural function of Re-Zr-TBP complex in dodecane is also shown in Fig. 3. Although Re is also co-extracted by TBP in the presence of Zr^{4+} like UO_2^{2+}, there are no interactions around Re expect for the interaction for the Re-O of ReO_4^-. This result suggests that Zr^{4+} would exist beyond 4.0 Å and the ReO_4^- seems to interact with Zr^{4+} through water.

References

1. Maacacek, F. and Kadrabova, J., J. Radioanal. Chem. **51**, 97 (1979).
2. Prutt, D. J., Radiochim. Acta **28**, 153 (1981).
3. Prutt, D. J., Radiochim. Acta **29**, 107 (1981).
4. Jassim, T. N., Liljenzin, J. O. and Persson, G., Radiochim. Acta **33**, 163 (1983).
5. Kanellakopulos, B. and Konig, C. P., Radiochim. Acta **33**, 169 (1983).
6. Neck, V. and Kanellakopulos, B., Radiochim. Acta **42**,135 (1987).
7. Garraway, J. and Wilson, P. D., J. Less-Common Met. **106**, 183 (1985).
8. Ressler, T., J. Synch. Rad. **5**, 118 (1998).
9. Zabinsky, S. I., Rehr, J. J., Ankudinov, A., Albers, R. C. and Eller, M. J., Phys. Rev. B. **52**, 2995 (1995).
10. Allen, P. G. *et al*., Radiochim. Acta **76**, 77 (1997).

Physica Scripta. Vol. T115, 308–311, 2005

C K-Edge NEXAFS of 6H-SiC and 3C-SiC Systems

M. Pedio*[1], A. Giglia[1], N. Mahne[1], S. Nannarone[1,3], S. Giovannini[2], C. Cepek[1], F. Boscherini[2], R. Carboni[2], M. Benfatto[4] and S. Della Longa[4,5]

[1]TASC-INFM Area Science Park, I-34012 Basovizza
[2]Dipartimento di Fisica, Universita' Bologna and INFM
[3]INFM-UdR Modena and Dip. Ingegneria dei materiali e dell'ambiente, Universita' Modena
[4]LNF-INFN P.O. Box 13, I-00044 Frascati
[5]Dipartimento Medicina Sperimentale, Università L'Aquila, 67100 L'Aquila, Italy

Received June 26, 2003; accepted December 4, 2003

PACS numbers: 78.70.Dm, 71.20.Nr

Abstract

Silicon carbide polytipes 6H-SiC and 3C-SiC were characterized by optical absorption at the C K edge in the near edge absorption region.

3C-SiC and 6H-SiC showed similarities for energies about 15 eV above the edge.

Marked differences were found in the near edge region. A picture based on the p distribution of empty states was suitable to describe the main features of 3C-SiC. 6H-SiC showed important absorption anisotropies traceable to the anisotropies of the scattering paths as shown by full multiple scattering calculation performed by MXAN code. The role of self consistency is also discussed.

1. Introduction

The interest in silicon carbide is increasing due to its promising properties in high power, high frequency and high temperature electronic applications [1]. Silicon Carbide is one of the compounds that show the most pronounced polytypism, with more than 200 SiC polytypes existing in nature. The existence of so many different polytypes is due to the many possible stacking sequences of the basic structural elements: the $\{111\}$ Si-C bilayers of the cubic (zincblende) structure or $\{0001\}$ layers of the hexagonal structure [2].

All SiC polytypes have the same nearest neighbor configuration, and differ in the long-range structure. The long range order influences deeply the electronic properties, which depend on the joint density of states between valence and conduction band. For example the band gap energy increases with increasing hexagonal character of the polytype: 2.2 eV in 3C-SiC, 3.0 eV in 6H-SiC and 3.5 eV in 2H-SiC. Experimental results [3] and theoretical calculations [4] show that the differences in the electronic properties are a consequence of the differences in the electronic structure of empty states. It is crucial to understand the long-range properties of the different polytypes, and significant efforts were made to characterize these systems [3, 4, 5, 6]. Nevertheless, a detailed knowledge of the correlation between electronic and structural properties is still lacking in literature. X-ray absorption spectroscopy gives insights on both aspects at the same time, giving information on the local density of the empty states, and providing the local atomic geometry around the absorbing atom.

This work reports on a C K-edge X-ray absorption study of 6H-SiC monocrystal and 3C-SiC ordered film. The sample orientations were (0001) for the 6H and (100) for the 3C system. The C K-edge NEXAFS spectra of the two systems showed similarities for energy above 295 eV (i.e. 15 eV above the absorption edge), while marked differences were found in the near edge region (within 10–15 eV above the edge). These differences are related both to the particular polytype and to the measurement geometry and light polarization used. Full multiple scattering self-consistent calculations were performed on these systems by using MXAN code.

For the C K-edge NEXAFS of 3C-SiC the assignment of the structures was made on the basis of the character of the empty electronic states and by using the full multiple scattering simulations. The C K-edge of the absorption spectra of 6H-SiC monocrystal showed a strong dependence on the polarization direction of the photon electric field that is explained in terms of the anisotropy of the electronic structure of the hexagonal 6H systems and also by the anisotropies of the scattering paths, as analyzed by the simulations. The role of self-consistency is also discussed.

2. Experimental

The cubic SiC sample was growth *ex-situ* by co-deposition of Fullerene and Silicon on Si(100) substrate at high temperature (about 1100 K). The thickness of the SiC film was 8000 Å. This growth procedure leads to 3C-SiC films that can show a good degree of order, without the presence of other polytypes [7]. The quality of the film was *ex-situ* evaluated by X-ray diffraction and by Low Electron Energy Diffraction (appearance of the (3×2) pattern) after a cycle of sputtering (Ar^+, 500 eV, 0.1 μA) and annealing (1000 K) in ultra high vacuum. Photoemission from the C 1s, Si 2p core levels and from the valence band were measured in order to characterize the system. 6H-SiC was a commercial CREE crystal, with a thickness of about 1 mm. Optical absorption measurements at the C K-edge were performed in a UHV chamber at the BEAR beamline of the ELETTRA synchrotron radiation facility in Trieste, Italy [8]. The light was linearly polarised with a photon flux of the order of 10^{10} ph/s. The energy resolution was 80 meV. The sample could be rotated along an axis normal to the synchrotron orbit plane, allowing switching from normal incidence (photon Electric field in the surface plane, p incidence conditions) to grazing incidence (photon Electric field almost normal to the surface plane).

The absorption of 3C-SiC thin ordered film was obtained in total electron yield (TY), by measuring the current drained by the sample; the dark current was stable and typically of the order of 0.1 pA. For the insulating 6H-SiC monocrystal the absorption was obtained by measuring the total fluorescence yield obtained from a calibrated photodiode (IRD AXUV100). Also in this case the dark current was stable, and typically of the order of 0.01 pA. The sample was biased at +1000 V in order to avoid any signal due to

*e-mail: pedio@tasc.infm.it

the electrons excited by the photon beam reaching the photodiode detector. The use of fluorescence yield guarantees that spectra are relative to bulk properties and unaffected by the surface condition. The photodiode surface normal formed an angle of 90° with the direction of the incident beam. Fluorescence yield (FY) spectra of concentrated samples can be distorted due to self-absorption [9]. The FY spectra were corrected for self-absorption as described in ref. [10].

Absorption signals were normalized to the incident flux, obtained by measuring the current drained by a tungsten grid inserted in the beam path. The grid was flashed in order to remove the contaminants, typically C and O.

3. Results and Discussion

The absorption spectrum (measured by TY) at the C K edge of 3C-SiC, taken at normal incidence, is shown in Fig. 1(a). In Fig. 1(b) the absorption at the same edge, taken by FY, is reported for 6H-SiC for two different grazing angles, 75° and 15°, respectively.

For 3C-SiC, the spectrum region above the C K edge shows a rich fine structure characterized by a group of peaks with prominent features at about 290 eV. The spectra did not show any dependence on the incidence direction of light, confirming the good crystal quality of the thin film with zinc-blend structure.

The 6H-SiC spectra show a similar fine structure, but with a dependence on the direction of the electric field with respect to the surface normal.

The following discussion is concentrated on the electronic and structural information that can be extracted from the analysis of the near edge spectra. The discussion will concern the first 15 eV above the edge, where marked differences occur. No significant differences are present above about 295 eV, where the NEXAFS spectra show similar features (indicated by the A and B labels of Fig. 1). The above experimental evidences are in agreement with inverse photoemission (IPES) measurements [6] and theoretical calculations [4], which show that the density of empty states of the conduction band extend significantly up to about 15 eV. In a framework based on the electronic states, the contribution to the K edge is related to the p character of the empty states. Band structure calculations [4] and cluster calculations performed by Xα molecular orbital [11] show that the unoccupied density of states of SiC both in cubic (3C-SiC) and hexagonal polytypes (applicable to the 6H-SiC in present case) is dominated by C 2p and C 2s empty electronic states. In particular the C 2p character is spread up to about 20 eV above the edge. In this framework the group of features in the IPES spectrum of 1×1 6H at 8 eV above the Fermi level has been attributed to the intrinsic bulk band of 6H-SiC due mainly to C 2p empty states. On this basis, the feature at 292 eV (present in the 6H-SiC, missing in the 3C-SiC) can be related to the bulk state at 8 eV detected by IPES, confirming the carbon origin of this state. Moreover the behavior of the 6H-SiC states as a function of the light incidence angle can be put into relation with the bond direction. In particular the most intense state at 290 eV suggests the presence of a state almost prominent from the basal plane of p character. This analysis is not able to assign the origin of the final state.

Information on both geometrical and electronic structure can be extracted by analyzing the experimental spectra with full multiple scattering calculations. Full multiple scattering simulations have been performed by MXAN [12] code. The code can provide fits of the experimental data by the absorption cross section calculation depending on the choice of structure and potential parameters. Preliminary non self consistent results will be shown here. Results obtained by using a self consistent

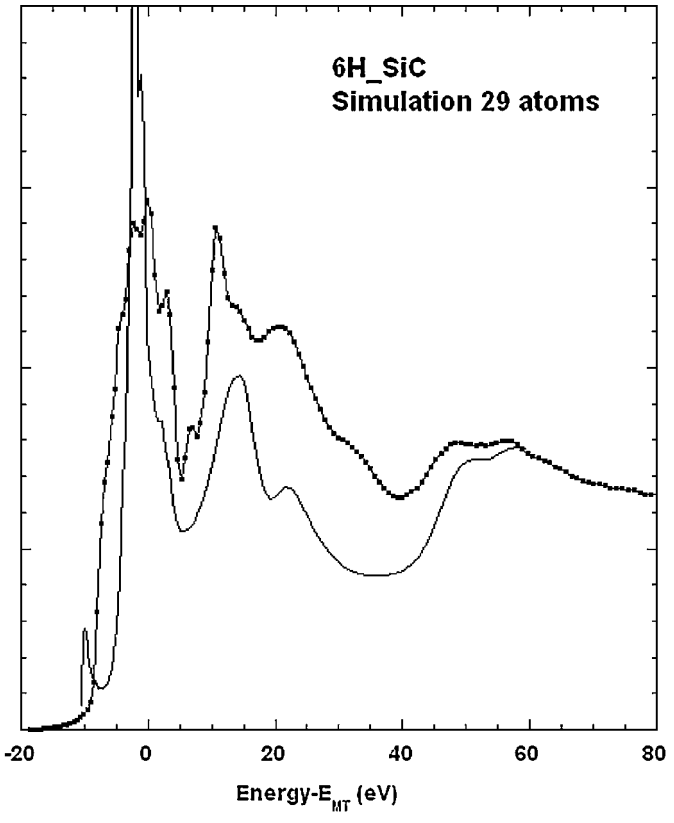

Fig. 1. (a) C K-edge NEXAFS of 3C SiC 8000 Å ordered film taken at normal incidence in total yield detection mode (b) 6H SiC monocrystal taken at nearly normal (75°) and grazing incidence (15°) in fluorescence yield mode.

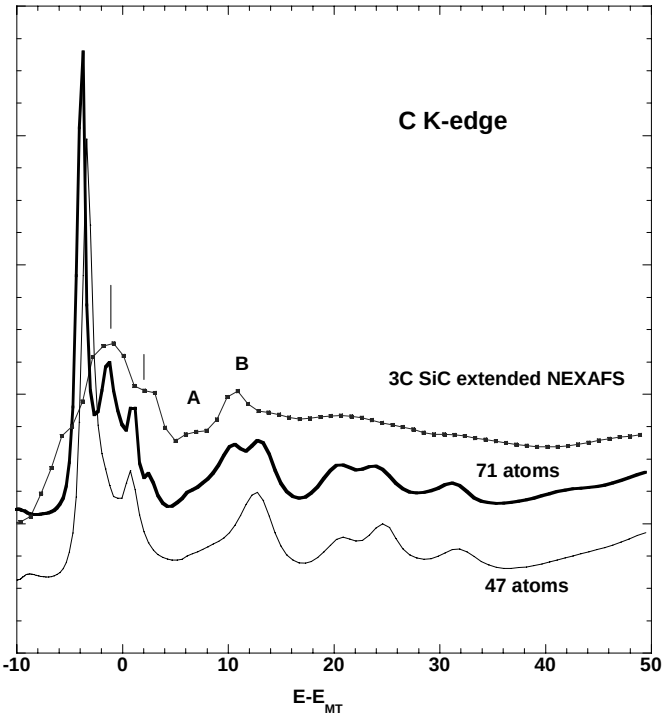

Fig. 2. Experimental spectrum (dots) of the C K-edge extended NEXAFS of 3C SiC compared with MXAN simulation performed with a cluster of 47 and 71 atoms around the central C atom. A and B indicate the features showing up in all the spectra of the SiC polytypes.

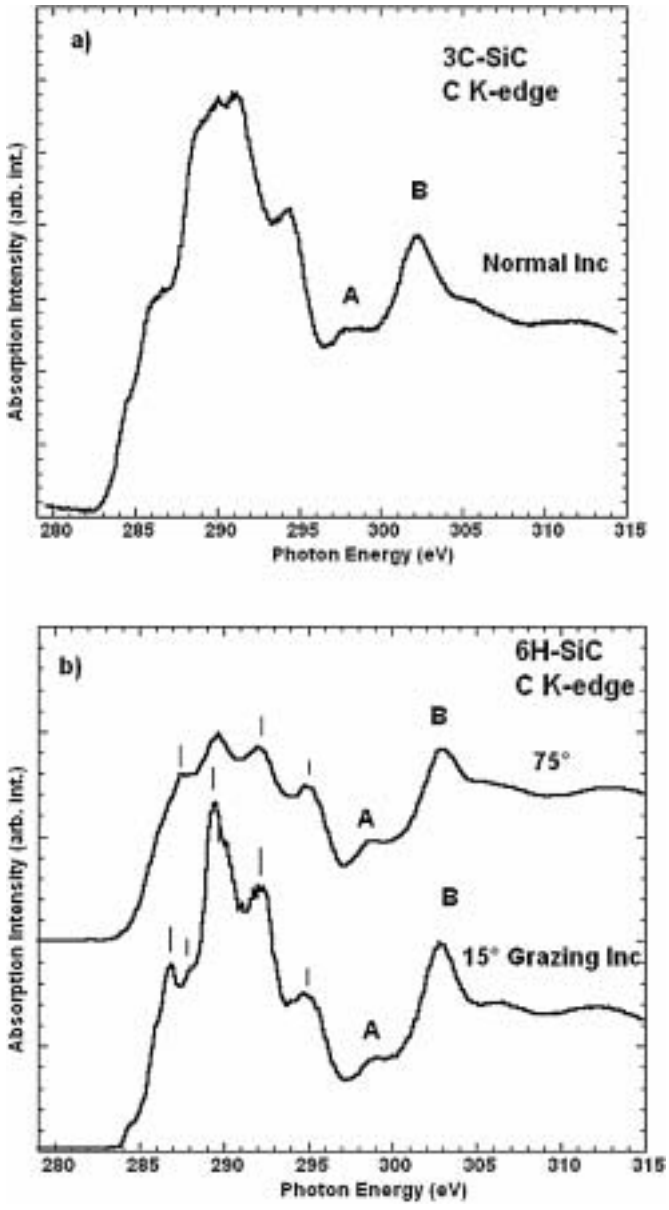

Fig. 3. Experimental spectrum (dots) of the C K-edge extended NEXAFS of 6H SiC taken at nearly normal incidence (75°) compared with MXAN simulation performed with a cluster of 29 atoms around the central C atom.

potential will be presented in a forthcoming paper. A Hedin-Lundqvist energy dependent potential was used to take into account the exchange and correlation. The atoms coordinates were fixed, while some potential parameters (e.g. interstitial potential values, overlap fraction between contiguous atoms and the Fermi energy) were treated as fitting parameters. The results are shown in Fig. 2 for 3C-SiC and in Fig. 3 for 6H-SiC.

Fig. 2 shows our results obtained with two 3C clusters of 47 atoms (cluster radius of about 4.7 Å) and of 71 atoms (cluster radius of about 5.3 Å) around the central C atom. The dependence of the simulation on the cluster dimension shows that to reproduce the high energy part of the spectrum it is enough to use a cluster of 3.6 Å. The NEXAFS part within 20 eV above the edge is reproduced only by using 71 atoms, and convergence in the simulations was achieved only at this cluster dimension. Apart from the over-estimation of the intensity at the very edge, the simulation gives a good account of the overall lineshape.

As in the case of the 3C polytype, in the case of 6H-SiC a simulation with 29 atoms (corresponding to a radius of 3.6 Å) is able to reproduce the spectrum at energies above the feature A of Fig. 1(b). The result is shown in Fig. 3 for the case of 75° of grazing incidence and compared with the experimental results reported in Fig. 1(b). The simulation gives a good account of the overall features of the spectrum though it overestimates the intensity in the near edge region.

The simulations (not shown here) performed with a larger cluster (56 atoms corresponding to a radius of 5.3 Å) gave a good account of the dependence of the intensities of the two features at about 293 eV and 295.5 eV on the direction of the electric field of light, as reported in Fig. 1(b). This is in agreement with the picture reported by Vvedensky [13] that demonstrates that the maxima of the absorption cross section correspond to those scattering paths involving atoms in a direction parallel to the direction of the electric field of the light. Closer to the edge the details of potential are more critical requiring the use of a self consistent approach mainly for low Z elements. In the case of low Z elements further difficulties arise from the effects due to the long e-h recombination life time. Moreover theoretical calculations in the case of carbon silicides [14] indicate that there is a large accumulation of electronic charge around the carbon atom generating a situation similar to that of ionic materials where, as discussed in ref. [15], self consistency is required to take into account the critical details of potentials. In order to test the possibility to correctly simulate the near edge part of NEXAFS corresponding to conduction band contribution of the local density of C electronic states, further calculations are in progress.

4. Conclusions

Silicon carbide polytipes 6H-SiC and 3C-SiC were characterized by optical absorption at the C K edge in the near edge absorption region. The NEXAFS spectra of both systems show important differences related to the peculiarities of the electronic and structural properties of the two systems well evident in the 0–20 eV photon energy region above the edge. Less evident differences were detected for higher energies.

The assignment of spectral features can be made on the basis of the partial empty density of states mainly of 2p character originating from C. This is further substantiated by the observation in the near edge region of the strong dependence of the absorption spectra, only for 6H poly-type, on the polarization direction of the photon electric field related to the anisotropy of the stacking sequence of the hexagonal structure.

Non self consistent multiple scattering analysis is able to describe the region close to the absorption edge; on the other side its failure in the about first 10 eV is in agreement with the critical dependence of the electronic potential substantiated by the possibility of interpretation on the basis of the density of empty states. The above point requires particular attention in the description of the potential. To this aim a self consistent analysis by the MXAN code is in progress.

Acknowledgment

This work was partially supported by the Istituto Nazionale per la Fisica della Materia (INFM) under project PURS-FLUX.

References

1. Pens, G. and Helbig, R., "Silicon Carbide – Recent Results in Physics and in Technology", Festkörperprobleme/Advances in Solid State Physics, Vol. 30, (ed. U. Rössler), (Vieweg, Braunschweig ,1990).
2. Wychoff, R. W. G., "Crystal Structures", (Wiley, New York, 1963).

3. Lüning, J., Eisebitt, S., Rubensson, J.-E., Ellmers, C. and Eberhardt, W., Phys. Rev. B **59**, 10573 (1999) and ref. therein.
4. Lambrecht, W. R. L., Limpijumnong, S., Rashkeev, S. N. and Segall, B., Phys. stat. sol. (b) **202**, 5 (1997).
5. Johansson, L. I., Owman, F., Mårtensson, P., Persson, C. and Lindefelt, U., Phys. Rev. B **53**, 13803 (1996); Soukiassian, P., Semond, F., Mayne A. and Dujardin, G., Phys. Rev. Lett. **79**, 2498 (1997).
6. Forbeaux, I., Themlin, J.-M. and Debever, J.-M., Phys. Rev. B **58**, 16396 (1998).
7. Volz, K. *et al.*, Mat. Sci. Engin. A**289**, 255 (2000); Cepek, C. *et al.*, "Improved β-SiC(100)/Si (100) Interface quality", unpublished.
8. Naletto, G., Pelizzo, M. G., Tondello, G., Nannarone, S. and Giglia, A., SPIE Proc. **4145**, 105 (2001); Nannarone, S. *et al*., SRI conference proceedings, to be published.
9. Goulon, J., Goulon-Ginet, C., Cortes, R. and Dubois, J. M., J. Phys. (Paris) **43**, 539 (1982); Tröger, L. *et al.*, Phys. Rev. **46**, 3283 (1992).
10. Carboni, R., Giovannini, S., Antonioli, G. and Boscherini, F., "Self-absorption correction strategy for fluorescence-yield soft X-ray near edge spectra", Physica Scripta, these proceedings.
11. Muramatsu, Y., Takenaka, H., Ueno, Y., Gullikson, E. M. and Perera, R. C. C., Appl. Phys. Lett. **77**, 2653 (2000).
12. Della Longa, S., Arcovito, A., Girasole, M., Hazemann, J. L. and Benfatto, M., Phys. Rev. Lett. **87** 155501 (2001); Benfatto, M., Physica Scripta, these proceedings.
13. Vvedenski, D. D., Surf. Sci. **162**, 909 (1985).
14. Ayma, D., Rérat, M., Orlando, R. and Lichanot, A., Acta Cryst. A**54**, 1019 (1998).
15. Wille, L. T., Durham, P. J. and Sterne, P. A., J. Physique C**8**, 43 (1986).

Physica Scripta. Vol. T115, 312–313, 2005

Zinc Oxynitride Powders Examined by X-ray Absorption Near Edge Spectroscopy

Toshihiro Moriga[1]*, Takashi Sakamoto[1], Ryoji Saki[1], Kei-ichiro Murai[1], Ichiro Nakabayashi[1] and James B. Metson[2]

[1]Department of Chemical Science and Technology, Faculty of Engineering, University of Tokushima, Tokushima 770-8506, Japan
[2]Department of Chemistry, The University of Auckland, Private Bag 92019, Auckland, New Zealand

Received June 26, 2003; accepted November 4, 2003

PACS number: 61.10.Ht

Abstract

Anti-bixbyite-type zinc oxynitride powders $Zn_3(N_{1-x}O_x)_{2-y}$ could be prepared by directly nitriding zinc powder under ammonia gas flow. $Zn_3(N_{0.91}O_{0.09})_{1.98}$ could be obtained after 168 hours of nitridation at 500 °C. X-ray absorption spectra near N and O K-edges for some zinc oxynitrides were recorded in both total electron yield and fluorescence modes. The two spectra provide complementary information on the near surface, and on what can be considered as the bulk of the powdered zinc oxynitride. O K-edge spectra clearly appeared for all the measured oxynitrides in both the total electron yield and fluorescence modes. However, only the N K-edge fluorescence yield spectrum was detected even for the nitrogen-richest oxynitride $Zn_3(N_{0.91}O_{0.09})_{1.98}$. These results imply that the prepared zinc oxynitrides were covered with some ten nanometers of oxide layers and that nitridation of zinc powders would proceed by thinning down the oxide layers.

1. Introduction

Various zinc compounds are actively investigated because of their significant properties. For example, impurity doped ZnO is a promising material for transparent conducting oxides [1, 2]. Recently, zinc ternary oxides such as Zn-In-O [3, 4] and Zn-Sn-O [5] systems have also drawn much attention as new transparent conducting oxides. However, Zn-O-N system has been scarcely studied. The anti-bixbyite-type Zn_3N_2 has been reported to show n-type conduction with a direct band gap of 1.23 eV [6] whereas the optical band gap of the wurtzite-type ZnO is determined to be around 3.2 eV. Futsuhara *et al*. tried to alter the optical band gap from 1.23 to 3.2 eV by varying the composition of Zn-O-N films, and showed that the gap decreased from 3.26 eV to 2.3 eV with increasing nitrogen concentration in the films [7].

In preparing such metal oxynitrides, ammonia gas is preferentially used as a nitrogen source. We have reported that the anti-bixbyite-type zinc oxynitrides $Zn_3(N_{1-x}O_x)_{2-y}$ could be prepared by directly nitriding zinc powder under ammonia gas flow [8]. The oxygen content x and amount of anion deficiency y decreased with increasing nitriding period at 500 °C. The nitrogen richest $Zn_3(N_{0.91}O_{0.09})_{1.98}$ could be obtained after 168 hours of nitridation at 500 °C. During the nitridation of zinc powder by ammonia gas flow, entire zinc oxide layers of a few millimeters covered forming oxynitrides and the oxynitrides enriched their nitrogen content in proportion to the nitriding period. Though these oxynitrides were detected as a single phase by X-ray diffraction, it is necessary to prove the microstructures by using methods which are sensitive to the local environment around the nitrogen and oxygen centers.

In this study, X-ray absorption spectra near N and O K-edge for the zinc oxynitrides were recorded in both total electron yield and fluorescence modes. The two spectra provide complementary information on the near surface, and on what can be considered as the bulk of powdered zinc oxynitride.

2. Experimental Procedures

Metallic zinc powder (analytical grade, particle size less than 45 μm, purchased from Merck) was used as a starting material. The zinc powder was laid in an alumina boat placed in an alumina tube of a horizontal Siliconit tube furnace. After evacuating the system, argon gas was introduced. The furnace temperature raised to the nitriding temperature of 400–600 °C in 1 hour, the gas was switched to ammonia flowing at a rate of 50 ml/min. Both the argon and ammonia gases were dried by passing through a soda lime cylinder and a coiled coolant trap (−30 °C). The product was cooled in the furnace down to room temperature.

Phase identification was performed by powder X-ray diffractometry (Rigaku RINT-2500VHF+) using monochromatized CuKα radiation with a source power of 40 kV and 100 mA. The oxygen and nitrogen contents of each oxynitride were analyzed using a Horiba EMGA-2800 device. The samples mixed with a Ni-Sn flux were reduced in a carbon crucible to convert the oxygen and nitrogen into carbon monoxide and N_2 in helium as a carrier gas, respectively. The amount of carbon monoxide was determined by measuring the IR absorbance and that of N_2 was detected by the thermal conductance. In calculations of composition of oxynitrides, the ratio of zinc to anion components (nitrogen and oxygen) was normalized to be "3". Hereafter, the composition of oxynitride is expressed as $Zn_3(N_{1-x}O_x)_{2-y}$, where x represents oxygen amount and y represents the anion deficiency in the oxynitride.

X-ray absorption spectroscopy was carried out at the Canadian Synchrotron Radiation Facility (CSRF) located at the Aladdin storage ring at the Synchrotron radiation Centre, University of Wisconsin, Madison, USA. The ring operated at 1 GeV and the average ring current was 190 mA. N K-edge and O K-edge spectra were recorded on the Spherical Grating Monochromator beamline, in both total electron yield (TEY) and fluorescence yield (FLY) modes [9]. The grating used on the spherical grating monochromator has 600 lines/mm, giving an energy range of 240–700 eV. The resolution of this beamline has been demonstrated to be around 70 meV in gas phase spectroscopy [10]. The photon beam is incident along the surface normal and the energy was typically scanned across 395 to 420 eV and 510 to 560 eV windows to collect the nitrogen and oxygen spectra, respectively. The beam on the sample has a size of 1 mm horizontal times 1 mm vertical. Spectra were normalized by division by the photon flux measured by a 90% transmission gold mesh.

*E-mail: moriga@chem.tokushima-u.ac.jp

3. Results and Discussion

The X-ray diffraction patterns showed that nitridation of metallic zinc under ammonia gas flow at 500 °C led to the formation of pure anti-bixbyite-type zinc oxynitrides. Interestingly, the zinc oxynitrides were covered with ZnO in the alumina boat. After removing the oxide cover carefully, the oxynitrides were examined. When the nitriding temperature was set at 500 °C, $Zn_3(N_{0.81}O_{0.19})_{1.97}$ and $Zn_3(N_{0.91}O_{0.09})_{1.98}$ was formed for 48 and 168 hours, respectively. The compositional analysis of the products suggested that the oxygen content x in $Zn_3(N_{1-x}O_x)_{2-y}$ fundamentally decreased with increasing nitriding period. The lattice constant a of the respective product was 9.762 Å after the 48-hour nitridation and 9.764 Å after the 144-hour nitridation, both of which were slight smaller than 9.769 Å of the reported one for Zn_3N_2. This trend in increased lattice constants agrees well with the results reported by Futsuhara *et al*. [7, 11], and these facts mean that the oxygen should be occluded in the zinc oxynitrides.

Figure 1 shows O K-edge TEY and FLY spectra observed for $Zn_3(N_{0.81}O_{0.19})_{1.97}$ and $Zn_3(N_{0.91}O_{0.09})_{1.98}$ at room temperature. No significant differences were observed between the spectra except that the edge jump height corresponding to the so-called white line, just after the absorption threshold, was smaller in the FLY spectra than that in the TEY spectra. Figure 2 shows N K-edge TEY and FLY spectra. No signals were detected in the TEY mode whereas definitive spectra were presented in the FLY mode for both specimens.

Kasrai *et al*. considered the electron mean free path and thus information depth in TEY and FLY modes, in the analysis of oxide films on silicon [9]. For the Si L-edge at around 100 eV the maximum sampling depth in TEY mode is found to be around 5 nm, while that of the fluorescence spectrum is around 70 nm. While sampling depths will be somewhat greater for the N and O K-edges at 400–550 eV due to the increased range of the primary Auger electrons which give rise to the TEY signal, the factor of >10 in the relative information depth will be retained. These results imply that the prepared zinc oxynitrides were covered with some ten nanometers of oxide layers where nitrogen scarcely existed. Note that the S/N (signal to noise) ratio was improved for the sample of nitrogen-rich $Zn_3(N_{0.91}O_{0.09})_{1.98}$. This fact would be mainly attributable to a decrease of thickness of the oxide layers, suggesting that nitridation of zinc powders would proceed by thinning down the oxide layers. The zinc nitrides will contain less amount of oxygen than detected by the compositional analysis.

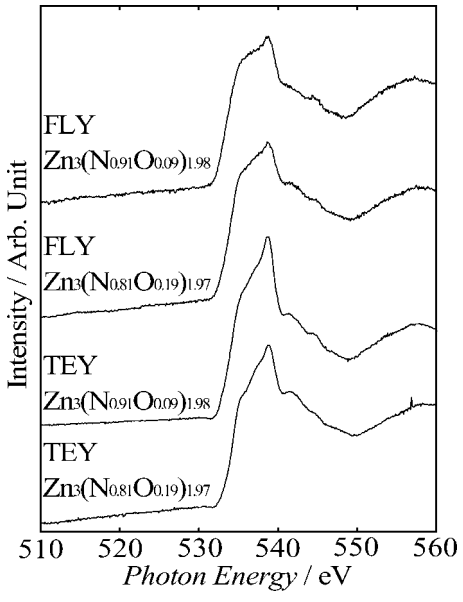

Fig. 1. O K-edge TEY (total electron yield) and FLY (fluorescence yield) spectra observed for $Zn_3(N_{0.81}O_{0.19})_{1.97}$ and $Zn_3(N_{0.91}O_{0.09})_{1.98}$.

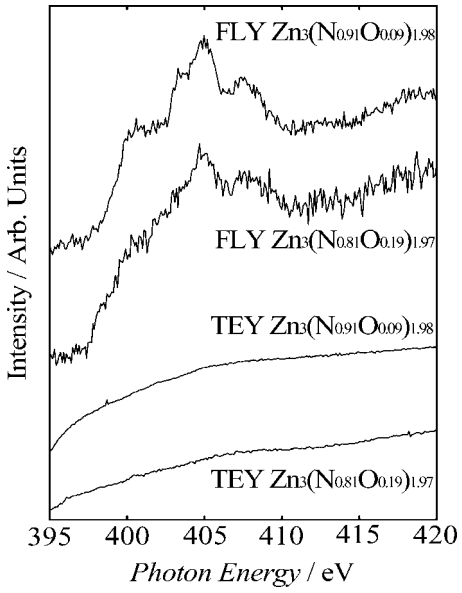

Fig. 2. N K-edge TEY (total electron yield) and FLY (fluorescence yield) spectra observed for $Zn_3(N_{0.81}O_{0.19})_{1.97}$ and $Zn_3(N_{0.91}O_{0.09})_{1.98}$.

Concerning the feature of N K-edge FLY spectrum of $Zn_3(N_{0.91}O_{0.09})_{1.98}$, a dominant peak observed at 405 eV and a shoulder peak at around 400 eV are consistent with that of the N K-edge FLY spectrum of crystalline GaN. In line with other works, including studies of BN, the sharp feature at around 400 eV and the broader peak at 405 eV can be correlated with nitrogen in sp^2 and sp^3 hybridization, respectively [12, 13]. Based on this model, the zinc oxynitride shows greater sp^3 character in the bonding of nitrogen. It is not clear how this should be interpreted, as it is apparent that the nitrogen will be in an octahedral environment in the anti-bixbyite-type zinc oxynitrides. Though early first transition metal nitrides such as TiN and VN possess metallic characters, they tend to show stronger covalent characters as their atomic number increases. Covalent nitrides refer to compounds containing heavier metals than copper in the periodic table. The greater sp^3 character, however, presumably relates to the greater p character, resulting from strong covalency between Zn-N bonds.

References

1. Minami, T., Nanto, H. and Takata, S., J. Appl. Phys. Lett. **41**, 958 (1982).
2. Tominaga, K., *et al*., Thin Solid Films **386**, 267 (2001).
3. Moriga, T., *et al*., J. Am. Ceram. Soc. **81**, 1310 (1998).
4. Moriga, T., *et al*., J. Solid State Chem. **155**, 312 (2000).
5. Minami, T., *et al*., Jpn. J. Appl. Phys. **33**, L1693 (1994).
6. Kuriyama, K., Takahashi, Y. and Sonohara, F., Phys. Rev. B**48**, 2781 (1993).
7. Futsuhara, M., Yoshioka, K. and Takai, O., Thin Solid Films **322**, 274 (1998).
8. Sakamoto, T., Saki, R., Moriga, T., Murai, K. and Nakabayashi, I., Int. J. Mod. Phys. B**17**, 1523 (2003).
9. Kasrai, M., *et al*., Appl. Surf. Sci. **99**, 303 (1996).
10. Yates, B. W., *et al*., J. Synchrotron Rad. **7**, 296 (2000).
11. Futsuhara, M., Yoshioka, K. and Takai, O., Thin Solid Films **317**, 322 (1998).
12. Soo, Y. L., *et al*., Phys. Rev. B **60**, 13065 (1999).
13. Terminello, L. J., Chaiken, A., Lapiano-Smith, D. A., Doll, G. L. and Sato, T., J. Vac. Sci. Technol. A **12**, 2462 (1994).

Physica Scripta. Vol. T115, 314–315, 2005

Local Structure of Six-Coordinated Silicon in Li_2O-SiO_2-P_2O_5 Glasses by Transmission XAFS Experiments

K. Handa[1*], J. Ide[2], K. Yamamoto[2], N. Kurosawa[2], K. Ozutsumi[2], T. Harami[2], K. Kojima[2] and N. Umesaki[3]

[1]Synchrotron Radiation Center, Ritusmeikan University, 1-1-1 Nojihigashi, Kusatsu, Shiga 525-8577, Japan
[2]Faculty of Science and Engineering, Ritsumeikan University, 1-1-1 Nojihigashi, Kusatsu, Shiga 525-8577, Japan
[3]Japan Synchrotron Radiation Research Institute (JASRI), SPring-8, Mikazuki, Sayo 679-5198, Japan

Received June 26, 2003; revised January 29, 2004; accepted January 30, 2004

PACS numbers: 61.10.Ht, 61.43.Fs

Abstract

Six-coordinated silicon [6]Si was observed by Si and P K-edge XAFS measurements in $x$$Li_2O$-$y$$SiO_2$-(100-$y$)$P_2O_5$ glasses (x = 25 and 33, y = 40, 45, 50, 55, and 60). Si K-edge EXAFS spectra of the glasses indicated the co-existence of [6]Si and four-coordinated silicon [4]Si. The proportion of octahedral [SiO_6^{6-}] to [6]Si depends upon the alkali content and the [SiO_6^{6-}]/[SiO_4^{4-}] tetrahedral ratios were estimated by Si K-edge XANES spectra. The interatomic distances were 1.88–1.90 Å for Si-O and 1.5 5–1.61 Å for P-O and the amounts of [SiO_6^{6-}] were 11.8–46.9%.

1. Introduction

It is thought that local structure of silicon in silicate glasses has usually a SiO_4 tetrahedral structure, but in case of SiO_2-P_2O_5 glasses and crystals with high phosphorus concentration, it was reported by NMR [1] and XANES [2] that six oxygen atoms bind with silicon. Moreover, the proportion of six-coordinated silicon [6]Si depends upon the alkali content [3]. XAFS spectra of Si and P K-edge were collected in the soft X-ray region under vacuum conditions, and usually measured by total electron yield [TEY]. However, TEY is very sensitive to the near surface structure of the sample. Therefore, it is not suitable to know the real network in structure formed glasses.

In the present study, we report the experimental method of transmission XAFS under atmospheric pressure and the local structure of [6]Si in octahedral [SiO_6^{6-}] in Li_2O-SiO_2-P_2O_5 glasses.

2. Experimental

$x$$Li_2O$-$y$$SiO_2$-(100-$y$)$P_2O_5$ (x = 25, 33, y = 40, 45, 50, 55, 60) glasses were prepared from extra-reagent grade SiO_2, P_2O_5 and Li_2CO_3. The glasses were melted in Pt crucibles in the range 1573–1673 K depending on the stoichiometry and then quenched by squashing between two stainless-steel plates. The Si and P K-edge XAFS spectra of glasses were obtained by transmission mode at BL-4 in the Ritsumeikan Synchrotron Radiation Center using InSb(111) double monochromater crystals and two ionization chambers filled with helium gas.

3. Results and discussion

Fig. 1 depicts Si K-edge XANES spectra of the glasses. It was reported by Li and Fleet *et al.* [2, 4, 5] that the white peak at the Si K-edge of [SiO_4^{4-}] and [SiO_6^{6-}] were observed at 1868 and 1840 eV, respectively. Each obtained spectrum was fitted by Gaussian components for [4]Si and [6]Si. This estimation method for [6]Si through deconvolution of the Si K-edge XANES spectra was first addressed by Li *et al.* [4] and subsequently revised by Fleet *et al.* [2, 6]. As shown in Fig. 2, the Si K-edge EXAFS spectra of the glasses are very similar for all glasses in the composition range investigated. On the other hand, the EXAFS oscillation of these glasses differs from the Si K-edge EXAFS of standard samples, such as Leucite and amorphous SiO_2. Coordination numbers obtained by XANES fitting analysis were used in the EXAFS curve fittings as an initial value. Results of the curve fitting procedure indicate that the Si-O interatomic distances of

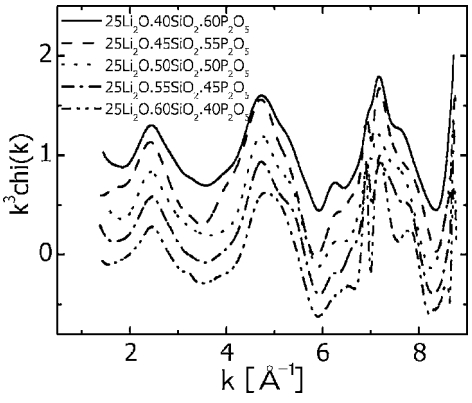

Fig. 1. Transmission mode Si K-edge XANES spectra of Li_2O-SiO_2-P_2O_5 glasses. The absorption edge peak of the glasses are observed at 1848.0 eV, and the shoulder peak by six-coordinated silicon are 1850.0 eV.

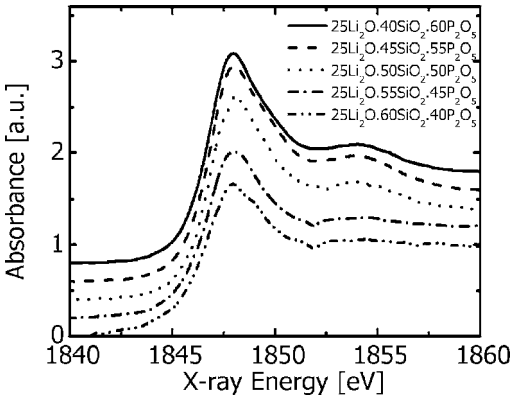

Fig. 2. EXAFS oscillation spectra obtained by transmission mode Si K-edge EXAFS spectra of Li_2O-SiO_2-P_2O_5 glasses.

*e-mail: handa@se.ritsaumei.ac.jp

Table I. *EXAFS structure parameters for $Li_2O.SiO_2.P_2O_5$ glasses.*

Samples	$N_{Si\text{-}O}/N_{P\text{-}O}$ [atoms]	$R_{Si\text{-}O}/R_{P\text{-}O}$ [Å]	SiO_6^{-6}/SiO_4^{-4} [%]
$25Li_2O.40SiO_2.60P_2O_5$	$4.5 \pm 0.3/3.8 \pm 0.2$	$1.89 \pm 0.04/1.61 \pm 0.03$	25.3/74.7
$25Li_2O.45SiO_2.55P_2O_5$	$4.7 \pm 0.3/4.0 \pm 0.2$	$1.88 \pm 0.04/1.55 \pm 0.03$	32.5/67.5
$25Li_2O.50SiO_2.50P_2O_5$	$4.5 \pm 0.3/4.0 \pm 0.2$	$1.89 \pm 0.04/1.57 \pm 0.03$	25.3/74.7
$25Li_2O.55SiO_2.45P_2O_5$	$4.4 \pm 0.3/3.8 \pm 0.2$	$1.88 \pm 0.04/1.57 \pm 0.03$	18.2/81.8
$25Li_2O.60SiO_2.40P_2O_5$	$4.3 \pm 0.3/4.0 \pm 0.2$	$1.88 \pm 0.04/1.58 \pm 0.03$	11.8/88.2
$33Li_2O.40SiO_2.60P_2O_5$	$4.6 \pm 0.3/4.0 \pm 0.2$	$1.90 \pm 0.04/1.58 \pm 0.03$	46.9/53.1
$33Li_2O.55SiO_2.45P_2O_5$	$4.4 \pm 0.3/3.8 \pm 0.2$	$1.90 \pm 0.04/1.58 \pm 0.03$	26.7/73.3
$33Li_2O.50SiO_2.50P_2O_5$	$4.3 \pm 0.3/3.8 \pm 0.2$	$1.90 \pm 0.04/1.58 \pm 0.03$	16.7/83.3
Leucite [$KAI(Si_2O_6)$]	4.0 ± 0.1/	1.64 ± 0.01/	
TEP	$/4.0 \pm 0.1$	$/1.58 \pm 0.01$	

the glasses are 1.88–1.90 Å, while the Si-O interatomic distance of tetrahedral [SiO_4^{4-}] in Leucite was 1.64 Å. The obtained structural parameters by EXAFS and XANES are summarized in Table I. The coordination numbers $N_{Si\text{-}O}$ and $N_{P\text{-}O}$ and the interatomic distances $R_{Si\text{-}O}$ and $R_{P\text{-}O}$ were estimated by EXAFS, and the ratio [SiO_6^{6-}]/[SiO_4^{4-}] by XANES fitting. Moreover, the Si-O distance of [SiO_6^{6-}] in a SiP_2O_7 crystal in which silicon is octahedrally coordinated to oxygen is 1.7345 Å [6]. Therefore, Si-O distances in Li_2O-SiO_2-P_2O_5 glasses are much larger than in the crystal composed of [SiO_6^{6-}] octahedral structure.

On the other hand, the P K-edge EXAFS spectra of Li_2O-SiO_2-P_2O_5 glasses can be divided roughly into two types, and the P-O distance in $25Li_2O$-$40SiO_2$-$60P_2O_5$ glass are larger than the other glasses as shown in Table I.

4. Conclusion

Six-coordinated silicon [6]Si was observed by Si K-edge EXAFS spectra in $x$$Li_2O$-$y$$SiO_2$-(100-$y$)$P_2O_5$ glasses ($x = 25$ and 33, $y = 40$, 45, 50, 55, and 60). The results indicate the co-existence of tetrahedral [SiO_4^{4-}] and octahedral [SiO_6^{6-}]. The proportion of [SiO_6^{6-}] octahedra depends upon the alkali content and the [SiO_6^{6-}]/[SiO_4^{4-}] ratios were estimated by Si K-edge XANES spectra and analysis of EXAFS. While the Si-O interatomic distance of [SiO_4^{4-}] in Leucite was 1.64 Å, the Si-O distance containing [SiO_6^{6-}] octahedral were 1.88 to 1.90 Å. Moreover, the Si-O distance in a SiP_2O_7 crystal in which Si atom is octahedrally coordinated to oxygen is 1.7345 Å [1], therefore, Si-O distances in Li_2O-SiO_2-P_2O_5 glasses are much larger than in the crystal composed of [SiO_6^{6-}] octahedral. On the other hand, P-O interatomic distances in the glasses were observed at 1.55–1.61 Å, while the distance in TEP was 1.58 Å.

References

1. Mudrakovskii, I. L. *et al.*, Chem. Phys. Lett. **120**, 424 (1985).
2. Fleet, M. E. *et al.*, J. Non-Cryst. Solids **220**, 85 (1997).
3. Dupree, R. *et al.*, J. Non-Cryst. Solids **106**, 403 (1988).
4. Li, D. *et al.*, Am. Mineral. **81**, 111 (1996).
5. Muthupari, S. *et al.*, J. Non-Cryst. Solids **238**, 259 (1998).
6. Poojary, D. M. *et al.*, J. Solid State Chem. **112**, 106 (1994).

Physica Scripta. Vol. T115, 316–317, 2005

A XANES Study at the Na and Al K-edge of Soda-Lime Aluminosilicate Glasses and Crystals

D. R. Neuville[1], L. Cormier[2], A.-M. Flank[3] and P. Lagarde[3]

[1]Physique des Minéraux et des Magmas, IPGP, CNRS UMR 7047, 4 place Jussieu, 75005 Paris, France
[2]Laboratoire de Minéralogie et de Cristallographie, CNRS UMR 7590, Universités PARIS 6 et 7, IPGP, 4 place Jussieu, 75005 Paris, France
[3]Laboratoire pour l'Utilisation du Rayonnement Electromagnétique, Bat 209D, Centre Universitaire Paris-Sud, B.P. 34, 91898, Orsay, France

Received June 26, 2003; accepted October 16, 2003

PACS number: 61.43.Fs

Abstract

X-ray absorption near edge structure (XANES) spectra, at the Na and Al K-edge, have been measured for Ca-Na aluminosilicate glasses. This allows a determination of the local cationic sites corresponding to 6–8 oxygen neighbours in a distorted first shell for Na and to 4 oxygen neighbours for Al. The Al XANES spectra show a strong dependence on the medium range organisation of the polymeric network.

1. Introduction

Soda lime aluminosilicate glasses are important glasses in glass industry or for geological melts but there have been relatively few structural studies of glasses in this system. Alkali and alkaline earth content are strongly affecting the physical properties (viscosity, electrical conductivity and heat capacity) and the microstructure of the glasses. Calcium and sodium in aluminosilicate glasses have a double structural role either as modifier, participating to the network depolymerization, or as charge compensator, near the $(AlO_4)^-$ tetrahedra. The local and medium range environment may be affected by the structural role played in the network by these cations. However, a detailed analysis of the cationic environment is lacking, which is important to understand the structural role of the alkali. Previous studies have mainly concentrated on the aluminosilicate network by NMR [1] or Raman [2] spectroscopies, indicating that Al and Si are present in tetrahedral coordination but the polymerization nature (rings, Si/Al ordering...) of the aluminosilicate network is still poorly understood.

In this paper, we present an extensive study on a wide range of composition of aluminosilicate glasses containing Ca and Na. The environment of Na and Al are investigated by X-ray Absorption Spectroscopy (XAS) to highlight the influence of the substitution Ca/Na or Si/Al and to determine the possible usefulness of this technique to investigate the cationic environment in complex multicomponent glasses.

2. Experimental

Soda lime aluminosilicate glasses (NCAS glasses) were synthesized by melting at 1900 K for 4 hours and then quenched by immersion of the bottom of the Pt crucible in water. Chemical compositions were obtained by electron microprobe analyses (with a Camebax SX50 at the Université Paris 7). We use the notation NCAx.y.z, where x, y and z refer to the molar percent of SiO_2, Al_2O_3 and Na_2O respectively, and 1-x-y-z is the CaO molar content.

We obtained XANES spectra at Na K-edge (1070.8 eV) and Al K-edge (1559 eV) on the SA32 beam line at the Super ACO storage ring at the LURE (Orsay, France). The spectra were collected at room temperature using a double-crystal monochromator equipped with beryl (10$\underline{1}$0) for the Na K edge and quartz (10$\underline{1}$0) for the Al K edge. The total yield of photoelectrons (TEY) was measured using the sample current for two or three scans with 0.1 eV step and 1 s integration time. Spectra were calibrated using the inflection point of the absorption edge of metallic Ge (1217 eV) and Al (1559 eV) foils for the Na and Al XANES spectra, respectively. The energy calibration was periodically checked during the measurements. A Victoreen pre-edge was removed for each spectrum and the data were normalized.

3. Results

Na K edge XANES spectra are shown in Figure 1 for NCA glasses and compared with crystalline references (albite $NaAlSi_3O_8$, nepheline $NaAlSiO_4$ and jadeite $NaAlSi_2O_6$). The quality of the XANES spectra for the crystalline references is significantly improved compared to a previous study [3] and in agreement with a more recent study for jadeite [4]. A weak pre-edge (peak *a*) at about 1074.4 eV is apparent on some samples. Absorption spectra present sharp features near threshold (1077.4 and 1082.4 eV) and broader resonances extending 60–90 eV above the threshold. The sharp lines close to the threshold can be attributed to core-level excitons, i.e., an excitation of a core-level electron into an unoccupied bound level. The first sharp feature in the absorption spectra, peak *b*, can be associated with a localized transition from the 1s core level to the 3p state of Na^+ [5]. Although the detailed interpretation of some peaks energetically close to the strong peak *b* is under discussion, there is a consensus that broad peaks above 1085 eV are due to photoelectron scattering resonances, i.e. the outgoing photoelectron wave from the absorbing atom and the single- or multiple-scattering from the surrounding atoms.

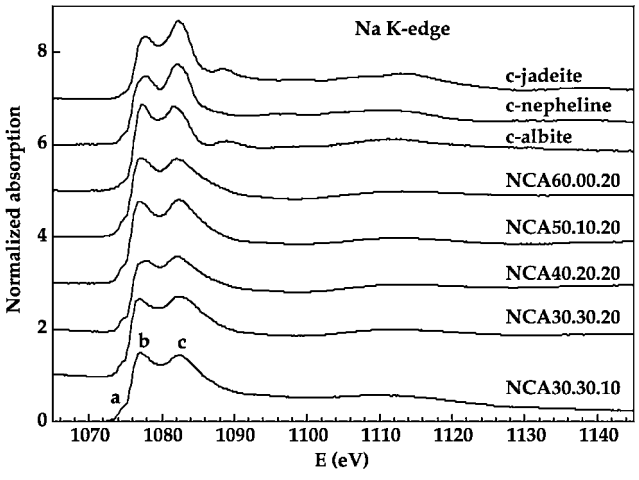

Fig. 1. Na K-edge XANES spectra for the NCA glasses compared with crystalline references.

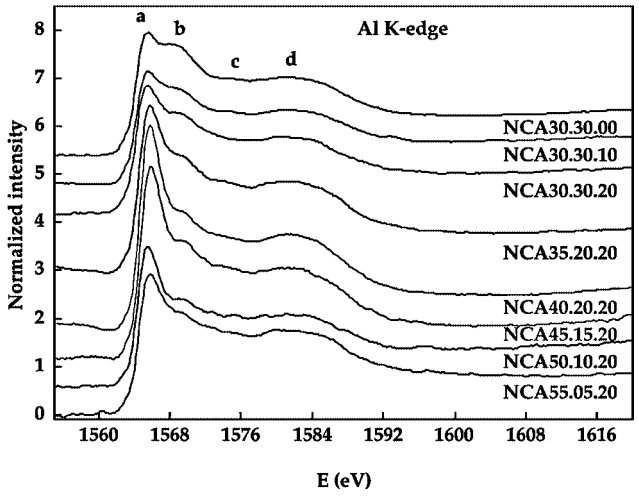

Fig. 2. Al K-edge XANES spectra for the NCA glasses.

The positions of peaks *b* and *c* are the same for the glasses and the references. Yet, the relative intensities of peak *b* and *c* change from jadeite to nepheline and albite. Peak *c* is more intense in jadeite than peak *b* and the reverse is observed for albite. XANES spectra for nepheline and albite have greater similitude with XANES spectra of glasses than the spectra of jadeite, in particular for the relative intensities of peaks *b* and *c*. The coordination number of Na in albite and nepheline corresponds to 8 oxygen neighbours with a wide range of Na-O distances between 2.5 and 3.15 Å. The Na site in jadeite is more regular with six oxygen neighbours at a mean Na-O distance of 2.391 Å and two further oxygen neighbours at 2.803 Å.

Al K-edge XANES spectra are presented in Figure 2 for the NCA glasses. A white line at 1565.6 eV is observed, followed by three ill-defined features a about 1568.1, 1574.5 and 1581 eV. These absorption features arise from transitions of core electrons to the first empty electronic bound states as well as from multiple scattering resonances inside the nearest neighbour coordination shell or among the first neighbours [6].

4. Discussion and conclusion

The Na K-edge XANES spectra of the NCA glasses are compared in Figure 1 with several Na- aluminosilicate crystals. Peaks *b* and *c* in glasses are broader which is likely due to a more disordered Na environment. Peak *c* in glasses present a broad tail at high energy which may overlap the feature present at 1088 eV in albite. In the crystalline references, the Na environment corresponds to 5 (albite) or 6 (jadeite and nepheline) oxygen neighbours at distances of 2.3–2.7 Å with two more oxygen neighbours at longer distances (2.8–3 Å). The similitude between the spectra of crystals and glasses indicate a similar distorted environment around Na in aluminosilicate glasses. This coordination number is close to that determined by EXAFS in sodium aluminosilicate glasses [3]. Similarly, computational simulation studies indicate a distorted environment around Na with 5 or more oxygen neighbours [7, 8].

As Si is replaced by Al, the structural role of Na is changing from a modifying position which depolymerises the glassy network to a charge compensating position near the $(AlO_4)^-$ tetrahedra. Such change in structural role implies small modification in the cation environment [9] but no clear modification of the Na XANES spectra are discernible which suggests that XANES spectra are not sensitive to such changes. Similarly, at constant content of SiO_2 and Al_2O_3 of 30 mol% (two lower curves in Figure 1), the effect of substituting one cation (Na) by another (Ca) does not modify the positions, the relative intensities and the widths of peaks *b* and *c*. This again suggests that the Na environment is poorly affected by such substitution or that such changes are too subtle to be observed in the Na XANES spectra.

The position and the shape of the white line in the Al XANES spectra indicate that Al is tetrahedrally coordinated for all glass compositions [6]. Among the various glasses, variation in the relative energy intensity of peaks *a* and *b* are observed on the Al K-edge XANES spectra. The intensity of peak *a* is the most intense for the NCA45.15.20 and NCA40.20.20 samples and becomes less intense as Si is replaced by Al (NCA30.30.20). With the Si/Al substitution, there is a repolymerization of the glassy network. The observed changes in the Al XANES spectra indicate that XANES spectra are highly sensitive to the degree of polymerization of the glassy network and to the number of Si and/or Al neighbours in the second coordinated shell. For a constant ratio of Si/Al, the intensities of peak *b* slightly increases when Na is replaced by Ca (three top curves in Figure 2). The origin of this contribution is still uncertain without simulations and multiple scattering calculations. This feature is not necessarily associated with the cations. Indeed, Ca atoms favour the microsegregation of Al due to the double charge of Ca^{2+} ions which requires two $(AlO_4)^-$ tetrahedra in their environment compared to one in the case of Na^+ ions. Therefore, peak *b* could be an indication of this Al distribution. This is confirmed by the low intensity of peak *b* in the glasses with low Al_2O_3 content, where a heterogeneous distribution of Al atoms is unlikely (NCA55.05.20).

In conclusion, Al and Na XANES spectra can give valuable structural information on the structure of complex disordered materials but theoretical analysis is required. Few changes are observed in the Na XANES spectra with Si/Al or Ca/Na substitution. By contrast, the Al XANES spectra present important changes upon these substitutions in relation with the nature of the aluminosilicate network.

Acknowledgments

The authors are grateful to Georges Calas and François Farges for fruitful discussions.

References

1. Maekawa, H., Maekawa, T., Kawamura, K. and Yokokawa, T., J. Phys. Chem. **95**, 6822 (1991); Merzbacher, C. I., Sheriff, B. L., Hartman, J. S. and White, W. B., J. Non-Cryst. Solids **124**, 194 (1990).
2. McMillan, P., Piriou, B. and Navrotsky, A., Geochim. Cosmochim. Acta **46**, 2021 (1982); Neuville, D. R. and Mysen, B. O., Geochim. Cosmochim. Acta **66**, 1727 (1996).
3. McKeown, D. A., Waychunas, G. A. and Brown, G. E. Jr., J. Non-Cryst. Solids **74**, 325 (1985).
4. Mottana, A., Murata, T., Wu, Z. Y., Marcelli, A. and Paris, E., Phys. Chem. Minerals **24**, 500 (1997).
5. Teodorescu, C. M., El Afif, A., Esteva, J. M. and Karnatak, R. C., Phys. Rev. B **63**, 233106 (2001); Murata, T., Matsukawa, T. and Naoe, S., Solid State Commun. **66**, 787 (1988).
6. Cabaret, D., Sainctavit, Ph., Ildefonse, Ph., Calas, G. and Flank, A.-M., Phys. Chem. Minerals **23**, 226 (1996).
7. Greaves, G. N., Fontaine, A., Lagarde, P., Raoux, D. and Gurman, S. J., Nature **293**, 611 (1981); Mazzara, C., Jupille, J., Flank, A.-M. and Lagarde, P., J. Phys. Chem. B **104**, 3438 (2000).
8. Oviedo, J. and Sanz, J. F., Phys. Rev. B **58**, 9047 (1998); Angeli, F. *et al.*, J. Non-Cryst. Solids **276**, 132 (2000); Cormack, A. N. and Du, J., J. Non-Cryst. Solids **293–295**, 283 (2001).
9. Cormier, L. *et al.*, Phys. Rev. B **59**, 13517 (1999).

Physica Scripta. Vol. T115, 318–319, 2005

XAFS Study of BI*ME*VOX Ionic Conductors for *ME* = Mg, Si, Zr, Zn

A. Twaróg[1,*], R. Bacewicz[1], A. Kozanecka[1], W. Wróbel[1], F. Krok[1] and I. Abrahams[2]

[1]Faculty of Physics, Warsaw University of Technology, 00-662 Warsaw, Poland
[2]Structural Chemistry Group, Department of Chemistry, Queen Mary, University of London, United Kingdom E1 4NS

Received June 26, 2003; accepted in revised form November 4, 2003

PACS numbers: 61.10.Ht, 66.10.Ed

Abstract

BI*ME*VOX ceramics with different molar fraction of *ME* = Mg, Si, Zr, Zn have been investigated. X-ray absorption spectra have been measured for K edges of vanadium and zinc. The XANES at the vanadium K edge undergoes a conspicuous change for the metal dopant concentrations exceeding dopant solubility limits. Position of the pre-edge peak indicates the valence state of vanadium to be 5+ in all studied BI*ME*VOX'es. Vanadium coordination, as inferred from the EXAFS data, shows similarity for all dopants used, with two characteristic distances to oxygen atoms. An estimate of oxygen occupation numbers is given. Local environment of zinc atoms has an average coordination number *ca.* 4, and exhibits shorter interatomic distances to oxygen atoms than vanadium.

1. Introduction

Fast oxide ion conductors have found use in devices such as fuel cells, oxygen sensors and gas separation membranes. In last years interest has been focused on a family of oxide ion conductors based on bismuth vanadate, $Bi_4V_2O_{11}$, which have high conductivities at relatively low temperatures (*ca.* 10^{-3} Scm^{-1} at 500 °C). The structure of the parent compound, $Bi_4V_2O_{11}$ consists of alternating layers of $[Bi_2O_2]_n^{2n+}$ and $[VO_{3.5}]_n^{2n-}$. Three main polymorphs have been identified and are associated with various ordering in the vanadate layer. The high oxide ion conductivity is found only in the high temperature γ-phase. Substitutional doping of vanadium by lower valency cations (in most cases divalent metals) leads to a stabilisation of the γ-phase at room temperature. This family of solid electrolytes has become known as the BI*ME*VOX system [1, 2].

Most of structural data concerning BI*ME*VOX'es comes from diffraction measurements, which do not distinguish between the sites of the vanadium and the dopant cation. In contrast, EXAFS spectroscopy is a local probe, which examines structure around a specific atom. Till now, two papers on EXAFS studies in BI*ME*VOX system concerning only few compositions have been published [3, 4].

In this work we studied X-ray absorption fine structure in BI*ME*VOX materials with bivalent and tetravalent dopants.

2. Experimental

BI*ME*VOX samples with *ME* = Si, Mg, Zr, Zn have been prepared from high-purity oxides by conventional solid state interdiffusion procedures. XAFS measurements have been carried out at HASYLAB (Hamburg) at the A1 station by the transmission method. Most measurements have been performed on vanadium K edge. Considering a local structure around a metal dopant, only the zinc K edge was experimentally attainable in this study.

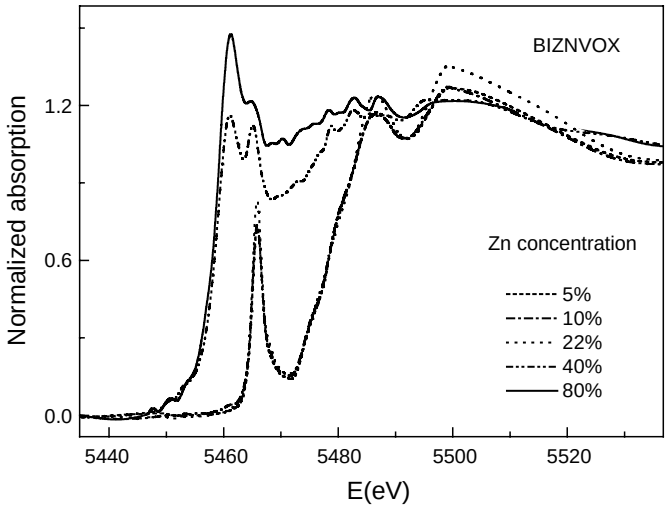

Fig. 1. XANES for BIZNVOX for different Zn content.

3. Results and Discussion

Fig. 1. presents the normalised XANES spectra for BIZNVOX with different zinc content. It shows quite dramatic change of the spectra between two compositions with 22% and 40% of zinc. This corresponds to crossing the zinc solubility limit and formation of polyphasic system. In the further analysis we will limit ourselves only to the single phase (γ-phase) compositions, which correspond to a dopant content well below 30% for all studied BI*ME*VOX materials. The distinct pre-edge peak has practically the same position for all studied BI*ME*VOX'es (Fig. 2). A comparison with V_2O_5 standard indicates that vanadium is almost exclusively in 5+ charge state [5]. The strength of the pre-edge feature indicates highly non-centrosymmetric position of vanadium atoms. As has been shown for V_2O_5 [6], the strength of this peak comes about almost exclusively from the short V-O bond and its asymmetry to the opposite bond. This suggests that "apical" oxygens in BI*ME*VOX materials are far from ideal octahedral positions. When two oxygen vacancies are present in equatorial positions, local environment of vanadium atom is effectively tetrahedral-like for which strong pre-edge feature is usually observed.

The EXAFS data in the k range 3–14 Å^{-1} have been extracted and analysed in a standard way, using the VIPER programme and ATHENA-ARTHEMIS package. The scattering amplitudes and phases have been calculated by the FEFF8 programme. Fig. 3. shows the Fourier transform of the EXAFS function measured at the vanadium K edge for all studied BI*ME*VOX'es and for the zinc K edge. The range of the useful data is limited to the nearest neighbour shell, because of disorder in higher shells. The data has been analysed, taking into account results of the combined X-ray and neutron powder diffraction [7, 8]. In particular they

*Corresponding author: A. Twaróg e-mail: twaruk@if.pw.edu.pl

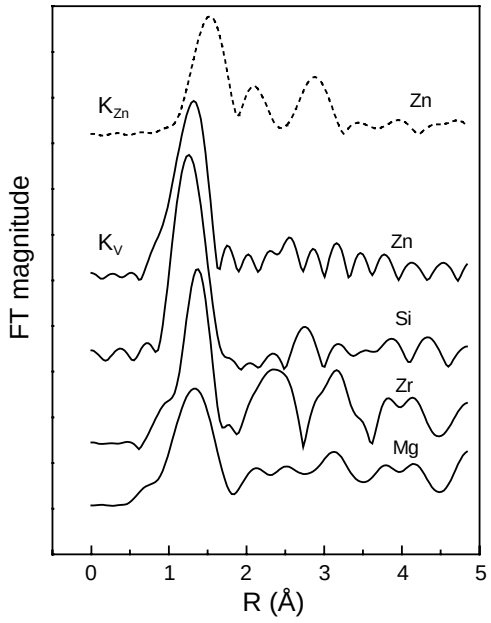

Fig. 2. Pre-edge peak for BI*ME*VOX with different *ME* dopants.

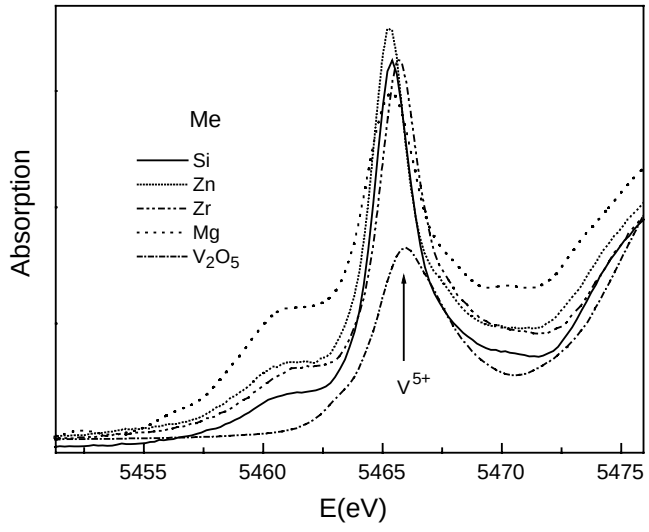

Fig. 3. Fourier transforms of $k^2\chi(k)$ for K edge of vanadium and K edge of zinc.

have revealed two main types of vanadium/dopant coordination viz. distorted octahedral and distorted tetrahedral. In a distorted "octahedral-like" coordination vanadium has 2 apical oxygen atoms at *ca.* 1.6 Å distance and 2 to 4 (depending on number of vacancies) equatorial oxygens at *ca.* 2.1 Å. For this reason, we performed two-shell fitting. The results are presented in Table 1. The parameter errors were estimated from comparison of the results from several scans and different fitting procedures. The shorter interatomic V-O distances (R_1) can be identified with the apical oxygen atoms and longer ones (R_2) with equatorial oxygen

Table I. *Fitting parameters for BIMEVOX with different dopants.*

ME	R_1 (Å)	N_1	R_2 (Å)	N_2
Mg	1.74	1.4	2.07	2.61
Si	1.7	1.5	2.13	3.4
Zn	1.73	2	2.13	3
Zr	1.67	1.7	2.08	2.8
error	0.03	0.4	0.03	0.4

atoms. The obtained coordination numbers bear a quite high uncertainty. Still, the EXAFS results indicate, shorter vanadium bonds with 1 or 2 oxygen atoms and longer bonds with 2 or 3 oxygen atoms. Analysis of zinc K edge EXAFS indicates, that the Zn-O distances are shorter than the V-O distances. The shorter bonds have 1.5 Å length and longer 1.95 Å. The total coordination number is for zinc closer to 4, what is expected in the equatorial vacancy model [2].

4. Conclusions

Vanadium K-edge XANES of the studied BI*ME*VOX materials appears to be a sensitive probe of their crystallographic phase. The high intensity of the pre-edge peak is associated with a strongly non-centrosymmetric environment of V atoms. Position of the pre-edge peak in the XANES spectra of vanadium indicates its valence state close to 5+ in all studied BI*ME*VOX'es. Vanadium coordination, as inferred from EXAFS data, shows also similarity for all BI*ME*VOX'es with two V-O bond lengths. It is, however difficult to determine exact occupation numbers for oxygen atoms from our data and to judge dominant location of oxygen vacancies (apical or equatorial positions). Zinc coordination number in BIZNVOX is close to 4, the interatomic distances to oxygen atoms are shorter than for vanadium.

Acknowledgments

This work was supported by the European Union CEPHOMA Project.

References

1. Abraham, F., Debreiull-Gresse, M. F., Mairesse, G. and Nowogrocki, G., Solid State Ionics **28–30**, 529 (1988).
2. Abrahams, I. and Krok, F., J. Mater. Chem. **12**, 3351 (2002).
3. Chadwick, A. V. and Franclin, A. J., Phil. Mag. A **68**, 787 (1993).
4. Chadwick, A. V. *et al*., Solid State Ionics **119**, 79 (1999).
5. McKeown, D. A., Muller, I. S., Matlack, K. S. and Pegg, I. L., J. Non-Cryst. Sol. **298**, 160 (2000).
6. Sipr, O., Simunek, A. and Bocharov, S., Kirchner, Th. and Draeger, G., Phys. Rev. B **60**, 14115 (1999).
7. Abrahams, I., Krok, F. and Nelstrop, J. A. G., Solid State Ionics **90**, 57 (1996).
8. Abrahams, I., Krok, F., Malys, M. and Bush, A. J., J. Mater. Sci. **36**, 1099 (2001).

Physica Scripta. Vol. T115, 320–322, 2005

Behavior of Sodium Deposited on SiO_2 at High Coverages

R. J. Prado[a], P. Lagarde[a,*], A.-M. Flank[a] and J. Jupille[b]

[a]LURE, Centre Universitaire Paris-Sud, Bat 209d, B.P. 34 91898 Orsay-cedex, France
[b]Groupe de Physique des Solides, Universités Paris 6 et 7, 75251 Paris cedex 05, France

Received June 26, 2003; accepted in revised form November 4, 2003

PACS numbers: 61.10Ht, 61.43Er, 78.70Dm

Abstract

By evaporation on a clean native or thermal silica film, sodium atoms incorporate into the silica network and Na becomes surrounded by a well defined local structure. Exposure to oxygen transforms this ($Na + SiO_2$) glassy system to a crystallized compound close to Na_2SiO_3. Higher Na coverage of the clean silica surface leads to a metallic sodium multilayer, which transforms after the same oxygen dosing to pure Na_2O.

1. Introduction

In previous papers [1, 2], we have studied by XAFS at the sodium K-edge the behaviour of this alkali metal deposited under UHV conditions on thin native or thermal silica layers. It has been shown that the sodium incorporates into the silica network and appears surrounded by a well defined local structure made of oxygen and silicon atoms at definite interatomic distances. After sodium deposition, the silica layer presents therefore a strong analogy with soda-silicate glasses of the (Na_2O - SiO_2) composition and a first conclusion is that sodium plays an active role in building the structure of these glasses. For moderate sodium evaporation conditions, the amount of sodium left on the sample, as measured by the absorption jump at the Na K-edge, presents a saturation behaviour which corresponds approximately to 35 at. % of sodium.

Nevertheless some definite differences exist between the glass and $Na + SiO_2$: since sodium is deposited as neutral atoms, while in the glass, the incorporation takes place through the oxide, the silica layer is oxygen-defective. This incorporation of sodium is thermally reversible since a 600 °C heating in vacuum removes the sodium from the SiO_2. Because of the oxygen stoichiometry of the final compound, it is likely that a dosing of oxygen could change the chemical composition of the mixed $Na + SiO_2$ layer. In this paper we then present results on the exposure of two samples to oxygen: the first one corresponds to a 'moderate' deposit with a local structure close to that of the previous experiments, and the second one is the result of a very long sodium evaporation beyond the saturation limit.

2. Experimental

XAS experiments have been done on the SA32 beam line at LURE-Super-ACO, running typically at 800 MeV with an average current of 300 mA. For sodium K-edge spectra, the line is equipped with a beryl ($10\underline{1}0$) double-crystal monochromator, allowing an energy resolution of about 0.5 eV at 1 keV. The incident flux is monitored by the total electron yield (TEY) from a 2 µm polyethylene film covered by 700 Å of titanium. The absorption signal is also measured by TEY inside the UHV chamber, the vacuum level being kept always, even during the Na evaporation, in the low 10^{-10} Torr range.

The data analysis follows the now classical scheme: the atomic background is modelled by a spline function and the normalization uses the Heitler formalism. Then the filtered Fourier transform of the $k.X(k)$ EXAFS data, weighted by an Hanning window spanning from 2.3 to 7.5 $Å^{-1}$ is fitted in k and R spaces by the FEFFIT code [3]. The phase shift parameters are *ab-initio* calculated by FEFF7 [4] and checked on the experimental results for the model compound Na_2SiO_3. This procedure has been detailed in the previous papers.

3. Results

3.1. *'Moderate' deposits*

In this case the SAES-getter cell was set to 4.8 A and the evaporation time was 45 min. The structural result is perfectly in line with previously published analysis and sodium is found surrounded by about 3 oxygen atoms at 2.30 Å and 2 silicon atoms at 3.80 Å. Moreover the Fourier transform exhibits the presence of other sodium atoms in the surroudings of one Na, at a distance close to 3 Å. These sodium neighbours have been shown to appear only at high sodium contents.

This sample is then exposed to oxygen at a pressure of 10^{-6} Torr for 20 min at room temperature. The local structure around Na appears definitely different, as indicated in Fig. 1 through a comparison between the near edge structures, while the similarity between the Fourier transforms immediately shows

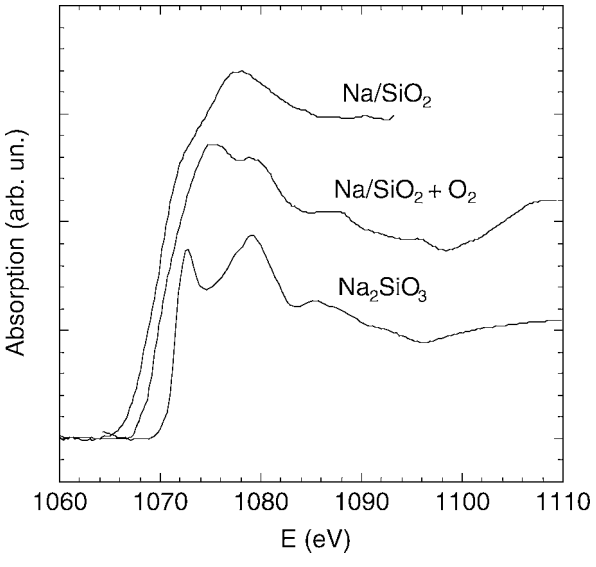

Fig. 1. Comparison of the near K-edge structure of sodium incorporated into silica (top), after exposition to oxygen (center) and in Na_2SiO_3 compound (bottom). The curves have been scaled for clarity.

*e-mail: pierre.lagarde@lure.u-psud.fr

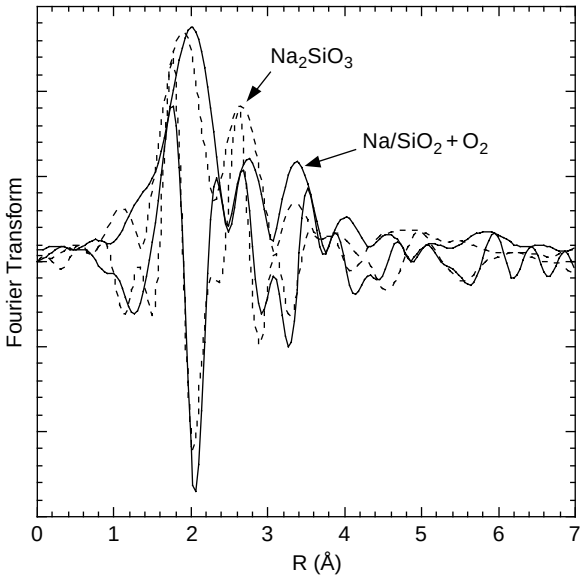

Fig. 2. Comparison between the Fourier transforms of $Na/SiO_2 + O_2$ (solid line) and Na_2SiO_3 (dotted line).

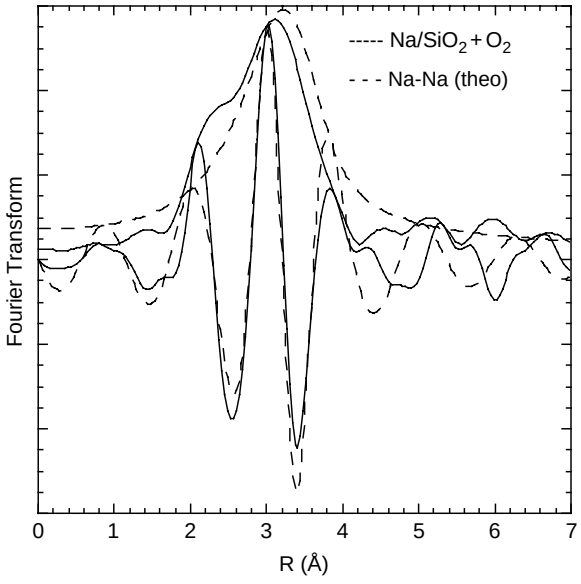

Fig. 3. Fourier transform of the 'large' sodium coverage EXAFS data (solid line) compared to the theoretical contribution from Na-Na pairs in pure sodium metal (dotted line).

that the sodium environment is very close to that of the crystalline Na_2SiO_3 compound (Fig. 2). Conclusions of this first experiment are then the following:

a) pure silica incorporates sodium atoms, leading to a still amorphous structure where the sodium presents a well defined environment. By increasing the evaporation time, the sodium cooncentration can reach about 35 at. %.
b) upon exposure to oxygen, the Na-SiO_2 layer absorbs oxygen, generating a compound with a local structure very close to that of crystalline Na_2SiO_3.

This behavior could explain why fused silica halogen lamps should not be touched by bare fingers: the hands bring sodium, which, with the oxygen of the air, transforms the pure silica (melting point of 1713 °C) into Na_2SiO_3 which has a much lower melting point at about 1089 °C, leading to the destruction of the fused quartz enveloppe.

3.2. *'Heavy' coverages*

Increasing the current of the sodium cell leads to, for the same time of deposit, a totally different structural result. The EXAFS Fourier transform is now dominated by a component at about 3 Å. This peak can be interpreted as a contribution from the first shell of metallic sodium. In Fig. 3, are superimposed the experimental result and the theoretical contribution of Na-Na at 3.76 Å calculated by FEFF7. On the lower *R* side of this main peak appears the sodium-oxygen contribution analoguous to the preceding result. Therefore, by a more intense sodium deposit, a pure metallic sodium multilayer is obtained once the saturation limit of the silica substrate has been reached. The energy position of the edge is found now about 3 eV lower than in the case of Na_2SiO_3 which is in line with an atomic Na (compared to Na+) electronic configuration of the sodium.

The same oxygen treatment as the one used for the first sample changes drastically the absorption spectrum at the sodium edge, which becomes characteristic of a crystallized compound. The modelling by FEFF8 shown in Fig. 4 indicates that the metallic sodium multilayer has been fully transformed into pure sodium oxide Na_2O. An analysis of the EXAFS data leads to the same conclusion.

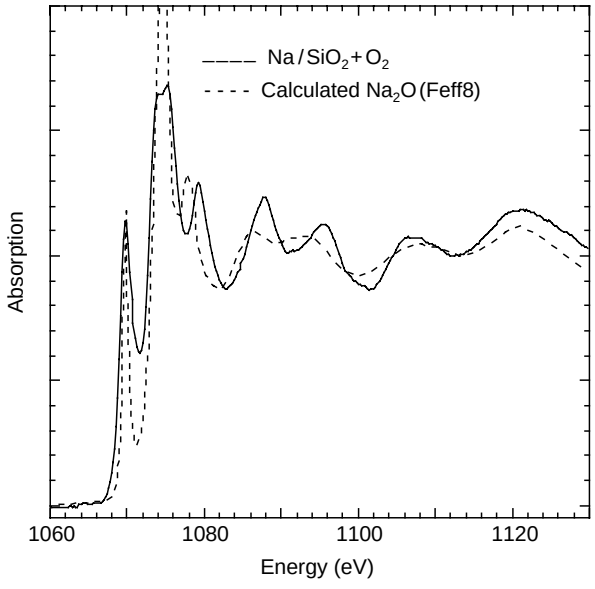

Fig. 4. The near edge spectrum of the 'large' deposit after an O_2 exposition compared to a FEFF8 calculation of Na_2O.

4. Conclusions

When exposed to oxygen the amorphous system made by the native or thermal silica layer incorporated with sodium in UHV conditions transforms into a compound which has a local structure around the sodium atom close to that of Na_2SiO_3. Because of the low melting temperature of Na_2SiO_3 compared to that of pure silicon oxide this behaviour could explain the sensitivity of pure fused silica used in high temperature halogen lamps to contact with fingers, which bring sodium atoms.

When the rate of sodium evaporation on the silica layer is strongly increased, it sticks on the substrate and forms a pure metallic multilayer. This behavior on silica differs from that of sodium on most clean crystalline surfaces, like silicon. An exposure to oxygen of this metal overlayer gives rise to pure sodium oxide, Na_2O. It is worth to point out that this experimental procedure is the only way to prepare a sample

of metallic sodium or sodium oxide for X-ray absorption experiments.

Acknowledgements

We thank the team in charge of the Super-ACO machine. R.J. Prado has been supported at LURE by a grant from CAPES (Brazil).

References

1. Lagarde, P., Flank, A.-M., Mazzara, C. and Jupille, J., Surf. Sci. **482–485**, 376 (2001).
2. Jupille, J., Flank, A.-M. and Lagarde, P., J. Am. Ceramic. Soc. **85**, 1041 (2002).
3. Newville, M. *et al.*, Physica B **154**, 208 (1995).
4. Ankudinov, A. L. and Rehr, J. J., Phys. Rev. B **56**, R1712 (1997).

Physica Scripta. Vol. T115, 323–325, 2005

Unoccupied Electronic States of MgS, CaS, FeS: X-Ray Absorption Fine Structure Theoretical Analysis

A. V. Soldatov[1,*], A. N. Kravtsova[1], M. E. Fleet[2] and X. Liu[2]

[1]Faculty of Physics, Rostov State University, Sorge 5, Rostov-on-Don, 344090, Russia
[2]Department of Earth Sciences, University of Western Ontario, London, Ontario, N6A 5B7, Canada

Received June 26, 2003; accepted in revised form November 4, 2003

PACS number: 71.20.Ps

Abstract

The distributions of unoccupied electronic states in the conduction bands of MgS and CaS have been determined. It has been found that the bottom of the conduction band of MgS is formed by Mg s and S s states, and of CaS by S d, s and p states. The partial electronic densities of S p and Fe d states in the conduction band of FeS (B8 phase) have been calculated. Interaction between these states in the bottom part of the conduction band of iron sulfide has been studied. A special kind of hybridization has been found: it has been shown that the sulfur p states are "squeezed out" of the energy region of the iron d states.

1. Introduction

The monosulfides of Ca and Mg have the rocksalt (B1) structure and occur in EH enstatite chondrite meteorites, where they appear to result from metamorphism under very reduced conditions [1]. Iron monosulfide has a hexagonal NiAs-type (B8) structure under ambient pressure and temperature. FeS is a nearly ubiquitous phase in most meteorites and is the iron sulfide of lunar rocks. It occurs also, albeit sparingly, in magmatic sulfide assemblages of mafic/ultramafic rocks.

One of the most fruitful methods allowing study of the local arrangement of atoms and electronic structure of the presently investigated compounds is X-ray absorption near-edge structure (XANES) spectroscopy [2]. But, in order to extract the necessary information from the experimental spectra, one needs to perform theoretical analysis.

Some of the physical properties of the studied sulfides cannot be explained without a detailed study of their electronic structure. The electronic structure of the valence band of many monosulfides has been widely investigated. In contrast, the electronic structure of the conduction band has received much less attention due to limitations of theoretical calculations and experimental approaches. Some experimental measurements carried out by different methods [3–7] have yielded information on aspects of the electronic structure of the investigated sulfides; for example, the experimental estimation of band gaps. But only theoretical methods yield a complete description of the electronic energy band structure. Attempts to understand the electronic structure of the metal sulfides were made earlier by different theoretical methods. Analysis of the electronic band structure of magnesium sulfide predicts an indirect (Γ-X) band gap [8–10]. In materials with an indirect band gap the bottom of the conduction band and the top of the valence band lie at different wavevectors. The band gap in MgS is bounded by S p states in the upper part of the valence band [8–10] and Mg s states [9, 10] (and to a less extent, S d) in the conduction band. Different estimates of the band gap width of MgS are given in the literature. Stepanyuk *et al.* [9] using the totally self-consistent linear augmented plane wave method have found that the value of band gap width is 2.69 eV. This result is in a good agreement with that calculated by Kalpana *et al.* [10] (2.7 eV) using the tight binding linear muffintin orbital (TBLMTO) method. But the Hartree-Fock calculation performed by Pandey *et al.* [8] has resulted in band gap value of 6.48 eV. Ching *et al.* [11] based on the MOLCAO method have determined that the gap width of MgS is equal to 4.59 eV.

In CaS the band gap (estimated variously as 2.143 eV [12], 3.2 eV [11] or 7.6 eV [8]) lies between the S p states [8, 12] in the valence band and Ca d states [12] in the conduction band. Pandey *et al.* [8] disagree with the view of Stepanyuk *et al.* [12] and Ching *et al.* [11] that CaS is an indirect (Γ-X) band dielectric. It is claimed [8] that CaS is a direct-band-gap material.

Moreover, several experimental measurements of band gaps in magnesium and calcium sulfides have been carried out. XPS measurements on bulk MgS and ZnSe/MgS supperlattice made by Suzuki *et al.* [3] indicate that the band gap width of MgS is 5.27–5.47 eV. Investigation of CaS single crystals by optical reflectivity and luminescence [4–5] resulted in an estimated indirect band gap width of 4.434 eV, a direct gap (X) of 5.343 eV, and a direct gap (Γ) of 5.80 eV. Optical absorption measurements in CaS evaporated thin film [6] yielded a band gap width equal to 5.38 eV. CaS : Eu2+ : Sm^{3+} thin films were studied by Zhang *et al.* [7], and a band gap equal to 4.48 eV was obtained. Thus, we can conclude that the experimental measurements of band gap width differ from the theoretical estimations. Overall, the experimental band gaps are significantly larger than the theoretical ones.

The above-mentioned theoretical results were obtained by analysing the band structure calculations and densities of states of studied compounds. But in the literature we can find only total DOS calculations for occupied [8, 10, 12, 13] or unoccupied states [10, 12] of MgS and CaS. The projected DOS of investigated sulfides has not been computed earlier.

In this paper we present the curves proportional to the projected electronic densities of unoccupied states in the conduction band of MgS, CaS, FeS calculated for the first time.

2. Method of calculation

For the calculation, the computer code G4XANES [14] was used. The algorithm of the full multiple scattering method was described earlier [14]. Atomic charge densities were obtained with the help of a self-consistent Dirac method. Phase shifts of the photoelectron were calculated in the framework of the crystal muffin-tin (MT) potential scheme with touching MT spheres. The MT radii and the MT constants were obtained according to an

*e-mail: soldatov@rsu.ru

established procedure of MT potential construction [14]. The MT approximation according to the Mattheiss prescription [15] with Slater exchange ($\alpha = 1.0$) was used while constructing the crystal potential.

3. Results and discussion

Some initial investigations of metal sulfides have been performed previously by X-ray absorption near edge structure (XANES) spectroscopy [16–18]. Sulfur K- and L-edge XANES spectra of MgS, CaS, FeS were collected at the Canadian Synchrotron Radiation Facility (CSRF), Aladdin storage ring (University of Wisconsin at Madison, Wisconsin) [16–17]. The theoretical analysis of experimental data was made by full multiple scattering method [17–18]. It has been found that the S K- and $L_{2,3}$-XANES spectra results from the multiple scattering of an excited photoelectron inside a large cluster of 13 shells (251 atoms) for MgS and CaS (B1 phase), although a cluster size of 4 shells (37 atoms) appears sufficient for FeS (B8 phase). A good agreement between theoretical and experimental spectra was obtained for all studied sulfides. For example, in Fig. 1(a) the comparison of experimental S K-XANES spectrum of magnesium sulfide with theoretical one is presented. Experimental and theoretical S $L_{2,3}$-XANES spectra of MgS are shown in Fig. 1(b). In order to compare the theoretical S K- and $L_{2,3}$-XANES spectra of MgS with experimental XANES, the Fermi distribution function and three main factors that cause the broadening of the spectra were taken into account. These factors were: 1.) the width of the core hole states, which is 0.59 eV for the S K-edge XANES and

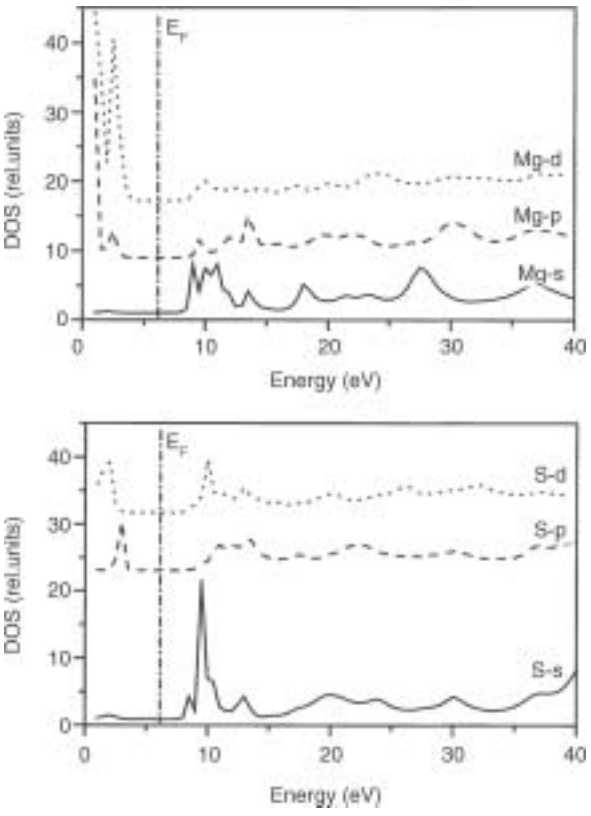

Fig. 2. Partial densities of unoccupied states in the conduction band of MgS, using a cluster of 13 shells (251 atoms). Origin of the energy scale corresponds to the zero of the MT potential. Vertical dotted line conforms to the location of Fermi level.

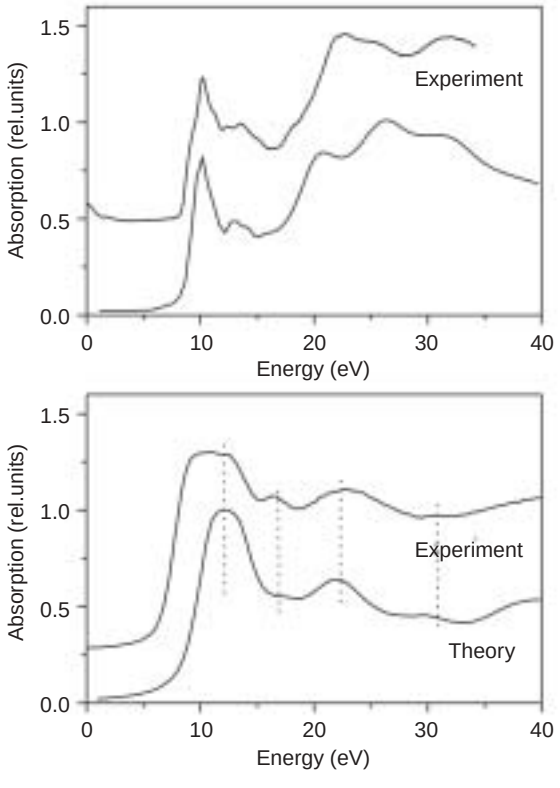

Fig. 1. a) Comparison of the experimental S K-XANES for MgS with theoretical XANES spectrum calculated for the cluster of 251 atoms; b) comparison of the S K $L_{2,3}$-edge absorption spectrum for MgS with the theoretical XANES. Origin of the energy scale corresponds to the zero of the MT potential. Vertical dotted lines correspond to the locations of peaks of experimental spectra.

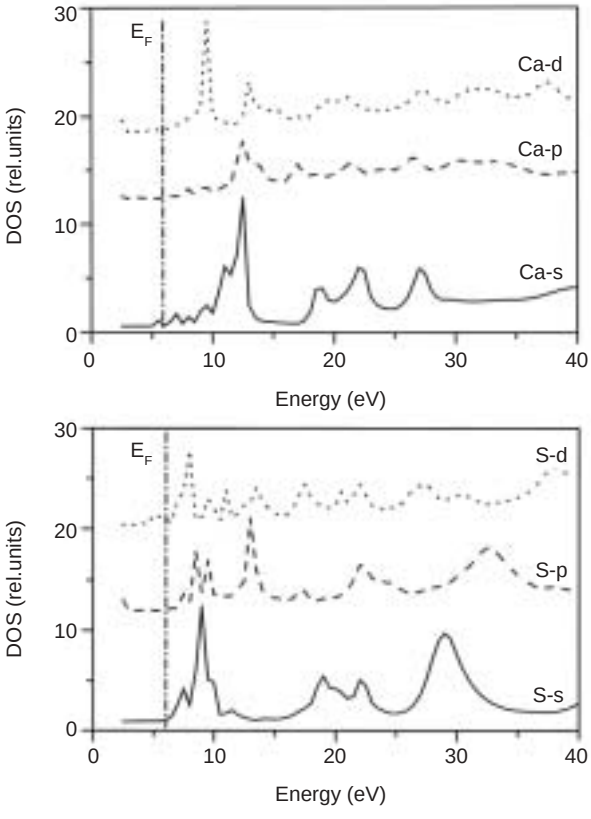

Fig. 3. Partial densities of unoccupied states in the conduction band of CaS, using a cluster of 13 shells (251 atoms). Origin of the energy scale corresponds to the zero of the MT potential. Vertical dotted line conforms to the location of Fermi level.

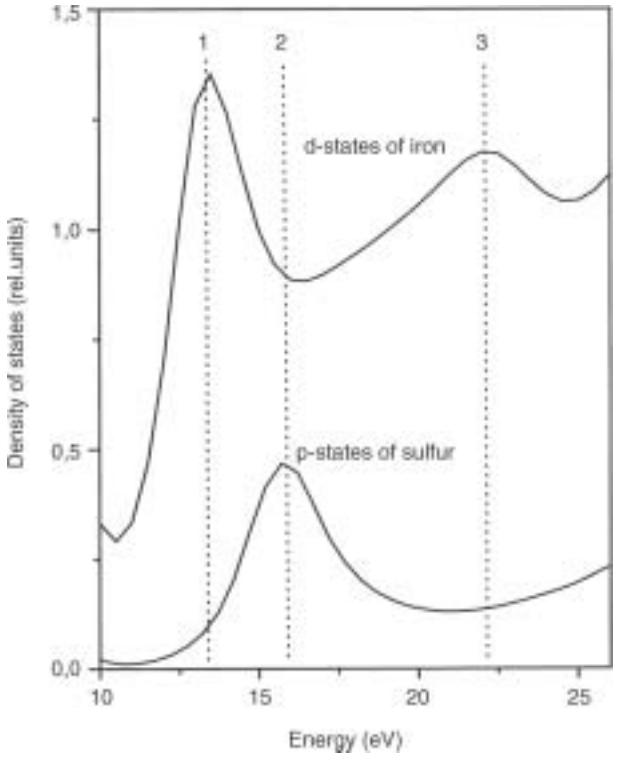

Fig. 4. Part of the densities of unoccupied states of FeS (B8 phase) where a repulsive hybridization is observed. Cluster of 4 shells (37 atoms) was taken into account. Origin of the energy scale corresponds to the zero of the MT potential.

0.05 eV for the S $L_{2,3}$-edge XANES; 2.) the mean free path of the photoelectron function [19]; and 3.) the experimental energy resolution, which is 0.9 eV for the S K-edge XANES and ∼0.1 eV for the S $L_{2,3}$-edge XANES. From Fig. 1 (a,b) one can see that theoretical spectra are in good agreement with correspondent experimental spectra in both shape and energy peaks positions. These results indicate that the present theoretical approach works well and calculations for partial densities of states can be done using the same MT potential.

In Fig. 2 the partial DOS in the conduction band of MgS are shown. It is seen that S p states lie at the top of the valence band of MgS. The bottom of conduction band is formed by Mg s states and S s states. Our calculations give an estimation of the band gap width for MgS to be about 4.6 ± 0.3 eV.

In Figure 3 the partial densities of states in the conduction band of CaS are presented. It shows that the bottom of the conduction band is mainly formed by sulfur states (S d and s states and, in lower degree, S p states). We estimate that the band gap width of CaS is about 3.5 ± 0.3 eV.

In the present work an interesting effect was found for electronic density of states of B8 phase iron sulfide. In Fig. 4 the unoccupied electronic p states of sulfur and d states of iron in the conduction band of FeS (B8) are shown. It can be seen that line 1 corresponds to the position of maximum of iron d states as well as to a minimum in the sulfur p states. At the position of line 2 there is a maximum of S p states. This feature aligns well with the minimum of d states of iron. Line 3 marks the next maximum of Fe d states. Note also that this line matches a minimum in the sulfur p states plot. Thus, the S p states in the conduction band of FeS (B8) have minima at the position of maxima in Fe d states. In these cases the S p states are "squeezed out" of the energy positions of Fe d states, as a result of the specific interaction between iron and sulfur states. For the unoccupied states such specific interaction between electronic states has been previously found for rare earth sulfides [20], CeO_2 [21], orthoferrites [22] and stishovite [23]. Thus, we can conclude that the interaction between S p states and Fe d states in the conduction band of FeS (B8) is a special kind of repulsive hybridization.

References

1. Fleet, M. E. and MacRae, N. D., Geochim. Cosmochim. Acta **51**, 1511 (1987).
2. Bianconi, A., "XANES Spectroscopy", in "X-ray Absorption: Principles, Applications and Techniques of EXAFS, SEXAFS and XANES". (Edited by Prins, R. and Koningsberger, D. C.) (John Wiley & Sons, New York, 1988), p. 573.
3. Suzuki, H., Nashiki, H., Hoshiyama, M. and Suemune, I., Nonlinear Opt. **18**, 227 (1997).
4. Kaneko, Y. and Koda, T., J. Crystal Growth **86**, 72 (1988).
5. Kaneko, Y., Morimoto, K. and Koda, T., J. Phys. Soc. Japan **52**, 4385 (1983).
6. Saum, G. A. and Hensley, E. B., Phys. Rev. **113**, 1019 (1959).
7. Zhang, J.-G. *et al.*, J. Mater. Res. **7**, 411 (1992).
8. Pandey, R., Jaffe, J. E. and Kunz, A. B., Phys. Rev. B **43**, 9228 (1991).
9. Stepanyuk, V. S. *et al.*, Phys. Stat. Sol. (b) **174**, 289 (1992).
10. Kalpana, G., Palanivel, B., Thomas, R. M. and Rajagopalan, M., Physica B **222**, 223 (1996).
11. Ching, W. Y., Gan, F. and Huang, M.-Z., Phys. Rev. **52**, 1596 (1995).
12. Stepanyuk, V. S. *et al.*, Phys. Stat. Sol. (b) **155**, 215 (1989).
13. Lichanot, A., Dargelos, A. and Larrieu, C., Solid State Commun. **90**, 189 (1994).
14. Della Longa, S., Soldatov, A. V., Pompa, M. and Bianconi, A., Comput. Mater. Sci. **4**, 199 (1995).
15. Mattheiss, F., Phys. Rev. **181**, 987 (1969).
16. Farrell, S. P. and Fleet, M. E., Solid State Commun. **113**, 69 (2000).
17. Farrell, S. P. *et al.*, Am. Miner. **87**, 1321 (2002).
18. Kravtsova, A. N., Stekhin, I. E., Soldatov, A. V., Liu, X. and Fleet, M. E., Phys. Stat. Sol. (b) **234**, R4 (2002).
19. Muller, J. E., Jepsen, O. and Wilkins, J. W., Solid State Commun. **42**, 365 (1982).
20. Soldatov, A. V. and Gusatinskii, A. N., Phys. Status Solidi B **125**, k129 (1984).
21. Soldatov A. V. *et al.*, Phys. Rev. B **50**, 5074 (1994).
22. Povahznaja, N. A., Shvejtzer, I. G. and Soldatov, A. V., J. Phys.: Condensed Matter **7**, 53 (1995).
23. Soldatov, A. V., Kasrai, M. and Bancroft, G. M., Solid State Commun. **115**, 687 (2000).

Physica Scripta. Vol. T115, 326–328, 2005

Characterization by XAS of NiO Thin Films Prepared by Pulsed LASER Deposition

J. Moscovici[1,2,*], I. Bouessay[3], A. Rougier[3] and A. Michalowicz[1,2]

[1]Groupe de Physique des Milieux Denses, Université Paris XII, 94010 Créteil, France
[2]LURE, Université Paris Sud, 91498 Orsay, France
[3]Laboratoire de Réactivité et Chimie des Solides, UMR6007, 33 rue St. Leu, 80039 Amiens, France

Received June 26, 2003; accepted in revised form June 28, 2004

PACS number: 61.10 Ht

Abstract

Further understanding of the electrochromic mechanism taking place in anodically colored nickel oxide was achieved by XAS. From EXAFS simulation we were able to determine the percentages of electrochemically active phases and confirm the dissolution of the oxidized one, which was previously assumed by electrochemical characterization.

1. Introduction

Since the early eighties, Nickel Oxide has received a great interest due to its brownish coloration associated to the presence of trivalent nickel ions when anodically oxidized. NiO thin films switch reversibly to a transparent state on reduction. Further interest comes from its association to the blue coloration of tungsten trioxide, yielding a neutral gray color of a complete device. However despite a large number of studies, many aspects of NiO electrochromic behavior remain poorly understood. To throw some light on the mechanism, NiO thin films were grown using Pulsed Laser Deposition (PLD). Among a wide range of growth parameters, good electrochromic properties were determined to be a 10^{-1} mbar oxygen pressure and a Room Temperature (RT) substrate [1]. Preliminary understanding of the electrochromic mechanism was deduced from the coupling of electrochemical test and X-ray diffraction, Scanning and Transmission Electron Microscopies. However, if the X-ray diffractogramms of the as-deposited film exhibit well defined peaks confirming the NiO cubic structure (SG: Fm-3m) with a [111] preferred orientation, on cycling the loss in resolution limits the benefit of this long range order technique. This paper presents further insights into the understanding of the electrochromic mechanism involved in NiO thin films, grown by PLD, using X-ray Absorption Spectroscopy (XAFS).

2. Experimental and Data Analysis

NiO thin films were deposited on SnO_2:F coated glass substrates in optimized conditions, namely a 10^{-1} mbar oxygen pressure and a RT substrate, by PLD using a KrF excimer laser (Lambda Physik, Compex 102, $\lambda = 248$ nm) and a laser fluence of 1–2 J · cm^{-2}. The duration of depositions last from few minutes to few hours, leading to thickness in the 10 to 500 nm range. The electrochemical properties of the films were characterized by cyclic voltammetry performed on an AUTOLAB PGSTAT 30 system with a NiO|KOH 1 M|Pt *versus* Hg/HgO cell configuration.

The XAS spectra were recorded at the Ni K edge at LURE (Laboratoire pour l'Utilisation du Rayonnement Electromagnétique) on the EXAFS13 (DCI D42) workstation in total electron yield mode. The monochromator was a channel-cut silicon with reflecting (331) faces. EXAFS data analysis was performed with "EXAFS 98" programs [2] using the Lengeler-Eisenberger standard procedure to normalize EXAFS function $\chi(k)$ [3]. The Fourier transform (FT) of $\chi(k)$ was performed with a k^3 weight and a Kaiser-Bessel apodization window function (the smoothness coefficient $\tau = 3$) in the range $1.5\,\text{Å}^{-1} < k < 12.52\,\text{Å}^{-1}$.

3. Results

Electrochromic performances (i.e. capacity, contrast) of PLD NiO thin films increase with decreasing film thickness [4]. Unfortunately, due to the very small amount of material ($\approx 10^{-6}$ g) EXAFS data could not be recorded on very thin films whereas the spectrum resolution increases with film thickness. Therefore, despite a lower electrochromic activity, the XAS study was focused on the thicker films knowing that a similar mechanism takes place whatever the film thickness.

3.1. *Cyclic Voltammetry*

Figure 1a shows the Cyclic Voltammogram (CV) of NiO | KOH 1 M|Pt *versus* Hg/HgO cell with 465 nm thick film. The CV is characterized by a set of reversible peaks, located at about 0.60 V in oxidation and 0.38 V in reduction, which is associated to a faradic process involving the Ni^{3+}/Ni^{2+} ions. The strong increase in current observed at the end of the anodic sweep corresponds to the oxygen evolution. The evolution of the relative capacity (deduced from the surface area below the CV shape) is plotted in Fig. 1b. The capacity curve can be separated in three domains, (I) the activation period, during which the capacity increases, (II) the steady state, and (III) the degradation period.

3.2. *XANES*

In this paper, we do not show any XANES spectrum but we observe that during the oxidation process, the inflection point of the edge shifts from 8344.97 eV to 8345.65 eV due to the transformation of Ni^{2+} to Ni^{3+}. As described in the following, the shift intensity is correlated to the amount of oxidized phase, which varies on cycling.

3.3. *EXAFS*

The evolution of the EXAFS spectra on coloration (recorded after the film was maintained in the oxidized state $V = 0.60$ V for 10

*e-mail: moscovic@univ-paris12.fr

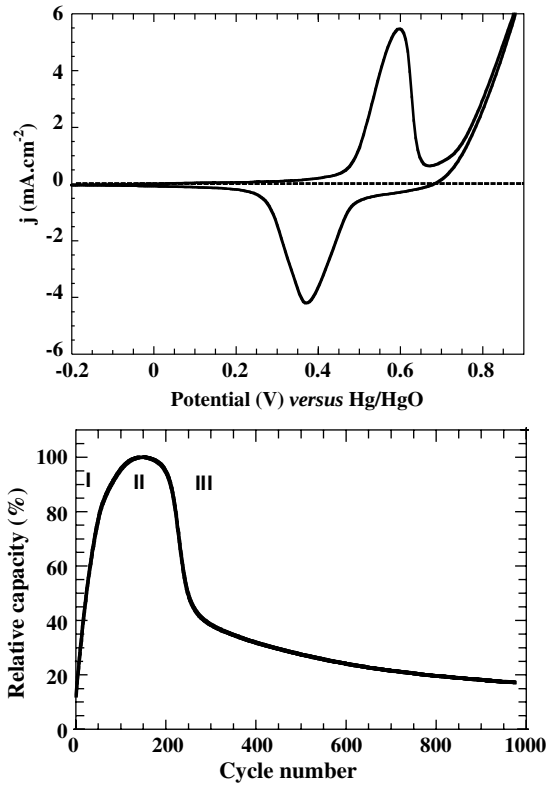

Fig. 1. (a) 50th Cyclic Voltammogram of NiO | KOH 1 M | Pt *versus* Hg/HgO cells of NiO 465 nm thick film. Cycling is performed between −0.20 V and 0.90 V at a sweep rate of 10 mV · s^{-1}. (b) Evolution of the relative capacity ($100 * Q/Q_{\max.}$) versus the number of cycles for NiO|KOH 1 M|Pt *versus* Hg/HgO cells of NiO 465 nm thick films. I, II, III represent the activation period, the steady state and the degradation period, respectively.

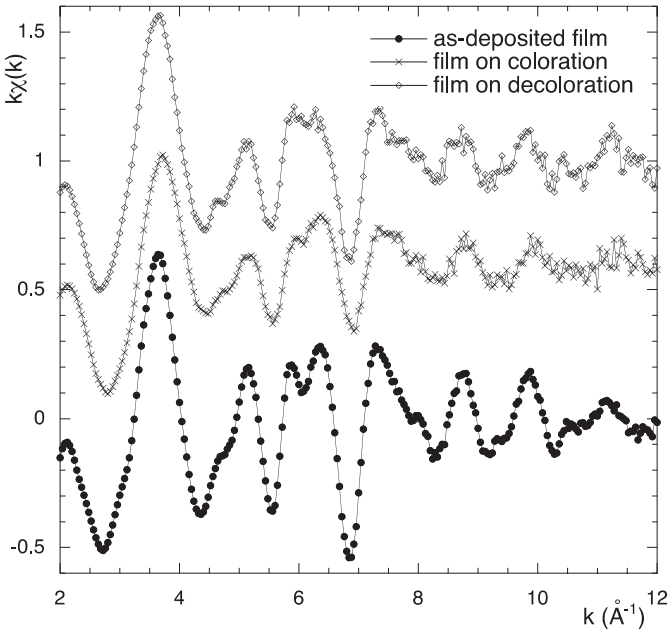

Fig. 2. Comparison between the EXAFS spectra of the as-deposited film, after coloration and decoloration. Both coloration and decoloration were performed after the film went through 100 cycles.

minutes) and decoloration (after the film was maintained in the reduced state $V = 0.2$ V for 10 minutes) is presented in Fig. 2 in comparison with the one of the as-deposited NiO film.

Based on the mechanism, previously deduced from electrochemical data, one may assume that the coloration/decoloration

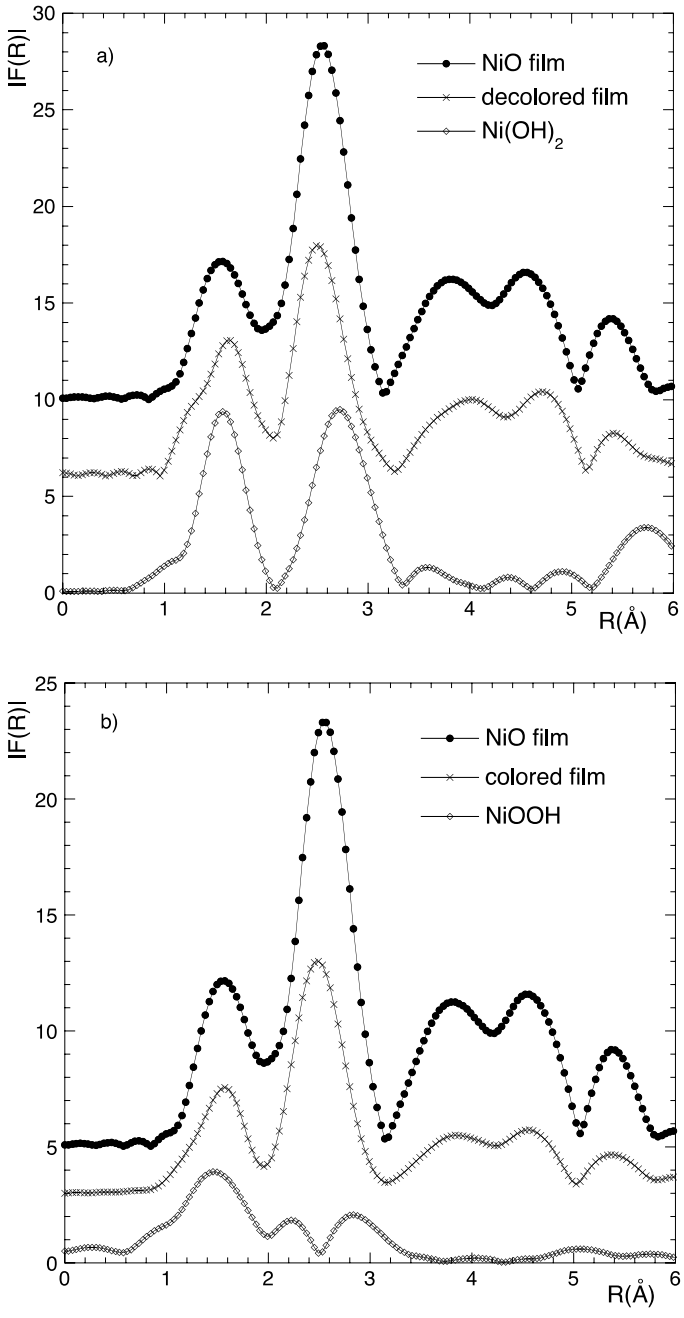

Fig. 3. (a) Comparison of the Fourier Transform of NiO film in the bleached state with NiO and β(II)Ni(OH)$_2$ and (b) in the colored state with NiO and β(III) NiOOH.

process involves electrochemically (oxy)-hydroxides phases, whereas NiO acts as a reservoir [4]. Therefore, the EXAFS spectra of the colored and bleached state correspond to the superimposition of nickel oxide and hydroxide phases. In this regard, EXAFS spectrum of the bleached state was compared to β(II)Ni(OH)$_2$ whereas EXAFS spectrum in the colored state was compared to β(III)NiOOH. The corresponding FT are presented in Fig. 3a,b. FT of NiO is decomposed in 5 shells of which meaning and amplitude are well described in the literature [5–6]. The loss in amplitude for region higher than 3.5 Å, observed for cycled films or hydroxides, is not surprising as multiple scattering phenomenon is enhanced in cubic symmetry in comparison to the hexagonal one (i.e. higher number of direct Ni-ONi paths). The evolution of the FT of the EXAFS spectra recorded on cycling at V_0 ($V_0 \approx 0.1$ V corresponds to the equilibrium state) is shown in Fig. 4. In first approximation, the FT of the film after 1000 cycles

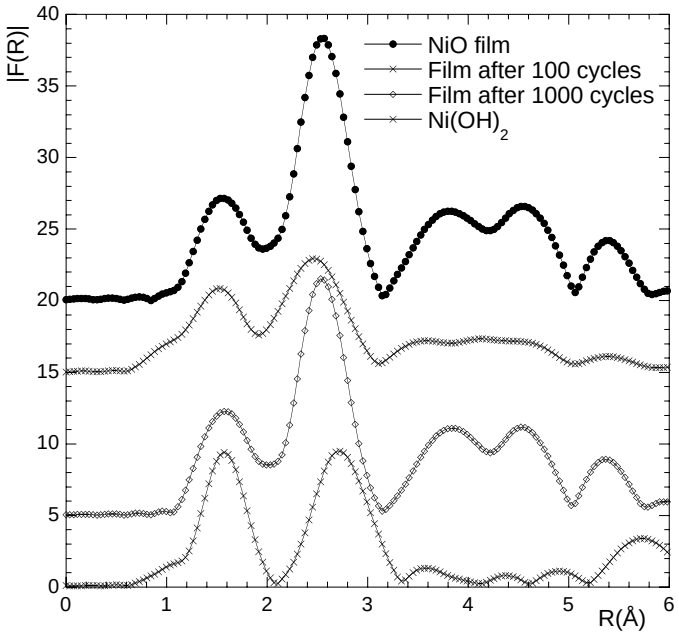

Fig. 4. Comparison of the Fourier Transform of films cycled 100 and 1000 times at V_0 with NiO and $Ni(OH)_2$.

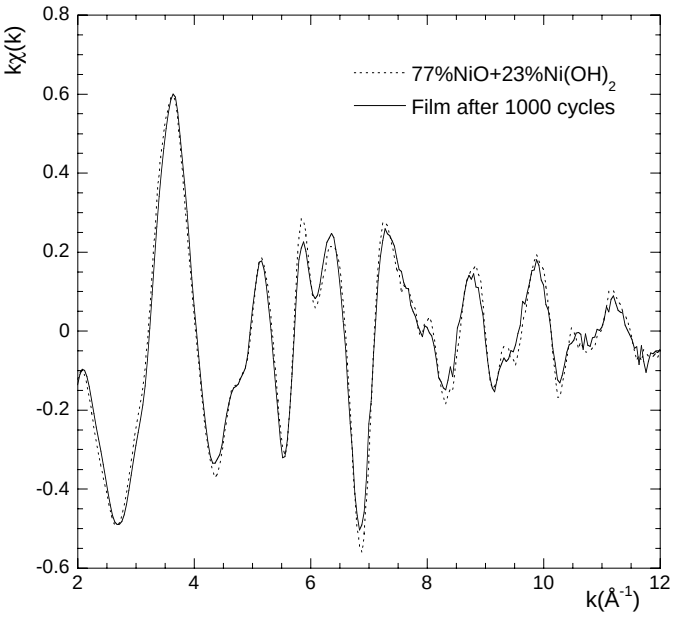

Fig. 5. EXAFS simulation of a 100 cycled films and $x\text{NiO} + (1 - x)$ $\beta\text{(II)Ni(OH)}_2$, $x = 77\%$.

exhibits similar features of the as-deposited film whereas the film cycled 100 times shows a rather different FT, associated to similar amplitudes for the first two shells and quasi no amplitude for the further shells. This trend would suggest that the film on cycling undergoes modifications, of which are not completely reversible, and tends to return to its initial state.

4. Discussion

Whatever the cycling stage, EXAFS spectra correspond to the superimposition of NiO and an (oxy)-hydroxide phase, namely $\beta\text{(II)Ni(OH)}_2$ in reduction and at V_0, or $\beta\text{(III)NiOOH}$ in oxidation. The proportion of the second phase was estimated from basic simulation performed by comparing the experimental EXAFS spectrum with the calculated sum of $x\text{(NiO)} + (1 - x)$ [$\beta\text{(II)Ni(OH)}_2$ or $\beta\text{(III)NiOOH}$] EXAFS spectra. The x values are evaluated by linear least squares fitting and the error bars are calculated using the statistical standard deviation (2σ). The various percentages are gathered in Table I whereas an example of simulation is given in Fig. 5 for the film cycled 100 times. For the colored phase, we have calculated the figure of merit with $\beta\text{(II)Ni(OH)}_2$ instead of $\beta\text{(III)NiOOH}$, the best fit is largely in favor of $\beta\text{(III)NiOOH}$ ($\chi^2 = 0.43$) compared to $\beta\text{(II)Ni(OH)}_2$ ($\chi^2 = 2.48$).

Table I. *Percentages of the (oxy)-hydroxide active phases, namely β(II)Ni(OH)$_2$ in reduction and β(III)NiOOH in oxidation, deduced from the simulation of the EXAFS spectra.*

Cycle Number	$(1 - x)$ % (EXAFS)
0	0% (100% NiO)
100 (V_0)	48% ± 4 $Ni(OH)_2$
1000 (V_0)	23% ± 2 $Ni(OH)_2$
100 on coloration	66% ± 1 NiOOH
100 on decoloration	39% ± 1 $Ni(OH)_2$

Table I shows two major trends: (*i*) a decrease in the amount of $\beta\text{(II)Ni(OH)}_2$ on cycling in good agreement with the decrease in capacity observed in Fig. 1b and (*ii*) a larger quantity of oxidized phase in coloration than of the reduced phase in the bleached state for the same cycle number. The presence of a higher amount of $\beta\text{(III)NiOOH}$ than of $\beta\text{(II)Ni(OH)}_2$ confirms that the capacity results from the addition of a reversible phenomenon associated to the $Ni(OH)_2/\text{NiOOH}$ reaction (39% in the case of the film cycled 100 times) to which is added an irreversible phenomenon previously identified as being due to the instability of the oxidized phase [4]. Moreover the existence of the dissolution mechanism is emphasized on cycling with a decrease in the $Ni(OH)_2$ percentage down to 23% for the film cycled 1000 times.

5. Conclusion

In this paper, we demonstrate the benefit of the XAS characterization in the understanding of the electrochromic mechanism involved in NiO thin films deposited by Pulsed Laser Deposition, which was simply assumed based on electrochemical tests. Simulation of the EXAFS spectra leads to the determination of the percentage of the various electrochemically (oxy)-hydroxide active phases, namely $\beta\text{(II)Ni(OH)}_2$ in reduction and $\beta\text{(III)NiOOH}$ in oxidation. Moreover the smaller percentage of the β(II) phase in the bleaching process compared to the β(III) phase proves the dissolution of the oxidized phase, which is thermodynamically less stable.

References

1. Bouessay, I., Rougier, A., Beaudoin, B. and Leriche, J. B., Appl. Surf. Sci. **186**, 490 (2002).
2. Michalowicz, A., J. Phys. IV **7**, 235 (1997).
3. Lengeler, B. and Eisenberger, P., Phys. Rev. **B21**, 4507 (1980).
4. Bouessay, I., Rougier, A. and Tarascon, J.-M., J. Electrochem. Soc., submitted.
5. Nam, K. W., Yoon, W. S. and Kim, K. B., Electrochim. Acta **47**, 3201 (2002).
6. Corrias, A., Mountjy, G., Piccaluga, G. and Solinas, S., J. Phys. Chem. B **103**, 10081 (1999).

Physica Scripta. Vol. T115, 329–331, 2005

EXAFS Study of SnO_2 Xerogel Doped with Sb and PTCDA

J. Padežnik Gomilšek[1,*], U. Lavrenčič Štangar[2,3], A. Šurca Vuk[2], G. Bratina[3], I. Arčon[3,4] and A. Kodre[4,5]

[1]Faculty of Mechanical Engineering, Smetanova 17, SI-2000 Maribor, Slovenia
[2]National Institute of Chemistry, Hajdrihova 19, SI-1000, Ljubljana, Slovenia
[3]Nova Gorica Polytechnics, Vipavska 13, SI-5000 Nova Gorica, Slovenia
[4]J. Stefan Institute, Jamova 39, SI-1000 Ljubljana, Slovenia
[5]Faculty of Mathematics and Physics, Jadranska 19, SI-1000 Ljubljana, Slovenia

Received June 26, 2003; accepted in revised form November 4, 2003

PACS Ref: 81.20.Fw, 61.10.Ht

Abstract

SnO_2 and doped Sb:SnO_2 sol, prepared by a precipitation-peptization sol-gel process, has been used as a host for the incorporation of an organic semiconductor, the perylene dye (PTCDA). The structure of the SnO_2 gel host together with the effect of inorganic (Sb) and organic (PTCDA) doping is studied with EXAFS at the Sn and Sb K-edge. Distinct neighbor shells are resolved only up to 4 Å. The corresponding radii are the same as in a cassiterite crystal structure with a 60% reduction in the Sn neighbor population. In the spectra at the Sn edge, the doping with Sb and/or a small concentration of PTCDA produces no detectable effect. At higher content of PTCDA, however, the number of the first oxygen neighbors is diminished by ∼30% indicating that the disordered organic groups from the dye molecule reach right into the Sn neighborhood. In the weaker Sb EXAFS spectra only the first shell of oxygen neighbors is resolved: again the static disorder is higher in the presence of the organic dopant.

1. Introduction

The sol-gel processing has been developed into an appropriate technique for producing inorganic and organic-inorganic glasslike materials [1]. Owing to mild processing conditions, organic molecules can be introduced into inorganic polymeric matrices. The inorganic matrix in this study is tin-oxide gel derived by alkaline aqueous sol-gel route [2]. For comparison, SnO_2 matrix was made also according to a peroxo route [3]. Pure or Sb-doped SnO_2 in thin film form is a promising material for transparent conductive electrodes, ion-storage electrodes or low-emitting coatings for advanced glazings [3–8].

In addition to inorganic doping, perylene tetracarboxylic acid dianhydride (PTCDA) as an organic semiconductor with attractive optical properties has also been introduced into the SnO_2 gel matrix. Generally, the photochemical and mechanical stability of the dye is increased by using inorganic host systems [9, 10]. PTCDA is highly insoluble in common solvents used for sol-gel synthesis (alcohol, water) so that a homogeneous dispersion in the sol-gel host is not easy to achieve. However, good solubility and distribution of perylene derivatives was found in alkaline medium of SnO_2 sol that was prepared by the aqueous precipitation-peptization sol-gel process.

From the structural point of view, SnO_2 can serve as an insertion compound (to be used for example as an optically passive counter electrode in electrochromic devices) since it has the rutile structure with existing tunnels expanding along the 001 direction, which enable the intercalation/deintercalation of small ions (Li^+) through the thin film. The ion-insertion properties can be additionally improved by: (*i*) decreasing electronic resistivity and the particle grain size with doping; and (*ii*) increasing the porosity and the number of redox centres [7]. The induced disorder of the rutile structure through doping can be investigated by EXAFS. Thus, EXAFS of various SnO_2 xerogel samples is used to study the structural environment around tin atom and the disordering effect of Sb and PTCDA guest species.

2. Synthesis

SnO_2 aqueous sol (*a*) was made according to ref. [2] from $SnCl_4 \cdot 5H_2O$ precursor (Table I). Doping with Sb was achieved by adding $SbCl_3$ (7 mol% vs. Sn) in the initial aqueous solution acidified with HCl to dissolve Sb-salt. A precipitate was formed with the addition of ammonia up to pH 3. After repeated washing with water the precipitate was peptised with 8 mL of concentrated aqueous ammonia, which resulted in a basic aqueous sol (pH ∼ 10). To this sol (undoped and Sb-doped) various amounts of PTCDA (0.5–5 mol%), previously dissolved in 9% KOH, were introduced. The gelling time of the sol in a closed vessel was a few days at room temperature.

SnO_2 peroxo sol (*p*) was made for comparison purposes according to ref. [3]. Conc. H_2O_2 was added dropwise to $SnCl_2 \cdot 2H_2O$ precursor leading to the strong exothermic reaction. The formed solution was evaporated at 70 °C to get a viscous opaque gel, which was diluted with ethanol. To this sol a small amount of bis end-capped triethoxysilane with a covalently linked mid polyether chain (ICS-PPG4000 [11], 1 mol%) was added to enhance the porosity of the oxide samples in order to improve ion-storage characteristics.

Xerogel powders were made from gels by drying them at ambient conditions.

Table I. *List of $Sn O_2$ xerogel samples (labels: a – inorganic from aqueous route, p – hybrid organic-inorganic from peroxo route, Sb – Sb doped, P_l – low concentration of PTCDA, P_h – high concentration of PTCDA).*

label	route	Sb	PTCDA
a	aqueous		
aSb	aqueous	7 mol% vs. Sn	
aP_l	aqueous		0.5 mol.%
aSbP_l	aqueous	7 mol% vs. Sn	0.5 mol.%
aP_h	aqueous		5 mol.%
p	peroxo		

*E-mail: jana.padeznik@uni-mb.si

3. Experiment

Samples of xerogel powders were prepared on multiple layers of adhesive tape to gain sufficient absorption jump: 0.2–0.6 at Sn K edge (29200 eV) and ∼0.2 at Sb K edge (30491 eV). Standard Sn and Sb K-edge EXAFS spectra were measured at the X1 station of HASYLAB synchrotron facility at DESY (Hamburg, Germany) using a two-crystal Si 311 monochromator with energy resolution of about 6 eV. Owing to the high photon energy, the incident beam is free of harmonic contamination. The energy scale at Sn edge was calibrated by a simultaneous absorption measurement of a thin Sn foil, while at Sb edge only the stability of the monochromator scale was monitoring by a simultaneous measurement of both Sb doped samples. Spectra were analysed by FEFF6 code [12, 13].

4. Results

The XANES spectra of all samples are very similar showing no detectable valence shift.

By EXAFS, the structure of pure inorganic SnO_2 gel host derived from aqueous sol (*a*) is compared to that of hybrid organic-inorganic xerogel made by peroxo sol-gel route (*p*). In both r-space spectra, a coherent signal is found only up to $r \sim 4$ Å indicating a short-range order. Obviously, the preparation route influences the local structure: a sharp first peak observed in the *a* spectrum is split into two smaller peaks in the *p* spectrum (Fig. 1).

For *a* spectrum, a very good fit of the first peak can be obtained with a model of 6 oxygen neighbors at 2.06 Å as in the cassiterite crystal [14]. With two subsequent shells of Sn neighbors the entire *a* spectrum is roughly described: the distances agree with crystal data but the occupation number is reduced to ∼40% due to disorder in the structure (Table II). The signal of farther oxygen neighbors in the cassiterite structure is small and their parameters cannot be reliably extracted from the xerogel data.

The nearest neighborhood of Sn in the hybrid organic-inorganic xerogel can be modeled with a combined model of a reduced number (∼4.5) of oxygen atoms at distances as in the cassiterite structure and of approximately 1.5 chlorine atoms at 2.40 Å as in a $SnCl_4$ structure [15]. Thus, a relatively large fraction of Sn atoms in the xerogel made by peroxo route remains as chloride while in the xerogel made by aqueous precipitation-peptization route no Sn-Cl bonds are detected, confirming that Cl from starting materials is efficiently washed out.

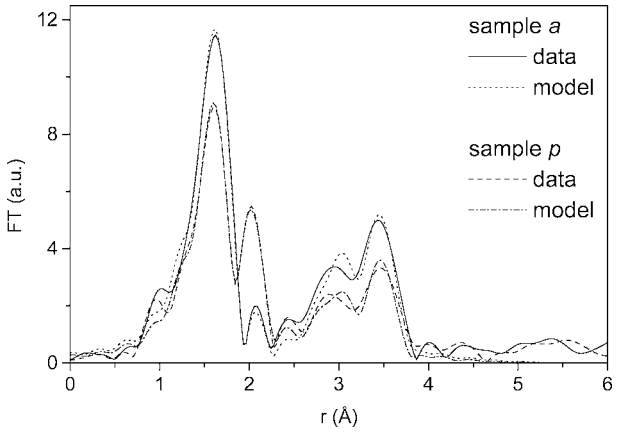

Fig. 1. Fourier transform of the Sn K edge EXAFS of the SnO_2 xerogel and its 3-path model in comparison with SnO_2 xerogel made by peroxo route and its 4-path model (k^3-weighted, 3–14 $Å^{-1}$).

Table II. *Model parameters for spectra at Sn K edge, k range 3–14 $Å^{-1}$, r range 1.3–4 Å (except for sample aP_h: 1.3–2.1), k^3-weighted, the numbers in parentheses indicate uncertainties of the last digit, for sample a the coordination number N_1 was kept fixed.*

	SnO_2 crystal	sample *a*	sample *p*	sample aP_h
r_{fit}	–	0.008	0.009	0.006
N_1 (**O**)	6	6	4.6(5)	4.2(4)
r_1 [Å]	2.05	2.06(1)	2.06(1)	2.06(1)
σ_1^2 [$Å^2$]	–	0.004(1)	0.005(1)	0.003(1)
N_2 (**Sn**)	2	0.9(1)	0.6(4)	–
r_2 [Å]	3.19	3.22(1)	3.22(1)	–
σ_2^2 [$Å^2$]	–	0.002(1)	0.003(1)	–
N_3 (**O**)	4	–	–	–
r_3 [Å]	3.59	–	–	–
N_4 (**Sn**)	8	3.1(9)	3.0(10)	–
r_4 [Å]	3.71	3.74(7)	3.74(1)	-
σ_4^2 [$Å^2$]	–	0.005(1)	0.006(2)	–
N_5 (**Cl**)	–	–	1.5(1)	–
r_5 [Å]	–	–	2.41(1)	–
σ_5^2 [$Å^2$]	–	–	0.002(1)	–

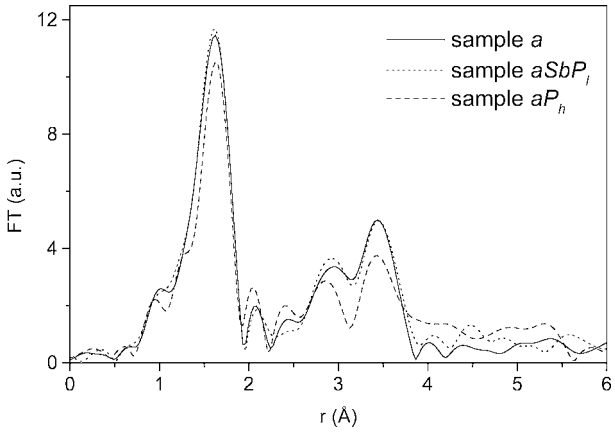

Fig. 2. The effect of doping the SnO_2 xerogel with Sb and low concentration of PTCDA in comparison with doping with high concentration of PTCDA (k^3-weighted, 3–14 $Å^{-1}$).

It can be seen from Fig. 2 that doping with Sb (7 mol% vs. Sn) and a small concentration of PTCDA (0,5 mol%) produces no detectable effect in the spectra at the Sn edge. Doping with high concentration of PTCDA (5 mol%), however, results in a lower signal of the first neighbors. A single-shell model differs from that of the *a* spectrum only in a lower occupation number while the distance and the Debye-Waller factor remain practically the same. The missing oxygen neighbors are not replaced with another species indicating that the disordered organic groups from the dye reach right into the Sn neighborhood.

The spectra at Sb K edge exhibit a higher level of noise due to the relatively small concentration of Sb atoms and a strong background absorption limiting the scope of modeling. Nevertheless, some information can be extracted: both Fourier spectra exhibit only one prominent peak indicating highly disordered Sb-sites (Fig. 3). The first shell around Sb consists of ∼5 oxygen atoms at ∼1.95 Å. In Sb-doped xerogels, the additional doping with PTCDA even at low concentration results in higher static disorder around Sb atoms (Table III).

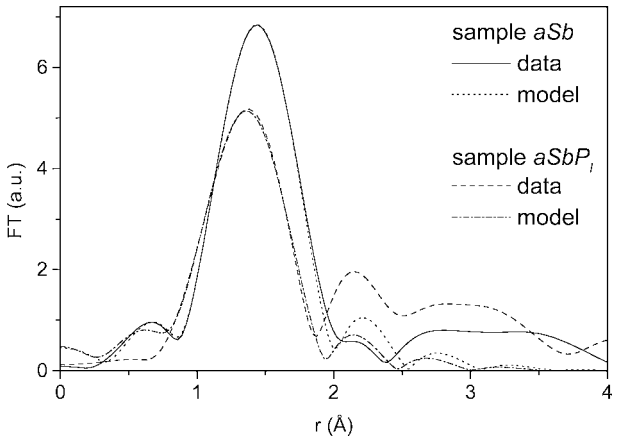

Fig. 3. Fourier transform of the Sb K edge EXAFS of the Sb-doped SnO_2 xerogel in comparison with Sb- and low concentration PTCDA-doped xerogel. Single-path models (k^3-weighted, 2.7–9.1 $Å^{-1}$) are also shown.

Table III. *Model parameters for spectra at the Sb K-edge, k range 2.7–9.1Å^{-1}, r range 1.0–1.8Å, k^3-weighted, the numbers in parentheses indicate uncertainties of the last digit.*

	sample *aSb*	sample *aSbP$_1$*
r_{fit}	0.001	0.002
N_1 (**O**)	4.9(5)	5.0(8)
r_1 [Å]	1.98(1)	1.93(1)
σ_1^2 [Å^2]	0.003(1)	0.006(2)

5. Conclusions

Tin-oxide gel was doped with Sb and/or PTCDA to tailor the electrochemical and optical properties of the final material, keeping the host structure nearly unchanged with evenly dispersed dopant in it. Indeed, all Sn EXAFS spectra are adequately modeled by the structure of SnO_2 cassiterite with reduced occupation numbers.

The disorder increases with the content of the organic dopant. Higher concentration induces a drop of the first neighbor signal indicating a homogeneous distribution of the organic dye.

Acknowledgements

The work was supported by the Slovenian Ministry of Science and Technology and the IHP-Contract HPRI-CT-1999-00040 of the European Commision. Advice on beamline operation by N. Haack of HASYLAB is gratefully acknowledged.

References

1. Brinker, C. J. and Scherer, G. W., "Sol-Gel Science, The Physics and Chemistry of Sol-Gel Processing" (Academic Press, San Diego 1990).
2. Orel, B., Lavrenčič Štangar, U., Crnjak Orel, Z., Bukovec, P. and Kosec, M., J. Non-Cryst. Solids **167**, 272 (1994).
3. Opara Krašovec, U., Orel, B., Hočevar, S. and Muševič, I., J. Electrochem. Soc. **144**, 3398 (1997).
4. Stjerna, B., Olsson, E. and Granqvist, C. G., J. Appl. Phys. **76**, 3797 (1994).
5. Olivi, P., Pereira, E. C., Longo, E., Varelly, J. and Bulhoes, L. O., J. Electrochem. Soc. **140**, L81 (1993).
6. Orel, B., Lavrenčič Štangar, U. and Kalcher, K., J. Electrochem. Soc. **141**, L127 (1994).
7. Orel, B., Lavrenčič Štangar, U., Opara, U., Gaberšček, M. and Kalcher, K., J. Mater. Chem. **5**, 617 (1995).
8. Lampert, C. M., Solar Energy Mater. **6**, 1 (1981).
9. Hofacker, S. and Schottner, G., J. Sol-Gel Sci. Technol. **13**, 479 (1998).
10. Schneider, M., Hagen, J., Haarer, D. and Muellen, K., Adv. Mater. **12**, 351 (2000).
11. Lavrenčič Štangar, U., Grošelj, N., Orel, B. and Colomban, P., Chem. Mater. **12**, 3745 (2000).
12. Stern, E. A., Newville, M., Ravel, B., Yacoby, Y. and Haskel, D., Physica B **208&209**, 117 (1995).
13. Rehr, J. J., Albers, R. C. and Zabinsky, S. I., Phys. Rev. Lett. **69**, 3397 (1992).
14. Seki, H., Ishizawa, N., Mizutani, N. and Kato, M., J. Ceramic Assoc. Japan YGKSA **92**, 219 (1984).
15. Barnes, J. C., Sampson, H. A. and Weakley, T. J. R., J. Chem. Soc. Dalton **1980**, 949 (1980).

Physica Scripta. Vol. T115, 332–334, 2005

XANES Study of Tribofilms Generated from Belt-Drive Continuously Variable Transmission Fluids

Yoshimu Iwanami[a,*], Hisayuki Wada[b] and Masaharu Nomura[c]

[a]Nippon Oil Corporation, Central Technical Research Laboratory, 8 Chidoricho, Naka-ku, Yokohama 231-0815, Japan
[b]Nippon Oil Corporation, Lubricants Research Laboratory, 8 Chidoricho, Naka-ku, Yokohama 231-0815, Japan
[c]Photon Factory, Institute of Materials Structure Science, High Energy Accelerator Research Organization, 1-1 Oho, Tsukuba, Ibaraki 305-0801, Japan

Received June 26, 2003; accepted in revised form January 28, 2004

PACS number: 81.40.Pq

Abstract

We have studied the chemistry of S species in tribofilms generated on steel blocks from belt-drive continuously variable transmission fluids using X-ray absorption near-edge structure (XANES) spectroscopy. First, we examined S K-edge XANES spectra of tribofilms generated using a friction tester from four kinds of fluid which have different friction properties. It is suggested that sulphides such as FeS, alkyl sulphide and ZnS in the tribofilms might increase the friction coefficients of the tribofilms. Second, we examined the XANES spectra of tribofilms collected in both fluorescent yield (FY) and conversion electron yield (CEY) modes. FY and CEY spectra of a fluid were compared and it is found that ZnS content in the surface region might be higher than that in the bulk. On the other hand, the chemistry of the S species in the other three tribofilms might be almost uniform as far as the near surface and the bulk are concerned.

1. Introduction

The fuel efficiency of vehicles will continuously be an important issue in order to conserve natural resources and protect the global environment. Under those circumstances, belt-drive continuously variable transmissions (B-CVTs) have attracted attention because B-CVTs give better fuel efficiency than conventional automatic transmissions (ATs), and they also enable the torque converter, if applied, to lock up at a slower vehicle speed than with ATs. Recently, B-CVTs have been adopted for some vehicles by automobile manufacturers, and it has become very important for oil manufacturers to develop transmission fluids suitable for B-CVTs, that is, belt-drive continuously variable transmission fluids (B-CVTFs) [1]. B-CVTFs are required to have not only the properties of conventional automatic transmission fluids (ATFs), such as good oxidation stability and antiwear performance, but also a high friction coefficient between metal surfaces.

In order to develop high-performance B-CVTFs, it is necessary to investigate the nature of the tribofilms that are generated on metal surfaces by lubrication and govern the lubrication performance. Although conventional surface analysis methods such as EPMA and XPS have been employed to investigate the tribofilms, the nature of the tribofilms has not been well elucidated yet. Therefore, we employed XANES spectroscopy which is more sensitive to the chemical environments of elements such as P and S contained in the tribofilms than other analytical techniques, in order to investigate the nature of the tribofilms.

In this paper, we report the chemistry of the S species of the tribofilms generated on steel blocks using a friction tester, from four B-CVTFs which include different additives such as antioxidant and antiware additives and have different friction properties. The S K-edge XANES spectroscopy in both the fluorescence yield (FY) and the conversion electron yield (CEY) modes was employed to characterize the S species in the tribofilms.

2. Experimental

2.1. *Tribofilm preparation*

The block-on-ring test [2], which is one of friction tests and a convenient method for surveying B-CVTF performance, was employed both to prepare tribofilms and to measure the friction coefficients for four test fluids: three designed for vehicles with high torque-capacity B-CVT units and one designed for vehicles with medium torque-capacity B-CVT units, which is also used as AT fluid as shown in Table I. A schematic diagram of the friction test is shown in Fig. 1. The load is applied on the rotating test ring, so the friction force is produced along a line contact between the block and the ring. The test fluid reaches a level over halfway above the test ring. The test conditions are summarized in Table II. The tribofilms generated on the test blocks were used for the XANES measurements.

2.2. *XANES measurement*

S K-edge XANES measurements were carried out on BL-9A [3] at the Photon Factory, High Energy Accelerator Research

Table I. *Test fluids.*

Test fluids Use		Fluid-1 B-CVT	Fluid-2 B-CVT	Fluid-3 B-CVT	Fluid-4 AT/B-CVT
Elements (mass %)	S	0.10	0.50	0.14	0.10
	P	0.03	0.06	0.03	0.02
	B	0.01	0.02	0.01	0.03
	Ca	0.03	0.13	0.02	0.04
	Zn	0	0.07	0	0.03

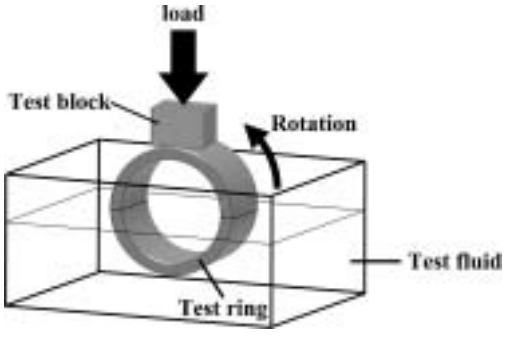

Fig. 1. Schematic diagram of the friction test.

*e-mail: yoshimu.iwanami@eneos.co.jp

Table II. *Test conditions.*

Load (N)	1,112
Fluid temperature (°C)	100
Sliding velocity (m/s)	1.0
Test block and ring	Steel

Organization, Tsukuba, Japan. X-rays were monochromatized with a Si(111) double crystal monochromator and higher orders were reduced by a pair of mirrors. The spectra were collected in both the FY and the CEY modes using a Lytle detector.

3. Results and Discussion

The test time dependences of the friction coefficients for the test fluids are very different: the friction coefficient of Fluid-1 barely varies with test time, while those for the other fluids vary with test time, as shown in Fig. 2. At the 30-minute point in the test, the fluids can be classified into two groups: fluids designed only for B-CVTs, which show high friction coefficients (Fluids-1 to 3), and fluid designed for both B-CVTs and ATs, which shows a medium friction coefficient (Fluid-4). Therefore, as the first step, we examined the S K-edge XANES spectra of the tribofilms generated at the test time of 30 min in the FY mode which indicates the chemistry of the bulk of the tribofilms, in order to understand the differences in the chemical nature of the tribofilms generated from B-CVTFs between the above-mentioned two groups.

The S K-edge XANES spectra of four tribofilms in the FY mode show different patterns (Fig. 3), suggesting that S species in the tribofilms are different, but each spectrum has four characteristic peaks (marked a, b, c and d). In order to identify

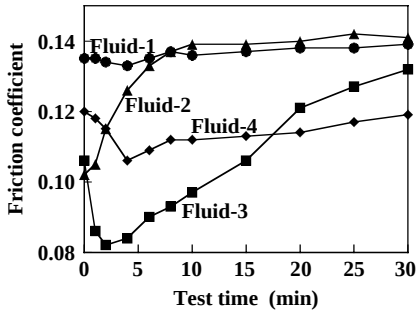

Fig. 2. Test time dependence of friction coefficient for test fluids.

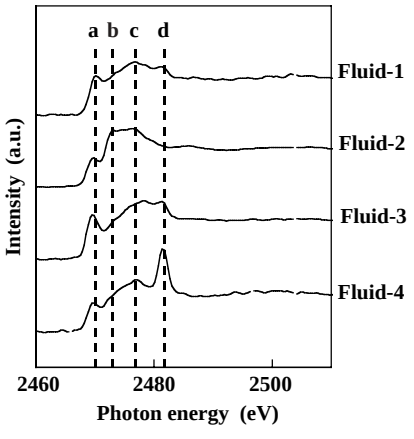

Fig. 3. S K-edge XANES spectra of B-CVT and AT/B-CVT tribofilms (at the 30-minute point).

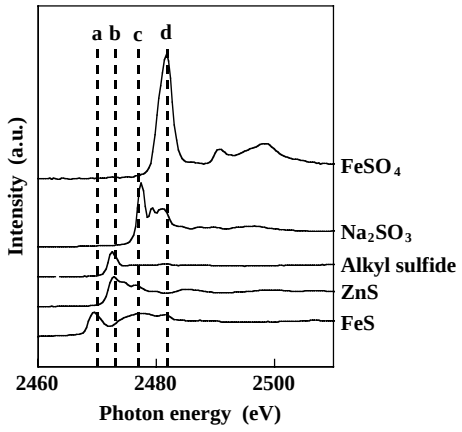

Fig. 4. S K-edge XANES spectra of model compounds of S species.

the nature of these peaks, we examined the S K-edge XANES spectra of several model compounds of S species that are supposed to be contained in the tribofilms. Comparison of the spectra of the tribofilms (shown in Fig. 3) with those of model compounds (shown in Fig. 4) suggests that peaks a and b are related to reduced forms of sulphur such as FeS, ZnS or alkyl sulphide [4]. On the other hand, peaks c and d are likely to be related to oxidized forms of sulphur such as sulphite (Na_2SO_3 as a typical example) and sulphate ($FeSO_4$ as a typical example). These results suggest that the bulks of tribofilms generated from B-CVTFs are composed of sulphide, sulphite and sulphate.

It is found that the sulphide peaks a and b in the XANES spectra of tribofilms generated from fluids designed only for B-CVTs use (hereafter referred to as B-CVT tribofilms, Fluids-1 to 3) are stronger than those in the spectrum of tribofilm of the fluid designed for both ATs and B-CVTs use (hereafter referred as AT/B-CVT tribofilm, Fluid-4) and the sulphate peak d in the spectrum of the AT/B-CVT tribofilm is stronger than those in the spectra of the B-CVT tribofilms. These results suggest that the bulks of B-CVT tribofilms are composed of more sulphides than are that of the AT/B-CVT tribofilm, while the bulk of the AT/B-CVT tribofilm is composed of more sulphate than are those of the B-CVT tribofilms.

In order to understand the chemical nature of tribofilms in detail, we estimated the composition of S species in the tribofilms by the following method. The S K-edge XANES spectra of the tribofilms were deconvoluted with four or five spectra of model compounds, that is, sulphides, a sulphite and a sulphate, by fitting the spectra of the tribofilms with those of model compounds using least squares method. In the deconvolutions of the XANES spectra of tribofilms generated from fluids containing Zn species (Fluids-2, 4), the spectra of FeS, ZnS and alkyl sulphide as sulphides were employed, while in the deconvolutions of the spectra of tribofilms from fluids not containing Zn species (Fluids-1, 3), the spectra of FeS and alkyl sulphide as sulphides were employed. As a result of the deconvolutions, it is found that the bulks of the B-CVT tribofilms are composed of over about 95% sulphides such as FeS, ZnS and alkyl sulphide, while the bulk of the AT/B-CVT tribofilm is composed of about 85% sulphides and 15% sulphite and sulphate as shown in Fig. 5.

Because the B-CVT tribofilms show high friction coefficients and the AT/B-CVT tribofilm shows a medium friction coefficient, it is suggested that the friction coefficients of the tribofilms might be governed by the type of S species contained in the tribofilms, that is, sulphides might increase the friction coefficients.

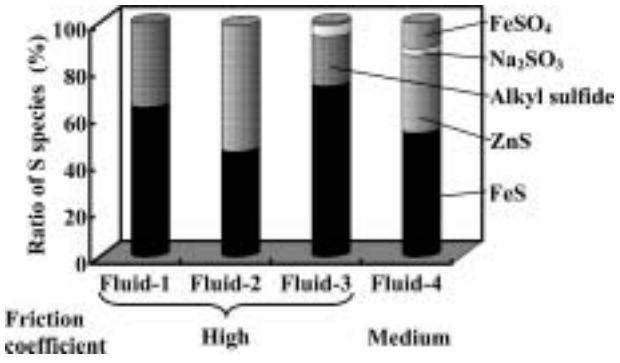

Fig. 5. Ratio of S species in the bulk of tribofilms (at the 30-minute point).

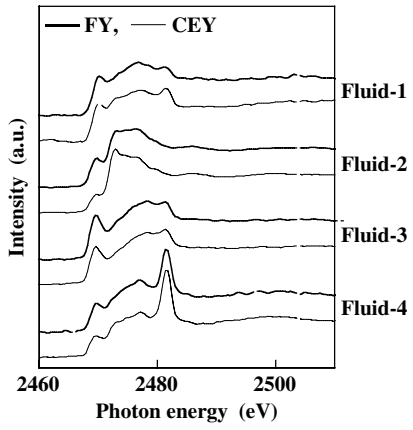

Fig. 6. S K-edge XANES in FY and CEY modes spectra of B-CVT and AT/B-CVT tribofilms (at the 30-minute point).

Further, in order to understand the uniformity of the chemistry of the S species in tribofilms, we compared the S K-edge XANES spectra of tribofilms collected in the FY mode and those collected in the CEY mode which indicates the chemistry in the near surface region of the tribofilms. Almost no significant differences in the XANES spectra of the tribofilms are observed between the two modes, except the spectra of the B-CVT tribofilm generated from Fluid-2, which gives a high friction coefficient and contains Zn species, as shown in Fig. 6. Fig. 6 suggests that the ZnS content in the near surface region of the B-CVT tribofilm generated from Fluid-2 might be higher than that in the bulk. On the other hand the chemistry of the S species in the other tribofilms might be almost uniform as far as the near surface and the bulk are concerned. In another report, the tribofilm prepared from Fluid-2 using another type of friction tester, that is a reciprocating type friction tester, showed no significant difference between the XANES spectra in both the FY and the CEY modes [5]. This suggests that the friction test conditions might affect the uniformity of the chemistry of the S species in tribofilms.

4. Conclusion

The following are suggested by the examination of the S K-edge XANES spectra of four tribofilms generated from B-CVTFs:

1. XANES spectroscopy is a useful analytical method to characterize the S species in the tribofilms in detail.
2. Sulphides such as FeS, alkyl sulphide and ZnS in the tribofilms might increase the friction coefficients of the tribofilms.
3. ZnS content in the near surface region of the tribofilm generated from Fluid-2, which gives a high friction coefficient and contain Zn species, might be higher than that in the bulk. On the other hand, the chemistry of the S species in the other three tribofilms might be almost uniform as far as the near surface and the bulk are concerned.

References

1. Mabuchi, Y., Kano, M., Ishikawa, T., Sano, A. and Wakizono, T., Trib. Trans. **43**, 229 (2000).
2. Ward, Jr., W. C., Sumiejski, J. L., Derevjanik, T. S., Fewkes, R. and Ikeda, M., '98 TVT Symposium, Yokohama 82 (1998).
3. Nomura, M. and Koyama, A., Nucl. Instrum. Meth. Phys. Res. **A467–468**, 733 (2001).
4. Kasrai, M. *et al*., Trib. Trans. **41**, 69 (1998).
5. Wada, H., Iwanami, Y. and Nomura, M., JSAE Paper No. 20030238 (2003).

Physica Scripta. Vol. T115, 335–338, 2005

Near Edge X-Ray Absorption Spectroscopy: a Novel Approach for Determining Conduction Band Edge States in Transition Metal Oxide Gate Dielectrics

G. Lucovsky[1,*], Y. Zhang[1], J. L. Whitten[2], D. G. Schlom[3] and J. L. Freeouf[4]

[1]Department of Physics, North Carolina State University, Raleigh, NC 27695-8202, USA
[2]Department of Chemistry, North Carolina State University, Raleigh, NC 27695, USA
[3]Department of Materials Science, Pennsylvania State University, College Park, PA 16802, USA
[4]Department of Electrical Engineering, Oregon Graduate Institute, Portland, OR 97291, USA

Received June 26, 2003; accepted October 22, 2003

PACS numbers: 71.15.Nc, 71.15.Qe, 78.20.−e, 78.40.−q, 78.70.Dm

Abstract

Spectroscopic studies of transition metal (Tm) and rare earth (Re) oxides, combined with *ab initio* theory identify the band edge electronic structure of alternative high-K dielectrics. The lowest conduction band states are derived from anti-bonding transition metal d*-states with a π symmetry and show strong final state effects. Applied to the complex Tm/Re mixed oxides of the general form $ReTmO_3$, this approach identifies a novel way for obtaining separate and independent control of band gap energies and dielectric constants through local bonding arrangements in which Tm and Re atoms are nearest neighbors to the same oxygen atom.

1. Introduction

The band edge electronic structure of the group IVB Tm oxides, TiO_2, ZrO_2, and HfO_2, has been obtained by X-ray absorption spectroscopy (XAS) and vacuum ultra-violet spectroscopic ellipsometry (VUV SE), coupled with *ab initio* calculations and provides the basis for a quantitative understanding of empirically-determined scaling of band gaps and band offset energies with respect to Si as function of the atomic d-state energies of the respective Tm/Re atoms. Based on this scaling, and confirmed by experiment, elemental oxides, and silicate and aluminate alloys containing Sc, Ti, Ta and Nb have band offset energies too small for reducing direct tunneling to levels required for advanced devices in spite of high dielectric constants and film thickness increases of 5 to 10 relative to SiO_2.

Spectroscopic studies of $GdScO_3$ provide an additional dimension to this scaling. Based on XAS and VUV SE measurements, and combined with an extension of *ab initio* calculations to complex oxides with Re-O-Tm bonding arrangements, it is shown that coupling of Re and Tm atomic d-states in these arrangements increases minimum band gaps and conduction band offset energies with respect to crystalline Si, thereby identifying novel and technologically important opportunities for band gap 'engineering' at the atomic scale.

2. Spectroscopic studies of group IVB Tm oxides and $GdScO_3$

The lowest conduction band states of ZrO_2 as determined from Zr $M_{2,3}$ and O K_1 XAS [1], and band edge optical absorption constants from VUV SE measurements [2] are associated with symmetry-split Zr 4d*-states, and a broader band derived form Zr5s*-states. Table I summarizes the relative energies of these spectral features for ZrO_2, as well as HfO_2 and TiO_2. Relative energies of these features in the $X_{2,3}$ spectra (X = L, M and N) normalized to the lowest d*-state energy, are essentially the same for ZrO_2 and HfO_2, except for a small difference in the d*-s* state splitting. In contrast, the d* state splitting in the TiO_2 $L_{2,3}$ spectra is smaller, and the d*-s* splitting is larger. Due to final state effects the d* state splitting show differences in the respective Tm $X_{2,3}$, O K_1 and absorption edge spectra. Figure 1 displays corresponding spectra for $GdScO_3$: the $L_{2,3}$ spectrum for Sc in Fig. 1(a), the O K_1 edge spectrum in Fig. 1(b), the optical absorption constant in Fig. 1(c), and additional absorption edge transmission for intra 4f-level transitions in Fig. 1(d) [3].

Table I. *Measured d*-d* and d*-s* splittings.*

oxide	$X_{2,3}$ d*-d* (d*-s*) ±0.2 eV	K_1 edge d*-d* (d-s) ±0.2 eV	band edge d*-d* (d*-s*) ±0.2 eV
TiO_2	2.0 (13)	1.8 (6)	1.4 (5)
ZrO_2	2.4 (12)	1.3 (4.5)	∼1.4 (<1)
HfO_2	∼2 (10)	1.5 (4.5)	∼1.4 (<1)

The features in the $L_{2,3}$ spectrum in Fig. 1(a) are associated with localized transitions between spin-orbit split Sc $2p_{1/2}$ and $2p_{3/2}$ states and symmetry split Sc 3d* states. Matrix element effects account for the lack of observable absorption from the Sc states to anti-bonding Sc 4s* states [4]. The spin-orbit splitting is ∼4 eV, the symmetry splitting of the 3d*-states is ∼2 eV, and the spectral width is <0.5 eV (the spectral resolution is ∼0.2 eV).

The two features at ∼532.5 and 536 eV in the O K_1 edge in Fig. 1(b) are associated with transitions to d*-states. Based on relative widths, the lower energy feature is Sc 3d*-like, and the higher is Gd 5d*-like. The splitting between these states, ∼3.5 eV is smaller than the splitting of ∼4.2 eV in ZrO_2 (4d*) and HfO_2(5d*), but larger than the 2.5 eV splitting in TiO_2 (3d*).

Figure 1(c) displays the optical absorption constant, α, at the band edge as a function of photon energy obtained from the analysis of VUV SE data. The transmission measurement in Fig. 1(d) establishes that the features between about 4.8 and 5.8 eV are due to intra 4f-level transitions characteristic of the partially occupied 4f-shell in Gd [5]. The rapid rise of absorption at approximately 5.8 eV in Fig. 1(c) marks the onset of transitions from the top of valence band, O 2p π non-bonding states, to the lower of the two d*-states. Since there is no distinct

*e-mail: lucovsky@unity.ncsu.edu

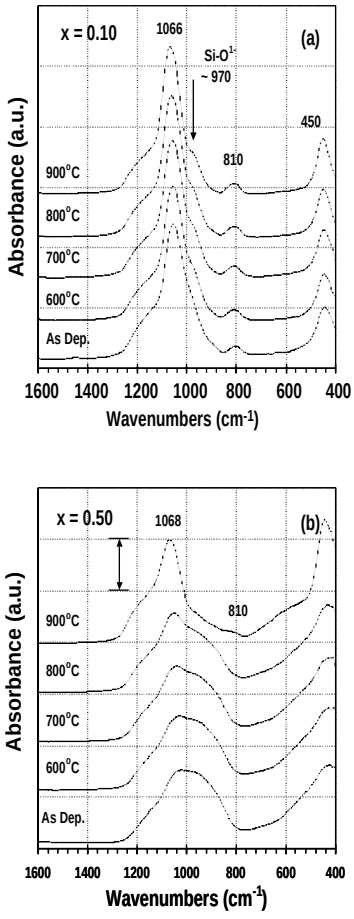

Fig. 1. $GdScO_3$ spectra: (a) $L_{2,3}$ spectrum for Sc, (b) O K_1 edge spectrum, (c) band edge absorption constant, and (d) transmission.

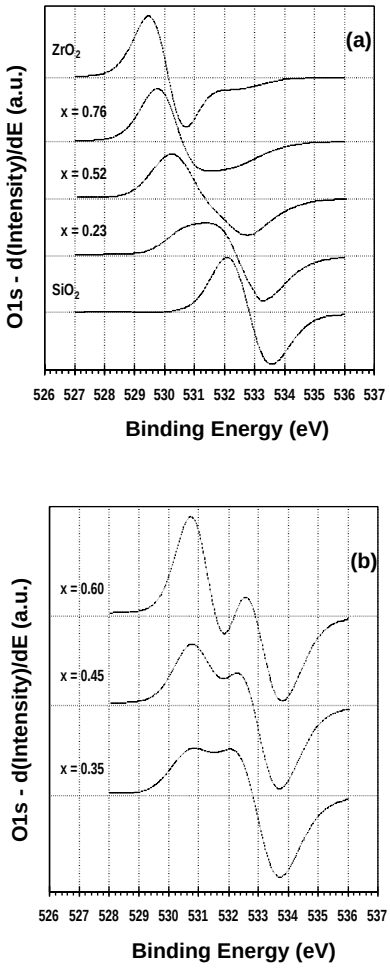

Fig. 2. Calculated band edge electronic structure of ZrO_2 and TiO_2. Energies are referenced to the top of the valence band.

spectral evident for the second d*-state, absorption above 6 eV is dominated by transitions to s*-states.

3. *Ab initio* calculations

The spectra for the group IVB oxides have been interpreted through *ab initio* calculations, the details of which will be published elsewhere [6]. The electronic structure calculations employ variational methods in which an exact Hamiltonian is used so that the variation principle applies. The calculations are done initially through a self-consistent field (SCF) Hartree-Fock calculation with a single determinant wave function, which does not include electron correlation. Following this, there is a configuration interaction (CI) refinement of the bonding orbitals based on a multi-determinant expansion wave function, and including electron correlation effects.

This method has been applied to small clusters that include the bonding of the transition metal atom to O neighbors terminated by H atoms. Calculations have been made for the ground state energy, and the Zr K_1, the Zr $M_{2,3}$, the O K_1, and the absorption edge transitions and the corresponding electronic structures for TiO_2, and HfO_2. Table I summarizes the relative energies of these spectral features for ZrO_2, as well as HfO_2 and TiO_2. Relative energies of these features in the $X_{2,3}$ spectra (X = L, M and N) normalized to the lowest d* state energy, are essentially the same for ZrO_2, HfO_2, and TiO_2 except for small differences in the d*-s* state splitting. The d*-d*, and d*-s* splittings are smaller in the K_1 edge and band edge spectra as well. The d*-s* splitting are greater for TiO_2, with no d*-s* overlap in the band edge spectra, as contrasted with marked overlap for both ZrO_2 and HfO_2. This trends have been are in agreement with theory.

Figure 2 compares the calculated band edge structures of ZrO_2 and TiO_2. All energies are referenced to the top of the valence band, which is comprised of oxygen atom 2p π non-bonding states. Consider first the valence band states. In order of increasing binding energy these are non-bonding O 2p π, and 3d Ti or 4d Zr π-bonded states, and 3d Ti or 4d Zr σ-bonded states with the corresponding O 2p π or σ orbitals. The overlap is larger for the Ti 3d-O 2p π-bonding than for Zr 4d-O 2p π-bonding, hence the difference of $\sim$2 eV. The differences in relative energy between the Ti 3d-O 2p and Zr 4d-O 2p σ-bonding states are similar as indicated by the dashed arrows. The separation of the conduction band d-states comes from the calculations, and the relative energy of the lowest conduction band state is from experiment. The energies of the lowest Tm conduction band states have a reversed π^*/σ^* ordering, and the energies relative the atomic Ti 3d and Zr 4d states and are respectively smaller consistent with the *bonding stabilization energy* being greater than the *anti-bonding destabilization energy*.

One of the more important features of Fig. 2 is the energy difference between the respective atomic d-states, 11.1 eV for the Ti 3d state, and 8.13 for the Zr 4d state, and the respective lowest anti-bonding states. This is approximately 2 eV, and is the basis for the scaling of elemental oxide band gaps with the energies of the respective atomic d-states that is displayed in Fig. 3. This explains the approximately linear dependence in the energy range between

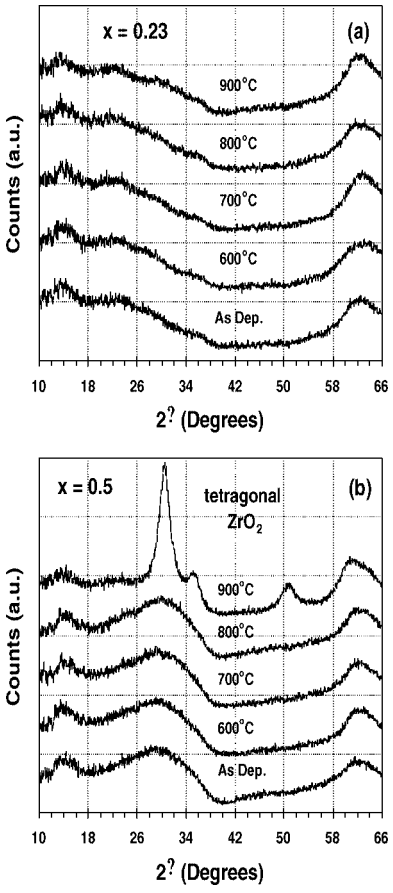

Fig. 3. (a) Empirical scaling of band gaps versus atomic d-state energy. Solid line – trend for transition metal oxides, dashed line – predicted scaling for complex oxides with d-state coupling. 3(b) Empirical scaling of conduction band offset energies with respect to Si versus atomic d-state energy. Solid line – trend for transition metal oxides, dashed line – predicted scaling for complex oxides with d-state coupling.

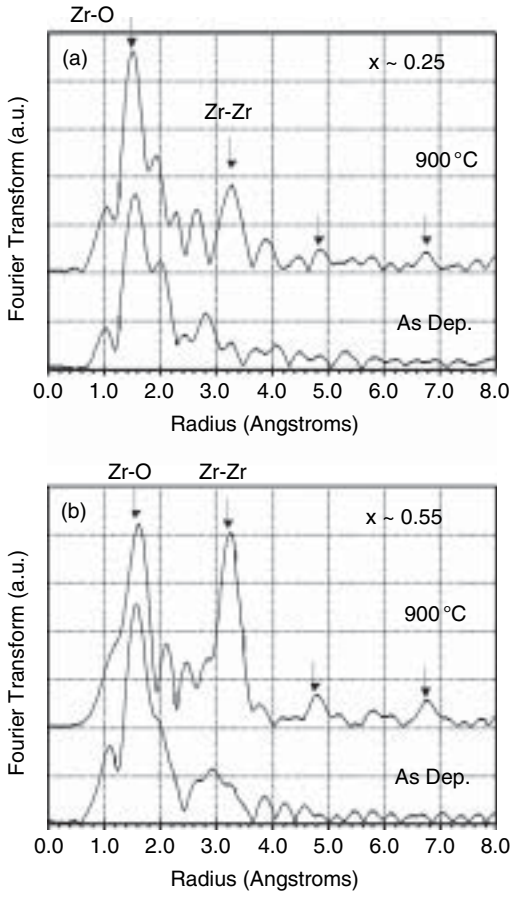

Fig. 4. Schematic representation of molecular orbitals for band edge electronic structure. Top: for elemental transition metal and rare earth oxides; bottom; for complex oxides with d-state coupling through O-atoms.

-11 and -8 eV, which includes in order of increasing (more positive) d-state energy, Ti, Nb, Ta, Sc, Zr and Hf. The bending over at higher energies, e.g., for Y or La, is a manifestation of interactions between higher lying $(n + 1)$ s*-states, and the n d*-σ–state band. The flattening out at lower energy occurs for oxides of Mo and W (not high-K candidates) where d-state occupancy is increased.

Based on this scaling, and results presented in Ref. [7], the minimum band gap in $GdScO_3$ is expected to be determined by transitions which terminate in d*-states with Sc 3d*-character. Since the top of the valence is O 2p p non-bonding, the valence band relative to vacuum are expected to be essentially the same in Sc_2O_3 and $GdScO_3$. The band gap for Sc_2O_3 as determined from transitions terminating in the lowest lying 3d*-state is a approximately 4.3 ± 0.1 eV [7], scaling arguments would place the lowest band gap in $GdScO_3$ at approximately the same energy, and less than 4.5 eV. This expectation is based on comparisons between the band gaps of TiO_2 and $SrTiO_3$, and Nb_2O_5 and $KNbO_3$ [8], where the respective band gaps differ by no more than 0.2 eV.

4. Interpretation of the spectra for $GdScO_3$

Since the lowest band gap in $GdScO_3$ is at ~4.9 eV, this represents a marked departure from the scaling discussed above. This is accounted for by considering differences between the bonding in $GdScO_3$ and the elemental oxides and oxides in Fig. 4. The local bonding in $GdScO_3$ includes arrangements in which both Gd and Sc atoms are bonded to the same O atom. This promotes a mixing of Sc 3d-states and Gd 5d-states, which contributes to both the valence band and conduction band electronic structure. Figure 4 presents an energy band scheme that applies. The upper part of the figure illustrates bonding in elemental Tm or Re oxides, e.g., Sc_2O_3 or Gd_2O_3, in which Tm or Re atoms, respectively, are second neighbors and bonded to a common O atom. The lower portion indicates changes that occur in complex oxides in which Tm and Re atoms are second neighbors through bonding to the same O atom. For $GdScO_3$, the overlap of the Sc 3d states both for π- and σ-bonding is greater than for the Gd 5d states, and this results in valence band, and anti-bonding states that are shifted in energy from their respective end member oxides, Sc_2O_3 and Gd_2O_3. Based on overlap integral differences, valence band π- and σ-states are at intermediate energies with respect to the corresponding elemental oxides states. This increases the energy of the lowest conduction band state with respect to Sc_2O_3, and also makes the separation between the two d*-states intermediate between those of a 3d-oxide and 5d-oxide. This is important for band gap/band offset energy scaling, and is included in Fig. 3.

The basis for the scaling comes from comparisons between $GdScO_3$ and ZrO_2, where the onsets of strong absorption occur respectively at 5.8 and 5.7 eV; this means that $GdScO_3$ has a band gap characteristic of a 4d Tm oxide. It is interesting to note that the average atomic d-state energy in $GdScO_3$, equal 0.5 $(-6.6\,\text{eV} + -9.4\,\text{eV}) = -8\,\text{eV}$ which approximately equal the atomic d-state energy of ZrO_2, -8.13 eV. In a parallel manner, the band gaps of ScO_3, ~4.5 eV and Gd_2O_3, ~6.3 eV average out

to a band gap of approximately 5.5 eV. This suggests that a virtual crystal model can be applied to complex Tm/Re oxides in which d-states of the constituent atoms are coupled through bonding to common O atoms. Bonding in Tm/Re silicates and aluminates is qualitatively different and has been addressed in Ref. [1] and [9]. The energies of Zr core states, and Si core states track across Zr silicate alloys with a constant separation [9]. This equivalent to the difference between the band edge transitions between O 2p π non-bonding states and Zr 4d* and Si 3s* states maintaining a constant energy separation that is shown in Ref. [1]. Tm (Re) silicate and aluminate alloys are the *two band* systems, where energies are maintained at relative end-member oxide levels, but relative absorptions change with relative concentration, whilst the complex $ReTmO_3$ display a qualitatively different *single band* behavior. Oxides with Gd_2O_3 and Sc_2O_3, with other than the 1 : 1 ratio are expected to display spectra characteristic of more than one environment; e.e., Sc_2O_3 rich alloys, should display multiple d*-state features at energies characteristic of both Sc-O-Sc, and Sc-O-Gd bonding arrangements.

5. Discussion

Figure 4 includes the application of the virtual crystal model to complex oxides. The square point is the experimental value for $GdScO_3$ and is plotted at the Sc atomic d-state energy of 9.35 eV. The diamond shape point is for a HfO_2 (5d) – Tio_2 (3d), 1 : 1 alloy, $TiHfO_4$, where the band gap is the average of HfO_2 (5.8 eV) and TiO_2 (3.1 eV) or 4.4 eV. The conduction band offset energies are estimated on the basis of the virtual crystal model. $GdScO_3$ is 'equivalent' to ZrO_2 with an offset of 1.5 eV, and $Hf(Zr)TiO_2$ is expected to have an offset energy of approximately 1 eV, whereas a Ta_2O_5-$2HfO_2$ alloy may have an offset as high as 1.4 eV. Thin film alloys are being prepared to test these predictions of the virtual crystal model. If they prove to be correct, then a virtual crystal behavior should occur in the dielectric constants as well, and therefore provide separate and independent control of offset energies and K. This would be particularly interesting for the TiO_2 and Ta_2O_5 complex oxides where the dielectric constants of the elemental Tm oxides, $\sim$50, and 30, respectively.

Acknowledgements

Supported by the SRC, ONR and NSF.

References

1. Lucovsky, G. *et al*., J. Vac. Soc. Technol. **B 20**, 1739 (2002).
2. Lim, S.-G. *et al*., Appl. Phys. **91**, 4500 (2002).
3. Haeni, J. H. *et al*., J. Appl. Phys. (2003), in process.
4. Condon, E. U. and Shortley, G. H., "Theory of Atomic Spectra" (Cambridge, London, 1935).
5. McClure, D. S., "Electroic Spectra of Molecules and Ions in Crystals" (Academic Press, NewYork, 1959).
6. Zhang, Y., Lucovsky, G. and Whitten, J. L., unpublished.
7. Tippins, H. H., J. Phys. Chem. Soilds **27**, 1069 (1966).
8. Cox, P. A., "Transition Metal Oxides" (Oxford Science Publications, Oxford, 1992), Chap. 2.
9. Rayner, Jr., G. B., Kang, D., Zhang, Y. and Lucovsky, G., J. Vac. Sci. Technol. **B 20**, 1748 (2002).

Physica Scripta. Vol. T115, 339–341, 2005

Determination of the Short-Range Structure of $ZnCl_2$ in its Liquid, Vitreous and Crystalline Phases by XAS, at High Pressure and High Temperature

C. Fillaux, B. Couzinet, C. Dreyfus, J. P. Itié and A. Polian

Physique des Milieux Condensés, CNRS UMR 7602, Université Paris 6, B77, 4 place Jussieu, 75252 Paris Cedex 05, France

Received June 26, 2003; accepted November 4, 2003

Abstract

In situ EXAFS spectra of liquid, vitreous and crystalline zinc chloride under pressure and temperature, have been obtained and analysed using advanced techniques for data analysis (GNXAS). A detailed experimental investigation of the short-range structural properties of zinc chloride is presented. X-ray absorption measurements of solid and liquid $ZnCl_2$ have been collected in the P = 0-12GPa and T = 296-800 K ranges of pressure and temperature, using synchrotron radiation. The analysis of the signal in vitreous and liquid $ZnCl_2$ has been performed using a technique that allows to extract information on the radial distribution function $g(r)$ obtained from molecular dynamics simulations or previous diffraction determination.

1. Introduction

The pressure and temperature dependence of the structural properties of liquids and glasses of tetrahedral oxides are of fundamental and technical interest. However, observing possible pressure-induced coordination changes in the liquid phase of MO_2-type oxide with tetrahedral network requires temperatures much too high for the diamond anvil cell experiments. Therefore, we have substituted the oxide by zinc chloride, a glass forming material which has relatively low melting and glass transition temperatures ($Tm = 593$ K, $Tg = 375$ K), at ambient pressure.

Zinc chloride is unusual among the halides for its high viscosity at the melting point and consequently its ability to supercool into a glass at a relatively low temperature. The generally accepted representation of the structure of non-crystalline $ZnCl_2$ is based upon a well-defined tetrahedral local structure in which chlorine anions surround the zinc cation [1, 2, 3, 4].

Crystallographic studies have clearly established the tetrahedral coordination of Cl^- ions about the Zn^{2+} ions in crystalline $ZnCl_2$. In 1963, Wyckoff [5] lists three polymorphs, α-$ZnCl_2$ ($I\bar{4}2d$), β-$ZnCl_2$($P2_1/n$) and γ-$ZnCl_2$ ($P4/nmc$). It was shown, however, by Brynestad and Yakel [6, 7] in 1978, that careful preparation of anhydrous $ZnCl_2$ leads to the formation of only one crystal structure, δ-$ZnCl_2$ which has the orghorhombic symmetry and space group $Pna2_1$. Recent work [8] confirm their conclusion tha the previously reported allotropic forms are the result of water contamination of δ-$ZnCl_2$. Raman and X-ray experiments have shown the existence of a second $ZnCl_2$ phase which has the $CdCl_2$-type layer structure with the zinc cations in a six-fold coordination [9, 10].

This paper presents a structural study based on X-ray absorption measurements of glassy, crystalline and liquid $ZnCl_2$ in the $P = 0$–12 GPa pressure range and $T = 296$–800 K temperature range, collected using synchrotron radiation. Determination of the local structure is performed using EXAFS refinement in the framework of the GNXAS method for data analysis [11, 12, 13].

2. Experimental techniques

2.1. *Sample preparation*

The $ZnCl_2$ glass samples were high-purity beads (99.99%, Aldrich chemicals). Due to the extreme hygroscopicity of the glass and subsequent devitrification to the cristobalite-type α-$ZnCl_2$ in the presence of minute amounts of water (as seen by Raman spectroscopy), all manipulation of the material took place in a helium-filled glovebox. The beads were finely ground in a mortar and then the powder was loaded without pressure medium in a 200μ-diameter sample chamber of a preindented rhenium gasket. The sample, fine ruby spheres and strontium borate doped with samarium were pressurized in a membrane driven diamond anvil cell.

The high temperature experiments have been performed with an external heater, which allows us to increase the temperature up to 800 K.

2.2. *Dispersive Extended X-ray Absorption Fine Structure*

X-ray absorption measurements were performed at the Zn K-edge, in LURE (Laboratoire pour l'Utilisation du Rayonnement Electromagnitique, Orsay, France) on the D11 beam line (Dispersive EXAFS, DCI storage ring). Figure 1 shows typical XAS spectra collected at different pressures and temperatures.

Measurements on crystalline $ZnCl_2$ have been recorded at ambient temperature, from 0.2 up to 11.8 GPa, with a pressure accuracy of about 0.1 GPa. As previously reported [9, 10], we observed a pressure-induced phase transition between $\gamma - ZnCl_2$

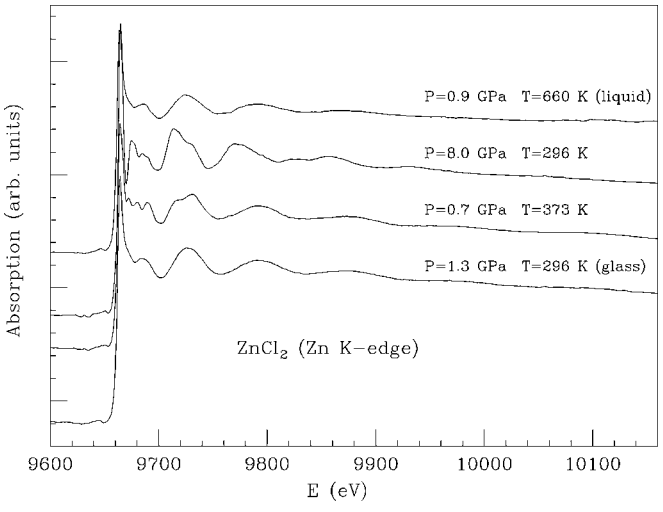

Fig. 1. X-ray absorption spectra of $ZnCl_2$ near the Zn K-edge, for four different pressures and temperatures in the glassy, liquid and two crystalline phases.

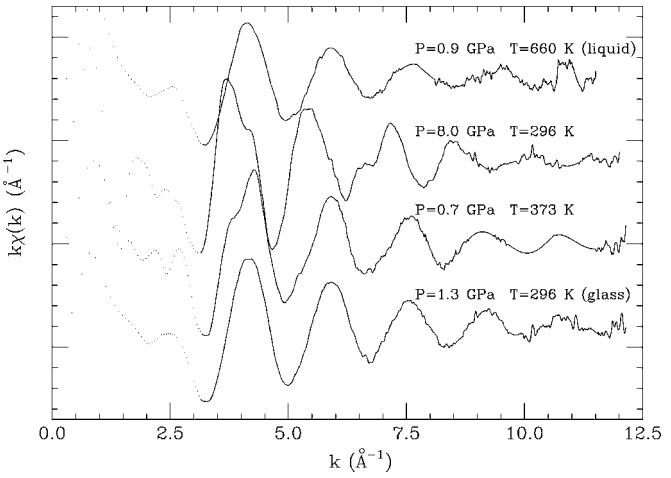

Fig. 2. Experimental XAFS data for four different phases of $ZnCl_2$.

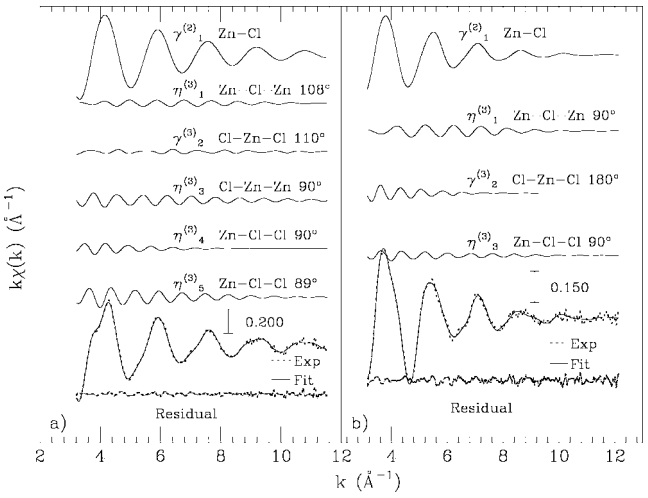

Fig. 3. Decomposition of the best-fit calculated multiple-scattering into individual two body ($\gamma^{(2)}$) and thr5ee-body ($\gamma^{(3)}$and$\eta^{(3)}$ including the two-body signal of the longest distance of the triplet) terms. a) Low-pressure crystalline phase $P =$ 0.3 GPa,$T = 396$ K. b) high-pressure crystalline phase $P = 2.6$ GPa,$T = 513$ K.

and a $CdCl_2-$type phase (see spectra at $P = 0.7$ and $P = 8.0$ GPa in Figure 1). Vitreous $ZnCl_2$ was measured only at ambient temperature and $P = 1.3$ GPa. By heating the sample above the glass transition temperature (3.73 K) we observed a crystallization of vitreous $ZnCl_2$, and then liquid was obtained at $P = 0.9$ GPa and $T = 660 \pm 10$ K.

The raw $k\chi(k)$ data for the four different phases are presented in Figure 2. The frequency difference between the two crystalline spectra is a direct manifestation of the increase of the first-shell average distance during the transition from the low-pressure crystalline phase (four-fold coordinated) to the high-pressure $CdCl_2-$type crystalline phase (six-fold coordinated). On the other hand, the vitreous, liquid and low-pressure crystalline phases have quite similar first-shell average distances, which is consistent with literature [4, 15]. We can see a softening of the oscillations for vitreous and liquid spectra which is a consequence of a lack of long-range order. The amplitude decrease for the liquid $ZnCl_2$ is due to an increase of thermal vibrations.

3. Results and discussion

3.1. *Methodology*

EXAFS data have been analyzed using the GNXAS package [13]. The experimental EXAFS signals of the four phases observed during the experiments are shown in Figure 3 and 4. They are compared with the corresponding best-fit model signals. Figure 3: low-pressure crystalline phase (a) and high-pressure crystalline phase (b). Figure 4: glassy phase (a) and liquid phase (b).

For the two crystalline phases the model signals include the first three coordination shells, modeled using asymmetric Γ-like distributions [12, 13]. The two-body and three-body signals of the model are calculated from the known structure at ambient conditions. Then only the more intense are kept for fitting experimental signals. In a first approach, average angle values have been kept fixed in order to minimize the number of free parameters.

For the disordered phases, we have used a method combining long-range information (tail) from MD and neutron diffraction data [14, 15], with the short-range sensitivity of the EXAFS ($\gamma^{(2)}$) [16].

In this paper, we present only the first-neighbour structural parameters R (interatomic distance) and σ^2 (Debye-Waller factor).

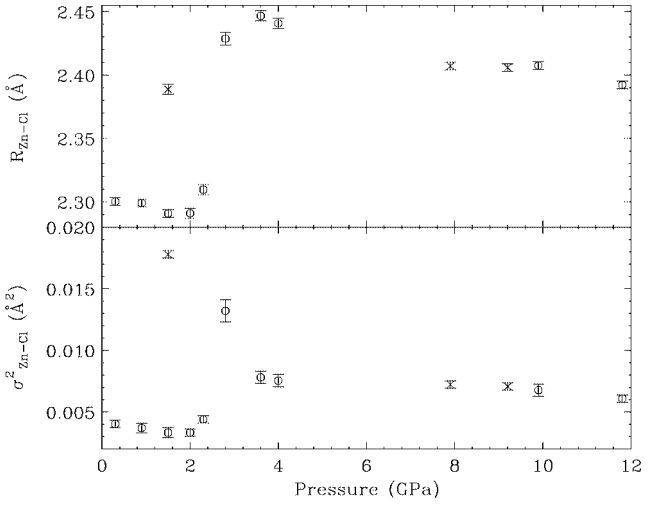

Fig. 4. Analysis of glassy and liquid $ZnCl_2$ spectra using a model $g(r)$ composed of two Γ -distribution peaks plus a tail contribution. a) Glassy phase $P = 1.3$ GPa, $T = 296$ K. b) Liquid phase $P = 0.9$ GPa, $T = 660$ K.

3.2. *Results*

The amount of water in the crystalline sample after loading was tested by Raman spectroscopy, that revealed a sharp peak at about 250cm^{-1}, characteristic of hydrated $\gamma - ZnCl_2$ according to other works [8, 9, 10]. Thus, low-pressure crystalline phase EXAFS analyses were done using $\gamma - ZnCl_2$ as a model for refinement.

The results of the ambient temperature structural refinement are reported in Figure 5. The error bars refer to a 95% confidence level and have been calculated using rigorous statistical methods accounting for correlations among parameters [13].

The pressure-induced phase transition from tetrahedral to octahedral $ZnCl_2$ occurs between 2 and 3.6 GPa. The first-neighbour distance starts from $R = 2.300 \pm 0.003$ Å at ambient conditions, then decreases on compression and shifts to $R = 2.446 \pm 0.004$ Å after the transition. Transition on decompression was not observed during these experiments because the lowest pressure reached was 1.5 GPa. However, the reverse transition began at this pressure, as seen from the high value of σ^2 and the decrease of R from 7.9 to 1.5 GPa.

The Debye-Waller factor, σ^2, is a parameter of disorder representing the sum of the static (configurational) and the

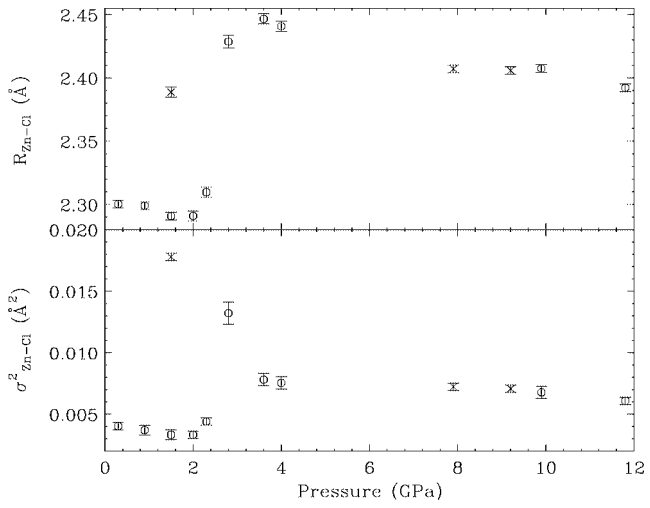

Fig. 5. First-shell parameters for solid $ZnCl_2$ determined by XAFS data-analysis as a function of pressure, at room temperature (o: compression, (×: decompression).

dynamic (thermal) disorder. During the isotropic compression of the low-pressure phase (up to 2 GPa) σ^2 decreases because of the decrease of the dynamic disorder. Actually, a decrease of σ^2. At the beginning of the transition, the increase of σ^2 is due to the increase of static disorder. A lot of atom positions are changing so the local structure is a mix of several configurations. In the high-pressure phase the static disorder is stabilized, and σ^2 decreases with the dynamic disorder, like in the low-pressure phase. However, the value of σ^2 is higher in the second phase because of longer interatomic distances.

Glassy $ZnCl_2$ was measured only at room temperature and P = 1.3 GPa. Structural refinement gives the value of R = 2.299 $\pm$ 0.004 Å and $\sigma^2 = 0.0036 \pm 0.004$Å^2. By annealing the sample above the glass transition temperature (373 K) we observed a crystallization.

Liquid $ZnCl_2$ was obtained at $P = 0.9$ GPa and $T = 660$ K from crystalline $ZnCl_2$. We obtained $R = 2.298 \pm 0.004$Å and $\sigma^2 = 0.0137 \pm 0.005$Å^2 as structural parameters. There is no significant difference between the first shell interatomic distance of crystalline, vitreous and liquid $ZnCl_2$ phases, at the same pressure, which shows the great stability of the tetrahedral configuration in this compound. We did not observe any thermal expansion by heating the low-pressure crystalline phase and the high-pressure one.

The values for R_{Zn-Cl} of the disordered phases obtained by Wong and Lytle [4] are quite different from those obtained in this work. The discrepancy is due to the need to involve a reference compound, in the EXAFS data-analysis method used in Ref. [4], in order to fix the phase factor of the EXAFS absorption coefficient. By contrast, the GNXAS data- analysis yields R_{Zn-Cl} directly like neutron or X-ray diffraction, which give R_{Zn-Cl} values closer to ours [1, 9, 15]. As a conclusion, we want to underline that EXAFS experiments combined with the GNXAS data analysis method is a really powerful tool to explore at the same time crystalline, vitreous and liquid $ZnCl_2$, at high pressure and high temperature.

References

1. Desa, A. E., Wright, A. C. and Sinclair, R. N., J. Non-Cryst. Solids 51, 57 (1982).
2. Angell, C. A. and Wong, J., J. Chem. Phys. 53, 2053 (1970).
3. Imaoka, M. and Konagaya, Y. and Hasegawa, HK., J. Ceram. Soc. Jap., 79, 97 (1971).
4. Wong, J. and Lytle, F. W., J. Non-Cryst. Solids, 37, 273 (1980).
5. Wyckoff, R. W. G., Crystal Structures, (Interscience, New York, 1989)
6. Brynestad, J. and Yakel, H. L., Inorganic Chemistry, 17, 5 (1978).
7. Yakel, H. L. and Brynestad, J., Inorganic Chemistry, 17, 11 (1978).
8. Yannopoulos, S. N., Kalampounias, A. G., Chrissanthopoulos, A. and Paptheodorou, G. N., J. Chem. Phys., 118, 3197 (2003).
9. Sakai, M., Kuroda, N. and Nishina, Y., J. Phys. Soc. Jpn., 54, (1985) 11
10. Polsky, C. H., Martinez, L. M., Leinenweber, K., VerHelst, M. A., Angell, C. A. and Wolf, G. H., Phys. Rev. B, 61, 5934 (2000).
11. Di Cicco, A., Minicucci, M. and Filipponi, A., Phys. Rev. Lett., 78 460 (1997).
12. Filipponi A., Di Cicco, A. and Natoli, C. R., Phys. Rev. B, 52, 15122 (1995).
13. Filipponi, A. and Di Cicco, A., Phys. Rev. B, 52, 15135 (1995).
14. Pusztai, L. and McGreevy, R. L., J. Non-Cryst. Solids, 117, 627 (1990).
15. Biggin, S. and Enderby, J. E., J. Phys. C: Solid State Phys., 14, 3129 (1981).
16. Filipponi, A., J. Phys. Condens. Matter, 6, 8415 (1994).

Physica Scripta. Vol. T115, 342–345, 2005

X-ray Absorption Studies of Borosilicate Glasses Containing Dissolved Actinides or Surrogates

C. Lopez, X. Deschanels, C. Den Auwer, J-N. Cachia, S. Peuget and J-M. Bart

Commissariat à l'Énergie Atomique (CEA) Valrhô/Marcoule, BP 17171, 30207 Bagnols-sur-Cèze, France

Received June 26, 2003; accepted in revised form November 4, 2003

PACS number: 81-05.kf

Abstract

The solubility of actinides and actinide surrogates in a nuclear borosilicate glass was studied with cerium, hafnium, neodymium, thorium and plutonium. Cerium is a possible surrogate for tetravalent and trivalent actinides such as plutonium, hafnium for tetravalent actinide such as thorium, and neodymium for trivalent actinides such as curium or americium. X-ray absorption spectroscopy was used to obtain data on the local environment of the dissolved elements in the glass network. For glasses melted at 1200°C, the solubility limits of the elements studied were as follows: Nd > Ce > Th > Pu > Hf. A correlation has been established between the cation bonding covalence, the oxygen polyhedron and the solubility limit of the elements: the greater the solubility, the larger the oxygen bonds.

1. Introduction

High-level radioactive waste in France containing actinides, fission products and activation products produced by spent fuel reprocessing is incorporated into "R7T7" borosilicate glass. The material must be as homogeneous as possible from both a chemical and a microstructural standpoint to ensure optimum radionuclide containment. Any possible heterogeneities observed arise from various processes including the excess loading of an element at a concentration that exceeds the solubility limit. It is thus essential to know the solubility limit of the elements.

Emerging industrial requirements have led the plant operators to increase the minor actinide and plutonium loading factors in these materials, in particular the reprocessing of high burn-up fuel. In this context a study [1] was undertaken to determine the solubility limit and understand the solubilization mechanisms of these elements in borosilicate glass.

2. Experimental Protocol

2.1. *Surrogate Element Selection Criteria*

Glass specimens in which the actinides were replaced by lanthanides or hafnium, are used to prepare and optimize the making of radioactive samples. This facilitated analysis of the inactive materials by the techniques used in this study (SEM, XAS).

The surrogates were selected on the basis of criteria such as the oxidation state, ionic radius, or coordination number. Cerium was selected as a plutonium surrogate since both elements can be stabilized in the glass at oxidation states +III and +IV. Two other elements, neodymium and hafnium, were also investigated as surrogates for actinides with only one stable oxidation state in the glass (oxidation states +III and +IV, respectively). The solubility variation of these two elements depending on the glass fabrication parameters can thus be estimated irrespective of any change in the oxidation state. Actinides with only a single oxidation state in the glass include curium (Assefa [2]) and americium (Karraker [3]) for oxidation state +III, and thorium (Petit-Maire [4]) for oxidation state +IV.

2.2. *Sample Preparation*

Samples were prepared from oxide, nitrate, and carbonate precursors or from previously fabricated glass frit containing the following elements (wt%): SiO_2 58.84; B_2O_3 18.15; Na_2O 7.00; Al_2O_3 4.28; CaO 5.23; Li_2O 2.56; ZnO 3.24; ZrO_2 0.7. The glass compositions were simplified to facilitate analysis and understanding of the phenomena involved, except for the samples containing plutonium and curium, which were more complex (22 oxides) and representative industrial glass. Zirconium was removed from the glass composition containing Pu, however, to avoid interfering with the EXAFS signal, as these two elements have absorption edges at comparable energies ($E_{Pu} = 18.066$ keV, $E_{Zr} = 17.955$ keV). The surrogates or actinides were incorporated in the glass in the form of oxides or nitric acid solutions obtained by dissolving the relevant element nitrate in water or in 1 N nitric acid. The glass was melted under neutral atmosphere (argon) for curium, plutonium and a few cerium glasses, or oxidizing atmosphere (air) for the others, at temperatures between 1100 and 1400°C in zirconia or platinum crucibles to limit glass-crucible interactions. The glass samples containing surrogates were then quenched in air at a rate of about 100°C/min to prevent the formation of crystalline phases. The glass samples containing plutonium or curium fabricated in a radioactive environment were cooled down to T_g by shutting off the heat source in the melter (≈5°C/min). Tests were carried out to check that heterogeneous phases did not precipitate during cooling. About 5 grams of glass containing plutonium and a few tens of grams of glasses containing the other elements were fabricated under these conditions.

A few glass samples containing cerium were fabricated under reducing conditions, i.e. aluminum nitride was added to reduce the cerium according to the following reaction, considered the most likely based on thermodynamic calculations by Diaz [5]:

$$3Ce^{4+} + N^{3-} \rightarrow 3Ce^{3+} + 1/2N_2.$$

Bubbles formed by this reduction were observed during sample preparation.

2.3. *Solubility Measurement : Notion of Conditional Solubility*

The solubility of an element is defined as the maximum concentration of this element that can be loaded in the glass while maintaining its homogeneity. The solubility limit is determined by gradually increasing the concentration in the glass of the element in question until a heterogeneous phase appears in the system (crystallization or demixing). The secondary phase is then characterized by optical microscopy, SEM and EDS.

The solubility limit value measured by microscopy varies, however, depending on the form (liquid or solid) or particle size of the precursor containing the surrogate when it was added to the glass. Similarly, when excess surrogate was added to obtain the formation of crystals in the glass, a surrogate concentration exceeding the limit determined by microscopy was measured in homogeneous vitreous zones of the sample. This suggests that thermodynamic equilibrium was not reached and that solubilization of the surrogate could be limited by the precursor dissolution step. For this reason the term "conditional solubility", by analogy with conditional thermodynamic constants, is more appropriate when referring to the quantity measured by microscopy. In the remainder of this article, conditional solubility is implied whenever the term "solubility" is used.

2.4. *X-ray Absorption Spectroscopy*

XANES spectroscopy was used to determine the oxidation state of cerium and plutonium since both elements are found at oxidation states +III and +IV in the glass.

EXAFS spectroscopy was used to determine the local environment (number of oxygen atoms, N, and cation-oxygen distance, d) around the elements studied in the glass. EXAFS spectra of glasses containing thorium(IV), plutonium(IV) and curium(III) were obtained at the Stanford Synchrotron Radiation Laboratory (SSRL), and those for glass containing cerium(III), neodymium(III) and hafnium(IV) were obtained at the Orsay Electromagnetic Radiation Application Laboratory (LURE). The analyses were performed at room temperature by L_{III}-edge fluorescence detection for these elements. Petit-Maire [4] showed that the local environment of thorium in borosilicate glass is not temperature-dependent. Based on these results, it may be assumed that quenching does not affect the local environment of the element analyzed.

The data were processed to determine the structural parameters of the first-neighbor shell using programs developed by Michalowicz [6].

3. Experimental Results – Discussion

3.1. *Element Solubility*

The measured solubility variation (in mol%) is indicated in Figure 1 versus the glass fabrication temperature for each of the elements studied. The upper value shown on the error bars of the experimental results corresponds to the first glass in which heterogeneity was observed, and the lower value to the final homogeneous glass. The solubility can be observed to increase with the processing temperature. The magnitude of this increase is greater for the elements at oxidation state +III (e.g. neodymium) than for the elements at oxidation state +IV (e.g. hafnium or thorium). The heterogeneities observed when the solubility limit is reached are silicates or oxides. Phase separation was observed for cerium and neodymium when their concentrations reached about 2.7 mol% at processing temperatures of 1200°C or higher.

The cerium oxidation state was characterized by chemical titration in borosilicate glasses fabricated at various temperatures. The analyses showed that glasses contain a mixture of cerium(+III) and cerium(+IV) and that the percentage of Ce(+III) drops from 53.8% to 88.1% of the total Ce when the glass fabrication temperature increases from 1100°C to 1400°C. These results were confirmed by XANES analysis. Cerium reduction at higher temperatures affects its solubility, as observed by Li [7]. Fabricating the glass under reducing conditions at 1200°C by adding aluminum nitride as a reducing agent increases the solubility limit from 0.45 mol% to 1.75 mol%. Under these conditions the cerium is completely reduced as shown by XANES analysis of the glass. Work is now in progress in an attempt to obtain similar results with plutonium. The only parameter that has been studied to date for this type of glass is the processing temperature. A homogeneous glass containing 0.076 mol% (i.e. 0.85 wt% plutonium oxide) was fabricated at 1200°C; XANES examination of the glass showed that under these conditions over 90% of the plutonium is at oxidation state +IV (Figure 2). Although the solubility results obtained for plutonium are still incomplete, there is no evidence to date of any variation in the Pu solubility with the glass processing temperature.

The results obtained for curium are not shown in Figure1. A glass sample containing 1.9 wt% CmO_2 (0.14 mol% Cm) fabricated at 1200°C was found to be homogeneous. This is consistent with the results of a study by Inagaki [8] in which

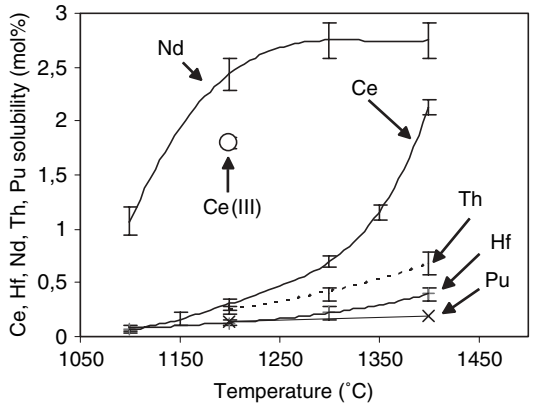

Fig. 1. Ce, Hf, Nd, Th, Pu solubility limits (mol%) determined experimentally in a borosilicate glass. At 1400°C the Pu solubility is lower than 0.192 mol%, works are in progress to have a better determination for the solubility of this element.

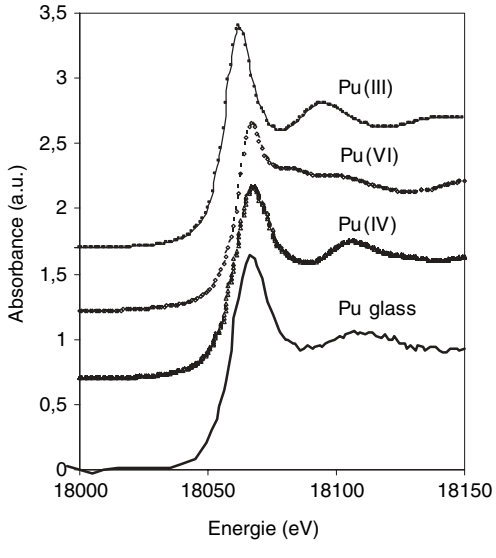

Fig. 2. XANES spectra of borosilicate containing 0.85 wt% of PuO_2 melted at 1200°C compared with the spectra of the reference compounds: Pu(III) in solution, Pu(IV) in PuO_2^{2+} in solution. To have a better understanding on the figure, the spectra are arbitrarily shifted along the vertical axis.

Table I. *Structural parameters of the first coordination sphere obtained from L_{III}-edge EXAFS spectra of the absorber atom (Nd, Ce(+III), Cm, Th, Pu, Hf) in borosilicate glass. The reference compound used to obtain the best fit for the experimental results is indicated in boldface type.*

	Structural parameters				
Samples	N	d(Å)	σ (Å)	r factor	Reference compounds
Nd glass	8.2 ± 1.6	2.49 ± 0.02	0.0662 ± 0.0014	1.52×10^{-3}	Nd_2O_3 P3m1, **$Nd_2Si_2O_7$P212121**
Ce(+III) glass	8.2 ± 1.6	2.44 ± 0.02	0.0383 ± 0.0009	2.19×10^{-3}	CeO_2 Fm3m, **$Ce_2Si_2O_7$P21/C**
Hf glass	7.5 ± 1.5	2.08 ± 0.02	0.001 ± 0.0002	5.47×10^{-3}	$HfSiO_4$ I41/AMD, HfO_2 P21/C
Th glass	6.9 ± 1.4	2.37 ± 0.02	0.0789	1.58×10^{-3}	**ThO_2 Fm3m**
Pu(+IV) glass	6.8 ± 1.4	2.25 ± 0.02	0.0713 ± 0.0008	4.97×10^{-3}	**PuO_2 Fm3m**
Cm glass	6.7 ± 1.4	2.45 ± 0.02	0.0139 ± 0.0034	9.45×10^{-3}	**CmO_2 Fm3m**

3.04 wt% curium oxide were homogeneously incorporated in a borosilicate glass.

3.2. *EXAFS Analysis of the Glass*

The purpose of these analyses was to propose hypotheses based on structural considerations to account for the observed differences in solubility of the elements studied. The result of EXAFS spectral analysis for each element are shown in Table I. The reference oxide compounds were analyzed by transmission; the silicates were simulated using the FEFF code [9] since we were unable to obtain these compounds.

The best simulations of the phase and the amplitude of Ce and Nd in borosilicate glass were obtained with the silicates $Nd_2Si_2O_7$ and $Ce_2Si_2O_7$. In the case of Ce-loaded glass, only the reduced glass samples containing exclusively Ce(+III) were analyzed. Its first neighbors are 8 oxygen atoms situated at a distance of 2.44 Å. It would be interesting to fabricate glass samples under more oxidizing conditions than in air to obtain Ce(+IV) in order to determine its environment. EXAFS analysis of glasses containing variable Nd concentrations showed that the local environment of this element was identical in each of the glasses containing 2.6, 0.52 or 0.26 mol%. The first-neighbor shell consists of 8 oxygen atoms at a distance of 2.49 Å.

The best fit of the experimental spectra for Pu(+IV) (Figure 3) and thorium were obtained using the PuO_2 and ThO_2 reference compounds. These results are consistent with published data for plutonium (Hess [10]) and for thorium (Petit-Maire [4], Farges [11]) in borosilicate glass.

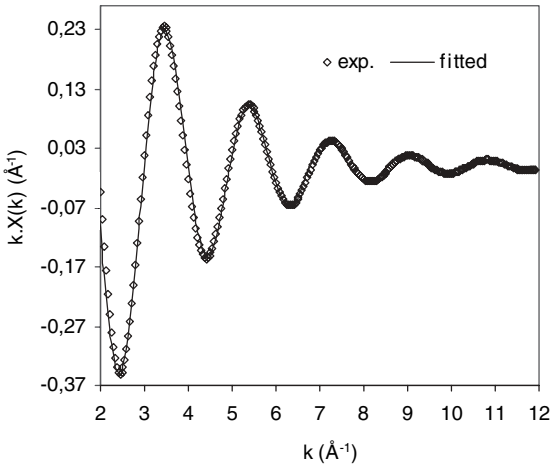

Fig. 3. Comparison between experimental EXAFS spectra and fitted spectra with PuO_2 reference compound for Pu in a borosilicate glass.

Table II. *Relation between field strength defined by Dietzel [12] and solubility of the considered element.*

Cation	Field strength (Dietzel)	Solubility at 1200°C (mol%)
Hf	0.92	0.1 ± 0.02
Pu	0.79	0.134 ± 0.06
Th	0.71	0.26 ± 0.04
Ce	0.5	1.6 ± 0.06
Nd	0.48	2.52 ± 0.06
Cm	0.5	

The length of the bonds established by actinides and surrogates with oxygen atoms in the glass network was determined by EXAFS analysis. Dietzel [12] defined the field strength parameter as the Z/d^2 ratio, where Z is the cation charge and d is the cation-oxygen distance. Network-forming cations such as B or Si exhibit a high field strength (between 1 and 2); conversely, network-modifying cations have a low field strength of between 0.1 and 0.4. Between these extremes are cations with intermediate field strength, including all the elements studied here (Table II). These intermediate cations occupy mixed positions in the glass network, i.e. they create bonds between chains of network-former tetrahedrons, or they may be either modifiers or formers depending on the particular glass composition. As shown in table II there is a correlation between the field strength as defined by Dietzel and the solubility limit of the element: the greater the field strength, the lower the solubility of the relevant element.

4. Conclusion

This investigation has shown that the solubility limits of the elements studied increase with the glass processing temperature. The elements at oxidation state +III exhibit higher solubility than the elements at oxidation state +IV. The greatest increase in solubility was observed for cerium: the higher solubility limit was attributable not only to the higher temperature but also to reduction of this element to Ce(+III).

The relatively similar behavior of the actinides at oxidation state +IV (Th, Pu) and hafnium, suggests that the surrogate elements are representative. Logically, therefore, by analogy with the results obtained with cerium, it should be possible to obtain a significant increase in plutonium solubility by reducing it to oxidation state +III.

References

1. Lopez, C., PhD thesis, Université d'Orsay, France (2002).
2. Assefa, Z., Haire, R. G. and Stump, N., Mater. Res. Soc. Symp. Proc. **556**, 359 (1999).
3. Karraker, D. G., J. Am. Ceramic Soc. **65**, 53 (1982).
4. Petit-Maire, D., PhD thesis, Université d'Orsay, France (1988).
5. Diaz, A., Verdier, P., Laurent, Y., Carrizosa, I. and Odriozola, J.A., Mater. Sci. Forum **383**, 87 (2002).
6. Michalowicz, A., J. Physique IV **7**, 235 (1997).
7. Li, H. *et al*., Ceram. Trans. **72**, 399 (1996).
8. Inagaki, Y., Furuya, H. and Idemitsu, K., Mater. Res. Soc. Symp. Proc. **257**, 199 (1992).
9. Ankudinov, A. L. and Rehr, J. J., Phys. Rev. **B56-4**, 1712 (1997).
10. Hess, N. J., Weber, W. J. and Conradson, S. D., J. Nucl. Mater. **254**, 175 (1998).
11. Farges, F., Brown, G. E. and Wu, Z., J. Physique IV **7**, 1009 (1997).
12. Dietzel, A. Z., Electrochemie **48**, 9 (1942).

Physica Scripta. Vol. T115, 346–348, 2005

Characterization of Lithium Battery Materials During their Functioning in Using Dispersive XAS

G. Ouvrard*[a], N. Bourgeon[a], D. Guyomard[a], F. Baudelet[b] and S. Belin[b]

[a]Institut des Matériaux Jean Rouxel, CNRS-Ecole Polytechnique de l'Université de Nantes UMR 6502, 2 rue de la Houssinière, BP 32229, 44322 Nantes Cedex 3, France
[b]LURE, Centre Universitaire Paris Sud, 91898 Orsay Cedex, France

Received June 26, 2003; accepted in revised form February 11, 2004

PACS numbers: 78.70.Dm, 82.45.Fk, 82.47.−a

Abstract

In order to understand precisely the changes induced by the reversible reaction of lithium with the electrode materials, XAS has been proved in many cases to be very efficient. The transformations generally concern the structure of the compound, at a short or a long range, and the oxidation state of the active element. We have studied, at the vanadium K edge, the behaviour of the compound $Li_{1.2}V_3O_8$, a promising electrode material for the lithium batteries. The XAS experiments have been performed, ex-situ or in-situ, in a classical way on systems close to equilibrium and, for the first time, during the battery cycling in using a dispersive XAS set-up. A plastic battery has been designed for this purpose and connected to an automated battery cycling system. The XANES part of the spectra has been decomposed into few simple mathematical functions and the results obtained at equilibrium and out of equilibrium are compared. The significant differences have been analysed in considering the voltage variations.

1. Introduction

Among the numerous materials which have been considered as positive electrodes in lithium batteries, the vanadium oxides occupy a primary role, especially when the negative electrode is made of lithium metal. This is due to their favorable voltage at about 3V versus the Li/Li^+ electrochemical couple. The reversible incorporation of lithium into all these materials induce, to various extent, structural modifications and redox processes due to the electron transfer from lithium to the host phase. X-ray absorption spectroscopy (XAS) is known to be a powerful tool to characterize the local structural environment of the atoms and to be highly sensitive to the oxidation states. In the last fifteen years, this technique has been largely used to characterize the lithium intercalated compounds [1–5], especially the vanadium oxides [6–8]. In the vanadium pentoxide V_2O_5, gradual changes in the vanadium coordination (V-O distances) and arrangement (V-V distances) have been put in evidence in considering the EXAFS part of the spectra and the changes of the pre edge peak intensities [8].

As for many battery materials, the experiments have been performed either ex-situ on samples prepared chemically or electrochemically, or in-situ on specially designed cells. The results obtained in these two different approaches are very similar, because in both cases the experiments are performed on materials very close to thermodynamic equilibrium. These conditions do not allow to characterize the phase during its functioning in the battery, i.e. when it is polarized during the discharge (lithium insertion) or the charge (lithium deinsertion) of the battery.

In this study we present XAS results obtained on $Li_{1.2}V_3O_8$, a vanadium oxide recently considered as a very good alternative to V_2O_5 as positive in metal lithium polymer batteries [9]. The experiments have been performed ex-situ or in-situ in static conditions, in the classical transmission mode, and, for the first time in dynamic conditions, during the battery functioning, in using a dispersive XAS experimental set-up.

2. Electrochemical results

Lithium trivanadate, $Li_{1.2}V_3O_8$, has been investigated as a positive electrode material for rechargeable lithium batteries during the past twenty years [10, 11]. Much research work has been focused on the structural characterization and cyclability of this compound. The crystal structure of $Li_{1.2}V_3O_8$ was first reported by Wadsley [12]. It has a monoclinic structure (space group $P2_1/m$) and is composed of two basic structural units, distorted VO_6 octahedra and VO_5 square pyramids. These two structural units share edges and corners to form layers [13]. Upon insertion, lithium atoms may occupy two different sites between the layers, octahedra and tetrahedra. The lithium insertion mechanism has been studied by X-ray diffraction (XRD) [13, 14]. When it is used as a positive in a lithium battery, the $Li_{1.2}V_3O_8$ compound can accommodate up to 3.8 lithium ions in the host structure with an operating voltage between 3.7V and 2V (figure 1). The lithium amount is determined by coulometric titration from the

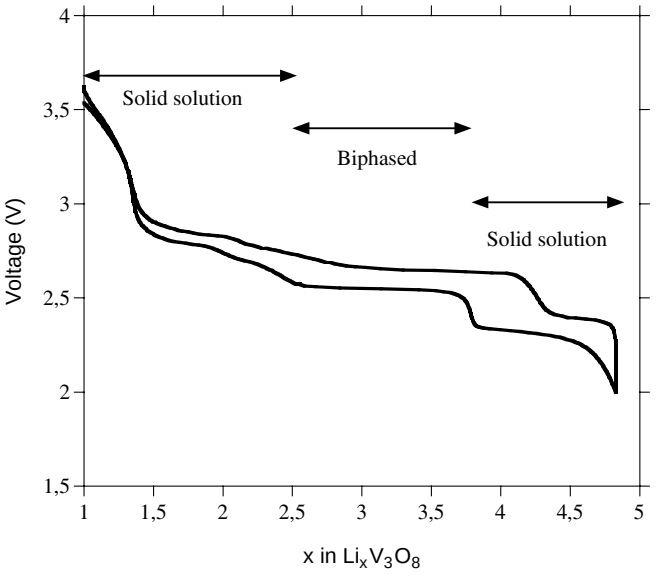

Fig. 1. Voltage versus composition curve in $Li_xV_3O_8$ system.

*e-mail: ouvrard@cnrs-imn.fr

current intensity passing through the battery in a given charge or discharge time. In considering the system $Li_xV_3O_8$, a combination of electrochemical and XRD results allow to conclude that

(*i*) for $1.2 \leq x \leq 2.6$, lithium is inserted in a single-phase reaction process. It corresponds to the gradual filling of empty sites changing mainly the stoichiometry without significant structural modifications.

(*ii*) the voltage plateau observed for $2.6 \leq x \leq 3.8$ is attributed to the coexistence of two phases whose compositions are close to $Li_3V_3O_8$ and $Li_4V_3O_8$. This last phase would have a defect rock salt structure, which is not significantly modified up to the composition $Li_5V_3O_8$.

3. Static experiments

Experiments have been performed at the vanadium K edge, in the transmission mode, on the DCI storage ring at LURE. Si_{111} and Si_{311} monochromators have been used to collect the data in the EXAFS and XANES parts of the spectra, respectively. EXAFS data treatment has followed a very classical procedure in using the WinXAS software [15] and the Feff phases and amplitudes [16].

Data have been collected for more than 20 different lithium contents and only few of them are displayed for the sake of clarity. The spectra have been normalized at the mid point of the first EXAFS oscillation. Figure 2 shows the changes of the edges with the lithium content upon lithium insertion and deinsertion. First we may notice that the process appears very well reversible. This is clearly evidenced by a comparison of the spectra for the pristine phase and the deintercalated one which are almost superimposed. There are two main tendencies in this spectra collection. The first one is a regular decrease of the pre-edge peak intensity upon lithium insertion. At the same time this peak is shifted towards the low energy part. This evolution is a clear signature of a reduction of vanadium and the evolution of its close oxygen environment towards a more centrosymmetrical one [7, 8]. The second clear change is a shift of the main edge towards the lower energy upon lithiation, in good agreement with a vanadium reduction. A lot of studies tried to correlate the shifts of the different singularities of the XANES spectra to the oxidation state of the element under study. In such an approach, there are two main difficulties. One of them is to take into account the fact that, for different compounds in which a given element has the same oxidation state, the edge shape and position are usually different [7]. The second one is to estimate the true position for the main edge whose the shape can be significantly modified by the oxidation state, as seen in figure 2. This is not surprising if we recall that the edge shape of a solid essentially reflects the electron density projected on the p orbitals of the considered element, and, therefore, is largely influenced by the atomic structure.

Most of the previous studies aiming to correlate the XANES spectra to the oxidation state define the singularities positions either in using first or second derivatives [8], or in considering the energy of the half height of the main edge as its position [7, 8]. In this study we have performed a complete and precise mathematical analysis of the first 30 eV of the normalized XANES spectra. We have chosen to model the continuum of empty electronic levels by an arc-tangent curve. Moreover, it is theoretically reasonable to simulate the shape of density of states by a gaussian curve. It is clear on the figure that a least three gaussian and one arc-tangent curve are necessary to simulate the first 30 eV of all the spectra. In order to minimize the freedom degree of the mathematical analysis we have limited the data treatment to this restricted hypothesis. The results are successful in the quality of the simulation (figure 3) and the gradual changes versus the lithium content of the positions of all the curves and the intensity of the pre-edge peak. From this analysis we have extracted precise positions and intensities, the last ones being given by the peak surface in the normalized spectra. As an example, figure 4 shows the variation of the pre-edge intensity versus the lithium content. It clearly demonstrates that the symmetry of the vanadium environment and the filling of the empty electronic states (redox process) vary linearly and reversibly with the lithium content.

This evolution is confirmed by the analysis of the EXAFS part of the spectra. Upon lithiation, we observe that the initial vanadium coordination of 5 (2+3) gradually tends toward a coordination of 6 with a unique V-O distance. The distance variations are very regular. The average distance increases with increasing vanadium size due to reduction.

This study in static conditions, identical to the one used in the XRD experiments, demonstrates that the oxidation state and

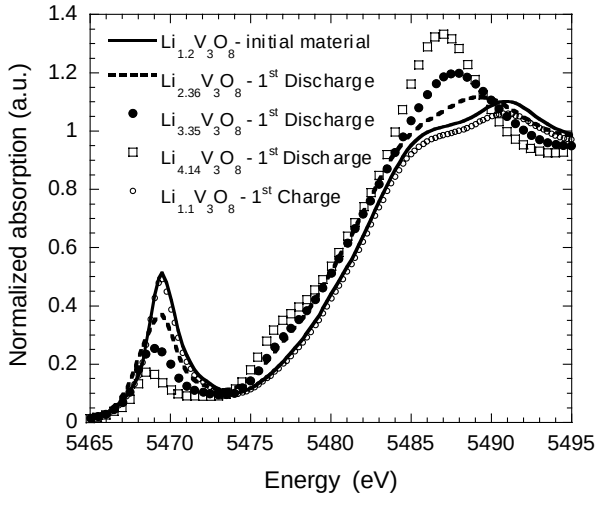

Fig. 2. Normalized absorption at the vanadium K edge for various compounds in the $Li_xV_3O_8$ system.

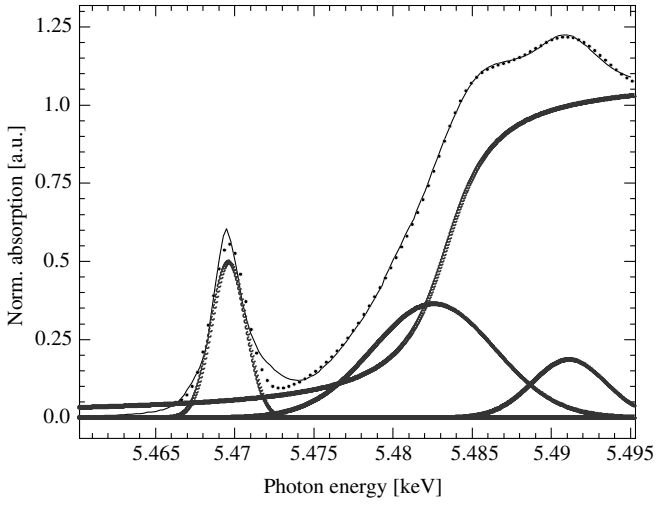

Fig. 3. Vanadium K edge simulation for $Li_{1.2}V_3O_8$. Full line: experimental data. Dotted curves: mathematical functions.

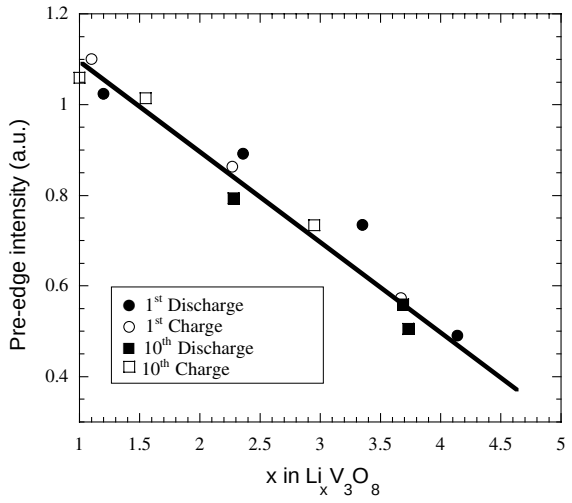

Fig. 4. Evolution of the vanadium K pre edge intensity on the first and tenth cycles, taken at thermodynamic equilibrium.

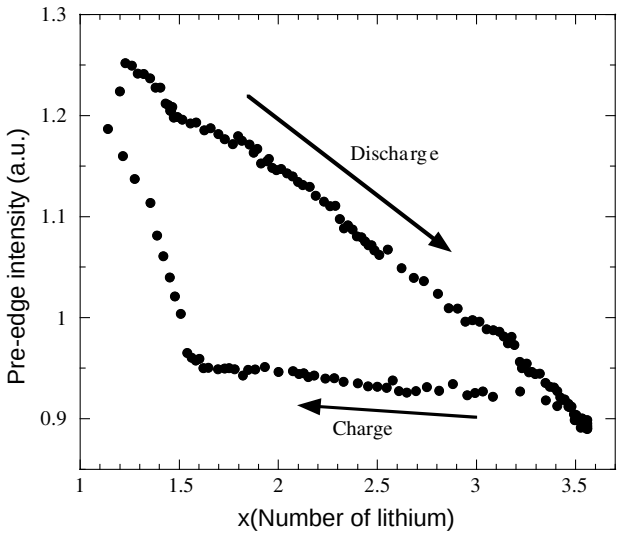

Fig. 5. Evolution of the vanadium K pre edge intensity during the battery functioning.

the structural environment of the vanadium atoms are modified very regularly and reversibly upon lithiation. This appears to be in contradiction with the XRD results which evidence the occurrence of defined phases with different structural arrangements. The only way to combine the results of these two techniques consists in considering a regular change of the V-O_n polyhedra and, at some peculiar degree of this transformation, the necessity to rearrange each other forming a different structure at long range order.

4. Dynamic experiments

Dynamic experiments have been performed on specially designed cells, in which a composite electrode containing the vanadium oxide is separated from a lithium sheet by a liquid electrolyte soaked in a separator, all the battery being inserted between sealed polymer films to protect the materials from moisture and oxygen. This battery is continuously cycled during the XAS data collection by an automated battery cycling test apparatus (Mac Pile). The lithium amount is continuously determined by coulometric titration. Due to polarization effect during the functioning and because we have chosen the same low voltage limit (2 volts), the maximum lithium content is lower in this case ($Li_{3.6}V_3O_8$) than in the equilibrium experiments ($Li_{4.2}V_3O_8$). The battery has been installed on the focussing point of the D11 beam line at DCI (LURE). Data have been collected, on an energy range of 500 eV, every 6 seconds with a bended Si_{111} monochromator.

At a first glance, the general evolution of the spectra, in both XANES and EXAFS, appears to go the same way as in the static experiments. The previously detailed treatment has been applied to the data. The evolution of the intensity of the pre-edge peak versus the lithium content is displayed on figure 5. It is remarkable that the changes on the discharge are almost perfectly linear, as observed in the static experiments, but that the process is, this time, largely irreversible. The variation on charge can be seen as an almost constant intensity followed by an abrupt modification at the composition $Li_2V_3O_8$. It is important to notice that this variation is, this time, similar to the voltage vs. Li content curve (see the charge curve on figure 1). We have no simple explanation to this surprising result, beyond the fact that, upon the functioning of the battery, there is certainly a large inhomogeneity of the lithium content inside each particle due to lithium diffusion. The lithium concentration is higher at the surface of the grain than in the heart during insertion (discharge) and the reverse can appear in some way upon deinsertion (charge). Presently, it is not possible to estimate the importance of this phenomenon but it appears that the vanadium is not able to react immediately and continuously, from a structural point of view, to the added lithium with its electron, giving rise to the observed hysteresis phenomenon.

This original study put clearly in evidence the importance of the kinetic for the local changes of the material when it is under the constraint of an electrochemical potential. Dispersive XAS appears as a unique tool to characterize the battery materials under their actual utilization, from a structural and redox point of view. Further experiments, including investigations on more cycles, will improve our understanding of the phenomenon, will allow to characterize the behavior upon polarization and relaxation, and will contribute to the improvement of the electrochemical performances.

References

1. Brec, R., Prouzet, E. and Ouvrard, G., J. Power Sources **26**, 325 (1989).
2. Ouvrard, G., Prouzet, E., Brec, R., Benazeth, S. and Dexpert, H., J. Solid State Chem. **86**, 238 (1990).
3. Moreau, P., Ouvrard, G., Gressier, P., Ganal, P. and Rouxel, J., J. Phys. Chem. Solids **57**, 1117 (1996).
4. Wu, Z. Y. *et al*., Phys. Rev. Lett. **77**, 2101 (1996).
5. Goward, G. R. *et al*., Electrochem. Solid State Lett. **2**, 367 (1999).
6. Leroux, F., Piffard, Y., Ouvrard, G., Mansot, J. L. and Guyomard, D., Chem. Mater. **11**, 2948 (1999).
7. Rossignol, C., Ouvrard, G. and Baudrin, E., J. Electrochem. Soc. **148**, A869 (2001).
8. Mansour, A. N., Smith, P. H., Baker, W. M., Balasubramanian, M. and McBreen, J., J. Electrochem. Soc. **150**, A403 (2003).
9. Jouanneau, S. *et al*., J. Mater. Chem. **13-4**, 921 (2003).
10. Bonino, F., Ottaviani, M., Scrosati, B. and Pistoia, G., J. Electrochem. Soc. **135**, 12 (1988).
11. West, K. *et al*., J. Electrochem. Soc. **143**, 820 (1996).
12. Wadsley, A. D., Acta Cryst. **10**, 261 (1957).
13. de Piccioto, L. A., Adendorff, K. T., Liles, D. C. and Thackeray, M. M., Solid State Ionics **62**, 297 (1993).
14. Kawakita, J., Katayama, Y., Miura, T. and Kishi, T., Solid State Ionics **107**, 145 (1998).
15. Ressler, T., J. Phys. IV **7**, C2-269 (1997).
16. Rehr, J. J., J. Appl. Phys. **32**, 8 (1993).

Physica Scripta. Vol. T115, 349–351, 2005

EXAFS Study on Disorder in Microstructure of Amorphous Mesoporous Titania with Large Surface Areas

Hideaki Yoshitake[1*], Tae Sugihara[2] and Takashi Tatsumi[2]

[1]Graduate School of Environment and Information Sciences, Yokohama National University, Yokohama 240-8501, Japan
[2]Division of Materials Sciences and Chemical Engineering, Graduate School of Engineering, Yokohama National University, Yokohama 240-8501, Japan

Received June 26, 2003; accepted in revised form November 4, 2003

PACS number: 82.75.Fq

Abstract

The mesoporous titania prepared by templating with hexadecylamine has an amorphous nature with a narrow pore size distribution centered at 2.8 nm and a Brunauer-Emmett-Teller (BET) surface area of $1230\,m^2\,g^{-1}$. The extremely large surface area implies that most of the atoms are exposed at the surface. XAFS spectroscopy was applied to investigate the microstructure of mesoporous titania. The EXAFS function, $k^3\chi(k)$, was considerably different from that of anatase. The amplitude decreased significantly in the large k region, suggesting large static and thermal disorders of the Ti-Ti bond. The third peak in the radial distribution function, which appeared at 3.4 Å in anatase and was attributed to the Ti atoms at the next nearest neighbouring site, was hardly observed in the Fourier transform of mesoporous titania. A comparison of the spectra at different temperatures revealed that the temperature dependence of the Debye-Waller factor for the Ti-Ti bond was significant. σ^2 was plotted against temperature and the effective surface Debye temperature of mesoporous titania was calculated to be 365 K. This is significantly lower than for the bulk titania crystals, 520 and 530 K for anatase and rutile, respectively.

1. Introduction

The templating using micelles of primary amine permits preparation of mesoporous inorganic oxides with a narrow pore size distribution and an extremely high surface area. Niobium [1], tantalum [2] and titanium [3, 4] oxides have been successfully synthesized by this method. Among those oxides titania attracts a great deal of attention due to its excellent performance in photocatalyst, photoelectronics, semiconductor etc. The BET specific surface area measured for mesoporous titania suggests that the majority of atoms are exposed at the surface [4]. The chemical bond and coordination structure of Ti in the bulk mesoporous titania can be influenced by the nature of the titania surface. The prominent peak in the preedge region of the Ti K edge XANES spectra has been attributed to 5-fold coordinated titanium [5]. The lack of peaks at $2\theta > 10^\circ$ in the Cu-K_α X-ray diffraction chart implies that the bulk phase is amorphous and, therefore, this physicochemical technique is not sufficient for analysing the nature of chemical bonds in this novel material. Since EXAFS spectroscopy requires structural order up to only a few Ångstrom around the target element, it can be a strong technique for structural studies, especially in a solid without periodic structure on the atomic scale. In this study we examine Ti K edge EXAFS spectra of mesoporous titania to clarify the local structure of Ti atom with emphasis on the static and thermal disorders of Ti-Ti bond.

2. Experimental

Mesoporous titania was prepared according to the literature [4] using hexadecylamine as a structural directing agent. The BET specific surface area was $1230\,m^2\,g^{-1}$ and a narrow mesopore size distribution peaking at 2.8 nm was obtained. X-ray absorption spectra of the Ti K edge were recorded on a BL-9A of the Photon Factory, High Energy Accelerator Research Organization, Tsukuba, Japan (Proposal #2002G269), with a ring energy of 2.5 GeV and a stored current of around 300–400 mA. A Si(111) double-crystal monochromator was used. The higher harmonics were removed by the total reflection on a Rh-Ni composite mirror and detuning the monochromator to 50%. The powder was diluted in boron nitride. A conventional transmission mode with detection using gas ion chambers was employed. The measurement of each spectrum was completed within 30 min. The drift of the monochromator between the measurements was 0.1 eV, which was estimated by the reproducibility of the edge position of Ti foil. This is comparable to the precision in the experiment [6] where a Si(111) double-crystal monochromator was also used and therefore the degree of drift does not cause any substantial errors in the following discussions.

EXAFS spectra were acquired five times under the same measuring conditions and from the extracted spectra, the average $\chi(k)$ was calculated. The EXAFS data were processed by a REX 2000 (Rigaku Co.) program assembly. The EXAFS oscillation is extracted by fitting a cubic spline function through the post edge region. After normalization using McMaster tables, the k^3-weighted EXAFS oscillation, $k^3\chi(k)$, in the 30–125 nm^{-1} region was Fourier transformed into a radial distribution function. The amplitudes and phase-shift functions for Ti-O and Ti-Ti bonds were calculated by FEFF 7.02 code. The amplitude reduction factor ($S_0{}^2$) was chosen to be 1 with a lifetime broadening (V_i) equal to 0.

3. Results and Discussion

The EXAFS spectra of the Ti K edge measured at 100 and 300 K are shown in Figure 1. Smaller amplitude and fewer oscillations are found in EXAFS of mesoporous titania than of anatase. As the measuring temperature of mesoporous titania rises, the oscillation in the high k region ($>9\,Å^{-1}$) smeared out and the amplitude in the low k region ($<4\,Å^{-1}$) decreased. These temperature dependent changes suggest large thermal vibration of the chemical bonds in the solid. Figure 2 shows Fourier transforms of EXAFS functions over 3–12.5 $Å^{-1}$. The peaks at 1.6, 2.7 and 3.4 Å in the FT of anatase are attributed to Ti-O, Ti-Ti and Ti-Ti bonds, respectively. The intensities of these peaks are reduced in

*e-mail: yos@ynu.ac.jp

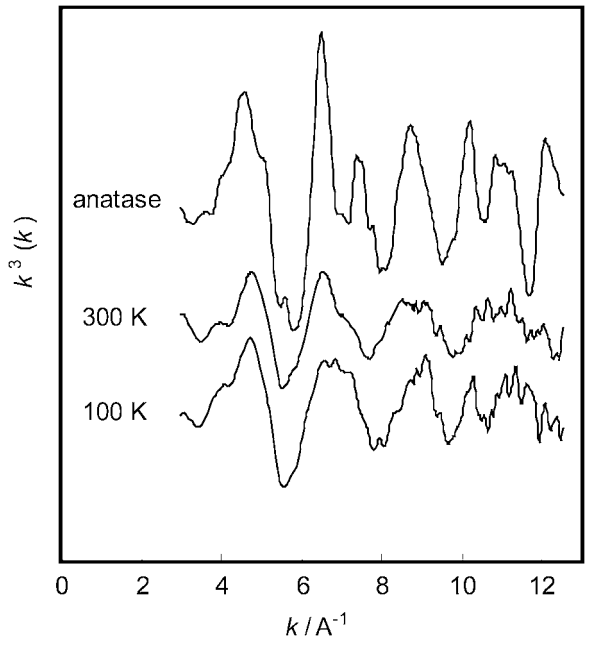

Fig. 1. EXAFS oscillations of mesoporous titania and anatase. The measurement temperature is shown.

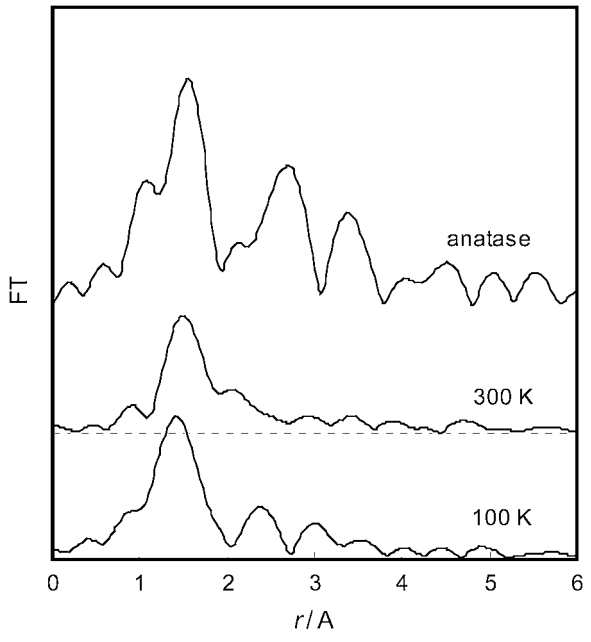

Fig. 2. Fourier transform of $k^3\chi(k)$ EXAFS of mesoporous titania and anatase. The measurement temperature is shown.

Table I. *Structural parameters of mesoporous titania determined by curve fitting analysis.*

	Ti-O				Ti-Ti				
Sample	N	r/Å	E/eV	σ/Å	N	r /Å	E/eV	σ/Å	R/%
Anatase[a]	6	1.96			4	2.99			
300 K[b]	2.78	1.91	2.68	0.061	0.52	2.77	3.1	0.081	3.5
100 K[b]	3.33	1.91	−10.3	0.055	0.45	2.69	6.18	0.061	3.8

a Data from X-ray crystallography. b Mesoporous titania.

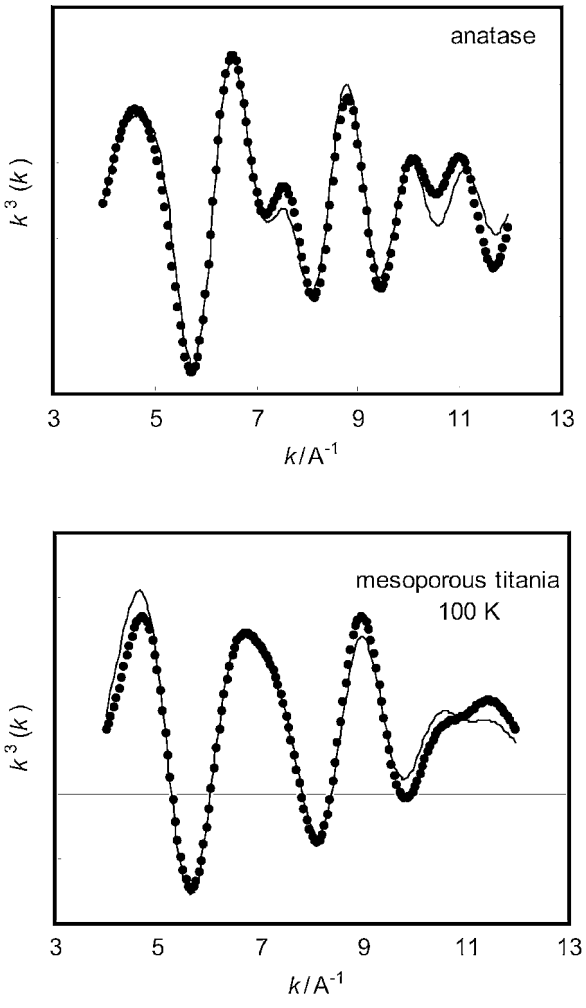

Fig. 3. Curve fitting results of $k^3\chi(k)$ EXAFS of mesoporous titania and anatase.

mesoporous titania. A small peak due to Ti-Ti bond appears in the spectrum measured at 100 K while it is hardly observed when the temperature is 300 K. The third peak around 3.4 Å almost disappeared at all temperatures. We filtered the peaks in radial distribution functions by the window between 0.7 and 3.1 Å and, after inverse Fourier transformation, the data were fitted with theoretical functions over 4–12 Å^{-1} in k-space. The best fitting results are summarized in Table I and Figure 3. The distances of Ti-O and Ti-Ti in mesoporous titania are shorter than those of anatase. This is apparently contradictory to the large thermal disorder observed in Figures 1 and 2. This can be reasonably explained by the anharmonicity of the pair distribution function that is not negligible in determining the structural parameters as have been reported in an oxide [7]. When the cumulant expansion technique was applied to these spectra, the bond lengths became larger than those in anatase: r(Ti-O) = 1.99–2.00 and r(Ti-Ti) = 3.04–3.09 Å.

Since σ for Ti-Ti bond is represented by $\sigma^2 = {\sigma_0}^2 + \sigma(T)^2$, where σ_0 is a disorder term due to static disorder independent of the temperature and $\sigma(T)$ is the temperature dependent term, and the latter term is correlated with the Debye temperature, σ^2 for Ti-Ti bond was plotted as a function of temperature in Figure 4. Since mesoporous titania is mostly composed of surface atoms, the Debye temperature can be more simply determined than in the formulations depending on the lattice. It has been claimed that the effective Debye temperature of a surface layer can be evaluated by emitting electron probes, e.g. low energy electron diffraction, X-ray photoelectron spectroscopy, valence band photoemission, and inverse photoemission [8, 9]. The intensity of the emerging photoelectron beam depends

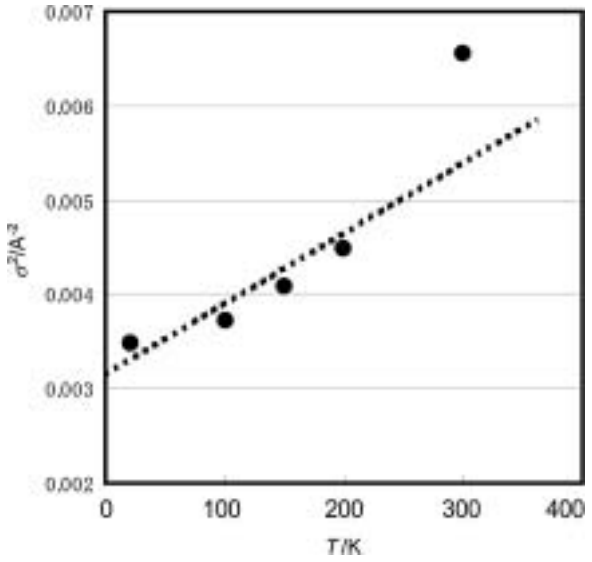

Fig. 4. Temperature dependence of Debye-Waller factors for Ti-Ti bond in mesoporous titania.

exponentially on the substrate temperature. The disorder factor in the index is inversely proportional to the Debye temperature squared. The large surface area allows us to apply this formulation to σ^2 for mesoporous titania. The Debye temperature thus deduced is 365 K, for mesoporous titania. This is significantly lower than the bulk titania crystals, 520 [10] and 530 K [11] for anatase and rutile, respectively. To the best of our knowledge, the Debye temperature of TiO_2 single crystal surface has not been reported. $\Theta_D(\text{surface})/\Theta_D(\text{bulk}) = 0.70$ will be smaller than the ratio in single crystal surface such as rutile(110), because both sides of the mesoporous wall are exposed while one side of the surface atomic layer in a single crystal is bound to the bulk lattice.

Acknowledgment

The authors thank Asahi Glass Foundation and Japan Society for the Promotion of Science for financial support.

References

1. Antonelli, D. M., Microporous Mesoporous Mater. **33**, 209 (1999); Antonelli, D. M., Nakahira, A. and Ying, J. Y., Inorg. Chem. **35**, 3125 (1996).
2. Antonelli, D. M. and Ying, J. Y., Chem. Mater. **8**, 874 (1996); Takahara, Y., Kondo, J. N., Takata, T., Lu, D. and Domen, K., Chem. Mater. **13**, 1194 (2001).
3. Antonelli, D. M., Microporous Mesoporous Mater. **30**, 315 (1999).
4. Yoshitake, H., Sugihara, T. and Tatsumi, T., Chem. Mater. **14**, 1023 (2002); Stud. Surf. Sci. Catal. **141**, 251 (2002).
5. Yoshitake, H., Sugihara, T. and Tatsumi, T., Phys. Chem. Chem. Phys. **5**, 767 (2003).
6. Mountjoy, G. *et al*., Chem. Mater. **11**, 1253 (1999) and references therein.
7. Lemaux, S., Bensaddik, A., van der Eerden, A. M. J., Bitter, J. H. and Koningsberger, D. C., J. Phys. Chem. B **105**, 4810 (2001).
8. Borca, C. N. *et al*., Appl. Phys. Lett. **77**, 88 (2000).
9. Waldfried, C. *et al*., Surf. Sci. **363**, 296 (1996).
10. Howard, C. J., Sabine, T. M. and Dickson, F., Acta Cryst. **B47**, 462 (1991).
11. Jacob, I., Moreh, R., Shahal, O. and Wolf, A., Phys. Rev. B **35**, 8 (1987).

Physica Scripta. Vol. T115, 352–355, 2005

Combining EXAFS and X-Ray Powder Diffraction to Solve Structures Containing Heavy Atoms

C. Hennig[1,*], T. Reich[2], W. Kraus[3], G. Reck[3], F. Prokert[4] and N. Schell[4]

[1]Forschungszentrum Rossendorf, Institut für Radiochemie, 01314 Dresden, Bautzner Landstr. 128, Germany
[2]Universität Mainz, Institut für Kernchemie, 55128 Mainz, Fritz Strassmann-Weg 2, Germany
[3]Bundesanstalt für Materialforschung und -prüfung, 12489 Berlin, Richard-Willstätter-Str. 11, Germany
[4]Forschungszentrum Rossendorf, Institut für Ionenstrahlphysik und Materialforschung, 01314 Dresden, Bautzner Landstr. 128, Germany

Received June 26, 2003; accepted in revised form November 4, 2003

PACS numbers: 61.10.Ht, 61.10.Nz

Abstract

Determination of structures using X-ray powder diffraction is complicated if the reflection intensities are mainly influenced by the scattering from heavy atoms and the atomic coordinates of light atoms remain uncertain. A method like EXAFS, which is sensitive to short range order, gives reliable atomic distances in the surroundings of heavy atoms with a precision of ±0.02 Å. The probability for obtaining the complete structure from X-ray powder diffraction increases if one includes parameters derived from EXAFS measurements as restraints during the procedure of structure solving. We demonstrate the potential of combining EXAFS and X-ray powder diffraction by solving the structure $UO_2[H_2AsO_4]_2{\cdot}H_2O$. The procedure starts with the determination of space group and cell parameters from XRD powder data. In a second step the absolute values of the structure factor |F| are separated by iterating a decomposition formula. The heavy atom positions are determined by direct methods. In the third step atomic distances of coordination polyhedra are estimated using EXAFS. Subsequently, the complete coordination geometries around the heavy atoms including reliable distances are used as restraints in the structure solving and refinement procedure.

1. Introduction

In crystal structures containing heavy atoms, the X-ray scattering process is only weakly influenced by light atoms, whereas the contribution of heavy atoms dominates. A determination of heavy-atom coordinates in the unit cell using X-ray powder diffraction is possible but sometimes it is difficult to locate the light atoms. This can happen under certain circumstances also for single crystal structures. On the other hand, a short-range order method like EXAFS gives reliable atomic distances in the surroundings of heavy atoms also in solid state and allows the characterisation of the coordination polyhedra more accurately. The advantage of EXAFS for determining heavy-atom structures was demonstrated in a recent study of $Cu[UO_2AsO_4]_2{\cdot}12H_2O$ and $Cu[UO_2AsO_4]_2{\cdot}8H_2O$ [1]. Furthermore, studies of local structural ordering effects are possible by including EXAFS measurements. This was demonstrated by the simultaneous refinement of EXAFS and XRD data [2] that were used to determine the structure of $Gd_2Ba_2CaCu_2Ti_3O_{14}$ [3], where neither of the heavy-element sites was accurately described by the long-range structural model.

However, the structure of coordination polyhedra is not completely independent and can be understood as a rigid unit. The introduction of molecule sequences or coordination polyhedra as rigid bodies in the powder diffraction refinement improves the probability to solve the structure [4] because the number of refinable parameters can be drastically reduced. In the case of X-ray powder pattern this is particularly useful since the ratio of reflection intensities to refinable parameters is typically low. In this paper a new procedure will be used to generate coordination polyhedra by obtaining experimental values from EXAFS. Including the information from EXAFS as restraints in the structure solving procedure and refinement, the probability increases to obtain the complete structure from powder diffraction data. The procedure is demonstrated using $UO_2[H_2AsO_4]_2{\cdot}H_2O$, which has a known crystal structure [5], as an example. For this example uranium and arsenic serve as heavy-atom framework whose coordinates will be analyzed by X-ray powder diffraction and serve as absorbing elements for U L_{III} and As K edge EXAFS measurements.

2. Experimental

EXAFS measurements were carried out on the Rossendorf Beamline (ROBL) [6] at the European Synchrotron Radiation Facility (ESRF) under dedicated ring conditions (6.0 GeV, 100–200 mA). X-ray powder diffraction measurements were performed twice, at a conventional X-ray source, and at ROBL. The monochromator of ROBL, which is equipped with a water-cooled Si(111) double-crystal system, was used in channel-cut measuring mode. Higher harmonics were rejected by two Pt coated mirrors. Energy steps in the EXAFS spectra were calculated giving corresponding k-space steps of 0.05 $Å^{-1}$. For EXAFS measurements the powder was mixed with boron nitride and pressed as pellet with a diameter of 13 mm. The amount of uranium used was calculated to give a jump of one in the ln(I0/I1) function across the uranium L_{III}-edge. The same sample was used for the measurements at the As K-edge. Uranium L_{III}-edge and arsenic K-edge EXAFS data were collected in transmission geometry using argon-filled ionization chambers. A closed-cycle He cryostat was used to analyze larger atomic distances by reducing thermal oscillations. First inflection points at the Y K-edge at 17038 eV and at the Au L_{III}-edge at 11919.7 eV were used for energy calibration of EXAFS spectra. The energy in the X-ray diffraction measurements were calibrated using silicon powder. EXAFS data were extracted from the raw absorption spectra by standard methods using the computer program EXAFSPAK [7]. Scattering phase and amplitude functions were calculated using FEFF 8 [8]. The X-ray diffraction data were analyzed using the programs PowderCell [9], CRYSFIRE [10] and SHELX-97 [11].

3. Results and discussion

The X-ray diffraction measurements with conventional Cu Kα radiation were performed in Bragg-Brentano geometry in order to obtain a high scattering intensity. The sample for diffraction measurements at the synchrotron was prepared in a quartz glass capillary with a diameter of 0.3 mm and measured by

*email hennig@esrf.fr

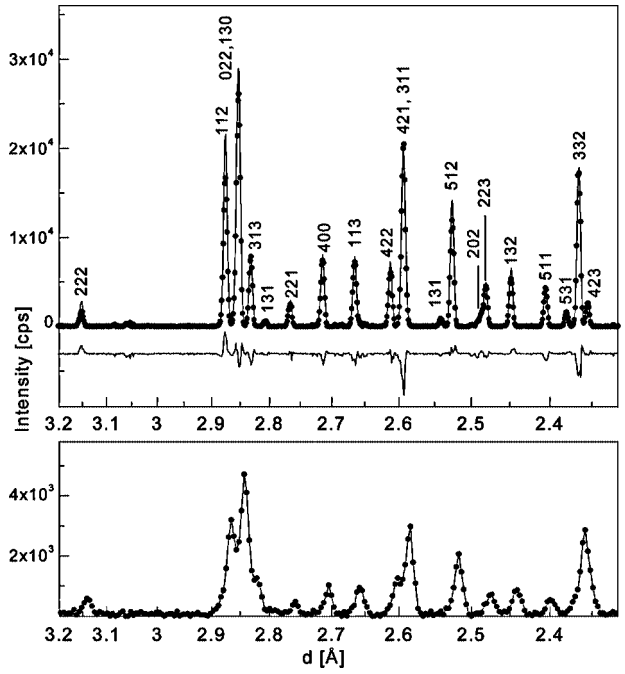

Fig. 1. Detail of X-ray powder diffraction pattern on $UO_2[H_2AsO_4]_2{\cdot}H_2O$, data obtained with Cu Kα radiation (bottom) and synchrotron radiation (top).

sample rotation in Debye-Scherrer geometry. The preparation in a capillary and the rotation reduce crystallite orientation effects. In Fig. 1 the diffraction patterns are given. For comparison the data are shown in *d*-space. A high angle resolution was achieved with the X-ray powder diffraction measurement at ROBL. The synchrotron based data show a Gaussian profile shape whereas the peak shape of the sample measured with the Cu Kα radiation was approximated with a Pseudo-Voigt profile.

The proposed procedure starts with the determination of space group and cell parameters from peak positions. The peak positions, separated from powder diffraction data, were analyzed using the program CRYSFIRE. In a second step, the individual intensities are extracted from powder pattern using the program PowderCell. The profile fitting procedure in this program does not need any structural model. It refines the cell parameters to be consistent with the angular position of the reflections according the Le Bail algorithm [12]. During each iteration step the lattice constants were refined according the chosen intensity distribution. Details of data collection and fit parameters obtained after final profile refinement are given in Tab. I.

Preliminary heavy-atom positions were found by direct methods using the intensities obtained by the first decomposition step of the X-ray powder pattern. In the third step, the coordination polyhedra and their connections were determined using EXAFS.

Table I. *Details of collected X-ray diffraction data collection and fit parameters of $UO_2[H_2AsO_4]_2{\cdot}H_2O$ (see Fig. 1).*

Source	X-ray tube	Synchrotron
Radiation	1.5406 Å	1.05087 Å
Diffractometer	URD 6	6-circle (Huber)
Scan geometry	Bragg-Brentano	Debye-Scherrer
2 θ range [°]	12.0–60.0	8.0–60.0
$\Delta 2\theta$ [°]	0.02	0.01
No. of reflections	124	401
Profile function	Pseudo-Voigt	Gauss
W	0.02	0.0043

W – reflex profil parameter.

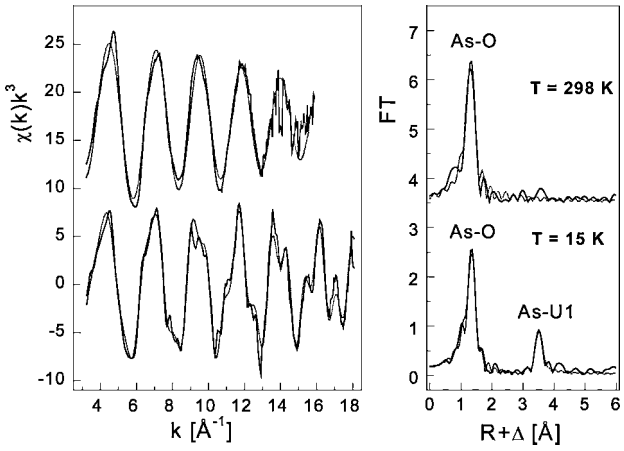

Fig. 2. As K-edge k^3-weighted EXAFS spectra of $UO_2[H_2AsO_4]_2{\cdot}H_2O$ (left) and their Fourier transforms (right).

Table II. *EXAFS structural parameters of the As K-edge of $UO_2[H_2AsO_4]_2{\cdot}H_2O$ at 289 K and 15 K (see Fig. 2).*

T [K]	shell	*R* [Å][a]	*N*[b]	σ^2 [Å^2]	ΔE [eV]
298	As-O	1.68	3.8(2)	0.0017	2.3
15	As-O	1.69	4.2(1)	0.0016	−4.9
	As-U1	3.71	1.9(2)	0.0029	−11.0

[a]Errors in distances *R* are ±0.02 Å, [b]errors in coordination numbers *N* are ±25% with standard deviations in parentheses.

Fig. 2 depicts the As K-edge k^3-weighted EXAFS spectra of $UO_2[H_2AsO_4]_2{\cdot}H_2O$. The corresponding fit results are presented in Tab. II. The measurement at room temperature (298 K) shows that As is surrounded by four oxygen atoms at an average distance of 1.68 Å indicating an $[AsO_4]$ tetrahedron. In order to reduce the thermal atomic movements, the same sample was measured at 15 K. This measurement shows that each $[AsO_4]$ tetrahedron is surrounded by two uranium atoms at a distance of 3.71 Å. The bond length points to a monodentate connection between the arsenate and the uranyl polyhedra. Corresponding to the $[H_2AsO_4]$ sequence of the chemical formula, two of the oxygen atoms are protonated.

EXAFS measurements of $UO_2[H_2AsO_4]_2{\cdot}H_2O$ at the U L_{III}-edge are shown in Fig. 3. The fit results are given in Tab. III. Two axial oxygen atoms (O_{ax}) are at a distance of 1.77 Å and five

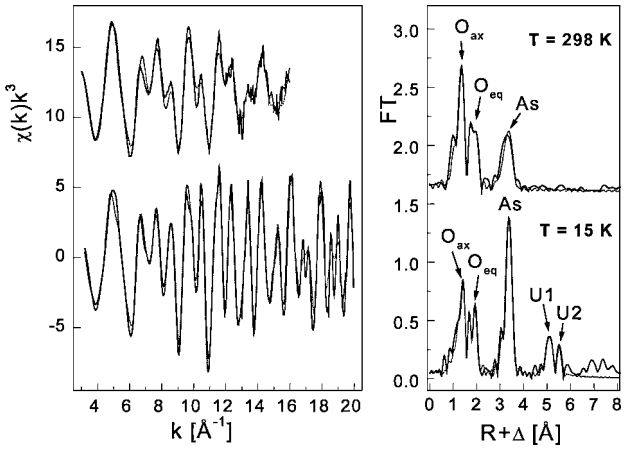

Fig. 3. UL_{III}-edge k^3-weighted EXAFS spectra of $UO_2[H_2AsO_4]_2{\cdot}H_2O$ (left) and their Fourier transforms (right).

Table III. *EXAFS structural parameters of the U L_{III}-edge of $UO_2[H_2AsO_4]_2{\cdot}H_2O$ at 289 K and 15 K (see Fig. 3).*

T [K]	shell	R [Å][a]	N[b]	σ^2 [Å^2]	ΔE [eV]
298	U-Oax	1.77	2.2(2)	0.0022	−1.2
	U-Oeq	2.38	5.1(4)	0.0068	/
	U-As	3.70	4.0(3)	0.0055	/
15	U-Oax	1.79	1.9(1)	0.0015	6.5
	U-Oeq	2.35	4.7(4)	0.0044	0.7
	U-As	3.70	4.2(2)	0.0019	1.2
	U-U1	5.38*	2.1(5)	0.0019	−14.0
	U-U2	5.73	6 (2)	0.0053	2.3

[a]Errors in distances R are ±0.02 Å, [b]errors in coordination numbers N are ±25 % with standard deviations in parentheses, *this value is influenced by the U-As shell at 5.45 Å.

equatorial oxygen atoms (O_{eq}) are detected at an average distance of 2.38 Å. The high Debye-Waller factor of 0.0068 Å^2 indicates that the equatorial oxygen atoms are not symmetry-equivalent. Taking into consideration that the errors in coordination numbers of distant shells are reduced at low temperatures, the uranium atom is coordinated by four As atoms via oxygen atoms. The EXAFS data show clearly that uranium is coordinated by 5 oxygen atoms in the equatorial shell. The fifth equatorial oxygen atom belongs to a H_2O molecule given in the chemical formula.

The position of light atoms in the unit cell are determined by including the EXAFS results as help for the interpretation of the first difference Fourier synthesis. Subsequently, average bond lengths of coordination polyhedra [$UO_{ax2}O_{eq5}$] and [AsO_4] obtained by EXAFS were used as restraints in the first cycles of structure solving. The polyhedron geometry was assumed as regular [AsO_4] tetrahedron and equal angle distribution in the equatorial shell of [$UO_{ax2}O_{eq5}$]. The structure was refined by cycles of powder pattern decompositions using the actual structural parameters and SHELXL-97 calculations (Tab. IV, Fig. 4). The structure refinement in the final step needed also the restraints from EXAFS, strong restraints for conventional powder diffraction data, and a reduced number of restraints for synchrotron data. Without any restraints the refinement procedure was unstable. The refinement converged with R1(on F) of 0.082 and 0.071 for 124 peaks of the conventional X-ray source and 401 reflections of the synchrotron, respectively.

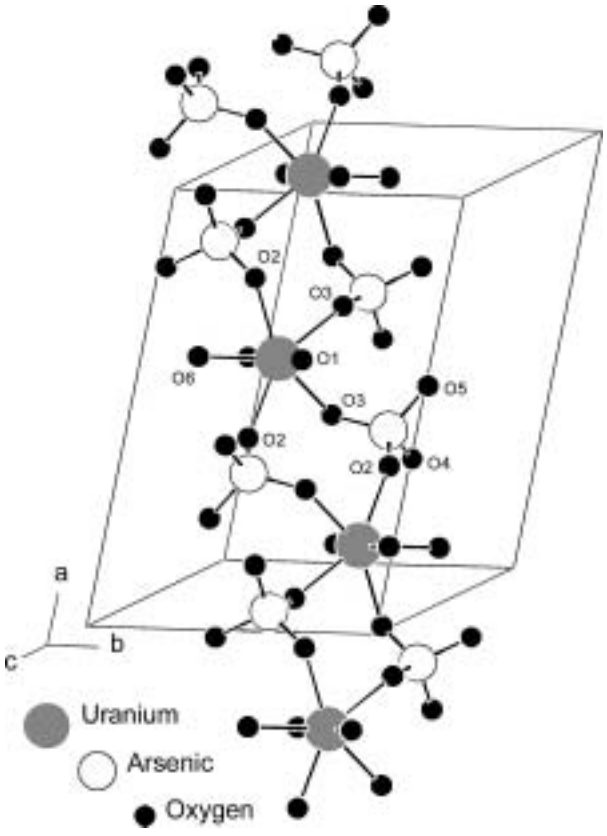

Fig. 4. Structure of $UO_2[H_2AsO_4]_2{\cdot}H_2O$.

Table IV. *Lattice parameters and atomic coordinates of $UO_2[H_2AsO_4]_2{\cdot}H_2O$, space group C2/c; first line: sample with CuKα radiation; second line: sample with synchrotron radiation; third line: single crystal from reference [5].*

a	b	c	β
13.172	8.860(3)	9.056(3)	124.49(3)
13.182	8.869(1)	9.062(1)	124.52(1)
13.164(3)	8.862(2)	9.050(3)	124.41(3)
Atom	x	y	z
U(1)	0.5	0.1548(2)	0.25
	0.5	0.1522(1)	0.25
	0.5	0.15300(3)	0.25
As(1)	0.6924(4)	0.4937(6)	0.4490(7)
	0.6892(2)	0.5033(2)	0.4430(2)
	0.68804(5)	0.5128(6)	0.44135(8)
O(1)	0.5	−0.1221(13)	0.25
	0.5	−0.1251(11)	0.25
	0.5	−0.1223(7)	0.25
O(2)	0.7457(7)	0.6204(10)	0.3717(11)
	0.7437(6)	0.6283(8)	0.3732(9)
	0.7354(5)	0.6404(5)	0.3640(7)
O(3)	0.5426(5)	0.1920(3)	0.4701(13)
	0.5348(12)	0.1654(10)	0.4685(12)
	0.5457(5)	0.1544(5)	0.4748(7)
O(4)	0.6362(8)	0.3453(8)	0.3159(8)
	0.6296(8)	0.3618(7)	0.3021(10)
	0.6236(4)	0.3634(5)	0.2885(6)
O(5)	0.5849(6)	0.5762(13)	0.4652(12)
	0.5767(5)	0.5847(10)	0.4490(9)
	0.5781(4)	0.5871(5)	0.4561(6)
O(6)	0.8095(7)	0.4393(12)	0.6563(8)
	0.7939(6)	0.4444(10)	0.6436(8)
	0.7995(4)	0.4419(5)	0.6456(6)

The procedure demonstrates that the combination of EXAFS with powder diffraction allows a complete crystal structure determination of heavy atom structures also when no single crystals are available.

Acknowledgment

We thank G. Grambole and M. Acker for sample preparation and K. Krogner for chemical analysis of the sample.

References

1. Hennig, C., *et al.*, Z. Krist. **218**, 37 (2003).
2. Binsted, N., Pack, M. J., Weller, M. T. and Evans, J., J. Am. Chem. Soc. **118**, 10200 (1996).
3. Weller, M. T., Pack, M. J. and Binsted, N., Angew. Chem. Int. Ed. **37**, 1094 (1996).
4. Dinnebier, R. E., Powder Diffraction **14**, 84 (1999).
5. Gesing, T. M. and Rüscher, C. M., Z. Anorg. Allg. Chem. **626**, 1414 (2000).

6. Matz, W., *et al.*, J. Synchrotron Rad. **6**, 1076 (1999).
7. George, G. N. and Pickering, I. J., EXAFSPAK, a suite of computer programs for analysis of X-ray absorption spectra. Stanford Synchrotron Radiation Laboratory, (Stanford 1995).
8. Ankudinov, A. L., Ravel, B., Rehr, J. J. and Conradson, S. D., Phys. Rev. B **58**, 7565 (1998).
9. Kraus, W. and Nolze, G., CPD Newsletter **20**, 274 (1998).
10. Shirley, R., CRYSFIRE An interactive powder indexing support program. University of Surrey, (Guildford 1999).
11. Sheldrick, G. M., SHELXS-97, (Göttingen 1997).
12. Le Bail, A., Duroy, H. and Fourquet, J. L., Mater. Res. Bull. **23**, 447 (1988).

Physica Scripta. Vol. T115, 356–358, 2005

Lattice Location of N in $In_xGa_{1-x}As_{1-y}N_y$ Dilute Nitrogen Alloys

G. Ciatto[1,*], F. Boscherini[2], F. D'Acapito[3], D. De Salvador[4], D. Batchelor[5], R. Carboni[2], L. Grenouillet[6], H. Mariette[6] and S. Mobilio[7]

[1]CNR c/o ESRF-Gilda CRG, 6 rue J.Horowitz, BP 220, 38043 Grenoble, France
[2]INFM and Department of Physics, University of Bologna, V. le C. Berti Pichat 6/2, 40127 Bologna, Italy
[3]INFM c/o ESRF-Gilda CRG, 6 rue J.Horowitz, BP 220, 38043 Grenoble, France
[4]INFM and Department of Physics, University of Padova, Via Marzolo 8, I-35131 Padova, Italy
[5]BESSY GmbH, Albert-Einstein-Str.15, 12489 Berlin, Germany
[6]CEA, 17 avenue des Martyrs, 38054 Grenoble, France
[7]Department of Physics, University of Rome III, Via della Vasca Navale 84, 00146 Roma, Italy

Received June 26, 2003; accepted in revised form November 4, 2003

PACS numbers: 61.10.Ht, 61.66.Dk, 81.05.Ea, 13.88.+e

Abstract

Dilute nitrides, in particular $In_xGa_{1-x}As_{1-y}N_y$ are very interesting alloys because of their actual and potential applications in the field of telecommunications and photovoltaics. A full knowledge of the local structure around each kind of atom, in particular the local ordering, is of fundamental importance because it is predicted to affect the electronics properties of these alloys. In this work we investigated the local environment of N and In by X-Ray absorption Fine Structure (XAFS). By exploiting the polarization dependency of XAFS we were able to demonstrate that N is fully substitutional to As. The lineshapes of the N K-edge XANES spectra are in fact identical, setting different grazing angles, which is a fingerprint of the cubic geometry of the N site. This information has been exploited to generate atomic clusters that very well simulate the experimental N K-edge XANES in the Full Multiple Scattering approach and to elaborate a multi-shell fit for XAFS data at the In K-edge. We concluded that N preferentially links In atoms, even if this short range ordering is by far weaker than the predicted one.

1. Introduction

In 1996 it was discovered that the substitution of a small fraction of As with N in $In_xGa_{1-x}As$ epitaxially grown on GaAs causes a giant reduction in the band gap of the alloy [1]. This effect, previously observed in GaAs:N since 1992 [2], became rapidly an object of theoretical studies addressed to understand its physics. The possibility to red-shift the band gap of $In_xGa_{1-x}As$ down to less than 1.0 eV is extremely important because these very long wavelengths are optimal for realizing modern Vertical Cavity Surface Emitting Lasers (VCSELs) employed in fibre optic communication; moreover the growth of InGaAsN on GaAs is quite simple and cheap. The light N atoms act as strain moderators, and permit to reach the required wavelengths limiting at the same time the indium content in the epilayers, which would otherwise relax because of the great difference in the lattice parameter between high In-content $In_xGa_{1-x}As$ and the GaAs substrate. Relaxation limits the performances of $In_xGa_{1-x}As_{1-y}N_y$-based optoelectronic and photovoltaic devices. Recently, a preferential In-N bonding has been predicted [3] for these alloys and some experimental reports have quantitatively confirmed this general trend measuring in hydrogenated [4] and annealed [5] $In_xGa_{1-x}As_{1-y}N_y$ a relative number of In-N bonds vs. In-As bonds greater than in a random alloy. Another recent experimental work qualitatively supports the hypothesis of the ordering induced by annealing [6]. Such an ordering has been predicted to inhibit the red shift of the band gap, resulting in severe material properties limitation. Blue shift has already been observed in annealed (nearer to equilibrium condition) samples [7], even if a conclusive demonstration of the parallelism between optical effects and structural ordering does not exist at present in literature. X-Ray Absorption Fine Structure is the ideal tool to address the issue of short range ordering (SRO). In order to build a simple structural model to fit EXAFS data, some preliminary information is of significant importance; first of all we have to know if N substitutes As atoms or if it precipitates forming other compounds, in the latter case we have to determine the substitutional fraction and the geometry of the N site in the precipitates. Finally we have to take into account the possibility for N atoms to occupy an interstitial site, forming As-N and N-N split interstitials as proposed by Li *et al*. [8].

Information on the geometry of the N sites can be obtained by exploiting the polarization dependence of the XAFS signal [9]:

$$\chi(k) = -3\frac{(\hat{\epsilon}\cdot\widehat{r_1})^2}{kr_1^2}\mathrm{Im}[e^{2ikr_1+2i\delta_1^1}f(k,\pi)]. \quad (1)$$

In this equation we underline the contribution to the EXAFS signal of a single neighbor located at distance r_1 relative to the absorber. $\hat{\epsilon}$ is the polarization direction of the X-rays, $\widehat{r_1}$ = unity vector in the absorber-scattered direction, k = photoelectron wave vector, $f(k,\pi)$ = backscattering amplitude, δ_1^1 = central atom phase shift. Turning the sample it is possible to set different angles between a definite crystallographic direction and the electric field of linearly polarized synchrotron radiation. Since cubic symmetry is isotropic from the standpoint of electron charge density, polarization dependence of N K-edge XANES should be absent in case of pure substitutional N, otherwise it should be significant in case of formation of hexagonal precipitates like GaN. In this paper we demonstrate that in our samples N is fully substitutional to As and how this information can be exploited to very well simulate N K-edge XANES in the full multiple scattering approach and to elaborate a robust multi-shell fit for XAFS data at the In K-edge.

2. Experimental

Two series of 140 nm thick $In_xGa_{1-x}As_{1-y}N_y$ epilayers were specifically grown by gas-source molecular beam epitaxy on (001) GaAs substrate in order to highlight the effects or SRO on the XAS data. The In and N concentration is in fact similar ($x \approx 0.04$, $y \approx 0.02$ in the first series and ≈ 0.03 in the second series), so the expected relative In-N coordination should be very high in the case of maximum In-N + Ga-As ordering (about 50% for series I and 90% for series II). Growth temperature was in the range 400–430 °C, thermal annealing was performed at 700 °C,

*ciatto@esrf.fr

for different times (90 and 300 s) [10]. Indium concentration was determined by Rutherford Backscattering Spectrometry, nitrogen concentration by combining (004) High Resolution X-Ray Diffraction (HRXRD) and Nuclear Reaction Analysis (NRA) measurements.

In K-edge measurements were performed at the European Synchrotron Radiation Facility in Grenoble (BM8, Gilda CRG beamline), exploiting a sagittally focusing monochromator equipped with Si [311] crystals, run in the dynamical mode [11]. The In K_α fluorescence signal was monitored using a thirteen-element hyper pure Ge detector. N K-edge measurements were performed at the BESSY II facility in Berlin (U49/2-PGM2, Cottbus beamline). Also in this case fluorescence detection was used in order to guarantee bulk sensitivity, using a window-less single element hyper pure germanium detector.

3. XAS Data Analysis

EXAFS oscillations at the In edge were extracted from the raw data with the AUTOBK code [12]: the pre-edge region was fitted with a linear function while the atomic background was interpolated by a cubic spline with 15 knots. Data analysis was performed by *ab-initio* modeling of the XAFS signal using the FEFF 8.00 code [13]. The theoretical signals were calculated using InGaAs and InN model clusters. Quantitative analysis was performed in the range $k = 3.0 \div 13.4\,\text{Å}^{-1}$ and $R = 1.6 \div 4.8\,\text{Å}$ (R values not corrected for the phase shift). The FEFFIT program [14] was used to extract the structural parameters: relative In-N coordination (and, as a consequence, In-As coordination), bond lengths and Debye-Waller factors.

N K-edge XANES spectra were simulated *ab-initio* in the real space full multiple scattering approach using self consistency for the potential; The FEFF 8.00 code, modified in order to treat large clusters, was exploited to perform the simulations. The cluster for simulating $GaAs_{1-y}N_y$ was generated by substituting an N impurity to the central As in a GaAs structure (GaAs:N) and relaxing the first and second shell distances through minimization of a valence force field potential [15] with appropriate force constants [16]. The same procedure was adopted for a N impurity in InAs. In order to simulate the quaternary alloys with different. In contents we exploited linear combinations of the simulated XANES spectra for GaAs:N and InAs:N.

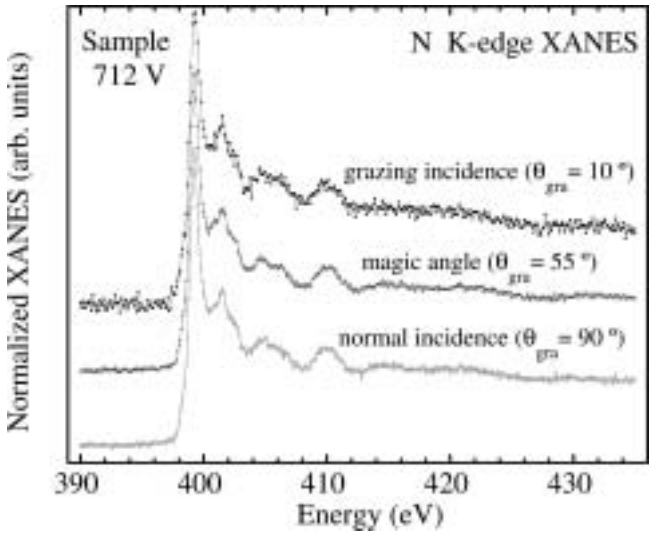

Fig. 1. N K-edge XANES taken on $In_{0.038}Ga_{0.962}As_{0.9665}N_{0.0335}$ for different grazing angles.

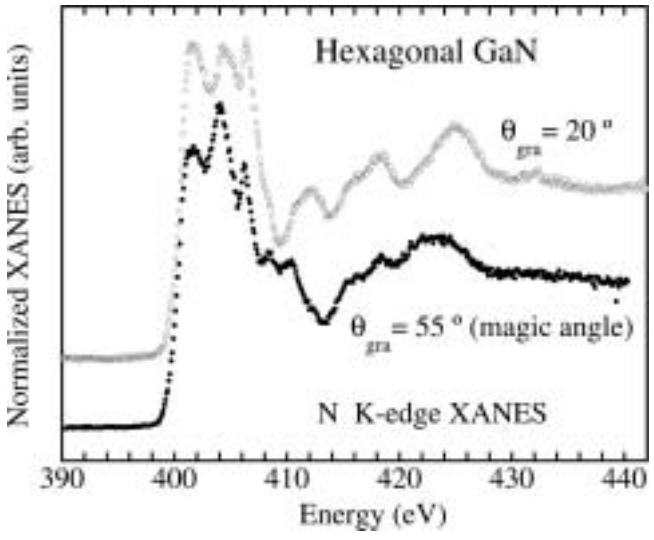

Fig. 2. N K-edge XANES of an hexagonal GaN standard for different grazing angles.

4. Substitutional Character of Nitrogen

In fig. 1 we report three N K-edge XANES spectra for sample 712 V ($In_{0.038}Ga_{0.962}As_{0.9665}N_{0.0335}$) taken with different incidence angles. The grazing angle (θ_{gra}) was respectively fixed to 10° (nearly grazing incidence), 55° and 90° (normal incidence). Straightforwardly θ_{gra} is also the angle between the electric field and the normal to the sample surface (in our case the [001] crystallographic direction referred to the substrate). In an hexagonal system $\theta_{gra} = 54.73°$ is the angle for which directional effects are like averaged, due to a cancellation in the expression of the squared cosine of the angle between the electric field vector and the direction of maximum electron charge density (δ), which enters the formulation for the absorption cross section [17], [18].

$$\cos^2\delta = \tfrac{1}{3} + \tfrac{1}{8}(1 + 3\cos 2\alpha)(\cos 2\theta_{gra} + \tfrac{1}{3}). \quad (2)$$

In this equation α is the angle between the direction of maximum electron density and the normal to the surface, for $\theta_{gra} = 54.73°$ the term in the last parenthesis becomes zero so that $\cos^2\delta$ and, as a consequence, the absorption cross section does not depend on α.

The three spectra in fig. 1 are virtually identical, evidencing there is no polarization dependence of N K-edge XANES: this is a fingerprint of the cubic symmetry of the structure. For a non-isotropic symmetry group (as the hexagonal) significant variations in the relative intensity of the XANES resonances would be otherwise observable; this is evident in fig. 2 where two N K-edge XANES spectra for an hexagonal GaN standard sample, respectively taken at $\theta_{gra} = 20°$ and $\theta_{gra} = 55°$, are reported. As concerns a possible different N location in the lattice, N complexes such as N-N and N-As split interstitials would give sharp resonances in the pre-edge region of the XANES, which are not observed in our case. The substitutional character of nitrogen is confirmed by comparing random and channelling NRA spectra, the latter obtaind aligning the deuterium beam used as probe along a definite crystallographic plane. The N substitutional fraction estimated by this technique is close to 100% for all samples, independent on the annealing [19].

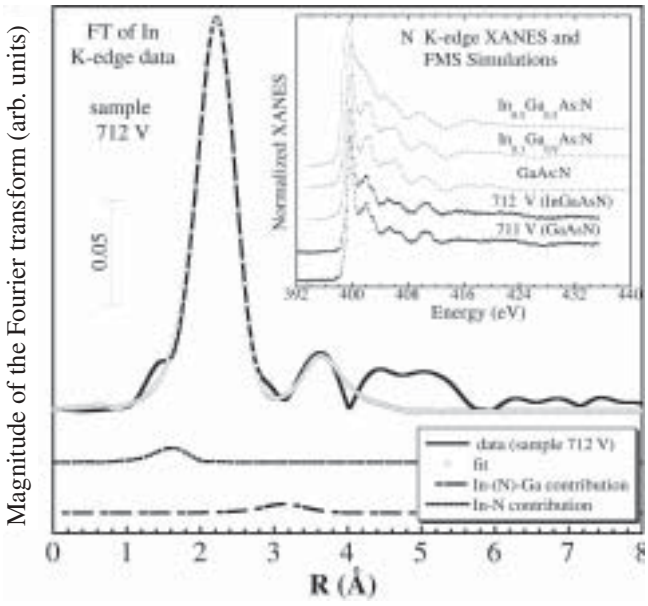

Fig. 3. Fit on the Fourier transform of the In K-edge EXAFS for sample 712 V with the relative N-related paths contributions (at the bottom); in the inset experimental XANES (the two bold lines at the bottom) and FMS simulations for x = 0%, 10%, 50%.

5. The Short Range Ordering

The knowledge of the kind of site occupied by N atoms in the alloy allows us to use the substitutional impurity model cited above for generating clusters employed in the FMS simulations of N K-edge XANES. The excellent results obtained, reported in the inset of fig. 3, proof the reliability of the model. At the bottom of the inset we reported the experimental XANES of the ternary sample 711 V ($GaAs_{0.9696}N_{0.0304}$) together with that of the quaternary 712 V. The two spectra are virtually identical and very well simulated starting by a simple GaAs:N "impurity" cluster (third line moving towards the top of the inset). This suggests that, if present, the N-In preferential bonding is quite weak. If it was stronger, according to the predictions based on Monte Carlo calculations [3], that would result in a very different lineshape, closer to the fifth line of the inset of fig. 3, which reports a simulation for an alloy where the indium content is 50%. On the other hand, 10% of indium in the alloy (fourth line) is not sufficient to sensibly modify the simulations i.e. we can neither exclude nor demonstrate the occurrence of weak ordering starting by the only N K-edge XANES. Fits of EXAFS spectra at the indium edge provide us with a quantification of the In-N preferential bonding. Having acquired knowledge of the substitutional character of nitrogen, we could use a single variable y_{In-N} in order to estimate the probability of an In nearest neighbor site to be occupied by a N atom ($1 - y_{In-N}$ for As). This variable allowed to easily model at the same time the second shell, where Ga atoms (the low In content made us unsensitive to the In-In coordination) were divided into those coordinated via a first shell As and the those coordinated via a first shell N. y_{In-N} weights the relative amplitude of the two subshells, situated at different distances from the absorber. In fig. 3 we report a fit on the Fourier Transform for sample 712 V, underling the contribution of first and second shell N-related paths (bottom). Details of this analysis and systematic discussion of the results achieved on all the samples at the indium edge have been object of a recent work [5]. We remind here of our conclusive finding: in annealed samples ordering has the same sign as predicted (In-N preferred to In-As) and the probability for an N atom to occupy an In-first neighbor site is up to three times the random one. Nevertheless our measured SRO parameters are about an order of magnitude smaller than those calculated via Monte Carlo simulations [3]. As grown samples, on the other hand, are virtually random alloys due to their far from equilibrium condition.

6. Conclusions

We addressed in this paper the issue of short range ordering (SRO) in $In_xGa_{1-x}As_{1-y}N_y$, a diluted nitride of great technological interest. We concentrated particularly on demonstrating how N is totally substitutional to As (i.e. cubic symmetry of the structure) by means of crossed N K-edge XANES, exploiting the linear polarization of synchrotron radiation, and NRA-channelling measurements. Holding this information we could elaborate simple model clusters to simulate N K-edge XANES and to fit In K-edge EXAFS data. The latter allowed us to give a quantitative estimation of SRO which, in annealed samples, holds the same sign as in predictions (preferential In-N vs. In-As bonding) but is about one order of magnitude weaker.

References

1. Kondow, M. *et al.*, Jpn. J. Appl. Phys. **35**, 1273 (1996).
2. Weyers, M., Sato, M. and Ando, H., Jpn. J. Appl. Phys. **31**, L853 (1992).
3. Kim, K. and Zunger, A., Phys. Rev. Lett. **86**, 2609 (2001).
4. Ciatto, G. *et al.*, Nucl. Instr. Meth. Phys. Res. B **200**, 34 (2003).
5. Ciatto, G. *et al.*, Phys. Rev. B **68**, 161201(R) (2003).
6. Lordi, V. *et al.*, Phys. Rev. Lett. **90**, 145505 (2003).
7. Spruytte, S. G. *et al.*, J. Appl. Phys. **89**, 4401 (2001).
8. Li, W., Pessa, M. and Likonen, J., Appl. Phys. Lett. **78**, 2864 (2001).
9. Lee, P. A., Citrin, P. H., Eisenberger, P. and Kincaid, B. M., Rev. Mod. Phys. **53**, 769 (1981), part I.
10. Grenouillet, L. *et al.*, J. Appl. Phys. **91**, 5902 (2002).
11. Pascarelli, S. *et al.*, J. Synchrotron. Radiat. **3**, 147 (1996).
12. Newville, M., Livins, P., Yacoby, Y., Rehr, J. J. and Stern, E. A., Phys. Rev. B **47**, 14126 (1993).
13. Ankudinov, A. L., Ravel, B., Rehr, J. J. and Conradson, S. D., Phys. Rev. B **58**, 7565 (1998).
14. Newville, M. *et al.*, Physica B **208&209**, 154 (1995).
15. Keating, P. N., Phys. Rev. **145**, 637 (1966).
16. Wright, A. F., J. Appl. Phys. **82**, 2833 (1997).
17. Katsikini, M., Paloura, E. C. and Moustakas, T. D., J. Appl. Phys. **83**, 1437 (1998).
18. Brouder, C., J. Phys.: Condens. Matter **2**, 701 (1990).
19. Bisognin, G. *et al.*, J. Appl. Phys. **95**, 49 (2004).

Physica Scripta. Vol. T115, 359–361, 2005

XAFS Study of Local Structure Change in Perovskite Titanates

K. Sato[1], T. Miyanaga[1], S. Ikeda[1] and D. Diop[2]

[1]Department of Materials Science and Technology, Faculty of Science and Technology, Hirosaki University, Aomori 036-8561, Japan
[2]Department of Physics, Faculty of Science and Technique, University Anta Cheikh Diop of Dakar, Dakar, Senegal

Received June 26, 2003; accepted in revised form June 23, 2004

PACS numbers: 02.40.−k, 12.39.Dc, 14.80.Hv

Abstract

The Ti K-edge EXAFS for $PbTiO_3$ measured in the temperature range including the critical temperature (763 K) due to the phase transition from tetragonal to cubic phase is discussed from the local point of view. Three kinds of atomic pairs, shorter Ti-O(1), medium Ti-O(2) and longer Ti-O(3) were analyzed independently. The interatomic distance of Ti-O(3) changes at T_c discontinuously and shows a "displacive" type transition. On the other hand, EXAFS shows that the lattice distortion remains even in cubic phase, which indicates "order-disorder" type transition. The peak intensity at the pre-edge region in XANES, which indicates the distortion of Ti atoms along the *c*-axis of the oxygen octahedron, corresponds to the distortion obtained from EXAFS analysis.

1. Introduction

X-ray absorption fine structure (XAFS) has become a technique to study local structures as a complementary technique to diffraction methods which are based on long-range order [1]. $PbTiO_3$ has long been considered as "displacive" type ferroelectrics: The perovskite $PbTiO_3$ shows tetragonal structure at $T < T_c$ (=763 K) (lattice parameters $a = b = 3.89$ Å and $c = 4.15$ Å at 300 K [2]) and cubic structure at $T > T_c$ ($a = b = c = 3.905$ Å at 773 K). On the other hand, if the local distortion does not change with temperature across T_c the transition is "order-disorder" type. In this case, only the orientations of the distortion within a small domain change with temperature; the orientation is arranged along the preferable direction below T_c, but it is disordered above T_c.

The local structural change of $PbTiO_3$ has been extensively studied by Sicron *et al*. using XAFS of both Pb L_{III} and Ti K-edges [3, 4]. These results show that an essential element of "order-disorder" is present even in this normally pure ferroelectric crystal, which displays a soft mode and a dielectric constant of typical "displacive" type ferroelectrics. Recently, a more detailed study by Pb L_{III} edge EXAFS for $PbTiO_3$ has been carried out [5] where three kinds of atomic pairs Pb-O(1,2,3) are analyzed independently. Shorter atomic pairs of Pb-O(1,2) show "order-disorder" type behavior, on the other hand, the longest Pb-O(3) shows "soft mode" behavior [5].

In this paper, we study the local structural change around Ti atoms in $PbTiO_3$ crystal through T_c in more detail. Actually, there exist three types of Ti-O pairs by tetragonal distortion; longer and shorter interatomic distances along the *c*-axis and a medium Ti-O pairs perpendicular to the *c*-axis. Our results show that the local distortion remains above T_c in which $PbTiO_3$ shows cubic phase.

2. Experimental and Data Analyses

The powder sample of $PbTiO_3$ (99.99%) was purchased from Soeakwa Co. Ltd. and was checked by X-ray powder diffraction to assure its crystal structure. The powder was mixed with BN and was dry pressed for producing a pellet that could be easily handled and placed within the furnace. X-ray absorption spectra of Ti K-edge (4.95 keV) were measured at BL9A of Photon Factory (KEK) in transmission mode. A Si(111) double crystal monochrometer was used. The temperature range for measurement was from 300 K to 923 K.

The EXAFS analysis was performed according to XANADU code [6] and it is given only briefly here. The normalized EXAFS interference function, $\chi(k)$, was multiplied by a Hamming window function to reduce the ripples in the Fourier-transformed spectra in *r*-space. The *k*-range for the Fourier transform was from 2.95 to 8.8 $Å^{-1}$.

3. Results and Discussion

We discuss here the result for Ti K-edge XAFS. Figure 1 shows the EXAFS oscillation functions, $k^2\chi(k)$, of Ti K EXAFS for $PbTiO_3$ crystal at various temperatures obtained by transmission measurement. Although the signal in the transmitted ionization chamber is not so large due to the absorption by Pb atoms, satisfactory data quality has been obtained up to 8.5 $Å^{-1}$ for EXAFS analyses even at high temperatures. As the temperature increases the amplitude of the EXAFS function decreases gradually. Figure 2 shows the Fourier transforms of Ti K EXAFS for $PbTiO_3$ crystals at various temperatures as shown in Fig. 1. The peak intensity decreases as temperature increases and change of the fine structure is observed. The atoms are distorted along the *c*-axis at tetragonal phase: There are three kinds of Ti-O atomic pairs; shorter Ti-O(1), medium Ti-O(2) and longer Ti-O(3) as shown in Fig. 3. The peaks from 1 to 2 Å include three Ti-O pairs. In the case of Ti K-edge we tried to perform 3 shell-fitting in order to obtain the structural parameters and reasonable results were obtained. Our unknown parameters for the fitting are *r* and σ^2 for each shell and the total number of them is 6.

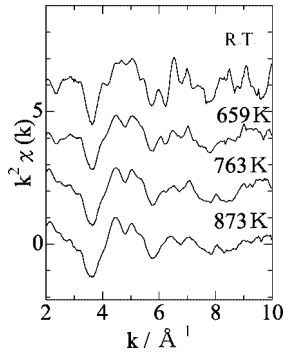

Fig. 1. EXAFS oscillation functions, $k^2\chi(k)$, of Ti K-edge EXAFS for $PbTiO_3$ crystal at various temperatures.

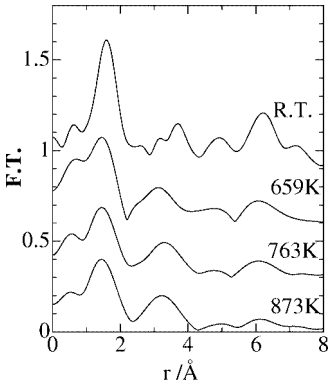

Fig. 2. Fourier transforms of Ti K-edge EXAFS for $PbTiO_3$ crystals at various temperatures as shown in Fig. 1.

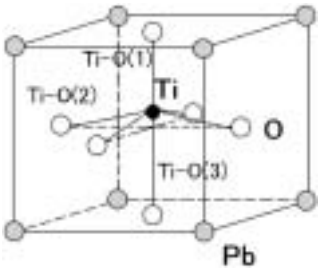

Fig. 3. Schematic structure of $PbTiO_3$ in the tetragonal phase. The central atom is Ti (Black circles), white circles represent O atoms and gray circles represent Pb atoms.

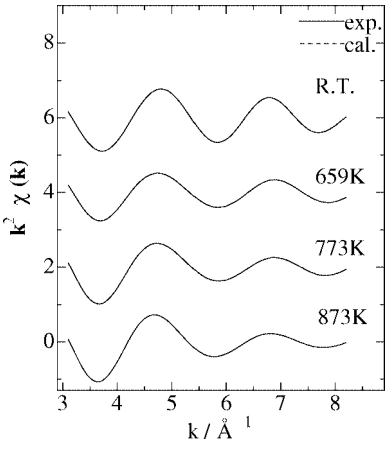

Fig. 4. Example of the quality for 3-shell fitting in the present study at various temperatures.

Figure 4 shows an example of the quality of 3-shell fitting in the present study at various temperatures. The fitting results reproduce the experimental spectra well. Figure 5 shows the contributions of each shell as a function of r which is obtained from the theoretical fitting for the Ti K-edge of $PbTiO_3$. Figure 6 shows the variations of three kinds of Ti-O interatomic distances with temperature. We also easily find the tetragonal distortion below T_c as shown in Pb L_{III}-edge EXAFS [5]. For example in the tetragonal phase at 300 K, the distance for Ti-O(1) is about 1.8 Å, that for Ti-O(2) is about 2.0 Å and that for Ti-O(3) is 2.4 Å. From these values we can estimate the distortion of Ti atoms with O atoms in the tetragonal phase. The distortion of Ti atoms from O atoms for c-axis is about 0.35 Å at 300 K for the tetragonal phase, which is the same value as that obtained by Sicron *et al.* [3, 4].

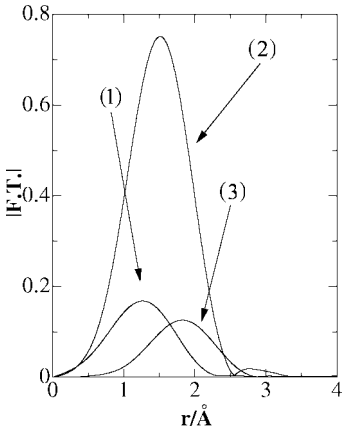

Fig. 5. The contributions of each shell in Ti K-edge fitting for $PbTiO_3$ as a function of r at 300 K.

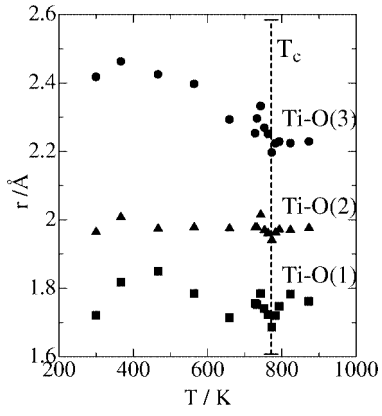

Fig. 6. Variations of three kinds of Ti-O interatomic distances with temperature.

The interatomic distance of Ti-O(2) is almost constant in the whole temperature range including T_c. That of Ti-O(3) decreases as temperature increases up to T_c and does not change with temperature at $T > T_c$. As for Ti-O(1), we find complex behavior between Ti-O(2) and Ti-O(3). That is: the longest Ti-O(3) shows typical "displacive" behavior and Ti distortion remains at temperatures above T_c. These phenomena are quite similar to the result of Pb-O obtained from Pb L_{III}-edge EXAFS study [5]. At $T > T_c$, the interatomic distance for Ti-O(1) is 1.75 Å, that for Ti-O(2) is 2.0 Å, and that for Ti-O(3) is 2.25 Å. This difference in Ti-O distance shows that atomic distortion remains at the cubic phase.

Figure 7 shows X-ray absorption near edge structure (XANES) of Ti K-edge for $PbTiO_3$ at various temperatures. We can find two clear peaks (A and B) before the edge. The origins of these two peaks are assigned to the transition from 1s to $3d_{xy}$ and $3d_z^2$ from the symmetry of the orbital, respectively. Although these transitions are forbidden generally in the dipole approximation, they are allowed by mixing with oxygen p-state orbitals due to the distortion of Ti atoms from the oxygen octahedron. That is the existence of these peaks indicates that Ti atoms are distorted.

Figure 8 shows the temperature variations of the intensity of peak A in Fig. 7 (solid circle). The peak intensity of A decreases gradually as the temperature increases up to T_c and decreases discontinuously at T_c and it is almost constant at $T > T_c$. The peak intensity of A ($= I_A$) is known to be approximately proportional to the amplitude to the Ti atom distortion as [7],

$$I_A = C\boldsymbol{e} \cdot d, \tag{1}$$

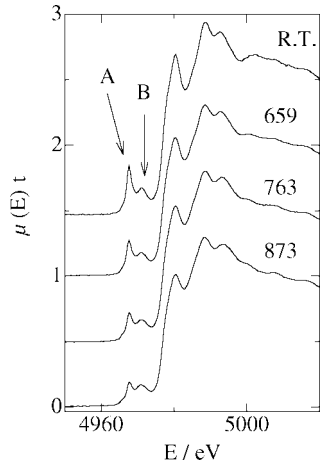

Fig. 7. X-ray absorption near edge (XANES) spectra of Ti K-edge for $PbTiO_3$ at various temperatures.

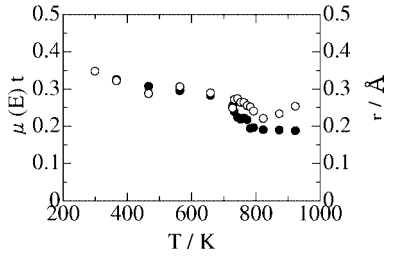

Fig. 8. Temperature variations of the intensity of peak A in XANES (Solid circle) and Ti atom distortion from the center of the oxygen octahedron (open circle).

where $\boldsymbol{e}$ and d are the unit vector in the direction of the electric field of incident X-rays and the distortion of a Ti atom from the center of an oxygen octahedron, respectively. C is a proportionality constant. The behavior in Fig. 8 indicates that the distortion of Ti atoms from O octahedron decreases as temperature increases and it remains finite at $T > T_c$. The values of the Ti atom distortion (d) along the c-axis with temperature evaluated from the present EXAFS by

$$d = (r_{\text{Ti-O(3)}} - r_{\text{Ti-O(1)}})/2 \quad (2)$$

are also presented (open circle) in Fig. 8. When we put the constant C to be 1.0, the curve of d vs T coincides approximately with that of I_A vs T at room temperature. d shows the same behavior as I_A and decreases as temperature increases up to T_c. As discussed previously 0.35 Å of d is the same as the value Sicron *et al*. reported [3, 4]. However they concluded that d is almost constant at the temperature range from low temperature to T_c and decreases slightly with 30% at $T > T_c$. On the other hand, our result shows clear decreasing of d in the ferroelectric phase ($T < T_c$).

4. Conclusion

We measured Ti K-edge EXAFS for $PbTiO_3$ in the temperature range including T_c. The structural changes were discussed from the viewpoint of short-range order. Three kinds of atomic pairs, shorter Ti-O(1), medium Ti-O(2) and longer Ti-O(3) were analyzed independently. The longest Ti-O(3) is discontinuously changed at the transition. The distortion of Ti atoms evaluated from EXAFS indicates that tetragonal distortion remains above T_c. The XANES study supports the temperature dependence the Ti distortion from EXAFS. The proposed solution may not be unique and further measurements, e.g. fluorescence mode for Ti K-edge XAFS, will hopefully confirm the obtained results.

Acknowledgements

The synchrotron radiation experiments were performed at Photon Factory in KEK under Proposal No. 2003G233.

References

1. Koningsberger, D. C. and Prins, R. (1998) "X-ray Absorption: Principles, Application Techniques of EXAFS, SEXAFS and XANES", (John Wiley and Sons Co, New York).
2. Shirane, G., Pepinsky, R. and Frazser, B. C., Acta Cryst. **9**, 131 (1956).
3. Sicron, N., *et al.*, Phys. Rev. B **50**, 13168 (1994).
4. Ravel, B., *et al.*, Ferroelectrics **164**, 265 (1995).
5. Miyanaga, T., Diop, D., Ikeda, S. and Kon, H., Ferroelectrics **274**, 41 (2002).
6. Sakane, H., *et al.*, Jpn. J. Appl. Phys. **32**, 4641 (1993).
7. Ravel, B., Stern, E. A. Vedrinski, R. I. and Kraizman, V., Ferroelectrics, **206–207**, 407 (1998).

Physica Scripta. Vol. T115, 362–364, 2005

XAFS Study of Cu(II), Ni(II) and Co(II) β-Aminovinylketone Complexes

V. G. Vlasenko[1], A. I. Uraev[2] and A. D. Garnovskii[2]

[1]Institute of Physics, Rostov State University, Stachki Ave. 194, 344090 Rostov-on-Don, Russia
[2]Institute of Physical and Organic Chemistry, Rostov State University, Stachki Ave. 194/2, 344090 Rostov-on-Don, Russia

Received June 26, 2003; accepted December 4, 2003

PACS numbers: 61.10.Ht, 82.40.Qt

Abstract

A series of mononuclear complexes with 1-phenyl-3-(2-phenylsulfanyl-phenyl-amino)-pent-2-en-1-one (**Ia**) and 1-phenyl-3-(2-phenylsulfanyl-phenylamino)-but-2-en-1-one (**Ib**) ligands, which mimics the active site of copper, cobalt and nickel proteins, have been synthesized and structurally characterized by EXAFS.

EXAFS analysis has shown that NiL_2 and CoL_2 complexes with $L =$ **Ia** are hexacoordinated by added Ni-S and Co-S bonds in contrast with square-planar NiL_2 (CoL_2) complexes with $L =$ **Ib**. The CuL_2 complexes with both $L =$ **Ia** and $L =$ **Ib** ligands have the CuN_2O_2 planar coordination.

1. Introduction

The diversity in the structures of active site of metalloproteins is reflected in many different functions that they perform. The functional properties of the metallic cores in a metalloproteins depend on the coordination geometry of metal, the number and the nature of coordination ligands. The structure of many metalloproteins has been elucidated from single crystal X-ray diffraction. Despite this fact, detailed understanding both the structural and functional properties of the metallic cores of many proteins is often limited. In recent years the synthesis of small-molecule complexes, structural and functional mimics of native metalloproteins has become an intensive area of research in chemistry. A numerous model compounds of mononuclear copper- and nickel-containing metalloenzymes, such as cytochrom oxidase, azurin, plastocyanin etc. have been synthesized and reported [1–3].

In this paper we report the synthesis and EXAFS study of novel copper, cobalt and nickel complexes as a models for the $MeN_2O_2(S_2)$ active site in metalloproteins.

2. Experiments and Data Analysis

2.1. *Preparation*

The ligands 1-phenyl-3-(2-phenylsulfanyl-phenylamino)-pent-2-en-1-one (**1a**, $R_1 = H$, $R_2 =$ Ph) $C_{21}H_{17}NOS$ and 1-phenyl-3-(2-phenylsulfanyl-phenylamino)-but-2-en-1-one (**1b**, $R_1 = CH_3$, $R_2 =$ Ph) $C_{22}H_{19}NOS$ were prepared according to the technique described in our previous works [4, 5]. The Cu, Ni and Co complexes **II** and **III** were synthesized as follows. The corresponding ligand and metal acetate were dissolved in methanol. The reaction mixture was stirred and boiled for 40 min. The solids formed were filtered and purified in methanol. The resulting product was recrystallized from toluene and dried.

2.2. *XAFS measurements*

The Cu, Co and Ni K-edge XAFS spectra were measured in transmission at the EXAFS-spectrometer of Synchrotron Radiation Siberian center with the storage ring, operating at an energy beam of GeV and a current of 80 mA. A Si (111) double-crystal monochromator determined X-ray energy. The intensities of both incident and transmitted X-ray beams were measured with ionization chambers filled with Ar gas. Samples were prepared as sandwich between two layers of Maylar film. The thickness of the samples was calculated in order to obtain an absorption jump at the edge $\Delta\mu x \cup 1.0$, where μ is "free" atom absorption, x is a thickness of a sample.

XAFS data analysis was carried out using a standard procedure. The EXAFS functions $\chi(k)$ were obtained from the X-ray absorption spectra by subtracting a Victoreen curve background removal, normalization on the height of the edge and reduction of the absorption data $\mu(E)$ to the EXAFS functions $\chi(k)$ where k is the photoelectron wavevector. The threshold energy E_0 was defined as the maximum of the first derivative of the absorption edge.

The Fourier transformations of EXAFS were performed in the k range 2.6–13.0 Å^{-1}. A Bessel window $w(k)$ with smoothness coefficient 2 and k^2 weighting were used. The structural models were built by a least-squares curve-fitting utilizing *ab initio* calculation for amplitude and phase of the scattering factors by means of FEFF7 [6]. The initial parameters for fit were obtained from crystallographic data of **II**(Ni) for Ni and Co complexes [5], and $Cu(OC(NH_2)(NHNH_2))_2Cl_2$ [7] for Cu-complexes. The fitting refined parameters were: E_0, R (the radii of coordination spheres (CS)), σ^2 (the Debay-Waller factor). Coordination numbers N were fixed. The quality of the fit was determined using a least-squares fitting parameter, Q, defined as:

$$Q(\%) = \frac{\sum[k\chi_{\exp}(k) - k\chi_{\text{th}}(k)]^2}{\sum[k\chi_{\exp}(k)]^2}.$$

3. Results and discussion

The Ni-complex **II** with **Ia** ligands differs from the Ni-complex with **Ib** ligands replacement of $R^1 =$ H by CH_3 (Figure 1). However such replacement leads to considerable difference of physic-chemical properties of these compounds. The Ni-complex **II** is brown and paramagnetic, while the Ni-complex **III** is green and diamagnetic. It indicates that the surroundings of Ni atoms in these complexes is essentially different.

The Fourier transforms (FT) of Ni K-edge EXAFS spectra of the Ni complexes are shown at Figure 2. For both complexes the first major peak at the FT corresponds to the Ni first CS from two nitrogen and two oxygen atoms. For the Ni-complex **II** the second prominent peak at $r = 2.05$ Å is attributed to two

[1] e-mail: vlasenko@ip.rsu.ru

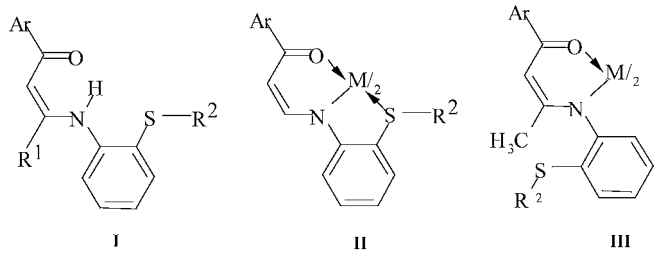

I II III

R^1=H **(Ia)** and CH_3 **(Ib)**; M=Cu, Ni; Co; R^2=Ph and CH_3.

Fig. 1. Structures of the **Ia** and **Ib** ligands, and the **II**, **III** Cu, Co and Ni complexes.

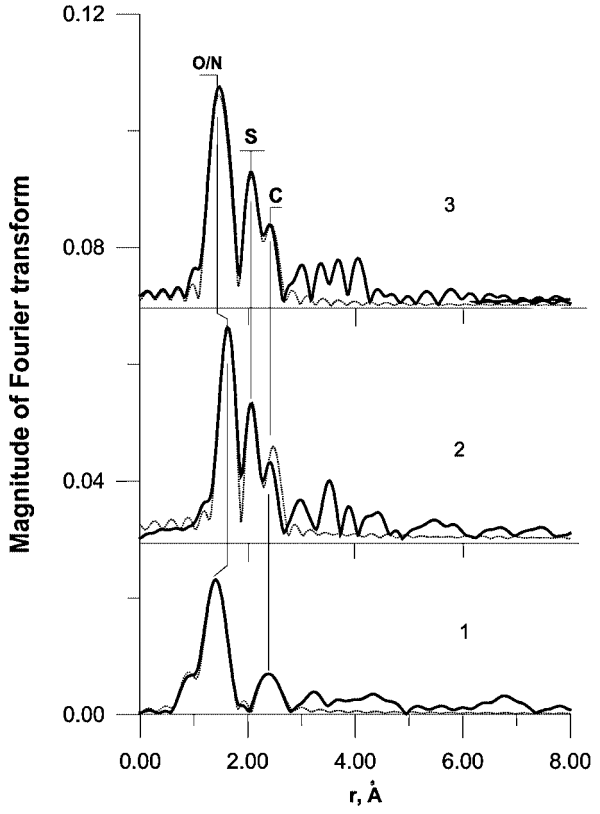

Fig. 2. Experimental (solid line) and calculated (dashed line) Fourier transforms of the Ni and Co K-edge EXAFS for **III** (Ni)-1, **II** (Ni)-2 and **II** (Co)-3 complexes.

coordinated sulfur atoms. The EXAFS function was calculated by FEFF7 using the atomic coordinates, which were taken from single crystal diffraction data for this compound [5]. A fit results are listed in Table I. The bond lengths obtained are in good agreement with the crystallographic data. The average value of the Ni-O/N bond lengths for this Ni complex **III** is lower than that for the complex **II** ($R = 1.88$ Å versus $R = 2.05$ Å). The absence of the sulfur atom coordination and such short Ni-O/N bond lengths point on a square-planar configuration of the **III**(Ni) complex. Figure 2 (Co K-edge) shows that FT of the Co complex is very similar to FT of **II**(Ni). Thus, local surroundings of these metal atoms are similar and Co complex has the square-planar structure **II** as well (results of the EXAFS analysis are shown in Table I).

In opposite to Ni and Co complexes, the FT of Cu-complexes with **Ia** and **Ib** ligands are close to each other (Figure 3). The FT of Cu complexes has a major peak, corresponding to four nitrogen and oxygen atoms of the first CS. The outer shells of the Cu complexes represented by the several small peaks can be simulated by four carbon atoms at 2.89–2.98 Å. The results of the

Table I. *Fit results for Ni, Co and Cu complexes. N is coordination number, R is bond length (the values in the parentheses are derived from diffraction data [5]), and σ^2 is the Debye-Waller factor.*

compound	R^c, Å	N^a	σ^2, Å^2	CS	Q, %
III(Ni)	1.88(1)	4	0.0026(3)	N/O	
R^2 = Ph	2.89(4)	6	0.0056(5)	C	3.6
II(Ni)	2.05(2)	4	0.0020(3)	N/O	
R^2 = Ph	(2.009, 2.024, 2.002, 2.009)	(4)			2.8
	2.47(2)	2	0.0039(4)	S	
	(2.4634, 2.4723)	(2)			
II(Co)	2.01(2)	4	0.0043(7)	N/O	
R^2 = Ph	2.55(3)	2	0.0063(3)	S	2.6
	2.98(5)	6	0.0071(7)	C^b	
II(Cu)	1.86(3)	2	0.0026(3)	O	
R^2 = Ph	2.02(3)	2	0.0026(6)	N	2.9
	2.89(4)	4	0.0088(1)	C^b	
II(Cu)	1.88(1)	2	0.0017(3)	O	
$R^2 = CH_3$	2.00(3)	2	0.0023(4)	N	3.0
	2.93(3)	4	0.0070(6)	C^b	
III(Cu)	1.87(2)	2	0.0029(9)	—	
R^2 = Ph	2.06(2)	2	0.0022(2)	N	3.5
	2.92(4)	4	0.0079(3)	C^b	
III(Cu)	1.89(3)	2	0.0031(1)	—	
$R^2 = CH_3$	2.03(1)	2	0.0041(2)	N	3.9
	2.92(5)	4	0.0088(6)	C^b	

[a]Coordination numbers were fixed. [b]Additional shells of 4-6C atoms were included in the fit. [c]Uncertainties in the distances arise primary from errors in the calculation of phase shifts. The first-shell distances are typically accurate to ±0.02 Å.

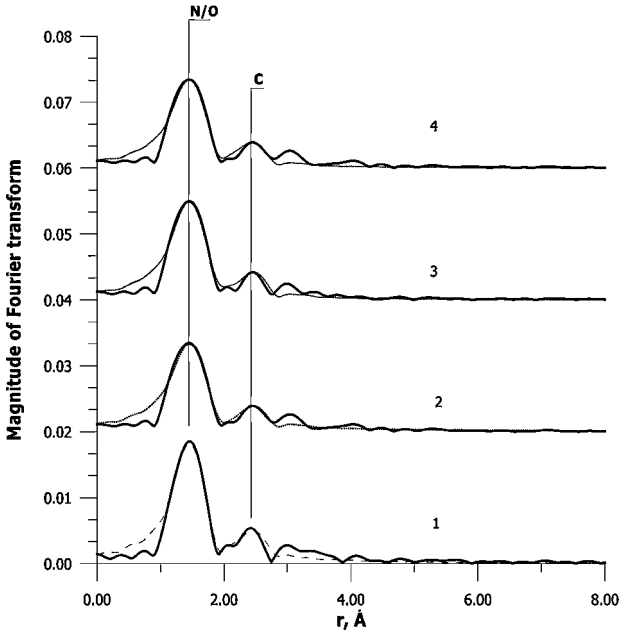

Fig. 3. Experimental (solid line) and calculated (dashed line) Fourier transforms of the Cu K-edge EXAFS for **II** (Cu, R^2 = Ph)-1, **II** (Cu, $R^2 = CH_3$)-2, **III** (Cu, R^2 = Ph)-3 and **III** (Cu, $R^2 = CH_3$)-4 complexes.

EXAFS analysis are shown in Table I. Thus, fit results indicate on a square-planar configuration **III** for the Cu-complexes with both the **Ia** and the **Ib** ligands, that can be related to the Jahn-Teller distortion.

Acknowledgments

This work was supported by RFBR (Grant 04-03-32366) and scientific program "Universities of Russia" (Grant UR.05.01.006).

References

1. Uraev, A. I., *et al*., Polyhedron **19**, 2361 (2000).
2. Fernandez, J. M., *et al*., Trans. Metal. Chem. **25**, 511 (2000).
3. Pereira, E., Gomes, L. and de Castro, B., J. Chem. Soc., Dalton Trans **4**, 629 (1998).
4. Kurbatov, V. P., Osipov, O. A., Kovalenko, K. N. and Tihonova, A. S., J. Inorg. Chem. USSR **13**, 770 (1968).
5. Uraev, A. I., *et al*., Russ. Chem. Bull. **51**, 1924 (2002).
6. Zabinski, S. I., Rehr, J. J., Ankudinov, A. and Albe, R. C., Phys. Rev. B **52**, 2995 (1995).
7. Nardelli, M., Gasparri, G. F., Boldrini, P. and Battistin, I. G., Acta Crystal. **19**, 491 (1965).

Physica Scripta. Vol. T115, 365–368, 2005

Determination of Tm Charge State in PbTe(Tm) by XANES Method

A. I. Lebedev[1], I. A. Sluchinskaya[1*], S. G. Nikitenko[2] and S. G. Dorofeev[3]

[1]Physics Department, Moscow State University, Leninskie gory, 119899 Moscow, Russia
[2]Institute of Catalysis, 630090 Novosibirsk, Russia
[3]Chemistry Department, Moscow State University, Leninskie gory, 119899 Moscow, Russia

Received June 26, 2003; accepted November 4, 2003

PACS numbers: 61.10.Ht, 72.80.Jc, 81.05.Hd

Abstract

The local environment and the charge state of Tm atoms in PbTe were studied by EXAFS and XANES techniques at the L_{III} absorption edge of Tm (8.648 keV). It was revealed that Tm atoms predominantly substitute for Pb atoms in PbTe and are surrounded by Te atoms at a distance of 2.99 ± 0.02 Å. Tm atoms were found to be in Tm^{3+} charge state independently of the section of the phase diagram used for Tm doping. These results are in agreement with the results of previous investigation of the Pb-Tm-Te phase diagram.

Electrical studies of PbTe(Tm) with large deviation from stoichiometry revealed that the electron concentration was about one order of magnitude lower than the total Tm concentration and remained nearly constant (about 10^{19} cm^{-3}) while varying the sample composition. Reduced electrical activity of the Tm impurity in PbTe was explained by effect of selfcompensation.

1. Introduction

Narrow-gap IV-VI semiconductors have attracted considerable attention due to their wide application in infrared (IR) optoelectronics. They are mainly used for production of photodiodes and photoresistors, as well as for lasers, working in middle and far IR regions. At the present time the development of new types of photodetectors is closely connected with utilizing of unusual impurity effects recently discovered in doped IV-VI semiconductors. The study of impurity states created by doping of these semiconductors with some of III-group elements [1], transition [2] and rare-earth metals [3], each of which can have several charge states, revealed unusual physical properties, such as the pinning of the Fermi level and giant IR photoconductivity. The appearance of these effects in PbTe(In) was attributed to the In^{+}-In^{3+} valence switching [4]. It should be noted, that if the doping impurities have magnetic moment, the doped semiconductor may exhibit interesting magnetic properties [2, 3].

It is well known that Tm atom in thulium chalcogenides can also exist in two charge states (Tm^{2+} and Tm^{3+}) or exhibit intermediate valence [5–9]. Thulium ion is divalent in bulk stoichiometric TmTe [9] and trivalent in bulk TmS [6], while in thin surface layer of TmS the Tm ion is divalent [6, 7]. The transition from Tm^{2+} to Tm^{3+} in bulk materials may be related to an increase of splitting of 5d states in a crystal field with the decrease of the lattice parameter, which results in disappearing of energy gap in the case of TmS. In Tm_2Te_3 [9] as well as in Tm_2O_3 [10] Tm atom is in trivalent state. It should be noted that the lattice parameter in TmTe is larger than in Tm_2Te_3, so the transition from Tm^{2+} state in TmTe to Tm^{3+} state in Tm_2Te_3 can be explained in a similar way. The pressure, temperature and component concentration are also the factors, which can affect the charge state of Tm in compounds and solid solutions [11]. The anion radius of Se^{2-} and the lattice parameter in TmSe have intermediate values between the corresponding data for TmS and TmTe and, therefore, the charge state of Tm in TmSe is difficult to predict from simple reasons. Based on experimental data, the authors of [8] came to a conclusion that Tm has a mixed valence in bulk TmSe.

As follows from all the above, thulium impurity in PbTe may have different valence, and so we decided to carry out direct measurements of the Tm charge state in Tm-doped PbTe and to compare the results with those obtained from electrical measurements on these solid solutions.

XAFS spectroscopy is known to be a powerful tool for studies of the charge state and local environment of rare-earth atoms with different valence in compounds and solid solutions. XAFS technique has two main advantages:

1) it can measure directly the ratio of number of ions in different charge states by analyzing the structure of the spectrum near the absorption edge;
2) it enables to obtain the instantaneous radial distribution function of the distances to neighbors of possibly unstable (in valence) ions from the analysis of EXAFS data.

Strong white lines at the absorption edge distinguish the L_{III} X-ray absorption spectra of the rare-earth metals. These lines arise from transitions from atomic $2p_{1/2}$ (L_{II}) and $2p_{3/2}$ (L_{III}) levels into partially filled large density d states. The shape and structure of these lines depend on the electron configuration and charge state of the atom. Therefore the study of these lines can give information on charge states, in particular, charge state of the Tm atom in PbTe. XANES and EXAFS techniques have been already used for investigation of the charge states and local environment of Tm atoms in all thulium monochalcogenides [12, 13] and some their solid solutions [10]. XAFS spectroscopy data confirmed that Tm is divalent in TmTe, Tm is trivalent in TmS, but in TmSe it exhibits an intermediate valence state in the bulk and the divalent state at surface [10, 12]. The value of bulk mean valence in TmSe was shown to be sensitive to the stoichiometry of samples.

To our knowledge, there are only few published XAFS data on the charge state of the Tm impurity in other crystals, besides monochalcogenides. Detailed results on ZnS(Tm) [14] and $CaSO_4$(Tm) [15] are only available. Although lead chalcogenides have received particular attention, the systematic study of the impurity charge states in them by X-ray absorption was not undertaken yet.

*e-mail: Irinasluch@nm.ru

In this paper we present new results on EXAFS, XANES and electrical studies of Tm-doped PbTe.

2. Samples and experimental

All measurements were carried out on polycrystalline samples and single crystals of PbTe(Tm).

XANES measurements on PbTe(Tm) were performed on single crystals grown by Bridgman method along the PbTe-TmTe and PbTe-Tm_2Te_3 sections of the phase diagram and on polycrystalline samples of TmTe, Tm_2Te_3 and Tm_2O_3. The concentrations of thulium in PbTe(Tm) were 0.85 and 3.0 at.%, correspondingly. The samples were synthesized from binary compounds PbTe, TmTe or Tm_2Te_3 in evacuated quartz ampoules. Before XANES measurements the crystals were powdered in argon atmosphere and placed into a special argon-filled camera. Argon atmosphere prevented the oxidation of samples, the manifastation of which was detected in our previous EXAFS study of Tm-doped PbTe samples. All single crystals of PbTe(Tm) had the NaCl crystal structure, while Tm chalcogenides had either the NaCl structure (for TmTe) or the NaCl-based superstructure (defect NaCl structure with Tm vacancies of the Sc_2S_3 type for Tm_2Te_3) at 300 K. Oxide Tm_2O_3 had the Mn_2O_3 structure at 300 K.

EXAFS measurements on PbTe(Tm) were performed on the samples grown by Bridgman method along the PbTe-TmTe sections of the phase diagram. The Tm concentrations in Tm-doped PbTe were 3.0 and 5.0 at.%. It should be noted that no special efforts were undertaken to prevent the sample oxidation in this EXAFS experiment.

Electrical measurements were performed on a series of polycrystalline PbTe(Tm) samples with different deviation from stoichiometry. The samples were prepared by alloying the beforehand synthesized $(PbTe)_{0.985}(Tm_2Te_3)_{0.015}$ compound with extra lead or tellurium in evacuated quartz ampoules. Concentration of Tm in all these samples was 3.0 at.%. The samples were annealed at 800 °C for 60 hours.

EXAFS experiments were carried out on station 7.1 of the synchrotron radiation source of Daresbury Laboratory (UK) with an electron beam energy of 2 GeV and maximum storage ring current 250 mA. The synchrotron radiation was monochromatized by two flat Si (111) crystals. Spectra were measured at the L_{III} absorption edge of Tm (8.648 keV) in fluorescence mode at 300 K. Before EXAFS measurements the samples were powered, the powders were sifted through a sieve and then rubbed onto the surface of adhesive tape. The thick-sample limit for the fluorescence measurements was achieved by folding the tape (8…16 layers). More detailed description of the experiment and EXAFS spectra processing can be found elsewhere [16].

XANES data were collected on EXAFS station at VEPP-3 (Novosibirsk, Russia) with an electron beam energy of 2 GeV and maximum storage ring current 100 mA. Measurements were performed at 300 K at the L_{III} absorption edge of Tm in fluorescence mode in oxygen-free atmosphere. The standards for Tm^{2+} and Tm^{3+} valence states were TmTe, Tm_2Te_3 and Tm_2O_3.

The measurements of conductivity and Hall effect were done by standard technique on rectangular-shaped samples with typical dimensions of $4 \times 1 \times 5\,mm^3$ at room temperature. The current and potential contacts to the samples were soldered by indium.

3. Results and discussion

Figure 1 shows the EXAFS spectrum for $Pb_{0.95}Tm_{0.05}Te$ sample obtained at the Tm L_{III} edge. The analysis of the first shell revealed that Tm atoms substitute for the metal atoms in PbTe and are surrounded by tellurium atoms at a distance of 2.99 ± 0.02 Å. Moreover, in the first shell a contribution from the atoms, located at 2.26 ± 0.02 Å was found. The comparison of the obtained distances with known bond lengths in TmTe [12], Tm_2Te_3 [13] and Tm_2O_3 [17] compounds showed that, apparently, Tm atoms in PbTe are in the trivalent state, that is indicated by negligible difference in distances of Tm-Te in PbTe(Tm) (2.99 Å) and Tm-Te in Tm_2Te_3 (3.02 Å). Concerning the atoms located in the first shell at a distance of 2.26 Å, one can see that this distance is close to mean Tm-O distance in Tm_2O_3 (2.25 Å). Therefore we think that, except Te, the oxygen atoms are also present in first shell of Tm. The appearance of oxygen in our samples may be a result of oxidation of samples during their synthesis, preparation and measurement.

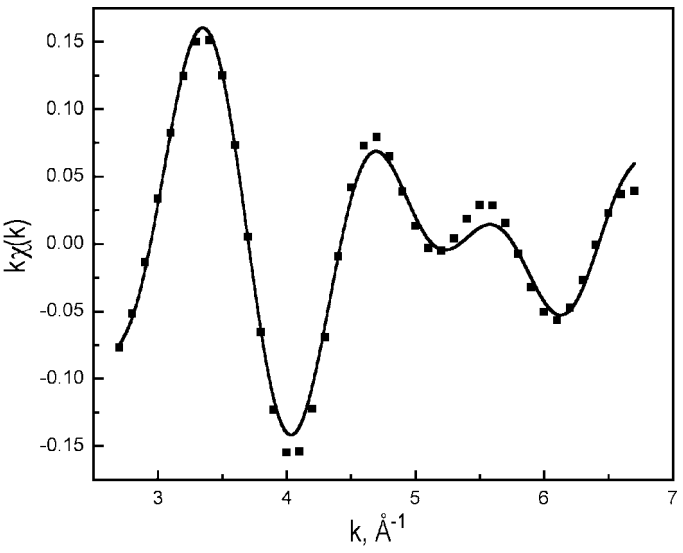

Fig. 1. EXAFS data corresponding to the first shell of $Pb_{0.95}Tm_{0.05}Te$ obtained at the Tm L_{III} edge at 300 K. Points are experimental data and the line is its best theoretical approximation.

In spite of the presence of oxygen in the samples, the conclusion that Tm impurity atoms in PbTe substitute predominantly for Pb atoms is still valid. However, uncontrolled oxidation may prevent the reliable determination of the charge state of Tm in PbTe. That is why we decided to carry out additional XANES measurements in oxygen-free atmosphere with a special care to prevent oxidation during the sample preparation.

Figure 2 presents the XANES spectra for two samples of PbTe(Tm) with different Tm concentration, as well as for TmTe and Tm_2Te_3 compounds. It is seen that the L_{III} absorption edge of Tm is denoted by a strong white line. This line is in fact a general feature of L_{III} edges for all rare-earth atoms in 2+ and 3+ valence states and is mainly due to transitions into empty 5d state. As follows from this figure, the spectra corresponding to the different electron configurations and charge states of Tm, differ considerably. The edge structure of Tm in Tm_2Te_3 (Tm^{3+} charge state) consists of one strong white line. The same structure was observed in Tm_2O_3. The XANES spectra of Tm in TmTe (Tm^{2+} charge state) have characteristic doublet structure, in which the long-wavelength white line has nearly the same shape as that of Tm^{3+} in Tm_2Te_3, but is shifted by nearly 8 eV towards lower energy.

Comparative analysis of spectra obtained for Tm-doped PbTe crystals and standard samples leads to a conclusion that Tm

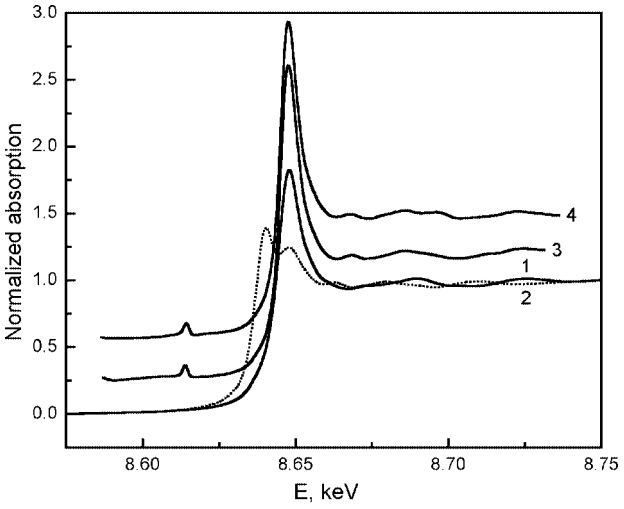

Fig. 2. Normalized XANES spectra obtained at the Tm L_{III} edge for Tm_2Te_3 (1), TmTe (2), PbTe-Tm_2Te_3 solid solution (3) and PbTe-TmTe (4) solid solution at 300 K.

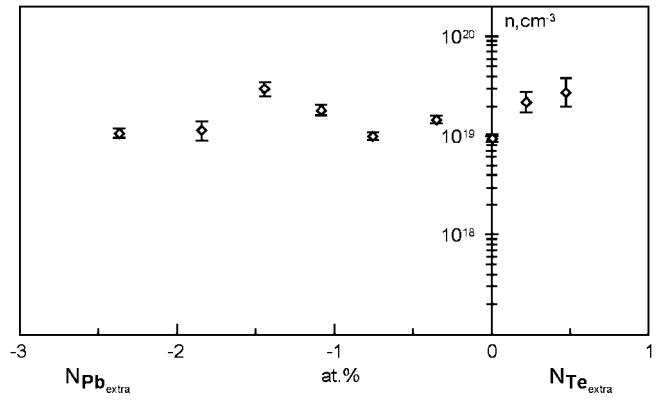

Fig. 3. Dependence of the electron concentration on the deviation from the stoichiometry for $Pb_{0.97}Tm_{0.03}Te$ samples at 300 K.

atoms in PbTe are in the Tm^{3+} charge state independently of the section of the phase diagram used for Tm doping. Indeed, in XANES spectra for PbTe(Tm) we failed to detect even the minor contribution of the second line observed for Tm^{2+} states. This result is in agreement with the data of our EXAFS measurements and the results of the Pb-Tm-Te phase diagram investigation [18], which established that the PbTe-TmTe section of the phase diagram is not quasibinary and at high Tm concentration in samples the Pb precipitations may even arise.

Data obtained from EXAFS and XANES spectra give evidence that Tm atoms in PbTe substitute for Pb atoms and are in the trivalent state and, therefore, must play a role of a single charged donor in these crystals. This conclusion was confirmed by our electrical measurements. Indeed, all investigated PbTe(Tm) samples had n-type conductivity; however, the expected direct relation between Tm and free carrier concentrations in the samples was not found. Measured electron concentration was about one order of magnitude lower than the value expected for single charged donors. To study the origin of this discrepancy, additional experiments on non-stoichiometric samples were performed.

Assuming the single charged donor behavior of the Tm atom, one could expect that addition of extra Pb within the homogeneity region of PbTe(Tm) would result in an increase of free electron concentration, while the addition of extra Te would decrease it. The dependence of the carrier concentration on the deviation from the stoichiometry is shown in figure 3. It is seen that the electron concentration remains nearly constant when varying the sample composition. There are two ways to explain these results.

The first explanation is the pinning of the Fermi level by Tm impurity, by analogy with the action of the In impurity. In the case of indium the In atoms are present simultaneously in both charge states (In^+ and In^{3+}) and the addition of extra Pb or Te changes only their relative concentrations. The pinning of the Fermi level in this case is provided by In^+ ions, which are negative-U centers (centers with negative correlation energy). However, the supposition that Tm has the same properties in PbTe disagrees with our XANES data, which indicates the existence of only one charge state of Tm.

The second explanation of the obtained dependence of the carrier concentration on the composition supposes that the donor action of Tm is compensated by the acceptor behavior of intrinsic defects in PbTe, such as Pb vacancies. It is known that the doping of lead chalcogenides with high concentration of I, Cl, In or Ga donor impurities results in an increase (by more than one order of magnitude) in solubility of extra stoichiometric Te, while doping them with Tl or Na acceptor impurities leads to an increase in solubility of excess Pb [19–21]. The nature of such a selfcompensation effect is that the doping of a sample with electrically active impurities makes it energetically favorable the formation of intrinsic point defects that have an opposite electrical sign. Due to selfcompensation, the change of the carrier concentration is always smaller than the concentration of the doping impurities. In our opinion this explanation seems to be more preferable.

4. Conclusions

In conclusion, the X-ray absorption and electrical studies of Tm-doped PbTe crystals revealed that Tm atoms predominantly substitute for Pb atoms and are in Tm^{3+} charge state independently of the section of the phase diagram used for Tm doping. This conclusion is in agreement with the results of investigation of the Pb-Tm-Te phase diagram. Reduced electrical activity of Tm impurity in PbTe is explained by the effect of selfcompensation.

Acknowledgements

The authors are very grateful to Dr. O. I. Tananaeva for valuable discussions and continuous interest in the present work.

References

1. Kaidanov, V. I. and Ravich, Yu. I., Uspekhi Fiz. Nauk **145**, 51 (1985) (in Russian).
2. Khokhlov, D. *et al*., Int. J. Modern Phys. B **16**, 3343 (2002).
3. Ivanchic, I. I. *et al*., Phys. Rev. B **61**, R14889 (2000).
4. Drabkin, I. A. and Moizhes, B. Ya., Fiz. Tekh. Poluprovodn. **15**, 625 (1981) (in Russian).
5. Bucher, E. *et al*., Phys. Rev. B **11**, 500 (1975).
6. Martensson, N., Reihl, B., Pollak, R. A., Holtzberg, F. and Kaindl, G., Phys. Rev. B **25**, 6522 (1982).
7. Kaindl, G. *et al*., Phys. Rev. B **26**, 1713 (1982).
8. Batlogg, B., Ott, H. R., Kaldis, E., Thoni, W. and Wachter, P., Phys. Rev. B **19**, 247 (1979).
9. Ott, H. R. and Hulliger, F., Z. Phys. B **49**, 323 (1983).
10. Brewer, W. D., Kalkowski, G., Kaindl, G. and Holtzberg, F., Phys. Rev. B **32**, 3676 (1985).

11. Zhuze, V. P. and Smirnov, I. A., in: "Rare-earth semiconductors" (Nauka, Moscow 1977), p. 152 (in Russian).
12. Launois, H., Rawiso, M., Holland-Moritz, E., Pott, R. and Wohlleben, D., Phys. Rev. Lett. **44**, 1271 (1980).
13. Materlic, G., Muller, J. E. and Wilkins, J. W., Phys. Rev. Lett. **50**, 267 (1983).
14. Dexpertghys, J., Charreire, Y., Estebanpuges, P., Albert, L. and Dexpert, H., J. Electrochem. Soc. **135**, 383 (1988).
15. Barkyoumb, J. H., Mansour, A. N., Chakrabarti, K. and Mathur, V. K., Radiation Protection Dosimetry **47**, 59 (1993).
16. Lebedev, A. I., Sluchinskaya, I. A., Demin, V. N. and Munro, I. H., Phys. Rev. B **55**, 14770 (1997).
17. ICSD database (CD ROM version).
18. Dorofeev, C. G., Volodin, B. D., Tyurin, A. V., Zlomanov, V. P. and Tananaeva, O. I., Izv. RAN. Neorgan. Mater. **35**, 934 (1999) (in Russian).
19. Bytenskii, L. I., Kaidanov, V. I., Melnik, R. B., Nemov, S. A. and Ravich, Yu. I., Fiz. Tekh. Poluprovodn. **14**, 74 (1980) (in Russian).
20. Veis, A. N., Kaidanov, V. I., Melnik, R. B. and Ukhanov, Yu. I., Fiz. Tekh. Poluprovodn. **7**, 928 (1973) (in Russian).
21. Bytenskii, L. I. *et al*., Fiz. Tekh. Poluprovodn. **15**, 981 (1981) (in Russian).

Physica Scripta. Vol. T115, 369–371, 2005

Lattice Relaxation around Arsenic and Selenium in CdTe

V. Koteski[1], H. Haas, E. Holub-Krappe, N. Ivanovic[1] and H.-E. Mahnke[*]

Hahn-Meitner-Institut Berlin GmbH, Bereich Strukturforschung, D-14109 Berlin, Germany

Received June 26, 2003; accepted in revised form November 4, 2003

PACS numbers: 61.72.Ji, 61.72.Vv, 61.10.Ht, 71.15.Mb, 71.55.Gs

Abstract

We have investigated the lattice relaxation around impurity atoms at the anion sublattice in CdTe, such as As acting as acceptor and Se which is isovalent to Te, with fluorescence detected EXAFS. We experimentally verify the lattice relaxation with a bond length being reduced by 8% around the As atom as inferred indirectly from *ab-initio* calculations of the electric field gradient in comparison with the measured value in a PAC experiment (S. Lany *et al*., Phys. Rev. B **62**, R2259 (2000)). In the case of the isovalent impurity atom Se, the bond length is similarly reduced as determined experimentally by EXAFS and by model calculations with the density functional theory implemented in the WIEN97 program. In contrast to this inward relaxation, preliminary calculations for Br in CdTe, the next element in the series As, Se, and Br, which acts as donor at the Te sublattice, indicate an increase in bond length, an interesting prediction waiting for experimental verification.

1. Introduction

The incorporation of impurity atoms is often accompanied with lattice distortions and the formation of defect complexes. Local strain fields introduced by the impurities can drastically influence electrical and optical properties. Knowledge about these local effects is mainly derived from measurements, which determine the local structure only indirectly (like e.g. Electron Spin Resonance, Perturbed Angular Correlation (PAC), Zeeman- and Piezoscopic FTIR studies). A rather direct experimental access to lattice distortions is provided by the X-ray absorption spectroscopy (EXAFS). In this contribution we report on measurements of the lattice relaxation around the acceptor dopant As, and the isovalent impurity Se at the Te sublattice in CdTe with EXAFS. The experimental challenge lies in the necessary compromise between a concentration high enough for an EXAFS detection, but low enough to avoid compensation and clustering of the dopants in the semiconductors. In the case of As in CdTe, the aim was to experimentally verify the lattice relaxation around the impurity atom as determined theoretically with the LAPW method used to calculate the electric field gradient in comparison with the measured value in a PAC experiment [1]. In order to understand the driving force for the lattice relaxation we also determined the relaxation around Se, the neighbouring element to As and isovalent to Te, for which no doping effects in CdTe are known. Finally we have extended our calculation to the next neighbouring element, Br, acting as donor when incorporated substitionally at the Te sublattice.

2. Experiment and theory

2.1. *Experimental details*

The incorporation of arsenic as the acceptor dopant in CdTe was done by ion implantation at the tandetron of FZ Rossendorf. A total dose of $7 \times 10^{15}\,\mathrm{cm}^{-2}$ As atoms was almost uniformly distributed up to a depth of 3 µm. The samples, originally from Crystec GmbH[2], were thermally treated before and after the implantation following the approaches [2] in which As was predominantly incorporated as acceptor at the Te site as checked by photoluminescence (PL) measurements. To reduce background in the fluorescence detected EXAFS from undoped sample material, the crystals were thinned from the back to a total thickness of about 30 µm. For the case of Se in CdTe we used mixed $CdTe_{1-x}Se_x$ crystals, provided by M. Fiederle[3], which were powdered, mixed with graphite or polyethylene, and pressed into pellets.

To determine the local structure around As and Se we have measured the K-edge absorption at the X1-beamline of HASYLAB at DESY. In the case of As we measured the absorption in the fluorescence mode with the 5-segment Ge-detector, the fluorescence being detected in line with the polarisation vector of the incoming synchrotron radiation. To reduce the influence from elastic and inelastic scattering of the incoming radiation, critical absorption was employed using a foil made out of Ge powder mixed with polyethylene. In the case of Se, the absorption could be measured in transmission on the powdered samples. The absorption on Cd and Te was measured in transmission, too. For the measurements, the samples were mounted on a He gas flow cryostat, keeping the temperature at approximately 18 or 300 K.

The analysis of the observed absorption spectra was done following the standard FEFF procedure [3, 4] including the background treatment with AUTOBK [5]. In the case of Se in the mixed crystal, a combined multiple data set fitting procedure of the data recorded for Se as well as for Cd and Te data could be applied.

2.2. *Theoretical details*

Complementing our experimental work we have performed *ab-initio* calculations based on the density functional theory (DFT) with the WIEN97 package [6] which uses the linearised augmented plane wave (LAPW) method and with the FHI96md program [7] which uses first-principles pseudo-potentials (PP) and a plane-wave basis set. The latter was used to investigate the size dependence of the super-cells constructed around one substitutional As atom in CdTe. The calculations yielded good agreement with our EXAFS experiment (see Table I) so that the determined relaxations can be used as a solid basis for further interpretations of derived parameters such as hyperfine interaction parameters of defect complexes (for further details see [1, 8]).

[*]Corresponding author: E-mail: mahnke@hmi.de

[1]Permanent address: VINČA Institute of Nuclear Science, POB 522, 11001 Belgrade, Serbia and Montenegro.

[2]Crystec GmbH, D-12555 Berlin.

[3]M. Fiederle, Freiburger Materialforschungszentrum, private communication.

Table I. *Comparison of experimentally determined nearest neighbour and next-nearest neighbour distances around impurity (dopant) atoms in CdTe with calculated values obtained with LAPW (super-cell size 32 atoms) and with PP methods (super-cell size up to 216 atoms). The calculated values are given for the charged configuration in the case of As and Br. Distances for the neutral configuration are closer to the undoped material values by 0.01–0.02 Å in the case of As and approximately 0.04 Å in the case of Br. (All values are given in Å).*

		R_{nn} (theo)			R_{nnn} (theo)	
System	R_{nn} (exp)	LAPW	PP	R_{nnn} (exp)	LAPW	PP
CdTe	2.806*			4.583*		
As in CdTe	2.58(2)	2.57#	2.57	4.50(6)	4.52#	4.55
Se in CdTe	2.67(1)	2.66		4.53(1)	4.55	
Br in CdTe	?	2.90		?	4.57	

*Values derived from the standard lattice parameter.
#Values as presented in ref. [1]

3. Results and discussion

An example of our EXAFS result at low temperature is given in Fig. 1. As checked for two different samples, the main features of the absorption spectra at 20 K and at room temperature remain the same. Since our main concern was that the concentration may be too close to the doping limit, we checked the uniqueness of the As configuration. The mentioned temperature behaviour may be taken as a first, although weak proof for the structural uniqueness of the As configuration. Similarly, the detected PL corresponding to the As acceptor line in CdTe may not be a sufficient proof for the occurrence of the As-on-Te-site configuration as the main or sole As configuration either. As an additional test, we have inspected the XANES region of the absorption spectra and compared it to model spectra assuming As in various configurations (see Fig. 2). The modelling was performed according to [9]. Only the description of As being substitutionally at the Te site matches the experimental spectra. The occurrence of a "white line" in our experiment allows to safely state that the contribution from other As configurations cannot exceed a few percent of the total As concentration. We can therefore adopt the determined bond length as representative for As in CdTe at the substitional Te site.

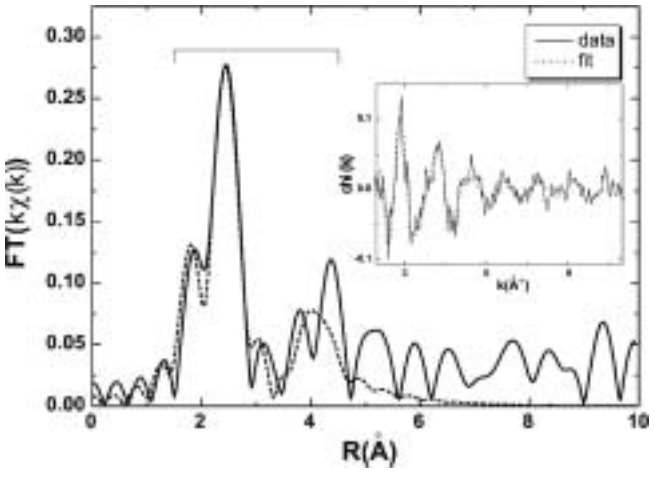

Fig. 1. Radial distribution function of As in CdTe obtained from the EXAFS spectrum, weighted linearly with k and Fourier transformed. The fit region in R-space is indicated by the bar. The insert shows the EXAFS spectrum $\chi(k)$.

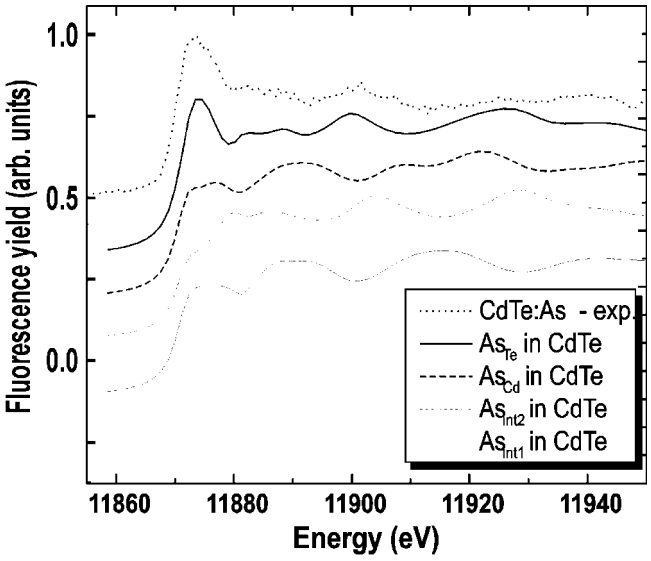

Fig. 2. Comparison of the experimental XAFS signal with XANES spectra calculated for different configurations around As in CdTe: (*i*) As substitutionally on the Te site (As_{Te}), (*ii*) As on the substitutional Cd site (As_{Cd}), and As located interstitially with (*iii*) either Te (As_{int1}) or (*iv*) Cd (As_{int2}) as first-shell neighbours. The theoretical spectra are normalised to the experimental edge step and shifted in y-direction for easier comparison.

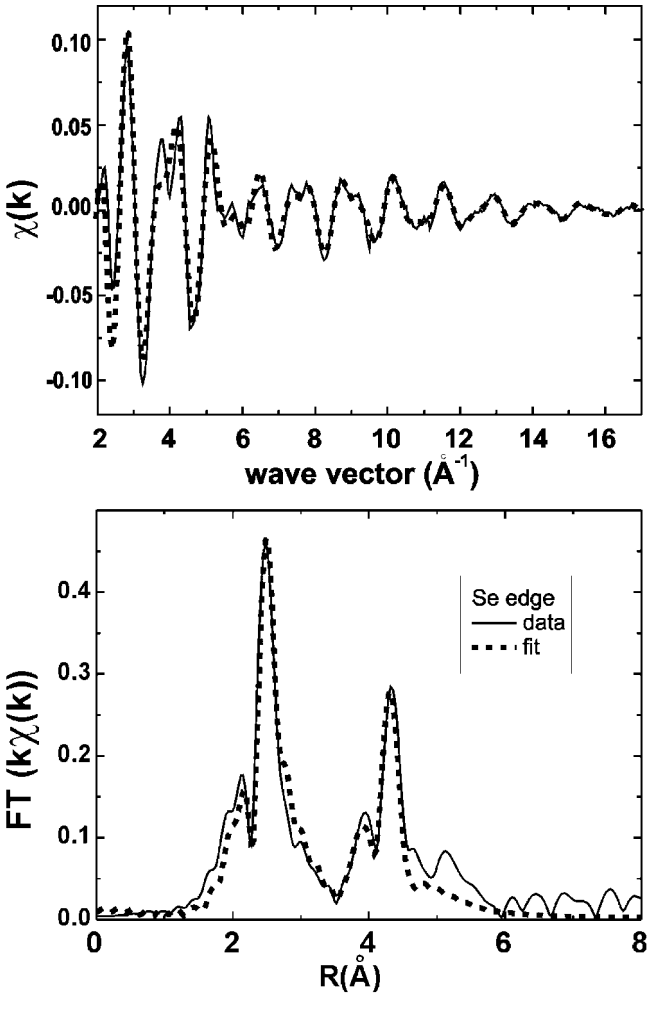

Fig. 3. EXAFS spectrum $\chi(k)$ (top) and radial distribution function (bottom) of Se in $CdTe_{1-x}Se_x$ for $x = 0.04$, obtained from the EXAFS spectrum, weighted linearly with k and Fourier transformed. The fitting range in R-space runs from 1.9 to 5 Å.

In Tab. I we compare our measured bond length with the results obained from the pseudo-potential calculations as well as the LAPW values according to ref. [1]. The agreement is very good. A distinction between the two possible impurity charge states cannot be made, the difference is too small to be noticeable in our data taken our experimental accuracy into account. There is, however, a tendency that the bond length extracted from our XAFS data is shorter by approximately 0.04 Å at room temperature than at 20 K which could be the result of a change of the charge state, or at least of a shift in the occupation of the possible impurity charge states.

Our EXAFS data on Se and the corresponding calculated values can be considered as an additional support to the good agreement obtained for As in CdTe between experiment and model calculation. The experimental results for Se in $CdTe_{1-x}Se_x$ are illustrated in Fig. 3. The extracted values are included in Tab. I. We have chosen a concentration of $x = 0.04$ which comes close to the super-cell size of 32 atoms. The agreement is very good and gives confidence to attack more sophisticated configurational doping problems both by modelling and the experimental verification of proposed model description. In this context we present our result of bond length calculation for the donor Br in CdTe, included in the Tab. I. Contrary to the As and Se case, it shows a sizeable increase in bond length. This prediction is awaiting experimental verification, which would probably help us to understand the formation of Br A-centre in CdTe.

Acknowledgement

The authors are grateful to the HASYLAB staff at DESY, in particular to N. Haack and E. Welter. We thank H. Rossner for his advice on analysis and fitting of the data, for P. Szimkowiak for his help in sample preparation as well as M. Fiederle from the Freiburger Materialforschungszentrum for the $CdTe_{1-x}Se_x$ sample. Help in sample preparation is also acknowledged for the As implantation by M. Friedrich (FZ Rossendorf), and crystal thinning and PL tests by S. Lany, F. Wagner and H. Wolf (University Saarbrücken). We further thank J. Bollmann and J. Weber from the TU Dresden and S. Lany and T. Wichert from the U Saarbrücken for fruitful discussions on the problem of lattice relaxation around dopants in semiconductors. Finally, we gratefully acknowledge the help of G. Schwarz from the FHI Berlin in setting up the input parameters for the FHI96md computer code.

References

1. Lany, S. *et al*., Phys. Rev. **B62**, R2259 (2000).
2. e.g. Lany, S. *et al*., Physica **B302–303**, 114 (2001) and ref. therein.
3. Rehr, J. J., Mustre de Leon, J., Zabinsky, S. I. and Albers, R. C., J. Am. Chem. Soc. **113**, 5135 (1991).
4. Stern, E. A., Newville, M., Ravel, B., Yacoby, Y. and Haskel, D., Physica **B208&209**, 117 (1995).
5. Newville, M., Livins, P., Yacoby, Y., Rehr, J. J. and Stern, E. A., Phys. Rev. **B47**, 14126 (1993).
6. Blaha, P., Schwarz, K. and Luitz, J., WIEN97, A Full Potential Linearised Augmented Plane Wave Package for Calculating Crystal Properties, (Karlheinz Schwarz, TU Wien, Austria, 1999), ISBN 3-9501031-0-4.
7. Bockstedte, M., Kley, A., Neugebauer, J. and Scheffler, M., Comp. Phys. Commun. **107**, 187 (1997).
8. Koteski, V., Ivanovic, N., Haas, H., Holub-Krappe, E. and Mahnke, H.-E., Nucl. Instr. Meth. **B200**, 60 (2003).
9. Ankudinov, A., Ravel, B., Rehr, J. J. and Conradson, S., Phys. Rev. **B58**, 7565 (1998).

Physica Scripta. Vol. T115, 372–374, 2005

XAFS Study of A-site-Deficient $La_{0.63}Ti_{0.92}Nb_{0.08}O_3$ Perovskite

Akira Yoshiasa[1*], Maki Okube[1], Hiroki Okudera[1], Akihiko Nakatsuka[2], Masatomo Yashima[3], Atsushi Sakai[3], Mizuki Mori[3] and Roushown Ali[3]

[1]Department of Earth and Space Science, Graduate School of Science, Osaka University, Toyanaka, Osaka 560-0043, Japan
[2]Department of Advanced Material Science and Engineering, Faculty of Engineering, Yamaguchi University, Ube, Yamaguchi 755-8611, Japan
[3]Department of Material Science and Engineering, Interdisciplinary Graduate School of Science and Engineering, Tokyo Institute of Technology, Nagatsuda, Midori-ku, Yokohama 226-8502, Japan

Received June 26, 2003; accepted in revised form November 3, 2003

PACS number: 61.10.Ht

Abstract

The temperature dependence of EXAFS Debye-Waller factors in $La_{0.63}Ti_{0.92}Nb_{0.08}O_3$ perovskite with cation deficiency was investigated with the cumulant expansion method. The measurements of the Ti and Nb K-edge and La L3-edge EXAFS spectra were carried out in the transmission mode at temperatures up to 800 K. The obtained local bond distances of 1.95(1) Å for Ti-O, 1.98(1) Å for Nb-O and 2.65(1) Å for La-O are significantly smaller than the expected values on Shannon's radii. This characteristic is attributable to the presence of the cation deficiency. The effective pair potentials, $V(u) = \alpha u^2/2 + \beta u^3/3$, were evaluated and the potential coefficients α and β for the Ti-O bond in $La_{0.63}Ti_{0.92}Nb_{0.08}O_3$ are 6.6(1) eV/Å^2 and −42(3) eV/Å^3, respectively. The Ti-O bond in the A-site-deficient $La_{0.63}Ti_{0.92}Nb_{0.08}O_3$ has relatively larger anharmonic and soft potential coefficient than that in ordinary $CaTiO_3$ perovskites.

1. Introduction

$La_{2/3}TiO_3$-based compounds with an *A*-site-deficient perovskite-type ABO_3 structure exhibit high ionic conductivities and dielectric constants. The orthorhombic (Cmmm) – tetragonal (P4/mmm) phase transition occurs reversibly and continuously at 623(2) K in $La_{0.63}Ti_{0.92}Nb_{0.08}O_3$ [1]. Cation vacancies in the compounds are ordered in a lattice site at lower temperature. Yashima *et al*. [2] determined the temperature dependence of the $La_{0.63}Ti_{0.92}Nb_{0.08}O_3$ structure by means of high-resolution synchrotron X-ray powder diffraction. The unit-cell parameters were found to change continuously with increasing temperature even near the phase transition. No hysteresis was observed in the lattice parameters between heating and cooling processes. Because La^{3+} and Nb^{5+} have larger valence than alkali earth elements and Ti^{4+} in ordinary $ATiO_3$ (A = Ca,Sr,Ba) perovskites, respectively, it is interesting to investigate its influence on the local structure, ionic conductivity and phase transition. The ionic conductivities are strongly dependent on the local structure.

Detailed knowledge of local structure and thermal properties for each atom in perovskite-type compounds is of great importance for understanding the mechanisms of favorable physical properties [3]. The analysis of the temperature-dependent EXAFS Debye-Waller factor allows us to evaluate the interatomic force constants for neighboring atoms [4, 5].

2. Experimental and analysis

$La_{0.63}Ti_{0.92}Nb_{0.08}O_3$ perovskite was synthesized by a solid-state reaction reported previously [1, 2]. Starting materials were high-purity powders of La_2O_3, TiO_2 and Nb_2O_3 (>99.9%). The dried powders were weighted and well mixed. The mixture was calcined in air. The process of grinding and calcination was repeated four times. Obtained powders were ground and pressed into pellets under a uniaxial pressure of 150 MPa. The pellets were sintered at 1630 K for 12 hours in air. The sintered material was crushed and ground to obtain a fine powdered sample. The crystal of $La_{0.63}Ti_{0.92}Nb_{0.08}O_3$ perovskite was identified by X-ray diffraction.

The appropriate amount of fine powder sample and boron nitride powder was mixed and pressed into pellets of < 0.2 mm in thickness and 10.0 mm in diameter. Measurements of the Ti and Nb K-edge and La L3-edge EXAFS spectra were carried out in transmission mode at beam line BL-9A and BL-10B of the Photon Factory in KEK, Tsukuba (Proposal No. 2002G276). Because $La_{0.63}Ti_{0.92}Nb_{0.08}O_3$ contains a relatively small amount of Nb atoms, the sample for Nb K-edge had only edge-jumps with 0.2 ($\Delta\mu d$), where μ is the linear absorption coefficient and d is the thickness. X-ray absorption measurements were made in the temperature range from 300 to 800 K. The synchrotron radiation was monochromatized by a Si(111) double crystal monochromator. Mirrors are used to eliminate higher harmonics. Details of the measurement and analysis were given in references [5, 6].

The EXAFS interference function, $\chi(k)$, was extracted from the measured absorption spectra using the standard procedure [7]. The $\chi(k)$ was normalized using MacMaster coefficients according to the EXAFS workshop report [8]. Figure 1(a) shows the Ti K-edge EXAFS oscillation $k^3\chi$ at 333 K. Figure 1(b) shows examples of Fourier transforms of the Ti K-edge EXAFS spectra in the ranges of $2.5 < k < 10.7$. In quantitative analyses we carried out the Fourier-filtering technique and a nonlinear least-squares fitting method by comparing the observed $\chi(k)_{\mathrm{exp}}$ and calculated $\chi(k)_{\mathrm{calc}}$. We used the EXAFS formula in the single scattering theory with the cumulant expansion up to the fourth order term [9]:

$$\chi(k) = \sum_B (N_B/kR_{AB}^2)\,|f_B(k;\pi)|\exp(-2R_{AB}/(k/\pi)) \times \exp(-2\sigma 2k^2 + (2/3)\sigma 4k^4) \times \sin(2kR_{AB} - (2k/R_{AB}) \times(1 + 2R_{AB}/(k/\eta))\sigma 2 - (4/3)\sigma 3k^3 + \psi_{AB}(k))$$

where N_B is the coordination number of scattering atoms B at distance R_{AB} from the absorbing atom A, $|f_B(k;\pi)|$ the backscattering amplitude of photoelectrons and $\psi_{AB}(k)$ the phase shift function. Values of the function $|f_B(k;\pi)|$ and $\psi_{AB}(k)$ were calculated using the FEFF3 program [10]. σn denotes the nth cumulant. The mean free path λ of the photoelectron is assumed to depend on the wave number, $\lambda(k) = k/\eta$, where η is a constant.

*Corresponding author: Akira Yoshiasa: yoshiasa@sci.kumamoto-u.ac.jp

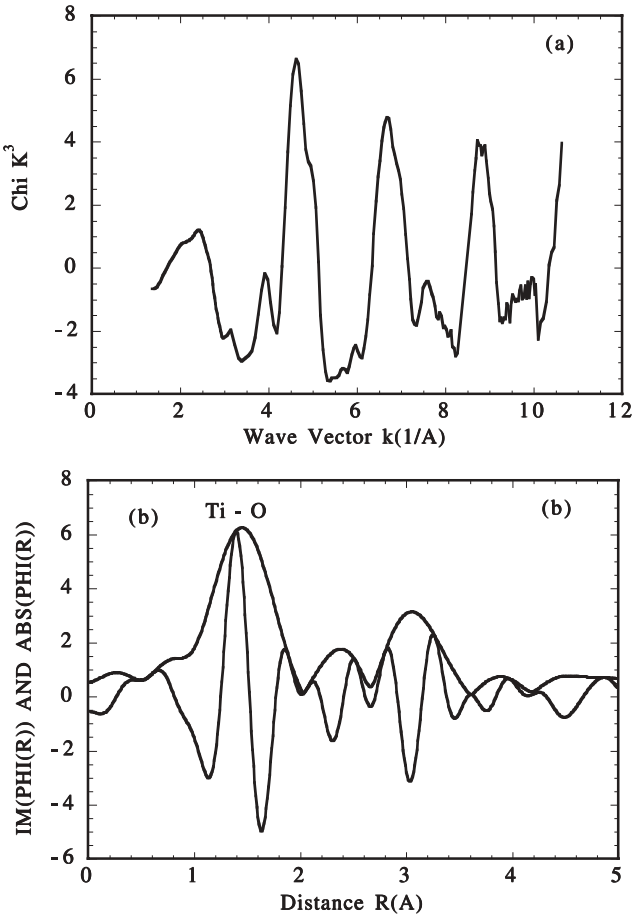

Fig. 1. (a) Observed Ti K-edge EXAFS oscillation $k^3\chi$ of $La_{0.63}Ti_{0.92}Nb_{0.08}O_3$ at 333 K. (b) Fourier transforms of the Ti K-edge EXAFS for $La_{0.63}Ti_{0.92}Nb_{0.08}O_3$ at 333 K. No phase shift corrections are made.

Single-shell fitting was carried out for each nearest-neighbor distance, where the number of neighboring atoms was fixed at the crystallographic value as $N_B = 6$ for the Ti-O and Nb-O distances and $N_B = 12$ for the La-O distances. We assumed that η and ΔE_0 have negligible temperature dependences. Here ΔE_0 is the difference between the theoretical and experimental threshold energies. The values of η and ΔE_0 are determined so as to give the best fit to the spectrum at the lowest temperatures. Because the fourth-order term was negligible, the refinement was performed to the structure parameters $R_{AB}, \sigma 2$ and $\sigma 3$ in each shell by use of the fixed η and ΔE_0 values. The reliability of the fit parameters,

$$R = \sum \left| {k_s}^3 \chi_s(k_s)_{\text{exp}} - {k_s}^3 \chi(k_s)_{\text{calc}} \right| / \left| {k_s}^3 \chi(k_s)_{\text{exp}} \right|,$$

between the experimental and calculated EXAFS functions was less than 0.032.

3. Results and Discussion

Figure 2 shows a portion of the crystal structure of $La_{0.63}Ti_{0.92}Nb_{0.08}O_3$ determined by X-ray diffraction experiment at room temperature [2]. There are two crystallographically nonequivalent La site (La1 and La2 sites) in the orthorhombic phase. The La1 sites are occupied 98% by La^{3+} and vacancies in the La1 sites are 2%. On the other hand, the La2 sites are occupied only 29% by La^{3+} and vacancies in the La2 sites are 71%. The average La1-O and La2-O distances determined by

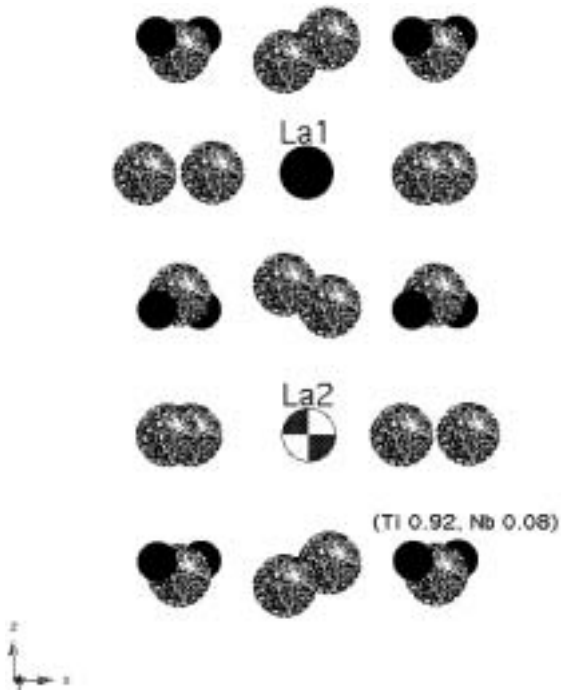

Fig. 2. Portion of the crystal structure (space group Cmmm) of *A*-site deficient $La_{0.63}Ti_{0.92}Nb_{0.08}O_3$ perovskite with double ideal cubic ABO_3 unit along the c-axis at room temperature.

diffraction are 2.691 and 2.802 Å, respectively. The deficient La2 site has significantly larger bond distance. EXAFS spectroscopy is effective for investigating the local environment around the La ions, while the average of the occupied and unoccupied sites is obtained by diffraction experiments. The local bond distance determined by EXAFS method is 2.65(1) Å for La-O bond, which is an average value for all La ions in both La1 and La2 sites. The La-O distance obtained by EXAFS represents the actual nearest-neighbor distance and is shorter than those obtained by diffraction experiments, indicating that the unoccupied sites are larger than the occupied sites.

The Ti and Nb ions in the orthorhombic phase are located at crystallographically equivalent positions. Diffraction method provide the $(Ti_{0.92}Nb_{0.08})$-O distance (1.950 Å), which is an average of Ti-O and Nb-O distances. The local bond distances obtained by EXAFS are 1.95(1) and 1.98(1) Å for Ti-O and Nb-O bonds, respectively.

Based on the ionic radii of Shannon, Ti-O, Nb-O and La-O distances are expected to be 1.985, 2.02 and 2.74 Å, respectively. The obtained local bond distances of 1.95(1) Å for Ti-O, 1.98(1) Å for Nb-O and 2.65(1) Å for La-O are significantly smaller than the expected values on the Shannon radii. The same tendency was observed by diffraction experiment [2], though diffraction method gives the averaged bond distances over occupied and unoccupied *A*-sites and over the Ti-O and Nb-O distances in the B-site. This characteristic is attributable to the cation deficiency. The coordination number of oxygen decreases with increasing cation deficiency, which leads to a decrease in ionic radii of O^{2-}. The O^{2-} ions shift from unoccupied sites toward occupied sites, and lattice sites become dilate around vacancies.

Figure 3 shows XANES spectra of Ti K-edge at 300 and 800 K. It is known that the relative peak intensity of the pre-edge peaks change with the local Ti atom distortion [10, 11]. No change in XANES spectra and in threshold energies of the Ti K-, Nb K- and La L3-edges was observed among the examined temperatures.

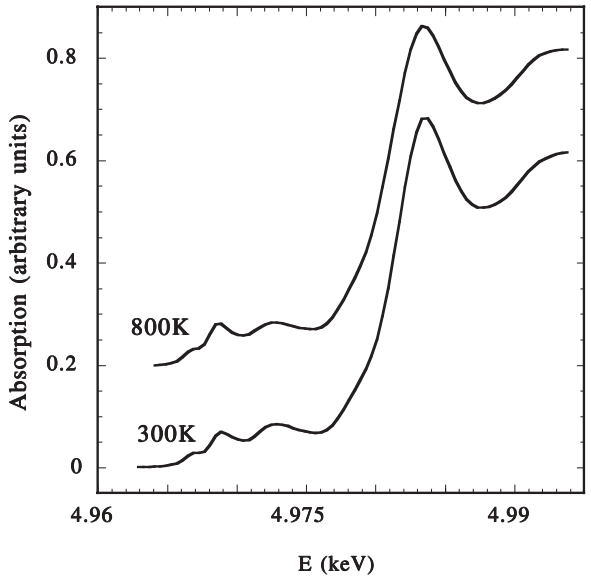

Fig. 3. XANES spectra of Ti K-edge in $La_{0.63}Ti_{0.92}Nb_{0.08}O_3$ at 300 K and 800 K.

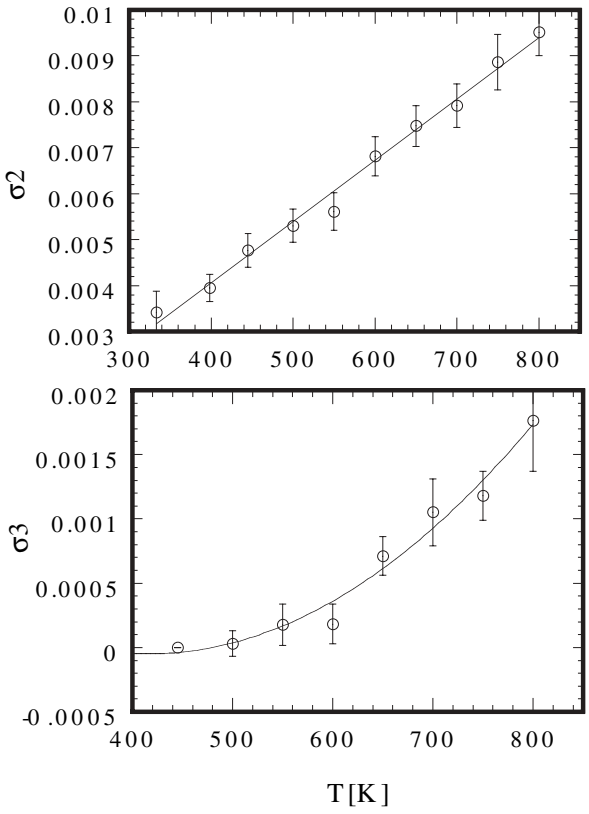

Fig. 4. Temperature (K) dependence of $\sigma 2$ and $\sigma 3$ for the Ti-O bond in $La_{0.63}Ti_{0.92}Nb_{0.08}O_3$ perovskite.

No significant difference in local distortion for each cation site near the phase transition point and at the higher temperatures is recognized.

Figure 4 shows the temperature dependence of $\sigma 2$ and $\sigma 3$ for Ti-O bond in $La_{0.63}Ti_{0.92}Nb_{0.08}O_3$. The Debye-Waller type factor $\sigma 2$ includes the effects of static and dynamic disorders. The static disorder is configuration disorder, while the dynamic disorder arises from thermal vibrations of atoms. The contribution of thermal vibrations, σ_{thermal}, can be estimated under the assumption of classical statistical dynamics by the temperature dependence of $\sigma 2$ [5]. A steep slope in the figure represents a weak bonding. The gradient for the experimental $\sigma 2$ is equal to k_B/σ, if we evaluate the anharmonic effective pair potential $V(u) = \alpha u^2/2 + \beta u^3/3!$ from the contribution to the thermal vibration, where k_B is the Boltzmann constant, α and β are the potential coefficients and u is the deviation of the bond distance from the location of the potential minimum. β is calculated from the values of $\sigma 2$ and $\sigma 3$ [9].

The potential coefficients α and β for the Ti-O bond in $La_{0.63}Ti_{0.92}Nb_{0.08}O_3$ are $6.6(1)\,\text{eV}/\text{Å}^2$ and $-42(3)\,\text{eV}/\text{Å}^3$, respectively, while those for the Ti-O bonds in $CaTiO_3$ [6] are $6.9(1)\,\text{eV}/\text{Å}^2$ and $-38(2)\,\text{eV}/\text{Å}^3$, respectively. The Ti-O bond in the *A*-site-deficient $La_{0.63}Ti_{0.92}Nb_{0.08}O_3$ has relatively larger anharmonic and soft potential coefficient than that in ordinary $CaTiO_3$ perovskites. The potential coefficient α for the Nb-O bond in $La_{0.63}Ti_{0.92}Nb_{0.08}O_3$ is estimated as $27(7)\,\text{eV}/\text{Å}^2$ with large error. The Nb^{5+}-O bond is considerably stronger than the Ti^4-O bond.

References

1. Ali, R. *et al.*, J. Solid State Chem. **164**, 51 (2002).
2. Yashima, M., Ali, R., Tanaka, M. and Mori, T., Chem. Phys. Lett. **363**, 129 (2002).
3. Sicron, N. *et al.*, Phys. Rev. **B50**, 13168 (1994).
4. Yoshiasa, A., Koto, K., Maeda, H. and Ishii, T., Jpn. J. Appl. Phys. **36**, 781 (1997).
5. Yoshiasa, A., Nagai, T., Ohtaka, O., Kamishima, O. and Shimomura, O., J. Synchrotron Rad. **6**, 43 (1999).
6. Yoshiasa, A., Nakajima, K., Murai, K. and Okube, M., J. Synchrotron Rad. **8**, 940 (2001).
7. Maeda, H., J. Phys. Soc. Jpn. **56**, 2777 (1987).
8. Lytle, F. W., Sayers, D. E. and Stern, E. A., Physica B **158**, 701 (1989).
9. Ishii, T., "Principle of the theory of EXAFS", (Shokabo, Tokyo, 1994).
10. Rehr, J. J., Mustre de Leon, J., Zabinski, S. I. and Albers, R. C., Am. Chem. Soc. **113**, 5135 (1991).
11. Ravel, B., Stern, E. A., Vedrinski, R. I. and Kraizman, V., Ferroelectrics **206–207**, 407 (1998).

Physica Scripta. Vol. T115, 375–377, 2005

XAFS Study of the Perovskite-Type Proton Conductor $SrZr_{0.9}Yb_{0.1}O_{3-\delta}$

Maki Okube[1,*], Akira Yoshiasa[1], Masatomo Yashima[2], Kentaro Ohuchi[2], Taijyu Ishimura[2], Chiya Numako[3] and Kichiro Koto[3]

[1]Department of Earth and Space Science, Graduate School of Science, Osaka University, Toyanaka, Osaka 560-0043, Japan
[2]Department of Material Science and Engineering, Interdisciplinary Graduate School of Science and Engineering, Tokyo Institute of Technology, Nagatsuda, Midori-ku, Yokohama, 226-8502, Japan
[3]Faculty of Integ. Arts and Sci., Tokushima University, Tokushima, 770-8502, Japan

Received June 26, 2003; accepted in revised form November 3, 2003

PACS number: 61.10.Ht

Abstract

Temperature dependence of XAFS spectra of the Perovskite-type proton conductor $SrZr_{0.9}Yb_{0.1}O_{3-\delta}$ at Sr and Zr K-edges and Yb L3, L2 and L1-edges have been investigated. Chemical shifts to lower energy and change in XANES spectra are observed with increasing temperature. No change in the XANES spectra and in the threshold energies of the Yb L3-, L2- and L1-edge was observed. This indicates that the effective charges (oxidation states) of the Sr and Zr ions change with oxygen loss while the effective charge of the Yb ions were maintained. The unit cell volumes increase with increasing temperature with a slight bend between 700 and 950 K. This bend of the unit cell volumes vs. temperature is considered to be due to the loss of oxygen, which is consistent with the result of a weight loss in TGA observed in the same temperature range. The mean-square relative displacements (MSRD) of the backscattering atoms with respect to the absorbing atom were also determined by EXAFS. Its temperature dependence increases with a slight bend between 700 and 950 K, which is considered to be due to a local structure change accompanied by the loss of oxygen rather than that by the phase transition at 948 K. It is proposed that the changes of local structure and effective charges of Sr and Zr ions must play an important role in the protonic conductivity.

1. Introduction

Perovskite-type oxides such as Ln^{3+} doped $SrCeO_3$ and $BaCeO_3$, where Ln^{3+} represents trivalent lanthanide elements, have been found to exhibit appreciable proton conduction in hydrogen-containing atmospheres at high temperature [1, 2, 3, 4, 5]. Among these, the chemical stability of $SrZrO_3$-based oxides is much better, and Yb-doped $SrZrO_3$ oxide shows the highest proton conductivity. The proton conductivity depends on the amount of dopant Yb ions and shows a maximum value when substituted for Yb ions by 10 mol%. The oxide ion vacancies and/or electron holes are produced by substitution of tetravalent zirconium ions by trivalent ytterbium ions. In our previous studies [6, 7], the mass loss and gain of oxygen in the Yb-doped $SrZrO_3$ was observed in the heating and cooling processes, respectively. Four polymorphs of SrZrO3 were reported [8]. The temperature dependence of local structure in $SrZr_{0.9}Yb_{0.1}O_{3-\delta}$ is not known yet. Detailed knowledge of the local structure and thermal properties for each atom in $SrZr_{0.9}Yb_{0.1}O_{3-\delta}$ perovskite is of great importance for understanding the mechanisms of protonic conduction.

2. Experimental and analysis

The $SrZr_{0.9}Yb_{0.1}O_{3-\delta}$ perovskite was synthesized by the solid-state reaction reported previously [6, 7]. The sample were sintered at 1975 K for 30 h and kept in air for a week. The crystals were characterized by high temperature X-ray powder diffraction analyses. Space group and detail structure for each phase are determined using synchrotron radiation and Rietveld refinements.

The measurements of Sr K-, Zr K-, Yb L3-, Yb L2- and Yb L1-edges EXAFS spectra were carried out in the transmission mode at beam line BL-10B of the Photon Factory, KEK. X-ray absorption measurements were made in the temperature range from 300 to 1250 K. Details of the measurement and analysis were given in reference [9, 10].

The EXAFS interference function was extracted from the measured absorption spectra and was normalized MacMaster coefficients according to the EXAFS workshop report. The radial structure function was obtained by the Fourier transform over the k range of 3.5–12.5 $Å^{-1}$ for the Sr K- and Zr K-edge and of 3.5–11 $Å^{-1}$ for the Yb L3-edge. In quantitative analyses, we carried out the Fourier-filtering technique and a nonlinear least squares fitting method by comparing the observed and calculated EXAFS interference function. We used the EXAFS formula in

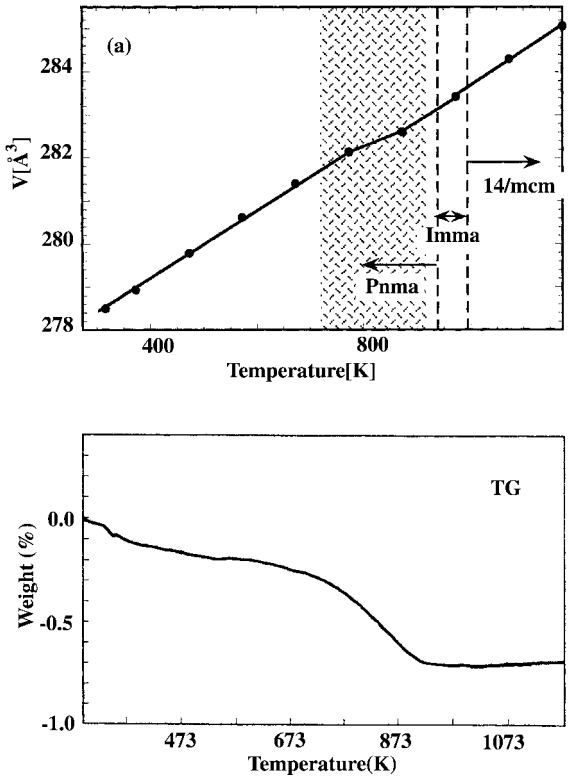

Fig. 1. TGA thermogram from 300 K to 1200 K for the sample of $SrZr_{0.9}Yb_{0.1}O_{3-\delta}$. (a) The unit cell volumes of $SrZr_{0.9}Yb_{0.1}O_{3-\delta}$ vs. temperature. (b) The space group of each phase is also shown.

*Corresponding author: Maki Okube: makisan@ess.sci.osaka-u.ac.jp

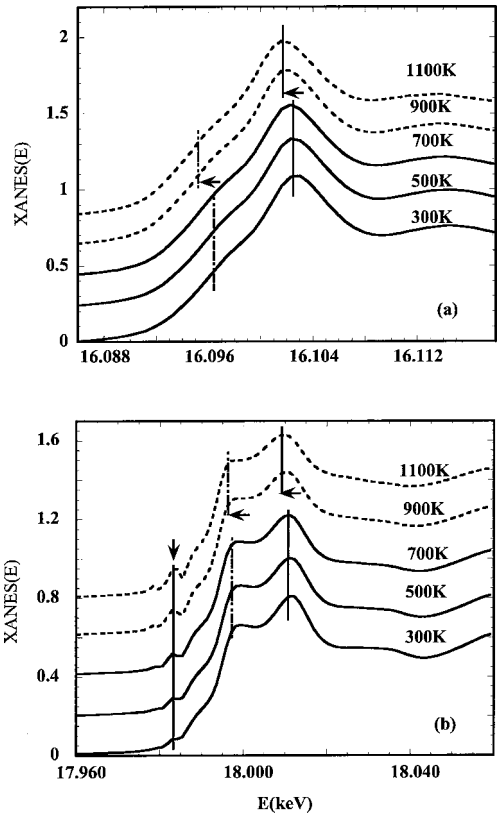

Fig. 2. Temperature (K) dependence of XANES spectra of $SrZr_{0.9}Yb_{0.1}O_{3-\delta}$ at the Zr K- (a) and Sr K-edges (b).

the single scattering theory with the cumulant expansion up to the fourth order term.

3. Results and Discussion

The unit cell volumes increase with increasing temperature with a slight bend between 700 and 950 K (Fig. 1). This bend of the unit cell volumes vs. temperature is considered to be due to loss of oxygen, which is consistent with the result of a weight loss in TGA observed in the same temperature range [7]. The amount of oxide ion vacancies was estimated to be 3.3 atom% [7]. In $SrZr_{0.9}Yb_{0.1}O_{3-\delta}$, the Pnma-Imma-I4/mcm-Pm-3m phase transitions were observed reversibly at 948, 993 and 1223 K, respectively, in our detail structure analyses. The weight loss of oxygen occurs at a lower temperature than phase transition temperatures.

Figure 2 shows the temperature dependence of XANES spectra of $SrZr_{0.9}Yb_{0.1}O_{3-\delta}$ at the Sr K- and Zr K-edges. Chemical shifts to lower energy and changes in XANES spectra are observed with increasing temperature and are considered due to the mass loss of oxygen. Changes of the oxidation states of Sr and Zr ions can be expected above the temperature of a mass loss of oxygen. No change in XANES spectra and in threshold energies of the Yb L3-, L2- and L1-edge was observed (Fig. 3).

This indicates that the effective charges (oxidation states) of Sr and Zr ions change with oxygen loss while the effective charge of Yb ions were maintained. The shifts of threshold energies for Sr K- and Zr K-edges are 1.4 and 1.2 eV, respectively. The data suggests that the total electric charges for Sr and Zr ions are less than 2 and 4, respectively. It is considered that the changes of local structure and effective charge of Sr and Zr ions must play an important role in the protonic conductivity.

At room temperature, the Zr-O distance of 2.094 (3) Å in $SrZr_{0.9}Yb_{0.1}O_{3-\delta}$ by EXAFS is in good agreement with that of 2.091(1) Å in $SrZrO_3$ by diffraction. The obtained Sr-O distance of 2.735(5) Å in $SrZr_{0.9}Yb_{0.1}O_{3-\delta}$ is larger than that of 2.698(4) Å in $SrZrO_3$. The sum of the effective ionic radii [11] between 4-coordinated oxide ions and 6-coordinated Yb ions is 2.248 for Yb-O distance. The Yb-O distance of 2.168(3) Å in $SrZr_{0.9}Yb_{0.1}O_{3-\delta}$ obtained by EXAFS is 0.08 Å smaller than expected value from ionic radii. This suggests that Yb ion is less than 6-coordination of oxygen and the oxide ion vacancies are localized around Yb ions at lower temperature. No significant difference in local bond distance for each cation at the higher temperatures is seen within the experimental error.

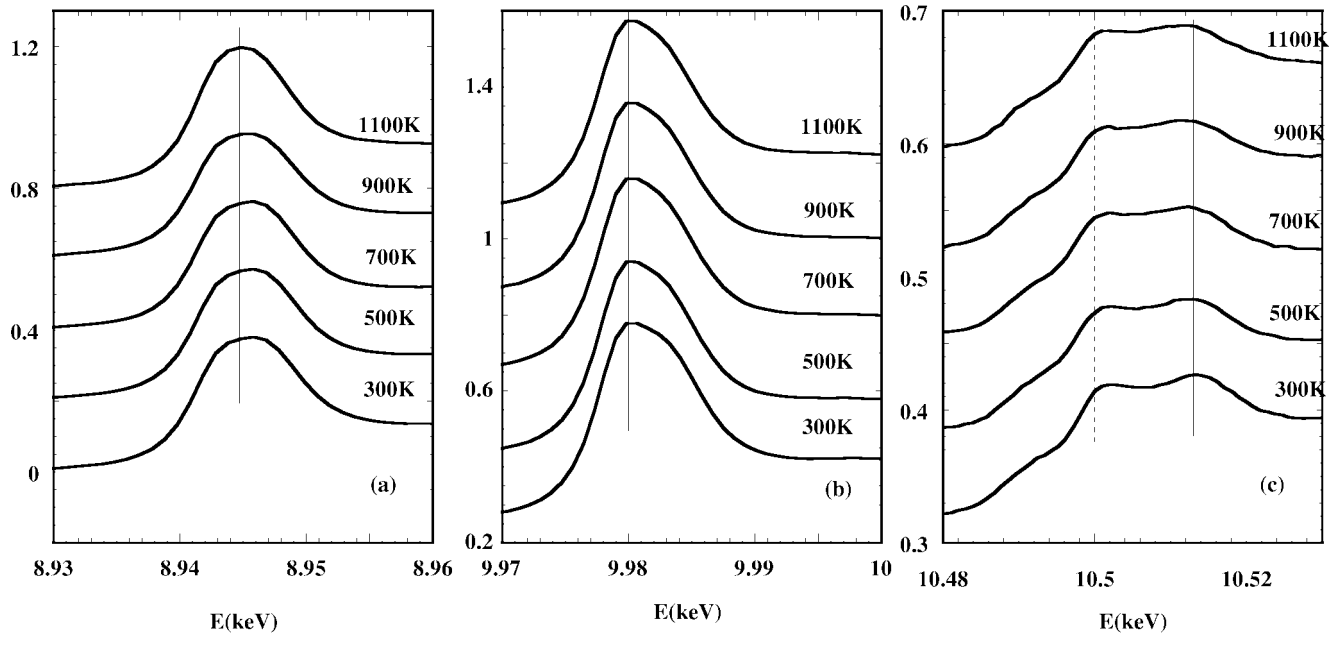

Fig. 3. Temperature (K) dependence of XAFS spectra of $SrZr_{0.9}Yb_{0.1}O_{3-\delta}$ at the Yb L3, L2 and L1 edges.

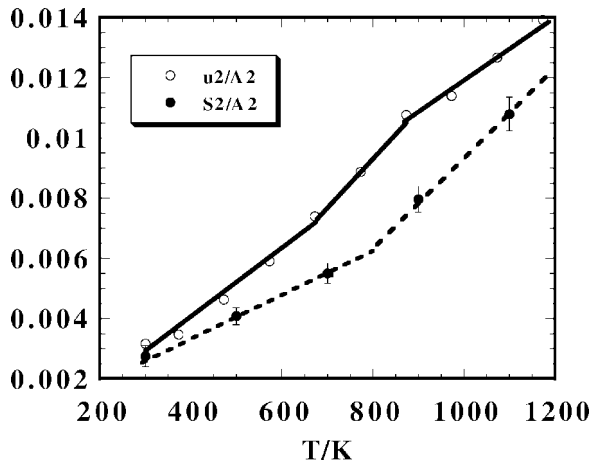

Fig. 4. Temperature (K) dependence of the Debye-Waller factor of EXAFS analysis (σ_2) for the Zr-O bond and that of diffraction analysis (u^2) for Zr(+Yb) atom in $SrZr_{0.9}Yb_{0.1}O_{3-\delta}$.

The Debye-Waller factor determined by EXAFS spectroscopy (σ_2) is sensitive to short-range correlations of the atomic motion. The mean-square relative displacement (MSRD) of the backscattering atoms with respect to the absorbing atom can be determined by EXAFS. The mean-square displacement (MSD: u^2) of each atom at crystallographically equivalent positions is determined by diffraction methods. The MSRD contains the contribution from the MSD of both absorbing and backscattering atoms and the displacement correlation function (DCF) [12, 13]: $\mathrm{MSRD_{AB}} = \mathrm{MSD_A} + \mathrm{MSD_B} - 2\mathrm{DCF}$.

Figure 4 shows the temperature dependence of σ_2 for the Zr-O bond and u^2 for the Zr (+10%Yb) atoms in $SrZr_{0.9}Yb_{0.1}O_{3-\delta}$. The amplitudes of both Debye-Waller factors are nearly the same. The amplitude of u^2 for Zr atom increases with increasing temperature with a slight bend between 700 and 950 K. This bend may be correlated to the loss of oxygen and to the change of effective charge of the Zr ion. The bend of the amplitude of σ_2 versus temperature is also observed at temperatures higher than 700 K, which is considered to be due to a local structure change accompanied by the loss of oxygen rather than the phase transition at 948 K. A detailed study on thermal properties for each atom in $SrZr_{1-x}Yb_xO_{3-\delta}$ ($x = 0.0$, 0.05 and 0.1) perovskite is now in progress. The gradient for the experimental σ_2 is equal to k_B/α, if we evaluate the harmonic effective pair potential $V(u) = \sigma u^2/2$ from the contribution to the thermal vibration, where k_B is the Boltzmann constant, α is the potential coefficient and u is the deviation of the bond distance from the location of the potential minimum [14]. The potential coefficient α for the Zr-O bonds in $SrZr_{0.9}Yb_{0.1}O_{3-\delta}$ at lower temperature is 9.1 eV/Å^2, which is larger than the potential coefficients for the Ti-O bonds (7.0 eV/Å^2) in $SrTiO_3$ and $CaTiO_3$ [15]. This is consistent with properties such as the melting temperature.

4. Conclusion

The effective charges (oxidation states) of both Sr and Zr ions change with oxygen loss while the effective charge of the Yb ions were maintained.

The oxide ion vacancies produced by trivalent Yb substituted for tetravalent Zr are localized near Yb ions. The oxygen vacancies derived by oxygen loss at the high temperature are considered to be localized Sr ions and Zr ions. The changes of local structure and effective charge of Sr and Zr ions play an important role in the protonic conductivity.

References

1. Iwahara, H., *et al*., Solid State Ionics **3/4**, 359 (1981).
2. Iwahara, H., *et al*., J. Electrochem. Soc. **135**, 529 (1988).
3. Bonanos, N., *et al*., Solid State Ionics **44**, 305 (1991).
4. Yajima, T., *et al*., Solid State Ionics **47**, 271 (1991).
5. Yajima, T., *et al*., Solid State Ionics **51**, 101 (1992).
6. Osaka, T., *et al*., Mater. Res. Bulletin **34**, 11 (1999).
7. Koto, K., Solid State Ionics **154–155**, 741 (2002).
8. Carlsson, L., Acta Crystallogr. **23**, 901 (1967).
9. Yoshiasa, A., *et al*., J. Synchrotron Rad. **6**, 43 (1999).
10. Yoshiasa, A., *et al*., Jpn. J. Appl. Phys. **36**, 781 (1997).
11. Shannon, R. D., Acta Crystallogr. **A32**, 751 (1976).
12. Beni, G. and Platzman, P. M., Phys. Rev. **B14**, 1514 (1976).
13. Ishii, T., J. Phys.: Condens. Matter **4**, 8029 (1991).
14. Yoshiasa, A., *et al*., J. Synchrotron Rad. **6**, 1051 (1999).
15. Yoshiasa, A., *et al*., J. Synchrotron Rad. **8**, 940 (2001).

Physica Scripta. Vol. T115, 378–380, 2005

XANES Study of Lanthanum-Doped Lead Titanate Ceramics

P. P. Neves[1], V. R. Mastelaro[1,*], A. Michalowicz[2], J. A. Eiras[3], Luiz P. Lopes[1], A. C. Doriguetto[1] and Y. P. Mascarenhas[1]

[1]Instituto de Física de São Carlos, USP - São Carlos – SP, Brazil
[2]GPMD, Université Paris XII-Val de Marne, 94010 Creteil cedex - France
[3]Departamento de Física, UFSCar, SP, Brazil

Received June 26, 2003; accepted in revised from November 4, 2003

PACS numbers: 61.10.Ht, 61.66.Fn, 64.70.Kb

Abstract

X-ray absorption spectroscopy was used to probe the short-range structure in lanthanum-doped lead titanate ceramics ($Pb_{1-x}La_xTiO_3$) for x ranging from 0.0 to 0.30. A comparison of the XANES spectra and the X-ray diffraction (XRD) results indicates that the local structure around Ti atoms had a different compositional dependence. According to the XANES data, even for the sample containing 30% of lanthanum, for which the XRD analysis indicated the existence of a cubic structure, a local distortion around Ti atoms persisted. The intensity of the pre-edge feature of the PLT30 sample decreased by a factor of only two when compared with the lanthanum-free sample.

1. Introduction

$Pb_{1-x}La_xTiO_3$ (PLT) ceramic materials have been studied extensively due to their interesting physical properties [1]. The isomorphic replacement of lead atoms by lanthanum atoms induces some interesting changes in the physical properties. Upon increasing the lanthanum content ($x > 0.25$), a diffuse character of the ferroelectric-paraelectric phase transition (DPT) is observed. This variation in the phase transition character is followed by a linear decrease of the Curie temperature (T_c) to room temperature [1, 3]. It has been suggested that the lanthanum-induced modification of $PbTiO_3$ causes structural changes that can be directly related to the nature of the phase transition [4]. Although the physical properties of the PLT system have been studied in some detail [1–7], the literature contains few reports concerning the structural characteristics of the PLT system.

The $PbTiO_3$ crystal structure has been exhaustively studied [8–10]. Its room temperature structure is tetragonal P4mm ($a = 3.902(3)$ and $c = 4.156(3)$ Å) [11]. The notation on perovskite structures labels the Pb and Ti sites *A* and *B*, respectively and according to the literature, the La^{3+} ion replaces the Pb^{2+} ion rather than the Ti^{4+} ion in Pb-based perovskites [12]. To maintain the neutrality of the charge when lead atoms are replaced by lanthanum atoms, *A* site vacancies are created [12].

Using the Raman scattering technique, E.C.S. Tavares *et al.* [13] probed the short-range structure in lanthanum-doped lead titanate ceramics for x ranging from 0.0 to 0.30. According to their report, X-ray diffraction measurements of highly doped samples ($x>0.27$) indicated a cubic structure. On the other hand, in highly doped samples ($x>0.27$), measurements of Raman scattering at temperatures above and below the tetragonal phase transition showed a residual short-range structural disorder in the cubic phase. These authors suggested that the existence of this short-range structural disorder may be correlated to the relaxor behavior in highly doped samples.

Despite this system's scientific and technological importance, there is still a paucity of conclusive investigations regarding its crystalline structure. In this paper, we discuss a short-range structural study of $Pb_{1-x}La_xTiO_3$ ceramic samples as a function of the lanthanum content. X-ray Absorption Spectroscopy (XAS) was used to probe the local structure around Ti atoms.

2. Sample Preparation and Experimental Details

Polycrystalline $Pb_{1-x}La_xTiO_3$ (PLTx) samples with $0.0 \leq x \leq 0.30$ were prepared by the conventional mixed oxides method. PbO, TiO_2 and La_2O_3 were mixed with distilled water in an alumina ball mill. Monophasic PLT powders were obtained after calcination in air for 3 h at 1123 K. The calcined powders, pressed into pellets, were sintered in a covered alumina crucible at 1473 K for 3 h. Further details of sample preparation are reported elsewhere [2].

The titanium K-edge X-Ray absorption spectra were collected at the LNLS (National Laboratory of Synchrotron Light) in Campinas, Brazil, a facility that uses the D04B-XAS1 beam line [14]. The LNLS storage ring was operated at 1.36 GeV and 100–160 mA. The pelletized samples obtained after sintering were ground for XAS measurements. XAS data were collected at the Ti K-edge (4966 eV) in transmission mode and at room temperature, using a Si(111) channel-cut monochromator. Ionization chambers were used to detect the incident and transmitted flux. XANES (X-ray absorption near edge structures) at the Ti K-edge were recorded for each sample between 4910 and 5200 eV, using energy steps of 0.5 eV. A qualitative interpretation of XANES spectra obtained at the Ti K-edge was performed using the software package developed by Michalowicz and Noinville [15]. For purposes of comparison among different samples, all the spectra were background removed and normalized, using as unity the first EXAFS oscillation.

3. Results and Discussion

Figure 1 shows the XANES spectra obtained at the Ti K-edge of PLT samples. The pre-edge region of the K-edge XANES spectra of some transition metal oxides are characterized by a pronounced feature several volts before the main rising edge [16–18]. In transition metal oxides that crystallize in centrosymmetric structures, this pre-edge feature is very small or absent; in noncentrosymmetric structures it can be quite large [16–18]. According to the literature, the physical origin of the peak labeled A in Figure 1 is the transition of the metallic 1s electron to an unfilled d state [16]. This forbidden electronic dipole transition is normally allowed by the mixture of p character from surrounding oxygen atoms in the unfilled d states. On the other

*e-mail: valmor@if.sc.usp.Br

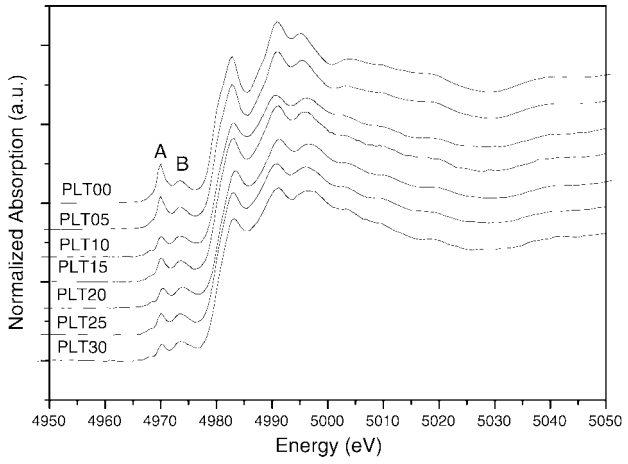

Fig. 1. Ti K-edge XANES spectra of PLTx powder samples with $0.0 \leq x \leq 0.30$.

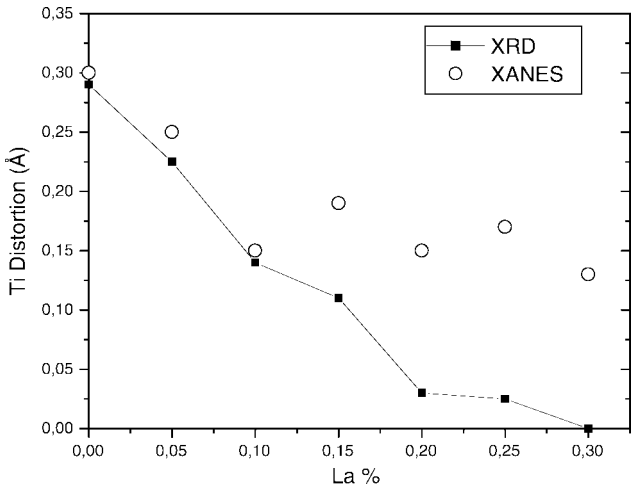

Fig. 2. Variation of the intensity of A pre-edge peak in XANES spectra and Ti atom distortion along the c-axis obtained from XRD data.

hand, the peak labeled B in Figure 1 was found to be caused by Ti 1s electron transition to the unoccupied 3d-originated e_g-type molecular orbitals of TiO_6 polyhedra neighboring the absorbing Ti atoms, which are weakly affected by the core hole potential [18]. The peak B area does not depend strongly on small displacements of the atoms from their sites in a cubic crystal lattice, but it changes significantly when 4d atoms appear in the vicinity of the absorbing Ti atom, for instance, Zr atoms in the PZT solid solution [18].

As can be seen in Figure 1, the intensity of the A feature in the PLT05 sample is similar to that of the undoped sample. A 10% increase in the amount of lanthanum causes a significant drop in the intensity of the A feature. A further increase of lanthanum to a concentration of up to 30% shows a slight variation in the intensity of the A feature, indicating a slight dependence of the A feature's intensity on the concentration of lanthanum. The intensity of the A feature was compared with that of the undistorted $EuTiO_3$ cubic compound. In $EuTiO_3$, which is centrosymmetric, the intensity of the pre-edge A feature is very small [16]. This comparison PLT suggests that the local distortion around Ti atoms persisted as the amount of lanthanum increased, even in the PLT30 sample. Thus, the XANES results of all the samples containing lanthanum shows that Ti atoms were located in distorted sites.

With regard to the analysis of the B pre-edge feature, since we found no significant variation in its shape and amplitude when the content of lanthanum was increased, it is reasonable to assume that La atoms preferably replaced Pb atoms rather than Ti atoms. This assumption is in good agreement with our XRD results.

The magnitude of Ti atom distortion from the center of the oxygen octahedron can be evaluated by measuring the intensity of the A feature [16, 19]. The intensity of the A feature was extracted from the XANES spectra by least-square fitting in the interval from 4965 to 4980 eV. A single Gaussian function was used to model the A pre-edge feature. The results have an uncertainty of 0.1 eV in energy and 0.02 in intensity. Figure 2 compares the magnitude of Ti atoms distortion by measuring the intensity of the A feature present in the XANES spectra with the Ti atom distortion obtained from XRD data. The values of Ti atom distortion obtained from XRD data were obtained by making a difference between Ti-O distances situated along the c-axis divided by 2.

As illustrated in Figure 2, the amplitude of the distortion of Ti atoms decreased as the content of lanthanum increased and was in good agreement with Ti atom distortion obtained from XRD data for compositions containing up to 10% of La. For the PLT00 sample, the amplitude of Ti distortion was found to be equal to 0.29 Å, a very close value to that found by other authors [16, 19]. For the samples containing more than 10% of La, the amplitude of Ti atom distortion obtained by measuring the intensity of the pre-edge A feature indicate that a local distortion around Ti persisted, whereas the analysis of XRD data suggested that Ti atoms returned to the center of the TiO_6 octahedron, presenting a point $m\bar{3}m$ symmetry in the sample containing 30% of La. A certain structural discrepancy exists between XAS and XRD results concerning the PLT30 sample.

The same kind of discrepancy between XAS and XRD results involving local and long-range structural data was observed by Sicron *et al*. in their study of the nature of the ferroelectric phase transition in the $PbTiO_3$ compound [20]. Whereas the XAS results showed that the local distortion around lead and titanium atoms were nonzero above the transition temperature, the XRD data suggested that Ti and Pb atoms returned to the center of the atom site [20].

According to the literature, as long as some long-range order is present, the diffraction pattern is composed essentially of δ functions, even if structural disorder is present [16]. In this case, there is also a weak broad background, which is usually ignored. The disorder does, however, affect the relative integrated intensities of the various δ functions. Thus, in principle, the diffractogram do contain information on the disordered structural distortions. To obtain this information, it is necessary to introduce the disordered distortions to the fitting model and to have a sufficient range of k space to solve the disordered distortions. Since most X-ray diffraction powder models do not take disordered distortions into account, these experiments provided information only on the average structure.

4. Conclusions

The qualitative analysis of the XANES spectra indicated that the local structure around Ti atoms had a different compositional dependence than that indicated by the results obtained from the X-ray diffraction analysis. According to the XANES data, for the sample containing 30% of lanthanum, for which the XRD analysis clearly indicated the existence of a cubic structure, a local distortion around Ti atoms persisted. The intensity of the A feature of this sample decreased by a factor of only two when compared to the lanthanum-free sample. Our results are in good

agreement with the results obtained by Raman Spectroscopy, in which the existence of a local disorder in highly doped lanthanum samples was observed.

Acknowledgments

Research partially performed at LNLS – National Laboratory of Synchrotron Light, Brazil. We are also grateful to FAPESP, CNPq (Brazil) and USP-COFECUB for their financial support.

References

1. Keizer, K., Lansink, G. J. and Burggraaf, A. J., J. Phys. Chem. Solids **39**, 59 (1978).
2. Garcia, D. and Eiras, J. A., Ferroelectrics **123**, 51 (1991).
3. Bhaskar, S., Majumder, S. B. and Katiyar, R. S., Appl. Phys. Lett. **80**, 3997 (2000).
4. Dai, X., Xu, Z. and Viehland, D., J. Appl. Phys. **51**, 4356 (1996).
5. Hennings, D., Mat. Res. Bull. **6**, 329 (1971).
6. Keizer, K., Bouwama, J. and Burgraaf, A. J., Phys. Status Solid A **35**, 281 (1976).
7. Kuwabara, M., Goda, K. and Oshima, K., Phys. Rev. B **42**, 10012 (1990).
8. Shirane, G., Pepinsky, R. and Frazer, B. C., Phys. Rev. **97**, 1179 (1995).
9. Shirane, G., Pepinsky, R. and Frazer, B. C., Acta Crystallographica **9**, 131 (1956).
10. Glazer, A. M. and Mabud, S. A., Acta Crystallographica B **34**, 1065 (1970).
11. Nelmes, R. J. and Kuhs, W. F., Solid State Commun. **54**, 721 (1985).
12. Shannon, R. D., Acta Crystallogr., Section A: Cryst. Phys., Diffr., Theor. Gen. Crystallogr. **32**, 751 (1976).
13. Tavares, E. C. S., Pizani, P. S. and Eiras, J. A., Appl. Phys. Lett. **72**, 897 (1998).
14. Tolentino, H. C. N., *et al*., J. Synchrotron Rad. **8**, 1040 (2001).
15. Michalowicz, A. and Noinville, V., In Gallad 2.0 code, LURE, Orsay, France (1992).
16. Ravel, B. and Stern, E. A., Physica B **208–209**, 316 (1995).
17. Ravel, B., Stern, E. A., Vedrinskii, R. I. and Kraizman, V., Ferroelectrics **206–207**, 407 (1998).
18. Veddrinskii, R. V., Kraizman, V. L., Novakovich, A. A., Demekhin, Ph. V. and Urazhdin, S. V., J. Phys.: Condensed Matter **10**, 9561 (1998).
19. Miyanaga, T., Diop, D., Ikeda, S. I. and Kon, H., Indian Geotechnical Conference (2002), in press.
20. Sicron, N., *et al*., Phys. Rev. B **50**, 13168 (1994).

Physica Scripta. Vol. T115, 381–383, 2005

Pressure Induced Phase Transitions in Amorphous Ge

E. Principi[1], F. Decremps[2], A. Di Cicco[1], F. Datchi[2], S. De Panfilis[3], A. Filipponi[4] and A. Polian[2]

[1]INFM, Università di Camerino, dip. di Fisica, via Madonna delle Carceri 62032, Camerino (MC), Italy
[2]PMC, Université Pierre et Marie Curie, 4 place Jussieu 75252 Paris, France
[3]ESRF Experimental Division – BM29, B.P. 220 38043 Grenoble Cedex, France
[4]INFM, Università dell' Aquila, dip. di Fisica, via Vetoio 67010 Coppito, L'Aquila, Italy

Received June 26, 2003; accepted February 6, 2004

PACS numbers: 60.10.Ht, 61.43.Dq, 64.70.Kb

Abstract

Amorphous germanium (a-Ge) structure is known to show a complex behavior upon pressurization. Here an XAS experiment on a-Ge at high pressure and temperature is presented, which is aimed to investigate such behavior and verify the presence of "polyamorphism". High quality a-Ge EXAFS spectra (Ge K-edge) have been collected up to 8.3 GPa. The data analysis, realized using the GNXAS package, gives precise values of the first neighbor bond lengths at various pressures. Two well defined behaviors of the a-Ge local atomic structure have been observed, depending on the sample temperature. At 475 K a-Ge starts to crystallize above 8 GPa. On the other hand, at room temperature, the data seem to indicate the occurrence of a transition toward a different amorphous structure, well before the start of the process of crystallization.

1. Introduction

Elemental amorphous semiconductors (a-Si, a-Ge) play an important role in scientific and technological research since the 1960s. Great progresses have been made in the industrial applications of semiconducting materials, which are at the basis of the modern integrated device technology. Nevertheless the structural characteristics of these systems and their response to temperature and pressure are still subject of debate in condensed matter physics. Still today several questions are open, for example the existence of different pressure-induced amorphous phases (termed "polyamorphism") is not experimentally confirmed.

Here we focus our attention on amorphous Ge. a-Ge is known to undergo an abrupt decrease of the resistivity at 6 GPa and room temperature [1] due to a semiconductor-metal transition. This experimental result can be explained by a "two-fluid" model [2] based on thermodynamical calculations. Nevertheless there is still no experimental confirmation that the resistivity change is associated with a first order structural transition between a low density (LDA) and a high density (HDA) amorphous phase as obtained by numerical simulations. In the last 15 years several experimental and theoretical efforts have been devoted to shed light onto this matter, but no definitive results have been obtained [3, 4, 5, 6, 7, 8]. Differences in the results collected so far, could be related to the processes of "amorphization" used to obtain the a-Ge samples (melt quenching, ions sputtering, glow discharge, evaporation onto substrate). Depending on the preparation methods, different kinds of amorphous Ge structures can be generated which are characterized by different bulk densities [9], voids distributions and impurities concentration. Similar problems can affect computational models, because there are several ways to define the initial amorphous configuration in numerical simulations [10, 11].

Accurate experimental investigations on a-Ge polyamorphism are possible using X-ray absorption spectroscopy (XAS) which allows the study of subtle variations of local order. XAS is particularly suited to this scope due to its unique structural sensitivity. In the next sections we present a preliminary study of a-Ge local structure probed by XAS technique, covering a wide range of pressures between 0 and 8.3 GPa, at room temperature and at 495 K.

2. Experimental

The a-Ge measurements have been carried out at the ESRF, using the advanced set up available at the BM29 beamline [12] which is designed to collect simultaneously both X-ray absorption spectroscopy (XAS) data and energy-scanning X-ray diffraction (ESXD) patterns.

a-Ge samples of suitable thickness have been prepared by evaporation onto Kapton polyimide films of high-purity Ge. The deposition has been performed under high vacuum conditions (10^{-5} mbar) and the Kapton substrate was placed at about 5 cm from the Ge source. A mixture of BN and LiF powders, used as pressure markers, has been compacted in a 1.5 mm diameter cylinder with a small piece of wrapped Kapton/a-Ge foil, placed in a 2 mm graphite hollow cylinder and in a 7 mm boron-epoxy gasket to be used in the "Paris-Edinburgh" large-volume press.

High quality a-Ge XAS spectra (Ge K-edge) and related ESXD patterns have been collected up to 8.3 GPa, both at room temperature and at 475 K. The absence of Bragg peaks associated with Ge crystalline phases was confirmed by the powerful seven-channel collimator system available at BM29 (see [13] and ref. therein). Absence of sample oxidation was also confirmed by near-edge XAS spectra. The experimental XAS data have been analyzed using the GNXAS package [14, 15], taking into account the presence of double electron excitations in the atomic background and multiple scattering in the EXAFS signal [16].

3. Results and discussion

Two sets of EXAFS signals collected at various pressures up to 8.3 GPa are presented in figure 1, for two different sample temperatures (295 K and 475 K). The quality of the raw EXAFS signals is very good, also higher pressures, thanks to the advanced XAS set-up installed at the beamline BM29 (ESRF) [12]. The high sensitivity to the local structure which characterizes the XAS technique, make us able to detect very small variations in the a-Ge bond length and variance.

At room temperature (fig. 1 upper panel) the smooth decrease of the EXAFS frequency is associated with the compression of the first neighbor distance upon pressurization. Nevertheless, a clear increase of frequency, is observable above 8.0 GPa (P_c).

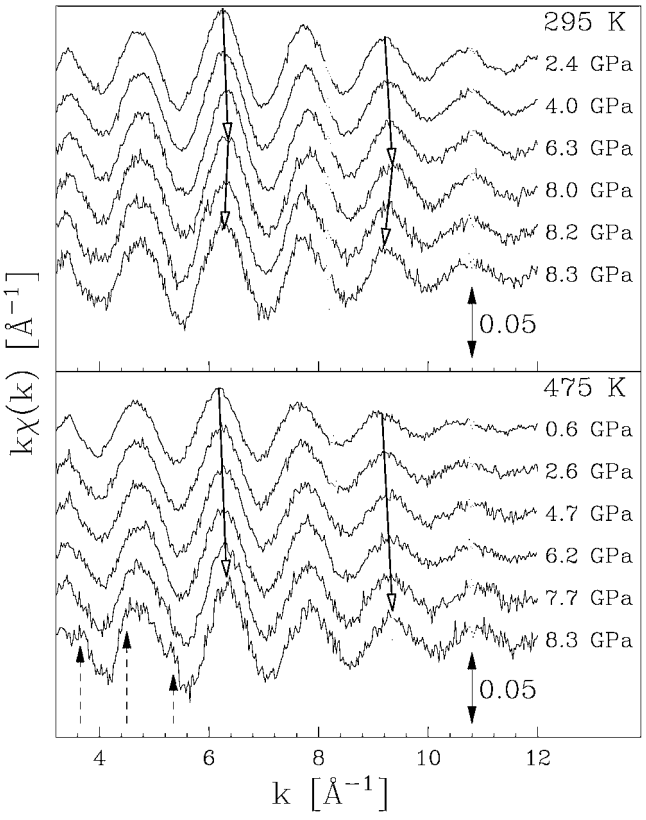

Fig. 1. EXAFS signals collected at 295 K and 475 K are shown at various pressures. The long arrows are drawn as guides for the eyes. At 295 K (upper panel) the signal frequency decreases gradually up to 8.0 GPa (P_c), then an increase of the frequency can be observed. At 475 K (lower panel) the signal frequency decreases gradually up to 8.3 GPa. The dashed arrows at low wave numbers (k) indicate the appearance of high frequency signals at 8.3 GPa.

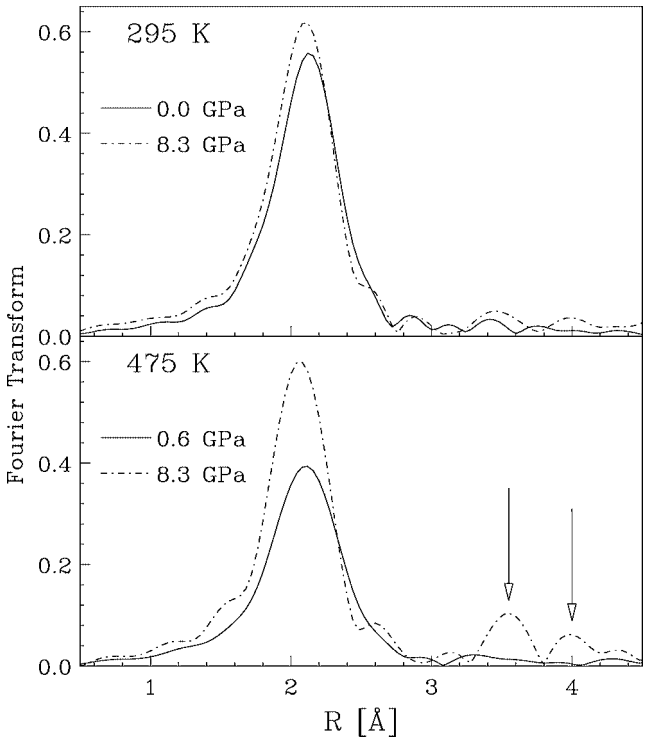

Fig. 2. Fourier transforms of selected experimental EXAFS signals. At 475 K (lower panel) the high frequency present in the total signal, causes the growth of two small peaks in the transform at $R \simeq 3.5$ Å, 4.0 Å (vertical arrows) which are not present at room temperature (upper panel). The position of the principal peaks is shifted due to the decrease of the main signal frequency.

This indicates the presence of a structural change. In order to investigate the nature of this change, the ESXD patterns collected above the transition pressure P_c have been analyzed confirming the absence of c-Ge diffraction peaks. Moreover high frequency multiple scattering signals usually present in ordered c-Ge crystals [16] have not been detected in the low k region of the EXAFS signals. A possible explanation of these findings is that at P_c a-Ge undergoes a structural phase transition toward another (denser) amorphous phase, as recently obtained by numerical calculations [5].

At 475 K the a-Ge structure shows a different response to the pressure (fig. 1 lower panel). In fact there is no sign of sudden modifications in the first neighbor distance, which gradually decreases upon compression. In the same figure a high frequency oscillation becomes evident in the EXAFS signal at 8.3 GPa for $k < 6\,\text{Å}^{-1}$ (dashed arrows in fig. 1 lower panel). This high frequency signal is probably due to the medium range order in the amorphous structure, which starts to increase above 8 GPa, but similarly to the room temperature case, the diffraction patterns do not show any evidence of c-Ge peaks at 475 K and 8.3 GPa.

In figure 2 the Fourier transforms of selected EXAFS signals are shown. The main difference between the room temperture (upper panel) and the high temperature (lower panel) results, is the presence of small peaks ($R \simeq 3.5$ Å, 4.0 Å) at 475 K and 8.3 GPa, which are due to the multiple scattering high frequency in the total EXAFS signal. Similar peaks have been detected in previous EXAFS experiments [7, 17] which studied the gradual crystallization of a-Ge at ambient pressure induced by high temperature annealing. In agreement with those experiments, we deduce that above P_c the simultaneous action of pressure and temperature has induced the ordering of the a-Ge structure. In our data the crystallization process is probably at the first stage and limited to small c-Ge embryos, noticeable only by the extreme sensitivity to the local environment of EXAFS and not visible by diffraction. Increasing the pressure further, we expect that the final process of crystallization can take place starting from these small crystalline clusters similarly to a nucleation process. It is remarkable that a limited increase of the temperature ($\Delta T \sim 200$ K), induces clear differences in the evolutions of the a-Ge structure upon pressurization. In fact in previous experiments [7, 17] traces of crystallization have been detected after annealing above $T = 675$ K.

In figure 3 the whole set of measured first neighbor Ge–Ge distances is presented. EXAFS offers a very accurate evaluation of these distances, which have been measured with a maximum uncertainty of ± 0.005 Å at both temperatures. As expected the average Ge–Ge distance in the hotter sample is larger. Also the overall trend of the experimental points in figure 3 as a function of pressure is comparable, indicating that the a-Ge bulk compressibility values at 295 K and 475 K are similar. The most remarkable difference is the sudden change in the Ge-Ge distance ($\Delta d_{\text{Ge-Ge}} \simeq 0.02$ Å) at P_c at room temperature, which is totally absent at 475 K. Although the first shell distance undergoes this unexpected elongation, the bulk density upon pressurization is expected to increase. This happens to c-Ge which changes at higher pressures from diamond ($N = 4$) to a denser β-tin structure ($N = 6$), characterizated by a longer first neighbor distance. Also a-Ge has been seen to crystallize at high pressure in the β-tin phase [4, 8]. Nevertheless in our case the coordination number of a-Ge increases only slightly ($N_0 = 4.0 \rightarrow N_{P_c} \sim 4.5$). Therefore one can conjecture that the HDA phase packing is more similar to

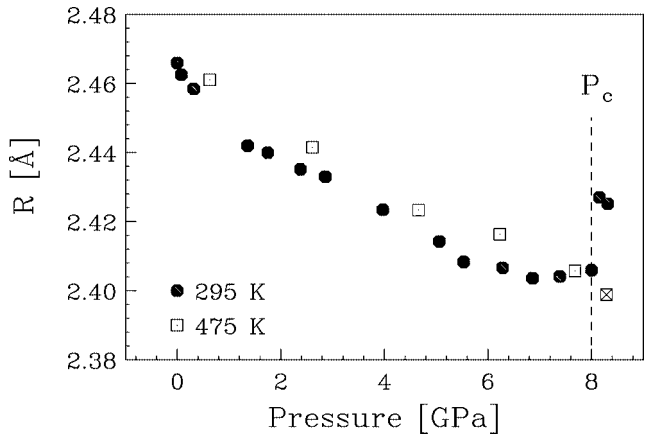

Fig. 3. First neighbor Ge–Ge distance in a-Ge obtained from EXAFS analysis at 295 K and 475 K. Above the transition pressure P_c structural changes take place at both temperatures: at room temperature the Ge-Ge distance becomes suddenly shorter indicating a drastic change of the amorphous structure, on the contrary at 475 K multiple scattering signals are detectable (crossed square) which could be associated to the starting of the process of crystallization. The maximum uncertainty affecting the data is ±0.005 Å at both temperatures.

a disordered ST12 [18] structure ($N = 4$), than a β-tin structure ($N = 6$), but more work is necessary to confirm this hypothesis.

4. Conclusions

Amorphous Ge structure has been analyzed at high pressure and temperature and the presence of a phase transition (at $P_c \simeq 8$ GPa) has been observed at room temperature, well before the crystallization. Upon this transition the a-Ge structure remains amorphous in agreement with existing numerical simulations. Other investigations are necessary for the high pressure phase in order to clarify its structural and electronic properties. At 475 K the a-Ge structure shows a different response to the pressure. The higher thermal energy, combined with pressurization, seems to favor crystallization at a pressure close to P_c, above which our results indicate the starting of the crystallization process. All these results have been obtained using the XAS technique which is a unique tool to investigate amorphous systems due to its high sensitivity to subtle modifications of the local atomic structure.

References

1. Shimomura, O. *et al*., Phil. Mag. **29**, 547 (1974).
2. Aptekar, L. I., Sov. Phys. Dokl. **24**, 993 (1979).
3. Freund, J., Ingalls, R. and Crozier, E. D., J. Phys. Chem. **94**, 1087 (1990).
4. Tanaka, K., Phys. Rev. B **43**, 4302 (1991).
5. Durandurdu, M. and Drabold, D. A., Phys. Rev. B **66**, 41201 (2002).
6. Tanaka, K., Non-Cryst. Solids **150**, 44 (1992).
7. Wakagi, M. and Maeda, Y., Phys. Rev. B **50**, 14090 (1994).
8. Itié, J. P. *et al*., J. Physique IV **7**, C2 (1997).
9. Tatsumi, Y., Honda, H., Ikegami, K. and Naito, S., J. Phys. Soc. Japan **57**, 2977 (1987).
10. Wooten, F., Winer, K. and Weaire, D., Phys. Rev. Lett. **54**, 1392 (1985).
11. Djordjević, B. R., Thorpe, M. F. and Wooten, F., Phys. Rev. B **52**, 5685 (1995).
12. Filipponi, A. *et al*., Rev. Sci. Instrum. **71**, 2422 (2000).
13. Filipponi, A. *et al*., Rev. Sci. Instrum. **74**, 2654 (2003).
14. Filipponi, A., Di Cicco, A. and Natoli, C. R., Phys. Rev. B **52**, 15122 (1995).
15. Filipponi, A. and Di Cicco, A., Phys. Rev. B **52**, 15135 (1995).
16. Filipponi, A. and Di Cicco, A., Phys. Rev. B **51**, 12322 (1995).
17. Paesler, M. A. and Sayers, D., Phys. Rev. B **28**, 4550 (1983).
18. Crain, J., Ackland, G. J. and Clark, S. J., Rep. Prog. Phys. **58**, 705 (1995).

Physica Scripta. Vol. T115, 384–386, 2005

Local Order Around Er^{3+} Ions in thin Silicon Oxide Layers Grown in Si by MBE

F. d'Acapito*[1], S. Mobilio†[2], A. Terrasi[3], S. Scalese[3], G. Franzó[3] and F. Priolo[3]

[1]INFM – OGG, c/o GILDA CRG – ESRF, B.P.220 F-38043 Grenoble, France
[2]Dipartimento di Fisica, Universitá Roma Tre, Via della Vasca Navale 84, I-00146 Roma, Italy
[3]INFM and Dipartimento di Fisica, Universitá di Catania, Corso Italia 57, I-95129 Catania, Italy

Received June 26, 2003; accepted November 26, 2003

PACS Ref: 61.72.-y

Abstract

Er doped Si represent an interesting class of materials for the realization of light emitting devices based on Si technology. The local structure around Er ions is known to strongly affect the luminescence properties of the Rare Earth. In this work the Er site in Er + O doped silicon samples prepared by Molecular Beam Epitaxy has been investigated by X-ray Absorption Spectroscopy at the Er L_{III} edge. Samples with different preparation parameters such as the O/Er ratio and thermal treatments were investigated. Data were fitted using a model consisting in a first shell of O atoms and a second shell of Si atoms and accounting for multiple scattering effects. The rare earth is found to be linked to 5–6 O atoms at around 2.23 Å whereas a well defined Er-O-Si bond angle of ≈136 deg is evidenced.

1. Introduction

Er doped Si has been extensively studied in the recent years due to its potential application in optoelectronics [1]. The $^4I_{13/2} \rightarrow 4I_{153/2}$ transition indeed occurs at 1.54 μm coinciding with one of the minimum absorption windows of commercial silica based optical fibers. This transition is forbidden by electrical dipole selection rules, but becomes possible whenever the Er ions is embedded in a non centrosymmetric environment and can be excited both optically [2] and electrically [3] in such systems. The major problem with the Er : Si system is the low solubility of this rare earth ion in the matrix being of the order of 2×10^6 Er/cm^2 [4]. Using non-equilibrium techniques to raise the Er concentration above the solubility limit (namely ion implantation) leads to the precipitation of Er in Er silicide [5, 6]. This compound, having cubic symmetry around the Er ion produces no luminescence from the Rare Earth. An efficient way to enhance the solubility of Er is in Si is the co-doping with O. In this way Er binds to O ions and concentrations as high as 10^{19} Er/cm^3 can be incorporated in crystalline Si [7]. In samples with Er : O ratio equal to 1 : 10, strong luminescence at 1.54 μm has been observed at 77 K, with a moderate quenching as the temperature is increased. The X-ray Absorption Fine Structure (EXAFS) technique [8] has revealed to be effective in describing the local site of Er in crystalline Si [5, 6, 9–11], and amorphous hydrogenated Si [12, 13]. These studies show that Er is generally 6-coordinated to O ions at a distance of 2.24–2.26 Å. When Er is coordinated to less O ions [12] the Er-O bond lengths shrink to 2.09–2.14 Å. The use of the Multiple Scattering formalism on the other hand, revealed extremely effective in describing the site of Er and Yb beyond the O shell in glassy matrices like silicate [14, 15] and phosphate [16] glasses. The aim of this study was to determine, the site of the Er ion in differently prepared Er + O doped crystalline Si samples by EXAFS.

Table I. *Description of the preparation and thermal treatments of the samples used in the present investigations.*

Sample	Nominal molar ratio O/Er	Annealing temperature	Annealing time
33	1.8	—	—
33E	1.8	900 °C	30 s
49	5	—	—
49E	5	900 °C	30 s

2. Sample Preparation

Samples were prepared by Molecular Beam Epitaxy (MBE) onto (001) oriented Czochralsky Si wafers. Si evaporation was carried out by electron gun in presence of an Er flux arising from an effusion cell and a molecular oxygen leak into the MBE chamber. A pure Si buffer layer 100 nm thick was always deposited prior to the Er : O co-doped layer whose thickness was in the range 240–270 nm. The substrate temperature during the growth was kept at 550 °C to ensure a good epitaxy. Two samples were also annealed to check the stability of the obtained layers. With this procedure $Si : Er_x : O_y$ layers with $x \approx 10^{-3}$ and $y/x = 1.8$ and 5 were grown as resumed in Tab. I.

3. Experimental Details and Results

The experiments at the Er L_{III} edge were carried out at the GILDA CRG beamline at the European Synchrotron Radiation Facility. The monochromator was equipped with a pair of Si(311) crystals and was run in the so-called *Dynamic Focusing* Mode [17]. This means that at each energy point the radius of curvature of the second crystal is changed in order to fix the focal position on the sample spot. Harmonic rejection was achieved by using a pair of Pd coated mirrors with an energy cutoff of 21 keV. The absorption coefficient was measured by collecting the fluorescence yield from the samples using a 13 elements Hyper Pure Ge detector at Liquid Nitrogen Temperature. For each sample 2 to 4 scans were collected and averaged to increase the Signal to Noise (S/N) ratio. Finally a spectrum on Er_2O_3 finely powdered and deposited on a millipore membrane was collected in transmission mode as reference compound. EXAFS spectra with the relative fits are shown in Fig. 1 whereas the Fourier Transforms (FT) are shown in Fig. 2. From these spectra it is evident the presence of a coordination peak at an apparent distance just below 2 Å due to the Er-O bond plus a further peak at ≈ 3.0 Å that can be ascribed to an Er-Si coordination. This is reasonably not due to a direct Er-Si bond, because in this case the related peak is usually observed at a somewhat shorter apparent distance, ≈2.5 Å as shown in the FT shown in [6, 10]. Thus, the hypothesis is made that Er is not

*Electronic address: dacapito@esrf.fr
†Also at INFN, Laboratori Nazionali di Frascati, P.O. Box 13, I-00044 Frascati (Roma), Italy.

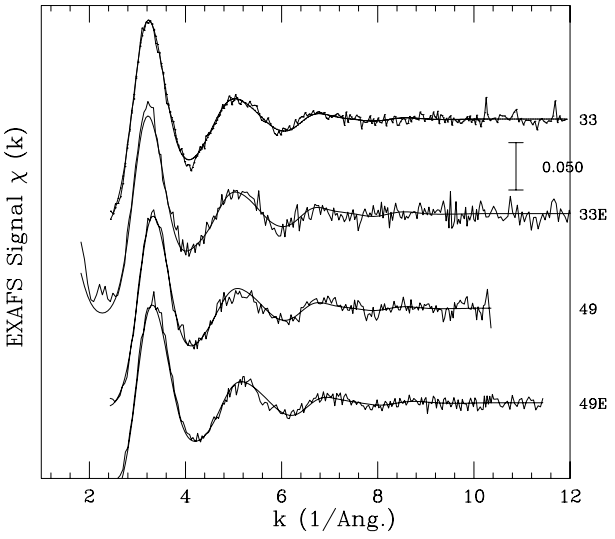

Fig. 1. EXAFS spectra of the samples with the fitting function superimposed.

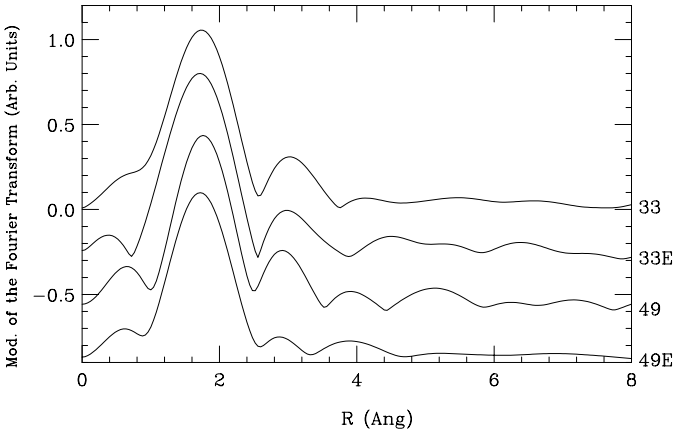

Fig. 2. Fourier Transforms of the EXAFS spectra. The transform was carried out in the range $k = 2.5 \ldots 9\,\text{Å}^{-1}$ using a k^2 weight.

directly bound to si but the interaction happens *via* the O nearest neighbor. Data analysis was carried out by using the GNXAS code [18, 19]. The theoretical signals were calculated from a cluster derived from the crystalline structure of $Er_2Si_2O_7$ [20]. Data were analyzed in an average range $k = 2.5 \ldots 11\,\text{Å}^{-1}$ working directly on the absorption spectrum. To reproduce the spectra we considered a Single Scattering (SS) Er-O path described by a bond length R_{Er-O} and Debye-Waller factor σ^2_{Er-O} and Multiple Scattering (MS) Er-O-Si path (that includes both the MS and the Er-Si SS path) described by the Er-O SS parameters plus the Si-O bond length R_{O-Si}, the Debye-Waller factor σ^2_{Si-O} and the angular parameters $\Theta_{Er-O-Si}$ and $\sigma^2_{\Theta Er-O-Si}$. The Er-Si bond length and Debye-Waller factors are derived automatically from these data by the program code. At each Er-O bond is thus associated one Er-Si and one triangular Er-O-Si bond. This comes from the fact that, being O bound to both Er and Si, a well defined Er-O-Si bond angle should exist as indeed found in glassy matrices [14, 16]. In the fitting procedure all the cited parameters plus the Er-O coordination number N_{Er-O} and the edge position E_0 were varied with the exception of σ^2_{Si-O} (fixed to literature data $0.0001\,\text{Å}^2$ [21]), and the R_{O-Si} and $\sigma^2_{\Theta Er-O-Si}$ parameters, defined in the fit of sample 33 and then fixed for the others. The s_0^2 parameter was defined in the fit of the Er_2O_3 compound ($s_0^2 = 0.92$) and then kept fixed. The results are shown in Tab II.

Table II. *Results of the quantitative fits. For all spectra $R_{O-Si} = 1.60$ Å, $\sigma^2_{Si-O} = 0.0001\,\text{Å}^2$ and $\sigma^2_{\Theta Er-O-Si} = 30\,\text{deg}^2$. Errors were determined by a χ^2 analysis with a confidence level of 95%.*

Sample	N_{Er-O} ±0.6	R_{Er-O} ±0.02 Å	σ^2_{Er-O} ±0.003 Å^2	$\Theta_{Er-O-Si}$ ±4 deg	R_{Er-Si} ±0.03 Å	σ^2_{Er-Si} ±0.007 Å^2
33	5.7	2.22	0.015	134	3.55	0.020
33E	5.5	2.23	0.014	137	3.60	0.018
49	5.0	2.23	0.013	135	3.58	0.019
49E	4.8	2.24	0.013	136	3.59	0.017

4. Discussion

All the samples exhibit the same local environment despite the different preparation conditions. This means that an equilibrium configuration is attained already during the growth and that successive thermal treatments have only minor effects on the local structure. An opposite situation was found in similar systems obtained by ion implantation [6] where the Er environment was found to progressively evolve from a silicide structure to an oxide structure under thermal annealing. In all samples the average site appears to be a 5–6 fold oxygen-coordinated Rare Earth ion with a first coordination shell of ≈2.23 Å. A high Er-O coordination is present also in samples with a nominal low O/Er ratio (33) and its origin is under investigation at present. A possible explanation could be the diffusion of O species present in the Si substrate that came in contact with Er like already found in Er implanted Czochralsky Si [5]. Further studies will be devoted to the elucidation of this point. A well defined Er-O-Si bond angle is found, of around 135 deg, leading to an Er-Si distance of ≈3.5 Å. The Er-O bond length falls in the typical range of previous investigations [5, 6, 9, 11] whereas the Er-Si distance and Er-O-Si the bond angle approach the values found in silicate ($R_{ErSi} = 3.59$ Å and $\Theta_{Er-O-Si} = 140$ deg) [14] and phosphate ($R_{ErSi} = 3.61$ Å and $\Theta_{Er-O-Si} = 143$ deg) [16] glasses. No evidence of a possible Er-Er coordination is found due to the dilution of the Er species in the matrix.

5. Conclusion

In this work the site of Er in Er + O doped Si samples obtained by MBE has been studied by EXAFS. Er is bound to 5 to 6 O neighbors linked in turn to Si atoms from the matrix. A well defined Er-O-Si bond angle of around 136 deg is found as already pointed out for glassy matrices.

References

1. Coffa, S., Polman, A. and Schwartz, R. N., eds., Rare Earth doped semiconductors II, no. 301 in MRS Symposia Proceedings (Materials Research Society, Pittsburgh, 1996).
2. Coffa, S., Priolo, F., Franzó, G., Bellani, V., Carnera, A. and Spinella, C., Phys. Rev. B **48**, 11782 (1993).
3. Franzó, G., Priolo, F., Coffa, S., Polman, A. and Carnera, A., Appl. Phys. Lett. **64**, 2235 (1994).
4. Ren, F. Y. G., Michel, J., Sun-Paduano, Q., Zheng, B., Kitagawa, H., Jacobson, D. C. and Kimlerling, J. P. L. C., Rare Earth doped semiconductors, no. 301 in MRS Symposia Proceedings (Materials Research Society, Pittsburgh, 1993).
5. Adler, D. L., Jacobson, D. C., Eaglesham, D. J., Marcus, M. A., Benton, J. L., Poate, J. M. and Citrin, P. H., Appl. Phys. Lett. **61**, 2181 (1992).
6. Terrasi, A., Franzó, G., Coffa, S., Priolo, F., d'Acapito, F. and Mobilio, S., Appl. Phys. Lett. **70**, 1712 (1997).

7. Coffa, S., Franzó, G., Priolo, F., Polman, A. and Serna, R., Phys. Rev. B **49**, 16313 (1994).
8. Lee, P. A., Citrin, P. H., Eisenberger, P. and Kincaid, B. M., Rev. Mod. Phys. **53**, 769 (1981).
9. Ishii, M., Ishikawa, T., Ueki, T., Komuro, S., Morikawa, T., Aoyagi, Y. and Oyanagi, H., J. Appl. Phys. **85**, 4024 (1999).
10. Terrasi, A., Priolo, F., Franzó, G., Coffa, S., d'Acapito, F. and Mobilio, S., J. Lumin. **80**, 363 (1999).
11. Pizzini, S., Binetti, S., Calcina, D., Morgante, N. and Cavallini, A., Mat. Sci. Eng. B **72**, 173 (2000).
12. Piamonteze, C., Iniguez, A. C., Tessler, L. R., Alves, M. C. M. and Tolentino, H., Phys. Rev. Lett. **81**, 4652 (1998).
13. Tessler, L. R., Piamonteze, C., Alves, M. C. M. and Tolentino, H., J. Non-Cryst. Sol. **266–269**, 598 (2000).
14. d'Acapito, F., Mobilio, S., Gastaldo, P., Barbier, D., Santos, L. F., Martins, O. and Almeida, R. M., J. Non-Cryst. Solids **293–295**, 118 (2001).
15. d'Acapito, F., Mobilio, S., Santos, L. and Almeida, R. M., Appl. Phys. Lett. **78**, 2676 (2001).
16. d'Acapito, F., Mobilio, S., Bruno, P., Barbier, D. and Philipsen, J., J. Appl. Phys. **90**, 265 (2001).
17. Pascarelli, S., Boscherini, F., d'Acapito, F., Hrdy, J., Meneghini, C. and Mobilio, S., J. Synch. Rad. **3**, 147 (1996).
18. Filipponi, A., di Cicco, A. and Natoli, C. R., Phys. Rev. B **52**, 15122 (1995).
19. Filipponi, A. and di Cicco, A., Phys. Rev. B **52**, 15135 (1995).
20. Smolin, Y. I. and Shepelev, Y. F., Acta Crystallogr. B **26**, 484 (1970).
21. Greaves, G. N., Fontaine, A., Lagarde, P., Raoux, D. and Gurman, S. J., Nature **293**, 611 (1981).

Physica Scripta. Vol. T115, 387–389, 2005

The Structural Role of Ag in Galena (PbS). A XANES Study

Gabriele Giuli[1], Eleonora Paris[1], Ziyu Wu[2], Simone De Panfilis[3], Giovanni Pratesi[4] and Curzio Cipriani[4]

[1]Dip. di Scienze della Terra e Unita' INFM – Universita' di Camerino, Italy
[2]Beijing Synchrotron Radiation Facility, Institute of High Energy Physics, Chinese Academy of Sciences, 100039 Beijing, P.R. China
[3]ESRF – Grenoble, France
[4]Dip. di Scienze della Terra – Universita' di Firenze, Italy

Received June 26, 2003; accepted in revised form November 4, 2003

Abstract

A number of Ag-bearing galena samples (PbS) has been investigated by Ag K-edge XAS in order to determine the Ag structural role within the host galena structure. Despite the very low absorber concentration and the high absorbance of the PbS matrix, XANES spectra were successfully collected for samples with Ag content down to 500 ppm. Theoretical spectra have been calculated with the CONTINUUM code in order to discriminate the contributions from Ag located in the two possible sites in the galena structure: the Pb site (located at Wyckoff position 4b, octahedral S coordination, site symmetry m3m), and an interstitial site (located at Wyckoff position 8c, tetrahedral S plus tetrahedral Pb coordination, site symmetry $\underline{4}3m$). Experimental spectrum of diaphorite (a Ag-bearing mineral phase forming nano- to micro inclusions in Ag-rich galena) have been used for comparison.

The XANES experimental spectra show two different types of Ag environment:

a) the samples with high Ag content display spectra similar to that of diaphorite, as evidenced by the theoretical spectra, suggesting that, when present in considerable amount, most of the Ag partitions into the diaphorite inclusions rather than entering the galena structure;
b) trace level Ag-bearing samples display spectra very different from that of diaphorite. In view of the absence of micro- and nano-inclusions in the latter samples (confirmed by electron microscopy), these spectra are taken as representative of the Ag environment in the host galena structure. In these samples the comparison between experimental and theoretical spectra shows that the spectrum can be interpreted as the sum of the two contributions from Ag located in the 8c and 4b positions in the galena structure, in approximately the same proportions. Therefore, the data suggest that in this type of galena sample, half of the Ag occupies the vacant Pb site whereas the remaining part is located in the interstitial 4b site.

1. Introduction

In spite of its precious metal nature, Ag can be present in sulphides as a trace impurity in solid solution. Of particular economical importance is the presence of Ag in natural galena (PbS), as this represents the major ore for the extraction of Ag world-wide. In galena, PbS, whose structure is NaCl-type, Ag partly can substitute for Pb, and partly can form micro-inclusions of diaphorite, a mineral phase of composition $Pb_2Ag_3Sb_3S_8$ where Ag is located in octahedral sites. Substitution mechanism in the galena structure can be attained by two exchange reactions [1]: the first, $2Ag^+ = Pb^{2+}$, can lead only to modest Ag content because at least half of the Ag should be located in interstitial sites; the second exchange reaction, $Ag^+ + (Sb, Bi)^{3+} = 2Pb^{2+}$, can lead to higher Ag contents. The investigation of the type of mechanism for Ag incorporation in the PbS structure is the aim of this study, which has been carried out on selected samples of natural galena, already chemically and structurally well characterized. The major analytical difficulty in this study is the very low amount of Ag in the galena matrix, below the electron microprobe detection limit (500 ppm) coupled with the presence of a heavy matrix (Pb). The determination of the role of Ag requires therefore the use of methods which are able to overcome this problems.

X-ray Absorption Spectroscopy (XAS) can give insight on the Ag structural role in the galena structure thanks to such characteristics as element-selectivity and sensitivity to the local structural and chemical environment around the absorber, even at low concentrations of the absorber and in presence of a matrix composed of heavy elements. However, the determination of Ag location in the galena host structure is an experimentally challenging task because of the very low Ag content involved, a problem we tried to overcome by using fluorescence detectors and very long acquiring time. To better characterize the experimental data and obtain structural information on the Ag location in the galena host structure we made use of theoretical XAS spectra, calculated using the structure refinements available.

2. Experimental methods

2.1. *Samples and their characterization*

A group of Ag-bearing galena samples has been selected among those currently available at the "Museo di Mineralogia e Litologia" of the University of Firenze (I) and the mineralogical collection of the "Dip. Scienze della Terra" of the University of Camerino (I). The samples were checked for purity by powder X-ray diffraction, whereas polished sections were examined by Scanning Electron Microscopy in order to check for the eventual presence of micro inclusions. Chemical compositions were obtained by means of a JEOL JXA 8600 electron microprobe operating at 15.0 kV and 10.0 nA, and with the electron beam focused to a radius of 10 μm. Data were corrected according to the method by Bence and Albee [2]. The data are averages of eight individual analyses, and show the GalYuk to contain 0.23 wt% Ag, whereas all the other samples contain less than 500 ppm Ag (which is the detection limit of Ag as measured with electron microprobe).

2.2. *Data collection and reduction*

Samples for XAS measurement were prepared by smearing finely ground powder on a kapton tape. XANES spectra were collected at the beamline BM-29 of the ESRF (European Synchrotron Radiation Facility) storage ring (Grenoble, F) operating at 6 GeV and with the ring current ranging from 150 to 200 mA. Radiation was monochromatised by means of two channel-cut Si (311) crystals. Spectra were recorded in step-scan mode measuring the incident beam intensity with a ionisation-chamber and the fluorescence yield with a high purity Ge detector. Scans ranged from 25200 eV to 25700 eV with a variable energy step in order to get a constant energy step in the XANES region and a constant K step in the EXAFS region. The reported spectra are the average of three different scans. A Ga filter was placed in front of the Ge detector in order to reduce the Pb fluorescence, thus avoiding the detector saturation and allow to analyze the trace amounts of Ag in the samples.

Experimental XANES spectra were reduced by background subtraction with a linear function and then normalised for atomic absorption on the average absorption coefficient of the spectral

region from 25600 to 25700 eV. Energy was calibrated against a standard of Ag metal (25514 eV). The threshold energy was taken as the first maximum of the first derivative of the spectra, whereas peak positions were obtained by calculating the second derivative of the spectra.

2.3. *Theoretical spectra*

Theoretical XANES spectra were calculated in the frame of the one-electron multiple-scattering theory of Lee & Pendry [3], with refinements and computational methods progressively introduced by Natoli *et al*. [4], Durham *et al*. [5], Natoli & Benfatto [6], Durham [7]. The calculations were carried out by means of the CONTINUUM code [4, 6] using clusters of increasing size till convergence was achieved (at about 5 Å from the absorber in this case). The cluster density has been defined according to Mattheiss [8] and the Coulomb part of the potential was obtained by superposition of neutral atomic charge densities using the Clementi & Roetti basis set [9]. We used the $Z + 1$ approximation (final state rule) to simulate the charge relaxation around the core hole in the absorber, and for the exchange-correlation part of the potential we used the energy- and position-dependent complex Hedin-Lundquist potential. Muffin-Tin radii were chosen according to Norman's criterion, and allowing a 10% overlap between contiguous spheres to simulate the atomic bond. Convolution has been obtained with a Lorentzian shaped function to account for the core hole lifetime.

3. Results and discussion

3.1. *Experimental spectra*

Representative Ag K-edge experimental spectra of the Ag- bearing PbS samples are shown in Fig. 1 along with the spectrum of a diaphorite sample, used for comparison. It is evident that the spectra can be divided into two groups: 1) spectra like that of GalYuk sample closely resembles that of diaphorite both in peak positions and intensity; 2) spectra like those of G-1786 (G-15653 and GaIBg) have a more complex shape than that of diaphorite, and display a larger number of more resolved peaks.

The resemblance of the GalYuk spectrum to that of diaphorite can be easily explained by the presence of diaphorite inclusions in this sample in the form of needles up to 200 μm long. The presence of diaphorite in this sample was known before XAS analysis and this sample was chosen and used therefore to indicate the effect on the XANES spectrum due to the local environment of Ag in diaphorite included in the galena structure. However, it must be noted that SEM microchemical analysis of the same sample revealed the presence of small amounts (below the electron microprobe detection limit) of Ag also in the PbS matrix, away from the diaphorite needles. The XANES spectra clearly indicates that most of the contributions to the spectrum are due to Ag located in the diaphorite inclusions, whereas the Ag diluted in the galena matrix, as expected, shows negligible contributions to the XANES spectrum.

The second type of spectra (G-1786 type) is certainly different from the diaphorite-bearing galena spectra. However, a more detailed interpretation, given the absence of standard materials, requires the use of theoretical spectra. This procedure will allow to give information on the site preference of Ag in the galena structure and how the individual Ag sites contribute to the total spectrum [10].

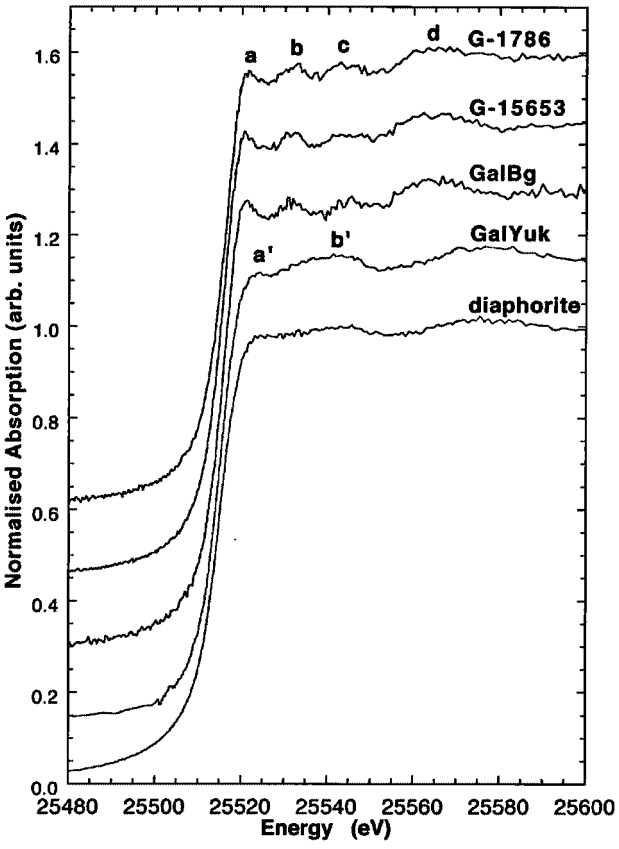

Fig. 1. Experimental Ag K-edge XANES spectra of Ag-bearing PbS samples along with a diaphorite standard.

3.2. *Theoretical spectra*

The theoretical Ag K-edge XANES have been calculated for two clusters of about 80 atoms up to 7.3 Å from the absorber. The calculations for Ag in the octahedral (Oh) and tetrahedral (Td) sites are shown in Fig. 2a. The spectra (dotted line) have been convoluted with a 6.75 eV wide lorentzian [11] in order to account for core-hole lifetime (solid line). Despite the severe dumping of the spectral features after convolution, the two spectra still differ significantly in shape, thus allowing to discriminate the contribution of each Ag site to the total spectrum. In particular, the contributions from the two sites differ both for energy position and intensity of the peaks in the edge region (about + 10 eV in the energy of the main peak between Oh and Td configurations), reflecting the different coordination environment, but also differ for the overall shape at high energy, due to the different structural and chemical composition of the two clusters used in the calculations.

3.3. *Discussion and conclusions*

The comparison of the experimental spectrum of Ag-bearing galena sample with the theoretical single site spectrum (Oh or Td) does not show a good agreement, suggesting that the substitution mechanism of Ag in the galena host structure cannot be related to a single site partitioning (Ag in Oh or in Td). Therefore, we can be certain that Ag in the galena structure cannot be located in only one site. Infact, a better agreement between experimental and theoretical spectra is obtained when using theoretical spectra calculated by combination of the two single site contributions in different proportions (Fig. 2b). The best fit has been found when comparing the experimental spectra with the weighted sum of 50% of Ag in the octahedral and 50% in the tetrahedral site (Fig. 3)

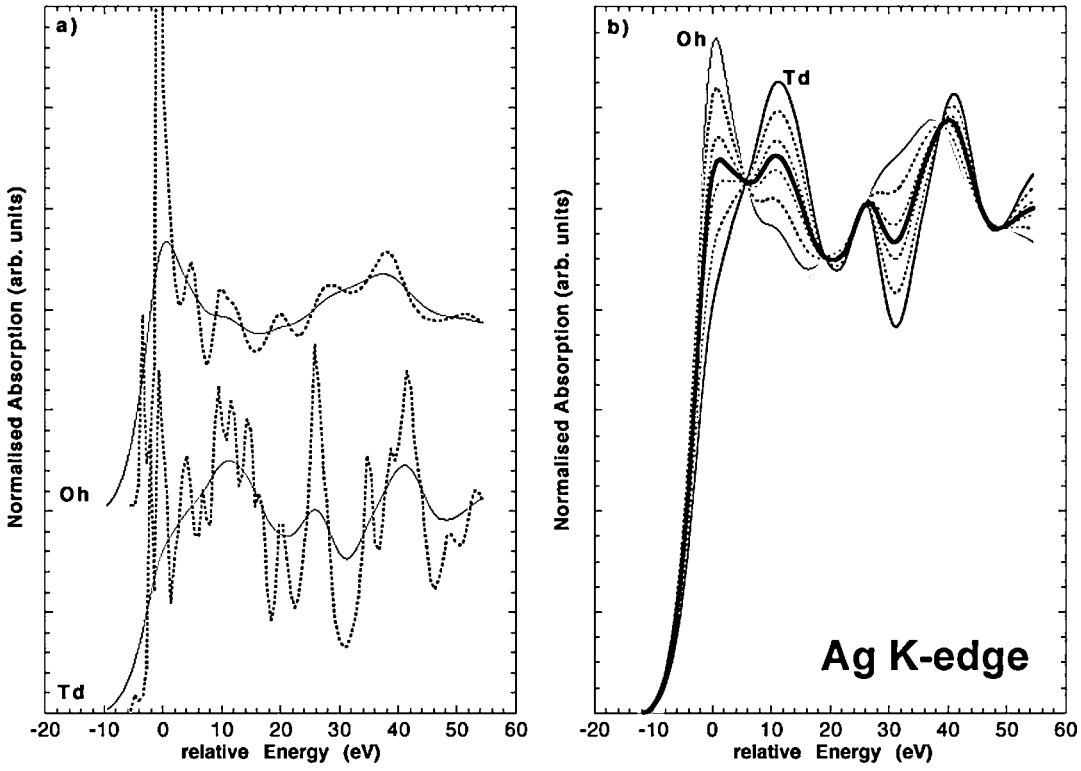

Fig. 2. a) Theoretical Ag K-edge XANES spectra for Ag located in the octahedral (Oh) and tetrahedral (Td) site in the PbS structure (see text). The theoretical spectra (dotted lines) have been convoluted by a 6.75 eV wide Lorentian to take into account Ag K-edge core-hole lifetime; b) weighted sums of the theoretical spectra: it can be clearly noted that the relative intensity of the two peaks at the low energy side change dramatically as a function of Ag partition in the two sites.

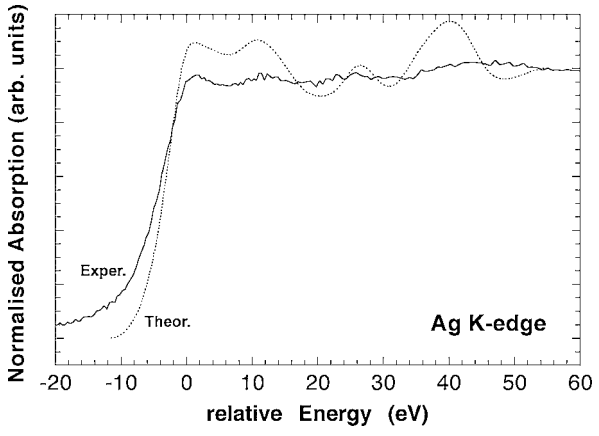

Fig. 3. Comparison between the theoretical and experimental Ag K-edge spectra. The relative position and intensity of the XANES features a and b are satisfactorily reproduced by a theoretical spectrum obtained by taking into account equal amounts of octahedrally and tetrahedrally coordinated Ag.

showing that the peak energy and intensity are well reproduced (peak b-peak a energy difference is 10.5 eV for the experimental and 11.2 eV for the theoretical). If we look at the ratio between the intensity of peaks b and a as another indication of similarity between the spectra [12, 13], we find that the values of this ratio in the experimental and in the theoretical spectrum are very close. These information are in favor of the goodness of the fit and strongly support the hypothesis that the $2Ag^{+} = Pb^{2+}$ exchange reaction can be considered appropriate for describing the presence of Ag in galena in the samples studied. In fact, from the XANES spectra we found the direct evidence that half of the Ag atoms is located in the octahedral sites, whereas the other half of the Ag atoms is located in the interstitial sites. This type of distribution appears to be realistic when Ag is in trace amounts in galena, whereas when Ag is more concentrated a Ag-rich phase like diaphorite segregates and the $2Ag^{+} = Pb^{2+}$ exchange reaction cannot take into account a higher proportion of Ag in the structure, as evidencd by the spectrum of sample GalYuk.

Regarding the second possible exchange reaction $Ag^{+} + (Sb,Bi)^{3+} = 2Pb^{2+}$, we did not detect Sb or Bi in our samples, not even in trace amounts. Therefore the investigation of this type of substitution has to be postponed until suitable samples will be found.

Acknowledgements

Grants from MIUR to EP (confin02 and confin03). Z.Y. Wu acknowledges the financial support of the Outstanding Youth Fund of the National Natural Sciences Foundation (10125523) and the Pilot Project of the Knowledge Innovation Program of Chinese Academy of Sciences (KJCX2-SW-N11).

References

1. Sharp, T. G. and Buseck, P. R., Am. Mineral. **78**, 85 (1993).
2. Bence, A. E. and Albee, A. L., J. Geol. **76**, 382 (1968).
3. Lee, P. A. and Pendry, J. B., Phys. Rev. B **11**, 2795 (1975).
4. Natoli, C. R., Misemer, D. K., Doniach, S. and Kutzler, F. W., Phys. Rev. A **22**, 1104 (1980).
5. Durham, P. J., Pendry, J. B. and Hodges, C. H., Comput. Phys. Commun. **25**, 193 (1982).
6. Natoli, C. R. and Benfatto, M., J. de Phys. **47**, C8, 11 (1986).
7. Durham, P. J., In "X-ray absorption" (edited by Koningsberger, D. C. and Prins, R.), Chemical Analysis Series, (J. Wiley, New York 1988), Vol. 92, p. 72–84.
8. Mattheiss, L., Phys. Rev. A **134**, 970 (1964).
9. Clementi, E. and Roetti, C., At. Data Nucl. Data Tables **14**, 177 (1974).
10. Giuli, G., Paris, E., Wu, Z., Berrettoni, M., Della, Ventura, G. and Mottana, A., Phys. Rev. B **62**, 5473 (2000).
11. Krause, M. O. and Oliver, J. H., Phys. Chem. Ref. Data **8**, 329 (1979).
12. Paris, E. and Tyson, T., Phys. Chem. Minerals **21**, 299 (1994).
13. Giuli, G., Paris, E., Wu, Z., Mottana, A. and Seifert, F., Eur. J. Mineral. **14**, 429 (2002).

Physica Scripta. Vol. T115, 390–392, 2005

Reflection mode XAFS at the Ti K-edge of Lithium Intercalated TiO_2 Electrodes

D. Lützenkirchen-Hecht[1,*], M. Wagemaker[2], A. A. van Well[2] and R. Frahm[1]

[1]Institut für Materialwissenschaften und Fachbereich Physik, Bergische Universität Wuppertal, Gaußstr. 20, D-42097 Wuppertal, Germany
[2]Interfaculty Reactor Institute, Delft University of Technology, Mekelweg 15, 2629 JB Delft, The Netherlands

Received June 26, 2003; accepted December 8, 2003

PACS numbers: 82.47.Aa, 71.20.Tx, 61.10.Ht, 61.10.Kw

Abstract

Lithium intercalation and deintercalation in crystalline TiO_2-electrodes (rutile and anatase modifications) was investigated ex situ using grazing incidence reflection mode X-ray absorption spectroscopy in a specialized cell which permits the removal of the electrolyte and the subsequent measurement of grazing incidence X-ray absorption spectra under a protecting noble gas atmosphere. Small changes observed in near edge X-ray absorption spectra indicated that the Ti^{4+} ions are reduced by the electrochemical lithiation, depending on the TiO_2 modification, $Ti^{3.5+}$ states as well as Ti^{3+} states are observed for rutile and anatase, respectively. Angle dependent experiments reveal that the intercalation is not complete for rutile, while anatase seems to be fully intercalated. In addition, a certain amount of Li remains in the anatase electrode after a complete intercalation – deintercalation cycle. The results suggest that Li-ions are generally accumulated at the electrode/electrolyte interface during both intercalation and deintercalation.

1. Introduction

Rechargeable lithium ion batteries are attractive for their potential use as lightweight, compact energy storage device in applications ranging from portable electronics to vehicles. Therefore lithium ion insertion into metal oxides is one of the main objectives of recent battery research. In this contribution, we will report on ex-situ EXAFS studies of the electrochemical insertion of Li into smooth thin film TiO_2 rutile electrodes. The reversible storage of Li in TiO_2 finds its application in the use as anode material in non-aqueous rechargeable lithium batteries [1, 2]. Based on the change in color from transparent to dark blue when lithium is inserted, electrochromic devices can be realized using lithiated TiO_2 electrodes [3, 4]. In spite of the large number of studies, the origin of the electrochromic effect in Li- inserted TiO_2 remains unclear up to date. Compared to rutile, TiO_2 anatase can accommodate much more Li in its crystal lattice [5–8]. In fact, most of these studies report that hardly any Li inserts into bulk rutile at room temperature [5, 7, 8]. While the originally tetragonal anatase bulk phase undergoes an orthorhombic distortion upon Li insertion resulting in a lithium titanate structure characterised by the *Imma* space-group [9], the structure of Li-intercalated rutile has not yet been investigated in detail.

In this context, grazing incidence X-ray absorption spectroscopy is a well suited technique to obtain structural and electronic information about the electrode surfaces during the intercalation and deintercalation. Unfortunately, the parasitic absorption of the electrolyte is a significant drawback for real in situ studies at energies in the vicinity of the Ti K-edge (4966.4 eV) even if sophisticated detector equipment is employed at 3rd generation synchrotron sources. We therefore designed a new cell, which enables the electrochemical processing of samples which are sensitive towards oxidation by air or humidity. Additionally, it permits grazing incidence X-ray absorption experiments after the controlled emersion of the electrodes from the electrolyte; first results have been published recently [10, 11]. In this contribution, we will address the electrochemical intercalation of Li in two different TiO_2 modifications (rutile and anatase) and compare the observed structures.

2. Experimental

The X-ray absorption experiments were performed at the X-ray undulator beamline BW1 [12] at the DORIS III storage ring at HASYLAB (Hamburg, Germany) operating with 4.45 GeV positrons and injection currents of about 150 mA. The incident monochromatic X-ray beam from a Si(111) double-crystal monochromator with an energy resolution of about 0.9 eV was collimated to a vertical size of about 240 μm and 10 mm horizontally. Incident and reflected intensities were measured by means of argon filled ionization chambers. A second slit system in front of the second ionization chamber suppresses the intensity of non specularly reflected X-rays and shields this detector from the direct beam. All components of the reflectometer, i.e. the sample position, the angle of the detector arm and the slit system can be adjusted by stepper motors. The reflection mode XANES and EXAFS data were collected in the vicinity of the Ti K-edge (4966.4 eV) at ambient temperature. A Ti metal foil was measured in transmission between the second and a third ionization chamber in order to calibrate the energy scale of the monochromator simultaneously with each of the samples. Thin film TiO_2 working electrodes (thickness ≈25 nm, length 40 mm, width ≈25 mm) were prepared by RF sputter deposition on gold covered single crystal quartz substrates. Li intercalation was performed in an electrolyte consisting of 1 M $LiClO_4$ in propylene carbonate (PC). High purity copper wires served both as counter and reference electrodes in a three electrode compartment which is controlled by a potentiostat. Li intercalation and deintercalation was performed under potentiostatic conditions. After the electrochemical treatment, the electrolyte was removed from the samples surface and remaining electrolyte drops were removed by a jet of high purity He prior to the X-ray investigations. Rutile as well as anatase TiO_2, TiO, Ti_2O_3, $Li_4Ti_5O_{12}$ (Li-Ti-spinell) and $Li_{0.6}TiO_2$ samples – the latter with space group *Imma* (nr. 74, [9]) – were investigated in transmission geometry to obtain reference spectra. Further details are given elsewhere [10, 11].

3. Results and Discussion

In Figure 1(a), near edge XANES data determined from reflection mode spectra from a rutile electrode are presented for different

*e-mail: dirklh@uni-wuppertal.de

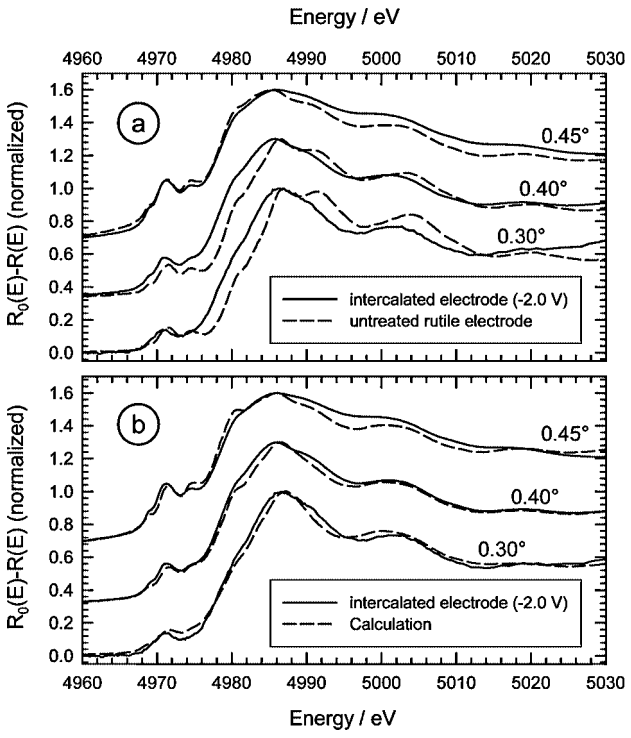

Fig. 1. (a) Comparison of absorption spectra determined as the normalized difference $|R_0(E) - R(E)|$ for the intercalated (-2.0 V for 1 h) and the untreated electrode for several glancing angles. (b) Comparison of the experimental XANES spectra of the intercalated electrode (full lines) to calculations for a multilayered structure (dashed lines) for different grazing angles as indicated. Assumed was a top layer of 5.7 nm $Li_{0.6}TiO_2$ on an underlying rutile TiO_2 layer with a thickness of 20 nm and a 12.5 nm thick gold backing electrode on the quartz substrate. (The spectra are shifted vertically by 0.3 for each angle for a better visualization.)

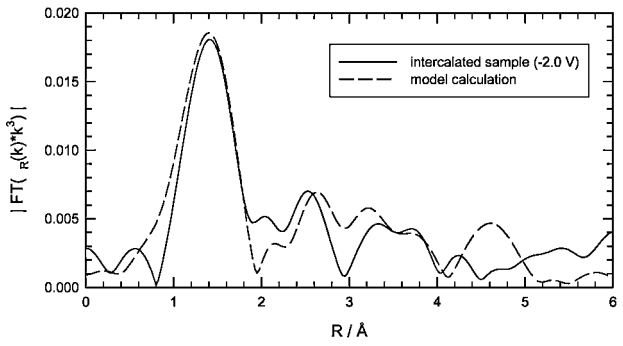

Fig. 2. Comparison of the magnitude of the Fourier- transform of the reflection mode fine structure spectrum of the intercalated rutile electrode ($\Theta = 0.30°$, full line) with that of a model calculation assuming a multilayered structure consisting of 5.7 nm $Li_{0.6}TiO_2$ on 20 nm rutile layer and 12.5 nm gold on the quartz substrate (dashed lines) (Data are not corrected for phase shifts. The k-range for the Fourier-transform is $2.2\,\text{Å}^{-1} \leq k \leq 10.2\,\text{Å}^{-1}$).

grazing angles. The spectra were calculated as the normalized difference between a linear pre-edge background $R_0(E)$ and the reflection mode XANES spectrum $R(E)$ in order to obtain a measure of the absorption (see ref. [10]). Spectra from the untreated electrode and intercalated rutile (-2.0 V vs. Cu) are shown.

Obviously, distinct differences between both data sets were observed, especially for $\Theta = 0.30°$ and $\Theta = 0.40°$. The most prominent is the shift of the absorption edge from about 4979.4 eV to about 4978.0 eV after the intercalation. The critical angle of total reflection is about 0.42°. Accordingly, the penetration depth of the X-rays amounts to ca. 3–4 nm at 0.30°, 5–10 nm at 0.40° to more than 50 nm at 0.45°. We can therefore conclude that the near surface region of the rutile is modified by the intercalation. The observed edge shift corresponds to a reduction of the rutile Ti^{4+} states to a Ti-valence of ca. 3.6 [10]. Thus a spinell type Li-Ti-O compound such as $Li_2Ti_2O_4$ [9] is very unlikely present due to its Ti^{2+} valence. Furthermore, significant changes can be observed above the edge, for example the double peaked structure in the spectrum of the untreated rutile electrode between ca. 4985 eV and 4992 eV was transformed to a single peak centered at about 4986 eV after the Li insertion. The comparison of the XANES spectra of the intercalated rutile electrode with those of other Li-Ti-oxide reference compounds and Ti-oxides shows that the near edge structures are very similar to those of $Li_{0.6}TiO_2$ [10].

We therefore conducted model calculations, results of which are presented in Fig. 1(b). For these calculations, the complex refractive index $n = 1 - \delta - i * \beta$ was extracted from transmission mode EXAFS spectra of the reference compounds by means of a Kramers-Kronig analysis, and the reflection mode spectra were calculated by applying the Fresnel theory for multilayered systems [13]. For the calculations shown in Fig. 1(b), a $Li_{0.6}TiO_2$ top layer with 5.7 nm thickness (t) on an underlying rutile TiO_2 layer ($t = 20$ nm) and a thin film gold backing electrode ($t = 12.5$) on the quartz substrate (dashed lines) was assumed. As can be seen, a good fit to the experimental data was achieved for all grazing angles. Therefore the structure of the Li intercalated rutile seems to be at least very similar to that of $Li_{0.6}TiO_2$. This is further supported by the results of reflection mode extended X-ray absorption spectra of the intercalated electrode. A typical result is presented in Fig. 2. Here, the Fourier-Transform of the reflectivity fine structure $\chi_R(E)$ extracted from the experimental data is compared to that of a model calculation. It has to be mentioned that similar calculations were performed using multilayered systems with different Li-Ti-O compounds and Ti-oxides such as $Li_2Ti_2O_4$, $Li_4Ti_5O_{12}$, TiO and Ti_2O_3. However, these calculations only fit poorly to the experimental data. Therefore it can be concluded that the structure of the lithiated rutile layer is very similar to that of $Li_{0.6}TiO_2$ (anatase type space group imma, [9]) in which Ti has a valence of 3.5 and Ti is surrounded by 6 nearest neighbour oxygen atoms in a strongly distorted octahedron with bond distances between 1.94 Å and 2.13 Å, and two different Ti-Ti coordination distances at 2.89 Å and 3.13 Å.

A completely different picture was observed for Li intercalation in anatase TiO_2. First of all, the electrochemical intercalation occurs for a significantly smaller negative potential, i.e. the intercalation requires a significantly smaller overpotential compared to Li intercalation in rutile. XANES spectra calculated from reflection mode EXAFS spectra measured after lithiation at -1.6 V (vs. Cu) for 1 h are presented in Fig. 3(a). In this figure, we also show XANES data of the untreated anatase electrode and data measured after a galvanostatic deintercalation (20 min with a current density of about $1\,\mu A/\text{cm}^2$).

The dramatic shift of the absorption edge towards smaller energies after the intercalation is evident. We obtained a value of 4976.2 eV compared to 4979.0 eV for the untreated electrode. This value corresponds well to the position of the Ti_2O_3 absorption edge at 4976.0 eV, i.e. the presence of a Ti^{3+} species is very likely after the intercalation. To our best knowledge, Li-Ti-oxide reference compounds with a Ti^{3+} valence have not been reported up to now. Therefore we simply compared the derivative spectrum of the intercalated anatase electrode with that of polycrystalline Ti_2O_3 measured in transmission in Fig. 3(b). The similarity of both derivative spectra is evident: Both derivative spectra show

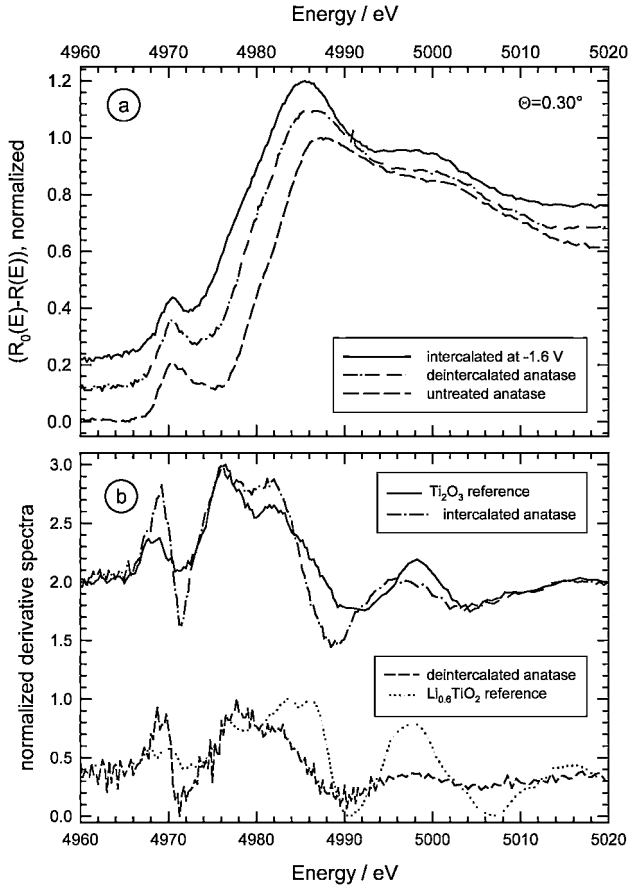

Fig. 3. (a): Normalized difference spectra $(R_0(E) - R(E))$ obtained ex situ from an anatase TiO_2 electrode in 1 M $LiClO_4$ in propylene carbonate for a glancing angle $\Theta = 0.30^\circ$ for untreated anatase, the intercalated and the deintercalated electrode. (b): Comparison of derivative spectra of the intercalated and deintercalated anatase sample with those of reference compounds measured in transmission.

minima and maxima at very similar energies. It should be noted at this point, that the effect of the anomalous dispersion influences the intensities of the peaks derived from the reflection data which might therefore be different [10]. Nevertheless, we can conclude from our measurements that the Ti atoms at the surface of the intercalated anatase electrode have a very similar electronic structure compared to Ti_2O_3 as was proved by preliminary model calculations using a layered structure with a Ti_2O_3 top layer of 4–5 nm thickness.

After deintercalation, an edge position of about 4978.2 eV was found. This energy corresponds well to that of the $Li_{0.6}TiO_2$ reference (4977.6 eV). Also the derivative spectrum of the deintercalated electrode is very similar to that of $Li_{0.6}TiO_2$. Thus the anatase electrode is not completely discharged but some of the intercalated Li remains within the sample. Angle dependent measurements show that the edge shifts to higher values for higher grazing angles, i.e. a larger X-ray penetration depth. Thus it can be concluded that the inserted Li is accumulated at the outer surface towards the electrolyte during deintercalation. The same observation was made for the intercalated material, i.e. the oxidation state seems to increase with increasing distance from the electrode/electrolyte interface. Therefore it can be deduced that only a surface layer of the lithiated material is in the Ti^{3+} state. More detailed model calculations are however necessary to clarify this point.

Acknowledgements

We like to thank P. Keil and U. Haake for their help at the beamline. Financial support by the MWF Nordrhein-Westfalen and HASYLAB is greatfully acknowledged.

References

1. Huang, S. Y., Kavan, L., Exnar, I. and Grätzel, M., J. Electrochem. Soc. **142**, L142 (1995).
2. Ohzuku, T., Kodama, T. and Hirai, T., J. Power Sources **14**, 153 (1985).
3. Hagfeldt, A. and Grätzel, M., Chem. Rev. **95**, 49 (1995).
4. Cantão, M. P., Cisneros, J. I. and Torresi, R. M., Thin Solid Films **259**, 70 (1995).
5. Stashans, A., Lunell, S., Bergsträm, R., Hagfeldt, A. and Lindquist, S. E., Phys. Rev. **B 53**, 159 (1996).
6. Ohzuku, T., Takehara, Z. and Yoshizawa, S., Electrochim. Acta **24**, 219 (1979).
7. Zachau-Christiansen, B., West, K., Jacobsen, T. and Atlung, S., Solid State Ionics **28–30**, 1176 (1988).
8. Kavan, L., Grätzel, M., Gilbert, S. E., Klemenz, C. and Scheel, H. J., J. Am. Chem. Soc. **118**, 6716 (1996).
9. Cava, R. J., Murphy, D. W., Zahurak, S., Santoro, A. and Roth, R. S., J. Solid State Chem. **53**, 64 (1984).
10. Lützenkirchen-Hecht, D., Wagemaker, M., Keil, P., van Well, A. A. and Frahm, R., Surf. Sci. **538**, 10 (2003).
11. Wagemaker, M., Lützenkirchen-Hecht, D., Keil, P., van Well, A. A. and Frahm, R., Physica **B 336**, 119 (2003).
12. Frahm, R., Weigelt, J., Meyer, G. and Materlik, G., Rev. Sci. Instrum. **66**, 1677 (1995).
13. Borthen, P. and Strehblow, H.-H., Physica **B 208&209**, 421 (1995).

Physica Scripta. Vol. T115, 393–395, 2005

Linearly Polarized Carbon K-edge X-ray Absorption Spectroscopic Study of Heavily *p*-Doped Polyacetylene Film with Preferred Orientation

M. G. Kim[1], H. J. Lee[2], B. H. Kim[2], J. S. Kim[2] and Y. W. Park[2*]

[1]Beamline Research Division, Pohang Accelerator Laboratory, Pohang University of Science and Technology, Pohan, South Korea
[2]School of Physics and Condensed Matter Research Institute, Seoul National University, Seoul 151-747, South Korea

Received June 26, 2003; accepted December 9, 2003

PACS numbers: 78.66.Qn, 61.10. Ht

Abstract

The structures of polyacetylene (PA) films with oriented chains have been intensively investigated with linearly polarized carbon K-edge near edge X-ray absorption fine structure (NEXAFS) for the first time. The angular dependence of linearly polarized peak feature has been observed from normal to glancing incidence, with respect to the stretched direction of the PA film. The polymeric chain orientation of the stretched *trans*-PA has been determined with the strong angular dependence of $\pi^*_{C-C}, \sigma^*_{C-H}$, and π^*_{C-C} resonance. Heavily doped PA films with 6% $FeCl_4^-$ or ClO_4^- show different near-edge peak features from the undoped PA films, especially in the energy region of ~285 eV corresponding to electronic transition of C ls electron to unoccupied π^*_{C-C} molecular level. Upon doping, the resonance peak position for sp^2 hybridization of unsaturated C−C bonding is shifted to higher energy and the peak intensity is reduced significantly, which indicates that the cleavage of conjugated π bonds by p-doping occurs in the *trans* polymeric chain reducing the alternating double bond chain length. Although the peak features for σ^*_{C-H} and σ^*_{C-C} have been effectively changed, no angular dependence of the NEXAFS spectra are observed in the doped PAs.

Polyacetylene (PA) is the simplest sp^2-hybridized conjugated system and is therefore of special fundamental importance. From the first discovery of the insulator-metal transition by doping [1], PA has been widely studied both experimentally and theoretically [2]. At low doping level, the soliton-based conduction process is known to be dominant and yet the electronic structure in the heavily doped regime is not well understood due to the complex morphology of the randomly entangled fibrillar morphology of PA film [3]. Recently, the photo generation of soliton pairs has been well demonstrated in femto-second spectroscopy study [4]. Also the low temperature *I–V* characteristics of PA nanofiber has been investigated under magnetic field to understand the intrinsic conduction mechanism [5].

On the one hand, spectroscopic research of soft X-ray absorption, mostly concentrated on carbon K-edge, has been carried out for the quantitative study of the local structure in various organic-inorganic materials, such as chemisorbed molecules [6, 7, 8] and polymeric systems [9, 10, 11]. Direct information of unoccupied molecular level can be obtained from the intensive absorption peaks of carbon K-edge near-edge X-ray absorption fine structure (NEXAFS). The electric dipole-allowed transitions of ls electron to molecular orbitals provide a direct spectral probe of nature as well as the orientation for various chemical bonds in the materials. In the present study, spectroscopic studies of p-doped PA films with oriented chains have been carried out with linearly polarized carbon K-edge NEXAFS for the first time to investigate the local distortion of polymer chains around the dopant ions.

High-density PA films are synthesized according to the modified Shirakawa method [12], which is described elsewhere in detail [13, 14]. The PA films were oriented by stretching with $l/l_0 \sim 2$–3 or $l/l_0 \sim 5$–6, where l is the final stretched length and l_0 is the unstretched length. The oriented samples were doped with $FeCl_4^-$ or ClO_4^- from solution up to a saturation level of ~ 7–8 *molar%* Carbon K-edge NEXAFS measurements on the PA films were performed on the BL2B1 beamline in the storage

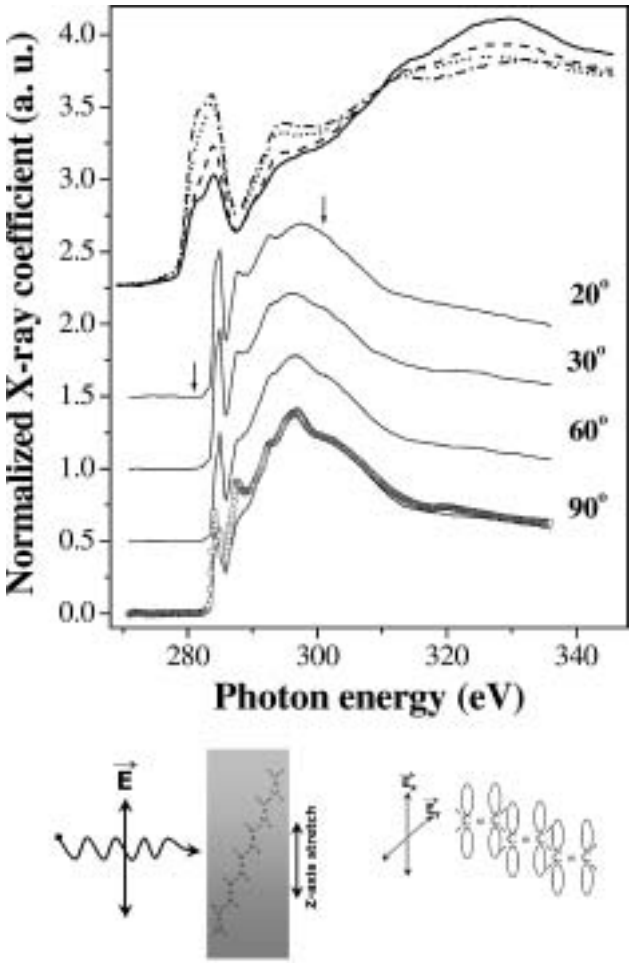

Fig. 1. Angular dependence of Carbon K-edge NEXAFS spectra for 2 times-stretched *trans*-form PA film. In the normal incidence angle, the electric field vector ***E*** of linear polarized X-ray is paralled to the hydrocarbon chain orientation. The open circles mean unstretched *trans*-PA film. The upper NEXAFS spectra from 281 to 301 eV have been magnified for clarity.

*e-mail : ywpark@phya.snu.ac.kr

ring of 2.5 GeV with ring current of 120 ∼ 160 mA at Pohang Light Source (PLS). The PA film with thickness of about 10 μm was attached on Ta foil substrate. The NEXAFS were taken in a total electron yield mode by recording the sample current. The energy resolving power ($E/\Delta E$) in the entire measurement range was greater than 2000. The base pressure of the experimental chamber was in the 10^{-9} torr range. The experimental spectra were normalized by a reference signal from Au mesh with 90% transmission. The angular dependence of stretched PA films on linearly polarized incident X-rays has been obtained by rotating from normal to 20° with respect to the plane of the PA film.

Trans- and *cis*-form PA films with oriented chains have been intensively investigated with linearly polarized carbon K-edge NEXAFS. Figure 1 shows NEXAFS spectra of PA films for incident X-ray angles from normal to 20° with respect to the electric field vector E. The angular dependence of NEXAFS spectra for 2-times stretched PA film is presented in Figure 1, in comparison with those of pristine *cis*- and *trans*-PA films. Since the linearly polarized X-ray is very sensitive to C-H and C-C orientations within the hydrocarbon frame, the peak position and the intensity give important structural information about the chemical bonding between atoms.

The NEXAFS spectra show a typical absorption peak feature of unsaturated hydrocarbon with three kinds of resonance for $\pi^*_{C-C}, \sigma^*_{C-H}$, and σ^*_{C-C} levels. In the present PA films, the intense absorption peak (peak A) at ∼285 eV corresponds to electronic transition of carbon ls electron to unoccupied π^*_{C-C} molecular orbital (MO) level [15, 16]. The appearance of the π^* resonance indicates a distinct existence of a conjugation system, -[HC=CH−CH=CH]$_{n-}$, in the PA film. The broad higher energy peaks (peaks B and C) above 285 eV can be assigned to σ^*_{C-H} and σ^*_{C-C} MO levels, respectively. The intensity of peak A gradually increases with the incident X-ray angle, from normal to glancing ($\Theta \sim 20°$), meaning the systematic increase of interaction between the p-orbital for π bonding and the incident X-ray. The rotation to glancing leads to an increase of the peak intensity for σ^*_{C-H} resonance and a decrease for the σ^*_{C-C} resonance.

Such angular dependence of NEXAFS spectra can be described with the relationship between the PA chain orientation and the ***E*** vector of linearly polarized X-ray. For oriented molecules, the C−H or the C−C resonance generally exhibits a large angular dependence for electric field vector ***E*** parallel to the chain direction. When the C−C bond of saturated hydrocarbon is in the basal plane, the intensity of σ^*_{C-C} resonance is relatively large. However, the intensity of σ^*_{C-H} resonance is small since the bonding orientation is perpendicular to that of the C−C bond. For unsaturated hydrocarbon, the angular dependence is similar to that of the saturated hydrocarbon although both C−H and C−C bonds exist within the basal plane with sp^2 hybridization.

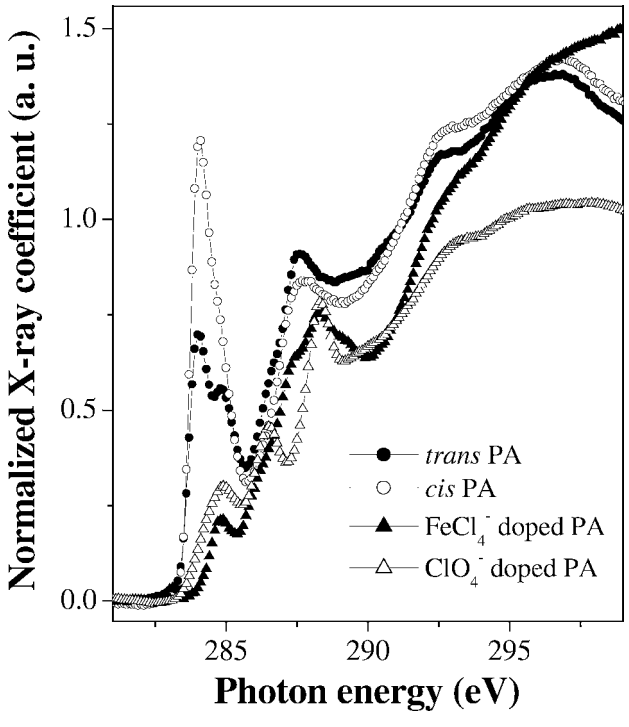

Fig. 2. Carbon K-edge NEXAFS spectra for *p*-doped PA films for normal incidence.

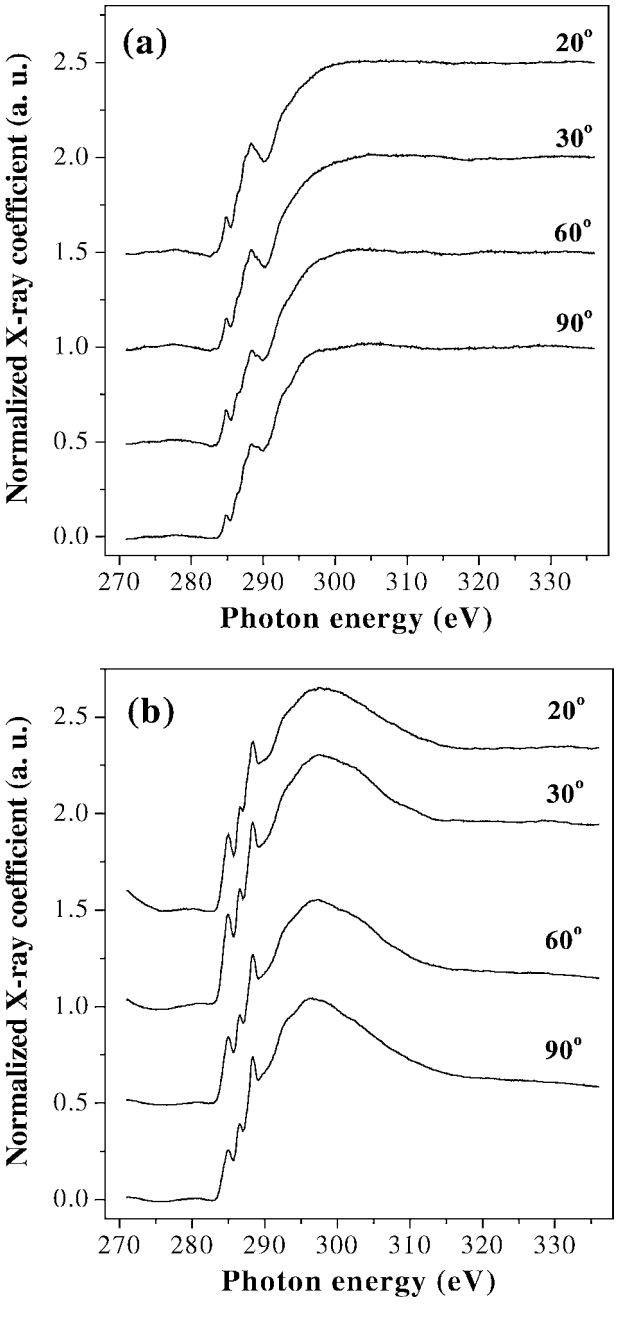

Fig. 3. Carbon K-edge NEXAFS spectra for (a) $FeCl_4^-$ and (d) ClO_4^--doped PA films with 2 times-stretch from the normal incidence angle to 20°.

In the present study, the PA chain orientation by stretching has been determined with the angular dependence of NEXAFS, based on earlier spectroscopic results of other organic materials [6, 7, 8]. The spectral change of PA film with respect to the incident X-ray angle directly shows a preferred orientation of the hydrocarbon chain, here $-$HC=CH$-$CH=CH$-$ acetylene chain. The σ^*_{C-C} resonance is dominant at glancing incidence of $\Theta = 20^\circ$, as shown in Figure 1. It means that the π conjugated orbitals are oriented nearly normal to the surface plane, which can be supported with the intensity variations of σ^*_{C-H} and σ^*_{C-C} resonance peaks.

Figure 2 shows NEXAFS spectra of p-doped PA films measured parallel to the hydrocarbon oriented direction. The results are compared to those of pristine *trans*- and *cis*-PA films. $FeCl_4^-$ or ClO_4^- doped PA films show different near-edge peak features from those of undoped PA film, especially in the energy region of $\sim$285 eV corresponding to the unoccupied π^*_{C-C} molecular level. Upon doping, the resonance peak intensity for sp^2 hybridization of unsaturated C=C bonding dramatically decreases and the peak position is shifted to the higher energy side, which indicates that the cleavage of conjugated π bonds by p-doping occurs in the *trans*-PA chain reducing the chain length of the alternating double bonds. The weak π* resonance means coexistenc of unsaturated and saturated C$-$C bonding in the p-doped PA films. The peak features for σ^*_{C-H} and σ^*_{C-C} have also been effectively changed in the doped PAs.

For the 2 times stretched p-doped PA films, however, no angular dependence of the peak feature has been observed from normal to glancing incidence angles, as shown in Figure 3. The peak intensities of the π* and σ* resonances are non-sensitive to the incident angle and the chain orientation, unlike in the case of both *trans*- and *cis*-PA films, which shows strong angular dependence of π^*_{C-C}, σ^*_{C-H}, and σ^*_{C-C} resonances.

The angle independent spectra for p-doped PA films are related to the disappearance of C=C bonding and to the increase of bonding disorder by local structural distortion, upon doping. The introduction of dopants into well-ordered hydrocarbon chain leads to local distortion around the doping site *i.e.*, creating solitons in the chain. The long range order of C$-$C, C$-$H, and C=C bonding breaks down, which causes a short range order around the doping site in the ordered PA films.

In summary, angular dependence with linearly polarized X-ray has been observed for *trans*-PA with preferred orientation from normal to glancing incidence. The strong angular dependence shows polymeric chain orientation of the stretched *trans*-PA. Upon $FeCl_4^-$ or ClO_4^- doping, the cleavage of conjugated π bonds by p-doping occurs in the *trans* polymeric chain. For p-doped PAs, NEXAFS spectra are independent of incident X-ray angle, in spite of the effective spectral change in doped PAs with respect to those of *trans*- and *cis*-PA films.

Acknowledgments

We are grateful to authorities concerned of Pohang Light Source (PLS) for XAS measurements. This work was supported by he National Research Laboratory program under Contract No. M1-0104-00-0023, Ministry of Science and Technology (MOST), Korea.

References

1. Chiang, C. K., *et al*., Phys. Rev. Lett. **39**, 1098 (1977).
2. Skotheim, T. A., Elsenbaumer, R. L. and Reinodds, J. R., "Handbook of Conducting Polymer", (Marcel Dekker Inc., New York, 1998).
3. Hegger, A. J., Kivelson, S., Schrieffer, J. R. and Su, W.-P., Rev. Mod. Phys. **60**, 781 (1988) and references therein.
4. Miranda, P. B., Daniel, M., Hegger, A. J. and Park, Y. W., Phys. Rev. B **66**, 125202 (2002).
5. Kaiser, A. B. and Park, Y. W., Curr. Appl. Phys. **2**, 33 (2002).
6. Stöhr, J., Outka, D. A., Baberschke, K., Arvanitis, D. and Horsley, J. A., J. Phys. Rev. B **36**, 2976 (1987).
7. Solomon, J. L., Madix, R. J. and Stöhr, J., J. Chem. Phys. **89**, 5316 (1988).
8. Solomon, J. L., Madix, R. J. and Stöhr, J., J. Chem. Phys. **89**, 8379 (1990).
9. Evans, C. E., *et al*., J. Phys. Chem. B **106**, 9036 (2002).
10. Urquhart, S. G., *et al.*, J. Electron Spectrosc. **100**, 119 (1999).
11. Okajima, T., *et al.*, J. Phys. Chem. A **102**, 7093 (1998).
12. Akagi, K., *et al*., Synth. Met. **D1**, 27 (1989).
13. Park, Y. W., *et al.*, Solid State commun. **65**, 147(1988).
14. Suh, D.-S., *et al*., Phys. Rev. B **65**, 165210 (2002).
15. Sodhi, R. N. S. and Brion, C. E., J. Electron Spec. Related Phenom. **37**, 1 (1985).
16. de Brito, A. N., *et al*., J. Electron Spec. Related Phenom. **59**, 293 (1992).

Physica Scripta. Vol. T115, 396–398, 2005

Cs 3d Absorption and Resonant Photoemission Study of Caesium Halogenides

R. Ruus[1,*], K. Kooser[1], E. Nõmmiste[1], A. Saar[1], I. Martinson[2] and A. Kikas[1]

[1]Institute of Physics, University of Tartu, Riia 142, EE51014 Tartu, Estonia
[2]Department of Atomic Spectroscopy, Lund University, Professorsgatan 1, S-22100 Lund, Sweden

Received June 26, 2003; accepted in revised form November 4, 2003

PACS numbers: 32.80.Hd and 78.70.Dm

Abstract

The highly localized 4f electrons play an important role in forming of the electronic structure and properties of compounds. The 3d photoabsorption and resonant decay spectra of Cs halides represent an interesting case showing both the localized and spatially extended f wavefunction features. We present and discuss the Cs 3d X-ray absorption and resonant photoelectron emission spectra of the Cs halides. The Cs 3d absorption spectra exhibit a strong atom-like shape resonance behavior, solid-state effects play a minor role. The appearance of the spectral features, which are intrinsic to a localized state, in the decay spectra show that the Cs 3d photoelectron, temporally and spatially trapped in the Cs 3d shape resonance due to the potential barrier for εf electrons near threshold, has substantially localized nature.

1. Introduction

The highly localized 4f electrons play an important role in forming of the electronic structure and magnetic properties of lanthanide compounds. It is shown [1] that the localization of the 4f wave function may take place at 3d and 4d excitations also in pre-lanthanides where the 4f electrons are not present in the ground state. The collapse, *i.e.* sudden compression of the radial wave function of 4f electrons arises because of specific, double-well features of the effective potential for 4f electrons. In the 3d spectra the collapse of the 4f wave functions is expected to show up along the series Xe to Ba. Experimental results on the 3d photoabsorption of xenon-like ions I^-, Cs^+, Ba^{2+}, and La^{3+} in various halides [2, 3] show the collapse of the 4f wave functions in Ba halides. The 3d photoabsorption spectra of Cs halides represents an interesting intermediate case showing both the bound state and continuum features in the spectra.

To understand the nature of the photoabsorption at the 3d edge of Cs, we performed a careful study of the nonradiative decay processes at the 3d photoabsorption edge of the Cs halides by using resonant photoemission spectroscopy. The photoemission spectra have been recorded, over an energy domain of 150 eV covering up to the 4d levels, for selected exciting photon energies along the Cs 3d absorption curves. We use Hartree–Fock (HF) calculation in conjunction with the Watson sphere model to demonstrate potential barrier effects on the development of shape resonances in 3d photoabsorption spectrum.

2. Experiment

The experiments were performed on the beamline D1011 at the MAX-II storage ring. The electron spectra are excited by a photon beam from a modified SX-700 plane-grating monochromator with an energy resolution 0.2 eV at the caesium M_5 edge (around 730 eV) and analyzed by a hemispherical electron spectrometer Scienta SES-200. A 200 eV pass energy gave a kinetic energy resolution of about 0.2 eV. The thin films ∼100 Å of Cs halides were prepared in situ by thermal evaporation onto a polished stainless steel substrate in a preparation chamber at a pressure 10^{-7} Torr, and then transferred to the experimental chamber operated at a pressure 10^{-10} Torr. The Cs M_{45} absorption spectra were obtained by measuring X-ray-induced photoconduction current through the sample.

3. Results and discussion

Figure 1 shows the photoabsorption spectrum of Cs halides. The vertical bars mark the energy positions of the Cs $3d_{5/2}$ and $3d_{5/2}$ thresholds in Cs halides, which were found by measuring Cs 3d binding energies with respect to the top of the valence band and adding the band-gap energies [4]. The measured absorption

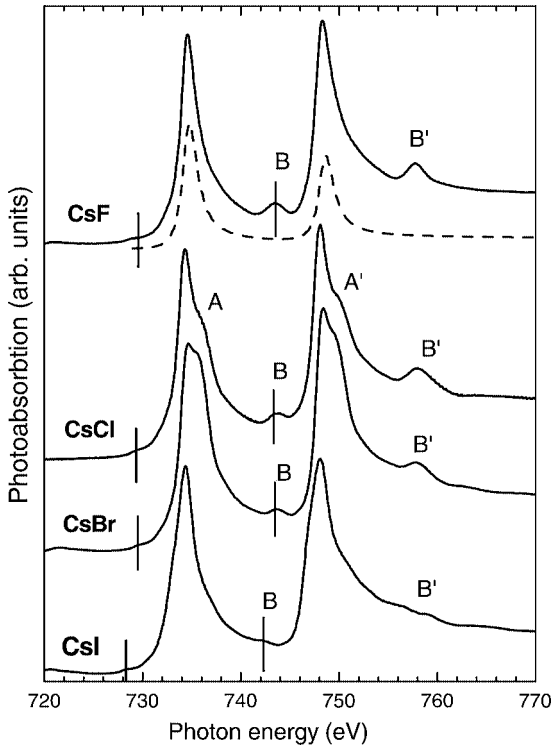

Fig. 1. Cs 3d X-ray absorption spectra of Cs halides (solid line). Vertical bars indicate the binding energies for Cs $3d_{5/2}$ and $3d_{3/2}$ levels relative to the conduction band. The calculated Cs^+ 3d subshell photoionization cross-sections (dotted). A value of −0.31 a.u. = −5.7 eV for the depth of the Watson sphere was used in calculating the cross-sections. A shift of 2.1 eV in the energy scale for the calculated curve was applied to align the first peak with the experimental one.

*e-mail: rein@fi.tartu.ee

spectra exhibit two strong peaks, asymmetric toward the high-energy side bands corresponding to the Cs $3d_{5/2}$ and $3d_{3/2}$ photoexcitations. These peaks are clearly above the ionization thresholds, thus the final states can be considered as the continuum states. In contrast to CsF and CsI where the main M_4 and M_5 peaks are similar to those found for the Cs atom [5], in CsCl and CsBr we see the high-energy shoulders (labeled as A and A' in Fig. 1) of the main line. These additional structures reflect the influence of the solid-state environment on the potential barrier for f electrons.

The experimental spectra show also two additional peaks (labeled as B and B′ in Fig. 1), which are very weak in CsI and are strongest in CsF. Since these peaks are absent from the atomic spectrum, the presence of these peaks should presumably be ascribed to the solid-state effects.

The absorption spectrum exhibits also a weak structure near the Cs $3d_{5/2}$ threshold. From the energy considerations it follows that this weak band may be due to transitions to the εp continuum of conduction band states.

The Hartree–Fock calculation of the 3d excitations shows that 4f orbital is collapsed in the free Cs^+ ion. But in crystals ions are completely screened by the surrounding ions. In the simplest approximation the electrostatic screening effects due to the solid environment can be described theoretically by the Watson sphere model [6]. In this model, the crystalline environment of an ion is approximated with a spherical shell of charge centered at the ion. The charge on the sphere is chosen to be equal in magnitude but opposite in sign to the charge of the ion.

For the present study, we modified the HF configuration average code of Cowan [7] by including Watson sphere model. Our calculations of the 3d excitations for the Cs^+ ion using the HF approximation in conjunction with the Watson sphere model show that the radial part of the 4f wave function crucially depends on the depth (V_c) of the potential well; if V_c becomes greater than -5 eV the mean 4f radius abruptly increases from 1.5 to 17 a.u. [8], i.e. 4f orbital becomes uncollapsed. Such strong changes we can see also for the 3d excited continuum states with f symmetry.

In Fig. 2 we display the results of the calculations of the photoionization cross section for the Cs^+ ion for different values of V_c . The curves show the development of the delayed onset of absorption for Cs^+, which is caused by the effective radial potential barrier effects for εf electrons. An electron excited above the 3d threshold into the εf channel will have to tunnel through the centrifugal barrier before it can escape from the atom. The increase of the depth (V_c) of the Watson potential well leads to the increase of the potential barrier for f electrons. At low kinetic energies of the εf photoelectron, the potential barrier prevents penetration of the εf wave into the inner region of the ion. Hence, the 3d-εf overlap is small as is the 3d → εf photoionization cross section. For higher kinetic energies, the εf probability strongly increases in the spatial region of the 3d electrons as also the 3d-εf overlap and the 3d → εf cross-section.

Another interesting feature to note in Fig. 2 is a gradual increase of width and asymmetry of the shape resonance with increasing height of the potential barrier. In the region of relatively small heights of the potential barrier, i.e. with $-V_c$ in the range of about 0.2–0.3 a.u., the intensity of the photoionization is concentrated in a narrow single peak that looks like a bound state. Note that in contrast to the strong potential barrier effects exhibited in the εf channel photoionization, the εp channel photoionization shows only very weak dependence on the choice of the parameters of the Watson sphere and is several orders of magnitude smaller than the εf channel cross-section.

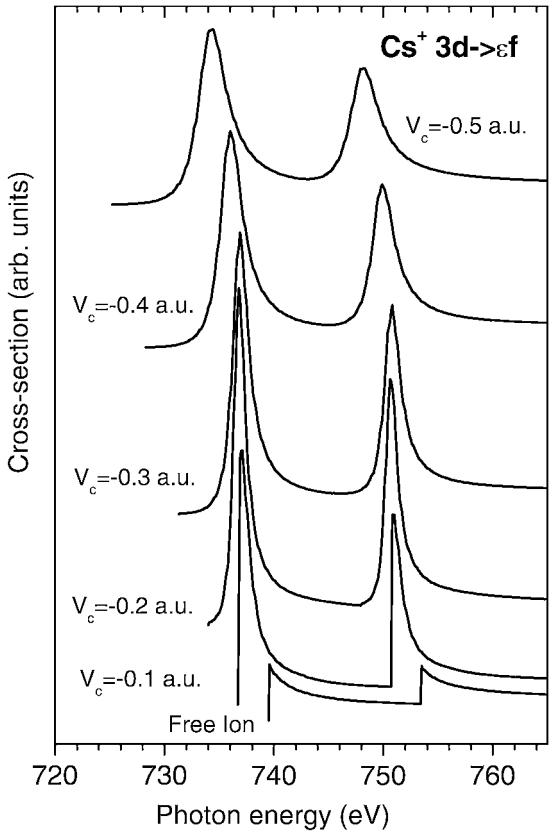

Fig. 2. Theoretical Cs^+ 3d photoionization cross sections calculated for different values of the depth of the Watson sphere V_c.

Unfortunately, the choice of the parameters of the Watson sphere (V_c) for a particular compound is substantially optional. Nevertheless, for the ionic crystals the physically justified parameters associated with the Watson sphere are the total charge Q, which equals the ionicity of the ion, and the $-V_c$, which is equal to the Madelung potential in the ion site, i.e. the potential ($-V_c$) at the ionic site coincides with the Coulombic crystal potential at that site. In Fig. 1, for CsF we show the comparison of the calculated photoabsorption cross-sections by using the Madelung potential value for Cs^+ ion ($V_c = -0.31$ a.u.) with the measured absorption spectrum.

The overall profile of the experimental spectrum is in good general agreement with the calculation, apart from an energy shift of ∼2.1 eV. However, the widths of the computed resonances are narrower than those observed experimentally, and relative peak intensities do not coincide exactly.

More detailed insights into the mechanisms of the Cs 3d absorption resonance can be gained from resonant decay spectra. The resonant photoemission studies are a very useful probe of the creation of localized states that are not accessible by other spectroscopic methods [9]. Since a shape resonance is considered as a temporary trapping of the photoelectron by the potential barrier and when the de-excitation time is comparable to the trapping time, the resonant decay spectra show spectral features, characteristic to the decay of the excited bound states. As an example we look into the details of the decay of the M_5 shape resonance in CsCl.

In Fig. 3 we present the photon energy dependence of the intensities of the peaks in resonant Auger spectra, obtained by the curve fitting analysis. The upper panel shows the intensities of 4d and 4p photoelectron lines, i.e. population of final 4d and 4p hole

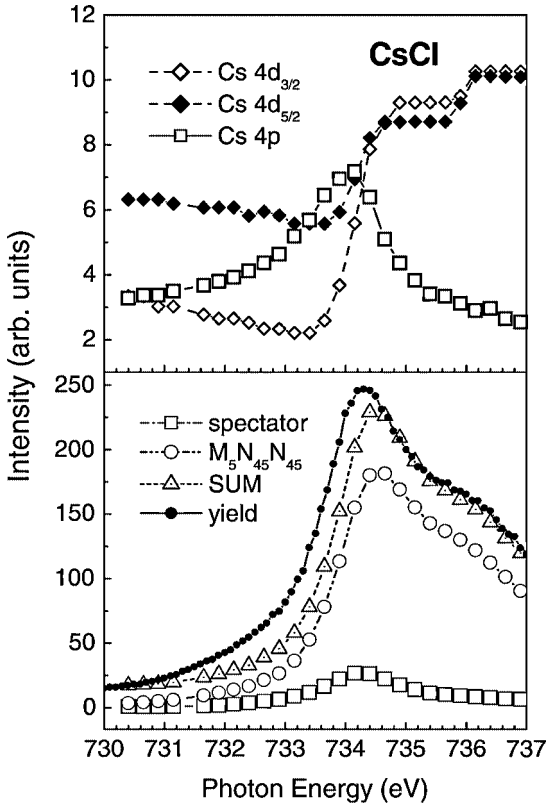

Fig. 3. The photon energy dependence of the different decay channels of the continuum Cs $3d_{5/2}$ resonance in CsCl, obtained from curve fits. The upper panel shows the cross-section of 4d and 4p participator channels while the lower one represents the spectral behavior of $M_5N_{45}N_{45}$ normal and 4f spectator Auger channels; a sum over the contributions of all these decay channels (labeled as SUM in Figure) and photoabsorption curve (labeled as yield).

states as a function of photon energy. These spectra thus represent the partial photoionization cross-section into a particular ionic state (Cs $4d^{-1}$ and $4p^{-1}$) and show enhancements in the region of the M_5 absorption resonance. As one can see in Fig. 3 the Cs $4d^{-1}$ partial photoionization cross-section show unexpectedly strong enhancement at the shoulder of the M_5 shape resonance. At the same time the enhancement of the Cs $4p^{-1}$ and $M_{45}N_{45}N_{45}$ 4f spectator intensities (in the lower panel of Fig. 3) is negligible. Moreover, as seen in Fig. 3 the spectral behavior of the Cs 4p partial photoionization cross-section is very different from that for the 4d spectral profiles. The similarity between the 4p cross-section and the 4f spectator photoemission signal (in the lower panel of Fig. 3) provides evidence that the observed spectral behavior of the 4p cross-section at Cs 3d absorption resonances originates from the $M_{45}N_{45}N_{45}$ 4f spectator transitions rather than from the participant decay transitions. However, because of strong configuration mixing of the $4d^84f + 4p^5$ final states, it is not exactly correct to separate the transitions to the single ($4p^5$) hole and double ($4d^84f$) hole states.

The different behavior of the 4d and 4p partial photoionization cross-sections can result from two different mechanisms. First, only the temporally and spatially trapped by the potential barrier εf electrons can gain additional intensity of the 4d partial photoionization cross-sections through the participator decay of the resonantly excited states, $3d^9\varepsilon f \rightarrow 4d^9$.

The second one may be considered as a result of the interaction of a low-energy εf photoelectron (de-excitation will take place after the electron has tunneled through the barrier) with a fast Auger electron *via* post-collision interaction, leading to the recapture of the photoelectron by the ionized core and, subsequently, to the transitions $3d^9\varepsilon f \rightarrow 4d^84f + 4p^5$, i.e. the enhancement of the 4f spectator as well as the 4p partial photoionization cross-sections.

Summarizing, we conclude that the appearance of the spectral features, which are intrinsic to a localized state, in the decay spectra show that the Cs 3d photoelectron, temporally and spatially trapped in the Cs 3d shape resonance due to the potential barrier for f electrons near threshold, has substantially localized nature. Our calculations of the 3d photoionization for the Cs^+ ion using the HF approximation in conjunction with the Watson sphere model show the importance of potential barrier effects in forming the shape resonances in the Cs 3d absorption.

Acknowledgment

This work is financially supported by the Estonian Science Foundation, by the European Community through the 5th Framework project "Access to Research Infrastructure Action of the Improving Human Potential Programme", and by "Centre of Excellence" Program. The authors are grateful to the staff of MAX laboratory for the assistance and co-operation.

References

1. Connerade, J. P., Contemp. Phys. **19**, 415 (1978); Kuchas, S. A., Karosene, A. V. and Karaziya, R. I., Izv. Akad. Nauk SSSR Ser. Fiz. **40**, 270 (1976).
2. Ruus, R. *et al.*, Phys. Rev. **B 49**, 14836 (1994).
3. Maiste, A. A., Ruus, R. E., Kuchas, S. A., Karaziya, R. I. and Elango, M. A., Zh. Eksp. Teor. Fiz. **78**, 941 (1979) [Sov. Phys. JETP **51**, 474 (1980)].
4. Poole, R. T., Phys. Rev. **B 11**, 5179 (1975).
5. Arp, U. *et al.*, J. Phys. B: At. Mol. Opt. Phys. **32**, 1295 (1999).
6. Watson, R. E., Phys. Rev. **111**, 1108 (1958).
7. Cowan, R. D., "The Theory of Atomic Structure and Spectra" (University of California Press, Berkeley, 1981).
8. Ruus, R., Ph.D. thesis, University of Tartu, (1999).
9. Wang, H. *et al.*, Phys. Rev. **A 50**, 1359 (1994).

Physica Scripta. Vol. T115, 399–401, 2005

In-situ XAFS Studies on Local Structures of Molten InSb Compounds

Shiqiang Wei[1*], Kunquan Lu[2], Chenxi Li[2], Wenjie Zhong[1], Wensheng Yan[1], Tomaya Uruga[3], Wei Chen[2], Xiaojuan Niu[2], Zhonghua Wu[4], Dongliang Chen[1] and Zhihu Sun[1]

[1]National Synchrotron Radiation Laboratory, University of Science and Technology of China, Hefei 230029, P. R. China
[2]Institute of Physics, Chinese Academy of Sciences, Beijing 100080, P. R. China
[3]Japan Synchrotron Radiation Research Institute, Kouto, Mikazuki, Sayo-gun, Hyogo 679-5198, Japan
[4]Institute of High Energy Physics, Chinese Academy of Sciences, Beijing 100039, P. R. China

Received June 26, 2003; accepted in revised form February 11, 2004

PACS numbers: 61.10.Ht, 61.25.Mv, 64.70.Dv.

Abstract

The local structures of semiconductor InSb compound have been studied by *in-situ* XAFS in the temperature range of 300 and 823 K. Reverse Mont Carlo calculation is used to simultaneously fit both In and Sb K-edge EXAFS functions $k\chi(k)$ of InSb compound. The fitting results indicate that the average bond length R_1 (2.80 Å) and the average coordination number N_1 (4.0) of the first In-Sb (or Sb-In) shell of InSb (723 K) are similar to those (2.79 Å, 4.0) of crystalline InSb (300 K) with a zinc-blende structure, in spite of InSb compound possessing a large thermal disorder degree at 723 K. At the temperature of 828 K ($T_{m(InSb)} = 798$ K), the R_1 and N_1 of the first In-Sb shell are 2.90 Å and 5.8, and the R_1 and N_1 of the first Sb-In shell are 2.90 Å and 5.5 for molten InSb, respectively. For molten InSb (828 K), the coordination numbers of the In-Sb (or Sb-In) first shell are mostly 5 and 6, and a few percent of In-In (or Sb-Sb) coordination appears in the first shell. It implies that the tetrahedron structures of the In-Sb (or Sb-In) covalent bonds of InSb compound have been destroyed in the liquid state.

1. Introduction

The studies of the structures and properties of molten matters have attracted wide interest recently, since some fundamental problems in liquid physics are not clear enough [1, 2], e.g., the mechanism of solid-liquid transition, the atomic and electronic structures of liquid semiconductors, metals and alloys. In particular, the III-V semiconductors with zinc-blende structure have exhibited some special properties upon the melting point, such as that the covalent bonds are destroyed, the density increases and a semiconductor-metal transition occurs. In the last two decades, Möller *et al.* [3], and Bellissent–Funel *et al.* [4] have succeeded in studying the structures of liquid metallic Sb and Ga with X-ray diffraction (XRD) and neutron diffraction (ND). However, normal XRD and ND techniques are not useful to study the structure of multi-component liquid matter, although the total partial correlation function can be obtained for GaAs [5] and GaSb [6]. In order to determine the partial correlation function of a multi-component system, a complicated experiment technique of anomalous X-ray scattering performed at different wavelengths or neutron scattering with isotopic substitution must be used [7].

Fortunately, X-ray absorption fine structure (XAFS) that is sensitive to the short-range order and atomic species surrounding the absorbing atom in a complicated matter, can obtain nice data with high ratio of signal to noise for molten matters, because of the applications of high brilliance synchrotron radiation light sources. Filipponi *et al.* [8] and Wang *et al.* [9] have investigated the local structures of liquid Rh, Pd and InSb with *in situ* XAFS. However, there are two difficulties in performing reliable XAFS data analysis for a large disorder system. One is that an unreasonable model-dependent pair distribution function used for the data analysis of a disorder system may lead to a large deviation. Another is that the multi-electron excitation can strongly affect the EXAFS oscillation signals of the molten matters. Hence, it is essential to propose a reasonable way for analyzing the XAFS data of condensed matters in the molten state.

In the present paper, *in situ* XAFS has been used to probe the local structures of pre-molten and liquid InSb compounds. The model-independent method of reverse Mont Carlo (RMC) calculation is used to simultaneously fit both In and Sb K-edge EAXFS functions $k\chi(k)$. It is possible to accurately and reliably determine the local structural changes of InSb compound from the solid state to the liquid state.

2. Experimental

An InSb sample used for XAFS measurement was prepared as the following procedures. Fine powder of InSb with sizes of about 10 μm prepared from single crystal was homogenously mixed with crystalline LiF powder. Then, the mixed powder was pressed into a tablet with diameter of 10 mm and thickness of 1 mm. The ratio of InSb to LiF powder was optimized by making the absorption jump $\Delta\mu x \approx 1$ at the In or Sb K-edge. The InSb tablet was sealed in a quartz sample holder that was composed of two thin quartz windows with thickness of 200 μm in a vacuum of 10^{-3} Pa. Our previous work has verified that InSb did not react with LiF at high temperature, even at temperatures above the melting point of InSb semiconductor [9].

The In and Sb K-edge XAFS spectra of InSb compound were measured in the XAFS station of BL01B1, SPring-8 of Japan Synchrotron Radiation Research Institute. The electron beam energy was 8.0 GeV and the maximum stored current was about 100 mA. X-rays covering a wide energy range ($4 \sim 113$ keV) is coming from the bending magnets. Si (311) double crystal was used as monochromator. A Rh-coted quartz mirror was used for the higher harmonics rejection. XAFS data were collected in transmission mode using ion chambers filled with mixed Kr/Ar gas at temperatures of 300, 723 and 828 K, respectively. The sample temperature was monitored by a Platinum-rhodium thermocouple placed between the sample and holder. XAFS data were analyzed by USTCXAFS [10] and UWXAFS3.0 codes [11].

3. Results and discussions

The normalized XAFS spectra and μ_0 background for the In and Sb K-edge of InSb measured at the temperatures 300, 723 and 828 K are shown as solid and dot lines in Fig. 1 (a) and

*Correspondent: Shiqiang Wei, E-mail: sqwei@ustc.edu.cn

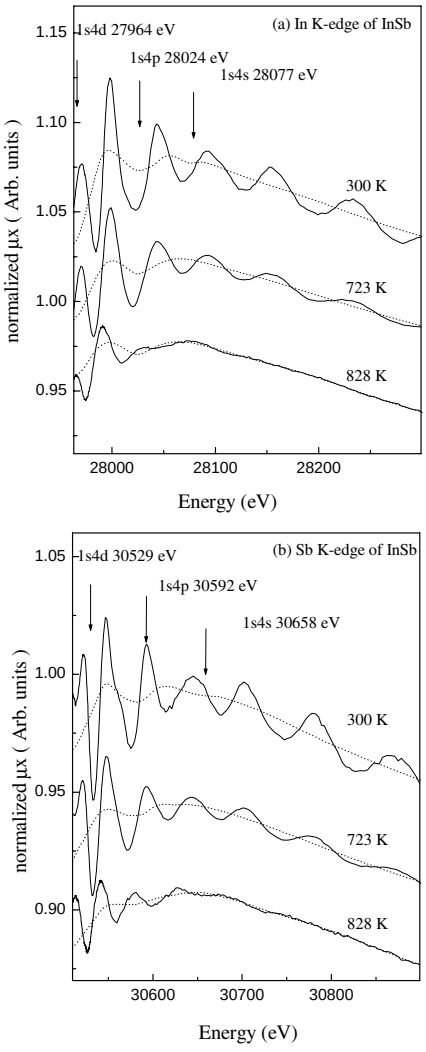

Fig. 1. Normalized XAFS spectra with μ_0 background removals for (a) In and (b) Sb K-edge of InSb fitted by arctangent functions.

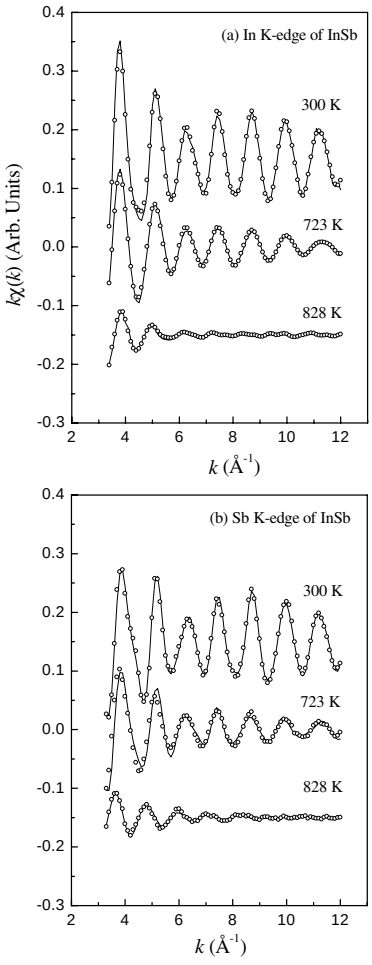

Fig. 2. RMC fitting results for (a) In and (b) Sb K-edge $k\chi(k)$ EXAFS functions of InSb at room temperature, pre-molten InSb (723 K) and molten InSb (828 K): experiment (solid line), fitting (open circle).

1 (b), respectively. The [1s4d], [1s4p] and [1s4s] double-electron excitations of In and Sb atoms in the InSb compound are noted by the arrows. Seen from both In and Sb K-edge XAFS spectra of InSb (300 K), the jump of [1s4d] excitation is much larger than that of the EXAFS oscillation peak. With going to [1s4p] and [1s4s] excitations, the jumps in the EXAFS oscillation curves of InSb (300 K) decrease greatly. For liquid InSb (828 K) ($T_m = 798$ K), the intensity of its EXAFS oscillations decreases significantly compared with that of crystalline InSb (300 K). One can observe unambiguously that the signals of double-electron excitation seriously affect the EXAFS oscillations of pre-molten and liquid InSb in the energy region of 20 $\sim$ 200 eV above the In and Sb K-edge. Here the μ_0 background, as shown in Fig. 1 (a) and (b), is fitted by an empirical model in which the jump is an arctangent function depending on amplitude, width and inflection point position [12].

Figure 2 (a) and (b) demonstrate the In and Sb K-edge EXAFS functions $k\chi(k)$ of the pre-molten and liquid InSb compounds (solid lines). It can be clearly seen that the positions of the oscillation peaks of InSb (723 K) are the same as those of InSb (300 K), whereas the intensity of oscillations strongly decreases with temperature from 300 K to 723 K. Compared with that of pre-molten InSb (723 K), the oscillation intensity of liquid InSb (828 K) further decreases, especially in the high k region. Moreover, the oscillation intensity of the In K-edge EXAFS functions in the high k-range drops faster than that of the Sb K-edge EXAFS functions in the liquid InSb (828 K). These results indicate that during the solid-liquid transition of InSb compound, the local structures around Sb and In atoms change markedly and the disorder degree around In atoms is slightly larger than that of Sb atoms for liquid InSb.

In order to quantitatively obtain local structural information of the pre-molten and liquid InSb, RMC calculation [13], a model-independent method, is used to simultaneously fit the In and Sb K-edge EXAFS functions $k\chi(k)$ of InSb compound. In the RMC simulation, the initial configuration having 512 In and Sb atoms in a cubic cell with length L of 24.8466 Å is used to fit the experimental $k\chi(k)$ spectra of molten InSb compound. The atomic number is determined by the chemical composition and mass density of InSb at the measurement temperature. The range for the EXAFS fitting is in R space of 0 $\sim$ 6 Å and k space of 2.5 $\sim$ 12.0 $Å^{-1}$. A new configuration is generated by random motion of one particle (In or Sb atom). A new partial correlation function $g'(r)$ is then calculated from this configuration. If the simulated $k\chi(k)$spectrum is in good agreement with the experiment data, the fitting is completed and $g(r)$ is obtained by calculating the average result of the last 200 configurations. The fitting curves are shown in Fig. 2 (a) and (b) (opened circles).

Figure 3 displays the $g(r)$ partial correlation functions of In-Sb and Sb-In shells of InSb compound measured at pre-molten and liquid states. In the temperature region from 300 to 723 K, the sharp peaks corresponding to the first and the second In-Sb (or

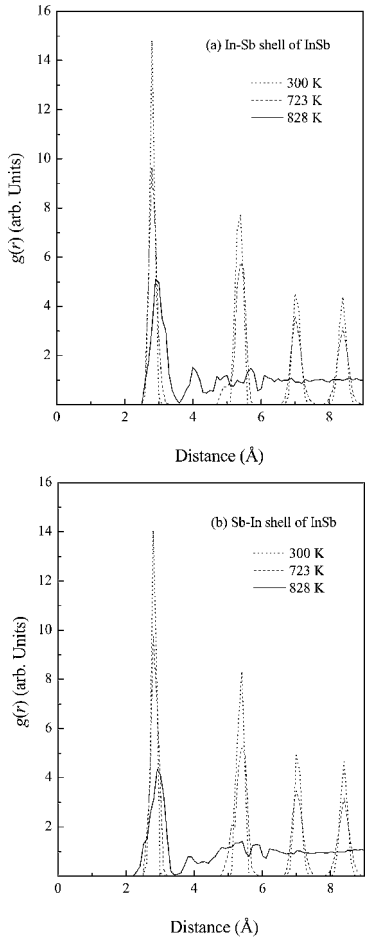

Fig. 3. Partial correlation functions of (a) In and (b) Sb atoms of InSb at 300, 723 and 828 K.

Sb-In) shells have the same positions at 2.8, 5.4 Å, respectively. For liquid InSb (828 K), only the main peak of the first nearest neighbor of In-Sb (or Sb-In) shell appears while the peaks of the higher shells are much lower. Moreover, the main peak shifts to 2.9 Å and its intensity strongly decreases and broadens for liquid InSb (828 K), as compared with that of the pre-molten InSb (723 K). The average coordination number N_1 calculated from the partial correlation functions of the first nearest neighbor around In (or Sb) atoms is 4.0 (or 4.0), 4.0 (or 4.0) and 5.8 (or 5.5) for the In-Sb (or Sb-In) shell at temperatures of 300, 723 and 828 K, respectively. Upon the melting point, the N_1 of In-Sb shell increases 1.8 and the N_1 of Sb-In shell increases 1.5 for the liquid InSb (828 K). It means that the coordination number in the In-Sb first shell is about 0.3 larger than that in the Sb-In first shell for the liquid InSb (828 K). This shows that there is a difference in the local structures around the In and Sb atoms in molten InSb (828 K).

It is well known that the In (or Sb) atoms in solid InSb crystal with zinc-blende structure are coordinated by four Sb (or In) atoms in the form of In-Sb covalent bond in the first nearest neighbor. Our fitting results show that R_1 and N_1 of the first In-Sb (or Sb-In) shell are 2.80 Å and 4.0 for pre-molten InSb (723 K), identical to those of InSb (300 K). This implies that the RMC calculation is reliable, since the RMC structural parameters of InSb compound in the pre-molten solid state is equal to those of crystalline InSb semiconductor. For liquid InSb (828 K), R_1 of In-Sb (or Sb-In) shell slightly elongates to 2.90 Å and the average coordination number N_1 of In-Sb (or Sb-In) shell largely increases to 5.8 (or 5.5). This means that the tetragonal covalent coordination of In (or Sb) atoms in the molten state is destroyed. Wang *et al.* [9] have reported that the coordination number N_1 of the In-Sb shell was 5.2 from the In K-edge XAFS results of liquid InSb. Wang's result is close to our results. With neutron diffraction, Bergman *et al.* [14] have studied the structure of liquid GaAs, and Mizuki *et al.* [6] have studied the structure of liquid GaSb. They both reported the coordination number of the first nearest neighbor to be $5.4 \sim 5.5$. These results are similar to ours, suggesting the similarity of the local structures in liquid GaAs, GaSb and InSb. Calculated from the final configuration of our fitting results, the coordination numbers of the In-Sb (or Sb-In) first shell are mostly 5 and 6 and about few percent In-In (or Sb-Sb) coordination is in the first shell around In (or Sb) atoms for molten InSb (828 K). Moreover, Wang *et al.* [9] considered that there is heterogeneous atomic coordination in the first shell of liquid GaSb, i.e., Ga is mainly surrounded by Sb atoms and partly coordinated by Ga atoms.

In conclusion, the XAFS results obtained from In and Sb K-edge XAFS spectra indicate that the melting destroys the tetragonal covalent network in crystalline InSb semiconductor. In the molten state, the average coordination number N_1 and the average bond length R_1 of the first nearest neighbor around In (or Sb) increases by $1.5 \sim 1.8$ and 0.1 Å for liquid InSb (828 K), and a few percent In-In (or Sb-Sb) coordination appears in the first shell of molten InSb (828 K). These results are key-factors in interpreting the transition of semiconductor-metal and the increase of density during the solid-liquid transformation of InSb semiconductor.

Acknowledgments

We would like to thank SPring-8 for giving us beam time for XAFS measurement. This work was supported by the Chinese National Science Foundation Committee (Grant No.10174068), the development of high-level university of University of Science and Technology of China and Knowledge Innovation Program of the Chinese Academy of Sciences.

References

1. Crozier, E. D., Physica B **208–209**, 330 (1995).
2. Filipponi, A., J. Phys.: Condens. Matter **13**, R23 (2001).
3. Möller, H. K. F. and Hendus, H., Z. Naturforsch. **12a**, 102 (1957).
4. Bellissent-Funel, M. C., Levesque, D. and Weis, J. J., Phys. Rev. A **39**, 6310 (1989).
5. Zhang, Q. M., Chiamtti, G., Selloni, A., Car, R. and Paninello, M., J. Non. Cryst. Solids **117**, 8930 (1990).
6. Mizukil, J., Kakimotot, K., Misawat, M., Fukunagas, T. and Noboru, W., J. Phys.: Condens. Matter **5**, 3391 (1993).
7. Enderby, J. E., North, D. M. and Egelstaff, P. A., Philos. Mag. **14**, 961 (1966).
8. Filipponi, A., Di Cicco, A. and Panfilis, S. D., Phys. Rev. Lett. **83**, 560 (1999); J. Phys.: Condens. Matter **11**, L43 (1999).
9. Wang, Y. R., Lu, K. Q. and Li, C. X., Phys. Rev. Lett. **79**, 3644 (1997).
10. Zhong, W. J. and Wei, S. Q., J. Univ. Sci. Tech. China **31**, 328 (2001).
11. Stern, E. A., Newville, M., Ravel, B., Yacoby, Y. and Haskel, D., Physica B **208&209**, 117 (1995).
12. Li, G., Bridges, F. and Brown, G. S., Phys. Rev. Lett. **68**, 1609 (1992).
13. Gurman, S. J. and McGreevy, R. L., J. Phys. CM **2**, 9463 (1990).
14. Bergman, C., Bichara, C., Chieux, P. and Gaspard, J. P., J. de Physique **C8**, 97 (1985).

Physica Scripta. Vol. T115, 402–404, 2005

XAFS Study on Cathode Materials for Li-ion Batteries using X-ray Microbeam

Takamasa Nonaka*, C. Okuda, H. Nakano, Y. Ukyo and Y. Seno

TOYOTA Central Research & Development Laboratories, Inc., Nagakute, Aichi, 480-1192, Japan

Received June 26, 2003; accepted October 15, 2003

Abstract

We attempted to investigate whether the Ni valences change homogeneously in a grain of $LiNi_{0.8}Co_{0.2}O_2$ during charging/discharging Li-ion batteries. *In situ* XAFS measurements using X-ray microbeam with the size of about 1–2 μm were applied to measure position dependencies of Ni (Co) valences in a grain. In order to investigate the electronic changes caused by capacity fading, three types of coin cells for *in situ* XAFS measurements were prepared, the cell after one charge/discharge cycle, after 100 cycles at 60 °C and after aging at 60 °C for 21 days, respectively. Two-dimensional fluorescence maps of Ni and Co were obtained to determine measuring points in a grain (the center of a grain, the edge of a grain, etc.). Ni and Co K-edge XAFS spectra were collected in transmission mode for each point. As a result, no apparent differences depending on positions were observed for all types of the cells. It was concluded that the changes of Ni valences during charging/discharging batteries occur homogeneously in a grain, not depending on the degree of capacity fading.

1. Introduction

$LiNi_{0.8}Co_{0.2}O_2$ is one of the current candidates as a cathode material for advanced rechargeable batteries having high capacities. It is known that the stability of $LiNi_{0.8}Co_{0.2}O_2$ is superior to that of $LiNiO_2$ because it exhibits a single-phase region upon oxidation from 3.0 V to 4.1 V [1]. However, capacity fading occurs not only during charge/discharge cycling but also when batteries are stored at high temperatures. Thus, capacity fading is the most important problem facing practical use. From the standpoint of overcoming capacity fading, it is essential to understand the electronic and structural changes that accompany capacity fading. In our previous work, these changes have been studied by *in situ* XAFS measurements, where the relationship between these changes and the capacity fading were revealed [2].

In our practical uses of Li-ion batteries, $LiNi_{0.8}Co_{0.2}O_2$ is formed into grains with the size of about 10–20 μm. If the electronic changes have position dependencies in each grain, (for example, the Ni valence at the center of a grain is higher than that at the edge of a grain), our understanding of capacity fading has to be modified. So it is worth investigating whether the electronic and structural changes occur homogeneously in each grain. Furthermore, the information about homogeneity of Ni (Co) valences is of great significance in developing batteries with this cathode material. In this work, we studied the local valence changes in a grain by *in situ* XAFS using X-ray microbeam with the size of about 1–2 μm.

2. Experimental

Fig. 1 shows a drawing of the coin cell developed for *in situ* XAFS measurements in transmission mode. By using 0.4 mm Beryllium windows, the X-rays can penetrate through the cell. XAFS data can be obtained at various voltages without taking the cathode material out of the cell. In order to make each spectrum reflect the information from only one grain, the thickness of cathode was controlled to be less than 100 μm. To investigate the changes resulting from cycling and storing at high temperatures, three types of cells were prepared, the cell after one charge/discharge cycle, after 100 cycles at 60 °C and after aging at 60 °C for 21 days, respectively. The conditions of cells used in this study are listed in Table I.

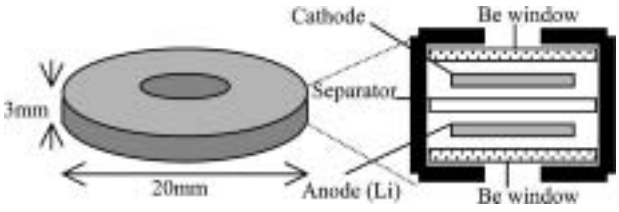

Fig. 1. Schematic drawing of an *in situ* coin cell.

Table I. *Conditions of in situ coin cells.*

Condition	Capacity (relative value)
After one charge/discharge cycle	100
After 100 charge/discharge cycles at 60 °C	66
After storing at 60 °C for 21 days	91

The experiments were carried out on BL16XU [3] at SPring-8. BL16XU has an X-ray optical system to generate X-ray microbeam using two elliptical mirrors with a Kirkpatric-Baez (KB) configuration [4]. Comparing with other methods for microbeam generation such as zone plates, KB mirror method is suitable for XAFS measurements because X-ray energy is tuneable with the focus point fixed. The KB mirrors can focus X-rays in a small area ranging from microns to submicrons in size at the sample position. The full width at half maximum of the microbeam used in this study was about 1–2 μm, estimated from knife-edge test results. Fig. 2 illustrates the experimental setup for this study. X-ray microbeams are irradiated to a sample mounted on a high-precision two-dimensional moving stage. Fluorescence and transmission maps can be obtained by scanning the sample with respect to the microbeams. A silicon semiconductor detector (SSD) and an ionization chamber are employed to collect fluorescent and transmitted X-rays, respectively.

The experimental procedure was as follows. A coin cell was mounted on the sample stage with its voltage kept at 3.0 V. Ni and Co distribution maps were obtained at 9.0 keV to determine points for XAFS measurements. At several points, Ni and Co K-edge

*e-mail: nonaka@mosk.thtlabs.co.jp

XAFS spectra were collected in transmission mode. After XAFS measurements for all points were finished, the cell was charged to a voltage of 4.2 V. XAFS measurements were performed at the same points as 3.0 V. The same procedure was repeated to obtain XAFS spectra for the cell after discharging.

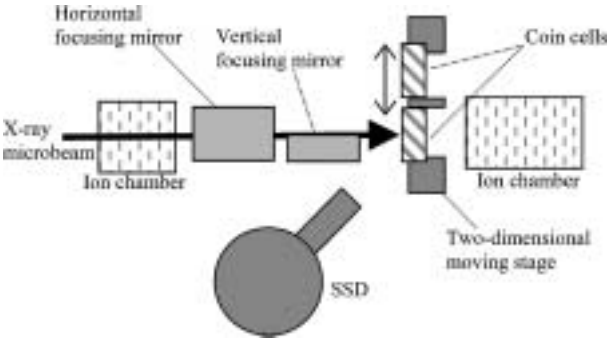

Fig. 2. Experimental setup for microscopic XAFS in transmission mode (top view).

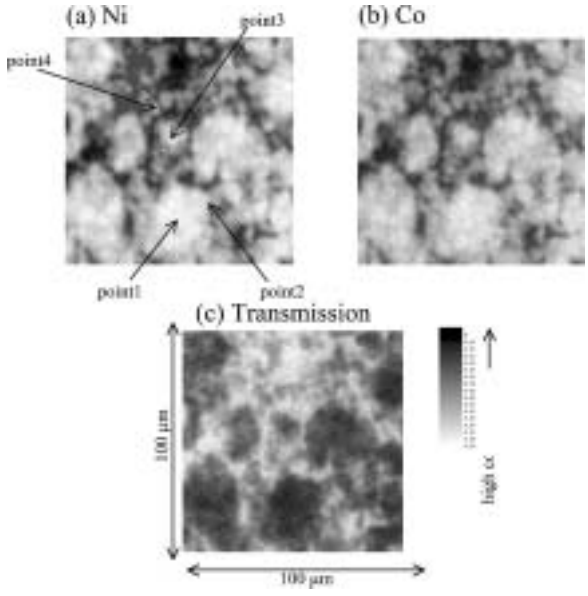

Fig. 3. (a) Ni fluorescence map, (b) Co fluorescence map, (c) transmission map for the cell after one charge/discharge cycle. All maps were obtained at initial state (before charging the cell).

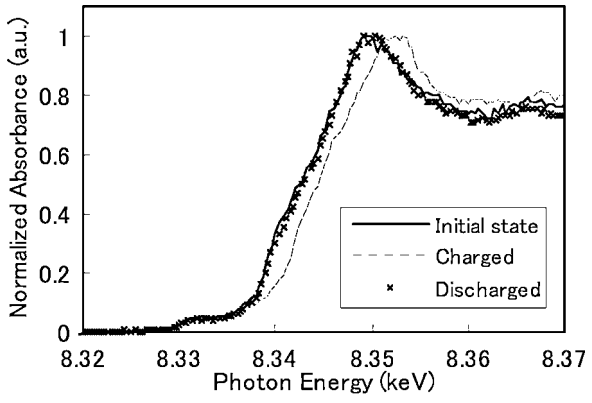

Fig. 4. Ni K-edge XANES spectra measured at point 2 (the edge of a grain) for the cell after one charge/discharge cycle.

3. Results and Discussion

3.1. *Cell after one charge/discharge cycling*

Ni (Co) fluorescence and transmission maps are shown in Fig. 3. Grains of cathode materials with the size of 10–20 μm can be clearly recognized in the fluorescence maps. The distribution of Co appears to be perfectly equal to that of Ni, indicating uniform mixing of Ni and Co. The transmission map is seen to be the "negative image" of Ni and Co fluorescence maps, which demonstrates that the thickness of the cathode is thin enough to prevent grains from piling up along the path of X-rays. Fig. 4 shows the change of Ni K-edge spectra upon charging/discharging at the edge of a grain (point 2). The absorption edge shifts to higher energy after

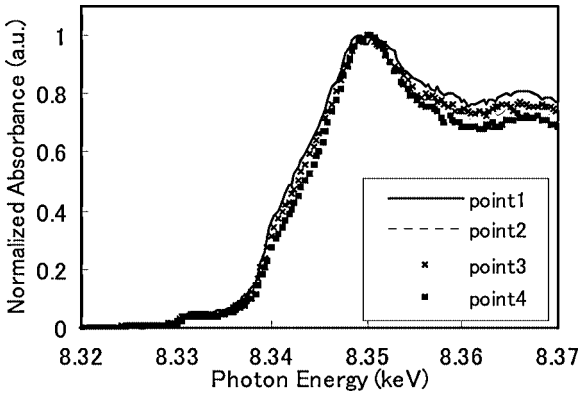

Fig. 5. Comparison of Ni K-edge XANES spectra measured at several points for the cell after one charge/discharge cycle (initial state).

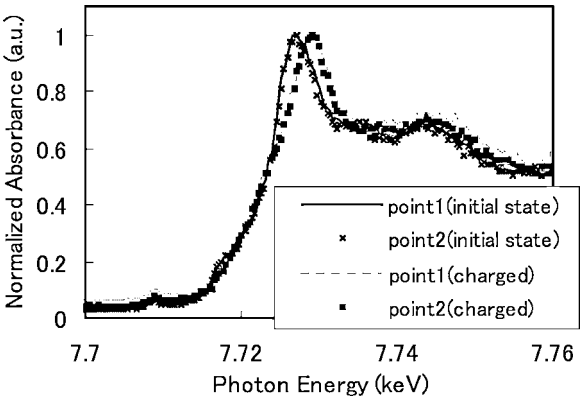

Fig. 6. Co K-edge XANES spectra for the cell after one charge/discharge cycle.

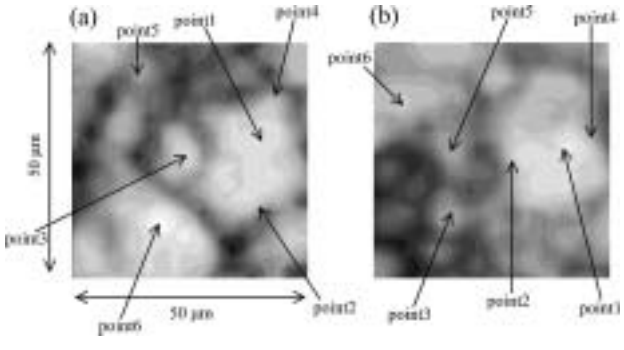

Fig. 7. Ni fluorescence maps for (a) cell after 100 cycles at 60 °C (b) cell after aging at 60 °C for 21 days.

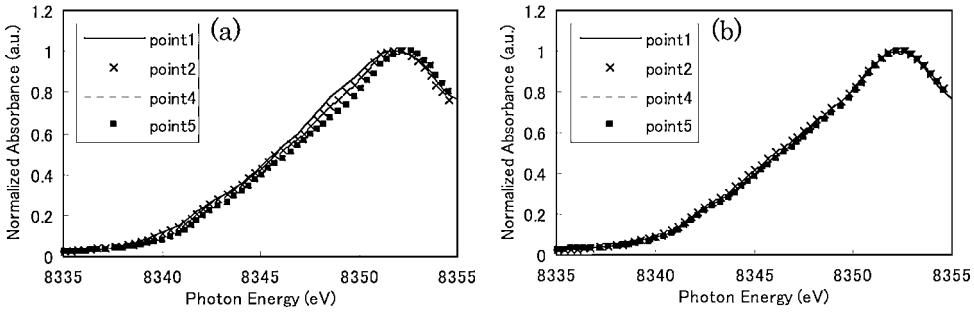

Fig. 8. Comparisons of Ni K-edge XANES spectra measured at several points for (a) cell after 100 cycles at 60°C (b) cell after aging at 60°C for 21 days (charged state (4.2V)).

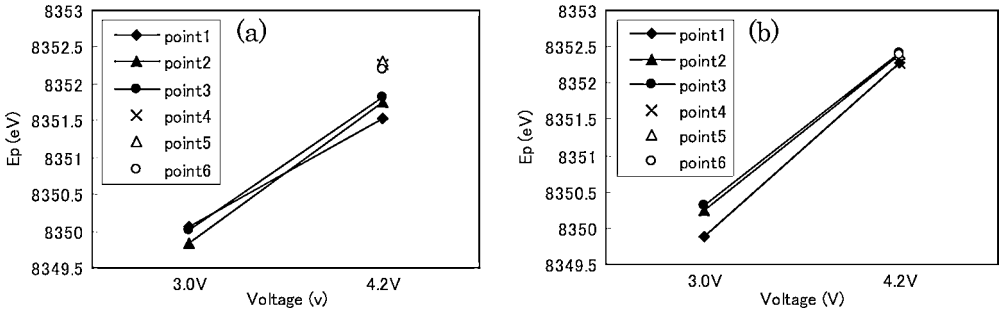

Fig. 9. Comparisons of Ni K-edge peak energies as a function of cell voltages for (a) cell after 100 cycles at 60°C (b) cell after aging at 60°C for 21 days. Ep: the energy at the maximum height of the edge jump.

charging the cell and returns to the same energy as the initial state reversibly after discharging. These chemical shifts corresponds to the change of Ni valence (from 3+ to 4+ upon charging, from 4+ to 3+ upon discharging) caused by the removal/insertion of lithium [5]. The position dependency of Ni K-edge spectra in its initial state is shown in Fig. 5. No apparent position dependency was found. Also in charged state, position dependency was not found. These results indicate that the changes of Ni valences occur homogeneously in a grain and have no dependency on grain size.

An example of Co K-edge spectra is shown in Fig. 6. As well as the result of Ni, we could not find any difference between each spectrum measured at different position.

3.2. *Cell after 100 cycles at 60°C, cell after aging at 60°C for 21 days*

Ni fluorescence maps are shown in Fig. 7 and the position dependencies of Ni K-edge XANES spectra obtained at charged state (4.2V) are shown in Fig. 8. The S/N ratios of these spectra are better than those of the cell after one charge/discharge cycling. It is supposed that the difference in S/N ratios is due to the difference in X-ray intensities. (The measurement described in 3.1 was done on another day from the day for the measurements described in 3.2.) XANES spectra shown in Fig. 8(a) seem to have position dependencies. In order to make this difference clear, a quantitative analysis was performed as follows. Graphical comparisons of the edge peak energies as a function of cell voltages are shown in Fig. 9. The edge peak energy E_p is defined here as the energy at the maximum height of the edge jump. In the cell after 100 cycles, the edge peak energies of point 4–6 are higher than those of point 1–3 (Fig. 9(a)). There is, however, possibility that these gaps of energies originate from the effect of X-ray irradiation. The measurements for point 4–6 were done once, on the other hand, the measurements for point 1–3 were done twice (at 3.0V and 4.2V). It is assumed that X-ray microbeams could cause local alterations of electrolytes and lead to lower oxidation states of Ni at points irradiated twice. The further experiments with increasing measuring points are needed to confirm this assumption. Except for the gaps described above, any apparent position dependency was found. At the present time, we concluded that the changes of Ni valences with charging a capacity faded cell occur homogeneously in a grain and have no dependency on grain size.

4. Conclusion

We attempted to investigate whether the Ni Valences change homogeneously in a grain of $LiNi_{0.8}Co_{0.2}O_2$ during charging/discharging Li-ion batteries. *In situ* XAFS measurements using X-ray microbeam with the size of about 1–2 μm were applied to measure position dependencies of Ni (Co) valences in a grain. As a result, no apparent differences depending on positions were observed for all types of the cells. It was concluded that the changes of Ni valences during charging/discharging batteries occur homogeneously in a grain, not depending on the degree of capacity fading.

The information obtained with this study is of great significance in developing batteries with this cathode material and also in understanding capacity fading. The experimental techniques described here can become strong tool in the analysis of Li-ion batteries.

References

1. Levi, E. *et al.*, Solid State Ionics **126**, 97 (1999).
2. Nonaka, T., Okuda, C., Ukyo, Y. and Okamoto, T., J. Synchr. Radiat. **8**, 869 (2001).
3. Hirai, Y. *et al.*, SPring-8 Annual Report 1999, 100 (1999).
4. Hasegawa, M. and Hirai, Y., J. Appl. Phys. **90**, 2792 (2001).
5. Nakai, I., J. Power Sources **68**, 536 (1997).

Physica Scripta. Vol. T115, 405–407, 2005

Tin and Niobium in Dry and Fluid-Rich (H_2O, F) Silicate Glasses

P. C. Piilonen[1,2,*], F. Farges[1,3], R. L. Linnen[4] and G. E. Brown Jr.[3,5]

[1]Laboratoire des Géomateriaux, Université de Marne-la-Vallée, CNRS FRE 2455, 77454 Marne-la-Vallée cedex 2, France
[2]Canadian Museum of Nature/Musée canadien de la nature, Ottawa, Ontario K1P 6P4, Canada
[3]Department of Geological and Environmental Sciences, Stanford University, California 94305-2115, USA
[4]Department of Earth Sciences, University of Waterloo, Waterloo, Ontario N2L 3G1, Canada
[5]Stanford Synchrotron Radiation Laboratory, Menlo Park, California 94025, USA

Received June 26, 2003; accepted in revised form November 24, 2003

PACS numbers: 61.10.Ht, 61.43.Fs, 91.65.Nd, 91.65.Rg

Abstract

The speciation of niobium and tin in 29 silicate glasses was investigated by XAFS at the Nb and Sn K-edges using beamline 4-3 and 11-2 at SSRL (Stanford, USA). The metal content in the glasses varies between 100 ppm and 5 wt.% (to examine the effects of Nb_2O_5 and SnO_2 saturation in the melt composition prior quenching). The glasses show variation in composition from peralkaline to peraluminous, with either zero or ∼2 wt.% fluorine. In addition, hydrous glasses were quenched from water-saturated melts at 850 °C and 2 kbar under relatively reducing conditions. Three "haplogranitic" compositions (a model granite in the system Na_2O-K_2O-AlO_3-SiO_2) were investigated: peralkaline (labeled "ASI 0.6"), metaluminous ("ASI 1.0") and peraluminous ("ASI 1.2"). One series of haplogranitic glasses ("SQ") were synthesized at intermediate oxygen fugacity conditions (∼10^{-9} atm.). In addition, 15 model oxide and silicate compounds of tin and niobium were investigated.

The tin-bearing glasses show Sn K-edge XAFS spectra that resemble that displayed by eakerite, a Ca-Sn silicate in which Sn(IV)O_6 octahedra share corners with SiO_4 tetrahedra (⟨Sn-O-Si⟩: 150°). However, the most reduced glasses show significant contributions arising from weakly bound Sn(II)O_n complexes. The niobium-bearing glasses show Nb K-edge XAFS spectra that most closely resemble that displayed by vuonnemite, a Na-Ti-Nb silicophosphate. Niobium forms NbO_6 clusters, also bonded to Si/Al second neighbors. The coordination geometry of niobium in the glasses is strongly influenced by both Nb content and alkalinity; H_2O content does not strongly influence the speciation of niobium. Fluorine-bearing Nb-glasses show unusual XANES spectra, which might be related to a decrease in the coordination number of niobium from 6 to 4 (or 5). However, based on Nb K-edge XANES calculations (FEFF 8), fluorine does not appear to complex niobium.

1. Introduction

Tin and niobium are geochemically unusual, because they concentrate into late-stage magmas and hydrothermal fluids [5]. A growing body of evidence suggests that the behavior of such elements is highly dependent on the alkalinity and the presence of volatile elements (such as water, fluorine) of the parental melt/fluid. Recent experimental studies [1–4] involving these elements have focused on their solubility, diffusivity and mobilization in both hydrous and anhydrous melts and glasses. However, no speciation studies are available to ascertain these macroscopic properties. In this study, we utilize XAFS spectroscopy to elucidate the speciation and coordination geochemistry of tin and niobium in anhydrous, water-saturated and fluorine-bearing alkaline and haplogranitic melts in order to better understand their behavior in natural magmatic systems.

*Corresponding author (e-mail: ppiilonen@mus-nature.ca)

2. Experimental Methods

The tin-bearing glasses studied were quenched from water-saturated melts at 800 °C and 2 kbar. Three haplogranitic compositions were investigated: (1) peralkaline (labeled "ASI 0.6", where the 0.6 is the "alumina saturation index", i.e., the $Al_2O_3/(Na_2O + K_2O)$ molar ratio), (2) metaluminous ("ASI 1.0") and (3) peraluminous ("ASI 1.2"). One series of glasses ("SQ") were synthesized at the Bayerisches Geoinstitut, Bayreuth (Germany) at intermediate oxygen fugacity (f_{O_2}) conditions (∼ 10^{-12} atm. at 800 °C). Two other series ("AL" and "GB") were synthesized at the CRSCM (Orléans, France) at more oxidized and more reduced conditions, respectively. The amounts of Sn^{4+} were predicted based on cassiterite solubility measurements [2].

The niobium-bearing glasses (1000 ppm Nb to 5 wt.% Nb_2O_5) were quenched from melts at 850 °C and 2 kbar. Two haplogranitic compositions were investigated: (1) peralkaline (ASI 0.6) and (2) peraluminous (ASI 1.2). Niobium-bearing glasses of these compositions were either dry, wet (water saturated, ∼5 wt.% H_2O) or contained ∼2 wt.% F. Additional anhydrous sodium silicate glasses (NS2 and NS3) were synthesized at ENS (Lyon, France) at 1200 °C and 1 bar containing between 1000 ppm Nb and 3 wt.% Nb_2O_5.

X-ray absorption spectroscopy was performed at the Stanford Synchrotron Radiation Laboratory (SSRL) using spectrometers 4-1 and 11-2. Room temperature X-ray absorption fine structure (XAFS) spectra were collected at the Nb K absorption edge (∼19 keV) and the Sn K-edge (∼29 keV) using a Si(220) double crystal monochromator and a Stern-Held fluorescence detector (3 mm Zr filter and Ag Soller-slits) filled with Xe. Energy resolution is ∼ 4 eV. Nb and Sn foils were used for calibration purposes.

3. Results and Discussion

3.1. *Sn model compounds and glasses*

The tin-bearing crystals investigated included cassiterite (Bolivia and Malaysia), eakerite [$(Ca_2SnAl_2Si_6O_{18}(OH)_2 \cdot 2(H_2O)$] various perovskite-based polymorphs ($SnSrO_3$, $CaSnO_3$ and $CdSnO_3$), SnO , $SnCl_2$ and metallic Sn. No clear shift of the edge between Sn^{2+} and Sn^{4+} is observed due to low resolution at the Sn K-edge (∼6 eV). However, Sn^{2+}-O and Sn^{4+}-O distances are very different (due to ionic radii differences). Finally, Sn-O bonds are much more ionic, adding to the challenge of collecting noise-free EXAFS spectra in Sn^{2+}-rich samples. No evidence of SnO_2 saturation was observed at the Å-scale in any of the glasses studied, which validates previous macroscopic measurement on tin solubility in these glasses (see [1–4]).

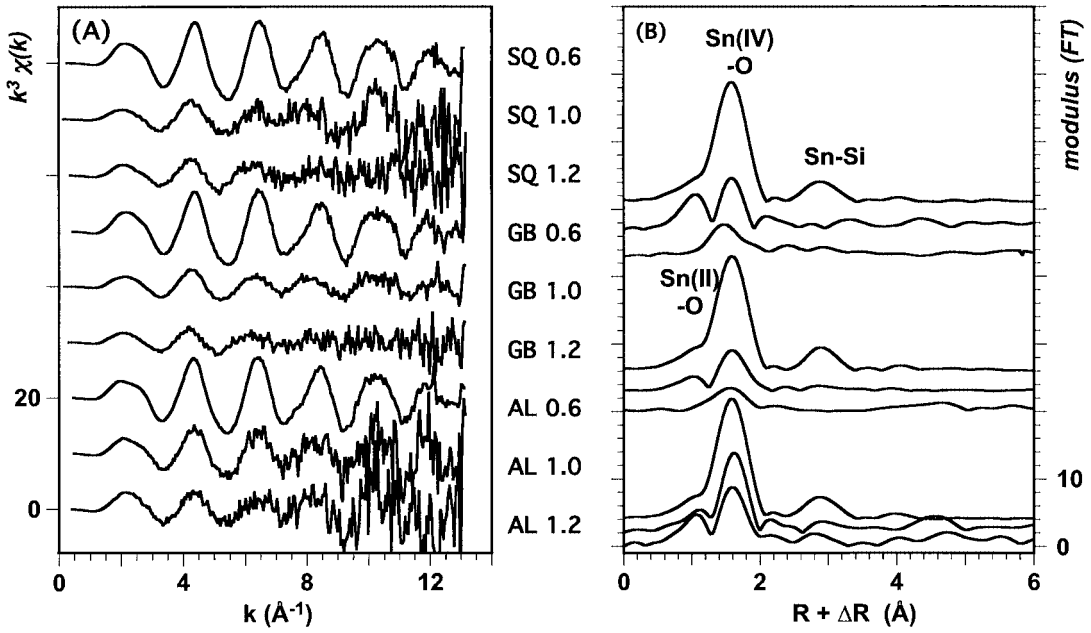

Fig. 1. Sn-bearing glasses. A. Sn K-edge normalized (k^3-weighted) EXAFS spectra for each series of glasses investigated. B. Fourier-transforms of normalized EXAFS spectra shown in (A), showing contributions arising from first oxygen neighbors and distant network formers such as Si in eakerite model compound.

Large changes detected in the XANES spectra of the tin-bearing glasses are related to changes in the oxidation state of tin and its local environment. In general, tetravalent tin displays environments (Fig. 1) close to those measured in eakerite [6], suggesting that Sn bonds to the tetrahedral framework and is charge-compensated by network modifiers such as sodium. $Sn^{4+}O_6$ octahedra share corners with SiO_4 tetrahedra (⟨Sn-O-Si⟩: 150°). By contrast, Sn^{2+} forms more ionic complexes which are less connected to the glass structure. However, changes in melt composition (such as peralkalinity and water content) does not change drastically the tin speciation in these glasses.

3.2. *Nb model compounds and glasses*

Niobium model compounds include the silicates vuonnemite (from Canada and Russia), labuntsovite (Russia), the orthophosphate olmsteadite (USA) and the oxides pyrochlore (Canada) and columbite (Africa and Canada). Niobium in natural minerals is always found as Nb^{5+} in octahedral-coordination. Distances to nearest neighbors in niobium minerals span a range from 1.76 to 2.26 Å. There is no evidence for a change in oxidation state in the model compounds from Nb^{5+}.

Changes detected in the XANES spectra of the Nb-bearing glasses (Fig. 2) are dominantly the result of changes in niobium content and alkalinity. The presence or absence of H_2O in the melt does not appear to have an effect on the local structure of Nb, in agreement with [8]. Niobium occurs solely as Nb^{5+} and is present in 6-coordinated environments. The local coordination geometry of niobium in the silicate glasses is similar to that of $^{[6]}$Nb in the silicophosphate mineral vuonnemite [7]. In vuonnemite, the dominant contribution in the EXAFS spectra is due to Nb-O bonds. A weaker and more distant contribution arises from

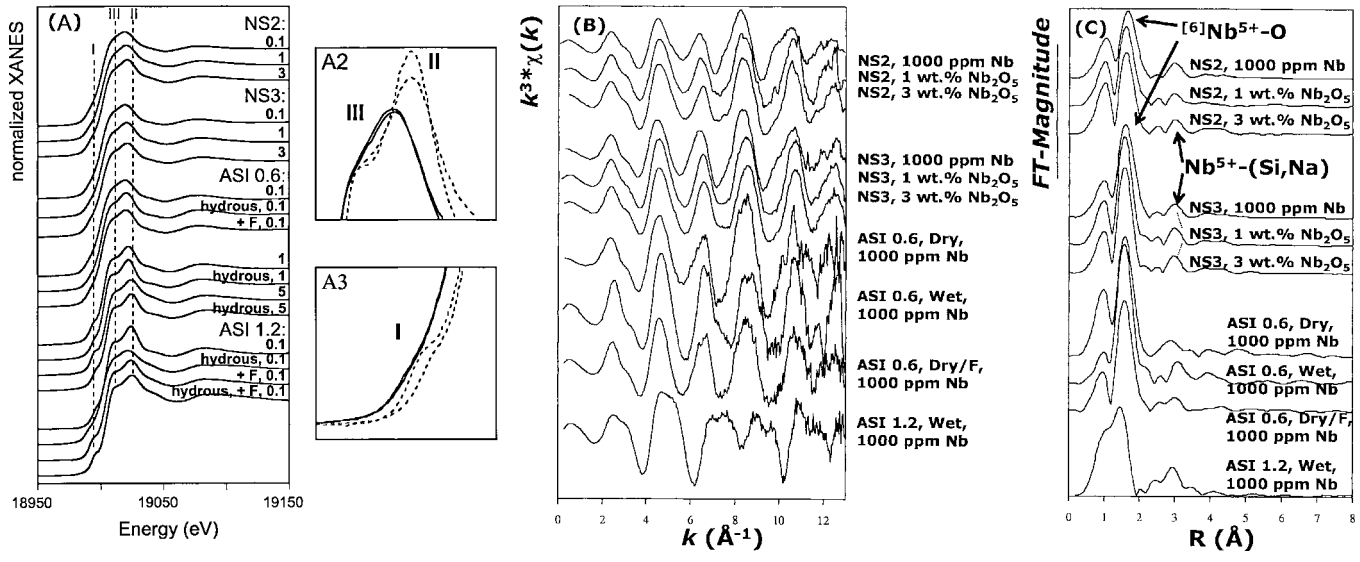

Fig. 2. Nb-bearing glasses. A. XANES spectra; A2: zoom on edge crests in 0.1 wt.% Nb glasses. The relative magnitude of the low energy shoulder increases with decreasing alkalinity; A3: zoom the on pre-edge (feature I). Feature I increases in height with decreasing alkalinity. B. Normalized (k^3-weighted) EXAFS spectra. C. Corresponding Fourier transforms.

next-nearest (Si, Na) neighbors. Development of a stronger pre-edge feature is observed in ASI 0.6 and 1.2 glasses with >1 wt.% Nb_2O_5 (Fig. 2) and is related to a Nb_2O_5 saturation of the melts. An even more intense and well-defined pre-edge is found in hydrated glasses containing 2 wt.% fluorine. Preliminary FEFF calculations on various model compounds indicates this pre-edge to be related to a decrease in niobium coordination from 6 to either 5 or 4 (but no direct complexation of Nb by F is found). The main edge crest features of the niobium K-edge XANES spectra for most glasses resemble those of model compounds such as vuonnemite (Fig. 2). A shift in the main edge crest to higher energies and an increase in the relative intensity of the first EXAFS oscillation is observed with increasing alkalinity and decreasing niobium content. The appearance of such a feature may be related to decreasing radial distortion around the $^{[6]}$Nb.

These preliminary results show that the behaviour of tin and niobium in these glasses: the melt structure exerts a much stronger influence on niobium (peralkalinity, presence of water and fluorine) than tin. Spectra from rare model compounds of tin and niobium (such as eakerite and vuonnemite), together with ab-initio FEFF 8 XANES calculations, help to provide a better understanding the local structure around these elements in glasses. The derived structural information not only has major implications to the understanding of the geochemistry of these elements in natural magmatic systems, but also on nuclear waste glasses in which niobium is a highly nucleating component.

References

1. Linnen, R. L. *et al.*, Geochim. Cosmochim. Acta **59**, 1579 (1995).
2. Linnen, R. L. *et al.*, Geochim. Cosmochim. Acta **60**, 4965 (1996).
3. Linnen, R. L. and Keppler, H., Contrib. Mineral. Petrol. **128**, 213 (1997).
4. Horng, W-S. *et al.*, Geochim. Cosmochim. Acta **63**, 2419 (1999).
5. Moller, P., "Lanthanides, Tantalum and Niobium," (Springer-Verlag, **103** 1986).
6. Kossiakoff, A. A. and Leavens, P. B., Am. Mineral. **61**, 956 (1976).
7. Ercit, T. S. *et al.*, Can. Mineral. **36**, 1311 (1998).
8. Linnen, R. L., Lithos, submitted (2003).

Physica Scripta. Vol. T115, 408–411, 2005

XANES Study on Solid Electrolyte Interface of Li Ion Battery

T. Akai[1*], H. Ota[1], H. Namita[1], S. Yamaguchi[2] and M. Nomura[3]

[1]Mitsubishi Chemical Group Science and Technology Research Center, Inc., 1000 Kamoshida-cho Aoba-ku, Yokohama 227-0033, Japan
[2]Mitsubishi Chemical Corporation, Battery Materials Department, 33-8 Shiba 5-chome, Minato-ku, Tokyo 108-0014, Japan
[3]Institute of Materials Structure Science, High Energy Accelerator Research Organization, Oho, Tsukuba 305-0801, Japan

Received June 26, 2003; accepted November 4, 2003

Abstract

We have investigated solid electrolyte interfaces (SEI) of lithium ion batteries containing sulfur additive for electrolyte with S K-edge XANES spectra. Graphite anode and $LiCoO_2$ cathode were used as electrodes and ethylene sulfite (ES) was used as an additive for propylene carbonate electrolyte. Compared with XANES spectra of standard compounds, it is elucidated that the SEI layer on the graphite anode includes Li_2SO_3, $ROSO_2Li$, Li_2SO_4 and organic sulfur with C-S-C and/or C-S-S-C bonding. The XANES spectrum of the cathode shows that Li_2SO_4 and organic sulfur compounds with C-S-C and/or C-S-S-C are included in the SEI on the cathode. In the discharge state, the sulfur compounds in SEI layers on the anode dissolve into the electrolyte under high temperature around 120 °C although the dissolution of the sulfur species is not observed in the charge state. On the other hand, it is found that the rate of dissolution of the sulfur compounds in SEI layers on $LiCoO_2$ cathode is lower in the discharge state than in the charge state.

1. Introduction

In comparison to other rechargeable battery types, lithium ion rechargeable batteries have been more widely used in cellular phones or personal computers because they provide higher energy density and generate high voltage. They are also being exploited as batteries for electric vehicles. There have been many studies about materials used in lithium ion cells to improve the performances. In the development of electrolytes, the role of additives for electrolytes has been given more importance recently in an effort to prevent undesirable reactions on electrodes [1–6].

Propylene carbonate (PC) has a low melting point and high conductivity at low temperatures. It is attractive solvent for the use at low temperatures. However, PC is usually decomposed on electrodes and it is hardly utilized in commercial batteries. Ethylene sulfite (ES) is known as a good additive for PC based electrolytes [5]. It is considered to produce an effective passivation film, which is called a solid electrolyte interface (SEI), to suppress the decomposition of PC. Several studies on SEI layers including ES have been reported so far [7].

X-ray absorption near edge structure (XANES) is a useful tool for structural studies of many kinds of materials because it includes useful information about coordination geometry and electronic structures such as valency or symmetry of unoccupied orbitals of X-ray absorbing atom [8]. In particular, the fingerprints analysis of XANES is a convenient and reliable method for assignment of compounds if there are suitable reference compounds. There are many studies with Sulfur K-edge XANES spectrum to get direct information about sulfur compounds in many fields, for example, coal [9], asphaltenes [10] and soil humic substances [11]. The S K-edge XANES has been already utilized for the SEI analysis of lithium batteries, and has generated useful information about the SEI including sulfur compounds [12].

In this research, we have applied the S K-edge XANES to the SEI on electrodes in lithium ion cell to get more information about sulfur compounds and their thermal stability when ES is used as an additive to PC based electrolytes. The thermal stability of the SEI is an important factor in terms of the performance and the safety in lithium ion batteries. It is necessary to improve the thermal stability in commercial rechargeable batteries.

2. Experimental

The anode was prepared by coating a copper foil with a mixture of graphite (Mitsubishi Power Graphite (MPG), Mitsubishi Chemical Corporation) and poly vinylidene difluoride (PVdF). The cathode was prepared by coating an aluminum foil with a mixture of $LiCoO_2$ and acetylene black and PVdF. The electrolyte was a 1 M $LiPF_6$/PC solution containing 10% ES by weight (Sol-Rite™, Mitsubishi Chemical Corporation). The cell was galvanostatically charged and discharged at 0.16 mA/cm^2 within the potential range of 3.0–4.2 V. After one cycle, the cell was disassembled in an argon globe box. The samples for the XANES measurements were transferred by use of a sealed container with argon gas. The heating of the electrodes was carried out in the electrolyte at the rate of 1 °C per minute.

The S K-edge XANES measurements were performed at BL-9A in the Photon Factory of High Energy Accelerator Research Organization. The operation energy was 2.5 GeV and the stored current was between 300 and 450 mA. Si(111) double crystals were used as a monochromator and higher orders were reduced with a pair of Ni coated quartz mirrors. The photon energy was calibrated with the largest peak (2482.0 eV) in the S K-edge XANES spectrum of Na_2SO_4 powder. The incident X-rays were detected with an ion chamber filled with helium gas. Both conversion electron yield and fluorescence yield were detected simultaneously with the modified Lytle detector. All measurements were carried out in helium atmosphere. Therefore, we could measure samples with high vapor pressure, even in the liquid state. Powder samples and electrode samples were put on conductive tapes and drops of liquid samples were dried on conductive tapes for measurement. The XANES spectrum of the conductive tape showed that there are subtle sulfur compounds. Since the intensity of the XANES spectrum of the conductive tape was very weak, it did not substantially interfere with the spectra of reference samples. The X-ray beam was irradiated just on the electrodes in case of measuring the electrode samples. Therefore, the spectra of the electrode samples were not interfered with sulfur compounds on the conductive tape.

3. Results and Discussion

Figure 1 shows the S K-edge normalized electron yield XANES spectra of the graphite anode and the $LiCoO_2$ cathode before heating and heated up to 120 °C in 1 M $LiPF_6$/PC + ES10%

*e-mail: akai.toshio@mp.m-kagaku.co.jp

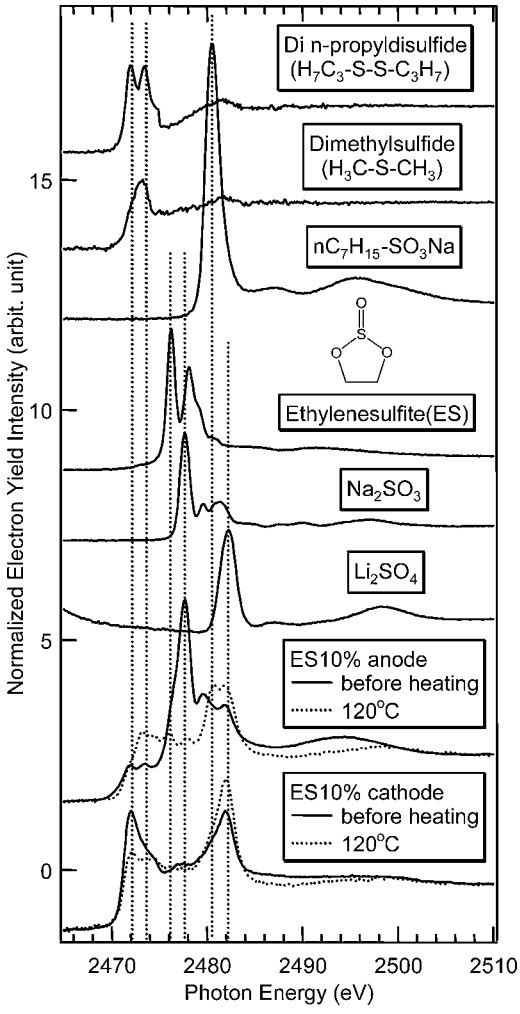

Fig. 1. Normalized S K-edge XANES spectra of the graphite anode and $LiCoO_2$ cathode before heating (solid line) and heated up to 120 °C (dashed line) in 1 M $LiPF_6$/PC + ES10% compared with some reference sulfur compounds with electron yield.

Table I. *The peak energy in S K-edge XANES spectra of the graphite anode, $LiCoO_2$ cathode in 1 M $LiPF_6$/PC+ES10%, and some reference sulfur compounds.*

Sample	Peak energy (eV)			
PC+ES10%				
anode	2471.9	2473.5	2477.7	2479.7
120°C	2473.2	2476.2	2480.7	2481.9
PC+ES10%				
cathode	2472.0			2482.0
120°C	2472.0			2482.0
Na_2SO_3			2477.6	2479.6
Li_2SO_4				2482.1
nC_7H_{15}-SO_3Na				2480.5
Ethylenesulfite (ES)		2476.3	2478.1	
Dimethylsulfide (H_3C-S-CH_3)		2473.3		
Di n-propyldisulfide (H_7C_3-S-S-C_3H_7)	2471.9	2473.4		

respectively compared with some reference compounds. The values of some peak energies are listed in Table I. There are four peaks in the anode samples before heating. The peaks at 2477.7 eV and 2479.7 eV are assigned to Li_2SO_3 because the values are attributed to the peaks energies of Li_2SO_3. The shoulder around 2482 eV in the spectrum of the anode shows that the anode also contains Li_2SO_4 whose peak energy is 2482.1 eV. We consider that the peaks at 2471.9 eV and 2473.5 eV on the anode are derived from organic sulfur having C-S-C and/or C-S-S-C bonding because the values of 2471.9 eV and 2473.5 eV are close to the values of peak energy in the spectrum of dimethylsulfide (H_3C-S-CH_3) which has a peak at 2473.3 eV and of din-propyldisulfide (H_7C_3-S-S-C_3H_7), which has two peaks at 2471.9 eV and 2473.4 eV. These two peaks have been assigned to $1s \rightarrow \sigma^*$(S-S) and σ^*(S-C) transitions, respectively in previous study [8]. It is reported that these compounds are produced by the reductive decomposition of ES [7].

Large two peaks at 2480.7 eV and 2481.9 eV, and small two peaks at 2473.2 eV and 2476.2 eV are observed in the spectrum of the anode heated up to 120 °C in the discharge state. Each peak is assigned to $ROSO_2Li$ (2480.5 eV), Li_2SO_4 (2482.1 eV), organic sulfur compounds (2473.3 eV) and ES (2476.3 eV), respectively.

Two peaks at 2472.0 eV and at 2482.0 eV are found in the spectrum of the cathode shown in Fig. 1. The peak at 2482.0 eV is attributed to Li_2SO_4. Most of Li_2SO_4 must be derived from impurities contained in $LiCoO_2$ in comparison with a cathode blank spectrum. The peak at 2472.0 eV has an unsymmetrical shape, which broadens to higher energy region. The unsymmetrical shape implies that the peak at 2472.0 eV may include another peak around 2473 eV. Therefore, we consider that the cathode also contains organic sulfur compounds with C-S-C and/or C-S-S-C bonding. In the spectrum of the cathode heated up to 120 °C in the discharge state, the intensity at 2472.0 eV decreases and the intensity at 2482 eV increases relatively compared with the spectrum before heating.

The background subtracted fluorescence yield spectra of the anodes heated up to 80 °C and 120 °C in the discharge state are shown in the upper part of Fig. 2(a) compared with the spectrum before heating. Since all spectra were measured under the same sensitivity and the same sample configuration, we consider the intensity of the background subtracted spectra shows the content of sulfur on the electrodes to some extent. The spectrum of the anode heated up to 80 °C is almost the same as that before heating. However, the shape and the intensity of the spectrum of the anode heated up to 120 °C are quite different from those of the other two spectra. The decrease in the intensity of the spectrum of the anode heated up to 120 °C shows that the sulfur compounds in SEI have dissolved into the electrolyte under high temperature around 120 °C. In particular, Li_2SO_3 is not found clearly in the spectrum. These results indicate that Li_2SO_3 dissolves into the electrolyte faster than $ROSO_2Li$, Li_2SO_4 and organic sulfur. We consider that both $ROSO_2Li$ and Li_2SO_4 exist in the SEI even before heating and are left in the SEI after heating although those peaks are not clearly detected in the spectrum before heating.

On the other hand, there is no large difference between the spectra of the anode samples in the charge state except that the intensity of the peaks in the 80 °C spectrum at 2477.7 eV and 2479.7 eV, which is attributed to Li_2SO_3, is a little stronger than those of other two spectra shown in the lower part of Fig. 2(a). This result is considered that both dissolution and production occur in the charge state. Lithium is intercalated into graphite anode in the charge state. The intercalated lithium has a capability of the SEI formation. As a result, the production of SEI by the intercalated lithium and dissolution by high temperature occur simultaneously in the charge state. Therefore, the large differences between the spectra of the anode samples are not found in the

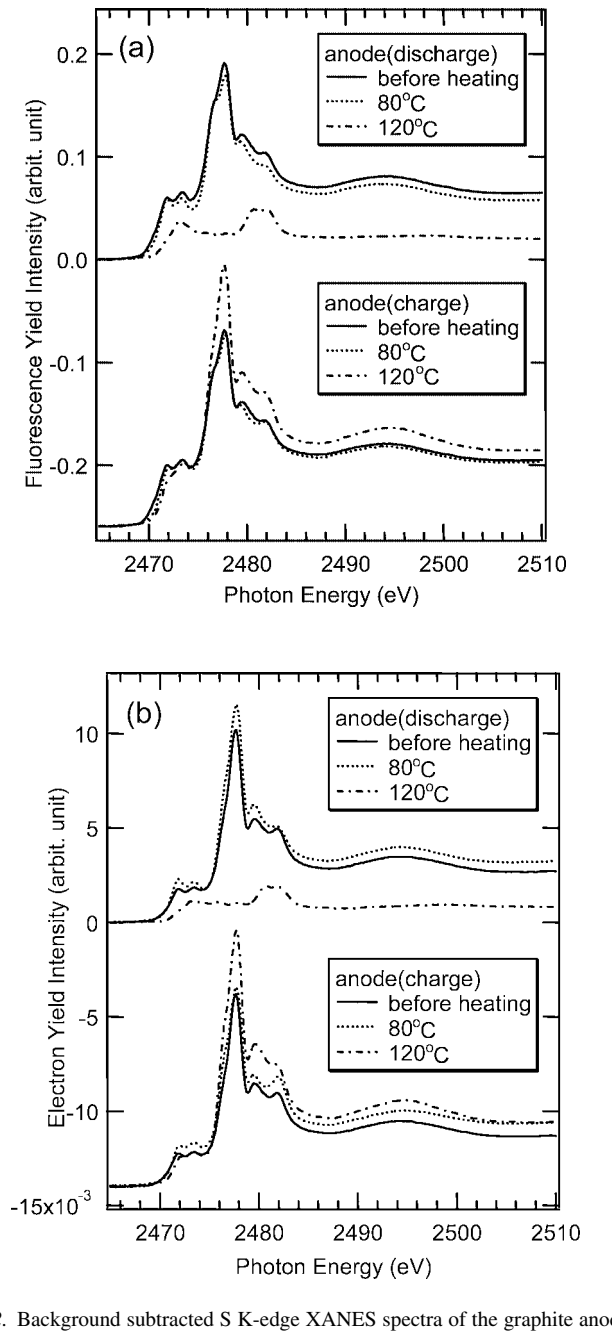

Fig. 2. Background subtracted S K-edge XANES spectra of the graphite anodes heated up to 80 °C and 120 °C (a) with fluorescence yield, and (b) with electron yield.

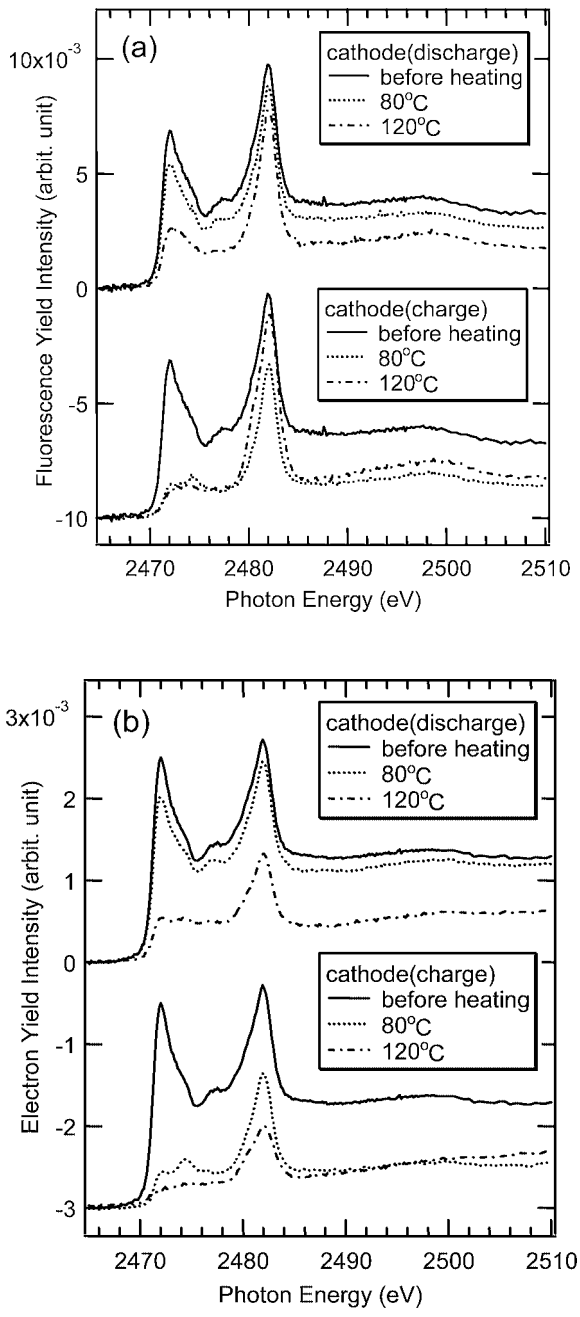

Fig. 3. Background subtracted S K-edge XANES spectra of the $LiCoO_2$ cathodes heated up to 80 °C and 120 °C (a) with fluorescence yield, and (b) with electron yield.

spectra in the charge state. Due to the same reason, the intensity of the peaks related to Li_2SO_3 (2477.7 eV, 2479.7 eV) increases in the spectrum of anode heated up to 80 °C. In this case, the rate of production is considered to be slightly higher than that of dissolution.

The spectra of anode samples with electron yield are shown in Fig. 2(b). The dependency on temperature is mostly the same as the result obtained from the spectra with fluorescence yield. The intensity derived from Li_2SO_3 in electron yield is slightly stronger than that measured in fluorescence yield. The concentration of Li_2SO_3 seems to be higher in surface than in bulk of SEI.

Figure 3(a) shows the background subtracted fluorescence yield spectra of the cathodes heated up to 80 °C and 120 °C in the discharge state (upper part) and in the charge state (lower part). The intensity around 2720 eV gradually decreases with temperature in the discharge state. The decrease in the intensity around 2720 eV in the charge state is larger than that in the discharge state in the case of 80 °C. These results imply that the dissolution rate of organic sulfur compounds in the charge state is larger than that in the discharge state at 80 °C. This trend in the cathode is opposite to that in the anode, explained as the following. As lithium atom is extracted from $LiCoO_2$ in the charge state, it changes into Li_xCoO_2, where x is less than 1.0. The Li_xCoO_2 in the charge state has a higher oxidation activity than the $LiCoO_2$ in the discharge state. Therefore, it is considered that the sulfur compounds contained in SEI dissolve faster in charge state than in discharge state under high temperature.

The electron yield spectra of the cathodes heated up to 80 °C and 120 °C are shown in Fig. 3(b). The dependency on temperature is almost the same as the result obtained from the fluorescence yield spectra. The large difference is found in the intensities derived from organic sulfur compounds. The intensity of the

peak at 2472.0 eV in electron yield is stronger than that in the fluorescence yield. This means organic sulfur compounds exist more on the surface of SEI on the cathode.

4. Conclusions

The S K-edge XANES has been applied to analyze the SEI containing sulfur in lithium ion batteries. It is found that the S K-edge XANES is very effective in studying the SEI. It is also found that the SEI on anode includes Li_2SO_3, $ROSO_2Li$, Li_2SO_4 and organic sulfur having C-S-C and/or C-S-S-C bonding. The XANES spectrum of cathode shows that Li_2SO_4 and organic sulfur compounds with C-S-C and/or C-S-S-C are included in the SEI on the cathode. Most of Li_2SO_4 must be derived from impurities contained in $LiCoO_2$ in comparison with the blank spectrum of $LiCoO_2$ only.

The authors have also investigated the thermal stability of the sulfur compounds in SEI layer. In the case of the graphite anode, the sulfur compounds in SEI layer in the discharge state dissolve under high temperature around 120 °C. Such dissolution is not found in the charge state. It is considered that the SEI layer on the anode is more stable under high temperature in the charge state than in the discharge state. It is also observed that Li_2SO_3 dissolves more easily than other sulfur compounds. On the other hand, it is found that the rate of dissolution of the sulfur compounds in SEI layer on the $LiCoO_2$ cathode is lower in the discharge state than in the charge state, which implies that the SEI on the $LiCoO_2$ cathode is more stable in the discharge state than in the charge state.

References

1. Shu, Z. X., McMillan, R. S. and Murray, J. J., J. Electrochem. Soc. **140**, 922 (1993).
2. Aurbach, D., Ein-Eli, Y. and Cusid, O., J. Electrochem. Soc. **141**, 603 (1994).
3. Ein-Eli, Y., Thomas, S. R. and Koch, V. R., J. Electrochem. Soc. **142**, 1159 (1997).
4. Aurbach, D. *et al*., J. Electrochem. Soc. **145**, 3024 (1998).
5. Wrodnigg, G. H., Besenhard, J. O. and Winter, M., J. Electrochem. Soc. **146**, 470 (1999).
6. Eriksson, T. *et al*., J. Electrochem. Soc. **149**, A69 (2002).
7. Ota, H., Sato, T., Suzuki, H. and Usami, T., J. Power Sources **97–98**, 107 (2001).
8. Chauvistre, R. *et al*., Chem. Phys. **223**, 293 (1997).
9. Xia, K. *et al*., Soil Sci. Soc. Am. J. **62**, 1240 (1998).
10. Sarret, G., Connan, J., Kasrai, M., Eybert-Berard, L. and Bancroft, G. M., J. Synchrotron Rad. **6**, 670 (1999).
11. Vairavamurthy, M. A. *et al*., Energy Fuels **11**, 546 (1999).
12. Ota, H., Akai, T., Namita, H., Yamaguchi, S. and Nomura, M., J. Power Sources, **119–121**, 567 (2003).

Physica Scripta. Vol. T115, 412–414, 2005

Comparison of Photo-Degradation of Polyimide Film by UV Irradiation in Air and in Vacuum

Tomoaki Tanaka[1,2*], Kyoko K. Bando[1], Nobuyuki Matsubayashi[1], Motoyasu Imamura[1] and Hiromchi Shimada[1]

[1]National Institute of Advanced Industrial Science and Technology, 1-1-1 Higashi, Tsukuba, Ibraki, 305-8565, Japan
[2]New Energy and Industrial Technology Development Organization, Sunshine 60 Bldg., 3-1-1 Higashi Ikebukuro, Toshima-ku, Tokyo 170-6028, Japan

Received June 26, 2003; accepted in revised form November 4, 2003

PACS number: 82.35.−x

Abstract

Structural changes of pyromellitimido-oxydianiline (PMDA-ODA) polyimide (PI) films by UV irradiation were studied by means of XAFS and XPS. UV irradiation in air was found to cause oxidative cleavage of the imide ring of the PMDA part, whereas that in vacuum changed the conjugated structure involving nitrogen but did not likely open the imide ring. The results indicate that the combined analysis of XAFS and XPS is a powerful tool for polymer surfaces.

1. Introduction

Changes in properties of polymers by UV irradiation are of significant industrial and scientific interest. There have been many investigations on the structural changes of polymers by UV irradiation in relation to, for example, degradation of mechanical properties or improvements of adhesion properties. Because the structural changes start from the surface, surface analytical methods are very often used for the investigation. In this context, many scientists have used X-ray photoelectron spectroscopy (XPS) that gives chemical information on specific elements based on the binding energies of the core electrons. XPS can discriminate a specific element with different chemical states and can give reliable semi-quantitative analytical results. X-ray absorption fine structure (XAFS) has an advantage over XPS in the respect that XAFS is more sensitive than XPS for the changes in the local structure around a specific atom. Although recent progress of synchrotron radiation technology has made it relatively easy to measure the XAFS spectra of light elements such as C, N and O, there still remained a problem to measure the XAFS spectra of bulk insulators by surface-sensitive electron yield methods. Recently, however, we developed a system consisting of a partial electron yield detector, hemispherical analyzer and charge-neutralization flood gun that enables us to measure XAFS and XPS spectra of bulk insulators [1]. In the present paper, we report the photo-degradation behavior of pyromellitimido-oxydianiline (PMDA-ODA) polyimide (PI, Fig. 1) films using the above system.

PMDA-ODA PI films have excellent heat-resistance properties and are used in wide applications as thermal blankets. When PI films are used as the thermal blanket in the aerospace industry, photo-degradation of the films is of significant importance, because the films are subject to very strong UV irradiation for a long period. In a previous paper [2], we reported photo-degradation of PI films in air. The results suggested that the imide ring in the PMDA part was cleaved by an oxidative reaction. In the present study, we monitor the spectral changes of the PI films by UV irradiation in vacuum that is more similar to the conditions for aerospace applications. We compare the XPS and XAFS spectra of the PI films irradiated in air and in vacuum and discuss the difference in the degradation behavior of the PI films. Through the results and discussions, we show that the combined analysis of XPS and XAFS is a powerful tool for the analysis of polymer surfaces.

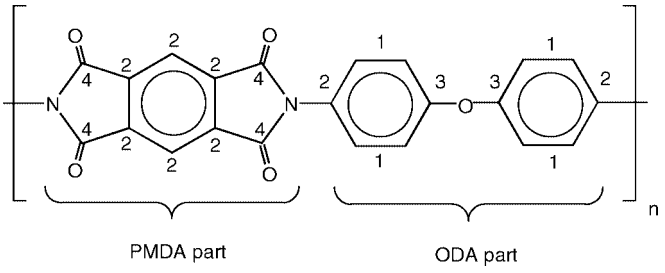

Fig. 1. Structural formula of PMDA-ODA polyimide films.

2. Experimental

The XAFS spectra were measured at a soft X-ray beam line BL-13C of the Photon Factory at the Institute of Materials Structure Science (KEK-PF). An ultra high vacuum (UHV) chamber with an electron yield detector and a hemispherical analyzer was equipped at the end of BL-13C. The experimental setup of the measurement system is shown in Fig. 2. The electron flood gun and low-energy Ar ion gun equipped in the UHV chamber performs charge-neutralization of sample surface and enables spectral measurements of insulators. The experimental method was already described in a previous paper [1]. The XPS spectra in the present paper were measured with Al Kα X-ray excitation ($h\nu = 1486.6\,\mathrm{eV}$).

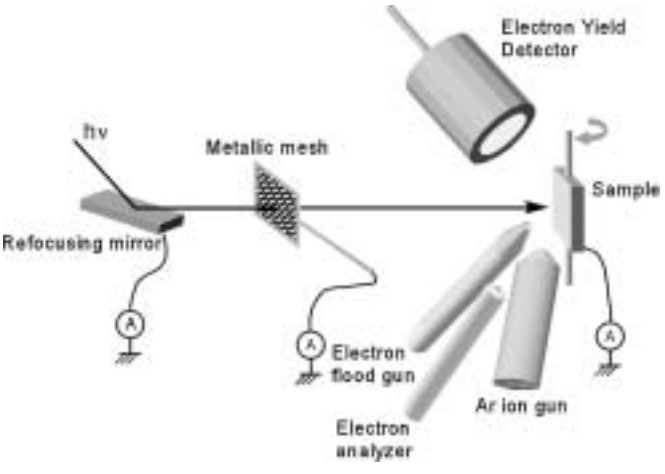

Fig. 2. Experimental setup of XPS and XAFS measurement.

*e-mail: tanaka-t@aist.go.jp

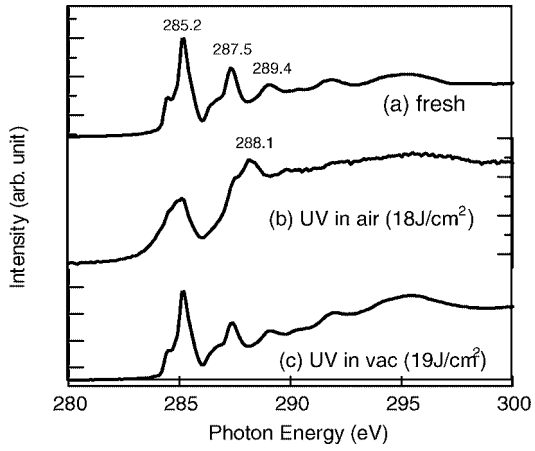

Fig. 3. C K-edge XAFS spectra of fresh and irradiated PI films; (a) fresh, (b) 18 (J/cm^2) under air, (c) 19 (J/cm^2) under vacuum.

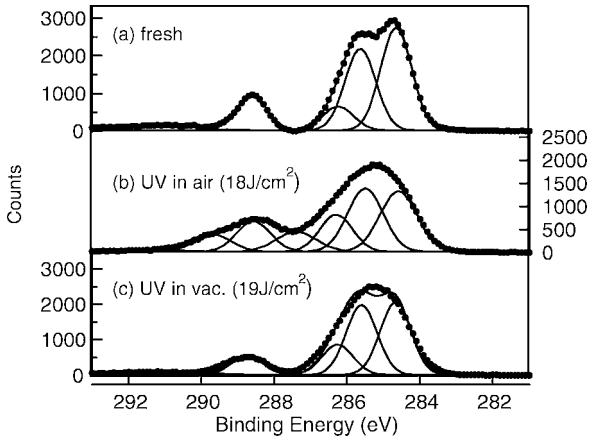

Fig. 4. C1s XPS spectra of fresh and irradiated PI films.

As a UV light source, a low-pressure mercury lamp with wavelengths of 184.9 nm and 253.7 nm was used. For UV irradiation in vacuum, a PI film with a diameter of 5 mm and a thickness of 20 μm was set in the UHV chamber and irradiated through a view-port made by synthetic fused silica. The background pressure of the irradiation chamber was $\sim 1 \cdot 10^{-8}$ torr. Before introduction to the UHV chamber, the topmost surface of the PI films was removed by scraping, because the surface of the films was contaminated with adventitious carbon.

3. Results and discussion

3.1. *C K-edge XAFS analysis*

Figure 3 shows the C K-edge XAFS spectra of fresh and UV irradiated PI films in air and in vacuum. According to a literature [3], the most sharp and intense doublet peak observed at about 285 eV and the peak at 289.4 eV in the spectrum of the fresh PI film were assigned to the π^* resonance (C=C) of PMDA and ODA aromatic rings. Similarly, the sharp peak at 287.5 eV was assigned to the π^* resonance (C=O) and the peaks observed at higher energies than 290 eV were assigned to σ^* resonance. UV irradiation in air significantly changed the spectrum; the intensities of the π^* peaks assigned to the aromatic rings decreased, whereas a new peak appeared at 288.1 eV. Compared with the past literatures, the peak at 288.1 eV is most likely assigned to π^* resonance (C=O) of carboxyl (-COO-) groups [4]. In contrast, UV irradiation in vacuum did not cause evident changes in the spectrum.

Figure 4 shows the C1s XPS spectrum of the fresh and irradiated PI films. The spectrum of the fresh PI film could be deconvoluted into four components that were assigned to two kinds of aromatic carbon (1, 2 in Fig. 1), C-O (3 in Fig. 1) and C=O (4 in Fig. 1) from the low energy side. Note that the relative intensity of each component is consistent with the atomic ratio in the PMDA-ODA structure. By UV irradiation in air, the intensities of the peaks assigned to aromatic carbon (1, 2) decreased, whereas new peaks appeared at 287.3 eV and 290.0 eV. On the basis of the literatures [5, 6], the peaks at 287.3 eV and 290.0 eV are respectively assigned to carbonyl and carboxyl groups. Thus, both XAFS and XPS spectra suggested that UV irradiation in air caused the cleavage of the imide ring of the PMDA part. Similar to XAFS, no significant change was observed in the spectrum of the PI film by UV irradiation in vacuum.

3.2. *O K-edge XAFS analysis*

Figure 5 shows the O K-edge XAFS spectra of fresh and UV irradiated PI films. The spectrum of the fresh PI film showed a sharp peak at 530.1 eV assigned to π^* resonance (C=O) and a broad peak at 539.7 eV assigned to σ^* resonance (C=O). Two small peaks observed at 532.3 eV and 534.7 eV were not exactly assigned but probably assigned to π^* resonance related to C=O, such as -N-C=O-. After UV irradiation in air, the intensities of the two small peaks decreased and the sharp peak at 530.1 eV was broadened. These results are likely attributed to the structural change of the imide ring. UV irradiation in vacuum did not cause detectable changes in the O K-edge XAFS spectrum.

Figure 6 shows the O1s XPS spectra before and after UV irradiation. All the spectra exhibited a peak with a shoulder at the higher energy side. No obvious changes in the spectral shapes were observed during UV irradiation. However, the relative peak area ratio of O1s relative to C1s increased by 17% after UV irradiation in air. This indicates surface oxidation of the PI film during UV irradiation in air.

3.3. *N K-edge XAFS analysis*

Figure 7 shows the N K-edge XAFS spectra of fresh and UV irradiated PI films. The two sharp peaks at 400.4 eV and 403.0 eV observed in the fresh PI film were likely assigned to

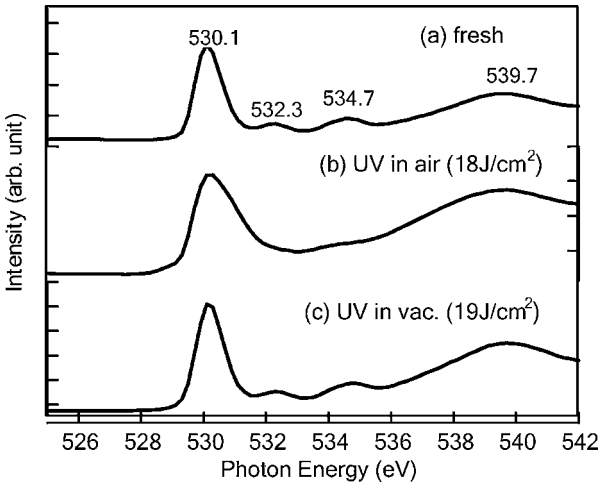

Fig. 5. O K-edge XAFS spectra of fresh and irradiated PI films.

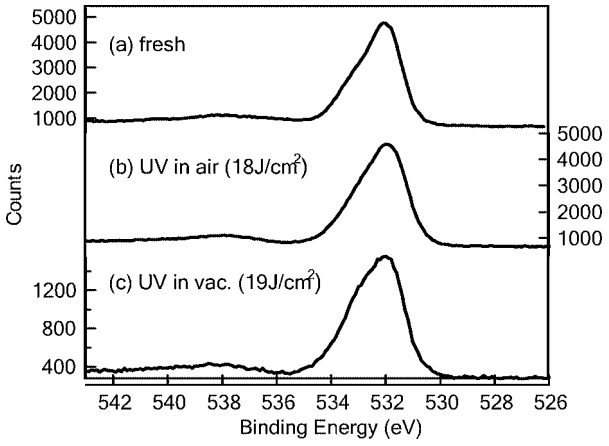

Fig. 6. O1s XPS spectra of fresh and irradiated PI films.

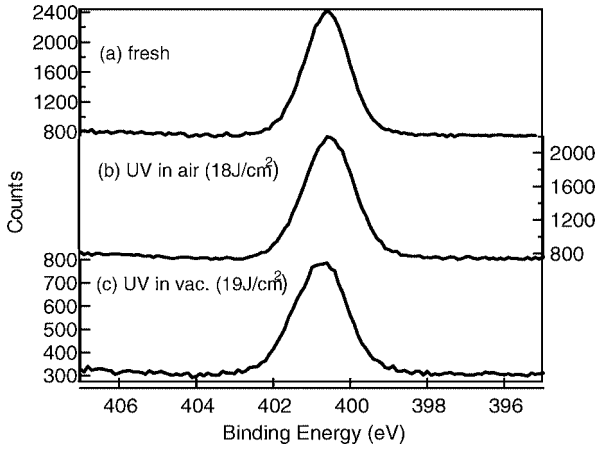

Fig. 8. N1s XPS spectra of fresh and UV irradiated PI films.

π^* resonance (-N-C=O). By UV irradiation in air, the intensities of the both peaks decreased in line with the changes in the C K-edge and O K-edge XAFS spectra. In contrast to the C K-edge and O K-edge XAFS spectra, an evident change was observed in the spectrum of the UV irradiated PI film in vacuum. The intensity of a small peak at 399.0 eV observed in the spectrum of the fresh PI film increased after UV irradiation in vacuum. According to past literatures [7–10], a feature observed below 400.0 eV was assigned to a pyridine-like ring or CN triple bond that leads to a more strongly conjugated system than imide rings.

Figure 8 shows the N1s XPS spectra before and after UV irradiation. All the spectra exhibited a symmetric peak and no meaningful difference was observed among them.

3.4. *Discussion and summary*

The XAFS and XPS results presented here may not be sufficient to conclude the structural changes of the PI films occurring by UV irradiation, however, below we discuss possible changes of the PMDA-ODA structure. UV irradiation in air most likely caused the cleavage of the imide ring of the PMDA part. The cleavage between -CO- and −N< likely formed -COO- with the addition of oxygen from air. As a next step, the active -COO- readily reacts with the aromatic ring of the neighbor polymer chain. This resulted in the decrease in the intensities of the features arising from the aromatic carbon with no substituted functional group in both XAFS and XPS spectra (Figs. 3 and 4). The above discussion is also consistent with the changes observed in the O K-edge XAFS spectra (Fig. 5) and the increased O1s/C1s ratio in XPS spectra. Note that the above discussion is slightly different from a recent paper by Okajima *et al*. [11] who claimed formation of an aldehyde group from an ester group by UV irradiation of a poly-butylentelephthalate (PBT) film. The change in the local structure around N by UV irradiation in air is not clear, but the change in the N K-edge XAFS spectrum suggested a change in the local structure around N from −N< to $-NH_2$ that has no π^* resonance. Thus, UV irradiation in air caused cleavage of the imide ring followed by bridging between the polymer chains via –COO- groups.

The structural change of the PI film by UV irradiation in vacuum was relatively smaller than those by UV irradiation in air. The spectral changes indicated no cleavage of the imide ring but suggested reformation of the imide ring that resulted in the changes in the conjugated structure. Note that the changes in the local structure around N and O could not be detected by XPS. The present results implicate that the combined analysis of XAFS and XPS is a powerful tool for the polymer surface, because the two techniques give supplementary information each other on the polymer components.

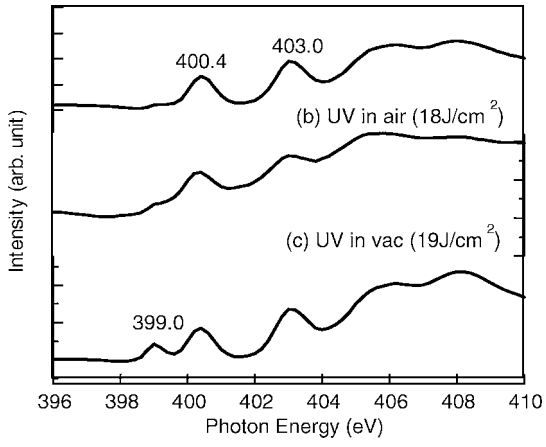

Fig. 7. N K-edge XAFS spectra of fresh and UV irradiated PI films.

Acknowledgment

We appreciate the collaboration with the staff responsible for the insertion device at the Photon Factory. This work was done under the approval of the PF advisory committee (2001G108).

References

1. Tanaka, T., Bando, K., K., Matsubayashi, N., Imamura, M. and Shimada, H., J. Electron Spectrosc. Related Phenom. **114–116**, 1077 (2001).
2. Tanaka, T. *et al*., Anal. Sci. **17**, 1077 (2001).
3. Jordan-Sweet, J. L., J. Chem. Phys. **89**, 2482 (1988).
4. Outka, D. A. *et al*., Surf. Sci. **185**, 53 (1987).
5. Beamson, G. and Briggs, D., "High Resolution XPS of Organic Polymers-The Scienta ESCA300 Database", (Wiley, 1992), p. 214.
6. Clark, D. T. and Dilks, A., J. Poly. Sci. **17**, 957 (1979).
7. Oichi, K. *et al*., Jpn. J. Appl. Phys. **32**, 818 (1993).
8. Sakai, T. *et al*., J. Phys. Chem. B **105**, 9191 (2001) .
9. Mitra-Kirtley, S. *et al*., J. Am. Chem. Soc. **115**, 252 (1993).
10. Pavlychev, A. A., Hallmeier, K. H., Hennig, C., Hennig, L. and Szargan, R., Chem. Phys. **201**, 547 (1995).
11. Okajima, T. *et al*., J. Phys. Chem. A **102**, 7093 (1998).

Physica Scripta. Vol. T115, 415–417, 2005

Structure Determination by EXAFS of Nb-Peroxo-Citrato Complexes in Aqueous Solution-Gel Systems

M. K. Van Bael[1*], I. Arčon[2], K. Van Werde[1], D. Nelis[1], J. Mullens[1] and L. C. Van Poucke[1]

[1]Laboratory of Inorganic and Physical Chemistry, IMO, Limburgs Universitair Centrum, B-3590 Diepenbeek, Belgium
[2]Nova Gorica Polytechnics, Vipavska 13, SI-5000 Nova Gorica, and Institute Jožef Stefan, Ljubljana, Slovenia

Received June 26, 2003; accepted October 15, 2003

PACS numbers: 61.10Ht, 81.20Fw

Abstract

A structural study of a niobium-peroxo-citrato complex in an aqueous solution, used as a precursor for the synthesis of ceramic oxides by an aqueous solution-gel route is performed by Nb K-edge EXAFS analysis. The results clearly indicate the formation of niobium-peroxo-citrato dimers via Nb-O-Nb links. Nb(V) ions are seven-coordinated including one Nb=O bond of a niobyl group and two Nb-O bonds from a side-on metal-peroxo group. The results are consistent with a previously proposed structural model based on Raman and UV spectroscopy studies.

1. Introduction

There has been a lot of interest in the preparation of electroceramic metal oxides containing niobium by solution techniques. From an economical and ecological point of view, aqueous routes are preferred. The aqueous solution-gel route involves the formation of a gel network by hydrolysis, condensation and complexation reactions in an aqueous solution of metal salts and chelating or bridging ligands [1–3]. Drying and a suitable heat treatment convert the amorphous gel into the desired ceramic oxide.

Aqueous solution chemistry of high valent metals such as Nb(V) is however very complicated because they are extremely sensitive towards hydrolysis, leading to precipitation and undesired phase segregation. Despite the additional fact that the only available water-soluble Nb compound – an oxalate – is not appropriate for gel formation and combination with other metal ions, we succeeded to transform it into a water-soluble Nb precursor, suitable for gel formation, by reaction with peroxide and complexation with citric acid.

In order to understand the mechanism of the solution-gel processes on the molecular level it is crucial to know the structure of the Nb complex formed in the precursor solution. Up to date only one model was proposed for a niobium-peroxo-citrato complex in aqueous solution by Narendar and Messing [4], based on Raman and UV spectroscopy studies of the solution and additional IR data on the condensed phase. However, to our knowledge, there are no XRD or other direct data on the structure of the Nb complex.

The objective of this work is to study the structure of the Nb-peroxo-citrato complex in the aqueous solution by Nb K-edge EXAFS. We analyse the local niobium environment and compare the structural results with the model proposed by Narendar and Messing.

2. Experimental

The aqueous niobium solution was synthesized according to the procedure of Nelis *et al*. [2] by first oxidizing niobium(V) ammonium oxalate with hydrogen peroxide in an aqueous solution of citric acid. The pH is then raised to 7.5 with ammonia which allows the citrate groups to co-ordinate the metal ions and to form a stable water-soluble Nb(V)-peroxo-citrato complex.

The Nb K-edge EXAFS spectrum of the solution was measured at the BM20 beamline of the ESRF synchrotron radiation facility. The station provided a Si(111) fixed-exit double-crystal monochromator with about 3 eV resolution at the Nb K-edge. Harmonics were effectively suppressed (below 8×10^{-4}) by a slight detuning of the monochromator crystals, keeping the intensity at 70% of the rocking curve with the beam stabilization feedback control. The beam was focused using two mirrors with silicon reflecting stripes on a silicon substrate. The first mirror is bent for horizontal collimation of the synchrotron radiation from the bending magnet on the monochromator, while the second mirror, placed after the monochromator, allows a vertical focusing of the monochromatic beam onto the sample. The beam size on the sample was 1 mm × 8 mm.

The solution was inserted in a polyethylene cuvette with a path length of 8.5 mm. The Nb concentration of 0.15 M was chosen to obtain an optimal absorption thickness of about 1 above the Nb K-edge. The intensity of the incident and transmitted beam was measured with Ar filled ionisation cells. The standard stepping progression within [−250 eV–1000 eV] region of the Nb K-edge was adopted for EXAFS spectra with an integration time of 2s/step. The exact energy calibration is established with simultaneous absorption measurements on an Nb metal foil.

3. Results

Nb EXAFS spectrum (Fig. 1) was analyzed by the University of Washington analysis programs using FEFF6 code for ab initio calculation of scattering paths [5, 6]. Nb neighbour shells are discerned in the k^3 weighted Fourier transforms of the EXAFS spectrum shown on Fig. 2 together with a best-fit EXAFS model. A very good fit is found in the R range from 1.3 Å to 4.0 Å with seven oxygen atoms in the first coordination shell, and one Nb atom and several carbon atoms in a second shell. The quality of the fit is shown also on Fig. 1. A complete list of best-fit parameters is presented in Table I.

To describe the first coordination shell we included in the model three different Nb-O distances that can be expected in similar metal-peroxo complexes [7–11]. Indeed, we found one oxygen at a short distance of 1.75 Å, corresponding to niobyl group (Nb=O)

*e-mail: marlies.vanbael@luc.ac.be

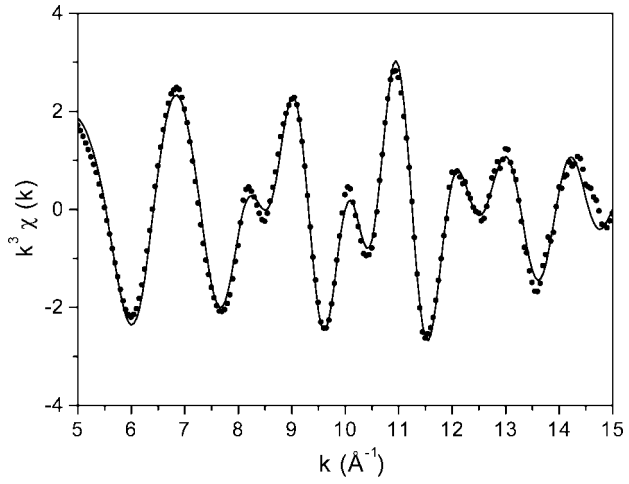

Fig. 1. k^3 weighted Nb K-edge EXAFS spectra of Nb-peroxo-citrato complex in the solution. Dots – experiment; solid line – EXAFS model.

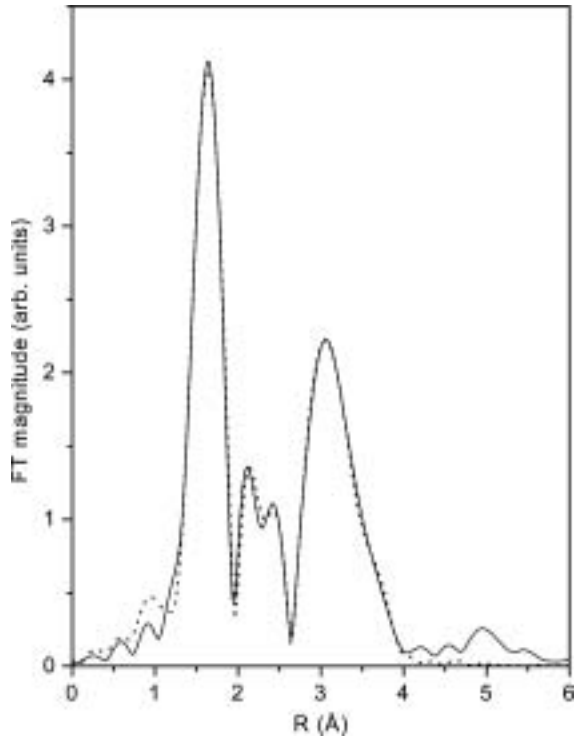

Fig. 2. k^3 weighted Fourier transforms of Nb EXAFS spectra of Nb-peroxo-citrato complex in the solution calculated in the k range of 5 Å^{-1} to 15 Å^{-1}. Solid line-experiment, dotted line–EXAFS model.

which is consistent with bond lengths of metal-oxo groups, e.g. Mo=0 (1.66 Å) [8] and V=O (1.60 Å) [10]. The remaining six oxygens are found to be distributed into two groups: first three centered at the distance of 2.03 Å and the remaining three at a much longer distance of 2.59 Å. A metal-oxygen distance of about 2.0 Å is characteristic for side-on metal-peroxo bonds [12, 13], while the longer distance indicates the presence of carboxylate oxygens coordinated to Nb. Due to large correlations between fitting parameters it was not possible to obtain a more precise distribution of oxygen neighbours in the first shell. Even at this level of details we obtained relatively large uncertainties for number of neighbours and Debye-Waller factors.

Similarly, due to high correlations of the second shell parameters, we were not able to determine the exact number of carbon atoms, which were found at non-equal distances in that shell. However, the Nb neighbour parameters could be reliably determined since they were not affected by the correlations.

Table I. *Structural parameters of the nearest coordination shells around the Nb atom in aqueous solution of the Nb-peroxo-citrato complex: type of neighbour atom, number N, distance R, and Debye-Waller factor σ^2. Uncertainties of the last digit are given in the parentheses.*

Neigh.	*N*	*R* (Å)	σ^2 (Å^2)
O	0.8(1)	1.75(2)	0.005(2)
O	2.6(4)	2.03(1)	0.004(2)
O	2.9(4)	2.59(1)	0.007(3)
C	1.5(4)	2.98(3)	0.008(3)
Nb	1.0(1)	3.30(1)	0.004(1)
C	5(1)	3.76(2)	0.004(2)
C	2(1)	4.08(2)	0.004(2)

4. Discussion

The structural parameters obtained by Nb EXAFS can be compared with the proposed model for the niobium-peroxo-citrato complex in aqueous solution by Narendar and Messing [4]. Their model consists of a dimeric structure in which each Nb(V) ion is surrounded by seven oxygens, one from a niobyl group, two from a side-on peroxo group and four from citrate ligands.

In our case the presence of a single Nb neighbour at 3.30 Å clearly indicates the formation of dimers via Nb-O-Nb links. We also find seven-coordinated Nb with one short Nb=O bond of a niobyl group. Two of the three oxygens at about 2.0 Å may be ascribed to side-on metal-peroxo bonds, for which we have additional evidence from the UV spectrum of the solution, showing the characteristic ligand-metal charge-transfer band at 255–260 nm [14]. The remaining four oxygens most probably originate from carboxylate and α-hydroxy groups of citric acid ($C(OH)(COOH)(CH_2COOH)_2$). The hydroxy coordination is expected because the complex synthesized with a modified ligand without the α-OH group is not stable. The oxygens at a relatively long distance of about 2.6 Å may be ascribed to carboxylate groups for which a closer approach is hindered by increased strain within the citrate ligands. The carbon atoms in the second shell found at 3.0 Å, 3.8 Å and 4.1 Å originate from citrate functional groups.

Our results are consistent with the structural model of Narendar and Messing [4]. Other structural studies of metal-peroxo-carboxylato complexes in condensed phases based on IR spectroscopy, thermal analysis and X-ray diffraction [4, 7–15] also support our findings: most of them reveal a structure with a pentagonal bipyramid coordination of the metal which is then sp^3d^3 hybridized. Additionally, in many cases dimer units are formed in amorphous precipitates or in a crystalline form of similar peroxo-carboxylato complexes [4, 9–11]. However, we find some differences compared to the XRD data obtained on crystalline samples with the same dimeric structural units. In the solution we observed three long Nb-O distances instead of one reported for the crystalline samples of other metal complexes [9–11]. Therefore our results suggest that the dimers may have slightly different structure in solution than in a condensed phase.

Acknowledgements

This work was partly financed by the Fund for Scientific Research of Flanders (F.W.O.-Vlaanderen) (Belgium) via the research program G0257.95 CRG/DUBBLE. We acknowledge the European Synchrotron Radiation Facility for provision of synchrotron radiation facilities (experiment ME-246) and we would like to thank T. Reich and A. Bauer for assistance in using the Radiochemistry and materials research ROBL-CRG beamline (BM20).

I. Arčon is supported by the Slovenian Ministry of Education, Science and Sport. M.K. Van Bael and D. Nelis are respectively a post-doctoral fellow and a research assistent of the F.W.O.-Vlaanderen. K. Van Werde is indebted to the 'Instituut voor de aanmoediging van Innovatie door Wetenschap en Technologie in Vlaanderen' (I.W.T.).

References

1. Nelis, D. *et al.*, J. Sol-Gel Sci. Tech. **26**, 1125 (2003).
2. Nelis, D. *et al.*, Integr. Ferroelectrics **45**, 205 (2002).
3. Van Werde, K. *et al.*, J. Mater. Chem. **11**, 1192 (2001).
4. Narendar, Y. and Messing, G. L., Chem. Mater. **9**, 580 (1997).
5. Stern, E. A., Newville, M., Ravel, B., Yacoby, Y. and Haskel, D., Physica B **208** & **209**, 117 (1995).
6. Rehr, J. J., Albers, R. C. and Zabinsky, S. I., Phys. Rev. Lett. **69**, 3397 (1992).
7. Djordjevic, C., Wilkins, P. L., Sin, E. and Butcher, R. J., Inorg. Chim. Acta **230**, 241 (1995).
8. Flanagan, J., Griffith, W. P., Skapski, A. C. and Wiggins, R. W., Inorg. Chim. Acta **96**, L23 (1985).
9. Djordjevic, C., Gundersen, J. L., Jacobs, B. A. and Sin, E., Polyhedron Commun. **8**, 541 (1989).
10. Djordjevic, C., Lee, M. and Sin, E., Inorg. Chem. **28**, 719 (1989).
11. Djordjevic, C., Lee, M. and Sin, E., Inorg. Chim. Acta **233**, 97 (1995).
12. Bayot, D., Tinant, B. and Devillers, M., Catal. Today **78**, 439 (2003).
13. Bayot, D., Tinant, B., Mathieu, B., Declerq, J. P. and Devillers, M., Eur. J. Inorg. Chem. **2003**, 737 (2003).
14. Van Werde, K., Ph.D. Thesis – Limburgs Universitair Centrum, Belgium (2003).
15. Griffith, W. P. and Wickens, T. D., J. Chem. Soc. A, 397 (1968).

Physica Scripta. Vol. T115, 418–420, 2005

Debye-Waller Factor Study of Co, Cu and CoCu Granular Alloy

J. C. Cezar, N. P. Abreu and H. C. N. Tolentino

Laboratório Nacional de Luz Síncrotron, CP 6192, Campinas, SP, Brazil, 13084-971

Received June 26, 2003; accepted in revised form November 4, 2003

PACS numbers: 65.40.De, 61.10.Ht, 75.47.De

Abstract

Granular solids composed of Co dispersed in a Cu matrix attracted the attention of magnetism community due to several interesting characteristics. One of their most striking properties is the giant magnetoresistance. In this work we used EXAFS to study the Debye-Waller factor, or disorder, of a $Co_{10}Cu_{90}$ sample as a function of the temperature. Using the correlated Einstein model, we were able to separate the thermal from the static contribution to the disorder. We concluded that the granular alloy has static disorder comparable to that of bulk well crystallized Co. In other words, for the $Co_{10}Cu_{90}$ sample around Co atoms, most of the disorder has thermal origin at room temperature. This is explained basically as the influence of the Cu matrix on the atoms at the interface of the well defined Co particles.

1. Introduction

Granular magnetic systems have been extensively studied in the last few years because they display a number of interesting physical properties which, besides the prospective technological use, settle a challenge to the physics community to be properly understood. Among these properties one can mention giant magnetoresistance, superparamagnetism, spin-glass-like behavior and the kinetics of growth of nanocrystalline grains. The system studied in the present work displays all the above mentioned properties, and therefore it is a unique setting to investigate the physical properties of granular solids.

In granular solids composed of cobalt particles embedded in a copper matrix, as is the case of the $Co_{10}Cu_{90}$ sample, it was observed that the relative disorder ($\Delta\sigma^2$) around Co atoms, taking bulk Co as reference, has a non-monotonous behavior and decreases for increasing annealing conditions (fig. 1) [1]. In EXAFS the disorder is represented by a Debye-Waller factor $\exp -\sigma^2 k^2$, where σ^2 represents the absolute mean square relative displacement (MSRD) and $\Delta\sigma^2$ is the relative value compared to a reference. The annealing enables an increase of the Co particles within the matrix and tends to better organize their interface with the matrix, leading to a smaller overall disorder. Nevertheless, the disorder can be of thermal or static origin and it is not yet understood which one contributes more. In order to disentangle both contributions, we used EXAFS spectroscopy to study the dynamical behavior of the Co-Cu sample, by comparison with the bulk Co and Cu metals.

2. Experiment

The studied Co-Cu sample was a melt-spun ribbon, 0.05 mm thick and 5 mm wide, of 10 at.% of Co embedded in a 90 at.% Cu matrix. The annealing was performed allowing a constant electric current of 4 A, flow through the sample length during one minute (Joule annealing [3]). Both bulk Co and Cu were also measured for comparison. The EXAFS measurements were performed at the D04B-XAS beamline at LNLS [2], Brazil, for sample and bulk metals from 10 K up to 600 K, in transmission mode. The data analysis followed the standard Fourier filtering procedure: initially a straight line (fitted in the pre-edge region) was subtracted from the raw spectra. The $\chi(k)$ signal was then extracted subtracting a seven segment spline. The Fourier transform was performed with k^2 weighting, from 2.5 up to 14.5 $Å^{-1}$. The back Fourier transform was done in an interval of 1 Å centered around the first neighbors peak. The EXAFS equation for the first neighbor shell was fitted using experimental amplitudes and phases, as will be described later in this paper. In these fits the coordination number was fixed at 12, the number of neighbors in the coordination shell for HCP and FCC structures. From the fitting procedure we obtained inter-atomic distances, relative Debye-Waller factors and energy shifts of the absorption edge. The following discussion will be based on Debye-Waller factors results solely.

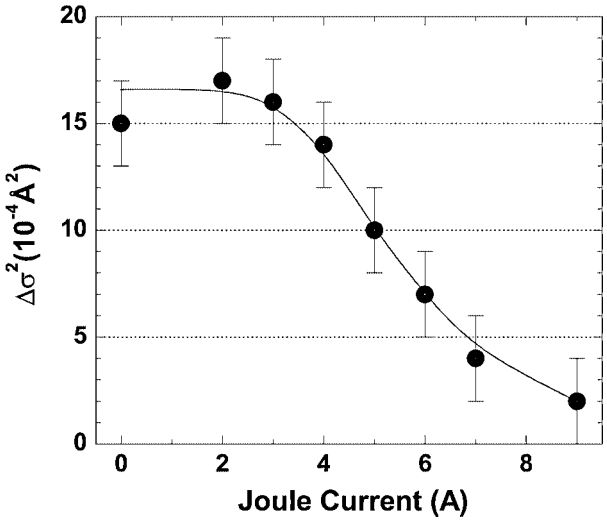

Fig. 1. Variation of the relative total disorder (static and thermal) around Co atoms with the annealing, for a series of $Co_{10}Cu_{90}$ samples. The reference bulk Co and all samples were measured at room temperature. The annealing was performed by Joule heating the samples during one minute with different currents. Details about these results can be found in reference [1].

3. Results and discussion

The $\chi(k)k^1$ signals for bulk Co and Co-Cu sample around Co K-edge, and Cu around Cu K edge are shown in figure 2 for some selected temperatures. It can be clearly seen the effect of the temperature in damping the EXAFS oscillations.

In the first approach to the analysis, the Co K-edge spectra of the Co-Cu sample, measured from 10 up to 600 K, were analyzed using the extracted experimental phases and amplitudes from the spectrum of the sample measured at the lowest temperature, i.e., from the Co-Cu spectrum at 10 K. So, the disorder found at different temperatures are relative to the sample at 10 K. These

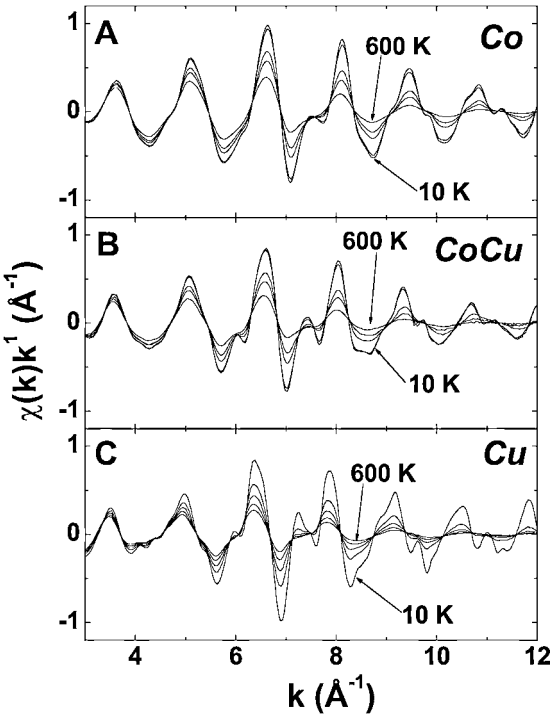

Fig. 2. Representative examples of EXAFS signal obtained for the bulk Co (a), $Co_{10}Cu_{90}$ sample (b), and bulk Cu (c). The measurement temperatures shown are 10, 100, 300, 400 and 600 K for Co and $Co_{10}Cu_{90}$. For Cu they are 10, 300, 400, 500 and 600 K. The arrows indicate only the minimum and maximum temperature.

data, carrying just the thermal contribution $\Delta\sigma^2_{TH}$ to the total disorder, were fitted using the correlated Einstein model [4, 5], according to the following equation:

$$\Delta\sigma^2_{TH}(\Theta_E, T) = \frac{\hbar^2}{2\mu k_B \Theta_E} \coth\left(\frac{\Theta_E}{2T}\right) - \sigma_0^2 \qquad (1)$$

where Θ_E is the Einstein temperature, T the absolute temperature and μ is the reduced mass of the pair of atoms involved in the bond. The σ_0^2 constant is introduced because our data give the disorder relative to the lowest temperature. In fact, the σ_0^2 represents the zero-point thermal fluctuation. So, the equation (1) has two adjustable parameters to vary in the fit, namely Θ_E and σ_0^2.

The same procedure was used for the bulk Co and Cu standards, using experimental phase and amplitudes from each metal measured at 10 K as reference. As result, we found the effective Einstein temperature Θ_E, and the absolute zero-point thermal fluctuation σ_0^2 for each sample (see Table I). In fig. 3, the experimental results and the absolute thermal disorder fitted to the correlated Einstein model are plotted against the temperature. The experimental points are shifted from zero by the zero-point thermal fluctuation value.

Table I. *Results of the fits shown in fig. 3.* Θ_E *and* Θ_D *are the Einstein and Debye temperatures obtained using the correlated Einstein model.*

	Co	$Co_{10}Cu_{90}$	Cu
$\sigma^2_{0K}(10^{-4}$ Å$^2)$	30 ± 1	32 ± 1	36 ± 2
Θ_E (K)	285 ± 3	269 ± 3	233 ± 3
Θ_D (K)	380 ± 4	359 ± 4	311 ± 4
f (N/m)	69 ± 1	61 ± 1	50 ± 1

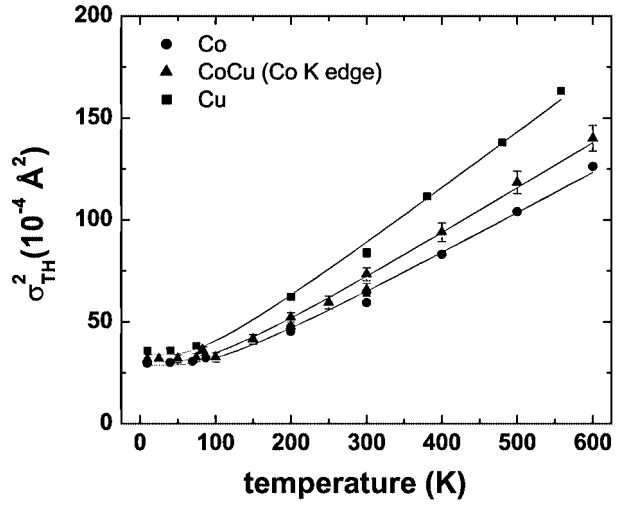

Fig. 3. Absolute thermal disorder variation as function of temperature for bulk Co and $Co_{10}Cu_{90}$ sample around Co K-edge and for bulk Cu around Cu K-edge. The continuous lines represent the fits to the correlated Einstein model.

The Einstein temperature can be considered as a measure of the effective bond-stretching force constant, given by $f = \mu k_B^2 \Theta_E^2/\hbar$[5]. The values corresponding to all samples (Table I) can be used to compare the strength of different bonds. The smaller Einstein temperature obtained for bulk Cu in comparison with bulk Co reflects the fact that Cu atoms present a greater thermal disorder at a given temperature. In other words, Cu-Cu bonds are weaker than Co-Co bonds, as shown by the effective force constants. For the $Co_{10}Cu_{90}$ sample, we observed an intermediate situation. That can be understood as the following: if individual Co atoms were dispersed in the Cu matrix, they would be bound to Cu atoms with weaker bonds compared to Co-Co bonds, and therefore would have a greater thermal disorder. Co atoms on the surface of the Co particles would have their lattice dynamics affected by the matrix, while atoms within the core of Co particles would tend to preserve the bulk Co properties. EXAFS gives the average over all Co atoms. Depending on the surface/volume ratio of the particles in the sample, the effective Einstein temperature Θ_E will tend to the bulk Cu (small particles) or Co (big particles) values. In the $Co_{10}Cu_{90}$ sample studied here, the Co atoms are forming particles with an average size close to 4 nm, whose surface/volume ratio corresponds to approximately 30% [1]. As expected, the thermal behaviour of the Co atoms in the $Co_{10}Cu_{90}$ sample is closer to that of the bulk Co sample. The Debye temperatures, estimated simply by $\Theta_D \approx 4\Theta_E/3$ [4], are listed in table I. The behavior of Θ_D follows that of Θ_E and compares very well to the values reported in the literature (315 and 385 K for Cu and Co respectively [6]).

Another approach to the data analysis was to fit the Co K-edge spectra of the Co-Cu sample using bulk Co, measured at the same temperature, as reference. Even if in the Co-Cu sample, Co atoms have Co and Cu as first neighbors, these atoms are very similar and can hardly be distinguished as scatters [1]. With this approach, the obtained Debye-Waller factor contains not only the disorder from thermal origin, but also the additional static disorder of Co-Cu sample relative to bulk Co. These experimental results are shown in fig. 4 for each temperature (squares). In addition, it is shown in the same figure (continuous line) the relative thermal disorder between the $Co_{10}Cu_{90}$ sample and the bulk Co, obtained by the difference between the respective fitted curves shown in fig. 3. One can observe that the experimental points lie above but fairly close to the expected relative thermal disorder of

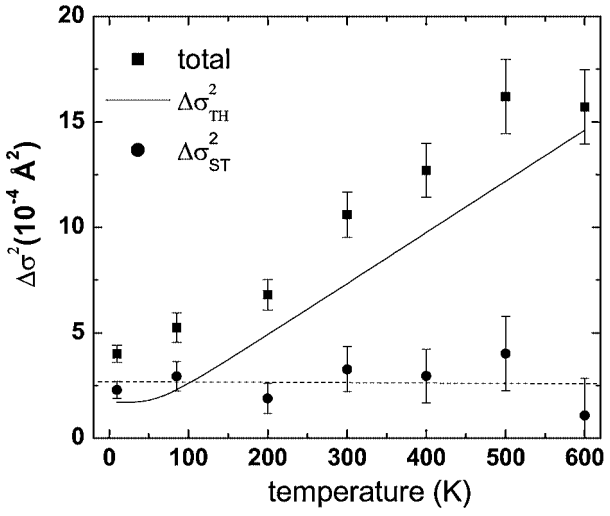

Fig. 4. Variation of the relative total disorder (squares) around Co atoms with temperature, in annealed $Co_{10}Cu_{90}$ sample. The bulk Co was used as reference and measured at each temperature together with the sample. The continuous line represents the expected relative thermal disorder. The circles represent the static contribution to the disorder ($\Delta\sigma^2_{ST}$).

$Co_{10}Cu_{90}$. The difference between the experimental points and the calculated curve arises due to a small amount of static disorder. This difference is also plotted in fig. 4 (circles), and the dashed horizontal line is a linear fit of these points, showing (as expected) a constant value for the static disorder ($\approx 3\times10^{-4}$ Å^2). One can note that the relative static disorder is very small compared with the thermal component.

4. Conclusions

In this work we investigated the behavior of the disorder in a Co-Cu granular alloy. The temperature dependence of the EXAFS Debye-Waller factor, compared with the same measurements on bulk Co and Cu, allowed us to conclude that most of the disorder in the granular alloy is of thermal origin, and that the static disorder is negligible and nearly the same as bulk Co.

Acknowledgments

This work has been supported by the Brazilian Synchrotron Light Source (LNLS) under proposal D04B–XAS1 1286. J. C. Cezar and N. P. Abreu acknowledge FAPESP and CNPq for grants.

References

1. Cezar, J. C., Tolentino, H. C. N. and Knobel, M., Phys. Rev. B **68**, 055329 (2003).
2. Tolentino, H. C. N. *et al.*, J. Synchrotron Rad. **8**, 1040 (2001).
3. Allia, P., Tiberto, P., Baricco, M. and Vinai, F., Rev. Sci. Instrum. **64**, 1053 (1993).
4. Sevillano, E., Meuth, H. and Rehr, J. J., Phys. Rev. B **20**, 4908 (1979).
5. Dalba, G. and Fornasini, P., J. Synchrotron Rad. **4**, 243 (1997).
6. Ashcroft, N. W. and Mermin, N. D, "Solid State Physics", (Saunders College Publishing, 1976).

Physica Scripta. Vol. T115, 421–423, 2005

Microstructures of Mechanically Alloyed $Fe_{60}Ni_{40}$ Studied by XAFS and XRD

Shilong Yin*[1], Zhi Xie[2], Jing Zhang[3], Qing Bian[4], Wensheng Yan[2], Zheng Jiang[2] and Shiqiang Wei[2]

[1]Institute of Science, Hohai University, Nanjing 210098, P.R. China
[2] National Synchrotron Radiation Laboratory, University of Science and Technology of China, Hefei, 230029, P.R. China
[3]Beijing Synchrotron Radiation Facility, Beijing 100039, P.R. China
[4]Institute of Science, PLAUST, Nanjing 210016, P.R. China

Received June 26, 2003; accepted in revised form November 4, 2003

PACS numbers: 61.10.Ht, 75.50.Bb, 81.40.Rs.

Abstract

The structures of mechanically alloying $Fe_{60}Ni_{40}$ milled for 5, 10, 20 and 40 hours were investigated by XAFS and XRD. The XRD patterns indicate that the α-Fe phase almost disappears and only the fcc phase remains after milling for 10 hours. The XAFS results further show that the RSF shape of Fe atoms is similar to that of Ni atoms for the MA $Fe_{60}Ni_{40}$ (10 h) alloy. The Debye-Waller factors σ_1 of the Fe and Ni atoms in the MA $Fe_{60}Ni_{40}$ (10 h) increase from 0.071 and 0.091 Å to 0.102 and 0.105 Å, respectively. These results demonstrate that the local structure of most Fe atoms in the MA $Fe_{60}Ni_{40}$ (10 h) has changed from bcc structure to fcc one after milling for 10 hours. With the milling time going to 40 hours, the σ_1 of both Fe and Ni atoms increase to about 0.117 Å, the $R_1 = 2.48$ Å and $N_1 = 11.9$ around Fe atoms are equal to $R_1 = 2.48$ Å and $N_1 = 11.9$ around Ni atoms and the magnitude peaks of the higher shells disappear for MA $Fe_{60}Ni_{40}$ (40 h). These results imply that the changes of local structure around Fe atoms are identical with that around Ni atoms in MA $Fe_{60}Ni_{40}$ alloys. We consider that the MA $Fe_{60}Ni_{40}$ (40 h) alloy is a homogenous solid solution.

1. Introduction

Recently, a lot of studies have revealed that the mechanical alloying (MA) can strongly increase the solid solubility of the completely immiscible alloys with a positive heat (or small negative heat) of mixing. For example, the solid solubility of Fe-Ni, Fe-Cu and Cu-Ta alloys increase from 3–6% of the thermodynamics balance to about 30% of the supersaturated one [1–4]. The MA Fe-Ni alloy has been widely applied in the fields of magnetic read-write header, accurate instruments and the laser techniques due to its crystal lattice constant invariableness in a wide temperature range, good soft magnetism ability as well as its nice property in absorption of microwave [5–10].

Kaloshkin *et al*. [1, 5] have studied the structure of as-prepared and annealed $Fe_{100-x}Ni_x$ alloys using X-ray diffraction (XRD). Their results indicate that the $Fe_{100-x}Ni_x$ alloy is a single fcc phase for $x \geq 28$, a single bcc phase for $x \leq 22$ as well as coexisting phases with fcc and a bcc structures for x in the range of $22 < x < 28$. Baldokhin *et al.*'s results have shown that the single-phase (bcc) $Fe_{100-x}Ni_x$ $(10 < x < 20)$ alloys transfer to coexistence of fcc and bcc alloy phases after annealing at 923 K [6]. Kuhrt *et al*. [7, 8] reported the martensitic transformation of $Fe_{100-x}Ni_x$ alloys from their XRD, DSC and VSM results. They have found that the microstructure of the MA $Fe_{100-x}Ni_x$ alloy can influence considerably the kinetics of the martensitic transformation, and that its high density of grain boundaries and lattice defects can hinder the martensite growth of the MA $Fe_{100-x}Ni_x$ alloy. However, no a detailed investigation on the local structure of the MA $Fe_{100-x}Ni_x$ alloys has been done yet.

In the present paper, the long-range and short-rang structures of $Fe_{60}Ni_{40}$ alloys with various milling times have been studied by XRD and X-ray absorption fine structure (XAFS). The results are useful to understand the local structural change and the mechanism of forming supersaturating Fe-Ni solid solutions during the MA process.

2. Experimental

Crystalline iron and nickel powders with purity higher than 99.8% and with particle sizes less than 200 mesh were mixed to the desired composition $Fe_{60}Ni_{40}$. The mixture and tungsten carbide balls were sealed inside a cylindrical stainless-steel vial filled with argon gas. The weight ratio of the milling ball to the mixed powder is 40-1. The MA was performed in a planetary ball miller with a rotation speed of about 220 r/min. The various samples of $Fe_{60}Ni_{40}$ were obtained after $Fe_{60}Ni_{40}$ mixtures were milled for 5, 10, 20, 40 h, respectively. The standard Fe (or Ni) powder for XAFS measurement was prepared by milling the Fe (or Ni) powder in an agate mortar. The XRD patterns of the samples were measured on a D/max-rA rotating target diffractometer using Cu K_α radiation ($\lambda = 1.5418$ Å, 40 kV and 60 mA), with a 0.02 degree step (set time is 0.1 s), DS = SS = 1°, RS = 0.3 mm.

X-ray absorption spectra of $Fe_{60}Ni_{40}$ samples at Fe and Ni K-edge were measured at the U7C beamline of National Synchrotron Radiation Laboratory (NSRL) and the beamline of 4W1B of Beijing Synchrotron Radiation Facility (BSRF). The storage ring of NSRL was operated at 0.8 GeV with a maximum current of 160 mA, and the hard X-ray beam from a three-pole superconductor wiggler with a magnetic field intensity of 6 T was used. The storage ring of BSRF was run at 2.2 GeV with a maximum current of 100 mA. Fixed-exit Si(111) flat double crystals were used as monochromator. The XAFS spectra in NSRL were collected in transmission mode with ionization chambers filled with Ar/N_2 at room temperature, using a Keithley Model 6517 Electrometer to record the electron charge directly. XAFS data were analyzed by NSRLXAFS3.0 software package compiled by Zhong *et al*. and UWXAFS3.0 according to the standard procedures [11, 12].

3. Results and discussions

The XRD patterns of α-Fe, metallic Ni and the MA $Fe_{60}Ni_{40}$ alloys with different milling times are displayed in Fig. 1. For comparison, the intensity of the diffraction peaks of α-Fe and metallic Ni is decrease by a factor of 1/5 and 1/15, respectively. After the $Fe_{60}Ni_{40}$ mixture is milled for 5 hours, the XRD profile shows that the peaks corresponding to the crystalline face (110),

*Correspondent: Shilong Yin, e-mail: slyin@vip.sina.com

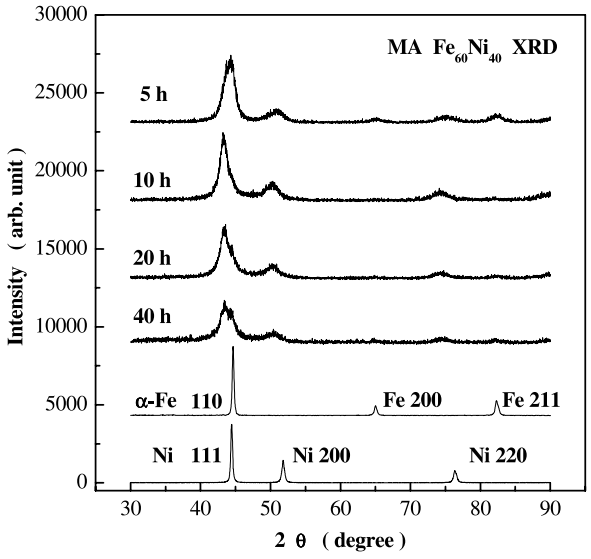

Fig. 1. XRD patterns of the MA $Fe_{60}Ni_{40}$ alloys.

(200) and (211) of bcc structural α-Fe and the crystalline face (111), (200) and (220) of fcc structural Ni are markedly clear in Fig. 1, but their intensities are much lower than those of the standard Fe and Ni references. Moreover, their diffraction peaks become broader. This indicates that the lattices of Fe and Ni powders become distorted. With the milling time going to 10 hours, the characteristic peaks of α-Fe phase almost disappear and only the peaks with fcc structure remain in the XRD pattern of the MA $Fe_{60}Ni_{40}$ (10 h), and the peak corresponding to the crystalline face (111) of the fcc structure shifts about 1.0 degree to the low angle direction. This implies that α-Fe and metallic Ni have formed the MA $Fe_{60}Ni_{40}$ alloy with fcc structure driven by the mechanical alloying, and that the lattice of the fcc structural Fe-Ni alloy has been expanded due to the diffusing of Fe atoms into the Ni lattice. The results (The MA $Fe_{60}Cu_{40}$ alloys) reported by Yavari *et al*. [4] and us [13] are in agreement with this work of the MA $Fe_{60}Ni_{40}$ alloys. Eckert *et al*. [14] have considered that the expansion of the lattice is induced by the elastic strain and magnetovolume effect. After milled for 40 hours, the peak associated with the crystalline face (111) for the MA $Fe_{60}Cu_{40}$ alloy becomes much weaker and broader, showing that the lattice distortion of the fcc Fe-Ni alloys increases further.

The EXAFS functions $k^3\chi(k)$ from both K-edge spectra of Fe and Ni atoms in the MA $Fe_{60}Ni_{40}$ alloys are shown in Figure 2. The radial structural functions (RSF) by Fourier transforming (FT) $k^3\chi(k)$ functions are shown in Figure 3. It can be observed that there are the following characteristics in the RSF functions of the α-Fe and metallic Ni powders. As shown in Fig. 3 (a), the RSF curve of bcc α-Fe powder has a strongest peak at 2.2 Å which corresponds to the first and second nearest Fe-Fe coordination shells, and the stronger peak at 4.48 Å associated with the fourth nearest coordination shell has an intensity of about 60% of that of the first peak. In the RSF curve of fcc metallic Ni powder as shown in Fig. 3 (b), the main peak located at about 2.15 Å is related to the first shell of Ni-Ni coordination, and two small peaks at about 4.0 and 4.6 Å correspond to the third and fourth nearest neighbor shells.

Seen from Fig. 3 and Table I, the main peak intensities of the $Fe_{60}Ni_{40}$ alloy decrease evidently for the sample milled for 5 hours, and the Debye-Waller factors of Fe and Ni atoms in the MA in $Fe_{60}Ni_{40}$ (5 h) increase to $\sigma_{\text{Fe-M}} = 0.086$ Å, and $\sigma_{\text{Ni-M}} = 0.095$ Å. The bond length R_1 and the coordination number N_1 of the first shell of the MA $Fe_{60}Ni_{40}$ (5 h) alloy ($R_{\text{Ni-M}} = 2.49$ Å, $N_{\text{Ni-M}} = 12.2$; $R_{\text{Fe-M}} = 2.49$ Å $N_{\text{Fe-M}} = 8.9$) are likely identical to those of metallic Ni ($R_1 = 2.55$ Å, $N_1 = 12$) and α-Fe ($R_1 = 2.48$ Å, $N_1 = 8.0$) powders. These results quantitatively manifest that the lattices of α-Fe and metallic Ni in the MA $Fe_{60}Ni_{40}$ (5 h) sample have been distorted in the beginning of the mechanical milling. Schultz has reported [14] that the structure change happens in the initial milling stage for the Fe-Zr and Ni-Zr binary systems, using XRD and DSC techniques. Their results are consistent with the conclusion of this work.

With the milling time increasing to 10 h, the main peak intensities in the RSF curves of Fe and Ni atoms of the MA $Fe_{60}Ni_{40}$ (10 h) decrease further, and the Debye-Waller factors of both $\sigma_{1\text{Fe-M}}$ and $\sigma_{1\text{Ni-M}}$ increase to about 0.102 Å. This implies that the disorders around Fe and Ni atoms in the MA $Fe_{60}Ni_{40}$ (10 h) alloy increase with the milling times. From the RSF curve of the Fe K-edge EXAFS spectrum of the MA $Fe_{60}Ni_{40}$ (10 h)

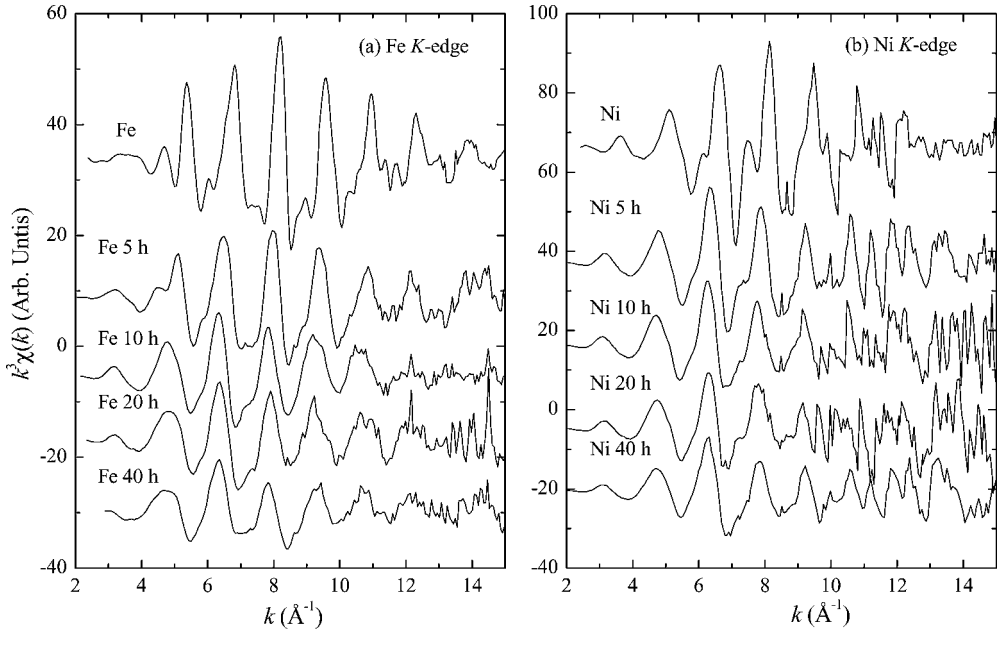

Fig. 2. $k^3\chi(k)$ curves of the MA $Fe_{60}Ni_{40}$ alloys: (a) Fe K-edge and (b) Ni K-edge.

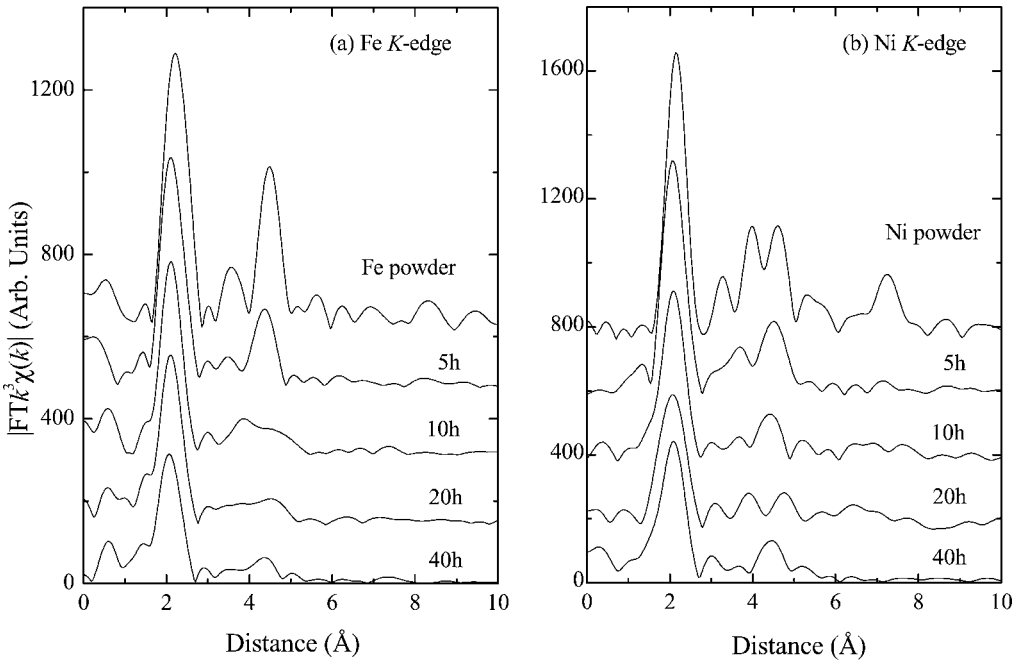

Fig. 3. RSF curves of the MA $Fe_{60}Ni_{40}$ alloys: (a) Fe K-edge and (b) Ni K-edge.

Table I. *Structural parameters of the MA $Fe_{60}Ni_{40}$ alloys obtained by fitting the (a) Fe, and (b) Ni K-edge EXAFS spectra.*

milling time (hour)	Bond type	N	R/Å	σ/Å
(a) Fe K-edge				
5	Fe-M	8.9 ± 1.1	2.49 ± 0.01	0.086 ± 0.010
10	Fe-M	10.3 ± 1.2	2.49 ± 0.02	0.102 ± 0.012
20	Fe-M	11.2 ± 1.5	2.49 ± 0.02	0.102 ± 0.012
40	Fe-M	11.9 ± 1.5	2.48 ± 0.02	0.117 ± 0.011
Fe foil	Fe-Fe	8.0 ± 0.5	2.48 ± 0.01	0.071 ± 0.007
	Fe-Fe	6.0 ± 0.5	2.86 ± 0.01	0.084 ± 0.007
(b) Ni K-edge				
5	Ni-M	12.2 ± 1.0	2.49 ± 0.02	0.095 ± 0.020
10	Ni-M	12.3 ± 1.0	2.49 ± 0.02	0.105 ± 0.018
20	Ni-M	11.8 ± 1.5	2.49 ± 0.02	0.113 ± 0.022
40	Ni-M	11.9 ± 1.5	2.48 ± 0.02	0.117 ± 0.021
Ni powder	Ni-Ni	12.0 ± 0.6	2.49 ± 0.02	0.091 ± 0.005

alloy, the peak at 4.48 Å disappears and two new peaks appear at the positions of 4.0 and 4.6 Å. Meanwhile, the peak shape and intensity of the RSF curve from the Fe K-edge EXAFS spectrum is almost the same as that of the Ni K-edge EXAFS spectrum. This means that the local structure around Fe atoms has changed from bcc structure to fcc. However, $N_{1\text{Fe-M}}$ is about 10.3, which is larger than that of the bcc-phase α-Fe powder ($N = 8$) and smaller than that of fcc metallic Ni powder ($N = 12$). These results indicate that the local structures of most Fe atoms have transformed from bcc to fcc structure, and the main MA production is fcc structural Fe-Ni alloy, and part of bcc structural Fe-Ni alloy remains. When the milling time is increased to 40 hours, the magnitudes of the main peaks in the Fe and Ni RSF curves of MA $Fe_{60}Ni_{40}$ (40 h) obviously decrease, and are about half of those of α-Fe and metallic Ni powder. The Debye-Waller factor of $\sigma_{1\text{Fe-M}}$ and $\sigma_{1\text{Ni-M}}$ increases to about 0.117 Å for the MA $Fe_{60}Ni_{40}$ (40 h) alloy. Furthermore, $R_1 = 2.48$ Å and $N_1 = 11.9$ around Fe atoms are equal to $R_1 = 2.48$ Å and $N_1 = 11.9$ around Ni atoms for the MA $Fe_{60}Ni_{40}$ (40 h) alloy. It suggests that the MA $Fe_{60}Ni_{40}$ (40 h) alloy forms a homogenous solid solution after milling for 40 hours.

In summary, the XAFS and XRD results indicate that α-Fe and metallic Ni mixture start to form Fe-Ni alloy in the initial MA stage, and the local structures around Fe and Ni atoms in the fcc structural MA $Fe_{60}Ni_{40}$ alloys are greatly distorted with the milling time, finally, the middle range order has been almost destroyed for the MA $Fe_{60}Ni_{40}$ (40 h) alloy. A homogenous MA $Fe_{60}Ni_{40}$ alloy solid solution with large lattice distortion is produced after milling for 40 hours. These results are greatly different from those of MA $Fe_{60}Cu_{40}$ alloy reported in the literature [15, 16], in which there are both fcc Fe-rich and bcc Cu-rich regions in the $Fe_{60}Cu_{40}$ solid solution.

Acknowledgment

This work was supported by the development of high-level university of University of Science and Technology of China, key-project of Beijing Synchrotron Radiation Facility, and key-program of the Chinese Academy of Sciences.

References

1. Kaloshkin, S. D., Tcherdyntsev, V. V., Baldokhin, Yu. V., Tomilin, I. A. and Shelehov, E. V., J. Non-Cryst. Solid. **287**, 329 (2001).
2. Yavari, A. R., Desre, P. J. and Benameur, T., Phys. Rev. Lett. **68**, 2235 (1992).
3. Schultz, L., Mater. Sci. Eng. **97**, 15 (1988).
4. Fukunaga, T., Mori, M., Inou, K. and Mitzutani, U., Mater. Sci. Eng. A**134**, 863 (1991).
5. Kaloshkin, S. D., Tcherdyntsev, V. V., Baldokhin, Yu. V., Tomilin, I. A. and Shelehov, E. V., Physica B **299**, 236 (2001).
6. Baldokhin, Y. V., Tcherdyntsev, V. V., Kaloshkin, S. D., Kochetov, G. A. and Pustov, Y. A., J. Magn. Magn. Mater. **203**, 313 (1999).
7. Kuhrt, C. and Schultz, L., J. Appl. Phys. **73**, 1975 (1993).
8. Kuhrt, C. and Schultz, L., J. Appl. Phys. **73**, 6588 (1993).
9. Hong, L. and Fultz, B., J. Appl. Phys. **79**, 3946 (1993).
10. Lapina, T. M., Shabashov, V. A., Sagaradze, V. V. and Arbuzov, V. L., Mater. Sci. Forum **294–296**, 767 (1999).
11. Zhong, W. J. and Wei, S. Q., J. Univ. Sci. Technol. China **31**, 328 (2001).
12. Stern, E. A., Newville, M., Ravel, B., Yacoby, Y. and Haskel, D., Physica B **208&209**, 117 (1995).
13. Wei, S. Q., *et al*., Physica B **305**, 135 (2001).
14. Eckert, J., Holzer, J. C. and Johnson, W. L., J. Appl. Phys. **73**, 131 (1993).
15. Schultz, L., Mater Sci. Eng. **97**, 15 (1998).
16. Wei, S. Q., Oyanagi, H., Wen, C. E., Yang, Y. Z. and Liu, W. H., J. Phys. **9**, 11077 (1997).

Physica Scripta. Vol. T115, 424–427, 2005

Multiple Scattering Analysis of O K-Edge NEXAFS in Iron Oxides

S. Giovannini[1], F. Boscherini[1], R. Carboni[1], L. Signorini[1], L. Pasquini[1], N. Mahne[2], A. Giglia[2], M. Pedio[2*], S. Nannarone[2,3], M. Benfatto[4] and S. Della Longa[4,5]

[1]INFM and Dip. di Fisica, Universita' Bologna
[2]TASC-INFM Area Science Park, I-34012 Basovizza
[3]TASC-INFM Area Science Park, I-34012 Basovizza and Dip. Ing. dei materiali e dell'ambiente, Un. di Modena e Reggio Emilia
[4]LNF-INFN P.O. Box 13, I-00044 Frascati
[5]Dipartimento Medicina Sperimentale, Università L'Aquila, 67100 L'Aquila, Italy

Received June 26, 2003; accepted in revised form November 4, 2003

PACS number: 78.70.Dm

Abstract

We report a detailed analysis of O K-edges near edge X-ray absorption of maghemite, hematite and magnetite iron oxides. Measurements were performed on powder in Fluorescence Yield mode of detection.

Iron forms several stable oxides and its phase diagram is more complicated than that of other transition metal as Ni or Co. The differences in the local symmetry of the three iron oxides are related with the distinguishable NEXAFS spectra. In particular the spectra are characterized by a sharp doublet ascribable to transitions to the empty metal d-bands involving the t_{2g} and e_g states whose energy splitting and intensities depend on the structure and state of ionicity.

The NEXAFS spectra have been simulated and fitted by MXAN code. The aim of these simulations was the test of light *Z* element NEXAFS spectra calculation performed by phenomenological no-self-consistent potential in the near edge region, the most sensible to electronic properties details; a fit procedure of the potential parameters was performed in the extended NEXAFS photon energy range and subsequently used for near edge calculations. The MXAN simulations obtained in this way, reproduce the experimental data with good agreement and evidentiate the differences in the spectra of the three compounds. In particular maghemite, that has oxygen in two different sites, has been well simulated using potential details found for the other oxides hematite and magnetite.

1. Introduction

Iron forms several stable oxides and its phase diagram is more complicated than that of other transition metal as Ni or Co [1, 2, 3]. Iron oxides are used as catalyst materials and for their magnetic properties in the high-density magnetic recording media technology. For these reasons the investigation of iron oxides has gained increasing attention in the past years.

We report a detailed analysis of iron oxide near edge X-ray absorption fine structure (NEXAFS) performed at the O K-edge. NEXAFS spectra of maghemite, hematite and magnetite (in powder form) were performed by Fluorescence Yield detection mode. The differences in the local structure and symmetry around the central oxygen atom of the three iron oxides lead to distinguishable NEXAFS spectra. A detailed discussion on transition metal oxides trend in O K-edge spectra is reported in ref. [1]. The O K-edge spectra of iron oxides are characterized [1, 3] by a sharp doublet ascribable to transitions to the empty metal d-bands involving the t_{2g} and e_g states and showing different energy splitting and intensities as a function of the O-Fe structure and state of ionicity. The higher energy part is due to the 4sp contribution of Fe to the O 2p density of empty states.

This work is focussed on hematite, magnetite and maghemite oxides. In the three studied compound oxygen nearest neighbor shell is formed by 4 Fe anion in a pseudo tetrahedrical configuration. The oxidation state of Fe is a mixture of +2 and +3 for magnetite and exclusively +3 for maghemite and hematite. Hematite (α-Fe_2O_3) has a corundum structure, magnetite (Fe_3O_4) has a cubic inverse spinel, while maghemite presents a distorted spinel (γ-Fe_2O_3) structure with oxygen in two different sites both in a tetrahedral symmetry; it can be thought as derived by magnetite structure with all Fe^{3+} cations.

Total Yield spectra for magnetite and hematite, with an energy resolution of 500 meV, were previously reported by Wu *et al*. [3]; the spectra we present have better resolution of 200 meV. The results of this work measured in Fluorescence yield are similar, but show relative intensity ratios between the doublet peak and the higher energy feature group that are similar in the three compounds. Different intensity ratios of the 3d band relative to the 4 sp transition metal orbitals have been explained in terms of the diminished hybridisation of the metals 3d states with the O 2p states [1, 3].

Hematite is characterized by a structure at about 546 eV. This peak is much more pronounced with respect to literature data, taken at lower resolution.

The structure of the sample has been checked by O K-edge and Fe K-edge EXAFS [4].

The NEXAFS spectra have been simulated and fitted by MXAN code [5]. Our aim was the test of the calculation of light *Z* element (oxygen) near edge XAS spectra performed by phenomenological no-self-consistent potentials and analyse the simulated results in the near edge region, the most sensible to electronic properties details. These were obtained by a fit procedure of the potential parameters performed in the extended NEXAFS photon energy range (70 eV). Our simulations by phenomenological potential reproduce the experimental data with good agreement. The maghemite O K-edge spectrum has been calculated by multiple scattering for the first time. The procedure to obtain the phenomenological potential used here to get the simulated spectrum of the two different oxygen sites is detailed discussed in the following.

2. Experimental

Measurements at the O absorption K-edge were performed on the BEAR beamline of the ELETTRA synchrotron radiation facility in Trieste, Italy. The energy resolution was 200 meV for a typical photon flux on the sample of the order of 10^{10} ph/s [6]. All measurements were performed in the fluorescence yield mode using a photodiode (IRD AXUV100) operated in the current mode; the typical photodiode dark current was of the order of

*e-mail: pedio@tasc.infm.it

0.1 pA with an overall long term stability of the order of 0.01 pA. Use of fluorescence yield guarantees that spectra are relative to average bulk properties and unaffected by surface-specific structure. The samples were smeared on carbon tabs and then placed on a sample holder consisting of a steel plate mounted on a vertical rotary feedthrough. The samples were polarized at +1000 V in order to avoid electrons excited by the photon beam reaching the photodiode detector.

Fluorescence yield spectra of concentrated samples can be distorted due to self-absorption [7]. In order to minimize spectral distortions the angle between the impinging photon beam and the sample surface was fixed at 70°. Since some distortions can in any case be present the raw data was corrected according to a method developed by some of the co-authors which involves the scaling of the experimental spectrum to tabulated atomic cross-sections [8]. All the O K-edge data have been thus corrected for self-absorption. Absorption signals were normalized to the incident flux obtained by measuring the current drained by tungsten grid inserted in the beam path. The grid was flashed in order to remove contaminants, typically C and O.

3. Results and Discussion

Fig. 1 shows O K-edge NEXAFS spectra of hematite (α-Fe_2O_3), maghemite (γ-Fe_2O_3) and magnetite (Fe_3O_4) as measured by Fluorescence Yield of powder samples.

In the low photon energy region, within 5 eV above the edge, a sharp doublet is present in all the three spectra. The doublet was interpreted in the literature as due to transitions to the empty metal d-bands involving the t_{2g} and e_g states as projected on to the p O empty states and whose degeneracy is removed by the breaking of symmetry of the octahedral configuration in pure Fe while the higher energy is due to the 4sp iron contributions to the O 2p density of states.

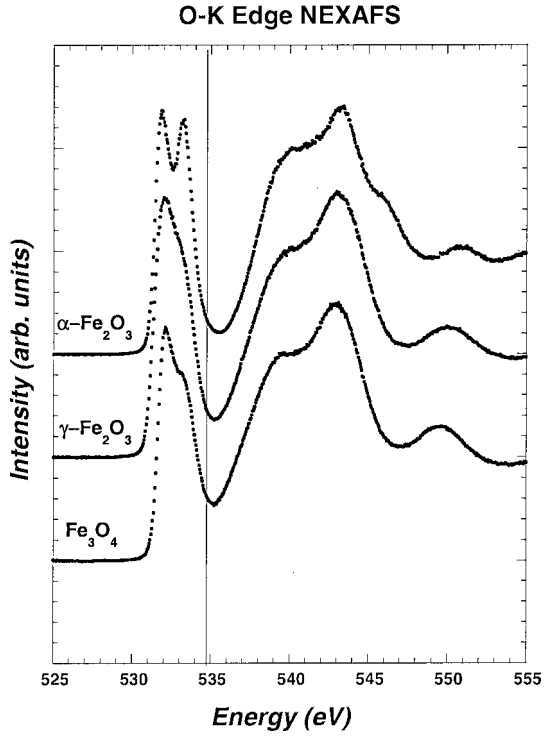

Fig. 1. Fluorescence yield experimental spectra of O K-edge NEXAFS of (a) hematite (α-Fe_2O_3), (b) maghemite (γ-Fe_2O_3) and (c) magnetite (Fe_3O_4).

Table I. *List of distances in hematite (α-Fe_2O_3), magnetite (Fe_3O_4) and maghemite (γ-Fe_2O_3) in the two different O sites.*

	α-Fe_2O_3	Fe_3O_4	γ-Fe_2O_3 (site 1)	γ-Fe_2O_3 (site 2)
Fe1	1.94 (×2)	1.887 (×1)	1.840 (×1)	1.888 (×1)
Fe2	2.11 (×2)	2.059 (×3)	2.099 (×3)	1.967 (×1)
Fe3				2.034 (×1)
Fe4				2.099 (×1)
O1	2.67 (×2)	2.853 (×3)	2.792 (×3)	2.792 (×1)
O2	2.77 (×2)	2.968 (×6)	2.904 (×3)	2.887 (×2)
O3	2.88 (×4)	3.081 (×3)	2.953 (×3)	2.903 (×3)
O4	3.03 (×4)		3.061 (×3)	2.953 (×1)
O5				3.05 (×2)
O6				3.06 (×3)
⟨O-O⟩	2.876	2.968	2.958	2.956

The distances to the central oxygen atom in the three iron oxides are reported in Table I up to a radius of about 3 Å; note that the oxygen surrounding of hematite is sensibly different in symmetry and distances to the other two compounds.

In Fig. 1 the doublet is very well resolved for hematite and remains clearly detectable for the three compounds. The differences in the energy splitting and intensities are functions of the O-Fe structure: the energy splitting is larger in hematite (1.45 eV) and decreases to about 1.05 eV for the other two compounds, magnetite and maghemite; the peak at about 532 eV is related to the t_{2g} state with π character and the other at about 533 eV is due to the e_g states, with σ character [2]. The spectrum for maghemite is similar to that of magnetite but exhibits a significant shift towards lower energies of most features, including a −0.35 eV shift of the absorption edge itself.

The higher energy region is characterized by broader features that have been proved to be due in hematite and magnetite [3] to multiple scattering induced by atoms lying above 5 Å from the central oxygen atom. Moreover hematite is characterized by a structure at about 546 eV. This peak is much more pronounced with respect to literature data, taken at lower resolution. Total Yield NEXAFS spectra of hematite and magnetite have been reported in the literature at a resolution of 500 meV and analysed by multiple scattering formalism [3]. The spectra of the present work are measured in Fluorescence yield are similar, indicating the correctness of our procedure for correcting for self-absorption. Moreover the spectra presented here have the better resolution of 200 meV and show a similar weight of the 3d-band region intensity with respect to the 4sp region (for the implication of this result see the discussion of refs. [1] and [3]).

Here we use the well characterized systems hematite and magnetite O K-edge spectra (refs. [1] and [3]) to test the MXAN fitting procedure in order to analyse the reliability of the code in finding the no-self-consistent phenomenological potential parameters for near edge low Z element spectra. No multiple scattering simulation is present in the literature on maghemite.

Full multiple scattering simulations have been performed by MXAN code [5] that is based on the comparison between the experimental spectrum and several theoretical calculations generated by a fit procedure. The X-ray photoabsorption cross section is calculated using the general MS scheme within the muffin tin (MT) approximation. For the exchange and correlation part of the potential we used no-self-consistent phenomenological potentials: energy-independent Xα potential, the complex Hedin-Lundqvist (HL) and the real energy-dependent HL potential plus

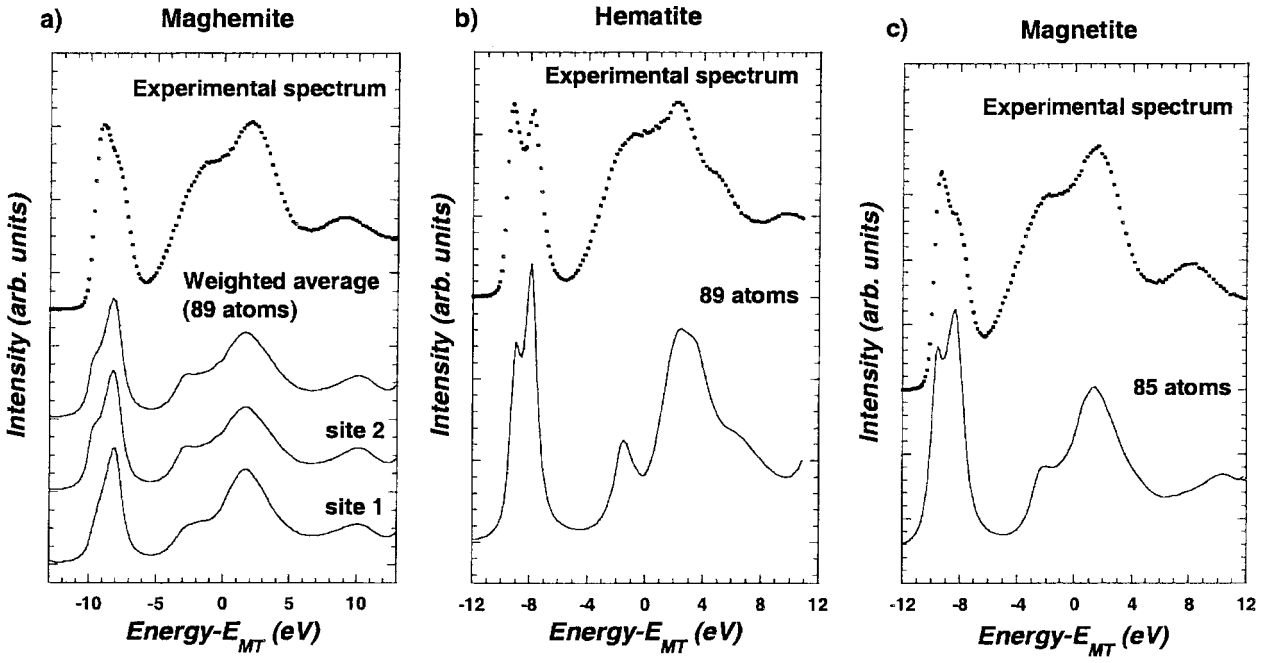

Fig. 2. Comparison of the NEXAFS simulations by MXAN and the experimental O K-edge spectra of (a) maghemite, (b) hematite and (c) magnetite. The number of atoms used in the input cluster of the simulation is indicated.

a damping factor [5]. In the fit procedure the coordinate structure was fixed while some potential parameters were fit, like the values of the interstitial potential, of the overlap between contiguous atoms, the Fermi energy. These are fit parameters which are changed at every step in order to minimize the square residual between the theoretical and the experimental spectra.

Figure 2 shows the O K-edge NEXAFS for the three oxides and the best fit obtained by MXAN. The calculation and fit procedure was the following: the extended NEXAFS part (up to about 600 eV) of the hematite and magnetite spectra were fitted by MXAN fixing the structure coordinates at 75 atoms for hematite, and 85 for magnetite, leaving as fitting parameters the interstitial potential and the overlap between contiguous atoms. This has been done both for HL and Xα potentials. We obtained similar parameter values for both hematite and magnetite, even though they have different nominal ionicity [9] (not surprising for the higher energy part of NEXAFS [10]). Note that in the muffin tin potentials calculated in this way (i.e., non self consistent) all the atoms are neutral.

The so obtained potential parameters were used to simulate the NEXAFS spectra for the three compounds: two distinct oxygen sites spectra of maghemite that were then weighted averaged and NEXAFS spectra for hematite and magnetite. In this way we obtained the simulation shown in fig. 2.

For hematite and magnetite we found good agreement with the experimental data, with some improvement in the higher part of the spectra with respect to the simulations performed in ref. [3]. The best simulations in both cases were obtained by using HL real potential with phenomenological dumping factor. The agreement with the experimental spectra of maghemite is good and a slightly better agreement was found for Xα real potential with respect to HL.

The broad peaks in the higher part of NEXAFS of hematite and magnetite are due to multiple scattering paths involving atoms above 5 Å away from the central oxygen atom. Their energy separation and relative intensities result to be different in the three compounds and can be related to the regularity of the octahedron formed by the metal surrounded by the oxygen atoms; actually the energy separation between the two features decreases from magnetite (3.37 eV), which presents all regular octahedron, to maghemite (3.0 eV), that has some distorted octahedron, to hematite (2.9 eV), which has all distorted octahedron.

Due to the better resolution in hematite the characterizing feature at about 546 eV can be clearly singled out; it is well reproduced by using input an cluster with a number of atoms higher than 75 i.e., is due to scattering paths involving the atoms within 5.5 Å from the absorber.

With the potentials obtained as described above we focussed our analysis on the doublets. It is worth noting that the simulations presented here are made in the single particle approximation. We were able to reproduce the doublets of the three compounds, even though we found differences in their relative intensities. Several tests have been performed and we found that this low energy part is extremely sensitive to the details of the potential.

Fig. 3 shows a shell by shell analysis of the doublet as performed by increasing the number of atoms in the input cluster. For hematite the doublet appears in simulation based on a cluster with more than 27 atoms. This cluster is formed by the central oxygen atom surrounded by 4 Fe, 12 O, 6 Fe and 4 O within 4 Å by the absorber. Whereas for magnetite and maghemite the splitting is present from a cluster of 17 atoms (4 Fe and 12 O around the absorber) in a radius of 3 Å from the central oxygen atom. In maghemite we do not found striking differences in site 1 and site 2 (Fig. 2a) results but in doublet splitting that is slightly higher in the case of site 1 (3.2 eV) with respect to site 2 (3.0 eV) and in some details of the higher energy peak group.

We found differences with ref. [3] in the at edge simulations relative intensities in doublets. We infer that these discrepancies are due to differences in potential details as found by fit procedure. The low energy part differences are ascribable to details in the potentials: actually playing *a priori* with the potential parameters in the calculations, it is possible to obtain an intensity ratio closer to the experimental value. It is worth noting that for ionic compounds it was found that the lower spectrum part is affected

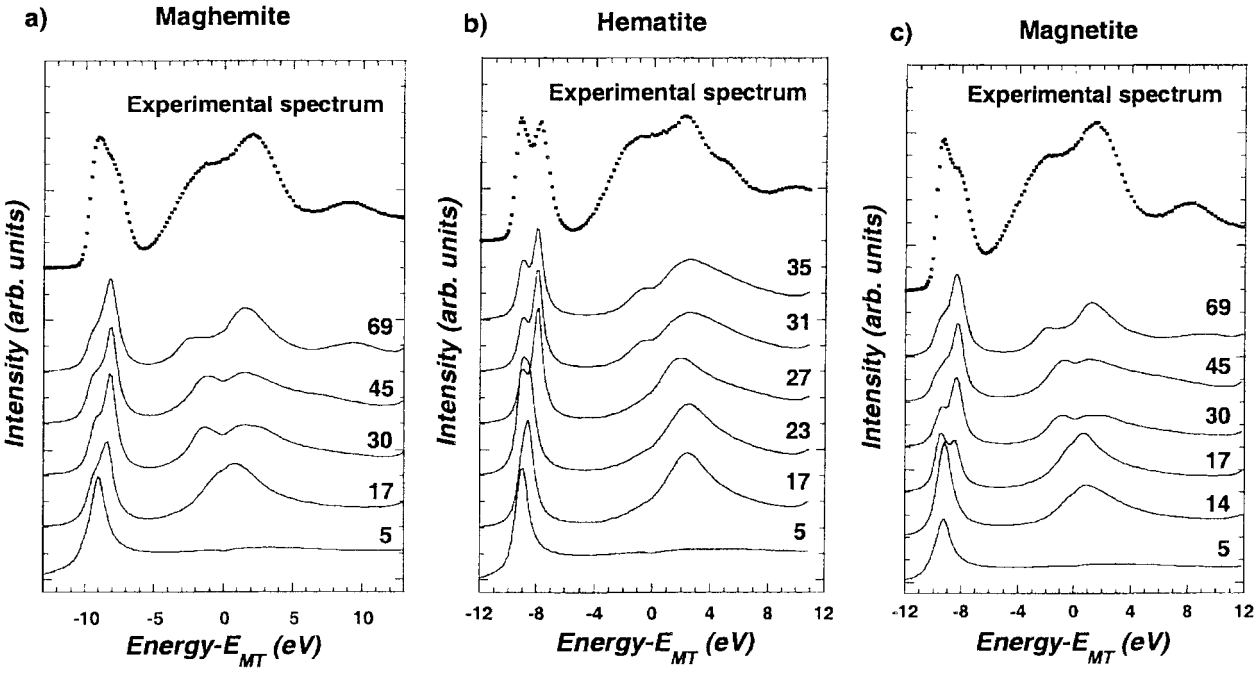

Fig. 3. Shell by shell NEXAFS simulation as a function of the number of atoms used in the input clusters for (a) maghemite, (b) hematite and (c) magnetite.

by potential details especially in case of O K-edge [9] and that the effect of self consistency allowing for charge transfer on the shape of the spectra are localized in the first region above the edge, namely at 25 eV. In order to improve the agreement with the experimental data we intend to perform further simulations by self consistent potentials by using the correct charge transfer between Fe and oxygen atoms in the systems, in the next future. In any case our results confirm that the muffin tin prescription for non self consistent potential is reasonable and the effects are quantitative at higher energies.

4. Conclusions

We measured the O K-edge NEXAFS spectra of hematite, magnetite and maghemite iron oxides in fluorescence detection mode with a resolution better than 200 meV. Spectra show a similar weight of the 3d-band region intensity with respect to the 4sp region.

We used the well characterized systems (refs. [1] and [3]) hematite and magnetite O K-edge spectra to test the MXAN fitting procedure in order to analyse the reliability of the code in finding the no-self-consistent phenomenological potential parameters for near edge low Z element spectra.

We report the Multiple Scattering analysis of iron oxides; we successfully simulated the three oxides. The fit procedure of the potential parameters has been performed in the extended part of the NEXAFS spectra of hematite and magnetite. The parameters found in this way for the no-self consistent potential have been used to calculate the near edge part of the three compounds spectra. Maghemite structure shows two different O sites and its NEXAFS O K-edge spectrum was well simulated, for the first time, by using potential parameters found by a fitting procedure of the hematite and magnetite oxides.

Simulations correctly reproduced the energy separation trend of the d-Fe state projection onto the O p states, forming the part of the spectra immediately above the O K-edge.

Acknowledgment

This work was partially supported by the Istituto Nazionale per la Fisica della Materia (INFM) under project PURS-FLUX and by a LdS-INFM fellowship.

References

1. de Groot, F. M. F. *et al.*, Phys. Rev. B **40**, 5715 (1989).
2. Schedel-Niedrig, Th., Weiss, W. and Schlögl, R., Phys. Rev. B **52**, 17449 (1995).
3. Wu, Z. Y. *et al.*, Phys. Rev. B **55**, 2570 (1997).
4. Signorini, L. *et al.*, submitted to Phys. Rev. B.
5. Benfatto, M. and Della Longa, S., J. Synchrotron Rad. **8**, 1087 (2001); Della Longa, S., Arcovito, A., Girasole, M., Hazemann, J. L. and Benfatto, M., Phys. Rev. Lett. **87**, 155501 (2001); Benfatto, M., these proceedings.
6. Naletto, G., Pelizzo, M. G., Tondello, G., Nannarone, S. and Giglia, A., SPIE Proc. **414**, 105 (2001); Nannarone, S. *et al.*, SRI conference proceedings, to be published.
7. Goulon, J., Goulon-Ginet, C., Cortes, R. and Dubois, J. M., J. Phys. (Paris) **43**, 539 (1982); Tröger, L., *et al.*, Phys. Rev. **46**, 3283 (1992).
8. Carboni, R., Giovannini, S., Antonioli, G. and Boscherini, F. "Self-absorption correction strategy for fluorescence-yield soft x-ray near edge spectra", Physica Scripta, these proceedings.
9. As noted by different authors the transition metal oxides show a high covalent contribution in the O-Metal bond.
10. Wille, L. T., Durham, P. J. and Sterne, P. A., J. Physique **C8**, 43 (1986).

Physica Scripta. Vol. T115, 428–430, 2005

Local Structure in $LaMnO_3$ Across the Jahn-Teller Transition

Raquel A. Souza[1,2], Aline Y. Ramos[1,3], Helio C. N. Tolentino[1] and Eduardo Granado[1]

[1]Laboratório Nacional de Luz Síncrotron, Campinas, SP, Brazil
[2]Universidade Estadual de Campinas, IFGW, Campinas, SP, Brazil
[3]LMCP, UMR7590 CNRS – France

Received June 26, 2003; accepted in revised form December 17, 2003

PACS numbers: 75.47.Lx, 61.10.Ht, 71.90.+q

Abstract

We report on an EXAFS study of the local environment of manganese atoms in $LaMnO_3$ across the cell ordering transition temperature. During the EXAFS analysis the phase derivative method was used prior to conventional fits in order to prevent possible mistakes arising from the correlation between parameters in the fitting method. The combination of the two procedures assert the result that the local splitting in the Mn-O distance is maintained above the Jahn-Teller transition and support the order-disorder character predicted for this transition in $LaMnO_3$.

1. Introduction

The lanthanum manganite and its doped alloys have attracted much attention in the last decade, in large part due to the potential applications of the so-called Colossal Magnetoresistance. These compounds show very unusual physical properties, arising from intricate interrelations between spin, charge and local structure. Many of these phenomena still remain to be elucidated, even in the parent undoped compound $LaMnO_3$. At room temperature, $LaMnO_3$ is an A-antiferromagnetic insulator. The oxygen octrahedron surrounding the manganese is strongly distorted due to the tough Jahn-Teller (JT) character of the Mn^{3+} ion. Mn-O bonds with three different lengths coexist (1.91 Å, 1.97 Å, 2.15 Å) [1]. Cooperative ordering of the distorted octahedra results in the crystallization of $LaMnO_3$ in an orthorhombic variant of the cubic perovskite structure. Above $T_{JT} \simeq 700$–750 K, the lattice becomes metrically cubic [1, 3] and the resistivity decreases by about two orders of magnitude [2]. At the local scale this so called Jahn-Teller (JT) transition is not yet well understood. On the first hand, thermodynamical calculations have shown that the energy needed to remove the local Jahn-Teller should be far above the thermal energy at T_{JT}. The transition would happen as an order-disorder transition in the sequence of the distorted octahedra. Experimentally, the two pioneers works of Granado *et al*. [3] and Araya-Rodriguez *et al*. [4] supported the hypothesis of the upkeep of the local JT distortion, respectively from Raman results [3] and from the analysis of the overall disorder in the EXAFS data across T_{JT} [4]. On the other hand, the theory that the local Jahn-Teller distortion may vanish and the Mn-O distances collapse like the cell parameters was sustained by J. H. Song *et al*. [5], as result of the fitting procedure in the data reduction of their EXAFS spectra in thin $LaMnO_3$ films. More recently Sanchez *et al*. [6], using the same procedure of data reduction, have reached opposite conclusions in $LaMnO_3$ polycrystals. This disagreement may call into question the validity of the fitting method applied to high temperature data of this complex system and request definitive analysis methodology. In the present work we report on an EXAFS study of the manganese environment in a high quality $LaMnO_3$ manganite across T_{JT}. The Phase Derivative Method (PDM) [7] was combined to the fitting procedure to fully assert the results of the data analysis.

2. Experimental

The ceramic $LaMnO_3$ sample studied in this work was prepared by standard ceramic methods and shows a JT transition around 710 K [3]. Fine grained powder was pressed between two thin beryllium windows and placed in an electrical furnace for measurements from 300 K to 870 K. The EXAFS data were collected at the LNLS D04B-XAS1 beam line in the transmission mode up to 600 eV above the Mn K-edge (6550 eV). This extension in the data range ($k_{max} = 12.5$ Å^{-1}) establishes the value $\delta R_{min} = 0.13$ Å as the minimum difference between two close distances that can be resolved in the EXAFS analysis. The two distances at 1.91 Å and 1.97 Å are seen as one unique short distance Mn-O_s = 1.94 Å, easily resolved from the long distance Mn-O_l = 2.15 Å (δR = 0.21 Å).

The EXAFS oscillations were extracted following the standard procedure using the WinXAS program [9]. The signal corresponding to the oxygen coordination shell is then selected by Fourier filtering and analysed first using the Phase Derivative Method then using the fitting subroutine of the WinXAS code. In the fitting procedure the number of free parameters is limited to $n \approx 2\Delta k \Delta R/\pi$, where Δk is the useful range and ΔR is interval corresponding to the selected signal in the real space. Fitting procedures involving more than this limit of parameters may lead to systematic errors. On the other hand the number of parameters ideally requested for a joint fit of two subshells of the same backscatter is 8 (2 numbers of neighbours (N_1, N_2), 2 distances (R_1, R_2) and 2 Debye-Waller (DW) factors (σ_1^2, σ_2^2), the energy shift ΔE_0 and the amplitude-reduction factor (S_0^2)).

The PDM exploit the modulation in the EXAFS signal occuring when the contributions of two close shells separated by δR are combined. For two shells with the same backscatter atom, it can easily be shown [7, 8] that this modulation results in a minimum in the total amplitude, at $k = k_B$ given by $k_B = \pi/2\delta R$. The presence of this extremum – or beat – is widely used to identify the occurence of close shells. At the beat value also occurs an extremum in the total phase derivative [7]. Even when the EXAFS signal is strongly damped by thermal or static disorder, the determination of the position of the beat from the derivative (PDM method) is very accurate [8]. Due to and various sources of systematic errors $\delta R_B = \pi/2k_B$ does not give exactly the bond length separation [8]. However any modification in this separation will be detected by a shift in the beat position.

3. Results and Discussion

The k^2-weighted $\chi(k)$ spectrum and its Fourier transform (FT) are presented in fig. 1 for $LaMnO_3$ at 300 K. The first peak in the FT corresponds to the coordination shell and a back-FT is

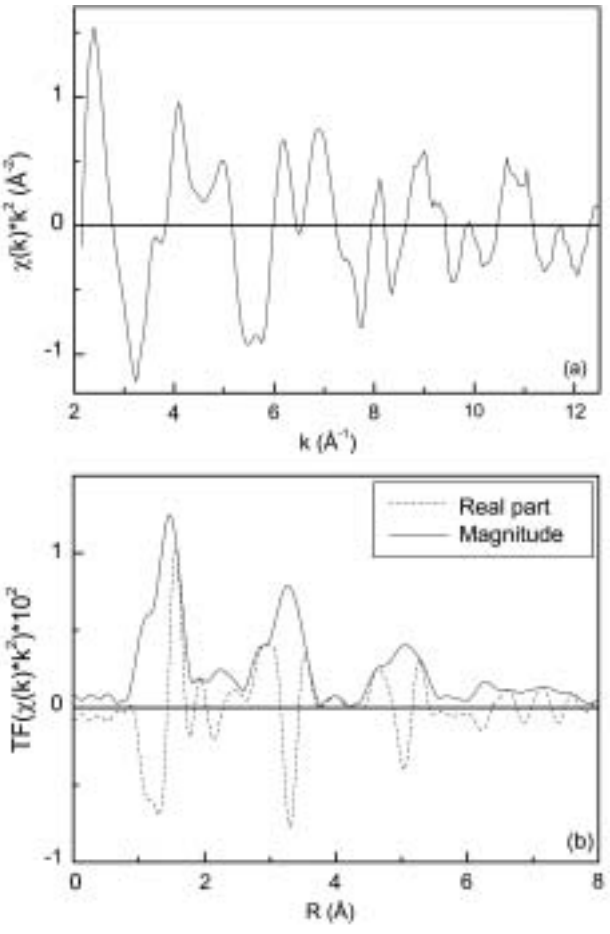

Fig. 1. (a) $LaMnO_3$ k^2-weighted EXAFS signal and (b) its Fourier transform.

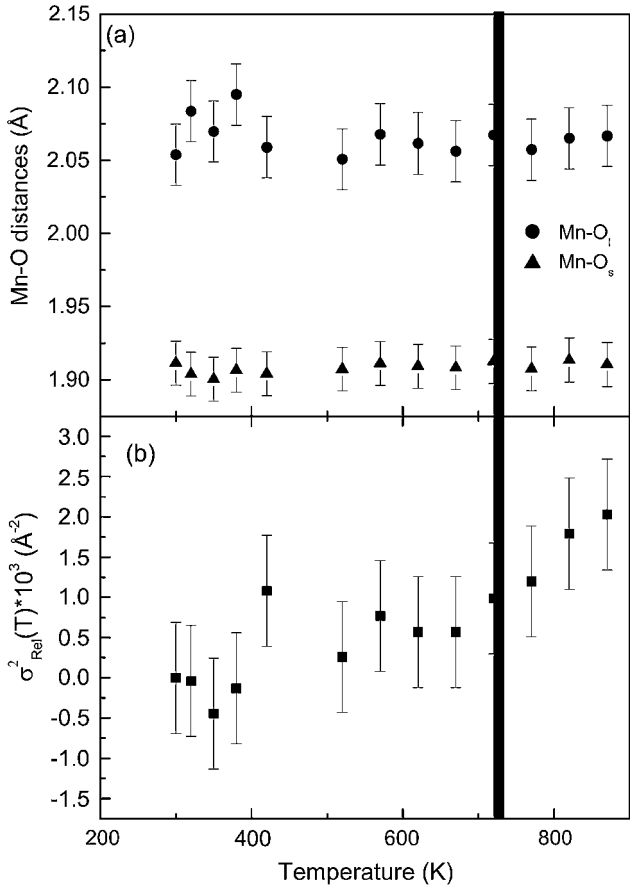

Fig. 3. Results of the fitting procedure: (a) distances Mn-O_s and Mn-O_l and (b) relative Debye-Waller factor: $\Delta\sigma^2(T) = \sigma^2(T) - \sigma^2(300\,\mathrm{K})$. The vertical line correspond to the Jahn-Teller temperature transition.

applied in real space over the interval $R_{min} = 0.9$ to $R_{max} = 2.1\,\text{Å}$ to separate this signal. When applying to PDM to the selected signal, we observe at $k_B(300\,\mathrm{K}) = 9.5\,\text{Å}^{-1}$ a beat corresponding to the separation δR between the short and long Mn-O distances.

The same procedure was repeated for all temperatures. $\delta k_B(T) = k_B(T) - k_B(300\,\mathrm{K})$ is plotted in fig. 2 as a function of temperature. Any reduction of the Jahn-Teller distortion around Mn^{3+}, would result in a decrease of δR and be detected as positive shift in the beat position ($\delta k_B \approx 0$). Actually, we observe a small minimum in the beat position at the JT temperature. This minimum could correspond to a maximum increase of 5% in the distances splitting, but is more likely associated to a small variation in the disorder. Within the errors bars, we can certify that the beat value does not increase above the transition temperature. The bond length splitting is kept unchanged across the JT transition.

When applying the conventional fitting method [9] with $\Delta k = k_{min} - k_{max} \approx 10\,\text{Å}^{-1}$ and $\Delta R = R_{min} - R_{max} \approx 1.2\,\text{Å}$, we found 7 independent points, maximum number of parameters ideally requested for this analysis. During the fitting procedure, the numbers of neighbours were fixed to $N_1 = 4$ and $N_2 = 2$ and the values of the DW factor σ^2 were taken identical in the two subshells: $\sigma_1^2 = \sigma_2^2 = \sigma^2$. The fit was performed in k space using theoretical scattering paths calculated using FEFF7 code. The conditions of the fit were kept the same for all temperatures. The distances and the DW factor obtained as result of the fit are plotted in fig. 3. There is no significant change in the behaviour of the σ^2 and the distances are almost constants over the whole temperature range. Like the PDM, the fitting procedure leads to the conclusion that the local Jahn-Teller splitting in the Mn-O bond length is kept constant across the transition temperature.

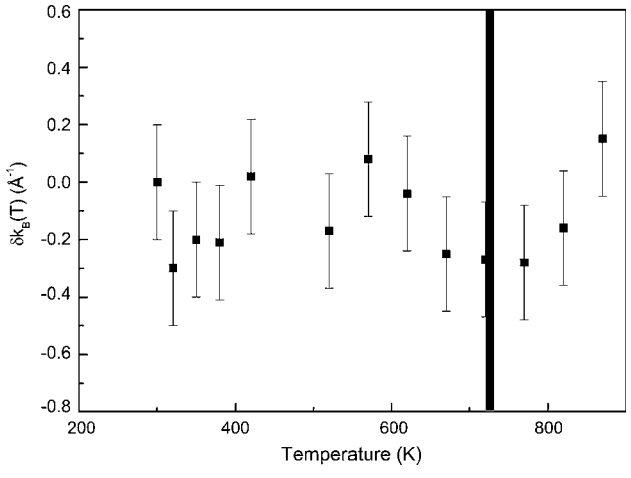

Fig. 2. PDM results: relative values of the beat position: $\delta k_B(T) = k_B(T) - k_B(300\,\mathrm{K})$. The vertical line correspond to the Jahn-Teller temperature transition.

4. Conclusions

The evolution of the local environment of manganese atoms in $LaMnO_3$ across Jahn-Teller transition was studied by EXAFS, using two independent methods of data reduction. We showed that the splitting in the Mn-O distances is kept unchanged across

the Jahn-Teller temperature and that there is no significant change in the Debye-Waller factor. Local distortion within the MnO_6 octahedra still exist above T_{JT}. Our results support the model of an order-disorder transition at T_{JT}, where the cooperative distortion vanishes, but the local distortion is maintained.

Acknowledgments

This work is partially supported by LNLS/ABTLuS/MCT. RAS acknowledges the PIBIC/CNPq. AYR acknowledges the grant from CNPq/PCI.

References

1. Rodriguez-Carvajal, J. *et al*., Phys. Rev. B **57**, R3189 (1998).
2. Zhou, J.-S. and Goodenough, J. B., Phys. Rev. B **60**, R15002 (1999).
3. Granado, E. *et al*., Phys. Rev. B **62**, 11304 (2000).
4. Araya-Rodriguez, E. *et al*., J. Magn. Magn. Mater. **233**, 88 (2001).
5. Song, J. H. *et al*., Phys. Rev. B **66**, 020407(R) (2002).
6. Sánchez, M. C. *et al*., Phys. Rev. Lett. **90**, 045503 (2003).
7. Martens, G. *et al*., Phys. Rev. Lett. **39**, 1411 (1977).
8. Jaffrès, H. *et al*., Phys. Rev. B **61**, 14628 (2000).
9. Ressler, T., J. Synchrotron Radiation **5**, 118 (1998).

Physica Scripta. Vol. T115, 431–432, 2005

Fluorescence EXAFS Analysis of Nanoscale Zinc-Blende MnAs Dots Grown on GaAs(001) by Molecular Beam Epitaxy

H. Ofuchi[1*], J. Okabayashi[2], M. Mizuguchi[2,3], M. Yamada[2], K. Ono[4], Y. Takeda[1], M. Oshima[2] and H. Akinaga[3]

[1]Nagoya University, Furo-Cho, Chikusa-Ku, Nagoya 464-8603, Japan
[2]University of Tokyo, 7-3-1 Hongo, Bunkyo-Ku, Tokyo 113-8656, Japan
[3]SYNAF-NRI-AIST, Tsukuba Central 4, 1-1-1 Higashi, Tsukuba, Ibaraki 305-8562, Japan
[4]Photon Factory, Institute of Material Structure Science, Oho, Tsukuba 305-0801, Japan

Received June 26, 2003; accepted in revised form November 4, 2003

PACS numbers: 78.70.Dm, 75.50.Pp, 68.55.Jk, 61.10.Ht, 81.07.−b

Abstract

In this work, geometric structures for ferromagnetic nanoscale zinc-blende MnAs dots grown on a sulfur-passivated GaAs(001) were investigated by using fluorescence EXAFS measurement. EXAFS measurements revealed that MnAs dots grown on GaAs(001) substrate did not form NiAs-type structure but zinc-blende structure. The Mn-As bond length in the MnAs dots is about 2.48 Å, which is close to that which was estimated from lattice constant of zinc-blende MnAs obtained by density-functional calculations. Existence of zinc-blende MnS (β-MnS) phase was also observed by EXAFS measurements.

1. Introduction

The thermal-equilibrium MnAs possess as NiAs-type structure. Very recently, it is predicted by density-functional calculations that the band structure of zinc-blende MnAs in the ferromagnetic state becomes half-metallic [1]. We have successfully fabricated zinc-blende MnAs dots grown on GaAs(001) by molecular-beam epitaxy (MBE) [2]. However, the geometrical structure of the MnAs dots is not yet clear, because it is difficult to evaluate the geometrical structure of the MnAs dots with average height of a few nm by conventional methods such as X-ray diffraction.

In the present work, geometric structures for ferromagnetic nanoscale zinc-blende MnAs dots grown by MBE were investigated by fluorescence extended X-ray absorption fine structure (XAFS) measurements using synchrotron radiation. The fluorescence XAFS measurement is a powerful technique for investigating local structures around a specific element and is suitable for evaluating the geometric and electronic structures around a specific element in the present study [3, 4].

2. Experimental

The nanoscale MnAs dots were grown on sulfur-passivated GaAs(001) substrates by MBE. Details of the growth procedure are described in ref. [2]. Deposition temperature was about 200 °C. The MnAs dots were capped by a 10 nm GaAs layer to prevent the oxidation.

The EXAFS measurements were performed at the beam line BL12C at the Photon Factory in Tsukuba with a Si(111) double crystal monochromator and a bent cylindrical mirror using the SR from the 2.5 GeV storage ring [5]. The EXAFS spectra were measured in the fluorescence-detection mode at a temperature of 70 K. The incident X-ray beam intensity was monitored with a nitrogen-filled ionization chamber, while the fluorescence X-ray signal was detected by an array of 19 elements Ge solid-state detector (SSD). The EXAFS spectra of the (Ga,Mn)As ([Mn] = 3%) film and NiAs-type MnAs film were also measured as references.

3. Results and discussion

Figure 1 displays the Fourier transformed Mn K-edge EXAFS spectra $k^2\chi(k)$ for MnAs dots, (Ga,Mn)As, and NiAs-type MnAs film. In the radial distance of 1.5–2.8 Å, we observed main peaks due to the first coordination shell around the Mn atoms were observed. The main peak in the MnAs dots was located at a shorter radial distance than those of the (Ga, Mn)As and NiAs-type MnAs film, suggesting that the local structure around Mn atoms in the MnAs dots is different from that in the (Ga, Mn)As and NiAs-type MnAs reference films.

In order to analyze the details of the measured spectra, curve-fitting of the EXAFS spectra was carried out with theoretically

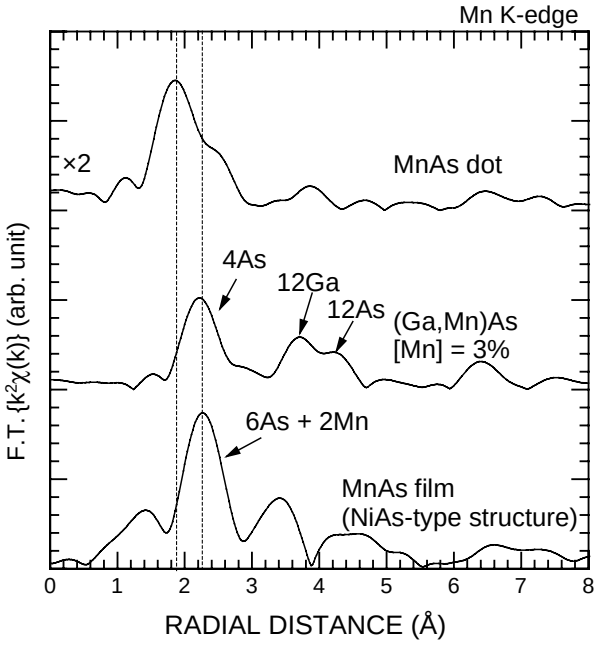

Fig. 1. Fourier transform of the Mn K-edge EXAFS oscillation function spectra $k^2\chi(k)$ of nanoscale zinc-blende MnAs dots, (Ga,Mn)As ([Mn] = 3%) film, and NiAs-type MnAs film. Dotted vertical lines at 1.9 Å and 2.3 Å indicate positions of the main peak for the MnAs dots and NiAs-type MnAs film, respectively.

*e-mail: ofuchi@numse.nagoya-u.ac.jp

calculated spectra using FEFF6 [6]. From the curve-fitting result, it is found that for the MnAs dots the Mn atoms are coordinated by As and S atoms. The Mn-As bond length is ≈ 2.48, which is close to that which was estimated from the lattice constant (≈ 5.6–5.7) of zinc-blende MnAs obtained by density-functional calculations [7]. The Mn-S bond length is 2.43 Å, which is close to that of zinc-blende MnS (β-MnS). The sum of coordination number of As and S atoms around Mn atoms is about 4, coinciding with that of zinc-blende MnAs and MnS. Thus, it is considered that zinc-blende MnAs and β-MnS coexist in the present film. It is considered that the formation of β-MnS phase is due to the sulfur which was passivated on GaAs substrate.

Acknowledgment

This work was supported by the New Energy and Industrial Technology Development (NEDO). XAFS studies were performed as part of Project No. 2002G238 accepted by the Photon Factory Program Advisory Committee, the Ministry of Education, Science, Sports and Culture, Japan.

References

1. Shirai, M. *et al*., J. Magn. Magn. Mater. **177–181**, 1383 (1998).
2. Ono, K. *et al*., J. Appl. Phys. **91**, 8088 (2002).
3. Jaklevic, J. *et al*., Solid State Commun. **23**, 679 (1977).
4. Ofuchi, H. *et al*., Appl. Sur. Sci. **117/118**, 781 (1997).
5. Nomura, M. *et al*., KEK Report **95-15** (1996).
6. Zabinsky, S. I. *et al*., Phys. Rev. B **52**, 2995 (1995).
7. Sanvito, S. *et al*., Phys. Rev. B **62**, 15553 (2000).

Physica Scripta. Vol. T115, 433–434, 2005

Soft X-ray XAFS Experiments of SiO_2-P_2O_5 Sol-Gel Film

J. Ide[1], K. Handa[2], H. Takakura[1], K. Ozutsumi[1] and N. Umesaki[3]

[1]Faculty of Science and Engineering, Ritsumeikan University, 1-1-1 Nojihigashi, Kusatsu, Shiga 525-8577, Japan
[2]Synchrotron Radiation Center, Ritsumeikan University, 1-1-1 Nojihigashi, Kusatsu, Shiga 525-8577, Japan
[3]Japan Synchrotron Radiation Research Institute (JASRI, SPring-8), 1-1-1 Kouto Mikazuki-cho, Sayo-gun, Hyogo 679-5198, Japan

Received June 26, 2003; accepted in revised form February 10, 2004

PACS numbers: 61.10.Ht, 61.43.Fs, 81.20.Fw

Abstract

Structural evolutions in a heat-treatment process have been studied using Si and P K-edge XAFS in SiO_2-P_2O_5 sol-gel layers on silicon substrates. The Si K-edge EXAFS results indicate that structural changes occur between 1173 K and 1273 K. In the case of heat-treated samples at 1273 K, the Si-O interatomic distance is 1.63–1.64 Å. On the other hand, the distances are 1.66 Å–1.68 Å below 1273 K. Furthermore, structural properties around Si and P in the sol-gel process have been studied. In the XAFS spectra, the ratio of P to Si shows 84% decrease after heat-treatment above 1073 K. For the Si-O and P-O distances, wet-gel has shorter interatomic distance than sol-gel raw solution, TEOS and TEP, respectively.

1. Introduction

The amount of energy supplied by the sun to the earth is more than five orders of magnitude larger than the world electric power consumption level that currently keeps modern civilization going [1]. Energy supply by solar systems has very important meanings for the future because of the direct conversion system of clean-solar energy into electric energy.

The sol-gel method is widely applied to produce functional coatings on substrates of metals, plastics, semiconductor materials and ceramics. It can also be used to fabricate coatings on desired shapes and areas homogeneously [2]. Recently, we have succeeded in the extraction of electromotive force from a solar cell that was made from the viewpoint of cost-reduction, using sol-gel procedure. In the process of manufacturing silicon solar cells, P_2O_5 glasses are generally used for n-type diffusion layers, but it is very difficult to handle them because of their delicate nature. Therefore, SiO_2-P_2O_5 glasses are adopted for the diffusion and protecting layer. In this study, the structural properties of Si and P in the SiO_2-P_2O_5 layer on silicon substrates are investigated by X-ray absorption fine structure (XAFS) measurements [3].

2. Experimental procedure

SiO_2-P_2O_5 coating layers have been deposited onto p-type single crystalline silicon substrates by the sol-gel method. Sol-gel starting solution was prepared by mixture solution of 0.5 mol% $Si(OC_2H_5)_4$ (tetraethyl orthosilicate, TEOS) (HIGH PURITY CHEMICALS), 0.5 mol% $PO(C_2H_5)_3$ (triethyl phosphate, TEP), (HIGH PURITY CHEMICALS), 4 mol% C_2H_5OH, and 4 mol% distilled water [2–5]. To avoid contamination, catalysts were not added to the mixture solution. After the removal of the SiO_2 layer on the silicon substrates using hydrofluoric acid, the substrates were dipped into the sol-gel solution and withdrawn at a rate of 4 cm s^{-1}. The substrates were dried at room temperature for 5 minutes and then given heat-treatment at 1073–1273 K for 30 min. In addition to these samples, other samples were prepared, which experienced different heat-treatment time from 30–120 min at 1273 K with the same technique. SiO_2-P_2O_5 wet-gels were also prepared by the generation of the mixture solution of TEOS, TEP, ethanol and distilled water in a sealed container at room temperature for 240 hours.

Si K-edge XAFS measurements were performed for SiO_2-P_2O_5 layer samples in total electron yield (TEY) mode at BL-4 XAFS spectrometer in Ritsumeikan University [6, 7]. Furthermore, the amount of out-diffusion of phosphorus in both hydrolysis reactions and heat-treatment processes were estimated from transmission XAFS measurements using the fundamental jump ratios of Si to P K-edge in mixture solutions of different composition of TEOS and TEP. The Si K-edge XAFS spectra for leucite ($K[AlSi_2O_6]$) were measured by both TEY and transmission mode as a standard sample to compare the spectra. EXAFS analysis was carried out by standard techniques.

3. Results and discussion

Fig. 1 shows normalized XANES spectra at the Si K-edge of the SiO_2-P_2O_5 layer. There is a weak pre-edge feature at about 1842 eV in the spectra for heat-treated samples below 1273 K. This feature decreases with increasing heat-treatment temperature and is not observed in spectra at 1273 K. The pre-edge feature is the peak by the Si-Si correlation. Furthermore, the position of the absorption edge in spectra at 1273 K was slightly changed. The XANES spectra at the Si K-edge of TEOS, wet-gel and leucite were also obtained. The spectral change was not observed in the several wet-gel samples. However, the position of the absorption edge was changed in the spectra of TEOS, wet-gel and leucite. Fig. 2 shows extracted EXAFS spectra at the P K-edge for $AlPO_4$, TEP and wet-gel. There is little change in the phase and the amplitude of EXAFS oscillations. Because the spectral change was not observed in the wet-gel samples, only one spectrum of wet-gel is shown in Fig. 1. The results of the EXAFS analysis relating to the first coordination shell around the

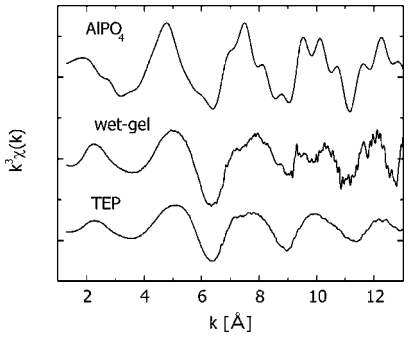

Fig. 1. Normalized XANES spectra at the Si K-edge in SiO_2-P_2O_5 layers. SiO_2-P_2O_5 coating layers have been deposited onto p-type single crystalline silicon substrates by the sol-gel method from the mixture solution of 0.5 mol% TEOS, 0.5 mol% TEP, 4 mol% C_2H_5OH and 4 mol% distilled water.

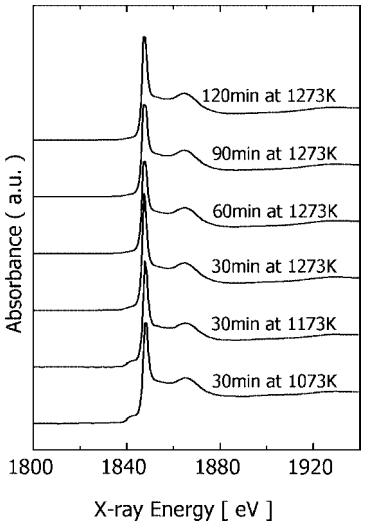

Fig. 2. Normalized EXAFS oscillation of the P K-edge in $AlPO_4$, wet-gel and TEP.

absorbing atom in SiO_2-P_2O_5 layers are summarized with TEOS, TEP, wet-gel and leucite in Table I.

The P-O coordination numbers in TEP and wet-gel are all 4.0, but the P-O distance for wet-gel is shorter than that for TEP. The decrease of the distance suggests that reticular structure was formed with P-O linkage by heat-treatment because of progress of the hydrolysis reaction.

The Si K-edge EXAFS results for SiO_2-P_2O_5 layers show that the coordination number is 3.7–3.8 and the Si-O interatomic distance is 1.63–1.68 Å. In sol-gel process, the alkyl group in the metallic alkoxide such as TEOS separates between metal ion and alkyl radical by external thermal energy. Metal-oxygen-metal bonding is usually formed, but imperfect reaction remains especially on the surface. In case of TEOS sol-gel process, -Si-$(O-)_3$ units with unpaired electrons were formed on the surface. It is observed as a decrease of the coordination number by TEY measurements because TEY method is sensitive to the surface structure. The Si-O interatomic distance decreases with increasing heat-treatment temperature from 1073 K to 1273 K and it was not changed by heat-treatment time at 1273 K. It is estimated by these results that the heat-treatment at 1273 K causes the separation of alkyl radical and causes re-bonding with oxygen in air and re-location of atoms.

The concentration ratios of P to Si in the mixture solution and wet-gel consisting of 0.5 mol% TEOS and 0.5 mol% TEP were 1.01 and 0.96, respectively. On the other hand, the ratios in the SiO_2-P_2O_5 layers were about 0.16. As a result, the heat-treatment above 1073 K causes phosphorus atoms to diffuse into the n-type Si substrate and to air. Thus, phosphorus atoms hardly exist in the glass layers after heat-treatment above 1073 K in air.

Table I. *Structural parameters estimated by EXAFS analysis.*

Sample	M[atoms]	R[Å]	method	
• SiO_2-P_2O_5				
30min,1073 K	Si-O	3.7 ± 0.2	1.68 ± 0.04	TEY
30min,1173 K	Si-O	3.6 ± 0.2	1.66 ± 0.04	TEY
30min,1273 K	Si-O	3.7 ± 0.2	1.64 ± 0.04	TEY
60min,1273 K	Si-O	3.8 ± 0.2	1.64 ± 0.04	TEY
90min,1273 K	Si-O	3.8 ± 0.2	1.63 ± 0.04	TEY
120min,1273 K	Si-O	3.8 ± 0.2	1.64 ± 0.04	TEY
• Leucite	Si-O	4.0 ± 0.1	1.64 ± 0.01	TR*
	Si-O	4.0 ± 0.2	1.63 ± 0.03	TEY
• TEOS	Si-O	4.0 ± 0.1	1.72 ± 0.03	TR*
• wet-gel	Si-O	4.0 ± 0.1	1.67 ± 0.03	TR*
• TEP	P-O	4.0 ± 0.1	1.56 ± 0.02	TR*
• wet-gel	P-O	4.0 ± 0.1	1.54 ± 0.02	TR*

* TR: transmission mode.

4. Conclusion

Structural evolutions have been studied, by XAFS techniques, in heat-treatment processes around Si in SiO_2-P_2O_5 sol-gel layers on silicon substrates. EXAFS results indicate that structural changes occur between 1127 K and 1273 K. The Si-O distance decreases from 1.68 to 1.64 Å with increasing heat-treatment temperature from 1073 to 1273 K and it was not changed by heat-treatment time at 1273 K. These results indicate that heat-treatment at 1273 K removed alkyl radical completely and causes re-bonding with oxygen atoms in the air.

References

1. Hamakawa, Y., ISAP International **No. 5** (2002).
2. John, D. W. and Nico, A. M. J. W., "Sol-Gel Materials" (Taylor & Francis, 2001).
3. Teo, B. K., "EXAFS: Basic Principles and Data analysis" (Springer-Verlag, 1986).
4. Zhang, Y. and Wang, M., Mat. Sci. & Eng. **B67**, 99 (1999).
5. Gallardo, J. *et al*., J. Non-Cryst. Solids **298**, 219 (2002).
6. Handa, K. and Ozutsumi, K., Phys. Chem. Glasses **44**, 171 (2003).
7. Ozutsumi, K. and Handa, K., Rev. Sci. Instrum. **75**, 111 (2004).

Physica Scripta. Vol. T115, 435–438, 2005

XAFS Study on Silica Glasses Irradiated by High-Energy Particles

Tomoko Yoshida[1*], Tetsuo Tanabe[1] and Hisao Yoshida[2]

[1]Center for Integrated Research in Science and Engineering, Nagoya University, Nagoya 464-8603, Japan
[2]Department of Applied Chemistry, Graduate School of Engineering, Nagoya University, Nagoya 464-8603, Japan

Received June 26, 2003; accepted in revised form November 4, 2003

PACS Ref: 61.80.Hg

Abstract

X-ray absorption technique was applied to analyze the local structures of fused and synthesized silica glasses before and after irradiation in a nuclear reactor. Si K-edge EXAFS revealed changes in the SiO_4 tetrahedron structure by the irradiation, i.e. a distorted tetrahedron in the silica glass returned to more regular one but the connection between neighboring tetrahedrons became looser. In addition, the detailed analysis of EXAFS spectra gave evidence for the formation of direct Si-Si bonding after prolonged irradiation, suggesting the appearance of Si precipitates in silica glass.

1. Introduction

Irradiation effects by high-energy particles such as neutron and ions on silica glasses are one of the main concerns for their application as optical windows, insulators and optical fibers in nuclear environments. The chemical states and density of defects in silica glasses should be closely related to their optical and physical properties such as transparency and hardness. Therefore, defects in silica glasses such as oxygen vacancy-related ones and Si precipitates caused by displacement damage have been widely studied by optical techniques and ESR measurements [1–6]. However, it is still difficult to observe the structures of the defects at an atomic scale in a SiO_2 glass, because the structural changes in its amorphous nature does not allow us to apply diffraction techniques. In the present work, we have investigated the change of the local structure of the SiO_2 glass before and after in-reactor (i.e., neutron and γ-ray) irradiation by Si K-edge X-ray absorption fine structure.

2. Experimental

Samples used in this work were a fused silica (SiO_2) glass (T-2030) and a synthesized silica glass (T-4040) of 13 mm diameter and 2 mm thickness produced by Toshiba Ceramics, Japan with different OH contents of ca. 1 ppm and 800 ppm, respectively.

The samples were irradiated in the nuclear reactor YAYOI at the University of Tokyo. YAYOI was operated with a power of 1.5 kW, where a neutron flux was about 6×10^{11} n/m^{2}s with an average neutron energy of 1.3 MeV and the γ-ray level was about 3.0 kGy/h [7]. The irradiation temperature was ambient and kept below 323 K because of the small output power of the reactor.

Si K-edge X-ray absorption spectra were recorded under vacuum ($<10^{-6}$ Pa) at room temperature at the BL-7A station of UVSOR, or at the BL-11B station of the Photon Factory, Institute of Materials Structure Science, High Energy Accelerator Research Organization (KEK-PF), using a two-crystal InSb(111) monochromator. Two different recording modes, i.e. a total

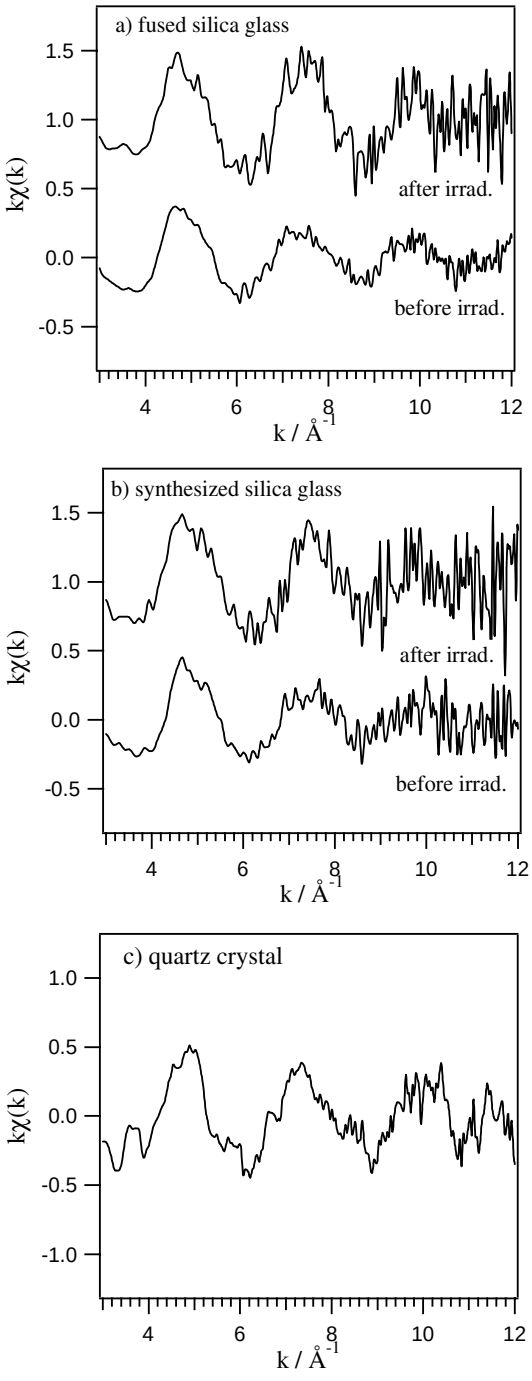

Fig. 1. k-weighted Si K-edge EXAFS spectra of (a) the fused silica glass before and after in-reactor irradiation, (b) the synthesized silica glass before and after in-reactor irradiation, and (c) a quartz crystal. The EXAFS spectra of silica glasses (a,b) and that of a quartz crystal (c) were recorded by fluorescent X-ray yield mode and total electron yield mode, respectively. The neutron fluence of the irradiated fused and synthesized silica glasses are 2.8×10^{19} n/m^2 and 2.7×10^{20} n/m^2, respectively.

*e-mail: yoshida@cirse.nagoya-u.ac.jp

Table I. *Results of curve-fitting analyses.*

Sample	Shell	coordination number	interatomic distance (Å)	$\Delta\sigma^{2a)}$ (Å^2)
Quartz	Si-O	4.0	1.61	0
	Si-Si	4.0	3.02	0.00285
Fused silica (unirradiated)	Si-O	3.7	1.61	0.00276
	Si-Si	1.1	3.05	0.00008
Syn.silica (unirradiated)	Si-O	3.7	1.61	0.00269
	Si-Si	0.8	3.09	0.00332
Irrad. fused silica	Si-O	4.2	1.60	−0.00074
(2.8×10^{19} n/m^2)	Si-O	1.4	2.92	0.00118
Irrad. syn. silica	Si-O	4.3	1.60	0.00114
(2.7×10^{20} n/m^2)	Si-O	1.5	2.91	0.00150
	Si-Si[b)]	2.0	3.86	−0.00358

The region of 0.8–3.2 Å in RSFs were inversely Fourier transformed. Si-O shell and Si-Si shell were extracted from EXAFS of quartz crystal and silicon crystal, respectively. The errors in coordination number and interatomic distance are ±20% and ±0.02 Å, respectively. [a)]$\Delta\sigma^2$ is the difference between the Debye-Waller factors of the sample and the reference sample (quartz), [b)]The region of 3.2–3.8 Å in RSFs were inversely Fourier transformed.

electron yield (TEY) mode and a fluorescent X-ray yield (FY) mode were employed with detectors consisting of an electron multiplier and a gas-flow proportional counter, respectively [8].

3. Results and Discussion

3.1. *The changes of SiO_4 tetrahedron structure and the connection of SiO_4 tetrahedrons in silica glasses by in-reactor irradiation*

Fig. 1 shows the *k*-weighted Si K-edge EXAFS spectra of the silica glasses before and after in-reactor irradiation together with that of a SiO_2 crystal (quartz) sample as a reference, and Fig. 2 compares their radial structure functions (RSFs) obtained from Fourier transforms of the EXAFS. We also performed curve-fitting analysis of the Fourier-filtered EXAFS by the least-squares method. In Fig. 2, the peaks in the region of 0.8–3.2 Å were isolated with a Hanning window, and inversely Fourier transformed. The curve-fitting analysis was carried out with Si-O and Si-Si shells. The amplitude and the phase shift of Si-O and Si-Si shells were extracted from EXAFS of the quartz crystal and a silicon crystal, respectively. The curve-fitting results are summarized in Table I.

The EXAFS oscillation of the quartz crystal (Fig. 1c) has distinct shoulders at around 3.6, 5.8, 6.6 and 8.5 Å^{-1}, which are characteristic of the long-range periodic nature in the quartz sample. In a SiO_2 crystal, a regular SiO_4 tetrahedron is connected to four neighbors to form an ordered structure. Correspondingly, the peak at ca. 1.2 Å attributed to the first neighboring oxygen atoms (Si-O) appeared very intense and sharp (Fig. 2(c)). The peak observed at ca. 2.6 Å in the RSF originates from the second neighboring Si atoms (Si-O-Si). The distance between two Si atoms situated at the center of neighboring SiO_4 tetrahedrons estimated from the curve-fitting is nearly equal to the tabulated value for SiO_2 crystal, and the coordination number was 4 as expected.

The EXAFS spectra and their RSFs of the silica glasses were clearly different from those of the quartz crystal. In their RSFs, the intensity of the 1.2 Å peak corresponding to Si-O is smaller than that for the crystal and the peaks at ca. 2.6 Å attributed to the neighboring Si atoms are also reduced. The absence of the intense peaks relating to the second nearest neighbors indicates

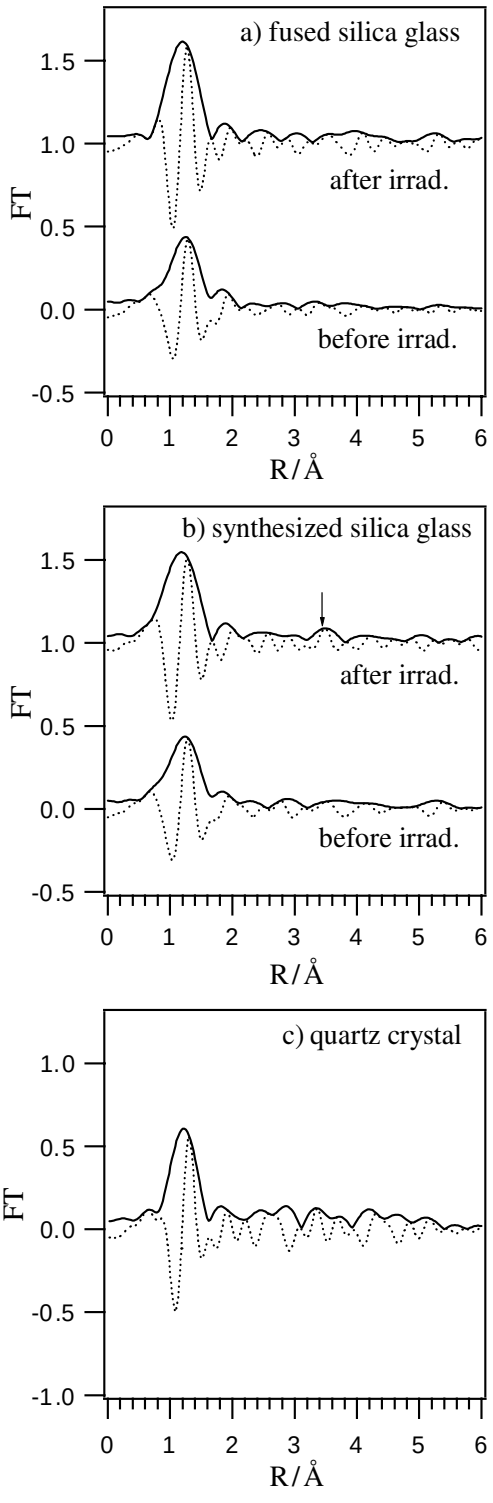

Fig. 2. Radial structure functions of *k*-weighted Si K-edge EXAFS spectra of (a) the fused silica glass before and after in-reactor irradiation, (b) the synthesized silica glass before and after in-reactor irradiation, and (c) a quartz crystal. The neutron fluence of the irradiated fused and synthesized silica glasses are 2.8×10^{19} n/m^2 and 2.7×10^{20} n/m^2, respectively.

weaker or less linkage of the neighboring tetrahedrons in the glasses compared to that of the crystal, reflecting the disordered network of SiO_4 tetrahedrons [9], i.e. in the silica glass there are some variance in the distance between Si atoms in the center of neighboring tetrahedrons. Accordingly the estimated coordination numbers of the unirradiated silica glasses from the curve-fitting analyses were ca. 1, much less than the 4 for quartz crystal (Table I). Simultaneously, the symmetry of the SiO_4 tetrahedron

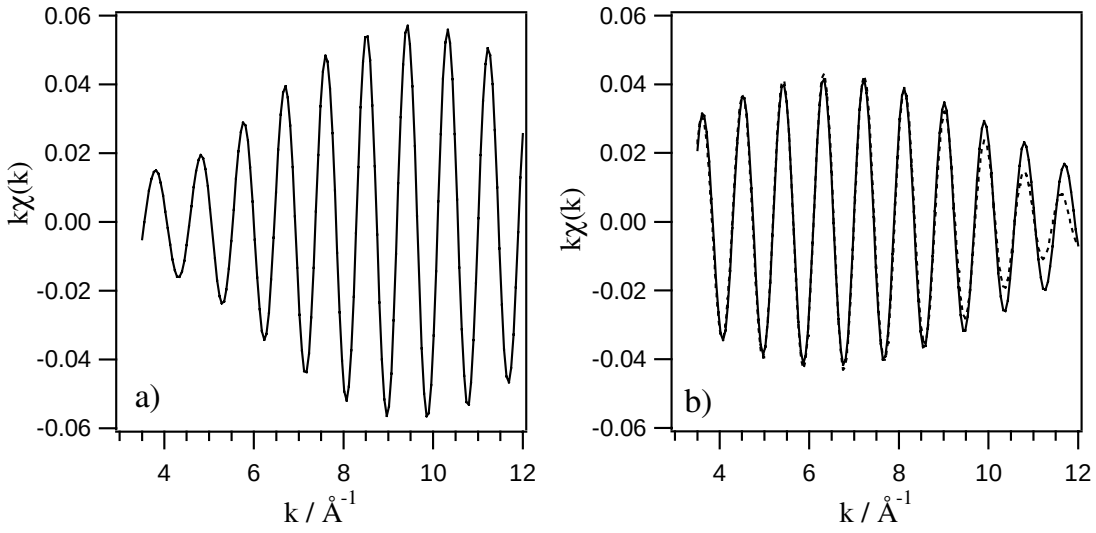

Fig. 3. Inversely Fourier transformed spectra of RSFs of a quartz crystal (a) and the synthesized silica glass after the irradiation of 2.7×10^{20} n/m^2 (b, solid line) and the curve-fitting by Si-Si shell (b, dashed line).

in the silica glass should be slightly distorted from a regular SiO_4 tetrahedron, resulting in the reduction of the peak intensity at 1.2 Å in RSFs.

The EXAFS spectra of the silica glasses irradiated with low neutron fluence (less than ca. 1×10^{19} n/m^2) were fundamentally the same as those of their unirradiated ones (not shown here). A structural change was recognized in the EXAFS spectra of the silica glasses irradiated with more than 2×10^{19} n/m^2 as shown in Fig. 1. The EXAFS oscillations in the range of $k = 6.5$–7.5 Å^{-1} were larger for the irradiated silica glasses than for the unirradiated one. In the RSFs, it should be noted that the peak intensity at 1.2 Å due to the Si-O bond increased to a level similar to that of the quartz crystal. Moreover, the coordination numbers of the first neighboring oxygen atoms increased from ca. 3.7 to ca. 4.2 after in-reactor irradiation (see Table I). At the same time the coordination number of the second neighboring Si atoms decreased, i.e., the Fourier-filtered EXAFS spectra of the irradiated silica glasses were not fitted well using a Si-Si shell. However, the curve-fitting using a Si-O shell instead of a Si-Si shell was successful. The distance 2.92 Å thus evaluated corresponds to the path length of multiple scattering for Si-O-O in the regular SiO_4 tetrahedron. These results suggest some decoupling of neighboring distorted SiO_4 tetrahedrons in a silica glass via the atomic displacement by neutron irradiation. Accordingly, the decoupled distorted SiO_4 tetrahedrons could relax and return to regular or isolated SiO_4 tetrahedron and the O-Si-O angles would be more uniform after irradiation, as observed in the growth of the peak assigned to Si-O in RSFs. This does not mean recovery of long range order (or recrystallization). The irradiation certainly gave more disorder in long range as the appearance of Si precipitates discussed below, or each tetrahedron became more isolated.

3.2. *The appearance of Si precipitates in silica glasses by in-reactor irradiation*

It is also noteworthy that a small but distinct peak around at 3.5 Å appeared in the RSF of synthesized silica glass after the irradiation by 2.7×10^{20} n/m^2. Then, for the irradiated synthesized silica glass, inverse Fourier transforms were also performed for the RSF peaks in the region of 3.2–3.8 Å. The results were compared with that for a quartz crystal (Fig. 3). The envelope of the spectrum for the irradiated synthesized silica glass is clearly different from that of the quartz crystal. The maximum of the envelope appeared at around 6 Å^{-1} in the irradiated synthesized silica glass while that of the quartz crystal was around 9 Å^{-1}. Our separate FEFF analysis [10] for a quartz crystal indicated that RSF peaks in the 3.2–3.8 Å region are caused by a single scattering of the third neighboring oxygen atom (Si-O) and/or multiple scatterings by the first and the third neighboring oxygen atoms (Si-O-O). Actually, the inversely Fourier transformed spectrum of the quartz crystal (Fig. 3(a)) could not be fitted well by the Si-Si shell, supporting the FEFF analysis.

The inversely Fourier transformed spectrum of the irradiated synthesized silica glass could be fitted by Si-Si shell as shown in Fig. 3(b). This indicates the formation of direct Si-Si bonding in the heavily irradiated silica glass. The interatomic distance of the Si-Si pair was estimated as ca. 3.86 Å by the curve-fitting analysis, which is very close to 3.84 Å of the second neighboring distance in a Si crystal. This is another evidence for the appearance of Si precipitates in the irradiated silica glass. Formation of Si precipitates of less than 1 nm in size in SiC by electron irradiation has been reported, and attributed to the preferential displacement of C-atoms [11]. Although the detailed mechanism of the formation of Si precipitates in the irradiated silica glasses is still unclear, and needs more work. Nevertheless, the present work clearly demonstrates that XAFS is a powerful technique to detect the change of local structure even in amorphous materials like silica glasses as well as the nucleation in atomic scale.

Acknowledgements

The authors are very grateful to Prof. Shunsuke Muto at Nagoya University for his helpful discussion.

References

1. Skuja, L. N., Streletsky, A. N. and Pakovich, A. B., Solid State Commun. **50**, 1069 (1984).
2. Skuja, L. N. and Etzian, W., Phys. Status Solidi A **96**, 191 (1986).
3. Anedda, A. *et al.*, Nucl. Instr. Meth. B **91**, 405 (1994).
4. Anedda, A., Carbonaro, C. M., Corpino, R. and Raga, F., Nucl. Instr. Meth. B **141**, 719 (1998).

5. Tanabe, T. *et al*., J. Nucl. Mater. **212–215**, 1050 (1994).
6. Edwards, A. H., Fowler, W. B. and Robertson, J., "Structure and imperfections in amorphous and crystalline silicon dioxide" (John Wiley & Sons, LTD, New York, 2000) p. 258.
7. Nakazawa, M. and Sekiguchi, A., Radiation Dosimetry Data for Reactor YAYOI, Interior Report of University of Tokyo, R0037, in Japanese.
8. Kitajima, Y., J. Phys. IV France **7**, 705 (1997).
9. Tanabe, T. *et al*., Fusion Eng. Design **29**, 435 (1995).
10. Ankudinov, A. L., Ravel, B., Rehr, J. J. and Conradson, S. D., Phys. Rev. B **58**, 7565 (1998).
11. Asaoka, N., Muto, S. and Tanabe, T., Diamond Related Mater. **10**, 1251 (2001).

Physica Scripta. Vol. T115, 439–441, 2005

Quantum Dots Microstructure and Energy Spectrum Peculiarities

S. B. Erenburg[1,*], N. V. Bausk[1], L. N. Mazalov[1], A. I. Nikiforov[2] and A. I. Yakimov[2]

[1]Institute of Inorganic Chemistry SB RAS, Lavrentiev Ave.3, Novosibirsk, 630090, Russia
[2]Institute of Semiconductors Physics SB RAS, Lavrentiev Ave.13, Novosibirsk, 630090, Russia

Received June 26, 2003; accepted in revised form July 1, 2004

PACS numbers: 61.10.Ht, 81.07.Ta, 68.35.Fx

Abstract

The pyramid-like Ge islands deposited on Si(001) substrate using molecular beam epitaxy at 300 °C reveal quantum dots (QDs) properties. Measurements of X-ray absorption fine structure at the germanium K edge (GeK XAFS measurements) have been performed using total electron yield and fluorescent detection mode. The influence of effective thickness of the germanium film, Ge nanocluster sizes and Si deposition temperature on the QDs microstructure parameters is revealed. Some information concerning the energy structure of the free states of the quantum dot was extract from X-ray absorption near edge structure (XANES) spectra for the first time.

1. Introduction

Here we report the use of EXAFS (Extended X-ray Absorption Fine Structure) [1, 2] and XANES (X-ray Absorption Near Edge Structure) spectroscopy to study the spatial and electronic structure of Ge/Si heterostructures.

Development of techniques allowing to determine spatial and electronic structure parameters on the surface or interfaces of materials will provide the controllable fabrication of structures containing nanoclusters with discrete electronic spectra. The fabrication of such systems will allow success in the traditional trend toward miniaturization and in element engineering for quantum computers [3, 4]. In semiconductor nanostructures with spontaneously ordered inclusions of a narrower band gap material within a broader bandgap matrix the limiting case of the dimensional quantization is realized. Zero-dimensional quantization exist within a certain interval of microinclusion sizes with the formation of so-called quantum dots (QDs) characterized by discrete electronic spectra.

In a heteroepitaxial system with a mismatch between the lattice constants, the initial growth may occur by layers. Formation of thicker layers leads to a tendency toward elastic strain relaxation and elastic energy decrease by disturbing the two-dimensional growth and forming isolated islands, so-called Stranski-Krastanov growth. In a series of comparatively recent studies it was shown by different experimental methods (capacitance spectroscopy [5], hopping transport [6], admittance spectroscopy [7], optical spectroscopy [8]) that at a certain thickness of the epitaxial Ge film on Si(001) in the electronic spectra of the heterostructures there appear features associated with the zero-dimensional density of the states. These features are due to the dimensional quantization of the hole spectrum in the Ge islands appearing during disturbed two-dimensional growth.

The spectrum of states in the self-organizing nanoclusters may be largely influenced by the elastic deformation at the boundaries arising from a mismatch of the lattice parameters of the nanocluster and substrate. In the Ge/Si system the lattice mismatch amounts to 4.2%. This will cause changes in the local structure: local distortions of the symmetry, changes in the valence angles and interatomic distances. Such structural changes may change the energy spectrum by a magnitude of the order of 0.1 eV [9], which is comparable with the dimensional quantization energy in a QD.

The local structural changes in the thin layers and nanoclusters are not detectable by traditional X-ray structural analysis or electron diffraction, because such systems have no long-range ordering. EXAFS (extended X-ray absorption fine structure) spectroscopy [1, 2] provides a unique possibility for solving such problems [10]. These methods allow determination of parameters of the local environment of atoms and electronic parameters of nanoclusters. Thus in [11], using XANES (X-ray absorption near-edge structure) spectroscopy, a broadening of the forbidden gap with decreasing size of the CVD grown germanium nanoclusters in silicon was found. In [12, 13], using EXAFS spectroscopy, the local environment of Ge adatoms on Si(001), the structure of thin Ge layers on Si(001) and a superlattice with strained $(Ge_4/Si_4)_5$ layers were studied. It is revealed in [14–16] using GeK XAFS measurements that Ge QDs are characterized by interatomic Ge-Ge distances of 2.41 Å which is 0.04 Å less than in bulk Ge.

The growth of self-organizing Ge islands and later of the blocking Si layer is evidently accompanied by the temperature-dependent surface diffusion of Si and Ge atoms, affecting the composition of the wetting layer and the composition and width of the intermediate layer at the Si-Ge interface. These characteristics of the transitional layers should have a substantial influence on the features in the QD energy spectrum. Therefore, energy spectrum calculation for QD, interpretation peculiarities of their experimental energy spectra as well as design of elements with given electronic properties must take into account variations of the QD local structure.

2. Experimental

In this work, a surface-sensitive EXAFS measurement based on total electron yield and fluorescent detection was used to study peculiarities of Ge/Si structures.

The effective thickness varied from two to ten monolayers for the studied Ge films. Two-dimensional pseudomorphous Ge films have been grown up to a critical thickness of four monolayers on Si(001). As a result of continuing deposition, pyramid-like Ge islands were grown in Stranski-Krastanov mode.

Germanium K edge (GeK) EXAFS and XANES spectra in Ge/Si (100) heterostructures were measured using synchrotron radiation (SR) of the VEPP-3 storage ring at the Budker Institute of Nuclear Physics in Novosibirsk. The X-ray energy was defined by a double crystal monochromator with a channel-cut Si(111)

*E-mail: simon@che.nsk.su

single crystal. The obtained data were processed using the EXCURV92 software package [17]. In the data processing, the phase and amplitude characteristics were calculated in the X_α-DW approximation, using the procedures of the package [17]. For the analysis of the Ge local environment the Fourier-filtered data were fitted using the k and k^2-weighting procedure in the photoelectron wave vector interval from 2.5 Å^{-1} to 13 Å^{-1}. The error in determining interatomic distances with the fitting procedure was ±0.01 Å. The amplitude-damping factor $S_0{}^2$ was determined by data fitting for massive Ge and was equal to 0.8.

3. Results and discussion

Simplest models afford ground for inclusion of one averaged variant of the environment for Ge atoms with distances R_1(Ge-Ge), R_2(Ge-Si) and the coordination numbers of Ge with respect to germanium atoms (n_1(Ge)) and to silicon atoms (n_2(Si)). Such models are most likely correct for 4-monolayer Ge films in Si [16]. The better model should include at least two types of Ge atoms for the samples with QDs: 1) Ge atoms in the 2-monolayer thick transition layer on both sides of the boundary, 2) the atoms inside the quantum dots. The thickness of the transition layer was estimated using the conclusion from [16] that the pseudomorphous 4-monolayer Ge films are embedded in the Si matrix and the two transition layers on both sides of the boundary contain about 50% of Si atoms. This assumption turned out to be true, since with the use of the quantum dots of the same transition layer parameters (of the interatomic distances R_1(Ge-Ge), R_2(Ge-Si) and the coordination numbers n_1(Ge) in germanium and n_2(Si) in silicon) as in the 4-monolayer films, the Ge atoms within the quantum dots have practically no silicon atoms in the first sphere of their environment for the samples with effective thickness equal to 8–10 ML [16]. This samples were prepared at temperatures: 300 °C (film growth) and 500 °C (deposition temperature of the blocking Si layer).

Fig. 1 illustrates the monotonic growth of a fraction of Ge atoms inside pure germanium islands with only Ge atoms in their environment as the effective thickness of the germanium film increases from 4 to 10 monolayers, i.e. the monotonic size evolution of germanium nanoclusters as a function of film thickness in this series. It was of interest to study analogous systems prepared using slightly different temperatures for the film growth and the deposition of the blocking silicon layer. First, structures were prepared using the same temperature for the film growth (300 °C) but a lower (300 °C) deposition temperature of the blocking Si layer.

Table I. *Comparison of parameters obtained by the fitting procedure for pseudomorphous Ge films and structures with pyramid-like Ge islands on Si(001) with blocking Si layer deposited at 500 °C and 300 °C. R_1(Ge-Ge)-, R_2(Ge-Si) – interatomic distances; n_1(Ge)-, n_2(Si) – coordination numbers of Ge with respect to germanium atoms and to silicon atoms; T – blocking Si layer deposition temperature.*

T °C	sample	R_1	R_2	n_1	n_2
500 °C	Film	2.41 Å	2.37 Å	1.7	2.3
300 °C	Film	2.42 Å	2.37 Å	2.7	1.3
500 °C	QD	2.40 Å	2.36 Å	2.6	1.4
500 °C	QD	2.41 Å	2.37 Å	1.7	2.3
		2.41 Å	2.37 Å	3.7	0.3
300 °C	QD	2.42 Å	2.37 Å	2.7	1.3
		2.42 Å	2.38 Å	4.0	0.0

Table I displays influence of blocking Si layer deposition temperature on local structure parameters (n_1(Ge), n_2(Si)). As is seen from Table I with the change in the temperature conditions there is no appreciable change in interatomic distances but the partial coordination numbers of germanium with respect to Ge-n_1(Ge) and Si-n_2(Si), are seriously altered. I.e. such decrease in the temperature leads to a substantial decrease of the diffusion between the phases Ge/Si and the formation of sharper phase boundaries.

As is seen from Fig. 2 the amplitude characteristics of the EXAFS spectra for such films do not differ from those of bulk Ge

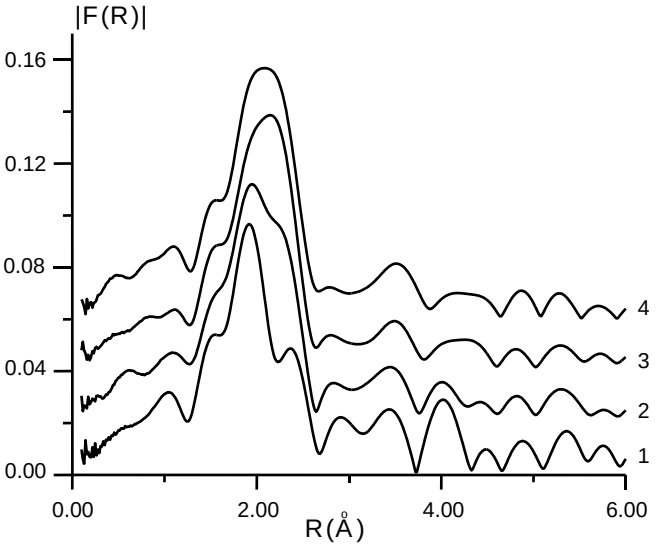

Fig. 1. Fourier transform magnitude of $k^3\chi(k)$ GeK EXAFS data: for pseudomorphous 4-monolayer (4 ML) 2D-films on Si(001) – *curve 1*, for Ge nanoclusters on pseudomorphous 4-monolayer films on Si(001) with effective thickness equal to 6ML – *curve 2*, equal to 8ML – *curve 3*, equal to10 ML – *curve 4*.

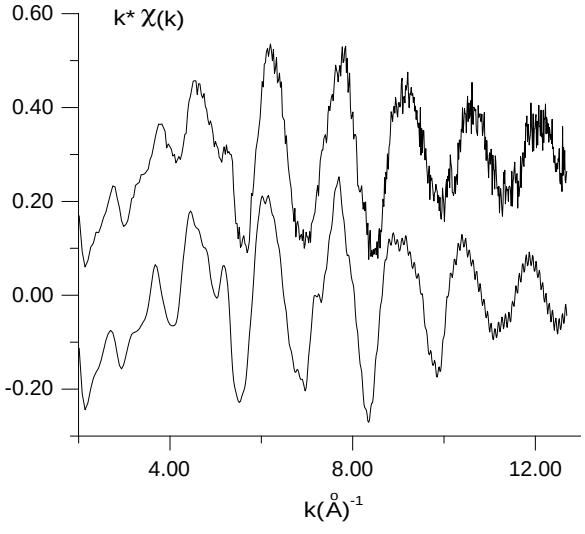

Fig. 2. GeK k-weighted normalized oscillating part of the X-ray absorption coefficient measured on pure Ge film (1000 Å) – *bottom curve* and on Ge nanoclusters (∼15 nm × ∼1.5 nm) on Si(001) with blocking Si layer deposited at 300 °C – *top curve*.

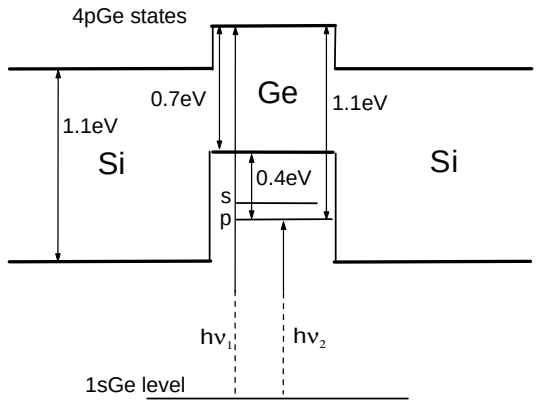

Fig. 3. Scheme of hole states and X-ray absorption electron transitions in the Ge quantum dots with boron dopant.

and there is only a small phase shift. This effect may be explained by the scattering potentials of the environment for the absorbing atoms being similar not only in the first sphere of its environment. On the other hand, the phase shift at large energies for nanoclasters relative to bulk germanium is apparently due to a decrease in the Ge-Ge interatomic distances.

Thus, the strong influence on the microstructural parameters of Ge/Si heterosystems by elastic deformation at the boundaries due to mismatch of lattice parameters of nanocluster and substrate was detected by direct measurement showing that EXAFS spectroscopy is a very perceptive tool to study materials containing nanostructures.

In addition, the interatomic distances R_1(Ge-Ge) and R_2(Ge-Si) obtained from the EXAFS data are in agreement with the interatomic distances derived from the spatial distribution of elastic deformation calculated within the valence force field (VFF) model. The calculation was performed by the procedure based on the use of the Green function of the "atomistic" elastic problem, which was further developed in [18].

In conclusion, a few words about the first attempt to extract from X-ray absorption spectra some information concerning the energy structure of the free states of the quantum dot itself. XANES spectra of two samples were compared. One sample was synthesized using the conventional conditions. The other sample was doped with boron (B) by a special procedure so that Ge in nanoclusters had a substantial deficit of electron charge.

A detailed comparative analysis of the obtained spectra show the presence of an absorption maximum in the spectrum of the doped sample at a distance of -1.8 eV from the point of inflection of the main GeK absorption edge (the position of the GeK absorption edge). Such maximum is absent in the sample with no dopant. The maximum has an intensity of the order of 0.2% of the absorption jump in the main GeK absorption edge. It was established that the maximum is due to the appearance of free levels in the quantum dot at a depth of the order of 1.1 eV from the bottom of the Ge conduction band or 0.4 eV from the top of the Ge valence band (Fig. 3) in accordance with previous experimental and calculation results [19].

Acknowledgement

Financial support from the Russian State Scientific and Engineering Program on "Basic Research in Physic" (theme 01.40.01.09.04, public contract 40.072.1.1.1176), from the Siberian Branch of Russian Academy of Sciences Program "Integration" (grant № 117) and from the Federal Principal Program "Integration of Science and Education in Russia" (public contract №0761/1353) is greatly appreciated.

References

1. Sayers, D. E., Stern, E. A. and Lytle, F. W., Phys. Rev. Lett. **27**, 1204 (1971).
2. Rehr, J. J. and Ankudinov, A. L., J. Synchrotron Radiation **8**, 61 (2001).
3. Shchukin, V. A. and Bimberg, D., Appl. Phys. A. **67**, 687 (1998).
4. Barenco, A., Deutsch, D., Ekert, A. and Jozsa, R., Phys. Rev. Lett. **74**, 4083 (1995).
5. Yakimov, A. I., Dwurechenskii, A. V., Nikiforov, A. I. and Pchelyakov, O. P., JETP Lett. **68**, 125 (1998).
6. Yakimov, A. I., Dwurechenskii, A. V., Nikiforov, A. I. and Pchelyakov, O. P., Phys. Low-Dim. Struct. **3/4**, 99 (1999).
7. Yakimov, A. I., *et al.*, Phys. Rev. B **59** 12598 (1999).
8. Yakimov, A. I., Dvurechenskii, A. V., Stepina, N. P. and Nikiforov, A. I., Phys. Rev. B **62**, 9939 (2000).
9. Rieger, M. M. and Vogl, P., Phys. Rev. B **48**, 14276 (1993).
10. Koninsberger, D. C. and Prins, R., "X-ray Absorption: Principles, Applications, Techniques of EXAFS, SEXAFS and XANES," (New York, Wiley 1988), pp. 710.
11. Kakar, S., *et al.*, in Abstracts of MRS 1998 Spring Meeting, V2.5, (San Francisco, California 1998), p. 350.
12. Oyanagi, H., Sakamoto, K. and Shioda, R., J. Phys. IV France **7**(C2), 669 (1997).
13. Wei, S., Oyanagi, H., Sakamoto, K., Takeda, Y. and Pearsall, T. P., J. Synchrotron Rad. **6**, 790 (1999).
14. Erenburg, S. B., *et al.*, Russian J. Structural Chem. **41**, 802 (2000).
15. Erenburg, S. B., *et al.*, Solid State Ion. Diff. Reactions **141–142**, 137 (2001).
16. Erenburg, S. B., *et al.*, Nucl. Instr. Meth. Phys. Res. A. **470**, 283 (2001).
17. Binsted, N., Campbell, J. W., Gurman, S. J. and Stephenson, P. C., SERC Daresbury Lab. Rep., (1991).
18. Nenashev, A. V. and Dvurechenskii, A. V., J. Exp. Theor. Phys. **117**, 570 (2000).
19. Dvurechenskii, A. V., Nenashev, A. V. and Yakimov, A. I., Nanotechnology **13**, 75 (2002).

Physica Scripta. Vol. T115, 442–444, 2005

Orbital Ordering in $Pr_{0.5}Sr_{0.5}MnO_3$: Pr K-Edge XAFS Study

K. R. Priolkar[1*], V. D. Kulkarni[1], P. R. Sarode[1], R. Kumashiro[2] and S. Emura[3]

[1]Department of Physics, Goa University, Taleigao Plateau, Goa 403 206
[2]Department of Material Science, Faculty of Science, Osaka City University, Sugimoto, 3-3-138, Sumiyoshi-ku, Osaka 558-8585, Japan
[3]Institute of Scientific and Industrial Research, Osaka University, Mihoga-oka 8-1, Ibaraki, Osaka 567-0047, Japan

Received June 26, 2003; accepted in revised form March 11, 2004

PACS number: 61.10.Ht

Abstract

Pr K-edge XAFS spectrum as a function of temperature in $Pr_{0.5}Sr_{0.5}MnO_3$ has been recorded on BL01B1 beam line at Spring-8, in order to study the effect of lattice distortions as the sample passes from a paramagnetic insulator phase at room temperature to ferromagnetic metal phase below 265 K and to an antiferromagnetic insulator phase at low temperatures. It is found that when the ferromagnetic to antiferromagnetic transition takes place, the MnO_6 octahedra rotate in the ab-plane and tilt away from the vertical along the c-axis. The tilting of the MnO_6 octahedra is responsible for the A-type antiferromagnetic phase.

1. Introduction

$Pr_{0.5}Sr_{0.5}MnO_3$ has been of great interest because of its peculiar magnetic and transport properties. This compound undergoes magnetic as well as structural transitions from a paramagnetic insulator (PMI) phase to ferromagnetic metal (FMM) phase at ~265 K and to an antiferromagnetic insulator (AFI) phase at ~140 K [1, 2]. The structure also changes from body centered tetragonal to face centered orthorhombic phase [3]. The antiferromagnetic ordering is A-type rather than CE-type and hence does not exhibit charge ordering. An important role in this context is played by the steric effects, macroscopic cooperative distortions, usually called tilting or buckling and the local deformations of the MnO_6 octahedra caused by size effects. Extended X-ray absorption fine structure (EXAFS) spectroscopy is an ideal tool to explore such distortions and local deformations and has been used quite successfully in lanthanum based manganites [4–7]. However, EXAFS at the Mn K-edge in other rare-earth based compounds is severely affected by the L edges of the rare-earth ions. One possible solution to observe the local structural changes in such perovskite oxides is by recording EXAFS at the K-edge of the rare-earth ion. Such a study requires EXAFS beamlines operating in the 40 keV range like the BL01B1 beamline at SPring-8. The present study was therefore undertaken with an aim to study the local structural changes around the Pr ion in $Pr_{0.5}Sr_{0.5}MnO_3$ as it traverses from PMI to FMM to AFI phase and to understand these changes in context of orbital ordering in $Pr_{0.5}Sr_{0.5}MnO_3$.

2. Experimental

Polycrystalline $Pr_{0.5}Sr_{0.5}MnO_3$ sample was synthesized using the conventional solid-state reaction method, which involved firing of stoichiometric amounts of starting materials at about 900 °C in a furnace three to four times with intermediate thorough grindings. Just before final sintering the sample was pressed into pellet and heated at 1000 °C for 16 hours. Powder X-ray diffraction pattern showed a single phase tetragonal perovskites structure without any detectable impurities. Further characterization was done by a.c. susceptibility and resistivity measurements. The results obtained were similar to those reported earlier [1, 3, 8]. XAFS spectra at the Pr K-edge were recorded using the BL01B1 XAFS beamline at SPring-8. A Si (311) crystal plane served as the monochromator. The first mirror and the monochromator were fully tuned in order to get optimal resolution. The slit width of the monochromator exit was 0.3 mm vertical and 6 mm horizontal to ensure good signal to noise ratio. During the measurements the synchrotron was operated at an energy of 8 GeV and a current between 80 to 100 mA. The spectra were scanned in the range 41.6 to 43.3 keV for the Pr K-edge EXAFS. The photon energy was calibrated for each scan with the first inflection point of the Pr K-edge in Pr metal (42002 eV). Both the incident (I_o) and transmitted (I) synchrotron beam intensities were measured simultaneously using ionization chambers filled with a mixture of 15% Ar and 85% N_2 gases and 100% Ar gas respectively. The absorbers were made by pressing the samples into pellets of 10 mm diameter with boron nitride as binder. The thickness of the absorber was adjusted such that $\Delta\mu_o x$ was restricted to a value ≥ 1, where $\Delta\mu_o$ is edge step in the absorption coefficient and x is the sample thickness. Data analysis was done using the UWXAFS program [9].

3. Results and Discussion

EXAFS spectra at the Pr K-edge of the sample were recorded at room temperature, 180 K and 50 K so as to study the local structural changes in each of the three phases. The Fourier transforms (FT) of these spectra are presented in Fig. 1. The FT

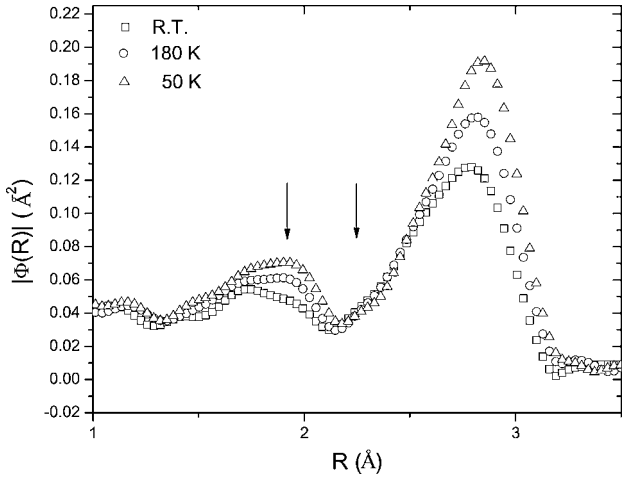

Fig. 1. FT spectra of Pr K-edge EXAFS in $Pr_{0.5}Sr_{0.5}MnO_3$ at different temperatures.

*Email: krp@unigoa.ac.in

Table I. *Structural parameters for $Pr_{0.5}Sr_{0.5}MnO_3$ at different temperatures obtained from EXAFS analysis.*

Bond Type	Coordination Number	Bond Length (Å)	σ^2 (Å^2)
R.T.			
Pr-O	4.0	2.527 (8)	0.007 (1)
Pr-O	4.0	2.701 (8)	0.006 (1)
Pr-O	4.0	2.880 (9)	0.006 (1)
Pr-Mn	8.0	3.339 (2)	0.005 (1)
180 K			
Pr-O	4.0	2.520 (9)	0.005 (1)
Pr-O	4.0	2.668 (8)	0.005 (1)
Pr-O	4.0	2.810 (8)	0.004 (1)
Pr-Mn	8.0	3.327 (2)	0.004 (1)
50 K			
Pr-O	4.0	2.690 (9)	0.002 (1)
Pr-O	4.0	2.810 (8)	0.002 (1)
Pr-O	4.0	2.533 (20)	0.003 (1)
Pr-O	2.0	2.869 (9)	0.001 (1)
Pr-Mn	8.0	3.315 (5)	0.002 (1)

Figures in brackets indicate uncertainties in the last digit.

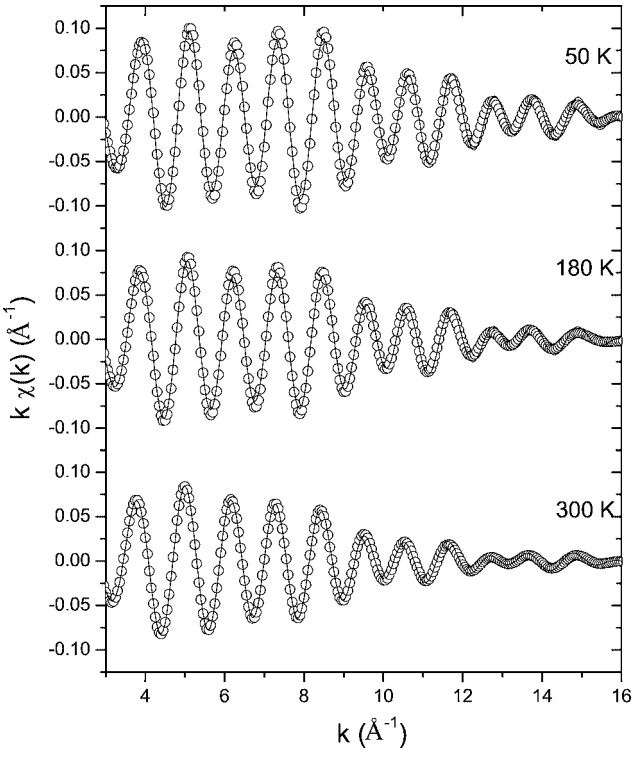

Fig. 2. k – weighted backtransformed EXAFS spectra (circles) along with fitted curves (lines) in $Pr_{0.5}Sr_{0.5}MnO_3$.

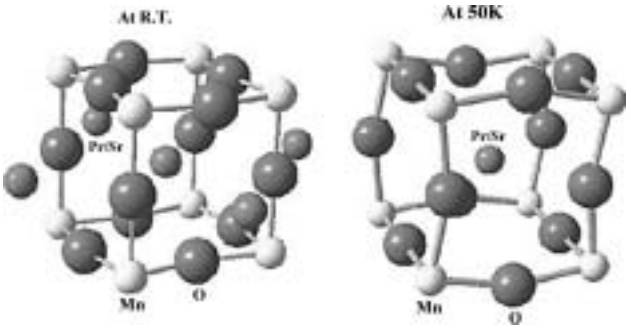

Fig. 3. Local structures around Pr ion at room temperature and 50 K in $Pr_{0.5}Sr_{0.5}MnO_3$.

spectra are not corrected for phase shift however; the values of bond lengths reported in the paper are the corrected values. The room temperature (R.T.) pattern shows two distinct correlations in the region 1.5 and 2 Å due to Pr-O bonds and a broad and most intense maximum at 2.8 Å comprising of a Pr-O and a Pr-Mn correlation. The FT spectrum at 180 K is similar to the one at R.T. One notable change however, is in the 1.5 to 2 Å range wherein there is a change in weight from first correlation to second. The 50 K spectrum has an additional subtle feature at about 2.3 Å, probably an indication of change of symmetry of the compound.

The EXAFS spectrum at R.T. was fitted using three Pr-O and a Pr-Mn correlations obtained from FEFF 6.01 [10] for I4/mcm symmetry. To reduce the number of fitting parameters the coordination numbers for all Pr-O correlations were constrained to be around 4.0 each and that of Pr-Mn correlation to be around 8.0. The final fitted parameters obtained are presented in Table I and the fitting in back transformed *k*-space is shown in Fig. 2. A good fit is obtained to the experimental data. For fitting low temperature data, the final parameters obtained for R.T. data served as starting guess parameters. In the first cycle only the debye-waller factors were varied followed by bond lengths to account for effect of lowering of temperature. A reasonably good fit was obtained for 180 K data. Although the metal – insulator transition in $Pr_{0.5}Sr_{0.5}MnO_3$ occurs only at about 140 K [11], neutron diffraction studies [3] have clearly shown that the structural transition starts around 180 K. This could be the reason for similarity between 180 K and 50 K F.T. spectra, especially in the 1.5 to 2.0 Å range. However, to fit the 50 K data the coordination number also had to be varied and resulted in physically unacceptable numbers. This data was therefore fitted with correlations obtained using FEFF for *Fmmm* symmetry with four Pr-O correlations two of which are four coordinated and two are two coordinated. For this fitting cycle also, the coordination numbers were constrained to be around the theoretically obtained values. The resulting fit was quite good and is shown in Fig. 2 and the fitted parameters are tabulated in Table I.

The local structure of Pr in $Pr_{0.5}Sr_{0.5}MnO_3$ is depicted in Fig. 3. This structure has been drawn using the bond lengths obtained from above analysis and structural information. It can be seen that the MnO_6 octahedra rotate in the ab-plane and tilt away from the vertical along the c-axis when the sample undergoes ferromagnetic metal to antiferromagnetic transition. This leads to two Pr-O bond lengths at 2.534 Å and 2.810 Å instead of one at 2.701 Å at R.T. in the plane of Pr atom. Furthermore due to rotation of MnO_6 octahedra, the 2.880 Å and 2.527 Å Pr-O bond lengths at R.T. change to 2.691 Å, 2.869 Å and 2.534 Å. This rotation and tilting of the MnO_6 octahedra result in ordering of Mn d_{x2-y2} orbitals along the *x*-axis that is responsible for A-type ordering in $Pr_{0.5}Sr_{0.5}MnO_3$.

4. Conclusions

(a) EXAFS at the Pr K-edge has been studied for the first time to explore structural changes in $Pr_{0.5}Sr_{0.5}MnO_3$ as the material undergoes a PMI to FMM to A-type AFI transition.

(b) In the AFI phase the EXAFS spectra can only be fitted using Pr-O and Pr-Mn correlations obtained from *Fmmm* type orthorhombic structure.

(c) This results in rotation in the a-b plane and tilting away from the vertical of MnO_6 octahedra that result in ordering of Mn d_{x2-y2} orbitals along the *x*-axis that is responsible for A-type ordering in $Pr_{0.5}Sr_{0.5}MnO_3$.

Acknowledgements

The authors (K.R.P. and P. R. S.) would like to gratefully acknowledge JASRI for beam time on BL01B1 under proposal No. 2002A0036-Nx-np, travel assistance from Department of Science and Technology, Government of India, New Delhi and local hospitality from Spring-8, JASRI, Japan.

References

1. Knížek, K., Jirák, Z., Pollert, E., Zounová, F. and Vratislav, S., J. Solid State Chem. **100**, 292 (1998).
2. Tomioka, Y., Asamitsu, A., Moritomo, Y., Kuwahara, H. and Tokura, Y., Phys. Rev. Lett. **74**, 5108 (1995).
3. Damay, F. *et al.*, J. Magn. Magn. Mater. **184,** 71 (1998).
4. Tyson, T. A. *et al*., Phys. Rev. B **53**, 13958 (1996).
5. Booth, C. H. *et al*., Phys. Rev. B **54**, 15606 (1996).
6. Lanzara, A. *et al.*, Phys. Rev. Lett. **81**, 878 (1998).
7. Agrestini, S., Saini, N. L., Lanzara, A., Natali, F. and Bianconi, A., Int. J. Mod. Phys. B **14**, 2852 (2000).
8. Pollert, E. *et al.*, J. Magn. Magn. Mater. **246**, 290 (2002).
9. Newville, M., Livins, P., Yacobi, Y., Rehr, J. J. and Stern, E. A., Phys. Rev. B **47**, 14126 (1993).
10. Zabinski, S. I., Rehr, J. J., Ankudinov, A., Albers, R. C. and Eller, M. J., Phys. Rev. B **52**, 2996 (1995).
11. Chainani, A. *et al.*, Phys. Rev. B **56**, R15513 (1997).

Physica Scripta. Vol. T115, 445–447, 2005

An Investigation of Valence State and Structural Geometry of Polyvalent Fe and Ti Ions in Sodium Borosilicate Glasses by X-Ray Absorption Spectroscopy

X. C. Yang[1], M. Dubiel[1*], D. Ehrt[2] and A. Schütz[2]

[1]Department of Physics, Friedemann-Bach-Platz 6, Martin Luther University of Halle-Wittenberg, D-06108 Halle, Germany
[2]Otto-Schott-Institute, University of Jena, Fraunhoferstrasse 6, D-07743 Jena, Germany

Received June 26, 2003; accepted December 10, 2003

PACS numbers: 61.10.Ht, 61.43.Fs

Abstract

Valence states and structural environments of polyvalent Fe and Ti ions in two different borosilicate glasses have been studied by X-ray Absorption Near Edge Structure (XANES) and Extended X-ray Absorption Fine Structure (EXAFS) techniques. The results indicate that different valence states of polyvalent metal ions usually exist simultaneously in glass matrix. Doping C favours the formation of reduced state of metal ion. Especially, Fe^{2+} ion can be reduced into neutral iron atom. Fe^{2+} ion generally occupies octahedrally coordinated site. Fe^{3+} ion tends to be in tetrahedral coordination with increasing total iron concentration. Adding oxidising agent can transfer the octahedral iron ions into tetrahedral Fe^{3+} ions. Ti^{4+} ions mainly occupy five-fold coordination sites in NBS1 and four-fold coordination sites in NBS2, depending on the existence of non-bridging oxygen ions in the glass matrix.

1. Introduction

Valence state and structural environment of iron and titanium ions have been widely studied using optical absorption [1], Mössbauer [2], electron spin resonance [3], square-wave voltammeter [4] and X-ray absorption techniques [5–8]. However, the coordination nature of iron and titanium ions by oxygen has been controversially discussed due to the difference in glass composition and in preparation condition. In Fe-bearing silicate glasses melting at ambient conditions, it is generally reported that Fe^{2+} occupy octahedral net-modifying sites. Fe^{3+} have two possibilities of occupying tetrahedral or octahedral sites depending on melting conditions of silicates. For instance, Hayashi *et al.* [9] proposed that Fe^{3+} ions tend to be in octahedral symmetry at large ratios of the number of Fe^{3+} ions to that of nonbridging oxygen ions, and to be in tetrahedral symmetry when the glass matrix is basic. Hannoyer *et al.* [8] suggested that Fe^{3+} is in both tetrahedral and octahedral coordination. The proportion of octahedral Fe^{3+} is found to decrease with increasing amounts of Fe^{3+} in soda-lime silicate glasses containing the same total iron. The relative number of octahedral Fe^{3+} increases with increasing total iron in oxidised soda-lime silicate glasses. Kukkadapu *et al.* [10] reported that the majority of ferric ions likely occupy the octahedral sites, $Fe^{3+}{}_{oct}$, that were isolated and were readily convert into ferrous ions, $Fe^{2+}{}_{oct}$, without changing its coordination. The limited tetrahedral sites for ferric ions are stable against reduction to ferrous ions even under strong reducing condition.

Sandstrom *et al.* [11] found that the oxidation state of titanium in SiO_2 was always Ti^{4+}. Nevertheless, change in Ti geometry occurred with concentration. For example, below 7 wt% TiO_2 all of the Ti was fourfold coordinated with a Ti-O bond length of 1.81 Å. At higher concentrations, some sixfold coordinated Ti occurred with a Ti-O bond length of 2.15 Å. Grunes's research [12] indicated that Ti^{4+} ions in oxides and silicate compounds are four-fold or six-fold coordinated. Dumas and Petiau [13] observed similar intermediate behavior of Ti environment in aluminosilicate glasses. However, Ti^{4+} is possibly five-fold coordinated just like in $Ba_2TiSi_2O_8$ and $Ba_2TiSi_2O_8$ crystals.

In this report, the valence state and coordination geometry of iron and titanium ions in sodium-borosilicate glasses have been studied by changing the redox condition, glass basicity and metal ion concentration. The XANES reflects the chemical bonding of the element and the local symmetry. Especially, the position of the absorption edge is shifted in dependence on the valence state. On the other hand, the EXAFS experiments enable to obtain structural information of local environment like the coordination species and coordination numbers (CN) surrounding the detected atom, interatomic distance, r, and mean-square relative displacement, σ^2, the so-called Debye-Waller factor (DWF) [14, 15].

2. Experimental procedures

NBS1 and NBS2 are sodium borosilicate glasses with compositions of $16Na_2O$-$74SiO_2$-$10B_2O_3$ and $4.3Na_2O$-$74SiO_2$-$20.7B_2O_3$-$1Al_2O_3$ (mole percentage), respectively. No non-bridging oxygen ions were found in NBS2. Fe_2O_3, $FeC_4H_4O_6$, TiO_2 and Ti_2O_3 powders were added into samples NBS1 and NBS2 and were melted at 1500 °C for NBS1 series and at 1600 °C for NBS2 series by an electric resistance furnace. In some cases, graphite or $NaNO_3$ powder was added as redox agent to change the valence states of Fe and Ti ions. Platinum crucible was used for the normal and oxidising melts and quartz crucible was used for the reducing melts [16].

X-ray absorption experiments at Fe and Ti K-edges were carried out at the beam line E4 of HASYLAB in Hamburg (Germany) in transmission mode, utilizing Si (111) double-crystal monochromator. Harmonic rejection was achieved by detuning the monochromator crystals between 40 and 50%. References and glasses were milled into powders by Mixer Mill MM 200 produced by Retsch Company, and then mixed with polyethylene and pressed into tablets with optimum thickness. Absorption edge energies were determined from the half-height of normalised absorption spectra.

The normalised spectra $\chi(k)$ were weighted by k^2 and Fourier transformed using a Hanning window function. Parameters were

*e-mail: dubiel@physik.uni-halle.de

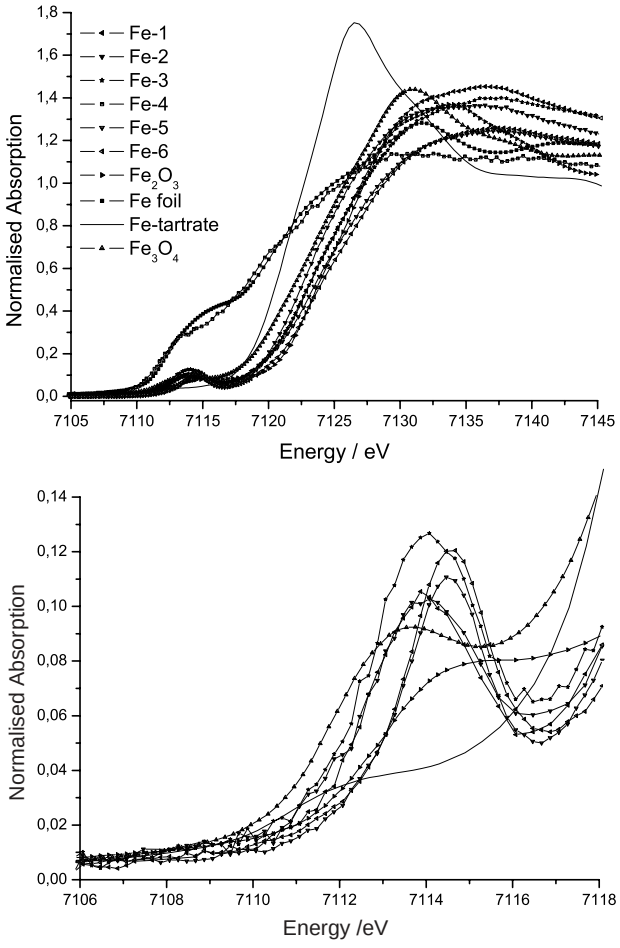

Fig. 1. The normalised Fe K-edge XANES spectra of Fe-containing references and sodium-borosilicate glasses. The prepeaks were enlarged to compare the position and height. Fe-1 = NBS1 + 0.5 mol% Fe_2O_3; Fe-2 = NBS2 + 0.5 mol% Fe_2O_3; Fe-3 = NBS1 + 0.5 mol% Fe_2O_3+$NaNO_3$; Fe-4 = NBS1 + 1.0 mol% Fe-tartrate + C; Fe-5 = NBS2 + 5.0 mol% Fe_2O_3; Fe-6 = NBS1 + 5.0 mol% Fe_2O_3.

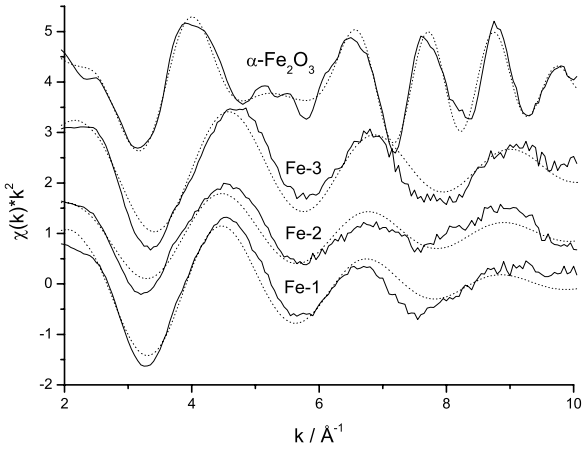

Fig. 2. Fe K-edge EXAFS spectra and fitting curves of samples Fe-1, Fe-2 and Fe-3.

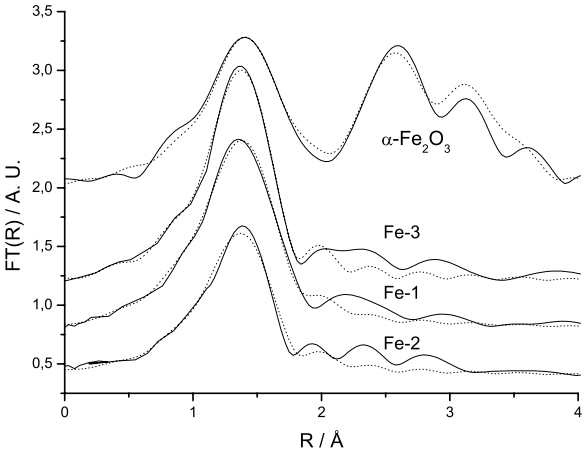

Fig. 3. Fourier transformation of the corresponding EXAFS oscillations weighted by k^2 and their fitting curves.

fitted based on theoretical amplitude and phase function calculated by FEFF7 and FEFF8. The amplitude reducing factor, 0.7, was used to fit Fe K-edge EXAFS spectra of Fe-bearing borosilicate glasses. The k range used for the Fourier transformation was 2–10 Å^{-1} for the glass samples. In the real space, the fit range was 1–3 Å.

3. Experimental results and discussion

Fig. 1 shows the normalised Fe K-edge XANES spectra of Fe_2O_3 doped sodium-borosilicate glasses. Fe K-edge EXAFS spectra of samples Fe-1, Fe-2 and Fe-3 are given in Fig. 2. The corresponding FT spectra and fitting curves (dotted line) are given in Fig. 3. The fitted structural parameters are shown in Table I.

For transition-metal oxides it has been found experimentally that edge energy shift increases with increasing valence state of the metal ions in oxides or compounds [17] though it is difficult to give a quantitative relationship to explain the magnitude of edge shift because edge shift can be induced by many factors like effective nuclear charge, oxidation state, coordination number, type of chemical bonding, electronegativity, hybridisation, relaxation energy, screening and inner level shift. For example, the edge energies Fe-tartrate, Fe_3O_4 and Fe_2O_3 are 7120.4 eV, 7121.8 eV and 7123.6 eV, respectively. The absorption edge shifts 3.2 eV from bivalent iron ion to trivalent iron ion.

For NBS1 and NBS2 glasses doped by 0.5 mol% Fe_2O_3, the Fe-K edge energies are 7122.9 eV and 7122.4 eV, respectively, indicating the coexistence of Fe^{2+} and Fe^{3+}. Increasing the doped concentration of Fe_2O_3 from 0.5 mol% to 5 mol%, the edge energies move to 7123.7 eV for NBS1 and 7123.3 eV for NBS2, indicating that the majority of iron ions in NBS1 and NBS2 doped by 5.0 mol% Fe_2O_3 are in trivalent states. The lower edge energies in NBS2 series indicate that there are more Fe^{2+} ions in NBS2 series than in NBS1 series because NBS2 series have lower basicities and were melted at higher temperature. Higher melting temperature and lower basicity favour the formation of reduced states of iron ion. In addition, the energy and the intensity of Fe-K prepeak are larger in 5.0 mol% Fe_2O_3 doped NBS series than in the corresponding 0.5 mol% Fe_2O_3 doped NBS series, indicating

Table I. *The fitted structural parameters of first Fe-O coordination in some samples. The uncertainties for nearest neighbour distance and Debye-Waller Factor are 0.01 Å and 0.002 Å^2, respectively.*

Sample	R (Å)	DWF (Å^2)	CN	ΔE_0 (eV)	R-factor
Fe_2O_3	1.96	0.0056	3	−3.0	0.016
	2.09	0.0103	3 (set)		
Fe-1	1.89	0.010	5.0 ± 0.7	−3.6	0.016
Fe-2	1.88	0.0075	4.7 ± 0.7	−5.1	0.041
Fe-3	1.86	0.0047	4.4 ± 0.4	−3	0.018

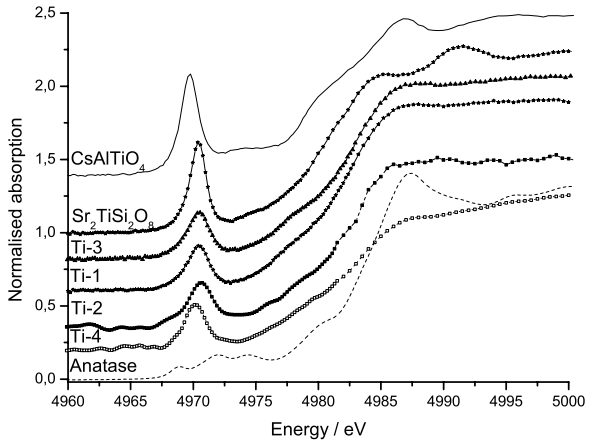

Fig. 4. The normalised Ti K-edge XANES spectra of Ti-containing model compounds and glasses. Ti-1 = NBS1 + 0.5 mol% Ti_2O_3; Ti-2 = NBS1 + 1.0 mol% TiO_2; Ti-3 = NBS1 + 1.0 mol% TiO_2 + C; Ti-4 = NBS2 + 1.0 mol% TiO_2.

that more Fe ions occupy tetrahedral sites with increasing the concentration of Fe_2O_3.

C-containing glasses have lower edge energies compared to the corresponding samples prepared in normal conditions, indicating that Fe^{2+} content increases due to the reduction of Fe^{3+} into Fe^{2+} by C. When C was doped into NBS1+1.0 Fe^{2+}-Tartrate, Fe^{2+} ion was reduced towards its neutral state by comparing near-edge features between the sample and Fe foil. Doping $NaNO_3$ into NBS1 does not change the position of absorption edge energy. However, it makes an increase in the prepeak height, indicating that more Fe^{3+} ions are in tetrahedral symmetries in the oxidised sample. EXAFS analysis also shows that the nearest neighbour distance and coordination number decrease for the oxidised sample. The increase in the relative number of tetrahedral Fe^{3+} ion may be attributed to the tranformation of octahedral Fe^{3+} ion into tetrahedral Fe^{3+} by adding oxidising agent.

Fig. 4 is the normalised Ti K-edge XANES spectra of Ti-containing compounds and borosilicate glasses.

Ti K-edge energies of Ti_2O_3 and anatase are 4975.8 eV and 4982.1 eV, respectively. When 0.5 mol% Ti_2O_3 was doped into glass NBS1, the edge energy shifted to 4980.2 eV, indicating that partial Ti^{3+} ion was oxidised into Ti^{4+} ion. Ti-K edge energies of samples Ti-2 and Ti-4 are 4981.8 eV and 4981.1 eV, respectively, indicating that the majority of titanium ion is four valence when anatase was doped into samples NBS1 and NBS2, and sample NBS2 contains more Ti^{3+} ions than NBS1 because higher melting temperature and lower glass basicity favour the formation of lower valent Ti ions. When C was doped into sample Ti-2, T-K edge energy decreases to 4981.0 eV, indicating that some of Ti^{4+} ions were reduced into Ti^{3+} ions.

Farges *et al.* [18] showed that the use of either position or normalised peak height alone is not sufficient to derive reliable coordination numbers for Ti when it is present in several coordinations. In our case, the evaluation of Ti coordination structures was further complicated due to the existence of trivalent Ti. The position and height of Ti-K edge prepeak are 4969.7 eV and 0.68 for $CsAlTiO_4$, 4970.4 eV and 0.61 for $Sr_2TiSi_2O_8$. For anatase there exist three prepeaks with decreasing heights due to the increase of symmetry. The position and height of the second prepeak are 4971.9 eV and 0.17, respectively. The prepeak position of sample Ti-2 is 4970.6 eV, larger than that of $Sr_2TiSi_2O_8$, indicating that Ti^{4+} ions in sample Ti-2 mainly occupy five-fold coordination sites. The shoulder observed in the main prepeak indicates the existence of some amounts of six-fold coordinated Ti^{4+} ions, which makes the prepeak height reduction to 0.31. The prepeak position of sample Ti-4 is 4970.2 eV, between that of $CsAlTiO_4$ and $Sr_2TiSi_2O_8$, indicating that Ti^{4+} ions mainly occupy four-fold coordination sites. The reduction in prepeak height can be attributed to the existence of some amounts of trivalent titanium ions. Similarly, Ti^{4+} ions in samples Ti-1 and Ti-3 mainly occupy five-fold coordination sites. The reduction in prepeak height compared to that of $CsAlTiO_4$ and $Sr_2TiSi_2O_8$ can be attributed to the existence of some amounts of trivalent titanium ions in the glasses. The conclusions concerning the coordination numbers could be confirmed by EXAFS calculations that yield Ti-O coordination numbers within the range of 4 to 5. Further experiments should be done to determine the concentration of Ti^{3+} ion in sodium borosilicate glasses and the effect of the concentration of Ti^{3+} ion on the position and height of Ti-K edge prepeak.

4. Conclusions

Valence state and structural geometry of polyvalent ions in glasses depends on doped cationic charge, glass composition and redox condition. Higher melting temperature and lower glass basicity favour the formation of lower valence ions. Doping C favours the formation of reduced state of metal ion. Especially, Fe^{2+} ion can be reduced into neutral iron atom. Fe^{2+} ion generally occupies octahedrally coordinated site. Fe^{3+} is in both tetrahedral and octahedral coordination in 0.5 mol% doped sodium borosilicate glasses, and tends to be in tetrahedral coordination with increasing the relative number of trivalent iron ions by doping $NaNO_3$ or increasing total iron concentration. Ti^{4+} ions in NBS1 with non-bridging oxygen ions mainly occupy five-fold coordination sites. In NBS2 without non-bridging oxygen, however, Ti^{4+} ions mainly occupy four-fold coordination sites.

Acknowledgements

The authors would like to thank SCHOTT JENAer Glas Stiftungsfonds for the financial support.

References

1. Steele, F. N. and Douglas, R. W., Phys. Chem. Glasses **6**, 246 (1965).
2. Williams, K. F. E., Johnson, C. E. and Thomas, M. F., J. Non-Cryst. Solid **226**, 19 (1998).
3. Sunandan, C. S. and Jagannathan, R., Solid State Commun. **53**, 985 (1985).
4. Wiedenroth, A. and Ruessel, C., J. Non-Cryst. Solids **318**, 79 (2003).
5. Yang, X. C., Brunsch, S. and Dubiel, M., HASYLAB Annual Report (2001), P. 796.
6. Greaves, G. N., *et al.*, Philos. Mag. B **58**, 271 (1988).
7. Booth, C. H., *et al.*, J. Mater. Res. **14**, 2628 (1999).
8. Hannoyer, B., Lenglet, M., Duerr, J. and Cortes, R., J. Non-Cryst. Solid. **151**, 209 (1992).
9. Hayashi, M., Hori, M., Susa, M., Fukuyama, H. and Nagata, K., Phys. Chem. Glasses **41**, 49 (2000).
10. Kukkadapu, R. K., Li, H. and Smith, G. L., J. Non-Cryst. Solids **317**, 301 (2003).
11. Sandstrom, D. R., J. Non-Cryst. Solids **41**, 201 (1980).
12. Grunes, L. A., Phys. Rev. B **27**, 2111 (1983).
13. Dumas, T. and Petiau, J., J. Non-Cryst. Solids **81**, 201 (1986).
14. Koningsberger, D. C. and Prins, R. eds., "X-Ray Absorption: Principles, Applications, Techniques of EXAFS, SEXAS, and XANES", (Wiley, New York, 1988).
15. Iwasawa, Y. eds., "X-ray absorption fine structure for catalysts and surfaces", (World Scientific Publ. Co., Singapore, 1996).
16. Schütz, A., *et al.*, Glass Sci. Technol. **75** C2, 242 (2002).
17. Lytle, F. W., Greegor, R. B. and Panson, A. J., Phys. Rev. B **37**, 1550 (1988).
18. Farges, F., Brown, G. E. and Rehr, J. J., Phys. Rev. **56**, 1809 (1997).

Physica Scripta. Vol. T115, 448–449, 2005

Zr K-Edge EXAFS Study of PZT Thin Film Formation From Sols

I. Arčon[1,2*], B. Malič[2], M. Kosec[2] and A. Kodre[2,3]

[1]Nova Gorica Polytechnics, Vipavska 13, POB 301, SI-5001 Nova Gorica, Slovenia
[2]Jožef Stefan Institute, Jamova 39, POB 3000, SI-1001 Ljubljana, Slovenia
[3]Faculty of Mathematics and Physics, University of Ljubljana, Jadranska 19, SI-1000 Ljubljana, Slovenia

Received June 26, 2003; accepted November 4, 2003

PACS numbers: 61.10.Ht, 61.43.Er, 61.25.Em, 78.70.Dm

Abstract

We examined the local environment of zirconium atoms in the $Pb(Zr_{0.53}Ti_{0.47})O_3$ (PZT) sol, prepared from lead acetate and transition metal n-propoxides in 2-methoxyethanol, and in the as-pyrolyzed amorphous film deposited on (0001) sapphire. The immediate neighborhood of Zr atoms changes markedly upon transition from the sol to the amorphous film. Clustering of Zr species in the process of film formation in the form of Zr oxide nanoparticles is indicated.

1. Introduction

Ferroelectric thin films have been widely studied for a range of applications such as memories, capacitors, sensors or micro-electromechanical devices [1, 2]. In comparison to solid-state synthesis, alkoxide based sol-gel processing of multicomponent materials is recognized to yield more homogeneous products at lower processing temperatures, due to the formation of heterometallic bonding already in solution. In chemical solution deposition (CSD) of thin films the main processing steps include the synthesis of a heterometallic precursor, typically in a nonaqueous medium, the deposition of the film, and the processes occurring upon thermal treatment: drying, consolidation and crystallization of the target ferroelectric phase [3]. Understanding the structural transitions in the process of film formation from the sol would allow a better tailoring of the properties of the final product.

In 2-methoxyethanol-based processing of $Pb(Zr_{0.53}Ti_{0.47})O_3$ (Zr-rich PZT) thin films an inorganic network arises in the reaction between transition metal alkoxides and lead acetate. Thermodynamically stable perovskite film on sapphire (0001) substrate crystallizes at 700 °C from the amorphous phase through the transitory pyrochlore-type phase [4] as generally observed for CSD PZT thin films [3]. It is known that the crystallization temperature of the perovskite phase is higher for Zr-rich PZT thin films than for Ti-rich thin films. Furthermore, the intermediate nanocrystalline pyrochlore-type (or fluorite) phase exists in a broader temperature range in Zr-rich PZT films [5, 6]. So far there are no reports on the structure of the amorphous phase of the PZT films, even though there are indications that it crucially influences the perovskite crystallization temperature in the film.

In this work Zr K-edge EXAFS of amorphous $Pb(Zr_{0.53}Ti_{0.47})O_3$ thin film pyrolyzed at 350 °C and its precursor prepared by the 2-methoxyethanol route is studied to provide insight into the structural changes in the process of the formation of amorphous Zr-rich PZT film from the sol.

2. Experimental

PZT sol, corresponding to the target composition of $PbZr_{0.53}Ti_{0.47}O_3$ with 10 mol% PbO excess, was prepared in a 100 ml batch by diluting zirconium and titanium n-propoxides in 2-methoxyethanol and by adding anhydrous lead acetate in the required quantity. The metal contents of all compounds were determined gravimetrically. The reaction mixture was heated to approximately 60 °C to get a clear solution. After 2 hours of refluxing and distillation of the ester formed during the reaction a stable 0.5 M sol was obtained. All manipulations were performed in dry nitrogen atmosphere. PZT thin film was deposited on sapphire substrate (0001) by spin-coating and pyrolyzed at 350 °C for 1 minute. The film thickness was about 200 nm. X-ray diffraction showed that the film was amorphous.

Zr K-edge EXAFS spectra of the PZT sol and thin film were recorded at the X1 station in HASYLAB at DESY (Hamburg, Germany). A Si(311) double-crystal monochromator was used with 3 eV resolution at 18 keV. Harmonics were effectively eliminated by detuning the monochromator crystal using a stabilization feedback control.

Absorption spectrum of the PZT sol was measured in a standard transmission mode. The sol, concentrated to approximately 1 M solution in order to increase the signal-to-noise ratio, was inserted in a liquid absorption cell with 0.5 mm lucite windows. Sample thickness of about 1 mm was chosen to obtain total absorption thickness of about 2 above the Zr K-edge. An empty absorption cell served as a reference spectrum measured under identical conditions. The intensities of the incident and transmitted beams were measured with Ar filled ionization cells. The standard stepping progression within the (−250 eV, 1000 eV) interval relative to the Zr K-edge was adopted with an integration time of 1 s/step.

Zr EXAFS spectrum of the PZT film was measured in a fluorescence detection technique using a 4-channel Ge fluorescence detector. The absorption spectra were obtained as the ratio of the fluorescence detector signal and the signal of the incident photon beam from the ionization cell filled with argon at ambient pressure. The same stepping progression was adopted as in the case of the sol with an integration time of 4 s/step. To improve the signal to noise ratio, eighteen consecutive runs were superimposed.

3. Results and discussion

Zirconium EXAFS spectra of PZT sol and thin film were analyzed by the University of Washington analysis programs using FEFF6 code for *ab initio* calculation of scattering paths [7, 8]. A comparison of both spectra (Fig. 1) shows that the signal-to-noise

*Corresponding author: e-mail: iztok.arcon@p-ng.si

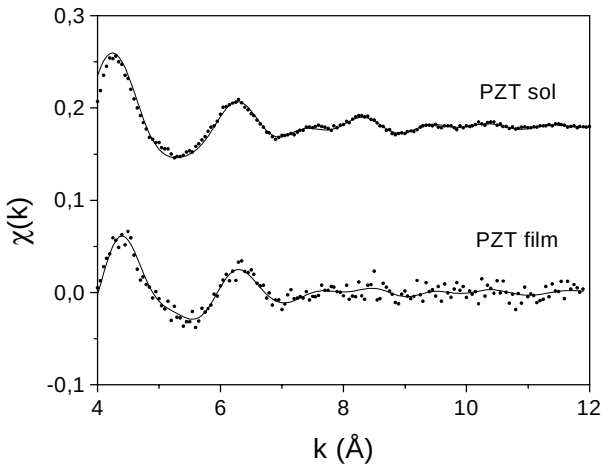

Fig. 1. Zr K-edge EXAFS spectra of PZT sol and amorphous thin film on (0001) sapphire: (dots) – experiment, (solid line) – EXAFS model.

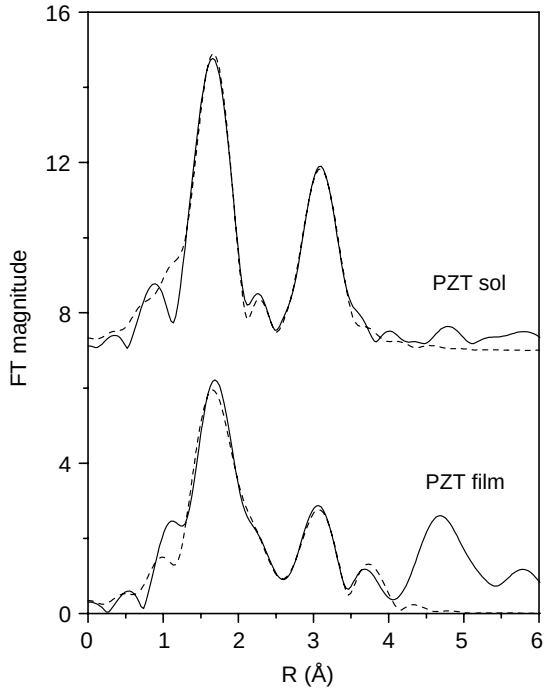

Fig. 2. The k^3 weighted Fourier transforms of zirconium EXAFS spectra of PZT sol and amorphous thin film on (0001) sapphire, calculated in the k range of 4–11 Å^{-1}: (Solid line)- experiment, (dashed line) – EXAFS model.

ratio of the fluorescence EXAFS spectrum measured on the film is about an order of magnitude lower, in spite of the much longer detection time. Nevertheless, a quantitative analysis reveals that the local neighborhood of Zr atoms in the film is different from that observed in the sol. The difference can be clearly seen in Fig. 2, where k^3-weighted Fourier transforms of the EXAFS spectra are shown.

Two shells of neighbors are discerned in the local neighborhood of Zr atoms in the sol. A fit of the EXAFS spectrum in the R range of 1.3 Å to 3.8 Å shows that the immediate neighborhood of Zr atoms is populated with about seven O atoms at two slightly different distances 2.11 Å and 2.23 Å, while the wide second shell of neighbors consists of zirconium atoms at 3.47 Å and carbon atoms at about 3.3 Å and 3.7 Å, in agreement with our previous study of PZT sols [4]. Carbon atoms belong to the functional groups of the starting compounds and the solvent. The number of Zr neighbors points to clustering of zirconium species.

Table I. *Parameters of the nearest coordination shells around zirconium atom in PZT sol and amorphous thin film: atomic species, average number N, distance R and Debye-Waller factor σ^2. Uncertainty of the last digit is given in parentheses.*

Zr	N	R (Å)	σ^2 (Å^2)
PZT sol			
O	3.8(5)	2.11(4)	0.002(1)
O	3.2(5)	2.23(4)	0.002(1)
C	3(1)	3.29(1)	0.003(1)
Zr	2(1)	3.47(2)	0.006(2)
C	5(2)	3.63(5)	0.003(1)
PZT film			
O	4.0(7)	2.14(4)	0.003(1)
O	2.8(7)	2.67(4)	0.002(1)
Zr	3(1)	3.43(2)	0.006(2)
O	6(1)	4.19(5)	0.007(3)

The local structure around Zr formed in the sol is not retained in the amorphous film. The fit of the EXAFS spectrum of the film (in the same R range of 1.3 Å to 3.8 Å) shows that the distribution of oxygen atoms around Zr is significantly altered: there are about four oxygens at 2.14 Å and about three at a much larger distance of 2.67 Å. In the second coordination shell Zr and O atoms are found, but no C atoms. The complete list of structure parameters is given in Table I. Relatively high uncertainties in the number of neighbors in individual shells are due to the high correlation of the shell parameters N and σ^2.

We attribute the difference between the amorphous film and the sol to the partial decomposition of organic functional groups upon heating to 350 °C [3]. Namely, the local structure around Zr atoms in the film is similar to the Zr neighborhood in the tetragonal ZrO_2 [9]. Most probably nano-clusters of zirconium oxide are forming within the film.

It is conceivable that the segregation of Zr species in the film – possibly as zirconia nanoparticles within the amorphous matrix-hinders the crystallization of the perovskite phase by the formation of the transient pyrochlore-type phase, so that the crystallization of the perovskite phase is shifted to higher temperature.

Acknowledgment

Support by the Ministry of Science and Technology of the Republic of Slovenia within the National Research Program, by Internationales Buero BMBF (Germany), and by the IHP-Contract HPRI-CT-1999-00040 of the European Commision is acknowledged. L. Troeger and N. Haack of HASYLAB provided expert advice on beamline operation.

References

1. Inoue, N., IEEE Trans. Electron Devices **49**, 1572 (2002).
2. Muralt, P., Micromech. Microeng. **10**, 136 (2000).
3. Tuttle, B. A. and Schwarz, R. W., Mater. Res. Soc. Bull. **21**, 49 (1996).
4. Malič, B. *et al.*, Integrated Ferroelectrics **20**, 81 (2000).
5. Huang, Z., Zhang, Q. and Whatmore, R. W., J. Appl. Phys. **85**, 7355 (1999).
6. Wilkinson, A. P., Speck, J. S., Ceetham, A. K. and Natarajan, S., Chem. Mater. **6**, 750 (1994).
7. Stern, E. A., Newville, M., Ravel, B., Yacoby, Y. and Haskel, D., Physica B **117**, 208 (1995).
8. Rehr, J. J., Albers, R. C. and Zabinsky, S. I., Phys. Rev. Lett. **69**, 3397 (1992).
9. Teufer, G., Acta Crystallographica **15**, 1187 (1962).

Physica Scripta. Vol. T115, 450–453, 2005

EXAFS and XRD Characterization of Iron Thin Films Prepared by Sputtering at Very Low Temperatures

F. Jiménez-Villacorta*, A. Muñoz-Martín*, M. Vila*, C. Prieto*,# and A. Traverse**

*Instituto de Ciencia de Materiales de Madrid. Consejo Superior de Investigaciones Científicas. Cantoblanco, 28049- Madrid, Spain
**Laboratoire pour l'Utilisation du Rayonnement Électromagnetique, Centre Universitaire Paris-Sud, BP34. 91898-Orsay Cedex, France

Received June 26, 2003; accepted in revised form November 4, 2003

PACS numbers: 75.50.Tt, 75.75.+a

Abstract

Iron thin films of less than 100 nm have been grown on Si(100) wafers by DC magnetron sputtering at well-controlled substrate temperatures. Three different sets of samples have been prepared in order to study the influence of the preparation conditions on their magnetic properties: *i*) natural oxidized samples, *ii*) "*in-situ*" partially oxidized and *iii*) non-oxidized iron thin films. For the last two sets, a gold film prior to expose the air capped the samples. XRD and EXAFS experiments have been performed to obtain the size and the shape of the grains. They provide a columnar growth for samples prepared at room temperature and a diminution of the grain size along the normal to the surface when the preparation temperature decreases.

1. Introduction

Ultrafine particles of metals and alloys can be prepared by several techniques. In order to obtain thin film samples thermal evaporation [1], electron beam [2], or ion beam sputtering sources [3] have been used. An important improvement of these methods is to cool the substrate down to liquid nitrogen temperature. Nevertheless, no such a cooling technique has been extensively used to prepare thin films samples. Ultrafine particles are interesting because of spectacular changes in physical properties by decreasing the size of a material from the bulk to the atomic level. In particular, small grain size ferromagnetic materials exhibit different magnetic properties mainly as a result of the finite size effect. Enhanced magnetic anisotropy and coercivity have been observed in the materials with particle size close to the single domain size [4]; they are of interest for magnetic recording applications. Fe-based materials are the most promising candidates for high-density recording media [5] due to its high saturation magnetization and coercivity.

We have prepared iron thin films by sputtering at very low temperatures. After partial oxidation, they showed a very interesting magnetic behaviour: the coercive field evaluated at 5 K gave higher values for samples prepared at temperatures near 200 K, additionally, they had an exchange bias with a similar behaviour [6]. That behaviour has been correlated with the partial oxidation of the samples, as well as, with the grain size lowering [7].

The aim of the present work is to characterize iron thin films microstructures by X-ray absorption and diffraction techniques in order to give light to study their magnetic properties as a function of their characteristic lengths. It is known that both diffraction and absorption techniques provide data to estimate the characteristic size of the crystallographic grains. Generally, the results obtained by both techniques are comparable, but not in full agreement. It is also presented in this paper a method to explain the possible discrepancies by studying the grain shapes crystallographically.

2. Experimental

Iron thin films were grown on naturally oxidized Si(100) substrates using a DC-operated two-inches planar magnetron source. Base pressure was in the range of 10^{-7}mbar and Ar pressure for sputtering deposition was 5.0×10^{-3} mbar. The experimental set-up has a possibility of maintaining the substrate at constant temperature during deposition by use of a cold finger attached to a home-modified continuous flow Oxford CF-100 cryostat in the vacuum chamber. An Oxford ITC-502 temperature controller set the substrate temperature with a precision of 0.1 K; substrate temperature can be selected from 5 to 400 K. Additionally, in order to deposit a cap layer, the set-up has a possibility of changing sputtering targets maintaining the sample at the base pressure and at low temperatures.

Deposition rate was about 1 nm/min, the power (about 4 W) applied to the magnetron and deposition time were kept constant for the whole set of samples. Three sets of samples were prepared: the first one was exposed to the air, being passivated at room temperature and room pressure; the second set was capped with a gold film inside the preparation chamber in order to prevent oxidation; and the third set was intentionally oxidized inside the preparation chamber at room temperature under an oxygen partial pressure of 1×10^{-2} mbar for 1h, and subsequently a gold cap film was deposited in order to prevent further oxidation.

X-ray diffraction (XRD) was performed on the Bragg-Brentano geometry on a standard two-circle diffractometer (Siemens D-500) in order to determine the texture of the samples, as well as, the film grain size by evaluating the coherence length of the diffracted peaks.

X-ray absorption experiments have been carried out at LURE (DCI, XAS-13 beamline) with electron beam energy of 1.85 GeV and average current of 250 mA. Data of the Fe K-edge were obtained by using a fixed exit monochromator with two flat Si(311) crystals, with the total electron yield on a biased electrode in a He atmosphere sample chamber at liquid nitrogen temperature [8]. The experimental geometry was chosen in a way that the X-ray polarization vector was contained in the film and the incoming X-ray beam forms an angle of 70° with the normal to the surface. Details of the polarization experiments have been explained carefully elsewhere [9].

A standard EXAFS analysis was performed by using the VIPER program [10]. Oscillations were obtained after removing the background by a cubic spline fitting polynomial and EXAFS signal ($\chi(k)$) was obtained by normalizing the magnitude of the

#Correspondant author: e-mail: "cprieto@icmm.csic.es"

oscillations to the edge jump. The corresponding pseudo Radial Distribution Function around the three component atoms has been obtained by weighting by the wavenumber ($k\chi(k)$), multiplying by a Hanning window and Fourier transforming. For comparative study, the Fourier transform of EXAFS signal was performed within the same k-range. The here presented analysis is based on the fit of the oscillations obtained by back-Fourier transform of the first coordination sphere (between 1.5 and 2.8 Å). The amplitude and phase were calculated by the FEFF code version 6.01 reported by J. Rehr [11]. The S_0^2 amplitude loss factor was obtained by using the spectrum of a Fe foil as the reference.

3. Results and Discussion

Figure 1 shows the normalized XANES signal of the three sets of samples. The intensity of the main feature at 7130 eV clearly shows that gold-capping prevents the sample oxidation effectively (see Fig. 1(a)) and that the partial oxidation becomes more enhanced for the samples prepared at low temperatures (see Figs. 1(b) and (c)). X-ray diffraction study [6] indicates that the crystallographic grain size of a thin film decreases by preparing at low temperatures. It is reflected in the present XANES results, because oxidation of Fe grains should be more effective when the surface/volume ratio becomes bigger. This is the case for small grains.

$k\chi(k)$ EXAFS signals and their Fourier transforms of the three sets of samples are shown in Figs. 2 and 3, respectively. These data show that iron remains in the bcc structure for the whole set of conditions and temperature preparations, although a decrease of the EXAFS signal amplitude is observed for the samples prepared at low temperatures. It may be interpreted as a lost of the average coordination number due to the finite size effect.

Table I summarizes the parameters obtained by the EXAFS data analysis. The results indicate that remarkable variations are obtained neither in the Fe-Fe distance nor in the Debye-Waller factor, but a clear decrease in the coordination number (CN) is obtained.

From the CN, it is possible to calculate the characteristic size of the grains that forms the thin film. By using the model proposed by Borowski [12] for spherical clusters, we derived the dependence of the Fe-Fe CN as a function of the Fe grain size. Nevertheless, the large values obtained for the coercive field (about 2500 Oe) of oxidized samples [6] suggest the existence of grains with very elongated shape. Figure 4 presents calculated curves that relate the CN to the grain size with an elliptical form in order to compare

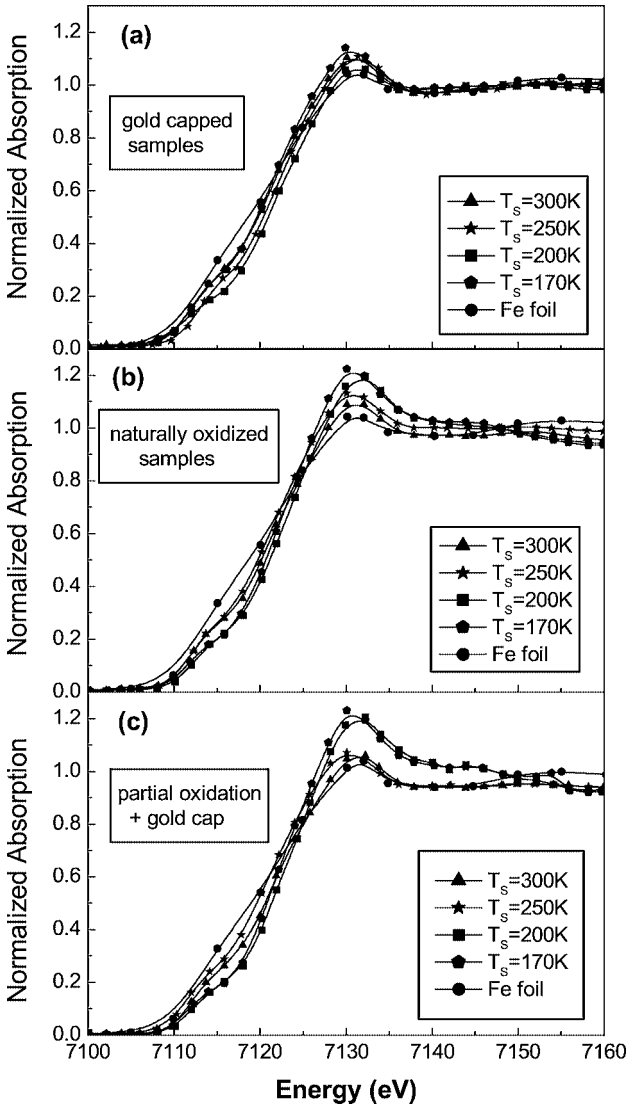

Fig. 1. Normalized XANES spectra from the samples prepared at different temperatures. (a) non-oxidized gold capped samples; (b) naturally oxidized samples; (c) *in-situ* partially oxidized and gold capped samples.

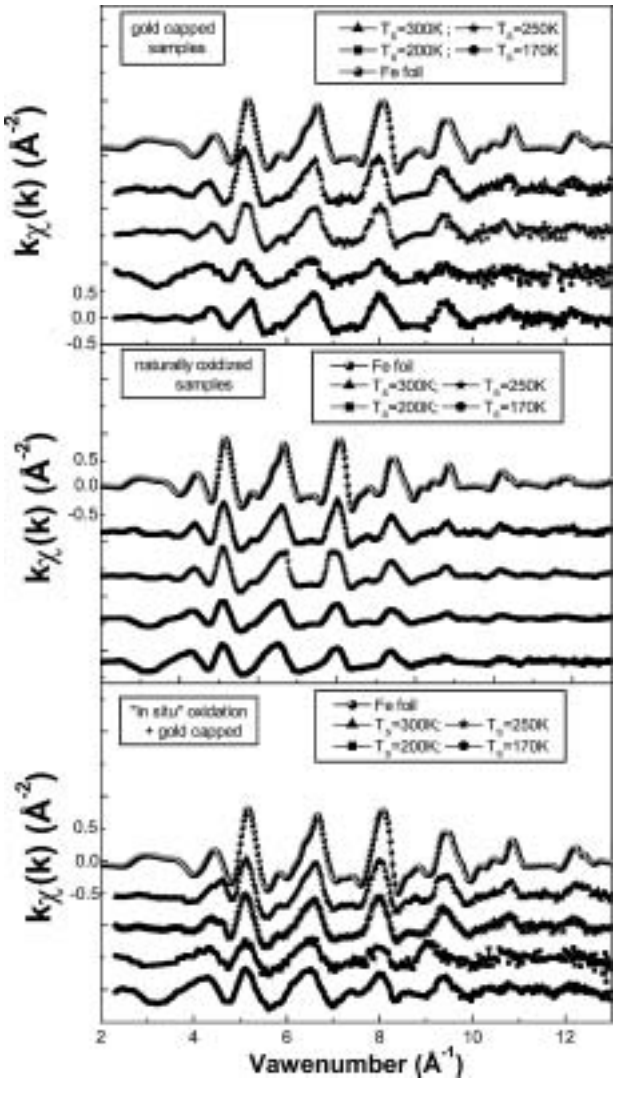

Fig. 2. k-weighted EXAFS signals from the samples shown in Fig. 1.

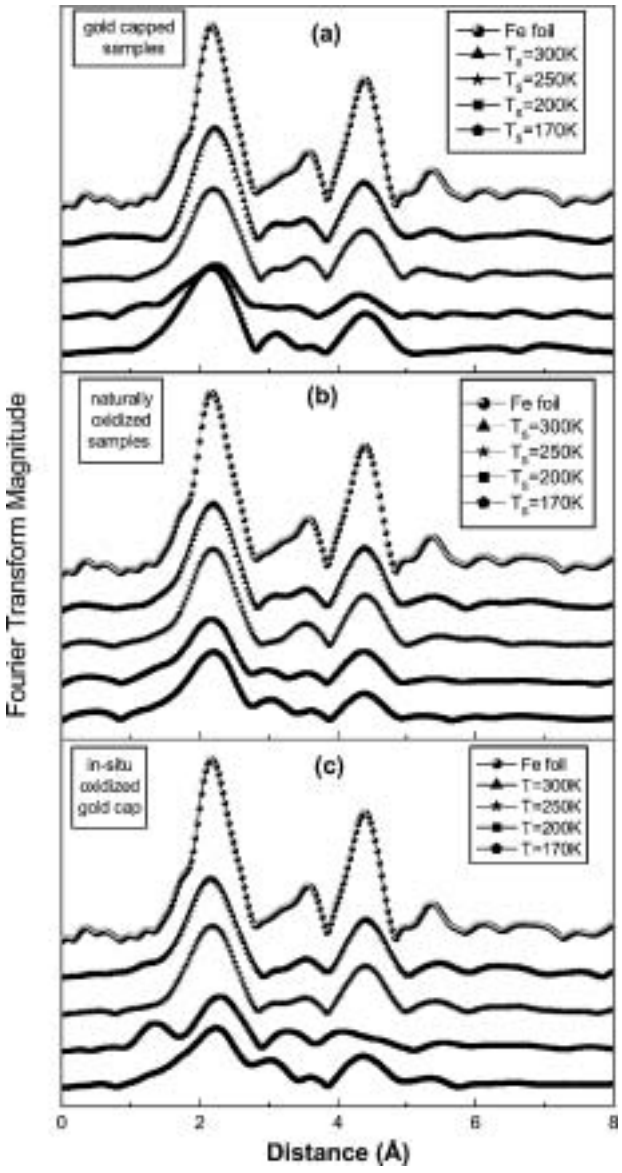

Fig. 3. Fourier Transform of the $k\chi(k)$ signals of Fig. 2.

Table I. *Parameters obtained by the EXAFS analysis. Samples are classified in three sets depending on their preparation procedures. T_S is the substrate temperature at preparation; R_j is the bond distance that contributes to the first peak of the Fourier Transform magnitude; N_j is the number of neighbours; and σ_j is the Debye-Waller factor.*

Sample	T_S (K)	N_j	R_j (Å)	σ_j (Å)
Fe foil	300	8.00	2.48	0.071
		6.00	2.48	0.071
Natural oxidation	300	6.68	2.49	0.077
		4.66	2.85	0.077
	250	5.69	2.49	0.071
		3.62	2.86	0.071
	200	3.90	2.49	0.070
		1.47	2.86	0.070
	170	3.64	2.50	0.065
		1.85	2.87	0.065
Gold-capped	300	6.74	2.51	0.080
		4.69	2.89	0.080
	250	5.16	2.50	0.076
		3.74	2.88	0.076
	200	3.64	2.50	0.084
		1.47	2.88	0.084
	170	6.21	2.49	0.073
		3.73	2.84	0.073
In-situ oxidation and gold-capped	300	6.74	2.49	0.075
		4.15	2.85	0.075
	250	5.67	2.49	0.070
		3.07	2.85	0.070
	200	3.31	2.54	0.070
		2.31	2.89	0.070
	170	4.30	2.50	0.074
		1.74	2.87	0.074

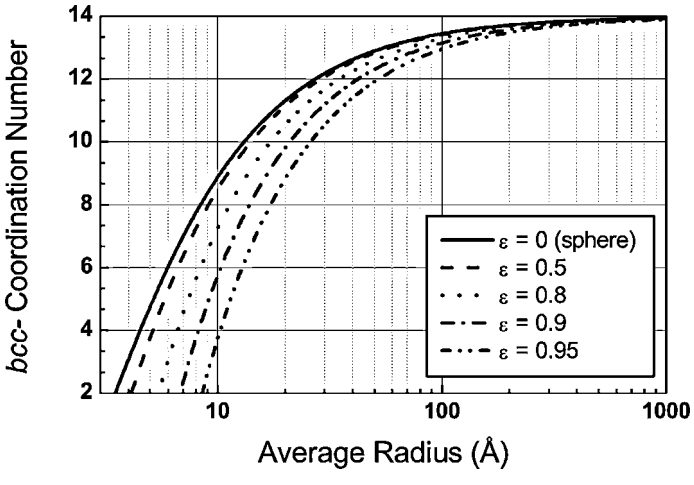

Fig. 4. Coordination number as a function of grain size for ellipsoids with different eccentricity (ε). ε is defined as $\varepsilon = 1 - b/a$, where b is the long ellipse axis and a is the short ellipse axis.

with the spherical form (calculations should be presented as a function of the averaged diameter). It is clear that for ellipse with higher eccentricity values the grain needs a bigger size to reach the maximum CN where the finite size effects are neglectable.

Moreover, in order to evaluate the dimensions of the grains along the perpendicular to the film, one can use the coherence length obtained from the width of X-ray diffraction (XRD) peaks. The studied samples have a (110)-bcc texture and it is possible to estimate the grain size from the FWHM of this diffraction peak by using the Scherrer formula. It should be noted that the measured characteristic length is along the direction of the transferred momentum ($\boldsymbol{Q}$) according to the XRD experiment. For textured films, a Bragg-Brentano geometry was used where the thin film was placed symmetrically respect to the beam incidence and the detector (at a specular position); this experimental arrangement maximizes signal for textures normal to the surface being the transferred $\boldsymbol{Q}$ perpendicular to the film.

As our films are not highly textured, "rocking curves" extend over $\pm 20^\circ$ from the normal. This fact allows performing measurements with transferred $\boldsymbol{Q}$ along directions different from the perpendicular. The analysis of these data [13] provides a general behaviour of iron thin films on silicon. Samples prepared at room temperature clearly exhibit a columnar growth and samples prepared below 200 K have grains of spherical shape.

The competition between this change of shape and its characteristic size should be taken into account in order to explain the reported magnetic coercivity behaviour [6, 7]. The film grains shape is independent of the oxidation process and the coercivity

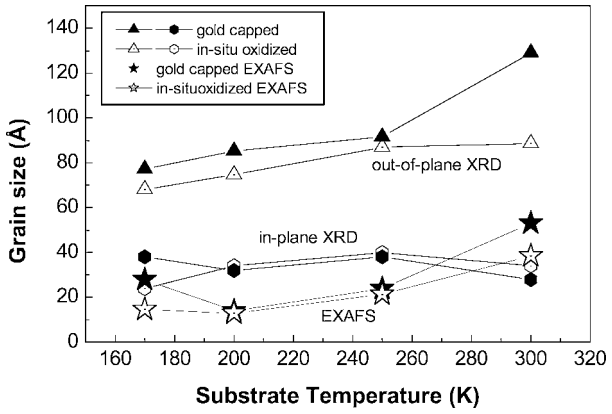

Fig. 5. "Out-of-plane" and "in-plane" characteristic sizes obtained from the coherence length in X-ray diffraction experiments. Partially oxidized gold capped and non oxidized gold capped samples are presented. Grain sizes obtained from the EXAFS data are given for comparison.

behaviour should be explained as follow. The film grains shape provides an increase of the coercivity when columns diminish in size respect to the obtained at room temperature and that increase drops for grains with nearly spherical form, as it occurs for samples prepared down 200 K.

Figure 5 shows the dependence of the characteristic "out-of-plane" and "in-plane" lengths obtained by XRD for *in-situ* oxidized and non-oxidized (gold capped) samples. We estimated the eccentricity and average size for each sample from the corresponding calculation curve as presented in Fig. 4. The sizes obtained by EXAFS are also shown in Fig. 5, compared with the characteristic lengths obtained by XRD.

The EXAFS results are in agreement with the "in-plane" XRD lengths, but not with the "out-of-plane" ones. This fact can be explained as follows. For the particle size determination of a thin film with randomly distributed elongated particles the XRD gives the larger dimension due to their sharper contribution to the diffraction peak, while the EXAFS is directly related to the shorter dimension because it controls the coordination number. This can be easily understood for an infinitely sharp needle (or wire) where the averaged CN only depends on the number of neighbouring atoms along the axis and is independent of the larger dimension size.

Additionally, there is another experimental parameter. The incoming X-ray polarization is parallel to the film plane, thus the polarization dependence makes that "in-plane" distances are highly weighted than the perpendicular ones in the EXAFS contribution [9]. This fact explains the reduction of the grain sizes obtained by EXAFS with respect to the "in-plane" dimensions obtained by XRD.

4. Conclusions

EXAFS spectroscopy and XRD have been used to study the microstructure of sputtered iron thin films prepared at low temperatures. The size and shape of the thin film grains were determined by two independent methods. They change with the substrate temperature at preparation.

The columnar growth of the films gives shorter characteristic sizes along "in-plane" than along "out-of-plane" directions. It has been proved that the smaller grain dimension is the characteristic length that governs the effect of the finite grain size in the EXAFS experiments. This effect should be taken into account in order to compare both EXAFS and XRD data.

A columnar growth explains results obtained for samples prepared near room temperature. At preparation, by decreasing the substrate temperature, a strong diminution of the column height is observed and, consequently, the grain shape changes for samples prepared at low temperature. This behaviour should be taken into account in order to explain the magnetic anomalies reported elsewhere [6].

Acknowledgements

Authors thank LURE for technical assistance and the inclusion in the European Training and Mobility Program. This work has been supported by the Spanish DGCYT under contract No. MAT2000-1384.

References

1. Sánchez-López J. C. *et al.*, Nanostruct. Mater. **7**, 813 (1996).
2. Gunther, B. and Kumpmann, A., Nanostruct. Mater. **1**, 27 (1992).
3. Terauchi, S., Koshizaki, N. and Umehara, H., Nanostruct. Mater. **5**, 71 (1995).
4. Kneller, E., in "Magnetism and Metallurgy", (Ed. by Berkowitz, A. E. and Kneller, E.), (Academic Press, New York, 1969).
5. Tasaki, A., Tomiyana, S. and Idia, S., Jpn. J. Appl. Phys. **4**, 707 (1965).
6. Muñoz-Martín, A., Prieto, C., Ocal, C., Martínez, J. L. and Colino, J., Surf. Sci. **482**, 1095 (2001).
7. Muñoz-Martín, A., Vila, M., Prieto, C., Ocal C. and Martínez J. L., Vacuum, **67**, 583 (2002).
8. Mimault, J., Faix, J. J., Girardeau, T., Jaouen, M. and Tourillon, G., Meas. Sci. Technol. **5**, 482 (1994).
9. Castañer, R. *et al.*, J. Phys.: Cond. Matter **6**, 4981 (1994).
10. Klementiev, K. V., "VIPER for Windows", freeware: www.desy.de/ ∼klmn/viper.html; and Klementev, K. V., J. Phys. D: Appl. Phys. **34**, 209 (2001).
11. Rehr, J. J., Jpn. J. Appl. Phys. **32**, 8 (1993).
12. Borowski, M., J. Phys. IV France **7**, C2-259 (1997).
13. Jiménez-Villacorta, F., Muñoz-Martín, A. and Prieto, C., J. Appl. Phys. (at the press).

Physica Scripta. Vol. T115, 454–456, 2005

EXAFS Characterization of Nickel Clusters in Ni/Si_3N_4 Sputtered Thin Films

M. Vila*, F. Jiménez-Villacorta*, C. Prieto*# and A. Traverse**

* Instituto de Ciencia de Materiales de Madrid. Consejo Superior de Investigaciones Científicas. Cantoblanco, 28049- Madrid, Spain
**Laboratoire pour l'Utilisation du Rayonnement Électromagnetique, Centre Universitaire Paris-Sud, BP34. 91898-Orsay Cedex, France

Received June 26, 2003; accepted in revised form January 13, 2004

PACS numbers: 75.50.Tt; 75.75.+a

Abstract

Ni and Si_3N_4 layers have been alternatively deposited by sputtering in order to study Ni clusters embedded in amorphous Si_3N_4. The nominal Ni layer thickness has been varied from 2 to 60 Å and the number of layers was planned to have a similar total amount of Ni. The decrease in the Ni-Ni coordination number observed by Extended X-ray Absorption Fine Structure spectroscopy has been used to study the microstructure of the Ni clustering. For small Ni layer thickness, the actual Ni layer becomes discontinuous and an average cluster diameter of Ni clusters can be determined. Ni metallic cluster in the Ni/Si_3N_4 system show a magnetization smaller than in bulk nickel, the decrease of magnetization of the cluster should be attributed to a dead skin at the surface of the Ni-clusters.

1. Introduction

Nano-scale structures have drawn a great deal of attention. By decreasing the material size from the bulk to the atomic level, many physical properties undergo spectacular changes. Small clusters have an average magnetic moment per atom larger than the bulk value [1]. In particular, materials with small grain size exhibit unique magnetic properties such as magnetization [1], superparamagnetic behaviour [2] or giant magnetoresistance [3].

Granular materials composed of magnetic clusters embedded in non-magnetic matrix can be prepared by typical thin film techniques such as sputtering [4] or ion implantation where clusters size can be controlled by the preparation parameters. We chose to study the $Ni\text{-}Si_3N_4$ system.

Materials with Ni clusters embedded in another ceramic matrix, AlN, have been prepared by ion implantation and their magnetic properties have been studied [5, 6]. The aim of the present work is to check the possibility to synthetize Ni clusters in another ceramic by sputtering and to perform the microstructural characterization to study their magnetic properties as a function of their characteristic length.

The effect of the matrix on the magnetization at saturation measured at low temperature will be discussed in view of the results presented in Ref. [6].

2. Experimental

$Ni\text{-}Si_3N_4$ multilayer films were grown at room temperature on Si(100) by using two planar 2″ magnetron source (Angstrom Science) operated by both Huttinger DC and RF-power supply, respectively. Circular targets were mechanically clamped to the water-cooled electrode. The vacuum system provides a residual pressure near 1×10^{-7} mbar. Using Ar as sputtering gas, a DC power of typically 20 W was used to deposit nickel by, and using N_2 as reactive sputtering gas, a RF power of 100 W was used to deposit silicon nitride from a pure silicon target. The compositional characterization of silicon nitride prepared in this way has been reported elsewhere [7, 8].

Within our preparation conditions, when the Ni layer average thickness ranges from 2 to 60 Å, their roughness makes that X-ray reflectivity spectra do not show a multilayer, but nevertheless, metallic nickel is present at the sample. Changing the Ni average thickness and the Ni concentration it is possible to control the cluster size and distance between clusters.

The Ni deposition rate was determined previously by X-ray reflectivity, but, due to the very short time to prepare each layer, some error cannot be avoided. Thus, we have determined the total amount of Ni by Rutherford Backscattering Spectroscopy (RBS) at the Centro Nacional de Aceleradores (Sevilla, Spain) by using the 3 MV Tandem ion beam accelerator.

X-ray absorption experiments have been carried out at LURE (DCI, XAS-13 beamline) with electron beam energy of 1.85 GeV and an average current of 250 mA. Ni K-edge data were obtained by using a fixed exit monochromator with two flat Si (311) crystals. Signal detection was made by collecting the total electron yield on a biased electrode placed in a He atmosphere sample chamber at liquid nitrogen temperature [9].

A standard EXAFS analysis was performed by using the VIPER program [10]. Oscillations were obtained after removing the background by a cubic spline fitting polynomial and EXAFS signal ($\chi(k)$) was obtained by normalizing the magnitude of the oscillations to the edge jump. The corresponding pseudo Radial Distribution Function around the Ni atoms has been obtained by weighting by the wavenumber ($k\chi(k)$), multiplying by a Hanning window and Fourier transforming. For comparative study, the Fourier transform of EXAFS signal was performed within the same k-range. The here presented analysis is based on the fit of the oscillations obtained by back-Fourier transform of the first coordination sphere (between 1.2 and 2.5 Å). The backscattering amplitude and phase were calculated by the FEFF code version 6.01 reported by J. Rehr [11]. The $S_0{}^2$ amplitude loss factor was obtained by using the spectrum of a Ni foil as the reference.

Magnetization hysteresis loops were measured at 4 K in a SQUID magnetometer (MPMS-5S from Quantum Design). Magnetic fields were applied up to 40 kOe in order to saturate the magnetization of the samples.

3. Results and Discussion

EXAFS signals of the studied set of samples are shown in Fig. 1(a). Samples with nominal Ni layer thickness more than 30 Å present a clear fcc-like EXAFS structure. However, the samples with nominal Ni thickness less than 30 Å, have no more fcc structure,

#Correspondant author: e-mail: cprieto@icmm.csic.es

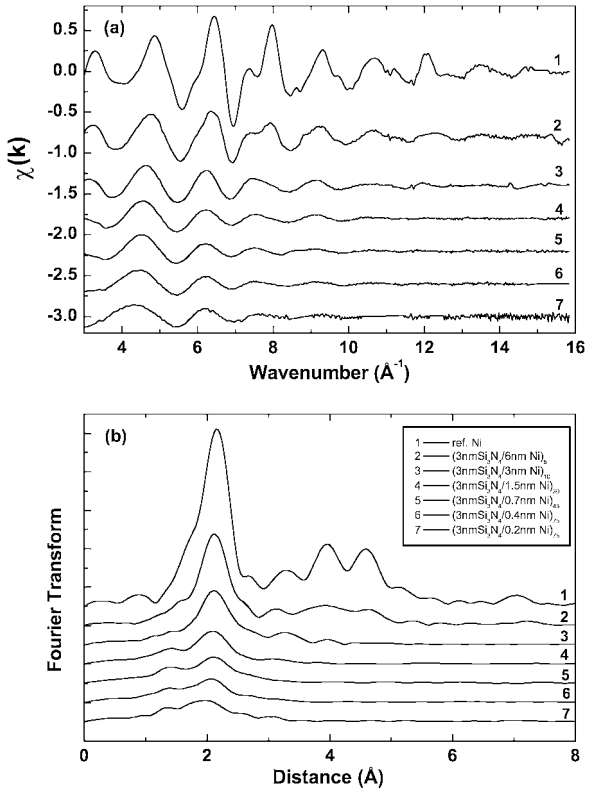

Fig. 1. (a) *k*-weighted EXAFS signal of samples prepared with a Ni deposition rate of 3.5 nm/min. (b) Fourier Transform of the precedent $k\chi(k)$ signals.

but amorphous. Figure 1(b) shows the Fourier transforms of the precedent data. The signal corresponding to the first Ni-Ni neighbours decreases with the nominal Ni thickness. Moreover, a small EXAFS contribution appears at distances shorter than the Ni-Ni one.

Table I summarizes the parameters obtained after the fitting of the EXAFS data. Two possible pairs (Ni-N and Ni-Si) have been

Table I. *Parameters obtained after EXAFS analysis. Samples are labelled by the nominal thickness of each individual layer with the number of bilayers at the subindex. N_j, number of neighbours, R_j, bond distance and $\sigma_j{}^2$, Debye-Waller factor. The last column is the average Ni-layer thickness obtained by RBS.*

Sample	Deposition rate (nm/min)	Pair	N_j	R_j (Å)	$\sigma_j{}^2$ (Å^2)	Ni-layer thickness (Å)
Ni-reference	3.5	Ni-Ni	12.0	2.49	0.0052	200
(30 Å Si_3N_4/60 Å Ni)$_5$	3.5	Ni-Ni	9.6	2.49	0.09	59.0
		Ni-N	1.0	1.89	0.011	
(3 Å Si_3N_4/30 Å Ni)$_{10}$	3.5	Ni-Ni	5.7	2.49	0.0089	32.6
		Ni-N	2.3	1.931	0.011	
(30 Å Si_3N_4/15 Å Ni)$_{20}$	3.5	Ni-Ni	3.6	2.49	0.009	18.5
		Ni-N	2.8	1.87	0.011	
(30 Å Si_3N_4/7 Å Ni)$_{43}$	3.5	Ni-Ni	2.8	2.49	0.009	9.1
		Ni-N	3.2	1.87	0.011	
(30 Å Si_3N_4/4 Å Ni)$_{75}$	3.5	Ni-Ni	2.6	2.49	0.010	6.6
		Ni-N	2.8	1.90	0.013	
(30 Å Si_3N_4/2 Å Ni)$_{75}$	3.5	Ni-Ni	2.2	2.48	0.009	4.5
		Ni-N	2.6	1.92	0.011	
(30 Å Si_3N_4/30 Å Ni)$_{10}$	7.2	Ni-Ni	9.0	2.49	0.0089	36.7
		Ni-N	1.1	1.931	0.011	
(30 Å Si_3N_4/15 Å Ni)$_{15}$	7.2	Ni-Ni	6.0	2.49	0.009	19.4
		Ni-N	3.1	1.87	0.011	

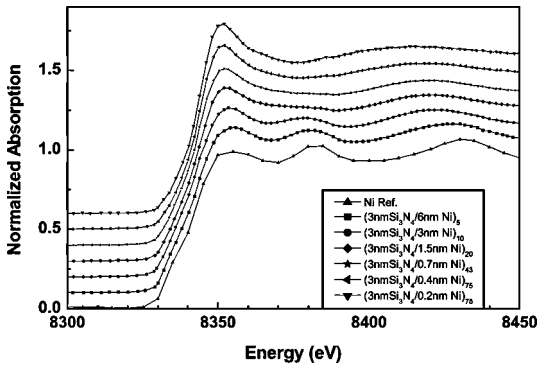

Fig. 2. Normalized XANES spectra corresponding to samples prepared with a Ni deposition rate of 3.5 nm/min.

taken into account in order to explain the distance that appears shorter than Ni-Ni, but we have found that the Ni-Si contribution is negligible. EXAFS analysis provides a decrease of the Ni-Ni coordination number that is associated with the finite size effect. Hence we could suggest that Ni clusters have been formed surrounded by the N atoms of the nitride.

Fig. 2 shows the normalized XANES signals. In agreement with EXAFS data, samples with nominal Ni layer thickness more than 30 Å present a clear fcc-like XANES structure and for the samples less than 30 Å, the increase of the feature at 8350 eV indicates that nickel atoms loose the fcc crystallographic structure and some of them are coordinated to the nitrogen of the silicon nitride. This suggests, a decrease of the Ni cluster size by lowering the nominal Ni layer thickness.

Next, we determined the average Ni layer thickness by measuring the total Ni atomic amount by RBS and normalizing by the number of layers. Results are given also in Table I, showing a good agreement between the nominal Ni layer thickness and the obtained data. However, for the thinner layers, there is a small increment of the actual Ni amount because there is an excess of the growing time coming from the time needed to position the substrate over the Ni source.

In Fig. 3, the EXAFS coordination numbers are plotted as a function of the Ni layer thickness determined by RBS. A monotonous increase is observed for the Ni-Ni coordination number that tends to the Ni coordination number (CN) in the bulk fcc phase. On the other hand, the Ni-N CN decreases to zero with the Ni layer thickness.

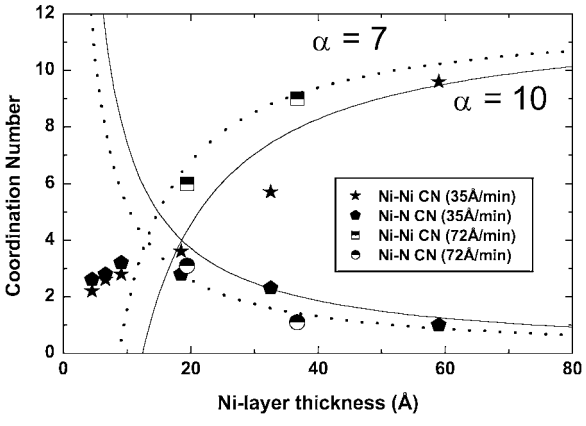

Fig. 3. Coordination number as a function of layer thickness. Points are EXAFS obtained results for Ni-Ni and Ni-N pairs. Lines are calculated as it is indicated in the text (solid line corresponds to $\alpha = 10$ and doted line to $\alpha = 7$).

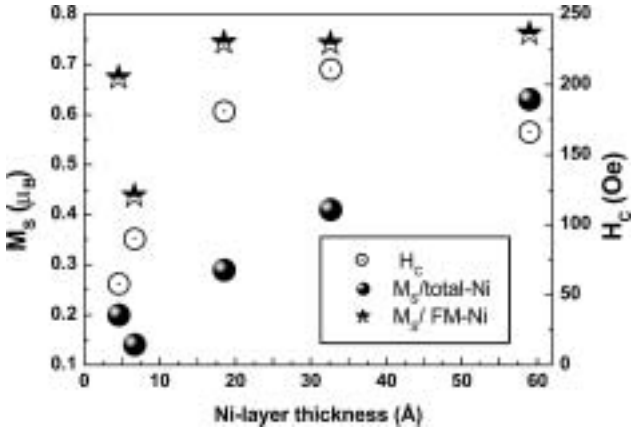

Fig. 4. Atomic saturation magnetization (M_S) and coercive field (H_C) vs. the Ni-layer thickness. Black circles are used to plot the magnetization normalized to the total amount of nickel and stars represent the atomic magnetization by considering only the Ni atoms in the ferromagnetic metallic phase.

It is possible to calculate the CN behaviour of a layer as a function of their thickness. By using a similar model as that proposed by Borowski [12] for spherical clusters, the following equation is derived for the Ni-Ni CN in a nickel layer: $CN_{(Ni\text{-}Ni)} = CN_{bulk}(1 - \alpha d/2t) = 12(1 - \alpha d/2t)$; where d is the distance between the nearest neighbour Ni atoms, t is the thickness of the layer and the bulk coordination number (CN_{bulk}) is 12 for the fcc phase; α is a parameter ($\alpha > 1$) in order to take into account the roughness of the layer that makes a bigger ratio for atoms situated at the surface of the layers. Additionally, the nickel atoms located at the surface of the layer and that can coordinate to the nitrogen atoms of Si_3N_4 can be estimated as: $CN_{(Ni\text{-}N)} = (1/4)CN_{bulk}(2\alpha d/t) = 3\alpha d/t$; where CN_{bulk} has been taken equal to 6 as typically for an octahedral coordination.

In Fig. 3 are represented the calculated curves relating the average CN to the layer thickness. In order to roughly fit the EXAFS-obtained CN for the higher layer thickness, the α factor has been taken as $\alpha = 10$ and $\alpha = 7$ for samples prepared at 3.5 nm/min and 7.2 nm/min deposition rate, respectively. This result shows that, within this range of deposition range, the Ni layer roughness decreases for higher deposition rate.

The set prepared with Ni deposition rate of 3.5 nm/min supplies very thin Ni layer samples. For thickness less than 15 Å, the obtained CN does not follow the calculated behaviour. This is because the roughness is bigger than the average thickness, which makes that Ni must not be considered yet as a continuous layer appearing in the sample as dispersed metallic clusters, this thickness can be considered as the percolation limit.

Finally, hysteresis loops have been measured at low temperature ($T = 4$ K) in order to obtain saturation magnetization (M_S) and coercive field (H_C). M_S has been determined by extrapolating the magnetization data for a magnetic field of 4 T. In order to obtain the atomic magnetization one can normalize by the total amount of Ni in the sample; results are given in Fig. 4 vs. the Ni-layer thickness. Compared with the bulk Ni ($0.63\mu_B$), samples present a significant decrease for thinner Ni-layers. Such a similar decrease of the magnetization has already been observed in Ref. [13] for Ni and Co clusters embedded in AlN whatever the preparation technique, sputtering or ion implantation. Moreover, coercive field also decreases for Ni-layer thickness less than 10 Å in coincidence with the percolation limit obtained from the EXAFS analysis, indicating that small size clusters have a super-paramagnetic character.

The large drop of magnetization for the thin Ni layers should be ascribed to a dead skin effect. The surface of the Ni layer is covered by a Ni-N wrap. In order to calculate the magnetization per metallic Ni atom, the amount of nickel forming Ni-N bonds should be excluded from the normalization. In order to estimate what is the relative amount of Ni atoms in the magnetic metallic phase, we have used the ratio between the obtained CN for Ni-Ni and Ni-N bonds. After performing this new normalization, the atomic M_S remains at roughly constant values (values are also plotted in Fig. 4). The reduction obtained for samples having very small coercive field can be attributed to an underestimation of the magnetic saturation due to the super-paramagnetic shape of the hysteresis loops.

4. Conclusions

EXAFS spectroscopy has been used to study the microstructure of sputtered Ni/Si_3N_4 multilayer system. For small Ni-layer thickness samples should be considered as Ni clusters embedded in amorphous Si_3N_4. It has been determined that the magnetization per Ni atom decreases with the Ni-layer thickness and that, is due to a magnetically dead skin where the Ni is coordinated to the nitrogen of the Si_3N_4 amorphous matrix. Additionally, the atomic magnetization of Ni atoms in the magnetic metallic phase seems to be independent of the nanometric characteristic size of the Ni.

Acknowledgements

Authors thanks LURE for technical assistance and the inclusion in the European Training and Mobility Program. This work has been supported by the Spanish DGCYT under contract No. MAT2000-0767-C02.

References

1. Billas, I. M. L., Chatelain, A. and de Heer, W. A., Science **265**, 1682 (1994).
2. Dormann, J. L., Rev. Appl. Phys. **26**, 1381 (1981).
3. Berkowitz, A. *et al*., Phys. Rev. Lett. **68**, 3745 (1992).
4. Babonneau, D. *et al*., Appl. Phys. Lett. **76**, 2892 (2000).
5. Zanghi, D., Delobbe, A., Traverse, A. and Krill, G. J., Phys.: Condens. Matter **10**, 9721 (1998).
6. Zanghi, D. *et al*., J. Appl. Phys. **89**, 6329 (2001).
7. Vila, M., Prieto, C., Garcia-López, F. J. and Respaldiza, M. A., Nucl. Instrum. Meth. B **211**, 199 (2003).
8. Vila, M. *et al.*, Vacuum **67**, 513 (2002).
9. Mimault, J., Faix, J. J., Girardeau, T., Jaouen M. and Tourillon, G., Meas. Sci. Technol. **5**, 482 (1994).
10. Klementev, K. V., "VIPER for Windows", freeware: www.desy.de/∼klmn/viper.html; and Klementev, K. V., J. Phys. D: Appl. Phys. **34**, 209 (2001).
11. Rehr, J. J., Jpn. J. Appl. Phys. **32**, 8 (1993).
12. Borowski, M., J. Phys. IV France **7**, C2-259 (1997).
13. Zanghi, D. *et al.*, J. Appl. Phys. **90**, 6367 (2001).

Physica Scripta. Vol. T115, 457–458, 2005

Local Structure of $Sr_2FeMo_xW_{1-x}O_6$ Double Perovskites Studied by EXAFS

F. Bardelli[1,2], C. Meneghini[1,2], S. Mobilio[1,3], Sugata Ray[4] and D. D. Sarma[4,5]

[1]Dip di Fisica Univ. di "Roma Tre" Via della vasca navale 84, I-00146 Roma Italy
[2]INFM-GILDA c/o ESRF Grenoble, France
[3]INFN Laboratori Nazionali di Frascati, Italy
[4]Solid State and Structural Chemistry Unit, Indian Institute of Science, Bangalore-560 012, India
[5]Jawaharlal Nehru Centre for Advanced Research, Bangalore, India

Received June 26, 2003; accepted November 4, 2003

PACS numbers: 71.30th, 72.15Eb, 72.25−b, 75.47Np

Abstract

Sr_2FeMoO_6 double perovskits display low field MR at a relatively high temperature and unusual ferromagnetic properties. These compounds depicts metal to insulator transition increasing x above $x_c \sim 0.25$. A comparative analysis of the near edge regions (XANES) suggests that iron is Fe^{3+} in the metallic range. Checking the end compounds, we found that the doped samples can be viewn as inhomogeneous distributions of the end compounds. This could help to distinguish between the two scenarios proposed to explain the metal to insulator transition. Moreover, the local atomic structure of $Sr_2FeMo_xW_{1-x}O_6$ as a function of composition ($0 \leq x \leq 1$) has been investigated by Extended X-ray absorption spectroscopy (EXAFS) a the Fe, Mo, Sr K-edges and W L_{III}-edge.

1. Introduction

Recently, the double perovskits system, $Sr_2FeMo_xW_{1-x}O_6$, has attracted the interest of the solid state scientists because of its remarkable magnetoresistive properties. The ordered undoped end compound Sr_2FeMoO_6 ($x = 1$) has alternating occupancy of Fe^{2+} and Fe^{3+} ions at the B sites of the double perovskits A_2BO_6 structure, where A and B represent two cations. The interest in this compound derives from the rather high temperature of their ferrimagnetic transition (∼450 K). In this phase it is believed to be ordered with each B site sublattice of Fe^{3+} and Mo^{5+} arranged ferromagnetically, while the two sublattices are coupled to each other antiferromagnetically. It has been suggested [1] that high structural order in Fe^{3+} and Mo^{5+} occupancy leads to a half metallic ferromagetic state (HMFM), with only minority spin carriers present at the Fermi level.

This compound exhibits a large negative magnetoresistance (MR) at 5 K as well as at 300 K [1–3]. Such large magnetoresistance is believed to be driven by the complete spin polarization at the Fermi energy in the HMFM state. The other end compound, $x = 0$ (Sr_2FeWO_6), belong to the same double perovskite family but shows very different electrical transport and magnetic properties. It is insulating throughout the temperature range with antiferromagnetic ordering below 37 K [5, 6].

Since Sr_2FeMoO_6 and Sr_2FeWO_6 have contrasting transport properties, it is expected that an alloy system of these compounds, such as the $Sr_2FeMo_xW_{1-x}O_6$ series, would exhibit a metal insulator transition (MIT) as a function of x. Two models have been proposed to explain the MIT. In one scenario [5], Fe is believed to be in the 3+ state in the metallic range ($x_c \gtrsim 0.25$) and Mo and W in the 5+ state; one itinerant electron is provided by each Mo^{5+} ($4d^1$) and W^{5+} ($5d^1$) site. For $x < x_c$, Fe transforms into the 2+ state converting Mo and W into the 6+ state (W, $5d^0$). This gives rise to the insulating behavior since, for the $5d^0$ electronic configuration of the W^{6+} sites, the Fe^{2+} ions couple antiferromagnetically with each other via the Fe-O-W-O-Fe type super exchange interaction. In this scenario a valence transition is the driving force for the MIT.

In a more recent work [1], it has been proposed that Mo remains in the 5+ state in the entire composition range while W is in the 64+ state. This implies that there is no valence transition Mo and W ions at the critical concentration. The substitution of W^{6+} in place of Mo^{5+} requires the transformation of one Fe^{3+} to Fe^{2+} for charge neutrality. Thus the system is viewn as an inhomogeneous distribution of metallic Sr_2FeMoO_6 and insulating Sr_2FeWO_6 parts; in the scenario the MIT at the critical composition is driven by the percolation threshold of the system. Above x_c the system is in a macroscopically metallic ferromagnetic state of Sr_2FeMoO_6 with a distribution of small clusters of insulating antiferromagnetic Sr_2FeWO_6. At higher W doping, the insulating Sr_2FeWO_6 clusters grow in size, eventually engulfing the metallic Sr_2FeMoO_6 clusters for $x < 0.3$, giving rise to the observed MIT.

2. Results

X-ray absorption spectroscopy (XAS) experiments were performed at the GILDA (General Italian Line for Diffraction and Absorption) beam line [7] at the European Synchrotron Radiation Facility (ESRF) in Grenoble, France. X-ray beam energies were tuned using a double crystal, sagittal focusing monochromator mounting Si [311] crystals. High quality XAS spectra at the Fe (7112 eV), Mo (20000 eV) and SR (17998 eV) K edges and at the W L_{III} edge (10207 eV) have been collected in transmission mode: incident (I_o) and transmitted (I_t) beam intensities were recorded using ionization chambers and the absorption signal was defined as: $\mu(E) = \ln(I_o/I_1)$. Data were collected keeping the samples at low temperature (77 K) in order to reduce the effects of thermal disorder.

A qualitative analysis of the XANES region of the absorption spectra (figure 1) does not reveal appreciable differences in the W and Mo absorption edges over the entire concentration range indicating that the valence of the W and Mo ions does not change with the concentration. This is incompatible with the valence transition scenario proposed to explain the MIT and discussed above. Data refinement (to be compared with diffraction data [4]) in the EXAFS [8–10] region shows no changes even in the local structure near the Mo and W ions.

On the contrary the Fe edge absorption spectra show large effects in the XANES region while crossing the critical concentration value indicating a valence transition of Fe ions from 3+ above x_c to 2+ below x_c.

Moreover, we checked the possibility of fit the spectra to a weighted sum of the end compounds: $\mu_{FIT}(x) = \alpha \cdot \mu_{exp}(x = 1) +$

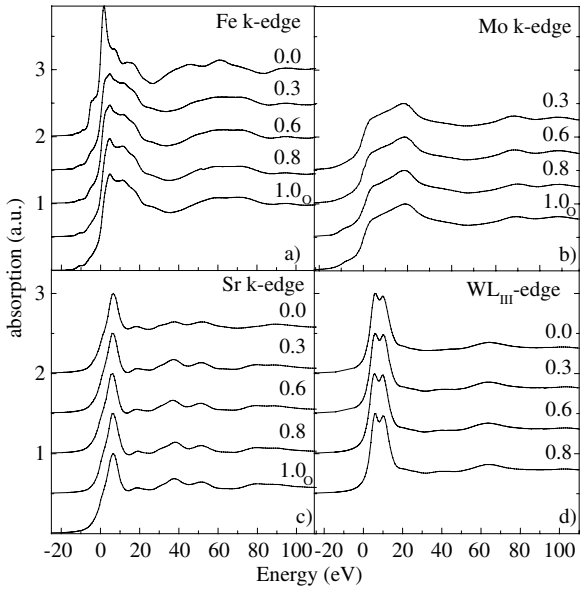

Fig. 1. The figure reports the raw absorption spectra for the Fe, Mo, W and Sr edges. As can be seen only the spectra of the Fe edge show appreciable variations as a function of the composition.

$(1-\alpha)\cdot\mu_{exp}(x=0)$ where α is a free parameter in the fitting procedure. We found an excellent agreement using this procedure. This result demonstrates without any doubt that the doped compounds are an inhomogeneous distribution of the end compounds. Moveover, this result is again incompatible with the valence transition scenario, because, in such scenario a shift in the edge position should be observed, and this will result in the failure of the fits.

Figure 2 reports the values of α and $1-\alpha$ obtained by fitting different concentrations samples. Keeping in mind the correspondence between the Mo^{5+} concentration x and the concentration of Fe^{3+} ions (together with that between W^{6+} and Fe^{2+} ions) from figure 2 we can deduce that the concentration of Fe^{3+} remains constant above x_c. This seems to be in contrast with the percolative transition scenario, because, in this case, the concentration of end compound necessary to best fit the doped compounds spectra should equal the nominal concentrations, i.e. the values of α and $1-\alpha$ should be on the straight lines reported in the figure.

3. Conclusions

Our work strongly excludes the valence transition scenario but even the other scenario proposed the percolation transition one,

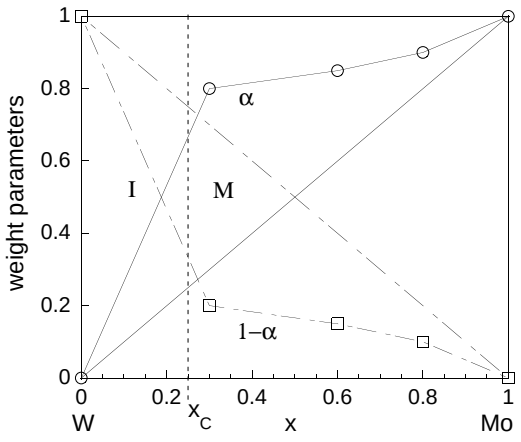

Fig. 2. Figure reports the values of the weight parameters α and $(1-\alpha)$. The straight lines shows the hypothetical behavior of the same parameters as expected by the percolative transition scenario.

does not seem to be totally compatible with our results. On the one hand, the goodness of the fits described above agrees with the idea that the doped compounds are an inhomogeneous distribution of the end compounds, as proposed by the percolative scenario. On the other hand, the values, resulting from the same fits, do not agree with the ones involved by the percolative scenario. To agree with this scenario something should balance the excess of Fe^{3+} (i.e. of α in the fits) in the metallic range above x_c introduced by the W^{6+} doping. So, more physics is required to accord our results with the percolative transition scenario. We suppose that the excess of 3+ valence Fe ions could arise from an unwanted oxygen deficiency present in our samples.

References

1. Kobayashi, K.-I., Kimura, T., Sawada, H., Terakura, K. and Tokura, Y., Nature **395**, 677 (1998).
2. Niebieskikwiat, D. *et al*., Phys. Rev. B **62**, 3340 (2000).
3. Ray, S., Kumar, A., Majumdar, S., Sampathkumaran, E. V. and Sarma, D. D., J. Phys.: Cond. Matter **13**, 607 (2001).
4. Chmaissem, O. *et al*., Phys. Rev. B **62**, 14197 (2000).
5. Nakakawa, T., Yoshikawa, K. and Nomura, S., J. Phys. Soc. Japan **27**, 880 (1969).
6. Kawanaka, H., Hase, I., Toyama, S. and Nishihara, Y., Physica B **281–282**, 1428 (2000).
7. Pascarelli, S. *et al.*, J. Synchrotron Rad. **3**, 147 (1996).
8. Lee, P. A. and Pendry, J. B., Phys. Rev. B **11**, 2795 (1975).
9. Lee, P. A., Citrin, P. H., Eisenberger, P. and Kincaid, B. M., Rev. Mod. Phys. **53**, 769 (1981).
10. Ankudinov, A. I., Ravel, B., Rehr, J. J. and Conradson, S. D., Phys. Rev. B **58**, 7565 (1998).

Physica Scripta. Vol. T115, 459–461, 2005

Local Structure of Ag Nano-Clusters Deposited on Silicon Wafer by Total Conversion Electron Yield XAFS

Y. Suzuki[1], T. Miyanaga[*1], K. Kita[1], T. Uruga[2] and I. Watanabe[3]

[1]Department of Materials Science and Technology, Faculty of Science and Technology, Hirosaki University, Hirosaki, Aomori 036-8561, Japan
[2]JASRI/SPring-8, Mikazuki-cho, Hyogo 679-5198, Japan
[3]Faculty of Science, Osaka Women's University, Sakai, Osaka 590-0035, Japan

Received June 26, 2003; accepted in revised form November 4, 2003

PACS number: 03.30+p

Abstract

We have investigated the local structure of Ag nano-clusters deposited as thin films on silicon substrate by using a total conversion electron yield XAFS (X-ray absorption fine structure) method at Ag K-edge. High quality spectra were obtained from samples with thicknesses of 1–10 nm. We have found that these clusters have an *fcc* structure and that the interatomic distance does not depend on the thickness. The coordination number, N, however, changes with the thickness of the film. The N value for the first nearest shell as a function of the film thickness is compared with the theoretically expected value by taking account of the surface effect. For thinner films, the observed N values are smaller than the expected values. We have observed a correlation between the N value and the electromagnetic field intensity at the surface evaluated from IR measurement. The morphology of Ag nano-cluster particles must affect the local electric field intensity at the surface.

1. Introduction

The research on interfaces between metals and semiconductors is playing a very important role in the recent developments of science and technology. Silver thin film deposited on silicon substrate is one of the typical examples for the metal/semiconductor system and has been studied by several techniques [1]. It is well known that a thin noble metal film exhibits anomalous light absorption in the visible and infrared regions, i.e. the local electric field is enhanced at the thin film surface. Such systems as Ag on Ge and Si have been extensively studied [2] and it is known that this phenomenon has not been explained well by classical theory and effective dielectric functions. In order to reveal this electric field enhancement, it is necessary to obtain structural information about Ag clusters deposited on the Si surface, since the local structure of Ag clusters might be related to this phenomenon. X-ray absorption fine structure (XAFS) has become apparent to be a technique for studying the local structure in a material from the short-range point of view and complementary to the conventional diffraction method based on long-range order.

The total conversion electron yield (TCEY) method used in the present work is a simpler and more convenient means than the fluorescence detection method for the XAFS study of thin films deposited on thick substrates. It detects mainly the Auger electrons emitted from the sample. Since the X-ray absorption coefficient is smaller for heavier atoms and heavy atoms with a hole in the core shell relax through fluorescence emission with higher probability than the Auger process, very thin films composed of heavy atom Ag could be expected to be a difficult system to study by the TCEY method [3, 4]. Our present experiments, however, indicate that the method was an appropriate choice for the present samples.

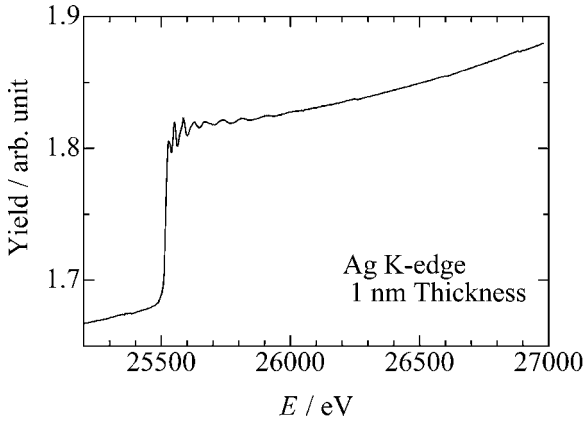

Fig. 1. X-ray absorption spectrum at Ag K-edge for 1 nm Ag film on Si wafer by a TCEY method.

2. Experimental

Silver films with various thickness, T, 1–10 nm in mass thickness were deposited on silicon wafer by electron-beam evaporation method in a vacuum chamber at 5×10^{-10} torr at room temperature. The thickness was evaluated by a quartz oscillator.

XAFS spectra at Ag K-edge (25.5 keV) were obtained at BL01B1 of SPring-8 by the TCEY technique. The sample wafers were stuck on a sample current electrode by conductive adhesive tape and helium gas was introduced into the CEY cell. The wafers were rotated within the sample plane in order to remove the diffraction peaks from Si substrate and Ag sample [5]. A Si(311) double-crystal monochromator was used. The incident X-ray was introduced to the sample surface at a grazing incidence angle of two degrees and the electric vector of X-ray was polarized in the plane of the sample. The photon flux and the stability of the beam at BL01B1 were high enough for measuring high energy XAFS employing the TCEY method for surface study. As an example, the Ag K-edge X-ray absorption spectrum for a sample with 1 nm Ag deposited on Si surface is shown in Fig. 1. The qualities of the XAFS data for very thin films by the TCEY technique were quite satisfactory.

The EXAFS analyses were performed by using XANADU [6] and FEFF 6.01 code [7]. For the curve-fitting procedure, the non-linear least square fitting method was applied to the experimental data as described in the following expression,

$$\chi(k) = \sum_j \frac{S_0^2 N_j}{k r_j^2} f_j(k, r_j) \exp(-2\sigma_j^2 k^2) \exp(-2r_j/\lambda(k)) \times \sin[2kr_j + \varphi_j(k)] \quad (1)$$

*e-mail: takaf@cc.hirosaki-u.ac.jp

where r, N and σ are the interatomic distance, the coordination number and the root mean square displacement, respectively, for each atomic pair. The phase shift $\varphi(k)$, the backscattering amplitude $f(k, r)$ and the electron mean free path $\lambda(k)$ are obtained from the FEFF6.01 calculation [4].

3. Results and Discussion

Figure 2 shows EXAFS $k\chi(k)$ spectra for several different Ag films in thickness. The amplitude of the oscillation function decreases as the Ag thickness decreases. Figure 3 shows the Fourier transforms of the EXAFS oscillations in the k-range of 3.3–13.3 Å^{-1}. Every spectrum has a strong peak at almost the same distance. It means that all these Ag films have an *fcc* structure and almost equal interatomic distances as Ag bulk. The intensity of |FT(r)|, however, changes with the thickness of the film. The intensity is closely related with the coordination number, N. The peak intensities for the nearest neighbor (2.8 Å) are almost the same for 10–7 nm samples, however, they become smaller when the films are thinner than 7 nm.

In order to obtain more detailed structural parameters, we applied the non-linear least square fitting (curve fitting) method to the first nearest peak. The results are summarized in Table I.

The coordination numbers, N, for the first nearest atoms are plotted in Fig. 4 as a function of Ag thickness, T. For the TCEY technique, it is not easy to determine the scale factor S_0^2 from the standard foil sample because of the self-absorption effect. Therefore we assume that the N value for a 10 nm Ag film is 12 because of the independence of the values for 7–10 nm samples on the thickness. The samples with smaller thickness are expected to have smaller N values than 12, which is caused by the surface effect. The expected values for the ideally flat *fcc* layer of Ag are calculated using the method proposed by Crozier *et al.* [8]. The calculated values are plotted in the same Figure by the X mark, in which the polarization of incident photons is not considered. For the case that the polarization is in the plane of the flat sample, the effective coordination number does not depend on the thickness and should be a constant of 12. The calculated N values clearly demonstrate the surface effect in the smaller thickness region (1–5 nm).

Table I. *Structural parameters obtained from EXAFS analyses.*

T/nm	r/nm	$\sigma/10^{-3}$ nm	N	L/nm	D/nm
1.0	0.288	9.7	8.9	1.8	5–10
2.0	0.287	9.7	9.9	2.1	—
3.0	0.289	9.7	10.8	3.6	10–20
5.0	0.288	9.5	11.4	8.8	30–40
7.0	0.288	9.9	12.1	—	—
8.0	0.288	9.7	12.0	—	—
10.0	0.288	9.7	12.0	—	—

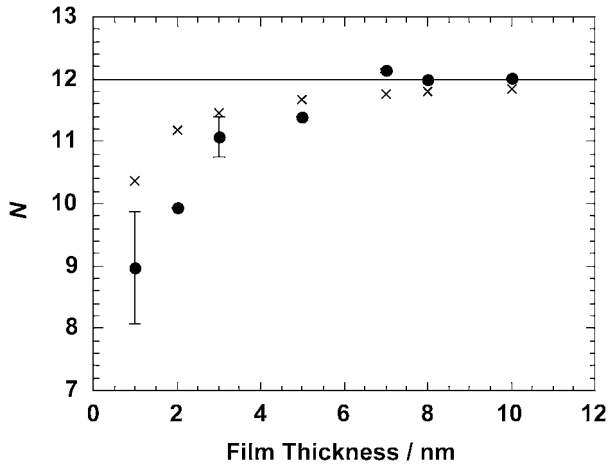

Fig. 4. Coordination number, N, of the first nearest neighbor as a function of film thickness (solid circle). Crosses indicate the values for ideally flat films [8].

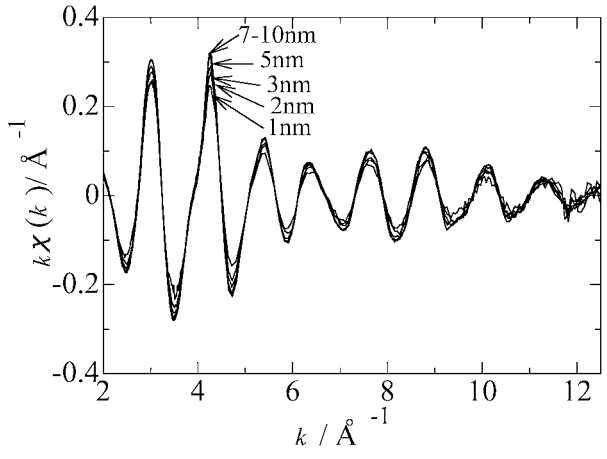

Fig. 2. $k\chi(k)$ spectra of Ag K-edge XAFS for 1–10 nm Ag films deposited on Si wafer.

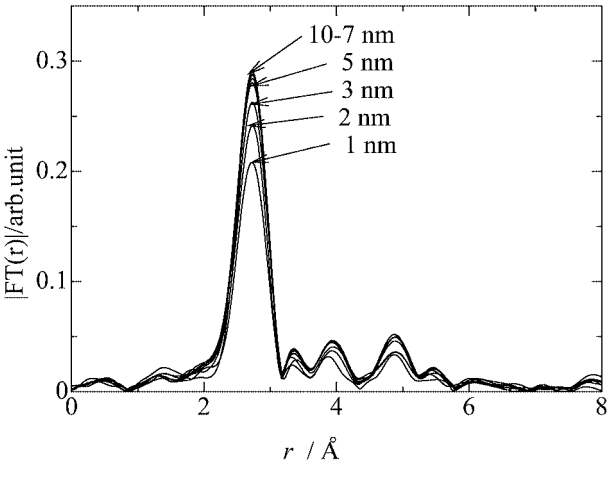

Fig. 3. Fourier transforms of Ag K-edge EXAFS for 1–10 nm Ag films deposited on Si wafer.

Very thin Ag films are known to form islands on the solid surface. Figure 5 shows FE-SEM (Field Emission Scanning Electron Microprobe) photographs for the present Ag films on Si wafer. Each scale bar in the photographs indicates 40 nm. The photographs display the island structure of Ag films and these islands are merged together gradually into larger islands with the increase of the thickness. Since the total area of superficies of island-shaped film is larger than that of the planar ones, we assume that this causes the decreased coordination numbers compared to the calculated N values for ideally flat samples. If the Ag clusters are assumed to form cubes with the edge length L, we can evaluate the L values from the effective coordination number [8], which are listed in Table I. In the table are also listed the average diameters, D, of the islands estimated from the FE-SEM images. While the L values obtained from the EXAFS should be compared with the D values from the FE-SEM for the ideal system, the L values are far smaller than the D values: For example, the 3 nm thickness sample gives 3.6 nm of L from the EXAFS but 10–20 nm of D from the FE-SEM images. For this discrepancy, we assume that

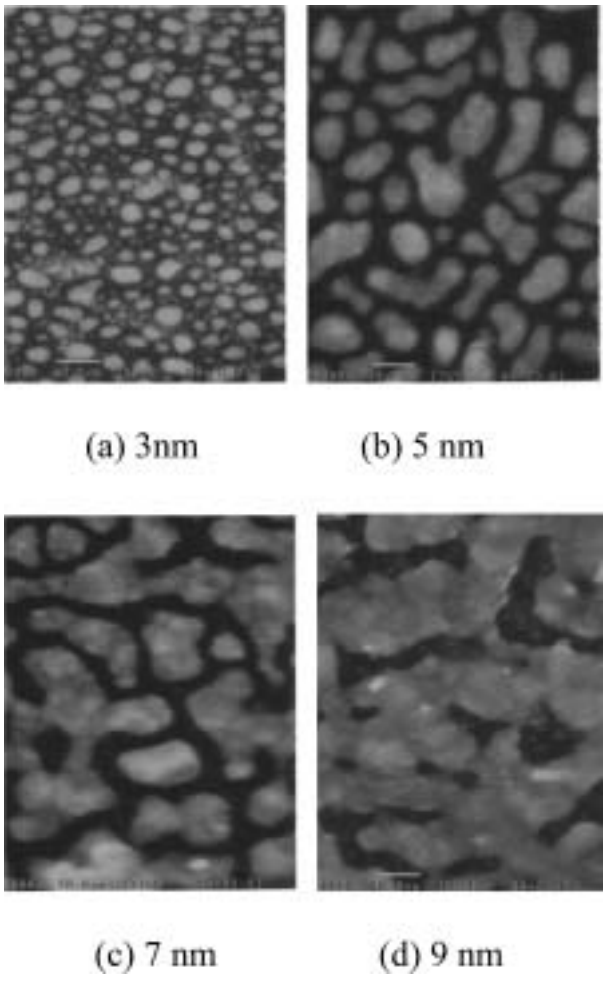

Fig. 5. FE-SEM (Filed Emission Scanning Electron Microprobe) photographs of Ag films on Si wafer with different films in thickness.

there exist vacancies or dislocations in the Ag clusters. As a result the net coordination number from the EXAFS is smaller than that expected from the real scale of clusters.

In the present EXAFS analysis, we have assumed that the mean free path (MFP) (or imaginary part of the self-energy) of the photoelectron does not depend on the size of Ag cluster. However, the MFP can possibly depend on the size of the system as pointed out by Zhao and Montano [9]. For more accurate analysis, such a higher order effect for X-ray absorption must be taken into account.

Finally we discuss the enhancement of the electric field at the surface as observed in the IR spectra. Figure 6 shows electromagnetic (EM) field intensities evaluated from the IR absorption coefficient for a $1025\,\mathrm{cm}^{-1}$ peak due to methanol molecules adsorbed on Ag film as a function of the film thickness [10]. The EM field intensity becomes the most intense at around 7 nm in film thickness. It is interesting to observe that the position of the peak in Fig. 6 coincides to the position where the N value levels off at 12 as shown in Fig. 4. In general, physical properties of Ag film or particle depend on the number of free electrons in Ag, which is considered to decrease if the coordination number of Ag atoms decreases. The electric field intensity changes as the number of free electrons: that is the smaller number of free electrons or the smaller coordination number of Ag, the weaker electric field intensities in the thickness range of film smaller than 7 nm. On the other hand, when Ag film covers the whole region of Si wafer, the interaction between electromagnetic wave and free

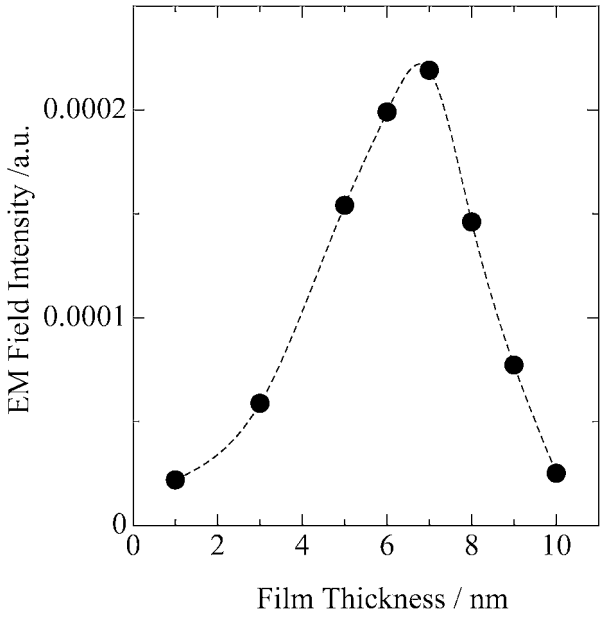

Fig. 6. Electromagnetic (EM) field intensity evaluated from the IR absorption coefficient for a $1025\,\mathrm{cm}^{-1}$ peak of methanol molecules adsorbed on Ag films as a function of the film thickness.

electron decreases. So the EM field intensity decreases again in the thickness range larger than 7 nm.

4. Conclusion

We have investigated the local structure of Ag nano-clusters deposited on silicon wafer surface. Total conversion electron yield method was applied to obtain Ag K-edge XAFS. It is found that these clusters take an *fcc* structure and have the same interatomic distances irrespective of the film thickness. The coordination number of the Ag atom, however, varies with the thickness of the film. Coordination number for the first nearest atoms as a function of the film thickness is compared with the theoretically expected values taking into account the surface effect. For thinner films, the observed coordination numbers are smaller than the expected values. We observed a good correlation between the dependencies of the coordination number and electromagnetic field intensity at the surface upon the film thickness. The local electric field at the surface must be related to the morphology of Ag nano-cluster particles on Si substrate.

Acknowledgement

The XAFS experiments were performed at SPring-8 under the approval of JASRI (Proposal No. 2001A0221-NX-np/BL01B1, No. 2001B0165-NX-np/BL01B1, and No. 2002B0544-NX-np/BL01B1).

References

1. *for example*, Matsuda, I., *et al*., Phys. Rev. B **63**, 125325 (2001).
2. Suzuki, Y., *et al*., Surf. Sci. **433–435**, 261 (1999).
3. Yanase, E., *et al*., Anal. Sicence **15**, 225 (1999).
4. Takahashi, M., *et al*., J. Synchrotron Rad. **6**, 222 (1999).
5. Uruga, T., Tanida, H. and Yasukawa, K., unpublished.
6. Sakane, H., *et al*., Jpn. J. Appl. Phys. **32**, 4641 (1993).
7. Zabinsky, S. I., Rehr, J. J., Ankudinov, A., Albers, R. C. and Eller, M. J., Phys. Rev. B **52**, 2995 (1995).
8. Crozier, E. D., Seary, A. J., McManus, M. K. and Jiang, D. T., J. Phys. IV France **7**, C2, 251 (1997).
9. Zhao, J. and Montano, P. A., Phys. Rev. B **40**, 3401 (1989).
10. Kita, K., Master Thesis, Department of Physics, (Hirosaki University 2001).

Physica Scripta. Vol. T115, 462–463, 2005

EXAFS Study of $PbPb_{1/3}Ta_{2/3}O_3$ Perovskite

V. G. Vlasenko[1], I. V. Pirog, I. P. Raevskii, O. N. Razumovskaya, S. I. Raevskaya and L. A. Shilkina

Institute of Physics, Rostov State University, Stachki Ave. 194, Rostov-on-Don, 344090, Russia

Received June 26, 2003; accepted December 4, 2003

PACS numbers: 61.10.Ht, 61.66.Fn

Abstract

We have synthesized a new lead-based oxide $Pb(Pb_{1/3}Ta_{2/3})O_3$ of the $PbB'_nB''_mO_3$ perovskite-type, where B′-sites are occupied by Pb^{2+} ions. The perovskite-type structure with cell parameter $a = 4.14$ Å was determined by powder X-ray diffraction. We have studied the XAFS of the Pb L_{III}-edge in $Pb(Pb_{1/3}Ta_{2/3})O_3$. Our analysis confirms the presence of Pb^{2+} = B′-site cations having a distorted octahedral oxygen coordination with a nearest-neighbour Pb-O bond length of $R = 2.45$ Å. The Pb-O distances for Pb^{2+} = A-site cations was found to be equal to $R = 2.89$ Å, that is typical of perovskites. The presence of superstructural lines on the X-ray diffraction pattern as well as non-diffused permittivity maximum strongly support the presence of 1 : 2 long-range ordering in $Pb(Pb_{1/3}Ta_{2/3})O_3$.

1. Introduction

Lead-based ternary 1 : 2 perovskites of the $A(B'_{1/3}Ta_{2/3})O_3$ type are technologically important microwave ceramics for use as a dielectric resonators because these compounds have a high dielectric constant, low losses (high quality Q values) and a small temperature coefficient of resonant frequency. When disordered $A(B'_{1/3}Ta_{2/3})O_3$ (B′ and Ta ions arranged randomly on the B-site) has a cubic perovskite structure in which corner shared, BO_6 octahedra describe a cubooctahedral A-site interstice. Mg^{2+}, Ni^{2+}, Co^{2+}, Zn^{2+} and other ions with relatively small ionic radii can occupy the B′-site in the perovskite structure. The ordered compound in which B′ and Ta ions occupy alternate (111)-planes of the pseudocubic structure in a 1 : 2 ratio, adopts a trigonal symmetry [1–3]. We have synthesized a new lead-based oxide $Pb(Pb_{1/3}Ta_{2/3})O_3$, where B′-sites are occupied by Pb^{2+} ions with considerably larger ionic radius.

In this paper, crystal structure and local surroundings of the Pb atoms in novel $Pb(Pb_{1/3}Ta_{2/3})O_3$ perovskite by X-ray powder diffraction and EXAFS are investigated.

2. Experimental procedure

Polycrystalline sample of $PbPb_{1/3}Ta_{2/3}O_3$ was synthesized by solid state reaction. High purity powders of $PbCO_3$ and Ta_2O_5 were used. Sample was characterized by X-ray powder diffraction. X-ray powder diffraction data were measured at room temperature with a DRON-3M diffractometer using Cu $K\alpha_1$ radiation at 33 kV and 25 mA. The diffraction pattern was scanned in the 2Θ range of 10°–90° with a counting time 4 s step^{-1}. The XRD pattern was analyzed by the Rietveld method, using the PCW-2,3 refinement program [4]. The initial unit cell parameters and atomic coordinates for the Rietveld refinement were calculated. Rietveld refinement was performed using a pseudo-Voigt function to describe the reflection profile. The seven-order polynomial background, zero point shift, scale factor, unit cell parameters and peak shape parameters were varied in the fitting procedure. The overall thermal parameters and atomic coordinates were not refined.

The Pb L_3-edge XAFS spectra were measured in transmission at the EXAFS-spectrometer of Synchrotron Radiation Siberian center with the storage ring, operating at beam energy of 2 GeV and current of 80 mA. The X-ray beam was monochromatized using a Si (111) double crystal in the energy range of 12500–14100 eV (the Pb L_3-edge energy is 13040.6 eV). The intensities of both incident and transmitted X-ray beams were measured with ionization chambers filled with Ar gas. Samples were prepared as a sandwich between two layers of Maylar film.

Data analysis has been performed using UWXAFS code [5]. XAFS data analysis was carried out using standard procedure. The EXAFS functions $\chi(k)$ were obtained from the X-ray absorption spectra by subtracting a Victoreen curve background removal, normalization on the height of the edge and reduction of the absorption data $\mu(E)$ to the EXAFS functions $\chi(k)$, where k is the photoelectron wavevector. The threshold energy E_0 was defined as the maximum of the first derivative of the absorption edge.

Fourier transform of the k^2-weighted spectra has been performed over the range $3.0 < k < 13$ Å^{-1}. The fitting to the experimental spectra has been performed using theoretical spectra simulated by means of FEFF7 [6]. The initial parameters refined in fit were obtained from crystallographic data of $BaPb_{1/3}Ta_{2/3}O_3$ [7].

3. Results and discussion

Figure 1 shows the powder X-ray diffraction pattern and refinement of $PbPb_{1/3}Ta_{2/3}O_3$. XRD analysis using the Rietveld method was carried out and it was found that this lead-based

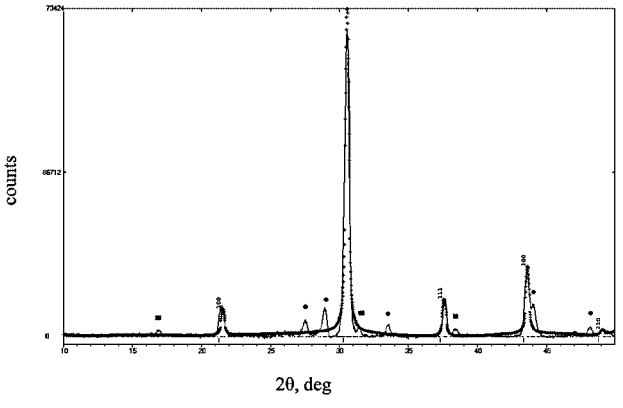

Fig. 1. Powder X-ray diffraction pattern of $PbPb_{1/3}Ta_{2/3}O_3$. The experimental data are represented by solid line, while the calculated pattern is shown by crosses. Peaks marked by ■ correspond to the superstructure Bragg lines; peaks marked by ● correspond to the $Pb_3Nb_4O_{13}$ pyrochlore phase.

[1] vlasenko@ip.rsu.ru

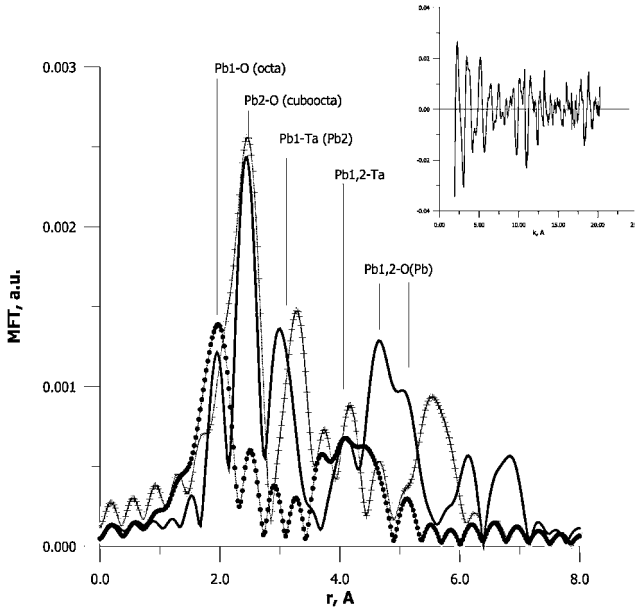

Fig. 2. Fourier Transforms for $\chi(k)$ Pb L_{III} EXAFS spectra of $PbPb_{1/3}Ta_{2/3}O_3$ (solid line), the models $PbTaO_3$ (open circles) and $PbPb_{1/3}Ta_{2/3}O_3$ (filled circles). The inset shows the experimental $\chi(k)$ Pb L_{III} EXAFS.

oxide $Pb(Pb_{1/3}Ta_{2/3})O_3$ has a cubic perovskite structure with the Pm-3 m (221) space group. The lattice parameter was found to be $a = 4.14$ Å. In the XRD pattern some weak extra peaks that do not correspond to the $Pb(Pb_{1/3}Ta_{2/3})O_3$ are observed. These reflections can be indexed to lead tantalate compound with the pyrochlore structure similar to $Pb_3Nb_4O_{13}$ [8].

According to Fig. 1, a weak superstructure reflections, that originate from the 1 : 2 order are visible in XRD pattern of the $Pb(Pb_{1/3}Ta_{2/3})O_3$. This is likely to be due to the fact that the Pb^{2+} and Ta^{5+} cations are distributed on individual (111) planes of the perovskite subcell with alternating (Pb, Ta, Ta) layers. This assumption is strongly supported by the non-diffused permittivity maximum observed at about 220 °C.

Fourier transform of k^2-weighted $\chi(k)$ for the $PbPb_{1/3}Ta_{2/3}O_3$ is presented at Fig. 2. The inset illustrates the experimental PbL_{III}-edge EXAFS. The Fourier transforms of models calculated for $PbYb_{1/2}Ta_{1/2}O_3$ [9] (where Yb was replaced by Pb) and $BaPb_{1/3}Ta_{2/3}O_3$ [7] (where Ba was replaced by Pb) are shown together with experimental Fourier transform. As seen, the Fourier transform of the experimental spectrum exhibits two well-resolved peaks at about $r = 1.98$ Å and $r = 2.52$ Å corresponding to the first and the second coordination shells around the Pb^{2+} ions. According to our models the first peak originates from 6 oxygen atoms in octahedral positions, while the second one corresponds to 12 oxygen atoms in cubooctahedral positions. The fitting obtained interatomic distances are $R = 2.45$ Å and $R = 2.89$ Å for Pb^{I}-O and Pb^{II}-O bonds correspondingly. Thus, the results obtained clear show that the Pb^{2+} ions occupy 1/3 octahedral positions in the $Pb(Pb_{1/3}Ta_{2/3})O_3$ perovskite.

4. Conclusion

A new lead-based oxide $Pb(Pb_{1/3}Ta_{2/3})O_3$ has a perovskite-type structure with Pm-3m space group and a cell parameter $a = 4.14$ Å. Some evidence of the 1 : 2 long-range ordering for the perovskite cell is found. The Pb^{2+} ions occupy 1/3 octahedral positions in the $Pb(Pb_{1/3}Ta_{2/3})O_3$ perovskite.

Acknowledgments

This work was supported by RFBR grants 01-03-33119 and 02-02-17781.

References

1. Quzi, I., Reaney, I. M. and Lee, W. E., J. Eur. Cer. Soc. **21**, 2613 (2001).
2. Kolodiazhnyi, T. V., Petric, A., Johari, G. P. and Belous, A. G., J. Eur. Cer. Soc. **22**, 2013 (2002).
3. Hu, X., Chen, X. M. and Wu, Y. J., Mat. Lett. **54**, 279 (2002).
4. Kraus, W. and Nolze, G., "Powder Cell for Windows", version 2.3, Federal Institute for Materials Research and Testing, (Berlin, Germany 1999).
5. Stern, E. A. *et al*., Physica B **208**/**209**, 117 (1995).
6. Zabinski, S. I., Rehr, J. J., Ankudinov, A. and Alber, R. C., Phys. Rev. **B52**, 2995 (1995).
7. Galasso, F., Pule J. Inorgan. Chem. **2**, 482 (1963).
8. Beech, F. *et al*., J. Solid State Chem. **77**, 322 (1988).
9. Bokov, V. A. and Mylnikova, I. E., Sov. Phys. Solid State **2**, 2728 (1960).

Physica Scripta. Vol. T115, 464–466, 2005

Changes in the Local Structure of Nanocrystalline Electrochromic Films of Hydrated Nickel Vanadium Oxide upon Ozone-Induced Coloration

E. Avendaño[1,*], A. Kuzmin[2], J. Purans[2], A. Azens[1], G. A. Niklasson[1] and C. G. Granqvist[1]

[1]Department of Materials Science, The Ångström Laboratory, Uppsala University, P. O. Box 534, SE-751 21 Uppsala, Sweden
[2]Institute of Solid State Physics, University of Latvia, Kengaraga street 8, LV-1063 Riga, Latvia

Received Month XX, 2004; accepted Month XX, 2004

PACS numbers: 61.10.Ht, 78.70.Dm, 68.55.−a, 78.66.−w, 78.20.Jq, 78.40.−q, 81.15.Cd

Abstract

Hydrated thin films of nickel vanadium oxide ($Ni_{1-x}V_xO_y$), made by reactive DC magnetron sputtering, were studied by X-ray absorption spectroscopy at the Ni and V K-edges using synchrotron radiation. The XANES signals were analysed within the full-multiple-scattering formalism, whereas EXAFS data were modelled within the multi-shell multiple-scattering approach. We found that transparent films exhibit a nanocrystalline NiO-type structure with homogeneous distribution of V ions substituting Ni ions. Exposure of the films to ozone resulted in dark brown coloration associated with an appearance of Ni^{3+} ions and accompanied by a modification of the local electronic and atomic structures of the V and Ni ions. The largest changes occurred in the environment of the V ions, which presumably change their valence state from V^{4+} to V^{5+} and displace into off-centre positions by ∼0.4 Å.

1. Introduction

Electrochromic (EC) materials are able to reversibly alter their optical properties upon charge insertion-extraction caused by the application of an external voltage [1]. These materials can be used for a variety of applications, such as in architectural "smart widows capable of changing their transmittance thereby providing improved visual and thermal comfort for the occupants in conjunction with energy efficiency for the building. An EC device is characterised by a number of features, such as optical modulation, physical size, durability, etc.

Thin films of hydrated nickel oxide and nickel based oxides are of much interest. One reason for this is their ability for coloration upon ozone exposure [2], which allows charge balancing in order to make the films ready for facile device assembly consistent with large-scale production. Recent reviews of EC devices are found in [3].

The present paper presents X-ray absorption spectroscopy data of $Ni_{1-x}V_xO_y$ thin films at the Ni and V K-edges. The emphasis is on changes of the local atomic and electronic structures of Ni and V ions in transparent and ozone-coloured states of the films.

2. Experimental details and data analysis

Transparent hydrated $Ni_{1-x}V_xO_y$ thin films were deposited onto quartz and Kapton foil substrates by reactive DC magnetron sputtering from a non-magnetic $Ni_{93}V_7$ (wt %) target with a diameter of 5 cm. A base pressure of $\sim 4 \cdot 10^{-5}$ mTorr was reached in the deposition unit, and sputtering was carried in a mixture of $Ar/O_2/H_2$ (99.998% pure) at 35 mTorr and 200 W. The gas flows ratios were 50/2/4. Coloured films were produced by exposure during 6 minutes to ozone using a UV lamp [2].

Optical measurements were carried out on a Perkin-Elmer double-beam spectrophotometer operating at 300 to 2500 nm in wavelength.

X-ray absorption spectra of transparent and coloured thin films, and of reference compounds (crystalline *c*-NiO and *c*-V_2O_5), were recorded at the Ni and V K-edges using synchrotron radiation from the LURE DCI storage ring. A standard transmission setup at the D21 (XAS-2) beam-line, with a Si(311) double-crystal monochromator and two ion chambers containing N_2 gas, was used. All experiments were done at room temperature with an energy resolution of 1 to 2 eV.

The X-ray absorption spectra were analysed, following standard procedures, by the EDA software package [4, 5]. The EXAFS part of the spectra was singled out by the Fourier filtering procedure and best-fitted within the multi-shell Gaussian/cumulant models using the theoretical amplitudes and phase shift functions, calculated by the FEFF8 code [6], for the two reference compounds. The E_0 position, defining the zero-photoelectron wave-number ($k = 0$), was set to provide the best match of the experimental and calculated EXAFS signals for the reference compounds. The XANES signals were analysed qualitatively by comparison of experimental spectra with the ones calculated by the FEFF8 code [6] within the full-multiple-scattering (FMS) approach. In all calculations, the complex Hedin-Lundqvist exchange-correlation potential [7] was used to account for the inelastic losses of the photoelectron, and the cluster potential was calculated self-consistently.

3. Results and discussion

Figure 1 shows the optical response of a ∼650-nm-thick $Ni_{1-x}V_xO_y$ thin film upon ozone exposure. The spectral absorptance $A(\lambda)$ was calculated from measured transmittance $T(\lambda)$ and reflectance $R(\lambda)$ as $A(\lambda) = 1 - T(\lambda) - R(\lambda)$. A huge modulation of the optical properties is observed within the solar range; it corresponds to a change of the visible colour from transparent to dark brown.

X-ray absorption spectra, measured at the Ni and V K-edges, allowed us to follow the modifications in the local electronic and atomic structures as the films were coloured in ozone.

Experimental XANES signals are shown in Fig. 2(a). At the Ni K-edge, a difference between the *c*-NiO reference and a $Ni_{1-x}V_xO_y$ film is present in the pre-edge peak intensity and in the fine structure located above the edge. The pre-edge peak is associated with a transition from the 1s(Ni) state to the 3d(Ni) states mixed with the 2p(O) states. The pre-edge intensity is smaller in the films than in *c*-NiO, as was also observed previously in pure nanocrystalline NiO films [8]. This effect was interpreted

*Esteban.Avendano@angstrom.uu.se

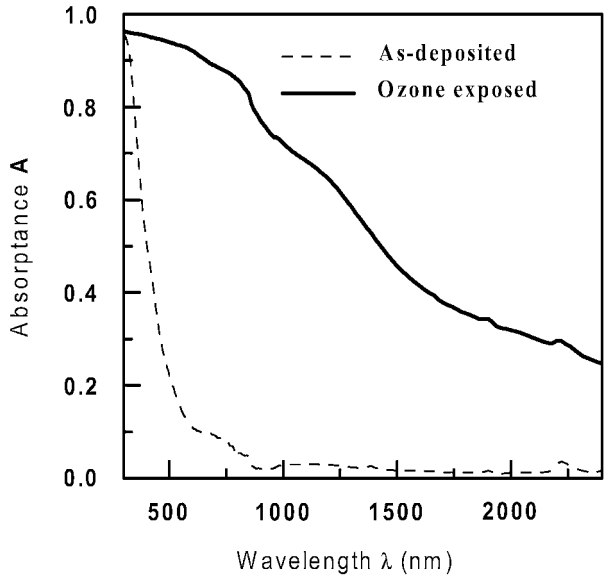

Fig. 1. Spectral absorptance within the solar range of $Ni_{1-x}V_xO_y$ thin films in the as-deposited (transparent) and ozone-exposed (coloured) states.

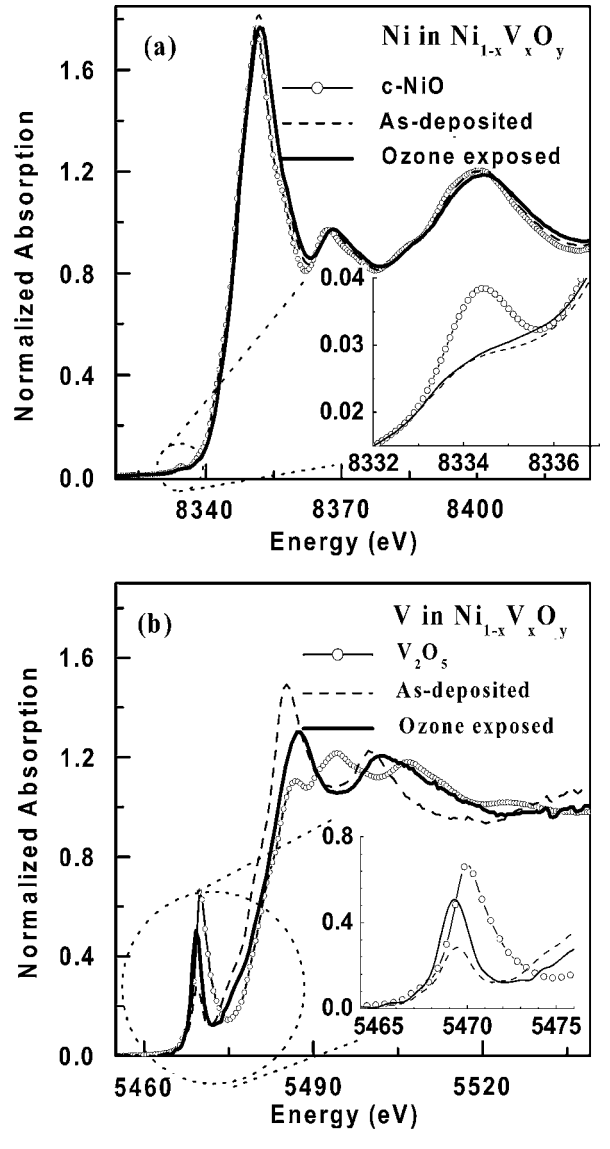

Fig. 2. Experimental XANES signals for the Ni (a) and V (b) K-edges in as-deposited (transparent) and ozone-exposed (coloured) $Ni_{1-x}V_xO_y$ thin films. XANES data for the reference compounds *c*-NiO and *c*-V_2O_5 are shown in parts (a) and (b), respectively.

within the Zaanen-Sawatzky-Allen model [9] as being due to an increase of the oxygen-nickel charge transfer energy accompanied by a reduction of the amount of ground state configurations with holes in the 2p(O) states. Thus a decrease of the pre-edge in the films can be associated with the fact that the Ni-O bonding becomes less covalent. It is noted that no significant change of the pre-edge peak occurs upon ozone exposure.

The V K-edge in the thin films is compared with data for *c*-V_2O_5 in Fig. 2(b). The pre-edge peak is related to the transition $1s(V) \rightarrow 3d(V) + 2p(O)$. A comparison of two reference compounds, i.e. *c*-NiO and *c*-V_2O_5, shows that the intensity of the pre-edge peak is much higher in vanadium oxide because the 3d(V) states are more strongly mixed with 2p(O) states due to shorter V-O bonds and lower local symmetry at the V sites. The pre-edge intensity is relatively small in a transparent film but increases strongly upon coloration. Such behaviour can be associated with the change of valence states from V^{4+} to V^{5+} [10]. Our preliminary FMS calculations suggest that this process is accompanied by an increase of the local distortion, responsible for a modification of fine structure located above the V edge.

Figure 3 shows Fourier transforms (FTs) of the EXAFS signals for the Ni and V K-edges. A comparison of the FT signals for the films and for *c*-NiO allows to conclude that the films have a nanocrystalline structure; specifically, the peak amplitudes decrease more for the outer shell due to the

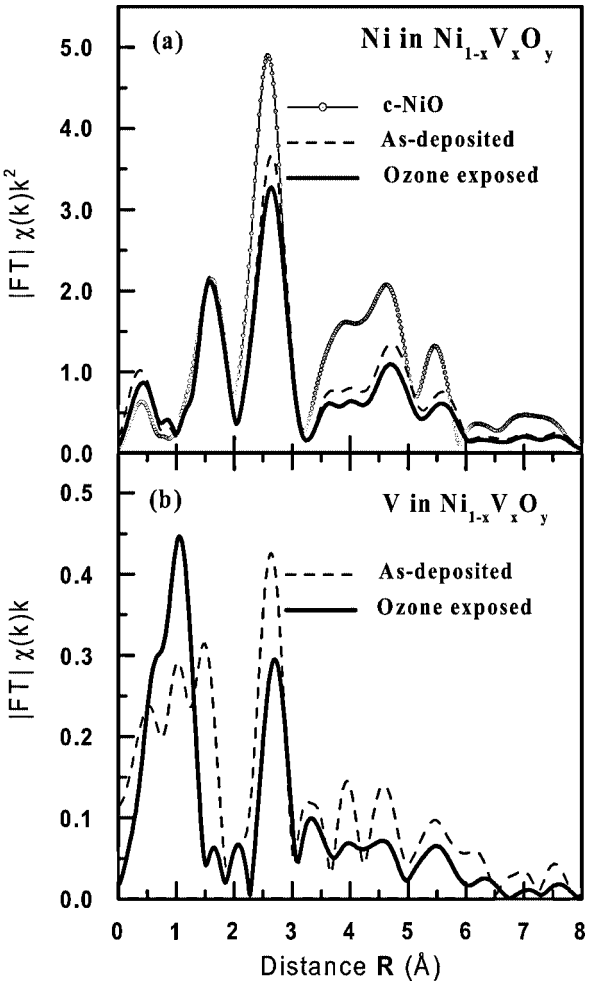

Fig. 3. Fourier transform (FT) moduli of EXAFS signals at the Ni (a) and V (b) K-edges in *c*-NiO (part a) and $Ni_{1-x}V_xO_y$ thin films in the as-deposited (transparent) and ozone-exposed (coloured) states.

size effect [8, 11]. The first peak at 1–1.5 Å corresponds to the first coordination shell of Ni/V ions, composed of six oxygen atoms. The second peak at about 2.5–2.7 Å is due to three contributions: (*i*) nickel (Ni_2) atoms in the second shell; (*ii*) oxygen (O_3) atoms in the third shell; (*iii*) two double-scattering signals, generated within the 90°-triangular paths as $M_0 \rightarrow O_1 \rightarrow O_1 \rightarrow M_0$ and $M_0 \rightarrow O_1 \rightarrow Ni_2 \rightarrow M_0$ where M_0 is the Ni_0 or V_0 central/absorbing atom. Our multi-shell fitting procedure of the Ni K-edge EXAFS signals suggests that, on average, the film structure resembles that of *c*-NiO. However, some relaxation of the first coordination shell of the Ni ions, comprising six oxygen atoms, occurs in the films and leads to a decrease of the mean Ni-O distance by ∼0.02 to 0.04 Å. At the same time, the second shell Ni-Ni distance increases by ∼0.01 to 0.02 Å. The difference between the two films is mainly related to some increase of the disorder in the coloured film, which is probed by the Debye-Waller factor and resulted in a relative decrease of the peaks for the outer shells in the FT. The nanocrystallite size was estimated roughly by an approach proposed before [8]; it is based on the model of Ref. [11] and gave a nanocrystal diameter of ∼10 Å.

The analysis of the V K-edge EXAFS signals suggests that V ions substitute Ni ions in the NiO-type structure and are distributed without any evidence for clustering. This conclusion is derived from the comparison of the experimental V K-edge EXAFS signals with the theoretical ones, calculated by the FEFF8 code for the V ion(s) placed at the Ni ions sites in NiO structure. Our best-fit modelling suggests no presence of vanadium ions in the second coordination shell of vanadium, but indicates clearly the vanadium first shell modification upon coloration. In transparent films, V ions are located at the centre of oxygen octahedra, whereas they shift to off-centre positions upon coloration. The displacement is ∼0.4 Å in the [100] direction towards the nearest oxygen atom. Thus, V ions introduce a significant degree of disorder into the NiO-type structure of coloured thin films.

4. Conclusions

X-ray absorption spectroscopy at the Ni and V K-edges allowed us to reconstruct the local electronic and atomic structures of nickel vanadium oxide thin films in transparent and coloured states. We found that, while the main contribution to the optical properties of the films ensues from the Ni sublattice, the V ions are strongly affected by an ozone treatment.

Acknowledgements

We thank the LURE DCI D21 beam-line staff (Prof. S. Bénazeth, Dr. I. Nicolis and Dr. E. Curis) for their technical collaboration. The Latvian Government (grants 1.0811 and 1.0821), the National Swedish Energy Authority and the Swedish Foundation for Strategic Environmental Research supported this work. E.A. acknowledges a scholarship from the University of Costa Rica.

References

1. Granqvist, C. G., "Handbook of Inorganic Electrochromic Materials" (Elsevier, Amsterdam, 1995).
2. Azens, A., Kullman, L. and Granqvist, C. G., Solar Energy Mater. Solar Cells **76**, 147 (2003).
3. Granqvist, C. G., Solar Energy Mater. Solar Cells **60**, 201 (2000); Granqvist, C. G., Avendaño, E. and Azens, A., Thin Solid Films, to be published.
4. Kuzmin, A., Physica B **208**/**209**, 175 (1995).
5. Aksenov, V. L., Kuzmin, A. Y., Purans, J. and Tyutyunnikov, S. I., Phys. Part. Nucl. **32**, 675 (2001).
6. Ankudinov, A. L., Ravel, B., Rehr, J. J. and Conradson, S. D., Phys. Rev. B **58**, 7565 (1998).
7. Rehr, J. J., Mustre de Leon, J., Zabinsky, S. I. and Albers, R. C., J. Am. Chem. Soc. **113**, 5135 (1991); Mustre de Leon, J., Rehr, J. J., Zabinsky, S. I. and Albers, R. C., Phys. Rev. B **44**, 4146 (1991).
8. Kuzmin, A., Purans, J. and Rodionov, A., J. Phys.: Cond. Matter **9**, 6979 (1997).
9. Zaanen, J., Sawatzky, G. A. and Allen, J. W., Phys. Rev. Lett. **55**, 418 (1985).
10. Wong, J., Lytle, F. W., Messmer, R. P. and Maylotte, D. H., Phys. Rev. B **30**, 5596 (1984).
11. Löffler, J. and Weissmüller, J., Phys. Rev. B **52**, 7076 (1995).

Physica Scripta. Vol. T115, 467–470, 2005

Application of a Metal Ion-Implantation for the Preparation of Visible-Light Sensitive Zeolite Photocatalyst: V Ion-Implanted Ti-Containing HMS Mesoporous Molecular Sieves

Hiromi Yamashita*, Yukiya Kanazawa, Keiko Kida and Masakazu Anpo

Department of Applied Chemistry, Osaka Prefecture University Gakuencho 1-1, Sakai, Osaka 599-8531, Japan

Received June 26, 2003; accepted in revised form November 4, 2003

Abstract

Visible light sensitive zeolite photocatalysts have been prepared by metal ion-implantation of Ti-containing mesoporous molecular sieves with V ions (V/Ti-HMS) which can operate under visible light irradiation ($\lambda > 450$ nm). The metal ion-implantation with V ions was effective to shift the absorption band of Ti-containing molecular sieves to longer wavelengths. This V/Ti-HMS performed the photocatalytic reactions for the NO decomposition under visible light irradiation, while no reaction proceeded on the original Ti-HMS. XAFS analysis indicated that implanted V-oxide moieties existed having tetrahedral coordination and interacted with the tetrahedrally coordinated titanium oxide moieties. These XAFS results as well as the analysis with UV-VIS absorption measurements indicate that the charge transfer excited state of the tetrahedrally coordinated titanium oxide moieties interacting with the tetrahedrally coordinated vanadium oxide moieties plays a significant role in the photocatalytic reaction under visible light irradiation.

1. Introduction

Zeolites involving transition metal ions within the zeolite framework have opened new possibilities in many research areas not only for catalysis but also for various photochemical processes [1–6]. Especially the titanium oxide species prepared within the zeolite framework have revealed a unique local structure as well as a high selectivity in the oxidation of organic substances with hydrogen peroxide [2, 3]. Although TiO_2 has octahedral coordination, titanium oxide having tetrahedral coordination can be prepared in silica matrix such as zeolites and mesoporous molecular sieves. Ti-zeolites with tetrahedrally coordinated titanium oxide moieties showing unique reactivities for various photocatalytic reactions under UV-irradiation (220–260 nm) [5–10] are good candidates as efficient and selective photocatalysts. Although these tetrahedrally coordinated Ti-oxide moieties can exhibit the unique photocatalytic reactivity, they can only adsorb and utilize UV light at around 220–260 nm to form the charge transfer excited state as active species. It is also vital to develop Ti-zeolites which can operate efficiently under visible light irradiation. Recently it has been successfully made the application of metal ion-implantation using accelerated metal ions to design unique TiO_2 photocatalyst realizing a breakthrough in the development of the efficient photocatalytic system and the utilization of solar light energy [11–13]. Metal ions are the charged atoms whose kinetic energies can be controlled by acceleration of the metal ions under a controlled electronic field. The application of metal ion-implantation [11] to modify the Ti-zeolites is very interesting. In this study, it has been found that metal ion-implantation with V ions has been applied on Ti-containing mesoporous molecular sieves to design photocatalysts which can operate under visible light irradiation.

*Present address: Department of Materials Science and Processing Graduate School of Engineering Osaka University.
E-mail: yamashita@mat.eng.osaka-u.ac.jp

2. Experimental

2.1. *Catalysts*

Ti-containing mesoporous molecular sieves (Ti-HMS) (Si/Ti = 50) were synthesized using tetraethylorthosilicate and titanium-isopropoxide as the starting materials and dodecylamine as a template [14–16]. The gelation of the material mixtures were carried out at room temperature for 24 h. The product was collected by centrifugal filtration, washed with distilled water, and dried in air at 353 K. To remove the occluded organic molecules, the samples were heated under a flow of dry air at 773 K for 5 h. The surface area of Ti-HMS is about 700 m^2/g.

This Ti-HMS photocatalyst (100 mg) was pressed into a wafer of 13 mm diameter and 1 mm thickness. V ions implanted Ti-HMS (V/Ti-HMS) was prepared by the metal ion-implantation method. The implantation of V^+ ions to Ti-HMS was carried out using an ion-implanter consisting of a metal ion source, mass analyzer, and high voltage ion accelerator (150 keV) [11–13]. In this method, the metal ions are accelerated in the electronic field and injected to the sample target (Ti-HMS wafer) as an ion beam. The ion-implanted samples were heated under a flow of dry air at 773 K for 5 h.

2.2. *Photocatalytic reaction*

Prior to spectroscopic measurements and photocatalytic reactions, the powdered catalysts were degassed at 723 K for 2 h, heated in O_2 at the same temperature for 2 h and then finally evacuated at 473 K for 2 h to 10^{-6} Torr. The photocatalytic reactions of NO molecules were carried out with the catalysts (100 mg of the catalyst involving zeolite) in a quartz cell with a flat bottom (90 ml) connected to a conventional vacuum system (10^{-6} Torr range) [7]. The light irradiation of the catalysts in the presence of NO (17 μmol) was carried out under visible light ($\lambda > 390$, 420 nm) using a 75 W high-pressure Hg lamp at 275 K and color filters. The reaction products were analyzed by gas chromatography. The photocatalytic oxidation of propene (16 μmol) with O_2 (32 μmol) was carried out with the catalysts (50 mg) under UV light irradiation ($\lambda > 250$ nm, $\lambda > 340$ nm) at 295 K. The products collected in the gas phase and after heating of catalysts at 573 K were analyzed by gas chromatography.

2.3. *Characterization*

The diffuse reflectance absorption spectra were recorded with a Shimadzu UV-2200A spectrometer at 295 K. The XAFS spectra (XANES and EXAFS) were measured at the BL-9A facility [17] of the Photon Factory at the National Laboratory for High-Energy Physics, Tsukuba. A Si(111) double crystal was used to monochromatize X-rays from the 2.5 GeV electron storage ring. The Ti K-edge absorption spectra were recorded

in the fluorescence mode at 295 K. In a typical experiment, 50 mg of the sample pressed in to a disc was loaded into the *in situ* cell having Kapton windows. The normalized spectra were obtained by a procedure described in previous literature [18] and Fourier transformation was performed on k^3-weighted EXAFS oscillations in the range of 3–10 $Å^{-1}$. The preedge peaks in the XANES regions were normalized for atomic absorption, based on the average absorption coefficient of the spectral region from 5050–5200 eV [19]. Curve-fitting of the EXAFS data was carried out by employing an iterative nonlinear least-squares method and the empirical backscattering parameter sets extracted from the shell features of reference compounds.

3. Results and discussion

The results of the XRD analysis indicate that Ti-HMS has the structure of HMS mesoporous molecular sieves having pores larger than 20 Å and the Ti-oxide moieties are highly dispersed in the framework, while no other phases are formed [14, 15].

Figure 1 shows Ti K-edge XANES spectra of the Ti-HMS. The XANES spectra of the Ti containing compounds at the Ti K-edge show several well-defined preedge peaks that are related to the local structures surrounding the Ti atom. These relative intensities of the preedge peaks provide useful information on the coordination number surrounding the Ti atom [4, 19]. As shown in Fig. 1, Ti-HMS exhibits an intense single preedge peak, indicating that the titanium oxide species in the Ti-HMS has a tetrahedral coordination. Figure 1 also shows Fourier transforms of Ti K-edge EXAFS of Ti-HMS. The data are given without corrections for phase shifts. Ti-HMS exhibits a strong peak at around 1.6 Å (uncorrected for the phase shift) which can be assigned to the neighboring oxygen atoms (a Ti-O bond), indicating the presence of a highly dispersed titanium oxide species on Ti-HMS. From the results obtained by the curve-fitting analysis of the EXAFS spectra, it was found that the Ti-HMS consist of tetrahedrally coordinated titanium ions with an atomic distance of 1.83 Å.

The metal ion-implantation with V ions on Ti-HMS was carried out at 150 eV and the implanted sample was calcined in O_2 at 723 K after ion-implantation. Figure 2 shows diffuse reflectance UV-Vis absorption spectra of the original Ti-HMS and the V/Ti-HMS with various amounts of implanted V ions. Ti-HMS exhibited absorption bands in the wavelength region of 220–260 nm, shifting into the shorter wavelength region as compared to the bulk TiO_2. This absorption band is attributed to the LMCT (ligand-to-metal charge transfer) band of the highly dispersed

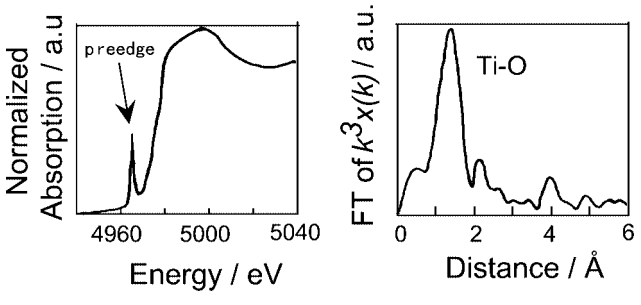

Fig. 1. Ti K-edge XANES spectrum (left) and Fourier transform of EXAFS (right) of Ti-HMS.

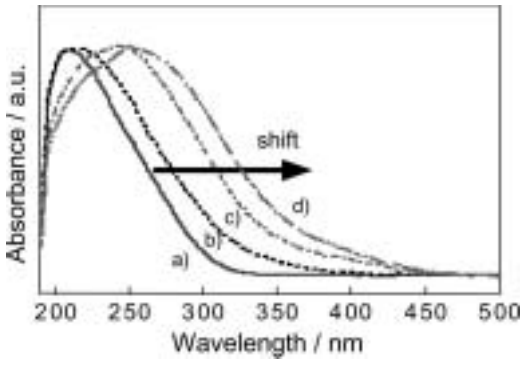

Fig. 2. Diffuse reflectance UV-Vis absorption spectra of the Ti-HMS (a) and V/Ti-HMS (b–d) with various amounts of V ion-implanted. Implanted V ions: (b) 0.66, (c) 1.3, (d) 2.0 (μmol/g-cat).

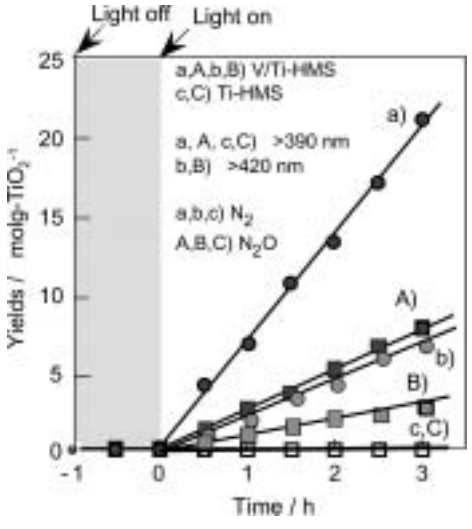

Fig. 3. Reaction time profiles of the photocatalytic decomposition of NO on Ti-HMS and V/Ti-HMS (V: 2.0 μmol/g-cat) under visible light irradiation ($\lambda > 390$ nm, 420 nm) .

titanium oxide species having a tetrahedral coordination [8, 9]. As shown in Fig. 2, the absorption band of V/Ti-HMS is found to shift to the longer wavelength region, the extent depending on the amount of V ions implanted. These V/Ti-HMS can absorb light at the visible light region (~450 nm). These results indicate that the metal ion-implantation is effective to modify the Ti-HMS to absorb the visible light and exhibit the photocatalytic reaction under visible light irradiation.

These V/Ti-HMS showed the photocatalytic reactivity under visible light irradiation ($\lambda > 420$ nm). As shown in Figure 3, visible light irradiation of these V/Ti-HMS in the presence of NO led the selective decomposition of NO into N_2 and O_2 and the yield of the photo-formed N_2 increased linearly with the irradiation time. On the other hand, the NO decomposition did not proceed on the un-implanted original Ti-HMS under visible light irradiation. These results clearly show that V ions implanted into the framework structures of Ti-containing zeolite does work to modify the electronic properties of the tetrahedrally coordinated titanium oxide moieties.

Table I shows the results of the photocatalytic oxidation of propene with O_2 under irradiation of light with various wavelengths ($\lambda > 250$ nm, $\lambda > 340$ nm). Under light irradiation with longer wavelengths ($\lambda > 340$ nm), the photo-epoxidation of propene with O_2 to form propene oxide proceeded on the

Table I. *The products in the photocatalytic oxidtion of propene with O_2 on V/Ti-HMS and Ti-HMS under light irradiation with various wavelengths.*

Catalysts	Light /nm	Conv. /%	PO-yield /%	Selectivity / %			
				PO	HO	HC	COx
V/Ti-HMS	>340	0.8	0.2	26	66	8	0
Ti-HMS	>340	0	0	0	0	0	0
Ti-HMS	>250	7	1.5	22	57	11	10

PO: propylene oxide, HO: oxidized hydrocarbon (acetone etc.).
HC: hydrocarbon, COx: CO_2 and CO.

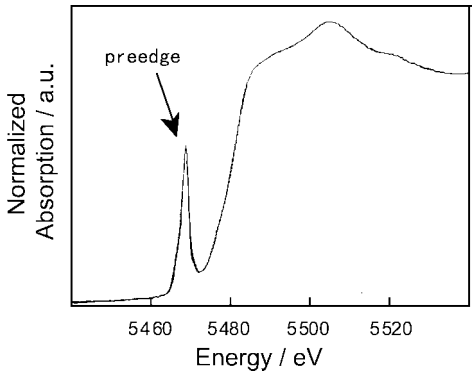

Fig. 4. V K-edge XANES spectrum of V/Ti-HMS (V: 1.3 μmol/g-cat).

ion-implanted V/-HMS, while no reaction occurred on the original un-implanted Ti-HMS.

Figure 4 shows V K-edge XANES spectra of the V/Ti-HMS. V/Ti-HMS exhibits an intense single preedge peak. The characteristic feature of both XANES spectra is the appearance of a preedge peak due to the so-called 1s-3d transition which is mainly caused by the mixing of the 2p orbitals of the oxygen molecules with the 3dp orbitals of the vanadium atoms. This p-d mixing suggests the presence of a terminal monoxo-vanadyl group (V = O). It was also found that the shape of the XANES spectrum of V/Ti-HMS is quite similar to that of the VO(O-i-$C_3H_7)_3$ complex, indicating that V/Ti-HMS consists of vanadium oxide moieties having a tetrahedral coordination in C_{3v} symmetry [20]. Figure 5 shows Fourier transforms of V K-edge EXAFS of V/Ti-HMS and V_2O_5 as reference and the data are given without corrections for phase shifts. V/Ti-HMS exhibit a peak at around 1.4 Å (uncorrected for the phase shift) which can be assigned to the neighboring oxygen atoms (V-O bonds), indicating the that vanadium ions are highly dispersed in the catalyst. On the other hand, the reference V_2O_5 exhibits two intense peaks at around 1.5 and 2.8 Å ascribed to the V-O bond and V-O-V linkage, respectively. For V/Ti-HMS, it was found that the second peak shifts to a shorter distance and its intensity is much lower than that of the reference V_2O_5. These results indicate that the next-neighbors of the V environment is not the same V-based ones but is the Ti-based tetrahedra forming V-O-Ti linkages.

The analysis using XAFS measurements indicate that the implanted V ions are highly dispersed in the tetrahedrally coordination and exist in the next neighbor position of tetrahedrally coordinated titanium oxide moieties having the formation of the Ti-O-V linkage which leads to the modification of the electronic properties of tetrahedrally coordinated titanium oxide moieties. This direct interaction between the implanted V ions and the tetrahedrally coordinated titanium oxide moieties can realize the absorption of visible light and leads to selective photocatalytic NO decomposition into N_2 and O_2 even under visible light irradiation. These results indicate that the metal ion implantation is also useful to create efficient and selective Ti-containing zeolite catalysts which can operate even under visible light irradiation.

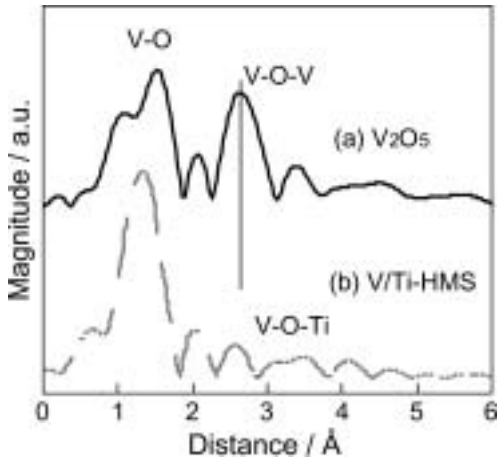

Fig. 5. Fourier transforms of V K-edge EXAFS of (a) V_2O_5 (reference) and (b) V/Ti-HMS (V: 1.3 μmol/g-cat).

4. Conclusions

The metal ion-implantation with V ions was effective to shift the absorption band of Ti-containing mesoporous molecular sieves to longer wavelengths. The ion-implanted V/Ti-HMS were found to exhibit photocatalytic decomposition of NO under visible light irradiation with longer wavelength ($\lambda >$ 450 nm). The direct interaction between the implanted V ions with a tetrahedral coordination and the tetrahedrally coordinated titanium oxide moieties can realize the absorption of visible light and create efficient photocatalytic reactivity even under visible light irradiation.

Acknowledgements

This work has been supported by the Ministry of Education of Japan for Grant-in-Aid Scientific Research (Grant No. 12042271 and No. 13650845). The X-ray absorption experiments were performed at the Photon Factory of KEK (2001G115) with helpful advice from Prof. M. Nomura.

References

1. Notari, B., Ad. Catal. **41**, 253 (1996).
2. Corma, A., Chem. Rev. **97**, 2373 (1997).
3. Wu, P. and Tatsumi, T., J. Phys. Chem. B **106**, 748 (2002).
4. Thomas, J. M. and Sankar, G., Acc. Chem. Res. **34**, 571 (2001).
5. Anpo, M. and Che, M., Ad. Catal. **44**, 119 (1999).
6. Yamashita, H., Zhang, J. L., Matsuoka, M. and Anpo, M., in "Photofunctional Zeolite", (ed. Anpo, M., NOVA Science Publishers, New York, 2000), p. 129.
7. Yamashita, H. *et al*., J. Phys. Chem. **100**, 16041 (1996).
8. Yamashita, H., Ikeue, K., Takewaki, T. and Anpo, M., Top. Catal. **18**, 95 (2002).
9. Ikeue, K., Yamashita, H., Takewaki, T. and Anpo, M., J. Phys. Chem. B **105**, 8350 (2001).

10. Zhang, J. *et al*., J. Phys. Chem. B **105**, 8395 (2001).
11. Yamashita, H., Harada, M., Ichihashi, Y. and Anpo, M., J. Phys. Chem. B **102**, 10707 (1998).
12. Anpo, M., Ichihashi, Y., Takeuchi, M. and Yamashita, H., Res. Chem. Intermed. **24**, 143 (1998).
13. Yamashita, H., Ichihashi, Y., Takeuchi, M., Kishiguchi, S. and Anpo, M., J. Synchrotron Rad. **6**, 451 (1999).
14. Zhang, W., Tanev, P. T. and Pinnavaia., T. J., J. Chem. Soc., Chem. Commun. 979 (1996).
15. Yamashita, H. *et al*., Chem. Commun. 435 (2001).
16. Yamashita, H. *et al*., J. Synchrotron Rad. **6**, 453 (1999).
17. Nomura, M. and Koyama, A., J. Synchrotron Rad. **6**, 182 (1999).
18. Yamashita, H., Matsuoka, M., Tsuji, K., Shioya, Y. and Anpo, M., J. Phys. Chem. **100**, 397 (1996).
19. Yoshitake, H., Sugihara, T. and Tatsumi, T., Phys. Chem. Chem. Phys. **5**, 767 (2002).
20. Zhang, S. G., Higashimoto, S., Yamashita, H. and Anpo, M., J. Phys. Chem. **102**, 5590 (1998).

Physica Scripta. Vol. T115, 471–473, 2005

XAS Study of A_2FeMoO_6 Double Perovskite

J. Herrero-Martín[1], J. García[1*], G. Subías[1,2], J. Blasco[1] and M. C. Sánchez[1]

[1]Instituto de Ciencia de Materiales de Aragón, CSIC-Universidad de Zaragoza, 50009 Zaragoza, Spain
[2]European Synchrotron Radiation Facility, B. P. 220, 38043 Grenoble, France

Received June 26, 2003; accepted in revised form November 4, 2003

PACS numbers: 61.10.Ht; 75.70.Pa; 75.50.Gg

Abstract

The electronic and geometrical structure of A_2FeMoO_6 (A = Ca, Sr, Ba, $Ba_{1/2}Sr_{1/2}$) compounds has been investigated by means of X-ray absorption spectroscopy at the iron and molybdenum K-edges. The Mo-O distances extracted from the Mo K-edge EXAFS spectra are almost identical for all compounds while XANES spectra show small differences depending on the divalent metal. The XAS spectra at the Fe K-edge showed significant differences instead. Our analysis suggests an influence of the divalent A-metal in the electronic state of iron and molybdenum. Both the chemical shift at the iron K-edge and the interatomic Fe-O distances, closely correspond to Fe^{3+} for Sr_2FeMoO_6 and Ca_2FeMoO_6 while a mixed valence state (between +2 and +3) is deduced for the Ba sample. Accordingly, the Mo valency is higher for the barium sample.

1. Introduction

Recently, the emerging field of magnetoelectronics has spurred up interest in studying some ordered double perovskites $A_2BB'O_6$ (A = Ca, Sr, Ba; BB' = FeMo, FeRe, CrRe, etc.) that show half metallicity [1]. The perovskite B sites are occupied alternatively by different B and B' cations in these compounds. Among them, A_2FeMoO_6 are known to be ferrimagnetic with critical temperature (T_C) ranging between 330 and 420 K [2]. The lowest T_C corresponds to the Ba_2FeMoO_6 compound that shows the largest crystallographic cell with cubic symmetry [3]. The replacing of Ba with smaller cations leads to a diminution of the unit cell size together with a lowering of the crystal symmetry. In this way, Sr_2FeMoO_6 has the highest T_C and a tetragonal cell [3, 4] while Ca_2FeMoO_6 crystallises in a monoclinic cell [3, 5]. All of the samples have metallic behaviour in the whole temperature range studied. In addition, the T_C of Ca_2FeMoO_6 is slightly lower than that for Sr_2FeMoO_6, showing a competition effect between cell volume and structural distortion.

Previous band calculations proposed the antiferromagnetic coupling between localised Fe^{3+} and the single itinerant downspin electron provided by the Mo^{5+} [1]. However, later studies suggest that the physical properties strongly depends on the 2p (O) – 4d (Mo) hybridization [6]. Therefore, the knowledge of the oxidation states is very important to gain insight into both the conduction mechanism and the magnetic interactions. Previous attempts to ascertain the atomic electronic state of Mo and Fe gave rise to serious controversies. In this way while some X-ray magnetic circular dichroism data did not show any observable spin magnetic moment on Mo in the Sr_2FeMoO_6 [7], other authors report a measurable moment of $-0.32\,\mu_B$ confirming the ferrimagnetic ordering [8]. The Fe valency was also the subject of contradictory results. X-ray absorption spectroscopy data of Sr_2FeMoO_6 at the Fe L-edge conclude that iron is either in +3 state [7] or in an intermediate valence Fe^{2+}/Fe^{3+} [8, 9]. Furthermore, Mössbauer experiments were also interpreted in terms of Fe^{3+} [10] or in terms of Fe^{2+}/Fe^{3+} [11]. Accordingly, the oxidation state for Fe and Mo in these compounds is not well understood so far.

We here report X-ray spectroscopy data of both K-edges, Fe and Mo, in order to gain insight into the local electronic structure correlating the changes observed in both atoms. We have performed experiments on a selected set of samples with different A-atoms. This allows us to ascertain the role of the alkaline-earth atom, if any, in the electronic structure of Fe and Mo atoms. From XANES and EXAFS we will show that the charge state depends on the substituted divalent metal. The Ca_2(or Sr_2)$FeMoO_6$ samples are nearly described as Fe^{3+} Mo^{5+}, while for barium compounds an intermediate valence for Mo and Fe was found.

2. Experimental

The samples were prepared by solid state reaction. Stoichiometric amounts of $BaCO_3$, $SrCO_3$, $CaCO_3$, Fe_2O_3, 2/3 MoO_3 and 1/3 Mo were mixed, grounded, pressed into pellets and heated at 1200 °C during 4 h in a pure atmosphere of Ar. The Mo : MoO_3 ratio is higher than the theoretical one (1/6 : 5/6) to compensate further oxidation. This step is enough to form the Ca_2FeMoO_6 sample with minor impurities of CaO. The other samples instead contain significant amounts of secondary phases such as A_2MoO_4 (A = Ba, Sr). In order to remove the secondary phases, the samples were grounded, pressed and sintered at 1200 °C in a stream of H_2/Ar (2/98) during 1 h. The samples were characterised by X-ray powder diffraction using D-max Rigaku system with a Cu rotating anode. They were all single phases.

The X-ray absorption experiments were carried out in transmission mode at the beamline BM29, ESRF, Grenoble (France). The storage ring operating conditions were 6 GeV electron energy and 150–190 mA electron current. A Si(311) double-crystal monochromator was used for Fe K-edge and Mo K-edge measurements. The incident and transmitted beams were detected by means of ionization chambers. The energy resolution $\delta E/E$ was estimated to be about 6×10^{-5}. The spectra were collected at 30 K using a closed-cycle helium cryostat whose accuracy was estimated to be ±1 K.

3. Results

The Fe K-edge XANES spectra for A_2FeMoO_6 samples compared to $LaFeO_3$ (as reference) are shown in Fig. 1. Spectra for the different samples are very similar, as expected for the same crystallographic structure. A main resonance at the threshold (hereafter denoted as peak A), a weak pre-peak structure (denoted as peak B) at ∼15 eV below the peak A and a shoulder at intermediate energies between the previous features (denoted as C) can be seen. Features A and C correspond to dipolar transitions whose shape is due to the local geometrical structure.

*e-mail: jgr@unizar.es

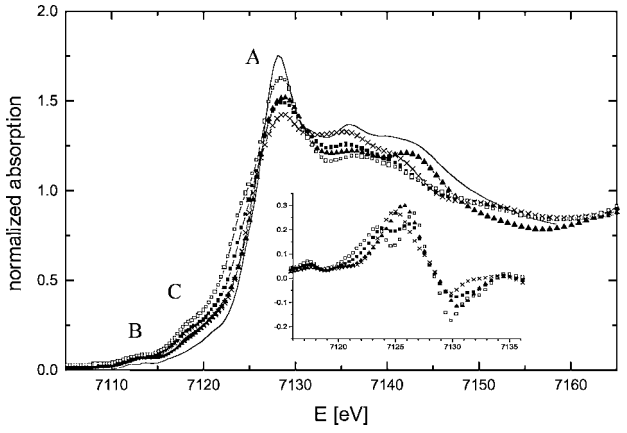

Fig. 1. XANES spectra of the series A_2FeMoO_6, *A*: Ba_2 (open squares), $Ba_{1/2}Sr_{1/2}$ (solid squares), Sr_2 (crosses) and Ca_2 (triangles) at the Fe-K absorption edge and at 30 K. The solid line corresponds to the reference $LaFeO_3$. Inset: first derivative near the absorption edge of the spectra (same symbols).

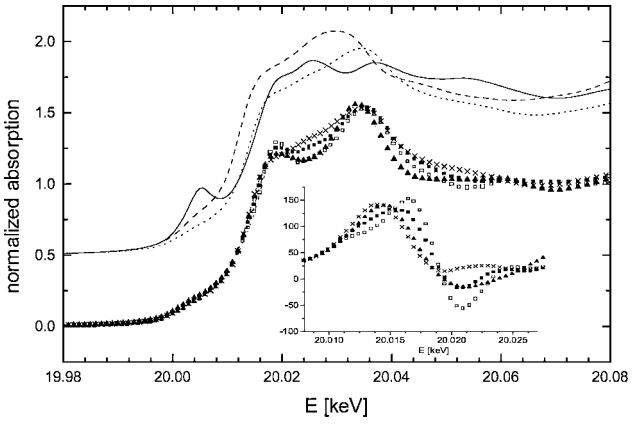

Fig. 2. XANES spectra of the series A_2FeMoO_6 at the Mo-K edge and at 30 K, where *A*: Ba (open squares), $Ba_{1/2}Sr_{1/2}$ (solid squares), Sr (crosses) and Ca (triangles). References are also plotted shifted upwards: The solid, broken and dotted lines correspond to MoO_3, $SrMoO_3$ and $SrFe_{2/3}Mo_{1/3}O_3$, respectively. Inset: The first derivative near the absorption edge of A_2FeMoO_6.

Differences among the spectra come from the different scattering power of the divalent metals and may be also due to small differences in the crystal symmetry. The intensity of the white line for A_2FeMoO_6 samples could be correlated with the change of symmetry in the series, from cubic to monoclinic. The weak pre-peak B is ascribed to $1s \rightarrow 3d$ transitions either quadrupole-allowed or dipole-forbidden. The latter becomes allowed due to strong mixing of O 2p and Fe 3d states. Some authors claimed that the mixing of d states between different neighbouring transition metal atoms, through hybridisation with the oxygen p-band, give rise to these pre-peaks [12]. Within this interpretation, the intensity of these pre-peaks shows a large mixing between 3d-Fe and 4d-Mo states.

The main important difference among the XANES spectra concerns the energy position of the absorption edge. The edge position is mainly ascribed to the Fe oxidation state in this case. Different contributions from geometrical effects to the absorption edge position should be negligible due to the very similar crystallographic structures. The edge (taken as the first inflection point at the derivative) with the highest energy corresponds to $LaFeO_3$, the reference for octahedral Fe^{3+}. Ca_2FeMoO_6 and Sr_2FeMoO_6 have their edges at energies slightly lower than the reference compound. Ba_2FeMoO_6 has the edge at the lowest energy whereas the value for $BaSrFeMoO_6$ is intermediate. Therefore, the maximum chemical shift is 1.5 eV between the spectra of Ba and Ca samples. It is noteworthy that the chemical shift between Fe^{3+} and Fe^{2+} is about 4 eV [13]. The derivative spectra are shown in the inset of fig. 1. The presence of two peaks in the derivative spectra for Ba and $Ba_{1/2}Sr_{1/2}$ samples indicate a fluctuating intermediate valence of the iron atom for both samples.

The Mo K-edge spectra for A_2FeMoO_6 samples are plotted in Fig. 2 together with selected reference samples: MoO_3 (Mo^{6+}), $SrFe_{2/3}Mo_{1/3}O_3$ (Mo^{6+}-perovskite structure) and $SrMoO_3$ (Mo^{4+}-perovskite structure). The Mo K-edge XANES of MoO_3 is characterised by a clear pre-peak at ~12 eV below the absorption edge. Such pre-peak has been reported in previous works as a shoulder of the main edge. The better energy resolution of our experimental set-up allows us to discern a peak that arises from the distorted octahedral coordination of α-MoO_3. The pre-peak transforms into a weak shoulder for the rest of the spectra in agreement with the nearly regular MoO_6 octahedra presented in either the double perovskites or the two other reference compounds. We note a chemical shift of 3.5 eV between $SrFe_{2/3}Mo_{1/3}O_3$ and $SrMoO_3$ attributed to the chemical shift between Mo^{4+} and Mo^{6+} in a perovskite structure. The spectra of the double perovskites show a relatively weak white line and strong resonances above the edge related to multiple scattering contributions that are absent in the reference compounds (see Fig. 2). The main absorption edge for Mo^{6+} references is located at 20015.5 eV. A chemical shift is present for double perovskites that can be better noticed in the derivative of the absorption coefficient, plotted in the inset of Fig. 2. The displacements of the absorption edges follow the opposite pattern to the previously observed at the Fe K-edge. The maximum edge energy corresponds to Ba_2FeMoO_6 (20016.4 eV) and the difference with respect to Sr_2FeMoO_6 and Ca_2FeMoO_6 is about 2.5 eV. The edge for $BaSrFeMoO_6$ lies at intermediate values of the previous samples. The EXAFS spectra, $\chi(k)$, of the series were also analysed using the XOP package [14]. The experimental EXAFS signal was extracted from the raw spectra following standard methods [15]. Background removal was performed and the atomic absorption coefficient was determined by a low order polynomial fit of the spectra. The Fourier transform (FT) of the $k\chi(k)$ spectra was

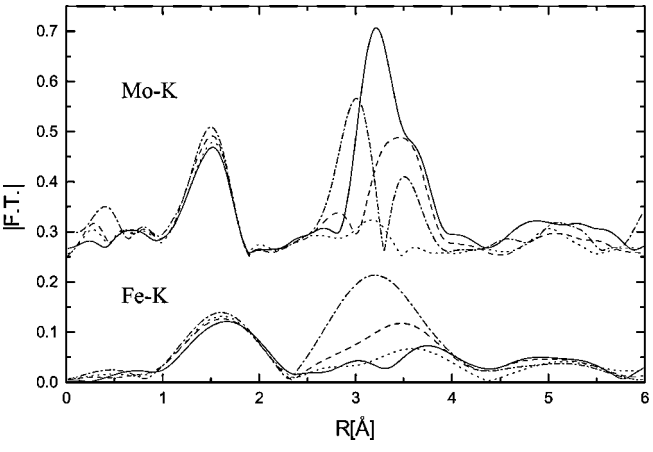

Fig. 3. Top: Fourier Transform spectra corresponding to the EXAFS at the Mo-K edge for the series A_2FeMoO_6 series, *A* being Ba (solid line), $Ba_{1/2}Sr_{1/2}$ (dashed line), Sr (dashed-dotted line) or Ca (dotted line). Bottom: Fourier Transforms of the EXAFS curves at the Fe K-edge for the A_2FeMoO_6 series, *A* being Ba (solid line), $Ba_{1/2}Sr_{1/2}$ (dashed line), Sr (dashed-dotted line) or Ca (dotted line).

Table I. *Distances r[Fe(Mo)-O] and relative Debye-Waller factors $\Delta\sigma^2$ obtained by comparison with experimental phases of the reference compounds ($LaFeO_3$ for the Fe K-edge and $SrMoO_3$ for the Mo K-edge) for the A_2FeMoO_6 samples. All the spectra were collected at 30 K. The estimated errors in bond-lengths are all less than 1%.*

	Fe K-edge		Mo K-edge	
A	$\langle r\rangle$	$\langle\Delta\sigma^2\rangle$	$\langle r\rangle$	$\langle\Delta\sigma^2\rangle$
Ba	2.06	0.0017	1.98	0.0019
$Ba_{1/2}Sr_{1/2}$	2.02	0.0020	1.95	0.0008
Ca	2.00	0.0016	1.96	0.0012
Sr	1.99	0.0014	1.94	0.0002

extracted using a gaussian window between 3 and 18 $Å^{-1}$ for the Mo K-edge and between 4.5 and 11 $Å^{-1}$ for the Fe K-edge. FT spectra are plotted in Fig. 3(b). They provide a qualitative description of the local structure around photoabsorber atoms. The radial distribution is different for each sample though they have a similar first peak in both edges. This peak corresponds to the six-oxygen first coordination shell. We observe a small variation of the first peak position for the Fe K-edge spectra, indicating an increase of the interatomic Fe-O distances on going from Ca/Sr to Ba samples. While for the Mo K-edge, the first peak position is nearly the same, showing that the Mo-O interatomic distance does not depend on the divalent metal. Further peaks, corresponding to higher distances, arise from different contributions: Fe(Mo)-*A* and Fe(Mo)-Mo(Fe) distances, and multiple scattering paths such as O-Fe(Mo)-O and Fe(Mo)-O-Mo(Fe). The shapes of these peaks depend strongly on the sample due to either the crystallographic symmetry or the different scattering power of the divalent cations. The most symmetric structure, cubic Ba_2FeMoO_6, presents a strong second peak at the Mo K-edge corresponding to a narrow distribution of Fe(Mo)-*A* distances. On the contrary, at the Fe K-edge the strongest peak is found for the tetragonal Sr_2FeMoO_6 sample. The monoclinic Ca_2FeMoO_6 instead, shows several weak peaks as expected for a broad distribution of interatomic distances.

The first shell contribution was extracted by Fourier filtering of the FT spectra between 0.8 and 2.3 Å at the Fe K-edge and between 0.9 and 1.9 Å at the Mo K-edge. The spectra were analysed by curve fitting using the first shell Fourier filtered experimental signals of $SrMoO_3$ and $LaFeO_3$ as references for the Mo K-edge and the Fe K-edge, respectively. Coordination number and ΔE_0 have been fixed to six and zero, respectively. The Fe(Mo)-O interatomic distances (r) and Debye-Waller factors (σ^2) were the fitting parameters. The best-fit results are summarised in table I. The data seem to be reasonable and agree with those reported from crystallographic studies. The main result is that Fe-O interatomic distances increase with increasing size of *A*.

4. Discussion

The description of the charge state of molybdenum and iron in A_2FeMoO_6 double perovskites is nowadays a matter of controversy. From the K-edge XANES spectra, we obtain that the Fe valency is close to 3+ for Sr_2FeMoO_6 and Ca_2FeMoO_6 samples, lower than 3+ for $BaSrFeMoO_6$ and Ba_2FeMoO_6 seems to have an intermediate value close to 2.6+. These results correlate fairly well with the Fe-O interatomic distances obtained from EXAFS analysis. Sr_2FeMoO_6 and Ca_2FeMoO_6 show interatomic Fe-O distances similar or slightly higher than the theoretical Fe^{3+}-O, 1.995 Å from ref. [15], while Fe-O in Ba_2FeMoO_6 has an intermediate value between the former and the expected for Fe^{2+}-O (2.13 Å). Accordingly, the Mo K-edge XANES spectra of Ca_2FeMoO_6 and Sr_2FeMoO_6 suggest an intermediate ionic state between Mo^{5+} and Mo^{6+} for these two samples. Meanwhile, electronic charge on the Mo atom in Ba_2FeMoO_6 and $BaSrFeMoO_6$ is higher (absorption edges are at higher energies) and very close to +6. This is not reflected in the interatomic distances deduced from Mo K-edge EXAFS. Mo-O bond-length differences in this series are lower than those obtained for Fe-O. Nevertheless, Mo-O distances seem to be few noticeable to the Mo valency. This may be due to the very similar ionic radii [16] of Mo^{6+} and Mo^{5+} (0.59 and 0.61 Å, respectively).

Our results show the high sensitivity of the charge state to the substituted divalent metal. Moreover, macroscopic properties of these materials (as saturation magnetization, or T_C) do not strongly depend on such substitution. These facts support that the description of these materials in terms of localized ionic states (Fe^{3+}/Mo^{5+} or Fe^{2+}/Mo^{6+}) seems to be meaningless. We think of an antiferromagnetic coupling between localized Fe^{3+} moments and an itinerant downspin electron as the best model to describe these compounds. The electronic and spin density of this electron projected in either Fe^{3+} or Mo^{6+} sites will highly depend on the substituted divalent metal and may also depend on the synthetic details. The latter could also explain that different research groups reported different results in their X-ray magnetic dichroism and L_2/L_3 X-ray absorption experiments on Sr_2FeMoO_6 [7, 8].

Acknowledgements

This work was supported by the Spanish CICyT MAT02-01221 project and DGA. We thank ESRF for beam time granting.

References

1. Kobayashi, K.-I., Kimura, T., Sawada, H., Terakura, K. and Tokura, Y., Nature **395**, 677 (1998).
2. Galasso, F., Douglas, F. C. and Kasper, R., J. Chem. Phys. **44**, 1672 (1966).
3. Ritter, C. *et al.*, J. Phys.: Condens. Matter **12**, 1 (2000).
4. Chmaissem, O. *et al.*, Phys. Rev. B **62**, 14197 (2000).
5. Alonso, J. A. *et al.*, Chem. Matter. **12**, 161 (2000).
6. Fang, Z., Terakura, K. and Kanamori, J., Phys. Rev. B **63**, 180407 (2001).
7. Ray, S. *et al.*, Phys. Rev. Lett. **87**, 097204-1 (2001).
8. Besse, M. *et al.*, Europhys. Lett. **60**, 608 (2002).
9. Moreno, M. S. *et al.*, Solid State Commun. **120**, 161 (2001).
10. Sarma, D. D. *et al.*, Solid State Commun. **114**, 465 (2000).
11. Balcells, Ll. *et al.*, Appl. Phys. Lett. **78**, 781 (2001).
12. Joly, Y., Cabaret, D., Renevier, H. and Natoli, C. R., Phys. Rev. Lett. **82**, 2398 (1999).
13. Benfatto, M., Solera, J. A., García, J. and Chaboy, J., Chem. Phys. **282**, 441 (2002).
14. Sánchez del Rio, M. and Dejus, R., http://www.esrf.fr/computing/scientific/xop
15. Koningsberger, D. C. and Prins, R., "X-ray absorption: Principles, application, techniques of EXAFS, SEXAFS and XANES" (John Wiley, New York 1988).
16. Shannon, R. D., Acta Cryst. A**32**, 751 (1976).

Physica Scripta. Vol. T115, 474–476, 2005

Confined Lead Nano-Granules Investigated with X-ray Absorption Spectroscopy

A. Witkowska[1,*], J. Rybicki[1], A. Trapananti[2], E. Principi[2] and A. Di Cicco[2]

[1]Department of Solid State Physics and TASK Computer Center, Gdansk University of Technology, 80-952 Gdansk, Poland
[2]INFM UdR, Department of Physics, University of Camerino, I-62032 Camerino, Italy

Received June 26, 2003; accepted February 6, 2004

PACS number: 78.55.Qr, 61.46.+w, 61.10.Ht

Abstract

In the present contribution we show that X-ray absorption spectroscopy may be an effective way to obtain a detailed insight into nano-granular structures embedded in a glass matrix. For the first time we have employed the single energy X-ray absorption detection method to determine the diameter distribution of metallic granules embedded in a glass matrix. In particular, we have estimated the diameter distribution of Pb granules confined in a $PbOSiO_2$ matrix.

1. Introduction

Lead-silicate glasses, due to their interesting and useful properties, find many industrial applications. As special materials they are used in the production of plate image amplifiers and scintillators [1]. For our present considerations it is most important that lead-silicate glasses submitted to reduction process (e.g. in hydrogen atmosphere), undergo dramatic structural changes. In particular, metallic Pb granules and/or separate neutral Pb atoms appear in reduced glasses. The structural changes are accompanied by remarkable changes of optical properties [2] and in surface electrical conductivity [3]. Moreover, reduced glasses have very high secondary emission coefficients, thus finding an application in the production of electron channel multipliers [3]. The metallic granules confined in a glassy matrix have been the subject of our recent studies [4, 5, 6, 7, 8]. The structural parameters describing the nearest neighbourhood of lead atoms (Pb-Pb and Pb-O pair distribution functions) and the mean size of metallic granules have been obtained for xPbO $(1-x)SiO_2$, $x = 0.3,\ 0.5,\ 0.7$ glasses. In the present contribution, we outline a new method of determination, or at least estimation, of the distribution of diameters of metallic granules embedded in a glass matrix using an X-ray absorption method called single-energy X-ray absorption detection [9].

The X-ray absorption coefficient in homogeneous sample of constant thickness d and atomic density ρ is given by a simple formula: $\alpha = \sigma\rho d$, where σ is the cross section for radiation absorption. During the first order phase transition a significant change in the absorption coefficient can be expected in the whole energy range, related to a change of structural and electronic properties. The most drastic changes in the absorption coefficient α are observed in the vicinity of the absorption edge. Thus, performing measurements of the X-ray absorption coefficient as a function of temperature for a given fixed radiation energy at which the greatest difference in the value of α appears, one can determine the phase transition temperature, and many other related physical quantities, as relative contributions of various phases, overheating/overcooling parameters, as well as structural parameters of the subsequent phases (due to the possibility of performing simultaneous X-ray diffraction and quick EXAFS measurements at each temperature).

As this method is sensitive enough to detect variations of the absorption coefficient at the phase transition of the first order even for nanometer-size objects, an effort to determine or at least estimate the nanogranule diameter distribution for Pb granules confined in a silica matrix has been undertaken.

2. Experimental details

The preparation procedure of the considered 0.7PbO $0.3SiO_2$ glass sample has been described in detail elsewere [8]. The reduction process was realised in hydrogen atmosphere at the temperature of $T_{red} = 400\,^{\circ}\mathrm{C}$, during time periods of $t_{red} = 70\,\mathrm{h}$. The presence of nano-sized granules was established by EXAFS/MD analysis and X-ray diffraction measurement.

The X-ray absorption measurements were conducted at the BM29 beam-line at the European Synchrotron Radiation Facility (Grenoble). Details on the experimental setup can be found in reference [10]. The raw results of the single-energy X-ray absorption measurements of the reduced glass and pure crystalline lead (as reference data) are shown in the lower panel of figure 1. In order to determine the optimal energy for the $\alpha(T)$ measurement, i.e. the energy corresponding to the most pronounced variations of the absorption coefficient during the phase transition, XANES spectra have been measured for each sample in the temperature range from 23 °C to 350 °C. The upper panel of figure 1 shows two such spectra, obtained for crystalline lead under and above the phase transition temperature $T_m \approx 327\,^{\circ}\mathrm{C}$. For all samples the greatest difference between the $\alpha_S(E)$ (solid) and $\alpha_L(E)$ (liquid) curves appeared at the energy of 13061 eV. This energy was used in our experiment. The heating/cooling rate of about 0.5 deg/s was applied.

3. Results

During heating, in the case of crystalline Pb a sharp discontinuity at $T_m \approx 327\,^{\circ}\mathrm{C}$ is observed, whereas for hydrogen-reduced 0.7PbO $0.3SiO_2$ glass the transformation takes place in a finite temperature range. The pattern recorded in the upstroke is not reversible in the downstroke (undercooling effect). The magnitude and shape of the obtained $\alpha(T)$ loop depend on the magnitude of changes in the short-range environment, on the presence of impurities, on the coupling strength between Pb clusters and the matrix, on the surface melting effect, and on the granule size distribution [9].

*e-mail: agnieszka@mif.pg.gda.pl

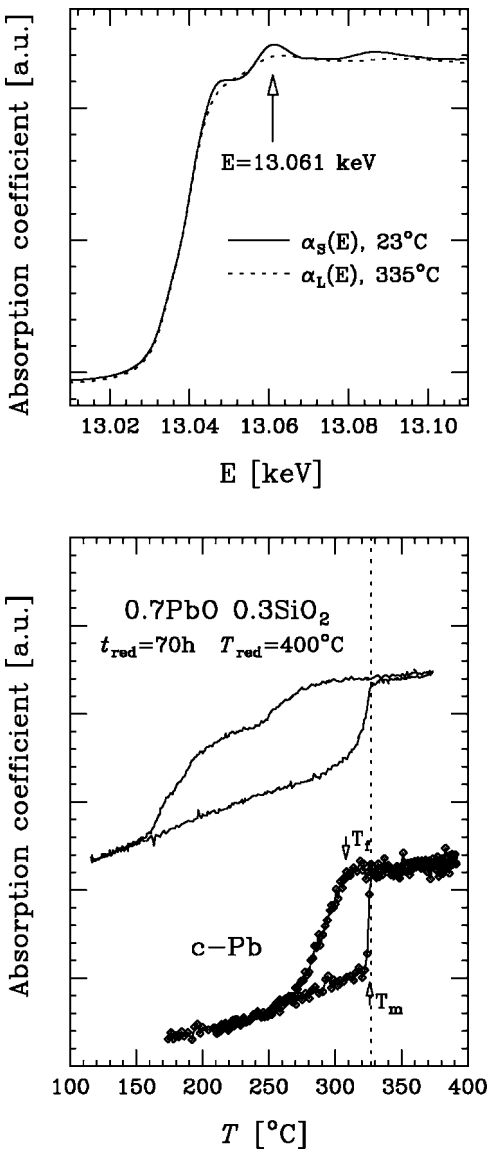

Fig. 1. The Pb L_3 edge measurement in the solid (23 °C) and liquid (335 °C) phases of crystalline lead (upper panel). Single-energy (13061 eV) X-ray absorption measurement results for samples containing powdered crystalline Pb and hydrogen-reduced 0.7PbO 0.3SiO_2 glass (lower panel).

In the simplest interpretative scheme for a lead granular structure confined in a glassy matrix, we assume that the shape of the $\alpha(T)$ melting curve is related mainly to the dependence between the melting temperature (T_m) and the granules' radii (r_g).

The melting of small particles has been described by two main models: (a) the homogeneous melting model [11], and (b) the liquid-skin melting model [12] (for details see [13, 14] and references therein). In numerous experimental and theoretical works dealing with the dependence of the melting temperature on the confined granule size (e.g. [15, 16, 17]), the homogeneous melting model (without a liquid skin) has been used in the first approximation. This model predicts a size-dependent melting temperature, T_m, that varies with the granule radius as follows:

$$T_m = T_0 - \frac{2T_0}{L\rho_S r_g}\left[\gamma_S - \left(\frac{\rho_S}{\rho_L}\right)^{2/3}\gamma_L\right], \tag{1}$$

where T_0 is the bulk melting temperature, L is the latent heat of fusion, ρ_S and ρ_L are densities in the solid and liquid phases, respectively, and γ_S and γ_L are surface energies in the solid and liquid phases, respectively. Assuming $T_0 = 327.5\,^\circ$C, $L = 23.2\,$J/g, $\rho_S = 11.34\,$g/cm^3, $\rho_L = 10.66\,$g/cm^3, and $\gamma_S = 0.61\,$J/m^2 [18], $\gamma_L = 0.48\,$J/m^2 [19], one can determine the $r_g(T_m)$ dependence from equation (1).

Simultaneously, a single-energy X-ray absorption detection experiment enables accurate determination of the relative atomic fraction melted at the temperature $T_m^{(i)} = T_i + \frac{T_{i+1}-T_i}{2}$, defined as:

$$\Delta f(T_m^{(i)}) = \frac{\alpha(T_{i+1}) - \alpha(T_i)}{\alpha_L - \alpha_S}. \tag{2}$$

Fitting the polynomial function to the experimentally obtained data, $\alpha(T)$, one can calculate this fraction with sufficient accuracy. In our analysis, $T_m^{(i)}$ was determined with the step $(T_{i+1} - T_i)$ equal to 0.1 °C. The $\Delta f(T_m^{(i)})$ dependence for 0.7PbO 0.3SiO_2 glass is shown in figure 2(a).

Then correlation between $\Delta f(T_m^{(i)})$ and the volume of granules melted at a temperature close to $T_m^{(i)}$ (equation (1)):

$$\Delta f(T_m^{(i)}) \sim N_g(T_m^{(i)}) \cdot \rho_L \cdot r_g^3(T_m^{(i)}),$$

leads to the distribution of granule size, $N_g(r_g)$.

The obtained distribution for reduced 0.7PbO 0.3SiO_2 glass is presented in figure 2(b). A maximum at $r \sim 75$Å can easily be distinguished. However, a single continuous diameter distribution covers the interval of 55–4000 Å. These results are compatible with our previous EXAFS/MD analysis [8].

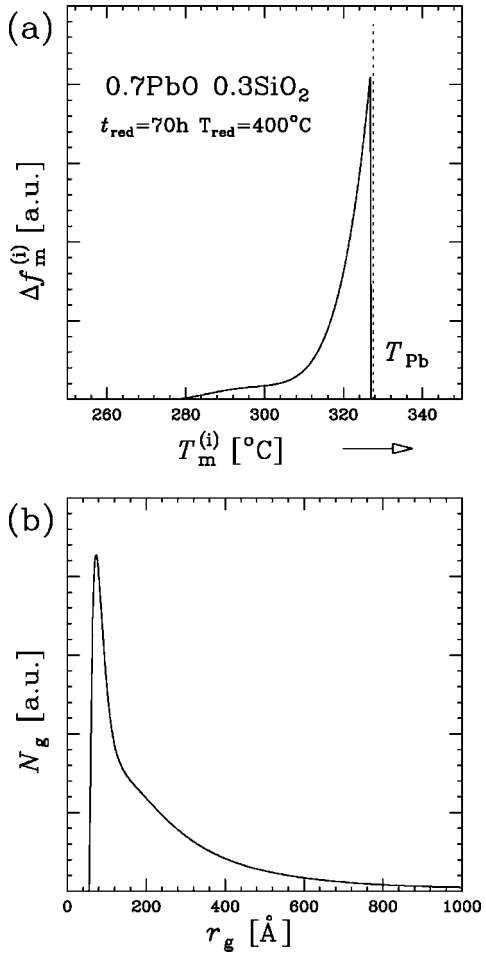

Fig. 2. a) Relative atomic fraction melted in the temperature range $[T_i, T_{i+1}]$ versus $T_m^{(i)}$. The dotted line marks the melting temperature of bulk Pb. b) Estimated granule radii distribution for reduced 0.7PbO 0.3SiO_2 glass.

4. Conclusions

The measurements and analysis of the $\alpha(T)$ characteristic for hydrogen-reduced lead-silicate glass have shown that the single-energy X-ray absorption method can be a useful source of information on confined granules embedded in glassy matrices.

Our interpretation scheme and usage of equation (1) may be considered merely as a first approximation. More precise analysis should take explicitly into account, first of all, the granules' confinement (i.e. the confinement-induced pressure, exact values of surface energy in the solid and liquid state specific for a given matrix, etc.) and the surface melting effect. Thus, the detailed results presented in the paper should only be considered as preliminary. However, we believe to have thus demonstrated the potential of the method for estimating the granule diameter distribution.

Acknowledgement

We gratefully acknowledge the support of the European Synchrotron Radiation Facility in provision of their synchrotron radiation facilities for the HS1663 experiment and would like to thank the BM29 staff members.

References

1. Wiza, J. L., Nucl. Instrum. Meth. **62**, 587 (1979).
2. Pan, Z., Henderson, O. O. and Morgan, S. H., J. Non-Cryst. Solids **171**, 134 (1994).
3. Trzebiatowski, K. *et al.*, Proc. Conf. Fundamentals of Glass Science and Technology, Växjő, Sweden (1997).
4. Trzebiatowski, K., Witkowska, A. and Murawski, L., Mol. Phys. Rep. **27**, 115 (2000).
5. Witkowska, A., Rybicki, J. and Feliziani, S., Opt. Appl. **30**, 685 (2000).
6. Witkowska, A. *et al.*, J. Non-Cryst. Solids **276**, 19 (2000).
7. Witkowska, A. *et al.*, IEEE Trans. Dielectrics Electrical Insulation **8**, 385 (2001).
8. Witkowska, A., Rybicki, J. and Di Cicco, A., J. Non-Cryst. Solids, (2003) (submitted).
9. Filipponi, A. *et al.*, J. Phys. CM **10**, 235 (1998).
10. Filipponi, A. *et al.*, Rev. Sci. Instrum. **71**, 2422 (2000).
11. Pawlow, P., Z. Phys. Chem. **65**, 545 (1909).
12. Reiss, H. and Wilson, B. I., J. Colloid. Sci. **3**, 551 (1948).
13. Buffat, Ph. and Borel, J-P., Phys. Rev. **A 13**, 2287 (1976).
14. Peters, K. F., Cohen, J. B. and Chung, Y-W., Phys. Rev. **B 57**, 13430 (1998).
15. Grabaek, L. *et al.*, Phys. Rev. **B 45**, 2628 (1992).
16. Goswami, R. and Chattopadhyay, K., Appl. Phys. Lett. **69**, 910 (1996).
17. Itoigawa, H., Kamiyama, T. and Nakamura, Y., J. Non-Cryst. Solids **210**, 95 (1997).
18. Heumann, Th. and Johannisson, J., Acta Met. **20**, 617 (1972).
19. Melfort, D. A. and Hoar, T. P., J. Inst. Metals **85**, 197 (1957).

Physica Scripta. Vol. T115, 477–479, 2005

Structural Analysis of Manganese Borate Glasses by XAFS Measurement

A. Kajinami*[1], S. Deki[1] and K. Handa[2]

[1]Department of Chemical Science and Engineering, Faculty of Engineering, Kobe University, 1-1 Rokko-dai, Nada-ku, Kobe Hyogo, 657-8501, Japan
[2]SR Center, Ritsumeikan University, 1-1-1 Noji-Higashi, Kusatsu, Shiga, 528-8577, Japan

Received June 26, 2003; accepted in revised form November 3, 2003

PACS numbers: 61.10.Ht; 61.43.Fs

Abstract

The composition dependence of short-range structure was investigated for manganese borate glasses ($(MnO)_X(B_2O_3)_{1-X}$, $X = 0.21$, 0.30, 0.44, 0.52) by XAFS measurement. The manganese K-edge XAFS spectra of the glasses were measured at the beamline 4 (BL-4) station of the synchrotron radiation facility at Ritsumeikan University in Japan. From the XANES spectra, it was found that the manganese ion is divalent in the glasses and it does not vary with the MnO content. The EXAFS spectra indicate that the manganese ion is surrounded by four oxygen atoms with an interatomic distance of *ca.* 2.1 Å. A notable composition dependence of the Mn-O correlation is not observed for the glasses.

1. Introduction

It is well known that composition dependences of physico-chemical properties, such as density and thermal expansion coefficient, have maxima or minima from $X = 0.3$ to 0.4 for alkali borate glasses ($(M_2O)_X(B_2O_3)_{1-X}$ glasses, where M is an alkali metal). This is called the 'boric oxide anomaly' [1, 2]. For examining these irregularities, the structure of alkali borate glasses has been extensively investigated, e.g., by X-ray and neutron diffraction [3, 4], Raman spectroscopy [5], B^{11}-NMR [6], molecular dynamics simulation [7], IR spectroscopy [8]. It is proposed from these studies that various structural groups, such as boroxol ring, diborate, triborate, metaborate ring, and so on, are formed from the tetrahedral BO_4 units and the triangle BO_3 units in the alkali borate glasses [9]. However, we are not aware of any structural studies on glasses containing other metal ions, although the structural analysis is important for elucidating the effect of other metal ions on the structural group.

In a previous study, we investigated the short-range structure of manganese borate glasses ($(MnO)_X(B_2O_3)_{1-X}$) by high energy XRD (HEXRD) [10]. It was found that the coordination number of B-O increases with increasing MnO content. However, the coordination number of Mn-O has not been elucidated from the HEXRD because the Mn-O correlation is overlapped with B-B or O-O correlations in the total correlation function, $T(r)$. Especially, for manganese-containing oxide crystals, the coordination number and interatomic distance of Mn-O depend on the valency of manganese ion and its composition [11–14]. Therefore, it is important to investigate the valency and the short-range structure of manganese ions in different glasses.

In the present study, the structure of manganese borate glasses ($(MnO)_X(B_2O_3)_{1-X}$, $X = 0.21, 0.30, 0.35, 0.44$) was investigated by Mn K-edge XAFS measurements at the synchrotron radiation facility of Ritsumeikan University in Japan. We discuss the composition dependence of the valency and short-range order of the manganese ion from the XANES and EXAFS data, respectively.

2. Experimental

2.1. *Preparation of manganese borate glass*

The manganese borate glasses ($(MnO)_X(B_2O_3)_{1-X}$) were prepared in the range from $X = 0.21$ to 0.52. B_2O_3 and $MnCO_3$ were used as starting materials, mixed and then heated in alumina crucibles at 1373 K for 2 hours. The melt was rapidly quenched to ambient temperature by the twin-roller method [15]. The quenching rate was around 10^3–10^4 K/s. The amorphicity of the glasses was verified by the absence of sharp peaks in the XRD pattern. The composition of the glasses was analyzed by inductively coupled plasma atomic emission spectroscopy (ICP-AES) (Seiko Instruments Inc., SPS1500VR).

2.2. *XAFS measurement*

The glass samples were well-ground, mixed with boron nitride (BN) powder and then pressed into pellets of 10 mm diameter. Manganese K-edge XAFS spectra were recorded in transmission mode at BL-4 beam line with synchrotron radiation from the 575 MeV storage ring of the SR facility in Ritsumeikan University, Shiga, Japan. The absorption spectra were measured using a Ge(220) ($d = 2.000$ Å) double monochromator and two ionization chambers. The absorption coefficients, $\mu t (\mu t = \ln(I_0/I))$, were measured from 6300 to 7500 eV with a fixed accumulation time of 5 s per data point. The EXAFS interference function ($k^3\chi(k)$) and radial distribution function (RDF) were calculated by Rigaku, EXAFS Software (REX2, RIGAKU). The k^3 weighted $\chi(k)$ was extracted from the observed absorption spectrum by a cubic spline method. These were then Fourier-transformed with a Hanning window to evaluate the radial distribution functions (RDFs) [16].

3. Results and discussion

3.1. *XANES spectra of manganese borate glasses*

Figure 1 shows normalized XANES spectra at the Mn K-edge of $(MnO)_X(B_2O_3)_{1-X}$ ($X = 0.21$, 0.30, 0.44, 0.52) glasses. The spectra of manganese carbonate and manganese dioxide are also displayed for reference. The absorption edges of Mn for the manganese glasses are found in the range from 6450 to 6550 eV. It is noted that the position of the Mn K-edge of the glasses does not change with the MnO content, X. The XANES spectra of the glasses show that the absorption edge energy is similar to the one of manganese carbonate ($MnCO_3$), which indicates

*e-mail: kajinami@kobe-u.ac.jp

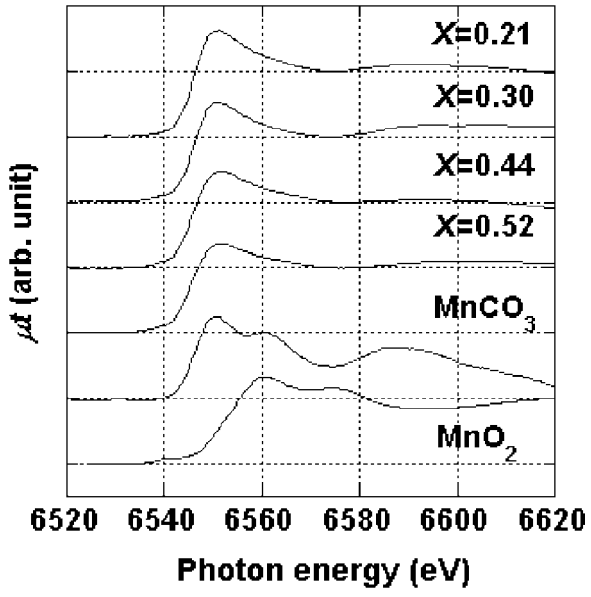

Fig. 1. XANES spectra of $(MnO)_X(B_2O_3)_{1-X}$ glasses, manganese carbonate, and manganese dioxide.

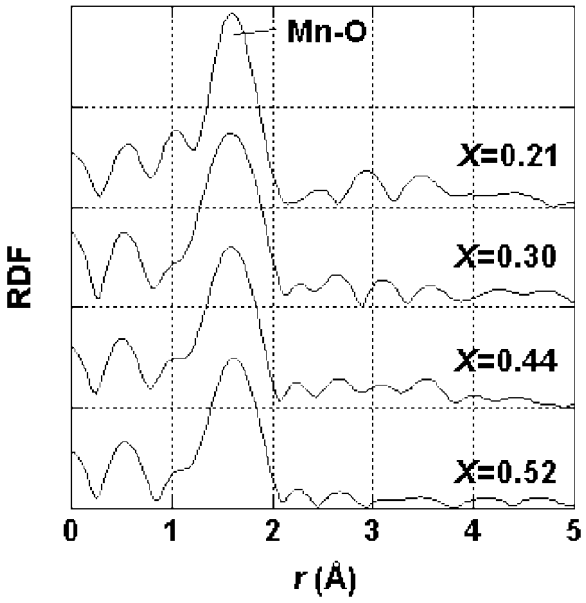

Fig. 3. EXAFS radial distribution functions (RDFs) of $(MnO)_X(B_2O_3)_{1-X}$ glasses.

that manganese ion is divalent (Mn^{2+}) in the glasses. A notable composition dependence of the valency is not observed in these glasses.

3.2. *EXAFS spectra of manganese borate glasses*

Figure 2 shows interference functions, $k^3\chi(k)$s, of the glasses, which include oscillations up to 10 Å^{-1}. It is found that the functions have similar frequency and amplitude, which implies that there is no composition dependence of the short-range structure of the manganese ion in the glasses. Figure 3 shows radial distribution functions (RDFs) of the glasses, calculated by Fourier transformation of the $k^3\chi(k)$s without correction for the phase shift. All patterns show a peak at *ca.* 1.6 Å, which is assigned to Mn-O correlation. The RDF was back Fourier-transformed from 1.2 to 2.1 Å to reproduce the interference function, $k^3\chi(k)$, of the Mn-O correlation. The structural parameters were evaluated by the standard EXAFS equation,

$$\chi(k') = \frac{N}{k'r^2} f(k') \exp(-2\sigma^2 k'^2) \cdot \exp\left(\frac{-2r}{\lambda}\right) \cdot \sin[2k'r + \phi(k')], \tag{1}$$

where $N, r, \sigma, \phi(k')$, $F(k')$ and λ are coordination number, interatomic distance, Debye-Waller factor, phase shift, back-scattering factor, and mean free path length of the electron, respectively [17]. k' denotes the corrected wave number as

$$k' = (k^2 - 2m\Delta E_0/\hbar^2)^{\frac{1}{2}}, \tag{2}$$

where ΔE_0 is the energy shift of the Mn K-edge ionization potential. Using Mckale's parameters [18], these structural parameters, r, N, σ, and ΔE, and λ are used to reproduce the $k^3\chi(k)$ oscillation of the Mn-O correlation by a least square fitting method [16]. Table I summarizes the optimized structural parameters. The results indicate that the interatomic distance of Mn-O correlation is about 2.1 Å for all glasses. A composition dependence of the Mn-O correlation is not observed in the range from $X = 0.21$ to 0.44. It is known that the Mn-O distances vary with composition of manganese ions in the range from 1.8 to 2.3 Å for other manganese containing glasses [19–21], where the composition dependence is related to the Mn oxidation state and the number of surrounding

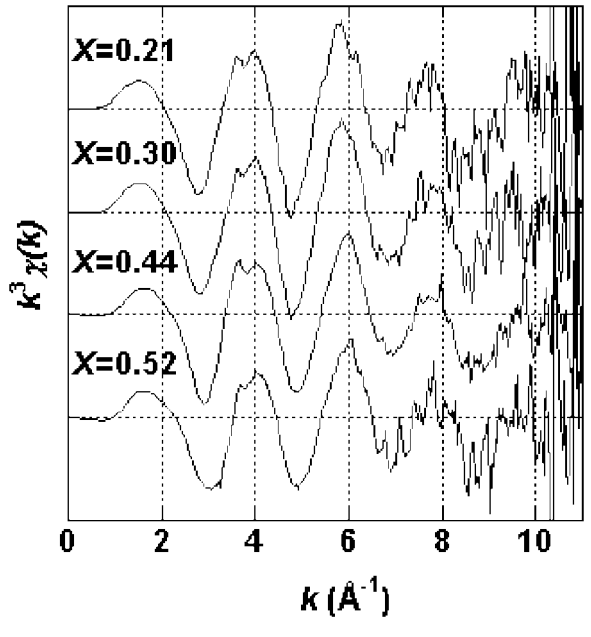

Fig. 2. EXAFS interference functions, $k^3\chi(k)$s of $(MnO)_X(B_2O_3)_{1-X}$ glasses.

Table I. *Structural parameter of $(MnO)_X(B_2O_3)_{1-X}$ glasses obtained by the curve fitting method. N: coordination number of Mn-O correlation, r: Mn-O distance (Å), σ: Debye-Waller factor (Å), ΔE: E_0 shift (eV), and λ: mean free path length of photo-electron (Å).*

X	N	r	σ	ΔE	λ
0.21	3.96	2.13	0.086	1.61	3.79
0.30	3.96	2.12	0.093	1.88	4.00
0.44	3.86	2.11	0.094	2.51	3.63
0.52	3.67	2.11	0.086	5.07	3.37

ions. In the crystalline structure, the Mn-O distances become shorter with increasing oxidation state [11–14]. The fixed value of Mn-O distances in Table I may be due to the unchanged valency of the manganese ion in the glasses.

From Table I, it is found that the coordination number for the Mn-O is about four, which indicates that the manganese ion has tetrahedral structure with oxygen. In the crystalline structure of MnB_4O_7 (i.e. $(MnO)_{0.33}(B_2O_3)_{0.66}$), there is a similar short-range structure, in which the manganese ion is surrounded by four oxygen atoms at *ca*. 2.1 Å [22]. The deconvolution of the total correlation function, $T(r)$, from HEXRD measurements [10] also shows that the coordination number is about four, which agrees with the assignment to the tetrahedral structure of manganese ion in the glasses.

4. Conclusions

The interatomic distance and coordination number of the Mn-O correlation were investigated by XAFS measurements to study the modification of the short-range structure in manganese borate glasses. It is found that no composition dependence of the short-range structure was observed for the glasses, in which the manganese ion is bivalent and has tetrahedral structure with oxygen ions. The detailed structure will be elucidated by further studies such as neutron diffraction, IR, Raman measurements and NMR by the authors.

Acknowledgment

The authors wish to thank Ritsumeikan University SR center and SPring-8 for supporting the XAFS measurements by 'Nanotechnology Comprehensive Support Project' of Ministry of Education, Culture, Sports, Science and Technology (MEXT) in Japan. We would like to thank to 'Center for instrumental analysis' in Kobe University for using the ICP-AES spectrometer.

References

1. Sakka, S., Kamiya, K. and Kato, K. J., Non-Cryst. Solids **52**, 77 (1982).
2. Shelby, J. E., J. Am. Ceram. Soc. **66**, 225 (1983).
3. Paschina, G., Piccaluga, G. and Magini, M., J. Chem. Phys. **81**, 6201 (1984).
4. Herm, G., Derno, M. and Stiel, H., J. Non-Cryst. Solids **88**, 381 (1986).
5. Meera, B. N. and Ramakrishna, J., J. Non-Cryst. Solids **159**, 1 (1993).
6. Bray, P. J., J. Non-Cryst. Solids **96**, 45 (1987).
7. Handa, K., Iwadate, Y. and Umesaki, N., Jpn. J. Appl. Phys. Suppl. **38-1**, 140 (1999).
8. Doweidart, H., Abou Zeid, M. A. and El-Damrawy, G. M., J. Phys. D **24**, 2222 (1991).
9. Konijnendijk, W. L. and Stevels, J. M., "Borate Glasses" (Plenum Press, New York 1977), p. 259.
10. Kajinami, A., Kotake, T., Deki, S. and Kohara, S., Nucl. Instrum. Meth. Phys. Res. Sect. B **199**, 34 (2003).
11. Millini, R., Gagriardi, M. F. and Piro, G., J. Mater. Sci. **29**, 4065 (1994).
12. Christensen, N. A. and Olliver, G., J. Solid State Chem. **4**, 131 (1972).
13. Battle, P. D., *et al*., J. Chem. Mater. **9**, 552 (1997).
14. Battle, P. D., *et al*., J. Chem. Mater. **9**, 1042 (1997).
15. Nassau, K., Wang, C. A. and Grasso, M., J. Am. Ceram. Soc. **62**, 74 (1979).
16. Teo, B. K., "EXAFS: basic principles and data analysis" (Springer-Verlag, Berlin 1986), p. 23.
17. Sayers, D. A., Stern, E. A. and Lytle, F. W., Phys. Rev. Lett. **35**, 204 (1971).
18. McKale, A. G., Veal, B. W., Paulikas, A. P., Chan, S.-K. and Knapp, G. S., J. Am. Chem. Soc. **110**, 3763 (1988).
19. Staneva, A. D., Gattef, E. M. and Dimitriev, Y. B., Phys. Chem. Glasses **41**, 403 (2000).
20. Matsubara, E., Waseda, Y., Hashimoto, S. and Inomata, K., Phys. Stat. Sol. **117**, K1 (1990).
21. Georgieva, I., Ivanov, I. T., Dimitrov, V., Gattev, E. and Dimitriev, Y., J. Mater. Sci. **31**, 3197 (1996).
22. Abraham, S. C., Bernstein, J. L., Gibart, P. and Sherwood, R. C., J. Chem. Phys. **60**, 1899 (1974).

Physica Scripta. Vol. T115, 480–482, 2005

Chemical State Analysis of 0.2 mass% Mo in Steel by XAFS

M. Nagoshi*, T. Kawano, K. Sato, M. Funakawa, T. Shiozaki and K. Kobayashi(1)

Steel Research Laboratory, JFE Steel Corporation, 1-1 Minamiwatarida, Kawasaki-ku, Kawasaki 210-0855, Japan
(1)Photon Factory, High Energy Accelerating Research Organization, 1-1 Oho, Tsukuba, 305-0801, Japan

Received June 26, 2003; accepted in revised form November 4, 2003

PACS numbers: 61.10.Ht, 64.75.+g, 81.05.Bx

Abstract

0.2 mass% Mo in a high-strength steel has been investigated using X-ray absorption fine structure (XAFS) technique. Mo-K edge X-ray fluorescence XAFS spectra show the transition from Mo in solution in α-Fe matrix to Mo in carbides when the steel is annealed at 650 °C. We have evaluated the atomic fraction of Mo atoms in solution and in carbides from curve fitting parameter of XANES spectra and from coordination number of iron surrounding Mo in the α-Fe matrix derived from an EXAFS analysis.

1. Introduction

Metals added into steel (micro-alloying elements) dramatically change many properties of steel product, such as strength and anti-corrosion property. It is important to understand the mechanisms of improvement of the properties by adding the elements in order to design micro alloyed steel with superior performance. The micro alloying elements often play very important roles on the properties by forming precipitates with a small size. Transmission electron microscopy (TEM) is a powerful tool for direct observation, and compositional and structural analysis of precipitates with sizes down to a few-nm [1]. Atom-probe field-ion microscopy (AP-FIM) has been applied to direct imaging of atoms in steel [2]. There are difficulties however in obtaining structural and quantitative information of precipitates with sizes of less than a few-nm especially at the early stage of precipitation.

X-ray absorption fine structure (XAFS) spectroscopy is widely used in material science to clarify the short-range structure of the elements in interest. Although this technique has been often applied to amorphous metals [3], the study on the micro-alloying steel (crystal) is few [4–6]. In this study, we present Mo K-edge XAFS spectra recorded for a 0.2 mass% Mo-added high-strength steel and discuss the results in terms of change of chemical states of Mo with annealing. We also discuss the quantitative chemical state analysis of Mo using the XAFS spectra.

2. Experimental

The 0.04 wt% C–1.5 wt% Mn steel containing Mo of 0.2 mass% was soaked at 1250 °C and then water-quenched from about 650 °C (starting material). The starting material was water-quenched just after the annealing at 650 °C for 0.5 min–60 min. A piece of steel with the same composition was quenched from 900 °C after the soaking is prepared as a reference of Mo which is substitutional in α-Fe matrix (a bcc structure). A residue extracted from steel aged at 675 °C by electrolytic extraction method was prepared as a reference of Mo in precipitated carbides. The measured surfaces of the steel specimens were carefully mirror polished.

The XAFS measurements were carried out at BL27B of Photon Factory, KEK (2.5 GeV, Tsukuba, Japan), with a two-crystal Si (111) monochrometor. The Mo-K edge XAFS spectra were measured in an X-ray fluorescence mode using a Lytle-type detector (a photon-pass length of 100 mm) with a solar slit and Kr gas for the steel and residue specimens. The spectra were analyzed using a commercial software (Rex 2000, Rigaku corp.).

3. Results and Discussion

3.1. *Chemical states of Mo*

Figure 1 shows Mo-K edge XAFS spectra for the 0.2 mass% Mo steel annealed at 650 °C for 0.5 min–60 min [spectra (c)–(f)] as well as the spectra for the starting material [spectrum (b)], the specimen quenched from 900 °C [spectrum (a)], the residue electrically extracted from the thermal aged steel [spectrum (g)], and Mo_2C [spectrum (h)]. The X-ray absorption near-edge structures (XANES) for the starting material are indistinguishable from those for the specimen quenched from 900 °C. This shows that Mo atoms in the starting material are almost all substitutional in the Fe matrix. The spectra gradually change during the annealing, which shows that the annealing induces changes in the local environment of Mo atoms. A broad peak at about 20060 eV decreases in intensity and a peak at about 20045 eV increases with the annealing. The differential spectrum obtained by subtracting the spectrum of the starting materials from that of the specimen annealed for 60 min is shown in Fig. 2. Peak positions of the differential spectrum are close to those of the spectrum for the

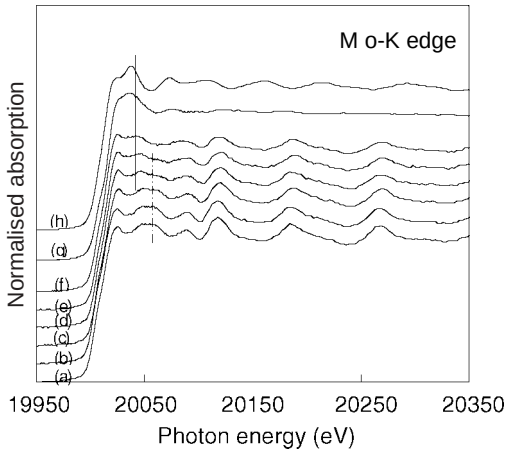

Fig. 1. Normalized Mo-K edge X-ray fluorescence XAFS spectra for 0.2 mass%-Mo steel. (a) water-quenched from 900 °C, (b) starting material, annealed at 650 °C for (c) 0.5 min, (d) 2 min, (e) 10 min and (f) 60 min. Spectra for residue electronically extracted from thermal aged steel (g) and Mo_2C (h) are also presented.

*e-mail: m-nagoshi@jfe-steel.co.jp

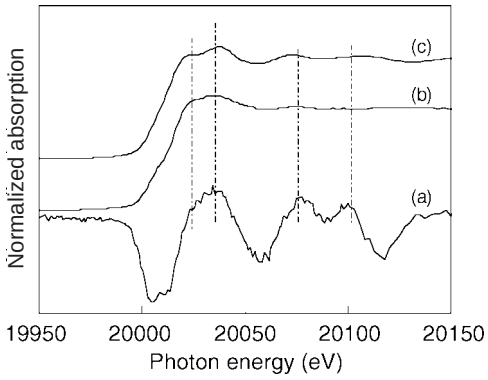

Fig. 2. Differential Mo-K XANES spectrum obtained by subtracting the starting material from the specimen annealed at 650 °C for 60 min. Spectra for residue electronically extracted from thermal aged steel and Mo_2C are compared.

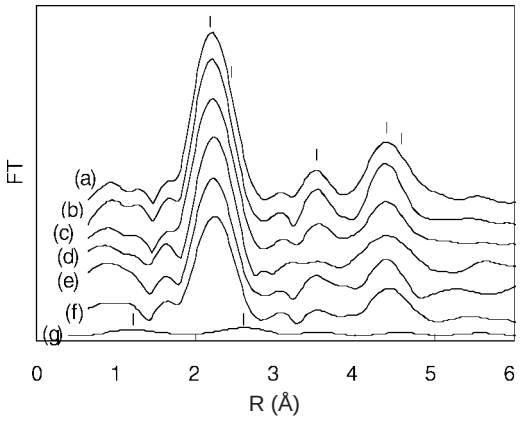

Fig. 3. Fourier transforms of k^3-weighted Mo-K edge EXAFS spectra for 0.2 mass%-Mo steel. (a) water-quenched from 900 °C, (b) starting material, annealed at 650 °C for (c) 0.5 min, (d) 2 min, (e) 10 min and (f) 60 min. FT for residue electronically extracted from thermal aged steel is also presented (g).

residue and Mo_2C, which strongly suggests that a part of Mo forms carbides in the annealed specimen.

The amplitude of extended X-ray absorption fine structure (EXAFS) oscillation in the photon energy range from 20050 eV to 20300 eV decreases by annealing, see Fig. 1. This phenomenon is clearly demonstrated in the Fourier transforms (FT) of the k^3-weighted EXAFS spectra shown in Fig. 3. The radial distribution (phase-shifts were not corrected) shows that peaks in the FT decrease in intensity by the annealing. The FT curves have a typical bcc structure for all steel specimens, which shows that the EXAFS oscillation is dominated by photoelectrons being scattered at Fe atoms surrounding Mo. The precipitated carbides show only weak amplitudes even for the thermal aged steel [spectrum (g) in Fig. 1 and Fig. 3]. The weak EXAFS amplitude for the precipitates may be due to their small size and structural deformation. From the above discussion, the reduction of the EXAFS amplitude is attributed to the decrease of the number of Mo atoms in solution in α-Fe matrix.

The XANES and EXAFS spectra show the transition from Mo in solution in α-Fe matrix to Mo in carbides when the steel is annealed at 650 °C.

3.2. *Quantitative chemical state analysis of Mo*

The XAFS spectra shown in Fig. 1–Fig. 3 provide us a chance to analyze the chemical states of Mo quantitatively. We have evaluated the atomic fraction of Mo in solution in the α-Fe matrix and in precipitates from the XANES and EXAFS spectra.

Table I. *Results of curve-fitting analysis for Mo-K EXAFS spectra.*

	$(Mo\text{-}Fe)_{1st}$			$(Mo\text{-}Fe)_{2nd}$	
Treatments	CN	R (Å)	$\sigma^2 \cdot 10^{-3}$ (Å^2)	R (Å)	$\sigma^2 \cdot 10^{-3}$ (Å^2)
Starting material	7.8	2.54	3.84^F	2.84	5.93^F
650 °C × 0.5 min	7.2	2.54	3.84^F	2.86	5.93^F
650 °C × 2 min	6.5	2.55	3.84^F	2.83	5.93^F
650 °C × 10 min	5.6	2.55	3.84^F	2.84	5.93^F
650 °C × 60 min	5.1	2.55	3.84^F	2.85	5.93^F
650 °C + WQ	8.0^F	2.54	3.84	2.86	5.93

F: fixed numbers, CN of 2nd shell is fixed as 0.75×(CN of 1st shell).

A curve-fitting parameter of the XANES spectra is adopted for quantitative analysis. The reference spectra for dissolved and precipitated Mo are represented by those for the specimen quenched from 900 °C and for the residue from the thermal aged steel, respectively. The XANES spectra in the photon energy range between −50 eV and +100 eV from the absorption edge are used for the cave fitting after they are subtracted the background and normalized by μ_0. The atomic ratio of the two Mo states is evaluated for each specimen as a ratio of two reference spectra, in which the ratio well reproduces each spectrum.

The decrease of the coordination number of Fe atoms surrounding dissolved Mo atoms is another index (see Fig. 3). This is valuable because the EXAFS signal reflects mainly the dissolved Mo atoms as mentioned above. The coordination number was evaluated by a curve fitting of inverse FT curves (k^3-weigted) for the 1st and 2nd nearest neighbors (the strongest peak of FT in Fig. 3). The k-range for the FT is 3–12 Å^{-1} and the ratio of the 1st and 2nd nearest neighbors was fixed to 8/6. A backscattering factor, a phase shift, and a Debye-Waller factor were derived from the analysis of the reference specimen quenched from 900 °C and fixed in the analysis of other specimens. The results of the curve-fitting analysis are shown in Table I. The R-factors were between 0.8 and 1.3 for all specimens. The atomic fraction of Mo atoms in solution in the matrix was estimated from the coordination number assuming that the coordination number for the specimen quenched from 900 °C (a reference of dissolved Mo in Fe) is unity.

Figure 4 shows the atomic fraction of precipitated Mo estimated by the above two methods. Both curves show the same

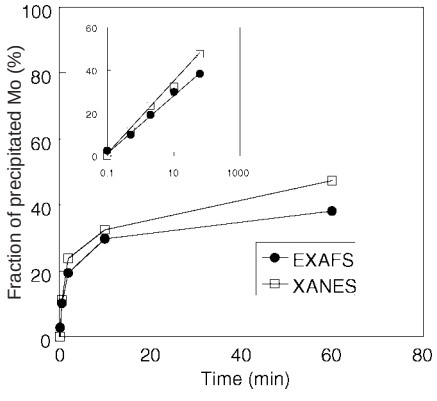

Fig. 4. The atomic fraction of precipitated Mo estimated from XANES and EXAFS spectra as a function of annealing time at 650 °C. Insert plots the results versus a legalistic time scale.

tendency as a function of the annealing time, although the values from the XANES spectra are higher than those from the EXAFS spectra. The insert in the figure clearly shows that the precipitation of Mo has already started even at an annealing time of 0.5 min and proceeds in proportion to the square root of time up to at least 60 min. These phenomena are first clarified by XAFS.

The atomic fraction of precipitated Mo estimated from the XAFS was compared with that from an electrolytic extraction method combined with chemical analysis for the thermal aged specimen. The EXAFS analysis provides about 15% higher value than the electrolytic extraction method. Precipitates with small size could dissolve into solution and/or leak through the filter during the extraction process for the latter method. Our results are indicative of the possibility that XAFS becomes a powerful tool for a quantitative chemical state analysis of small precipitates in steel. The XAFS technique, providing spatially averaged quantitative information on chemical states of micro-alloying elements, must be complemental to direct imaging techniques such as TEM and AP-FIM. This method is easily applied to bulk specimens, which is an advantage when compared with TEM, AP-FIM, and chemical analysis.

The difference in the atomic fraction of the precipitated Mo derived from XANES and EXAFS analysis (in Fig. 4) is a still problem. Two reasons should be considered. One is a selection of reference spectra for precipitated Mo. Residues extracted from steel are not always suitable when precipitates are very small. Another one is the difference of the spatial range probed by XANES and EXAFS analysis (the former would be wider than the latter).

4. Conclusion

The 0.2 mass% Mo in steel was studied by X-ray fluorescence yield XAFS. The XAFS spectra clearly show the transition from Mo in solution to carbides in steel at 650 °C. We demonstrate that the XAFS is applicable to non-destructive quantitative chemical state analysis of micro-alloying elements in steel.

Acknowledgements

The three of authors (M.N., T.K. and K.S.) would like to thank to the High Energy Accelerating Research Organization (KEK) for fruitful collaboration and Dr. N. Usami, Photon Factory, KEK, for her experimental support and helpful discussion.

References

1. For example, Williams, D. B. and Carter, C. B., "Transmission Electron Microscopy", (Plenum Press, New York, 1996).
2. For example, Buswell, G. M. *et al*., J. Nucl. Mater. **148**, 107 (1987).
3. For example, Sakurai, M. *et al*., Mater. Sci. Eng., **A179**/**A180**, 469 (1994).
4. Pizzini, S., Roberts, K. J., Phythian, W. J., English, C. A. and Greaves, G. N., Phil. Mag. Lett. **61**, 223 (1990).
5. Watanabe, T. *et al*., User Expriment Report Spring-8(2002A) **No. 9**, 177 (2002).
6. Nagoshi, M. *et al*., User Expriment Report Spring-8(2003A) **No. 11**, 12 (2003).

Physica Scripta. Vol. T115, 483–485, 2005

Ce 2p3d Resonant Inelastic X-ray Scattering in Ce–Ni Intermetallic Compounds

J.-M. Mariot[1], L. Journel[1], R. Delaunay[1], J.-P. Rueff[1], G. Schmerber[2], J.-P. Kappler[2], N. Jaouen[3], F. Wilhelm[3], A. Rogalev[3], C. F. Hague[1*] and G. Krill[4]

[1]Laboratoire de Chimie Physique–Matière et Rayonnement (UMR 7614), Université Pierre et Marie Curie, 11 rue Pierre et Marie Curie, F–75231 Paris Cedex 05, France
[2]IPCMS, GEMME (UMR 7504), Université Louis Pasteur, 23 rue du Loess, F–67037 Strasbourg, France
[3]ESRF, 6 rue Jules Horowitz, BP 220, F–38043 Grenoble Cedex, France
[4]LURE, Centre Universitaire Paris Sud, Bât. 209D, BP 34, F-91898 Orsay Cedex, France

Received June 26, 2003; accepted November 4, 2003

PACS numbers: 78.70.Ck, 78.70.Dm

Abstract

Resonant inelastic X-ray scattering is well suited to studying pre-edge features in x-ray absorption spectra. Here it is applied to the Ce L_3 edge in CeNi, $CeNi_2$, and $CeNi_7$. A relatively strong feature is observed corresponding to $4f^2$ final states. We show that its presence is not the consequence of $2p \rightarrow 4f$ quadrupole transitions but rather to final state interactions with conduction electrons and Ni $3d$ states.

1. Introduction

The interesting electronic properties of the lanthanides are due to the presence of itinerant (band-like) 5d6s valence electrons and of an integral number of localized (atomic-like) 4f electrons at similar energies [1]. The situation is less clear cut for elements at the beginning of the series where hybridization between the 4f electrons and the valence electrons can arise. This is notably the case for the mixed-valence behavior of Ce-based compounds [2]. High-energy spectroscopies have long played a major role in the investigation of the f-count in these materials. For instance, the comparison between X-ray absorption spectroscopy (XAS) at the Ce 3d edge and theoretical multiplet calculations of the $3d^{10}4f^n \rightarrow 3d^9 4f^{n+1}$ transitions have been used to determine the weights of the f^n configurations in the ground state [3]. In the case of the Ce $L_{2,3}$-edge XAS, empirical models are used to arrive at the f-count [4, 5]. X-ray photoelectron spectroscopy (XPS) on the Ce 3d core levels is another technique widely used to investigate both f-count and hybridization effects despite its high surface sensitivity [6]. The results of these core-level spectroscopies are usually interpreted within the framework of a single-impurity Anderson model proposed by Gunnarsson and Schönhammer (GS) [7]. The same set of parameters have been shown to account for Ce 3d XPS spectra, 4f photoemission experiments, and bremsstrahlung isochromat spectroscopy (BIS) of several Ce–TM (transition metal) compounds within the GS model [8].

Recently some limitations to the GS model have been put forward. For instance, configuration-dependent hybridization terms have been introduced leading to a significant improvement in the description of the XPS and BIS experiments, even for systems where the hybridization is strong [9]. New progress has also been made on the experimental side by recording high-energy Ce 3d photoemission spectra, which enhance bulk sensitivity and allow bulk information to be extracted [10].

Over the past decade, the availability of synchrotron radiation sources with increased brightness has made it possible to develop resonant inelastic X-ray scattering (RIXS) at intermediate energies, i.e., at the rare earth $L_{2,3}$ edges (see for instance Ref. [11]). In such experiments empty states are also probed, but because X-ray scattering leaves behind a weakly bound core hole (in the 3d shell for instance), fine structure can be identified. The latter is usually masked by the shorter lifetime of the 2p core-hole in the standard XAS experiment. Like XAS, RIXS is element selective, and like XAS studied in the fluorescence yield mode, it is bulk sensitive being a photon-in–photon-out process. The latter is a particularly important feature in respect to reactive materials.

Here we show that Ce 2p3d RIXS for three Ce–Ni intermetallic compounds (CeNi, $CeNi_2$ and Ce_2Ni_7) reveals the presence of a strong f^2-like feature at the Ce L_3-edge. This finding is discussed in relation to the standard interpretation of Ce L_3-edge XAS data.

2. Experimental

The RIXS experiments were performed at the European Synchrotron Radiation Facility on beamline ID12 which is equipped with a two Si(111) plane-crystal monochromator [12]. The incoming monochromatized radiation is focused to a spot of $\approx$40 μm in the vertical plane. This spot is the source of an ultra-high vacuum compatible cylindrically-bent quartz $(20\bar{2}3)$ spectrometer dispersing in the vertical plane [11]. The overall resolution for the present experiment is estimated to be $\approx$1.5 eV as determined from a study of the elastic scattering from the samples. The absorption spectra were recorded in the total yield fluorescence mode. All the experiments were performed at room temperature with bulk samples prepared by arc-melting under an argon atmosphere of high-purity constituents. X-ray diffraction was used to check the quality of the samples.

3. Results and Discussion

The Ce 2p3d RIXS spectra of CeNi, $CeNi_2$ and Ce_2Ni_7 are given in Figs 1, 2 and 3 respectively. The intensity of the scattered radiation is given as a function of the energy transfer, i.e., the difference $(\Omega - \omega)$ between the energy Ω of the incoming photon and the energy ω of the outgoing photon. The Ce L_3 XAS spectra are also given as an inset to each figure. The arrows on the XAS spectrum indicate the energies of the resonant excitation used.

*Also at LURE, Centre Universitaire Paris Sud, Bât. 209D, BP 34, 91898 Orsay Cedex, France.

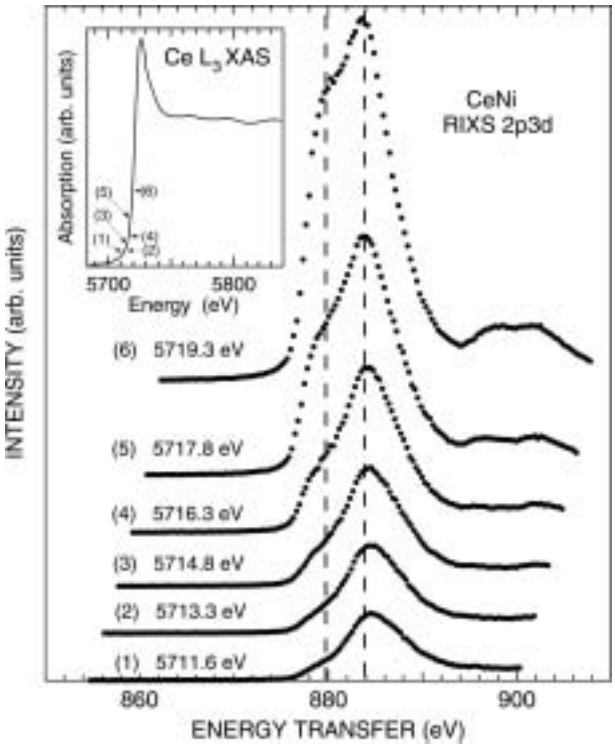

Fig. 1. Ce 2p3d RIXS spectra in CeNi excited at the energies shown by arrows on the Ce L_3 X-ray absorption spectrum (given in the inset).

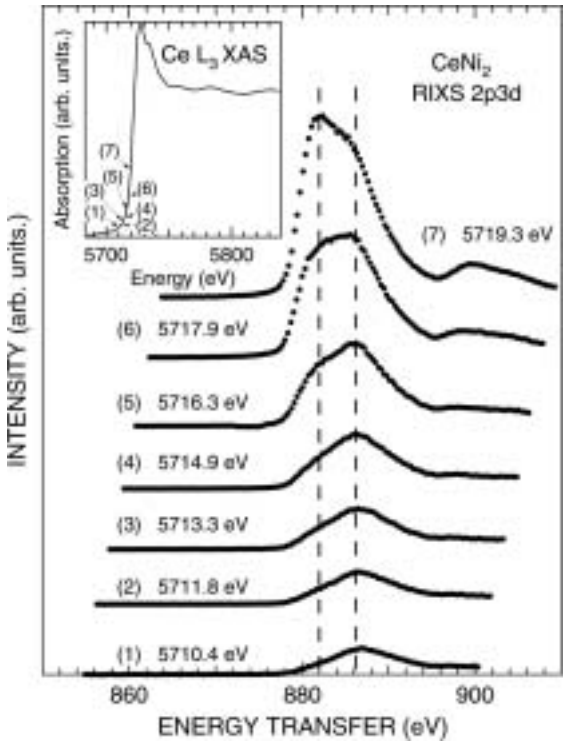

Fig. 2. Ce 2p3d RIXS spectra in $CeNi_2$ excited at the energies shown by arrows on the Ce L_3 X-ray absorption spectrum (given in the inset).

The XAS spectra exhibit a strong white line followed by a shoulder at ≈7 eV on the high energy side which are generally attributed to dipole transitions originating from respectively $4f^1$ and $4f^0$ configurations in the ground state. The higher energy shoulder increases in relative intensity across the series as the nickel content increases.

The RIXS data reported here correspond to excitation energies below the Ce $2p_{3/2}$ ionization threshold. When plotted on an energy transfer scale they clearly show-up two peaks at the Ce L_3-edge. The extra component in the pre-edge region is situated at ≈882 eV and the main peak at ≈886 eV with different relative intensities depending on the compound. We attribute the peak at lower energy transfer to a well screened Ce 3d core hole with a $4f^2$-like configuration. Excitation to the $4f^0$ peak is omitted because the signal is then mixed in with normal fluorescence from the ionized $4f^1$-edge.

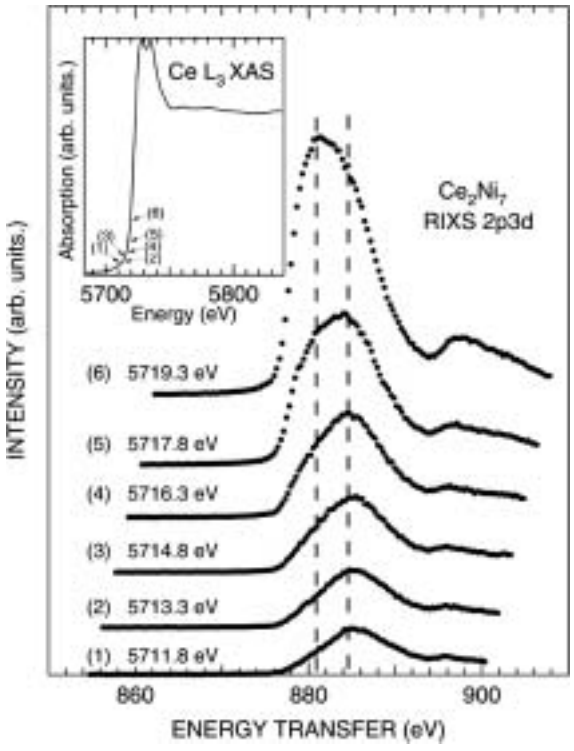

Fig. 3. Ce 2p3d RIXS spectra in Ce_2Ni_7 excited at the energies shown by arrows on the Ce L_3 X-ray absorption spectrum (given in the inset).

The role played by $2p \rightarrow 4f$ quadrupole transitions in rare-earth systems has been extensively discussed particularly in relation with the interpretation of X-ray absorption magnetic circular dichroism (see, e.g., Nakazawa *et al*. [13] for a recent discussion). RIXS performed on ionic CeF_3 [14] and LaF_3 [15] and confronted to theoretical calculations clearly corroborate the presence of a $2p \rightarrow 4f$ quadrupole transition but indicate that its intensity is only about 2% of the $2p \rightarrow 5d6s$ dipole transition. Thus in the following we examine the origin of the unexpectedly high intensity of the $4f^2$-like configuration in the Ce–Ni intermetallics.

Calculations involving both itinerant and localized electron states in the presence of a core hole are extremely diffcult to implement. Thus to analyse our RIXS data quantitatively we use a model already successfully applied to La 2p3d RIXS for lanthanum compounds [15]. In the ground state $|g\rangle$ La is known to have a purely $4f^0$ configuration with the $4f^1$ states lying too high in energy to make any significant contribution. Similarly the contribution from $4f^2$ in the ground state of Ce can be neglected but, as already stressed, both $4f^1$ and $4f^0$ contribute in the Ce mixed valent compounds:

$$|g\rangle = \sum_{i=0}^{2} a_i |f^i\rangle \quad (i = 0, 1, 2,), \tag{1}$$

where coefficient a_2 is negligible. In the intermediate (final) state the presence of an extra 2p (3d) hole, pulls the $4f^1$ and $4f^2$ states down (the hole is better screened) thus modifying the interaction

between the 4f and valence electrons. For the final state, we write

$$|\text{“}f^n\text{”}\rangle = \sum_{i=0}^{2} c_i^{(n)} |f^i\rangle \quad (i = 0, 1, 2,). \tag{2}$$

If we include the transition matrix elements implicitly in the *ac* terms, the intensity to the final state will be:

$$I(f^i) = \left| \sum_{j=0}^{2} a_0 c_j^{(i)} + \sum_{j=0}^{2} a_1 c_j^{(i)} \right|^2 . \tag{3}$$

In our model the densities of states are simulated by semi-ellipses located at different energies according to the whether the excitation is towards mainly $4f^2$, $4f^1$ or $4f^0$ states. The width is assumed to be determined by the 5d6s states themselves hybridized with the Ni conduction states. The RIXS spectrum is then built from a Gaussian excitation function whose amplitude is scaled according to the overlap with each configuration represented by the density of states convoluted with the 2p Lorentzian profile. As the width of the excitation is small compared to that of the 2p broadening we can simulate the final state by the convolution of the narrow 3d final state core hole with the sum of three gaussians centered at the excitation energy. Finally, further broadening is introduced to take into account the Gaussian spectrometer function. The energy offsets between the semi-ellipses and their width are chosen to give the best fit to the full set of experimental spectra using the excitation energy as the only variable. For more detail of the procedure see Ref. [15]. An example of the fit is shown in Fig. 4 for CeNi.

The values for the full-width at half-maximum of the 2p and 3d core-levels were taken to be 4.0 eV and 1.4 eV respectively. The width of the semi-ellipse was 5.5 eV. Other parameters are shown in the figures and the relative intensity of the $4f^2$ and $4f^1$ components are summarized in Table I. Values obtained by XPS are also given in this table.

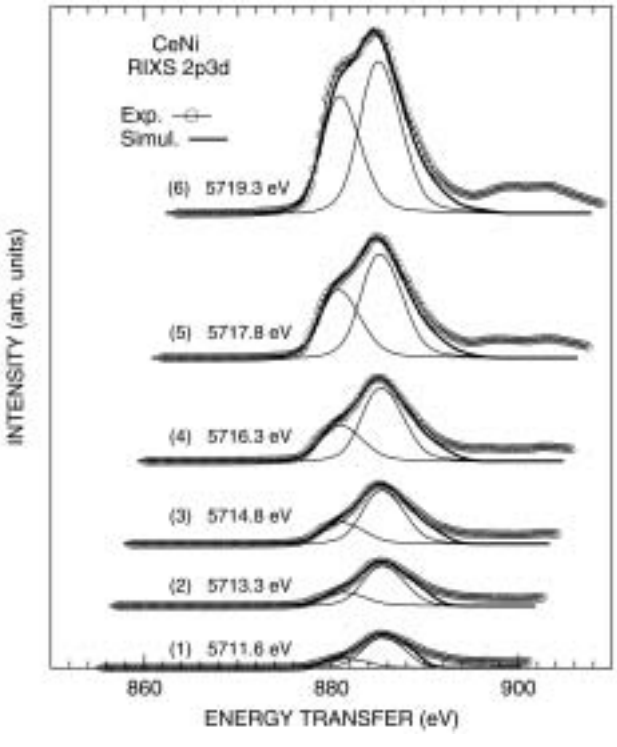

Fig. 4. Simulated Ce 2p3d RIXS spectra for CeNi.

Table I. *Relative intensities of f^2 and f^1 peaks as given from the simulation of the Ce 2p3d RIXS spectra. Values deduced from Ce 3d XPS spectra are also given.*

	$f^2/(f^1 + f^2)$			
	CeNi	$CeNi_2$	Ce_2Ni_7	$CeNi_5$
RIXS	0.16	0.21	0.20	—
XPS[a]	0.16	0.23	—	0.19

[a]From Ref. [6].

In the more straightforward case of La–Ni compounds where the ground state is not mixed valent it was found that the relative intensity of a $4f^1$-like final state increased as interaction with Ni 3d states in the final state increased. XAS measurements at the Ce L_3 edge show that the $4f^0$ peak increases in relative intensity as the Ni content increases. In such a case it is generally taken as directly related to the ground state coeffcients a_0 and a_1. It explains that XAS is widely used to measure f-count directly.

Our results indicate however that the structure at the Ce XAS L_3-edge is made up of two peaks one of which results from interaction with conduction states leading to a $4f^2$-like configuration. It is much stronger than would be expected from a quadrupole transition. It is also stronger in the two compounds with the larger Ni content. The values for the $f^2/(f^1 + f^2)$ ratios taken from XPS [6] are similar though they concern an ionized system unlike RIXS.

4. Conclusions

Ce 2p3d RIXS is able to reveal structure not observed in XAS measurements. The indications are that XAS may not be used as a straightforward method for estimating ground state f-counts because 4f–conduction-electron interactions in the intermediate state significantly modify the relative intensities of the peaks attributed to dipole transitions from the ground state configuration. The XAS peak originating from transitions from the mainly $4f^1$ ground state configuration has a component whose intensity increases with Ni content as its main component decreases. Because of the diffculty of constructing a reliable theoretical model, more detailed analysis across a large series of Ce compounds is required before quantitative corrections to XAS can be applied.

References

1. Elliott, R. J., “Magnetic Properties of Rare Earth Metals” (Plenum Press, New York, 1972).
2. Varma, C. M., Rev. Mod. Phys. **48**, 219 (1976).
3. Fuggle, J. C. *et al*., Phys. Rev. B **27**, 4637 (1983).
4. Röhler, J., “Handbook on the Physics and Chemistry of Rare Earths” (edited by K. A. Gschneider Jr, L. Eyring and S. Hüfner) (North-Holland, Amsterdam 1987), Vol. 10, Ch. 71.
5. Capehart, T. W. *et al*., Phys. Rev. B **55**, 11496 (1983).
6. Fuggle, J. C. *et al*., Phys. Rev. B **27**, 7330 (1983).
7. Gunnarsson, O. and Schönhammer, K., Phys. Rev. B **28**, 4315 (1983).
8. Allen, J. W. *et al*., Adv. Phys. **35**, 275 (1986).
9. Witkowski, N., Bertran, F. and Malterre, D., Phys. Rev. B **56**, 15040 (1997).
10. Braicovich, L. *et al*., Phys. Rev. **56**, 15047 (1997).
11. Hague, C. F. *et al*., J. Electron Spectrosc. Related Phenom. **110–111**, 179 (2000).
12. Goulon, J. *et al*., Physica B **208**, 199 (1995).
13. Nakazawa, M. *et al*., Phys. Rev. B **66**, 113104 (2002).
14. Mariot, J.-M. *et al*., Physica B **259–261**, 1136 (1995).
15. Journel, L. *et al*., Phys. Rev. B **66**, 045106 (2002).

Physica Scripta. Vol. T115, 486–488, 2005

XANES Study of Titanium Environment in $BaO\text{-}B_2O_3\text{-}TiO_2$ System

Valmor R. Mastelaro[1], Carlos A. C. Feitosa[1], Lauro J. Q. Maia[1], Antonio C. Hernandes[1], Alain Ibanez[2] and Alain Michalowicz[3]

[1]Instituto de Física de São Carlos, Universidade de São Paulo, São Carlos, S.P. Brazil
[2]CNRS – Laboratoire de Minéralogie e Cristallographie, Grenoble, France
[3]GPMD, Universite Paris XII-Val de Marne, 94010 Creteil cedex, France

Received June 26, 2003; accepted in revised form December 10, 2003

PACS numbers: 81.05.Kf, 81.05.Pj, 81.20.Fw

Abstract

The coordination environment of titanium atoms in the $x_1TiO_2\text{-}x_2BaO\text{-}x_3B_2O_3$ system, where $x_1 = 4\%$, 8%, 15% and $x_2/x_3 = 8/9$ (molar %), has been determined by X-Ray Absorption Near-Edge Structure (XANES) spectroscopy at the Ti K-edge. The environment of Ti atoms in BBT powder amorphous samples prepared using a chemical method is composed by $^{[4]}$Ti as the predominant specie but the $^{[6]}$Ti specie is also detected. After crystallization, titanium environment in powder samples is predominately composed by $^{[6]}$Ti species. The environment of titanium atoms in glassy samples produced by melting is very similar to that observed on the amorphous powdered samples. On the other hand, the environment of titanium in glass-ceramic samples is completely different from that of powder crystallized samples. A significant amount of $^{[4]}$Ti specie was found after the crystallization in the glass-ceramic samples.

1. Introduction

The crystallization process of the $BaO\text{-}B_2O_3\text{-}TiO_2$ (BBT) ternary system has been systematically studied [1, 2]. Depending on the composition, TiO_2 can act as a nucleating agent promoting the crystallization or inhibiting the crystallization process. According to the composition and the temperature of heat-treatment, the crystallization process can lead to the formation of interesting crystalline phases as the β-BaB_2O_4 (or β-BBO) phase [1, 2]. This phase has attracted the attention of many researches due its interesting optical non-linear properties, for example, a large effective second harmonic generation coefficient [3].

Recently, glass-ceramics samples containing non-centrosymmetric BaB_2O_4 (β-BBO) crystals by controlled devitrification of $x_1TiO_2\text{-}x_2BaO\text{-}x_3B_2O_3$ glasses, where $x_1 = 4\%$, 8%, 15% and $x_2/x_3 = 8/9$ (molar %) were prepared [2]. According to this work, for the $x_1 = 4\%$ sample we observed the formation of only the β-BBO crystalline phase whereas for the $x_1 = 8$ and $x_1 = 15\%$ samples the presence of a $BaTi(BO_3)_2$ phase was identified.

In order to better understand the role of TiO_2 on the crystallization process on the $BaO{-}B_2O_3\text{-}TiO_2$ system, we carried out the XANES analysis at the titanium environment from powder, glasses and glass-ceramics samples obtained from the $x_1TiO_2\text{-}x_2BaO\text{-}x_3B_2O_3$ system, where $x_1 = 4\%$, 8%, 15% and $x_2/x_3 = 8/9$ (molar % ratio).

2. Experimental details

Power samples (PW) from the $x_1TiO_2\text{-}x_2BaO\text{-}x_3B_2O_3$ system with $x_1 = 4\%$, 8%, 15% and $x_2/x_3 = 8/9$ (molar %), were prepared using the polymeric precursor method (Pechini Method) [4]. The heat treatments to produce powder samples were carried out in two stages: initial heating to 330 °C/5 h in an oxygen atmosphere at a heating rate of 10 °C/min to pyrolize the organic materials and "puff", followed soon thereafter by heating to 450 and 750 °C with a heat treatment time of 2 h.

Glass samples (GL) were prepared by mixing appropriate amounts of Commercial powders of reagents grade $BaCO_3$, TiO_2 and B_2O_3, and then melted in a platinum crucible in an electrically heated furnace for 3 hour at 1100 °C. To obtain glass-ceramics samples (GC), glass samples were mechanically polished to get a mirror surface, and then heat-treated in air in an electrically heated furnace at 620 °C during 120 h.

Ti K-edge edge X-Ray Absorption spectra were collected at the LNLS (Laboratório Nacional de Luz Sincrotron, Campinas, Brazil) facility using the XAS beam line [5]. The LNLS storage ring was operated at 1.37 GeV with a nominal ring current of 130 mA. Data were collected at the Ti K-edge (4966 eV) in transmission mode using a Si (111) "channel-cut" monochromator. Ionization chambers were used to detect the incident and transmitted flux. An energy step equal to 0.4 eV and 1.0 eV was used to collect the data at the near the region of the absorption edge. Due to the low critical energy of the machine, harmonic contamination from the monochromator is negligible at the energy of measurements [6]. To monitor the energy calibration, XANES spectra of a metallic foil was recorded at the same time as XANES spectra of the samples, using a third ionization chamber. From XANES data, the intensity of the pre-edge feature was obtained using a single Gaussian function. To compare the intensity and the position of the pre-edge features, all the XANES spectra were background corrected and normalized on the first EXAFS oscillation.

3. Results and discussion

The pre-edge region of the K-edge XANES spectra of some transition metal oxides are characterized by a pronounced feature several volts before the main rising edge. In transition metal oxides that crystallize in centrosymmetric structures, this pre-edge feature is very small or absent; in noncentrosymmetric structures it can be quite large. This pre-edge feature before the edge is commonly attributed to transitions from 1s energy levels of Ti to the Ti3d/O2p molecular orbital [7, 8]. A $1s \rightarrow 3d$ transition is Laporte forbidden by dipole selection rules but becomes allowed when p-d orbital mixing occurs such as which is located in a TiO_4 tetrahedron or a $(^{[5]}TiO)O_4$ site (i.e., without a center of symmetry) [8]. The height and position of this pre-edge feature are direct functions of the degree of p-d mixing, site distortion, oxidation state and experimental resolution [7, 8].

Recently, Farges *et al.* [8] showed empirically that the average coordination number of Ti in a range of titanium

e-mail: Valmor@if.sc.usp.br

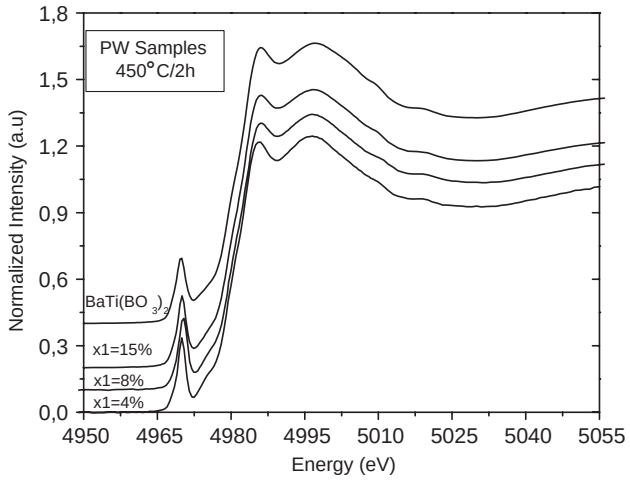

Fig. 1. Ti K-edge XANES spectra for powder amorphous samples (PW) compared to the XANES spectrum of $BaTi(BO_3)_2$ glassy phase.

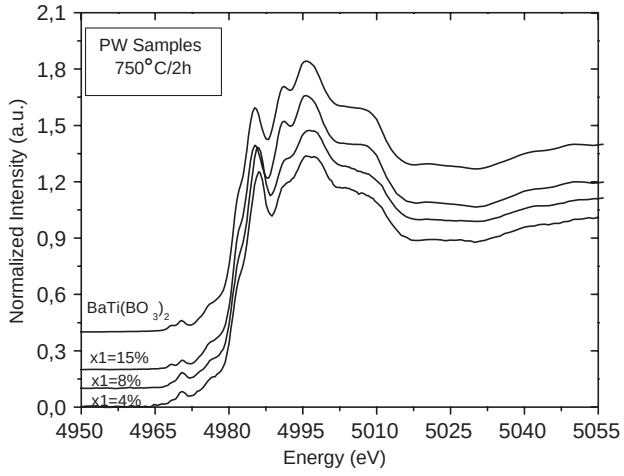

Fig. 2. Ti K-edge XANES spectra for powder samples (PW) crystallized at 750 °C during 2 h compared to the XANES spectrum of $BaTi(BO_3)_2$ crystalline phase.

oxide reference materials and titanium silicate glasses can be extracted reasonably well from plots of pre-edge intensity versus peak positions. Indeed, 4-, 5- and 6-fold coordinated Ti atoms appear to give pre-edge peaks at 4969.5, 4970.5 and 4971.5 ± 0.2 eV, respectively. Thus, the work of Farges *et al*. show that [4]Ti, [5]Ti and [6]Ti are distinguishable according to the position and height of the pre-edge peak [8]. This was the basis of a XANES study by Farges *et al*. in a large variety of minerals and glassy compounds [8].

Figure 1 shows the Ti K-edge XANES spectra of BBT powder samples (PW) heat-treated at 450 °C during 2 h. For comparison, the XANES spectrum of $BaTi(BO_3)_2$ glassy composition is also shown. According to X-ray diffraction measurements these samples are amorphous. The characteristics of the pre-edge structure for these PW amorphous samples and fot the $BaTi(BO_3)_2$ glassy composition are given in Table I. The pre-edge structure in all the amorphous PW samples is a unique and prominent peak at $4970,0 \pm 0.2$ eV, the same position of [4]Ti compounds [8]. However, the intensity of the pre-edge feature is lower than observed in [4]Ti compounds. The analysis of the pre-edge position and height in this series of samples, including the $BaTi(BO_3)_2$ glassy composition is characteristic of a mixture of [4]Ti and [6]Ti species.

Table I. *Pre-edge parameters for the pre-edge structure in PW (powder), GL (glass) and GC (glass-ceramic) samples and $BaTi(BO_3)_2$ glassy and crystalline phases.*

Sample	Position (eV) ± 0.2 eV	Normalized height (a.u.)
$BaTi(BO_3)_2$ glassy phase	4969.6	0.23
$BaTi(BO_3)_2$ crystalline phase	4970.3	0.04
PW $x_1 = 4\%$ TiO_2 450 °C/2 h	4970.0	0.30
PW $x_1 = 8\%$ TiO_2 450 °C/2 h	4970.4	0.28
PW $x_1 = 15\%$ TiO_2 450 °C/2 h	4970.1	0.28
PW $x_1 = 4\%$ TiO_2 750 °C/2 h	4970.4	0.05
PW $x_1 = 8\%$ TiO_2 750 °C/2 h	4970.4	0.05
PW $x_1 = 15\%$ TiO_2 750 °C/2 h	4970.5	0.03
GL $x_1 = 4\%$ TiO_2	4970.1	0.03
GL $x_1 = 8\%$ TiO_2	4970.1	0.03
GL $x_1 = 15\%$ TiO_2	4969.9	0.03
GC $x_1 = 4\%$ TiO_2	4969.8	0.23
GC $x_1 = 8\%$ TiO_2	4970.4	0.13
GC $x_1 = 15\%$ TiO_2	4970.0	0.16

Figure 2 shows the Ti K-edge XANES spectra of BBT powder samples (PW) heat-treated at 750 °C during 2 h. For comparison, the XANES spectrum of $BaTi(BO_3)_2$ crystalline phase is also shown. The characteristics of the pre-edge structures for these crystallized PW samples and for the $BaTi(BO_3)_2$ crystalline phase are also given in Table I. The pre-edge structure in all the PW samples heat-treated at 750 °C during 2 h is composed of two contributions at $4968,3 \pm 0.2$ and at $4970,3 \pm 0.2$ eV, the same position of [6]Ti compounds [8]. The intensity of the second contribution (associated to the dipolar transition) decreases as the amount of titanium increases. According to the literature, Ti atoms in the $BaTi(BO_3)_2$ crystalline phase are coordinated by 6 oxygen atoms located at 1.92 Å in regular octahedra [9]. This fact explains why the intensity of the pre-edge feature in this sample is smaller.

According to X-ray diffraction experiments, the $x_1 = 4\%$ and $x_1 = 8\%$ PW samples heat-treated at 750 °C could present the contribution of two crystalline phases, $BaTiO_3$ and $BaTi(BO_3)_2$. To verify this hypothesis, we simulated a mixing of the XANES spectra of these two crystalline phases. A good agreement was achieved when the simulated XANES spectra was supposed to the composed of 75% of the $BaTi(BO_3)_2$ phase and 25% of the $BaTiO_3$ phase. A similar result was obtained for the $x_1 = 8\%$ PW sample heat-treated at 750 °C.

Figure 3 shows the Ti K-edge XANES spectra of BBT glass samples (GL). For comparison, the XANES spectrum of $BaTi(BO_3)_2$ glassy composition is also shown. The characteristics of the pre-edge structures for these GL samples are given in Table I. As was observed for the PW amorphous samples, the pre-edge structure in all the GL samples is a unique and prominent peak at $4970,0 \pm 0.2$ eV, the same position of [4]Ti compounds [10]. Again, the intensity of the pre-edge feature is lower than observed in [4]Ti compounds. Thus, the pre-edge feature in these GL samples is characteristic of a mixture of [4]Ti and [6]Ti.

Figure 4 shows the Ti K-edge XANES spectra of BBT glass-ceramic samples (GC). For comparison, the XANES spectrum of $BaTi(BO_3)_2$ crystalline phase is also shown. The characteristics of the pre-edge structure for these glass-ceramic samples and that of $BaTi(BO_3)_2$ crystalline phase are also given in Table I. The pre-edge structure in all the GC samples is quite different when compared with the PW crystalline samples. Firstly, the XANES of GC samples presents a unique peak which intensity depends

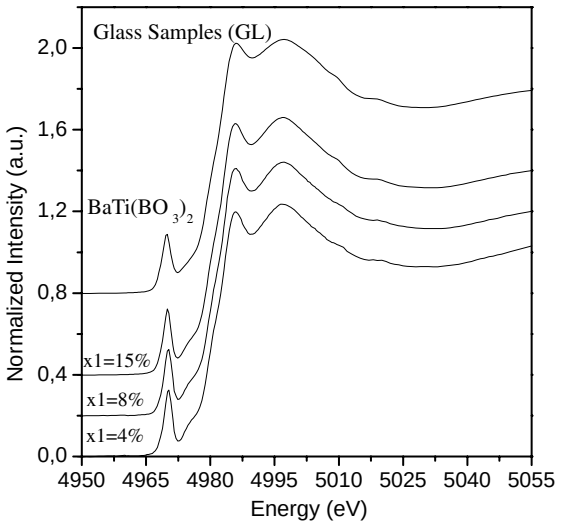

Fig. 3. Ti K-edge XANES spectra for glassy samples (GL) compared to the XANES spectrum of $BaTi(BO_3)_2$ glassy phase.

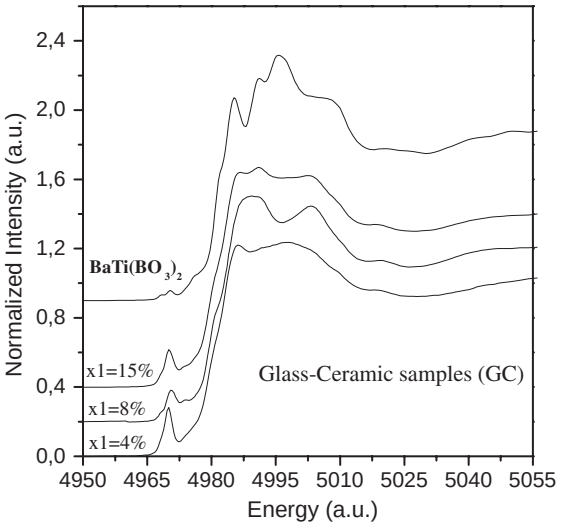

Fig. 4. Ti K-edge XANES spectra for glass-ceramic samples (GC) compared to the XANES spectrum of $BaTi(BO_3)_2$ crystalline phase.

on the amount of TiO_2: the intensity of the pre-edge feature for the $x_1 = 4\%$ GC sample is higher and comparable to that of the glass sample whereas in the $x_1 = 8\%$ and $x_1 = 15\%$ the intensity lower. For the three GC samples, the pre-edge feature is very different from that observed on the $BaTi(BO_3)_2$ crystalline phase. It seems that, although powder samples and glass-ceramic samples were obtained from a material presenting the same nominal composition, the crystallization process is influenced by the method used to prepare the samples, a chemical solution method and the melting method. According to the intensity and the position of the pre-edge feature of GC samples, we can infer that the pre-edge feature is characteristic in these samples contains the contribution from $^{[4]}$Ti and $^{[6]}$Ti, with the predomination of the $^{[4]}$Ti species.

4. Conclusions

XANES studies revealed that the local structure around Ti atoms in amorphous powder samples obtained using the polimeric precursor method is very similar to the local structure in glassy samples of same composition obtained by melting. In both set of samples, the pre-edge feature of the XANES spectra is characteristic of a mixture of $^{[4]}$Ti and $^{[6]}$Ti species. After crystallization, powder and glass-ceramic samples presents a different titanium local structure: in the powder samples, titanium atoms is present dominantly as $^{[6]}$Ti whereas in glass-ceramic samples, a mixing of $^{[4]}$Ti and $^{[6]}$Ti was observed. This difference can explain why we observed the crystallization of different phases on powder and glass-ceramic samples.

Acknowledgments

Research partially performed at LNLS – National Laboratory of Synchrotron Light, Brazil. We are also grateful to FAPESP and CNPq (Brazil) for their financial support.

References

1. Cerchez, M., Boroica, L. and Hülsenberg, D., Phys. Chem. Glasses **41**, 233 (1998).
2. Pernice, P., Esposito, S. and Aronne, A., Phys. Chem. Glasses **39**, 222 (1998).
3. Chen, C. T., Wu, B., Jiang, A. and You, G., Sci. Sinica **B28**, 235 (1985).
4. Pechini, M. P., U.S. Patent No. 3.330.697 (1967).
5. Tolentino, H. *et al*., J. Synchr. Radiation **5**, 521 (1998).
6. Ramos, A. Y., Tolentino, H., Barrea, R. and Alves, M. C. M., Laboratório Nacional de Luz Sincrotron (LNLS), Internal Report MeT-02/99 (1999).
7. Farges, F., J. Non-Cryst. Solids **204**, 53 (1996).
8. Farges, F., Brown, Jr G. E. and Rehr, J. J., Geoch. Cosmoch. Acta **60**, 3023 (1996).
9. Zhang, S. Y. *et al*., Mater. Res. Bulletin **38**, 783 (2003).

Physica Scripta. Vol. T115, 489–491, 2005

Mineralogy of Greigite Fe_3S_4

I. Letard[1], Ph. Sainctavit[1], N. Menguy[1], J.-P. Valet[2], A. Isambert[2], M. Dekkers[3] and A. Gloter[4]

[1]Laboratoire de Minéralogie - Cristallographie de Paris, Université Pierre et Marie Curie, 4, place Jussieu, F-75 252 Paris Cedex 05
[2]Institut de Physique du Globe de Paris, France
[3]Paleomagnetic Laboratory, Utrecht University, The Netherlands
[4]Laboratoire de Physique des Solides, Orsay, France

Received June 26, 2003; accepted in revised form November 4, 2003

Abstract

Greigite Fe_3S_4 is one of the two natural magnetic iron sulphides. Its formula and structure make it the sulphide equivalent of magnetite Fe_3O_4, leading to frequent confusions between these two spinelles in paleomagnetic studies and possible wrong interpretation of some paleaomagnetization measurements.

We have carried out high resolution EELS experiments and recorded X-ray magnetic circular dichroic spectra at the iron $L_{2,3}$ edges on natural and synthetic samples. The natural samples present a core-shell structure of crystallized greigite surrounded by an amorphous iron oxide phase. The differences observed on the XMCD signal of Fe_3S_4 compared to Fe_3O_4 could be explained by the presence of iron vacancies, Fe_3S_4 being a lacunary iron sulphide.

1. Introduction

The study of rock magnetization gives information about the magnetic history of the Earth. Paleomagnetism, in association with other methods, allows to date precisely geological events like appearances and disappearances of animal species or to follow the movements of the lithospheric plates. Dating events thanks to this method is possible because the Earth magnetic field reverted its orientation several times at the geological scale of time.

Among the numerous iron-sulphide minerals, only two are ferrimagnetic, all the others being antiferromagnetic or having complicated magnetic structure (van Vleck paramagnetism). These two magnetic iron sulphides are pyrrhotite Fe_7S_8 and greigite Fe_3S_4. These minerals keep a print of the inversions of the Earth magnetic field. Thus their remanent magnetization is used as the starting point of paleomagnetic studies. Nevertheless, their electronic properties are not well known because they often occur as mixed phases and with an oxidized surface layer.

Fe_3S_4 is a sulphospinelle. Fe_3S_4 and magnetite Fe_3O_4 have the same cubic crystalline structure with octahedral and tetrahedral sites. They only differ by their anions. However, the repartition of Fe^{2+} and Fe^{3+} is not known in Fe_3S_4. Moreover, Fe_3S_4 presents a saturation magnetization by formula unit 2.5 times lower than Fe_3O_4 [1]. It has a different easy-magnetization axis ([100] instead of [111]) [2]. It shows no Verwey transition: whereas at temperature lower than 120 K, a distorsion of the cubic structure has been observed in Fe_3O_4, accompanied by a brutal decrease of the magnetic susceptibility, no such phenomenon has been seen on Fe_3S_4.

All these differences occur despite a similar crystal structure. Iron sulfiphides require a reducing environment. Iron should thus be mainly present as Fe^{2+}. But this would not be sufficient to account for the observed reduction of the magnetization. An other explaination for the reduced magnetization could be the presence of iron vacancies on the octahedral sites.

We have studied both natural and synthetic samples. The complexity of natural samples needs a preliminary observation by transmission electronic microscopy (TEM) associated with energy electron loss spectroscopy (EELS) in order to study the composition and crystalline structure of the sample and to investigate its stability on a period of time of several weeks. The study of the magnetic properties implies the use of X-ray absorption spectroscopy (XAS) and in particular X-ray magnetic circular dichroism (XMCD). To separate the contributions of Fe^{2+} and Fe^{3+} in the octahedral and tetrahedral sites, we followed an approch similar to that exposed in a companion paper by S. Brice-Profeta. However, in iron sulphides, the covalence of the bonds is stronger than in oxides. This implies that the multiplet structures are less visible than in oxides. In consequence, the selectivity of site and of oxidation state is less precise in sulphides than in oxides.

2. Samples description

The natural samples have been collected in the marine sediments uncovered by the errosion caused by the Crostolo River, Po Valley, Italy [3]. Fe_3S_4 is probably of biogenic origin, synthetized inside or around bacteria. Fe_3S_4 particles are separated from the sediment by a magnetic extraction in desoxygenized water. Using this method, we clear the sample from non-magnetic materials which can contain iron and disturb the XAS measurements. However, the resulting extracted sample may contain other magnetic particles among which some might bear iron.

We compared these natural biogenic samples to synthetic ones obtained by hydrothermal synthesis from Mohrs solution $Fe(NH_4)_2(SO_4)_2$ and sodium sulphide NaS_2 in desoxygenized water solution [4].

3. Experimental results

The TEM and EELS experiments have been carried out on the High Resolution TEM Akashi Topcon EM-002B of the LPS (Orsay, France) and on the 2010F Jeol microscope of the CP2M (Marseille, France). XAS measurements have been carried out on the SU23 beamline at LURE (Orsay, France) and on the BACH beamline at Elettra (Trieste, Italy). Spectra have been recorded at the iron $L_{2,3}$ edges.

3.1. *EELS: the core-shell structure of the particles*

The TEM study of the natural samples showed grains of about 50–200 nm wide, as presented in fig. 1. These grains are constituted of a core and a shell. The shell is about 10 nm thick when observed a few days after the extraction. It constitutes the totality of the grains after a few weeks. In the core, diffraction features appear clearly whereas the shell appears amorphous. We have recorded EELS spectra on both the core and the shell of several particles. We recorded spectra from a few eV after the

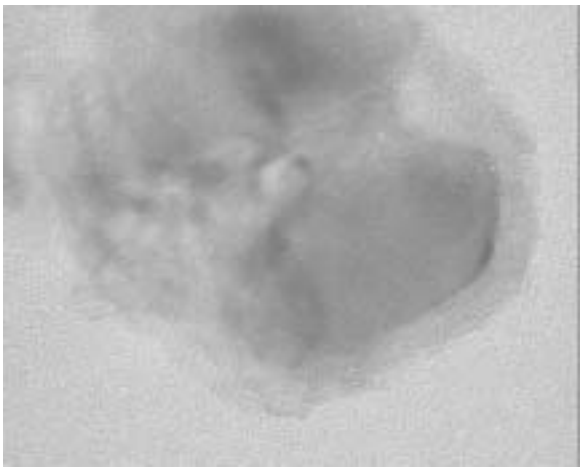

Fig. 1. TEM picture of a grain of crystalline iron sulphide surrounded by a shell of amorphous iron oxide.

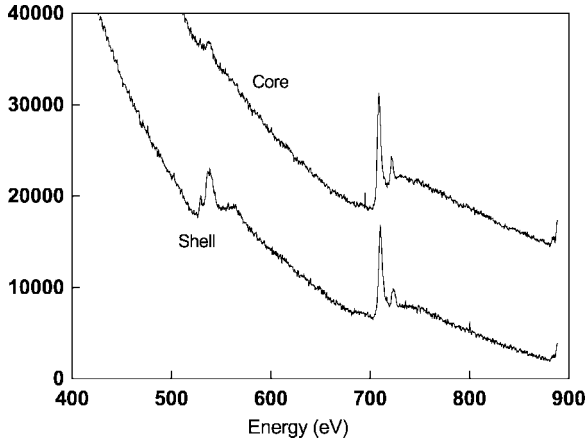

Fig. 2. EELS spectra recorded separately on the core and on the shell of a particle of natural Fe_3S_4: oxygen K-edge and iron $L_{2,3}$ edges.

elastic feature to 900 eV. The O K-edge to Fe $L_{2,3}$ edges range is shown on fig. 2. The spectrum recorded on the core shows absorption at the S and at Fe $L_{2,3}$ edges and slight absorption at the O K-edge. On the contrary, the spectrum recorded on the shell presents strong absorption at the O K-edge and Fe $L_{2,3}$ edges but not at the S $L_{2,3}$ edges. The Fe $L_{2,3}$ edges feature is typical of spectra obtained on iron oxides. The shell is thus contituted of an amorphous iron oxide phase. An electron diffraction on the core confirms that this crystalline iron sulphide phase is greigite.

TEM observations on the synthetic samples have shown crystallized greigite particles of a few hundred nanometers wide. The synthetic particles were observed a few days after the synthesis and did not present any feature of oxidation. No measurement was carried out after a few weeks or months thus we have no idea of the way synthetic greigite oxidizes when aging.

EELS spectra have also been recorded with a better energy resolution on both the core and the shell of several particles. The spectra are shown on fig. 3. One can notice that the signal recorded on the sulphide part of the particle also contains the contribution of the surface. Indeed, to reach the core of the particle, the electron beam goes accross the oxide shell, which can contitute up to 20% of the explored volume depending on the oxidation rate of the particles.

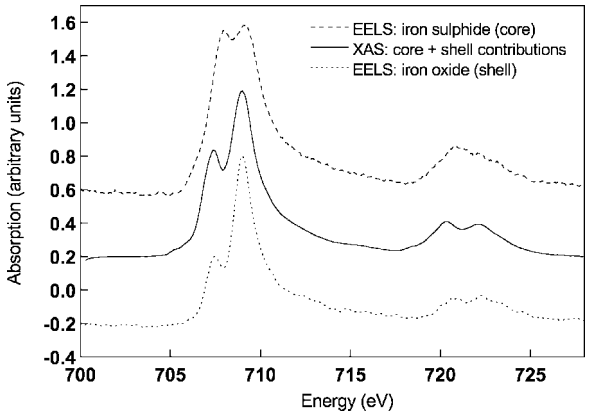

Fig. 3. Comparison of the iron $L_{2,3}$ edges spectra recorded by EELS respectively on the sulphur and on the oxide part of a particle and by XAS (fresh natural sample).

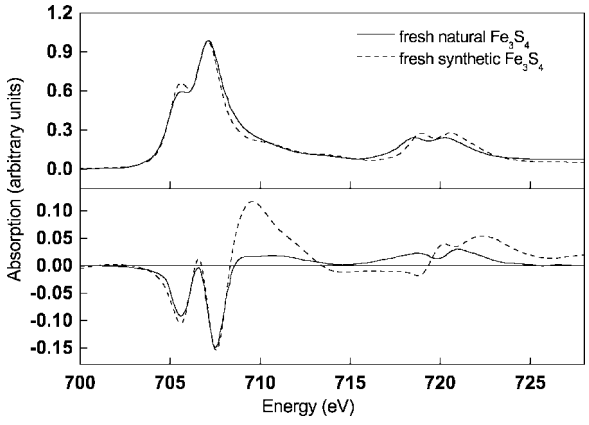

Fig. 4. Isotropic and dichroic spectra recorded at 4.2 K in a magnetic field of $+/-2$T on the natural and synthetic samples. The magnetization is saturated.

3.2. *XAS and XMCD*

Contrary to EELS, XAS and XMCD can give information on the magnetic properties. This spectroscopy does not bring as good spatial resolution as EELS, but brings a better energy resolution. The XAS spectra of natural greigite are the result of both contributions of the core and the shell of the particles (see fig. 3). In the same way, the XAS spectra of recently synthetized greigite is intermediate between the hematite spectra and the iron sulphur EELS spectra. It may be the result of a similar oxidation process that may yield a core-shell structure.

In order to determine the repartition between Fe^{3+} and Fe^{2+} in Fe_3S_4, we have recorded XMCD spectra on natural and synthetic Fe_3S_4. The signals are shown on fig. 4.

4. Interpretation

In samples as complexe as natural magnetic minerals, coupling the two techniques, EELS and XMCD, is necessary.

4.1. *Oxidation towards hematite*

XAS spectra on synthetic greigite have been recorded a few weeks after the synthesis and six months after. The isotropic spectra presented on fig. 5 show that the aging of greigite leads to an iron oxide very close to hematite α-Fe_2O_3, mineral containing only Fe^{3+} in octahedral sites. The spectrum of recently

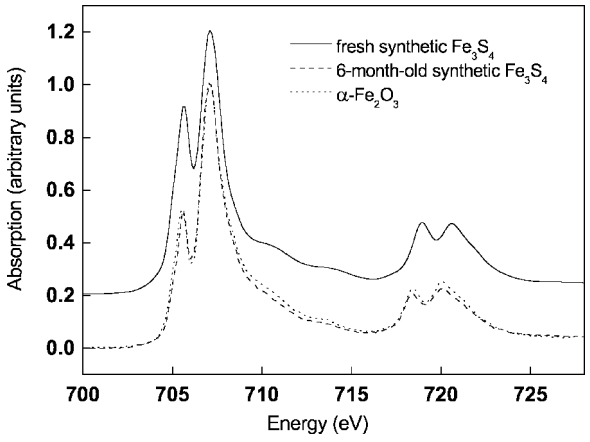

Fig. 5. XAS at iron $L_{2,3}$ edges spectra showing the evolution of synthetized Fe_3S_4 toward hematite.

synthetised Fe_3S_4 presents a stronger contribution for feature B. Fresh synthetic Fe_3S_4 shows dichroism (see fig. 4) whereas older synthetic Fe_3S_4 does not show any dichroic signal. Since the oxidized phases are stable, this result may evidence that the dichroic signal observed on fresh Fe_3S_4 is due to sulphide and not to oxide.

4.2. *No oxide contribution to the dichroic signal*

EELS spectra showed that the surrounding shell is contituted of amorphous iron oxide. This oxide probably leads to ferrihydrite or hematite α-Fe_2O_3. At 4 K, hematite is antiferromagnetic. The magnetic contribution of the shell to the spectra is thus a paramagnetic or antiferromagnetic contribution. Thus, whereas the isotropic spectra is the sum of oxide and sulphide contributions, the observed dichroic signal may be only due to the Fe_3S_4 core.

4.3. *Comparison between natural and synthetic samples*

The two samples present similar isotropic cross sections though XMCD signals are pretty different. We attribute the differences to various ratio of oxide *vs* sulphide contributions. The large positive bump after the L_3 edge is a clear sign of Fe-S hybridization. Fe_3S_4 structure can accomodate for various electronic and crystallographic modifications (Fe^{2+}/Fe^{3+} ratio or presence of vacancies) so that, even without spurious oxidation contributions, similar phases could yield quite different XMCD spectra. To illustrate this point, XMCD signals of γ-Fe_2O_3 and Fe_3O_4 are quite different although they are almost indistinguishable by diffraction techniques.

Compared to the dichroic signal obtained on Fe_3O_4 (presented on fig. 6), at the L_3 edge, the ratio of the two peaks is reverted: in Fe_3S_4, feature A is weaker than feature A′ and it is the contrary

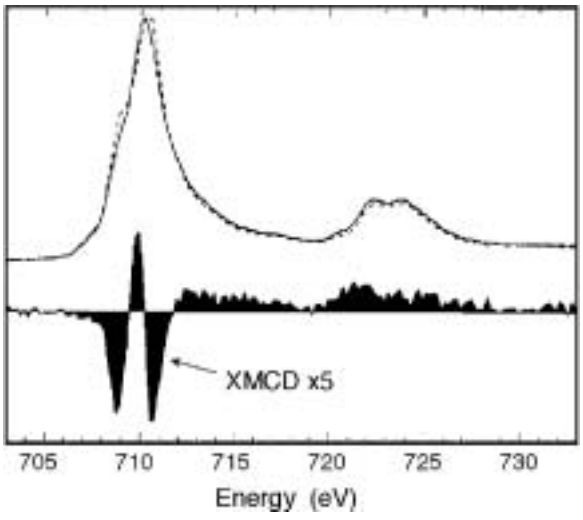

Fig. 6. Isotropic and dichroic spectra recorded on Fe_3O_4 [5].

in Fe_3O_4. This can be attributed to a contribution of Fe^{2+} in octahedral sites weaker in Fe_3S_4 than in Fe_3O_4.

5. Conclusion

EELS on natural greigite showed a core-shell structure composed of a core of well-crystalized Fe_3S_4 and a shell of amorphous iron oxide, possibly precursor of hematite α-Fe_2O_3. XMCD spectra more probably take into account only the sulphur contribution. The differences observed between the XMCD spectra of Fe_3S_4 and Fe_3O_4 can be explained by the presence of iron vacancies in Fe_3S_4 leading to a lacunary iron sulphide similar to the lacunary iron oxide maghemite γ-Fe_2O_3.

Acknowledgements

We would like to thank François Bertran and Franck Fortuna (SU23 beamline, LURE, Orsay, France), Marco Zangrando and Michele Zacchigna (BACH beamline, Elettra, Trieste, Italy), Jean-Paul Kappler and Christophe Cartier dit Moulin for their help in the experimental part of the work. This is IPGP contribution No. 1926.

References

1. Hoffmann, V., Phys. Earth Planet. Interiors **70**, 288 (1992).
2. Heywood, B. R., Mann, S. and Frankel, R. B., Mat. Res. Soc. Symp. Proc. **218**, 93 (1991).
3. Tric, E. *et al.*, Phys. Earth Planet. Interiors **65**, 319 (1991).
4. Dekkers, M. J. and Schoonen, M. A. A., Geochim. Cosmochim. Acta, **58**, 4147 (1994).
5. Kuiper, P., Searle, B. G., Duda, L.-C., Wolf, R. M. and van der Zaag, P. J., J. Electron Spectrosc. Rel. Phenom. **86**, 107 (1997).

Physica Scripta. Vol. T115, 492–494, 2005

Evolution of an Iron Film on GaAs(001)-4 × 6

R. A. Gordon[1], P. S. Budnik[1], D. T. Jiang[2] and E. D. Crozier[1,*]

[1]Department of Physics, Simon Fraser University, 8888 University Drive, Burnaby, BC, Canada V5A 1S6
[2]Canadian Light Source, Saskatoon, SK, Canada S7N 2X8

Received June 26, 2003; accepted in revised form November 4, 2003

PACS numbers: 61.10.Ht, 68.55.Jk, 75.50.Bb, 81.15.Hi

Abstract

The process of iron film epitaxial growth on the 4 × 6 reconstructed surface of GaAs(001) proceeds through a transition between island (Volmer-Weber) and layer (quasi-Frank-van-der-Merwe) growth. We have examined the growth of iron on GaAs(001)-(4 × 6) *in-situ* by polarization-dependent XAFS in the total reflection mode. The onset of greater ordering in the film has been observed through the development of tetragonally-distorted iron. The distortion towards lattice-matching between the iron in-plane and the GaAs substrate is clearly evident immediately after the transition between growth modes. The resulting body-centered tetragonal structure persists to 30 monolayers, the largest thickness studied.

1. Introduction

Iron films on GaAs substrates continue to attract interest for magnetic applications owing to the small (1.4%) mismatch between body-centred cubic (bcc) Fe and half the lattice constant of GaAs. Studies of the evolution of film stress, surface morphology and magnetic behavior have been performed [1–3] using the (4 × 6) reconstruction of the GaAs surface. Using this reconstruction minimizes reaction between the iron and substrate [4] and results in high-quality epitaxially-grown films [5] but with the possibility of macroscopic defects for thicker films [2].

Missing from the picture of iron on GaAs(001)-(4 × 6) is an understanding of how the structure changes with increasing thickness. There is a transition in growth modes from Volmer-Weber (island) to quasi-Frank-van-der-Mewe (layer) growth [5] that occurs near 4 monolayer (ML) thickness, and the iron is reported to be distorted to a body-centred tetragonal (bct) structure near 10 ML that favors lattice-matching to the substrate [6]. We have extended our polarization-dependent XAFS structural study [6] of the bct distortion with measurements above and below the transition in growth modes to better understand how these iron films on GaAs(001) evolve as a function of thickness.

2. Experimental

Samples were prepared and measured *in-situ* using the molecular beam epitaxy (MBE) facilities of the Pacific Northwest Consortium Collaborative Access Team (PNC-CAT) beamline – sector 20 of the Advanced Photon Source, Argonne National Laboratory [7]. Gallium arsenide (001) n-type wafer sections (American Xtal Technology) underwent a thermal desorb treatment before sputtering (500 eV Ar^+) and anneal to achieve the (4 × 6) reconstruction. Room temperature deposition was done with RHEED monitoring using Omicron EFM3 evaporators and growth rates of ∼0.5 ML per minute. Samples with Fe thicknesses of (ML-equivalent) 0.5, 2, 3.5, 5, 6, 9.3, 15, 16 and 30 were prepared. The 15 ML sample was prepared on top of the 3.5 ML sample; the 30 ML was on top of the 16 ML sample, after XAFS data on the first thickness were obtained. RHEED oscillations were not observed for the second thicknesses deposited.

XAFS measurements were done on the undulator beamline of the PNC-CAT. The Si(111) double-crystal monochromator was detuned to 75% of the maximum intensity at 7500 eV to reduce harmonic contributions. X-rays were incident in the total-reflection geometry with the polarization vector either (near) perpendicular or in the plane of the substrate (within 2° of (110), (−110) or (010) orientations). To minimize distortion of the spectra due to dispersion effects in the sample and adjacent media, the angle of incidence was set to approximately 2/3 of the critical angle at 7500 eV [8]. Fluorescence XAFS data were obtained using Argon-filled ionization chambers [9] or, for the two thinnest samples, a 13-element Ge(Li) detector (Princeton-Gamma-Technology). Helium-filled transmission chambers were used for normalization and reference data.

3. Results

EXAFS interference functions, $\chi(k)$, were extracted from the absorption spectra using AUTOBK [10]. Figure 1 shows the averaged EXAFS interference functions for perpendicular polarization measurements on each of the thicknesses measured. A reference Fe foil and a sample in-plane (16 ML) plot are also shown for comparison. The 16 ML in-plane and foil bear a much stronger resemblance to each other than to any of the out-of-plane data. This is particularly noticeable in the region 2.3–7 $Å^{-1}$. Noticeable differences exist between foil and film (out-of-plane) that indicate the persistence of the bct distortion up to and including the 30 ML film. In particular, both the reduced amplitude of the oscillation at 5 $Å^{-1}$ when compared to the foil and the absence of a feature at 6 $Å^{-1}$ for the out-of-plane 30 ML data are strong indications that the thickest film measured has not relaxed to body-centred-cubic. With decreasing thickness, fine structure in the $\chi(k)$'s decreases to the point that the two thinnest samples appear almost as single frequencies.

Fourier transforms, with k^2-weighting and 10% Gaussian windows, were taken and analyzed using WINXAS [11] and FEFF7 [12]. Transforms were taken over the range 2.37 $Å^{-1}$ to the end as plotted in Fig. 1, typically 14.2 $Å^{-1}$. Analysis was done over the first peak in the Fourier transform, as shown for the 16 ML and 6 ML samples in Figure 2 in order to extract nearest-neighbour and next-nearest-neighbour (*c*-axis) information. To allow for the presence of Ga or As beneath, on-top or within the film, alloying models were used in the FEFF simulations. Since gallium and arsenic are essentially indistinguishable in backscattering from each other and the element in between them,

*crozier@sfu.ca

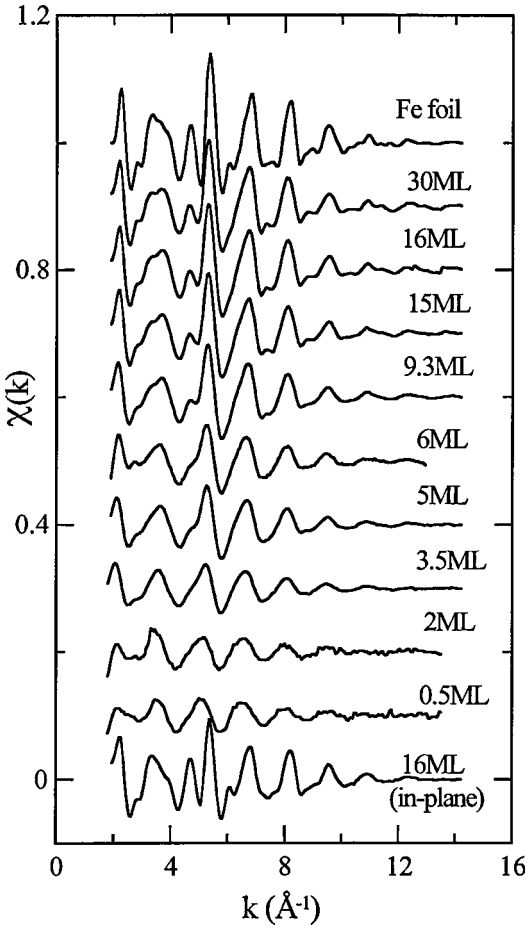

Fig. 1. Iron EXAFS interference functions, $\chi(k)$ for X-ray polarization perpendicular to (along the normal to) the GaAs(001) substrate for films of thickness equivalents from 0.5 to 30 monolayers. A reference iron foil $\chi(k)$ (top) and polarization-parallel (in-plane) $\chi(k)$ (bottom) are shown for comparison.

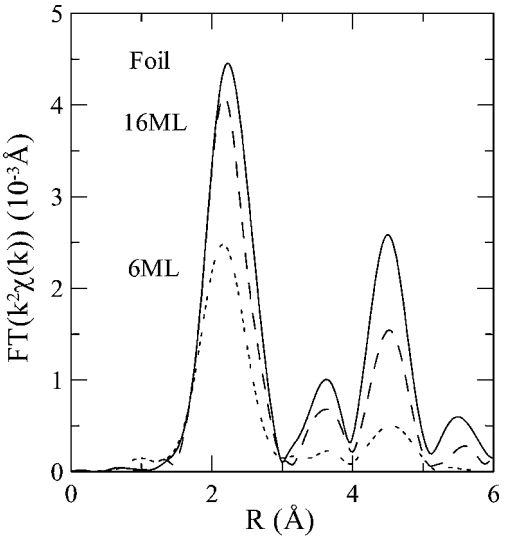

Fig. 2. Comparison of k^2-weighted Fourier transforms for Fe foil, 16 ML and 6 ML samples.

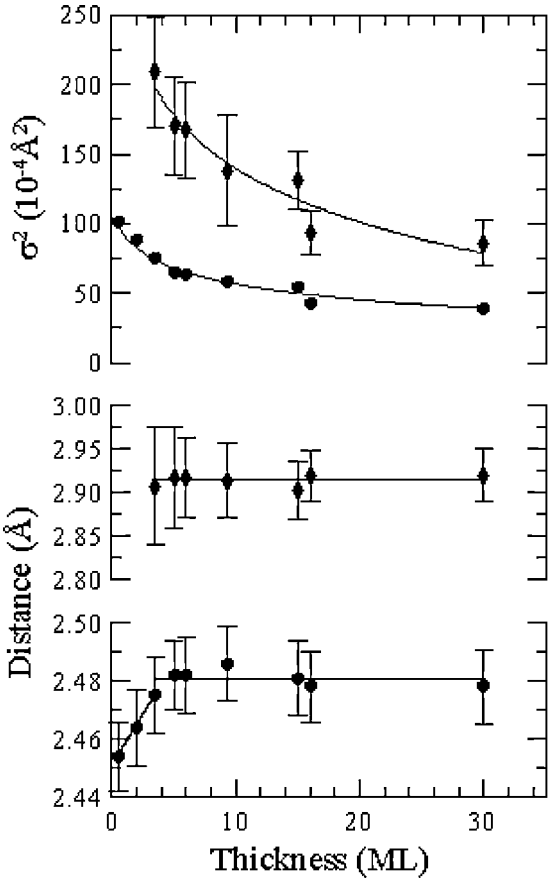

Fig. 3. Distances and mean-square relative displacements for the two shells (nearest-neighbour, lattice constant) contained in the first peak of the Fourier transform. Error bars for nearest-neighbour σ^2 are comparable to the size of the point. Curves are drawn as a guide for the eye.

germanium, we simplified the calculations by using Ge as the average of both. It is also challenging to distinguish Fe from Ga or As in backscattering. The extent of alloying (fraction non-iron species in film) was increased in the simulations with decreasing film thickness. This was done based on a starting structural model of a bct iron film capped below by Ga (for the gallium-rich 4×6 substrate surface) and above by As (As segregating to the film surface [5]), with the simplification of using Ge for Ga and As. With coordination numbers fixed according to this model, the influence of non-Fe species decreases for the average Fe atom with increasing Fe thickness. For 9.3 ML and higher, a pure Fe model give comparable fit results, indicating an insensitivity to non-Fe species at the 10% level or below.

Fit results for these two shells are summarized in Figure 3. Small offset corrections of order 0.01 Å were applied based on reference iron foil fit results. Distances for both Fe and non-Fe atoms (Ge in place of Ga and As) in a given backscattering path were constrained to be the same for both species present in that shell. The mean-square-relative-displacements for both species were similarly constrained. This did not result in any difficulty in fitting that would mandate a splitting of these into independent parameters. We were unable to obtain second shell information for the 2 ML and 0.5 ML samples. At 3.5 ML, we are at the transition point between growth modes and are able to obtain some second shell information. For 3.5 ML and higher, we observe fairly constant values for the nearest-neighbour and c-axis distances, with no detectable dependence of the distortion to bct on thickness up to 30 ML (30 ML roughly corresponds to a film 44 Å thick).

The σ^2 values increase with decreasing thickness, consistent with an increasing ratio of surface to interior atoms (fewer atoms bound inside the film) and may also reflect an increasing influence of substrate atoms within the iron film. For comparison, the foil and 16 ML in-plane values (in Å^2) for ${\sigma_1}^2$ and ${\sigma_2}^2$ are 0.0050(2) and 0.0064(5) for the foil, and 0.0051(5) and

0.0067(9) for the 16 ML film. The $\sigma_2{}^2$ values for the out-of-plane polarization plotted in fig. 3 are considerably larger than the in-plane or foil values. This may be due to increased disorder or (surface) roughness in the out-of-plane direction, but may also be due to the strained nature of the film itself. For both polarizations, the nearest-neighbour interactions are largely in-plane, since the nearest-neighbour in a bcc or bct structure is located approximately 36° above the plane (the angle between the [111] and [110] directions). Next-nearest neighbour interactions for in-plane are also in-plane, but, for the out-of-plane measurements, the next-nearest neighbour is 90° above the plane – entirely out of plane. The out-of-plane direction is the direction of response to the in-plane stress. It is not unreasonable to expect a larger dynamic contribution to the mean-square-relative-displacement in this case, but a temperature-dependent study would be required to confirm this.

For the 3.5 ML and below, the nearest neighbour distance appears to contract relative to the thicker films, approaching the Ga-As bond length in GaAs (2.448 Å) for the average iron atom as the Fe coverage tends towards zero monolayers. This suggests some reaction with the substrate where Fe could be occupying As or Ga vacancies at or near the surface. This is consistent with the observed tensile stress in such films [1] whose origin was attributed to diffusion of Ga or As out of the substrate and the possible re-occupation of the resultant voids by iron.

Acknowledgments

Experiments at the PNC-CAT beamline were made possible by support from the Natural Sciences and Engineering Research Council of Canada, through major facilities access and operating grants. Research at the PNC-CAT and the APS is also supported by the U.S. Department of Energy, Basic Energy Sciences under contracts W-31-109-Eng-38 (APS) and DE-FG03-97ER45628 (PNC-CAT).

References

1. Wedler, G., Wasserman, B., Nötzel, R. and Koch, R., Appl. Phys. Lett. **78**, 1270 (2001).
2. Schönherr, H.-P., Nötzel, R., Ma, W. and Ploog, K. H., J. Appl. Phys. **89**, 169 (2001).
3. Xu, Y. B. *et al*., Phys. Rev. B **58**, 890 (1998).
4. Freeland, J. W., Coulthard, I., Antel, W. J. Jr. and Stampfl, A. P. J., Phys. Rev. B **63**, 193301 (2001).
5. Monchesky, T. L. *et al*., Phys. Rev. B **60**, 10242 (1999).
6. Gordon, R. A., Crozier, E. D., Jiang, D.-T., Monchesky, T. L. and Heinrich, B., Phys. Rev. B **62**, 2151 (2000).
7. Heald, S. *et al*., J. Synch. Rad. **8**, 342 (2001).
8. Jiang, D. T. and Crozier, E. D., Can. J. Phys. **76**, 621 (1998).
9. Gordon, R. A., Crozier, E. D., Shoults, J. and Jiang, D.-T., Rev. Sci. Instrum. **73**, 2849 (2002).
10. Newville, M., Livins, P., Yacoby, Y., Stern, E. A. and Rehr, J. J., Phys. Rev. B **47**, 14126 (1993).
11. Ressler, T., J. Phys. IV **7**, C2-269 (1997).
12. Zabinsky, S. I., Rehr, J. J., Ankudinov, A., Albers, R. C. and Eller, M. J., Phys. Rev. B **52**, 2995 (1995).

Physica Scripta. Vol. T115, 495–497, 2005

Structure of the Magnetic Trilayer System Fe/Pd/Fe Epitaxially Grown on GaAs(001)-4×6

P. S. Budnik, R. A. Gordon and E. D. Crozier*

Physics Department, Simon Fraser University, Burnaby, B.C., V5A 1S6, Canada

Received June 26, 2003; accepted in revised form November 4, 2003

PACS numbers: 61.10.Ht, 68.55.Jk, 75.50.Bb, 81.15.Hi

Abstract

The magnetic behaviour of ferromagnetic/non-ferromagnetic/ferromagnetic trilayers is strongly dependent on the nature of the interface between layers, the strain in the layers and the extent of any interdiffusion or reaction between layers and substrate. In this paper, results are presented from a polarization-dependent *in situ* XAFS study of Fe/Pd/Fe trilayers epitaxially grown on GaAs(001)-(4 × 6). Fe and Pd K-edge spectra were obtained both above and below the critical angle for total reflection. The structure of iron grown on the Ga-terminated 4 × 6 reconstructed surface of the GaAs(001) substrate, for thicknesses greater than 6 monolayers, is tetragonally distorted from its natural bcc structure with contracted and expanded lattice constants in the in-plane and out-of-plane directions, respectively. The intermediate Pd layer shows distortion from its natural fcc structure. Alloying at the interface with the underlying Fe is restricted to a depth of 0.5–1.0 monolayers (ML). The upper layer of Fe shows tetragonal distortion similar to the layers of Fe grown on GaAs(001)-4 × 6. However, the upper distortion is stronger. There is also evidence of alloy formation at the interface involving the underlying Pd with the thickness of the alloy region being 2–2.5 ML.

1. Introduction

The small lateral dimensions of spintronic devices and high density memory bits require the employment of magnetic ultrathin metallic film structures. In magnetic trilayer systems of the form F/M/F the magnetic moments in the ferromagnetic film F are locked together by exchange coupling through the non-magnetic spacer layer M. The magnetic behaviour in these systems – the magnetic anisotropy and interlayer coupling – is strongly dependent on the thickness of the layers, the nature of the interface between layers, the strain in the layers and the extent of any interdiffusion or reaction between layers and substrate. Understanding the structure is a critical component of developing the correct interpretation of the magnetic behaviour. A molecular beam epitaxy facility was developed for use on the PNC-CAT undulator beamline to permit *in situ* epitaxial growth of metal films and their structural characterization by synchrotron radiation techniques.

In an earlier study [1] we used polarization-dependent XAFS in the total reflection mode to characterize the epitaxial growth of Fe on GaAs(001)-(4 × 6). The small lattice mismatch of 1.4% between bcc iron ($a = 2.866$ Å) and GaAs ($a/2 = 2.827$ Å) has made it a model system for growth of ferromagnetic materials on semiconductors. Quantitative analysis of our *in situ* XAFS data [1, 2] indicated a body-centered tetragonal (bct) structure with $c/a \sim 1.03$ starting at ~ 5 ML (monolayers) and persisting to 30 ML, the thickest film studied.

Here, we present *in situ* results of a polarization-dependent XAFS study both above and below the critical angle for total reflection from Fe/Pd/Fe trilayers epitaxially grown on GaAs(001)-(4 × 6). Palladium was chosen as the spacer layer for three reasons. 1) Pd is easily influenced magnetically by ferromagnetic species such as iron. 2) Pd has been grown on single crystal Fe(001) [3] and Fe has been grown on the surface of Pd(001) grown on MgO [4–6], but with different structural conclusions. 3) The lattice mismatch between the naturally occurring fcc structure of Pd and the in-plane lattice of bct Fe grown on GaAs(001)-4 × 6 is smaller than for single crystal bcc Fe(001). Thus Pd in the GaAs trilayer system will have a different elastic strain, different structure and consequently different magnetic response than when substrates of Fe(001) or Pd(001) are used.

2. Methods and Materials

Samples on GaAs(001)-(4 × 6) were prepared *in situ* by MBE on epiready n-type GaAs (American Xtal Technology) wafers as described elsewhere [1, 2]. Layer deposition was monitored by reflection high energy electron diffraction, RHEED, with the number of oscillations of specular (anti-Bragg) spot intensity giving the layer thickness in ML. These measurements were used as calibration for the rate of deposition.

In growing the Fe/Pd/Fe trilayer sample, 30 ML of Fe were first deposited. Ar^+ sputtering was then used to remove the less than 1 ML of As from the GaAs that is known to float to the surface during Fe deposition [1, 7]. The sample was annealed for 30 minutes at ∼150 °C and another 8.5 ML of Fe were deposited at the anneal temperature. This is referred to as the 38.5 ML Fe sample. Subsequently the following overlayers were grown: 3.5 ML Pd; 3.5 ML Pd for a total of 7 ML Pd; 4 ML Fe; and 6 ML Fe for a total of 10 ML Fe. The Fe and Pd deposition rates were ∼0.4 ML/min and ∼0.3 ML/minute, respectively.

XAFS measurements were made using the PNC-CAT undulator beamline, ID-20 [8]. The Si(111) double-crystal monochromator was detuned above the Fe and Pd K-edges to 75% of the maximum intensity to reduce harmonic contributions. X-rays were incident in the total-reflection geometry with the electric vector either (near) perpendicular, $\boldsymbol{E}_{\perp}$, or in the plane of the substrate, $\boldsymbol{E}_{||}$ (within 2° of (110) and (−110) orientations). To minimize distortion of the spectra due to anomalous dispersion effects in the sample and adjacent media, the angle of incidence was set to approximately 2/3 of the critical angle φ_C, at 250 eV above the respective K-edges [9]. Fe K-edge measurements, $\boldsymbol{E}_{||}$, were also made at $\sim 2\varphi_C$ after deposition of 3 ML Pd in order to examine the effect of growing overlayers of Pd on the structure of the underlying Fe. All XAFS data on the trilayers were acquired using total electron yield.

The EXAFS interference functions were extracted using AUTOBK [10] while fixing E_o at the first inflection point.

*crozier@sfu.ca

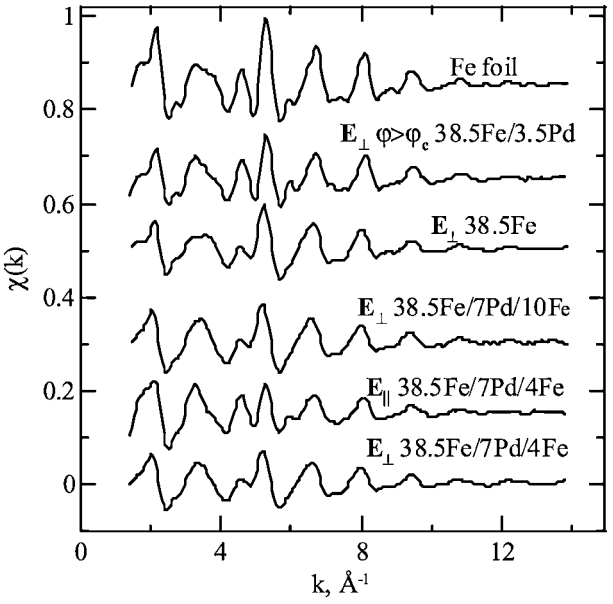

Fig. 1. The Fe K-edge EXAFS interference functions $\chi(k)$ for the X-ray polarization perpendicular to (along the normal to) and parallel to the GaAs(001) substrate for Pd and Fe films of different thickness. A reference iron foil $\chi(k)$ (top) is shown for comparison. The angle of incidence on the films is 2/3 the critical angle φ_C, except for the upper $\chi(k)$ where $\varphi = 2\varphi_C$.

Polarization-dependent XAFS amplitudes and phase shifts were calculated using FEFF 7 [11] and non-linear least squares fitting of the Fourier transform of $k\chi(k)$ was done using WINXAS [12].

3. Results

The characteristic differences between the $\chi(k)$ of iron foil over the range 3 to 7 Å^{-1} in Fig. 1 and $\boldsymbol{E}_\perp$ of the 38.5 ML sample indicate that the latter has a bct structure [1, 2]. When 3.5 ML of Pd are deposited and the structure of the iron probed by XAFS measurements at $2\varphi_C$, the similarity of $\boldsymbol{E}_{||}$ to iron foil indicates that the overlayer of Pd has not significantly changed the bct structure of the underlying 38.5 ML Fe. When 10 ML Fe are deposited on 7 ML of Pd, the $\boldsymbol{E}_\perp\chi(k)$ is similar to the $\boldsymbol{E}_\perp\chi(k)$ for the bct 38.5 ML Fe. However, for the initial 4 ML Fe grown on Pd, inspection of the $\chi(k)$ for $\boldsymbol{E}_\perp$ and $\boldsymbol{E}_{||}$ indicates differences over the 3 to 4 Å^{-1} range.

The $\chi(k)$ for the Pd K-edge are shown in Fig. 2. Relative to Pd foil, at high k, the $\chi(k)$ of the films have decreased amplitudes and appear to contain only a single frequency. There are differences over the range 3 to 5 Å^{-1}. The change of slope at 4 Å^{-1} is less pronounced for $\boldsymbol{E}_{||}$ in the 7 ML data than in the Pd foil. The $\chi(k)$ for $\boldsymbol{E}_{||}$ for 7 ML has a change of slope at 3 Å^{-1} not observed in the foil. $\boldsymbol{E}_\perp$ is different from $\boldsymbol{E}_{||}$ over the range 3 to 5 Å^{-1}. In the 3.5 ML data the $\chi(k)$ for $\boldsymbol{E}_\perp$ is similar to that for 7 ML. There are subtle differences between $\boldsymbol{E}_{||}$ and $\boldsymbol{E}_\perp$ in the 3.5 ML data.

Detailed analysis, done in R-space, indicates that in our Fe/Pd/Fe trilayer system in all three layers the Fe and Pd are distorted from their natural bcc and fcc structures, respectively. Alloy is formed at both Fe/Pd and Pd/Fe interfaces. The amount of alloying is smaller at the first interface compared to the second. Main aspects of the analysis are given below.

The magnitudes of the Fourier transforms of $k\chi(k)$ for the Pd data are shown in Fig. 3. Polycrystalline Pd has a fcc structure with n.n. distance $R_1 = 2.75$ Å and second n.n. $R_2 = 3.89$ Å.

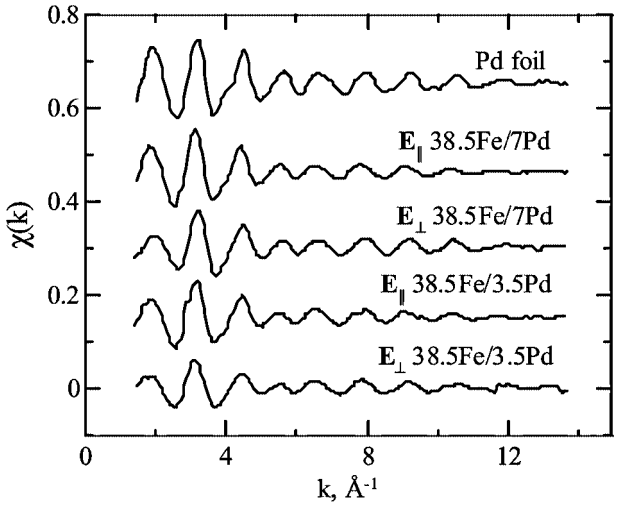

Fig. 2. The Pd K-edge $\chi(k)$ for the X-ray polarization perpendicular to and parallel to the GaAs(001) substrate for Pd films of different thickness. A reference Pd foil $\chi(k)$ (top) is shown for comparison.

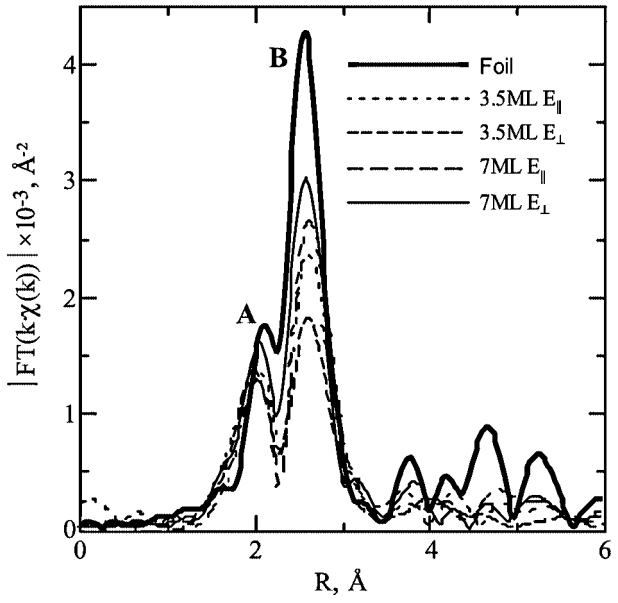

Fig. 3. The magnitude of the Fourier transform of $k\chi(k)$ for the Pd films and Pd foil. The transforms were calculated with a 20% Gaussian window over the k-space range 2.3–12.3 Å^{-1}.

The splitting of the main peak into A and B is produced by the k-dependence of the Pd backscattering amplitude, $f(k, \pi)$, when convolved with the n.n. distribution function. Using FEFF 7 the offset between the fit and crystallographic distances for Pd foil are ~0.01 Å for R_1 and 0.03 Å for R_2. Inspection of Fig. 3 reveals the peak ratio B/A decreases as the thickness of the film decreases. This is caused by backscattering from the underlying Fe, some of which has alloyed with Pd.

Fig. 4 shows the result of fitting 3.5 ML Pd with the electric vector parallel to the substrate. The imaginary parts of the Fourier transform for Pd-Fe and Pd-Pd are almost in-phase under peak A but become out-of-phase under peak B. This interference makes the fit sensitive to the Pd-Fe interface. Also shown in Fig. 4 is the magnitude of the Fourier transform obtained from a fit to the n.n. Pd-Fe distance and three Pd-Pd distances to 4.7 Å.

Analysis of $\boldsymbol{E}_\perp$ and $\boldsymbol{E}_{||}$ for the 3.5 ML Pd sample revealed that Pd has a fct structure expanded in-plane and contracted

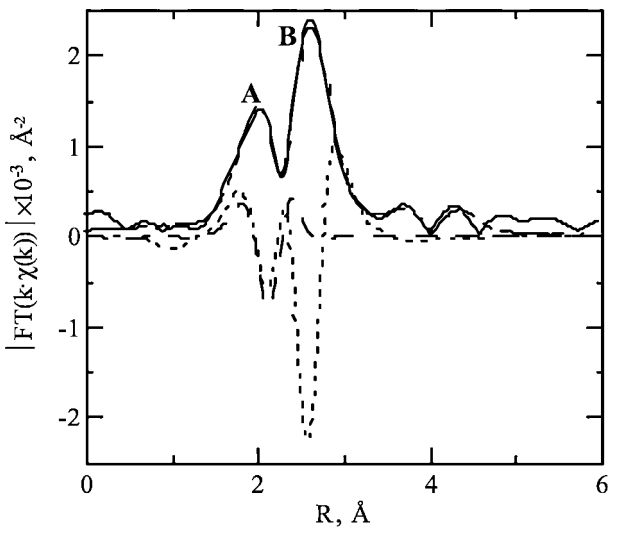

Fig. 4. The contribution of Fe and Pd to the transform of 3.5 ML Pd in the $\boldsymbol{E}_{||}$ configuration. The solid line is the magnitude of the FT of the data. The dashed and dotted lines are the imaginary parts of the Pd-Fe and Pd-Pd contributions to the fit of the data, respectively. The broken line indicates the magnitude of the fit including the n.n. Pd-Fe distance and three Pd-Pd distances out to 4.7 Å.

out-of-plane (with respect to fcc Pd) with $a = 3.93$ Å and $c = 3.87$ Å. Both polarizations indicate the presence of Fe under the first peak of the Fourier transform. The coordination number for the n.n. Pd-Fe distance and this distance itself, 2.60 Å (same for both polarizations) suggest the formation of an alloy within the first 0.5–1 ML Pd.

Analysis of 7 ML Pd showed that the fct structure of Pd is preserved. Analysis of $\boldsymbol{E}_{||}$ showed no presence of Fe, while $\boldsymbol{E}_{\perp}$ revealed a small amount of Fe, correlated through coordination numbers and Pd-Fe distance with the 3.5 ML Pd data, allowing one to speculate that no further alloying between Fe and Pd occurred when the additional 3.5 ML of Pd were deposited.

Analysis of the upper 4 ML Fe, both $\boldsymbol{E}_{||}$ and $\boldsymbol{E}_{\perp}$, revealed Pd to be present in greater amounts than the traces of Fe at the 38.5 ML Fe/Pd interface. Coordination numbers yield around 2–2.5 ML of Fe-Pd alloy consistent with Le Fevre and Chanderis [4]. Fe-Fe distances show that Fe has a bct structure with $a = 2.85$ Å and $c = 2.96$ Å which is more distorted from bcc than Fe grown on GaAs(001)-(4 × 6). Analysis of $\boldsymbol{E}_{\perp}$ for 10 ML of Fe, is in agreement with the 4 ML data, showing the same tetragonal distortion and the presence of some Pd. The Fe-Pd n.n. distance stays the same as for the 4 ML sample and equal to 2.63 Å.

Acknowledgments

This work was supported by the Natural Sciences and Engineering Research Council of Canada through major facilities access and operating grants. Research at the PNC-CAT beamline, Advanced Photon Source, Argonne National Laboratory is also supported by the US Department of Energy under contracts W-31-109-Eng-38 (APS) and DE-FG03-97ER45628 (PNC-CAT).

References

1. Gordon, R. A., Crozier, E. D., Jiang, D.-T., Monchesky, T. L. and Heinrich, B., Phys. Rev. B **62**, 2151 (2000).
2. Gordon, R. A., Budnik, P. S., Jiang D. T. and Crozier, E. D., XAFS 12 conference proceedings.
3. Fullerton, E. E. *et al.*, Phys. Rev. **B 51**, 6364 (1995).
4. Boeglin, C. *et al*., Phys. Rev. **B 60**, 4220 (1999).
5. Meyerheim, H., Vedpathak, M., Shah, V., Lu, Y. and Kirschener, J., private communication.
6. Vogel, J. *et al*., Phys. Rev. **B 55**, 3663 (1997).
7. Monchesky, T. L. *et al*., Phys. Rev. B **60**, 10242 (1999).
8. Heald, S. *et al*., J. Synch. Rad. **8**, 342 (2001).
9. Jiang, D. T. and Crozier, E. D., Can. J. Phys. **76**, 621 (1998).
10. Newville, M., Livins, P., Yacoby, Y., Stern, E. A. and Rehr, J. J., *Phys. Rev.* B. **47**, 14126 (1993).
11. Zabinsky, S. I., Rehr, J. J., Ankudinov, A., Albers, R. C. and Eller, M. J., Phys. Rev. B **52**, 2995 (1995).
12. Ressler, T., J. Phys. IV **7**, C2-269 (1997).

Physica Scripta. Vol. T115, 498–500, 2005

Valence State of Ru at the Mn sites in $Pr_{0.5}Sr_{0.5}MnO_3$

J. S. Kim[1], B. H. Kim[1], D. C. Kim[1], M. G. Kim[2], A. Maignan[3], B. Raveau[3] and Y. W. Park[1*]

[1]School of Physics and Condensed Matter Research Institute, Seoul National University, Seoul 151-747, Korea
[2]Beamline Research Division, Pohang Accelerator Laboratory, Pohang University of Science and Technology, Pohang 790-784, Korea
[3]Laboratoire CRISMAT, UMR CNRS ISMRA 6508, 6bd Maréchal Juin 14050, Caen Cedex, France

Received June 26, 2003; accepted December 9, 2003

PACS numbers: 75.30.Kz, 61.10.Ht, 75.47.Gk

Abstract

The valence of Ru at the Mn sites in $Pr_{0.5}Sr_{0.5}MnO_3$ has been studied using Ru K- and L_{III}-edge X-ray absorption near edge structure (XANES) spectroscopy. In comparison with XANES of tetravalent and pentavalent ruthenates, it was found that the Mn-site doped Ru is mainly in tetravalent state with a small amount of pentavalent Ru. This result indicates that the change of carrier density with Ru doping is not sufficient to induce the drastic enhancement of ferromagnetism observed in transport properties of Ru-doped $Pr_{0.5}Sr_{0.5}MnO_3$. The mixed valence state of doped Ru suggests that 4d orbitals of Ru are involved in electronic transport of the Mn^{3+}-O-Mn^{4+} network with the valence fluctuation $Ru^{5+} + Mn^{3+} \leftrightarrow Ru^{4+} + Mn^{4+}$. The prime role of Ru has been discussed in terms of Mn valence change and magnetic interactions between Mn and doped Ru ions.

$Pr_{0.5}Sr_{0.5}MnO_3$ has attracted great interest because of its particular magnetic and transport properties. In $Pr_{0.5}Sr_{0.5}MnO_3$, two magnetic ground states coexist in different temperature regimes, which results in the two magnetic phase transitions: the paramagnetic (PM) to ferromagnetic (FM) near 270 K and the FM to antiferromagnetic (AFM) transition around 150 K [1]. Furthermore its AFM ground state at low temperatures has an A-type structure [2] where the FM metallic planes are antiferromagnetically coupled to each other. This intriguing AFM state is related to the $d_{x^2-y^2}$ orbital ordering which is responsible for the 2-dimensional (2D) characteristics in magnetic and transport properties [2, 3].

Previously, several cations [4, 5, 6] were used to explore the Mn-site doping effects on $Pr_{0.5}Sr_{0.5}MnO_3$. Compared to the doping with variation of Pr and Sr contents, Mn-site doping will cause not only the changes of the carrier density and lattice distortion of the Mn^{3+}-O-Mn^{4+} network, but also the interesting interactions between Mn ions and the substituted cations. In the case of nonmagnetic cations, the valence and size of the substituted cation were suggested to govern the change of the magnetic phases. When the valence of Mn ion is increased by doping with divalent or trivalent cations, the AFM and PM phases were extended at the expense of the FM phase [5]. On the other hand, the pentavalent cation doping which decreases the Mn valence suppressed the AFM phase and induced the FM phase at low temperatures. In the case of the magnetic cation, Cr, the AFM insulating phase at low temperatures was rapidly destroyed and the FM metallic phase was induced with decrease of T_C [6]. Considering that Cr exists as trivalent cation in the Mn^{3+}-O-Mn^{4+} network [7] this insulator-to-metal transition caused by Cr doping at low temperatures indicates that the Mn-site doping with magnetic cations does not have the similar effects observed in the case of nonmagnetic cation doping. In order to understand such an exceptional effect it was proposed that magnetic elements could participate in the carrier transport with Mn ions, even introducing the FM phase by double exchange (DE) interaction [8].

Recently, Mn-site doping with Ru was reported to destroy the A-type AFM insulating state in $Pr_{0.5}Sr_{0.5}MnO_3$ [9]. In contrast to Cr doping, however, Ru doping increases T_C, which indicates that Ru could play a unique role in the Mn^{3+}-O-Mn^{4+} network compared to the other cations. Thus Ru can be considered as a most promising candidate for participating in carrier transport, as well as the DE interaction with Mn ions. In order to understand the origin of these drastic effects of Ru doping, it is important to address the valence state of doped Ru ion. In this paper, we have determined the valence of the Mn-site doped Ru in $Pr_{0.5}Sr_{0.5}MnO_3$ using X-ray absorption near edge structure (XANES) studies at the Ru K- and L_{III}-edge with reference samples, $SrRuO_3$ and Sr_2YRuO_6.

Polycrystalline samples of $Pr_{0.5}Sr_{0.5}Mn_{1-x}Ru_xO_3$ ($0.00 \leq x \leq 0.10$) and the reference materials for XANES measurements, $SrRuO_3$ and Sr_2YRuO_6 were prepared using the solid-state reaction method [9]. All samples were characterized as a single phase with nominal stoichiometry by X-ray diffraction patterns. The standard 4-probe method was used for resistivity measurement under magnetic fields, zero and 6 T using a 7 T superconducting magnet system. XANES experiments on Ru K-edge and L_{III}-edge were carried out at Pohang Accelerator Laboratory (PAL). Ru K-edge spectra were collected using a Si(311) double-crystal monochromator in transmission mode on the 7C1 Electro-Chemistry beam line. Ru L_{III}-edge spectra were recorded on the 3C1 EXAFS beam line using Si (111) double-crystal monochromator in fluorescence mode. Background subtraction and normalization for XANES data were carefully done according to the standard procedure.

Figure 1 presents the temperature dependence of resistivity for $Pr_{0.5}Sr_{0.5}Mn_{1-x}Ru_xO_3$ under zero and 6 T magnetic fields. For $Pr_{0.5}Sr_{0.5}MnO_3$, apparent slope changes in $\rho(T)$ are observed at $T_C \sim 270$ K and $T_N \sim 165$ K, which denote the boundaries of the PM, FM, and AFM states. Below T_N, $\rho(T)$ increases rapidly with decrease of temperature. When Mn is substituted by Ru, the low temperature AFM phase is drastically destroyed as shown in Fig. 1. $\rho(T)$ of $Pr_{0.5}Sr_{0.5}Mn_{0.98}Ru_{0.02}O_3$ displays a metallic behavior down to 2 K with a slightly increasing behavior below 120 K. As Ru concentration increases, the PM to FM transition shifts to higher temperature up to 317 K for 10% of Ru doped sample. This transition temperature is almost same with that of $Pr_{0.5}Sr_{0.5}MnO_3$ under 6 T magnetic field. Therefore the Ru doping at Mn-site extends the FM phase similarly to the application of magnetic field, but with greater efficiency.

Ru K-edge XANES spectra of $Pr_{0.5}Sr_{0.5}Mn_{0.9}Ru_{0.1}O_3$ are shown in Fig. 2 with those of the reference materials: well-known tetravalent ($SrRuO_3$) and pentavalent (Sr_2YRuO_6) ruthenates. The

*e-mail: ywpark@phya.snu.ac.kr

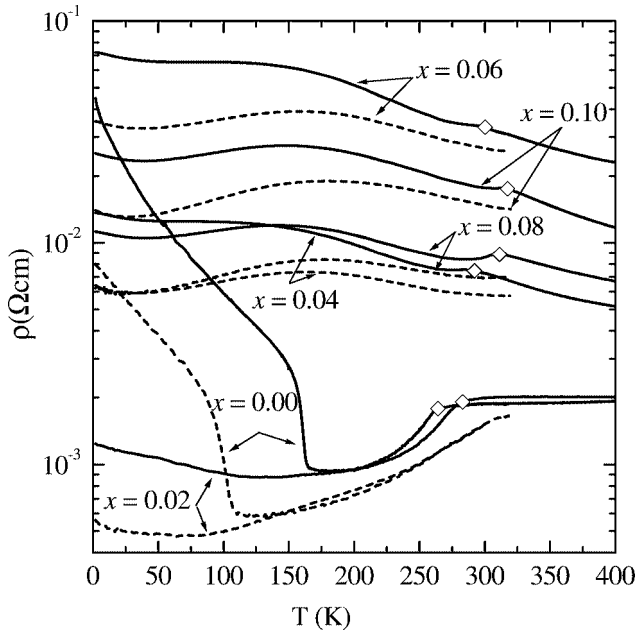

Fig. 1. Temperature dependence of resistivity under zero (solid lines) or 6 T (dashed lines) magnetic field for $Pr_{0.5}Sr_{0.5}Mn_{1-x}Ru_xO_3$ ($0.00 \leq x \leq 0.10$). FM transition point at zero magnetic field is indicated with the open diamond symbol on each solid curve.

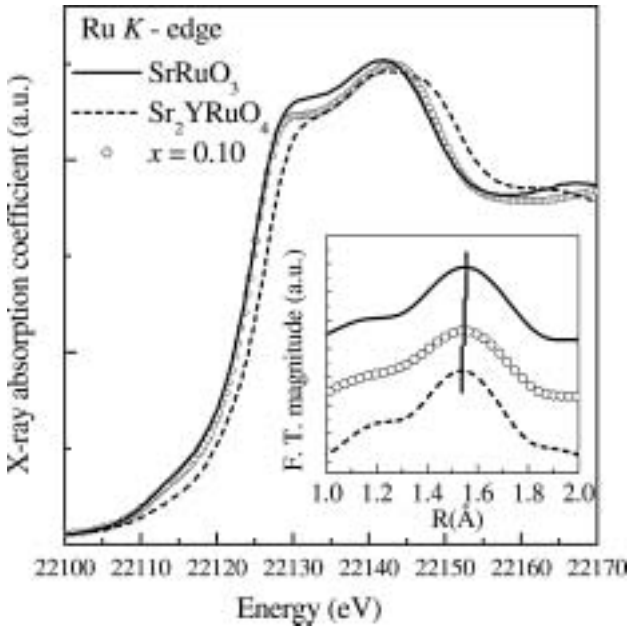

Fig. 2. Normalized Ru K-edge X-ray absorption spectra for $Pr_{0.5}Sr_{0.5}Mn_{0.9}Ru_{0.1}O_3$ compared to the reference ruthenates, $SrRuO_3$ and Sr_2YRuO_6. The inset shows the Ru-O bond peak in the plot of the *r*-space data for three samples.

main edge peak is assigned to a dipole-allowed transition from 1s to 5p states. From comparison of XANES spectra between tetravalent and pentavalent ruthenates, it is clearly shown that the main edge is shifted to higher energy by ∼1 eV as Ru valence increases from 4+ to 5+ [10]. The transition energy shift is attributed to the enhancement of Coulomb energy due to an increase of the effective charge for Ru ion. For Ru doped $Pr_{0.5}Sr_{0.5}MnO_3$, XANES spectra are similar to those of tetravalent ruthenates, which shows that the valence of the doped Ru is close to 4+. The inset of Fig. 2 presents the *r*-space data for three samples obtained from the Fourier Transform of the EXAFS

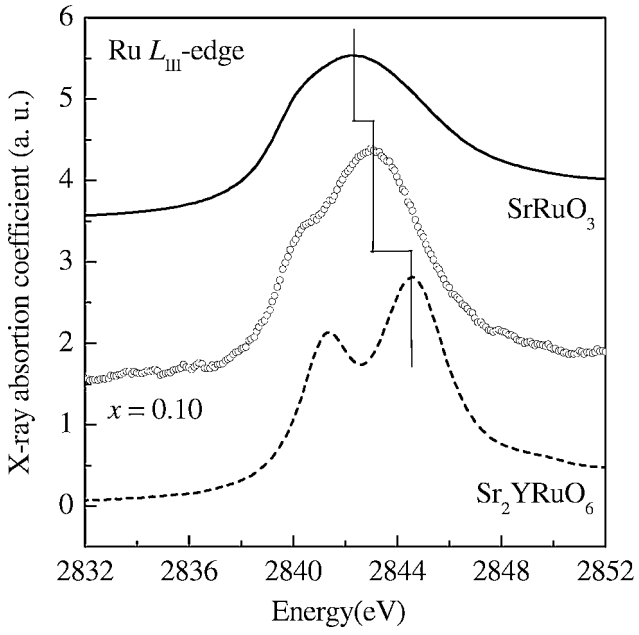

Fig. 3. Normalized Ru L_{III}-edge X-ray absorption spectra for $Pr_{0.5}Sr_{0.5}Mn_{0.9}Ru_{0.1}O_3$ compared to the reference ruthenates, $SrRuO_3$ and Sr_2YRuO_6.

oscillations above the edge. For comparison of Ru-O bond length between the samples, we plot the first peak corresponding to the Ru-O bond, which is sensitive to the Ru valence state. As shown in the inset of Fig. 2, the Ru-O bond length of $Pr_{0.5}Sr_{0.5}Mn_{0.9}Ru_{0.1}O_3$ is in between those of tetravalent and pentavalent ruthenates. These results indicate that Ru valence at the Mn-site is not exactly same as 4+ but probably, mixed-valence between 4+ and 5+.

The mixed valent state of Ru is more clearly observed in Ru L_{III}-edge XANES as shown in Fig. 3. In octahedra configuration, degenerate 4d orbitals of Ru are split into t_{2g} and e_g orbitals separated by crystal field. Two peaks in L_{III}-edge spectra are corresponding to $2p \rightarrow t_{2g}$ (lower energy peak) and $2p \rightarrow e_g$ (higher energy peak) transitions, which are observed in both cases of tetravalent and pentavalent Ru oxides. However, there are clear differences between L_{III}-edge spectra of Ru^{4+} and Ru^{5+}. The peak energy of t_{2g}-related and e_g-related peaks for tetravalent Ru is much closer to each other than pentavalent Ru case. Also, spectral weight for e_g-related peak becomes enhanced compared to t_{2g}-related peak and the peak position shifts to higher energy by ∼1.5 eV with increase of Ru valence from 4+ to 5+ as shown the XANES spectra for $SrRuO_3$ and Sr_2YRuO_6. The spectrum of Ru at the Mn sites in $Pr_{0.5}Sr_{0.5}MnO_3$ is similar to that of $SrRuO_3$, which is also consistent with Ru K-edge XANES result. However, the significant increase of spectral weight for e_g-related peak is observed in the L_{III}-edge spectra of Mn-site doped Ru. Also, there is a clear energy shift by ∼0.6 eV with respect to that of $SrRuO_3$. Such a chemical shift for Ru doped $Pr_{0.5}Sr_{0.5}MnO_3$ is attributed to the change of Ru valence [14]. Therefore the valence state of Ru at the Mn sites in $Pr_{0.5}Sr_{0.5}MnO_3$ is mixed valent state. This mixed valence state of Ru is crucial to understand the unusual enhancement of T_C.

Figure 4 displays Mn-site doping dependence of T_C for various dopants, Ga, Al, Sn, Ti, Cr and Ru in $Pr_{0.5}Sr_{0.5}MnO_3$. [4, 5, 6, 9, 11] For nonmagnetic cations, T_C is decreased rapidly with Mn-site doping concentration. In consideration of phase diagram of $Pr_{1-x}Sr_xMnO_3$, T_C is enhanced as Mn valence decreases from 3.5+, while T_C is suppressed as Mn valence increases. If T_C is determined dominantly with the change of Mn valence, T_C

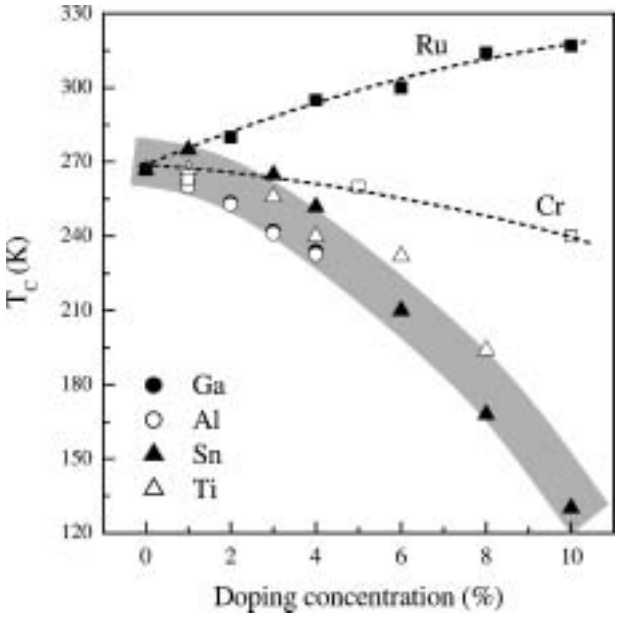

Fig. 4. T_C versus Mn-site doping concentration plot for $Pr_{0.5}Sr_{0.5}Mn_{1-x}M_xO_3$ (M = Al, Ga, Sn, Ti, Cr and Ru).

is expected to increase for tetravalent dopant such as Sn^{4+} or Ti^{4+} and to decrease for trivalent dopant such as Al^{3+} or Ga^{3+}. However, T_C decreases in both cases as shown in Fig. 4. In both cases, T_C was reduced as the concentration of the substituted cation increases, which indicates that the Mn-site doped cations disturb the carrier transport and weaken DE interaction in the Mn^{3+}-O-Mn^{4+} network. This reduction of T_C was strongly related to the lattice distortion due to the size difference between Mn and the substituted ion; for instance, smaller trivalent cation, Al^{3+} decreases T_C more drastically compared to Ga^{3+} and In^{3+}. Similarly Cr exists as a trivalent ion at the Mn sites and disturbed the carrier transport. However empty d orbitals of Cr can induce magnetic exchange interaction with Mn ions, so that T_C is not so much suppressed as the cases of other trivalent nonmagnetic dopants such as Al^{3+} or Ga^{3+}. Ru also have empty d orbitals like Cr, and 4d e_g^0 state of Ru^{4+} or Ru^{5+} is ferromagnetically coupled with e_g^1 state of Mn^{4+} [12]. In contrast to Cr doping, T_C is enhanced with Ru doping as shown in Fig. 4. Since Ru valence estimated from XANES study is between 4+ and 5+, which is higher than Cr valence, such difference could be attributed to Mn valence change due to Mn-site doping. However, T_C of 10% Ru doped $Pr_{0.5}Sr_{0.5}MnO_3$ is even higher than the maximum T_C in the series of $Pr_{1-x}Sr_xMnO_3$ as mentioned above. Moreover, Mn-site doping dependence of T_C for nonmagnetic dopants follows a general trend irrespective of valence of dopant, which suggests that valency effect is not a dominant origin for T_C enhancement.

Instead, the peculiar role of Ru is related to presence of the extended 4d orbitals. The mixed valence state for the Mn-site doped Ru found in XANES reveals that extended 4d orbitals of Ru are strongly hybridized with Mn orbitals and contributes to the band formation with valence fluctuation $Ru^{5+} + Mn^{3+} \leftrightarrow Ru^{4+} + Mn^{4+}$ [13]. Ru reinforces the ferromagnetism by FM coupling with Mn ions and does not hinder DE interaction within the Mn^{3+}-O-Mn^{4+} network. As a result, T_C is unusually enhanced by Ru doping in $Pr_{0.5}Sr_{0.5}MnO_3$.

In summary, XANES studies using Ru K- and L_{III}-edge spectra have shown that the valence state of Mn-site doped Ru in $Pr_{0.5}Sr_{0.5}MnO_3$ is mixed valent state, which is close to tetravalent state. The presence of mixed valent state of doped Ru is strong evidence for the valence fluctuation in the type of $Ru^{5+} + Mn^{3+} \leftrightarrow Ru^{4+} + Mn^{4+}$. Through this valence fluctuation, conduction path is formed in Ru-O-Mn path and delocalization of e_g carrier is maintained in contrast to other dopant. These effects of Ru doping enhance the ferromagnetism and increases T_C in $Pr_{0.5}Sr_{0.5}MnO_3$.

Acknowledgments

This work was supported by the National Research Laboratory program under Contract No. M1-0104-00-0023, Ministry of Science and Technology (MOST), Korea. XANES experiments at PAL were supported in part by MOST and POSCO, Korea.

References

1. Tomioka, Y., Asamitsu, A., Moritomo, Y., Kuwahara, H. and Tokura, Y., Phys. Rev. Lett. **74**, 5108 (1995).
2. Kawano, H. *et al.*, Phys. Rev. Lett. **78**, 4253 (1997).
3. Jung, J. H. *et al.*, Phys. Rev. B **61**, 14656 (2000).
4. Maignan, A. and Raveau, B., Z. Phys. B **102**, 299 (1997).
5. Maignan, A., Martin, C. and Raveau, B., Z. Phys. B **102**, 19 (1997).
6. Martin, C. *et al.*, J. Magn. Magn. Mater. **202**, 11 (1999).
7. Toulemonde, O. *et al.*, Eur. Phys. J. B **4**, 159 (1998).
8. Young Sun, Xiaojun Xu and Yuheng Zhang, Phys. Rev. B **63**, 054404 (2001); Young Sun, Wei Tong, Xiaojun Xu and Yuheng Zhang, Phys. Rev. B **63**, 174438 (2001).
9. Maignan, A., Martin, C., Hervieu, M. and Raveau, B., J. Appl. Phys. **89**, 500 (2001).
10. Jin-Ho Choy, Jung-Young Kim, Sung-Ho Hwang, Seung-Joo Kim and Demazeau Grared, Inter. J. Inorg. Mater. **2**, 61 (2000).
11. Kim, J. S. *et al.*, Phys. Rev. B **66**, 224427 (2002).
12. Goodenough, J. B., Wold, A., Arnott, R. J. and Menyuk, N., Phys. Rev. **124**, 373 (1961).
13. Martin, C., Maignan, A., Hervieu, M., Autret, C. and Raveau, B., Phys. Rev. B **63**, 174402 (2001).
14. Sundar Manoharan, S., Sahu, R. K. and Rao, M. L., Europhys. Lett. **59**, 451 (2002).

Physica Scripta. Vol. T115, 501–503, 2005

Soft X-ray Absorption Spectra of Amorphous Carbon

Yasuji Muramatsu[1], Eric M. Gullikson[2] and Rupert C. C. Perera[2]

[1]Kansai Research Establishment, Japan Atomic Energy Research Institute (JAERI), 1-1-1 Kouto, Mikazuki, Sayo-gun, Hyogo 679-5148, Japan
[2]Center for X-Ray Optics, Lawrence Berkeley National Laboratory, Berkeley, 1 Cyclotron Road, Berkeley, California 94720, USA

Received June 26, 2003; accepted in revised form November 4, 2003

PACS number: 61.10. Ht

Abstract

Information about the local structure of amorphous carbon (*a*-C) films was obtained by comparing soft X-ray absorption spectra in the CK region of sputtered *a*-C films to reference carbon compounds such as hydrofullerene ($C_{60}H_{36}$), highly oriented pyrolytic graphite (HOPG), and carbon black. The spectra of the *a*-C films exhibited fine structures, which consisted of at least different six portions. Comparing the spectral features of the *a*-C films with the reference compounds and the spectral analysis by discrete variational (DV)-Xα molecular orbital calculations indicated that the fine structures of the *a*-C films are due to a hybrid of sp^2 and sp^3 carbon atoms.

1. Introduction

Amorphous carbon (*a*-C) films are important and interesting materials in industry and materials science. It is believed that they consist of a random structure of sp^2- and sp^3-configured carbon atoms and that the local structure or chemical bonding states determine their mechanical and optical properties. Thus, numerous researchers have conducted characterization studies of *a*-C films using various analytical methods such as Raman spectroscopy, X-ray photoelectron spectroscopy (XPS), Auger electron spectroscopy (AES), and electron energy loss spectroscopy (EELS) in order to clarify local structures and chemical bonding states. Recently, various carbon films have been characterized by soft X-ray emission and absorption spectroscopy using highly brilliant synchrotron radiation [1–6]. This method is effective for obtaining electronic-structure information about occupied and unoccupied orbitals, which directly reflects the local structure and chemical bonding states. However, the spectral features observed in the X-ray emission and absorption spectra of the *a*-C films have yet to be clearly assigned.

In our previous study [6], fine structures were clearly observed in the soft X-ray absorption spectra of sputtered *a*-C films, which were systematically deposited by various sputtering methods under varying conditions. These fine structures have rarely been measured by EELS [7, 8], which generally has a lower energy resolution than soft X-ray absorption spectroscopy using synchrotron radiation. Thus, in order to extract information on the local structures of *a*-C films from the fine structures, soft X-ray absorption spectra of *a*-C films were compared to reference carbon compounds. Reference compounds should be selected if they are fairly large molecules, which were composed of sp^2 and sp^3 carbon atoms. Hence, this study used hydrofullerene ($C_{60}H_{36}$), which is composed of twenty-four sp^2 carbon atoms and thirty-six sp^3 carbon atoms, as the reference compound.

This paper describes the comparison on the soft X-ray absorption spectral features between *a*-C films and reference compounds such as $C_{60}H_{36}$, highly oriented pyrolytic graphite (HOPG), and carbon black.

2. Experiments

The total-electron-yield (TEY) X-ray absorption spectra in the C*K* region of commercially available *T*-symmetry $C_{60}H_{36}$ [9], HOPG, and carbon black were measured in beamline BL-6.3.2 [10] at the Advanced Light Source (ALS). Powder samples of $C_{60}H_{36}$ and carbon were pressed and held on indium-sheet substrates. The estimated resolving power ($E/\Delta E$) of the TEY absorption measurements was approximately 1600 using a 600 lines/mm variable-line-spacing grating and a 20 μm exit slit. The incident angle to the sample surface was fixed at 45 degrees. The measurement conditions were the same as the previous measurement of sputtered *a*-C films [6]. The energy calibration was achieved by tuning the π^* peak energy of HOPG to 285.5 eV.

3. Results and Discussion

Figure 1 shows the TEY X-ray absorption spectra of the *a*-C films and reference compounds, $C_{60}H_{36}$, HOPG, and carbon black. The spectra of the *a*-C films were extracted from previously measured data [6]. The *a*-C films were deposited by RF, ion-beam, and electron-cyclotron-resonance (ECR) sputtering methods under various deposition conditions. For the RF-sputtered carbon films, the pressure of the source gas was 5×10^{-2} (R1), 1×10^{-1} (R2), and 1×10^{-2} Torr (R3). For the ion-beam-sputtered carbon films, the annealing temperature was 'not annealed' (I1), 400 °C (I2), and 700 °C (I3). For the ECR-sputtered carbon films, the acceleration voltage was −20 (E1), −75 (E2), and −100 V (E3). The spectra of *a*-C films displayed two peaks at 285.5 eV and 293 eV, which correspond to the energy portions of π^* and σ^* peaks in HOPG, respectively. Therefore, these peaks in *a*-C films are assigned to be π^* and σ^* peaks, respectively. Four other structures are also observed at 284.5 eV (denoted by *a*), at 287 eV (*b*), 288 eV (*c*), and 289 eV (*d*) among the *a*-C films. Although the relative peak intensities among these six structures depended on the deposition methods/conditions, the peaks were observed at constant energy positions, which suggests common local structures in the *a*-C films, but at different ratios. Similar structures, which correspond to the π^*, *c*, *d*, and σ^* in $C_{60}H_{36}$, were noted in the spectral feature of the *a*-C films. Therefore, it is estimated that the *a*-C films have local structures similar to $C_{60}H_{36}$. A broad π^* peak is observed in carbon black at 285.5 eV and the energy position of the lower-energy portion in this π^* peak corresponds to the lowest-energy fine structure *a* in *a*-C films. Carbon black is essentially composed from randomly-ordered polycyclic-aromatic-structures [11]. Hence, it is estimated that similar polycyclic- aromatic-structures partially exist in *a*-C films.

The local structures of *a*-C films were further estimated by comparing the spectral similarities to the spectral features of $C_{60}H_{36}$, which were analyzed by discrete variational (DV)-Xα molecular orbital (MO) calculations [12–13]. Figure 2 shows

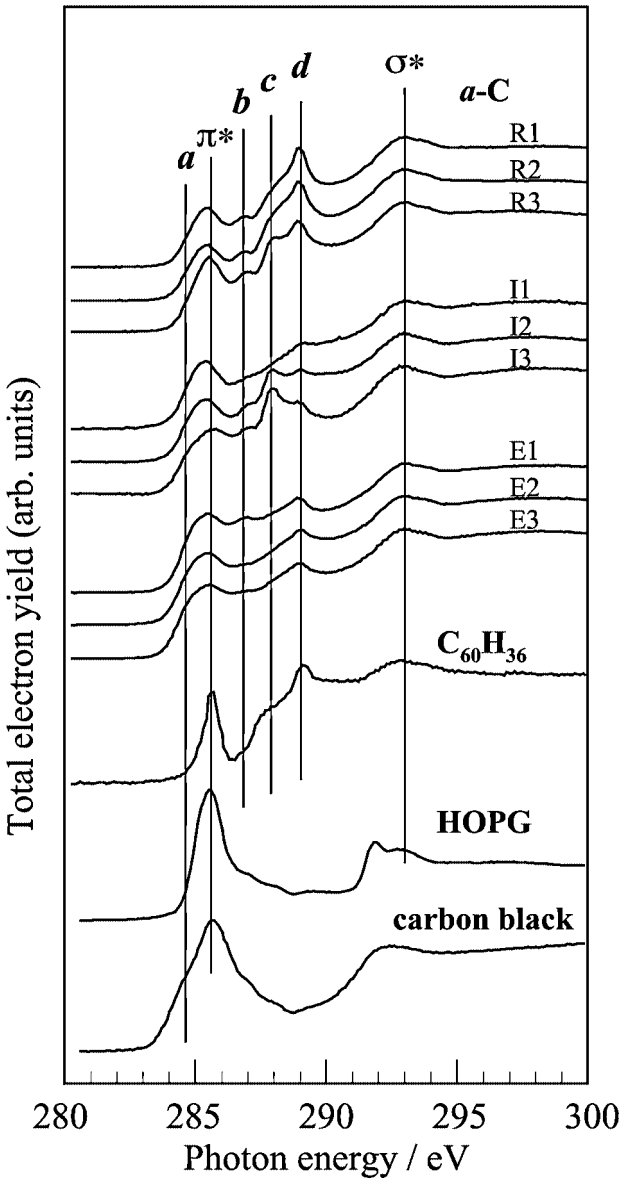

Fig. 1. TEY X-ray absorption spectra of *a*-C films for three different conditions when deposited by RF (R1-3), ion-beam (I1-3), and ECR sputtering (E1-3) [6] and $C_{60}H_{36}$ [9], HOPG, and carbon black are shown as references. *A*-*d*, π^*, and σ^* denote the specific spectral features consisting of at least six portions in the *a*-C films.

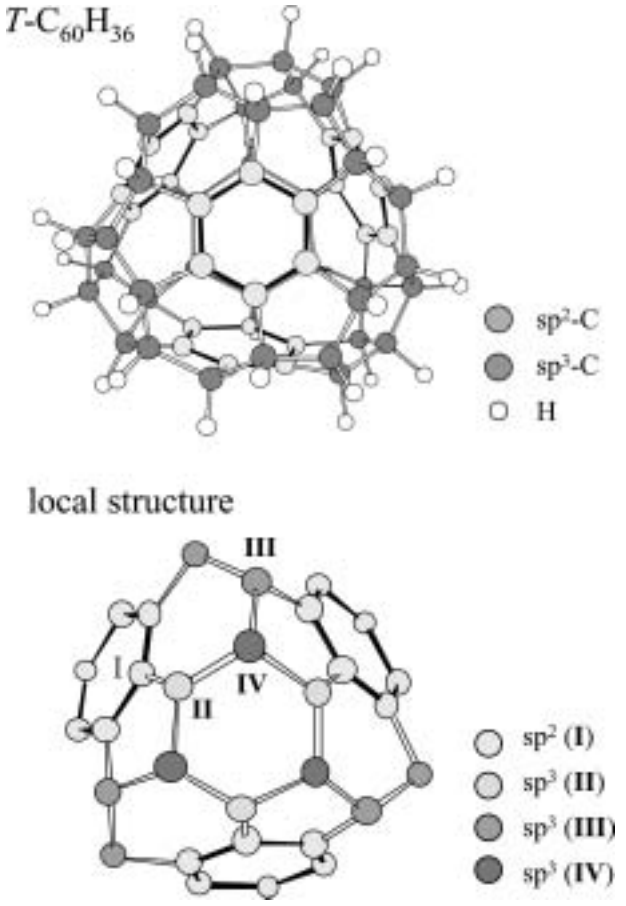

Fig. 2. Molecular structure (upper panel) and local structure (lower panel) of T-$C_{60}H_{36}$. Hydrogen atoms bound to sp^3 carbon atoms are not shown in the local structure. I–IV denote the four different types of carbon atoms.

the molecular structure of the T-symmetry $C_{60}H_{36}$ and its local structure. In T-$C_{60}H_{36}$, thirty-six of the carbon atoms are bound to hydrogen atoms that have a sp^3 configuration. The remaining twenty-four carbon atoms are sp^2 and form four six-membered benzene rings located in the tetrahedral positions. There are four structurally unique carbon atoms in T-$C_{60}H_{36}$. The twenty-four sp^2-C atoms (I) are identical and each is bound to two sp^2-C atoms and one sp^3-C atom. There are three types of sp^3-C atoms, twenty-four are sp^3-C atoms (II, III) each bound to two sp^3-C atoms, one sp^2-C atom, and one H atom, while the other twelve sp^3-C atoms (IV) are each bound to three sp^3-C atoms and one H atom. For the spectral analysis of the X-ray absorption, DV-Xα MO calculations on the electronic structure of the excited states, with the inner core holes and electrons in unoccupied orbitals, should be necessary to exactly reproduce the measured X-ray absorption spectral features [14]. However, the calculations on excited states are generally more difficult than those on the ground states, and the ground-state calculations provide approximated information on the X-ray spectral analysis especially in K-shell excitations. Thus, we show here the calculated spectra on the ground states as the first-order approximation. Figure 3 shows the unoccupied C2p- and C2s-DOS spectra of the individual sp^2- and sp^3-C atoms. The total C2p-DOS spectrum approximately reproduces the measured X-ray spectral features of π^*, c, d, and σ^*. Table I lists the unoccupied orbital populations of the individual carbon atoms. The π^* peak originates from π^* orbitals since the 2p orbitals of the sp^2-C (I) account for approximately 90% of the population at peak π^*. The orbital populations of peaks c, d, and σ^* peaks are shared by sp^2-C (I), sp^3-C (II, III), and sp^3-C (IV) with 11–45% of the 2p orbitals and up to 11% of 2s orbitals. In particular, the 2p orbitals of both sp^2-C (I) and sp^3-C (II, III) account for more than 30% of the population at peak c and the 2p orbitals of both sp^3-C (II, III) and sp^3-C (IV) account for more than 30% of peak d. This indicates that peak c has more sp^2 character than peak d. The σ^* peak is mainly due to the σ^* orbitals, which are mostly composed of sp^3-C (II, III) and sp^2-C (I). From this analogy, it can be estimated that the fine structures π^*, c, d, and σ^* in *a*-C films result from the hybridization of sp^2 and sp^3 carbon atoms. In addition, the higher the energy positions of the fine structure peaks, the more sp^3 character the hybridized carbon atoms have in the local structure.

4. Conclusion

The soft X-ray absorption spectra of *a*-C films, which were measured using synchrotron radiation, were compared to

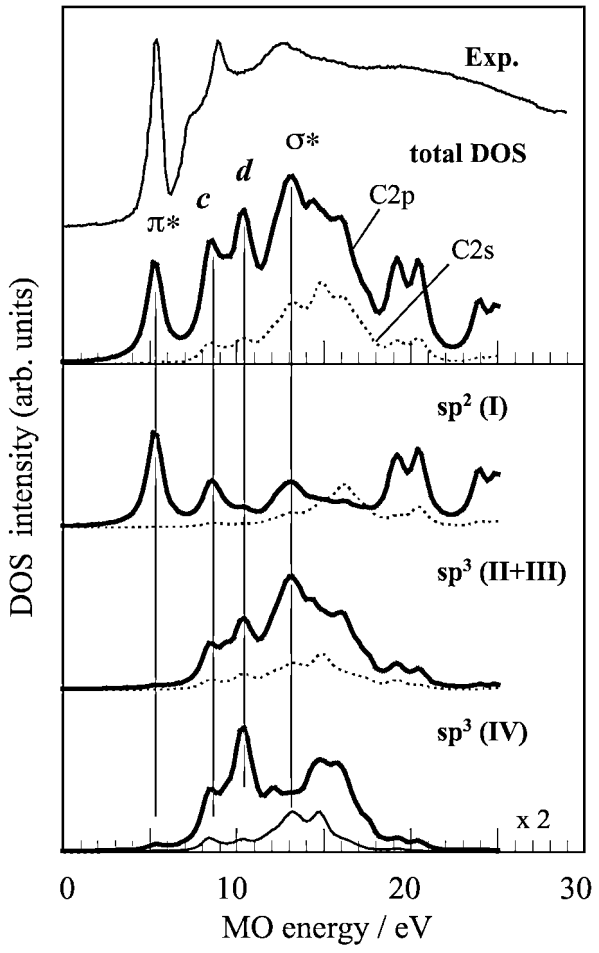

Fig. 3. Calculated total DOS spectrum and DOS spectra of individual carbon atoms (I–IV) in *T*-$C_{60}H_{36}$. The measured X-ray absorption spectra are also shown on the total DOS spectrum.

reference compounds, *T*-$C_{60}H_{36}$, HOPG, and carbon black. The *a*-C films had fine structures, which consisted of at least six portions.Four portions (π^*, *c*, *d*, σ^*) in the fine structure corresponded to the energy positions of four peaks in *T*-$C_{60}H_{36}$. Spectral analysis of *T*-$C_{60}H_{36}$ using DV-Xα MO calculations indicated that the origin of these peaks is the hybridization of sp^2 and sp^3 carbon atoms. Therefore, it is estimated that the fine structures observed between π^* and σ^* peaks in *a*-C films originated from the hybridization of sp^2 and sp^3 carbon atoms. The lowest-energy fine structure *a* in *a*-C films corresponded to the lower-energy portion in the broad π^* peak in carbon black.

Table I. *Orbital populations of the four different types of carbon atoms (I–IV) in unoccupied orbitals corresponding to the measured X-ray absorption peaks denoted by π^*, c, d, and σ^*.*

		Orbital population/%					
		sp^2-C(I)		sp^3-C(II&III)		sp^3-C(IV)	
peak	MO energy/eV	2s	2p	2s	2p	2s	2p
π^*	5.2	0.6	89.6	1.1	4.1	0.9	3.8
c	8.6	3.1	31.9	7.1	31.5	4.6	21.7
d	10.4	2.3	11.1	8.9	39.6	3.6	34.5
σ^*	13.2	6.1	17.9	11.0	45.0	8.1	12.0

Hence, it is estimated that the lowest-energy fine structure *a* in the *a*-C films originated from polycyclic-aromatic-structures. The reference compounds did not display the fine structure *b*. Thus, further experiments using different reference compounds are necessary to estimate the origin of the fine structures in *a*-C films.

Acknowledgments

We would like to thank Dr. Shigeru Hirono of NTT-AFTY Corporation and Dr. Takayoshi Hayashi of Corning Japan K. K. for useful discussions. This work has been supported by the a Grant-in-Aid from the Ministry of Education, Culture, Sports, Science, and Technology in Japan under contract No. 15550081 and by the US Department of Energy under contract No. DE-AC03-76SF00098.

References

1. Coffman, F. L. *et al*., Appl. Phys. Lett. **69**, 568 (1996).
2. Gruen, D. M. *et al*., Appl. Phys. Lett. **68**, 1640 (1996).
3. Anders, S., Diaz, J., Agerll, J. W., Yu Lo, R. and Bogy, D. B., Appl. Phys. Lett. **71**, 3367 (1997).
4. Skytt, P. *et al*., Diamond Related Mater. **3**, 1 (1993).
5. Gutierrez, A., Lopez, M. F., Garcia, I. and Vazquez, A., J. Vac. Soc. Technol. A **15**, 294 (1997).
6. Muramatsu, Y. *et al*., Carbon **39**, 1403 (2001).
7. Berger, S. D., McKenzie, D. R. and Martin, P. J., Philosophical Magazine Lett. **57**, 285 (1998).
8. Yamazaki, H., Katashima, M., Bekku, I., Mihara, M. and Okuyama, N., Jpn. J. Appl. Phys. **29**, L2108 (1990).
9. Muramatsu, Y. *et al*., J. Electron Spectrosc. Relat. Phenom. **107**, 177 (2000).
10. Underwood, J. H. *et al*., Rev. Sci. Instrum. **67**, 3372 (1996).
11. Fabish, T. J. and Schleifer, D. E., Carbon **22**, 19 (1984).
12. Adachi, H., Tsukada, M. and Satoko, C., J. Phys. Soc. Jpn. **45**, 875 (1978).
13. Satoko, C., Tsukada, M. and Adachi, H., J. Phys. Soc. Jpn. **45**, 1333 (1978).
14. Nakamatsu, H., J. Jpn. Soc. Syn. Radiat. Res. **13**, 10 (2000).

Physica Scripta. Vol. T115, 504–506, 2005

Glancing Angle Fluorescence XAFS Study on Metal Oxide Thin Films Obtained by Oxygen Gas Cluster Ion Beam Assisted Deposition Techniques

H. Kageyama[1,5*], T. Asanuma[1], T. Takeuchi[1], K. Kadono[1], J. Matsuo[2,5], T. Seki[2,5], T. Kitagawa[3,5], N. Toyoda[3,5], Y. Shimizugawa[3,5] and T. Uruga[4]

[1]National Institute of Advanced Industrial Science and Technology, Midorigaoka 1-8-31, Ikeda 563-8577, Japan
[2]Ion Beam Engineering Experimental Laboratory, Faculty of Engineering, Kyoto University, Sakyo, Kyoto 606-8501, Japan
[3]Laboratory of Advanced Science and Technology for Industry, Himeji Institute of Technology, 3-1-2 Koto, Kamigoori-cho, Ako-gun, Hyogo 672-1025, Japan
[4]Experimental Facilities Division, Japan Synchrotron Radiation Research Institute, 1-1-1 Koto, Mikazuki-cho, Sayo-gun, Hyogo 679-5198, Japan
[5]Collaborative Research Center for Cluster Ion Beam Process Technology

Received June 26, 2003; accepted November 4, 2003

PACS numbers: 61.10.Ht, 68.55.Jk, 61.43.Er, 41.75.Lx, 36.40.Wa

Abstract

Glancing angle fluorescence XAFS analysis of Ta and Ti oxide thin films, which were obtained by oxygen gas cluster ion beam assisted deposition techniques (GCIB), was made to analyze the valence states and the structures of the 'amorphous' thin films at atomic level. Glancing angle XAFS measurement was made for Ta L_3-edge of the Ta oxide thin films and Ti K-edge of the Ti oxide thin films with 200 nm thickness, respectively, using the detection method of electron yield by conversion with He flow gas counter (CEY) at the beam line BL01B1 in the SPring-8. The Ta L_3-XANES results indicate that the assistance of the oxygen GCIB leads to the higher oxidation state of the Ta atom. The Ta L_3 and Ti K EXAFS results suggest that these metal oxide films obtained by the oxygen GCIB assisted deposition techniques have amorphous-like structure.

1. Introduction

The thin films metal oxides, for example Ta_2O_5 and TiO_2, will be widely used for semiconductor devices and multi-layer thin film for optical devices. The improvement of the optical properties requires accurate control of the refractive index and the optical transparency of the Ta_2O_5 and TiO_2 layer, i.e. high stoichiometry and so-called 'amorphous' structure. Glancing angle XAFS analysis is a suitable tool to analyze the structure of such 'amorphous' thin films at the atomic level instead of thin film X-ray diffraction [1]. Moreover, glancing angle XAFS analysis in the fluorescence mode, especially using the detection method of electron yield by conversion with He flow gas counter (CEY), is a highly sensitive and powerful tool to analyse the local structure of these 'amorphous' thin films.

In this study we measured the Ta L_3-XAFS of Ta oxide thin films and Ti K-XAFS of Ti oxide thin films, which were obtained by a recently developed innovative deposition technology, i.e. oxygen gas cluster ion beam assisted deposition techniques [2, 3] with different deposition conditions using glancing angle XAFS analysis in the CEY mode measurement.

2. Experimental

Glancing angle XAFS measurements were made using Si(111) monochromator and sample table with multi-rotation and translation axes, which are used for setting the glancing angle incidence condition, at the beam line BL01B1 of SPring-8 (Proposal No. 2001A0254-NX-np, 2002A0063-NX-np). The Ta oxide thin films with 200 nm thickness used in the Ta L_3-XAFS measurement are 1) Ta oxide thin film on Si wafer which were fabricated from a Ta oxide target by oxygen gas cluster ion beam assisted deposition (GCIB) with acceleration energy of 3 keV, 7 keV and 11 keV, respectively, 2) Ta oxide thin films deposited on Si wafer which were fabricated from a Ta metal target by GCIB with acceleration energy of 7 keV, ion current of 1 $\mu A/cm^2$ and deposition rate of 0.24 Å/s and acceleration energy of 7 keV, ion current of 0.2 $\mu A/cm^2$ and deposition rate of 1.2 Å/s, respectively, and 3) that by conventional electron beam deposition 4) together with those of 'Ta metal' deposited on Si wafer in the same chamber. Also the Ta L_3-XAFS of Ta film, low temperature form and high temperature form Ta_2O_5 crystalline powders were measured as reference spectra. Ti oxide thin films with 200 nm thickness used in the Ti K-XAFS measurement are 1) Ti oxide thin films which were formed by oxygen GCIB with acceleration energy of 3 keV and 2) that by conventional electron beam deposition. Also the Ti K-XAFS of Ti metal, two polymorphs of TiO_2, rutile and anatase, were measured as reference spectra. For thin film samples we measured typically four scans of Ta L_3-XAFS and Ti K-XAFS with energy range of 500 eV below and 1100 eV above the absorption edge in the CEY mode while the Ta L_3-XAFS and Ti K-XAFS of the reference samples were measured in both CEY and transmittance modes. Data were analyzed by the procedure proposed by Maeda *et al* [4]. The radial distribution functions were obtained by the Fourier transform of the k^3-weighted EXAFS functions typically in the k ranges between 2.0 and 15.3 $Å^{-1}$. The curve fitting analysis for the first Ta-O coordination shell typically between 1.1 Å and 2.0 Å in the radial structure functions was performed using the theoretical phase shifts and back-scattering amplitudes derived from FEFF code [5, 6].

3. Results and discussion

Fig. 1.a shows the first derivative Ta L_3-XANES spectra $d\mu/dE$ of Ta oxide thin films which were fabricated from the Ta oxide target together with those of Ta film, low temperature form and high temperature form Ta_2O_5. Comparison of the spectra of the films with the different deposition conditions indicates that the absorption edge, which corresponds to the first peak in $d\mu/dE$, shifts toward higher energy in the order of the electron beam, 3 keV, 7 keV and 11 keV GCIB conditions. This suggests that the assistance of the oxygen GCIB leads to a higher oxidation state

*E-mail: h-kageyama@aist.go.jp

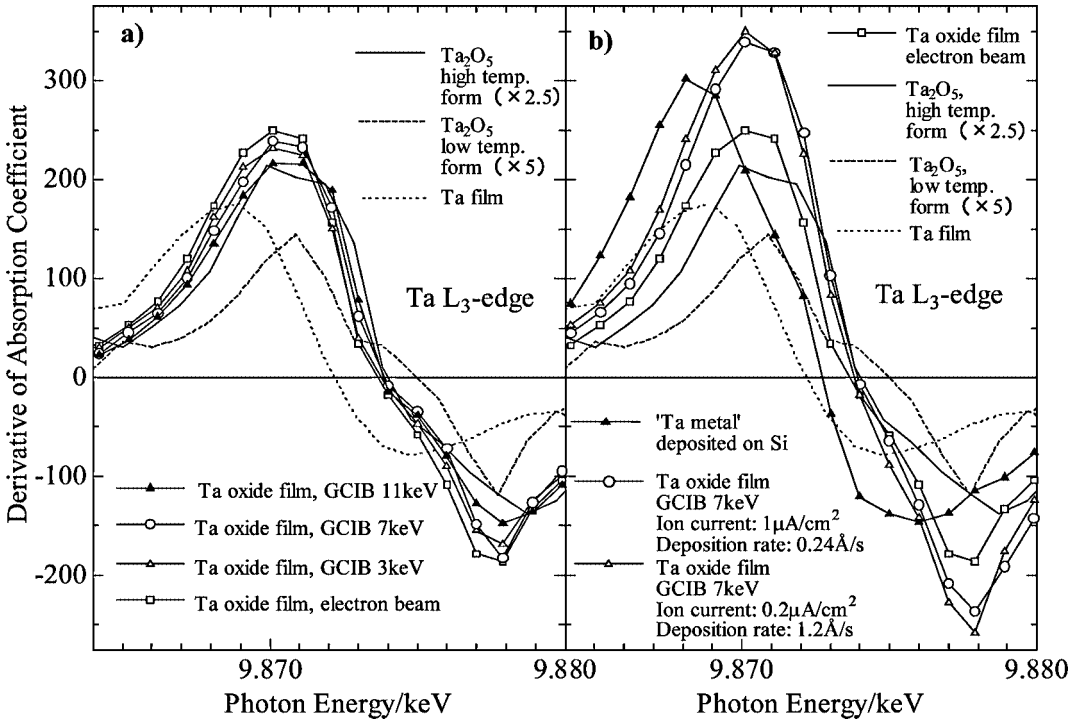

Fig. 1. The first derivative Ta L_3-XANES spectra $d\mu/dE$ of Ta oxide thin films which were fabricated from a Ta oxide target by oxygen gas cluster ion beam assisted deposition (GCIB) with acceleration energy of 3 keV, 7 keV and 11 keV, respectively, and electron beam deposition together with those of Ta film, low temperature form and high temperature form Ta_2O_5 (a). The first derivative Ta L_3-XANES spectra $d\mu/dE$ of Ta oxide thim films fabricated from a Ta metal target by oxygen GCIB with acceleration energy of 7 keV, ion current of 1 μA/cm^2 and deposition rate 0.24 Å/s and acceleration energy of 7 keV, ion current of 0.2 μA/cm^2 and deposition rate of 1.2 Å/s, respectively, and by the electron beam deposition together with those of 'Ta metal' deposited on Si in the same chamber, Ta film, low temperature form and high temperature form Ta_2O_5(b).

of the Ta atom. Fig. 1.b shows the first derivative Ta L_3-XANES spectra $d\mu/dE$ of Ta oxide thin films which were fabricated from the Ta metal target and those of 'Ta metal' deposited on Si in the same chamber. Also the comparison of the spectra of the films with the different deposition conditions indicates that an absorption edge shift toward higher energy is observed in the order of the electron beam, 7 keV, ion current of 0.2 μA/cm^2 and deposition rate of 1.2 Å/s, 7 keV, ion current of 1 μA/cm^2 and deposition rate of 0.24 Å/s GCIB conditions. This means that the assistance of the oxygen GCIB with higher dose per unit time would lead to the formation of the higher oxidation state of the Ta atom.

Fig. 2 shows k^3-weighted Ta L_3-EXAFS of Ta oxide thin films which were fabricated from the Ta oxide and Ta metal targets by different oxygen GCIB conditions and by electron beam deposition together with those of 'Ta metal' deposited on Si in the same chamber, Ta film, low temperature form and high temperature form Ta_2O_5. Comparison of the Ta L_3-EXAFS oscillations under the different deposition conditions indicates that the significant loss of long-range-order in the high k region above 10 Å^{-1} is observed for the thin films deposited with the assistance of the oxygen GCIB, especially for acceleration energy of 7 keV. This result suggests that the assistance of the oxygen GCIB would be effective for Ta oxide thin films with 'amorphous-like' structure compared with the electron beam deposition. Also a significant loss of long-range-order in the high k region is found for films deposited with assistance of oxygen GCIB, especially for acceleration energy of 7 keV, ion current of 1 μA/cm^2 and deposition rate of 0.24 Å/s. This result suggests that the assistance of the higher dose oxygen GCIB with optimum acceleration energy would be more effective for Ta oxide thin films with 'amorphous-like' structure than the conventional electron beam deposition. Table I shows results of curve fitting

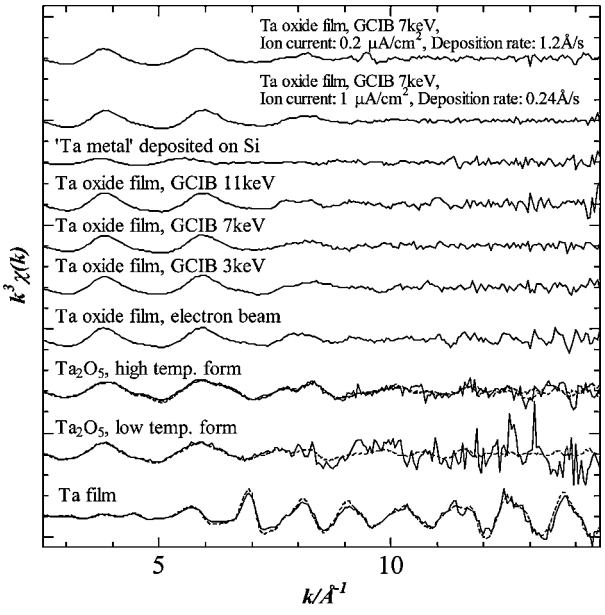

Fig. 2. k^3-weighted Ta La_3-EXAFS of Ta oxide thin films fabricated from a Ta oxide target by oxygen gas cluster ion beam assisted deposition (GCIB) with acceleration energy of 3 keV, 7 keV, and 11 keV respectively, those of Ta oxide thin films which were fabricated from a Ta metal target by the oxygen GCIB with acceleration energy of 7 keV, and ion current of 1 μA/cm^2 and deposition rate of 0.24 Å/s and acceleration energy of 7 keV, ion current of 0.2 μA/cm^2 and deposition rate of 1.2 Å/s, respectively, and that by the electron beam deposition together with those of Ta film, low temperature form and high temperature form Ta_2O_5. Solid line: electron yield (CEY) mode, broken line: transmittance mode.

analysis for the first Ta-O coordination shell. The shortest Ta-O distance is observed for the film deposited by assistance of 7 keV oxygen GCIB with ion current of 1 μA/cm^2 and deposition rate of 0.24Å/s although all the thin film samples have shorter

Table I. *Results of curve fitting analysis for the first Ta-O coordination shell using the theoretical phase shifts and back-scattering amplitudes derived from FEFF code [5, 6]. The lattice parameters and the atomic coordinates used for FEFF calculation were referred from the crystal structure in the ICSD database [7].*

Sample	Coordination number N	Interatomic ditance R [Å]	Mean square relative displacement σ^2 [Å^2]
Ta_2O_5, Crystallographic [7]	Short 5 and Long 1	1.931, 1.937 1.937, 1.947 1.947, 2.030	—
	Distances	Av. 1.955	
Ta_2O_5, Low temperature form	5.2(7)	1.961(3)	0.013(2)
Ta oxide film, Electron beam	5.3(11)	1.935(1)	0.0136(12)
Ta oxide film, GCIB 3 keV	4.9(7)	1.929(3)	0.0139(3)
Ta oxide film, GCIB 7 keV	4.9(5)	1.928(3)	0.0130(4)
Ta oxide film, GCIB 11 keV	5.1(11)	1.939(5)	0.0145(4)
Ta oxide film, GCIB 7 keV Ion current: 1 μA/cm^2, Deposition rate: 0.24 Å/s	5.0(5)	1.914(9)	0.0130(8)
Ta oxide film, GCIB 7 keV Ion current: 0.2 μA/cm^2, Deposition rate: 1.2 Å/s	5.0(11)	1.938(15)	0.0152(13)

Ta-O distances than those of low temperature form Ta_2O_5 and averaged one of the known crystallographic data. Lüzenkirchen-Hecht and Frahm mentioned that the thin films reveal smaller bond distances compared with the bulk reference in general and that this apparently reduced bond distance is a further indication for a highly disordered material and originates from the highly asymmetric pair distribution functions in amorphous solid [1].

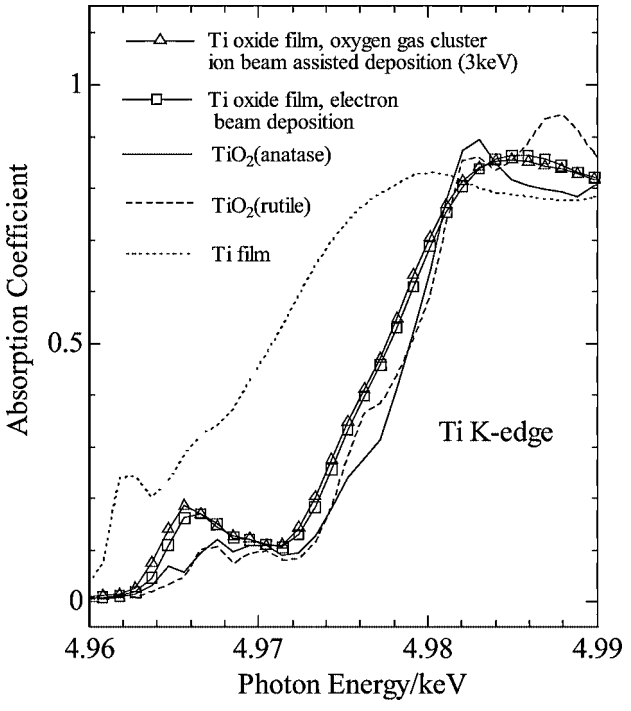

Fig. 3. Ti K-XANES of Ti oxide thin films, formed by the oxygen gas cluster ion beam assisted deposition (3 keV) and electron beam deposition together with those of Ti metal, TiO_2 (rutile) and TiO_2 (anatase).

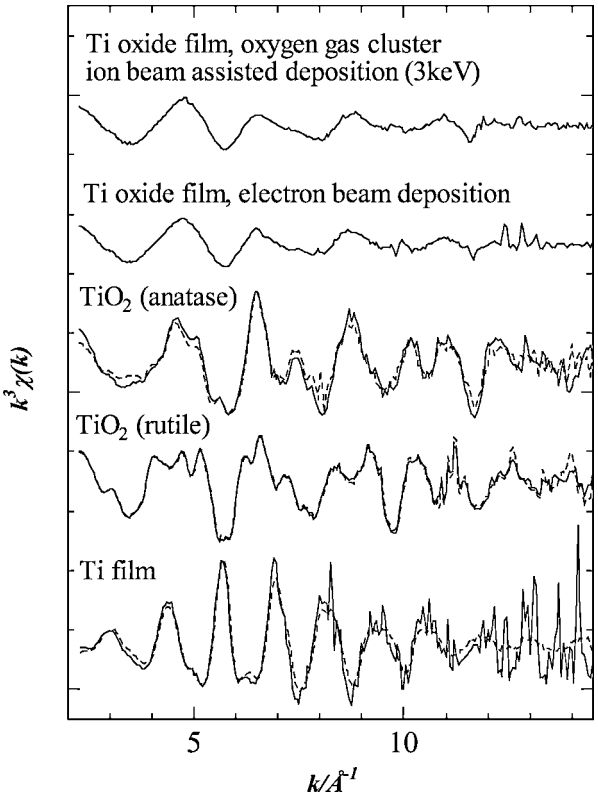

Fig. 4. Ti K-EXAFS of Ti oxide thin films, which were formed by oxygen gas cluster ion beam assisted deposition (3 keV) and electron beam deposition together with those of Ti metal, TiO_2 (rutile) and TiO_2 (anatase). Solid line: electron yield (CEY) mode, broken line: transmittance mode.

According to this discussion it is suggested that the film that was deposited by the oxygen GCIB assistance especially under the optimum deposition condition of 7 keV acceleration energy with ion current of 1 μA/cm^2 and deposition rate of 0.24 Å/s has the most amorphous-like structure.

Fig. 3 shows a comparison of the Ti K-XANES of the samples. A significant difference of the spectral features is observed between the films under electron beam and 3 keV oxygen GCIB conditions, and two polymorphs of TiO_2. This suggests that these thin films have different electronic state and/or local coordination structures from two polymorphs of TiO_2. Fig. 4 shows a comparison of the Ti K-EXAFS of the samples. Also a significant loss of long-range-order in the high k region is found for both films deposited with assistance of 3 keV oxygen GCIB and electron beam deposition. This suggests that these Ti oxide thin films have similar amorphous-like structures.

Acknowledgement

Authors would like to express gratitude to the New Energy and Industrial Technology Development Organization (NEDO) for support of this work.

References

1. Lützenkirchen-Hecht, D. and Frahm, R., J. Synchrotron Rad. **8**, 478 (2001).
2. Yamada, I., Proc. 14th Symp. Ion Sources and Ion-Assisted Technology, Tokyo, The Ion Engineering Society of Japan, Tokyo, 227 (1991).
3. Yamada, I., Radiation Effects Defects Solids **124**, 69 (1992).
4. Maeda, H., *et al*., Jpn. J. Appl. Phys. **21**, 1342 (1982).
5. Rehr, J. J., Mustre de Leon, J., Zabinsky, S. I. and Albers, R. C., J. Am. Chem. Soc. **113**, 5135 (1991).
6. Mustre de Leon, J., Rehr, J. J., Zabinsky, S. I. and Albers, R. S., Phys. Rev. **B44**, 4146 (1991).
7. Hummel, H. U., Fackler, R. and Remmert, T., Chem. Berichte **125**, 551 (1992).

Physica Scripta. Vol. T115, 507–509, 2005

Pseudo Jahn-Teller Effect Observed in Eu@C_{60}

Shuichi Emura[1], Koun Shirai[1] and Yoshihiro Kubozono[2,3]

[1]ISIR, Osaka University, Mihoga-oka 8-1, Ibaraki, Osaka 567-0047, Japan
[2]Department of Chemistry, Okayama University, Okayama 700-8530, Japan and
[3]CREST, Japan Science and Technology Corporation, Kawaguchi, 332-0012, Japan

Received June 26, 2003; accepted in revised form November 4, 2003

PACS number: 71.20.Tx

Abstract

Structures and electronic states in the ground state of endohedral fullerence are investigated by XAFS analysis and XANES spectrum. The distances between the Eu ion and the neighboring C atoms show clearly that the Eu ion is inside the C_{60} cage. The endohedral element, Eu, in C_{60} is located away from the central position of C_{60} cage by 1.4 Å. We show the detailed location of the Eu ion in the C_{60} cage by XAFS and the first principles calculation. The perturbation theory indicates that the distortion of C_{60} cage and the shift of the Eu ion are attributed to electron-nuclear interaction, pseudo-Jahn-Teller type interaction. XANES spectrum of Eu L_{III}-edge shows that the valence of the Eu ion is close to +2. The electron configuration is thus f^7, showing the total symmetry (A_{1g}) of I_h group. The details of the structures and the electronic states will be discussed with both the experimental and theoretical results.

1. Introduction

In the last few years, endohedral metallofullerences as new hopeful materials became of great interest [1]. In these materials, the $M@C_{60}$ (M = alkaline earth and lanthanide metal atoms) is the most fundamental molecule, and was discovered in the early stage of fullerene science. Several pioneers are trying to synthesize, to characterize, and to study the physics of these materials [2]. However, since the specimens of high quality are obtained with difficulty, not many publications, especially for $M@C_{60}$, are found in literature. In such situation, we have successfully isolated Y, Ba, Ce, Pr, Nd, and Gd@C_{60}'s for the first time [3–5]. Recently, Eu@C_{60} is extracted with aniline solvent from soot produced by arc heating of a graphite/Eu_2O_3 composite. We measured XAFS and XANES spectra for Eu@C_{60} to obtain the environmental information around endohedral Eu ions.

Electron-lattice interaction plays an important role in many fields of solid state physics. As one type of electron-lattice interactions, the Jahn-Teller effect is a well-known origin for lattice instability in the local environment or in the whole lattice [6–8]. Here, we will examine the pseudo Jahn-Teller type instability to explain the location of Eu ion in a large C_{60} cage. Recently the first principles calculation has been developed as powerful tool to study material properties. We will discuss the result of the first principles calculation with the pseudo Jahn-Teller effect.

2. Experimental

The specimen preparation is briefly described here. The detailed treatment is given in Ref. [3]. The soot containing Eu@C_{60} was prepared by an arc-discharge of graphite/Eu_2O_3 composite rod at 26 V and 80 A under He pressure of 80 Torr. Four-stage HPLC (High Performance Liquid Chromatography) was performed with Buckyclutcher I column and aniline solvent (flow rate: 0.75 ml/min.) after extraction from the soot with the aniline. The four steps HPLC shows a single peak. To confirm the existence of Eu@C_{60}, time-of-flight mass spectrum was observed, which suggested an endohedral structure in Eu@C_{60}. The solid sample for XAFS measurements was obtained by removing aniline solvent from the fraction under reduced pressure, and was dried by dynamical pumping at 10^{-6} Torr for 12 hours.

XAFS spectra were observed at BL12C of Photon Factory and at BL01B1 of SPring-8. The standard methods in both the transmittance and fluorescence modes were employed. Monochromatic X-ray beams were obtained through a double-Si [111]-crystal monochromater. The X-ray photon energy was calibrated with a Cu foil by assigning 8.9788 keV to pre-edge peak on the Cu absorption K-edge. The third harmonics were removed by two mirrors. The measurements were performed at room temperature. As the performance of the sample is of critical importance in the fluorescence mode, great attention was paid on the thickness and the mounting condition of the samples [9, 10].

3. Theoretical calculation

3.1. *Method*

A program "Osaka 2000" [11] with an *ab-initio* pseudopotential method based on local-density approximation (LDA) [12, 13] was used. This program expresses wavefunctions with a plane-wave expansion. Troullier-Martins potentials [14] with modification of Kleinman-Bylander type [15] were used for the pseudopotenials, and Ceperley-Alder formula [16] was used for the exchange-correlation functional.

At present, this program code is limited to non-spin polarization and non-relativistic case, which may have some consequences on the properties of 4f elements. Even if these effects can be ignored, the plane-wave expansion method has a disadvantage in studying 4f elements, because of their deep potentials and the slow convergence. In spite of these disadvantages, we examined this method in order to explore further study on the dynamical properties in future developments. In creating the pseudopotential of Eu, all components of s, p, d, and f orbital are included in valence electrons. Initially, the cutoff radius of the f potential was set to be 1.41 Å. In this case, the cutoff energy E_{cut} for plane-wave expansion becomes large (~1090 eV) in order to obtain a moderate convergence. Hence, the cutoff radius of the f potential was increased to 1.85 Å. In this setting, the plane-wave expansion shows acceptable convergence at E_{cut} = 490 eV, with 0.1 eV per atom.

E-mail: emura@sanken.oasaka-u.ac.jp

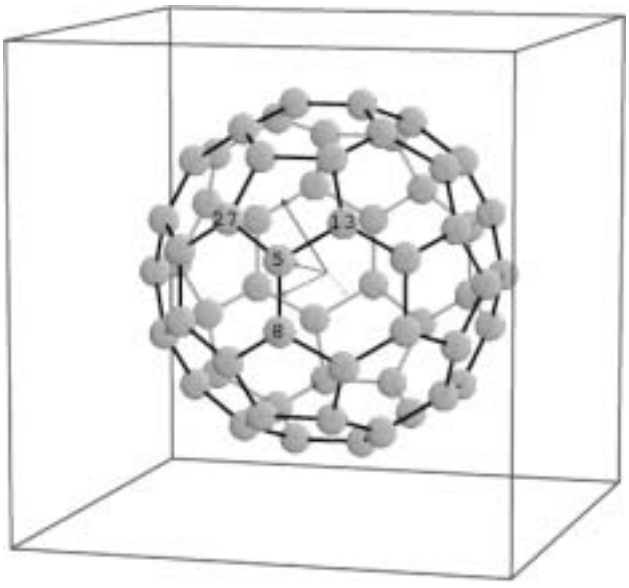

Fig. 1. A crystal model of C_{60} in this study.

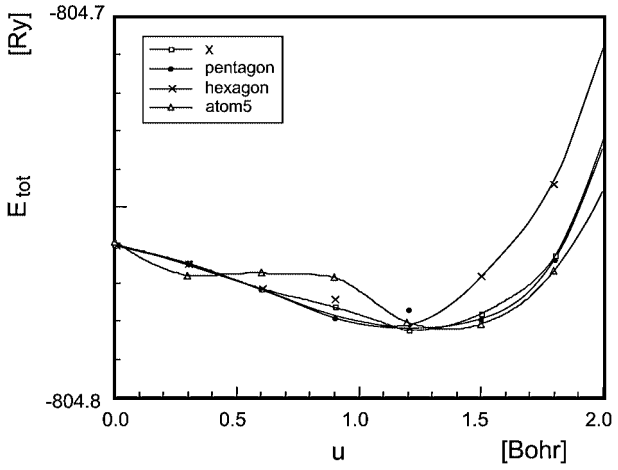

Fig. 2. The total energy versus Eu position measured from the center of C_{60}.

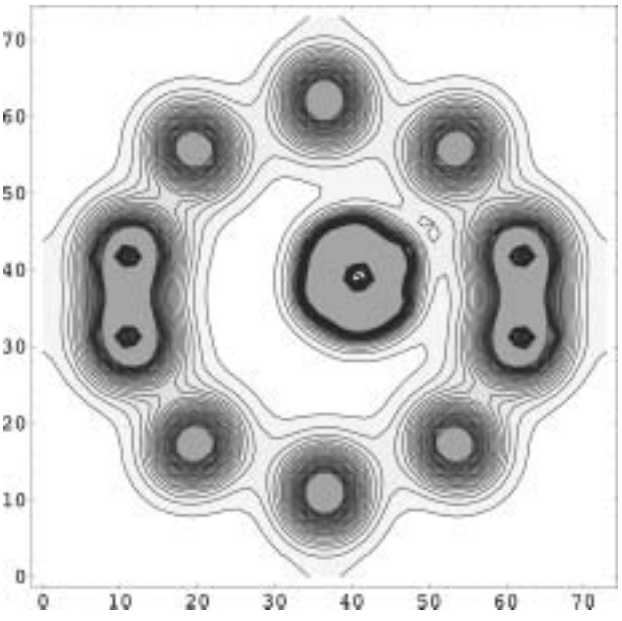

Fig. 3. The charge distribution of Eu@C_{60}. The contour map is divided by 20 from 0 to 0.2 [el/Bohr^3].

3.2. *Structural models*

The crystal structure of C_{60} is complicated due to a fact that many polymorphous phases, which have been found [17]. Any structure contains at least four units of C_{60} in the primitive cell. The differences between these phases are however only slight, for example, those differences in the orientation among different C_{60} units. The basic structure of C_{60} is almost the same; the radius of C_{60} is 3.62 Å, and the bond lengths of the intra C-C bonds are almost the same. Hence, we simplify the crystal structure of C_{60} by constructing a simple cubic structure containing only one C_{60} unit at the center, keeping the inter-molecular distance as shown in Fig. 1. This largely reduces computational task. The lattice parameter is set to be 10 Å, by considering the fact that the distance of adjacent C_{60} in the phase of $Pa\bar{3}$ is 9.92 Å.

3.3. *Calculated Results*

First, the pure C_{60} has been optimized with respect to all the atom positions. The intra C-C bond lengths are 1.404 (1.401 experiment) Å in the hexagonal edge and 1.437 (1.485) Å in the pentagonal edge. The agreement with experiment is good. Then, a Eu atom is inserted in the C_{60} crystal. When the Eu atom is placed at the center, the charge distribution shows that there is essentially no covalent bond between Eu and C atoms. The charge state is estimated by integrating the charge density inside a sphere with the center at Eu position. Taking the radius of the sphere a half the distance between the Eu and C atoms, we found that 1.33 electrons are deficient at the Eu position. This infers a singly ionized state.

We examined the total energy $E_{\rm tot}$ of the crystal as a function of the position of the Eu, with all the C atoms fixed. In Fig. 2, variations of $E_{\rm tot}$ are shown in four symmetry lines from the center to the cell boundaries. In all the directions examined, the energy minimum is located at a distance of 0.64 Å from the center. The value is different from the present experiment. We reexamined the adiabatic energy curves by raising the cutoff energy of the plane-wave expansion to 720 eV, with almost the same result. It seems that ignoring relativistic effects and spin polarization is the primary cause of this discrepancy. The spin polarization may affect those states near the Fermi level in this system.

The curvature of the adiabatic potentials at the energy minima is about 1 mdyn/Å. This amounts to the strong force constant of a Si stretching bond. This result seems rather surprising, because there is no strong covalent bond between Eu and C atoms. The strength of individual bonds Eu-C is still small. However, there are many C atoms surrounding the Eu atom, and accordingly the force constant becomes large enough as a whole. In Fig. 3, the charge distribution of the optimized structure is shown in the [020] plane. The charge density at the midpoint between Eu and C is 1/20 times smaller than that of Si covalent bond. An analysis of the charge distribution shows that 2.18 electrons are deficient in the Eu site. Thus, we can say that the charge state of Eu atoms at their equilibrium position is a doubly ionized one, Eu^{2+}.

4. Results and Discussion

The bond distances between the Eu atom and C atoms up to the second nearest neighbors were found by XAFS analysis. These values are 2.34 and 2.84 Å. Only the distance to the first nearest neighbors and the configuration number are not enough to decide if the Eu atom locates inside the C_{60} cage or at some position outside of C_{60}. The distance of the second neighbors gives the key information for it. Figure 4 shows the relation of distances. The dots in the figure indicate the distance between the Eu atom and

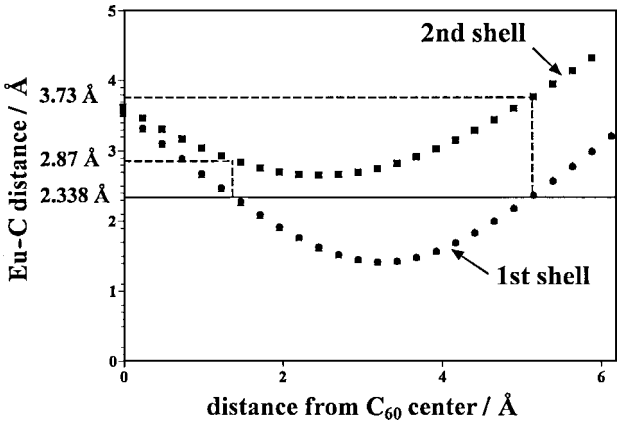

Fig. 4. Correlations of the distances between the Eu atom and the first neighbors and the second neighbors.

the C atom of the first and the second neighbors along the suitable line from the center of C_{60}. This figure indicates that the Eu atom is inside C_{60} cage, and furthermore that it locates away from the center of C_{60} cage by 1.4 Å toward the center axis of hexagonal network of the C atoms. XANES spectra of Eu C_{60} suggested that the valence of Eu atom is about +2 [5]. The electron configuration is thus f^7, showing the total symmetry (A_{1g}) of the I_h group.

The central instability of the Eu ion in the cage of C_{60} is also presented by first principles calculation. The calculated valency of the Eu atom is +2.18. This value excellently agrees with the experimental one. We will at first start with just +2 valency at the central position of the Eu atom. Under the condition, the charge distribution of the Eu^{++} (f^7) ion is spherical. The lowest unoccupied molecular orbital (LUMO) of C_{60} is a T_{1u} state, as well known. The +2 valence of the Eu atom means that the two electrons of the Eu atom transfer to C_{60} cage and occupy the T_{1u} state with a parallel spin. The two electrons may distribute uniformly over the whole C_{60} cage, giving total symmetry because of the repulsion force between the electrons. These situations suggest that the central position in the C_{60} cage is most stable inside the cage for the +2 valenced Eu ion, which is also the viewpoint of electro-static theory. However, the experimental observation and the first principles calculation indicate that the central position is unstable. Thus, we have to consider *ungerade* type instability to explain the observed phenomenon that the Eu atom shifts from the center along the high symmetric axis, that is, an *ungerade* charge distribution of the Eu ion and on the C_{60} cage should be taken into consideration. The electron density calculated by the first principles theory well simulates this state (see figure 3). However, two electrons in the T_{1u} orbital give a gerade symmetry in the wave function. As the cage of C_{60} with about 7 Å diameters is very big for an electron, the correlation of electrons should not be so strong. Thus, we may be able to treat the electrons independently. Under this assumption, the small shift of the Eu^{++} ion from the center of the cage lets itself recognize one electron. A vibrational mode of ungerade type plays an important role in this situation. It makes wave functions of gerade type mix those of ungerade type. The Hamiltonian for the expression of the interaction is represented as $\boldsymbol{H} = \lambda \boldsymbol{Q}_{T_{1u}}$, where λ is the coupling constant and $\boldsymbol{Q}_{T_{1u}}$ the normal coordinate with T_{1u} symmetry. Solving the interaction among the one electron with symmetry on the C_{60} cage and the f^7 electrons of the Eu^{++} ion, we obtain a double minimum potential along the $\boldsymbol{Q}_{T_{1u}}$ normal coordinate. It means the central instability of the Eu atom. This is just the pseudo Jahn-Teller effect.

Acknowledgements

The experiments in this study were performed at Photon Factory through Grant No. 1998G-289 and 2000G 248 and at SPring-8 through Proposal No. 1997B0087-NX-np, 1998A0219-CX- np, and 2000A0002-NX-np.

References

1. Saunders, M. *et al*., Science **259**, 1428 (1993).
2. Rose, H. R. *et al*., J. Chem. Soc. Chem. Commun. 1361 (1993).
3. Kubozono, Y. *et al*., Chem. Lett. 457 (1996).
4. Kubozono, Y. *et al*., J. Am. Chem. Soc. **118**, 6998 (1996).
5. Takabayashi, Y. *et al*., Chem. Lett. 1019 (1997).
6. Nagasaka, S., J. Phys. Soc. Jpn. **50**, 1570 (1981) and *ibid* **52**, 898 (1982).
7. Emura, S. and Ishiguro, M., Phys. Rev. B**38**, 12851 (1988).
8. Emura, S. *et al*., Phys. Rev. B**38**, 3280 (1988).
9. Emura, S. *et al*., Phys. Rev. B**47**, 6918 (1993).
10. Emura, S. and Maeda, H., Rev. Sci. Instrum. **65**, 25 (1994) and Jpn. J. Appl. Phys. **32**, 734 (1993).
11. Shirai, K., see http://www.cmp.sanken.osaka- u.ac.jp/∼koun/osaka.html
12. Car, R. and Parrinello, M., Phys. Rev. Lett. **55**, 2417 (1985).
13. Payne, M. C., Teter, M. P., Allan, D. C., Arias, T. A. and Joannopoulos, J. D., Rev. Mod. Phys. **64**, 1045 (1992).
14. Troullier, N. and Martins, J. L., Phys. Rev. B**43**, 1993 (1991).
15. Kleinman, L. and Bylander, D. M., Phys. Rev. Lett. **48**, 1425 (1982).
16. Ceperley, D. M. and Alder, B., Phys. Rev. Lett. **45**, 566 (1980).
17. Weaver, J. H. and Poirier, D. M., in "Solid State Physics", (H. Ehrenreich and F. Spaepen eds.) **48**, 1 (1994).

Physica Scripta. Vol. T115, 510–512, 2005

The Hybridized M3d-F2p Character of Low-Energy Unoccupied Electron States in 3d Metal Fluorides Observed by F 1s Absorption

A. S. Vinogradov[1*], S. I. Fedoseenko[1], S. A. Krasnikov[1,2], A. B. Preobrajenski[1,3], V. N. Sivkov[1], D. V. Vyalikh[1,4,5], S. L. Molodtsov[1,4,6], V. K. Adamchuk[1], C. Laubschat[6] and G. Kaindl[5]

[1]V. A. Fock Institute of Physics, St. Petersburg State University, St. Petersburg, 198504 Russia
[2]W. Ostwald-Institut für Physikalische und Theoretische Chemie, Universität Leipzig, D-04103, Leipzig, Germany
[3]MAX-lab, Lund University, S-22100 Lund, Sweden
[4]Russian–German Laboratory at BESSY II, D-12489 Berlin-Adlershof, Germany
[5]Institut für Experimentalphysik, Freie Universität Berlin, D-14195 Berlin, Germany
[6]Institut für Festkörperphysik, Technische Universität Dresden, D-01062 Dresden, Germany

Received June 26, 2003; accepted in revised form November 7, 2003

PACS numbers: 78.70.Dm, 71.20.−b, 71.70.Ch

Abstract

The near-edge fine structure of the F 1s absorption spectra of 3d metal fluorides was studied for the first time with high energy resolution. The spectra of these, the most ionic compounds of the 3d atoms, are analyzed comparing with the F 1s absorption spectrum of the molecular TiF_6^{2-} anion in solid K_2TiF_6. The latter spectrum was afore interpreted considering the fluorine spectra of the molecular PF_6^- anion in a KPF_6 crystal and of the gas-phase SF_6 molecule. The low-energy empty electron states in the 3d metal fluorides are shown to be formed due to covalent mixing of the metal 3d and fluorine 2p electron states.

1. Introduction

The covalent mixing (hybridization) between the transition-metal (TM) 3d electrons and ligand valence electrons leads to delocalization of the 3d states, decreasing the 3d electron density on the TM atoms and thus lowering the role of the 3d electron correlations. Although X-ray Absorption Spectroscopy (XAS) has been widely used for several decades for obtaining information on the energy distribution and spatial localization of unoccupied electron states in TM compounds, systematic XAS studies of the role of hybridization in the formation of the electronic structure of these compounds are nearly not available.

This paper presents F 1s absorption spectra measured for the first time with high photon-energy resolution for a series of binary fluorides TiF_4, VF_4, VF_3, CrF_3, CrF_2, MnF_3, MnF_2, FeF_3, FeF_2, CoF_2, NiF_2, CuF_2, and ZnF_2. We have selected fluorides because they are the most ionic among the simplest 3d-metal compounds. Their spectra and the electronic structure may provide a basis for understanding electronic properties of more complicated covalent compounds. The obtained spectra are analyzed in order to (*i*) elucidate the character of the covalent bonding and the way it is displayed in X-ray absorption spectra and (*ii*) study the conduction-band electronic structure along the whole series of TM fluorides.

2. Experiment

We investigated the Near-Edge X-ray Absorption Fine Structure (NEXAFS) of the F 1s spectra in binary fluorides KF, TiF_4, VF_4, VF_3, CrF_3, CrF_2, MnF_3, MnF_2, FeF_3, FeF_2, CoF_2, NiF_2, CuF_2, and ZnF_2, as well as in the gas-phase SF_6 molecule and in the PF_6^- and TiF_6^{2-} molecular anions of the solid compounds KPF_6 and K_2TiF_6. The 2p absorption spectra of titanium in TiF_6^{2-}, TiF_4, TiO_2 and of potassium in KF were investigated additionally as a tool for interpretation of the F 1s absorption structures in the spectra of titanium and potassium fluorides. Most of these spectra were measured at the Russian-German beamline (RGB) of the electron storage ring BESSY II [1], while the spectra of KF and CuF_2 were taken under similar experimental conditions at the D1011 beamline of the electron storage ring MAX II. Spectra from the solid samples (powders) were obtained by detecting the total electron yield. The absorption spectra of gas-phase SF_6 and Ne were measured with a gas cell by detecting the photoionization yield. Based on the linewidth analysis for the Ne 1s → 3p transition, the photon-energy resolution of the RGB in the range of the F 1s absorption edge (∼690 eV) was estimated to be approximately 115 meV. The absorption spectra were normalized to the incident photon flux. Photon energies in the range of the fine structure of the F 1s absorption spectra were calibrated using the known position (683.9 eV) of the first narrow peak in the F 1s absorption spectrum of K_2TiF_6 [2], which was recorded before and after measurement of each spectrum of all fluorides.

3. Results and discussion

The high-resolution F 1s absorption spectra of the TM fluorides were measured over a wide photon-energy range (675–760 eV) and normalized to the same absorption jump at the photon energy of 760 eV. Figures 1 and 2 show NEXAFS spectra in the photon-energy range of 678–710 eV. To our knowledge the high-resolution F 1s spectra of the majority of the binary TM fluorides under study are presented for the first time. Previously only the spectra from some difluorides of 3d atoms [3] and from ScF_3 [4] were measured although with essentially lower resolution. Evidently, the obtained spectra differ very strongly both from the F 1s spectrum of K_2TiF_6 containing covalent molecular anions TiF_6^{2-} and along the series of the 3d-metal fluorides (with increasing number of TM 3d electrons: TiF_4-⋯-ZnF_2). Nevertheless, one can distinguish two spectral ranges, whose structural features are similar for all the spectra, including that of covalent TiF_6^{2-}. The first range contains narrow resonances *a*, *a*′, *b*, and *b*′ located below the F 1s absorption edge (∼690 eV). The second range is dominated by the broader absorption bands *c*, *d*, and *e* that are located slightly above the edge and significantly overlap with each other.

Since for all fluorides under study an octahedral, or nearly octahedral, coordination of the 3d atoms by fluorine is typical,

*Corresponding author E-Mail: Alexander.Vinogradov@pobox.spbu.ru

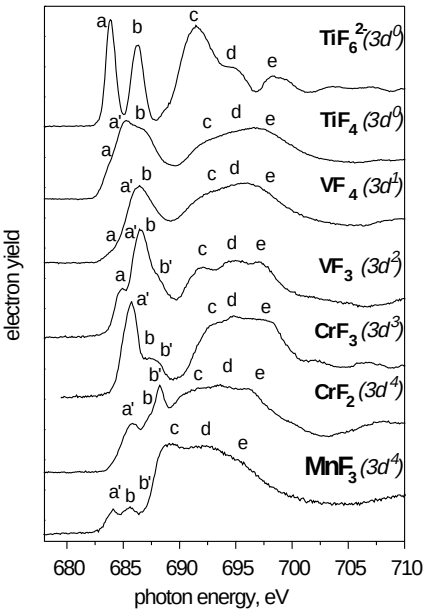

Fig. 1. High-resolution F 1s absorption spectra of 3d-metal fluorides K_2TiF_6, TiF_4, VF_4, VF_3, CrF_3, CrF_2, and MnF_3. The spectra were normalized to the same absorption jump at the photon energy of 760 eV.

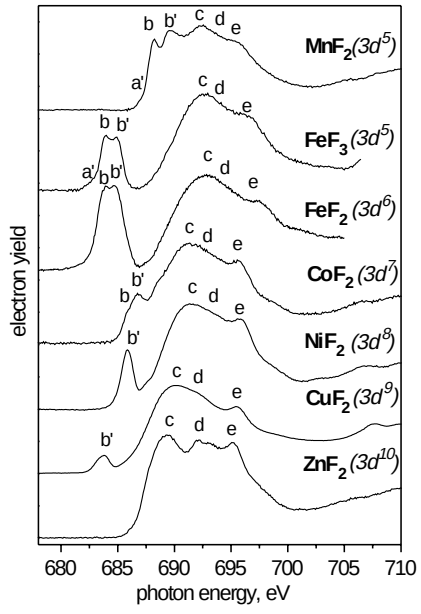

Fig. 2. High-resolution F 1s absorption spectra of 3d-metal fluorides MnF_2, FeF_3, FeF_2, CoF_2, NiF_2, CuF_2, and ZnF_2. The spectra were normalized to the same absorption jump at the photon energy of 760 eV.

these crystals are commonly considered as three-dimensional arrays of interlinked perfect or distorted MF_6 octahedra [5]. In this case, possible covalent bonding between the 3d atom M and surrounding fluorine atoms in ionic crystals can, evidently, take place within the octahedron due to the mixing of the valence M 3d, 4s, 4p and F 2p electron states. In order to follow how this hybridization of the valence states can be reflected in the F 1s absorption spectra of binary TM fluorides, first we discuss the origin of the absorption features in the spectra of the covalent molecular TiF_6^{2-} anion in solid K_2TiF_6.

In Fig. 3 we compare the F 1s NEXAFS spectra for the following isostructural covalent systems: the gas-phase SF_6 molecule and the solid-state molecular anions PF_6^- and TiF_6^{2-} representing isolated regular octahedra [5]. The absorption

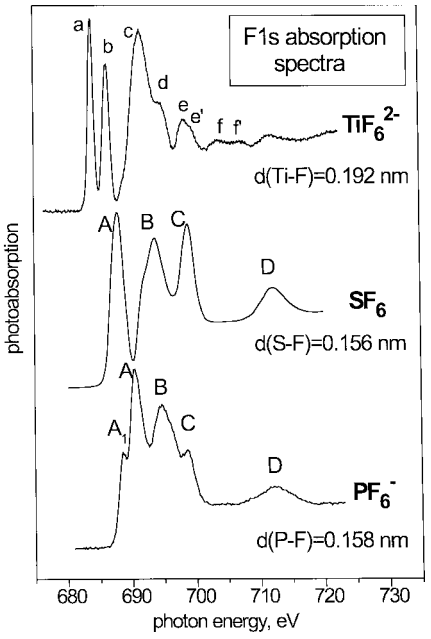

Fig. 3. Near-edge fine structure of the F 1s absorption spectra for covalent anions TiF_6^{2-} and PF_6^- in solid K_2TiF_6 and KPF_6 as well as for gas-phase molecule SF_6.

spectrum of SF_6 exhibits well-developed structures A-D, which result from the transitions of the F 1s electrons into unoccupied molecular orbitals (MOs) of a_{1g}, t_{1u}, t_{2g}, and e_g symmetry [6–9]. Bands C and D appear in the continuum significantly above the absorption edge resulting from the transitions to MOs t_{2g} and e_g. These MOs are formed due to covalent mixing of the S 3d states and the F 2p states, so that the corresponding peaks can be observed in the absorption spectra of both sulfur and fluorine at almost the same energy positions above the vacuum level. The latter is also true for the covalent molecular anion PF_6^- in solid KPF_6 showing absorption spectra similar to those of SF_6 [10].

Whereas the F 1s NEXAFS spectra of SF_6 and PF_6^- are similar to each other, they differ considerably from the spectrum of TiF_6^{2-}. Indeed, resonances C and D vanish from the continuum, two very narrow and intense absorption peaks *a* and *b* arise in the low-energy spectral range and the onset of the F 1s absorption becomes shifted by several eV to low energies. It is remarkable that the energy half widths of peaks *a* and *b* (∼1 eV) in the spectrum of solid K_2TiF_6 are significantly smaller than the half width of the lowest-energy peak A (2.3 eV) in the spectrum of gaseous SF_6 molecule. By comparison between absorption structures in the F 1s and the Ti 2p spectra it can be easily shown that the low-energy peaks *a* and *b* are related to electron transitions into the unoccupied Ti $3dt_{2g}$ and $3de_g$ states hybridized with the F 2p electron states [10]. Thus, the Ti 3d states in the TiF_6^{2-} anion can be probed by the F 1s NEXAFS. In going from SF_6 and PF_6^- to TiF_6^{2-} one can clearly observe (*i*) a large (∼15 eV) low-energy shift of the absorption bands related to the 3d states of the central atom (bands C and D for SF_6 and PF_6^- and peaks *a* and *b* for TiF_6^{2-}) and (*ii*) a considerable decrease in their energy half width (Fig. 3). These spectral changes result definitely from the collapse and the subsequent increase of localization of the 3d states of the central atom in going from the atoms at the end of the second row to the atoms of the first transition series [11].

Based on the local and space-oriented character of the covalent bonds and taking into account the results of our comparative

consideration for F 1s spectra of TiF_6^{2-}, TiO_2, KF, and TiF_4 [10], we believe that it is possible to consider the octahedral quasi-molecule MF_6 formed by the 3d atom and surrounding fluorine atoms as the main building block of the crystal not only in rather covalent 3d systems, but also in the case of ionic TM fluorides.

The similarity in overall lineshape and energy position for the NEXAFS in the spectra of the ionic fluorides and the covalent molecular anion TiF_6^{2-} allows us to assign the structures observed in both cases to the unoccupied electron states with the mixed TM 3d – F 2p character resulting from the significant covalent bonding between the valence electrons of the metal and fluorine atoms. However, in going from the TiF_6^{2-} anion to the binary fluorides and further along the series TiF_4- $\cdots$ -ZnF_2 the spectra in Figs. 1 and 2 exhibit remarkable changes in number and relative intensity of the resonances, as well as in their energy positions with respect to each other and to the onset of the F 1s continuum. These changes are likely caused by (*i*) a decrease in the number of unoccupied TM 3d states, (*ii*) an exchange interaction between the 3d electrons in partially filled shells, (*iii*) changes in size of MF_6 and the character of its distortion, and (*iv*) a different impact of the remaining part of the crystal on the quasi-molecule MF_6 that may particularly influence the coupling between these structural units.

Nevertheless, we can make some assumptions about the origin of these low-energy structural features. Taking into account the results of our comparative quasi-molecular analysis of the XAS spectra of TiF_6^{2-}, TiO_2, and KF [10], we can assume first of all that the coupling between the octahedra MF_6 in the TM fluorides affects only slightly the lineshape of the fluorine spectra. Calculations of the electronic structure for oxides of the 3d atoms [12] show that accounting for the exchange interaction between the 3d electrons leads to additional splitting of the $3dt_{2g}$ and $3de_g$ electron states of MO_6 into $t_{2g}\uparrow$, $e_g\uparrow$ and $t_{2g}\downarrow$, and $e_g\downarrow$ components related to the two possible spin orientations in both states: up ($\uparrow$) or down ($\downarrow$), respectively. Evidently, a similar situation must hold for MF_6 in the TM fluorides. It is also clear that the ordering of these split 3d components depends on the ratio between the magnitudes of the crystal-field and the exchange splitting. More detailed discussion [10] allows us to suppose that the crystal-field splitting for the fluorides under study is larger than the exchange splitting and, as a consequence, the ordering of the 3d components is $t_{2g}\uparrow$, $t_{2g}\downarrow$, $e_g\uparrow$, and $e_g\downarrow$.

Based on the formal valence, we assume that the titanium atom (with $3d^24s^2$ valence electrons) actually has the same electronic configuration of the Ti^{4+} ion in the molecular anion TiF_6^{2-} and in solid TiF_4, which contains no 3d electrons at all. In this case, the 3d – 3d exchange interaction is absent and peaks *a* and *b* in the spectrum of TiF_6^{2-} can be related to the electron transitions into the spin degenerate $3dt_{2g}$ and $3de_g$ states. The changes in the low-energy absorption structure in going from TiF_6^{2-} to TiF_4 result from the considerable tetragonal distortion of the octahedra in TiF_4 [5], which causes a splitting of the $3dt_{2g}$ and $3de_g$ bands each into two components and a merge of the low-energy absorption bands into one broad band *a*-*a*′-*b*.

In contrast to that, in other binary (V, Cr, etc.) fluorides these states are additionally split due to the exchange interaction between the 3d electrons, which occupy the $t_{2g}\uparrow$, $t_{2g}\downarrow$, $e_g\uparrow$, and $e_g\downarrow$ states successively according to their statistical weights: 3 and 2 for the t_{2g} and e_g components, respectively. In the case of VF_4 one available 3d electron partly occupies the lowest $3dt_{2g}\uparrow$ band, which may be additionally split into two components owing to the considerable distortion of the VF_6 octahedron (as in TiF_4). As a consequence, one broad band *a*-*a*′-*b* is observed at the low-energy onset of the F 1s absorption spectrum. The formal valence configuration $3d^2$ for the vanadium ion V^{3+} in VF_3 with the nearly perfect VF_6 octahedra indicates that the corresponding F 1s absorption spectrum may also exhibit all four 3d components, since the lowest $t_{2g}\uparrow$ state remains not fully occupied. Due to the ideal octahedral shape of VF_6 the absorption spectrum of VF_3 is characterized by better resolved structures as compared to the VF_4 and TiF_4 spectra. The overall lineshape of its low-energy structures *a*-*a*′-*b*′ does not rule out the possibility of existence of an additional unresolved component *b* in the range of the broad peak *a*′. In the case of CrF_3, CrF_2, MnF_3, MnF_2, and FeF_3 the lowest $t_{2g}\uparrow$ state is already completely occupied, so that only three low-energy features *a*′, *b*, and *b*′ (related to the transitions to the $t_{2g}\downarrow$, $e_g\uparrow$, and $e_g\downarrow$ states) are observed in the spectra.

Similarly, only two transitions to the $e_g\uparrow$ and $e_g\downarrow$ states are found in the spectra of FeF_2 and CoF_2, since the $t_{2g}\downarrow$ state in these compounds is filled. For NiF_2 and CuF_2 only the last absorption peak *b*′ is observed in the low-energy part of the F 1s spectra, since only one electron state $e_g\downarrow$ remains unfilled. In the spectrum of ZnF_2 the low-energy structure is absent because all 3d electron states are fully occupied.

In conclusion, the basic results of our study provide a strong experimental evidence for importance of covalent mixing in the formation of unoccupied electron states in crystalline 3d-TM fluorides. The F 1s absorption spectra are found to be very promising in probing unoccupied 3d states of the TM atoms in these compounds.

Acknowledgements

This work was supported by the Russian Foundation for Basic Research (project no. 01-03-32285), the Ministry of Industry and Science of the Russian Federation (project no. 40.030.1.1.11.17), the Deutsche Forschungsgemeinschaft (SFB 463, TP B4 and B16), and the bilateral program Russian-German Laboratory at BESSY II. We thank the staff of BESSY II for valuable technical assistance. A. S. Vinogradov gratefully acknowledges the financial support by the Technische Universität Dresden. A. B. Preobrajenski acknowledges the support by the Swedish Foundation for International Cooperation in Research and Higher Education (STINT).

References

1. Fedoseenko, S. I. *et al.*, Nucl. Instrum. Meth. Phys. Res. A **470**, 84 (2001).
2. Vinogradov, A. S. *et al.*, Fiz. Tverd. Tela (Leningrad) **24**, 1417 (1982) [Sov. Phys. Solid State **24**, 803 (1982)].
3. Nakai, S. *et al.*, Phys. Rev. B **37**, 10895 (1988).
4. Umeda, M., Tezuka, Y., Shin, S. and Yagishita, A., Phys. Rev. B **53**, 1783 (1996).
5. Wells, A., "Structural Inorganic Chemistry", 5th ed. (Oxford University Press, Oxford, UK, 1984).
6. Zimkina, T. M. and Vinogradov A. S., J. Phys. (Paris) **32**, C4-3 (1971).
7. Dehmer, J. L., J. Chem. Phys. **56**, 4496 (1972).
8. Hudson, E. *et al.*, Phys. Rev. A **47**, 361 (1993).
9. Francis, J. T. *et al.*, Phys. Rev. A **52**, 4665 (1995).
10. Vinogradov, A. S. *et al.*, to be published.
11. Karazia R. I., Usp. Fiz. Nauk **135**, 79 (1981) [Sov.Phys.-Usp. **24**, 775 (1981)].
12. Suzuki, C., Kawai, J., Adachi, H. and Mukoyama, T., Chem. Phys. **247**, 453 (1999).

Physica Scripta. Vol. T115, 513–515, 2005

Investigation of Structural and Electronic Properties in Ru Perovskite Oxides by XAFS Measurements

M. Mizumaki[a], K. Yoshii[b], Y. Hinatsu[c], Y. Doi[c] and T. Uruga[a]

[a]Japan Synchrotron Radiation Research Instituite, 1-1-1 Kouto Mikazuki-cho, Sayoh-gun 678-5198, Japan
[b]Japan Atomic Energy Research Institute, 1-1-1 Kouto Mikazuki-cho, Sayoh-gun 678-5148, Japan
[c]Division of Chemistry, Hokkaido University, Kita 8, Nishi 10, Kita-ku, Sapporo 153-8505, Japan

Received June 26, 2003; accepted in revised form November 4, 2003

PACS numbers: 78.70.Dm, 74.25.Jb

Abstract

The electronic and structural properties of Ru oxides were investigated by utilizing X-ray absorption spectroscopy (XAS). We estimate the valence of Ru in perovskite ruthenium oxides by XAS measurements. XAS measurements were carried out at room temperature around Ru K-edge. The valence of Ru in A_2(A = Ba, Sr)LnRuO$_6$ and A(A = Ca, Ba, Sr)RuO$_3$ was 4+. The valence of Ru in Ln$_3$RuO$_7$ was 5+. The valence of Ru in PbRuO$_3$ showed an intermediate value between 4+ and 5+. We calculated XAS spectra around the Ru K-edge by FEFF 8.0. Theoretical calculation reproduced the experimental spectra. We analyzed XAS spectra and obtained information of local structure. The bond length between Ru and O was consistent with the results of neutron diffraction.

1. Introduction

The perovskite-type oxides have the general formula ABO_3, in which A represents a large electropositive cation and B represents a small transition metal ion. The perovskite structure can be described as a framework of corner-shared BO_6 octahedra which contain A cations at 12-coordinate sites. Recent studies of ruthenium oxides with the formula ABO_3 have shown a wide variety of electrical and magnetic properties such as unconventional superconductivity, and ferromagnetism accompanied by spin glass behavior [1]–[3]. Double perovskite-type oxides have the formula $A_2B'BO_6$, in which the primes indicate the different ions in different oxidation states, and in some cases, the cations at the B sites, B' and B'', regularly order, i.e., 1 : 1 arrangement of B' and B'' ions has been observed over the six-coordinate B-sites. Since the B cations generally determine the physical properties of perovskites, different kinds of B' and B'' ions should show a variety of the physical properties of double perovskites. We have been interested in the properties of the perovskites containing tetra- or pentavalent ruthenium ions. The electronic structure of $Ru^{4+(5+)}$ is [Kr]$4d^{4(3)}$ ([Kr] = krypton core). Such highly oxidized cations from the second transition series sometimes show quite unusual magnetic behaviour. In the compounds A_2BRuO$_6$ (where A is alkaline-earth metal and B is a lanthanide (Ln) and a 3d transition metal (TM)), ruthenium ions are in the tetravalent state in the case of B = 3d TM and in the pentavalent state in the case of B = Ln. In the case of B = 3d TM, these compounds sometimes show ferromagnetic order [7]. In the case of B = Ln, these compounds show long range magnetic ordering at low temperature. For example, Sr_2YRuO_6 [4] and Sr_2LuRuO_6 [5] are antiferromagnetic below 26 and 30 K, respectively, and Sr_2ErRuO_6 [6] shows antiferromagnetic ordering involving both Ru^{5+} and Er^{3+} at 40 K. However, previous work is limited to the compounds in which the paramagnetic ions are only Ru^{5+} ions, except for Sr_2ErRuO_6. But direct measurements of Ru ion valence in A_2BRuO$_6$ and A(A = Sr, Ca, Ba, and Pb)RuO$_3$ have not been carried out before. Especially, the valence of Ru ions in $Pb_2Ru_2O_6$ could not be determined. In this study, we estimate directly the valence of ruthenium ions in the perovskites. We investigated the electronic and structural propertries of these Ru compounds by means of X-ray absorption spectroscopy (XAS) measurements.

2. Experimental

Polycrystalline samples of A(A = Sr, Ca, Ba, and Pb)RuO$_3$ and A(A = Sr, Ba, Ca, and La)$_2B$(B = La, Eu, Mn, and Ni)RuO$_6$ were prepared by the conventional solid state reaction as noted in Ref. [8 and 9]. These products were shown to be perovskite-like single phase materials by powder X-ray diffraction. The XAS spectra of the Ru K-edge for Ru oxides were obtained at the beamline BL39XU and BL01B1 of SPring-8, Japan. The beamline was composed of a double-crystal monochormator equipped with a Si 111 crystal and a Si mirror for eliminating higher harmonics. The XAS spectra were recorded under transmission mode. The X-ray intensity was monitored using ionization chambers filled with N_2 gas before and after observing samples. For the XAS measurements, powdered samples were uniformly spread on Scotch tape and then the thickness of samples were adjusted so that the edge jump was 1. All the XAS data were obtained at room temperature. The energy resolution was about 2 eV around the Ru K-edge. In order to investigate the electronic properties and local structure of Ru oxides, we carried out calculations of XAS spectra by utilizing the code FEFF 8.0 [10].

3. Results and Discussion

Figure 1 shows normalized XANES spectra of A(A = Ca, Sr, Ba)RuO$_3$ and $Pb_2Ru_2O_{6.5}$ around the Ru K-edge. The Ru K-edge correponds to transition from 1s to 5p. From bottom to top, six curves show CaRuO$_3$, SrRuO$_3$, BaRuO$_3$, $Pb_2Ru_2O_{6.5}$ and Eu_3RuO_7 respectively. The valence of Ru ions in Eu_3RuO_7 is known to be pentavalent. These spectra were composed of two peaks denoted A and B. According to Ref. [11 and 12], the two peaks of A and B correspond to $5p_x$ and $5p_{y(z)}$ respectively. This result means that RuO$_6$ octahedra are distorted and the apical Ru-O bond length is longer than the Ru-O bond length in the ab-plane. The spectral shape of these Ru compounds are very similar to each other. These results show that the

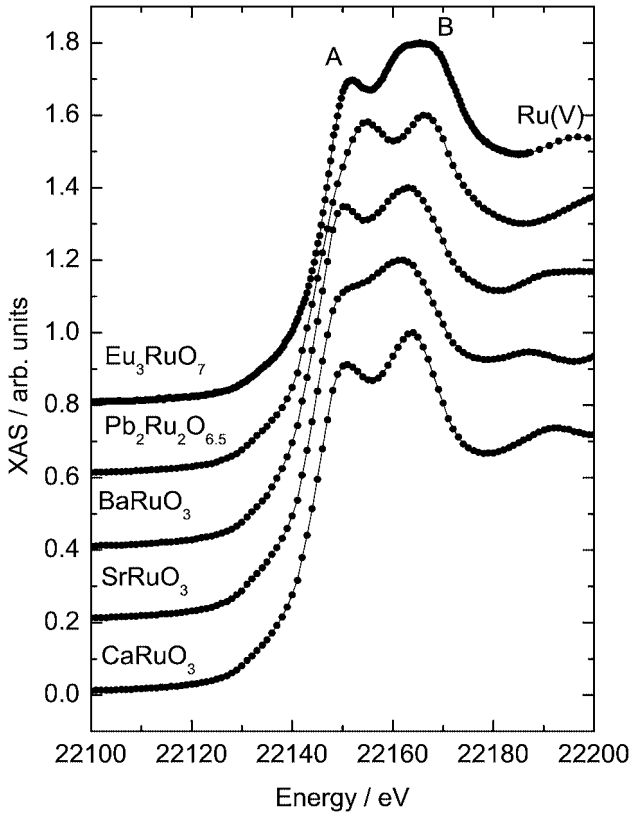

Fig. 1. XAS spectra in $A(A = \text{Ca, Sr, Ba})RuO_3$ and $Pb_2Ru_2O_{6.5}$ around the Ru K-edge.

compounds have the same local symmetry around the Ru ion. But the absorption edge in $Pb_2Ru_2O_{6.5}$ shifted to higher photon energy by 2 eV compared with the other compounds. This means that the valence of Ru ions in $Pb_2Ru_2O_{6.5}$ is higher than that of the other compounds and could be pentavalent. Therefore, we propose that the valence of Pb ions is nearly divalent.

Figure 2 shows normalized XANES spectra of $A_2B(B =$ Ni, Mn, Eu, La)RuO_6 around the Ru K-edge. From bottom to top, seven curves show Ca_2MnRuO_6, La_2NiRuO_6, Ba_2EuRuO_6, Ba_2LaRuO_6, Sr_2EuRuO_6 and Eu_3RuO_7. These spectra were composed of two peaks denoted A and B. The spectra are very similar. The width of peak B in the case of $B =$ Ln is broader than in the case of $B =$ 3d TM. But the absorption edge of La_2NiRuO_6 shifted to lower photon energy by 2 eV compared with the other compounds and is close to the absorption edge of $SrRuO_3$. This means that the valence of Ru ions in La_2NiRuO_6 is lower than for the other compounds and could be tetravalent [13].

In order to investigate the local strucutre and the electronic states of Ru ions in $A(A =$ Ca, Sr, Ba)RuO_3, we calculate the Ru K-XAS spectra by means of FEFF 8.0 [10]. The atomic position and space group were obtained in previous papers [14], [15]. We used that the space group of $BaRuO_3$ is $R\bar{3}m$ and that of $CaRuO_3$ is Pnma and that of $SrRuO_3$ is $Pm\bar{3}$ and Pnma. Figure 3 shows theoretical and experimental spectra around the Ru K-edge of Ru oxides. The solid lines represent theoretical spectra and solid circles represent experimental spectra. For $SrRuO_3$, the solid line shows (I)$Pm\bar{3}$ and the broken line shows (II)Pnma. The bottom panel shows $SrRuO_3$ and the upper panel shows $CaRuO_3$. For both compounds, theoretical spectra reproduced experimental spectra very well.

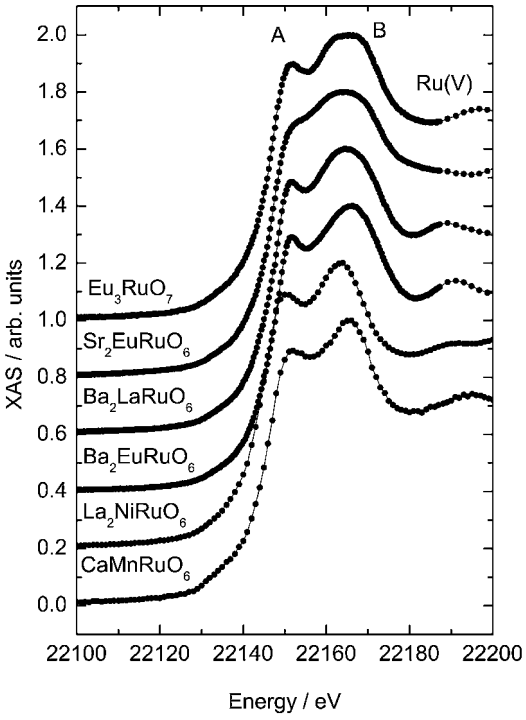

Fig. 2. XAS spectra in Ca_2MnRuO_6, La_2NiRuO_6, Ba_2EuRuO_6, Ba_2LaRuO_6, Sr_2EuRuO_6 and Eu_3RuO_7 around the Ru K-edge.

Especially, for $SrRuO_3$, theoretical spectra were calculated for two different models of the crystal structure in order to confirm the structure of $SrRuO_3$. In the case of Pnma, the theoretical spectral shape of XAS reproduced the experimental one. The intensity ratio of the peaks A and B was almost the same

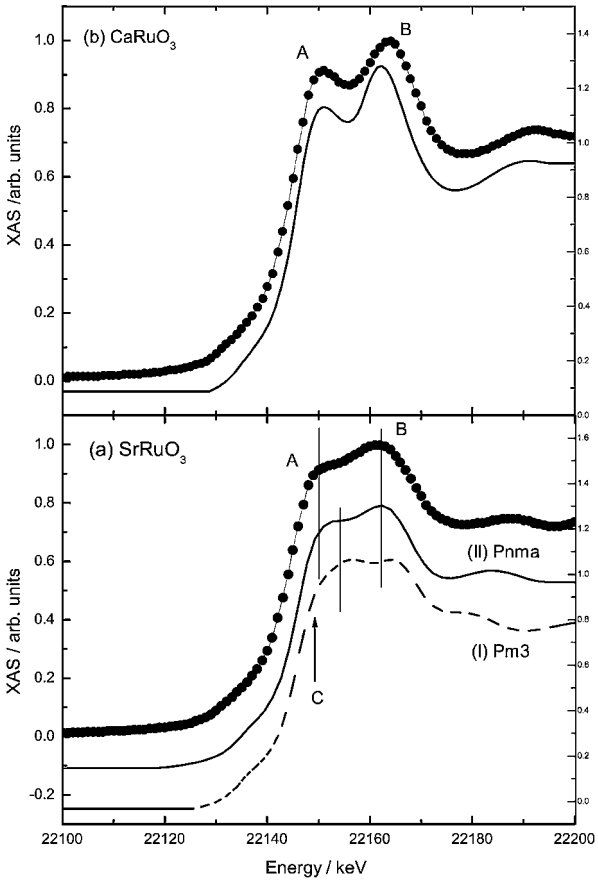

Fig. 3. Theoretical and experimental XAS spectra in $A(A =$ Ca, Sr)RuO_3 around the Ru K-edge.

between experimental and theoretical spectra. In the case of $Pm\bar{3}$, the difference between peaks *A* and *B* in theoretical XAS is closer than the difference of experimental one. The shoulder C was found. In this calculation, the spectrum of Pnma is reproduced better than that of $Pm\bar{3}$. Therefore, we conclude that the crystal structure of $SrRuO_3$ is Pnma and that the bond length between Ru and O, which were estimated by means of XAS measurements, is consistent with the results of neutron diffraction [16].

4. Summary

In summary, we measured XANES spectra around the Ru K-edges for Ru oxides at BL39XU and BL01B1 of SPring-8, Japan. We estimate the valence of eight Ru compounds. The valence of Ru ion in $Pb_2Ru_2O_{6.5}$ and Ca_2RuMnO_6 are close to pentavalent. The valence of Ru ions in Ba_2EuRuO_6, Ba_2LaRuO_6 and Sr_2EuRuO_6 are pentavalent. The other compounds are tetravalent. In order to investigate the local strucutre and the electronic states of Ru ions in $A(A = \text{Ca, Sr, Ba})RuO_3$, we calculate the Ru K-XAS spectra by means of FEFF 8.0. We conclude that the crystal structure of $SrRuO_3$ was Pnma [16].

Acknowledgment

I would like to thank Dr. H. Tanida and Dr. M. Suzuki for experimental help and fruitful discussions.

References

1. Maeno, Y. *et al.*, Nature (Lond) **372**, 532 (1994).
2. Felner, I., Nowik, I., Baradaric, I. and Gospodinov, M., Phys. Rev. B **62**, 11332 (2000).
3. Reich, S., Tsabba, Y. and Cao, G. J., Magn. Magn. Mater. **202**, 119 (1999).
4. Battle, P. D. and Macklin, W. J., J. Solid State Chem. **52**, 138 (1984).
5. Battle, P. D. and Jones, C. W., J. Solid State Chem. **78**, 108 (1989).
6. Battle, P. D., Jones, C. W. and Studer, R., J. Solid State Chem. **90**, 302 (1991).
7. He, T. and Cava, R. J., Phys. Rev. B **63**, 172403-1 (2001).
8. Battle, P. D. and Jones, C. W., Mater. Res. Bull. **22**, 1623 (1987).
9. Doi, Y. and Hinatsu, Y., J. Phys. Condens. Matter **11**, 4813 (1999).
10. Ankudinov, A. L., Ravel, B., Rehr, J. J. and Conradson, S. D., Phys. Rev. B **58**, 7565 (1998).
11. Hankel, D. *et al.*, Phys. Rev. B **61**, 7055 (2000).
12. Oyanagi, H. *et al.*, J. Syncrotron Rad. **5**, 1001 (1998).
13. Yoshii, K. *et al.*, J. Alloys Comp. **348**, 236 (2003).
14. Kobayashi, K. *et al.*, Mater. Res. Bull. **29**, 1271 (1994).
15. Felser, C. and Cava, R. J., Phys. Rev. B **61**, 10005 (2000).
16. Yoshii, K. *et al.*, J. Magn. Magn. Mater. ICM proceedings (to be published).

Physica Scripta. Vol. T115, 516–519, 2005

Correlation Between Local Structure and Ionic Conductivity of Potassium-Doped Siloxane Poly(propyleneoxyde) Ormolytes

Juliano Chaker[1,2,3], Karim Dahmouche[1], Valérie Briois[2], Celso V. Santilli[1], Sandra H. Pulcinelli[1] and Patrick Judeinstein[3]

[1]Instituto de Química/UNESP, C. P. 355 CEP 14800-900 Araraquara-SP, Brazil
[2]LURE, Centre Universitaire Paris-Sud, BP 34, 91898 Orsay Cedex, France
[3]RMN en Milieu Orienté, Centre Universitaire Paris-Sud, Bât 410, 91405 Orsay, France

Received June 26, 2003; accepted in revised form February 6, 2004

Abstract

The local order around K for $K(CF_3SO_3)$ doped Siloxane-Poly(propyleneoxide) hybrids at different doping concentration was investigated by X-ray absorption spectroscopy (EXAFS and XANES) at the potassium K-edge. The results indicate that the use of HCl as hydrolytic catalyst for gelation induces the precipitation of KCl. The ionic conductivity is strongly related to the presence of oxygen atoms as first neighbours around potassium and to the amount of KCl precipitate.

1. Introduction

The search for new efficient solid polymer electrolytes is one of the clues for the development of various electrochemical devices such as rechargeable batteries, sensors, data storage or electrochromic displays [1]. These new advanced materials should combine good ionic conductivity, thermal and electrochemical stabilities, reasonable mechanical properties, and processing abilities, but also, optical transparency could be required for some of the cited applications [2]. The need for such a combination of properties explains the recent development of ion-conducting hybrids systems in which alkali salts are dissolved inside an organic-inorganic matrix. Such materials (also called Ormolytes – ORganically MOdified electroLYTEs) can be obtained by the sol-gel route by mixing and/or grafting together polyether chains with an inorganic network [3]. Then, these materials combine the solvent behavior of the polymer component (generally poly(ethyleneoxide) (PEO, $-(CH_2CH_2O)_n-$) or poly (propyleneoxide) (PPO, $-(CH_2CHCH_3O)_n-$) and the mechanical properties of a network grafted by silica nodules (SiO_2). The versatility of the "chimie douce" synthetic route allows to tailor the properties of the final materials by the choice of the starting component and the synthetic conditions. Then, strong effects of the catalyst which is used during the hydrolysis and condensation steps are well established, allowing to control the microsegregation of the two phases and the tuning of the thermo-mechanical properties of the organic component [4]. Less is known about the influence of the catalyst on the ionic conduction properties of the ormolytes.

Recently we have reported that in siloxane-PPO ormolytes doped with different potassium salts ($KClO_4$, KI, KCF_3SO_3 and KNO_2) [5], potassium ions are present in several forms: some of them are dissolved inside the PPO matrix because of the interactions with the ether-type oxygens, while the low solubility of these salts leads also to crystalline or amorphous KX(X = ClO_4, I and NO_2) precipitates. Besides of the low solubility of the salts inside the polymeric matrix, the use of HCl as catalyst for the gelation of the hybrid precursor induces the formation of a KCl phase. The set of results so-obtained have suggested that the ionic conductivity is correlated to the presence of oxygen atoms as first neighbours around potassium. Nevertheless, the existence of several sites for most of the samples studied in [5] did not make easy the correlation between ionic conductivity and the local order around the cation. To go further in this way, two families of almost equivalent materials are studied herein, differing only by the amount of HCl catalyst. Large variations of the ionic conductivity are observed and related to the study of the local order around the potassium salt by X-ray absorption spectroscopy (EXAFS and XANES) at the K K-edge.

2. Experimental

2.1. *Sample preparation*

The preparation of potassium-doped siloxane-PPO hybrid sols and gels has already been described [5]. Equimolar amounts of 3-isocyanatopropyltriethoxysilane (IsoTrEOS) and O,O′Bis(2-aminopropyl(polypropyleneoxide) were stirred together in tetrahydrofuran (THF) under reflux for 15 hours. THF was evaporated and a hybrid precursor $_3$(EtO)Si-(PPO)-Si(OEt)$_3$ was obtained. This process was adopted for PPO polymers with molecular weight (M_W) of 2000 and 4000 g/mol (labelled as PPO2000 and PPO4000). 0.5 g of the precursor was mixed with 0.6-mL of ethanol containing HCl at 0.001 M and 0.128 M for routes A and B, respectively. The amount of HCl in route B being two orders of magnitude higher than that in route A, we will speak about a non-catalysed route for route A and a catalysed one for route B. Then 0.15 mL of KCF_3SO_3 aqueous solution was added leading to ratios $[H_2O]/[Si] = 21.9$ and 38.4 for PPO2000 and PPO4000, respectively. The potassium amount so-added was defined as a function of the number of the ether-type oxygen of PPO chains (O): $R = [O]/[K] = 4$, 15, 20, 30 and 50. Monolithic pieces with thickness of 0.5 mm were obtained after slow drying under vacuum at 80 °C for 24 h.

2.2. *Conductivity measurements*

Ionic conductivity measurements were performed at room temperature (RT) with a SOLARTRON SI1260 apparatus in the range of 1 Hz to 10 MHz, with an applied tension of 300 mV.

2.3. *XAS measurements and data analysis*

XAS measurements were carried out at LURE (Orsay, France) on the D44 station installed on the DCI storage ring (1.85 GeV and 300 mA). Potassium K edge (3609 eV) data were recorded in transmission mode at RT using ionization chambers filled with He/Ne and a Ge(111) (Si(111)) double crystal monochromator for EXAFS (XANES). Harmonics rejection was done by using two mirrors cut-off. As-prepared rubbery samples were measured under primary vacuum leading to typical absorption jumps ranging from 0.05 to 0.5.

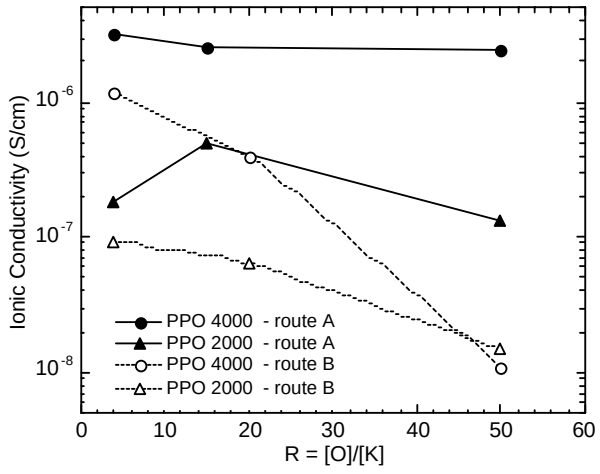

Fig. 1. Ionic conductivity of the different ormolytes as a function of R.

The EXAFS and XANES normalization were performed as previously described in [5]. Structural parameters were determined by a least square fitting procedure using experimental phase and amplitude functions extracted from KF and KCl. The transferability of the fluor electronic functions extracted from the rocksalt structure of KF to simulate oxygen contribution around potassium was checked onto $KClO_4$. Electronic phase and amplitude functions for carbon atoms were extracted from the McKale tables [6].

3. Results

The ionic conductivities measured for the different samples as a function of the molar ratio R are shown in Figure 1. These hybrids exhibit tunable ionic conductivities at RT ranging between $3 \cdot 10^{-6}$ and 10^{-8} S cm^{-1} depending on M_W and R. The ionic conductivity increases with the potassium content, but whatever M_W, the ionic conductivities of ormolytes prepared without HCl (route A) are higher than the values measured on the samples prepared with HCl (route B) by a factor 10 or 100.

Figure 2 presents XANES spectra of the corresponding ormolytes. On one hand, the XANES spectra of ormolytes prepared without HCl are superimposable for all samples. So only the spectrum recorded for route A ormolytes with the lower potassium content is presented in Fig. 2. On the other hand, the shapes of the XANES spectra of hybrids prepared with HCl are very dependent to the doping concentration. As the amount of KCF_3SO_3 decreases, the spectrum becomes more structured with resonances in phase with those observed on the XANES spectrum of KCl. In fact as demonstrated in the insert of Figure 2, a spectrum with a shape similar to the one observed for the K doped siloxane PPO2000 ormolyte with $R = 50$ is obtained from a linear combination of the XANES spectra of KCl and of route A ormolyte, in the ratio $\approx 1:1$.

Figure 3a and b reports $k\chi(k)$ EXAFS spectra and corresponding Fast Fourier Transforms (FFT) of the different samples. Due to the similarity of XANES spectra of the ormolytes prepared by route A only the PPO2000 sample with $R = 15$ has been presented. The first intense peak is related to the oxygen first shell of coordination whereas the second can be related to a chlorine or carbon contribution or both depending on the routes and dopant content. The structural parameters obtained by a least-square fitting procedure are gathered in Table I for ormolytes

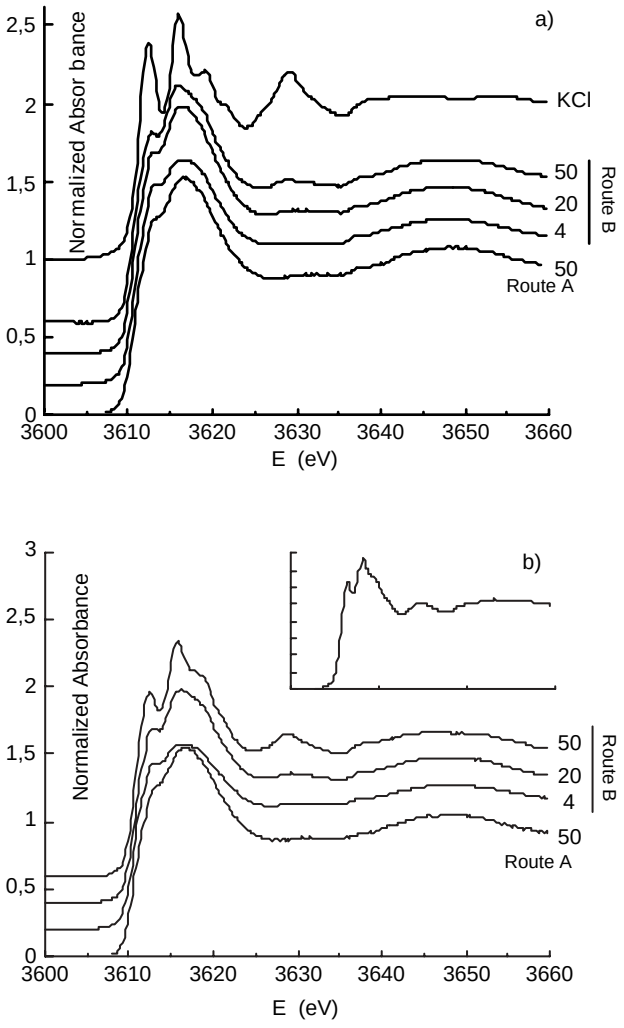

Fig. 2. Potassium K-edge XANES spectra of a) PPO4000- and b) PPO2000-based ormolytes. The XANES spectrum of KCl is given for comparison in a) whereas the insert in b) is the 1 : 1 linear combination of the XANES spectrum of KCl and of the typical XANES spectrum of route A ormolytes.

prepared with PPO2000. They are in agreement with the XANES analysis.

4. Discussion

4.1. *Local order around potassium for ormolytes of route A*

Irrespective to the KCF_3SO_3 content, the local order of potassium doping PPO2000 and PPO4000 ormolytes prepared by route A is identical. A potassium ion is coordinated by 6.6 ± 0.7 oxygens located at 2.77 ± 0.02 Å. The large Debye-Waller factor (0.16 Å) accounts for a large distribution of distances as reported for crystalline polymer-salt complexes PEO_4:KSCN [7] and PEO:KCF_3SO_3 [8]. Indeed in the PEO based-systems the average K-O distance was found at 2.85 Å with bond distances ranging from 2.49 to 3.09 Å. Note also that the coordination number of potassium determined by EXAFS is also in good agreement with the 7-fold coordinence reported for potassium in these published crystallographic structures. A common characteristic of PEO salt complexes [7, 8] is that anions participate in the coordination sphere of potassium together with ether-type oxygens of the polymer and the proportion in the number of anions and ether-type oxygens in the first coordination sphere depends on the proportion of salt in the complexes. In the case of siloxane-PPO hybrids doped by potassium salts, we have strong experimental evidence

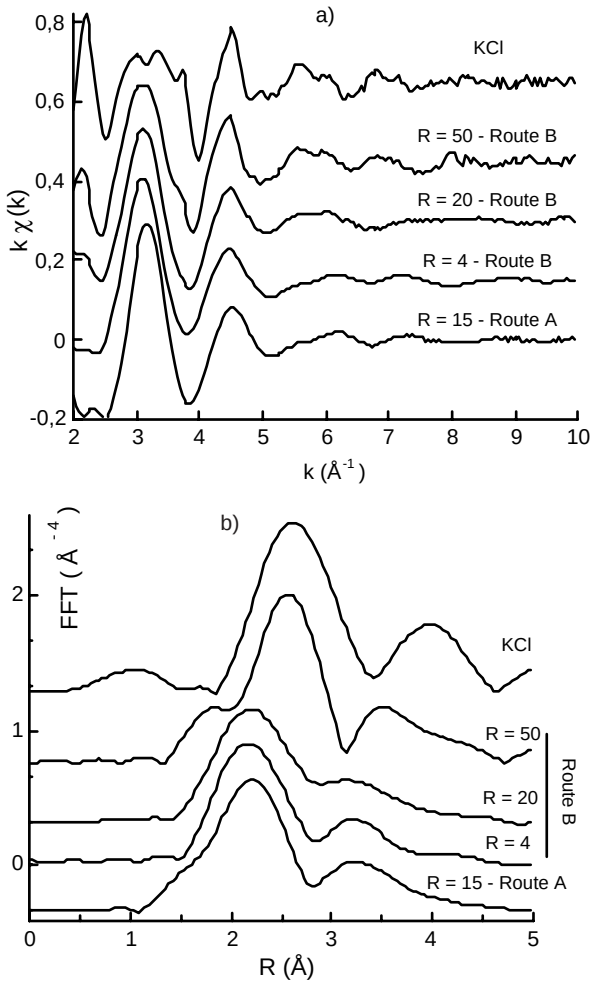

Fig. 3. a) Potassium K-edge $k\,.\,\chi(k)$ EXAFS spectra of the different PPO2000-based ormolytes and b) FFT of the $k^3\,.\,\chi(k)$, using a Kaiser apodization window from 2.7 to 9.3 Å^{-1} with $\tau = 4$. The spectrum of KCl is given for comparison.

that potassium is only coordinated by ether-type oxygens since the local order around potassium is the same using KSCN, KI or KCF_3SO_3 salts to prepare PPO2000 hybrids [9]. The anion is totally dissociated from the potassium atom, in agreement with some preliminary Raman experiments obtained with the potassium triflate salt [9]. This result allows us to unambiguously attribute the second peak of the FFT of ormolytes prepared by route A to a carbon contribution of the polymer backbone. The average number of carbon atoms, 6.4 ± 0.6, is equal to the average oxygen coordination number and the average distance is equal to 3.28 ± 0.02 Å. As for the K-O bond distance, the K-C correlation distance is shorter in the siloxane-PPO ormolytes than the average distance found for PEO_4:KSCN [7] (3.53 Å). Possible explanations should be the amorphous character of the polymer backbone in the PPO samples and the different conformation of the PEO and PPO skeletons.

Table I. *Results of curve-fitting analysis of potassium K-edge EXAFS spectra of the different PPO2000-based ormolytes. The inverse Fourier transforms were carried out from 1.30 to 3.60 Å, except for the route B sample with $R = 50$ for which the window was 1.40 to 3.05 Å. Uncertainty of the last digits is given in parentheses. The residual ρ factor is defined as:*
$\rho = [\Sigma(k^3\chi_{\mathrm{exp}}(k) - k^3\chi_{\mathrm{theo}}(k))^2/\Sigma(k^3\chi_{\mathrm{exp}}(k))^2]^{1/2}$

PPO2000-based ormolytes	Shell	N	R (Å)	σ (Å)	ρ (%)
Route A	K-O	6.6 (7)	2.77 (2)	0.16 (3)	0.14
R = 15	K-C	6.4 (6)	3.26 (2)	0.14 (3)	
Route B	K-O	6.2 (6)	2.79 (2)	0.16 (3)	0.14
R = 4	K-C	4.7 (5)	3.29 (2)	0.14 (3)	
Route B	K-O	5.4 (5)	2.79 (2)	0.15 (3)	0.19
R = 20	K-C	6.8 (7)	3.25 (2)	0.15 (3)	
Route B	K-O	4.2 (4)	2.81 (2)	0.16 (3)	0.50
R = 50	K-Cl	4.1 (4)	3.14 (2)	0.17 (3)	

4.2. *Local order around potassium for ormolytes of route B*

Potassium atoms are embedded for these ormolytes into two phases: a crystalline KCl phase and the phase in which potassium is in interaction with ether oxygens. The proportion of both phases is dependent on the doping level. This result has already been reported for iron(III) doped siloxane-PEO ormolytes prepared in presence of HCl [10]. Due to the constant amount of HCl introduced in the synthesis, the formation of KCl phase in the sample is a dominant phenomenon at low potassium concentration but decreases as the potassium amount increases. It is noteworthy that at equivalent doping level, the XANES spectra of PPO4000 ormolytes are less structured than PPO2000 ones suggesting that the KCl dissociation is more efficient for longer polymeric chains.

4.3. *Ionic conductivity and local order around potassium*

It is commonly accepted that in these materials ionic conductivity is obtained within the amorphous phase of the material via a liquid-type migration of the cations assisted by segmental motions of polymeric chains. A mechanism of charge hopping between adjacent sites having equivalent coordination symmetries is generally proposed and the ionic conductivity depends both on the number and the nature of the charge carriers [11]. Our structural results are in agreement with this viewpoint. Indeed for ormolytes prepared by route A, the local order around potassium is the same for all doping level and characteristic of potassium in interaction with ether-type oxygens of polymers. Ormolytes prepared with PPO4000 have better ionic conductivity than PPO2000 ormolytes: this is due to a better mobility of the longest chains ($n = 68$ (CH_2CHCH_3O) units) compared to the shortest ones ($n = 34$). The observed increase of ionic conductivity with R for route A PPO4000 ormolytes is due to an increase of the number of charge carriers. For route A PPO2000 ormolytes, we assume that the observed decrease of ionic conductivity for $R = 4$ results from the formation of O-K^+-O crosslinks leading to the decrease of chains mobility as it was reported for $LiClO_4$ doped ormolytes [12]. Ormolytes prepared by route B have a lower ionic conductivity than ormolytes prepared by route A whatever their composition. This could be explained by the lower number of charge carriers. Interestingly, route B PPO2000 ormolytes do not present the maximum of ionic conductivity with the doping level in the concentration range investigated. In fact, as a part of potassium atoms are embedded into KCl phase, we assume that the level in which O-K^+-O crosslinks are formed to strengthen the polymeric matrix is shifted to higher potassium concentration. This feature suggests that the KCl precipitate should play the role of plasticizer, as that reported for propylene carbonate in high molecular weight PEO-$LiCF_3SO_3$electrolytes [13]. To summary, it appears that the addition of HCl catalyst in the preparation is prejudicial for ionic

conduction at the lowest potassium concentrations ($R \geq 20$). For $R = 4$ the ionic conduction of ormolytes prepared by both routes is of the same order of magnitude.

5. Conclusion

This study describes some relationships between the ionic conductivity in ormolytes and the local order around the cation as measured by X-ray absorption. It evidences the strong influence of even small changes in the synthetic route and the need to control it severely to tune the properties of advanced materials.

Acknowledgements

This work has been financially supported by FAPESP (Brazil) and CNRS (France) organisms and a CAPES/COFECUB program. We thank the LURE storage ring staff for providing the synchrotron radiation.

References

1. Gray, F. M., "Polymer Electrolytes", RSC Materials Monographs, Royal Society of Chemistry, Cambridge, (1997).
2. Meyer, W. H., Adv. Mater. **6**, 439 (1998).
3. Judeinstein, P. and Sanchez, C., J. Mater. Chem. **6**, 511 (1996).
4. Lesot, P. *et al.*, J. Mater. Chem. **8**, 147 (1998).
5. Chaker, J. *et al*., J. Sol-Gel Sci. Techno **26**, 1075 (2003).
6. McKale, A. G., Veal, B. W., Paulikas, A. P., Chan, S. K. and Knapp, G. S., J. Am. Chem. Soc. **110**, 3763 (1988).
7. Lighfoot, P., Nowinski, J. L. and Bruce, P. G., J. Am. Chem. Soc. **116**, 7469 (1994).
8. MacGlashan, G. S., Andreev, Y. G. and Bruce, P. G., J. Chem Soc., Dalton Trans. **6**, 1073, (1998).
9. Chaker, J. *et al*., in preparation.
10. Chiavacci, L. *et al*., J. Appl. Cryst. **36**, 405 (2003).
11. Armand, M., Adv. Mater. **2**, 127 (1990).
12. Dahmouche, K., Santilli, C. V., Pulcinelli, S. H. and Craievich, A. F., J. Phys. Chem. B **103**, 4937 (1999).
13. Frech, R. and Chintapalli, S., Solid State Ionics **85**, 61 (1996).

Physica Scripta. Vol. T115, 520–522, 2005

Solvation Structure of Bromobenzene Molecule Doped in Supercritical Xenon Studied with Fluorescent XAFS Measurement

Zhaohui Jin[1], Kazumichi Nakagawa[2*], Masahito Tanaka[1], Iwao Shimoyama[1], Fusae Kaneko[2] and Takatoshi Murata[3]

[1]Graduate School of Science and Technology, Kobe University, Nada-ku, Kobe 657-8501, Japan
[2]Faculty of Human Development, Kobe University, Nada-ku, Kobe 657-8501, Japan
[3]Kyoto University of Education, Kyoto 612-8522, Japan

Received June 26, 2003; accepted in revised form November 4, 2003

PACS number: 8233De

Abstract

On the basis of the first successful determination of the solvation structure of 1-bromonaphthalene (BrNaph) in supercritical xenon (sc-Xe) fluid (BrNaph/sc-Xe), we measured bromine K-edge fluorescent XAFS of bromobenzene (BrBz) doped in supercritical xenon (BrBz/sc-Xe), in an attempt to study the detailed characteristics of the solvation structure in supercritical fluids. Observed spectra of BrBz/sc-Xe showed obviously different pattern from that of BrBz liquid and that of BrBz/Hexane in the near-edge region. The small peak at 13470 eV which appeared in the case of BrBz liquid was not observed in sc-Xe, and the broad peak around 13490 eV was deformed especially at the higher energy side. On the basis of these spectral changes, we tentatively concluded that the local structure in BrBz liquid was destroyed in sc-Xe and a new solvation structure was formed. Theoretical calculation is now being planned.

1. Introduction

Supercritical fluid is well known to be useful as a substitute of organic solvents to extract some specific organic materials in a variety of fields such as food industries and medical supplies [1, 2]. However, it is not clear what sort of solvation structure is responsible to the excellent solubility. Pioneer works [3, 4] have revealed from a macroscopic point of view that the excellent solubility originated from the cluster formation around the solute molecules. Many efforts were devoted to obtain the microscopic view of the solvation structure with spectroscopy [5, 6], neutron diffraction [7], and NMR [8] techniques. Recently, X-ray Absorption Fine Structure (XAFS) technique becomes to attract much attention because of the rapid advances in synchrotron radiation [9, 10].

The first successful measurement of XAFS spectra was reported by our group [11], in which XAFS spectra was observed by X-ray transmission mode for 1-bromonaphthalene (BrNaph) molecule doped in supercritical xenon (sc-Xe). In the case of BrNaph/sc-Xe, a new peak was observed in the near edge region of Br K-edge (13470 eV ∼ 13480 eV). This peak was not observed in the case of hexane solution (BrNaph/Hexane) and that of pure BrNaph liquid. Using the full multiple scattering calculation technique, K. Hayakawa *et al.* [12] succeeded at the first time to suggest a possible solvation structure of a molecule in supercritical fluid. According to their result, about six Xe atoms are surrounding a Br atom of BrNaph with distance of about 0.5 nm. The next step is to get information about the interaction between the Br and the benzene ring. Bromobenzene (BrBz) was selected in this work as the solute instead of BrNaph, because the size of BrBz is smaller than that of BrNaph. The reasons for choosing supercritical xenon as the solvent are as follows. (*i*) The critical temperature of xenon (289.73 K), the critical pressure (5.84 MPa) and the critical number density ($4.59 \cdot 10^{21}$ cm^{-3}) is relatively low. Thus, the handling is easy. (*ii*) Because of its large atomic number, the back-scattering cross section for photoelectron of Xe atom is large. (*iii*) Xenon is inert.

In this paper, we will report results of fluorescent XAFS measurement of BrBz/sc-Xe. Comparing the obtained results with those for BrBz/Hexane and for pure liquid of BrBz, we will discuss about possible solvation structure of BrBz/sc-Xe system.

2. Experiment procedure and results

The BrBz liquid was purchased from Aldrich Chemical Co. and used without further purification. Xenon gas was purchased from Tokyo Kasei Co. and purified by degassing and passing the molecular sieves column activated at 650 K.

A droplet of BrBz liquid was injected in a high-pressure cell which has a pair of beryllium windows with 3 mm thickness and 15 mm diameter. After the cell was evacuated, xenon was introduced into the cell from gas handling system which was described in detail elsewhere [10]. Density of Xe gas was determined by careful adjustment of pressure at room temperature. Values of pressure were converted into number densities according to data reported by A. Michels *et al.* [13]. In this experiment the Xe density was varied from zero to $8.7 \cdot 10^{21}$ cm^{-3}.

The XAFS measurement was performed at the beamline BL-12C of the Photon Factory (PF), Japan. In Fig. 1, we show the experimental setup schematically. Energy resolution of the Si(111) double crystal monochromator was better than 2 eV at $h\nu \approx 9$ keV, and the backlash of the main axis rotation was

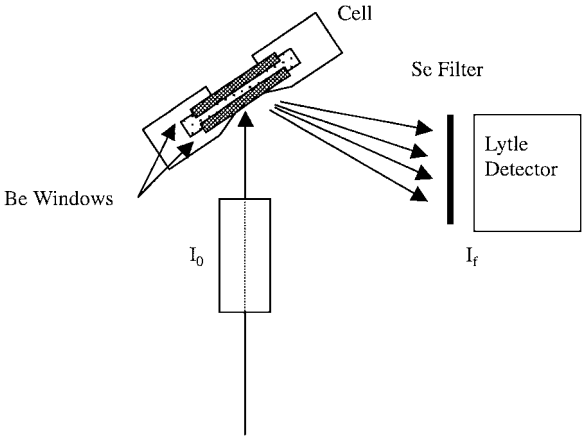

Fig. 1. Schematic diagram of the experimental setup for fluorescent XAFS measurement. I_o and the Lytle detector (I_f) are ion chambers used to measure the incident and fluorescent X-ray.

*Correspondence person e-mail: nakagawa@kobe-u.ac.jp

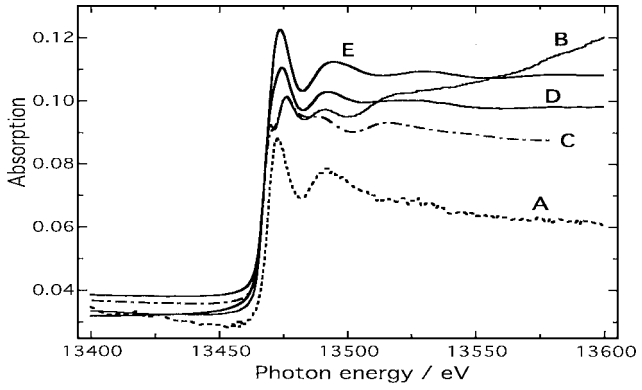

Fig. 2. The fluorescent XAFS spectra. A: BrBz vapor, B: pure BrBz liquid, C: BrBz doped in Hexane (transmission mode), D: BrBz dissolved in low-density Xe ($0.7 \cdot 10^{21}$ cm^{-3}), E: BrBz dissolved in supercritical Xe ($8.7 \cdot 10^{21}$ cm^{-3}).

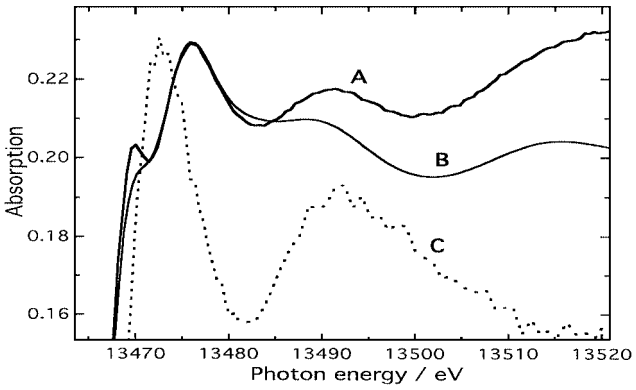

Fig. 3. Magnification of the near edge region of fluorescent XAFS spectra. A: Pure BrBz liquid, B: BrBz doped in Hexane (transmission mode), C: BrBz vapor.

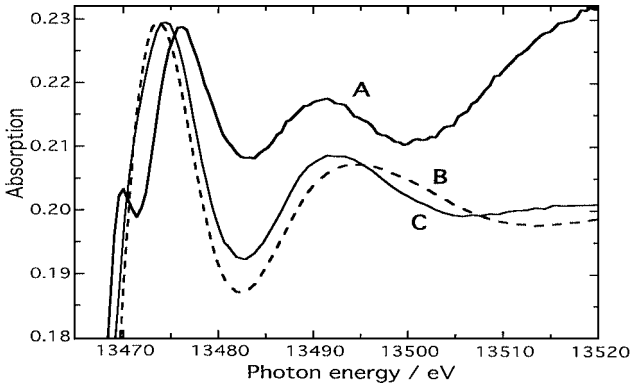

Fig. 4. Magnification of the near edge region of fluorescent XAFS spectra. A: Pure BrBz liquid, B: BrBz dissolved in supercritical Xe ($8.7 \cdot 10^{21}$ cm^{-3}), C: BrBz dissolved in low-density Xe ($0.7 \cdot 10^{21}$ cm^{-3}).

0.0006 degree according to M. Nomura *et al.* [14]. The storage ring of PF was operated with the positron energy of 2.5 GeV and a stored current of 250 to 350 mA. The energy calibration was performed with the K-edge absorption of the Cu foil to be 8980.3 eV.

As shown in Fig. 1, in order to measure the XAFS signal of low concentration solute, we used the fluorescent XAFS technique. The Lytle detector [15] was used to detect the X-ray fluorescence. The Selenium filter was equipped to eliminate the scattering component of incident X-ray beams. In order to make the characteristic feature of sc-Xe clear, we also measured the spectra of BrBz vapor, pure BrBz liquid and BrBz doped in hexane liquid (BrBz/Hexane). The spectrum of BrBz/Hexane was measured in transmission mode.

Obtained spectra are summarized in Fig. 2; BrBz vapor (curve A), BrBz liquid (curve B) and BrBz/Hexane (curve C). Among a series of fluorescent XAFS spectra of BrBz/sc-Xe from low-density to high-density, typical two spectra at Xe = $0.7 \cdot 10^{21}$ cm^{-3} (curve D) and $8.7 \cdot 10^{21}$ cm^{-3} (curve E) are plotted in the figure. It should be noted that the curve D was obtained for just Xe gas under supercritical state and the curve E was obtained for the supercritical xenon.

As seen from Fig. 2, in the case of BrBz vapor, only one peak at 13473 eV was observed at the Br K-edge region. On the contrary, two peaks at 13470 eV and 13476 eV were observed for pure BrBz liquid. The 13470 eV peak shrank to a shoulder for BrBz/Hexane. In the $0.7 \cdot 10^{21}$ cm^{-3} xenon, the 13470 eV peak became smaller than that for BrBz/Hexane. Finally this peak disappeared in the case of sc-Xe ($8.7 \cdot 10^{21}$ cm^{-3}).

Onset energies of each spectrum were examined. The highest and the lowest onset energies were found for the case of BrBz vapor and for the case of pure BrBz liquid, respectively. In the case of the solvents with middle density, namely, for Xe gas, sc-Xe and hexane, onset energies were just between that for vapor and pure liquid. This tendency is natural in terms of the density effect of solvent.

Finally, we examined energy positions of the strong peak around 13475 eV. As seen from the magnified illustration shown in Fig. 3 and Fig. 4, the peak energy difference between pure BrBz liquid (peak: 13476 eV) and BrBz vapor (peak: 13473 eV) is larger than the energy resolution 2 eV of the monochromator and thus meaningful. On the contrary, the energy difference between Xe gas (peak: 13474.3 eV) and sc-Xe (peak: 13473.6 eV) is clearly smaller than the energy resolution of the monochromator and thus it is meaningless in the view of our experimental accuracy.

3. Discussion

In order to discuss about the solvation structure microscopically, we started from the pioneer work by H. Bertagnolli *et al.* [16]. They measured XAFS, X-ray and neutron diffraction and suggested the local order, in other word, solvation structure in BrBz liquid. Although they did not analyze, a small peak is observed in their XAFS spectrum (Fig. 1 of their paper), which is believed to be the 13470 eV peak shown our Fig. 2, 3 and Fig. 4. Using Fig. 3 of our paper, we will try to discuss the nature of the 13470 eV peak. In Fig. 3 and 4, magnitude of the vertical axis was normalized to the same order.

As seen from Fig. 3 and as mentioned above, the small peak observed at 13470 eV in pure BrBz liquid become to be only a small shoulder in BrBz/Hexane. Because this peak was not observed in vapor spectrum (curve C in Fig. 3), it is natural that this peak is originated from the local structure between a BrBz molecule and other BrBz molecules, which was described by H. Bertagnolli *et al.* [16]. The small shoulder in BrBz/Hexane may means that a BrBz molecule is still surrounded by other BrBz molecules to remain the $(BrBz)_n$ cluster partially. In vapor state, BrBz molecules may be separated each other and just isolated; thus, there was no 13470 eV peak in vapor.

Using Fig. 4, we will examine the solvation effect of sc-Xe. As seen from the figure, in Xe gas and in sc-Xe, 13470 eV peak disappeared, which means that the local structure in pure BrBz liquid was destroyed. It should be noted that for the sc-Xe ($8.7 \cdot 10^{21}$ cm^{-3}) the broad peak around 13490 eV was deformed especially at the higher energy side. This deformation imply that

the BrBz-$(Xe)_n$ cluster may be produced in sc-Xe. The tendency of spectral change is different from the case of BrNaph/sc-Xe, in which a new peak appeared in the lower energy side of the largest peak. This difference between BrBz/sc-Xe and BrNaph/sc-Xe may be due to different surrounding structure of xenon. On the basis of this difference in two similar molecules doped in same solvent Xe, we tentatively concluded that a new structure formed in BrBz/sc-Xe, which should be different from the solvation structure of BrNaph/sc-Xe.

Theoretical calculation with the full multiple scattering theory is now being planned together with theoretical scientists.

4. Conclusions

The fluorescent XAFS spectra were measured for BrBz vapor, pure BrBz liquid, BrBz dissolved in low-density Xe ($0.7 \cdot 10^{21}\,\mathrm{cm}^{-3}$) and in supercritical Xe ($8.7 \cdot 10^{21}\,\mathrm{cm}^{-3}$), as well as the transmission XAFS spectra of BrBz doped in Hexane. On the basis of careful comparison of these spectra, we tentatively concluded that the $(BrBz)_n$ structure in the pure BrBz liquid was completely destroyed in sc-Xe and a new structure BrBz-$(Xe)_n$ might be formed in sc-Xe. Theoretical calculation is being planned.

Acknowledgments

This work was supported by the Joint Study Program of the Photon Factory numbers 2001G105 and 98G291. Authors thank Dr. M. Nomura and Mr. A. Koyama for strong support.

References

1. Johnston, K. P. *et al.*, "Supercritical fluid Science and Technology", (ACS Press 1989).
2. Morita, A. *et al.*, J. Phys. Lett. **244**, 149 (1995).
3. Franck, E. U., Z. Pysik. Chem. Neue Folge **6**, 345 (1956).
4. Roessling, G. L. and Franck, E. U., Ber. Bunsenges. Phys. Chem. **87**, 882 (1983).
5. Kajimoto, O., Chem. Rev. **99**, 355 (1999).
6. Nakagawa, K. *et al.*, J. Electron Spectrosc. Relat. Phenom. **78**, 415 (1996).
7. Narten, A. H. and Levy, H. A., J. Chem. Phys. **55**, 2263 (1971).
8. Matubayashi, N. *et al.*, J. Chem. Phys. **107**, 9133 (1997).
9. Wallen, S. L. *et al.*, Rev. Sci. Instrum. **67**, 2843 (1996).
10. Murata, T. *et al.*, Rev. Sci. Instrum. **66**, 1437 (1995).
11. Murata, T. *et al.*, J. Synchrotron Rad. **5**, 1004 (1998).
12. Hayakawa, K. *et al.*, Jpn. J. Appl. Phys. **38**, 6423 (1999).
13. Michels, A. *et al.*, Physica **20**, 99 (1954).
14. Nomura, M. *et al.*, KEK Report 95-15 (1996).
15. Lytle, F. W. *et al.*, Nucl. Instr. Meth. Phys. Res. **226**, 542 (1984).
16. Bertagnolli, H. *et al.*, Ber. Bunsenges. Phys. Chem. **91**, 1287 (1987).

Physica Scripta. Vol. T115, 523–524, 2005

XAFS Observations of Initial Growth of (0001) ZnO on $\{11\bar{2}0\}$ Sapphire Substrates

P. Fons[1], K. Nakahara[2], A. Yamada[1], K. Matsubara[1], K. Iwata[1], H. Takasu[2] and S. Niki[1]

[1]National Institute of Advanced Industrial Technology, Umezono 1-1-1, Tsukuba Japan 305
[2]Rohm Corporation, Kyoto Japan

Received June 26, 2003; accepted in revised form February 10, 2004

PACS numbers: 61.10Ht, 61.10.Nz, 61.72.Dd, 68.47.Gh

Abstract

We have investigated the initial stages of growth and relaxation of ZnO grown on $\{11\bar{2}0\}$ (**a**-sapphire) films ranging from 2.5 to 100 nm in thickness. A significant feature of this process is the change in symmetry in going from the two-fold symmetry of the **a**-sapphire surface to the six-fold symmetry of ZnO. As-grown films were investigated by atomic force microscopy (AFM), high-resolution (X-ray diffraction, and polarized XAFS. AFM measurements indicated planar growth even from the earliest stages of epitaxy reflective of the long surface diffusion length of Zn. High-resolution X-ray diffraction measurements demonstrated resolution-limited (0002) rocking curves for films up to 30 nm thick (early growth) upon which the onset of diffuse scattering was observed, eventually coming to completely dominate for films thicker than 100 nm (late-growth). Polarized XANES and EXAFS measurements were performed on the Zn edge to elucidate structural changes from early to late-growth. Analysis of EXAFS data indicated an anisotropic accomodation of misfit with large in-plane bond rotations and with only a slight outward relaxation of the ZnO lattice along the [0001] direction. Electrical measurements indicate that the electron concentration in this initial layer is degenerate.

Recent research into wide bandgap materials for photoelectronic applications has focused on III-V materials, in particular GaN. Another class of materials, the II-VI oxide-based semiconductors also holds great promise for optoelectronics applications. In particular, the II-VI oxide semiconductor ZnO is a harbinger for such applications with its direct bandgap of 3.7 eV and large excitonic binding energy of 60 meV. The most significant problems facing the practical use of ZnO remains the reduction of residual carrier defect-related carrier concentration and p-type doping. It has been recently demonstrated that it is possible to eliminate the 30° rotation twins observed in epitaxial ZnO films grown on (0001) sapphire substrates by growing on the $(11\bar{2}0)$ face of sapphire despite the apparent symmetry mismatch between the (6-fold) epilayer and the (2-fold) substrate [1]. These rotation twins most likely are a consequence of the large mismatch strain present between the ZnO epilayer ($\mathbf{a} = 0.3250$ nm, $\mathbf{c} = 0.5213$ nm) and the underlying (0001) sapphire ($\mathbf{a} = 0.4754$ nm, $\mathbf{c} = 1.299$ nm) substrate.

To further optimize the growth process with the ultimate goal of yet further reducing the defect-related residual carrier concentration, we have studied the relaxation process for thin films of ZnO grown on **a**-sapphire. The as-grown films were characterized using a combination of *in-situ* RHEED, X-ray pole figure analysis, HRXRD, AFM, and polarized XAFS.

Samples were grown on $(1\bar{1}20)$ sapphire substrates after the substrates were degreased with organic solvents and thermally cleaned *in-situ* at a temperature of 600 °C. ZnO layers were then grown using a thermal Zn source (7N) and a RF (300 W) oxygen (6N) source. Details of the chamber and growth process have been published elsewhere [2].

All samples were grown using a substrate temperature of 350 °C. Diffraction measurements made *in-situ* using RHEED showed that the films were c-oriented with the in-plane epilayer/substrate orientation $\langle 11\bar{2}0\rangle \| [0001]$. Films of differing thickness were made by stopping growth after 15, 30, 45, 60, 120, 600, and 3600 seconds. X-ray reflection was used to confirm that the thickness of these samples was approximately 3, 5, 8, 10, 20, 100, and 600 nm, respectively. As stated earlier for films less than ∼10 nm thick, the RHEED patterns, while being single-domain epitaxial, were diffuse. The patterns became streaky after about 10 nm with a 3×3 streaky reconstruction pattern becoming visible after ∼20 nm.

The HRXRD measurements utilized a Philips MRD goniometer with a 15° asymmetric Bartels Ge (220) monochromator and a triple-reflection Ge (220) analyzer. The ω and 2θ axes of the goniometer were fitted with optical encoders resulting in a quoted absolute positioning error of 10^{-4} degrees for ω and θ. Experiments on near-perfect Si wafers indicated that the lateral coherence of the source was on the order of ∼2 μm.

XAFS measurements were taken using the Zn Kα-edge at the Photon Factory at KEK in Tsukuba, Japan using line BL-12c. Measurements were taken at glancing angle in fluorescence mode using a liquid nitrogen cooled Ge detector array with both horizontal (incident beam polarization along the in-plane direction of the sample) and vertical (incident beam polarization along the c-axis of the sample) polarizations. The samples were at room temperature.

Fig. 1 (left) shows a reciprocal space area map for a (30 s) ∼5 nm thick ZnO epilayer near the ZnO (0002) reciprocal lattice point (RLP). In the figure, a resolution limited (∼0.003°) streak is visible with no intensity present outside the central streak. For these measurements the zero of ω was calibrated using the sapphire $(11\bar{2}0)$ reflection. The slight tilt observable along the RLP diffraction streak reflects the substrate miscut; the normal

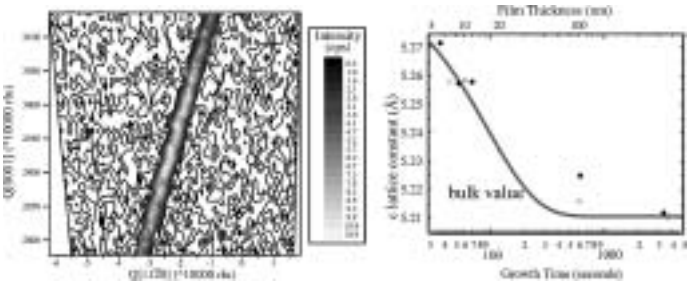

Fig. 1. (left) Triple axis X-ray reciprocal space map near the ZnO (0002) reflection for a ZnO film grown on approximately 5 nm thick (right). Thickness dependence of c-lattice constant values determined from reciprocal space mapping.

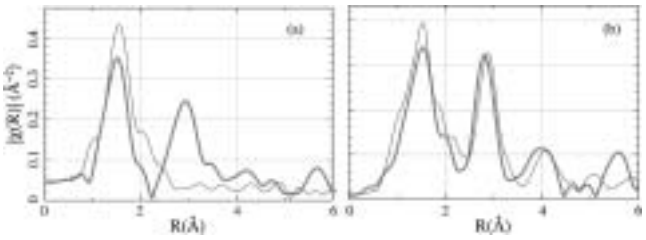

Fig. 2. Real space Fourier transform $|\chi(R)|$ for a 5 nm thick film taken in vertical (thick line) and horizontal (thin line) polarizations. The transforms were taken over the range from 3 to 12 inverse Ångstroms.

to the surface corresponding to the elongation direction of the RLP. A similar diffraction pattern was observed for 8 nm and 10 nm thick films with a slight narrowing of the diffraction streaks along the Q_z direction parallel to the substrate normal due to increased film thickness. No diffuse scattering was visible outside the central RLP streak and the transverse component was again resolution limited. In contrast, for a 20 nm thick (120 s) film, the reciprocal space map (not shown) indicated the presence of diffuse scattering in addition to the strong central streak indicating the likely presence of dislocations with a screw component were formed.

As can be discerned from the Fig. 1 (right) as film thickness decreases, the value of the c-lattice constant as determined from the center of the (0002) RLP increases. The strong intensity of the (0002) RLP is indicative of the presence of long-range order along the c-axis.

Fig. 2 shows real-space Fourier transforms of $|\chi(R)|$ for the same 5 nm thick film shown in Fig. 1 (left). From the figure, it is clear that the second shell is strongly attenuated when the incident beam polarization is in-plane (thin line), but, in contrast, is still very strong for the case in which the incident beam polarization in aligned along the c-axis. This result is consistent with large in-plane bond angle distortions. These distortions have only a minor effect on the atomic ordering along the c-axis direction as is clearly shown by the strong diffraction present in Fig. 1. In contrast, for the 10 nm thick film as can be seen in Fig. 2 (right), the strong anisotropy is no longer present.

To further elucidate the thickness trend, the experimental $|\chi(R)|$ were fitted to a model using the packages *Artemis* and *Ifeffit* [3] in which the values of the a and c lattice constants were allowed to vary independently with the appropriate changes in path lengths calculated geometrically. The scattering paths for the simulation were obtained using feff8 [4] using the ideal wurtzite structure and the appropriate polarization cards. As can be seen in Fig. 3,

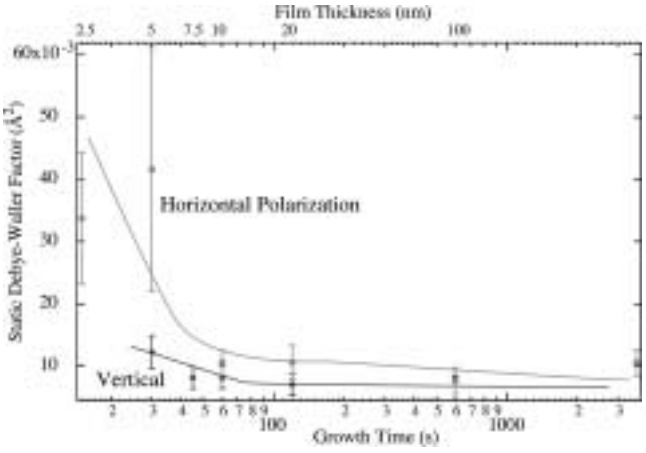

Fig. 3. Static two-center Debye-Waller disorder parameters as a function of film thickness.

there is virtually no change in the second shell static disorder with thickness for the case of vertical polarization. For the case of horizontal polarization in which bond angle disorder is probed in-plane, there is in contrast, a sharp increase in disorder for films $\leq$5 nm thick.

In conclusion, we have undertaken preliminary observations of the film relaxation processes occurring in the heteroepitaxial growth of ZnO on **a**-sapphire. From HRXRD and polarized EXAFS measurements, it is clear that there is strong anisotropy in the relaxation process with large in-plane bond distortions accommodating the different symmetry of the underlying sapphire surface. Concomitant with appearance of diffuse scattering in the 0002 reciprocal space maps, the in-plane distortion is greatly reduced and film quality improves markedly. This is suggestive of the generation of misfit dislocations which act to relieve the interfacial stress associated with growth on sapphire. Glancing incidence HRXRD suggest that initially random in-plane bond distortions reorganize into domains for thicker films as evidenced by omega peak half-widths for reciprocal lattice vectors nearly in-plane.

References

1. Fons, P. *et al*., J. Crystal Growth **209**, 523 (2000).
2. Fons, P., Iwata, K., Niki, S., Yamada, A. and Matsubara, K., J. Crystal Growth **201–202**, 627 (1999).
3. Newville, M., J. Synchrotron Rad. **8**, (2001) 322.
4. Ankudinov, A. L., Ravel, B., Rehr, J. J. and Conradson, S. D., Phys. Rev. B **58**, 7565 (1998).

Physica Scripta. Vol. T115, 525–527, 2005

Ge Coordination States in SiO_2-GeO_2 Glasses at High Pressure, Inferred from *in situ* XAFS at the Ge K-Edge

Odile Majérus[1], Laurent Cormier[1], Jean-Paul Itié[2] and Georges Calas[1]

[1]Laboratoire de Minéralogie Cristallographie de Paris (LMCP), UMR CNRS 7590, Universités Paris 6 et 7, IPGP, 4 place Jussieu, F-75252 Paris cedex 05, France
[2]Laboratoire de Physique des Milieux Condensés (LPMC), UMR CNRS 7602, Université Paris 6, 4 place Jussieu, F-75252 Paris cedex 05, France

Received June 26, 2003; accepted February 13, 2004

Abstract

In SiO_2-GeO_2 glasses submitted to high pressure conditions, germanium atoms undergo a coordination change from four to six on a pressure-range depending on the composition. In the transition region, the possibility of having a mixture of tetrahedra and octahedra for Ge instead of the intermediate fivefold coordination state has been studied. Through comparison of the informations extracted from XANES and EXAFS, the model of a mixture of IV and VI coordination states, with a possible small amount of fivefold coordinated Ge appearing on the compression, is favoured.

1. Introduction

In oxide glasses as in crystals, the major pressure-induced structural transformation is the coordination change of the network former, from the fourfold to the sixfold coordination state. However, the transformation process should be different in glasses with respect to crystals, because of the configurational variety of the former. Such a transformation has been recently investigated in a series of SiO_2-GeO_2 glasses, by *in situ* high pressure X-ray Absorption Spectroscopy (XAS) measurements at the Ge K-edge [1]. These experiments have put in evidence the existence of an intermediate phase on a large pressure range, stemming from the disruption of the low-pressure tetrahedral framework, and conducting to the high-pressure phase based on octahedral units. Two possibilities can be envisaged: either the intermediate structure consists of a mixture of the fourfold and sixfold Ge coordination states, or it involves an intermediate fivefold coordinated unit. These two alternatives refer to different underlying thermodynamic natures for the transformation, which can be of first order or continuous, respectively.

This proceeding focuses on the problem of determining mixtures of coordinences from the XAS spectra at the Ge K-edge. To this purpose, the XANES spectra have been decomposed in components representative of the low-pressure and high-pressure states. The analysis suggests a mixture of fourfold and sixfold coordinated units, with a possible small amount of the fivefold coordination state formed during the compression. However, limitations of this qualitative approach are outlined.

2. Experimental

$_x SiO_{2\ (1-x)} GeO_2$ glasses with $x = 30, 50, 65$ and 80 were obtained through a sol-gel process followed by heat-treatment of the gels. Compositions measured by microprobe analysis correspond to the nominal ones within 2 mol%. The details of the sample preparation are described elsewhere [1]. The XAS experiments were performed at the D11 beamline of the Laboratoire pour l'Utilisation du Rayonnement Electromagnétique (LURE, Orsay, France), using synchrotron radiation emitted by the DCI storage ring. The experimental dispersive set-up has been explained in [2]. A Si(111) curved monochromator selects the energy-range of the incident white beam and focuses the Bragg-reflected photons on the sample through a diamond anvil cell in which the sample is loaded, with silicone oil as a pressure transmitting medium. An accessible energy range of about 420 eV was obtained at the Ge K-edge. The pressure range explored was typically 0–25 GPa.

The XAS spectra were normalized in absorbance using Victoreen and spline functions. The k^3-XAFS signal was Fourier transformed using a Kaiser window with $\tau = 2.5$ and a k range of about 4 to 10 $Å^{-1}$. The E_0 value and the k-range for the Fourier transform (FT) were maintained constant over all the spectra of a pressure cycle. The FT-filtered oscillations corresponding to the Ge-O peak were fitted using phase and amplitude parameters extracted from reference spectra.

3. Results

Three reference spectra at the Ge K-edge are shown in the top of Fig. 1: GeO_2 of quartz structure (q-GeO_2) and vitreous GeO_2 (v-GeO_2), both based on corner-connected GeO_4 tetrahedra, and GeO_2 of rutile structure (r-GeO_2) in which Ge is in a sixfold coordinated state. q-GeO_2 XANES spectrum shows three features beyond the white line: the C feature, at about +21.2 eV above the absorption threshold and assigned to scattering inside the tetrahedron, and the lower-energy features A ($\sim$ +10 eV) and B ($\sim$+13 eV) corresponding to interactions extending beyond the tetrahedron. By comparison, v-GeO_2 XANES spectrum presents a C feature at the same energy, and only one broad resonance at $\sim$+11.5 eV in place of the A and B peaks. This is consistent with a structure of corner connected tetrahedra as in q-GeO_2, but with disorder beyond the first shell due to a distribution of the intertetrahedral angles. The r-GeO_2 XANES spectrum is characterized by a white line of higher intensity and subsequent features at +16.5 (B′) and +26 eV (C′). The edge crest is shifted by about 1 eV and appears broader with respect to that in q-GeO_2. Finally, the XANES spectra of the SiO_2-GeO_2 glasses show a C feature as in q- and v-GeO_2, but the resonance at +11.5 eV does not appear, indicating a higher degree of disorder on the medium-range scale, of both structural and chemical nature and induced by the SiO_2-GeO_2 mixing.

With increasing pressure up to about 25 GPa, the XANES shape of the SiO_2-GeO_2 glasses evolves toward a XANES shape similar to that of Ge in r-GeO_2 (center of Fig. 1, sample with 30 mol% SiO_2): the relative intensity of the edge crest increases, while the C feature progressively vanishes, consistently with the break-down of the tetrahedra. At high pressure, a very smoothed resonance appears at about +28 eV above the absorption threshold, which may correspond to the C′ resonance in r-GeO_2. The +2 eV shift may be related to a compression effect, according

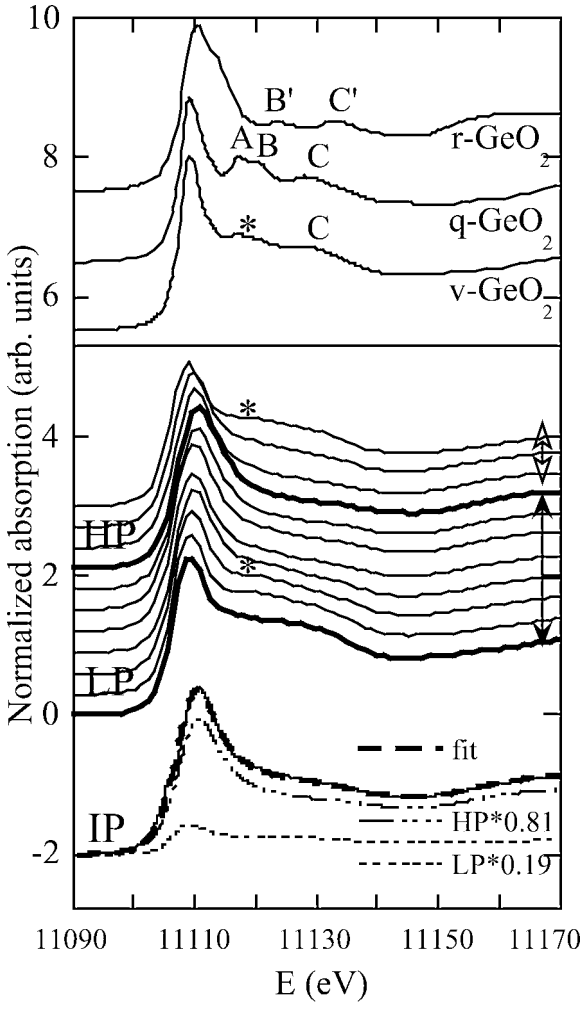

Fig. 1. Top: Ge K-edge XANES in rutile GeO_2 (r-GeO_2), quartz GeO_2 (q-GeO_2) and vitreous GeO_2 (v-GeO_2). Centre: Ge K-edge XANES in a SiO_2-GeO_2 glass with 30 mol% SiO_2, at different pressures: on compression at 0.7; 5.0; 9.9; 13.2; 15.7; 18.8; 22.0; 26.8 GPa from bottom to top (black double arrow) and on decompression at 8.8; 5.1; 0 GPa (white double arrow). Bottom: Example of a XANES decomposition of a spectrum (IP) in terms of low pressure (LP) and high pressure (HP) components.

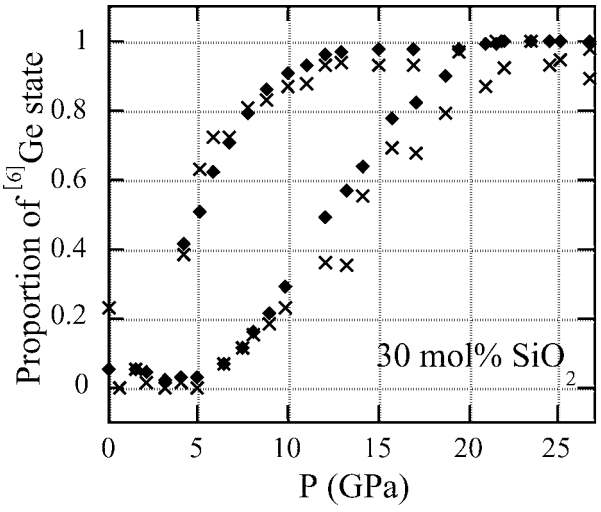

Fig. 2. Proportion of [6]Ge state derived from XANES linear decomposition (full diamonds) and double-shell fitting of EXAFS (crosses).

to the $1/r^2$ dependence invoked for the energy of multiple scattering resonances [3]. Moreover, the edge crest broadens and shifts by about +1 eV. Therefore, the XANES spectrum at high pressure (26.8 GPa for this sample) is assigned to Ge in mainly sixfold coordination state. The mean Ge-O distance of 1.81 Å, extracted from the EXAFS on the same measurement, corroborates this assignment [1]. Finally, in the limited pressure-range during the compression, then on decompression, we observe the growing of a smoothed resonance similar to that in v-GeO_2 (it is marked by a * in Fig. 1). This is related to changes on the medium-range scale, whose origin is difficult to ascribe without an analysis based on structural models.

A spectrum at intermediate pressure (17.1 GPa) is reproduced on the bottom of Fig. 1. This spectrum is refered to as IP, while the low-pressure and high-pressure spectra are respectively noted LP and HP and indicated as bold lines in the center of Fig. 1. These latter spectra are chosen as references for [4]Ge and [6]Ge respectively. Considering that the IP spectra result from a mixture of both [4]Ge and [6]Ge, we have decomposed the IP XANES spectra as a linear combination of the LP and HP XANES spectra, by use of a least-squares fitting procedure. The result of the fit is depicted on the bottom of Fig. 1 along with the weighted LP and HP components. Two hypotheses are made in this procedure. Firstly, the absence of the fivefold coordination state is assumed. Indeed, such a contribution can hardly be established from the XANES spectra, because the shape of the XANES of [5]Ge is not known and may be close to that of [4]Ge + [6]Ge. Secondly, we suppose that the [4]Ge and the [6]Ge sites remain unaltered under pressure, so that they give identical XANES signals, whatever the pressure.

The linear combination fits very well the shape of the IP XANES spectra at each intermediate pressure (Fig. 2). Only the resonance (*) appearing on the first stage of the compression could not be reproduced, confirming its assignment to pressure-induced changes on the medium-range scale. Further confirmation of this decomposition is obtained from the EXAFS signal, which has been fitted using two shells of oxygen neighbours, as explained elsewhere [1]. In Fig. 2 are compared the proportions of [4]Ge and [6]Ge obtained by XANES decomposition and double-shell-EXAFS fitting. The agreement is very good for both the compression and decompression measurements. The discrepancy of 10% at high pressure represents the total uncertainty over both procedures.

4. Discussion and conclusion

In situ high pressure XAFS experiments have been carried out on GeO_2-SiO_2 glasses at the Ge K-edge, in a dispersive mode using a diamond anvil cell. The XANES spectra can be adequately modelled using a linear combination of the 4-fold and 6-fold coordination states for Ge. On compression and on decompression, the XAS spectra thus reflect the coexistence of the fourfold and sixfold coordination states, without the presence of a significant amount of other intermediate species (possible amount is less than 10%).

The different behaviours on compression and on decompression may be due to different extension of the metastability field of each coordination state. The metastability of the sixfold coordinence on pressure release is likely to be important, because the GeO_6 octahedron is energetically favoured (r-GeO_2 is the most stable phase in ambient conditions). At the metastability limit [6]Ge may revert back to [4]Ge in an abrupt way, precluding any observation of an intermediate state. The reversibility of the transformation suggests that some memory of the initial glass is

maintained in this ambient-temperature process, preventing from the retention of an octahedral network.

The presence of $^{[5]}$Ge can not be completely excluded in this study, without knowing the shape of the $^{[5]}$Ge XANES. Ge in fivefold coordination has been reported in crystalline potassium germanate [5], which should be used for XAS measurements. We note that in alkali germanate glasses of low alkali compositions, the occurrence of $^{[5]}$Ge is also controversial, partly because of the small amount of $^{[5]}$Ge possibly involved (about 15% [6]), and because the differences expected between the $^{[4]}$Ge, $^{[5]}$Ge and $^{[6]}$Ge species in the radial distribution functions and spectroscopic signals are weak. Another important question is the pressure-dependence of the Ge K-edge XANES of $^{[4]}$Ge or $^{[6]}$Ge site, owing to the compression of the site itself and the changes in medium-range ordering. Simulations and XANES calculations are needed to assess the influence of the isotropic medium-range order of such glasses on the XANES signal. Finally, a principal component analysis (PCA) of both the XANES and EXAFS signals is in progress to determine independent components in the series of spectra and possibly rule out the presence of intermediate species in the transformation [7].

Acknowledgments

We are grateful to Guillaume Morin (LMCP) for providing the least-squares fitting procedure adapted to XANES spectra. Pascal Munsch (LURE) and Daniel Neuville (IPGP) are gratefully thanked for their help in loading the DAC and during the data acquisition. Laurence Galoisy and Delphine Cabaret (LMCP) are acknowledged for fruitful discussions.

References

1. Majérus, O., Cormier, L., Itié, J.-P. and Calas, G., J. Non-Cryst. Solids, accepted.
2. Dartyge, E., *et al*., Nucl. Instrum. Meth. **A246**, 452 (1986).
3. Bianconi, A., Fritsch, E., Calas, G. and Petiau, J., Phys: Rev. B **32**, 4292 (1985).
4. Itié, J.-P., *et al*., Phys. Rev. Lett. **63**, 398 (1989).
5. Fay, V. D., Vollenkle, H. and Wittmann, A., Z. Kristallogr. Bd. **138**, 439 (1973).
6. Hoppe, U., *et al*., J. Non-Cryst Solids **278**, 99 (2000).
7. Wasserman, S. R., *et al*., J. Synchrotron Rad. **6**, 284 (1999).

Physica Scripta. Vol. T115, 528–530, 2005

Measurement of Luminescence from Silica Glasses: an Optical X-Ray Absorption Fine Structures Study at Si K-Edge

Tomoko Yoshida[1*], Tetsuo Tanabe[1], Shogo Takahara[2] and Hisao Yoshida[3]

[1]Center for Integrated Research in Science and Engineering, Nagoya University, Nagoya 464-8603, Japan
[2]Department of Nuclear Engineering, Graduate School of Engineering, Nagoya University, Nagoya 464-8603, Japan
[3]Department of Applied Chemistry, Graduate School of Engineering, Nagoya University, Nagoya 464-8603, Japan

Received June 26, 2003; accepted October 14, 2003

PACS number: 61.80.Cb

Abstract

Soft X-ray excited optical luminescence (XEOL) of silica glasses was studied with respect to the excitation X-ray energy (near the Si K-edge) and irradiation time. The luminescence spectra showed emission bands at 3.1 eV and 2.7 eV, assigned to $B_{2\beta}$ and $B_{2\alpha}$ oxygen deficient centers in silica glasses, and the luminescence yields of these bands changed drastically before and above the Si K-edge. Si K-edge photoluminescence yield (PLY) spectrum of the band at 3.1 eV was similar to Si K-edge XANES spectrum recorded in the photocurrent mode for the same silica sample, except for the negative edge jump in the PLY spectrum.

The time evolutions of the band intensity at 3.1 eV were also investigated under the excitation by soft X-ray below and above Si K-edge. The band intensity in both cases decreased slightly with the irradiation. These results indicate that a part of $B_{2\beta}$ centers in the silica glass probably changed to other types of oxygen deficiencies by the electron excitation effect. In the early stage of the irradiation, a rapid increase in the intensity of the 3.1 eV band was also observed, indicating that soft X-ray irradiation produced luminescence sites such as $B_{2\beta}$ centers.

1. Introduction

Radiation effects on silica glasses are one of the main concerns for their application as optical windows, insulators and optical fibers in fusion and fission environments [1]. Although the radiation damage of silica in nuclear environments has been widely studied, the detailed damaging process and damaged structure has not been fully understood. That is mainly because the effect of ionizing radiation, which is very important in optical materials like silica, is mixed up with the displacement effect.

The present work is our trial to observe soft X-ray radiation effects on silica. Since the energy region of soft X-rays covers the K-edges of silicon and oxygen, it is possible to study the dynamic and specific radiation effect of silica under the preferential excitation of these inner-shell electrons. In this study, we have measured the luminescence from silica glasses under soft X-ray irradiation near the Si K-edge, and discussed the origin and the variation of the luminescence sites.

2. Experimental

The samples used in this work were unirradiated low-OH and high-OH fused silica glasses (T-2030 and T-1030, produced by Toshiba Ceramics, Japan) and high-OH fused silica glass after irradiation in a nuclear reactor. The diameter and thickness of each sample was 13 mm and 2 mm, respectively. The measurement of luminescence of these silica glasses induced by soft X-ray irradiation (1.8–1.9 keV) was carried out on the beam line 7A at UVSOR, Institute for Molecular Science with a stored current of 100–200 mA. The luminescence was focused by a lens in the UHV chamber to the monochromator (CP-200, JOBIN YVON) and detected by a multi-channel analyser (OMA III, EG&G PRINCETON APPLIED RESEARCH). The photon energy (E) from ca. 4 eV to 1.5 eV was measured because the photon detecting efficiency in the region $E < 1.5$ eV and $E > 4$ eV were reduced drastically. The luminescence yield spectrum was also measured using a photomultiplier (Hamamatsu Photonics R955).

3. Results and discussion

3.1. *X-ray excited optical luminescence (XEOL)*

Fig. 1 shows observed luminescence spectra from various types of silica glasses under soft X-rays near Si K-edge (1848 eV). The low-OH fused silica glass (T-2030) showed an intense emission band at around 3.1 eV (Fig. 1(a)), while no distinct

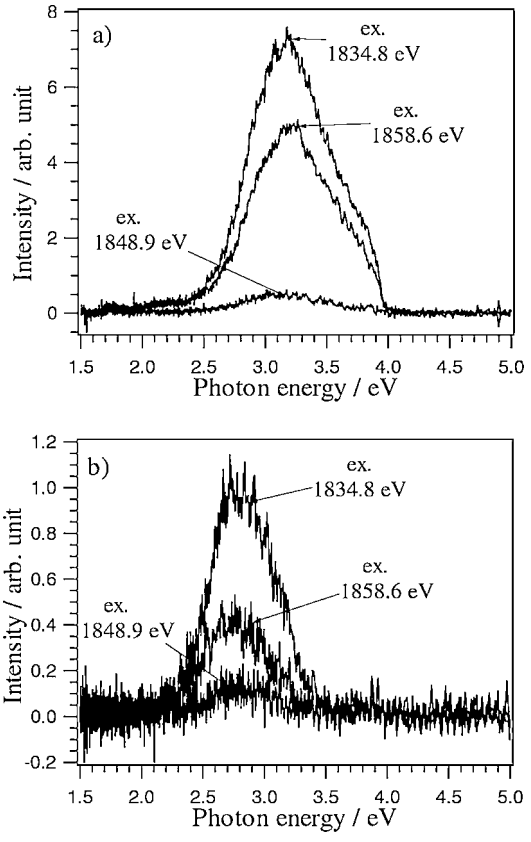

Fig. 1. Optical luminescence spectra of silica glasses excited by soft X-rays with energy of 1834.8 eV, 1848.9 eV and 1858.6 eV. (a) Low-OH fused silica glass. (b) High-OH fused silica glass after neutron irradiation.

*e-mail: yoshida@cirse.nagoya-u.ac.jp

emission band was observed for the high-OH fused silica glass (T-1030) (not shown here). However, after neutron irradiation in a nuclear reactor, the latter silica glass showed an emission band at 2.7 eV and not at 3.1 eV. Similar luminescence spectra have been measured for silica glasses under in-reactor or UV irradation [2, 3], and we have concluded that the origin of the present XEOL is likely due to electron excitation of oxygen deficiencies in silica glasses by soft X-rays. Based on the photon energy of the emission bands, the 3.1 eV band should be related to the intrinsic $B_{2\beta}$ center in the low-OH silica glass (T-2030), while 2.7 eV band to $B_{2\alpha}$ center produced in silica glasses (T-1030) by the atomic displacement effect of neutron irradiation [4]. In this short paper, we focused on the luminescence at 3.1 eV attributed to $B_{2\beta}$ center.

3.2. *The photoluminescence yield (PLY) spectrum of the 3.1 eV band*

It is noteworthy that the intensities of the 3.1 and 2.7 eV emission bands change with the excitation energy of soft X-rays (Fig. 1). We measured a photoluminescence yield (PLY) spectrum of the 3.1 eV band which is shown in Fig. 2(a) together with a Si K-edge XANES spectrum (Fig. 2(b)) recorded in the photocurrent mode for the same fused silica glass. One can clearly see that both PLY and XANES spectra are similar, although the former jump negatively whereas the latter positively at Si K-edge. The outline of the phenomenological theory for the shape of the PLY spectrum has been proposed previously [5, 6] and is due to the competitive absorption of sites being responsible for the luminescence and those being not. Since in both cases the total absorption condition applies, the key factors that decide the direction of the edge jump are relative luminescence yield of the absorption events above and below the edge. By applying this theory to the present case, above Si K-edge, the transition of Si 1s electron to 3p orbital and/or continuum state occurs and simultaneously the relative luminescence yield reduces; therefore, the PLY spectrum may show negative and similar feature to the XANES spectrum. This is also the reason why the intensities of the 3.1 eV emission band change with the soft X-ray excitation energy in Fig. 1.

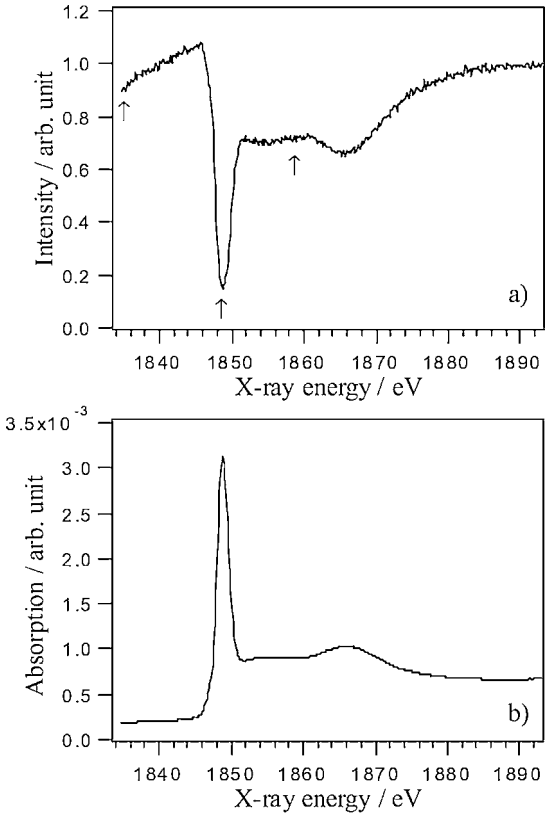

Fig. 2. Comparison between a) the luminescence yield spectrum of the 3.1 eV band and b) Si K-edge XANES spectrum of a fused silica glass.

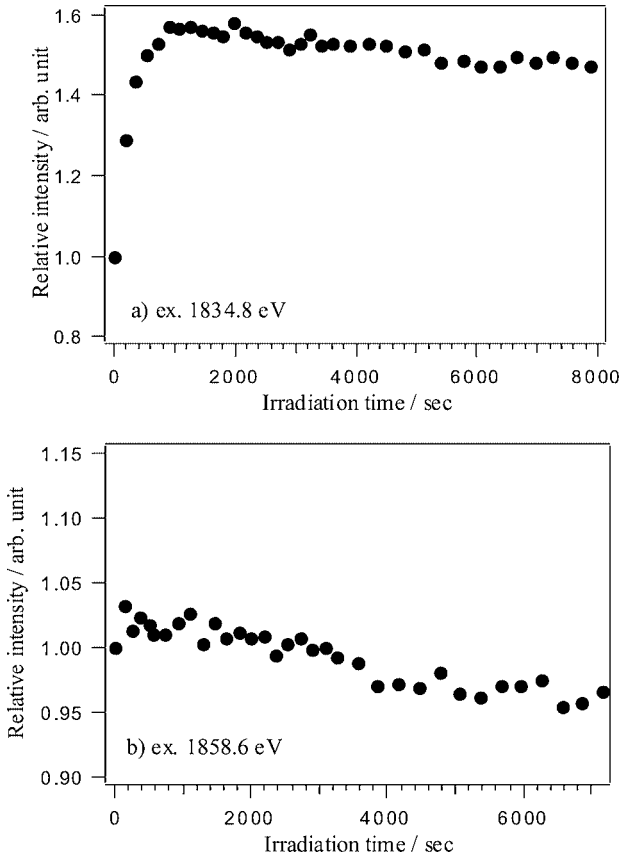

Fig. 3. Variation of the relative intensity of the band at 3.1 eV with the irradiation time. Excitation X-ray energies are a) 1834.8 eV (below Si K-edge) and b) 1858.6 eV (above Si K-edge), respectively.

3.3. *Time evolution of the intensity of XEOL*

We have investigated the long term change of 3.1 eV XEOL intensity with the irradiation time of soft X-rays. Fig. 3 shows the variation of the band intensity at 3.1 eV due to $B_{2\beta}$ center under the excitation by X-rays with energy of 1834.8 eV (below Si K-edge) and 1858.6 eV (above Si K-edge). The intensities were normalized by the intensity at the beginning of the soft X-ray irradiation. Except the very early stage of the irradiation, the relative intensity in both cases decreased slightly with the irradiation time. Ishii *et al.* and Skuja [7, 8] have reported that the $B_{2\beta}$ centers in silica are easily changed to E′ centers by electron excitation under the UV laser irradiation. In addition, the transformation of $B_{2\beta}$ centers to E′ centers had been observed in our separate γ-ray irradiation experiment for silica glasses [3]. Therefore, we have concluded that some of the $B_{2\beta}$ centers probably changed to other types of oxygen deficiencies such as E′ centers by electron excitation effect, but the $B_{2\beta}$ centers were fundamentally stable against the present irradiation condition. This result may be partially due to the weak intensity of X-ray from the synchrotron in this energy region.

On the other hand, in the very early stage of the irradiation, the increase of the 3.1 eV band intensity is appreciable (Fig. 3(a)). This result may indicate that soft X-ray irradiation produced luminescence sites such as $B_{2\beta}$ centers. The increasing rate was quite different with excitation X-ray energies at 1834.8 eV and 1858.6 eV. In the present stage, the origin of the difference of the initial increasing rate are not clear. However, such a dynamic phenomenon was observed for the first time, so far as we know, and the present results clearly indicate that the *in-situ* observation is a potential technique to study the dynamic radiation effects of soft X-ray on silica.

References

1. Clinard, F. W. Jr. and Hobbs, L. W., "Physics of Radiation Effects in Crystal" (Elsevier, Amsterdam 1986), p. 442.
2. Yoshida, T. *et al.*, Nucl. Instr. Meth. B **166–167**, 476 (2000).
3. Ii, T. *et al.*, J. Nucl. Mater. **283–287**, 898 (2000).
4. Tohmon, R. *et al.*, Phys. Rev. B **55**, 1337 (1989).
5. Emura, S., Maeda, H. and Nomura, M., Physica B **208–209**, 108 (1995).
6. Murata, T., Jiang, D. T., Sham, T. K., Feng, X. H. and Frigo, S. P., J. Electr. Spectr. Related Phenom. **79**, 155 (1996).
7. Ishii, K., Ohki, Y. and Nishikawa, H., UVSOR (Inst. Mol. Sci., Okazaki, Japan) Activity Report 130 (1993).
8. Skuja, L., J. Non-Cryst. Solids **239**, 16 (1998).

Physica Scripta. Vol. T115, 531–533, 2005

Sodium Adsorption on the TiO_2(110) Surface: an XAFS Structural Study

R. J. Prado[a], P. Lagarde[a,1], A.-M. Flank[a], J. Jupille[b] and S. Bourgeois[c]

[a]LURE, Bat 209d, Centre Universitaire Paris-Sud, BP 34 91898 Orsay-cedex, France
[b]GPS, Université P&M Curie, Place Jussieu, 75251 Paris-cedex 06, France
[c]Laboratoire de Recherche sur la Réactivité des Solides, Université de Bourgogne, BP 47870, 9, Av. Alain Savary, 21078 Dijon-cedex, France

Received June 26, 2003; accepted November 4, 2003

PACS numbers: 61.10Ht, 68.43FG, 78.70Dm

Abstract

The adsorption site of sodium atoms deposited onto a clean TiO_2(110) surface has been determined by EXAFS. The best result is obtained for an 'in-between' site where the sodium is bound to two bridging oxygen atoms at 2.25 Å and one in-plane one at 2.40 Å, in full agreement with DFT calculations. At higher coverage the site becomes a hollow site where Na is equidistant to the three oxygen atoms at 2.30 Å.

1. Introduction

Among the numerous metal/oxide interfaces, deposit of alkali metals on titanium-dioxide play a special role since these atoms induce specific properties of the interface [1], and their atomic or electronic structure is far from fully understood. In this paper we have carried out X-ray absorption spectroscopy measurements (XAFS) on low and high sodium coverages at the sodium K-edge and we compare our experimental results on the local environment of the sodium atoms with the most recent theoretical models [2].

2. Experimental and data analysis

The preparation method of the TiO_2(110) surface is nowadays very well documented. Successive phases of cleaning by 500 eV Ar^+ ions, followed by annealing in UHV at 600 °C using electron bombardment have been used. The surface has then been checked by Auger spectroscopy, which does not show any contamination by carbon or calcium. This procedure has been applied to two samples, which both present a sharp (1×1) LEED pattern but differ by the orientation of the [001] bonding oxygen rows which have been set parallel or normal to the photon electric field.

XAS experiments have been done on the SA32 beam line at LURE-Super-ACO. For sodium K-edge spectra, the line is equipped with a beryl (10$\underline{1}$0) double-crystal monochromator, allowing an energy resolution of about 0.5 eV at 1 keV. The incident flux is monitored by the total electron yield (TEY) from a 2 µm polyethylene film covered by 700 Å of titanium. The absorption signal is also measured by TEY inside the UHV chamber. The vacuum level has been kept always, even during the Na evaporation, in the low 10^{-10} Torr range.

The Fourier transform of the kX(k) XAFS data uses an Hanning window spanning from 2.3 to 7.5 $Å^{-1}$. Structural parameters are then obtained by a fitting procedure using the FEFFIT [3] code, the phase shift parameters being *ab-initio* calculated by FEFF7 [4] and tested on the crystallized model compound Na_2SiO_3 [5]. It is worth to point out here that we have to fit two independant polarization experiments with the same structural environment.

3. Results

3.1. *Low sodium coverages*

We have at first deposited an almost equal small amount of sodium on the two samples. The position of the edge is identical to that of pure sodium chloride, 3 eV higher than that of metallic sodium. This indicates that the sodium is nearly fully ionized when deposited onto the surface, a result in agreement with the theoretical calculations of the energetics of this system as well as photoemission results [1, 2].

The first step of the analysis consists in building a model cluster, shown in Fig. 1, from which the different phase shifts can be calculated by FEFF7. Sodium atoms have been located on the site that the theoretical results [2] consider to be the more stable. It is the so-called 'in between' site where the sodium is linked to two bridging oxygen at 2.25 Å and to one in-plane oxygen at 2.40 Å. Therefore all interatomic distances and apparent coordination numbers are defined. The fitting procedure then involves only the energy position of the edge and the Debye-Waller factors of each bond. The best results of the fits are given in Table I while Fig. 2 shows the corresponding theoretical and experimental Fourier transforms.

According to photoemission experiments [1] and also to theoretical calculations [2] on the stability of the sodium site, adsorption of sodium induces a derelaxation of the surface, then the model described in Table I assumes bulk-terminated positions for the titanium and oxygen atoms surrounding Na. During the fitting procedure, it appears that the result is definitely improved when one allows the last Na-O distance to vary, the final value being 3.6 Å instead of 3.8 Å. We believe that this discrepancy is

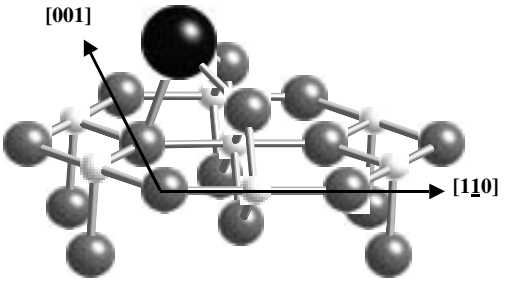

Fig. 1. Schematic view of the sodium site described in table I. Small, medium and large spheres are respectively titanium, oxygen and sodium atoms.

[1]e-mail: pierre.lagarde@lure.u-psud.fr

Table I. *Best fit results for the local environment of the sodium atom set to a position described in ref [2]. The energy edge shift is −5.5 ± 1 eV for both pannels. O (B) and O (P) are the bridging and planar oxygens, Ti (V) and Ti (VI) the pentagonal and octahedral titanium. The fixed values are set in bold, and the numbers in parenthesis are the changes to the expected values for the best fit.*

	E//[001]			E//[1$\underline{1}$0]		
Neighbour	Apparent coordination number	Distance (Å)	D.W. Factor (Å^2 ± 0.02)	Apparent coordination number	Distance (Å)	D.W. Factor (Å^2 ± 0.02)
O (B)	**2.6**	**2.25**	0.0001	**2.1**	**2.25**	0.0001
O (P)	**0.0**	**2.40**	0.00001	**0.8**	**2.40**	0.0003
Ti (VI)	**0.0**	**2.67**	0.001	**0.8**	**2.67**	0.03
Ti (V)	**1.2**	**3.33**	0.0125	**2**	**3.33**	0.004
O	**3.7**	3.6 (−0.2)	0.001	**2.1**	3.5 (−0.3)	0.02

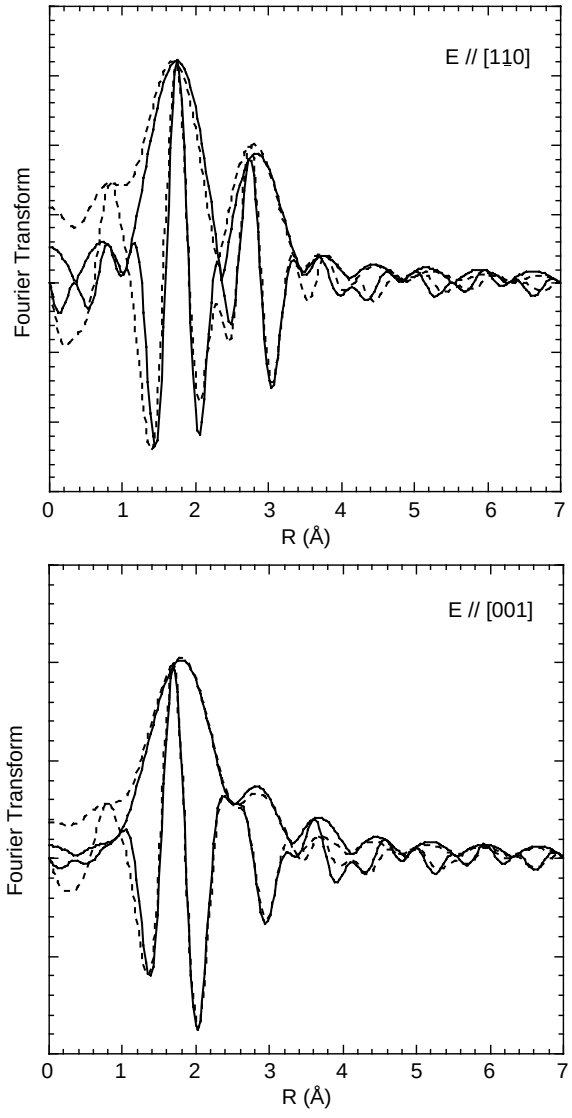

Fig. 2. Experimental (solid lines) and model (dashed lines) Fourier transforms for the two polarizations for a low sodium coverage described by Table I.

not real but corresponds to the limit of our modelling of the data, given the signal to noise ratio and the EXAFS energy domain available.

In both orientations, the introduction of sodium-sodium interactions, assumed for both the [1$\underline{1}$0] direction or the [001] one at distances corresponding to the occupancy of equivalent neigbouring sites, is destroyed by the fitting procedure which returns a very large Debye-Waller factor for the corresponding interatomic distance. This means that the sodium atoms should be isolated, in line with the presence after evaporation of still a definite (1 × 1) LEED pattern, although less sharp than that of the clean surface. According to the findings by Nerlov *et al*. [1], this means a coverage less than one monolayer.

The above results only prove that the site of the sodium determined by *ab-initio* density functional calculations is fully in agreement with EXAFS experiments. We then attempted to check if other published structural solutions could also be in agreement with our experimental results:

1- Albaret *et al*. [2] have also considered the 'adjacent' site, where the sodium is bound to one bridging oxygen and two planar ones. It presents a very short (2.09 Å) and two very long (2.56 Å) Na-O distances. This splitting is not compatible with the experimental results and the fitting procedure never reaches a reasonable value.

2- In most of the sodium compounds where sodium is bound to oxygen, the distance Na-O lies close to 2.30 Å which is close to the sum of the two ionic radii. We have therefore attempted to simulate our experimental data assuming for sodium an hollow site where the alkali atom is equally distant, at about 2.30 Å, from three oxygen atoms. Whatever is the site considered (either 'adjacent' or 'in-between') the fit is only obtained if some distances between the sodium and the surface atoms are allowed to vary in a way not really grounded physically.

3.2. *High sodium coverages*

The above samples have been first cleaned and then a long deposit of sodium has been made giving a relative jump at the edge about five times higher. Albaret *et al*. [2] have also modelled the relative stability of different adsorbate configurations at a coverage of half a monolayer: the alkali atoms are now in a nearly perfect 'in between' hollow site. Assuming that this site remains the same at full coverage, the fitting procedure returns the values listed in Table II. The changes, in both crystallographic directions, induced by the occupation of all possible equivalent sites by the sodium atoms are well described by the analysis of the EXAFS experimental results. Here again (see Table II) the fit is improved by a change of the more distant shells. Photoemission experiments [1] suggest the existence, at high sodium coverage, of metallic sodium which could form disordered metallic clusters. As a matter of fact, Fig. 3 compares the near edge spectra of the very low coverage analyzed in section 3.1 (curve a) to that of the high coverage (curve b). This last spectrum exhibits a pre-edge

Table II. *Best fit results for the local environment of the sodium atom at a coverage of 1 ML as described in ref [2]. The energy edge shift is −0.2 ± 1 eV for both pannels.*

	E//[001]			E//[1$\underline{1}$0]		
Neighbour	Apparent c.n.	Distance (Å)	D.W. Factor (Å^2 ± 0.02)	Apparent c.n.	Distance (Å)	D.W. Factor (Å^2 ± 0.02)
O (B)	**2.5**	**2.28**	0.000037	**2.6**	**2.28**	0.00006
O (P)	**0.0**	**2.35**	0.00001	**0.3**	**2.35**	0.0007
Ti (VI)	**0.0**	**2.71**	0.0001	**1.**	**2.71**	0.04
Na	**6**	**2.95**	0.020	**3**	**3.05**	0.0002
Ti (V)	**1.3**	3.18	0.01	**1.9**	3.16	0.04
O	**3.8**	3.53 (−0.18)	0.02	**2.1**	3.53 (−0.18)	0.0001

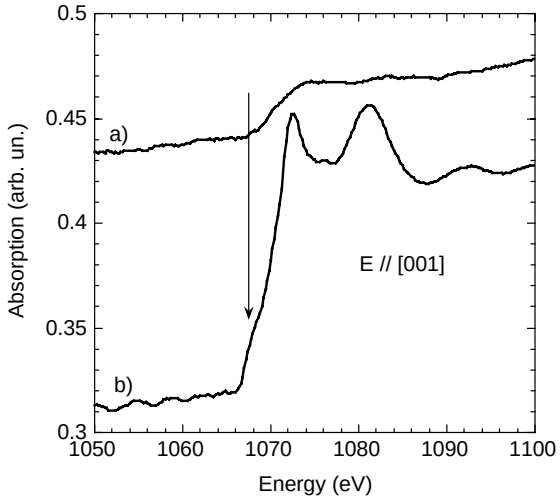

Fig. 3. Near edge structure of sodium for a low coverage (curve a) and for the high coverage (curve b). The amount of sodium is related to the relative jump at the edge and the arrow points to the position of a pre-edge feature which could be the signature of metallic sodium.

feature, around 3 eV below the main edge, attributed to sodium metal which, because of its very low Debye temperature, appears only in the edge jump.

4. Conclusions

A direct determination of the sodium adsorption site on a clean TiO_2(110) surface has been obtained by XAFS. The experimental results agree very well with density-functional calculations: at low coverages when sodium atoms do not interact the sodium locates on an 'in between' site with a distance to the bridging oxygens (2.25 Å) shorter than that with the in-plane one (2.40 Å). When the sodium amount increases to reach a full coverage, the Na-O distances become nearly equal, the presence of sodium neigbours is well evidenced in the experiments while the near edge spectra shows a signature from metallic sodium clusters on top of the surface.

Acknowledgements

We thank the team in charge with the Super-ACO machine. R. J. Prado has been supported at LURE by a grant from CAPES (Brazil).

References

1. Nerlov, J., Christensen, S. V., Weichel, S., Pedersen, E. H. and Moller, P. J., Surf. Sci. **371**, 312 (1997).
2. Albaret, T., Finocchi, F. and Noguera, Cl., Phys. Rev. B **65**, 035402 (2001).
3. Newville, M. *et al.*, Physica B **154**, 208 (1995).
4. Ankudinov, A. L. and Rehr, J., J. Phys. Rev. B **56**, R1712 (1997).
5. Lagarde, P., Flank, A.-M., Mazzara, C. and Jupille, J., Surf. Sci. **482–485**, 376 (2001).

Physica Scripta. Vol. T115, 534–537, 2005

XANES Studies of Thallium Compounds and Valence States and Local Environment of Thallium in Some of its Superconducting Cuprates

Arvind Agarwal* and A. N. Vishnoi+

Department of Physics, M.N. National Institute of Technology, Allahabad, 21004, India

Received June 26, 2003; accepted in revised form November 4, 2003

PACS number: 61.10.Ht

Abstract

The position and shape of X-ray absorption discontinuities have been used to deduce structural and chemical bonding information on model compounds of thallium and its superconducting cuprates. The L X-ray absorption spectra were recorded on a Rigaku X-ray Spectrometer and monochromatized using a flat crystal of Si (1, 1, 1). The background subtraction was done using Victoreen function. The normalized absorption coefficient is plotted as a function of X-ray photon energy. It is observed that the XANES of L_I edge has fewer features as compared to those of L_{III} edge. The L_{II} edge spectra of thallium are similar to L_{III} edge spectra. The L_{III} absorption discontinuity of thallium splits into three components whereas no splitting is observed in L_I edges. Thallium L_{III} edge spectra show a single absorption peak for monovalent compounds whereas in trivalent compounds a weak peak followed by a shoulder on rising absorption which culminates into a strong absorption peak. The important difference between the spectra of monovalent and trivalent compounds is the shift in the inflexion point energy of L_{III} edges and a shift of the main absorption maximum. The X-ray absorption spectra of superconducting cuprates show similarities with the spectra of Tl_2O_3 suggesting the presence of Tl^{3+} ions in octahedral configuration in these cuprates.

1. Introduction

It is well known [1–5] that monovalent and trivalent thallium compounds have interesting chemistry as a consequence of 6s and 6p electrons present in the valence band. The nature of the bonding in these compounds varies widely. Covalent contributions to the bondings [6] in thallium (I) halides reach a maximum with thallous iodide, which has a double-layered orthorhombic structure [7]. A feature of fundamental importance which influences the structure and bonding in thallium compounds is that the 6s, 6p and 6p levels are sufficiently close and hybridization of these orbitals is energetically favorable in several thallium compounds. Hybridization alters the character of the otherwise pure and vacant 6p and 6d levels of monovalent and trivalent thallium in covalently bonded compounds. In the absence of hybridization, like in ionically bonded Tl^{1+} or Tl^{3+} compounds, the same 6p and 6d levels are subjected to strong crystal fields. The effects of the coordination sphere of ligands and the point group symmetry of the thallium atom lift the degeneracies of the p and d manifolds. This suggests that X-ray absorption spectroscopy is a very strong informative experimental approach to study the coordination geometry and bonding relation in thallium compounds. The near-edge features involve the transition from some core state to allowed lowest unoccupied empty states in the valence region of a given atomic center. XANES reveal the identity of the allowed transitions and also the mixing or splitting of the final state orbitals [8, 9]. Using known structural data, informative deductions on structure – bonding relations have been made. Both Tl L_I and Tl L_{III} edge XANES spectra have been used since they probe $2s \rightarrow 6p$ and $2s \rightarrow 6d$ transitions respectively. The study was extended to a new class of superconducting oxides containing thallium [10–15] to collect information on atomic environment and valence states of thallium ions.

2. Origin of Data

The analyzed data were collected in the in-house EXAFS laboratory. X-rays emitted from a conventional X-ray tube were monochromatized by a flat silicon (1,1,1) crystal and allowed to pass through the sample. The transmitted X-rays were then detected through a detector by moving the sample in and out of the X-ray beam. The voltage pulses produced were fed into a digital scalar and counted for a certain time, the number of counts per unit time is directly proportional to the number of photons entering into the detector. The ratio of counts of detector reading without the sample and with the sample gave I_0/I. The logarithms of this are proportional to the absorption coefficient μ. The I_0/I was then recorded as a function of the monochromator crystal position. The crystal was mounted on a goniometer driven by a step motor. The monochromator steps were proportional to the incident angle of the X-ray beam on the crystal face. The data analyzed was originally in the form of monochromator steps versus I_0/I.

3. Numerical Analysis

The L absorption of model thallium compounds and superconducting oxides containing thallium were normalized by fitting a linear function to the pre-edge data and fitting cubic splines to the XANES region of the data up to 100 eV, extrapolating both functions to zero energy i.e. the inflexion point energy, subtracting the pre-edge data function from each point in the experimental spectrum and dividing by the step height. This procedure results in a normalization of the data to the unit step height.

The profiles of absorption edges were obtained by averaging the results of a large number of spectra recorded in turn from each sample. The inflection point in the L_{III}-edge in Tl_2O_3 was taken as a reference point. Its energy was found to be 12665 eV.

4. Results and Discussions

The normalized L_{III} and L_I absorption spectra of model thallium compounds and superconducting oxides containing thallium are presented in Figs. 1–6. These normalized X-ray absorption spectra suggest that the XANES of L_I-edge have far fewer features as compared to those of L_{III} edge. The L_{II}-edge spectra of thallium were similar to L_{III}-edge spectra, therefore, the profiles of L_{II}-edge

* e-mail: a_arvind@hotmail.com
+Department of Physics, University of Allahabad, Allahabad 211002, India

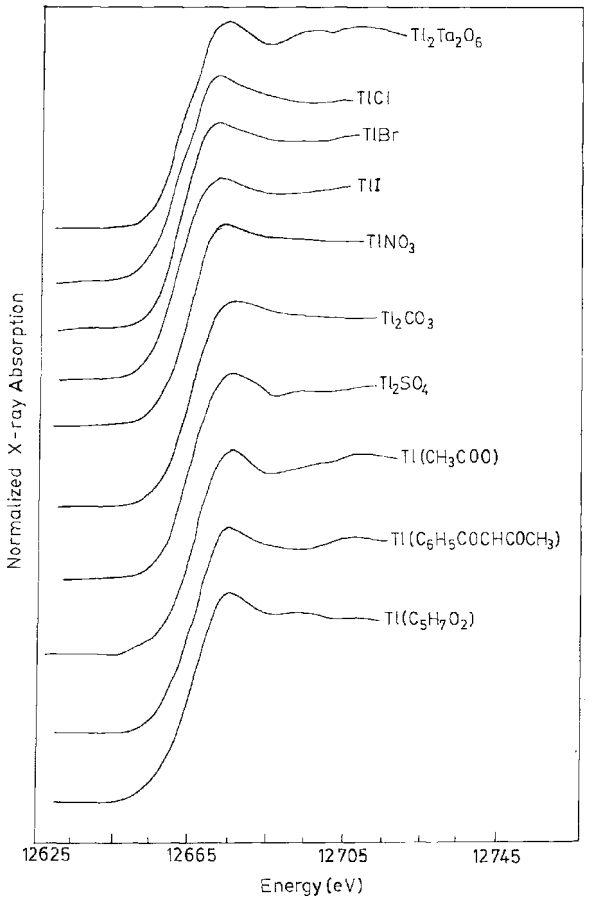

Fig. 1. Normalized Tl L_{III} absorption spectra of monovalent compounds.

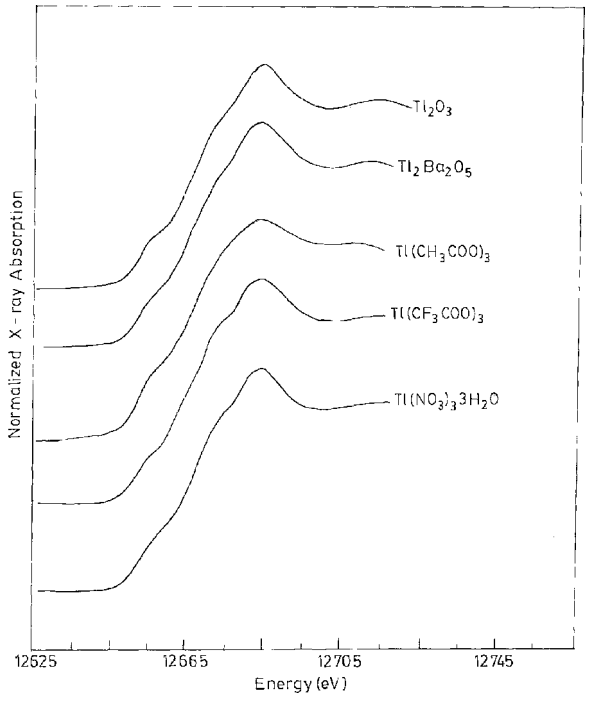

Fig. 2. Normalized Tl L_{III} absorption spectra of trivalent compounds.

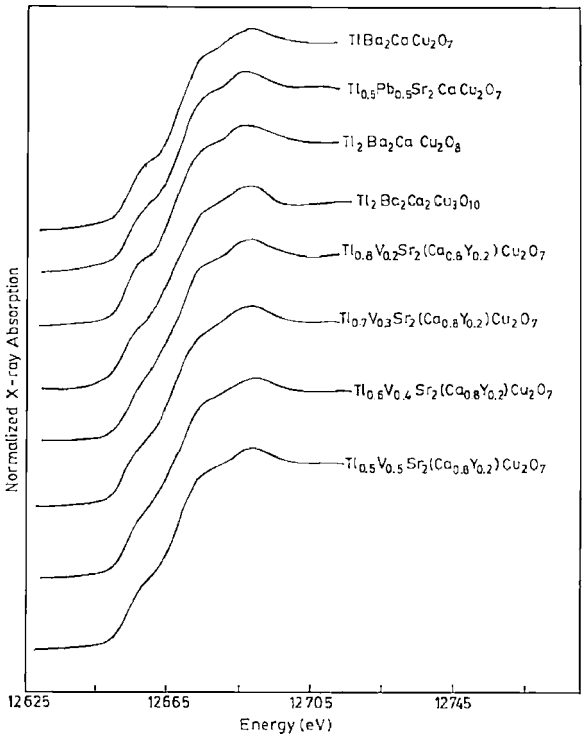

Fig. 3. Normalized Tl L_{III} absorption spectra of cuprates.

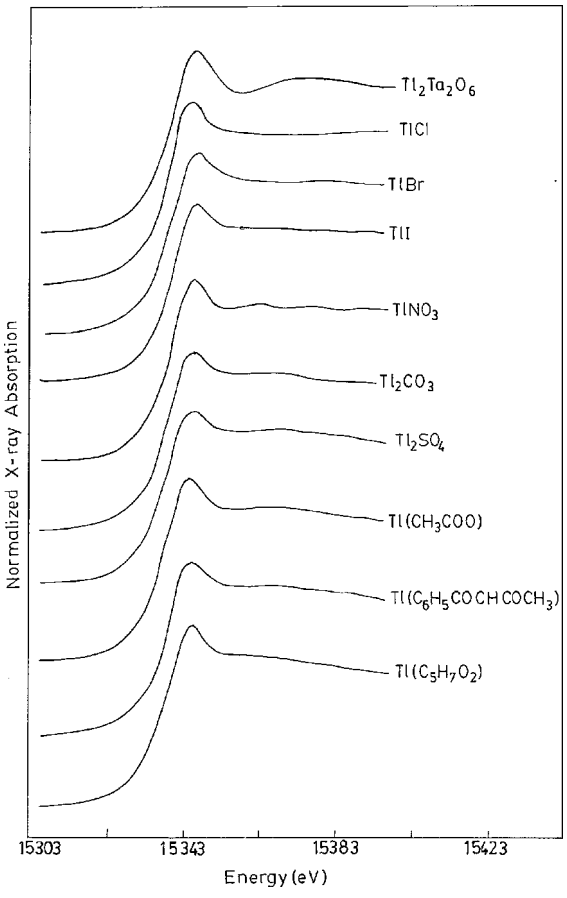

Fig. 4. Normalized Tl L_I absorption spectra of monovalent compounds.

are not presented. The L-absorption spectra of pure thallium metal could not be recorded as it is easily oxidized in air at normal temperature [2]. Figures 1–6 show that the L_{III} absorption discontinuity of thallium splits into three components whereas no splitting was observed in L_I-edge.

4.1. *Thallium L_{III}-edge Spectra*

Fig. 1 shows a single absorption peak for monovalent compounds whereas in the spectra in Fig. 2 for trivalent compounds a weak peak is followed by a shoulder on rising absorption which

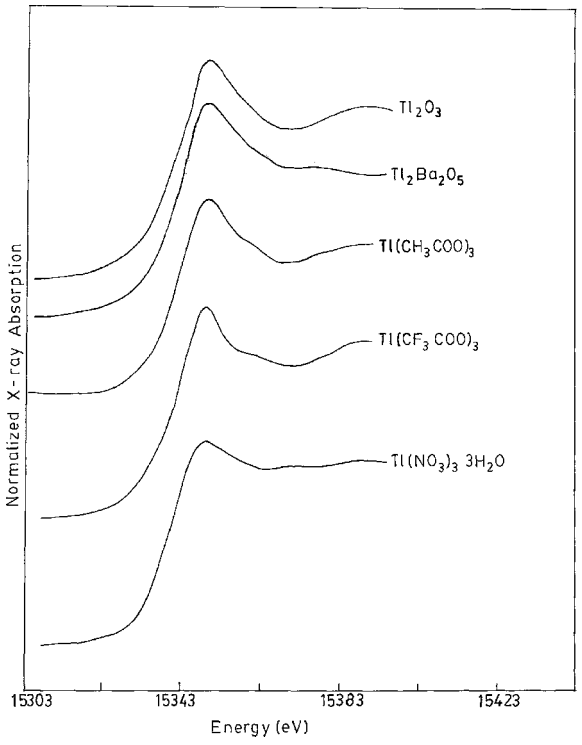

Fig. 5. Normalized Tl L_I absorption spectra of trivalent compounds.

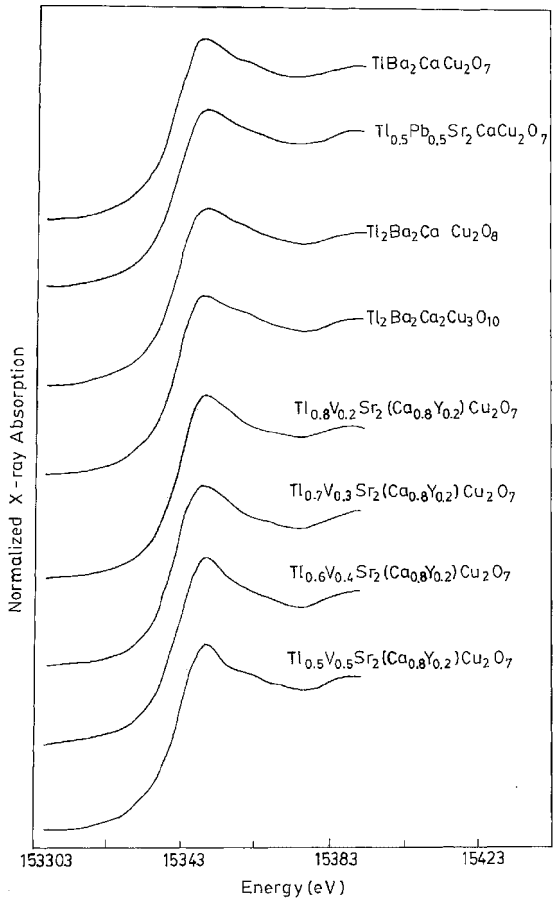

Fig. 6. Normalized Tl L_I absorption spectra of cuprates.

culminated into a strong absorption peak. The outer electronic configuration of monovalent thallium is: $6s^2\ 6p^0\ 6d^0$ hence the single absorption peak observed in the monovalent thallium compounds corresponds to the allowed transition of an $2p_{3/2}$ electron to 6p state which is admixed with 6d and 2s characters of metal and ligands respectively. In trivalent thallium compounds 6s, 6p and 6d states being completely vacant, a weak peak, the shoulder and the main absorption peak can be attributed to the transitions to hybridized states $2p_{3/2} \rightarrow 6s$, $2p_{3/2} \rightarrow 6p$, $2p_{3/2} \rightarrow 6d$ respectively. The transition $2p_{3/2} \rightarrow 6s$ becomes allowed by mixing of 6d character from metal and 2s character of ligating atom. In monovalent thallium compounds, no peak corresponding to the electronic transition, $2p_{3/2} \rightarrow 6s$ is observed. In fact, the transition probability for p to d transition is higher than that for p to s transition [16]. On the basis of these absorption spectra of thallium model compounds, the states concerning the valence states of thallium ions in well-characterized superconductors can be described. The overall profiles of these oxides shown in Fig. 3 are very similar to those of Tl_2O_3 and other trivalent thallium compounds. The L_{III}-edge peaks in these superconductors are slightly different from those observed for trivalent compounds as the octahedron of ligands around thallium ions is distorted. This distortion was studied by analyzing the EXAFS spectra of these compounds. The results obtained are in good agreement with those reported by Studer *et al.* [17–18] and Vijayakrishnan *et al.* [19]. Vijayakrshnan *et al.* [19] proposed the Tl^{1+} like state in cuprate superconducters suggesting the presence of a 6s state. The L_I-edge profiles have ruled out this possibility.

4.2. *Thallium L_I-edge Spectra*

The L_I-edge spectra for monovalent, trivalent and superconducting oxides were simple in all cases. Splitting of the edge was not observed. In the monovalent compounds the 6s orbital is occupied, but 6d is completely vacant. Therefore a main peak corresponding to $2s \rightarrow 6p$ transition was expected and since 6s is unavailable for transition to occur, no splitting of the L_I-edge was observed. In trivalent compounds, the 6s and 6p orbitals being vacant, a pre-edge peak corresponding to the forbidden transition $2s \rightarrow 6s$ was expected. However no such peak was observed. In these compounds, like monovalent compounds, only the main absorption peak corresponding to $2s \rightarrow 6p$ was observed.

The L_I-edge spectra of all the superconducting oxides were similar to Tl_2O_3 and other trivalent thallium compounds. The intensity of this peak is slightly less in superconducting oxides as compared to that in Tl_2O_3. Similar results were obtained by Studer *et al.* [17–18] in 1212, 2212, 1223 and 2223 superconducting oxides. Thus L_I XANES also leads to the conclusion that the thallium ions exist in +III state in superconducting oxides, i.e. the absence of electrons in the 6s levels.

5. Conclusions

1) The shoulder peak of trivalent compounds and the main absorption peak of monovalent compounds occur almost at the same energy positions in L_{III}-edge spectra. The only difference is the shift in the inflexion point energy of L_{III}-edges and a shift of the main absorption maximum.

2) The observations indicate the presence of octahedraly coordinated Tl^{3+} ions in the well-characterized superconducting oxides.

3) The X-ray absorption spectra of vanadium doped cuprates show similarity with the spectra of Tl_2O_3, thereby suggesting the presence of Tl^{3+} ions in octahedral configuration in these cuprates.

4) The only difference in the L_I-edge profiles of monovalent and trivalent thallium compounds is the shift of the inflexion point and the shift of the main absorption peak.

5) It was also observed in the L_I-edge profiles that the main absorption peaks were located at the same energy positions. The only difference was the intensity of the peak corresponding to 2s to 6p transition.

Acknowledgements

The authors warmly thank Professor Dr. P. R. Sarode (Goa University, India) for providing samples of superconducting cuprates and helpful discussions on the subject. The authors also warmly thank Dr. K. R. Priolkar (Goa University, India) for the help in recording the spectra and Mr. Joao Luiz Azevedo de Carvalho (University of Brasilia, Brazil) for preparing the figures in the print format.

References

1. Lee, A. G., "The Chemistry of Thallium", (Elseiver, Amsterdam 1971).
2. Wade, K. and Banisfer, A. J., "Comprehensive Inorganic Chemistry", (Edited by J. C. Bailer *et al.*) (Pergamon Press, New York 1933), vol. I, ch. XII, p. 993.
3. Meller, J. W., "A Comprehensive Treatise on Inorganic and Theoretical Chemistry", (Longman, London 1924), vol. V.
4. Scriver, D. F. and Wharf, I., Inorg. Chem. **8**, 2167 (1969).
5. Carty, A. J., Coord. Chem. Rev. **4**, 29 (1969).
6. Waddington, T. C., "Advances in Inorganic Chemistry and Radiochemistry", (Edited by H. J. Emeleus and A. G. Sharpe) (Academic Press, New York 1959), vol. I, p. 158.
7. Wells, A. F., "Structural Inorganic Chemistry", (Oxford University Press, London 1962).
8. Nagel, D. J. and Boun, W. L., "X-ray Spectroscopy", (Edited by L. V. Azaroff) (McGraw-Hill Book Co., New York 1974).
9. Srivastava, U. C. and Nigam, H. L., Coord. Chem. Rev. **9**, 275 (1973).
10. Sheng, Z. and Hermann, A. M., Nature **332**, 55 (1988).
11. Sheng, Z. and Hermann, A. M., Nature **332**, 138 (1988).
12. Politis, C. and Luo, H., Modern Phys. Lett. B **2**, 793 (1988).
13. Domenges, B., Hervieu, M. and Raveau, B., Solid State Commun. **68**, 303 (1988).
14. Parkin, S. S. P. *et al.*, Phys. Rev. Lett. **61**, 1103 (1988).
15. Liu, R. S. and Edwards, P. P., J. Solid State Chem. **91**, 407 (1991).
16. Teo, B. K. and Lee, P. A., J. Am. Chem. Soc. **101**, 2815 (1979).
17. Studer, F. *et al.*, Physica C **159**, 609 (1989).
18. Studer, F. *et al.*, Intl. J. Mod. Phys. B**3**, 1085 (1989).
19. Vijayakrishnan, V., Kulkarni, G. U. and Rao, C. N. R., Mod. Phys. Lett. B**4**, 45 (1990).

Physica Scripta. Vol. T115, 538–540, 2005

High-Pressure EXAFS and XRD Investigation of Unit Cell Parameters of SnO

H. Giefers[†*], F. Porsch[‡] and G. Wortmann[†]

[†]Department Physik, Universität Paderborn, D-33095 Paderborn, Germany
[‡]Mineralogisch-Petrologisches Institut, Universität Bonn, D-53115 Bonn, Germany

Received June 26, 2003; accepted November 4, 2003

PACS numbers: 61.10.Ht; 61.10.Nz; 62.50.+p; 61.66.Fn

Abstract

This study combining X-ray diffraction and X-ray absorption spectroscopy reveals the variation of the lattice parameters a and c and the atomic position parameter z(Sn) of tetragonal stannous oxide SnO under pressure up to 10 GPa. The observed strong elastic anisotropy of the SnO crystal can be attributed to its layered structure. The axial ratio c/a decreases from 1.27 to 1.16 whereas the position parameter z(Sn) increases from 0.237 to 0.269.

1. Introduction

Recently, stannous oxide (SnO) has received much attention due to its technological applications. Powders of SnO can be used as anode materials in lithium rechargeable batteries, as coating materials or as effective catalysts for several acid syntheses [1]. The oxidation and disproportionation process of SnO thin films enables the production of thin tin dioxide films, which are used as transparent electrodes in liquid crystal displays (LCDs) and solar-electrical energy conversion devices or as chemical sensors [2].

At ambient conditions tin oxide SnO has a tetragonal litharge-type structure with one free atomic positional parameter z for Sn. Above 1.5 GPa a transition to an orthorhombic phase has been reported [3, 4], but is also discussed controversially [5]. In order to get more insight into the high pressure behaviour of SnO we performed EXAFS and energy dispersive X-ray diffraction (EDXRD) experiments to receive the structural parameters a, c and z(Sn) and to prove the existence of the reported tetragonal to orthorhombic phase transition.

2. Experimental

The blue-black metallic shining sample material SnO obtained from Chempur (99.9%) was grounded for the EDXRD and EXAFS measurements. After grounding a pale-brown mat powder was obtained.

EDXRD measurements were carried out at beamline F3 of HASYLAB (DESY Hamburg) with white synchrotron radiation from a bending magnet with a critical energy of 16 keV. The diffracted beam is recorded by a nitrogen-cooled Ge-detector with an energy resolution of 360 eV at 20 keV. The diffraction angle Θ was chosen to 3.91° so that the fluorescence lines of Sn do not interfere with the important diffraction lines. The beam was collimated to $0.2 \times 0.2\,\mathrm{mm}^2$. A diamond anvil cell (DAC) with 1 mm flats was used for the EDXRD measurements with inconel as gasket material and liquid nitrogen as pressure transmitting medium. The sample diameter was 0.4 mm. The diffraction patterns were analysed with the computer programme EDXPowd [6]. The pressure was determined from the diffraction lines of gold [7], which was mixed into the sample.

EXAFS measurements at the Sn-K edge (29.2 keV) were performed at the HASYLAB beamline X1 using a Si(311) double crystal monochromator. The beam was collimated to $0.8 \times 0.8\,\mathrm{mm}^2$. A high pressure cell with boroncarbide (B_4C) as anvil material and copper as gasket material was used in this study [8]. The sample diameter was 1.3 mm. Polyethylene was used as pressure transmitting medium and silver powder as pressure marker, using the known pressure dependence of the Ag-Ag distance [9] derived from the EXAFS signal measured at the Ag-K edge (25.5 keV). EXAFS data reduction and analysis were performed using the software WinXAS 2.3 [10].

3. Results and Discussion

The litharge type structure of SnO consists of Sn-O-Sn layers with weak bindings between adjacent layers. Sn is square-pyramidal coordinated by oxygen with a Sn-O distance of 2.22 Å [11]. Our EDXRD analysis at ambient conditions reveals the lattice parameters $a = 3.800$ Å and $c = 4.836$ Å ($c/a = 1.272$) in good agreement with the values of c/a from 1.2687 to 1.2745 given in the literature [3, 11–14]. The position z of Sn above the O plane is given to $z = 0.2369$ [11]. An investigation concerning the pressure dependence of z(Sn) has not been published yet.

The high-pressure EDXRD study reveals the variation of the lattice parameters a and c. However, due to the strong preferred orientation of SnO in the high-pressure cell, the free atomic position parameter z(Sn) could not be determined from the diffraction intensities. The EDXRD study revealed no phase transition up to 11 GPa. At pressures above 5 GPa the diffraction lines (hkl) with $h \neq k$ became broadened (Fig. 1). The broadening is less than 2% at 11 GPa for the (200) reflection, where [4] reports a line splitting of more than 7% for that reflection in the orthorhombic phase at 9 GPa. Because [4] used LiF as pressure transmitting medium we performed control experiments with other pressure transmitting media, MgO, NaCl and mineral oil, known for their nonhydrostatic performance, which revealed also line broadening of 5% and more for the (200) reflection. Hence, we attribute this line broadenings to tensil stress conditions in the high pressure cell. It seems that SnO is very sensitive to tensil stress as has already been assumed by [5].

The pressure variation of the lattice parameters a and c of the tetragonal phase is shown in Fig. 2 as well as the decrease of the volume V. A fit of the Birch equation of state to the p-V

*e-mail: wo_hg@physik.upb.de

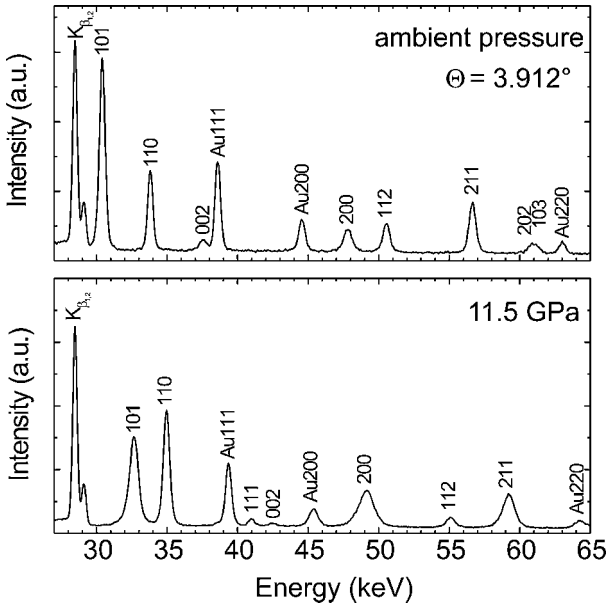

Fig. 1. EDXRD spectra of SnO at ambient pressure (top) and 11.5 GPa (bottom). Diffraction lines (*hkl*) with $h \neq k$ are broadened with pressure, the (200) reflex stronger than the (101) and (211) reflexes.

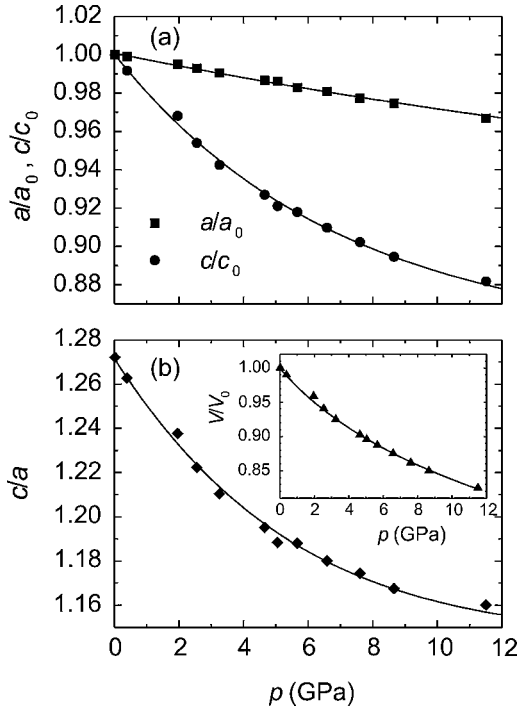

Fig. 2. (a) Normalized lattice parameters a and c. (b) Pressure dependence of c/a. The inset shows the normalized unit cell volume fitted with a Birch equation of state.

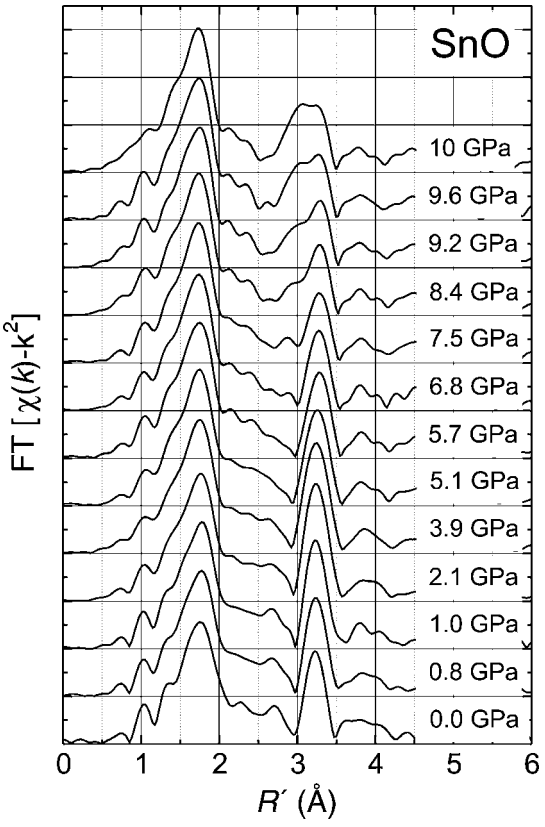

Fig. 3. Fourier transformation of the pressure dependent EXAFS signal. The Sn-O distance was obtained from a fit to the peak around $R' = 1.8$ Å.

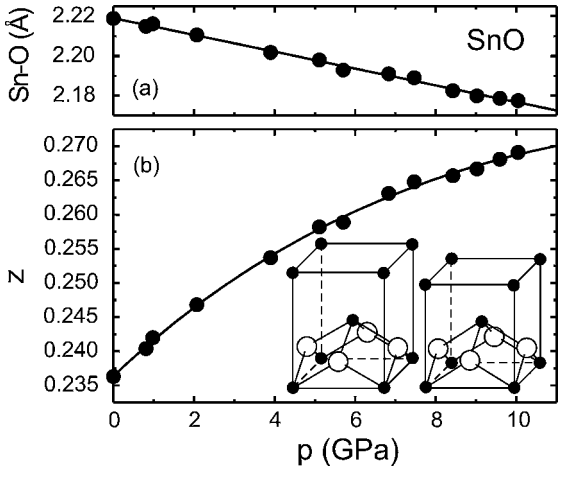

Fig. 4. (a) Pressure dependence of the Sn-O distance determind from EXAFS and (b) pressure dependence of the position parameter z(Sn) in SnO, determined from EXAFS and EDXRD studies. The inset shows the unit cell of tetragonal SnO at 0 GPa (left) and 10 GPa (right). Large spheres are O atoms; small spheres are Sn atoms.

data of SnO provides a bulk modulus $K_0 = 33.5(11)$ GPa and a first derivative of $K_0' = 6.1(5)$.

The variation of the z(Sn) parameter is determined from the X-ray absorption spectra providing the Sn-O distance and using in addition the lattice parameters from the EDXRD experiments, as done previously by [15]. Fig. 3 shows the Fourier transforms of the normalized X-ray absorption spectra at the Sn-K edge for SnO at different pressures up to 10 GPa. The analysis of the nearest neighbour distances (Sn-O) in the range form $R' = 0.85$ to 2.5 Å yield the distance R and the 2nd cumulant σ^2. The nearest neighbour distance decreases from 2.219 Å at ambient pressure to 2.178 Å at 10 GPa and the 2nd cumulant decreases from $5.3 \cdot 10^{-3}$ Å^2 to $4.3 \cdot 10^{-3}$ Å^2. The apparent change in the second neighbours peak around $R' = 3.2$ Å in Fig. 3 at pressures above 8 GPa is due to the approach of the adjacent Sn layers and has not been evaluated here because it involves three different Sn shells.

From the pressure dependence of the Sn-O distance and the lattice parameters a and c one can calculate the position parameter z(Sn). As seen from the EXAFS experiment the compressibility of the Sn-O bonding is quite small which means that this bonding is rather strong. From purely geometrical considerations one can

see that the strong compression of the c-axis together with a negligible variation of the Sn-O distance causes an increase of z with increasing pressure. When the Sn-O-Sn layers come closer with pressure the repulsion increases and the increase of z(Sn) flattens under increasing pressure (Fig. 4).

References

1. Han, Z. *et al.*, Mater. Lett. **48**, 99 (2001) and ref. therein.
2. Choi, W. K. *et al.*, J. Mater. Sci. Lett. **16**, 1551 (1997) and ref. therein.
3. Adams, D. M., Christy, A. G., Haines, J. and Clark, S. M., Phys. Rev. **B46**, 11358 (1992).
4. Serebryanaya, N. R., Kabalkina, S. S. and Vereshchagin, L. F., Dokl. Akad. Nauk SSSR **14**, 307 (1969).
5. Kapitanov, E. V. and Yakovlev, E. N., Phys. Stat. Sol. **A51**, 641 (1979).
6. Porsch, F., EDXPowd 3.13, Windows Version, RTI GmbH Paderborn, Germany (1996).
7. Anderson, O. L., Isaak, D. G. and Yamamoto, S., J. Appl. Phys. **65**, 1534 (1989).
8. Strecker, M., PhD thesis, Universität Paderborn (2000).
9. Carter, W. J. *et al.*, NBS Special publ. **326**, 147 (1971).
10. Ressler, T., J. Synch. Rad. **5**, 118 (1998).
11. Izumi, F., J. Solid State Chem. **38**, 381 (1981).
12. Moore, W. J. and Pauling, L., J. Am. Chem. Soc. **63**, 1392 (1941).
13. Swanson, H. E. *et al.*, NBS Circular **539** Vol. IV, 28 (1953).
14. Pannetier, J. and Dennes, G., Acta. Cryst. **B36**, 2763 (1980).
15. San-Miguel, A., Itié, J. P. and Polian, A., Physica **B208&209**, 506 (1995).

Physica Scripta. Vol. T115, 541–544, 2005

Mn on the Surface of ZnO(0001) – a Resonant Photoemisson Study

E. Guziewicz[1,2,*], K. Kopalko[2], J. Sadowski[3,4,2], M. Guziewicz[5], Z. Golacki[2], J. Kanski[6] and L. Ilver[6]

[1]Los Alamos National Laboratory, Los Alamos, NM 87544, USA
[2]Institute of Physics, Posish Academy of Sciences, Warszawa, Poland
[3]Niels Bohr Institute fAFG, Ørsted Laoratory, University of Copenhagen, Denmark
[4]MAX-lab, Lund University, Lund, Sweden
[5]Institute of Electron Technology, Warszawa, Poland
[6]Chalmers University of Technology and Göteborg University, Göteborg, Sweden

Received June 26, 2003; accepted June 23, 2004

PACS number: 73.20.−r

Abstract

The electronic structure of Mn/ZnO system has been invesigated by synchrotron radiation photoemission. Manganese vacuum deposition was done at room temperature onto a ZnO(0001) single crystal for coverage $\Theta_{Mn} \leq 4$ ML. Photoemission spectra taken near the Mn3p–Mn3d absorption edge after each deposition step show resonant enhancement of Mn3d states within 10 eV of the Fermi edge. The experimentally deduced partial Mn3d density of states for $\Theta \geq 1.2$ ML shows at least three features: a major Mn3d structure at 3.8–4.5 eV below the Fermi edge, a valence structure at lower binding energy (1–3 eV) and a broad satelite in the 5.5–9 eV range. The branching ratio of satellite/main structure increases with depostion from 0.33 for 0.4 ML to 0.65 for 4 ML. After annealing up to 500 °C the satellite/main ratio decreases to 0.43 indicating a high degree of hybridization between the Mn3d states and valence band of ZnO. After annealing no manganese cap layer was found at the crystal surfaces as was confirmed by the lack of metallic Fermi edge in photoemission spectra and by scanning Auger spectroscopy experiment. The photoemission Mn3p core level spectra taken after annealing consist of two components separated by about 4 eV, which shows that at least two manganese states are observed in the Mn–ZnO interface region.

1. Introduction

The wide bandgap semiconductor ZnO doped with one of the 3d Transition Metals (TM) is a promising material for short wavelength magneto-optical applications [1], especially for transparent magnets. Manganese and cobalt are the most interesting TM admixtures for ZnO because their solubility in the ZnO matrix is significantly higher than other TMs. In addition, theoretical calculations point out that a ferromagnetic state of ZnMnO is expected even at room temperature [2].

Manganese ions are usually incorporated *in situ* during ZnO flux growth [3], combinatorial lase molecular-beam epitaxy method [4] or pulsed-laser deposition [5]. In the experiment presented here we used the method of Mn diffusion into the ZnO matrix after heating up to 500 °C of Mn/ZnO interface with 4 ML of manganese deposited onto the ZnO(0001) surface. We investigated the experimental Mn3d partial density of states in order to determine interactions between this magnetic electron shell and valence band of the ZnO single crystal.

2. Experimental conditions

The single ZnO wurzite crystal was grown in the Insitute of Physics, Polish Academy of Sciences by chemical vapor transport using chlorine as transporting agent. The orientation of the crystal was determined by X-ray diffraction. A clean (0001) surface of ZnO monocrystal was prepared in an ultra-high vacuum system ($p \approx 4 \cdot 10^{-10}$ Torr) using argon ion bombardment ($U = 600$ V, $t = 40$ min) and annealing to 300 °C. The experiment was performed at BL41 beamline at the MAX I storage ring in Lund, Sweden. Angle-resolved photoemission spectra were recorded with the overall energy resolution of 200 meV at photon energy of 50 eV. Mn was deposited in the III-Mn-V MBE system vacuum connected to the photoemission chamber. During Mn deposition all the sources other then Mn were cooled down to low temperatures. The Mn coverage of the ZnO surface was estimated from precise calibrations of Mn flux used for III-Mn-V MBE growth [6]. We sequentially deposited small amounts (from 0.2 to 4 ML) of manganese on a clean ZnO(0001) surface under ultra-high vacuum and, via photoemission spectra, we follow changes in the valence band of Mn/ZnO system and in the experimental Mn3d partial density of states. After deposition of 4 ML of manganese the Mn/ZnO system was heated up to 500 °C in order to promote diffusion of manganese atoms.

The photoemission spectra were taken at room temperature, normalized to the photon flux and the secondary electron background has been subtracted. The binding energy scale is referred to the Fermi level of a thick manganese film.

3. Results and discussion

Energy Distribution Curves (EDC's) were taken after each step of deposition at various photon energies between 30 and 110 eV. We have investigated the Mn contribution in the valence band region by resonant-photoemission spectroscopy at the Mn3p-Mn3d absorption threshold. At resonance the Mn3p electron is excited into the empty part of the Mn3d states. This excited state decays via autoionization in which the Mn3d electron drops down to fill the Mn3p hole and its energy is transferred to another Mn3d electron that is ejected into the continuum:

$$\mathrm{Mn3p^6 3d^5} + h\nu \rightarrow \mathrm{Mn3p^5 3d^6} \rightarrow \mathrm{Mn3p^6 3d^4} + \mathrm{e}.$$

The final state of the process is the same like in direct photoemission from the Mn3d shell:

$$\mathrm{Mn3p^6 3d^5} + h\nu \rightarrow \mathrm{Mn3p^6 3d^4} + \mathrm{e}.$$

The interference between the two channels of photoemission leads to the increase in the photoemission intensity as the photon energy is swept through the 3p-3d threshold. The asymmetric Fano line shape characterizes the intensity variations.

In Fig. 1 we show the set of normal photoemission spectra of Mn/ZnO interface measured at the maximum of Mn3p-3d resonance ($h\nu = 51$ eV). All the spectra in Fig. 1 were

*email: ela@lanl.gov

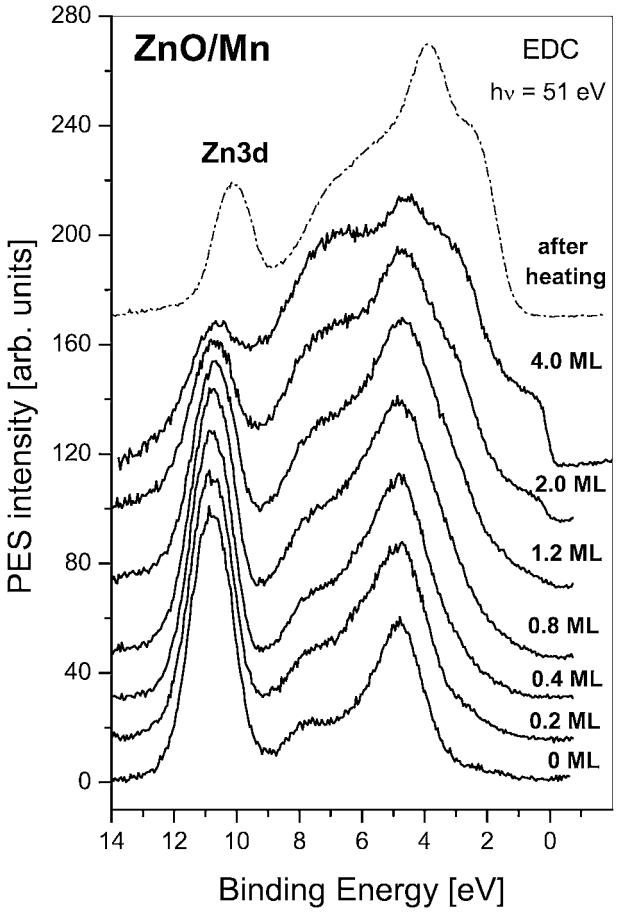

Fig. 1. EDC's for Mn/ZnO(100) system measured after each step of deposition for $h\nu = 51$ eV (maximum of Mn3p-3d resonance). The spectra intensities were normalized to 100 in their maximum.

normalized to constant height to emphasize line-shape changes. The bottom spectrum shows clean ZnO(0001) valence band and Zn3d emission taken before Mn deposition. The spectrum was shifted by 0.12 eV towards higher binding energies in order to compensate the binding energy shift due to a Shottky barrier formation. Contribution from the ZnO substrate is visible at around 4.8 eV up to the 4 Mn ML depositions. For $\Theta = 4$ ML the position of this highest valence band peak is shifted about 0.3 eV towards lower binding energy which results from contribution of the manganese emission in this binding energy region. The manganese contribution is also observed between 6.5 and 8 eV starting from coverage of 1.2 ML. For $\Theta = 2$ ML a metallic shoulder at the Fermi edge is created. This means that part of manganese atoms do not diffuse into the interface region and remains at the crystal surface. For $\Theta = 4$ ML the metallic shoulder is three times higher than for $\Theta = 2$ ML. The structure between 6.5–8 eV is more pronounced and we can see a new shoulder created at around 3.2 eV.

The upper curve in Fig. 1 (dashed line) was taken after 18 hours of annealing in 500 °C in the MBE chamber. After annealing the metallic shoulder at the Fermi edge has disappeared and the rest of photoemission spectra is shifted towards lower binding energies. The Zn3d core level after annealing is located at 10.1 eV, which is 0.6 eV lower than for clean ZnO single crystal. The main structure of the valence band is now situated at 3.8 eV below the Fermi level and the spectra in 9 eV of the Fermi edge is very similar to the Mn3d contribution in another II-VI based ternary compounds reported in the papers published before [7–10]. The Zn3d core level photoemission peak is sharp and its full width at half maximum (FWHM) is exactly the same as in single ZnO and equals 1.6 eV. The sharpness of the peak indicates that manganese does not lead to the disorder in the ZnO cation sublattice.

The scanning Auger microprobe measurements were taken for Mn/ZnO system after annealing. Auger spectra from the surface were measured during ion etching of a small spot of the crystal. There was no Mn capping layer and Zn was abundant at the surface. The Mn/Zn ratio measured on the surface was 0.43. During etching the oxygen concnetration was constant and Zn gradually replaced Mn. The transition region width had an extension of about 20 Å with gradually lower Mn concentration.

The experimental Mn3d partial density of states is presented in Fig. 2. The method exploits an asymmetrical lineshape of the photoemission intensity near the resonant Mn3p-Mn3d threshold. Below the maximum of the resonance ($h\nu = 51$ eV in the experiment) one can observe a minimum where the photoemission from Mn3d shell can be neglected ($h\nu = 47$ eV). The contribution of the Mn3d states to the valence band can be obtained from

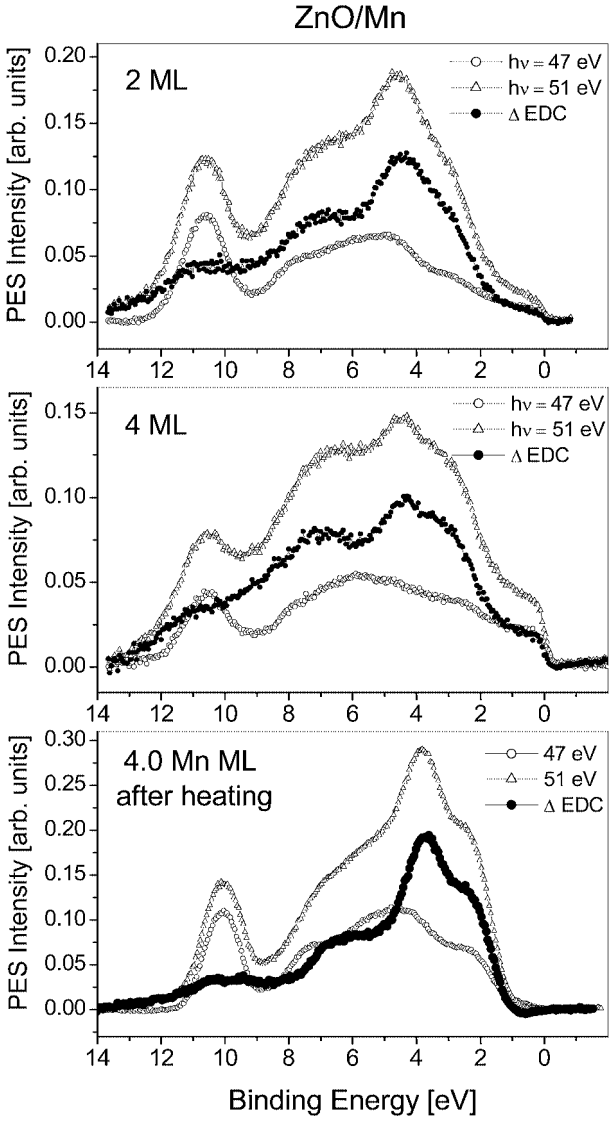

Fig. 2. The set of difference ΔEDC spectra (resonance-antiresonance) obtained for $\Theta = 2$ and 4 ML, and after annealing of Mn/ZnO system. Open triangles show resonant spectra ($h\nu = 51$ eV), open circles antiresonant spectra ($h\nu = 47$ eV) and solid circles calculated ΔEDC spectra.

difference between EDC spectra taken on and off resonance. The results of the procedure for $\Theta = 2$ and 4 ML, and after annealing are presented in Fig. 2.

The ΔEDC = EDC(51 eV)-EDC(47 eV) spectra consists of three structures typically found in II-VI ternary compounds with manganese [7–10]. The main structure is situated at 3.8–4.5 eV, valence structure at 0–3 eV and a broad satellite between 5.5 and 9 eV below the Fermi edge. For $\Theta = 2$ and 4 ML the low energy shoulder of the main peak contains two contributions: a metallic shoulder located at the Fermi edge and structure around 3 eV below.

Electronic structure calculations are available for $Cd_{1-x}Mn_xTe$ [11, 12] ternary compound. They are also used to interpret the Mn-derived structures of other Mn-substituted II-VI compounds. The main peak in the overall structure of the Mn3d partial density of states represents part of the Mn3d electrons only weakly influenced by hybridization. The valence structure presumably originates from the Mn3d states hybridized with the valence band. The satellite structure is not related to the partial density of Mn3d states, but represents a shake-up-like satellite of the main Mn3d peak, which is not described in the one-electron picture.

The binding energy of the main Mn3d structure of Mn/ZnO system is 4.4 eV and 4.38 eV for $\Theta = 2$ and 4 ML, respectively, and 3.8 eV below the Fermi edge after annealing. The intensity of satellite/main peak ratio changes from 0.33 for $\Theta = 0.4$ ML to 0.89 for $\Theta = 4$ ML and drops to 0.43 after annealing. The relative satellite/main intensity of the Mn3d peak in ZnMnY (Y = S, Se, Te) compounds was regarded in dependence of V_{pd} hybridization parameter [7]. The 0.43 value obtained for ZnMnO alloy follow the trend toward higher hybridization as we move up in the Periodic Table, which was found in ZnY compounds (Table I).

According to the results obtained for ZnMnY (Y = S, Se, Te) ternary compounds V_{pd}, a parameter describing the amount of the Mn3d-anion p hybridization, increases with decrease of satellite/main branching ratio. Therefore for Mn/ZnO system we may expect hybridization effect comparable to ZnMnS compound and higher than in the case of ZnMnSe or ZnMnTe. It is also higher than the hybridization effect in the widely investigated $Ga_{1-x}Mn_xAs$ compounds [13].

It is worth to mention that the experimental Mn3d partial density of states presented here follows very well the trend found the chalogenide-based semiconductors [7]. The similarity is much better than in the case of $Zn_{1-x}Mn_xO$ thin films obtained by pulsed-laser deposition [14].

Table I. *The energy of the main Mn3d peak and branching ratio of the satellite to the main structure in Zn-VI ternary alloys with Mn. The data of ZnY (Y = Te, Se, S) are taken from ref. [7].*

	E_{main}	satellite/ main ratio
$Zn_{0.68}Mn_{0.32}Te$	3.8 eV*	1.05
$Zn_{0.81}Mn_{0.19}Se$	3.7 eV*	0.90
$Zn_{0.81}Mn_{0.19}S$	3.5 eV*	0.4
Mn/ZnO after annealing	3.0 eV*	0.43

*The binding energy is given in respect to the valence band edge.

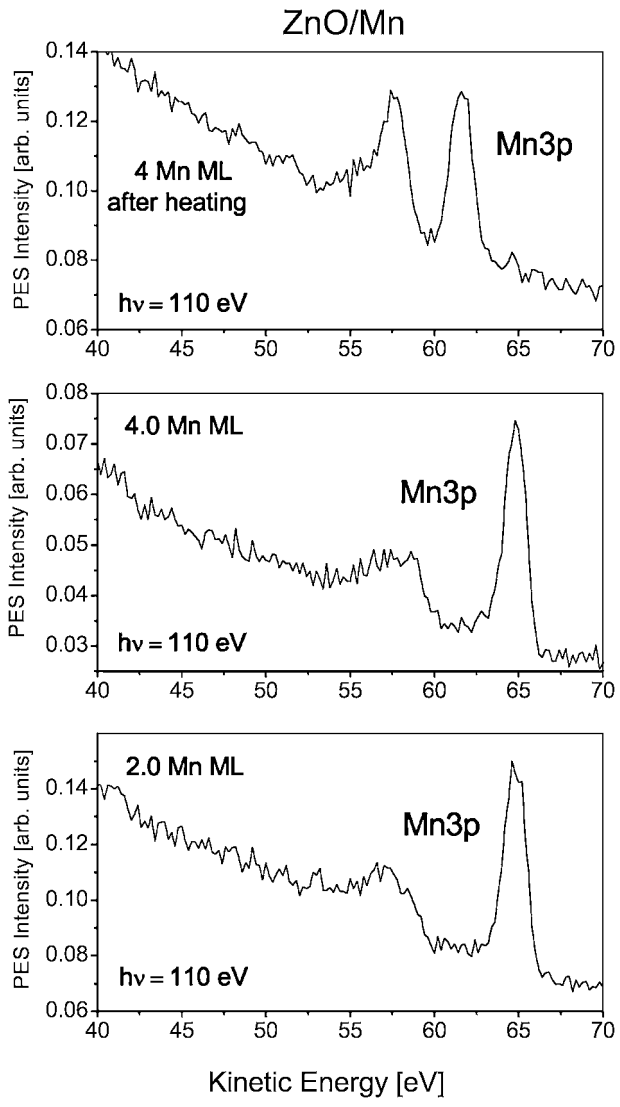

Fig. 3. Mn3p core EDC's measured with photon energy of 110 eV. Spectra show two Mn3p components chemically shifted by about 4 eV.

In Fig. 3 we show the photoemission spectra of Mn3p core level measured at $h\nu = 110$ eV after deposition of 2 and 4 Mn ML, and after annealing. EDC's show two Mn3p features observed at kinetic energies 57.5 eV and 64.9 eV before annealing and 57.7 eV and 61.7 eV after this process. The intensity of the structure observed at lower kinetic energy increases after annealing and presumably it consists of two photoemission peaks. This is the evidence that we have at least two manganese states in the Mn-ZnO interface retion.

4. Conclusions

In conclusion, we have measured Mn/ZnO(0001) system by synchrotron radiation photoemission. After deposition of 4 ML of manganese on clean ZnO(0001) surface and annealing up to 500 °C the metallic shoulder at the Fermi edge disappeared and no Mn capping layer has been found at the surface. The intensity of satellite/main peak in the experimental Mn3d partial density of states was determined as 0.43. This is evidence that the hybridization effect in $Zn_{1-x}Mn_xO$ surface alloy is comparable to $Zn_{1-x}Mn_xS$ and much higher than in $Zn_{1-x}Mn_xSe$, $Zn_{1-x}Mn_xTe$ and $Ga_{1-x}Mn_xAs$ semimagnetic compounds.

Acknowledgements

Measurements at MAX-Lab Swedish national synchrotron radiation facility have been supported by the European Community within the "Access to Research Infrastructure action of the Improving Potential Programme". The work was also supported by KBN (Poland) project 7 T08A 006 20.

References

1. Fukumura, T., Jin, Z., Ohtomo, A., Koinuma, H. and Kawasaki, M., Appl. Phys. Lett. **75**, 3366 (1999).
2. Dietl, T., Ohno, H., Matsukura, F., Cibert, J. and Ferrant, D., Science **287**, 1019 (2000).
3. Ohashi, N. *et al.*, Jpn. J. Appl. Phys. **38**, 5028 (1999).
4. Jin, Z. *et al*., Appl. Phys. Lett. **78**, 3824 (2001).
5. Fukumura, T., Jin, Z., Ohtomo, A., Koinuma, H. and Kawasaki, M., Appl. Phys. Lett. **75**, 3366 (1999).
6. Sadowski, J. *et al*., J. Vac. Sci. Technol. B **18**, 1697 (2000).
7. Weidemann, R., Gumlich, H.-E., Kupsch, M., Middelmann, H.-U. and Becker, U., Phys. Rev. B **45**, 1172 (1992).
8. Taniguchi, M. *et al*., Phys. Rev. B **51**, 6932 (1995).
9. Wall, A., Raisanen, A., Haugstad, G., Vanzetti, L. and Franciosi, A., Phys. Rev. B **44**, 8185 (1991).
10. Happo, N. *et al*., Phys. Rev. B **50**, 12 211 (1994).
11. Wei, S.-H. and Zunger, A., Phys. Rev. B **35**, 2340 (1987).
12. Gunnarsson, O., Andersen, O. K., Jepsen, O. and Zaanen, J., Phys. Rev. B **39**, 1708 (1989).
13. Okabayashi, J. *et al*., Phys. Rev. B **59**, R2486 (1999).
14. Mizokawa, T., Nambu, T., Fujimori, A., Fukumura, T. and Kawasaki, M., Phys. Rev. B **65**, 85209 (2002).

Physica Scripta. Vol. T115, 545–547, 2005

X-ray Excited Optical Luminescence Studies of PPh_3AuCl: Site-Specificity at the C and P K-Edges and the Au $M_{5,4}$-Edges

P.-S. G. Kim[1], Y. F. Hu[2], R. J. Puddephatt[1] and T. K. Sham[1*]

[1]Department of Chemistry, University of Western Ontario London, Ontario, N6A 5B7 Canada
[2]Canadian Synchrotron Radiation Facility, Synchrotron Radiation Center, University of Wisconsin-Madison, Stoughton, Wisconsin, 53589 U.S.A.

Received June 26, 2003; accepted November 4, 2003

PACS numbers: 78.55.−m, 61.10.Ht

Abstract

The luminescence of a prototype gold(I) compound, PPh_3AuCl, which is a building block compound for many light emitting organo-gold complexes and polymers, has been studied by the X-ray excited optical luminescence (XEOL) technique in conjunction with the X-ray Absorption Fine Structures (XAFS) at the C and P K-edge as well as the Au $M_{5,4}$-edges. We present the site and excitation channel specificity of XEOL and its chemical implications.

1. Introduction

Since Dori *et al*. [1] reported the luminescence of the gold(I) complex, $[(PPh_3)_3AuCl]$, a variety of mono- and multinuclear gold(I) complexes as well as gold(I) polymers and oligomers has been synthesized. These materials often show interesting photophysical and photochemical properties [2–5]. For example, a number of symmetrical binuclear gold(I) complexes with various diphosphine or diacetylides ligands exhibit strong luminescence in both solution and solid state [2–4]. The luminescence is generally assigned as phosphorescence from the metal-centered or metal-to-ligand charge transfer excited states. Along with small molecules (eg. Alq_3, $q = 8$ hydroxyquinoline, and $Ru(bipy)_3^{2+}$, bipy = bipyridene) [6, 7] and organic polymer light emitters (eg. poly-phenylene vinylene and derivatives) [8], gold containing complexes have potential applications in organic light emitting diodes (OLED). OLED are based on layers of thin organic films that are the hole-injection/transport, emissive and the electron injection/transport layers sandwiched by two electrodes. Upon applying an appropriate voltage to the cell, the injected positive (holes) and negative (electrons) charges recombine in the emissive layer to produce light (electroluminescence).

The present study aims to investigate the optical properties of the representative mononuclear gold(I) complex, PPh_3AuCl, (Au is linearly bonded to P and Cl through σ and π interactions) using the X-ray Excited Optical Luminescence (XEOL) technique, which has shown promising applications in the characterization of thin films, organometallic compounds, as well as polymers [6–8]. Larson, *et al*. reported the optical and optically detected magnetic resonance (ODMR) studies of the excited states of PPh_3AuCl and found weak high energy (3.9 eV and 3.4 eV) emissions, which were attributed to the phenyl-localized $\pi\pi^*$ state [9] as well as low energy emissions at ∼2.3–2.7 eV (charge transfer phosphorescence). XEOL with synchrotron light as an excitation source is an X-ray in, optical photons out technique [6–8]. An excitation of a core electron with tunable X-rays to the LUMO and beyond is the primary photoabsorption process, which is followed by the decay of the core hole. These processes lead to the production of photoelectrons, Auger electrons, fluorescence photons, and the associated secondary processes, which result in the formation of thermalized holes and electrons, respectively, in the valence band/HOMO and the conduction band/LUMO. The radiative recombination of holes and electrons produces luminescence. The de-excitation of an exciton, an excimer or exciplex can also lead to luminescence. The XEOL technique involving core level excitation can be site- and excitation-channel specific when the excitation energy is tuned across the absorption edge of the element of which the local electronic structure is effectively coupled to the luminescence channel [6–8].

2. Experimental

The compound was prepared by standard methods from reagent-grade materials [10]. The specimens were prepared as a fine powder film on an indium foil. The Near Edge X-ray Absorption Fine Structures (NEXAFS) at the C and P K-edges and Au $M_{5,4}$-edges were recorded at the Spherical Grating Monochromator (SGM) beamline (bending magnet) and the Double Cystal Monochromator (DCM) beamline, respectively, of the Canadian Synchrotron Radiation Facility (CSRF) at the Synchrotron Radiation Center, University of Wisconsin-Madison. The NEXAFS were monitored simultaneously by total electron yield (TEY), fluorescence yield (FLY) and photoluminescence yield (PLY) collecting all the optical photons (zero order) as well as partial yields at a selected emission channel. At the SGM, the monochromatic soft X-ray beam has an energy resolution of ∼0.3 eV at the carbon K-edge of ∼286 eV with a slit size of 100 μm × 100 μm. The energy resolution at the DCM is ∼0.8 eV with InSb (111) crystals in these experiments. It should be noted that the TEY spectrum resembles that of the absorption while the PLY is sensitive to the chemical environment of the absorbing atom and the excitation channel that may or may not couple to the luminescence chromophore effectively, leading to site and excitation channel specificity [6–8]. The optical photons were collected with a J-YH100 monochromator. All spectra were normalized with the intensity of the incident beam.

3. Results and Discussion

Fig. 1 (a) shows the normalized XEOL of the gold(I) compounds obtained with various excitation energies across the C, P K-edge and Au $M_{5,4}$-edge. It should be noted that the emission profiles remained the same regardless of the excitation energy across the edges although the intensity was noticeably different depending on the excitation energy. The XEOL exhibits well-defined structures with luminescence peaks at 455 nm (2.72 eV), 486 nm (2.55 eV), and 533 nm (2.33 eV). This is in good agreement with the emission spectra at room temperature for the phosphine

*e-mail: sham@uwo.ca

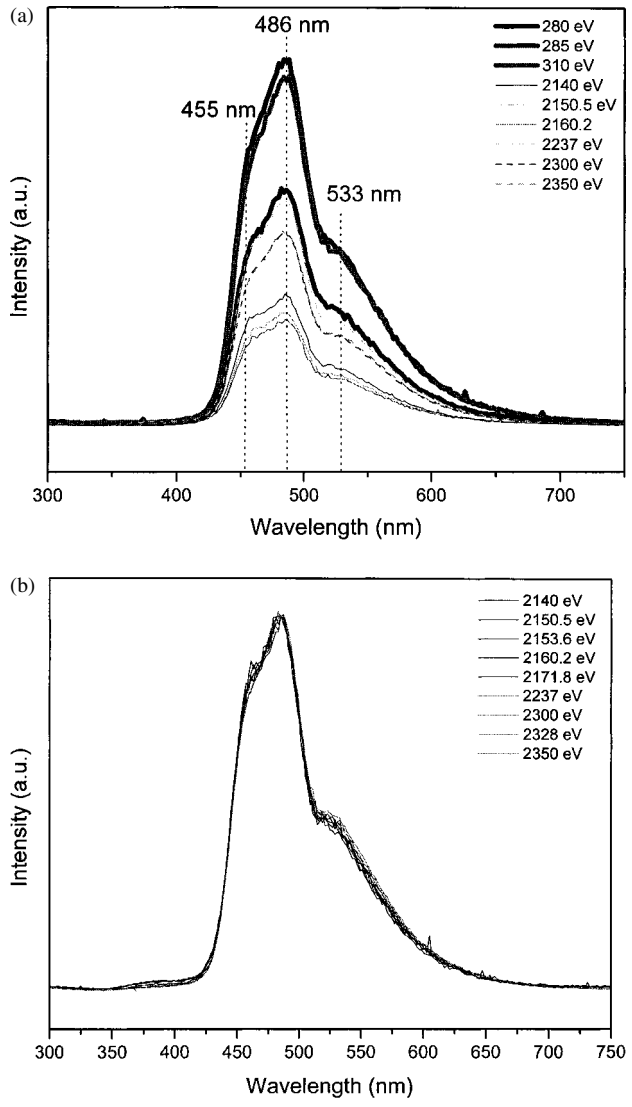

Fig. 1. (a) XEOL at the excitation energies across the C, P K-edge and Au $M_{5,4}$-edge; (b) XEOL spectra have been normalized at 486 nm.

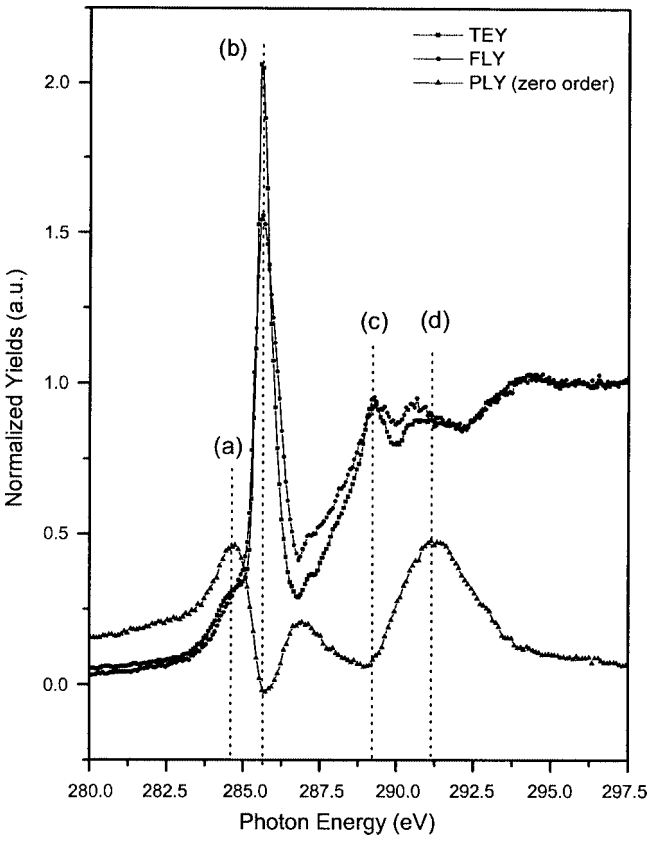

Fig. 2. The normalized yields of PPh_3AuCl at the C K-edge in TEY, FY, PLY (zero order) modes.

complexes, following pulsed laser excitation at 337 nm reported by Larson *et al*. [9]. One would expect higher intensity from the higher excitation energies, however, the luminescence intensities were higher across the C K-edge than the P K-edge and the Au $M_{5,4}$-edge. However, as noted in the experimental section, two different beamlines have been utilized, a comparison cannot be quantified without the absolute flux. Qualitatively, however, this may be due to a higher absorption cross-section at the C K-edge. A closer examination of the XEOL spectra at the P K-edge and Au $M_{5,4}$-edge reveals that the relative intensities of the three peaks are slightly different between the edges as shown in Fig. 1(b). Upon normalizing of all the spectra at the strongest peak at 486 nm, it becomes apparent that the intensity of the peak at the higher wavelength (533 nm) increases at the expense of the peak at the lower wavelength (455 nm), as the excitation energies decrease from the Au $M_{5,4}$-edge to the P K-edge. An emission at the shorter wavelengths (385 nm ∼ 3.22 eV) becomes noticeable. This situation can be understood in terms of the increase in the population of the more energetic states.

Fig. 2 shows the C K-edge NEXAFS of PPh_3AuCl in TEY and FLY as well as zero order PLY. NEXAFS measures the photoabsorption cross-section for the excitation of tightly bound core electrons to LUMO and LUMO +1 orbital, etc. and is recorded by scanning the incident X-ray photon energy across an absorption edge. It provides informations about the local structure and bonding of the absorbing atom [11]. For unsaturated organic molecules such as aromatics, the C K-edge typically exhibits two types of main transitions. The intense and narrow feature at low energy (∼285–286 eV) represents a C 1s → π^* (bound state) transition, whilst the broad transition at higher energy (∼290–292 eV) represents a C 1s → σ^* (quasi bound state involving carbon-carbon interaction) transition. There are also weak resonances in between associated with C 1s → σ^* transition of the C-H bond. It is apparent that there are two peaks in π^* transition regions, an intense and sharp peak at ∼286 eV (peak (b)) and a weak broad shoulder (peak (a)) at slightly lower energy region. These absorption peaks can be attributed to C 1s to π^* transitions of nonequivalent carbons on the phenyl rings. It should be noted that the specimen was a reasonably thin and uniform film as indicated by the exact profiles of TEY (surface sensitive) and FLY (bulk sensitive).

The phosphorus K-edge absorption spectrum collected in the TEY mode is shown in Fig. 3, together with the photoluminescence yields. Two sharp peaks are apparent, which represent the two main transitions as in the case of the C K-edge, a P 1s → π^* transition at the lower energy region and a 1s → σ^* transition at a slightly higher energy. Similar to the C K-edge, the TEY and FLY are identical, indicating a thin and uniform film. The TEY at the Au $M_{5,4}$-edge is displayed in Fig. 4, which only shows a weak edge jump. This is not unexpected since the Au $M_{5,4}$-edge jump (d – p transition) has a low cross-section and a large lifetime broadening.

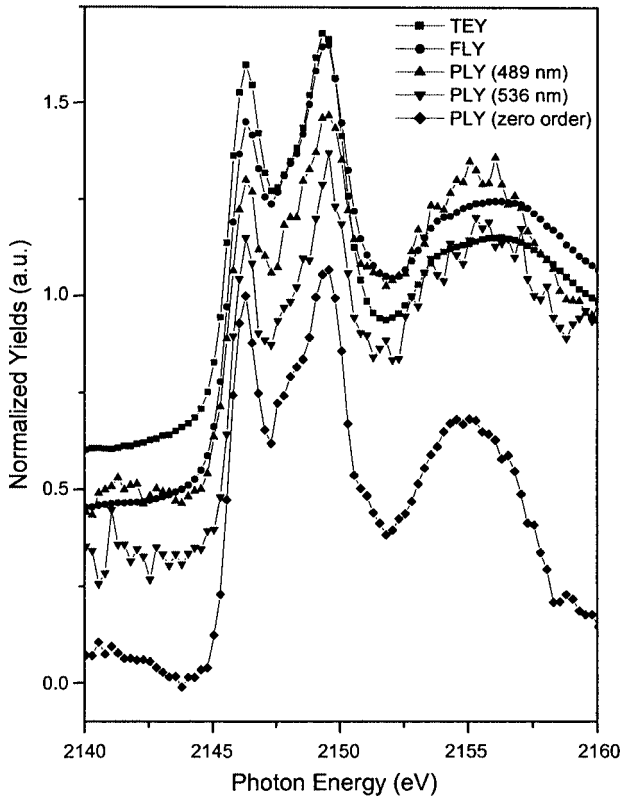

Fig. 3. The normalized yields of PPh_3AuCl at the P K-edge in TEY, FY, PLY (zero order and partial yields) modes.

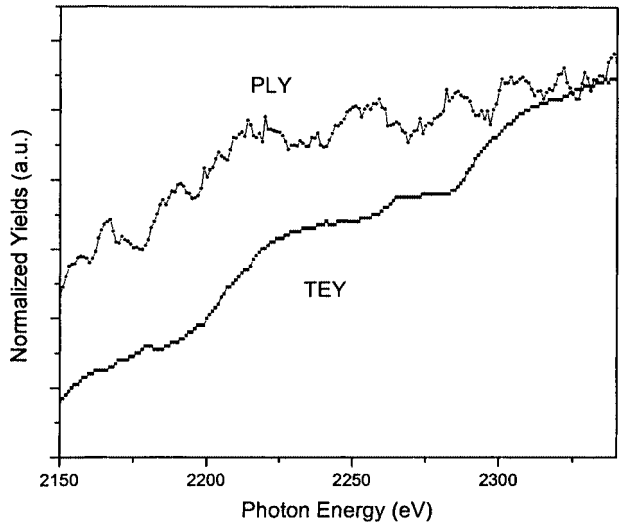

Fig. 4. TEY and PLY (zero order) of PPh_3AuCl at the Au $M_{5,4}$-edge.

Returning to the C K-edge (Fig. 2), the most interesting feature is in the PLY in which all optical photons of the gold(I) complex are collected. A close examination of the TEY and the PLY of the PPh_3AuCl reveals that the first π^* resonance, peak (a), is enhanced in PLY relative to TEY, whilst the main π^* resonance, peak (b), is inverted in the PLY. The inversion can be explained as follows. First, the splitting in the π^* resonance occurs due to the nonequivalent carbon atoms in the phenyl rings and only those carbon atoms (most likely those bonded directly to P) that are associated with the transition are coupled effectively to the luminescence. Second, the inversion could be due to the total absorption phenomenon in which the strong π^* channel absorbs a major fraction of the incoming photons. If the luminescence quantum yield is less efficient than the absorption elsewhere, the PLY would invert. It is interesting to note that the transition from C 1s to σ^* quasi bound states at ~290 eV peak (d) shows a broad peak in the PLY. This observation is in contrast to a previous XEOL study of Ru(2,2'-bipy)$_3^{2+}$ in which the σ^* transition was significantly suppressed [7].

The total (zero order) and partial photoluminescence yields (PLY) at the P K-edge NEXAFS shown in Fig. 3 exhibit the same profile as the TEY and the FLY indicating that local excitations at the P K-edge is strongly coupled to the luminescent chromophore. Thus the emission can be assigned to the decay of an excited state having both P and Au character. This is also supported by the observation of an intense Au $L_{3,2}$-edge whiteline for PPh_3AuCl, indicating that the P-Au-Cl moiety has high densities of unoccupied states of Au d character. According to Larson *et al.* [9], the vibronic analysis of the emission in PPh_3AuCl was consistent with an assignment of a LMCT state, but the vibrational frequencies disagreed with Raman frequencies. They then attributed that a severely perturbed trap or an adventitious impurity was responsible for the emission in PPh_3AuCl. They concluded in a more recent study that the low energy emission is a phosphorescence of gold-based $\sigma^* \rightarrow \sigma$ parentage [12]. Based on the C, P K-edge, the Au $M_{5,4}$-edge PLY, and Au $L_{3,2}$-edge XANES, our results indicate that the excited state has considerable Au-P character.

4. Conclusions

We have reported experimental observations of soft X-ray induced luminescence of the PPh_3AuCl complex by exciting the system with photon energies tuned across the carbon, and the phosphorus K-edge as well as the gold $M_{5,4}$-edge. We find that the luminescence is dominantly at low energy and the origin of the luminescence is primarily from the P – Au σ^* to σ of primarily Au d character.

Acknowledgment

We thank the NSERC (Canada) and EMK (Ontario) for financial support and NSERC for a PGS B scholarship to PSK. The Synchrotron Radiation Center, University of Wisconsin-Madison is supported by the NSF grant # DMR-0084402. We also thank Drs. Kim Tan and Astrid Jürgensen of the Canadian Synchrotron Radiation Facility for their technical supports.

References

1. Ziolo, R. F., Lipton, S. and Dori, Z., J. Chem. Soc. Chem. Commun. **17**, 1124 (1970).
2. King, C., Wang, J.-C., Khan, Md. N. I. and Fackler, J. P., Jr., Inorg. Chem. **28**, 2145 (1989).
3. King, C., Khan, Md. N. I., Staples, R. J. and Fackler, J. P., Jr., Inorg. Chem. **31**, 3236 (1992).
4. Puddephatt, R. J., Coord. Chem. Rev. **216**, 313 (2001).
5. Brandys, M.-C., Jennings, M. C. and Puddephatt, R. J., J. Chem. Soc. Dalton Trans. **24**, 4601 (2000).
6. Naftel, S. J. *et al*., Appl. Phys. Lett. **78**, 1847 (2001).
7. Kim, P.-S. *et al.*, J. Am. Chem. Soc. **123,** 8870 (2001).
8. Rogalev, A. and Goulon, J., "Chemical Applications of Synchrotron Radiation, Part II", (Edited by T. K. Sham) (World Scientific, New Jersy 2002), ch. 15, p. 707.
9. Larson, L. J., McCauley, E. M., Weissbart, B. and Tinti, D. S., J. Phys. Chem. **99**, 7218 (1995).
10. McAuliffe, C. A., Parish, R. V. and Randall, P. D., J. Chem. Soc. Dalton Trans. **11**, 1730 (1979).
11. Stöhr, J., "NEXAFS Spectroscopy" (Springer-Verlag, Berlin 1992).
12. Weissbart, B., Toronto, D. V., Balch, A. L. and Tinti, D. S., Inorg. Chem. **35**, 2490 (1996).

Physica Scripta. Vol. T115, 548–551, 2005

The P(1s) and P(2p) XAFS Spectra of Elemental Phosphorus, Theory and Experiment

Astrid Jürgensen*

Canadian Synchrotron Radiation Facility, Synchrotron Radiation Center, 3731 Schneider Drive, Stoughton, WI, USA 53589-3097

Received June 26, 2003; accepted in revised form July 1, 2004

PACS numbers: 78.70.Dm, 33.20.Rm, 31.15.Ar

Abstract

X-ray absorption spectroscopy was used to study the local structure and chemical bonding of elemental phosphorus. Three allotropes of this element exist in the solid state. The most common of these is the amorphous red phosphorus. The other two are crystalline: white phosphorus and black phosphorus. In the gas phase tetrahedral P_4 molecules are stable up to ~800 °C. At higher temperatures P_2 molecules become dominant.

Theoretical P(1s) and P(2p) XAFS spectra of gaseous and solid state phosphorus were calculated by *ab initio* FEFF and GSCF3 methods. These were compared and the spectral features were related to structural and electronic properties of the different allotropes of elemental phosphorus. The calculation results were then used to explain the features observed in the experimental P(1s) and P(2p) spectra of red phosphorus that were measured using synchrotron radiation.

1. Introduction

Three structural allotropes of the element phosphorus exist in the solid state. Crystalline black-P is the most stable allotrope, a semiconducting material with an orthorhombic puckered layer structure [1]. Two high pressure phases exist: a semi-metallic rhombohedral form that is formed reversibly at 40–80 kbar, and a metallic simple-cubic phase, formed reversibly at 110 kbar. Crystalline white-P, the least stable allotrope, is composed of tetrahedral P_4 molecules. At room temperature it is in the β-phase, a plastic crystal [2, 3]. Its structure is similar to that of α-Mn with the P_4 molecules in the positions of the Mn atoms [2]. The low temperature α-phase, formed reversibly at −77 °C, has a structure comparable to γ-Pu [2]. The most common allotrope is red-P. Like white-P, it is composed of P_4 molecules. It is usually an amorphous solid, but a crystalline form with a very complex 3D network structure can be prepared [4]. Tetrahedral P_4 molecules are stable in the gas phase up to ~800 °C. At higher temperatures they decompose into P_2 molecules that have a shorter P-P bond length and, like N_2, a formal triple bond [4].

2. Calculations

The molecular geometry of gaseous P_2 and P_4 was optimised with GAMESS US [5]. The Huzinaga minimal basis set 533/53, expanded to 322121/3221, with one d polarisation function was employed. The resulting P-P single bond length for tetrahedral P_4 is 2.2095 Å, in good agreement with experimental values for the P-P single bond [2, 6]. The bond length of 1.8797 Å of linear P_2 is significantly shorter, as expected for a triple bond.

Theoretical P(1s) and P(2p) XANES spectra were calculated for the gas phase using the GSCF3 computer code [7, 8]. The atom positions for P_2 and P_4 correspond to the optimised geometry, and the same basis set was employed. However, in the calculation of the core-hole states, it was expanded to 2111111111/2111111 with one d-polarisation function for the excited P atom. To generate the spectra, Gaussian peaks are used with the peak area set equal to the calculated oscillator strength, and the peak width at half maximum (FWHM) was set to 0.1 eV and 1.0 eV for the P(2p) and P(1s) XANES, respectively.

The theoretical P(1s) EXAFS interference function $\chi(k)$ was calculated with the FEFF 7.0 computer code [9] for the P_4 molecule (optimised geometry) and for the crystalline phases of solid state P that exist at room temperature and atmospheric pressure. The experimental crystal lattice parameters and atom positions were used for black-P [1]. Individual P atoms were placed into the unit cell of the β-phase of white-P [2] using the optimised P_4 structure with the centre of the molecule at the fractional coordinates corresponding to the atom positions of α-Mn [10]. The calculations were done for radial distances up to 10 Å which correspond to clusters containing between 150 and 215 atoms. Only single scattering (SS) and triangular multiple scattering (MS) paths were included. The unit cell of white-P contains several symmetry unique P atoms (9 in the β-phase). The FEFF calculation was done for each of these as the central atom, and the overall $\chi(k)$ was then taken as a weighted average. This was not necessary for black-P, as there is only one symmetry unique atom in the unit cell. The Fourier Transform (FT) of the k^3 weighted $\chi(k)$ was obtained over the k-range from 2 to 15 $Å^{-1}$ using a 30% Gaussian window function.

3. Experiment

P(1s) and P(2p) XAFS spectra of red-P were measured at the double crystal monochromator (DCM) [11] and Grasshopper [12] beamlines of the Canadian Synchrotron Radiation Facility (CSRF), respectively. The spectra were measured simultaneously by total electron yield (TEY), using the photoelectron current, and by fluorescence yield (FY), using a multi-channel-plate detector. The incident photon beam was at normal incidence to the sample surface. Normalisation with respect to the photon flux (I_0) was achieved through simultaneous TEY measurement of a Ni mesh at the Grasshopper and a gas cell with ~1 torr N_2 at the DCM, both located upstream from the sample. The red-P was obtained commercially from Alfa Aesar (99% purity) and used without further purification.

The EXAFS was extracted from the P(1s) absorption spectrum using WINXAS [13]. The edge energy E_0 was set to 2143.6 eV, and the atomic absorption μ_0 was approximated by a cubic spline function with 9 sections over a range from 2 to 15 $Å^{-1}$. A weighing factor of k^3 was applied to the data. The FT of $k^3\chi(k)$ was obtained over the same k-range using a 30% Gaussian window function.

*e-mail address: ajurgens@uwo.ca

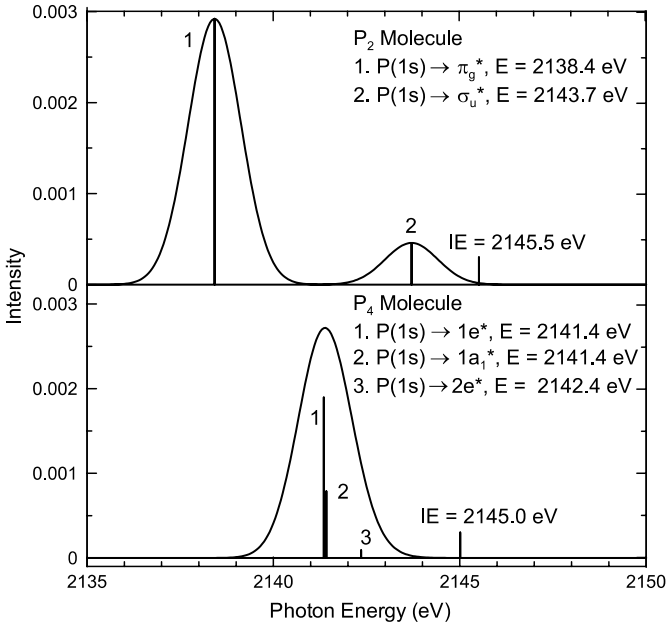

Fig. 1. The theoretical P(1s) XANES spectra of the P_2 (top) and P_4 (bottom) molecules.

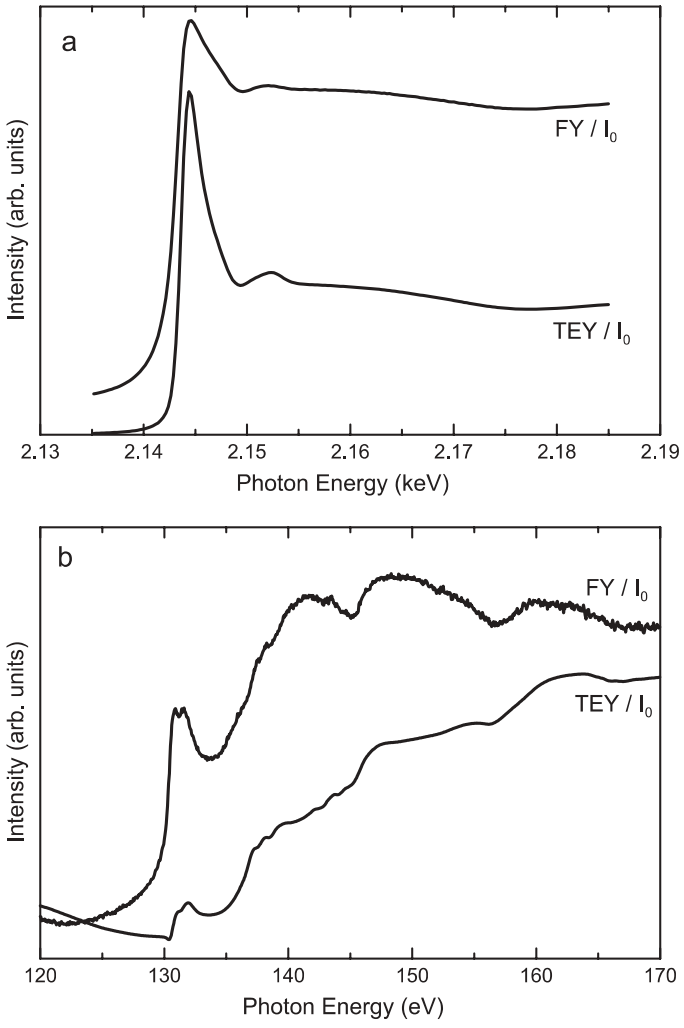

Fig. 2. The experimental (a) P(1s) and (b) P(2p) XANES spectra of red-P.

4. Results and Discussion

The theoretical P(1s) XANES spectrum of P_2 has two absorption peaks that result from the P(1s) $\rightarrow \pi_g^*$ and P(1s) $\rightarrow \sigma_u^*$ transitions (Fig. 1). There is only one feature in the XANES of P_4 that is at an energy intermediate to the peaks of P_2. It arises from the overlap of three unresolved absorption peaks (Fig. 1). The $1e^*$ and $1a_1^*$ orbitals of P_4 correspond to the π_g^* and σ_u^* of P_2, respectively. The orbital lobes of π_g^* are perpendicular to the P_2 bond axis, thus minimising repulsion. In the $1e^*$ of P_4 they lie more along the bond axes. They point towards each other, destabilising the orbital, and hence increasing the transition energy. The opposite effect occurs for the σ_u^*-$1a_1^*$ pair. The σ_u^* lies along the P_2 bond axis and is thus destabilised relative to the $1a_1^*$ of P_4. The $2e^*$ orbital of P_4, another P-P antibonding orbital, has no equivalent in P_2. A transition to the last antibonding orbital of P_4, $1a_2^*$, is not observed, because it is forbidden by symmetry constraints.

The main absorption peak in the experimental P(1s) XANES of red-P (Fig. 2a) occurs at 2144.4 eV, 5.5 eV below the ionisation edge [6]. It corresponds to the XANES feature of the P_4 molecule. The smaller height observed in the FY spectrum relative to TEY, suggests distortion due to self-absorption in the former. The second XANES peak at 2152.4 eV might be caused by a small amount of phosphate in the sample. It could also be a post-edge shape resonance of red-P.

The P(2p) XANES of P_2 has four features resulting from the spin-orbit pairs of the P(2p) $\rightarrow \pi_g^*$ and P(2p) $\rightarrow \sigma_u^*$ transitions. Due to the molecular field splitting of the P(2p) orbitals ($\Delta E = 0.085$ eV for the ionisation energy (IE) and $\Delta E = 0.23$ eV for the excited molecular states), they are partially resolved double peaks.

Convergence problems were encountered for the calculation of the P(2p) XANES of P_4. One solution, using the unrestricted Hartree-Fock method for the excited states, resulted in an increase of the calculated IE by ~10.5 eV. Furthermore, it reduced the molecular symmetry, splitting all e-orbital pairs ($2p_{x,y}$, $1e^*$ and $2e^*$). Hence, three P(2p) IE's were calculated with energy differences of 0.013 and 0.341 eV. Seven P(2p)-hole excited states with a transition energy below the IE were found, the six states with the electron in a P-P antibonding orbital, and one additional state with the electron in a P(3d) orbital. The P(2p) $\rightarrow 1a_1^*$ and P(2p) $\rightarrow 1e^*$ transitions occur between 6 and 7.5 eV below the IE, and the P(2p) $\rightarrow 2e^*$ and P(2p) $\rightarrow$ P(3d) transitions are between 1 and 2.5 eV below the IE. A P(2p) $\rightarrow 1a_2^*$ transition, 1.9 eV below the IE, is not observed. The most intense feature in the spectrum is the spin-orbit pair resulting from the P(2p) $\rightarrow 1e^*$ transition. Due to molecular field effects each of these peaks is split into three that are partially resolved.

The experimental P(2p) XANES spectrum of red-P (Fig. 2b) has one pre-edge feature peaking at 130.9 and 131.6 eV followed by several shape resonances in the ionisation continuum. The pre-edge peak corresponds to the most intense feature in the XANES of the P_4 molecule, the P(2p) $\rightarrow 1e^*$ transition, but only the spin-orbit splitting is barely resolved. The TEY spectrum is shifted by ~0.3 eV towards higher energy relative to the FY spectrum, probably due to sample charging effects.

The k^3-weighted FT of the P(1s) EXAFS interference function for the P_4 molecule has a single peak corresponding to the P-P single bond distance (Fig. 3). A negative phase shift causes the peak to appear at a lower R value then expected. The P_4 molecule is the main building block of white- and red-P, and the atoms in black-P also form three P-P single bonds. Thus this peak is observed in the P(1s) EXAFS of all forms of solid state P.

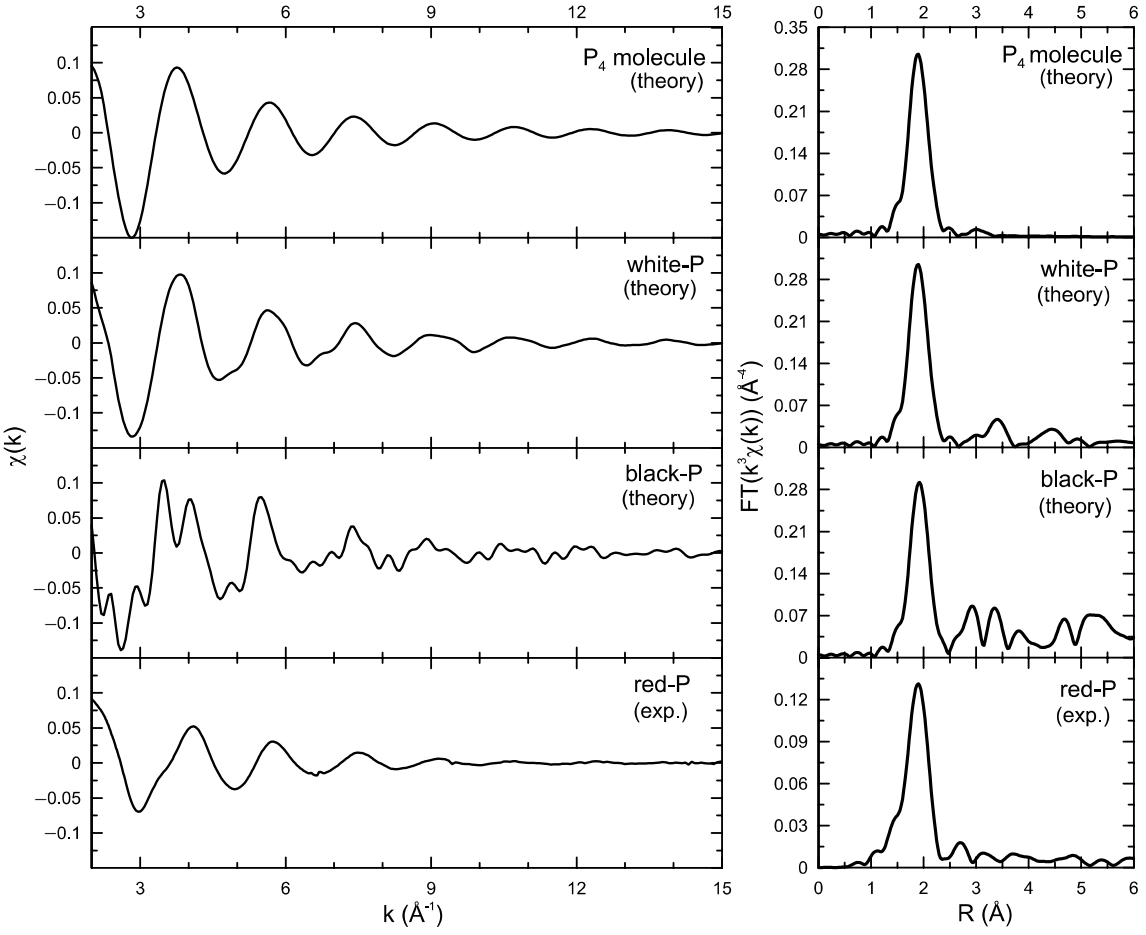

Fig. 3. The EXAFS interference function $\chi(k)$ and the magnitude of its k^3 weighted FT for the P_4 molecule (theory), white-P (theory), black-P (theory) and red-P (experiment).

For white-P the contribution from other shells is minor, because there are so many paths with slightly different radial distances that their scattering waves tend to be out of phase with each other, and thus cancel out. In the experimental $\chi(k)$ of the β-phase of white-P even less contribution from higher shells is expected, because this phase is a plastic crystal and the P_4 molecules can rotate about their centres [3]. In black-P there are significantly fewer scattering paths, so peaks are observed at larger R-values in the FT (Fig. 3). The second and third peaks result from the combination of six SS paths and four MS paths with scattering distances between 3.3 and 4.0 Å. These include scattering from second and third neighbours within the layer and two SS paths involving atoms in an adjacent layer.

As expected, only one dominant peak is observed in the FT of the $k^3\chi(k)$ that was extracted from the P(1s) TEY spectrum of red-P (Fig. 3). It was fitted using the FEFF paths calculated for the P_4 molecule (one SS path and one MS path). The coordination numbers were fixed, ΔE_0 was limited to one value, and R and σ^2 of the MS path were correlated to the corresponding value of the SS path. The results are shown in Fig. 4. The R-value of 2.212 Å obtained for the P-P single bond length is in good agreement with literature values [2, 6]. Attempts to fit the low-R shoulder using P-O scattering paths were unsuccessful, indicating that phosphate, if present, is a very minor impurity in the sample.

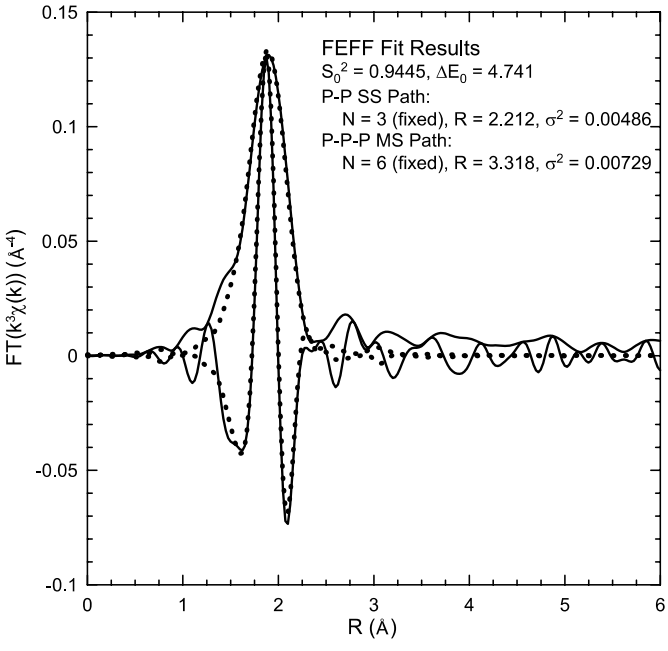

Fig. 4. The imaginary part and the magnitude of the experimental FT($k^3\chi(k)$) of red-P (solid lines), and the fit results using the theoretical $\chi(k)$ of the P_4 molecule (dotted lines).

Acknowledgements

The experimental work was done at the Canadian Synchrotron Radiation Facility (CSRF), located at the Synchrotron Radiation Center (SRC) in Stoughton, WI, USA. Funding for CSRF is provided by the National Research Council (NRC) of Canada and the Natural Sciences and Engineering Research Council (NSERC) of Canada. SRC is operated by the University of Wisconsin, Madison and funded by NSF under grant No. DMR-0084402.

References

1. Chang, K. J. and Cohen, M. L., Phys. Rev. B **33**, 6177 (1986).
2. Simon, A., Borrmann, H. and Horakh, J., Chem. Ber./Recueil **130**, 1235 (1997).
3. Schnering, H. G. v., Angew. Chem. Int. Ed. Engl. **20**, 33 (1981).
4. Shriver, D. F., Atkins, P. W. and Langford, C. H., "Inorganic Chemistry" (W. H. Freeman and Company, New York, 1990), p. 373.
5. Schmidt, M. W. *et al.*, J. Comput. Chem. **14**, 1347 (1993).
6. Küper, G., Hormes, J. and Sommer, K., Macromol. Chem. Phys. **195**, 1741 (1994).
7. Kosugi, N., Theor. Chim. Acta **72**, 149 (1987).
8. Kougi, N. and Kuroda, H., Chem. Phys. Lett. **74**, 490 (1980).
9. Ankudinov, A. L. and Rehr, J. J., Phys. Rev. B **56**, R1712 (1997).
10. Gazzara, C. P., Middleton, R. M., Weiss, R. J. and Hall, E. O., Acta. Cryst. **22**, 859 (1967).
11. Yang, B. X. *et al.*, Nucl. Instr. Meth. Phys. Res. **A316**, 422 (1992).
12. Tan, K. H., Bancroft, G. M., Coatsworth, L. L. and Yates, B. W., Can. J. Phys. **60**, 131 (1982).
13. Ressler, T., J. de Physique IV **7**, 269 (1997).

Physica Scripta. Vol. T115, 552–555, 2005

XANES, EXAFS and RMN Contributions to Follow the Structural Evolution Induced by Alkali-Silica Reaction in SiO_2 Aggregate

L. Khouchaf[1,*], J. Verstraete[1], R. J. Prado[2,3] and M. H. Tuilier[4]

[1]Centre de Recherche de l'Ecole des Mines de Douai, 941 rue Charles Bourseul, BP.838 59508 DOUAI, France
[2]LURE, Centre Universitaire Paris-Sud, Bât 209D, B.P.34, 91898 ORSAY Cedex, France
[3]Instituto de Física, USP, C.P. 66318, 05315-970, São Paulo, SP, Brazil
[4]Equipe de Recherche Technologique, Université de Haute-Alsace, 61 rue Albert Camus, F-68093 – Mulhouse Cedex France

Received June 26, 2003; accepted in revised form June 23, 2004

PACS numbers: 61.10.Ht

Abstract

In this work, we analyze and correlate information obtained from XANES, EXAFS and NMR on a SiO_2 aggregate attacked by Alkali Silica Reaction (ASR). EXAFS and XANES results enable local order evaluation during the amorphization process within the aggregate. NMR results show the presence of amorphous and crystalline phases of silica during ASR attack. Besides, theoretical simulations of XANES spectra were performed and the atomic structure that generates the peak located 8 eV above the white-line (feature C in the text) was identified. The results lead us to deduce a change in the local order around silicon.

1. Introduction

The Alkali-Silica Reaction (ASR) is one of the main phenomena that damage the concrete in the world. Many studies were carried out in order to explain the ASR mechanism [1]. In recent studies we evaluated the damage caused by ASR in a flint aggregate by Environmental Scanning Electron Microscopy (ESEM) and X-ray Diffraction (XRD) [2, 3]. Both results support the formation of new phases, which precipitate in the aggregate.

A relationship between the concrete degradation and its structural behavior has been established [4]. Today, most authors agree with the idea that the beginning of the ASR is the rupture of the siloxane bonds Si-O-Si when the aggregate used in the concrete contains SiO_2 as in our study. Thus, any attempt to understand the ASR mechanism must consider the local changes around silicon and/or oxygen.

The studies performed by Dien Li *et al.* [5] showed the utility of the XANES technique to examine the amorphization process in crystalline SiO_2. Then we used, for the first time, X-ray absorption spectroscopy (XANES and EXAFS) to analyze the structural evolution of a flint aggregate. Nuclear magnetic resonance (NMR) results obtained on the flint aggregate submitted to ASR are also presented. Further, using FEFF8 [6], we show how to identify the origin of the XANES structures found in the spectra.

2. Materials and Methods

The aggregate used in this work is a natural SiO_2 flint from the north of France. It contains 99.1% SiO_2. X-ray diffraction shows that it is made of α-quartz phase with moganite traces. Sample preparation and the ASR procedure used have been previously described [3, 7].

In the ASR mechanism, the ions present in the concrete (such as OH^-, K^+ and Ca^{++}) can penetrate the poorly crystallized and porous parts of the aggregate [8]. The attack is initiated by hydroxyl ions, as indicated below

$$2SiO_2 + OH^- \Rightarrow SiO^-{}_{5/2} + SiO_{5/2}H \quad (1)$$

inducing the rupture of Si-O-Si bonds between two tetrahedrons SiO_2, called Q_4, and producing $SiO^-{}_{5/2}$ and $SiO_{5/2}H$, called Q_3 or silanols. The equation of the reaction could be written as: $2Q_4 + OH^- \Rightarrow SiO^-{}_{5/2} + Q_3$. The cations, which are abundant in the porous structure of the material, are attracted to the sites of negative charge and participate in the reaction. The calcium cations are likely to react with silica species to form calcium silicate hydrate [8].

The flint aggregate was powdered and the distribution of the average particle size showed two maxima, at 160 µm and 630 µm, before the reaction. 1 g of crushed flint was subjected to accelerated ASR at 80 °C with a mixture of 0.5 g of portlandite $Ca(OH)_2$ and 10 ml of potash solution KOH at 0.79 mol/l [3, 7]. The pH of the solution was 13.9. In this study we will present results from samples of flint aggregate after 30, 72 and 168 hours of ASR attack, respectively named 30 h, 72 h and 168 h. In order to probe the surrounding of silicon atoms in the sample, solid-state ^{29}Si magic angle spinning nuclear magnetic resonance (MAS-NMR) and both EXAFS and XANES spectra at the Si K-edge were collected.

MAS-NMR spectra were obtained using a Bruker MSL 300 spectrometer operating at 59.631 MHz with a 2.5 mm Bruker CP/MAS probe spinning at 4 kHz. Tetramethylsilane (TMS) was used as a reference for chemical shifts measurements. Spectra were recorded with a pulse angle of 30° and a recycle delay of 80 s. The number of scans was 2150 for each sample.

The XANES and EXAFS data were recorded using the SA32 beam-line of the Super-ACO ring at LURE, Orsay, France. The data were collected in the total electron yield (TEY) detection mode, using a 0.2 eV step for XANES and 1 eV step for EXAFS. The beam was monochromatized by a double-crystal monochromator, equipped with two InSb (111) single crystals, and calibrated on a c-Si sample (1839 eV at the Si K-edge threshold). The software "*EXAFS pour le Mac*" [9] was used to perform the initial data treatment and first shell simulations. A 6th degree polynomial function was used to reproduce the atomic absorption, and the signal was normalized using the Lengeler-Eisenberger method. A k^2 weighting and a Kaiser apodization window between approximately 2.8 and 11.3 $Å^{-1}$, with $\tau = 1.0$, were used to calculate the Fourier transform of the EXAFS signal shown here.

The FEFF8 code was used to simulate the XANES signal of α-quartz [10]. We used the Hedin-Lundqvist interaction potential

*e-mail: khouchaf@ensm-douai.fr

and determined the local interstitial atomic potential around the absorbing atom. In order to identify the multiple scattering paths (atomic structure) responsible for the generation of feature C (see Fig. 1), we first identified the size of the cluster necessary to reproduce this feature.

Subsequently, in order to identify the atoms that are involved in the multiple scattering process generating feature C, we generated several different sub-clusters. For each of these sub-clusters, we deleted only one different atom of the initial cluster (except the absorber atom) and performed a FMS calculation. If the deleted atom contributes to the generation of feature C, then this feature is weakened or disappears for this specific calculation. With this procedure, we were able to identify the only atoms that are involved in the multiple scattering process generating feature C.

3. Results

3.1. *Experimental*

Figure 1 shows the XANES spectra from samples 30 h, 72 h and 168 h compared to the flint before ASR attack. The main peaks are noted A, B, C, D and E. The positions of all peaks are the same for all samples: peaks A, C and E are located respectively at 1846.8 eV, 1854.4 eV and 1864.2 eV, corresponding to the value of the same peaks for α-quartz. The origin of the XANES peaks is only described in a general way in the literature [5, 11]. With the exposition to ASR, one can notice decreasing intensity and/or broadening of the features.

The EXAFS study enabled us to follow the evolution of the short-range order (SRO) around silicon under the effect of ASR. Figure 2 shows Fourier Transforms (FT) of the EXAFS signal from flint aggregate before and after 30, 72 and 168 hours of exposure to ASR. One can observe that the amplitude of the first shell (Si-O bonding) peak slightly increases during ASR attack, due to the equivalence of the Si-O distances in the SiO_2 tetrahedra after amorphization. However, silicon atoms are always surrounded by four oxygen atoms at a mean distance of 1.60 ± 0.02 Å. In addition, the amplitude of the peaks for the second and third neighbors decreases, due to the amorphization of the material.

The analysis of the EXAFS Fourier transforms shows that the SRO above the first shell around Si atoms is almost preserved during ASR attack, however the amplitude of the peaks for the second and third neighbors decreases, due to the amorphization of the material.

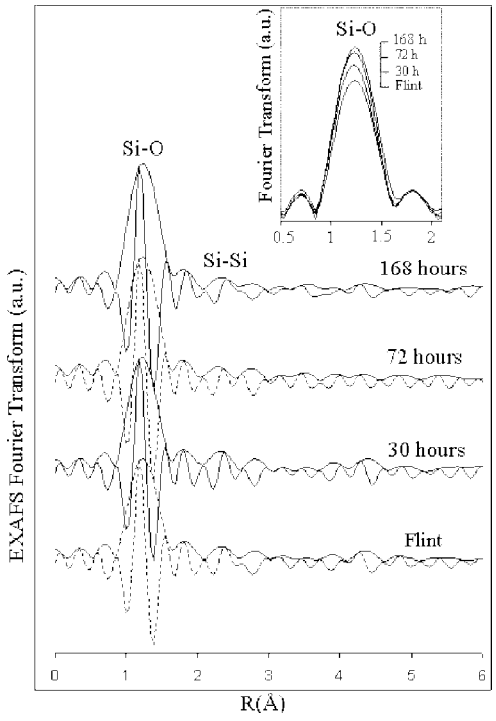

Fig. 2. EXAFS Fourier Transforms from flint aggregate before ASR attack, and after 30, 72 and 168 hours of exposition to ASR.

In figure 3 MAS-NMR ^{29}Si spectra from samples 30 h, 72 h and 168 h are compared to that of the flint aggregate before ASR attack. On the spectrum of the flint aggregate we can notice the presence of a sharp peak at −107 ppm, related to the presence of Q_4 (crystalline) sites, and another peak at −100 ppm, related to Q_3 sites [12]. After 72 hours of attack, one can observe an increase in the number of Q_3 sites in the aggregate. Moreover, a new peak appears around −110 ppm, also increasing its intensity with the time of attack, being attributed to poorly crystallized or amorphous silica [12].

3.2. *Calculation*

In agreement with other results [11], theoretical simulations of the XANES spectra show that feature C appears when a cluster having 53 atoms (diameter of 10.5 Å) is used.

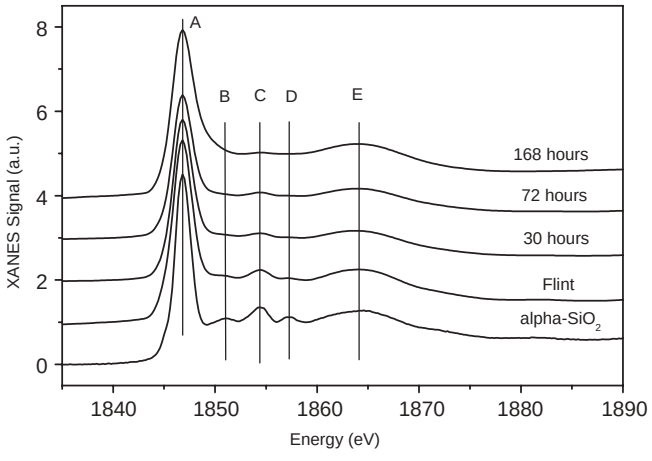

Fig. 1. XANES spectra of the samples 30 h, 72 h, 168 h, flint aggregate before ASR attack and α-SiO_2.

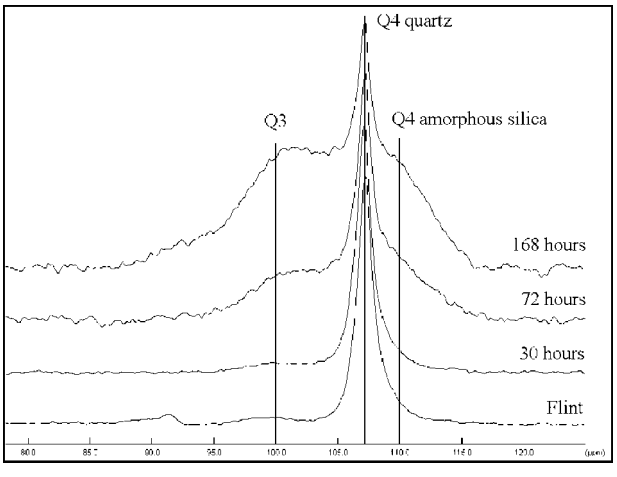

Fig. 3. MAS NMR ^{29}Si spectra of the samples submitted to ASR during 30h, 72h and 168h compared to flint aggregate before ASR.

Table I. *Position and distances from the central Si atom, set at the origin, for the six atoms that generate feature C (see Fig. 1) by multiple scattering in the α-SiO_2 structure.*

atom	shell	*x* (Å)	*y* (Å)	*z* (Å)	Distance (Å)
Si	6th	−2.27367	−3.93810	1.80168	4.86
Si	6th	−4.54733	0.00000	−1.80165	4.86
O	3rd	−2.90895	−2.96759	0.66283	4.20
O	3rd	−4.02448	−1.03543	−0.66283	4.20
O	7th	−1.15813	−4.84909	1.13883	5.10
O	7th	−4.77850	1.42152	−1.13883	5.10

Subsequently, we generated 52 sub-clusters. For each of these sub-clusters, we deleted one different atom of the initial cluster (except the absorber atom) and performed a FMS calculation. Finally, the absence of only 6 (4 O and 2 Si atoms) of the 52 atoms analyzed influenced the intensity of feature C during simulation. The positions of these six atoms are listed in Table I. These are the sole atoms that influence the generation of this XANES structure and, as one can see, their atomic positions are symmetric, as expected.

Figure 4 shows simulation of results for some sub-clusters (from sub-cluster without atom 33 to that without atom 46 of the FEFF input list of atoms) and compare them to the experimental spectra. In this figure, the original energy range of the theoretical spectra, obtained with the Hedin-Lundqvist interaction potential, was scaled to provide the coincidence of both A and E features in both theoretical and experimental spectra. However, the use of the Dirac-Hara interaction potential gives automatically a good energy scale but also a less realistic whiteline. Simulations without feature C were obtained for sub-clusters without atoms 39 and 40 of the FEFF input list, that is, the Si atoms in table I.

4. Discussion

The data collected by MAS-NMR show that the flint aggregate is not perfectly crystalline, confirming previous results [3]. As expected, the quantity of Q_3 sites increases with ASR attack. Simultaneously, a new peak located at −110 ppm, related to the presence of amorphous silica (amorphous Q_4 sites) [12], appears only after attack and also increases its intensity with duration of ASR.

These data show that the formation of a Q_3 site during ASR attack causes, simultaneously, the creation of amorphous Q_4 sites by deformation/relaxation of its direct neighborhood. Therefore, the presence of a crystalline phase within all samples shows that, at least, amorphous and crystalline phases coexist in the aggregate during ASR attack, corroborating previous results [13], in which flint aggregates attacked by ASR are heterogeneous, presenting what seems to be different phases.

In order to check this assumption and correlate the NMR data with the respective phases, it will be important to carry out experiments of micro-XAFS on each one of the different zones identified in our samples.

XANES results clearly show the effects of the structural deterioration during ASR attack (figure 1), confirming that this technique can give significant information about the amorphization process generated by ASR in the concrete.

The positions of the peaks in the XANES spectra are identical for all samples, and also identical to those for α-quartz, indicating that the crystalline phase of the samples has always the same basic structure. However, with the exposition to ASR, the decreasing intensity of peak C and broadening of features A and E are remarked, pointing out the amorphization of the material.

Since the first coordination sphere of Si is preserved with 4 oxygen atoms, the EXAFS data corroborates the fact that the agent of the ASR is the hydroxyl ion, as shown in equation (1). Also, the Fourier transforms of the EXAFS signal illustrate the evolution process of the SRO around silicon with ASR.

Theoretical simulations of the XANES spectra were also performed and the set of atoms responsible for the generation of feature C is identified, but the intensity of this peak is underestimated by FEFF8 code, despite our efforts to reduce the broadness of the spectra or to increase the intensity of the peak by changing the FEFF8 parameters. On the other hand, the size of the cluster necessary to generate the feature is in agreement with other similar works, as well as the position of the feature, corroborating our result. This feature disappears only when deleting one of the six atoms listed in table I. In addition, separating these atoms into two groups of 3 (1st, 3rd, 5th and 2nd, 4th, 6th in table I) one can see that both groups are symmetric by a 180° rotation. This result enables us to deduce that the origin of feature C in SiO_2 can be attributed to the MS of the photoelectron by the ensemble of atoms listed in table I.

Due to the fact that feature C is generated by the atomic structure inside a small cluster with a radius of 5.1 Å, it is clear that the initial structural order of the flint is deteriorated in sample 168 h, as confirmed by EXAFS. However, since the depths probed by NMR and EXAFS measured in TEY mode are different, NMR being more bulk sensitive, this result is not in opposition to the existence of a crystalline phase in the flint aggregate after ASR. It indicates that the surface of the aggregate is more damaged than the bulk.

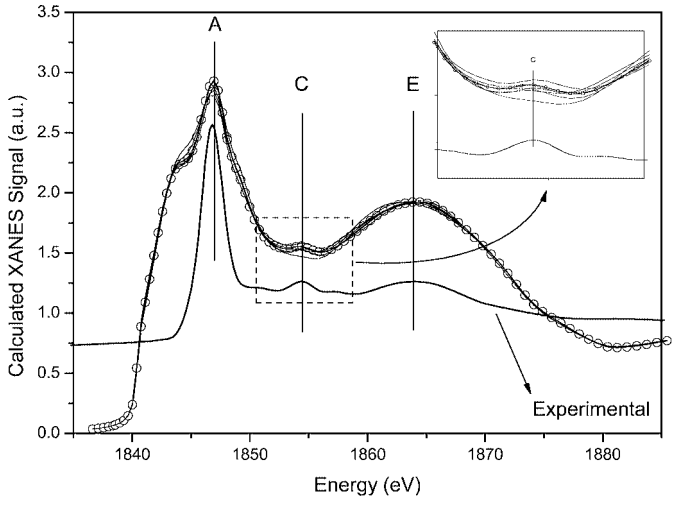

Fig. 4. Comparison between experimental and XANES simulation spectra for several sub-clusters, as explained in the text.

5. Conclusions

The XAFS results complement and agree with other studies performed by Dien Li *et al.* using model materials, providing extra information and helping us to better understand the mechanisms of the ASR in concrete. The NMR data give additional information about the ASR process, showing the coexistence of different

phases such as Q_3 rich zones, well-crystallized and amorphous zones within the aggregate. Additionally, we developed a method to identify the set of atoms that generates a specific structure in the XANES spectra. As an example, we identified the origin of feature C in the experimental spectra of α-quartz.

Acknowledgements

Authors would like to thank M. Delmot and M. D. Bulteel. Thanks are also due to CAPES (Brazil), for the post-doc support of R. J. Prado at LURE.

References

1. Chatterji, S. and Thaulow, N., in Proc. 11th Int. Conf. Alkali-Aggregate Reaction in Concrete, (Edited by Berube *et al.*), (Quebec, Canada 2000), p. 21.
2. Bulteel, D. *et al*., J. Phys. IV. **10**, 513 (2000).
3. Verstraete, J. *et al*., Cement and Concrete Research, submitted (2002).
4. Poole A. B., "Alkali-Aggregate Reaction in concrete", (Edited by Van Nostrand) (New-York 1992), p. 1.
5. Li, D. *et al*., Solid State Commun. **87**, 613 (1993). Li, D. *et al*., Am. Mineral. **79**, 622 (1994).
6. Ankudinov, A. L., Ravel, B., Rehr, J. J. and Conradson, S. D., Phys. Rev. **B 58**, 7565 (1998).
7. Bulteel, D., Garcia-Diaz, E., Vernet, C. and Zanni, H., Cement Concrete Res. **32**, 1199 (2002).
8. Kurtis, K. E., Monteiro, P. J. M., Brown, J. T. and Meyer-Ilse, W., Cement Concrete Res. **28**, 411 (1998).
9. Michalowicz, A., "*EXAFS pour le MAC*", in "Logiciels pour la Chimie", (Société Française de Chimie, Paris 1991), p. 102.
10. Smith, G. and Alexander, L. E., Acta Cryst. **16**, 462 (1963).
11. Wu, Z. Y., Jollet, F. and Seifert, F., J. Phys.: Condens. Matter **10**, 8083 (1998).
12. Faugere, M. P. *et al*., in "Nuclear Magnetic Resonance Spectroscopy of Cement-Based Materials", (Edited by P. Colombet, A.-R. Grimmer, H. Zanni, and P. Sozzani), (Springer 1998) p. 217.
13. Verstraete, J., Khouchaf, L. and Tuilier, M. H., J. Scanning Microscopies submitted (2003).

Physica Scripta. Vol. T115, 556–558, 2005

EXAFS Study of Pressure-Induced Phase Transition in $SrWO_4$

A. Kuzmin[1,*], R. Kalendarev[1], J. Purans[1], J. P. Itié[2,3], F. Baudelet[2,3], A. Congeduti[3] and P. Munsch[3]

[1]Institute of Solid State Physics, University of Latvia, Kengaraga street 8, LV-1063 Riga, Latvia
[2]Physique des Milieux Condensés, Université Pierre et Marie Curie, B 77, F-75252 Paris, Cedex 05, France
[3]LURE, Université Paris-Sud, Bat 209D, B.P. 34, F-91898 Orsay Cedex, France

Received June 26, 2003; accepted in revised form November 13, 2003

PACS number: 61.10.Ht, 78.70.Dm, 61.50.Ks

Abstract

Pressure-induced scheelite-to-wolframite structural phase transition in $SrWO_4$ was studied using two complementary techniques – X-ray absorption spectroscopy and X-ray diffraction (XRD). In situ XRD and W L_3-edge EXAFS measurements were performed using the synchrotron radiation. The experiments were done at room temperature in the pressure range from 0 to 30 GPa using the diamond anvil cell. The XRD results unambiguously show that $SrWO_4$ transforms from the tetragonal scheelite phase to the monoclinic wolframite-type phase at about 11.7 GPa. Locally this transition appears as a change of the tungsten ions coordination from regular tetrahedral to distorted octahedral. The analysis of the EXAFS data suggests that tungsten ions displace from the centres of the tetrahedra by about 0.04 Å and some nearest oxygen atoms relax by about 0.23 Å.

1. Introduction

Strontium tungstate $SrWO_4$ belongs to scheelite-type ABO_4 compounds which are commonly used as solid-state laser hosts when doped with rare-earth ions [1]. In scheelites [2], tungsten ions are surrounded by four equidistant oxygen atoms, forming regular tetrahedra, whereas the A^{2+} ions are located between WO_4 units and are eight-fold coordinated by oxygen atoms.

At high pressure, the scheelite structure transforms into the wolframite one, in which both tungsten and A^{2+} ions are expected to be six-fold coordinated by oxygen atoms. Pressure-induced scheelite-to-wolframite phase transition in ABO_4 compounds has been studied for many years [2]. It is associated with a displacement of B cations, leading to the change of their coordination from tetrahedral to distorted octahedral (Fig. 1).

Until now most works on the scheelite-to-wolframite phase transition have been performed by Raman spectroscopy and X-ray diffraction. In particular, the Raman studies of tungstates indicate that the transition occurs at 6.5 GPa for $BaWO_4$ [3], at 10 GPa for $CaWO_4$ [4] and at 11.5 GPa for $SrWO_4$ [4, 5].

In this work we present for the first time in situ X-ray absorption spectroscopy (XAS) and X-ray diffraction (XRD) measurements of the high-pressure phase transition in $SrWO_4$. A combination of two complementary structural methods allowed us to follow precisely pressure-induced modifications of the $SrWO_4$ structure and to probe directly the transformation of WO_4 tetrahedron to WO_6 octahedron. Note that this work is the first observation of the scheelite-to-wolframite phase transition from the local viewpoint.

2. Experimental details and data analysis

In-situ pressure-dependent (0–30 GPa) energy-dispersive XAS and XRD experiments were performed at D11 (XAS10) and DW11A (WDIS) beamlines using synchrotron radiation from the LURE DCI storage ring, operated at the energy 1.85 GeV and the current 230–300 mA. Polycrystalline $SrWO_4$ (99.9%) sample was commercial powder, obtained from Alfa Aesar. It was finely ground, and some quantity was placed together with few pieces of ruby into the standard diamond anvil cell. A water-ethanol-methanol mixture was used as a pressure-transmitting medium. Pressure was measured before and after pair of XAS and XRD experiments using the standard ruby fluorescence technique. The position of the cell was adjusted during each XAS experiment to improve the quality of the spectra, thus minimising the appearance of extra absorption peaks associated with Bragg reflections from the diamonds. The energy scale of the W L_3-edge XAS experiments was calibrated relative to the measurement of $SrWO_4$ powder in transmission mode on a conventional spectrometer (beamline D21 at LURE) with a double-crystal Si(311) monochromator. All experiments were done at room temperature.

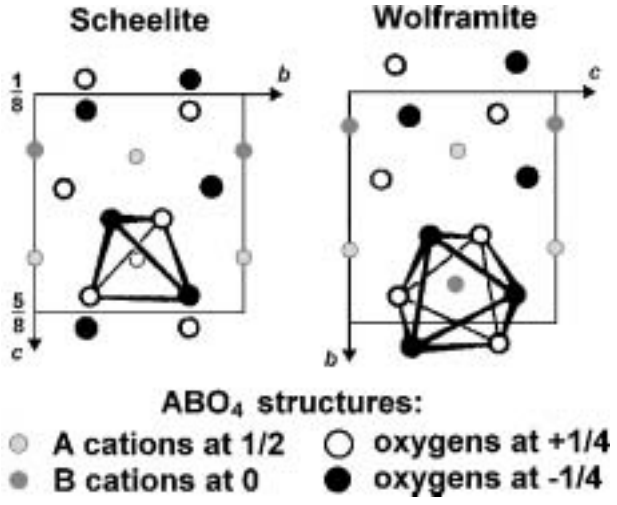

Fig. 1. Comparison of scheelite and wolframite ABO_4 structures [2].

After energy scale calibration [6], the W L_3-edge X-ray absorption spectra were analysed by the EDA software package [7, 8] following standard procedure. The EXAFS part of the spectra was singled out by the Fourier filtering procedure and best-fitted within the multi-shell Gaussian/cumulant model [7, 8]. Theoretical scattering amplitudes and phase shift functions, calculated by the FEFF8 code [9] for the $SrWO_4$ structure [10], were utilised in the model. The complex Hedin-Lundqvist exchange-correlation potential [11] was used to account for the inelastic losses of photoelectron, and the cluster potential was calculated self-consistently.

*e-mail: a.kuzmin@cfi.lu.lv

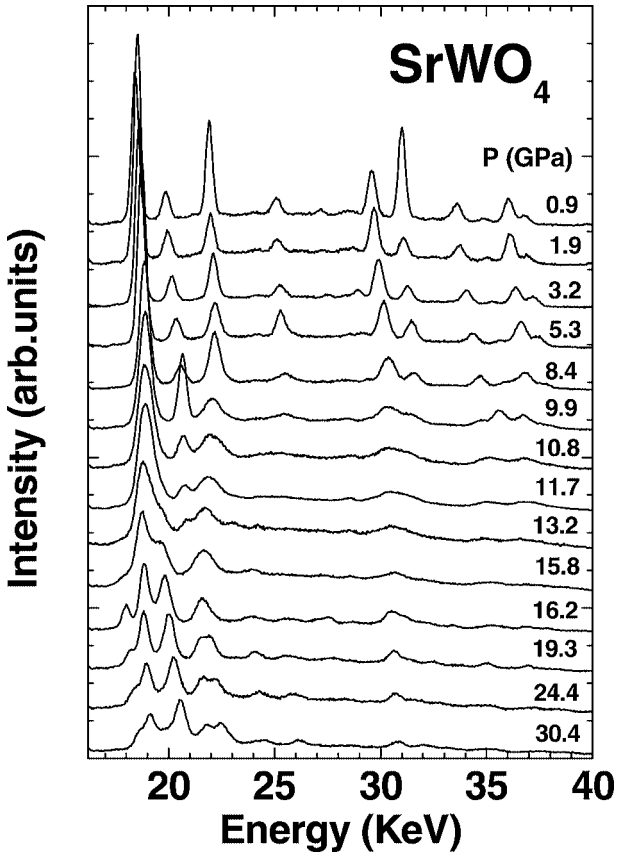

Fig. 2. Energy-dispersive X-ray powder diffraction patterns of polycrystalline $SrWO_4$. All visible peaks belongs to $SrWO_4$. Note a transition from tetragonal to monoclinic phase at about 11.7 GPa.

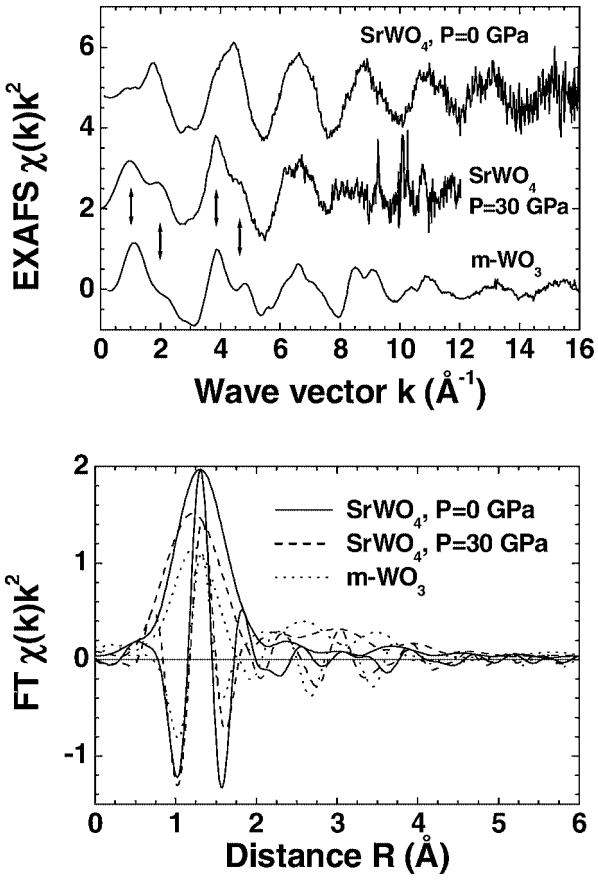

Fig. 3. The experimental W L_3-edge EXAFS $\chi(k)k^2$ signals and their FTs in $SrWO_4$ (at $P = 0$ and 30 GPa) and m-WO_3 [12]. Arrows in the upper panel indicate well visible similarities in the EXAFS signals of $SrWO_4$ at 30 GPa and m-WO_3, in which tungsten ions are six-fold coordinated. Note that the FTs are not corrected for the phase shifts.

3. Results and discussion

XRD patterns of $SrWO_4$ at different pressures are shown in Fig. 2. The transition from tetragonal scheelite phase to monoclinic wolframite phase is observed at about 11.7 GPa, when a new peak starts to grow at 20 KeV on the right side of the first strong peak. This result is in perfect agreement with Raman studies in [4, 5].

The analysis of the W L_3-edge EXAFS spectra confirm and complements the results of XRD. The W L_3-edge EXAFS spectra are strongly sensitive to the local environment around tungsten atoms. In Fig. 3 we present two EXAFS spectra and their Fourier transforms (FTs), corresponding to the extreme points at 0 and 30 GPa. Large modifications caused by the phase transition are well visible. Comparison of the spectrum at 30 GPa with the one of monoclinic WO_3, in which tungsten atoms have distorted octahedral environment, shows their similarity. The FTs are dominated by the first coordination shell peak at 1.25 Å. The group of peaks located above the first one are due to outer coordination shells and multiple-scattering effects.

The best-fit analysis of the first peak at 1.25 Å (Fig. 4) within the multi-shell Gaussian/cumulant models allowed us to determine the variation of the local environment around tungsten atoms. The fits were performed using the one-shell and two-shells and three-shells models with and without the cumulants [7, 8]. We found that at low pressure the one-shell Gaussian model is adequate to describe the experimental EXAFS signal. Thus, in scheelite phase, tungsten atoms are four-fold coordinated by oxygen atoms with the mean distance R(W-O) = 1.78 Å and the Debye-Waller (DW) factor σ^2(W-O) = 0.002 Å^2. Next nearest oxygen atoms are expected at 3.08 Å [10] and do not contribute under the first peak in FT. An increase of pressure results in the rise of the DW factor to

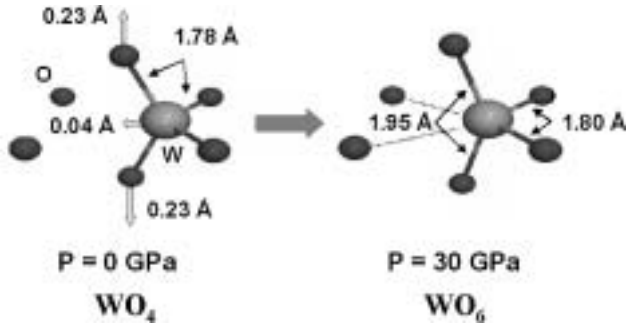

Fig. 4. Model of the local structure modification around tungsten atoms in $SrWO_4$ upon high-pressure phase transition. Large grey spheres are tungsten atoms, small black spheres are oxygen atoms. Wide arrows in the left part of the figure indicate directions of atomic displacements. The bonds of two weakly bound oxygen atoms, which complete the octahedron at high-pressure, are shown by dotted lines in the right part of the figure.

σ^2(W-O) = 0.007 Å^2, that indicates an increase of static disorder due to the beginning of tungsten atoms displacements.

Above the phase transition, the two-shells model becomes more adequate to describe the experimental EXAFS signals. The results suggest that there are two oxygen atoms at R(W-O) = 1.80 Å with σ^2(W-O) = 0.002 Å^2 and two oxygen atoms at R(W-O) = 1.95 Å with σ^2(W-O) = 0.005 Å^2 and C_3 = 0.006 Å^3.

Thus, the application of pressure forces tungsten atoms to displace by about 0.04 Å in the direction of the tetrahedron edge to reconstruct it till octahedron (Fig. 4). At the same time, two oxygen

atoms displace in opposite directions by about 0.23 Å, to allow for the tungsten to pass. As a result, the coordination of tungsten atoms at 30 GPa becomes distorted octahedral with two short (1.80 Å), two middle (1.95 Å) and two long bonds (not detectable in our experiment due to probably their large DW factors). The values of the W-O bonds in high-pressure phase are typical for octahedral coordination of tungsten atoms [13]. However, stronger bonding of tungsten atoms with four oxygen atoms show that tungstens tend to preserve tetrahedral-like environment. This conclusion is supported by recent high-pressure Raman studies [5]. It was found [5] that the frequency of the stretching $A_g(\nu_1)$ mode of the WO_4 tetrahedra changes smoothly across the phase transition pressure, suggesting sufficient stability of tetrahedral units.

4. Conclusions

The pressure-induced scheelite-to-wolframite structural transition in $SrWO_4$ was studied for the first time by in situ XAS and XRD techniques. We confirmed the occurrence of the phase transition at about 11.7 GPa. The analysis of the W L_3-edge EXAFS spectra allowed us to follow in details a transformation of tungsten coordination polyhedron from regular tetrahedron in scheelite phase to distorted octahedron in wolframite phase.

Acknowledgements

This work was supported by EC FP5 program "Access to Research Infrastructures", the CAMART project (WP-31) and Latvian Government grants 1.0811 and 1.0821.

References

1. Kaminskii, A. A., "Laser Crystals" (Springer, Berlin, 1981).
2. Sleight, A. W., Acta Cryst. B **28**, 2899 (1972).
3. Jayaraman, A., Phys. Rev. B **28**, 4774 (1983).
4. Christofilos, D., Ves, S. and Kourouklis, G. A., Phys. Stat. Sol. (b) **198**, 539 (1996).
5. Christofilos, D., Papagelis, K., Ves, S., Kourouklis, G. A. and Raptis, C., J. Phys. Condens. Matter **14**, 12641 (2002).
6. Comez, L., *et al.*, J. Synchrotron Rad. **8**, 776 (2001).
7. Kuzmin, A., Physica B **208**/**209**, 175 (1995).
8. Aksenov, V. L., Kuzmin, A. Y., Purans, J. and Tyutyunnikov, S. I., Phys. Part. Nucl. **32**, 675 (2001).
9. Ankudinov, A. L., Ravel, B., Rehr, J. J. and Conradson, S. D., Phys. Rev. B **58**, 7565 (1998).
10. Guermen, E., Daniels, E. and King, J. S., J. Chem. Phys. **55**, 1093 (1971).
11. Rehr, J. J., Mustre de Leon, J., Zabinsky, S. I. and Albers, R. C., J. Am. Chem. Soc. **113**, 5135 (1991); Mustre de Leon, J., Rehr, J. J., Zabinsky, S. I. and Albers, R. C., Phys. Rev. B **44**, 4146 (1991).
12. Kuzmin, A. and Purans, J., J. Phys.: Condens. Matter **5**, 9423 (1993).
13. Kuzmin, A. and Purans, J., Rad. Measurements **33**, 583 (2001).

Physica Scripta. Vol. T115, 559–561, 2005

Electrochemical Lithium Intercalation into Transition Metal Oxides

U. Haake, D. Lützenkirchen-Hecht* and R. Frahm

Institut für Materialwissenschaften und Institut für Experimentalphysik – FB 8, Bergische Universität Wuppertal, Gaußstr. 20, D-42097 Wuppertal, Germany

Received June 26, 2003; accepted December 18, 2003

PACS numbers: 82.47.Aa, 71.20.Tx, 61.10.Ht, 61.10.Kw

Abstract

Lithium intercalation and deintercalation in amorphous MoO_3-electrodes was investigated *in situ* using grazing incidence reflection mode X-ray absorption spectroscopy. Small changes observed in the near edge X-ray absorption spectra indicated that the Mo^{6+} ions are reduced by the electrochemical lithiation, leading to a formal Mo^{5+} oxidation state. Angle dependent experiments reveal that the intercalation is not complete for the applied conditions, i.e. the Li-ions are not homogeneously distributed in the entire volume of the amorphous working electrode. In addition, a certain amount of Li remains in the Mo-oxide electrode after a complete intercalation/deintercalation cycle. The results suggest that Li ions are accumulated at the electrode/electrolyte interface during both intercalation and deintercalation.

1. Introduction

Lithium ion intercalation in metal oxides is one of the main objectives of recent battery research (see, e.g. [1–3]). Rechargeable lithium ion batteries are attractive for their use as lightweight, compact energy storage devices in applications ranging from portable electronics to vehicles. Up to now, the published work mainly dealt with Li intercalation in crystalline oxide materials. The intercalation processes are in many cases limited by the diffusion of the Li ions into the electrode material, and thus amorphous electrodes should have principal advantages: Due to their more open structures, the diffusion of the inserted Li ions into the electrode should be significantly facilitated. Up to now, however, only few publications dealing with Li intercalation in amorphous electrode materials have appeared in the literature [4, 5]. These studies are based on electrochemical techniques and thus no information about the structural changes occurring during the intercalation could be derived so far. In this context, grazing incidence X-ray absorption spectroscopy is a well suited technique to obtain structural and electronic information about the electrode surfaces during the intercalation and de-intercalation *in situ*. We have studied Li-intercalation in different transition metal oxides such as Ta_2O_5, Nb_2O_5, MoO_3 and WO_3 [6]. In the present paper, we will focus on grazing incidence X-ray absorption near edge structure investigations of the lithiation of amorphous MoO_3-thin films.

2. Experimental

The X-ray absorption experiments presented here were performed at the bending magnet station RÖMO II [7] at the DORIS III storage ring at HASYLAB (Hamburg, Germany). A double-crystal monochromator with two flat Si(311) crystals was used. Reflectivity EXAFS data were collected at room temperature in the vicinity of the Mo K-edge (20000 eV). The incident, monochromatic X-ray beam was collimated to a size of about 240 µm (vert.) and 10 mm (horiz.). Incident and reflected intensities were measured by argon and argon/krypton filled ionization chambers. A second slit system in front of the second ionization chamber suppresses the intensity of non specularly reflected X-rays and shields this detector from the direct beam. All components of the reflectometer, i.e. the sample position, the angle of the detector arm and the slit system can be adjusted by stepper motors. Simultaneously with each EXAFS scan, a Mo metal foil was measured in transmission between the second and a third ionization chamber in order to calibrate the energy scale of the monochromator. Reference spectra were obtained in transmission from a Mo metal foil and polycrystalline MoO_2 and MoO_3 powders.

Thin film working electrodes (thickness ≈60 nm, length 10 mm, width ≈35 mm) were prepared by reactive magnetron sputtering from a Mo-metal target in an O_2-containing atmosphere. Smooth float glass covered with a thin electrical gold contact of about 10–20 nm thickness was used as substrate. The electrode was glued into the PTFE body of the electrochemical cell, which was sealed by two thin Kapton foils which served as X-ray windows. High purity Cu-wires were used as reference and counter electrodes and all the electrochemical preparations were performed in an electrolyte containing 1 M $LiClO_4$ in propylene carbonate (PC). The whole assembly was mounted in a metal vessel which was continuously flooded with He-gas in order to maintain an inert atmosphere for the experiments. The metal vessel has two X-ray windows for the impinging and the reflected beam and a third window in the top flange to visualize the surface of the electrode with a small video camera even during the X-ray experiments. More details about the cell will be given elsewhere [8].

3. Results and Discussion

In Figure 1, a near edge reflection mode XANES spectrum of the untreated Mo-oxide working electrode measured *in situ* under open circuit conditions is presented for a glancing angle $\Theta = 0.07°$. The edge position at about 20015 eV as well as the intense pre-edge feature at 20005 eV which are typical for MoO_3 [9] are clearly resolved. For the further data processing, a linear pre-edge background $R_0(E)$ was fitted to the experimental data as shown in Fig. 1 (a) and extrapolated to the post edge region. The normalized difference $R_0(E) - R(E)$ was calculated subsequently in order to obtain a measure of the absorption. In Fig. 1(b), these data are compared to the absorption of polycrystalline MoO_3 measured in transmission. Obviously, both spectra are very similar with respect to the edge position, the pre-edge peak and its intensity.

It is well known that electronic excitations can be observed in near edge X-ray absorption spectra depending on the

*e-mail: dirklh@uni-wuppertal.de

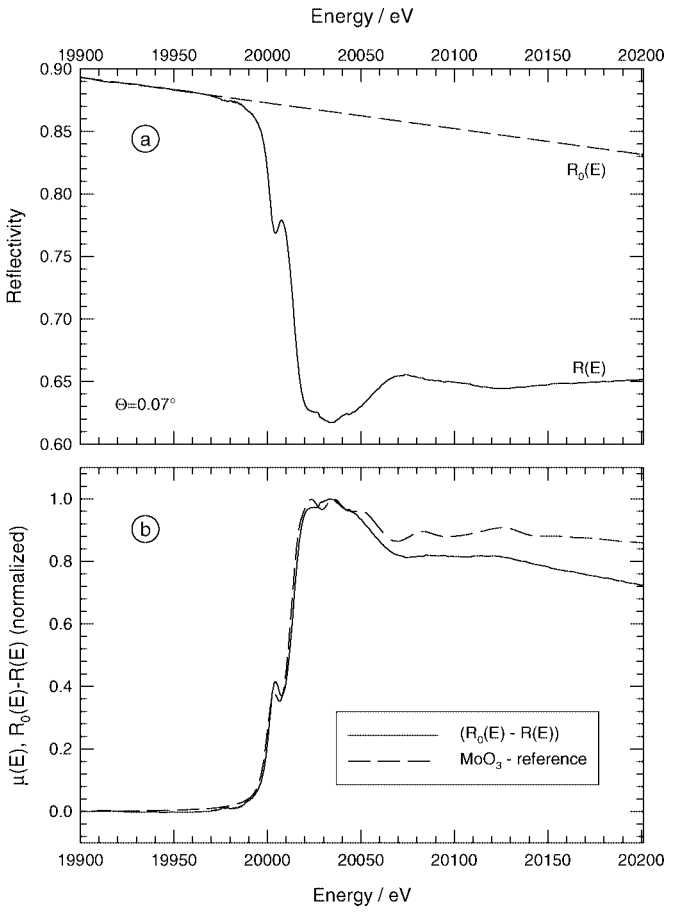

Fig. 1. (a) *In situ* reflection mode XANES spectrum of an amorphous MoO_3 working electrode ($\Theta = 0.07°$) in 1M $LiClO_4$ + propylene carbonate at the Mo K-edge. The pre-edge background $R_0(E)$ was subtracted from the spectrum in order to give approximate values for the absorption, which is compared to the normalized absorption of polycrystalline MoO_3 in (b).

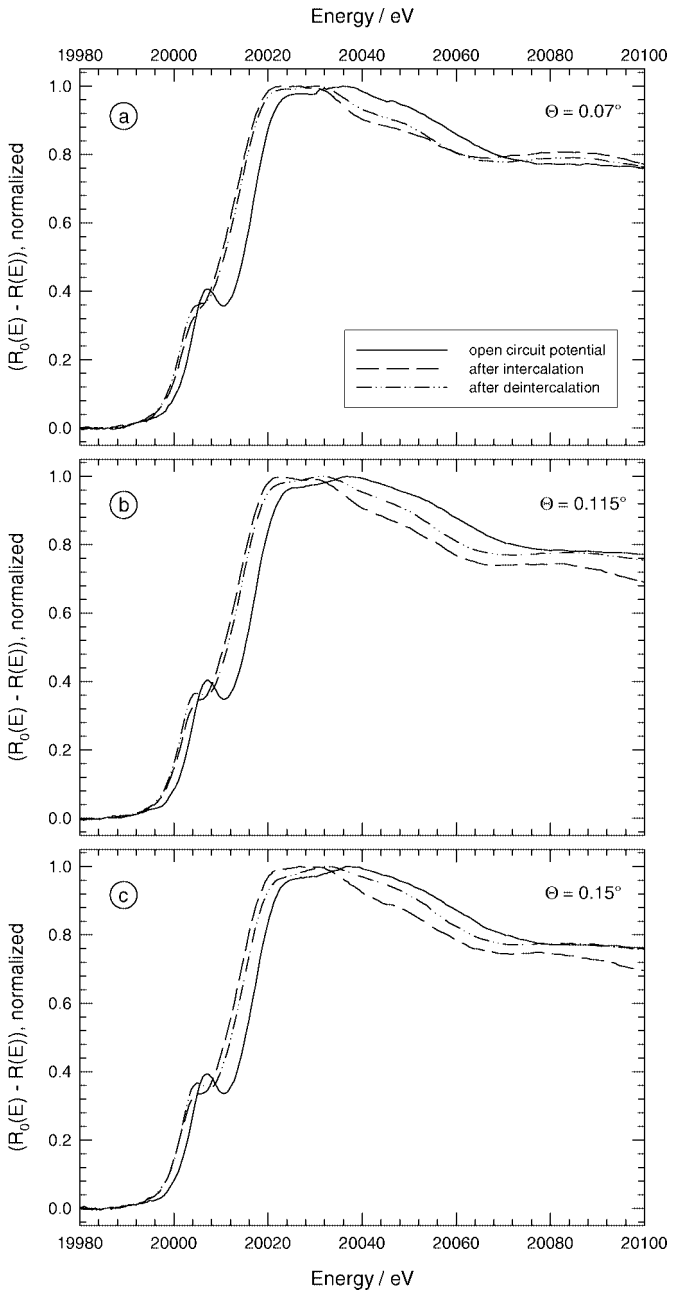

Fig. 2. Normalized difference spectra ($R_0(E) - R(E)$) obtained *in situ* from an amorphous MoO_3 electrode in 1 M $LiClO_4$ + propylene carbonate for different conditions and glancing angles.

local geometry [9, 10]. A pseudo-atomic model leads to the conclusion that the observed pre-edge structures may be due to $1s \rightarrow 4d$, $1s \rightarrow 5s$ and $1s \rightarrow 5p$ transitions [11]. The first of these transitions is partially allowed in a tetrahedral oxygen surrounding, but it is strictly forbidden in an octahedral oxygen geometry [11]. In crystalline MoO_3, the first Mo-O coordination consists of a complex structure with four short Mo-O distances between 1.67 and 1.94 Å with a structure close to a tetrahedron, and two additional long Mo-O distances of 2.25 and 2.33 Å which complete a deformed octahedral coordination [12]. This is the reason why a prepeak is observed for MoO_3, but not for MoO_2, which crystallizes in the rutile structure in which Mo is surrounded by 6 oxygen in a distorted Mo-O octahedra [9, 11, 12]. For an ideal tetrahedral Mo-O coordination, the intensity of the prepeak is even much more enhanced and a shift toward higher binding energy is observed, i.e. the position and the intensity of the prepeak are a sensitive tool for detailed studies of the Mo-O coordination [10, 13]. Thus, it can be concluded that the first coordination in the amorphous films does not consist of ideal tetrahedral structures but is more similar to that of polycrystalline MoO_3. Furthermore, also post edge features at about 20022–20050 eV are located at similar energies for both samples, whereas their intensity differs significantly. These differences may be related to the influence of the rather simple treatment of the reflectivity data and the influence of the anomalous dispersion – it has to be kept in mind that both the imaginary and the real part of the refractive index $n(E) = 1 - \delta(E) - \mathrm{i} * \beta(E)$ contribute to the reflectivity [14].

In Fig. 2, normalized difference spectra $R_0(E) - R(E)$ are shown for several grazing angles and different experimental conditions. Spectra of the sample at open circuit conditions prior to any electrochemical treatment are compared to those after the Li-intercalation at −1.54 V (vs. Cu) for 2 h and to spectra measured after the deintercalation at +0.9 V (vs. Cu) for 2 h. The most obvious change after the intercalation is the shift of the Mo K-edge position towards smaller values, i.e. the Mo^{6+} states of the amorphous MoO_3-electrode are electrochemically reduced. Furthermore, the position of the prepeak is also shifted to smaller energies and its intensity is reduced. After the electrochemical deintercalation, a slight shift of the edge towards higher energies is observed. However, the edge position of the untreated MoO_3 electrode is not reproduced, suggesting that a certain amount of Li remains within the Mo-oxide sample.

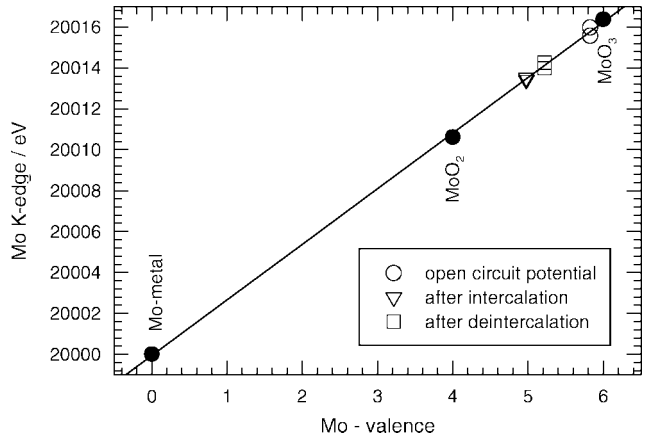

Fig. 3. Mo K-edge positions and chemical valences of polycrystalline Mo-reference compounds (Mo-metal, MoO_2, MoO_3). Indicated are the edge positions and the determined valences calculated from *in situ* measured grazing incidence Mo K-edge spectra prior to the lithiation (open circuit potential), after intercalation at -1.54 V and deintercalation at $+0.9$ V.

A closer inspection of the graphs also shows that the observed features change as a function of the grazing angle. For example, the shift between the XANES spectrum of the intercalated sample and that of the deintercalated sample is larger for a grazing angle $\Theta = 0.15^\circ$ compared to $\Theta = 0.07^\circ$ and $\Theta = 0.115^\circ$. This observation can easily be understood if a layered structure consisting of a thin Li_xMoO_3 layer on top of the bare MoO_3-oxide is assumed as follows. The penetration depth for the X-rays is about 3–4 nm for $\Theta = 0.07^\circ$, ca. 40 nm for 0.115° and ca. 300 nm for 0.15°. For the intercalated sample, the measured spectra at 0.07° and 0.115° are very similar, while small changes are observed for the spectrum at 0.15°. Therefore it can be assumed that the intercalated layer has a thickness of about 40–50 nm, and that the inner region of the MoO_3 layer towards the gold contact is not affected by the intercalation. Furthermore, after deintercalation, changes are visible between the spectrum recorded at 0.07° and 0.115°, thus the Mo-oxide electrode is not deintercalated completely. Still, Li ions are accumulated in a thin surface layer of about 10–20 nm thickness.

The edge positions and the chemical valences derived from the reflection mode near edge spectra measured at 0.07° are compared to those of Mo-oxide reference compounds in Fig. 3. First of all, the edge position of the electrode under open circuit conditions is almost identical to that of polycrystalline MoO_3 as already deduced from Fig. 1. Assuming a linear relation between the Mo K-edge position and the valence, we determined a value of about +5 for the Mo valence after the intercalation at -1.54 V for 2 h, and a slightly increased value of about +5.2 after the deintercalation at +0.9 V. Since the penetration depth is only some few nm for these experiments, the similarity of the derived edge positions clearly indicate that Li ions are accumulated at the electrode/electrolyte interface during the both the intercalation and the deintercalation. This agrees quantitatively with the edge positions determined for higher grazing angles, for which the edge positions are shifted to higher energies as can be seen in Fig. 2(b) and (c). This data interpretation is also consistent with results of extended X-ray absorption spectroscopy investigations [6, 8]. In the future, further time dependent grazing incidence XAFS experiments are very desirable in order to obtain a comprehensive picture of the structural changes of the amorphous Mo-oxide electrodes during the intercalation and deintercalation at different potentials. This also comprises a detailed analysis of EXAFS data.

Acknowledgement

We like to thank P. Keil and K. Bruder for their help at the beamline. Financial support by the MWF Nordrhein-Westfalen and HASYLAB is greatfully acknowledged.

References

1. Huang, S. Y., Kavan, L., Exnar, I. and Grätzel, M., J. Electrochem. Soc. **142**, L142 (1995).
2. Bonino, F., Busani, L., Manstretta, M., Rivolta, B. and Scosati, B., J. Power Sources **6**, 261 (1981).
3. Ohzuku, T., Kodama, T. and Hirai, T., J. Power Sources **14**, 153 (1985).
4. Frenning, G., Nilsson, M., Westlinder, J., Niklasson, G. A. and Strømme-Mattson, M., Electrochim. Acta **46**, 2041 (2001).
5. Frenning, G., Engelmark, F., Niklasson, G. A. and Strømme, M., J. Electrochem. Soc. **148**, 418 (2001).
6. Haake, U., Diploma Thesis, Universität Wuppertal (2003).
7. Frahm, R., Rev. Sci. Instr. **60**, 2515 (1989).
8. Haake, U., Lützenkirchen-Hecht, D. and Frahm, R., Electrochimica Acta, in preparation.
9. von Hippel, L. M. J., Hilbrig, F., Schmelz, H., Lengeler, B. and Knözinger, H., Collect. Czech. Chem. Commun. **57**, 2465 (1992).
10. Kutzler, F. W., Natoli, C. R., Misemer, D. K., Doniach, S. and Hodgsen, K. O., J. Chem. Phys. **73**, 3274 (1980).
11. Chiu, N. S., Bauer, S. H. and Johnson, M. F. L., J. Catal. **89**, 226 (1984).
12. Gmelin, "Handbuch der Anorganischen Chemie", 8. Aufl., Molbydän, Ergänzungsband B2, (Springer Verlag: Berlin, Heidelberg, New York, 1986).
13. Lützenkirchen-Hecht, D. and Frahm, R., J. Phys. Chem. **B 105**, 9988 (2001).
14. Heald, S. M., Rev. Sci. Instrum. **63**, 873 (1992).

Physica Scripta. Vol. T115, 562–563, 2005

Local Structures of Liquid Semi-Metal Sb Studied by *in-situ* XAFS

Wensheng Yan[1], Chenxi Li[2], Shiqiang Wei[1*], Zhonghua Wu[3], Xiaojuan Niu[1], Wei Chen[2], Kunquan Lu[2] and Tomaya Uruga[4]

[1]National Synchrotron Radiation Laboratory, University of Science and Technology of China, Hefei 230029, P.R. China
[2]Institute of Physics, Chinese Academy of Sciences, Beijing 100080, P. R. China
[3]Institute of High Energy Physics, Chinese Academy of Sciences, Beijing 100039, P.R. China
[4]Japan Synchrotron Radiation Research Institute, Kouto, Mikazuki, Sayo-gun, Hyogo 679-5198, Japan

Received June 26, 2003; accepted January 8, 2004

PACS numbers: 61.10.Ht, 61.25.Mv; 64.70.Dv

Abstract

The local structures of semi-metal Sb have been studied by *in-situ* XAFS in the temperature range of 298 and 913 K. The radial structural functions of Sb atoms reveal that the local structure of the pre-molten Sb (893 K) is similar to that of crystalline Sb (298 K), except the increase of thermal disorder degree. With the temperature increasing up to 913 K, the position of the first peak located at 2.63 Å in the liquid Sb is kept the same as that in the pre-molten Sb, while the intensity of the first peak is strongly reduced by about 30% during the solid-liquid transition. This feature indicates that the melting results in a large increase of disorder degree of the liquid Sb, and that there exists covalent bonded clusters $(Sb)_n$ in the liquid Sb (913 K).

1. Introduction

It is well known that there are larger difficulties in performing a reliable structural study on the molten matters from the viewpoint of theory and experiment [1]. Up to date, no clear structural information in the liquid area has been shown for most of phase diagrams of metals, alloys and compounds [2]. However, it is essential to understand the structures and properties of the molten matter, since these high quality materials such as semiconductors, metals and alloys, are generally coming from their molten states. In the last two decades, Möller *et al*. [3] Bellissent -Funel *et al*. [4] Zhang *et al*. [5] and Mizuki *et al*. [6] have studied the structures of liquid metallic Sb, Ga, GaAs and GaSb with X-ray diffraction (XRD) and neutron diffraction (ND). More recently, because of the applications of the high brilliance synchrotron radiation light source, a high ratio of signal to noise could be obtained for the data of the liquid matters by X-ray absorption fine structure (XAFS). Filipponi *et al*. [7] and Wang *et al* [8] have investigated the local structures of liquid Rh, Pd and GaSb (or InSb) with *in situ* XAFS.

Sb is a unique element, which is a semi-metal at ambient condition with the density of 6.684 g/cm^3 and conductance of 1.11×10^3 $(\Omega{\cdot}\mathrm{cm})^{-1}$, and that is a liquid metal at above melting point (903 K) with the density of 6.53 g/cm^3 and conductance of 5.45×10^3 $(\Omega{\cdot}\mathrm{cm})^{-1}$ [9]. In early stage, Lamparter *et al*. [10] have studied the structure of the liquid Sb with neutron diffraction (ND) technique, and reported that the coordination number N of the first shell of liquid Sb is about 4.6. Whereas, Waseda *et al*. [11] have showed that the N of the first shell of liquid Sb is about 8.7 from their ND results. They have given a contradictory interpretation on the structure of the molten Sb. In order to understand the structure and property of the liquid Sb, it is necessary to make a reliable study for the structure of the liquid Sb.

In the present paper, *in situ* XAFS has been used to measure the local structures of the pre-molten and liquid element Sb.

2. Experimental

The fine powders of Sb (about 10 μm size), which were prepared from single crystals by grinding and sieving, were sufficiently mixed with LiF powder made from a single crystal. The mixed powder was pressed into tablets of diameter 10 mm and thickness 1 mm. The ratio of Sb to LiF powder was optimized as the X-ray absorption jump $\Delta\mu \approx 1$ at the Sb K-edge. The tablet was sealed in a vacuum quartz tube and sintered at 880 K for about 4 h, and then put into a quartz sample holder with two thin windows (of thickness 200 μm) sealed in the vacuum.

The measurements of Sb K-edge XAFS spectra were performed at the BL01B1 of SPring-8 of Japan Synchrotron Radiation Research Institute. The electron energy was about 8 GeV with a maximum current of 100 mA. The Si(311) double crystal was used as monochromator. For the higher harmonics rejection an Rh-coted quartz mirror was used. Data were collected in transmission mode using ion chambers filled with the mixed gas of Kr/Ar at the temperatures of 298, 893 and 913 K, respectively. XAFS data of Sb samples were analyzed by USTCXAFS3.0 [12] and UWXAFS3.0 codes [13].

3. Results and discussions

The Sb K-edge XAFS spectra for the antimony at the temperatures of 298, 893 and 913 K are shown in Fig. 1 (the melting point of crystalline Sb is 903 K). It can be observed clearly that the shape of the XAFS spectrum for the pre-molten Sb (893 K) is similar to that of crystalline Sb (298 K). In the energy range from 50 to 400 eV above the K-edge for crystalline Sb (298 K), there are six XAFS oscillation peaks located at 30550, 30586, 30635,

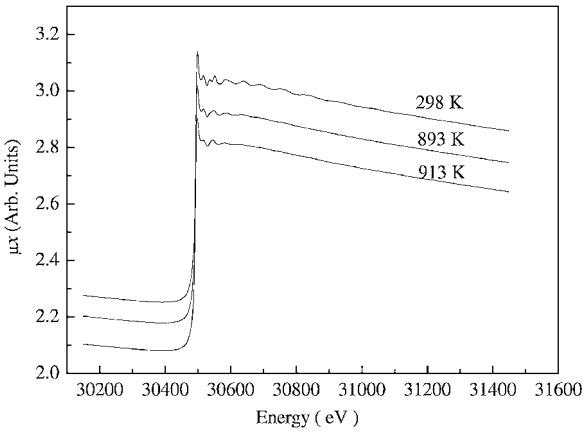

Fig. 1. The Sb K-edge XAFS spectra for the Sb at the temperatures of 298, 893 and 913 K.

*Correspondent: Shiqiang Wei, E-mail: sqwei@ustc.edu.cn

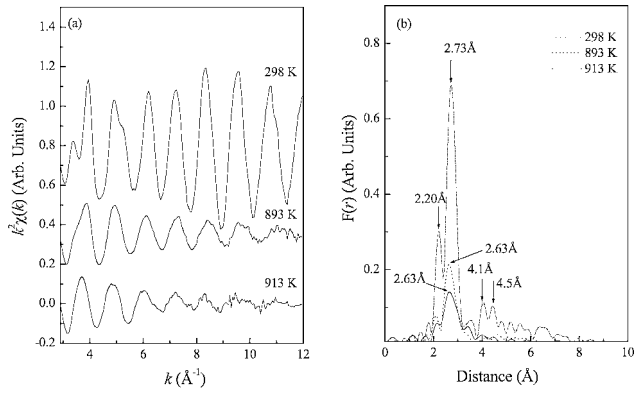

Fig. 2. (a) The Sb K-edge XAFS functions $k^2\chi(k)$, (b) the radial structural functions for the Sb at the temperatures of 298, 893 and 913 K.

30688, 30759 and 30835 eV, respectively. As the temperature increases to 893 K, the oscillation amplitudes of the pre-molten Sb (893 K) drop markedly for these peaks from the fourth to the sixth. This feature shows that the local structure of the pre-molten Sb (893 K) is mostly identical with that of Sb (298 K), except a large increase in the disorder degree. When the temperature rises to 913 K, only three peaks located at 30546, 30581 and 30625 eV can be observed evidently in the XAFS spectrum of the liquid Sb (913 K) in the energy range from 50 eV to 400 eV above the K-edge. The positions of these oscillation peaks shift to the lower energy side by about $4 \sim 10$ eV and the amplitudes drop obviously as compared with those of Sb (298 K). This result indicates that the coordination environment and the disorder degree around Sb atoms in the liquid Sb (913 K) change largely in the process of solid-liquid transition.

Fig. 2 (a) and (b) demonstrates the Sb K-edge XAFS functions $k^2\chi(k)$ and the radial structural functions (RSF) for the Sb samples at the temperatures of 298, 893 and 913 K. Seen from Fig. 2 (a), the magnitude of the oscillations of the liquid Sb (913 K) strongly decreases in the high k range, compared with that of the pre-molten Sb (893 K). It means that the melting can increase the disorder degree around Sb atoms greatly. Furthermore, Fig. 2 (b) shows that there are three peaks located at 2.73, 4.1 and 4.5 Å in the RSF curve for the Sb (298 K). The main peak at 2.73 Å (un-calibrated) is corresponding to the first coordination shell of Sb in which the bond length R_1 and coordination number N_1 of the first sub-shell are 2.90 Å and 3, and that the R_2 and N_2 of the second sub-shell are 3.36 Å and 3. The shoulder peak at 2.20 Å originates from the non-linearity of the phase shift function of back-scattering atom Sb. The two peaks located at 4.1 and 4.5 Å are contributed to the XAFS signals of the Sb-Sb second shell and the Sb-Sb-Sb multiple scattering paths. Compared with the RSF of the Sb (298 K), the intensity of main peak for the pre-molten Sb (893 K) drops abruptly by about 70%, and its position moves by about 0.1 Å toward low-R direction. Moreover, the peaks at 4.1 and 4.5 Å corresponding to the high coordination shells almost disappear for the pre-molten Sb (893 K). With the temperature further increasing to 913 K (exceeding the melting point of Sb), the position of the main peak of the liquid Sb corresponding to the first coordination shell is kept the same as that of the pre-molten Sb (893 K), while its intensity decreases by about 30% of that of the pre-molten Sb (893 K).

In the previous studies of liquid matters [14], Stern *et al.* [15], Wei *et al.* [16] as well as Di Cicco *et al.* [17] have investigated the local structures of Pb and Ga with XAFS. They have found that the positions of the first RSF peak for both Pb and Ga atoms move by about $0.1 \sim 0.2$ Å toward the low-R direction during the process of solid-liquid transition. Hoshino *et al.* [18] have reported the local structures of As_2Se_3 covalent compound in the solid and liquid states. Their XAFS results have shown that the positions of the first RSF peak of both As and Se atoms always remain at about 2.5 Å in the liquid or solid state of As_2Se_3. Tamure *et al.* [19] have studied the local structures of solid and liquid Te with XAFS. Their results indicate that the position of the first peak of the solid Te shifts by about 0.1 Å toward the low-R direction when the temperature increases from 298 to 573 K, but the melting does not change the RSF peak position of Te. Summarizing above results, one can find that in temperature range of the solid state, the change of RSF curves of the Sb with temperature is similar to those of metallic elements (i.e., Pb, Ga and Te), but is different from those of As and Se in the A_2Se_3 covalent compound. However, in the process of solid-liquid transition, the change of RSF curves of the Sb is similar to those of element Te and covalent compound As_2Se_3. In addition, Menelle *et al.* [20] and Yamagcuchi *et al.* [21] have investigated the structure of the liquid Te using the neutron diffraction technique. Their results imply that there are fragmented-chains $(Te)_n$ connected by the covalent bonds in the liquid Te. Hence, the local structural change of Sb with the temperatures is in good agreement with that of Te in the solid and liquid state. Similarly, we consider that there may exist $(Sb)_n$ clusters combined by the covalent bonds in the liquid Sb (913 K). The quantitative structural studies of the pre-molten and liquid Sb by the reverse Monte Carlo calculation will be published elsewhere.

Acknowledgments

We would like to thank SPring-8 for giving us the beam time for XAFS measurement. This work was supported by the Chinese National Science Foundation Committee (Grant No.10174068) and the development of high-level university of University of Science and Technology of China.

References

1. Crozier, E. D., Physica B **208–209**, 330 (1995).
2. Wisterdam, Jaime, "Phase diagram: a literature source book" (Elsevier Scientific Pub. Co., Amsterdam, 1981).
3. Möller, H. K. F. and Hendus, H., Z. Naturforsch. **12a**, 102 (1957).
4. Bellissent-Funel, M. C., Levesque, D. and Weis, J. J., Phys. Rev. A **39**, 6310 (1989).
5. Zhang, Q. M., Chiamtti, G., Selloni, A., Car, R. and Paninello, M., J. Non-Cryst. Solids **117**, 8930 (1990).
6. Mizukil, J., Kakimotot, K., Misawat, M., Fukunagas, T. and Noboru, W., J. Phys.: Condens. Matter **5**, 3391 (1993).
7. Filipponi, A., Di Cicco, A. and Panfilis, S. D., Phys. Rev. Lett. **83**, 560 (1999); J. Phys.: Condens. Matter **11**, L43 (1999).
8. Wang, Y. R., Lu, K. Q. and Li, C. X., Phys. Rev. Lett. **79**, 3644 (1997).
9. Warren, W. W. and Clark, W. G., Phys. Rev. **177**, 600 (1969).
10. Lamparter, P., Martin, W., Steed, S. and Freyland, W., J. Non-Cryst. Solids **61**, 279 (1984).
11. Waseda, Y., "The Structure of Non-Crystalline Materials: Liquids and amorphous Solids" (McGraw-Hill, New York, 1980).
12. Zhong, W. J. and Wei, S. Q., J. of Univ. Sci. Technol. China **31**, 328 (2001).
13. Stern, E. A., Newville, M., Ravel, B., Yacoby, Y. and Haskel, D., Physica B **208–209**, 117 (1995).
14. Filipponi, A., J. Phys.: Condens. Matter **13**, R23 (2001).
15. Stern, E. A., Living, P. and Zhang, Z., Phys. Rev. B. **43**, 8850 (1991).
16. Wei, S. Q., *et al.*, J. Non-Cryst. Solids **275**, 160 (2000).
17. Di Cicco, A. and Filipponi, A., Europhys. Lett. **27**, 407 (1994).
18. Hoshino, H., Yamamoto, I., Miyanaga, T., Ikemoto, H. and Endo, H., J. Non-Cryst. Solids **250–252**, 478 (1999).
19. Tamura, K., *et al.*, J. Phys.: Condens. Matter **3**, 7495 (1991).
20. Menelle, A., Bellissent, R. and Flank, A. M., Physica B **156–157**, 174 (1989).
21. Yamaguchia, T., Ohtanib, H. and Yonezawab, F. J., Non-Cryst. Solids **250–252**, 437 (1999).

Physica Scripta. Vol. T115, 564–566, 2005

In situ X-ray Absorption Spectroscopic Study of Oxide Film on Fe Alloy

Jin Suk Kim, Chang Hwan Chang* and Kyoo Young Kim

Department of Materials Science and Engineering, Pohang University of Science and Technology, San 31, Hyoja-Dong, Nam-gu, Pohang 790-784, Korea
*Materials Analysis Team, Research Institute of Industrial Science & Technology PO Box 135, Pohang 790-600, Korea

Received June 26, 2003; accepted November 4, 2003

PACS number: 61.10.Ht

Abstract

The nature of passive film grown on the bulk surface of Fe-20Cr alloy in a pH 8.4 boric-borate buffer was investigated with *in situ* synchrotron X-ray absorption spectroscopy. The main electrochemical test method was potentiostatic polarization and various potentials were applied from −1.0 V to 0.6 V vs. saturated calomel electrode (SCE). X-ray absorption data from the passive film formed in the boric-borate buffer were collected from an *in situ* reflection X-ray absorption spectroscopic experiment in a grazing-incident geometry that is suitable for investigating the nanometer-thick passive film. It was observed in the Fe K-edge XANES (X-ray absorption near-edge structure) region that the Fe absorption edge moved from the absorption edge of metal Fe to that of Fe oxide as the applied potential increased. It was observed from an analysis of the Radial Distribution Function (RDF) from Fe K-edge EXAFS (Extended X-ray Absorption Fine Structure) data that the Fe-Fe bond intensity of the first shell decreased and Fe-O bond intensity increased as the applied potential increased. The RDF of the Fe oxide is consistent with γ-Fe_2O_3.

1. Introduction

Despite many investigations, the nature and stability of the passive film on Fe alloy in borate buffer solution is still poorly understood. Much of the research performed has been on the iron/borate buffer system. The system was chosen due to the high efficiency of film formation and the thin, protective passive film that is formed. But, one of the major problems in investigating the passive film is that the separation of the behavior of passive film from that of the underlying metal or alloy is not a straightforward task. In order to obtain information purely on the passive film, studies on model systems such as synthetic bulk or thin film oxides are necessary. Sugimoto *et al.* studied the chemical stability of synthetic (Fe, Ni, Cr)-oxide films prepared by metal-organic chemical vapor deposition in a strong HCl solution and showed that the corrosion rate is mainly determined by the chromium content of the mixed oxides [1]. However, the reaction mechanism of oxide in a certain solution can be explained with using synthetic oxide but the experiment using synthetic oxide cannot give an account of the oxide structure formed on the bulk metal surface. Another problem is that the passive film formed in an aqueous solution could be analyzed in an *in-vacuo* condition by XPS and AES so far. The passive film formed on the surface of metal in a solution is likely to vary its physical and chemical property with time out of the solution. Thus, we have not been able to define the nature of passive film in a solution exactly. Bardwell *et al.* found that Cr(IV) ion in passive film on Fe-26Cr was completely absent several hours after air exposure [2]. Recently, in order to overcome the problem, an attempt on *in-situ* passive film in solution were made with synchrotron radiation [3–7].

In situ XANES studies by Nagayama and Cohen provided considerable insight into the nature of the passive film on iron [8]. They suggested that the passive film is a multi-layer structure, consisting of an inner layer of Fe_3O_4 and an outer layer of γ-Fe_2O_3, which is cation deficient at the surface. Davenport *et al.* reported that the passive film on iron at 0.4 V mercurous sulfate electrode (MSE) in a pH 8.4 borate buffer resembled a ferric oxide such as γ-Fe_2O_3 [3]. A recent *in situ* X-ray diffraction measurement of the passive film on iron in a borate buffer confirms the spinnel structure although the oxide differs from the standard bulk γ-Fe_2O_3 and Fe_3O_4 [9]. But most *in situ* corrosion studies have been performed with a sputtered thin film metal or oxide, so the properties of passive films on these samples may be different from the passive film formed on the bulk metal surface. The main purpose of this study is to investigate the passive film grown on the bulk metal surface by *in situ* synchrotron X-ray absorption spectroscopy. In this study, XANES and EXAFS data are collected from passive film on Fe-Cr alloy at a specific potential in the pH 8.4 boric-borate buffer solution.

2. Experimental Procedure

Synchrotron X-ray absorption data were collected at 8C1 XRD/XAS beamline at the Pohang Light Source (PLS). For the analysis of thin passive film on the alloy surface, the reflection XAS method in grazing-incident geometry was used. In reflection XAS (X-ray Absorption Spectroscopy) measurements, the angle of incident X-ray beam was adjusted to be lower than the critical angle of the alloy for inducing a total reflection of X-rays, and a Si(Li) scintillation detector counted the reflected X-rays. Before the *in situ* XAS experiment, the critical angle for the total reflection was determined to be 0.375° from X-ray reflectivity measurement of the alloy. The incident angle of X-ray beam was fixed at 0.3° during the *in situ* XAS measurement. The focused size of X-ray beam used for the XAS experiment was 3 mm(H) 0.5 mm(V).

The specimen having a dimension of 1.8 mm(w) × 10 mm(l) × 4 mm(t) was prepared from Fe-20Cr alloy. The bulk specimen sat at the center of a chemical cell for the *in situ* XAS experiment, held by an epoxy regin that also provided an electrical connection (Figure 1). Ports in the cell allowed insertion of a platinum wire counter electrode and saturated calomel electrode (SCE) reference. A polymide film was used as an X-ray window. The test solution was a pH 8.4 boric-borate buffer solution. The passive film was grown artificially by applying potentials of 0.0, 0.2, 0.4, 0.6 V for a passivation time of 120 min. The EXAFS data were collected after the passivation time. In order to minimize X-ray absorption through the test solution, the specimen width was reduced to 1.8 mm and the real path length of X-rays in the cell was 2.0 mm.

*Electronic address: chchang@rist.re.kr

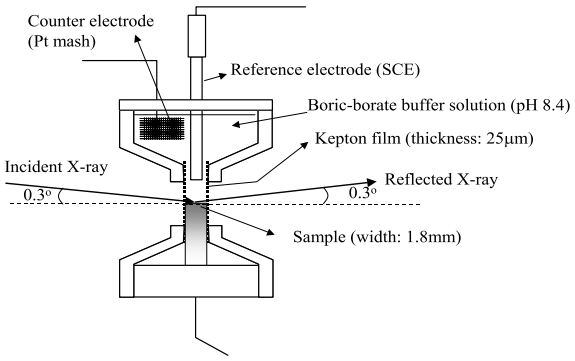

Fig. 1. Schematic diagram of *in situ* electro-chemical cell.

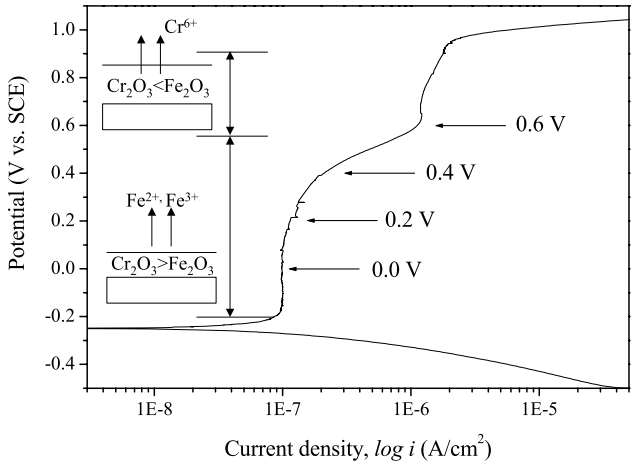

Fig. 2. Potentiodynamic curve of Fe-20Cr in pH 8.4 boric-borate buffer solution.

3. Results and Discussion

For the determination of applied potential, a potentiodynamic test was performed. Figure 2 shows a potentiodynamic curve of Fe-20Cr alloy in pH 8.4 borate buffer solution at room temperature. There are several reports explaining the passive film structures in the distinct potential regions [10, 11]. For low passive potentials below 0.6 V, the film consists of a mixture of Fe_2O_3 and Cr_2O_3 but in this potential range Cr_2O_3 is predominantly formed on the steel surface. Above a potential of 0.6 V, Cr_2O_3 is dissolved out in solution as Cr(VI) ion and Fe_2O_3 is the dominant element of the passive film.

Figure 3 shows the variation of normalized Fe K-edge XANES and EXAFS spectra as a function of applied potential. The XANES curves below the potential of 0.6 V are nearly similar to the pure Fe, but a shift of absorption edge is clearly observed at the potential of 0.6 V. Generally, the edge energy of Fe is shifted to higher values as the average valence of iron increases, thus, the edge position is a clear indication of the valence number. So, the edge shift observed from Figure 3 indicates that Fe is correlated with the metal elements in passive film below the potential of 0.6 V. In this region, although the surface of an alloy can be covered with a Fe-Cr complex oxide, Cr oxide may be more stable than Fe oxide because Fe oxide can be dissolved out as Fe^{2+} and Fe^{3+}. In this case, Fe oxide can not be observed dominantly in the XAFS measurement. However, Cr oxide can be dissolved out as Cr^{6+} above the potential of 0.6 V and the ratio of Fe oxide to Cr oxide increases with the passivation time [12]. From this time, Fe oxide can be measured in XAFS.

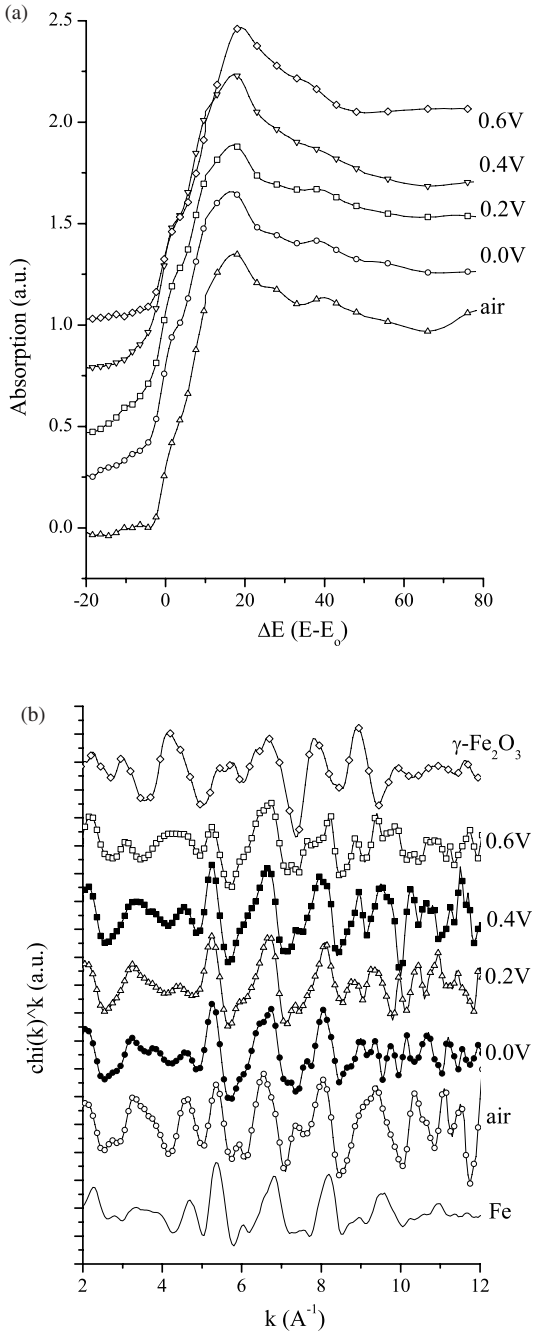

Fig. 3. XANES and EXAFS spectrum from Fe-20Cr alloy measured at Fe K-edge of 7112 eV as a function of applied potential in pH 8.4 buffer solution. (a) XANES spectra, (b) EXAFS spectra.

Figure 4 (a) shows the magnitude of Fourier transformations of the XAFS data at potentials of 0.2 V and 0.6 V, and those of pure Fe and various oxides. The RDF was calculated from the measured XAFS data by using UWXAFS program. The XAFS data was not good enough to obtain chemical information of Fe atom with simulation. So the nature of passive film was identified in comparison with Radial Distribution Functions (RDF) of pure Fe and various Fe oxides. The first shell of pure Fe and γ-Fe_2O_3 was calculated from data measured from reference sample as shown in Figure 4 (b). At an applied potential of 0.2 V, the RDF of the first shell is analogous to that of pure Fe. At this potential, Cr oxide may be more stable than Fe oxide. The penetration depth of X-rays in the passive layer at the incident angle of 0.3° was calculated to be $\sim$ 40 Å [13]. Generally, the thickness of the passive film formed on stainless steel has a range from 10 to 40 Å. In addition, the

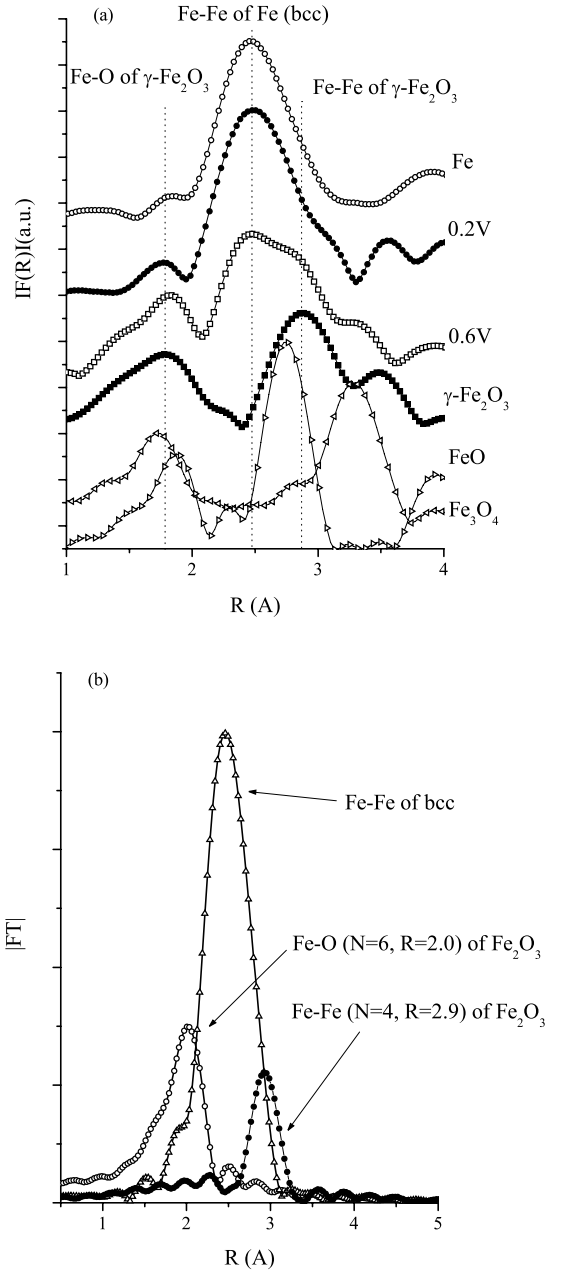

Fig. 4. (a) Magnitude of Fourier transformation of EXAFS data from applied potential of 0.2 V and 0.6 V, and those of pure Fe and other Fe-oxide sample. All spectra have been transformed over $k = 3.0\,\text{Å}^{-1}$ to $k = 11\,\text{Å}^{-1}$ using a hannig window function times k. (b) First shell of Fe and γ-Fe_2O_3 calculated from theoretical data.

thickness of passive film composed of Cr oxide has a range from 5 to 30 Å. Thus, in this potential range, the substrate effect cannot be completely ruled out even with the grazing-incident reflection method. However, as the potential increases, the intensity of Fe-Fe bond decreases and the Fe-O and Fe-Fe single scattering bond of γ-Fe_2O_3 appear clearly at a potential of 0.6 V. The thickness of Cr oxide in passive film may have a limitation by dissolution of Cr oxide in the high potential range. The potentiodynamic curve also shows an increase of current density from 0.6 V, presumably due to the dissolution of Cr oxide as CrO_4^{2-}. Due to the dissolution of Cr_2O_3 by oxidation, the passive film becomes porous and the ratio of Fe oxide to Cr oxide may increase. From the RDF analysis, the valid Fe oxide seems to be γ-Fe_2O_3.

4. Conclusion

We have studied the passive film grown on bulk metal surface as a function of applied potential by *in situ* reflection XAS method for Fe K-edge. In boric-borate buffer solution, Fe oxide in passive film seems to be unstable at potentials below 0.6 V. The RDF analysis indicates that Fe appears to be correlated with metallic element in this region. However, at a potential of 0.6 V, it was observed that the absorption edge of Fe moved from metal Fe absorption edge to Fe oxide absorption edge. It seems that the Fe oxide formed on Fe-20Cr alloy at the potential 0.6 V is γ-Fe_2O_3.

Acknowledgment

The authors thank M. K. Joo, Materials Analysis Team at RIST, for his help with XAS measurements at the 8C1 POSCO XRD/XAS beamline. This work was supported by RIST (Project No. 2001H082).

References

1. Sugimoto, K., Seto, M., Tanaka, S. and Hara, N., J. Electrochem. Soc. **140**, 1586 (1993).
2. Bardwell, J. A. *et al.*, J. Electrochem. Soc. **139**, 371 (1992).
3. Davenport, A. J. and Sansone, M., J. Electrochem. Soc. **142**, 275 (1995).
4. Schmuki, P., Virtanen, S., Davenport, A. J. and Vitus, C. M., J. Electrochem. Soc. **143**, 574 (1996).
5. Schmuki, P., Virtanen, S., Davenport, A. J. and Vitus, C. M., J. Electrochem. Soc. **143**, 3997 (1996).
6. Oblansky, L. J., Davenport, A. J., Ryan, M. P., Isaacs, H. S. and Newman, R. C., J. Electrochem. Soc. **144**, 2398 (1997).
7. Schmuki, P. *et al.*, J. Electrochem. Soc. **145**, 791 (1998).
8. Nagayama, M. and Cohen, M., J. Electrochem. Soc. **109**, 781 (1962).
9. Ryan, M., Newman, R. C. and Thompson, G. E., J. Electrochem. Soc. **142**, L177 (1995).
10. Tanaka, S., Hara, N. and Sugimoto, K., Mater. Sci. Eng. A. **198**, 63 (1995).
11. Haupt, S. and Strehblow, H.-H., Corros. Sci. **37**, 43 (1995).
12. Doh, S. J. *et al.*, Nucl. Inst. Meth. B. **199**, 211 (2003).
13. Qvarfort, R., Corros. Sci. **40**, 215 (1998).

Physica Scripta. Vol. T115, 567–569, 2005

XAFS Analyses of Zinc Compound in Corrosion Product for Magnesium Alloy of Super Plastic Processing

T. Honma[1*], H. Mori[2], K. Higashi[3], H. Okado[1], K. Maehara[4], I. Hirosawa[1] and N. Umesaki[1]

[1]Japan Synchrotron Radiation Research Institute, Mikazuki, Hyogo 679-5198, Japan
[2]Railway Technical Research Institute, Kokubunji, Tokyo 185-8540, Japan
[3]Graduate School of Engineering, Osaka Prefecture University, Sakai, Osaka 560-0043, Japan
[4]Nittech Research Corporation, Himeji, Hyogo 671-1116, Japan

Received June 26, 2003; accepted November 4, 2003

PACS numbers: 61.10.Ht, 82.45.Bb, 62.20.Fe

Abstract

X-ray absorption fine structure measurements at zinc K-edge in the corrosion product of super plastic processed zinc doped magnesium alloy has been performed to clarify the corrosion mechanism. The XANES spectra and the radial distribution functions obtained from Fourier transformed EXAFS oscillations of the corrosion product of zinc doped magnesium alloy and reference compounds of ZnO, zinc carbonate ($2ZnCO_3{\cdot}Zn(OH)_2{\cdot}H_2O$), $ZnCl_2$ and zinc foil suggest that the local structure of Zn compound in corrosion product is close to that of zinc carbonate.

1. Introduction

Magnesium (Mg) alloy is an advanced material for applications of light weight metal. Recently, it is adopted in electric appliances, such as TV case and Compact Disks, and applications of railway vehicles and automobile are future demands [1]. It is difficult to process parts using Mg alloy under cold working, because these alloy systems with a hexagonal close-packed structure hardly slip. So new process method is important for Mg alloy application.

One recent advantage of processing of Mg alloy, super plastic behavior which shows high ductility, more than 300%, has been applied to light weight metal such as aluminum and titanium alloy. The super plastic behavior has also occurred in high strength zinc (Zn) doped Mg alloy (ZK) for structure material, and middle strength aluminum (Al) doped Mg alloy (AZ) for electric appliances. Super plastic processed Mg alloy is given attention due to its toughness and lightness. Zn doped Mg alloy is studied as a good candidate of super plastic processed Mg alloy. Super plasticity is one of the metallurgical reactions such as creep. It can be possible to elongate so long under specific temperature, elongated velocity [2]. In order to apply the super plastic property in metallic materials processing, microstructural treatment such as the control of the grain size is important. The super plastic behavior in Mg alloy would be applied for the processing of the parts [3–5].

Mg alloy is very sensitive to corrosion, because Mg has the property of the lowest galvanic voltage in metallic material and a sensitive surface [6]. Therefore, the corrosion mechanism has been investigated and factor analysis for the corrosion has been done. It has been reported that [7] the effect of precipitation on the grain, ratio of Fe/Mn contents, surface active layer after processing is large. With these reports, Zn shows advantages for corrosion in Mg alloy.

Among other alloying elements in Mg alloy, Zn is generally believed not to have a significant effect on the corrosion behavior of Mg alloys [8]. However, the super plastic processed ZK alloy has one severe problem corroded more easily than conventional processed alloy. ZK alloy is a good candidate for the high strength one. Clarifying the corrosion mechanism is an urgent subject because the corrosion causes trouble to put super plastic processed ZK alloy to practical use.

We have done corrosion tests in water of super plastic processed AZ and ZK alloys. We observed the conditions of corrosion by Scanning Electron Microscopy (SEM). In Zn doped Mg alloy, it was found that corrosion pits occurred and corroded easily by the corrosion test. On the other hand, as for Al doped Mg alloy that Zn is very poor, it is confirmed that no corrosion pits occurred though the material is corroded. The existence of Zn compound contained in the corrosion product is confirmed by Energy Dispersion Spectrum analysis (EDS) measurement.

It is very important in the realization of super plastic processed Mg alloy to clear the corrosion mechanism investigating the influence which a small amount of element contained in Mg alloy exerts on the corrosion. The main ingredient of the corrosion product in the Mg and Mg-Al alloy is MgO which shows amorphous structure [9]. The corrosion product of ZK alloy also show amorphous like structure obtained by X-ray diffraction. In order to clarify the corrosion process of super plastic processed Zn doped Mg alloy, we have investigated the local structure of Zn compound in the corrosion product using X-ray absorption measurements, paying attention to Zn which exists in the alloy in a small quantity.

2. Experimental

2.1. *Specimen*

Two types of Mg alloys, super plastic processed Al doped Mg alloy (AZ) and Zn doped one (ZK), were prepared in corrosion test. The specimens are screw shaped and were processed by rolling with super plastic works. The chemical compositions of specimens are listed in Table I. On processing screw, solid solution treatments were done in 573 K for 10 hours to solve the precipitation into grains for Mg alloy matrix. After that, screw processing was performed by a rolling machine under 646 K that is the condition of super plastic behavior. The grain size is larger than 10 μm before the rolling process, while it becomes less than 1 μm after the process; the numbers were obtained by optical microscope observation.

*e-mail: honma@spring8.or.jp

Table I. *Chemical compositions of used specimens (unit : Mass%).*

	Al	Zn	Zr	Mn	Fe	Si	Cu	Ni	Ca	Mg
AZ31	3.5	0.2	—	0.2	0.003	0.08	0.02	0.003	0.025	Bal.
ZK61	—	4.8	0.45	—	—	—	0.02	0.003	—	Bal.

2.2. *Corrosion tests*

The specimens were put into water and corrosion was accelerated during 5 months with constant temperature of 298 K and constant humidity of 60%.

2.3. *Evaluation of corrosion*

Scanning Electron Microscope (SEM) was performed to investigate the surface microstructure of specimens after the corrosion test and Energy Dispersion Spectrum analysis (EDS) was done to analyze the chemical composition of the corrosion product. Accelerated voltages in SEM observation were 15 kV. The point focus analyses for corrosion products by EDS were estimated.

X-ray absorption fine structure (XAFS) experiments of the corrosion product were carried out on the beam lines BL38B1 and BL19B2 at SPring-8 to investigate the local structure of Zn compound. A Pt mirror was inserted to eliminate the harmonics. Zn K-edge XAFS were measured in the transmission mode at room temperature with a Si(111) monochromator. As reference samples, ZnO, $ZnCl_2$, Zinc carbonate ($2ZnCO_3{\cdot}3Zn(OH)_2{\cdot}H_2O$) were also measured because it could be considered that Zn compound in the corrosion product is oxide, chloride and/or carbonate.

3. Results and discussion

Figure 1 shows SEM micrographs of the cross section view of screws (sample AZ and ZK) which are made of AZ and ZK alloys with super plastic works. The corrosion was shown in both samples, and then the corrosion damage in ZK sample was more serious than that of AZ in this corrosion test. It was found that the charge up image in SEM photographs in the surface of AZ sample and the corrosion area of ZK. In general, it has not observed the charge up image in SEM for electrical conducted samples. Following these results, the corrosion products were aggregated in the area of the charge up image of AZ and ZK samples. From EDS spectra of AZ and ZK samples, Mg, Al, Cu and Si was found in the corrosion product of AZ sample and Mg, Zn and Si in that of ZK. It was reported that Zn hardly contributes to corrosion mechanism in Mg alloy by protection of anode reaction in galvanic corrosion [7].

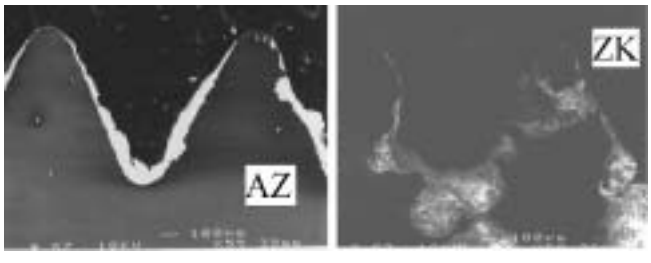

Fig. 1. SEM micrographs show surface of specimens of AZ and ZK alloys (cross section view).

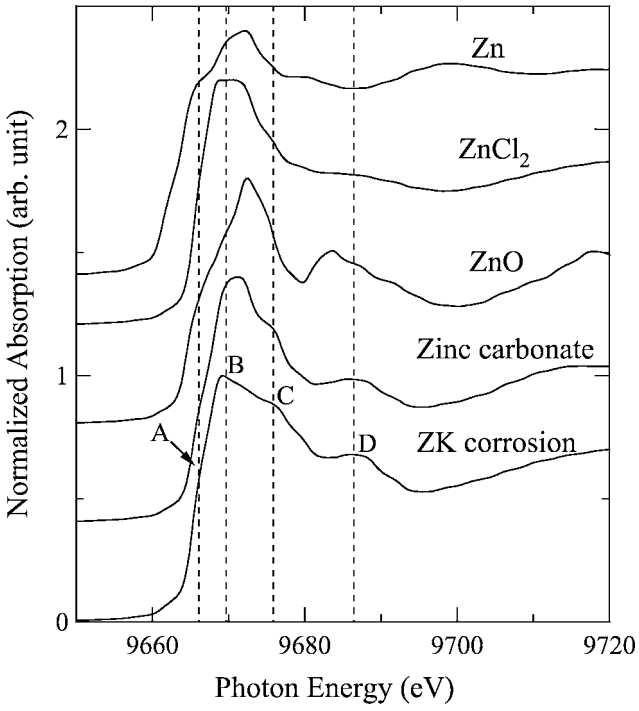

Fig. 2. Zn K-edge XANES spectra of the corrosion product of ZK sample and references.

However, the component of Zn in the corrosion product of super plastic processed ZK sample was found in this case. Therefore, we have focused on Zn compound contained in the corrosion product of ZK sample and performed XAFS analyses that is useful for investigating the amorphous materials as this corrosion product.

Figure 2 shows Zn K-edge XANES spectra of the corrosion product of ZK alloy and reference compounds of ZnO, $ZnCl_2$, Zinc carbonate and Zn foil. The Zn K absorption edge energy E_0 of these samples, except for Zn foil, is about 9665 eV. This indicates that the valences of those samples are almost +2. The spectrum of the corrosion product shows a slight shoulder A around 9666 eV, a peak B (white line) around 9670 eV, a shoulder C around 9676 eV and a small peak D around 9687 eV. In ZnO, a sharp peak (white line) is shown in the position higher than 3 eV from the peak B of the corrosion product and a small peak lower than 3 eV from peak D. The spectrum of $ZnCl_2$ shows a plateau (white line) around peak B and a broad peak around peak D. The spectrum of Zinc carbonate is similar to that of the corrosion product, except for the structure of the white line.

Figure 3 shows the Fourier transforms (radial structure function (RSF)) without corrections for errors in the phase shift of k^3-weighted Zn K-edge EXAFS of the corrosion product of ZK sample and reference compounds of ZnO, $ZnCl_2$ and Zinc carbonate. The profile of the corrosion product of ZK alloy shows a peak at ~0.15 nm, which is due to Zn-O bond. The distance of the Zn-O bond in ZnO is a little longer than that in the corrosion product and a clear peak structure shows around 0.3 nm of the Zn-Zn bond. In $ZnCl_2$, there is only a peak around 0.18 nm, which is due to Zn-Cl bond. The profile of FT in zinc carbonate has a peak around 0.15 nm and a small peak around 0.28 nm. The profile of the corrosion product is very similar to that of zinc carbonate.

The profiles of XANES and FT of the corrosion product of ZK sample and references indicate that the local structure of Zn in the corrosion product of ZK alloy is very similar to that of

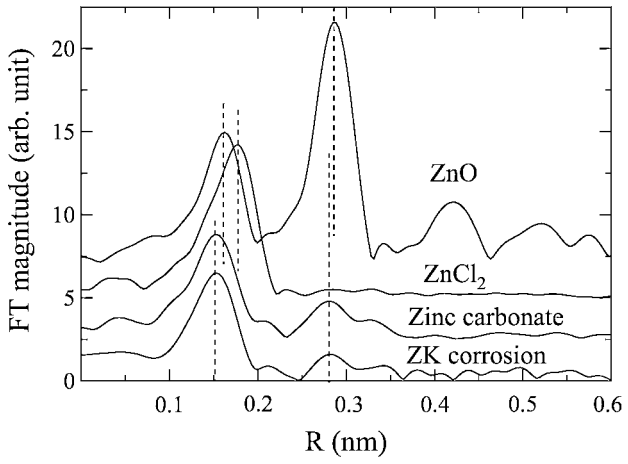

Fig. 3. Fourier transformed $k^3\chi$(K) at Zn K-edge of the corrosion product of ZK sample and references.

zinc carbonate. These results obtained by XAFS measurements suggest that Zn in the super plastic processed ZK alloy is corroded by carbonic acid in the water.

4. Conclusions

Corrosion tests have been done in super plastic processed Al doped and Zn doped Mg alloys (AZ and ZK). The corrosion damage in ZK sample was more serious than that of AZ. The point focus analysis by EDS for corrosion products of ZK alloy indicates that Zn is contained in the corrosion product. These results suggest that Zn in the super plastic processed ZK alloy influences the corrosion.

In order to clarify the corrosion process of super plastic processed Zn doped Mg alloy, we have investigated the local structure of Zn compound in the corrosion product using XAFS measurements, paying attention to Zn which exists in the alloy in a small quantity. The XANES spectra and RSF obtained from Fourier transformed EXAFS oscillations of the corrosion product of ZK sample and reference compounds of ZnO, zinc carbonate ($2ZnCO_3{\cdot}3Zn(OH)_2{\cdot}H_2O$), $ZnCl_2$ and Zn foil suggest that the local structure of Zn compound in corrosion product of super plastic processed ZK alloy is close to that of zinc carbonate.

From the above results, it is important to consider the role of Zn in corrosion mechanism on super plastic processed Zn doped Mg alloy. The XAFS analyses will provide the important information to investigate the corrosion products in microscopic terms.

Acknowledgments

The XAFS experiments were performed at SPring-8 with the approval of Japan Synchrotron Radiation Research Institute (JASRI) (Proposal No. 2002B0614-NI-np, 2002A0409-NX-np). We would like to thank the JASRI beamline staff Dr. Tanida for support and help.

References

1. Hama, S. and Watanabe, F., J. Inst. Light. Metals **51**, 514 (2001).
2. "Light Metal workshop", Report of light metal body, No. 6, 31 (2000).
3. Watanabe, H., Kumai, T. and Higashi, K., Metal **71**, 502 (2001).
4. Watanabe, H. *et al*., J. Japan Inst. Light. Metals **49**, 401 (1999).
5. Chino, Y. and Mabuchi M., J. Japan. Inst. Metals **51**, 498 (2001).
6. Iglesias-Rubianes, L. *et al*., J. Japan. Inst. Metals **50**, 538 (2000).
7. Nisancioglu, K. and Nordlien, J. H., J. Japan. Inst. Metals **50**, 429 (2000).
8. Emley, E. F., "Principles of Magnesium Technology", (Pergamon Press, Oxford 1966).
9. Nordlien, J. H. *et al*., J. Electrochem. Soc. **143**, 2564 (1996).

Physica Scripta. Vol. T115, 570–572, 2005

X-ray Absorption Studies of Al-Mn System

L. K. Mehta[1], S. K. Joshi[1*] and A. P. Deshpande[2]

[1]Physics Department, Government Post-Graduate Arts & Science College, Ratlam - 457001, India
[2]Amolakchand College, Yavatmal - 445001, India

Received June 26, 2003; accepted in revised form November 10, 2003

PACS number: 78.70.Dm

Abstract

X-ray K-absorption studies have been carried out on Al-Mn system comprising $Al_{90}Mn_{10}$, $Al_{88}Mn_{12}$, $Al_{86}Mn_{14}$, $Al_{84}Mn_{16}$, $Al_{82}Mn_{18}$ and $Al_{81}Mn_{19}$ samples. These samples have been characterized by X-ray diffraction (XRD) studies which support the formation of icosahedral phase. The X-ray K-absorption discontinuities in case of the Al-Mn system have been found to be shifted towards the high energy side with respect to the K-absorption edge of pure metal Mn, which indicates the behaviour of manganese atom as the cation. The X-ray absorption chemical shifts suggest a covalent bonding. The studies also indicate that with the increase in Mn concentration chemical shifts also increase.

We have attempted to correlate the values of the electron to atom ratio (e/a) with the chemical shifts (ΔE). The nature of relationship between e/a and ΔE is quite similar to that between ΔE and Mn concentration. Further, we have estimated the density of states at the Fermi level $D(E_F)$ for these samples and plotted them against chemical shift values. Extrapolation from this graph between $D(E_F)$ and ΔE indicates a $D(E_F)$ value for Al metal which is quite near to the actual value for Al metal. These studies establish the existence of a pseudo gap in the case of presently investigated Al-Mn samples. The present studies also support our assumption of assigning the chemical shift values to the Fermi level in the case of Al-Mn system under present investigation.

1. Introduction

Various aspects of the Al-Mn system have been studied by many workers [1–8], even then the Al-Mn system still remains of interest in the scientific community. In the present paper, we have reported the X-ray spectroscopic studies on Al-Mn system. The data on the chemical shifts (ΔE) of the Al-Mn quasicrystalline system have been reported in order to know the nature of bonding in such materials. The samples studied are:

(*i*) $Al_{90}Mn_{10}$, (*ii*) $Al_{88}Mn_{12}$, (*iii*) $Al_{86}Mn_{14}$,
(*iv*) $Al_{84}Mn_{16}$, (*v*) $Al_{82}Mn_{18}$ and (*vi*) $Al_{81}Mn_{19}$.

2. Experimental

The Al-Mn samples have been prepared by standard method. XRD results support the formation of icosahedral phase [9–11].

X-ray absorption spectra (K-absorption discontinuity of Mn) have been recorded using a Cauchois type bent crystal spectrograph of 0.4 m diameter. The analyzing crystal used in the present work was mica with (100) reflecting plane. The detailed experimental procedure for the X-ray spectroscopic investigations has been described in an earlier publication [12].

3. Results and discussion

The X-ray diffraction (XRD) studies carried out in the present investigations reveal that there is a mixing of fcc Al, and icosahedral phases. The XRD results are in conformity with those of others [13–16]. The grain size of the samples was found to be of the order of 90 to 400 Å.

Table I. *Data for X-ray K-absorption spectra of Mn in Al-Mn system.*

Sample	E_K (eV)	Chemical Shift (ΔE_K) (eV)	Edge-width ($E_A - E_K$) (eV)	e/a	$D(E_F)$
$Al_{90}Mn_{10}$	6546.5	9.9	6.9	2.2	3.10×10^{45}
$Al_{88}Mn_{12}$	6546.8	10.2	9.7	2.4	3.58×10^{45}
$Al_{86}Mn_{14}$	6547.1	10.5	12.4	2.5	3.83×10^{45}
$Al_{84}Mn_{16}$	6547.6	11.0	13.0	2.6	3.98×10^{45}
$Al_{82}Mn_{18}$	6547.9	11.3	14.1	2.7	4.27×10^{45}
$Al_{81}Mn_{19}$	6548.3	11.7	15.5	2.8	4.35×10^{45}
Mn Metal	6536.6	—	—	—	—

The values of energy of K-absorption discontinuities of manganese in Al-Mn system have been reported in Table I. The values of the edge-widths are also included in the same table.

From Table I, it can be seen that the K-absorption discontinuities in case of the Al-Mn system have been found to be shifted towards the high energy side with respect to that of pure Mn metal. This shift of the absorption discontinuities is referred to as the chemical shift which indicates the behaviour of manganese atom as the cation. It is well known that the chemical shifts of the X-ray absorption discontinuity in compounds are governed by the nature of chemical bonding [17–18]. The general observation regarding the chemical shifts is that whenever the absorbing atom is a cation, X-ray absorption discontinuity shifts towards the high energy side and whenever the absorbing atom is an anion it shifts towards the low energy side with respect to that of pure metal. In a binary compound the more electronegative atom should behave as an anion while the less electronegative atom behaves as a cation. In the case of Al-Mn system, the electronegativity difference between Al and Mn is zero as per the Pauling electronegativity scale [19]. On the basis of other electronegativity scales, for Al (1.61) and Mn (1.55) the electronegativity difference is too small in order to be used to conclude upon the cationic or anionic behaviour of Mn in Al-Mn system. The Al-Mn system in the present case shows the quasicrystalline nature having the icosahedral structure as proposed by XRD studies of these samples. Keeping into consideration the quasicrystalline nature of these samples, such a magnitude of chemical shifts of the quasicrystalline materials can be interpreted as due to iono-covalent bonding. It is important to note that the Al-Mn system although appearing to be an alloy of Al and Mn, shows insulating behaviour instead of metallic one [20–21]. A strong covalent bond may be responsible for such a behaviour. The magnitude of chemical shifts observed by us in the case of Al-Mn system

*e-mail: skjoshi_rlm@sancharnet.in

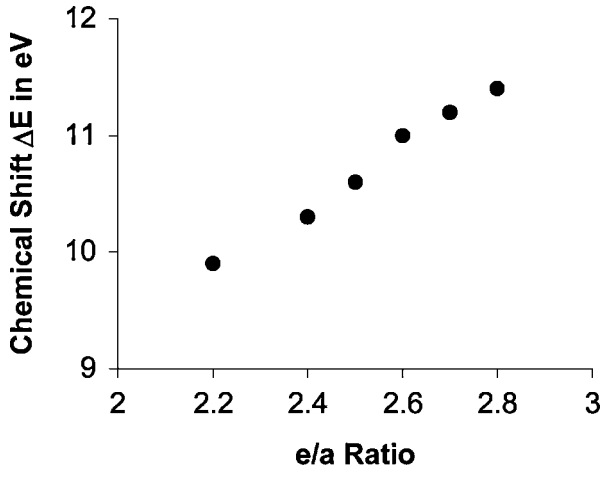

Fig. 1. Variation of Chemical Shift ΔE with electron to atom ratio (e/a).

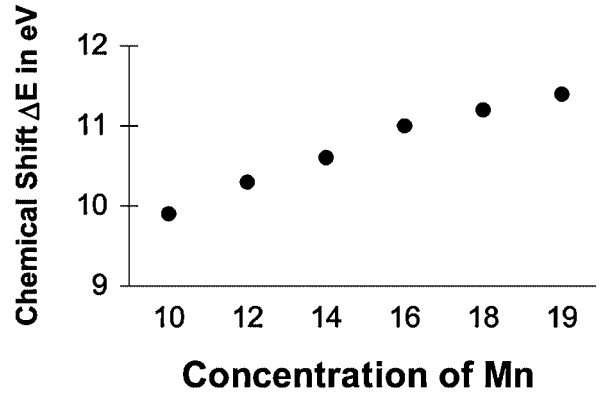

Fig. 2. Variation of Chemical Shift ΔE with concentration of Mn.

are indicative of their strong covalent bonding character. The Al-Mn in quasicrystalline form has the icosahedral decagonal phase. A change in concentration of Mn distorts the decagonal phase which in consequence is responsible for change in ionicity. The X-ray diffraction analysis of the present samples gives evidence for distortion in the icosahedral decagonal phase.

The electron to atom ratio plays a very important role in bonding. The values (e/a) for the presently studied system have been estimated following a procedure described elsewhere [22]. We have plotted in Fig. 1 the values of the electron to atom ratio (e/a) against the chemical shift (ΔE) in the case of the Al-Mn system. In Fig. 2 we have also plotted chemical shift vs. Mn concentration. Roughly an exponential relationship between e/a and ΔE is observed. The nature of this relationship is quite similar to that obtained between ΔE and Mn concentration in the Al-Mn system studied in the present investigations. The effect of the ionicity and in turn the e/a ratio on the chemical bonding as reflected in the chemical shift can be obviously seen from the above relationship.

As per the tight binding approximation, in many cases, the density of states is determined mainly by the actual potential of the atom and its nearest neighbours. The valence band and conduction band then tell whether or not they overlap with each other. When they overlap, the density shows a minimum which is called a pseudo gap. Such a pseudo gap was shown by Weaire [23] and Heine [24] for amorphous covalent materials such as Si.

It has been shown by several workers [25–27], that the inflection point on the K-absorption discontinuity in the case of pure metals corresponds to the Fermi energy. The Fermi level shifts in the case of different alloys have been studied by a number of workers [28–29]. In the case of compounds, however, the Fermi energy being uncertain, the inflection point on the absorption discontinuities can not be attributed to the Fermi level. The transition in such cases takes place from the inner level to the first available unoccupied states in the conduction band. It has been further shown [25–27], that there are a sizable number of holes on the top of the valence band where there is a reasonable transition probability. In the case of the present Al-Mn system, the conduction band is composed of manganese 3d and aluminium p-orbitals and higher orbitals of manganese. The band picture for the system is that of the valence band and the conduction band separated by a wide energy gap with the Fermi level lying in a pseudo gap. The inflection point of K-absorption discontinuity of the Al-Mn system can be attributed to the half filled Fermi level. Since there is an appreciable number of holes on the top of the valence band, the absorption discontinuity can extend from the top of the valence band to the first available state in the conduction band, which we may assume to be the bottom of the conduction band. Thus the edge width of K-absorption discontinuities of manganese in Al-Mn system can be regarded as the band gap.

Following Kimura and Takeuchi [30], we have obtained the density of states at the Fermi energy $D(E_F)$ given by:

$$D(E_F) = m/\hbar^2(M/d)^{3/2}\{3(e/a)N_A/4\}^{1/3}. \quad (1)$$

Here, $D(E_F)$ = density of states at Fermi level; M = effective atomic number; d = density of atoms; e/a = electron/ atoms; N_A = Avogadro's number; and $\hbar = h/2\pi$, where h is Planck's constant.

The density of states at the Fermi level $D(E_F)$ drops drastically when the electron density approaches 2.1 in units of (e/a) showing thereby the existence of a pseudo gap at the Fermi level [31]. In Table I, we have reported the e/a values and $D(E_F)$ for the Al-Mn samples.

We have plotted in Fig. 3 $D(E_F)$ vs. chemical shift ΔE. $D(E_F)$ varies linearly with the chemical shifts. If we extrapolate this curve to the lower energy side, we reach the $D(E_F)$ value for Aluminium metal which is equal to 2.05×10^{45} from the graph. The actual value of $D(E_F)$ for pure Aluminium is 2.17×10^{45}. The agreement between the two values establishes our assumption of assigning the chemical shifts to the Fermi level in case of Al-Mn system. The $D(E_F)$ value for pure manganese is 2.17×10^{45}. This means that if we want to extrapolate the same curve on the other side towards pure manganese, the curve should show a maximum somewhere midway and then show a decreasing trend until it reaches $D(E_F)$ for pure manganese. The dependence of electronic

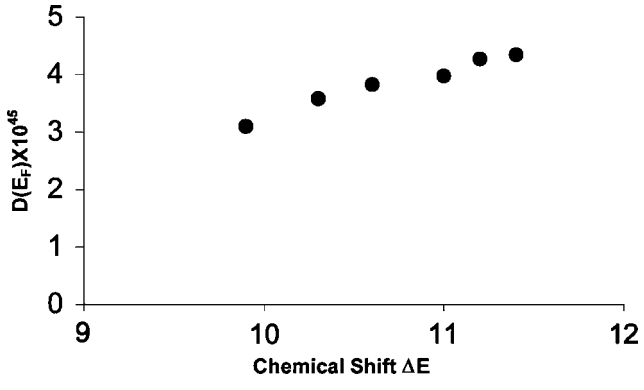

Fig. 3. Chemical Shift ΔE versus density of states at the Fermi level $D(E_F)$.

specific heat coefficient on Mn concentration of Al-Mn system shows a broad bump and a rapid increase at lower concentration while a rapid decrease at the higher concentration of Mn. This means the existence of a pseudo gap at E_F [32]. Also soft X-ray emission spectra have shown a decrease in the partial density of states of s and d electrons at E_F for Al-Mn icosahedral phase [33, 34].

Acknowledgements

We are thankful to M. P. Council of Science and Technology, Bhopal – 462 004, India for providing the financial support to carry out the present work in the form of a research project (P-100/90).

References

1. Lalla, N. P., Tiwari, R. S. and Srivastava, O. N., J. Phys. Condens. Matter **1**, 7603(1989).
2. Daulton, T. L., Kelton, K. F. and Gibbons, P. C., Philos. Mag. B **63**, 687 (1991).
3. Kelton, K. F., Int. Mater. Rev. **38**, 105 (1993).
4. Fujiwara, T., de Laissardiere Trambly and Yamamoto, S., Mater. Sci. Eng. **179**, 118 (1994).
5. Higginson, R. L., Aindow, M. and Bate, P. S., Philos. Mag. Lett. **72**, 193 (1995).
6. Belin, E., Dankhazi, Z., Mizutani, U. and Sadoc, A., J. Non-Cryst. Solids **192&193**, 312 (1995).
7. Bian, W. and Zhu, Y., Acta Cryst. A **53**, 175 (1997).
8. Hafner, J. and Krajci, M., Phys. Rev. B **57**, 2849 (1998).
9. Knapp, J. A. and Follstaedt, D. M., Phys. Rev. Lett. **55**, 1591 (1985).
10. Saito, Y., Jpn. J. Appl. Phys. **25**, L693 (1986).
11. Sekhar, J. A., Current Sci. **54**, 94 (1985).
12. Shrivastava, B. D., Joshi, S. K. and Pandeya, K. B., X-ray Spectrom. **17**, 127 (1988).
13. Kramer, P. and Neri, R., Acta. Crystallogr. A **40**, 580 (1984).
14. Field, R. D. and Fraser, H. L., Mat. Sci. Eng. **68**, L17 (1984).
15. Bak, P., Phys. Rev. Lett. **54**, 1517 (1985).
16. Levine, D. and Steinhardt, P. J., Phys. Rev. Lett. **53**, 2477 (1984).
17. Kondawar, V. K. and Mande, C., X-ray Spectrom. **5**, 793 (1976).
18. Kumar, A., Nigam, A. N. and Shrivastava, B. D., X-ray Spectrom. **10**, 25 (1981).
19. Pauling, L., "The Nature of Chemical Bond" (Cornell. Univ. Press. Ithaca, New York 1960).
20. Pool, S. J., Dreshman, A. J. and Lawless, K. R., Phys. Rev. Lett. **55**, 2324 (1985).
21. Wong, K. M. and Pool, S. J., Phys. Rev. **34**, 7371 (1986).
22. Athanasiou, N. S., Int. J. Mod. Phys. B **11**, 2443 (1997).
23. Weaire, D., Phys. Rev. Lett. **26**, 985 (1971).
24. Heine, V., J. Phys. C **24**, 1 (1970).
25. Deshpande, A. P. and Mande, C., Solar Cell **16**, 429 (1986).
26. Chattopadhyay, S. and Deshpande, A. P., J. Phys. Soc. Jap. **55**, 2320 (1986).
27. Deshpande, A. P., "Advances in Physics of Materials" (Edited by Z. H. Zaidi and M. Hussain) (Today and Tomorrow Publishers, New Delhi 1989).
28. Lokhande, N. R. and Mande, C., Phys. Stat. Sol. B **102**, K11 (1980).
29. Lokhande, N. R. and Mande, C., Pramana **17**, 1 (1981).
30. Kimura, K. and Takeuchi, S., "Quasicrystals: The State of the Art" (Edited by D. P. DiVincenzo and P. J. Steinhardt) (World Scientific, Singapur 1991).
31. Fujiwara, T., Phys. Rev. B **40**, 942 (1989).
32. Gudinho, M., Berger, C., Lasjaunias, J. C., Hosselbach, K. and Bethoux, O., Non-Cryst. Solids **117&118**, 808 (1990).
33. Machado, F. L. A., Kang, W. W., Canfield, P. C. and Clark, W. G., Phys. Rev. B **38**, 8088 (1988).
34. Machado, F. L. A. *et al*., Solid. Stat. Commun. **61**, 145 (1987).

Physica Scripta. Vol. T115, 573–576, 2005

X-Ray K-Absorption Studies of Cobalt (II) Imidazoles

S. K. Joshi[1*] and B. D. Shrivastava[2]

[1]Government Post Graduate Arts and Science College, Ratlam 457001, India
[2]School of Studies in Physics, Vikram University, Ujjain 456010, India

Received June 26, 2003; accepted in revised form January 19, 2004

PACS number: 78.70.Dm

Abstract

X-ray K-absorption edges along with their extended X-ray absorption fine structure (EXAFS) have been recorded using a laboratory XAFS spectrometer for the Co(II) imidazoles viz., $Co(etImz)_2Cl_2$, $Co(iprImz)_2Cl_2$, $Co(tvImz)_2Cl_2$, $Co(vImz)_4Cl_2$, $Co(vImz)_4(SCN)_2$, $Co(tvImz)_4Cl_2$, and $Co(tvImz)_4(SCN)_2$. The chemical shifts for these samples have been reported and the present studies reveal that the anions in $Co(ligand)_4Cl_2/(SCN)_2$ do not interact strongly with the metal ion. The studies further show that the complexes have tetrahedral structure in which anions $Cl_2/(SCN)_2$ remain outside the first coordination shell in $Co(ligand)_4Cl_2/(SCN)_2$ type complexes. The total phase shifts δ_1 and phase parameters β_1 for these samples have been estimated using the modified graphical method for the determination of bond distances. The values for phase parameter β_1 explain the dominance of backscattering in the various complexes studied.

1. Introduction

Imidazole is a molecule of biological importance. It is contained in the structure of several biomolecules like amino acids and peptides and serves as ligand to the metal ions in a variety of metalloenzymes. Metal complexes of imidazole and substituted imidazole are therefore important biological entities. The substituted imidazoles included in the present studies are: $Co(etImz)_2Cl_2$, $Co(iprImz)_2Cl_2$, $Co(tvImz)_2Cl_2$, $Co(vImz)_4Cl_2$, $Co(vImz)_4(SCN)_2$, $Co(tvImz)_{4D}\ Cl_2$, $Co(tvImz)_4(SCN)_2$ where etImz = ethyl imidazole; iprImz = isopropyl imidazole; vImz = vinyl imidazole and tvImz = thiovinyl imidazole.

1.1. *Structure*

Imidazoles normally form tetrahedral complexes with most of the transition metal ions. The complexes included in the present investigations may be grouped into two classes:

$Co(ligand)_2Cl_2$ and $Co(ligand)_4Cl_2/(SCN)_2$. Further it is obvious that all the ligands have only one nitrogen group available for coordination so that they will behave as a monodentate nitrogen donor ligands. All the $Co(ligand)_2Cl_2$ type complexes may therefore be given a tentative structure, as proposed and represented in [Fig. 1(a)]. $Co(ligand)_4Cl_2/(SCN)_2$ complexes may also be assigned the tetrahedral structure if only four substituted imidazole molecules are included in the coordination sphere and the interactions from the anions (Cl or SCN) are negligible [Fig. 1(b)]. Alternatively, if the anions interact significantly with the metal they are also included in the coordination sphere and a distorted octahedral structure may result [Fig. 1(c)]. The motivation behind the present work is to find whether the anions Cl and SCN are included in the first coordination shell and contribute to the X-ray absorption chemical shifts on the central metal ion cobalt. However, the results of the present studies reveal that the anions in $Co(ligand)_4\ Cl_2/(SCN)_2$ do not interact strongly with the metal ion and hence they are outside the first coordination shell. So structure as proposed in Fig. 1(b) is confirmed by X-ray absorption studies.

2. Experimental

The X-ray absorption spectra for the above samples including the fine structure up to nearly 280 eV have been recorded using a 40 cm curved crystal spectrograph of Cauchois type. Tungsten ($_{74}$W) L-emission line or Ni Kα_1 line has been used as a reference line; the other reference line being the Kα_1 emission line of copper. The remaining experimental details have been in general similar to those described earlier [1, 2]. The K-edge positions have been estimated using the derivative spectra.

3. Results and Discussion

Figure 2 shows the cobalt K-absorption edge along with the EXAFS features of the Co (II) imidazoles. In Table I, the values of the energies of the K-absorption edges of the samples, chemical shift values and phase parameter β_1 for these complexes have been included. In Table II, we have included the energy values of the EXAFS features, k in (Å^{-1}) and total phase parameter δ_1 in rad.

3.1. *Chemical shift*

Earlier also X-ray chemical shifts [3–7] and XAS studies [8, 9] have been utilised to obtain important chemical information regarding the coordination in the complexes belonging to transition metals.

The edge shift ΔE (known as chemical shift) is defined as follows $\Delta E = E_{K(Compound)} - E_{K(Metal)}$. The position of the X-ray K-absorption edge depends on the valence of the absorbing ion [10]. But valence state is not the only factor that governs the magnitude of the chemical shift. At least three factors that must be considered to explain the chemical shift values in metal complexes are valence state, the effective charge on the central metal ion [11, 12], stereochemistry and covalent bonding. Here we have observed that the chemical shifts are positive and lie in the range 6.6 to 8.9 eV. On the basis of previous reports [13–15] for cobalt (II) complexes, and our chemical shift values, we infer that all the presently studied cobalt imidazole samples possess oxidation state +2. A perusal of the values of the chemical shift in Table I indicates that among $Co(ligand)_2Cl_2$ type complexes, Co $(etImz)_2Cl_2$, (7.1 eV) and $Co(iprImz)_2Cl_2$, (7.3 eV) show nearly the same values of chemical shifts. This indicates that merely a change in the chain length of R has little effect on the chemical shift value. The chemical shift value of $Co(tvImz)_2Cl_2$ (6.8 eV) is definitely lower than those of $Co(etImz)_2Cl_2$ (7.1 eV)

*e-mail: skjoshi_rlm@sancharnet.in

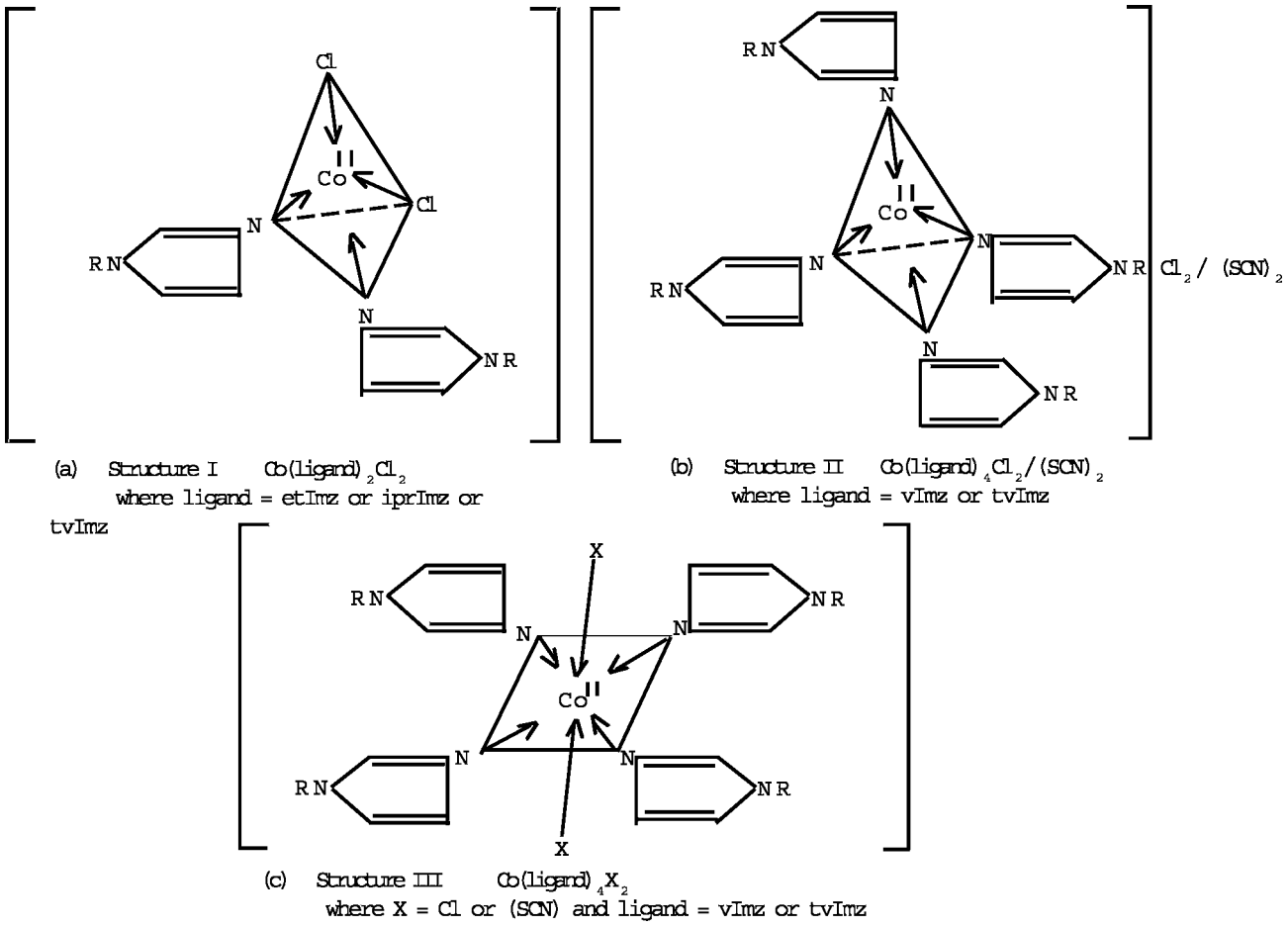

Fig. 1. Structures of Co(II) Imidazole complexes.

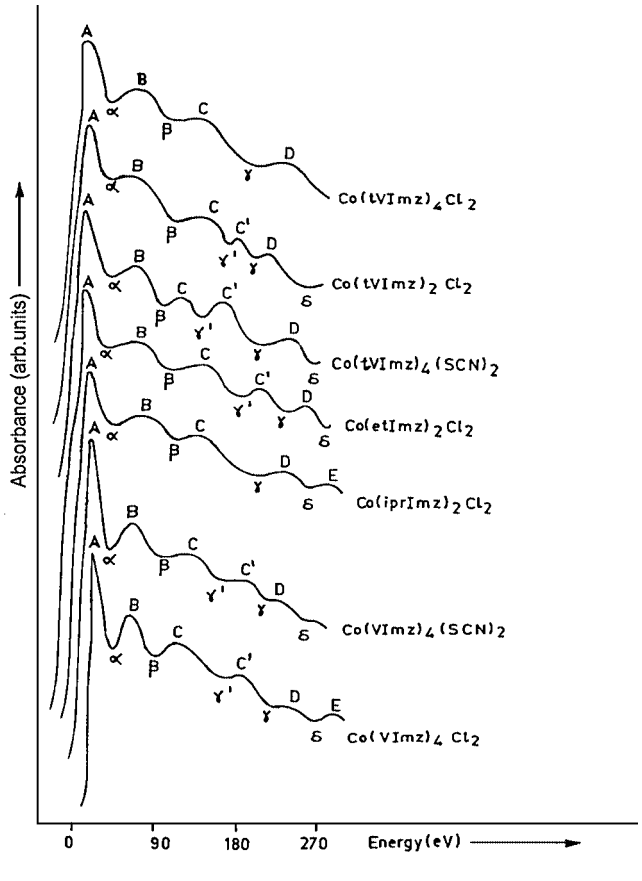

Fig. 2. EXAFS at the K-absorption edge of Cobalt in its Imidazoles.

Table I. *Chemical shift of K-absorption edge of Cobalt in Co(II) imidazole and phase parameter* β_1.

S. No.		E_K (eV)	Chemical shift ΔE_K (eV)	Phase Parameter β_1 (Rad.)
	Cobalt Metal	7709.7	—	—
I.	Co $(etImz)_2Cl_2$	7716.8	7.1	−1.88
II.	Co $(iprImz)_2Cl_2$	7717.0	7.3	−3.53
III.	Co $(tvImz)_2Cl_2$	7716.5	6.8	−1.88
IV.	Co $(vImz)_4Cl_2$	7718.6	8.9	−0.47
V.	Co $(vImz)_4(SCN)_2$	7718.5	8.8	−0.78
VI.	Co $(tvImz)_4Cl_2$	7716.3	6.6	−1.72
VII.	Co $(tvImz)_4(SCN)_2$	7716.7	7.0	−2.67

and $Co(iprImz)_2Cl_2$ (7.3 eV). Thus a major change in the nature of *R* can certainly influence the donor properties of the coordinated nitrogen atom and hence the effective charge of the metal ion.

Compounds $Co(vImz)_4Cl_2$ and $Co(vImz)_4(SCN)_2$ show nearly the same values of chemical shift; similarly compounds $Co(tvImz)_4Cl_2$ and $Co(tvImz)_4(SCN)_2$ also show nearly the same values of chemical shift indicating that there is no change in the value of chemical shift when Cl_2 is replaced by $(SCN)_2$. Therefore Cl_2 and $(SCN)_2$ are outside the coordination sphere.

A perusal of Table I also reveals that the value of chemical shift for $Co(vImz)_4Cl_2$; (8.9 eV) is greater than the value of chemical shift for $Co(tvImz)_4Cl_2$; (6.6 eV). Similarly the shift

Table II. *EXAFS parameters for Co(II) Imidazoles.*

(I) Co (etImz)$_2$Cl$_2$									
E (eV)	11.2	43	75	116	144	212	238	267	277
k	1.71	3.36	4.44	5.52	6.15	7.46	7.91	8.37	8.55
δ_1 (rad)	3.98	4.49	4.83	5.16	5.35	5.76	5.90	6.04	6.50
(II) Co (ipr Im z)$_2$Cl$_2$									
E (eV)	11.1	40	71	108	139	205	236	265	279
k	1.70	3.24	4.32	5.32	6.04	7.34	7.87	8.34	8.56
δ_1(rad)	5.63	6.10	6.44	6.75	6.97	7.37	7.54	7.68	7.75
(III) Co (tv Im z)$_2$Cl$_2$									
E(eV)	13.8	43	69	116	147	218	243	270	—
k	1.90	2.36	4.25	5.52	6.21	7.57	7.99	8.42	—
δ_1(rad)	4.04	4.49	4.77	5.16	5.37	5.80	5.93	6.06	—
(IV) Co (v Im z)$_4$Cl$_2$									
E(eV)	7.2	31	50	89	114	198	232	249	270
k	1.37	2.85	3.62	4.83	5.47	7.21	7.81	8.09	8.42
δ_1(rad)	2.46	2.92	3.16	3.53	3.73	4.27	4.46	4.55	4.65
(V) Co (et Im z)$_4$Cl$_2$									
E(eV)	9.4	32	55	100	130	198	234	257	—
k	1.57	2.90	3.80	5.12	5.84	7.21	7.84	8.22	—
δ_1(rad)	2.84	3.25	3.53	3.94	4.16	4.58	4.78	4.90	—
(VI) Co (tv Im z)$_4$Cl$_2$									
E(eV)	13.6	41	68	118	147	211	245	—	—
k	1.89	3.28	4.22	5.57	6.21	7.44	8.02	—	—
δ_1(rad)	3.87	4.31	4.60	5.02	5.21	5.60	5.78	—	—
(VII) Co (tv Im z)$_4$Cl$_2$									
E(eV)	12.9	44	77	127	149	218	245	265	281
k	1.84	3.40	4.50	5.77	6.25	7.57	8.02	8.34	8.59
δ_1(rad)	4.81	5.29	5.63	6.03	6.18	6.59	6.73	6.82	6.90

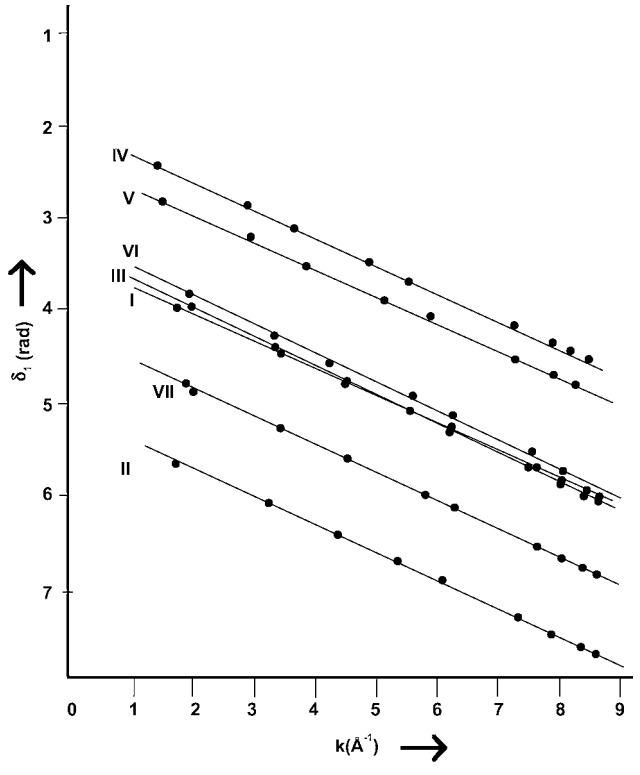

Fig. 3. δ_1 against k for Co (II) Imz.

for Co(tvImz)$_4$(SCN)$_2$; (8.8 eV) is greater than the value of shift for Co(tvImz)$_4$(SCN)$_2$; (7.0 eV). Thus when imidazole is replaced by thioimidazole the other factors remaining the same there is a decrease in the chemical shift indicating more covalent nature of thiovinyl-imidazoles.

3.2. *Data generation*

The values of the wave vector k (Å^{-1}) have been obtained using the expression

$$k = (0.263E)^{1/2}, \tag{1}$$

where E is the energy (in eV) of the peaks in the EXAFS measured from the inflection point on the component K of the absorption curves. The phase parameter β_1 and the average metal – ligand bond length R_1 have been estimated [16] with expression (2) where R_1 (in Å) is the radius of the first coordination sphere and n is the order of the position of EXAFS maxima and minima,

$$(\tfrac{1}{2} + n) = 2k(R_1 - \alpha_1) + 2\beta_1 - \pi. \tag{2}$$

Finally the total phase shifts δ_1 have been calculated [17] from the expression

$$\delta_1 = -\alpha_1 k + \beta_1 - \tfrac{1}{2}\pi. \tag{3}$$

It is well known that the sine term in the EXAFS equation determines periodicity. The determination of phase shifts is very important for this purpose. Several attempts [16–18] have been made to determine phase shifts theoretically. The total phase shift given by Equation (3) may be compared with the theoretical phase shift given by Teo and coworkers [16–18].

$$Q_{ab} = Q_a(k) + Q_b(k) - \pi. \tag{4}$$

This indicates that the phase parameter $2k\alpha_1$ resembles Q_a, the phase shift due to the central atom, while the phase parameter $2\beta_1$ resembles Q_b, the back scattering phase shift.

The values of δ_1 when plotted against the wave vector k (Fig. 3) give a curve similar in character to the theoretical curves obtained by Mckale *et al.* [19]. It has usually been assumed that the total phase shift for compounds belonging to a given system should be the same. However, in the present case we found that δ_1 vs. k curves (Fig. 3) are different for the Co(II)) imidazole complexes. The δ_1 vs. k plots are straight lines and are nearly parallel to each other. Hence, we can conclude that there is a linear variation between the total phase shift δ_1 and k. Earlier workers have applied the modified SLS (Stern, Lytle and Sayer's) method for the determination of the total shift (δ_1) in the case of ternary compounds [20], cobalt (III) complexes of ethylene diamine [21] etc. We have attempted to estimate the total phase shift (δ_1) and phase parameter (β_1) for the seven Co (II) imidazole complexes for the first time.

Phase shift determinations have been carried out by several workers in various systems [22–28]. Stearns and Stearns [22], using the Fourier transformation method, have observed that the parameter α_1 (b in their case) can be interpreted as corresponding to the scattering size of the atoms, whereas the parameter β_1 (a in their case) is associated with the depth of the potential well in which the absorbing atom is placed. They have further shown that an atom pair in any condensed material has a unique linear phase function in the operating k range.

A close perusal of Table II shows that the phase parameter β_1 for samples Co(etImz)$_2$Cl$_2$ i.e., sample (I) and Co(iprImz)$_2$Cl$_2$ i.e. sample (II) are respectively -1.88 and -3.53. This clearly indicates that as the chain length increases from ethyl to isopropyl, the back scattering phenomenon in the first coordination shell dominates and this is reflected in the larger value of phase parameter β_1 for sample (II). The phase parameter β_1 for sample (IV) i.e., Co(vImz)$_4$Cl$_2$ and sample (VI) i.e., Co(tvImz)$_4$Cl$_2$ are respectively -0.47 and -1.72. Similarly for Co(vImz)$_4$(SCN)$_2$ [sample (V)] and Co(tvImz)$_4$(SCN)$_2$ [sample(VII)] the phase

parameter values are -0.78 and -2.67 respectively. Hence, the conclusion may easily be drawn that in going from (vImz) to (tvImz) in both the pairs the contribution of backscattering from sulphur present in the thiovinyl imidazole is perceptible to be dominating the back scattering process. As discussed above on the basis of chemical shift values it has been proposed that $Cl_2/(SCN)_2$ are outside the first coordination shell in complexes of the type $Co(ligand)_4Cl_2/(SCN)_2$. The $Cl_2/(SCN)_2$ groups are in the second coordination shell and their contribution to the phase parameter β_1 is visible as seen obviously from different values of β_1 for the four complexes of $Co(ligand)_4Cl_2/(SCN)_2$ type. Further, β_1 values indicate strong backscattering from $(SCN)_2$ group as compared to Cl_2 group on the basis of slightly higher values i.e., $Co(vImz)_4(SCN)_2$ $(-0.78) > Co(vImz)_4Cl_2$ (-0.47) and also $Co(tvImz)_4(SCN)_2$ $(-2.67) > Co(tvImz)_4Cl_2$ (-1.72). The present method of phase shift determination using the modified graphical technique is simple and comparable to the above theoretical methods [22–28]. The above analysis provides a physical picture of the X-ray absorption process. This method may be used for studying systems such as amorphous materials, metallic glasses and bio molecules in which knowledge of the environment of atoms is desired.

References

1. Shrivastava, B. D., Joshi, S. K. and Pandeya, K. B., X-ray Spectrom. **17**, 127 (1988).
2. Shrivastava, B. D., Shrivastava, Bhakta Darshan, Joshi, S. K., Pandeya K. B. and Mishra, A., J. Synchrotron Rad. **8**, 713 (2001).
3. Wakita, H., Yamaguchi, T., Yoshida, N. and Fujiwara, M., Jpn. J. Appl. Phys. **32**, 836 (1993).
4. Joshi, S. K., Shrivastava, B. D. and Mahajan, N. K., J. Phys. IV France **7**, C2-643 (1997).
5. Katare, R. K., Joshi, S. K., Shrivastava, B. D., Pandeya, K. B. and Mishra, A., X-ray Spectrom. **29**, 187 (2000).
6. Katare, R. K., Joshi, S. K., Shrivastava, B. D., Patel, R. N. and Mishra, A., Ind. J. Pure Appl. Phys. **40**, 908 (2002).
7. Joshi, S. K., Shrivastava, B. D. and Deshpande, A. P. (Eds.), "X-ray Spectroscopy and Allied Areas" (Narosa Publishing House, New Delhi 1998).
8. Furenlid, L. R., Renner, M. W. and Fujita, E., Physica B **208&209**, 739 (1995).
9. Kau, L. S., Spira-Solomon, D. J., Penner-Hahn, J. E., Hodgson, K. O. and Solomon, E. I., J. Am. Chem. Soc. **109**, 6433 (1987).
10. Choy, J. H., Kim, D. K., Hwang, S. H. and Demazean, G., Phys. Rev. **B 50**, 16631 (1994).
11. Mehta, C. P. and Chetal, A. R., Phys. Stat. Sol. **B 179**, 579 (1993).
12. Pong, W. F., *et al*., Phys. Rev. **B 50**, 7371 (1994).
13. Kumar, A., Nigam, A. N. and Agarwala, U., Z. Phys. Chemie, Leipzig **262**, 908 (1981).
14. Kumar, A., Nigam, A. N. and Agarwala, U., Z. Phys. Chemie Leipzig **262**, 34 (1981).
15. Joshi, S. K., Shrivastava, B. D., Pandeya, K. B. and Mahajan, N. K., "X-ray Spectroscopy and Allied Areas" (Edited by S. K. Joshi, B. D. Shrivastava and A. P. Deshpande), (Narosa Pub. House, New Delhi 1998) p. 212.
16. Teo, B. K., Kijima, K. and Bau, R., J. Am. Chem. Soc. **100**, 6211 (1978).
17. Teo, B. K. and Lee, P. A., J. Am. Chem. Soc. **101**, 2815 (1979).
18. Teo, B. K., Eisenberger, P., Reed, J., Barton, J. K. and Lippard, S. J., J. Am. Chem. Soc. **100**, 75 (1978).
19. Mckale, A. G., Veal, B. W., Paulikas, A. P., Chan, S. K. and Knapp, G. S., J. Am. Chem. Soc. **110**, 63 (1988).
20. Deshpande, A. P., Sapre, V. B. and Mande, C., Phys. Stat. Sol. **B 145**, 77 (1988).
21. Khadikar, P. V., Joshi, S., Mangalson, N. F. and Silk, J. E., X-Ray Spectrom. **23**, 137 (1994).
22. Stearns, D. G. and Stearns, M. B., Phys. Rev. **B 27**, 3842 (1983).
23. Mustre de Leon, J., Rehr, J. J., Zabinsky, S. I. and Albers, R. C., Phys. Rev. **44**, 5135 (1991).
24. Rehr, J. J., Mustre de Leon, J., Zabinsky, S. I. and Albers, R. C., J. Am. Chem. Soc. **113**, 5135 (1991).
25. Rehr, J. J. and Albers, R. C., Phys. Rev. **B 41**, 8139 (1990).
26. Rehr, J. J., Albers, R. C. and Zabinsky, S. I., Phys. Rev. Lett. **69**, 3397 (1992).
27. Rehr, J. J., Jpn. J. Appl. Phys. **32**, 8 (1993).
28. Rehr, J. J., Booth, C. H., Bridges, F. and Zabinsky, S. I., Phys. Rev. **B 49**, 12347 (1994).

Physica Scripta. Vol. T115, 577–579, 2005

XAFS Study on $Li_{1-x}Ni_{0.5}Mn_{0.5}O_2$ Cathode Materials for Li-Ion Batteries

Yoshinori Arachi*[1], Hironori Kobayashi[2], Shuichi Emura[3], Yoshiyuki Nakata[4], Minoru Tanaka[1] and Takeshi Asai[1]

[1]Unit of Chemistry, Faculty of Engineering, Kansai University, Suita, Osaka 564-8680, Japan
[2]National Institute of Advanced Industrial Science and Technology (AIST), Ikeda, Osaka 563-8577, Japan
[3]ISIR, Osaka University, Ibaraki, Osaka 567-0047, Japan
[4]Faculty of Science and Engineering, Iwakimeisei University, Iwaki, Fukushima 970-8551, Japan

Received June 26, 2003; accepted November 4, 2003

PACS number: 71.20.Ps

Abstract

The structural change and charging process for $Li_{1-x}Ni_{0.5}Mn_{0.5}O_2$ were determined by X-ray diffraction and XAFS measurement. XAFS has been employed to investigate the change in electronic structure of cathode material. As the cell charged, the Ni K-edge XANES spectra showed chemical shift towards higher energy, while Mn K-edge showed no significant shift. Divalent nickel metal is oxidized to trivalent with Li-deintercalation, in association with the phase transition from hexagonal (*R3m*) to monoclinic (*C2/m*).

1. Introduction

In the field of Li-ion batteries, new cathode materials with high theoretical energy density and good cycleability alternatives to $LiCoO_2$ have been extensively pursued such as $LiNiO_2$ or $LiMn_2O_4$. Several problems, including thermal stability and capacity fading at elevated temperatures, limit practical utilization, and few materials satisfy all properties that support high performance. $LiNi_{0.5}Mn_{0.5}O_2$ is one of the promising cathode materials of lithium secondary battery. It adopts a hexagonal unit cell like a layered $LiCoO_2$ or $LiNiO_2$, and the cell performance using Li exhibits a specific capacity of 150 mAh/g in the voltage range of 2.5 to 4.3 V which corresponds to one-half of the theoretical capacity (280 mAh/g) [1]. In addition, this material shows the superior characteristics of a larger capacity than $LiMn_2O_4$ and better thermal stability than $LiNiO_2$. Dahn *et al.* reported that Ni^{2+} and Mn^{4+} coexist in the layered materials [2]. When the cell is charged, Ni^{2+} is oxidized to Ni^{4+}, while Mn^{4+} retains its oxidation state. The charging process corresponds to the electrochemical Li extraction from the layered structure of $Li_{1-x}Ni_{0.5}Mn_{0.5}O_2$. However, the details of the crystal structure of charged $Li_{1-x}Ni_{0.5}Mn_{0.5}O_2$ and the charging process are still ambiguous. In a previous study, we determined the crystal structure of this material by neutron powder diffraction. It was found that $LiNi_{0.5}Mn_{0.5}O_2$ has a hexagonal lattice, and the parameters are $a = b = 2.89109$ Å, $c = 14.297$ Å and the ion distribution can be expressed as $[Li_{0.91}Ni_{0.09}]_{3b}[Li_{0.09}Mn_{0.5}Ni_{0.41}]_{3a}O_2$ [3, 4]. In this study, the structure of charged $Li_{1-x}Ni_{0.5}Mn_{0.5}O_2$ ($x = 0.5$), which corresponds to the composition for showing rechargeable capacity, was determined and XAFS of Ni, Mn and O K-edges were used to investigate the charging process and the electronic structure changes during Li-deintercalation.

2. Experimental

Samples were prepared from $LiOH{\cdot}H_2O$ and dry precipitates of $Ni(OH)_2$ and $Mn(OH)_2$ which were kindly supplied by TOSOH Company. They were mixed and then calcinated at 873 K for 12 h. The obtained powders were pressed into a disk under a pressure of 5 t/cm^2, and sintered at 1273 K for 12 h. Lithium was electrochemically deintercalated at a rate of 170 μA/cm^2, by use of a coin-type cell. The cathode material was composed of the following materials; sample : acetylene black : poly vinylidene fluoride (PVDF) = 86 : 4 : 10 in wt%, and 1 M $LiClO_4$ in propylene carbonate (PC) : 1,2-dimethoxycarbonate (DMC) = 1 : 1 by volume was used as the electrolyte. X-ray diffraction measurement was performed by use of synchrotron radiation, at a wavelength of $\lambda = 0.500$ Å on BL02B2 at SPring-8. Rietveld crystal structural refinement was carried out by use of the program RIETAN-2000 [5]. X-ray absorption measurements at the Mn- and Ni-K edges by transmission mode were performed on BL01B1 at SPring-8. The software programs WinXAS2.1 [6] and FEFF8.10 [7] were used for XAFS analysis. Oxygen K-edge XANES was measured on BL8B1 at UVSOR (Okazaki, Japan) in total electron yield and fluorescence yield mode.

3. Results and discussion

3.1. *X-ray diffraction*

Figure 1 shows X-ray diffraction patterns for electrochemically lithium-deintercalated samples, using synchrotron radiation source. Each sample corresponds to the composition in the charge curve. Rietveld analysis showed that a structural change occurred with the phase transition from hexagonal (*R3m*) to monoclinic (*C2/m*) resulting from the ordering of cations in the layered structure. Electron diffraction patterns by HR-TEM support these results. The change of lattice parameter during the charging process is summarized as follows: *a* and *b* in the plane of the structure decrease linearly, and *c* of the vertical axis increases. The charging process proceeds with the electrochemical Li extraction from the layered structure of $Li_{1-x}Ni_{0.5}Mn_{0.5}O_2$, associated with the oxidation reaction of transition metals (Ni or Mn). The change in lattice parameters can be explained by decreased ionic radius of oxidized transition metals and electrostatic repulsive force between oxygen ions, after lithium is extracted.

3.2. *XAFS*

Figure 2 shows Ni and Mn K-edge XANES spectra for $Li_{1-x}Ni_{0.5}Mn_{0.5}O_2$ together with spectra of NiO, $LiNiO_2$ and Li_2MnO_3 as reference compounds for Ni^{2+}, Ni^{3+} and Mn^{4+}.

*e-mail: arachi@ipcku.kansai-u.ac.jp

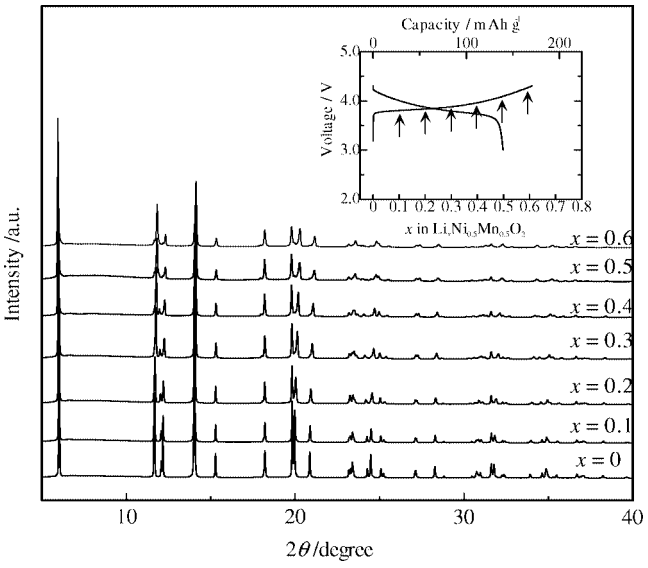

Fig. 1. X-ray diffraction patterns for $Li_{1-x}Ni_{0.5}Mn_{0.5}O_2$. The insert shows Charge and Discharge curves of the $Li/Li_{1-x}Ni_{0.5}Mn_{0.5}O_2$ measured with a current density of 0.1 mA/cm^2 and cut-off voltages of 3.0 and 4.3 V.

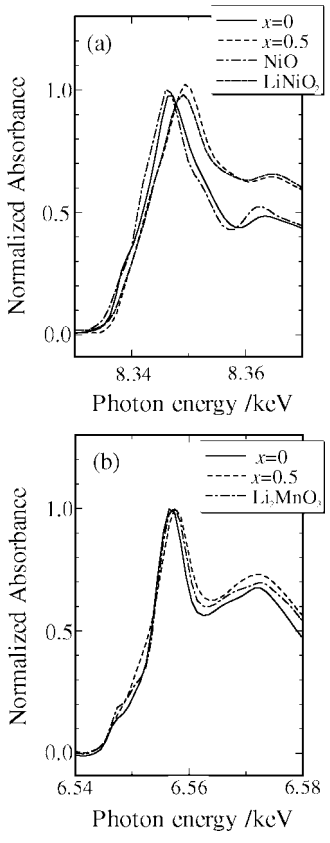

Fig. 2. XANES spectra of (a) Ni and (b) Mn K-edge for $Li_{1-x}Ni_{0.5}Mn_{0.5}O_2$ and reference compounds.

As the cell charged, XANES spectra of Ni K-edge showed a chemical shift towards higher energy in the voltage range of 2.5–4.1 V and no remarkable shift was observed up to 4.5 V. On the other hand, in the Mn K-edge no chemical shift was observed. The Ni K-edge XANES spectra correspond to a valence state of Ni^{2+} for the $x = 0$ sample and show a change in the valence state to Ni^{3+} for the $x = 0.5$ sample, while the Mn K-edge XANES spectra almost correspond to a valence state of Mn^{4+} for the $x = 0$ sample and show essentially small deviation from the valence state of Mn^{4+} for the $x = 0.5$ sample. These results demonstrate

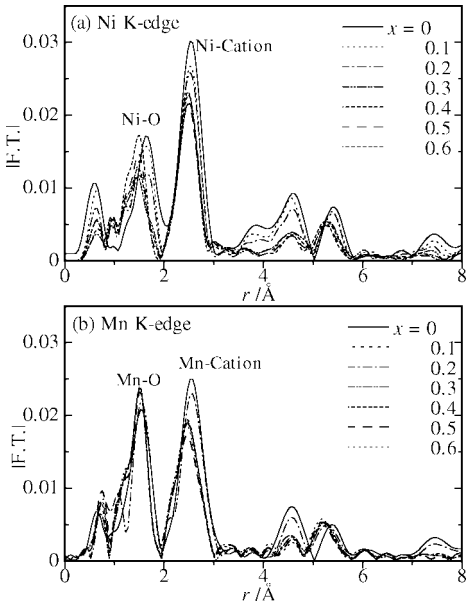

Fig. 3. Fourier transforms of (a) Ni and (b) Mn K-edge EXAFS for $Li_{1-x}Ni_{0.5}Mn_{0.5}O_2$.

that $Li_{1-x}Ni_{0.5}Mn_{0.5}O_2$ ($x = 0$ and 0.5) can be represented as $Li(Ni^{2+}{}_{0.5}Mn^{4+}{}_{0.5})O_2$ and $Li_{0.5}(Ni^{3+}{}_{0.5}Mn^{4+}{}_{0.5})O_2$ respectively. Thus, the charging process of this material up to $x = 0.5$ is proceeded by continuous oxidation of Ni, not oxidation of Mn. Figure 3 shows XANES spectra of O K-edge obtained by fluorescence yield (F.Y.) for charged $Li_{1-x}Ni_{0.5}Mn_{0.5}O_2$. The sample of $x = 0.7$ was prepared at different electrochemical conditions from that of Fig. 1. The sampling depth in F.Y. mode is much deeper than that in the electron yield. These spectra reflect on the internal chemical state of the sample. The broad peak at about 547–552 eV may correspond to the transition to the band composed of transition metal (Ni,Mn) 3d and O2p. The slight peak shift towards lower energy implies that oxygen participates in the oxidation of the material. Explanation of O K-edge spectra in details using first principle calculation are under progress. Figure 4 shows Fourier transforms of (a) Ni and (b) Mn K-edge for $Li_{1-x}Ni_{0.5}Mn_{0.5}O_2$ after the charging process. The spectra show similar features in relation to the radial distribution, in reflection of

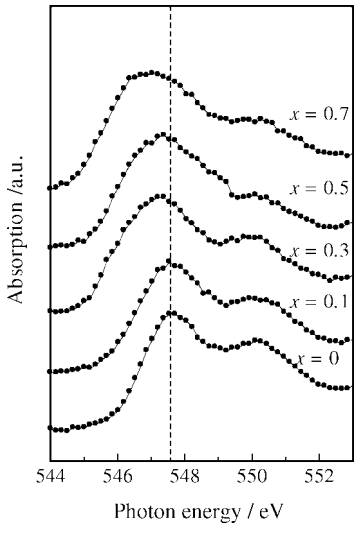

Fig. 4. O K-edge XANES spectra of $Li_{1-x}Ni_{0.5}Mn_{0.5}O_2$.

the two metals being placed in similar environment. In Figure 4(a), the first peak in the FT corresponds to the first neighbor of Ni; i.e., a Ni-O shell in the structure. The second peak in the FT corresponds to the second neighbor of Ni; i.e., a Ni-Cation shell where the cation can be either Ni or Mn. The first peak shifted to shorter distance after charging, since the oxidation of Ni^{2+} to Ni^{3+} shortens the bonding length of Ni-O. On the other hand, no shift is observed in the Mn K-edge. By use of the structural model obtained by X-ray diffraction analysis, backscattering amplitude and phase parameter were calculated by FEFF and fitting was carried out. The results show that as the cell charged, the distance of the first neighbor, Ni-O, decreased as a result of reduction in the ionic radius of nickel. A structure model using two shells yielded good fitting for the composition of $x = 0.5$ ($R = 2.49\%$), because Ni and O in monoclinic phase show two different bonding distances (2.053 Å for $x = 0$, 1.915 Å (C.N. = 4.0) and 2.043 Å (C.N. = 2.0) for $x = 0.5$).

In summary, the structural change and charging process for $Li_{1-x}Ni_{0.5}Mn_{0.5}O_2$ were determined by X-ray diffraction and XAFS measurement. The $x = 0$ sample has a hexagonal lattice in which a small part of Ni occupies the Li(3b) site, and as the cell charged the monoclinic phase appeared from the composition of $x = 0.3$. Lithium was mainly removed by the oxidation of Ni, resulting in the ordering of cations in the layer; that is, appearance of the monoclinic phase. However, it is likely that oxygen participates in the charging process. It was found that nickel was divalent and manganese tetravalent at the octahedral site respectively. The results of EXAFS analysis showed that as the cell charged, the distance of the first neighbor Ni-O decreased. It results from the decrease of the ionic radius for nickel by oxidation. Therefore, it can be concluded that the main role of charging reaction in the cell is the oxidation of nickel, Ni^{2+} to Ni^{3+}.

Acknowledgement

The synchrotron radiation experiments were performed at SPring-8 with the approval of the Japan Synchrotron Radiation Research Institute (JASRI) (Proposal 2001B0484-NX-np, 2002A0370-ND1-np). Oxygen K-edge XANES was performed on BL8B1 at UVSOR (Okazaki, Japan).

References

1. Ohzuku, T. and Makimura, Y., Chem. Lett. **8**, 744 (2001).
2. Lu, Z., MacNeil, D. D. and Dahn, J. R., Electrochem. Solid-State Lett. **4**, A191 (2001).
3. Arachi, Y. *et al.*, Chem. Lett. **1**, 60 (2003).
4. Kobayashi, H. *et al.*, J. Mater. Chem. **13**, 590 (2003).
5. Izumi, F. and Ikeda, T., Mater. Sci. Forum **321–324**, 198 (2000).
6. Ressler, T., J. Physique IV **7**, C2-269 (1997).
7. Rehr, J. J. and Albers, R. C., Rev. Mod. Phys. **72**, 621 (2000).

Physica Scripta. Vol. T115, 580–582, 2005

Magnetic Moment in the Top Pt Layer of Co/Pt Bilayers

M. Suzuki[1], H. Miyagawa[1], N. Kawamura[1], H. Muraoka[2], Y. Inaba[2], T. Shimatsu[2], Y. Sonobe[3], Y. Isohama[4], N. Nakamura[4], N. Ishimatsu[4] and H. Maruyama[4]

[1]SPring-8/JASRI, Mikazuki, Hyogo 679-5198, Japan
[2]RIEC, Tohoku University, Sendai, Miyagi, 980-8577, Japan
[3]IBM Almaden Research Center, San Jose, CA 95120, USA
[4]Graduate School of Science, Hiroshima University, Higashi-Hiroshima, Hiroshima 739-8526, Japan

Received June 26, 2003; accepted in revised form December 4, 2003

PACS numbers: 75.70.−i, 75.50.Ss, 75.70.Cn, 78.70.Dm

Abstract

The magnetic properties of a few atomic Pt layers on a 15 nm thick Co film were studied by X-ray magnetic circular dichroism spectroscopy at the Pt $L_{2,3}$ edges. The spin and orbital magnetic moments of the Pt 5d electrons were separated using the magneto-optical sum rules. The Pt magnetization profile as a function of distance from the Co-Pt interface was determined using data from a series of films with various Pt thicknesses. This magnetization profile was approximated by an exponential function with a decay length of 0.41 nm, which characterizes the effective range of the magnetic coupling between Co and Pt. The total magnetic moment of a Pt atom at the interface was 0.7 μ_B/atom including a 13% orbital moment. This is discussed in the context of the thermal stability of magnetic recording media capped with a thin layer of Pt.

A high recording density of 100 Gbits/in^2 was recently developed in magnetic recording media, and now researchers aim to achieve even higher recording densities in the range of 1 Tbits/in^2. An alternative to present longitudinal recording for storing data is perpendicular recording. Perpendicular recording can reduce the area needed for unit data bit storage on a medium and consequently, will significantly increase the recording density. The target size of a single recording bit is $10 \times 45 \times 20\,\text{nm}^3$ for some perpendicular media being developed. This small size requires reducing the magnetic grain size to the nanometer scale for reliable reading/writing operations with a good signal-to-noise ratio. However, even in perpendicular recording, thermal decay may limit further reductions in the grain size because the magnetic grain thermal stability depends on the anisotropy constant K_u and the volume V using the relationship $K_u V/k_B T$, where k_B is the Boltzmann constant and T is temperature. Thus, higher magnetic anisotropy is required to maintain thermal stability of the material used in high density perpendicular media with a smaller grain volume. Sonobe *et al.* reported that capping with a 1 nm thick Pt layer improved the thermal stability of granular $CoCr_{18}Pt_{12}$ perpendicular media [1]. They pointed out that the Pt cap layer possibly has induced ferromagnetism, which gives rise to the large perpendicular anisotropy and increases the in-plane exchange coupling. As reported in Co/Pt multilayer systems [2] and Co-Pt alloys [3–5], Pt atoms that are paramagnetic in the bulk are significantly polarized in the vicinity of the ferromagnetic atoms such as Co due to their large Stoner factor, and have crucial effects for magnetism of the system.

This paper reports the magnetic properties of single Pt layers less than 2 nm thick located on a Co film, studied using X-ray magnetic circular dichroism (XMCD) spectroscopy at the Pt $L_{2,3}$ edges. The aim of this study is to determine the role of the surface Pt layer of the CoCrPt perpendicular media in improving the thermal stability. Several Co/Pt bilayer films were investigated as models for real perpendicular media that contains Pt in the host granular layer. We use the element specificity of the XMCD technique to probe the magnetization of only the Pt, which was a few atomic layers, with high sensitivity. The spin and orbital moment of the Pt 5d electrons were separated using the sum rules [6]. The distributions of the both moments as a function of the distance from the Co-Pt interface were determined from a series of XMCD data taken with samples of varying Pt layer thickness.

Table I. *Characteristics of Co/Pt bilayer films. The $\Delta\theta_{50}$ denotes the angular dispersion of the c-axis, which is determined by the full width at the half maxima of the X-ray rocking curve profile.*

Pt thickness (nm)	Co thickness (nm)	$\Delta\theta_{50}$ of Co (°)
0.15	14.3	13.4
0.5	15.1	9.5
1.0	15.0	10.8
2.0	14.6	9.04

Co/Pt bilayer films of four different Pt thicknesses were prepared by dc magnetron sputtering. A magnetic Co layer, approximately 15 nm thick, was deposited onto a glass substrate following a 10 nm thick Ti seed layer, and a Pt layer was deposited on the top. The samples were grown at room temperature to minimize the interface diffusion. Table I summarizes the characteristics of these samples. The thickness of the Pt layer was estimated from the amount of sputter growth time after a carefully calibrating the Pt deposition rate. The Pt thickness was measured by the XAS edge jump at the Pt $L_{2,3}$ edges and is consistent with the designed value. In the present study, Co was chosen as the magnetic layer instead of granular CoCrPt used in real perpendicular recording media, so that the magnetic properties of the top Pt layer could be studied using element specificity of XMCD technique. Consequently, the present Co/Pt bilayers did not show perpendicular magnetic anisotropy.

XMCD experiments at the Pt $L_{2,3}$ edges were conducted in the fluorescence mode at BL39XU of SPring-8 [7]. Monochromatic X-rays were incident on a Co/Pt sample perpendicularly to the film plane. A magnetic field of 20 kOe was applied perpendicular to the film plane to attain saturation magnetization. Intensities of fluorescent X-rays were detected using a silicon drift detector. The detector allowed total count rates as high as 10^5 counts/s and efficient separation of the Pt Lα (L_3 excitation) and the Lβ (L_2 excitation) lines from the elastic scattering, which mainly

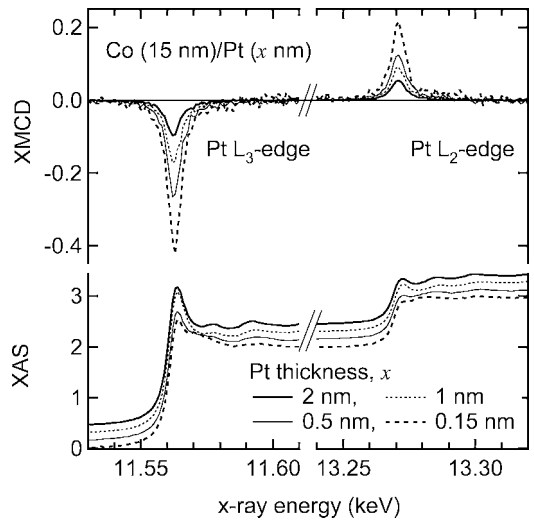

Fig. 1. X-ray magnetic circular dichroism spectra (top) at the Pt $L_{2,3}$ edges in Co/Pt bilayer films of different Pt thickness x, compared with spin-averaged XAS spectra (bottom). The XAS spectra are shown with vertical shifts for better display.

originates from the substrate. A 2.7 mm thick diamond crystal was used as an X-ray phase retarder to generate circular polarization incident on the sample and to switch the photon helicities every two seconds. The degree of circular polarization was higher than 90%. The difference in sample fluorescence yields for right- and left-circular polarizations was recorded as a function of the X-ray energy, while the direction of the applied magnetic field was fixed. This setup allowed the XMCD spectra in a few atomic Pt layer on Co film to be successfully obtained with a high signal-to-noise ratio.

Figure 1 shows the observed XMCD spectra in Co/Pt films with various Pt thicknesses, and at the bottom spin-averaged XAS spectra are compared. The XMCD and XAS amplitude include the same scale factor so that the XAS step height at the L_3 and L_2 edges is 2.07 and 1.00, respectively. This branching ratio was experimentally determined from XAS measurement for the present samples. The sign of the XMCD spectra was negative at the L_3 edge and positive at the L_2 edge, which indicates that the Pt magnetization is parallel to the external field and to the magnetization of Co. At both the L_3 and L_2 edges, the XMCD amplitude decreased as the Pt thickness increased, indicating that the Pt magnetization decreases as the distance from the interface with Co increased. The shape of the XMCD spectrum was independent of the Pt thickness. The 0.15 nm Pt thick sample showed the largest XMCD amplitude, 22% with respect to the XAS edge jump. To the best of our knowledge, this XMCD value is larger than any XMCD data of Pt in Pt-transition metal alloys [3–5], Pt/Co [2] or Pt/Ni [8] multilayers reported to date. The Pt atoms located very close to the Co-Pt interface may have a considerable magnetic moment.

The spin and orbital magnetic moments of the Pt layer was determined by applying the sum rules [6]. We have used a Lorenz function to fit the XMCD and XAS components arising from the dipole transition to the 5d band. The continuum background in the XAS spectrum was subtracted using an arctangent curve. When applying the spin sum rule, the magnetic dipole term was neglected. It is noteworthy that results of the spin sum rule for XMCD data taken with in-plane magnetization [9] differ from the present one by less than 15% even for the 0.15 nm thick Pt. We consider that this anisotropy is due to either the real anisotropy in the spin moment or the magnetic dipole term, or both. Therefore, the spin moment presented below may include up to a 15% contribution from the magnetic dipole term.

Table II. *The magnetic moments per 5d hole in the top Pt layer of Co/Pt bilayers of different Pt thickness x.*

x (nm)	m_{spin} (μ_B/hole)	m_{orb} (μ_B/hole)	m_{total} (μ_B/hole)
0.15	0.36	0.053	0.41
0.5	0.21	0.036	0.25
1.0	0.14	0.021	0.16
2.0	0.079	0.011	0.09

Table II shows the observed 5d magnetic moments in the Pt layer. A larger magnetic moment was observed for the sample with a thinner Pt layer. For the 0.15 nm thick Pt layer the total moment was 0.41 μ_B/hole. This value gives 0.7 μ_B/atom when using the Pt 5d hole number 1.7, which was reported in a theoretical calculation for a similar system [10]. This value is two and three times larger than the Pt moments reported in $Co_{50}Pt_{50}$ alloy thin films [5] and Ni/Pt multilayers [8], respectively. The orbital moment was 0.053 μ_B/hole (0.09 μ_B/atom), which is a 13% contribution to the total magnetization.

The results shown in Table II give the average moment per Pt atom over the entire layer. From these, the distribution of the Pt magnetization as a function of the distance from the Co-Pt interface can be obtained [11]. For this analysis, we made products of the average moment listed in Table II and the corresponding Pt thickness, then took the difference one from the other.

Figure 2 plots the result of the analysis. The total moment of the Pt 5d electrons was determined to be $m_{spin} + m_{orb} = 0.41\ \mu_B$/hole (0.7 μ_B/atom) for a Pt atom that is in contact with Co atoms at the interface. An exponential function, $m(d) = m_0 \exp(-d/\delta)$, well reproduces the variation in the the total moment $m(d)$, where d is the distance from the interface, and m_0 and the decay distance,

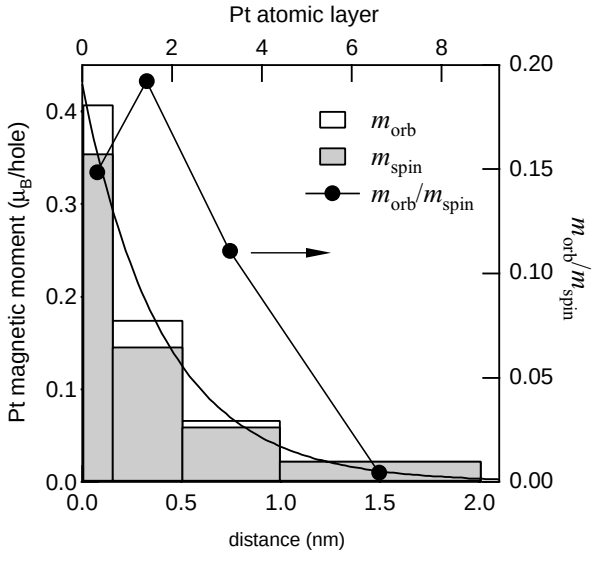

Fig. 2. Distribution of the Pt magnetic moment as a function of the distance from the Co-Pt interface. The top axis shows the corresponding Pt atomic layer number. The m_{orb} and m_{spin} denote the orbital and the spin moments, respectively. The solid curve shows an exponential function fitted to the total magnetic moment $m_{spin} + m_{orb}$. Solid circles, referred to the right axis, show the ratio of m_{orb} to m_{spin}.

δ are the fit parameters. The decay distance $\delta = 0.41$ nm gives the best fit. This value corresponds to two atomic layers of Pt and characterizes the effective range of magnetic coupling between Co and Pt. The fit curve is shown by the solid line in Fig. 2.

From these results, we can conclude that only four or less atomic Pt layers have a substantial amount of induced magnetic moments and contribute to the thermal stability of magnetic films. Regarding the orbital moment, it decreases more rapidly than the spin moment, and almost vanishes at 1.5 nm away from the interface. The magnetic anisotropy in a Co magnetic film may be enhanced by two or three atomic Pt layers, which show considerable amount of the orbital moment, near the Co-Pt interface.

The present result is consistent with the reported magnetization profile determined by resonant X-ray magnetic reflectometry in another Co/Pt bilayer [12], except the regime within 0.3 nm from the Co-Pt interface, where our results show larger magnetization values. In addition to the total magnetization profile, which can be obtained by the magnetic reflectometry, we have separately determined the distribution of the spin and orbital magnetization. Moreover, the magnetization in single atomic layer of Pt located very close to the interface has been observed.

In this study, the distribution of Pt magnetization induced by the Co underlayer was quantitatively determined and effective range of magnetic coupling was estimated in the vicinity of the Co-Pt interface. In future studies, the magnetic anisotropy of the Pt layer, which may be crucial for the thermal stability of the perpendicular media. needs to be investigated. Angular dependent XMCD experiments [9, 13] would provide useful information related to the magnetic anisotropy.

Acknowledgments

This work was performed with the approval of Japan Synchrotron Radiation Research Institute (JASRI) as Nanotechnology Support Project of The Ministry of Education, Culture, Sports, Science and Technology (Proposal No. 2002B0648-NS2-np/BL39XU).

References

1. Sonobe, Y., *et al.*, IEEE Trans. Mag. **38**, 2006 (2002).
2. Rüegg, S., *et al.*, J. Appl. Phys. **69**, 5655 (1991).
3. Maruyama, H., Matsuoka, F., Kobayashi, K. and Yamazaki, H., J. Mag. Mag. Mater. **140–144**, 43 (1995).
4. Grange, W., *et al.*, Phys. Rev. B **58**, 6298 (1998).
5. Grange, W., *et al.*, Phys. Rev. B **62**, 1157 (2000).
6. Thole, B. T., Carra, P., Sette, F. and van der Laan, G., Phys. Rev. Lett. **68**, 1943 (1992); Carra, P., Thole, B. T., Altarelli, M. and Wang, X., Phys. Rev. Lett. **70**, 694 (1993).
7. Maruyama, H., *et al.*, J. Synchrotron Rad. **6**, 1133 (1999).
8. Wilhelm, F., *et al.*, Phys. Rev. Lett. **85**, 413 (2000).
9. Suzuki, M., *et al.*, in preparation.
10. Ederer, C., Komelj, M., Fähnle, M. and Schütz, G., Phys. Rev. B **66**, 094413 (2002).
11. Vogel, J., *et al.*, Phys. Rev. B **55**, 3663 (1997).
12. Geissler, J., *et al.*, Phys. Rev. B **65**, 020405 (2001).
13. Weller, D., *et al.*, Phys. Rev. Lett. **75**, 3752 (1995).

Physica Scripta. Vol. T115, 583–585, 2005

CO Induced Spin Reorientation Transition of Co/Pd(111) Studied by XMCD and XPS

D. Matsumura[1], T. Yokoyama[2], K. Amemiya[1], S. Kitagawa[1] and T. Ohta[1,*]

[1]Department of Chemistry, Graduate School of Science, The University of Tokyo, 7-3-1 Hongo, Bunkyo-ku, Tokyo 113-0033, Japan
[2]Institute for Molecular Science, Myodaiji-cho, Okazaki, Aichi 444-8585, Japan

Received June 26, 2003; accepted October 14, 2003

PACS numbers: 75.70.Ak, 75.30.Gw, 68.43.Fg, 79.60.Dp

Abstract

The effect of CO adsorption on the magnetic easy axis of Co/Pd(111) magnetic thin films has been studied by C 1s X-ray photoelectron spectroscopy (XPS) and Co L-edge X-ray magnetic circular dichroism (XMCD) in absorption spectroscopy. We found by the XMCD measurements that the CO adsorption at 200 K induces the spin reorientation transition of a 4–6 monolayer (ML) Co thin film, but it does not cause spin reorientation at 300 K. Simultaneous XPS measurement showed that the C 1s spectrum has a single peak at 285.8 eV at 300 K, while it has an additional shoulder at 285.3 eV at 200 K. The main peak is associated with the CO atop adsorption, and the shoulder might be ascribed either to bridge or hollow site adsorption. Temperature and CO coverage dependences of XMCD and C 1s XPS spectra reveal that the bridge or hollow site CO adsorption is responsible for the spin reorientation of the Co thin film. This is the first direct observation to correlate the magnetic anisotropy of a magnetic thin film with the molecular adsorption site.

Co thin films on Au, Pt, and Pd(111) surfaces exhibit a strong perpendicular magnetic anisotropy (PMA) [1, 2, 3, 4] and have widely been studied. In particular, multilayer systems have attracted much attention, because they have a wider range of perpendicular magnetic easy axis than single layer systems. XMCD studies reveal that the perpendicular orbital magnetic moment is enhanced at the interface of these systems [4–6]. We can also expect a large anisotropy of the orbital magnetic moment at the surface of the magnetic thin films because there is no atom above the surface. However, it has not widely been examined due to difficulty of preparing a clean surface.

Recently, it has been revealed that the magnetic anisotropy and the magnetic easy axis of thin films are influenced by gaseous adsorption on the surfaces [7, 8, 9, 10, 11]. This is phenomenologically explained by the reason that atomic or molecular adsorption reduces the absolute value of the surface magnetic anisotropy constant which favors parallel magnetization, and as a result, perpendicular magnetization becomes energetically stable [10, 11]. In addition, induced magnetization of the adsorbates has also been studied [12]. The sign of the magnetic coupling between adsorbates and thin films was found to be related to the magnetic easy axis of the films. These facts suggest that the magnetic anisotropy of thin films is affected by the adsorption of gaseous molecules.

In the present work, we have observed the spin reorientation transition of Co/Pd(111) induced by CO chemisorption by means of XMCD and XPS measurements. XMCD provides information on the magnetization of the Co thin film. We found that quenching of the surface parallel magnetic orbital moment by CO adsorption is a key of PMA stabilization [13, 14]. On the other hand, XPS is a powerful surface analytical method, which is sensitive to the chemical environment. Especially for CO adsorption systems, their adsorption sites can be discriminated by the XPS cheical shift and high resolution. Thus, we have examined the correlation between the CO surface adsorption fashion and the spin reorientation transition of Co thin film induced by stepwise CO adsorption and desorption. It is a new approach to observe magnetism of a thin film from the view of surface chemistry.

All the experiments have been performed at the soft X-ray bending magnet station, BL-7A, which is equipped with a varied-line-spacing plane grating monochromator, in the Photon Factory of the Institute of Materials Structure Science, High Energy Accelerator Research Organization (KEK-PF) [15].

Co thin films were prepared on a Pd(111) single crystal by the following procedure. The Pd(111) substrate was cleaned by repeated cycles of Ar sputtering (2 keV) and annealing at 1000 K in an ultrahigh vacuum chamber. The cleanliness and order of the surface were confirmed by NEXAFS (near-edge X-ray absorption fine structure), LEED (low-energy electron diffraction) and XPS. Co thin films were deposited on Pd(111) at room temperature with the electron-beam evaporation method. As RHEED (reflection high-energy electron diffraction) oscillation has not been observed in the present system, we estimated the thickness of each film by the edge jump of NEXAFS and the Auger intensity ratio between Co and Pd.

The C 1s X-ray photoelectron spectra were taken with a hemispherical electrostatic analyzer (GAMMADATA-SCIENTA, SES-2002) with an incident X-ray energy of 430 eV. The X-ray incident angle was fixed at $\theta = 30^\circ$ from the surface and normally emitted photoelectrons were detected. For Co L-edge XMCD measurements, we used elliptically polarized X-rays emitting downwards from the electron orbital plane by -0.4 ± 0.1 mrad. The circularly polarization factor was estimated to be 0.85. The absorption spectra were recorded with the partial-electron-yield mode with a retarding voltage of 500 V using a microchannel plate (MCP), which was placed below the sample. The XMCD spectra were obtained by reversing the magnetization of the films. Each sample was mounted in a Helmholtz coil and was magnetized by a current pulse (0.1 T) along the incident X-rays and the remnant magnetization was examined. We could measure XPS and XMCD in absorption spectroscopy under the same conditions without changing the sample and/or detector position.

Figures 1 and 2 show the perpendicular and parallel effective spin magnetic moments of Co/Pd(111) magnetic thin films with various thicknesses, which were obtained by the observation of Co L-edge XMCD and the application of the magnetic sum rule analysis. In order to check the magnetic easy axis of each thin film, XMCD measurements were performed at normal incidence ($\theta = 90^\circ$) for the detection of perpendicular magnetization, and at

*ohta@chem.s.u-tokyo.ac.jp

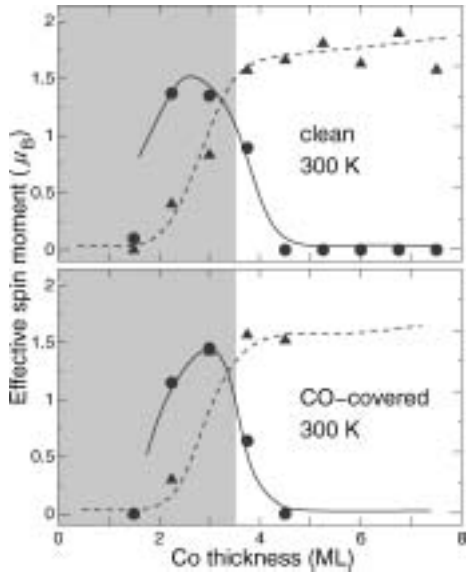

Fig. 1. Effective spin magnetic moments of clean (up) and CO-covered (down) Co thin films on Pd(111) at 300 K as a function of Co thickness. Circles and solid lines correspond to the surface normal direction, while triangles and dashed lines correspond to the surface parallel one. Hatched areas indicate the PMA regions.

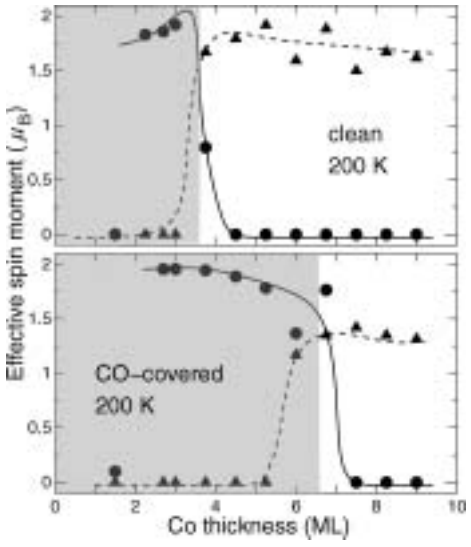

Fig. 2. Effective spin magnetic moments of clean (up) and CO-covered (down) Co thin films on Pd(111) at 200 K as a function of Co thickness. Circles and solid lines correspond to the surface normal direction, while triangles and dashed lines correspond to the surface parallel one. Hatched areas indicate the PMA regions.

grazing incidence ($\theta = 30^\circ$) for the detection of surface parallel magnetization. For the clean Co/Pd(111) system, the region of the perpendicular magnetic easy axis is below 3.5 ML at both 300 K and 200 K. CO adsorption at 300 K does not shift the critical thickness of the Co/Pd(111) at all. On the other hand, in the case of 200 K, CO-covered films show a wider region of perpendicular magnetic easy axis than the clean one by about 3 ML. Co films with thickness of 4–6 ML inherently show a parallel magnetic easy axis and undergo a spin reorientation transition from surface parallel to perpendicular direction upon CO adsorption at 200 K. These results indicate that PMA is stabilized by CO adsorption at 200 K and not affected by that at 300 K.

Figure 3 shows C 1s photoelectron spectra of CO adsorbed on Co/Pd(111) taken at 300 K and 200 K. The C 1s spectrum at 300 K consists of a single peak at 285.8 eV, while that at 200 K has an additional shoulder at 285.3 eV, suggesting two

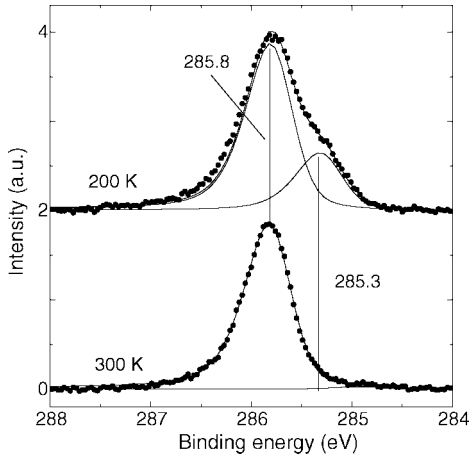

Fig. 3. C 1s X-ray photoelectron spectra from CO adsorbed on 4.5 ML Co film on Pd(111), taken at temperatures of 300 K and 200 K. The vertical lines indicate the positions of peaks assigned to atop (285.8 eV) and bridge or hollow (285.3 eV) adsorptions sites (see text).

kinds of adsorption sites at 200 K. Previous XPS experiments for CO adsorbed on *hcp* Co(0001) single crystal suggest that CO molecule occupies atop sites at 300 K and bridge or hollow sites as well as atop sites at 200 K [16]. Photoelectron diffraction study indicated that epitaxially grown Co films have a *fcc* structure up to 20 ML [17], which is different from the *hcp* structure in the bulk. Although it is not certain that the CO adsorption behavior on the Co film is the same as that on *hcp* Co (0001), the C 1s peak of bridge and hollow sites generally appears at the lower energy position than that of atop sites by 0.5–1.0 eV on several metal surfaces. Thus, we can deduce that CO molecules are adsorbed exclusively on atop site of Co/Pd(111) at 300 K and both on atop and bridge (or hollow) sites at 200 K.

In order to examine both the surface adsorption behavior of CO molecule and the change in magnetism of the Co thin film, C 1s XPS and Co L-edge XMCD spectra were measured at stepwise CO adsorption. Figure 4 shows the relationship between C 1s and

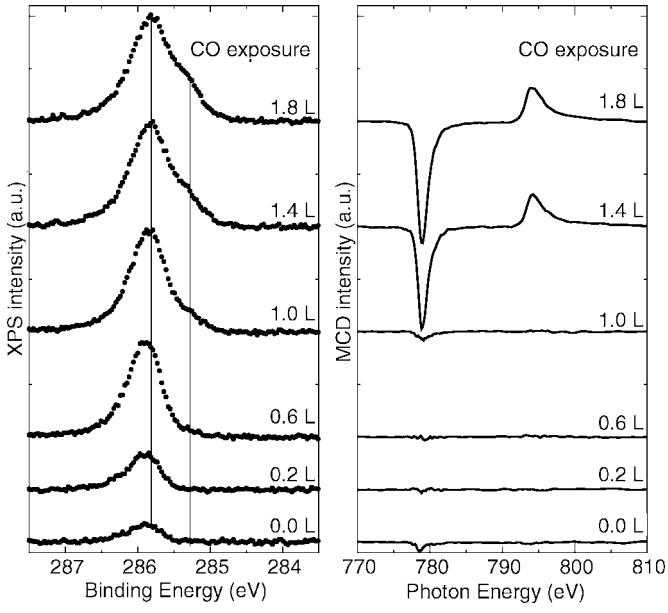

Fig. 4. C 1s X-ray photoelectron spectra (left) and normal incident Co L-edge XMCD spectra (right) from 4.5 ML Co thin film on Pd(111) during step by step CO adsorption at 200 K.

Co XMCD spectra for a 4.5 ML Co film during CO dosage at a temperature of 200 K. The Co film undergoes spin reorientation transition from surface parallel (before CO adsorption) to perpendicular magnetization (after being completely covered with CO). Note that the X-ray incident angle was normal so as to detect only perpendicular magnetization for the XMCD measurements. Nearly zero XMCD signal during the low CO coverage does not indicate that the Co thin film is not magnetized, but is fully magnetized in parallel direction before CO dosage, as confirmed by the XMCD observation at grazing incidence (not shown). The growth manner of the main XPS peak at 285.8 eV suggests that the atop sites are occupied at the low coverage. At around 1.0 L (1 L = 10^{-6} Torr · s; 1 Torr = 133 Pa) CO dosage, the main peak became saturated and the shoulder at 285.3 eV gradually grew up. At the same time, Co XMCD gradually appeared, which means that the easy axis of Co had just begun to rotate the orientation of spin from surface parallel to perpendicular direction. At around 1.8 L CO exposure, both C 1s and XMCD peak intensities were saturated, which means that CO adsorption was completed and Co was fully magnetized perpendicularly. We observed the same correlation between CO occupation of bridge or hollow sites and the perpendicular magnetization of Co thin film in thermal heated desorption process. We found that the spin reorientation transition in Co/Pd(111) is induced as a consequence of CO adsorption on bridge or hollow site and not induced by CO adsorption on atop site which is the most energetically favored adsorption position. We have repeated these adsorption and desorption experiments for several films which consist of 4–6 ML Co films on Pd(111) and observed similar behavior.

As for the behavior of the spin reorientation transition induced by surface adsorption, we compare CO on Co/Pd(111) with H or CO on Ni/Cu(001). A linear shift of the critical thickness accompanied with the coverage of H or CO on Ni/Cu (001) was pointed out by using magneto-optical Kerr effect (MOKE) [10, 11]. It was concluded that H or CO adsorption reduces the absolute value of the surface magnetic anisotropy constant with the adsorption coverage. On Ni/Cu(001), CO resides at atop sites at 300 K and H resides at fourfold hollow sites at 200 K. For both cases the site occupation is unique. Our result shows that the chemisorption-driven spin reorientation transition of Co/Pd(111) is induced only when CO is adsorbed on bridge or hollow sites, while it is not induced when CO occupies the atop site which is the most favorable adsorption site. This suggests that the change of the surface magnetic anisotropy is expressed not only by the coverage, but also by the adsorption structure of the surface.

Surface and interface magnetic anisotropies of the thin films originate in structural and electronic effects. Some studies point out that the in-plane interatomic distance of a few ML Co film on Pd(111) seems to be the same as that of Pd due to the epitaxial growth [17]. From the view of the structural effect, such an elongated interatomic distance at the interface creates an interface magnetic anisotropy. CO adsorption on the atop site does not affect the Co-Co interatomic distance much, while CO atoms adsorbed on bridge or hollow sites might push in the Co substrate and elongate the Co interatomic distance. This could be the reason why CO adsorbed on atop sites does not change the surface magnetic anisotropy while occupation of bridge or hollow sites creates the PMA.

We have reported the chemisorption-driven spin reorientation transition of the Co/Pd(111) magnetic thin film by simultaneous measurements of XPS and XMCD on the same system in order to solve the correlation between the surface adsorption structure and the magnetic anisotropy of the thin film. We found that the spin reorientation transition of Co/Pd(111) induced by CO chemisorption is exclusively accomplished by CO adsorbed on bridge or hollow sites and occupation of atop sites has no effect on the spin reorientation transition. We would like to emphasize that if one considers surface magnetic anisotropy of a thin film, it is important to know the surface structure of adsorbates. Because surface adsorption shows various structures under certain conditions, these results allow us to have a new research field between surface chemistry and magnetic thin films.

Acknowledgments

This study was supported by a Grant-in-Aids for scientific research (No. 14204069) and the 21st Century COE Program from the Ministry of Education, Culture, Sports, Science and Technology. The authors gratefully acknowledge Mr. Hirokazu Watanabe and Mr. Hitoshi Abe for their support in the experiments and data analysis. The present work has been performed under the approval of the Photon Factory Program Advisory Committee (PF-PAC No. 2001S2-003).

References

1. Chappert, C., Renard, D., Beauvillain, P., Renard, J. P. and Seiden, J., J. Magn. Magn. Mater. **54–57**, 795 (1986).
2. Engel, B. N., Wiedmann, M. H., Van Leeuwen R. A. and Falco, C. M., J. Appl. Phys. **73**, 6192 (1993).
3. Tatnall, C. J., Schille, J. P., Grundy, P. J. and Lord, D. G., J. Magn. Magn. Mater. **165**, 391 (1997).
4. Weller, D. *et al*., Phys. Rev. B **49**, 12888 (1994).
5. Sang-Koog Kim and Kortright, J. B., Phys. Rev. Lett. **86**, 1347 (2001).
6. Oh, S.-J. *et al*., Appl. Surf. Sci. **169–170**, 127 (2001).
7. Chen, J. and Erskine, J. L., Phys. Rev. Lett. **68**, 1212 (1992).
8. Hope, S., Gu, E., Choi, B. and Bland, J. A. C., Phys. Rev. Lett. **80**, 1750 (1998).
9. Robach, O. *et al*., Phys. Rev. B **65**, 054423 (2002).
10. Vollmer, R., Gutjahr-Löser, Th., Kirschner, J., van Dijken, S. and Poelsema, B., Phys. Rev. B **60**, 6277 (1999).
11. van Dijken, S., Vollmer, R., Poelsema, B. and Kirschner, J., J. Magn. Magn. Mater. **210**, 316 (2000).
12. Yokoyama, T. *et al*., Phys. Rev. B **62**, 4191 (2000).
13. Matsumura, D., Yokoyama, T., Amemiya, K., Kitagawa, S. and Ohta, T., Phys. Rev. B **66**, 024402 (2002).
14. Yokoyama, T. *et al*., J. Phys.: Condens. Matter **15**, S537 (2003).
15. Amemiya, K., Kondoh, H., Yokoyama, T. and Ohta, T., J. Electron Spectrosc. Relat. Phenom. **124**, 151 (2002).
16. Lahtinen, J., Vaari, J. and Kauraala, K., Surf. Sci. **418**, 502 (1998).
17. Atrei, A. *et al.*, Surf. Sci. **372**, 91 (1997).

Physica Scripta. Vol. T115, 586–588, 2005

Limitations of Integral XMCD Sum-Rules for the Early 3d Elements

A. Scherz[1*], H. Wende[1], C. Sorg[1], K. Baberschke[1], J. Minár[2], D. Benea[2] and H. Ebert[2]

[1]Institut für Experimentalphysik, Freie Universität Berlin, Arnimallee 14, D-14195 Berlin-Dahlem, Germany
[2]Institut für Physikalische Chemie, Universität München, Butenandtstraße 5-13, D-81377 München, Germany

Received June 26, 2003; accepted in revised form November 4, 2003

PACS numbers: 78.70.Dm, 75.70.−i, 71.20.Be

Abstract

We report on XMCD measurements at the $L_{2,3}$ edges of the early 3d transition metals, Ti, V and Cr, polarized by Fe. In contrast to the classical ferromagnets Fe, Co and Ni, the XMCD spectra reveal a complex and detailed fine structure. We analyze the experimental data with the help of full-relativistic *ab initio* calculations of the X-ray absorption cross section $\mu(E)$ that provide the energy-dependent XMCD spectrum and the correlated magnetic moments μ_s and μ_l. We demonstrate that the use of the so-called integral sum-rules, which interrelate certain areas of the XMCD spectra to μ_s and μ_l, yield erroneous results for the early 3d elements due to 2p–3d core hole correlations in $L_{2,3}$ absorption spectra.

To study the magnetic properties of thin films and magnetic nanostructures the determination of element-specific magnetic moments and the separation into their spin and orbital components (μ_s and μ_l) is one of the striking applications of the X-ray magnetic circular dichroism (XMCD). Concerning the spin and orbital magnetic moments of 3d transition metals (TM's) the magneto-optical sum-rules [1] interrelate certain areas of the $L_{2,3}$ absorption spectra to the magnetic ground state of the d valence shell. Even though certain approximations might limit the validity of the sum-rules [2], it has been demonstrated that they can successfully be applied to the late 3d transition metals (TM's), i.e. Fe and Co bulk metals [3]. In this way orbital and spin magnetism of thin films, multilayers, clusters and one-dimensional chains have been explored by means of XMCD, since most of the magnetic nanostructures are composed of the 3d ferromagnets Fe, Co, and Ni. On the other hand investigations of the induced magnetic moments in the non-ferromagnetic constituent of magnetic multilayers, e.g. Fe/TM with TM = V, and Cr [4, 5], have also attracted considerable interest. The observation of circular dichroism at the L edges of the early 3d TM's can evidence the existence of a net magnetic moment. However, the application of the sum-rules to the early 3d TM's in order to determine quantitatively the spin and orbital moments has several drawbacks: (*i*) The $L_{2,3}$ edges partially overlap which makes a deconvolution of the individual contributions of the L_3 and L_2 edge difficult. (*ii*) The branching ratio, i.e. the fraction of the $2p_{3/2}$ transition channel, strongly deviates from the statistical 2 : 1 due to the 2p–3d core-hole interaction [6]. (*iii*) According to (*i*) and (*ii*) the core hole interaction may become competitive to the small spin-orbit coupling in the core shell (few eV) resulting in apparent spin moments derived by the spin sum-rule. This has been demostrated for Mn, Fe, Co and Ni ions on the basis of atomic calculations [7] where deviations between 30% and 8% were found for Mn and Ni, respectively. (*iv*) Early 3d TM's are either non-magnetic (Ti, V) or antiferromagnetic (Cr) in their bulk configurations and it makes an independent validation of the sum-rule results difficult.

In this work, we extend the discussion of the sum-rule limitations to the early 3d TM's Cr, V and Ti. The question is how information contained in the XMCD spectra can safely be transferred to spin and orbital moments. Contrary to the idea of integral sum-rules, it has been proposed to analyze the spectral line shape of the circular dichroism in more detail [8, 9]. This approach deals with deriving magnetic moments from the absorption fine structure of the circular dichroism which depends on the magnetic ground state properties of the 3d band. For this purpose we compare the experimental absorption spectra to *ab initio* calculations based on a full-relativistic spin-polarized Korringa-Kohn-Rostoker (SPR-KKR) Greens-function method, for details see Ref. [2]. The theory provides both the energy-dependence of the $L_{2,3}$ absorption coefficient $\mu^+(E)$, $\mu^-(E)$ for left- and right-circularly polarized light, respectively, and the corresponding spin and orbital magnetic moments. Recently, we have demonstrated that the application of the spin sum-rule to V-XMCD spectra of a $Fe_{0.90}V_{0.10}$ standard sample yields erroneous moments that are 5 times smaller [10]. Hereby, systematic errors introduced exclusively by the commonly used procedure do not account for the strong deviation. Here, we assign this concept to Ti and Cr in order to provide trends across the 3d series in view of 2p–3d core-hole interaction.

All the samples were prepared *in situ* under ultrahigh vacuum conditions ($\sim 2 \times 10^{-10}$ mbar) by evaporation from high-purity rods on an annealed Fe(110) buffer layer (10 nm) on a Cu(100) single crystal. The Fe/Ti/Fe(110) and Fe/Cr/Fe(110) trilayers were deposited successively at 300 K similar to the prototype Fe/V/Fe(110) trilayers in Ref. [11]. The Fe/V alloy has been prepared by co-evaporation from a triple-e-beam evaporator that allows for individual control of the deposition rates, for details see Ref. [10]. Interestingly, for the Fe/Ti trilayers we observed that the Ti-XMCD signal is independent of the deposited Ti-thickness (<1.5 nm). This suggests that in average all Ti-atoms became equally polarized through Fe. This result can be understood from considering the formation of a $TiFe_2$ structure in our trilayers as it was recently reported for Fe/Ti multilayers in Ref. [12]. The XMCD measurements were carried out at the third generation synchrotron radiation facility of Berlin (BESSY II). At the insertion device beamline UE56/1-PGM the so-called 'gap-scan' technique, driving both the undulator and the monochromator simultaneously, allows for absorption measurements with a constant high degree of circularly polarized light (90%) and high photon-flux in the required energy-range (Ti-Cr: 420–640 eV). The XMCD spectra at the $L_{2,3}$ edges were obtained by reversing the sample magnetization with an electric pulse-driven coil and alternatively, by inverting the helicity of the X-rays. The samples

*Corresponding author, electronic address: babgroup@physik.fu-berlin.de; URL: http://www.physik.fu-berlin.de/~ag-baberschke/index.html

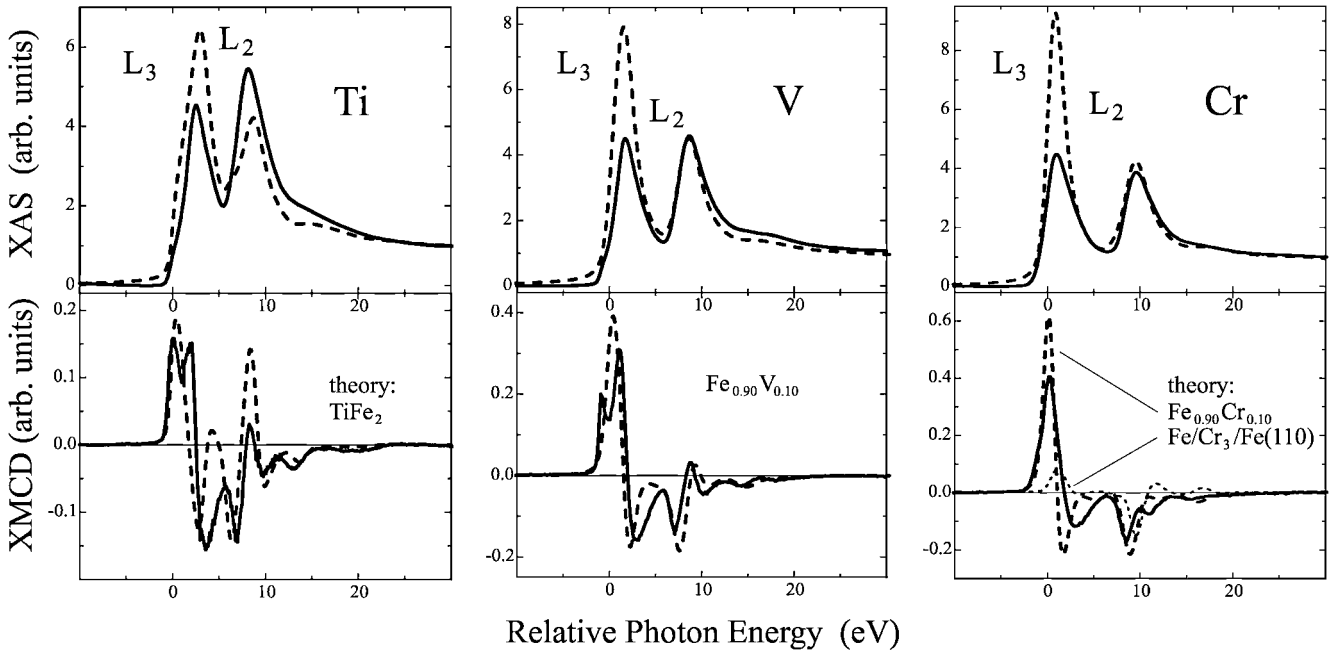

Fig. 1. Normalized (above) XAS and (below) XMCD spectra for the early 3d TM's Ti, V, and Cr at the $L_{2,3}$ edges: (solid lines) experimental data versus (dashed lines) *ab initio* calculations. The experimental data have been corrected corresponding to measurements with 100% circularly polarized light with the *k* vector parallel to the magnetization. Note that scaling factors between theory and experiment as well as between the XAS and XMCD intensities do not exist.

were probed in magnetic remanence using the total electron yield detection mode. The easy-axis of magnetization for all the present samples is in-plane along the [001] Cu direction. Therefore, the absorption measurement were performed under 20° grazing incidence of the X-rays and consequently, all spectra have been corrected for saturation effects. To ensure that the XMCD spectra can be safely transferred to magnetic moments the Fe-XMCD signals have been cross-checked with the one of bulk Fe/Cu(001).

In Figure 1 the experimental XAS and XMCD spectra (solid lines) are presented for Ti, V and Cr at the $L_{2,3}$ edges together with the *ab initio* calculations (dashed lines). The positive onset of the dichroism at the L_3 edge reveals antiparallel orientations of the net magnetization of Ti, V, and Cr with respect to Fe in agreement with theory. Because core-hole correlation effects [6] were not taken into account in the calculations, the branchings ratios in the XAS spectra for the experiment and theory are different. Those effects result in a transfer of spectral weight in favor of the L_2 edge and govern the XAS spectra of 3d TM's towards lower d-counts as it can be clearly observed in Figure 1. The overlap of the $L_{2,3}$ edges hinders to distinct band-structure related features in vicinity to both edges. However, there are broad satellites slightly above the L_2 edge that stem from van Hove singularities in the bcc-Brillouin zone identified by the theory.

The XMCD spectra (average of 4 couples) are almost free of noise bringing the detailed absorption fine structure to light. For the investigated samples, the XMCD to XAS peak height ratio at the L_3 edge is ∼3%, ∼7%, and ∼9% for Ti, V, and Cr, respectively. In contrast to the ferromagnets Fe, Co and Ni the XMCD spectra of early 3d TM's show dispersive line shapes at the $L_{2,3}$ edges. The lower the filling of the d-valence band the more the peaks become asymmetric. In case of Ti we can demonstrate that the XMCD signal even turns completely asymmetric. This tendency across the 3d series has been modeled in terms of multipole moments of the ground state [8]. A better description of the energy-dependent XMCD spectrum can be obtained including band-dispersion [9, 10] as it is shown in Figure 1. Interestingly, calculations of the XMCD spectrum assuming perfect interfaces for the $Fe/Cr_3/Fe$ sample reveal a different XMCD spectrum. However, the agreement with the experiment improves considering partly interdiffused interfaces which in turn demonstrates the sensitivity of the XMCD signal to the electronic band-structure. Hence, we included the theoretical spectra for a $Fe_{0.90}Cr_{0.10}$ alloy serving as a reference in Figure 1. Furthermore, the theory can separately evaluate contributions of the L_3 and L_2 edge. This allows for a rough deconvolution of the edges in experimental spectra and give an estimate for systematic errors of the spin sum-rule. In correspondence to the XAS spectrum the circular dichroism for Ti, V, and Cr reveals an oscillatory fine structure above the L_2 edge that originates from the spin-dependent band structure and is perfectly reproduced by the calculations. On the other hand, the splitting of the L_3 peak in the experimental XMCD spectrum for Ti and V can be attributed to multiplets. The atomic-like features indicate that the 3d electrons remain partly correlated in early 3d TM's which might be supported by the fact that the features are missed by the SPR-KKR calculations.

The theory provides both the XMCD to XAS peak ratios and the corresponding spin and orbital magnetic moments which are listed in Table I. In order to test the validity of the integral sum-rules we compared those values with the one derived from the application of the commonly used procedure, for details see e.g. Ref. [3, 10]. The number of d-holes was taken from theory being 7.36, 6.44, and 5.45 per atom for Ti, V, and Cr, respectively. Instead of separating the $L_{2,3}$ contributions we used a simple energy cut-off determined by the local minimum between the edges. In case of V we recently reported the breakdown of the spin sum-rule since the apparent spin moments deviate by a factor 5 with respect to theory [10] and polarized neutron studies [13]. The V orbital moment shows reasonable agreement with theory, even the antiparallel alignment of the spin and orbital moments can be correctly deduced. Note that the orbital sum-rule can be applied

Table I. *The apparent magnetic moments derived by application of the sum-rules to the experimental data and the spin and orbital magnetic moments as calculated by ab initio theory corresponding to the theoretical XAS and XMCD spectra in Fig. 1. The spin moment ratio R reveals a considerable underestimation of the 'real' values by the sum-rule analysis, see text.*

	theory		sum-rules		
	μ_s (μ_B)	μ_l (μ_B)	μ_s (μ_B)	μ_l (μ_B)	R
Ti	−0.70	0.014	−0.17	0.069	0.24(10)
V	−1.01	0.020	−0.20	0.016	0.20(3)
Cr	−0.95	0.014	−0.28	0.011	0.47(15)

without deconvoluting the $L_{2,3}$ edges. Ti acquires an induced spin moment of $-0.7\,\mu_B$ predicted by theory for the Fe_2Ti structure. Even though the XMCD to XAS peak ratios are in reasonable agreement between experiment and theory the spin sum-rule fails similar to V. The experimental Cr data indicate a magnetic moment of about $-0.6\,\mu_B$ in comparison with the $Fe_{0.90}Cr_{0.10}$ reference and with XMCD measurements on Fe/Cr trilayers reported by Idzerda *et al.* [5], while the application of the spin sum-rule yields $-0.28\,\mu_B$. Finally, the apparent spin moment (sum-rule) to expected spin moment ratio R is given in Table I. It appears that going towards the late 3d elements the deviation of the spin sum-rule reduces systematically from 80% (Ti) to 50% (Cr) while it varies for the late 3d ions between 30% (Mn) to 8% (Ni) in atomic calculations [7]. The deviation of the spin sum-rule is related to the remixing of the 2p transitions channels and elucidates why the sum-rule holds for Fe and Co [3]. In case of the early 3d TM's the influence of the core hole is much stronger, because the core hole interaction increases with the vacancy of the d-band while the spin-orbit coupling in the core shell decreases. It is valuable to note that the orbital sum-rule provides the correct sign. This means accordingly that the spin and orbital moments are antiparallel aligned for Ti, V and Cr and aligned in parallel for Fe and Co in agreement with the theoretical expectations.

In summary we have compared state-of-the-art experimental XMCD measurements with *ab initio* theory. This allows a detailed analysis of the fine structure in the $L_{2,3}$ absorption spectra and moreover, provides the XMCD-related spin and orbital magnetic moments. The absorption fine structure of early 3d TM's reveal band-structure-related features as well as multiplet structures. We have extended the discussion of the validity of the spin sum-rule to the early 3d TM's which suffer from 2p–3d core hole correlations in $L_{2,3}$ absorption measurements. We give quantitative deviations of the sum-rules that allows to estimate realistic magnetic moments from XMCD spectra.

Acknowledgments

We thank the Bessy crew for the excellent experimental conditions. The work was supported by the BMBF (05KS1 KEB4) and BMBF (05SC8 WMA7).

References

1. Thole, B. T., Carra, P., Sette, F. and van der Laan, G., Phys. Rev. Lett. **68**, 1943 (1992); Carra, P., Thole, B. T., Altarelli, M. and Wang, X., *ibid.* **70**, 694 (1993).
2. Ebert, H., Rep. Prog. Phys. **59**, 1665 (1996).
3. Chen, C. T. *et al*., Phys. Rev. Lett. **75**, 152 (1995).
4. Schwickert, M. M. *et al*., Phys. Rev. B **57**, 13681 (1998).
5. Idzerda, Y. U. *et al*., Phys. Rev. B **48**, 4144 (1993).
6. Schwitalla, J. and Ebert, H., Phys. Rev. Lett. **80**, 4586 (1998); Ankudinov, A. L., Nesvizhskii, A. I. and Rehr, J. J., Phys. Rev. B **67**, 115120 (2003).
7. Teramura, Y., Tanaka, A. and Jo, T., J. Phys. Soc. Japan **65**, 1053 (1996).
8. van der Laan, G., Phys. Rev. B **55**, 8086 (1997).
9. Guo, G. Y., Phys. Rev. B **57**, 10295 (1998).
10. Scherz, A. *et al*., Phys. Rev. B **66**, 184401 (2002).
11. Scherz, A. *et al*., J. Appl. Phys. **91**, 8760 (2002).
12. Fnidiki, A. *et al*., J. Appl. Phys. **84**, 3311 (1998).
13. Mirebeau, I., Parette, G. and Cable, J. W., J. Phys. F: Met. Phys. **17**, 191 (1987).

Physica Scripta. Vol. T115, 589–590, 2005

Local Structure in Strained Manganite thin Films

N. M. Souza-Neto[1,2,*], A. Y. Ramos[1,3], H. C. N. Tolentino[1], E. Favre-Nicolin[4] and L. Ranno[4]

[1]Laboratório Nacional de Luz Síncrotron - LNLS, P.O. Box 6192, 13084-971, Campinas, São Paulo, Brazil
[2]Instituto de Física "Gleb Wataghin", IFGW - UNICAMP, Campinas, SP, Brazil
[3]Laboratoire de Minéralogie-Cristallographie de Paris, LMCP -UMR 7590 -CNRS, Paris, France
[4]Laboratoire Louis Néel, UPR 5051 CNRS-UJF Grenoble, France

Received June 26, 2003; accepted in revised form November 4, 2003

PACS numbers: 78.70.Dm, 31.15.Ar, 68.55.−a, 75.47.Lx, 33.15.Dj

Abstract

We report on a polarized X-ray absorption spectroscopy study, combining experimental measurements and *ab initio* calculations, of $La_{0.7}Sr_{0.3}MnO_3$ films, epitaxially grown on tensile and compressive substrates. Measurements show significant modifications in the coordination shell around manganese atoms in the film plane for both substrates. We show that biaxial strain is locally accommodated in the coordination shell, by distortion of the MnO_6 octahedron, without change in the tilt angle. The modifications of the near edge spectra were correlated to modification in the average Mn−O bond distance and distortion of the MnO_6 octahedra. This distortion tending to localize the charge carriers may account for the decrease of the Curie temperature observed in thin films with respect to bulk systems.

1. Introduction

Among the materials exhibiting the Colossal Magnetoresistance effect [1], mixed manganite films have received special attention due to their potential application for a new generation of magneto-electronic devices [2]. From a fundamental point of view they show a variety of interesting phenomena due to the interplay of several, opposite magnetic interactions highly correlated with the crystal structure and the hole doping (metal-insulator transition, charge ordering, orbital ordering, phase segregation . . .). Moreover, high quality thin films of manganites can be brown using deposition techniques similar to the ones developed for high-TC superconductors. Structural and magnetic studies of thin films on slightly mismatched substrates have showed significant sensitivity of manganite properties to the induced strain. The temperature of the ferromagnetic transition, for example, has been observed to decrease as the external strain is increased. This would open up large possibilities to the design of tunable magnetic devices, if it were possible to address the explicit connection between the cell induced strains and the local structure around the manganese atoms, the Mn−O distances (coordination length) and the Mn−O−Mn angle (octahedral tilt), key parameters for the versatility of the magnetic and transport properties. X-ray absorption spectroscopy has been already used to investigate local order around the manganese atoms in some manganites films [3, 4], but there is no consensus yet about the relative importance of these two key parameters.

We report here on a polarized X-ray absorption spectroscopy study in $La_{0.7}Sr_{0.3}MnO_3$ (LSMO) thin films epitaxially grown on tensile and compressive substrates. Experimental measurements and *ab initio* calculations were combined to elucidate the strain induced local modification around the manganese ions.

*Electronic address: narcizo@lnls.br

2. Experimental

LSMO thin films (pseudo-cubic perovskite structure, $a = 3.87$ Å) were epitaxially grown by pulsed laser deposition under tensile ($SrTiO_3$ (STO) [001]) and compressive ($LaAlO_3$ (LAO) [001]) substrates with cubic and pseudo-cubic structures ($a = 3.905$ Å and $a = 3.793$ Å respectively). The low lattice mismatch between LSMO, STO and LAO allows a pseudomorphic growth for film thickness below 100 nm and 50 nm respectively [5]. MgO substrate (cubic, with $a = 4.21$ Å) was used to obtain a non pseudomorphic 3d-texturized fully relaxed film. For similar thickness the strain factor ($\epsilon_{zz} - \epsilon_{xx}$, see table I) is about twice for the film grown on LAO than for the film grown on the STO substrate.

The X-ray absorption experiments at the Mn K-edge (6539 eV) were performed at the LNLS D04B-XAS beamline using a Si (111) channel-cut crystal monochromator. The incident beam was monitored by an ion chamber and the data were collected in fluorescence mode using a Ge 15-elements solid state detector. Selective information about the bonds in a plane parallel to the film surface (IP) and perpendicular to this plane (OP) of the same film are obtained by setting the angle between electric field vector of the incident photon beam and the film surface to values close to 0 and 90 degrees (10 and 75 degrees, respectively).

3. Results and Discussion

Figure 1 shows XANES spectra of the tensile (STO substrate) and compressive (LAO substrate) strained films. The energy shift at the spectra collected can be associated to local changes on average Mn−O bond distance. We should note that the shifts for the tensile and compressive films are in opposite directions. For LSMO/STO the negative energy shift (−0.4 eV) shows that the Mn−O bond length is larger in the IP plane, as compared to the OP plane. On the contrary, in the film under compressive strain, LSMO/LAO,

Table I. *Strain components ε_{xx} and ε_{zz} (defined as $\epsilon_{xx} = \epsilon_{yy} = \frac{a_{film} - a_{ref}}{a_{ref}}$ and $\epsilon_{zz} = \frac{c_{film} - c_{ref}}{c_{ref}}$) in LSMO films.*

Substrate	film thickness	$\epsilon_{xx} = \epsilon_{yy}$	ϵ_{zz}
$SrTiO_3$ (STO)	60 nm	0.9%	−0.8%
MgO (MO)	60 nm	0%	0%
$LaAlO_3$ (LAO)	45 nm	−2.0%	2.3%

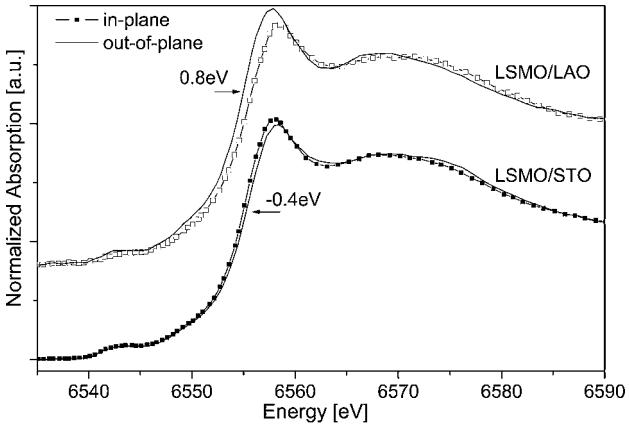

Fig. 1. Near Edge X-ray absorption spectra at the Mn K edge for the tensile ($SrTiO_3$) and compressive ($LaAlO_3$) LSMO film in plane and out of plane measurements. The energy shifts are in opposite directions and differ by a factor 2.

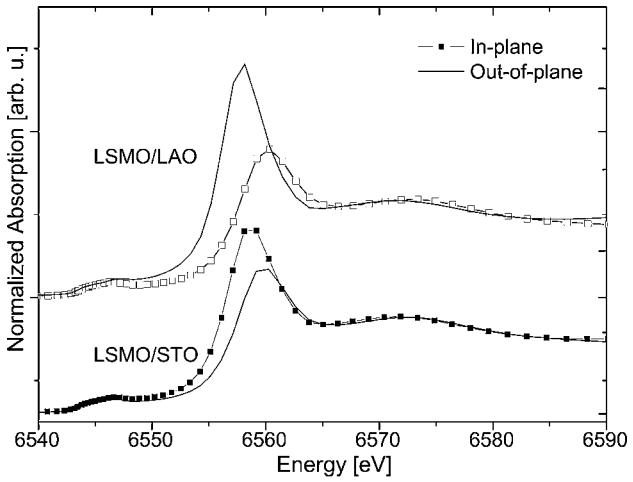

Fig. 2. XANES *ab initio* calculations of the LSMO structure in the compressive and tensile films, considering tetragonal distortion of the Mn−O octahedron. Comparison between the in plane and out of plane orientations for each film.

the positive energy shift (+0.8 eV) indicates that the Mn−O bond length is smaller in IP plane than in the OP plane of the film.

Moreover the amplitude of the shift for the LSMO/LAO film is about twice that for the LSMO/STO one and of the same order as the ratio of the long range strain factor among these films ($\epsilon_{zz} - \epsilon_{xx}$, on table I). The strain on the cell parameters is then directly related to average octahedral modifications. This indicates that the strain should be fully accommodated by changes in the coordination shell (Mn−O), without any modification of the Mn−O−Mn angle.

Slight modifications of the first line shape and intensity are observed in the XANES spectra. Such modifications already reported in the literature have been associated to distortions of the local structure.

We performed *ab initio* simulations using the full multiple scattering approach, to investigate the effect of octahedral distortion on the XANES spectra. Self-consistent calculation of the atomic potentials were performed using the Feff8.2 code [6]. The real part of the potential is modeled by an exchange-correlation Hedin-Lundqvist potential. All calculated absorption spectra were normalized by the value at 50 eV above the absorption edge allowing the *ab initio* calculations to be compared in position and intensity. Simulations were performed in a LSMO cluster considering isotropic MnO_6 and anisotropic distortions. The calculations shown in figure 2 were performed for clusters with tetragonal distortion using local order parameters scaling with the cell parameters of the films. The calculations do not take into account structural disorder or dispersion of the Mn−O length, so that for the calculated XANES spectra the differences in amplitude are higher and the rising slope steeper than in the experimental data. With this restriction, the calculated structures (figure 2) reproduce well the main differences in the features of the experimental results (figure 1) among the two orientations of the films: the energy shift amplitude and direction, and the relative reduction of the amplitude of the white line. Based on these calculations we can then certify that a model of anisotropic distortion of the MnO_6 octahedron accounts for the experimental XANES spectra.

In the LSMO system, the contribution of the spontaneous energy-lowering Jahn-Teller distortion of the $Mn^{3+}O_6$ is too small to be associated to a measurable average octahedral distortion. The substrate strain induces a larger and measurable static anisotropic distortion of the MnO_6 octahedron, with splitting of the in-plane and out-of-plane Mn−O bond lengths. This distortion leading to an increase of the splitting of the e_g levels, tends to localize the charge carriers and may account for the decrease of the Curie temperature observed in thin films with respect to bulk systems [5] .

We must point out that the XANES modifications are mainly correlated with modifications on the O−O−O angle (between the oxygens of the octahedron) by splitting of the Mn−O bond length. This splitting can appear due to different in-plane and out-of-plane bond lengths, as occurred for a tetragonal local distortion of the MnO_6 octahedron, but also in more complex distortion, as for example an orthorhombic distortion, were different Mn−O bond lengths are in the film plane. This later non-isotropic distortion in the plane may take place due to the nature of the Mn^{3+} and Mn^{4+} ions and is suggested by our EXAFS study [7]. Unfortunately, the change in the density of unoccupied states between these two situations is very small and *ab initio* calculations yield almost the same results for tetragonal and orthorhombic distortions.

4. Conclusions

In summary, we present here a combination of experimental measurements and *ab initio* calculations of polarized X-ray absorption to investigate the local scale structural distortion induced by substrate strain around manganese atoms in $La_{0.7}Sr_{0.3}MnO_3$ films. We show that biaxial strain is locally accommodated in the coordination shell, by distortion of the MnO_6 octahedron, without change in the tilt angle.

Acknowledgments

This work is partially supported by LNLS/ABTLuS/MCT. NMSN acknowledges a grant from CAPES. AYR acknowledges a grant from CNPq.

References

1. Millis, A. J., Nature **392**, 147 (1998).
2. Prellier, W., Lecoeur, P. and Mercey, B., J. Phys.: Condens. Matter **13**, R915 (2001).
3. Miniotas, A., Vailionis, A., Svedberg, E. B. and Karlsson, U. O., J. Appl. Phys. **89**, 2134 (2001).
4. Qian, Q. *et al*., Phys. Rev. B **63**, 224424 (2001).
5. Ranno, L., Llobet, A., Tiron, R. and Favre-Nicolin, E., Appl. Surf. Sci. **188**, 170 (2002).
6. Ankudinov, A. L., Bouldin, C., Rehr, J. J., Sims, J. and Hung, H., Phys. Rev. B **65**, 104107 (2002).
7. Ramos, A. Y. *et al.*, AIP Conf. Proc. **652**, 456 (2003).

Physica Scripta. Vol. T115, 591–593, 2005

Ga Magnetic Polarization in Mn_3GaC under High Pressure Probed by Ga *K*-Edge XMCD

N. Kawamura[1,*], N. Ishimatsu[2], M. Isshiki[1], Y. Komatsu[2] and H. Maruyama[2]

[1]SPring-8/JASRI, Mikazuki, Hyogo 679-5198, Japan
[2]Graduate School of Science, Hiroshima University, Higashi-Hiroshima, Hiroshima 739-8562, Japan

Received June 26, 2003; accepted December 10, 2004

PACS numbers: 75.50.Cc, 75.30.Kz, 61.10.Ht, 07.35.+k

Abstract

To study pressure-induced ferromagnetic state in Mn_3GaC perovskite, we have performed X-ray absorption spectroscopy (XAS) and X-ray magnetic circular dichroism (XMCD) spectroscopy at the Ga *K*-edge under high pressure up to 29.4 GPa at room temperature. Ga *K*-edge XMCD was observed under pressure ranging from 4.5 to 29.4 GPa and results indicate that the Ga atom is magnetically polarized under high pressure. From the XMCD spectral profile, it is suggested that the pressure-induced ferromagnetic state has a canted ferromagnetic structure.

1. Introduction

The Mn_3MC (M = Al, Zn, Ga, In and Sn) system shows characteristics typical of itinerant-electron system and has received extensive interest because it exhibits a great variety of magnetic phase transitions [1]. In particular, Mn_3GaC shows a first-order phase transition at $T_t = 170$ K from a ferromagnetic (F) phase to an anti-ferromagnetic (AF) phase upon decreasing temperature [1–4], and in the AF phase metamagnetism occurs under high magnetic fields [5]. In addition, pressure-induced ferromagnetism has been reported near the Curie temperature T_C; when pressure is applied, magnetization is significantly enhanced and the T_C increases above the value of 260 K observed at ambient pressure (AP) [4]. To date, there is no evidence for the existence of magnetically polarized states.

The crystal structure of Mn_3GaC is cubic-perovskite type. Mn atoms occupy the face centers of the cubic lattice formed by Ga atoms, and C atoms are sited at the body-centered position. According to neutron diffraction experiments [3], the Mn moments are aligned along the [111] direction and coupled parallel (antiparallel) with the adjacent (111) planes in the F (AF) phase. Kaneko *et al*. [4] measured the AC susceptibility of Mn_3GaC under high pressure and found an intermediate magnetic structure between the AF and F phases. Furthermore, it was found that high pressure led to an increase in T_C and an enhancement of the F state. Kamishima *et al*. [6] recorded magnetization curves for the same substance under pulsed high magnetic field and found that pressure stabilized the F phase and enhanced the Mn moment in the F phase. They have pointed out that large spin fluctuations may play an important role in the anomalous increase of the Mn moment with pressure. However, their investigation was restricted within a relatively low-pressure region (<1 GPa) because of the difficulty in performing magnetization measurement or neutron diffraction using a high-pressure diamond-anvil-cell (DAC). Therefore, a spectroscopic method is needed to investigate the magnetic properties under high pressure using a DAC.

X-ray magnetic circular dichroism (XMCD) has attracted much interest as a tool to investigate magnetic states [7]. It is accepted that *K*-edge XMCD spectrum arises from the $4p$ orbital polarization induced by mixing with the $3d$ states of neighboring sites [8, 9]. It is possible to observe XMCD for non-magnetic constituents, because the p states of non-magnetic atoms may be polarized by the $4p$-$3d$ hybridization with neighboring magnetic atoms. Recently, Ishimatsu *et al*. established a method for measuring XMCD using a DAC [10, 11]. Then we applied this method for studying the electronic and magnetic states of Mn_3GaC under high pressure. XAS and XMCD spectra at the Ga *K*-edge were measured at room temperature (RT) up to a pressure of 29.4 GPa. In this paper, we present pressure-dependent XMCD spectrum at the Ga *K*-edge, and discuss the magnetic structure from the viewpoint of Mn electronic states.

2. Experimental

XMCD experiment were performed using the helicity-reversal method under a fixed magnetic field of 0.6 T and were carried out at the beamline 39XU of SPring-8 [12]. X-rays emitted from a linear undulator were monochromatized by Si 111 double crystals and higher harmonics rejected by a Pt coated mirror. Circularly polarized X-rays were generated using a diamond X-ray phase plate [13], 2.7 mm thick. The circularly polarized X-ray beam passed through a slit of aperture 70 × 70 μm. High pressure was applied using a DAC made of Cu-Be alloy [10]. A pair of diamond anvils, 1.0 mm thick and 0.45 mm in culet diameter, was used. Mn_3GaC powder was loaded into a hole in a SUS gasket together with several pieces of ruby and a methanol/ethanol mixture (4 : 1) as a pressure medium. The generated pressure was monitored using the ruby fluorescence method. Incident and transmitted beam intensities were monitored using an ionization chamber with flowing N_2 and Ar gases, respectively. All measurements were performed at RT.

The XMCD spectrum was recorded near the Ga *K*-edge (E_0 = 10.367 keV) at energy intervals of 0.5 eV. To obtain a thickness-independent spectrum, XAS was normalized at the higher energy region, which is the conventional method.

To determine the compressibility of Mn_3GaC at RT, X-ray diffraction (XRD) experiments under high pressure were performed at BL04B2 [14]. This beamline is dedicated to high pressure XRD experiments, and utilizes an imaging plate system for the data acquisition. Sample quality and crystallographic phase were also verified by XRD measurements.

3. Results and Discussion

Figure 1 (a) shows the pressure variation of the XAS spectrum at the Ga *K*-edge in Mn_3GaC as a function of X-ray energy.

*e-mail: naochan@spring8.or.jp

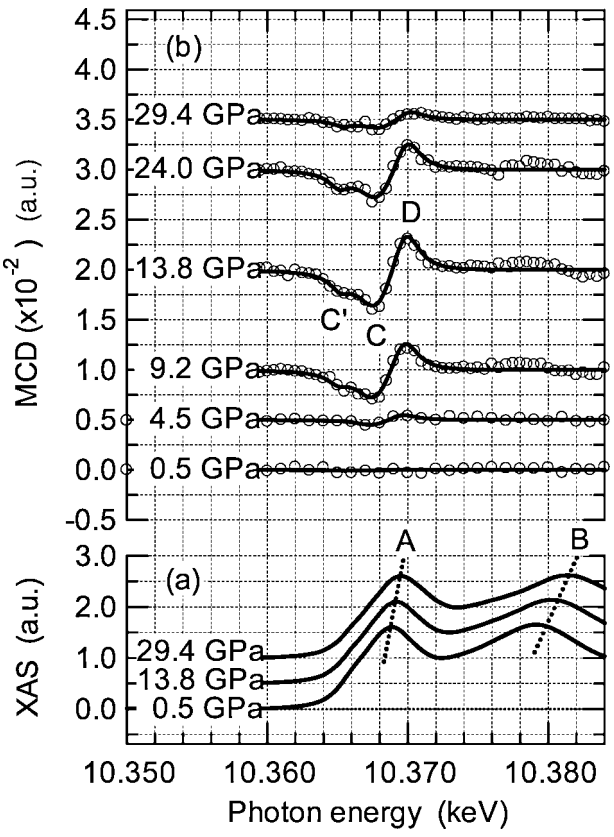

Fig. 1. Pressure variation of (a) XAS and (b) XMCD spectra at the Ga *K*-edge in Mn_3GaC.

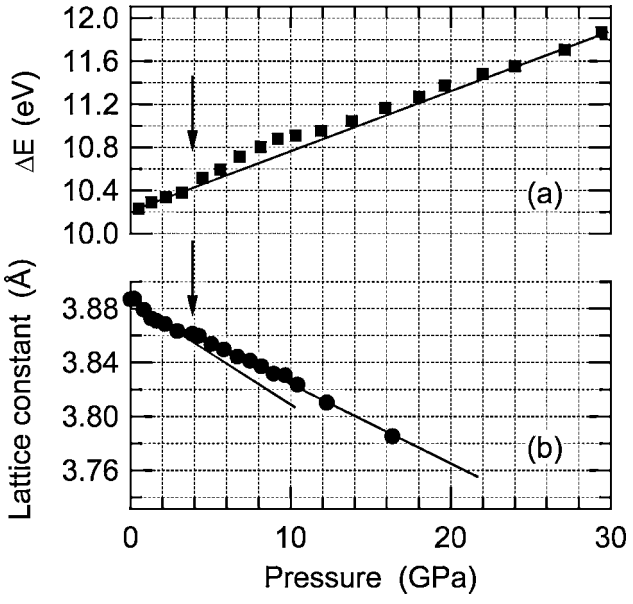

Fig. 2. (a) Energy difference ΔE between peak A and B in the XAS spectrum of Mn_3GaC (see in Fig. 1 (a)), and (b) lattice constant as a function of applied pressure. Solid lines are for an eye-guide.

The XAS spectrum consists mainly of two peaks, labeled A and B. The energy difference between the peaks (ΔE) is about 10.0 eV at 0.5 GPa. At higher pressure, the peaks A and B shift to higher energy and ΔE becomes larger. The plot of ΔE as a function of applied pressure (Fig. 2 (a)) shows that ΔE increases approximately linearly with increasing pressure. Closer inspection reveals that ΔE deviates from linearity in a convex manner above 4.5 GPa (indicated by an arrow). The lattice constant of Mn_3GaC decreases in an approximately linear manner with increasing pressure (Fig. 2(b)) but is more accurately described by two lines of distinct slope for pressures above and below 4.5 GPa. These anomalies are probably related to the ferromagnetic state resulting from the pressure applied over 4.5 GPa. For both XAS and XRD experiments, it was confirmed that the crystal structure was preserved over the pressure range.

Figure 1 (b) shows the variation with pressure of the XMCD spectrum at the Ga *K*-edge in Mn_3GaC. In the pressure range from AP to 4.5 GPa, there is no significant XMCD signal because the Mn_3GaC exists in a paramagnetic state. As more applied pressure is augmented, a dichroic spectrum appears resulting from induced polarization in the Ga $4p$ states. This XMCD profile is characterized by a dispersion-type profile changing form negative to positive sign with three peaks apparent: a negative peak (labeled C) with a smaller peak at lower energy (labeled C′) and a positive peak (labeled D). When the pressure is increased furthermore, the XMCD intensity grows until it reaches a moderate maximum at 13.8 GPa, after which it begins to gradually decrease. The dichroic signal does not disappear even at 29.4 GPa; the critical pressure to suppress the dichroic signal is estimated by extrapolation to be 32 GPa.

According to the magneto-optical sum rule for *K*-edge [8], the integrated intensity of the XMCD spectrum can be related to the expectation value of orbital angular momentum of p states. For the spectra in Fig. 1 (b), energy integration yields a negative intensity, although the value is very small. Therefore, the $4p$ moment of Ga atom is aligned parallel with the magnetic field. It is reasonable to explain Ga $4p$ polarization as being caused by $4p$–$3d$ hybridization with Mn $3d$ states at neighboring sites.

The magnetic structure under high pressure can be predicted from the spectral profile of XMCD. Experiments observing the effects of the temperature variation of the XMCD spectrum were performed at the *M K*-edge for Mn_3MC (M = Zn and Ga) under AP and results indicate that the XMCD spectral profile is closely associated with magnetic structure resulting from the magnetic states of Mn atoms [15]. This study suggests that under high pressure Mn_3GaC has a canted ferromagnetic (CF) structure because of two observations: (1) The existence of the additional peak C′ is a similar feature to the spectral profile at the Zn *K*-edge of Mn_3ZnC in a CF phase, and (2) the observed maximum XMCD intensity of 0.34% is smaller than the 0.6% intensity observed for the F phase at 200 K under AP. On the assumption that T_C linearly increases with pressure, it is predicted that an F phase has a critical pressure of 10 GPa from the results of Kaneko *et al.* [4]. However, the observed value of 4.5 GPa is much lower, so that it is suggested that a new magnetic phase exists under high pressure.

Figure 3 shows the intensity of peaks C and C′ as a function of the applied pressure. The peaks were decomposed using a multi-Lorentzian method. From this figure it is observed that peaks C and C′ exhibit the same behavior under pressure. In Mn_3ZnC, the intensity of peak C′ decreases with temperature in the CF phase, while that of peak C increases [15]. This difference may be attributed to the correlation between the magnitude of Mn magnetic moments and the canted angle of these moments in the CF phase.

According to the band calculation for Mn_3MC (M = Zn, Ga, In and Sn) by a self-consistent augmented plane wave method [16], the number of electrons in the M atom leads to a shift of the Fermi level, although the type of M atoms does not affect the overall shape of the density of states. The compression of interatomic distance when pressure is applied changes the density of states around the Fermi level. The magnitude in overlap

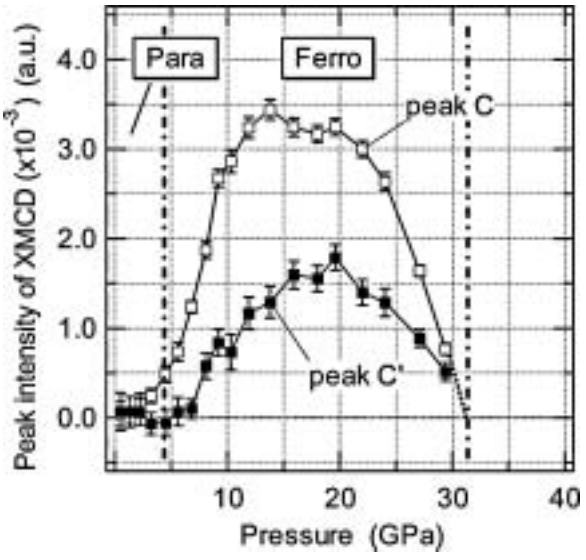

Fig. 3. The XMCD intensities of the peaks C and C′ as a function of pressure, after multi-Lorentzian curve fitting. Error bars indicate standard deviation of the fit.

between Mn 3*d* and Ga 4*p* orbitals is considered to play an important role in the underlying mechanism of the appearance of magnetism in the Mn_3MC system.

4. Conclusions

We have measured the pressure variation of XAS and XMCD spectra near the Ga *K*-edge at RT. The XMCD spectrum has been observed under pressures ranging from 4.5 to 29.4 GPa and the critical pressure that suppresses the dichroic signal is estimated to be 32 GPa. An anomaly in the result of XAS and XRD experiments has also been observed at about 4.5 GPa, and is related to the existence of a pressure-induced ferromagnetic phase. Ga 4*p* polarization is thought to originate from 3*d* polarization at neighboring Mn atoms, and for the Mn_3GaC system, calculation using the sum rule reveals the 4*p* moment is aligned parallel with the magnetic field. Consideration of the spectral profile suggests that the magnetic structure in the ferromagnetic phase is a canted ferromagnetic structure similar to that of Mn_3ZnC in low temperature phase.

Mn_3GaC exhibits interesting magnetic characteristics under high pressure near temperature T_t. Further detailed investigation, including theoretical calculation, is required to elucidate the relationship between the observed magnetism and Mn 3*d* and Ga 4*p* electronic states in different environments.

Acknowledgment

The authors express their thanks to Dr. D. Fruchart of Laboratoire de Cristallographie, CNRS, for supplying the high quality sample.

References

1. Fruchart, D. and Bertaut, E. F., J. Phys. Soc. Jpn. **44**, 781 (1978).
2. Bouchaud, J. P., *et al*., J. Appl. Phys. **37**, 971 (1966).
3. Fruchart, D., *et al*., Solid State Commun. **8**, 91 (1970).
4. Kaneko, T., Kanomata, T. and Shirakawa, T., J. Phys. Soc. Jpn. **56**, 4047 (1987).
5. Kaneko, T., Kanomata, T., Miura, S., Kido, G. and Nakagawa, Y., J. Magn. Magn. Mater. **70**, 261 (1987).
6. Kamishima, K., Bartashevich, M., Goto, T., Kikuchi, M. and Kanomata, T., J. Phys. Soc. Jpn. **67**, 1748 (1998).
7. Schütz, G. and Winke, R., Hyperfine Interaction **50**, 457 (1989).
8. Igarashi, J. and Hirai, K., Phys. Rev. **B50**, 17820 (1994).
9. Igarashi, J. and Hirai, K., Phys. Rev. **B53**, 6442 (1996).
10. Ishimatsu, N., *et al*., Nucl. Inst. Meth. Phys. Res. **A467–8**, 1061 (2001).
11. Ishimatsu, N., *et al*., J. Phys. Soc. Jpn. **72**, 2372 (2003).
12. Maruyama, H., *et al*., J. Synchrotron Rad. **6**, 1133 (1999).
13. Hirano, K., Izumi, K., Ishikawa, T., Annaka, S. and Kikuta, S., Jpn. J. Appl. Phys. **30**, L407 (1991).
14. Isshiki, M., Ohishi, Y., Goto, S., Takeshita, K. and Ishikawa, T., Nucl. Inst. Meth. Phys. Res. **A467–8**, 663 (2001).
15. Kawamura, N., in preparation for publication.
16. Motizuki, K. and Nagai, H., J. Phys. C: Solid State Phys. **21**, 5251 (1988).

Physica Scripta. Vol. T115, 594–596, 2005

Jahn-Teller Dynamic Distortions in $LaMnO_3$ Determined by EXAFS

J. García[1*], G. Subías[1,2], M. C. Sánchez[1] and J. Blasco[1]

[1]Instituto de Ciencia de Materiales de Aragón. Consejo Superior de Investigaciones Científicas y Universidad de Zaragoza, 50009 Zaragoza, Spain
[2]European Synchrotron Radiation Facility, Boite Postale 220, 38043 Grenoble, France

Received June 26, 2003; accepted in revised form November 4, 2003

PACS numbers: 61.10.Dp, 61.10.Eq, 71.90.+q

Abstract

The geometric and electronic local structure of $LaMnO_3$ across the cooperative Jahn-Teller (JT) transition at $T_{JT} = 750$ K has been studied by means of X-ray Absorption Near Edge Structure (XANES) and Extended X-ray Absorption Fine Structure (EXAFS) at the Mn K-edge. XANES spectra, as a function of temperature, do not show significant changes either in the pre-peak structures or at the absorption edge indicating similar electronic local structure for the Mn atom above and below T_{JT}. Analysis of the EXAFS spectra shows that dynamical tetragonal JT distortion of the MnO_6 octahedron is also present above T_{JT}. The structural transition is explained in terms of an orientated ordering of tetragonal distorted octahedral complexes. Above T_{JT}, the e_g electron jumps between the three degenerate vibronic states being localized and ordered below the transition.

1. Introduction

Rare-earth manganite perovskites have recently been the focus of a large number of experimental and theoretical studies [1]. This is due to the extraordinary magnetic, electronic and structural properties such as colossal magnetoresistance, different crystallographic phases (the so-called charge ordering phases) or structural changes induced by applying a magnetic field. In spite of the large number of studies performed, there is lack of a unified explanation for this large and rich phenomenology. One of the main ingredients which seems to be responsible of these properties is the existence of Mn^{3+} in octahedral coordination. This ion is unstable to the local octahedral symmetry through the Jahn-Teller effect. The distortion removes the degeneracy of the e_g orbitals in the $t_{2g}{}^3e_g{}^1$ electron configuration of the Mn^{3+} ions and stabilizes the $3d_{3z2\text{-}r2}$ orbital respect to the $3d_{x2\text{-}y2}$ one.

At ambient conditions stoichoimetric $LaMnO_3$ is a paramagnetic insulator with orthorhombic perovskite structure (space group *Pbnm* [2, 3]). The structure, can be described as formed by tetragonal distorted MnO_6 octahedron disposed in such a way that long and short Mn-O bonds alternate in the *ab* plane along the Mn-O-Mn path. In terms of the Jahn-Teller coupling, the ordering of distortions implies a spatial ordering of d-orbitals. Upon heating, $LaMnO_3$ undergoes a structural phase transition at $T_{JT} = 750$ K above which the orbital ordering disappears [3, 4]. This transition is accompanied by an abrupt change in the electrical resistivity, thermoelectric power and Weiss constant at T_{JT} [5].

Several mechanisms have been proposed to explain the orbital ordering in 3d transition metal oxides with orbital degeneracy. Some authors attribute it to the superexchange interaction between atoms in different sites [6, 7]. Other authors instead, locate its origin in cooperative Jahn-Teller effect where the lattice distortion occurs cooperatively and lifts the orbital degeneracy at the transition metal ion [8, 9]. Other mechanisms, including the combined influence of superexchange and electron-phonon interactions have also been proposed [10]. In spite of the theoretical effort to understand the orbital ordering in $LaMnO_3$ [6–10], direct experimental evidences shedding light on the mechanism responsible for the structural transition at $T_{JT} = 750$ K are not still provided. High resolution neutron diffraction experiments show that above T_{JT} the MnO_6 octahedron becomes nearly regular and the thermal parameters of the oxygen atoms are anomaly high, although there is not change of crystal symmetry [3]. The observed pseudocubic lattice would arise from the average of dynamic spatial fluctuations of the orthorhombic distortion. This result was the origin of the Zou and Goodenough [5] vibronic mechanism proposed to explain the electrical conductivity above T_{JT}.

Within this work, we study the electronic and local structure across the cooperative Jahn-Teller transition by X-ray absorption spectroscopy at the Mn K edge. We will show from the XANES and EXAFS spectra that the MnO_6 octahedra are locally distorted above T_{JT}, so the structural phase transition can reasonably be described as an ordering of local distortions that are thermally disordered above T_{JT}.

2. Experiment

The preparation and characterization of stoichiometric $LaMnO_3$ was reported elsewhere [2]. X-ray absorption experiments were performed at the ESRF's beamline BM29 (Grenoble, France). Pellets were prepared by mixing the powdered samples with boron nitride in order to optimize the thickness. A fixed-exit Si(311) double-crystal monochromator was used, the estimated energy resolution being $\Delta E/E = 7 \times 10^{-5}$. Spectra were recorded in transmission mode using ionization chambers as detectors. Another $LaMnO_3$ pellet was simultaneously measured at room temperature for energy calibration. A Displex cryostat from Oxford Instruments was used for low temperature measurements (20 K–300 K), whereas high temperature experiments were performed with a furnace.

XANES spectra were normalized to the high part of the spectrum (100 eV) after a linear background subtraction [11]. EXAFS spectra ($\chi(k)$) were obtained by removing the smooth atomic absorption coefficient (μ_0) by means of a cubic spline [14]. The spectra were analyzed using the FEFF 8.10 code that allows to correlate the Debye-Waller factor (D-W) with the interatomic distances. The structural analysis was performed in *R*-space fitting mode including multiple scattering terms up to 4 Å [12].

3. Results and Discussion

XANES spectra for several temperatures below and above T_{JT} are shown in fig. 1. The spectral shape for $LaMnO_3$ shows two

*E-mail: jgr@posta.unizar.es

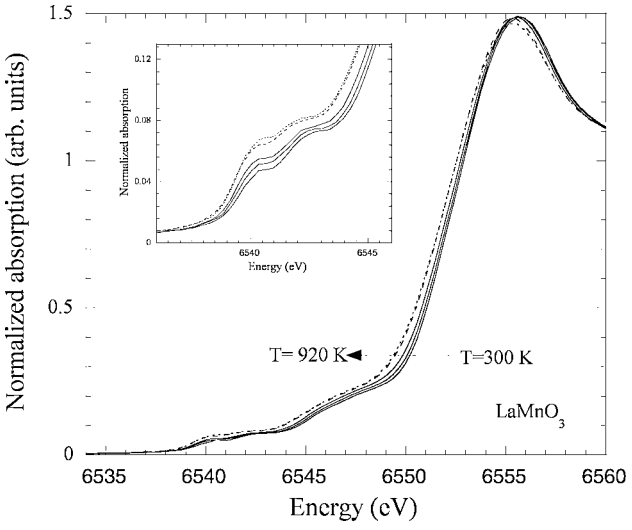

Fig. 1. Normalized XANES spectra of $LaMnO_3$ as a function of temperature. A small shift of the spectra is shown increasing temperature. Solid and dashed lines correspond to spectra taken below and above T_{JT} respectively. Inset shows a detail of the pre-peak structures.

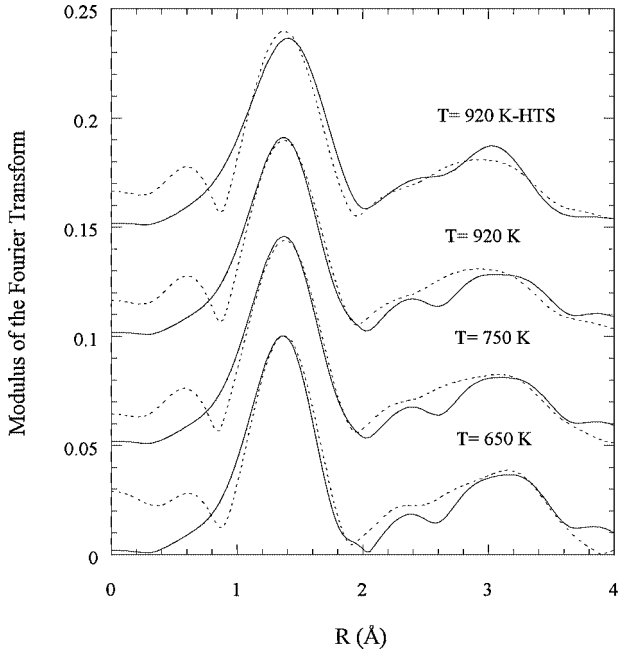

Fig. 2. Fourier Transform of the EXAFS spectra (discontinuous line) measured at temperatures closed T_{JT} and the best-fit simulation (continuous line) with the FEFF 8.10 package. Upper figure shows the best fit simulation at 920 K, above T_{JT}, using the high temperature crystallographic structure (HTS).

separate regions: The pre-edge region related with transitions to empty Mn d-states due to the covalency with the adjacent oxygen p-states and the main-edge region corresponding to dipolar transitions to the empty Mn p-band. The spectra at different temperatures are very similar to each other indicating that no large changes of the local electronic structure occur between 300 and 920 K. We note that the spectra shift to lower energies with increasing temperature, the maximum shift being of about 0.5 eV. These small differences can be ascribed to minor thermal effects: An increase of atomic vibration leads to a smoothing of the absorption features. Accordingly, an apparent shift of the absorption edge and an increase of the broadness of the main peak are observed. Moreover, as it is shown in the inset, the same pre-edge features are observed above and below the transition temperature showing that the splitting of the projected d-states occurs above T_{JT}.

EXAFS spectra of $LaMnO_3$ were recorded at fixed temperatures from 20 K up to 920 K. The spectra at low temperatures ($T < 300$ K) were measured up to $k = 12\,\text{Å}^{-1}$ in order to obtain reliable structural parameters. The Fourier Transforms of the spectra above and below T_{JT} are shown in fig. 2. We observe that the intensity of the different peaks, associated to different coordination shells, decrease with increasing temperature. This is expected for a standard evolution due to the increase of the thermal motion. It is noteworthy that no discontinuity was observed in the EXAFS spectra at T_{JT}, indicating a similar local structure for the Mn^{3+} ions above and below T_{JT}. If the tetragonal distortion disappeared at the phase transition, an increase of the intensity of the first oxygen shell peak should be expected above T_{JT}, reflecting a more symmetrical oxygen environment. In order to verify it, we have performed an accurate quantitative study. First, we have analyzed the first oxygen coordination shell by fitting the Fourier filtered first-shell contribution between 1 and 2 Å, at different temperatures. We have used the signal obtained from the room temperature EXAFS spectrum as reference. The Fourier filtered signals can be well reproduced from the room temperature spectrum by changing only the relative D-W ($\Delta\sigma^2$) factor. $\Delta\sigma^2$ increases with increasing temperature as expected for a system without changes in the local structure. In order to quantify the tetragonal distortion, we have fitted the spectra using the FEFF 8.10 code's theoretical amplitudes and phases. First and second coordination shells were included in the fitting process and multiple scattering paths were also considered. Fig. 2 shows the best-fit results for spectra in the neighborhood of T_{JT}. The obtained interatomic Mn-X (X = O, Mn, La) distances agree with the crystallographic values, except for $T > T_{JT}$. Our results show that the MnO_6 octahedron remains tetragonal distorted above T_{JT}. For instance, the interatomic distances resulting from the fit at 840 K are, $d(\text{Mn-O}_{\text{short}}) = 1.92$ Å, $d(\text{Mn-O}_{\text{long}}) = 2.13$ Å, $d(\text{Mn-Mn}_{\text{short}}) = 3.85$ Å, $\text{d(Mn-Mn}_{\text{long}}) = 4.01$ Å, similar to the values at room temperature. As comparison, we have performed the fit with the symmetric interatomic distances obtained of the crystallographic data at temperatures above T_{JT} [3]. It is observed that the fit is worse that the one using the crystallographic data at room temperature (i.e. tetragonally distorted MnO_6 octahedra). Moreover, the obtained Debye-Waller factor for this fit is anormally high, $\sigma^2 = 16 \times 10^{-3}\,\text{Å}^2$ (comparable to the tetragonal distortion). Fig. 3 shows the D-W factors of the different Mn-X contributions as a function of temperature. It is worth mentioning that long and short Mn-X bonds show close D-W factors, as expected. A small change in the $\sigma^2(T)$ evolution is observed at the phase transition for the Mn-O, Mn-La and Mn-Mn shells indicating the occurrence of the phase transition.

In conclusion, EXAFS spectra demonstrate that the MnO_6 octahedron is also tetragonal distorted at temperatures above T_{JT}. The interaction time for the photoabsorption process is lower than for the thermal motion and consequently, the local structure probed by EXAFS provide the instantaneous local structure around the absorbing atom. On the other hand, diffraction data provide the periodicity of the average structure as Rodriguez-Carvajal *et al.* [4] claim. From both experiments, we can infer that below T_{JT} the tetragonal local distortion is three-dimensional ordered giving rise to the well-known *Pbnm* structure. On the other hand, above T_{JT}, the local distortions are dynamically disordered and the average lattice is cubic.

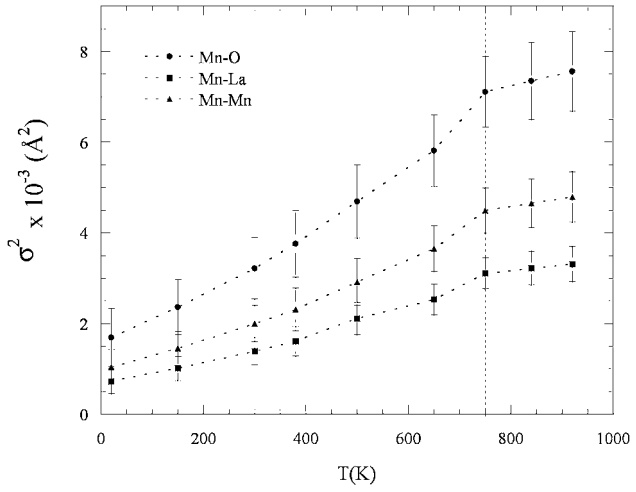

Fig. 3. Debye-Waller factor as a function of temperature for the three coordination shells. The vertical line indicates T_{JT}.

This result shows that Mn^{3+} ion displays a strong Jahn-Teller coupling giving rise to the called static JT regime [13]. Above T_{JT} each Mn octahedron is instantaneously distorted and it jumps among the three equivalent tetragonal distortions. Below T_{JT}, the tetragonal distortions are periodically ordered. From this point of view, the phase transition can be classified as an order-disorder phase transition where the statistical occupation corresponds to the three possible orientations of the tetragonal distortions on each octahedron. This also agrees with the lack of modification of the pre-peak features of the XANES spectra.

Summarizing, the following relevant results can be concluded from these experiments [14].

i) The orbital degeneracy of the Mn^{3+} ion is already lifted at temperatures above T_{JT}. XANES spectroscopy shows that the empty Mn^{3+} electronic *d*-states are unaltered crossing the JT transition whereas EXAFS spectroscopy shows that the JT tetragonal distortion remains in the pseudocubic phase above T_{JT}.

ii) The structural phase transition is then produced by the ordering of the local distortions by elastic coupling with the macroscopic strain field, giving rise to the low temperature *Pbnm* crystal symmetry.

iii) In the frame of the Jahn-Teller effect, the lowest energy for the e_g electron is coupled with the three possible distortions giving rise to three degenerate electronic states [13] $d_{x2\text{-}r2}$, $d_{y2\text{-}r2}$ and $d_{z2\text{-}r2}$ where the electron thermally jumps among them above T_{JT} and is localized and ordered below T_{JT}. In this sense the orbital ordering proposed for $LaMnO_3$ is arising from the ordering of the JT local distortions so a direct electronic origin for orbital ordering (i.e. superexchange between orbitals, or cooperative Jahn-Teller mechanisms with simultaneous lattice distortion) lifting the orbital degeneracy, should be discarded.

iv) The high temperature phase can be described as a dynamically local distorted phase with strong antiferrodistortive first neighbor coupling. Therefore, a schematic picture of the vibronic conductivity mechanism proposed by Zhou and Goodenough [5] could be the following: Above T_{JT}, the e_g electron jumps among the degenerate three orbitals on each Mn^{3+} ion. This electron can also jump to the orbital of the nearest neighbor manganese, due to the covalency with the oxygen, giving rise to a mobility of the carrier in the lattice. In the low temperature phase, the e_g electrons are ordered and localized and they cannot jump between adjacent octahedra. Although this conduction mechanism is assisted by phonons, it cannot be considered as polaronic.

Acknowledgments

Supported be the Spanish CICyT project n° MAT2002-01221. The authors warmly thank ESRF for beam time granting.

References

1. Dagotto, E., Hotta, J. and Moreo, A., Phys. Reports **344**, 1 (2001).
2. Ritter, C. *et al*., Phys. Rev. B **56**, 8902 (1997).
3. Rodriguez-Carvajal, J. *et al*., Phys. Rev. B **57**, R3189 (1998).
4. Norby, P. *et al*., J. Solid State Chem. **119**, 191 (1995).
5. Zhou, J. S. and Goodenough, J. B., Phys. Rev. B **60**, R15002 (1999).
6. Okamoto, S., Ishihara, S. and Maekawa, S., Phys. Rev. B **65**, 144403 (2002).
7. Kugel, K. I. and Khomskii, D. I., Zh. Eksp. Teor. Fiz. **64**, 1429 (1973) [Sov. Phys. JETP **37**, 725 (1973)].
8. Höck, K.-H., Schröder, G. and Thomas, H., Z. Physik B **30**, 403 (1978).
9. Millis, A. J., Phys. Rev. B **53**, 8434 (1996).
10. Bala, J., Olés, A. M. and Sawatzky, G. A., Phys. Rev. B. **65**, 184414 (2002).
11. Koningsberger, D. C. and Prins, R., "X-ray Absorption Tecniques of EXAFS, SEXAFS and XANES", (Wiley, New York, 1988).
12. Stern, E. A. *et al*., Physica B **208&209**, 117 (1995). http://FEFF.phys.washington.edu/.
13. Abragam, A. and Bleaney, B., "Electron paramagnetic resonance of transition ions", (Clarendon Press, Oxford, 1970) 792.
14. Sánchez, M. C., Subías, G., García, J. and Blasco, J., Phys. Rev. Lett. **90**, 045503 (2003).

Physica Scripta. Vol. T115, 597–599, 2005

XAFS Study of Epitaxial $Co_xTi_{1-x}O_{2-x}$ Anatase

S. M. Heald*[1,2], S. A. Chambers[1] and T. Droubay[1]

[1]Pacific Northwest National Laboratory, Richland, WA, 99352, USA
[2]Bldg. 435E, Advanced Photon Source, Argonne, IL, 60439, USA

Received June 26, 2003; accepted November 4, 2003

PACS numbers: 75.50.Pp, 78.70.Dm

Abstract

Co doped TiO_2-anatase is a promising candidate for a room-temperature ferromagnetic semiconductor. XAFS measurements have been used to investigate the local Co environment and Co valence for several Co-anatase films. The samples were grown on $LaAlO_3$ (001) by oxygen plasma assisted molecular beam epitaxy and on $SrTiO_3$ by atomic oxygen assisted MBE. Co concentrations were about 5%. The measurements were made at the PNC-CAT bending magnet and undulator beamlines at the Advanced Photon Source. For the films on $LaAlO_3$, the near edge clearly shows the presence of only Co(2+), and no evidence for metallic Co, while the films on $SrTiO_3$ showed significant metallic Co. Analysis of the extended fine structure for the $LaAlO_3$ films finds that the Co substitutes for Ti with some distortion of the lattice. Both in-plane and out-of-plane Co-O bonds are expanded from the Ti-O bonds in anatase. The in-plane bonds are expanded approximately twice as much. A deficit in the oxygen coordination number suggests a correlation of oxygen vacancies with Co sites.

1. Introduction

Spintronics devices utilize the spin of carriers, and offer the promise of new devices with enhanced functionality. Dilute magnetic semiconductors (DMS) are promising candidates for spin injectors in spintronics devices. DMS materials can have spin polarized states in their valence or conduction bands. At interfaces with nonmagnetic semiconductors they can then be used for spin polarized carrier injection, allowing for the fabrication of novel devices utilizing spin. Theory and measurements indicate that they can be much more efficient spin injectors than ferromagnetic metals.

Most traditional DMS materials require cryogenic cooling, a major disadvantage for practical devices. Therefore, extensive theoretical and experimental searches have been underway for DMS materials that exhibit ferromagnetic behavior above room temperature. To date the most robust candidate appears to be Co doped TiO_2-anatase. The ferromagnetic properties of this material were first discovered by Matsumoto *et al.* [1]. Their films were produced by pulsed laser deposition (PLD) on $LaAlO_3$ and $SrTiO_3$ substrates. The saturation moment was found to be $0.3\,\mu_B$/Co atom.

Since then films have been grown using a number of methods, and show a range of values for the saturation moments. Many of the PLD films show evidence for Co nanoparticles that could explain some of the magnetic results. Therefore, it is essential to use techniques that can distinguish the different Co oxidation states, especially techniques that average the entire film thickness. XANES provides such a tool.

In the present work, molecular beam epitaxy (MBE) techniques were used to grow the films. Either oxygen plasma or atomic oxygen was used in an attempt to prevent the production of Co nanoparticles. The oxygen plasma assisted MBE (OPAMBE) films showed a saturation moment of $1.26\,\mu_B$/Co [2]. Bulk Co has a saturation moment of $1.7\,\mu_B$/Co atom, and its formation can complicate the measurement of magnetic properties. We will demonstrate that X-ray absorption near edge measurements are a sensitive and simple probe for the formation of metallic particles. The Co is primarily in the 2+ oxidation state, although metal is detected in some of the films.

The extended fine structure (EXAFS) has been also measured to look at a number of other questions about these materials [3]. The first is the location of the Co in the anatase lattice. The Co 2+ ion is significantly larger than the Ti 4+ ion in anatase. Theory suggests that the Co may be residing in an interstitial site [4]. However, we will show that Co resides in a distorted substitutional site. There is also the question of the oxygen vacancies. For charge balance, each substitution of a Co for Ti should result in the formation of an oxygen vacancy. Additional oxygen vacancies are required to dope the films n-type. If these oxygen vacancies are associated with the Co sites they may be observable in the EXAFS coordination number. Finally, a wide range of surface morphologies have been observed in nominally identical films. Films range from atomically flat to particle laden. Scanning Auger and high resolution TEM indicates that the particles remain in the anatase structure, but have a much higher concentration of Co than the bulk film. In this paper we compare the EXAFS from films with and without these particles.

2. Samples and Measurements

Results from five samples are presented. Two of the samples were grown on $LaAlO_3$ (100) [5], and three of the samples were grown on $SrTiO_3$ on Si. The samples on $LaAlO_3$ were grown by oxygen plasma assisted MBE, and will be referred to as LAO1 and LAO2. Sample LAO1 showed no evidence for Co-rich particles, while LAO2 had about 1% of the surface area covered by Co-rich particles that seems to contain most of the Co in the film. The samples grown on $SrTiO_3$/Si were grown by MBE with atomic oxygen used in an attempt to maintain stoichiometry. These three nominally identical films will be referred to as STO1, STO2 and STO3. The films were all approximately 20 nm thick with Co concentration of about 5%.

The X-ray measurements were made at the PNC-CAT beamlines at Sector 20 at the Advanced Photon Source. Most of the measurements were made at the insertion device beamline 20-ID. Some of the LAO1 measurements were made on the bending magnet beamline 20-BM. The measurements were made at glancing angles of 1-2 deg using a focused beam of less then 10 μm in diameter (30 μm for 20-BM). The focusing mirrors also effectively rejected the beam harmonics. The fluorescence was detected using a 13-element Ge detector. 50–100 μm of Al was

*e-mail: heald@aps.anl.gov

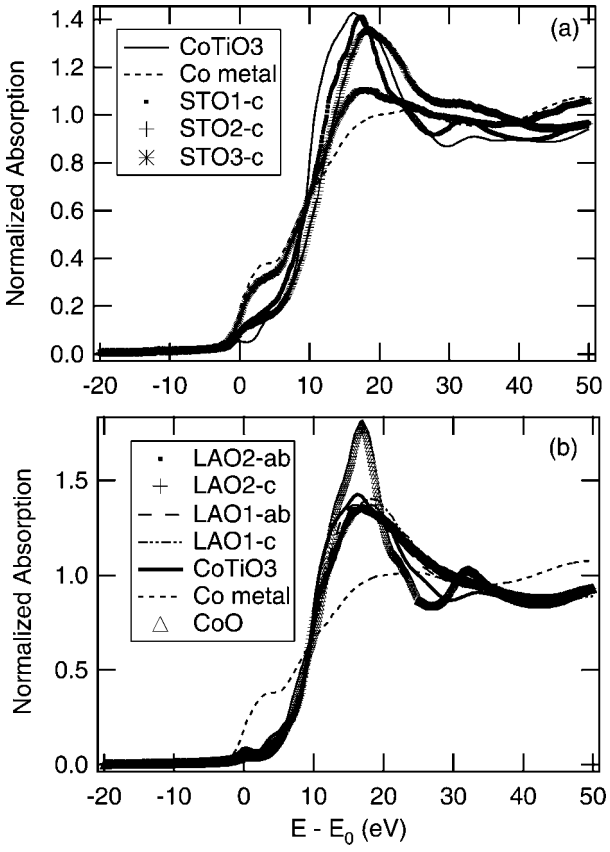

Fig. 1. Near edge plots for the Co-doped anatase samples as compared to CoO, $CoTiO_3$ (Co^{+2}) and Co metal. a) The three samples grown on $SrTiO_3$ on Si. Only the c axis polarization is shown since the ab data was similar. b) The two samples grown on $LaAlO_3$ are shown. ab indicates the polarization is in the ab plane and c indicates the X-ray polarization is out of the plane of the film.

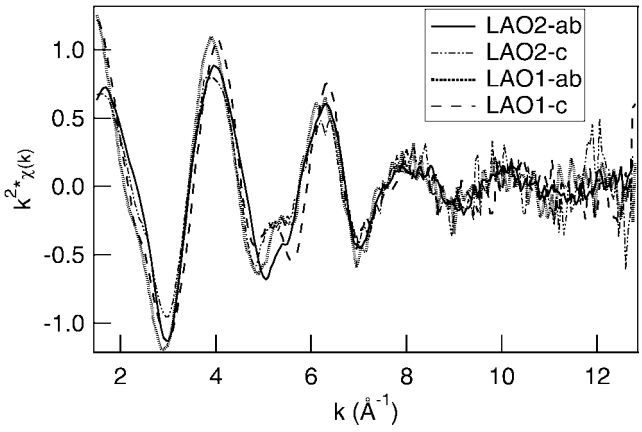

Fig. 2. k^2 weighted $\chi(k)$ for the two samples grown on $LaAlO_3$. ab indicates the X-ray polarization is in the ab plane and c indicates the polarization is along the c-axis.

Table I. *Fitting results compared to standard compounds. For the standards the crystallographic N and R are given. For the Co standards σ^2 is derived from the EXAFS analysis.*

Sample	*N*	*R* (Å)	σ^2 (Å^2)
$CoTiO_3$	3	2.054	0.0056 (0.0005)
	3	2.172	0.0082 (0.0007)
CoO	6	2.133	0.0069 (0.0005)
Anatase-c	2	1.966	–
Anatase-ab	4	1.937	–
CoLAO1-c	1.8 (0.2)	2.01 (0.01)	0.010 (0.001)
CoLAO1-ab	3.6 (0.3)	2.04 (0.01)	0.0095 (0.001)
CoLAO2-c	1.4 (0.3)	2.03 (0.02)	0.0079 (0.0015)
CoLAO2-ab	3.5 (0.3)	2.03 (0.01)	0.0086 (0.001)

used to filter out the Ti and La fluorescence. A Si(111) double crystal monochromator provided an energy resolution of about $\Delta E/E = 1.4 \times 10^{-4}$. The energy was calibrated using Co metal with the peak in the derivative set to 7708 eV. $CoTiO_3$ and CoO were measured in absorption as Co^{2+} standards, and to calibrate the FEFF 7 [6] calculations used to analyze the data.

The films grow with their c-axis normal to the surface. Measurements were made with the X-ray polarization in the ab-plane and along the c-axis. All of the samples except for LAO1 were measured with the samples spinning about the surface normal to minimize Bragg peak interference. Sample LAO1 seemed to have fortuitous alignment and did not need spinning. Figure 1 shows the near edge results compared to the standards. The films on STO in Fig. 1(b) show clear evidence for Co metal ranging from approximately 30–70%. In contrast the LAO films show no evidence for Co metal, and have a near edge similar to $CoTiO_3$. The edges to not look like CoO, which has been suggested as a component of some pulsed laser deposited films [7].

Since they contain significant Co metal, we did not attempt to analyze the EXAFS from the STO samples. Fig. 2 shows the extracted k^2 weighted EXAFS for the two LAO samples. The EXAFS was extracted using the autobak method as implemented in IFEFFIT [8]. The EXAFS dies off quickly indicating significant disorder about the Co site. There is a relatively small contribution from higher shells. There are small differences between the two films with the amplitude for the LAO2 film consistently smaller for both polarizations.

3. Analysis and Discussion

IFEFFIT was used to fit the first shell data. Table I compares the Co or Ti environment for TiO_2-anatase, $CoTiO_3$ and CoO. For each polarization dependent measurement, we expect a single Co-O distance if the Co is substituting for Ti. However, the distance for the two polarizations could be different. A typical single shell fit is shown in Fig. 3, and the results for all the samples are given in table I. Also, shown in Fig. 3 is a fit to a model for an interstitial site calculated using density functional theory [9]. This site has two

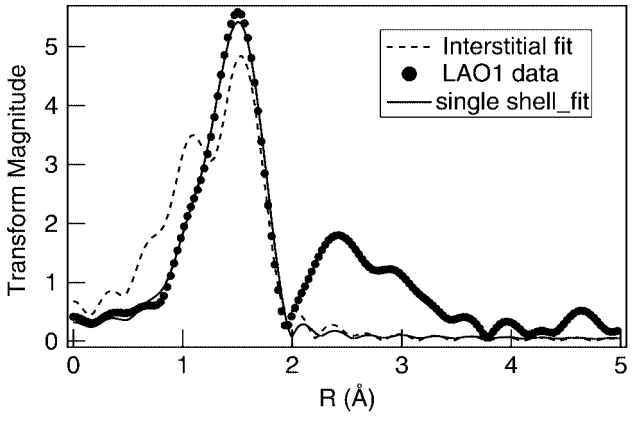

Fig. 3. Fitting for sample LAO1. The transform range is 2–11 Å^{-1}, and the fitting was carried out over the r-space range of 0.8–1.9 Å, giving approximately 7 independent data points. A single shell fit is compared to the interstitial model discussed in the text.

short Co-O bonds and four long bonds all at different distances. For the fitting an overall Δr was varied, along with an overall σ^2. If a separate σ^2 was used for the short and long bonds, the short bond value fit to a large value effectively removing them from the model. It is obvious that the interstitial model does not fit the data.

The fitting results in table I show that the Co-O bond lengths in the films are intermediate between the Co-O bond length in the typical Co compound and the Ti-O bond lengths in Anatase. This is to be expected if the larger Co ion is substituting for the Ti in anatase. In general the disorder has increased. Again this is expected due to the strains introduced into the lattice by the larger Co ion. Note that the bonds lengths along the c-axis are equal to or smaller than the ab-plane bonds. In anatase the c-axis bonds are longer. However, in the anatase structure the Co (or Ti) oxygen bonds form a linear chain along the c-axis while in the ab plane the oxygen atoms are alternately slightly above or below the plane. It is reasonable that the oxygen atoms in the plane can more easily accommodate the larger Co atom by changing the amount of buckling. The c-axis oxygen atoms are more constrained from moving away from the Co atoms.

The higher shell structure in anatase is fairly complicated, and the measured EXAFS from the higher shells is relatively weak. Therefore, detailed fitting of the higher shells was not attempted. A comparison was made with a calculated model for Co in anatase, and it does appear the measurements are consistent with disordered anatase-like higher shell structure.

The coordination numbers for the CoLAO samples are somewhat lower than for anatase. The numbers in table I are given assuming the Co is in the Ti site. For this case the two oxygens along the c-axis would give the same EXAFS amplitude as the four bonds distributed in the ab-plane. From charge neutrality we expect an oxygen vacancy is produced for each Co^{2+} ion substituted for a Ti^{4+} ion. In addition, excess oxygen vacancies are required to make the material semiconducting. The question is whether these oxygen vacancies are correlated with the Co sites. Such vacancy correlation could provide a mechanism for strain relief.

If all of the vacancies are next to the Co sites then there should be a deficit in coordination of at least one atom. This does not seem to be the case for the LAO1 film, but a partial correlation is indicated. The measured reduction in coordination is similar to our uncertainties but appears in measurements for both polarizations. A larger reduction in O neighbors is indicated for the LAO2 film. The total reduction is about 1 atom. In neither sample is there a large preference for location of the O vacancy in the c-axis or ab-plane sites.

4. Summary

The results show that XAFS is a powerful tool for looking at Co-anatase films. The near edge is very sensitive to the presence of Co nanoparticles. For films grown using OPAMBE on $LaAlO_3$, no metallic Co was detected and all of the Co was found to be in the 2+ valence. The use of atomic oxygen was less successful in avoiding metal formation, and the films studied had Co metal particles accounting for 30–70% of the total Co. In contrast to surface sensitive techniques, this XAFS result is a true average of all the Co in the film.

For the films without metal, the extended fine structure provided strong evidence for the Co occupying the Ti sites in the anatase lattice. An interstitial model is definitely ruled out, and the Co-O bond lengths are significantly shorter than typical Co^{2+} bonds with oxygen in standard compounds. This is expected if the Co is substituting for the smaller Ti atoms. Comparison of films with and without Co-rich particles found very similar results. Both results showed indications of reduced oxygen coordination with a larger reduction for the particle rich film. Oxygen vacancies are required for charge balance and to dope the films n-type. A reduced coordination indicates that there is some correlation of the O vacancies with the Co sites. This correlation might be a strain relief mechanism. The larger Co ions are undoubtedly inducing significant strain into the lattice, which could be partially relieved by an oxygen vacancy moving close to a Co. The lattice strain is indicated in the measurements by an increased Debye-Waller factor, and by a much reduced higher shell contribution as compared to the pure materials.

Acknowledgements

This work was supported by the PNNL Nanoscience and Technology Initiative, the US DOE, Office of Basic Energy Sciences, and the DARPA Spins in Semiconductors Initiative. PNC-CAT facilities and research at these facilities is supported by the US DOE Office of Science grant no. DE-FG03-97ER45628. Use of the Advanced Photon Source was supported by the U.S. DOE, under Contract No. W-31-109-ENG-38.

References

1. Matsumoto, Y. *et al*., Science **291**, 854 (2001).
2. Chambers, S. A. *et al*., Appl. Phys. Lett. **79**, 3467 (2001).
3. Parts of this work are also presented in Chambers, S. A., Heald, S. M. and Droubay, T., Phys Rev. **B67**, 100401(R) (2003).
4. Sullivan, J. M. and Erwin, S. C., unpublished.
5. Chambers, S. A. *et al*., Thin Solid Films **418**, 197 (2002).
6. Zabinsky, S. I. *et al*., Phys. Rev. B **52**, 2995 (1995).
7. Kim, J.-Y. *et al*., Phys. Rev. Lett. **90**, 017901 (2003).
8. Newville, M., J. Synchroton Rad. **8**, 322 (2001).
9. Sullivan, J. M., private communication.

Physica Scripta. Vol. T115, 600–602, 2005

Temperature Dependence of Magnetic EXAFS for Rare Earth Elements

H. Wende*[1], A. Scherz[1], C. Sorg[1], Z. Li†[1], P. Poulopoulos‡[1], K. Baberschke[1], A. L. Ankudinov[2], J. J. Rehr[2], F. Wilhelm[3], N. Jaouen[3], A. Rogalev[3], D. L. Schlagel[4] and T. A. Lograsso[4]

[1]Institut für Experimentalphysik, Freie Universität Berlin, Arnimallee 14, D-14195 Berlin-Dahlem, Germany
[2]Department of Physics, Box 351560, University of Washington, Seattle, Washington 98195, USA
[3]European Synchrotron Radiation Facility (ESRF), BP 220, 38043 Grenoble, France
[4]Ames Laboratory, Iowa State University, Ames, Iowa 50011, USA

Received June 26, 2003; accepted in revised form November 4, 2003

PACS numbers: 61.10.Ht, 78.70.Dm, 75.25.+z

Abstract

A systematic study of the X-ray magnetic circular dichroism at the L_3 edge is presented for Gd and Tb single crystals in the extended energy range (MEXAFS). The investigation of the dichroic signal in this energy range is especially interesting for rare earth metals because the relative intensity of the magnetic EXAFS to the near edge signal (XMCD) is much larger compared to 3d transition metals. This is because the MEXAFS for the rare earth elements is essentially proportional to the total 4f magnetic moment, whereas the XMCD is dominated by dipole transitions to the spin-dependent 5d densities of states only. The temperature dependence of the magnetic EXAFS originates both from spin fluctuations and lattice vibrations. We present a new procedure to separate these contributions by modeling the absorption coefficients $\mu^+(E)$ and $\mu^-(E)$ for right and left circularly polarized X-rays, by the energy shifted experimental spin-averaged spectra. The temperature dependence of the MEXAFS can then be described by a temperature-dependent energy shift $\Delta E(T)$ which is proportional to the temperature-dependent magnetization $M(T)$. Furthermore, multiple and single scattering contributions in the MEXAFS are separated by comparison of the experimental data to *ab initio* calculations using the FEFF8 code.

The magnetic EXAFS (MEXAFS) is the extended energy range counterpart of the near-edge X-ray magnetic circular dichroism (XMCD). Interestingly, the temperature dependence of the MEXAFS is different from the one of XMCD because in the extended energy range the dynamic disorder due to lattice vibrations adds to the effect of the spin dynamics and therefore a larger damping with temperature is found in comparison to the near-edge signal [1–4]. Hence, the temperature dependence of the MEXAFS is a superposition of both effects. Surprisingly, the contribution of the EXAFS Debye-Waller factor is often neglected in various MEXAFS works. Therefore, the results might be questionable if simply the Fourier transform intensities are compared [5] without correcting for the effect of the lattice vibrations. In this work we will present a new experimental approach to disentangle the two contributions by modeling the MEXAFS with the energy-shifted EXAFS data. This is especially important when the MEXAFS intensity for various systems is correlated to the spin moment as for instance for rare earth metals in comparison to 3d transition metals. The Debye-temperature for the rare earth elements is in the range of $\theta_D \approx 170\,\mathrm{K}$ whereas one finds $\theta_D \approx 450\,\mathrm{K}$ for the 3d transition metals. Therefore, the mean square relative displacement σ^2 is about a factor of two larger for the rare earth metals compared to the 3d metals even at 100 K. The data at the L_3 edges were recorded on Gd and Tb single crystals at the ID12 beamline at the ESRF. We made use of the so-called gap-scan technique which enabled us to combine a high photon flux with a high degree of circular polarization [6] and detected the fluorescence yield. The data were corrected for self-absorption effects (see [7] for details). The single crystals have the shape of a plate and were mounted at normal incidence to the X-rays with the magnetic field aligned along the photon k-vector. By means of element specific hysteresis loops the saturation fields at the specific temperatures were determined [4]. The EXAFS and MEXAFS oscillations were extracted with the conventional spline analysis (see [8] for details).

The procedure applied in this work to disentangle the effect of the lattice vibrations from the spin fluctuations is based on the description of the MEXAFS in various theoretical works: The MEXAFS fine structure is related to the energy derivative of the DOS which is linked to the derivative of the spin-averaged EXAFS [9–12]. Ebert and coworkers showed that the MEXAFS fine structure is connected to the spin and orbital polarization $(\mathrm{d}/\mathrm{d}E)\langle\sigma_z\rangle$ and $(\mathrm{d}/\mathrm{d}E)\langle l_z\rangle$ by analyzing sum rules in their differential form [13–16]. Even in the near-edge range similar theoretical treatments can be found [17, 18]. In a simplified picture the MEXAFS can be described as the difference of the spin-dependent scattering at the potentials which are modeled from the normal EXAFS scattering potentials being shifted in energy by an exchange-related energy $\Delta E(T)$. In this case the MEXAFS oscillations could be simulated with χ_M^{sim} by calculating the difference of the regular EXAFS oscillations χ which are shifted in energy by $\pm 1/2\,\Delta E$:

$$\chi_M^{sim}(E,T) = \chi\left(E - \tfrac{1}{2}\Delta E(T)\right) - \chi\left(E + \tfrac{1}{2}\Delta E(T)\right). \qquad (1)$$

To test this assumption we applied this procedure to the experimental Gd and Tb MEXAFS data at 10 K and simulated them with the experimental EXAFS spectra at the same temperature. The only free parameter is the energy shift ΔE which is varied until the simulated MEXAFS intensities match the experimental ones. The results are given in Fig. 1. Surprisingly, this simple approach can reproduce various fine structures of the experimental MEXAFS seen for instance at $k = 4.0\,\text{Å}^{-1}$ for Gd and at $k = 8.0\,\text{Å}^{-1}$ for Tb. Also the enveloping amplitude of the MEXAFS is correctly described. This demonstrates that the rigid-band model as suggested by Brouder *et al.* [10] holds for the modeling of the MEXAFS even up to large k-values of about $11\,\text{Å}^{-1}$. Therefore, the shift of the EXAFS by ΔE to model $\mu^+(E)$ and $\mu^-(E)$ is a way to determine the spin-dependent densities of states. It turns out that the shape of the L_3-edge MEXAFS can be described by the first derivative of the EXAFS $\mathrm{d}\chi/\mathrm{d}E$ and $\Delta E(T)$ is there to scale the intensity. Thinking in terms of a Taylor series

*Corresponding author electronic address: babgroup@physik.fu-berlin.de; URL: http://www.physik.fu-berlin.de/~ag-baberschke/index.html
†Present address: Department of Chemistry, University of Georgia, Athens, GA 30602, USA.
‡Present address: Materials Science Department, University of Patras, Gr-26504 Patras, Greece.

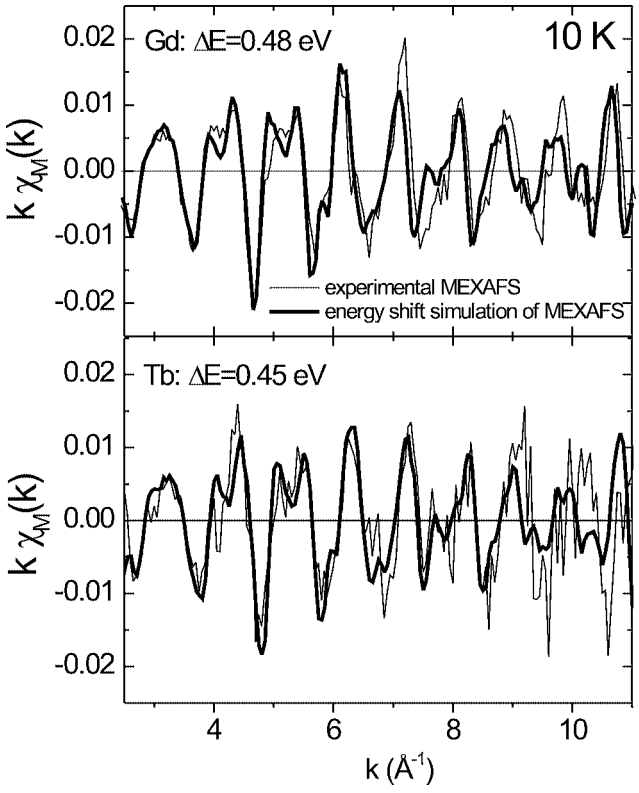

Fig. 1. Experimental MEXAFS data for Gd (top) and Tb (bottom) single crystals at 10 K in comparison to simulation of the MEXAFS with the spin-averaged EXAFS data. For the simulation the difference of the energy shifted EXAFS oscillations $\chi(E - \frac{1}{2}\Delta E) - \chi(E + \frac{1}{2}\Delta E)$ was analyzed.

the higher order terms can be neglected because of the smallness of $\Delta E(T)$. This is not the case for K-edge MEXAFS where Brouder *et al.* [10] showed that the MEXAFS is proportional to the second derivative of the EXAFS $\mathrm{d}^2\chi/\mathrm{d}E^2$ and Ebert *et al.* discussed these results on the basis of the differential form of the sum rules [15]. We also applied successfully the simple model given by eq. (1) to the MEXAFS of 3d elements (not shown). There the $L_{3,2}$ edges overlap strongly in contrast to the rare earth metals presented here, where the $L_{3,2}$ edges are well separated by several hundred eV (Tb: ∼730 eV). Furthermore, the procedure of simulating the MEXAFS at the specific temperature T with the experimental EXAFS data at the same temperature automatically takes the reduction by the EXAFS Debye-Waller factor into account. Hence, the temperature dependence of the energy shift ΔE is not due to the lattice vibrations but spin fluctuations only and therefore these two contributions can be separated.

Now, the temperature dependence of $\Delta E(T)$ will be analyzed in detail: $\Delta E(T)$ is determined by fitting the temperature-dependent MEXAFS oscillations with the procedure described by eq. (1). The experimental results for Gd are given in Fig. 2. Obviously, the temperature dependence of ΔE follows the one of the magnetization $M(T)$ [19] as it is also suggested in recent theoretical works [20]. This shows that the entire temperature dependence of the MEXAFS can be described by the factor $M(T) \cdot \mathrm{e}^{-2\sigma^2(T)k^2}$. Therefore, one has to correct not only for the amplitude reduction by the reduced temperature T/T_C but also for the EXAFS Debye-Waller factor when the MEXAFS intensity is correlated to the spin moment. In various MEXAFS works the latter effect was neglected although there is a strong influence by the factor $\mathrm{e}^{-2\sigma^2(T)k^2}$, e.g. when the MEXAFS intensity of 3d

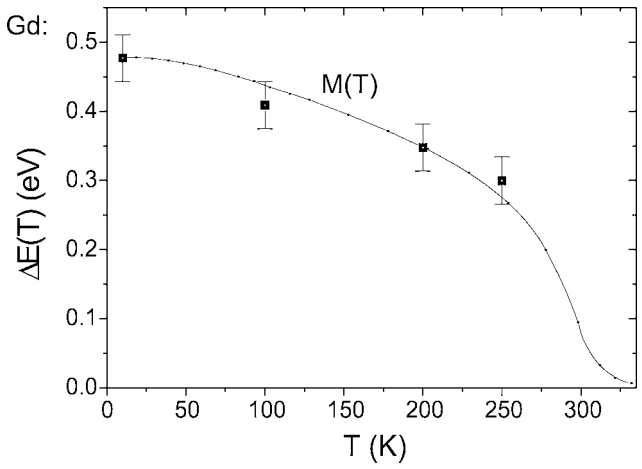

Fig. 2. Temperature dependence of the exchange related energy shift $\Delta E(T)$ for a Gd single crystal in comparison to the temperature dependence of the magnetization taken from the literature [19].

transition metals is compared to the ones of the rare earths (see above).

For a more detailed investigation of the Tb EXAFS and MEXAFS data we compared the experimental results to *ab initio* calculations using the FEFF8.2 code [21] (Fig. 3). Since the FEFF8.2 calculations are not self consistent with respect to the spin dependence, the MEXAFS data were scaled down to match the experiment. The calculations for the EXAFS and the MEXAFS agree quite well with the experiment in k-space as well as in R-space since all the fine structures are reproduced by the calculation. Interestingly, various fine structures of the MEXAFS that were already seen in the energy shift simulation in Fig. 1, e.g. at about $k = 5.3$, 6.8 and 7.8 Å^{-1}, can also be detected in the FEFF8.2 calculation. The splitting of the main peak in the Fourier transforms, which is due to a minimum in the enveloping amplitude at about $k = 9$ Å^{-1}, is accurately modeled. Even all the peaks in the Fourier transform for the EXAFS and the MEXAFS with respect to their position as well as their relative intensity are well described by the theory. In order to disentangle those peaks into their multiple- (MS) and single-scattering (SS) contributions, we used the advantage to switch on/off those effects in the theory. The result of this separation is given in Fig. 4. All the peaks up to 6.0 Å can be described by single-scattering contributions. The

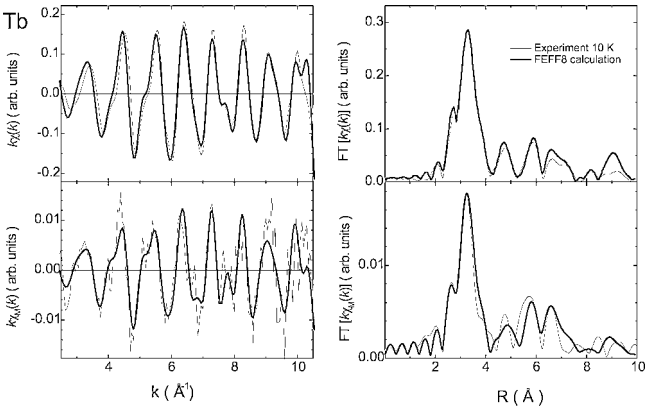

Fig. 3. Experimental Tb EXAFS (top) and MEXAFS (bottom) oscillations $k \cdot \chi(k)$ and $k \cdot \chi_M(k)$ (left) and the corresponding Fourier transforms (right) in comparison to *ab initio* calculations (FEFF8.2).

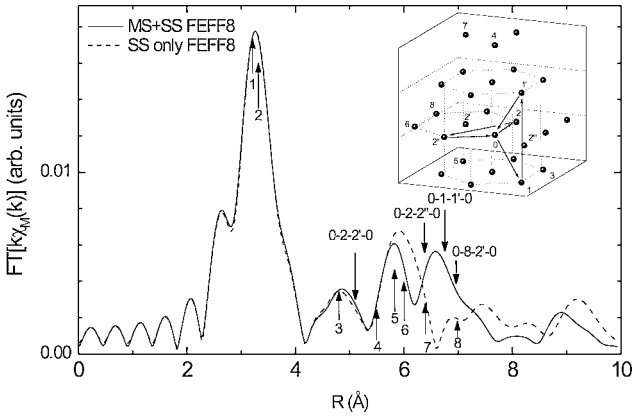

Fig. 4. Theoretical separation of multiple and single scattering contributions in the Tb MEXAFS (FEFF8.2).

triangular scattering path 0–2–2′–0 (inset of Fig. 4) at about 3.0 Å hardly contributes to the overall intensity. However, at distances larger than 6.0 Å clear contributions from various triangular paths can be found. Surprisingly, smaller intensities are found for the multiple-scattering calculation (solid line) above 7.5 Å. This demonstrates that the multiple- and the single-scattering paths interfere destructively as it was also determined for the Gd MEXAFS [22]. Contrary, such an effect was not seen for the L-edge MEXAFS of the 3d metals Fe and Co where even an enhancement of MS paths was found [2].

In conclusion, we have shown that the temperature-dependent MEXAFS can be modeled by the difference of the energy-shifted EXAFS spectra. This procedure allows to disentangle the effect of spin fluctuations from lattice vibrations. We find experimentally that the temperature-dependent energy shift follows the temperature dependence of the magnetization. This demonstrates that the MEXAFS intensities have to be corrected for the reduced temperature T/T_C **and** the effect of the EXAFS Debye-Waller factor when the MEXAFS intensities are correlated to the spin-moment. Furthermore, we find by means of *ab initio* calculations that the multiple-scattering contributions in the rare earth MEXAFS interfere destructively with the single-scattering ones in contrast to the findings for the 3d L-edge MEXAFS.

Acknowledgements

We thank G. Ceballos for his help during the experiments. This work was supported by the BMBF (05 KS1 KEB 4) and ESRF (HE-536 and HE-756).

References

1. Wende, H. *et al.*, J. Appl. Phys. **83**, 7028 (1998).
2. Wende, H. *et al.*, J. Synchrotron Rad. **6**, 696 (1999).
3. Wende, H. *et al.*, In "Theory and Computation for Synchrotron Radiation Spectroscopy", (edited by Benfatto, M., Natoli, C. R. & Pace, E.), AIP Conference Proc. **514**, 140 (2000).
4. Wende, H. *et al.*, J. Synchrotron Rad. **8**, 419 (2001).
5. Ahlers, D., Attenkofer, K. and Schütz, G., J. Appl. Phys. **83**, 7085 (1998).
6. Rogalev, A. *et al.*, J. Synchrotron Rad. **5**, 989 (1998).
7. Tröger, L. *et al.*, Phys. Rev. B **46**, 3283 (1992).
8. Wende, H., (1999). PhD. thesis: "Extended X-ray Absorption Fine Structure Spectroscopy of Surfaces and Thin Films: Local Structure, Dynamic and Magnetic Properties", (Verlag Dr. Köster, Berlin (1999)) ISBN3-89574-341-0.
9. Ankudinov, A. and Rehr, J. J., Phys. Rev. B **52**, 10214 (1995).
10. Brouder, C., Alouani, M., Gioretti, C., Dartyge, E. and Baudelet, F., In "Spin–Orbit-Influenced Spectroscopies of Magnetic Solids", Herrsching Proc., (edited by Ebert, H. and Schütz, G.), (Springer, Berlin, 1996) 259–274.
11. Brouder, Ch., Alouani, M. and Bennemann, K. H., Phys. Rev. B **54**, 7334 (1996).
12. Dartyge, E. *et al.*, Physica B **208&209**, 751 (1995).
13. Ahlers, D., Schütz, G., Popescu, V. and Ebert, H., J. Appl. Phys. **83**, 7082 (1998).
14. Ebert, H. *et al.*, Europhys. Lett. **42**, 295 (1998).
15. Ebert, H., Popescu, V. and Ahlers, D., Phys. Rev. B **60**, 7156 (1999).
16. Popescu, V., Ebert, H. and Ahlers, D., J. Magn. Magn. Mat. **191**, 368 (1999).
17. Erskine, J. L. and Stern, E. A., Phys. Rev. B **12**, 5016 (1975).
18. Gotsis, H. J. and Strange, P., J. Phys.: Condens. Matter **6**, 1409 (1994).
19. Nigh, H. E., Legvold, S. and Spedding, F. H., Phys. Rev. **132**, 1092 (1963).
20. Ankudinov, A. L., Rehr, J. J., Wende, H. and Baberschke, K., these proceedings.
21. Ankudinov, A. L., Ravel, B., Rehr, J. J. and Conradson, S. D., Phys. Rev. B **58**, 7565 (1998).
22. Wende, H. *et al.*, Nucl. Instrum. and Meth. in Phys. Res. A **467–468**, 1426 (2001).

Physica Scripta. Vol. T115, 603–605, 2005

X-Ray Resonant Scattering in Fe_3O_4, $MnFe_2O_4$ and $CoFe_2O_4$ Ferrites

G. Subías*[1,2], J. Garcia[1], M. G. Proietti[1], J. Blasco[1], H. Renevier[3], J. L. Hodeau[3] and M. C. Sánchez[1]

[1]Instituto de Ciencia de Materiales de Aragón. CSIC-Universidad de Zaragoza, 50009 Zaragoza, Spain
[2]European Synchrotron Radiation Facility, B.P. 220, 38043 Grenoble, France
[3]Laboratoire de Cristallographie, C.N.R.S., B.P. 166, 38042 Grenoble Cedex 09, France

Received June 26, 2003; accepted in revised form April 16, 2004

PACS numbers: 61.10.Eq, 78.70.Ck, 71.30.+h, 71.90.+q, 75.50.Gg

Abstract

X-ray resonant scattering experiments at (002) and (006) forbidden Bragg reflections were performed on Fe_3O_4, $MnFe_2O_4$ and $CoFe_2O_4$ single crystals. The intensity of these reflections in Fe_3O_4 shows three characteristic features as a function of energy. A pre-peak resonance related to dipolar-quadrupolar transitions coming from the tetrahedral Fe ions and a main resonance at the absorption edge and the energy-extended oscillating part ascribed to the anisotropy of the octahedral Fe ions. X-ray resonant scattering experiments on $MnFe_2O_4$ (normal spinel) and $CoFe_2O_4$ (inverse spinel) ferrites verify experimentally the origin of these resonances, the main peak is caused by the dipole transition of the octahedral site iron and the pre-edge peak is due to the dipole-quadrupole transition of the tetrahedral site iron, independently of the formal valency or chemical specie. These experimental results show that anisotropic tensor susceptibility (ATS) scattering cannot be simply considered as a direct proof of orbital ordering.

1. Introduction

X-ray resonant scattering experiments are used to find experimental proof of the existence of orbital and charge ordering in transition metal compounds. Within this framework, lots of studies have been recently reported on manganites [1–3], NaV_2O_5 [4], V_2O_3 [5] and other transition metal oxides. The interpretation of the observed X-ray resonant scattering patterns in terms of an ionic charge/orbital ordering model has been criticized by different authors who propose instead a structural origin for the observed X-ray resonant scattering reflections [6–9].

In order to investigate the charge/orbital ordering phenomena in transition metal compounds, we studied first the classical archetypical compound magnetite (Fe_3O_4). Magnetite has been considered as prototype of charge ordering systems where octahedral Fe^{3+}/Fe^{2+} iron ions are dynamically disordered above the Verwey transition temperature (Tv) and periodically ordered below Tv [10]. We carried out X-ray resonant scattering experiments at the (002) and (006) forbidden reflections, fingerpoint of the Verwey model, above and below Tv [11, 12]. Our results demonstrate that no ionic charge ordering is present in magnetite at low temperatures, at least for ionic configurations satisfying the Anderson condition [12]. Moreover, the temporal existence of localized Fe^{3+} and/or Fe^{2+} ionic states in the high-temperature phase was also completly discarded [11]. On the other hand, the experimental facts can be easily explained in terms of a structural model, based on the anisotropy of the anomalous atomic scattering factor of the octahedral Fe ions (anisotropic tensor suceptibility (ATS) scattering).

The intensities of the (002) and (006) forbidden Bragg reflections in magnetite show three clear features as a function of energy, a pre-peak resonance, a main-edge resonance and an energy-extended oscillating part. Both theoretical simulations and the q-dependence of the experimental X-ray resonant spectra indicate that the pre-peak resonance has its origin from a dipolar-quadrupolar excitation-deexcitation channel at the tetrahedral iron ions. On the other hand, the main-edge resonance and the energy-extended oscillatory part are both ascribed to 1s-εp dipolar transitions at the octahedral iron ones. The azimuthal dependence of these reflections follows a $\pi/2$-periodicity. We note that the point symmetry of the octahedral sites is not octahedral (O_h) but trigonal-distorted (D_{3d}) so anisotropy coming from this trigonal symmetry should be expected. Moreover, it also explained satisfactorily the azimuthal and q-dependencies of these reflections. The atomic scattering tensor is defined in the trigonal symmetry by,

$$\begin{pmatrix} f_\perp & 0 & 0 \\ 0 & f_\perp & 0 \\ 0 & 0 & f_\parallel \end{pmatrix} \tag{1}$$

$f_\parallel$ and $f_\perp$ being the component parallel and perpendicular to the trigonal axis, respectively. Then, we obtain that the structure factor scattering tensor is given by

$$F_{00l} = \frac{16}{3}\begin{pmatrix} 0 & (f_\parallel - f_\perp) & 0 \\ (f_\parallel - f_\perp) & 0 & 0 \\ 0 & 0 & 0 \end{pmatrix} \tag{2}$$

and the respective azimuthal and q-dependencies are given by

$$I^T_{00l} \propto \left|\tfrac{16}{3}(f_\parallel - f_\perp)\right|^2 (\sin^2\theta + \cos^2\theta \sin^2(2\varphi)). \tag{3}$$

The aim of this work is to demonstrate experimentally 1) the assignation of the pre-peak resonance to atoms at tetrahedral sites and 2) the structural origin of the main-edge resonance elucidating whether it reflects or not a claimed d-orbital ordering in some way. We have performed X-ray resonant scattering experiments at the (002) and (006) forbidden reflections of two selected spinel ferrites, $MnFe_2O_4$ and $CoFe_2O_4$, at the Fe, Mn and Co K-edges. Spinel ferrites are of general formula AB_2O_4, A and B being the tetrahedral and octahedral sites, respectively. They are derived from Fe_3O_4 by partial substitution of iron ions by other divalent transition metal element such as Mn, Co, Ni, Cu or Zn. It is known that Mn^{2+} mainly substitutes the tetrahedral A-sites in the spinel structure whereas Co^{2+} mainly goes into the octahedral B-sites [13]. Considering this cation distribution between the tetrahedral and octahedral sites, no pre-peak resonance should be observed, neither at the Fe K-edge in $MnFe_2O_4$ nor at the Co K-edge in $CoFe_2O_4$. Moreover, no resonance at the Mn K-absorption edge should be detected. On the other hand, Fe K-edge spectra should show the resonance at the absorption edge in both samples.

In this paper, we will show that the measured energy and azimuthal behaviour of the (002) and (006) forbidden reflections for these spinel ferrites completely confirms our previous results

*e-mail: gloria@unizar.es

for magnetite and it adds a new experimental proof of the structural origin of resonant forbidden reflections in transition metal oxides. Finally, we note that the formal valency of octahedral iron ions in the studied (Mn, Co) spinel ferrites is +3 compared to +2.5 of magnetite. The effects of the valence state and the d-electronic configuration will be briefly discussed.

2. Experiment

X-ray resonant scattering experiments were performed at the French CRG D2AM beam line at the European Synchrotron Radiation Facility [14]. A Si(111) double crystal with an energy resolution of about 1 eV was used to monochromatize the incident σ–polarized beam. The incident polarization vector was perpendicular to the diffraction plane (σ incident geometry) and no polarization analysis to separate σ and π components of the scattering beam was performed in this case. Single crystals of Fe_3O_4, $MnFe_2O_4$ and $CoFe_2O_4$ ferrites were melt-grown by floating-zone method. (001) surfaces were cut and polished with fine diamond paste. The physical characterization has been reported elsewhere [12]. All the crystals are single phase at room temperature with lattice constants $a = 8.396$ Å, $a = 8.499$ Å and $a = 8.391$ Å for magnetite, Mn and Co ferrites, respectively.

3. Results and Discussion

The energy dependence of the intensity at the maximum of the forbidden reflections (002) and (006) of Fe_3O_4, $MnFe_2O_4$ and $CoFe_2O_4$ ferrites near the iron K absorption edge at room temperature is shown in Figure 1. A main resonance is observed at similar energies around the K edge (7125 eV) for all the samples.

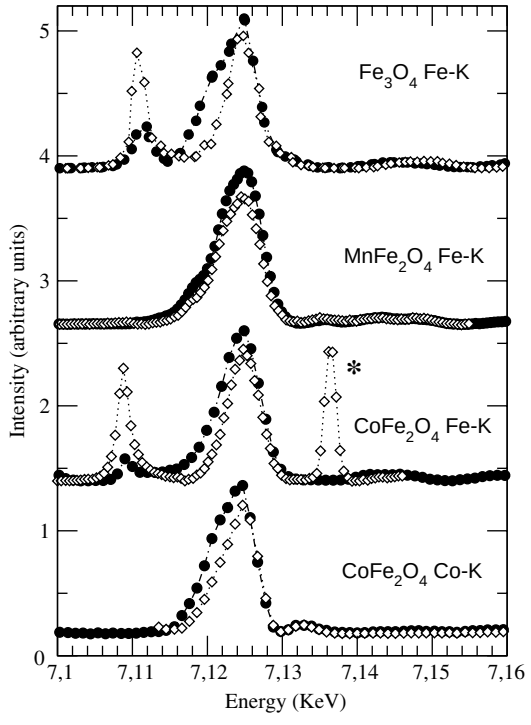

Fig. 1. Energy dependence of (002) (closed circles) and (006) (open diamonds) forbidden reflections at room temperature for Fe_3O_4, $MnFe_2O_4$ and $CoFe_2O_4$ spinel ferrites around the Fe and Co K-edges. The Co K-edge spectrum has been shifted in energy for comparison. Lines are a guide for the eye and asterisks mark spurious Renninger reflections.

This resonance was assigned to the dipolar transitions from the 1s core level to the εp bands in Fe_3O_4 due to the anisotropy of the atomic scattering factor of the octahedral Fe ion that results from the trigonal symmetry of the B-sites ($\bar{3}$m) [11]. A second resonance at about 7111 eV appears only for Fe_3O_4 and $CoFe_2O_4$ samples. This resonance corresponds to the pre-peak energy in the fluorescence spectrum and in the case of Fe_3O_4 was explained as arising from dipolar-quadrupolar excitation-deexcitation channels at the tetrahedral Fe ion by using *ab-initio* multiple scattering simulation [11]. Moreover, the intensity of this pre-peak resonance in Co ferrite shows the same q-dependence as in pure magnetite. The energy dependence of the (002) and (006) reflections at the Co K absorption edge at room temperature is also shown at the bottom of Figure 1. In this case, only the resonance at energies close to the Co K-edge (7725 eV) is observed.

The distribution of the metal ions between the tetrahedral and octahedral sites in spinel ferrites has drawn much attention in literature because of its influence in their physical properties [13]. In the case of Fe_3O_4, an inverse distribution of cations occurs; the Fe^{2+} ions are located on the octahedral B-sites and the Fe^{3+} ions are uniformly distributed over the remaining octahedral-B and tetrahedral-A sites. For Co ferrite, the inverse structure is also found where Co^{2+} ions prefer the octahedral B-site positions. On the other hand, in Mn ferrite, Mn^{2+} ions occupy predominantly the tetrahedral A-site positions. Taking into account this cation distribution between the octahedral and tetrahedral sublattice, the following conclusions can be inferred: 1) the absence of a pre-peak resonance in both the Fe K-edge spectra of $MnFe_2O_4$ and the Co K-edge spectra of $CoFe_2O_4$ (where no Fe or Co ions, respectively, occupy the tetrahedral sites) confirms that this feature comes directly from the tetrahedral ions and 2) the appearance of a resonance at the absorption edge for all the samples and K-edges considered, except for the Mn K-edge in agreement with the absence of Mn ions at the octahedral sites, confirms its dipolar origin at the octahedral B-sites. In addition, the fact that the valence state of the octahedral Fe ions in $MnFe_2O_4$ and $CoFe_2O_4$ is +3, instead of +2.5 as for Fe_3O_4, and that the resonance is observed for transition metal ions with different d-orbital occupation (Fe^{3+} is a $3d^5$ and Co^{2+} is a $3d^7$) proves that the X-ray resonant scattering intensity at these forbidden reflections arises mainly from the anisotropy of the transition metal environment, i.e. it has a structural origin.

Let us now discuss briefly the energy line shape and the azimuthal dependence of the (002) and (006) forbidden reflections in these spinel ferrites. A shift of about 2 eV to lower energies is observed for the pre-peak resonance at the Fe K-edge in $CoFe_2O_4$, indicating that the d electronic configuration of the tetrahedral Fe ions in Fe_3O_4 and $CoFe_2O_4$ are slightly different. This result also corroborates the dipolar-quadrupolar character of this resonance. Moreover, the energy line shape of the resonance at the Fe K-edge is also slightly different for the three studied samples. The dependence of the (002) and (006) scattered total intensity on the azimuthal angle φ for the Co ferrite compared to the magnetite [11] at $E = 7124.5$ eV (Fe K) and at $E = 7725$ eV (Co K) is shown in Figure 2a and 2b, respectively. The same $\pi/2$ φ-periodicity as in Fe_3O_4 is found for the Co ferrite at both Fe and Co K-edges. The dependence on the Bragg angle (θ) is clearly shown at zero azimuthal angle where the scattered intensity is about 5% of the maximum for the (002) reflection and 30% for the (006) one for both absorption edges and samples. It reasonably compares to the theoretical simulations (calculated by equation (3)) considering only the anisotropy of the atomic scattering factor

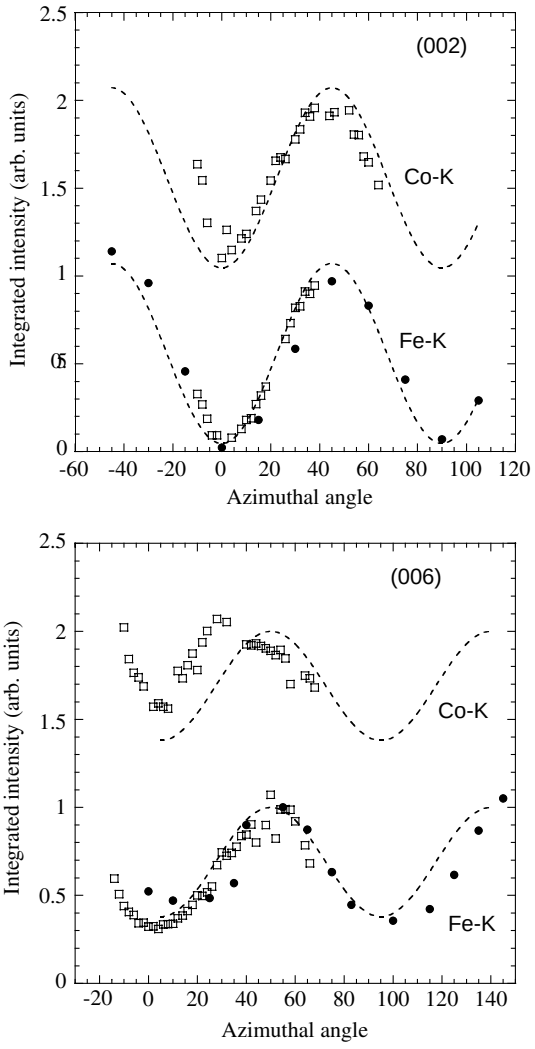

Fig. 2. (upper panel) Total integrated intensity of the (002) forbidden reflection as function of the azimuthal angle φ at the maximum of the resonance at the Fe(Co) K absorption edge. Closed circles: Fe_3O_4 sample and open squares: $CoFe_2O_4$ sample. Dashed lines show theoretical simulations calculated by equation (3). Co K-edge data have been artificially shifted by 1 unit in the vertical scale as a matter of illustration. (lower panel) Total integrated intensity of the (006) forbidden reflection as function of the azimuthal angle φ at the maximum of the resonance at the Fe(Co) K absorption edge. Closed circles: Fe_3O_4 sample and open squares: $CoFe_2O_4$ sample. Dashed lines show theoretical simulations calculated by equation (3). Co K-edge data have been artificially shifted by 1 unit in the vertical scale as a matter of illustration.

of the Fe (or Co) ions at the octahedral *B*-sites due to the trigonal distortion (dipolar transitions). Inhomogeneities in the mosaic structure of the samples at different azimuthal angles may cause the dispersion in the scattered intensities. Moreover, the energy-dependent spectra of $CoFe_2O_4$ at both Fe and Co K-edges, taken at different azimuthal angle values, are almost identical to each other except for a scale factor.

4. Conclusions

X-ray resonant scattering experiments at the respective transition metal K-edges of Fe_3O_4, $MnFe_2O_4$ and $CoFe_2O_4$ have been reported providing *direct* experimental evidence of the theoretically predicted origin for the several resonances observed in these materials: **1)** the resonance at energies corresponding to the prepeak of the fluorescence spectrum is clearly demonstrated to arise from dipolar-quadrupolar contributions from the tetrahedral iron ions and **2)** the main resonance associated to the 1s-εp dipolar transition is confirmed to be mainly of structural origin due to the anisotropy of the local symmetry at the octahedral *B*-sites.

We note that the energy and azimuthal dependence of the scattered intensity for the dipole transition does not depend on the formal valency of the octahedral *B*-site atom (Fe atom has a formal valency of +2.5 in magnetite and +3 in the other two spinels) or on the type of transition metal atom which occupies this octahedral site (the Co K-edge resonance shows similar behavior as the resonance at the Fe K-edge). On the contrary, the pre-peak resonance coming from the tetrahedral atom seems to be sensitive to the atomic specie and the chemical composition.

In conclusion, these results imply that the dipolar X-ray resonant scattering cannot be simply viewed as a *direct* observation of orbital ordering as it has been claimed for transition-metal oxides. Moreover, the lack of sensitivity of the dipolar resonant scattering signal to the formal 3d electronic configuration points out that a band description approach is the best option to explain the electronic, magnetic and transport properties in spinel ferrites.

Acknowledgments

We thank the financial support of the Spanish CICyT project n° MAT2002-01221. We also acknowledge ESRF and the French CRG D2AM beam line for granting beam time.

References

1. Murakami, Y., *et al*., Phys. Rev. Lett. **80**, 1932 (1998).
2. Murakami, Y., *et al*., Phys. Rev. Lett. **81**, 582 (1998).
3. Zimmermann, M. V., *et al*., Phys. Rev. B **64**, 195133 (2001).
4. Nakao, H., *et al*., Phys. Rev. Lett. **85**, 4349 (2000).
5. Paolasini, L., *et al*., Phys. Rev. Lett. **82**, 4719 (1999).
6. Benfatto, M., Joly, Y. and Natoli, C. R., Phys. Rev. Lett. **82**, 636 (1999).
7. García, J., Sánchez, M. C., Blasco, J., Subías, G. and Proietti, M. G., J. Phys.: Condens. Matter **13**, 3243 (2001).
8. García, J. and Benfatto, M., Phys. Rev. Lett. **87**, 189701 (2001).
9. García, J. and Subías, G., Phys. Rev. B **68**, 127101 (2003).
10. Verwey, E. J. W., Nature (London) **144**, 327 (1939).
11. García, J., *et al*., Phys. Rev. Lett. **85**, 578 (2000).
12. García, J., *et al*., Phys. Rev. B **63**, 054770 (2001).
13. Brabers, V. A. M., in "Handbook of Magnetic Materials" (Edited by K. H. L. Buschow) (North-Holland Publ. Co. Amsterdan 1995) vol. **8**, ch. 3, p. 189.
14. Ferrer, J. L., *et al*., J. Synchrotron Rad. **5**, 972 (1998).

Physica Scripta. Vol. T115, 606–608, 2005

Atomic Structure and the Magnetic Properties of Zr-Doped Sm_2Co_{17}

B. Ravel and K. Gallagher

Naval Research Laboratory, Washington, DC 20375, USA

Received June 26, 2003; accepted November 4, 2003

PACS number: 61.10.Ht

Abstract

Permanent magnets based on Sm_2Co_{17} are of significant technological interest due to their high coercivities and elevated Curie temperatures. In this paper we examine the local environment of Zr-doped Sm_2Co_{17}. The presence of Zr in Sm_2Co_{17}-based magnets causes the formation of hexagonal Sm_2Co_{17} lamellae in the microstructure in the commercial materials. These lamellae serve as diffusion paths, enabling the development of good magnetic properties. While it is presumed that the Zr enters the lattice into either the Sm or Co dumbbell sites, there is, to date, no direct evidence of this assumption. In this paper, we present evidence of how the Zr does substitutes into the Sm_2Co_{17} lattice. We discuss the implication of this result on the magnetic properties and grain structure of the Zr-doped material.

1. Introduction

Magnetic materials of the nominal stoichiometry Sm_2Co_{17} are attractive for applications requiring high temperature, permanent magnets due to their high coercivity and Curie temperature above 900 K [1]. As engineered for commercial application, Sm_2Co_{17}-type magnets possess complex microstructures resulting from the addition of various dopants and the application of multiple heat treatments. The microstructure of a typical $Sm(Co, Fe, Cu, Zr)_z$ sample consists [1] of a cellular structure with $\sim$100 nm cells separated by fairly thick (4–10 nm) cell walls. Superposed over this structure are thin, parallel lamellae which are a few nm thick and permeate the cellular structure. Upon proper heat treatment, the dopants segregate [2] into different regions of the microstructure. The Cu migrates to the cell walls which are stabilized in the hexagonal $SmCo_5$ structure. The cells in $Sm(Co, Fe, Cu, Zr)_z$ are Fe rich and stabilize in the rhombohedral Sm_2Co_{17} structure. The lamellae are Zr rich and of the hexagonal Sm_2Co_{17} structure.

The magnetic properties result from domain-wall pinning at the cell boundaries, which is made possible by the Cu-rich 1–5 structure of the cell-walls. With low Cu content, only small sample volumes can be stabilized in the 1–5 phase and so the cell walls [3] remain thin. The addition of Zr to the sample promotes a uniform cellular microstructure as well as the formation of the Zr-rich lamellae. It is understood that the formation of the lamellae provide a path for the migration of Cu to the cell walls during thermal processing, thus promoting uniformity of the cellular structure as well as significantly increased coercivity.

While the microstructural phenomena discussed above are well established empirically, the underlying physical mechanisms remain poorly understood. Although the addition of Zr is known to promote the growth of the desired microstructure, very little is known about how Zr incorporates into the lattice of the lamellar portion of the $Sm(Co, Fe, Cu, Zr)_z$ microstructure or about the energetics of that substitution. In this work we investigate Zr-doped Sm_2Co_{17} in order to begin addressing this question. Because of the complexity of the $Sm(Co, Fe, Cu, Zr)_z$ microstructure and the presence [2] of small Zr concentrations in the cell region, we chose to focus on the Sm_2Co_{17} material in the absence of this complex microstructure by preparing samples with a few percent Zr to fall along the Sm_2Co_{17} line of the Sm–Co–Zr phase diagram [4]. In this report, we present results of EXAFS measurements on Zr-doped Sm_2Co_{17} and their structural implications.

There is scant investigation in the Sm–Co magnet literature into the details of the structure of Zr-doped material. Ray has long suggested [6, 7] that Zr enters the Sm_2Co_{17} lattice by substituting either for the Sm atom or for the Co dumbbells. Derkaoui, *et al.* [4] suggest the same on the strength of microscopy and X-ray diffraction measurements. Neither author, however, presents any direct evidence of the sort offered by an EXAFS experiment. The one report of EXAFS [8] on Zr-doped Sm_2Co_{17} presents data and conclusions at odds with our findings.

2. Sample Preparation and Data Collection

Samples of Zr-doped Sm_2Co_{17} were prepared by arc-melting stoichiometric ratios of high-purity metals under an argon atmosphere and in a water-cooled copper vessel. A few atomic percent additional Sm was added to each sample to compensate for loss of Sm during melting and annealing. In this paper, we present results on two samples prepared in this manner. Sample A was sealed in a quartz ampule under vacuum and annealed for 24 hours at 1050 °C and cooled to room temperature at a rate of 5 °C per minute. The stoichiometry of this sample was determined by inductively coupled plasma optical emission spectroscopy to be $Zr_{2.33}Sm_{8.62}Co_{89.05}$. Sample B was sealed in a quartz ampule under argon and annealed for 96 hours at 1150 °C and quenched to room temperature by immersion of the sealed ampule in water. Its stoichiometry was found to be $Zr_{3.36}Sm_{9.86}Co_{86.78}$. Purity of phase for each sample was checked by x-ray diffraction. Neither sample was pure of phase. Evidence for both the hexagonal and rhombohedral forms of Sm_2Co_{17} was seen, although both samples appeared to be predominantly hexagonal Sm_2Co_{17}. Neither sample showed significant evidence of the $SmCo_5$ phase.

EXAFS data were measured in fluorescence at NSLS beamline X11A using ionization chambers to measure both the incident and fluorescent flux. The bulk samples were mounted on a copper sample holder on the cold finger of a Displex two-stage helium compressor cryostat for low temperature measurement. Data were collected at 15, 100, 200, and 300 K. Measuring data at multiple temperatures allows us to better characterize our fitting models by verifying the temperature dependence of the fitting parameters. For example, we expect that parameters such as S_0^2 and E_0 will be independent of temperature while others, like σ^2, should be monotonically increasing in temperature.

For all data, the background removal was performed using the ATHENA [9] program, which uses the AUTOBK algorithm [10]. Data analysis was made using theoretical standards computed by FEFF6 [11]. The fits were performed using the ARTEMIS [9] program, which uses IFEFFIT [12] for all numerical operations.

3. EXAFS Results

There was significant structural variation between these two samples, as is clear from the data presented in Figures 2 and 3. The data from sample A are much larger in amplitude than from sample B and the main peak in $\bar{\chi}(R)$ is at a larger value of R, indicating a longer near-neighbor distance.

For our fits to these data, we considered the possibility that the Zr might substitute for any site in the Sm_2Co_{17} lattice. For each data set, the possibility of Zr substituting for any of the Co sites comprising the ring structures seen in Figure 1 was rejected. The nearest-neighbor distance for each of the ring sites is too short – about 2.45 Å – to be supported by either data set. The previous EXAFS report [8] reported the Zr to be in one of these sites, thus is at odds with the current results. The remaining possibilities, substitution into the Sm site or into a dumbbell Co site, are both consistent with the suggestions of Ray and of Derkaoui, *et al*. [4, 6, 7].

For sample A, the most successful model has Zr substituting for Sm but slightly displaced from the Sm site of symmetry by 0.065(9) Å. This sample also shows evidence of a small oxide component. 6.5(3)% of the Zr atoms are in an oxide environment. E_0 and the various σ^2 parameters were all reasonable and displayed reasonable temperature dependences.

The most striking result from these data was a significant statistical preference for the Zr atom to be in a local environment consistent with the rhombohedral Sm_2Co_{17} structure rather than the hexagonal. The main difference, as seen in Figure 1, is the presence of a dumbbell Co atom at 2.84 Å in the $\hat{z}$ direction in the rhombohedral structure. Excluding this scatterer from the fit, i.e. placing the Zr atom at the hexagonal Sm site, results in a statistically significantly worse fit, as seen in the lower panel of Figure 2. This result seems to be at odds with the XRD, which shows that the sample is predominantly hexagonal, and suggests that the presence of Zr in the lattice may serve to stabilize the rhomobohedral local structure under certain sample preparation conditions.

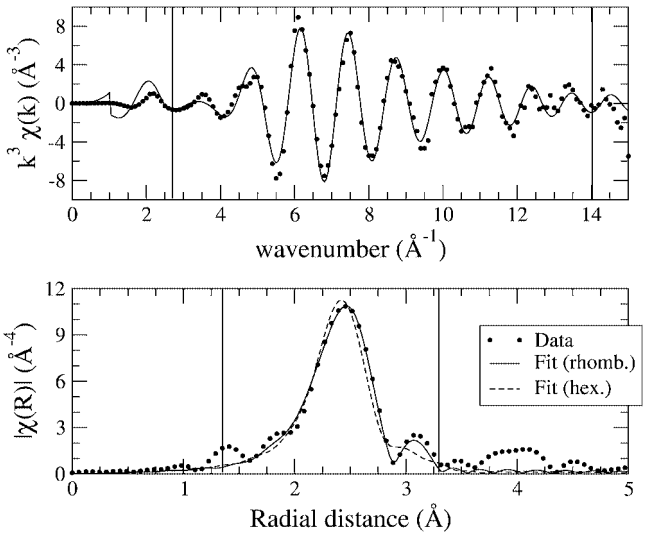

Fig. 2. Fit to the data measured on sample A using the model which places the Zr atom near a Sm site in rhombohedral Sm_2Co_{17} structure. The upper panel shows the fit in k-space with k^3 weighting. The vertical lines denote the extent of the Fourier transform. The lower panel shows the Fourier transform of the data in the upper panel. The vertical lines denote the fitting range in R. The fit with the hexagonal structure fails to fit the full width of the main peak.

The only structural model which yielded acceptable fit results for sample B places the Zr atom near the position of one of the dumbell Co atoms, although slightly farther displaced from the plane containing the ring of Co atoms surrounding the dumbbell site. The fit finds the Zr atom displaced from that plane by 1.789(61) Å as compared to the Co distance of 1.704 Å, according to the crystal data.

Although none of the other fitting models considered proved successful, the model described above is not entirely satisfying. The misfit on the high-R side of the peak in Figure 3 is significant

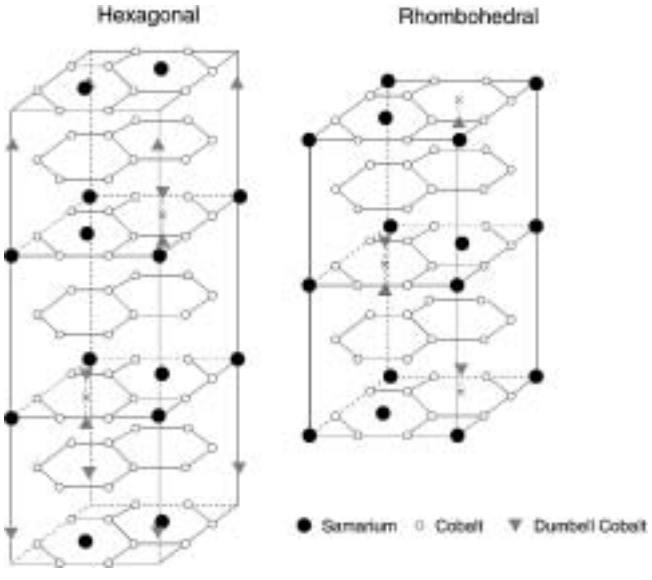

Fig. 1. Structures of hexagonal (left) and rhombohedral (right) Sm_2Co_{17} [5]. The Sm atoms (•) are at the centers of some Co (○) ring structures. Others have Co "dumbbells" at their centers.

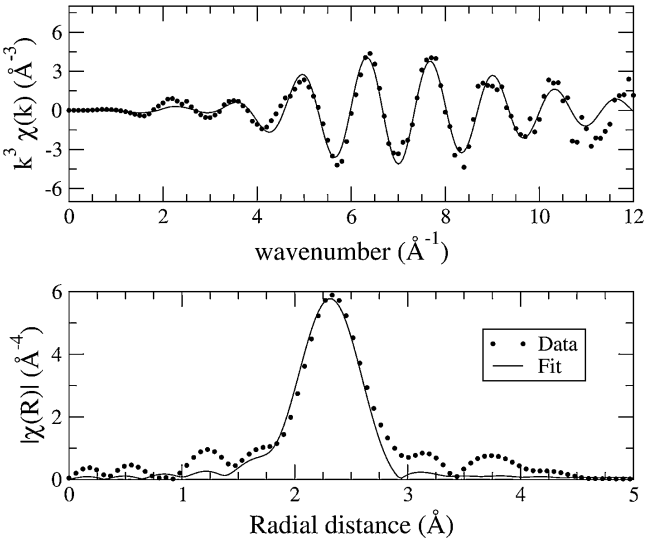

Fig. 3. Fit to the data measured on sample B using the model which places the Zr atom near a Co1 site in the hexagonal Sm_2Co_{17} Structure. The upper panel shows the fit in k-space with k^3 weighting. The vertical lines denote the extent of the Fourier transform. The lower panel shows the Fourier transform of the data in the upper panel. The vertical lines denote the fitting range in R.

and the small peak above 3 Å is not fit at all. We considered the possibilities of Zr oxide, Zr metal clusters, higher shells around the Col site, and the presence of a scatterer at the other dumbbell position. The data support none of the possibilities. Furthermore, the measured σ^2 values are large, ranging from 0.0098(33) Å^2 at 10 K to 0.0118(45) Å^2 at 300 K. Together these results suggest either that the placement of a Zr atom at a dumbell Co site introduces significant local disorder or that the model of Zr at the dumbbell site is suspect.

4. Conclusions

For sample A, the best fit to the data was obtained by placing the Zr atom near the Sm site in the rhombohedral Sm_2Co_{17} structure. For sample B, the best fit corresponds to a Zr atom near a copper dumbbell site in the hexagonal Sm_2Co_{17} structure. Both results confirm the speculations of previous authors [4, 6, 7] that Zr would replace a Sm atom or a Co dumbbell in this lattice and contrast the previous EXAFS report [8] on Zr in Sm–Co magnets.

The purpose of measuring the ternary alloy was to avoid the complexities introduced by the microstructure of the commercial $Sm(Co, Fe, Cu, Zr)_z$ materials. This did not prove to be a wholly successful strategy. Small differences in the heat treatment of our two samples lead to significant differences in structure about the Zr atom. It seems that the fabrication of the ternary alloy is, itself, a formidable materials science problem.

We plan much future work in this area. Future EXAFS studies of the ternary alloy prepared under various conditions are needed to fully elucidate the role of Zr in the Sm_2Co_{17} lattice. Clearly sample conditions lead to variations in local structure about the Zr atom. It is important to understand this variability, particularly in the temperature range in which the lamellar structure forms in the commercial alloy. Also important will be to study the role of Zr in the Sm_2Co_{17} lamellae in the commercial $Sm(Co, Fe, Cu, Zr)_z$ magnet. Electron nanoprobe energy loss studies [2] show that the Zr is concentrated in the lamellae, although some Zr remains in the cell regions of the $Sm(Co, Fe, Cu, Zr)_z$ microstructure. From those results, we estimate that about 80% of the total Zr atoms lie in the lamellae, thus making it possible to consider deconvolving the lamellar Zr portion of an EXAFS spectrum measured from the commercial magnet. These future studies on the ternary and commercial alloys will clarify the structural aspects of the Zr substitution into the Sm_2Co_{17} lattice. Detailed structural knowledge should deepen our understanding of the poorly understood physical mechanisms leading to the rich microstructure and outstanding magnetic properties of the commercial magnets.

Acknowledgments

We thank R. Gunning for preparing sample A. One of us (KG) is supported by the National Research Council.

References

1. Hadjipanayis, G. C., J. Magn. Magn. Mater. **200**, 373 (1999).
2. Yang, J.-M., Shindo, D., Takeguchi, M., Kawasaki, M. and Oikawa, T. J., J. Japan Inst. Metals **63**, 542 (1999).
3. Tang, W., Zhang, Y. and Hadjipanayis, G. C., J. Appl. Phys. **87**, 399 (2000).
4. Derkaoui, S., Valignat, N. and Allibert, C., J. Alloys Compds. **232**, 296 (1996).
5. Ostertag, W. and Strnat, K. J., Acta Cryst. **21**, 560 (1966).
6. Ray, A. E., J. Appl. Phys. **55**, 2094 (1984).
7. Ray, A. E., J. Appl. Phys. **67**, 4972 (1990).
8. Rabenberg, L., Barrera, E. V., Maury, C. E., Allibert, C. H. and Heald, S. M., J. Appl. Phys. **69**, 5568 (1991).
9. Ravel, B. and Newville, M., "ATHENA and ARTEMIS: Interactive graphical data analysis using IFEFFIT", in these proceedings.
10. Newville, M., Līviņš, P., Yacoby, Y., Rehr, J. J. and Stern, E. A., Phys. Rev. B **47**, 14126 (1993).
11. Zabinsky, S. I., Rehr, J. J., Ankudinov, A., Albers, R. C. and Eller, M. J., Phys. Rev. B **52**, 2995 (1995).
12. Newville, M., J. Synchrotron Radiat. **8**, 322 (2001).

Physica Scripta. Vol. T115, 609–610, 2005

Theoretical Analysis of Spin-Dependent Mn K-Edge X-Ray Absorption of MnP

G. Smolentsev and A. V. Soldatov*

Department of Physics, Rostov State University, 5, Sorge street, 344090 Rostov-on-Don, Russia

Received June 26, 2003; accepted June 28, 2004

PACS number: 78.70.Dm

Abstract

Spin-dependent X-ray absorption near edge structure (XANES) spectra measured by selectively monitoring of the Mn K-beta emission while scanning the excitation energy through the Mn K absorption edge were analyzed. The method of calculation is based on a combination of self-consistent spin-polarized calculation of muffin-tin potential and a full multiple scattering theory for interpretation of X-ray absorption. This approach allows to separate influence of dipole transition matrix elements and density of empty electronic states on spin-dependent XANES. It is found that matrix elements affect the splitting between spin-up and spin-down spectra only near the absorption threshold, while differences in densities of states slightly shift spectra in the region 35–55 eV above the main edge. Effects of multielectron term dependent broadening of spin-dependent XANES spectra and different mean free paths of photoelectrons with spin-up and spin-down in ferromagnetic phase were taken into account. It is shown that these factors also contribute to the splitting of spectra with different spin directions near the absorption threshold.

1. Introduction

Recent progress in construction of synchrotron sources and X-ray fluorescence detectors opened new possibilities for development of X-ray absorption measurements. By selectively monitoring one of the fluorescence components and scanning the incident photon energy through the absorption edge one can then do X-ray absorption measurements in Raman mode (or inelastic X-ray scattering mode). This experimental technique has several advantages if compared with traditional methods of X-ray absorption spectroscopy. One of them is a possibility to measure spin-dependent X-ray absorption fine structure. This method does not require long-range magnetic order and can therefore be applied to paramagnetic, antiferromagnetic as well as ferromagnetic systems. As a result of the exchange interaction between the 3p and 3d electrons in the final state (in the case of 3d-transition metals), the fluorescence spectrum shows pronounced satellite structure. On the base of multiplet splitting calculations it has been found that the spectra measured with fluorescence energy fixed on the main emission peak and on the satellite corresponds to the spin-polarized XANES spectra. After the pioneer publication of Hamalainen [1] such method was applied to the Mn K-edge in MnP [2], $LaMnO_3$ [3], complexes of Mn(II) with octahedral arrangement of metal ion [4] and Fe K-edge in protein rubredoxin [5] and Fe porphyrins [6].

Simultaneously with development of experimental techniques, theoretical methods explaining the spin-dependent X-ray absorption spectra were developed. In our preliminary paper [7] we reported first multiple scattering calculations of spin-polarized X-ray absorption fine structure (SPXANES) of MnF_2 and MnO. Besides the SPXANES the spin effects have been found to be very important in X-ray magnetic circular dichroism [8], magnetic extended X-ray absorption fine structure [9] and calculation of X-ray absorption under spin transitions in protein active centers [10]. Influence of spin-orbital interaction of final states on SPXANES is negligible (in contrast with magnetic circular dichroism), therefore using non-relativistic theory, but with inclusion of exchange splitting of final states, is appropriate for the interpretation of SPXANES.

Beside combination of multiple scattering theory with self-consistent field (SCF) calculations of potential, other methods to obtain SPXANES were proposed. Dufek [11] interpret MnF_2 SPXANES using linearized-augmented-plane-wave approximation. Taguchi and Kotani [12] reported multiplet splitting calculations of MnO and MnF_2 spectra based on empirical densities of unoccupied states.

In the present paper we report multiple scattering calculations of SPXANES of MnP.

2. Method of calculation

In order to obtain two sets of potentials for spin-up and spin-down configurations we performed self-consistent spin-polarized calculation of the electronic structure of small MnP_6 cluster that is a fragment of MnP crystal. The method we used is based on self consistent field scattered waves (SCF X_α-SW) technique with Slater X_α local density approximation (LDA) [13]. The charges of Mn and P ions were chosen according to the formal oxidation levels. Furthermore we have assumed that three 3d-electrons of Mn^{3+} are spin-up and one electron is spin-down. This correlates with recent results [14]. It has been found, that the difference between charges with various spin directions and d-character within the Mn muffin-tin spheres is 2.12 electrons.

Two sets of potentials, corresponding to the different spin states, obtained in the spin-polarized self-consistent calculations of small MnP_6clusters, were used to calculate partial phase shifts of the photoelectron, scattering on these potentials and dipole transition matrix elements. Then we performed full multiple scattering XANES calculations using these spin-dependent phase shifts and transition matrix elements in the same manner as in our previous work [7]. The algorithm of full multiple scattering method was described earlier [15]. Cluster containing 7 nearest to absorbing atom shells were chosen according to the convergence criterion.

3. Results and discussion

The spin dependence of the X-ray absorption is a result of interplay of two effects: different densities of spin-up and spin-down states and different transition matrix elements. Using multiple scattering formalism it is possible to separate these two factors. As one

*e-mail: Soldatov@rsu.ru

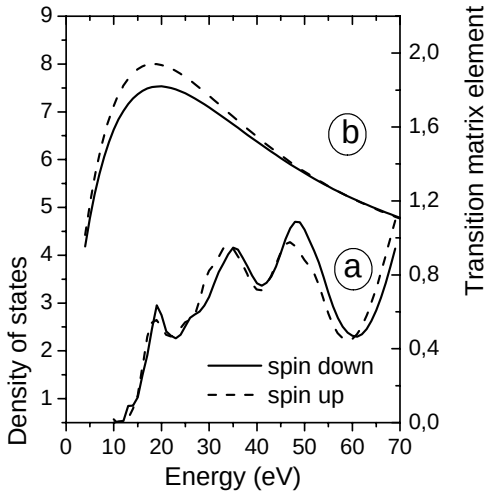

Fig. 1. (a) Spin-dependent densities of Mn unoccupied states with p-symmetry and (b) normalized squared dipole transition matrix elements as a function of photoelectron energy.

can see in fig. 1a there is an overall shift of spin-up density of states (DOS) towards low energy and a small decrease of intensity of peaks A and E. The relative shift of spin-up and spin-down DOS is due to the exchange interaction of 3d electrons with the photoelectron. It is clearly visible in the experimental spectra near the minimum F, where spin-dependence of transition matrix element is negligible. Such trend is observed also in other Mn and Fe SPXANES [1–6].

In Fig. 1b we present calculated matrix element of dipole transition. Its spin dependence influences XANES in the energy range 5–45 eV. Difference between matrix elements is significant (more than 10% in maximum). Therefore the assumption used by Taguchi [12] for MnF_2, that matrix elements for spin-up and spin-down states are equal is not valid. Besides spin dependence, the matrix element also shows considerable energy dependence. It can not be treated as a constant (as it was done for MnF_2 [11]) because it will result in wrong relative intensities of the low energy features.

In order to directly compare theoretical and experimental spectra one must take into account the broadening of the experimental spectrum according to the finite mean free path of a photoelectron, experimental resolution and spin-dependent factor equal to the width of 3p level for spin down and 3p + 1s for spin-up spectra. Recently it has been shown both experimentally [16] and theoretically [17], that for ferromagnetic samples the mean free path of photoelectrons is also spin-dependent. To test the influence of this factor on SPXANES we have performed calculations with non-spin-polarized energy-dependent broadening function obtained by Muller [18] and spin-polarized function from [17]. Results of such simulations are presented in fig. 2. Broadening factor as a function of energy is also shown. As one can see, the spin dependence of the mean free path influences the intensity of pre-edge feature and peak A. Another broadening factor mentioned above, partially compensates the differences between broadening of pre-edge peaks.

A novel method of data processing to exclude the effect of multiplet dependent broadening has been reported [2]. Probably, during this empirical data analysis the average differences between energy-dependent broadening functions were also taken into account. In fig. 3 we compare our calculations with these spectra. As one can see, good agreement with experiment was obtained.

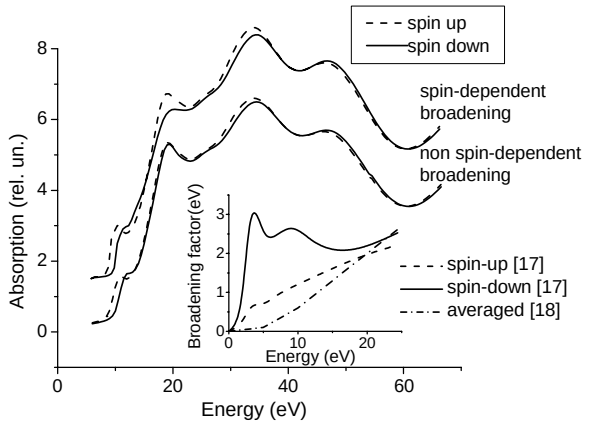

Fig. 2. Theoretical spin-dependent spectra calculated with non-spin-polarized energy-dependent broadening function [18] and spin-polarized function from [17]. The inset shows broadening factor as a function of energy.

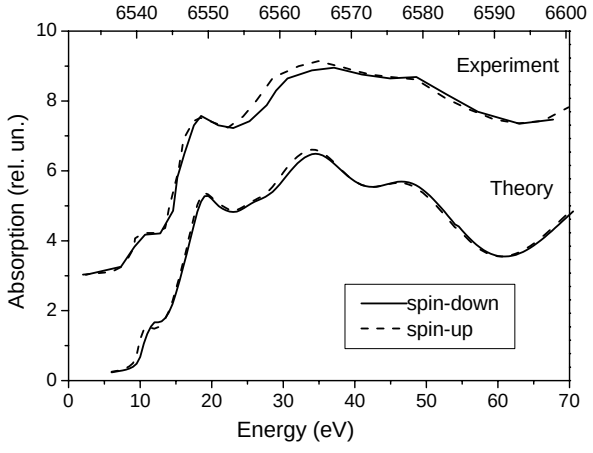

Fig. 3. Experimental Mn K-edge spin-dependent X-ray absorption of MnP after data processing [2] compared with theoretical spin-polarized X-ray absorption.

Acknowledgment

This work was supported by RFBR (Grant No. 02-02-17922a).

References

1. Hamalainen, K., *et al.*, Phys. Rev. B. **46**, 14274 (1992).
2. De Groot, F. M. F., *et al.*, Phys. Rev. B. **51**, 1045 (1995).
3. Qian, Q., Tyson, T. A., Kao, C. C., Croft, M. and Ignatov, A. Yu., Appl. Phys. Lett. **80**, 3141 (2002).
4. Peng, G., *et al.*, J. Am. Chem. Soc. **116**, 2914 (1994).
5. Wang, X., Grush, M. M., Froeschner, A. G. and Cramer, S. P., J. Synchrotron Rad. **4**, 236 (1997).
6. Wang, X., Randall, C. R., Peng, G. and Cramer, S. P., Chem. Phys. Lett. **243**, 469 (1995).
7. Soldatov, A. V., Ivanchenko, T. S., Kovtun, A. P., Della Longa, S. and Bianconi A., Phys. Rev. B. **52**, 11757 (1995).
8. Brouder, Ch., Alouani, M. and Bennemann, K. H., Phys. Rev. B. **54**, 7334 (1996).
9. Ebert, H., Popescu, V. and Ahlers, D., Phys. Rev. B. **60**, 7156 (1999).
10. Della Longa, S., *et al.*, Eur. Biophys. J. **27**, 541 (1998).
11. Dufek, P., Schwarz, K. and Blaha, P., Phys. Rev. B. **48**, 12672 (1993).
12. Taguchi, M. and Kotani, A., Tech. rep. of ISSN Ser. A. №3082 (1996).
13. Slater, J. C., J. Chem. Phys. **43**, 228 (1965).
14. Contienza, A., Picozzi, S., Geng, W. T. and Freeman A. J., Phys. Rev. B. **64**, 085204 (2001).
15. Della Longa, S., Soldatov, A. V., Pompa, M. and Bianconi, A., Comp. Mater. Sci. **4**, 199 (1995).
16. Hopster, H., J. Electr. Spec. Relat. Phenom. **98**, 17 (1999).
17. Hong, J. and Mills, D. L., Phys. Rev. B. **62**, 5589 (2000).
18. Muller, J. E., Jepsen, O. and Wilkins, J. W., Solid State Commun. **42**, 365 (1982).

Physica Scripta. Vol. T115, 611–613, 2005

Direct Observation of the Fe Substitution Effect on the MCD Spectra of the Dysprosium Iron Garnet Family

A. Agui[a], M. Mizumaki[b], T. Matsushita[b], N. Kawamura[b] and T. Nakatani[a]

[a]Japan Atomic Energy Research Institute, SPring-8, 1-1-1 Kouto Mikazuki-cho, Sayo-gun 678-5148, Japan
[b]Japan Synchrotron Radiation Research Institute, SPring-8, 1-1-1 Kouto Mikazuki-cho, Sayo-gun 678-5198, Japan

Received June 26, 2003; accepted in revised form November 4, 2003

PACS numbers: 78.70.Dm, 75.50.Ww, 72.80.Ga, 71.20.Eh

Abstract

Soft X-ray magnetic circular dichroism (MCD) and absorption spectra (XAS) were measured at the Fe $L_{2,3}$-edges and the Dy $M_{4,5}$-edges for a family of dysprosium iron garnets. The Fe ions sit in either O_h symmetry sites or T_d symmetry sites in $Dy_3Fe_5O_{12}$. Only Fe ions in the O_h sites are substituted with In ions in $Dy_3Fe_{4.25}In_{0.75}O_{12}$ and only Fe ions in the T_d sites are substituted with Ga ions in $Dy_3Fe_{4.25}Ga_{0.75}O_{12}$. The XAS spectrum profiles of the three-dysprosium iron garnets are very similar. The MCD signals of both the Fe $L_{2,3}$-edges and the Dy $M_{4,5}$-edges of $Dy_3Fe_{4.25}Ga_{0.75}O_{12}$ are similar to that of $Dy_3Fe_5O_{12}$, but $Dy_3Fe_{4.25}In_{0.75}O_{12}$ is remarkably different. The results directly show that the spin moment of Fe in the T_d sites play a major role in determining the total magnetization of $Dy_3Fe_5O_{12}$.

1. Introduction

$R_3Fe_5O_{12}$(Rare Earth Iron Garnet: RIG) is a typical ferri-magnet composed of a rare earth element (R) and iron. The iron and rare earth valences are both positive trivalent, while oxygen is negative divalent. RIG has a crystal structure called "garnet structure". In RIG, an Fe^{3+} ion is surrounded by O^{2-} ions and has either O_h symmetry or T_d symmetry [1, 2]. It was found that the Fe^{3+} ions sit in tetrahedral and octahedral sites and the R^{3+} ions sit in dodecahedral sites. The ratio of the T_d sites to the O_h sites is 3 : 2.

The magnetic properties of RIG can be interpreted based on a collinear Neel model. In the formula $R{\downarrow}_3Fe{\downarrow}_2\ Fe{\uparrow}_3O_{12}$ (up (down) arrow represents the majority (minority) spin), the magnetic moments of the T_d and O_h sites of the iron sublattices are anti-parallel yielding a net moment of one Fe^{3+} ion, which corresponds to $5\mu_B$ directed towards the tetrahedral sites. The magnetization of the rare earth sublattice is anti-parallel to the net iron.

Dysprosium iron garnet ($Dy_3Fe_5O_{12}$: DyIG) belongs to the RIG family. $Dy_3Fe_{4.25}In_{0.75}O_{12}$ is made by site-selectively replacing 37.5% of the Fe ions in the O_h symmetry sites in $Dy_3Fe_5O_{12}$ with In ions. On the other hand, site-selectively replacing 25% of Fe ions in the T_d sites in $Dy_3Fe_5O_{12}$ with Ga ions makes $Dy_3Fe_{4.25}Ga_{0.75}O_{12}$. The ordinal magnetic property measurements macroscopically represent the overall magnetic property of the system. On the other hand, the core level absorption spectroscopy measures the electronic and spin states in a conduction band for selected elements and orbitals. For example, when an Fe 2p electron is excited, the soft X-ray absorption spectrum (Fe $L_{2,3}$ XAS) reflects the 3d electron state following the dipole moment selection rule. (When a Dy 4f electron is excited, the spectrum is a Dy $M_{4,5}$ XAS.) The difference between the right- and left-handed circular polarized X-ray excited XAS is called circular dichroism. The spectrum reflects the spin state in a magnetic material. Kawamura *et al*. reported Dy $L_{2,3}$ magnetic circular dichroism (MCD) spectra [3].

The MCD signal direction is dependent on the ion, Dy ions or Fe ions either in T_d symmetry and O_h symmetry, that has the majority spin moment. In this study, the substitution effect of Fe on MCD spectra in $Dy_3Fe_5O_{12}$, $Dy_3Fe_{4.25}Ga_{0.75}O_{12}$ and $Dy_3Fe_{4.25}In_{0.75}O_{12}$ at the Fe $L_{2,3}$-edges and the Dy $M_{4,5}$-edges was directly measured to investigate the magnetic properties of Fe in the T_d and the O_h symmetry site.

2. Experiments

MCD and XAS spectra at the Fe $L_{2,3}$ and the Dy $M_{4,5}$-edges for the DyIG compounds were measured using synchrotron radiation at the soft X-ray beamline BL23SU at SPring-8, Japan [4, 5, 6]. An APPLE2-type undulator was the light source and a varied space plane grating type monochromator was installed at the beamline. The obtained energy-resolution $E/\Delta E$ was higher than 7000 around the Fe $L_{2,3}$-edges [7]. The XAS spectra were recorded in total electron yield (TY) mode. It is empirically known that the TY spectrum well represents the photo absorption spectrum in the core-level excitation region. The sample current (I_1) is normalized by the incident photon intensity (monitored current (I_0)) and the normalized absorption intensity (I) is determined by $I = I_1/I_0$. The XAS intensities using parallel and anti-parallel photon helicity to the magnetic field are denoted by I_+ and I_-, respectively. The XAS of isotropic polarization is defined as $I_{iso} = (I_+ + I_-)/2$, and the MCD intensity is denoted as $I_{MCD} = (I_+ - I_-)$. The most unique performance of the APPLE2-type undulator is that shifting the phase of the magnet rows of the undulator switches the photon helicity in a few seconds from right-handed to left-handed circularly polarized X-rays. During MCD measurements, the undulator and the monochromator were synchronously controlled, *i.e*., the photon helicity was switched at each photon energy point. This method is advantageous for avoiding the energy disparity between the two different circularly polarized X-rays, caused by the repeatability of a monochromator [8].

$Eu_3Fe_5O_{12}$, $Dy_3Fe_{4.25}Ga_{0.75}O_{12}$ and $Dy_3Fe_{4.25}In_{0.75}O_{12}$ powder samples were uniformly pasted on a sample holder using carbon tape. A static magnetic field of 0.4 Tesla was applied to the sample at room temperature (about 300 K). The magnetic moment of DyIG was saturated at $H = 0.4$ Tesla. The incident angle of the photon beam was set parallel to the magnetic field.

3. Results and Discussion

Figure 1 shows the XAS spectra of $Dy_3Fe_5O_{12}$, $Dy_3Fe_{4.25}Ga_{0.75}O_{12}$ and $Dy_3Fe_{4.25}In_{0.75}O_{12}$ at the Fe $L_{2,3}$-edges. Spectra of I_{iso}, I_+, and I_- are shown as solid, dashed, and dotted curves, respectively. The inset shows the detailed spectra at the L_3-edge.

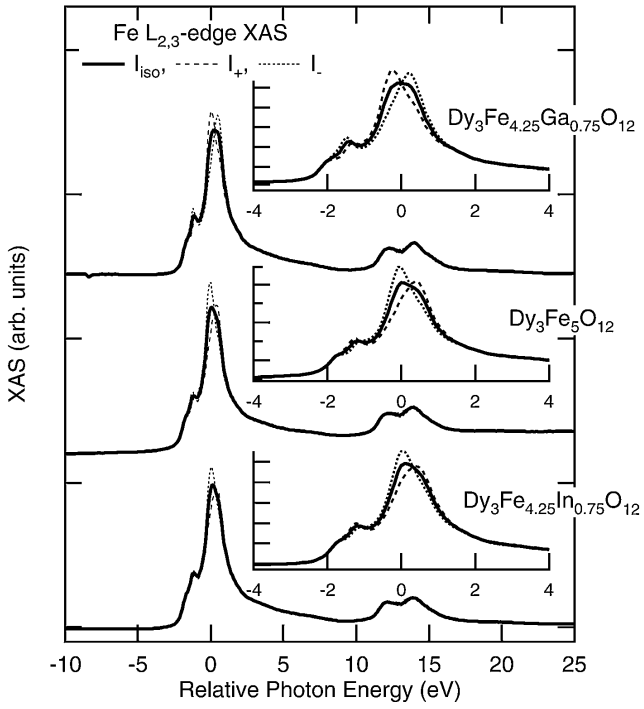

Fig. 1. Fe $L_{2,3}$ XAS of $Dy_3Fe_5O_{12}$, $Dy_3Fe_{4.25}Ga_{0.75}O_{12}$ and $Dy_3Fe_{4.25}In_{0.75}O_{12}$ in a magnetic field of 0.4 Tesla at room temperature in a relative energy scale. The L_3 peak is set to 0 eV and the edge jump is set to 1. Spectra of I_{iso}, I_+ and I_- are shown in as solid, dashed, and dotted curves, respectively. The inset shows detailed spectra at the L_3-edge.

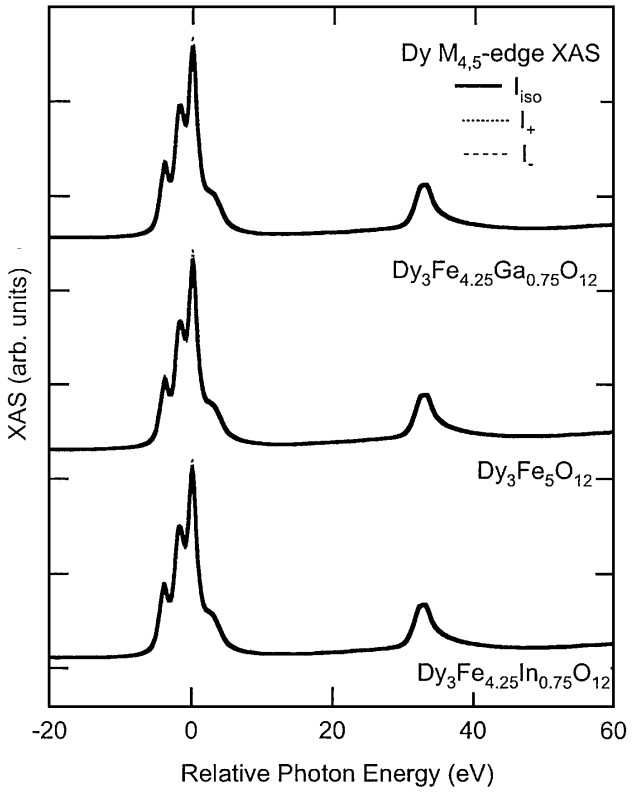

Fig. 2. Dy $M_{4,5}$ XAS of $Dy_3Fe_5O_{12}$, $Dy_3Fe_{4.25}Ga_{0.75}O_{12}$ and $Dy_3Fe_{4.25}In_{0.75}O_{12}$ in a magnetic field of 0.4 Tesla at room temperature in a relative energy scale. The M_5 peak is set to 0 eV and the edge jump is set to 1. Spectra of I_{iso}, I_+ and I_- are shown in as solid, dashed, and dotted curves, respectively.

Here the photon energy of the Fe L_3 peak of I_{iso} is nominally set to 0 eV and the edge jump of I_{iso} is normalized to be 1 for each specimen. The white lines of L_3 and L_2 are clearly observed. There is a small shoulder at the lower energy side of the L_3 peak, which originates from orbital mixing of Fe 3d and O 2p that is found in Fe oxides such as a ferrite and an ilmenite [9, 10]. Figure 2 shows the XAS spectra of $Dy_3Fe_5O_{12}$, $Dy3Fe_{4.25}Ga_{0.75}O_{12}$ and $Dy_3Fe_{4.25}In_{0.75}O_{12}$ at the Dy $M_{4,5}$-edge. The spectra of I_{iso}, I_+, and I_- are shown as solid, dashed and dotted curves, respectively. Here the photon energy of the Dy M_5 peak is nominally set to 0 eV and the edge jump of I_{iso} is normalized to 1 for each specimen. The white lines of M_5 and M_4 are clearly observed. The fine structure of the M_5 peak is due to the multiplet effect.

All three samples have similar Fe $L_{2,3}$ XAS and the Dy $M_{4,5}$ XAS line shapes. These results imply that the displacement of the Fe ion does not substantially change the Fe 3d and the Dy 4f electronic states. I_+ and I_- of the Fe $L_{2,3}$-edges show differences between samples.

Figures 3 and 4 show MCD spectra (I_{MCD}: solid curves) of $Dy_3Fe_5O_{12}$, $Dy_3Fe_{4.25}Ga_{0.75}O_{12}$ and $Dy_3Fe_{4.25}In_{0.75}O_{12}$ at the Fe $L_{2,3}$-edges, and at the Dy $M_{4,5}$-edges, respectively. The photon energy of the Fe L_3 peak and the Dy M_4 peak are nominally set to 0 eV and the zero level of the Fe $L_{2,3}$ MCD and the Dy $M_{4,5}$ MCD spectra are shifted by 0.3 and 0.15, respectively.

The MCD signal signs are the same for the Fe $L_{2,3}$-edges and the Dy $M_{4,5}$-edges of $Dy_3Fe_5O_{12}$ and $Dy_3Fe_{4.25}In_{0.75}O_{12}$, but $Dy_3Fe_{4.25}In_{0.75}O_{12}$ has the opposite sign. The Dy $M_{4,5}$-edges MCD signal is in opposite direction of the Fe $L_{2,3}$-edges. For all the samples, the net Fe spin moment is opposite the net Dy spin moment. The Fe ions in O_h sites decrease when the Fe ions are replaced with In ions, but the MCD signal of $Dy_3Fe_{4.25}In_{0.75}O_{12}$ and $Dy_3Fe_5O_{12}$ are the same. The MCD signal of $Dy_3Fe_{4.25}Ga_{0.75}O_{12}$ and $Dy_3Fe_5O_{12}$ are in opposite

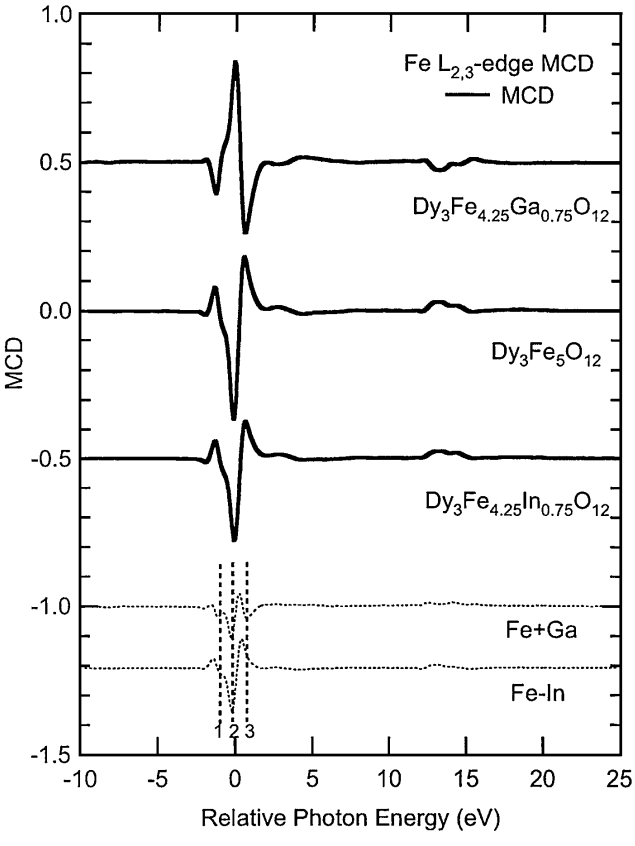

Fig. 3. Fe $L_{2,3}$ MCD of $Dy_3Fe_5O_{12}$, $Dy_3Fe_{4.25}Ga_{0.75}O_{12}$ and $Dy_3Fe_{4.25}In_{0.75}O_{12}$ in a magnetic field of 0.4 Tesla at room temperature in a relative energy scale.

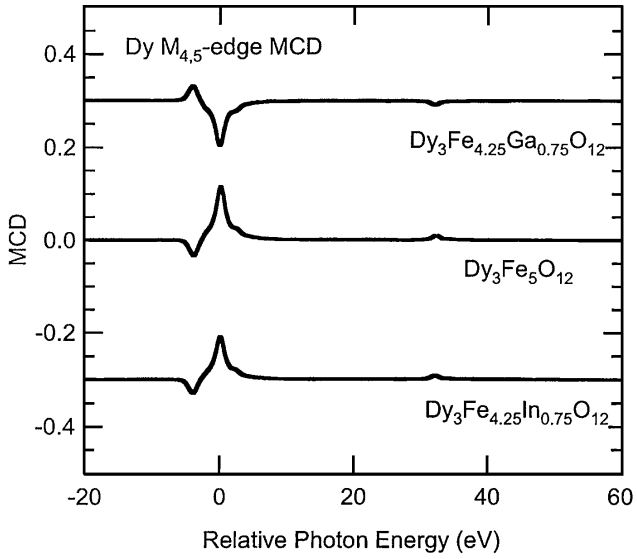

Fig. 4. Dy $M_{4,5}$ MCD of $Dy_3Fe_5O_{12}$, $Dy_3Fe_{4.25}Ga_{0.75}O_{12}$ and $Dy_3Fe_{4.25}In_{0.75}O_{12}$ in a magnetic field of 0.4 Tesla at room temperature in a relative energy scale.

directions and the majority spin moment in $Dy_3Fe_5O_{12}$ is changed from that in $Dy_3Fe_5O_{12}$. Here, the magnetic moments of Fe and Dy are defined as M_{Fe} (about $5\mu_B$) and M_{Dy}. The number of Fe ions in O_h and T_d sites is defined as N_{Oh} and N_{Td}, respectively. The macroscopic magnetic moment is written as $(N_{Td}\text{-}N_{Oh})\ M_{Fe}\text{-}3M_{Dy}$. $Dy_3Fe_5O_{12}$ has a positive moment, by $Dy_3Fe_{4.25}Ga_{0.75}O_{12}$ has a negative moment. The magnetic moment of the Dy ions itself is large, but they disordered at room temperature and the total magnetic moment of Dy is estimated to be $0.42\mu_B < M_{Dy} < 1.67\mu_B$.

In Fig. 3, the dotted curves show the difference spectra of $Dy_3Fe_{4.25}In_{0.75}O_{12}$ from $Dy_3Fe_5O_{12}$ MCD spectra and to make the number of Fe ions the same, the intensity of $Dy_3Fe_{4.25}In_{0.75}O_{12}$ (I_{Fe-In}) is reduced by a factor 0.85. For the $Dy_3Fe_{4.25}Ga_{0.75}O_{12}$ spectra (I_{Fe+Ga}), the difference specra is achieved by adding the spectra of $Dy_3Fe_{4.25}Ga_{0.75}O_{12}$ and $Dy_3Fe_5O_{12}$. Again, the intensity of $Dy_3Fe_{4.25}In_{0.75}O_{12}$ is reduced to 0.85 to scale the number of Fe ions in an unit. In the I_{Fe+Ga} spectrum, the signal from the O_h sites is enhanced and in the I_{Fe-In} spectrum, the T_d signal is enhanced. The line shapes of the XAS and MCD spectra are strongly dependent on the electronic states or the electronic configuration of the atom. In order to provide a better qualitative description of the spectral feature, the line shapes of the XAS and MCD spectra were further investigated by calculating by the ionic model [11]. Figure 5 shows the corresponding calculated Fe $L_{2,3}$ MCD spectrum (I_{MCD}) for Fe^{3+} (d^5) in the T_d symmetry

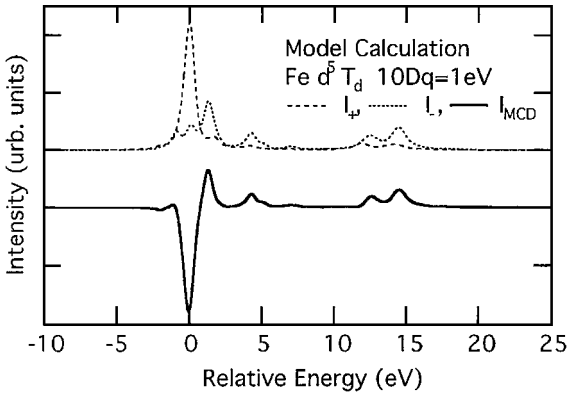

Fig. 5. Calculated XAS and MCD spectra using the ionic model, at the Fe $L_{2,3}$-edge for Fe^{3+} ion in a T_d symmetry crystal field for $10Dq = 1$ eV.

crystal field (I_+ and I_-) and where the crystal field energy from the ligand state to the 3d level $10Dq = 1$ eV. The claculated spectrum reproduces the line shape of the I_{Fe-In} spectrum. Comparing Fig. 5 and Fig. 3, it is assumed that in Fig. 3 the O_h site structures are observed at 1 and 3 and the T_d site structure is observed at 2.

In summary, the substitution effect of Fe on the total magnetic moment direction of $Dy_3Fe_5O_{12}$ was directly investigated. The XAS and MCD spectra were measured at the Fe L and the Dy M-edge of $Dy_3Fe_5O_{12}$, $Dy_3Fe_{4.25}Ga_{0.75}O_{12}$ and $Dy_3Fe_{4.25}In_{0.75}O_{12}$ with element selectivity. The Fe ions in the T_d symmetry sites play an important role in determining the direction of the total magnetization.

Acknowledgments

The authors are grateful to the JASRI staff including Drs. H. Tanaka, and M. Takao for their help for the helicity switching of the undulator. BL23SU is supported by the JAERI soft X-ray staff, including Dr. A. Yoshigoe.

References

1. Wolfarth, E. P., Ferro Magn. Mater. **2**, 1 (1980).
2. Geller, S. and Gilleo, M. A., J. Phys. Chem. Solids **3**, 30 (1957).
3. Kawamura, N., Suzuki, M., Maruyama, H. and Ishikawa, T., J. Synchrotron Rad. **8**, 425 (2001).
4. Yokoya, A. *et al*., J. Synchrotron Rad. **5**, 10 (1998).
5. Nakatani, T., Saitoh, Y., Teraoka, Y., Okane, T. and Yokoya, A., J. Synchrotron Rad. **5**, 536 (1998).
6. Yoshigoe, A. *et al*., J. Synchrotron Rad. **8**, 502 (2001).
7. Saitoh, Y., Teraoka, Y., Agui, A., Yoshigoe, A. and Yokoya, A., Nucl. Instr. Meth. Phys. Res. **A474**, 253 (2001).
8. Agui, A. *et al*., Rev. Sci. Inst. **72**, 3191 (2001).
9. Agui, A. *et al*., Surface Sci. Lett. **9**, 843 (2002).
10. Agui, A. *et al*., J. Synchrotron Rad. **8**, 907 (2001).
11. Deb, A., Mizumaki, M., Muro, T., Sakurai, Y. and Tsurkan, V., Phys. Rev. B **68**, 14427 (2003).

Physica Scripta. Vol. T115, 614–615, 2005

Fluorescence EXAFS Study on Local Structures around Mn and Fe Atoms Doped in ZnO

H. Ofuchi[1*], Z. W. Jin[2], T. Fukumura[3], M. Kawasaki[3], Y. Matsumoto[4], T. Hasegawa[4], H. Fujioka[5], M. Oshima[5] and H. Koinuma[6]

[1]Nagoya University, Furo-Cho, Chikusa-Ku, Nagoya 464-8603, Japan
[2]National Institute for Materials Science, 1-2-1 Sengen, Tsukuba, Ibaraki 305-0047, Japan
[3]Institute for Materials Research, Tohoku University, Sendai 980-8577, Japan
[4]Frontier Collaborative Research Center, Tokyo Institute of Technology, Yokohama 226-8503, Japan
[5]University of Tokyo, 7-3-1 Hongo, Bunkyo-Ku, Tokyo 113-8656, Japan
[6]Materials and Structures Laboratory, Tokyo Institute of Technology, Yokohama 226-8503, Japan

Received June 26, 2003; accepted in revised form November 4, 2003

PACS numbers: 78.70.Dm, 78.66.Hf, 68.55.Jk,75.50.Pp

Abstract

In this work, geometric structures for *TM*-doped (*TM* = Mn and Fe) ZnO film grown by combinatorial laser molecular beam epitaxy (CLMBE) were investigated using fluorescence EXAFS measurement. The EXAFS analysis has revealed that the majority of *TM* ions heavily doped in ZnO ([Mn] ∼ 20% and [Fe] ∼ 1%) substituted the Zn atoms in ZnO lattice.

1. Introduction

Diluted magnetic semiconductors have attracted much interest as materials with both optical and magnetic properties. Recently, ZnO-based diluted magnetic semiconductor (DMS) with high Curie temperature above room temperature has been predicted by mean field theory [1]. High *Tc* is beneficial in utilizing ZnO-based DMS for novel magneto-electronic devices.

In the present work, Fe- and Mn-doped ZnO thin films grown by combinatorial laser molecular beam epitaxy (CLMBE) were investigated by fluorescence extended X-ray absorption fine structure (EXAFS) measurements using synchrotron radiation. We have successfully fabricated 3d transition-metal-doped (TM-doped) ZnO films by CLMBE [2, 3]. However, the geometric structures for the heavily TM-doped ZnO has not been clear yet. The fluorescence EXAFS measurement is a powerful technique for investigating local structures around a specific element and is suitable for evaluating the geometric and electronic structures around TM ions in the present study [4, 5].

2. Experimental

Mn- and Fe-doped ZnO films were grown on sapphire (0001) substrate by CLMBE. Details of the film growth procedure are described in ref. [2]. Concentration of Fe and Mn ions were determined by electron probe microanalysis (EPMA).

EXAFS measurements were performed at the beam line BL12C at the Photon Factory in Tsukuba using the SR from the 2.5 GeV storage ring with a Si(111) double crystal monochromator and a bent cylindrical mirror [6]. The EXAFS spectra were measured in the fluorescence-detection mode at a temperature of 70 K. The intensity of incident X-ray beam was monitored by a nitrogen-filled ionization chamber, while the fluorescence X-ray signals were detected by 19 elements Ge solid-state detector (SSD).

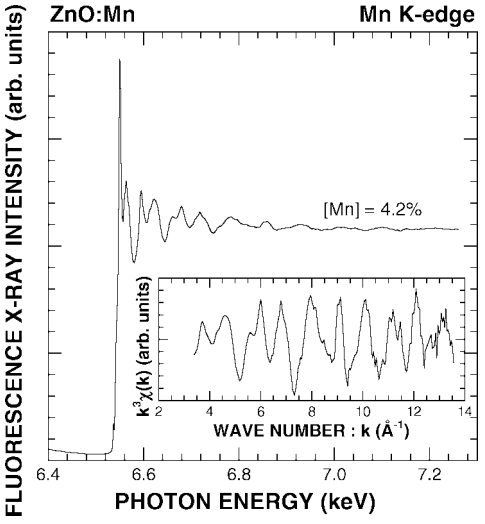

Fig. 1. Fluorescence X-ray intensity of Mn-doped ZnO film (Mn concentration : [Mn] = 4.2%) at Mn K-edge. Inset shows Mn-K-edge EXAFS oscillation function spectrum $k^3\chi(k)$.

3. Results and discussion

Figure 1 and 2 display the fluorescence X-ray intensities for Mn- and Fe-doped ZnO thin films at Mn and Fe K-edge, respectively. EXAFS oscillations were clearly observed for each sample. Figures 3 and 4 represent the Fourier transformed Mn and Fe ions K-edge EXAFS spectra $k^3\chi(k)$ for Mn- and Fe-doped ZnO thin films and the theoretical EXAFS spectra $k^3\chi(k)$ for substitutional Mn and Fe ions on the Zn site in the ZnO lattice are compared. Theoretical EXAFS spectra were generated by FEFF6 program [7]. Despite the high level of *TM* ions doped in the ZnO, several peaks are clearly observed at a longer radial distance, indicating that the local structures around the *TM* ions are well-ordered with respect to short-range ordering. In addition, the experimental spectra correspond well to the theoretical ones. Thus, it is expected that *TM* ions in heavily doped ZnO substitute the Zn-site in the ZnO lattice.

In order to analyze the details of the measured spectra, curve-fitting for the EXAFS spectra was carried out with theoretically calculated spectra using FEFF6 [7]. For all the samples, species of neighboring atoms and coordination numbers show good agreement with those of the ZnO film. Although we also carried out curve-fitting for models of various TM oxides, reliable parameters for such models were not obtained. We therefore

*e-mail: ofuchi@numse.nagoya-u.ac.jp

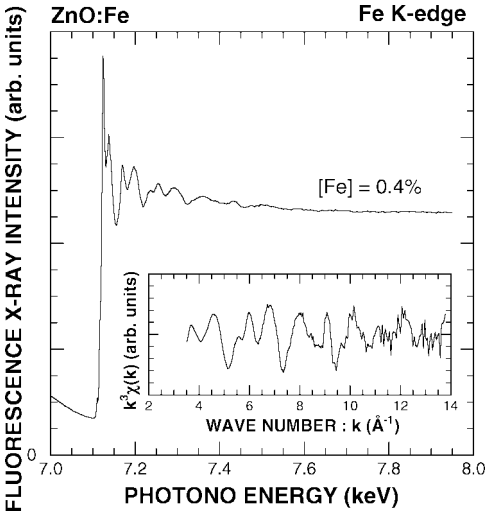

Fig. 2. Fluorescence X-ray intensity of Fe-doped ZnO film (Fe concentration: [Fe] = 0.4%) at Fe K-edge. Inset shows Fe-K-edge EXAFS oscillation function spectrum $k^3\chi(k)$.

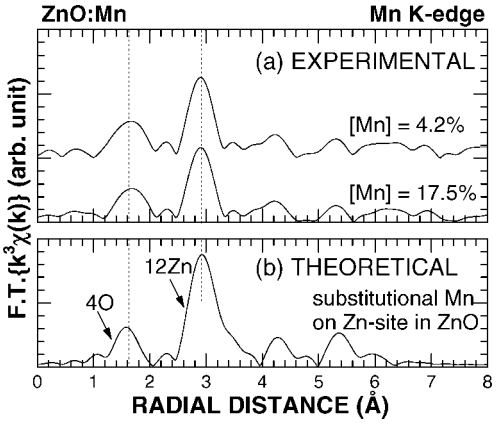

Fig. 3. Fourier transform of Mn K-edge EXAFS oscillation function spectra $k^3\chi(k)$ of (a) Mn-doped ZnO film and (b) theoretical EXAFS spectrum for the substitutional Mn ion on the Zn site in the ZnO lattice. The Fourier transformation was performed in the k range of 4.0–13.0 Å^{-1}. The Debye-Waller factor was assumed as 0.05 Å for bond length below 3.5 Å and 0.075 Å for bond length above 3.5 Å. The theoretical EXAFS spectra were generated by FEFF6 [7].

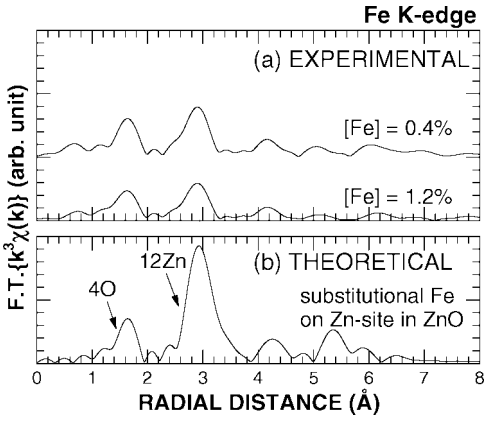

Fig. 4. Fourier transform of Fe K-edge EXAFS oscillation function spectra $k^3\chi(k)$ of (a) Fe-doped ZnO film and (b) theoretical EXAFS spectrum for the substitutional Fe ion on the Zn-site in the ZnO lattice. The Fourier transformation was performed in the k range of 4.0–13.0 Å^{-1}. The Debye-Waller factor was assumed as 0.05 Å for bond length below 3.5 Å and 0.075 Å for bond length above 3.5 Å. The theoretical EXAFS spectra were generated by FEFF6 [7].

conclude that the majority of *TM* ions (above 80% of the total *TM* ion amounts) in all the samples substitute the Zn-site in ZnO, which indicates the formation of a ZnO-based DMS layer. For the Mn-doped ZnO thin films, Mn-O bond lengths were determined to be 2.01–2.02 Å, and for the Fe-doped ZnO thin films, the Mn-O bond length is 1.97–1.98 Å.

Acknowledgment

This work was supported by Proposal Based Program of NEDO (99S12010) and JSPS Research for the Future Program in the area of Atomic-Scale Surface and Interface Dynamics. XAFS studies were performed as part of a project (Project No. 2001G078) accepted by the Photon Factory Program Advisory Committee, the Ministry of Education, Science, Sports and Culture, Japan.

References

1. Dietl, T. *et al.*, Science **287**, 1019 (2000).
2. Jin, Z. W. *et al.*, J. Cryst. Growth. **214**/**215**, 55 (2000).
3. Fukumura, T. *et al.*, Appl. Phys. Lett. **75**, 3366 (1999).
4. Jaklevic, J. *et al.*, Solid State Commun. **23**, 679 (1977).
5. Ofuchi, H. *et al.*, Appl. Surf. Sci. **117**/**118**, 781 (1997).
6. Nomura, M. *et al.*, KEK Report **95-15** (1996).
7. Zabinsky, S. I. *et al.*, Phys. Rev. B **52**, 2995 (1995).

Physica Scripta. Vol. T115, 616–619, 2005

Temperature Dependence of X-Ray Magnetic Circular Dichroism in Rare Earth Iron Garnets (Rare Earth = Gd, Dy and Sm)

Hayato Miyagawa*, Naomi Kawamura and Motohiro Suzuki

SPring-8/JASRI, 1-1-1 Kouto Mikazuki-cho, Hyogo 679-5198, Japan

Received June 26, 2003; accepted November 11, 2003

PACS numbers: 75.50.Gg, 78.70.Dm, 78.90.+t

Abstract

We studied the feasibility of magnetic circular dichroism (MCD) in the hard X-ray region for determining 4f magnetic moments by measuring the temperature dependence of MCD spectra at rare earth L_2-edge in systems of rare earth iron garnets (R-IG) for R = Gd, Dy and Sm. Two components arising from the magnetization of the Gd and Fe sublattices, which were combined into the MCD spectrum of Gd-IG, were separatively deduced. For Dy- and Sm-IG, we successfully obtained the temperature dependence of the MCD component that comes from only R sublattice magnetization under the assumption that the MCD spectra of the series of R-IG contain the same contribution of the iron sublattice.

1. Introduction

Since the first theoretical prediction of magnetic circular dichroism (MCD) in X-ray absorption spectra (XAS) by B. T. Thole in 1985 [1], a lot of MCD measurements have been preformed for various ferromagnetic and ferrimagnetic materials [2–5] using synchrotron radiation sources, which produce high brilliant X-rays with good tunability of the circular polarization. The physical origin of MCD can be understood qualitatively by the excitation of partially spin-polarized photoelectrons from an unpolarized initial core state to spin-split empty final states [6–8]. The interest in the use of MCD is well understood by its ability to provide highly selective information: (1) the absorption process is atomic selective and (2) owing to the selection rules, it is possible in principle to determine independently the magnetic contribution of all open shells in an atom. These advantages of MCD are encountered in not only macroscopic magnetization measurements such as VSM or SQUID but also microscopic measurements using polarized neutrons or electrons.

The MCD in the region of hard X-rays has feasibility in some experimental aspects; a little surface sensibility which gives information of bulk magnetism, and good transmission through substances which can collect good statistical accuracy, and no necessity of high vacuum chambers. The first stage of the MCD measurements using hard X-ray was brought in the late 1980s by G. Schütz *et al.* [3]. Subsequently, extensive studies at the K-edge of transition metals ($1s \rightarrow 4p$) or at the L-edge of rare earths ($2p \rightarrow 5d$) has been reported [4–7] with experimental data and theoretical calculations. Unfortunately, however, the explanation of the MCD spectra at these edges were not so straightforward because we do not directly observe the shells that mainly contribute to the magnetization. On the contrary we measure at L-edges of transition metal ($1s \rightarrow 3d$) or M-edges of rare earths ($3d \rightarrow 4f$) in the soft X-ray region. Especially, the MCD spectra of rare earth L-edges in 4f-3d magnetic materials, in which more than two magnetic elements exist, have complicated structures. This complexity is interpreted as a consequence of the following effects. (a) There is an unignorable effect of E2 (quadrupole) transition, which contaminates the spectra produced by E1 (dipole) transition. (b) The polarization of 5d electrons is due to both the 4f-5d *inter*-atomic interaction and (c) the 5d-3d *intra*-atomic interaction with the adjacent transition metal. Quantitative and systematic calculations of MCD in the series $R_2Fe_{14}B$ were performed by Fukui *et al.* including the above effects [8]. K. Asakura and H. Ogasawara have proceeded the calculation with the hybridization effect of R 5d and Fe 3d in $R_2Fe_{14}B$ [9] and $CeFe_2$ [10]. They pointed out the importance of the additional effects to the 4f-5d interaction caused by the contraction of 5d orbital in the real space. This effect of '5d-contraction' may reverse the sign of the MCD signal in some cases [11, 12]. The spectra reproduced from their calculations were in good agreement with experimental results. The significance of the effects described above for other materials is, however, still unclear for a lack of empirical inspections.

In this paper we report the temperature dependence of MCD spectra at the R L_2-edge of rare-earth iron garnets (R-IG, $R_3Fe_5O_{12}$; R = Gd, Dy, and Sm). In R-IG, there exist two ferric sites; one contains three Fe^{3+} in tetrahedral symmetry and the other contains two Fe^{3+} in octahedral symmetry per formula unit. Magnetic moments of iron at these two sites align antiparallel by super-exchange through oxygen atoms. The R^{3+} ions are antiferromagnetically coupled to the net moment of the iron ions in the case of heavy rare earths and ferromagnetically in the case of light rare earths, but this coupling is much weaker than that among iron ions. The sublattice magnetization of R-IG was studied by means of the subtracting method [13, 14], in which the magnetization of the R sublattice was estimated from the subtraction of the magnetization of Lu-IG from that of R-IG under the assumption that the Fe sublattice has almost the same value of the magnetic moment in the series of R-IG. Lu has a filled 4f shell which has no magnetic moment and the whole magnetic moment of Lu-IG originates in the Fe sublattice. The magnetic moment of Gd and Dy at low temperature were estimated as 21.0 μ_B and 21.9 μ_B in this subtracting method [14], and the temperature dependences of these magnetic moments were well explained by the molecular field theory [15]. A reliable result for Sm sublattice magnetization was, however, not obtained because the magnetic moment of Sm is too small to be determined correctly by the subtracting method [16].

The purpose of this study is to investigate the temperature dependence of MCD spectra in R-IG, and to evaluate the validity of the *element specific* measurement of MCD in the hard X-ray region comparing with the R sublattice magnetic moment estimated from macro magnetization by the subtracting method.

*e-mail: miyagawa@eng.kagawa-u.ac.jp

Present address: AMS, Facul. Eng. Kagawa Univ. 2217-20, Hayashi-cho, Takamatsu, 761-0396, Japan

2. Experiments

MCD measurements were made on SPring-8 BL39XU. A detail description of the optical configuration at this beamline was reported in [17]. The energy resolution of the incident X-rays was about 1.5 eV at the absorption edges measured in this study. The degree of circular polarization, about 90%, was switched between right and left at 30 Hz by using a diamond phase retarder [18]. The powdered samples, which were put uniformly on a scotch tape, were mounted in a magnetic field of 2 T. The magnetic field was generated by a super-conducting magnet for measurements at temperature below 30 K, and by an electromagnet at higher temperature. The intensities of the incident and of the transmitted X-rays were converted to voltage, V_0 and V, using ion chambers are in the front and back of the sample position. The photo absorption, $\mu(\omega)$, is measured as the time-average of V/V_0, and MCD, $\Delta\mu(\omega)$, is measured as the output of a lock-in signal which averages V/V_0 with modulation of the circular polarization of X-rays. In this scheme, we define

$$\text{XAS:} \quad \mu(\omega) = \frac{\mu_+(\omega) + \mu_-(\omega)}{2}, \tag{1}$$

$$\text{MCD:} \quad \Delta\mu(\omega) = \mu_+(\omega) - \mu_-(\omega). \tag{2}$$

Here $+$, $-$ means right and left circular polarization of the incident X-ray when the external magnetic field is parallel to the X-ray direction. The spectra of $\mu(\omega)$ and $\Delta\mu(\omega)$ were measured in the energy range of 40 eV around the absorption edges at temperatures between 2 K and 300 K with a step of about 10 K. The MCD spectra in this study have been normalized by the 'edge jump' of XAS spectra, which was estimated as the difference of $\mu(\omega)$ at ± 20 eV from the absorption edges. The MCD peak due to the effect for the quadrupole transition has been undetected in the L_2-edge of these compounds, so no considerations or procedures for its effect were needed. The MCD spectrum of Gd-IG and Dy-IG flips its sign below and above the compensation temperature, T_{comp}, so we have adapted the sign of MCD below this temperature and have reversed MCD spectra that were measured above T_{comp}.

3. Results and discussion

The Gd L_2-edge MCD spectra of Gd-IG measured at 2, 50, 100, 200 and 300 K are shown in Fig. 1. The temperature dependence of these spectra shows continual changes of both the shape and the magnitude of MCD. The reduction of the intensities of MCD with the rise of temperature evokes analogous with the depression of the magnetization of Gd sublattice. The change of the spectral shape, however, means that the MCD value at each energy point has different temperature dependence. In order to understand the behavior of these spectra, we have taken the proposition as follows. MCD at Gd L_2-edge contains two components. (1) First, $\Delta\mu_{Gd}(\omega)$, which is the direct spectrum reflecting the magnetic states of Gd sites, that is, the magnetization of the 4f shell. This component varies corresponding to the 4f-5d *intra-atomic* interaction. (2) Next, $\Delta\mu_{Fe}(\omega)$, which comes from the magnetization of the iron sublattice through 5d-3d *inter-atomic* super-exchange interaction. The observed MCD spectrum is a linear combination of these components.

$$\Delta\mu_{exp.} = \Delta\mu_{Gd}(\omega) \cdot m_{Gd}(T) + \Delta\mu_{Fe}(\omega) \cdot m_{Fe}(T), \tag{3}$$

here, $m_M(T)$ means the magnetization of the M atom sublattice. Both terms in the right side of the equation change only their size according to the magnetization of each sublattice, which depends

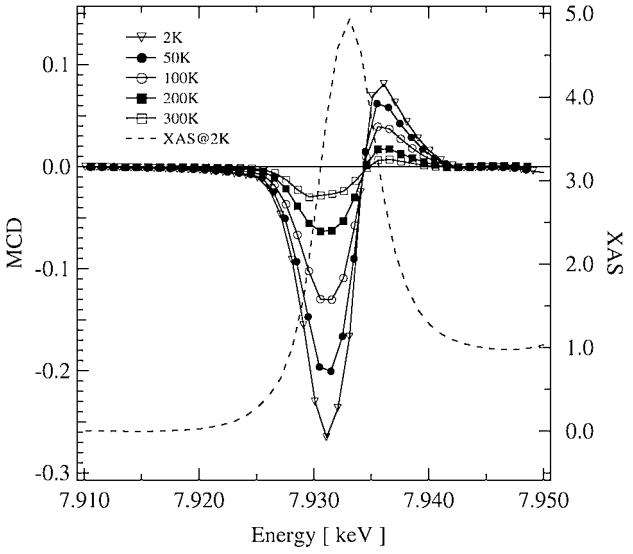

Fig. 1. MCD spectra of Gd L_2-edge in Gd-IG measured at 2 K, 50 K, 100 K, 200 K and 300 K. All spectra have been normalized by the edge jump of XAS.

to temperature, and do not change shape. The shape of $\Delta\mu_{exp.}$ is determined as the ratio between $m_{Gd}(T)$ and $m_{Fe}(T)$ at each temperature.

In order to extract $\Delta\mu_{Gd}(\omega)$ and $\Delta\mu_{Fe}(\omega)$ independently from obtained MCD spectra, we set them as parameters and preformed a fitting at each energy. For $m_{Gd}(T)$ and $m_{Fe}(T)$, the sublattice magnetic moments for Gd and Fe were used, which were estimated by means of the subtracting method of the macroscopic magnetization measurements of Gd-IG and Lu-IG.

In Fig. 2, the obtained two components are plotted. These fitting results can reproduce the experimental MCD spectra, $\Delta\mu_{exp.}$, at each temperature with good precision. The Fe components in Fig. 2 are very similar in shape to the MCD spectrum of Lu L_2-edge in Lu-IG, measured by N. Kawamura [19]. The 4f shell in Lu has no hole and no magnetic moment; therefore 5d spin polarization reflects only the magnetization of the Fe sublattice. This means that the $\Delta\mu_{exp.}$ of Lu-IG contains only the second term

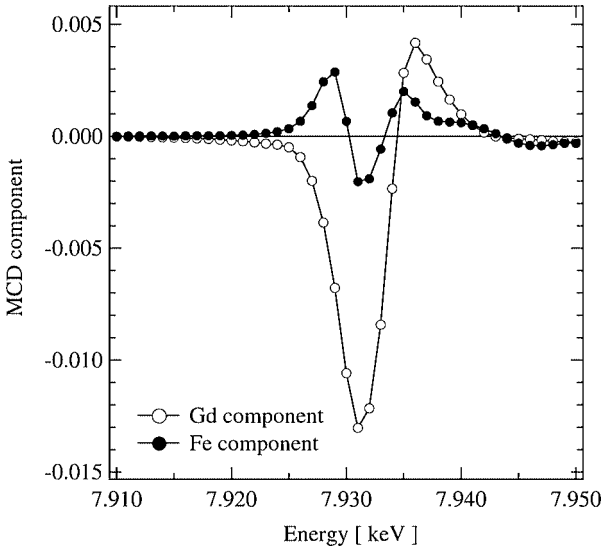

Fig. 2. The components of Gd (open) and Fe (filled) that contribute to MCD of Gd-IG L_2-edge. Both components are plotted as the size as the each sublattice has the magnetic moment 1 μ_B.

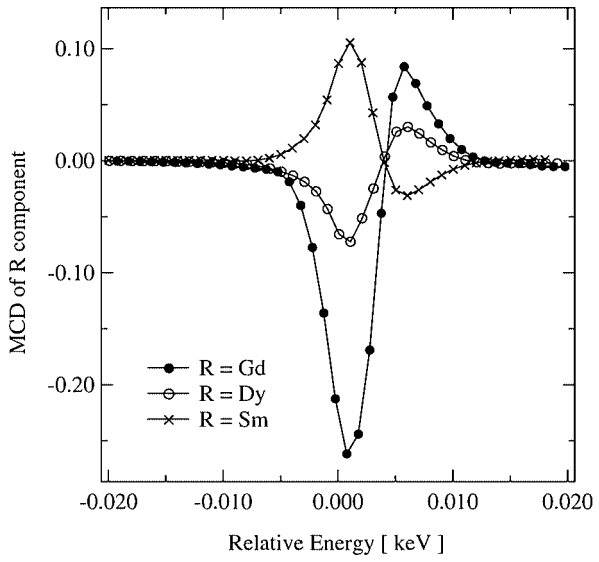

Fig. 3. The rare earth components in the MCD spectra of Gd-IG (filled), Dy-IG (open), and Sm-IG (cross) at 2 K. The magnetic moments of all R sublattices are parallel to the applied field in these samples.

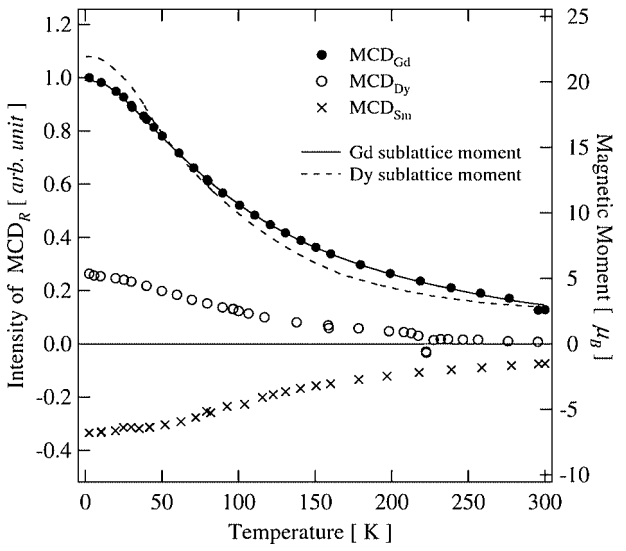

Fig. 4. The temperature dependence of the MCD components of Gd (filled), Dy (open), and Sm (cross), normalized by the value of Gd at 2 K. The magnetic moments of sublattice R estimated by means of the subtracting method are also plotted with the right axis as a solid line and a dashed line for Gd-IG and Dy-IG, respectively.

in Eq. (3). The similarity of the MCD spectrum in Lu-IG and the Fe component in Gd-IG supports the validity of the fitting analysis in this study and also demonstrates the possibility that $\Delta\mu_{Fe}(\omega)$ in Fig. 2 is appropriable to other R-IGs.

The measured MCD spectra of L_2-edge in Dy-IG and Sm-IG have the same trend of the temperature dependence as that of Gd-IG; the value for those decreases with increasing temperature, changing the shape of spectra. From these spectra, we have extracted the rare earth component, $\Delta\mu_R(\omega) \cdot m_R(T)$, which corresponds to the first term in Eq. (3), on the assumption that the component from the magnetization of the iron sublattice is also included in MCD spectra of Dy-IG and Sm-IG. In this procedure, we needed to shift the energy of $\Delta\mu_{Fe}(\omega)$ to the absorption edge of Dy or Sm. These energy-shifts were estimated as the differences of the first inflection points of XAS and were tuned finely to create the experimental spectra most closely.

The obtained spectra of Dy and Sm components at 2 K are shown in Fig. 3. In Fig. 3 are also plotted Gd component deduced from the fitting analysis in Gd-IG. With increasing temperature, these components change sizes according to the magnetization of the R sublattice, $m_R(T)$, being invariable in shape. In Fig. 4, the thermal variation of these R components in Dy-IG, Sm-IG and Gd-IG are shown where these are normalized so that of Gd equals 1 at $T = 2$ K. The magnetization-temperature curves of R sublattice estimated by means of the subtraction method of macro measurements are also in the same figure as a solid line for Gd and a dashed line for Dy. In Fig. 4, the right axis and the left axis are scaled approximately as the Gd sublattice magnetization should superpose to the MCD component of the Gd sublattice.

For Gd-IG and Dy-IG, the rare earth MCD components in Fig. 3 are similar in shape; they show a prominent minimum at $E = 1$ eV followed by a maximum located at about $E = 6$ eV, and the ratio between these peaks is about 1 : 3. The spectrum of the Sm component has also the same similarity with reversed sign. It is expected that the shape of these components may apply to the L_2-edge MCD spectra of other rare earth iron garnets.

The temperature dependence of the Dy component in Fig. 4 is consistent with the sublattice magnetization estimated from macroscopic measurements. Its value is, however, too small. The result of the MCD component of Sm, which is larger than that of Dy in absolute value and has a minus sign through the measured temperature, shows the discrepancy that the magnetic moment of Sm estimated from macroscopic measurement is expected to be small compared to that of Dy, and to have a plus sign versus the applied field. From this result, it is inferred that the L_2-edge of MCD at the rare earth reflects a value that is proportional to the total magnetization of the R sublattice, but it is not easy to compare among the samples that have different R elements. The reason seems to be the degree of 4f-5d interaction or an effect of the contraction of the 5d shell. Further investigations of MCD in the hard X-ray region for various 4f-3d compounds are needed. It is noteworthy that the temperature dependence of the Sm magnetic moment in Sm-IG, which is difficult to estimate by means of macroscopic measurement for its small 4f magnetic moment, is clearly obtained in this study as shown in Fig. 4.

4. Conclusion

We presented a verification of the *element specific* magnetic measurement of rare earth L_2-edge MCD spectra in R-IG comparing to the magnetization of the R sublattice, which is deduced from macroscopic magnetization measurements of R-IG and Lu-IG by means of the subtraction method. All measured MCD of Gd-IG, Dy-IG, and Sm-IG contain the same component from Fe sublattice magnetization, and the contribution of the R sublattice has been simply obtained by subtracting the Fe component from the measured spectra. The R component of MCD spectra in R-IG indicates a thermal variation similar to the estimated magnetization of the R sublattice from the macroscopic measurements, but the sign and the magnitude of MCD signals includes an uncertainty, which is expected to be related to the 4f-5d interaction with the effect of the spatial contraction of the rare earth 5d shell. The temperature dependence of the Sm sublattice magnetization in Sm-IG has been obtained without contamination from the Fe sublattice.

Acknowledgment

The authors are grateful to Dr. A. Koizumi and Mr. T. Nagao for their help in the magnetization measurements at Faculty of Science, Himeji Institute of Technology.

References

1. Thole, B. T., Phys. Rev. B **55**, 2086 (1985).
2. Laan, V. D., Phys. Rev. B **34**, 6529 (1986).
3. Schütz, G., Phys. Rev. Lett. **58**, 737 (1987).
4. Ebert, H., Solid State Commun. **69**, 485 (1989).
5. Fischer, P., Solid State Commun. **70**, 777 (1990).
6. Imada, S. and Jo, T., J. Phys. Soc. Jpn. **59**, 3358 (1990).
7. Ebert, H., J. Appl. Phys. **63**, 3055 (1988).
8. Fukui, K., Phys. Rev. B **64**, 104405 (2001).
9. Asakura, K., J. Phys. Soc. Jpn. **71**, 2771 (2002).
10. Ogasawara, H., J. Phys. Chem. Solids **63**, 1485 (2002).
11. Matsuyama, H., J. Phys. Soc. Jpn. **66**, 337 (1997).
12. Veenendaal, M. V., Phys. Rev. Lett. **78**, 1162 (1997).
13. Wolf, W. P., Phys. Rev. **124**, 449 (1961).
14. Geller, S., Phys. Rev. **137**, A1034 (1965).
15. Litster, J. D., J. Appl. Phys. **37**, 1320 (1966).
16. Geller, S., Phys. Rev. **131**, 1080 (1963).
17. Maruyama, H., J. Synchrotron Rad. **6**, 1133 (1999).
18. Suzuki, M., Jpn. J. Appl. Phys. **37**, L1488 (1998).
19. Kawamura, N., *private communication*.

Physica Scripta. Vol. T115, 620–622, 2005

X-ray Absorption Fine-Structure Determination of Interfacial Polarization in $SrTiO_3$ Thin Films Grown on Si(001)

J. C. Woicik[1,*], F. S. Aguirre-Tostada[2], A. Herrera-Gomez[2], R. Droopad[3], Z. Yu[3], D. Schlom[4], E. Karapetrova[5], P. Zschack[5] and P. Pianetta[6]

[1]National Institute of Standards and Technology, Gaithersburg, Maryland 20899, USA
[2]CINVESTAV-Quertero, Apartado Postal 1-798, Queretaro 76001, Mexico
[3]Physical Sciences Research Labs, Motorola, 2100 East Elliot Road, Tempe, Arizona 85284, USA
[4]Materials Science and Engineering, Pennsylvania State University, University Park, PA 16802, USA
[5]University of Illinois, APS-UNICAT, Argonne National Laboratory, Argonne, IL 60439, USA
[6]Stanford Synchrotron Radiation Laboratory, Stanford, CA 94309, USA

Received June 26, 2003; accepted in revised form December 8, 2003

Abstract

Polarization-dependent X-ray absorption fine structure together with X-ray diffraction have been used to study the local structure in $SrTiO_3$ thin films grown on Si(001). Our data indicate that an interfacial polarization of the $SrTiO_3$ layer by the Si substrate results in a tetragonal distortion of the $SrTiO_3$ unit cell.

At room temperature, $SrTiO_3$ (STO) exemplifies the ideal, cubic perovskite structure [1]. It is formed by placing Sr^{+2} atoms at the corners of a cube, a Ti^{+4} atom at the cube center, and O^{-2} atoms at the face centers, in perfect octahedral coordination with the Ti^{+4} atom, as shown in Figure 1a. STO is often referred to as an "incipient" ferroelectric because it exhibits quantum paraelectric behavior below 4 °K in which the ferroelectric phase transition is suppressed by the non-vanishing zero-point motion of the ions [2]. It also possesses a competing, antiferroelectric distortion at 105 °K that involves the rotation of the oxygen octahedra coupled with a small, <0.01%, tetragonal c/a distortion [3]. Additionally, it is well known that strain induces ferroelectricity in STO at liquid-helium temperatures [4], and a recent theoretical study has suggested that the "mismatch" strain imposed on a thin STO layer when grown on a substrate with a dissimilar lattice constant can lead to ferroelectricity at room temperature [5].

To examine the effects of epitaxial strain on thin STO films, films with thicknesses of 40 Å, 60 Å, 80 Å, and 200 Å were grown on Si(001) substrates using molecular-beam epitaxy. Details of the sample preparation have been given elsewhere [6]. Near and extended X-ray absorption fine-structure data were collected at the Ti K edge. All data were recorded at room temperature. The data were recorded by monitoring the Ti K fluorescence using a single-element SiLi detector. The absorption data were collected with the polarization vector of the synchrotron radiation aligned both parallel and perpendicular to the Si(001) surface. In addition, the X-ray absorption spectrum from finely ground STO powder was recorded in transmission; it was used as the phase and amplitude standard to determine the Ti–O bond lengths within the films.

In order to characterize the strain state of the STO films, high-resolution X-ray diffraction measurements were performed. Figure 2 shows the results of the diffraction experiment for both the parallel (in-plane) and perpendicular (out-of-plane) lattice constants of the STO films. Notably is the observation that the lattice constant in the in-plane direction; i.e., the lattice constant parallel to the STO/Si interface, is significantly larger than the bulk STO lattice constant. This effect is due to the different thermal expansion coefficients of STO and Si. It has been observed for GaAs on Si hetero-epitaxy and results from the relaxation of the film at growth temperature [7]. Even more surprising, however, is that the out-of-plane lattice constant of the thinner films becomes larger than the corresponding in-plane lattice constant with a c/a distortion approaching ∼0.33. This distortion is close to the c/a distortion observed for the tetragonal, ferroelectric phases of $BaTiO_3$ (∼1%) [8].

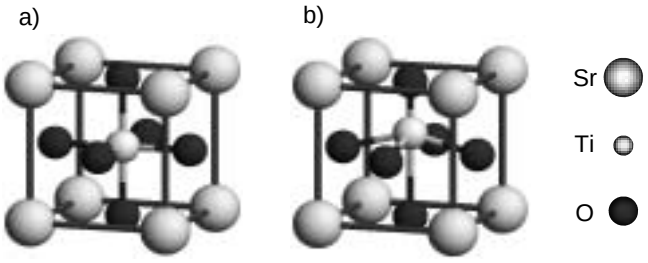

Fig. 1. STO unit cell. a) Cubic. b) Tetragonal.

Figure 3 shows the Ti K X-ray absorption near-edge spectra from the thin films studied. The main edge occurring near 4980 eV is associated with dipole transitions from the Ti 1s to the Ti 4p conduction-band levels. The first two features occurring below the edge are associated with dipole-forbidden transitions from the Ti 1s to the crystal-field split Ti 3d states that have a splitting of ∼2.1 eV, as we have indicated in the figure [9]. Our data show a

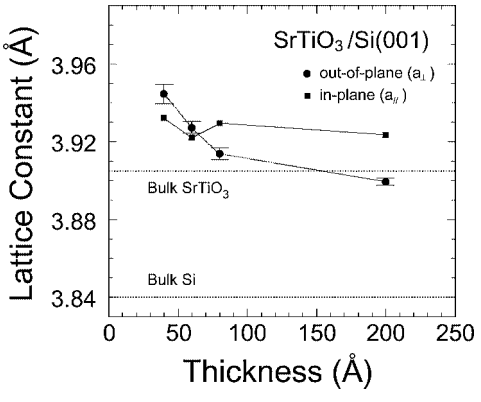

Fig. 2. Perpendicular lattice constants of the 40 Å, 60 Å, 80 Å, and 200 Å STO films as determined by X-ray diffraction. The dotted line shows the cubic lattice constant of STO.

*E-mail: woicik@bnl.gov

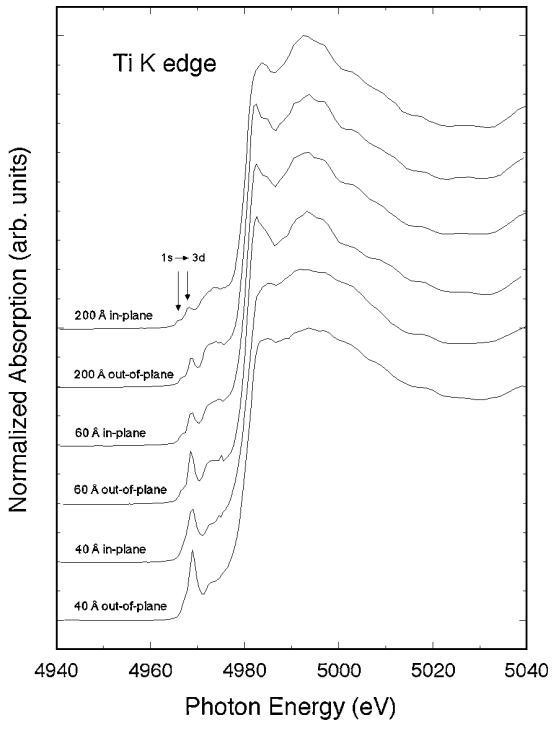

Fig. 3. Ti K pre-edge spectra from the thin STO films recorded with the polarization vector in-plane and out-of-plane. The data have been normalized to equal edge jump.

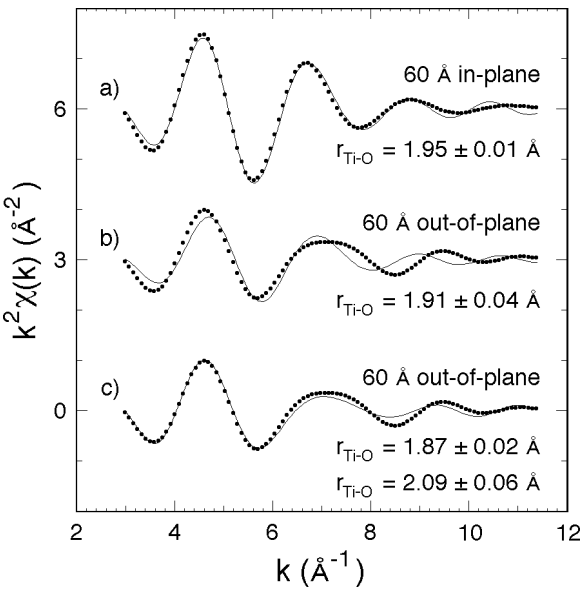

Fig. 4. Fits to the Fourier-filtered, first-shell contributions to the k^2-weighted fine structure from the 60 Å film using the phase and amplitude functions obtained from the STO powder. The dots are the data points of the backtransform, and the solid lines are the fits. a) In-plane data using one Ti-O distance. b) Out-of-plane data using one Ti-O distance. c) Out-of-plane data using two Ti-O distances.

large increase in the intensity of the second but not the first Ti K pre-edge feature with increasing strain. In crystals that possess an inversion center, the d states that are even with respect to inversion are symmetry forbidden from mixing with the p states that are uneven. In crystals that lack an inversion center, this symmetry restriction is lifted, and the p states are allowed to mix with the d states making 1s transitions to the second of the two pre-edge features dipole allowed [9, 10]. The intensity of the second pre-edge feature therefore has been correlated with the loss of inversion symmetry that accompanies ferroelectricity in the perovskite structure [11]. Consequently, these data suggest that the presence of the STO/Si interface results in the polarization of the STO layer. As evidenced by the data from the thicker films, this polarization decreases away from the interface, and it is likely caused by the ionic rearrangement of the first STO layer.

To quantify the extent of this distortion, we now examine our extended X-ray absorption fine-structure data. The Ti-O radial shell was modeled with the phase and amplitude standards obtained from the STO powder. The results of the modeling for the 60 Å film are shown in Figure 4. The top panel (a) shows the fit to the data from the film recorded with the polarization vector in-plane, and the middle panel (b) shows the fit to the data recorded with the polarization vector out-of-plane, both assuming a single Ti-O bond length. Clearly, a beat occurs in the out-of-plane data near $k = 7\,\text{Å}^{-1}$ that is not modeled by a single Ti-O distance. Our analysis using two Ti-O distances (c) finds the Ti-O bond length to be split by 0.22 ± 0.06 Å along the Si[001] surface-normal direction. (We note that due to the limited data range attainable from such thin films, only the coordination numbers and bond lengths were fit.)

It is interesting to compare our determination of the splitting of the Ti-O distance to that determined by neutron scattering for the tetragonal, ferroelectric phase of $BaTiO_3$ [12]. This distortion results in three distinct Ti-O bond lengths, one within the contracted a plane, $r_{\text{Ti-O}} = 2.00$ Å, and two along the elongated c axis, $r_{\text{Ti-O}} = 1.83$ Å and $r_{\text{Ti-O}} = 2.20$ Å. These bond lengths compare with our determination of the in-plane, $r_{\text{Ti-O}} = 1.95 \pm 0.01$ Å, and out-of-plane, $r_{\text{Ti-O}} = 1.87 \pm 0.02$ Å and $r_{\text{Ti-O}} = 2.09 \pm 0.06$ Å, Ti-O bond lengths within the strained STO film.

Our model of the strained STO tetragonal unit cell is shown in Figure 1b. The model possesses three distinct Ti-O bond lengths (one within the contracted a plane and two along the expanded c axis) concomitant with the loss of inversion symmetry around the central Ti ion. The intrinsic relationship between strain, polarization, and chemical hybridization had been observed experimentally.

Acknowledgments

Research carried out (in whole or in part) at the National Synchrotron Light Source, Brookhaven National Laboratory, which is supported by the U.S. Department of Energy, Division of Materials Sciences and Division of Chemical Sciences, under Contract No. DE-AC02-98CH10886. The UNICAT facility at the Advanced Photon Source (APS) is supported by the Univ. of Illinois at Urbana-Champaign, Materials Research Laboratory (U.S. DOE, the State of Illinois-IBHE-HECA, and the NSF), the Oak Ridge National Laboratory (U.S. DOE under contract with UT-Battelle LLC), the National Institute of Standards and Technology (U.S. Department of Commerce) and UOP LLC. The APS is supported by the U.S. DOE, Basic Energy Sciences, Office of Science under contract No. W-31-109-ENG-38. Additional support was provided by the Consejo Nacional de Ciencia y Tecnologia of Mexico (CONACyT Project No. 34721-E, 33901-U) and the Stanford Linear Accelerator Center (CRADA-Project No. 158).

References

1. Kittel, C., "Introduction to Solid State Physics", (Wiley, New York, 1976), Chap. 13.
2. Muller, K. A. and Burkard, H., Phys. Rev. B **19**, 3593 (1979).
3. Shirane, G. and Yamada, Y., Phys. Rev. **177**, 858 (1969).
4. Uwe, H. and Sakudo, T., Phys. Rev. B **13**, 271 (1976).

5. Pertsev, N. A., Tagantsev, A. K. and Setter, N., Phys. Rev. B **61**, R825 (2000).
6. Yu, Z. *et al*., J. Vac. Sci. Technol. B **18**, 1653 (2000).
7. Lucus, N., Zabel, H., Morkoc, H. and Unlu, H., Appl. Phys. Lett. **52**, 2117 (1988).
8. Mitsui, T. *et al*., "Ferro- and Antiferroelectric Substances", Landolt-Bornstein, Group III, Vol. 3, (edited by Hellwege, K.-H. and Hellwege, A. M.), (Springer-Verlag, Berlin, 1969).
9. Cotton, F. A., "Chemical Applications of Group Theory", (Wiley, New York, 1971), Chap. 8.
10. Wong, J., Lytle, F. W., Messmer, R. P. and Maylotte, D. H., Phys. Rev. B **30**, 5596 (1984).
11. Ravel, B., Stern, E. A., Vedrinskii, R. I. and Kraizman, V., Ferroelectrics **206–207**, 407 (1998).
12. Kwei, G. H., Lawson, A. C., Billinge, S. J. L. and Cheong, S.-W., J. Phys. Chem. **97**, 2368 (1993).

Physica Scripta. Vol. T115, 623–625, 2005

XAS Characterization of Growth Parameter Effects for Pulsed Laser Deposited $Co_xTi_{1-x}O_{2-\delta}$ Films

A. Lussier*, J. Dvorak[1], Y. U. Idzerda[1], S. R. Shinde[2], S. B. Ogale[2] and T. Venkatesan[2]

[1]Department of Physics, Montana State University, Bozeman, MT 59717, USA
[2]Center for Superconductivity Research, University of Maryland, College Park, MD 20742-4111, USA

Received June 26, 2003; accepted in revised form November 4, 2003

PACS number: 75.50.Pp

Abstract

Films of cobalt-doped titanium dioxide ($Co_xTi_{1-x}O_{2-\delta}$) can be stabilized in the thermodynamically unfavorable anatase phase if they are grown on appropriate substrates. We performed X-ray Absorption Spectroscopy (XAS) measurements at the oxygen, titanium, and cobalt edges of PLD grown samples. Our data shows the success of this substrate-induced stabilization of the anatase phase occurs only at elevated temperatures (~700 °C or more) and elevated oxygen partial pressures (~1×10^{-5} Torr or more). The effects of post annealing in vacuum are also considered.

1. Introduction

Magnetic semiconductors have recently received considerable attention because of their potential applications in combining conventional semiconductor technology and spin transport electronics. Spin polarized current injection in semiconductors is an obstacle of particular concern that may be overcome by the development of a suitable ferromagnetic semiconductor. When injecting spin polarized electrons from ferromagnetic metals into traditional semiconductors, scattering can occur because of band structure mismatch [1]. Ferromagnetic semiconductors, if successfully synthesized, could solve this problem.

Cobalt doped anatase TiO_2 has been shown to have a hysteretic signature at and above room temperature [2–4]. However, it is thermodynamically unfavorable [5] and will, at elevated temperatures, revert to the more stable rutile structure [6]. For most spin transport electronics applications, it is essential that these materials be grown as thin films. As has been well demonstrated in other systems, it is possible to stabilize the anatase phase by growing it on an appropriate substrate. Two substrates have been identified by the scientific community as good candidates to stabilize the anatase phase: $SrTiO_3(001)$ and $LaAlO_3(001)$ [5, 7, 8]. The lattice match between the cubic $SrTiO_3$ ($a = 3.905$ Å) and the tetragonal anatase TiO_2 ($a = 3.784$ Å, $c = 9.515$ Å) helps promote the growth of anatase with the c axis perpendicular to the film plane. The rutile structure of TiO_2 is also a tetragonal crystal but with a poor lattice match ($a = 4.585$ Å, $c = 2.953$ Å) [9].

The Co-doped anatase is properly described by $Co_xTi_{1-x}O_{2-\delta}$, where the "δ" represents oxygen vacancies, which must exist to maintain charge neutrality of the sample by compensating for the cobalt (valence 2+) substituted titanium (valence 4+) atoms. It is therefore not surprising that the sample's structure depends strongly on the oxygen partial pressure during growth. Note additionally that oxygen vacancies are necessary for conductivity. According to Chambers *et al*. [1], oxygen vacancies make TiO_2 an n-type semiconductor; it would otherwise be an insulator. They also suggests the ferromagnetic coupling between cobalt atoms is electron mediated and would not be possible without oxygen vacancies in excess of those required for charge neutrality.

2. Experimental

In this study, $Co_xTi_{1-x}O_{2-\delta}$ films ($x = 1\%$ and 7%) were grown on $SrTiO_3$ by pulsed laser deposition (PLD) at various temperatures and partial pressures of oxygen (PO_2). Rutherford backscattering, X-ray diffraction, and vibrating sample magnetometry measurements on some of the samples have been published elsewhere (see Shinde *et al.* [3]). The samples were shown to exhibit ferromagnetism at high temperatures and high temperature treatment was found to dramatically enhance Co incorporation in the matrix. Subsequent XAS results (this study) allowed us to determine the necessary conditions that enable the substrate induced stabilization of the desired anatase structure. We used X-ray Absorption Spectroscopy (XAS) to measure the $L_{2,3}$ edges of cobalt and titanium, and the K edge of oxygen. Measurements were performed at the MSU Materials X-ray Characterization Facility located at beamline U4B of the National Synchrotron Light Source at Brookhaven National Laboratory.

Rutile and anatase TiO_2 have been studied extensively. The XAS intensity profiles of oxygen and titanium, in rutile or anatase, are available for comparison with our spectra. Our spectra are in fair agreement with calculations by F. M. F. de Groot [10, 11] and in very good agreement with XAS spectra measured by Ruus *et al*. [12] and Soriano *et al*. [13]. By comparing our oxygen and titanium XAS spectra with previously measured spectra we can determine whether our Co-doped samples are in the anatase, rutile, or some other TiO_2 structure.

3. Results

To make the structure identification, the revealing feature is a double peak at around 460 eV. For the anatase structure the left peak dominates while for the rutile structure the right peak is the larger of the two. Similarly, the oxygen spectral shapes reveal whether the probed oxygen is in an anatase or rutile structure. Having both oxygen and titanium spectra for comparison allows us to determine our sample's structure with confidence.

3.1. *Substrate growth temperature dependence*

Titanium and oxygen XAS measurements on samples grown at various substrate temperatures (see Fig. 1) reveal a lower limit to the temperature at which films can be stabilized in the

*E-mail: lussier@physics.montana.edu

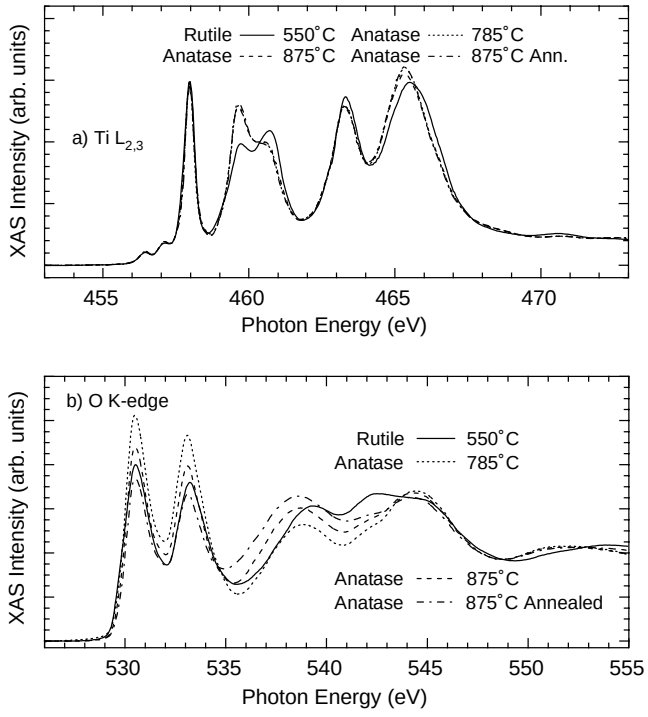

Fig. 1. The titanium $L_{2,3}$ XAS (a) for 7% cobalt doped TiO_2 films grown at various substrate temperatures. Only the lowest growth temperature yielded the rutile structure while all others resulted in anatase. Annealing the sample resulted in no significant difference in the titanium spectra. The oxygen K edge spectra (b) confirm the titanium results. Spectra from all samples have the same general features except for that of the sample grown at 550 °C, which is characteristic of the rutile structure.

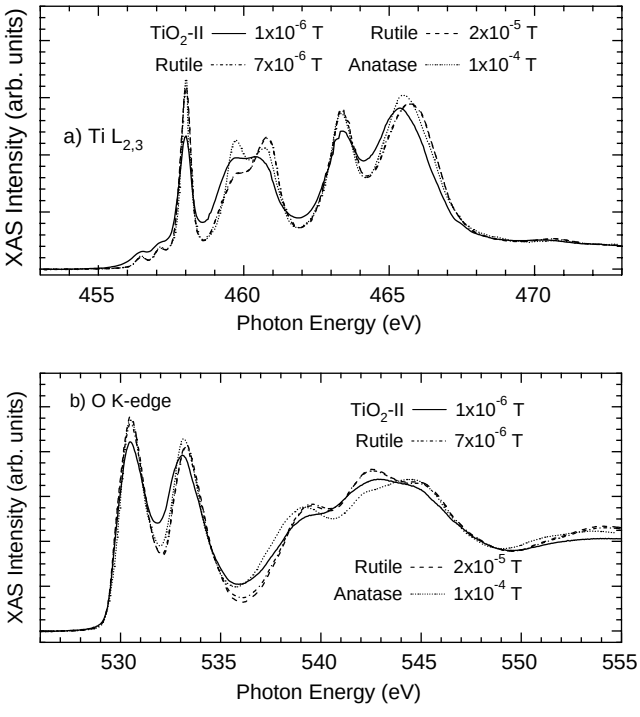

Fig. 2. Titanium spectra (a) for 1% Co samples grown at various PO_2. Oxygen partial pressures above 1×10^{-4} are necessary to ensure growth in the anatase structure. The oxygen spectra (b) for the same samples confirm the conclusions reached from the titanium spectra. For partial pressures below approximately 5×10^{-6} Torr we obtain a spectrum similar to that of the $CoTiO_2$-II structure.

anatase structure for Co-doped TiO_2. For successful substrate induced stabilization, the titanium, cobalt, and oxygen atoms must have a minimum mobility, allowing them to conform to the substrate. At low temperatures the reduced mobility causes the substrate induced anatase structure growth to be lost and the films then revert to the more thermodynamically stable rutile structure.

3.2. *Dependence on oxygen partial pressure during growth*

The oxygen partial pressure (PO_2) dependence was determined for two sets of samples grown at 700 °C with 1% and 7% cobalt doping. There is a minimum PO_2 required to obtain the anatase structure (see Fig. 2). Indeed, below a certain PO_2 the films grow in the rutile structure, or at very low PO_2, they may adopt the so-called TiO_2-II structure. Although the TiO_2-II XAS spectral shape resembles a mixture of anatase and rutile, this structure is an entirely different (orthorhombic) structure [12]. We understand the PO_2 effect by recognizing that oxygen has a lower sticking coefficient on a fully oxidized surface. Titanium then, likely dictates film growth kinetics and anatase growth must occur at an overpressure of oxygen (well above stoichiometric ratios). Oxygen deficiency will again compromise the substrate induced anatase structure stabilization. Interestingly, at the threshold oxygen partial pressure between the formation of anatase and rutile there appears to be a region of mixed phase. This was revealed by the sample grown at the threshold PO_2 of 2×10^{-5} T, for which the surface region is in the rutile structure while the bulk appears to be in the anatase structure (as revealed by XRD measurements by Shinde *et al*. [3]). The titanium spectra and oxygen spectra share the same general features whether samples are grown with 1% or 7% cobalt doping so the 7% spectra were omitted in Fig. 2. The conclusions we draw concerning PO_2 effects on growth are by and large independent of cobalt doping concentration.

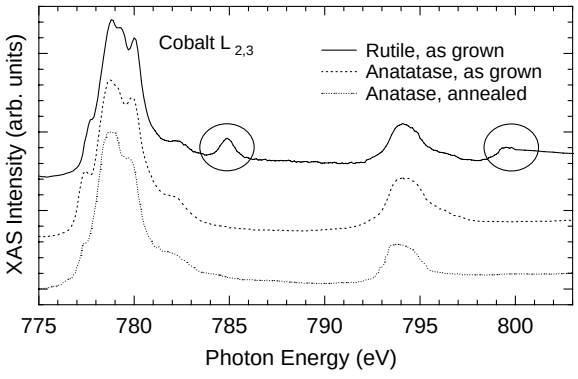

Fig. 3. Cobalt $L_{2,3}$ spectra. Samples that were shown to be in the rutile phase from the oxygen and titanium spectra have additional features that are circled in the figure. The effect of annealing on the cobalt spectra of 7% Co-doped samples is also shown. The sharpening, and partial loss of shoulder features suggests a partial transformation to metallic cobalt.

3.3. *Cobalt Spectra*

The cobalt $L_{2,3}$ XAS spectra shown in Fig. 3 are in agreement with those published by Chambers *et al*. for Co doped anatase TiO_2 [1]. They very closely resemble $CoTiO_3$ spectra, providing evidence that cobalt atoms take on substitutional lattice sites [4]. The spectral shapes display minimal change with varying growth conditions or resultant structure. Nevertheless, we identified an additional sharp feature above both the L_2 and L_3 edges in the Co spectra from samples that were determined to be in the rutile phase (by inspection of the oxygen and titanium scans). The origin of this spectral feature (circled in Fig. 3) is still

unknown but is currently being investigated by band structure calculations.

Also included in Fig. 3 is the cobalt $L_{2,3}$ XAS spectrum for a sample that was post annealed in vacuum at 875 °C to create conductivity enhancing oxygen vacancies and disperse clustered cobalt atoms in the film [3]. Although cobalt clusters in a semiconducting matrix exhibit macroscopic ferromagnetism, an intrinsic ferromagnetic semiconductor is necessary to achieve successful interfacing with traditional semiconductors. Cluster dispersal is therefore desirable. The present work shows that annealing also causes out-diffusion towards the surface. This is substantiated by the sharpening and loss of shoulder features of the L_3 edge of the annealed spectrum in Fig. 3, which both suggest a partial transformation to metallic cobalt. Because XAS is surface sensitive, and previous work shows dispersal in the bulk [3], we conclude that metallic clustering occurs near the surface. Our conclusions apply to our sample which was annealed in vacuum. Other studies show that annealing in an oxygen environment leads to similar results [14] and annealing in argon caused dispersal but no clustering [3].

4. Conclusion

We have determined suitable oxygen partial pressure and substrate temperature conditions that allow for substrate induced stabilization of cobalt doped anatase TiO_2 grown by PLD. The phase diagram shown in Fig. 4 best describes our conclusions. High enough growth temperatures are necessary to induce mobility of deposited atoms and epitaxial conformation to the substrate. A minimum PO_2 ensures enough oxygen is present during growth in spite of oxygen's higher volatility compared to titanium and cobalt. Post-annealing leads to out-diffusion of cobalt and metallic surface clustering. Finally, we have identified a new feature in the cobalt scans of Co-doped rutile TiO_2 that is absent for samples in the anatase structural phase.

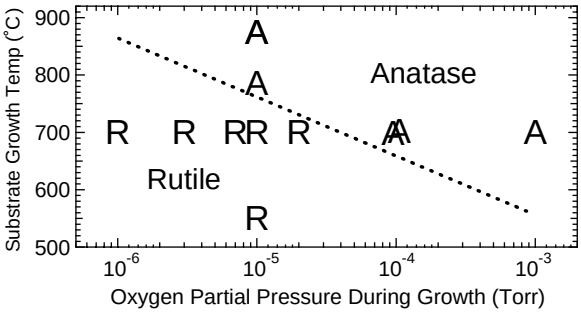

Fig. 4. Phase diagram for partial oxygen pressure and substrate growth temperature requirements that allow for substrate induced anatase structure stabilization on $SrTiO_3$.

Acknowledgments

This work is supported by DOD. The National Synchrotron Light Source is supported by DOE. Some of us (U. of Maryland) would like to acknowledge NSF-MRSEC grant No. DMR-00-80008 and DARPA support under SpinS program (N000140210962).

References

1. Chambers, S. A., Materials Today, pp. 34–39, (April 2002).
2. Matsumoto, Y. *et al*., Science **291**, 854 (2001).
3. Shinde, S. R. *et al*., Phys. Rev. B **67**, 115211 (2003).
4. Chambers, S. A. *et al*., Appl. Phys. Lett. **79**, 3467 (2001).
5. Shim, I.-B., An, S.-Y., Kim, C. S., Choi, S.-Y. and Park, Y. W., J. Appl. Phys. **91**, 7914 (2002).
6. http://mineral.galleries.com/minerals/oxides/anatase/anatase.htm
7. Matsumoto, Y. *et al*., Appl. Surf. Sci. **189**, 344 (2002).
8. Murakami, M. *et al*., Appl. Phys. Lett. **78**, 2664 (2001).
9. http://ruby.colorado.edu/∼smyth/min/tio2.html
10. de Groot, F. M. F., Fuggle, J. C., Thole, B. T. and Sawatzky, G. A., Phys. Rev. B **41**, 928 (1990).
11. de Groot, F. M. F. *et al*., Phys. Rev. B **48**, 2074 (1993).
12. Russ, R. *et al*., Solid State Commun. **104**, 199 (1997).
13. Soriano, L. *et al*., Monatshefte für Chemie **133**, 849 (2002).
14. Kim, J. Y. *et al*., Phys. Rev. Lett. **90**, 017401 (2003).

Physica Scripta. Vol. T115, 626–628, 2005

XMCD Investigation of Spin Disorder in γ-Fe_2O_3 Nanoparticles at the Fe $L_{2,3}$ Edges

S. Brice-Profeta[1], M.-A. Arrio[1], E. Tronc[2], I. Letard[1], Ch. Cartier dit Moulin[4,3] and Ph. Sainctavit[1,3]

[1]ENSEEG/LTPCO1, 1130 rue de la Piscine, 38U02 Saint Routin d Hères, Cedex, France
[2]Laboratoire de Chimie de la Matière Condensée, UMR 7574 CNRS/UPMC, Case 174, F-75252 Paris Cedex
[3]Laboratoire pour l'Utilisation du Rayonnement Électromagnétique, UMR 130 CNRS/CEA/MENRT, BP 34, F-91898 Orsay
[4]Laboratoire de Chimie Inorganique et Matériaux Moléculaires, UMR 7071 CNRS/UPMC, Case 42, F-75252 Paris Cedex

Received June 26, 2003; accepted in revised form November 4, 2003

PACS numbers: 75.25.+z, 71.70.Ch, 78.70.Dm

Abstract

We use XMCD at the $L_{2,3}$ edges of iron to analyze the site-specific magnetic contributions of ions in nanoparticles of maghemite, γ-Fe_2O_3. Maghemite is the oxidized form of magnetite Fe_3O_4. We report results of the study of the magnetic order on tetrahedral and octahedral magnetic sublattices in γ-Fe_2O_3 nanoparticles as a function of the applied magnetic field. Magnetic contributions of Fe^{3+}_{Oh} and Fe^{3+}_{Td} are determined using the Ligand Field Multiplet theory. It is found that when the external field decreases, the magnetic contribution of Fe^{3+} ions on octahedral sites is significantly reduced by comparison to the contribution of Fe^{3+} ions on tetrahedral ones. This shows that a higher degree of canting exits on octahedral sites.

1. Introduction

Size reduction of ferrimagnetic spinel oxides results in modifications of their magnetic properties. For instance, particles of some nanometer are superparamagnetic at room temperature. Furthermore, when there is no appreciable relaxation of the magnetization, the value of the non-relaxing magnetization of ferro- and ferrimagnetic particles is lower than the saturating magnetization of the bulk material. Cationic disorders and atoms located at the surface are responsible for this lowering of the non-relaxing magnetization.

Maghemite is the oxidized form of magnetite. It has the following crystallographic structure: $(Fe^{3+}_{Td})[Fe^{3+}_{5/3}\square_{1/3}]_{Oh}O_4$ ($Fd\bar{3}m$), where $\square$ stands for a vacancy, *Td* for the tetrahedral crystallographic sites of spinel and *Oh* for the octahedral ones. Moments on octahedral and tetrahedral sites are coupled antiferromagnetically. Magnetic disorders in nanoparticles of maghemite have been widely investigated by means of zero- and in-field Mössbauer spectroscopy, magnetization measurements under high and moderate field and AC susceptibility [1]. Many experimental results indicate that spin disorder arises from surface spins, that experience fewer magnetic exchanges with the neighboring atoms. There is also opposite results, assigning the magnetic disorder to the existence of chemical defects in all the volume of a particle [2].

Site-specificity of X-Ray Magnetic Circular Dichroism (XMCD) makes it a powerfull tool to analyze the magnetic contributions of the different atoms in nanoparticles of spinel oxides. This piece of work focuses on the case of small maghemite nanoparticles of average diameter 3 nm. These particles are synthetized using soft chemistry in a two-step process. Aqueous co-precipitation of Fe^{2+} and Fe^{3+} ions at room temperature yields to magnetite particles. Magnetite is oxidized to maghemite under acidic conditions. Details of the synthesis can be found in reference [3]. This synthesis gives well-crystallized monodisperse particles. SQUID magnetometry measurements and Mössbauer spectroscopy have been carried out previously on these particles [4]. We use XMCD at the $L_{2,3}$ edges of iron to study the magnetic order on tetrahedral and octahedral sites in those particles at 4,2 K, as a function of the external magnetic field.

2. Experimental and calculations

Isotropic absorption spectra (XAS) and XMCD signals have been recorded at the Elettra synchrotron source (Trieste, Italy) on the BACH beamline [5]. The experimental end-station is a UHV chamber cooled thanks to a pumped ^{4}He cryostat. A superconducting coil allows to apply a magnetic field up to $+/-$ 7 T on the sample. The sample is a power of γ-Fe_2O_3 nanoparticles. A copper sample holder ensures electrical and thermal conductions. The absorption is measured by total electron yield. Exit and entrance slits are set to 20 µm. The beam is monochromatized using a plane mirror and a spherical grating of groove density 400 lines.mm^{-1}. The resulting resolving power is of $E/\Delta E \simeq 2000$. The photon flux on the sample is larger than 10^{11} photons.s^{-1}. The XMCD signal is extracted from four absorption spectra, recorded reversing both the phase of the high-energy APPLE II undulator and the magnetic field applied along the X-ray propagation direction. The absorption cross-sections for a right-circularly polarized beam and for a magnetic field applied paralled and antiparallel to the propagation vector $\boldsymbol{k}$ are denoted as $\sigma^{\downarrow\uparrow}$ and $\sigma^{\downarrow\downarrow}$. In the same manner, for a left-circularly polarized beam, the corresponding cross-sections for parallel and antiparallel fields are denoted as $\sigma^{\uparrow\uparrow}$ and $\sigma^{\uparrow\downarrow}$. The XMCD signal is obtained following $\sigma_{\mathrm{XMCD}} = \frac{(\sigma^{\downarrow\uparrow}+\sigma^{\uparrow\downarrow})}{2} - \frac{(\sigma^{\downarrow\downarrow}\, n+\, \sigma^{\uparrow\uparrow})}{2}$.

XAS and XMCD signals are simulated by Ligand Field Multiplet calculations. Multiplets calculations are multi-electronic calculations taking into account the ground $2p^63d^5$ configuration and the excited $2p^53d^6$ configuration. The inter-electronic interactions (e.g. the Slater integrals) and the spin-orbit coupling on the 2p (ζ_{2p}) and 3d shell (ζ_{3d}) are calculated using Cowan's atomic Hartree-Fock code [6]. Furthermore, in a solid, Slater's integrals are scaled by a reduction factor κ, to account for the electronic delocalization. The Hamiltonian also contains crystal field and Zeeman terms. Reduced matrix elements are calculated by Th. Thole's code, using Butler's group subduction theory in the ground and the excited configurations [7, 8]. The transitions are calculated in the electric dipole approximation for right- and left-circularly polarized radiations. Transition lines are convoluted by a Lorentzian function ($\Gamma(L_3) = 0.2$ eV and $\Gamma(L_2) = 0.4$ eV), accounting for the core-hole broadening, and by a

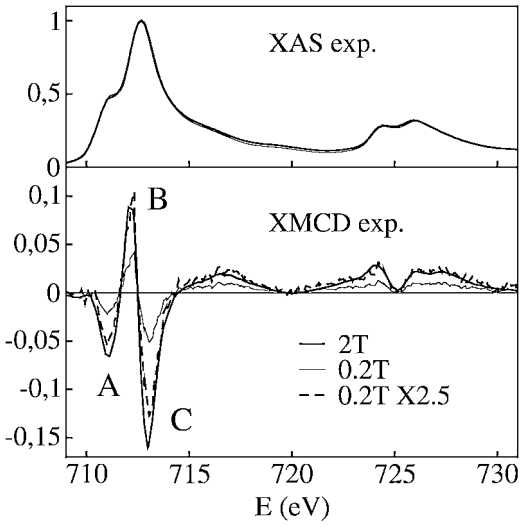

Fig. 1. Experimental isotropic absorption (XAS) and XMCD signals of γ-Fe_2O_3 nanoparticles of average size 3 nm for $H_{ext} = 2$ T and $H_{ext} = 0.2$ T.

Gaussian function ($\sigma = 0.25$ eV), accounting for the experimental broadening.

3. Results and discussion

XAS and XMCD obtained for external fields of 0.2 and 2 T are reported on figure 1. There is a reduction of the dichroic intensity, evaluated as the integral of $|\sigma_{\mathrm{XMCD}}|$. This reduction reflects the dependence of the magnetization of nanoparticles on the external field. At 4,2 K, the ratio of the XMCD intensity between 2 T and 0.2 T is $(M(2\,\mathrm{T})/M(0.2\,\mathrm{T}))_{\mathrm{XMCD}} = 2.5$. This value can be compared to magnetization measurements at the same temperature: $M(2\,\mathrm{T}) = 60\,\mathrm{A.m^2.kg^{-1}}$ and $M(0.2\,\mathrm{T}) = 29\,\mathrm{A.m^2.kg^{-1}}$, yielding $(M(2\mathrm{T})/M(0.2\,\mathrm{T}))_{\mathrm{SQUID}} = 2.0$. In addition to the variation of intensity, the shape of the XMCD signal is also modified when the magnetic field decreases. Figure 1 also presents the XMCD signals recorded at 0.2 T multiplied by 2.5, so as to have equal intensities for the positive B peaks at 0.2 and 2 T. From the rescaled signal, it appears that the intensities of the two negative A and C peaks at 0.2 T are reduced comparatively to their value at 2 T. The A peak is decreased by 12% and the C peak is decreased by 20%. In the following, it is shown using Ligand Field Multiplet calculations that the A and C peaks are due to the magnetic contribution of Fe^{3+}_{Oh} ions and that the B peak is due to the magnetic contribution of Fe^{3+}_{Td} ions. As moments of Fe^{3+}_{Oh} and Fe^{3+}_{Td} ions are coupled antiferromagnetically, their contributions to XMCD are of opposite sign.

The calculations are performed separately for Fe^{3+}_{Oh} and Fe^{3+}_{Td} ions. The XAS and XMCD signal arising from each site are presented on figure 2. The value of crystal field parameters can be inferred from optical spectra for tetrahedral [9] and octahedral [10] Fe^{3+} ions. We used 10 Dq (Fe^{3+}_{Oh}) = 1.5 eV and 10 Dq (Fe^{3+}_{Td}) = 0.7 eV. The reduction of Slater's integrals gives a Racah B parameter of 88 meV, that is close to the experimental Racah B parameter of 72 meV for maghemite [10, 11]. The total magnetic field experienced by Fe^{3+} ions is simulated by the Zeeman hamiltonian with $\mu_B g H = 20$ meV in $\hbar$ units. As the crystallites are oriented at random with respect to the external field, the dichroic spectra are calculated for three crystallographic orientations of the applied field: $H_{ext}//[111]$, $H_{ext}//[110]$ and $H_{ext}//[100]$ (see figure 2). The average over space

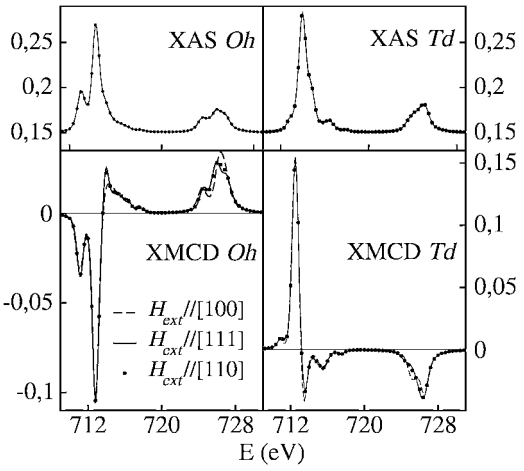

Fig. 2. Calculated XAS and XMCD for $H_{ext}//[111]$, $H_{ext}//[110]$, and $H_{ext}//[100]$.

of the absorption cross-sections is evaluated from these three orientations according to reference [12]:

$$\sigma_{\mathrm{powder}} = \frac{100}{385}\sigma_{H_{ext}//[100]} + \frac{99}{385}\sigma_{H_{ext}//[111]} + \frac{176}{385}\sigma_{H_{ext}//[110]}$$

XMCD signals of Fe^{3+}_{Td} and Fe^{3+}_{Oh} ions are similar for $H_{ext}//[110]$ and $H_{ext}//[111]$, but they are slightly modified for $H_{ext}//[100]$. However, the effect of the orientation of the external magnetic field is weaker for Fe^{3+} ions, that have an almost pure sextet ($^6A_{1g}$) orbital non-degenerated ground state in octahedral symmetry, than for anisotropic Fe^{2+} ions for instance [13].

XAS and XMCD of γ-Fe_2O_3 are then reproduced by linear combinations of the separate octahedral and tetrahedral contributions, as shown on figure 3. The shoulder at 714 eV is too intense by comparison with the experimental signal. It is probably due to covalency effects, that influence noticeably the shape of the XMCD signal between L_3 and L_2 edges. Simulating such effects would require configurations interactions in the calculations. XMCD signals of figure 3 are obtained assuming an ideal ferrimagnetic ordered bulk structure ($Td/Oh = 3/5 = 0.6$) and a reduced magnetic contribution of Fe^{3+}_{Oh} ions ($Td/Oh = 0.65$). The former XMCD signal is rescaled to have equal intensities of the

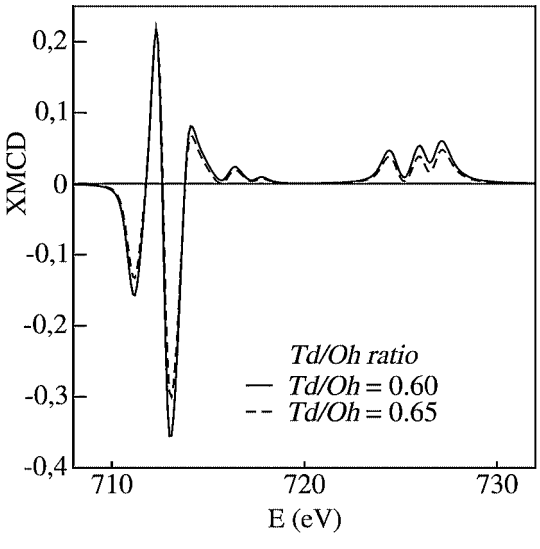

Fig. 3. Calculated XMCD (XAS normalized to 1 at the maximum of the L_3 edge) for two Td/Oh ratios.

B positive peaks in the two calculated signals. For the reduced magnetic contribution of Fe^{3+}_{Oh} ions, the intensity of the A peak is lowered by 15%, and the intensity of the B peak by 16%, which is close to the experimental evolution observed going down from 2 T to 0.2 T. The simulation agrees with an additional decreases of 8% of the magnetization on octahedral sites compared to the global lowering of the magnetization on both of the *Td* and *Oh* sublattices awaited if one considers a same degree of spin disorder for the two sublattices.

4. Conclusion

XMCD at the $L_{2,3}$ edges allows to investigate the respective magnetic contributions of Fe^{3+} ions on octahedral and tetrahedral sites in γ-Fe_2O_3. The use of multiplet calculations allows to assign the experimental field-dependence of XMCD to a greater degree of spin disorder on the octahedral magnetic sublattice relatively to the tetrahedral one. From XMCD measurements on a single size of particles, it is not possible to conclude whether this magnetic disorder is a surface or a core effect. Similar measurements have been performed on larger particles, that have a lower surface to volume ratio. A greater magnetic disorder on octahedral sites still exists when low magnetic fields are applied. But the effect is reduced compared to the 3 nm particles. Those results are consistent with a magnetic disorder located at the surface of the particles. We have also investigated particles coated with phosphate ligands. The ligands create a total magnetic disorder of the first atomic layer at the surface of the particles. The comparison of coated particles with uncoated ones evidences that magnetically disordered surface sites are mainly octahedral sites. These results stand in agreement with former in-field Mössbauer results [4]. Details of these investigations will be published in a forthcoming publication.

Acknowledgements

This work has been carried out using the very-low temperature crystat designed by J. P. Kappler and one of us. We are grateful to the staff of the BACH beamline for experimental help.

This is IPGP contribution number 1927.

References

1. Dormann, J. L., Fiorani, D. and Tronc, E., "Magnetic relaxation in fine-particle systems", (Edited by I. Prigogine and Stuart A. Rice) (Advances in Chemical Physics, John Wiley and sons, 1997), vol. XCVII, p. 366.
2. Morales, M. P., Serna, C. J., Bødker, F. and Mørup, S., J. Phys.: Condens. Matter **9**, 5461 (1997).
3. Vayssière, L., Chanéac, C., Tronc, E. and Jolivet, J.-P., J. Colloid Interface Sci. **205**, 205 (1998).
4. Tronc, E. *et al*., J. Magn. Magn. Mater. **221**, 63 (2000).
5. Zangrando, M. *et al*., Rev. Sci. Instrum. **72**, 1313 (2001).
6. Cowan, R. D., "The theory of atomic structure and spectra", (Los Alamos series in basic and applied sciences, University of California Press, 1981).
7. Butler, P. H., "Point Group Symmetry Applications: Methods and Tables", (Plenum Press, 1981).
8. Thole, B. T. *et al*., Phys. Rev. B **32**, 5107 (1985).
9. Melamed, N. T., de S. Barrow, F., Viccaro, P. J. and Artman, J. O., Phys. Rev. B **5**, 3377 (1972).
10. Sherman, D. M. and Waite, T. D., Am. Min. **70**, 1262 (1985).
11. The Racah B parameter can be expressed using Slater's integrals as $B = \frac{1}{49}F^2 - \frac{5}{441}F^4$.
12. Ayant, Y., Belorizky, E., Guillot, M. and Rosset, J., Le Journ. de Phys. **26**, 27 (1965).
13. van Elp, J. and Searle, B. G., J. Electron. Spectrosc. Relat. Phenom. **86**, 93 (1997).

Physica Scripta. Vol. T115, 629–631, 2005

A Universal Relationship Between Magnetization and the Local Structure in $La_{1-x}Ca_xMnO_3$; a Probe of the Magnetization Process

L. Downward[1], F. Bridges[1], S. Bushart[1], J. Neumeier[2] and L. Zhou[3]

[1]Department of Physics, University of California, Santa Cruz, CA 95064, USA
[2]Department of Physics, Montana State University, Bozeman, MT 59717, USA
[3]Stanford Synchrotron Radiation Laboratory, Stanford Linear Accelerator Center, Menlo Park, CA 94025, USA

Received June 26, 2003; accepted November 4, 2003

PACS number: 61.10.Ht

Abstract

We report X-ray Absorption Fine Structure (XAFS) measurements of the colossal magneto-resistance (CMR) samples $La_{0.79}Ca_{0.21}MnO_3$ and $La_{0.7}Ca_{0.3}MnO_3$ at high magnetic fields. For T near T_c, the width parameter of the pair distribution function, σ, decreases significantly as the applied magnetic field is increased. For a given magnetization, M, the decrease in σ^2 from the disordered polaron state is the same, irrespective of whether M was achieved through a change in temperature or the application of an external magnetic field. This universal behavior can be modeled as a quadratic function of magnetization, and suggests a new model for the magnetization process.

In many previous studies, σ^2, the width the Mn-O pair distribution function, decreases rapidly as the temperature (T) is lowered below the ferromagnetic transition temperature (T_c) for the CMR manganites. This has been attributed to a decrease in the amount of polaron-induced disorder in the magnetized state; similar results have also been observed in neutron pair distribution function (NPDF) analysis studies [1–7]. Furthermore, for several different CMR samples, we have shown that the change in σ^2 ($\Delta\sigma^2$) below T_c can be described by an exponential function of the magnetization, although no theoretical model predicts such behavior [1, 2]. The more extensive study presented here shows that the change $\Delta\sigma^2$ is only a function of the magnetization M, irrespective of how M is produced; it also provides evidence for a new relationship between $\Delta\sigma^2$ and M, based on a physical model.

Mn K-edge data were collected on powdered samples of $La_{0.79}Ca_{0.21}$ MnO_3 and $La_{0.7}Ca_{0.3}MnO_3$ as a function of temperature and magnetic field on beamline 7-2 (Si ⟨111⟩ monochromator crystals) at the Stanford Synchrotron Radiation Laboratory (SSRL). The data were reduced using standard procedures and Fourier transformed to r-space. The r-space Mn-O peak was then fit using the RSFIT program, using standards calculated from FEFF6 [8]. The number of neighbors was constrained to 6, and only the r-space peak position and the width parameter of the pair distribution function, σ, were allowed to vary. (S_o^2 and E_o were determined at low T and then held constant for fits to higher temperatures.) Then σ provides a single local structure parameter for comparison with M. Although one might attempt to model the system as two (or more) Mn-O peaks, there would then be two amplitudes and two σ's which are partially coupled; a local structure parameter for comparison with M is then not well defined. For each temperature, independent fits were made to four traces and the average value of σ obtained; the relative errors, the rms fluctuation about the average, is comparable to the symbol size, except where error bars are shown. The absolute errors for σ^2, which depend on S_o^2, may be of order 10%; they shift the plot vertically.

These first results indicate a significant temperature and magnetic field dependent change in σ^2, near and above T_c (∼190 K for the 21% Ca sample, and ∼260 K for the 30% Ca Sample) (see Fig. 1 and Fig. 2). At low temperatures, the sample is ordered and σ^2 is small while at high temperatures there is a large amount of polaron-induced disorder, as observed previously. Furthermore, there is a field dependent change in σ^2. Near T_c, σ^2 decreases as the applied field is increased indicating that the application of a magnetic field removes polaron disorder from the sample (see Fig. 1 and Fig. 2).

The change in σ^2 is defined as

$$\Delta\sigma^2 = \sigma^2_{\mathrm{T}} + \sigma^2_{\mathrm{FP}} + \sigma^2_{\mathrm{static}} - \sigma^2_{\mathrm{Mn-O}}, \tag{1}$$

where σ^2_{T} is the thermal contribution calculated from $CaMnO_3$ [9], $\sigma^2_{\mathrm{static}}$ is the excess (above σ^2_{T}) contribution at low temperatures, $\sigma^2_{\mathrm{Mn-O}}$ is calculated from fits to r-space data and is plotted in Fig. 1 and Fig. 2. The difference between $\sigma^2_{\mathrm{T}} + \sigma^2_{\mathrm{static}}$ and $\sigma^2_{\mathrm{Mn-O}}$ at high

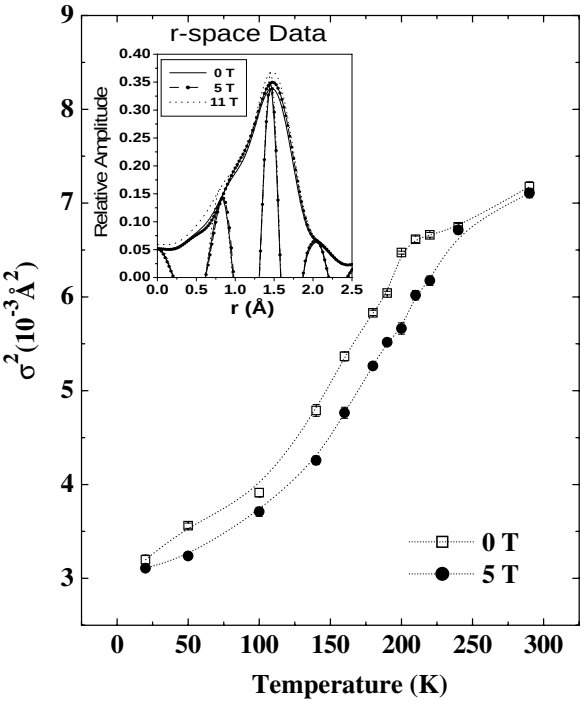

Fig. 1. σ^2 vs T for the Mn-O nearest neighbor peak for the 21% Ca sample. The dotted lines are guides to the eye. The inset shows the corresponding r-space changes in the Mn-O peak at T_c (190 K) – the amplitude increases (σ^2 decreases) with increasing field.

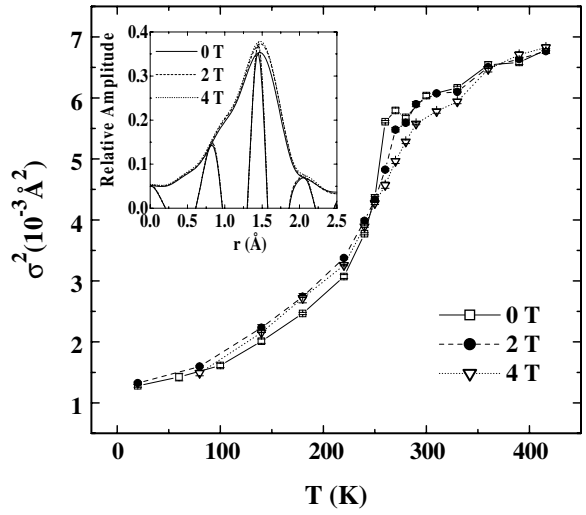

Fig. 2. σ^2 vs T for the Mn-O nearest neighbor peak for the 30% Ca sample. The lines are guides to the eye. The inset shows the corresponding r-space changes in the Mn-O peak at T_c (260 K) – the amplitude increases (σ^2 decreases) with increasing field.

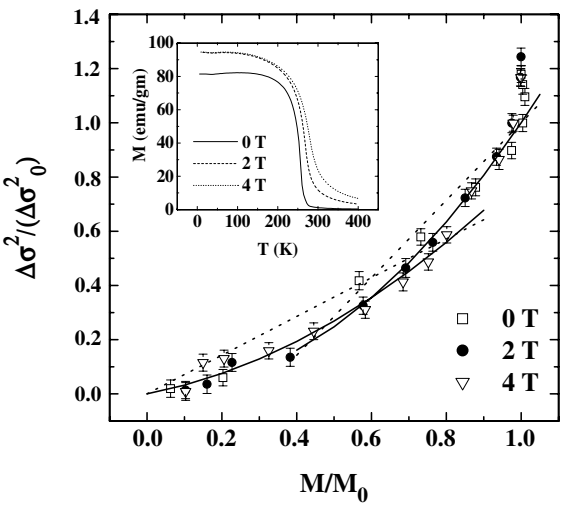

Fig. 4. $\Delta\sigma^2$ vs relative magnetization for the 30% Ca sample. $\Delta\sigma^2$ and M have been normalized to the value at 150 K, when the the sample becomes fully magnetized. The curves show the theoretical dependence of $\Delta\sigma^2$ on magnetization given by the quadratic function described in Eq. (2). The dotted lines show the dependence of a linear fit assuming the distortions are first removed in pairs of distorted Mn^{+3} and undistorted Mn^{+4} sites, as described in the text. The inset shows the magnetization curve for each field in the plot demonstrating that the sample magnetization is saturated (remains constant) below 150 K. The vertical part near $M/M_0 = 1$ is evidence that polaron distortions are continuing to be removed after the sample has become fully magnetized.

temperatures is called the full polaronic distortion, σ^2_{FP} in Eq. (1) above [1, 2].

In Fig. 1, we show that for the 21% sample, σ^2 decreases as the applied B-field is increased at constant temperature. A similar dependence on B-field can be seen for the 30% sample at temperatures near T_c. However, at lower temperatures for this sample, the change in σ^2 is independent of field and $\Delta\sigma^2$ continues to increase as T is lowered after the magnetization saturates which occurs at ∼150 K (compare magnetization data in Fig. 4 inset and Fig. 2).

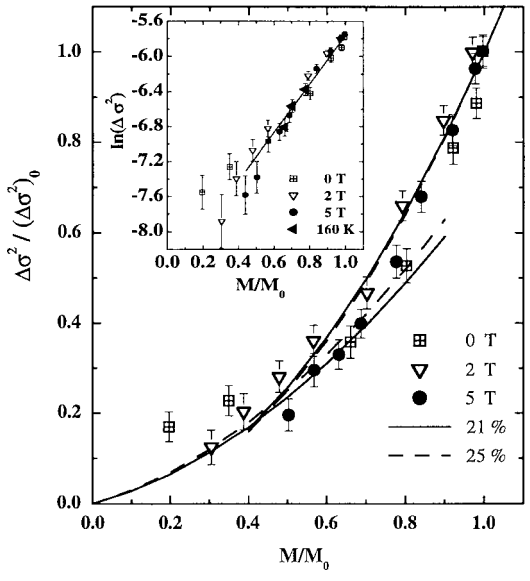

Fig. 3. $\Delta\sigma^2$ vs relative magnetization for the 21% Ca sample. $\Delta\sigma^2$ and M have been normalized to the maximum value for each field. $\Delta\sigma^2$ is the decrease in σ^2 as T is lowered below T_c that is attributed to the loss of polaronic distortion. The curves show the theoretical dependence of $\Delta\sigma^2$ on magnetization given by the quadratic function described in Eq. (2). The inset shows a logarithmic plot of $\Delta\sigma^2$ vs normalized magnetization; it shows that over this available range in M, a semi-log plot describes the data quite well. In both plots many of the data points are at a different temperature (i.e. for fixed field, varying T). To show more clearly that one can keep T fixed and vary M (via a change in B-field) several points are plotted for $T = 160$ K. These points lie along the same line in the semi-log plot indicating a universal dependence on M.

The observed changes in $\Delta\sigma^2$ can be modeled by either an exponential function or a polynomial function of magnetization where there are regions of differing behavior see Fig. 3 and Fig. 4. A semi-log plot for the 30% sample is similar to the inset for the 21% sample. The magnetization has been normalized to the saturation value while $\Delta\sigma^2$ has been normalized to the value at which the sample becomes fully magnetized; this occurs at the lowest temperature for the 21% sample, but at ∼150 K for the 30% sample. The relatively slow change in $\Delta\sigma^2$ at low M indicates that the lowest-distortion sites must become magnetized first. Since the "Mn^{+4}" site is thought to be essentially undistorted, the magnetization process may proceed in pairs – an undistorted "Mn^{+4}" site and a distorted "Mn^{+3}" site; this allows an electron to hop back and forth between two Mn sites as required in the double exchange model but only required that one of the distorted sites become undistorted. Once all the "Mn^{+4}" sites become magnetized (60% of the sample is magnetized for the 30% sample), further increases in M require that every additional Mn site must become undistorted. Since a significant cluster must be magnetized in ferromagnetic systems it is likely that the magnetized clusters form filaments through the sample and the magnetic and non-magnetic regions are intertwined. For the 30% sample, the vertical part near $M/M_0 = 1$ in Fig. 4 is evidence that polaron distortions are continuing to be removed after the sample has become fully magnetized, which indicates that the Mn sites can be magnetized but still have a small local distortion. A possible explanation is that the polarons are still partially localized at 150 K. Only at the lowest temperatures are the polarons essentially delocalized.

The magnetization process described above can be described by the following model. Let the smallest polaron distortions removed be α_0, and assume that there is a distribution of distortions that are removed with the largest distortions removed when $M \sim M_o$. The distortion that is removed at various states of magnetization (f is the fractional magnetization (M/M_o)), can be

described as $\alpha = \alpha_o(1 + \gamma f)$, where γ is a measure of the range of distortions. Below the critical value of f (twice the Calcium concentration, $2x$) the distortion removed per pair is only α; above this value of f the distortion removed per pair is 2α. This leads to the following normalized expressions which were used to fit the $\Delta\sigma^2$ data:

$$\frac{\Delta\sigma^2}{\Delta\sigma_0^2} = \begin{cases} \frac{1}{2}Af(1+\gamma f) & \text{for } f \le f', \\ \frac{1}{2}Af'(1+\gamma f') + A(f-f')(1+\gamma f) & \text{for } f > f', \end{cases} \quad (2)$$

where f' is the critical value of f (twice the Calcium concentration, $2x$), and A is a normalization constant equal to $\frac{1}{\Delta\sigma_0^2}$, where $\Delta\sigma_0^2$ is value of $\Delta\sigma^2$ when $f = 1$. $\gamma = 2$ gives good agreement with the data in Figs. 3 and 4.

We have extended our previous results [1, 2] to show that the relationship between σ^2 and magnetization, is more universal. Changing the sample magnetization by either varying the applied field or varying the temperature produces similar changes in σ^2. Further analysis needs to be done to investigate the full nature of this relationship.

Acknowledgments

The experiments were carried out under NSF grant DMR0301971 and were performed at SSRL, which is operated by the U.S. DOE, Division of Chemical Sciences, and by the NIH, Biomedical Resource Technology Program, Division of Research Resources.

References

1. Booth, C. H. *et al*., Phys. Rev. Lett. **80**, 853 (1998).
2. Booth, C. H. *et al*., Phys. Rev. B **57**, 10440 (1998).
3. Billinge, S. J. L., DiFrancesco, R. G., Kwei, G. H., Neumeier, J. J. and Thompson, J. D., Phys. Rev. Lett. **77**, 715 (1996).
4. Cao, D., Bridges, F., Worledge, D. C., Booth, C. H. and Geballe, T., Phys. Rev. B **61**, 11373 (2000).
5. Cao, D., Bridges, F., Booth, C. H. and Neumeier, J. J., Phys. Rev. B **62**, 8954 (2000).
6. Subías, G., García, J., Proietti, M. G. and Blasco, J., Phys. Rev. B **56**, 8183 (1997).
7. Tyson, T. A. *et al*., Phys. Rev. B **53**, 13985 (1996).
8. Zabinsky, S. I., Rehr, J. J., Ankudinov, A., Albers, R. C. and Eller, M. J., Phys. Rev. B **52**, 2995 (1995).
9. Cao, D. *et al*., Phys. Rev. B **64**, 184409 (2001).

Physica Scripta. Vol. T115, 632–634, 2005

Mn K-Edge Magnetic EXAFS for Ni-Mn Alloys

T. Miyanaga*[1], T. Okazaki[1], R. Maruko[1], S. Nagamatsu[2], T. Fujikawa[2] and Y. Sakisaka[1]

[1]Department of Materials Science and Technology, Faculty of Science and Technology, Hirosaki University, Hirosaki, Aomori 036-8561, Japan
[2]Graduate School of Science, Chiba University, Yayoi-cho 1-33, Inage, Chiba 263-8522, Japan

Received June 26, 2003; accepted in revised form January 19, 2004

PACS number: 03.30+p

Abstract

We have measured Mn K-edge magnetic EXAFS for $Ni_{0.76}Mn_{0.24}$ alloy. The 2nd peaks in the Fourier transform attributed to Mn-Mn pairs in the ordered phase are enhanced in comparison with those in non-magnetic EXAFS. This result suggests that some Ni atoms in the 2nd shell are replaced by Mn atoms, which have large magnetic moment in comparison with Ni atoms, due to heat-treatment induced atomic ordering. Semi-relativistic theoretical calculations well explain the observed magnetic EXAFS. We estimate the ratio of the magnetic moments of Ni to Mn atom in Ni-Mn alloy, within a single scattering limit.

1. Introduction

The correlation between the structure and magnetism of 3d transition metal alloys has long been an important topic in condensed matter physics. Among the 3d transition metal alloys, the Mn based alloys have recently attracted special attention because of their potential applications in magnetic recording technology. Ni_3Mn alloy has been an interesting example of such alloys and can undergo a structural phase transition where the magnetic behavior is sensitive to the atomic arrangement [1]. Cable and Child studied the magnetic moment distributions in disordered Ni_xMn_{1-x} ($x = 0.80$–0.95) alloys by polarized-neutron diffuse-scattering [2]. They showed that the magnetic moment of isolated Mn atom in $Ni_{0.95}Mn_{0.05}$ alloy is 3.50 μ_B, which decreases with Mn concentration. Two possible explanations are proposed: (1) The ferromagnetic component of Mn moment decreases by becoming randomly oriented or antiferromagneically coupled. In this case the local magnetic moment of Mn atom is conserved even in the disorder state. (2) Averaging over up-spin and down-spin magnetic configurations on Mn atoms. In this case, the net local moment of Mn atom decreases. They concluded that the magnetic distribution is complicated and not specifically defined by the neutron-cross-section measurement, since the neutron scattering technique is based on long-range order.

On the other hand, magnetic XAFS is a powerful tool for the investigation of local magnetic structures with short-range order in alloys, and uses circular polarized X-ray beam from a synchrotron radiation source [3–7]. The interpretation of magnetic EXAFS is clear and direct for the study of local magnetic structures, although the signal is much smaller than that of magnetic XANES. Recently, some theoretical approaches have been developed for magnetic EXAFS analyses [8–10]. Recent measurements of magnetic XAFS have been reported for alloys [11] and theoretical analyses have been applied to FeCo and FePt alloys [9] and disordered GdCo alloys [12].

In this paper, we experimentally and theoretically study magnetic EXAFS for ordered $Ni_{0.76}Mn_{0.24}$ alloys prepared by heat treatments.

*e-mail: takaf@cc.hirosaki-u.ac.jp

2. Experimental and Theory

A 21 μm foil sample of $Ni_{0.76}Mn_{0.24}$ was prepared by polishing carefully and annealing for 100 hours at 693 K under Ar atmosphere in order to make certain an ordered state. The reason why we study this concentration is that the ordered phase of $Ni_{0.76}Mn_{0.24}$ alloy is easily obtained by the shorter heat treatment time than that of $Ni_{0.75}Mn_{0.25}$ alloy, in which the residual oxygen can oxidize the sample. The saturation magnetization of this sample is 56.4 emu/g and the degree of order S is deduced to about 0.74. Magnetic EXAFS of Mn k-edge (6.4–7.2 keV) for $Ni_{0.76}Mn_{0.24}$ foil was measured at BL28B of Photon Factory in KEK (2.5 GeV) with circularly polarized X-rays that were generated by an ellipsoid multi-pole wiggler and monochromatized using a Si(111) double-crystal monochromator [13, 14]. The absorption spectra were measured in transmission mode at 30 K. Instead of switching helicity of the incident photons, the applied magnetic field, about 0.6 T which is still enough to saturate the magnetization of the sample, was reserved every 4 seconds to obtain MCD effect.

We perform semi-relativistic theoretical calculation of the magnetic EXAFS for binary alloy as the ordered model of Ni_3Mn including up to 4th shell atoms (∼5 Å). In the case of the binary system, it is important to determine the electronic state for each atom. To calculate the phase shift for magnetic EXAFS, we refer to the electronic structures obtained from FLAPW method [15]. The details of the present theoretical approach are discussed elsewhere [15, 16]. In this calculation, multiple scattering effect, the amplitude reduction factor by Debye-Waller factor and many-body effects are not taken into account.

3. Results and Discussion

First we discuss the result for non-magnetic EXAFS. Figure 1 (a) shows the non-magnetic EXAFS oscillation function, $k\chi(k)$, for experimental Mn K-edge for $Ni_{0.76}Mn_{0.24}$ foil sample (solid line) and theoretical calculation by a model of ordered *fcc* Ni_3Mn (dashed line). For experimental spectra the magnetic EXAFS signal is normalized by the edge jump of the non-magnetic X-ray absorption spectrum to be unity. Similar experimental spectrum was observed in a previous paper [15]. However, the present result is much better than the previous one. As the figure shows, the main oscillating parts for experimental and theoretical calculation are coinciding. On the other hand, a more fine oscillation is found in the experimental spectrum. Figure 1 (b) shows a comparison between experimental and theoretical Fourier transforms (FT) of the non-magnetic EXAFS $k\chi(k)$ shown in Fig. 1 (a). For the data processing we use the XANADU code [17]. The k-range of the Fourier transform is $2.0 \sim 10.8\,\text{Å}^{-1}$. Solid line (dashed line) shows the result for the experimental (theoretical) EXAFS. Vertical arrows in Fig. 1 (b) denote the crystallographic positions

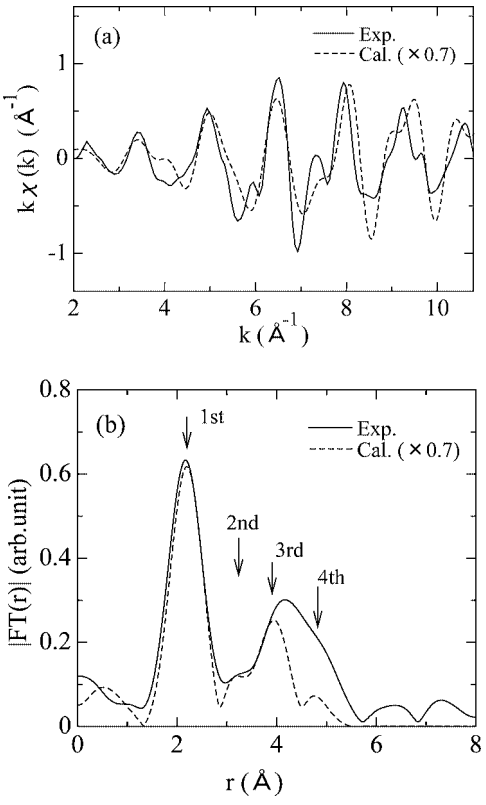

Fig. 1. (a) Non-magnetic EXAFS $k\chi(k)$ spectra for the Mn K-edge of experimental data for $Ni_{0.76}Mn_{0.24}$ alloy (solid line) and theoretical calculation as a model of ordered Ni_3Mn (dashed line). (b) Fourier transforms of non-magnetic EXAFS $k\chi(k)$ shown in (a).

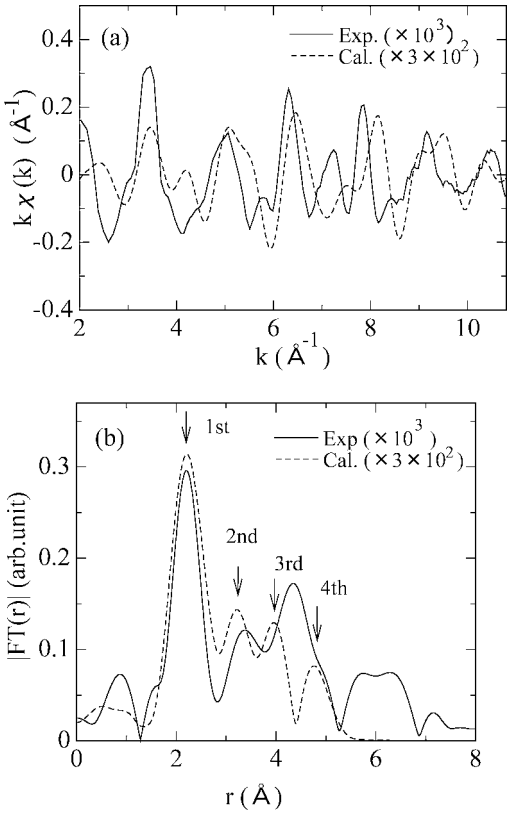

Fig. 2. (a) Magnetic EXAFS $k\chi(k)$ spectra for the Mn K-edge of experimental data for $Ni_{0.76}Mn_{0.24}$ alloy (solid line) and theoretical calculation as a model of ordered Ni_3Mn (dashed line). (b) Fourier transforms of the magnetic EXAFS $k\chi(k)$ shown in (a).

of nearest neighbor atoms in Ni-Mn *fcc* lattice from the central Mn atom. First nearest neighbor atoms are located at 2.54 Å, second at 3.59 Å, third at 4.5 Å and fourth at 5.08 Å. In Fig. 1 (b), the phase shift correction is not considered, so the peak position is not equal to these crystallographic data. The amplitude of the calculated EXAFS is larger than that for the experimental one, since we neglect thermal vibration, electron mean-free and many-body effects in the present analyses (the factor is about 0.7). The FT of the first and second peak for the theoretical calculation almost overlapp the experimental one. However, deviation is found between theoretical calculation and experimental spectrum for the third and fourth peaks (experimental peaks is enhanced in comparison to theoretical). This phenomenon is considered as a multiple scattering effect; especially a focusing effect is expected in the fourth shell atoms. In the present theoretical calculation, multiple scattering is not taken into account. Since our present calculation cannot reproduce such an effect, we discuss mainly the results for the first and second shells.

Next we discuss the result for magnetic EXAFS. Figure 2 (a) shows a comparison between experimental magnetic EXAFS $k\chi(k)$ spectrum and theoretical one. The main oscillating part almost coincides with that of non-magnetic EXAFS. On the other hand, the fine oscillating structure is more pronounced than in the case of non-magnetic EXAFS. Figure 2 (b) presents a comparison between experimental and theoretical calculation for the FT of magnetic EXAFS shown in Fig. 2 (a). Deviation is found in the third and fourth peaks between experimental and theoretical. This is considered as multiple scattering or focusing effect as for non-magnetic EXAFS. For the first and second peaks, we can find clear enhancement of the second peak in magnetic EXAFS in comparison to non-magnetic one (Fig. 1 (b)). This result can be interpreted as follows. After appropriate heat treatment, the Ni-Mn alloys are ordered. In the ordered phase, Mn atoms with large magnetic moment ($\sim$3.5 μ_B from neutron diffraction [2]) are exchanged to Ni atoms that are located in the second shell around an X-ray absorbing Mn atom. Therefore the second nearest Mn atoms strongly contribute to the magnetic EXAFS.

Another important effect we should consider is a strong multiple scattering effect, which was reported in the higher shell of magnetic EXAFS by Ahlers & Shutz [6] and Wende *et al.* [7]. Wende *et al.* have shown the quite interesting result that the multiple scattering effect is enhanced in magnetic EXAFS and the FT peak for the second shell overlaps the triangle multiple scattering path for *bcc* structure [7]. In their case, if the first nearest distance is 2.49 Å (as a typical model for Fe), the distance for the third shell is 4.06 Å and the corresponding triangle path is 3.92 Å, in which it is difficult to distinguish them with the FT method [7]. On the other hand, in the present *fcc* Ni_3Mn case, the distance for the second shell is 3.59 Å and the corresponding triangle path is 3.81 Å (the difference is 0.22 Å). We carefully checked the simulation of FT (k-range is 2–10.8 Å^{-1}) for various situations and certify that the peaks of 3.59 Å and 3.81 Å do not overlapped and can be distinguished from each other. The peak of the triangle path (3.81 Å) should be included at longer distance than the second peak. However, since the second peak position is slightly shifted in Fig. 2 (b), a small portion of the triangle path effect may be mixed into the second shell contribution. Unfortunately our present calculation cannot take the multiple scattering process into account. So we have to consider a single scattering limit.

ptIn the theoretical calculation for magnetic EXAFS, we can handle the electronic configuration and also magnetic moments of each Ni and Mn atom. For the ordered Ni_3Mn model, the 1st and

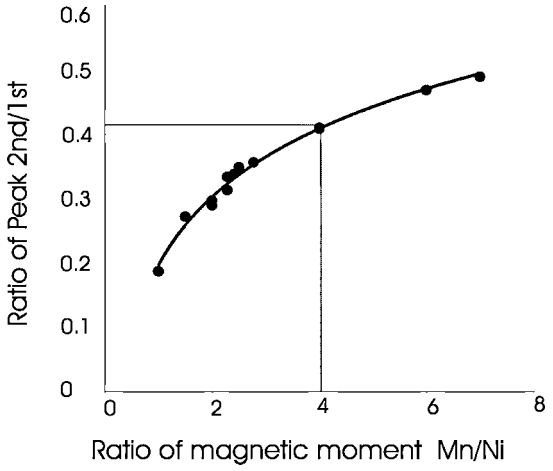

Fig. 3. The ratio of the calculated Fourier peak intensity Mn/Ni as a function of the ratio of magnetic moments Mn/Ni atom used for the theoretical calculation.

2nd peak in the Fourier transform are attributed to the Ni and Mn atom. The ratio of the peak intensities of the 1st to 2nd peak in the FT of the magnetic EXAFS depends on the magnetic moment of Ni and Mn atoms. Figure 3 shows calculated Fourier peak intensity Mn (2nd peak)/Ni (1st peak) as a function of the ratio of magnetic moments of Mn and Ni atom used for the theoretical calculation.

From the FT in Fig. 2 (b), we obtain the ratio of 2nd/1st peaks 0.41. Using the theoretical curve shown in Fig. 3, we estimated the ratio of the magnetic moment Mn/Ni ~ 4.0 (as shown in Fig. 3). This value is much smaller than that obtained from neutron study (Mn/Ni ~ 10) [18], however it is fairly close to the result derived from a recent band calculation using FLAPW method (Mn/Ni ~ 4.8) [15]. As a reason for the small value of the ratio of magnetic moments Mn/Ni, the ordered Ni_3Mn model is not adequate for the present $Ni_{0.76}Mn_{0.24}$ sample ($S \sim 0.74$). The electronic states used in the theoretical calculation are still inaccurate or the multiple scattering effect cannot be neglected in the contribution of second shell peak. While there are still problems we should solve in this simple method to derive the ratio of the magnetic moments of each atom, this method has a potential for disordered magnetic systems in which neutron diffraction cannot be applied. To improved this method, more accurate analyses of magnetic EXAFS, *e.g.* multiple scattering process [7], thermal vibration and spin disorder [5] and many body effect, are necessary to take into account.

4. Conclusion

We measure the Mn K-edge magnetic EXAFS for $Ni_{0.76}Mn_{0.24}$, where the 2nd peaks in the Fourier transform are enhanced in comparison with those in non-magnetic EXAFS. This result suggests that some Ni atoms in the 2nd shell are replaced by Mn atoms with larger magnetic moment than Ni atom, due to heat-treatment induced atomic ordering. Semi-relativistic theoretical calculation well explains the observed magnetic EXAFS. We propose a simple method to evaluate the ratio of the magnetic moments for each atom in Ni-Mn alloy from magnetic EXAFS, which is applicable to disordered systems, even within a single scattering approximation.

Acknowledgements

The authors thank Dr. T. Iwazumi, Dr. Y. Watanabe and Dr. T. Nakamura for kindly supporting the measurement of magnetic XAFS. One of the authors (T.M.) thanks Prof. Yu. A. Babanov and Prof. A. Z. Menshikov for a fruitful discussion and to Prof. E. D. Crozier for encouragement of this work. This work was performed under the approval of proposal No. 98G236 and No. 2001G232 of the Photon Factory (PF) at KEK.

References

1. Okazaki, T., Jpn. J. Appl. Phys. **34**, 1537 (1995).
2. Cable, J. W. and Child, H. R., Phys. Rev. B **10**, 4607 (1974).
3. Schutz, G., *et al.*, Phys. Rev. Lett. **58**, 737 (1987).
4. Lovesey, S. W. and Collins, S. P., "X-ray Scattering and Absorption by Magnetic Materials," (Oxford Science Publisher, 1996), pp 151.
5. Wende, H., *et al.*, J. Appl. Phys. **83**, 7028 (1998).
6. Ahlers, D. and Shutz, G., Phys. Rev. B **57**, 3466 (1998).
7. Wend, H., *et al.*, J. Synchrotron Rad. **6**, 696 (1999).
8. Ankdinov, A. L. and Rehr, J. J., Phys. Rev. B **52**, 10214 (1995).
9. Popescu, V., Ebert, H. and Jenkins, C., J. Synchrotron Rad. **6**, 711 (1999).
10. Nagamatsu, S. and Fujikawa, T., J. Synchrotron Rad. **8**, 416 (2001).
11. Pizzini, S., *et al.*, Phys. Rev. B **50**, 3779 (1994).
12. Yamamoto, I., Nagamatsu, S., Nakamura, T., Fujikawa, T. and Nagao, S., J. Elect. Spect. **125**, 89 (2002).
13. Iwazumi, T., Koyama, A. and Sakurai, Y., Rev. Sci. Instrum. **66**, 1691 (1995).
14. Kobayashi, K., Maruyama, H., Iwazumi, T. and Yamazaki, H., Solid State Commun. **97**, 491 (1997).
15. Miyanaga, T., *et al.*, J. Synchrotron Rad. **10**, 113 (2003).
16. Fujikawa, T. and Nagamatsu, S., Jpn. J. Appl. Phys. **41**, 2005 (2001). Fujikawa, T. and Nagamatsu, S., J. Electr. Spectr. **129**, 55 (2003).
17. Sakane, H., *et al.*, Jpn. J. Appl. Phys. **32**, 4641 (1993).
18. Paoletti, A. and Ricci, F. P., J. Appl. Phys. **34**, 1571 (1963).

Physica Scripta. Vol. T115, 635–637, 2005

XMCD Signals of the High Spin Molecules Fe_8

I. Letard[1], Ph. Sainctavit[1,5], D. Gatteschi[2], Ch. Cartier dit Moulin[3,5], G. Champion[3] and J.-P. Kappler[4,5]

[1]Laboratoire de Minéralogie – Cristallographie de Paris, Université Pierre et Marie Curie, 4, place Jussieu, F-75 252 PARIS Cedex 05
[2]Dipartimento di Chimica, Universita di Firenze, Italy
[3]Laboratoire de Chimie Inorganique et Matériaux Moléculaire, Paris, France
[4]Institut de Physique et des Chimie des Matériaux de Strasbourg, France
[5]Laboratoire pour l'Utilisation du Rayonnement Electromagnétique, Orsay, France

Received June 26, 2003; accepted in revised form November 4, 2003

PACS number: 75.75.+a

Abstract

Fe_8 clusters are molecules which show quantum spin tunneling at very low temperature. They have eight iron ions that are six-fold coordinated and magnetically coupled through oxygen bridges. The net magnetization ($M_s = 20\,\mu_B$ per molecule) results from competing antiferromagnetic interactions between the Fe^{3+} ions ($S = 5/2$). Because of the structural anisotropy of these molecules, the magnetization curve presents a hysteresis loop with staircases below 2 K. The staircases of the hysteresis loop are due to the quantum spin tunneling, which is temperature dependent for 400 mK $< T <$ 3 K and temperature independent below 400 mK. Using a ^{3}He–^{4}He dilution refrigerator, we have recorded XMCD spectra at iron $L_{2,3}$ edges at 300 mK for this molecule. It has been possible to record an XMCD remnant signal, without magnetic field applied, on these high spin molecules. XMCD coupled with Ligand Field Multiplet calculations has allowed to determine the spin and orbit magnetizations of Fe^{3+}.

1. Introduction

High spin molecules show peculiar magnetic properties at very low temperature: remnant magnetization and spin tunneling effect below $\simeq$1 K. In order to determine the role of the anisotropy of the molecule in the remnant magnetization process and to know the contributions of the spin and orbit magnetic moments to the total magnetization, we carried out X-ray absorption spectroscopy (XAS) and X-ray magnetic circular dichroism (XMCD) experiments at the iron $L_{2,3}$ edges at 300 mK. The spectra have been simulated in the ligand field framework. A first part presents the Fe_8 high spin molecules and their properties. In the two following parts, the experimental set up that permits XMCD recordings at 300 mK and the simulation of the experimental signals are described. Then the results are presented and discussed.

2. High spin molecules

2.1. *Structure of the molecules*

Molecule – magnets present a high remnant magnetic moment at low temperature (remnant magnetization higher than $5\,\mu_B$ per molecule below 300 mK) [1]. This behaviour makes these molecules good candidates for the small memory elements searched for spintronics. The properties expected to obtain such magnetic response are high structural anisotropy and high magnetic moment. Thus, it shall contain a sufficiently high number of transition elements and particular geometry which can favour one magnetization direction among the others. The structure of the molecule $[(C_6H_{15}N3)_6Fe_8O_2(OH)_{12}]Br_7(H_2O)$ $Br–8H_2O$ (Fe_8) is shown on fig. 1. It contains 8 iron atoms (Fe^{3+}, $S = 5/2$). The iron ions are magnetically coupled through bridging oxygens. Spin-polarized neutron diffraction measurements showed that six iron magnetic moments stand in a direction and the two other ones stand in the opposite direction. The resulting spin of the molecule is $S_{tot} = 10$.

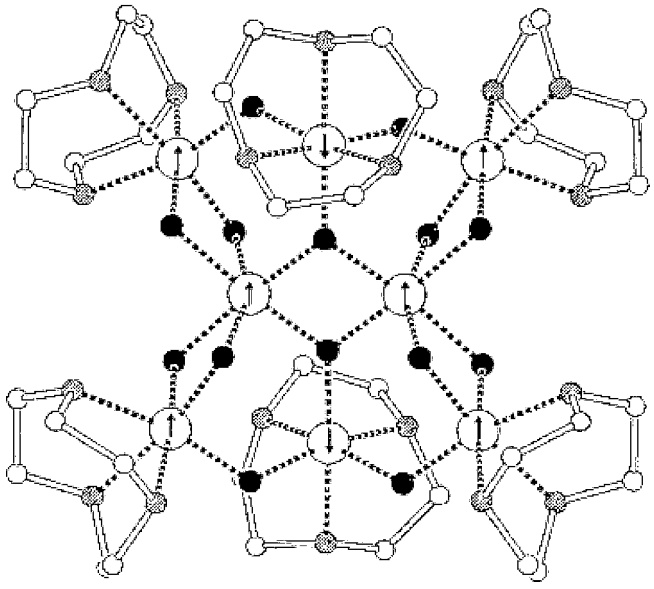

Fig. 1. Fe_8 molecule [1]. The wide circles represent iron atoms, the small black ones oxygen atoms, the small grey ones nitrogen atoms and the small white ones carbon atoms.

2.2. *Magnetic properties of Fe_8 molecules*

The temperature at which the hysteresis loop opens on the magnetization curve depends on the rate of variation of the magnetic field. When the loop opens, one observes staircases that are due to the spin tunneling effect [1]. Indeed, contrary to the majority of magnetic compounds, the magnetization of this magnet-molecule is quantized. The spin-tunneling effect and the remnant magnetization are observed only below $\simeq$1 K but the relaxation is slow enough to be studied by XMCD below $\simeq$300 mK (75% of the saturation magnetization is kept after one hour, time needed to record the XMCD signal).

3. Experimental set up

The experiments have been carried out on the SU23 beamline at LURE (Orsay, France) with a dilution refrigerator set up [3].

A liquid ^{4}He cryostat reaches temperatures no lower than 4.2 K. If one pumps on the liquid ^{4}He phase, one can reach 1 K and 0.3 K if it is ^{3}He instead of ^{4}He. To reach lower temperatures, we used a ^{3}He–^{4}He dilution refrigerator. This device is constituted of a

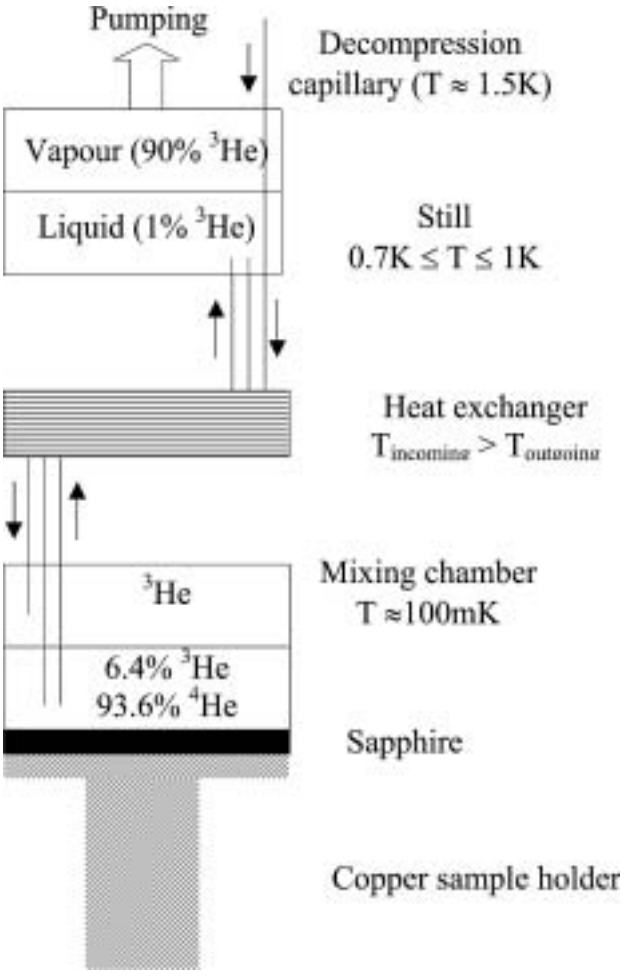

Fig. 2. Scheme of the inner part of the dilution refrigerator.

classical $^4He_{liq}$–N_{2liq} cryostat and of an inserted cooling device containing the ^{3}He–^{4}He mixture. Below 1 K, a phase separation occurs between ^{3}He and ^{4}He. The device is cooled by pumping on the two-phase mixture, inducing the transfert of ^{3}He molecules from the ^{3}He rich phase to the poor one. The cooling happens because of the large latent heat absorbed when a ^{3}He molecule crosses the interface. A sample holder is fixed to the colder part of the device through a sapphire that permits at the same time the thermal conduction and the electrical insulation necessary to the detection in the total electron yield mode.

A scheme of the experimental set up is shown on fig. 2. With this type of device, one can reach 0.1 K in a closed chamber. For XAS utilisations, the cryostat must include windows permitting the entry for the X-ray beam. This reduces the thermal insulation. Moreover, the application of the magnetic field needed for the XMCD measurements induces Foucault currents that also limit the minimum temperature. The ^{3}He–^{4}He dilution refrigerator developped at LURE reaches a stable temperature of 300 mK under the X-ray beam.

Motivations for carrying out XAS and XMCD experiments at these very low temperatures are multiple. They include the study of small particles in which the blocking temperature is very low: the smaller the particles, the lower the blocking temperature.

4. Modelisation of the spectra: multiplets calculations

We used the ligand field multiplet theory in order to simulate the isotropic and XMCD spectra at the Fe $L_{2,3}$ edges. This method takes into account the local environement of the absorbing atom through the crystal field parameters and the hybridization of the chemical bond (by the means of the Slater integrals). A trigonal distorsion of the octahedral sites have been used in agreement with the actual symmetry around Fe ions. The obtained signals are convoluted by a Lorentzian function in order to take into account the lifetime of the core hole and by a Gaussian function to take into account the instrumental broadening.

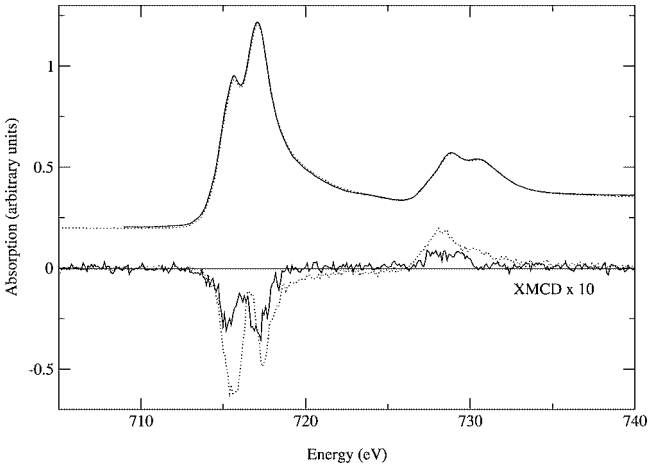

Fig. 3. Dot line: XAS and XMCD signals with T = 300 mK and H = ±5 T. Solid line: remnant XAS and XMCD signals with T = 300 mK and H = 0 T after saturation in a field of ±5 T.

5. Results and discussion

5.1. *Experimental results*

We have recorded the absorption and dichroic signals under 300 mK. Fig. 3 shows the XAS and XMCD signals obtained in a magnetic field of ±5 T and the XAS and remnant XMCD signals obtained under 0 T after saturation in a magnetic field of ±5 T. The remnant signal at 717.5 eV is attributed to Fe^{3+}. It represents only 65% of the corresponding feature observed under the 5 T magnetic field. This is the consequence of the relaxation of the magnetization. This reduction is in agreement with the values obtained by SQUID measurements [1]. However, this remnant dichroic spectrum shows that the relaxation is slow enough to acquire the remnant signal. This constitutes one of the first observations of a remnant XMCD signal on molecular systems, the other being at the Cr and Ni K-edge [4]. If one takes into account the polarization rate and the relaxation of the magnetization, the intensity of the dichroic signal has the expected order of magnitude. Nevertheless, even if these experiments were carried out on samples from the same batch as Ghigna *et al.* [2], the obtained signal is different.

Besides, one can notice that the dichroic feature at 716 eV is stronger in the spectrum recorded with magnetic field than in the spectrum recorded without magnetic field. This contribution to the spectra can be attributed to paramagnetic Fe^{2+} present on the surface of the grains and giving a dichroic signal only when the field is applied. Working in remanence sets free from the contribution of this species that is not part of the molecule. The calculations have thus been compared to the remnant signal.

5.2. *Modelisation*

The calculated signals are presented in fig. 4, compared to the experimental spectra recorded without magnetic field after

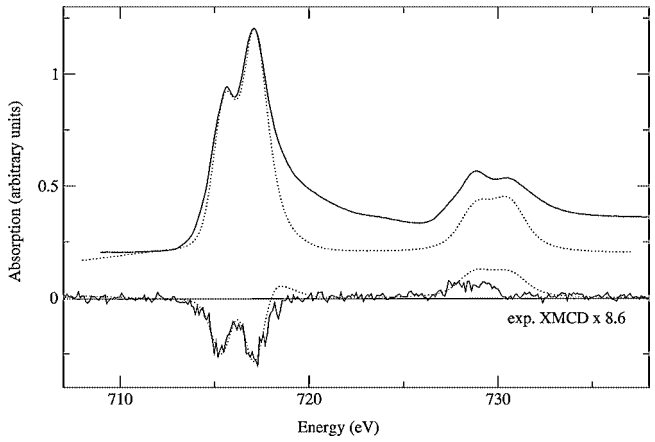

Fig. 4. Comparison between experimental and calculated signals.

application of $H = \pm 5\,\mathrm{T}$. The signal calculated with Fe^{3+} ions in distorted octahedral sites gives a good simulation of the spectra at the L_3 edge. The signal is not so well reproduced at the L_2 edge.

The values obtained for the crystal field ($10\,\mathrm{Dq} = 1.7\,\mathrm{eV}$) and for the reduction of the Slater integrals ($\kappa = 0.31$) are consistent with the values used for the simulation of Fe^{3+} signals in analogous molecular compounds.

The calculations give a spin moment of $5/2$ and no orbital moment on the Fe^{3+} ions, which is in agreement with the predicted values for an ion with the $3d^5$ configuration. The distorsion of the octahedral sites, which is necessary to the fit, does not change significantly the value obtained for the orbital moment. This zero value is not incompatible with the existence of a magnetic anisotropy in Fe_8. Indeed, Ghigna and coworkers have observed that on the Mn_{12} molecule, the orbital magnetic moment is 0 though a strong anisotropy is observed [2].

Nevertheless, the value of the L_z/S_z ratio obtained by the use of the sum rules on the experimental signal is not 0 but about 0.1, which leads to an orbital magnetic moment of $0.5\,\mu_B$. The discrepancy comes from the differences between the experimental and calculated signals at the L_2 edge.

6. Conclusion

The ^{3}He–^{4}He dilution refrigerator makes possible measurements of XMCD signals at the $L_{2,3}$ edges at very low temperature (300 mK). This method gives the dichroic signal due to the Fe^{3+} contained in the molecule and not to spurious contributions of eventual paramagnetic iron ions. Multiplets calculations tend to show that the existence of a remnant magnetization does not imply a non-zero orbital magnetic moment.

Acknowledgements

We would like to thank François Bertran and Franck Fortuna from the SU23 beamline (LURE, Orsay, France) for their help in the experimental part of the work and Sandrine Brice for her useful advice in the multiplet calculations. This is IPGP contribution No. 1925.

References

1. Sangregorio, C., Ohm, T., Paulsen, C., Sessoli, R. and Gatteschi, D., Phys. Rev. Lett. **78**, 4645 (1997).
2. Ghigna, P. *et al*., Phys. Rev. B **64** 132413 (2001).
3. Sainctavit, Ph. and Kappler, J.-P., In "Magnetism and Synchrotron Radiation", (Editions de Physique, 2000), pages 235–253.
4. Train, C., Giorgetti, C., Baudelet, F., Champion, G. and Cartier dit Moulin, Ch., Comptes-Rendus de Chimie, **6**, 337 (2003).

Physica Scripta. Vol. T115, 638–640, 2005

Co/Cu/Ni Trilayers Near Their Curie Temperature Studied by XMCD

C. Sorg*, A. Scherz, H. Wende, T. Gleitsmann, Z. Li†, S. Rüttinger, Ch. Litwinski and K. Baberschke

Institut für Experimentalphysik, Freie Universität Berlin, Arnimallee 14, D-14195 Berlin-Dahlem, Germany

Received June 26, 2003; accepted in revised form November 4, 2003

PACS numbers: 75.70.Ak, 75.70.−i, 78.70.Dm

Abstract

The elements-specific magnetizations of Co/Cu/Ni trilayers are studied near their Curie temperature by X-ray magnetic circular dichroism. Small magnetic fields are applied during the measurements to rule out the formation of magnetic domains. The experiments confirm that the Curie temperature of the Ni magnetization is shifted up to $\Delta T_{Ni} \approx 80\,\mathrm{K}$ in presence of an interlayer exchange coupling. In agreement with *ab initio* theory, we evidence the tail of the Ni magnetization in the trilayer.

Co/Cu/Ni trilayers have been used as a prototype system to study the interlayer exchange coupling J_{inter} [1–3]. In these trilayers the ferromagnetic layers of Ni and Co are coupled through the Cu spacer. The coupling strength and the relative alignment of the Ni magnetization to the Co magnetization (parallel or antiparallel) are mainly determined by the thickness of this Cu spacer [3]. Pioneering experiments, which were carried out in remanence, revealed a separate onset of the magnetization for the different ferromagnetic Ni and Co layers [1]. In the case of 4 ML Ni and 2 ML Co the ordering temperature of Ni is below the one of Co. A remarkable increase ΔT of the lower ordering temperature was observed in the presence of J_{inter} [1, 2]. Theoretical investigations addressed this effect to enhanced 2D spin-fluctuations [4]. The exchange coupling of the Co film acts on the Ni film not only as static exchange field but it influences also by higher order contributions the dynamics of the fluctuating spins. Therefore, a tail in the temperature-dependent magnetization is expected near the ordering temperature [4, 5]. However, this tail was not observed in the earlier experiments.

Up to now, the magnetization of coupled trilayers has only been investigated in remanence. Effects that possibly arise due to the formation of magnetic domains near the ordering temperature cannot be entirely excluded. Therefore, investigations under a small applied field were carried out here. To clarify the question of a tail of the Ni magnetization in coupled trilayers small signals close to the Curie temperature have to be measured precisely with a high density of temperature points. Such a clarification contributes to the investigations of the temperature dependence of the interlayer exchange coupling, as studied e.g. in [6]. The absence of the Ni tail would imply that J_{inter} vanishes when the magnetization of one ferromagnetic component in the trilayer vanishes. The recent development of the new undulator beamlines at third generation synchrotrons has very much improved the technical possibilities.

In the present work the individual magnetizations of Co and Ni in coupled Co/Cu/Ni trilayers are studied by the virtue of the element-specific X-ray magnetic circular dichroism (XMCD) in remanence as well as in a small applied magnetic field. Hysteresis loops and temperature-dependent magnetization curves are investigated. In particular we draw our attention to the Ni magnetization near the Ni Curie temperature. New results bring new insight into the critical behavior of exchange coupled ferromagnetic thin films near their ordering temperature.

The Co/Cu/Ni trilayers were prepared *in situ* like in the earlier experiments as described for example in Refs. [1, 3]. The measurements were carried out in ultrahigh vacuum (base pressure $p < 2 \cdot 10^{-10}$ mbar) at the undulator beamline UE56/1-PGM at BESSY II. We measured the drain current while applying a positive voltage to a metallic grid near the sample to ensure the complete extraction of the emitted electrons also under a small magnetic field. The substrate crystal was oriented such that we measured along [110], which is the easy axis for Co/Cu/Ni/Cu(100) trilayers. The XMCD signal at the maximum of the L_3 edge (normalized to a constant edge jump) is proportional to the element-specific magnetization $M(T)$. For the hysteresis loops we measured the field-dependent XMCD signal at the L_3 maximum. Taking advantage of the high photon-flux together with the high circular polarization-degree at the new undulator beamlines at third generation synchrotrons small XMCD signals near the Curie temperature can be determined more precisely. Better statistics can be obtained in shorter time and therefore, measurements close to T_C^{*Ni} with a relativly high density of data points have become achievable.

Figure 1 presents the magnetization of a 6 ML Ni film covered with 5 ML Cu in the temperature range from ∼80 K up to room

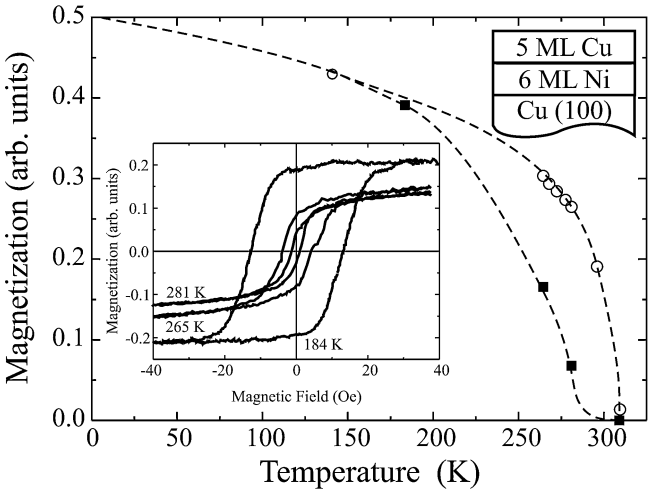

Fig. 1. Temperature-dependent Ni magnetization of a 5ML Cu/6ML Ni/Cu(100) bilayer system in a constant applied magnetic field ($H = 40$ Oe, open circles), and at remanence determined from hysteresis loops (solid squares). The dashed lines serve as guides to the eyes. The inset shows the Ni hysteresis at three different temperatures.

*Corresponding author electronic address: babgroup@physik.fu-berlin.de; URL: http://www.physik.fu-berlin.de/~ag-baberschke/index.html

†New address: Department of Chemistry, University of Georgia, Athens, GA 30602, USA.

temperature in remanence (solid squares) and under a constant applied magnetic field of $H = 40\,\mathrm{Oe}$ (open circles). Hysteresis loops at three different temperatures are shown in the inset of Fig. 1. At $T = 184\,\mathrm{K}$ the coercitive field is $H_C = 13\,\mathrm{Oe}$ and the magnetization saturates for $H \gtrsim 30\,\mathrm{Oe}$. Above $T \approx 200\,\mathrm{K}$ the remanent magnetization decreases considerably faster than the one in the applied magnetic field. Such a behavior has been observed in ultrathin Co/Cu(100) films [7] and Ni/Cu(100) films [8] using the polar magneto-optic Kerr effect. In both cases it was addressed to the formation of magnetic domains near the Curie temperature of these films. Magnetic domains with different directions of magnetization lead to a reduction of the remanent magnetization. Applying a small magnetic field of $H \approx 30\,\mathrm{Oe}$ is, in our case, sufficient to bring the sample into a single domain state even close to the Ni ordering temperature. Only by measuring on a single domain film one will obtain the proper magnetization in vicinity of T_C. However, the applied magnetic field should be small so that it does not produce additional field-induced magnetization in the sample. It is worth while to mention that operating in very low magnetic fields of a few Oe only it is important to pay attention to small stray fields. Zero current in the electro-magnet is not equal to zero magnetic field in the sample. Already a very small magnetic field like e.g. the earth field displaces the hysteresis loops, and creates a mismeasurement of the proper magnetization.

In Fig. 2 the temperature-dependent magnetization of Ni in a coupled trilayer measured at $H = 40\,\mathrm{Oe}$ both before (open circles) and after evaporation of the Co layer (solid circles) is shown. Measuring under a small static magnetic field we ensure a single-domain state of the sample. Therefore, we can rule out artifacts that stem only from a formation of domains. At first, a 4 ML Ni film capped with 4 ML Cu was studied (open circles). For this bilayer the Ni magnetization vanishes at $T_C^{Ni} \approx 210\,\mathrm{K}$. Then we 'turned on' the coupling by evaporating 2.8 ML Co onto the same sample. The Ni magnetization in the trilayer (solid circles) vanishes at a critical temperature $T_C^{*Ni} \approx 290\,\mathrm{K}$ which is $\Delta T_{Ni} \approx 80\,\mathrm{K}$ higher than for the bilayer system. The Curie temperature of the Co film is well above room temperature and its magnetization (not shown) is nearly constant in the investigated temperature range. The large ΔT_{Ni} confirms the results of Refs. [1, 2] so that they cannot be addressed to effects of domain formation.

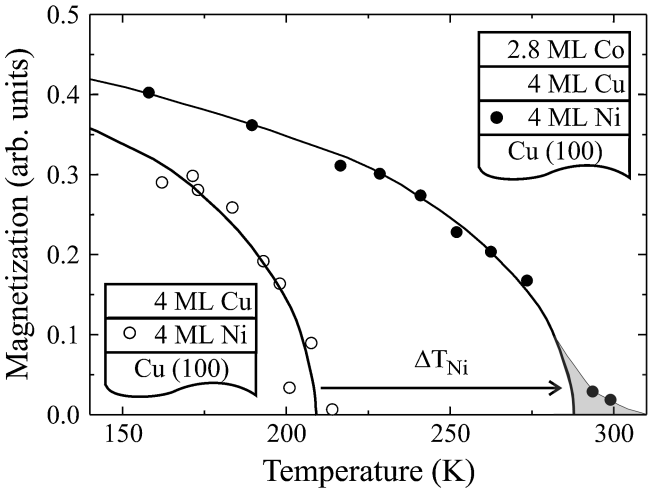

Fig. 2. Ni magnetization of a trilayer before (open circles) and after (solid circles) evaporation of the Co layer measured at $H = 40\,\mathrm{Oe}$.

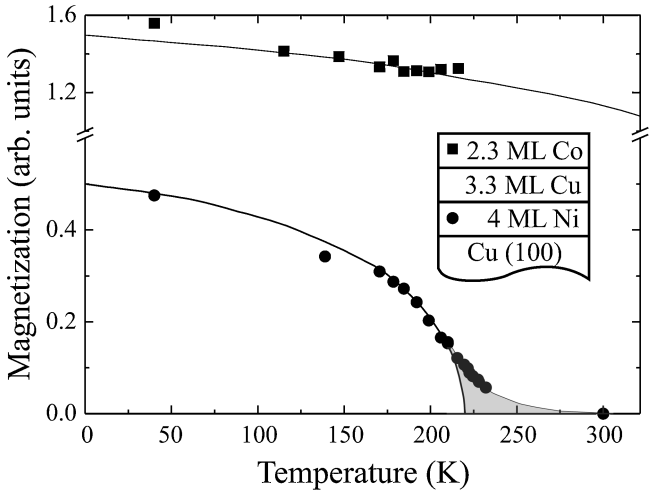

Fig. 3. Individual Ni and Co magnetization of a Co/Cu/Ni trilayer. A tail in the Ni magnetization near the ordering temperature is clearly visible.

Theoretical investigations of coupled trilayers revealed that the Curie temperature shift is related to the strength of the interlayer exchange coupling. For the description of the magnetic behavior in the ultrathin magnetic layers spin-fluctuations have to be taken into account in a localized picture [4]. In two-dimensional systems such spin-fluctuations reduce the magnetization more strongly than in bulk systems. Another theoretical study uses the so-called spectral density approach, that is within an itinerant single-band Hubbard model, to investigate coupled trilayers [5]. Although an itinerant model is more appropriate for 3d transition metals, the results of both approaches are in good agreement with the experiment yielding a strong shift ΔT_{Ni} to higher values after the Co film has been evaporated on top, i.e. after the exchange coupling has been switched on.

Figure 3 shows the individual Ni and Co magnetization curves exemplarily for a trilayer consisting of 4 ML Ni, 3.3 ML Cu and 2.3 ML Co for temperatures with $40\,\mathrm{K} \leq T \leq 300\,\mathrm{K}$. Both curves were measured under a small applied field. In our new experiments in a temperature range close to T_C, we observe a tail of the Ni magnetization which is clearly out of the noise. This tail in $M(T)$ is predicted in both theoretical investigations the itinerant approach and the localized Heisenberg model [4, 5].

In summary, we have presented the element-specific magnetizations of Co/Cu/Ni/Cu(100) trilayers close to the Curie temperature of the Ni film. For the measurements the formation of magnetic domains close to T_C has to be excluded. We have demonstrated that in our case applying a small magnetic field of $H = 30\,\mathrm{Oe}$ is sufficient. The shift ΔT_{Ni} of the Ni magnetization in the trilayer compared to the Cu/Ni bilayer is remarkably large and cannot be induced by a static magnetic field only. The existence of a tail of the Ni magnetization was evidenced. Our results are in agreement with theoretical predictions in a Heisenberg model as well as in an itinerant approach. They demonstrate that spin fluctuations, i.e. higher order contributions in the spin dynamics, are of more importance in ultrathin films than 3D bulk magnetism.

Acknowledgments

We thank the BESSY crew for the good operational conditions of the beamline and the technical assistance. This work was supported by the BMBF (05 KS1 KEB 4).

References

1. Bovensiepen, U. *et al*., Phys. Rev. Lett. **81**, 2368 (1998).
2. Scherz, A. *et al*., J. Magn. Magn. Mat. **236**, 1 (2001).
3. Poulopoulos, P. and Baberschke, K., "Lecture Notes in Physics", Springer **580**, 283 (2001).
4. Jensen, P. J. *et al*., Phys. Rev. B **60**, R14994 (1999).
5. Wu, J. H., Herrmann, T., Potthoff, M. and Nolting, W., J. Phys: Cond. Mat. **12**, 2847 (2000).
6. Zhang, Z., Zhou, L., Wigen, P. E. and Ounadjela, E., Phys. Rev. Lett. **73**, 336 (1994).
7. Kerkmann, D., Pescia, D. and Allenspach, R., Phys. Rev. Lett. **68**, 686 (1992).
8. Poulopoulos, P., Farle, M., Bovensiepen, U. and Baberschke, K., Phys. Rev. B **55**, R11961 (1997).

Physica Scripta. Vol. T115, 641–644, 2005

XAS Study of $LaMn_{1-x}Ga_xO_3$ Series

M. C. Sánchez[1], G. Subías[1,2*], J. García[1] and J. Blasco[1]

[1]Instituto de Ciencia de Materiales de Aragón, CSIC-Universidad de Zaragoza, 50009 Zaragoza, Spain
[2]European Synchrotron Radiation Facility, B.P. 220, 38043 Grenoble, France

Received June 26, 2003; accepted in revised form November 4, 2003

PACS numbers: 61.10.Ht; 75.47.Lx; 75.50.Lk; 74.47.De

Abstract

The $LaMn_{1-x}Ga_xO_3$ series has been studied by means of X-ray absorption spectroscopy (XAS) at the Mn and Ga K-edges. The local electronic and geometric structure around Ga^{3+} barely changes along the series showing that Ga^{3+} only acts as a constructive element of the crystal structure. On the contrary, the intensity of the pre-edge structures at the Mn K-edge shows a continuous decrease as the content of Ga increases. This result indicates a strong mixing of the 3-d states among near-neighbours Mn^{3+} ions. The local geometric structure around Mn^{3+} (MnO_6 octahedron) also changes along the series. Namely, Mn^{3+} evolves from a cooperative static Jahn-Teller regime, as in $LaMnO_3$, to a non-correlated dynamic Jahn-Teller regime ($x > 0.5$). Moreover, this result points to the lack of local tetragonal distortion for isolated Mn^{3+} ions.

1. Introduction

$R_{1-x}A_xMnO_3$ (R = rare earth; A = divalent cation) compounds show a large variety of phase transitions and magnetic arrangements as result of a strong interplay among orbital, lattice, magnetism and transport properties [1, 2]. $LaMnO_3$ [3–5] with an orthorhombic unit cell and a cooperative tetragonal deformation of the MnO_6 octahedron (Jahn-Teller type) at room temperature shows antiferromagnetic (AFM) ordering of A-type below $T_N = 140$ K. The manganese moments are aligned in the [010] direction with the spins coupled ferromagnetically in the *a-b* plane and antiferromagnetically along the c axis. Variations in the oxygen stoichiometry [5] or doping [1, 2] induce ferromagnetic interactions in these compounds. The substitution of La by a divalent cation leads to ferromagnetic and conductive compounds without tetragonal deformations of the MnO_6 octahedron. This ferromagnetic (FM) interaction is ascribed to the double exchange mechanism between Mn^{3+} and Mn^{4+} [6]. FM interactions can also be induced by substitution of Mn by another transition metal [7–12]. In $LaMn_{1-x}Ni_xO_3$, ferromagnetism can be explained by a strong superexchange [11, 12] FM interaction between Mn^{4+} and Ni^{2+}. However, the replacement of Mn^{3+} by a non-magnetic trivalent ion such as Ga^{3+} or Sc^{3+} also induces ferromagnetism [8, 10].

$LaMn_{1-x}Ga_xO_3$ series was matter of our interest with the aim to determine the change of properties as a function of the dilution of manganese with a non-magnetic trivalent metal as gallium [13]. We note that substitution with gallium does not change the valence state of manganese. The replacement of Mn by Ga induces a continuous decrease of the tetragonal distortion of the MO_6 (M = Mn, Ga) octahedron being practically regular for $x \geq 0.6$. Simultaneously, a FM component appears that it is explained in terms of a canting of the A-type AFM structure. The FM component increases with the Ga content up to $x = 0.5$ where a collinear ferromagnetism is observed. For $x \geq 0.6$, the system evolves from collinear ferromagnetism into superparamagnetism. The pure A-type AFM structure only appears for the undoped sample, $LaMnO_3$, in which a complete cooperative ordering of the local tetragonal distortions occurs. The ordering degree of this tetragonal distortion, observed by the decrease of the cell distortion in the orthorhombic structure, seems to be the origin of the sign change in the magnetic interactions. Recently we have studied the local structure above the Jahn-Teller transition temperature (T_{JT}) obtaining that the MnO_6 octahedron is already distorted above T_{JT} and consequently, the change of magnetic interaction observed in this system should be due to an order-disorder transition [14].

To determine the origin of the change from antiferromagnetism to ferromagnetism with Mn dilution, an accurate characterisation of the series is needed. Previous diffraction studies give information on the average of interatomic distances and geometry for atoms, manganese and gallium. In order to obtain information on the local geometry on each individual atom, a selective technique was used in the present study. We report here, the study of the electronic and local structure around the two metals by means of X-ray absorption spectroscopy at Mn and Ga K-edges in $LaMn_{1-x}Ga_xO_3$ series. As we will show, the tetragonal distortion of the MnO_6 octahedra decreases with x and it results in a decrease of the orthorhombic distortion of the unit cell. In other words, the crystal structure and the magnetic ordering changes with increasing the content of gallium and this effect is due not only to the disorder induced by the substitution but also to the change on the local structure at the manganese atom.

2. Experimental

We have studied $LaMn_{1-x}Ga_xO_3$ samples with $x = 0$, 0.1, 0.2, 0.4, 0.6, 0.8 and 1. The synthetic route and crystallographic structure have been reported elsewhere [13]. All samples were characterised as single-phase perovskites by X-ray powder diffraction at room temperature. The oxygen content of the samples was analysed using standard redox titration with $KMnO_4$ and Mohr salt. The samples were oxygen-stoichiometric within the analysis accuracy (± 0.02).

X-ray-absorption measurements at the metal K-edge were carried out at the BM29 beam line at the European Synchrotron Radiation Facility (Grenoble, France). A fixed-exit Si(311) double crystal monochromator was used, the estimated energy resolution being $\Delta E/E = 6 \times 10^{-5}$. The absorption spectra were recorded in transmission mode at room temperature using ionisation chambers as detectors. EXAFS spectra ($\chi(k)$) were obtained by removing the smooth atomic absorption coefficient (μ_0) by means of a cubic spline [15]. The spectra were analysed using FEFF 8.10 package that allows correlating Debye-Waller factor (DW) with the interatomic distances. The structural analysis was performed

*email: gloria@unizar.es

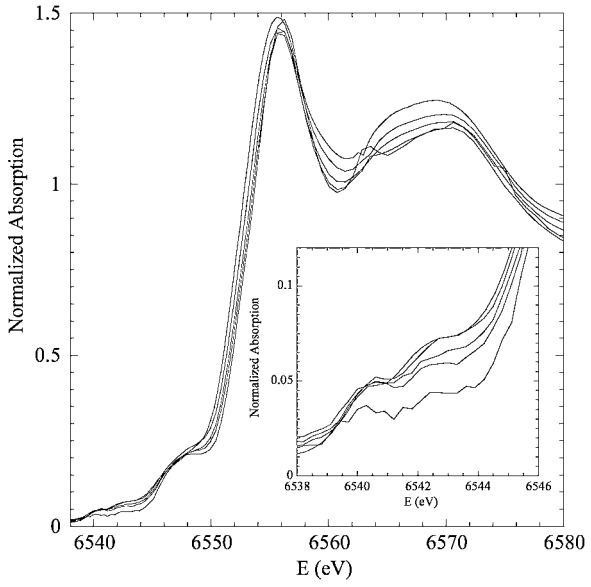

Fig. 1. Normalized Mn K-edge XANES spectra for $LaMn_{1-x}Ga_xO_3$ samples (from left to right $x = 0.0$, 0.2, 0.4, 0.6 and 0.8). Inset: Detail of the pre-peak structures.

in the R-space fitting mode including multiple scattering terms up to 4 Å [16]. XANES spectra were normalized to the high part of the spectrum (around 100 eV above the absorption edge) after a linear background subtraction [15].

3. Results

The Mn K-edge XANES spectra of $LaMn_{1-x}Ga_xO_3$ ($x = 0$, 0.2, 0.4, 0.6 and 0.8) at room temperature are shown in figure 1. The spectra are characterised by a main resonance at the edge corresponding to $1s \rightarrow \varepsilon p$ transitions and a pre-peak structure around 15 eV below the edge. The pre-peak is displayed in more detail in the inset of figure 1. All the spectra are very similar to each other as expected for compounds with a similar perovskite structure. A continuous chemical shift to higher energies is observed from $LaMnO_3$ to $LaMn_{0.2}Ga_{0.8}O_3$. The chemical shift, correlated with the valence state, between $LaMnO_3$ (Mn^{3+}) and $CaMnO_3$ (Mn^{4+}) has been determined to be 4.3 eV [11]. In the $LaMn_{1-x}Ga_xO_3$ series, a maximum shift of 0.5 eV was found. Accordingly, we can deduce a similar valency for the Mn along this series, as expected from the homovalent substitution between Mn^{3+} and Ga^{3+}.

The pre-peak structure is ascribed to $1s \rightarrow 3d$ transitions either quadrupole-allowed or dipole-forbidden. The latter becomes allowed due to a strong mixing of O 2p and Mn 3d states. It has been recently suggested [17] that the pre-peaks have their origin in the density of d-states of the neighbouring transition metal atoms, showing the mixing of d states between different atoms, through hybridisation with the oxygen p-band. The intensity of the pre-peaks decreases with increasing the content of Ga. According to the previous model [17], near neighbours Mn atoms are replaced with Ga that has 3d orbitals fully filled. Therefore, $LaMn_{1-x}Ga_xO_3$ samples have less available empty 3d states with increasing x. We also note that the pre-peak shape is unaltered after dilution indicating a similar splitting of the Mn d-band for all samples.

The Ga K-edge room-temperature XANES spectra of the $LaMn_{1-x}Ga_xO_3$ series, not shown here, are very similar to each other, indicating that the local electronic and geometrical structures around Ga^{3+} do not change along the series.

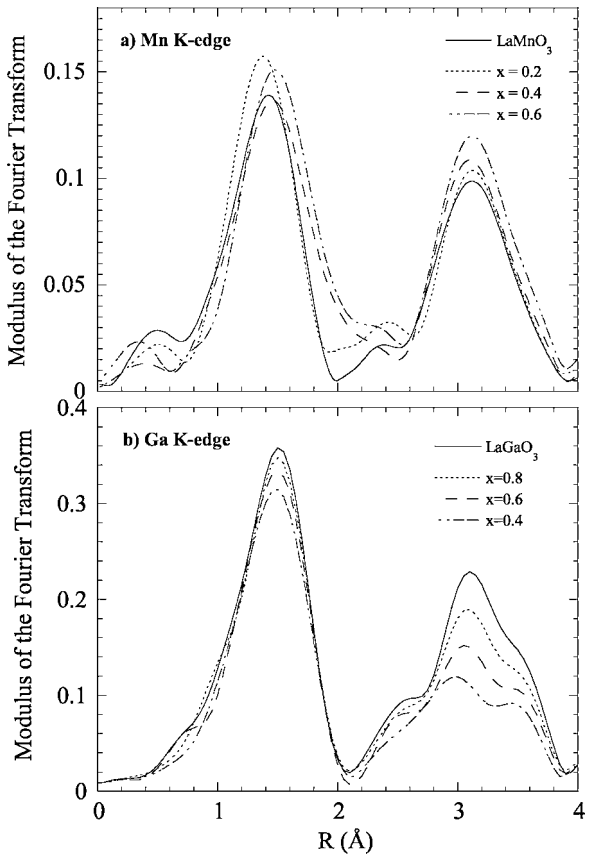

Fig. 2. Modulus of the k-weighted Fourier Transform of the EXAFS spectra of $LaMn_{1-x}Ga_xO_3$ samples at a) Mn K-edge and b) Ga K-edge.

Figure 2a shows the modulus of the Fourier transform at the Mn K-edge. The k-weighted Fourier Transform between 3.0 and 12.0 $Å^{-1}$ was calculated using a Gaussian window. Two main peaks corresponding to first (Mn-O) and second (Mn-La, Mn-Mn, Ga and Mn-O) coordination shells are noticeable. The peak corresponding to the second coordination shell increases as the Ga content increases in agreement to the diminution of the crystallographic orthorhombic distortion. However, the first peak corresponding to the Mn-O coordination does not show a monotonic evolution with the Mn dilution. If the tetragonal distortion decreased with the content of gallium in the sample, a continuous increase of the peak height should be observed. The quantitative analysis of the EXAFS spectra indicates that Mn-O environment is highly distorted in the whole series. Nevertheless, we note a continuous change along the series between two types of MnO_6 distortions that, in principle, can be ascribed to two different Jahn-Teller regimes (static or dynamic) [18]. The main results of the structural analysis are summarised in Fig. 3. This analysis gives interatomic (Mn-X (X = O, Mn or Ga, La) distances in agreement with the crystallographic data [13, 14]. For instance, Mn in $LaMnO_3$ is surrounded by four oxygens at 1.94 Å (hereafter denoted as Mn-O_{short}) and by two oxygens at 2.17 Å (Mn-O_{long}). It is worth realizing that the best fits at the Mn K-edge were obtained using four Mn-O_{short} and two Mn-O_{long} in samples with high content of Mn. Samples with low Mn-content instead, showed better fits using a unique Mn-O distance although with a high Debye-Waller factor. Therefore, the MnO_6 local geometry strongly changes along the series. It evolves from a tetragonal-distorted MnO_6 configuration in low Ga-doped samples to a regular MnO_6 octahedron at $x = 0.6$. This result agrees with previous crystallographic studies [13]

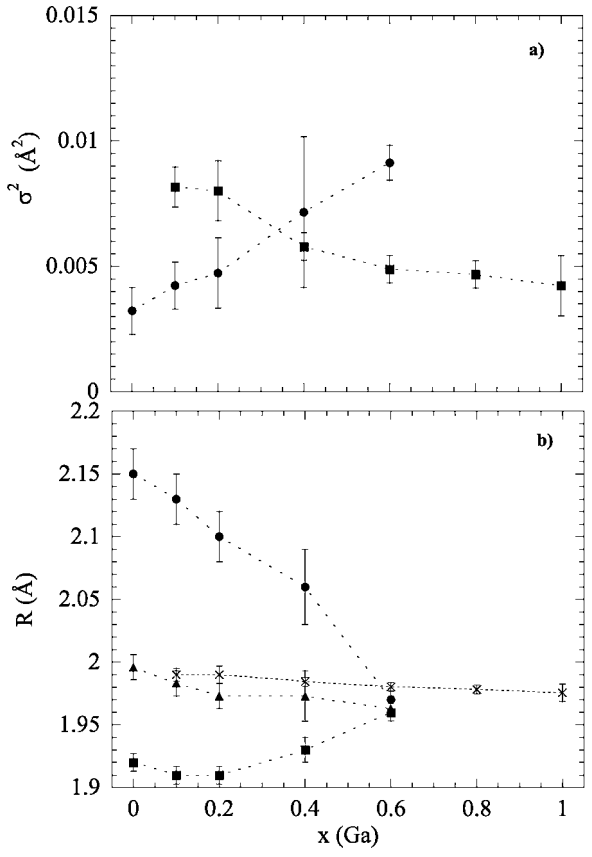

Fig. 3. (a) Average Debye-Waller factor versus x for Mn-O (circles) and Ga-O (squares) distances. (b) Interatomic Mn-O and Ga-O distances. Crosses, circles, squares and triangles refer to Ga-O, Mn-O_{long}, Mn-O_{short} and average Mn-O, respectively.

showing regular MeO_6 octahedra (Me = Mn, Ga) at the same composition. Nevertheless, we observe a significant increase of the Mn-O Debye-Waller factor coupled to the decrease of the tetragonal distortion. In fact, the average mean deviation for the Mn-O distances, obtained from the Debye-Waller factor values, is comparable to the tetragonal distortion observed in the other samples of the series.

Figure 2b shows the modulus of the Fourier Transform at the Ga K-edge taken between 2.4 and 12.5 Å^{-1}. It was obtained from the k-weighted EXAFS spectra for all samples. Two peaks corresponding to first and second coordination shells are also observed. In this case, the intensity of both peaks increases as the content of Ga does. The first peak (first coordination shell) is alike for all the samples. Only a slight decrease in the intensity can be observed with decreasing the content of Ga. It can be related to the structural stress induced by the neighbouring anisotropic Mn^{3+} ions. Anyway, the shape and intensity of this peak seems to indicate a high symmetrical oxygen environment around the Ga^{3+} ions for all samples.

The structural analysis for the Ga-edge is also displayed in Fig. 3. All samples show regular GaO_6 octahedra. The interatomic Ga-O distance remains almost constant for the whole series although we observe a continuous increase of the Ga-O Debye-Waller factor with decreasing the content of Ga. This is related to the mentioned intensity decrease of the first peak in Fig. 2b and we think it is a hallmark of the local structure stress induced by neighbouring MnO_6 with tetragonal distortion.

Finally, we also note that the average Mn-O interatomic distance (triangles in fig. 3) is very similar to the Ga-O distances, in agreement with the formation of a solid solution between Mn and Ga.

4. Discussion

The XAS study performed on this series allows us to provide a complete structural description of this system. The $LaMn_{1-x}Ga_xO_3$ compounds are formed by two kinds of octahedra: regular GaO_6 and distorted MnO_6, as expected. The non-magnetic Ga^{3+} ion ($3d^{10}$ configuration) acts as a building element of the crystal structure without participating in the magnetic interactions. On the other hand, the evolution of the distortion of the MnO_6 octahedron along the series should be matter of a detailed discussion. $LaMnO_3$ is formed by MnO_6 octahedra with a tetragonal distortion. At $T < T_{JT}$, the tetragonal-distorted octahedra are ordered in an antiferrodistortive pattern, *i.e.* Mn-O_{long} and Mn-O_{short} are alternated in the two directions of the *ab* plane (considering the frame of the Pbnm space group) whereas at $T > T_{JT}$, these tetragonal distortions are dynamically disordered [14]. The local tetragonal distortion on each MnO_6 octahedron is thought to be originated by the Jahn-Teller effect that removes the degeneration of the e_g states. Within this framework, one would expect that substitution of Mn by Ga give rise to a set of distorted MnO_6 octahedra randomly located in the bulk structure. However, we have shown that tetragonal distortion decreases continuously as the content of Mn does, MnO_6 being regular for $x = 0.6$. It is well known that Jahn-Teller theory differentiate two coupling regimes. These regimes give rise to different type of distortions: dynamic and static [18]. The dynamic regime is characterised by a linear coupling term higher than the anisotropic coupling one. Accordingly, the minimum of the Q3Q2 distortion modes lies in the so-called 'Mexican hat'. This means that MnO_6 freely fluctuates between the compressed and expanded tetragonal distortions along the three octahedral axes. On the other hand, the static regime can be viewed as the transformation from the 'Mexican hat' into a 'tricorn hat'; so only three tetragonal distortions (compressed or expanded) are accessible to the system. Taking into account that the MnO_6 octahedron is described by a regular octahedron with an unusual high Mn-O Debye Waller factor for $x \geq 0.6$, it can be described as a Jahn-Teller system in the dynamic regime. On the contrary, the tetragonal distortion of $LaMnO_3$ belongs to the static Jahn-teller regime where the distortions are oriented below T_{JT} [14]. Summarising, the dilution by gallium of the $LaMnO_3$ lattice produces a continuous change from the cooperative static Jahn-Teller regime of the MnO_6 octahedra into a non-correlated dynamic Jahn-Teller regime for $x \geq 0.6$ samples. Finally, we can also conclude that the increase of the ferromagnetic interactions with the gallium content is correlated with the regime change of the Jahn-Teller effect.

Acknowledgements

This work was supported by the Spanish CICyT MAT02-01221 project. We thank ESRF for granting beam time.

References

1. Coey, J. M. D., Viret, M. and Von Molnar, S., Adv. Phys. **48**, 167 (1999).
2. Dagotto, E., Hotta, J. and Moreo, A., Phys. Rep. **344**, 1 (2001).
3. Wollan, E. O. and Koehler, W. C., Phys. Rev. **100**, 545 (1955).
4. Huang, Q. *et al.*, Phys. Rev. B **55**, 14 987 (1997).
5. Ritter, C. *et al.*, Phys. Rev. B **56**, 8902 (1997).
6. Zener, C., Phys. Rev. **82**, 403 (1951).

7. Goodenough, J. B., Wold, A., Arnott, R. J. and Menyuk, N., Phys. Rev. **124**, 373 (1961).
8. Zhou, J.-S., Yin, H. Q. and Goodenough, J. G., Phys. Rev. B **63**, 184423 (2001).
9. Hébert, S. *et al.*, Phys. Rev. B **65**, 104420 (2002).
10. Goodenough, J. B., Dass, R. I. and Zhou, J., Solid State Sci. **4**, 297 (2002).
11. Sánchez, M. C., García, J., Blasco, J., Subías, G. and Pérez-Cacho, J., Phys. Rev. B **65**, 144409 (2002).
12. Blasco, J. *et al.*, Eur. Phys. J. B **30**, 469 (2002).
13. Blasco, J., García, J., Campo, J., Sánchez, M. C. and Subías, G., Phys. Rev. B **66**, 174431 (2002).
14. Sánchez, M. C., Subías, G., García, J. and Blasco, J., Phys. Rev. Lett. **90**, 45503 (2003).
15. Koningsberger, D. C. and Prins, R., "X-ray absorption: Principles, application, techniques of EXAFS, SEXAFS and XANES" (John Wiley, New York 1988).
16. Stern, E. A., Newville, M., Ravel, B., Yacoby, Y. and Haskel, D., Physica B **208&209**, 117 (1995). http://FEFF.phys.washington.edu/.
17. Joly, Y., Cabaret, D., Renevier, H. and Natoli, C. R., Phys. Rev. Lett. **82**, 2389 (1999).
18. Abragam, A. and Bleaney, B., "Electron paramagnetic resonance of transition ions" (Clarendon Press, Oxford 1970), p. 792.

Physica Scripta. Vol. T115, 645–647, 2005

Analysis for Fe-*M* (*M* = Si, Al, Sn) Alloys by Multiple Scattering X-Ray Magnetic Circular Dichroism of Fe K-Edge

K. Okamoto[1*], S. Nagamatsu[2], E. V. Voronina[3], T. Miyanaga[4] and T. Fujikawa[1]

[1]Grad. School for Sci., Chiba Univ., 1-33, Yayoi-cho, Inage, Chiba 263-8522, Japan
[2]Center for Frontier Electronics and Photonics Chiba Univ. 1-33, Yayoi-cho, Inage, Chiba 263-8522, Japan
[3]Physical-Technical Institute of UrDRAS, 132 Kirov Str, Izhevsk 426001, Russia and
[4]Department of Materials Science and Technology, Faculty of Science and Technology, Hirosaki Univ. Hirosaki, Aomori 036-8561, Japan

Received June 26, 2003; accepted November 4, 2003

Abstract

We have measured Fe K-edge XMCD of Fe-metalloid (Si, Al, Sn) in the ferromagnetic and glass-like phases, where the latter phases are only observed for Fe-Al and -Sn systems in the high-concentration region. The observed characteristic features of the XMCD spectra for this state can be explained by use of full multiple scattering relativistic theory within Mattis' magnetic model.

1. Introduction

Spin-glasses show specific magnetic properties conditioned by frustration and randomness of exchange interaction. Sometimes they have small amount of magnetic atoms (about 0.1–10%) randomly distributed in metals, which have competitive exchange interaction.

Cannela and Mydosh measured susceptibility of gold alloy mixed with low concentration Fe atoms, which showed a sharp cusp near the critical temperature [1]. This result was explained by randomly frozen magnetic moments. Ylsukov *et al*. measured the Mössbauer effect for Fe-metalloid (Si, Al, Sn) alloys to study magnetic properties, which demonstrated in the high-concentration range some unusual magnetic behavior [2]. Detailed explanation of this interesting behavior has not been given yet. Mattis [3] considers a theoretical model of spin structure in which the magnetic moments are oriented in two opposite directions in such a way that each of the magnetic moments are randomly distributed in the lattice, whereas the magnetic moments are in the same directions in the same domains [4]. In the literature, this state is known as a Mattis' magnets or Mattis' spin glass.

The study of such random spin structures by XMCD approach is of great interest in virtue of its sensitivity to the value and direction of particular local magnetic structures. In this work, we have studied Fe-metalloid (Si, Al, Sn) alloys by Fe K-edge XMCD to clarify the local geometric, electronic and magnetic structures. In particular, we focus our attention on spin glass models.

2. Theory

The multiple scatterings play an important role in the analyses of XANES spectra; that is also the case for the XMCD analyses in the near edge region. As long as we neglect the relativistic effects at the nearby atoms (this approximation is proved to be reliable as shown in Ref [5]), we can easily renormalize the multiple scattering series,

$$T^{\infty} = T^{(0)} + T^{(1)} + \cdots \tag{1}$$

which is crucial in the near-edge XMCD analyses. The details are shown elsewhere [6].

Here we use a relativistic XMCD theory developed by us. We have observed good convergence in regard to the cluster size for ∼60 atoms.

3. Experiment

Nanocrystalline disordered powders of Fe-Si, -Al and -Sn alloys obtained by mechanical grinding in a planetary ball mill were taken for investigation. The average size of the powder particles was 2 μm for Fe-Si, 1–2 μm for Fe-Al and 4 μm for Fe-Sn alloys. XMCD spectra for Fe K-edge (7.130–7.180 keV) for the Fe-metaloid (Si, Al, Sn) samples were measured at BL28B OF Photon Factory in KEK (2.5 GeV) with circularly polarized X-rays that were generated by an ellipsoid multi-pole wigler and monochromatized using a Si(111) double-crystal monochromator [7, 8]. The absorption spectra were measured in transmission mode at 20 K. The XMCD signals were detected by ionization chambers filled by N_2 gas. Instead of switching helicity of the incident photons, the applied magnetic field, about 0.6 T which was still enough to saturate the magnetization of the sample, was reserved every 4 seconds to obtain MCD effect.

4. Results and Discussion

The magnetic structures of Fe-*M* (*M*=Si, Al, Sn) alloys depend on the metalloid concentration. When the metalloid concentration increases, we find a specific change of the magnetic moment on the Fe atom and of the geometric structure by using Mössbauer spectroscopy and XRD [4]. Figure 1 shows experimental Fe K-edge XMCD spectra for Fe-Al and Fe-Sn alloys, which only show the change of the intensity through the phase transition from ferromagnetic phase to spin glass phase. To explain these specific feature we calculate the Fe K-edge XMCD spectra for these systems.

First we calculate the Fe K-edge XMCD for crystalline ferromagnetic Fe_3Si, and compare it with the experimental one.

Table I. *The magnetic moment of Fe atoms at site Fe-1 and Fe-2 in Fe-M (M = Si, Al, Sn) alloys [9].*

Fe-M	Fe-1 (μ_B)	Fe-2 (μ_B)
Fe_3Si	2.30	1.35
Fe_3A1	2.18	1.50
Fe_3Sn	2.30	2.30

*Electronic address: Okamoto@graduate.chiba-u.jp

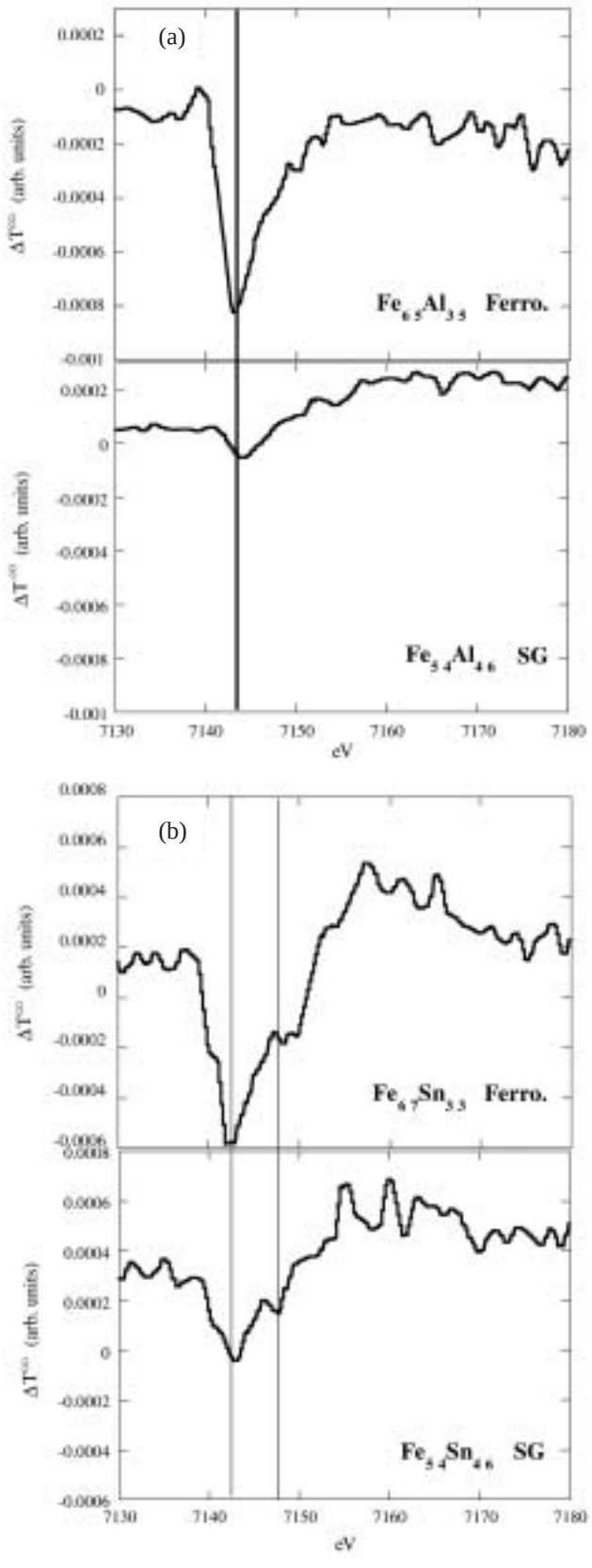

Fig. 1. Experimental Fe K-edge XMCD for ferromagnetic (Ferro.) $Fe_{65}Al_{35}$ and $Fe_{67}Sn_{33}$, spin glass (SG) $Fe_{54}Al_{46}$ and $Fe_{54}Sn_{46}$. In both alloys, XMCD shows no energy shift of the negative main peak, but changes the intensity in different magnetic phases.

We should note that there exist two different Fe sites, Fe-1 and Fe-2 with the ratio 1 : 2. For the present calculation we refer to the spin magnetic moments estimated by first-principle density-functional calculations based on ultrasoftpseudopotentials and all electron methods [9], which are listed in Table I. Figure 2 shows the calculated result compared with the experimental one; the energy 0 is set to be the onset of the Fe K-edge absorption. Satisfactory agreement is obtained. We have also obtained good results both for ferromagnetic Fe_3Al and Fe_3Sn.

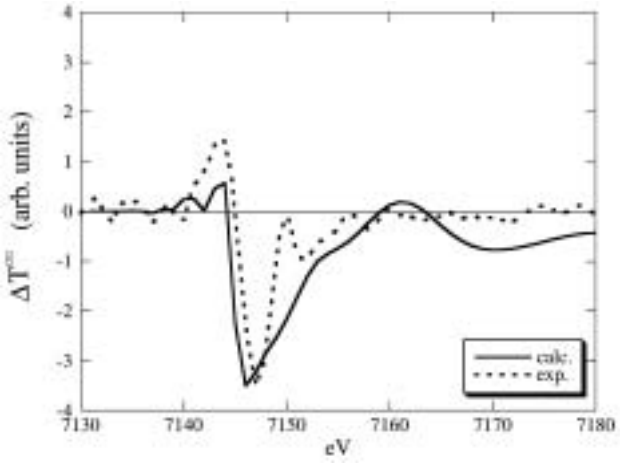

Fig. 2. Calculated (solid line) and experimental (dotted line) Fe K-edge XMCD in crystalline ferromagnetic Fe_3Si.

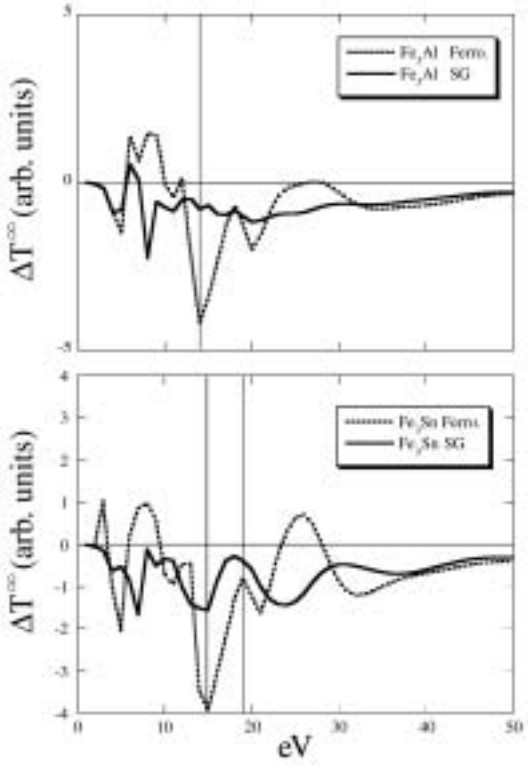

Fig. 3. Calculated XMCD spectra for Fe_3Al and Fe_3Sn glass-like models (solid lines) compared with the ones in ferromagnetic phase (dotted lines).

We next calculate the Fe K-edge XMCD spectra for some glass-like models where the spin orientation is randomly distributed in the whole space. To study these models we consider a simplified model where half of the Fe atoms in the first and second shells around an X-ray absorbing atom *A* have (−) spin whereas the others including the atom *A* have (+) spin for simplicity. Figure 3 shows the calculated XMCD spectra for the Fe_3Al and Fe_3Sn alloys according to this model compared with the ones in the ferromagnetic phase. We show the sum of the site-1 and -2 XMCD

with the weights of the different sites

$$\frac{1}{3}\Delta T^{\infty}(1) + \frac{2}{3}\Delta T^{\infty} \tag{2}$$

where $\Delta T^{\infty}(1)$ is the XMCD at the Fe-1 site whose fraction is $1/3$. In Fe_3Al the sharp prominent negative peak at about 14 eV observed for the ferromagnetic model is lost but observed at about 8 eV for the classical spin glass model, and the smaller negative peak at 20 eV for the former is lost for the latter. In Fe_3Sn the prominent sharp negative peak at 15 eV shows no peak shift for these models; the classical spin glass model gives rise to a broad shallow peak there. The small negative peak observed at 21 eV for the former is lost but observed at 23 eV for the latter. These calculated results for these glass-like models are not in accordance with the observed experimental results as shown in Fig. 1. We thus can rule out the possibility of glass-like model for these systems.

On the other hand the Mattis spin glass model simply predicts the XMCD

$$x^{+}\Delta T^{\infty}(+) + (1 - x^{+})\Delta T^{\infty}(-) = (2x^{+} - 1)\Delta T^{\infty}(+) \tag{3}$$

where x^{+} is the fraction of magnetic Fe atoms with (+) spin and $\Delta T^{\infty}(+)$ is the XMCD for those magnetic atoms and $\Delta T^{\infty}(+) = -\Delta T^{\infty}(-)$. We should note that each of $\Delta T^{\infty}(\pm)$ are calculated by use of the sum (2). We only expect the overall scale down of the XMCD observed for the ferromagnetic systems depending on x^{+} and no peak shift. The observed spectral changes as shown in Fig. 1 for $Fe_3X(X = \text{Al, Sn})$ are just what we expect from the above equation (3).

5. Concluding Remarks

In this work we have measured iron metalloid Fe K-edge XMCD in ferromagnetic and spin glass phases. The latter phase is only observed for Fe_3A1 and Fe_3Sn. The observed characteristic features in the observed XMCD spectra for the spin glass phase are well explained with aid of Mattis spin glass model. With increase of the metalloid concentration the small domain could be randomly broken into smaller pieces of magnetic domains, which gives rise to scale down of the XMCD. We have assumed the domain size is large enough to apply the simple additive rule as shown by eq. (3), however we should carefully study the interface effects of the domain when the domain size is of the order of $\approx$10 Å.

References

1. Cannella, V. and Mydosh, J. A., Phys. Rev. B **6**, 4220 (1972).
2. Ylsukov, E. P., Voronina, E. V. and Barinov, V. A., J. Magn. Magn. Mat. **115**, 271 (1992).
3. Mattis, D. C., "The Theory of Magnetism 2", (Springer-Verlag, 1985).
4. Ylsukov, E. P., Voronina, E. V., Korolyvo, A. V. and Konygin, G. N., The Phys. Met. Metallogr. **92**, s133 (2001).
5. Fujikawa, T. and Nagamatsu, S., Jpn. J. Appl. Phys. **41**, 2005 (2002).
6. Fujikawa, T. and Nagamatsu, S., J. Elect. Spect. **129**, 55 (2003).
7. Iwazumi, T., Koyama, A. and Sakurai, Y., Rev. Sci. Instrm. **66**, 1691 (1995).
8. Kobayashi, K., Maruyama, H., Iwazumi, T. and Yamazaki, H., Solid Sate Commun. **97**, 491 (1996).
9. Moroni, E. G., Wolf, W., Hafner, J. and Podloucky, R., Phys. Rev. B **59**, 12860 (1998).

Physica Scripta. Vol. T115, 648–650, 2005

Evolution of Ni Local Structure in $NdNiO_3$ Perovskite Across the Metal-Insulator Transition

C. Piamonteze[1,2], H. C. N. Tolentino[1], A. Y. Ramos[1,3], N. E. Massa[4], J. A. Alonso[5], M. J. Martínez-Lopes[5] and M. T. Casais[5]

[1]Laboratório Nacional Luz Síncrotron, Caixa Postal 6192 - 13084-971 - Campinas, SP, Brazil
[2]IFGW, UNICAMP, Campinas, SP, Brazil
[3]LMCP, CNRS-UMR7590, University of Paris VI, Paris, France
[4]LANAIS-CEQUINOR, Universidad Nacional de La Plata, La Plata, Argentina
[5]Instituto de Ciencia de Materiales de Madrid, CSIC, Madrid, Spain

Received June 26, 2003; accepted in revised form December 17, 2003

PACS numbers: 61.10.Ht, 71.30.+h, 72.80.Ga

Abstract

$NdNiO_3$ presents a metal-insulator (*MI*) transition at 200 K with decreasing temperature. This system was characterized by neutron diffraction as orthorhombic with a very symmetric Ni site and almost no modification at the NiO_6 octahedra is observed across the transition. We carried out EXAFS measurements on $NdNiO_3$ from room temperature down to 10 K, crossing the *MI* transition and observed important local modifications at the Ni site. The phase derivative method shows that there are distorted Ni sites, with at least two different Ni-O distances, along all the temperature range measured. The modification across the *MI* transition concerns the increasing of the distorted phase. This hypothesis is sustained by the behavior of the Debye-Waller factor (σ^2) with temperature. With decreasing temperature, when the sample is around T_{MI} σ^2 rapidly increases due to the growing amount of distorted sites. These results give basis for a discussion in terms of a percolative transition.

Transition-metal oxides with perovskite structure exhibit a variety of interesting properties like high-T_C superconductivity and colossal magnetoresistance. These systems have in common a complex interplay between its magnetic, electronic and structural properties. In particular, RNiO$_3$ perovskites (R = rare earth), except for $LaNiO_3$, display metal-insulator phase transition as temperature decreases [1]. RNiO$_3$ systems have a distorted perovskite structure, where the NiO_6 octahedra tilt and rotate to fill the empty space left around the rare earth. Both the degree of distortion and the MI transition temperature, T_{MI}, increase as the R ion becomes smaller. Neutron diffraction results show that the crystallographic structure for systems with R = Pr, Nd and Sm has Pbnm symmetry where the unique Ni site has all Ni-O separations almost equal. Across the transition, minimum modifications at Ni-O distances and a slight change at Ni-O-Ni angles were observed. On the other hand results on Raman spectroscopy together with electron diffraction measurements have showed a structural modification for $NdNiO_3$ thin films across the MI transition that was associated to a Ni orbital ordering [2]. Moreover, also in $NdNiO_3$ films, a charge ordering was observed at the insulating phase [3]. Nevertheless, for systems with smaller R ions (Ho, Y, Er, Tm, Yb and Lu), Alonso *et al.* [4, 5] observed a monoclinic distortion which leads to the existence of two unequivalent Ni sites. When crossing the electronic transition the Pbnm symmetry is established [6] at the metallic phase.

This work presents results on EXAFS (Extended X-ray Absorption Fine Structure) at the Ni K edge (E = 8333 eV) for $NdNiO_3$ (T_{MI} = 200 K) showing modifications at the NiO_6 octahedra across the *MI* transition. The measurements were performed using a Si(111) channel-cut monochromator at the D04B-XAS beamline at LNLS, Campinas, Brazil. In order to perform the measurements, the powder sample is deposited over a cellulose membrane, such that a homogeneous sample optimized for transmission measurements is obtained. A He cryogenerator was used to decrease the sample temperature down to 10 K.

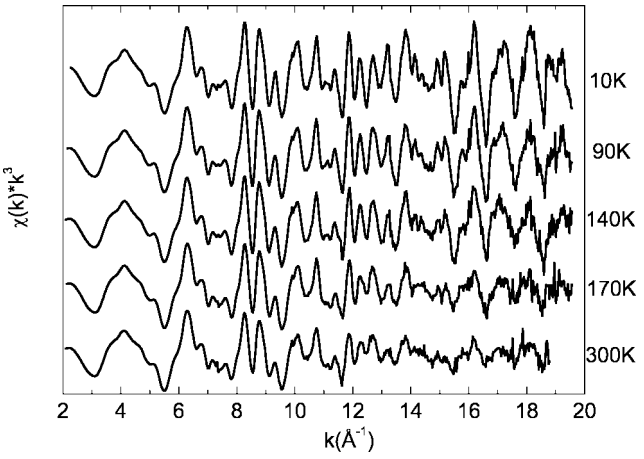

Fig. 1. EXAFS signal weighted in k^3 ($\chi(k) * k^3$) for $NdNiO_3$ (T_{MI} = 200 K). The spectra were translated in vertical for a better visualization.

The EXAFS signal was measured until 19.5 Å^{-1} for several temperatures varying from room temperature down to 10 K. In figure 1 the EXAFS signal is shown for some of the temperatures measured. There are no dramatic changes on the EXAFS signal as the *MI* transition is crossed. It is seen only a continuous increase of the oscillation amplitude with decreasing temperature.

The Fourier Transformed spectra for the measurements at 10 K and at room temperature are shown in figure 2. The dependence of the FT amplitude with temperature is evidenced by the peaks above 2 Å. As temperature is decreased the FT amplitude increases due to smaller thermal damping. However, looking at the first peak on the FT spectra, which comes from the Ni-O coordination shell, it is seen that the amplitude is almost the same, despite the great difference in temperature. Moreover, the Ni-O peak for the data at 10 K shows a splitting that probably comes from the existence of different Ni-O distances.

The multiple Ni-O distances were analyzed using the phase derivative method [7, 8]. This method is based on the fact that a filtered EXAFS signal that is formed by different interatomic distances presents a beating in the amplitude function and an inflexion point on the phase function. The position of this inflexion point (named k_b) gives a numeric estimate of the separation among the interatomic distances, in the case of being only two, given by $\Delta R = \pi/(2k_b)$. Figure 3 shows the phase functions for all temperatures measured. At the right side of figure 3 the correspondent first derivative of the phase functions are shown

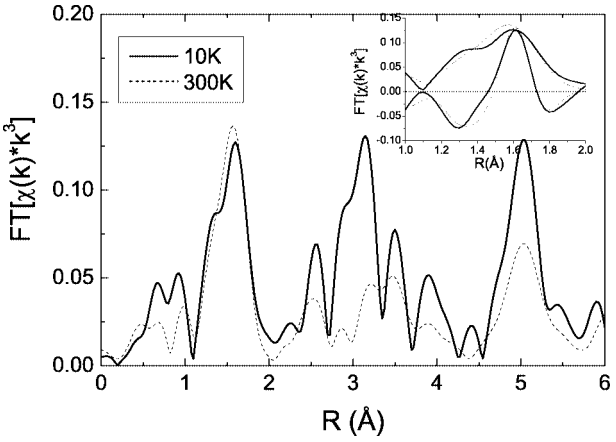

Fig. 2. Fourier Transform of the EXAFS signal for $NdNiO_3$ ($T_{MI} = 200$ K) at 10 K and room temperature.

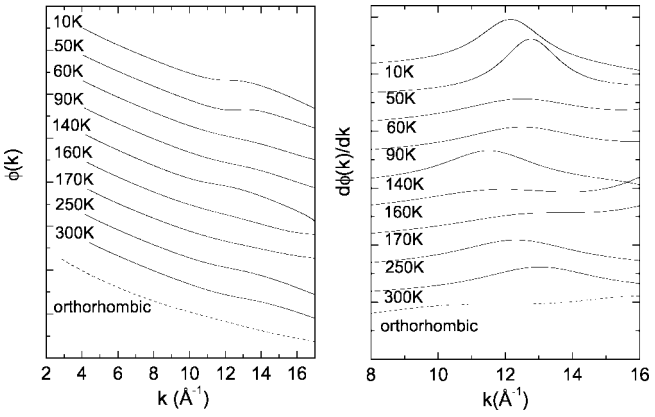

Fig. 3. Left, phase functions, and right, their corresponding first derivative. The curves were translated in vertical in order to have a better visualization.

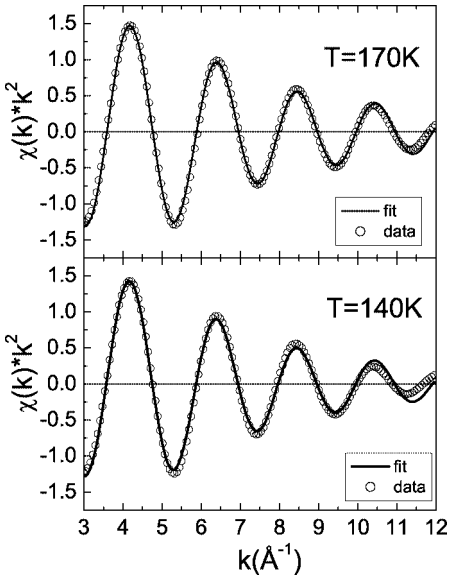

Fig. 4. Fit of the filtered EXAFS signal with one Ni-O distance.

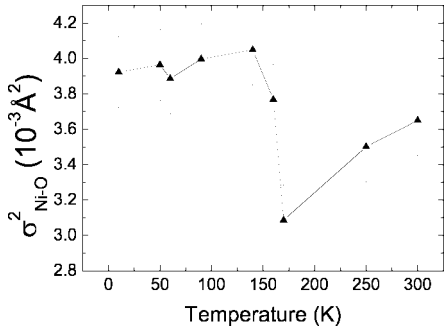

Fig. 5. Debye-Waller factor obtained from the fit of the $NdNiO_3$ data. See text for details.

to facilitate the visualization of the inflexion point. Taking the position of the inflexion point from these curves we obtain a separation of 0.13 Å between the different Ni-O distances. The most interesting result of the phase derivative method is that the inflexion point does not completely disappear at the metallic phase, indicating that some portion of distortion is still present and, then, that the structural transition is wider than the *MI* transition. The dotted line in figure 3 shows the phase function (and its first derivative) extracted from a simulated EXAFS signal using the crystallographic parameters found for $NdNiO_3$ [9]. Since the Ni-O distances found from diffraction are practically identical, the inflexion point is not seen for the simulated signal. Therefore, for none of the temperatures measured it is seen such a symmetric site for Ni from our EXAFS data.

The fitting of the filtered EXAFS signal with two different Ni-O distances using the complete range measured turned out to be very difficult due to the number of free parameters. Instead, we analyzed the data upto $k = 12\,\text{Å}^{-1}$. From figure 3 it is seen that the beating is localized between 12 and 13 Å^{-1}. Therefore, cutting the data at $12\,\text{Å}^{-1}$ we reduce the resolution and the different Ni-O distances are no longer distinguishable. So, a fitting with a unique Ni-O distance is possible. Figure 4 shows the fitted curve compared to the experimental signal for two spectra measured at different temperatures. The fitting was carried out using theoretical phase and amplitude functions obtained considering symmetric NiO_6 octahedra. The amplitude reduction factor (S_0^2) was maintained constant between different temperatures. From this figure it is seen that a unique Ni-O distance fits very well the data in this reduced k-range. Note that the data measured at 140 K show a stronger damping in the end of the spectrum compared to the data measured at higher temperature (170 K). The reason for this will be clarified in the following discussion.

Figure 5 shows the evolution of Debye-Waller factors obtained from the fitting as a function of temperature. σ^2_{Ni-O} shows a normal smooth decrease, with decreasing temperature, down to 170 K. Below this temperature, it suddenly increases. The increase in σ^2_{Ni-O} below 170 K is explained by an increase of the structural disorder contribution to the total Debye-Waller measured by EXAFS. Since the phase derivative method shows that distorted Ni sites exist in the metallic and insulating phases, such increase in σ^2_{Ni-O} can be attributed to a growth on the amount of distorted sites. In our fit it was considered only an average Ni-O distance when, in fact, there are more than one different interatomic distance. The width of this distance distribution is included in the Debye-Waller factor, that is also an average over all Ni sites. With the increase of the amount of distorted sites, the average disorder also increases, as figure 5 shows.

All the evidence presented here point to important modifications at Ni sites. The main modification across the *MI* transition comes from an increase of the amount of distorted Ni sites, which are present both in metallic and insulating phases. The fact that this distortion at the NiO_6 octahedra has not been seen by diffraction measurements [9] indicates that it takes place at a local scale and it does not have long range coherence. The

results shown by the phase derivative method together with the behavior of σ^2 with temperature give basis for a discussion over a percolative transition in $R\mathrm{NiO_3}$ systems.

References

1. Lacorre, P. *et al.*, J. Solid State Chem. **91**, 225 (1991).
2. Zaghiroui, M., Bulou, A., Lacorre, P. and Laffez, P., Phys. Rev. B **64**, 81102 (2001).
3. Staub, U. *et al.*, Phys. Rev. Lett. **88**, 126402 (2002).
4. Alonso, J. A. *et al.*, Phys. Rev. Lett. **82**, 3871 (1999).
5. Alonso, J. A., Martínez-Lope, M. J., Casais, M. T., García-Muñoz, J. L. and Fernández-Díaz, M. T., Phys. Rev. B **61**, 1756 (2000).
6. Alonso, J. A. *et al.*, Phys. Rev. B **64**, 94102 (2001).
7. Martens, G., Rabe, P., Schwentner, N. and Werner, A., Phys. Rev. Lett. **39**, 1411 (1977).
8. Jaffrès, H. *et al.*, Phys. Rev. B **61**, 14628 (2000).
9. García-Muñoz, J. L., Rodríguez-Carvajal, J., Lacorre, P. and Torrance, J. B., Phys. Rev. B **46**, 4414 (1992).

Physica Scripta. Vol. T115, 651–653, 2005

Information in Magnetic EXAFS

A. L. Ankudinov[1], J. J. Rehr[1], H. Wende[1,2] and K. Baberschke[2]

[1]Dept. of Physics, Box 351560, University of Washington, Seattle, Washington 98195, USA
[2]Institut für Experimentalphysik, Freie Universität Berlin, Arnimallee 14, D-14195 Berlin-Dahlem, Germany

Received June 26, 2003; accepted February 6, 2004

PACS numbers: 78.70.Dm, 78.20.Ls, 75.50.Cc

Abstract

To understand the information one can obtain from MEXAFS, we develop a theory of MEXAFS within the spherical wave approximation. We show that the dominant signal is directly proportional to the magnetic moment per atom and smaller than regular EXAFS by an order of magnitude. We show that this explains the observed temperature dependence of MEXAFS. The higher order correlation functions can, in principle, be determined from double scattering paths, but they give contributions which are smaller by another two orders of magnitudes compared to that from the spin moment. Thus MEXAFS can serve as an alternative method for the element specific extraction of total spin magnetic moments. This can be achieved by modification of the regular EXAFS fitting routines and the output of the spin-dependent FEFF8 code.

Magnetic EXAFS is defined as the difference between the EXAFS signal for right and left circular polarized X-rays. This signal is typically very small, and one needs 3rd generation synchrotron sources to determine its temperature dependence. Thus accurate measurements of this effect became possible only recently [1–6]. The first theory and calculations of MEXAFS were developed assuming perfect ordering of spins (i.e., zero temperature) [7, 8]. Even the first experiment showed that MEXAFS amplitude is dominated by the total spin moment per atom [1, 2]. In this paper we generalize the theory of MEXAFS for nonperfect spin ordering, and determine the sensitivity of MEXAFS to the moments of the spin distribution.

For a ferromagnet at zero temperature the MEXAFS signal has been shown to be proportional to the difference in absorption between spin-up and spin-down electrons [7]. Using the spherical wave approximation [9] to facilitate understanding, the MEXAFS signal in Eq. (17)–(19) of [7] can be rewritten as a sum over individual path contributions:

$$\chi_M^{N-1}(k) = \mathrm{Im} C_{jl}\, \hat{\rho}_1 \cdot \hat{\rho}_N \prod_{n=1}^{N} \frac{\mathrm{e}^{\mathrm{i}\rho_n}}{\rho_n} \left[\mathrm{e}^{\mathrm{i}2\delta_\uparrow} \prod_{n=1}^{N-1} f_n^{\uparrow}(\theta_n) - \mathrm{e}^{\mathrm{i}2\delta_\downarrow} \prod_{n=1}^{N-1} f_n^{\downarrow}(\theta_n) \right], \quad (1)$$

where k is the wavevector of the photoelectron produced from an initial state with total momentum j, $\uparrow$ and $\downarrow$ indicate the direction of the photoelectron spin $s = \pm 1/2$. Here the scattering path consists of $N-1$ scatterers at positions $\boldsymbol{R}_\mathrm{i}$ and one absorbing atom at $\boldsymbol{R}_0 = \boldsymbol{R}_N$; $\boldsymbol{\rho}_n = k(\boldsymbol{R}_n - \boldsymbol{R}_{n-1}) = \hat{\rho}_n \rho_n$, and $\rho_n = |\boldsymbol{\rho}|$; θ_n is angle between $\boldsymbol{\rho}_n$ and $\boldsymbol{\rho}_{n+1}$; f_n^s is a scattering amplitude at n-th scatterer; and δ_s is the central atom phase shift. We will denote the corresponding phase factor as $f_N^s = \exp(\mathrm{i}\delta_s)$, as this will simplify our expressions.

Thus we take the standard picture of MEXAFS and separate the process into a) the production of spin-polarized photoelectrons, which is determined by atomic physics (i.e., the Fano effect), and b) the propagation of spin-polarized photoelectrons through the solid. Due to the strong spin-orbit interaction in the initial state, right (left) circularly polarized light produces more photoelectrons with spin-up (spin-down) along the X-ray k-vector. The excess is determined by Clebsh-Gordon coefficients and leads to a prefactor $C_{jl} = (-)^{j-l-1/2} l/(2j+1)$ in the Eq. (1), that depends on the initial state total j and orbital l momenta. For the initial s-states ($l = 0$) one has to include the small spin-orbit interaction in the final state. The approximate expression for this case is given by Eq. (9) [10]. Assuming that spin-orbit splitting is approximately constant, one can show that Eq. (1) for MEXAFS still holds with a different prefactor proportional to a derivative of signal with respect to energy $C_{1/2,0} = (\Delta_{so}/3)\delta/\delta E$. Notice that for each scattering path the derivative may be replaced with $2\mathrm{i}R/k$, since the fastest changing term with energy is $\mathrm{e}^{2\mathrm{i}kR}$ with $2R$ being the total path length.

During propagation the photoelectron scatters from sites which possess spin moments $\boldsymbol{s}_i$. In this work we will neglect the spin-flip processes and assume that scattering depends on the projection of $\boldsymbol{s}_i \cdot \boldsymbol{s}$. The scattering amplitudes are directly connected with the spin-dependent potentials at a given site, which are small perturbations on the average scattering potential. Thus the scattering amplitude is dominated by linear dependence on both spins. For example, the phase shifts and scattering amplitudes can be calculated via a generalized Born approximation. Since according to density functional theory [11] the spin-dependent potential is determined by the total spin-density, we can always write the spin dependent scattering amplitude as a linear combination:

$$f_n^s(s_n) = f_{n,0} + s\, s_n f_{n,1}, \quad (2)$$

where s_n is the projection of total spin on a scatterer on the X-rays k-vector. Higher order terms in $(\boldsymbol{s} \cdot \boldsymbol{s}_n)$ can be included in the above expansion, since this scattering amplitude should stay the same if we switch the sign for photoelectron spin and spin s_n. But such higher order terms will give an order of magnitude smaller contribution for each consecutive term, as demonstrated in Fig. 1.

The ratio $f_{n,1}/f_{n,0}$ for the central atom and for the backscattering amplitude for Gd metal (Fig. 1) exhibit significant energy dependence. However the typical ratio is about 0.1, which implies that magnetic scattering is an order of magnitude smaller. This is true even for the $4f^7$ configuration of Gd where one can expects the largest magnetic scattering, since all 4f electrons have spin-up in this case.

Since MEXAFS, apart from an atomic prefactor, is given by the difference between the absorption for spin-up and spin-down photoelectrons, one can generalize the MEXAFS calculation for arbitrary spin distributions using spin-dependent scattering

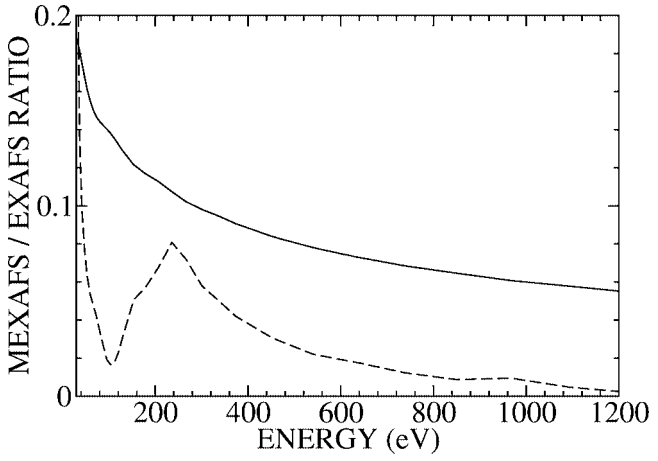

Fig. 1. The Gd metal ratio of $s_n f_{n,1}/f_{n,0}$ for the absorbing atom phase shift (solid) and the nearest neighbor backscattering amplitude (dashes) vs. energy above the L_3 edge. The ratio is plotted for the zero temperature with $s_n = 7/2$, which is appropriate for the ratio between MEXAFS and EXAFS (see Eq. (9)). Since the ratio is mostly below 0.1 the MEXAFS signal is proportional to the total spin on each site as discussed in text.

amplitudes as

$$\chi_M^{N-1}(\{s_n\}) = \mathrm{Im}\frac{C_{jl}\,\mathrm{e}^{2ikR}\hat{\rho}_1\cdot\hat{\rho}_N}{\prod_n \rho_n}\sum_s 2s\prod_n f_n^s(s_n), \tag{3}$$

where $2R$ is the total path length, and the spin of the photoelectron is $s = \pm 1/2$, and $\{s_n\}$ denotes the spin configuration: spin s_1 on atom 1, s_2 on atom 2 and s_N on atom N.

To obtain the observed signal we need to sum the results calculated for a given spin configuration $\{s_n\}$, weighted with the probability $P(s1, s2, \ldots, s_N)$ to find that spin configuration,

$$\chi_M^{N-1} = \int \mathrm{d}(s_1)...\mathrm{d}(s_N)\chi(\{s_n\})P(\{s_n\}). \tag{4}$$

Experimentally it is found that the main contribution to MEXAFS signal comes from single scattering paths and multiple scattering paths with three or fewer atoms [1, 3]. This means that the MEXAFS signal can be calculated if the 4-point spin-distribution function $P(s_1, s_2, s_3, s_4)$ is known. Fortunately, one does not need to know the distribution function precisely to analyze the MEXAFS data. This is because an expansion of the scattering amplitudes in powers of ss_i only picks up certain moments of the distribution function.

First, we demonstrate this for the single scattering contribution to MEXAFS. Within the spherical wave scattering limit,

$$\chi_M^1(s_1, s_2) = \mathrm{Im}\frac{C_{jl}\mathrm{e}^{2ikR}}{\rho_1\rho_2}(s_1 f_{1,1} f_{2,0} + s_2 f_{2,1} f_{1,0}), \tag{5}$$

so integrating over distribution functions, we obtain

$$\chi_M^1 = \mathrm{Im}\frac{C_{jl}\mathrm{e}^{2ikR}}{\rho_1^2}(\langle s_1\rangle f_{1,1} f_{2,0} + \langle s_2\rangle f_{2,1} f_{1,0}). \tag{6}$$

Thus the single scattering MEXAFS can be used to measure the average spin on each element, and is independent of spin-spin correlation function.

A similar procedure for the double scattering term, again within the spherical wave scattering limit, leads to

$$\chi_M^2(s_1, s_2, s_3) = \mathrm{Im}\frac{C_{jl}\mathrm{e}^{2ikR}\hat{\rho}_1\cdot\hat{\rho}_3}{\prod_n \rho_n}(s_1 f_{1,1} f_{2,0} f_{3,0} + s_2 f_{2,1} f_{1,0} f_{3,0} + s_3 f_{3,1} f_{1,0} f_{2,0} + s_1 s_2 s_3 f_{1,1} f_{2,1} f_{3,1}), \tag{7}$$

and we obtain

$$\chi_M^2 = \mathrm{Im}\frac{C_{jl}\mathrm{e}^{2ikR}}{\prod_n \rho_n}(\hat{\rho}_1\cdot\hat{\rho}_3)(\langle s_1\rangle f_{1,1} f_{2,0} f_{3,0} + \langle s_2\rangle f_{2,1} f_{1,0} f_{3,0} + \langle s_3\rangle f_{3,1} f_{1,0} f_{2,0} + \langle s_1 s_2 s_3\rangle f_{3,1} f_{1,1} f_{2,1}). \tag{8}$$

Thus in principle the double scattering term contains information about the 3-point correlation function $\langle s_1 s_2 s_3\rangle$. However this is expected to be two orders of magnitude smaller, since it contains two more powers of $f_{i,1}$ (see Fig. 1). Therefore this signal is practically undetectable. Notice that all even power correlation functions do not enter the result, due to the symmetry with respect to inversion of both spins on the photoelectron and on the atom. The summation over the photoelectron spin leaves only odd power moments of the spin distribution.

The above expression also explains why the neglect of the spin-flip processes is justified. For X-ray absorption calculations, the photoelectron must come back with the same spin as it left with. Thus for the single scattering term spin-flip cancels exactly, while for double scattering the spin-flip scattering must happen on both scatterers, which lead to an amplitude one order of magnitude smaller than the dominant term in spin conserving scattering. This will also be true for higher order scattering.

Similar manipulations can be done for the triple scattering term with the same conclusion. The dominant signal is proportional to the spin on each scattering site. The higher order correlation functions ($\langle s_1 s_2 s_3\rangle$, $\langle s_1^2 s_2\rangle$, etc.) can be hardly be measured from experiment, since they are suppressed by about 2 orders of magnitude.

From these equations one can also understand why the ratio of the multiple scattering to the single scattering contribution is larger for MEXAFS than for EXAFS. For systems with a single magnetic atom, one can assume that all ratios $f_{i,1}/f_{i,0}$ are nearly the same

$$\begin{aligned}\chi_M^1/\chi^1 &= 2\langle s\rangle f_{i,1}/f_{i,0},\\ \chi_M^2/\chi^2 &= 3\langle s\rangle f_{i,1}/f_{i,0},\\ \chi_M^3/\chi^3 &= 4\langle s\rangle f_{i,1}/f_{i,0}.\end{aligned} \tag{9}$$

This shows that relative magnitude of the multiple scattering peaks should be 1.5–2 times larger than the single scattering contributions. This is in agreement with previous works [4, 5].

Thus we find that for mono-atomic systems, only one magnetic parameter $\langle s\rangle$ can be obtained from MEXAFS experiment. The Debye-Waller factors arise from the averaging the $\exp(2ikR)$ factor with respect to atomic motion or disorder. Therefore they should be the same for EXAFS and MEXAFS. However a further reduction of the MEXAFS amplitude with temperature can be attributed to the reduction in the average spin per atom, i.e., which is proportional to the total temperature dependent magnetization. Wende et al. experimentally observe a close proportionality of the ratio between MEXAFS and EXAFS signals to the temperature dependence of the magnetization or $\langle s\rangle(T)$ [6]. In that work, authors suggest as an approximation, simply to differentiate the EXAFS signal with respect to energy and multiply it by a fitting parameter Δ_{ex}. This parameter is an estimate of the exchange splitting between spin-up and -down bands, which should be proportional to $\langle s\rangle$. Such an approximation is justified if the signal is dominated by the shortest single scattering path, which is usually the case in practice. The derivative with respect to energy automatically weights the larger distances stronger, since $\mathrm{d}/\mathrm{d}k\exp(2ikR) = 2iR\exp(2ikR)$. This seems to weight the single

scattering paths with large distances incorrectly. However, the signal is strongly dominated by the nearest neighbor single scattering path. As a results the direct proportionality of Δ_{ex} to $\langle s \rangle$ or magnetization has been observed for the temperature dependent measurement [12].

As we discussed above the MEXAFS signal is directly proportional to the total spin moments on each site. To extract $\langle s_i \rangle$ one can use calculations to estimate the the proportionality factors $f^M_{\mathrm{eff},i}$. Thus analogous to EXAFS, the MEXAFS can be parameterized as

$$\chi_M = S_0^2 \mathrm{Im} \sum_{paths} \frac{\sum_i f^M_{\mathrm{eff},i} \langle s_i \rangle}{kR^2} \mathrm{e}^{2\mathrm{i}kR + 2\mathrm{i}\delta_l} \mathrm{e}^{-2\sigma^2 k^2}. \quad (10)$$

Notice that we added S_0^2 and Debye-Waller factors to this equation but they should be the same as for EXAFS. Thus unlike the standard EXAFS equation, where FEFF8 [13] can be used to calculate one f_{eff} for each path, for MEXAFS one may need several $f^M_{\mathrm{eff},i}$, which are essentially derivatives of a particular path contribution with respect to spin on particular atom type. To obtain such derivatives one needs a few calculations of XMCD for some particular spin configurations (e.g. all $s_i = 0$ except one $s_{i0} = 1$). Notice that such calculation may include spherical wave corrections and spin-orbit interaction in final state. Thus the extraction of spin moment for systems with several magnetic atoms requires one to modify the FEFF8 output as well as the input to EXAFS fitting programs.

In conclusion, MEXAFS can be viewed as a method to extract the total spin moment for each element. There is, however, a significant distinction between these moments and the spin moments extracted from the sum rules. The MEXAFS spin is the total spin on each site, while the sum rules can be used to split this total spin in partial angular momentum contributions. For example, the Tb L_3 edge XMCD near the absorption edge can be used to obtain s_{5d}, while MEXAFS should be proportional to $\langle s_{4f} + s_{5d} \rangle$. The higher order correlation functions are practically undetectable by MEXAFS technique, since they are expected to give contributions two orders of magnitude smaller. As a consequence of that we suggest that MEXAFS analysis can be done similar to EXAFS analysis to extract information on site specific total spin moments.

References

1. Schütz, G., Knulle, M. and Ebert, H., Phys. Scripta **T49A**, 302 (1993).
2. Pizzini, S., Fontaine, A., Dartyge, E., Giorgetti, C., Baudelet, F., Kappler, J. P., Boher, P. and Giron, F., Phys. Rev. B **50**, 3779 (1994).
3. Lemke, L. *et al.*, J. Phys. Cond. Matt. **10**, 1917 (1998).
4. Wende, H., Srivastava, P., Arvanitis, D., Wilhelm, F., Lemke, L., Ankudinov, A., Rehr, J. J., Freeland, J. W., Idzerda, Y. U. and Baberschke, K., J. Synchrotron Rad. **6**, 696 (1999).
5. Wende, H., Wilhelm, F., Poulopoulos, P., Baberschke, K., Freeland, J. W., Idzerda, Y. U., Rogalev, A., Schlagel, D. L., Lograsso, T. A. and Arvanitis, D., AIP Conf. Proceedings **514**, 140 (2000).
6. Wende, H., Wilhelm, F., Poulopoulos, P., Rogalev, A., Schlagel, D. L., Lograsso, T. A., Baberschke, K., J. Synchrotron Rad. **8**, 419 (2001).
7. Ankudinov, A. and Rehr, J. J., Phys. Rev. B **52**, 10214 (1995).
8. Ebert, H., Popescu, V. and Ahlers, D., J. Phys. IV **7**, 131 (1997).
9. Rehr, J. J. and Albers, R. C., Phys. Rev. B **41**, 8139 (1990).
10. Ankudinov, A. L. and Rehr, J. J., Phys. Rev. B **56**, R1712 (1997).
11. von Barth, U. and Hedin, L., J. Phys. C **5**, 1629 (1972).
12. Wende, H. *et al.*, these proceedings.
13. Ankudinov, A. L., Ravel, B., Rehr J. J. and Conradson, S. D., Phys. Rev. B **58**, 7565 (1998).

Physica Scripta. Vol. T115, 654–657, 2005

Resonant Photoemission Study of $La_{1-x}Sr_xMnO_3$ Single Crystals

L. L. Lev[1*], M. B. Tsetlin[1], M. Leandersson[2], H. Nylen[3], I. Lindau[3], M. N. Mikheeva[1] and A. M. Balbashev[4]

[1]ISSPh, RRC "Kurchatov Institute", 1, Kurchatov sq., Moscow, Russia
[2]MAX-Lab, Lund University, Box 118, S-221 00 Lund, Sweden
[3]Department of Synchrotron Radiation Research, Lund University, Box 118, S-221 00 Lund, Sweden
[4]Moscow Power Institute, Moscow

Received June 26, 2003; accepted February 6, 2004

PACS numbers: 78.70.Dm, 79.60.−i, 75.47.Lx

Abstract

A feature at a binding energy of ∼2.5 eV which has not previously been discussed in the literature is observed in the photoemission spectra of the valence band of $La_{1-x}Sr_xMnO_3$ single crystals. To reveal the origin of this feature measurements of resonant photoemission on $La_{1-x}Sr_xMnO_3$ were performed as well as absorption spectra at the La N and Mn $L_{2,3}$ edges at liquid nitrogen and room temperatures. Only for Mn L edge we observed a clear resonance for a binding energy corresponding to the feature of interest. Comparison with the calculated density of states led to the conclusion that the feature corresponds to Mn t_{2g} states.

1. Introduction

Transition metal oxides with the composition $La_{1-x}Sr_xMnO_3$ have attracted tremendous interest during the last several years due to the discovery of colossal magnetic resistance (CMR) effect that occurs near room temperature [1] and therefore opens up possible technology applications. The parent compound $LaMnO_3$ is an A-type antiferromagnetic insulator with a Neel temperature $T_N \approx 140$ K. Doping $LaMnO_3$ with strontium transforms it into a magnetic metal at low temperatures.

For $x \geq 0.175$ near the magnetic transition temperature T_C the ferromagnetic transition is accompanied by a metal-insulator transition. For $0.1 < x < 0.175$ $La_{1-x}Sr_xMnO_3$ is an insulator for both $T > T_C$ and $T < T_C$. The CMR effect occurs when an external magnetic field gives rise to a temperature increase of this phase transition and a dramatic decrease of the resistance is observed [1].

For a proper description of such unusual properties the double-exchange mechanism with a strong Hund coupling [2] is needed as well as electron-phonon coupling (Jahn-Teller distortion) [3].

The local configuration of the Mn^{3+} ion in $LaMnO_3$ is $t^3{}_{2g}e^1{}_g$. With divalent metal substitution part of the ions turns into Mn^{4+}. But according to recent work [4, 5, 6] the doped holes have O 2p character, opposite to the usual double-exchange mechanism.

In this work we present resonant photoemission and X-ray absorption near edge structure (XAS) data of $La_{1-x}Sr_xMnO_3$ single crystals in the range of x from 0 (insulator) to 0.33 (metal) at both room temperature and close to the liquid nitrogen temperature near the Mn 2p and La 4d edges. These results were partly published in [7].

2. Experimental

Single crystals of $La_{1-x}Sr_xMnO_3$ (for $0 < x < 0.33$) were obtained by the floating zone method by light heating on the device URN 2-3 M made at the Moscow Power Institute. First, a ceramic bar was made from La_2O_3, $SrCO_3$ and Mn_3O_4 with purity no less than 99.99. The concentration of Mn_3O_4 was increased by 0.5 at% to compensate for evaporation of Mn. Original synthesis was performed during the annealing of a powder mixture at 1200 °C during 24 hrs. After pressing the bar was clinkered at 1350 °C during 24 hrs. Single crystals with $x < 0.075$ were grown in inert Ar atmosphere and single crystals with composition range $0.075 < x < 0.5$ were grown in air in the open crystallization chamber. Typical growing speed was 7–10 mm/hour and rotation speed was 60 rpm.

The crystal structure was determined by neutron and X-ray diffraction. It should be noted that the deviations of the slightly distorted orthorhombic and rhombohedral structures from cubic are negligible, so we will use cubic notations in the text of the present paper.

Photoemission spectra were obtained at the synchrotron radiation source MAX-I at the MAX-Lab laboratory, Lund University, Sweden. We used beamlines 22 and 41.

Beamline (BL) 22 is equipped with a modified SX-700 plane grating monochromator and a 200 mm mean radius hemispherical electron energy analyzer with a multi channel plate detector. The angle between the exciting radiation and the analyzer axis was 40°. The total resolution of the beamline was 0.1 eV in the valence band and 1 eV for resonance series around the Mn 2p absorption threshold.

BL 41 is equipped with a toroidal grating monochromator with three gratings and a goniometer mounted angle-resolved electron energy analyzer (VSW HA50). The acceptance angle of the analyzer is ±1° and the total energy resolution in these measurements was about 0.25 eV.

Samples were introduced into the experimental chamber via a load-lock system.

The energy calibration was made using a gold reference foil in electrical contact with the samples. The investigations were performed in the experimental chambers at 10^{-10} torr pressure and at two temperatures: room temperature (RT) and close to liquid nitrogen temperature (LT).

Single crystals were cleaved *in situ* by an anvil-knife cleaving system. The (001) axis was perpendicular to the sample surface. The resulting surfaces were rough but well defined since LEED images could be obtained. The method of *in situ* cleavage leads to samples with the surface quality much better than in the case of polycrystalline and thin film samples or by scraping samples in vacuum.

3. Results and discussion

Fig. 1 presents typical electron spectra for different strontium concentrations x in a binding energy E_b region up to 30 eV,

*e-mail: lev@isssph.kiae.ru

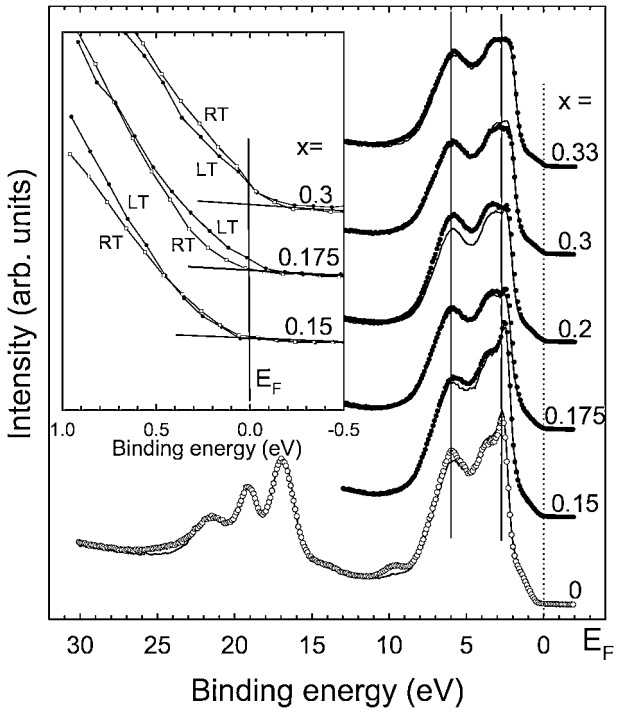

Fig. 1. Valence band photoemission spectra for samples with different strontium concentrations x measured at RT (solid lines) and LT (dots) for $h\nu = 130$ eV. All spectra were normalized to the La $5p_{3/2}$ peak taking into account a La concentration of $1 - x$ and shifted along the ordinate axis. For $x = 0$ the open circles show a spectrum obtained after several hours of measurements. The inset shows binding energy range close to E_F for $x = 0.15$, 0.175 and 0.3. Open circles shows curves for RT, black circles for LT. Spectra for different x shifted along ordinate axis.

measured at RT (solid lines) and LT (dots) for $h\nu = 130$ eV at BL 22 under the normal emission conditions. All spectra were normalized to the La $5p_{3/2}$ peak taking into account a La concentration of $1 - x$ and shifted along the ordinate axis. Zero value of the binding energy corresponds to the Fermi level E_F. A valence band is located at E_b 0 to 9 eV. In the figure for $x = 0$ one can see the following features: the La $5p_{3/2}$ and La $5p_{1/2}$ shallow core levels at $E_b \sim 16.8$ eV and ~19 eV respectively, and the O $2s$ peak at ~21.3 eV. The insulator $LaMnO_3$ samples were only measured at RT because of the charging effect. A comparison of the spectra of the clean sample surface (measured just after the cleavage, solid line) and of the contaminated surface (several hours after the cleavage, open circles) of the $LaMnO_3$ sample shows that, firstly, the spectrum of the contaminated surface has a feature at a binding energy of 9.5 eV, secondly, the emission from the states with binding energy of 5–8 eV increases compared to the maximum of the valence band spectrum and the background at high binding energies also increases. Thirdly, the intensity of the feature with a binding energy of ~2.5 eV decreases only slightly with contamination.

In fig. 1 can be seen a valence band shift towards lower binding energy with an increase of strontium concentration. The leading edge of the valence band (low E_b) moves monotonically in the whole range of x. The valence band is modified in such way that the high E_b edge remains almost constant (therefore an increase in x leads to the widening of the valence band spectrum). A shift of the binding energy for several features of photoemission spectra was also observed in [4] on ceramic samples. This shift qualitatively corresponds to a decrease in the Mn 3d count.

The integrated intensity of the valence band spectra decreases for $x \geq 0.175$. This is correlated with the transition of $La_{1-x}Sr_xMnO_3$ into a metal with increasing Sr concentration.

Analysis of the photoemission spectra near the Fermi edge (see inset in fig. 1) indicate that for $x = 0.15$ (and for all $x \leq 0.15$) the density of states at E_F is close to zero both for high and low temperatures, for $x = 0.3$ (actually for $x \geq 0.2$, which is metallic samples for all temperature range) the density of states at E_F differs from zero for high and low temperatures, but for $x = 0.175$ the density of states differs from zero at LT, and is close to zero at RT. This dependence of the density of states upon x agrees with our resistance and magnetic susceptibility data (not shown here).

It is worth mentioning that in spite of the fact that overall photoionization cross-sections for La and Sr valence band states are ~100 times less than for O 2p and Mn 3d states at a photon energy of 130 eV [8] the valence band changes significantly with Sr concentration. This fact is in contradiction to the x-dependence obtained in [9] on polycrystalline $Pr_{1-x}Sr_xMnO_3$, where the shape of the valence band did not change with Sr doping.

The changes in the valence band (fig. 1) are basically connected with a clear feature at ~2.5 eV binding energy. This feature diminishes when the strontium concentration is increased. Together with the entire valence band in the low binding energy region, this feature shifts toward lower E_b values as the Sr concentration increases: from $E_b = 2.7$ eV ($x = 0$) to $E_b = 2.3$ eV ($x = 0.33$). Below we refer to this feature as «~2.5 eV feature». This feature was also seen in earlier work on polycrystalline samples of $La_{1-x}Ca_xMnO_3$ [10], in $Pr_{1-x}Sr_xMnO_3$ systems [9] and on $Nd_{1-x}Sr_xMnO_3$ single crystals [11]. But for our samples this feature was much more pronounced, especially for low Sr concentrations, and we observed a Sr doping dependence (and also an angular dependence, [12]).

As we showed above, the part of the valence band, in which this feature is observed, does almost not change with surface contamination (the spectra for $x = 0$ on fig. 1). Therefore it is unlikely that the feature can be attributed to surface state emission. In order to determine a relationship between this feature and atomic electron orbitals of one of the sample elements, we investigated the valence band spectrum by resonance photoemission spectroscopy near the La 4d and Mn 2p absorption thresholds.

Fig. 2 presents a series of curves, measured at photon energies near the La 4d absorption threshold ($h\nu = 95$–134 eV) at LT for the sample with strontium concentration $x = 0.15$. Spectra were measured at BL41. The spectra are normalized to the photon flux by measuring the photocurrent from a gold mesh.

As can be seen from the figure, there are two processes that are happening near the La 4d absorption threshold. Firstly, the shape of the valence band changes with increasing $h\nu$ from 95 to 133.5 eV. At $h\nu = 130$ eV the ~2.5 eV feature becomes higher than the rest of the valence band, due to the decreasing emission from the 3–9 eV states. The second observation is that the intensity of the valence band is changing during the resonance photoemission process. Emission from the valence band states has a maximum for a photon energy of 117 eV, which corresponds to the maximum of the absorption curve (see inset to fig. 2). The emission increase is highest for ~3.5 eV and lower for ~2.5 eV.

Our results from measurements near the La 4d threshold lead us to the conclusion that the local density of states on the La atoms is created by states with binding energies across the entire valence band and the states at $E_b \cong 2.5$ eV are not uniquely contributing to the La 4d resonance emission. In addition, the contribution from

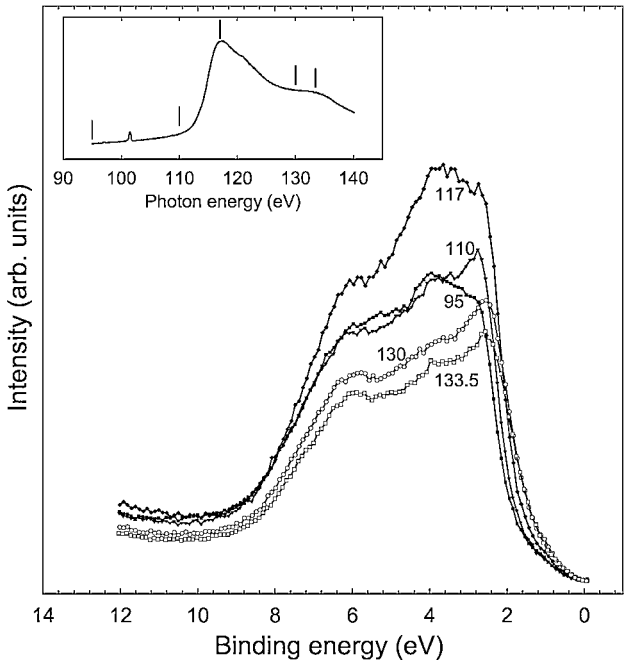

Fig. 2. Valence band photoemission spectra for the sample with $x = 0.15$, measured at a photon energy near the La 4d absorption threshold under normal emission conditions at LT. The spectra are normalized to the photon flux. The inset shows the absorption spectrum and the photon energies used in the photoemission measurements.

La states in the valence band for off-resonance photon energies, as mentioned above, is negligible due to a small photoionization cross-section. So one may suggest that the feature seen at ∼2.5 eV should not be contributed to La states.

Moving to fig. 3, we can see that the Mn 2p resonance displays the opposite properties: the ∼2.5 eV energy states become clearly distinguishable at a photon energy of 642 eV, i.e. at the maximum of the manganese absorption (the inset in figure 3), with a background of increasing emission from the entire valence band. Further increase of the photon energy leads to decreasing emission from the valence band. In the figure we can see the Auger-peak onset at $E_b = 6$ eV and its movement to the left with increasing photon energy. A sharp increase in the resonance of the emission near the Mn 2p absorption threshold allows us to draw the following conclusions: the manganese states exist in the entire valence band from 0 to 9 eV, and the ∼2.5 eV feature corresponds to a state that is strongly localized on the Mn atoms. In [4] authors attributed the state with binding energy ∼2.7 eV in $LaMnO_3$ to Mn 3d state with t_{2g} symmetry. The same conclusion was made in work [11] for $Nd_{1-x}Sr_xMnO_3$ single crystals.

We have recorded a full set of resonance spectra but in fig. 3 we show spectra only for typical $h\nu$. For all resonance spectra we plot constant initial state (CIS) spectra for the maximum of valence band, binding energy range around 2.3–2.6 eV (t_{2g} states, fig. 4, dotted lines) and for binding energy range 0–0.3 eV (e_g states, fig. 4, solid lines) for two temperatures: above (black circles) and below (open circles) the magnetic transition that occurs at 225 K according to our susceptibility data. The spectra are normalized to unity at $h\nu = 638$ eV, corresponding to the onset of the resonance. One can see that for temperatures below the magnetic transition the resonance is less pronounced for both binding energies, a fact that implies that the localization effect is less for the ferromagnetic phase than for the paramagnetic. More intensive resonance for t_{2g} states than for e_g states we also attribute to more localized character of t_{2g} states [4].

In [13] the authors suggested that the absence of the ∼2.5 eV feature in photoelectron spectra of ceramic samples is due to the poor quality of the surfaces. In our opinion, however, this feature in our experiment can be seen for both a clean surface and single crystal structure. However, we do not observe any dispersion of this state with changes in photon energy and emission angle [12]. For now we cannot definitely reject the band-related explanation

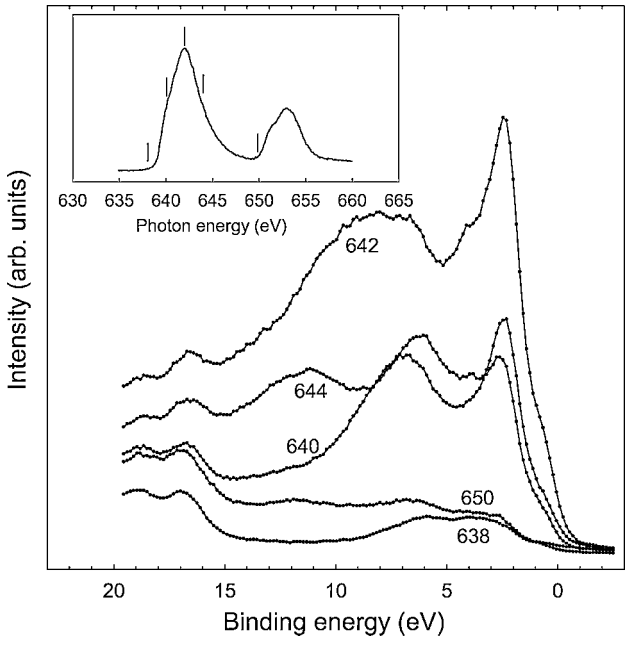

Fig. 3. Valence band photoemission spectra for the sample with $x = 0.15$, measured at a photon energy near the Mn 2p absorption threshold under normal emission conditions at LT. The spectra are normalized to the current in the storage ring. The inset shows the absorption spectrum and the photon energies used in the photoemission measurements.

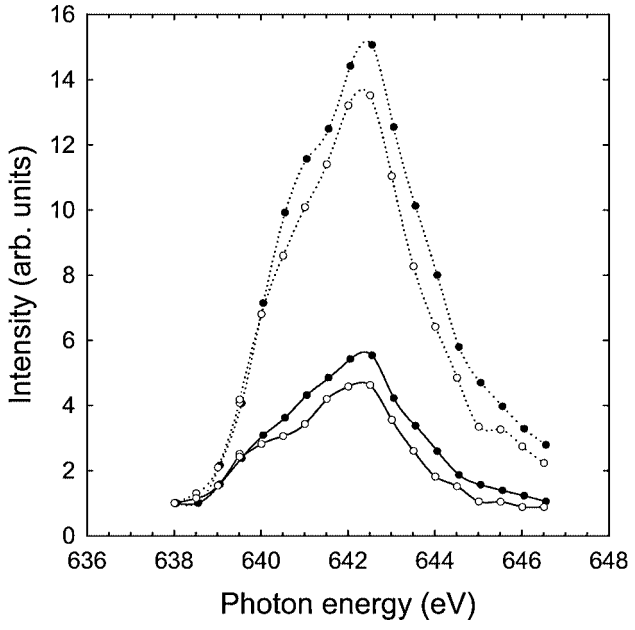

Fig. 4. CIS spectra for binding energy ∼2.3 eV (dotted lines) and ∼0 eV (solid lines) for two temperatures, above (black circles) and below (open circles) the magnetic transition and plotted for the set of photoelectron spectra measured at different $h\nu$ near the Mn 2p absorption edge. The spectra are normalized to unity at $h\nu = 638$ eV, corresponding to the onset of the resonance.

because theoretical calculations of the $LaMnO_3$ band structure [14] show that the dispersion of t_{2g} is also small. Elaborate measurements of the valence band photoemission spectra with high angular resolution and at different photon energies are required for a final conclusion.

4. Conclusion

Photoemission, XAS and resonant photoemission studies have been performed for $La_{1-x}Sr_xMnO_3$ single crystals with x ranging from 0 (dielectric) to 0.33 (metal) at two temperatures.

In agreement with previous results we observe an increase of the density of states at the Fermi level with increasing Sr doping level, providing direct evidence for a metal-insulator transition. A shift of the features in the photoemission spectra qualitatively corresponds to an increase of the hole concentration.

For single crystals we monitored the Sr-concentration dependence of the feature with a binding energy of $\sim$2.5 eV .The relative intensity of this feature decreases with divalent metal doping. Results of our resonant photoemission study together with cross-section dependence and theoretical calculations led us to assign this feature to Mn 3d t_{2g} states.

The relative intensity of the $\sim$2.5 eV feature changes only weakly with contamination of the sample surface, a fact supporting that this state is bulk related.

Acknowledgements

We are grateful to RFFI for grant No. 17847 and to the Royal Swedish Academy of Sciences for financial support. We are indebted to the personal of MAX-lab for their help in the experiments.

References

1. Urushibara, A. *et al*., Phys. Rev. B **51**, 14103 (1995).
2. de Gennes, P.-G., Phys. Rev. **118**, 141 (1960); Zener, C., Phys. Rev. **82**, 403 (1951).
3. Millis, A. J., Littlewood, P. B. and Shraiman, B. I., Phys. Rev. Lett. **74**, 5144 (1995).
4. Saitoh, T. *et al*., Phys. Rev. B **51**, 13942 (1995).
5. Pellegrin, E. *et al*., J. Electron Spectrosc. Relat. Phenom. **86**, 115 (1997).
6. Ju, H. L., Sohn, H.-C. and Krishnan, Kannan M., Phys. Rev. Lett. **79**, 3230 (1997).
7. Lev, L. L. *et al*., Poverhnost' Issue # 6, 37 (2001).
8. Yeh, J. J. and Lindau, I., At. Data Nucl. Data Tables **32**, 1 (1985).
9. Kang, J.-S. *et al*., Phys. Rev. B **60**, 13257 (1999).
10. Park, J.-H. *et al*., Phys. Rev. Lett. **76**, 4215 (1996).
11. Sekiyama, A. *et al*., Phys. Rev. B **59**, 15528 (1999).
12. To be published in the proceedings of ICESS-9.
13. Pickett, W. E. and Singh, D. J., Phys. Rev. B **53**, 1146 (1996).
14. Satpathy, S., Popovic, Z. S. and Vukaylovic, F. R., Phys. Rev. Lett. **76**, 960 (1996); Satpathy, S., Popovic, Z. S. and Vukaylovic, F. R., J. Appl. Phys. **79**, 4555 (1996).

Physica Scripta. Vol. T115, 658–660, 2005

XAFS and XRD Studies on Structures of $Nd_9Fe_{85-x}Mn_xB_6$ Nanocomposites

Shilong Yin[1*], Shiqiang Wei[2], Guozhi Xie[1], Qing Bian[3], Jing Zhang[4], Ou Chen[2] and Hongwei Yang[2]

[1]College of Sciences, Hohai University, Nanjing 210098, P. R. China
[2]National Synchrotron Radiation Laboratory, University of Science and Technology of China, Hefei 230029, P. R. China
[3]Institute of Science, PLAUST, Nanjing 210007, P. R. China
[4]Beijing Synchrotron Radiation Facility, Beijing 100039, P. R. China

Received June 26, 2003; accepted in revised form February 10, 2004

PACS numbers: 61.10.Ht, 75.50.Bb, 81.40Rs

Abstract

The short- and long-range structures of $Nd_9Fe_{85-x}Mn_xB_6$ ($x = 0.0$, 0.5 and 1.0) nanocomposites have been investigated by X-ray absorption fine structure (XAFS) and X-ray diffraction (XRD). The results indicate that the as-spun $Nd_9Fe_{85}B_6$ is mainly composed of amorphous $Nd_2Fe_{14}B$ and α-Fe phases. With the addition of the element Mn of about 0.5% (or 1.0%), the change of the disorder degree σ implies that the medium-range order around Fe atoms in the as-spun $Nd_9Fe_{85-x}Mn_xB_6$ is strongly increased. In particular, the third peak ($R = 4.50$ Å) shows that the increase of medium-range order of the as-spun $Nd_9Fe_{85-x}Mn_xB_6$ is attributed to forming an α-Fe phase. We consider that during the melt-spun process, the element Mn diffuses into the $Nd_9Fe_{85-x}Mn_xB_6$ mixture and forms alloy phases of $Nd_2Fe_{14}B(Mn_y)$ and $Fe(Mn_y)$ nano-crystals. The $Fe(Mn_y)$ alloy with a bcc α-Fe structure keeps a medium-range order around Fe atoms.

1. Introduction

Recently, the potential nanocomposite $Nd_2Fe_{14}B/\alpha$-Fe two-phase permanent magnets that possess the feature of high coercivity from $Nd_2Fe_{14}B$ and high saturation magnetization from α-Fe, have attracted much attention because of their novel magnetic performance and lower cost [1–3]. In order to further improve the magnetic performance of the rare earth permanent magnets, a lot of studies have been devoted to the magnetic properties and the structures of Nd-Fe-B systems by changing the chemical compositions and adding some metallic or rare earth elements [4–8]. It has been found that the addition of element Mn into $Nd_2Fe_{14}B/\alpha$-Fe cast ingots can strongly modify their magnetic and electronic properties [9]. However, the relationship between the structure of the $Nd_2Fe_{14}B/\alpha$-Fe nanocomposites and the addition of element Mn is not clear enough . In order to understand the magnetic properties of nanocomposite $Nd_2Fe_{14}B/\alpha$-Fe doped by Mn, it is essential to perform structural characterization.

In the present work, X-ray absorption fine structure (XAFS) and X-ray diffraction (XRD) are used to study the structures of $Nd_9Fe_{85-x}Mn_xB_6$ modified by the added element Mn. We aim to find the structural changes induced by the addition of small amounts of Mn.

2. Experimental

Ribbons of $Nd_9Fe_{85-x}Mn_xB_6$ ($x = 0.0$, 0.5 and 1.0) were prepared by using mixed metals and alloys of Fe (99.5 at%), Mn (99.8 at%), Nd (99.8 at%) and FeB alloy (B 24.99 at%). Ingot alloy with a homogeneous composition was obtained by arc melting 3 times, and then the molten alloy was spun with a molybdenum wheel at a linear speed of 20 m/s in argon atmosphere from a crucible. It is denoted as the as-spun sample.

The XRD patterns of $Nd_9Fe_{85-x}Mn_xB_6$ samples were measured on a Y-4ϕ rotating target diffractometer (Dandong X-ray photometer Co. LTD) using Cu K_α radiation ($\lambda = 1.5406$ Å, 40 kV and 100 mA). Fe K-edge XAFS spectra of $Nd_9Fe_{85-x}Mn_xB_6$ were collected at the U7C beamline of National Synchrotron Radiation Laboratory (NSRL) and the 4W1B beamline of Beijing Synchrotron Radiation Facility (BSRF). The storage ring of NSRL was operated at 0.8 GeV with a maximum current of 160 mA. The hard X-ray beam was from a three-pole superconducting Wiggler with a magnetic field intensity of 6 Tesla. Fixed-exit Si(111) flat double crystals were used as monochromator. The X-ray harmonics were minimized by detuning the two flat Si(111) crystal monochromator to about 70% of the maximum incident light intensity. Ionization chambers filled with Ar/N_2 mixed gases were used to collect XAFS spectra. The XAFS spectra were recorded in a transmission mode at room temperature. The XAFS data were analyzed by NSRLXAFS software packages [10].

3. Results and Discussions

XRD patterns of the as-spun $Nd_9Fe_{85-x}Mn_xB_6$ ($x = 0.0$, 0.5 and 1.0) nanocomposites are shown in Fig. 1. It can be observed that there are obviously different characteristics in the as-spun $Nd_9Fe_{85-x}Mn_xB_6$ with various concentrations of Mn. A weak and wide amorphous peak in the angle region (2θ) from 30° to 50°

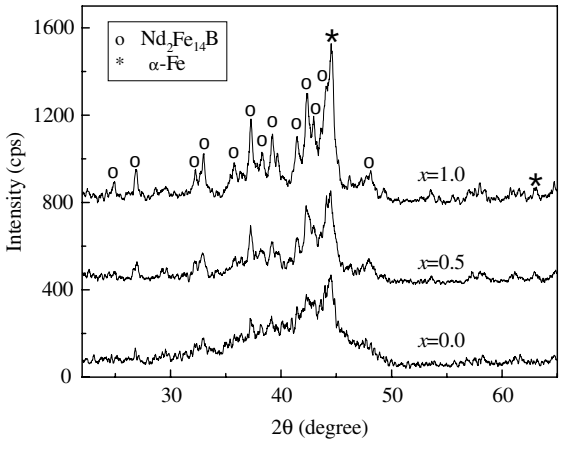

Fig. 1. XRD patterns of the as-spun $Nd_9Fe_{85-x}Mn_xB_6$ ($x = 0.0$, 0.5 and 1.0) nanocomposites quenched at 20 m/s.

*Correspondent, E-mail: slyin@vip.sina.com

where some weak diffraction peaks are appended appears in the Mn-free $Nd_9Fe_{85}B_6$ sample. For the as-spun $Nd_9Fe_{84.5}Mn_{0.5}B_6$ with Mn concentration of $x = 0.5$, the magnitude of its amorphous peak decreases to about two-thirds of that of the Mn-free sample. Furthermore, some diffraction peaks corresponding to the phases of crystalline $Nd_2Fe_{14}B$ and α-Fe can be observed. The peaks located at 44.67° and 64.80° come from the (110) and (200) reflections of the α-Fe phase, and the diffraction peaks at 32.88°, 37.24°, 39.14°, 42.28°, 42.82° and 44.01° correspond to the (311), (214), (313), (410), (411) and (314) reflections of the $Nd_2Fe_{14}B$ phase, respectively. With the amount of Mn going to $x = 1.0$, the intensities of all the diffraction peaks strongly increase to about twice those of the $Nd_9Fe_{84.5}Mn_{0.5}B_6$. This result indicates that the long-range order of nanocomposite $Nd_2Fe_{14}B$ and α-Fe grains in $Nd_9Fe_{85-x}Mn_xB_6$ increases sharply with the amount of element Mn. Hence, a small amount of Mn can promote the $Nd_9Fe_{85}B_6$ alloy to form crystalline $Nd_2Fe_{14}B$ and α-Fe phases in the melt-spun process.

Figure 2 shows radial structural functions (RSF) of Fe atoms of the as-spun $Nd_9Fe_{85-x}Mn_xB_6$ nanocomposites, which are obtained from Fourier transform (FT) of their XAFS oscillation functions $k^3\chi(k)$. It can be seen clearly that the increase of Mn concentration in the as-spun $Nd_9Fe_{85-x}Mn_xB_6$ does not change the position (2.10 Å) of their first peaks, but the intensity increases slightly. However, a drastic change of their RSF curves occurs in the higher shells with Mn concentration. For the Mn-free sample, no strong RSF peaks appear in the higher shells, indicating the amorphousness of the as-spun $Nd_9Fe_{85}B_6$. As the Mn concentration x increases to 0.5, two strong peaks located at 3.60 and 4.50 Å are apparently present in the as-spun $Nd_9Fe_{85-x}Mn_xB_6$. The positions and heights of these two peaks remain almost the same as x increases further to 1.0. From the XAFS and XRD results, one can deduce that the short- and medium-range order structures of the as-spun $Nd_9Fe_{85-x}Mn_xB_6$ ($x = 0.0$, 0.5 and 1.0) change remarkably with the Mn concentrations from 0.0 to 1.0.

The space group of $Nd_2Fe_{14}B$ is $P4_2/mnm$ [11], and there are six different Fe sites with inter-atomic distances of the first neighbors ranging from 2.46 to 2.78 Å. This complicated structure makes the XAFS signal of Fe atoms in $Nd_2Fe_{14}B$ much lower than that in α-Fe. In the fitting procedure, the number of independent

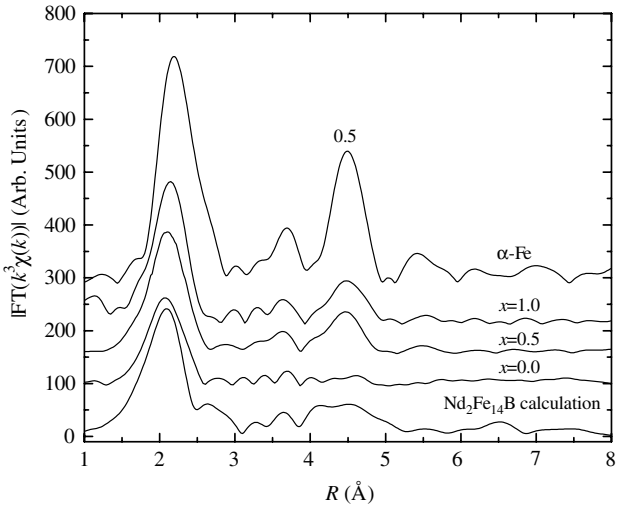

Fig. 2. FT magnitude of Fe K-edge XAFS spectra for the α-Fe powder multiplied by a factor of 0.5 and the as-spun $Nd_9Fe_{85-x}Mn_xB_6$ ($x = 0.0$, 0.5 and 1.0) samples.

Table I. *Structural parameters of Fe atoms from XAFS data of the as-spun $Nd_9Fe_{85-x}Mn_xB_6$ ($x = 0.0$, 0.5 and 1.0) nanocomposites, α-Fe and $Nd_2Fe_{14}B$ reference compound.*

Sample	Fe-Fe sub-shell	N	R (Å)	σ (Å) ±0.007
$x = 0.0$	1	4.5 ± 0.5	2.48 ± 0.02	0.108
	2	2.6 ± 0.4	2.59 ± 0.03	0.120
	3	1.8 ± 0.4	2.74 ± 0.03	0.120
$x = 0.5$	1	4.6 ± 0.5	2.48 ± 0.02	0.105
	2	2.5 ± 0.4	2.59 ± 0.03	0.115
	3	1.9 ± 0.4	2.74 ± 0.03	0.115
$x = 1.0$	1	4.4 ± 0.5	2.49 ± 0.02	0.094
	2	2.7 ± 0.4	2.59 ± 0.02	0.104
	3	1.8 ± 0.4	2.75 ± 0.03	0.104
α-Fe		8	2.48	
$Nd_2Fe_{14}B$	1	4	2.46–2.53	
	2	3	2.55–2.66	
	3	2	2.71–2.78	

data points N_d ($N_d = 2\Delta k \Delta R/\pi + 2$) is about 12 where the ranges Δk and ΔR are 11 $Å^{-1}$ and 1.5 Å, respectively. Since the first SRF peak is mainly due to Fe-Fe pairs, it is practically impossible to use more than three sub-shells in the XAFS fitting, due to the limitation of N_d. Hence, in order to properly model a reasonable structure for the data analysis of our samples, we need to seriously consider the structural feature of $Nd_2Fe_{14}B$ and α-Fe. Three sub-shells with average bond lengths $R_1 = 2.50$ (2.46–2.53), $R_2 = 2.59$ (2.55–2.66), $R_3 = 2.75$ (2.71–2.78) Å and with adjustable parameters of 10, are used for the XAFS simulation of the as-spun $Nd_9Fe_{85-x}Mn_xB_6$ ($x = 0.0$, 0.5 and 1.0) nanocomposites. The fitting results are summarized in Table I.

Seen from Fig. 2, the theoretical XAFS spectrum of crystalline $Nd_2Fe_{14}B$ calculated by the FEFF7 software packages [12] is significantly different from the experiment XAFS spectrum of α-Fe. In particular, by comparing with α-Fe, the crystalline $Nd_2Fe_{14}B$ has a lower peak intensity for the first shell and no strong magnitude peaks for the higher shells. Hence, the stronger RSF peak at 4.50 Å for the as-spun $Nd_9Fe_{85-x}Mn_xB_6$ ($x = 0.5$ and 1.0) nanocomposites comes from the α-Fe phase. Deducing from the composition of the as-spun $Nd_9Fe_{85-x}Mn_xB_6$, the ratio of $Nd_2Fe_{14}B$ phase to α-Fe phase is about 70% to 30% under ideal conditions. Therefore, we consider that the lower intensity in the RSF curves of the as-spun $Nd_9Fe_{85-x}Mn_xB_6$ ($x = 0.5$ and 1.0) is mainly attributed to Fe atoms coexisting in the two phases of crystalline $Nd_2Fe_{14}B$ and α-Fe. Moreover, table I has shown that the coordination number N_1 (about 4.5) of the as-spun $Nd_9Fe_{85-x}Mn_xB_6$ ($x = 0.5$ and 1.0) nanocomposites is slightly larger than the nominal value N_1 (4) of the $Nd_2Fe_{14}B_6$ alloy. This suggests further that a small amount of Fe phase with α-Fe structure-like exists in the as-spun $Nd_9Fe_{85-x}Mn_xB_6$ ($x = 0.5$ and 1.0) alloy. The reason is that there are 8 Fe-Fe pairs at 2.48 Å in the first shell of the bcc structural α-Fe. With the increase of Mn concentration, the disorder degrees of σ as shown in table I indicate that σ_1 (or σ_2 and σ_3) of the as-spun $Nd_9Fe_{85-x}Mn_xB_6$ is 0.108 Å (or 0.120 and 0.120 Å), 0.105 Å (0.115 and 0.115 Å), 0.094 Å (0.104 and 0.104 Å) for $x = 0.0$, 0.5 and 1.0, respectively. These results mean that the addition of Mn can strongly increase the medium-range order around Fe atoms in the as-spun $Nd_9Fe_{85-x}Mn_xB_6$. In particular, the RSF peak intensity at 4.50 Å corresponding to the α-Fe phase largely increases for the as-spun $Nd_9Fe_{85-x}Mn_xB_6$ ($x = 0.5$ and

1.0) nanocomposites, indicating that the increase of medium-range order happens mainly in the Fe phase with a bcc α-Fe structure-like. We consider that during the melt-spun process, the element Mn has diffused into the $Nd_9Fe_{85-x}Mn_xB_6$ mixture and results in forming alloy phases of $Nd_2Fe_{14}B(Mn_y)$ and $Fe(Mn_y)$ nano-crystals where Mn significantly promotes the medium-range order around Fe atoms in the $Fe(Mn_y)$ phase with a bcc α-Fe structure. Hence, we propose that the as-spun $Nd_9Fe_{85-x}Mn_xB_6$ ($x = 0.5$ and 1.0) is composed of crystalline $Nd_2Fe_{14}B(Mn_y)$ and α-$Fe(Mn_y)$ nanocomposites with a nice medium-range order.

Acknowledgment

We would like to thank National Synchrotron Radiation Laboratory (NSRL) and Beijing Synchrotron Radiation Facility (BSRF) for giving us beam time for XAFS measurement. This work was supported by the Natural Science Foundation of China under Grant No.10174068 and the National Key Project of Fundamental Research of China (973) No. G1999064508.

References

1. Kneller, E. F. and Hawig, R., IEEE Trans. Magn. **27**, 3588 (1991).
2. McCormick, P. G., Miao, W. F., Smith, P. A. I., Ding, J. and Street, R., J. Appl. Phys. **83**, 6256 (1998).
3. Hadjipanayis, G. C., J. Magn. Magn. Mater. **200**, 373 (1999).
4. Hirosawa, S., Kanekiyo, H. and Uehara, M., J. Appl. Phys. **73**, 6488 (1993).
5. Chang, W. C., Chiou, D. Y., Wu, S. H., Ma, B. M. and Bounds, C. O., Appl. Phys. Lett. **72**, 121 (1998).
6. Yamasaki, M., *et al.*, Scripta Mater. **44**, 1375 (2001).
7. Li, S. D., Dai, Y. D., Gu, B. X., Tian, Z. J. and Du, Y. W., J. Alloys Compounds **339**, 202 (2002).
8. Jurczyk, M. and Jakubowicz, J., J. Alloys Compounds **311**, 292 (2000).
9. Cheng, B. P., Fu, S. C., Yang, Y. C. and James, J. J., J. Appl. Phys. **64**, 5543 (1988).
10. Zhong, W. J. and Wei, S. Q., J. Univ. Sci. Technol. China **31**, 228 (2001).
11. Powder Diffraction Files, International Center for Diffraction Data, Swarthmore, PA, (1989).
12. Mustre de Leon, J., Rehr, J. J., Zabinsky, S. I. and Albers, R. C., Phys. Rev. B **44**, 4146 (1991).

Physica Scripta. Vol. T115, 661–663, 2005

Temperature Dependence of the Growth of Cerium Oxide Nanoparticles investigated by SAXS and XANES

J. Zhang, Z. Y. Wu*, L. X. Rong and B. Z. Dong

Beijing Synchrotron Radiation Facility, Institute of High Energy Physics, Chinese Academy of Science, Beijing 100039, P.R. China

Received June 26, 2003; accepted in revised form November 4, 2003

PACS numbers: 61.10.Ht; 61.10.Eq; 81.07.Bc

Abstract

The growth process of cerium oxide nanoparticles has been investigated by synchrotron Small-Angle X-ray scattering (SAXS) and X-ray absorption near edge spectroscopy (XANES) as a function of the annealing temperature in the range from 298 K to 973 K in atmosphere. The SAXS experimental intensity increases dramatically with increasing annealing temperature, corresponding the nucleation and growth of CeO_2 nanoparticles. SAXS also indicates that the growth of CeO_2 nanoparticles shows a fractal behaviour. When the annealing temperature increases CeO_2 nanoparticles changes from a volume to surface fractal index. The XANES of CeO_2 nanoparticles at the Ce L_3 edge reveals the increase of the relative intensity of the transition from Ce 2p to $4f^1$ 5d $e_g\underline{L}$, with increasing temperature up to 873 K. Because XANES does not show any significant change for temperature higher than 873 K, this result supports the fractal growth properties of CeO_2 nanoparticles addressed by SAXS.

1. Introduction

CeO_2 nanoparticles are of interest as catalysts in photocatalytic reactions, as a solid oxide fuel cell electrolyte material, and for gas sensors, optical coatings, high-T_c superconductors, and high storage capacitor devices. Therefore, not only is synthesizing CeO_2 nanoparticles important but also understanding its growth characteristics at the nanolevel is essential [1, 2, 3].

Small-angle scattering of X-rays (SAXS) is a technique of choice for probing structural features that occur on length scales between approximately 10 Angstroms and 1000 Angstroms [4]. It can offer opportunities to study nanoparticle systems, e.g. directly probing the self-similar structure behavior or fractal structures during the growth of nanoparticles.

X-ray absorption near edge structure (XANES) spectroscopy, a unique element-specific technique sensitive to the local structure, can provide insight into local environment as well as electronic structures of materials [5]. In particular, XANES at Ce L_3 thresholds can reveal oxidation states of cerium and covalence with oxide ligand [6].

In this paper, we prepare CeO_2 nanoparticles by sol-gel process. The SAXS and XANES are used to investigate the nanoparticle sizes, fraction behavior and binding property in CeO_2. Further the formation and growth mechanisms of CeO_2 nanoparticles are discussed.

2. Experiment

The cerium oxide for the present study was prepared by mixing 0.1 M $Ce(SO_4)_2{\cdot}4H_2O$ solution with ammonia solution. The precipitate obtained was filtered, washed with distilled water and dried at room temperature in an oven. To further study the effect of annealing temperature, the as-prepared sample was annealed at 423 K, 473 K, 573 K, 673 K, 773 K, 823 K, 873 K, 923 K, 973 K for 2 hours under air condition.

The SAXS data were collected on the 4B9A beamline at the SAXS station at Beijing Synchrotron Radiation Facility (BSRF) [7]. X-rays from a bending magnet are focused in both horizontal and vertical directions by a Pt coated toroidal mirror, monochromatized by a double Si(111) crystal monochromator with fixed exit. The energy range of the beamline is 3 keV to 12 keV with $3 \cdot 10^{-4}$ resolution when the storage ring is operated at 2.2 GeV. In our experiments, the data accumulation time was 50 seconds. The angular range was chosen to provide data from $h = 0.005\,\text{Å}^{-1}$ to $h = 0.15\,\text{Å}^{-1}$, where the magnitude of scattering vector $h = 4\pi \sin\vartheta/\lambda$, 2θ and λ being respectively the scattering angle and incident X-ray wavelength of 1.54 Å. The distance between the sample chamber and the detector is 1.495 m. The detector for SAXS data collection is an image plate (IP) system Fuji BAS-2500, with an active area of 400 mm by 200 mm and a minimum pixel size of 100 μm. Two ionization chambers were used to measure the sample transmission. Background scattering from the slit collimator and the residual air path between the vacuum chamber and the detector was measured and subtracted. Excess SAXS scattering from CeO_2 nanoparticles was also corrected for incident beam decay and sample transmission.

XANES spectra at the Ce L_3 edge were measured in transmission mode by using synchrotron radiation with a Si (111) double crystal mono-chromater at the EXAFS station (Beam line 4W1B) of the Beijing Synchrotron Radiation Facility. The storage ring was run at typical energy 2.2 GeV with an electron current of about 80 mA. To suppress unwanted harmonics, the angle between the monochromator crystal faces was adjusted to mistune the incident beam by 30%. The incident and output beam intensities were monitored and recorded using nitrogen gas and a 50% argon-doped nitrogen flowing ionization chamber. The spectra were scanned in the range of 5.5–6.2 keV, which cover the L_3 edge absorption of Cerium atoms. The energy resolution was about 1.5 eV for XANES.

3. Results

3.1. *SAXS*

Figure 1 shows SAXS plots of scattering intensity $I(h)$ versus scattering vector h for CeO_2 nanoparticles with different annealing temperatures. The scattering intensity increases feebly as the annealing temperature changes from 298 K to 823 K. As the temperature increases to 873 K, a drastic enhancement of the scattering intensity is observed, and in the following procedure little variation of the scattering intensity occurs at 923 K and 973 K in our work. These evolutions correspond to the nucleation and growth of CeO_2 nanoparticles, as reported from ref [8, 9].

*Corresponding author: E-mail: wuzy@ihep.ac.cn

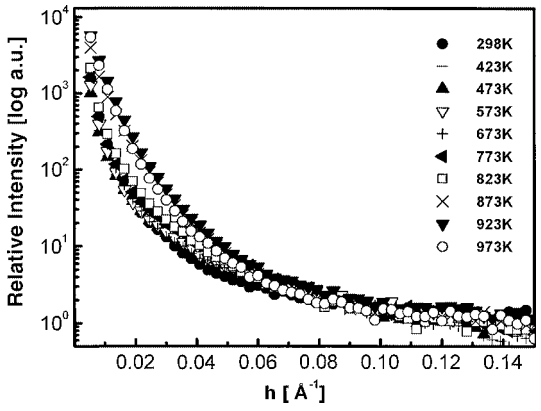

Fig. 1. SAXS plots of CeO_2 nanoparticles at different annealing temperatures.

To further characterize the microstructure of the nanoparticles, a fractal exponent is also extracted from the SAXS curves. Fig. 2 shows a log-log plot of I *vs* h as a function of annealing temperature. All spectra exhibit an almost linear behavior. As shown in Fig. 3, the value of the modulus of the slope (α) for 298 K–873 K is 2.0 $\sim$ 2.15. For further increasing temperature, α increases up to 3.45 $\sim$ 3.50. This reveals that the growth of CeO_2 nanoparticles follows a fractal rule, and the fractal dimension changes from mass fractals to surface fractals as the temperature increases in the range of 298 K and 973 K.

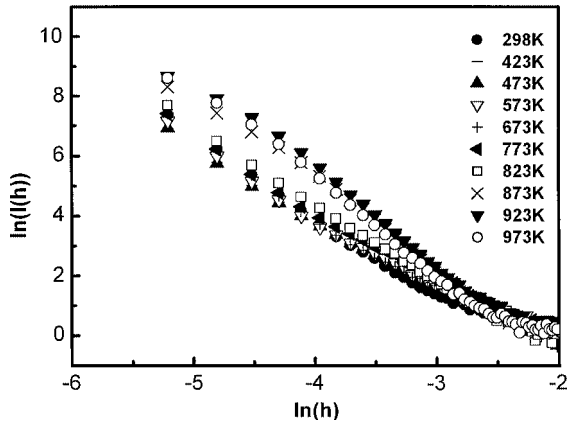

Fig. 2. Plots of $\ln(I(h))$ vs $\ln h$ of CeO_2 nanoparticles on different annealing temperature.

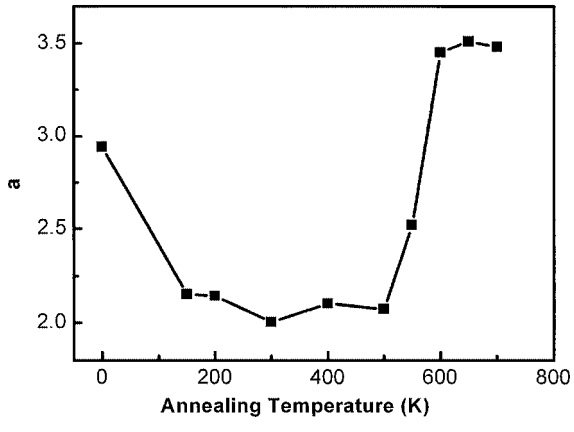

Fig. 3. Plot of α against annealing temperature for CeO_2 nanoparticles.

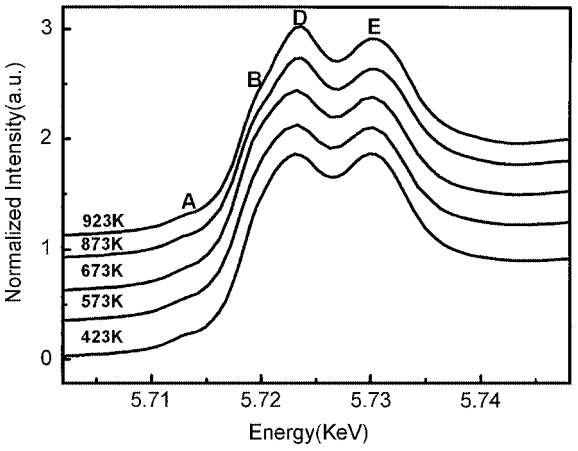

Fig. 4. XANES at Ce L_3-edge of CeO_2 nanoparticles at different annealing temperatures.

3.2. *XANES*

XANES is used to characterize the electric structure of CeO_2 nanoparticles during sintering. Figure 4 compares normalized Ce L_3-edge XANES spectra of select samples. The assignments of Ce L_3-edge spectra are based on references [10, 11]. The pre-edge structure, labeled A, is assigned to final states with delocalized d character at the bottom of the conduction band. Due to the cubic crystal-field splitting of Ce 5d states, features B and D are associated to the transitions of Ce 2p to the Ce $4f^1$ 5d $e_g\underline{L}$ and Ce $4f^1$ 5d $t_{2g}\underline{L}$ states, where $\underline{L}$ denotes an oxygen ligand 2p hole; $4f^1$ refers to an electron from an oxygen 2p orbital to a cerium 4f one (charge transfer-like). The energy separation between peaks B and D is about 3.6 eV, which is in agreement with previous work. The feature E is attributed to the contribution of a different final state configuration $4f^0$ 5d. Generally, the Ce spectrum has a distinct double-peaked structure (D, E) with the higher-lying peak corresponding to the Ce^{4+} valence state.

With increasing calcination temperature up to 873 K, the relative intensity of transition D increases, but further increasing temperature does not show a significant change in these parameters. The results suggest the decrease of oxygen vacancies in CeO_2 nanoparticles during sintering, as in ref [6, 12].

4. Discussion

In nanocrystalline ceramic particles like CeO_2, one would expect an increase in the concentration of oxygen vacancies with decreasing nanoparticle size below 20 nm [12]. From XRD and TEM, the size of CeO_2 nanoparticles in 423 K, 623 K, 873 K, 923 K are 2.3 nm, 4.6 nm, 17.2 nm, 65.3 nm, respectively. Hence, it appears that large concentration of oxygen vacancies may exist within the nanoparticles in lower temperature such as 423 K, 623 K. When the annealing temperature increase, the oxygen vacancies may drastically reduce. This in turn would cause an increase in the relative intensity of the transition Ce 2p to the Ce $4f^1$ 5d $e_g\underline{L}$ and Ce $4f^1$ 5d $t_{2g}\underline{L}$ states in XANES, as temperature increases.

An increase in oxygen vacancies is also known to accelerate mass-transport during sintering. By reducing the density of oxygen vacancies one could conceivably retard the grain growth [13, 14]. Therefore, the scattering intensity increases drastically as the annealing temperature changes from 823 K to 873 K, and little variation of the scattering intensity occurs at 923 K and 973 K.

Further analyzing from SAXS curves, aggregation of CeO_2 nanoparticles changes from a mass fractal structure to surface fractal structure. The mass fractal dimension is indicative of an irregular mass distribution or non-uniform density distribution in the material, whereas the surface fractal dimension indicates the presence of a rough surface in the material [15]. One of the main reasons is as follows: when the annealing temperature is in the range of 298–873 K, the size of CeO_2 nanoparticles is below 10 nm and there are lots of oxygen vacancies in the nanoparticles, which can accelerate the mass-transport during sintering. The aggregation of CeO_2 nanoparticles shows mass fractal structure. With increasing temperature, the sizes of the nanoparticles increase above 20 nm, and their oxygen vacancy density decreases dramatically, which can reduce the activation energy for mass compactness [14]. Therefore, the growth of CeO_2 nanoparticles is not controlled by mass fractal structure. CeO_2 nanoparticles become coarsen and coalesce, further their aggregation changes to surface fractal structure.

5. Conclusion

In summary, we prepare CeO_2 nanoparticles by sol-gel process. SAXS and XANES are used to investigate the formation and growth properties of CeO_2 nanoparticles. SAXS indicates that the growth of CeO_2 nanoparticles shows a fractal behavior. When the annealing temperature increases, CeO_2 nanoparticles change from volume to surface fractal index. The XANES of CeO_2 nanoparticles at the Ce L_3 edge reveal the increase of the relative intensity of the transition from Ce 2p to $4f^1\,5d\,e_g\underline{L}$, with increasing temperature up to 873 K, but further increasing temperature does not significant change the transition. These properties are assumed to be due to the formation of oxygen vacancies.

References

1. Chen, L. X., Rajh, T., Wang, Z. and Thurnauer, M. C., J. Phys. Chem. B **101**, 10688 (1997).
2. Mogensen, M., Sammes, N. M. and Tompsett, G. A., Solid State Ionics **127**, 63 (2000).
3. Walkenhorst, A., Schmitt, M., Adrian, H. and Petersen, K., Appl. Phys. Lett. **65**, 1030 (1994).
4. Hackley, V. A., Anderson, M. A. and Spooner, S., J. Mater. Res. **7**, 2555 (1992).
5. Bianconi, A., in "X-ray Absorption: Principles, Applications, Techniques of EXAFS, SEXAFS, XANES", (Edited by Prins, R. and Koningsberger, D.) (Wiley, New York, 1988).
6. Nachimuthu, P., Wen, C. S., Ru, S. L., Ling, Y. J. and Jin, M. C., J. Solid State Chem. **149**, 408 (2000).
7. Dong, B. Z., Shen, W. J., Yang, H. L. and Zhang, Z. J., J. Appl. Crystallogr. **30**, 877 (1997).
8. Zhang, J., Rong, L. X., Liu, Y. and Dong, B. Z., Mater. Sci. Eng. A **351**, 224 (2003).
9. Liu, W. *et al*., Phys. Rev. B **59**, 11755 (1999).
10. Soldatov, A. V. *et al*., Phys. Rev. B **50**, 5074 (1994).
11. Douillard, L., Gautier, M., Thromat, N. and Duraud, J. P., Nucl. Instrum. Meth. B **97**, 133 (1995).
12. Zhou, X. D. and Huebner, W., Appl. Phys. Lett. **79**, 3512 (2001).
13. Coble, R. L. and Burke, J. E., in "Progress in Ceramic Science", (edited by Burke, J. E.) (1963), Chap 4, 197.
14. Hackley, V. A., Anderson, M. A. and Spooner, S., J. Mater. Res. **7**, 2555 (1992).
15. Mandelbrot, B. B., "The Fractal Geometry of Nature", (Freeman, San Francisco, 1982).

Physica Scripta. Vol. T115, 664–666, 2005

Study on the Thermal Degradation of CeO_2-ZrO_2 Solid Solution by XAFS and XRD

Y. Nagai[1]*, T. Yamamoto[2], T. Tanaka[2], T. Nonaka[1] and A. Suda[1]

[1]TOYOTA Central R&D Labs., Inc., Nagakute, Aichi 480-1192, Japan
[2]Department of Molecular Engineering, Kyoto University, Kyoto 606-8501, Japan

Received June 26, 2003; accepted in revised form November 4, 2003

PACS number: 61.10.Ht

Abstract

A homogeneous CeO_2-ZrO_2 solid solution has an ordered cation arrangement and exhibits the highest oxygen storage/release capacity (OSC) among several types of CeO_2-ZrO_2 with the same composition (Ce/Zr = 1). The crystal structure of this CeO_2-ZrO_2 solid solution is usually termed the "κ-$CeZrO_4$ phase". Its OSC performance degrades upon high-temperature treatment under an oxidative atmosphere. Using Ce K- and Zr K-edges XAFS and powder XRD, this research investigated the structural change along with the thermal degradation of κ-$CeZrO_4$. The fresh sample was aged at 973 K, 1273 K and 1473 K under an oxidative atmosphere. Their OSC performances were characterized at 773 K by a thermo-gravimetric method. The OSC performance deteriorated in the order: the fresh sample $\approx$973 K > 1273 K > 1473 K-aged samples. We also found that, if the temperature went beyond 1273 K, the Ce/Zr ordered arrangement would collapse, and the local structure around Ce and Zr ions would also be changed remarkably. These results indicated that the OSC was strongly dependent on the atomic structure.

1. Introduction

Oxygen storage/release capacity (OSC) is one of the important functions required for automotive three-way catalysts (TWCs) and plays a critical role in efficiently detoxifying harmful compounds, such as hydrocarbons, CO and NOx in automotive exhaust gases [1]. In TWCs, ceria is widely used for its high OSC based on the reversible redox reaction ($CeO_2 \longleftrightarrow CeO_{2-x} + x/2\ O_2$; $x = 0$–0.5). The OSC performance and the durability of the pure CeO_2 were inadequate for practical application in the actual TWCs. More than ten years ago, we discovered that the addition of ZrO_2 to CeO_2 enhanced the OSC as well as improved its thermal stability [2]. Following this discovery, CeO_2-ZrO_2 has been widely utilized in the commercial catalysts. So far, a considerable number of studies have focused on the physical properties and structure of CeO_2-ZrO_2, and significant progress has been achieved to deepen our understanding of this material. Recently, we discovered that a homogeneous CeO_2-ZrO_2 solid solution had an ordered cation arrangement and exhibited the highest OSC among several types of CeO_2-ZrO_2 with the same composition (Ce/Zr = 1) [3]. The crystal structure of this CeO_2-ZrO_2 solid solution is usually termed the "κ-$CeZrO_4$ phase" [4]. Its OSC performance degrades upon high-temperature treatment under an oxidative atmosphere. In order to develop more efficient TWCs, it is really meaningful to investigate and clarify what caused this thermal degradation. We assumed that this thermal degradation resulted from a structural change. In this research, using XAFS and powder XRD, we tried to investigate what exactly happened to its structure along with the thermal degradation of κ-$CeZrO_4$ and correlated that with its OSC performance.

*e-mail: e1062@mosk.tytlabs.co.jp

2. Experimental

CeO_2-ZrO_2 solid solution (Ce : Zr = 1 : 1 molar ratio), which has a κ-$CeZrO_4$ structure, was prepared by a coprecipitation process using $Ce(NO_3)_3$ and $ZrO(NO_3)_2$ aqueous solutions. The precipitate was reduced at 1473 K for 4 h with pure CO flowing and was then oxidized in air at 773 K for 3 h. This sample is referred to as "fresh". Portion of the fresh sample were aged in air for 3 h at 973 K, 1273 K and 1473 K. These obtained samples are referred to as "aged". All the samples were finally calcined in air at 773 K prior to XAFS and XRD measurements. Through the above treatment, oxygen was fully stored in the Ce oxides.

The OSC was measured by a thermo-gravimetric analysis [5]. The fresh and aged samples with 1 wt% platinum loading were cyclically reduced with 20% H_2 (N_2 balance) for 5 min, then oxidized with 50% O_2 (N_2 balance) for 5 min at 773 K. The weight loss and gain were quantified by a thermo-gravimetric analyzer (TGA-50, Shimadzu Corp.). The reductive/oxidative conditions were maintained until the weight became constant. The sample's weight change between the reductive and oxidative conditions corresponds to the total OSC at 773 K.

The powder XRD experiments were carried out using a RINT2000 (Rigaku Co., Ltd.) diffractometer with Cu-K_α radiation (1.5406 Å). The Ce K-edge (40.45 keV) and Zr K-edge (18.00 keV) XAFS spectra were measured at BL16B2 of SPring-8 (Hyogo, Japan). The measurements were carried out using a Si (311) double crystal monochromator in the transmission mode at room temperature. Data reduction of the XAFS was carried out as described elsewhere [6]. A quantitative curve-fitting analysis of the EXAFS spectra was performed for the inverse Fourier transforms on the cation-oxygen (cation = Ce, Zr) shells. Empirical parameters in the analysis were obtained from standard compounds, e.g., cubic CeO_2 for Ce-O bonding, 8 mol% Y-doped cubic ZrO_2 for Zr-O bonding.

3. Results and discussion

Table I lists the OSC performances of the samples. The Ce efficiency means the ratio of $Ce^{3+}/(Ce^{3+} + Ce^{4+})$ under the reductive condition. The Zr oxidation state in the CeO_2-ZrO_2 remains at Zr^{4+} under both the reductive and oxidative conditions at 773 K [7]. Thus, only the Ce atoms contribute to the OSC through the Ce^{3+}/Ce^{4+} redox couple. The fresh sample exhibited a high OSC, and its Ce efficiency was 90.0%. It is noteworthy that almost all of the Ce in the CeO_2-ZrO_2 contributes to the OSC. The OSC value of the 973 K-aged sample is almost equal to that of the fresh sample, while the OSC performance gradually decreases with increasing aging temperature.

Table I. *OSC properties of the fresh and the aged samples.*

Sample[a]	OSC [b] (μmol-O_2/g)	Ce efficiency[c] (%)
Fresh	750	90.0
973 K-aged	772	91.0
1273 K-aged	483	56.9
1473 K-aged	283	35.0

[a]The fresh sample was aged in air at the indicated temperatures.
[b]OSC (Oxygen Storage/Release Capacity) was measured at 773 K.
[c]The ratio $Ce^{3+}/(Ce^{3+}+Ce^{4+})$ under the reductive condition.

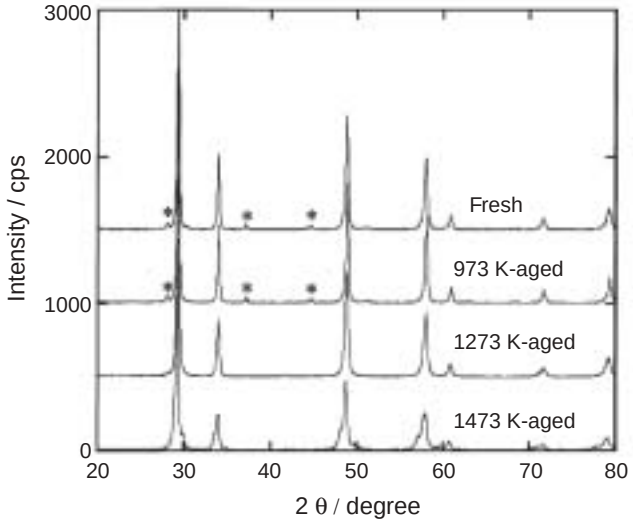

Fig. 1. X-Ray diffraction patterns of the fresh and aged samples. Small peaks marked with asterisks are characteristic of κ-$CeZrO_4$ due to the ordered arrangement of the cations, see ref. [4].

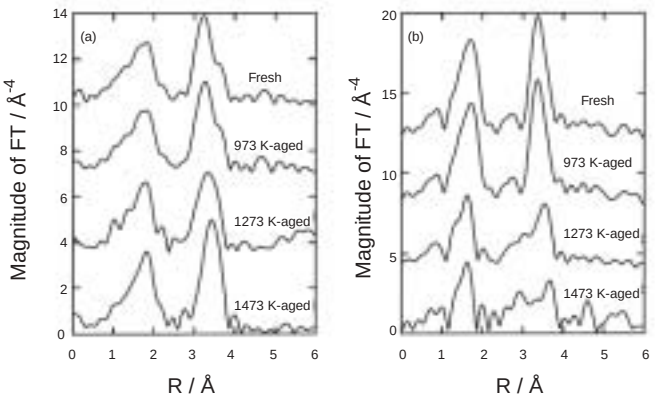

Fig. 2. k^3-weighted EXAFS spectra (left) and their Fourier-transforms (right) for (a) Ce K-edge and (b) Zr K-edge EXAFS of the fresh and aged samples.

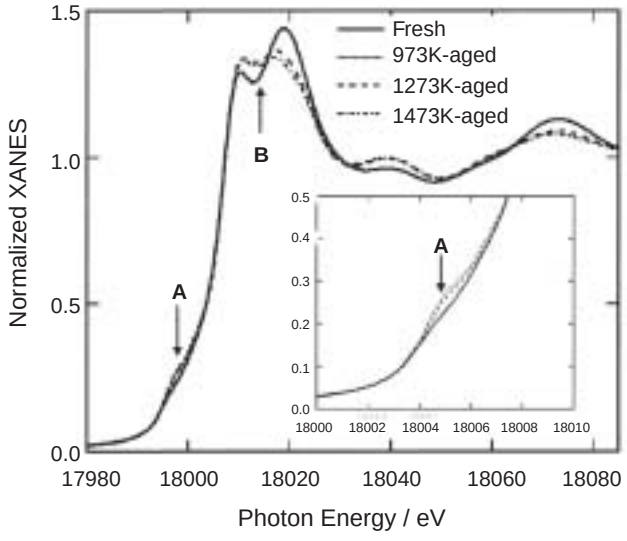

Fig. 3. Zr K-edge XANES spectra of the fresh and aged samples.

Fig. 1 shows the XRD patterns of the samples. For the fresh sample, we could observe small peaks, which marked here with an asterisk, except for the principal peaks which were attributed to the cubic fluorite $CeZrO_4$. These small peaks are ascribed to the ordered arrangement of the cations along the ⟨110⟩ direction [4]. This crystal structure of the cubic fluorite $CeZrO_4$, termed the "κ-$CeZrO_4$ phase" [4], has an ordered arrangement of the cations. Its structure was still maintained upon aging at 973 K. However, the ordering peaks disappear upon aging at 1273 K or higher, and only the principal peaks of cubic $CeZrO_4$ remain observable. In addition, the principal peaks for the 1473 K-aged sample become broad and begin to split partially. Therefore, we can assume that a phase separation occurred at 1473 K, and that the $CeZrO_4$ solid solution becomes partially divided into more stable CeO_2 and ZrO_2.

Fourier transforms (FTs) were carried out the Ce K- and Zr K-edges EXAFS spectra in about the 3.0–16 $Å^{-1}$ region. FTs of the Ce K-edge are presented in Fig. 2(a). The first peak at 1.8 Å and the second peak at 3.5 Å correspond to the Ce-O and Ce-cation (cation = Ce, Zr) bonds, respectively. The Ce-O and Ce-cation peaks of the 973 K-aged sample are located at the same positions as those of the fresh sample and have the same amplitude. On the other hand, the shapes of the FTs for the 973 K, 1273 K and 1473 K-aged samples are obviously different. Fig. 2(b) shows the FTs of the Zr K-edge EXAFS spectra. The first peak at 1.7 Å was assigned to Zr-O bonds and the second peak at 3.5 Å to Zr-cation bonds. The same observation for the Ce K-edge also applies to the Zr K-edge XAFS. The spectra of the fresh and 973 K-aged samples have the same features. The spectra of the aged samples are different from each other.

The XANES spectra at the Zr K-edge are shown in Fig. 3. A careful comparison of the spectra labeled A and B across the samples reveals several interesting facts. First, peak A, a weak shoulder on the steeply rising absorption edge, is more apparent for the 1273 K and 1473 K-aged samples than those of the fresh and 973 K-aged ones. This pre-edge absorption can be assigned to the $1s \rightarrow 4d$ which is sensitive to the Zr-O geometry. This transition is considerably strong in the case of pure tetragonal ZrO_2 [8]. In fact, the features of the XANES spectra of the 1273 K and 1473 K-aged samples are very similar to that of the pure tetragonal ZrO_2 [8]. Thus, it is clear that the 1273 K and 1473 K-aged samples have a tetragonal environment of the Zr-O coordination. As for peak B, it is in the form of a slight splitting in the 1273 K and 1473 K-aged samples, although it exhibits a clear splitting in the fresh and 973 K-aged samples. A clear splitting like this could also be observed for cubic ZrO_2 [8]. In addition, it is well-known that the peak A is weaker in cubic ZrO_2 than in tetragonal ZrO_2 [8]. Clearly, the fresh and 973 K-aged samples have a cubic environment of the Zr-O coordination.

Table II. *Curve-fitting analysis for Ce-oxygen shells*[a].

Sample	Bond	*CN*	*R* (Å)	$\Delta\sigma^2$ [b] (Å^2)
Fresh	Ce-O	8.0(2)	2.27(0)	0.0044(2)
973 K-aged	Ce-O	8.0(1)	2.27(0)	0.0035(1)
1273 K-aged	Ce-O	8.0(1)	2.29(0)	0.0039(1)
1473 K-aged	Ce-O	8.0(1)	2.30(0)	0.0032(1)

[a]The standard deviation at the last digit is given in parentheses.
[b]Relative Debye-Waller factor.

Table III. *Curve-fitting analysis for Zr-oxygen shells*[a].

Sample	Bond	*CN*	*R* (Å)	$\Delta\sigma^2$ [b] (Å^2)
Fresh	Zr-O	8.0(2)	2.27(0)	−0.0046(2)
973 K-aged	Zr-O	8.0(5)	2.26(0)	−0.0081(2)
1273 K-aged	Zr-O	4.0(5)	2.18(0)	−0.0072(5)
	Zr-O	4.0(5)	2.36(2)	0.0063(45)
1473 K-aged	Zr-O	— [c]	— [c]	— [c]

[a]The standard deviation at the last digit is given in parentheses.
[b]Relative Debye-Waller factor.
[c]Reasonable fit could not be obtained.

The quantitative curve-fitting results of Ce and Zr K-edges EXAFS are summarized in Tables II and III, respectively. Only the results for the cation-oxygen bonding around 1.0–2.0 Å in the FTs are presented here to focus on cation-oxygen geometry in the samples. First, all the Ce-O shells were fitted with a single Ce-O bond, and the CN for all samples was 8. This indicates that Ce-O coordination for all samples has a symmetric 8-fold coordination. Secondly, the Zr-O shells for the fresh and 973 K-aged samples were fitted with a single Zr-O bond. In contrast, the Zr-O shell for the 1273 K-aged sample was fitted with two sets of short and long Zr-O bond lengths. These short and long bond lengths and the CN (4 + 4) of Zr-O are close to the values for the typical tetragonal ZrO_2 [8]. But the distances of Zr-O for the 1273 K-aged sample is not equal to the values for the pure tetragonal ZrO_2, because a $CeZrO_4$ solid solution in the 1273 K-aged sample forms. These results indicate that Zr-O coordination in the fresh and 973 K-aged samples have a symmetric 8-fold coordination, while Zr-O coordination in the 1273 K-aged sample has two sets of nonequivalent tetrahedral geometry. This result is in agreement with the Zr K-edge XANES data. Although we could not obtain a reasonable fitting for the Zr-O shell of the 1473 K-aged sample caused by the partial phase separation, we can determine from the Zr K-edge XANES that this sample also has the above tetrahedral geometry.

We summarize our results and analysis as follows. The OSC performance deteriorated in the order: the fresh sample $\approx$973 K > 1273 K > 1473 K-aged samples. Furthermore, we found that, if the temperature went beyond 1273 K, the Ce/Zr ordered arrangement would collapse and the local structure around Ce and Zr ions was also changed remarkably. These results indicated that the OSC strongly depends on the atomic structure and provided us a key point on how to enhance or optimize the oxygen storage performance involved in three-way catalysts.

Acknowledgements

The X-ray absorption experiments were performed at the SPring-8 with the approval of the Japan Synchrotron Radiation Research Institute (JASRI) (Proposal No. C01A16B2-4020N).

References

1. Matsumoto, S., Toyota Tec. Rev. **44**, 10 (1994).
2. Ozawa, M., Kimura, M. and Isogai, A., J. Alloys Comp. **193**, 73 (1993).
3. Nagai, Y. *et al.*, Catal. Today **74**, 225 (2002).
4. Kishimoto, H. *et al.*, J. Alloys Comp. **312**, 94 (2000).
5. Suda, A. *et al.*, J. Ceram. Soc. Japan **109**, 177 (2001).
6. Tanaka, T. *et al.*, J. Chem. Soc., Farad. Trans. **84**, 2987 (1988).
7. Fornasiero, P. *et al.*, J. Catal. **151**, 168 (1995).
8. Li, P., Chen, I.-W. and Penner-Hahn, J. E., Phys. Rev. B **48**, 10063 (1993).

Physica Scripta. Vol. T115, 667–670, 2005

Study of the Probe Molecule Adsorption on Co-Mo Sulfide Model Catalysts by Means of XAFS

Takeshi Kubota, Masatoshi Kawano and Yasuaki Okamoto*

Department of Material Science, Shimane University, Matsue 690-8504, Japan

Received June 26, 2003; accepted November 4, 2003

PACS number: 8245Jn

Abstract

The changes of the active sites of the Co-Mo sulfide model catalysts by the adsorption of NO or O_2 were investigated by means of Co K-edge XAFS and FT-IR techniques. It is clearly shown that the coordinatively unsaturated edge sites of MoS_2 are decorated by Co atoms by employing a CVD method using a vapor of $Co(CO)_3NO$. It is found from Co K-edge XANES spectra that Co atoms are scarcely oxidized by the adsorption of NO. On the other hand, with the O_2 adsorption in a closed system, Co atoms are gradually oxidized with adsorption time. It is also found that O_2 adsorption on a Co-Mo catalyst is significantly suppressed by pre-adsorption of NO.

1. Introduction

Alumina-supported Co(Ni)-Mo(W) sulfides have been extensively used as hydrodesulfurization (HDS) catalysts. These catalyst systems have attracted much attention, because it is well known that very strong synergy effects are observed between Co(Ni) and Mo(W) in these catalysts [1, 2]. Numerous studies have been conducted to clarify the cause of the synergy effects by means of a variety of spectroscopic techniques; EXAFS, Mössbauer emission spectroscopy (MES), XPS and so on [3–5]. Since the proposal by Topsøe *et al*. [3, 6], it is generally accepted that the so-called "Co(Ni)-Mo-S" phase is catalytically active for HDS reaction in these catalyst systems. In recent years, a structure for the Co-Mo-S phase is proposed in which Co atoms are atomically dispersed and located, most likely in front of the square sulfur faces of the MoS_6 trigonal prisms along the edges of the MoS_2 crystallites [7]. However, a detailed structure on the Co-Mo-S phase is still open to question [8–11].

NO and O_2 have been used as probe molecules for the characterization of active sites of the Co-Mo sulfide catalysts because these molecules adsorb on the unsaturated sites of metal atoms, which form active sites of the catalysts [1]. NO adsorption on metal sulfide catalysts has been studied by several workers [6, 11–13]. In particular, FT-IR spectra of adsorbed NO have been used for characterization of metal sulfide catalysts, since Co sites and Mo sites can be distinguished on the basis of the positions of absorption bands [6, 12, 13]. The adsorption capacity of probe molecules such as NO and O_2 are also used for the estimation of the number of the active sites of HDS catalysts. However, the influences of adsorption of these probe molecules are uncertain on the chemical state of the metal atoms (oxidation of the metal atoms, changes of the adsorption behavior caused by the preadsorbed molecules and so on). XAFS techniques have advantages that it can analyze the local structure of X-ray absorbing atoms under in situ conditions and are suitable for the investigation of probe molecule adsorption. Hence, XAFS techniques were applied to the characterization of Ni-Mo catalysts using NO adsorption [14]. Although Nielsen *et al*. have reported that oxidation of Ni occurs on Ni-Mo sulfide catalysts by NO adsorption [14], the XAFS investigation on the effects of NO and O_2 adsorption has not been carried out for Co-Mo catalysts, which are mainly used for HDS reaction. However, it is difficult to selectively extract the information on the Co-Mo-S structure for catalysts prepared by a conventional method, since besides the Co-Mo-S phase, several Co species are simultaneously formed in these catalysts such as Co_9S_8 and Co^{2+} ions bound to the support [1–5].

In our previous studies, we have reported that MoS_2 edge sites are selectively decorated with Co atoms to form the Co-Mo-S phase by employing a CVD method using a $Co(CO)_3NO$ vapor [15, 17]. This model catalyst system can be regarded as an ideal catalyst for spectroscopic studies. In this paper, we will clarify the influence of the adsorption of probe molecules, NO and O_2 on the chemical states of the Co atoms forming the Co-Mo-S phase by means of Co K-edge XANES and FT-IR.

2. Experimental

2.1. *Catalyst preparation*

An alumina-supported Mo oxide catalyst (MoO_3/Al_2O_3) was prepared by a conventional impregnation method using $(NH_4)_6Mo_7O_{24}4H_2O$ as a precursor. Al_2O_3 was supplied by the Catalysis Society of Japan as Reference Catalysts (JRC-ALO-6; $180\,m^2\,g^{-1}$, 250–500 mesh). The catalyst was dried at 373 K overnight and calcined at 773 K for 5 h. MoO_3/Al_2O_3 was sulfided at 673 K in a flow of $H_2/H_2S = 90/10$ for 1.5 h (MoS_2/Al_2O_3). A model catalyst [15, 16], CVD-$Co/MoS_2/Al_2O_3$, was prepared by a CVD method using $Co(CO)_3(NO)$. MoS_2/Al_2O_3 (0.1 g) was evacuated ($<10^{-3}$ Pa) at 673 K for 1 h and then exposed to a $Co(CO)_3(NO)$ vapor at room temperature for 5 min, followed by evacuation for 10 min at room temperature to remove $Co(CO)_3(NO)$ molecules physisorbed on the surface of MoS_2/Al_2O_3. Detailed preparation procedures have been reported previously [15, 16]. A catalyst prepared by a conventional impregnation method using $Co(CH_3COO)_2$ is denoted Co-MoS_2/Al_2O_3. The Mo and Co contents were 8.7 and 2.7 wt.% for the CVD catalyst and 8.7 and 2.0 wt% for the impregnation catalyst, respectively.

2.2. *XAFS measurement*

The Co K-edge XAFS spectra for Co-Mo catalysts were measured in a fluorescence mode at BL-7C of the Photon Factory in the Institute of Material Structure Science, High Energy Accelerator Research Organization (KEK-IMSS-PF) in Japan under in situ conditions. The synchrotron radiation was monochromatized by a Si(111) double-crystal monochromator. The storage ring was operated in 2.5 or 3.0 GeV. The photon flux was 1×10^{11} photons/s. The estimated energy resolution at 9 keV was

*e-mail: yokamoto@riko.shimane-u.ac.jp

about 2 eV and the monochromator was scanned in a 0.5 eV step for the Co K-edge region. The higher harmonics were eliminated by detuning the incident X-ray to 60%. The fluorescence detection was carried out by using a Lytle type detector with flowing Ar. The incidence X-ray was monitored by an ion chamber with flowing N_2. The spectra were obtained by collecting signals I_f/I_0, where I_0 indicates the intensity of incidence X-ray and I_f the intensity of fluorescence X-ray. Normalized XANES spectra were obtained by subtracting the pre-edge background from the raw data assuming a straight line. Normalization was carried out by the edge height.

The catalyst was evacuated at room temperature after sulfidation and then transferred to an XAFS cell with Kapton windows without exposure to air. After the XAFS measurement of the sample in a vacuum, 6.7 kPa of NO or O_2 was introduced to the cell and the XAFS spectra of the catalyst exposed to the probe molecule were recorded again. After keeping for 2–3 h, the NO or O_2 gas was evacuated for 5 min to replace NO (O_2) by O_2 (NO). Subsequently, 6.7 kPa of O_2 or NO was introduced to the cell. After the replacement, XAFS spectra were measured again.

2.3. *FT-IR and NO adsorption capacity measurement*

The FT-IR spectra of NO adsorption on the catalysts were measured by FT/IR620 (JASCO) using an in situ cell. A self-supporting disk of the catalyst was presulfided at 673 K and transferred to the cell in a glove-box filled with N_2. The disk was resulfided at 673 K in the cell and evacuated, followed by introduction of 6.7 kPa of NO. The amounts of NO and O_2 adsorption capacity on the catalysts were measured using a pulse method between 200 K and 323 K [11].

3. Results and discussion

Figure 1 shows the FT-IR spectra of NO adsorbed on the metal sulfide catalysts. With MoS_2/Al_2O_3, a doublet peak appeared at 1776 and 1685 cm^{-1}, assigned to NO adsorbed on coordinatively unsaturated sites (cus) of Mo sulfides [6, 12, 18]. After the addition of Co atoms by the CVD method, a new doublet peak appeared at 1851 and 1805 cm^{-1}. These peaks are assigned to NO adsorbed on cus Co sulfides as a dinitrosyl form [6, 12]. The intensity of the peak at 1677 cm^{-1} was extremely weak, indicating that cus sites at MoS_2 edges are almost completely covered with Co atoms after the addition of Co by the CVD method. On the other hand, with Co-MoS_2/Al_2O_3, three peaks were observed at 1685, 1794 and 1846 cm^{-1}. These peaks are interpreted as overlapping of two doublet peaks due to adsorbed NO on cus Co and Mo sulfides [6, 12]. It is concluded from the FT-IR spectra that cus sites at MoS_2 edges of the catalyst prepared by the CVD method are covered with Co atoms more effectively than those of the catalyst prepared by a conventional impregnation method. It is revealed that the edge sites of MoS_2 are essentially fully covered with Co atoms by the CVD method.

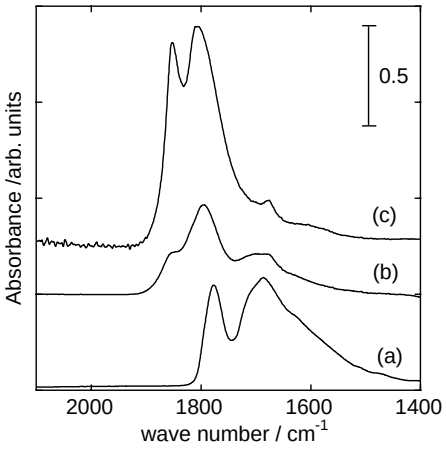

Fig. 1. FT-IR spectra of NO adsorbed on the metal sulfide catalysts. (a) MoS_2/Al_2O_3, (b) Co-MoS_2/Al_2O_3 prepared by a conventional impregnation method (Co 2.0 wt%), (c) CVD-Co/MoS_2/Al_2O_3 prepared by the CVD method.

Figure 2(A) shows the Co K-edge XANES spectra of the metal sulfide catalysts, $CoAl_2O_4$ and Co_9S_8. With the spectra for the catalysts prepared by the impregnation method, a small peak was observed at 7726 eV, characteristic of Co^{2+} in $CoAl_2O_4$, indicating that a part of Co atoms bind with Al_2O_3 surface to form Co^{2+} as in $CoAl_2O_4$, in agreement with other workers [1–3]. This is highlighted by the difference spectrum, in Fig. 2(B) (Fig. 2(A) (b)–(c), close to the XANES of Co^{2+} in $CoAl_2O_4$). However, with the catalyst prepared by the CVD method, XANES

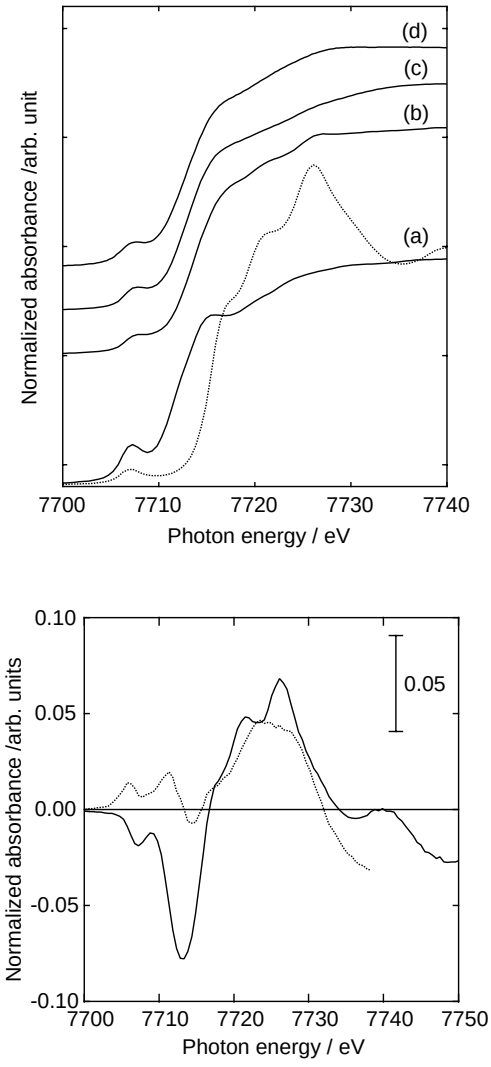

Fig. 2. (A) Co K-edge XANES spectra of Co-Mo sulfide catalysts and reference compound. (a) Co_9S_8 (solid line) and $CoAl_2O_4$ (dotted line), (b) Co-MoS_2/Al_2O_3 prepared by an impregnation method (2.0 wt% Co), (c) CVD-Co/MoS_2/Al_2O_3 prepared by the CVD method, (d) CVD-Co/Al_2O_3 prepared by the CVD method. (B) Co K-edge XANES difference spectra of Co-Mo sulfide catalysts obtained by subtracting the spectrum of CVD-Co/MoS_2/Al_2O_3 prepared by the CVD method. Solid line; (b)–(c) and dotted line (d)–(c).

spectrum in Fig. 2(A) showed no peak at 7726 eV except a weak s-d transition peak. Furthermore, no formation of bulk Co_9S_8 in CVD-Co/MoS_2/Al_2O_3 is confirmed by the absence of a shoulder peak characteristic of bulk Co_9S_8 (7715 eV), when the spectra for CVD-Co/MoS_2/Al_2O_3 and Co_9S_8 in Fig. 2(A) are compared. The XANES spectrum of CVD-Co/Al_2O_3 is also shown in Fig. 2(A). The difference XANES spectrum in Fig. 2(B) between CVD-Co/Al_2O_3 and CVD-Co/MoS_2/Al_2O_3 shows a broad feature around 7725 eV, suggesting interactions between Co atoms in CVD-Co/Al_2O_3 and oxygen atoms on the support or the presence of highly dispersed Co_9S_8 clusters (see Fig. 2(B)). These results clearly demonstrate a selective formation of Co species characteristic of the CoMoS phase in the model catalyst. A linear correlation between Co content in CVD-Co/MoS_2/Al_2O_3 and NO adsorption capacity of MoS_2/Al_2O_3 also supports a selective formation of the Co-Mo-S phase [15].

Figure 3(a) and (b) present the Co K-edge XANES spectra of CVD-Co/MoS_2/Al_2O_3 before and after adsorption of probe molecules, NO and O_2, respectively. With the NO adsorption, a small but reproducible shift of the absorption edge was observed (0.5 eV). The same shift (0.5 eV) was also observed for the catalyst after NO adsorption by the pulse method. These results indicate the changes of electronic state of the Co atoms by the NO adsorption. It is considered from a comparison of XANES that dissociation of NO and concomitant oxidation of the Co sites do not take place even after 3 h, since no changes were observed characteristic of oxidation of Co atoms (appearance of the white line at 7726 eV or a large shift of the absorption edge). However, Nielsen *et al*. reported that about 30% of Ni atoms were oxidized by NO adsorption for Ni-Mo catalysts at room temperature [14]. The difference is interpreted in terms of the difference between Co and Ni in the tendency toward dissociation of NO molecules. On the other hand, as shown in Fig. 3(b), O_2 adsorption caused a larger shift of the absorption edge (ca. 1.0 eV), accompanying an evolution of a peak at 7727 eV, characteristic of the oxidized Co atoms (Co^{2+} in $CoAl_2O_4$, Fig. 2(A)). The intensity of this peak increased with time, indicating a gradual oxidation of Co atoms by O_2 adsorption at room tempetature. These results clearly indicate that NO is superior to O_2 as a probe molecule for the characterization of Co-Mo HDS catalysts.

Figure 3(c) and (d) show the Co K-edge XANES spectra of CVD-Co/MoS_2/Al_2O_3 after NO or O_2 adsorption following the pre-adsorption of O_2 or NO, respectively. The Co K-edge XANES spectrum was scarcely changed by O_2 adsorption following the NO adsorption after 5 min. Only a small peak at 7725 eV was observed after 2 h. This indicates that O_2 adsorption on cus Co sites is strongly inhibited by the pre-adsorption of NO. It is considered that NO and O_2 molecules adsorb on the same Co sites, and that cus Co sites, which cause the dissociation of O_2 , are blocked by the adsorbed NO molecules. On the other hand, the NO adsorption following the O_2 adsorption caused a decrease in the intensity of the peak induced by the O_2 adsorption. It is considered that the pre-adsorbed oxygen reacts with NO, and the adsorbed O_2 molecules are gradually replaced by NO. These XANES spectra clearly show the difference of the adsorption property of NO and O_2.

To clarify the effects of pre-adsorbed molecules, the amounts of NO and O_2 adsorption were measured at various temperatures, as shown in Fig. 4. It is confirmed from Fig. 4 that O_2 adsorption is significantly suppressed by the pre-adsorption of NO. Furthermore, it is also found that the O_2 adsorption capacity is monotonously increased with adsorption temperature, while NO adsorption capacity is almost constant over a wide range of adsorption temperature. These results suggest that O_2 is inappropriate as a probe molecule, since it is considered from XANES results that Co atoms are oxidized by the O_2 adsorption under static conditions (Fig. 3) and the adsorption amount of O_2 depends strongly on the adsorption temperature (Fig. 4).

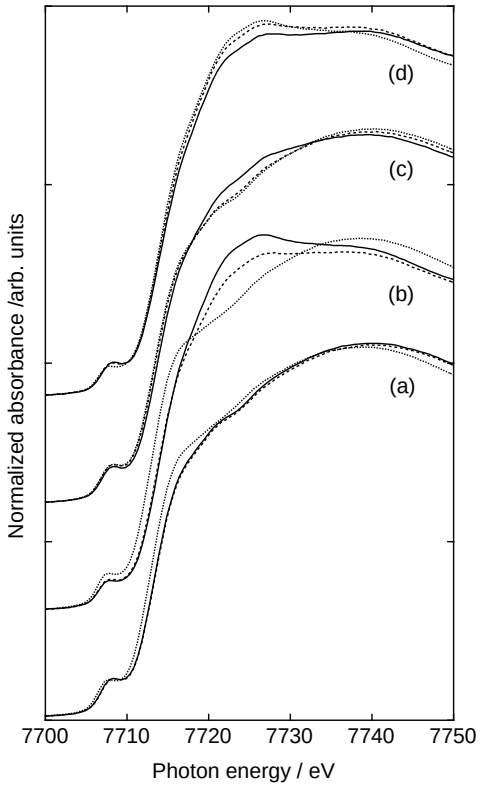

Fig. 3. Co K-edge XANES spectra of CVD-Co/MoS_2/Al_2O_3. (a) before adsorption (dotted line), after 10 min (dashed line), and after 3 h (solid line) for NO adsorption. (b) before adsorption (dotted line), after 6 min (dashed line), and after 2 h (solid line) for O_2 adsorption. (c) O_2 adsorption following the NO adsorption and (d) NO adsorption following the O_2 adsorption. Pre-adsorbed (dotted line), after 5 min (dashed line), and after 2 h (solid line) for the second adsorption. Adsorption of probe molecules was carried out under static conditions at room temperature.

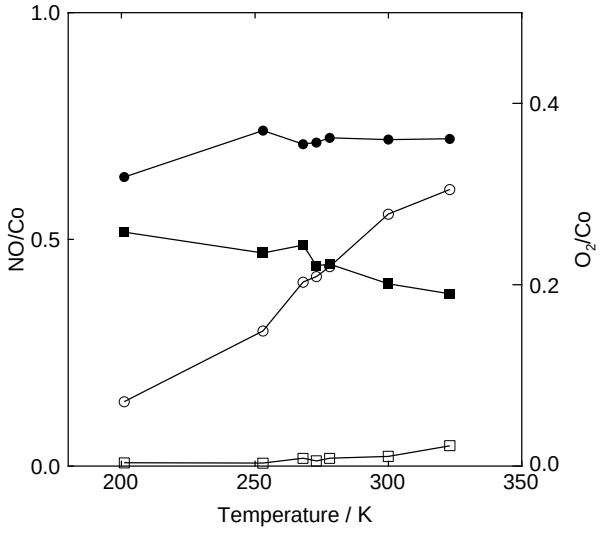

Fig. 4. Amounts of adsorbed NO and O_2 per Co atom as a function of adsorption temperature. Closed circle: NO/Co, open circle: O_2/Co, closed square: NO/Co after the O_2 adsorption, and open square: O_2/Co after the NO adsorption.

4. Conclusions

1) The Co K-edge XANES spectra show that Co species characteristic of the CoMoS phase are selectively formed in a Co-Mo sulfide model catalyst by a CVD method using $Co(CO)_3NO$.

2) NO or O_2 adsorption on Co atoms changes the Co K-edge XANES spectrum. NO is more appropriate probe molecule for the Co-Mo-S phase because the Co atoms in the Co-Mo-S phase are oxidized by O_2 adsorption at room temperature as shown by Co K-edge XANES.

3) Significant suppression of O_2 adsorption by the pre-adsorption of NO is observed by XAFS in agreement with the adsorption capacity measurement.

Acknowledgment

This work has been entrusted by the New Energy and Industrial Technology Development Organization under a subsidy of the Ministry of Economy, Trade and Industry.

References

1. For example; Topsøe, H., Clausen, B. S. and Massoth, F. E., "Hydrotreating Catalysis" Catalysis Science and Technology, (ed. J. R. Anderson and M. Boudard), Springer-Verlag, Berlin, 1996), vol. 11.
2. Gates, B. C., Katser, J. R. and Shuit, G. C. A., "Chemistry of Catalytic Process", (McGraw-Hill, New York, 1979), p. 390–447.
3. Topsøe, H., Clausen, B. S., Topsøe, N. and Pederson, E., Ind. Eng. Chem. Fundam. **25**, 25 (1986).
4. Chianelli, R. R., Daage, M. and Ledoux, M. J., Adv. Catal. **40**, 177 (1994).
5. Prins, R., de Beer, V. H. J. and Somorjai, G. A., Catal. Rev.-Sci. Eng. **31**, 1 (1989).
6. Topsøe, H. and Topsøe, N., J. Catal. **84**, 386 (1983).
7. Bouwens, S. M. A. M., van Veen J. A. R., Koningsberger, D. C., de Beer, V. H. J. and Prins, R., J. Phys. Chem. **95**, 123 (1991).
8. Byskov, L. S., Nørskov, J. K., Clausen, B. S. and Topsøe, H., J. Catal. **187**, 109 (1999).
9. Raybaud, P., Hafner, J., Kresse, G., Kasztelan, S. and Toulhoat, H., J. Catal. **190**, 128 (2000).
10. Lauritsen, J. V., Helveg, S., Lagsgaad, E., Stensgaad, I., Clausen, B. S., Topsøe, H. and Besenbacher, F., J. Catal. **197**, 1 (2001).
11. Okamoto, Y., Kawano, M. and Kubota, T., J. Chem. Soc. Chem. Commun. 1086 (2003).
12. Yamada, M., Catal. Surv. Jpn. **3**, 3 (1999).
13. Yamada, M., Koizumi, N. and Yamazaki, M., Catal. Today **50**, 3 (1999).
14. Nielsen, L. P., Ibsen, L., Christensen, S. V. and Clausen, B. S., J. Mol. Catal. A **162**, 375 (2000).
15. Okamoto, Y., Ochiai, K., Kawano, M., Kobayashi, K. and Kubota, T., Appl. Catal. A **226**, 115 (2002).
16. Okamoto, Y., Ishihara, S., Kawano, M., Sato, M. and Kubota, T., J. Catal. **217**, 12 (2003).
17. Okamoto, Y. and Kubota, T., Catal. Today **86**, 31 (2003).
18. Okamoto, Y., Katoh, Y., Mori, Y., Imanaka, T. and Teranishi, S., J. Catal. **70**, 445 (1981).

Physica Scripta. Vol. T115, 671–674, 2005

In-situ X-ray Absorption Spectroscopy Investigations During the Conditioning Procedure of PtRu Colloid Catalysts

H. Modrow[1,*], G. Köhl[1], J. Hormes[2], H. Bönnemann[3], U. Endruschat[3] and R. Mörtel[3]

[1]Physikalisches Institut der Universität Bonn, Nussallee 12, 53115 Bonn, Germany
[2]Center for Advanced Microstructures and Devices, 6980 Jefferson Hwy, Baton Rouge LA70806, USA
[3]Max-Planck Institut für Kohlenforschung, Kaiser-Wilhelm Platz1, 45470 Mülheim a.d. Ruhr, Germany

Received June 26, 2003; accepted November 4, 2003

PACS numbers: 78.70 Dm, 82.45 Yz, 82.45 Jn

Abstract

We present the first *in situ* characterization of the conditioning process of a Vulcan supported precatalyst based on PtRu nanoparticles with either aluminumorganic or tetraalcylammonimum protection shells, obtained by X-ray absorption spectroscopic measurements on the Pt L_{III}-edge. To perform these measurements, a suitable reaction cell was developed. In combination with results from transmission electron microscopy, these data provide the basis for a detailed understanding of the abovementioned process. In detail, we find that whereas the increase in particle size during this process and thus agglomeration of particles is rather small, there is a reduction of disorder in both types of particles, especially in the ones with an aluminumorganic protection shell. Furthermore, we observe different behavior of the Pt component in the two different types of particles during the oxidative step of the conditioning process, as only in aluminumorganically stabilized particles Pt atoms are subject to oxidation, whereas in the other sample they remain strictly zerovalent. Tentatively, these findings can be related to the internal structure of the as synthesized particles as obtained from preliminary evaluation of Pt L_{III} EXAFS-spectra.

1. Introduction

Presently, PtRu nanoparticles supported by Vulcan [Cabit corp] are discussed intensely as an promising electrode material for the PEMFC [2–9], mainly due to the small particle sizes (<3 nm) which promise a large active surface contribution. Naturally, it is essential to analyze whether this property of the nanoparticles is maintained during the conditioning process and whether this process might change the intrinsic catalytic properties of the material, which would lead to changes in the electronic structure of such catalysts. The aim of this study is to provide a detailed characterization of the changes in electronic properties and particle size which electrocatalysts made of nanoparticles undergo during the formation process. Whereas the changes in particle size of this material during conditioning were investigated *ex situ* using transmission electron microscopy (TEM), the electronic structure was investigated in situ using the X-ray Absorption Near Edge Structure (XANES). Such an *in situ* study is essential for two reasons: First of all, the direct extrapolation of results obtained from *ex situ* techniques performed after a change of the ambient conditions, especially those obtained under UHV such as XPS, seems at least questionable and needs verification. For example, in the previous XPS studies [3–5] no information could be obtained about the oxidation-state of the metals before the first conditioning step because of several experimental restrictions, mainly overlapping signals which prevented direct access to certain stages of the process. Secondly, even if one assumes that results obtained from *ex situ* investigations can be extrapolated, such studies can elucidate changes induced in the sample during the process of conditioning, but they provide no information on the mechanism which caused these changes and thus no starting point for a possible refinement of the formation process.

XANES spectroscopy is especially suited for *in situ* investigations during an ongoing reaction because it offers direct access to the electronic bulk structure of a given sample while it is being exposed to a given atmosphere. It is, however, well known that particle size effects can exert a considerable influence on the electronic structure of a sample. The addition of systematic TEM measurements on the identical set of samples and EXAFS (extended X-ray absorption fine structure) analysis of the morphology of the starting material which is discussed in detail elsewhere [1] enables us to separate chemical and particle size effects on a given sample, thus allowing for a detailed understanding of the conditioning process.

2. Experimental

2.1. *Synthesis and supporting procedure*

Two types of colloids have been investigated in this study: The first class of colloids were obtained by coreduction of $PtCl_2$ and $RuCl_3$ with $N(oct)_4[B(et)_3H]$ [2, 10, 11]. The resulting PtRu nanoparticles have an average diameter of about 1.6 nm and a metal content of 6.9 wt.% Pt and 3.6 wt.% Ru which corresponds well to the results obtained in previous studies [2, 10]. The particles are stabilized by the *in-situ* generated surfactant. The colloids were supported on high surface area carbon (20 wt.% metal content) by combining a THF dispersion of the PtRu-colloid with a suspension of Vulcan in THF. After 24 h the solvent was evaporated from the remaining solution. The supported pre-catalyst was washed and dried at room temperature in vacuum (10^{-3} mbar).

The second type of colloids consists of particles, which were synthesized by the reaction of Pt-acetylacetonates and $Al(alkyl)_3$, and are only about 1.1 nm small. The elemental analysis shows 13.2 wt.% Pt, 6.8 wt.% Ru and 12.4 wt.% Al. The particles are surrounded by a stabilizing matrix of aluminiumorganic compounds, which still contains Al-methyl groups. Therefore, the matrix can be modified with protic agens, whereby the particles for themselves are not significant growing [3, 4]. To support the aluminumorganic PtRu colloid on the high area support Vulcan XC 72 (20 wt.% metal content), a dispersion of the colloid in toluene was dropped at 40 °C to a vigorously stirred suspension of Vulcan in the same solvent. The resulting suspension was stirred for 24 h again at 40 °C. The solvent was evaporated and the remaining powder was dried in vacuum for 24 h (10^{-3} mbar, 60 °C).

*modrow@physik.uni-bonn.de

2.2. *Conditioning*

The precatalyst cannot be used in electrocatalysis directly, because the protecting shell is still present and blocks the particle surface for the electrochemical reaction. It is removed quantitatively by application of a "conditioning process" which consists of three succeeding steps:

1. Heating the sample in an inert gas (Ar) atmosphere to the necessary conditioning temperature (300 °C for the $N(octyl)_4$-stabilized colloids and the modified aluminiumorganic colloids; 250 °C for the non-modified aluminiumorganic colloids).
2. Annealing of the sample with an O_2/Ar-mixture for 30 minutes, which yields a complete removal of the stabilizer molecules from the particle surface.
3. Annealing of the sample with H_2 for 30 minutes, which leads a complete reduction of the active metals in the sample.

2.3. *In-situ-XANES-measurements*

Pt LIII-XANES measurements have been recorded in transmission mode at beamline BN3 at the Electron Stretcher and Accelerator ELSA [12] at the University of Bonn running in storage ring mode at an electron energy of 2.7 GeV with an average current of 25 mA. A modified Lemonnier-type [13] double crystal X-ray monochromator, equipped with a pair of plane Ge(422)-crystals ($2d = 2.304$ Å) was used. Ionization chambers were filled with 300 mbar Argon as detection system. Energy-calibration was made relative to the first inflection point in the spectrum of the Pt-foil, which was set to 11564 eV. The photon energy was scanned from 11500 to 11650 eV with an integration time of 800 ms per point. For a quantitative comparison, a linear background was fitted to the pre-edge region (11500–11550 eV) of the spectra and subtracted from the raw data. To normalize the spectra, the inflection point of the broad shape resonance at 11637 eV was assigned a value of 1.

2.4. *The in situ cell*

A special designed heating cell for air-sensitive samples, which is presented in figure 1, was used to perform the conditioning. The heating cell consists of two parts. One part is a slightly modified inert gas sample holder described elsewhere [4]. Part of a cylindric mini press (SPECADIE P/N 3550 from Graseby Specac) was mounted at the end of the sample holder. Pellets of the sample could be made inside an Argon-filled glove-box by tightening two screws of the mini press at the sample holder. With a special outlet at the sample holder, a thermocouple was led through the holder, whose end was placed directly on the sample. After sample preparation the sample holder was sealed and transferred to the beamline. The ionization chambers and the sample chamber were filled with Argon before the sample holder was opened.

The second part of the heating cell consists of a 2 mm spiral heating cable (Thermocoax) mounted onto a second holder which was placed perpendicular to the sample holder and the beam onto the experiment. The spiral heating cable could be sled directly to the sample leaving a cylindric hole for the synchrotron beam to pass through. Before the conditioning procedure an *ex-situ* XANES-spectrum of the sample was recorded. After each conditioning step in situ spectra were taken. No measurements could be performed at the Ru L-edges of the PtRu- samples because pellets cannot be used at low energies as the absorption becomes too strong. Also, the temperature used in the conditioning process prevents the use of tape as carrier material for the powder. Measurements at the Ru K-edge were not possible due to the limited spectral range of the Bonn synchrotron radiation source.

3. Results and Discussion

3.1. *In-situ-XANES-measurements*

3.1.1. *PtRu-N(octyl)$_4$Cl-stab.-catalyst.* Figure 2 presents the XANES spectra ot the PtRu-$N(octyl)_4$-catalyst at the Pt L_{III} edge during the course of the conditioning. Changes in the Pt L_{III} XANES-spectra of the catalyst are small, but significant. A comparison between the spectrum of the catalyst and the

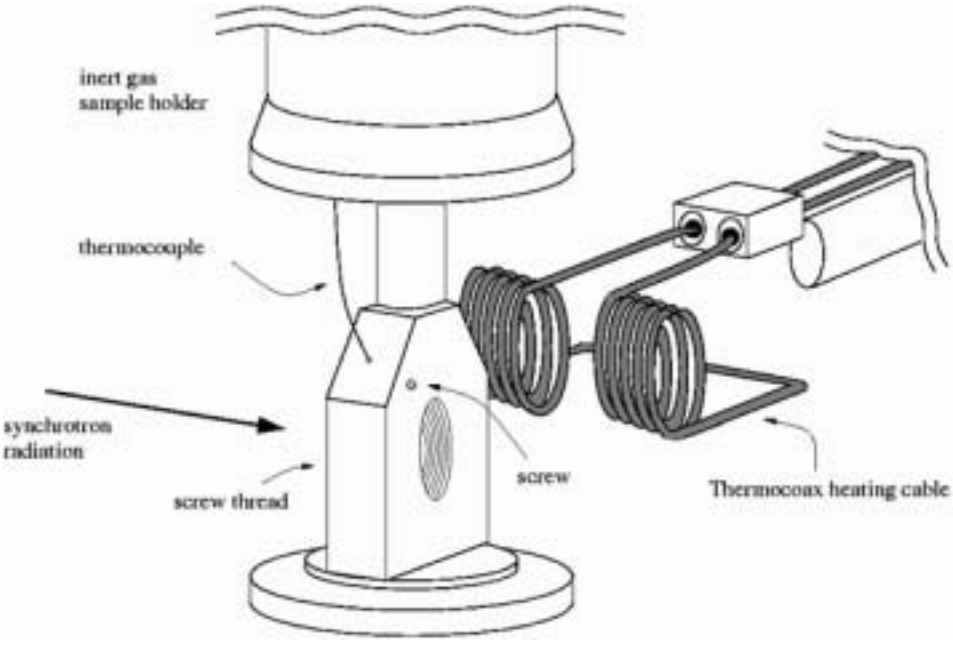

Fig. 1. Sample cell for the heating of airsensitive samples.

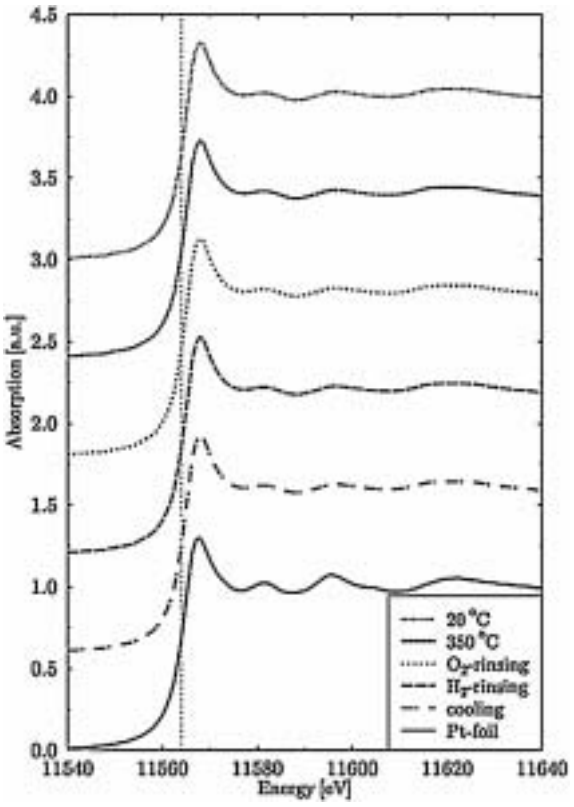

Fig. 2. Pt L_{III}-XANES: Conditioning of the PtRu-N(octyle)$_4$-catalyst.

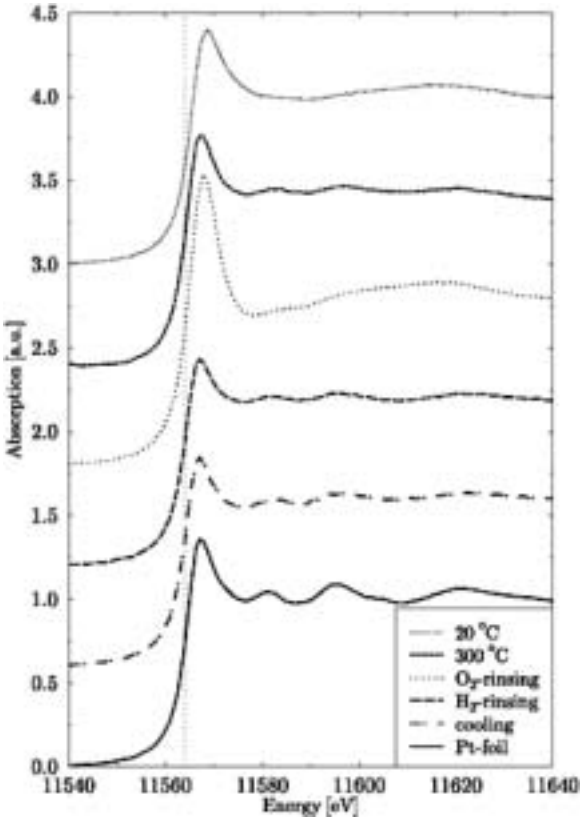

Fig. 3. Pt L_{III}-XANES: Conditioning of the aluminumorganic PtRu-catalyst.

one obtained from a Pt reference foil shows the coincidence of the energy positions of the first inflection point and the shape resonances. This indicates a zerovalent character of the Pt component in the catalyst and shows that Pt is mostly surrounded by Pt atoms, indicating segregation of Pt and Ru in the particles. The spectrum of the catalyst is in perfect agreement with the spectrum of the unsupported colloid presented in [10]. This shows that supporting the colloids on Vulcan has no influence on the metal core of the colloid as long as the protection shell is present. The only change during the conditioning procedure is the slightly more distinct presence of the three shape resonances during the heating of the sample in Ar atmosphere, which might partly reflect a slight particle growth from $d_{vol} = 2.7$ to 3.3 nm observed by TEM, but is more likely to be a result of crystallisation/ordering of the particles during the heating process of the first step. During the subsequent conditioning steps, oxidation and reduction, no further changes in the shape resonances are observed. Also, no shift in the absorption edge and no increase in white-line intensity could be observed during the oxidative step. This shows clearly that the oxidation state of the completely reduced Pt does not change during the floating of the catalyst with O_2. This result is in agreement with former XPS-measurement [10]. The chemically more noble Pt remains resistent to oxidation. In literature, one finds the observation that an O_2 rich atmosphere usually leads to a segregation of Ru atoms to the particle surface. XPS results [10] indicate that Ru is oxidized after the oxidative step. A Ru oxide-layer at the surface of the particles could act as a protective coating for underlying particles and therefore preventing the Pt atoms from oxidation. In the last conditioning step, the reduction of the catalyst, again no changes are observed at the Pt L_{III} edge. The possible reduction of Ru [10] has no influence on the Pt. From the spectra it cannot be concluded if a segregation of the Ru component on the surface is taking place during the conditioning procedure.

3.1.2. *PtRu-Alorg.-catalyst.* Figure 3 presents the XANES spectra of the PtRu aluminumorganic-catalyst at the Pt L_{III} edge during the course of the conditioning. Again, XANES spectra of the pure colloid and the supported catalyst are identical, as in the case discussed above indicating again that the supporting procedure has no influence on the metal core of the nanoparticles. Although the edge position of the catalyst spectrum is slightly shifted to higher energies (0.4 eV) compared to the edge position of the Pt foil spectrum, this shift lies within the measurement error, as 1 motorstep is equal to 0.7 eV. The small intensity of the observed whiteline suggests that again Pt is present in a zerovalent state at the beginning of the reaction. However, during the first conditioning step, the heating of the sample under Ar atmosphere, weak shape resonances arise. Again, this might be attributed partly to the particle growth observed in TEM from 1.1 to 1.3 nm, whose relevance is supported by a U-test [15], but is more likely to be related to the increasing order in the particles, as this difference in size corresponds at most to the addition of one shell to the particle.

While rinsing the sample with oxygen in the next conditioning step, a clear increase in the white-line intensity can be observed, which indicates the partial oxidation of the Pt atoms. During rinsing with H_2 the intensity of the white-line is decreased again which now corresponds to the reduction of the Pt. This is in strong contrast to the above results of the PtRu-N(octyl)$_4$-catalyst where no changes in white-line intensity could be observed, but in good agreement with XPS measurements [4], where an oxidation and reduction of Pt in the second and third conditioning step was also found. The reduced intensity of the whiteline in the spectrum compared to the spectrum before the conditioning procedure indicates the removal of the organic ligands. This was previously shown only indirectly by XPS, as no C(1s) signal could be detected after the conditioning. The initally formed shape resonances are still observed after the conditioning process.

Naturally, the observed differences, especially with respect to the behavior of the Pt atoms during the oxidative step, need further discussion. Based on the preliminary analysis of our Pt-L-III EXAFS spectra, which is discussed in detail elsewhere [1], we find clear evidence for a ragged, incompact, surface rich structure of the aluminumorganically stabilized particles in contrast to a more compact structure in which stricter segregation is observed for the tetraalkylammonium-stabilized particles. Allowing for some degree of speculation, this might also account for the observed stability against oxidative processes during the conditioning process: Whereas in a ragged particle the formation of a protecting shell of (oxidized) Ruthenium is not easily possible, in a compact atomic arrangement the formation of such a core shell structure is much easier to accomplish. An alternative attempt of an explanation might be a different degree of protection of the varying organic ligands. However, the latter approach seems questionable due to the observed successful removal of the protection shell in the course of the conditioning process.

4. Conclusions

Using a specially designed reaction cell, we have been able to apply Pt LIII-XANES successfully to investigate *in-situ* the conditioning process of two different types of catalysts based on PtRu nanoparticles. No significant changes between the XANES spectra of the nanoparticles and the catalysts made thereof by supporting them on Vulcan were observed. By correlation of the results of these measurements with particle size information obtained by TEM, we obtained evidence for ordering within the particles during the first step of the conditioning process, whereas the trend to induce agglomeration of particles is comparatively small. XANES spectra also allowed the observation of the oxidation state. The experiment showed that the $N(octyl)_4$-stabilized colloid catalysts are far more stable against oxygen exposure then the aluminumorganic catalysts. This can either be explained by the bigger size of the $N(octyl)_4$-stabilized catalysts, but more likely by differences in the initial internal structure of the PtRu nanoparticles shown by the analysis of *ex situ* EXAFS data. Comparison of *ex-situ* XPS- and *in situ* XANES-measurements yields a consistent picture of the conditioning process.

Acknowledgements

The authors would like to thank the DFG for financial support under contract numbers BO1135 and HO887.

References

1. Bönnemann, H. *et al*., Fuel Cells, in print (2004).
2. Schmidt, T. J. *et al*., Langmuir **13**, 2591 (1997).
3. Bönnemann, H. *et al*., J. New. Mat. Electrochem. Systems **3**, 199 (2000).
4. Paulus, U. A. *et al*., J. Catal. **195**, 383 (2000).
5. Schmidt, T. J. *et al*., J. Electrochem. Soc. **145**, 925 (1998).
6. Carette, L., Friedrich, K. A. and Stimming, U., Chem. Phys. Chem. **1**, 162 (2000).
7. Kordesch, K. and Simader, G. "Fuel Cells and Their Applications", (VCH Weinheim 1996).
8. Crown, A. *et al*., J. New Mat. Electrochem. Syst. **3**, 275 (2000).
9. Liu, L., Viswanathan, R., Fan, Q., Liu, R. and Smotkin, E. S., Electrochim. Acta **43**, 3657 (1998).
10. Vogel, W., Britz, P., Bönnemann, H., Rothe, J. and Hormes, J., J. Phys. Chem. B **101**, 11029 (1997).
11. Bönnemann, H. *et al*., Angew. Chem. **103**, 1344 (1991).
12. Althoff, K. H. *et al*., Part. Accel. **27**, 101 (1990).
13. Lemonnier, M., Collet, O., Depautex, C., Esteva, J.-M. and Raoux, D., Nucl. Instr. Meth. **152**, 109 (1978).
14. Rothe, J. *et al*., J. Fres. J. Anal. Chem. **355**, 372 (1996).
15. Müller, P., „Lexikon der Stochastik", (Akademie Verlag, Berlin, 1991).

Physica Scripta. Vol. T115, 675–677, 2005

Monolayer Dispersive Supported $CuO/\gamma\text{-}Al_2O_3$ Catalysts Studied by XAFS

Dongliang Chen[1], Xinyi Zhang[2], Yuhai Hu[3], Yi Chen[3], Shaobo Zou[1] and Shiqiang Wei[1*]

[1]National Synchrotron Radiation Laboratory, University of Science and Technology of China, Hefei, 230029, P. R. China
[2]Synchrotron Radiation Research Center, and The state Key Laboratory of Surface Physics, Fudan University, Shanghai, 200433, P. R. China
[3]Institute of Mesoscopic Solid State Chemistry, and Department of Chemistry, Nanjing University, Nanjing 210093, P. R. China

Received June 26, 2003; accepted November 13, 2003

PACS numbers: 61.10.Ht, 61.46.+w, 82.45.Jn

Abstract

The local structures of supported $CuO/\gamma\text{-}Al_2O_3$ monolayer dispersive catalysts with different CuO loadings have been investigated by XAFS. For the $CuO/\gamma\text{-}Al_2O_3$ catalyst with CuO loading of 0.4 mmol/100 m^2, the XAFS results indicate that only one peak corresponding to the Cu-O first shell appears in the radial structural function of Cu atoms, and that the bond length $R_{Cu\text{-}O}$ and coordination number N are 1.95 Å and 3.8, respectively. We consider that the CuO active species on the surface of $\gamma\text{-}Al_2O_3$ are in the form of isolated atomic clusters $(CuO_4)_m{}^{n+}$ with distorted structure for the $CuO/\gamma\text{-}Al_2O_3$ (0.4 mmol/100 m^2) catalyst. It has been found that small amount of CuO nano-grains is formed on the surface of $\gamma\text{-}Al_2O_3$ for $CuO/\gamma\text{-}Al_2O_3$ (0.8 mmol/100 m^2) catalyst while the CuO loading is just equal to the threshold 0.8 mmol/100 m^2. For the catalyst with CuO loading of 1.2 mmol/100 m^2, the local structure of Cu atoms in $CuO/\gamma\text{-}Al_2O_3$ is similar to that of CuO powder. On the basis of the XAFS results, a schematic monolayer dispersion model has been proposed for $CuO/\gamma\text{-}Al_2O_3$ catalysts.

1. Introduction

The elimination of atmosphere pollutants and automobile exhaustions, such as the reduction of NO and CO concentrations, have attracted considerable attention in the last two decades [1–4]. Although the noble metals catalysts of $Pt/\gamma\text{-}Al_2O_3$ and $Pd/\gamma\text{-}Al_2O_3$ show a nice catalytic property in reduction of NO in the presence of CO or oxidation of CO [3, 4], they are not widely used due to their expenses. Hence, one needs to find a cheaper catalyst. A number of studies by Kummer [5], Kapteijn *et al*. [6], and Chen *et al*. [7] have indicated that the supported $CuO/\gamma\text{-}Al_2O_3$ monolayer-dispersed catalysts possess higher catalytic activity at room temperature for the reduction of NO in the presence of CO or oxidation of CO. Especially, $CuO/\gamma\text{-}Al_2O_3$ catalyst has a lower price than those of the noble metal catalysts [8, 9]. It means that $CuO/\gamma\text{-}Al_2O_3$ is a promising candidate for applications in controlling environmental pollutions.

Xie *et al*. [10], Chen *et al*. [7, 11] and Friedman *et al*. [12] have reported that under proper calcination conditions, the copper oxide species can be spontaneously dispersed as a monolayer on the surface of $\gamma\text{-}Al_2O_3$ support. The threshold for CuO monolayer dispersion on the surface of $\gamma\text{-}Al_2O_3$ is about $0.8 \sim 1.6$ mmol/100 m^2 [7, 11]. The monolayer dispersion has been confirmed by X-ray diffraction (XRD). No peaks corresponding to the crystalline CuO phase appear in the XRD pattern of $CuO/\gamma\text{-}Al_2O_3$ when the CuO loading is lower than its monolayer dispersive threshold. However, peaks of crystalline CuO phase can be observed in $CuO/\gamma\text{-}Al_2O_3$ while the CuO loading is higher than its monolayer dispersive threshold. Unfortunately, even if a lot of studies have been done on $CuO/\gamma\text{-}Al_2O_3$ monolayer dispersive catalysts, the occupations of Cu^{2+} ions on the surface of $\gamma\text{-}Al_2O_3$ support are not clear enough yet [7, 11–13].

In this present approach, the local structures of supported $CuO/\gamma\text{-}Al_2O_3$ monolayer dispersive catalysts prepared via impregnations have been investigated by XAFS. Three different CuO loadings of 0.4, 0.8 (equal to the monolayer dispersion threshold of 0.8 mmol/100 m^2) and 1.2 mmol/100 m^2 are used to study the local structures of $CuO/\gamma\text{-}Al_2O_3$ catalysts. On the basis of the XAFS results, a simple monolayer dispersion model has been proposed to interpret the structures of $CuO/\gamma\text{-}Al_2O_3$ catalysts.

2. Experimental

$\gamma\text{-}Al_2O_3$, obtained from Fusun Petrochemical Institute in China, had been calcined at 973 K for 5 hours before using for preparing supported catalysts; the BET surface area was 195 $m^2 \cdot g^{-1}$. The supported $CuO/\gamma\text{-}Al_2O_3$ catalyst was prepared by incipient wetness impregnation of $\gamma\text{-}Al_2O_3$ support with an aqueous solution containing the requisite amount of copper nitrate hexahydrate. The catalyst was dried at 373 K for 24 hours, and subsequently calcined at 923 K in air for 3.5 hours. The $CuO/\gamma\text{-}Al_2O_3$ catalysts with different CuO loadings were as follows, $CuO/\gamma\text{-}Al_2O_3$ (0.4 mmol/100 m^2), $CuO/\gamma\text{-}Al_2O_3$ (0.8 mmol/100 m^2) and $CuO/\gamma\text{-}Al_2O_3$ (1.2 mmol/100 m^2).

The Cu K-edge absorption spectra of $CuO/\gamma\text{-}Al_2O_3$ catalysts were measured at the XAFS station of 4W1B beamline of Beijing Synchrotron Radiation Facility. The electron beam energy was 2.2 GeV and the maximum stored current was about 80 mA. Fixed-exit Si (111) flat double crystals were used as monochromator. The X-ray harmonics were minimized by detuning the two flat Si (111) crystals to about 70% of the maximum incident light intensity. Data were collected in transmission mode using ion chambers with mixed Ar/N_2 fill gas at room temperature. XAFS data were analyzed by using USTCXAFS3.0 [14] and UWXAFS3.0 codes [15].

3. Results and Discussion

The Cu K-edge EXAFS functions $k^3\chi(k)$ and their Fourier transformations (FT) for CuO powder and $CuO/\gamma\text{-}Al_2O_3$ catalysts with different CuO loadings are shown in Figure 1 and Figure 2, respectively. The FT is performed using the k region from 2.5 to 12 $Å^{-1}$ and a Hanning window. It can be observed that several stronger oscillations as shown in Figure 1 appear in the high-k region extended to 12 $Å^{-1}$ for the CuO powder. The oscillation feature of $CuO/\gamma\text{-}Al_2O_3$ catalyst with CuO loading

*Correspondent: Shiqiang Wei, E-mail: sqwei@ustc.edu.cn

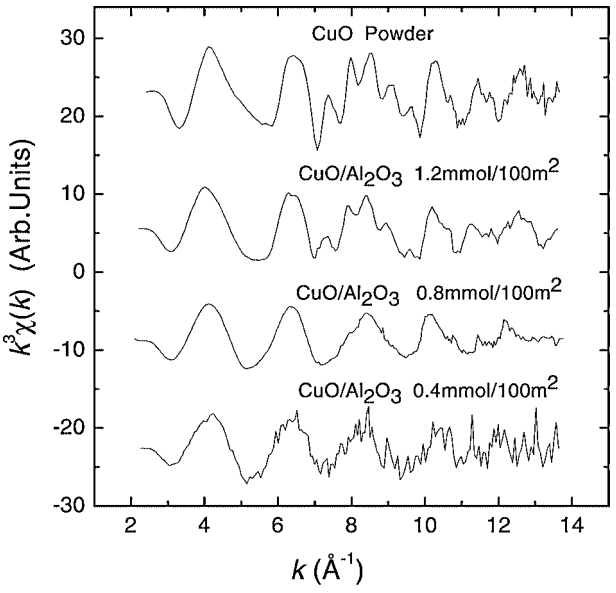

Fig. 1. $k^3\chi(k)$ functions of CuO powder and CuO/γ-Al_2O_3 with different CuO loadings.

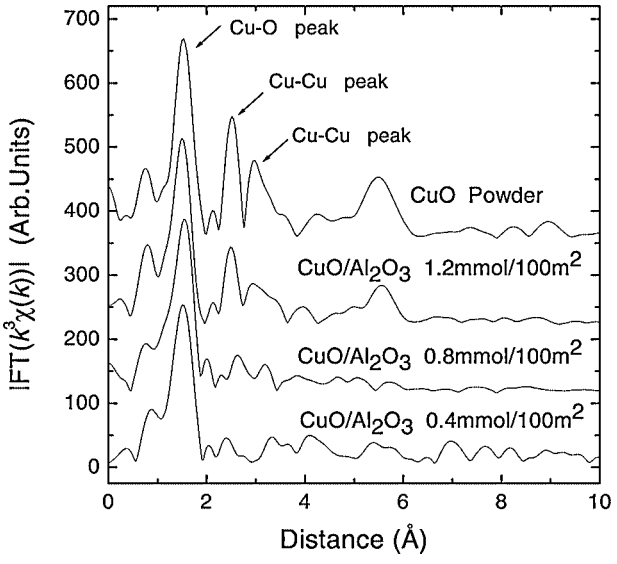

Fig. 2. RSF curves of CuO powder and CuO/γ-Al_2O_3 with different CuO loadings.

of 1.2 mmol/100 m^2 is similar to that of CuO powder, unless its magnitude in the high-k region is slightly deceased. With the CuO loadings decreasing to 0.8 or 0.4 mmol/100 m^2, the magnitude of the oscillation peaks for the CuO/γ-Al_2O_3 catalyst is further deceased by compared with that of CuO/γ-Al_2O_3 (1.2 mmol/100 m^2). Figure 2 demonstrates that there are three stronger peaks located at about 1.5, 2.5 and 3.4 Å in the FT curve of the CuO powder. The first and second peaks correspond to the first shell of four Cu-O pairs with bond length of 1.96 Å, the second shell of two Cu-O pairs with bond length of 2.78 Å and ten Cu-Cu pairs with an average bond length of 3.03 Å, respectively. With the CuO loading changing from 1.2 to 0.4 mmol/100 m^2, only the peak of the first shell exists and the peaks of the higher shells disappear for the monolayer dispersive CuO/γ-Al_2O_3 catalyst.

For obtaining the structural parameters of CuO/γ-Al_2O_3 catalysts, least-squares curve fit was performed for the data analysis by using the USTCXAFS3.0 code [14]. The theoretical amplitude functions and phase shifts were calculated by FEFF7.0

Table I. *The structural parameters of CuO powder and CuO/γ-Al_2O_3 with different CuO loadings.*

Sample	Bend type	R/Å	σ^2/Å^2	N	ΔE/eV
CuO/γ-Al_2O_3	Cu-O	1.95	0.0052	3.8	−1.9
(0.4 mmol/100 m^2)	Cu-O	2.78	0.0161	0.1	−1.9
	Cu-Cu	2.97	0.0220	0.2	−1.9
CuO/γ-Al_2O_3	Cu-O	1.95	0.0050	3.9	−1.6
(0.8 mmol/100 m^2)	Cu-O	2.78	0.0153	0.2	−1.6
	Cu-Cu	2.97	0.0214	3.4	−1.6
CuO/γ-Al_2O_3	Cu-O	1.95	0.0049	4.0	−1.9
(1.2 mmol/100 m^2)	Cu-O	2.78	0.0139	2.0	−1.9
	Cu-Cu	2.97	0.0221	8.1	−1.9
CuO Powder	Cu-O	1.95	0.0042	3.9	2.1
	Cu-O	2.78	0.0050	2.0	2.1
	Cu-Cu	2.97	0.0220	9.6	2.1

[15]. The curve fits, based on single-scattering theory, were performed in R-range between 1.0 and 2.9 Å for the two first nearest Cu-O sub-shells ($R_1 = 1.96$, $R_2 = 2.78$ Å) and one Cu-Cu second shell ($R_3 = 3.03$ Å). The fitting results are summarized in Table I.

Seen from Table I, the structural parameters of the Cu-O first sub-shell are almost the same for all the CuO/γ-Al_2O_3 catalysts with CuO loadings of 0.4, 0.8 and 1.2 mmol/100 m^2. Their bond lengths R and the coordination numbers N are 1.95 Å and 3.8, 1.95 Å and 3.9, 1.95 Å and 4.0, respectively. However, the N of the Cu-O second sub-shell ($R = 2.78$ Å) is about 2.0 for CuO/γ-Al_2O_3 (1.2 mmol/100 m^2) while those of CuO/γ-Al_2O_3 (0.8 or 0.4 mmol/100 m^2) are close to zero, and the N of the Cu-Cu second shell ($R = 2.97$ Å) are 8.1, 3.4 and 0.2 for CuO loadings of 1.2, 0.8 and 0.4 mmol/100 m^2, respectively. These structural parameters have clearly shown that only the XAFS signal corresponding to the Cu-O first shell appears in the CuO/γ-Al_2O_3 (0.4 mmol/100 m^2) catalyst that is lower than the monolayer dispersion threshold of 0.8 mmol/100 m^2. When the CuO loading is increased to the monolayer dispersion threshold or exceeds it, the peaks of their higher shells appear in the FT curves as shown in Figure 2. It is noteworthy that the bond lengths ($R = 1.95$ Å) and coordination numbers ($N = 3.8$) of the Cu-O first shell of CuO/γ-Al_2O_3 (0.4 mmol/100 m^2) catalyst is almost the same as those ($R = 1.95$ Å and $N = 4.0$) of CuO powder, CuO/γ-Al_2O_3 (0.8 mmol/100 m^2) and CuO/γ-Al_2O_3 (1.2 mmol/100 m^2) catalysts. This feature implies that the first nearest neighbors of Cu^{2+} in CuO/γ-Al_2O_3 catalysts are similar to that of crystalline CuO powder, which is independent of the CuO loadings. Xie *et al.* [10], Chen *et al.* [7, 11] and Friedman *et al.* [12] have considered that CuO species are highly dispersed (or monolayer dispersive) on the surface of γ-Al_2O_3 under the monolayer dispersive threshold of CuO, since their XRD patterns indicate that no diffraction peaks corresponding to crystalline CuO were observed for CuO loadings of 0.8 mmol/100 m^2. In fact, there are two possible reasons for the disappearance of CuO diffraction peaks. One is that CuO species are monolayer dispersive on the surface of γ-Al_2O_3, which is just as the results reported by Xie *et al.* [10] and Chen *et al.* [7, 11]. The other is that CuO species are much smaller clusters with high dispersion on the surface of γ-Al_2O_3. XRD technique is difficult for detecting the diffraction signals while the grain sizes of the particles are small enough [16]. Our XAFS results indicate that Cu^{2+} ions are in the form of atomic clusters $(CuO_4)_m^{n+}$

with distorted structure on the surface of γ-Al_2O_3, even for the CuO/γ-Al_2O_3 catalyst in which CuO loading is lower than the threshold of 0.8 mmol/100 m^2. Meanwhile, the disappearance of higher Cu-O and Cu-Cu coordination shells for CuO/γ-Al_2O_3 (0.4 mmol/100 m^2) catalyst indicates that there are no Cu^{2+} ions existing in incorporated form on the surface vacant sites of the γ-Al_2O_3 support, or in other words, there are no Cu-Cu or Cu-Al second coordination shells in CuO/γ-Al_2O_3 (0.4 mmol/100 m^2). Otherwise, the peak associated with the Cu-Cu or Cu-Al second shell should appear in the monolayer-dispersed CuO/γ-Al_2O_3 catalysts [12]. This result suggests that CuO species on the surface of γ-Al_2O_3 do not exist in the form of Cu_2O [17] or spinal $CuAl_2O_4$ [18]. In addition, the present results seem to indicate that it is impossible to have Cu^{2+} coordinated by 5 oxygen atoms in the first nearest neighbor as claimed in Refs. [11] and [12]. In order to well interpret the XAFS results, we consider that the CuO active species on the surface of γ-Al_2O_3 are in the form of isolated atomic clusters $(CuO_4)_m{}^{n+}$ with distorted structure. This result means that the $(CuO_4)_m{}^{n+}$ cluster as a basic structural element occupies the surface vacant site of the γ-Al_2O_3 support for the monolayer-dispersed supported CuO/γ-Al_2O_3 catalyst after calcined at a lower temperature of 723 K.

The weak peaks of the higher coordination shells for the CuO/γ-Al_2O_3 catalyst with CuO loading of 0.8 mmol/100 m^2 show that most of the Cu^{2+} ions are in the form of isolated atomic clusters $(CuO_4)_m{}^{n+}$, but there is also a small amount of CuO nano-grains forming on the surface of γ-Al_2O_3 support. For the CuO/γ-Al_2O_3 catalyst with CuO loading of 1.2 mmol/100 m^2, Cu^{2+} ions on the surface of the γ-Al_2O_3 support are mainly in the form of poly-crystalline CuO. Our results are consistent with those reported by Shi *et al*. [19]. They have studied the local structures around Mo for monolayer-dispersed MoO_3/γ-Al_2O_3 catalysts with XAFS, and show that below the monolayer dispersive threshold of MoO_3 loadings, the dispersion phase of MoO_3 active species on the surface of γ-Al_2O_3 support consists of [MoO_4] polyhedrons that are not connected to each other.

In summary, we propose a schematic mechanism to interpret the local structural change for monolayer dispersive CuO/γ-Al_2O_3 catalyst during the preparation by impregnation. After the mixture of γ-Al_2O_3 support and copper nitrate aqueous solution is dried, Cu^{2+} ions exist in the form of $Cu(NO_3)_2$ absorbed randomly onto the surface of γ-Al_2O_3 support. Then, the $Cu(NO_3)_2$ compound with the crystal water are probably decomposed at the calcinating temperature of 723 K in air for 3.5 hours, the CuO species are in the form of atomic clusters $(CuO_4)_m{}^{n+}$ (or $(Cu(OH)_4)_m{}^{n+}$) with distorted structure as a basic cluster element occupying the surface vacant sites of the γ-Al_2O_3 support.

Acknowledgment

This project was supported by the Chinese Nature Science Foundation Committee (Grant No.10174068), the development of the high-level university of University of Science and Technology of China and Key-program of Beijing Synchrotron Radiation Facility.

References

1. Radwan, N. R. E., Fagal, G. A. and EI-Shobaky, G. A., Colloids Surf. A **178**, 277 (2001).
2. Curtin, T., Regan, F. O., Deconinck, C., Knuttle, N. and Hodnett, B. K., Catal. Today **55**, 189 (2000).
3. Pisanu, A. S. and Gigola, C. E., Appl. Catal. B: Environmental **20**, 179 (1999).
4. Klimish, R. L. and Talor, K. C., Environ. Sci. Technol. **7**, 127 (1993).
5. Kummer, J. T., Prog. Energy Combust. Sci. **6**, 177 (1980).
6. Kapteijn, F., Stegenga, S., Dekker, N. J. J., Bijsterboach, J. W. and Moulijn, J. A., Catal. Today **16**, 273 (1993).
7. Hu, Y. H., Dong, L., Wang, J., Ding, W. P. and Chen, Y., J. Mol. Catal. (A): Chem. **162**, 307 (2000).
8. Parvulescu, V. I., Grange, P. and Delmon, B., Catal. Today **46**, 233 (1998).
9. Olsbye, M., Wendelbo, R. and Akporiaye, D., Appl. Catal. A **152**, 127 (1997).
10. Xie, Y. C. and Tang, Y. Q., Adv. Catal. **37**, 1 (1990).
11. Chen, Y. and Zhang, L. F., Catal. Lett. **12**, 51 (1992).
12. Friedman, R. M., Freeman, J. J. and Lytle, F. W., J. Catal. **55**, 10 (1978).
13. Strohmeier, B. R., Leyden, D. E., Field, R. S. and Hercules, D. M., J. Catal. **94**, 514 (1985).
14. Zhong, W. J. and Wei, S. Q., J. Univ. Sci Tech. China **31**, 328 (2001).
15. Stern, E. A., Newville, M., Ravel, B., Haskel, D. and Yacoby, Y., Physica B **208&209**, 117 (1995).
16. Lagarde, P. and Dexpert, H., Adv. Phys. **33**, 567 (1984).
17. Yamaguti, T., Proc. Physico-Math. Soc. Japan **20**, 230 (1938).
18. Passerini, L., Gazzetta Chimica Italiana GCITA **60**, 389 (1930).
19. Shi, W. P. *et al*., Surf. Interface Anal. **32**, 202 (2001).

Physica Scripta. Vol. T115, 678–680, 2005

In situ Study of the Crystallisation of Nano-Sized Zinc and Cobalt Aluminate Spinel Catalysts from Ion-Exchanged Zeolite Precursors

A. M. Beale[1*], G. Sankar[1], D. G. Nicholson[2] and W. van Beek[3]

[1]Davy Faraday Research Laboratory, The Royal Institution of GB, 21 Albemarle Street, London W1S 4BS, UK
[2]Department of Chemistry, Realfagsbygget, Norwegian University of Science & Technology, N-7491 Trondheim, Norway
[3]ESRF, BP 220, F-38043 Grenoble Cedex, France

Received June 26, 2003; accepted February 4, 2004

PACS number: 81.20

Abstract

Heat induced amorphisation of cobalt and zinc ion-exchanged zeolites A and Y has been used as a synthetic method to prepare the spinel phases $CoAl_2O_4$ and $ZnAl_2O_4$. We report here some of our early results from an *in situ* investigation into the formation of these phases and we discuss the possibilities of estimating spinel particle size from the magnitude of the second peaks in the EXAFS Fourier transform.

1. Introduction

Transition metal oxide spinels have been used in many industrial applications including semiconductors, magnetic storage media and in sensor technology [1]. However, their thermal stability, high oxygen anion mobility and the ease with which other ions can be accommodated into the spinel framework mean that they are often considered to be potentially good candidates for use in heterogeneous catalysis. Although it is possible to prepare spinels possessing large surface areas by means of co-precipitation procedures (this method is preferred to the mixing of the solid oxides), these methods normally involve calcination temperatures in excess of 1000 °C and are often plagued with problems such as the crystallisation of additional unwanted phases and phase transformation to an inactive form. As such new approaches have been developed for the preparation of such materials, including the crystallisation of spinels from collapsed ion-exchanged zeolite precursors and hydrothermal procedures [2, 3]. Normally zeolites collapse to first form an amorphous material before transforming to dense phase systems, at elevated temperatures [2, 4]. The abundance of silicon and oxygen in the zeolite framework means that quartz and cristobalite are some of the common phases that crystallise at elevated temperatures. However, zeolites containing high concentrations of aluminium require an equal amount of charge balancing monovalent ions such as sodium and yield other phases such as nepheline ($NaAlSiO_4$) [2]. These extra-framework sodium ions can be readily replaced with other metal ions, for example Co^{2+} or Zn^{2+}. It was soon discovered that other materials such as the spinel phases $CoAl_2O_4$ and $ZnAl_2O_4$ can be obtained by collapsing these Co^{2+} and Zn^{2+} exchanged zeolites [2, 5]. More recently [1, 6] this work has been developed further resulting in a viable, reproducible and cheap method for the preparation of the transition metal aluminates $CoAl_2O_4$, $NiAl_2O_4$ and $ZnAl_2O_4$ with surface areas often in excess $100\,m^2/g$.

Although the recent investigation showed the formation of small particles by XRD, the results did not show whether a highly disordered spinel phase was produced in the amorphous phase. Thus, we focussed our attention on a detailed investigation by combined XRD/QuEXAFS (since this method combines both the techniques that are sensitive to long-range and short-range ordering). For this purpose we investigated the formation of $CoAl_2O_4$ and $ZnAl_2O_4$ spinels from various heat-treated cobalt and zinc ion exchanged zeolites. We performed both *in situ* and *ex situ* experiments to investigate the structures that are formed prior, during and after transformation of the amorphous phase to the final dense crystalline product. X-ray absorption spectroscopy, in particular, allowed us to clearly distinguish the formation of either Co_3O_4 or $CoAl_2O_4$ phase in the heat-treated cobalt exchanged zeolites.

2. Experimental

Zeolites A (Si : Al = 1) and Y (Si : Al = 2.52) were used since they had previously been employed successfully to prepare spinel phases [1, 4–6]. In a typical experiment 5 g of zeolite was added to 250 ml of distilled water containing 0.1 M of either cobalt acetate/nitrate or zinc nitrate. Ion exchange was carried out at 70 °C for 30 minutes before the solid materials (pink in colour for cobalt exchanged samples but white for zinc) were filtered, washed and dried overnight at 100 °C. Combined *in situ* XRD/QuEXAFS experiments of the oven-dried samples were carried out on station 9.3 at the SRS Daresbury Laboratory. In a typical experiment 20 mg of the zeolite samples were pressed into a disc of 13 mm diameter and placed into an *in situ* cell permitting combined measurement [6–8]. Samples were heated at 5 °C/minute to 950 °C with XAS and XRD data collected sequentially. XAS data was collected for 380 s and XRD for 180 s resulting in a total cycle time of 10 minutes. XRD data were collected on an INEL detector at a wavelength of 1.661 Å. XAS data were processed using the Daresbury Laboratory suite of programmes namely EXCALIB, EXBROOK and EXCURV98. Based on the *in situ* study we focused our *ex situ* measurements on samples heated at 850 °C and 950 °C. For this purpose, pellets were pressed from 0.3 g portions of the ion-exchanged zeolites and these were placed in a ceramic crucible before firing began at a heating rate of 5 °C/minute. Samples were withdrawn and the reaction quenched at 850 °C and 950 °C respectively before they were subjected to *ex situ* XRD and XAS measurements. XRD patterns were recorded using a Siemens D500 diffractometer with Cu-Kα_1 radiation. Cobalt and zinc K-edge XAS measurements on 20 mg portions (of 20 mm diameter) of the as-prepared and calcined samples were carried out on the Swiss-Norwegian beamline at the ESRF.

*email: andrewb@ri.ac.uk

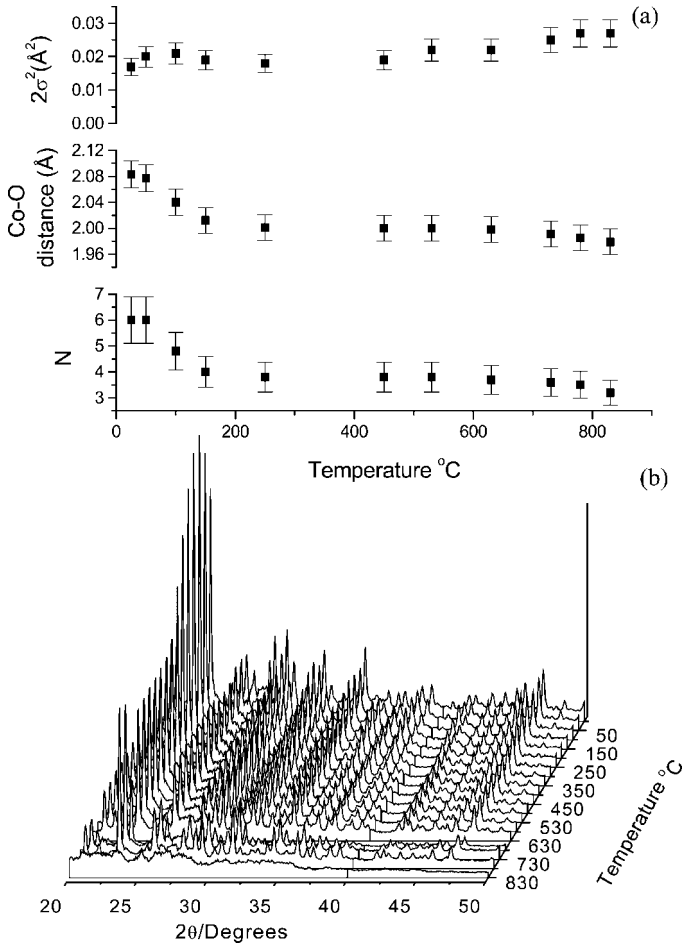

Fig. 1. Plot of the data obtained from a single scattering first shell analysis of the QuEXAFS data (a) and a stacked plot of the XRD data (b) collected sequentially with the QuEXAFS during calcination of cobalt exchanged zeolite Y. The estimated error in the determination of bond distance (as shown by the error limits in marked in 1(a)) is approximately 1% whereas for the occupancy and disorder this is in the order of 15%.

Table I. *Structural parameters determined from Co/Zn K-edge EXAFS of ion exchanged zeolites A.*

Zeolite	Salt	M-O distance[1] (Å)	N^1	$2\sigma^2$ (Å^2)[1]	*R*-factor (%)
A	Cobalt acetate	2.08	5.9	0.016	20.2
A	Cobalt nitrate	2.08	5.7	0.016	19.8
A	Zinc nitrate	1.97	4.4	0.017	25.7
Y	Cobalt nitrate	2.09	6.0	0.016	17.7

[1]The estimated error for the M-O distance is *ca* 0.02 Å and for the occupancy and disorder is *ca* 10 percent.

The results of the detailed analysis of the cobalt and zinc K-edge EXAFS data of the as-prepared (oven-dried) samples, recorded ex-situ, employing single scattering analysis procedures are given in table I. It is clear from this analysis that the cobalt ions are coordinated to six oxygen atoms with an average metal oxygen distance of 2.08 Å, whereas the zinc ions are connected to four oxygen atoms at a distance of 1.98 Å with both results similar to previously reported measurements for ion-exchanged cobalt and zinc ions in zeolites [2, 9].

As noted above in the *in situ* XRD/QuEXAFS measurements, after calcination of the samples, both the XRD and XAS data, recorded *ex situ*, underwent a number of changes. A typical best fit to the EXAFS data and the associated Fourier transforms are shown in figure 2 for the cobalt and zinc nitrate ion-exchanged zeolite A samples calcined at 950 °C. It is clear from a simple first shell analysis that the Co-O and Zn-O distances have shortened after the heat treatment to *ca* 1.95 Å, which is consistent with the formation of tetrahedral Co^{2+} and Zn^{2+} containing spinel structures [10, 11]. The XRD patterns, which are not shown here, also contain reflections pertaining to the spinel phases. Higher coordination shells have also been fitted in an attempt to obtain information on particle size. For this purpose XAS data were collected first on the bulk $CoAl_2O_4$ and $ZnAl_2O_4$

3. Results and discussion

In order to follow the formation of spinel phases from the amorphised zeolites a combined XRD/QuEXAFS study was carried out during calcination of cobalt-exchanged zeolite Y to 950 °C. In figure 1 we show the a stacked plot of the XRD data collected sequentially with the QuEXAFS data and the variation of structural parameters obtained from the analysis of the Co K-edge data of cobalt ion-exchanged zeolite A sample; the EXAFS data of the first shell was analysed for this purpose employing single scattering procedures. The XRD data clearly showed that the crystalline zeolite structure is lost above 830 °C and no appreciable structural modification is seen at temperatures below 800 °C. However, the EXAFS results clearly showed several gradual changes during the heat treatment process. In particular the average Co-O distance and the coordination number decreased during the initial stages of the heat treatment, which may be attributed to the loss of adsorbed water. The changes observed by both techniques suggest that the formation of the cobalt spinel phase occurs via a reduction in coordination number and bond length of the local cobalt environment in the initial stages (at temperatures *ca* 250 °C most probably as a result of zeolite dehydration) before the cobalt spinel forms from the amorphised zeolite at temperatures *ca* 850 °C.

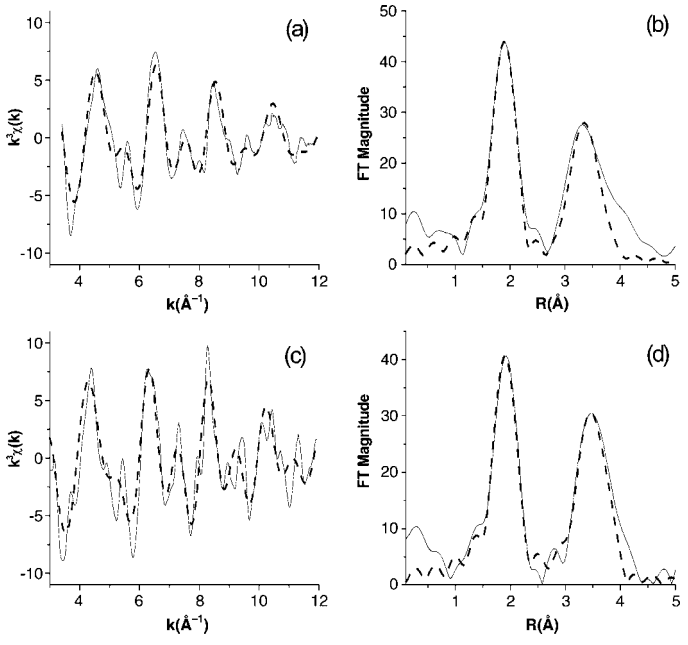

Fig. 2. Best fit between experimental Co (a) and Zn (c) K-edge EXAFS data (solid line) and the calculated best fit (dashed line) and associated Fourier transforms (b and d) for cobalt/zinc nitrate exchanged zeolite A samples calcined at 950 °C.

Table II. *Structural parameters determined from Co/Zn K-edge EXAFS of ion exchanged zeolites A after heat treatment at 850 and 950°C respectively.*

Structure	Calcination temperature (°C)	M-O[1] distance (Å)	N1[1]	$2\sigma^2$ (Å^2)[1]	M-Al[2] distance (Å)	N2[2]	$2\sigma^2$ (Å^2)[2]	M-M[2] distance (Å)	N3[2]	$2\sigma^2$ (Å^2)[2]	R-factor (%)
$CoAl_2O_4$	—	1.95	4.0	0.004	3.32	12	0.013	3.52	4.0	0.007	42.5
$ZnAl_2O_4$	—	1.95	3.8	0.009	3.29	12	0.019	3.52	4.0	0.008	58.0
Zeolite A*	850	1.98	4.0	0.004	3.24	1.7	0.013	—	0	0.007	31.4
Zeolite A*	950	1.96	3.6	0.004	3.27	3.9	0.013	3.50	1.9	0.007	51.0
Zeolite A$^+$	850	1.97	4.0	0.004	3.23	2.4	0.013	3.48	0.4	0.007	48.8
Zeolite A$^+$	950	1.96	4.0	0.004	3.28	5.1	0.013	3.50	2.0	0.007	52.4
Zeolite A$^?$	850	1.97	5.1	0.009	3.14	2.1	0.019	—	0	0.008	21.0
Zeolite A$^?$	950	1.95	3.8	0.009	3.29	5.0	0.013	3.52	2.5	0.008	48.7

M = Cobalt/Zinc
* Cobalt acetate exchanged
$^+$ Cobalt nitrate exchanged
$^?$ Zinc nitrate exchanged
[1]The estimated error for the M-O distance is *ca* 0.02 Å and for the occupancy and disorder is ca 10 percent.
[2] The error associated with M-Al and M-M distances representing higher shells have slightly higher error of *ca* 0.04 and the respective coordination number and Debye-Waller factors have 15 percent.

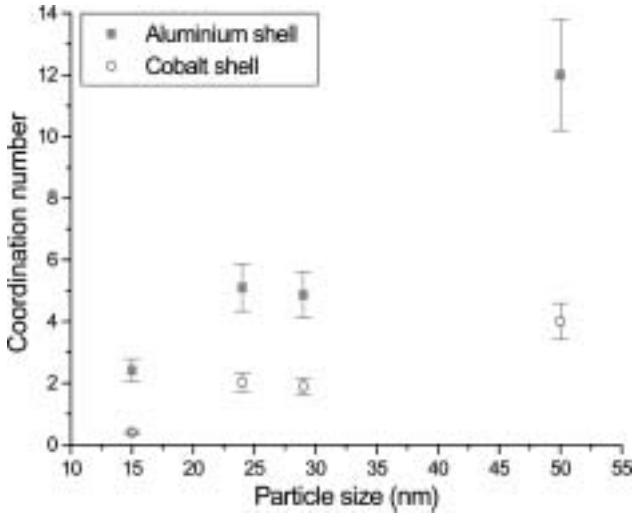

Fig. 3. Comparison of second and third shell coordination numbers and the particle size estimated from the FWHM of the 311 reflection in the XRD pattern using the Scherrer equation.

structures and the data refined with the coordination numbers for the higher aluminium and cobalt/zinc shells fixed to 12 and 4 respectively to avoid correlation effects. It is clear from a comparison of second and third shell coordination numbers of the bulk with the samples prepared from zeolite that the latter ones has much smaller particles compared to the bulk; the particle size estimated from the FWHM of the 311 reflection in the XRD pattern using the Scherrer equation support the findings of the EXAFS results (Table II and figure 3). Similar to many other nano-sized oxide systems, a coordination number of 4 for the first shell indicated that irrespective of the particle size the particles terminate with oxygen. Further work is necessary to determine accurately the coordination number of the higher-shell data, by perhaps carrying out measurements at very low temperatures to remove the dynamic disorder contribution and estimate only the static disorder resulting from the small particle nature of the systems prepared from zeolites.

4. Summary

Cobalt and zinc ion exchanged zeolites A and Y have successfully been used to prepare the spinel phases $CoAl_2O_4$ and $ZnAl_2O_4$. Evidence suggests that the spinels form directly from the amorphised zeolites and therefore it does not appear that the spinel formation promotes zeolite collapse. A comparison of the coordination numbers obtained from a second shell analysis of the calcined materials revealed small spinel oxide particles are formed by employing this procedure. These results suggested that the preparative process could be controlled to yield nano-sized cobalt and zinc aluminate particles for applications in particular in the area of catalysis.

Acknowledgments

The authors thank EPSRC for financial support, CCLRC, Daresbury Laboratory and ESRF for the provision of beam time and facilities. GS thanks the Leverhulme Trust for a Senior Research Fellowship. We also thank Professor H-P. Weber and Dr. H. Emerich at SNBL, ESRF and Ian Harvey at the SRS, Daresbury Laboratory for help with the experiments and for useful discussions.

References

1. Schmidt, W. and Weidenthaler, C., Chem. Mat. **13**, 607 (2001).
2. Colyer, L. M., Greaves, G. N., Carr, S. W. and Fox, K. K., J. Phys. Chem. B. **101**, 10105 (1997).
3. Chen, Z. *et al*., Mater. Lett. **55**, 281 (2002).
4. Greaves G. N. *et al*., Jpn. J. Appl. Phys. **38**, 202 (1999).
5. Colyer, L. M. *et al*., Nucl. Instr. Meth. Phys. Res. B. **97**, 107 (1995).
6. Weidenthaler, C. and Schmidt, W., Chem. Mater. **12**, 3811 (2000).
7. Clausen, B. S., Topsøe, H. and Frahm, H., Adv. Catal. **42**, 315 (1998).
8. Sankar, G. *et al*., J. Phys. Chem. B. **97**, 9550 (1993).
9. Sankar, G. and Thomas, J. M., Top. Catal. **8**, 1 (1999).
10. de Bont, P. W. *et al*., Appl. Catal. A-Gen. **236**, 205 (2002).
11. Cooley, R. F. and Reed, J. S., J. Am. Ceram. Soc. **55**, 395 (1972).
12. G. Toriumi, K., Ozima, M., Akaogi, M. and Saito, Y., Acta Cryst. B. **34**, 1093 (1978).

Physica Scripta. Vol. T115, 681–684, 2005

Structure of Dioxygen Binding Xerogels Incorporating Cyclams Complexed with $CuCl_2$ Salts

C. Goulon-Ginet[1*], J. Goulon[1], A. Rogalev[1], F. Wilhelm[1], N. Jaouen[1], G. Dubois[2], S. Brandès[2], G. David[2], R. Guilard[2], R. Corriu[3], D. Cabaret[4] and Y. Joly[5]

[1]ESRF, BP 220, F-38043 Grenoble Cedex, France–* also Université J. Fourier, Faculté de Pharmacie, F-38706 La Tronche, France
[2]LIMSAG, UMR 5633 CNRS-AIR LIQUIDE, Université de Bourgogne, Faculté des Sciences Gabriel, Bd. Gabriel, F-21100 Dijon, France
[3]LCMOS, UMR 5637 Université de Montpellier II, Place E. Bataillon, F-34095 Montpellier, France
[4]LMCM, UMR 7590 Université P. et M. Curie, case 115, 4 Place Jussieu, F-75252 Paris Cedex 05, France
[5]Laboratoire de Cristallographie du CNRS, associé à l'Université J. Fourier, B.P. 166, F-38042 Grenoble Cedex, France

Received June 26, 2003; accepted January 19, 2004

PACS number: 7870Dm

Abstract

X-ray absorption/emission spectroscopies were combined in order to elucidate how hybrid xerogels complexed with $CuCl_2$ could bind reversibly O_2. *Difference* EXAFS analyses at the Cu K-edge revealed the existence of binuclear structures with long Cu . . . Cu distances, *i.e.* $R_{Cu-Cu} \approx 3.98$ Å and 3.87 Å for the oxygenated and *oxygen-free* xerogels. In oxygenated xerogels, dioxygen would bridge two Cu atoms in a μ–$\eta^1 : \eta^1$ peroxo-like conformation. The Cu-O signal found at short distance ($R_{Cu-O1} = 1.85 \pm 0.01$ Å) is fully consistent with 40% of O_2 molecules being chemisorbed per Cu site. In oxygen-free xerogels, Cl K-edge EXAFS revealed the presence of Cu^I sites with short Cl-Cu bond lengths ($R_{Cl-Cu} = 2.11 \pm 0.03$ Å) and of pentacoordinated Cu^{II} sites with longer Cl-Cu bond lengths ($R_{Cl-Cu} = 2.45 \pm 0.03$ Å). Another signal at $R_{Cl \ldots Cu} \approx 2.73$ Å may suggest that Cl could bridge [Cu^I, Cu^{II}] sites. Deconvoluted XANES spectra of the active xerogels exhibit a strong pre-edge resonance that was assigned to the Cu^I sites. The chemical shifts of the Cu K$\beta_{1,3}$ lines also confirmed the coexistence of Cu^I, Cu^{II} sites.

1. Introduction

Advanced industrial applications require AIR LIQUIDE to remove trace amounts of dioxygen in inert gases. Recently, organic-inorganic hybrid polymers or xerogels incorporating metal chelating ligands such as the 1,4,8,11-tetrazacyclotetradecane (Cy = cyclam) macrocycle have attracted much attention for trapping dioxygen since it was found that hybrid xerogels complexed with $CuCl_2$ along route (B) could bind *reversibly* O_2 whereas xerogels prepared by a similar Sol-Gel process but along route (A) were inactive [1, 2] (Fig. 1). It was our aim to elucidate how xerogels of type (B) could bind dioxygen [3]. Materials and methods are briefly reviewed in section 2. As illustrated with section 3, much information was extracted from difference EXAFS analyses carried out at both the Cu and Cl K-edges. In section 4, it is shown that numerically deconvoluted XANES spectra exhibit a strong, characteristic pre-edge resonance signal in *all* active xerogels. XANES simulations performed beyond the *muffin-tin* approximation led us to assign this signal to Cu^I sites. The chemical shifts of the Cu K$\beta_{1,3}$ lines confirmed the coexistence of Cu^I and Cu^{II} sites.

2. Materials and Methods

All samples, including model compounds were synthesized and characterized at the LIMSAG in Dijon. Active, oxygen-free xerogels were handled under controlled atmosphere in a glove box and stored as powdered pellets in a vacuum-tight cell carefully designed for this project. Hereafter, **XB1** denotes *oxygen-free* xerogels of type (B) complexed with $CuCl_2$ and **XB2** the corresponding oxygenated xerogels; **XB3** denotes *oxygen-free*

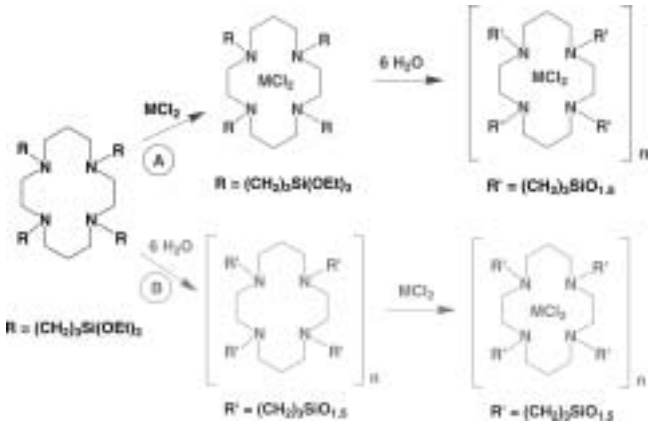

Fig. 1. Alternative routes to yield metalled xerogels.

xerogels of type (B) complexed with $CuBr_2$ and **XB4** the corresponding oxygenated xerogels. In contrast, **XA1** will denote an inactive xerogel of type (A). Relevant model compounds which were investigated include [3]: **1** = [TPP Cu^{II}]; **2** = [Cy Cu^{II}] $2ClO_4^-$; **3** = [TMCy Cu^{II}] $2BF_4^-$; **4** = [TMCy $Cu^{II}Cl$] BF_4^-; **5** = [$N(Me)_2N(CH_2\text{-}Pyr)_2$ Cy Cu^{II}] $2BF_4^-$; **6** = [$N(Pr)_4$ Cy $Cu^{II}Cl$] Cl^-.

High quality EXAFS and XANES spectra were recorded at the windowless ESRF beamline ID12 which is equipped with helical undulator sources [4, 5]. All data were taken at low temperature ($T = 80$ K) in the fluorescence detection mode using an array of 8 PNN^+ photodiodes. At the Cu K-edge, the μ-step gap scan technique made it possible to detect useful EXAFS signal over 2000 eV ($k_{max} \leq 23$ Å^{-1}). At the Cl K-edge, the spectra had to be truncated ($k_{max} \leq 14.4$ Å^{-1}) due to a contamination with a weak potassium K-edge signal. The Cu K$\beta_{1,3}$ lines emission spectra were collected using a spherically bent Si (440) crystal analyzer operated at 46.17° Bragg angle. The high signal/noise ratio allowed us to increase artificially the energy resolution by numerical deconvolution.

Hereafter we will display *optical* FT EXAFS spectra corrected for the amplitude and phase shifts of a selected (dominant) shell j [6, 7, 8].

$$\bar{\chi}_j(R) = \int_0^\infty \mathrm{d}k \cdot W(k) \cdot \chi_j^{(cor)}(k) \cdot \exp[-2\mathrm{i}kR] \tag{1}$$

where $W(k)$ is the Kaiser-Bessel window and:

$$\chi_j^{(cor)} = \chi(k) \cdot \frac{kR_j^2 \cdot \exp[2\sigma_j^2 k^2 - \mathrm{i}\psi_j(k, R_j)]}{F_j(k, R_j) \cdot D_j(\Gamma; k; R_j) \cdot S_0^2(k)} \tag{2}$$

in which F_j, ψ_j are the scattering amplitude and phase-shift of shell j, whereas $D_j \cdot S_0^2$ describes the multielectron response of the system. All corrections were generated by running the FEFF8.9 code [9]. Fits and simulations (in $k + R$ spaces) were performed with code x0 [6, 7, 8]. The numerical deconvolution of the XANES spectra (4096 data pts) was carried out using a Voigt lineshape accounting for both the core hole lifetime and instrumental broadening. For simplicity, we used $\Delta E_G(fwhm) = \Delta E_L(fwhm) \approx 1.4\,\text{eV}$ at the Cu K-edge [3]. XANES simulations were carried out with the advanced code FDMNES [10].

3. EXAFS Analyses

The Cu K-edge FT EXAFS spectra $\Im m\,\bar{\chi}_N(R)$ of xerogels **XB1** and **XB2** are compared in Fig. 2A. Given that the signatures assigned to the Cu…N and Cu…C_α shells of the cyclam macrocycle were nicely superimposed, we carried out the analysis of the difference $\Delta\chi$ [**XB2-XB1**]. The most striking feature in the FT difference spectrum (Fig. 2B) is a well resolved peak assigned to a short Cu-O bond: $R_{Cu-O(1)} = 1.855 \pm 0.005$ Å. Fitting this Fourier-filtered signal led to an average number of bound oxygen atoms $N_{O(1)} = 0.76 \pm 0.06$ *per* Cu site in remarkable agreement with the BET isotherms measured at 77 K. Note that the fitted distance $R_{Cu-O(1)}$ is very close to the bond length (1.852 Å) found in binuclear [Cu^I-O_2] model compounds of oxy-hemocyanin [11], *e.g.* in end-on μ–$\eta^1 : \eta^1$ *trans*-peroxo complexes [12]. In the FT difference spectrum (Fig. 2B), there is also at *ca.* 4 Å, a characteristic signal which is most likely resulting from a small variation of the distance $R_{Cu\,\ldots\,Cu}$ when dioxygen is bound to Cu. From tentative simulations, we obtained: $R_{Cu\,\ldots\,Cu} = 3.99 \pm 0.03$ Å for the oxygenated xerogel **XB2** and $R_{Cu\,\ldots\,Cu} = 3.89 \pm 0.03$ Å for the oxygen-free xerogel **XB1**. Most encouraging, the number density $N_{Cu(2)} \approx 0.76$ went out identical to $N_{O(1)}$ As far as our assignment is correct, we may rule out any *side-on* peroxo configuration for which $R_{Cu\,\ldots\,Cu} \leq 3.56$ Å [11]. At this stage, the assignment of the long distance $R_{Cu-O(2)} \approx 2.96$ Å to the most intense peak found between 2–4 Å is much more tentative. Nevertheless, if we admit that the distance $d_{O(1)\,\ldots\,O(2)}$ is of the order of 1.44 Å (as suggested by the vibrational RAMAN spectrum), we would expect the angle [Cu-O_1-O_2] to be 128° whereas Quantum Chemistry calculations would predict 130° [13]. This would have the important implication that the sequence [$Cu_{(1)}$-$O_{(1)}$-$O_{(2)}$-$Cu_{(2)}$] could not be coplanar, the $Cu_{(1)}$-$O_{(1)}$ and $Cu_{(2)}$-$O_{(2)}$ bonds being rotated by *ca.* 93° with respect to each other.

The Cl K-edge FT EXAFS spectra $\Im m\,\bar{\chi}_{Cu}(R)$ of xerogels **XB1** and **XB2** are compared in Fig. 3A and the corresponding FT difference spectrum is displayed in Fig. 3B. In Fig. 3A, we may identify a triplet of well resolved Cl…Cu distances: the shortest one ($R_{Cu-Cl} = 2.11 \pm 0.03$ Å) is characteristic of a Cu^I-Cl bond; the next one ($R_{Cu-Cl} = 2.45 \pm 0.03$ Å) was typically

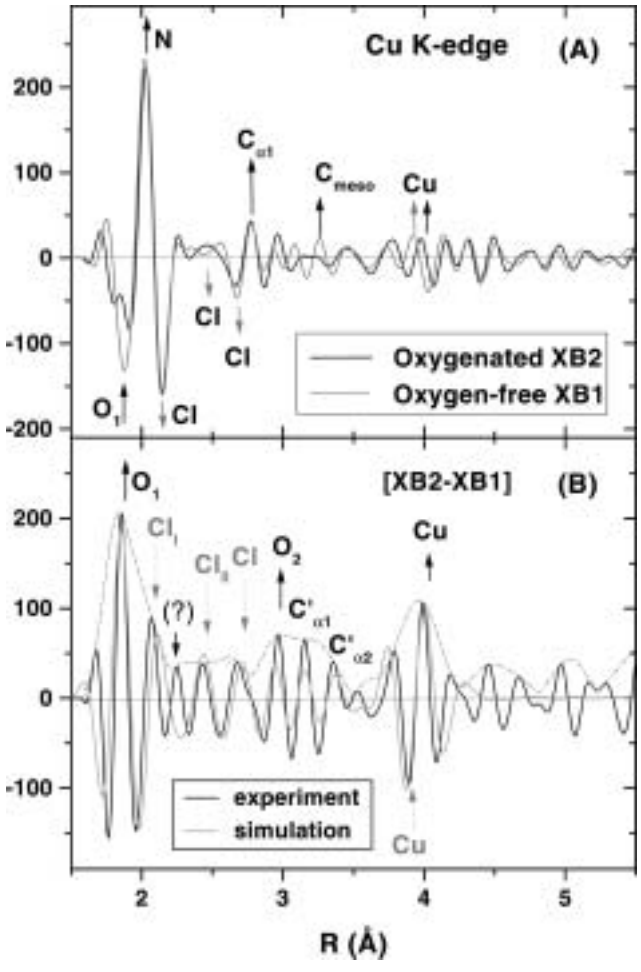

Fig. 2. Cu K-edge FT spectra of active xerogels. (A): Comparison of $\Im\ m\,\bar{\chi}(R)$ of the oxygen-free xerogel **XB1** (dotted line) and of the oxygenated xerogel **XB2** (full line); (B): FT spectra of the difference $\Delta\chi$ [**XB2-XB1**]. A simulated FT difference spectrum is also shown (dotted line). Identified contributions of the chlorine atoms are marked with arrows.

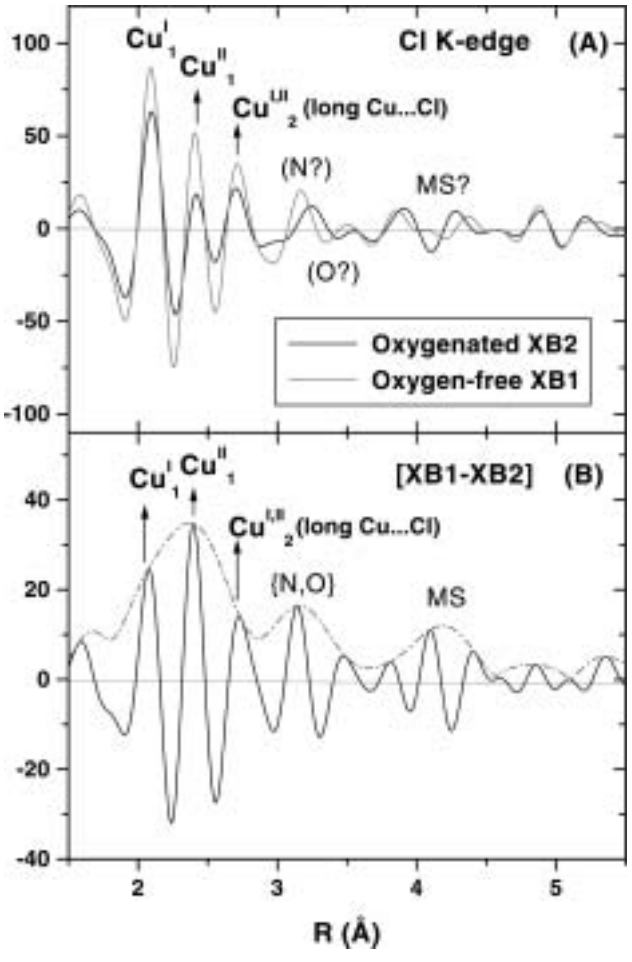

Fig. 3. Cl K-edge FT spectra of active xerogels. (A): Comparison of $\Im\ m\,\bar{\chi}(R)$ of xerogels **XB1** (dotted line) *vs* **XB2** (full line); (B): FT difference spectra.

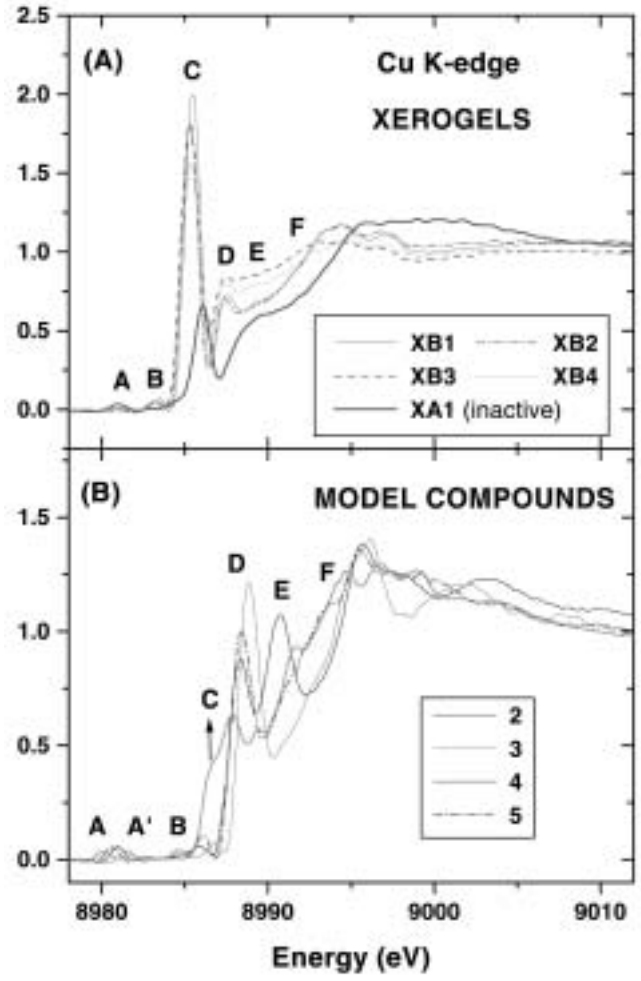

Fig. 4. Numerically deconvoluted Cu K-edge XANES spectra.

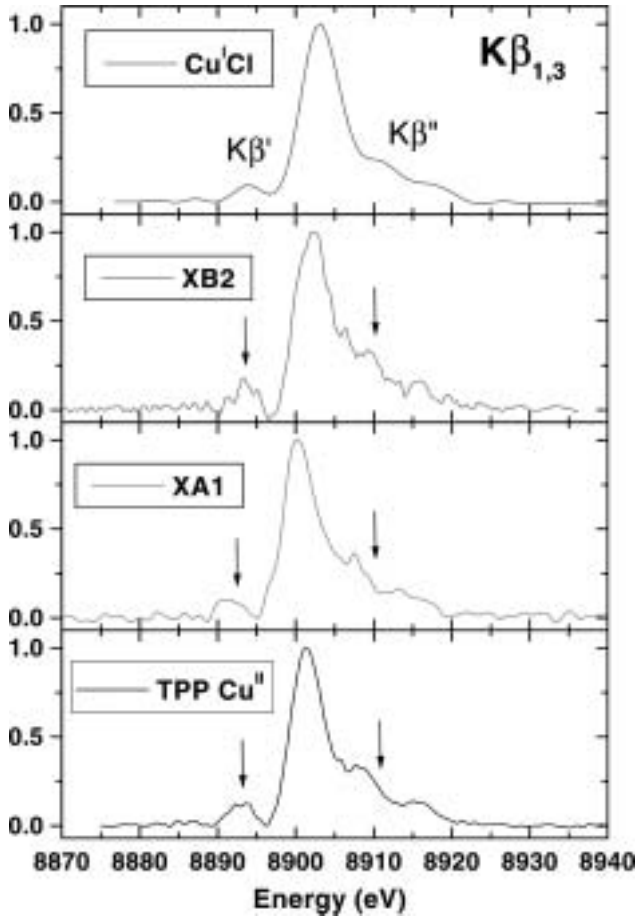

Fig. 5. Chemical shifts of the Cu $K\beta_{1,3}$ fluorescence lines.

found in pentacoordinated model compounds (*e.g.* species **6**) for a Cu^{II}-Cl; there is an additional signal at long distance ($R_{Cu\ldots Cl} = 2.71 \pm 0.03$ Å) which may be characteristic of Cl atoms bridging [Cu^{I}, Cu^{II}] sites [14]. The FT difference spectrum of Fig. 3B clearly indicates that the signal assigned to the pentacoordinated $Cu^{(II)}$ site nearly totally vanishes in the oxygenated xerogel **XB2**.

We have regrouped in Fig. 4A the deconvoluted Cu K-edge XANES spectra of various active/inactive xerogels. For the sake of comparison, we have also reproduced in Fig. 4B the deconvoluted XANES spectra of several model compounds of known structure. Most striking is the systematic presence of a strong resonance peaking at 8985.33 eV – labelled (C) – in all active xerogels. Note that its intensity decreases by only 15% in the oxygenated xerogels. Whereas we were rather successful in simulating the XANES spectra of all model compounds of known structure using the MSW option of the code FDMNES, we systematically failed in reproducing the resonance (C) using binuclear clusters of stereogeometry consistent with the EXAFS study. A very promising result [3] was nevertheless obtained using the *Finite Difference* option of FDMNES which makes it possible to carry out XANES simulations beyond the common *muffin-tin* approximation: once we could get rid of the uncertainty associated with the *muffin-tin zero*, it became obvious that resonance (C) should be unambiguously associated with Cu^{I} sites. Another valuable advantage of the code FDMNES is to allow us to control the charge transfer from the ligand toward the metal: this proved to be important in the case of neutral cyclam ligands.

A perennial dificulty with XANES is that the information regarding the electronic structure (valence, charge transfer etc . . .) is often obscured by structural effects. It has long been argued that the chemical shifts of the Kβ fluorescence lines could as well yield valuable information regarding the population of the valence orbitals. We have reproduced in Fig. 5, the X-ray emission spectra of xerogels **XA1** and **XB2** in the energy range of the $K\beta_{1,3}$ fluorescence lines. The emission spectra of $Cu^{I}Cl$ and **1** = [TPP] Cu^{II}] were added for the sake of comparison. Note the presence of the well known Kβ′ and Kβ″ satellites. Selecting the copper porphyrin **1** as reference, the inactive xerogel **XA1** exhibits a *negative* chemical shift (−0.84 eV), whereas the active xerogel **XB2** has a *positive* chemical shift (+0.81 eV) which increases up to 1.2 eV in the case of $Cu^{I}Cl$. This confirms that the electron density is higher around Cu in the active xerogel than in the inactive one. This result is implicitly consistent with the coexistence of Cu^{I}, Cu^{II} sites in the active xerogels.

In conclusion, it appears that the active sites in the oxygenated xerogel **XB2** should not be viewed as *true* peroxo complexes involving $[O_2]^{2-}$ anions with a formal Cu^{II} valency: it would be more appropriate to refer here to a Cu^{I}-(O_2)-Cu^{I} adduct compound. This would be fully consistent with the reversible character of the dioxygen trapping.

References

1. Dubois, G. *et al.,* Chem. Commun. 2283 (1999).
2. Dubois, G. *et al.*, Angew. Chem. Int. Ed. Engl. **40**, 1087 (2001).
3. Goulon, J. *et al.*, Inorg. Chem., submitted.

4. Goulon, J. *et al.*, J. Synchrotron Radiat. **5**, 232 (1998).
5. Rogalev, A. *et al.*, "Magnetism and Synchrotron Radiation," Lecture Notes in Physics, (Beaurepaire, E. *et al.* Eds.) (2001), vol. 565, 60.
6. Goulon, J., Goulon-Ginet, C. and Gotte, V., "XAS applied to Porphyrin Chemistry," in: Handbook of Porphyrin Chemistry, (Kadish, K. M. *et al.* Eds.) (Academic Press, New-York, 2000, **Vol. 7**, 79).
7. Marchon, J.-C. *et al.*, Inorg. Chem. **29**, 57 (1990).
8. Gotte, V. *et al.*, J. Phys. Chem. **104**, 1927 (2000).
9. Rehr, J. J. *et al.*, J. Am. Chem. Soc. **113**, 5135 (1991).
10. Joly, Y., Phys. Rev. B **63**, 125120 (2001).
11. Blackman, A. G. and Tolman, W. B., "Metal-Oxo and Metal-Peroxo Species in Catalytic Oxidations," (Meunier, B. Ed.), Structure and Bonding, (Springer Verlag, Berlin 2000) **97**, 180.
12. Jacobson, R. R. *et al.*, J. Am. Chem. Soc. **110**, 3690 (1988).
13. Kitajima, N. *et al.*, J. Am. Chem. Soc. **114**, 1277 (1992).
14. Breeze, S. R. and Wang, S., Inorg. Chem. **35**, 3404 (1996).

Physica Scripta. Vol. T115, 685–687, 2005

EXAFS Study of Electrolytic Nanosolution Confined in Interstitial Nanospaces of Single-Wall Carbon Nanohorn Colloids

T. Ohkubo[1,2], Y. Hattori[3], H. Kanoh[1,4], T. Konishi[1,4], H. Sakai[2], M. Abe[2], D. Kasuya[5], M. Yudasaka[5], S. Iijima[5,6,7], T. Fujikawa[1,4] and K. Kaneko[*1,4]

[1]Department of Chemistry, Faculty of Science, Chiba University, 1-33 Yayoi, Inage, Chiba 263-8522, Japan
[2]Faculty of Science and Technology, Tokyo University of Science, 2641 Yamazaki, Noda, Chiba 278-8510, Japan
[3]Institute of Research and Innovation, 1201 Takada, Kashiwa, Chiba 277-0861, Japan
[4]Center for Frontier Electronics and Photonics, Chiba University, 1-33 Yayoi, Inage, Chiba 263-8522, Japan
[5]Japan Science and Technology Corporation, 34 Miyukigaoka, Tsukuba 305-8501, Japan
[6]Faculty of Science and Technology, Meijo University, 1501 Shiogamaguchi, Tenpaku, Nagoya 468-8502, Japan
[7]NEC Corporation, 34 Miyukigaoka, Tsukuba 305-8501, Japan

Received June 26, 2003; accepted December 15, 2003

PACS numbers: 61.10.Ht, 68.43.Hn

Abstract

The structure of RbBr aqueous solution confined in the interstitial nanospaces of single-wall carbon nanohorn (SWNH) assemblies was elucidated by using extended X-ray absorption fine structure (EXAFS) technique. The decrease of hydration number around a Rb ion is clearly observed. The EXAFS analysis indicates that the highly distorted and dehydrated structure around ions of aqueous solution confined in the nanospace (nanosolution: NSN) to form quasi one-dimensional structure in the interstitial nanospaces of SWNH assemblies. This unique hydration structures formed in nanospaces of SWNH is quite different from that not only of the bulk aqueous solution, but also confined in the slit-shaped nanospaces of activated carbon fiber (ACF).

1. Introduction

Nano-confined molecules surrounded by solid-pore walls have gathered much attention from the aspects of their unique structures and properties. This is because the nano-confinement has an intensive possibility to get an essential understanding of matters and it can be helpful to develop new technologies related to gas storage, gas separation, purification, and electronic devices [1, 2]. We have been challenged to elucidate the molecular nano-confinement using solid nanospaces from the above viewpoint, reporting that the molecules adsorbed in hydrophobic nanospaces tend to form highly ordered structures which depend sensitively on the nanospace geometry and the properties of adsorbate molecules [3]. Water and alcohol molecules, for instance, adsorbed in the slit-shaped carbon nanospaces form a highly ordered structure even at 303 K as revealed by *in situ* X-ray diffraction (XRD) technique [4–7]. Also CCl_4 [8], NO [9], and Xe [10] form a highly condense structure in the carbon nanospaces even at 303 K. This effect is named pseudo-compression effect.

Properties of ionic solutions have been studied to develop fundamental understanding of their natures. Classical hydration models, such as Frank-Wen model [11], are indeed helpful to understand the properties of electrolytic solution. However, it is quite difficult to elucidate more exactly the ionic solution structure. Furthermore, we wonder if such a model can be applied to nano-scale phenomena and structures. The ionic aqueous solution in the bulk phase has an isotropic structure. The chemical and physical natures of the isotropic bulk structure are understood from the hydration structure. A better understanding of the solution is requested on the points of the role of hydrogen bonding to form long-range hydration structure and the presence of local anisotropic structures. As nanospaces can induce an effective anisotropic molecular field for restricted molecules and ions, a new insight on solution chemistry can be expected. We have challenged this subject using well-characterized hydrophobic nanospaces with extended X-ray absorption fine structure (EXAFS) [12–14], because EXAFS has been applied to elucidate local structures around a target ion with an intensive theoretical background [15, 16].

Activated carbon fiber (ACF) having different pore widths is available and it has contributed to develop the studies on nano-confinement. Although abundant single-wall carbon nanotubes (SWNT) [17, 18] cannot be produced without metallic catalysts, high purity single-wall carbon nanohorn (SWNH) [19] which has a structure close to SWNT is available for studies on nano-confinement. Hence, comparative studies on the nano-confinement using SWNH and ACF are preferable. Here, the adsorption isotherm of nitrogen at 77 K on SWNH is of type II, although isotherms of two kinds of ACFs are of type I. The average slit pore widths of two kinds of ACFs are 0.7 nm and 1.1 nm, respectively, from the analysis of subtracting pore effect (SPE) method for high-resolution α_s-plot [20, 21]. Grand canonical Monte Carlo (GCMC) simulation on molecular adsorption in the interstitial nanospaces of SWNH indicates the presence of quasi one-dimensional pores between four SWNH particles [22]. Then we examined the hydration structure of RbBr aqueous solution confined in the interstitial nanospaces of SWNH assemblies with EXAFS and related analysis.

2. Experimental

Electrolytic aqueous solution of RbBr ($1\,mol/cm^3$) was introduced into the interstitial pores of SWNH and dried by evacuation to 0.1 mPa and 423 K for 2 hours. After the deposition of RbBr, water vapor was adsorbed to provide the corresponding solution only in the nanospaces of SWNH; we denote the NSN made by RbBr aqueous solution on SWNH as NH-NSN. In

* Corresponding author: kaneko@pchem2.s.chiba-u.ac.jp

addition, NSNs in the slit-shaped nanospaces of ACFs are also shown for comparison in this article which are denoted by ACF(x)-NSN. Here, x is the average pore width of ACFs obtained by N_2 adsorption isotherms at 77 K.

These samples were installed in an EXAFS glass cell with windows of Mylar film (350 μm: Toray Ind. Inc.). The EXAFS measurements were performed on both Rb and Br K-edges for the NSNs at the National Laboratory for High Energy Accelerator Research Organization (KEK) in Tsukuba after pre-examination with a laboratory XAFS measurement system (EXAC820: Technos Co. Ltd.) which was equipped with Mo rotating-anode X-ray source. The EXAFS spectra of the corresponding solutions were measured for comparison. The structure determination was carried out by the curve fitting of the reverse Fourier transformed function of the 1st shell in each radial structure function (RSF) with theoretical parameters calculated by FEFF code [23].

3. Results and Discussion

Fig. 1 shows the RSFs around a Rb ion for NSNs and bulk aqueous solution. The peak positions of 1st hydration shells for NSNs are shorter than that of bulk aqueous solution, indicating the pseudo-compression effect in the nanospaces. Also, the 1st hydration shell of NH-NSN includes another peak at longer distance. This peak comes from the carbon atoms of SWNH or the other hydration shell in the nanospaces. However we cannot predict the structure indicated by the additional shoulder-like peak. In this study, we included the additional shoulder-like peak of NH-NSN in the curve fitting.

Fig. 2 shows the RSFs around a Br ion for NSNs and bulk aqueous solution. The RSF of NH-NSN clearly contains two kinds of shells indicating the 1st hydration shell and another shell of carbon atoms of SWNH or the other hydration shell in the nanospaces. The determination of hydration structure around a Br ion is quite difficult because of the weak hydration of water molecules to a Br ion [24] and the double excitation effect of photoelectrons [25, 26]. The analysis of hydration shell around a Br ion needs theoretical calculation. Hence we must focus on the nano-confinement effect for the NSN with the hydration structures around a Rb ion.

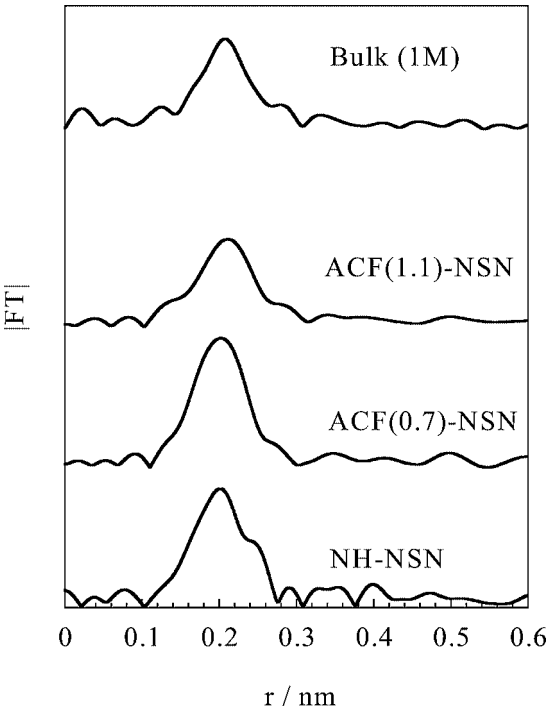

Fig. 1. Radial structure functions around a Rb ion.

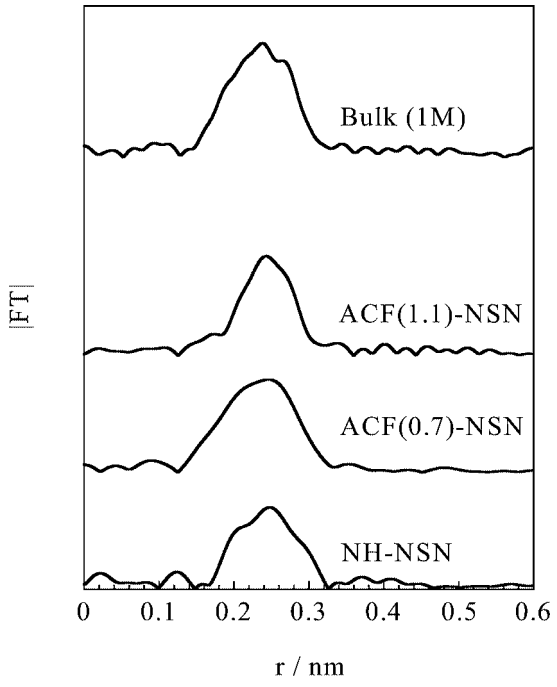

Fig. 2. Radial structure functions around a Br ion.

The structural parameters obtained by a least-squares fit of Fourier-filtered EXAFS spectra around a Rb ion are summarized in Table I. The fitting on a Rb ion for each sample was carried out by using an EXAFS formula including a 3rd order cumulant term C_3. This table shows that the structure around a Rb ion of NH-NSN is different from that of both ACF-NSN and bulk aqueous solution. The coordination number around a Rb ion for NH-NSN, which is only 2.6, is the least. On the other hand, the Rb-H_2O distance for NH-NSN is slightly longer than those of ACF-NSN. This result indicates that the hydration structure around a Rb ion in the quasi-one dimensional nanospace of SWNH is completely different from that in the slit spaces of ACFs. Furthermore, the DW factor for NH-NSN is much less than those for ACF-NSN and the 3rd order cumulant term is larger than for any other aqueous solutions, suggesting that the Rb-hydrated complexes form highly compressed structure with low dimension in the interstitial nanospaces of SWNH assemblies. Hence, this characteristic hydration anomaly of NH-NSN stems from the confinement in the quasi one-dimensional nanospaces. EXAFS study on NSN using nanospaces of different geometries is going to show the presence of different hydration structures.

However we must be cautious for giving an explicit conclusion on the above hydration structure, because the reliability of curve fitting for NH-NSN is relatively higher than any other samples. The fact that the 1st hydration shell of NH-NSN contains two kinds of structural shells should also be examined in future study with the theoretical model obtained by molecular simulation technique.

Table I. *Structural parameters obtained by a least-squares fit of Fourier-filtered EXAFS spectra around a Rb ion.*

Sample	r_{Rb-O}/nm	N_{Rb-O}	${\sigma^2}_{Rb-O}$/nm^2	$C_3/10^6$ nm^3	R/%
NH-NSN	0.290(±0.002)	2.6(±0.2)	1.07(±0.09)	4.2(±0.8)	14.9
ACF(0.7)-NSN	0.286(±0.001)	5.3(±0.1)	2.45(±0.03)	3.3(±0.2)	6.4
ACF(1.1)-NSN	0.283(±0.002)	3.8(±0.1)	2.35(±0.05)	2.0(±0.4)	7.4
RbBr solution (1M)	0.291(±0.002)	6.0*	2.58(±0.01)	3.6(±0.5)	8.2

Distance between two atoms r, coordination number N, DW factor σ, 3rd order cumulant term C_3, and reliability of fitting procedure R for each sample. Here, the R factor can be defined as:

$$R(\%) = \frac{\sqrt{\sum \left\{\chi^{data}(k) - \chi^{fit}(k)\right\}^2}}{\sqrt{\sum \left\{\chi^{data}(k)\right\}^2}} \times 100.$$

Here, $\chi^{data}(k)$ and $\chi^{fit}(k)$ are the EXAFS functions of the experimental data and the fitting function, respectively. The first and second elements in the subscripts denote the central and scattering atoms, respectively. The asterisk (*) shows the fixed parameter.

Acknowledgement

This work has been performed under the approval of the Photon Factory Program Advisory Committee (Proposal No. 2002G242). Also this work was supported by Research Fellowships of the Japan Society for the Promotion of Science (JSPS) for Young Scientists and Grant-in-Aid for Scientific Research (S) (No. 15101003) by JSPS.

References

1. Rouquerol, F., Rouquerol, J. and Sing, K. S. W., "Adsorption by Powders & Porous Solids", (Academic Press, London 1999).
2. Conway, B. E., "Electrochemical Supercapacitors: Scientific Fundamentals and Technological Application", (Kluwer, New York 1999).
3. Kaneko, K., Carbon **38**, 287 (2000).
4. Iiyama, T., Nishikawa, K., Otowa, T. and Kaneko, K., J. Phys. Chem. **99**, 10075 (1995).
5. Iiyama, T., Nishikawa, K., Suzuki, T. and Kaneko, K., Chem. Phys. Lett. **274**, 152 (1997).
6. Ohkubo, T., Iiyama, T., Nishikawa, K., Suzuki, T. and Kaneko, K., J. Phys. Chem. B **103**, 1859 (1999).
7. Ohkubo, T., Iiyama, T. and Kaneko, K., Chem. Phys. Lett. **312**, 191 (1999).
8. Iiyama, T., Nishikawa, K., Suzuki, T. and Kaneko, K., J. Phys. Chem. B **101**, 3037 (1997).
9. Kaneko, K., Fukuzaki, N. and Ozeki, S., J. Chem. Phys. **87**, 776 (1987).
10. Aoshima, M., Suzuki, T. and Kaneko, K., Chem. Phys. Lett. **310**, 1 (1999).
11. Frank, H. S. and Wen, W.-Y., Discuss. Faraday Soc. **24**, 133 (1957).
12. Ohkubo, T. *et al.*, J. Am. Chem. Soc. **124**, 11860 (2002).
13. Ohkubo, T., Kanoh, H., Hattori, Y., Konishi, T. and Kaneko, K., Stud. Surf. Sci. Catal. **146**, 61 (2003).
14. Ohkubo, T., Kanoh, H. and Kaneko, K., Aust. J. Chem. **56**, 1013 (2003).
15. Teo, B. K., "EXAFS: Basic Principles and Data Analysis", (Springer-Verlag, Berlin 1986).
16. Koningsberger, D. C. and Prins, R., "X-ray Absorption", (John Wiley & Sons, New York 1988).
17. Iijima, S. and Ichihashi, T., Nature **363**, 603 (1993).
18. Bethune, D. S. *et al.*, Nature **363**, 605 (1993).
19. Iijima, S. *et al.*, Chem. Phys. Lett. **309**, 165 (1999).
20. Kaneko, K. and Ishii, C., Colloid Surf. **67**, 203 (1992).
21. Setoyama, N., Suzuki, T. and Kaneko, K., Carbon **36**, 1459 (1998).
22. Tanaka, H., El-Merraoui, M., Steele, W. A. and Kaneko, K., Chem. Phys. Lett. **352**, 334 (2002).
23. Ankudinov, A. L., Ravel, B., Rehr, J. J. and Conradson, S. D., Phys. Rev. B **58**, 7565 (1998).
24. Tanida, H., Sakane, H. and Watanabe, I., J. Chem. Soc. Dalton Trans. **15**, 2321 (1994).
25. Li, G., Bridges, F. and Brown, G. S., Phys. Rev. Lett. **68**, 1609 (1992).
26. D'Angelo, P., Di Cicco, A., Filipponi, A. and Pavel, N. V., Phys. Rev. A **47**, 2055 (1993).

Physica Scripta. Vol. T115, 688–690, 2005

EXAFS Characterization of the Local Structure of Fe in Fe-ZSM-5: an Experimental and Theoretical Study

Sun Hee Choi[1*], Benjamin R. Wood[2], Jason A. Ryder[2] and Alexis T. Bell[2]

[1]Beamline division, Pohang Accelerator Laboratory, POSTECH, San 31, Hyogadong, Namgu, Pohang 790-784, Republic of Korea
[2]Department of Chemical Engineering, University of California, Berkeley, CA 94720-1462, USA

Received June 26, 2003; accepted November 4, 2003

PACS number: 61.10.Ht

Abstract

The local structure of Fe in Fe-ZSM-5 prepared by solid-state exchange was investigated with EXAFS. Fe K-edge spectra taken at liquid nitrogen temperature of He- and CO-pretreated sample show two main peaks, one at 1.6 Å and the other at 2.5 Å. To interpret the origin of these peaks, RSFs were simulated for a number of mono- and di-iron structures obtained from quantum chemical calculations. The peak at 1.6 Å is clearly identified with scattering from O atoms coordinated to a Fe atom. The peak at 2.5 Å has been used to argue for the presence of di-iron oxo species. However, the origin of this peak and its interpretation remains an open question. The imaginary part of the Fourier-transformed data for the peak at 2.5 Å has the same characteristics as that generated theoretically for Fe-Al scattering. This evidence strongly suggests that iron in Fe-ZSM-5 is present as isolated cations in an aluminum framework. Further evidence for such a structure is the absence of any change in the magnitude of the peak at 2.5 Å with sample treatment.

1. Introduction

It has been demonstrated that N_2O-pretreated Fe-ZSM-5 react with methane to methoxide species, which subsequently hydrolyze to form methanol. A number of studies have been carried out aimed at understanding the effects of catalysts preparation and pretreatment on the structure of Fe in Fe-ZSM-5 and relating this information to catalyst activity. Formally, the electronic state of iron is either +2 or +3, depending strongly on the pretreatment. The most difficult issue to address is the nuclearity of Fe once exchanged into the zeolite. Joyner *et al.* have concluded that Fe in Fe-ZSM-5 occurs in different forms, ranging from isolated metal ions to large oxide clusters and small oxygen-containing nanoclusters such as Fe_4O_4 and Fe_4O_3 [1]. Marturano *et al.* [2] and Battiston *et al.* [3] have reported evidence for binuclear iron-oxo complexes and diferric(hydroxy)oxo-bridged complexes based on EXAFS spectra of fully exchanged Fe-ZSM-5 ($Fe/Al \cong 1$). These di-iron structures resemble the core unit in methane monooxygenase (MMO) and are characterized by a Fe-Fe distance of approximately 3 Å. However, when the loading of Fe in Fe-ZSM-5 is such that $Fe/Al < 1$, isolated Fe species have been found as principal species [4].

The aim of the present work was to establish the effects of Fe/Al ratio and pretreatment conditions on the speciation of iron in Fe-ZSM-5. Fe-ZSM-5 with Fe/Al ratios of 0.33 to 0.80 was prepared by solid-state exchange and was characterized by EXAFS. The interpretation of EXAFS data was aided by simulations of radial structure function (RSF)s for iron-containing species proposed to exist in Fe-ZSM-5.

2. Experimental Method

Fe-ZSM-5 was prepared by solid-state exchange using $FeCl_3$ (Adrich, 99.99%). Without exposure to air, the calcined H-ZSM-5 ($Si/Al = 25$) was mixed with an appropriate amount of anhydrous $FeCl_3$ with resulting Fe/Al ratios of 0.33, 0.66, and 0.80, respectively. After the mixture was heated from 298 to 583 K, the sample was washed with deionized water.

The as-prepared material was contained in a specially designed cell and pretreated on three different conditions with He, O_2, and CO. XAFS measurements were conducted on beamlines 4-2 and 4-3 of Stanford Synchrotron Radiation Laboratory (SSRL). The radiation was monochromatized using a Si(111) double-crystal and the incident beam was detuned by 15% in order to minimize higher harmonics. Fe K-edge spectra were taken in transmission mode at liquid nitrogen temperature. The collected data were analyzed with the UWXAFS 3.0 package [5] and the FEFF 8 code [6]. The procedure for EXAFS data analysis is described elsewhere [7]. The reference materials used as standards for fitting the experimentally derived RSFs were generated with the FEFF 8 code and the Fourier-filtered data were fitted in momentum space.

3. Theoretical Method

The structures of both isolated and di-iron species were determined from quantum chemical calculations. For isolated sites, the Fe atom and a portion of the zeolite framework were represented by a 23-26-atom cluster. To represent a di-iron species, the two Fe atoms and the associated portion of the zeolite framework were represented by a 40-46-atom cluster. Quantum chemical calculations of the geometries were performed using non-local, gradient-corrected density-functional theory (DFT). The Jaguar 4.0 suite of programs (Schrödinger, Inc.) and Gaussian 98 were used for this purpose. With the exception of the terminal Si atoms, all of the atoms in the cluster were allowed to relax during the course of calculations. The atomic coordinates for each mono- and di-iron species, determined from the quantum chemical calculations, were then used to generate the theoretical EXAFS function $\chi(k)$.

4. Results and Discussion

Among the theoretically calculated isolated iron species, the structure of $Z^-[Fe(O)_2]^+$, where Z^- represents the zeolite framework, and its simulated RSF are presented in Fig. 1. The RSF exhibits a peak between 1 and 2 Å, a peak between 2 and 3 Å, and a pair of overlapping peaks centered near 3 Å.

*E-mail: shchoi@postech.ac.kr

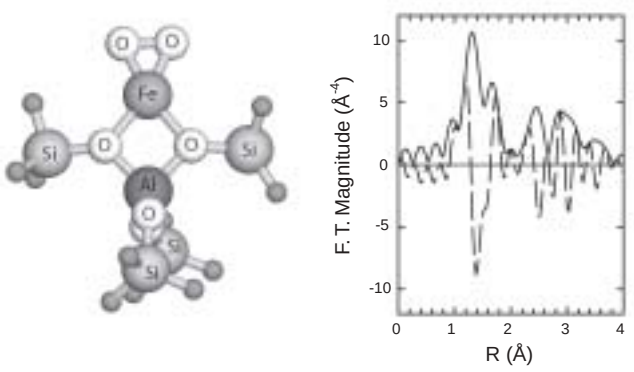

Fig. 1. Fourier transforms of theoretical data for isolated iron species of $Z^-[Fe(O)_2]^+$ in Fe-ZSM-5. The imaginary parts of Fourier transformed data are also plotted as dashed lines.

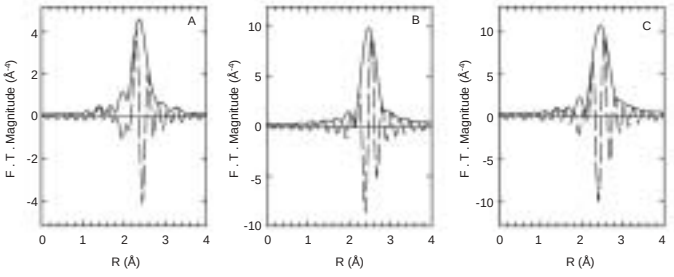

Fig. 2. k^3-weighted Fourier transformation about the Fe K-edges of theoretical data for (A) Fe-Al pair, (B) Fe-Fe pair, and (C) combined contribution of Fe-Al and Fe-Fe pairs. The theoretical EXAFS $\chi(k)$was generated with FEFF 8 for the structure of $Z^-[HOFe(OH)_2FeOH]^{2+}Z^{-1}$.

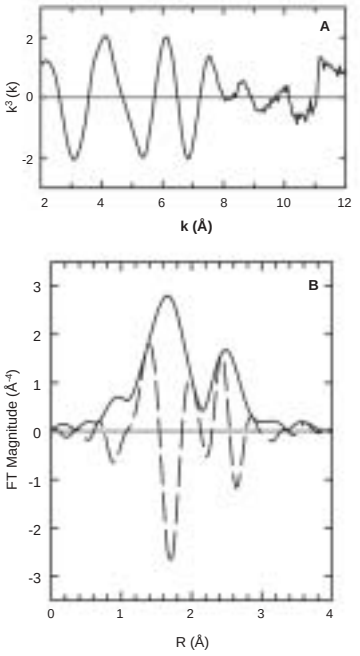

Fig. 3. k^3-weighted EXAFS function (A) and its Fourier transformation (B) about the Fe K-edge of Fe-ZSM-5 (Fe/Al = 0.33) pretreated with He.

Calculations using the FEFF 8 code show that the first of these features is attributable exclusively to scattering from O atoms bound to Fe. Similar calculations for the second peak in RSF indicate that the dominant contribution is due to scattering from the Al atom in the charge site. The theoretically derived RSF of $Z^-[Fe(OH)_2]^+$ shows close similarities to $Z^-[Fe(O)_2]^+$. The theoretical EXAFS spectra of di-iron species are more complicated than that for an isolated Fe species because of the greater number and variety of the scattering paths associated with the former species. For all di-iron structures, the peak appearing in the range of 1–2 Å can be assigned exclusively to Fe-O scattering. The peak appearing in the region of 2–3 Å is now comprised of two dominant parts – one due to Fe-Al scattering and the other due to Fe-Fe scattering. Figure 2 shows the contributions of Fe-Al and Fe-Fe scattering to the RSF peak at 2–3 Å for $Z^-[HOFe(OH)_2FeOH]^{2+}Z^-$. The results presented in Figure 2 suggest that it would be difficult to determine whether a peak appearing in the RSF for a sample of Fe-ZSM-5 is due to Fe-Fe or Fe-Al backscattering alone or is due to a combination of the two types of backscattering, if attention is given only to the magnitude function. This would be particularly true if the Fe-Fe and Fe-Al distances are nearly the same. Identification of which contribution dominates can be made, though, by comparison of the imaginary part of the RSF for the peak in the region of 2–3 Å with that characteristic of Fe-Al, Fe-Fe, or Fe-Al and Fe-Fe backscattering.

A plot of $k^3\chi(k)$and the RSF of for Fe-ZSM-5 (Fe/Al = 0.33) pretreated with He are shown in Fig. 3. Two distinct peaks are observed in the RSF when the sample pretreated in He or CO- one at about 1.6 Å and the other at about 2.5 Å. The RSF of the O_2-pretreated sample shows the same two peaks together with a new peak at about 1.1 Å. As noted earlier peaks in the region of 1–2 Å can be attributed to scattering from oxygen atoms coordinated to an iron absorber. The appearance of a new peak for Fe-O back scattering following O_2 pretreatment suggests that some of the Fe atoms have undergone a change in their environment. The peak at 2–3 Å is still observed in the RSF for O_2-pretreated sample. As discussed above this peak could be due to either Fe-Fe or Fe-Al scattering. Samples pretreated with He, O_2, and CO and non-pretreated show close similarities in the RSFs. Interestingly, the peak at 2.5 Å does not change with sample pretreatment. Even a fresh sample with no pretreatment has a magnitude comparable to that of pretreated samples. It is also evident that pretreatment in He, O_2, and then in CO has little effect on the intensities of the peaks at 1.6 Å and 2.5 Å. Comparison of RSFs of Fe-ZSM-5 with different Fe/Al ratios demonstrates that the RSF following He and CO pretreatment are virtually the same, the only significant difference being that the ratio of the peak at 1.6 Å to that 2.5 increases slightly with increasing Fe/Al ratio. After O_2 pretreatment, the peaks at 1.1 Å and 2.5 Å are independent of Fe/Al ratios, whereas the peak at 1.6 Å increases with increasing Fe/Al ratios.

The Fourier filtered EXAFS data were fitted using a model consisting of a single Fe absorber coordinated to one or two shells of O atoms and a shell of Al atoms. The decision to consider Fe-Al and not Fe-Fe, or a combination of Fe-Al and Fe-Fe backscattering was based on the shape of the imaginary portion of the RSF for the peak at 2.5 Å. Examination of Figs. 1 and 2 shows that the shape of the imaginary portion of this peak is very similar to that for Fe-Al back scattering. Only a single shell of O atoms was required to fit the data for samples pretreated in He and CO but two shells of O atoms were required to fit the data for samples pretreated in O_2. Table I shows that the coordination numbers and interatomic distances determined from a fit of the Fourier-filtered EXAFS data are virtually the same for samples of Fe-ZSM-5

Table I. *Fe K-edge EXAFS least-square fitting results for Fe-ZSM-5 with different Fe/Al ratios pretreated under different conditions.*

Pretreatment	shell	N^a	R (Å)^b	σ^2 ($\times 10^{-3}$ Å)^c	ΔE_0 (eV)^d	R-factor
Fe-ZSM-5 (0.33)						
He	O	3.5	2.14	15.8	2.2	0.0087
	Al	1.6	2.90	7.0	−2.2	
O_2	O	0.4	1.38	6.6	5.2	
	O	1.7	2.04	6.5	5.2	0.0148
	Al	1.4	2.92	4.2	6.1	
CO	O	3.9	2.12	14.8	0.43	0.0090
	Al	1.5	2.87	4.6	−4.4	
Fe-ZSM-5 (0.66)						
He	O	4.5	2.08	18.2	0.32	0.0417
	Al	1.1	2.88	1.8	−1.1	
O_2	O	0.4	1.40	5.3	3.2	
	O	2.4	2.02	4.9	3.2	0.0037
	Al	1.9	2.92	6.4	6.3	
Fe-ZSM-5 (0.80)						
He	O	4.6	2.11	12.9	−1.1	0.0159
	Al	1.9	2.82	5.3	−14.2	
O_2	O	0.4	1.44	7.7	4.1	
	O	2.4	2.03	3.8	4.1	0.0159
	Al	1.6	2.92	4.4	5.6	
CO	O	3.8	2.09	11.2	−1.3	0.0418
	Al	1.6	2.85	6.6	−9.7	

[a] Coordination number (±10%), [b] interatomic distances (±0.02 Å), [c] Debye-Waller factor, [d] energy shift and [e] R-factor gives a sum-of-squares measures of the fractional misfit, which is defined as

$$R = \sum_{i=1}^{N}\{[\mathrm{Re}(f_i)^2 + [\mathrm{Im}(f_i)]^2\} \Big/ \sum_{i=1}^{N}\{[\mathrm{Re}\,(\tilde{\chi}_{data}(k_i))]^2 + [\mathrm{Im}(\tilde{\chi}_{daai}(k_i))]^2\}$$

where $f_i = \tilde{\chi}_{data}(k_i) - \tilde{\chi}_{model}(k_i)$.

pretreated in He or CO, independent of the Fe/Al ratio. In all cases the coordination number of Fe with O is ∼4 and the Fe-O distance is approximately 2.1 Å. Both the coordination number and the bond distance are similar to that either $Z^-[Fe(O)_2]^+$ or $Z^-[Fe(OH)_2]^+$. The coordination number of Fe with Al ranges from 1.6 to 1.9, which is higher than that for either of the two model structures cited above. This apparent inconsistency could be a result of multiple scattering caused by the light O atoms lying along the scattering paths between Fe and Al.

5. Conclusions

The local structures of Fe in Fe-ZSM-5 with Fe/Al ratios between 0.33 and 0.80 were investigated with EXAFS. The RSF is characterized by two principal features located at 1.6 and 2.5 Å, irrespective of pretreatment conditions. The first of these peaks is associated with Fe-O scattering. Fourier analyses and EXAFS least-square fits indicate that the second peak originates from Fe-Al scattering, not from Fe-Fe scattering as has been proposed previously. The iron in Fe-ZSM-5, therefore, is present as isolated iron cations. For He- and CP pretreated samples, the structure of Fe in Fe-ZSM-5 is best described as $Z^-[Fe(O)_2]^+$ or $Z^-[Fe(OH)_2]_+$, where Z^- represents the charge-exchange site in the zeolite.

References

1. Joyner, R. and Stockenhuber, M., J. Phys. Chem. B **103**, 5963 (1999).
2. Marturano, P., Drozdova, L., Pirngruber, G., Kogelbauer, A. and Prins, P., Phys. Chem. Chem. Phys. **3**, 5585 (2001).
3. Battiston, A. A. *et al.*, J. Catal. **213**, 251 (2003).
4. Lobree, L. J., Hwang, I.-C., Reimer, J. A. and Bell, A. T., J. Catal. **186**, 242 (1999).
5. Stern, E. A., Newville, M., Ravel, B., Yacoby, Y. and Haskel, D., Physica B **208 & 209**, 117 (1995).
6. Ankudinov, A. L., Ravel, B., Rehr, J. J. and Conradson, S. D., Phys. Rev. B **58**, 7565 (1998).
7. Sayers, D. E. and Bunker, B. A., "X-ray Absorption: Principles, Applications, Techniques of EXAFS, SEXAFS and XANES". (Edited by Koningsberger, D. C. and Prins, R.) (John Wiley & Sons, New York, 1988), ch. 6, p. 211.

Physica Scripta. Vol. T115, 691–694, 2005

XAFS Study on the Visible-Light Sensitive Cr-Containing Zeolite Photocatalyst: Mesoporous Cr-HMS Molecular Sieves

Hiromi Yamashita*, Katsuhiro Yoshizawa, Keiko Kida, Satoshi Ohshiro and Masakazu Anpo

Department of Applied Chemistry, Osaka Prefecture University, Gakuencho 1-1, Sakai, Osaka 599-8531, Japan

Received June 26, 2004; accepted November 4, 2004

Abstract

The Cr-containing mesoporous molecular sieves (Cr-HMS) operated as efficient photocatalyst for the decomposition of NO into N_2 and O_2 even under visible light irradiation ($\lambda > 450$ nm). This photocatalyst exhibited a sharp and intense preedge peak in the XANES region which was characteristic of Cr-oxide species in tetrahedral coordination. In the Fourier transform of EXAFS spectrum, only a single peak due to the neighboring oxygen atoms was observed and the curve-fitting analysis indicated that 4-coordinated Cr-oxide moieties having two terminal Cr=O bonds were present. The results obtained with XAFS analysis as well as the analyses with UV-VIS absorption and photoluminescence measurements indicate that the charge transfer excited state of the tetrahedrally coordinated Cr-oxide moieties play a significant role in the photocatalytic reaction under visible light irradiation.

1. Introduction

It is of special interest to design ion and/or cluster size catalysts within zeolites [1–8] because these fascinating supports offer unique nano-scaled pore systems, unusual internal surface topology, and ion-exchange capacities. The highly dispersed transition metal oxides incorporated within the zeolites and mesoporous molecular sieves show unique reactivities not only for various catalytic reactions, but also for photocatalytic reactions under UV light irradiation [1–4]. Recently, unique and efficient photocatalytic systems incorporating the transition metal oxides (Ti, V, Mo, etc.) have been designed and developed using the cavities and frameworks of zeolites and mesoporous molecular sieves [4–8]. Especially Ti-zeolites with tetrahedrally coordinated titanium oxide moieties showing unique reactivities for various photocatalytic reactions under UV-irradiation (220–260 nm) are the good candidates as the efficient and selective photocatalysts. Although these tetrahedrally coordinated Ti-oxide moieties can exhibit the unique photocatalytic reactivity, they can only adsorb and utilize UV light at around 220–260 nm to form the charge transfer excited state as active species. The design of photocatalytic systems which can operate under visible light irradiation have been desired. Previously, we have found that the metal ion-implantation of TiO_2 with highly accelerated transition metal ions is useful to design photocatalysts which can operate efficiently under visible light irradiation [9]. Although this metal ion-implantation technique can be applied to the metal oxides incorporated in the zeolites, it has been desired earnestly that the photocatalysts responsive under visible light irradiation should be prepared by conventional chemical processes.

In the present study, Cr-containing mesoporous molecular sieves (Cr-HMS) have been prepared by the conventional chemical method. Their photocatalytic reactivities under visible light irradiation were investigated and the local structure of Cr-oxide active sites were studied by spectroscopic techniques such as XAFS, UV-Vis absorption, and photoluminescence measurements.

2. Experimental

The chromium containing mesoporous zeolite molecular sieves (Cr-HMS)(Si/Cr = 50, 635 m^2/g) was synthesized using tetraethylorthosilicate and $Cr(NO_3)_3 \cdot 9H_2O$ as the starting materials and dodecylamine as a template [10, 11]. The chromium-silicalite (CrS-1, 190 m^2/g) microporous zeolite (Si/Cr = 100) was hydrothermally synthesized using tetraethoxysilane and $Cr(NO_3) \cdot 9H_2O$ as starting materials and tetrapropyl ammonium hydroxide (TPAOH) as a template in accordance with previous literature [12]. Imp-Cr/HMS zeolite (Si/Cr = 50, 615 m^2/g) were prepared by impregnating HMS with an aqueous solution of $Cr(NO_3)_3 \cdot 9H_2O$. Calcination of the sample was carried out in a flow of dry air at 773 K for 5 h. Prior to spectroscopic measurements and photocatalytic reactions, the catalysts were degassed at 723 K for 2 h, heated in O_2 at the same temperature for 2 h and then finally evacuated at 473 K for 2 h to 10^{-6} Torr.

The photocatalytic reactions of NO molecules were carried out with the catalysts (100 mg of the catalyst involving zeolite) in a quartz cell with a flat bottom (80 ml) connected to a conventional vacuum system (10^{-6} Torr range) [7]. The light irradiation of the catalysts in the presence of NO (135 μmol/g-cat) was carried out at 275 K under UV light ($\lambda > 270$ nm) or visible light ($\lambda > 450$ nm) using a high pressure mercury lamp through water and color filters. The reaction products were analyzed by gas chromatography.

XRD patterns were obtained with a Shimadzu XD-D1 using Cu Kα radiation. The XAFS spectra (XANES and EXAFS) were measured at the BL-9A facility [13] of the Photon Factory at the National Laboratory for High-Energy Physics, Tsukuba. A Si(111) double crystal was used to monochromatize the X-rays from the 2.5 GeV electron storage ring. The Cr K-edge absorption spectra were recorded in the fluorescence mode at 295 K. In a typical experiment, 50 mg of the sample pressed into a disc was loaded into the *in situ* cell having the Kapton windows. The normalized spectra were obtained by a procedure described in previous literature [14] and Fourier transformation was performed on k^3-weighted EXAFS oscillations in the range 3–10 $Å^{-1}$. The curve-fitting of the EXAFS data was carried out by employing the iterative nonlinear least-squares method and the empirical backscattering parameter sets extracted from the shell features of reference compounds. The diffuse reflectance UV-Vis absorption spectra were recorded with a Shimadzu UV-2200A spectrometer at 295 K. The in situ photoluminescence spectra the catalysts were measured at 77 K with a Shimadzu RF-501 spectrofluorophotometer.

*Present address: Department of Materials Science and Processing, Graduate School of Engineering, Osaka University, e-mail: yamashita@mat.eng.osaka-u.ac.jp

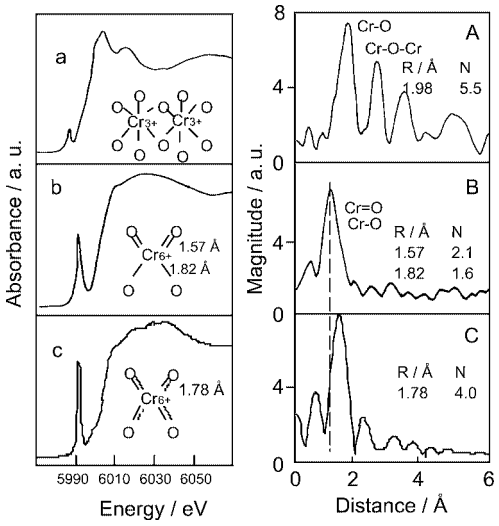

Fig. 1. Cr K-edge XANES spectra (a–c) and Fourier transforms of EXAFS (A–C). (a,A) imp-Cr-HMS, (b,B) Cr-HMS, (c,C) CrS-1. R: bond distance (Å), N: coordination number.

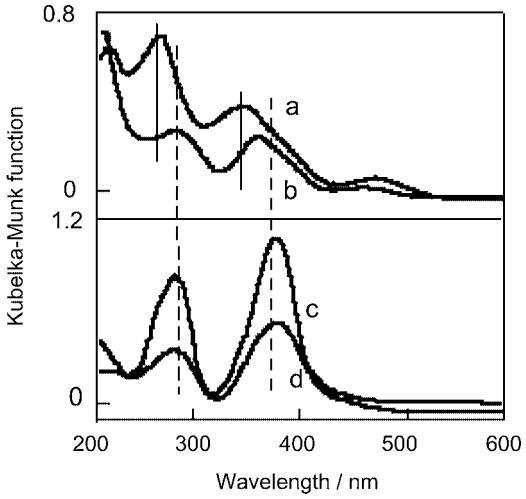

Fig. 2. Diffuse reflectance UV-Vis absorption spectra of (a) degassed Cr-HMS, (b) hydrated Cr-HMS by H_2O vapor addition (25 Torr), (c) degassed CrS-1 and (d) K_2CrO_4 solution.

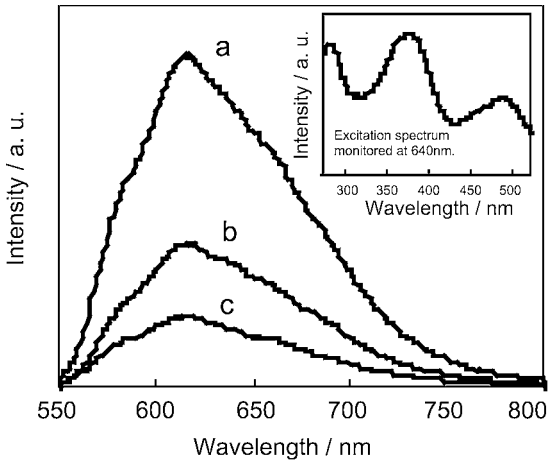

Fig. 3. The photoluminescence spectra of Cr-HMS at 77 K excited at (a) 280, (b) 370, (c) 500 nm. The enclosed figure shows the excitation spectrum of the photoluminescence monitored at 640 nm.

3. Results and discussion

Cr-HMS mesoporous molecular sieves exhibited a single peak at around 2° in the XRD patterns indicating that the Cr-HMS has the structure of the HMS mesoporous molecular sieves having pores larger than 20 Å and the Cr-oxide moieties are highly dispersed in the zeolite framework, while no other phases are formed [10, 11]. Also the results of XRD analysis indicated that imp-Cr/HMS keeps the mesoporous structure and CrS-1 has the MFI zeolite structure without a formation of crystalline Cr-oxide species.

Figure 1 shows the XAFS spectra of the pretreated imp-Cr/HMS, Cr-HMS and CrS-1. The imp-Cr/HMS exhibits a weak preedge peak in the XANES spectra and an intense peak due to the neighboring Cr atoms (Cr-O-Cr) in the Fourier transform of EXAFS, indicating that the catalyst consists of a mixture of tetrahedrally and octahedrally coordinated Cr-oxide species (Cr_2O_3-like cluster). Cr-HMS exhibits a sharp and intense preedge peak which is characteristic of Cr-oxide moieties in tetrahedral coordination [15–17]. In the Fourier transform of EXAFS, only a single peak due to the neighboring oxygen atoms (Cr-O) can be observed showing that Cr ions are highly dispersed in Cr-HMS. In the curve fitting analysis of the EXAFS of Cr-HMS, the best fitting was obtained with two oxygen atoms (Cr=O) in the shorter atomic distance of 1.57 Å and two oxygen atoms (Cr-O) in the long distance of 1.82 Å. CrS-1 also exhibits an intense preedge peak indicating the presence of Cr-oxide in tetrahedral coordination and only a single peak due to Cr-O bond can be observed. The peak position of Cr-O bond with CrS-1 is the longer than that of Cr-O bond observed with Cr-HMS. In the curve fitting analysis of the EXAFS of CrS-1, the best fitting was obtained with four oxygen atoms (Cr-O) in the atomic distance of 1.78 Å.

Figure 2 shows the diffuse reflectance UV-Vis absorption spectra of the degassed and hydrated Cr-HMS, degassed CrS-1, and K_2CrO_4 aqueous solution. The degassed Cr-HMS exhibit three distinct absorption bands at around 270, 370, 480 nm which can be assigned to the charge transfer from O^{2-} to Cr^{6+} of the tetrahedrally coordinated Cr-oxide moieties [18, 19]. The absorption bands assigned to the absorption of the dichromate of Cr_2O_3 cluster cannot be observed above 550 nm, indicating that tetrahedrally coordinated Cr-oxide moieties exist in an isolated state. On the other hand, the degassed CrS-1 exhibit two distinct absorption bands at around 280, 380 nm and the band in the visible light region ($\lambda > 450$ nm) can be hardly observed. These absorption bands are very similar to those of K_2CrO_4 aqueous solution which has the Cr^{6+} ions tetrahedrally coordinated by oxygen atoms in the same distance of Cr-O bond. In the hydrated Cr-HMS, the two bands in the region of UV light shift to the longer wavelengths (280, 380 nm) and the intensity of the band in the region of visible light (480 nm) decreases, indicating that the coordination geometry of Cr-oxide moieties in the hydrated Cr-HMS changes to be similar to those of CrS-1. These differences in the absorption spectra among the catalysts well reflect the changes in the coordination geometry of Cr-oxide moieties, as suggested in the XAFS analysis.

Cr-HMS evacuated at 473 K exhibited a photoluminescence spectrum at around 550–750 nm upon excitation of the absorption (excitation) band at around 250-550 nm. Figure 3 shows the photoluminescence spectra of Cr-HMS observed at 77 K upon the excitation at 280, 370, and 500 nm, respectively. The photoluminescence upon the excitation at these wavelengths observed at the same position, while the intensities of spectra depend on the wavelength of excitation. In the excitation spectrum

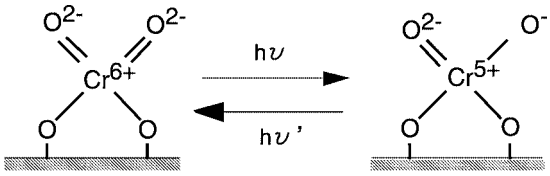

Scheme 1. Charge transfer processes on the tetrahedrally coordinated Cr-oxide moieties.

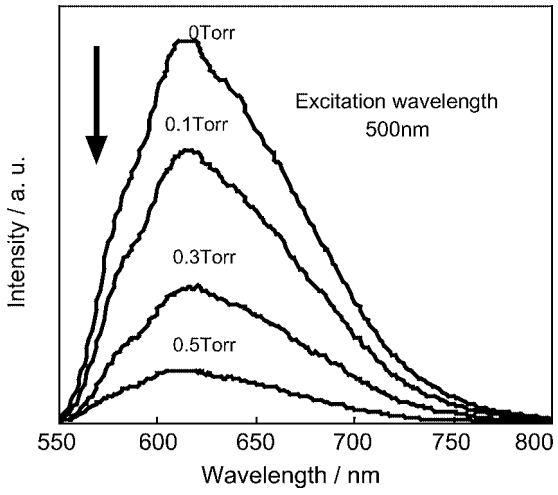

Fig. 4. Effects of the addition of NO on the photoluminescence spectra of the Cr-HMS at 77 K.

of Cr-HMS monitored at 640 nm, three excitation bands are observed at 280, 370 and 500 nm, which are almost corresponding to the absorption bands observed in the UV-Vis absorption spectra shown in Fig. 2. No change in the positions of these absorption bands is observed with changing the monitoring wavelength of photoluminescence, indicating that the photoluminescence occurs as the radiation decay process from the same excited state independently to the excitation wavelength. These absorption and photoluminescence spectra are similar to those obtained with well-defined highly dispersed Cr-oxides anchored on silica and can be attributed to the charge transfer processes on the tetrahedrally coordinated Cr-oxide moieties involving an electron transfer from O^{2-} to Cr^{6+} and a reverse radiative decay, respectively [20, 21]. These results indicate that the Cr-HMS mesoporous molecular sieve involves Cr-oxide moieties in tetrahedral coordination having two terminal Cr=O, being in good agreement with the results obtained by XAFS, and UV-Vis measurements. The estimated model for the local structure of the Cr-oxide moieties and the charge transfer processes are shown in Scheme 1.

Figure 4 shows the effects of the addition of NO on the photoluminescence spectra of the Cr-HMS at 77 K. The addition of NO onto the Cr-HMS leads to an efficient quenching of the photoluminescence in its yield, its extent depending on the amount of NO added. The observation of the efficient quenching by the NO addition indicates that the charge transfer excited state of the tetrahedrally coordinated isolated Cr-oxide moieties, $(Cr^{5+}-O^{-})^*$, easily interact with NO under UV light and visible light irradiation.

UV light irradiation ($\lambda > 270$ nm) of the Cr-HMS in the presence of NO led to the photocatalytic decomposition of NO and the evolution of N_2, N_2O and O_2 in the gas phase at 275 K. The Cr-HMS also shows photocatalytic reactivity even

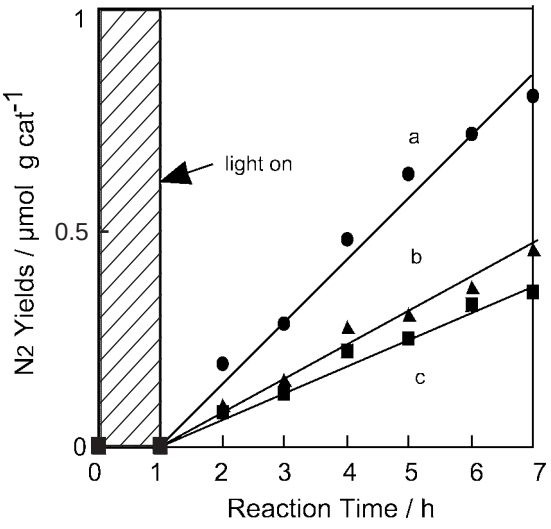

Fig. 5. Reaction time profile of the N_2 formation in the photocatalytic decomposition of NO on the Cr-HMS ($\lambda > 270$ nm) (a), imp-Cr/HMS ($\lambda > 270$ nm) (b), Cr-HMS ($\lambda > 450$ nm) (c) at 273 K.

under visible light irradiation ($\lambda > 450$ nm). As shown in Fig. 5, the N_2 yields increase linearly to the irradiation time. The formation of these reaction products were not detected in the dark conditions nor in irradiation of the HMS itself without Cr-oxide. These results clearly indicate that the presence of both Cr-oxide species included within HMS as well as light irradiation are indispensable for the photocatalytic reaction to take place and the direct decomposition of NO to produce N_2, O_2 and N_2O occurs photocatalytically on the Cr-HMS. Although the reaction rate under the visible light irradiation is smaller than under UV light irradiation ($\lambda > 270$ nm), the selectivity for N_2 formation (97 %) under visible light irradiation ($\lambda > 450$ nm) is higher than that of UV light irradiation (45 %). These results indicate that Cr-HMS can absorb visible light and act as an efficient photocatalyst under not only UV light but also visible light irradiation and especially Cr-HMS can exhibit the high selectivity to form N_2 under visible light irradiation. On the other hand, imp-Cr/HMS exhibit the smaller reactivity than the Cr-HMS and CrS-1 exhibited no reactivity under visible light irradiation. These results indicate that the presence of Cr-oxide having the tetrahedral coordination with the terminal Cr=O bond is essential to the demonstration of photocatalytic reactivity even under visible light irradiation.

4. Conclusions

The present results have clearly demonstrated that the Cr-HMS with mesoporous structure and tetrahedrally coordinated Cr-oxide moieties can exhibit the efficient reactivity for the photocatalytic decomposition of NO under visible light irradiation ($\lambda > 450$ nm). Cr-HMS contains tetrahedrally coordinated Cr-oxide moieties in the framework having two terminal Cr=O and that the charge transfer excited state of the Cr-oxide moieties are responsible for the efficient photoluminescence and photocatalytic reactivities. This photocatalytic system with tetrahedrally coordinated Cr-oxide moieties dispersed on mesoporous zeolite molecular sieves seems to be a good candidate to use abundant visible or solar light energy for the useful chemical synthesis.

Acknowledgements

This work has been supported by the Ministry of Education of Japan for Grant-in-Aid Scientific Research (Grant No. 12042271 and No. 13650845). The X-ray absorption experiments were performed at the Photon Factory of KEK (2001G115) with helpful advice from Prof. M. Nomura.

References

1. Corma, A., Chem. Rev. **97**, 2373 (1997).
2. Wu, P. and Tatsumi, T., J. Phys. Chem. B **106**, 748 (2002).
3. Thomas, J. M. and Sankar, G., Acc. Chem. Res. **34**, 571 (2001).
4. Xamena, F. X. L. I. *et al.*, J. Am. Chem. Soc. **125**, 2264 (2003).
5. Anpo, M. and Che, M., Ad. Catal. **44**, 119 (1999).
6. Yamashita, H., Zhang, J. L., Matsuoka, M. and Anpo, M., in "Photofunctional Zeolite", (ed. Anpo, M., NOVA Science Publishers, New York, 2000), p. 129.
7. Yamashita, H. *et al.*, J. Phys. Chem. **100**, 16041 (1996).
8. Yamashita, H., Ikeue, K., Takewaki, T. and Anpo, M., Top. Catal. **18**, 95 (2002).
9. Yamashita, H., Ichihashi, Y., Takeuchi, M., Kishiguchi, S. and Anpo, M., J. Synchrotron Rad. **6**, 451 (1999).
10. Zhang, W., Tanev, P. T. and Pinnavaia, T. J., J. Chem. Soc. Chem. Commun. 979 (1996).
11. Yamashita, H. *et al.*, Chem. Commun. 435 (2001).
12. Rigutto, M. S. and Bekkum, H. V., Appl. Catal. **687**, L1 (1991).
13. Nomura, M. and Koyama, A., J. Synchrotron Rad. **6**, 182 (1999).
14. Yamashita, H., Matsuoka, M., Tsuji, K., Shioya, Y. and Anpo, M., J. Phys. Chem. **100**, 397 (1996).
15. Thomas, J. M. and Sankar, G., J. Synchrotron Rad. **8**, 55 (2001).
16. Pak, C. and Haller, G. L., Micropor. Mesopor. Mater. **48**, 165 (2001).
17. Zhu, Z. D., Chang, Z. X. and Kevan, L., J. Phys. Chem. B **103**, 2680 (1999).
18. Weckhuysen, B. M., Schoonheydt, R. A., Mabbs, D. E. and Collison, D., J. Chem. Soc., Faraday Trans. **92**, 2431 (1996).
19. Weckhuysen, B. M., Verberckmoes, A. A., Buttiens, A. L. and Schoonheydt, R. A., J. Phys. Chem. **98**, 579 (1994).
20. Anpo, M., Takahashi, I. and Kubokawa, Y., J. Phys. Chem. **86**, 1 (1982).
21. Hazenkamp, M. F. and Blasse, G., J. Phys. Chem. **96**, 3442 (1992).

Physica Scripta. Vol. T115, 695–698, 2005

Annealing Temperature Dependence of C_{60} on Silicon Surfaces: Bond Evolution and Fragmentation as Detected by NEXAFS

M. Pedio*[1], F. Borgatti[1], A. Giglia[1], N. Mahne[1], S. Nannarone[2], S. Giovannini[3], C. Cepek[1], E. Magnano[1], G. Bertoni[4], E. Spiller[4], M. Sancrotti[1,4], L. Giovanelli[1], L. Floreano[1], R. Gotter[1] and A. Morgante[1,5]

[1]TASC-INFM, Strada Statale 14, km 163.5, I-34012, Trieste, Italy
[2]INFM and Dip. Ingegneria dei materiali e dell'ambiente, Universita' Modena e R. E.
[3]INFM and Dip. Fisica, Università di Bologna, Italy
[4]INFM and Dip. di Matematica e Fisica, Un. Cattolica del Sacro Cuore, Brescia, Italy
[5]INFM and Dip. Fisica, Università di Trieste

Received June 26, 2003; accepted December 4, 2003

PACS number: 78.70.Dm

Abstract

We report a near-edge X-ray absorption spectroscopy (NEXAFS) study of the C K-edge of C_{60} molecules interacting with Si(100) and Si(111) surfaces. Annealing the C_{60}/Si systems at 1050 K induces fullerene fragmentation and leads to SiC nucleation. Tuning the probing depth and studying polarization dependence, the NEXAFS results shed light on the evolution of the molecular states after thermal treatment, up to the fullerene fragmentation and SiC formation. The NEXAFS spectra of a single layer of C_{60} deposited at 670 K onto both surfaces show a strong C_{60}-substrate interaction. A polarization dependence of the spectra can be detected; this behaviour is similar to the results obtained on C_{60} covalently chemisorbed on Al surfaces. We find, for both substrates, that fullerene fragmentation starts at the C-Si interfaces, involving the C atoms lying close to the Si substrate, implying an increase of the number of C-Si bonds at the fragmentation stage.

1. Introduction

C_{60} interacts strongly with Si susbtrate atoms, forming a covalent C-Si bond. Decomposition of C_{60} takes place on Si(100) above $\cong$ 1000 K, and the SiC formation takes place by nucleation [1, 2, 3, 4]. STM results show that on both, Si(100) and Si(111) substrates, the fragmentation of the C_{60} cages starts locally. Large SiC islands are formed at temperatures higher than 1050 K, after cage decomposition. Under the appropriate growth conditions, it is possible to grow ordered phases on different Si substrates [5, 6] obtaining the cubic polytype 3C-SiC. A remarkable point is that with this procedure SiC can be grown at a temperature ($T \cong 1000$ K) significantly lower than with other methods ($T >$ 1300 K) and this could improve the structural quality of the interface between SiC and Si to integrate Si-SiC technology. Hamza *et al.* [1] showed that thermal fragmentation of C_{60} on Si(111)-(7 × 7) can lead to an ordered 3C-SiC thin film oriented in register with the substrate. X-Ray diffraction measurements [7] show that well ordered 3C-SiC can be obtained by depositing C_{60} precursors on Si(100) and demonstrate that the occurrence of extra-phases can be properly limited by choosing the appropriate substrate temperature and deposition rate during C_{60} deposition. Co-deposition of Si and C_{60} on heated Si substrate leads to higher quality SiC films.

NEXAFS is a mature technique to study the electronic structure of molecules deposited on surfaces [8]. Here NEXAFS spectroscopy is used to study the evolution of the C_{60} molecular empty states in C_{60}-Si interfaces as a function of the annealing temperature, up to the fullerene fragmentation and SiC formation. The study was performed by varying the probing depth by using different detection modes (Auger Yield and Total Yield with probing depth of 8 Å [9] and more than 50 Å, respectively), and by changing the light polarization direction with respect to the surface. The NEXAFS spectra of a single layer of C_{60} deposited at 300 K and annealed at 670 K onto both surfaces, show a strong C_{60}-substrate interaction, confirming literature results [10]. A polarization dependence of the spectra can be detected, similarly to the behavior observed when C_{60} is chemisorbed on Al surfaces [11]. In this latter case the C_{60} molecules interacted with the surface via a covalent bond, similar to the case studied here of C_{60} absorption on Si surfaces, even though for Si substrates the bond also involves the LUMO + 1 states. By changing the detection mode (Auger yield and total yield), we were able to distinguish the more external molecular states configuration with respect to the C-Si interface during thermal C_{60} fragmentation and SiC nucleation. Our results show that fullerene fragmentation starts from the C-Si interfaces, with the disruption of the C_{60} molecular states toward the bulk, i.e. involving the C atoms lying close to the Si substrate atoms. This result indicates the increase of the number of C-Si bonds at the interface during fragmentation.

2. Experimental

The C_{60}/Si systems were studied by XAS and photoemission spectroscopy. The preparation of Si(100) and Si(111) clean substrates and the C_{60} deposition from crucible were performed according the procedures of refs. [2] and [5]. Thermal treatments of C_{60} deposited on Si substrates were made for a time of 5 minutes at different temperatures in ultra high vacuum. Temperatures were measured by a pyrometer and thermocouple (experimental error about ±10 K). Islands of cubic SiC were produced by fullerene deposited on the Si(100) substrate and annealed at high temperature ($T >$ 1060 K) [1, 5, 6]. Measurements at the C absorption edge of C_{60} deposited on the Si(111) surface were taken at the ALOISA beamline of the ELETTRA synchrotron (Trieste, Italy) [12] by using the drain current detection mode. The energy resolution was 80 meV for the NEXAFS spectra, and the typical photon flux on the sample was of the order of 10^{11} photons/s. Spectra were recorded both in s and p incidence (with the $\boldsymbol{E}$ vector of the impinging light at respectively, 90° and 7° with respect to the surface normal).

NEXAFS of the fullerene interacting with Si(100) surface and 3C-SiC ordered films were performed on the BEAR beamline

*e-mail: pedio@tasc.infm.it

of ELETTRA [5]. The ***E*** light vector of the impinging photons was in the surface plane. The energy resolution was 80 meV for the XANES spectra, and the typical photon flux on the sample was of the order of 10^{10} photons/s. The NEXAFS spectra have been measured in total electron yield, drain current (sampling depth >50 Å) and Auger Yield modes. In the Auger Yield mode, a CMA analyser was tuned at the C LVV Auger line of Kinetic Energy ≈270 eV, estimated sampling depth ≈8 Å [9].

Photoemission from the C 1s and Si 2p and valence bands were measured by an electron analyser (an angular integrated CMA for BEAR and an angular resolved Hemispherical analyzer for ALOISA) for a deeper characterization of the systems.

All the spectra were measured at room temperature and normalized to the incident photon flux obtained by measuring simultaneously the current drained by a tungsten grid inserted in

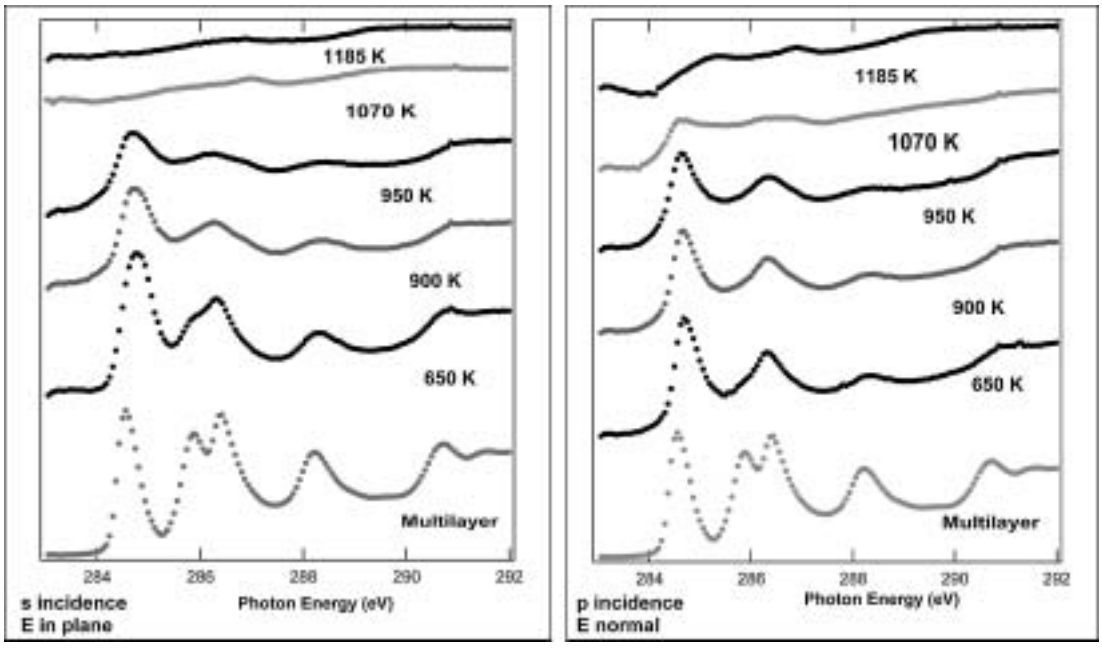

Fig. 1. The evolution of the C K-edge NEXAFS spectra (drain current) measured in s and p incidences for the C_{60}/Si(111) system as a function of annealing temperature. A thick C_{60} film (multilayer) is shown for comparison.

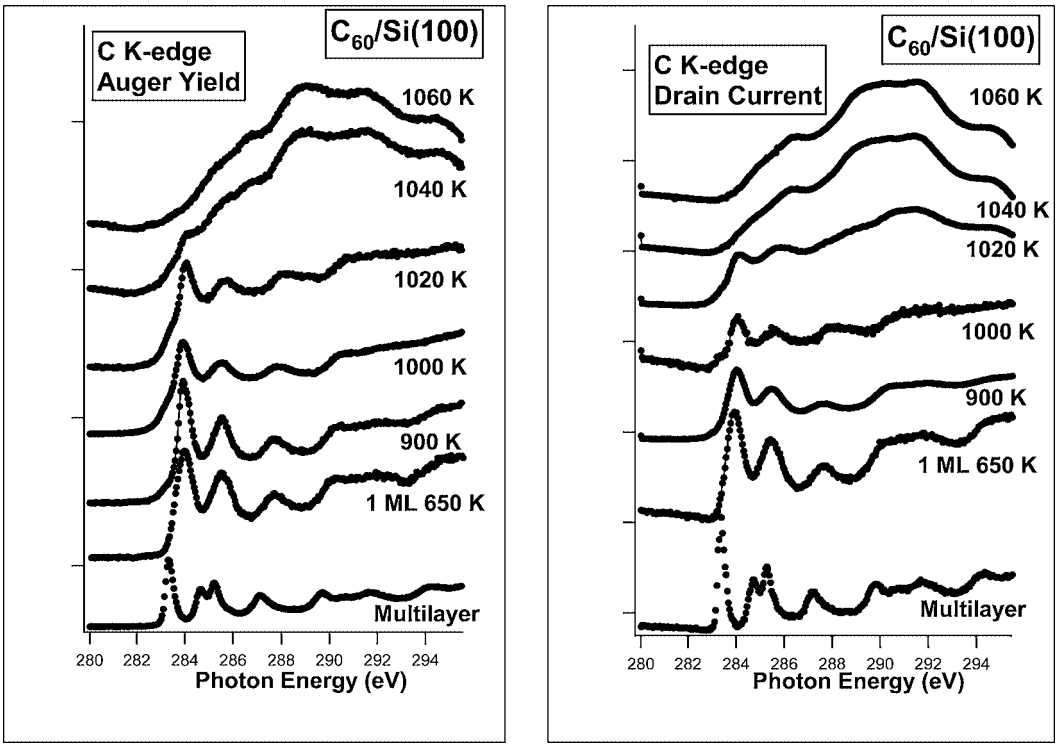

Fig. 2. Evolution of the C K-edge NEXAFS spectra for the multilayer C_{60} and 1 ML of C_{60}/Si(100) system after different annealing treatments as measured simultaneously in two detection mode: the most surface sensitive Auger Yield (left) and Drain Current (right). The geometry was such that the ***E*** light vector of impinging photon was in the surface plane. The temperature is indicated in Kelvin. Thick C_{60} film (multilayer) is shown for comparison.

the beam path. The tungsten grid was previously heated at high temperature to remove contaminants.

3. Results and Discussion

The NEXAFS spectra of the C K-edge of the C_{60}/Si(111) system as a function of annealing temperature are reported in Fig. 1. The multilayer C_{60} spectrum is shown for comparison. The evolution of the molecular empty states of the fullerene molecules as a function of annealing temperature was studied both in s (left panel) and p (right panel) light incidence mode, with the E vector of the impinging light at respectively, 90° and 7° with respect to the surface normal. Fig. 2 shows the C K-edge NEXAFS spectra for the 1 ML C_{60}/Si(100) system as a function of annealing temperature, measured in the two detection mode (Auger yield, left panel, and drain current, right panel) up to the molecule fragmentation and the SiC island formation. A C_{60} multilayer spectrum is shown for comparison. The spectra of the C_{60} multilayer are largely independent of the light incidence (s or p), the probing depth and the Si substrates. The first four peaks of the C_{60} multilayer NEXAFS correspond to molecular states with π character (ref. [10] and refs therein).

The NEXAFS spectra of a single layer of C_{60} deposited at 300 K on both surfaces and annealed at 670 K (Fig. 1 and Fig. 2), show a strong C_{60}-substrate interaction with a broadening of the transition involving mainly the LUMO and LUMO + 1 π character states, confirming literature results [10]. This behavior is similar to the one observed when C_{60} is chemisorbed on Al surfaces [11], where the C_{60} molecules interact with the surface with a bonding similar to the case here studied. In the case of Si substrates the effect of the anisotropy of the fullerene molecular states toward the bulk and out of the surface appears even more pronounced and involves also the LUMO + 1 state (see spectra annealed at 670 K), as already found by authors in ref. [10]. Similar results are found for the C_{60}/Si(100) single monolayer. The study of the connection between the NEXAFS data and the C_{60} orientation will be discussed in a forthcoming paper. Increasing the annealing temperature the molecular states become even broader and above 1060 K the SiC island formation takes place, with the gradual vanishing of molecular features. A polarization dependence of the spectra can be detected when the spectra are measured in s or p incidences for the C_{60}/Si(111) system (Fig. 1). The LUMO molecular state has a different broadening in the two different incidences (i.e. it is broader in s incidence) and at 1070 K it can be distinguished only in p incidence.

The NEXAFS spectra in both systems show that molecular states during fragmentation are more intense in p incidence geometry. Comparing the high annealing temperature spectra of C_{60}/Si(111) system, spectra obtained in p incidence show more pronounced features. This can be taken as evidence that the final state of the transitions have π character, pointing outward the surface.

The thermal treatment of the C_{60}/Si(100) system in the high temperature range of 950–1070 K (Fig. 2) induces a further broadening of the C_{60} molecular features, that still remain distinguishable, up to 1040 K. Fragmentation of the molecule starts for an annealing temperature above 1020 K. By varying the probing depth additional information is obtained. In fact, in the spectra obtained in the surface sensitive mode (Auger Yield probing depth of 8 Å, of the order of the fullerene dimension 7 Å), C_{60} features are recognizable, while they are washed out when using a higher probing depth, of the order of 50 Å. This result is shown by the data in Fig. 3a, where the NEXAFS spectrum taken with a probing depth of 8 Å for 1 ML C_{60}/Si(100) after annealing at 1000 K is compared with the difference curve obtained by subtracting the NEXAFS spectra after 1040 K minus

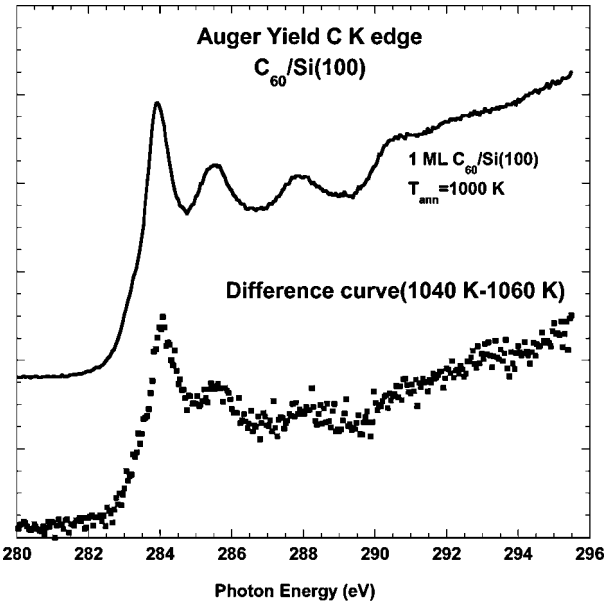

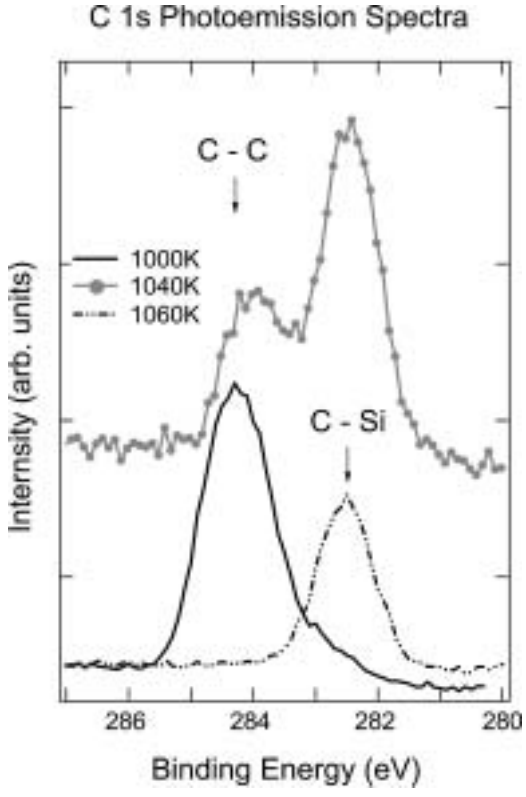

Fig. 3. (a) NEXAFS difference curve of the spectra taken in Auger yield mode on the C_{60}/Si(100) systems after 1040 K and 1060 K annealing temperature. The difference spectrum is compared with the spectrum in AY taken after an annealing treatment at 1000 K in Fig.2. (b) C 1s XPS spectra of one C_{60} ML annealed at different temperatures, measured at photon energy of 380 eV. In the bottom are shown the C 1s spectrum of the C_{60} ML annealed at 1000 K (straight line), where almost carbon are in the C-C bond, and the spectrum of the C_{60} ML annealed at 1060 K (dotted line), where all the C atoms reacted with the substrate to form SiC. The spectrum of the top (system annealed at 1040 K) clearly shows the two components due to C-C and C-Si bonds.

1060 K annealing temperature taken at the same probing depth. The difference curve was calculated in order to make evident the molecular features that are present in the 1040 K spectrum and completely vanish in the 1060 K spectrum, taken as reference for C in the SiC state. Note that the geometry was such that the E light vector of the impinging photon was parallel to the surface plane. This means that the set of C atoms in the external layer of the C_{60} cage is the last to be perturbed by the annealing and that C_{60} decomposition first takes place at the C atoms in contact with the Si substrate atoms with a gradual increase of the number of Si-C bonds [2, 5].

Photoemission results reported in Fig. 3b, indicate that two C inequivalent bonds are present after having annealed at 1040 K. The two different bonds are assigned [4] to the C-C bond at 284.2 eV and to the C-Si bond at 282.6 eV.

Summarizing our data indicates that the C_{60} fragmentation starts at a temperature of about 1020 K. By changing the probing depth of NEXAFS, after thermal C_{60} fragmentation and SiC nucleation, we found that the residual molecular states of the fragmented C_{60} cage are localized on the topmost surface layer, i.e. they are at the more external site with respect to the C-Si interface. The feature intensities behaviour of the electric field direction for the $C_{60}/Si(111)$ system show that the molecular fragment have π character and are likely directed almost orthogonal to the surface. This topic will be discussed in a forthcoming paper.

4. Conclusions

We studied the molecular state evolution of C_{60} deposited on silicon (100) and (111) surfaces. The study was based on optical absorption at the C K-edge and on its dependence on the direction of the electric field at the surface. Additional information was obtained by using different probing depths in the acquired spectra.

The NEXAFS C K-edge results on both systems during annealing show that the outer molecular states of the C_{60} cage endure up to annealing temperature as high as 1040 K. These residual fragment molecular states are π orbitals directed normal to the surface.

References

1. Hamza, A. V., Balooch, M. and Moalem, M., Surf. Science **317**, L1129 (1994).
2. Cepek, C., Schiavuta, P., Sancrotti, M. and Pedio, M., Phys. Rev. B **60**, 2068 (1999); Sakamoto, K. *et al.*, Phys. Rev. B **60**, 2579 (1999).
3. Wang, X. D. *et al.*, Jpn. J. Appl. Phys. Part 2 **31**, L983 (1992); Chen, D. and Sarid, D., Phys. Rev. B **49**, 7612 (1994).
4. Goldoni, A. *et al.*, Surf. Rev. Lett. **9**, 775 (2002).
5. Pesci, A. *et al.*, Surf. Sci. **482–485**, 829 (2001); Moras, P. *et al.*, Appl. Surf. Sci. **184**, 50 (2001).
6. Cepek, C. *et al.*, "Improved β-SiC(100)/Si (100) Interface quality", unpublished.
7. Volz, K. *et al.*, Mat. Sci. Engineering **A289**, 255 (2000).
8. Stöhr, J. "NEXAFS Spectroscopy", Springer Series in Surface Sciences, Vol. 25 (Springer-Verlag, Berlin, 1992).
9. Goldoni, A., Cepek, C. and Modesti, S., Synthetic Metals **77**, 189 (1996).
10. Kondo, D. *et al.*, Surf. Sci. **514**, 337 (2002).
11. Maxwell, A. J. *et al.*, Phys. Rev. B **57**, 7312 (1998).
12. Floreano, L. *et al.*, Rev. Sci. Instrum. **70**, 3855 (1999).
13. Naletto, G., Pelizzo, M. G., Tondello, G., Nannarone, S. and Giglia, A., SPIE Proc. **4145**, 105 (2001); Nannarone, S. *et al*., SRI conference proceedings, to be published.
14. Pedio, M. *et al.*, Surf. Sci. **437**, 249 (1999).

Physica Scripta. Vol. T115, 699–702, 2005

EXAFS and XANES Study of Two Novel Pd Doped Sn/SnO_x Nanomaterials

Didier Grandjean[1*], Robert E. Benfield[2], Céline Nayral[3], Laurent Erades[3], Katerina Soulantica[3], André Maisonnat[3] and Bruno Chaudret[3]

[1]Department of Inorganic Chemistry and Catalysis, Debye Institute, Utrecht University, Sorbonnelaan 16, 3584 CA Utrecht, The Netherlands
[2]Functional Materials Group, School of Physical Sciences, University of Kent, Canterbury CT2 7NR, U.K.
[3]Laboratoire de Chimie de Coordination CNRS, 205, route de Narbonne, 31077 Toulouse Cedex 04, France

Received June 26, 2003; accepted November 4, 2003

PACS numbers: 6110Ht; 6146+w

Abstract

EXAFS and XANES at the Pd and Sn K-edges have been used to characterise a novel palladium doped Sn/SnO_x nanocomposite that have found application in a new type of high performance solid-state gas sensor. The spherical nanoparticles (10 to 65 nm diameter) prepared either by co-decomposition of Sn and Pd organometallic precursors (doping in volume) or by decomposition of a palladium precursor on preformed Sn/SnO_x core-shell nanoparticles (doping in surface) consist of a tin metallic core surrounded by some small platelets of a well-crystallised material embedded in an outer layer of amorphous tin oxide. In this layer tin atoms in an oxidation state close to +IV, are four-fold coordinated to oxygen with bond distances slightly larger than in bulk cassiterite SnO_2. In both samples palladium was found to be always in a metallic state, only surrounded by Sn and Pd atoms located at unusually short distances. The two samples that differ mainly by their Pd coordination number present very different morphologies and electrical properties when fully oxidised. A possible location of the Pd atoms in these two materials is proposed.

1. Introduction

A new high performance gas sensor using the integrated circuit technology [1, 2] has been designed by depositing a drop of a suspension of a novel Sn/SnO_x nanocomposite [3, 4] doped with Pd onto a silicon die. This drop is then heated up to 600 °C using the integrated heater and a thin film of highly sensitive Pd doped nanostructured SnO_2 is generated onto the surface of the silicon wafer [2]. The suspension of monodisperse nanoparticles of Pd doped Sn/SnO_x [5] is prepared by a new chemical method based on the decomposition of Sn and Pd organometallic precursors in a controlled water/anisole mixture. Two different synthesis routes have been investigated: co-decomposition of Sn-based and Pd-based organometallic precursors (doping in volume) and decomposition of a palladium precursor on preformed Sn/SnO_x nanoparticles (doping in surface). A subsequent heat-treatment of these colloids carried out at 600 °C leads in all cases to Pd-doped SnO_2 nanoparticles that retain the same size and morphology. If the surface doping leads to a big improvement of the conducting properties of the oxidised sensor material, the volume doping produces a material that features poorer electrical properties than the undoped one. These contradictory results show that a detailed investigation of the structure and electronic properties of these nanocomposites is crucial to achieve a full understanding of the relationship between their structure and electrical properties. Mössbauer spectroscopy, XPS, HRTEM and X-ray diffraction have been already applied to characterise these colloids [4] but these techniques have shown some limitations due to the complex nature of these materials.

We report here an EXAFS and XANES study carried out both at the Sn and Pd K-edge of these two Pd doped Sn/SnO_x samples prepared by two different methods. The aim of this investigation is to complement the characterisation methods already used by a local order sensitive probe in order to better characterise the local structure and the electronic properties as well as to determine the dopant location in these colloids, precursors of the SnO_2-based sensor nanomaterials. This should allow for a better monitoring of the synthesis process that is essential to develop a reproducible low-cost synthetic method for large-scale production.

2. Experimental

2.1. *Preparation of the nanocomposites*

2.1.1. *Preparation of Pd doped in surface [Sn/SnO_x] colloidal suspension.* Preparation of the pure tin colloid from the $[Sn(NMe_2)_2]_2$ precursor in anisole containing traces of water follows the route described previously [3, 4]. The palladium precursor $[Pd(dba)_2]$ in anisol was added to a colloidal suspension of pure Sn/SnO_x ($[Pd]/[Sn] = 4\%$). After exposition to 1 bar of CO during 20 mn, depressurisation, decantation, filtration and drying under vacuum, a black powder was obtained and sampled by TEM.

2.1.2. *Preparation of Pd doped in volume [Sn/SnO_x] colloidal suspension.* The palladium precursor $Pd(OAc)_2$ was added to a solution of $[Sn(NMe_2)_2]_2$ in anisole containing traces of water in a Pd/Sn ratio of 8 wt%. The solution was then heated at 135 °C for 3 hours under magnetic stirring and a black suspension was obtained. After decantation the black precipitate was washed with anisole and sampled by TEM.

2.2. *Electron microscopy*

Samples for HRTEM studies were prepared in a glove box by slow evaporation of a drop of suitably diluted colloidal suspensions deposited on holey carbon-covered grids. The HRTEM experiments were performed at the "Service Commun de Microscopies de l'Université Paul Sabatier" on a JEOL JEM 2010 electron microscope working at 200 kV.

2.3. *X-ray Absorption Spectroscopy*

X-ray absorption data were collected on beamline 9.2 (CLRC Daresbury Laboratory, UK), operating under beam conditions of 2 GeV, 200 mA using a Si (220) double-crystal monochromator. XAS signals were measured in transmission mode at the Sn K-edge and in fluorescence mode using a 13-channel solid-state detector at the Pd K-edge. The spectra were recorded at 80 K by

*E-mail: D.Grandjean@chem.uu.nl

cooling the samples with a cold finger liquid-nitrogen cryostat. Appropriate amounts of sample were finely ground with boron nitride and pressed into 13 mm pellets producing a suitable edge jump. Data reduction of experimental X-ray absorption spectra was performed using the program EXBROOK [6]. EXAFS refinements with k^2 weighting were carried out with EXCURV98 [6] using Fourier filtering techniques with the same filter windows (0.8–4.0 Å).

3. Results and discussion

3.1. *Electron Microscopy*

Figure 1a shows the HRTEM image of a typical surface-doped nanoparticle in colloidal suspension that is clearly composed of a crystallised core of ca. 12 nm diameter surrounded by some small platelets of a well-crystallised phase embedded in an outer layer of amorphous material of ca. 4 nm thickness. XRD and Mössbauer results are consistent with the presence of an amorphous tin oxide surface layer surrounding a β crystallised tin core [4]. However, the coordination and oxidation state of tin in this layer as well as the exact nature of the platelets that are absent in the pure Sn/SnO_x material remain unclear. Figure 1b displays a HRTEM image of a typical volume-doped particle [5]. It is obvious that the particle size has increased dramatically to reach ca. 65 nm in diameter. As in the case of surface doped particles, the core of the particle appears to be surrounded by platelets of a rather crystalline material embedded in an outer amorphous layer.

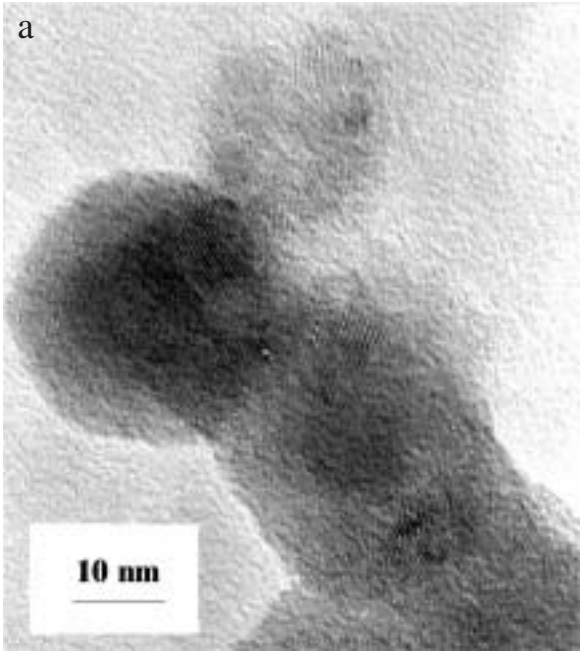

Fig. 1. HREM images of **a**: Pd surface-doped Sn/SnO_x nanoparticle; **b**: Pd volume-doped Sn/SnO_x nanoparticle.

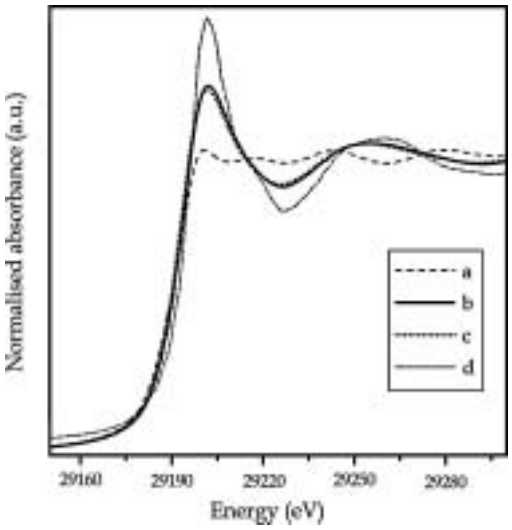

Fig. 2. Sn K-edge normalised XANES spectra of **a**: bulk Sn; **b**: Pd surface-doped Sn/SnO_x; **c**: Pd volume-doped Sn/SnO_x; **d**: bulk SnO_2.

3.2. *XANES*

3.2.1. *Sn K-edge.* Background corrected and normalised XANES of the two nanocomposites that are presented in Figure 2 along with Sn metal and bulk SnO_2 taken as references, show that the two nanomaterials have a very similar XANES profile. They both feature the white line characteristic of the oxide species but with a lower intensity than for the SnO_2 reference compound showing that the average oxidation state of Sn in this material is lower than in bulk SnO_2. Compared to SnO_2, the nanocomposites XANES spectra are also characterised by damped resonance peaks that usually shows the presence of a disordered phase and/or a large number of surface atoms. A mixture of an amorphous SnO_2 phase and a tin metallic phase is a possible explanation of the shape of this XANES profile.

3.2.2. *Pd K-edge.* Figure 3 shows the background corrected and normalised XANES of the two nanomaterials along with bulk PdO and bulk Pd presented as references. The two XANES spectra are almost identical and seem to have the same average electronic structure. The general profile of the spectrum of the Pd doped samples is similar to the one of bulk metallic Pd but with very much damped resonance peaks indicating the presence of disorder in the material and/or nanosize structures. The PdO spectrum has a totally different shape and its edge position is obviously shifted towards the higher energies as one might expect it for a higher oxidation state. The XANES analysis can already show that the Pd doped Sn/SnO_x samples are not oxidised and have an electronic

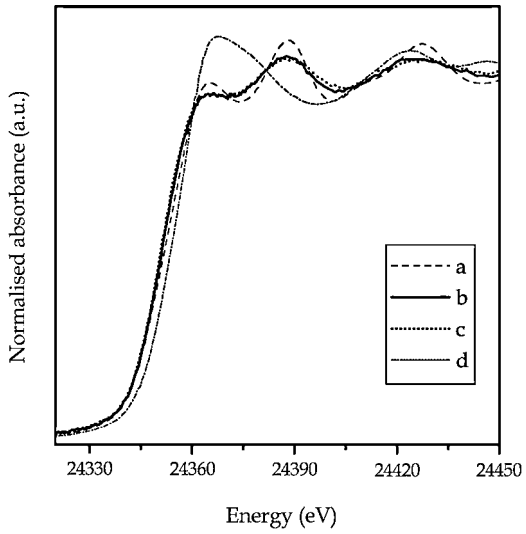

Fig. 3. Pd K-edge normalised XANES of **a**: bulk Pd; **b**: Pd surface-doped Sn/SnO$_x$; **c**: Pd volume-doped Sn/SnO$_x$; **d**: bulk PdO.

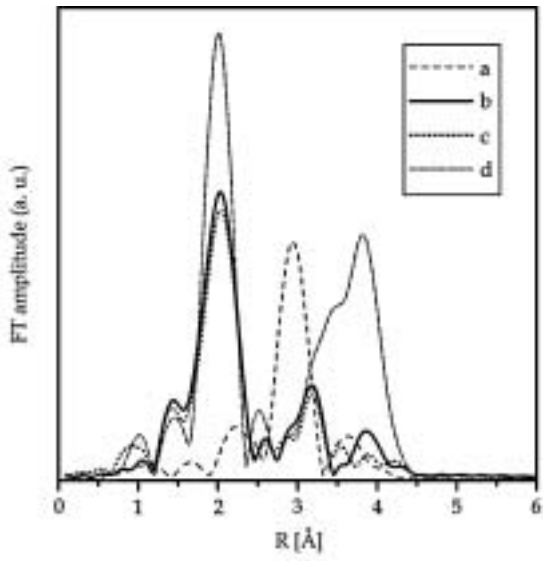

Fig. 4. Fourier Transforms of the k^3-weighted (references) or k^2-weighted Sn K-edge EXAFS of **a**: bulk Sn; **b**: Pd surface-doped Sn/SnO$_x$; **c**: Pd volume-doped Sn/SnO$_x$; **d**: bulk SnO$_2$.

Table I. *Summary of structural results of Sn and Pd K-edge EXAFS refinements of the two Pd-doped Sn/SnO$_x$ nano-materials.*

	Pd volume-doped Sn/SnO$_x$		Pd surface-doped Sn/SnO$_x$	
K-Edge	Sn	Pd	Sn	Pd
E_f (eV)	−8.5 (3)	−4.0 (8)	−6.8 (5)	−4.6 (4)
AFAC	1	0.80	1	0.80
k-range	2.5–15	3–14	2.5–15	3–14.5
N_1	3.3 (1) O	2.6 (5) Sn	3.3 (2) O	2.8 (4) Sn
R_1	2.071 (4)	2.55 (1)	2.073 (4)	2.58 (1)
A_1	0.010(1)	0.005(1)	0.008(1)	0.012 (1)
N_2	0.9 (3) Sn	0.5 (4) Pd	1.1 (4) Sn	2.3 (6) Pd
R_2	3.00 (1)	2.71 (4)	3.01 (1)	2.77 (1)
A_2	0.014 (5)	0.001 (2)	0.010 (4)	0.012 (3)
N_3	0.8 (3) Sn		1.9 (7) Sn	
R_3	3.25 (1)		3.27 (2)	
A_3	0.010 (4)		0.021 (8)	
N_4			0.6 (5) Sn	
R_4			3.75 (2)	
A_4			0.009 (8)	
N_5			0.1 (1) Pd	
R_5			2.58 (2)	
A_5			0.0006 (−)	
R (%)	15.1	16.4	18.6	14.3

E_f = contribution of the wave vector of the zero photoelectron relative to the origin of k [eV].
AFAC = amplitude reduction due to many-electron processes.
N_i = number of atom in the ith shell.
R_i = radial distance of atoms in the ith shell [Å].
A_i = Debye-Waller term of the ith shell ($A = 2\sigma^2$ with σ = Debye-Waller factor) [Å^2].
R factor in %.
*these parameters were kept fixed during the refinement.

structure close to the metallic state but with very small particle size and/or an amorphous character.

3.3. *EXAFS*

Results of the EXAFS structural refinements for the Sn and Pd K-edges measurements are summarised in Table I.

3.3.1. *Sn K-edge.* The phase corrected Fourier transforms (FT's) of the two Pd doped-samples are gathered in Figure 4. As the XANES data already showed, both nanocomposites feature a very similar FT. The first peak could be fitted for both samples with 3.3 O located at 2.071–2.073 Å from the central atom (Table I). This is similar to the values found for the undoped Sn/SnO$_x$ materials [7]. If we take into account the part of the Sn that belongs to the core of the colloid, the tin atoms in the oxidised phase are then likely to be 4 fold coordinated to oxygen [7]. The corresponding bond distances are only slightly larger than in bulk SnO$_2$ (2.045 Å) indicating that Sn has an oxidation state close to +IV. The second peak in the FT could be fitted with ca. 1 Sn atoms located at 3.00–3.010 Å from the Sn scatterer atom. This distance does not correspond to the Sn-Sn distance in SnO (3.515 Å) or SnO$_2$ (3.187 Å) tin oxides but to the bond distances in the tin metallic phase (3.022 Å) [8]. The relative amount of metallic tin atoms in the colloid was estimated using the Sn coordination number at ca. 25% [7]. The low intensity of the peaks beyond the metal tin shell show that the tin oxide phase is mainly in a disordered and/or amorphous state confirming the presence of a dispersed matter pointed out by HRTEM. The general fit of the surface-doped sample was slightly improved when a shell of ca. 0.1 Pd atoms located at 2.58 Å was added to the EXAFS model.

3.3.2. *Pd K-edge.* The Fourier transforms of the two nanomaterials presented in Figure 5 are different from one another. The results of the EXAFS refinement (Table I) show that the environment around the Pd atoms is composed for both samples of ca. 2.7 Sn atoms, located at a distance of 2.55 Å in the case of the volume-doped sample, and at a distance of 2.58 Å, consistent with the Sn K-edge fit results, in the surface-doped sample. These distances are shorter than tin-palladium bond lengths in alumina supported catalysts (ca. 2.63 Å) already reported by Choi *et al.* [9] and Pd-Sn distances in the Pd$_2$Sn phase (Pd-Sn 2.608 Å) [8]. Both samples feature a second shell of palladium atoms consisting of 2.3 atoms located at 2.77 Å for the surface-doped sample and of only 0.5 atoms located at 2.71 Å for the volume-doped sample. No other peaks could be detected indicating together with the XANES results that the Pd phase is rather amorphous and/or that this phase is composed of very small particles that are not oxidised but part of a metallic phase. The Pd-Pd distances found in these two samples (2.71–2.77 Å) are slightly different than the typical

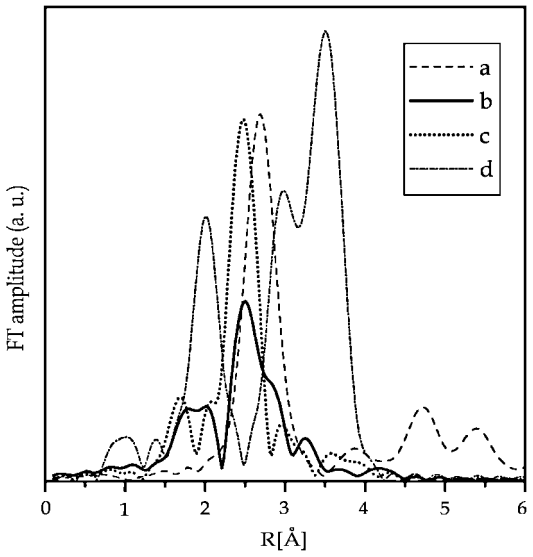

Fig. 5. Fourier Transforms of the k^3-weighted (references) or k^2-weighted Pd K-edge EXAFS of **a**: bulk Pd; **b**: Pd surface-doped Sn/SnO_x; **c**: Pd volume-doped Sn/SnO_x; **d**: bulk PdO.

bond distance of the palladium metallic phase (Pd-Pd 2.751 Å) [8]. The small discrepancy observed in the bond distances (ca. 1–2%) between the two samples may indicate that Pd atoms are in different locations and have different environments in each sample. The very low value of the Pd coordination number found for the volume-doped sample indicates that a better mixing of the Sn and Pd atoms occurs during the preparation process.

By combining the EXAFS results with the TEM images it is possible to propose two locations of the Pd dopant atoms in these nanomaterials. The first one is in small platelets of pure Pd surrounded by a tin/tin oxide interface located around the tin metallic core. These platelets were observed in both samples but mainly in the surface-doped one. The second location is in the Sn metallic core of the particle in which they form a bulk alloy with Sn and/or an Sn/Pd phase. A combination of these two locations seems to occur in the volume-doped sample.

Pd doped samples have been tested for their electrical properties after a full oxidation at 600 °C, in the working conditions of the gas sensor. The two Pd doped samples feature very different electrical properties. If the sample doped in surface shows an approximately 2-fold increase in its sensitivity to gases like CO compared to the undoped SnO_2 samples [10], the volume-doped sample features very poor electrical properties with a very high resistivity. The high amount of Pd (8 wt%) that has been used in this case as well as the different morphology could explain the dramatic change of the electrical properties in this sample.

4. Conclusion

The EXAFS and XANES results showed that the major part of tin in both Pd doped Sn/SnO_x nanocomposites is forming an amorphous oxide phase in which Sn atoms in an oxidation state close to +IV, are four-fold coordinated to oxygen atoms with an average bond distance slightly longer than in bulk cassiterite SnO_2. The presence of a metallic core estimated at ca. 25% of the total amount of tin atoms could also be pointed out. Pd is always in a metallic state and is surrounded by Sn and Pd atoms located at unusually short distances that vary according to the sample. A possible location of the palladium into the small crystalline platelets around the Sn core of the particle has been suggested for the sample doped in surface. For the sample doped in volume the formation both of a bulk Sn/Pd phase in the core part of the particle that could explain the huge increase in the particle size, together with the presence of Pd platelets around it has been suggested. When oxidised, the sample doped in surface features a large increased in its gas sensitivity compared to the pure one, whilst a very high resistivity have been measured in the sample doped in volume. This XAS study has allowed us in complement to the other techniques used, to fully characterise the structure of these materials by pointing out more specifically the location of the doping element in the two methods. These results should lead to significant improvement in the optimisation of the preparation method of these nanocomposites.

Acknowledgements

For financial support we thank the EU TMR programme contract number FMRX-CT98-0177. Access to the synchrotron facilities at the SRS was arranged through the general support of the EPSRC for the use of central facilities. We wish to acknowledge the assistance and advice of Dr. Fred Mosselmans (SRS 9.2) during the experimental measurements. We wish also to acknowledge the use of the EPSRC's Chemical Database Service at Daresbury.

References

1. Fau, P., Nayral, C., Chaudret, B. and Maisonnat, A., Motorola, European patent No. 98400246.9-2104.
2. Fau, P., *et al.*, Sensors and Actuators B **78**, 83 (2001).
3. Nayral, C., *et al.*, Adv. Mater. **11**, 61 (1999).
4. Nayral, C., *et al.*, Chem. Eur. J. **6**, 4082 (2000).
5. Nayral, C., *et al.*, Appl. Surf. Sci. **164**, 219 (2000).
6. Binstead, N., Campbell, J. W., Gurman, S. J. and Stephenson, P. C., EXAFS Analysis Programs, Daresbury Laboratory, Warrington (1991).
7. Grandjean, D., Benfield, R. E., Nayral, C., Maisonnat, A. and Chaudret, B., J. Phys. Chem. B **108**, 8876 (2004).
8. The United Kingdom Chemical Database Service, Fletcher, D. A., McMeeking, R. F. and Parkin, D., J. Chem. Inf. Comput. Sci. **36**, 746 (1996).
9. Choi, S. H. and Lee, J. S., J. Catal. **193**, 176 (2000).
10. Erades, L., *et al.*, submitted for publication.

Physica Scripta. Vol. T115, 703–704, 2005

Cd and Se Atomic Environments During the Growth of CdSe Nanoparticles in Glass

T. M. Hayes, P. D. Persans, A. Filin, C. Peng and W. Huang

Rensselaer Polytechnic Institute, Troy, NY USA

Received June 26, 2003; accepted November 7, 2003

PACS numbers: 61.46.+w; 78.70.Dm

Abstract

Thermal treatment of Cd and Se doped borosilicate glass yields CdSe nanoparticles that are interesting for applied and fundamental studies of quantum and size effects in semiconductors. Using X-ray absorption spectroscopy at both the Cd and Se K-edges, we have studied the local atomic structure for each of these reactants at several stages of particle growth. When the doped glass is quenched from 1050 °C, the Cd neighbor is mostly oxygen and the Se neighbor is mostly Zn. With heat treatment at 600–750 °C, the concentration of nearest neighbor Cd-Se bonds increases and becomes dominant while the optical spectrum evolves toward that of a composite containing CdSe.

II-VI semiconductor nanoparticles grown in glass have long been model systems for the study of quantum confinement and other size effects. Deep understanding of the environment of the reactant atoms is important for two reasons. First, interpretation of optical properties requires knowledge of the crystal order or disorder, defects, and interface bonds. Second, control of nucleation and growth of nanoparticles requires an understanding of the bonding of reactants both before and after particles are formed.

An often-cited, but untested, model of CdSe particle formation in glass is described by Weyl [1]. In this model, Se and Cd are present in the melt as ZnSe and CdO and should be predominant in quenched glass. At lower temperature CdSe is more stable than ZnSe and CdO. At the heat treatment temperature of 500–700 °C, ZnSe and CdO dissociate and Se and Cd diffuse through the glass and aggregate onto CdSe particles. The details of the precursor phases were not discussed by Weyl. We have addressed the question of the local bonding of Cd and Se atoms at various stages of particle growth using X-ray absorption spectroscopy near the respective K-edges. Optical absorption and resonant Raman spectroscopies were used to characterize particle size and composition [2].

Samples were prepared from commercial RG695 filter glass from Schott Glass Technologies. The base glass has as major components, SiO_2, B_2O_3, Na_2O, CaO, ZnO, and K_2O. Cd and Se are added. Glass composition was determined by the self-consistent interpretation of X-ray fluorescence, X-ray absorption, and electron microprobe measurements.

As-received RG695 glass has been heat-treated after quench to grow relatively large ($d > 5$ nm) nanoparticles with an absorption edge close to the bulk band gap of CdSe (1.8 eV). We prepared glass with nanoparticles in various stages of growth by dissolving the nanoparticles in commercial glass by heating to 1050 °C, followed by quenching. A 5 mm thick slab, contained by Pt shim stock, is typically quenched within 30 seconds to below 500 °C. Prior to cutting, the slab is annealed for one hour at 450 °C to reduce thermal stress. Many samples were cut from a single large ($40 \times 40 \times 5$ mm) slab of each glass to suitable thickness (3 mm for Cd edge XAS, 0.3 mm for Se edge XAS, and 0.5 mm for optics), polished, and heat treated. We focus in this paper on two samples i) as-received (heat treated) RG695 and ii) a sample quenched from 1050 °C.

X-ray absorption spectra were acquired by transmission using in-line gas ionization chamber detectors with the sample at 77 °K. The incident X-ray energy was scanned using a Si(220) "two bounce" monochromator on beamlines 4-2 and 10-2 at the Stanford Synchrotron Radiation Laboratory. Our optics yielded a resolution of 12 eV FWHM at the Cd K edge. The X-ray absorption spectra were reduced and analyzed using standard techniques [3].

In Fig. 1 we show the optical absorption spectra of heat treated and quenched glasses along with the scaled absorption spectrum of bulk CdSe. The absorption edge of commercial RG695 glass ("heat treated") is blue-shifted by ∼100 meV compared to bulk CdSe. This shift could be due to any combination of quantum confinement, composition variation from pure CdSe, or strain. The vibrational Raman scattering spectrum contraindicates substantial alloying ($Zn_xCd_{1-x}S_ySe_{1-y}$) or strain. (We have previously shown that Zn alloying can be significant in commercial CdS-doped glasses [4].) Assuming that the entire blue shift of the heat treated sample is due to quantum confinement yields an estimate of 6 nm for the particle diameter, consistent with broadening observed in X-ray diffraction. The sample that was quenched from 1050 °C exhibits extremely little absorption below 3.5 eV. Assuming that the edge is representative of quantum-confined CdSe particles, we estimate that there are very few particles with diameter larger than

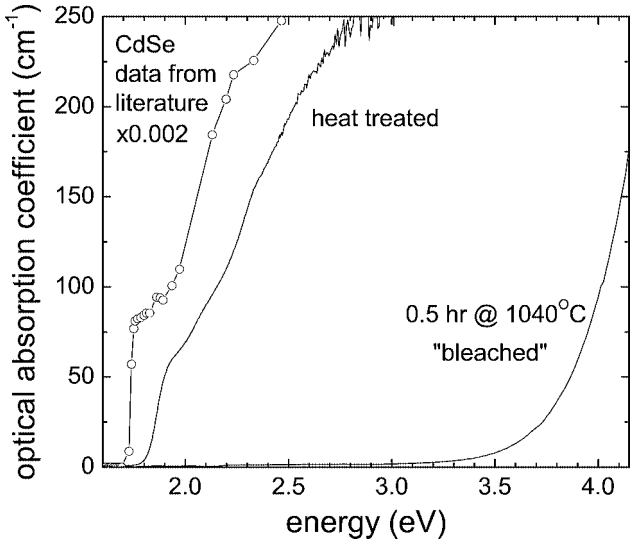

Fig. 1. The optical absorption coefficient α is shown as a function of photon energy for heat treated (as-received) RG695 glass, glass quenched from 1050 °C, and bulk CdSe.

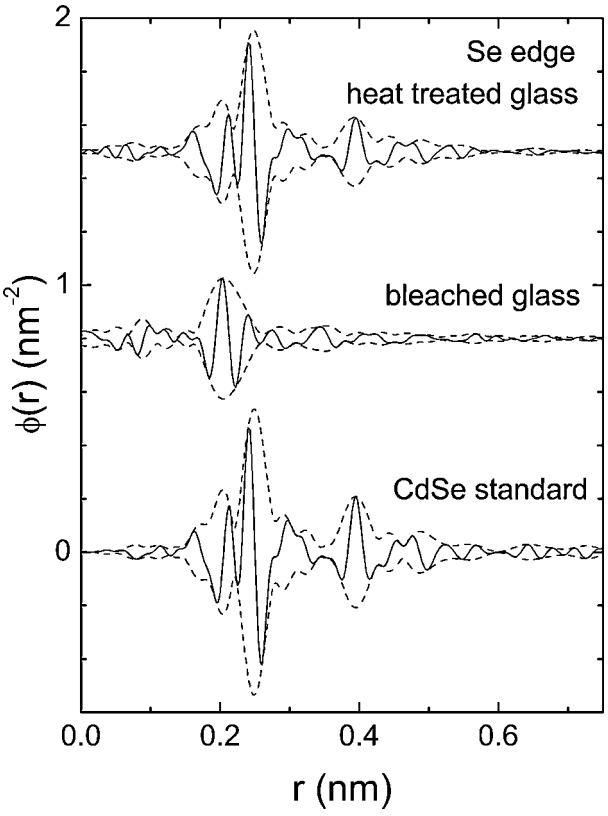

Fig. 2. The real part (solid line) and magnitude (dashed line) of $\phi(r)$, the Fourier transform of $k\chi$, extracted from the XAS data Se edge of three samples as labeled in the figure.

1.5 nm. Optics can tell us little else about the state of the particles or reactants in bleached material.

From XAS measurements we know that the Cd and Se concentrations in both glass samples are nearly equal, with 8.2×10^{19} Cd atoms/cm^3 and 6.5×10^{19} Se atoms/cm^3. The near balance of reactants makes it possible to perform meaningful XAFS analysis on both edges. In Fig. 2 we show the real part (solid line) and magnitude (dashed line) of $\phi(r)$, the Fourier transform of $k\chi$, measured at the Se edge for the heat treated glass, the bleached glass, and a CdSe standard. The CdSe standard exhibits two significant peaks in ϕ at 0.25 nm and 0.4 nm, corresponding to the Cd nearest neighbor and the Se second neighbor respectively. Similar structure is observed for the heat treated glass. The ϕ spectrum of the bleached glass is very different, with a single peak in ϕ centered close to 0.2 nm.

We fit the first neighbor region for Se using FEFF3 [5] signatures for Zn and Se. We fit the first neighbor region for Cd using signatures for O and Se. When possible, FEFF signatures were adjusted by fitting them to standards including CdSe, Se, and CdO.

Analysis of XAFS both edges gives the following results. In the bleached glass: 20% of the Se is bound to Cd and 60% of the Se is bound to Zn. The remainder of the Cd in the bleached glass is bound to O. In the heat-treated glass: 80% of the Se is bound to Cd in an ordered environment. The remainder of the Cd is bound to O. In both glasses, there is a 20% deficit in observed Se neighbors, presumably due to a very disordered environment for this phase.

We conclude that most of the Se is indeed bound to Zn and most of the Cd is bound to O in the quenched glass, consistent with the conventional model of Weyl [1]. A recent XAFS report identifies Se as the predominant first neighbor for Se in a similar quenched glass [6]. We have made a careful comparison of the fits for both Se and Zn first neighbors and conclude that Zn yields a significantly better fit. In the quenched glass, 20% of the Se is in CdSe, but optical absorption results demand that the CdSe must be in particles smaller than 1.4 nm diameter. Heat treatment causes the formation of CdSe in an ordered environment at the expense of ZnSe and CdO. In commercial glass, most of the available Se is incorporated into CdSe particles larger than 6 nm in diameter. There is no evidence for the formation of ZnSe and CdSe pseudobinaries.

Acknowledgments

We gratefully acknowledge funding by the Department of Energy (DOE) Office of Basic Energy Sciences grant DE-FG0297ER455662. The XAS measurements were made at SSRL, which is funded by the DOE Office of Basic Energy Sciences and the NIH Biotechnology Resource Program.

References

1. Weyl, W. A., "Coloured Glass", (Dawsons of Pall Mall, London,1959).
2. Persans, P. D. *et al.*, J. Appl. Phys. **87**, 3850 (2001).
3. Hayes, T. M. and Boyce, J., in "Solid State Physics", (edited by H. Ehrenreich, F. Seitz and D. Turnbull), (Academic Press, New York, 1982), Vol. 37, 173.
4. Persans, P. D., Lurio, L. B., Pant, J., Lian, G. D. and Hayes, T. M., Phys. Rev. B **63**, 115320 (2001).
5. Rehr, J. J., Mustre de Leon, J., Zabinsky, S. I. and Albers, R. C., J. Am. Chem. Soc. **113**, 5135 (1991).
6. Demourgues, A. *et al.*, Physica B **208**, 354 (1995).

Physica Scripta. Vol. T115, 705–708, 2005

Ni K- and Au L_3-edge XAFS of $[Au_6Ni_{32}(CO)_{44}]^{6-}$ and a Study of its Transformations in Acetonitrile Solutions

O. A. Belyakova[1,*], Y. Kubozono[2], S. Kashino[2] and Yu. L. Slovokhotov[1]

[1]Nesmeyanov Institute of Organoelement compounds, RAS, 28 Vavilov St., Moscow 119991, Russia
[2]Department of Chemistry, Okayama University, Okayama 700-8530, Japan

Received June 26, 2003; accepted November 4, 2003

PACS numbers: 81.07.−b, 61.10.Ht

Abstract

Oxidation of the $[Au_6Ni_{32}(CO)_{44}]^{6-}$ cluster anion in acetonitrile solutions by air and by Me_3NO has been monitored using Ni K- and Au L_{III}-edge XAFS spectroscopy. EXAFS data for the pristine cluster correspond reasonably well to its known crystal structure and point to a formation of bimetallic Ni-Au nanoparticles in the oxidation products. Air oxidation of the acetonitrile solutions without additional oxidants/promoters goes very slowly whereas addition of Me_3NO results in immediate precipitation. The nanoparticles formed upon the oxidation are suggested to have a core of gold atoms and an outer shell of nickel oxide.

1. Introduction

Transition metal nanoparticles have attracted significant attention over the last decade [1–3]. Their potential application areas encompass, among others, catalysis, medicine, and electronics. One of the most promising synthetic approaches to metal nanoparticles is a controlled chemical transformations of well-characterized molecular precursors, *e.g.* high-nuclearity cluster compounds [2]. Up to date, a wealth of stoichiometric cluster compounds with cluster cores ranging from highly ordered fragments of close packings to loose irregular agglomerates are known [3], which can be used as building blocks in a design of new metal-based nanostructured materials. An especially important class of these materials consists of bimetallic nanoparticles, which allow fine tuning of the materials' properties due to a variability of their chemical compositions and spatial distributions of the component metal atoms in cluster cores [4].

Recently, a new high-nuclear stoichiometric bimetallic carbonyl cluster $[Au_6Ni_{32}(CO)_{44}]^{6-}\cdot 6PPh_4\cdot 4.5CH_3CN$ was synthesized, isolated, and characterized by single-crystal X-ray diffraction by L. F. Dahl and his group [5]. According to the crystallographic data, the core of the cluster anion (Fig. 1) is built up of an inner Au_6 octahedron surrounded by a Ni_{32} shell. In the idealized D_{3d} point symmetry of the Au_6Ni_{32} bimetallic moiety, five types of Ni atoms are symmetrically non-equivalent (meanwhile, the crystallographic symmetry of the core is P-1 such that 16 Ni atoms are crystallographically independent). In overall, the structure is characterized by broad distributions of all interatomic contacts. Upon mild heating or chemical oxidation, this cluster readily loose its carbonyl ligands to form higher-nuclearity species. Therefore, it may be a convenient precursor in preparation of bimetallic Ni-Au nanoparticles.

XAFS spectroscopy is an important tool to study chemical transformations, which lead to a formation of nanoclusters, *e.g.* colloid metals [1, 6, 7]. Earlier, the oxidative aggregation of various stoichiometric palladium carbonyl-phosphine clusters exposed to air in toluene solutions, giving rise to f.c.c. Pd_n nanoparticles (where n is *ca.* 900) was monitored by us using Pd K-edge EXAFS and XRD [8].

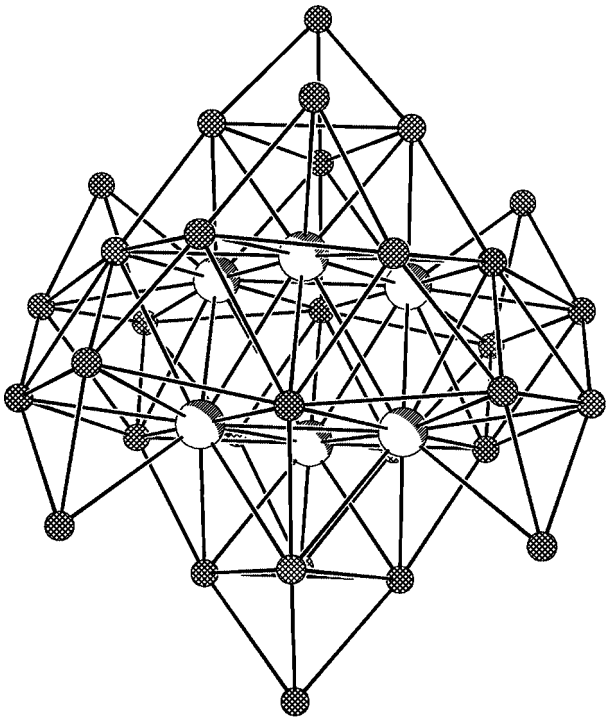

Fig. 1. Cluster core of the initial Au_6Ni_{32} cluster according to the X-ray crystallographic analysis [5]. Large spheres denote Au atoms, small spheres denote Ni atoms.

In this paper, we report on Au L_{III}- and Ni K-edge XAFS monitoring of the evolution of the $[Au_6Ni_{32}(CO)_{44}]^{6-}$ cluster anion in acetonitrile solutions upon oxidation. As it was shown elsewhere [9], Me_3NO readily transfer an oxygen atom to carbonyl ligands to form CO_2 and thus strongly promotes the overall oxidation of transition metal carbonyls in the presence of air. Thus, both oxidation routes with and without the promoter were studied.

2. Experimental

Polycrystalline cluster compound $[Au_6Ni_{32}(CO)_{44}]^{6-}\cdot 6PPh_4\cdot$ 4.5MeCN (hereinafter, referred to as Au_6Ni_{32}; 25 mg) was provided by Prof. Lawrence F. Dahl (University of Wisconsin-Madison, USA). Commercially available acetonitrile was further purified from air by Ar bubbling for 10 min. Two samples of dark brown acetonitrile solutions with a concentration of *ca.* 20 g/l for

*e-mail: obelyak@ineos.ac.ru

the first solution (**1**) and *ca*. 30 g/l for the second solution (**2**) were prepared by ultrasonication (1 min) of the respective amounts of Au_6Ni_{32} in *ca*. 0.5 ml of MeCN. For measurements, *ca*. 0.1 ml of both solutions were placed in small plastic cells, which were open to air. The rest of the two solutions, kept closed from air, maintained brown colour with some brown precipitate formed. In order to promote the oxidation, 3 mg of a mild oxidant Me_3NO (*ca*. 10 : 1 excess with respect to the initial cluster) dissolved in several drops of EtOH/MeOH mixture was added to the fraction of the solution **2** kept in a closed vessel for 10 hours. The brown colour of the solution immediatly disappeared and a brown flake-like precipitate evolved, which was separated afterwards onto a paper filter.

The polycrystalline powder of the initial Au_6Ni_{32} cluster (in Ar-blown polyethylene bags), solutions **1** and **2**, and the resulting precipitate were studied by XAFS in the fluorescence yield mode at the BL-9A bending magnet beamline of the Photon Factory synchrotron facility (KEK, Tsukuba, Japan) operated at 2.5 GeV with the electron current stored of 300 mA. The beam was focused on a sample by a system of conical Rh-coated mirrors to give a spotsize of $0.35 \times 1\,mm^2$. Intensity of the primary beam monocromatized by a Si(111) double crystal monocromator was measured by an ionization chamber filled with nitrogen; X-ray fluorescence yield was measured using a Lyttle detector. XAFS data for the air-exposed solutions **1** and **2** were collected repeatedly every 15–20 minutes (XANES) or 2–2.5 hours (EXAFS) with a total duration of 10 hours. The standard processing of EXAFS spectra was performed using the UWXAFS [10] software package with *ab initio* scattering amplitude and phase functions calculated by FEFF [11]. Normalized EXAFS curves $k^3\chi(k)$ over the k ranges of 2.6–12 $Å^{-1}$ for most of the spectra and 2.6–15 $Å^{-1}$ for the Au L_{III} spectrum of the precipitate were used in the curve-fitting.

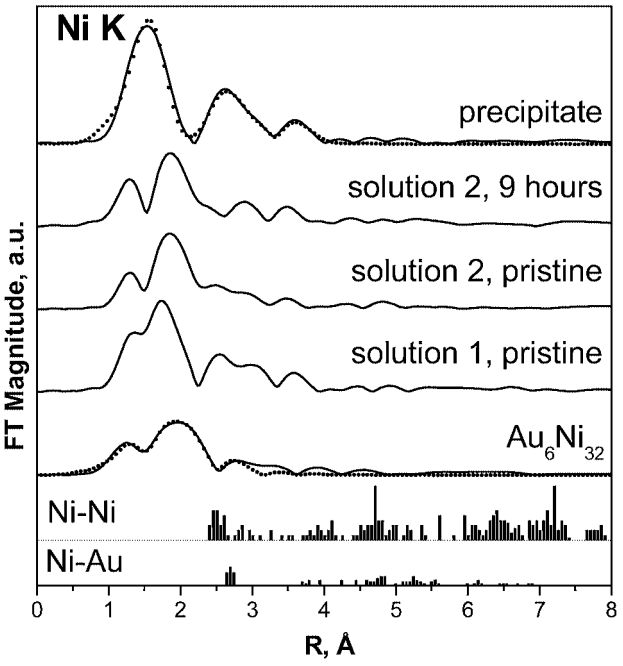

Fig. 2. Fourier transforms of Ni K-edge EXAFS spectra for the initial Au_6Ni_{32} cluster, pristine acetonitrile solutions **1** and **2**, solution **2** exposed to air for 9 hours, and the precipitate: experiment (solid lines) and best-fits (dots). Histograms of Ni-Ni and Ni-Au interatomic distances in the initial Au_6Ni_{32} cluster are shown for comparison.

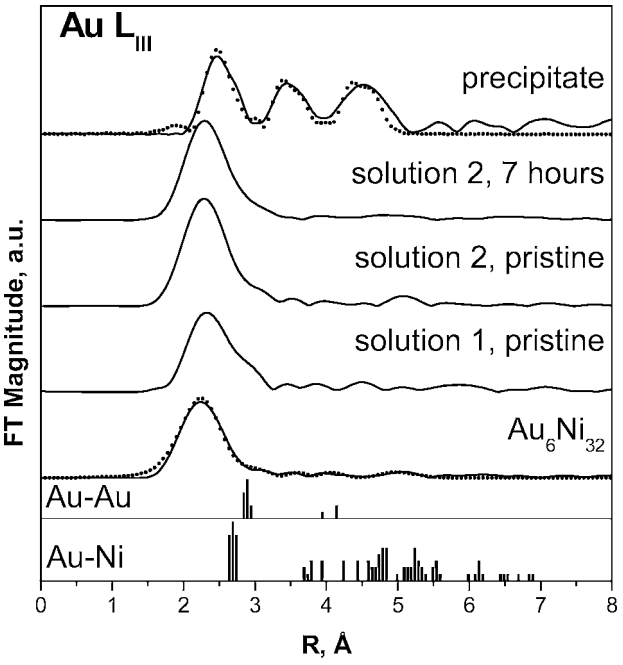

Fig. 3. Fourier transforms of Au L_{III}-edge EXAFS spectra for the initial Au_6Ni_{32} cluster, pristine acetonitrile solutions **1** and **2**, solution **2** exposed to air for 7 hours, and the precipitate: experiment (solid lines) and best-fits (dots). Histograms of Au-Ni and Au-Au interatomic distances in the initial Au_6Ni_{32} cluster are shown for comparison.

3. Results and discussion

Typical Fourier transforms (FTs) of Ni K- and Au L_{III}- edge EXAFS for the studied samples are shown in Figs. 2 and 3, respectively. Best-fit curves for the initial cluster and the resulting precipitate, are shown in dotted lines. Values of structural parameters corresponding to the best-fit structural models are summarized in Table I.

Due to the low symmetry of the Au_6Ni_{32} core in the initial cluster (see histograms of metal-metal distances shown in Figs. 2 and 3), fitting procedure of EXAFS spectra is challenging, especially in the case of Ni K-edge data. Nevertheless, a minimum required model of Au_6Ni_{32} composed of two Ni-C (Ni-C1 and Ni-C2), Ni-Ni, Ni-Au, and Ni . . . O spheres showed a pronounced similarity to the experimental Ni K-edge FT. The obtained best-fit values for the interatomic distances lie within the distribution limits of the respective parameters known from crystallographic data (see Table I). The FT pattern at Au L_{III}-edge even better corresponds to the structural model; its main peak is formed by overlapping contributions from closest Au-Ni and Au-Au distances. The pattern of relatively weak peaks at 3–5 Å can be well fitted to a set of outer spheres including non-bonding Au . . . C as well as Au . . . Ni and Au . . . Au separations in a good agreement with the crystallographic data.

The FTs of the precipitate are drastically different from those of the initial compound indicating a deep rearrangement of both the cluster core and the ligand shell due to the oxidation. The first dominant peak in the Ni K-edge FT can be well simulated with Ni-O scattering path at 2.03 Å that strongly suggests that a substitution of carbonyl ligands by oxygen atoms occurred. The shortest Ni-Ni distance is 2.93 Å according to the fitting results. Both these values are close to corresponding Ni-O and Ni . . . Ni distances in cubic crystalline nickel oxide NiO of NaCl type [12]. At Au L_{III}-edge, the FT is composed of three distinct peaks at *ca*. 2.45 Å, 3.45 Å, and 4.52 Å (not corrected for the phase shift). The high intensities of these peaks

Table I. *Best-fit values of EXAFS structural parameters for the initial Au_6Ni_{32} cluster and the final product of its oxidation by Me_3NO compared to X-ray diffraction data.*

	EXAFS			X-ray diffraction	
Path	R, Å	N	σ^2, Å^2	R/R_{mean}, Å	N_{mean}
Au_6Ni_{32}, Ni K-edge ($R_f = 0.03$)				Au_6Ni_{32} [5]	
Ni-C1	1.90	1.1	0.002	1.75–2.05/1.90	2.7
Ni-C2	2.08	1.6	0.002		
Ni-Ni	2.45	3.0	0.016	2.37–2.60/2.48	3.0
Ni-Au	2.74	1.5	0.007	2.62–2.76/2.68	1.5
Ni...O	2.77	2.7	0.009	2.83–2.94/2.89	2.7
Au_6Ni_{32}, Au L_{III}-edge ($R_f = 0.02$)				Au_6Ni_{32} [5]	
Au-Ni	2.64	8.0	0.014	2.62–2.76/2.68	8.0
Au-Au	2.92	4.0	0.021	2.83–2.94/2.89	4.0
Au...C	3.54	5.0	0.011	3.49–3.70/3.61	5.0
Au...Ni	3.76	3.0	0.020	3.66–3.94/3.79	3.0
Au...Au	4.05	1.0	0.005	3.95–4.15/4.07	1.0
Au...Ni	5.35	2.0	0.009	—	—
Precipitate, Ni K-edge ($R_f = 0.03$)				NiO [12]	
Ni-O	2.03	3.9	0.009	2.09	6
Ni-Au1	2.73	2.1	0.010		
Ni...Ni1	2.93	9.7	0.029	2.95	12
Ni...Au2	3.70	2.6	0.009		
Ni...Ni2	3.84	13.4	0.026	4.18	6
Precipitate, Au L_{III}-edge ($R_f = 0.05$)				Bulk Au [13]	
Au-Ni1	2.75	1.5	0.004		
Au-Au1	2.70	4.0	0.008	2.88	12
Au...Ni2	3.67	2.0	0.002		
Au...Au2	3.59	10.0	0.008	4.08	6
Au...Ni3	4.67	3.8	0.001		
Au...Au3	4.58	16.1	0.006	5.00	24

assume a relatively big cluster core with a well-ordered local environment of gold atoms [13]. According to the fitting results, both gold and nickel contribute to these three peaks with the gold contribution dominating. Furthermore, Ni-Au interatomic distances independently determined from Ni K- and Au L_{III}-edge data (Au-Ni1/Ni-Au1 and Au...Ni2/Ni...Au2 in Table I) are consistent. No fitting-improving Au-A contributions (where A denotes oxygen or other light atoms) were found.

In Ni K-edge XANES (Fig. 4), the pattern of the precipitate with a weak pre-edge feature and an intense main component ("white line"), is totally different from that of the initial cluster compound, which has a strong pre-edge peak and a weak white line. The pre-edge feature, which appears due to a forbidden $1s \rightarrow 3d$ electronic transitions is always prominent for compounds with direct Ni-Ni bonds. A strong reduction of this feature gives an evidence that a substantial part of Ni-Ni bonds was broken as a result of the oxidation in accordance with EXAFS data, where only non-bonding Ni...Ni closest distances are observed.

Therefore, our XAFS data indicate that nanoparticles composed of an Au core and a NiO outer shell are most probably formed upon the chemical oxidation of the initial $[Au_6Ni_{32}(CO)_{44}]^{6-}$ cluster anion with Me_3NO. It has to be mentioned that Au-Au interatomic distances (2.70 Å, 3.59 Å, and 4.58 Å) are significantly shorter than in the bulk f.c.c. gold (2.88 Å, 4.07 Å, and 4.99 Å, respectively) that may point to a different, *viz.* non-f.c.c, arrangement of Au atoms in cores of the Au-Ni nanoparticles. The Au-Au interatomic distances as short as 2.70 Å were also found in high-nuclearity gold cluster compounds by single crystal X-ray diffraction [14].

A comprehensive quantitative analysis of the FT patterns of acetonitrile solutions is too complicated since a lot of scattering

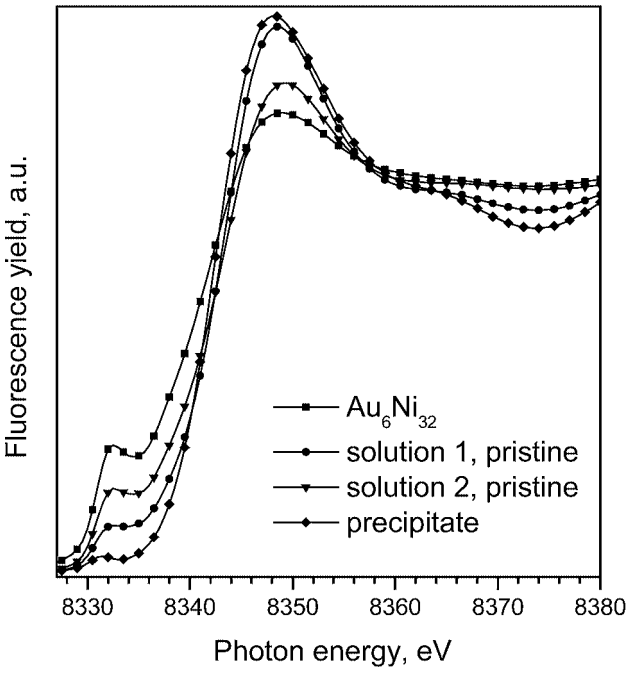

Fig. 4. Ni K-edge XANES spectra of the initial Au_6Ni_{32} cluster, pristine acetonitrile solutions **1** and **2**, and the precipitate.

paths has to be taken into account. Qualitatively, both pristine solutions show some differences in the shape of the first peak in Ni K-edge FT pattern as compared to that of the initial Au_6Ni_{32} cluster assuming a partial replacement of carbonyl ligands by oxygen species at Ni atoms. On the other hand, the two Au L_{III}-edge FTs of the solutions closely resemble that of Au_6Ni_{32} indicating that the Au_6 octahedron remains intact upon dissolution. Upon exposure to air for several hours, both solutions do not show any prominent changes as evidenced by time-resolved EXAFS and XANES series at Ni K- and Au L_{III}-edges (as a typical example, FTs for the solution **2** after 7–9 hours of air exposure are shown in Figs. 2 and 3). The changes, if any, can be reduced to an increase in the fraction of the unreacted Au_6Ni_{32} cluster. The most probable reason of that is a very slow oxidation of Au_6Ni_{32} in small amounts of MeCN solution by air (possibly, due to a formation of a thin film of oxidation products at a surface, which prevents further air access). Therefore, all the initial oxidation of the solutions **1** and **2**, most probably, takes place in a dissolution step, and thus the state of pristine solutions depend largely upon the preparation details, such as solvent pre-treatment. During air exposure, a slow precipitation withdraws insoluble oxidation products from the monitored area of the solution. In contrast, addition of Me_3NO causes immediate oxidation and precipitation of Au/Ni nanoparticles.

4. Summary and outlook

- An analysis of Ni K- and Au L_{III}-EXAFS spectra for the initial cluster compound $[Au_6Ni_{32}(CO)_{44}]^{6-}\cdot 6PPh_4\cdot 4.5CH_3CN$ yields values of structural parameters in a reasonable agreement with crystallographic data despite the heavy static disorder of the cluster core, which demonstrates applicability of EXAFS to similar high-nuclearity stoichiometric cluster compounds (see also [7, 8]).
- The oxidation product precipitated from the acetonitrile solution of the initial compound by Me_3NO was identified as a nanostructured material containing a core of Au atoms covered with a nickel oxide shell.

- Without addition of Me_3NO, the air oxidation of the acetonitrile solutions goes very slowly. A partial oxidation, most probably, occurs upon the preparation or ultrasonication of the solutions.
- In order to achieve a controlled oxidation of the initial cluster in a solution, chemical conditions of the reaction have to be adjusted (selection of protonic-aprotonic solvents mixtures, air blowing, or utilization of other mild oxidation promoters).
- Supplementary physical methods like XRD, IR, and HRTEM will be applied to verify the suggested structure of the final oxidation product.

Acknowledgements

Authors are indebted to Professor Lawrence F. Dahl (University of Wisconsin-Madison) who has kindly provided us with the initial Au_6Ni_{32} cluster and inspired this study. We are also grateful to Professor Edward Stern and Professor John Rehr (University of Washington, Seattle) for the UWXAFS and FEFF software, respectively. Authors also thank the KEK administration for the beamtime allocation and assistance in data collection. This work was supported by the Russian Foundation for Basic Research (grant #02-03-33225).

References

1. Schmid, G., Chem. Rev. **92**, 1709 (1992).
2. Guczi, L. *et al*., Top. Catal. **19**, 157 (2002).
3. Longoni, G. and Iapalucci, M. C. in "Clusters and Colloids. From Theory to Applications", (ed. by G. Schmid), (VCH, Weinheim, 1994), p. 91.
4. Vogel, W. *et al*., J. Phys. Chem. **101**, 11029 (1997).
5. Tran, N. T. *et al*., J. Am. Chem. Soc. **121**, 5945 (1999).
6. Moiseev, I. I. and Vargaftic, M. N. in "Catalysis by Di- and Polynuclear Metal Cluster Complexes", (ed. by R. D. Adams and F. A. Cotton), (Wiley-VCH, New York, 1998), p. 395.
7. Slovokhotov, Yu. L. in "Solid State Organometallic Chemistry: Methods and Applications", (ed. M. Gielen, R. Willem and B. Wrackmeyer), (Wiley, Chichester, 1999), p. 113.
8. Belyakova, O. A. *et al*., Book of abstracts, XAFS 11 conference (Ako, Japan, August 2000), P3-084, p. 274.
9. Shen, J.-K. *et al*., J. Am. Chem. Soc. **110**, 2414 (1988).
10. Newville, M. *et al*., Physica B **208&209**, 154 (1995).
11. Zabinsky, S. I. *et al*., Phys. Rev. B **52**, 2995 (1995).
12. Sasaki, S., Fujino, K. and Takeuchi, Y., Proc. Jap. Acad. **55**, 43 (1979)
13. Benfield, R. E. *et al*., J. Phys. Chem. B **105**, 1961 (2001).
14. Teo, B. K., Shi, X. and Zhang, H., J. Am. Chem. Soc. **114**, 2743 (1992).

Physica Scripta. Vol. T115, 709–713, 2005

Investigation of Size Effects in Magnetoelectric $BiFeO_3$

S. Chattopadhyay*[1,4], S. D. Kelly[2], V. R. Palkar[3], L. Fan[1] and C. U. Segre[4]

[1]CSRRI-IIT, MRCAT, Building 433B, Advanced Photon Source, Argonne National Laboratory, 9700 S. Cass Avenue, Argonne, Illinois 60439, USA
[2]Environmental Research Division, Argonne National Laboratory, 9700 S. Cass Avenue, Argonne, Illinois 60439, USA
[3]Tata Institute of Fundamental Research, Homi Bhabha Road, Mumbai 400005, India
[4]Biological, Chemical and Physical Sciences Department, Illinois Institute of Technology, Chicago, IL 60616, USA

Received June 26, 2003; accepted January 7, 2004

PACS number: 61.10.Ht

Abstract

Magnetoelectric materials may be applicable in magnetic and ferroelectric devices, because they exhibit both magnetic and electrical ordering over a range of temperatures. One of the few magnetoelectic materials is $BiFeO_3$. Large particles of (bulk) $BiFeO_3$ have a perovskite structure, a Neel temperature (T_N) of 380 °C, and a ferroelectric transition temperature (T_C) of 810 °C. Changing the particle size of $BiFeO_3$, to nanometer scale has been demonstrated to affect the magnetoelectric properties of this material. These changes may result from the small particle size of the nanoparticulate $BiFeO_3$ or may be due to local structural changes caused by the decrease in particle size. Nanoparticles of $BiFeO_3$ with a narrow size distribution are not easy to prepare. Nanoparticles were synthesized by using wet chemical techniques and were characterized by X-ray diffraction and scanning electron microscopy. Fe K-edge X-ray-absorption fine structure (XAFS) measurements were made of bulk and nanoparticulate $BiFeO_3$ to determine the local atomic structure about Fe. The XAFS results from the nanoparticulate $BiFeO_3$ show that the local structure about the Fe atoms to approximately 4.0 Å is the same as in the bulk $BiFeO_3$ sample. This result indicates that the decrease in the Neel Temperature (400° to 339 °C for these samples) with the decrease in particle size (1.4 μm to 20 nm) is not due to local structural changes about the Fe atoms as a result of the decrease in particle size.

1. Introduction

Magnetoelectric materials, also called multiferroics, exhibit both ferroelectric and magnetic ordering. Recent interest in these materials is driven by their potential application in sensors and memory devices. $BiFeO_3$ is one of the few magnetoelectric materials. The ferroelectric properties of $BiFeO_3$ exist in a wide range of temperatures vanishing at a high Curie temperature (T_C) of 820 to 850 °C [1, 2]. This material is also antiferromagnetic below the Neel temperature, T_N = 380 °C, exhibiting very weak magnetism at room temperature due to the presence of a residual moment arising from a canted spin structure [3, 4]. The structure of $BiFeO_3$ deviates from the ideal cubic perovskite structure due to displacement of the Bi sublattice, and a deformation and twist of the FeO_6 octahedra [5–8]. At room temperature, $BiFeO_3$ possesses rhombohedral symmetry ($a = b = c = 5.6343$ Å, $\alpha = 59.348°$), containing two formula units per unit cell. An alternative hexagonal unit cell [5–8] contains six formula units of $BiFeO_3$ ($a = 5.5787$ Å, $c = 13.8688$ Å) (Figure 1).

Studies of the effect of finite particle size on the physical properties of oxides and in particular ferroelectric oxides have attracted much attention [9], although most early studies were restricted to ceramic particles with micrometer grain size [10, 11]. The recent development of several wet chemical techniques (solgel, microemulsion, coprecipitation, spray-pyrolysis, etc.) have made it possible to produce many oxides in a pure phase with a narrow size distribution of ultrafine particles. In this study

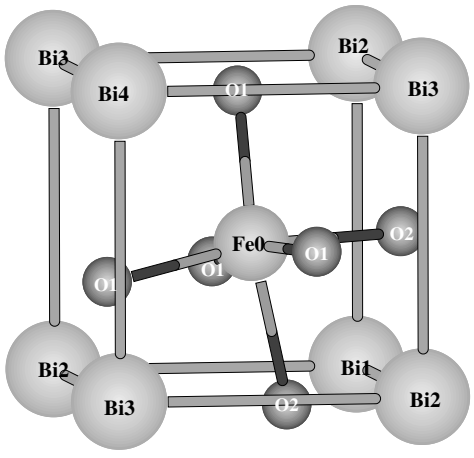

Fig. 1. Ball and stick model of one $BiFeO_3$ formula unit.

the coprecipitation technique was used to prepare the $BiFeO_3$ particles. $BiFeO_3$ is a partially covalent oxide. Previous studies have shown that as the particle size decreases for partially covalent oxides, there is an increase in unit cell volume and a distortion so that crystal symmetry increases [12]. In many of these compounds the physical properties are also affected by the decrease in particle size [13]. Size effect studies of nanoparticulate $BiFeO_3$ (23 to 80 nm) indicate that as the particle size decreases (a) the lattice expands, (b) the Neel temperature (T_N) decreases from 400 to 339 °C, and (c) the antiferromagnetic to paramagnetic transition becomes increasingly diffuse [14]. To understand these changes in the physical properties of $BiFeO_3$ as the particle size decreases, XAFS measurements have been made at the Fe and Bi edges at several temperatures and on several samples with varying particle sizes. This paper reports our first results on this large collection of data, where we compare the Fe K-edge data collected at 20 K for the BULK (1400 nm) and NANO (20 nm) $BiFeO_3$. Previous EXAFS studies of a similar material $BaTiO_3$ showed that the magnitude of the Ti atom's off-center displacement does not depend on particle size [15]. We are not aware of any previous EXAFS studies of nanoparticulate $BiFeO_3$.

2. Experimental Section

Pure single-phase particles of $BiFeO_3$ were prepared by using a wet-chemistry coprecipitation technique. Briefly, bismuth trioxide (Bi_2O_3) and ferric oxide (Fe_2O_3) of 99.9% purity were measured in stoichiometric proportions and dissolved in concentrated nitric acid. The solution was diluted with deionized water to bring the concentration level to 10% weight/volume. Bi and Fe cations were simultaneously coprecipitated with

*soma@agni.phys.iit.edu

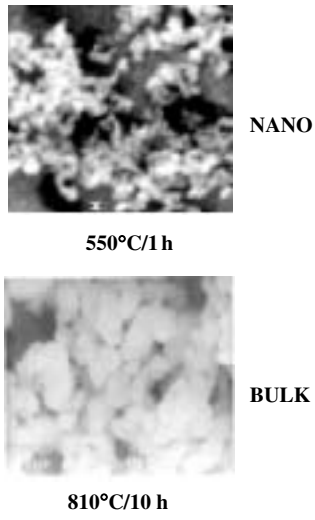

Fig. 2. SEM image of the NANO and BULK samples.

ammonium hydroxide. The precipitate was filtered and washed with deionized water until the pH reached 7. The washed precipitate was dried under an infrared lamp and thermogravimetric analysis (TGA) on the resultant precursor determined its calcination temperature. Weight loss was found to be complete by 500 °C, implying that the precursor should be heated above 500 °C to obtain $BiFeO_3$. Nanoparticulate (NANO 20 nm) and bulk (BULK 1400 nm) $BiFeO_3$ were synthesized by heating the precursor to 550 °C for 1 hour and 810 °C for 10 hours, respectively. The bulk heating temperature was chosen because Bi volatizes above 850 °C.

The samples were characterized with high-resolution X-ray diffraction (HR XRD) and scanning electron microscopy (SEM) measurements (see Fig. 2). HR XRD measurements (MRCAT ID-10 beamline at the Advanced Photon Source) verified the purity of the sample, and accurately determined the lattice parameters and particle sizes of the samples. The samples were packed in capillaries (2 mm diameter) that were rotated during the measurement in transmission mode. LaB_6 was used as a calibration standard. The size of the fine particle and the bulk samples was determined from full width at half maxima of the (012) peak using Scherrer's formula [16]. SEM measurements were used to determine the morphology of the particles.

The Fe K-edge EXAFS measurements were performed at the MR-CAT beamline [17] 10-ID at the Advanced Photon Source, Argonne National Laboratory. The samples were spread on tape. Several layers were stacked so that the thickness x of the samples corresponding to $\Delta\mu x = 0.5$, where $\Delta\mu$ is the jump of the absorption coefficient at the Fe K-edge energy. The samples were then loaded in a displex and cooled to 20 K. The energy of the monochromator was calibrated by simultaneously collecting the XAFS spectra from an iron foil. The undulator parameters (taper and gap) were optimized to obtain a large photon flux with nearly constant intensity within the scanned energy range of 6900 to 8400 eV. The Si(111) double crystal monochromator was scanned continuously so that the data was collected in quick EXAFS mode. A Rh harmonic rejection mirror was used to eliminate X-rays of higher harmonic energies. The incident and transmission photon intensity was measured by using ion chambers filled with the following gas mixtures, 80 : 20 $He : N_2$ and N_2, respectively. The size of the incident X-ray beam on the sample was 1 mm^2. The transmission measurements were collected over the scanned energy range of 6900 to 8400 eV with a step size of 0.4 eV and a dwell time of 0.5 s. For each sample, 10 scans were taken and then averaged.

Table I. *Size and lattice parameters for the fine particle sample (NANO) and the bulk sample (BULK) based on HR XRD measurements.*

SAMPLE	SIZE (nm)	a (Å)	c (Å)	Volume (Å^3)
BULK	1400	5.5789	13.8689	431.66
NANO	20	5.5824	13.8644	432.06

The data was processed using the FEFFIT package [18]. Background subtraction and data merging was done with Athena [19]. Theoretical models were constructed with the program FEFF7 [20] and the crystallographic atomic positions of $BiFeO_3$.

3. Results and Discussion

High resolution XRD data showed that the samples are phase pure. Table I gives the lattice parameters for the NANO and

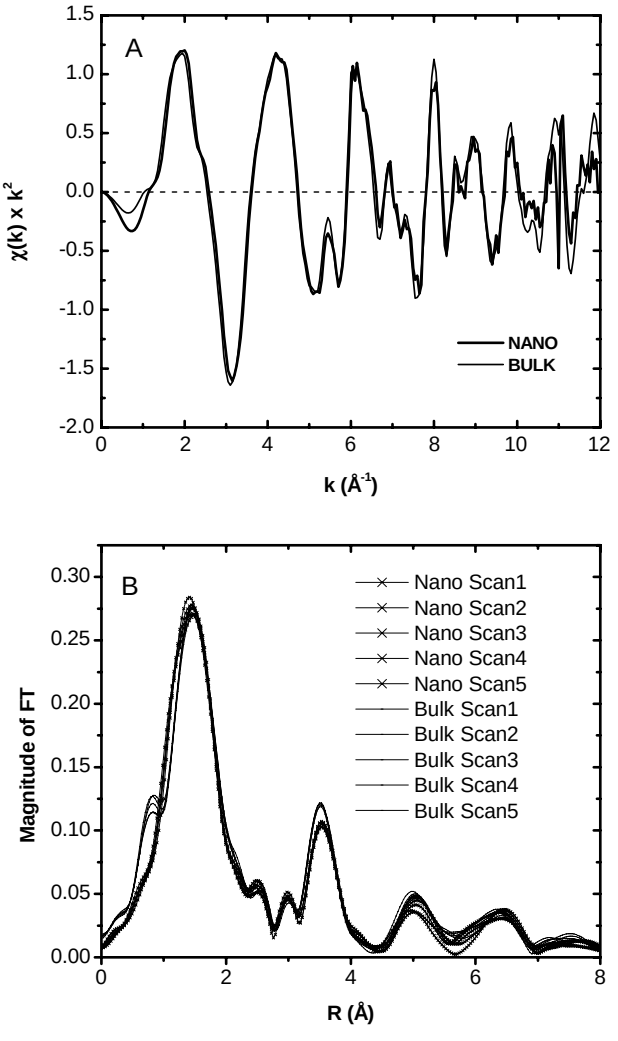

Fig. 3. Comparison of the EXAFS data from the NANO and BULK data sets. Panel A shows the average $\chi(k)$ data of 10 scans for the NANO and BULK data. The data ranges from 3.0 to 10.0 and 3.0 to 14.0 Å^{-1} are used for the fits to the NANO and BULK data sets, respectively. Panel B shows the magnitude of the Fourier transform (FT), k-weight of 1, for 5 of the Bulk and the NANO data sets using the data range from 3.0 to 10 Å^{-1} and a k-weight of 1. There is a systematic decrease in the second peak of the FT of the NANO data set as compared to the BULK data set.

BULK samples. These results show an expansion of the unit cell volume with the decrease in particle size from the BULK to NANO samples. However, for the first 7 coordination spheres this expansion corresponds to changes in distances between the Fe atoms and the neighboring atoms (0.000 to 0.002 Å) that are too small to resolve in an XAFS measurement. This result is confirmed by comparing the average $\chi(k) \cdot k^2$ data from the NANO and BULK samples (Fig. 3). Both data sets show the same phase (as the data sets cross zero at the same points) indicating that the distance between the Fe atoms and its neighbors are the same for both samples, but there is a systematic reduction in the amplitude of the signal from the NANO sample as compared to the BULK sample. This reduction in amplitude is small but reproducible for each of the 10 scans collected on both the NANO and BULK samples. To demonstrate the reproducibility of the data, Figure 3b shows the magnitude of the Fourier transform (FT) from 5 of the individual scans from the NANO and BULK data set showing a consistent and systematic decrease in the second peak height. Since each of the individual scans clearly shows a grouping that is tighter than the differences in the NANO to BULK data sets we are confident that this decrease in the amplitude of the EXAFS signal for the NANO data set relative to the BULK data set is larger than the uncertainty in the measurements.

Both data sets were fit simultaneously in *R*-space by using a *k*-weighting of 1, 2 and 3 in the FT of the data. The model for the data contains all paths from the reduced $BiFeO_3$ unit cell (Figure 1). Table II lists these paths and the EXAFS parameters. The model includes a $S_0{}^2$ value, a single third cumulant for the first and second oxygen shells, four energy shift values for each of the atom types and six σ^2 values grouped depending on the atom types and distances. This model has a total of 13 variables. The need for a third cumulant was tested by modeling the data with and without the third cumulant. The reduced-chi square value decreased by approximately 40% with the inclusion of a third cumulant (53 to 32); therefore it was included in the model. To test the NANO data for any changes relative to the BULK data, the model was simultaneously optimized to both data sets with exactly the same parameters. The magnitude and real part of the data and model are shown in Figure 4. Overall the model can describe most of the features in both data sets simultaneously, but the amplitude of the model is too large for the second peak in the FT for the NANO particulate data. The model can be corrected by fitting the second peak from 2.8 to 4.0 Å with an additional scaling factor for the coordination numbers of the Bi, Fe and O_3 shells for the NANO particulate data set. Parameters from shells in this region were re-optimized while parameters determined from the first shell were held to the values previously determined. The fit results for both of these fits to the data are listed in Table III. The coordination numbers were determined to be $7 \pm 4\%$ smaller in the NANO particulate sample than predicted by the $BiFeO_3$ crystal structure. The magnitude and real part of the data and model are shown in Figure 5.

The results of the simultaneous fit to the BULK and NANO data sets show very similar local structure for the nanoparticulate $BiFeO_3$ data relative to the bulk $BiFeO_3$ structure. The identical

Table II. *List of paths included in the XAFS model of the $BiFeO_3$ data. The path description includes the atom types (Path), the number of paths (Number), and the initial half path length (Reff). The XAFS parameters include a change in the half path length (Δr), the mean-square displacement of the half path length (σ^2), and an energy shift (ΔE). Changes in the half path lengths are parameterized in terms of a single expansion coefficient α. The values in Bold are the first occurrence of each parameter. In addition to the parameters listed an $S_0{}^2$ value and a third cumulant for the first two oxygen shells were determined in the fit. There are a total of 13 parameters for this model.*

Path	Number	*R*eff (Å)	Δr	σ^2	ΔE
Fe-O1	3	1.957	**α**·Reff	**σ^2o1**	**eo1**
Fe-O2	3	2.111	α·Reff	**σ^2o2**	eo1
Fe-Bi1	1	3.062	α·Reff	**σ^2bi1**	**ebi1**
Fe-Bi2	3	3.307	α·Reff	σ^2bi1	ebi1
Fe-O1-O2	24	3.447	α·Reff	**σ^2o1o2**	eo1
Fe-Bi3	3	3.579	α·Reff	σ^2bil	ebi1
Fe-Bi4	1	3.872	α·Reff	σ^2bi1	ebi1
Fe-Fel	6	3.964	α·Reff	**σ^2fe1**	**efe1**
Fe-Fe1-O1	12	4.016	α·Reff	σ^2fe1	0.5efe1+0.5eo1
Fe-O1-O2	6	4.051	α·Reff	$2 \cdot \sigma^2$ol	eo1
Fe-O1-Fe-O2	6	4.068	α·Reff	$2 \cdot \sigma^2$ol	eo1
Fe-O1-Fe1-O1	6	4.068	α·Reff	$4 \cdot \sigma^2$ol	0.7efel+0.3eo1
Fe-O3	6	4.053	α·Reff	**σ^2o3**	**eo3**
Fe-O1-O3	12	4.538	α·Reff	σ^2o3	eo3
Fe-O1-O3-O1	6	4.538	α·Reff	σ^2o3	eo3

Table III. *Best fit values from the simultaneous fits to the NANO and BULK data sets. For the first fit from 1.0 to 4.0Å there is an average of 7 variables for the model and 15 and 20 independent points for the NANO and BULK data sets. The best-fit value for $S_0{}^2$ is 0.80 ± 0.05, and for alpha is 0.003 ± 0.001, and for the third cumulant is 0.0003 ± 0.0001 Å^3 for both the data sets. The NANO data set has an additional energy shift relative to the BULK data set of 0.8 ± 0.4 eV. For the second fit from 2.8 to 4.0Å there is an average of 4 variables. The best-fit value for the reduction in amplitude of the Bi, Fe and O_3 shells is 7 ± 4%. Values without uncertainties were not determined in the fit but held at the values determined from the first fit.*

Paths	*N*	*R* (Å)	σ^2 ($\times 10^3$ Å^2)	ΔE (eV)
Fit range from approximately 1.0 to 4.0Å				
Fe-O1-Fe	3	1.963 ± 0.002	2.4 ± 0.5	1.2 ± 0.3
Fe-O2-Fe	3	2.117 ± 0.002	4.4 ± 0.8	1.2 ± 0.3
Fe-Bi1-Fe	1	3.071 ± 0.003	2.6 ± 0.2	3.7 ± 0.8
Fe-Bi2-Fe	3	3.317 ± 0.003	2.6 ± 0.2	3.7 ± 0.8
Fe-O1-O2-Fe (triangle)	24	3.457 ± 0.003	16.2 ± 8.0	1.2 ± 0.3
Fe-Bi3-Fe	3	3.590 ± 0.003	2.6 ± 0.2	3.7 ± 0.8
Fe-Bi4-Fe	1	3.884 ± 0.003	2.6 ± 0.2	3.7 ± 0.8
Fe-Fe1-Fe	6	3.976 ± 0.004	2.5 ± 0.5	3.6 ± 0.7
Fe-Fe1-O1-Fe	12	4.028 ± 0.004	2.5 ± 0.5	2.4 ± 0.5
Fe-O1-O2-Fe	6	4.029 ± 0.004	4.8 ± 1.0	1.2 ± 0.3
Fe-O1-Fe-O2-Fe	6	4.063 ± 0.004	4.8 ± 1.0	3.6 ± 0.7
Fe-O1-Fe-O1-Fe	6	4.080 ± 0.004	9.6 ± 2.0	2.0 ± 0.4
Fe-O3-Fe	12	4.082 ± 0.004	4.4 ± 6.8	5.4 ± 1.4
Fe-O1-O3-Fe	6	4.517 ± 0.004	4.4 ± 6.8	5.4 ± 1.4
Fe-O1-O3-O1-Fe	6	4.617 ± 0.004	4.4 ± 6.8	5.4 ± 1.4
Fit range from approximately 2.8 to 4.0Å				
Fe-Bi1-Fe	1	3.071	2.6 ± 0.1	3.7
Fe-Bi2-Fe	3	3.317	2.6 ± 0.1	3.7
Fe-Bi3-Fe	3	3.590	2.6 ± 0.1	3.7
Fe-Bi4-Fe	1	3.884	2.6 ± 0.1	3.7
Fe-Fe1-Fe	6	3.976	2.4 ± 0.1	3.6
Fe-Fe1-O1-Fe	12	4.028	2.4 ± 0.1	2.4
Fe-O3-Fe	12	4.082	5.4 ± 4.1	5.4
Fe-O1-O3-Fe	6	4.517	5.4 ± 4.1	5.4
Fe-O1-O3-O1-Fe	6	4.617	5.4 ± 4.1	5.4

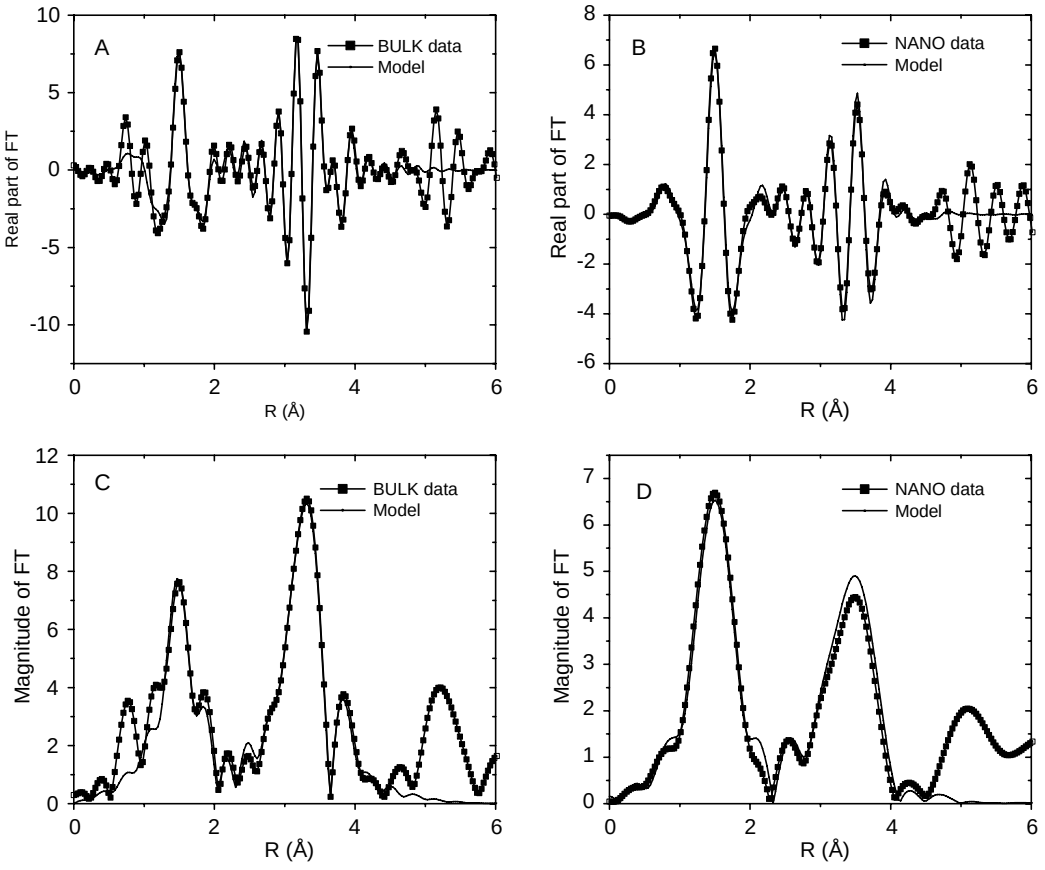

Fig. 4. The real part and magnitude of the Fourier transform (FT), k-weight of 3, of the NANO (B and D) and BULK (A and C) data and model fit. The fit range is from 1.0 to 4.0 Å.

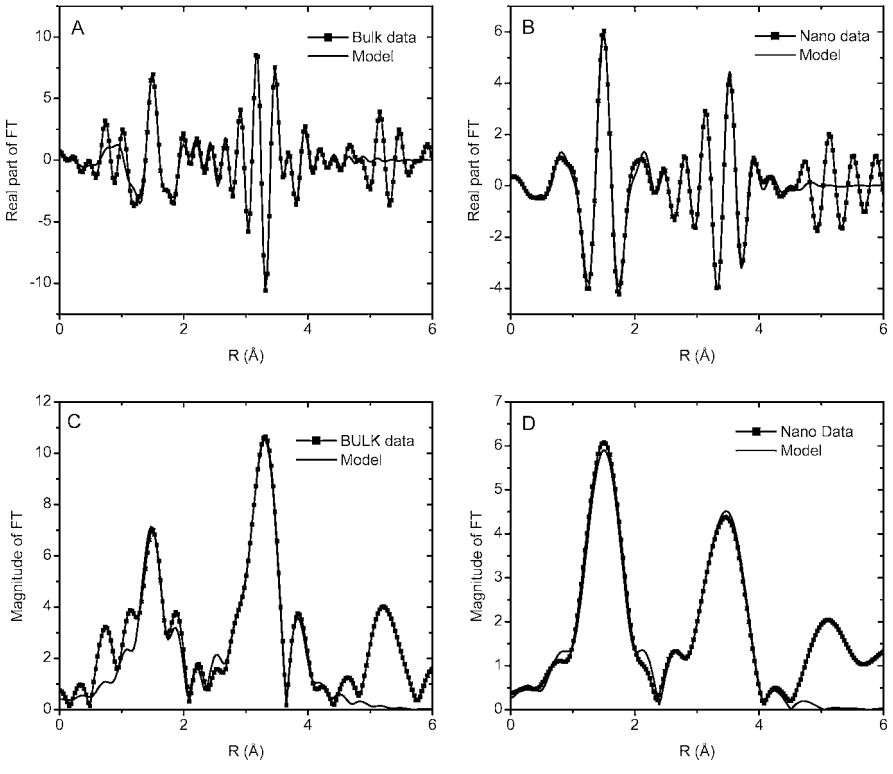

Fig. 5. The real part and the magnitude of the Fourier transform (FT), k-weight of 3, of the data and the fit for the NANO (B and D) and the BULK (A and C) samples. The fit range is from 2.8 to 4.0 Å.

model applied to both data sets as shown in Table III and Figure 4 illustrates the similarities in the data sets as the model describes both very well without the need of any independent parameters. This model only fails to reproduce the second peak height in the NANO data set by approximately 5%. By allowing the shells that contribute in this region to have reduced coordination number the model is able to describe both data sets (See Fig. 5). The decrease in the coordination number of $7 \pm 4\%$ for the NANO data set is consistent with the expected decrease in coordination number expected for 20 nm particles. A 20 nm particle should have an average coordination number of 7.6 Bi atoms at approximately 3.5 Å as compared to the bulk value of 8.0 Bi atoms. This calculation was made by assuming a uniform density of Fe atoms within a spherical particle with a 20 nm diameter and also with the assumption that the Fe atoms on the surface are coordinated with half as many (4) Bi atoms. So we infer that, though a decrease of particle size from 1400 nm to 20 nm is sufficient to bring about a decrease in the antiferromagnetic Neel temperature of the $BiFeO_3$ nanoparticles, it fails to affect the local structure of the Fe atoms in the NANO samples. We presume that this is a consequence of the presence of only ∼7% of the atoms on the surface of the material. With further decrease of the particle size and hence with increase in the number of surface atoms, it might be possible to see distinguishable changes in the local structure around Fe atoms and thereby further changes in the magnetic and electric properties of the material.

4. Conclusion

In conclusion, we have shown from our XAFS studies of the magnetoelectric $BiFeO_3$ system that, with decrease in particle size, there is no measurable change in the local structure within 4.0 Å of the Fe atoms in these samples. A more detailed study, currently in progress, which incorporates XAFS at the Bi L_{III} edge and multiple temperature measurements, may enable us to determine structural changes, if any. The results from this limited data set indicate that the changes in the physical properties of $BiFeO_3$ are likely due to the decreasing particle size rather than changes in the local structure about the Fe atoms.

Acknowledgements

MR-CAT is funded by the Department of Energy, Office of Energy Research under grant number DEFG0200ER45811. The APS is funded by the U. S. Department of Energy, Office of Science, Office of Basic Energy Sciences under Contract number W-31-109-Eng-38. The authors would like to thank Dr. Ken Kemner of Environmental Research division of Argonne National Laboratory and Prof. Vincent G. Harris of Northeastern University, Boston, for their comments and suggestions during manuscript preparation.

References

1. Roginskaya, Y. E., Tomoshpolskii, Y. Y., Venevstev, Y. N., Petrov, V. M. and Zhdanov, G. S., Sov. Phys. JETP **23**, 47 (1966).
2. Polomska, M., Kaczmarek, W. and Pajak, Z., Phys. Stat. Solidi A **23**, 567 (1974).
3. Smolenskii, G. A. and Yudin, V. M., Sov. Phys. Solid St. **6**, 2936 (1965).
4. Smolenskii, G. A. and Chupis, I., Sov. Phys. Usp. **25**, 475 (1982).
5. Kubel, F. and Schmid, H., Acta Cryst. B **46**, 698 (1990).
6. Bucci, J. D., Robertson, B. K. and James, W. J., J. Appl. Crystallogr. **5**, 187 (1972).
7. Michel, C., Moreau, J.-M., Achenbach, G. D., Gerson, R. and James, W. J., Solid State Commun. **7**, 701 (1969).
8. Moreau, J. M., Michel, C., Gerson, R. and James, W. J., J. Phys. Chem Solids **32**, 1315 (1971).
9. Anliker, M., Brugger, H. R. and Kanzig, W., Helv. Phys. Acta **27**, 99 (1954).
10. Martirena, T. and Burfoot, J. C., J. Phys. C: Solid State Phys. **7**, 3182 (1974).
11. Srinivasan, M. R., Multani, M. S., Ayuub, P. and Vijayraghavan, R., Ferroelectrics **51**, 137 (1983).
12. Ayyub, P., Palkar, V. R., Chattopadhyay, S. and Multani, M. S., Phys. Rev. B **51**, 6135 (1995).
13. Chattopadhyay, S., Ayyub, P., Palkar, V. R. and Multani, M. S., Phys. Rev. B **52**, 13177 (1995).
14. Shetty, S., Palkar, V. R. and Pinto, R., Pramana – J. Phys. **58**, 1027 (2002).
15. Frenkel, A. I., Frey, M. H. and Payne, D. A., J. Synch. Rad. **6**, 515 (1999).
16. Warren, B. E., "X-ray Diffraction", Page 256 (Addison-Wesley, NY, 1969).
17. Segre, C. U. *et al.*, Synchrotron Radiation Instrumentation: Eleventh U.S. Conference **CP521**, 419–422 (2000).
18. Stern, E. A., Newville, M., Ravel, B., Yacoby, Y. and Haskel, D., Physica B **208** & **209**, 117 (1995).
19. Newville, M., J. Synchr. Rad. **8**, 322 (2001).
20. Zabinsky, S. I., Rehr, J. J., Andukinov, A., Albers, R. C. and Eller, M. J., Phys. Rev. B **52**, 2995 (1995).

Physica Scripta. Vol. T115, 714–716, 2005

Nucleation and Growth of Copper Nanoparticles on Silicon Surfaces

A. Singh, K. Luening, S. Brennan, T. Homma[#], N. Kubo[#] and P. Pianetta[*]

Stanford Synchrotron Radiation Laboratory 2575 Sand Hill Rd, Stanford, CA 94309, USA

Received June 26, 2003; accepted December 17, 2003

PACS numbers: 81.65.Cf, 81.70.Jb, 82.45.Yz

Abstract

The recent adoption of copper interconnect technology by the semiconductor industry, has led to great interest in understanding the mechanisms of copper metal deposition onto silicon wafer surfaces from ultra pure water (UPW) solutions. We have studied these processes by using total reflection X-ray fluorescence (TXRF) and X-ray absorption near edge spectroscopy (XANES) in a grazing incidence geometry to determine the surface concentration and chemical state of copper atoms on intentionally contaminated Si surfaces. These measurements established that in deoxygenated UPW, copper is deposited on the silicon surface in the form of metallic nanoparticles with sizes up to 16 nm. However, in non-deoxygenated UPW, the copper is incorporated uniformly into the silicon surface oxide as Cu oxide.

1. Introduction

For over 30 years, the device density of silicon integrated circuits has been increasing, leading to more stringent requirements for surface cleanliness. Metallic impurities on the silicon surface can degrade the performance of the ultra-thin SiO_2 gate dielectrics that form the heart of the individual transistors resulting in reduced process yields and decreased device reliability. In particular, transition metals such as Co, Cu and Fe can introduce deep level traps that lead to threshold voltage shifts of MOS transistors and a reduction of minority carrier lifetimes [1]. Moreover, metals such as Cu and Au are fast diffusers in silicon and can spread into active device areas during various silicon processing steps [2–4]. Presently, transition metal impurities must now be reduced to concentrations lower than the mid-10^9 atoms/cm^2 region in order to achieve acceptable yields with current processing technologies [5].

Various cleaning solutions are used to remove metal atoms, particles and organics from practical silicon surfaces. Most silicon cleaning methodologies are based on the RCA clean which was originally developed by Kern [6]. In this process, silicon wafers are first immersed in a high-pH solution consisting of 5 H_2O: 1 H_2O_2: 1 NH_4OH to remove organics. This is followed by an HF dip to strip any oxides from the silicon surface, and finally the wafers are submerged in a low-pH solution consisting of 6 H_2O: 1 H_2O_2: 1 HCl to remove metallic ions. Between cleaning steps, the wafers are rinsed with ultra-pure water (UPW). It is vital that the chemicals, and more importantly the UPW used in the rinse steps, be very clean as any contaminants present in the solutions will be deposited on the silicon surface.

Since cleaning solutions, especially UPW, can often be a source of contamination, understanding how metal species in solution interact with silicon surfaces is vital. An especially important contaminant is copper, particularly since the implementation of copper interconnect technology has increased the presence of copper in the process environment. Copper contamination on silicon surfaces from solution is affected by a variety of factors including defects on the surface, doping in the semiconductor, and pH value [7]. For metal contamination during the wet cleaning process, there are two alternative reaction pathways determined by the pH value of the solution. In lower pH solutions, metal ions are electrochemically reduced and deposited on the surface as metallic particles [8]. Conversely, in higher pH solutions which grow an oxide on the silicon surface, metal ions are precipitated and included in the forming oxide layer as a metal oxide/hydroxide [9]. Since UPW has a neutral pH, both reaction mechanisms are available for deposition of copper, therefore it would be expected that other factors, such as the amount of dissolved oxygen, would play an important role in the deposition of Cu on silicon surfaces from UPW solutions.

In this study, the effect of dissolved oxygen in UPW on the deposition of Cu on Si wafer surfaces is examined by using a variety of techniques. By using total reflection X-ray fluorescence with a synchrotron X-ray source (SR-TXRF) it will be shown that the dissolved oxygen content influences the amount of copper deposited from UPW solutions. In addition, it is possible to ascertain whether the deposited copper is atomically dispersed or particle-like in nature by measuring the copper fluorescence signal as a function of the angle of incidence of the incoming X-rays. Finally, the chemical state of the deposited copper is determined with X-ray absorption near edge spectroscopy (XANES).

2. Experimental

Samples were prepared by cleaving silicon wafers into 20 mm $\times$ 10 mm pieces, which were subsequently cleaned using a 4 : 1 sulphuric acid/hydrogen peroxide mixture ($H_2SO_4 = 96$ vol%; $H_2O_2 = 30$ vol%) for 10 minutes followed by a rinse in UPW. These samples were then dipped into a solution of 0.5% HF for 1 minute to prepare a clean, hydrogen terminated surface. In order to study the influence of oxygen in UPW rinses, de-oxygenated UPW was prepared by Argon sparging, reducing the dissolved O_2 content to 0.3 ppm. The non-deoxygenated UPW contains about 3 ppm of dissolved oxygen. Copper in a 2% nitric acid matrix was then introduced into the UPW at concentration levels ranging from 0.01 ppb to 1000 ppb and surface contamination was then accomplished by immersing the hydrogen terminated silicon samples into these solutions for 5 minutes.

To determine the resulting surface concentration of copper, these samples were analyzed with SR-TXRF at the wiggler beam line 6-2 at the Stanford Synchrotron Radiation Laboratory (SSRL). The details of the experimental apparatus and procedures have been published elsewhere [10]. Briefly, X-ray fluorescence in a glancing incidence geometry (0.1° angle of incidence) is used for both elemental quantification and XANES measurements. In addition, the detailed shape of the fluorescence intensity as a

[#]Waseda University, Dept. of Applied Chemistry, Shinjuku, Tokyo 169-8555, Japan.

[*]e-mail: pianetta@stanford.edu

function of angle is used to distinguish between contaminants that reside in a uniform surface layer versus those that exist as particles on the surface [11].

The XANES spectra were obtained between 8.940 keV and 9.2 keV at increments of 0.5 eV between 8.97 keV and 8.99 keV near the copper K edge, 1 eV above the edge between 8.99 to 9.060 keV, and 5 eV between 9.06 and 9.2 keV. The signal was integrated for 10 seconds per point for each scan and up to 30 scans were accumulated on the low concentration samples to achieve a high signal to noise ratio. Reference spectra for Cu metal, CuO and Cu_2O were obtained from bulk samples. The bulk spectra were then used in a least squares fitting procedure to determine the percentage of each copper species present in the copper contaminated silicon samples. The energy calibration was maintained by simultaneously measuring the spectrum of a Cu foil behind the sample using the part of the beam that passed over the wafer without being reflected.

3. Results and Discussion

Figures 1a and 1b show SR-TXRF measurements on two sets of silicon samples contaminated in deoxygenated and non deoxygenated UPW with copper concentrations of 10 and 100 ppb, respectively. These results clearly demonstrate that the amount of copper deposited on the silicon surface strongly depends on whether the UPW has been deoxygenated or not. When the copper in solution is below approximately 15 ppb, less copper is deposited for the deoxygenated UPW, however, at solution concentrations greater than 15 ppb, more copper is deposited when the UPW is deoxygenated. This suggests that the mechanism for copper deposition is clearly different between deoxygenated and non-deoxygenated solutions.

In addition, the Cu 1s XANES results in figures 2a and 2b provide insights into the chemical state of the deposited copper. These spectra were obtained from silicon samples that were contaminated in non-deoxygenated (figure 2a) and deoxygenated (figure 2b) UPW solutions with an intentional copper concentration of 100 ppb. A linear background subtraction

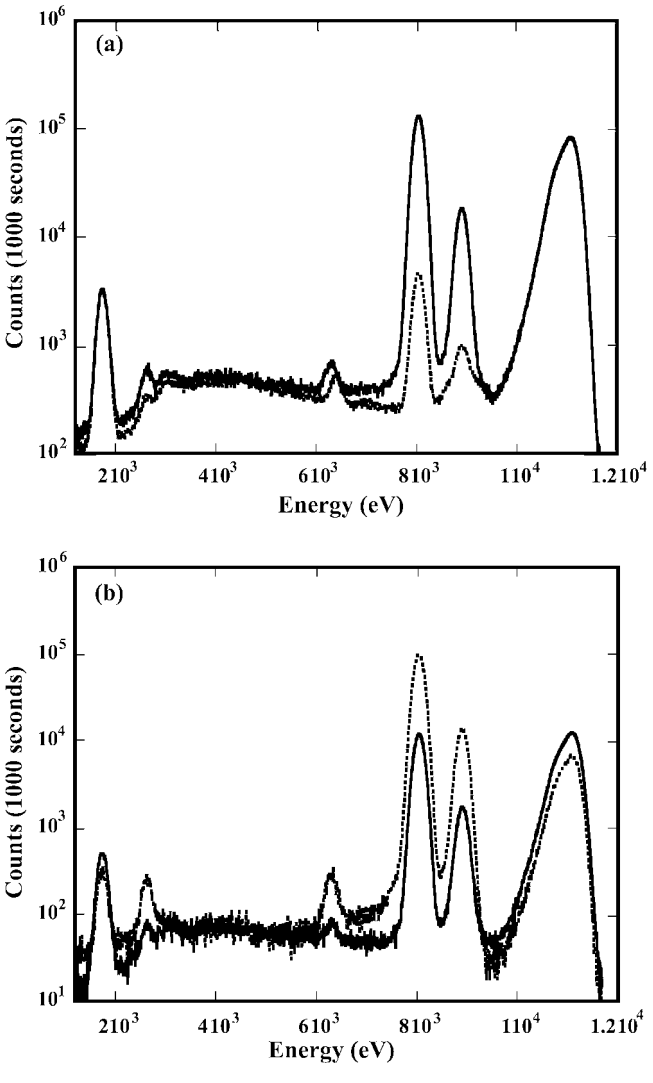

Fig. 1. TXRF spectra of silicon samples dipped in deoxygenated (dashed line) and non-deoxygenated (solid line) UPW contaminated with (a) 10 and (b) 100 ppb Cu. Note that at 10 ppb, less copper is deposited in the deoxygenated UPW and at 100 ppb, less copper is deposited in the non-deoxygenated UPW.

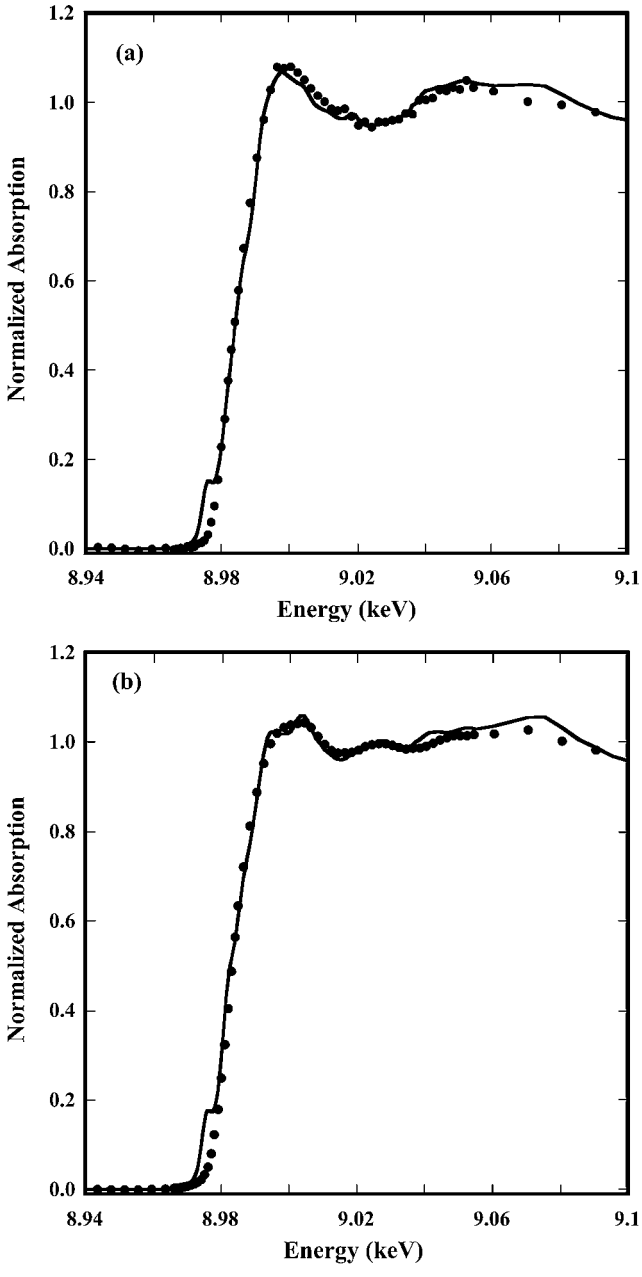

Fig. 2. Copper K-edge XANES spectra for silicon samples dipped in non-deoxygenated (a) and deoxygenated (b) UPW solutions that were contaminated with 100 ppb Cu. The overall fits are plotted as solid lines.

Table I. *Fractional contributions for the XANES fits shown in figure 2 for samples dipped in deoxygenated and non-deoxygenated UPW contaminated with 100 ppb Cu.*

	Deoxygenated	Non-deoxygenated
Cu metal	0.53	0.33
Cu (I) Oxide	0.30	0.27
Cu (II) Oxide	0.17	0.41

and normalization using a spline fit to the post edge region was conducted. Least squares fits were made between these spectra and the reference samples to determine the percentage contribution of copper metal, copper (I) oxide, and copper (II) oxide using the WinXAS program [12]. The numerical results of these fits are shown in table I. From these fits, it can be seen that the Cu deposited onto the silicon surface for the deoxygenated UPW has more metal character than that deposited from the non-deoxygenated UPW which contains less Cu metal and more of the Cu oxides. This provides evidence that, in the absence of dissolved oxygen, copper species in UPW will deposit reductively onto the silicon surface resulting in surface species that have significant metal character. On the other hand, the presence of dissolved oxygen inhibits reductive deposition and the copper species are preferentially incorporated into the growing oxide, resulting in surface species that are more oxide in character.

These results are further supported by measurements of the angular distribution of the fluorescence intensity as function of incidence angle which show that copper particle growth occurs in the deoxygenated UPW solution whereas the sample prepared in non- deoxygenated UPW gives a profile indicative of atomically dispersed copper near the silicon surface. A fit of the angle scan for the deoxygenated sample suggests the presence of nanoparticles with a mean diameter of 16 nm. This result is further confirmed by AFM measurements that show a large density of 20 nm high particles on the samples immersed in deoxygenated UPW.

In de-oxygenated solutions, our results confirm that the primary mode of Cu deposition is reductive, resulting in Cu metal cluster formation, while in non-deoxygenated solutions, Cu precipitates into the growing oxide as Cu oxide/hydroxide. However, at low concentrations such as 10 ppb, the concentration in the UPW is not high enough for metal cluster growth in deoxygenated solutions, and any deposited Cu is re-dissolved by the UPW solution. Therefore, the only Cu that is deposited at 10 ppb occurs by precipitation into the oxide. This mechanism results in higher amounts of deposited Cu for the air saturated solution, since an oxide grows more readily when compared to the deoxygenated solutions. Alternatively, at higher concentrations, such as 100 ppb, Cu cluster growth via the reductive mechanism can occur and therefore the amount of Cu deposited is higher for the de-oxygenated solutions since Cu is deposited both reductively and incorporated into the oxide.

4. Conclusion

It has been demonstrated that the deposition of copper onto silicon surface from ultra pure water solutions is strongly influenced by the presence of dissolved oxygen. TXRF measurements revealed that there is a concentration, above which the amount of copper deposited in deoxygenated UPW solutions was greater than that of non-deoxygenated UPW. Below this concentration threshold the reverse is true and the copper deposited is less for deoxygenated solutions. These differences suggest that the deposition mechanisms are influenced by the presence of dissolved oxygen and that reductive deposition occurs predominantly in deoxygenated UPW, while oxidative deposition primarily occurs in non-deoxygenated UPW. In addition, by measuring the Cu fluorescence as a function of angle, the presence of copper particles on the silicon surface was established for samples immersed in deoxygenated UPW. Finally, the chemical state of the deposited copper was determined using XANES. Samples immersed in deoxygenated UPW had a high metal Cu content, demonstrating that reductive deposition is the principal mechanism for deposition, while samples immersed in non-deoxygenated UPW had a high Cu(I) and Cu(III) oxide content, indicating that most the Cu deposited on the silicon surface was incorporated into the oxide.

Acknowledgements

We would like to thank the staff at SSRL for their expert technical assistance. This work was performed at SSRL, which is supported by the Department of Energy, Office of Basic Energy Sciences. The support of SIWEDS is also acknowledged.

References

1. Plummer, J. D., Deal, M. D. and Griffin, P. B., "Silicon VLSI Technology" (Prentice Hall, New Jersey, 2000) p. 155.
2. Weber, E. R., Appl. Phys. A **30**, 1 (1983).
3. Aboelfotoh, M. O. and Svendsson, B. G., Phys. Rev. B **44**, 742 (1991).
4. Shacham-Diamond, Y., Dedhia, A., Hoffstetterand, D. and Oldham, W. G., J. Electrochem. Soc. **140**, 2427 (1993).
5. "The International Technology Roadmap for Semiconductors 2002 Update" (Sematech, Austin 2002) p. 136.
6. Kern, W. and Puotinen, D. A., RCA Review **31**, 187 (1970).
7. Paunovic, M. and Schlesinger, M., "Fundamentals of Electrochemical Deposition" (Wiley and Sons, New York, 1998) pp. 133–161.
8. Morinaga, H., Suyama, M. and Ohmi, T., J. Electrochem. Soc. **141**, 2834 (1994).
9. Morinaga, H. *et al*., Mat. Res. Soc. Symp. Proc. **477**, 57 (1997).
10. Pianetta, P. *et al*., Thin Solid Films **373**, 222 (2000).
11. Klockenkaemper, R., "Total Reflection X-ray Fluorescence Analysis" (Wiley, New York, 1997).
12. Ressler, T., J. Synchrotron Radiation **5**, 118 (1998).

Physica Scripta. Vol. T115, 717–720, 2005

Electronic Characterization of the Single-Wall Carbon Nanotubes: a XANES Study

Z. Y. Wu[1,*)], I. Davoli[2], M. L. Terranova[3], S. Orlanducci[3], V. Sessa[3], M. Abbas[1], K. Ibrahim[1], J. Zhong[1] and S. Botti[4]

[1]Beijing Synchrotron Radiation Facility, Institute of High Energy Physics, P.O. Box 918, 100039 Beijing, China
[2]Dip. di Fisica and INFM, Università di Roma "Tor Vergata", Italy
[3]Dip. di Scienze e Tecnologie Chimiche and INFM, Università di Roma "Tor Vergata", Italy
[4]ENEA, Divisione Fisica Applicata, P.O. Box 65, 00044 Frascati, Italy

Received June 26, 2003; accepted November 4, 2003

PACS number: 61.10.Ht

Abstract

The electronic structure of two different samples of single wall carbon nanotubes (SWCNs) have been investigated using X-ray absorption near edge spectroscopy (XANES). The XANES data, detected around the C K edge, have been compared with that of a pure HOPG sample used as structural standard. The measurements have been carried out at the photoemission 4B9B beamline (Synchrotron Radiation Facility of the Institute of High Energy Physics of Beijing) using a surface-sensitive total electron yield technique. The samples were previously characterized using Raman spectroscopy, electron microscopy (SEM), and tunneling microscopy (STM). The bonding properties of C atoms (π^* and σ^* bands of sp^2–coordination) and the structural characteristics are identified by looking at the changes in both pre-edge and multiple-scattering regions of the XANES spectra.

The single-wall carbon nanotubes (SWCNs) were discovered in '93 [1] and are made purely of carbon atoms on a single sheet of graphite wrapped around a cylindrical axis. The same material with slight variations in the geometrical arrangement yields different electronic properties, ranging from metallic to semiconducting behavior. These nanosystems have fascinating chemical, mechanical and electrical properties which are remarkably different from those of any other carbon-based material and which suggest enormous potential applications in many technological areas, as catalysis, energy and gas storage, electron emitters, sensors, fast acting switches, molecular electronics, etc. [2–6]. In this contest it is very important to know and to control the electronic and chemical characteristics of the produced SWCNs.

Different methods were proposed to fabricate carbon nanotubes. The approach to the production of SWNCs used for this work relies on metal-catalysed reactions between atomic H and C nanopowders [7]. The amorphous C nanoparticles (diameter 40 ± 20 nm) are produced by cw-CO_2 laser-assisted pyrolysis of ethylene/acetylene mixtures in a flow-reactor [8]. The carbon nanotubes are generated using a CVD (Chemical Vapour Deposition) apparatus connected to a powder-flowing system formed by a powder reservoir, a mass flow controller and a final Mo nozzle which can be translated and rotated around the longitudinal axis. A scheme of the apparatus can be found in [9]. The C nanopowders are swept from the reservoir by Ar streams, and homogeneously distributed by the nozzle across the active area of the substrate where interaction with atomic H takes place. The main parameters of the synthesis process are: H_2 flowing rate 200 sccm; Ar flowing rate 40–60 sccm; substrate temperature 800–900 °C. The samples analyzed in this paper are representative of different kind or material which can be obtained by varying Ar flow rate and substrate temperature.

The produced nanotubes were deposited onto Si plates coated by a submicron dispersion of Fe particles.

Structural and morphological characterizations of SWCNs were carried out using Raman spectroscopy, electron microscopy (SEM), and tunneling microscopy (STM).

The SEM micrographs of Figs. 1 a) and b) show the morphology of two deposits formed by self-organized nanotubes joined together in bundles.

The STM analysis has been performed on a scanning probe microscope Jeol JSPM-4210, in low-vacuum conditions, at

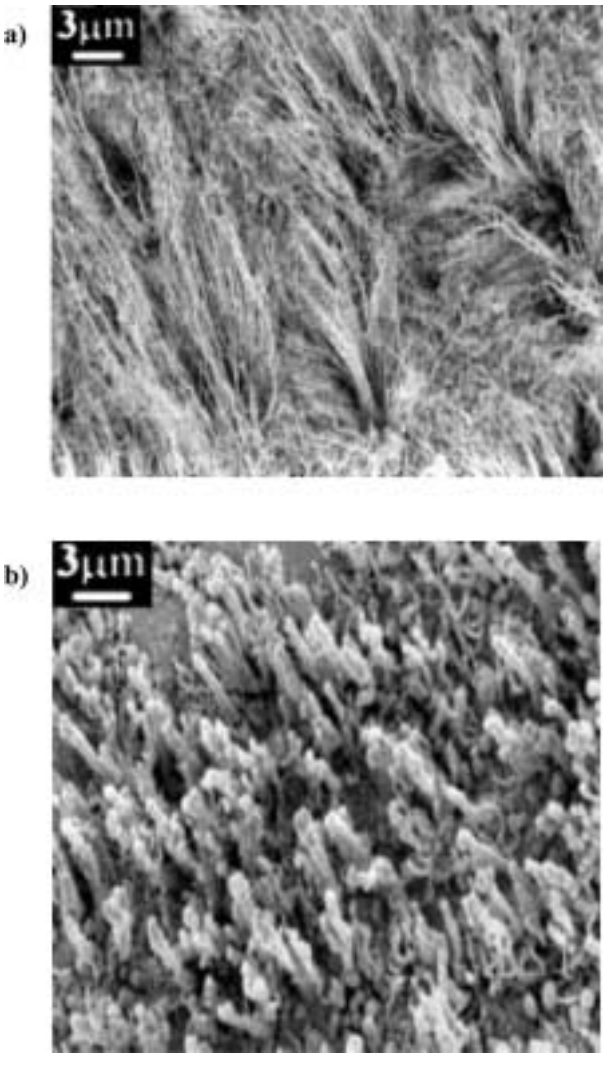

Fig. 1. SEM image of SWCNs deposits: a) sample 1; b) sample 2.

*)Electronic mail: wuzy@ihep.ac.cn and/or wuziyu@lnf.infn.it

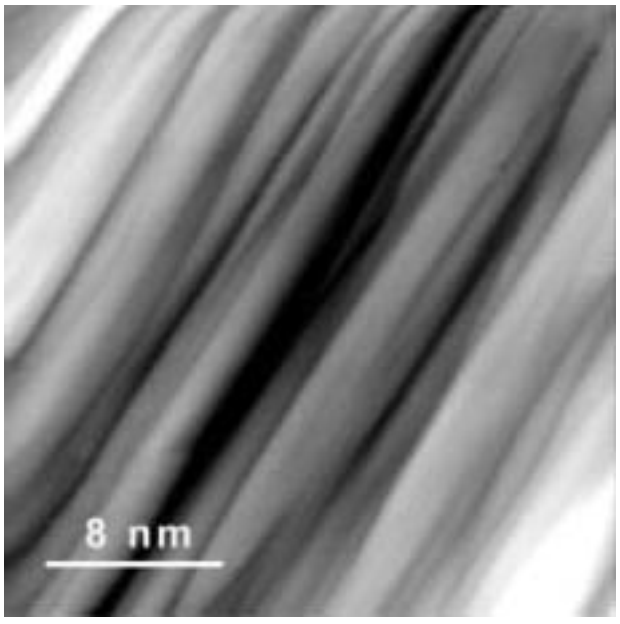

Fig. 2. STM image showing the assembling of the nanotubes in a bundle.

tunneling currents in the range 0.100–0.300 nA and at biases in the range 0.100–0.300 V.

STM image (Fig. 2) obtained from the same deposits of Fig. 1 a), allows to evidence a bundle formed by single wall carbon nanotubes aligned on a nanometric scale.

Further information about the structure of the nanotubes has been obtained by Raman analysis in the 80–400 cm^{-1} spectral region related to the Radial Breathing Mode (RBM) of SWCNs. The spectra were taken at room temperature in the backscattering configuration using an Ar^{-} ion laser beam (wavelength: 514.5 nm; laser power 10 mW; spectral resolution: 3 cm^{-1}). The analysis of the Raman spectra taken in the RBM region shows that under our catalytic growth conditions SWCNs are the dominant product (Fig. 3).

X-ray absorption spectroscopy (XAS) is a local structural technique of analysis based on the excitation of electronic transition from an inner level to outer unoccupied states. The photoabsorption process yields information on the local electronic structure and coordination environment around the absorbing atom. XAS techniques such as EXAFS (Extended X-ray Absorption Fine Structure) and XANES (X-ray Absorption Near Edge Structure) have been used extensively to investigate the local structure in the interior and at the surface, as well as bonding formation of a variety of solid-state materials [10–12].

The experimental set-up for the investigation of absorption spectra at the C K-edge is described in [13]. Samples were loaded in an ultrahigh vacuum chamber and maintained in a background pressure of $\sim 8 \times 10^{-8}$ Pa, although during the data acquisition the pressure rise up to $\sim 1 \times 10^{-7}$ Pa. The spectra are detected using the total electron yield (TEY) mode, a surface-sensitive detection method with a typical probing depth of a few nm. The photon energies used to record the C K-edge absorption spectrum range from 275 to 320 eV, and the experimental resolution at these photon energies is about 0.3 eV.

The C K-edge XANES spectra of the carbon nanotubes (samples 1 and 2) in TEY are reported in Fig. 4. According to the dipole-allowed transition selection rule, all spectral features are due to transitions from the carbon 1s core level to p-like final unoccupied states. The spectra show above the threshold well-resolved transition features (peaks *A* to *D*). From previous work [14–19], the two prominent transition features *A* and *C* at 285.5 and 293 eV may be associated with the existence of unoccupied π^* and σ^* bands, respectively. The behavior of transition peaks in both spectra are quite similar indicating that the short-range environment in both samples has the same structure. The spectral features *B* may be an indication of the σ^* resonance characteristic of C-H bonds [20–22] and are consistent with the growing conditions of our carbon nanotubes.

From the spectrum it is evident that the peaks of sample 2 are smoother compared to those of sample 1, which implies that the "medium-range" structure of SWCNs of sample 2 is more distorted and/or amorphous on the surface.

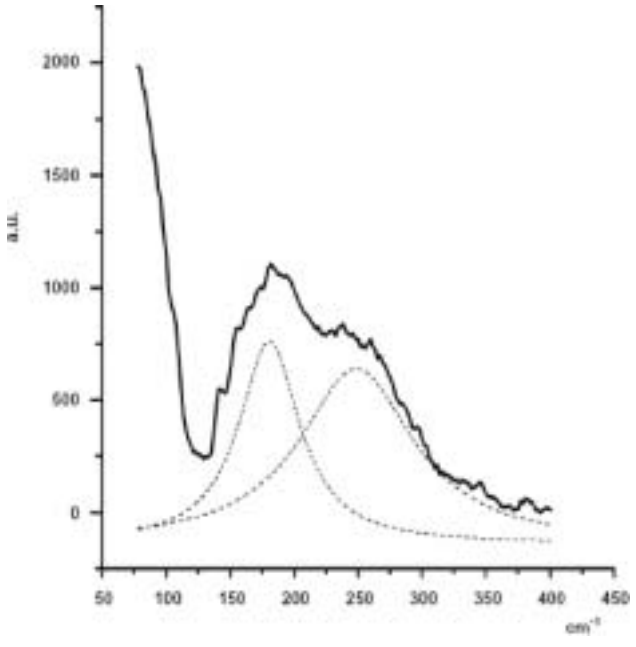

Fig. 3. Raman spectrum in the RBM region of a typical sample: the dashed line is the Lorentian fit to the experimental spectrum.

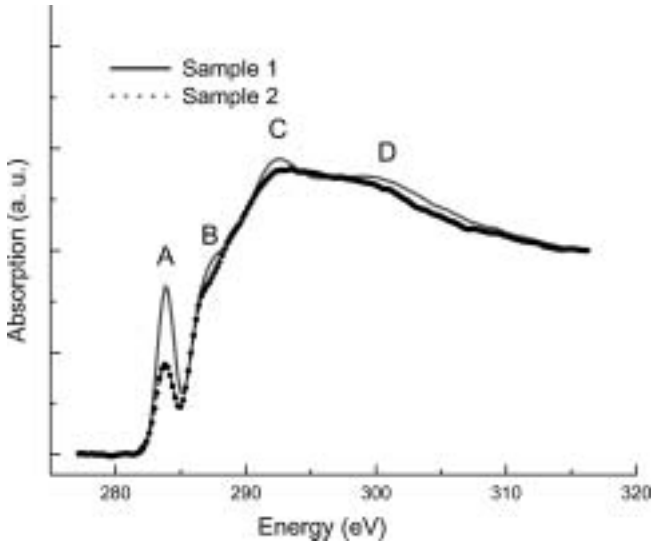

Fig. 4. The C 1s X-ray absorption spectra of sample 1 and sample 2 in total electron yield.

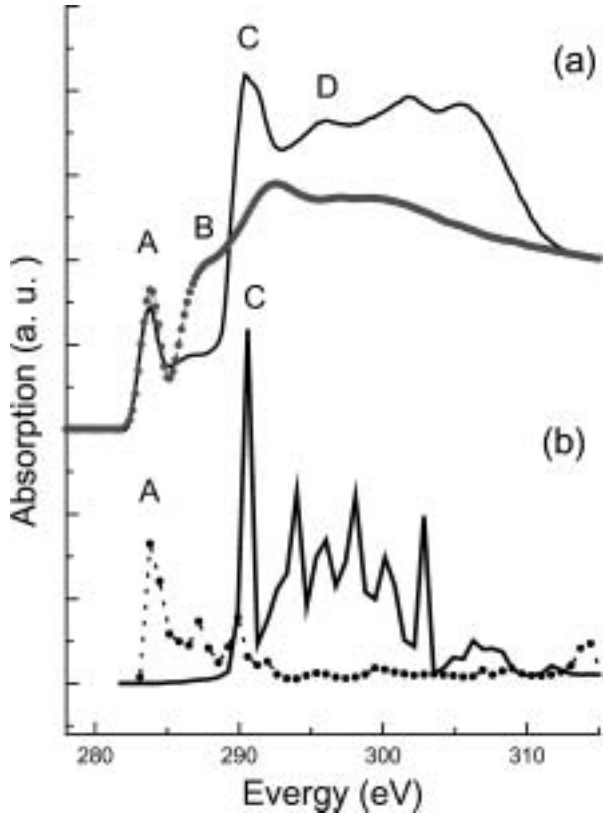

Fig. 5. (a) Comparison of the C K-edge XANES spectra of sample 1 (dot line) and highly oriented pyrolytic graphite (HOPG) in TEY (panel a). (b) Polarized multiple-scattering calculations of the C K-edge XANES of graphite: Z-component (dot line) and XY-components (solid line).

In Fig. 5(a) we present the comparison of the C K-edge XANES of sample 1 of SWCNs and the spectrum of highly oriented pyrolytic graphite (HOPG) in TEY. This latter spectrum exhibits a reasonable agreement with previous published data [14–18], i.e., as spectrum composed by three main features: an almost atomic contribution at about 285.5 eV, a peak (*A*) at about 293 eV (*C*) and the main large MS resonance centred at about 305 eV (*D*). The weak feature near 287.5 eV (*B*) was generally observed in the X-ray absorption spectra of graphite and attributed to the free-electron-like interlayer states in the graphite [23, 24]. If we look to the *A* structure, the intensity of this feature does not change significantly between CNT and HOPG, indicating that the structure just above the Fermi level is mainly a molecular interaction between the central atom and its nearest neighbour coordination shell (short-range effects), which addresses also a reasonable ordering of the carbon matrix. However, a difference between the spectra of SWCNs and HOPG can be recognized looking at the 289–320 eV region: the transition 1s $\rightarrow$ σ*-like states is less intense and fairly broadened in the SWCNs. This behaviour implies that the "long- or medium-range" atomic order deviates from graphite one (e.g. disorder and/or distortion effects). Actually in a bundle of self assembled nanotubes, carbon atoms experience an anisotropic geometry due to the fact that each C atom is bonded to the C atoms of the same graphene sheet and to the C atoms of the adjacent tubes. The anisotropic environment of the atoms can be certainly one of the causes of the distortion of the original trigonal structure. This mechanism, in turn, increases the number of distinct photoelectron scattering paths in a nanotube, yielding a broadening of the XANES spectrum. These effects may be due to a random phase decoherence among each set of closely similar multiple scattering paths and the variation in the threshold E_0 in the absorption coefficient [25]. Such effects could be also ascribed to the fact that the tubes in the bundles are not infinitely long neither perfectly straight. However, also the compositional disorder, i.e. the presence of H atoms of others impurities, leads to the smearing of near-edge features.

In Fig. 5(b) we present for comparison, the polarized XANES calculation of graphite using 215-atom cluster within a sphere of radius 7.5 A in the framework of the multiple scattering theory [26–30]. It is clearly evidenced in the dot line that the π* states (peak *A*) are reproduced in the Z-polarized component which corresponds to C $2p_x$ and $2p_y$ orbitals. This resonance is strong at grazing X-ray incidence, when the X-ray electric field vector has a large projection along the direction of the p orbital, and it is the weakest at normal X-ray incidence, when the electric field vector is perpendicular to the p orbital [19]. The corresponding 1s to σ* transitions around 293 eV appear in the XY-polarized calculation which contains the C $2p_z$ orbital and exhibits the opposite trend as expected since the σ* is orthogonal to the π*. It is work to notice that the position of σ* feature in SWCNs shifts towards higher energy than those in graphite indicating than the C-C distances in SWCNs are shorter than the one in graphite. The quantitative simulation are in progress and will be presented in a forthcoming paper.

The data at the C K edge in SWCNs and comparison with graphite show that structural and bonding configurations can be recognised looking at the characteristic pre-edge features. Moreover the investigation of the different features in the multiple-scattering region is found to be of fundamental importance to better understand topology and degree of order of these materials. These measurements can also be used to choose the chemical environment (i.e. H atmosphere) for the selected growth of SWCNs with specific properties.

Acknowledgements

Z.Y. Wu acknowledges the financial support by the *Key Important Nano-Research Program* (90206032) and of the *Outstanding Youth Fund* (10125523) of the National Natural Science Foundation of China, and also the Pilot Project of the Knowledge Innovation Program of Chinese Academy of Sciences (KJCX2-SW-N11).

References

1. Iijma, S. and Ichihashi, T., Nature **363**, 603 (1993).
2. Bockrath, M. *et al.*, Nature **397**, 598 (1999).
3. Yao, Z., Postma, H. W. J., Balents, L. and Dekker, C., Nature **402**, 273 (1999).
4. Avouris, P., Chem. Phys. **281**, 429 (2002).
5. Kasumov, Yu. *et al.*, Science **284**, 1508 (1999); Kociak, M. *et al.*, Phys. Rev. Lett. **86**, 2416 (2001).
6. Inagaki, M., "New Carbons – Control of Structure and Functions", (Elsevier Science, 2000).
7. Terranova, M. L. *et al.*, Mater. Chem. Phys. **874**, 1 (2000).
8. Botti, S., Coppola, R., Gourilleau, F. and Rizk, R., J. Appl. Phys. **88**, 3396 (2000).
9. Terranova, M. L. *et al.*, Chem. Phys. Lett. **327**, 284 (2000).
10. Hamad, K. S., Roth, R., Rockenberger, J., van Buuren, T. and Alivisatos, A. P., Phys. Rev. Lett. **83**, 3474 (1999).
11. Rehr, J. J. and Albers, R. C., Rev. Mod. Phys. **72**, 621 (2000).
12. Wu, Z. Y. *et al.*, Appl. Phys. Lett. **80**, 2973 (2002).
13. Liu, F. Q. *et al.*, J. Elect. Spectrosc. Rel. Phenom. **80**, 409 (1996).
14. Weng, X. D., Rez, P. and Ma, H., Phys. Rev. B **40**, 4175 (1989).
15. Bruhwiler, P. A. *et al.*, Phys. Rev. Lett. **74**, 614 (1995).
16. Bruley, J., Williams, D. B., Cuomo, J. J. and Pappas, D. P., J. Microscopy **180**, 22 (1995).
17. Tang, Y. H. *et al.*, Appl. Phys. Lett. **79**, 3773 (2001).

18. Imamura, M. *et al.*, Physica B **208&209**, 541 (1995).
19. Tang, Y. H., Sham, T. K., Hu, Y. F., Lee, C. S. and Lee, S. T., Chem. Phys. Lett. **366**, 636 (2002).
20. Stohr, J., "NEXAFS Spectroscopy", (Springer, New York, 1992).
21. Ishii, I. and Hitchcock, A. P., J. Electron Spectrosc. Relat. Phenom. **46**, 55 (1988).
22. Wesner, D. *et al.*, Phys. Rev. B **28**, 2152 (1983).
23. Fischer, D. A., Wentzcovitch, R. M., Carr, R. G., Continenza, A. and Freeman, A. J., Phys. Rev. B **44**, 1427 (1991).
24. Pickard, C. J., Ph.D. thesis, Christ's College, (1997).
25. Farges, F., Brown, G. E. and Rehr, J. J., Phys. Rev. B **56**, 1809 (1997).
26. Lee, P. A. and Pendry, J. B., Phys. Rev. **B 11**, 2795 (1975).
27. Natoli, C. R., Benfatto, M., Brouder, C., Ruiz Lopez, M. Z. and Foulis, D. L., Phys. Rev. B **42**, 1944 (1990); Tyson, T. A., Hodgson, K. O., Natoli, C. R. and Benfatto, M., Phys. Rev. B **46**, 5997 (1992).
28. Durham, P. J., Pendry, J. B. and Hodges, C. H., Solid State Commun. **38**, 159 (1981); Comput. Phys. Comm. **25**, 193 (1982).
29. Vvedensky, D. D., Saldin, D. K. and Pendry, J. B., Comput. Phys. Commun. **40**, 421 (1986).
30. Durham, P. J., in "X-ray Absorption: Principles, Applications, Techniques of EXAFS, SEXAFS, XANES", (edited by R. Prinz and D. Koningsberger), (Wiley, New York, 1988).

Physica Scripta. Vol. T115, 721–723, 2005

Structural Stability of Giant Polyoxomolybdate Molecules as Probed by EXAFS

Anatoly I. Frenkel*[1,2], Shira C. Frankel[2] and Tianbo Liu[3]

[1]Physics Department, Yeshiva University, 245 Lexington Avenue, New York, NY 10016, USA
[2]Stern College for Women, Yeshiva University, 245 Lexington Avenue, New York, NY 10016, USA
[3]Physics Department, Brookhaven National Laboratory, Upton, NY 11973, USA

Received June 26, 2003; accepted November 4, 2003

PACS numbers: 36.40.−c; 36.40.Qv; 61.10.Ht

Abstract

Recent progress in synthesis of "giant" polyoxomolybdate (POM) molecules that have a structure of hollow spheres or wheels and size of several nanometers in diameter has emphasized the need in their accurate structural investigation. Our temperature-dependent EXAFS studies demonstrated that the first generation POM molecules containing 132 Mo atoms, undergo irreversible structural transformations at ca. 500 K, while the recently synthesized second generation POM at ca. 400 K. The number of different structural units in these molecules can be accurately obtained from EXAFS analysis and compared with model structure calculations. In our method of analysis, we use theoretical calculations of pair radial distribution functions from the model structures as initial approximations to analyze the structures of these molecules. Our analysis allowed us to identify the new POM structure as a giant sphere, similar to the $\{Mo_{132}\}$ structure but containing 522 Mo atoms. Our results also demonstrate that the structural rigidity of different building blocks of these molecules can be quantitatively probed by EXAFS.

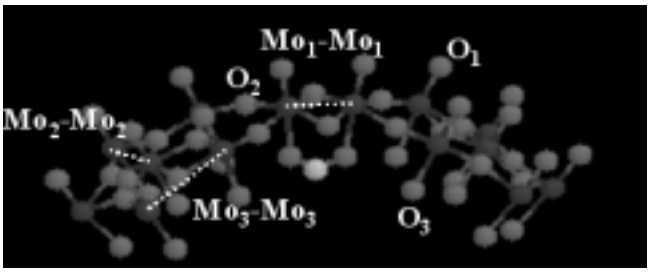

Fig. 1. Building blocks of the $\{Mo_{132}\}$ structure. Shown are $\{(Mo)Mo_5\}$ pentagons that have two types of Mo-Mo bonds: Mo_2-Mo_2 and Mo_3-Mo_3, and the $\{MO_2^{V}O_4\}$ bridges that have the third type of Mo-Mo bonds, denoted as Mo_1-Mo_1. Shown also are three types of oxygen atoms that belong to three distinct bond types: Mo-O_1, Mo-O_2, and Mo-O_3.

1. Introduction

In polyoxomolybdate (POM) molecules, that belong to a class of structurally underconstrained systems, a number of fascinating physical properties are expected. For example, in an analogous framework system, ZrW_2O_8, the presence of "rigid unit modes" (RUMs) was proposed to be the driving force of the recently discovered negative thermal expansion (NTE) [1]. These RUMs are a special class of "floppy modes" that were recently observed in amorphous and crystalline silicates, the transverse acoustic modes of a framework structure composed of rigid SiO_4 tetrahedra [2].

The building blocks of the $\{Mo_{132}\}$ structure can be visualized (Fig. 1) as containing 12 $\{(Mo)Mo_5\}$ pentagons with longer Mo-Mo distances and 30 $\{Mo_2^{V}O_4\}$ bridges that have shorter Mo-Mo bond lengths [3]. The structural data available from X-ray crystallography were processed by our software program that computes pair radial distribution functions (PRDF) $g_{AB}(r) = dN_{AB}/dr$ for A-B pairs (where element A is a central (absorbing) atom and element B is its neighbor. In the present case, the distributions were calculated for Mo-O and Mo-Mo neighbors. As it will be shown below, these calculations were essential to adequately analyze EXAFS data in the reference $\{Mo_{132}\}$ structure and apply the same analysis procedure to the unknown $\{Mo_N\}$ structure.

2. Synthesis and characterization of the 1st and 2nd generation "giant spheres"

The synthesis of the C_{60}-like $\{Mo_{132}\}$ and another even larger, hollow, spherical POM (likely to have the structure of 2nd generation of C_{60}-like) have been reported in literature [4, 5]. It is very easy to synthesize and grow $\{Mo_{132}\}$ single crystals that can be used for structure determination by single crystal X-ray diffraction experiments. However, for the larger POM, the final products are usually powders or tiny crystals. Small-angle X-ray scattering measurements showed ordered 5.2-nm primitive cubic packing of the single POM molecules, indicating the new POM molecules are extraordinarily large (for comparison, $\{Mo_{132}\}$ has the size of 2.9 nm), but the molecular structure of the new POM cannot be directly determined. We describe here that convincing evidence can be obtained from EXAFS measurements by realizing that the basic building units for various POMs are the same.

3. EXAFS measurements and analysis of the nano-spheres

EXAFS measurements were performed at the beamline X16C of the National Synchrotron Light Source (NSLS). Both types of samples, the $\{Mo_{132}\}$ and the 2nd generation $\{Mo_N\}$ spheres, were measured in transmission at different temperatures (from 140 K to 473 K) under nitrogen flow, using a custom-designed and built catalyst cell. Above ca. 500 K, the $\{Mo_{132}\}$ samples underwent irreversible structural transformations. The onset of the irreversible changes was lower (ca. 400 K) for the $\{Mo_N\}$ samples. Irreversibility was checked by comparing the data measured at 300 K before and after thermal treatment.

Different groups of Mo-O and Mo-Mo bonds can be observed in Fig. 2 that shows raw EXAFS data. Next to the horizontal axis in Fig. 2 (B), the PRDF plots are also shown. Comparison between the *r*-space data and X-ray crystallography results visualized by the PRDF plots demonstrates that EXAFS contains unique information on each of the structural groups (3 Mo-O groups and 3 Mo-Mo groups, Fig. 1). For example, the peak at ca.1.2 Å in Fig. 2 (B) corresponds to the Mo-O_1 axial pair in

*e-mail: frenkel@bnl.gov

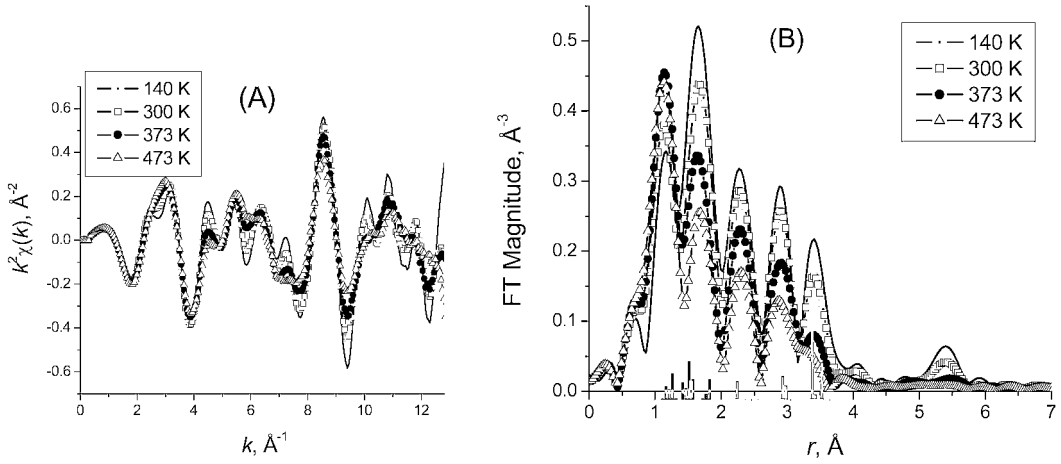

Fig. 2. EXAFS data (in k- and r-spaces) of the $\{Mo_{132}\}$. The radial distribution functions of Mo-O and Mo-Mo pairs, shifted toward lower r by 0.5 Å and 0.3 Å, respectively, are shown next to the horizontal axis in (B).

MoO_6 octahedra. The second peak, at ca. 1.7 Å corresponds to another axial Mo-O_3 and the equatorial Mo-O_2 bond groups of MoO_6 octahedra. From visual observation (the first peak intensity increases with temperature while that of the second peak decreases with temperature), one can hypothesize that the MoO_6 octahedral environment is not rigid. Rather, it should become progressively distorted at elevated temperatures.

FEFF6 [6] was used to calculate model Mo-O and Mo-Mo theoretical contributions to EXAFS. The theory that included three Mo-O and three Mo-Mo single-scattering paths was fitted to the data in r-space using FEFFIT [7]. The coordination numbers of each type of bond were dictated by the $\{Mo_{132}\}$ structure and fixed in the fits to be equal to the values obtained by our PRDF calculations. The bond lengths and disorders were varied independently for all bonds. Fit quality is shown in Fig. 3 for the lowest and highest temperatures analyzed.

The EXAFS data in the unknown sample, $\{Mo_N\}$ (Fig. 4) look strikingly similar to the $\{Mo_{132}\}$ standard (Fig. 3). Indeed, the peak positions align well for the Mo-O and Mo-Mo bonds between the two samples. Since the r-space data in the case of Mo_{132} structure mimics the PRDF obtained for a spherical particle that has $\{(Mo)Mo_5\}$ pentagons and $\{Mo_2^VO_4\}$ bridges with characteristic Mo_1-Mo_1, Mo_2-Mo_2 and Mo_3-Mo_3 bond lengths, the fact that

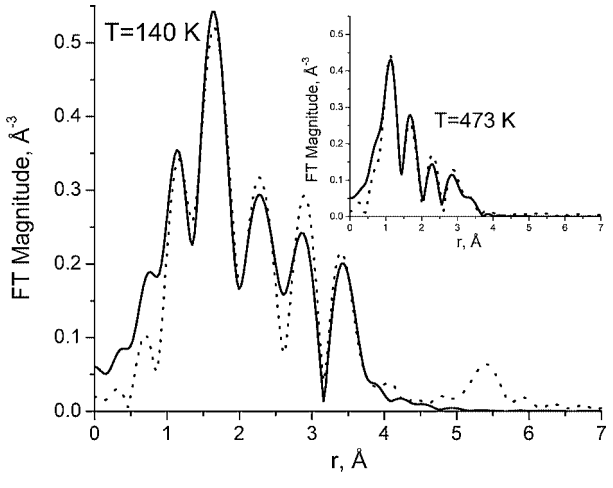

Fig. 3. Fourier transform magnitudes of EXAFS data and fits of the $\{Mo_{132}\}$ at 140 K and 473 K.

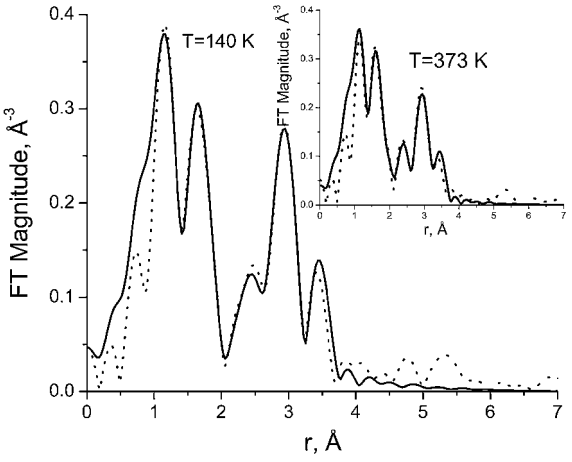

Fig. 4. Fourier transform magnitudes of EXAFS data and fits of the 2nd generation sphere at 140 K and 373 K.

our data for the unknown samples has signatures of the same groups indicates that the topological properties of the two types of particles, $\{Mo_{132}\}$ and $\{Mo_N\}$ should be very similar. In literature, one of the possible candidates for a spherical cluster that is larger in size than Mo_{132} is the 522-atom cluster that also has pentagons and bridges like the $\{Mo_{132}\}$ [8]. That justifies our analysis approach as nearly identical to that of the $\{Mo_{132}\}$ reference structure: we fixed the coordination numbers of each type of bond in accordance with the $\{Mo_{522}\}$ structure and varied the bond lengths and their disorders. The data and best fits are shown in Fig. 4 for the lowest and highest temperatures analyzed.

4. Results

σ^2 for the axial Mo-O_1 and Mo-O_3 bonds were found to be almost the same ($\sim$0.004(1) Å^2) throughout the temperature range (140 K to 473 K). The σ^2 for the equatorial Mo-O_2 bonds increased three-fold from 0.0050(9) Å^2 to 0.0142(15) Å^2 in the same temperature range.

The best fit values for the bond lengths for $\{Mo_{132}\}$ (shown by solid vertical lines in Fig. 5) were consistent with the PRDF calculations. The best fit results obtained in the 2nd generation sphere sample were also consistent with the same distance ranges for the three Mo-O bond groups and three Mo-Mo bond groups (shown by dashed vertical lines in Fig. 5), as in $\{Mo_{132}\}$ structure.

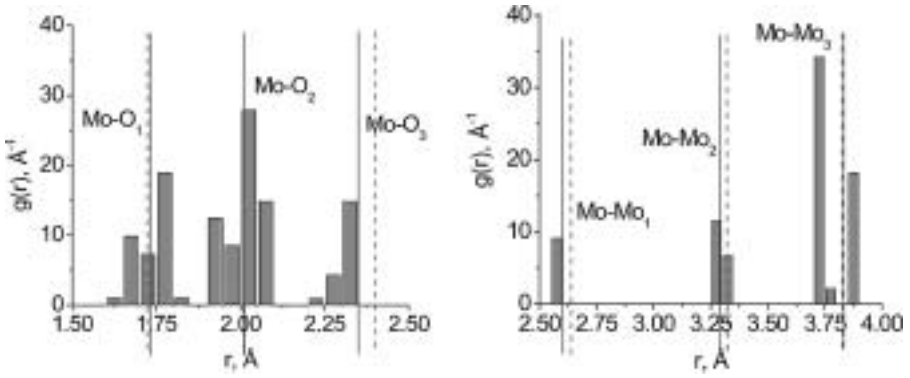

Fig. 5. PRDFs calculated from the crystallography data for Mo-O and Mo-Mo pairs. Shown by vertical lines are the best-fit EXAFS results for each group of distances obtained for the 1st and 2nd generation spheres.

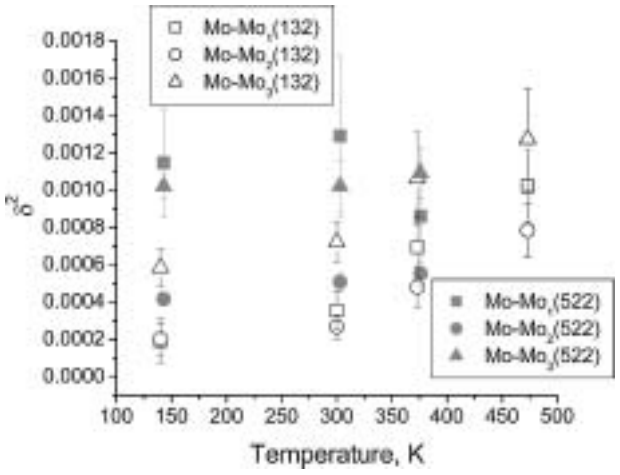

Fig. 6. Bond-length-normalized mean square displacement δ^2.

Figure 6 shows the normalized bond length disorder parameter, $\delta^2 = \sigma^2/R^2$ (where R is the bond length) that we calculated based on the best fit results obtained for σ^2 for each of the three Mo-Mo bonds in the both samples. The use of δ^2 is preferred because longer bonds may have larger σ^2 than shorter bonds not only due to the longer bonds' larger disorder but also due to the smaller correlation between the vibrations of their atoms. If σ^2 is normalized by R^2, the ambiguity caused by the Mo-Mo bond length differences in different structures will be partially lifted when the rigidities of the two structures are examined.

5. Discussion and Conclusions

The fit results for σ^2 of Mo-O bonds confirmed our hypothesis that the MoO_6 octahedra are not rigid in $\{Mo_{132}\}$. From the trend described above we infer that the MoO_6 octahedra are progressively distorted at elevated temperatures. This property has a familiar ring from the NTE materials where an asymmetric "tentpole" distortion of what previously was believed to be a rigid unit, a ZrO_4 tetrahedron, was proposed to be an alternative scenario to transverse O vibration in the W-O-Zr linkages in ZrW_2O_8 [9].

For the structure of the 2nd generation molecule, our results show that the topology of this molecule is analogous to that of $\{Mo_{132}\}$, as we assumed based on preliminary visual observation of the data. Because the number of Mo^V-Mo^V bonds (denoted by Mo_1-Mo_1 in Fig. 1) is much larger in this molecule (as determined by UV/vis. spectrometry, $\sim 87 \pm 8\%$ of Mo atoms in the POM are Mo^{VI}, compared to 55% in $\{Mo_{132}\}$) than in $\{Mo_{132}\}$, and due to the uniqueness of the topological characteristics of various POMs, the structure of this molecule must be that of $\{Mo_{522}\}$.

The non-monolithic nature of POMs has been discussed previously. As pointed out by A. Müller, *et al.* [10], most POMs consist of different $\{MO_x\}$-type building-block units that are highly stable. However, the linkages that connect these building blocks directly or via other coordinating centers [10] may be fragile and break even at moderate temperatures. As predicted by the different stability ranges of temperature in the $\{Mo_{132}\}$ and $\{Mo_{522}\}$ molecules, their structural rigidities should be different. Our EXAFS results indicate that the dominating factor responsible for this effect is the rigidity of the Mo^V-Mo^V bridges that connect the building blocks in these two structures. Figure 6 demonstrates that in Mo_{132}, these bridges are less disordered and therefore, more stiff than in Mo_{522}. We believe that the relative rigidity of these bond types, which serve as bridges between the $\{(Mo)Mo_5\}$ pentagon building blocks, revealed in our analysis of $\{Mo_{132}\}$ EXAFS data is the origin of these molecules' enhanced stability over the $\{Mo_{522}\}$ particles.

Acknowledgment

AIF and SCF were supported by Yeshiva University Research Foundation. TL acknowledges support by the U.S. Department of Energy, Division of Materials Science, No. DE-AC02-98CH10886. NSLS is supported by the U.S. Department of Energy.

References

1. Pryde, A. K. A. *et al.*, J. Phys.: Condens. Matter **8**, 10973 (1996).
2. Dove, M. T. *et al.*, Phys. Rev. Lett. **78**, 1070 (1997).
3. Müller, A. *et al.*, Coord. Chem. Rev. **222**, 193 (2001).
4. Müller, A. *et al.*, Angew. Chem. Int. Ed. Engl. **37**, 3360 (1998).
5. Liu, T. *et al.*, J. Am. Chem. Soc. **123**, 10966 (2001).
6. Zabinsky, S. I. *et al.*, Phys. Rev. B **52**, 2995 (1995).
7. Stern, E. A. *et al.*, Physica B **208&209**, 117 (1995).
8. Müller, A. *et al.*, Angew. Chem. **114**, 1210 (2002).
9. Cao, D. *et al.*, Phys. Rev. Lett. **89**, 215902 (2002).
10. Müller, A. *et al.*, Chem. Rev. **98**, 239 (1998).

Physica Scripta. Vol. T115, 724–726, 2005

In Situ XAFS Study on Mo Oxide Catalysts by Molten Salt Preparation

N. Matsubayashi[1*], K. Sato[1], M. Imamura[1], H. Shimada[1], P. Afanasiev[2] and C. Geantet[2]

[1]National Institute of Advanced Industrial Science and Technology, Tsukuba, Ibaraki 305-8565, Japan
[2]Institut de Recherches sur la Catalyse, 2 avenue Albert Einstein, 69626 Villeurbanne cedex, France

Received June 26, 2003; accepted December 12, 2003

PACS number: 03.61.20.Qg

Abstract

Preparation of catalysts in molten salt has great possibilities for producing excellent catalysts because the reaction in molten salt is quite different from that in water. MoO_3 dissolves in molten salt and finally becomes molybdate via intermediate oxoanions as catalytic active species. The structure of the oxoanions and the mechanism of stabilization on zirconia in the preparation process remain unknown. In the previous study, we have clarified the changes in the composition of molybdate species during the catalyst preparation procedures by quenching the samples. In the present paper, the structure of Mo oxoanions in molten nitrates at different temperatures was investigated by *in situ* XAFS.

Samples were prepared from MoO_3 in molten nitrate ($NaNO_3$). The mixture was heated up to various temperatures from 298 to 773 K. The *in situ* XAFS spectra of the molted samples were measured on Mo K-edge using an *in situ* cell at the BL-10B in the Photon Factory.

The EXAFS was analyzed quantitatively to obtain the structure and composition of Mo oxoanions in the molten nitrates by multi-component fitting based on a linear combination of $\chi(k)$ of reference samples and simulation using FEFF8 code in consideration of the Debye-Waller factor. The results show a change of composition of oxoanions in molten nitrate during the reaction.

1. Introduction

Catalyst preparation by the molten salt method has been shown to produce novel catalysts with high surface areas. In the preparation of molybdenum catalysts, MoO_3 is at first dissolved in the molten nitrate and subsequently transforms into some intermediates before completely changing to MoO_4^{2-} anions [1–4]. However, the structures and the reaction mechanisms of the intermediates have not been clarified yet. Because these intermediates do not have long-range ordered structures, we applied XAFS to the structural analyses involving composition determination of molybdate species in mixed KNO_3 and $NaNO_3$ salt [5]. In the previous study, we have clarified the changes in the composition of molybdate species during the catalyst preparation procedures [6].

In the present report, the reaction behavior of the preparation of unsupported molybdate catalysts in molten nitrate was investigated by *in situ* EXAFS. For this purpose, XAFS measurements were done using an *in situ* cell at various temperatures between 298 and 773 K.

2. Experimental

Unsupported molybdenum oxide catalysts were prepared from a MoO_3 precursor (5 mg) with 150 mg of $NaNO_3$ in an *in situ* cell of a quartz reactor with a thin window of 0.5 mm thickness to transmit X-rays. The cell tapers off at the bottom like a wedge to adjust X-ray path length by changing beam position. The amount of molten nitrate corresponds to a 10–20 fold molar excess. The mixture was heated up to 773 K at a heating rate of 1 K/min being kept for 1 h stepwise at 473, 523, 573, 623, 673, and 723 K and for 2 h at 773 K during an XAFS measurement as shown in Fig. 1. The Mo K-edge XAFS measurements were performed at the Photon Factory using BL-10B with a Si(311) channel-cut crystal monochromator. Fourier transformation was performed for $\Delta k = 80\,\mathrm{nm}^{-1}$ of Mo K-edge EXAFS. The phase shift and backscattering amplitude factor were corrected by using the calculated values of FEFF8 [7] for Mo as an absorber and O as a scatter in crystalline $Na_2MoO_4.2H_2O$.

Multi-component fitting of spectra was done using linear combination of experimental data of reference samples under non-negative constraint conditions. In particular, the k^3 weighted measured spectra were compared with synthesized spectra of reference spectra in k-space ($k = 30$–$110\,\mathrm{nm}^{-1}$) using the chemical composition as the parameter. MoO_3, $Na_2MoO_4.2H_2O$, and $Na_2Mo_2O_7$ were chosen as references.

3. Results and Discussion

It is not easy to *in situ* measure XAFS of molten salts because they are highly reactive with emission of NO_x gas and fundamentally heterogeneous in molten state. Figure 1 shows XANES spectra of Mo K-edge of $MoO_3/NaNO_3$ at 298–773 K plotted vs. time. A disturbance of the spectra occurred around the melting point. After the melting point, a precipitate was found in molten salt and a little NO_x gas bubbles rose up from the molten salt. Therefore temperature as increased very slowly. The X-ray beam irradiated on the precipitate. The color of the precipitate changed from yellow to white with the increase of temperature. The edge shape changed from that of MoO_3 to that of MoO_4^{2-} at the melting point indicating the change of dominant species.

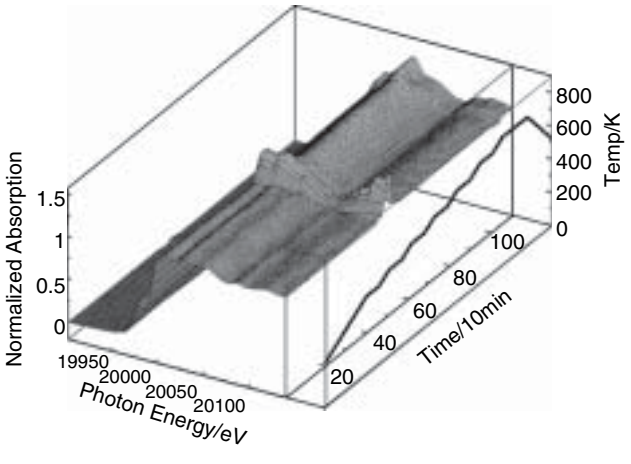

Fig. 1. In situ XANES spectra of Mo K-edge of $MoO_3/NaNO_3$ at 298–773 K.

*e-mail: n-matsubayashi@aist.go.jp

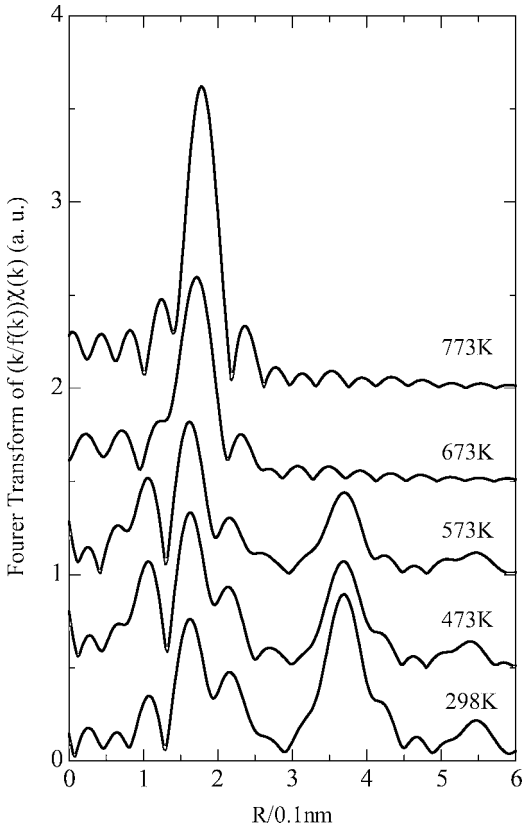

Fig. 2. Fourier transforms of $(k/f(k))\chi(k)$ of Mo K-edge EXAFS of $MoO_3/NaNO_3$ measured at 298–773 K.

Figure 2 shows the Fourier transforms of $(k/f(k))\chi(k)$ of Mo K-edge EXAFS of $MoO_3/NaNO_3$ measured at 298–773 K. The peak at 0.36 nm is assigned to Mo-Mo scattering of the MoO_3 structure. This indicates that the local structure of MoO_3 precursor remains intact before melting. With increasing temperature, the intensities of the peaks at 0.36 nm decrease, whereas the intensities of the peaks at 0.18 nm corresponding to Mo-O scattering in the highly symmetrical tetragonal MoO_4^{2-} structure increase. These results show that the MoO_3 precursor transforms into MoO_4^{2-} with increasing temperature.

In the reaction process of MoO_3 in the molten salts, many species of molybdenum oxides coexist as an amorphous state that seems to be important in catalyst activity. However, a quantitative analysis in a general idea of a crystal structure that has long range order measurable by X-ray diffraction is difficult. So, quantitative analysis according to local structure of a circumference of molybdenum by XAFS was attempted.

In the local structure around Mo of typical molybdenum oxides, the distance of Mo-O of four coordinates in tetrahedral MoO_4^{2-} is 0.18 nm and the distances of Mo-O of six coordinates in distorted octahedral MoO_3 are distributed in a range of 0.17–0.23 nm. The EXAFS signal of 6 coordinates in MoO_3 is smaller due to distortion than that of 4 coordinates in MoO_4^{2-}. In $Mo_2O_7^{2-}$, both structures coexist and the intensity of EXAFS is intermediate. This means that it is difficult to analyze quantitatively from the intensity of EXAFS signal in mixture of these oxide species.

In usual curve fitting analysis of EXAFS, three structural parameters of distance, R, coordination number, N, and Debye-Waller factor, σ, for each coordination shell are used mainly. The coordination shell should be ideally selected with a unique distance, but practically the coordination shell is often selected with intermediate distances such as six coordinates in a distorted octahedron. In this case, the distances are assumed to be distributed in gauss distribution to be fitted to a Debye-Waller factor. However, the assumption is obviously wrong for interatomic distances from crystal data.

The curve fitting for 4 coordinates in MoO_4^{2-} is easy. But in the curve fitting for 6 coordinates in MoO_3, if the coordination number is fixed to 6, the Debye-Waller factor would be large. Therefore the usual curve fitting analysis of EXAFS for a mixture of molybdenum oxides is difficult.

We have analyzed the $\chi(k)$ spectra using multi-component fitting with a linear combination of Mo species in mixtures consisting of $Mo_2O_7^{2-}$, MoO_4^{2-}, and MoO_3 according to the following formulas.

$$\chi_{cal}(k) = a\chi_a(k) + b\chi_b(k) + c\chi_c(k) + \cdots,$$

$$(\chi_{\exp}(k) - \chi_{cal}(k))^2 \rightarrow \min,$$

$$a, b, c \cdots \geq 0,$$

$$a + b + c + \cdots = 1.$$

Each $\chi(k)$ was weighted by k^3 in the fitting.

Correction with a Debye-Waller factor is necessary to compare the data of the *in situ* measurement at different temperatures. In the linear combination fitting, the correction was done by the data measured at the temperatures. We assumed that the static contribution of the Debye-Waller factor to the EXAFS amplitude is constant with temperature and the thermal contribution can be expressed as second and forth order cumulants. To interpolate for temperature, indexes σ_{2t}^2 and σ_{4t}^4 of exponential function like a Debye-Waller factor including anharmonic term ($\exp(-2\sigma_{2t}^2k^2 + 2\sigma_{4t}^4k^4/3)$), which are relative to $\sigma_{2t}^2 = 0$, $\sigma_{4t}^4 = 0$ at 298 K was introduced as fitting parameters to the $\chi(k)$ data of MoO_3, $Na_2Mo_2O_7$, and Na_2MoO_4 at each temperature using that at 298 K instead of a Debye-Waller factor of each coordination shell. The fitting parameters were increased with increasing temperature as shown in fig. 3.

In the fitting, some possible reference data including ammonium molybdate ($(NH_4)_6Mo_7O_{24}.4H_2O$) and phosphomolybdic acid ($P_2O_5.24MoO_3.nH_2O$) were attempted. The data that give a minus coefficient or large uncertainly were removed. As a result, fitting by reference data of MoO_3 $Na_2Mo_2O_7$, and MoO_4 was the best in the attempted data.

Figure 4 shows results of fitting of linear combination of $\chi(k)$. Since spectra around 600 K, the melting point indicated by a dashed line, are disturbed, stability of fitting is not good. However, just after the melting point, MoO_3 decreases, $Na_2Mo_2O_7$ increases at 673 K, and Na_2MoO_4 becomes a dominant species at 723 K.

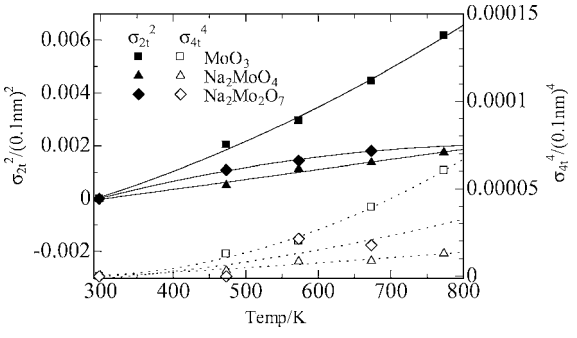

Fig. 3. Temperature dependency of total correction parameters for Debye-Waller factor, σ_{2t}^2 and σ_{4t}^4, experimentally determined by fitting on MoO_3, $Na_2Mo_2O_7$ and Na_2MoO_4.

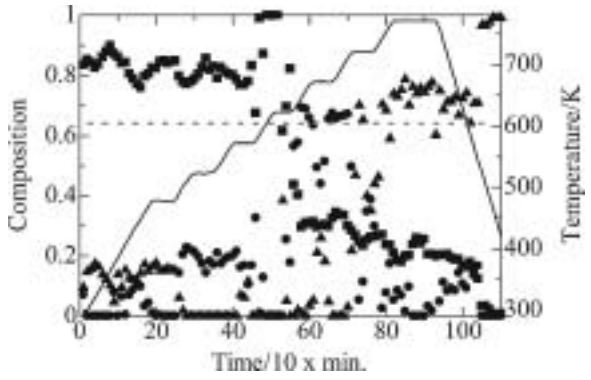

Fig. 4. Results of fitting of composition of Mo species in molten sodium nitrate obtained by EXAFS data fitting. ■ MoO_3, ● $Na_2Mo_2O_7$, ▲ Na_2MoO_4.

This tendency agrees with previous results obtained by quenching method. But the result of the *in situ* measurement revealed that MoO_3 and $Mo_2O_7^{2-}$ remained by about 15% in 773 K in a molten state and they become almost perfectly MoO_4^{2-} after freezing by cooling. Other molybdenum oxide species than the above three species may have formed in the mixture. The local structure of other polymolybdate species seemed to be similar to $Mo_2O_7^{2-}$, thus $Mo_2O_7^{2-}$ is a typical species of polymolybdate as a result. Thus, the total composition of the three species is normalized to 100%. Strictly speaking, the percentage obtained by this procedure does not necessarily correspond to the real percentage of components, but it indicates the relative contribution of the signal of the model to the EXAFS signal. Many other molybdenum oxide species, of which crystal data are not available, seems to coexist in the molten salt. It is necessary to add simulation models produced from the residual in the linear combination fitting to the reference data but the reliability of this procedure depends on the propriety of the model. At the next step, we will build reasonable models to explain the EXAFS results by combination with molecular mechanics and dynamics.

4. Conclusions

The *in situ* XAFS measurements of molten salts were performed by slowly increasing the temperature. A new fitting method of linear combination of reference $\chi(k)$ data was proposed for quantitative analysis by local structure around Mo of mixture system and estimated a change of composition of molybdenum oxide species with increasing temperature. MoO_3 and $Mo_2O_7^{2-}$ remained by around 15% as local structure even in 773 K after reaction in molten salt, and they were almost completely transformed to MoO_4^{2-} by cooling. This means that the analysis by quenching method does not exactly reflect the molten state.

Acknowledgment

This study was carried out under the collaboration between IRC and AIST in the PICS program. The XAFS measurements were performed under the approval of the Photon Factory Program Advisory Committee (Proposal 2001G327).

References

1. Afanasiev, P. and Geantet, C., Mater. Chem. Phys. **41**, 18 (1995).
2. Afanasiev, P., Geantet, C. and Kerridge, D. H., J. Mater. Chem. **41**, 347 (1995).
3. Afanasiev, P., Mater. Chem. Phys. **47**, 231 (1997).
4. Afanasiev, P. and Geantet, C., Coord. Chem. Rev. **178–180**, 1725 (1998).
5. Matsubayashi, N., Geantet, C., Afanasiev, P., Soldo, Y. and Hazemann, J. L., J. Phys. IV France **7**, 1179 (1997).
6. Matsubayashi, N. *et al*., J. Synchrotron Radiation **8**, 610 (2001).
7. Ankudinov, A. L., Ravel, B., Rehr, J. J. and Conradson, S. D., Phys. Rev. B **58**, 7565 (1998).

Physica Scripta. Vol. T115, 727–728, 2005

XAS and XRD Studies on the Structural Changes of Ni-Raney Catalyst after a Hydrogenation Process

N. Watanabe[1], A. Y. Ramos[1,2], J. A. M. Ferreira[3] and H. C. N. Tolentino[1]

[1]Lab. Nacional de Luz Síncrotron, P.O. Box 6192, 13083-970, Campinas, SP, Brazil
[2]Lab. Minéralogie-Cristallographie, CNRS-UMR7590, Univ. Paris VI, France
[3]Getec Guanabara Química Ind. S/A, Rua Joaquim Lemos 48, 24456-680, RJ, Brazil

Received June 26, 2003; accepted November 4, 2003

PACS numbers: 61.43.Gt, 61.10.Ht, 61.10.Nz, 68.47.De

Abstract

Ni-Raney catalysts have a sponge-like structure and are largely applied in reactions of organic hydrogenation. The industrial production has the advantages of low cost and simple process, however this catalyst has the inconvenient of the easy deactivation. The understanding of the deactivation mechanism has motivated several studies, some of them identifying a surface restructuration and loss of the active sites. In this work, we present XRD and XAS measurements at the Ni K edge of Ni-Raney samples obtained before and after an industrial reaction of olefin hydrogenation. We show that in the deactivation process, the porous structure of Ni grains becomes closer to the massive structure, presenting a higher number of first neighbors and an increase of the crystalline coherence. These results call into question the usual hypothesis of collapse of the porous structure.

1. Introduction

Ni-Raney catalysts are largely used in industrial processes of olefins and carbonyl groups hydrogenation reactions [1, 2]. Due to the easy deactivation of the catalyst, many efforts have been dedicated to elucidate the mechanism of this process [3]. The accumulation of organic species in the pores has been considered as a weak reason for the deactivation, and the main effect has been attributed to the collapse of the pore structure [4].

The main line of business of GETEC Guanabara Química Ind. S/A is the conversion of sugars into polyols by means of hydrogenation processes. X-ray absorption spectroscopy (XAS) and X-ray diffraction (XRD) were combined to analyze samples of freshly prepared and deactivated catalysts produced at GETEC.

2. Experimental

XAS, and XRD measurements have been performed at the LNLS (Laboratório Nacional de Luz Síncrotron), Campinas, Brazil. XAS samples were sealed with kapton tape immediately before the measurements. XAS spectra were performed at the Ni K edge in transmission mode. The X-ray beam was monochromatized with a "channel cut" Si (111) crystal. The instrumental resolution was 2.9 eV. The WINXAS program [5] was used for EXAFS data analysis. In XRD measurements, a sample holder with 5 mm window was used in an upside down position, aiming to minimize the interference of the water present in the fresh catalyst. XRD patterns were obtained at 8,200 eV, using a double crystal monochromator (Si (111)) with a sagital focusing in the second crystal.

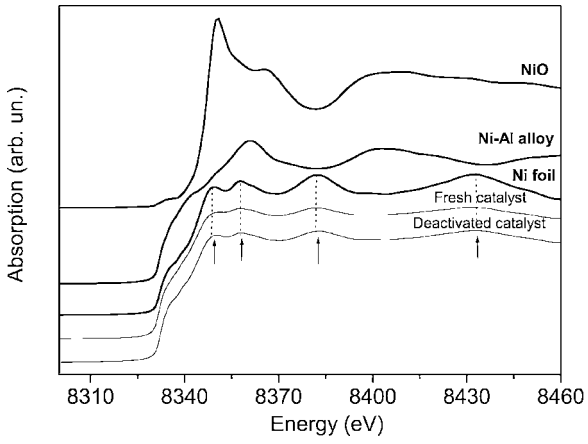

Fig. 1. XANES spectra at Ni K edge.

3. Results and discussion

3.1. *XAS measurements*

Figure 1 shows the XANES spectra of the freshly produced and deactivated catalyst at the Ni K edge. The XANES spectra demonstrate clearly that the chemical environment around the Ni atoms in the catalysts are identical to the metallic Ni foil, in which the structure on the threshold is related to the electronic transition from 1s level to the hybridized 3d-4p level [6]. The agreement of the energy position at the absorption edges (Ni K edge = 8,333 eV) demonstrates that even after the deactivation, the catalyst do not suffer changes in oxidation state, remaining in the metallic form of Ni^0. The structures indicated by the arrows (Figure 1), characteristic of nickel in FCC (face-centered cubic) packing, are preserved in the catalyst spectra, but with a reduction in amplitude of the oscillatory structures.

The Fourier Transform (FT) of the EXAFS oscillations (Figure 2) over the range 2.9–12.8 Å shows the decrease in the intensity of the peaks for the catalysts when compared to the metallic nickel. It can be related to the presence of a smaller average number of neighbors or a large increase of the disorder. The contribution of the first shell is selected by back Fourier filtering over the range 1.8–2.8 Å. Electronic parameters have been obtained from the metallic foil and used in the k-space least square fitting of the catalysts. This procedure certifies high reliability in the comparison of the structural parameters of the catalyst to those of the bulk nickel (Table I). The agreement between the experimental and adjusted curves is excellent. The σ^2 value is low, indicating a low disorder, with no lattice distortion or strain in the catalysts crystalline structure. The number of neighbors is reduced (around 6) in agreement to the XANES

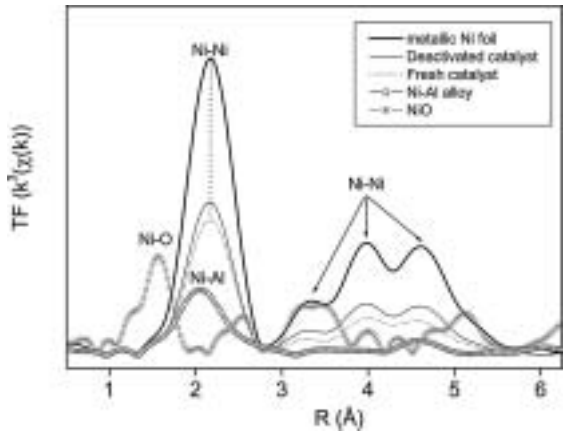

Fig. 2. FT of the EXAFS signal.

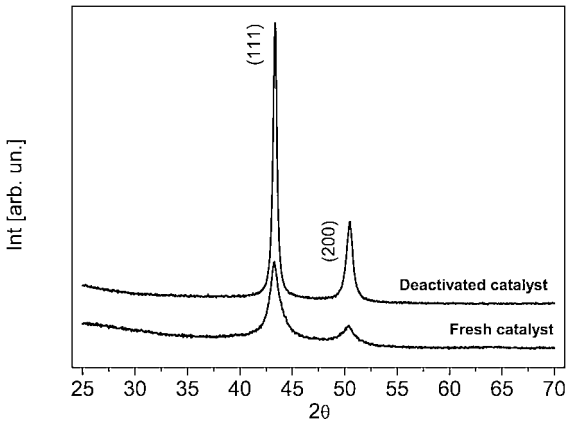

Fig. 3. X-Ray diffraction patterns.

Table I. *Quantitative analysis results of the coordination shell. N = number of neighbors, R = distance, $\Delta\sigma^2$ = Debye Waller factor in comparison to metallic Ni foil pattern.*

Sample	N	R (Å)	$\Delta\sigma^2$ (Å^2)
Fresh catalyst	5.90 ± 0.02	2.494 ± 0.003	0.0012 ± 0.0005
Deactivated catalyst	6.63 ± 0.03	2.495 ± 0.004	0.0014 ± 0.0004
FCC Ni foil	12	2.49	

results. There is no significant change in the Ni-Ni distances for the catalyst.

These results seem surprising since they do not obey the bond valence sum rule, in which low number of neighbors implies shorter distances. In spite of the fact that there is no evidence of aluminum or oxygen atoms participating on the chemical environment around the Ni atoms, it sounds reasonable to consider a surface with passivated dangling bonds.

We note that there is a significant increase of N after the deactivation effect that should be correlated to a decrease in the superficial area in the deactivated catalyst.

3.2. *XRD measurements*

The figure 3 shows the diffraction patterns of the catalyst samples. We observe broad peaks in the case of fresh catalyst and higher and sharper peaks after the deactivation [7]. This result indicates that in the deactivation process, the nickel framework not only gain more neighbors in a local order as demonstrated by XAS, but also gains crystalline coherence in a long-range order.

As demonstrated by XAS results, the broadness of the fresh catalyst can not be attributed to effects of lattice strain. Moreover, due to the morphological characteristic of the sponge-like structure, the calculation of crystallite sizes is fundamentally unfair. Even so, considering the approximations of the Scherrer equation [8], we can estimate the crystalline coherence length in the catalyst before and after the deactivation. This length is 7 nm for the fresh catalyst, and 17.5 nm for the deactivated one, in agreement to the hypothesis of enhancement of the crystalline coherence.

4. Conclusions

XAS and XRD measurements indicated that in the deactivation process, the porous Ni particles, become more close to the massive structure, presenting a higher number of first neighbors and an increase of the crystalline coherence length. With these evidences we propose the occurrence of a modification in the tridimensional connectivity of the solid during the deactivation process, that causes an increasing of the structural crystallinity of the catalyst. The precise mechanism involved is still an opened question, but the results presented in this work refuse the current hypothesis of pore collapse.

Acknowledgments

Getec Guanabara Química Ind. S/A is acknowledged for the financial support.

References

1. Raney, M., U.S. Patent 1 563 787, (1925).
2. Fouilloux, P., Appl. Cat. **8**, 1 (1983).
3. Mikkola, J.-P. *et al*., Appl. Cat. A **196**, 143 (2000).
4. Tanaka, S.-I., Hirose, N., Tanaki, T. and Ogata, Y. H., Int. J. Hydrogen Energy **26**, 47 (2001).
5. Ressler, T., J. Phys. IV France **7**, C2-269 (1997).
6. Rothe, J., Hormes, J., Schild, C. and Pennemann, B., J. Cat. **191**, 294 (2000).
7. Nakabayashi, I. *et al.*, J. Mater. Chem. **5**, 737 (1995).
8. Cullity, B. D., "Elements of X-ray Diffraction", 2nd Ed., (Addison-Wesley Publishing Company, Inc., Massachusetts, 1978), p. 102.

Physica Scripta. Vol. T115, 729–732, 2005

Investigation of Stress State of Silver Nanoparticles in Silicate Glasses by Means of EXAFS

M. Dubiel*, X. C. Yang and S. Brunsch

Department of Physics, Friedemann-Bach-Platze 6, Martin Luther University of Halle-Wittenberg, D-06108 Halle, Germany

Received June 26, 2003; accepted December 10, 2003

PACS numbers: 61.10.Ht, 61.46.+w, 61.43.Fs

Abstract

Nanosized spherical silver particles were formed in silicate glass by sodium/silver ion exchange and subsequent annealing in air or hydrogen atmosphere at elevated temperatures. Furthermore, the sol-gel procedure was used to prepare embedded Ag particles. Structural characterisation of these composite materials by temperature dependent EXAFS-spectroscopy with transmission and fluorescence experiments revealed distinct differences of the particle/matrix interaction across the interface. The Ag-O and Ag-Ag correlations could be separated by fit procedures. The Ag-Ag bond length of the crystalline particles sensitively reflects their state of stress depending on the formation conditions. It was found an increase as well as a decrease of the Ag-Ag distance, i. e. tensile and compressive stress states were formed, for ion-exchanged glasses as a result of different cooling procedures and after hydrogen treatments, respectively, and for sol-gel samples. The combination with high-resolution electron microscopy (HREM) experiments yields the confirmation of such effects. Furthermore, the size-dependent parameters of nanoparticles could be determined. The results can be interpreted by the size effect of nanoscaled particles and the influence of the surrounding matrix.

1. Introduction

Glasses containing metal nanoparticles were investigated mainly because of the specific optical absorption (see for example [1]). Recently, the preparation and characterization of such composites has been further stimulated by peculiar non-linear optical properties, especially an increased third-order susceptibility, making such glass a promising candidate for application in integrated optics and photonics [2]. Previous studies indicated that the optical properties of nanoparticle/glass composites strongly depend on the size, the structure and the concentration of the embedded nanoparticles as well as their interaction with the host matrix [3]. Therefore, different preparation methods like ion implantation, ion exchange, reducing atmosphere treatment, ion and laser irradiation and sol-gel technique have been used to fabricate specific configurations of nanoparticles in glasses. Structural information down to the atomic scale on the nanoparticulate composites may be obtained by high resolution electron microscopy (HREM) [4]. This does not only allow to determine size, size distribution, external shape and internal structure of metal particles, but also to evaluate surface/interface effects on their lattice parameter. X-ray absorption spectroscopy is another structure-sensitive method. From the extended X-ray absorption fine structure (EXAFS) spectra [5–7] of the corresponding metal atoms the lattice parameter may be determined, even with more accuracy than HREM. However, the EXAFS results are averaged parameters of atom-atom correlations summed up for all detected particles, different from data determined by HREM for individual particles. The combination of both methods should be advantageous for a precise structural characterization.

Here, the results of EXAFS spectroscopy will be demonstrated for silver nanoparticles prepared by different methods and with that by different thermal histories. The data of transmission and fluorescence techniques were used to evaluate the lattice parameters in comparison with bulk Ag materials. The HREM experiments should allow to confirm the variation of the lattice constants that are less than 0.001 nm. With that the nature and the origin of the stress state of nanoscaled particles as well as of interface effects should be discussed.

2. Experimental procedures

Commercial soda-lime glasses containing SiO_2 and Na_2O as main components were used either as base glass for ion exchange or as substrate for sol-gel layers. At first, glasses containing a large amount of iron oxide (0.865%) of small thickness (0.15 mm) were prepared by a long duration of exchange period (310–426 hours) and applying a two-step annealing procedure in the temperature range of 380 to 600 °C. This enables to produce a nearly homogeneous distribution of Ag species throughout the glass sample as well as a narrow size distribution of nanoparticles. That allows the application of transmission experiments as well as a precise comparison with HREM data. The particle sizes were between 2.8 and 7 nm. For a second set of glasses of a thickness of 4 mm, the silver ions were introduced into the glass matrix by immersing the samples in a mixed silver nitrate/sodium nitrate melt at 400 °C for 2 hours. The subsequent thermal treatment at 635 °C yields the formation of Ag particles of 3 nm mean size in a surface-near region only. That gives the possibility to test the influence of temper stresses within the glass surfaces that could be formed by quenching the samples. The reference sample has been cooled down slowly. The third part of samples was prepared by an ion exchange process (thickness of 0.15 mm) in nitrate mixed melts (330 °C, 310 hours) and a thermal treatment in reducing hydrogen atmosphere at 500 °C. This procedure results in the formation of particles of sizes of 2 to 11 nm. The sizes were determined by electron microscopy. The proportion of multiply twinned particles to single crystalline particles was increased compared with that of the ion-exchanged glasses. A fourth set of embedded silver particles was prepared by the sol-gel technique. The sols were prepared from tetraethoxysilane orthosilicate by adding dissolved silver nitrate. The sol-gel samples were produced via hydrolysis under acidic conditions and subsequent drying at 200 °C. The mean size of particles was found to be 6 nm.

Ag K-edge (25.514 keV) EXAFS at beam line X1 of HASYLAB (Hamburg, Germany) were measured in transmission mode utilizing Si (311) double-crystal monochromator. Harmonic

*e-mail: dubiel@physik.uni-halle.de

rejection was achieved by detuning the monochromator crystals between 40 and 50%. The Ag K-edge EXAFS spectra of Ag foil as a reference and Ag-containing glass were systematically measured in the temperature range from 10 K to 300 K using a liquid helium vapour flow cryostat equipped with an electric heater. The spectra measured in fluorescence mode were recorded at the ESRF at the beam line BM08/GILDA between liquid nitrogen and room temperature. The incident X-ray intensity was measured with an ionisation chamber, whereas the fluorescence intensity was collected by a plastic scintillator. Harmonic rejection was achieved by detuning the monochromator crystals at the mid point of the reflectivity curve. The parameters characterizing the Ag-O and Ag-Ag coordination shells (bond lengths, Debye-Waller factor, coordination number, third cumulant) were evaluated by fitting the EXAFS function by means of UWXAFS program package [8] by means of theoretical amplitude and phase functions calculated by FEFF 7 [9]. The data of the transmission experiments were calculated on the basis of the cumulant expansion technique up to third-order term to include also anharmonic vibrations [6, 10]. The procedure of data evaluation is described in detail in [6].

3. Experimental results and discussion

Fig. 1 shows the Fourier transformed EXAFS oscillations of the ion-exchanged glasses containing 0.865% Fe_2O_3, so-called green glasses. These spectra indicate the existence of crystalline silver particles incorporated into the glass matrix that can be confirmed by electron microscopy. Besides the Ag-Ag correlations, a small contribution of Ag-O environment is observed for glass samples. This part can be assigned to isolated silver ions, which are not incorporated in silver particles. This oxygen environment is well known from ion-exchanged samples. For the interesting Ag-Ag correlations, four neighbouring spheres were considered. The data of the first shell is shown in Fig. 2 together with the data of Ag foil as reference material. This data were calculated after Fourier transformation (k range of 2.6–18.6 $Å^{-1}$ for Ag foil and 2.6–16 $Å^{-1}$ for the glass samples) into the real space using a Hanning window function. The fit range was in each case 1.6–4 Å. The coordination number, the damping factor by many-body effects and the edge shift parameter were fitted at 12 K only. For higher temperatures this values were fixed. The parameters of Ag-Ag

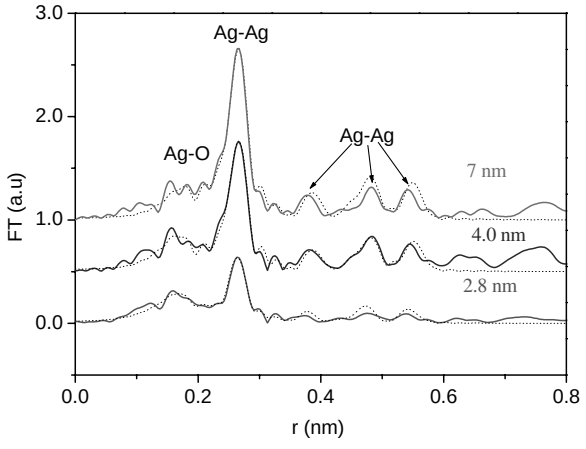

Fig. 1. Fourier transforms of the EXAFS oscillations of glass samples containing Ag particles of sizes of 2.8, 4 and 7 nm measured at 12 K and the corresponding fits (dashed lines) calculated by UWXAFS 3.0.

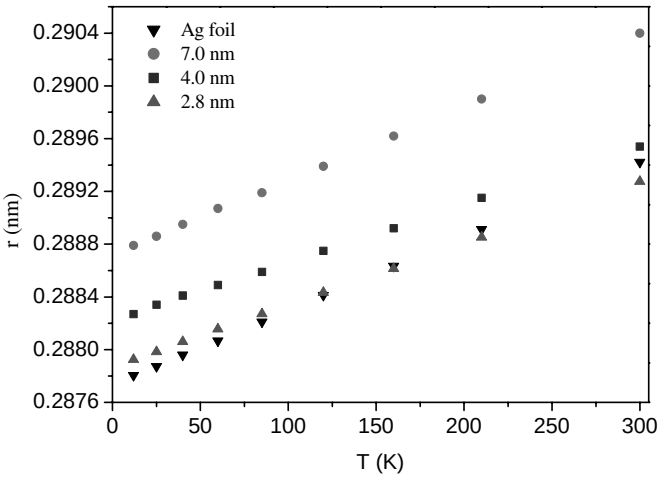

Fig. 2. Calculated Ag-Ag distances of Ag foil and of glasses represented in Fig. 1 in dependence on the temperature.

distance, Debye-Waller factor and third cumulant were fitted from 12 to 300 K. The EXAFS data for particles of 2.8 nm particles are similar to Ag foil values or slightly increased for larger particles (4 and 7 nm). These data demonstrate a lattice dilatation up to 0.001 nm for small particles after slowly cooling (duration of cooling was 24 hours) as investigated here. That means the typical lattice contraction of small particles is not observed in these glasses. High resolution electron microscopical investigations on this glass system confirm this effect for the parameters determined at 300 K [11]. However, the uncertainty of distance parameters determined by EXAFS resulting from the fit procedure is better (Δr = 0.0003 . . . 0.0005 nm) than the uncertainty of HREM data (Δr = 0.0006 . . . 0.0010 nm) resulting from the distribution of measured lattice parameters. The formation of such tensile stresses within the silver particles, i. e. the observed lattice dilatation, can be induced during the cooling procedure after the formation of silver particles at elevated temperatures due to the low thermal expansion coefficient of the silicate glass compared with that of bulk particles [6]. Furthermore, the starting temperature of cooling has to be considered [12]. Using the thermal expansion coefficient of Ag particles determined on the basis of third cumulant of EXAFS data (see [6]), such a behaviour can be explained quantitatively. It should be noted here, that there are small differences in interatomic distances determined by X-ray diffraction and EXAFS procedures for Ag foil [6]. Some authors [13–15] proposed that this effect originates from mean-squared vibrational disorder perpendicular to the line between the average position of the observed pair of atoms, here Ag-Ag. That requires theoretical calculations of vibrational disorder of Ag structures. However, the conclusions concerning the change of lattice parameters can be drawn without this because of the similar effect in bulk material and in nanoparticles.

Based on the previous results, the data of the other systems can be interpreted. Fig. 3 shows the Fourier transforms of EXAFS oscillations after strongly different cooling procedures, i. e. the formation of temper stresses inside the glass surface [16]. The compressive stress amounts to approximately 93 MPa. The experiments were performed by fluorescence method at 81 K because of the small concentration of particles. The data evaluation yield a reduced lattice parameter by 0.0005 nm for the quenched sample compared with the slowly cooled one and with the bulk sample too. That means, the expected compressive stress could be detected by the EXAFS method. The HREM experiments

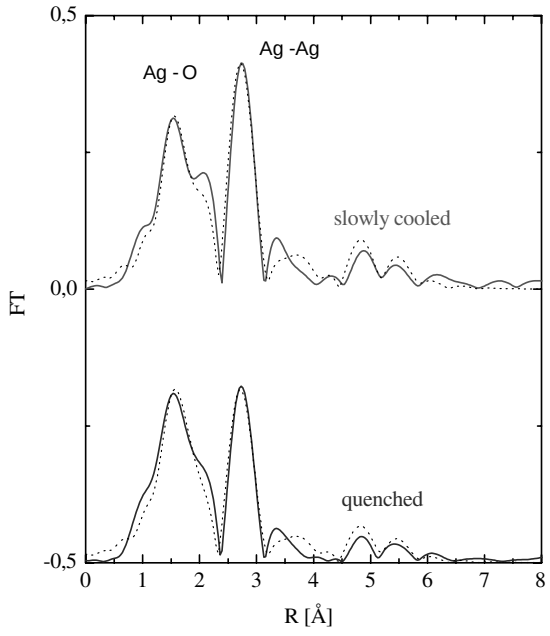

Fig. 3. Fourier transforms of EXAFS data measured by fluorescence method of quenched and slowly cooled samples together with the fitted curves (dashed lines).

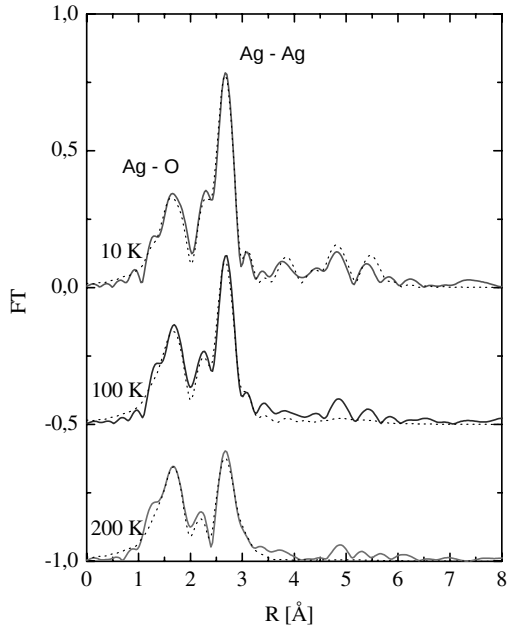

Fig. 4. Pair correlation functions as a result of particle formation due to treatment in hydrogen atmospheres. The dashed lines represent the fitted spectra.

do not allow to prove this effect. In the case of hydrogen treatment, the strongly increased concentration of silver particles enabled to perform absorption experiments. The corresponding spectra are represented in Fig. 4. The calculated Ag-Ag distances show a lattice dilatation up to 0.0001 nm for all temperatures. This increase of the Ag-Ag bond length is to explain by both the thermal expansion mismatch of particles and matrix and by the existence of twinned crystal structures. Fig. 5 shows the Ag-O and Ag-Ag spheres of the sol-gel glass containing Ag nanoparticles measured by fluorescence. The first Ag-Ag sphere shows a distinctly reduced bond length by 0.002 nm determined at 103 K. This lattice contraction corresponds to the behaviour of non-embedded nanoparticles that is caused by the increased number of surface atoms.

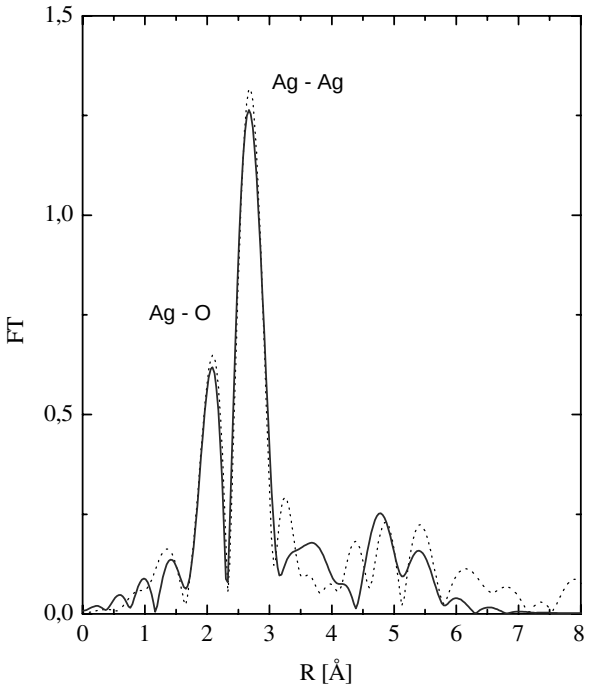

Fig. 5. Fourier transforms of fluorescence data of Ag nanoparticles prepared within a sol-gel layer and the corresponding fits (dashed lines).

Usually, small particles show reduced lattice parameters in comparison with bulk material due to the influence of surface atoms as mentioned above. This could be confirmed for isolated silver particles [17, 18] as well as for silver particles which were formed by precipitation processes in a sodium silicate glass as discussed before [19, 20]. Recently, similar results were obtained by EXAFS spectroscopy in fluorescence mode for particles formed by annealing, ion beam and laser beam irradiation [21]. In the same way, the local structure of silver clusters containing $8\,Ag^{+}$ ions or $6\,Ag^{0}$ atoms in the channels of a zeolite showed a slightly reduced lattice parameter compared with bulk material [22]. However, there are some experimental investigations that show the opposite behaviour of small particles of other types, i. e. a lattice dilatation has been measured. This was explained by interactions with ligands, the formation of oxide shells or the lattice mismatch between the particles and surface layers [23, 24]. Here, such explanations can be excluded because of investigations by electron microscopy.

4. Conclusions

It could be demonstrated that EXAFS spectroscopy represents a powerful tool to extract lattice parameters of nanocrystalline Ag particles in glasses with high accuracy. With that tensile and compressive stress states could be detected by changing the Ag-Ag bond lengths in the range of 0.0001 to 0.0020 nm. For ion-exchanged glasses and subsequent treatments in air or hydrogen atmosphere, the strength of interaction across the particle/matrix interface leads to lattice dilatation due to the thermal expansion mismatch of metal particle and glass matrix. The corresponding increase of Ag-Ag distances mainly in a surface near region of particles should be caused by Ag-O interactions across the particle/matrix interface. This effect does not exist for sol-gel samples. Here, the behaviour of particles is similar to isolated particles, i. e. the influence of Ag at the surface of particles dominates or there are no considerable interface effects,

respectively. The experiments on quenched Ag/glass composites demonstrated that even stresses of 93 MPa can be proved by EXAFS spectroscopy.

Acknowledgements

The authors would like to thank F. d'Acapito (ESRF/Grenoble) and the staff of HASYLAB (Hamburg) for their help during the EXAFS experiments. The work was supported by Deutsche Forschungsgemeinschaft (SFB 418).

References

1. Gonella, F. and Mazzoldi, P., "Metal nanocluster composite glasses", in "Handbook of Nanostructured Materials and Nanotechnology", (edited by H. S. Nalwa), (Academic press, vol. 1, p. 81 2000).
2. Haglund Jr., R. F., "Handbook of Optical Properties II: Optics of Small Particles, Interfaces, and Surfaces", (edited by R. E. Hummel and P. Wissmann), vol. 2, P.191-231, (CRC Press, New York 1997).
3. Flytzanis, C. F., Hache, F., Klein, M. C., Ricard, D. and Roussignol, P., "Nonlinear Optics in Composite Materials", in "Progress in Optics", vol. 29. (Edited by E. Wolf), (Elsevier, New York, p. 321 1991).
4. Hofmeister, H., Dubiel, M., Goj, H. and Thiel, S., J. Microsc. (Oxford) **177**, 331 (1995).
5. Yokoyama, T., Kimoto, S. and Ohta, T., Jpn. J. Appl. Phys. **28**, 851 (1989).
6. Dubiel, M., Brunsch, S. and Tröger, L., J. Phys.: Condens. Matter **12**, 4775 (2000).
7. d'Acapito, F., *et al*., Nucl. Instr. Meth. B **120**, 110 (1996).
8. Stern, E. A., Newville, M., Ravel, B., Yacoby, Y. and Haskel, D., Physica B **208**/**209**, 117 (1995).
9. Zabinsky, S. I., Rehr, J. J., Ankudinov, A. L., Albers, R. C. and Eller, M. J., Phys. Rev. B **52**, 2995 (1995).
10. Frenkel, A. I. and Rehr, J. J., Phys. Rev. B **48**, 585 (1993).
11. Dubiel, M., Brunsch, S., Seifert, W., Hofmeister, H. and Tan, G. L., Eur. Phys. J. D **16**, 229 (2001).
12. Dubiel, M., Brunsch, S. and Tröger, L., J. Synchrotron Rad. **8**, 539 (2001).
13. Stern, E. A., J. Physique Coll. **VI 7**, C2, 137 (1997).
14. Dalba, G., *et al*., Phys. Rev. B **58**, 4793 (1998).
15. Dalba, G., Fornassini, P., Grisenti, R. and Purans, J., Phys. Rev. Lett. **82**, 4240 (1995).
16. Seifert, W., Maschke, A. and Dubiel, M., Glastech. Ber. Glass Sci. Technol. **71**, 341 (1998).
17. Wassermann, H. J. and Vermaak, J. S., Surf. Sci. **22**, 164 (1970).
18. Montano, P. A., Zhao, J., Ramanathan, M., Shenoy, G. K. and Schulze, W., Z. Phys. D **12**, 103 (1989).
19. Hofmeister, H., Thiel, S., Dubiel, M. and Schurig, E., Appl. Phys. Lett. **70**, 1694 (1997).
20. Dubiel, M., Hofmeister, H. and Schurig, E., Recent Res. Devel. Appl. Phys. **1**, 69 (1998).
21. Battaglin, G., *et al*., Nucl. Instr. Meth. Phys. Res. B **200**, 183 (2003).
22. Miyanaga, T., Hoshino, H. and Endo, H., J. Synchrotron Rad. **8**, 557 (2001).
23. Rockenberger, J., *et al*., J. Phys. Chem. B **101**, 2691 (1997).
24. Hofmeister, H., Huisken, F. and Kohn, B., Eur. Phys. J. D **9**, 137 (1999).

Physica Scripta. Vol. T115, 733–735, 2005

Local Structures of Nanocomposite Co-C_{60} and Co-SiO_2 Thin Films Studied by Fluorescence XAFS

Bin Sheng[1], Dongliang Chen[1], Jiangwei Fan[1], Wenhan Liu[2], Xinfeng Zhang[1], Yong Jiang[1], Wensheng Yan[1] and Shiqiang Wei[1*]

[1]National Synchrotron Radiation Laboratory, University of Science and Technology of China, Hefei, 230029, P. R. China
[2]Department of Physics, University of Science and Technology of China, Hefei, 230026, P. R. China

Received June 26, 2003; accepted January 7, 2004

PACS numbers: 61.10.Ht, 75.50.Tt, 61.48.+c

Abstract

Local structures of nanocomposite Co-C_{60} and Co-SiO_2 thin films have been studied by fluorescence XAFS. The results indicate that the bond length R and coordination number N of the first Co-Co shell of Co-SiO_2 thin film are 2.49 Å and 11.8, respectively. It indicates that the local structure around Co atoms in the nanocomposite Co-SiO_2 thin film is similar to that of the metallic Co thin film. However, the local structure and the XANES spectrum of the Co-C_{60} thin film are much different from those of the Co-SiO_2 thin film. There are two Co-C and Co-Co coordination shells in the first neighbor of Co atoms of the Co-C_{60} thin film. For the Co-C_{60} thin film, the R, N and σ of the first Co-C and Co-Co shells are 1.88 Å 1.6, 0.050 Å, and 2.47 Å, 7.8, 0.110 Å, respectively. The decrease (4.0) of the coordination number and the contraction (0.04 Å) of the average band length for the first Co-Co shell in the Co-C_{60} thin film show that there is a strong interaction between the Co nano-particles and the C_{60} matrix. The XANES results further confirm that there is an electron transferring from Co atoms to C_{60} molecules in the Co-C_{60} thin film.

1. Introduction

The fabrications from nano-structural materials based on fullerenes have attracted considerable attention since an easy way was discovered for the synthesis of C_{60} in macroscopic quantities [1]. This is largely due to the unique properties of C_{60} such as an atom-like spherical molecular with an outer shell diameter of 1 nm, closed-cage molecular morphology, chemical inertness, stability at the pressure up to 20 GPa [2], and so on. In particular, the C_{60} modified by element metals have shown some novel properties. For example, superconductivity in K (or Rb, Cs)-doped fullerite crystal [3], higher coercivity magnetic materials Ni-C_{60} [4] and fast magnetic switching as well as high out of plane remanence materials Fe (or Co, CoFe)-C_{60} [5].

Zheng *et al*. [5] and Hou *et al.* [6] have reported that there is a strong interaction between C_{60} and metallic nano-particles in the nano-composite Fe (Co, CoFe)-C_{60} and Cu-C_{60} thin films, which results in the fascinating properties significantly different from those of both bulk metals and fullerenes. Zhao *et al*. [4] had studied the structures of the Ni nano-particles embedded in an amorphous C_{60} matrix by XRD and Raman spectra. Their results have demonstrated that the lattice expansion exists in the Ni particles and charge transfer is from Ni atoms to C_{60}. Hunt *et al.* [7] had studied the charge state and C_{60} monolayers desposited on Au (110), polycrystalline Ag, and Ni (110) with electron-energy-loss spectroscopy and low-energy electron diffraction. They found that the charge was transferred from the metallic surface of Au (110), Ag and Ni (110) to the C_{60}. Obviously, the properties of metal-C_{60} nano-composite thin films mainly depend on the interfacial interaction between metal particles and the C_{60} matrix. However, it is not clear enough of the local structures around the metallic atoms and C_{60} in the metal-C_{60} thin film yet.

In this paper, fluorescence XAFS has been used to investigate the local structures around the Co atoms in the nanocomposite Co-C_{60} and Co-SiO_2 thin films. We focus on the interaction between the metallic Co and the C_{60}. By comparing with the local structures of metallic Co and Co-SiO_2 thin film, it is possible to obtain the local structures around the Co atoms and the interactive distance $R_{Co\text{-}C}$ in the Co-C_{60} thin film. This result is useful to understand the electronic structures of C_{60} in the nanocomposite Co-C_{60} thin film modified by Co smaller particles.

2. Experimental

Nanocomposite Co-C_{60}, Co-SiO_2 and metallic Co thin films were prepared by magnetron sputtering. The base pressure of the growth chamber was 2.0×10^{-5} Pa. For the Co-C_{60} thin film, the metallic Cobalt (99.99%) target was sputtered with dc sputtering at an Ar pressure of 3.0 Pa, and the deposition rate was 0.1 Å/s. Meanwhile, a thermal heating source was used to sublimate C_{60} powder (99.9%) at a deposition rate of 0.6 Å/s. During the co-deposition, the Co target and the C_{60} heating source were separated from each other. The thickness of the Co-C_{60} thin film was 70 nm. Similarly, the Co-SiO_2 and metallic Co thin films were prepared by means of co-sputtering and dc sputtering, respectively. The thickness of Co-SiO_2 thin film was 72 nm and thickness of Co thin film was 36 nm. All three samples were deposited on the Si substrate at room temperature.

The Co K-edge XAFS spectra of metallic Co, nanocomposite Co-SiO_2 and Co-C_{60} thin films were measured at the XAFS station of 4W1B beamline of Beijing Synchrotron Radiation Facility. The electron beam energy was 2.2 GeV and the maximum stored current was about 80 mA. The fixed-exit Si (111) flat double crystals were used as monochromator. The X-ray harmonics were minimized by detuning the two flat Si (111) crystal monochromator to about 70% of the maximum incident light intensity. Data were collected at room temperature with fluorescence mode, using Lytle ion chamber detector filled with Ar gas. The USTCXAFS3.0 software packaged [8] was used for XAFS data analysis.

3. Results and Discussions

The Co K-edge EXAFS functions $k^2\chi(k)$ and their Fourier transformations (FT) of metallic Co, Nanocomposite Co-SiO_2 and Co-C_{60} thin films are shown in Fig. 1 and Fig. 2, respectively. It can be observed that the oscillation shape and peak intensity of

*Correspondent: Shiqiang Wei, E-mail: sqwei@ustc.edu.cn

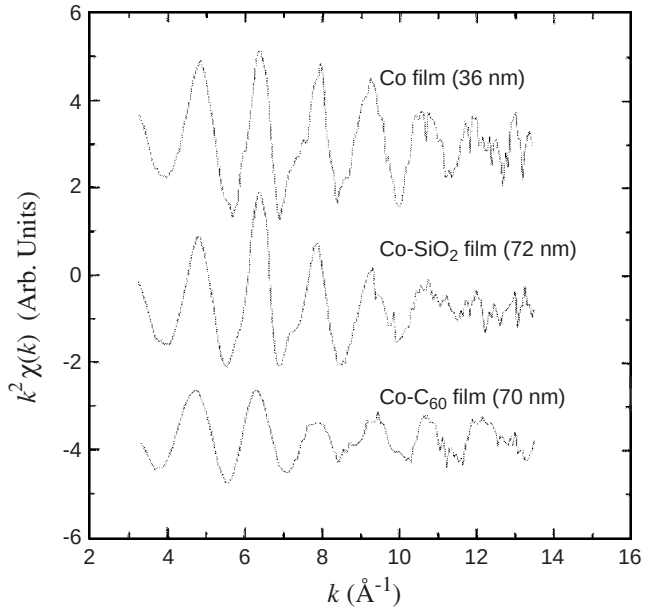

Fig. 1. Co K-edge EXAFS functions $k^2\chi(k)$ of metallic Co, nanocomposite Co-SiO_2 and Co-C_{60} thin films.

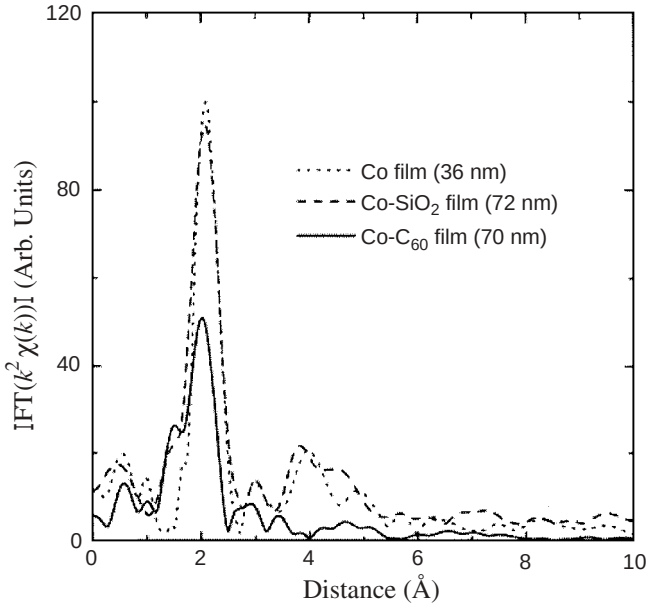

Fig. 2. The RSF functions of metallic Co, nanocomposite Co-SiO_2 and Co-C_{60} thin films.

$k^2\chi(k)$ curve of Co-SiO_2 thin film is similar to those of metallic Co thin film. However, the oscillation magnitude of Co-C_{60} thin film is about 50% weaker than those of the above two thin films. This result indicates that the local structure around Co atoms in the Co-C_{60} thin film is largely different from that in the Co-SiO_2 thin film. Furthermore, it can be clearly seen in Fig. 2 that the FT main peak of the metallic Co and Co-SiO_2 thin films appears at 2.09 Å, which corresponds to the first shell of the Co-Co coordination. However, the FT main peak shifts to 2.01 Å and its magnitude largely decreases for the Co-C_{60} thin film. In addition, a new small peak appears at 1.51 Å in the FT curve of the Co-C_{60} thin film, corresponding to the first shell of Co-C coordination. These results suggest that the local structure of Co atoms in the Co-C_{60} film has greatly modified by C_{60}.

Table I. *Structural parameters of the metallic Co, nanocomposite Co-SiO_2 and Co-C_{60} thin films.*

Sample		Bond type	R (Å)	σ (Å)	N	ΔE_0 (eV)
Co-C_{60}	(70 nm)	Co-C	1.88 ± 0.02	0.05	1.6 ± 0.6	-16.7
		Co-Co	2.46 ± 0.02	0.11	7.8 ± 0.8	-10.6
Co	(36 nm)	Co-Co	2.50 ± 0.01	0.090	12.0 ± 0.7	-2.84
Co-SiO_2	(72 nm)	Co-Co	2.49 ± 0.01	0.097	11.8 ± 1.0	-5.63

For obtaining the structural parameters of nanocomposite Co-C_{60} and Co-SiO_2 thin films, the least-squares curve fit is performed in the XAFS data analysis using the USTCXAFS3.0 code [8]. The theoretical amplitude and phase shifts functions are calculated by FEFF7.0 [9]. The curve fitting ranges of ΔR and Δk are from 1.1 to 2.5 Å and from 3.2 to 11.0 $Å^{-1}$, respectively. The structural parameters of the metallic Co, nanocomposite Co-SiO_2 and Co-C_{60} thin films are listed in the table I.

Seen from table I, the results indicate that the bond length R, coordination number N and Debye-Waller factor σ of the first Co-Co shell in the Co-SiO_2 thin film are 2.49 Å, 11.8 and 0.097 Å, respectively. It means that the local structure around Co atoms in the Co-SiO_2 thin film is similar to that of the Co thin film. Hence, the interaction between the Co nano-particles and SiO_2 matrix is very weak in the Co-SiO_2 thin film. This result is in good agreement with that reported by Murayama *et al*. [10] who have studied the interaction between the Co grains and the SiO_2 matrix in Co-SiO_2 thin film with Raman spectra. Furthermore, table I has shown that there are two coordination signals of Co-C and Co-Co shells around Co atoms in the Co-C_{60} thin film. The R, N and σ of the first Co-C sub-shell and the first Co-Co sub-shell are 1.88 Å, 1.6, 0.050 Å and 2.47 Å, 7.8, 0.110 Å for the Co-C_{60} thin film, respectively. It can be found that there is a large ratio (about 17%) of Co-C to Co-Co coordination number in the first shell of the Co-C_{60} thin film, and that the $N_{\text{Co-Co}} = 7.8$ and the $R_{\text{Co-Co}} = 2.46$ Å in the Co-C_{60} thin film is about 4.0 and 0.04 Å smaller than those of the metallic Co thin film, respectively. The

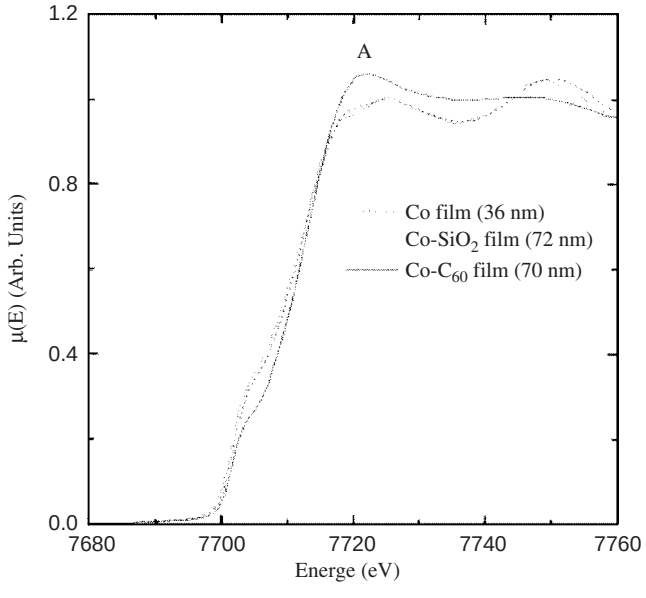

Fig. 3. XANES spectra of metallic Co, nanocomposite Co-SiO_2 and Co-C_{60} thin films.

decrease of the coordination number and the contraction of the bond length in the first Co-Co shell of the Co-C_{60} thin film indicate that there are a strong interaction between the Co nano-particles and the C_{60} matrix in the Co-C_{60} thin film. Kolobov *et al*. [11] have shown that the contraction of the average bond length of the first Co-Co shell in the Co nanocrystals embedded in carbon matrix. Their results are in good agreement with ours.

The X-ray absorption near-edge structure (XANES) spectra of the metallic Co, nanocomposite Co-SiO_2 and Co-C_{60} thin films are shown in Figure 3. The peaks A located at 7722 eV in the Co K-edge XANES spectrum of the Co-SiO_2 thin film is corresponding to the 1s $\rightarrow$ 4p electron transition of Co atoms. Moreover, the shape of XANES spectrum of the Co-SiO_2 thin film is similar to that of metallic Co thin film, in which the intensity of peak A is very lower. However, the XANES spectrum of the Co-C_{60} thin film is much different from that of the Co-SiO_2 thin film. The intensity of peak A in the Co-C_{60} thin film is stronger than those of the metallic Co and Co-SiO_2 thin films. Compared with the XANES spectra of CoO and Co_3O_4 studied by Modrow *et al*. [12] and Huffman *et al.* [13], the XANES spectrum of the Co-C_{60} thin film is close to those of CoO and Co_3O_4. Hence, we consider that there are electrons trasferring from Co atoms to C_{60} molecules in the Co-C_{60} thin film. Zhao *et al*. [4] have reported that there are $2 \sim 4$ electrons transferred to each C_{60} molecule Ni-C_{60} thin film from their results of Raman spectra. These indicate that the electronic structures of Co atoms are modified by C_{60} in the nanocomposite Co-C_{60} thin film.

Acknowledgement

This work was supported by the development of the high-level university of University of Science and Technology of China, a key-project of Beijing Synchrotron Radiation Facility, and a key-program of Chinese Academy of Sciences.

References

1. Kroto, H. W., Heath, J. R., O'Brien, S. C., Curl, R. E. and Smalley, R. E., Nature **318**, 162 (1985).
2. Duclos, S. J., Brister, K., Haddon, R. C., Kortan, A. R. and Thiel, F. A., Nature **351**, 380 (1991).
3. Hebard, A. F., Rosseinsky, M. J. and Haddon, R. C., Nature **350**, 600 (1991).
4. Zhao, Z. J., *et al.*, Phys. Rev. B **65**, 235413 (2002).
5. Zheng, L. A., Lairson, B. M. and Sarrera, E. V., Appl. Phys. Lett. **77**, 3242 (2000).
6. Hou, J. G., Li, X., Wang, H. Q. and Wang, B., J. Phys. Chem. Solid. **61**, 995 (2000).
7. Hunt, M. R., Modesti, S., Rudoli, P. and Palmer, R. E., Phys. Rev. B **51**, 10039 (1995).
8. Zhong, W. J. and Wei, S. Q., J. Univ. Sci. Tech. China **31**, 328 (2001), (in Chinese).
9. Brese, N. E., O'Keeffe, M., Ramakrishna, B. L. and Breele, R. B. V., J. Sol. Stat. Chem. **89**, 184 (1990).
10. Murayama, A., Kondoh, S., Miyamura, Miyamura, M., in Proc. 3rd Int. Symposium Physics at Magnetic Materials, edited by Kim, C. S., Lee, T. D., Oh, J. H., Hamlim, Seoul, Korea, p. 478 (1995).
11. Kolobov, A. V., Tominaga, J., Zvonareva, T. K., Ivanov Omskii, V. I. and Oyanagi, H., J. Appl. Phys. **92**, 6195 (2002).
12. Modrow, H., Bucher, S., Rehr, J. J. and Ankudinov, A. L., Phys. Rev. B **67**, 35123 (2003).
13. Huffman, G. P., *et al*., Catalysis **151**, 17 (1995).

Physica Scripta. Vol. T115, 736–739, 2005

EXAFS Study of Fe(3+) Interaction with ZrO_2 and TiO_2 Oxides

V. V. Kriventsov[1*], D. I. Kochubey[1], G. Colón[2], M. C. Hidalgo[2], J. A. Navio[2], M. V. Tsodikov[3] and Yu. V. Maksimov[4]

[1]Boreskov Institute of Catalysis, Lavrentiev prosp., 5, Novosibirsk, 630090, Russia
[2]Instituto de Ciencia de Materiales de Sevilla, Centro Mixto CSIC-Universidad de Sevilla and Dpto. De Quimica Inorganica, Universidad de Sevilla, Avda. Americo Vespucio, 41092, Sevilla, Spain
[3]Topchiev Institute of Petrochemical Synthesis, 29 Leninskii prosp., Moscow, 117912, Russia
[4]Institute of Chemical Physics, Kosygina st., 4, Moscow, 117977, Russia

Received June 26, 2003; accepted January 30, 2004

PACS numbers: 61.10.Ht; 82.65.Jv; 82.65.My

Abstract

The forms of Fe(3+) ions stabilization on TiO_2, ZrO_2 oxide nanoparticles and their composition were studied by EXAFS spectroscopy. The structure of the iron local surrounding was investigated with respect to: preparation method, coverage, support crystal modification, acidity of oxide surface and way of iron introduction into oxide matrix. For all oxides, it was shown that Fe(3+) ions stabilized mainly on the nanoparticle surfaces as isolated ions at low coverage. The location of these ions on the oxide surface depends on the correlation between Fe-O bond length and *Me*-O (Me = Ti, Zr) interatomic distances of oxide carriers. The increase of surface coverage results in formation of two-dimension layer structures. For the ZrO_2-TiO_2 composition, it should be noted that the iron cations interact mainly with zirconia. A few structural models of different iron locations were discussed.

1. Introduction

Irradiation of semiconductor particles suspended in water to catalyse oxidative or reductive processes of substrates present in solution is a well-known process, specially useful for the transformation of toxic substances into less harmful products. Although TiO_2 is the most useful photocatalyst, attention has been paid in recent years to iron-doped titania samples (testing efficiency) to replace the bare TiO_2. Results have been controversial, depending on multiple factors such as iron-loading, preparation method, calcination temperature, etc. [1–3]. Generally, no direct correlation between UV-VIS spectroscopic features and photochemical activity could be found, and the preparation method seems to be one of the most important factor for the reactivity of the catalyst.

In paper [4], concerning the iron-doped Degussa P25, it was shown that although wet impregnation method does not seem to be a suitable procedure to obtain a uniform distribution of the dopant into the matrix, the use of $Fe(acac)_3$ instead of $Fe(NO_3)_3$ yields a more homogeneous distribution of iron at the surface.

Structural study of the iron location at the surface seems to be a crucial step for understanding the correlation between the iron content and the preparation method with the catalytic activity of samples. Similar studies have been recently carried out using Fe/ZrO_2. ZrO_2 is also a semiconductor oxide that provides a suitable band-gap energy that enables it for photocatalytic uses.

In paper [5], the effect of iron doping on ZrO_2 was characterised and Fe/ZrO_2 system was tested for several photocatalytic reactions. EXAFS structural studies [6, 7] reveal that, for the sol-gel prepared samples, iron seems to form a two-dimensional layer structure that becomes a segregated oxide at higher loading. This segregated iron oxide could be in principle responsible for the low photocatalytic activity of systems.

This our paper is devoted to a study by EXAFS spectroscopy of iron doped ZrO_2-TiO_2 systems obtained by two different ways, co-precipitation and impregnation techniques.

2. Experimental

2.1. *EXAFS method*

EXAFS spectra of the Ti-K, Zr-K, Fe-K edges for all the samples were obtained at the EXAFS Station of Siberian Synchrotron Radiation Center. The storage ring VEPP-3, with electron beam energy of 2 GeV and an average stored current of 80 mA, has been used as the source of radiation. The X-ray energy was monochromated with a channel cut Si(111) monochromator. The EXAFS spectra of the Ti-K, Zr-K edges were recorded under transmission mode, using two ionization chambers as detectors. The EXAFS spectra of the Fe-K edge were recorded under fluorescent mode. For the Ti-K edge measurements, a harmonics rejection was performed by using a gold mirror. For transmission EXAFS measurements, the samples were prepared as pellets with thickness varied to obtain a 0.5–1.0 jump at the Ti-K, Zr-K absorption edges. The EXAFS spectra were treated using the standard procedures [8]. The background was removed by extrapolating the pre-edge region onto the EXAFS region in the forms of Victoreen's and 4-th power polynomials for transmission and fluorescent modes, respectively. Three cubic splines were used to construct the smooth part of the absorption coefficient. The inflection point of the edge of the X-ray absorption spectrum was used as initial point ($k = 0$) of the EXAFS spectrum. The modulus of Fourier transform (|FT|) was calculated from the EXAFS spectra in $k^3\chi(k)$ at the wave number interval 4.0–12.0 $Å^{-1}$. Curve fitting procedure with EXCURV92 [9] code was employed to determine precisely the distances and coordination numbers in similar wave number intervals after preliminary Fourier filtering using the known XRD data for the bulk zirconium, titanium and iron oxides. Debye-Waller factors are fixed (all the values are equal to 0.005 $Å^2$).

2.2. *Preparation of samples*

The samples studied were prepared by means of two different sol-gel techniques. The ZrO_2-TiO_2 system was prepared by using $ZrOCl_2 \cdot 8H_2O$ and TiO_2 Degussa P25 as precursors. The ZrO_2 content was about ~3–10 wt%. Iron doped systems were obtained by two different ways, co-precipitation and impregnation techniques. In both cases, iron loading was ~0.5–1.5 wt%

*e-mail: kriven@inp.nsk.su

Fe_2O_3. In the coprecipitation method, $Fe(acac)_3$ was settled in suspension jointly with $ZrOCl_2 \cdot 6H_2O$, commercial TiO_2 and urea as a precipitating agent. This solution was heated under reflux at about 80 °C for several hours and a precipitated was obtained after filtration. On the other hand, by the impregnation method, ZrO_2-TiO_2 mixed oxide was previously obtained by precipitation of $ZrOCl_2 \cdot 8H_2O$ on a TiO_2 suspension in distilled water at pH 10, and using ammonia as precipitating agent. The gel obtained was filtered and repeatedly washed in order to eliminate Cl- anions, and finally dried in oven at 110 °C. Fe was then incorporated into the ZrO_2-TiO_2 fresh mixed oxide by pouring down the corresponding amount of $Fe(acac)_3$ in ethanol. Two sets of samples were finally dried at 110 °C and then calcined at 600 °C during 2 hours. Those sets of samples were named as impregnation and co-precipitation samples prepared with/without Fe. Additionally all samples were characterized by XRD method.

3. Results and Discussion

Firstly it should be noted that the |FT| (modulus of Fourier transform) curves describing titanium local arrangement of all samples studied, not presented in this paper, are similar to that of TiO_2 (Degussa P25). |FT| curves describing iron local arrangement of two iron doped samples prepared by impregnation and co-precipitation are shown in Fig. 1(a,b). |FT| curves describing zirconium local arrangement for all the samples studied are shown in Fig. 1(c,d,e,f). EXAFS data (the interatomic distances and coordination numbers) of the studied samples for the iron and zirconium local arrangements are presented in Table I and Table II respectively.

As seen from Table I, there are three structural models describing the iron local arrangement for the doped impregnation and three model for the doped co-precipitation samples, which assume different iron localisation. For the trigonal α-Fe_2O_3, the

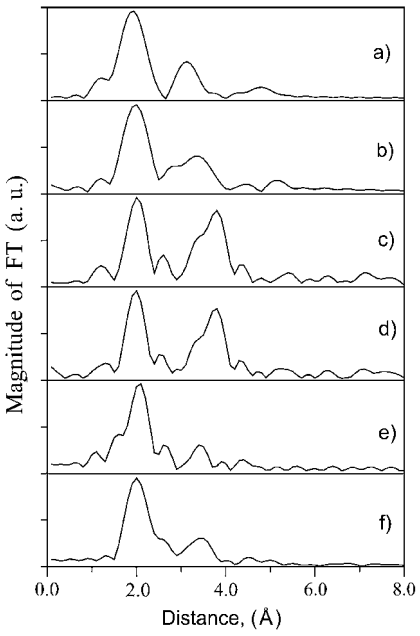

Fig. 1. |FT| curves describing iron local arrangement: a) Fe doped impregnation sample, b) Fe doped co-precipitation sample and zirconium local arrangement, c) impregnation sample, d) Fe doped impregnation sample, e) co-precipitation sample, f) Fe doped co-precipitation sample.

XRD data [10] show two Fe-O distances (1.941, 2.118 Å) and four Fe-Fe distances (2.895, 2.969, 3.361, 3.701 Å). All the models presented yield very similar results both for impregnation and co-precipitation samples: the first Fe-O distances of ∼1.97–2.00 Å and second Fe-Fe distances of ∼2.86–2.95 Å. The corresponding coordination numbers varied within ∼4.3–5.1 and ∼1.1–2.7, respectively. Analysis of the obtained set of distances evidenced for the presence of the Fe-O-Fe species seemingly as small iron oxide nanoclasters or layered structures located onto the

Table I. *EXAFS data (distances, coordination numbers) for iron local arrangement (in assumption of few structural models) of studied samples and known literature XRD data [10] for α-Fe_2O_3. Debye-Waller factors are fixed (all the values are equal to 0.005 Å^2).*

Preparation method	Model number	Bond type	Distance, Å (Error bar ∼1%)	Coordination number (Error bar ∼20%)	*R*-factor, %
Impregnation with Fe	1	Fe-O	1.97	4.3	23.9
		Fe-Fe	2.86	1.1	
		Fe-Ti	3.04	1.6	
	2	Fe-O	1.98	4.4	22.5
		Fe-Fe	2.88	1.5	
		Fe-Fe	3.04	1.6	
	3	Fe-O	1.98	4.4	22.0
		Fe-Fe	2.93	1.3	
		Fe-Zr	3.29	0.9	
Co-precipitation with Fe	1	Fe-O	1.97	4.8	15.6
		Fe-Fe	2.95	2.7	
		Fe-Ti	3.11	3.1	
	2	Fe-O	2.00	5.0	25.2
		Fe-Fe	2.92	1.2	
		Fe-Fe	3.49	2.1	
	3	Fe-O	2.00	5.1	24.6
		Fe-Fe	2.93	1.7	
		Fe-Zr	3.29	2.1	
α-Fe_2O_3		Fe-O	1.941, 2.118	3.0, 3.0	
		Fe-Fe	2.895, 2.969	1.0, 3.0	
		Fe-Fe	3.361, 3.701	3.0, 6.0	

Table II. *EXAFS data (distances, coordination numbers) for zirconium local arrangement (in assumption of few structural models) of studied samples and known literature XRD data [11] for $ZrTiO_4$. Debye-Waller factors are fixed (all the values are equal to 0.005 $Å^2$).*

Preparation method	Model number	Bond type	Distance, Å (Error bar ∼1%)	Coordination number (Error bar ∼20%)	*R*-factor, %
impregnation without Fe	1	Zr-O	2.12, 2.31	4.0, 2.3	21.6
		Zr-Zr	3.57, 3.66	1.1, 2.2	
impregnation with Fe	1	Zr-O	2.10, 2.30	3.9, 2.2	22.7
		Zr-Zr	3.55, 3.62	0.8, 2.1	
co-precipitation without Fe	1	Zr-O	2.12, 2.31	4.8, 1.8	26.5
		Zr-Zr	3.27, 3.39	0.6, 1.1	
	2	Zr-O	2.09, 2.20	4.0, 0.9	26.8
		Zr-Zr	3.36	0.7	
		Zr-Ti	3.49	0.4	
co-precipitation with Fe	1	Zr-O	2.06, 2.19	4.4, 0.8	23.7
		Zr-Zr	3.24, 3.36	0.8, 1.4	
	2	Zr-O	2.07, 2.21	4.5, 1.0	24.6
		Zr-Zr	3.32	0.9	
		Zr-Ti	3.58	0.6	
$ZrTiO_4$*		Zr-O	1.937		
		Zr-Zr	1.948, 2.228		
		Zr-Ti	3.328, 3.522, 3.632	2.0, 2.0, 2.0 2.0, 4.0, 4.0	
			3.328, 3.522 3.632	2.0, 4.0, 4.0	

surface and pre-surface region of the modified titania, ZrO_2/TiO_2 interface or ZrO_2.

Although the shapes of the |FT| curves (Fig. 1a,b) differ for the impregnation and co-precipitation samples that probably indicate on a few positions or different proportion between the iron localisation sites, a detail analysis is difficult because the choice of a preferred structural model is controversial in both cases.

Nevertheless, the EXAFS data (Table I) allows possibility that additionally both the Fe-O-Ti and Fe-O-Zr species, located on the surface/pre-surface region, could be formed. It should be noted that, for impregnation sample, the best is Model 3 which corresponds to Fe adsorbed on ZrO_2, while for co-precipitation sample the best is Model 1 more corresponding to Fe adsorbed on modified titania framework.

By analysis of the zirconium local arrangement of the impregnation samples, obtained from the |FT| curves (Fig. 1c,d) and EXAFS data (Table II), one may assume the formation of mainly tetragonal ZrO_2 phase located on TiO_2 surface.

The presence only of Zr-O distances of about ∼2.10–2.31 Å and long Zr-Zr distances of about ∼3.55–3.66 Å, which are typical for tetragonal ZrO_2 structure, clearly proves this suggestion. In our paper [6], a detailed discussion is presented about monoclinic/tetragonal zirconia determination by EXAFS data. It seems that iron doping does not influence on the formed structures because the shapes of |FT| curves as well as fitting results are similar for both samples. This our conclusion about ZrO_2 structures formed on the TiO_2 surface is in good agreement with the abovementioned hypothesis about iron localisation mainly on ZrO_2 surface.

For the co-precipitation samples, as seen from Fig. 1(e,f), the |FT| curves differ greatly from those for impregnation samples and have some differences between each other. So, amplitudes of the second Zr-Zr and/or Zr-Ti peaks are greatly decreased and the corresponding distances are shorter, while the amplitudes of first peaks are slightly increased as compared with those for impregnation samples. Such phenomena may be explained by assumption that the solid solution of ZrO_2 in the TiO_2 matrix is formed in addition to small amorphous ZrO_2 particles, and perhaps that a distorted $ZrTiO_4$ phase on TiO_2 surface is formed. It should be noted that the method limitation of the number of independed parameters for fitting does not allow to combine all the possibilities to elucidate the situation completely.

There are two structural models present in Table II for these cases. The first model corresponds more to small amorphous ZrO_2 particles, which have the an unusual structure with very short Zr-Zr distances of about ∼3.24–3.39 Å. Earlier such short Zr-Zr distances were shown for Fex/ZrO_2 system [6] and were explained by retaining the initial structures by anion residual after calcination. However, the Zr-O distances for doped and undoped co-precipitation samples are differerent: 2.06; 2.19 Å and 2.12; 2.31 Å respectively, the first is unusually short for the ZrO_2 structure and may be a subject for discussion. The second model corresponds more to a distorted $ZrTiO_4$ phase formed on the TiO_2 surface. Indeed, the presence of suitable Zr-Zr and/or Zr-Ti distances clearly proves this assumption but it should be noted that although the values of the Zr-Me distance are similar to those laying within ∼3.3–3.6 Å for the $ZrTiO_4$ structure, it seems that the bulk $ZrTiO_4$ phase is not formed, whereas the Zr-O distances of about 2.09–2.20 Å for the undoped co-precipitation sample and of about 2.07–2.2 Å for the doped co-precipitation sample, resulted from fitting (Table II), are longer than those corresponding to the $ZrTiO_4$ structure (1.937 Å; 1.948 Å; 2.228 Å). Because the both presented models may be realised in reality, the choice of the best variant is very complicated.

4. Conclusions

The local zirconium and iron arrangements of the iron doped ZrO_2-TiO_2, prepared by sol-gel method, were studied by EXAFS spectroscopy. Only a tetragonal ZrO_2 structure is located on TiO_2

surface for impregnation samples. It seems that the distorted $ZrTiO_4$ structure or small amorphous ZrO_2 particles are formed on the TiO_2 surface for the co-precipitation samples. The presence of the Fe-O-Fe species as well as the Fe-O-Ti and Fe-O-Zr species located on the surface/pre-surface region are shown. The small iron oxide nanoclasters or layered structures are located on the surface and pre-surface region of the modified titania, ZrO_2/TiO_2 interface or ZrO_2.

Acknowledgment

This research was supported by NATO (Ref. EST.CLG 979855), RFBR (03-03-32340a), RFBR (02-03-33053a) and RFBR (03-03-33104a) grants.

References

1. Litter, M. I. and Navío, J. A., J. Photochem. Photobiol. A **98**, 171 (1996).
2. Navío, J. A. *et al.*, Appl. Catal. B **16**, 187 (1998).
3. Navío, J. A. *et al.*, Appl. Catal. A **177**, 111 (1999).
4. Navío, J. A. *et al.*, J. Mol. Catal. **106**, 267 (1996).
5. Navío, J. A. *et al.*, Langmuir **17**, 202 (2000).
6. Vladimir Kriventsov *et al.*, J. Synchrotron Rad. **8**, 528 (2001).
7. Kriventsov, V. V. *et al.*, Nucl. Instr. Meth. A **470**, 341 (2001).
8. Kochubey, D. I., "EXAFS spectroscopy of catalysts" (Nauka, Novosibirsk 1992) (in Russian).
9. Binsted, N., Campbell, J. V., Gurman, S. J. and Stephenson, P. C., SERC Daresbury Laboratory, EXCURV92 code (1991).
10. Shin, H. S. and Kwon, S.-J., J. Korean Ceramic Soc. **30**, 499 (1993).
11. Newnham, R. E., J. American Ceramic Soc. **50**, 216 (1967).

Physica Scripta. Vol. T115, 740–743, 2005

EXAFS Study of Nb Doped $Sr(Co/Fe)O_{3-x}$ Perovskites

V. V. Kriventsov[1*], D. I. Kochubey[1], Z. R. Ismagilov[1], O. Yu. Podyacheva[1] and A. P. Nemudry[2]

[1]Boreskov Institute of Catalysis, Lavrentiev prosp. 5, Novosibirsk, 630090, Russia
[2]Institute of Solid State Chemistry and Mechanochemistry, Kutateladze 18, Novosibirsk, 630128, Russia

Received June 26, 2003; accepted December 17, 2003

PACS numbers: 61.10.Ht; 82.65.Jv; 82.65.My

Abstract

The local structure of the Fe, Co and Nb surroundings of niobium doped $Sr(Co/Fe)O_{3-x}$ perovskites was studied by EXAFS spectroscopy. The samples were prepared by ceramic method at $T = 1250\,^{\circ}C$. In order to vary the oxygen content, the samples were (*i*) slowly cooled in the furnace, (*ii*) quenched in liquid N_2 and electrochemically oxidised. According to EXAFS data, the Nb and Fe cations occupy octahedral positions even at low oxygen content. At the same time, the Co cations seemingly occupy highly distorted octahedral positions. It should be noted that the mean Co-O distance (∼1.84 Å) is much shorter than the mean Fe-O (∼1.92 Å) distance in this case. It was assumed that oxygen vacancies are mainly located near cobalt cation positions.

1. Introduction

Nonstoichiometric oxides $Sr(Co/Fe)O_{3-x}$ exhibiting the mixed electron/oxygen conductivity, are intensively studied as candidate oxygen membranes for catalytic partial methane oxidation and syn.gas production reactors [1–3].

Distribution and location of oxygen vacancies in a nonstoichiometric oxide are important for understanding the mechanism of oxygen transportation (the main functional property of an oxide) and structural transformations in the membrane material regarding the oxygen concentration.

Doping or introduction of different cations into the nonstoichiometric oxide crystal structure is a promising way to improve permeability, chemical and mechanical stability of oxygen membranes.

XRD is usually used to obtain information on the structure of doped oxides. Unfortunately, this method has a number of drawbacks. First, nonstoichiometric oxides can possess a number of point defects as oxygen vacancies, providing a distortion of the cation local surrounding. Since these vacancies are likely disordered, the standard diffraction methods can not be used for their analysis.

The second problem arises when oxides are doped by cations of elements with close scattering abilities. Sometimes these cations are located in several non-equivalent crystallographic positions and one should establish how different chemical element cations are distributed among these positions.

To distinguish them, one should apply some special techniques such as anomalous diffraction (using synchrotron radiation) along with the standard methods.

The above problems can be solved by EXAFS, which is both the local and selective method. This method permits one to study local structure of every chemical element surroundings regardless of the sample crystallization degree.

In this work EXAFS spectroscopy was used to study the $SrCo_{0.7}Fe_{0.2}Nb_{0.1}O_{3-x}$ perovskites with different oxygen concentrations.

2. Experimental

The $SrCo_{0.7}Fe_{0.2}Nb_{0.1}O_{3-x}$ samples were synthesized from stoichiometric amounts of $SrCO_3$, Fe_2O_3, Co_3O_4, and Nb_2O_5, which were thoroughly mixed in an AGO-2 planetary ball mill. Prior to this, ethanol was added to the reagents to prepare a paste-like mixture which was then treated in a mill for 30 seconds. After drying and calcination at 950 °C for 8 h, the mixture was retreated in a mill for 30 s. The pellets prepared from the oxide mixture were placed into a furnace at 1250 °C and held there for 12 h. To prepare $SrCo_{0.7}Fe_{0.2}Nb_{0.1}O_{3-x}$ with low oxygen concentration $(3 - x) \sim 2.5$, the samples were quenched in liquid nitrogen, if the samples were slowly cooled in the furnace oxygen content increased to $(3 - x) \sim 2.7$. The samples electrochemically oxidized in 1 M KOH [4] possessed the highest value $(3 - x) \sim 2.9$. According to XRD the samples with different oxygen content were monophasic and all X-ray reflections were indexed in perovskite cubic cell. The increase of oxygen concentration in $SrCo_{0.7}Fe_{0.2}Nb_{0.1}O_{3-x}$ samples is accompanied by the slight decrease of perovskite cubic parameter. XRD study was carried out on DRON-3M diffractometer with graphite monochromator using CuK_α radiation. Samples $SrCoO_{2.5}$, $SrFeO_{2.5}$ (brownmillerite type) and $SrCoO_3$, $SrFeO_3$ (perovskite type) were used as reference samples.

EXAFS spectra of the Nb-K, Co-K, Fe-K edges for all the samples were obtained at the EXAFS Station of Siberian Synchrotron Radiation Center (SSRC). The storage ring VEPP-3, with electron beam energy of 2 GeV and an average stored current of 80 mA, has been used as the source of radiation. The X-ray energy was monitored with a channel cut Si(111) monochromator. The all EXAFS spectra of the Nb-K, Co-K, Fe-K edges were recorded under transmission mode, using two ionization chambers as detectors. The samples were prepared as pellets with thickness varied to obtain a 0.5–1.0 jump at the Nb-K, Co-K, Fe-K absorption edges. The EXAFS spectra were treated using the standard procedures [5]. The radial distribution function of atoms (RDF) was calculated from the EXAFS spectra in $k^3\chi(k)$ as the modulus of Fourier transform at the wave number interval 3.8–12.0 $Å^{-1}$. Curve fitting procedure with EXCURV92 [6] code was employed to determine precisely the distances and coordination numbers in similar wave number intervals after preliminary Fourier filtering using the known XRD data for the $SrCoO_{2.5}$, $SrFeO_{2.5}$ (brownmillerite type) and $SrCoO_3$, $SrFeO_3$ (perovskite type) bulk compounds. Debye-Waller factors are fixed (all the values are equal to 0.005 $Å^2$).

EXAFS spectra of the cobalt, iron and niobium local surrounding were used to calculate effective coordination

*e-mail: kriven@inp.nsk.su

Table I. *EXAFS data (R – distances (Å); N – effective coordination numbers) describing Fe and Co local surroundings for reference samples.*

	Reference samples							
	$SrFeO_{2.5}$		$SrFeO_3$		$SrCoO_{2.5}$		$SrCoO_3$	
Bond type	*R*, Å	*N*	*R*, Å	*N*	*R*, Å	*N*	*R*, Å	*N*
Fe-O, Co-O	1.92	2.7	1.92	3.3	1.82	2.0	1.88	3.7
Fe-Sr, Co-Fe	3.19	0.8	3.29	1.5	3.19	1.1	3.25	1.1
Fe-Fe, Co-Co	3.96	1.7	3.95	7.5	3.87	1.5	3.86	5.6

Table II. *EXAFS data (R – distances (Å); N – effective coordination numbers) describing Nb local surrounding for $SrCo_{0.7}Fe_{0.2}Nb_{0.1}O_{3-x}$ samples.*

	$SrCo_{0.7}Fe_{0.2}Nb_{0.1}O_{3-x}$					
	$x \sim 0.5$		$x \sim 0.3$		$x \sim 0.1$	
Bond type	*R*, Å	*N*	*R*, Å	*N*	*R*, Å	*N*
Nb-O	1.95	6.2	1.95	6.9	1.94	7.7
Nb-Sr	3.35	1.9	3.36	3.0	3.34	3.9
Nb-Co, Fe	3.98	3.6	3.95	6.3	3.93	9.1

Table III. *EXAFS data (R – distances (Å); N – effective coordination numbers) describing Co local surrounding for $SrCo_{0.7}Fe_{0.2}Nb_{0.1}O_{3-x}$ samples.*

	$SrCo_{0.7}Fe_{0.2}Nb_{0.1}O_{3-x}$					
	$x \sim 0.5$		$x \sim 0.3$		$x \sim 0.1$	
Bond type	*R*, Å	*N*	*R*, Å	*N*	*R*, Å	*N*
Co-O	1.82	1.7	1.85	2.3	1.93	3.2
Co-Sr	3.19	0.6	3.22	0.7	3.33	1.3
Co-Co, Fe	3.89	1.4	3.89	2.7	3.94	4.9

Table IV. *EXAFS data (R – distances (Å); N – effective coordination numbers) describing Fe local surrounding for $SrCo_{0.7}Fe_{0.2}Nb_{0.1}O_{3-x}$ samples.*

	$SrCo_{0.7}Fe_{0.2}Nb_{0.1}O_{3-x}$					
	x ~ 0.5		x ~ 0.3		x ~ 0.1	
Bond type	*R*, Å	*N*	*R*, Å	*N*	*R*, Å	*N*
Fe-O	1.93	3.5	1.94	3.8	1.93	5.1
Fe-Sr	3.28	0.9	3.34	1.7	3.32	2.3
Fe-Co, Fe	3.93	2.8	3.94	5.0	3.93	7.0

numbers and distances Me-O and Me-Me in three coordination spheres (Tables I–IV). This way was chosen to analyze coordination numbers, because both doping and a change in the oxygen stoichiometry result in changes in average coordination numbers and distortion degrees of the coordination polyhedron. All nearby Me-O distances merge into one peak due to insufficient spatial resolution of the method. In this case, effective coordination number becomes the only available value providing the information on a true change in the coordination number due to oxygen vacancies and differences between interatomic Me-O distances.

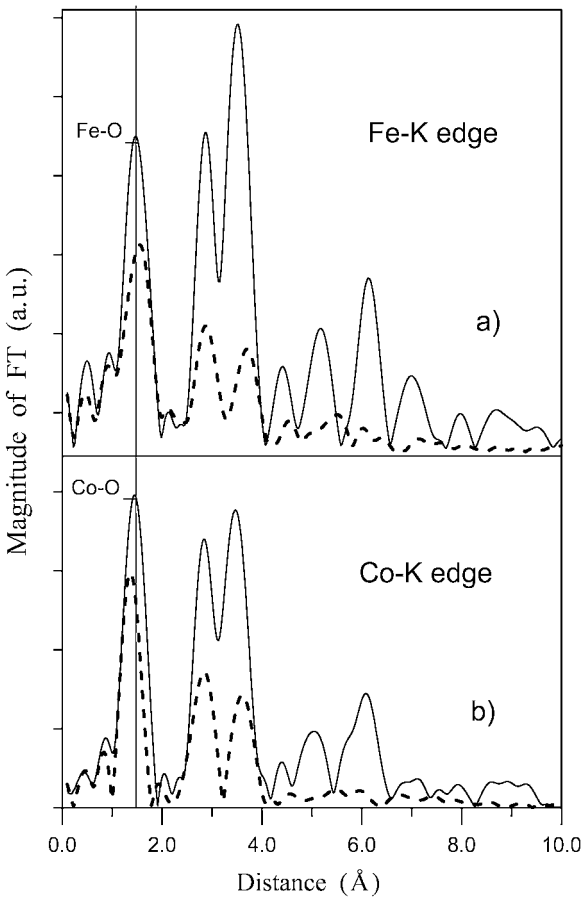

Fig. 1. Radial distribution function (RDF) curves describing a) Fe and b) Co local surrounding of reference samples: (solid line) – $SrFeO_3$, $SrCoO_3$; (dashed line) – $SrFeO_{2.5}$, $SrCoO_{2.5}$.

3. Results and Discussion

RDF curves, describing Fe and Co local surroundings, of reference samples are shown in Fig. 1. RDF curves, describing Co, Fe, Nb local surroundings of $SrCo_{0.7}Fe_{0.2}Nb_{0.1}O_{3-x}$ samples are presented in Fig. 2–4. EXAFS data (*R* – distances (Å); *N* – effective coordination numbers) for $SrCo_{0.7}Fe_{0.2}Nb_{0.1}O_{3-x}$ and reference samples are shown in Tables I–IV. XRD data, for reference and $SrCo_{0.7}Fe_{0.2}Nb_{0.1}O_{3-x}$ samples, are presented in Table V.

Structural data on cubic perovsikte AB_3 (A = Sr, B = Co, Fe, Nb) suggest that 6 oxygen atoms are observed in the cation first coordination sphere in position B. The second and third coordination spheres contain 8 strontium atoms and 6 metal atoms, respectively. The latter sphere can involve all metals, excepting strontium. A particular composition of the third coordination sphere depends on distribution of three metal cations through the compound bulk.

Reference samples: Diffraction data on samples $SrMeO_{3-x}$ (Me = Co, Fe; x = 0.5, 0.0) (Table V) comply with the literature evidence [7–10]. The oxides whose composition approximates the ideal perovskite $SrMeO_3$ have a cubic structure, but their effective coordination numbers (Fig. 1, Table I) for first spheres (Me-O) are low for both iron and cobalt containing perovskites. This indicates that random microdistortions exist in the structure as the long-range ordering (manifesting itself in diffraction) preserves. Note that the distortion degrees are close in both compounds.

Samples $SrMeO_{2.5}$ are crystallized in the brownmillerite type. It is of interest that for the cobalt sample, the unit cell parameter

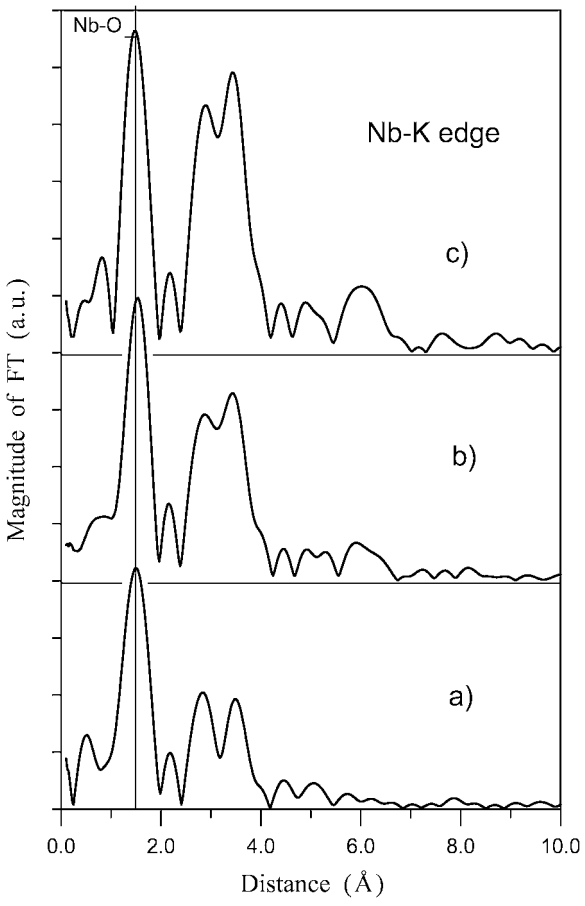

Fig. 2. Radial distribution function (RDF) curves describing Nb local surrounding of $SrCo_{0.7}Fe_{0.2}Nb_{0.1}O_{3-x}$ samples: a) $x \sim 0.5$; b) $x \sim 0.3$; c) $x \sim 0.1$.

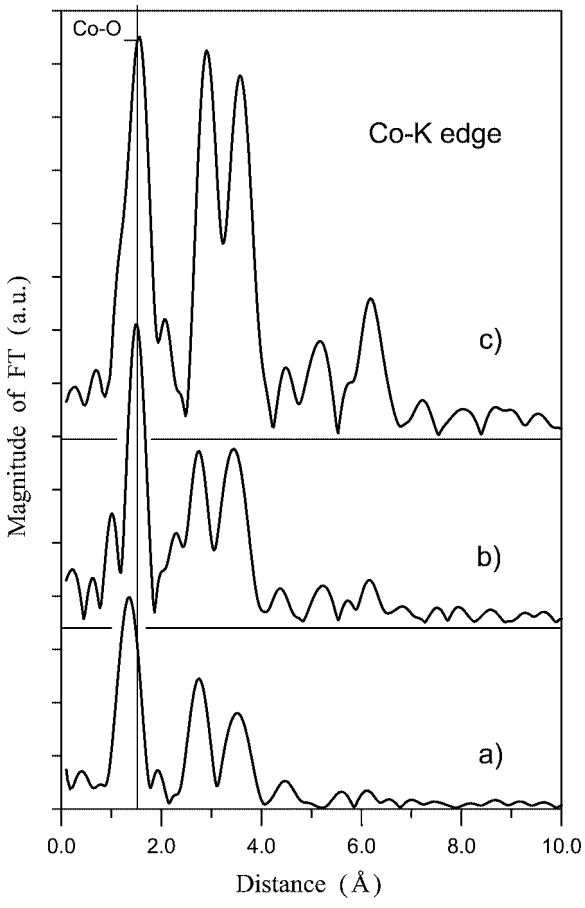

Fig. 3. Radial distribution function (RDF) curves describing Co local surrounding of $SrCo_{0.7}Fe_{0.2}Nb_{0.1}O_{3-x}$ samples: a) $x \sim 0.5$; b) $x \sim 0.3$; c) $x \sim 0.1$.

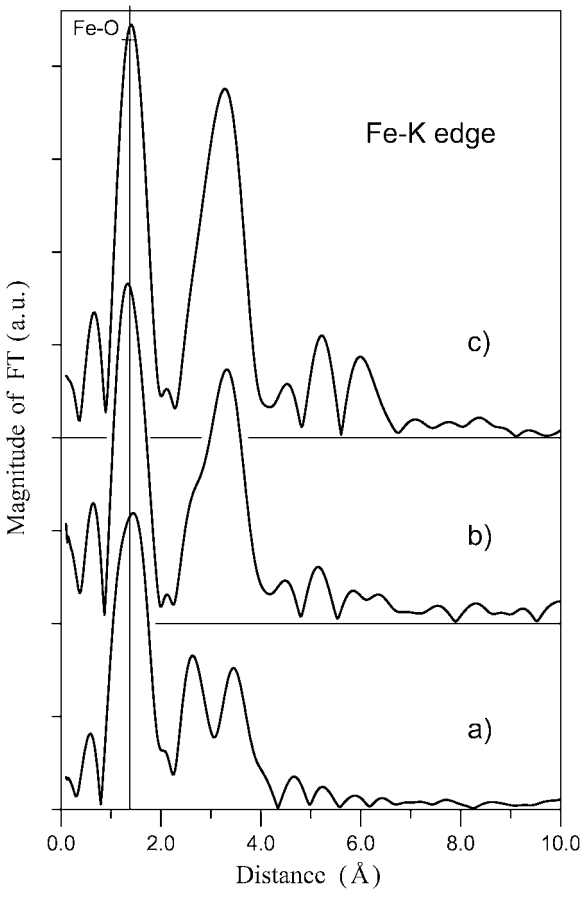

Fig. 4. Radial distribution function (RDF) curves describing Fe local surrounding of $SrCo_{0.7}Fe_{0.2}Nb_{0.1}O_{3-x}$ samples: a) $x \sim 0.5$; b) $x \sim 0.3$; c) $x \sim 0.1$.

along axis *a* significantly differs from that of the iron oxide. In EXAFS data (Fig. 1, Table I), this difference manifests itself as a decrease in the average interatomic distance Co-O by ∼0.1 Å. Whereas for the iron oxide, a transition to a brownmillerite structure does not affect average interactomic distances. For the cobalt sample, a great decrease in the effective coordination number of Co-O exceeds the probable decay value associated with a stoichiometry distortion and indicates large distortions in the cobalt environment with decreasing oxygen amount as compared to iron. Analysis of the changes in the interatomic distances and coordination numbers observed for the third coordination sphere permit one to arrive at the same conclusion. Therefore, though the iron and cobalt containing brownmillerite structures are similar in appearance, their local structures differ.

Additionally it should be noted that the sub-lattice of Co and Fe cations exhibits high symmetry. Some distortions are observed only in the oxygen sub-lattice and in the Me-Sr distances.

$SrCo_{0.7}Fe_{0.2}Nb_{0.1}O_{3-x}$ samples: XRD (Table V) suggests that all the synthesized samples (regardless of oxygen concentration) belong to the perovskite type and are crystallized into a cubic syngony. As oxygen concentration decreases, lattice parameters increase.

As noted above, all coordination numbers have relative values, which primarily evidence the degree of distortion of the local surrounding for given chemical element. According to the obtained data (Fig. 2, Table II), the niobium surrounding is highly symmetric and does not depend on the oxide stoichiometry. It is likely that the oxidation degree of niobium in all complexes is +5, the ion radius being small.

Table V. *XRD data for references and $SrCo_{0.7}Fe_{0.2}Nb_{0.1}O_{3-x}$ samples.*

	Reference samples								$SrCo_{0.7}Fe_{0.2}Nb_{0.1}O_{3-x}$		
	$SrCoO_{2.5}$		$SrFeO_{2.5}$		$SrCoO_3$		$SrFeO_3$		$x \sim 0.5$	$x \sim 0.3$	$x \sim 0.1$
	Brownmillerite (orth.)				Perovskite (cub.)				Perovskite (cub.)		
	Exper.	Lit. [7]	Exper.	Lit. [8]	Exper.	Lit. [9]	Exper.	Lit. [10]	Exper.		
a	5.477	5.456	5.664	5.671	3.824	3.840	3.855	3.855	3.926	3.886	3.856
b	15.746	15.664	15.553	15.590							
c	5.575	5.556	5.528	5.528							

The local surrounding of iron and cobalt radically differs (Fig. 3, 4; Tables III, IV). Thus, an increase in the oxygen concentration results in the increase in the iron coordination number only. For cobalt, changes in the effective coordination number are more complex. Since a change in the average coordination number is accompanied by an increase in the average interatomic distance Co-O. Within the limits of experimental error, distances Co-Co, Fe are constant. But the lattice parameter grows with oxygen removal. On studying the local distortions in cubic $KNbO_3$ [11–13], this observation was interpreted as a partial irregular shift of cations from their crystallographic positions and a turn of octahedrons being relative to each other, which is associated with a symmetry breakdown due to removal of some oxygen. Based on the above, one can assume that similar distortions are primarily associated with cobalt surrounding. Analysis of the EXAFS data suggest that local distortions accumulate with decreasing oxygen concentration on retention of macrosymmetry (long-range ordering). Thus, the introduced cations are not equivalent and the larger part of distortions is associated with cobalt. Indeed (Tables II–IV) a decrease in the oxygen concentration in the structure $SrCo_{0.7}Fe_{0.2}Nb_{0.1}O_{3-x}$ perovskites most strongly affects cobalt.

It is likely that iron and niobium are in the non-distorted octahedral at $(3 - x) = 2.5 - 3.0$, whereas cobalt can also occupy strongly distorted octahedral positions if oxygen is in deficiency. The cobalt local surrounding becomes more symmetric (more regular octahedral positions) with further decreasing oxygen deficiency.

It should be noted that the average distance Co-O for the modified perovskite in oxygen deficiency corresponds to that in $SrCoO_{2.5}$ having a brownmillerite structure.

On oxygen saturation the structure of all studied samples becomes more ordered, which manifests itself as appearance of new peaks in the region of large distances and a considerable rise in coordination numbers for the existing distances.

4. Conclusions

Using the EXAFS method to study modified perovskite-like $SrCo_{0.7}Fe_{0.2}Nb_{0.1}O_{3-x}$ system, it was shown that oxygen vacancies are mainly located near cobalt cation positions.

Acknowledgments

This research was supported by INTAS (00-00180), NATO (Ref. EST.CLG 979855), RFBR (03-03-32340a), RFBR (03-03-32192a), SB RAS Integ. Project No 42 and RAS Project (new materials) No 4.3.6 grants.

The authors also warmly thank Dr. S.V. Tsybulya and Dr. V.A. Ushakov (Boreskov Institute of Catalysis, Novosibirsk, Russia) for kindly presented XRD data and helpful discussions on the subject of the paper.

References

1. Bouwmeester, H. J. M. and Burggraaf, A. J., "Fundamentals of Inorganic membrane science and Technology" (Edited by A. J. Burggraaf and L. Cot) (Elsevier Science B. V., 1996) ch. 10.
2. Lee, T. H., Yang, Y. L., Jacobson, A. J., Abeles, B. and Zhou, M., Solid State Ionics **100**, 87 (1997).
3. Hendriksen, P. V., Larsen, P. H., Mogensen, M., Poulsen, F. W. and Wiik, K., Catalysis Today **56**, 283 (2000).
4. Nemudry, A. P., Koroleva, O. N., Pavlukhin, Yu. T., Podyacheva, O. Yu. and Ismagilov, Z. R., Izv. Ross. Akad. Nauk (seria Phys.) **67**, 952 (2003) (in Russian).
5. Kochubey, D. I., "EXAFS spectroscopy of catalysts" (Nauka, Novosibirsk 1992) (in Russian).
6. Binsted, N., Campbell, J. V., Gurman, S. J. and Stephenson, P. C., SERC Daresbury Laboratory, EXCURV92 code (1991).
7. Grenier, J. *et al.*, Mater. Res. Bull. **14**, 831 (1979).
8. Gallagher, *et al.*, J. Chem. Phys. **41**, 2429 (1964).
9. Shaplygin, I., Lazarev, V. and Russ, J., Inorg. Chem. (Engl. Transl.) **30**, 1828 (1985).
10. Takeda, Y., *et al.* Solid State Chem. **63**, 237 (1986).
11. Bugaev, L. A., Zhuchkov, K. N., Shuvaeva, V. A. and Rusakova, E. B., Japanese J. Appl. Phys. **38**, 215 (1999).
12. Bugaev, L. A., Shuvaeva, V. A., Zhuchkov, K. N., Rusakova, E. B. and Alekseenko, I. B., J. Synchrotron Rad. **6**, 299 (1999).
13. Bugaev, L. A., Shuvaeva, V. A., Zhuchkov, K. N., Rusakova, E. B. and Vedrinskii, R. V., J. Synchrotron Rad. **8**, 308 (2001).

Physica Scripta. Vol. T115, 744–748, 2005

Estimating Crystallite Size in Polydispersed Samples using EXAFS

S. Calvin*, C. J. Riedel, E. E. Carpenter, S. A. Morrison, R. M. Stroud and V. G. Harris

Naval Research Laboratory, Code 6344 Washington, DC 20375, USA

Received June 26, 2003; accepted November 4, 2003

PACS numbers: 81.07.Bc, 61.10.Ht

Abstract

It has long been understood that EXAFS is sensitive to crystallite size, since the average coordination number for a given scattering path is suppressed by a factor that depends upon the distance between the absorbing and scattering atoms. Careful analyses by other researchers have demonstrated the feasibility of determining crystallite size and even morphology in this way, but have in general been limited to well-characterized monodispersed samples. Here, we compare various techniques for estimating mean particle size in a polydispersed sample, using both EXAFS and conventional techniques. It is found that for polydispersed samples with an unknown size distribution, an analysis utilizing a simple spherical model performs nearly as well as more sophisticated models using realistic morphologies. Using simulations as well as experimental data, we demonstrate that EXAFS selects a "mean" size considerably smaller than that found by Scherrer analysis of XRD data; the two in combination can thus be used to give a crude estimate of polydispersion even in samples in which the form of the size distribution is unknown. Finally, we show that the sensitivity of EXAFS to the smallest crystallites present in the sample make it a useful adjunct to TEM in some cases.

1. Introduction

Since the extended X-ray absorption fine structure (EXAFS) of an element within a material is related to the radial distribution function about that element, it is necessarily true that even if a nanocrystalline material[1] adopts a structure identical to its bulk counterpart, the EXAFS will differ due to the reduced coordination numbers associated with atoms near the surface of the crystallites (here called the *termination effect*). In addition, the termination effect will be greater for longer direct scattering paths than for shorter ones, since the suppression is related to the number of atoms within half the path length of the crystallite boundary. Thus it is in theory possible to obtain information on the size and even the morphology of crystallites from analysis of the EXAFS data. Understanding of the termination effect is important for at least two reasons: it may be used to extract information regarding the size and morphology of a nanocrystalline sample; and, even if the sizes and morphologies of the particles in the sample are known, it is necessary to account for the termination effect to accurately analyze the EXAFS of the sample.

Several rigorous studies of the termination effect have been performed over the past several decades. Greegor and Lytle [1], for example, calculated the termination effect for particles in the shapes of spheres, cubes, and monolayer discs; they considered these shapes to be representative of more general classes of polyhedra. Using various metals supported on silica or alumina, they showed good agreement between the EXAFS results and size estimates based on chemisorption measurements. More recently, Frenkel *et al.* [2] and Arcon *et al.* [3] have both applied realistic geometries to the case of supported metal catalysts.

The aforementioned models assume that all of the crystallites in the sample are identical. For supported catalysts this is often a reasonable approximation. Almost all methods of synthesizing free nanoparticles, however, produce a distribution of particles of at least moderately different size, often approximating a log normal distribution [4]:

$$N(r) \propto \frac{1}{r \ln \sigma} \exp\left[\frac{-\left(\ln \frac{r}{r_0}\right)^2}{2(\ln \sigma)^2}\right] \Delta r. \quad (1)$$

In this equation, N is the number of particles with radii $r \pm \Delta r$; r_0 is the *geometric mean* and σ is the *geometric standard deviation* of the distribution.

Although it is possible in principle to extend the methods described above to polydispersed samples, in most cases where the distribution is not known by other means it is doubtful that an EXAFS spectrum contains sufficient information to unambiguously extract a complete size distribution. For the most part, therefore, the question of the termination effect in polydispersed samples has not been previously treated in the literature.

2. Comparison to Scherrer Analysis of X-Ray Diffractograms

An analogous situation holds in the field of X-ray (or, for that matter, electron) diffraction. It is well known that the Bragg peaks of samples comprising small crystallites are broadened due to the limited number of diffraction planes. In 1920, Scherrer computed the relationship between peak width and crystallite size for cubic crystallites [5]. This relationship is still frequently used to estimate the mean size of crystallites in a sample, despite the obvious drawbacks:

- The formula was derived for crystallites of equal size
- Other effects, such as strain, can contribute to the broadening of peaks in diffractograms
- In the case of powder samples, the formula assumes a cubic morphology
- The formula does not yield a measure of polydispersion; the Scherrer standard deviations sometimes reported in the literature measure the reproducibility of the technique when applied to different peaks in the diffractogram, and are unrelated to the width of the size distribution.

Considerable effort has gone into addressing these drawbacks (*e.g.* Bertaut tackled the issue of polydispersion [6]) or into using more sophisticated approaches such as the Fourier peak profile [7]. Nevertheless, the Scherrer formula continues to be the most widely applied method for determining mean size from X-ray diffractograms.

*e-mail: SCalvin@mailaps.org

[1] A sample consisting of single-crystal nanoparticles is, of course, itself a nanocrystalline material; the discussion in this paper is applicable to both freestanding nanoparticles and nanocrystals incorporated into a larger-scale matrix.

If "improved" techniques exist, why does the Scherrer formula continue to be used? In our opinion, the primary reason is its ease of use, combined with the poorly characterized nature of the samples to which it is often applied. A chemist or materials scientist attempting to synthesize nanoparticles, for example, frequently desires a rough estimate of the particle size. At an early stage, many new syntheses produce particles with irregular morphologies or size distributions (*e.g.* they may be contaminated with a few bulk-scale particles); in these cases, so little is known about the distribution that a sophisticated analysis is a waste of resources and the Scherrer analysis will produce a number which is nearly as accurate for much less effort.

In this paper, we discuss using EXAFS in a similar manner. Rather than computing the termination effect for precise morphologies, sizes, and size distributions, we utilize a simple spherical model. The remainder of this paper evaluates the properties and limitations of this model, and compares sizes determined in this way by those determined by Scherrer analysis and transmission electron microscopy (TEM).

3. Termination Effect for Homogenous Spheres

In this model, the crystallite is considered a homogeneous sphere of radius R. An atom a distance ρ from the center has an associated scattering sphere of radius r for each path. The fractional weight of this path relative to a bulk crystal is then equivalent to the fraction of the surface area of the smaller sphere that is contained with in the larger one. This fraction is equal to:

$$\frac{R^2 - (\rho - r)^2}{4\rho r}. \tag{2}$$

By integrating through the entire sphere and dividing by the volume, the formula for the average fraction of the surface area of a small sphere centered at a point in a larger one that is contained within the larger sphere (*i. e.* the fractional suppression of coordination number for direct scattering paths) is derived [8]:

$$1 - \frac{3}{4}\left(\frac{r}{R}\right) + \frac{1}{16}\left(\frac{r}{R}\right)^3. \tag{3}$$

Note that in the homogenous spherical model, atoms are not treated as residing on discrete lattice points, and no use is made of the crystal structure. For multiple-scattering paths, it is important to note that r in equation (3) is the distance from the absorbing atom to the most distant scattering atom, rather than half of the total path length.

4. Mean Size Determinations in Polydisperse Samples

Mean size is not a uniquely defined quantity for polydisperse samples, since it depends on the weighting scheme utilized. Number weighting, for example, counts each crystallite equally, and is therefore the natural scheme for determining size from microscopy images. Volume weighting, on the other hand, counts each atom equally (neglecting differences in density). X-ray absorption spectroscopy is, strictly speaking, volume-weighted. Eq. (3), however, deviates strongly from unity only as R becomes small, and does so in a nonlinear fashion. Thus the difference between the EXAFS spectrum of a sample containing small crystallites from a bulk sample of the same substance will be disproportionately influenced by crystallites toward the small end of the size distribution. Mean sizes determined in this way, therefore, will be somewhat smaller than the volume-weighted mean.

XRD amplitudes, on the other hand, are weighted by the square of the crystallite volume [9]. Because Scherrer analysis utilizes the full width of a diffraction peak at half its maximum value, the size as determined by Scherrer analysis is not identical to the mean weighted by the square of the volume, but it will generally be larger than that found by volume weighting, and thus larger than that found by EXAFS.

To examine the differences between the sizes determined by the two techniques, we constructed a numerical simulation of both EXAFS and Scherrer size determinations. In both cases, log normal distributions were used with specified geometric means and standard deviations. For the EXAFS simulation, simulated particles from 0.1 to 200.0 nm in diameter were included, with the sizes spaced by 0.01 nm (*i.e.* 0.01, 0.02, 0.03 . . . nm). Due to the need to construct a peak profile for each size simulated, the Scherrer simulation used fewer particle sizes, including particles from 0.75 to 19.5 nm in diameter spaced by 1.25 nm (*i.e.* 0.75, 2.00, 3.25 . . . nm).

The results for three log normal distributions are shown in Fig. 1, along with the volume and number weighted mean diameters. It is evident that all mean diameters are similar when the geometric standard deviation is 1.1 or below, while at 1.35 the Scherrer-determined mean is about 15% larger than that found by EXAFS.

More remarkable behavior is expected for samples with geometric standard deviations above a critical value of $e^{\sqrt{6}/6} \approx 1.50$ In these cases, it is straightforward to show that the mean of the distribution given in Eq. (1) diverges. A survey of the literature shows polydispersity of this degree is not uncommon [4, 10–12]. What, then, does this mean?

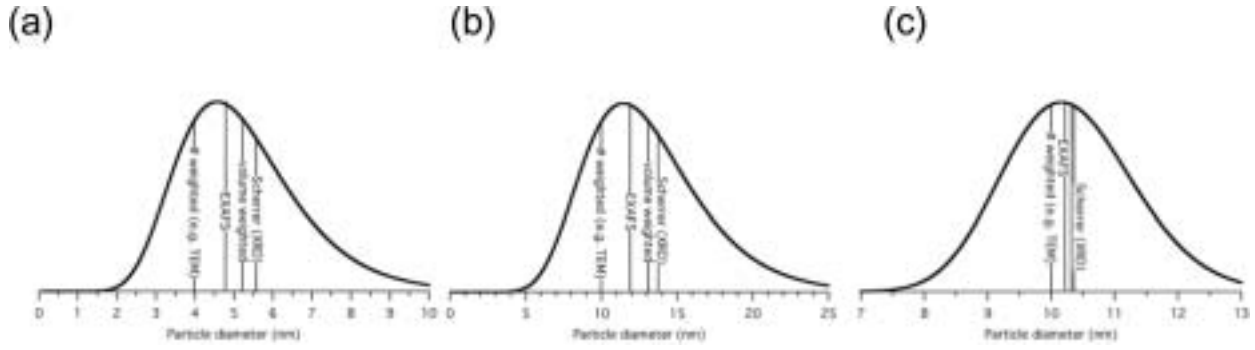

Fig. 1. Volume-weighted log normal size distributions for nanoparticles. The mean diameters as found using various weightings are also shown. Note the different scales on the x-axes. (a) $r_0 = 1.91$ nm, $\sigma = 1.35$; (b) $r_0 = 4.78$ nm, $\sigma = 1.35$; (c) $r_0 = 4.98$ nm, $\sigma = 1.11$. In (c), there is insufficient space to label the volume-weighted mean diameter; it is identified by the unlabeled line between the Scherrer and EXAFS sizes.

The answer lies in the log normal distribution, which includes particles of *all* sizes. In reality, of course, there must be a cut-off size at the high end, if for no other reason than that the sample itself is finite. (The low end also has a cut-off size – one atom!) When a particle distribution is reported as log normal, it is of course meant that the log normal distribution provides a good fit to the actual particle distribution over the size range of interest. The divergence of the theoretical Scherrer size for large polydispersion, then, suggests that Scherrer analysis of such samples is sensitive primarily to the details of the high end cut-off rather than the number or volume-weighted mean size. It is our assertion, therefore, that Scherrer analysis of a sample with a geometric standard deviation of more than 1.5 is not a meaningful measure of the mean particle size.

EXAFS, on the other hand, remains convergence until the volume-weighted mean itself diverges, *i.e.* until the geometric standard deviation exceeds $e^{\sqrt{3}/3} \approx 1.78$. Thus EXAFS size determinations are applicable over a wider range of polydispersity than Scherrer analysis.

5. Experimental Comparison to Atomic Models

In order to investigate these effects in a real system, nanoparticles of the element palladium were synthesized according to the method of Teranishi and Miyake [13] using polyvinylpyrrolidone (PVP) of molecular weight 29,000 Daltons in pure ethanol. Five samples were synthesized, using 75, 100, 255, 500, and 750 mg of PVP in 15 mL of ethanol. The greater the amount of PVP used in this synthesis, the smaller the expected particle size.

Samples were prepared by grinding the powders in a mortar and pestle, and then spreading thin layers of finely ground powder on multiple layers of Kapton tape. The number of layers of tape was chosen so that the total absorption was approximately one absorption length. Uniformity was confirmed at the beamline by measuring transmission as a function of beam position.

The prepared samples were taken to the National Synchrotron Light Source at the Brookhaven National Laboratory in Long Island, New York where X-ray absorption spectra were taken at beamline X-11A. Background subtraction was performed using the method described in Ref. [14], with the background region considered to extend up to 1.0 Å^{-1} in the Fourier transform. The k^2-weighted data is shown in Fig. 2, with the Fourier transform shown in Fig. 3. The typical decrease in amplitude with decreasing particle size is clearly evident.

The technique of curve-fitting to a FEFF8 theoretical standard was used to extract sizes from the data. First, a preliminary fit was performed on a bulk foil to determine $S_0{}^2$ (0.59 ± 0.01), ΔE_0 (-4.7 ± 0.3 eV), the lattice parameter (3.87 ± 0.01 Å), the mean square radial disorder (MSRD) for the nearest-neighbor path ($0.0033 \pm 0.002\ \text{Å}^2$), the MSRD for all other direct-scatterer paths ($0.0079 \pm 0.0014\ \text{Å}^2$), and the third cumulant for the nearest-neighbor path. Direct scattering paths out to the sixth co-ordination shell were included, as well as the fourteen most significant multiple-scattering paths. Multiple-scattering paths were constrained according to the method discussed in Ref. [15]. Because of a strong correlation between the value found for $S_0{}^2$ and the MSRD for the nearest-neighbor, $S_0{}^2$ was refined in a preliminary process that takes advantage of the different dependence on k of the two variables; see Ref. [16] for a complete description of this procedure. Likewise, the third cumulant for the nearest-neighbor was strongly correlated with the lattice parameter; applying the k-dependence procedure yielded a value of nearly zero for the nearest-neighbor third cumulant (the latter was therefore constrained to zero for the final fit). The R factor for this fit was 0.009.

Two models were then used to account for the termination effect: an "atomic" model in which the sample was assumed to be composed of perfect cuboctahedra, and the spherical homogenous model described in Section 3. In the atomic model, the possible mean size was made continuous by allowing for cuboctahedra of two sizes (*e.g.* 3-shell and 4-shell) to be present. All parameters were constrained to the values found for the foil except for the particle size and the lattice parameter; the lattice parameter was constrained to be the same for all nanoparticulate samples. For comparison, a fit that does not account for the termination effect was also performed. As can be seen from Fig. 3, both the atomic and spherical homogenous models yield very good fits, while the bulk (*i.e.* non-terminated) fit is poor. In the case of the sample

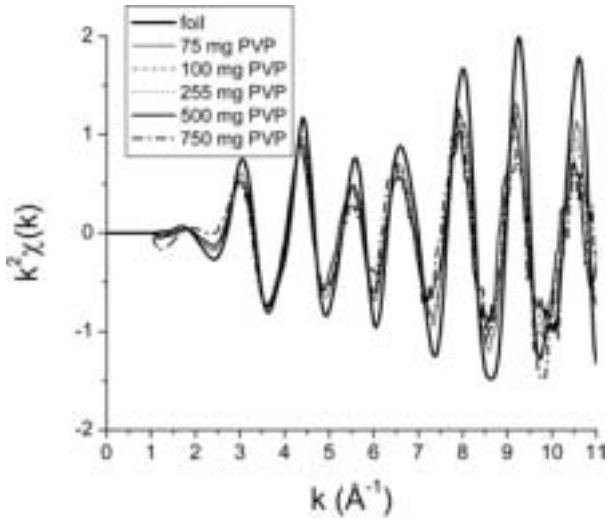

Fig. 2. $\chi(k)$ for palladium nanoparticle data, weighted by k^2.

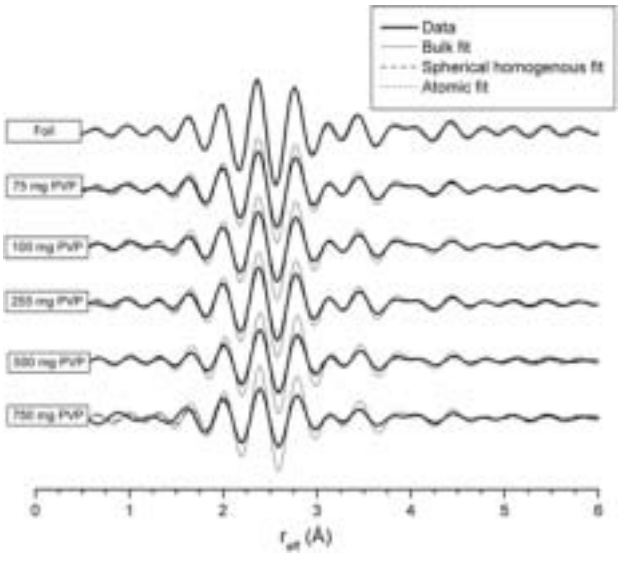

Fig. 3. Real part of Fourier transforms of data and fitted models. Atomic and spherical homogenous fits are essentially indistinguishable in these plots. Above r_{eff} of 2 Å atomic and spherical homogenous fits are essentially indistinguishable from the data as well. Only a bulk fit is shown for the foil, since the other two models would not be meaningful.

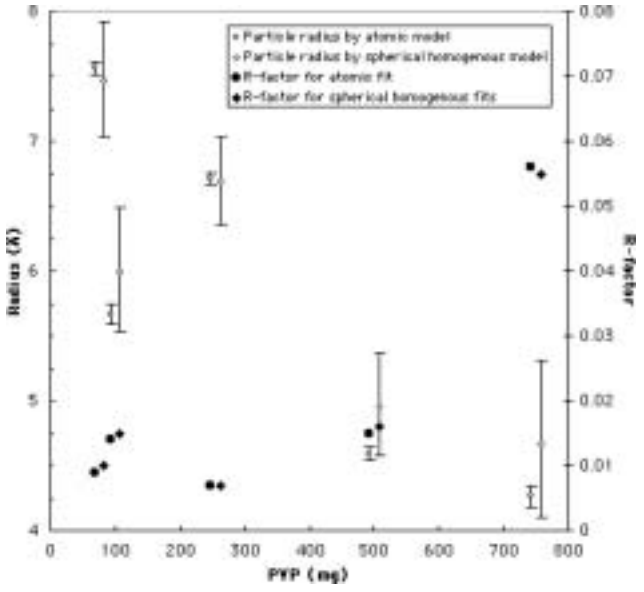

Fig. 4. Particle radius and *R* factor for atomic and spherical homogenous model fits. Results for the two models have been displaced horizontally from each other for visibility.

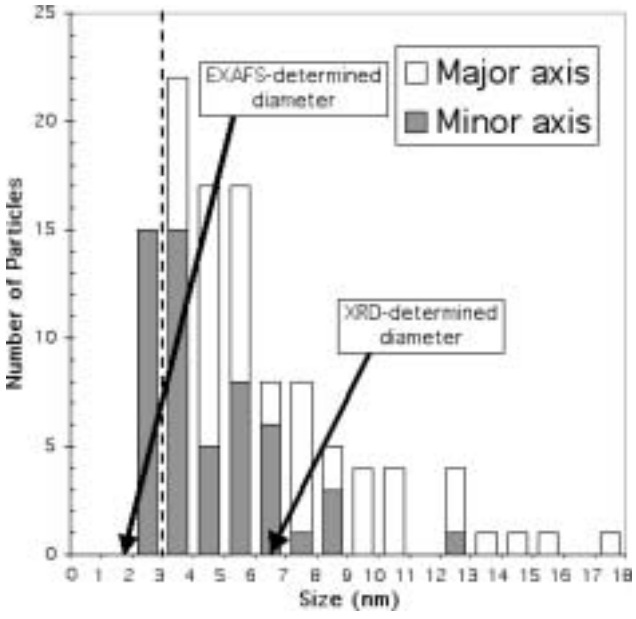

Fig. 5. Figure adapted from Ref. [17]. Histogram of nickel crystallite dimensions from TEM of a nanocrystalline sample. Crystallites with a major axis smaller than about three nanometers did not have sufficient diffracted intensity to be resolved by TEM; this limit is indicated by the dashed line. Note that the EXAFS indicated size is below this limit, and that the EXAFS and XRD determinations establish an interval that includes the majority of the crystallites found by TEM.

with the greatest amount of PVP there is a noticeable mismatch at low r; this may be due to residual PVP bound to the surface of the crystallite.

The results of the terminated fits are shown in Fig. 4 (the lattice parameter was found to be 3.88 Å in both cases). Both fits yield similar values for the radii of the particles, although the uncertainties in the atomic fits are considerably smaller. As expected, particle size is found to generally decrease with increasing PVP. Interestingly, both methods show an exception to this tend: the size of the sample prepared with 100 mg of PVP is found to be smaller than that prepared with 255 mg of PVP. This result was confirmed by TEM. Since TEM also showed the samples to be significantly polydispersed, the spherical homogenous model appears to be appropriate for obtaining a crude estimate of mean crystallite size.

6. Experimental Comparison to Scherrer Analysis

Fig. 5 is taken from a study published elsewhere [17] that compares the results of the spherical homogenous model, Scherrer analysis, and TEM for the same nanocrystalline sample. In that study, the method of using EXAFS to determine the mean size was especially crude, but also especially simple. Fourier transforms of the EXAFS spectra of both the sample and a bulk standard were taken, and the amplitude of the sample's Fourier transform was suppressed by the function given in Eq. (3), with r found by a single-variable fit. Note that this method requires no theoretical standard or multivariable fits. On the other hand, this method does not treat multiple-scattering paths correctly, care must be taken in accounting for the phase shift between EXAFS Fourier transforms and the true radial distribution function as well as artifacts introduced by the Fourier transform, and no allowance is made for relaxation of the nanocrystallites relative to the bulk sample. Nevertheless, the fits were quite good, yielding a mean EXAFS diameter of 1.8 nm. The Scherrer-determined diameter, in contrast, was 6.4 nm; in light of the discussion in Section 4, the difference between the two values suggests considerable polydispersion. TEM images confirmed polydispersion and increasing numbers of crystallites as the diameter dropped below 4 nm. Unfortunately, contrast was not sufficient to image crystallites smaller than 3 nm, and thus direct comparison to the EXAFS result could not be made. Nevertheless, Fig. 5 is qualitatively similar to Fig. 1, providing some confirmation for the ideas discussed above. Further studies are underway to provide additional experimental verification of the relation between mean size, polydispersion, and Scherrer, EXAFS, and TEM sizes.

7. Conclusions

In summary, we believe that EXAFS analyses using a simple homogenous spherical termination model show promise as a method of estimating crystallite sizes in polydispersed samples. Although the method does not provide the accuracy of atomic models, this is not a crucial drawback for samples with poorly characterized size distributions. In many cases, the ease with which this model can be applied may argue for its use over the more sophisticated techniques.

We also wish to emphasize that in samples with high polydispersion, Scherrer analysis is not sensitive to the mean crystallite size, making EXAFS an important alternative. In samples with more moderate polydispersion, the EXAFS determined size will generally be smaller than that determined by Scherrer analysis, with the difference between the two providing an indication of the degree of polydispersion that is present. Thus, the two techniques in combination can provide a first estimate of both size and polydispersion in cases where microscopy is difficult or unavailable.

References

1. Greegor, R. B. and Lytle, F. W., J. Catal. **63**, 476 (1980).
2. Frenkel, A. I., Hills, C. W. and Nuzzo, R. G., J. Phys. Chem. B **105**, 12689 (2001).
3. Arcon, I., Tuel, A., Kodre, A., Martin, G. and Barbier, A., J. Synchrotron Rad. **8**, 575 (2001).

4. Granqvist, C. G. and Burhman, R. A., J. Appl. Phys. **47**, 2200 (1976).
5. Zsigmondy, R. "Kolloidchemie" 3rd ed. (Spamer, Leipzig, 1920).
6. Bertaut, E. F., Acta Cryst. **3**, 14 (1950).
7. Rao, S. and Houska, C. R., Acta Cryst. A **42**, 6 (1986).
8. The same formula is derived by a different method in Borowski, M., J. Phys. IV **7**, C2–259 (1997).
9. Warren, B. E., "X-Ray Diffraction" (Dover, New York 1990).
10. Mitrikas, G., Trapalis, C. C. and Kordas, G., J. Non-Cryst. Solids 286, **41** (2001).
11. Wang, Q., Yang, H., Shi, J. and Zou, G., Mater. Sci. Eng. **A307**, 190 (2001).
12. Elihn, K. *et al*., Appl. Phys. A **72**, 29 (2001).
13. Teranishi, T. and Miyake, M., Chem. Mater. **10**, 594 (1998).
14. Calvin, S., Carpenter, E. E., Ravel, B., Harris, V. G. and Morrison, S. A., Phys. Rev. B **66**, 224405 (2002).
15. Calvin, S., Ph.D. Thesis (City University of New York, New York, 2001).
16. Ravel, B., Ph.D. Thesis (University of Washington, Seattle, 1997).
17. Calvin, S. *et al.*, J. Appl. Phys. **94**, 778 (2003).

Physica Scripta. Vol. T115, 749–752, 2005

XAFS and XRD Studies of PdO-CeO_2 Catalysts on χ-Al_2O_3

Wei Bing Li, Yuichiro Murakami, Masanao Orihara, Suminori Tanaka*, Kunio Kanaoka*, Kei-ichiro Murai†, Toshihiro Moriga, Eiji Kanezaki and Ichiro Nakabayashi

Faculty of Engineering, Tokushima University, Tokushima 770-8506, Japan
*Okura Industrial Co., Ltd.; 1515 Nakatsu-cho, Marugame-shi 763-8508, Japan

Received June 26, 2003; accepted November 4, 2003

Abstract

Alumina-supported PdO is largely accepted as an effective catalyst for the methane combustion reaction. In this study, we investigated the influence of the addition of CeO_2 to the PdO catalysts supported on χ-Al_2O_3 on their microstructures by XAFS spectroscopy and X-ray diffraction technique (XRD).

We obtained the radial structure functions (RSF) from Fourier transform of Pd K-edge EXAFS spectra of both fresh and as-tested catalysts for the PdO and PdO-CeO_2 system on alumina, respectively. A single peak, which is assigned to the nearest neighbor Pd-Pd bonds in Pd metal, was seen after the catalytic activity test at 573 K under a methane-oxygen stream. This is consistent with the fact that PdO in both the catalysts are reduced to metallic Pd at 573 K. In the fresh PdO-CeO_2 catalyst, the second- and third-neighbor peak intensities in the RSF were reduced to about one-half, compared with those in the fresh CeO_2-free catalyst, while these catalysts showed the same peak intensities for the nearest neighbor RSF. These results suggest that CeO_2 induces disordering of the outer shells of Pd scattering atoms in the PdO catalyst. It can be presumed that CeO_2 improves the dispersiveness of PdO particles over the support and depresses the aggregation among the particles.

1. Introduction

Combustion catalysts exert effects on the suppression of the evolution of dioxins, because the reaction is initiated at low temperature. As the combustion of iron oxides starts at 573 K, they are typical and widely used as combustion catalysts [1, 2]. Recently, PdO catalysts, which are supported on alumina, are used as combustion ones [3], and garbage bags or resin bags for daily procurement into which PdO catalysts are impregnated are in production. This is because PdO catalysts are colorless and transparent. In addition they burn at temperatures as low as 523 K. The effect of PdO catalysts on the depression of the evolution of dioxins is expected to be larger than that of iron oxides. Generally, γ-Al_2O_3, which is made by thermal treatment of boehmite (AlOOH), is used as a support. However, in a recent study we showed that the PdO catalyst supported on χ-Al_2O_3, whose precursor is gibbsite ($Al(OH)_3$), has a higher oxidation activity than that supported on γ-Al_2O_3 [4].

The most striking characteristic is that PdO has a high catalytic activity already at low concentration. As a matter of fact, the concentration of the PdO catalyst, which has been in practical use is less than 0.1 mol%. XRD is one of the conventional methods to determine the structure of catalysts. However it is less effective for highly dispersed and/or low concentration systems. X-ray absorption fine structure (XAFS) is applicable in such dilute systems to determine the local structure around X-ray absorbing atoms.

In this study, the X-ray absorption spectra near the Pd K-edge of catalysts of both fresh and as-tested PdO/Al_2O_3 and PdO-CeO_2/Al_2O_3, in which cerium oxides were added as promoters, were measured. In addition, XRD measurements were performed for synthesized high concentration catalysts. We discuss the role of CeO_2 promoters and the relationship between the catalytic activities of PdO catalysts and crystal structure of the catalysts as well as the local structure.

2. Experimental

2.1. *Catalyst preparation*

Weighed portions of $Al(OH)_3$ (gibbsite) and $Ce(NO_3)_3 \cdot 6H_2O$ were admixed together with deionized water with stirring for 0.5 h. An aqueous solution of $Pd(NO_3)_2$ (Pd content is 4.5 or 11.4 mass%) was added to the mixture of metal salts in atomic ratios from Ce/Pd = 0 to 5 while keeping the mass ratio of Al_2O_3/PdO = 9, resulting in a suspension. The suspension was calcined for 1 h at 773 K after stirring and drying for 1 h and 15 h, respectively. Samples for measurements were obtained after crushing the calcined solids and sieving into #10–#24 (1.68 mm–0.71 mm) mesh components.

2.2. *Catalytic reaction*

The catalytic experiments were performed in a fixed-bed continuous-flow quartz reactor operated at atmospheric pressure. Details of the reactor design have been described elsewhere [5]. A half-gram of the catalyst was loaded. The gas used was diluted with helium so that the pressure of methane and oxygen would be kept at 3.4 and 20.3 kPa, respectively. The reactants and products were analyzed with an on-stream gas chromatograph (Shimadzu GC-8APT) equipped with a TC detector and integrator (Shimadzu C-R6A).

2.3. *XRD measurements*

Powder X-ray diffraction data were collected using a high-performance diffractometer (Rigaku RINT2500VHF) with monochromatized CuKα radiation with a source power of 30 kV–100 mA for phase identification of the specimens.

2.4. *XAFS measurements and analysis*

Pd K-edge XAFS spectra for PdO/Al_2O_3 and PdO-CeO_2/Al_2O_3 were measured after the tests in a gas flow (CH_4: 2 ml/min, O_2: 2 ml/min) except for the fresh catalyst, in transmission mode at BL-10B of the Photon Factory, Tsukuba. The synchrotron radiation was monochromatized by a Si(311) channel-cut monochromator. The positron storage ring current and energy were approximately 300 mA and 2.5 GeV, respectively. Ionization chambers were applied as incident and transmission beam intensity detectors. Argon gas and krypton gas in the ionization chambers were employed for the incident and transmission monitors, respectively, to achieve optimum signal-to-noise ratio. The appropriate amounts of fine-powder sample and boron nitride powder were mixed and pressed into pellets of 1 mm thickness and

†e-mail: murai@chem.tokushima-u.ac.jp

10.0 mm diameter. All samples had edge-jumps of 1 ($\Delta\mu d$), where μ is the linear absorption coefficient and d is the thickness.

The EXAFS interference function, $\chi(k)$, was extracted from the measured absorption spectra using standard procedures [6], where k denotes the wave number of a photoelectron: $k = [2m(E - E_0)/\hbar^2]^{1/2}$. $\chi(k)$ was normalized using MacMaster coefficients according to the EXAFS workshop report [7]. The programs *XAFS93* and *MBF93* [6] were employed for the data analysis to determine local structure parameters. The EXAFS formula based on single-scattering theory is expressed by the cumulant expansion [8]:

$$\chi(k) = \sum_j \frac{N_j}{kR_j^2} \left|f_j(k,\pi)\right| \exp(-2\sigma_j^{(2)}k^2 + \tfrac{2}{3}\sigma_j^{(4)}k^4) \exp\left(-\frac{2R_j}{\lambda_j}\right) \times \sin\left[2kR_j - \frac{2k}{R_j}\left(1 + \frac{2R_j}{\lambda_j}\right)\sigma_j^{(2)} - \tfrac{4}{3}\sigma_j^{(3)}k^3 + \Psi_j(k)\right], \quad (1)$$

where N_j is the coordination number in the jth shell at distance R_j from the absorbing atom, $\left|f_j(k,\pi)\right|$ is the back-scattering amplitude of the photoelectron, and $\Psi_j(k)$ is the total phase shift function [9]. The quantities $\sigma_j^{(n)}$ are the nth cumulants. The mean free path λ_j of the photoelectron was taken to depend on the wave number k with the relationship $\lambda_j = k/\eta_j$. In this study, because we take a harmonic vibration model, the quantities $\sigma_j^{(3)}$ and $\sigma_j^{(4)}$ are zero. A Fourier-filtered EXAFS function of the peak in real space was compared with a theoretical EXAFS function. In the parameter fitting, the theoretical EXAFS function was filtered in the same way as the observed one in order to eliminate truncation effects in the Fourier transformation procedure.

3. Results and Discussion

Figure 1 shows the conversion of methane (C_M) on the catalysts. C_M was calculated by the following formula [2],

$$C_M(\%) = \frac{CO_2(P)}{CH_4(P) + CO_2(P)} \times 100 \quad (2)$$

where $CH_4(P)$ and $CO_2(P)$ represent the mole numbers of methane and carbon dioxide in the product stream. It was found that no methane oxidation occurred even at 873 K in the absence of the catalyst. The reaction started at temperatures as low as 473 K on the PdO catalysts. The conversions of both PdO and PdO-CeO_2 catalysts increased with increasing reaction temperature. Although the temperature at which C_M went up to 100% on PdO-CeO_2 catalysts was somewhat higher than that on Ce-free catalysts, the activity of PdO-CeO_2 catalysts was higher than that of Ce-free catalysts below 553 K. This result suggests that PdO-CeO_2 catalysts have higher catalytic activities than Ce-free catalysts.

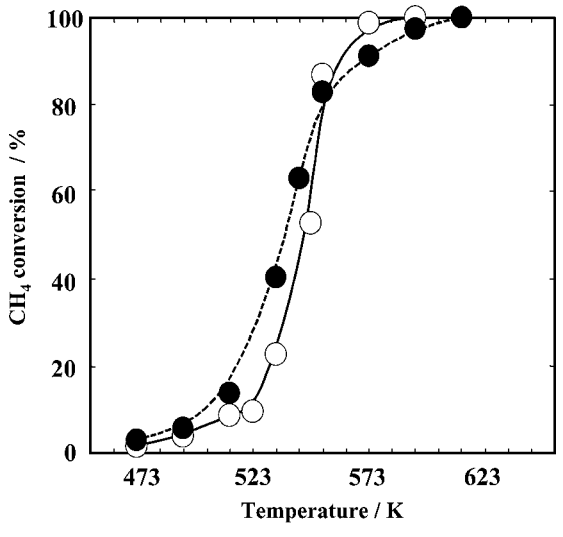

Fig. 1. Activity of methane oxidation of PdO and PdO-CeO_2 catalysts supported on χ-Al_2O_3. ○: PdO catalyst, ●: PdO-CeO_2 catalyst.

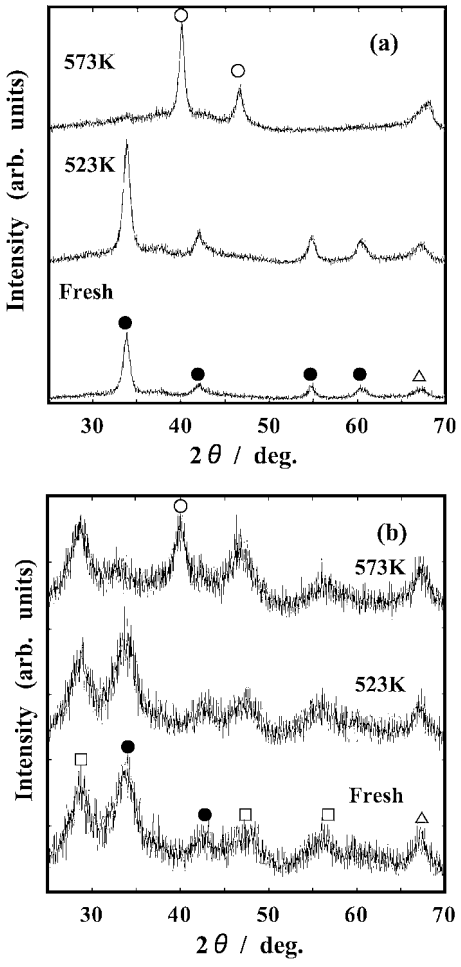

Fig. 2. XRD patterns for (a) the PdO and (b) the PdO-CeO_2 catalysts after tested in gases flow of CH_4 (2 ml/min) and O_2 (2 ml/min) at various temperatures. ○: Pd, ●: PdO, ⊡CeO_2, △: Al_2O_3.

Figure 2 shows XRD patterns for the PdO and PdO-CeO_2 fresh catalysts and those after tested in gas flow of CH_4 (2 ml/min) and O_2 (2 ml/min) at two different temperatures. All diffraction peaks for CeO_2-free catalysts could be assigned to PdO. The peaks were broadened after tested at 523 K. The diffraction profile at 573 K showed that PdO had been reduced to Pd metal. Equally, in the diffraction profile for PdO-CeO_2 catalysts at 573 K, no peaks for PdO were observed but those for Pd metal. In addition, the peaks for CeO_2 were still observed for PdO-CeO_2 catalysts. This suggests that the active species of the reaction is not CeO_2 but PdO. The diffraction profile for PdO-CeO_2 catalysts at each temperature was broader than that for PdO catalysts. It is obvious that PdO is remarkably affected by CeO_2. The results of XRD measurements indicate that the addition of CeO_2 prevents PdO from crystallization and PdO stays finely dispersed. Figure 3 shows a three dimensional structure of PdO and its projection down to the c-axis. The structure of PdO belongs to the tetragonal

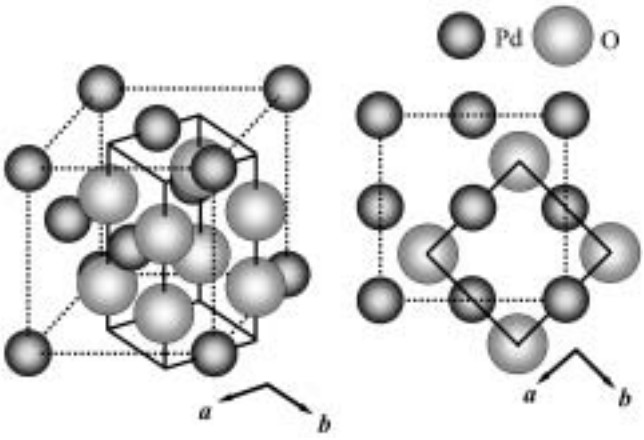

Fig. 3. A three dimensional structure of PdO and its projection down to the *c*-axis.

system. It is presumed that face-centered cubic lattices of Pd are formed just by removing oxygen atoms when PdO is reduced to Pd metal. In the EXAFS analyses, the distances between an absorbing Pd atom and its second-nearest neighbor are equal to the lengths of the *a*- or *b*-axes of the tetragonal PdO unit cell: they correspond to Pd-Pd bonds in Pd metal as shown in Figure 3.

Figure 4(a) shows normalized Pd K-edge XANES spectra of Pd foil (standard sample), fresh and as-tested PdO/Al_2O_3 catalysts at 523 K and 573 K. The XANES spectrum of as-tested catalyst at 523 K was nearly identical with that of fresh catalyst. On the other hand, the XANES spectrum of as-tested at 573 K was distinctly different from the above two spectra. The spectrum of as-tested at 573 K catalyst is characterized by a shift in the edge to lower energy and two peaks above the absorption edge. The normalized Pd K-edge XANES spectra of Pd foil, fresh and as-tested $PdO\text{-}CeO_2/Al_2O_3$ catalysts at 523 K and 573 K, as shown in Figure 4(b), have the same tendency as those of CeO_2-free catalysts. The shift of the absorption edge to lower energy corresponds to the reduction of the absorbing Pd atoms. These results are in agreement with the results of the XRD method. The spectral shapes above the absorption edge are roughly similar to that of Pd foil. These results indicate that PdO was reduced and is present in its metallic state on alumina. In a detailed comparison of the XANES spectra, the difference in the ratio of two peak intensities above the absorption edge was observed between catalysts for PdO and PdO-CeO_2 system on alumina after the catalytic activity test at 573 K. That is to say, the intensity ratio of the second peak around 24.37 keV to the first peak around 24.34 keV of $PdO\text{-}CeO_2/Al_2O_3$ catalyst after the test at 573 K is smaller than that of CeO_2-free catalyst after the test at 573 K. This characteristic of the spectral shape has been observed on a catalyst, which has high dispersiveness and activities [10]. This suggests that the addition of CeO_2 improves the dispersiveness of PdO on supports.

Fourier transformations were performed on Pd K-edge EXAFS spectra in the 3.0–16 $Å^{-1}$ region in *k*-space. The Fourier transforms of the Pd K-edge EXAFS spectra, which are the radial structure functions (RSF), are presented in Figure 5. No phase shift corrections are made. In Figure 5(a), the first-peak at 1.7 Å corresponds to the nearest Pd-O bonds and the second- (2.7 Å) and the third-one (3.1 Å) correspond to the second and the third Pd-Pd shells, respectively. Similarly, in Figure 5(b) the three peaks assigned to the nearest bonds (Pd-O), second-nearest neighbor (Pd-Pd) and the third-nearest neighbor (Pd-Pd) were observed at 1.7 Å, 2.7 Å and 3.1 Å, respectively. The three main peaks of

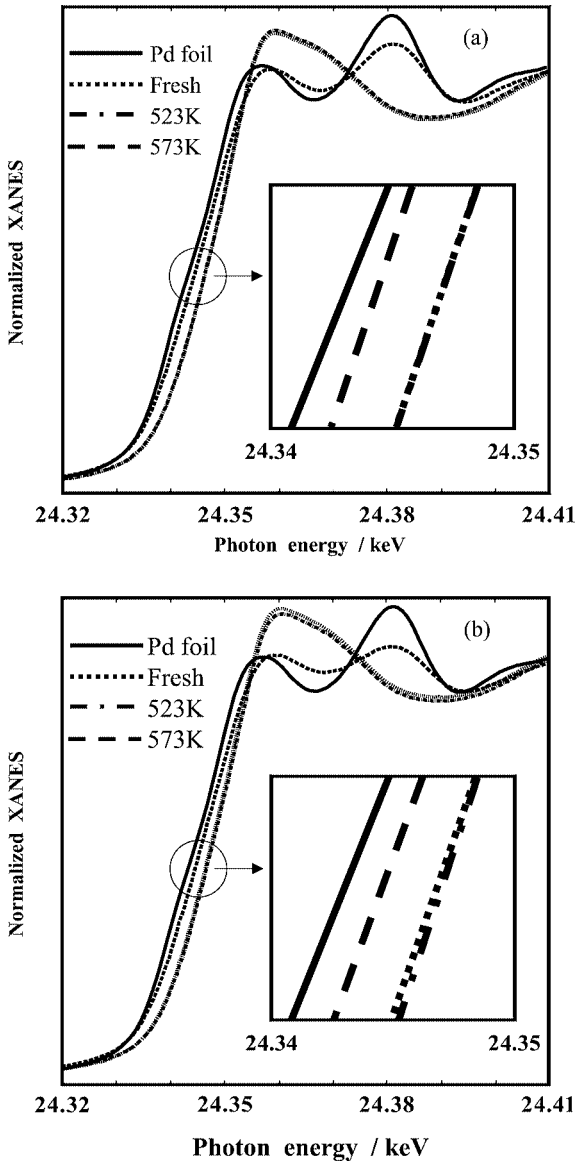

Fig. 4. Normalized XANES spectra for (a) the PdO and (b) the PdO-CeO_2 catalysts after tested in gases flow of CH_4 (2 ml/min) and O_2 (2 ml/min) at various temperatures with those for Pd metals.

PdO/Al_2O_3 are located almost at the same positions as those of $PdO\text{-}CeO_2/Al_2O_3$ catalyst in both results of the fresh catalyst and the catalyst tested at 523 K. However, in each result the two RSFs differ in terms of the amplitude. The amplitudes of the second and third peaks of $PdO\text{-}CeO_2/Al_2O_3$ catalyst were much weaker than those of the CeO_2-free catalyst in spite that the first peaks have the same amplitudes. This kind of phenomenon has been reported by Nakabayashi *et al*., 1995 [11], on Raney nickel catalyst. Such results indicate that there is crystal distortion in the $PdO\text{-}CeO_2/Al_2O_3$ catalysts, as supported by the broad peaks in the XRD patterns shown in Figure 2. CeO_2 induces disordering of the outer shell of Pd scattering atoms in the PdO catalysts. Figure 5(c) shows the FTs of the Pd K-edge EXAFS spectra for the sample after tested at 573 K and for Pd foil as a standard sample. All FTs for catalysts of PdO/Al_2O_3, $PdO\text{-}CeO_2/Al_2O_3$ and the Pd foil show the peaks corresponding to that for Pd-Pd in metal (Pd foil) at 2.4 Å. However, the intensity of the peak corresponding to the metallic Pd-Pd bond decreases in the order, Pd foil > PdO/Al_2O_3 > $PdO\text{-}CeO_2/Al_2O_3$, indicating that the Pd particle size decreases with support on Al_2O_3 and the addition

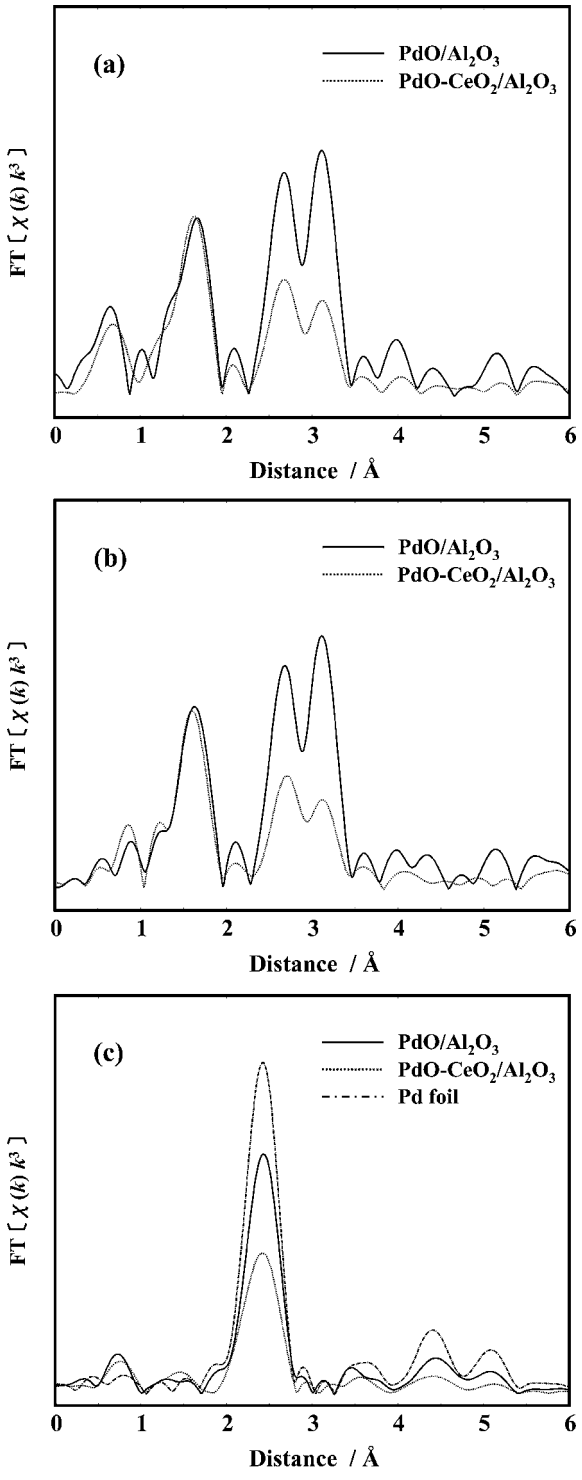

Fig. 5. The Fourier transforms of $\chi(k)k^3$ for (a) fresh, (b) tested at 523 K and (c) 573 K.

of CeO_2. This result shows that the addition of CeO_2 prevents PdO catalysts from being easily reduced to Pd metal and has an effect on the retention of catalytic activities. The results of local structure parameters fitting are shown in Table I. The reliability of fit parameters,

$$R = \sum_s \left| k_s^3 \chi(k_s)_{\exp} - k_s^3 \chi(k_s)_{calc} \right| \Big/ \left| k_s^3 \chi(k_s)_{\exp} \right|, \qquad (3)$$

Table I. *Local structure parameters of the catalysts and Pd foil (standard sample).*

Catalyst	T (K)	Shell	CN	R (Å)	$\sigma^{(2)}$ (10^{-2} Å^2)
PdO/Al_2O_3	fresh	first(Pd-O)	4.00(fix)	2.032(2)	4.28(18)
		second(Pd-Pd)	12.00(fix)	3.042(1)	6.83(9)
	523	first(Pd-O)	4.04(20)	2.022(2)	3.68(31)
		second(Pd-Pd)	11.98(82)	3.039(1)	8.54(31)
	573	first(Pd-Pd)	11.79(35)	2.727(1)	7.23(13)
$PdO\text{-}CeO_2/Al_2O_3$	fresh	first(Pd-O)	4.00(fix)	2.027(2)	3.51(16)
		second(Pd-Pd)	12.00(fix)	3.042(2)	8.73(17)
	523	first(Pd-O)	4.02(22)	2.019(2)	3.73(32)
		second(Pd-Pd)	11.60(49)	3.032(2)	1.10(65)
	573	first(Pd-Pd)	10.71(51)	2.727(1)	8.37(22)
Pd foil		first(Pd-Pd)	12.00(fix)	2.738(1)	0.0646(3)

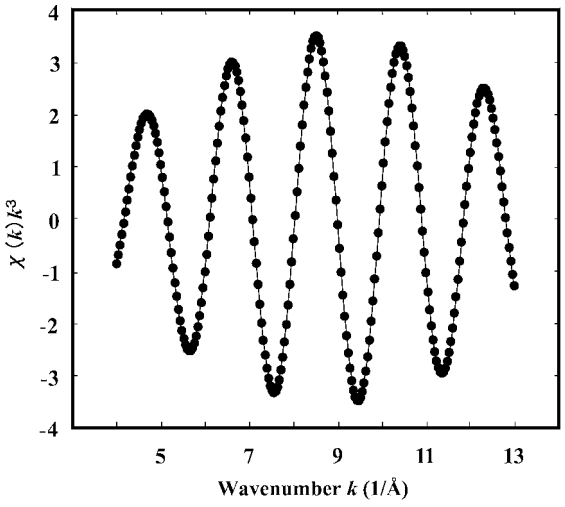

Fig. 6. Fourier-filtered EXAFS spectra (dotted curve) and least-squares fit (solid curve) for first-nearest Pd-O distance in fresh $Pd\text{-}CeO_2/Al_2O_3$ catalyst.

between the experimental and calculated EXAFS functions was less than 0.072. The quality of fit between $k^3\chi_{\exp}$ and $k^3\chi_{\mathrm{calc}}$ is shown in Figure 6.

References

1. Imai, T. *et al*., "Proc. 9th Annual Conference of the Japan Society of Waste Management Experts," (1998), p. 720. [In Japanese].
2. Katoh, M. *et al*., J. Solid State Chem. **156**, 225 (2001).
3. Thevenin, P. O., Alcalde, A., Pettersson, L. J., Järås, S. G. and Fierro, J. L. G., J. Catalysis **215**, 78 (2003).
4. Li, W. B. *et al*., (to be submitted).
5. Sugiyama, S., Minami, T., Moriga, T., Hayashi, H. and Moffat, J. B., J. Solid State Chem. **135**, 86 (1998).
6. Maeda, H., J. Phys. Soc. Jpn. **56**, 2777 (1987).
7. Lytle, F. W., Sayers, D. E. and Stern, E. A., Physica B **158**, 701 (1989).
8. Ishii, T., J. Phys.: Condens. Matter **4**, 8029 (1992).
9. MacKale, A. G., Veal, B. W., Paulikas, A. P., Chan, S. K. and Knapp, G. S., J. Am. Chem. Soc. **110**, 3763 (1988).
10. Imamura, S., Yamane, H., Kanai, H., Saito, Y. and Utani, K., J. Japan Petroleum Institute **45**, 222 (2002).
11. Nakabayashi, I. *et al*., Mater. Chem. **5**, 737 (1995).

Physica Scripta. Vol. T115, 753–755, 2005

XAS Investigation of Iron Substitution in Triclinic FeAPO-34

I. Arčon[1,2,*], A. Ristić[3], N. Novak Tušar[3], A. Kodre[2,4] and V. Kaučič[3]

[1]Nova Gorica Polytechnic, Vipavska 13, POB 301, SI-5001 Nova Gorica, Slovenia
[2]J. Stefan Institute, Jamova 39, POB 3000, SI-1001 Ljubljana, Slovenia
[3]National Institute of Chemistry, Hajdrihova 19, SI-1000 Ljubljana, Slovenia
[4]Faculty of Mathematics and Physics, University of Ljubljana, Jadranska 19, SI-1000 Ljubljana, Slovenia

Received June 26, 2003; accepted November 4, 2003

PACS numbers: 61.10.Ht , 82.75.Fq

Abstract

Iron-modified aluminophosphate with a triclinic form of the chabazite topology FeAPO-34, synthesized hydrothermally from a fluoride medium, is analyzed by Fe K-edge XANES and EXAFS. XANES analysis reveals that the as-synthesized sample contains approximately equal amounts of Fe(II) and Fe(III) cations, while the oxidation state of iron in the template-free sample is Fe(III). EXAFS analysis confirms the incorporation of iron into different framework sites of the as-synthesized FeAPO-34 with triclinic symmetry. In the template-free FeAPO-34 with rhombohedral symmetry, iron cations are located on tetrahedral sites, forming catalytically active acid and redox centers.

1. Introduction

The isomorphous substitution of aluminum sites in the framework of microporous aluminophosphates ($AlPO_4$-n, n denotes structure type) by small amounts of transition metal ions generates catalytically active acid and redox centers. In this way heterogeneous catalysts can be produced. The degree of incorporation of the metal atoms depends on the particular structure of the aluminophosphate.

In the triclinic form of aluminophosphate with chabazite topology ($AlPO_4$-34) successful substitutions of aluminum with Co, Mn, Ni and Zn cations were reported, producing CoAPO-34, MnAPO-34, NiAPO-34 and ZnAPO-34 aluminophosphates [1–3]. The aluminophosphate with triclinic form of chabazite topology ($AlPO_4$-34) can be synthesized from fluoride medium using morpholine or piperidine as structure-directing agents [4, 5]. There are three inequivalent aluminum sites in the framework of $AlPO_4$-34. Two aluminum sites are tetrahedrally coordinated while the aluminum at the third site is octahedrally coordinated with two fluoride atoms in addition to four oxygens. The fluoride ions bridge two Al atoms in a 4-ring connecting double-6-rings of the structure and thus break the rhombohedral symmetry of chabazite [4]. After the thermal treatment the template- and fluoride-free material adopts the rhombohedral symmetry of chabazite topology in which all aluminum atoms are tetrahedrally coordinated [5]. The framework structure of this phase reforms the triclinic symmetry of chabazite in the presence of water [6].

In this paper we examine the incorporation of iron into the framework of triclinic $AlPO_4$-34. We synthesized hydrothermally the FeAPO-34 aluminophosphate. XRD analysis confirmed that the as-synthesized sample had triclinic symmetry, while the framework of the template-free sample adopted the rhombohedral symmetry. The elemental analysis of the as-synthesized sample indicated isomorphous substitution of the framework aluminum by iron. Detailed information on the Fe cation location, however, was difficult to obtain by XRD, since Fe concentration was very low and Fe cations were randomly distributed in the structure. Therefore we used Fe K-edge XANES and EXAFS analysis to probe directly the valence state and the local environment of Fe cations in the as-synthesized and template-free FeAPO-34 samples.

2. Experimental

We synthesized hydrothermally triclinic FeAPO-34 from a fluoride medium using piperidine as a structure-directing agent [3]. A template-free sample was obtained by calcination in oxygen flow at 500 °C for 3 hours.

X-ray absorption spectra were measured in the transmission mode at E4 beamline of HASYLAB synchrotron facility at DESY in Hamburg. The E4 station provided a focused beam from an Au-coated torroidal mirror and a Si(111) double crystal monochromator with about 1 eV resolution at the Fe K-edge. Harmonics were effectively eliminated by a plane Au-coated mirror, and by a slight detuning of the monochromator crystals, keeping the intensity at 60% of the rocking curve with the beam stabilization feedback control. Powder samples of the as-synthesized and template-free FeAPO-34 materials and reference samples were prepared on multiple layers of adhesive tape and mounted on a sample holder in a vacuum chamber of the beamline, so that during measurements the samples were kept in high vacuum. The standard stepping progression within [−250 eV ... 1000 eV] region of the Fe K-edge was adopted with an integration time of 2s/step. The exact energy calibration was established with the simultaneous absorption measurements on the Fe metal foil.

3. Results and discussion

The Fe XANES spectra of the FeAPO-34 samples and reference compounds $Fe(III)PO_4$, $Fe(II)SO_4$, Fe(0) with known oxidation numbers are extracted by a standard procedure (Fig. 1) [7]. The zero energy is taken at the first inflection point in the Fe metal spectrum (7112 eV), i.e., at the 1s ionization threshold in the Fe metal. The shape of the K-edge and the pre-edge resonances is characteristic of the local symmetry of the investigated atom and can be used as a fingerprint in identification of its local environment [7, 8]. Tetrahedrally coordinated atoms are recognized by a single pre-edge peak, which can be assigned to the $1s \rightarrow 3d$ transition, as for example in the $FePO_4$ reference sample. The characteristic tetrahedral resonance is present in the template-free FeAPO-34 demonstrating that iron cations are incorporated into the tetrahedral sites. In the case of the as-synthesized sample

*E-mail: iztok.arcon@p-ng.si

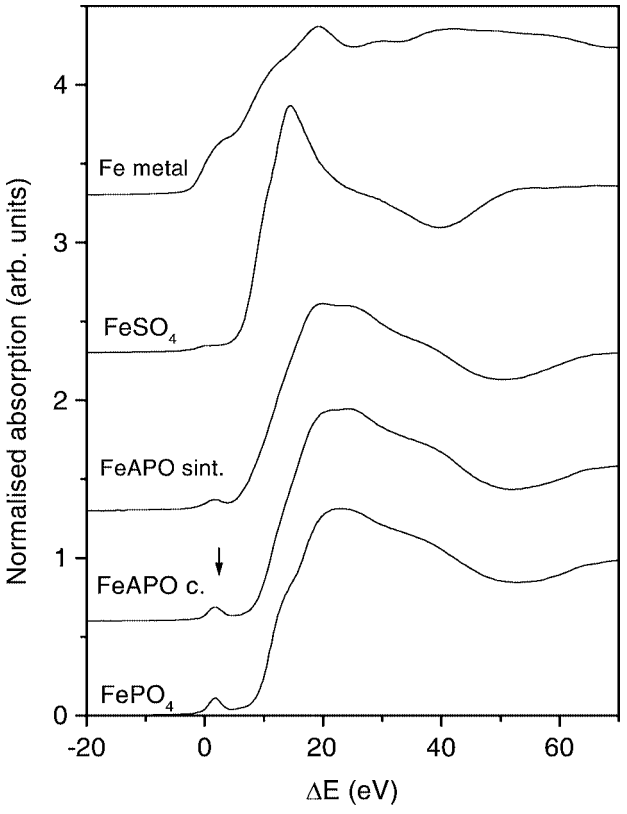

Fig. 1. Normalized Fe K-edge XANES spectra of the as-synthesized and template-free FeAPO-34 and reference samples: $FePO_4$, $FeSO_4$ and Fe metal. The zero energy is taken at the 1s ionization threshold in the Fe metal (7112 eV). The pre-edge resonance characteristic for tetrahedrally coordinated atoms is marked by the arrow.

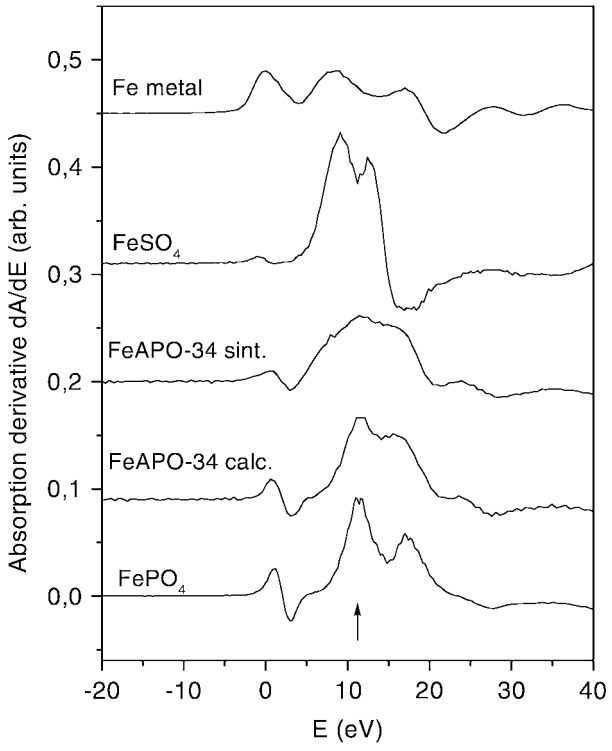

Fig. 2. Absorption derivative of the Fe K-edge profile of the as-synthesized and template-free FeAPO-34 and reference samples from Fig. 1. Vertical arrow is plotted at the energy position of Fe K-edge in $FePO_4$ sample.

the pre-edge peak is weaker, which indicates that only a fraction of iron cations in the sample occupy tetrahedral sites.

A change in the valence state of metal cations during calcination can be deduced from the energy shift of the Fe absorption edge. The precise energy position of the edge is taken at the edge inflection point, which can best be determined in the derivative spectrum (Fig. 2). A linear relation between the edge shift and the valence state has been established for the atoms with the same type of ligands [7–9]. From the spectra of the reference samples ($FeSO_4$ and $FePO_4$) with known iron oxidation states, we derive a Fe K-edge shift of about 3.0 eV per valence state. The Fe XANES spectra of the FeAPO-34 samples clearly indicate oxidation of iron cations during the calcination: the Fe K-edge in the template-free sample is shifted for 1.5 eV when compared to that in the as-synthesized sample. We obtained an average iron valence of about +2.5 in the as-synthesized and +3 in the template-free sample. The as-synthesized FeAPO-34 thus contains about the same amount of Fe(II) and Fe(III) cations, while during calcination all Fe(II) cations in the sample oxidize to Fe(III).

The Fe K-edge EXAFS spectra were quantitatively analyzed for the coordination number, distance, and Debye-Waller factor of the nearest coordination shells of neighbor atoms. The analysis was performed with the University of Washington UWXAFS package [10] using FEFF6 code [11] for ab initio calculation of scattering paths. The k^3 weighted Fourier transform magnitudes of Fe EXAFS spectra calculated in the k-range from 4.5 to 11.5 $Å^{-1}$ are shown in Fig. 3, together with the best fit EXAFS models.

In the case of the as-synthesized FeAPO-34 sample the fit of the first coordination shell shows that iron is coordinated on average

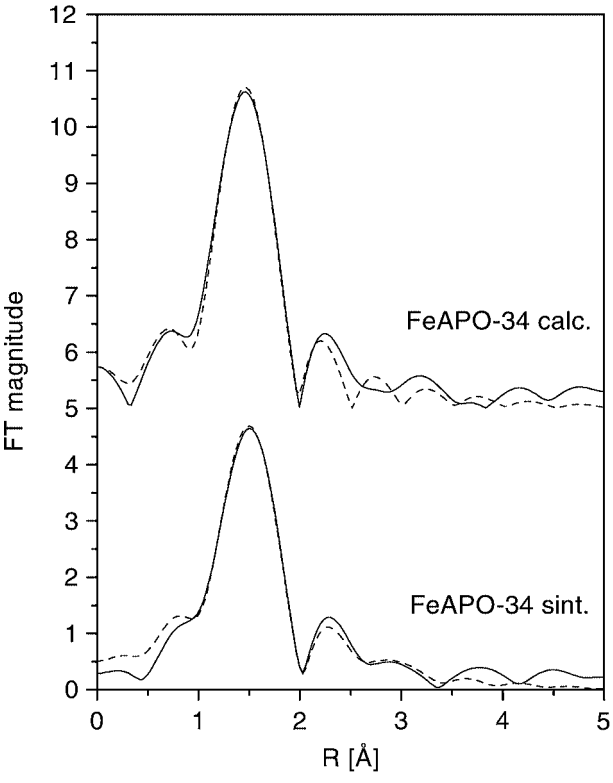

Fig. 3. Fourier transforms of k^3-weighted EXAFS spectra of the as-synthesized and template-free FeAPO-34 (experiment – solid line, EXAFS model – dotted line).

to five oxygen neighbors at 1.92 Å. This average Fe-O distance is consistent with Fe-O distances (1.91 Å) reported earlier for FeAPO-18 sample [12]. In addition, about 0.3 fluorine atoms on average are found at 2.18 Å. A presence of phosphorous atoms is

Table I. *Structural parameters of nearest coordination shells around iron in the as-synthesized and template-free FeAPO-34: neighbour atom, number of atoms (N), distance (R), and Debye-Waller factor (σ^2). Uncertainities of the last digit are given in the parentheses.*

Neighbour atom	N	R (Å)	σ^2 (Å^2)
as-synthesized (triclinic)			
O	4.9(5)	1.92(1)	0.007(2)
F	0.3(2)	2.18(1)	0.002(1)
P	0.6(4)	3.13(1)	0.002(1)
template-free (rhombohedral)			
O	3.8(5)	1.86(1)	0.004(1)

indicated in the second coordination shell at about 3.1 Å. Best fit parameters are listed in Table I.

This result supports isomorphous substitution of framework aluminum by iron in the as synthesized sample, as suggested by elemental analysis. Iron cations replace aluminum at all three inequivalent aluminum sites (tetrahedral and octahedral) in the framework of the triclinic $AlPO_4$-34 framework. In view of the limited sensitivity of the EXAFS signal it should be noted that fluorine neighbor atoms, expected on octahedral sites, cannot be reliably distinguished from oxygen atoms.

In the template-free sample we found four oxygen neighbors at a shorter distance of 1.86 Å in agreement with previously reported values for tetrahedrally coordinated Fe(III) cations [13]. This is in agreement with the rhombohedral symmetry of the template-free sample after the evacuation, when water molecules are removed from the pores. Taking into account also the XANES results we can conclude that in the template-free sample iron is incorporated into the tetrahedral framework sites in the form of Fe(III). The results are additionally supported by the IR spectroscopic analysis of adsorbed CO at 100 K, which gives clear evidence that the acidic Brønsted and redox centers are present in the template-free FeAPO-34 sample [3].

Acknowledgement

The work is supported by Slovenian Ministry of Education, Science and Sports through the research program P0-0516-0104 and the research project Z2-3457-0104 and by the IHP-Contract HPRI-CT-1999-00040 of the European Commision. Absorption spectra were measured at HASYLAB at DESY, Hamburg. Advice on beamline operation by Konstantin Klementiev of HASYLAB is gratefully acknowledged.

References

1. Rajić, N., Ristić, A., Tuel, A. and Kaučič, V., Zeolites **18**, 115 (1997).
2. Rajić, N., Arčon, I., Kaučič, V. and Kodre, A., Croatica Chemica Acta **72**, 645 (1999).
3. Ristić, A. *et al*., Micropor. Mesopor. Mater. **56**, 303 (2002).
4. Harding, M. H. and Kariuki, B. M., Acta Cryst. **C50**, 852 (1994).
5. Schott-Darie, C., Kessler, H. and Benazzi, E., "Proceedings of the International Symposium on Zeolite Microporous Crystals". (Edited by T. Hattori and T. Yashima) (Elsevier, Amsterdam 1994), p. 3.
6. Tuel, A. *et al*., J. Phys. Chem. B **104**, 5697 (2000).
7. Wong, J., Lytle, F. W., Messmer, R. P. and Maylotte, D. H., Phys. Rev. B **30**, 5596 (1984).
8. Arčon, I., Mirtić, I B. and Kodre, A., J. Am. Ceram. Soc. **81**, 222 (1998).
9. Ressler, T., Brock, S. L., Wong, J. and Suib, S. L., J. Synchrotron Rad. **6**, 728 (1999).
10. Stern, E. A., Newville, M., Ravel, B., Yacoby, Y. and Haskel, D., Physica B **208–209**, 117 (1995).
11. Rehr, J. J., Albers, R. C. and Zabinsky, S. I., Phys. Rev. Lett. **69**, 3397 (1992).
12. Zenonos, Ch. *et al*., Phys. Chem. Chem. Phys. **4**, 5421 (2002).
13. Ristić, A. *et al*., Chem. Mater. (2003) accepted.

Physica Scripta. Vol. T115, 756–758, 2005

Multiple Scattering Approach to Au L_3-edge XANES of spr-Au/Al_2O_3 Catalyst

Shin-ichi Nagamatsu[1*], Nobuyuki Ichikuni[2], Shogo Shimazu[2], Takashi Fujikawa[3], Kenzo Fukuda[4] and Takayoshi Uematsu[2**]

[1]Center for Frontier Electronics and Photonics, Chiba University, 1-33, Yayoi-Cho, Inage-Ku, Chiba 263-8522, Japan
[2]Faculty of Engineering, Chiba University, 1-33, Yayoi-Cho, Inage-Ku, Chiba 263-8522, Japan
[3]Graduate School for Science, Chiba University, 1-33, Yayoi-Cho, Inage-Ku, Chiba 263-8522, Japan
[4]The Institute of Applied Energy, Shinbashi SY Building 6F, 14-2, Nishi-shinbashi 1-chome, Minato-Ku, Tokyo 105-0003, Japan

Received June 26, 2003; accepted November 4, 2003

Abstract

Alumina supported gold catalyst prepared by spray reaction method (spr) provides gold particles with about 20 nm diameter. The gold particle size is larger than for conventional gold catalysts. However, the spr catalyst shows catalytic activity for NO-CO reaction. In the present paper, we discuss the local structures of spr-Au/Al_2O_3 catalyst by using Au L_3-edge XANES spectra. In order to investigate the local structures of Au-sites, multiple scattering approach to XANES analysis was applied. Calculated Au L_3-edge XANES spectrum for fcc-Au and Au_2O_3 were in good agreement with the observed spectra. XANES spectra for spr-Au/Al_2O_3 were characterized by 4 types of Au sites (bulk, interface, surface and peripheral). In this case, almost all gold sites (>90%) are bulk sites. Less than 10% of the gold particles are in interface sites. However, the experimental result for spr-Au/Al_2O_3 requires about 30% of gold oxide or hydroxide. Bulk of Al_2O_3 contains a certain number of gold nano-particles, which was incorporated in the Al_2O_3 support. In the interface area, gold oxide forms a few layers. This result was also supported by DV-Xα electronic structure calculations.

1. Introduction

Gold was known as inert material, before nanoscale gold particles dispersed on metal oxide supports were found to exhibit a remarkable catalytic activity and have become widely recognized for many reactions [1–4]. Catalytic properties of supported gold depend on the particle size of gold and the nature of the metal oxide supports. The various efforts have been focused on the preparation of gold catalysts by conventional methods (impregnation, co-precipitation, sol-gel, deposition-precipitation, etc.).

Using the advantage of spray technique [5–8], we have developed a new preparation method for multi-component composite systems and investigated various applications. We have applied the spray reaction method to supported metal catalysts (Ni/ZrO_2, Ru/Al_2O_3 and Ru/TiO_2) [5, 6]. We found high catalytic activities in multi-component nano-composite systems including Au. The spray reaction method (spr) provides Au nano-particles with diameters of 10–30 nm and catalytic activities. The Au particle size is larger than conventional Au catalysts (2–3 nm) which was expected as inert material in empirical assumptions.

In previous work, two kinds of supported Au catalysts, Au/TiO_2 and Au/Al_2O_3, were prepared by the spr method and we investigated their catalytic properties for CO oxidation over Au/TiO_2 and for NO-CO reaction over spr-Au/Al_2O_3, respectively [7, 8]. The synergy interactions between Au particles and supports will cause such catalytic activity. In this paper, we discuss the nano-structure based on Au L_3-edge XANES analysis of spr-Au/Al_2O_3 catalysts.

2. Theory

Multiple scattering approach to L_3-edge XANES formula [9] can be written as

$$\sigma = -\frac{2}{\pi}\mathrm{Im}\left[\frac{\rho_{3/2}(2)^2 e^{2i\delta_2^A}}{15\pi}(3\tau_{21,21} + 2\tau_{20,20}) + \frac{\rho_{3/2}(0)^2 e^{2i\delta_2^A}}{6\pi}\tau_{00,00} - \frac{2\sqrt{5}}{15\pi}\rho_{3/2}(2)\rho_{3/2}(0)e^{i(\delta_2^A+\delta_0^A)}\tau_{20,00}\right], \quad (1)$$

where A means absorption atom site and ρ means radial dipole integral. j_c is total angular momentum of initial core state,

$$\rho_{j_c}(l) = \int R_l(kr) r R_{j_c}(r) r^2 \, \mathrm{d}r. \quad (2)$$

In eq. (1), τ is a renormalized infinite order multiple scattering term and defined by

$$\tau_{L,L'} = [t^{-1}(1 - tG)^{-1}]^{\alpha\beta}_{L,L'}, \quad (3)$$

where t, G are angular momentum representation of t-matrix and Green's function. This matrix element describes a physical process where a photoelectron propagates from site β with angular momentum L' to site α and is scattered with angular momentum L. The t-matrix reflects the electronic structure, whereas G reflects the geometric structure. XANES analysis can give us useful information on electronic and geometric structures around the excited atom.

3. Experimental

The alumina-supported Au catalysts, Au/Al_2O_3 were prepared by a spray reaction (spr) and a conventional impregnation method (imp) [7, 8]. The catalytic activity was tested for NO-CO reaction with a 1 : 1 mixture gas after pre-treatment with O_2 and/or H_2. The O_2 pretreated catalyst showed remarkable activity (Fig. 1). We can expect the gold oxide and hydroxide to play important roles in this reaction.

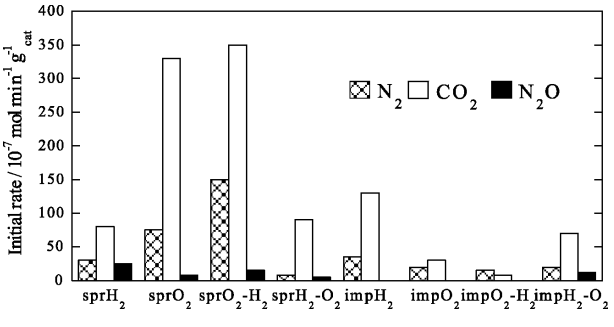

Fig. 1. Initial ratio of NO-CO reaction on Au/Al_2O_3 catalysts.

*e-mail: nagamatsu@restaff.chiba-u.jp
**e-mail: uematsu@faculty.chiba-u.jp

The properties of these catalysts were characterized by BET, XRD, XPS, EXAFS, XANES and other methods. BET surface areas were $22\,m^2/g_{cat}$ for spr catalyst and $97\,m^2/g_{cat}$ for imp catalyst, respectively. The crystallite sizes of Au (111) obtained by XRD analysis were 22 nm and 28 nm for spr catalyst and imp catalyst, respectively. The surface compositions of Au particles were obtained by XPS analysis of Au 4f spectra. The dispersion of Au was (0.29%) and (0.08%) for sprH$_2$ and impH$_2$, respectively. After H_2 pretreatment, Au particles were grown and surface areas decreased. However, sprH$_2$ kept large Au surface compositions.

There may be two interpretations; (1) The spr catalyst has a strong metal support interaction and hence sprH$_2$ keeps small particles during H_2 pretreatment, or (2) Au nano-particles are incorporated into the alumina support.

Figure 2.1 shows Au L_3-edge XANES spectra were measured at BL-10B of the Photon Factory (KEK) with a Si(311) channel cut monochromator (Proposal No. 2001G321). The supported Au particle catalysts are compose of bulk gold and gold oxide. Figure 2.2 shows linear combinations of observed Au foil and Au_2O_3 spectra. Comparison of white line intensity and peak structure at 11950 eV shows that there are 30% of Au_2O_3 in Au nano-particles on spr-Au/Al_2O_3.

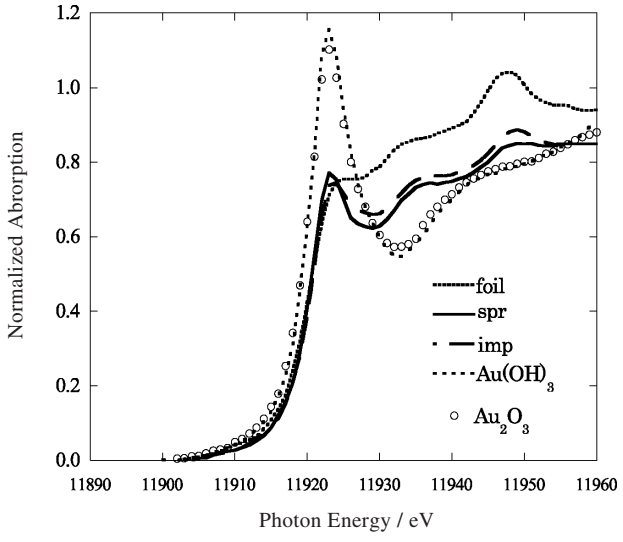

Fig. 2.1. Observed Au L_3-edge XANES spectra of Au foil compared to the results of spr-Au/Al_2O_3, imp-Au/Al_2O_3, $Au(OH)_3$ and Au_2O_3.

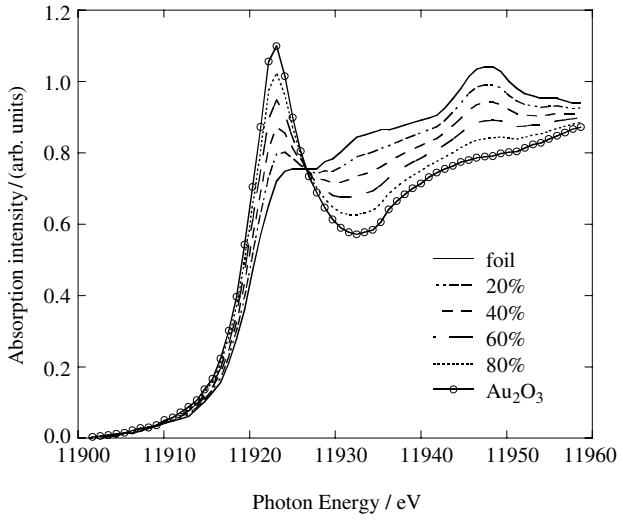

Fig. 2.2. Linear combination of Au L_3-edge XANES spectra of Au foil and Au_2O_3. The percentage means proportion of Au_2O_3.

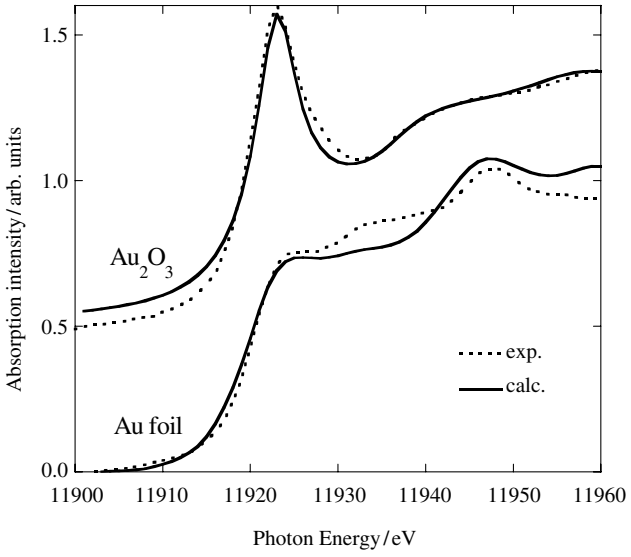

Fig. 3. Comparison of calculated Au L_3-edge XANES spectra for Au foil and Au_2O_3 and observed ones.

4. Result and discussion

First, we tried to calculate Au L_3-edge XANES spectra for fcc Au systems. The lattice constant is 0.408 nm, the nearest neighbor distance is 0.288 nm (12 atoms). The cluster includes 87 atoms and the radius is 0.7 nm. The electronic structure was obtained by FEFF8 [10] calculation [$(5d)^{9.6}$ $(6s)^{0.75}$ $(6p)^{0.65}$]. These values are close to relativistic tight-binding results [$(5d)^{9.6}$ $(6s)^{0.89}$ $(6p)^{0.51}$] [11]. In the case of Au_2O_3, the crystal structure is orthorhombic and Fdd2 [12]. There are two nonequivalent oxygen sites. The electronic structure was obtained by using FEFF8 code [10]. The results are Au [$(5d)^{9.29}$ $(6s)^{0.70}$ $(6p)^{0.61}$], O1 [$(2s)^{1.86}$ $(2p)^{4.40}$] and O2 [$(2s)^{1.87}$ $(2p)^{4.43}$]. The 5d-hole number is larger than that of bulk fcc gold, and two oxygen sites show similar electron occupation numbers. Figure 3 shows a comparison of experimental results and calculated Au L_3-edge for Au foil and Au_2O_3. Calculated results reproduced the observed one, except for the shoulder like structure around 11935 eV of Au foil.

The crystallite size of Au was calculated by Scherrer's equation from the half-width of Au (111). The XRD results show that the diameters of Au particles were 20–30 nm. The multiple scattering calculation uses atomic clusters with 0.5–1.0 nm diameter, and the catalyst particle size is large enough. Since less than 10% of the Au nano-particles are surface atoms, we can expect that the bulk like character is dominant. Furthermore, the metal-support interaction modifies the electronic structures of interface sites. We considered that 4 types of absorption sites (surface, bulk, peripheral, interface). The photoelectron mean free path is about 0.5–1.0 nm and thus these 4 sites are well independent. Observed XANES spectra were characterized by the linear combination of them.

A model structure was constructed with fcc Au and γ-alumina. The slight increase of statical disorder together with the general features of the XANES spectra allowed us to exclude structural changes from the fcc bulk metal structure to the icosahedral structure, even for clusters of 50 atoms [13]. The alumina support has γ-alumina structure, under these conditions.

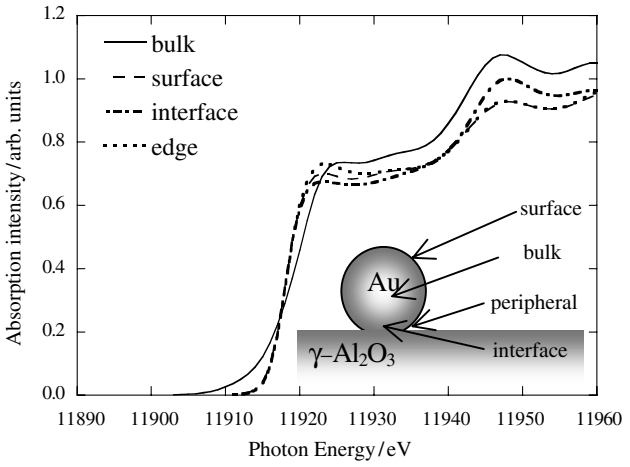

Fig. 4. Comparison of calculated Au L_3-edge XANES spectra for each atomic site.

4.1. *Au L_3-edge XANES spectra*

Figure 4 shows the calculated Au L_3-edge XANES spectra of each atomic site. For surface and peripheral sites, the peak height at 11950 eV is smaller than those for the bulk and the interface sites. These small coordination number sites show small peak heights at 11950 eV structure. On the other hand, the peak heights for Au L_3-edge XANES spectra of Au nano-particles were smaller than for bulk state [13] due to surface effect. There are two possibilities; Au nano-particles for spr-Au/Al_2O_3 are smaller than for other samples or gold oxide or hydroxide phase is rich.

4.2. *DV-Xα*

In order to estimate the effects of interface and surface depth, the local density of state for the different sites are calculated by DV-Xα method [14]. The atomic cluster models are very simple. They are flat surface and interface (fcc-Au (111) and O-terminated γ-alumina (111)). Figure 5 shows these results. For the surface and the interface site, these 5d local density of states (LDOS) were shifted to the high energy side. Interface effects modified the electronic structures a few layers from the interface. The peak shifts were larger than that for the surface.

5. Conclusion

Au/Al_2O_3 catalyst was prepared by spray reaction and impregnation method. We found that spr-Au/Al_2O_3 is more active than imp-Au/Al_2O_3 for NO-CO reaction. The activities depended on the pretreatment.

We tried to characterize the Au nano-particle on spr-Au/Al_2O_3 by using XANES spectra. 4 types of atomic sites characterize XANES spectra and multiple scattering theory allowed us to investigate this in more detail. In this case, bulk site is dominant. The other sites give similar spectra except for a peak structure at 11945 eV and white line structures. This result supports that simple analysis by the superposition of observed Au foil and Au_2O_3 (or $Au(OH)_3$). The spr-Au/Al_2O_3 contains 30–40% of gold oxide or hydroxide. They are distributed in the interface and the peripheral area. However, the surface area is less than 10% and the interface and the peripheral area are much smaller than the surface. It is too large to take the spr-Au/Al_2O_3 model

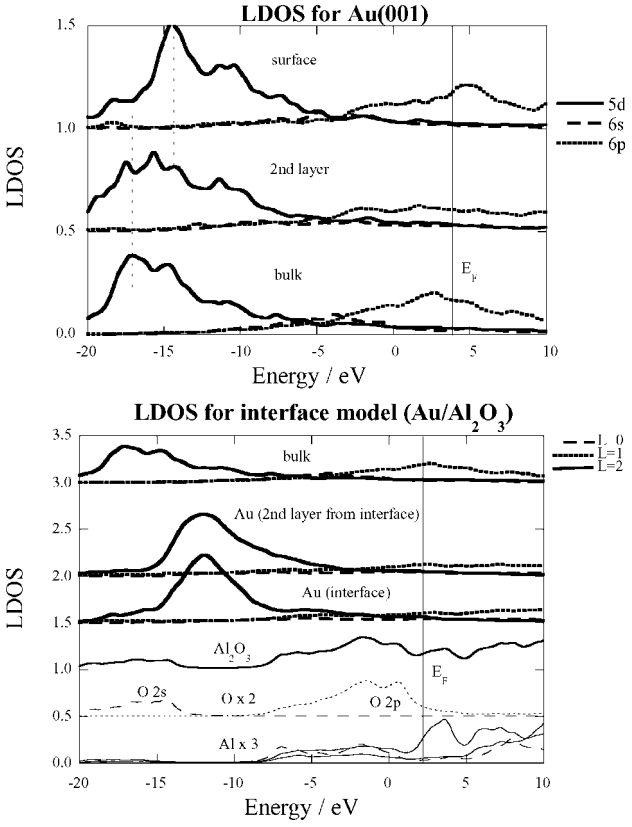

Fig. 5. Local density of states (LDOS) of surface and interface sites.

as 'gold particles on metal oxide'. There are Au nano-particles in the bulk of alumina support and a Au/Al_2O_3-interface are formed. However, Au particles with 20 nm diameter will supply only 10% of gold oxide. In order to investigate the effects of interface depth, we calculated LDOS for gold surface and gold/alumina interface. The LDOS structure of Au 5d is shifted by interface or surface effects. We found such peak shifts in 3–4 atomic layers from the interface. Therefore, it is a plausible model for spr-Au/Al_2O_3 that a part of Au nano-particles are distributed into the alumina.

References

1. Haruta, M. *et al.*, J. Catal. **144**, 175 (1993).
2. Tsubota, S., Cunningham, D. A. H., Bando, Y. and Haruta, M., Preparation of Catalysis VI, 227 (1995).
3. Kozlov, A. I., Kozlova, P., Lin, A. H. and Iwasawa, Y., Appl. Catal. A General **182**, 9 (1999).
4. Bond, G. C., Catalysis Today **72**, 5 (2002).
5. Uematsu, T. and Shimazu, S., Shokubai (Catalyst) **36** 252 (1994).
6. Li, D., Ichikuni, N., Shimazu, S. and Uematsu, T., Appl. Catal. A General **9**, 351 (1998).
7. Fan, L., Ichikuni, N., Shimazu, S. and Uematsu, T., Stud. Surf. Sci. Catl. **132**, 769 (2001).
8. Uematsu, T., Fan, L., Maruyama, T., Ichikuni, N. and Shimazu, S., J. Mol. Catal. A Chemical **209–214**, 182 (2002).
9. Fujikawa, T., J. Phys. Soc. Jpn. **62**, 2155 (1993).
10. Ankudinov, A., Ravel, B., Rehr, J. J. and Conradson, S. D., Phys. Rev. B **58**, 7565 (1996).
11. Mattheiss, L. F. and Dietz, R. E., Phys. Rev. B **22**, 1663 (1980).
12. Jones, P. G., Rumpel, H., Schwarzmann, E., Sheldrick, G. M. and Paulus, H., Acta Crystallographica B, **35** (1979).
13. Balerna, A. *et al.*, Phys. Rev. B **31**, 5058 (1985).
14. Adachi, H., Tsukada, M. and Satoko, C., J. Phys. Soc. Jpn. **45**, 875 (1978).

Physica Scripta. Vol. T115, 759–761, 2005

XANES Study of Carbon Nanotubes Grown without Catalyst

M. I. Abbas[1], Z. Y. Wu[1,2,*], K. Ibrahim[1], S. Botti[3], R. Ciardi[3] and A. Marcelli[2]

[1]Beijing Synchrotron Radiation Facility, Institute of High Energy Physics, Chinese Academy of Sciences, P.O. Box 918, 100039 Beijing, China
[2]Laboratori Nazionali di Frascati, Istituto Nazionale di Fisica Nucleare, Via Enrico Fermi 40, I-00044 Frascati, Italy
[3]ENEA, Divisione Fisica Applicata, P.O. Box 65, 00044 Frascati, Italy

Received June 26, 2003; accepted November 4, 2003

PACS numbers: 73.23.−f, 78.70Dm

Abstract

The structure of different carbon nanotubes grown without catalyst has been investigated and compared with graphite using XANES (X-ray Absorption Near Edge Structure) spectroscopy at the carbon K edge using surface-sensitive total electron yield technique. The surface and bonding properties (π^* and σ^* bands of sp^2 coordinate) are identified looking at the pre-edge features, while the structural characteristics of these materials have been identified looking at the structures in the multiple-scattering region of their XANES spectra.

1. Introduction

Since the discovery of carbon nanotubes [1], these hollow cylindrical molecules have been attracting great interest over the past decade, due to the fundamental scientific interest and their potential applications. Their one dimensional, hollow geometric structure and large surface area have made them manifest unique electronic [2] and mechanical [3] properties. Theoretical [4] and experimental [5, 6] studies have shown that single walled carbon nanotubes (SWNTs) can be metal, semiconductor or semimetal, depending on their chiral angle and diameter, which can be determined by Scanning Tunneling Spectroscopy (STM) [5–7] and other techniques [8]. Because of these properties, they can be used as electron field emission sources [9], scanning probes [10, 11], nanoelectronic devices [12], actuators [13], as well as selective molecular filter [14, 15], Li storage [16, 17], gas absorber [18–20], and so on. Experimental studies confirm that the electronic properties of SWNTs are very sensitive to the chemical environment and that a semiconducting tube can be converted to a metallic one through the exposure to air or oxygen [21]. Theoretical work [22] has also been carried out for the electronic properties of the oxidized carbon nanotubes and confirmed this sensitivity. However, recent high resolution photoemission spectroscopy study [23] of the interaction of molecular oxygen with single walled carbon nanotubes suggested that during the interaction, the surfactant contaminant caused by the extensive use of metal catalysts in the growth process and chemicals during tube purification and dispersion also play a major role, and these contamination traces are usually difficult to detect with conventional diagnostics, which limits the utilization of the intrinsic properties of the tubes. Therefore, a well-established technique [24, 25] to obtain carbon nanotubes without using metal catalysts is worth further investigation.

In this paper, we investigate the structure of carbon nanotubes grown without metal catalysts compared with graphite using XANES (X-ray Absorption Near Edge Structure) spectroscopy at the carbon K edge, and give a simple method for further treatment of the samples.

2. Experimental Details

Carbon nanotube samples were prepared [24, 25] by flowing amorphous carbon nano-sized (diameter 50 ± 20 nm) particles generated by laser-induced chemical vapor deposition [26] over a Joule-heated Si(100) substrate. The process was carried out in a controlled atmosphere reactor, with a residual base pressure of 10^{-6} atm. An inert gas carrier (Ar) was used to drive the nanoparticles from the reservoir in the deposition chamber with a controlled delivery rate. The nanoparticle flow accelerates through an expansion nozzle and then impacts on the substrate surface, placed along the expansion path. As the carrier gas flows by the substrate, the inertia of the particles causes them to travel across flow streamlines and collide with the surface. The high temperature of the substrate surface leads to self-assembled growth of the carbon nanotubes. The deposition parameters were Ar carrier flow = 300 sccm, $p = 0.04$ atm, substrate temperature is 950 °C, deposition time is 30 and 60 minutes for samples A and B, respectively.

As observed from SEM images, the carbon nanotubes grow directly from the particle surface, the mean tube diameter is 30–60 nm, very close to the particle size. A tube length of about 2–3 μm can be estimated. From Raman spectroscopy it can be deduced that the tubes consist mainly of bundles of several hundreds of SWNTs, and it can be estimated that a SWNT has a diameter ranging from 0.85 to 1.33 nm, with a mean of 1.1 nm.

The C K-edge near edge absorption spectroscopy measurements were performed at the Photoelectron Spectroscopy station of Beijing Synchrotron Radiation Facility of the Institute of High Energy Physics, Chinese Academy of Sciences. Samples were loaded in an ultrahigh vacuum chamber and maintained in a background pressure of $\sim 8 \times 10^{-10}$ Torr, reaching a pressure up to $\sim 1 \times 10^{-9}$ Torr during the data acquisition. The spectra were recorded using the total electron yield (TEY) mode, a surface-sensitive detection method with a typical probing depth of a few nm. The photon energies used to record the C K-edge absorption spectrum ranged from 275 to 320 eV, and the experimental resolution at these photon energies is about 0.3 eV.

3. Results and Discussions

In Fig. 1 we compare the C K-edge XANES spectra of carbon nanotube (sample A, prepared at the substrate temperature of 950 °C with deposition time for 30 minutes), graphite, pristine carbon nanopartical (CNP) and highly oriented polycrystalline graphite (HOPG). As labeled in the figure, we assign the common

*e-mail: wuzy@mail.ihep.ac.cn
Tel: +86-10-88235996; Fax: +86-10-88236229

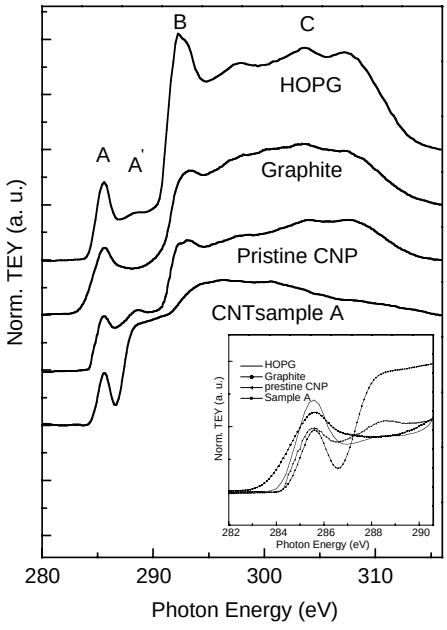

Fig. 1. C 1s x-ray absorption spectra in total electron yield of carbon nanotube sample A (with deposition time for 30 minutes), graphite, pristine carbon nanopartical (CNP) and highly oriented polycrystalline graphite (HOPG). Inset is the superposition of the four spectra in the energy range 282–290 eV.

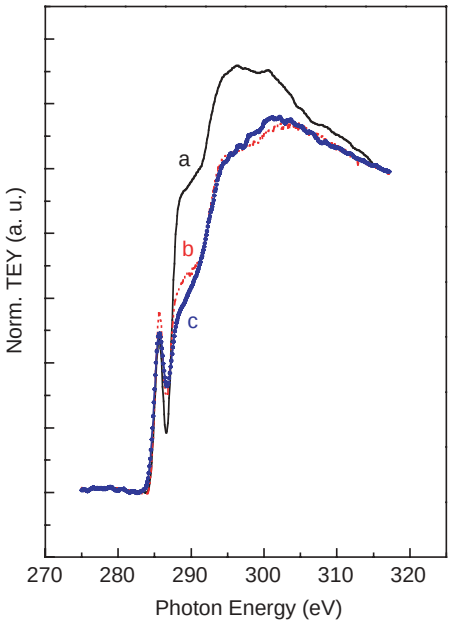

Fig. 2. Comparison of the C K-edge XANES spectra of sample A measured after different treating processes: (a) XANES of sample A as it was (solid line), (b) after annealing at 350 °C for 4 h (dashed line) and (c) a further Ar bombardment at 150 V and 20 mA for 1 h followed by an additional annealing of 1 h (dash-dotted line).

feature A at about 285.6 eV to the transition of C 1s to π^* unoccupied states, the feature B at about 292.5 eV to the 1s to π^* unoccupied states, and the quite broad and rich feature C to multiple scattering resonances. It can be observed that feature A, caused by C-C interaction (sp^2 bonding) of these four kinds of materials are similar in shape, despite a little broadening for the graphite. The intensity (all the spectra were normalized) of feature A of the nanotube sample, which is proportional to the DOS of the π^* bands, is almost the same as that of pristine carbon nanoparticle, but smaller than that of the graphite and HOPG, indicating that the nearest neighbor structure between the pristine carbon nanoparticles and the carbon nanotubes is nearly the same. However, significant differences can be noted for the feature between π^* and σ^* bands, labeled as A' in the figure. For HOPG, it was attributed to the free electron like interlayer states [27, 28], and it disappears for the amorphous graphite, confirming this argumentation. The more pronounced feature A' exhibites in the spectrum of amorphous pristine CNP, which has no free like electron states. Therefore this feature can be attributed to C-H σ^* like states, resulting from the hydrogenation of the pristine carbon nanoparticles [29]. The intensity of the feature is even more prominent for the nanotube sample, implying that more hydrogen atoms came out from the bulk of the pristine nanoparticles during the nanotube formation process to bond with the carbon atoms on the sidewall of the tubes. Since they are mostly on the surface, we can introduce a simple surface treating method to get pure nanotubes free from hydrogen atoms.

Fig. 2 shows C K-edge XANES spectra of sample A with and without surface treatment. (a) is the spectrum of the sample as it was, (b) is the one after annealing at 350 °C for 4 hrs in ultrahigh vacuum and (c) is the one after further modest Ar bombardment at 150 V and 20 mA for 1 h followed by annealing at 350 °C for 1 h. It can be noticed that feature A has no change after the treatment, implying that the short range structure is not affected during the treatment process, while the intensity of feature A′ decreases going from (a) to (c). This behavior immediately indicates that the surface is gradually cleaned from the hydrogen.

The C K-edge XANES spectrum of sample B (prepared at the substrate temperature of 950 °C with deposition time of 60 minutes after modest Ar ion bombardment for 1.2 h at 150 V and 20 mA beam current and further 1.5 h of annealing in ultrahigh vacuum chamber at 350 °C) is shown in Fig. 3 and compared with the spectrum of graphite. There is no evidence of bonding C-H σ^* structure in the spectrum of B, suggesting that the longer time of deposition during the formation of nanotubes is useful

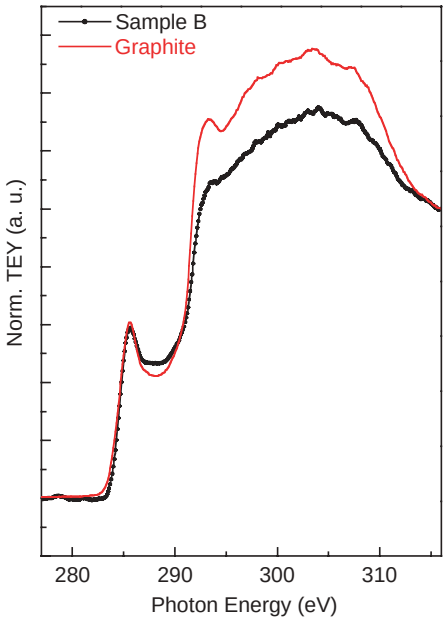

Fig. 3. C 1s XANES spectra in total electron yield of sample B (with deposition time for 60 minutes) and graphite. The XANES spectrum of sample B was measured following Ar ion bombardment for 1.2 h at 150 V and 20 mA beam current after 1.5 h of annealing in ultrahigh vacuum chamber at 350 °C.

for surface treatment of cleaning the tubes from hydrogen. It is worth noticing that XANES of sample B does not exhibit a complex pre-edge structure, which addresses also a reasonable ordering of the carbon matrix. However, a difference between the spectra of sample B and graphite can be recognized looking at the 289–320 eV region: the transition from 1s to σ^* like states is less intense and fairly broadened in the carbon nanotube of sample B. This behavior implies that the "long- or medium-range" atomic order deviates from the graphite one (e.g. disorder and/or distortion effects). Actually, in a nanotube more C atoms are surface ones, experiencing an anisotropic geometry, where a C atom is bonded to inner and outer atoms simultaneously. The anisotropic environment of the surface C atoms can certainly be one of the causes of the distortion of the original trigonal structure. This mechanism, in turn, increases the number of distinct photoelectron scattering paths in a nanotube, yielding a broadening of the XANES spectrum: B feature disappears and C broadens. These effects may be due to a random phase decoherence among each set of closely similar multiple scattering paths and the variation in the threshold E_0 in the absorption coefficient [30]. However, also the compositional disorder, i.e. the presence of residual amorphous carbon, leads to the smearing of near-edge features.

4. Conclusions

In summary, we investigated the carbon 1s XANES spectra of carbon nanotubes grown without catalyst, which are prepared by spraying the amorphous nanoparticals onto a silicon substrate at high temperature for different deposition time. The high temperature causes the transformation of amorphous hydrogenated nanoparticles into nanotubes and leaves some pristine particles (sample A). The data at the C K edge in both graphite and nanotubes show that structural and bonding configurations can be recognized looking at the characteristic pre-edge features but also the large differences in the multiple-scattering region can be investigated to better understand topology and degree of order of these materials. The achieved results are also consistent with the expected chemical environment of a carbon nanotube. It was found that a longer deposition time is preferable for obtaining pure tubes free from hydrogen with further surface treatment (sample B).

Acknowledgment

This work was supported by the Pilot Project of the Knowledge Innovation Program (KJCX2-SW-N11) of the Chinese Academy of Sciences and the Outstanding Youth Fund (10125523) and the Key Important Nano-Research Project (90206032) of the National Natural Science Foundation of China.

References

1. Ijima, S., Nature **354**, 56 (1991).
2. Sito, R., Dresselhaus, G. and Dresselhaus, M., "Physical Properties of Carbon Nanotubes" (College Imperial Press, London 1998).
3. Nardelli, M., Yakobson, B. and Bernholc, J., Phys. Rev. Lett. **81**, 4565 (1998).
4. Hamada, N., Sawada, S. and Oshiyama, A., Phys. Rev. Lett. **68**, 1579 (1992).
5. Wildoer, J. W. G., Venema, L. C., Rinzler, A. G., Smalley, R. E. and Dekker, C., Nature **391**, 59 (1998).
6. Odom, T. W., Huang, J. L., Kim, P. and Lieber, C. M., Nature **391**, 62 (1998).
7. Venema, L. C., Meunier, V., Lambin, Ph. and Dekker, C., Phys. Rev. B **61**, 2991 (2000).
8. Ijima, S. and Ichihashi, T., Nature **363**, 603 (1993).
9. de Heer, W. A., Chatelain, A. and Ugarte, D., Science **270**, 1179 (1995).
10. Dai, H., Hafner, J. H., Rinzler, A. G., Colbert, D. T. and Smalley, R. E., Nature **384**, 147 (1996).
11. Wong, S. S., Joselevich, E., Woolley, A. T., Cheung, C. L. and Lieber, C. M., Nature **394**, 52 (1998).
12. Tans, S., Verschueren, A. and Dekker, C., Nature **393**, 49 (1998).
13. Baughman, R. H., *et al*., Science **284**, 1340 (1999).
14. Tsang, S. C., Chen, Y. K., Harris, P. J. F. and Green, M. L. H., Nature **372**, 159 (1994).
15. Ayappa, K. G., Langmuir **14**, 880 (1998).
16. Beguin, F., *et al*., Synth. Met. **88**, 89 (1997).
17. Wu, G. T., *et al*., Electrochem. Soc. **146**, 1696 (1999).
18. Dillon, A. C., *et al*., Nature **386**, 377 (1997).
19. Ahn, C. C., Ye, Y., Ratnakumar, B. V., Witham, C., Bowman, R. C. Jr. and Fultz, B., Appl. Phys. Lett. **73**, 3378 (1998).
20. Chambers, A., Park, C., Teny, R., Baker, K. and Rodriguez, N. M., J. Phys. Chem. B **102**, 4253 (1998).
21. Collins, P. G., Bradley, K., Ishigami, M. and Zettl, A., Science **287**, 1801 (2000).
22. Jhi, S. H., Louie, S. G. and Cohen, M. L., Phys. Rev. Lett. **85**, 1710 (2000).
23. Larciprette, R., Goldoni, A. and Lizzit, S., Nucl. Inst. Meth. Phys. Res. B **200**, 5 (2003).
24. Botti, S., *et al.*, Appl. Phys. Lett. **80**, 1441 (2002).
25. Botti, S., *et al*., Chem. Phys. Lett. **355**, 395 (2002).
26. Botti, S., Coppola, R., Gourbilleau, F. and Rizk, R., J. Appl. Phys. **88**, 3396 (2000).
27. Fischer, D. A., Wentzcovitch, R. M., Carr, R. G., Continenza, A. and Freeman, A. J., Phys. Rev. B **44**, 1427 (1991).
28. Abbas, M. I., *et al*., submitted to Appl. Phys. Lett.
29. Tang, Y. H., *et al*., Appl. Phys. Lett. **79**, 3773 (2001).
30. Farges, F., Brown, G. E. and Rehr, J. J., Phys. Rev. B **56**, 1809 (1997).

Physica Scripta. Vol. T115, 762–764, 2005

XAFS Study on Active Iron Sites in MCM-41 as a Catalyst for Liquid Phase Oxidation

T. Shishido[1,*], Q. Zhang[2], Y. Wang[2], T. Tanaka[3] and K. Takehira[1]

[1]Graduate School of Engineering, Hiroshima University, 1-4-1 Kagamiyama, Higashi-hiroshima, Hiroshima 739-8527, Japan
[2]State Key Laboratory for Physical Chemistry of Solid Surfaces, Department of Chemistry, Xiamen University, Xiamen 361005, China
[3]Graduate School of Engineering, Kyoto University, Kyoto 606-8501, Japan

Received June 26, 2003; accepted November 4, 2003

PACS number: 61.10.Ht

Abstract

Iron-containing mesoporous molecular sieves (Fe-MCM-41) synthesized by both direct hydrothermal (DHT) and template-ion exchange (TIE) methods have been used as catalysts for the liquid phase oxidation of bulky organic compounds, *i.e.*, anthracene and *trans*-stilbene, with diluted hydrogen peroxide. In the case of Fe-MCM-41-DHT, analysis of Fe K-edge XAFS revealed that isolated and tetrahedrally coordinated Fe species exist in the framework of MCM-41. On the other hand, the Fe-MCM-41-TIE mainly contains small iron oxide clusters, which have octahedrally coordinated Fe species. The tetrahedrally coordinated Fe species in Fe-MCM-41-DHT showed both high activity and efficiency of hydrogen peroxide in the liquid phase oxidations, whereas the iron oxide clusters in the Fe-MCM-41-TIE showed low activity. Moreover, the iron cations incorporated inside the framework of MCM-41 do not leach during the reaction, whereas the small iron oxide clusters leach out into the liquid phase and do not contribute to the catalytic reaction.

1. Introduction

Metal ion-containing mesoporous silicates such as MCM-41 and MCM-48, which possess uniform nano-order mesopores and high concentration of isolated active sites, has attracted much attention as a new type of oxidation catalyst, especially for liquid phase oxidations of bulky organic compounds since a facile diffusion of relatively large molecules can be expected. Many studies have been done for synthesizing and characterizing metal ion-containing MCM-41. Some of these materials, *e.g.*, Ti-MCM-41 and V-MCM-41 showed unique catalytic properties for the reactions of a wide variety of organic substrates such as phenols, alkenes, naphthalenes, alcohols, and thioethers, etc. [1–5].

In order to introduce active metal centers to MCM-41, several kinds of methods have been proposed. The most popular method is the direct hydrothermal (DHT) method. The conventional impregnation, grafting [6] and the template ion exchange (TIE) methods [5] have been also reported. It can be expected that the metal cations with different environments in mesoporous material would result in various catalytic properties. Indeed, Ti-MCM-41 prepared by surface grafting method is more active than that prepared by the DHT method for the epoxidation of cyclohexene with TBHP (*tert*-butyl hydro peroxide) [7]. Vanadium species in V-MCM-41 prepared by the TIE method are dispersed on the surface of channel, preferring the oxidative dehydrogenation of propane, whereas vanadium sites prepared by the DHT method are incorporated in the framework of MCM-41, capable of oxidizing propane to acrolein with moderate selectivity [8]. On the other hand, iron functions as catalytic center in monooxygenase enzymes such as cytochrome P-450 and many selective oxidation systems containing iron, *i.e.*, Gif system and Fenton's reagent have also been developed. Iron is also the active center in many heterogeneous catalysts such as iron-containing microporous amorphous silica synthesized by a sol-gel method, Fe-ZSM-5, Fe-containing Y zeolite with Pd and $FePO_4$, for the selective oxidation of benzene and alkanes.

In the present work, we investigated the structure of iron species in Fe-MCM-41 prepared by two methods, *i.e.*, direct hydrothermal (DHT) and template-ion exchange (TIE) methods by means of Fe K-edge XANES/EXAFS. Iron cations were added into the synthesis gel before hydrothermal synthesis in the former method, while Fe^{3+} ions in the ethanol solution were exchanged with the template cations contained in the as-synthesized MCM-41 in the latter method. The catalytic performances of Fe-MCM-41 thus prepared were tested in the oxidation of both anthracene and stilbenes with H_2O_2, and the effects of the coordination environments of iron species on the catalytic performance are discussed.

2. Experimental

Fe-MCM-41 catalysts were prepared by both hydrothermal synthesis (DHT) and template ion exchanging (TIE) methods according to the previous report [5]. Sodium silicate, iron nitrate and hexadecyltrimethylammonium bromide were used as the sources of Si, Fe and template, respectively. The samples were finally calcined at 823 K for 6 h in a flow of dry air. The mesoporous structure of Fe-MCM-41 was confirmed by XRD and N_2 adsorption. FeO_x/Cab-O-Sil catalyst was also prepared by impregnation method as a reference. Cab-O-Sil is SiO_2, which has no pore structure.

The Fe K-edge XAFS spectra of samples were measured in a fluorescence mode at room temperature at BL7C of KEK-PF with a Si(111) channel cut monochrometor. Normalization of XANES and data reduction on EXAFS were carried out as described elsewhere [9]. Data treatments were carried out with the FACOM M1800 computer system of the DATA Processing Center of Kyoto University.

The liquid phase oxidations were performed using a batch type reactor. Products were identified by GC-MS and quantified by GC.

3. Results and discussion

The XRD patterns showed that all the Fe-MCM-41 with different iron contents had hexagonal regularity of mesopore and their pore diameters determined by N_2 adsorption were around 2.5–3.0 nm.

*e-mail: stetsuya@u-gakugei.ac.jp. Present Address: Department of Chemistry, Tokyo Gakugei University, 4-1-1 Nukui-Kita, Koganei, Tokyo 184-8501, Japan.

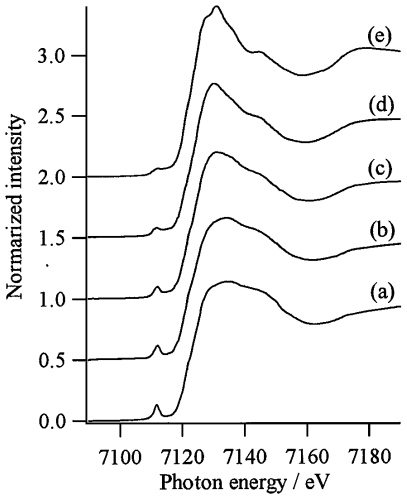

Fig. 1. Fe K-edge XANES spectra of Fe-MCM-41 and reference compounds. (a) Ferrisilicate (Si/Fe = 48), (b) Fe-MCM-41-DHT (Si/Fe = 105), (c) Fe-MCM-41-TIE (Si/Fe = 75), (d) FeOx/Cab-O-Sil (Si/Fe = 96), (e) α-Fe_2O_3. The numbers in parentheses are the Si/Fe atomic ratios.

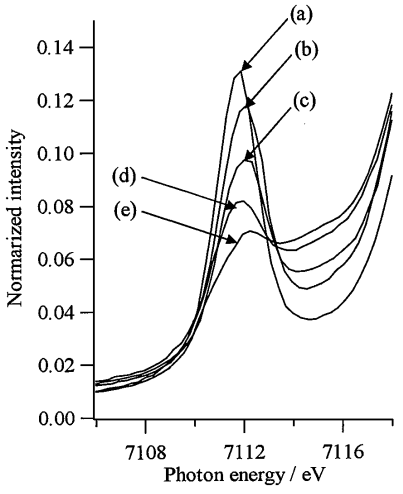

Fig. 2. Pre-edge region of Fe K-edge XANES spectra of Fe-MCM-41 and reference compounds. (a) Ferrisilicate (Si/Fe = 48), (b) Fe-MCM-41-DHT (Si/Fe = 105), (c) Fe-MCM-41-TIE (Si/Fe = 75), (d) FeOx/Cab-O-Sil (Si/Fe = 96), (e) α-Fe_2O_3. The numbers in parentheses are the Si/Fe atomic ratios.

Figure 1 shows the Fe K-edge XANES spectra of Fe-MCM-41 prepared by both DHT and TIE methods together with the reference compounds, ferrisilicate with MFI structure and α-Fe_2O_3. Iron atoms in ferrisilicate are mainly in tetrahedral coordination, and those in α-Fe_2O_3 are in octahedral coordination. A characteristic feature of these XANES spectra can be seen in the pre-edge peak at ca. 7112 eV, attributed to the 1s-3p dipolar forbidden transition. The 1s-3d pre-edge peak of Fe K-edge XANES spectra is sensitive to the electronic and geometric structure of the iron site. Principally, this forbidden transition gains additional intensity when the iron is in a noncentral symmetric environment or through mixing of 3d and 4p orbitals caused by the breakdown of inversion symmetry due to the structure distortion. Since the local symmetry around the iron is lowered from octahedral to tetrahedral coordination, the intensity of this peak tends to increase, *i.e.*, $I_{\text{tetrahedral}} > I_{\text{square pyramidal}} > I_{\text{octahedral}}$ [10] (Figure 2). Ferrisilicate which possessed regular tetrahedral coordination structure showed the largest intensity, whereas α-Fe_2O_3 with distorted octahedral coordination structure

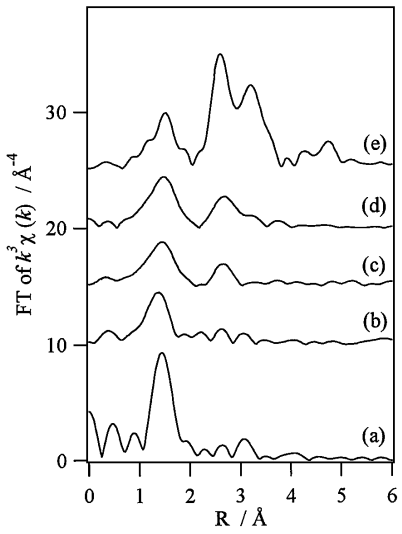

Fig. 3. Fourier transforms of k^3-weighted Fe K-edge EXAFS of Fe-MCM-41 and reference compounds. (a) Ferrisilicate (Si/Fe = 48), (b) Fe-MCM-41-DHT (Si/Fe = 105), (c) Fe-MCM-41-TIE (Si/Fe = 75), (d) FeOx/Cab-O-Sil (Si/Fe = 96), (e) α-Fe_2O_3. The numbers in parentheses are the Si/Fe atomic ratios.

showed very weak and broad absorption. The pre-peak intensity of the Fe-MCM-41-DHT was slightly lower than that of ferrisilicate. In the case of Fe-MCM-41-DHT, the oscillation by XANES which appears at high energy region (above ca. 15 eV from the absorption edge) is almost similar to that of ferrisilicate. These results indicate that the iron species in Fe-MCM-41-DHT exist in a tetrahedrally coordinated environment. The lower intensity of pre-edge peak may due to the difference in the framework structure of MCM-41 and that of the silicates zeolite. The wall of MCM-41 is essentially amorphous, while silicate zeolite is crystalline. Thus, the Si-O-Fe bonds in the amorphous framework of Fe-MCM-41-DHT may be connected with more relaxing angles than those in ferrisilicate. The pre-edge peak intensity of the Fe-MCM-41-TIE was lower than that of Fe-MCM-41-DHT, whereas higher than that of FeO_x/Cab-O-Sil.

Figure 3 shows the Fourier transforms (FTs) of k^3-weighted EXAFS spectra of Fe-MCM-41 FeOx/Cab-O-Sil, ferrisilicate and α-Fe_2O_3 (Phase shift was not corrected). The peak at 1.5 Å can be assigned to the contribution of the Fe-O shell. It should be noted that no considerable Fe-Fe shell, which is detected in the FTs for Fe-MCM-41-TIE, FeOx/Cab-O-Sil and α-Fe_2O_3 at around 2.8 Å, was observed for the Fe-MCM-41-DHT and ferrisilicate, suggesting that iron species dispersed as a monomer in the Fe-MCM-41-DHT and ferrisilicate. The curve-fitting analysis

Table I. *Results of curve-fitting analysis of Fe K-edge EXAFS*[a].

Samples[b]	bond	R	N	$\Delta\sigma^2$
Ferrisilicate (48)	Fe-O	1.85	3.9	−0.00071
Fe-MCM-41-DHT (105)	Fe-O	1.85	4.1	0.00083
Fe-MCM-41-TIE (102)	Fe-O	1.85	3.2	−0.00073
	Fe-O	1.99	3.2	−0.00086
	Fe-O-Fe	3.06	2.1	0.00893
α-Fe_2O_3	Fe-O	1.91	3.0	0.00070
	Fe-O	2.04	2.9	0.00230

a: R = bond length (Å), N = coordination number; $\Delta\sigma^2$ = Relative Debye-Waller factor (Å^2).
b: The number in the parenthesis is the Si/Fe atomic ratio.

Table II. *Epoxidation of trans-stilbene with hydrogen peroxide.*

Cat.(Si/Fe)[a)]	Fe content /wt%	Stilbene conv./%[b)]	Sel./%		H_2O_2[c), d)] conv./%
			Oxide[b)]	Benzald.	
MCM-41	0.0	13.5	84.6	15.4	53.5
Fe-MCM-41-DHT (105)	0.9	36.1	90.1	9.9	88.2
Fe-MCM-41-TIE (102)	0.9	23.8	88.8	11.2	86.1
Fe_2O_3/Cab-O-Sil (96)	1.0	17.5	86.4	13.6	86.5
Ferrisilicate (48)	1.9	6.2	87.4	12.6	78.5

Reaction conditions: catalyst, 0.2 g; reaction temp., 346 K; *trans*-stilbene, 1 mmol; H_2O_2, 9.8 mmol; DMF, 10 ml; reaction time, 2.5 h.
a: The numbers in parentheses are the Si/Fe atomic ratios of the fresh samples.
b: Stilbene, Oxide and Benzald. represent *trans*-stilbene, *trans*-stilbene oxide and benzaldehyde, respectively.
c: H_2O_2 (30 wt% aqueous solution), total 9.8 mmol, 2.45 mmol was added every 30 min in four times.
d: determined by iodometry.

of Fe K-edge EXAFS are summarized in Table I. As for the Fe-MCM-41-DHT, the incorporation of the majority of Fe^{3+} into the framework of MCM-41 with a tetrahedral coordination structure is inferred, since both the Fe-O distance (1.85 Å) and the coordination number (4.2) of Fe-MCM-41 were similar to those of the ferrisilicate with MFI structure. On the other hand, two kinds of Fe-O shells with the lengths of 1.85 and 1.99 Å and the coordination numbers of 3.2 and 3.2, respectively, were obtained in Fe-MCM-41-TIE. The iron in α-Fe_2O_3 possessed two kinds of Fe-O shells with the lengths of 1.91 and 2.04 Å and the coordination numbers of 3.0 and 2.9, respectively. The coordination number of Fe-Fe shell in Fe-MCM-41-TIE (2.1) was much smaller than that in α-Fe_2O_3 (7.9) [11]. These results suggest that small size iron oxide clusters exist in the channel of MCM-41.

The Fe-MCM-41 catalyzed efficiently the liquid phase oxidation of bulky organic compounds such as anthracene and *trans*-stilbene with H_2O_2. The activities of Fe-MCM-41 for the oxidations of anthracene and *trans*-stilbene were higher than those of FeO_x/Cab-O-Sil, which was prepared by a conventional impregnation, and ferrisilicate zeolite with MFI structure. Table II shows the results obtained with several catalysts in the epoxidation of *trans*-stilbene. *trans*-Stilbene oxide and benzaldehyde were formed in the oxidation of *trans*-stilbene. The Fe-MCM-41-DHT showed much higher conversion of *trans*-stilbene and slightly better selectivity to *trans*-stilbene oxide than the Fe-MCM-41-TIE at the same loading amount of iron. FeO_x/Cab-O-Sil showed not only lower conversion of *trans*-stilbene but also worse selectivity to *trans*-stilbene oxide. The low activity of ferrisilicate can be ascribed to its small pore size (0.51 nm × 0.54 nm) and narrow three-dimensional pore structure. The Fe-MCM-41-TIE showed slightly higher activity than FeO_x/Cab-O-Sil, while the surface area of the Fe-MCM-41-TIE is much higher than that of FeO_x/Cab-O-Sil. This indicates that the surface area of the catalyst is not important factor for the catalytic activity.

From these results mentioned above, we suggest that the isolated and tetrahedrally coordinated iron sites in the framework of MCM-41 over the Fe-MCM-41-DHT are responsible for the oxidations of both anthracene and *trans*-stilbene, whereas the small iron oxide clusters formed over the Fe-MCM-41-TIE are not effective. The Fe-MCM-41-DHT showed no leaching of iron species during the reaction. On the contrary, a large amount of iron cation in Fe-MCM-41-TIE leached out into the liquid phase and do not contribute to the catalytic reaction. Thus, the iron cations tetrahedrally coordinated and incorporated inside the framework of MCM-41 is stable towards leaching, whereas the small iron oxide clusters, which have octahedrally coordinated iron species, leach out.

Acknowledgment

The X-ray absorption measurements were performed under the approval of the Photon Factory (KEK-PF) Program Advisory Committee (Proposal No. 2002G097). The authors thank Dr. H. Yoshida (Nagoya University, Japan) for kind help in the measurements of the X-ray absorption spectra.

References

1. Corma, A., Chem. Rev. **97**, 2373 (1997).
2. Tanev, P. T., Chibwe, M. and Pinnavaia, T. J., Nature **368**, 321 (1994).
3. Thomas, J. M., Nature **368**, 289 (1994).
4. Ying, J. Y., Mehnert, C. P. and Wong, M. S., Angew. Chem. Int. Ed. **38**, 56 (1999).
5. Yonemitsu, M., Tanaka, Y. and Iwamoto, M., Chem. Mater. **9**, 2679 (1997).
6. Morey, M., Davidson, A., Eckert, H. and Stucky, G., Chem. Mater. **8**, 486 (1996).
7. Oldroyd, R. D. *et al.*, Angew. Chem. Int. Ed. **35**, 2787 (1996).
8. Zhang, Q., Wang, Y., Ohishi, Y., Shishido, T. and Takehira, K., J. Catal. **202**, 308 (2001).
9. Tanaka, T., Yamashita, H., Tsuchitani, R. Funabiki, T. and Yoshida, S., J. Chem. Soc. Faraday Trans. **84**, 2987 (1988).
10. Choy, J.-H., Yoon, J.-B., Kim, D.-K. and Hwang, S.-H., Inorg. Chem. **34**, 6524 (1995).
11. Wong, S., Lee, J., Cheng, S. and Mou, C., Appl. Catal. A **198**, 115 (2000).

Physica Scripta. Vol. T115, 765–768, 2005

In-Situ XAFS Study of Ag Clusters in Zeolite 4A

Y. Suzuki[1], T. Miyanaga[*1], H. Hoshino[2], N. Matsumoto[1] and T. Ainai[2]

[1]Faculty of Science and Technology, Hirosaki University, Hirosaki, Aomori 036-8561, Japan
[2]Faculty of Education, Hirosaki University, Hirosaki, Aomori 036-8560, Japan

Received June 26, 2003; accepted in revised form April 5, 2004

PACS number: 03.30+p

Abstract

In-situ Ag K-edge XAFS measurements have been carried out for fully Ag^+-exchanged zeolite 4A (Ag-4A) during continuous dehydration under vacuum in the temperature range between room temperature (r.t.) and 300 °C. The structural parameters (distance r, coordination number N and root mean square displacement σ) were derived by a three-shell (short and long Ag-O contacts and Ag-Ag contact) by curve-fitting analysis. The systematic dehydration effect on the structural change in the Ag clusters is studied by *in-situ* XAFS experiments. Ag^+ ions are reduced by removal of water molecules due to evacuation for 20 minutes at r.t. The formation of Ag clusters is suggested by full evacuation at r.t. With increasing dehydration temperature, N of Ag around a central Ag increases. For the Ag cluster formed at 300 °C the Ag-Ag contact distance is evaluated to be 2.79 ± 0.02 Å and N of Ag around a central Ag is 4.1 ± 0.3. The cluster formation is supported by XANES spectra which show that the Ag^+ ions in the fully hydrated Ag-4A change to Ag atoms in the dehydrated Ag-4A at 300 °C under vacuum.

1. Introduction

In the fully Ag^+-exchanged 4A (Ag-4A) the $12Ag^+$ ions are present inside zeolite cages, as needed to balance the anionic charge of the zeolite framework. The white color of the hydrated Ag-4A changes through yellow to brown by heating up to 400 °C under vacuum [1]. These changes in color by heating under vacuum are related to the formation of silver clusters due to the interaction of the silver atoms produced by reduction of Ag^+ ions during dehydration with the other silver atoms or Ag^+ ions [2]. X-ray diffraction experiments of the zeolite single crystal [3, 4] and EXAFS measurements on powder [5, 6] suggest the presence of the silver cluster in the zeolite cage. Recently it was found that the color of the white Ag-4A changes into pale yellow by full dehydration under vacuum at 27 °C for 7 hours [7]. It is interesting to study the changes in the local structure of the silver cluster for the same Ag-4A zeolite by heating at different temperatures under continuous evacuation. For this purpose an *in-situ* XAFS measurement was carried out using a special chamber [8] where the evacuation and heating are operated simultaneously. In this paper, we report results of *in-situ* EXAFS measurements on the Ag K-edge for the fully Ag^+-exchanged Ag-4A powder sample by continuous evacuation at room temperature (r.t.) and heating under vacuum, respectively.

2. Experimental and data analyses

Fully Ag^+-exchanged 4A (Ag-4A) powder samples were prepared by immersing Na-4A ($Na_{12}[(AlO_2)_{12}(SiO_2)_{12}]27.5H_2O$) zeolite in an aqueous $AgNO_3$ solution at 25 °C. The details of the sample preparation are described elsewhere [4, 6]. The white Ag-4A powder (fully hydrated) sample was packed in the cell. The cell was mounted in the *in-situ* XAFS measurement chamber. By holding the sample in the chamber XAFS measurements were carried out (1) under continuous evacuation at r.t. and (2) heating up to 300 °C under vacuum ($\sim 10^{-3}$ Pa) [8]. Ag K-edge X-ray absorption spectra were obtained at beamline BL-10B of the Photon Factory in KEK. A Si(311) channel-cut monochrometer was used, and energy and current of the storage ring were 3.0 GeV and 250∼400 mA, respectively. EXAFS spectra were recorded in transmission mode using ionization chamber detectors. The EXAFS interference function extracted from the absorption spectra was Fourier transformed by XANADU code [9]. In order to obtain the structural parameters, the EXAFS function was fitted by a non-linear least-squares method. The non-linear least square fitting method was applied to the experimental data as described below:

$$\chi(k) = \sum_j \frac{S_0^2 N_j}{k r_j^2} f_j(k, r_j) \exp(-2\sigma_j^2 k^2) \times \exp(-2r_j/\lambda(k)) \sin[2kr_j + \varphi_j(k)]$$

where r, N and σ are interatomic distance, coordination number and root mean square displacement, respectively, for each atomic pair. Phase shift $\varphi(k)$, backscattering amplitude $f(k, r)$ and electron mean free path $\lambda(k)$ are obtained from FEFF6.01 calculation [10]. The k-range for the curve-fitting method was $3.0 \sim 11.5$ Å^{-1}. Ag foil and $AgNO_3$ were used as standard samples for energy correction. In the present analyses, the multiple-scattering effect was neglected.

3. Results

Figure 1(a) shows the changes of $k\chi(k)$ EXAFS spectra obtained for Ag-4A during continuous evacuation from 0 to 20 minutes at r.t. In these experiments the sample was evacuated from 0.1 MPa to $\sim 10^{-3}$ Pa and the EXAFS spectra were recorded continuously for 2 minutes per one scan. It is found that at the evacuation for 20 minutes a few water molecules are removed from the unit zeolite cage [7]. The EXAFS spectra at the evacuation for 20 minutes were the same as those at the fully dehydrated condition after 7 hours. As seen in Fig. 1(a) $k\chi(k)$ profiles change clearly with increasing evacuation time. Especially the structure around $1 \sim 4$ Å^{-1} is changing as indicated by arrows in Fig. 1(a).

The corresponding change of Fourier transforms, |FT(r)|, is shown in Fig. 1(b). With increasing evacuation time, the intensity of the first peak (around 2 Å) decreases, while the intensity of the second peak (around 3 Å) increases considerably. The first peak corresponds to short Ag-O contact and the second peak to long Ag-O contact and Ag-Ag contact, respectively [5, 6]. As the evacuation proceeds, the positions of the first peak and the second peak shift to smaller r, which indicates that the contact

*e-mail: takaf@cc.hirosaki-u.ac.jp

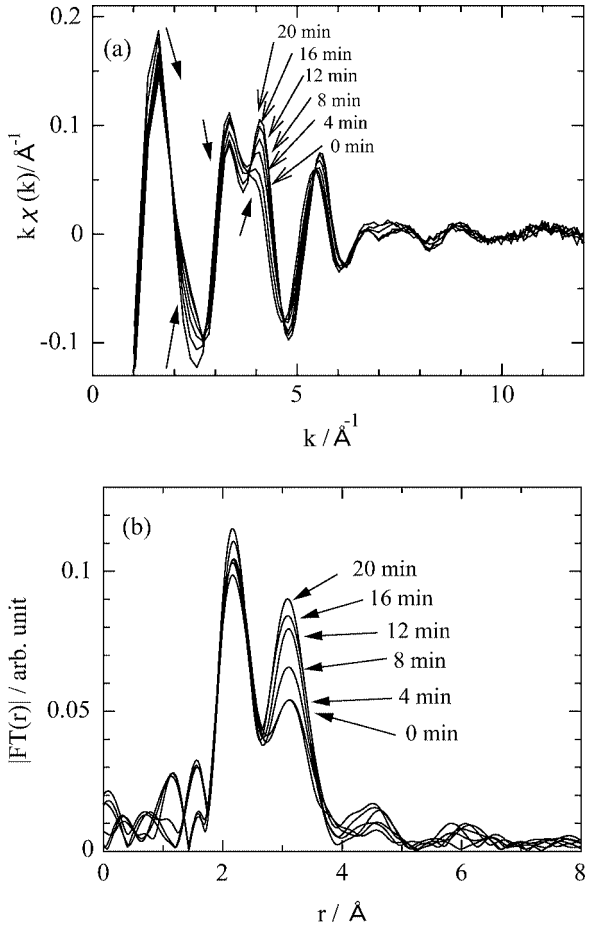

Fig. 1. Change of EXAFS $k\chi(k)$ spectra (a) and corresponding Fourier transform (b) for Ag-4A during evacuation as room temperature. The thick arrows indicate the change of evacuating time. The time interval for each spectrum is 4 minutes.

distances become short with increasing dehydration at r.t. It is interesting to point out that these changes in the contact distances for evacuation at r.t. are in qualitative agreement with those obtained for evacuation at high temperatures [6]. However, further analyses were not tried for the results obtained by 2 minutes per scan, because the quality of data was not high enough.

Figure 2(a) shows the changes of $k\chi(k)$ EXAFS spectra of the same Ag-4A sample obtained by scanning for more than 20 minutes. All spectra were measured at room temperature. The quality of data is good for further analyses. The curve represented by "A. 0.1 MPa" corresponds to the condition at 0.1 MPa and r.t. (Before evacuation and fully hydrated), "B. full evac." to full evacuation at r.t., "C. after 100 °C" to heating up to 100 °C under vacuum, "D. after 200 °C" to heating up to 200 °C under vacuum and "E. after 300 °C" to heating up to 300 °C under vacuum. In the $k\chi(k)$ curve for the fully hydrated Ag-4A (sample A) there appear a peak around 3.2 Å^{-1} and a shoulder around 4 Å^{-1}. After full evacuation at r.t. (sample B) the shoulder disappears and two peaks appear around 3 and 4 Å^{-1}. By further heating under vacuum up to 300 °C (samples C, D and E) the dip between two peaks becomes deeper.

Figure 2(b) shows the corresponding changes of $|\mathrm{FT}(r)|$. Two peaks appear around 2 Å and 3 Å. From A to E the intensities of the second peak (around 3 Å) increase, then the ratio of the intensity of the second peak to that of the first peak becomes large. The positions of the first and second peaks shift to smaller r from A to E.

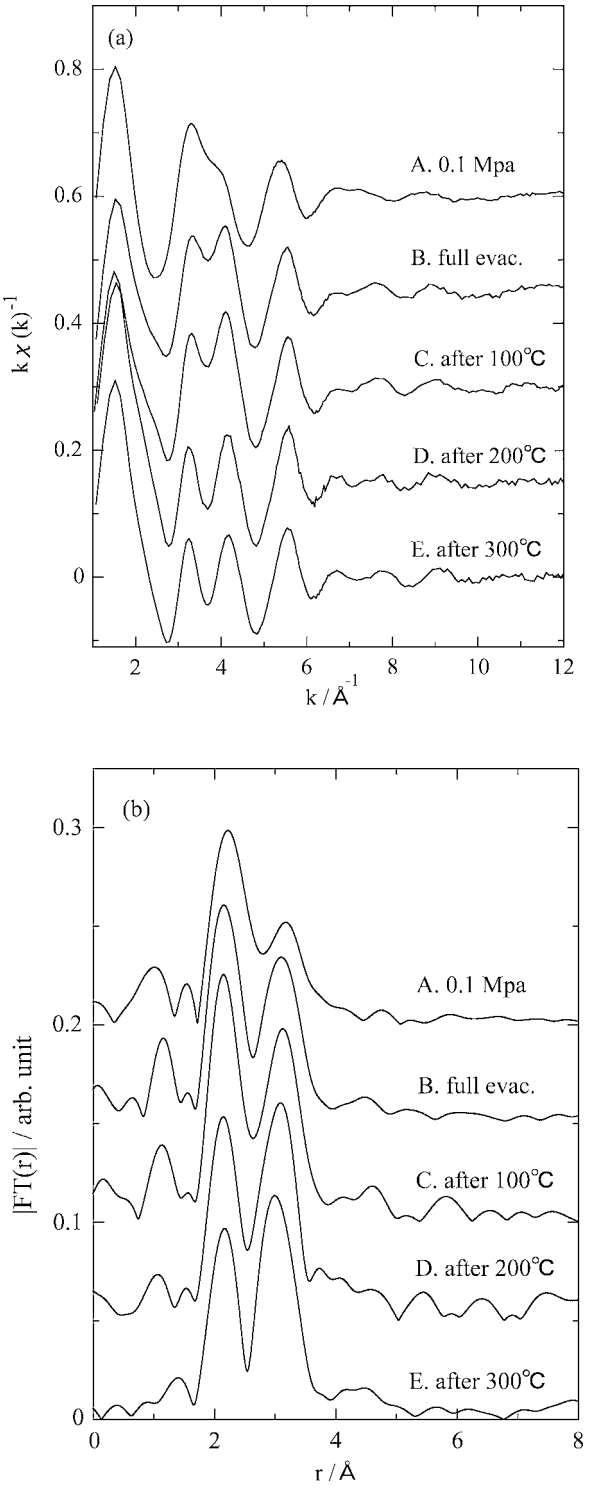

Fig. 2. Ag K-edge EXAFS $k\chi(k)$ spectra (a) and corresponding Fourier transform (b) for Ag-4A measured at r.t. A. measured at r.t. 0.1 MPa, B. measured at r.t. full evacuated, C. measured at r.t. after heating to 100 °C in vacuum, D. heating to 200 °C and E. heating to 300 °C.

4. Discussion

In order to derive the structural parameters, three-shell curve fitting analyses were carried out in the same way as in the previous work [6]: The three-shell model consists of two Ag-O contacts (short and long contact distances) and one Ag-Ag contact. An example of the fitting quality is shown in Fig. 3 for sample E. The fitting is fairly good. When the fitting was made by using the Ag-Si distance instead of the long Ag-O distance, the fitting quality was quite bad. The structural parameters obtained from the present

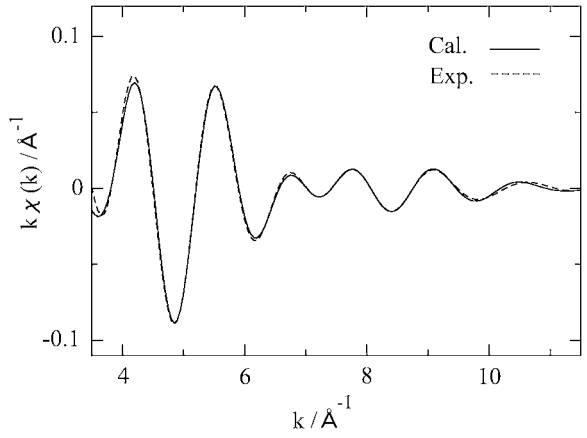

Fig. 3. Comparison for the Ag-K-edge EXAFS $k\chi(k)$ between experimental curve and calculated curve obtained by curve-fitting for the sample B.

Table I. *Structural parameters (r: contact distance, N: coordination number and σ: root mean square displacement) for Ag-4A.*

	Short Ag-O			Long Ag-O			Ag-Ag		
	r/Å	*N*	*σ*/Å	*r*/Å	*N*	*σ*/Å	*r*/Å	*N*	*σ*/Å
A	2.38	5.7	0.15	2.86	2.0	0.13	2.88	2.7	0.14
B	2.28	3.2	0.12	2.88	2.5	0.13	2.83	3.4	0.14
C	2.27	2.8	0.11	2.88	3.0	0.13	2.83	3.5	0.14
D	2.27	1.8	0.09	2.90	4.0	0.13	2.81	3.6	0.14
E	2.27	1.6	0.08	2.93	3.7	0.13	2.79	4.1	0.14

EXAFS spectra are summarized in Table I. Figure 4 shows the contribution from each shell in *r*-space (Fourier transform) as an example for sample E.

There are Ag^+ ions in the fully hydrated Ag-4A at 0.1 MPa and r.t. The short Ag-O distance decreases from 2.38 ± 0.02 Å (sample A) to 2.28 ± 0.02 Å (sample B) due to evacuation at r.t. The coordination number (*N*) of O around a central Ag^+ decreases from 5.7 ± 0.5 (sample A) to 3.2 ± 0.5 (sample B). In the fully hydrated Ag-4A there are water molecules in the vicinity of the Ag^+ ions. In common state, Ag^+ complex has tetrahedrally coordinated structure, for example, $Ag(H_2O)_4{}^+$ in aqueous solution [11], and the interatomic distance is reported to about 2.35–42 Å. On the other hand, in the distorted state, 5 or 6 coordinated complexes are reported [12] and the Ag^+ complex is expected to be distorted in the zeolite cavity. The large root mean square displacement *σ* of 0.15 shows the existence of distortion around the central Ag^+ ion and the coordination number of 5.7 includes the contributions from Ag-(OH_2) and Ag-O (zeolite cage). Therefore the interatomic distance of 2.38 Å is an average value for the widely distributed Ag-O pairs. By evacuation the water molecules are removed, then *N* of O around a central Ag^+ decreases. Since the Ag^+ ions in sample A have contact with oxygens in the zeolite framework and of water molecules, the interaction between the Ag^+ ion and the framework oxygen becomes strong by removal of water molecules, which results in a reduction of the short Ag-O contact distance. For the Ag-Ag contact the contact distance decreases from 2.88 ± 0.02 Å (sample A) to 2.83 ± 0.02 Å (sample B) and *N* of Ag^+ around a central Ag^+ increases from 2.7 ± 0.2 (sample A) to 3.4 ± 0.2 (sample B). The slight reduction of the distance and slight increment of *N* for the Ag-Ag contact by dehydration suggest that the Ag^+ ions are partly reduced to Ag atom by the removal of water molecules, since the Coulomb repulsion becomes weak when one of the Ag^+ ions is reduced to Ag atom between Ag^+ ions. For the long Ag-O contact the contact distance increases from 2.86 ± 0.02 Å (sample A) to 2.88 ± 0.02 Å (sample B) and *N* of O around a central Ag^+ increases from 2.0 ± 0.2 (sample A) to 2.5 ± 0.2 (sample B). It is noted that the appearance of Ag atoms produced by removal of water molecules makes the long Ag-O contact distance slightly longer due to an increase of the repulsive interaction. It is interesting to note that the partial reduction of the Ag^+ ions occur due to the removal of water molecules from the zeolite cages by full dehydration under vacuum at r.t., which results in the coloration of white Ag-4A at 27 °C [7] and the complete removal of water molecules has been confirmed by IR study of Ag-4A [8].

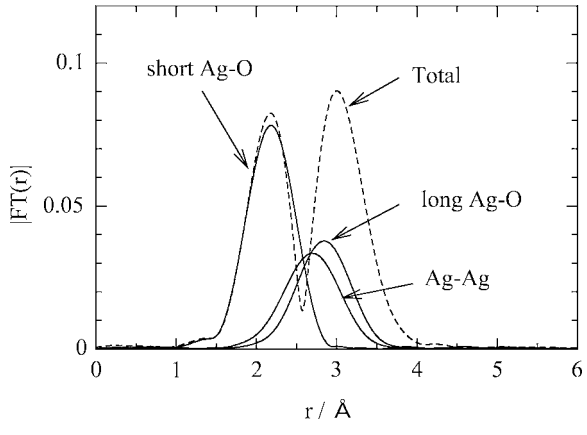

Fig. 4. Contributions from each shell (short Ag-O, long Ag-O, Ag-Ag, solid lines) in *r*-space (FT) for sample E. Dashed line is the FT from the total contribution.

For sample C to E the effect of the dehydration on the Ag-4A sample at high temperatures between 100 and 300 °C under vacuum is discussed. The short Ag-O contact distance remains at 2.27 ± 0.02 Å independent of temperature, while the *N* of O around a central Ag decreases from 2.8 ± 0.3 at 100 °C to 1.6 ± 0.3 at 300 °C, which arises from the increase of dehydration with increasing temperature under vacuum. This suggests that the reduction of the Ag^+ ion in the short Ag-O contact does not proceed at higher temperature. It is noted that, the distance of 2.27 Å for Ag-O is close to the value for linear or two-fold complex. The Ag-Ag contact distance decreases from 2.83 ± 0.02 Å at 100 °C to 2.79 ± 0.02 Å at 300 °C and the *N* of Ag around a central Ag increases from 3.5 ± 0.3 at 100 °C to 4.1 ± 0.3 at 300 °C. With increasing temperature the reduction of the Ag^+ ions proceed and the diffusion of the Ag atoms or Ag^+ ions is accelerated, which results in a decrease in the bond distance due to weaker repulsive interaction between Ag^+ ions and Ag atoms and the increase in the coordination number. For the long Ag-O contact the distance increases from 2.88 ± 0.02 Å at 100 °C to 2.93 ± 0.02 Å at 300 °C and the *N* of O around a central Ag increases from 3.0 ± 0.3 at 100 °C to 3.7 ± 0.3 at 300 °C. As the reduction of Ag^+ ion proceeds, the repulsion between Ag and the frame oxygen increases. This results in an increase of the long Ag-O distance. It is suggested that the contribution of the Ag atoms become dominant for the Ag-Ag and the long Ag-O contacts at high temperature [6].

The root mean square displacement *σ* for the short Ag-O contact decreases with increasing dehydration, while for the long Ag-O and Ag-Ag contacts *σ* remains unchanged.

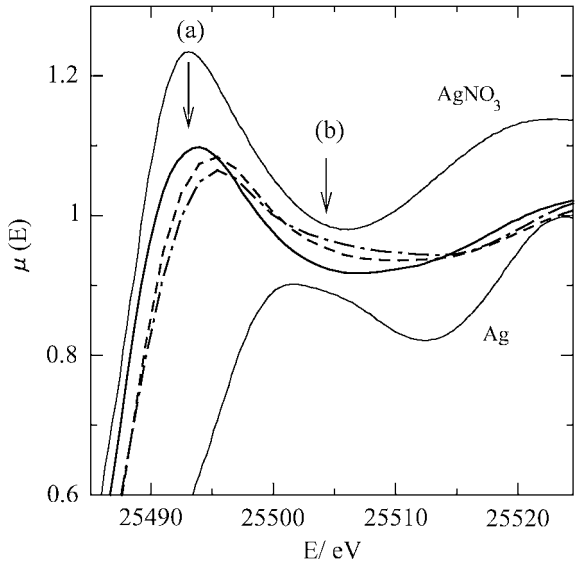

Fig. 5. XANES spectra of the Ag K-edge for Ag-4A: Solid line presents the result of sample A, dashed line does that of sample B, dot-dashed line does sample E. For comparison XANES's of $AgNO_3$ ($\mu(E)$ is shifted to $+0.1$) and Ag ($\mu(E)$ is shifted to -0.1) are also presented by thin solid line.

The fact that the coordination number N of Ag around a central Ag increases from 3.4 ± 0.3 for the Ag-4A fully evacuated at r.t. through 3.6 ± 0.3 at 200 °C to 4.1 ± 0.3 at 300 °C and the Ag-Ag contact distance decreases from 2.83 ± 0.02 Å for the evacuated sample at r.t. through 2.81 ± 0.02 Å at 200 °C to 2.79 ± 0.02 Å at 300 °C indicates that the formation of Ag clusters [3–7] in the zeolites cages sets on by dehydration under vacuum at r.t. and is accelerated by heating. The present systematic results for distance, coordination number and root mean square displacement are obtained for the first time by carrying out *in-situ* EXAFS experiments.

Figure 5 shows the changes of X-ray absorption near edge structure (XANES) for samples A, B and E. For comparison, XANES spectra of $AgNO_3$ and Ag foil are shown together. The XANES spectrum for sample A fully hydrated Ag-4A at r.t. is similar to that of $AgNO_3$ which is typical for the compounds with Ag^+-O pair. The peak (a) of the XANES spectra for samples B fully evacuated at r.t. and sample E heated to 300 °C under vacuum shift to higher energy and the intensity of the peak decreases with increasing dehydration. On the other hand, the intensity around the minimum (b) of XANES spectra for samples B and E increases with increasing temperature, which suggests the reduction of the valence state of the X-ray absorber from Ag^+ ions to Ag atom as indicated by XANES spectra of Ag foil. This behavior of the XANES spectra indicates that the Ag^+ ions in the hydrated Ag-4A is reduced to Ag atoms in the Ag-4A heated at 300 °C, which supports the formation of the Ag clusters with increasing dehydration temperature as we discussed on the EXAFS results.

5. Conclusion

The *in-situ* Ag K-edge EXAFS measurements have been carried out for fully Ag^+-exchanged zeolite 4A (Ag-4A) during continuous dehydration under vacuum in the temperature range between r.t. and 300 °C. The structural parameters (distance r, coordination number N and root mean square displacement) were derived by a three-shell (short and long Ag-O contacts and Ag-Ag contact) by curve-fitting analysis. The systematic dehydration effect on the structural change in the Ag clusters is discussed for the first time by carrying out the *in-situ* EXAFS experiments. It is found that the Ag^+ ions are reduced by removal of water molecules due to evacuation for 20 minutes. The formation of Ag clusters is suggested by full evacuation at r.t. With increasing dehydration temperature N of Ag around a central Ag increases. For the Ag cluster formed at 300 °C the Ag-Ag contact distance is evaluated to be 2.79 ± 0.02 Å and N of Ag around a central Ag of 4.1 ± 0.3. The cluster formation is supported by the XANES spectra which show that the Ag^+ ion in the fully hydrated Ag-4A change to Ag atoms in the dehydrated Ag-4A at 300 °C under vacuum.

Finally we should mention the limitation for the present analysis: our analysis is based on the three-shells model of short Ag-O, long Ag-O and Ag-Ag and the multiple scattering path was not taken into account. In our result the Ag coordination is indeed novel from the coordination chemistry point of view and a more sophisticated analysis using a later version of the theoretical EXAFS function (including the multiple scattering effect) will be needed to confirm the present results.

Acknowledgements

The synchrotron radiation experiments were performed at the Photon Factory in KEK under Proposal No. 2000G272 and 2002G279.

References

1. Hoshino, H., Bulletin of the Faculty of Education, Hirosaki University **75**, 29 (1996).
2. Sun, T. and Seff, K., Chem. Rev. **94**, 857 (1994).
3. Kim, Y. and Seff, K., J. Phys. Chem. **91**, 668 (1987).
4. Gellens, L. R., Mortier, W. J. and Uytterhoeven, J. B., Zeolites **1**, 11 (1981).
5. Miyanaga, T., Hoshino, H., Endo, H. and Sakane, H., J. Synchrotron Rad. **6**, 442 (1999).
6. Miyanaga, T., Hoshino, H. and Endo, H., J. Synchrotron Rad. **8**, 557 (2001).
7. Ainai, T., Master Thesis, Hirosaki University (2002).
8. Matsumoto, N., Master Thesis, Hirosaki University (2002).
9. Sakane, H. *et al*., Jpn. J. Appl. Phys. **32**, 4641 (1993).
10. Zabinsky, S. I., Rehr, J. J., Ankudinov, A., Albers, R. C. and Eller, M. J., Phys. Rev. B **52**, 2995 (1995).
11. Ohtaki, H. and Radnai, T., Chem. Rev. **93**, 1157 (1993).
12. Cotton, F. A. and Wilkinson, G., "Advanced Inorganic Chemistry", 4th ed (1988).

Physica Scripta. Vol. T115, 769–772, 2005

X-ray Absorption Spectroscopy on Heterogeneous Catalysts at the new XAS Beamline at ANKA

J.-D. Grunwaldt[1,*], S. Hannemann[1], J. Göttlicher[2], S. Mangold[2], M. A. Denecke[3] and A. Baiker[1]

[1]Institute for Chemical- and Bioengineering, Swiss Federal Institute of Technology, ETH Hönggerberg, CH-8093 Zürich, Switzerland
[2]Forschungszentrum Karlsruhe, Institut für Synchrochrotronstrahlung, P.O. Box 3640, D-76021 Karlsruhe, Germany
[3]Forschungszentrum Karlsruhe, Institut für Nukleare Entsorgung, P.O. Box 3640, D-76021 Karlsruhe, Germany

Received June 26, 2003; accepted November 4, 2003

PACS number: 6110Ht

Abstract

Ex situ and *in situ* XAFS studies have been performed at the new ANKA-XAS beamline on zirconia-silica mixed oxides for oxidation reactions, silver-gold based catalysts for CO oxidation and Cu/ZnO catalysts for methanol synthesis. Spectra were recorded both in the transmission geometry and in the fluorescence mode. The studies give insight into the structure of newly prepared catalysts and present first examples from the area of heterogeneous catalysis studied at this beamline, which is a new alternative in the network of European synchrotron radiation beamlines.

1. Introduction

The demand of synchrotron radiation in the field of X-ray absorption fine structure (XAFS) spectroscopy is increasing. To meet this demand, a new XAFS beamline at the synchrotron radiation source ANKA (Ångströmquelle Karlsruhe) of the Forschungszentrum Karlsruhe for the energy region 2.4 to 25 keV has recently been built and commissioned. This "ANKA-XAS" beamline focuses on applications in materials science, solid state chemistry, geo- and environmental sciences and the field of catalyst research. Already during the commissioning period the first test experiments on solid catalysts were performed and some results are presented herein.

Preparation of novel materials and their proper characterization are important for the design and discovery of new heterogeneous catalysts. XAFS plays a crucial role because it allows characterization of both amorphous and crystalline phases in heterogeneous catalysts [1, 2]. Moreover, it can be used not only *ex situ* but also under *in situ* conditions [2–4]. We present three examples demonstrating the possibilities and limitations of the new ANKA-XAS beamline. The first two examples emerge from the field of "new materials". Two interesting routes for the preparation of new materials are flame synthesis [5] and the synthesis of aerogels [6]. In both cases, materials with high surface area but different crystallinity, hydrophilicity and pore structure can be produced. Here, we investigate gold-silver based catalysts for CO-oxidation prepared by flame synthesis. ZrO_2-SiO_2 aerogels and their corresponding flame-synthesized material, used for cyclohexene oxidation, are also investigated. XAFS results of the well-known Cu/ZnO system [2, 7, 8], used as catalyst for methanol synthesis, methanol oxidation or steam reforming are reported as a representative example for an *in situ* and time-resolved study. The reduction behaviour of this catalyst is strongly dependent on the preparation method. These studies let us also discuss some of the limitations of the beamline during time-resolved studies.

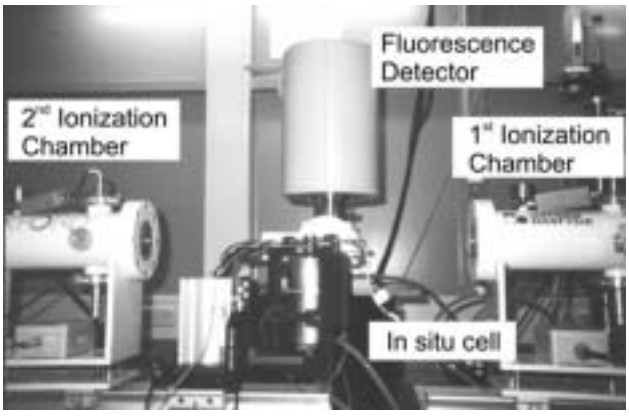

Fig. 1. Set-up of the XAFS experiment in transmission (ionization chambers) and fluorescence mode (detector at the back) at the ANKA-XAS beamline. Between the first and second ionization chamber there is an *in situ* EXAFS cell with furnace installed.

2. Experimental

2.1. *The ANKA-XAS beamline*

ANKA-XAS at the synchrotron radiation source ANKA, a storage ring operating at 2.5 GeV and a typical ring current of 85–180 mA, offers beamtime for scientific users and industrial customers. The beamline is equipped with a double crystal monochromator (DCM) with parallel mounted Si(111) and Si(311) crystal pairs for fast crystal changes. Studies in the energy range from 2.4 to 25 keV are possible [9], covering the S K-edge, L-edges of U up to the Pd K-edge. The optics includes a Zerodur mirror, deflecting downwards, which can be moved into the beam path behind the DCM to act as a low pass filter, suppressing higher harmonic reflections [10]. Three 300 mm ionization chambers are provided, which can be filled with counting gas at variable pressures (see Fig. 1). For our studies in fluorescence mode, a 5-element solid state detector (Canberra LeG 5-element) is used. A closed-loop He-cryostat allows measurements from about 15 K up to 310 K. User's own sample environment cells can be well adapted and thus easily set-up on the 200 × 100 cm optical table in the experimental hutch. Fig. 1 shows the set-up of our *in situ* fluorescence XAFS setup at ANKA-XAS. A chemical laboratory, located within the ANKA experimental hall, is now available for sample preparation during measurements. Thus the ANKA infrastructure is well-suited, e.g., for the characterization of new materials by XAFS also under *in situ* conditions.

2.2. *Preparation of the catalysts*

The gold and gold-silver catalysts (0.1–1 wt%Au, 1 wt%Ag) were synthesized in a methane/oxygen flame using a mixed solution of

*e-mail: grunwaldt@tech.chem.ethz.ch

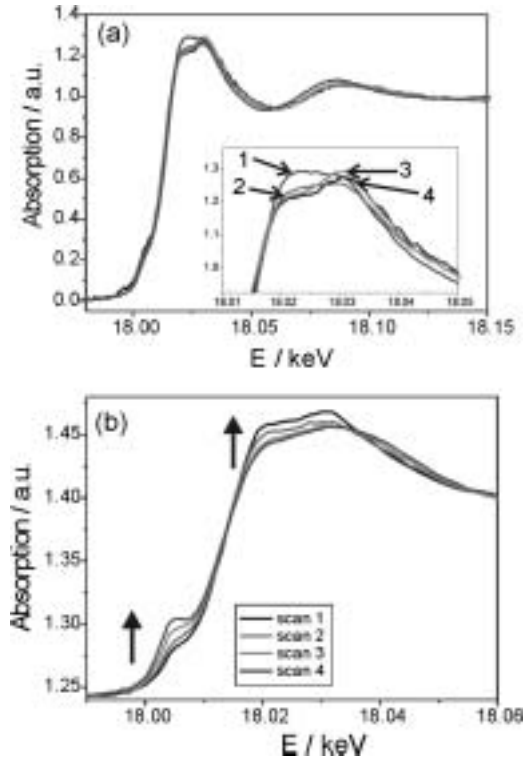

Fig. 2. Zr K-edge XANES for: (a) *ex situ* investigated samples: (1) 20%ZrO_2/SiO_2 (aerogel); (2) 5%ZrO_2/SiO_2 (flame-synthesis); (3) 5%ZrO_2/SiO_2 (aerogel); (4) 5%ZrO_2/-SiO_2 (aerogel, silylated); (b) 5%ZrO_2/SiO_2 (aerogel) during dehydration (scan 1: 50 °C, scan 2: 120 °C, scan 3: 180 °C, scan 4: 250 °C).

silver benzoate, dimethyl-acetylacetonato gold(III) and $Ti(O^iPr)_4$ precursors in an organic volatile solution. The catalysts were investigated as prepared and *in situ* reduction of the catalysts was performed in 5%H_2/He. ZrO_2/SiO_2 catalysts were prepared by aerogel synthesis using tetramethoxy silane and zirconium acetylacetonate as precursors, solvent extraction by supercritical CO_2 and subsequent calcination at 400 °C. The corresponding flame made precursors were prepared from the same precursors, similar as described in [11]. *In situ* dehydration was performed in a stream of He at a ramp rate of 5 °C/min. The 70%Cu/ZnO catalyst was prepared at pH = 8.5 and calcined at 330 °C (similar to as reported in [12]). The sample was reduced in 5%H_2/He at a heating rate of 1 °C/min.

3. Results

3.1. *ZrO_2/SiO_2 catalyst prepared by the aerogel and flame synthesis method*

Pre-investigations on the samples prepared by aerogel synthesis showed the samples are completely X-ray amorphous with high surface area (>200 m^2/g). Both XANES and EXAFS data on 5%ZrO_2/SiO_2 aerogels (without and with silylation) reveal zirconium to be mainly octahedrally coordinated. Fig. 2a displays the Zr K-edge XANES transmission mode data of several ZrO_2/SiO_2 samples. The absence of pre-edge features indicates octahedral coordination, as a pre-edge feature is expected for non-centrosymmetric Zr sites [13]. The XANES changes when 20 %ZrO_2 instead of 5%ZrO_2 is incorporated into the silica matrix. The change in the "fingerprint" at 18.02 keV is probably due to the formation of Zr-O-Zr species [13]. In contrast, the 5%ZrO_2/SiO_2 catalyst mainly contains Zr-O-Si species. Interestingly, the XANES fingerprint at the main absorption feature for the 5%ZrO_2/SiO_2 catalyst prepared by flame synthesis is intermediate to that of the 20%ZrO_2/SiO_2 catalyst and the corresponding sample prepared by the aerogel method. This indicates that during the flame synthesis more Zr-O-Zr species form than in the aerogel method. Probably, Zr-clusters originate from aggregation during the preparation process in the flame. The 5%ZrO_2/SiO_2 aerogel samples having a higher number of isolated Zr atoms showed a better catalytic performance in cyclohexene oxidation.

During dehydration of these samples (Fig. 2b) the pre-edge feature significantly increases, indicating an increase in tetrahedral coordinated Zr. A similar behavior is observed for TiO_2-SiO_2 aerogels [14], where Ti sites are mainly present as isolated species on the surface. Air moisture is sufficient to hydrate the Zr sites in the 5%ZrO_2-SiO_2 aerogel sample as also observed for Ti sites in TiO_2-SiO_2 aerogels and thereby change the coordination around the transition metal centres.

3.2. *Fluorescence EXAFS studies on 1%Au-1%Ag/TiO_2 and 0.1%Au-1%Ag/TiO_2*

Noble metal based heterogeneous catalysts have only rarely been prepared by flame pyrolysis. Recently, the technique was for the first time applied to bimetallic catalysts [15]. TEM investigations show that in order to achieve high noble metal dispersion during the preparation process, the noble metal loading has to be kept at a low level (<1 wt%). Fluorescence instead of transmission EXAFS studies are preferred at the Au L_3-edge in Au/TiO_2, since the TiO_2 support absorbs to a significant extent the X-rays and the gold concentration is low. Therefore the Au L_3 edge study is made in the fluorescence mode using a similar setup as described in ref. [16] and depicted in Fig. 1.

Fig. 3 shows the Au L_3 XANES of Au-Ag/TiO_2 samples used for CO-oxidation, indicating that most of the gold is in reduced state. This is supported by the fact that only slight spectral changes occur after *in situ* reduction of the catalyst. Based on simulations using the FEFF8.2 code [17], we found that only small variations in the near edge region are expected if gold is alloyed with silver. Therefore, we cannot exclude the possibility of alloy formation from the XANES. Analysis of the EXAFS (also shown in Fig. 3), however, point to the formation of alloyed Au-Ag particles, as can be e.g. seen by the altered Fourier transformed EXAFS spectra (cf. in [18]).

3.3. *In situ reaction combined with gas analysis: reduction of a CuO/ZnO catalyst*

The reduction of CuO/ZnO is a well-known example for *in situ* and time-resolved studies [2, 7, 8] greatly influenced by the preparation parameters. In a recent project, high throughput synthesis/testing has been combined with investigations by EXAFS [12]. Fig. 4 depicts typical XANES transmission spectra obtained during a scan of 7 min at the ANKA-XAS beamline. The simultaneously recorded mass changes in the mass spectrometer are also shown for comparison. The reduction of Cu^{2+} is clearly seen by the decrease in the white line and the formation of metallic copper by the increase of the pre-edge feature, starting at about 170 °C. The reduction is also reflected by hydrogen consumption ($m/e = 2$) and the formation of water ($m/e = 18$), observed in the mass spectrometer. The reduction covers a temperature span of 50 °C and thus about 7 spectra could be taken during the reduction of the catalyst. Modeling of the XANES through linear

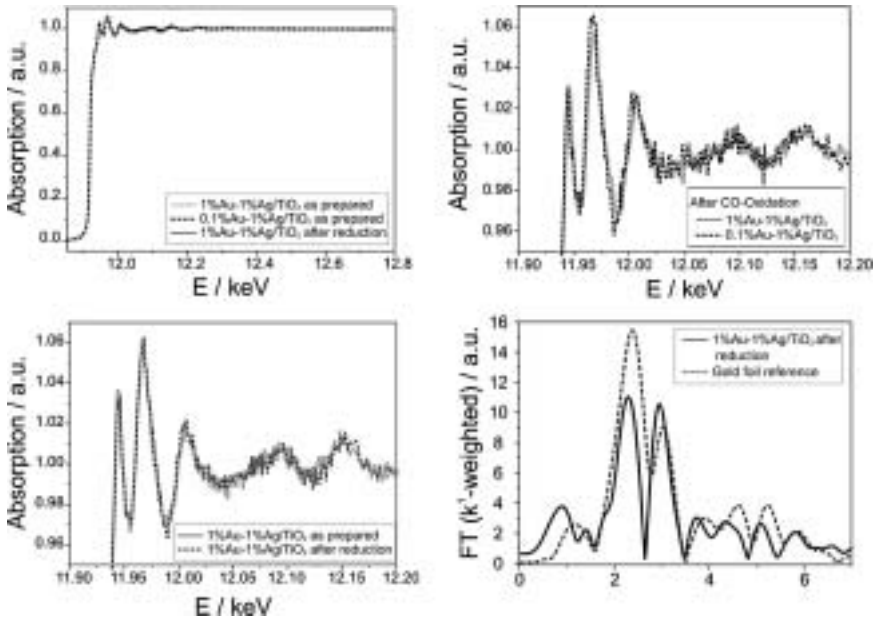

Fig. 3. Au L_3-edge fluorescence EXAFS data for Ag-Au/TiO_2 samples.

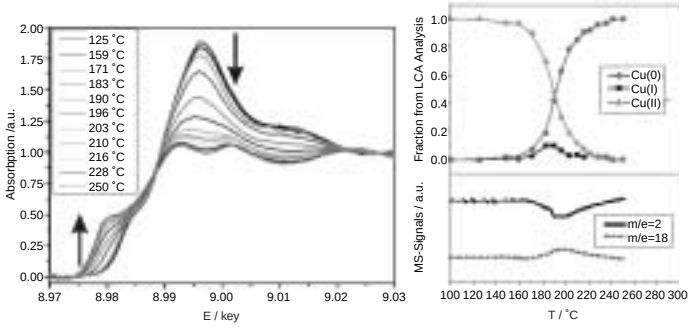

Fig. 4. In situ Cu K-edge XANES during reduction of 70%CuO/ZnO in 5%H_2/He with the corresponding results from fits to the data using a linear combination of reference spectra and mass spectrometric data.

combination of $Cu^{2+}/Cu^{+}/Cu^{0}$ reference data (LCA analysis) indicates that only a small fraction of Cu^{+} forms during the reduction. This is in agreement with previous studies [2, 7, 8]. Comparison to literature data and the extension of the study to further samples reveals that the reduction behaviour strongly depends on the preparation method (see also [19]). Hence, the effect of the preparation method on the reduction temperature and the catalytic activity is presently studied.

4. Conclusions

The examples illustrated here are the first studies on heterogeneous catalysts at the ANKA-XAS beamline. They demonstrate this beamline's potential for catalyst research. The beamline is well-suited for standard *ex situ* studies on new catalyst materials in the energy region 5–25 keV, providing new insight into the structure of flame-made and aerogel materials. The study on zirconia-silica materials revealed that the aerogel method and low ZrO_2 concentration result in optimal Zr dispersion and a high fraction of tetrahedrally coordinated Zr is found after dehydration of the samples. Bimetallic Au-Ag samples prepared by the flame method contain gold in metallic state already directly after preparation and Ag-Au alloy formation is observed after reduction. This example also shows that using a solid state detector for fluorescence detection not only *ex situ* studies but also *in situ* studies on a heterogeneous catalyst with the element of interest in the 1000 ppm range could be achieved (here 1000 ppm Au on TiO_2). The detector is, however, more bulky than the silicon drift detector [16]. Recently, studies of the Pt-reduction in PtO_x/Al_2O_3 during aerobic phenylethanol oxidation have also been performed successfully in the liquid phase at this beamline.

We confronted one of the beamline limitations during the CuO/ZnO catalyst study. Time-resolution, which is generally not too important during standard EXAFS scans but during dynamic studies, was low during the commissioning period of the beamline due to the preliminary set-up of the motor controllers and data acquisition software. This has been improved in the meantime. Recording good time resolved XANES spectra is limited to energies < 18 keV. The signal-to-noise ratio for EXAFS scans is only reasonably high at high k if the counting time is increased. This is due to the flux decrease at energies above $\sim$18 keV (the characteristic energy of the ANKA storage ring is 6.2 keV). However, EXAFS measurements with reasonable measurement times are feasible up to 20 keV.

In conclusion, the ANKA-XAS beamline has interesting potential for the characterization of heterogeneous catalysts or solids. The strength of the beamline is in the energy region 2.4–20 keV. It represents a new alternative in the network of existing European synchrotron radiation beamlines in catalyst research. This is important since the demand of hard X-rays at synchrotron rings in Europe cannot be met with the current number of existing beamlines.

Acknowledgements

We gratefully acknowledge beamtime at the ANKA-XAS beamline (Forschungszentrum Karlsruhe). We thank P. Kappen and C. Kiener for the help during the measurements and P. Hasselriis, W. J. Stark and C. Kiener for providing some of the catalyst samples. Our workshop at ETH is gratefully acknowledged for the assistance with construction of the *in situ* EXAFS set-ups, in particular the fluorescence EXAFS set-up tested at the ANKA-XAS beamline, and the Swiss Commission for Technology and Innovation (CTI, TopNano 21 grants 5978.2 TNS and 6740.1 TNS) for financial support of the flame-synthesized materials.

References

1. Koningsberger, D. C. and Prins, R., "X-ray Absorption: Principles, Applications, Techniques of EXAFS, SEXAFS, and XANES" (Wiley, New York 1988).
2. Clausen, B. S., Topsøe, H. and Frahm, R., Adv. in Catal. **42**, 315 (1998).
3. Bazin, D., Dexpert, H. and Lynch, J., in "X-ray Absorption Fine Structure For Catalysts and Surfaces" (Edited by Y. Iwasawa) (World Scientific, Singapore 1996), p. 113.
4. Grunwaldt, J.-D. and Clausen, B. S., Topics Catal. **18**, 37 (2002).
5. Stark, W. J., Pratsinis, S. E. and Baiker, A., Chimia **56**, 485 (2002).
6. Schneider, M. and Baiker, A., Catal. Rev. - Sci. Eng. **37**, 515–556 (1995).
7. Grunwaldt, J.-D. *et al*., J. Phys. Chem. B **105**, 5161 (2001).
8. Günter, M. M., Bems, B., Schlögl, R. and Ressler, T., J. Sync. Rad. **8**, 619 (2001).
9. ANKA-XAS in ANKA Beamlinebook (2003); www.fzk.de/anka
10. Absorption Beamline in "ANKA: Synchrotron Radiation Facility for Microfabrication and Analytical Services, Technical Specifications of the Front-ends, Beamlines, Experimental stations, Control System, and Parts of the Infrastructure" (Beamline Book Version 2.0, 1997), p. 2-49 – 2-60.
11. Stark, W. J., Pratsinis, S. E. and Baiker, A., J. Catal. **203**, 516 (2001).
12. Kiener, C. *et al*., J. Catal. **216**, 110 (2003).
13. Mountjoy, G., Anderson, R., Newport, R. J. and Smith, M. E., J. Phys. Condens. Matter **12**, 3505 (2000).
14. Grunwaldt, J.-D. *et al*., Phys. Chem. Chem. Phys. **4**, 3514 (2002).
15. Hannemann, S., Grunwaldt, J.-D., Baiker, A., (in preparation).
16. Kappen, P. *et al*., J. Sync. Rad. **9**, 246 (2002).
17. Ankudinov, A. L., Ravel, B., Rehr, J. J. and Conradson, S. D., Phys. Rev. B **58**, 7565 (1998).
18. Shibata, T. *et al*., J. Am. Chem. Soc. **124**, 11989 (2002).
19. Grunwaldt, J.-D., Kiener, C., Schüth, F. and Baiker, A., Physica Scripta **T115**, 819 (2005).

Physica Scripta. Vol. T115, 773–775, 2005

In-Situ X-Ray Absorption Near Edge Structure (Xanes) Spectroscopy of PtRu Colloid Catalysts at Operating Temperature

B. Brendebach[1,*], S. Bucher[1], J. Hormes[2], H. Bönnemann[3], K. S. Nagabhushana[3], R. Brinkmann[3] and H. Modrow[1]

[1]Physikalisches Institut der Universität Bonn, Nußallee 12, 53115 Bonn, Germany
[2]Center for Advanced Microstructures and Devices, 6980 Jefferson Highway, Baton Rouge, LA 70806, USA
[3]MPI für Kohlenforschung, Kaiser-Wilhelm-Platz 1, 45470 Mühlheim a. d. Ruhr, Germany

Received June 26, 2003; accepted November 4, 2003

PACS numbers: 78.70.Dm, 82.45 Jn, 82.45Yz

Abstract

In this study, *in-situ* XANES measurements of the Ru L_{III}-edge of one commercially available and a novel PtRu colloid catalyst, synthetized at the Max-Planck-Institut für Kohlenforschung, Mühlheim (Ruhr), Germany, at room temperature and at 80 °C in an atmosphere of 10% H_2 in N_2 are presented. During the process of heating at operating temperature, clear sample-specific changes are observed that can be correlated to structure and perfomance of the respective catalysts. The commercially available catalyst JM HiSpec 6000, Johnson Matthey company, and the freshly prepared novel colloid catalyst EUP-AA-25 show a reduction of the oxidation state of the Ru ions at operating temperature, demonstrating the existence of ruthenium sites which are accessible only under operating conditions. On the other hand, when examining the novel colloid catalyst extracted after 500 hours at working conditions, then declared as EUP-AA-21, no changes are observed while heating in a hydrogen containing atmosphere any more, indicating that the formerly active sites have been permanently blocked.

1. Introduction

PtRu nanoparticles are promising electrode materials for the Direct Methanol Fuel Cell (DMFC), because the small particle sizes (<3 nm) provide a large active surface [1–3]. The aim of this study is an improved characterization of the electronic structure of the Ru atoms, e.g. oxidation state, of such particles under conditions similar to the working conditions. Such an *in-situ* study is essential for two reasons: First of all, it is not clear whether the direct extrapolation of results obtained from *ex-situ* techniques is suitable for describing reactions occurring in the fuel cell under working conditions. Secondly, even if one assumes that results obtained from *ex-situ* investigations can be extrapolated, such studies cannot follow changes in the material that occur during operation and thus cannot provide a starting point for a possible refinement of the formation process. In fact, e.g. the reason for the higher CO and CO_2 tolerance of PtRu catalysts relative to pure Pt catalysts is still disputed, even though the effect was first observed in 1972 [4]. Possible explanations relate directly to H_2O activation by Ru [5] and electronic modification of the Pt d-DOS, which leads to a weakening of the Pt-CO bond [6, 7]. Consequently, obtaining direct access to the electronic structure at the Ru sites might open a promising pathway to the solution of this type of problems.

In-situ measurements at the Pt L_{III}-edge have e.g. been performed by Mukerjee *et al*. [8]. The *in-situ* access to the electronic structure of the ruthenium atoms is significantly more difficult, as the considerable life-time broadening smears out the K-edge structures, whereas photons in the Ru L-edge region lack the penetration depth. To our knowledge, this is the first investigation at working conditions at the Ru L_{III}-edge.

*e-mail: brendeba@physik.uni-bonn.de

2. Experimental

In-situ X-ray Absorption Near Edge Structure (XANES) measurements of the ruthenium L_{III}-edge of two PtRu-based catalysts were performed at the DCM-beamline at CAMD, Baton Rouge, USA, each at room temperature and at 80 °C in an atmosphere of 10% H_2 in N_2. A set of InSb(111) crystals was in use and spectra were taken in transmission mode. An argon spectrum was recorded for energy calibration setting the first inflection point to the 1s binding energy at 3205.9 eV [9]. Powder samples of metallic Ru, $RuBr_3$, RuO_2, and K_2RuO_4, purchased from the Sigma-Aldrich company, were measured as reference compounds, representing ruthenium atoms in oxidation states zero, three, four, and six, respectively. The maximum of the first derivative of the Ru powder spectrum, set to 2838 eV [9], was used for a refined energy calibration. The spectra were measured from 2750 eV to 2950 eV with a step size of approximately 1 eV in the pre- and post-edge region and 0.15 eV between 2810 eV and 2860 eV. A linear background was fitted to the pre-edge region and subtracted. The spectra were normalized to unity in the post edge region at 2900 eV.

3. Results

The focus of this study is centered on the description of the oxidation state of the binary nanocatalysts for fuel cells, as this elucidates the changes within the metal-metal and metal-oxygen-bonds between ambient and working conditions.

For example, within the commercially available catalyst JM HiSpec 6000 the Ru is highly oxidized at room temperature, but when heated at 80 °C in an atmosphere of partly hydrogen, a partial reduction reaction takes place as can be seen in the upper part of Fig. 1. Comparison with spectra of reference samples Ru powder, $RuBr_3$, RuO_2, and K_2RuO_4, shown in Fig. 2, clarify that the decrease of white line intensity at working conditions is related to a reduction of the number of oxidized Ru atoms. This behavior suggests the presence of active ruthenium sites within the catalyst which are only accessible under reaction conditions and appear oxidized otherwise.

To investigate whether these activated ruthenium sites are characteristic for highly active PtRu electrocatalysts, we have extended our analysis to a freshly prepared and a used sample of a novel Pt/Ru-based colloid catalyst, prepared by the MPI für Kohlenforschung, Mühlheim (Ruhr), Germany, by coreduction of $PtCl_2$ and $RuCl_3$ which initially shows similar electrocatalytic activity but whose performance is significantly worse after 500 hours of operation (c.f. Fig. 3).

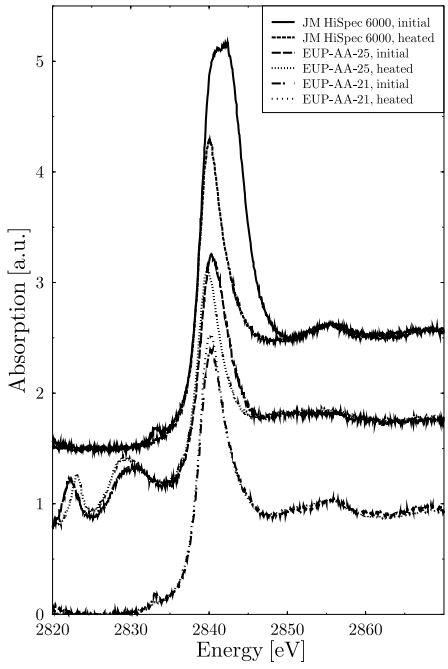

Fig. 1. XANES spectra of JM HiSpec6000 (upper), EUP-AA-25 (middle), and EUP-AA-21 (lower). Spectra are shifted along the *y*-axis for clarity.

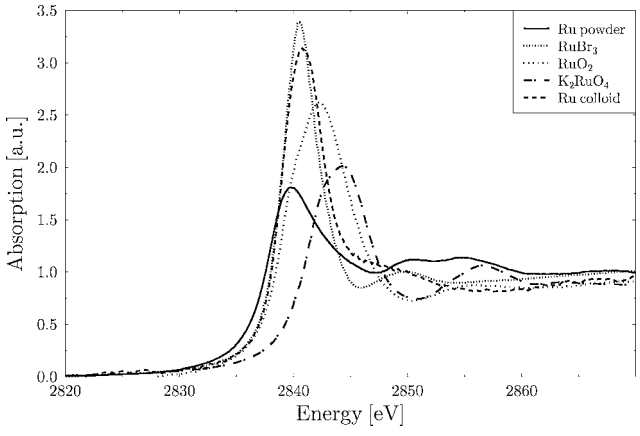

Fig. 2. XANES spectra of Ru reference compounds, the spectrum of the Ru colloid was taken out of [10].

The spectra of the freshly prepared catalyst, declared as EUP-AA-25, and after 500 hours at working conditions, then called EUP-AA-21, are shown in the middle and lower part of Fig. 1, respectively. Evidently, the pre-edge features in the spectra of sample EUP-AA-25 are relicts of the formation process. Platinum- and rutheniumchlorine are used as starting materials for the preparation of the nanoparticle catalysts. The positions of the peaks correspond to the Cl K-edge energy at 2833 eV. Interestingly, at room temperature the degree of oxidation observed for this catalyst is significantly lower than in the HiSpec sample, indicating a rather different site occupation. But under operating conditions the Ru L_{III} XANES spectra of the fresh catalyst – especially when correcting the normalization with respect to the influence of the Cl K-edge edge jump – are highly similar to the one acquired from the HiSpec catalyst, as shown in detail in Fig. 4. Thus, it seems reasonable to assume that in fact the spectrum of these two heated samples is a fingerprint for the electronic structure of the Ru atom which is favourable for electrocatalytic activity. This assumption is further supported

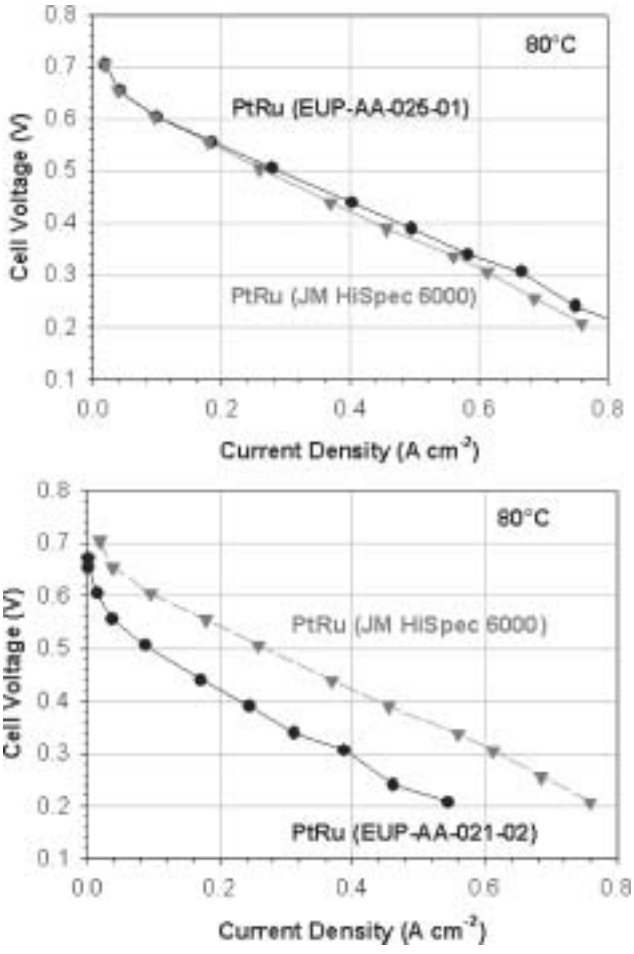

Fig. 3. Performance of EUP-AA-25 (upper) and EUP-AA-21 (lower) with respect to JM HiSpec 6000 [11].

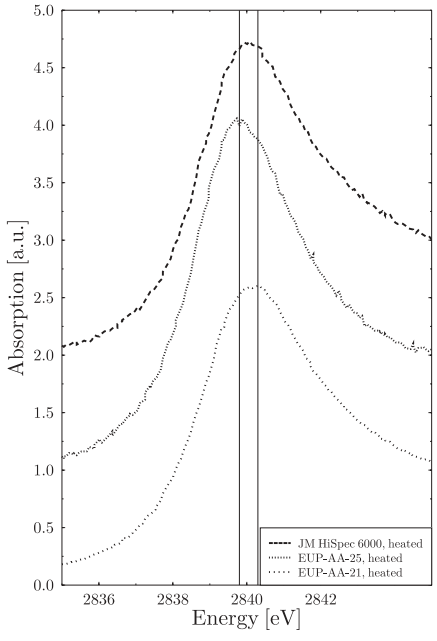

Fig. 4. XANES spectra of the catalysts at operating temperature (80 °C) in an atmosphere of 10% H_2 in N_2. Spectra are shifted along the *y*-axis for clarity.

by the observation that in contrast to the two cases discussed so far, after 500 hours of operation the Ru L_{III} XANES spectrum of the novel catalyst is clearly shifted to higher energies and is no longer susceptible to the change in the environmental conditions,

thus the deterioration of the electrocatalytical performance is accompanied by a clear change of the chemical environment at the Ru sites and it appears that the sites which are most active are blocked by permanent occupation with time. Unfortunately, so far, a sample of the JM HiSpec 6000 catalyst after 500 hours at working conditions, which would allow for the assessment whether this sample undergoes the identical aging process was not available.

Evidently, these results induce the desire to obtain an improved characterization of the active sites. Based on the data accumulated so far, only one statement can be made with respect to their nature: Earlier publications have shown that in a variety of Pt/Ru-based colloid catalysts enriched regions of Pt and Ru atoms, respectively, are formed and that a segregation of Pt atoms to the surface of the colloids is observed [12, 13]. When comparing the reference samples, only within the Ru powder and the $RuBr_3$ Ru-Ru bonds are present. Their spectra show a resonance at about 2850 eV which is missing the spectra of RuO_2 and K_2RuO_4, containing no Ru-Ru linkages. In addition, the spectrum of a pure Ru-containing colloid is also shown in Fig. 2, which as well shows a signature at the respective energy. Using that feature as a fingerprint for Ru-Ru bonds within a catalyst, the commercial JM HiSpec 6000 seems to be fully alloyed, because the spectra have a minimum at 2850 eV. When examining the spectra of the novel colloid catalyst small but significant features are visible at the respective energy which may lead to the assumption that they are not completely alloyed. If this should be the case, mixing of Pt and Ru states in the d-band should not be the decisive factor for the electrocatalytic activity of the sites. However, further detailed investigations are needed to solidify this hypothesis.

4. Conclusion

This study demonstrates that *in-situ* XANES measurements of the Ru L_{III}-edge at operating temperatures are feasible and monitor significant reactions at the Ru atoms and therefore serve as starting points for further refinements of Pt/Ru-based colloid catalysts which are promising anode materials for the Direct Methanol Fuel Cell (DMFC). In detail, *in-situ* XANES measurements of the ruthenium L_{III}-edge have been performed for one commercially available and one novel PtRu colloid catalyst at room temperature and at 80 °C in an atmosphere of 10% H_2 in N_2 simulating operating conditions, yielding a fingerprint for the Ru L_{III} XANES spectrum of the most active catalytic sites. Comparison with Ru reference samples in the oxidation state zero, three, four, and six show that the commercial catalyst and the freshly prepared novel catalyst contain active ruthenium sites which are accessible only under operating conditions and occupied under ambient conditions. In the case of the HiSpec catalyst, this occupation seems to lead to Ru(IV) states, which are not formed in the novel catalyst. Still, this material is also reduced to a lower oxidation state when heated in a hydrogen containing atmosphere in its initial state. Extracted after 500 hours at working conditions, the novel colloid catalyst remains unchanged and the active sites are no longer accessible. In spite of the significant differences in the XANES spectra under standard conditions, the active sites are identical. This is even more surprising as the novel colloid catalyst seems not to be fully alloyed whereas the spectra of the commercially available catalyst JM HiSpec 6000 do not show any indication of Ru-Ru bonds. Further studies are needed to elucidate the exact nature of the active sites and the mechanism which leads to their permanent occupation.

References

1. Bönnemann, H. *et al*., J. New. Mat. Electrochem. Syst. **3**, 199 (2000).
2. Paulus, U. A. *et al*., J. Catalysis **195**, 383 (2000).
3. Schmidt, T. J. *et al*., J. Electrochem. Soc. **145**, 925 (1998).
4. Binder, H., Köhling, A. and Sanstede, G., "From Electrocatalysis to Fuel Cells", (Edited by G. Sanstede) (University of Washington Press, Seattle 1972), p. 43.
5. Carette, L., Friedrich, K. A. and Stimming, U., "Review CHEMPHYSCHEM", (Wiley-VCH-Verlag, Weinheim 2000), p. 162.
6. Davies, J. C., Hayden, B. E. and Pegg, D. J., Electrochem. Acta **44**, 1181 (1998).
7. Gurau, B. *et al*., J. Phys. Chem. B **102**, 9997 (1998).
8. Mukerjee, S. and Mc Breen, J., J. Electrochem. Soc. **143**, 1409 (1996).
9. Williams, G. P., "X-ray Data Booklet", (Edited by A. C. Thompson and D. Vaughan) (Berkeley 2001), p. 1–3.
10. Köhl, G., dissertation thesis, BONN-IR-2001-14 (2001).
11. Bönnemann, H., Nagabhushana, K. S., Zeleney, P. and Zhen, Y., in preparation.
12. Nashner, M. S. *et al*., J. Am. Chem. Soc. **119**, 7760 (1997).
13. Hills, C. W., Nashner, M. S., Frenkel, A. I., Shapley, J. R. and Nuzzo, R. G., Langmuir **15**, 690 (1990).

Physica Scripta. Vol. T115, 776–780, 2005

EXAFS Studies of Bimetallic Ag-Pt and Ag-Pd Nanorods

Debdutta Lahiri[1*], Soma Chattopadhyay[2,3], B. A. Bunker[1], C. M. Doudna[4], M. F. Bertino[4], F. Blum[5], A. Tokuhiro[6] and J. Terry[1,2*]

[1]Physics Department, University of Notre Dame, Notre Dame, Indiana 46556, USA
[2]CSRRI-IIT, Advanced Photon Source, Argonne National Laboratory, 9700 S. Cass Avenue, Argonne, Illinois 60439, USA
[3]Biological, Chemical and Physical Sciences Department, Illinois Institute of Technology, Chicago, Illinois 60616, USA
[4]Department of Physics, University of Missouri-Rolla, Rolla, Missouri 65409, USA
[5]Department of Chemistry, University of Missouri-Rolla, Rolla, Missouri 65409, USA
[6]Department of Nuclear Engineering, University of Missouri-Rolla, Rolla, MI 65409, USA

Received June 26, 2003; accepted January 12, 2004

PACS number: 61.10.Ht

Abstract

Nanoparticles of Ag-Pt and Ag-Pd with high aspect ratios were synthesized using a radiolysis method. Gamma rays at dose rates below 0.5 kGy/h were used for irradiation. The nanoparticles were characterized by transmission electron microscopy (TEM), optical absorption spectroscopy and X-ray Absorption Fine Structure (XAFS) spectroscopy. Bright field micrographs show that Ag-Pt nanowires are composed of large particles with diameters ranging from 20–30 nm and joined by filaments of diameter between 2–5 nm. The Ag-Pd nanowires have diameters of 20–25 nm and lengths of 1.5 μm. For XAFS measurements, the Pt L_3 edge (11.564 keV), Ag K-edge (25.514 keV) and Pd K-edge (24.350 keV) were excited to determine the local structure around the respective atoms in the cluster. The Ag-Pt particles were found to possess a distinct core-shell structure with Pt in the core surrounded by Ag shell, with no indication of alloy formation. However, nanorods of Ag-Pd have formed an alloy for all the alloy compositions.

1. Introduction

Nanocrystalline materials are of great interest and are being widely studied because many physical and chemical properties of these materials are found to be dissimilar to those of conventional polycrystalline, coarse-grained materials. Such difference in properties arise because of the large fraction of atoms (5–50%) located at the surfaces and/or interfaces. Quantum size effects are observed in metal and semiconductor fine particles if their size is small enough so that the spacing between the discrete levels in the electronic energy spectrum becomes comparable with some of the characteristic energy parameters like kT, μH, $h\omega$, etc., thereby giving rise to changes in the thermodynamic, magnetic and optical properties respectively [1]. Nanocrystalline materials have been found to exhibit increased strength and hardness, enhanced diffusivity, improved ductility, reduced density, etc. compared to the bulk. Hence, these materials have found applications in microelectronic and optoelectonic devices, catalysis, sensing, drug delivery, etc. Metallic nanostructures with high aspect ratios are promising candidates for the development of sensors, catalysts and nanoscopic electrical connections.

Bimetallic nanoparticles are of greater interest than the monometallic ones, both technologically and scientifically [2]. The selective behavior of such bimetallic catalysts can be controlled by changing their composition ratios [3, 4]. Earlier studies have mostly been done on inorganic oxide-supported bimetallic nanoparticles [5]. Recently, novel techniques like microemulsion [6], decomposition of organometallic precursors [7], radiolysis [8], etc. have been developed for the synthesis of colloidal suspensions of these nanoparticle systems. Such systems are advantageous for study since the interference of substrate interaction is absent. A detailed review of bimetallic nanoparticles in dispersion has been published [9]. In this paper, we have used TEM and XAFS to investigate alloy formation in radiolytically synthesized Ag-Pt and Ag-Pd bimetallic nanoparticles in solution, possessing high aspect ratio. Such systems with high aspect ratio are particularly interesting because of their potential application as barcodes in sensors [3].

2. Experimental Section

2.1. *Synthesis*

Ag-Pt and Ag-Pd nanowires were synthesized by radiolysis [10, 11]. Radiolysis of aqueous solutions is an effective method to reduce metal ions and form homo- and heteronuclear clusters of transitions metals [10, 11]. In the radiolysis method, aqueous solutions are exposed to γ-rays (equation 1) to create solvated electrons, which in turn reduce the metal ions (equations (2) and (3)). The latter coalesce to form aggregates (equation (4)).

$$H_2O \rightarrow e^-_{aq}, H_3O+, H^*, OH^*, H_2O_2, \quad (1)$$

$$e^-_{aq} + M^{m+} \rightarrow M^{(m-1)+}, \quad (2)$$

$$e^-_{aq} + M^+ \rightarrow {M_0}^0, \quad (3)$$

$$n{M_0}^0 \rightarrow {M_2}^0 + (n-2)M0 \rightarrow \ldots\ldots\ldots {M^0}_n. \quad (4)$$

The samples were irradiated with γ radiation from the fission products of University of Missouri-Rolla's nuclear reactor pool. The reactor was operated at 180 kW for 1 hour and the samples were positioned 1 h after the reactor shutdown to prevent neutron bombardment and activation of samples. The dose rate was decreased exponentially from a value of 0.5 kGy/h in the first hour to about 0.05 kGy/h 48 hours after shutdown. Exposure to a total dose between 3 and 3.5 kGy typically required 36 to 48 hours. Total doses were measured with Thermoluminescent Dosimeters (TLD) placed in vials adjacent to the samples to be irradiated.

To obtain nanowires, parameters that were varied, were (a) total gamma ray dose and dose rate, (b) type of counterions added to the solution, (c) total and relative metal concentration, and, (d) polymer type and concentration. The most relevant parameters were the counter ions, the molar ratio between Ag and Pt or Pd, and the capping polymer. The data strongly suggests that polymer-metal ion complexes are formed, possibly in micellar form. Also, at least two conditions typical for nanowire formation, i.e. the presence of seeds and slow velocity of reduction, are met by the experiments. Samples were prepared with Ag-Pt and Ag-Pd

*Corresponding authors: dlahiri@u.washington.edu, terryj@iit.edu

Table I. *Conditions for formation of Ag-Pt and Ag-Pd nanowires by radiolysis.*

Conditions for nanowire formation	Ag-Pt System	Ag-Pd System
Total Dose (kGy)	3.5	3.5
Mole Ratio (%)	80-20 to 20-80	40-60 to 80-20
Salts	H_2PtCl_6 and Ag_2SO_4	Ag_2SO_4, Ag_2NO_3 and $PdSO_4$
Capping Polymer	Poly (vinyl alcohol)	Poly (vinyl alcohol)
PVA Molecular Mass (amu)	31000–170000	88600–97000
Metal ion concentration in solution (mol/L)	0.5 and 2×10^{-3}	0.5 and 2×10^{-3}
Scavenger for H^* and OH^* radicals	0.2 mol/L of 2-propanol	0.2 mol/L of 2-propanol
Hydrolysis Degree (%)	87–89	87–89

mole ratios varying from 100% to 0% of Ag in steps of 20%. The conditions for nanowire formation of Ag-Pt and Ag-Pd systems are listed in Table I.

2.2. *Characterization*

Samples were characterized for their size, shape and chemical composition prior to the XAFS measurements. TEM measurements and selective area electron diffraction (SAED) was carried out for microscopic structural characterization of the samples. The chemical composition of the nanoparticles was determined with Energy Dispersive X-ray analysis (EDAX).

XAFS measurements were performed at the MR-CAT undulator beamline at Advanced Photon Source, Argonne National Laboratory. The samples were sealed in plastic cuvettes before exposing them to the X-ray beam. For the Ag-Pt samples, Pt L3-edge (11.564 keV) and Ag K-edge (25.514 keV) were excited. The Ag-Pd samples were studied by exciting the Ag K-edge and the Pd K-edge (25.34 keV). For all the three edges, the undulator parameters were optimized to obtain a large photon flux with nearly constant intensity within the XAFS energy range. For the Ag and Pd edges, the undulator was tuned to its third harmonic.

A double crystal Si (111) monochromator was utilized for energy selectivity. For the Pt L3-edge, a Rh harmonic rejection mirror was used to eliminate the higher harmonics whereas Pt mirror was used for the Ag and Pd edges. The incident photon intensity was measured by an ion chamber filled with 80% He–20% N_2 gas mixture for Pt edge and full N_2 for Ag and Pd edges. Measurements were done in fluorescence mode with a 13-element solid state detector (Canberra with XIA electronics). For each sample, 10 scans were taken at the required edge and were then averaged. The spectra for all the samples were calibrated with reference Ag, Pt, Pd foils at the respective edges.

The data was processed using the University of Washington FEFFIT software package [14]. Theoretical models were constructed with the program FEFF7 [15]. The FEFFIT program was used to fit the structural parameters of the model [16].

3. Results and Discussion

Figure 1(a and b) shows typical bright field micrographs of Ag-Pt and Ag-Pd nanoparticles (growth conditions given in Table I), respectively. For Ag-Pt, the nanowires are composed of two types of particles: large particles, with typical diameters of 20–30 nm, are joined by thin filaments, with diameters of 2–5 nm. EDAX suggested that the larger particles have a typical composition

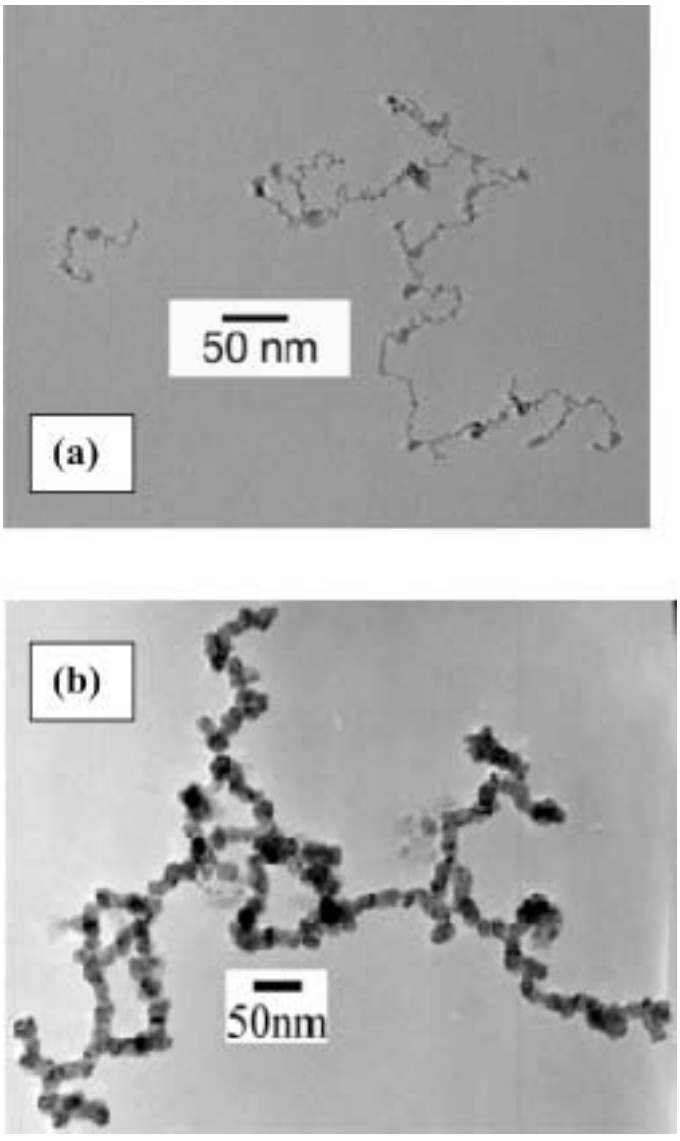

Fig. 1. Bright field TEM micrograph of Ag-Pt and Ag-Pd nanowires obtained after exposure to a total dose of 3.5 kGy, each.

of 80–90% of Ag and the filaments have composition close to 50% of silver. This implies that Ag particles are formed in the early stages of growth since reduction potential of Ag is more than that of Pt. The latter nucleated out of the Ag particles. In figure 1(b), we observe filament-like Ag-Pd particles with typical diameters of 20–25 nm and length of 1.5 μm. The lattice constant for the nanoparticles, calculated from the diffraction rings, showed an increase with the Ag concentration. The morphology of the particles was comparable for most metal mole ratios. EDAX showed that the ratio between the two metals varied within the same particle and between nanoparticles, but the variation was within ±20% of the mole ratio of the parent solution. The filaments have been observed to be polycrystalline in nature.

The XAFS data for all our samples have been shown in Figure 2. The lines in the Ag-edge data shows the frequency shift in *k*-space. The XAFS fit parameters for the Pt L3-edge from the Pt-Ag nanoparticles, are listed in Table II. A comparison of the fit with the data is shown in Figure 3. The apparent contraction in bond length can be explained from the effect of disorder in XAFS [17]. It suggests that the Pt atoms in this sample are in a disordered state compared to the Pt foil. The first shell does not show any conspicuous trace of Ag; the central Pt is coordinated by only Pt

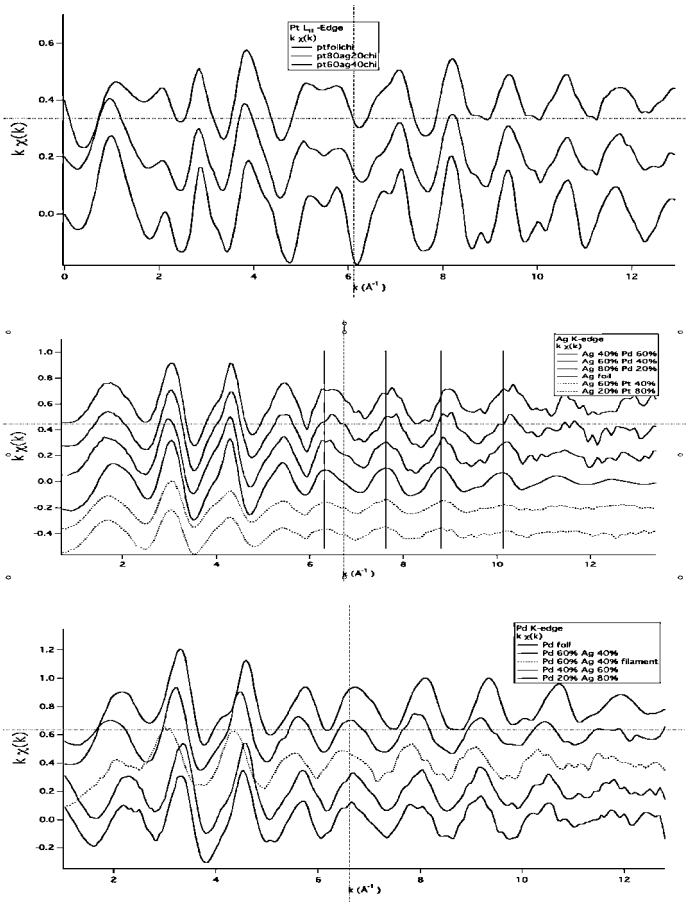

Fig. 2. Raw XAFS data for all the bimetallic nanoparticles at Pt, Ag and Pd edges. The plots are in the same order as they are listed in the figure legend.

atoms. The coordination number is much less than that of bulk Pt, which is reasonable because of the large surface to volume ratio of the nanoparticles. Alloy formation would instead have led to an expansion of the lattice parameter of Pt [18]. Such expansion has not been observed by us in this system. This implies that, in these Ag core-Pt shell particles, the two metals are not alloyed and retain their bulk lattice parameters.

The XAFS fit parameters for Pd-Ag samples were calculated from the fitting of Pd-edge and Ag-edge data. Since Pd and Ag are adjacent atoms in the periodic table, their backscattering amplitude and phase effects on the photoelectron wave are nearly identical. Hence, it is very difficult to distinguish between these two near neighbor species around the central atom and conclude

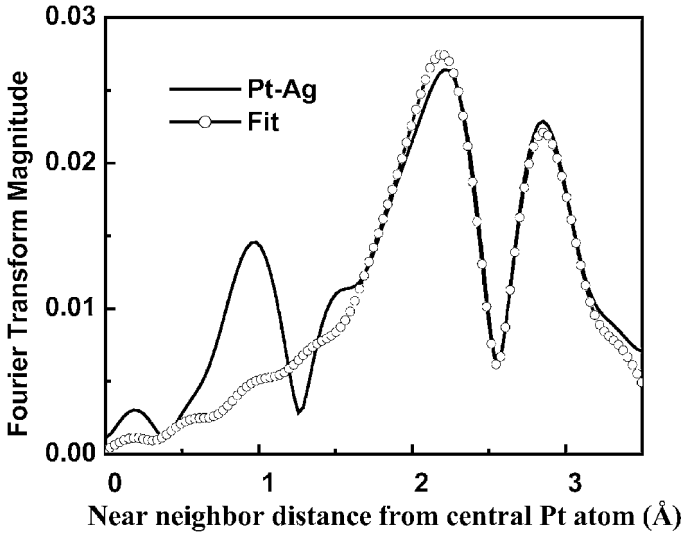

Fig. 3. Comparison of the fit with data for bimetallic nanorod system of Ag-Pt ($Ag_{0.6}Pt_{0.4}$) at Pt edge.

if they are alloying. Fortunately, the lattice parameters of Pd and Ag are significantly different. The shortest interatomic distance in Pd crystal is 2.75 Å while that in Ag crystal is 2.88 Å. Hence, in the case of alloying, the average interatomic distance around Pd in this bimetallic system should be observed to systematically increase from 2.75 Å towards 2.88 Å as more and more Ag is added. Correspondingly, the average distance around Ag should be observed to systematically decrease from 2.88 Å towards 2.75 Å with the decreased proportion of Ag.

Figures 4(a), 4(b) and 4(c) show the data (from Pd K-edge) and the fit for the samples (a) $Pd_{0.2}Ag_{0.8}$, (b) $Pd_{0.4}Ag_{0.6}$, and (c) $Pd_{0.6}Ag_{0.4}$. Of interest are the peaks in the region 2.25 and 3 Å since they represent the first shell or nearest neighbor distance. From figure 6(a), we observe that the nearest neighbor distance expands with increase in the mole percent of Pd. The results at the Pd edge are corroborated by results at the Ag edge. While doing the analysis for the Ag edge, the Debye-Waller factor was fixed from the fit results at the Pd-edge. Figures 5(a), 5(b) and 5(c) show the data (from Ag K-edge) and the fit for the samples (a) $Ag_{0.8}Pd_{0.2}$, (b) $Ag_{0.6}$ $Pd_{0.4}$, and (c) $Ag_{0.4}$ $Pd_{0.6}$. Around Ag atoms, we observe a contraction of the first shell. Figure 6(b) shows the change in the nearest neighbor distance with change in the mole percent of Ag in the bimetallic system. Together, these measurements indicate that the alloying of Ag and Pd has occurred in these nano-filaments. The detailed fit parameters are listed in Table II.

Table II. *Fit parameters for Ag-Pt and Ag-Pd nanowires.*

Sample Name	Edge	Near neighbor species	N^*	E_0 (eV)	R (Å)	σ (Å^2)
$Pt_{0.6}$ $Ag_{0.4}$	Pt	Pt	5 ± 1	3.56 ± 2.0	2.74 ± 0.01	0.005 ± 0.002
	Pt	Ag	2 ± 1	3.25 ± 2.0	2.75 ± 0.05	0.006 ± 0.002
$Pd_{0.2}Ag_{0.8}$	Pd	Pd	9 ± 1	-6.29 ± 0.8	2.79 ± 0.04	0.008 ± 0.001
$Pd_{0.4}Ag_{0.6}$	Pd	Pd	9 ± 5	-6.29 (fixed)	2.76 ± 0.04	0.007 ± 0.002
$Pd_{0.6}Ag_{0.4}$	Pd	Pd	9 ± 6	-6.29 (fixed)	2.77 ± 0.04	$0.006 \pm .0.002$
$Ag_{0.8}Pd_{0.2}$	Ag	Ag	10 ± 1	3.55 (fixed)	2.83 ± 0.02	0.008[1]
$Ag_{0.6}Pd_{0.4}$	Ag	Ag	9 ± 1	3.55 ± 0.2	2.8 ± 0.04	0.007
$Ag_{0.4}Pd_{0.6}$	Ag	Ag	12 ± 2	3.55 (fixed)	2.8 ± 0.01	0.006

[1]Debye-Waller factors at Ag-edge were fixed from Pd-edge results. When allowed to vary, they yielded values very close to those from Pd edge fitting.

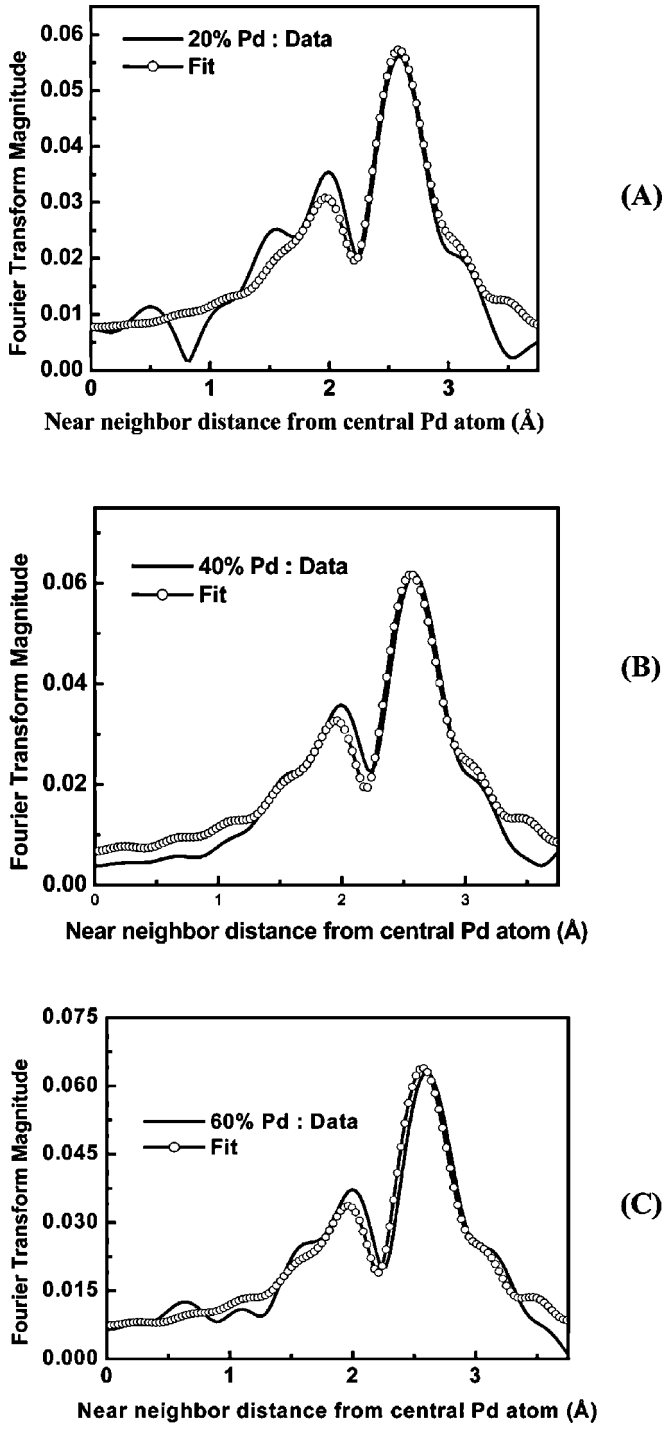

Fig. 4. Comparison of the fit with data for bimetallic nanorod system of Ag-Pd at Pd K-edge for the samples (a) $Pd_{0.2}Ag_{0.8}$, (b) $Pd_{0.4}Ag_{0.6}$ and (c) $Pd_{0.6}Ag_{0.4}$.

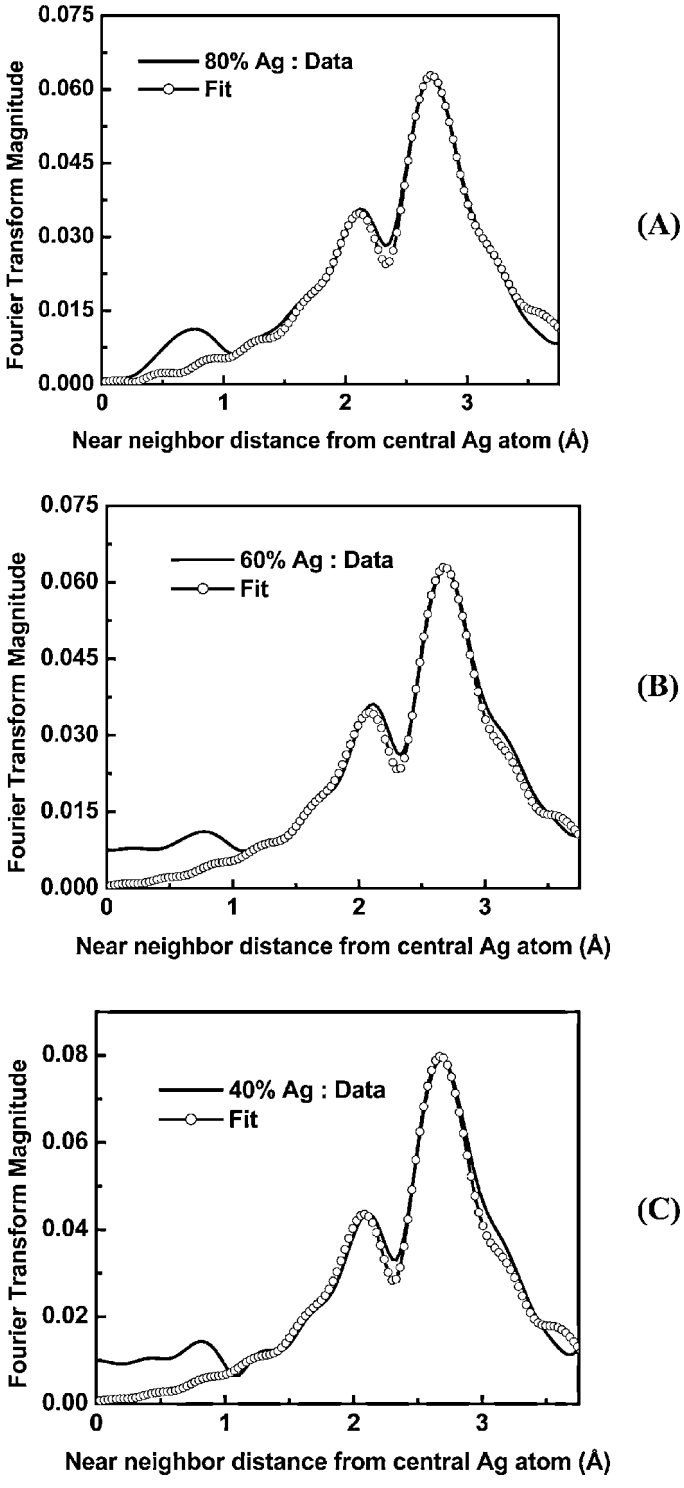

Fig. 5. Comparison of the fit with data for bimetallic nanorod system of Ag-Pd at Ag K-edge for the samples (a) $Ag_{0.8}$ $Pd_{0.2}$, (b) $Ag_{0.6}$ $Pd_{0.4}$ and (c) $Ag_{0.4}$ $Pd_{0.6}$.

The errors in the fitting parameters reflect a number of sources, one of which is the correlation between the various parameters. The fitting results varied as well, when we changed the near neighbor species. As mentioned in the previous paragraph, the backscattering amplitude and phase shift from Ag and Pd near neighbors are nearly indistinguishable. At each edge, we considered three different models for the nearest neighbors: (a) pure Pd atoms (b) pure Ag atoms and (c) a mixture of Ag and Pd atoms. The values obtained for the various fitting parameters varied slightly with the change in model. This variation has been included in our estimate of error. Despite all these errors, the change in the average near-neighbor distance, as a function of the % of impurity metal, is clearly systematic and significant. The change is however not linear and may be mistaken to be contradicting the well-established Vegard's law of alloying. This discrepancy may be resolved once we realize that Vegard's law is derived from diffraction experiments and depicts the average cell parameter from many unit cells. On the other hand, XAFS measurements probe the structure within a unit cell and hence the near neighbor distances, derived from XAFS, consist of a distribution of bond-lengths, which can lead to the observed deviation from linearity [19]. Also, in the case of our nanoparticle systems, there was a 10–20% distribution in the bimetallic composition ratios, which could contribute to the

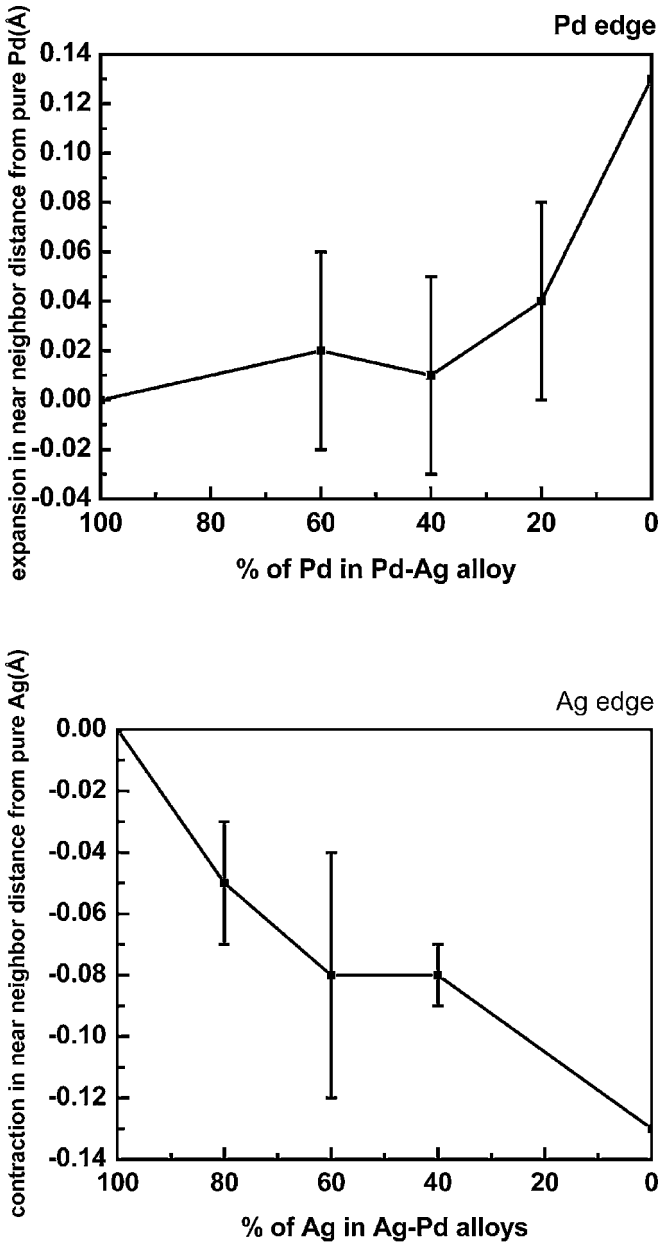

Fig. 6. (a) The expansion of the nearest neighbor distance in the Ag-Pd bimetallic nanoparticles as a function of the Pd molar ratio. (b): The contraction of the nearest neighbour distance in the Ag-Pd bimetallic nanoparticles as a function of the Ag molar ratio.

deviation. Surface relaxation could also contribute to the deviation from linearity. This nevertheless does not diminish our conclusion about alloying, since the changes in the near neighbor distance that we observe are clearly significant and systematic.

4. Conclusions

In conclusion, we have been successful in synthesizing bimetallic Ag-Pt and Ag-Pd nanowire systems by radiolysis. Ag-Pd nanowire systems have been found to form alloy whereas Ag-Pt does not form an alloy down to the lowest size obtained by us.

Acknowledgements

MR-CAT is funded by the Department of Energy, Office of Energy Research under grant number DEFG0200ER45811. The APS is funded by the U.S. Department of Energy, Office of Science, Office of Basic Energy Sciences under Contract number W-31-109-Eng-38.

References

1. Kubo, R., J. Phys. Soc. Jpn **17**, 975 (1962).
2. Sinfelt, J. H., J. Catal. **29**, 308 (1973).
3. Sheila, R. *et al.*, Science **294**, 137 (2001).
4. Lewis, L. N., Chem. Rev. **93**, 2693 (1993).
5. Meitzer, G., Visa, G. H., Lytle, F. W. and Sinfelt, J. H., J. Chem. Phys. **78**, 2533 (1983).
6. Zhang Xin and Chan Kwong-Yu, Chem. Mater. **15**, 451 (2003).
7. Cheng, P. *et al.*, J. Phys. Chem. B **103**, 10098 (1999).
8. Shibata T. *et al.*, J. Am. Chem. Soc. **124**, 11989 (2002).
9. Toshima Naoki and Yonezawa Tetsu, New J. Chem. 1179 (1998).
10. Doudna, C. M. *et al.*, J. Phys. Chem. B **107**, 2966 (2003).
11. Doudna, C. M. *et al.*, (manuscript under preparation).
12. Filankembo, A. and Pileni, M. P., J. Phys. Chem. B **104**, 5866 (2000).
13. Marignier, J. L., Belloni, J., Delcourt, M. O. and Chevalier, J. P., Nature **317**, 344 (1985).
14. Stern, E. A., Newville, M., Ravel, B., Yacoby, Y. and Haskel, D., Physica B **208** & **209**, 117 (1995).
15. Zabinsky, S. I., Rehr, J. J., Andukinov, A., Albers, R. C. and Eller, M. J., Phys. Rev. B **52**, 2995 (1995).
16. Newville, M., J. Synch. Radiation **8**, 96 (2001).
17. "X-Ray absorption: principles, applications and techniques of EXAFS, SEXAFS and XANES" (edited by Koningsberger, D. C. and Prins, R.), (1988).
18. Torigie, K., Nakajima, Y. and Esumi, K., J. Phys. Chem. **97**, 8304 (1993).
19. Boyce, J. B. and Mikkelsen, J. C., J. Cryst. Growth **98**, 37 (1989).

Physica Scripta. Vol. T115, 781–783, 2005

An XAFS Study on the Polymer Protected CuPd Bimetallic Nanoparticles – A Novel Heterobond-Philic Structure

K. Asakura[1,*], C. R. Bian[1], S. Suzuki[1], W.-J. Chun[1], N. Watari[2], S. Ohnishi[3], P. Lu[4] and N. Toshima[4]

[1]Catalysis Research Center, Hokkaido University, Sapporo 060-0811, Japan
[2]NEC Information Systems, Miyazaki 4-1-1, Miyamae-ku, Kawasaki 216-8555, Japan
[3]NEC Fundamental Research Laboratories, Miyukigaoka 34, Tukuba 305-8501, Japan
[4]Department of Materials Science and Engineering, Science University of Tokyo in Yamaguchi, Onoda-shi, Yamaguchi 756-0884, Japan

Received June 26, 2003; accepted December 10, 2003

PACS number: 61.10.Ht

Abstract

We have carried out EXAFS analyses on polymer-protected CuPd nanoparticles with sizes of about 1.4 nm. We found that the Cu-Pd heterobond was preferentially created in the CuPd nanoparticle and we called this type of structure a "heterobondphilic structure". DFT calculation indicated the electron transfer from Cu to Pd which stabilized the CuPd nanoparticle. The catalytic activities and their relation to the heterobondphilic structure were discussed.

1. Introduction

Bimetallic nanoparticles show interesting behavior and composition-dependent physical and chemical properties which can not be found in monometallic nanoparticles. Stable and homogenous bimetallic nanoparticles dispersed in solution can be obtained in the presence of protecting polymers [1]. We have applied EXAFS on polymer protected bimetallic nanoparticles and found that there are a variety of inner structures in the nanoparticles such as core-shell model, solid solution model, and cluster-in-cluster structure [1]. CuPd bimetallic nanoparticle dispersed in glycol solution show unique composition dependence for diene hydrogenation and nitrile hydration reactions as shown in Figs. 4 and 5 [2, 3]. We found a new structure of the polymer-protected CuPd bimetallic nanoparticles, where Cu-Pd bond is preferentially formed [4]. We named this new structure a "heterobondphilic" structure. We also carried out DFT calculations to find the stability of the CuPd nanoparticles. We would like to discuss the stability of CuPd heterobondphilic structure and its relation to catalytic properties.

2. Experimental

CuPd bimetallic nanoparticles were prepared as described in previous literature [2]. EXAFS measurements were carried out at BL12B (Cu K-edge) and BL10B (Pd K-edge) in Photon Factory (KEK-IMSS-PF) [4]. CuPd foils (1 : 9, 1 : 1 and 9 : 1) were purchased from Tanaka Noble Metal Ltd. EXAFS analyses were carried out using Rex2000 (Rigaku Co.). The EXAFS oscillations were extracted using a cubic smoothing method and were Fourier transformed with k^3-weight. Inversely Fourier filtered data were analyzed by non-linear least square curve fitting methods. Backscattering amplitude and phase shift functions were derived from FEFF8 [5, 6].

3. Results and Discussion

Fig. 1 shows the EXAFS oscillations for CuPd bimetallic nanoparticles for both Cu and Pd K-edges. The EXAFS oscillations are tremendously damped for the CuPd bimetallic nanoparticles compared to those for the pure Cu and Pd nanoparticles. This is due to the destructive interference between Cu-Cu and Cu-Pd (or Pd-Cu and Pd-Pd) EXAFS oscillations. Pd is located one row below Cu in the periodic table and hence their phase shift is π radians different. This means that we have to be careful to determine the amplitude and phase shift functions to obtain the correct structure nanoparticles from the EXAFS analysis. As mentioned in the experimental section, we used FEFF8 for the determination of backscattering amplitude and phase shift functions. We checked the validity of these theoretically derived parameters by analyzing reference compounds such as Pd, Cu and CuPd bimetallic alloy foils. EXAFS oscillation of Cu foil was well reproduced by FEFF8 but that of Pd foil was not at low k-region, around 40–60 nm^{-1} [4]. Thus we corrected the Pd theoretical parameters less than 60 nm^{-1} using empirical values [4]. Consequently, we could successfully analyze the CuPd foils using backscattering amplitude and phase shift functions as shown in Table I. Note that we can obtain coordination numbers for CuPd 1 : 1 alloy foil which are equal to those expected from the random alloy structure within the limit of error. We applied these backscattering amplitude and phase shift functions to CuPd bimetallic nanoparticles. The fitting results were tabulated in Table II. Effects of asymmetric pair distribution have not been taken into account because the surface relaxation would be lifted by the interaction of the protecting polymer [4]. The necessary conditions imposed on the analyses of bimetallic materials such as $N_{\mathrm{PdCu}}C_{\mathrm{Pd}} = N_{\mathrm{CuPd}}C_{\mathrm{Cu}}$, $\gamma_{\mathrm{CuPd}} = \gamma_{\mathrm{PdCu}}$ were checked and we found these conditions were satisfied in the limit of error. There are three types of inner structures for bimetallic cluster, namely core-shell model, cluster-in-cluster model, and solid solution model. In the core-shell model, one component located in the core region should give larger total coordination numbers than the others located in the shell region. But in the EXAFS results both components have similar total coordination numbers (about 8). In the cluster-in-cluster model, coordination numbers of like pairs should be larger than those for unlike pairs but it was not the case. The facts that total coordination numbers were the same for both metals and the coordination numbers ratio followed the composition agreed well with the formation of solid solution model. However, the coordination number for unlike pairs seems to be larger than the values expected from the solid solution model. Fig. 2 shows the ratio of coordination numbers

*e-mail: askr@cat.hokudai.ac.jp

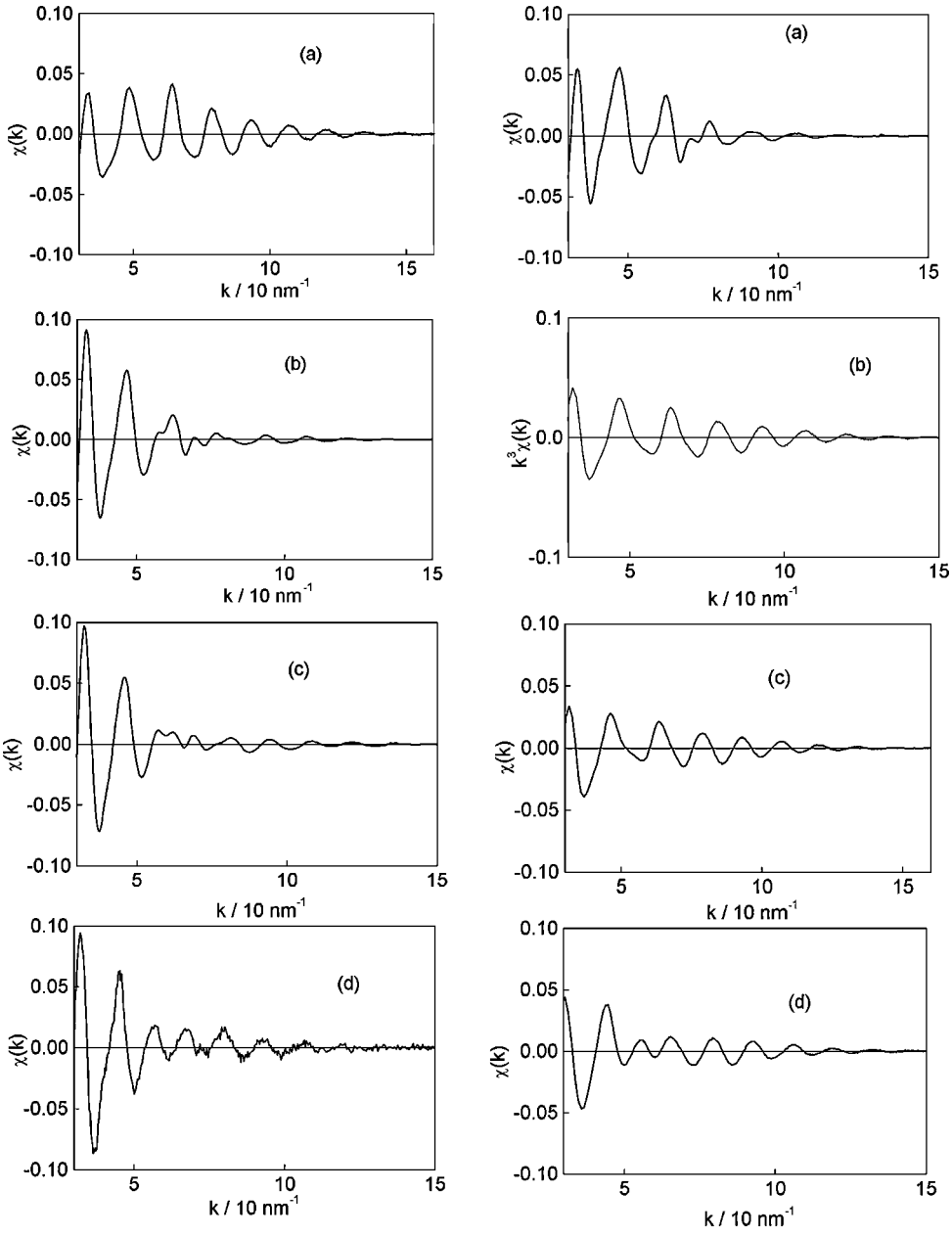

Fig. 1. EXAFS oscillations of CuPd bimetallic nanoparticles with compositions (a) Cu : Pd = 4 : 1, (b) Cu : Pd = 3 : 2, (c) Cu : Pd = 1 : 1 and (d) Cu : Pd = 1 : 4. The left and right panels are Cu and Pd K-edges, respectively. [4]

Table I. *Curve fitting results of Cu, Pd and CuPd alloy foils.*

Sample	Edge	Bond	N	r/nm	ΔE/eV	$\Delta\sigma^2/10^{-5}$ nm^2
Cu foil	Cu	Cu-Cu	[12]*	0.253(0.002) [0.256]*	3.5	4.6
Pd foil	Pd	Pd-Pd	[12]*	0.274(0.002) [0.276]*	−3.0	1.1
CuPd 1 : 9 foil	Cu	Cu-Cu	[1.2]	0.259(0.006)	−1(8)	4.5(1.5)
		Cu-Pd	[10.8]	0.268(0.002)	−5(3)	3.0(1.0)
	Pd	Pd-Cu	1.3(0.4)	0.267(0.004)	−5.4(5)	2.0(1.5)
		Pd-Pd	10.6(0.5)	0.272(0.002)	−1.2(3)	−2.0(1.0)
CuPd 1 : 1 foil	Cu	Cu-Cu	6.2(0.5)	0.257(0.003)	−4(4)	5.0(1.5)
		Cu-Pd	5.9(0.5)	0.262(0.004)	7(4)	4.5(1.5)
	Pd	Pd-Cu	6.1(0.5)	0.262(0.003)	−4(5)	4.0(1.5)
		Pd-Pd	5.8(0.5)	0.269(0.004)	0(5)	2.1(1.0)
CuPd 9 : 1 foil	Pd	Pd-Cu	[10.8]	0.258(0.002)	0(4)	2.0(1.0)
		Pd-Pd	[1.2]	0.265(0.005)	4(7)	2.5(1.0)

*The values in square brackets indicated the values obtained from crystallographic data.

of the unlike pairs to the total coordination numbers derived from EXAFS and calculated one based on solid solution model. The concave shape indicates that unlike pairs (hetero bond) such as Cu-Pd or Pd-Cu was preferably formed. We have carried out Monte Carlo simulations of the CuPd nanoparticle structure under the following simple assumptions. 1: The bond energy for Pd-Cu or Cu-Pd was larger than the average values for Cu-Cu and Pd-Pd. 2: The CuPd particle size was fixed to 1.3 nm (Average coordination number was 7.8). Table II contains the values expected from the model simulations. Thus the heterobondphilic structure can be realized if the unlike pair has a stronger bond than the like pair.

We have carried out DFT calculation based on 1, 3-atom clusters with fcc structure. When a Cu-Pd bond was formed, the total energies decreased as shown in Table III. Moreover, charge transfer from Pd to Cu occurred and the electron transfer from Cu 4s to Pd 4d stabilized the $CuPd_{12}$ or $PdCu_{12}$ cluster. The DFT calculations supported the stronger Cu-Pd heterobond than the homobond (Cu-Cu or Pd-Pd).

Table II. *Curve fitting results of bimetallic nanoparticles and coordination numbers expected from the model calculation.*

Cu : Pd	Edge	Bond	N	r/nm	ΔE/eV	$\Delta\sigma^2$/ 10^{-5} nm^2	N^*
4 : 1	Cu K	Cu-Cu	6.0(0.5)	0.253(0.003)	−4(3)	6.0(1.0)	6.1
		Cu-Pd	1.8(0.4)	0.258(0.005)	4(5)	4.9(2.0)	1.8
	Pd K	Pd-Cu	7.2(0.4)	0.257(0.002)	−2(3)	2.7(1.0)	7.0
		Pd-Pd	0.8(0.4)	0.270(0.005)	6(4)	1.3(2.0)	0.7
3 : 2	Cu K	Cu-Cu	3.9(0.4)	0.253(0.004)	−5(5)	4.5(2.0)	3.2
		Cu-Pd	3.8(0.4)	0.258(0.004)	6(5)	4.6(2.0)	4.2
	Pd K	Pd-Cu	5.5(0.5)	0.257(0.003)	4(5)	2.4(2.0)	6.3
		Pd-Pd	2.2(0.5)	0.270(0.004)	0(6)	3.7(2.0)	2.2
1 : 1	Cu K	Cu-Cu	2.8(0.5)	0.253(0.004)	−4(5)	5.0(1.0)	2.7
		Cu-Pd	5.0(0.5)	0.258(0.003)	4(5)	4.4(2.0)	5.1
	Pd K	Pd-Cu	5.1(0.4)	0.259(0.003)	−2(5)	2.4(2.0)	5.1
		Pd-Pd	2.8(0.3)	0.270(0.003)	7(6)	2.7(2.0)	2.7
1 : 4	Cu K	Cu-Cu	0.8(0.6)	0.255(0.005)	−3(5)	5.5(3.0)	0.7
		Cu-Pd	7.0(1.0)	0.264(0.005)	4(3)	5.0(3.0)	7.0
	Pd K	Pd-Cu	1.8(0.4)	0.265(0.004)	−3(4)	3.0(2.0)	1.8
		Pd-Pd	6.0(0.4)	0.273(0.002)	3(5)	3.6(1.0)	6.1

*The coordination numbers calculated from the calculation based on the heterobondphilic structure.

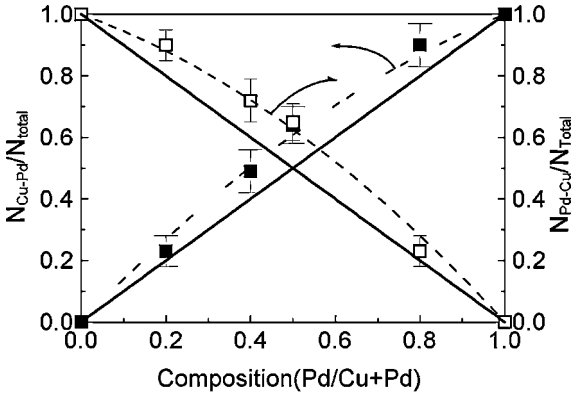

Fig. 2. Composition-dependence of the ratios of Cu-Pd (filled squares) and Pd-Cu(open squares) coordination numbers to the total coordination numbers together with those expected from a random alloy model (solid line). Broken lines are the least square fit of the data. [4]

Table III. *DFT calculations for M_{13} nanoparticle.*

		Muliken population		Central
	E_t/eV	Center	Peripheral	Charge
Pd_{13}	35.3	4.98	5.001	−0.018
$CuPd^*_{12}$	35.9	5.43	5.006	0.394
Cu_{13}	36.0	5.60	5.491	0.104
$PdCu^*_{12}$	36.9	5.23	5.480	−0.226

*Cu and Pd are located in the center of the nanoparticles of $CuPd_{12}$ and $PdCu_{12}$, respectively.

Figs. 3 and 4 show the composition-dependence of 1,3-cyclooctadiene hydrogenation activity and acrylonitrile hydration activity, respectively. The surface coordination number of Pd-Pd and Pd-Cu, which were obtained from the Monte Carlo simulation mentioned above, were also given in Fig. 3 and Fig. 4, respectively. In hydrogenation reaction, the reaction started with

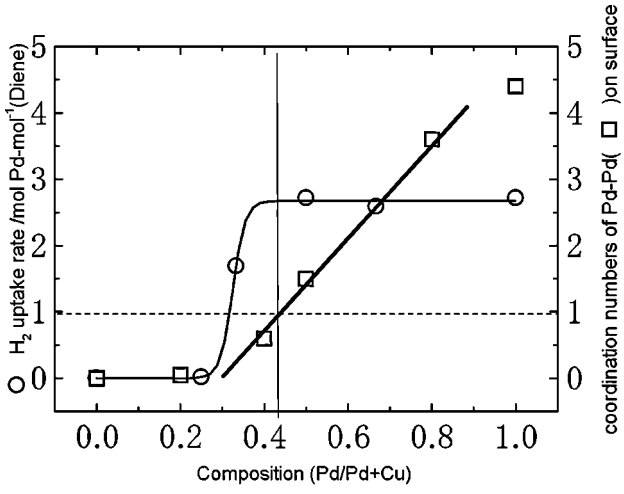

Fig. 3. Composition dependence of hydrogenation reaction rate (open circle) and surface coordination number of Pd-Pd (open square).

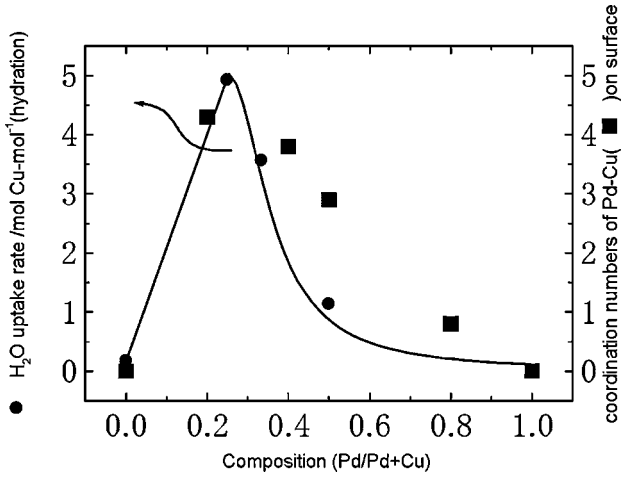

Fig. 4. Composition dependence of hydration reaction rate (filled circle) and surface Pd-Cu coordination number (filled square).

the appearance of Pd-Pd bond and the reaction was saturated when the Pd-Pd coordination number exceeded one. This result implies that the hydrogenation reaction requires at least one Pd-Pd ensemble. On the other hand, the hydration reaction requires Pd-Cu bond and the reaction rate is higher as the Pd-Cu coordination number increases. The hydration reaction may occur at the Pd-Cu ensemble in the synergistic catalysis of Pd and Cu [1].

The EXAFS analyses have shown that the Cu-Pd bimetallic nanoparticles have "heterobondphilic" structure as its inner structure. DFT calculation indicates that the Cu-Pd bond energy is stronger than that of homobond (Cu-Cu and Pd-Pd). The reactivity has a strong correlation with the composition of surface ensembles.

References

1. Toshima, N. and Yonezawa, T., New J. Chem. **22**, 1179 (1998).
2. Toshima, N. and Wang, Y., Chem. Lett. 1611 (1993).
3. Toshima, N. and Wang, Y., Adv. Mater. **6**, 245 (1994).
4. Bian, C. R., Suzuki, S., Asakura, K., Hei, L. and Toshima, N., *J. Phys. Chem.* **106**, 8587 (2002).
5. Rehr, J. J., Mustre de Leon, J., Zabinsky, S. I. and Albers, R. C., J. Am. Chem. Soc. **113**, 5135 (1991).
6. Rehr, J. J. and Albers, R. C., Rev. Mod. Phys. **72**, 621 (2001).

Physica Scripta. Vol. T115, 784–786, 2005

Local Structures of Ultra-Thin Pt Films Probed by Grazing Incidence Fluorescence XAFS

Zhi Xie[1], Isao Kojima[2], Yaning Xie[3], Bo He[1], Dongliang Chen[1], Tao Liu[3], Tiandou Hu[3], Xinyi Zhang[4] and Shiqiang Wei[1*]

[1]National Synchrotron Radiation Laboratory, University of Science and Technology of China, Hefei 230029, P. R. China
[2]National Institute of Advanced Industrial Science and Technology, AIST Tsukuba Central 5, 1-1-1, Higashi, Tsukuba 305-8565, Japan
[3]Institute of High Energy Physics, Chinese Academy of Sciences, Beijing 100039, P. R. China
[4]Synchrotron Radiation Research Center and Surface Physics Laboratory (National Key Laboratory), Fudan University, Shanghai 200433, P. R. China

Received June 26, 2003; accepted in revised form November 4, 2003

PACS numbers: 61.10.Ht, 81.05.Bx, 68.55.Jk

Abstract

The local structures of Pt thin films with thicknesses from 3 to 105 nm grown at 298 K have been studied by grazing incidence fluorescence XAFS technique. The results indicate that the bond length $R = 2.77$ Å and coordination number $N = 12.0$ of the first shell around Pt atoms in the Pt (105 nm) and Pt (30 nm) thin films are the same as those in Pt foil, except that the disorder degree σ increases by about 8%. The magnitude peaks (located at 2.77, 3.92, 4.80 and 5.55 Å) appearing in the radial distribution function curves suggest that the Pt (105 nm) and Pt (30 nm) thin films keep a long-range order. With thickness decreasing from 105 to 10 nm, the Debye-Waller factor σ^2 increases to 6.4×10^{-3} Å^2 ($\sigma^2 = 4.8 \times 10^{-3}$ Å^2 for the Pt foil). For the Pt (3 nm) ultra-thin film, R_1, N_1 and ${\sigma_1}^2$ are 2.78 Å, 10.1 and 7.1×10^{-3} Å^2, respectively. This implies that N_1 largely decreases and ${\sigma_1}^2$ strongly increases in the Pt (3 nm) ultra-thin film. Moreover, its magnitude peaks of the higher shells in the radial distribution function disappear for the Pt (3 nm) ultra-thin film. This result shows that the Pt lattice is largely distorted and the medium-range order around Pt atoms is completely destroyed for the Pt (3nm) ultra-thin film. We consider that the Pt lattice distortion of the Pt ultra-thin film originates from both interaction between Pt particles and SiO_2 substrate, and Pt grains with a smaller size forming a surface structure defect.

1. Introduction

Noble metal, such as Pt and Au, thin films are commonly used as electrodes extensively required for semiconductor devices with ultra-large-scale integration [1, 2]. In particular Pt thin film is a promising candidate for potential capacitor electrodes and gate metal material in gigabit dynamic random access memories and metal-oxide-semiconductor field effect transistors due to its high chemical stability in an oxidizing atmosphere and its high work function (5.6 eV) as well as other excellent electrical properties [3–5].

The performance of polycrystalline Pt thin film is strongly affected by its grain size distribution, impurity, defects, crystalline orientation, etc., and is intrinsically linked to the structure of the thin film [6–12]. Hiratani *et al*. [11] have found that the lattice shrinkage of Pt thin film fabricated by chemical vapor deposition increases with decreasing thickness below 35 nm, which can also lead to a higher resistance. Frenkel *et al*. [7] have reported that the bond length of the first nearest neighbors of Pt nano-clusters with an average size about 2.4 nm contracts. Lamber *et al*. [13] have shown a contraction in the lattice of Pd nano-clusters from their electron diffraction results. In order to clearly understand the nature of the Pt thin films and to optimize the growth conditions of Pt thin films, it is essential to determine the local structures of Pt thin films with different thicknesses from both fundamental and technological viewpoints.

In the present paper, grazing incidence fluorescence XAFS has been used to study the local structures of the Pt thin films fabricated by MBE in the thickness range from 3 to 105 nm. The local structures of Pt thin films depending on the thickness were accurately and reliably measured. This is favorable to optimize the growth conditions and fabrications of Pt film with a high quality.

2. Experimental

An ultrasmooth SiO_2 substrate with a surface roughness of 0.3 nm was cut into four pieces of approximately the same area. These small SiO_2 pieces were cleaned in acetone solution with an ultrasonic cleaner for 30 min. The Pt thin film was grown in a molecular-beam epitaxy (MBE) chamber. Before growing the Pt thin film, the SiO_2 substrate was cleaned by heating it to 1073 K for 1 h. Finally, the samples grown at room temperatures were fabricated with a growing rate of 0.10 nm/s. The thickness d of the samples is about 3, 10, 30, 105 nm, respectively. We have reported [6] that the surface topography of Pt (105 nm) thin film fabricated by MBE at 300 K is composed of three-dimensional, well-separated, mountain-like islands with about 1.81 nm roughness and grain sizes of about 10–20 nm.

The X-ray absorption spectra at the Pt L_{III}-edge for various Pt thin films were measured at the beamline of 4W1B of the Beijing Synchrotron Radiation Facility (BSRF) at room temperature. The electron beam energy was 2.2 GeV and the maximum stored current was about 80 mA. Fixed-exit Si (111) flat double crystals were used as monochromator. XAFS spectra of Pt thin films with thicknesses of 3 and 10 nm were collected in grazing-incidence fluorescence mode with an incidence angle of 0.19 degrees. The XAFS spectrum of Pt foil was collected in transmission mode. XAFS spectra of Pt thin films with thicknesses of 30 and 105 nm were collected in fluorescence mode with an incidence angle of 45 degrees. The XAFS data were analyzed by NSRLXAFS 3.0 software packages [14].

3. Results and discussion

Pt L_{III}-edge EXAFS functions $\chi(k)$ and their Fourier transformations (FT) for the Pt thin films with thicknesses of 3, 10, 30 and 105 nm are shown in Figure 1 and Figure 2, respectively. Figure 2 demonstrates that the FT curves of Pt (30 nm) and Pt (105 nm) thin films are similar to that of Pt foil. There are four obvious peaks located at 2.7, 3.9, 4.8 and 5.6 Å corresponding to the first four shells around Pt atoms in the fcc structural Pt crystal.

*Correspondent: Shiqiang Wei. E-mail: sqwei@ustc.edu.cn

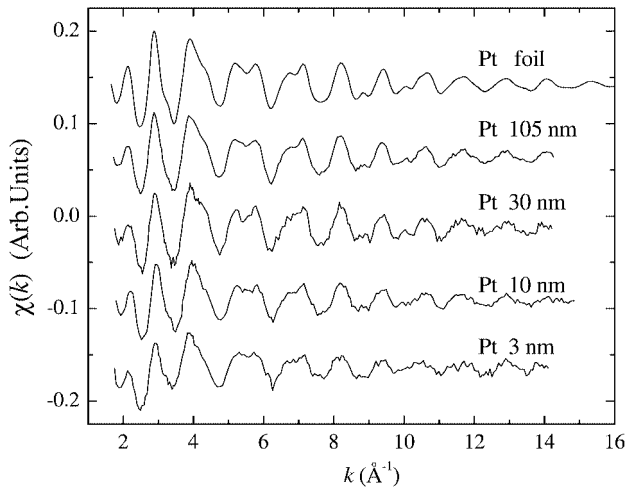

Fig. 1. EXAFS oscillation functions for Pt thin films with different thicknesses.

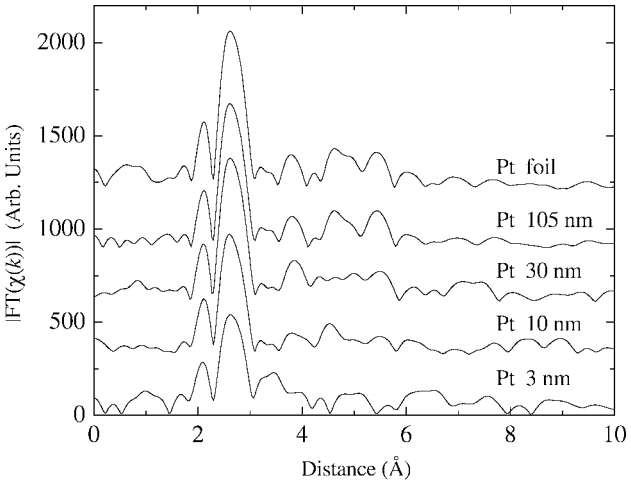

Fig. 2. Radial distribution functions for Pt thin films with different thicknesses.

For the Pt (3 nm) thinner film, the intensity of the first peak is much lower (about 70% of the Pt (105 nm) thin film), and the peaks of the higher shells disappear. It means that the medium-range order of Pt atoms has been destroyed for the Pt (3 nm) thinner film.

For obtaining the structural parameters of Pt thin films, a least-squares curve fit was performed for the data analysis by using the NSRLXAFS3.0 software packages [14]. The theoretical amplitude functions and phase shifts were calculated by FEFF7 [15]. The curve fits, based on single-scattering theory, were performed in the R-range between 1.9 and 3.1 Å. The fitting results are summarized in Table I.

Seen from Table I, the bond length R and the coordination number N is 2.77 Å and 12.0 for Pt foil, Pt (105 nm) and Pt (30 nm) thin films, respectively. However, the Debye-Waller factor σ^2 increases slightly from 0.0048 to 0.0052 and 0.0055 Å^2 with the reduction of the thickness of the Pt thin films. This indicates that the local structure of the Pt thin films with thicknesses of 30 and 105 nm are almost the same as that of Pt foil. This shows clearly that the Pt thin films keep the long-rang order and possess fcc structure when the thickness of the films is above 30 nm. An evident change occurs in the Pt (10 nm) thin film, and its R_1, N_1, and ${\sigma_1}^2$ is 2.77 Å, 11.3 and 0.0061 Å^2, respectively. This shows that there is a small lattice distortion in the Pt (10 nm) thin film. For the Pt (3 nm) thinner film, R_1, N_1, and ${\sigma_1}^2$ is 2.78 Å, 10.8 and 0.0077 Å^2, respectively. This result indicates that the local structure of the Pt (3 nm) thinner film is significantly different from those of the other Pt thin films.

In our previous work [16], it has been revealed that the densities of Pt thin films with thicknesses over 10 nm are larger than that of 94% of bulk Pt. This means that there is a smaller defect and a close compact in the as-deposited Pt thin films. Moreover, it has been shown that the root mean square (RMS) roughness on the surface of the Pt thin films is much lower than their thickness. Hence, the Pt atomic ratio of surface to bulk is very small for Pt thin films with thicknesses over 10 nm. This result is in good agreement with the XAFS results listed in Table I.

At the initial stage of growth of the Pt (3 nm) thinner film, it is favorable to grow the well-separated three-dimensional Pt islands that do not coalesce together. The lateral size of these grains is typically 10 nm as estimated by AFM [6], which has a higher ratio of surface to bulk in the Pt (3 nm) thin film. Therefore, we consider that the large lattice distortion is responsible for the reduction of coordination number (10.8) of the first shell in the Pt (3 nm) thin film as compared with that in bulk Pt foil. On the other hand, we have noted that σ^2 (0.0077 Å^2) of the Pt (3 nm) film is much larger than that ($\sigma^2 = 0.0052$ Å^2) of the Pt (105 nm) thin film. One of the most plausible explanations for the larger disorder degree is the relaxation of the bond lengths exhibited by surface atoms, driven by the substantial surface tension of a high curvature radius [17–19]. In response to this compressive tension, the atomic positions of the surface atoms shift away from the ideal fcc sites and cause lattice distortion. This process also destroys the medium-range order of the Pt (3 nm) thin film. Furthermore, the density measurement [16] shows that the density of Pt (3 nm) thin film is reduced to 87.8% of the density of bulk Pt, implying the existence of a large defect.

In summary, the fluorescence XAFS results show that the local structures of the Pt thin films with thicknesses between 30 and 105 nm remain of long-range order, and are nearly the same as that of Pt foil. With the Pt thin film thickness decreasing to 3 nm, the medium-range order around Pt atoms has been completely destroyed. We consider that the Pt lattice distortion of the Pt thin film with thickness of 3 nm originates from both the interaction between Pt particles and SiO_2 substrate, and Pt grains with smaller size forming a surface structure defect.

Table I. *Structural parameters of Pt ultra-thin film samples obtained from XAFS data.*

Sample	Bond	N	R (Å)	σ^2 (Å^2)	ΔE_o (eV)
Pt foil	Pt-Pt	12.0 ± 0.5	2.77 ± 0.002	0.0048 ± 0.0001	6.6 ± 0.4
105 nm Pt	Pt-Pt	12.0 ± 0.3	2.77 ± 0.003	0.0052 ± 0.0001	6.6 ± 0.5
30 nm Pt	Pt-Pt	11.9 ± 0.9	2.77 ± 0.004	0.0055 ± 0.0001	6.4 ± 0.8
10 nm Pt	Pt-Pt	11.3 ± 0.7	2.77 ± 0.006	0.0061 ± 0.0001	6.0 ± 0.7
3 nm Pt	Pt-Pt	10.8 ± 0.8	2.78 ± 0.010	0.0077 ± 0.0001	7.0 ± 0.6

Acknowledgment

This project was supported by the Chinese Nature Science Foundation Committee (Grant No.10174068), the development of high-level university of University of Science and Technology of China and Beijing Synchrotron Radiation Facility.

References

1. Scott, J. F., Ann. Rev. Mater. Sci. **28**, 79 (1998).
2. Kulkani, A. K. and Chang, L. C., Thin Solid Films **301**, 17 (1997).
3. Nayak, M., Ezhilvalavan, S. and Tseng, T. Y., "In Handbook of Thin Film Materials;" (Nalwa, H. S., Ed.); (Academic Press: San Diego, 2001); Vol. **3**, pp. 121–123.
4. Hiratani, M., Nabatame, T., Matsui, Y., Imagawa, K. and Kimura, S., J. Electrochem. Soc. **148**, C524 (2001).
5. Wilk, G. D., Wallace, R. M. and Anthony, J. M., J. Appl. Phys. **89**, 5243 (2001).
6. Wei, S. Q., Li, B., Fujimoto, T. and Kojima, I., Phys. Rev. B **58**, 3605 (1998).
7. Frenkel, A. I., Hills, C. W. and Nuzzo, R. G., J. Phys. Chem. B **105**, 12689 (2001).
8. Ball, M. J., Lucas, C. A., Markovic, N. M., Stamenkovic, V. and Ross, P. N., Surf. Sci. **518**, 201 (2002).
9. Aaltonen, T., Ritala, M., Sajavaara, T., Keinonen, J. and Leskela, M., Chem. Mater. **15**, 1924 (2003).
10. Block, J., Kolodziej, J. J., Rowe, J. E., Madey, T. E. and Shrodiner, E., Thin Solid Films **428**, 47 (2003).
11. Hiratani, M., Nabatame, T., Matsui, Y. and Kimura, S., Thin Solid Films **410**, 200 (2002).
12. Kuribayashi, K. and Kitamuura, S., Thin Solid Films **400**, 160 (2001).
13. Lamber, R., Weitjen, S. and Jaeger, N. I., Phys. Rev. B **51**, 10968 (1995).
14. Zhong, W. J. and Wei, S. Q., J. Univ. Sci. Tech. China **31**, 328 (2001).
15. Rehr, J. J., Zabinsky, S. I. and Albers, R. C., Phys. Rev. Lett. **69**, 3397 (1992).
16. Kojima, I., Wei, S. Q., Li, B. Q. and Fujimoto, T., J. Surf. Analysis **4**, 70 (1998).
17. Marcus, P. M., Qian, X. H. and Hübner, M., J. Phys.: Condens. Matter **12**, 5541 (2000).
18. Gazzadi, G. C. *et al*., Appl. Surf. Sci. **162**, 198 (2000).
19. Woltersdorf, J., Nepijko, A. S. and Pippel, E., Surf. Sci. **106**, 64 (1981).

Physica Scripta. Vol. T115, 787–789, 2005

Mo K-edge EXAFS Analysis of Mo/USY Zeolite – Effects of Extra-Framework Aluminum on the Location and Dispersion of Mo Sulfide Catalysts

Koichi Sato[1,*], Nobuyuki Matsubayashi[2], Motoyasu Imamura[2], Kyoko K. Bando[2] and Hiromichi Shimada[2]

[1]National Institute of Advanced Industrial Science and Technology (AIST), 4-2-1 Nigatake, Miyagino Sendai, Miyagi, 983-8551 Japan
[2]National Institute of Advanced Industrial Science and Technology (AIST), 1-1 Higashi, Tsukuba, Ibaraki, 305-8565 Japan

Received June 26, 2003; accepted November 4, 2003

PACS numbers: 82.75.−z; 82.75.Qt; 82.75.Vx; 89.30.Aa

Abstract

The local structures around Mo supported on USY zeolites containing different amounts of extra-framework Al species (EFAL) were investigated to elucidate the effects of EFAL on the location and dispersion of Mo sulfide catalysts. Mo K-edge EXAFS analysis indicated that Mo sulfide catalysts were highly dispersed and located, at least in part, in the micropores of USY zeolites, independent of the EFAL amounts. The dispersion of Mo sulfide was found to decrease with increasing amount of EFAL in the zeolites. EXAFS analysis of Mo oxide catalysts, the precursor of the sulfide catalysts, suggested that Mo oxide catalysts deposited on EFAL during the catalyst preparation were reluctant to disperse into micropores and formed larger MoS_2 clusters during sulfiding that lowered the dispersion.

1. Introduction

Y-type zeolites with Mo sulfide are promising catalysts for hydrocracking petroleum fractions. Because zeolitic micropores cannot accommodate large molecules in the heavy petroleum fractions, the active catalytic sites of Y-type zeolites are limited to the external surfaces, which are classified into two categories; the external surface of zeolite particles and the surface of mesopores with diameters between 2 nm and 50 nm. The roles of the mesopore surface in the cracking reactions are quite important because the external surface area of zeolite particles is not large enough to achieve high catalytic activity [1, 2]. Mesopores of Y-type zeolite are formed in many cases by steaming over 800 K that extracts Al from the zeolitic framework. During the following calcination procedure, the extracted Al forms so-called extra-framework Al species (EFAL), which are mainly deposited in the mesopores and micropores. EFAL is supposed to affect the location and dispersion of Mo sulfide catalysts on the zeolites that are important factors to control the catalytic activities. In the present study, we prepared a series of Mo/ultrastable Y-type (USY) zeolite catalysts with different amounts of EFAL and analyzed the local structure around Mo. Based on the results, we discussed the effects of EFAL on the dispersion and location of Mo sulfide catalysts in the USY zeolites.

2. Experimental

Three kinds of zeolites were used in the present study. Tosoh 330HUA (framework Si/Al = 9.7) was chosen as the starting USY zeolite (USY-A) containing a considerable amount of EFAL. USY-B was obtained by treating USY-A in a 0.1 mol/l HCl solution for 1 h at 298 K, followed by washing with water and drying at 393 K for 12 h. USY-C was obtained from USY-B by repeating the above procedure. Mo/USY catalysts were prepared by incipient wetness impregnation of the above zeolite powders with an aqueous solution of ammonium heptamolybdate ($(NH_4)_6Mo_7O_{24}$). The Mo loading was 6.7 wt% as MoO_3. After the impregnation, the catalysts were dried at 393 K and calcined at 823 K in dry air. The porosity and mesopore size distribution of the catalysts were calculated by using N_2 isotherm at 77 K. The bulk composition of zeolite was measured by chemical analysis, whereas the Al/Si ratio of the zeolitic framework was calculated from the unit cell parameters obtained by X-ray diffraction (XRD) [3].

The Mo K-edge EXAFS spectra of the catalysts before and after sulfidation were measured at the BL-10B of the Photon Factory at the High Energy Accelerator Research Organization (Tsukuba, Japan). The EXAFS spectra of the catalysts before sulfidation were obtained by measuring the absorption spectra of the self-supporting disk made of the catalyst powders in the transmission mode at an ambient atmosphere. The disk was then placed in a glass cell with Kapton windows and sulfided at 673 K in a flow of 5% H_2S/H_2 for 2 h. After purging the cell by N_2, the EXAFS spectra of the catalysts after sulfidation were obtained. The phase shift and backscattering amplitude factor were corrected by using the calculated values of FEFF6 [4]. In the analysis of the catalysts after sulfidation, the average coordination number of Mo-Mo (CN(Mo)) was obtained using the following relation [5, 6],

$$N(Mo) = BIr^2 \tag{1}$$

where B is the proportionality constant for Mo-Mo scattering obtained from the crystal of MoS_2 that has six Mo atoms around each Mo atom, I is the peak intensity of Mo-Mo scattering, and r is the distance between the Mo atoms. Note that it is assumed that the thermal and static disorders are constant.

3. Results and Discussion

3.1. *EXAFS measurements for Mo/USY before the sulfidation*

Table I shows the physical properties of the USY zeolites. For USY-A, the Si/Al ratio of the framework was 9.7, which was almost as three times as large as that of the bulk (3.2). The discrepancies between the Si/Al ratios of the framework and that of the bulk decreased in the order of USY-A < USY-B < USY-C. Table I also showed that the mesopore and micropore volumes increased in the order of USY-A < USY-B < USY-C. These results indicate that the HCl treatment effectively removed EFAL deposited in the mesopores and micropores of the starting USY-A.

*e-mail: koichi.sato@aist.go.jp

Table I. *Characterization of USY zeolites.*

zeolite	Si/Al molar ratio framework (XRD)	Si/Al molar ratio bulk (ICP)	relative crystallinity (%)[1)]	pore volume (cm^3/g) before Mo loading micropore[2)]	before Mo loading mesopore[3)]	after Mo loading micropore	after Mo loading mesopore
USY-A	9.7	3.2	83.7	0.244	0.145	0.223	0.130
USY-B	11.2	4.3	85.4	0.285	0.162	0.251	0.158
USY-C	12.8	9.1	93.6	0.321	0.186	0.264	0.191

1) Estimated by comparing the peak intensities of the XRD pattern referring to NaY(Si/Al = 2.8).
2) Calculated by the t-plot method.
3) Calculated by the BJH method.

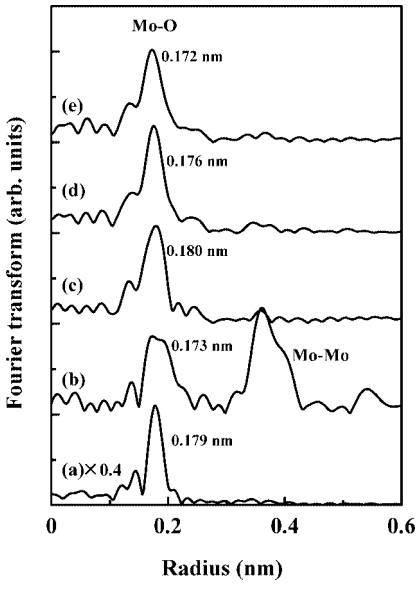

Fig. 1. Fourier transforms of the Mo K-edge EXAFS spectra for Mo/USY before the sulfidation. (a): $Na_2MoO_4 \cdot 2H_2O$, (b): MoO_3, (c): Mo/USY-A, (d): Mo/USY-B, (e): Mo/USY-C. The Mo-O distances are indicated in the figure.

Figure 1 shows the Fourier transformed EXAFS spectra of reference materials and Mo/USY catalysts before sulfidation. The spectrum of $Na_2MoO_4 \cdot 2H_2O$ (Fig. 1(a)) gave an intense peak at 0.178 nm that is assigned to tertahedrally coordinated Mo-O scattering. In contrast, the spectrum of MoO_3 (Fig. 1(b)) gave a broad peak between 0.17 nm–0.20 nm that is assigned to octahedrally coordinated Mo-O scattering and another peak at about 0.36 nm that is assigned to Mo-Mo scattering in the second nearest shell. Four oxygen atoms in MoO_4^{2-} are located at almost the same distance from Mo (0.175 nm–0.179 nm) [7], whereas MoO_6 octahedra are highly distorted and six oxygen atoms are located at 0.167 nm–0.223 nm with single or double bonding to Mo [8].

The spectra of all the three zeolites (Fig. 1(c)–(e)) gave peaks between 0.172 nm and 0.180 nm. Considering the relatively low and broad peaks, these peaks are likely assigned to Mo-O scattering of mixed MoO_4 tetrahedra and MoO_6 octahedra. Among the three USY zeolites, the Mo-O peak shifted from 0.180 nm of USY-A (c) to 0.172 nm of USY-C (e). The short Mo-O distance observed for USY-C is likely ascribed to dominant presence of octahedral Mo-O bonding, whereas the long Mo-O distance observed for USY-A is likely due to dominant presence of tetrahedral Mo-O bonding. Note that the Mo-O distance decreased with increasing EFAL amounts in zeolites.

Shimada *et al.* [9] reported EXAFS spectra of Mo oxide catalysts supported on various oxides. In their results, the ratio of tetrahedral Mo-O bonding relative to the total Mo-O bonding decreased in the order of $MgO > Al_2O_3 > SiO_2 > TiO_2$; the SiO_2 support favored the octahedrally coordinated MoO_3-like structure, whereas the Al_2O_3 support favored tetrahedral coordination around Mo particularly at low Mo loading. Their result is in good agreement with the present study described above. Namely, the relative ratio of octahedral Mo-O bonding increases with increasing amount of EFAL in the USY zeolites. Note that the surface of USY zeolite with high Si/Al ratios has similar chemical properties as those of SiO_2.

Previous papers [10, 11] indicate that Mo oxide catalysts are poorly dispersed on SiO_2 supports and sometimes give evidence to MoO_3-like structures. The spectrum of USY-C (Fig. 1(e)), however, showed no peak due to Mo-Mo scattering that was observed in the spectrum of MoO_3 (Fig. 1(b)). This suggests that Mo oxide species in USY-C are dispersed and distorted. Heptamolybdate anions ($Mo_7O_{24}^{6-}$), the precursor of Mo oxide catalysts, cannot penetrate into the micropores during the impregnation and are deposited on the mesopore surface. The deposited Mo oxide species are decomposed and can migrate into the micropores during calcination that is performed at higher temperatures than 573 K [12]. In the case of USY-C with the smallest amount of EFAL, Mo oxide species deposited on the USY zeolite surface relatively easily migrated and formed distorted octahedral Mo oxide in the micropores. Note that the USY micropores with a diameter of 0.74 nm hinder the growth of crystalline structures. On the other hand, heptamolybdate anions deposited on EFAL did not migrate into the micropores due to the relatively strong interaction between Mo oxide and EFAL. This is confirmed in the relatively large decrease in the mesopore volume of USY-A after Mo loading (Table I).

3.2. *EXAFS measurements for Mo/USY after the sulfidation*

Figure 2 shows the Fourier transformed EXAFS spectra of MoS_2 and Mo/USY catalysts after sulfidation. All the spectra exhibit two intense peaks at 0.239 nm and at 0.313 nm, which are assigned to Mo-S scattering and Mo-Mo scattering, respectively. The average coordination numbers (CN(Mo)) decrease in the order of Mo/USY-A (1.82) > Mo/USY-B (1.61) >Mo/USY-C (1.25). Because of high distortion of layered MoS_2 structures, the average size of MoS_2 clusters cannot be estimated directly from the CN(Mo) obtained from EXAFS [13–16]. Using a recently proposed relationship between the CN(Mo) and the average particle size of MoS_2 clusters that took into account the effects of the structural distortion and disorder on EXAFS [16], the

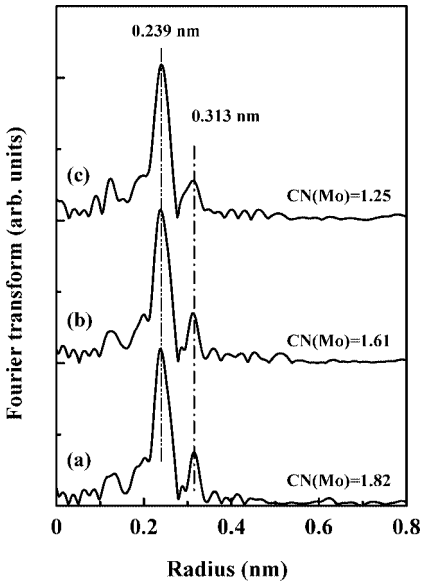

Fig. 2. Fourier transforms of the Mo K-edge EXAFS spectra for Mo/USY after the sulfidation. (a): Mo/USY-A, (b): Mo/USY-B, (b): Mo/USY-C.

average size of the MoS_2 clusters in the present catalysts were approximately estimated to 1.7 nm for USY-A, 1.6 nm for USY-B, and 1.4 nm for USY-C.

Considering the micropore size (0.74 nm) of USY zeolites, at least a part of the MoS_2 clusters were located inside the micropores. The above results on the CN(Mo) suggest that the relative ratio of the MoS_2 located inside the micropores to the total MoS_2 content decreases in the order of Mo/USY-C > Mo/USY-B > Mo/USY-A. This is consistent with the order of the micropore volumes after Mo loading (Table I). In other words, the amount of MoS_2 located on the mesopore surface increased with increasing EFAL in USY zeolites. This simultaneously resulted in the relatively large MoS_2 clusters in the zeolite with a large amount of EFAL. These discussions indicate that the location of Mo was likely fixed during the calcination, although it cannot be precluded that sulfidation promoted the migration of a part of Mo species from the mesopore surface into the micropores.

From the viewpoint of catalytic properties for advanced hydrocracking catalysts, even distribution of MoS_2 clusters in the mesopores and micropores is favorable to prevent overcracking or coking on the solid acid sites of USY zeolites. Furthermore, smaller MoS_2 clusters increase the number of active catalytic sites. The present results suggest that USY-C with the smallest EFAL has the most suitable properties as a support for hydrocracking catalysts.

4. Summary and conclusion

EXAFS spectroscopy was applied to the determination of the location and dispersion of MoS_2 clusters in three USY zeolites with different amounts of EFAL. The results indicated that a part of the MoS_2 clusters was located in the micropores, whereas the remainder was located on EFAL in the mesopores. This resulted in a better distribution and higher dispersion of MoS_2 clusters in the zeolite with a smaller amount of EFAL. Furthermore, large MoS_2 clusters suggested in Mo/USY-A might plug the mesopores of the USY zeolites. The analysis of the catalysts before sulfidation indicated that the location and dispersion of MoS_2 clusters were mostly fixed during the calcination procedure due to the stronger interaction between Mo oxide and EFAL than that between Mo oxide and the USY zeolite surface.

Acknowledgement

The EXAFS measurements were performed under the approval of the Photon Factory Program Advisory Committee (2002G134).

References

1. Sato, K., Nishimura, Y. and Shimada, H., Catal. Lett. **60**, 83 (1999).
2. Sato, K., Nishimura, Y., Honna, K., Matsubayashi, N. and Shimada, H., J. Catal. **200**, 288 (2001).
3. Fichtner-Schmittler, H., Lohse, U., Engelhardt, G. and Patzelous, V., Cryst. Res. Technol. **19**, K1 (1984).
4. Rehr, J. J., Mustre de Leon, J., Zabinsky, S. I. and Albers, R. C., J. Am. Chem. Soc. **113**, 5135 (1991).
5. Stern, E. A., Sayers, D. E. and Lytle, F. W., Phys. Rev. B **11**, 1009 (1975).
6. Shimada, H., *et al.*, Catal. Lett. **20**, 81 (1993).
7. Matsumoto, K., Kobayashi, A. and Sasaki, Y., Bull. Chem. Soc. Jpn. **48**, (1975).
8. Kihlborg, L., Ark. Kem. **21**, 357 (1963).
9. Shimada, H., *et al.*, J. Catal. **138**, 746 (1992).
10. de Boer, M., *et al.*, Catal. Lett. **11**, 227 (1991).
11. Leyrer, J., Mey, D. and Knozinger, H., J. Catal. **124**, 349 (1990).
12. Cid, R., *et al.*, J. Catal. **89**, 478 (1984).
13. Calais, C., *et al.*, J. Catal. **174**, 130 (1998).
14. Iwata, Y., *et al.*, Catal. Today **65**, 335 (2001).
15. Matsubayashi, M., *et al.*, J. Synchrotron Rad. **6**, 428 (1999).
16. Shido, T. and Prins, R., J. Phys. Chem. B **102**, 8426 (1998).

Physica Scripta. Vol. T115, 790–793, 2005

Characterization of Size Dependent Structural and Electronic Properties of CTAB-Stabilized Cobalt Nanoparticles by X-ray Absorption Spectroscopy

H. Modrow[1], N. Palina[1], Ch. S. S. R. Kumar[2], E. E. Doomes[2], M. Aghasyan[3], V. Palshin[2], R. Tittsworth[2], J. C. Jiang[4] and J. Hormes[2]

[1]Physikalisches Institut der Universität Bonn, Nussallee 12, 53115 Bonn, Germany
[2]Center for Advanced Microstructures and Devices, Baton Rouge LA70806, USA
[3]CANDLE, Acharyan 31, 375040, Yerevan, Armenia
[4]Department of Mechanical Engineering, Louisiana State University, Baton Rouge, LA 70803, USA

Received June 26, 2003; accepted June 28, 2004

PACS numbers: 61.10Ht, 6146w, 7322f

Abstract

CTAB (Cetyltrimethylammonium bromide) stabilized cobalt nanoparticles of three different sizes between 5.5 and 11 nm diameter were prepared using reverse-micelle method. Their geometric and electronic structure was characterized using X-ray Absorption Spectroscopy (XAS) at the Co-K-edge and Transmission Electron Spectroscopy (TEM). The as-prepared nanoparticles appear to have a cobalt core that is a "mixture" of the Co-α and β-phase and a shell, possibly, made of a cobalt(III) octahedral complex. The "shell" disappears when the particles are annealed to 250 °C and the particles are transformed into the "standard" hcp (α) phase. The short time stability of the particles against oxidation supports the presence of a core-shell structure with a Co core and a "protective shell". A longer exposure to air leads to a more or less complete oxidation of the entire particle to CoO.

1. Introduction

One of the most important challenges of nanoscience is to delineate the size-dependent properties of nanoparticles as it should – at least in principle – be possible to tune specific properties such as magnetism, heat capacity, optical, photoconductivity and charge transfer, electronic, melting point, catalytic by varying the size of the nanoparticles and/or the stabilizing surfactant coating. Despite the fact that several research groups have been focusing their attention to the correlation of macroscopic physical and chemical properties of nanoparticles with size [1], very little or no information is available about the size dependent electronic and geometric structure of nanoparticles [2]. In general, the power which changes morphology and thus also the electronic properties of nanoparticles is the increasing influence of the surface on the system. There are, however, several possibilities how these influences can modify the morphology and/or the electronic structure of such particles. On the one hand, especially for small metal particles, a chemical interaction at the surface may either lead to defined surface states or even influence the entire particle and its morphology [3]. On the other hand there is a pure crystallographic phase transformation, induced by the growing importance of the surface energy term to the total energy, in which the chemical composition of the sample remains identical and only changes in the arrangements of atoms and/or building blocks are responsible for changing particle properties. Examples for this effect occur rarely in a pure form [4], more often one finds that contributions of several phases are present simultaneously [5]. Finally, the formation of core-shell structures of different composition is possible [6]. Gaining this type of structural information is also crucial for an understanding of the magnetic properties of such particles, which deviate in most cases from what is expected from straightforward downscaling of the corresponding bulk magnetic properties.

In numerous recent studies, (e.g. ref. given in [3] and [4]) it has been shown that X-ray absorption spectroscopy can contribute significantly to the characterization of nanoparticles in general. Specifically, X-ray absorption spectroscopy is a useful technique for illuminating size dependent effects in these systems. This assertion is bolstered by calculation of theoretical spectra, which can at least partly compensate for the lack of "realistic" reference samples which is typical for investigations on nanoparticles.

Recently, cobalt nanoparticles have attracted a lot of interest not only because of their magnetic properties and potential to produce two and three dimensional self-assemblies [5, 7] but also as they are observed in various crystallographic phases as ε-Co [5, 7] bcc and fcc [8] but also a mixtures of hcp and fcc [9]. Until now it is not clear whether the actual phase depends on the size and/or the preparation route. The goal of this paper is to provide some additional information to solve these problems.

2. Experimental

2.1. *Reverse-micelle synthesis of cobalt nanoparticles*

Particles were synthesized using a reverse micelle technique. By varying the relative amount of water and surfactant used for preparation of microemulsion, three different sizes of cobalt nanoparticles were prepared. All the synthesis steps were carried out in Ar/N_2 atmosphere, using standard Schlenk technique, to avoid possible oxygen contamination.

2.2. *Transmission Electron Microscopy*

TEM studies were carried out using a JEOL TEM 2010 operating at 200 kV. The cobalt nanoparticles were dispersed in 5% octanol in octane and a drop of this solution was placed on a carbon-coated Formvar copper grid. The grids were allowed to dry undisturbed under ambient conditions for 15 min before TEM measurements were carried out.

2.3. *X-ray Absorption Spectroscopy*

Experiments were performed at the double crystal monochromator (DCM) and the X-ray Micro-Probe (XMP) beamlines at the 1.3 GeV electron storage ring of the Center for Advanced Microstructures and Devices (CAMD) synchrotron radiation facility at Louisiana State University. The experiments were performed in standard transmission using ionization chambers

filled with air at 1 atm. pressure as intensity monitor and as detector. The Lemmonier type monochromator was equipped with Si (311) crystals, and the photon energy was calibrated relative to the absorption spectrum of a standard 7.5 μm cobalt foil setting the first inflection point at an energy of 7709 eV. XANES spectra were collected in the −100 to +250 eV range relative to the Co K-edge, with approximate step sizes of 0.5 eV and 1 s integration time. Standard XANES data analysis was performed using the WINXAS97 software package, where raw spectra were normalized and background corrected by fitting the pre-edge region with a straight line, and the post-edge region with a third order polynomial.

To check the correlation between the XANES spectra and relevant model phases, the spectra of a number of reference phases were calculated using version 8.2 of the FEFF8 code [10].

3. Results and discussion

Average particle sizes as determined by TEM were 5.5, 8 and 11 nm respectively with a standard deviation of about 20%. Selected area electron diffraction (SAED) pattern analysis that averaged over several particles demonstrated that all three samples were composed of mixtures of hexagonal α-Co and face-centered cubic β-Co. No significant contributions from the ε-phase and/or any other compounds were detected.

Figure 1a shows the Co K-XANES spectra of CTAB-stabilized Cobalt nanoparticles of three different sizes. Evidently, clear and systematic changes in the spectra can be observed: with increasing particle size, the pre-edge structure located at 7708 eV gains intensity. In contrast to that, the maximum absorption in the edge region is reduced significantly.

Intuitively, one expects that with increasing particle size the similarity to the spectrum of hcp Cobalt, which is displayed in Figure 1b together with several other reference spectra, increases. At first sight, the observed size-dependent changes support this idea, as the observed changes in intensity in the spectra of the nanoparticle occur exactly at those energy positions where spectral features in the Co foil spectrum are located. However, even the spectrum of the largest particles with a diameter of about 11 nm is still significantly different from the one of pure hcp-Co. In fact, it is possible to reproduce the spectra of both the 11 nm and the 8 nm particles by linear superposition of the spectra of the smallest particles, whose average diameter is 5.5 nm, and that of hcp Co as shown also in Figure 1b. This basis set was chosen being aware of the fact that there are no "perfect" reference compounds available for the analysis of the spectra of nanoparticles. The spectrum of the 5.5 nm sample was chosen as it is a reasonable basis representing fcc contributions and the special (core-shell) structure of the here synthesized particles. From this fit, an hcp content of about 40% for the 11 nm particle and of about 19.5% for the 8 nm particle, respectively, can be derived. The error range for these numbers can be estimated to be ±5%. At the same time, the TEM pictures show homogenous (hcp and fcc) particles and no indication of additional phases and/or compounds. These observations together with the short time stability of the particles against oxidation (cf. below) can be interpreted assuming a core-shell type structure of the particles. Interestingly, a similar result has been obtained in a recent study on CTAB stabilized CeO_2 nanoparticles, which were reported to possess a Ce^{3+} shell.

If one assumes spherical particles, similar Co densities in core and shell, and the absence of significant amounts of hcp Co in the spectrum of the smallest particles, it is possible to extract the

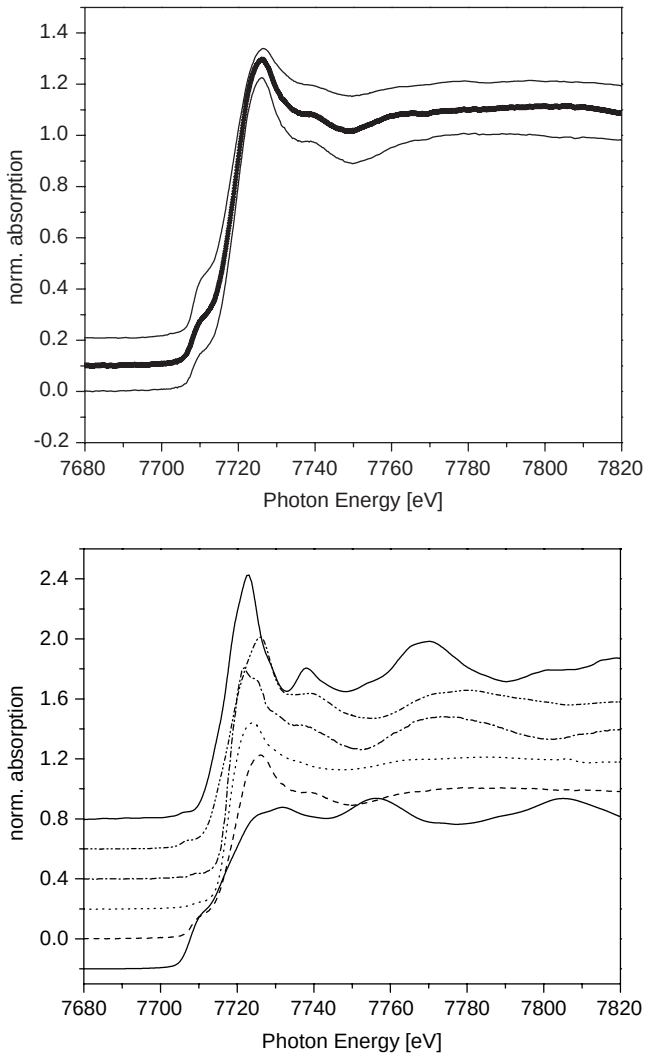

Fig. 1. a) Co-K-XANES spectra of the 3 nanoparticles: from top to bottom: 11 nm, 8 nm and 5.5 nm, the crosses in the spectrum of the 8 nm particles are the fitted spectrum (cf. text); b) Co-K-XANES spectra of some reference compounds: from top to bottom: CoO, Co_2O_3, $CoCl_2$, $CoBr_2$, Co (5 nm) sample Co-metal foil.

thickness of the respective cores and shells for the particles from the hcp Co contributions. For the 5.5 nm particle the hcp content can be estimated from the intensity of the pre-edge structure to be about 40%. The determined hcp Co contribution corresponds in this scenario to the quotient of the cube of the core radius r_c and the cube of the total radius r_t. Performing this calculation, we obtain a core radius of 4.75 nm for the particles with 11 nm diameter, a core radius of 3.15 nm for the particles with 8 nm diameter and a core radius of 2 nm for the 5.5 nm particle. Note that all values indicate an identical shell thickness for all three types of particles of about 0.8 nm, which in turn enhances the plausibility of the assumptions.

Evidently, this leaves us with the key problem of identifying the nature of the shell. Before tackling this problem directly, we shall gather some additional information on this shell based on the behavior of the particles during annealing and upon exposure to air.

Fig. 2 shows the Co-K- XANES spectra of samples exposed to air. First of all, it must be noted that there is a considerable resistivity against oxidation during short-term exposure to air, whereas after long-term exposure to air, the spectra of the particles are indistinguishable from the spectra of CoO. The degree to which conversion of the nanoparticles to CoO has happened at

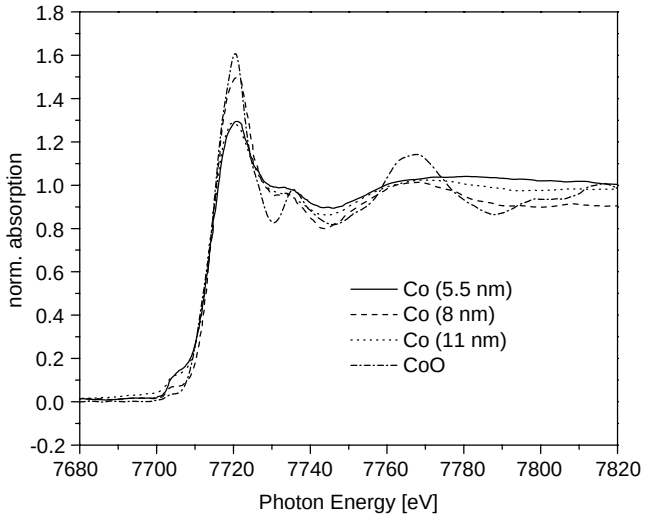

Fig. 2. Co-K-XANES spectra of the 3 nanoparticles after exposure to air for about 1 month in comparison with the spectrum of CoO.

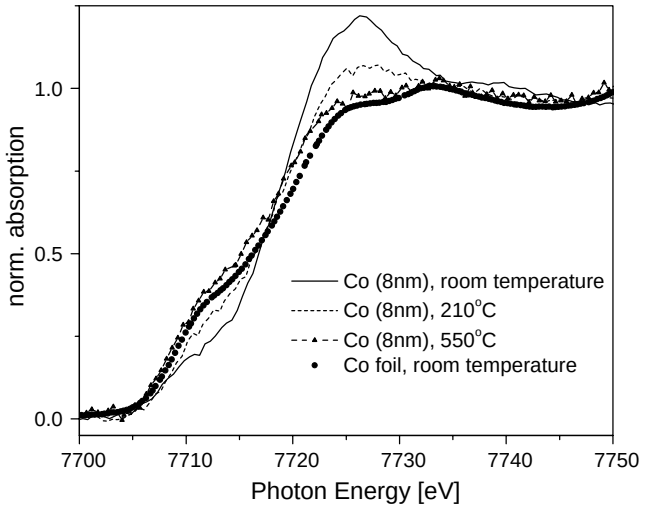

Fig. 3. Co-K-XANES spectra of Co (8 nm) measured *in situ* as a function of temperature in comparison with the spectrum of a Co-metal foil.

a given point of time is smallest for the smallest particles. At first sight, this is a seemingly counterintuitive behavior, as smaller particles usually show a significantly higher rate of oxidation, whereas here they appear to be most stable against exposure to air. This surprise is, however, quickly resolved if there is a core-shell structure of the particles, as already postulated above: The smaller the total particle size is, the higher is the relative contribution of the shell to the total spectrum. Consequently, a shell which offers more resistance against oxidation than the hcp Co core can easily induce the slower oxidation of a smaller particle, simply as the shell material oxidizes at a slower pace.

Figure 3 shows some of the Co-K-XANES spectra of the 8 nm sample recorded in situ during an annealing process under He-atmosphere. First significant changes in the intensity of white line and the structure in the rising edge are observed already at about 180 °C. Then, the spectra approach very fast that of the hcp-Co-foil. Already at about 360 °C there is hardly any difference between these two spectra indicating a complete transformation of the nanoparticles into hcp Co.

A likely candidate for the shell would be a cobalt oxide, such as CoO or Co_2O_3. (c.f. Fig. 1b). The latter compound appears to be the most likely candidate, as the similarity between the spectral features of this spectrum and the observed white line of the smallest nanoparticle is extremely. If this was the case, it should be possible to reproduce the XANES spectra of the smallest particle by a linear superposition of the spectra of hcp Co and the corresponding oxide, which fails completely for both types of Co-oxides as the white line intensity of the oxides is too high relative to their spectral contribution. One possible way to explain this observation is to postulate that we are witnessing indirectly a size effect on the spectrum of hcp cobalt. The pre-edge shoulder which is typical for the K-edge spectra of a 3d transition metal has been interpreted by several authors as an effect of pd-hybridization. If one follows this approach and bears in mind that decreasing the number of atoms in the system should decrease the width of the respective electronic bands and thus reduce their overlap, the intensity of the pre-edge structure should be reduced in a tiny Co particle. Consequently, the relative contribution of the Co spectrum, whose contribution is limited in the fit by the penalty obtained from an overshoot in the region of the pre-edge structure might be higher. In addition, the assumption of Co_2O_3 as being the compound forming the shell faces the problem that the long-time exposure to air converts the particles to CoO, which seems to be an unlikely reaction to happen from the thermodynamical point of view. Also the behavior upon annealing is of course inconsistent with assuming any type of oxide for the shell as all these compounds are very stable.

One of the factors which influence systematically the intensity of the whiteline of a given XANES spectrum is the formal electronegativity of the nearest neighbors. To visualize this effect, the Co-K-XANES spectra of CoO, $CoCl_2$ and $CoBr_2$ are also displayed in Figure 1b. As expected, the relative intensity of the white line decreases systematically, whereas the energy position of the spectral features of these Co(II) compounds varies only slightly. Whereas seemingly the shape and intensity of the whiteline of $CoBr_2$ agree rather well with the structures observed in the spectrum of the smallest nanoparticle, the attempt to achieve a good reproduction of the latter spectrum based on the linear superposition of the spectra of hcp Co and $CoBr_2$ fails.

However, the comparison of the spectrum of the smallest particle to the ones of the different Co(II) reference spectra indicates clearly that under the assumption that the shell material dominates the constituents of the smallest particle, this material must contain Co(III). Keeping also in mind that the shell gets destroyed completely at very low temperature of ∼210 °C, more likely candidates for the shell are Co(III) complexes such as $Co[(NH_3)_6]Br_3$ and $Co[(NR_3)_6]Br_3$. We are in the process of obtaining additional experimental evidence to confirm this assumption. The formation of these complexes and also the observed core-shell structure of the particles seem to be "typical" for CTAB as none of these effects had been reported for Co-nanoparticles stabilized with other surfactants.

Acknowledgements

Authors gratefully acknowledge financial support from NSF-EPSCoR (Grant No: NSF/LEQSF (2001-04) RII-03) through Louisiana Board of Regents and from the Deutsche Forschungsgemeinschaft (DFG) (Germany).

References

1. Kelly, L., Coronado, E., Zhao L. L. and Schatz, G. C., J. Phys. Chem. B **107**, 668 (2003).

2. Hills, C. W., Mack, N. H. and Nuzzo, R. G., J. Phys. Chem. B **107**, 2626 (2003).
3. Bucher, S. *et al*., Surface Sci. **497**, 321 (2002).
4. Palshin, V. G. *et al*., in: "Frontiers in Physics: From atom to the nanoscale" eds. J. McGuire, C. T. Whelan, American Institute of Physics, 2003, 99.
5. Puntes, V. F., Krishnan, K. M. and Alivisatos, P., Appl. Phys. Lett. **78**, 2187 (2001).
6. Wu, Z. *et al*., J. Phys. Chem. B **106**, 4569 (2002).
7. Sun, S. and Murray, C. B., J. Appl. Phys. **85**, 4325 (1999).
8. Dureuil, V., Ricolleau, C., Gandais, M. and Grigis, C., Eur, Phys. J. D **14**, 83 (2001).
9. Kato, Y. *et al*., Mater. Trans. **43**, 406 (2002).
10. Ankudinov, A. L., Ravel, B., Rehr, J. J. and Conradson, S. D., Phys. Rev. B **58**, 7565 (1998).

Physica Scripta. Vol. T115, 794–797, 2005

XAS In Situ Cell for Measurements of Mn and Fe Promoted Sulfated Zirconia Catalysts

R. E. Jentoft, A. H. P. Hahn, F. C. Jentoft and T. Ressler

Department of Inorganic Chemistry, Fritz Haber Institute of the MPG, Faradayweg 4-6, 14195 Berlin, Germany

Received June 26, 2003; accepted January 13, 2004

PACS numbers: 6110Ht, 8265+r

Abstract

Promotion of sulfated zirconia (SZ) with Mn or Fe results in an orders of magnitude more active catalyst for the skeletal isomerization of *n*-butane. One explanation for this promotion effect, consistent with rapid deactivation observed for these catalysts, suggests that the promoter participates in non-catalytic redox reactions. In order to test this hypothesis it was necessary to measure the Mn valence under reaction conditions (in situ). However, it was found that the catalysts have a reduced activity when pressed into pellets for measurement. Therefore, we designed an in situ cell that could be used to measure spectra of a powdered catalyst sample. The cell consists of an internal powder bed reactor (heatable to 773 K), which is enclosed in a He-filled, temperature controlled outer cell to ensure that the window to the inner cell, and the catalyst it contacts, are at a well-defined temperature. The reactor characteristics of the new cell are shown to be comparable to those of a quartz tubular reactor. Spectra are measured in fluorescence mode with simultaneous measurement of a reference foil in transmission using a section of the beam that bypasses the catalyst bed. Contrary to previous reports, data obtained in situ, show that the Mn valence remains constant during reaction with *n*-butane (333 K) after the catalyst has been activated in He. Additionally, EXAFS measurements indicate that the local environment of the Mn changes significantly during activation in He. Neither the XANES, nor the EXAFS for the Fe K-edge of FeSZ change during activation or reaction. These results suggest that the promotion effect is either catalytic, or is indirect, perhaps through modification of the zirconia bulk.

1. Introduction

The promotion of sulfated zirconia (SZ) with Fe or Mn ions results in a catalyst which is 1-2 orders of magnitude more active for the skeletal isomerization of light alkanes than sulfated zirconia alone [1]. Although there is some controversy due to non-uniform testing conditions, it is clear that 5 transition metal ions can promote the activity of SZ, the ions and their relative effectiveness as promoter are Mn $>$ Fe $\gg$ Co $\gg$ Ni $>$ Zn [2]. The function of the promoters is not yet understood. It has been suggested that they are involved in stoichiometric redox reactions [3, 4], but there are indications that one of the major effects of addition of promoters in SZ is to modify the zirconia bulk. Mn and Fe have both been found to incorporate into the zirconia lattice [5] as has been observed previously with non-sulfated zirconia [6]. Therefore, to obtain information on the promoter oxidation state and local structure we have measured the Mn and Fe K edge X-ray absorption spectra of promoted sulfated zirconia samples under the reaction conditions of *n*-butane isomerization. Sulfated zirconia based catalysts pose a particularly difficult problem for spectroscopic analysis. When the samples are ground or pressed, as is common in preparation for spectroscopy either to homogenize the sample or to form a pellet or wafer from powdered samples to support them in the beam path [7, 8] the catalytic activity is severely diminished [9]. In order to measure the active catalyst under reaction conditions it was necessary to construct a powder bed cell for fluorescence measurement.

2. Experimental

a) Sample preparation

The promoted SZ catalysts were produced using a commercially available sulfated zirconium hydroxide precursor (MEL Chemicals) containing 5–6 wt% SO_3. The promoters were added using the incipient wetness technique [10] with aqueous solutions of $Mn(NO_3)_2 * 4H_2O$ or $Fe(NO_3)_3 * 9H_2O$ (both Merck, p.a.) sufficient to result in a final 2 wt% nominal promoter content. The precursors were dried at room temperature prior to calcination in quartz boats containing 10 or 26 grams of precursor at 923 K (3 K/min ramp) for 3 hours in flowing 21% oxygen in nitrogen [10]. In the following, the samples will be designated as MnSZ and FeSZ for Mn promoted SZ and Fe promoted SZ, respectively.

b) X-ray diffraction

X-ray diffraction measurements were conducted using a STOE STADI-P diffractometer in Debye-Scherrer geometry with Cu Kα radiation and a primary monochromator. The samples were mixed 1 : 1 by weight with sieved α-Al_2O_3 (through gentle shaking) for an internal standard. Diffractograms were recorded between $2\theta = 0$ and 100° using a curved position sensitive detector. PowderCell v 2.4 [11] was used to fit the diffractograms with patterns calculated from single crystal data.

c) X-ray absorption spectroscopy

The necessity to characterize catalyst samples while they are operating, and the sensitivity of the sulfated zirconia based catalysts to mechanical stress [9] prompted us to construct an in situ cell for the measurement of powdered samples. A detailed report on the design of the cell is presented elsewhere [12]. The powdered catalyst is contained in an internal reactor body with a Kapton window to support the side of the powder bed into a vertical wall for measurement (Figure 1). The bed is rectangular and 4 mm from front to back, 10–14 mm wide with a 45° wall (parallel to the beam). A hole is drilled through the entire cell, and parallel to the 45° wall with a small area of intersection between the hole and the catalyst bed. The hole provides for a fraction of the beam to bypass the cell to obtain a reference spectrum in transmission. The catalyst is separated from the hole by a Kapton tube inserted in the hole. The catalyst is supported with a glass frit, and reactant gases flow from top to bottom through the catalyst bed. The temperature of the internal reactor body is controlled to the temperature measured by a thermocouple in the catalyst bed. An external body contains circulating He, and the temperature of the He is controlled to ensure that the Kapton window, and the volume of catalyst directly behind the window, is maintained at a defined temperature. Heaters on the external body are controlled to the temperature measured by

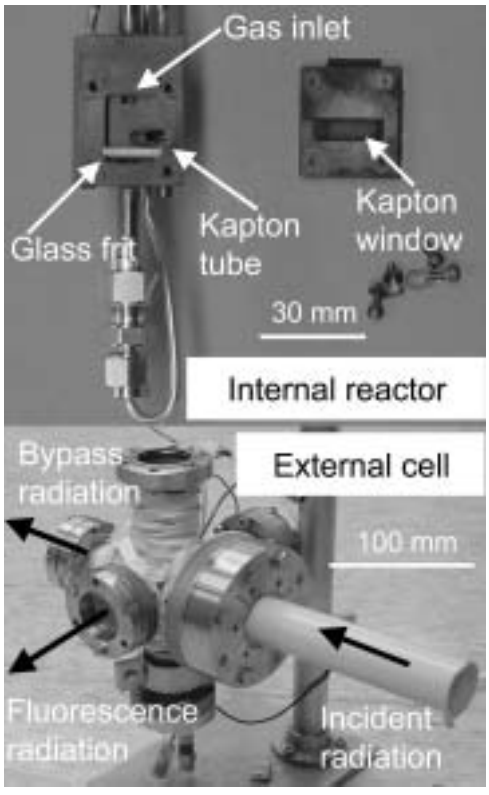

Fig. 1. New cell for measurement of powders under controlled gas phase and temperature. Internal reactor body to hold powder bed (top). External body for containment of constant temperature He (bottom).

a thermocouple terminating in the He near the window of the internal reactor. The cell can be operated with between 0.3 and 0.9 cm^3 of catalyst, and the interior reactor body can be heated to 723 K for catalyst activation or treatments. The gas phase is measured using an online mass spectrometer (Balzers, OmniStar). Conversion is calculated from the ratio of m/e = 29 to m/e = 42, and is calibrated using the fragmentation patterns for *n*-butane and isobutane.

X-ray absorption measurements were conducted at HASYLAB beamline E4 in the fluorescence mode using a single element Ge detector at 90° to the incident beam. The detector channels were windowed to a region of about 800 eV around the Mn or Fe Kα energy to minimize the measurement of scattered radiation. The spectra were energy calibrated to the first inflection point of the spectrum of a simultaneously measured Mn (6539 eV) or Fe (7112 eV) reference foil measured with the fraction of the incident beam that bypassed the catalyst bed. XANES spectra were taken from about 100 eV before the edge, and 200 eV after the edge with a total scan time of 11 minutes. Background correction and normalization was done with linear fits. The position of the Mn K-edge as measured by an arc tangent fit of the spectra is linearly related to the Mn valence [13]. The results of the Mn K-edge shift are summarized here, and presented in detail elsewhere [14]. The EXAFS measurements were about 90 minutes long and measured from 6480 to 6950 eV or 7030 to 7800 eV.

The samples were activated by heating in flowing He from room temperature to 703 K at 10 K/min and holding at 703 K for 30 minutes. Reactivation of the catalyst and reduction were carried out with the same heating program, but using 50% O_2 or 50% H_2 in He, respectively. Catalytic measurements were made at 333 K using a loading of 0.50 grams catalyst, 80 ml/min 1% *n*-butane in

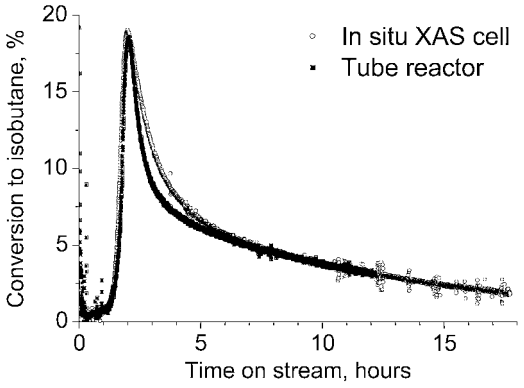

Fig. 2. Comparison of conversion vs. time on stream for a 2% FeSZ catalyst in a quartz, tubular plug flow reactor and the new in situ cell. Conditions: 0.5 g catalyst, 80 ml/min of 1% *n*-butane in He at atmospheric pressure, 333 K.

He at atmospheric pressure. The spectra were normalized using linear fits below and above the edge. The $\mu_0(k)$ fit for the Fe edge spectra was done between 2.65 and 11.5 $Å^{-1}$, and for the Mn edge spectra between 2.7 and 9.6 $Å^{-1}$ except for the spectrum of the reduced MnSZ sample which was fit between 2.2 and 9.6 $Å^{-1}$.

3. Results

Figure 2 shows a comparison of the time on stream behavior of the new cell, and of a quartz, tubular plug flow reactor. The time on stream behavior for both the in situ cell, and the standard laboratory reactor are nearly identical.

Figure 3 shows the Mn K-edge XANES during activation of Mn promoted sulfated zirconia. When MnSZ is activated in He the Mn valence reduces from an average valence of about 2.7 to about 2.5. The valence remains nearly constant during the skeletal isomerization of *n*-butane at 333 K, although the catalytic activity changes with time on stream as in Figure 2, and the valence remains constant during reactivation in 50% O_2 at 703 K. The valence is further reduced from 2.5 to about 2.3 when the catalyst is treated in 50% H_2 at 703 K [14]. The catalyst is active for isomerization after activation in He, and after reactivation in 50% O_2, but it is not active after the treatment in 50% H_2. The XANES spectra of the MnSZ sample presented in Figure 3, as well as those taken, in situ during the reaction, re-activation, and reduction treatments were all analyzed with principle component analysis (PCA). The differences among all

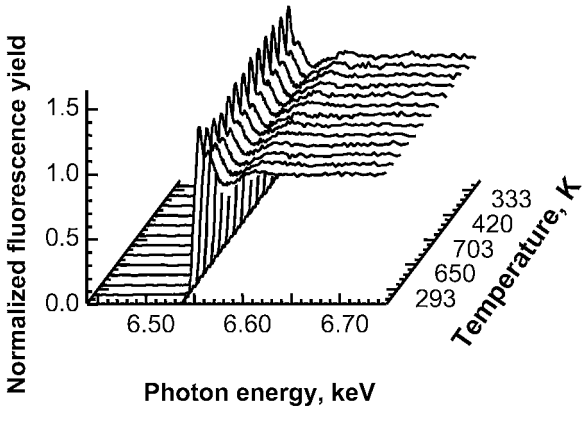

Fig. 3. Mn K-edge XANES measured in situ during the activation of a 2% MnSZ catalyst in flowing He.

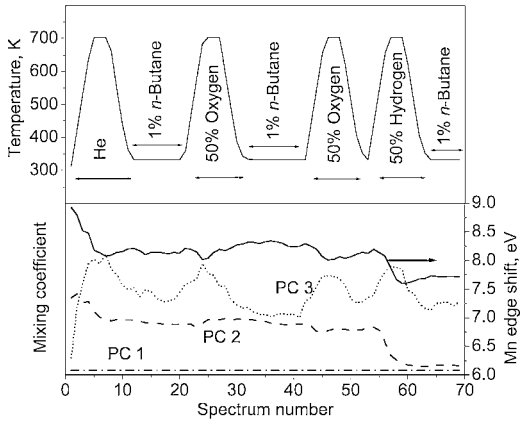

Fig. 4. PC analysis of Mn K-edge XANES measured in situ, during activation in He, reaction, reactivation, reaction, reactivation, reduction, and reaction. The upper part gives gas phase and temperature for each treatment. The lower graph gives the mixing coefficients for the three most significant principle components (broken lines), and the Mn K-edge energy shift relative to the Mn metal edge energy (solid line, right axis). Duration of experiment: 29 hours.

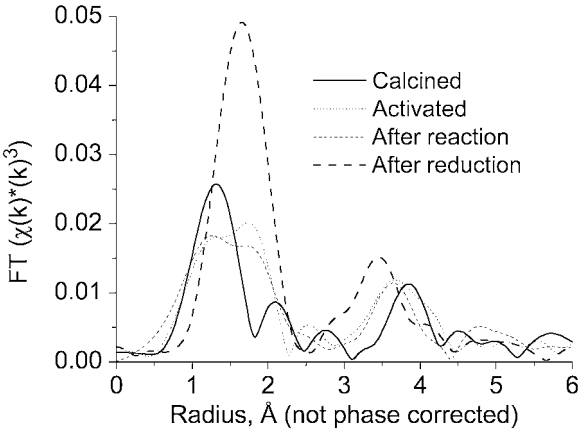

Fig. 5. The Fourier transformed ($\chi(k) * k^3$) of the Mn K-edge absorption spectra for MnSZ as calcined, after activation in He at 703 K for 30 minutes, after reaction with 1% n-butane at 333 K, and after reduction in 50% H_2 at 703 K for 30 minutes.

69 XANES spectra can be adequately described by three principle components. Figure 4 presents the mixing coefficients of the three most significant principle components along with the temperature and the gas phase composition in contact with the catalyst when the spectra were measured. In addition the Mn K-edge energy (relative to a Mn metal K-edge position) is given in the bottom half of Figure 4. It is clear that the second most significant component follows the Mn K-edge energy (and thus changes in the valence), and the third most significant component represents the effect of temperature on the XANES. The Fe K-edge XANES of the FeSZ catalyst taken in situ during activation in He, reaction with 1% n-butane, and reactivation in 50% oxygen show very little change during these treatments (spectra not shown). PC analysis of the XANES of the FeSZ sample indicated that two component were sufficient to describe the data. The mixing coefficients of the second most significant component followed changes in the temperature of the sample in a manner similar to that of the third component for the Mn K-edge XANES.

Extended spectra were taken at room temperature for the fresh catalyst and at 333 K for the catalyst before and after treatments (He, 50% O_2, or 50% H_2) and reaction (1% n-butane at 333 K). Distinctive in the $\chi(k)$ for these data are the lack of oscillations in the calcined MnSZ sample, and the much stronger oscillations after reduction. Figure 5 presents the Fourier transformed $\chi(k) * k^3$ (FT $\chi(k) * k^3$) for the MnSZ sample between the various treatments (not phase corrected). The calcined sample shows maxima at 1.3 and 3.85 Å. The sample as measured after activation, reaction, and reactivation, has quite similar structure, and shows maxima at 1.3, 1.75, and 3.65 Å. After reduction the FT $\chi(k) * k^3$ shows maxima at 1.65 and 3.45 Å. Figure 6 presents the radial distribution function for the FeSZ sample as calcined, and after activation, reaction, and reactivation. All measurements show a maximum at 1.57 and 2.7 Å with a shoulder at higher radius. For the calcined sample the first maximum has a higher magnitude, and there is an additional maximum at about 4.5 Å.

X-ray diffraction measurements were taken of the samples as calcined, and after the final reaction for the FeSZ sample, and after the final reduction and reaction for MnSZ (not shown). All reflections in the diffractograms can be attributed to the internal standard or tetragonal zirconia. For the FeSZ sample the structure of the zirconia did not change after treatment and reaction. For the MnSZ sample that underwent the additional treatment in 50% H_2 at 703 K there was a slight shift of the tetragonal lattice reflections to lower angles, and a slight increase in the amplitude of the reflections. A fit of the diffractograms for the MnSZ sample shows an increase in the unit cell volume of about 0.18% after the treatments.

4. Discussion

The new cell allows the measurement of powdered samples without the grinding and pressing necessary to produce a homogeneous self-supporting wafer. This can be critical for samples such as the SZ based catalysts, which are changed by such manipulations [9]. The time on stream profile of the new in situ cell is comparable to that of a tubular, plug flow reactor (Figure 2), and so the catalyst being characterized with XAS is the active catalyst. The utility for such measurements is highlighted by our results. When MnSZ is activated in He at 703 K, the Mn is reduced from an average valence of about 2.7 to about 2.5. When the MnSZ is exposed to 1% n-butane the Mn K-edge position does not change as indicated in Figure 4. PC analysis also tells us that, aside from the changes in the XANES that correlate to changes in the catalyst temperature (PC3, Figure 4), there are only two principle components required to describe the data. Therefore, changes in the XANES of the sample are due only to changes in two XANES spectra (more of one and less of the other), and both the reduction during activation in He, and the reduction in 50% H_2 are producing the same Mn species with a XANES distinct from a higher valent Mn species which is being reduced. In addition to these two Mn species there may be others which do not change. In contrast, the PC analysis of the FeSZ sample shows no changes in Fe K-edge XANES other than those attributable to changes in temperature. For the measurements during catalysis, this suggests that there are no detectable changes in the promoter ions during the reaction, and is contrary to earlier reports about the role of the promoter ions [3, 4, 15].

The EXAFS measurements taken in situ tell a similar story. The local structure around Mn in MnSZ does not change significantly during reaction, but the environment of the Mn does change during activation in He. The first maximum in the FT $\chi(k) * k^3$ of the calcined MnSZ sample is at about 1.3 Å. After activation, a second maximum appears at about 1.75 Å, and after reduction in 50% H_2

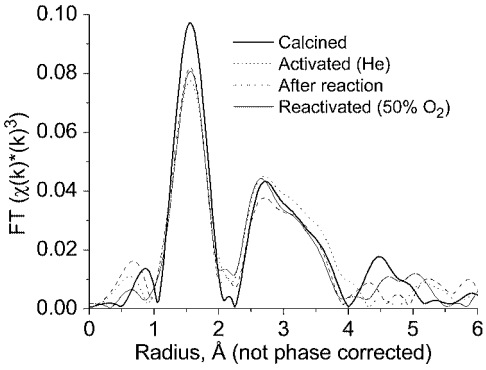

Fig. 6. The Fourier transformed ($\chi(k) * k^3$) of the Fe K-edge absorption spectra for FeSZ as calcined, after activation in He at 703 K for 30 minutes, after reaction with 1% *n*-butane at 333 K, and after reactivation in 50% O_2 at 703 K for 30 minutes.

the maximum at 1.3 Å is no longer discernable, but is replaced by a maximum of greater amplitude at about 1.65 Å. However, the meaning of the maxima in the FT $\chi(k) * k^3$ is problematic to determine. From the XANES we know that there are at least two species of Mn, one being reduced to the other during activation, and during heating in 50% H_2. Clearly the FT $\chi(k) * k^3$s show that this reduction causes a structural change in the Mn local environment. XRD results indicate that the zirconia lattice is tetragonal before and after all treatments for the MnSZ samples. Therefor, the changes in local order are either movement of the position of the Mn ions in the lattice, or more likely redistribution of the oxygen atoms around the reduced Mn ions. Additionally the decrease in valence is probably associated with an increase in oxygen vacancies in the zirconia lattice.

The FT $\chi(k) * k^3$s of the Fe in the FeSZ catalyst change very little during activation or reaction (Figure 6), consistent with the PCA analysis of the XANES which shows only one significant component other than that related to temperature. However, Fe oxide particles have been observed on the surface of promoted sulfated zirconia [16], and Fe also forms solid solutions with ZrO_2 [17]. Therefore, the FT $\chi(k) * k^3$s presented in Figure 6 represent the combination of at least two different structures.

5. Conclusions

The utility of the new in situ powder-bed, fluorescence mode XAS cell has been proven with the successful measurement of spectra from either Mn or Fe promoted SZ samples. The characteristics of the in situ cell as a reactor were demonstrated to be similar to that of a tubular laboratory reactor. The results demonstrate clearly that there is no detectable change in the Mn K-edge position during participation of the catalyst in the isomerization of *n*-butane. The majority of the Mn is not reduced. Additionally, neither the XANES nor the EXAFS of the Fe K-edge for the FeSZ catalyst change during activation in He or reaction. However, the Mn K-edge XANES for the MnSZ catalyst taken during activation, and during reduction in 50% H_2 do change, and one Mn species is changed into another during these treatments. EXAFS shows a consistent change in the local structure after activation and reduction.

Acknowledgements

The authors would like to thank Gisela Lorenz for sample preparation, Edith Kitzelmann for performing the XRD measurements, and Konstantin Klementiev and Edmund Welter at beamline E4, Hamburger Synchrotronstrahlungslabor. We also thank Prof. Robert Schlögl for his continuing support of this project.

References

1. Hsu, C.-Y., Heimbuch, C. R., Armes, C. T. and Gates, B. C., J. Chem. Soc. Chem. Comm. 1645 (1992).
2. Lange, F. C., Cheung, T.-K. and Gates, B. C., Catal. Lett. **41**, 95 (1996).
3. Wan, K. T., Khouw, C. B. and Davis, M. E., J. Catal. **158**, 311 (1996).
4. Morterra, C. *et al.*, Catal. Lett. **49**, 25 (1997).
5. Jentoft, F. C. *et al.*, J. Catal. **224**, 124 (2004).
6. Keshavaraja, A. and Ramaswamy, A. V., Appl. Catal. B **8**, L1 (1996).
7. Kampers, F. W. H., Maas, T. M. J., van Grondelle, J., Brinkgreve, P. and Koningsberger, D. C., Rev. Sci. Instrum. **60**, 2635 (1989).
8. Jentoft, R. E., Deutsch, S. E. and Gates, B. C., Rev. Sci. Instrum. **67**, 2111 (1996).
9. Klose, B. S. *et al.*, J. Catal. **217**, 487 (2003).
10. Hahn, A., Ressler, T., Jentoft, R. E. and Jentoft, F. C., Chem. Commun. 537 (2001).
11. Kraus, W. and Nolze, G., Federal Institute for Materials Research and Testing, Rudower Chaussee 5, 12489 Berlin, Germany.
12. Jentoft, R. E., Hahn, A., Jentoft, F. C. and Ressler, T., in preparation.
13. Ressler, T., Brock, S. L., Wong, J. and Suib, S. L., J. Phys. Chem. B. **103**, 6407 (1999).
14. Jentoft, R. E., Hahn, A., Jentoft, F. C. and Ressler, T., submitted to Phys. Chem. Chem. Phys.
15. Jentoft, R. E., Hahn, A., Jentoft, F. C. and Ressler, T., J. Syncrotron Rad. **8**, 563 (2001).
16. Scheithauer, M. *et al.*, J. Catal. **177**, 137 (1998).
17. Navío, J. A., Hidalgo, M. C., Colón, G., Botta, S. G. and Litter, M. I., Langmuir **17**, 202 (2001).

Physica Scripta. Vol. T115, 798–801, 2005

The Structure of a VO_x/TiO_2(anatase) Powder Catalyst under Reduction and Oxidation at 623 K

Geert Silversmit[a*], Jeroen A. van Bokhoven[b,#], Hilde Poelman[a], Ad van der Eerden[b], Guy B. Marin[c], Marie-Françoise Reyniers[c] and Roger De Gryse[a]

[a]Ghent University, Department Solid State Sciences, Krijgslaan 281 S1, B-9000 Gent, Belgium
[b]Utrecht University, Department of Inorganic Chemistry and Catalysis, Sorbonnelaan 16, 3584 CA Utrecht, The Netherlands
[c]Ghent University, Department Chemical Engineering, Krijgslaan 281 S5, B-9000 Gent, Belgium

Received June 26, 2003; accepted November 4, 2003

PACS numbers: 61.10.Ht, 68.47.Gh

Abstract

The structure of a TiO_2(anatase)-supported vanadium oxide powder catalyst was determined during a reduction-oxidation cycle at 623 K. A similar treatment was given to a pure V_2O_5 powder as reference system. The structural changes due to the reduction and oxidation on the supported and unsupported vanadium oxide were compared. A V_2O_5-like structure is present on the supported vanadium oxide after an initial oxidation at 623 K. The EXAFS fits point towards V_2O_5-clusters on the TiO_2 support. A reduction with H_2 at 623 K reduced the supported vanadium oxide to the V^{4+} valence state and had the same structural effect as on the V_2O_5. The successive re-oxidation restored the V_2O_5-structure on both systems.

1. Introduction

Vanadium oxides are important catalysts in different industrial processes, for instance in the oxidation of SO_2 to SO_3, in the partial oxidation of hydrocarbons like *o*-xylene to phthalic anhydride or *n*-butane to maleic anhydride, and in de-NO_x reactions [1, 2]. Supported vanadium oxides have better catalytic properties than unsupported ones and the effect can depend on the support type. In the oxidation of *o*-xylene to phthalic anhydride for instance, the TiO_2 anatase support is superior to other oxide supports like SiO_2, Al_2O_3 and MgO [3, 4].

The structure of calcined supported vanadium oxide on TiO_2(anatase) depends on its loading. Isolated VO_x species are present at very low concentrations ($\ll$1 monolayer); at higher loadings, but still less than one monolayer, a two dimensional surface phase is formed; a disordered V_2O_5 phase is found above one monolayer; and paracrystalline V_2O_5 forms at very high loadings (several monolayers), see [4] and references therein. The low surface coverages ($<$1 monolayer) favour tetrahedral co-ordination of supported vanadium oxide, while the higher coverages have more octahedral co-ordinated "VO_6" species. Furthermore, the tetrahedral co-ordination is the favoured bonding state in dehydrated samples [5].

In-situ reduction and oxidation measurements at reaction temperature are needed to reveal the structural changes of supported vanadium oxides during reactions. In this study a reduction and oxidation cycle was performed on a TiO_2(anatase) supported vanadium oxide powder catalyst at 623 K. The structural changes of the supported vanadium oxide are compared with a pure V_2O_5 powder.

2. Experimental

The V K-edge absorption spectra were collected at station D44 of the DCI storage ring at LURE (Laboratoire pour l'Utilisation du Rayonnement Electromagnétique) in Orsay (France) using a Si(111) monochromator with an energy resolution of 4×10^{-4} eV. The storage ring was filled with 1.85 GeV positrons and the storage ring current during measurements was 310 to 260 mA. All measurements were performed in transmission mode using ion chambers filled with air. The monochromator was detuned to 50% of the maximum intensity at the V K-edge (5465 eV) to minimise the presence of higher harmonics. To reduce noise, 6 scans were averaged for the VO_x/TiO_2(anatase) catalyst and 3 scans for the V_2O_5. The counting time was 1 to 5 s per data point, depending on the energy region. The V K-edge absorption spectra were recorded in five energy regions.

In-situ absorption spectra on the V_2O_5 and the VO_x/TiO_2 powder pellets were measured during a reduction/oxidation cycle at 623 K. The powders were first heated (10 °C/min) from room temperature (RT) to 623 K in He. Three spectra were recorded on the V_2O_5: one reference spectrum at RT in air (V_2O_5(RT)), a spectrum after reduction (V_2O_5(RED)) and after re-oxidation (V_2O_5(OX)). The VO_x/TiO_2 powder was first pre-oxidized (VO_x/TiO_2(pre-OX)), then reduced (VO_x/TiO_2(RED)) and finally re-oxidized (VO_x/TiO_2(OX)) at 623 K. Different V-O compounds were measured as references in air at RT.

Reduction and oxidation were carried out with flows of 100 ml/min at atmospheric pressure (5% H_2 in He and 5% O_2 in He respectively). The spectra were collected under flowing reducing or oxidizing atmospheres. Before measurements, the samples were pre-treated during several hours with the corresponding gas flow.

The samples were pressed in a stainless steel sample holder as self-supported pellets and mounted in an *in-situ* EXAFS cell equipped with beryllium windows [6]. The thickness of the pellets was chosen to give an absorption (μx) of 2.5 at the V K absorption edge for optimal signal to noise ratio. Typically 5 mg of V_2O_5 or VO_x/TiO_2 powder was pressed together with 40 mg of BN as inert filler. The VO_x/TiO_2(anatase) powder has 5.3 wt% vanadium and a BET surface area of 6.5–7.5 m^2/g. The VO_2(99%) powder was purchased from Alfa Aesar, the NH_4VO_3(99.99%), the $VOSO_4.3H_2O$(99.99%) and the BN (99%) powders were purchased from Sigma Aldrich and the V_2O_5(96%) powder from Merck.

The EXAFS data reduction and analysis were performed with the XDAP code [7]. The pre-edge was subtracted using a modified

*Corresponding author: Geert Silversmit: e-mail: Geert.Silversmit@UGent.be
#*Current address*: Laboratory for Technical Chemistry, ETH Hönggerberg, CH-8093 Zurich, Switzerland, (j.a.vanbokhoven@tech.chem.ethz.ch).

Victoreen curve [8] and the atomic background was obtained using a cubic spline routine [9]. The spectra were normalised by division of the absorption data by the edge-step at 50 eV above the edge position. No reference spectrum could be measured simultaneously with the sample under study, so that the coordinate axes of all absorption spectra have calibrated monochromator energy values. The main edge is chosen at the half height ($\mu x = 0.5$) of the normalised data. The EXAFS fit parameters were determined by multiple shell fitting in *R*-space, by applying the difference file technique using Fourier Transformations [10].

3. Results

3.1. *XANES spectra*

Wong *et al*. [11] have shown that the pre-edge and main-edge positions of V-Kα absorption spectra shift towards higher energies with increasing valence of the vanadium cation, and that the symmetry of the vanadium-ligand co-ordination can be deduced from the pre-edge intensity. Symmetrical vanadium–ligand co-ordinations, as regular "VO_6" octahedra, have very small pre-edge intensities, while co-ordinations with no inversion symmetry, like distorted "VO_6" units or "VO_4" tetrahedrons, have significant to large pre-edge intensities.

Because no absolute energy reference was available, we have taken the difference, Δ, between main- and pre-edge positions as an estimate for the valence of the V cations. In the vanadium oxide series V_2O_5, V_6O_{13}, VO_2 the valence of the V cation decreases from 5+ to 4+ and corresponding Δ values from 9.9 to 8.2 eV were found. An integrated pre-edge intensity of 2.5 is found for NH_4VO_3 that has an almost regular tetrahedral "VO_4" co-ordination [12] and 0.82 for $VOSO_4.3H_2O$ that has a slightly distorted "VO_6" co-ordination [13].

Figure 1 shows the normalised XANES spectra taken after the treatments performed on the V_2O_5 and VO_x/TiO_2 powders. The pre-edge intensities, Δ-values, and estimated valences and V-O co-ordinations are summarized in Table I. As compared to the references the pre-edge intensity for V_2O_5(RED) suggests a distorted "VO_6" octahedral co-ordination and the Δ-value a vanadium valence of 4+. After re-oxidation the XANES spectrum is identical to the one of V_2O_5(RT): pre-edge intensity and Δ retake the values of V_2O_5.

The supported vanadium oxide has a 5+ oxidation state after the pre-oxidation and a V_2O_5-like structure is present as can be seen from the good correspondence in the XANES spectra between the V_2O_5(RT) reference and VO_x/TiO_2(pre-OX) (Figure 1). The XANES signals are smaller, but the V_2O_5-shape is unambiguously present. Distorted "VO_6" octahedrae with a 4+ valence are present on the VO_x/TiO_2(RED). The re-oxidation restores the V_2O_5-like structure that is already found on VO_x/TiO_2(pre-OX).

3.2. *EXAFS spectra*

The $\chi(k)$ spectra of V_2O_5(RT) and V_2O_5(OX) could be fitted with the co-ordination numbers and bonding distances of the V_2O_5 crystal structure from [14]. The fitted and experimental k^2 Fourier transforms can be found in Figure 2. The fit parameters for V_2O_5(RT) are given in Table II. Similar parameters are obtained for V_2O_5(OX) (not shown). The V_2O_5(RED) is fitted with a distorted 1O + 2O + 2O + 1O octahedral co-ordination, the resulting distances can be found in Table II.

As for the XANES spectra, the k^2 FT for the oxidised supported samples resemble the one for V_2O_5(RT), although some differences are present: e.g. there is a clear loss of intensity in the V-shell around $R = 2.6$–2.7 Å (Figure 2). The EXAFS signals for VO_x/TiO_2(pre-OX) and VO_x/TiO_2(OX) could be fitted with the structural parameters of V_2O_5(RT). Compared to V_2O_5 however there is an extra V-O contribution at 2.7 Å and there are less V neighbours, as the V-V bond at 3.56 Å is not found,Table II. The fit parameters for VO_x/TiO_2(OX) are not given as they are similar to VO_x/TiO_2(pre-OX).

Identical V-O distances are obtained on the reduced VO_x/TiO_2 as on V_2O_5(RED), see Table II. Again less V-V neighbours are found than in the pure vanadium oxide.

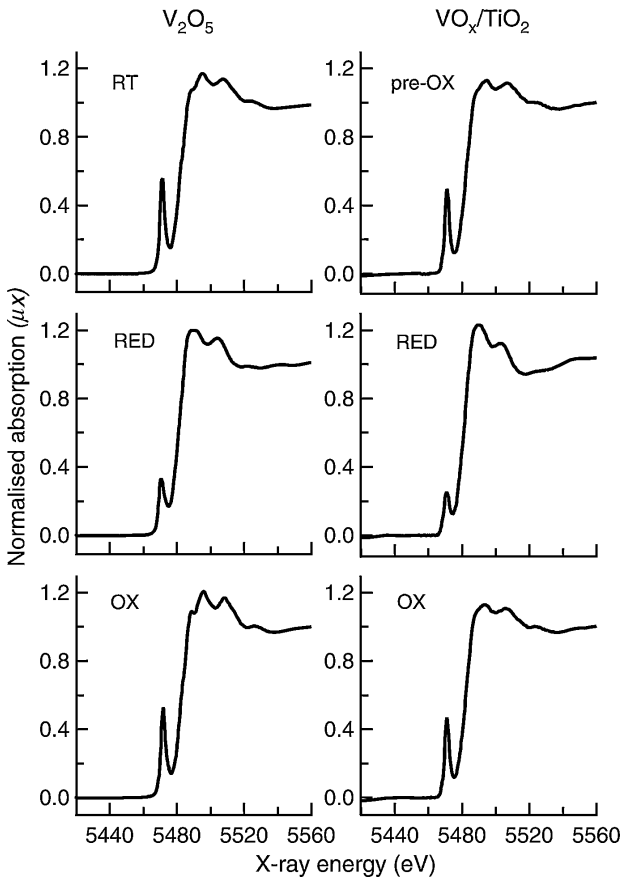

Fig. 1. Normalised XANES spectra of the V_2O_5 (left) and VO_x/TiO_2(anatase) (right) treatments.

Table I. *Pre-edge properties of the XANES spectra for the V_2O_5 and VO_x/TiO_2 treatments. Δ represents the difference between main-edge and pre-edge position.*

Sample	Δ (eV)	Estimated valence	Pre-edge intensity	Estimated co-ordination
V_2O_5(RT)	10.1	5	1.80	$= V_2O_5$
V_2O_5(RED)	9.1	~4	0.98	distorted "VO_6"
V_2O_5(OX)	9.9	5	1.80	$= V_2O_5$
VO_x/TiO_2(pre-OX)	10.5	5	1.53	V_2O_5-like
VO_x/TiO_2(RED)	9.0	~4	0.91	distorted "VO_6"
VO_x/TiO_2(OX)	10.5	5	1.57	V_2O_5-like

4. Discussion

The XAS measurements showed that a V_2O_5-like structure is present on the VO_x/TiO_2 after full oxidation. The number of deposited vanadium oxide monolayers can be calculated from the BET surface area of the support and the V_2O_5 loading.

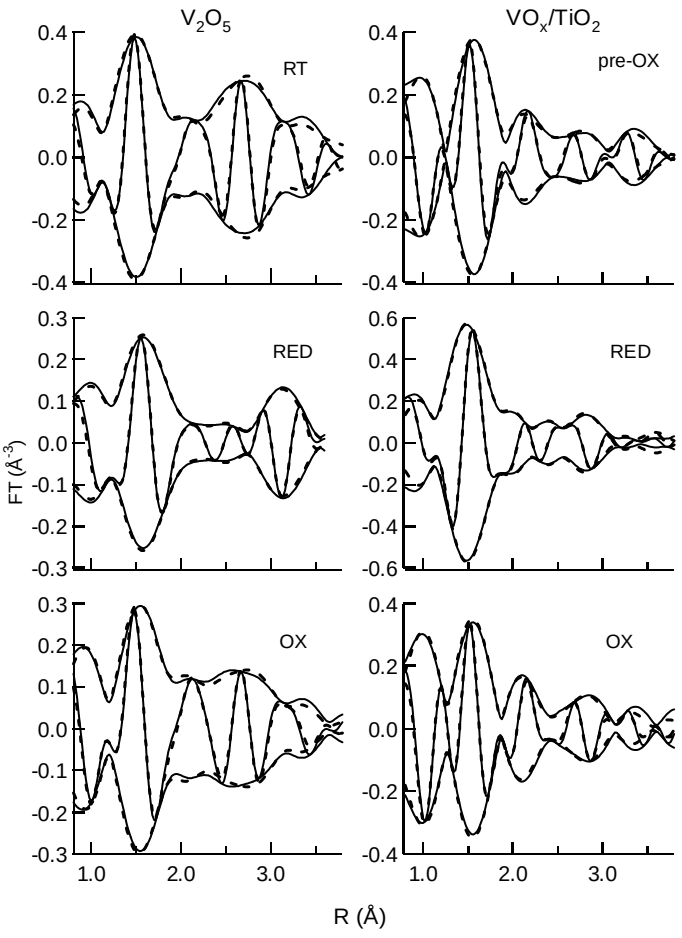

Fig. 2. k^2 Fourier transformations of the experimental χ (solid line) and fit (dotted line) for the V_2O_5 (left) and VO_x/TiO_2(anatase) treatments (right).

Table II. *EXAFS fit parameters for V_2O_5(RT), V_2O_5(RED), VO_x/TiO_2(pre-OX) and VO_x/TiO_2(RED).*

Sample	Absorber -Scatterer	EXAFS fit parameters R (Å)	N	$\Delta\sigma^2$	E_0
V_2O_5(RT)	V-O	1.60	1*	0.00168	−4.41
	V-O	1.78	1*	0.00210	10.00
	V-O	1.88	2*	−0.00261	−6.42
	V-O	2.01	1*	−0.00532	5.64
	V-V	3.10	2*	−0.00213	14.84
	V-V	3.45	1*	−0.00441	−11.56
	V-V	3.56	2*	0.00756	2.90
	k^2 variances: 3.80 (Imaginary) and 0.77 (Absolute)				
	Δk = 3.20–11.00 Å^{-1}, ΔR = 0.5–3.8 Å				
V_2O_5(RED)	V-O	1.65	0.99	0.00441	4.72
	V-O	1.89	2.12	0.00130	−1.59
	V-O	2.00	2.32	0.00162	10.00
	V-O	2.44	1.08	0.00975	−5.15
	V-V	3.07	1.97	0.00671	15.00
	V-V	3.34	1.97	0.00039	11.43
	k^2 variances: 3.30 (Imaginary) and 1.47 (Absolute)				
	Δk = 3.1–11 Å^{-1}, ΔR = 0.8–3.6 Å				
VO_x/TiO_2(pre-OX)	V-O	1.60	1*	−0.00330	−1.69
	V-O	1.78	1*	0.00145	10.00
	V-O	1.87	2*	0.00472	−4.60
	V-O	1.95	1*	−0.00121	7.41
	V-O	2.70	0.88	0.00138	−11.29
	V-V	3.16	2.45	0.00780	4.94
	V-V	3.39	0.65	−0.00454	−11.29
	k^2 variances: 1.94 (Imaginary) and 0.93 (Absolute)				
	Δk = 3.2–11 Å^{-1}, ΔR = 0.75–3.8 Å				
VO_x/TiO_2(RED)	V-O	1.64	0.99	0.00151	6.15
	V-O	1.88	2.11	−0.00409	1.16
	V-O	2.00	2.32	−0.00097	8.23
	V-O	2.45	1.08	−0.00184	7.71
	V-V	3.10	1.46	0.00688	9.56
	k^2 variances: 0.75 (Imaginary) and 0.47 (Absolute)				
	Δk = 3.1–11 Å^{-1}, ΔR = 0.8–4.0 Å				

*Fixed parameters, based on crystallographic data.

Unfortunately the BET surface area of the TiO_2 support is not known, therefore the BET of the VO_x/TiO_2 system is taken as an estimate, which amounted to 7 m^2/g. A support for this estimate can be found in the EUROCAT study [2]. This study on vanadium oxide supported on a 10 m^2/g TiO_2(anatase) powder has shown that the BET surface area changed less than 10% after depositions of V_2O_5 (1 and 8 wt%). For a complete coverage of a 7 m^2/g TiO_2 support with one bidimensional polyvanadate monolayer an amount of 1.05 wt% V_2O_5 is needed [2]. The supported vanadium oxide has 5.3 wt% V, which corresponds with 9.46 wt% V_2O_5. Several multilayers of vanadium oxide are thus present on the supported vanadium oxide. For such high loadings paracrystalline V_2O_5 is indeed found on supported vanadium oxides [1, 4]. The XANES features for VO_x/TiO_2 are smaller than for the unsupported V_2O_5 and less V-V neighbours are found in the EXAFS fits. Most likely V_2O_5 clusters are present on the supported vanadium oxide. No information on the cluster size could be obtained.

No structural support effect is found on the VO_x/TiO_2 during the H_2 reduction at 623 K as the structural changes on the VO_x/TiO_2 and V_2O_5 are similar. Probably the thickness and size of the V_2O_5-cluster on the anatase are large enough so that the supported vanadium oxide particles possess bulk properties.

The re-oxidation at 623 K restores the V_2O_5 structures on the supported and unsupported vanadium oxides showing that the H_2 reduction on the two vanadium oxide systems is reversible.

5. Conclusions

A reduction-oxidation cycle was given to a TiO_2(anatase) supported vanadium oxide (9.5 wt% V_2O_5) at 623 K. The structural changes of the supported vanadium oxide were followed with in-situ X-ray absorption measurements (XANES and EXAFS) and compared with unsupported pure V_2O_5. The supported vanadium oxide had a V_2O_5-like structure after full oxidation at 623 K. Most likely V_2O_5-clusters were present on the anatase support as less V-V neighbours were found in the EXAFS fits compared to unsupported V_2O_5. An H_2 reduction at 623 K had an identical effect on the structure of the supported vanadium oxide as on the unsupported V_2O_5: a distorted octahedral "VO_6" co-ordination was present and the mean vanadium oxidation state was V^{4+}. A re-oxidation restored the V_2O_5 structure on both systems.

No structural support effect was found for the supported vanadium oxide during this reduction-oxidation cycle at 623 K, as the supported V_2O_5 particles on the anatase behaved like bulk V_2O_5.

Acknowledgements

This work was supported by the Research Programme of the Fund for Scientific Research - Flanders (Belgium) (F.W.O. - Vlaanderen). We thank Dr. Stéphanie Belin of the D44 beam line staff for her support during the experiments.

References

1. Applied Catalysis A **157**, 1–420 (1997) special issue.
2. EUROCAT, Catal. Today **20**, 1–178 (1994) special issue.
3. Haber, J., Kozlowska, A. and Kozlowski, R., J. Catal. **102**, 52 (1986).
4. Bond, G. C. and Tahir, S. F., Appl. Catal. **71**, 1 (1991).
5. Eckert, H. and Wachs, I. E., J. Phys. Chem. **93**, 6796 (1989).
6. Kampers, F. W. H., Maas, T. M. J., van Grondelle, J., Brinkgreve, P. and Koningsberger, D. C., Rev. Sci. Instrum. **60**, 2635 (1989).
7. Vaarkamp, M., Linders, J. C. and Koningsberger, D. C., Physica B **208&209**, 159 (1995).
8. Vaarkamp, M., Dring, I., Oldman, R. J., Stern, E. A. and Koningsberger, D. C., Phys. Rev. B **50**, 7872 (1994).
9. Cook Jr. J. W. and Sayers, D. E., J. Appl. Phys. **52**, 5024 (1994).
10. Koningsberger, D. C., Mojet, B. L., van Dorsen, G. E. and Ramaker, D. E., Topics Catalysis **10**, 143 (2000).
11. Wong, J., Lytle, F. W., Messmer, R. P. and Maylotte, D. H., Phys. Rev. B **30**, 5596 (1984).
12. Evans Jr. H. T., Z. Kristallogr. **114**, 257 (1960).
13. Théobald, F. and Galy, J., Acta Cryst. B **29**, 2732 (1973).
14. Barnes, H. G., Ahmed, F. R. and Barnes, W. H., Z. Kristallogr. **115**, 110 (1961).

Physica Scripta. Vol. T115, 802–806, 2005

XAFS Study on the Local Atomic Structures of Cerium-Oxide Nanoparticles with Surface Coatings

Zhonghua Wu[1*], Jing Zhang[1], Xing Chen[1], Zhongjun Chen[1], Minhua Sun[1], Ziyu Wu[1] and Lin Guo[2]

[1]Beijing Synchrotron Radiation Lab, Institute of High Energy Physics, Chinese Academy of Sciences, P. O. Box 918, Bin 2-7, Beijing 100039, P. R. China
[2]School of Material Science and Engineering, Beijing University of Aeronautics and Astronautics, Beijing 100083, P. R. China

Received June 26, 2003; accepted November 4, 2003

PACS numbers: 81.07.Bc, 68.35.−p, 64.70.Nd, 61.10.Ht

Abstract

Four kinds of cerium oxide nanoparticles coated, respectively, with Sodium bis(2-ethylhexyl) sulfosuccinate (AOT), cetyltrimethyl ammonium bromide (CTAB), poly vinyl pyrrolidone (PVP) and those (naked) without surface coating were prepared using chemical method. The particle sizes were identified to be $2 \sim 3$ nm by using transmission electron microscope (TEM) and X-ray diffraction (XRD). Mixed valences of Ce^{3+} and Ce^{4+} were detected by X-ray absorption near-edge-structure (XANES) spectra. Extended X-ray absorption fine structure (EXAFS) spectra of Ce L_3-edge were fitted with a core-shell model. The core parts are almost the same as bulk CeO_2 with Ce^{4+} characteristic, however their shell parts change with surface coatings. The local atomic structures at shell parts (surface) and the contents and thicknesses of the shell parts were evaluated. The averaged Ce-O bond lengths at surface are changed from 2.504 Å (AOT), 2.568 Å (PVP), 2.628 Å (CTAB) to 2.634 Å (naked). The contents of surface are changed from 49% (AOT), 15% (PVP), 19% (CTAB) to 15% (naked). The results demonstrate that surface coatings have different influences on the surfaces of cerium oxide nanoparticles. A detailed discussion is given in this paper.

1. Introduction

Due to the special physical and chemical properties originating from a large ratio of surface to volume, small particle size and so on, the preparation, structural characteristics, property measurement and potential application of nanosized materials attract wide interest. There are many methods and techniques used to prepare nanosized materials. Even if the nanosized materials are the same species and have the same size, their atomic and electronic structures could be different because of different preparation methods. This will lead to different properties due to the difference in atomic and electronic structures. Therefore, studying and comparing the structures of nanosized materials, which have the same size but are prepared by different methods, is helpful to better utilize their unique properties.

Cerium oxides have been widely studied because of their complex electron structures[1–5]. In our previous report [6, 7], two kinds of cerium oxide nanoparticles coated by Sodium bis(2-ethylhexyl) Sulfosuccinate (AOT) and Cetyltrimethyl Ammonium Bromide (CTAB) were studied, respectively. Here, another two kinds of cerium oxide nanoparticles with almost the same particle size were prepared. One was modified with Poly Vinyl Pyrrolidone (PVP), another is without coatings (the naked one). We would like to compare the influence of the four kinds of surface modifications on the local atomic structure, especially on the surface atomic structures. X-ray absorption fine structure (XAFS) technique, as a powerful tool, was used to probe the local atomic and electronic structures. We hope to get a clearer understanding of nanosized materials with different preparation methods.

2. Experimental

The cerium oxide nanoparticles coated by PVP were prepared as follows: 20 ml of 0.001 mol/l of cerium chlorine ethanol solution was added to a solution of 0.35 g of PVP ($(C_6H_9NO)_n$, MW = 8000, Aldrich) in 40 ml of propanol under vigorous stirring, and the mixture solution was stirred rapidly for 0.5 h. While continuing to stir, 20 ml of 0.0035 mol/l ammonium hydroxide ethanol solution was slowly added dropwise. On the basis of the dehydrated properties of alcohol, the cerium-oxide nanoparticles organic-sol was obtained. The resulting sol was stored at room temperature under an ambient atmosphere, and showed no sign of precipitation for two months. The cerium-oxide nanoparticles powder was obtained by removing the solvent from the organic sol.

Two kinds of cerium oxide nanoparticles coated, respectively, with AOT ($C_{20}H_{37}NaO_7S$) and CTAB ($C_{16}H_{33}(CH_3)_3NBr$) were prepared by using the microemulsion method [6, 7]. For getting similar particles sizes, CTAB-coated cerium oxide nanoparticles were heated at 350 °C for 2 h. Another set of naked cerium oxide nanoparticles without coatings was prepared by precipitation method [8]. The preparation details of these cerium oxide nanoparticles can be found elsewhere [6–8]. X-ray diffraction (XRD) patterns of the four samples and bulk CeO_2 are shown in Fig. 1. The particle sizes were evaluated to be about $2 \sim 3$ nm for the four kinds of nanoparticles. Similar particle sizes were confirmed by transmission electron microscopy (TEM) as shown in Fig. 2 for PVP-coated cerium oxide nanoparticles.

Cerium L_3-edge XAFS spectra were collected at ambient temperature with transmission mode at the Extended X-ray Absorption Fine Structure (EXAFS) station of Beijing Synchrotron Radiation Laboratory (BSRF). Samples were homogeneously smeared on Scotch adhesive tape. Several layers were folded to reach the optimum absorption thickness ($\Delta\mu d \approx 1.0$, $\Delta\mu$ is the absorption edge step, d is the physical thickness of the sample). The storage ring was run at 2.2 GeV with an electron current about 80 mA. Higher harmonics were eliminated by detuning the double crystal Si(111) monochromator. The incident and transmission X-ray intensities were, respectively, detected by ion chambers that were installed in front of and behind the sample. The energy resolution ($\Delta E/E$) is about 2×10^{-4}. The absorption spectra were collected from 200 eV below the absorption threshold to over 500 eV above the threshold until the L_2 absorption edge appears.

3. Data Analysis and results

X-ray Absorption Near-Edge Structure (XANES) spectra of the four kinds of cerium oxide nanoparticles are shown in Fig. 3. For comparison, the XANES spectra of Ce L_3-edge of bulk CeO_2

*Corresponding author, e-mail: wuzh@mail.ihep.ac.cn

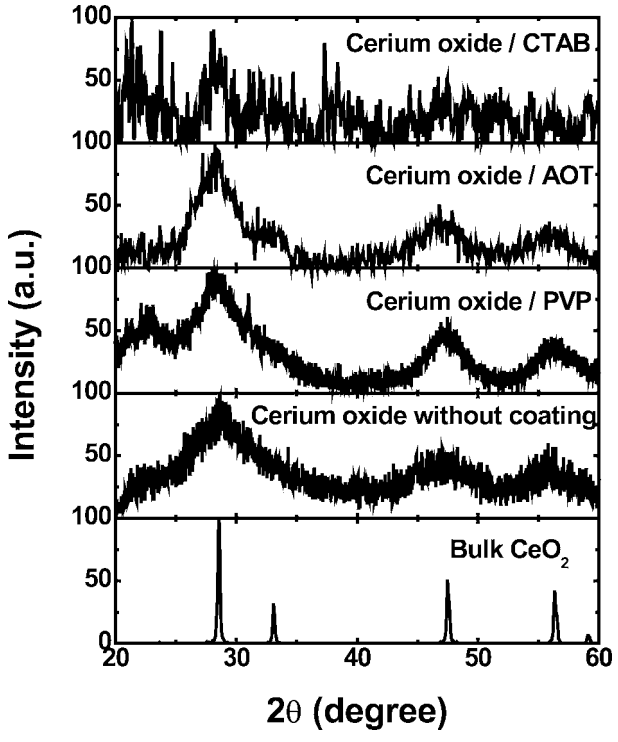

Fig. 1. X-ray diffraction patterns for bulk-CeO_2, cerium oxide nanoparticles without coating and those coated, respectively, by PVP, AOT and CTAB.

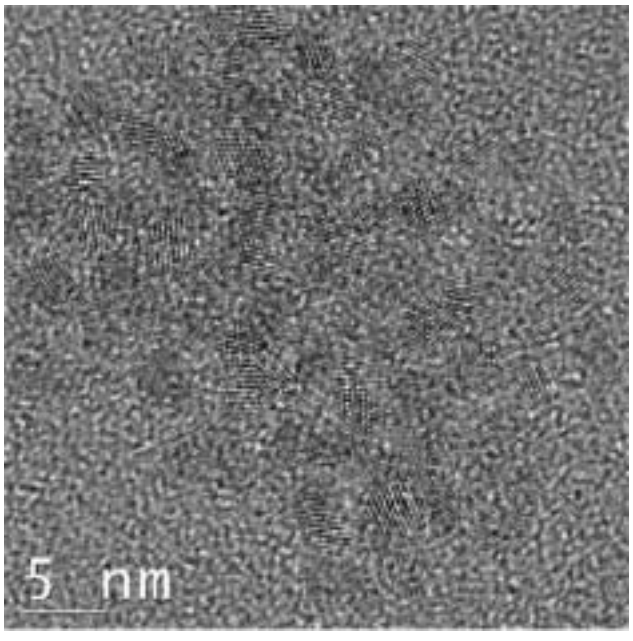

Fig. 2. High-resolution transmission electron micrograph of PVP-coated cerium oxide nanoparticles.

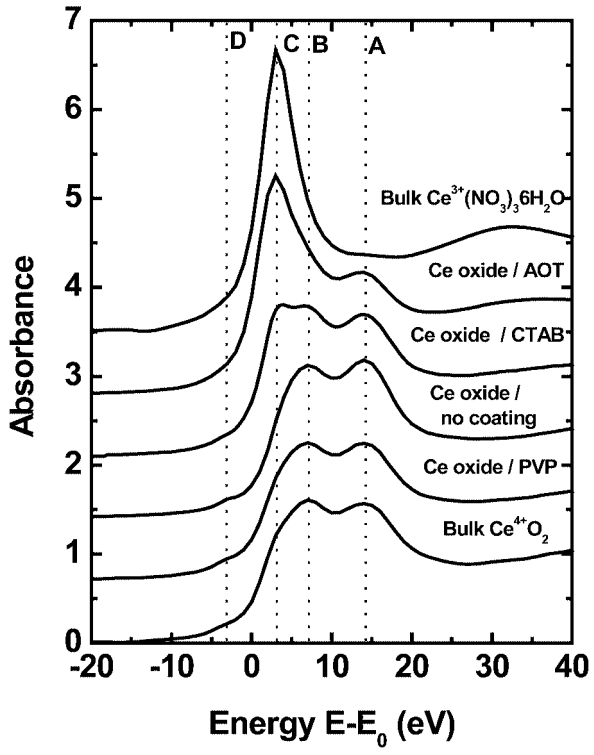

Fig. 3. XANES spectra of Ce-L_3 absorption for the four kinds of cerium oxide nanoparticles. For comparison, those of bulk CeO_2 and $Ce(NO_3)_36H_2O$ are also shown in this figure.

(quadrivalent Ce^{4+}) and bulk $Ce(NO_3)_36H_2O$ (trivalent Ce^{3+}) are also shown in Fig. 3. There are four XANES features [1] A, B, C, and D existing at the XANES spectrum of bulk CeO_2 and the nanoparticles. But the XANES spectrum of bulk $Ce(NO_3)_36H_2O$ only contains one main peak which coincides with the feature C of bulk CeO_2. The AOT- and CTAB-coated nanoparticles [6, 7] were identified to contain both Ce^{3+} and Ce^{4+} components. However, the PVP-coated cerium oxide nanoparticles and the naked ones have almost the same XANES features as bulk CeO_2. It implies that there are only Ce^{4+} components in the PVP-coated and the naked nanoparticles. The different spectral characteristics of the four kinds of cerium-oxide nanoparticles can be attributed to the different coatings and preparation procedures.

Four Gaussian-broadened Lorentzian functions were used to simulate the XANES features [9–10]. An arctan function was used to simulate the absorption background. The spectroscopic valences [9]were calculated to be about 3.48, 3.54, 3.52, 3.49, and 3.51, respectively, for AOT-coated, CTAB-coated, PVP-coated, the naked nanoparticles, and bulk CeO_2. The corresponding f-electron counts are 0.52, 0.46, 0.48, 0.51, and 0.49, respectively. The contribution from feature C is in the level as in bulk CeO_2 for PVP-coated and naked nanoparticles. This further demonstrates that the Ce^{3+} component is negligible in the PVP-coated and the naked nanoparticles. Their XANES spectra were also simulated by a linear summation of bulk CeO_2 and $Ce(NO_3)_36H_2O$ XANES spectra. The Ce^{3+} component is also negligible in the PVP-coated and the naked nanoparticles. While Ce^{3+} components were, respectively, reported to be 19% and 49% in the CTAB-coated and the AOT-coated nanoparticles [6, 7].

Multielectron excitation [11–18] affects seriously the EXAFS signal at the L_3-edge of Ce-absorption. After removing the multielectron excitation effect which was simulated with a Lorentzian function, the absorption curves were transferred to k space using the formula: $k = (2m(E - E_o)/\hbar^2)^{1/2}$. The post-edge absorption background was fitted and subtracted by using a spline function. Then, the resulting EXAFS functions were Fourier-transformed to R space with k^3-weight. Hanning windows were used in the Fourier transform and filter process. The Fourier transform and the first coordination peak filter regions are, respectively, about 7.8 Å^{-1} and 1.5 Å. More than seven fitting parameters are allowed for the nearest coordination. The Fourier-transform spectra and the nearest-neighbor coordination EXAFS functions were, respectively, shown in Fig. 4 and 5.

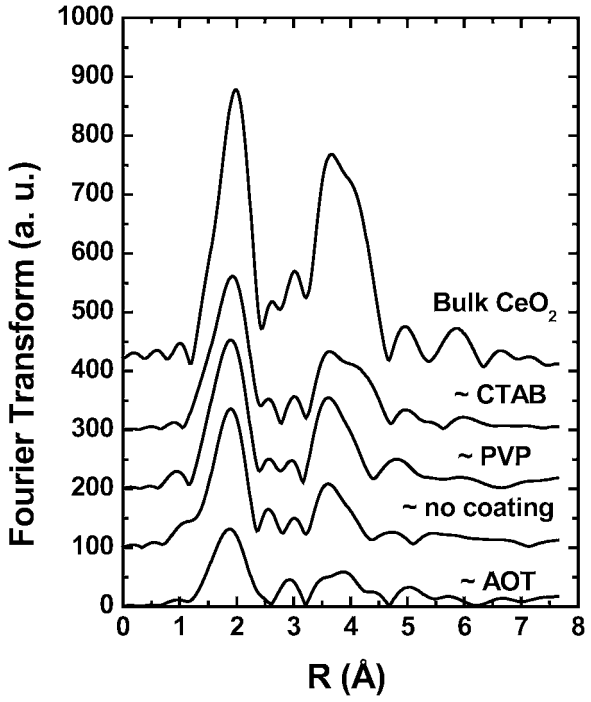

Fig. 4. Fourier transform spectra of Ce-L_3 absorption with k^3-weight for bulk-CeO_2 and the cerium oxide nanoparticles without coating and with coatings (AOT, PVP and CTAB).

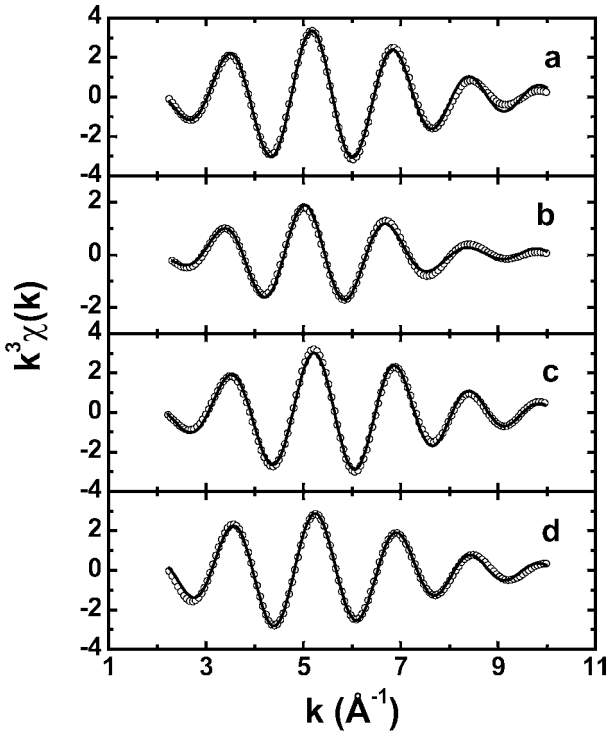

Fig. 5. EXAFS curves of Ce L_3-edge with k^3-weight, in cerium oxide nanoparticles coated by PVP (a), AOT (b), CTAB (c), and without coating (d). Symbols are experimental values, solid line are fitting ones.

Figure 1 shows that the nanoparticles have the same crystalline structure as bulk CeO_2, the wider diffraction peaks are due to the small particle-size and surface-effect. However, a single-shell fitting cannot give robust parameters. Two sub-shells (core-shell model [6, 7, 19]) were used to describe the local atomic structures. One corresponds to the core part; another corresponds to the shell (or surface). Bulk CeO_2 was used as a reference sample to get the amplitude and phase shift of Ce-O bond. The conventional EXAFS formula was used to fit the experimental signals. The first sub-shells were fixed to have the same structural parameters (8×2.343 Å) as the bulk CeO_2 [20] as indicated by X-ray diffraction patterns. It is the core parts that give the X-ray diffraction patterns as shown in Fig. 1 and these are less affected by the coatings (AOT, CTAB, or PVP). The second sub-shells are changeable with different coating, which describes the coating influence on the surface of nanoparticles. The fitting results are given in Table I. Although the second coordination peaks on the FT spectra could be well isolated, we cannot obtain its accurate structural parameters. This is because the mixed Ce-Ce and Ce-O multi-shells are included in the second coordination peak.

4. Discussion

Cerium oxide nanoparticles are well described by two sub-shells. The first sub-shell is almost the same as bulk CeO_2. We attribute this sub-shell to the contribution of the core-parts. Eight oxygen atoms surround the central cerium atom in the core part and these cerium atoms present Ce^{4+} characteristic. Another sub-shell describes the contribution of the shell-parts. The obtained coordination numbers as shown in Table I are nominal coordination numbers. The content (α) of the core part can be evaluated according to $\alpha = N_{\text{nom}}/N_{\text{true}}$. Here, N_{nom} is the nominal coordination number as listed in Table I, $N_{\text{true}} = 8$ is the real coordination number in core part as in bulk CeO_2. From the content $\beta(= 1 - \alpha)$ of the shell part, the real coordination number of shell part can be evaluated according to $N_{\text{true}} = N_{\text{nom}}/\beta$. Finally, the content of the core-part was evaluated to be about 51% (AOT), 81% (CTAB), 85% (PVP) and 85% (naked), respectively.

The second sub-shells are mainly the contribution of the shell part (surface) of the nanoparticles. The real coordination-numbers in the shell part were evaluated to be about 7 for AOT- and CTAB-coated cerium-oxide nanoparticles, and 8 for PVP-coated cerium-oxide nanoparticles and the naked ones. That is to say, there are about 7 oxygen atoms around cerium in an average Ce-O distance of 2.504 Å in the shell part of AOT-coated nanoparticles. Similarly, seven oxygen atoms surround the central cerium atom with an average Ce-O bond length of 2.628 Å in the shell part of CTAB-coated nanoparticles. But, eight oxygen atoms surround the central cerium atom, respectively with an average Ce-O bond length (2.568 Å and 2.634 Å) in the shell-part for PVP-coated nanoparticles and the naked ones. The shell part of AOT-coated nanoparticles is similar to Ce_2O_3 [21] (average, 7 O at 2.5047 Å). We also note that there are 9 oxygen atoms surrounding the central cerium atom in $Ce(OH)_3$ [22]. Here, six Ce-O bond lengths are 2.567 Å, which is similar to the surface Ce-O bond length (2.568 Å) in PVP-coated cerium oxide nanoparticles, the other three Ce-O bond lengths are 2.529 Å. The cerium atoms are coordinated by 10 oxygen in $Ce(NO_3)_3 4H_2O$ [23] with 10 different Ce-O bond lengths distributed from 2.487 to 2.689 Å in which one Ce-O bond length is 2.627 Å and similar to the surface Ce-O bond length (2.628 Å) in CTAB-coated cerium oxide nanoparticles. A total of 11 oxygen atoms around cerium in $Ce(NO_3)_3 6H_2O$ [24] have 11 different Ce-O bond lengths distributed from 2.494 to 2.882 Å in which two Ce-O bond lengths are, respectively, 2.632 and 2.635 Å and similar to the surface Ce-O bond length (2.634 Å) in naked cerium oxide nanoparticles. Partial cerium presents Ce^{3+} characteristics in AOT- and CTAB-coated nanoparticles, which just originate from the shell part

Table I. *Oxygen coordination parameters around Ce in naked cerium oxide nanoparticles (without coatings) and those coated, respectively, by AOT, CTAB, and PVP. N is the coordination number; R is the Ce-O bond length.* $\Delta\sigma^2$ *and* ΔE *are the difference of Debye-Waller factor and energy threshold corresponding to reference (Bulk* CeO_2*), respectively.* β *and* δ *are the content and thickness of shell part in these nanoparticles.*

Samples	N	R (Å)	$\Delta\sigma^2$ (Å^2)	ΔE (eV)	β(%)	δ(Å)
Bulk-CeO_2	8.0	2.343	0.0	0.0	0	0.0
Cerium oxide	4.1 ± 0.3	2.343 ± 0.010	0.0017 ± 0.0020	0.0 ± 1.0	49	2.0
Coated by AOT	3.4 ± 0.4	2.504 ± 0.020	0.0025 ± 0.0020	6.8 ± 1.0		
Cerium oxide	6.5 ± 0.4	2.343 (fix)	0.0054 ± 0.0020	0.2 ± 1.0	19	0.6
Coated by CTAB	1.4 ± 0.8	2.628 ± 0.020	0.0078 ± 0.0030	3.3 ± 2.0		
Cerium oxide	6.8 ± 0.4	2.343 (fix)	0.0043 ± 0.0020	0.6 ± 1.0	15	0.5
Coated by PVP	1.2 ± 0.8	2.568 ± 0.020	0.0010 ± 0.0030	3.6 ± 2.0		
Cerium oxide	6.8 ± 0.4	2.343 (fix)	0.0072 ± 0.0030	0.9 ± 1.0	15	0.5
Without coating	1.2 ± 1.0	2.634 ± 0.020	0.0053 ± 0.0030	2.8 ± 2.0		

of the nanoparticles. Obviously, the two kinds of cerium oxide nanoparticles are the mixtures [25–28] of Ce^{3+} and Ce^{4+}. While for PVP-coated cerium-oxide nanoparticles and the naked ones (without coating), there are always 8 oxygens surrounding the central cerium atom, but their Ce-O bond lengths in the shell part are different from the bulk one. Evidently in the later two cases, the shell-part Ce still keeps the Ce^{4+} characteristics. This is consistent with the XANES spectral characteristics as shown in Fig. 3.

Assuming the nanoparticles taking a spherical shape and having uniform mass density, and D is the diameter of the nanoparticle, then the thickness (δ) of the shell-part of the nanoparticles can be approximately evaluated as $\delta = D(1 - \alpha^{1/3})/2$. The naked nanoparticles have thinner shell thickness ($\delta \approx 0.5$ Å), because they are not affected by the coating. But in the surface modification nanoparticles, the shell thickness is, respectively, 0.5 Å (PVP), 0.6 Å (CTAB) and 2.0 Å (AOT). The obtained contents (β) of the shell-part and their thickness (δ) are listed in Table I.

Because of the small particle size, the surface effect of nanoparticles is not negligible. The content (β) and thickness (δ) of nanoparticles surface correspond to the surface effect. As the thickness is equal to zero, it means that the nanoparticles are exactly the same as bulk. While the thickness is equal to the radius of nanoparticles, it means that the nanoparticles are completely different from bulk. Therefore, the thickness of 0.5 Å in PVP-coated and naked cerium oxide nanoparticles demonstrates that: even on the surface there are still partial Ce atoms keeping the same coordination number and bond lengths as in bulk. In other word, the surface coatings only cause partial Ce atoms on the surface having different Ce-O coordination number and bond lengths. Obviously in the core-shell model, the content (β) and thickness (δ) of nanoparticles surface are only relevant to the partial volume which has different Ce-O bond length compared with bulk.

From Table I, it can be seen that more than 80 percent of absorbed atoms (Ce) locate at the core part of the nanoparticles except the AOT-coated ones. Even on the surface of the nanoparticles, it is easy for the cerium atoms to get oxygen from the atmosphere to occupy and compensate the oxygen vacancies originating from the surface effect. Besides, the possible O and N atoms that come from the coatings and the preparation procedure are also bonded to the surface Ce atoms. These always result in a high coordination (coordination number: 7 or 8) of the cerium at the surface of the nanoparticles. Evidently, for pure metallic nanoparticles prevented from oxidation, due to the small particle size, the coordination number of surface atoms and the average coordination number over the whole nanoparticles will dramatically decrease.

By comparing the four kinds of nanoparticles, their shell-part atomic structures were found to be different from the core part, and the Ce-O bond length in the shell part is elongated. We attribute these to the different coatings and sample-preparation methods. AOT is an anionic surfactant, CTAB is a cationic surfactant. But PVP is a neutral coating. AOT- and CTAB-coated nanoparticles have the same starting materials $Ce(NO_3)_3 6H_2O$, their shell-part all present Ce^{3+} characteristics and the same coordination number (7), although their contents and thickness are different. However, the neutral coating PVP has less effect on the nanoparticles surface, it likes the case without coating. Although the starting materials for PVP-coated nanoparticles and the naked ones are different (respectively, $CeCl_3$ and $Ce(SO_4)_2 4H_2O$), their shell-parts only present the Ce^{4+} characteristics and have the same coordination number (8) as in bulk. It seems that the chemical valence (Ce^{3+} or Ce^{4+}) of surface cerium is related to the coatings and the preparation procedure. Certainly, a suitable heat treatment for the nanoparticles will make the Ce^{3+}transfer to Ce^{4+}, and the nanoparticles transfer to pure CeO_2 [6].

Due to the large ratio of surface to volume and the small particle size, these nanoparticles show larger Debye-Waller factor. Surface modification makes the length of partial Ce-O bonds different. In the four kinds of nanoparticles, the naked nanoparticles have the longest Ce-O bond length at the shell part, and then CTAB-coated and PVP-coated nanoparticles. The AOT-coated ones have the shortest Ce-O bond length at the shell part. However, because of the different thickness of the shell part in the four kinds of nanoparticles, the total average coordination number and Ce-O bond length over the core and shell parts are listed as follow: 7.5×2.416 Å in AOT-coated nanoparticles, 7.9×2.394 Å in CTAB-coated nanoparticles, 8.0×2.387 Å in the naked nanoparticles (without coating) and 8.0×2.377 Å in the PVP-coated nanoparticles.

5. Conclusion

Four kinds of cerium oxide nanoparticles with different coatings were prepared. The local atomic structures of shell parts (surface) in these nanoparticles were obtained. The conclusion are summarized as follows:

The local atomic structures, thickness and contents of the shell part are affected by the surface modification in the nanoparticles. The anionic surfactant (AOT) has the strongest influence on the thickness and contents of surface, and then it is the cationic surfactant (CTAB) and the neutral coating (PVP). The naked nanoparticles (without coating) have the longest surface Ce-O bond length, while AOT-coated nanoparticles have the shortest surface Ce-O bond length.

Except the AOT-coated nanoparticles, the other three kinds of nanoparticles have almost the same average atomic structures. Except the elongated Ce-O bond lengths, the average atomic structures are quite similar to the bulk CeO_2.

The chemical valence of cerium at the shell part seems to be related to the coatings, the starting materials and the preparation procedure. In our cases, starting material $Ce(NO_3)_36H_2O$ with AOT or CTAB surfactants results in a shell part with Ce^{3+} characteristics. While starting materials $CeCl_3$ and $Ce(SO_4)_24H_2O$ with neutral coatings (PVP) or without coatings result in a shell part with Ce^{4+} characteristics. These were confirmed by the XANES features of cerium L_3-absorption.

Acknowledgment

This work is supported by the Chinese National Science Foundation Project No. 10374087.

References

1. Bianconi, A. *et al.*, Phys. Rev. B **35**, 806 (1987); Soldatov, A. V., Ivanchenko, T. S., Kotani, A. and Bianconi, A., Physica B **208&209**, 53 (1995).
2. Soldatov, A. V. *et al.*, Phys. Rev. B **50**, 5074 (1994).
3. Dexpert, H. *et al.*, Phys. Rev. B **36**, 1750 (1987).
4. Beaurepaire, E., Kappler, J. P., Malterre, D. and Krill, G., Europhys. Lett. **5**, 369 (1988).
5. Malterre, D., Phys. Rev. B **43**, 1391 (1991).
6. Wu, Z. H. *et al.*, J. Phys. Chem. B **106**, 4569 (2002).
7. Wu, Z. H. *et al.*, J. Phys.: Condensed Matter **13**, 1 (2001).
8. Nachimuthu, P., Shih, W. C., Liu, R. S., Jang, L. Y. and Chen, J. M., J. Solid State Chem. **149**, 408 (2000).
9. Capehart, T. W. *et al.*, Phys. Rev. B **55**, 11496 (1997).
10. Vandormael, D. *et al.*, Phys. Rev. B **56**, 6100 (1997).
11. Kodre, A. *et al.*, Physica B **208&209**, 379 (1995).
12. Fonda, E., Andreatta, D., Colavita, P. E. and Vlaic, G., J. Synchrotron Rad., **6**, 34 (1999).
13. Li, G., Bridges, F. and Brown, G., Phys. Rev. Lett., **68**, 1609 (1992).
14. Mukoyama, T. and Ito, Y., Nucl. Instrum. Meth. Phys. Res. B **87**, 26 (1994).
15. Chaboy, J., Marcelli, A. and Tyson, T. A., Phys. Rev. B **49**, 11652 (1994).
16. Benfield, R. E., Filipponi, A., Bowron, D. T., Newport, R. J. and Gurman, S. J., J. Phys.: Condens. Matter **6**, 8429 (1994).
17. D'Angelo, P., Di Cicco, A., Filipponi, A. and Pavel, N. V., Phys. Rev. A **47**, 2055 (1993).
18. Filipponi, A., Tyson, T. A., Hodgson, K. O. and Mobilio, S., Phys. Rev. A **48**, 1328 (1993).
19. Wu, Z. H., Guo, L., Li Q. S. and Zhu, H. S., J. Phys.: Condensed Matter **11**, 4961 (1999).
20. Whitfield, H. J., Roman, D. and Palmer, A. R., J. Inorg. Nucl. Chem. **28**, 2817 (1966).
21. Baernighausen, H. and Schiller, G., Less-Common Metals **110**, 385 (1985).
22. Mullica, D. F., Oliver, J. D. and Milligan, W. O., Acta Crystallographica, B **35**, 2668 (1979).
23. Milinski, N., Radivojevic, P., Ribar, B. and Djuric, S., Crystal Structure Commun. **11**, 1241 (1982).
24. Milinski, N., Ribar, B. and Sataric, M., Crystal Structure Commun. **9**, 473 (1980).
25. Zhou, Y. C. and Mohamed, N. R., Acta Materialia **45**, 3635 (1997).
26. Tschopea, A. and Birringera, R., Nanastruct. Mater. **9**, 591 (1997).
27. Palmqvist, A. E. C., Wirde, M., Gelius, U. and Muhammed, M., Nanastruct. Mater. **11**, 995 (1999).
28. Pfau, A. and Schierbaum, K. D., Surface Science **321**, 71 (1994).

Physica Scripta. Vol. T115, 807–809, 2005

Preparation of Mesoporous Silica Supported Nb Catalysts and *in-situ* XAFS Characterization During Carburization Process

N. Ichikuni*[1], H. Hachiya[1], K. K. Bando[2], S. Shimazu[1] and T. Uematsu[1]

[1]Department of Materials Technology, Faculty of Engineering, Chiba University, Chiba 263-8522, Japan
[2]National Institute of Advanced Industrial Science and Technology, Tsukuba 305-8565, Japan

Received June 26, 2003; accepted November 4, 2003

Abstract

Mesoporous silica supported Nb catalyst (imp Nb/SBA-3) was prepared by impregnation of $NbCl_5$ to the SBA-3 support. The mesoporous silicate-wall incorporated Nb catalyst (inc Nb-SBA-3) was synthesized by introducing $NbCl_5$ into an SBA-3 precursor solution. Both catalysts were carburized by a temperature programmed reaction (TPR) method under CH_4/H_2 gas stream. Nb K-edge *in-situ* XAFS analysis revealed that Nb_2O_5 was reduced to NbO_2 in the first stage of TPR and converted into NbC in the second stage. The silica-wall incorporated Nb species were highly dispersed and hardly reduced nor fully carburized. The difference in the carburization process between imp Nb/SBA-3 and inc Nb-SBA-3 was clarified.

1. Introduction

It is well recognized that an introduction of nitrogen or carbon into molybdenum lattice significantly alters its physical and chemical properties [1, 2]. Although early transition metal carbides (ETMC) are well known for their superior refractory, electronic and magnetic properties [3], not yet developed are their applications as catalysts. It is known that ETMC have demonstrated their resemblance in activities to those of the group 8-10 metals (Pt, Pd, Rh, etc.).

Most of the work on the catalytic application of early transition-metal carbides have been focused on Mo_2C and WC [3], and very few results have been reported on other compounds such as NbC. The focus on Mo_2C and WC has occurred in part because they can be prepared in high surface area form at moderate synthesis temperatures in the range between 900–1100 K. On the other hand, it is reported that the carburization of bulk Nb_2O_5 into NbC requires high temperatures as 1370 K [4]. The high temperature was required to carburize Ta oxide to TaC causing a sintering process and diminished surface area [5]. We have demonstrated that the carburizing temperature could be lowered to 1073 K by supporting the Nb species to amorphous silica [6]. Moreover, the smaller particle size of NbC could be prepared by using the highly ordered mesoporous material SBA-3, possessing 1.5–5 nm pores, instead of amorphous silica.

The conversion of Nb oxide to NbC and the particle size growth were not fully understood yet. X-ray Absorption Fine Structure (XAFS) is a suitable technique for the structural analysis of the conversion process under *in-situ* conditions. In this study, we prepared NbC/SBA-3 catalysts and SBA-3 wall incorporated NbC catalysts, and collected *in-situ* XAFS data to investigate the growth process of NbC on the support. The differences between imp Nb/SBA-3 and inc Nb-SBA-3 are discussed.

2. Experimental

2.1. *Catalyst preparation*

Hexagonal mesoporous silica SBA-3 was synthesized using tetraethylorthosilicate (TEOS) and $[CH_3(CH_2)_{15}N(CH_3)_3]Br$ (CTMABr) at 293 K for 24 h, followed by calcination under dry-air flow at 823 K. The SBA-3 was impregnated with $NbCl_5$ methanol solution overnight. The solvent was evaporated and calcined at 773 K in air [imp Nb/SBA-3]. The mesoporous silica-wall incorporated Nb catalyst was synthesized under acidic conditions using TEOS, $NbCl_5$ and CTMABr at 293 K for 24 h. Products were dried and calcined under dry-air flow at 823 K [inc Nb-SBA-3]. Carburization of Nb species was performed by TPR method. The precursor oxides were carburized in 20% CH_4/H_2 mixed gas stream to produce NbC samples by TPR process; the samples were heated at a linear rate of $10\,K \cdot min^{-1}$ or $5\,K \cdot min^{-1}$ to the final temperature, and kept there for 30 min.

2.2. *XAFS measurements*

The XAFS measurements were performed at BL-10B of the Photon Factory of the Institute of Materials Structure Science, Higher Energy Accelerator Research Organization (PF, KEK-IMSS). Nb K-edge spectra were collected in transmission mode with a Si(311) channel cut monochromator by using two ion-chambers filled with (50% Ar + 50% N_2) and (100% Ar) for I_0 and I, respectively. The monochromator was stepwise scanned for 1 s dwelling per each point in TPR process.

Catalysts were pressed into self-supporting disks and settled in a cell designed for carburization process as depicted in Fig. 1. The specially designed SUS cell can be heated up to 1273 K by an infrared gold-image furnace. The cell has two acrylic windows (3 mm thickness) at both ends of the X-ray path. The absorption of X-rays by the windows seemed to be sufficiently small at the Nb K-edge [7]. Carburization by TPR process was performed from room temperature to the final temperature under a flow of CH_4 ($30\,cm^3 \cdot min^{-1}$) and H_2 ($120\,cm^3 \cdot min^{-1}$). The heating rate was regulated to $5\,K \cdot min^{-1}$.

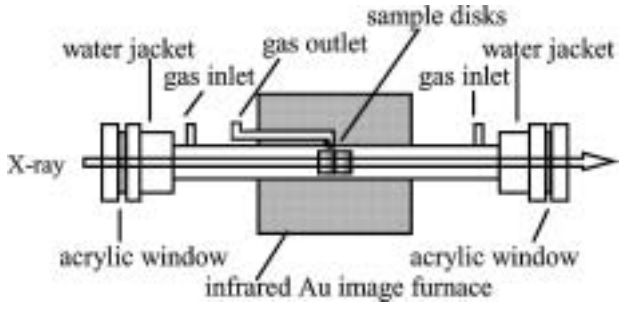

Fig. 1. Schematic of *in-situ* XAFS cell for carburization process.

*e-mail: ichikuni@faculty.chiba-u.jp

The collected data were analyzed by using the program REX2000 (Rigaku Co.). Curve-fitting (CF) analysis was conducted on $k^3\chi(k)$ in k-space, where k indicates the wave number of a scattered photoelectron and χ represented normalized EXAFS oscillations. Model parameters for curve-fitting analysis (back scattering amplitude and phase shift) were extracted from an EXAFS oscillation observed for bulk NbC ($N_1 = 12$, $r_1 = 0.315\,\text{nm}$).

3. Results and discussion

3.1. *Static structures*

The hexagonal mesoporosity of synthesized SBA-3 was confirmed by X-ray diffraction (XRD) pattern and transmission electron microscopy (TEM) measurements. The BET surface area was determined to be $1100\,\text{m}^2 \cdot \text{g}^{-1}$.

3wt% of Nb loaded SBA-3 was also characterized. Although the mesoporosity was maintained for imp Nb/SBA-3 and inc Nb-SBA-3 by XRD analysis, XRD peaks corresponding to d_{100} diffraction became weaker as TPR carburization performed. BET surface areas of both imp Nb/SBA-3 and inc Nb-SBA-3 was $1040\,\text{m}^2 \cdot \text{g}^{-1}$, the same as that of original SBA-3. On the other hand, BET surface areas of imp NbC/SBA-3 and inc NbC-SBA-3 were 730 and $870\,\text{m}^2 \cdot \text{g}^{-1}$, respectively. This surface area diminishment by carburization corresponded to the decrease of the mesoporosity. No Nb_2O_5 phase was observed for both imp Nb/SBA-3 and inc Nb-SBA-3 catalysts, suggesting high dispersion of Nb species.

3.2. *In-situ measurements*

Nb K-edge *in-situ* XANES spectra during TPR carburization for imp Nb/SBA-3 and inc Nb-SBA-3 are shown in Fig. 2 and Fig. 3, respectively. It takes about 10 min to collect one spectrum. NbC shows the distinct band at around 19040 eV, however, Nb_2O_5 does not show [6] this. Although there is no change at around 19040 eV for imp Nb/SBA-3 in the TPR process (solid lines), band growth is observed for the second stage of TPR (maintained at 1223 K, dotted lines) as shown in Fig. 2. Moreover, the 1s-4d

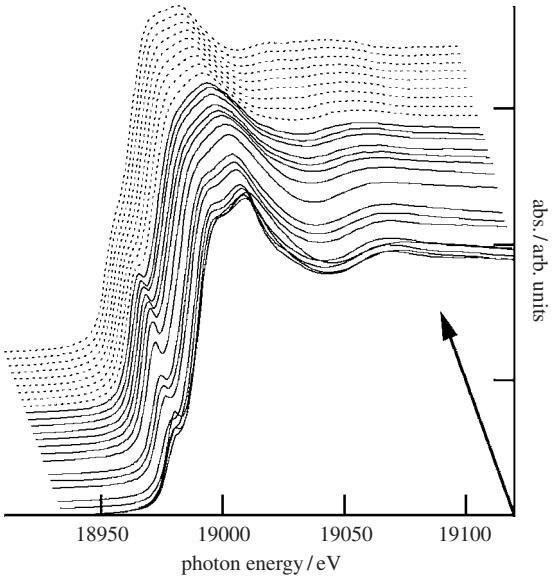

Fig. 2. In-situ XANES spectra observed during TPR carburization (dotted lines show retention stage) for imp Nb/SBA-3.

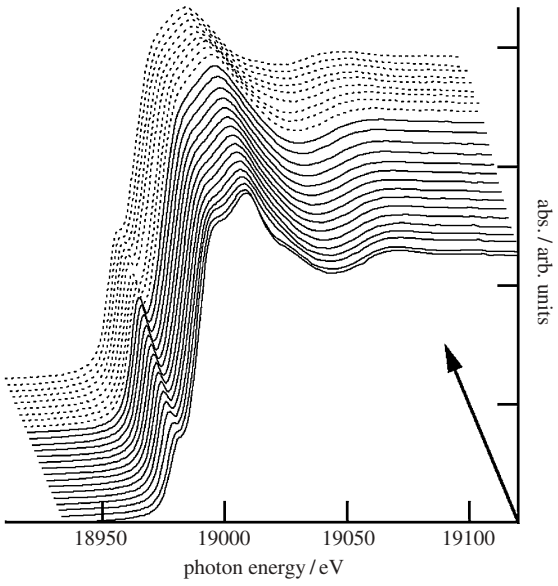

Fig. 3. In-situ XANES spectra observed during TPR carburization (dotted lines show retention stage) for inc Nb-SBA-3.

transition peak (at around 18990 eV), which was observed for starting materials, decreased gradually in the second TPR stage. Thus, it can be said that Nb_2O_5 on the SBA-3 support was reduced to NbO_2 in the first stage of TPR and converted into NbC in the second stage.

In the case of inc Nb-SBA-3, NbC band (at around 19040 eV) was not clearly observed at the end of TPR carburization. Moreover, the pre-edge peak did not fully disappear as shown in Fig. 3. It can be said that the silica-wall incorporated Nb species hardly carburized and remained as oxide. The pre-edge peak became more distinct in the first few spectra and then became smaller. These phenomena can be explained as dehydration from Nb-oxide. Thus, all Nb species in inc Nb-SBA-3 were not fully incorporated into silica-walls. Some of the Nb species remains on the mesoporous silica walls as imp Nb/SBA-3.

To clarify the growth process of NbC, CF analysis to the second TPR stage was carried out by using empirically extracted Nb-Nb parameters (from bulk NbC). The second stage of TPR kept the high temperature (1223 K and 1173 K for imp Nb/SBA-3 and inc Nb-SBA-3, respectively) under 20% CH_4/H_2 flow. To remove the thermal effect on the Debye-Waller (DW) factor, temperature dependencies of the DW factor were measured for bulk NbC under He flow and applied for the CF analysis. Figure 4 shows the

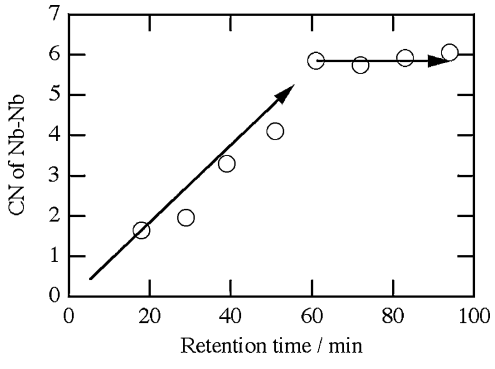

Fig. 4. Nb-Nb coordination number in the second stage of TPR (retention stage) at 1223 K for imp Nb/SBA-3.

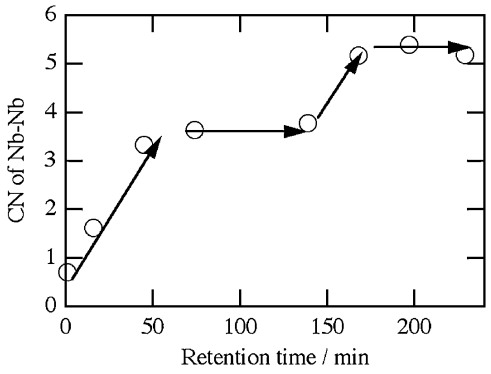

Fig. 5. Nb-Nb coordination number in the second stage of TPR (retention stage) at 1173 K for inc Nb-SBA-3.

change of CN for imp Nb/SBA-3. CN of Nb-Nb coordination increased gradually from ca. 1 to ca. 6, and did not change by further carburization at 1223 K. Thus, it can be said that the growth of NbC occurred in the second stage of TPR as reported before [8].

In the case of inc Nb-SBA-3, increase of CN took place in 2 steps as shown in Fig. 5; (1) CN increased from 1 to 4, (2) CN increased from 4 to 5.5. These phenomena can be explained from the Nb site. The Nb species existed in two sites, one is on the silica-wall and the other is in the silica-wall, as explained above. In the first step, exposed Nb species were reduced and carburized to produce NbC with CN of ca. 4. Further carburization treatment at 1173 K lead to carburization of silica-wall incorporated Nb species, which migrated to the NbC particles previously produced at the first step. At this point, CN became up to 5.5. However, there still remained un-carburized Nb species in the silica-wall, which showed oxide character. It can be said that highly dispersed silica-wall incorporated Nb species were hardly reduced and carburized.

4. Conclusion

Mesoporous silica SBA-3 with high surface area was synthesized and applied to the support. SBA-3 supported Nb catalyst and SBA-3 wall incorporated Nb catalyst were prepared and characterized. Both Nb loaded SBA-3 were carburized to produce supported NbC species under 20% CH_4/H_2 stream by TPR process.

The conversion and growth process of NbC during the TPR process were characterized by *in-situ* XAFS technique and revealed that the conversion to NbC and the growth of NbC occurred in the second stage of TPR. Conversion of SBA-3 wall incorporated Nb species to NbC followed two steps; (1) carburization of exposed Nb species on the wall, (2) carburization of incorporated Nb species inside the wall. The transformation of the Nb oxides to NbC species and their structure during carburization process could be observed by this *in-situ* XAFS technique.

Acknowledgement

This work was partially supported by a Grant-in-Aid from the Ministry of Education, Science, Sports and Culture of Japan (No. 12740311, 14740322).

References

1. Muller, J. M. and Gault, F. G., Bull. Soc. Chim. Fr. **2**, 416 (1970).
2. Levy, R. and Boudart, M., Science **181**, 547 (1973).
3. Oyama, S. T., in "The Chemistry of Transition Metal Carbides and Nitrides" (ed. Oyama, S. T.), (Blackie A&P 1 1996).
4. Teixeira da Silva, V. L. S., Ko, E. I., Schmal, M. and Oyama, S. T., Chem. Mater. **7**, 179 (1995).
5. Choi, J. G., Appl. Catal. A: General **184**, 189 (1999).
6. Ichikuni, N., Sato, F., Shimazu, S. and Uematsu, T., Topics Catal. **18**, 101 (2002).
7. Bando, K. K. *et al*., J. Synchrotron Rad. **8**, 581 (2001).
8. Ichikuni, N., Sato, F., Shimazu, S. and Uematsu, T., Stud. Surf. Sci. Catal. **132**, 781 (2001).

Physica Scripta. Vol. T115, 810–812, 2005

XAS Studies on Incorporation of Mn and Co into Silicalite-1

I. Arčon[1,2,*], N. Novak Tušar[3], A. Ristić[3], A. Kodre[2,4] and V. Kaučič[3]

[1]Nova Gorica Polytechnic, Vipavska 13, POB 301, SI-5001 Nova Gorica, Slovenia
[2]J. Stefan Institute, Jamova 39, POB 3000, SI-1001 Ljubljana, Slovenia
[3]National Institute of Chemistry, Hajdrihova 19, 1000 Ljubljana, Slovenia
[4]Faculty of Mathematics and Physics, University of Ljubljana, Jadranska 19, SI-1000 Ljubljana, Slovenia

Received June 26, 2003; accepted in revised form November 4, 2003

PACS numbers: 61.10.Ht, 82.75.Fq

Abstract

Mn- and Co-containing silicalite-1 (MnS-1 and CoS-1) were synthesized hydrothermally. Template-free samples were obtained by calcination at 550 °C for 6 hours in oxygen flow. X-ray diffraction, elemental, thermogravimetric and cation exchange analyses suggested a possible incorporation of Mn and Co cations into the framework positions of the silicalite-1. The valence state and local environment of both cations in the samples were examined by XANES and EXAFS analyses. Results show that Mn and Co cations isomorphously substitute silicon in the silicalite-1 framework only if they are in trivalent oxidation state. Divalent cations are incorporated on extra-framework positions. In the template-free MnS-1 sample all Mn cations are in trivalent state and substitute Si in the framework, forming a distorted and coordinatively unsaturated 3-fold symmetry, which is characteristic for Lewis acid sites. In the template-free CoS-1 sample only part of Co cations are in trivalent state substituting silicon in the framework.

1. Introduction

Zeolites with aluminosilicate framework are crystalline oxides comprising corner-sharing TO_4 tetrahedra (T = Si, Al) [1]. They possess regular pore system with diameters in the range from 0.3–1.4 nm and act as sieves at molecular level.

Silicalite-1 is an aluminium-free zeolite with the MFI structural topology [1]. Modification of silicalite-1 by isomorphous substitution of silicon by transition-metal elements enhances its catalytic activity. Incorporation of tetravalent (e.g. Ti, V) transition metals into the framework of silicalite-1 results in novel molecular sieves with selective oxidation properties [2]. Incorporation of trivalent (e.g. Cr, Fe) transition metals into the framework of silicalite-1 results in high-quality inorganic membranes used for catalytic membrane reactors [3]. So far all attempts of incorporation of divalent transition metals (e.g. Mn, Co) lead to the formation of the silicalite-1 with divalent cations on extra-framework positions [4].

In this paper we report on the isomorphous substitution of silicon in the framework of silicalite-1 by manganese and cobalt cations. Mn and Co K-edge XANES analysis is used to probe directly the valence state of the transition metal cations in the as-synthesized and template-free samples, while their local environment and therewith the site of the incorporation is examined by EXAFS.

2. Experimental

Manganese-containing silicalite-1 (MnS-1) was syntesized hydrothermally using tetraethylammonium hydroxide (TEAOH) as a structure-directing agent (template) [5]. Cobalt-containing silicalite-1 (CoS-1) was synthesized by similar procedure using tetrapropylammonium hydroxide (TPAOH) as a template. Template-free products were prepared by calcination at 550 °C for 6 hours in oxygen flow. Cation exchange was performed at room temperature by stirring the solid sample in a 1 M solution of NaCl for 24 hours with solid/liquid mass ratio 1/10. X-ray powder diffraction (XRPD) patterns of the products were collected on a Siemens D-5000 diffractometer with CuK_α radiation. Thermogravimetric analysis (TGA) was performed on a TA 2000 thermal analyzer in static air. Elemental analysis was carried out using an EDXS (energy dispersive X-ray spectroscopy) anaysis within the LINK ISIS 300 system, attached to the scanning electron microscope JEOL JSM 5800.

X-ray absorption spectra of MnS-1, CoS-1 and reference samples in the respective energy regions of the Mn and Co K-edge were measured at E4 beamline of HASYLAB synchrotron facility at DESY in Hamburg. The beamline provided a focused beam from an Au-coated torroidal mirror and a Si(111) double crystal monochromator with about 1 eV resolution at 7 keV. Harmonics were effectively eliminated by a plane Au-coated mirror, and by a slight detuning of the monochromator crystals, keeping the intensity at 60% of the rocking curve with the beam stabilization feedback control. Powder samples were prepared on multiple layers of adhesive tape. Several layers were stacked to obtain optimal attenuation above the K-edge of the investigated element. Reference spectra were measured under the same conditions on empty tapes without the sample. The standard stepping progression within [−250 eV ... 1000 eV] region of the Mn and Co K-edge was adopted for EXAFS spectra with an integration time of 4 s/step. Exact energy calibration was established with the simultaneous absorption measurements on Mn and Co metal.

3. Results and discussion

The as-synthesized MnS-1 and CoS-1 were identified from XRPD patterns as single crystalline phase products with MFI structure. Elemental and thermogravimetric analyses of the as-synthesized and template-free MnS-1 and CoS-1 suggested that 0.5% Si was isomorphously substituted by Mn and Co, respectively. Cation exchange procedure revealed that there were no exchangeable cationic sites in the template-free MnS-1, while some exchangeable cationic sites were present in the template-free CoS-1 sample. This indicated that all incorporated manganese atoms in the template-free sample isomorphously substituted framework silicon in the silicalite-1, while the Co substitution in the template-free CoS-1 sample was only partial.

To determine the valence state of the transition metal cations in the as-synthesized and calcined samples we examined Co and Mn K-edge energy shifts in the absorption spectra of the samples. The

*e-mail: iztok.arcon@p-ng.si

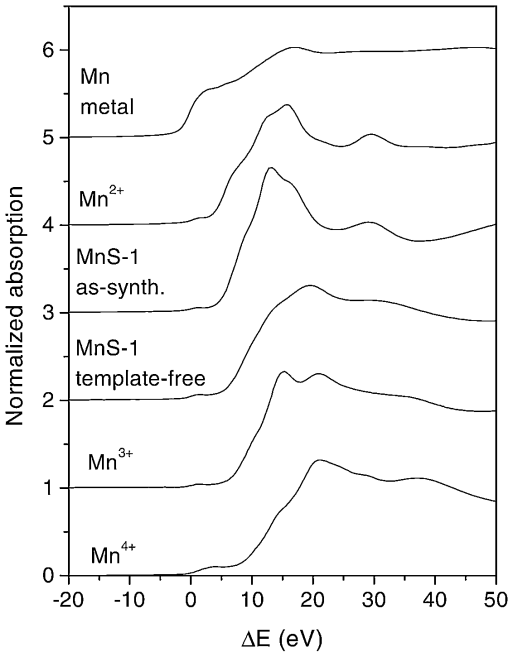

Fig. 1. Normalized Mn K-edge XANES spectra of the as-synthesized and template-free MnS-1 and Mn reference samples Mn metal, $Mn^{2+}O$, $K_3[Mn^{3+}(C_2O_4)_3].3H_2O$, and $Mn^{4+}O_2$. The spectra are displaced vertically for clarity. The zero energy is taken at the first inflection point of the Mn K-edge in the spectrum of Mn metal (6539.0 eV).

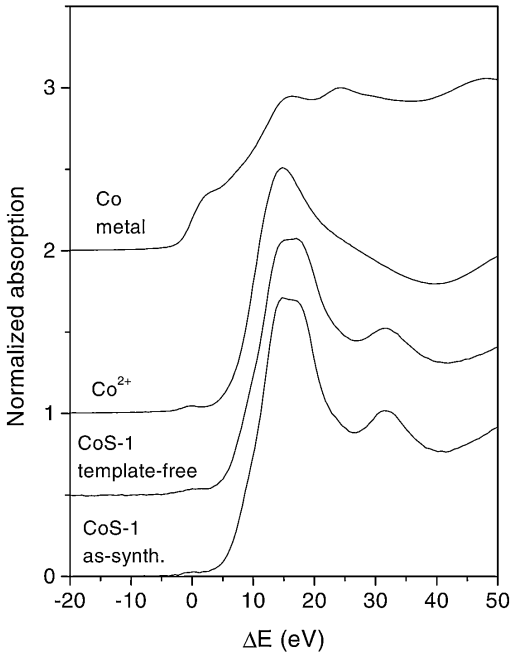

Fig. 2. Normalized Co K-edge XANES spectra of the as-synthesized and template-free CoS-1 and Co reference samples Co metal and $Co^{2+}(CH_3COO)_2.4H_2O$. The spectra are displaced vertically for clarity. The zero energy is taken at the first inflection point of the Co K-edge in the spectrum of Co metal (7709.0 eV).

precise energy position of the edge was taken at the edge inflection point. A linear relation between the edge shift and the oxidation state was established for the atoms with the same type of ligands [6–9]. For manganese atoms coordinated to oxygen atoms a shift of 3.5 eV per oxidation state was found [7], while for cobalt atoms shifts of 1.5–3 eV per valence were reported [9].

In Fig. 1 the Mn XANES spectra of the as-synthesized and template-free MnS-1 sample together with the spectra of the reference manganese compounds $Mn^{2+}O$, $K_3[Mn^{3+}(C_2O_4)_3].3H_2O$, and $Mn^{4+}O_2$ with known oxidation states are shown. The edge shift in the as-synthesized MnS-1 is the same as in the $Mn^{2+}O$ compound, indicating that the average oxidation state of manganese in the as-synthesized MnS-1 is 2+. The Mn K-edge in the template-free MnS-1 sample is shifted and coincides with the edge shift in the $K_3[Mn^{3+}(C_2O_4)_3].3H_2O$ compound. We can thus conclude that during calcination all Mn^{+2} cations oxidize to Mn^{+3}.

The Co XANES spectra (Fig. 2) reveal completely different behaviour of Co cations in the CoS-1 samples. The same energy position of Co K-edge is found in both as-synthesized and template-free CoS-1 samples, demonstrating that the valence state of the incorporated Co cations does not change during the process of calcination. Furthermore, the Co K-edge in the CoS-1 samples is shifted for about 1 eV relative to the edge in the reference Co^{2+} acetate sample, which indicates the presence of Co^{2+} and Co^{3+} cations in the silicalite samples.

Mn and Co K-edge EXAFS spectra of the as-synthesized and template-free MnS-1 and CoS-1 samples were quantitatively analyzed for the coordination number, distance, and Debye-Waller factor of the nearest coordination shells of neighbor atoms using the University of Washington UWXAFS package [10] and FEFF6 code [11]. The amplitude reduction factor ($S_0^2 = 0.80$) is kept fixed in the fits of all spectra. Its value is obtained from previous experimental results [12]. Fourier transforms of Mn and Co EXAFS spectra are shown in Figs. 3 and 4 together

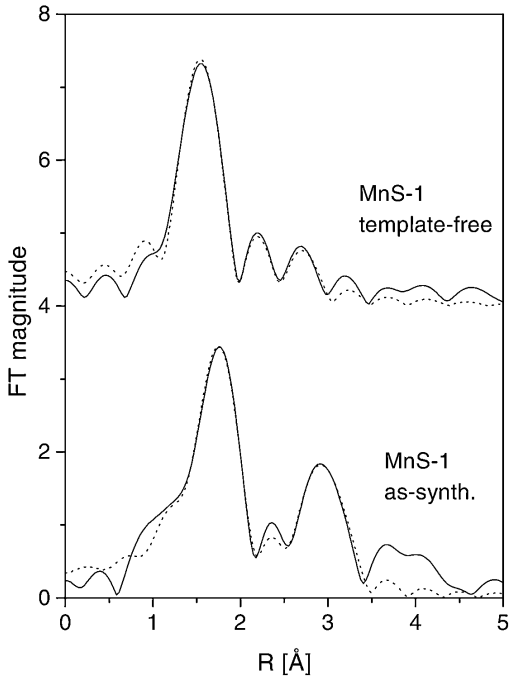

Fig. 3. Fourier transforms of the k^3-weighted Mn EXAFS spectra of the as-synthesized and template-free MnS-1 sample, calculated in the k range of 5–12 $Å^{-1}$ (solid line – experiment, dotted line – EXAFS model).

with best-fit EXAFS models. Complete lists of best-fit parameters are given in Tables I and II.

Two shells of neighbours are found around Mn cations in the as-synthesized MnS-1 sample. The fit in the R range from 1.2 Å to 3.5 Å shows that the first shell is composed of four oxygen atoms at 2.18 Å, while the second shell comprises about two Mn atoms at 3.35 Å. The presence of Mn-O-Mn links indicates

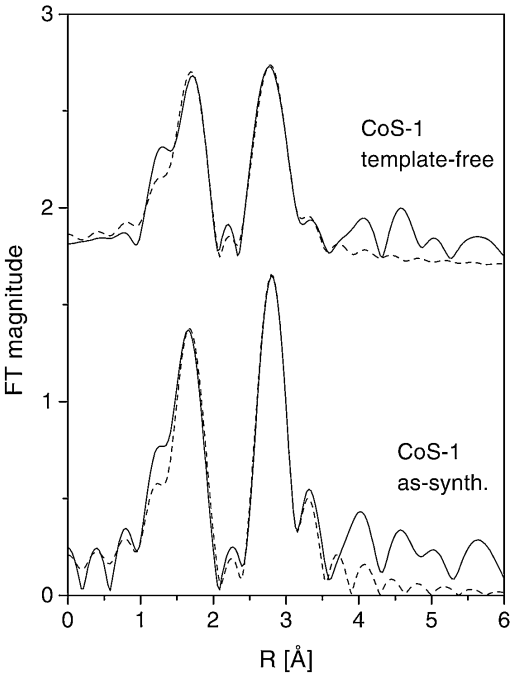

Fig. 4. Fourier transforms of the k^2-weighted Co EXAFS spectra of the as-synthesized and template-free CoS-1 sample, calculated in the k range of 3.5–12 Å^{-1} (solid line – experiment, dotted line – EXAFS model).

Table I. *Structural parameters of the nearest coordination shells around Mn atom in as-synthesized and template-free MnS-1: type of neighbor atom, average number N, distance R, and Debye-Waller factor σ^2. Uncertainties in the last digit (estimated by UWXAFS fitting program) are given in the parentheses.*

Neighbor	*N*	*R* (Å)	σ^2 (Å^2)
As-synthesized MnS-1			
O	3.6(3)	2.18(1)	0.008(1)
Mn	1.6(3)	3.35(1)	0.008(1)
Template-free MnS-1			
O	2.1(2)	1.93(1)	0.003(1)
O	0.8(2)	2.15(2)	0.005(2)
O	1.0(5)	2.81(2)	0.004(2)
O	1.1(5)	3.04(2)	0.004(2)
Si	0.9(6)	3.52(2)	0.020(5)

that Mn cations (divalent as shown by XANES) are located at extraframework sites, most probably in the form of metal-oxo species coordinated to the framework, but simultaneously bearing extra-framework oxygen atoms [7].

Significantly different local Mn neighborhood (within the same R range) is found in the template-free MnS-1 sample. Mn is coordinated to three oxygen atoms in the first coordination shell, two of them at a shorter distance of 1.93 Å and one at a longer distance of 2.15 Å. The short distance of 1.93 Å is consistent with the average tetrahedral Mn^{+3}-O distance of 1.93(4) Å reported for $MnAsO_4$ [13]. In the second coordination shell two oxygen atoms were identified at 2.81 Å and 3.04 Å. Additionally, at a larger distance of about 3.5 Å a presence of silicon atoms is indicated. Taking into account XANES results we can conclude that Mn^{3+} cations substitute Si in the framework of the template-free MnS-1, forming a distorted and coordination-wise unsaturated 3-fold symmetry, which is characteristic for Lewis acid sites (manganese framework sites) [14].

Table II. *Structural parameters of the nearest coordination shells around Co atom in as-synthesized and template-free CoS-1: type of neighbor atom, average number N, distance R, and Debye-Waller factor σ^2. Uncertainties in the last digit (estimated by UWXAFS fitting program) are given in the parentheses.*

Neighbor	*N*	*R* (Å)	σ^2 (Å^2)
As-synthesized CoS-1			
O	3.8(7)	2.11(1)	0.002(1)
Co	3.2(7)	3.16(1)	0.002(1)
O	4(1)	3.64(3)	0.002(1)
Template-free CoS-1			
O	2.9(4)	2.12(1)	0.002(1)
Co	3.2(5)	3.16(1)	0.005(2)
Si	2.5(5)	3.50(3)	0.011(2)

In modeling Co EXAFS spectra, the fit in the R range 1.3 Å–3.5 Å shows that in the as-synthesized sample cobalt atoms are coordinated to four oxygen atoms at 2.10 Å, while the second shell is composed of Co and O atoms. The local Co neighborhood in the template-free sample is slightly different (Fig. 4, Table II) but the Co-O-Co links are retained. Combining Co cation exchange, XANES and EXAFS results, we may conclude that the template-free CoS-1 sample contains two Co species (Co^{2+} and Co^{3+}), where trivalent cobalt cations substitute silicon in the framework sites while divalent Co cations are located at extra-framework sites in the form of metal-oxo species.

In conclusion, the results show that Mn and Co cations substitute silicon in the silicalite-1 framework isomorphously only if they are in the trivalent oxidation state. Divalent cations incorporate into the silicalite-1 on the extra-framework positions.

Acknowledgment

We acknowledge the support by the Slovenian Ministry of Education, Science and Sport through the research program P0-0516-0104 and the project Z2-3457-0104, by Internationales Buero BMBF (Germany), and by the IHP-Contract HPRI-CT-1999-00040 of the European Commission. Advice on beamline operation by Konstantin Klementiev of HASYLAB is gratefully acknowledged.

References

1. Depmeier, W., "Handbook of Porous Solids". (Edited by F. Schüth, K. S. W. Sing and J. Weitkamp) (Wiley-VCH, Weinheim 2002), vol. II, p. 728.
2. Mal, N. K. and Ramaswamy, P., Appl. Catal. A: General **143**, 75 (1996).
3. Li, S., Tuan, V. A., Falconer, J. L. and Noble, R. D., Micropor. Mesopor. Mater. **58**, 137 (2003).
4. Wichtelová, B., Sobalík, Z. and Dědeček, J., Appl. Catal. B: Environmental **41**, 97 (2003).
5. Tušar, N. N. *et al*., Chem. Mater., sent for publication.
6. Wong, J., Lytle, F. W., Messmer, R. P. and Maylotte, D. H., Phys. Rev. B **30**, 5596 (1984).
7. Ressler, T., Brock, S. L., Wong, J. and Suib, S. L., J. Synchrotron Rad. **6**, 728 (1999).
8. Arčon, I., Mirtič, B. and Kodre, A., J. Am. Ceram. Soc. **81**, 222 (1998).
9. Barrett, P. A., Sankar, G., Catlow, C. R. A. and Thomas, J. M., J. Phys. Chem. **100**, 8977 (1996).
10. Stern, E. A., Newville, M., Ravel, B., Yacoby, Y. and Haskel, D., Physica B **208–209**, 117 (1995).
11. Rehr, J. J., Albers, R. C. and Zabinsky, S. I., Phys. Rev. Lett. **69**, 3397 (1992).
12. Tušar, N. N. *et al*., Microporous Mesoporous Mat. **55**, 203 (2002).
13. Aranda, M. A. G., Attfield, J.-P. and Bruque, S., Inorg. Chem. **32**, 1925 (1993).
14. Zibrowius, B. and Loffler, E., "Handbook of Porous Solids". (Edited by F. Schüth, K. S. W. Sing and J. Weitkamp) (Wiley-VCH, Weinheim 2002), vol. II, p. 983.

Physica Scripta. Vol. T115, 813–815, 2005

Quantitative Determination of Platinum Oxidation State by XANES Analysis

H. Yoshida*, S. Nonoyama, Y. Yazawa and T. Hattori

Department of Applied Chemistry, Graduate School of Engineering, Nagoya University, Nagoya 464-8603, Japan

Received June 26, 2003; accepted in revised form November 4, 2003

PACS Ref.: 82.80.Ej

Abstract

Quantitative determination of platinum oxidation state on supported platinum catalyst was examined by using Pt L_{III}-edge XANES spectra. The nano-sized platinum particles on the support were partially oxidized under oxidative atmosphere. The atomic ratio of oxygen to platinum (O/Pt) for these particles could be determined by the amount of desorbed oxygen in He carrier (O_2-TPD) during elevated temperature. On the other hand, the XANES spectrum of the platinum catalysts oxidized under each corresponding condition was recorded under the same condition, then the area intensity of the white line of these spectra was evaluated by a simple simulation using a set of Gaussian and arctangent functions. A good linear relationship was confirmed between the white line intensity and the atomic ratio of oxygen to platinum, meaning that the oxidation state of the platinum could be quantitatively determined by a simple XANES analysis.

1. Introduction

It is known that the catalytic performance of supported platinum catalyst is affected by the properties of the support material and additive as well as the particle size of platinum. Further, in oxidative reactions such as catalytic combustion, the oxidation state of platinum is also one of the important factors to determine the catalytic activity, since the platinum of metallic state usually shows higher catalytic performance than in oxidized state [1, 2].

Since we reported that the use of solid super acid as the support remarkably enhanced the catalytic activity of platinum in propane combustion [3, 4] and that the self-inhibition effect of oxygen was much greater over basic support [5, 6], we have investigated the effect of the support [6–10] and the additive [10–12] as well as the particle size of platinum [7] on the supported platinum catalyst by focusing on the oxidation state of platinum. It has been confirmed that more metallic state of platinum is suitable for propane combustion. Further, it has been clarified that more electrophilic property of support materials and additive elements provide more metallic state of platinum, resulting in higher catalytic performance [6–12].

In these studies, the oxidation state of platinum has been discussed on the basis of the white line intensity at Pt L_{III}-edge XANES, which was evaluated by a simple curve fitting method. Since the white line, intense absorption peak, at the Pt L_{III}-edge is mainly assigned to electron transition from $2p_{3/2}$ to $5d_{3/2}$ and $5d_{5/2}$, it is an informative index for the oxidation state of platinum; a large white line is observed on oxidized platinum due to electron vacancy in the d-orbital, while a small while line is observed on metallic platinum due to lack of electron vacancy. However, the quantitative correlation between the platinum oxidation state and the white line intensity has not been clarified. It is very important to confirm the correlation between them for the further detailed quantitative study of platinum catalyst. In the present study, we evaluated both the oxidation state of platinum on supported catalyst by O_2-TPD method and the white line intensity at Pt L_{III}-edge XANES, and confirmed the relationship between them.

2. Experimental

The support materials used in the present study were MgO, Al_2O_3 and SiO_2-Al_2O_3, all of which were reference catalysts of Catalysis Society of Japan (MGO-1, ALO-4 and JRC-SAL-2) [13, 14]. The acid strengths (H_0) of them was 22.3, 3.3 and −12.0, respectively [8]. The sieved support material (+25 − 50 mesh) was immersed in $Pt(NO_2)_2(NH_3)_2$ aqueous solution, and excess water was removed by a rotary evaporator with suction at room temperature. After drying at 383 K for 12 h, the resultant powder were calcined at 673 K for 3 h, and then reduced at 623 K for 3 h in a flow of hydrogen. The platinum loading was 2 or 5 wt% as platinum. Additional reduction at 623 K for a moderate period was carried out on some samples in order to obtain catalysts having similar platinum dispersion to others. The CO uptake of platinum catalyst was measured by pulse-adsorption of CO in a flow of helium at room temperature [13, 14]. The platinum dispersion was calculated from the total CO uptake by assuming that carbon monoxide was adsorbed on surface platinum atom at a 1 : 1 stoichiometry.

The oxidation state of the oxidized catalyst was evaluated by O_2-TPD (Temperature Programmed Desorption of Oxygen) method on a TPD instrument (Bel Japan, Inc.) as follows. Prior to measurement, the sample was sequentially treated in H_2 (66.7 kPa), in vacuo and in O_2 (66.7 kPa) at selected temperature (473, 673 or 823 K) for 30 min each, followed by cooling down to room temperature and evacuation. Then, under monitoring O_2 desorbed from the sample by mass spectrometer (ANELVA, AQA-100R), the temperature of the sample bed was elevated (5 K min^{-1}) in a flow of He and held at 1073 K for more than 30 min. From the total area intensity of the spectrum, the amount of desorbed oxygen was evaluated, and the ratio of desorbed oxygen atom to platinum (O/Pt) was calculated.

Pt L_{III}-edge XANES spectra of the samples were recorded in transmission mode by a laboratory EXAFS instrument [15], EXAC820 (Technos Co. Ltd). The X-ray source was a rotating anode X-ray generator (22 kV, 200 mA, target anode: Mo, filament: LaB_6). A single monochromator was employed using a Johansson-type Ge(400) bent crystal curved with Rowland circle geometry ($R = 300$ mm) and the 1st order of the reflection was used. The sample disk was put in an *in-situ* cell in which temperature and flowing gas composition could be controlled. Before each measurement, the same treatment as that before TPD experiment was done. The measurement of such oxidized samples

*e-mail: yoshidah@apchem.nagoya-u.ac.jp

was carried out at room temperature in a flow of He. The X-ray intensity before passing the sample, I_0, was detected with a semi-transmitting sealed proportional counter (S-PC) filled with 0.5 atm of Ar and the intensity after the sample, I, was detected with a pure-Ge solid state detector (SSD).

The background subtraction and normalization were performed by using a modified Victoreen equation with a constant correction term (eq. (1)) [16]. The white line area intensity of normalized Pt L_{III}-edge XANES spectrum was evaluated by a curve fitting analysis [17] using a set of a Gaussian and an arctangent function (eq. (2)):

$$\mu(\lambda) = \mathrm{A} + \mathrm{C}\lambda^3 - \mathrm{D}\lambda^4, \quad (1)$$

$$I(E) = a(E) + g(E), \quad (2)$$

$$a(E) = h_1[0.5 + \pi^{-1}\tan^{-1}\{(E - E_1)/w_1\}],$$

$$g(E) = h_2\exp[-\ln 2(E - E_2)^2/w_2^2]$$

where I: simulated spectrum, E: X-ray energy (eV), $a(E)$: arctangent function, $g(E)$: Gaussian, h_i: height, w_i: width, E_1: inflection point (eV), E_2: peak position (eV). In the present simulation, h_1 was 1 and w_1, which is related to the lifetime of 2p electron, was fixed as 0.33, and the relative energy positions of the two functions were fixed as $E_1 = E_2 - 5.4$. E_1 was around 11567 eV.

3. Results and discussion

Six kinds of catalysts with different acid strengths of support and particle size of platinum were systematically prepared. There were two groups of prepared catalysts; one is catalysts of 2 wt% loading with 60% dispersion, while the other is catalysts of 5 wt% loading with around 30% dispersion. The mean particle size of these catalysts was estimated to be around 2 and 3.7 nm, respectively.

Fig. 1 shows O_2-TPD profiles of the representative samples. PtO_2 (Fig. 1a) exhibited two sequential desorption peaks around 800 K, which corresponds to the decomposition temperature of PtO_2 to Pt and O_2. The amount of oxygen desorption was determined and the ratio of oxygen to platinum (O/Pt) was calculated to be 2.02 for PtO_2 (Table I). This result indicates

Table I. *The ratio of O/Pt and white line intensity.*

Catalyst	Oxidation temperature (K)	O/Pt from O_2-TPD	White line intensity (arb. unit)
PtO_2	–	2.02	6.6
2wt.% Pt/MgO	823	1.72	6.1
2wt.% Pt/MgO	673	1.32	4.9
2wt.% Pt/MgO	473	0.72	3.4
2wt.% Pt/Al_2O_3	823	0.69	3.2
2wt.% Pt/SiO_2-Al_2O_3	823	0.92	2.0
5wt.% Pt/MgO	823	1.68	5.8
5wt.% Pt/MgO	673	1.40	4.7
5wt.% Pt/MgO	473	0.67	3.6
5wt.% Pt/Al_2O_3	823	0.44	2.4
5wt.% Pt/SiO_2-Al_2O_3	823	0.48	2.5

that this method is available for determination of O/Pt. As for the catalyst samples, the oxygen desorption peak was observed at different temperature from that of PtO_2. This means that the stability of the oxidized platinum particles on the support was affected by the support [10]. Especially on the MgO support, the decomposition temperature was clearly higher than the others, which means that oxidized platinum was well stabilized as reported [8, 10, 18]. However, in the present study, we want to focus not on the property of this oxidized platinum but the ratio of oxygen to platinum. Further studies are required to discuss the differences in the profiles.

The peak area intensity of the supported catalyst was obviously lower than that of the bulk PtO_2, which is due to low platinum contents on the supported samples. The O/Pt values for these oxidised catalyst samples were listed in Table I. The O/Pt values of the supported catalyst samples were obviously lower than 2, indicating that the platinum on the support was not fully oxidized. As a whole, the O/Pt of the catalyst sample was widely ranged from 0.4 to 1.7 with the variations of particle size, support material and oxidation temperature.

Fig. 2 shows Pt L_{III}-edge XANES spectra of the representative samples, which were measured by the laboratory EXAFS instrument. PtO_2 (Fig. 2a) exhibited the largest white line at 11567 eV among the samples, while the Pt foil (Fig. 2e) showed a very small white line. The white line intensity for the supported catalyst was larger than that of Pt metal and smaller than that

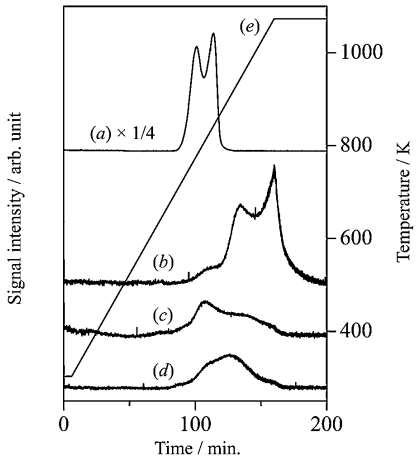

Fig. 1. The O_2-TPD profiles of (a) bulk PtO_2, (b) 2wt% Pt/MgO, (c) 2wt% Pt/Al_2O_3 and (d) 2wt% Pt/SiO_2-Al_2O_3. The sample was oxidized under oxygen (66.7 kPa) at 823 K for 30 min before measurement. The signal intensity of (a) was reduced to one fourth. The line (e) indicates the programmed temperature of the sample.

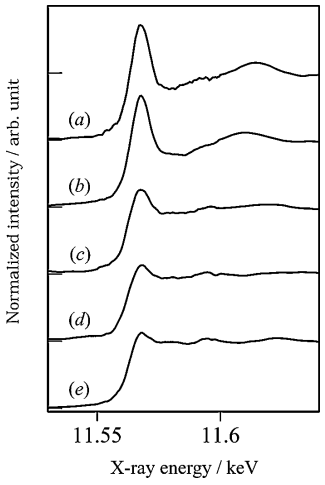

Fig. 2. Pt L_{III}-edge normalized XANES of (a) PtO_2, (b) 2wt% Pt/MgO, (c) 2wt% Pt/Al_2O_3 and (d) 2wt% Pt/SiO_2-Al_2O_3, and (e) Pt foil. The catalyst sample was oxidized at 823 K before measurement.

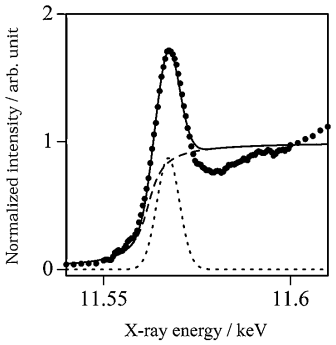

Fig. 3. A curve fitting analysis of XANES by using a set of an arctangent function (broken line) and a Gauss function (doted line). The dots show the experimental spectrum and the solid line shows the simulated curve.

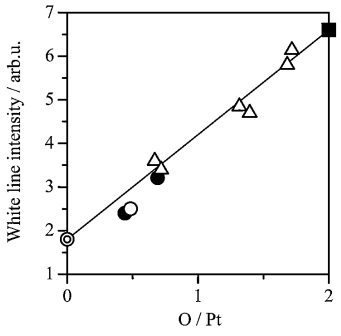

Fig. 4. Relation between the atomic ratio of oxygen to platinum (O/Pt) and the white line intensity of Pt L_{III}-edge XANES of PtO_2 (closed square), Pt foil (double circle) and supported Pt catalyst samples; Pt/MgO (open triangle), Pt/Al_2O_3 (closed circle), and Pt/SiO_2-Al_2O_3 (open circle). O/Pt was determined by O_2-TPD (see text).

of PtO_2, indicating that these platinum particles on the support materials partially oxidised.

To evaluate the white line intensity, a simple curve fitting analysis was carried out by using a set of a Gaussian (dotted line) and an arctangent function (broken line) as shown in Fig. 3. The simulated curve (solid line) seems to fit the experimental spectrum in the lower energy region including the white line. The white line intensity was expressed by the area intensity of the Gauss function and listed in Table I. Note that this simulation method was employed not for strict determination of the transition from 2p to 5d but simply for evaluation of the spectrum intensity.

As for PtO_2, Pt metal and supported catalysts, the obtained white line intensity was plotted versus O/Pt in Fig. 4. The plots clearly show a linear relationship between the two parameters, white line intensity and O/Pt. This means that the measurement of Pt L_{III}-edge XANES followed by a simple curve fitting analysis provides a quantitative estimation of platinum oxidation state even though the samples exhibited much different TPD profiles from each other. The linear relation can be described as:

$$R_{O/Pt} = A \times I_W - B \quad (3)$$

where $R_{O/Pt}$ denotes the ratio of oxygen to platinum, I_W denotes the white line area intensity, A and B are constants. In the present case, A was 0.42 and B was 0.73. This clear result suggests that, once the relationship and the constant values were confirmed in the given conditions, the oxidation state of platinum could be quantitatively evaluated from the white line intensity.

At the same time, both O_2-TPD and the white line intensity at Pt L_{III}-edge XANES were confirmed to be available for quantitative determination of the oxidation state of platinum. Although the H_2-TPR (Temperature programmed Reduction) method is often employed to know the platinum oxidation state, a reduction of support materials might occur under such conditions. It seems better to employ the O_2-TPD to know the oxidation state of platinum.

This linear relationship allows us to find the oxidation state of platinum quantitatively through the measurement of XANES; in other words, measurement of the EXAFS region was not necessary for this purpose. This would provide the following advantages: 1) quick measurement is possible even when we use a normal set up of EXAFS instruments since the region for recording is not wide. 2) Since the signal intensity of XANES is apparently larger than the EXAFS oscillation, it would also be possible to find the oxidation state of low loading platinum catalyst from even a very noisy or small XAFS spectrum. These advantages make it possible, for example, to record the dynamic variation of the platinum oxidation state in situ under reaction conditions.

4. Conclusion

The study of the oxidation state of platinum nano-particles through measurements of O_2-TPD profile and Pt L_{III}-edge XANES clarified the linear relationship between the ratio of oxygen to platinum (O/Pt) and the white line intensity. Thus, the O_2-TPD method and the simple simulation of the white line intensity of Pt L_{III}-edge XANES are confirmed to be suitable for quantitative determination for the ratio of oxygen to platinum.

References

1. Volter, J., Lietz, G., Spindler, H. and Lieske, H., J. Catal. **104**, 375 (1987).
2. Nunan, J. G., Robota, H. J., Cohn, M. J. and Bradley, S. A., J. Catal. **133**, 309 (1992).
3. Ishikawa, A., Komai, S., Satsuma, A., Hattori, T. and Murakami, Y., Appl. Catal. A **110**, 61 (1994).
4. Sugaya, T. *et al*., Trans. Mat. Res. Soc. Jpn. **15A**, 103 (1994).
5. Yazawa, Y. *et al*., Catal. Lett. **72**, 157 (2001).
6. Yazawa, Y. *et al*. T., Stud. Surf. Sci. Catal. **130**, 2189 (2000).
7. Yazawa, Y., Yoshida, H. and Hattori, T., Appl. Catal. A **237**, 139 (2002).
8. Yazawa, Y. *et al*. T., Appl. Catal. A **233**, 103 (2002).
9. Yoshida, H. *et al*., J. Synchrotron Rad. **6**, 471 (1999).
10. Yoshida, H., Yazawa, Y. and Hattori, T., Catal. Today, **87**, 19 (2003).
11. Yazawa, Y., Yoshida, H., Komai, S. and Hattori, T., Appl. Catal. A **233**, 113 (2002).
12. Yazawa, Y., Yoshida, H. and Hattori, T., J. Synchrotron Radiation **8**, 560 (2001).
13. Hattori, T., Matsumoto, H. and Murakami, Y., "Preparation of Catalysts IV". (Edited by B. Delmon, P. Grange, P. A. Jacobs and G. Poncelet) (Elsevier, Amsterdam, 1987), p. 815.
14. Uchijima, T., "Catalytic Science and Technology". (Edited by S. Yoshida, N. Takezawa and T. Ono) (Kodansha-VCH, Tokyo-Weinheim, 1990), Vol. 1, p. 393.
15. Udagawa, Y., "X-ray Absorption fine structure for catalysts and surfaces". (Edited by Y. Iwasawa) (Word Scientific, Singapore, 1996), p. 131.
16. Asakura, K., *ibid*., p. 34.
17. Yoshida, S. and Tanaka, T., *ibid*., p. 304.
18. Asakura, K., Nagahiro, H., Ichikuni, N. and Iwasawa, Y., Appl. Catal. A **188**, 313 (1999).

Physica Scripta. Vol. T115, 816–818, 2005

Spontaneous Dispersion of PdO and Generation of Metal Pd cluster in Zeolites Studied by Means of *in situ* DXAFS

Kazu Okumura*, Ryosuke Yoshimoto, Shigeru Yokota†, Kazuo Kato†, Hajime Tanida†, Tomoya Uruga† and Miki Niwa

Department of Materials Science, Faculty of Engineering, Tottori University, Koyama-cho, Tottori 680-8552, Japan
†Japan Synchrotron Radiation Research Institute, 1-1-1 Kouto, Mikazuki-cho, Sayo-gun, Hyogo 679-5198, Japan

Received June 26, 2003; accepted January 27, 2004

Abstract

Spontaneous dispersion and clustering processes of Pd were measured by means of energy-dispersive XAFS. The spontaneous dispersion of bulky metal Pd into highly dispersed PdO was directly observed on the H-type zeolite in the atmosphere of O_2. Various clustering processes of metal Pd was observed over different kind of zeolite supports. The selective formation of Pd_6 and Pd_{13} clusters were found over H-ZSM-5, H-Mordenite and H-Y supports, respectively. It was concluded that the crystal structure and acid sites of zeolites had significant influences on the dynamic behavior and the genesis of Pd clusters.

1. Introduction

Metal-support interaction in supported metal catalysts is important in understanding the structure and catalysis of supported metal. Previous studies concerning palladium catalysts revealed that the catalysis of the Pd center was significantly affected by the acid property of the support [1]. For instance, Brønsted acidity of zeolite was essential for selective reduction of NO by methane over Pd. In addition, the methane combustion activity of Pd was affected by the support surface [2]. One of the reasons for these effects could be the strong interaction between Pd and acid sites of supports. Indeed, we have observed spontaneous migration of agglomerated metal Pd into the highly dispersed PdO on acid sites under O_2 atmosphere at elevated temperature [3, 4]. This spontaneous dispersion of PdO was reversible upon repetition of reduction and oxidation treatments. The highly dispersed PdO was considered to be active center in the selective reduction of NO by methane in the presence of O_2 [4]. These observations imply that the interaction between palladium and acid sites of zeolites play an important role in the determination of dynamic behavior as well as the structure of palladium clusters generated in zeolite pore system. In this study, in order to elucidate the dispersion process of PdO onto acid sites of zeolites and to elucidate the clustering process of metal Pd, zeolites with various structures and cations were employed as supports for Pd. Although previous studies were primarily carried out under static conditions, the dynamic structural change could be directly observed using *in situ* and quick measurement of Pd structure. For this purpose, energy-dispersive XAFS (DXAFS) technique was undertaken for structural analysis of Pd loaded on various kinds of zeolite in an atmosphere of oxygen and hydrogen.

2. Experimental

Na-, H-ZSM-5 ($Si/Al_2 = 23.8$), H-Mordenite ($Si/Al_2 = 20$) and H-Y ($Si/Al_2 = 5.5$) were used as supports for Pd. Pd was loaded on these zeolites through an ion exchange method using $Pd(NH_3)_4Cl_2$ solution. The prepared samples were calcined in an N_2 flow at 773 K as a pretreatment. 0.4 wt% of Pd was loaded on each zeolite.

Pd K-edge DXAFS was measured at BL28B2 station of Japan Synchrotron Radiation Research Institute (SPring-8). The storage ring was operated at 8 GeV. Si polychrometer crystal was switched to a Laue configuration with (422) net plane to obtain an X-ray beam with dispersed energy region. The X-ray energy was calibrated with Pd foil as a reference. The sample was placed in a quartz *in situ* cell. The thickness of the sample was 1.5 cm. The sample was heated from room temperature to 773 K with a ramping rate of $5\,K\,min^{-1}$ in an O_2 flow ($50\,mL\,min^{-1}$) or 8% H_2 diluted with He ($90\,mL\,min^{-1}$) flow at atmospheric pressure. Typically, spectra measured for 0.3 s were accumulated 10 times for every 10 K. For extended X-ray absorption fine structure (EXAFS) analysis, the oscillation was extracted from the EXAFS data by a spline smoothing method [5]. The oscillation was normalized by the edge height around 50 eV above the threshold. The Fourier transformation of the k^3-weighted EXAFS oscillation from k space to r space was performed over the range 20–110 nm^{-1} (temperature programmed oxidation) or 30–120 nm^{-1} (temperature programmed reduction) to obtain a radial distribution function. The inversely Fourier filtered data were analyzed with a usual curve fitting method. For the curve fitting analysis, the empirical phase shift and amplitude functions for Pd-O and Pd-Pd were extracted from the data for bulk PdO and Pd foil, respectively. Debye-Waller factors of Pd-Pd (metal Pd) and Pd-O, Pd-(O)-Pd (Pd scattering in Pd oxide) were extracted from the spectra of Pd powder and PdO, respectively. In the analysis of spectra of samples, the Debye-Waller factors were extracted from the reference materials measured at the same temperature.

3. Results and Discussion

3.1. *Spontaneous dispersion of Pd onto acid sites of ZSM-5 [6]*

Fourier transforms of the $k^3\chi(k)$ EXAFS for Pd loaded zeolites are given in Figure 1. Initially, the formation of metal Pd was confirmed from the appearance of an intense nearest-neighboring Pd-Pd peak situated at 0.25 nm in every sample. From the coordination number of the Pd-Pd peak, the diameter of metal Pd was estimated to be larger than 1 nm. This indicates the generation of agglomerated metal Pd after the calcination of ion-exchanged Pd complex in N_2. In the case of Pd/Na-ZSM-5 (Figure 1(a)), the intensity of Pd-Pd (metal) gradually reduced accompanied by raising the temperature in an oxygen flow. Alternatively, new peaks appeared at 0.15 and 0.32 nm. These peaks could be assigned to the Pd-O and Pd-(O)-Pd characteristic of bulk PdO from a comparison with the reference spectrum of bulk PdO. In the spectra of Pd/HZSM-5 (Figure 1(b)), the Pd-Pd peak steeply

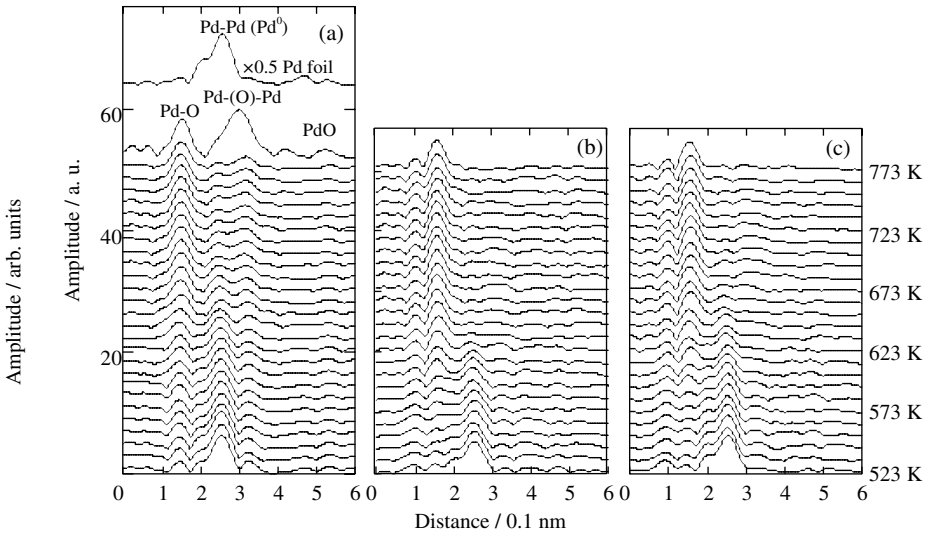

Fig. 1. Pd K-edge EXAFS Fourier transforms for Pd loaded on (a) Na-ZSM-5, (b) H-ZSM-5, (c) H-Mordenite measured in an O_2 flow; Pd loading, 0.4 wt%; Temperature ramping rate, 5 K min^{-1}; The spectra of PdO and Pd foil were measured at room temperature.

disappeared at 643 K. At the same time, the intensity of the Pd-O peak increased, indicating the oxidation of metal Pd progressed with increasing temperature. However, no Pd-(O)-Pd peak due to agglomerated PdO appeared. Although a similar feature was observed in Pd/H-Mordenite (Figure 1(c)), the temperature for disappearance of Pd-Pd and growth of Pd-O was higher than that of Pd/H-ZSM-5.

Figure 2 shows the coordination numbers (CN) of Pd-O, nearest-neighboring metal Pd-Pd, Pd-(O)-Pd of Pd oxide plotted as a function of oxidation temperature. The CN values were calculated based on the curve fitting analysis. As shown in Figure 2(a), Pd-O and Pd-(O)-Pd peaks appeared in place of the decrease in Pd-Pd due to metal on Na-ZSM-5 accompanied by increase in temperature. The generation of Pd-(O)-Pd meant that Pd metal was simply transformed into agglomerated PdO on the external surface of Na-ZSM-5 at elevated temperature. On H-ZSM-5 ($Si/Al_2 = 23.8$), the disappearance of Pd-Pd peak and the growth of Pd-O was observed at 643 K. However, in contrast to the Na-form of zeolites, Pd-(O)-Pd peak which is a characteristic of the agglomerated PdO did not appear even after the disappearance of metal Pd. This means that the agglomerated metal Pd migrated into the acid sites of zeolite to generate a highly dispersed PdO, because the intensity of Pd-(O)-Pd shell seemed to reflect the size of PdO. In addition, the data suggested that the migration of Pd occurred immediately after the oxidation of metal Pd particles, since the oxidation and the dispersion of Pd took place at the same time. Another dispersion process of PdO was revealed from the comparison with findings on H-ZSM-5 and Na-ZSM-5. Namely, the transformation of metal Pd-Pd into Pd-O was sharp and occurred at lower temperature over the H-ZSM-5 with respect to on the Na-ZSM-5. Taking this fact into account, it could be supposed that, in addition to the spontaneous dispersion of PdO, the oxidation of metal Pd was promoted through a strong metal-support interaction between acid sites of H-ZSM-5 and PdO, which possessed basic character. The disappearance of metal Pd-Pd and the alternative growth of Pd-O accelerated over H-ZSM-5 with respect to that for H-Mordenite. Thus it could be noted that the dispersion of Pd on H-ZSM-5 was easier than that of Pd/H-Mordenite. Probably, the pore structure of zeolite or the character of acid center affected the oxidation and migration process of Pd.

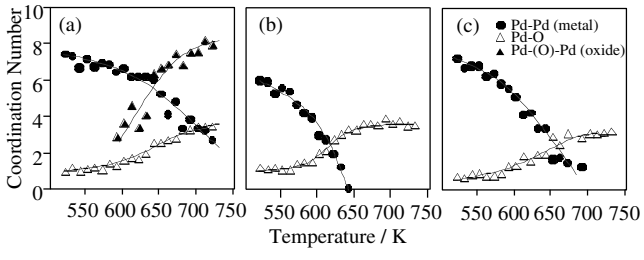

Fig. 2. Dependence of coordination number on temperature for Pd loaded on (a) Na-ZSM-5, (b) H-ZSM-5, (c) H-Mordenite measured during temperature programmed oxidation with O_2.

3.2. *Generation of metal Pd cluster in zeolites [7]*

In order to elucidate the clustering process of metal Pd in zeolite, DXAFS was measured every 10 K during the temperature programmed reduction (TPR) of Pd. Three kinds of zeolites, namely Na-ZSM-5, H-Mordenite and H-Y, were used as supports for Pd. The samples were preliminarily oxidized in an O_2 flow at 773 K for 4 h. After cooling to room temperature, an 8% H_2 flow was introduced to the *in situ* cell. Figure 3 gives the Fourier transforms of DXAFS spectra measured during TPR. After the oxidation pretreatment of Pd/Na-ZSM-5, the generation of agglomerated PdO was confirmed from the appearance of Pd-(O)-Pd peak at 0.3 nm in Fourier transform, which is characteristic of bulk PdO. In contrast, highly dispersed PdO was generated on H-Mordenite and H-Y type zeolites, no Pd-(O)-Pd peak was observed in the spectra of these zeolites. Then the flowing gas was switched to H_2 (8%) and the TPR measurement was conducted. The coordination numbers (CN) of nearest-neighboring Pd-Pd peaks calculated based on the curve-fitting method are summarized in Figure 4. In the beginning of the TPR over Pd/Na-ZSM-5, the formation of agglomerated Pd metal was already confirmed from the appearance of an intense Pd-Pd (metal) peak. The diameter of the agglomerated metal Pd could be estimated to 2 nm. The CN gradually increased with increasing reduction temperature from room temperature to 773 K. This fact indicated that the simple sintering and growth of metal Pd particles progressed when raising the temperature. However the feature

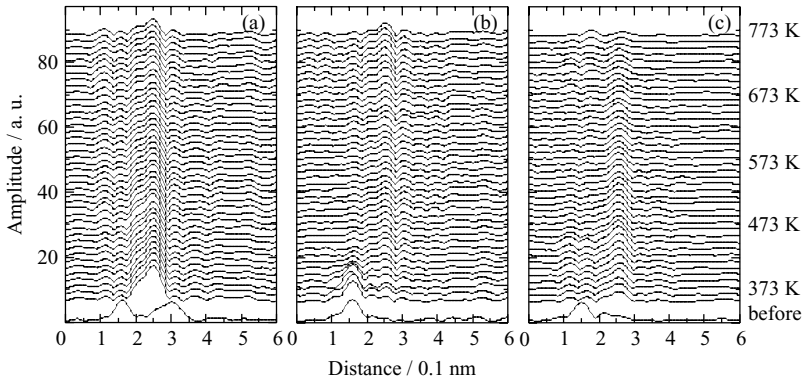

Fig. 3. Pd K-edge EXAFS Fourier transforms for Pd loaded on (a) Na-ZSM-5, (b) H-Mordenite, (c) H-Y measured in an 8% H_2 flow; Pd loading, 0.4 wt%; Temperature ramping rate, 5 K min^{-1}.

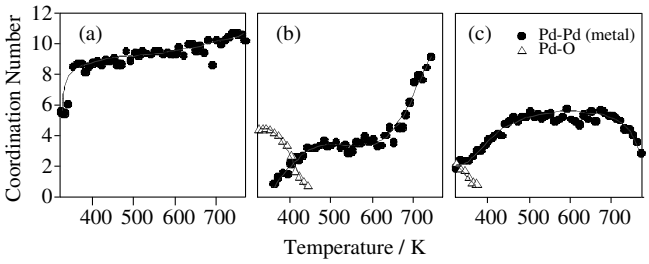

Fig. 4. Dependence of coordination number on temperature for Pd loaded on (a) Na-ZSM-5, (b) H-Mordenite, (c) H-Y measured during temperature programmed reduction with H_2.

of Pd loaded on H-Mordenite was considerably different from that of Pd/Na-ZSM-5 (Figure 4(a)). A slight increase in Pd-Pd was observed between 363 K and 443 K. At the same time, the reduction of PdO into Pd^0 proceeded, which could be seen from the reduction of the Pd-O peak. After the completion of the reduction, a plateau could be observed in the temperature range between 443 and 623 K. This suggests the generation of stable metal Pd clusters in the pore of H-Mordenite. From the Pd-Pd coordination number, the Pd cluster was estimated to be composed of 6 atoms. A similar phenomenon was observed on Pd/H-ZSM-5 ($Si/Al_2 = 23.8$).

Figure 4(c) shows CN plotted as a function of temperature for reduction of Pd loaded on H-Y type zeolites. The CN of Pd-Pd increased in the temperature range between 323 K and 503 K. Alternatively, the Pd-O bond decreased, suggesting the reduction of PdO progressed at this temperature similarly to the Pd/H-Mordenite case. After completion of the reduction, the CN of Pd-Pd became constant between 463 K and 673 K. Therefore, the generation of stable Pd metal cluster was suggested in the temperature region. Judging from the CN of nearest-neighboring Pd-Pd bond, the size of stable metal Pd in H-Y was slightly larger than those observed in H-ZSM-5 and H-Mordenite. Interestingly, further raising the temperature resulted in the decrease of CN of nearest-neighboring Pd-Pd. After the treatment of Pd/H-Y at 773 K, highly dispersed metal Pd cluster composed of three Pd atoms was generated. The fact was confirmed from the EXAFS data measured at room temperature. The tendency was different from those observed on other zeolites, namely Pd/Na-ZSM-5 and H-Mordenite, which exhibited simple agglomeration and the growth of metal Pd at high temperature above 673 K.

4. Conclusions

DXAFS technique was successfully applied for the measurement of dynamic structural change of Pd induced by the interaction of zeolite support and Pd. Firstly, we observed the spontaneous dispersion process of PdO over acid sites of H-ZSM-5 and H-Mordenite. On these zeolites the dispersion of PdO and oxidation of Pd took place at the same time, which was considerably different from the oxidation process observed on Pd loaded on Na-ZSM-5. Secondly, we observed the generation of stable metal Pd clusters in H-Mordenite and H-Y zeolites after the completion of the reduction. The phenomenon was quite different from that of Pd loaded on Na-ZSM-5, which had no acid sites.

References

1. Okumura, K. and Niwa, M., Catal. Survey Japan **5**, 121 (2002).
2. Chin, Y. H. and Resasco, D. E., in "Catalysis", Vol. 14 (Royal Society of Chemistry, London, 1999).
3. Okumura, K., Amano J. and Niwa, M., J. Phys. Chem. B **104**, 1050 (2000).
4. Okumura, K., Amano, J. and Niwa, M., J. Phys. Chem. B **104**, 9670 (2000).
5. Van Zon, J. B., Koningsberger, D. C., Van Blik, H. F. J. and Sayers, D. E., J. Phys. Chem. **82**, 5742 (1985).
6. Okumura, K., *et al*., Chem. Lett. **32**, 636 (2003).
7. Okumura, K., *et al*., J. Phys. Chem. B **108**, 6250 (2004).

Physica Scripta. Vol. T115, 819–821, 2005

X-ray Absorption Spectroscopy on Cu/ZnO Catalysts Selected by High-Throughput Experimentation Techniques

J.-D. Grunwaldt[1,*], C. Kiener[2], F. Schüth[2] and A. Baiker[1]

[1]Institute for Chemical- and Bioengineering, Swiss Federal Institute of Technology, ETH Hönggerberg, CH-8093 Zürich, Switzerland
[2]Max-Planck-Institut für Kohlenforschung, Kaiser-Wilhelm-Platz 1, D-45470 Mülheim a. d. Ruhr, Germany

Received June 26, 2003; accepted November 4, 2003

PACS number: 61.10.Ht

Abstract

CuO/ZnO catalysts, prepared in an automated synthesis by coprecipitation, were tested for methanol synthesis by high throughput screening using a 49-channel parallel flow reactor. The activity strongly depended on the preparation conditions and the calcination temperature. Interesting samples were selected for deeper characterization by EXAFS including *in situ* spectroscopic studies during temperature programmed reduction. Both ageing time and calcination temperature had a strong influence on the reduction behaviour of CuO/ZnO samples and thus resulted in an altered catalytic activity. In all cases, only a small fraction of Cu(I) species was formed during reduction.

1. Introduction

X-ray absorption spectroscopy is known to be a powerful technique in catalysis research. It does not only provide structural information on the crystalline phases but also gives (element-specific) information on the amorphous part of the catalyst [1–5]. In addition, structural transformations of solid catalysts both in gaseous or liquid reaction environment can be studied *in situ* and in a time-resolved manner [4–7], which allows to establish structure-activity relationships.

High-throughput experimentation (HTE)-technology for the preparation of heterogeneous catalysts using synthesis robots and multichannel parallel flow reactor systems has emerged as a powerful tool in catalysis research in recent time [8–11]. The method is effective to screen catalysts with respect to composition or preparation parameters.

Although a number of materials can be produced and tested using both synthesis robots and parallel reactor technology, this approach cannot substitute a rational design of catalysts, considering that the number of materials to be prepared is principally unlimited. Therefore, a combination of both approaches seems most promising. A structural characterization of all samples tested would be extremely time-consuming. More efficient is the selection of samples with distinct properties, as indicated from pre-characterization and catalytic tests for gaining structure-activity relationships. In this contribution, we illustrate how the EXAFS technique can contribute to this strategy.

For this purpose, the Cu/ZnO system is a well-suited example. During the past years it has been thoroughly investigated [12–19], also with respect to preparation parameters (composition, pH dependence of precipitation, calcination temperature, ageing). In particular, calcination and ageing seem to play a crucial role. Testing of the catalyst samples usually takes about one week considering the activation and equilibration time and thus parallel testing is advantageous. The future role of EXAFS in this area is discussed in this contribution.

2. Experimental

2.1. *Catalyst preparation and testing*

Automated synthesis and a 49-fold parallel reactor system, applicable at elevated pressure (50 bar), were used for the preparation of the samples and for activation/catalytic testing in methanol synthesis, respectively. The principal procedure is shown in Figure 1. Catalysts were precipitated at constant pH. During ageing, the pH just recorded and samples were taken from the suspension at certain times. More detailed information on the preparation procedure and the catalyst testing conditions can be found in ref. [20]. The prepared samples were characterized by X-ray diffraction, thermal analysis, and for selected samples reactive frontal chromatography was used to determine the copper surface area.

2.2. *X-ray absorption spectroscopy*

Reduction of the Cu/ZnO samples is an important feature in the understanding of the catalytic performance of the catalysts, which can be monitored with respect to Cu^{II}, Cu^{I} and Cu^{0}-species with X-ray absorption near edge structure. The XAS experiments were performed at beamline BM1B (Swiss-Norwegian Beamline) at ESRF (Grenoble, France) and at ANKA-XAS (Karlsruhe, Germany) in a reactor for pellet-shaped samples. Pellets with diameter of 13 mm and thickness of 1.5 mm were pressed from finely ground catalyst diluted with boron nitride and loaded in an *in situ* reactor cell with X-ray transparent windows and oven. The XAS data were obtained in transmission geometry using a Si(111) monochromator in both cases and EXAFS and XANES data were taken around the Cu K-edge (8.979 keV). The fraction of Cu^{II}, Cu^{I}

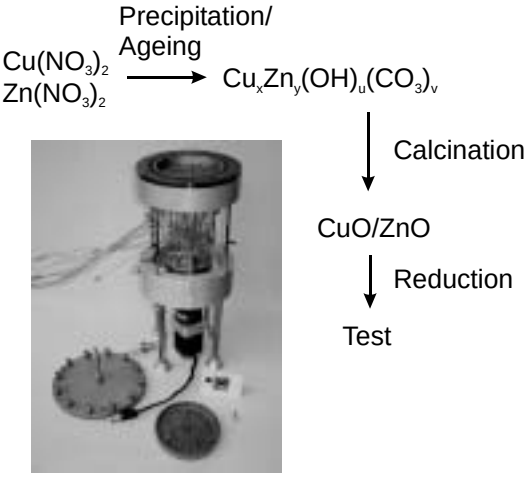

Fig. 1. Synthesis procedure of Cu/ZnO catalysts used in high throughput screening activity tests at 50 bar (picture depicts 49-fold high throughput reactor).

*e-mail: grunwaldt@tech.chem.ethz.ch

and Cu^0-species was determined by linear combination analysis (LCA).

3. Results and Discussion

Figure 2 gives an overview on the catalytic performance of selected catalysts calcined at different temperatures and aged for different time intervals. In particular, the ageing time turned out to be an important parameter in the synthesis process.

It shows that there are extreme dependencies on the ageing times of the (Cu,Zn)-hydroxycarbonate precipitates. In addition, calcination of the samples was necessary before activation by the reduction in hydrogen. One interesting series turned out to be the differently aged samples precipitated at pH 8.5 and calcined at a temperature of 330 °C. With increasing ageing time the methanol production rate first increased, but at very long ageing times the activity decreased again.

The typical reduction behaviour of sample 1 in Figure 2 is depicted in Figure 3 while the data of all five selected samples are gathered in Figure 4. It turned out that the fraction of formed Cu^I was relatively low (<10%) and that the formation of Cu^0 started right from the beginning. This can also be concluded from the fact that the pre-edge feature at 8.879 keV, typical for Cu^0, principally appeared just when the reduction started. These observations were similar for all five selected samples and thus the reduction directly to Cu^0 is fast, as also concluded in previous publications [4, 21, 22]. The reduction temperature is, however, strikingly different depending on the ageing time. The two most active samples, 3 and 4, are reduced at lower temperature than the less active samples. In all cases, a small fraction of Cu(I) species (<10%) occurs as intermediate from the beginning of the reduction until its end. This trend that in the more active catalysts copper is easier reduced has also been found for further catalysts in Figure 2. For the most active samples 3 and 4 we observe a higher reduction temperature for the more active sample. This may be due to a change in phase composition and will be investigated in further detail since the copper surface area increases slightly from sample 3 to 4. Note that a too long ageing time results in a catalyst with low activity, as it does for short ageing times. The EXAFS analysis

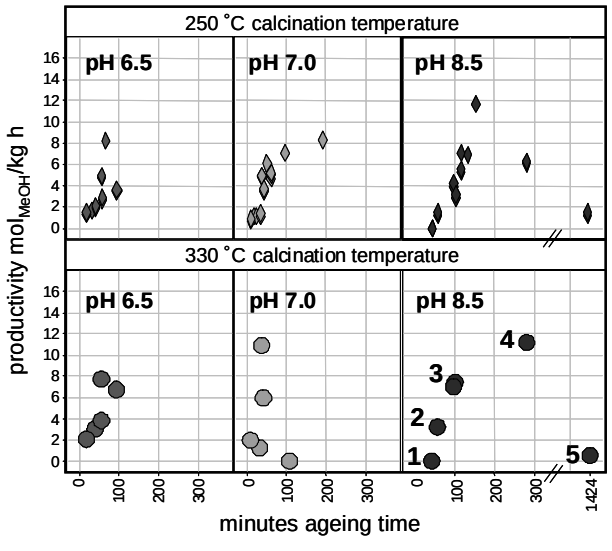

Fig. 2. Effect of ageing time, different starting pH values and calcination temperatures (trapezoid: 250 °C, circle: 330 °C) on catalyst activity dependence. All samples were tested by high throughput screening. Samples of pH 8.5/330 °C were chosen for detailed studies.

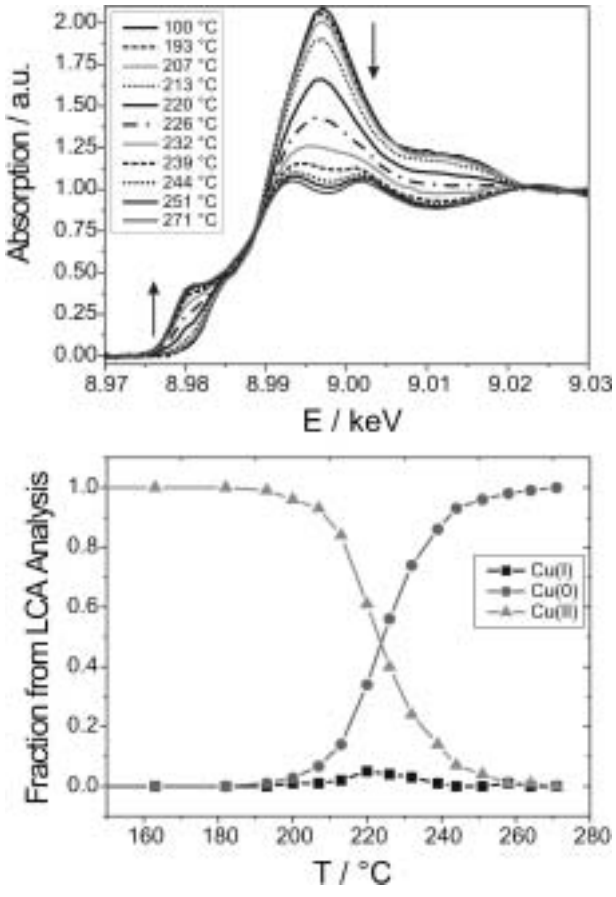

Fig. 3. Reduction of a CuO/ZnO sample monitored by *in situ* EXAFS and the analysis of the copper species by linear combination analysis (LCA).

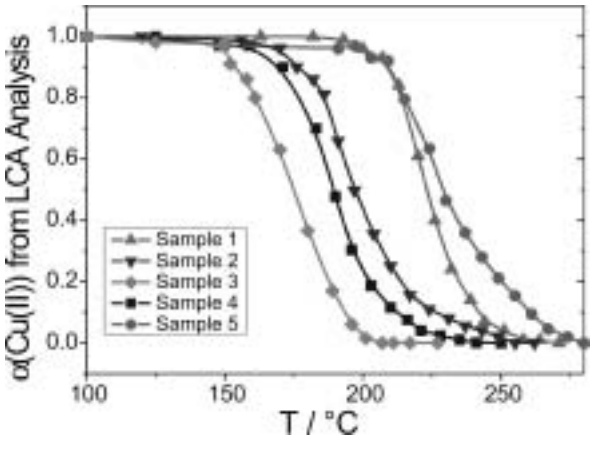

Fig. 4. Reduction behaviour of the 5 selected samples marked in Figure 2 (from starting pH 8.5/330 °C calcination). High activity was found for those samples, which are reduced at low temperature.

of all samples after reduction uncovered the presence of relatively large Cu particles with a coordination number of nearly 12 and a typical Cu-Cu distance of 2.55 Å. This is not surprising, since the copper loading is relatively high (typical for commercial catalysts) in comparison to previous EXAFS studies on Cu/ZnO model catalysts [4]. In previous temperature-programmed reduction experiments it was speculated that ZnO promotes the reduction of CuO [15]. The combined activity/characterization results indicate that the behaviour is more complex. It obviously depends on the phases formed during the ageing process and also the CuO-ZnO interface. Their formation is probably kinetically controlled

during the preparation process [13], i.e. in the beginning the formation of separate copper hydroxide and zinc hydroxide or hydroxycarbonates could be favoured while after longer ageing periods the formation of mixed hydroxides or hydroxycarbonates is preferred. Too long ageing periods probably lead to more crystalline samples that are more difficult to reduce than the amorphous or microcrystalline materials.

4. Conclusions and Outlook

The study shows that the catalytic activity is strongly dependent on different preparation parameters. A systematic approach can only be achieved by thorough catalyst testing and the use of automated synthesis procedures to guarantee reproducibility. The proper characterization of some selected series can lead to a more fundamental understanding. Combination with EXAFS is a useful approach since it can give direct information on the structure and the temperature controlled reduction mechanism. It turned out that a low reduction temperature is beneficial for the final activity, but not the only criterion. Hence, the studies are presently extended by combination with further characterization methods.

Acknowledgements

We gratefully acknowledge beamtime at the Swiss-Norwegian Beamline at ESRF (Grenoble) and at the ANKA-XAS beamline (Karlsruhe). The support by the beamline staff at SNBL (H. Emmerich, W. van Beek) and at ANKA-XAS (J. Göttlicher) is greatfully acknowledged. Moreover, we thank S. Hannemann for help during the EXAFS measurements and ESRF, ETH Zürich and OFG (SFB 558TP B2) for financial support.

References

1. Koningsberger, D. C. and Prins, R., "X-ray Absorption: Principles, Applications, Techniques of EXAFS, SEXAFS, and XANES" (Wiley: New York, 1988).
2. Iwasawa, Y., "X-ray absorption fine structure for catalysts and surfaces" (World Scientific: Singapore, 1996).
3. Thomas, J. M. and Sankar, G., J. Synchr. Rad. **8**, 55 (2001).
4. Clausen, B. S., Catal. Today **39**, 293 (1998).
5. Grunwaldt, J.-D. and Clausen, B. S., Topics Catal. **18**, 37 (2002).
6. Dent, A. J., Topics Catal. **18**, 27 (2002).
7. Grunwaldt, J.-D., Keresszegi, C., Mallat, T. and Baiker, A., J. Catal. **213**, 191 (2003).
8. Moates, F. C. *et al*., Ind. Eng. Chem. Res. **35**, 4801 (1996).
9. Cong, P. *et al*., Angew. Chem. Int. Ed. **38**, 483 (1999).
10. Senkan, S., Angew. Chem. **113**, 322 (2001).
11. Schüth, F. *et al*., Topics Catal. **21**, 55 (2002).
12. Klier, K., Adv. Catal. **31**, 243 (1982).
13. Chinchen, G. C., Denny, P. J., Jennings, J. R., Spencer, M. S. and Waugh, K. C., Appl. Catal. **36**, 1 (1988).
14. Clausen, B. S. *et al*., Topics Catal. **1**, 367 (1994).
15. Fierro, G. *et al*., Appl. Catal. A **137**, 327 (1996).
16. Grunwaldt, J.-D. *et al*., J. Catal. **194**, 452 (2000).
17. Günter, M. M., *et al*., Catal. Lett. **71**, 37 (2001).
18. Hansen, P. L. *et al*., Science **295**, 2053 (2002).
19. Bems, B. *et al*., Chemistry Eur. J. **9**, 2039 (2003).
20. Kiener, C. *et al*., J. Catal. **216**, 110 (2003).
21. Grunwaldt, J.-D. *et al*., J. Phys. Chem. B **105**, 5161 (2001).
22. Günter, M. M. *et al*., J. Sync. Rad. **8**, 619 (2001).

Physica Scripta. Vol. T115, 822–824, 2005

In Situ X-Ray Absorption Fine Structure Studies on the Structure of Ni_2P Supported on SiO_2

T. Kawai[1*], S. Sato[1], W.-J. Chun[1,2], K. Asakura[1], K.-K. Bando[3], T. Matsui[3], Y. Yoshimura[3], T. Kubota[4], Y. Okamoto[4], Y-K. Lee[5] and T. S. Oyama[5]

[1]Catalysis Research Center, Hokkaido University and [2]CREST, JST, Sapporo 060-0811, Japan
[3]National Institute of Advanced Industrial Science and Technology, Tsukuba, 305-8562, Japan
[4]Department of Material Science, Interdisciplinary Faculty of Science and Engineering, Shimane University, Matsue, 690-8504, Japan
[5]Environmental Catalysis and Materials Laboratory, Departments of Chemical Engineering and Chemistry, Virginia Polytechnic Institute and State University, Blacksburg, Virginia 24061-0211, USA

Received June 26, 2003; accepted November 3, 2003

Abstract

The local structure around Ni in a nickel phosphide catalyst supported on SiO_2 was investigated by an *in situ* X-ray absorption fine structure (XAFS) method during the reduction process of the catalyst and the hydrodesulfurization (HDS) reaction of thiophene. In the passivated sample, the Ni phosphide was partially oxidized but during the reduction process Ni_2P particles were regenerated. The particles had Ni-P and Ni-Ni distances of 0.220 and 0.259 nm, respectively, corresponding closely to those of bulk Ni_2P. *In situ* XAFS clearly revealed that Ni_2P structure was stable under the reaction conditions at atmospheric pressure and was an active structure for the HDS process.

1. Introduction

Regulations for S content in petroleum feedstock have become increasingly more severe year by year. For this reason there is great interest in the development of highly active hydrodesulfurization (HDS) catalysts. It has recently been found that metal phosphides show high activity for the HDS reaction [1]. A survey of different phosphides shows that Ni_2P is the most active compound for HDS [2]. When the Ni phosphide was supported on SiO_2, the activity and the lifetime were much improved. In this work we investigated the structure of Ni phosphides on a SiO_2 support by *in situ* XAFS spectroscopy during the preparation and the reaction processes.

2. Experimental

The Ni phosphide supported on SiO_2 (Cabosil L90, Cabot corporation, $90\,m^2\,g^{-1}$) was prepared by the reduction of Ni phosphate on SiO_2 [2]. The SiO_2 was impregnated with nickel nitrate and ammonium phosphate, followed by calcination at 773 K for 6 hours to give nickel phosphate. The SiO_2-supported nickel phosphate was reduced to Ni phosphide by means of temperature-programmed reduction (TPR) in H_2 flow using a heating rate of 5 K/min up to 773 K. After the reduction, the catalyst was passivated in 1% O_2/He at room temperature to protect the particle from bulk oxidation and was stored in Ar atmosphere. The passivated sample was then placed in a XAFS measurement cell [3] in a N_2-filled glove box and reduced again to activate the sample. The reduction was carried out in a temperature programmed manner with a ramping speed of 5 K/min up to 723 K under a H_2 flow. The reduction process was monitored by XANES spectroscopy. After the reduction, the sample was cooled down to 323 K and the EXAFS spectrum was measured in order to identify the active structure. The thiophene hydrodesufurization reaction was carried out at 573 K in a H_2 + thiophene mixture. (H_2 flow rate = 42 ml/min, thiophene flow rate = 1.3 ml/min.)

XAFS measurements were carried out at BL9A of Photon Factory (KEK-IMSS-PF) operated at 2.5 GeV and 300 mA. The X-ray was monochromatized by a Si(111) double crystal and focused on the sample using a bent conical mirror. Obtained XAFS data were analyzed by REX2000 (RIGAKU Co.) software [4] using theoretical standards calculated by FEFF 8.2 [5].

3. Results

Fig. 1 shows the EXAFS oscillation and the Fourier transform of a Ni_2P standard compound. The coordination numbers for Ni-O and Ni-Ni were determined to be 2.5 and 7, respectively. Fig. 2 shows the EXAFS oscillation and its Fourier transform of the passivated catalyst before reduction. The EXAFS oscillation is different from that of the Ni_2P standard compound, especially in the low *k*-region. The Fourier transform gives two peaks resembling that of the Ni_2P standard compound but the first peak is shifted to the low *r* side. Curve fitting analysis shows correspondence to a Ni-O bond distance (0.201 nm) in addition to the Ni-P (0.232 nm) and Ni-Ni (0.265 nm) distances. Thus during the passivation process, the Ni phosphide particle on the SiO_2 support was partially oxidized, probably only in the surface region. Fig. 3 shows the XANES spectra of the sample before and after the reduction. The first strong edge peak, indicating the presence of Ni-O, was

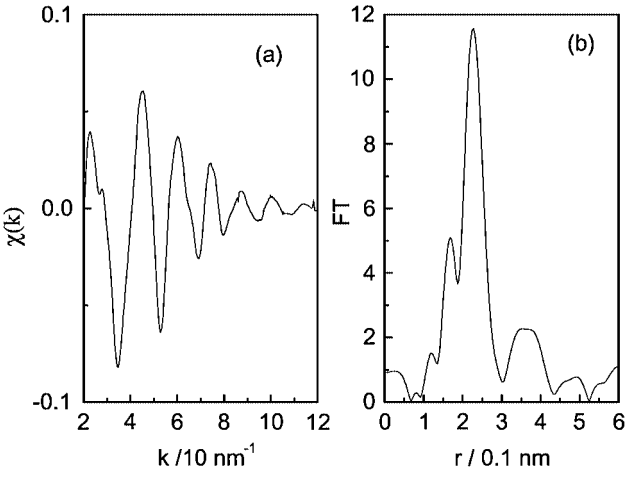

Fig. 1. EXAFS oscillation of Ni_2P powder (a) and its k^3-weighted Fourier transform (b).

*e-mail kawai@cat.hokudai.ac.jp

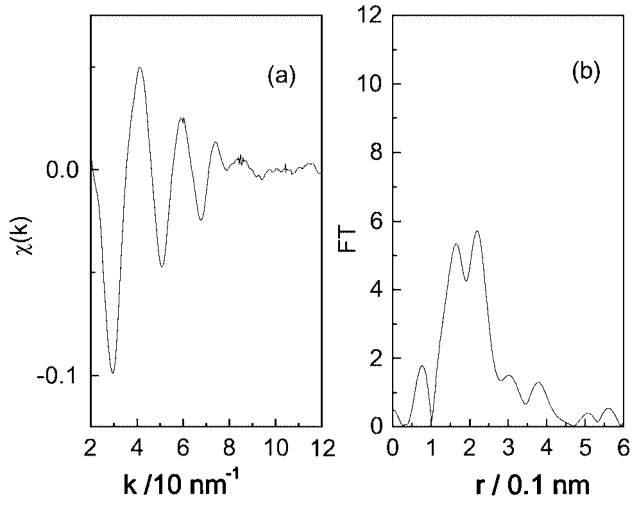

Fig. 2. EXAFS oscillation of Ni_2P powder SiO_2 (a) and its k^3-weighted Fourier transform (b).

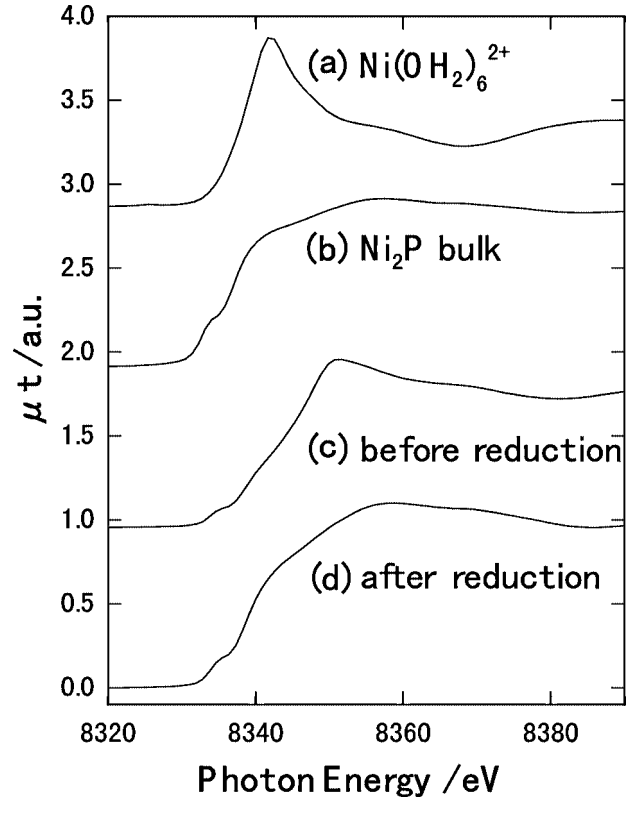

Fig. 3. XANES spectra of references and Ni_2P/SiO_2. (a) $Ni(OH_2)_6^{2+}$, (b) Ni_2P bulk, (c) before reduction (passivated sample) and (d) after reduction.

completely removed by the reduction process. We followed the reduction process by monitoring the sample with *in situ* XANES. Fig. 4 shows the *in situ* XANES traces in the course of the reduction process. Changes in the XANES traces start at 350 K. The reduction proceeds gradually and is completed at about 500 K. In the passivated sample, only the surface region is oxidized and is reduced easily. Fig. 5 shows the EXAFS oscillation and its Fourier transform of the sample after the reduction, and it can be seen that they are very similar to those of the Ni_2P standard compound shown in Fig. 1, indicating that the Ni_2P structure is generated by the reduction process. Ni-P and Ni-Ni bonds are found at 0.220 nm and 0.260 nm, respectively. The coordination numbers for Ni-P and Ni-Ni are 2.5 and 6.2, respectively. Assuming a spherical

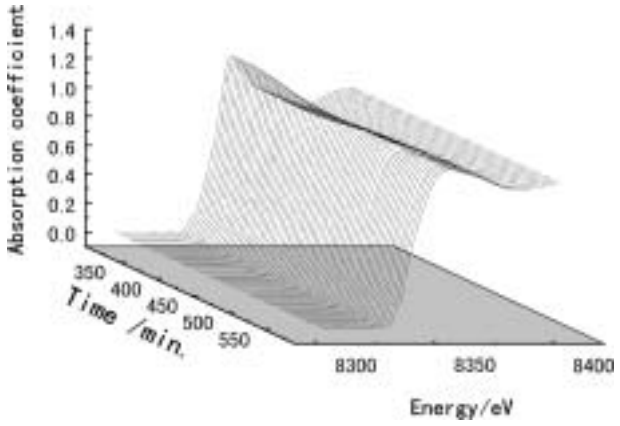

Fig. 4. Series of XANES spectra taken during the reduction process in a quick scan mode. Temperature ramping rate = 5 K/min.

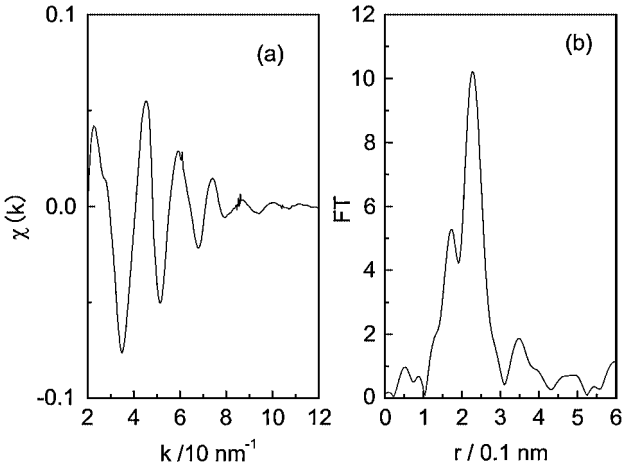

Fig. 5. EXAFS oscillation of Ni phosphide on SiO_2 after reduction (a) and its k^3-weighted Fourier transform (b).

shape of the Ni_2P particle [6], we calculated the particle-size dependence of coordination numbers. Comparing the observed and calculated values, the particle sizes are estimated to be 7.0 nm well corresponding to TEM results (10 nm).

The Ni_2P was heated up to a temperature at 573 K (reaction temperature) and employed in the thiophene HDS reaction. Fig. 6 shows the EXAFS oscillations just before the reaction and 2 hours after the start of reaction. Both XAFS oscillations are reduced

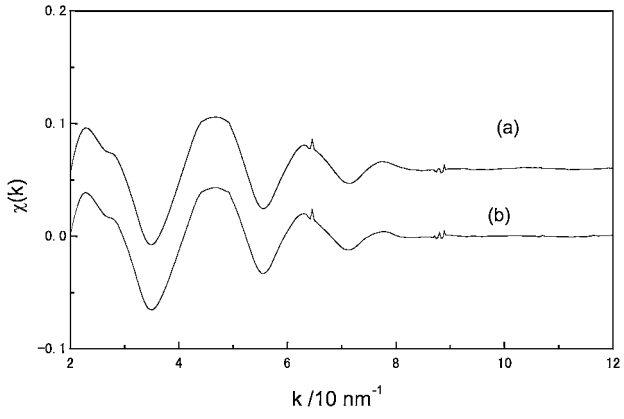

Fig. 6. EXAFS oscillations of Ni phosphide on SiO_2 before the HDS reaction (a) and 2 hours after the start of reaction.

in their amplitude due to the thermal disorder. However, the main features of Ni_2P are maintained after heating to 573 K. We find that little change occurs between the two spectra. Thus the Ni_2P structure is stable during the thiophene HDS reaction.

4. Conclusions

1. Ni phosphides are partially oxidized during the passivation process.
2. The passivated Ni phosphide is easily reduced by H_2 at 350–500 K.
3. The reduced catalyst consists of Ni_2P crystallites with size around 7 nm.
4. The Ni_2P structure is stable during the thiophene HDS reaction.
5. The Ni_2P is an active structure for HDS reaction.

Acknowledgment

This work was financially supported by NEDO International Joint Research Program (01EF1), and the U.S. Department of Energy, Office of Basic Energy Sciences, through Grant DE-FG02-963414669. The authors would like to express their gratitude to the PF staffs, especially to Prof. M. Nomura, Dr. N. Usami and Dr. A. Koyama for their technical supports.

References

1. Li, W., Dhandapani, B. and Oyama, S. T., Chem. Lett. 207 (1998).
2. Oyama, S. T., Wang, X., Requejo, F. G., Sato, T. and Yoshimura, Y., J. Catal. **209**, 1 (2002).
3. Bando, K. K., Saito, T., Kato, K., Tanaka, T., Dumeignil, F., Imamura, M., Matsubayashi, N. and Shimada, H., J. Synchrotron Rad. **8**, 581 (2001).
4. Asakura, K., "X-ray Absorption Fine Structure for Catalysts and Surfaces," ed. By Y. Iwasawa, World Scientific, Singapore (1996), p. 33.
5. Ankudinov, A. L., Ravel, B., Rehr, J. J. and Conradson, S. D., Phys. Rev. B **58**, 7565 (1998).
6. Sawhill, S. J., Phillips, D. C. and Bussell, M. E., J. Catal. **215**, 208 (2003).

Physica Scripta. Vol. T115, 825–827, 2005

Structural Analysis of Photo-Chemically Anchored Molybdenum Oxide Catalysts by EXAFS

H. Murayama[1], N. Ichikuni*[1], K. K. Bando[2], S. Shimazu[1] and T. Uematsu[1]

[1]Department of Materials Technology, Faculty of Engineering, Chiba University, Chiba 263-8522, Japan
[2]National Institute of Advanced Industrial Science and Technology, Tsukuba 305-8565, Japan

Received June 26, 2003; accepted February 6, 2004

PACS number: 82.65+r

Abstract

Silica supported molybdenum oxide catalysts were prepared from Mo dimer complex ($Mo_2(CH_3CO_2)_4$) by using photochemical anchoring (PCA) method. The local environments of Mo atoms on both attached and oxidized catalysts were investigated by Mo K-edge EXAFS, XANES, Raman spectroscopy and thermal gravimetric analysis. The bond distance between dimeric Mo atoms could be changed depending on the energy of UV irradiation. By using the lower irradiation energy ($\lambda > 350$ nm), the attached structure was close to the original Mo dimer complex. After oxidation of the catalyst, dimeric structure was formed with bridging oxygen and the Mo-(O)-Mo bond distance was 0.316 nm. On the other hand, in the case of higher irradiation energy ($\lambda > 250$ nm), the Raman spectrum of the attached catalyst had bands due to acetate ligands except a band at 405 cm^{-1} due to Mo-Mo skeleton bond. It means that $Mo_2(CH_3CO_2)_4$ is decomposed by UV irradiation. The oxidized form of the higher energy irradiated catalyst showed monomer-pair structure.

1. Introduction

Compounds of group V, VI and VII transition metals, particularly Mo, V, Re and W compounds, are widely used as catalysts for various reactions in industry such as metathesis of hydrocarbons [1–6]. Local structure of metal oxide is one of the most important parameters, which determines the activity. Anchoring metal oxide on support enables to design the local structure around active sites and to increase the number of active sites. Wide varieties of preparation methods, precursors and supports have been investigated in order to control the local structures [7]. For instance, $VOCl_3$ is attached to porous Vycor glass by using UV irradiation. Photo-activated $VOCl_3$ reacts with OH group on the Vycor glass surface. Since this reaction occurs quantitatively at room temperature, vanadium oxides are not aggregated. Vanadium oxides are attached uniformly with high dispersion [8]. Grafting of organometallic di- and tri-nuclear cluster complexes, such as $Mo_2(CH_3CO_2)_4$ and $Mo_3O(CCH_3)(CH_3CO_2)_6(CH_3OH)_3Cl$ to mesoporous FSM-16 generate dimer and trimer structure of Mo oxide, respectively [9, 10].

In this study, light sensitive $Mo_2(CH_3CO_2)_4$ was anchored on silica under UV irradiation. It is expected that the local structures of Mo oxides can be finely designed by controlling the irradiation energy. Local structures of catalysts for each preparation step were determined by using XAFS spectroscopy. Structural difference caused by irradiation energy was compared and discussed.

2. Experimental

5 wt% Mo/SiO_2 catalysts were prepared *in vacuo* by mixing without solvents (solid-solid reaction) in a quartz reactor under UV irradiation (photo-chemical anchoring (PCA) method). The UV irradiation was carried out by a 75 W high pressure Hg lamp through a UV cut-filter ($\lambda > 350$ nm) or without filter ($\lambda > 250$ nm) at room temperature for 1 h. The catalysts were designated with UV irradiation wavelength as PCA35 and PCA25, respectively. PCA35 and PCA25 catalysts were treated with H_2, followed by O_2 at 473 K for 1 h to convert into oxide form denoted as PCA35-ox and PCA25-ox, respectively.

The structures of the catalysts were characterized by X-ray absorption fine structure (XAFS), Raman spectroscopy, and thermal gravimetric analysis (TG). Mo K-edge XAFS measurements were carried out at BL-10B in the IMSS-PF, Tsukuba, Japan (Proposal No. 2000G286). The spectra were collected at room temperature in transmission mode with a Si(311) channel cut monochrometer by using two ion-chambers filled with (50% Ar + 50% N_2) and (100% Ar) for I_0 and I, respectively. The pretreated samples were sealed in an Al cell with Kapton windows in order to protect from contact with air. Coordination number (CN) and atomic distance (r) were evaluated by curve-fitting analysis in k-space using the REX2000 program (Rigaku Co.). Standard reference materials, Mo foil, MoO_3 and K_2MoO_4 were used to extract back scattering amplitude and phase shift function for Mo-Mo, bridging Mo-O and terminal Mo=O bonding, respectively. Raman spectra were taken with the 514.5 nm line of an Ar^+ laser on a JASCO NRS-2100 laser Raman spectrometer, and detected by a CCD cooled at 77 K. Samples were sealed in a quartz cell in order to protect from contact with air.

3. Results and discussions

The Mo K-edge XANES spectra can provide information on the local structural symmetry about X-ray absorbing Mo atoms. The peak positions of Mo K-edge XANES spectra were 20020.5 eV for PCA25, 20021.6 eV for PCA35, and 20022.2 eV for $Mo_2(CH_3CO_2)_4$. The peak position and the near-edge feature of PCA35 were close to those of $Mo_2(CH_3CO_2)_4$. However, the peak position of PCA25 was shifted to lower energy and the near-edge feature was gentler than that of $Mo_2(CH_3CO_2)_4$, suggesting that the average electronic structure and site symmetry around Mo atoms in the PCA25 were different from those in $Mo_2(CH_3CO_2)_4$.

Raman bands due to acetate ligands of $Mo_2(CH_3CO_2)_4$ were observed at 691, 951 and 1434 cm^{-1} [11] in both spectra of PCA25 and PCA35. In addition, a band at 405 cm^{-1} due to the Mo-Mo multiple bond of Mo dimer complex [11] was observed in the PCA35, but not in the PCA25.

The weight loss is 11.7% if all acetate ligands are released from 5 wt% $Mo_2(CH_3CO_2)_4/SiO_2$. The gap between the weight loss of all acetate ligands (11.7 wt%) and the observed weight loss by TG measurements for PCA25 and PCA35 (5.79 and 11.01 wt%, respectively) was assigned to the lost of acetate ligands by photo-decomposition. Thus, the number of acetate

*e-mail: ichikuni@faculty.chiba-u.jp

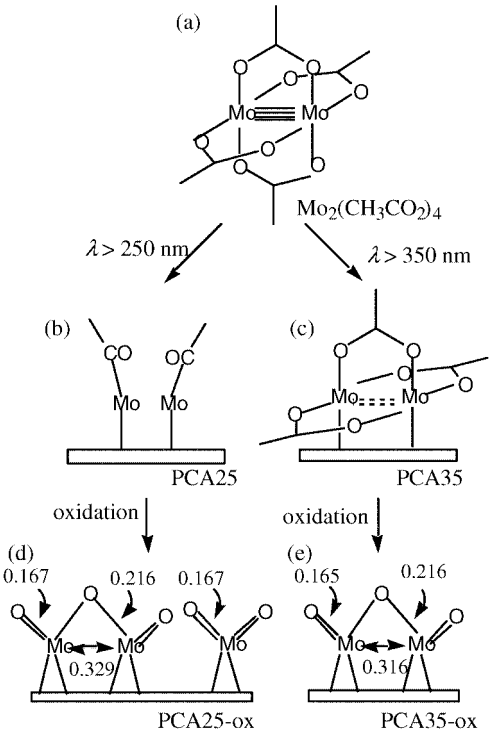

Fig. 1. Proposed structures of Mo species obtained by PCA process; (a) original Mo dimer complex, (b) PCA25, (c) PCA35, (d) PCA25-ox and (e) PCA35-ox.

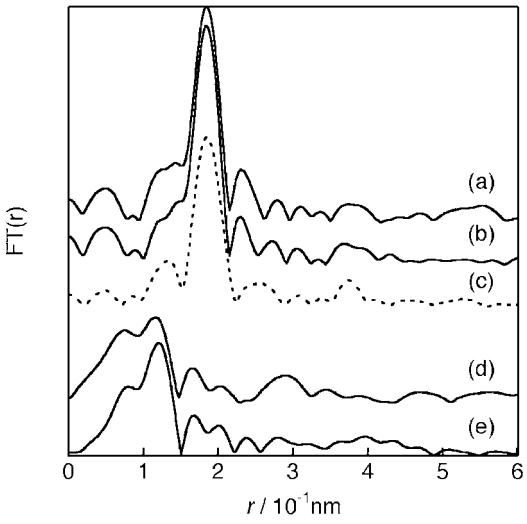

Fig. 2. Fourier transforms of EXAFS spectra for the original dimer complex and the catalysts; (a) PCA25, (b) PCA35, (c) $Mo_2(CH_3CO_2)_4$, (d) PCA25-ox and (e) PCA35-ox.

Table I. *Curve-fitting results for $Mo_2(CH_3CO_2)_4$, PCA25 and PCA35.*

compound	coordination	CN	r/nm	DW/nm
PCA25	Mo-O	3.3	0.221	0.0035
	Mo-Mo	0.5	0.239	0.0090
PCA35	Mo-O	3.5	0.219	0.0056
	Mo-Mo	0.9	0.211	0.0068
$Mo_2(CH_3CO_2)_4$	Mo-O	4.0	0.220	0.0066
	Mo-Mo	1.0	0.212	0.0082

ligands remaining on the PCA25 and PCA35 was 0.33 and 3.56, respectively.

The above results of XANES, Raman and TG measurement reveal that the degree of photo-decomposition of $Mo_2(CH_3CO_2)_4$ depends on the energy of UV irradiation. The structure models of PCA25 and PCA35 were proposed as Figure 1(b) and (c). PCA35 kept an original Mo-Mo skeleton with three acetate ligands. On the other hand, most acetate ligands were removed by photo-decomposition with higher UV energy ($\lambda > 250$ nm).The structure of PCA25 is different from $Mo_2(CH_3CO_2)_4$.

Crucial information about bonding properties of the two PCAs and the oxide catalysts were provided by Mo K-edge EXAFS spectroscopy. Figure 2(a), (b) and (c) show the Fourier transforms of the k^3-weighted Mo K-edge EXAFS spectra for the two PCAs and $Mo_2(CH_3CO_2)_4$ obtained from the 40–167 nm^{-1} k-range. A peak at 0.15–0.22 nm was attributed to Mo-O and Mo-Mo pairs [10]. The results of curve-fitting analysis are summarized in Table I. $Mo_2(CH_3CO_2)_4$ contains contributions from Mo-Mo bonds, $r = 0.212$ nm (CN = 1.0), and Mo-O bonds, $r = 0.220$ nm (CN = 4.0). They are in good agreement with the molecular structure of $Mo_2(CH_3CO_2)_4$ as shown in Figure 1(a). The Mo-O bond distances were determined to be 0.219 nm and 0.221 nm for PCA35 and PCA25, respectively. These values are close to that of the original $Mo_2(CH_3CO_2)_4$. The Mo-Mo bond distance for the PCA35 is also similar to that in $Mo_2(CH_3CO_2)_4$. The CN of Mo-O bond for PCA35 is in good agreement with the number of remaining acetate ligands given by TG measurement. On the PCA35 that anchored by irradiation with lower energy ($\lambda > 350$ nm), the Mo_2 initial framework was unchanged and about 3/4 of the acetate ligands remained (Figure 1(c)). On the contrary, the Mo-Mo bond distance for PCA25 is larger than that of $Mo_2(CH_3CO_2)_4$. The Mo_2 initial framework was broken and two Mo atoms were supported apart from each other (Figure 1(b)). The CN for the Mo-O bonds of PCA25 is larger than that expected by TG measurement. PCA25 seems to have two kinds of Mo-O bonds: one bound directly to silica and another bound to acetate ligands. Therefore the local structure of Mo can be controlled by irradiation energy.

Figure 2(d) and (e) show the Fourier transforms of k^3-weighted Mo K-edge EXAFS spectra for Mo/SiO_2 catalysts obtained from the 37–147 nm^{-1} k-range. The peak at about 0.25–0.35 nm in the FTs spectra can be attributed to neighboring Mo atoms. As shown in Table II, PCA35-ox had shorter Mo-(O)-Mo bonds at $r = 0.316$ nm than PCA25-ox ($r = 0.329$ nm). Those Mo-(O)-Mo bond distances reflected photo-chemical anchored Mo structure. The structure of PCA35 was similar to original complex, but in PCA25, the Mo_2 framework was broken down. The peaks observed at about 0.095–0.195 nm could be assigned to Mo-O bonds. A curve-fitting analysis indicated that the Mo species has two kinds of Mo-O bond. The shorter one ($r \sim 0.17$ nm) was attributed to the terminal Mo=O bond and the longer one ($r \sim 0.22$ nm) to the bridged Mo-O bond or to the Mo-O bond directly to the silica surface. The CN of terminal Mo=O bond and Mo-O bond were 1.2 and 0.5 for PCA25-ox and 1.0 and 1.2 for PCA35-ox, respectively. The PCA25-ox had larger CN of Mo=O bond and smaller CN of Mo-O bond than those in the PCA35-ox. Considering that two Mo atoms were supported apart from each other in PCA25, Mo oxide tend to be isolated in the PCA25-ox. The Mo K-edge XANES spectra of MoO_3 and K_2MoO_4 have representative structure for MoO_6 (octahedral coordination) and MoO_4 (tetrahedral coordination), respectively. The XANES spectrum of K_2MoO_4 exhibited a high intensity preedge peak due to the 1s-4d transition. It has been reported that Mo complexes with tetrahedral geometry have strong 1s-4d transition peaks

Table II. *Curve-fitting results for PCA25-ox and PCA35-ox.*

compound	coordination	CN	r/nm	DW/nm
	Mo=O	1.2	0.167	0.0072
PCA25-ox	Mo-O	0.5	0.216	0.0040
	Mo-(O)-Mo	0.4	0.329	0.0069
	Mo=O	1.0	0.165	0.0065
PCA35-ox	Mo-O	1.2	0.216	0.0065
	Mo-(O)-Mo	0.5	0.316	0.0075

[12, 13]. PCA25-ox possessed the strong preedge peak and the near-edge feature was close to that of K_2MoO_4. This suggests that the Mo oxide in the PCA25-ox had mainly tetrahedral geometry and was isolated. The preedge peak intensity of PCA35-ox was weaker than that of PCA25-ox. Thus, the Mo oxide in PCA35-ox was not isolated and made few Mo-(O)-Mo networks. According to the EXAFS and XANES analyses, local structures of Mo/SiO_2 catalysts were proposed as Figure 2(d) and (e). The structure of PCA25-ox was substantially monomer-pair without Mo-(O)-Mo bonding and that of PCA35-ox was dimeric.

4. Conclusion

From the results presented above, we conclude the following:

1. The degree of photo-decomposition of $Mo_2(CH_3CO_2)_4$ could be controlled by the energy of UV irradiation. The acetate ligands of the Mo dimer complex decreased to about 0.33 with higher irradiation energy ($\lambda > 250$ nm). The Mo-Mo bond distance of PCA25 was 0.239 nm. It was much longer than that of $Mo_2(CH_3CO_2)_4$ (0.212 nm). Two Mo atoms were supported apart from each other. On the other hand, about 3/4 of the acetate ligands were left in PCA35, and the Mo-Mo bond distance was 0.211 nm. The structure was close to the original Mo dimer complex. The framework of the Mo dimer complex was maintained.
2. Monomer-pair and dimetric Mo oxide structures were formed by oxidation of PCA25 and PCA35, respectively. PCA25-ox was monomer-pair without Mo-(O)-Mo bonding structure but it was not completely isolated. The Mo-(O)-Mo bond distance for PCA35-ox was 0.316 nm. The local structure of the Mo oxide catalysts was designed by the energy of UV irradiation.

Acknowledgement

This work was partly supported by a Sasakawa Scientific Research Grant from The Japan Science Society.

References

1. Haber, J., "Studies in Inorganic Chemistry, Molybdenum: An Outline of its Chemistry and Uses", (ed. by Braithwaite, E. R. and Haber, J.), (Elsevier, Amsterdam 1994).
2. Zhuang, Q., Fukuoka, A., Fujimoto, T., Tanaka, K. and Ichikawa, M., J. Chem. Soc., Chem. Commun. 745 (1991).
3. Takenaka, S., Tanaka, T., Funabiki, T. and Yoshida, S., J. Chem. Soc., Faraday Trans. 1 **94**, 695 (1998).
4. Murayama, H., Ichikuni, N., Shimazu, S. and Uematsu, T., Stud. Surf. Sci. Catal. **132**, 793 (2001).
5. Martin, C., Martin, I. and Rives, V., J. Chem. Soc., Faraday Trans. 1 **89**, 4131 (1993).
6. Jvin, K. J. and Mol, J. C., "Olefin Metathesis and Metathesis Poymerization", (Academic Press, London 1997).
7. Iwasawa, Y., Adv. Catal. **35**, 187 (1987).
8. Anpo, M., Sunamoto, M. and Che, M., J. Phys. Chem. **93**, 1187 (1989).
9. Ichikawa, M., *et al.*, Stud. Surf. Sci. Catal. **75A**, 529 (1992).
10. Zama, K., Imada, Y., Fukuoka, A. and Ichikawa, M., Appl. Catal. A **194**, 285 (2000).
11. Bratton, W. K., Cotton, F. A. and Debeau, M., J. Coord. Chem. **1**, 121 (1971).
12. Cramer, S. P., Hodgson, K. O., Gillum, W. O. and Mortenson, L. E., J. Am. Chem. Soc. **100**, 3398 (1978).
13. Mensch, C. T. J., van Veen, J. A. R., van Wingerden, B. and van Dijk, M. P., J. Phys. Chem. **92**, 4961 (1988).

Physica Scripta. Vol. T115, 828–830, 2005

In-Situ XAFS Analysis of Dynamic Structural Change of Pd-Pt Nano-Particles Supported on Catalyst Surface Under Sulfidation Conditions

K. K. Bando*[1], T. Matsui[1], Y. Ichihashi[2], K. Sato[3], T. Tanaka[4], M. Imamura[1], N. Matsubayashi[1] and Y. Yoshimura[1]

[1]National Institute of Advanced Industrial Science and Technology 1-1-1, Higashi, Tsukuba, Ibaraki 305-8565, Japan
[2]Department of Chemical Science and Engineering, Kobe University 1-1, Rokkodai, Nada, Kobe 657-8501, Japan
[3]AIST Tohoku, National Institute of Advanced Industrial Science and Technology 4-2-1, Nigatake, Miyagino, Sendai 983-8551, Japan
[4]National Institute for Environmental Studies 16-2, Onogawa, Tsukuba, Ibaraki 305-8506, Japan

Received June 26, 2003; accepted February 6, 2004

PACS numbers: 82.65.+r, 82.80.Ej

Abstract

In-situ XAFS observation of Pd-Pt catalysts supported on SiO_2, Al_2O_3 and USY was carried out during reduction and sulfidation processes. Under sulfidation conditions, Pd-Pt species on USY was the most seriously sulfided, whereas, no contribution of sulfur was observed in Pt L_{III}-edge EXAFS of sulfided Pd-Pt/SiO_2. Pd-Pt species on Al_2O_3 showed intermediate properties for sulfidation. It is found that Pd and Pt metal species formed relatively uniform alloy particles on SiO_2 and Al_2O_3, whereas, on USY, Pd and Pt atoms were segregated in the alloy particles.

1. Introduction

Supported Pd-Pt catalysts are known as efficient catalysts for deep hydrodearomatization (HDA) of diesel fuel [1, 2]. The activity varies with not only the composition of alloy species but also the kinds of the support [3–5]. In this work, the Pd-Pt alloy species supported on three kinds of supports were investigated: SiO_2, Al_2O_3 and ultra stable Y-type zeolite (USY). The order of total HDA activity was as follows: Pd-Pt/USY $\gg$ Pd-Pt/Al_2O_3 > Pd-Pt/SiO_2 [3]. Though Pd-Pt/USY and Pd-Pt/Al_2O_3 have almost the same number of exposed metal atoms determined by CO adsorption [3], the activity of Pd-Pt/USY was 6 times higher than Pd-Pt/Al_2O_3 [3]. The turn over frequency (TOF) of Pd-Pt/Al_2O_3 was similar to that of Pd-Pt/SiO_2, even though the average size of metal particles on SiO_2 was larger than that on Al_2O_3 [3]. Thus it is strongly suggested that the intrinsic activity of each metal site is different, probably due to difference in surface structure. *In-situ* XAFS (X-ray adsorption fine structure) technique was applied to surface structure analysis of the three catalysts. In the present work, the *in-situ* XAFS observation of the catalysts was carried out during reduction and sulfidation processes and the surface structure is discussed based on the structural change under these conditions.

2. Experimental

2.1. *Sample preparation*

Supported Pd-Pt (molar ratio of Pd/Pt was 4) catalysts were prepared by impregnation method. Al_2O_3 (Catalysts and chemicals Industry), SiO_2 (Fuji Silysia chemical), and an ultra stable Y-type zeolite (USY, $SiO_2/Al_2O_3 = 13.9$, Catalysts and chemicals Industry) were used as supports. The precursors for Pd and Pt were $Pd(NH_3)_4Cl_2 \cdot xH_2O$ and $Pt(NH_3)_4Cl_2 \cdot xH_2O$, respectively. The total metal content was 1.2–2 wt%. The impregnated samples were dried in vacuum at 333 K for 6 h, then calcined at 573 K under oxygen for 3 h. A round disk of 10 mm in diameter was made out of the calcined catalyst (0.2 g) and was set in an *in-situ* cell.

2.2. *XAFS measurements*

In-situ XAFS measurements were carried out at BL7C, 9A and 10 B of the Photon Factory in the Institute of Materials Structure Science, High Energy Accelerator Research Organization (PF-IMSS-KEK) in Japan. A Si(311) channel-cut and Si (111) double crystal monochromators were used for Pd K-edge and Pt L_{III}-edge XAFS measurements, respectively. All the spectra were obtained in transmission mode by using two ionization chambers in front and back of the cell (represented as I_0 and I, respectively). The ionization chambers filled with Ar (for I_0) and Kr (for I) were used in the Pd K-edge energy region, and in the Pt L_{III}-edge energy region, the gases were exchanged with N_2 (for I_0) and 15% Ar/N_2 (for I).

A flow reaction system including an *in-situ* XAFS cell [6, 7] was assembled at the end of the X-ray beam line. All the reaction conditions like temperature, pressure and gas flow rate could be monitored and controlled outside the radiation shield room. The exhaust gas contained H_2S and H_2. H_2S was removed with 20% NaOHaq absorber and H_2 was converted into H_2O with a burner. No toxic and/or flammable gases were detected at the end of the gas flow line.

The sample was initially reduced under a flow of 20%H_2/He. The flow rate was 120 cm^3/min. The temperature was increased stepwise by 50 K from ambient temperature to 573 K and kept for 1 hour at 573 K. After reduction, sulfidation of the sample was done at 553 K under a diluted H_2S (composed of 100 ppm H_2S + 20%H_2/He) at a flow rate of 120 ml/min.

XAFS spectra were observed in-situ in the course of all treatments every 10 min in a step-scanning mode with data accumulation time of 0.5–1 s for each step. XAFS analysis of the obtained data was conducted with commercially available software (REX, Rigaku Co.). Parameters for backscattering amplitudes and phase shift functions were extracted from the oscillations of standard substances (Pd foil, Pt foil, Pd-Pt alloy foil, PdS and PtS_2) observed at reaction temperature in order to exclude influence of thermal oscillations at higher temperature from analysis.

*e-mail: kk.bando@aist.go.jp

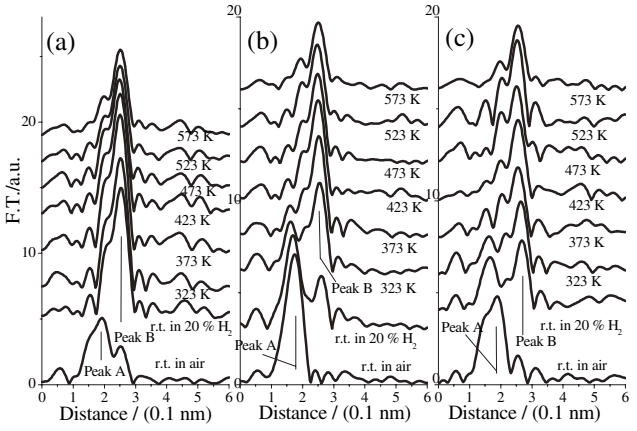

Fig. 1. Fourier transform of Pd K-edge EXAFS spectra ($k^3\chi(k)$) obtained during reduction under a flow of 20%H_2He: (a) Pd-Pt/SiO_2, (b) Pd-Pt/Al_2O_3 and (c) Pd-Pt/USY. The bottom function in each figure was obtained in air before reduction.

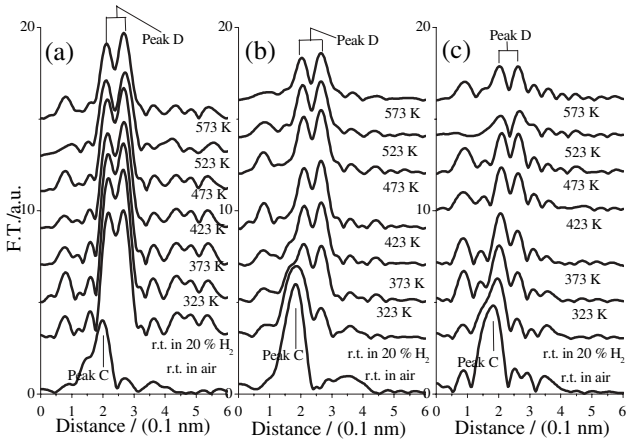

Fig. 2. Fourier transform of Pt L_{III}-edge EXAFS spectra ($k^3\chi(k)$) obtained during reduction under a flow of 20%H_2/He: (a) Pd-Pt/SiO_2, (b) Pd-Pt/Al_2O_3 and (c) Pd-Pt/USY. The bottom function in each figure was obtained in air before reduction in air.

3. Results and Discussion

3.1. *Reduction*

Figure 1 shows Fourier transform of Pd K-edge EXAFS ($k^3\chi(k)$) observed for the three catalysts during reduction under a flow of 20%H_2/He, except for the bottom spectra, which were observed before reduction. Initially, strong bands appeared at 0.18 nm in all catalysts (Peak A), and they were assigned to Pd-O and Pd-Cl scattering. For Pd-Pt/SiO_2, upon introduction of 20%H_2/He, the peak at 0.18 nm completely disappeared and a new peak appeared at 0.26 nm (Peak B), which is assigned to metal-metal scattering: Pd-Pd and Pd-Pt. The Peak B remained almost the same during subsequent reduction upto 573 K. For Pd-Pt/Al_2O_3, the Peak A was weakened by introduction of 20%H_2/He and correspondently the Peak B emerged at 0.26 nm, but contribution by Pd-O or Pd-Cl still remained at 0.18 nm. As the temperature increased, the Peak A became weak and finally disappeared at 373 K, while, the Peak B became intense and dominant. The change of spectra for Pd-Pt/USY was similar to that of Pd-Pt/Al_2O_3. One difference between Pd-Pt/USY and Pd-Pt/Al_2O_3 was that Pd in Pd-Pt/USY was more easily reduced at ambient temperature.

Figure 2 shows the Fourier transform of Pt L_{III}-edge EXAFS ($k^3\chi(k)$) observed under the same conditions as Fig. 1. The change of spectra is almost the same as that of Pd K-edge. Before reduction (the bottom line), a strong band assigned to Pt-O or Pt-Cl appeared at 0.18 nm (Peak C). During reduction, the Peak C decreased, while a new peak appeared near 0.26 nm (Peak D), which is assigned to metal-metal scattering: Pt-Pd and Pt-Pt. Reduction of Pt atoms on SiO_2 completes at ambient temperature as in the case of Pd, whereas, the Pd – (O, Cl) contribution (Peak C) disappeared at 373 K for both Al_2O_3 and USY supported catalysts.

Figure 3 shows the change in coordination numbers (CN) during reduction. The coordination numbers of Pd-Pd and Pt-Pd for Pd-Pt/SiO_2 are larger than those for Pd-Pt/Al_2O_3 and Pd-Pt/USY. This fact indicates that the averaged particle size of metal species on SiO_2 is larger than on Pd-Pt/Al_2O_3 and Pd-Pt/USY. The coordination number of Pt-Pd for Pd-Pt/SiO_2 and Pd-Pt/Al_2O_3 is larger than that of Pd-Pt/USY. A possible explanation for this difference is that the Pd and Pt atoms are relatively uniformly distributed in metal particles in Pd-Pt/SiO_2 and Pd-Pt/Al_2O_3, and segregated in Pd-Pt/USY (Fig. 4). The CN(Pt-Pd) gradually increases with temperature for all catalysts.

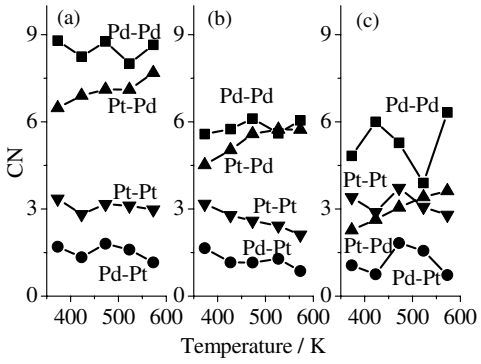

Fig. 3. Change of coordination numbers of metal-metal atomic pairs during reduction under a flow of 20%H_2/He: (a) Pd-Pt/SiO_2, (b) Pd-Pt/Al_2O_3 and (c) Pd-Pt/USY. Squares represent CN(Pd-Pd), circles CN(Pd-Pt), triangles CN(Pt-Pd), and inverted triangles CN(Pt-Pt).

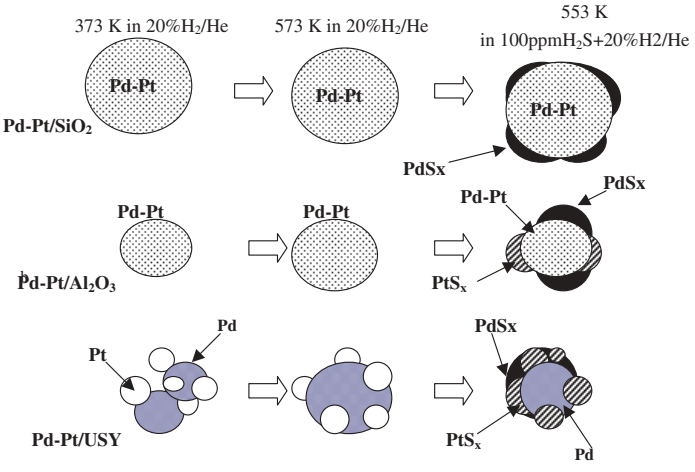

Fig. 4. Proposed structural change of Pd-Pt alloy particles during reduction and sulfidation.

It suggests that the mixing of Pt and Pd atoms increases with temperature.

3.2. *Sulfidation*

After reduction, the catalyst was cooled to 553 K and diluted H_2S (100 ppm H_2S + 20%H_2/He) was introduced. The catalyst was kept at 553 K under diluted H_2S until the sulfidation was

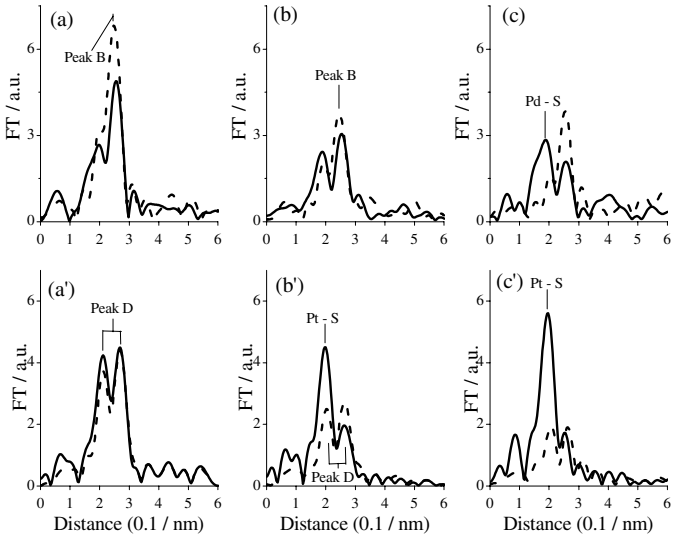

Fig. 5. Fourier transform of Pd K-edge (top figures) and Pt L_{III}-edge (bottom figures) EXAFS spectra ($k^3\chi(k)$) obtained after sulfidation at 553 K under a flow of 100 ppm H_2S + 20% H_2/He (solid lines), compared with those of reduced samples obtained in 20%H_2/He at 573 K (dashed lines) : (a, a′) Pd-Pt/SiO_2, (b, b′) Pd-Pt/Al_2O_3, and (c, c′) Pd-Pt/USY.

completed. Figure 5 shows Fourier transform of Pd K-edge and Pt L_{III}-edge EXAFS ($k^3\chi(k)$) observed after sulfidation at 553 K (solid lines) under diluted H_2S, compared with those obtained after reduction at 573 K (dashed lines). For Pd-Pt/SiO_2, the Peak B decreased in the Pd K-edge spectrum, whereas, in the Pt L_{III}-edge spectrum, the spectrum remained almost unchanged. For Pd-Pt/Al_2O_3, the Peak B decreased as in the case of Pd-Pt/SiO_2, and the Peak D in the Pt L_{III}-edge spectrum also decreased and a new peak due to Pt-S scattering appeared at 0.20 nm. For Pd-Pt/USY, the change was more noticeable than the other catalysts, that is, contribution of Pd-S was observed at 0.20 nm in the Pd K-edge spectrum and the peak of Pt-S scattering became dominant in the Pt L_{III}-edge spectrum after sulfidation. Table I shows curve-fitting (CF) results of reduced and sulfided catalysts. Although CN(Pd-S) was 1.0 in sulfided Pd-Pt/SiO_2, no contribution of Pt-S was found by CF analysis. For Pd-Pt/Al_2O_3, CN(Pd-S) was 0.9 and CN(Pt-S) was 4.2, meaning that higher degree of sulfidation of Pt rather than Pd occurred. For Pd-Pt/USY, sulfidation of the catalyst preceded more deeply, that is, CN(Pd-Pd) decreased from 6.3 to 2.9 and CN(Pt-S) became 6.3, indicating that almost all the Pt atoms were sulfided.

Judging from the contribution of sulfur in EXAFS spectra, it is concluded that sulfidation of metal species occurs favorably in the following order: Pd-Pt/USY > Pd-Pt/Al_2O_3 > Pd-Pt/SiO_2.

Table I. *Coordination numbers determined by curve-fitting analysis of reduced and sulfided catalysts.*

		Coordination Number (CN)					
Sample	Condition	Pd-Pd	Pd-Pt	Pd-S	Pt-Pd	Pt-Pt	Pt-S
Pd-Pt/SiO_2	Reduced*	9.0	1.0		7.7	3.1	
	Sulfided**	5.8	—	1.0	6.8	4.5	—
Pd-Pt/Al_2O_3	Reduced*	6.1	1.3		5.7	2.1	
	Sulfided**	5.0	—	0.9	3.9	—	4.2
Pd-Pt/USY	Reduced*	6.3	0.7		3.6	2.8	
	Sulfided**	2.9	—	1.9	1.9	—	6.3

*After reduction at 573 K for 1 h.
**After sulfidation at 553 K for 4.5 – 6 h.

As mentioned in 3.1, Pt and Pd atoms were segregated in the metal particles in Pd-Pt/USY. If it is assumed that Pt atoms formed small clusters and were mainly located on the outer surface of metal particles, then it is understandable that Pt sulfidation proceeded prior to Pd sulfidation (Fig. 4). On the other hand, in Pd-Pt/SiO_2 and Pd-Pt/Al_2O_3, Pd and Pt atoms were mixed more homogeneously and less Pt atoms were exposed to the outer surface. As a result, sulfidation of Pt was suppressed or limited, compared to Pd-Pt/USY (Fig. 4). In addition to that, it is suggested that Pt and Pd atoms in homogeneous bimetallic alloy are less active toward sulfur compared with pure Pt or Pd, because, according to CO adsorption, Pd-Pt/Al_2O_3 and Pd-Pt/USY have almost the same number of exposed metal atoms, but the number of sulfur adsorbed on Pd and Pt in Pd-Pt/Al_2O_3 was smaller than that in Pd-Pt/USY. The highest sulfur tolerance of Pt in Pd-Pt/SiO_2 might be due to highly homogeneous alloy formation or presence of Pd atoms on the surface, protecting Pt from sulfur.

Ackknowledgement

The XAFS measurements were carried out under the approval of PF PAC (Program Advisory Committee) as projects No. 2002G274 and No. 2000G283.

References

1. Lui, W.-Q., Zhao, L., Sun, G.-D. and Min, E.-Z., Catal. Today **51**, 135 (1999).
2. Yasuda, H. and Yoshimura, Y., Catal. Lett. **46**, 43 (1997).
3. Yasuda, Y., Kameoka, Y., Sato, T., Kijima, N. and Yoshimura, Y., Appl. Catal. A:General **185**, L199 (1999).
4. Shawn, D. J. and Song, C., Catal. Today **31**, 93 (1996).
5. Yasuda, H., Sato, T. and Yoshimura, Y., Catal. Today **50**, 63 (1999).
6. Bando, K. K. *et al.*, Topics Catal. **18**, 59 (2002).
7. Bando, K. K. *et al.*, J. Sync. Rad. **8**, 5b1 (2001).

Physica Scripta. Vol. T115, 831–833, 2005

Monitoring of fast Transformations in Solid State Chemistry and Heterogeneous Catalysis by QEXAFS in the Second Scale

D. Lützenkirchen-Hecht[1,*], J.-D. Grunwaldt[2], M. Richwin[1], B. Griesebock[1], A. Baiker[2] and R. Frahm[1]

[1]Institut für Materialwissenschaften und Fachbereich Physik, Bergische Universität Wuppertal, Gaußstr. 20, D-42097 Wuppertal, Germany
[2]Institute for Chemical and Bioengineering, Swiss Federal Institute of Technology, ETH Hönggerberg, CH-8093 Zürich, Switzerland

Received June 26, 2003; accepted November 4, 2003

PACS numbers: 61.10.Ht, 61.10.Kw, 82.20.−w

Abstract

The present paper points out the possibility of investigating solid-solid transformations using time dependent X-ray absorption spectroscopy (QEXAFS) on a second scale. For this purpose, new crystal driving mechanics were developed which enable the measurement of complete X-ray absorption spectra extending over up to 2000 eV with repetition frequencies of up to 40 Hz and the possibility of monitoring a reference sample simultaneously. This permits to detect even very small changes of the edge position – and thus the chemical valency of the species of interest – with a high accuracy. The application of the new set up is demonstrated for the in situ analysis of the thermal decomposition of Co-oxalate-hydrate in different gas atmospheres. The results prove that the details of the decomposition process and the formed reaction products depend sensitively on the composition of the gas atmosphere.

1. Introduction

A number of solid-solid transformations such as decomposition reactions or the reduction/oxidation of heterogeneous catalysts occur relatively fast, i.e. within less than a minute. Time resolved investigations are thus important in order to gain insight into the mechanisms of such solid-solid transformations (e.g. during changes of temperature or gas atmosphere). Since intermediate phases are usually present in an amorphous form, XANES or EXAFS experiments seem to be appropriate methods. In a previous in situ study [1], X-ray absorption near edge spectra were taken in the subsecond scale using the piezo-QEXAFS technique. In many cases full EXAFS spectra are needed for a proper interpretation. Hence, the monochromator needs to be moved over a larger angular range. For this purpose, we developed new crystal driving mechanics making use of a tilt table which is moved by an excenter disc [2]. While the description of this new monochromator will be subject of a forthcoming publication [3], we will report on time resolved investigations of decomposition reactions of inorganic materials and heterogeneous catalysts in this paper. More specifically, we succeeded in monitoring the decomposition of cobalt oxalate at the Co K-edge in different gas atmospheres.

2. Experimental

The experiments described here were performed at the undulator beamline 1-ID at the Advanced Photon Source (Argonne, Illinois, USA) operating with 7 GeV electrons and 100 mA of stored current in the topping up mode [4]. The polychromatic radiation from the X-ray source was monochromatized using a Si(111) channel-cut crystal, which was indirectly cooled via a hollow copper block and liquid nitrogen in a closed cycle [2]. The cooler with the crystal was mounted on a tilt table with two solid state hinges which was driven by an excenter disc. This excenter disc is directly mounted on the shaft of a DC-motor the turning speed of which is controlled by a computer and can be varied from about 0.1 Hz to 40 Hz [2, 3]. Several different excenter discs with different asymmetries enable to modify the angular range of the tilt table from about 0.05° to about 1.52°. Using a Si(111)-crystal in the vicinity of e.g. the Cu K-edge (8980 eV), these values correspond to an available energy range for the EXAFS experiments from about 100 eV to more than 2500 eV. The EXAFS data were obtained in transmission geometry. N_2-filled ionization chambers were used as detectors for the intensity of the incoming and the transmitted radiation. A slit system in front of the first ionization chamber was used for the horizontal and vertical definition of the beam which was typically $(0.3\,\mathrm{mm})^2$. The current signals from the ionisation chambers were converted and amplified by Keithley 428 current-to-voltage amplifiers. Their output signals were directly sampled by a fast A/D converter (4 channels with up to 200 kHz simultaneously) and stored on a PC computer. Further details of this setup are given elsewhere [2, 3].

The *in situ* cell for the experiments (design similar to that used in refs. [5, 6]) consists of a quartz glass capillary tube with 0.5 mm diameter and 10 μm wall thickness, which was loaded with the samples of interest, i.e. Co-oxalate-dihydrate in the present case (diluted with alumina). Different pre-mixed gases from a gas manifold could pass through the capillary reactor cell with a typical gas flow of ca. 5 ml/min. Heating of the *in situ* cell microreactor up to 600 °C was performed by passing a defined flow of hot N_2 gas besides the capillary encapsulated in a shield of Kapton foil (cf. description in [5]).

3. Results and Discussion

Due to their relatively low decomposition temperatures, transition metal oxalates are of high interest e.g. as precursors for the preparation of fine metal or oxide powders of the respective element, as well as for the synthesis of catalyst materials. Furthermore, thermal decomposition of metal oxalates is often used for the preparation of catalytically active solid products (see [7, 8] and references therein). Co-oxalate is of special interest due to its use for the preparation of catalysts for the Fischer-Tropsch-synthesis. We investigated the thermal decomposition of Co-oxalate-dihydrate ($CoC_2O_4 \cdot 2H_2O$) in different gas mixtures *in situ* at the Co K-edge (7709 eV). In Fig. 1(a), the room temperature spectrum of a Co-oxalate-dihydrate sample is shown together with that of the Co metal reference measured simultaneously within about 250 ms (2 Hz oscillation frequency, 10 kHz sampling rate). Besides the different EXAFS structures

*e-mail: dirklh@uni-wuppertal.de

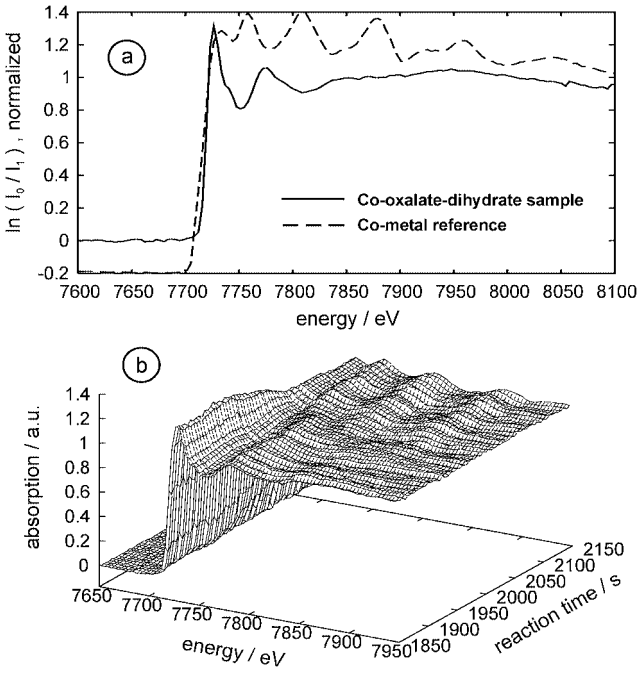

Fig. 1. (a) Co K-edge EXAFS spectrum of $CoC_2O_4{\cdot}2H_2O$ measured *in situ* within 250 ms prior to the initiation of a decomposition reaction together with the Co-metal reference measured simultaneously. (b) *In situ* Co K-edge absorption spectra measured during the thermal decomposition of $CoC_2O_4{\cdot}2H_2O$ in $Ar + 4\%\ H_2$. Each spectrum was measured within 250 ms. The displayed spectra belong to the temperature region between ca. 340 °C and ≈400 °C.

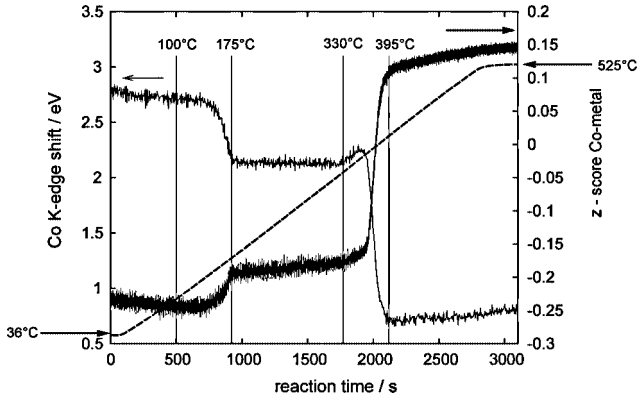

Fig. 2. EXAFS data analysis for the *in situ* decomposition reaction of Co-oxalate-dihydrate in Ar + 4% H_2. The dashed line shows the temperate as a function of time, some essential points are highlighted by vertical lines. The regular line belongs to the observed edge shift of the Co K-edge during the experiment (left ordinate) and the bold line corresponds to the principal component of Co-metal (z-score, right ordinate). Negative and positive values of the z-score belong to small and high Co-metal concentrations, respectively.

above the edge, in particular the small edge shift between both materials is evident – this is one of the big advantages of the set up used. Due to the use of a reference foil even small edge shifts can be very sensitively monitored. Fig. 1(b) depicts EXAFS spectra measured *in situ* in the vicinity of the Co K-edge during the thermal decomposition of Co-oxalate-dihydrate in a mixture of Ar + 4% H_2 in the course of a temperature ramp (10 K/min) from 35 °C to about 530 °C. More than 9000 spectra were measured for each single experiment. The shown spectra belong to the temperature region between ca. 340°C and ≈400 °C.

Obviously, both the structures at the edge and above the edge change dramatically at around 2000 s reaction time: while the white line intensity at the edge decreases significantly, the absorption maximum at about 7770 eV shifts to a lower energy of ca. 7750 eV and further structures appear at around 7900 eV. Besides the determination of accurate values for the edge energy position as a function of the reaction time (and temperature), a principal component analysis [9] was performed using the software package R [10] in order to identify the number and the type of the contributing phases. We found only two contributing principal components during the decomposition which could be identified as the Co-oxalate and Co-metal, i.e. Co(II)oxalate is directly transformed to metallic Co. More detailed results are compiled in Fig. 2. Between about 150 °C and 175 °C, a slight decrease of the absorption edge position to smaller energies by about 0.4 eV was observed. In agreement with previously published data [7, 8], this decrease can be understood in terms of the dehydration of the oxalate-hydrate according to the reaction

$$CoC_2O_4{\cdot}2H_2O \rightarrow CoC_2O_4 + 2H_2O. \quad (1)$$

The small edge shift indicates that the oxalate-hydrate has a slightly increased valence compared to pure CoC_2O_4. In addition, the z-score of Co-metal, which is related to the Co-metal concentration in the sample, shows a slight increase accordingly. It should be noted that the z-score is in general not simply proportional to the concentration, the latter has to be determined from the z-score by means of a target transformation and a least square fit of model compounds [9, 11–13]. However, this is a non-trivial task because of the large number of spectra which are involved in the current experiment. Nevertheless, by comparison with the z-score of the reference compounds (CoC_2O_4 and Co-metal) we can conclude that a negative z-score of the metal corresponds to a high concentration of CoC_2O_4 and positive values belong to a high metal concentration [2].

A further increase of the temperature to about 340 °C results in a steep decrease of the Co K-edge position by about 2.5 eV within a time frame of less than 100 s. At the same time, the Co metal z-score increases from about −0.2 to ca. 0.15 in parallel. Thus it is very likely that the decomposition

$$CoC_2O_4 \rightarrow Co + 2CO_2 \quad (2)$$

occurs in this temperature interval. For comparison, the z-score of metallic Co is 0.16, therefore we can conclude that the decomposition of the oxalate results not only in Co metal, i.e. a small fraction of Co-O species (such as cobalt oxide CoO) is formed.

For comparison, decomposition experiments were also performed in pure Ar atmospheres [2]. These experiments show that course of the reaction is sensitive to the composition of the gas atmosphere, in agreement with recent studies [7]. Our experiments show that the separation of the crystal water according to eqn. (1) occurs for a broader temperature interval compared to the hydrogen containing atmosphere, i.e. it starts at a lower temperature of about 100 °C and is finished at a slightly elevated temperature of ca. 195 °C as can be seen in Fig. 3.

The decomposition of the formed oxalate starts at about 300 °C and is finished at ca. 345 °C, as can be seen in the temperature dependency of the z-score, thus also the decomposition of the oxalate occurs at a lower temperature compared to the H_2-containing Ar atmosphere. However, a closer inspection shows that no shift of the Co K-edge position was observed in this temperature range. In general, the total shift in the Co K-edge position as well as the change in the z-score are smaller compared to the decomposition experiment in Ar + H_2: while the edge shift

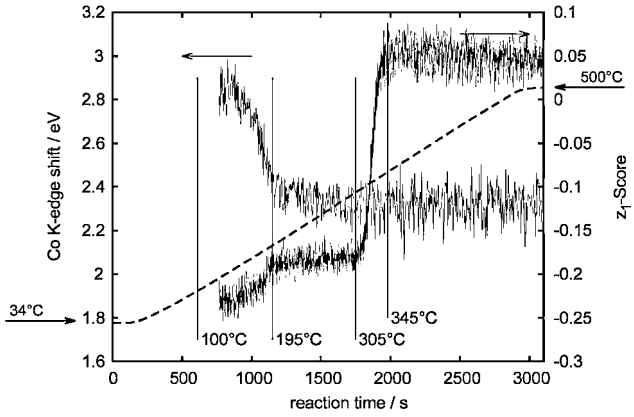

Fig. 3. Analysis of the *in situ* EXAFS data obtained during the decomposition of Co-oxalate-dihydrate in pure Ar. The dashed line shows the temperate as a function of time, some essential points are highlighted by vertical lines. The regular line belongs to the observed edge shift of the Co K-edge during the experiment (left ordinate) and the bold line corresponds to the principal component of Co-metal (z-score, right ordinate).

observed for the decomposition in Ar + H_2 was ≈2 eV, it is only about 0.5 eV in pure Ar. The corresponding changes for the z-score are about 0.3 and 0.4 for the decomposition without and with H_2, respectively. The results indicate that not all Co oxalate is completely decomposed according to eqn. (2) but also some Co-oxide forms directly. This is in agreement with Maciejewski *et al.*, who found about 13% of CoO in samples which were subjected to a decomposition in pure He [7]. Furthermore, the application of the principal component analysis also suggests the presence of three contributing species (i.e. CoC_2O_4, CoO and metallic Co) in the course of the complete experiment, thus it is very likely that the originally existing Co(II)oxalate phase is transformed to Co-metal and Co(II)-oxide. Our experiments suggest that CoO and Co metal exist in equal amounts which may be related to the fact that some residual oxygen in the Ar-atmosphere oxidizes metallic cobalt during the decomposition process. In addition, our samples consisted of Co oxalate diluted with alumina and thus some oxygen exposure may also result from this oxide support. The application of a target transformation is very desirable especially for this experiment to determine accurate values for the respective concentrations (see, e.g. [12, 13]).

Acknowledgements

We would like to thank the team of the SRI-CAT of beamline 1-ID at the Advanced Photon Source, especially D. Haeffner, A. Mashayekhi and P. Lee, for their invaluable help and manifold support at the beamline. The use of the Advanced Photon Source (APS) was supported by the U.S. Department of Energy, Office of Science, Office of Basic Energy Science, under contract no. W-31-109-ENG-38. Furthermore, we would like to thank M. Maciejewski for discussion.

References

1. Grunwaldt, J.-D., *et al*., J. Phys. Chem. **B 105**, 5161 (2001).
2. Richwin, M., PhD-dissertation, Universität Wuppertal, (2003).
3. Frahm, R., Richwin, M. and Lützenkirchen-Hecht, D., Physica Scripta (2003), submitted.
4. Gluskin, E., J. Synchrotron Rad. **5**, 189 (1998).
5. Clausen, B. S., Graebaek, L., Steffensen, G. and Topsoe, H., Catal. Lett. **20**, 23 (1993).
6. Grunwaldt, J.-D., Molenbroek, A. M., Topsoe, N.-Y., Topsoe, H. and Clausen, B. S., J. Catal. **194**, 452 (2000).
7. Maciejewki, M., Ingier-Stocka, E., Emmerich, W.-D. and Baiker, A., J. Therm. Anal. Calorimetry **60**, 735 (2000).
8. Malecka, B., Drozdz-Ciesla, E. and Malecki, A., J. Therm. Anal. Calorimetry **68**, 819 (2002).
9. Jackson, J. E., "A user's guide to principal components", (John Wiley & Sons), (New York, 1991).
10. Ihaka, R. and Gentleman, R., J. Comp. Graph. Statistics **5**, 299 (1996).
11. Malinowski, E. R. and Howery, D. G., "Factor analysis in chemistry", (John Wiley & Sons), (New York, 1980).
12. Ressler, T., Wong, J., Roos, J. and Smith, I. L., Environmental Sci. Technol. **34**, 950 (2000).
13. Wasserman, S. R., J. Phys. IV (France) **7**, C2-203 (1997).

Physica Scripta. Vol. T115, 834–836, 2005

XAFS Study on the Local Structure of Zirconium Containing Mesoporous Silicas, Zr-MCM-41 and Their Catalytic Properties

A. Yamaguchi[1,*], M. Yokoyama[1], A. Suzuki[3], Y. Iwasawa[3], H. Sakai[1,2], M. Yuasa[1,2] and M. Abe[1,2]

[1]Faculty of Science and Technology, Tokyo University of Science, Noda, Chiba 278-8510, Japan
[2]Institute of Colloid and Interface Science, Tokyo University of Science, Shinjuku, Tokyo 162-8601, Japan
[3]Department of Chemistry, Graduate School of Science, the University of Tokyo, Hongo, Bunnkyo-ku, Tokyo 113-0033, Japan

Received June 26, 2003; accepted November 4, 2003

PACS number: 6110Ht

Abstract

Zirconium-containing mesoporous silicas Zr-MCM-41 were prepared by two different methods and characterized by XRD, TEM, nitrogen adsorption and EXAFS. In one method, tetraethoxysilane (TEOS) and zirconium tetra-n-propoxide (ZTNP) were mixed and TEOS and ZTNP were hydrolyzed and condensed in aqueous cetyltrimetylammonium bromide solution. EXAFS analysis revealed that zirconium species in Zr-MCM-41 prepared by this method aggregated each other and formed the bonds of Zr-O-Zr. This catalyst had a low catalytic activity for the peroxidative bromination of phenol red. In the other method, $ZrCl_4$ and pure silica MCM-41 were used for impregnation. Zirconium species in this Zr-MCM-41 were highly dispersed as shown in the result of EXAFS analysis. This catalyst exhibited a high catalytic activity for the peroxidative bromination of phenol red. Zirconium species aggregated each other by calcination at 573 K, which caused reduction of catalytic activity.

1. Introduction

Periodic mesoporous silica MCM-41 is a promising material for catalyst support because of its high surface area and uniform pore dimensions [1, 2]. MCM-41 is suitable for transformation of relatively large molecules because the pores of mesoporous materials (2–50 nm diameter) are larger than those of zeolites. Association of transition metals with silica framework of MCM-41 forms catalytic active sites for the reactions. Mesoporous materials containing zirconium have been applied to certain reactions, such as hydroxylation of 1-naphthol [3], photocatalytic generation of hydrogen [4] and chiral alkene polymerization [5]. Tuel *et al.* used zirconium-containing mesoporous silica for the oxidation of large organic molecules using H_2O_2 in the liquid phase [6, 7] and found that it had an acidic character. In this study, we applied this character of Zr-MCM-41 to the peroxidative bromination of phenol red using H_2O_2 as an oxidant [8], according to the following reaction formula:

$$H_2O_2 + Br^- + \text{R-H} + H^+ \rightarrow \text{R-Br} + 2H_2O \quad (1)$$

where R-H and R-Br represent phenol red and bromophenol blue, respectively.

We have synthesized Zr-MCM-41 by two different methods and characterized the product by X-ray diffraction (XRD), transmission electron micrograph (TEM) and extended X-ray absorption fine structure (EXAFS) in order to reveal the effect of local structure of zirconium species on the catalytic activity for the peroxidative bromination of phenol red. EXAFS can provide the interatomic distances and coordination numbers of neighboring atoms for an X-ray absorbing atom in materials with no long-range structural order such as catalysts. O'Brien *et al.* measured Zr K-edge EXAFS in order to characterize organometallic zirconium-grafted siliceous MCM-41 [5] and revealed that the intact ligand existed after immobilization. We present the structural details of zirconium species in zirconium-containing MCM-41 in this article. We found that aggregation of zirconium species occurred by calcination and that it caused reduction of the catalytic activity.

2. Experimental

Zirconium-containing mesoporous silicas, Zr-MCM-41, were prepared by two different methods. In one method, tetraethoxysilane (TEOS) and zirconium tetra-n-propoxide (ZTNP) were used. First, TEOS and ZTNP were mixed in a molar ratio Si/Zr of 49. The mixture was added to an aqueous cetyltrimetylammonium bromide (CTAB) solution, the pH of which was adjusted to 12 by addition of sodium hydroxide. Hydrolysis and condensation of TEOS and ZTNP in the aqueous solution occurred while the mixture was stirred for 1 h and kept for 24 h at ambient temperature with no stirring. The molar ratio of the final gel mixture was 0.12 CTAB : 130 H_2O : 0.5 NaOH : 0.98 TEOS : 0.02 ZTNP. The solid product was filtered, washed with distilled water, and dried at 393 K for 10 h. The product was finally calcined at 773 K for 6 h in air. This product was denoted hereinafter as Zr-MCM-41(mix).

In the other method, zirconium chloride dissolved in ethanol was used as the source of zirconium for impregnation. Only TEOS was added to an aqueous 1.8 wt% CTAB solution, the pH of which was adjusted to 12 by addition of sodium hydroxide. Mesoporous silica without zirconium was obtained in the same way as the first method. Mesoporous silica calcined at 773 K was impregnated with an ethanolic zirconium chloride solution. The molar ratio of the total procedure was 0.12 CTAB : 130 H_2O : 0.5 NaOH : 0.98 SiO_2 : 0.02 $ZrCl_4$. After being dried at 393 K for 3 h, the product was finally calcined at 573, 773, and 1273 K. The product before and after calcination at 573, 773, and 1273 K was denoted hereinafter as Zr-MCM-41-393(imp), Zr-MCM-41-573(imp), Zr-MCM-41-773(imp) and Zr-MCM-41-1273(imp), respectively. The amount of zirconium in Zr-MCM-41(mix) and Zr-MCM-41-X(imp) samples were determined to be ca. 49 in Si/Zr by X-ray fluorescence technique.

The order of the structure of mesoporous materials was investigated by X-ray diffraction (XRD) using nickel filtered Cu Kα radiation. XRD patterns were recorded in the 2θ range from 1 to 10 degrees. Specific surface area was determined by nitrogen adsorption. In order to investigate the local structure around zirconium, the extended X-ray absorption fine structure (EXAFS) spectra at Zr K-edge (18.0 keV) of the catalysts were measured using a Si(111) double-crystal monochromator at BL-12C of KEK-PF. Data analysis was performed by UWXAFS package [9] and the backscattering amplitudes and phase shifts

*e-mail : aritomo@rs.noda.tus.ac.jp

were calculated with FEFF8 code [10]. The k^3-weighted EXAFS functions were Fourier transformed and fitted in R space. The k range of the Fourier transformation of EXAFS data was 30–150 nm^{-1} and the fitting R range was 0.13–0.38 nm. The spectra were fitted by two shells at most; Zr-O and Zr-(O)-Zr. The fitting parameters were coordination number, interatomic distance and Debye-Waller factors for each shell, and a correction of the threshold energy (ΔE_0). The value was determined so that the average residual factor got minimum. The number of free parameters should be smaller than the number of independent parameters calculated from the Niquest law.

Catalytic activities of Zr-MCM-41 for the peroxidative bromination of phenolsulfonephthalein (phenol red) were studied. In the reaction, 3 ml of an aqueous solution containing 0.2 mM phenol red, 0.1 M potassium bromide, and 10 mM hydrogen peroxide in HEPES buffer (pH 6.5) was stirred in the presence of 7.2 mg of the catalyst [8], to give 3′,3″,5′,5″-tetrabromophenolsulfonephthalein (bromophenol blue). Phenol red and bromophenol blue have an absorption peak at 450 and 589 nm, respectively, and the reaction was analyzed with a UV-vis spectrometer.

3. Results and discussion

3.1. *Characterization by XRD, TEM and nitrogen adsorption*

The XRD patterns of pure silica MCM-41 and Zr-MCM-41(mix) exhibited four distinguishable peaks before calcination, due to the hexagonal phase MCM-41. After calcination, the hexagonal structure of the MCM-41 and Zr-MCM-41(mix) samples was found to be retained, though the structural order decreased as evidenced by the weaker XRD peak. We investigated the unit cell parameters (***a***) obtained from XRD patterns and the specific surface areas derived from nitrogen adsorption technique. The calcination in air at 773 K caused 14 and 12% lattice contraction for pure silica MCM-41 and Zr-MCM-41(mix), respectively. Impregnation with ethanolic $ZrCl_4$ solution reduced the XRD peak for Zr-MCM-41-393(imp).

The XRD peaks for Zr-MCM-41-393(imp), Zr-MCM-41-573(imp), Zr-MCM-41-773(imp), and Zr-MCM-41-1273(imp) at $2\theta \sim 2.8$ (100 reflection line) revealed that Zr-MCM-41(imp) retained its structure after calcination at 573 and 773 K, whereas the structure of Zr-MCM-41(imp) completely collapsed after calcination at 1273 K. The specific surface areas of Zr-MCM-41(mix) and Zr-MCM-41-393(imp) were 676 and 831 $m^2\,g^{-1}$, respectively, in almost agreement with the value in the literature [11].

TEM images of MCM-41 and Zr-MCM-41-393(imp) also showed that they had ordered mesoporous structures.

3.2. *EXAFS analysis*

Figure 1 shows the Fourier transformed k^3-weighted EXAFS functions (phase shift uncorrected) for Zr-MCM-41(mix), Zr-MCM-41-393(imp), and a reference sample ZrO_2, together with the calculated functions derived from the curve fitting analysis. Two peaks were observed at 0.16 and 0.29 nm in Fig. 1 (a) for Zr-MCM-41(mix), distances similar to those corresponding to the peaks for ZrO_2, and were assigned to Zr-O and Zr-(O)-Zr contributions, respectively. Zirconium species in Zr-MCM-41(mix) aggregated each other and formed Zr-O-Zr bonds. XRD pattern in the 2θ range of 20–80 degrees for Zr-MCM-41(mix) did not show the peaks of ZrO_2 crystal indicating that Zr species

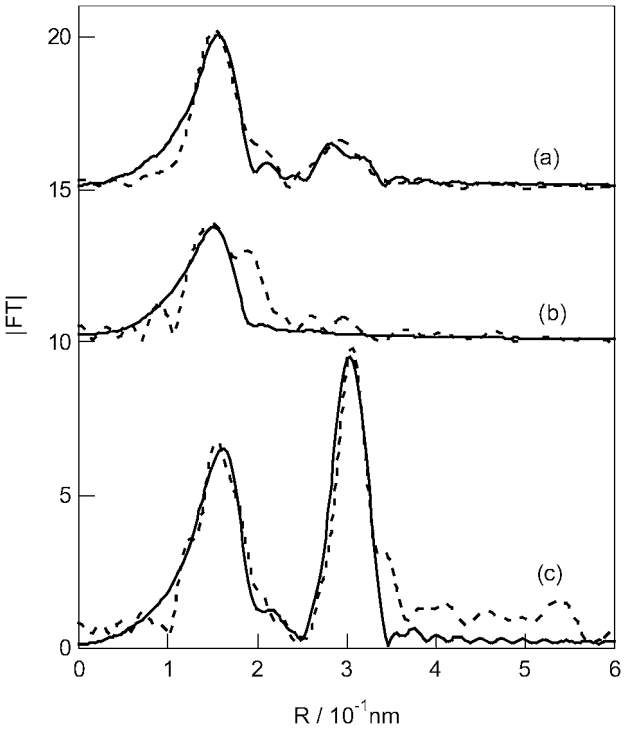

Fig. 1. Fourier transformed k^3-weighted EXAFS functions (·····) for (a) Zr-MCM-41(mix), (b) Zr-MCM-41-393(imp) and (c) reference sample ZrO_2, together with the results of curve fitting (———).

for Zr-MCM-41(mix) aggregated each other at amorphous phase. The higher shells in Fig. 1 (a) are different from those in Fig. 1 (c) because Zr species in Fig. 1 (a) and (c) are amorphous and crystal ZrO_2, respectively. As Zr species at amorphous phase does not have long-range order, the higher shells of Fourier transformed function decrease or disappear. Zr-MCM-41-393(imp) showed two peaks at 0.16 and 0.20 nm in Fig. 1 (b), which were assigned to Zr-O and long Zr-O contributions, respectively. Zr species in Zr-MCM-41-393(imp) were highly dispersed because no Zr-(O)-Zr bond was observed. Figure 2 shows the Fourier transformed k^3-weighted EXAFS functions (phase shift uncorrected) for Zr-MCM-41-573(imp), Zr-MCM-41-773(imp), and Zr-MCM-41-1273(imp), together with the calculated functions derived from the curve fitting analysis. The Fourier transform peaks at 0.29 nm in Fig. 1 (a) and Fig. 2 were fitted by Zr-(O)-Zr rather than Zr-(O)-Si, exhibiting better fits in the region, which indicated that zirconium were not incorporated in the Si framework of MCM-41 and that Zr species aggregated each other.

3.3. *Catalytic activity*

The catalytic activity of pure silica MCM-41 for the peroxidative bromination of phenol red was studied using spectral changes in UV-vis absorption. The peak at 440 nm did not decrease, which indicated that the concentration of phenol red did not change and MCM-41 without zirconium was inactive in the peroxidative bromination of phenol red. We investigated changes in the UV-vis spectrum during the reaction in the presence of Zr-MCM-41(mix) and Zr-MCM-41-393(imp). The peak at 440 nm decreased and that at 589 nm increased, a fact indicating that the reaction (phenol red changed to bromophenol blue) occurred and Zr-MCM-41(mix) and Zr-MCM-41-393(imp) showed catalytic activity in the reaction. Zirconium species in MCM-41 formed active sites for the peroxidative bromination reaction of phenol red. ZrO_2 crystal was inactive in the reaction. Zr-MCM-41-393(imp) had an activity

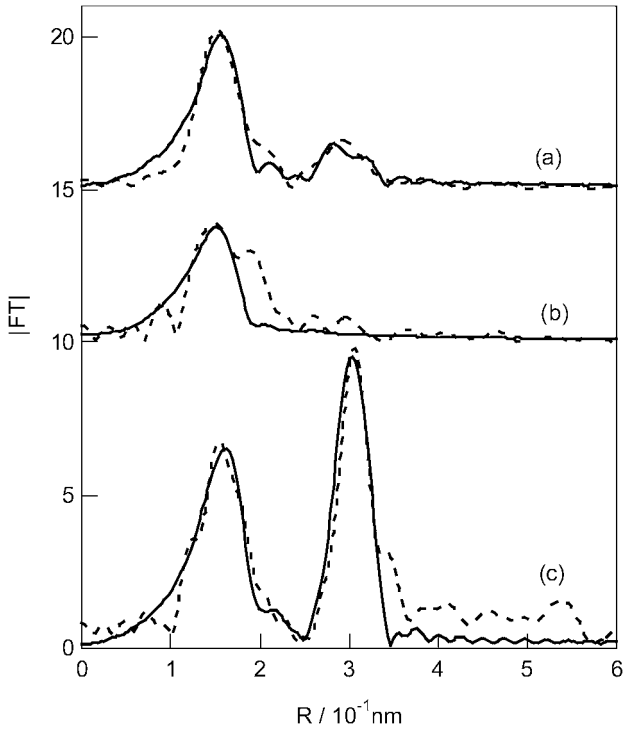

Fig. 2. Fourier transformed k^3-weighted EXAFS functions (· · · · · · · · ·) for (a) Zr-MCM-41-573(imp), (b) Zr-MCM-41-773(imp) and (c) Zr-MCM-41-1273(imp), together with the results of curve fitting (———).

higher than that for Zr-MCM-41(mix). Aggregation of zirconium species was observed in Zr-MCM-41(mix) as suggested by the results of EXAFS analysis, while zirconium species was found to be highly dispersed on the mesopore silica wall in Zr-MCM-41-393(imp), thus suggesting that the number of active site is relatively large. Zr-MCM-41-573(imp) has lower activity for the peroxidative bromination reaction of phenol red than that of Zr-MCM-41-393(imp) and that the activity for the reaction decreases with calcination temperature. As revealed in the results of EXAFS analysis, zirconium species aggregate each other by calcination at 573 K. The aggregation of zirconium species caused reduces the catalytic activity for the reaction.

Acknowledgement

The EXAFS measurements were done by the approval of the PAC committee (proposal No: 2001G298).

References

1. Biz, S. and Occelli, M. L., Catal. Rev. -Sci. Eng. **40**, 329 (1998).
2. On, D. T., Desplantier-Giscard, D., Danumah, C. and Kaliaguine, S., Appl. Catal. A **222**, 299 (2001).
3. Chaudhari, K., Bal, R., Srinivas, D., Chandwadkar, A. J. and Sivasanker, S., Micropor. Mesopor. Mater. **50**, 209 (2001).
4. Liu, S.-H. and Wang, H. P., Int. J. Hydrogen Energy **27**, 859 (2001).
5. O'Brien, S., Tudor, J., Maschmeyer, T. and O'Hare, D., Chem. Commun. 1905 (1997).
6. Tuel, A., Gontier, S. and Teissier, R., Chem. Commun. 651 (1996).
7. Gontier, S. and Tuel, A., Appl. Catal. A **143**, 125 (1996).
8. Walker, J. V., *et al*., J. Am. Chem. Soc. **119**, 6921 (1997).
9. Stern, E. A., Newville, M., Ravel, B., Yacoby, Y. and Haskel, D., Physica B **208**, 117 (1995).
10. Ankudinov, A. L., Ravel, B. and Rehr, J. J., Phys. Rev. B **58**, 7565 (1998).
11. Kostova, N. G., *et al.,* Catal. Today **65**, 217 (2000).

Physica Scripta. Vol. T115, 837–840, 2005

Structure and Magnetism of Ni Clusters in AlO_x: Importance of XAS in the Synthesis Optimization

E. Fonda[1*], D. Babonneau[2], F. Pailloux[2], S. R. Teixeira[3] and A. Traverse[1]

[1]Lab. pour l'Utilisation du Rayonnement Electromagnétique, BP 34, 91898 Orsay, France
[2]Lab. de Métallurgie Phys., UMR6630 CNRS, 86962 Futuroscope Chasseneuil, France
[3]Instituto de Fisica –UFRGS, P.O.Box 15051, 91501-970, Porto Alegre, RS, Brazil

Received June 26, 2003; accepted November 4, 2003

PACS numbers: 6110Ht, 6146+w

Abstract

X-ray absorption spectroscopy has been used to optimize the synthesis of Ni nano particles between thin layers of AlO_x in an Al matrix. Al deposition is used to reduce previously oxidized Ni clusters. Ex-situ characterization shows absence of Ni/Al intermixing and of Ni oxidation for a wide range of Ni thickness and exposures to dry air. The system shows new magnetic properties reported here for the first time.

1. Introduction

Al or AlO_x coating of ferromagnetic metals (FM) or anti-ferromagnetic oxides is a step of the fabrication of magnetic tunnel junctions. In this step mixing can occur at the interface between Al and the ferromagnetic metal or incomplete oxidation of the AlO_x barrier can reduce a part of the underlying anti-ferromagnetic oxide.

Recently, Egelhoff *et al.* suggested employing oxygen to suppress intermixing at the Al/*FM* interface [1]. The authors showed by X-ray reflectometry that oxidation of the first atomic layers of the ferromagnetic metal is sufficient to stop intermixing with Al in the case of $X = $ Co, Ni and $Ni_{80}Fe_{20}$ for stacks of the type SiO_2\10 nm X\4 nm Al. The same authors reported that Al is able to reduce the first few atomic layers of the ferromagnetic metal (*FM* = Ni, Co or Fe) and form an AlO_x diffusion barrier. R. Schad *et al.* [2] observed the stability of the AlO_x barrier and its capacity to protect the *FM* metal from oxidation even at an AlO_x thickness of about 0.6 nm. The authors employed reflectometry or X-ray photo-emission spectroscopy (XPS), but no detailed structural data are available by these techniques. Room temperature spontaneous mixing at the Al/Ni interface has already been successfully characterized by combining XAS and magnetic measurements (SQUID). Ni/Al (111) bi-layers [3] as well as Ni/Al multilayers [4] have been investigated. Ni and Al quickly react and below a thickness of 8 ML, Ni is fully mixed with Al, thus non-magnetic [5, 6].

We have studied stacks of the type SiO_2\Al*FM* t(nm)\Al produced by metal vapor deposition (MVD) in high vacuum (HV). After the deposition of each Ni or Al film, samples are exposed in-situ to a dry synthetic air flux. When optimal exposure time and pressures are found, no sign of FM\Al intermixing or of FM oxidation can be detected for t_{Ni} as low as 0.7 nm, even if exposure to oxygen is by two orders of magnitude larger than that reported by Egelhoff *et al.* [1].

XAS is sensitive both to oxidation state and local structure, it proves to be a unique tool to optimize the synthesis conditions: stopping intermixing and prevent oxidation of the thin ferromagnetic layer. We have been able to make *FM* clusters at the scale of a few nm or less in Al/AlO_x.

Grazing incidence small angle X-ray scattering (GISAXS) and transmission electron microscopy sustain XAS observations and provide upper limits for cluster size and cluster-cluster distances.

Finally, first magnetic results are shown. Peculiar magnetic properties are found and the possible origin of these features will be shortly discussed.

2. Experimental

Samples of the type SiO_2/Al 20 nm (p_{air})/Ni t(nm) (p_{air})/Al 20 nm were prepared in a HV chamber by metal vapor evaporation on a room temperature substrate. Maximum pressure during evaporation of the metals is in the low 10^{-7} mbar range. After the deposition of each different layer of the film, we raise the pressure in the chamber with a flux of synthetic air: nitrogen is necessary to avoid damages to the turbo pump. The pressure is kept for 5′ and then it is lowered back to the base value in almost the same time. The values of air pressure (20% O_2) are reported in Tab. I and discussed in section 3 with the results. Al and Ni thicknesses have been measured by a calibrated quartz micro-balance during deposition. Growth speeds are 10^{-2} and 10^{-1} nm s^{-1} for Ni and Al, respectively.

XANES (in Fig. 1) and EXAFS (not shown) spectra have been recorded at beam line D42 LURE with Si111 channel cut monochromator; a ionization chamber filled with air was used to monitor the incoming monochromatic beam and spectra were collected in the conversion electron yield (CEY) mode at liquid nitrogen temperature (LNT). The CEY cryostat employed is described in [7]. Spectra have been analyzed towards

Table I. *Post oxidation pressure dependence of the structure of Ni clusters. Ni thickness is 1.5 nm for all samples.*

Air Pressure (10^{-2} mbar)		N	R (nm)	σ^2 (10^{-5} nm^{-2})	Average Particle Diameter (nm)
0.0	Al	5.6(3)	2.424(6)	7.1(9)	/
0.1	Al	1.1(3)	2.42(1)	7(1)	
	Ni	8.7(4)	0.2479(2)	5.5(3)	14(4)
0.3	Ni	8.9(6)	0.2478(3)	5.4(5)	15(3)
0.6	Ni	9.2(8)	0.2473(5)	5.4(6)	16(6)
1.2	Ni	9.1(7)	0.2476(4)	5.0(5)	15(5)
Bulk	Ni	12.0(5)	0.2478(2)	3.1(3)	/

*e-mail: fonda@lure.u-psud.fr

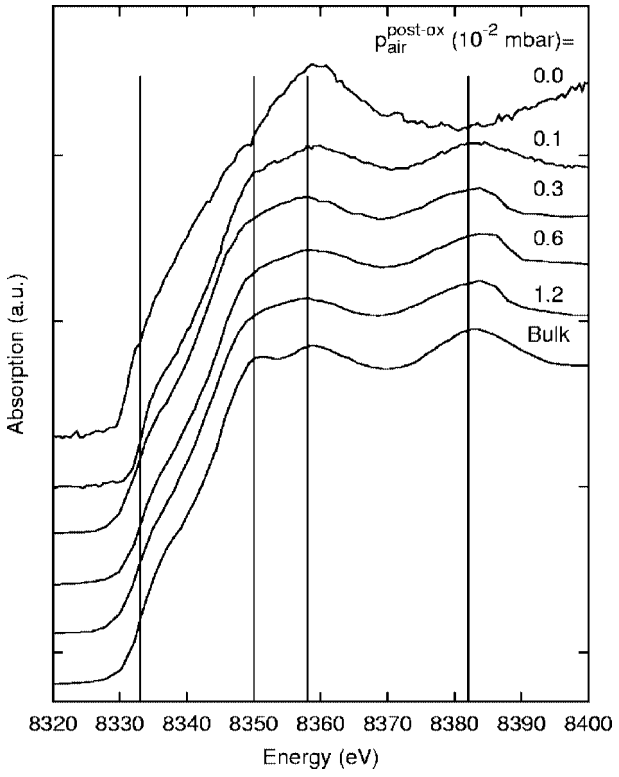

Fig. 1. XANES spectra at the Ni K-edge on samples SiO_2/Al 20 nm/Ni 1.5 nm/Al 20 nm versus different exposures to synthetic air (20% O_2/80% N_2). Exposure time is constant, 300 s. See Section 2. experimental for details.

theoretical standards obtained with code Feff8.1 [8] and self consistent MS calculations. EXAFS extraction and refinements have been performed by Autobk [9] and IFeffit codes [10], respectively.

The morphology and arrangement of the clusters was investigated by grazing incidence small-angle X-ray scattering (GISAXS) [11]. Measurements were carried out on DW31B LURE beam-line at a wavelength of 0.168 nm. GISAXS spectra are not shown.

The microstructure of the films was investigated by a JEOL 3010 high resolution transmission electron microscope (HRTEM) operating at 300 kV. A cross section of the sample with $t_{Ni} = 1.5$ nm and $p_{air} = 10^{-3}$ mbar is shown in Fig. 2.

Magnetization cycles have been measured with a superconducting quantum interference device (SQUID) at different temperatures and are reported in Fig. 3 and 4. Diamagnetic background coming from the thick SiO_2 substrate has been removed by a linear fit of the magnetization at high negative fields. A magnetization measurement of a blank SiO_2 substrate has been used to check the procedure and ensure background linearity.

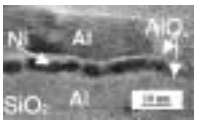

Fig. 2. Transmission electron microscopy image on a cross section of sample SiO_2/Al 20 nm/Ni 1.5 nm/Al 20 nm with $p = 3.0 \cdot 10^{-3}$ mbar. Ni clusters are in black at the center embedded in a thin layer of amorphous AlO_x.

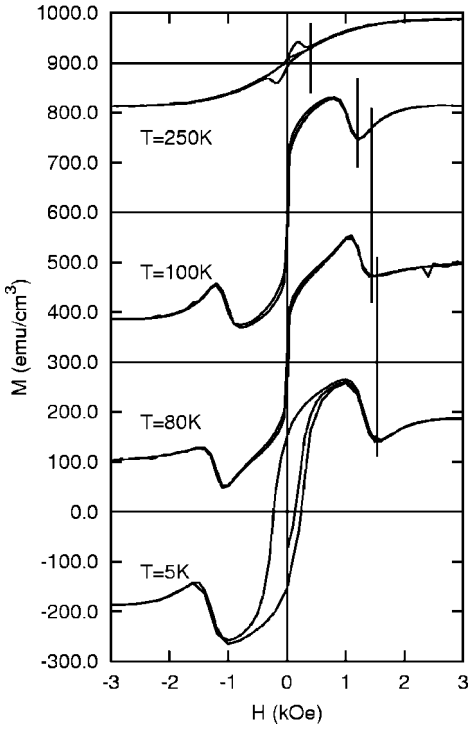

Fig. 3. Magnetization-demagnetization cycles of sample SiO_2/Al 20 nm/[Ni 1.5 nm/Al 8.3 nm]$_3$ with $p = 10^{-3}$ mbar.

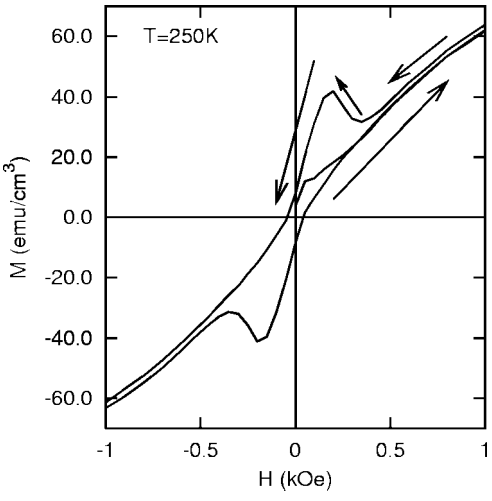

Fig. 4. An expanded view of the magnetization-demagnetization cycle at $T = 250$ K of sample SiO_2/Al 20 nm/[Ni 1.5 nm/Al 8.3 nm]$_3$ with $p = 10^{-3}$ mbar. The arrows indicate the magnetization path.

3. Results

3.1. *X-ray absorption spectroscopy*

XANES spectra in Fig. 1 well describe how XAS is effective in detecting Ni/Al intermixing and in driving synthesis optimization: when no air is introduced in the chamber after the deposition (in Fig. 1. $p_{air} = 0.0$ mbar), Ni and Al diffuse and XANES is typical of a disordered Ni aluminide like AlNi, Al_3Ni or Al_3Ni_2 [3, 4]. At pressures above $p_{air} = 10^{-3}$ mbar spectra are similar to bulk Ni, but smeared. This can be due to disorder or size distribution and small size of the particles. At $p_{air} = 10^{-3}$ mbar XANES is similar to bulk Ni, but the peak above 8358 eV is displaced at higher energy and is broader. This is simply due to the presence of a small Ni aluminide fraction that contributes to XANES [4]. The analysis of EXAFS spectra (not shown here)

Table II. *Thickness dependence of the structure and size of Ni clusters.*

Ni thickness t (nm)		N	R (nm)	σ^2 (10^{-5} nm^{-2})	Average Particle Diameter (nm)
0.7	Al	3(1)	2.41(2)	12(8)	
	Ni	4.9(7)	2.482(6)	5(1)	0.63(9)
1.5	Ni	8.9(6)	0.2478(3)	5.4(5)	1.5(3)
3.0	Ni	10.4(4)	0.2482(2)	4.8(3)	2.8(7)
6.0	Ni	11.3(6)	0.2481(3)	4.4(4)	>4
12.0	Ni	11.9(4)	0.2485(2)	4.6(2)	/
20.0	Ni	12.1(4)	0.2487(2)	4.4(2)	/
Bulk	Ni	12.0(5)	0.2478(2)	3.1(3)	/

gives a more quantitative description of the system. Results for samples at different oxidation pressures and $t_{Ni} = 1.5$ nm are shown in Tab. I. In agreement with XANES qualitative perusal, sample labeled $p_{air} = 0.0$ mbar contains a diluted Ni aluminide, while rising the pressure to $p_{air} = 10^{-3}$ mbar separates Ni and Al except for a small fraction. At higher pressures the local structure contains only contributions of a small Ni cluster and it does not change significantly from sample to sample. From the diminished Ni-Ni coordination number we can estimate the average particle size that is 1.5(5) nm.

EXAFS analysis results on samples obtained with variable Ni thickness and $p_{air} = 3 \cdot 10^{-3}$ are shown in Tab. II. The Ni-Ni coordination number increases as t_{Ni} and the average particles size obtained is close to the layer thickness. Disorder decreases in the series as we move from a fine particulate system to an almost continuous film. Ni-Ni distance marginally changes, but there is no clear trend in its evolution. In the case of $t_{Ni} = 0.7$ nm (about 3 Ni atomic layers), instead of a Ni-O contribution a Ni-Al signal is found. Assuming that it comes from the particles interfaces, we can deduce an average particle size of 0.63(9) nm.

3.2. *GISAXS*

GISAXS results (Tab. III) are of difficult interpretation for Ni thickness above 1.5 nm, since the system is almost coalescent. In Tab. III, numerical results for samples obtained with $p_{air} = 3 \cdot 10^{-3}$ mbar are shown. For $t_{Ni} = 0.7$ and 1.5 nm two small nonspecular diffuse peaks appear along the q_y axis. Integration of narrow stripes in the q_z and q_y directions provides information on vertical and horizontal particle sizes and average inter particle distance.

Actually, at $t_{Ni} = 1.5$ nm (and both p_{air}) half of the matter is apparently lost and it could be in the form of smaller particles or in a quasi continuous layer. This point will be discussed later.

Table III. *GISAXS results for $p_{air} = 3 \cdot 10^{-3}$ mbar.*

t_{Ni} (nm)	p_{air} (mbar)	Particle size (nm × nm)	Particle-Particle Distance (nm)
0.7	$3 \cdot 10^{-3}$	3.0 × 1.7	4.9
1.5	$3 \cdot 10^{-3}$	3.0 × 1.5	5.6
1.5	$1 \cdot 10^{-3}$	3.0 × 2.0	6.0

3.3. *Electron Microscopy*

A cross section of sample $p_{air} = 3 \cdot 10^{-3}$ mbar and $t_{Ni} = 1.5$ nm is shown in Fig. 2. Clusters are visible as dark objects in the central layer. Around them, a thin film is observable in light contrast. This is most likely AlO_x as will be discussed in the next section. Then, lower and upper Al films are visible; in the upper film there is a Al grain oriented as such to diffract the electrons and reveal interference fringes.

3.4. *Magnetometry*

Up to now, only sample (SiO_2/Al 20 nm/[Ni 1.5 nm/Al 8.3 nm]$_3$, $p_{air} = 1 \cdot 10^{-3}$ mbar) has been investigated. Magnetization cycles are shown in Fig. 3 for temperatures below and above the blocking (T_B) and Curie (T_C) temperature. Blocking temperature is about 50 K at 100 Oe and Curie temperature at about 250 K (corresponding zero-field-cooled/field-cooled cycles are not shown here). Lowering of the saturation magnetization ($M_S = -250$ emu/cm^3 at $T = 250$ K and 1 kOe) and increase of the coercitive field (H_C about 240 Oe at 5 K) with respect to bulk ($M_S = 484$ emu/cm^3, $H_C = 6$ Oe) are observed.

Another important feature appears at H about 1 kOe: the total magnetization drops of about 40% and at higher field it increases again, but at slower rate. This happens at 1 kOe at 5 K and at lower fields at higher temperatures.

A more detailed view of the magnetization cycle at 250 K is shown in Fig. 4 and reveals a second feature. The path it is not reversible and the total magnetization increases in a narrow region at low field while decreasing applied field. To our knowledge, these two features have never been described before in the literature.

4. Discussion

X-ray absorption data give direct and indirect information on the Ni structure. The first important information is that Ni oxide is not found in all samples within the sensitivity of XAS (a few %). Sample $t_{Ni} = 0.7$ nm should be the more sensitive, since it has the most important surface to bulk ratio; in this sample Ni-Al contributions are found instead of Ni-O. This finding is in accordance with the more negative potential for the oxidation of Al than that of Ni, then Ni and Al mixing is favorable in thermodynamic terms and occurs spontaneously at room temperature [3, 4] Al deposited on the top of oxidized Ni completely reduces it, thus Ni is surrounded by AlO_x.

The size of the particles as evaluated by XAS, GISAXS and observed by TEM is quite different. XAS results indicate a dense packing of particles with an average diameter close to the layer thickness for $t_{Ni} < 3$ nm. Actually, for values of t_{Ni} equal to or larger than 3 nm, it is not appropriate to speak in terms of particles, since GISAXS shows that particles are coalescent and no more nonspecular peaks are visible.

On the other hand, if we restrain our discussion to values of t_{Ni} equal to or smaller than 1.5 nm, GISAXS estimate does not take into account a large part of matter. Larger, well ordered particles contribute much more to the nonspecular signal than smaller particles. This justifies that the Ni amount calculated on the basis of GISAXS for sample $t_{Ni} = 1.5$ nm is less than half of the real Ni quantity even considering a compact packing in the plane. Thus, EXAFS average can be retained, but GISAXS gives a good estimate of the larger particles. This is in part confirmed by TEM cross section in which largest particles are almost 2–3 nm in

size, while particle-particle distance cannot be easily determined since we are observing the projection in the plane of the particles at different depths.

Magnetic properties of embedded nano particles are quite complex, since they are dominated by competing factors. While small size should favor an increased magnetic moment of the surface particles as observed in free particles [12], the interaction with the matrix can induce a loss [4, 13] or an increase [14] of the magnetization or more complicate exchange effects [15]. In addition, inter particle interactions play a role when the distance between particles is comparable to their size, as it is the case here.

This complexity makes difficult to find a model to explain magnetization cycles reported in Fig. 3 and 4. The irreversible path in Fig. 4 can be partially explained by the nucleation of vortex and its propagation during magnetization reversal as described by Guslienko *et al.* [16]. Actually, the authors described the vortex inside a particle and its propagation in an array of particles, but the same scheme could be applied to a vortex structure of magnetically interacting particles.

The drop of magnetization observed at all temperatures could be caused by a partial antiferromagnetic (AF) coupling of particles or of the particle shell. The origin of this coupling is at present undetermined. While the presence of a significant fraction of Ni oxide, which is AF, has been excluded and it has been demonstrated that Ni should be in contact with Al rather oxygen, this point is open and it is the subject of our active research.

5. Conclusions

A dense layer of Ni clusters with sizes below 3 nm can be produced in a thin AlO_x cage embedded in Al. XAS shows to be the best method to characterize the clusters and optimize the synthesis for particle sizes of a few nanometers.

Magnetization measurements reveal new properties of these systems that are reported here for the first time. The work to understand them is currently in progress.

Acknowledgment

E. Fonda has been fully supported during this research by a Marie Curie Fellowship of the E. U. program "Human Potential" (Contract HPMF-CT-20001-01125).

The authors thank O. Lyon of LURE (CNRS) for its helpful assistance during GISAXS measurements on beam-line DW31B.

References

1. Egelhoff, W. F. Jr., *et al.*, J. Appl. Phys. **89**, 5209 (2001).
2. Schad, R., *et al.*, J. Appl. Phys. **89**, 6659 (2001).
3. Damoc, L., Fonda, E., Le Fevre, P. and Traverse, A., J. Appl. Phys. **92**, 1862 (2002).
4. Fonda, E., Petroff, F. and Traverse, A., J. Appl. Phys. **93**, 5937 (2003).
5. Min, B. I., Freeman, A. J. and Jansen, H. J. F., Phys. Rev. **B37**, 6757 (1998).
6. Robles, R., Longo, R. C., Vega, A., Rey, C. and Gallego, L. J., Surf. Sci. **482–485**, 976 (2001).
7. Mimault, J., Faix, J. J., Girardeau, T., Jaouen, M. and Tourillon, G., Meas. Sci. Technol. **5**, 482 (1994).
8. Ankudinov, A. L. and Rehr, J. J., Phys. Rev. **B62**, 2437 (2000).
9. Newville, M., Livins, P., Yacoby, Y., Rehr, J. J. and Stern, E. A., Phys. Rev. **B47**, 14126 (1993).
10. Newville, M., J. Synchrotron Rad. **8**, 96 (2001).
11. Naudon, A. and Thiaudiere, D., J. Appl. Cryst. **30**, 822 (1997).
12. Billas, I., Chatelian, A. and de Heer, W. A., Science **265**, 1682 (1994).
13. Eastham, D. A., *et al.*, J. Phys. Condens. Matter **9**, L 497 (1997).
14. Respaud, M., *et al.*, Phys. Rev. B **57**, 2925 (1998).
15. Krishnan, K. M., Acta Mater. **47**, 4233 (1999).
16. Guslienko, K. Yu., Novosad, V., Otani, Y., Shima, H. and Fukamichi, K., Phys. Rev. **B65**, 024414 (2001).

Physica Scripta. Vol. T115, 841–843, 2005

Effects of Boron and Phosphorous on Nano-Amorphous Ni-B and Ni-P Alloys Studied by X-ray Spectroscopy

Shiqiang Wei[1]*, Zheng Jiang[1], Zheng Wei[1], Xinyi Zhang[2] and Shaobo Zou[1]

[1]National Synchrotron Radiation Laboratory, University of Science and Technology of China, Hefei 230029, P.R. China
[2]Synchrotron Radiation Research Center and Surface Physics Laboratory (National Key Laboratory), Fudan University, Shanghai 200433, P.R. China

Received June 26, 2003; accepted in revised form November 19, 2003

PACS number(s): 61.10.Ht, 61.43.Dq, 61.46.+w

Abstract

Both XAFS and XRD techniques have been used to investigate the effects of boron and phosphorous in nano-amorphous Ni-B and Ni-P alloys annealed at various temperatures. The XAFS and XRD results indicate that the initial Ni-B and Ni-P samples are amorphous alloys with large disorder. The static disorder factor (σ_S) of the nearest Ni-Ni sub-shell is 0.33 and 0.28 Å for the initial Ni-B and Ni-P alloys, respectively. Under an annealing temperature of 573 K, the nano-amorphous Ni-B alloy is crystallized into mixed phases of a crystalline Ni_3B and a metastable intermediate with smaller grain size and metallic Ni-like structure whose average grain size is about 30 nm, and the nano-amorphous Ni-P alloy forms two phases of crystalline Ni and Ni_3P with an average grain size of about 120 nm. It means that boron can retard the growth of Ni-B alloy into particles with larger size, in comparison with phosphorous. When the annealing temperature is increased to 773 K, most of the nano-crystalline Ni_3B is decomposed into crystalline Ni with larger grain size, but crystalline Ni_3P is rather stable. The XAFS results further show that the local structure around Ni atoms in the NiB sample annealed at 773 K is almost the same as that of Ni foil. However, the static disorder σ_S (0.125 Å) of the Ni-P sample annealed at 773 K is still much larger, which is attributed to the existence of some amount of crystalline Ni_3P. These results suggest that there is a great difference in the crystallization mechanism between nano-amorphous Ni-B and Ni-P alloys.

1. Introduction

Recently, much attention has been paid to the industrial applications of catalytic hydrogenation of nano-amorphous metal-metalloid Ni-B (P) alloy powders prepared by chemical reduction, since they have shown much higher activity and selectivity in the hydrogenation of furfural, cyclopentadiene and benzene as compared to the conventional industrial catalyst of Raney Ni [4–9]. In order to well understand and modify the catalytic nature of nano-amorphous Ni-B and Ni-P alloys, it is essential to study the effect on their structures of boron and phosphorous.

A lot of studies have been performed to elucidate the roles of boron and phosphorous in amorphous Ni-B (P) alloys. Li *et al*. [10, 11], Keong *et al*. [12] have studied the long-range structures of Ni-B and Ni-P alloys with X-ray diffraction (XRD). Their results have shown that the initial Ni-B and Ni-P samples are amorphous alloys. After annealing at 573 K, the amorphous Ni-B alloy crystallized to form a mixture of Ni, Ni_2B and Ni_3B [10, 11], and amorphous Ni-P alloy crystallized to produce a mixture of Ni, Ni_2P and Ni_3P [12]. With the annealing temperature rising to 773 K, most of the Ni_3B alloy in the Ni-B alloy decomposes into metallic Ni with a large grain size [11, 13, 16], while the crystalline Ni_3P in the NiP alloy kept its stability [12, 14, 15]. Although Li *et al*. have studied the structure of Ni-B and Ni-P with XAFS [10, 11, 14, 15], they only showed the radial structural functions of Ni atoms for the initial and annealed Ni-B and Ni-P alloys. Their results indicate that the amorphous Ni-B and Ni-P alloys are crystallized at annealing temperatures of 573 or 773 K. However, they have not performed a deeper and quantitative data analysis for the local structures of the amorphous Ni-B and Ni-P alloys due to the difficulty in analyzing XAFS spectra with large disorder.

In this work, both XRD and XAFS are used to study the long-range and local structures of initial and annealed nano-amorphous Ni-B and Ni-P alloys prepared by chemical reduction. We aim to investigate the influence of boron and phosphorous on the structures and the thermal stability of the nano-amorphous NiB and NiP alloys. These results are useful to understand the relationship between the structures and catalytic activity for nano-amorphous Ni-B and Ni-P alloys.

2. Experimental

Nano-amorphous Ni-P alloy powders were prepared via the following procedures: 22.5 g $NiCl_2{\cdot}6H_2O$, 20 g $NaH_2PO_2{\cdot}H_2O$ and NaAc were dissolved in water, and the volume of this mixed aqueous solution was 150 ml. The pH of this mixed solution was adjusted to 11 using 0.1 mol NaOH solution. Then, the aqueous solution was heated and kept at 313 K in a water bath for 4 hours. After the reaction had finished, the product was filtered and washed thoroughly with ammonia solution, subsequently washed by distilled water and 99.9% ethanol (EtOH) several times. The final product was kept in EtOH. The preparation of nano-amorphous Ni-B was described elsewhere [16]. Inductively coupled plasma spectrometry showed that the atomic composition of Ni-B and Ni-P powder was $Ni_{70}B_{30}$ and $Ni_{80}P_{20}$ (denoted as Ni-B and Ni-P hereafter). The crystallization process of the nano-amorphous Ni-B (or Ni-P) is described as follows. First, initial Ni-B (or Ni-P) powder of 2 g was placed in a pipe furnace, in a flow of high purity Ar gas. Second, the sample was slowly elevated to an annealing temperature designed in advance, and kept at various annealing temperatures for 2 hours. Finally, the annealed Ni-B (or Ni-P) samples were obtained after cooling naturally to room temperature.

The X-ray absorption spectra at the Ni K-edge for the initial and annealed $Ni_{70}B_{30}$ samples were measured at the beamline of U7C of the National Synchrotron Radiation Laboratory (NSRL) and 4W1B of the Beijing Synchrotron Radiation Facitlity (BSRF). The storage ring of NSRL was operated at 0.8 GeV with a maximum current of 160 mA. The hard X-ray beam was from a three-pole superconducting Wiggler with a magnetic field intensity of 6 Tesla. Fixed-exit Si(111) flat double crystals were used as a monochromator. The XAFS spectra were recorded in transmission mode with ionization chambers filled with Ar/N_2 at room temperature, using a Keithley Model 6517 Electrometer to

*Correspondent: Shiqiang Wei, E-mail: sqwei@ustc.edu.cn

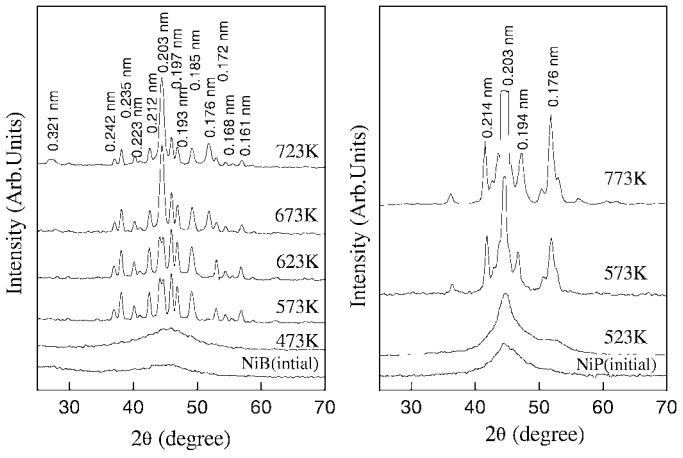

Fig. 1. XRD patterns of the nano-amorphous Ni-B (left) and Ni-P (right) alloy samples annealed at different temperatures.

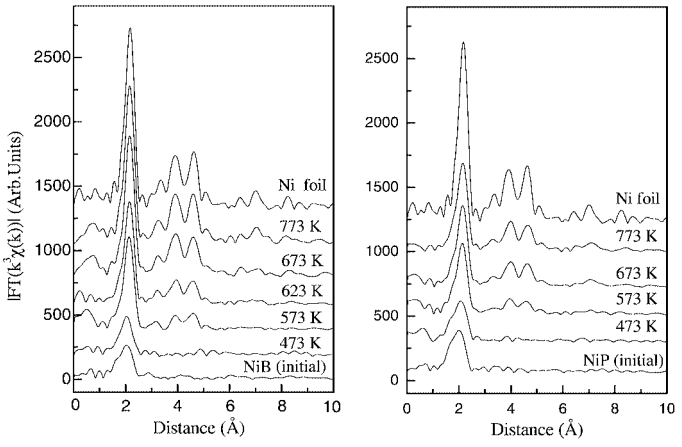

Fig. 2. RSFs of nano-amorphous Ni-B (left) and Ni-P (right) alloys annealed at different temperatures.

collect the electron charge directly. XAFS data of Ni-B and Ni-P samples were analyzed by USTCXAFS3.0 software packages compiled by Zhong and Wei according to the standard procedures [17].

The X-ray diffraction (XRD) patterns of the initial and annealed nano-amorphous NiB and NiP alloys were measured on a Y-4ϕ rotating target diffractometer (Dandong X-ray photometer Co. LTD) using Cu K_α radiation ($\lambda = 1.54056$ Å, 40 kV and 100 mA).

3. Results and Discussion

From the XRD patterns as shown in Fig. 1, it can be observed that there is a broad and weak peak located at $2\theta = 45^\circ$ in the initial nano-amorphous NiB and NiP alloys, which demonstrates that the initial Ni-B and Ni-P are typical amorphous alloys. Moreover, the peak of the initial Ni-B sample is much broader and weaker than that of the initial Ni-P sample, indicating the Ni-B sample possessing a higher amorphization than that of the Ni-P one. After annealing at 573 K, sharp peaks appear in the XRD curves of the NiB and NiP samples. By comparing with the standard XRD spectra of JCPDS-ICDD, it can be found that the crystalline Ni_3B and small amount of crystalline Ni_2B are formed for the nano-amorphous Ni-B alloy, and crystalline Ni_3P and metallic Ni are produced for the nano-amorphous Ni-P alloy. By using of the Scherrer Formula to estimate the grain size from the main peak of their XRD patterns, the average grain sizes are found to be about 30 nm and 120 nm for the Ni-B and Ni-P samples annealed at 573 K, respectively. These results indicate that boron plays a more important role in inhibiting the growth of nano-crystalline grains than phosphorous does. Our results about the grain-sizes of the annealing Ni-B and Ni-P alloys are consistent with those reported by Deng *et al*. [18] and Li *et al*. [19].

After annealing at 773 K, the strongest diffraction peak corresponding to crystalline Ni appears and the peaks associated with Ni_3B become much weaker for the Ni-B sample. This indicates that most of the Ni_3B has been decomposed to form crystalline Ni. The XRD pattern for the Ni-P sample annealed at 773 K is similar to that annealed at 573 K, except that the peaks corresponding to crystalline Ni and Ni_3P are much stronger. This means that there still remains some amount of crystalline Ni_3P in the Ni-P sample annealed at 773 K. We consider that the thermodynamic stability of nano-crystalline Ni_3P with larger grain size (120 nm) is higher than that of nano-crystalline Ni_3B with smaller grain size (30 nm).

The radial structural functions (RSF) of the nano-amorphous Ni-B and Ni-P alloys are shown in Fig. 2. In order to obtain the local structural parameters of Ni-B and NiP samples, the asymmetric pair distribution function of $G(R)_{\text{asym}}$ assumed as a convolution of Gaussian function, P_G, and exponential function, P_E, is used to fit the Ni K-edge XAFS spectra of the nano-amorphous Ni-B and Ni-P alloys. $G(R)_{\text{asym}}$ has been reported elsewhere [20, 21]. The structural parameters of the Ni-B and Ni-P samples annealed at various temperatures are summarized in Table I. In Fig. 2 only one main peak at 2.05 Å is observed for the initial Ni-B and Ni-P samples. This further shows the amorphous feature of the initial Ni-B and Ni-P alloys. The static disorder factor (σ_S) of the first nearest Ni-Ni sub-shell for the initial Ni-B alloy is 0.33 Å, which is larger than that ($\sigma_S = 0.28$ Å) of the initial Ni-P alloy. It indicates obviously that the disorder of the nano-amorphous Ni-B alloy is larger than that of the nano-amorphous Ni-P alloy. This result is consistent with that obtained from our XRD. Li *et al*. [10, 11] and Keong *et al*. [12] have reported that only one strong peak appears at the R-range of 1.3–2.8 Å, and that no peaks can be observed at longer distances.

After annealing at 573 K, the position of the first peak of the Ni-B and Ni-P samples shifts from 2.05 to 2.14 Å and its magnitude intensity increases about twice. Furthermore, it can be found that two small peaks corresponding to the second and third coordination shells appear at the positions of $R = 3.9$ Å and $R = 4.8$ Å. This result indicates that the nano-amorphous Ni-B and Ni-P alloys are crystallized at the annealing temperature of 573 K. The structural parameters in Table I have shown that the bond length R and σ_S for the Ni-Ni sub-shell undergo large changes for the Ni-B and Ni-P alloys annealed at 573 K, and decrease from 2.75 Å and 0.33 Å to 2.55 Å and 0.11 Å, and from 2.71 Å and 0.28 Å to 2.58 Å and 0.16 Å, respectively. These XAFS results are in good agreement with those from XRD. Moreover, the XAFS results indicate that two phases of nano-crystalline Ni with small grain size and crystalline Ni_3B are formed in the nano-amorphous Ni-B alloy annealed at 573 K, despite that no diffraction peaks corresponding to crystalline Ni appear in its XRD pattern [16]. Hence, we consider that boron can inhibit the nano-crystalline Ni to grow into grains with large sizes.

With the annealing temperature increasing to 773 K, the RSF curve of the Ni-B sample is almost the same as that of the metallic Ni foil. From the structural parameters of the Ni-B alloy annealed at 773 K in Table I, the coordination number N decreases from 2.6 to 0.3 for the first Ni-B sub-shell, and the bond length R and the

Table I. *Structural parameters of the nano-amorphous Ni-B and Ni-P alloys at different annealing temperatures.*

Sample	Temp. (K)	Bond	R (Å)	R_0 (Å)	N	σ_T (Å)	σ_S (Å)	ΔE_0 (eV)
Ni-B	Initial	Ni-Ni	2.74	2.41	11.0 ± 1.0	0.069	0.33	−0.2
		Ni-B	2.18	2.15	2.7 ± 0.3	0.046	0.034	−4.7
Ni-P	Initial	Ni-Ni	2.71	2.43	10.0 ± 1.0	0.060	0.28	−2.9
		Ni-P	2.23	2.15	1.6 ± 0.3	0.040	0.080	5.3
Ni-B	573	Ni-Ni	2.55	2.43	9.9 ± 1.0	0.060	0.11	−0.9
		Ni-B	2.18	2.15	2.6 ± 0.3	0.060	0.034	5.0
Ni-P	573	Ni-Ni	2.58	2.42	10.1 ± 1.0	0.063	0.16	−1.3
		Ni-P	2.22	2.15	0.8 ± 0.3	0.049	0.065	8.7
Ni-B	623	Ni-Ni	2.55	2.43	10.0 ± 1.0	0.058	0.10	−0.6
		Ni-B	2.18	2.15	2.6 ± 0.3	0.060	0.033	5.0
Ni-B	773	Ni-Ni	2.49	2.45	10.8 ± 1.0	0.070	0.039	1.6
		Ni-B	2.17	2.15	0.3 ± 0.3	0.056	0.023	−5.0
Ni-P	773	Ni-Ni	2.56	2.43	10.4 ± 1.0	0.060	0.125	−2.8
		Ni-P	2.25	2.19	0.6 ± 0.3	0.040	0.056	7.6
Ni foil		Ni-Ni		2.49	12.0	0.074		

*Average distance $R = R_0 + \sigma_S$, the uncertainties (or error bar) of R, σ_T and σ_S are about ±0.02 Å, ±0.005 Å, ±0.01 Å, respectively.

static disorder factor σ_S is 2.49 Å and 0.029 Å for the second Ni-Ni sub-shell, respectively. This indicates that most of the crystalline Ni_3B has decomposed. However, the intensity of the RSF first peak of the Ni-P alloy annealed at 773 K is only about half of that of metallic Ni foil, but is still similar to that of the Ni-P alloy annealed at 573 K. R and σ_S are 2.55 Å and 0.125 Å for the Ni-Ni sub-shell of Ni-P sample annealed at 773 K, respectively. Considering the XRD results, it can be believed that the thermodynamic stability of nano-crystalline Ni_3P is much higher than that of nano-crystalline Ni_3B. Hence, Ni_3P does not decompose at a temperature of 773 K.

Acknowledgement

This work was supported by the development of high-level university of University of Science and Technology of China, key-project of Beijing Synchrotron Radiation Facility, and key-program of Chinese Academy of Sciences.

References

1. Linderoth, S. and Morup, S., J. Appl. Phys. **69**, 5256 (1991).
2. Chen, Y., Catalysis Today **44**, 3 (1998).
3. Liebermann, H. H., "Rapidly Solidified Alloys" (M. Dekker, New York, 1993).
4. Hu, Z., Fan, Y. N. and Chen,Y., Appl. Phys. A **68**, 225 (1999).
5. Deng, J. F., Li, H. X. and Wang, W. J., Catalysis Today **51**, 113 (1999).
6. Moorjani, K. M. and Coey, J. D., "Magnetic Glasses", (Elsevier, Amsterdam, 1984), Chap. VIII.
7. Molnar, A., Smith, G. V. and Bartok, M., Adv. Catalysis **36**, 329 (1989).
8. Li, H. X. and Xu, Y. P., Mater. Lett. **51**, 101 (2001).
9. Lee, S. P. and Chen, Y. W., Industrial Engin. Chem. Res. **38**, 2548 (1999).
10. Li, H. *et al.*, Appl. Surface Sci. **152**, 25 (1999).
11. Li, H., Li, H. X. and Deng, J. F., Mater. Lett. **50**, 41 (2001).
12. Keong, K. G., Sha, W. and Malinov, S., J. Alloys Compounds **334**, 192 (2002).
13. Rojo, J. M. *et al.*, Phys. Rev. Lett. **76**, 4833 (1996).
14. Li, H. X., Wang, W. J., Li, H. and Deng, J. J., J. Catalysis **194**, 211 (2000).
15. Li, H. X. and Xu, Y. P., Mater. Lett. **51**, 101 (2001).
16. Wei, S. Q. *et al*., Phys. Rev. B **62**, 224201 (2001).
17. Zhong, W. J., He, B. and Wei, S. Q., J. University Sci. Technol. China **31**, 328 (2001).
18. Deng, J. F., Yang, J., Sheng, S. S., Chen, H. R. and Xiong, G. X., J. Catalysis **150**, 434 (1994).
19. Li, T. X. *et al*., J. Catalysis (in Chinese) **16**, 299 (1995).
20. Wei, S. Q. *et al*., J. Non-Crystalline Solids **275**, 160 (2000).
21. De Crescenzi, M. *et al*., Solid State Commun. **37**, 921 (1981).

Physica Scripta. Vol. T115, 844–846, 2005

The Manganese Complex of Oxygenic Photosynthesis: Conversion of Five-Coordinated Mn(III) to Six-Coordinated Mn(IV) in the S_2-S_3 Transition is Implied by XANES Simulations

Holger Dau*, Peter Liebisch and Michael Haumann

Freie Univ. Berlin, FB Physik, Arnimallee 14, D-14195 Berlin, Germany

Received June 26, 2003; accepted November 4, 2003

PACS numbers: 87.64.Fb; 87.14.Ee

Abstract

Photosynthetic water oxidation proceeds at a tetra-manganese complex bound to a cofactor-protein complex denoted as Photosystem II (PSII). To understand this process of fundamental importance for life on Earth, the crucial changes of the active-site occurring upon the individual transitions in the catalytic S-state cycle have been investigated by X-ray absorption spectroscopy at the Mn K-edge. For the S_2-S_3 transition, the changes in position and shape of the X-ray edge have been interpreted to be either associated with oxidation of Mn(III) to Mn(IV) or to formation of a ligand radical without manganese oxidation. Here we simulate XANES spectra of simple Mn-complexes using modern multiple-scattering code. Features of the XANES spectra are assigned to molecular orbitals by means of comparative semi-empirical calculations. It is concluded that the changes in position and shape of the edge spectra observed for the S_2-S_3 transition are explainable by the transformation of five-coordinated Mn(III) in a square-pyramidal geometry to six-coordinated Mn(IV).

1. Introduction

Photosynthetic water oxidation occurs at a manganese complex bound to a cofactor-protein complex denoted as Photosystem II (PSII). This complex contains four manganese atoms and, possibly, one calcium [1]. In the course of photosynthetic water oxidation the manganese complex of PSII acquires four distinct semi-stable oxidation states: S_0, S_1(dark-stable), S_2, and S_3. Light-driven oxidation of the S_3-complex is assumed to result in formation of S_4 which immediately is transformed to S_0, a transition coupled to the release of dioxygen. As reviewed elsewhere [2–5], by X-ray absorption spectroscopy (XAS) at the Mn K-edge changes in the arrangement of the nuclei as well as in the electronic structure (oxidation states, orbital occupancies) can be monitored as the Mn-complex of PSII advances through its catalytic S-state cycle. These changes are crucial with respect to the final goal to understand the mechanism of photosynthetic water oxidation at the atomic level.

Empirically it is found that the position of the X-ray edge shifts to higher energies upon oxidation of the X-ray absorbing transition metal (for a detailed discussion, see [5]). As shown in Fig. 1, for all oxidizing S-state transitions of the PSII manganese complex the Mn K-edge indeed shifts to higher energies [3, 6–10]. For the S_2-S_3 transition, however, the extent and especially the interpretation of the shift in the X-ray edge position is still debated. Using the inflection-point energy (zero-crossing point of the second derivative) as a marker for the edge position, Roelofs *et al.* [7] and Messinger *et al.* [9] found that the edge-shift determined for the S_2-S_3 transition is clearly smaller (by a factor of 4 to 7!!) than the ΔE_{edge} of the S_1-S_2 or S_0-S_1 transitions; they concluded that the S_2-S_3 transition does not involve manganese oxidation, but formation of a ligand radical instead. Using various alternative approaches to quantify the edge position, we determined the edge-shift to be of comparable magnitude for all oxidizing S-state transitions [3, 5, 8, 10, 11]. Consequently, we have concluded that Mn-centered oxidation is more likely than ligand-radical formation. It should be noted that the recent data of Dau *et al.* [3] and Messinger *et al.* [9] are mostly similar. We feel that the diverging conclusions are not rooted in the minor differences between these recent data sets, but in inappropriate analysis approaches (as discussed in [5]) and, especially, in an incomplete understanding of the structural and electronic factors that determine the XANES (X-ray absorption near-edge structure) spectra.

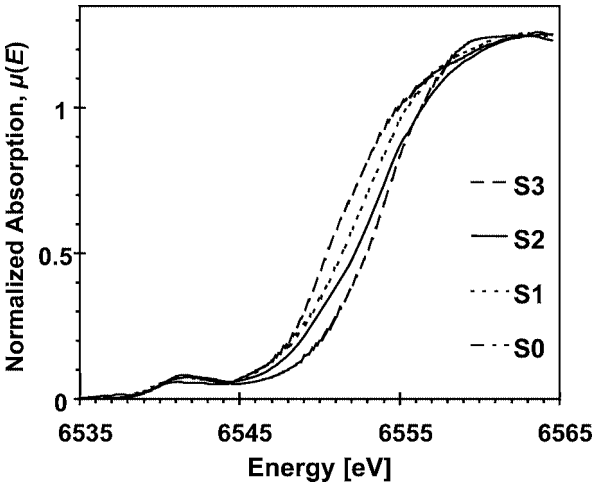

Fig. 1. XANES spectra of the PSII manganese complex for all four semi-stable intermediate states of the catalytic cycle.

In the S_2-S_3 transition the edge shape changes more pronouncedly than in the other oxidizing transitions. A particularly pronounced edge-shift is observed in the rising region of the edge (μ(E) < 0.4) which is continuously decreasing at higher energies. In clear contrast to the S_1-S_2 transition, no shift of the spectrum is observed around 6560 eV; instead an increase in the absorption is detectable (increase in the integrated area of the edge peak). Similarly pronounced changes in edge shape are not observed for the S_1-S_2 transition, which is commonly assumed to involve oxidation of Mn(III) to Mn(IV). Thus it has been argued that the edge-shape changes point towards the absence of Mn oxidation in the S_2-S_3 transition [7, 9], a conjecture which is rendered unlikely by the here presented XANES simulations.

Analysis of EXAFS (extended X-ray absorption fine-structure) spectra measured at 20 K (freeze-quench approach; [3, 4, 12]) and at room temperature [10, 13] indicate an increase in the number of di-μ-oxo bridges between Mn ions from two, in the S_1 and

*e-mail: holger.dau@physik.fu-berlin.de

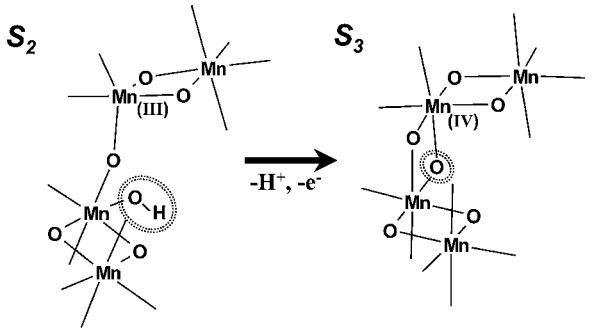

Fig. 2. Hypothesis on the structural changes of the PSII manganese complex associated with the S_2-S_3 transition [3]. The increase in the number of di-μ-oxo bridges upon the S_2-S_3 transition is strongly suggested by the analysis of EXAFS spectra collected for layered PSII membrane particles [3, 10, 12, 13]. The depicted arrangements of nuclei was chosen for clarity. The arrangement that is in best agreement with the linear dichroism in the EXAFS data of partially oriented samples [14, 15] and the structural information stemming from protein crystallography [16] differs slightly; for a more precise structural model of the PSII manganese complex in its S_1- and S_2-state, see [4, 17, 18]. The release of one proton from the manganese complex concomitant to the S_2-S_3 transition is indicated by time-resolved investigations on the proton release into the bulk phase and by analysis of electrochromic effects (Stark-shift in the spectra of nearby pigments); for review see [19]. The presence of five-coordinated Mn(III) can be energetically particularly favorable (Jahn-Teller effect) whereas Mn(IV) clearly prefers an octahedral coordination geometry. The proposed transformation of five-coordinated Mn(III) to six-coordinated Mn(IV) is confirmed by the XANES simulations discussed further below.

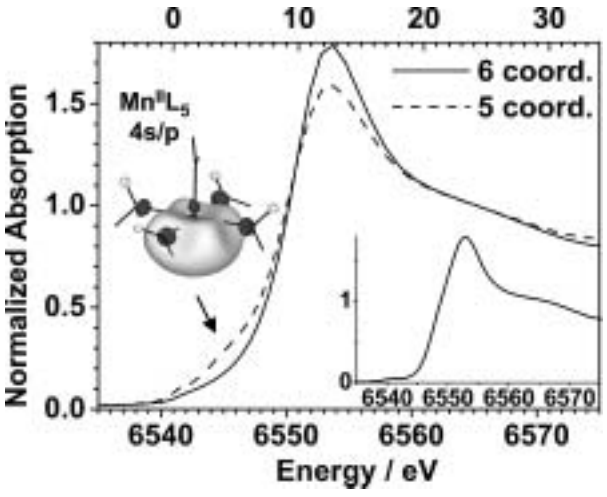

Fig. 3. XANES simulations of five-coordinated (square-pyramidal) and six-coordinated (octahedral) Mn(II). Solid line – $[Mn(H_2O)_6]^{2+}$; broken line – $[Mn(H_2O)_5]^{2+}$. For both complexes the Mn-O distance had been 2.195 Å. For comparison, the measured spectrum of $[Mn(H_2O)_6]^{2+}$ in aqueous solution is shown as an inset. The five-coordinated complex represents a purely hypothetical complex that had been obtained by omitting one of the six ligands of the six-coordinated complex. The molecular orbital (MO) is depicted that can be assigned to the shoulder-like feature in the simulated XANES spectrum of the five-coordinated complex. For the corresponding MO of the six-coordinated complex (not shown) we find that of all atomic orbitals of manganese only the 4s orbital contributes whereas in the five-coordinated complex significant s-p mixing is present (see inset). The s-p mixing facilitates the formally dipole forbidden 1s-4s transition in the five-coordinated complex. For details see [5].

S_2-state, to three, in the S_3-state. We have proposed that the μ-oxo bridge formation upon the S_2-S_3 transition is facilitated by transformation of five-coordinated Mn(III) to six-coordinated Mn(IV) [3]; a hypothetical scheme for the involved structural changes is depicted in Fig. 2. By XANES simulations it is shown that the occurrence of a transition from five-coordinated Mn(III) to six-coordinated Mn(IV) may indeed explain the distinct edge-shape changes observed upon the S_2-S_3 transition.

2. Materials and Methods

The experimental spectra shown in Fig. 1 correspond to the spectra presented in Dau *et al*. [3], but the shown spectra are renormalized such that their similarity with the data of Messinger *et al*. [9] is emphasized. For a description of experimental details, see [8].

To investigate the influence of coordination-number changes, XANES spectra were calculated using the *ab-initio* multiple-scattering code FEFF 8.2 of Rehr and coworkers (self-consistent potentials, full-multiple scattering calculations [20], for further details see [5]). Features of the XANES spectrum were assigned to molecular orbitals (MOs) by means of comparative semi-empirical MO-calculations [21] using the rationale described in Dau *et al*. [5].

3. Results and Discussion

In Figure 3, XANES spectra simulated for the Mn-hexaquo complex are shown; the simulated spectrum compares favorably well with measured spectra (inset in Fig. 3). By omission of one of the six water ligands a hypothetical five-coordinated complex (square-pyramidal coordination) is obtained which is characterized by a distinctly different XANES spectrum: (1) an additional shoulder is present in the rising part of the edge, and (2) the area of the principal absorption peak is diminished. Oscillator strength seems to shift from the edge peak towards the region of the initial edge rise.

The principal absorption maximum can be assigned to transition of the 1s core electron (of Mn) to unoccupied anti-bonding MOs with strong contributions of the 4p-orbitals of the X-ray absorbing manganese [5]. The energy level of the Mn 4s-orbital is in the rising part of the edge (∼7 eV above the onset of the pre-edge peak). In the six-coordinated complex the 1s-4s transition is dipole forbidden. In the five-coordinated complex, however, the corresponding molecular orbital gains significant p-character (see inset in Fig. 3). Due to this s-p mixing, a shoulder in the rising part of the spectrum is predicted for the five-coordinated complex. For a more complete discussion, see [5].

In the above considerations the Mn-ligand distances were assumed to be identical in the five-coordinated and in the six-coordinated Mn(II)-complex. To obtain spectra more closely related to the S_2-S_3 transition, we carried out XANES simulations for five-coordinated and six-coordinated Mn(III) and Mn(IV) ions using distances between manganese and its oxygen ligands that are typical for the respective oxidation-state/coordination-number combination.

As shown in Fig. 4, the transformation of Mn(III)L_6 to Mn(IV)L_6 is accompanied by an edge shift that (a) is relatively small in the region of the initial rise of the edge ($\mu(E) < 0.4$) and (b) continuously increases up to the edge maximum; the height of the edge maximum remains essentially unchanged. Upon the transition from five-coordinated Mn(III) to six-coordinated Mn(IV), however, the edge shift (1) is maximal in the region of the initial rise and minimal at the edge maximum; and (2) a clear increase in the area of the edge peak is observed.

In comparison to the simulated spectra of Fig. 4, in PSII (Fig. 1) the edge peak is clearly broader and lower, an observation easily explained by the pronounced spread of Mn-ligand distances [5] as

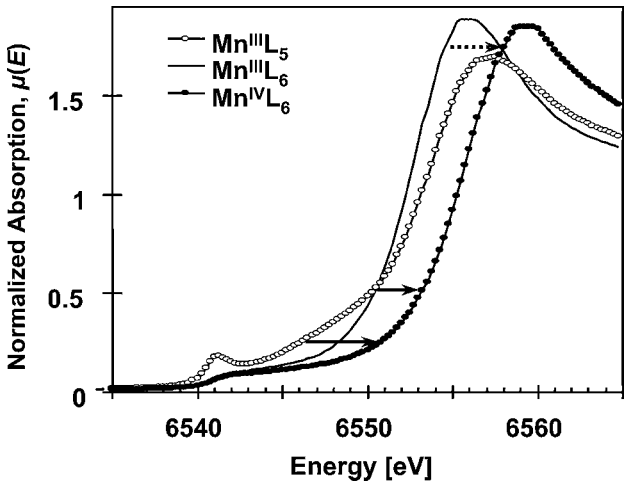

Fig. 4. XANES simulations for five- and six-coordinated Mn(III), and for six-coordinated Mn(IV). Open circles: $Mn(H_2O)_2(OH)_3$, Mn-O distance of 1.95 Å, square-pyramidal geometry. Solid line: $Mn(H_2O)_3(OH)_3$, Mn-O distance of 2.02 Å, octahedral geometry. Black circles: $Mn(H_2O)_2(OH)_4$, Mn-O distance of 1.90 Å, octahedral geometry.

it is encountered in the PSII manganese complex (see, e.g. [15]); the lower symmetry of the Mn coordination environment in PSII likely also contributes. The pre-edge peak is not appropriately simulated for two reasons: (*i*) The used multiple-scattering simulations can be anticipated to be of relatively low accuracy for low-lying bound states. (*ii*) The pre-edge peak depends strongly on details of the ligand environment (enhancement by broken inversion symmetry). The presence of di-μ-oxo bridges, e.g., leads to a significantly enhanced pre-edge magnitude. Such structural details, however, have not been considered in the shown XANES simulations. The most apparent difference between experimental spectra (Fig. 1) and simulated spectra (Fig. 4) is the magnitude of the edge shift that is roughly by a factor of four greater in the simulations. However, since in the tetra-manganese complex of PSII only one out of four Mn-ions is oxidized on each individual S-state transition, the magnitude of the observed edge shifts are anticipated to be by a factor of four smaller than in the simulations of Fig. 4.

Keeping in mind the above considerations, the comparison of the experimental spectra shown in Fig. 1 and of the simulated spectra shown in Fig. 4 can be approached. We find that the changes in the edge spectra detected for the S_1-S_2 transition resemble qualitatively the predicted changes for transformation of a Mn(III)L_6 complex to a Mn(IV)L_6 complex (see above, (a) and (b)). Most importantly, however, the major characteristics of the changes in the XANES spectra upon the S_2-S_3 transition are remarkably well modeled by simulating a transition from a square-pyramidal Mn(III)L_5 complex to an octahedral Mn(IV)L_6 complex (see above, (1) and (2)).

In the simulations described above we used the most simple structures (single Mn ion, all 5 or 6 Mn ligands at the same distance, idealized coordination geometries) that allow for a qualitatively correct description of the edge-shape changes. By XANES simulations on basis of clearly more sophisticated structural models of the tetra-manganese complex of PSII, a closer similarity between experimental and simulated spectra can be achieved (data not shown; see also contribution of Liebisch *et al.* in this volume), but the changes in the XANES spectra upon changes in the Mn oxidation and/or coordination geometry are similar to the here described edge-shape changes. To illustrate the principal effect and to facilitate a qualitative understanding of the underlying reasons for the edge-shape changes (in terms of molecular orbitals), we have deliberately chosen particularly simple structures.

In conclusion, the changes in the shape of the edge spectra observed for the S_2-S_3 transition are explainable by the transformation from five-coordinated Mn(III) to six-coordinated Mn(IV). That these changes in the edge spectra are associated with oxidation of a manganese ligand is a supposition we consider to be unlikely.

Acknowledgements

Financial support by the Deutsche Forschungsgemeinschaft (SFB 498, projects C6 and C8) and the German BMBF (program: Erforschung kondensierter Materie, grant 05/KS1KEA-6) is gratefully acknowledged.

References

1. Debus, R. J., Biochim. Biophys. Acta **1102**, 269 (1992).
2. Penner-Hahn, J. E., in "Metal Sites in Proteins and Models". (Edited by H. A. O. Hill and A. Thomson) (Springer Verlag, Heidelberg 1999), vol. 3, p. 1.
3. Dau, H., Iuzzolino, L. and Dittmer, J., Biochim. Biophys. Acta **1503**, 24 (2001).
4. Dau, H. and Haumann, M., J. Sync. Rad. **10**, 76 (2003).
5. Dau, H., Liebisch, P. and Haumann, M., Anal. Bioanal. Chem. **376**, 562 (2003).
6. Ono, T. *et al.*, Science **258**, 1335 (1992).
7. Roelofs, T. A. *et al.*, Proc. Natl. Acad. Sci. USA **93**, 3335 (1996).
8. Iuzzolino, L., Dittmer, J., Dörner, W., Meyer-Klaucke, W. and Dau, H., Biochem. **37**, 17112 (1998).
9. Messinger, J. R. *et al.*, J. Am. Chem. Soc. **123**, 7804 (2001).
10. Haumann, M. *et al.*, to be submitted (2004).
11. Haumann, M. *et al.*, J. Sync. Rad. **9**, 304 (2002).
12. Dau, H., Iuzzolino, L., Dittmer, J., Dörner, W. and Meyer-Klaucke, W., in "Photosynthesis: Mechanisms and Effects". (Edited by G. Garab) (Kluwer Academic Publishers, Budapest 1998), vol. 2, p. 1327.
13. Haumann, M., Grabolle, M., Neisius, T. and Dau, H., FEBS Lett. **512**, 116 (2002).
14. Dittmer, J. and Dau, H., J. Phys. Chem. B **102**, 8196 (1998).
15. Schiller, H. *et al.*, Biochem. **37**, 7340 (1998).
16. Zouni, A. *et al.*, Nature **409**, 739 (2001).
17. Haumann, M. *et al.*, in "Proc. 12th International Congress on Photosynthesis". (CSIRO Publishing, Collingwood 2001) p. S10_013 1.
18. Pospisil, P., Haumann, M., Dittmer, J., Sole, V. A. and Dau, H., Biophys. J. **84**, 1370 (2003).
19. Junge, W., Haumann, M., Ahlbrink, R., Mulkidjanian, A. and Clausen, J., Phil. Transactions: Biol. Sci. **357**, 1407 (2002).
20. Ankudinov, A. L., Ravel, B., Rehr, J. J. and Conradson, S. D., Phys. Rev. B **12**, 7565 (1998).
21. Zerner, M. C., Loew, G. H., Kirchner, R. F. and Mueller-Westerhoff, U. T., J. Am. Chem. Soc. **102**, 589 (1980).

Physica Scripta. Vol. T115, 847–850, 2005

The Location of Calcium in the Manganese Complex of Oxygenic Photosynthesis Studied by X-Ray Absorption Spectroscopy at the Ca K-Edge

Claudia Müller, Peter Liebisch, Marcos Barra, Holger Dau and Michael Haumann*

Inst. f. Experimentalphysik, Freie Universität Berlin, Arnimallee 14, D-14195 Berlin, Germany

Received June 26, 2003; accepted December 17, 2003

PACS numbers: 87.64.Fb, 82.39.Jn

Abstract

The tetra-manganese complex of photosystem II is the site of the production of most of the atmospheric dioxygen. To understand its function, an atomic-resolution structural model is required. X-ray absorption spectroscopy and protein crystallography yielded models for the arrangement of the four Mn atoms. The location of the functionally essential calcium cofactor within the complex, however, is still debated. To dwell on this point, XAS was performed at the Ca K-edge. Simulations of Ca EXAFS spectra reveal that at least two Mn atoms are located at a distance of ~3.3 Å to one Ca ion. Ca bound to the complex seems not to be fully hydrated. On basis of the complementary structural information derived from XAS at the Mn and Ca K-edge, a model of the Mn_4/Ca complex in its S_1-state is proposed which predicts intimate links between the Ca ion and Mn, possibly by bridging substrate-water molecules.

1. Introduction

Photosynthetic water oxidation is accomplished at a tetra-nuclear manganese complex bound to the lumenal side of the D1 subunit of photosystem II (PSII). Driven by light energy, from two water molecules, presumably bound to the Mn complex, dioxygen is produced in a five-stepped catalytic cycle. This biologically most important reaction generates the atmospheric oxygen [1, 2]. It has been shown that, besides of the Mn atoms, calcium is essential for the functioning of water oxidation [2]. Specifically, one Ca ion has been proposed to be in close vicinity to the Mn atoms [3–5] but this interpretation has been questioned [6].

Based on X-ray absorption spectroscopy (XAS) studies on all semistable oxidation states and on the crystallographic structure at 3.8 Å resolution [7, 8], we have previously proposed an atomic-resolution model of the Mn complex in its S_1-state [5, 9–11] with the following features: The four Mn atoms are arranged in two di-μ-oxo bridged pairs (Mn-Mn distance ~2.7 Å), the Mn-Mn vectors are about perpendicular to the membrane normal, and two Mn atoms of the dimers are separated by ~3.1 Å. The precise location and coordination of calcium has remained an open question. XAS data have been interpreted as indicating its location at about 3.3 Å from Mn [3–5, 11]; this attribution allowing for several positions of Ca with respect to the Mn atoms.

In this work we studied the coordination of Ca by XAS at the Ca K-edge on PSII preparations which contain about two Ca atoms per PSII center (one is supposedly close to Mn, the other one may be bound to an antenna protein [2]). It is shown that Ca is not fully hydrated and located at ~3.3 Å from minimally two Mn atoms which possibly belong to the same Mn dimer.

2. Materials and Methods

Highly active PSII membrane fragments (~1200–1400 μmol O_2/mg chlorophyll (Chl) × h at 28 °C) and partially dehydrated multilayer samples for XAS were prepared with betaine (0.5 M) in all media as a stabilizing agent as detailed in [11]; multilayers were deposited on Ca-free Mylar tape as a support; a pre-flash procedure was employed to quantitatively populate the S_1-state of the Mn complex [12]. Depletion of bulk Ca was achieved by gentle stirring of a solution of PSII membrane fragments (0.5 mg Chl/ml) with Chelex-100 (1.5 g/mg chl.) at 4 °C for 60 min at pH 6.5 and in darkness. Afterwards, Chelex was removed by filtration and then centrifugation. Pellets were resuspended in a buffer containing 25 mM MES, pH 6.5, 15 mM NaCl, and 1 M betaine, aliquots were taken for O_2-assays and AAS (atomic absorption spectroscopy) and samples were immediately used for preparation of multilayers.

AAS measurements were employed to quantify the Mn and Ca contents of the samples. Samples used for XAS contained 2 ± 1.5 Ca atoms per 4 Mn atoms. Chelex-treated samples possessed at least 90% of the oxygen-evolution activity of untreated controls.

XAS at the Ca K-edge was performed at the ESRF (Grenoble, France) at undulator beamline ID26 [13]. A newly constructed cryostat was used; samples were mounted on a helium-cooled turnable coldfinger. Samples were rapidly frozen to 50 K under evacuation of the cryostat; vacuum (~10^{-5} mbar) was maintained throughout the measurements. XAS spectra were collected in fluorescence mode using a large-area photodiode as a detector mounted within the cryostat (the angle between the electric field vector of the X-ray beam and the sample normal was 45°). A Ca-free, 150 nm thick Si-nitrite window was used for I_0 detection; no other foils were passed by the incident X-ray beam (spot size ~1 mm^2) or the X-ray fluorescence prior to detection. XAS spectra were measured using the rapid-scan mode of ID26 within 30 s (scan range 3900–4500 eV); only one scan was performed per sample spot. Measurements of reference substances revealed that the energy axis was stable by ±0.2 eV during the scans. Raw XAS spectra were normalized and EXAFS oscillations were extracted as previously described [5, 13]. Simulations of EXAFS spectra were carried out with the in-house software SimX [14] using an E_0 of 4030 eV (E_0 was allowed to refine by ±1.5 eV in the simulations) and phases calculated by FEFF 7 (J. Rehr and coworkers, Univ. of Washington). Fourier transforms were calculated from unfiltered EXAFS oscillations ranging over 23–400 eV above E_0 using cosine windows extending over 10% at both sides of the k-space. Backtransforms were calculated from 0–5 Å of reduced distance. EXAFS simulations were performed solely on unfiltered k^3-weighted oscillations (~30 scans averaged, k = 2.3–10.2 $Å^{-1}$, ${S_0}^2 = 0.9$).

*e-mail: haumann@physik.fu-berlin.de

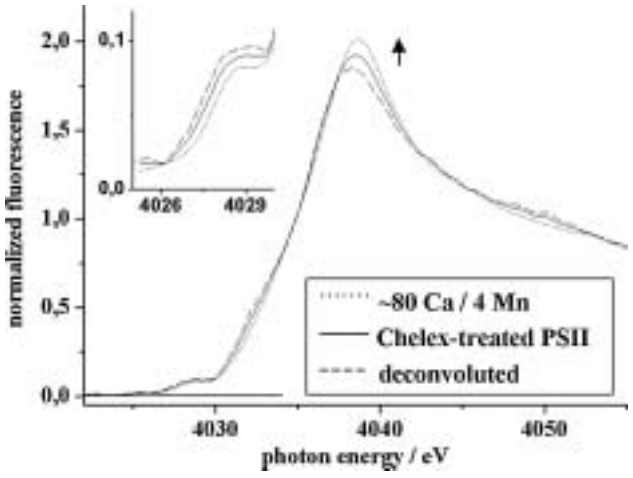

Fig. 1. Ca XANES spectra of samples containing ~80 Ca/4 Mn (dotted line) and where the Ca content has been drastically reduced by Chelex-treatment (solid line). The dashed line shows a tentative pure spectrum of the Ca bound to the Mn complex obtained by deconvolution. Inset: the pre-edge peak region. Arrow: difference between spectra at 4038 eV (see text).

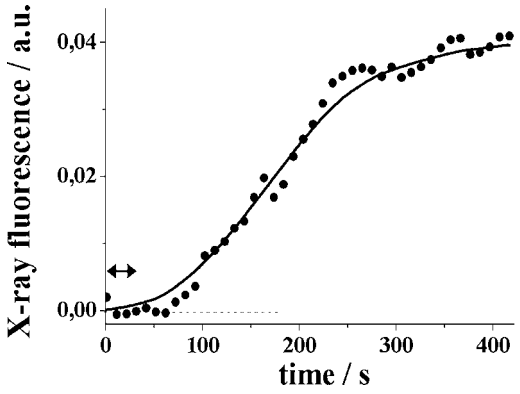

Fig. 2. Timescan of X-ray fluorescence at an excitation energy of 4038 eV. The solid line has been drawn to guide the eye; five scans were averaged; arrow: the duration of the XAS scans.

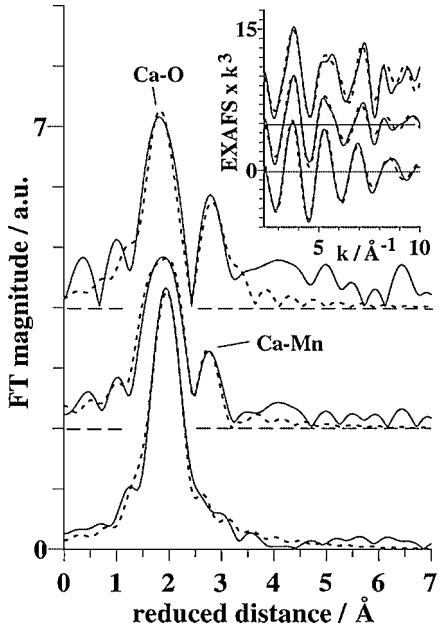

Fig. 3. Fourier-transforms of EXAFS oscillations (insets, backtransforms) of a sample containing ~80 Ca/4 Mn (bottom) and of a Chelex-treated sample (middle). Upper trace: tentative pure spectrum of the Ca within the Mn complex. Solid lines, experimental data; dashes, simulations (Table I; bottom, fit I; middle, fit IV; top, fit VI).

3. Results and Discussion

Figure 1 compares the XANES spectra at the Ca K-edge of PSII multilayer samples which contained ~80 Ca per four Mn ions (Ca was added as $CaCl_2$ to the buffer) (dashed line) and of a preparation where the Ca content was reduced to ~2 Ca/4 Mn by Chelex-treatment (solid line). Subtle but reproducible differences in the XANES are observed. A higher pre-edge peak (enhancement of dipole-forbidden $1s \rightarrow 3d$ transitions, inset in Fig. 1), a by 0.3 eV reduced edge energy ($E_{edge} = 4032.5$ eV vs. 4032.8 eV at 50% of normalized intensity), and a lower principal maximum are likely indicative of a lower coordination number and/or lower symmetry of Ca bound to PSII in Chelex-treated samples compared to its more symmetric coordination by 7–8 oxygens from water molecules in the bulk [15].

It has been shown by XAS measurements at the Mn K-edge that photoreduction of the Mn complex ("radiation damage") occurs within minutes at photon fluxes of $\sim 10^{13}\,s^{-1}$ even at cryogenic temperatures [13, 16–18]. This process produces Mn(II) which is released, presumably together with Ca, from its binding site [5, 13]. The problem may be even more severe in XAS measurements at the Ca K-edge where the X-ray absorption of the low-Z atoms of the samples is increased. To address the question whether radiation damage occurs, we employed the difference in the Ca K-edge magnitudes (most pronounced at 4038 eV, arrow in Fig. 1) of Ca bound to PSII or hydrated in the bulk. At an excitation energy of 4038 eV the X-ray fluorescence was recorded as function of time [17, 18] with Chelex-treated samples. Indeed, an increase of the fluorescence intensity is observed (Fig. 2) which likely indicates the release of specifically bound Ca (and Mn) from their binding sites into the bulk. At 50 K, Ca release seemed to occur within ~400 s. However, within the duration of the XAS scans (30 s) the fluorescence intensity at 4038 eV and, hence, the Ca K-edge magnitude remained about unchanged (Fig. 2, arrow). We conclude that Ca stayed bound to the Mn complex during the XAS scans; it is likely that also photoreduction was negligible and that the Mn complex was kept in its S_1-state.

Figure 3 shows the respective Fourier-transforms (FTs) of EXAFS oscillations (inset) of the ~80 Ca/4 Mn and the Chelex-treated samples. The spectrum of the high-Ca sample (lower traces) is well simulated using a single Ca-O shell with a coordination number of 7–8 and an average bond length of ~2.4 Å (Table I, fit I), parameters which are anticipated for hydrated Ca [15]. Thus, Ca is mainly present in its fully hydrated form in this sample, as expected. The FT of the EXAFS oscillations of the Chelex-treated sample is distinctly different (Fig. 3, middle traces). The magnitude of the main peak at ~2 Å of reduced distance is significantly diminished and the peak is broadened. Furthermore, a pronounced second peak at ~2.7 Å of reduced distance emerges in the FT. Such a peak is expected if Ca-Mn interactions are present. We first simulated this EXAFS spectrum by using only two backscatterer shells, O and Mn. The result is not satisfying as the error factor (R_F) is relatively large (Table I, fit II). Involving two oxygen shells significantly improved the fit, now revealing two Ca-O vectors of ~2.26 Å and ~2.43 Å lengths with a total coordination number of about 6 (Table I, fit III). The longer distance was similar to the one found in the high-Ca sample. A significant fraction of the Ca obviously is not bound to the Mn complex but present in a coordination which resembles the one of Ca in bulk water. The total coordination

Table I. *Parameters of EXAFS simulations (N_1, coordination number; R_i, absorber-backscatterer distance; σ_i^2, Debye-Waller parameter; R_F, weighted error sum [13]; (*), parameters fixed in the simulations).*

spectrum	fit	shell	N_i [per Ca]	R_i [Å]	σ_i^2 [10^{-3} Å^2]	R_F (1–3 Å) [%]
~80 Ca/4 Mn	I	Ca-O	7.32	2.42	12.3	13.7
Chelex-treated	II	Ca-O	6.43	2.38	16.1	17.6
PSII		Ca-Mn	1.49	3.27	15.0	
	III	Ca-O	2.30	2.26	1.5	12.7
		Ca-O	3.37	2.43	2.5	
		Ca-Mn	1.65	3.26	15.5	
	IV	Ca-O	3.33*	2.27	6.7	13.7
		Ca-O	2.33*	2.44	2.5	
		Ca-Mn	1.33*	3.26	14.5	
	V	Ca-O	2.50*	2.26	2.0	15.8
		Ca-O	3.50*	2.43	2.0	
		Ca-Mn	1.50*	3.26	16.8	
deconvoluted	VI	Ca-O	5.00*	2.29	11.2	14.3
(Ca in the Mn complex)		Ca-Mn	2.00*	3.27	9.3	

number of the Ca-O vectors was close to 6. This implies that the Ca bound to the Mn complex is not fully hydrated but coordinated by presumably only 5–6 oxygens, in line with the changes in the XANES spectrum. In both fit approaches, the number of Mn atoms as "seen" by the absorber, Ca, is well above unity, close to 1.5. If exactly two Ca atoms are present per 4 Mn atoms and only one is bound to the Mn complex, one would expect that the coordination number of the Ca-Mn vector is unity if one Ca is located at the same distance from two Mn ions. The found coordination number of the Ca-Mn vector of ~1.5 thus may mean that the average Ca : Mn stoichiometry in the Chelex-treated sample is truly 1.5 : 4 (compatible with the error in Ca quantification by AAS), or, alternatively, that three Mn ions are close to the Ca. The results of simulations on basis of the latter two possibilities (further assuming 7-coordinated Ca not bound to Mn and 5-coordinated Ca bound to Mn) are listed in Table I (fit IV, Ca : Mn = 1.5 : 4, 2 Mn-Ca vectors; fit V, Ca : Mn = 2 : 4, 3 Ca-Mn vectors). Both approaches yield reasonable fit qualities; two Ca-Mn vectors being slightly better. In summary, Ca is at about the same distance, ~3.3 Å, from minimally two Mn atoms. We tentatively deconvoluted the XAS spectrum of the Chelex-treated sample on basis of fit IV (by subtraction of 33% of the spectrum from the high-Ca sample). For the deconvoluted XAS spectra see Fig. 1 (dashed line) and Fig. 3 (upper trace). The EXAFS oscillations now attributed to Ca in the Mn complex are well simulated using only two backscatterer shells, Ca-O with $N = 5$ and Ca-Mn with $N = 2$ (two Ca-Mn vectors, Table I).

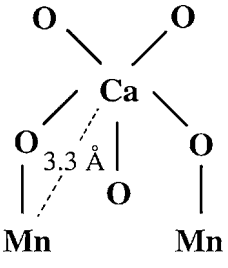

Fig. 4. The possible coordination of calcium within the Mn complex on basis of Ca XAS data.

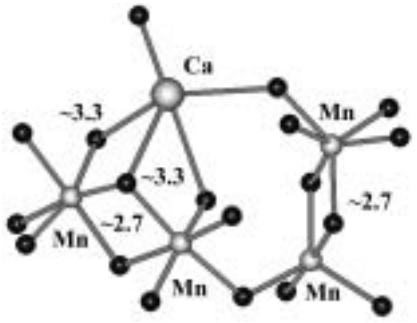

Fig. 5. Tentative model of the Mn_4/Ca complex in its S_1-state. Black dots, oxygens; two di-μ-oxo and one mono-μ-oxo bridge between Mn atoms are depicted (the model has been rotated with respect to previous drawings [10, 11]). Distances are given in Å.

On basis of the Ca XAS results we construct a model for the coordination of Ca in the Mn complex. It is shown in Fig. 4. Each distance between Ca and Mn is compatible with the presence of an intervening oxygen. The Mn complex in its S_1-state likely consists of a pair of di-μ-oxo bridged Mn dimers [5, 9, 10, 18]. If we combine the coordination of the Ca with the previously derived structural model of the Mn complex in S_1 [5, 9–11], one favored location of Ca within the complex is depicted in Fig. 5. We note that the five metal ions in this arrangement fit into the electron density of the Mn complex derived from crystallography [7, 8]. Interestingly, a Ca ion in this position would be at the same distance (~3.3 Å) from minimally the two Mn atoms of one dimer and furthermore, possibly coordinated by four oxygens that are, in turn, ligands to Mn. It is tempting to speculate that at least one of these oxygens belongs to substrate water which thereby becomes bound to both, Mn and Ca.

4. Conclusions

The location of the Ca ion within the Mn complex of PSII was investigated by XAS at the Ca K-edge. The shape of the XANES spectrum and EXAFS simulations imply that Ca is coordinated by 5–6 oxygens and that it is at ~3.3 Å distance from at least two Mn atoms. Combining information from Ca and Mn XAS we arrive at a structural model of the Mn_4/Ca complex in its S_1-state which is compatible with recent crystallographic data. The Mn atoms and the Ca in the complex may together form a binding site for the substrate water molecules. Investigations on the coordination of Ca in higher S-states of the catalytic cycle of water oxidation are underway.

Acknowledgements

Financial support from the Deutsche Forschungsgemeinschaft within SFB 498 (projects C6 and C8), from the Bundesministerium für Bildung und Wissenschaft (grant 05/KS1KEA-6) and from the Volkswagen-Foundation (grant I77/575) is gratefully acknowledged. We thank Dr. T. Neisius (ESRF, beamline ID26) for excellent support and Dr. K. Irrgang (TU-Berlin) for generous help with the AAS measurements.

References

1. Haumann, M. and Junge, W., Biochim. Biophys. Acta **1411**, 86 (1999).
2. Debus, R. J., Biochim. Biophys. Acta **1102**, 269 (1992).
3. Cinco, R. M. *et al.*, J. Phys. Chem. B **102**, 8248 (1998).
4. Cinco, R. M. *et al.*, Biochemistry **41**, 12928 (2002).
5. Pospisil, P., Haumann, M., Dittmer, J., Sole, V. A. and Dau, H., Biophys. J. **84**, 1370 (2003).

6. Riggs-Gelasco, P. J., Mei, R., Ghanotakis, D. F., Yocum, C. F. and Penner-Hahn, J. E., J. Am. Chem. Soc. **118**, 2400 (1996).
7. Zouni, A. *et al.*, Nature **409**, 739 (2001).
8. Kamiya, N. and Shen, J. R., Proc. Natl. Acad. Sci. USA **100**, 98 (2003).
9. Dau, H., Iuzzolino, L. and Dittmer, J., Biochim. Biophys. Acta **1503**, 24 (2001).
10. Dau, H., Liebisch, P. and Haumann, M., Anal. Bioanal. Chem. **376**, 562 (2003).
11. Haumann, M. *et al.* In: PS2001 Proceedings, CSIRO Publishing, Collingwood, Australia, contribution S10-013, pp 1–5 (2001).
12. Iuzzolino, L., Dittmer, J., Doerner, W., Meyer-Klaucke, W. and Dau, H., Biochemistry **37**, 17112 (1998).
13. Meinke, C., Sole, A. V., Pospisil, P. and Dau, H., Biochemistry **39**, 7033 (2000).
14. Dittmer, J., PhD Thesis, Christian-Albrechts-Universität Kiel, Germany (1999).
15. Jalilehvand, F. *et al.*, Am. Chem. Soc. **123**, 431 (2001).
16. Dau, H. and Haumann, M., J. Synchrotron Radiat. **10**, 76 (2003).
17. Haumann, M. *et al.*, J. Synchrotron Radiat. **9**, 304 (2002).
18. Haumann, M., Grabolle, M., Neisius, T. and Dau, H., FEBS Lett. **512**, 116 (2002).

Physica Scripta. Vol. T115, 851–854, 2005

NEXAFS Study of Amino Acid Analogues Assembled on Gold

Rodrigo M. Petoral Jr.* and Kajsa Uvdal

Laboratory of Applied Physics, Department of Physics and Measurement Technology, Linköping University, SE-581 83 Linköping, Sweden

Received June 26, 2003; accepted in revised form December 18, 2003

PACS number: 6843Hn

Abstract

In this work, near-edge X-ray absorption fine structure spectroscopy (NEXAFS) experiment is done to obtain the chemical and structural information about the occurrence and the average orientation of unoccupied molecular orbitals within the organic films. Amino acid, such as Tyrosine and 3,4-dihydroxyphenylalanine (DOPA), is linked to a thiol through a peptide bond and is adsorbed and self-assembled to polycrystalline gold surfaces. Results from the C k-edge and O k-edge spectra serves as fingerprints to each amino acid analogues. The average orientation of the molecules relative to the gold surface is determined from the polarization effects observed as intensity changes of the peaks in the spectra when the X-ray incidence angle is varied. It is assumed that the average tilt angle of the main molecular axis of amino acid linked to short amidethiol is based on the deduced orientation of the peptide bond.

1. Introduction

Immobilizing biomolecules such as amino acid and peptide derivatives can be used as model surfaces for studying specific interactions with other molecules which is important for biomaterial and biosensor application. Amino acids with aromatic side chains are interesting to study because they play an important role in many biochemical reactions. Tyrosine is one amino acid involved in the phosphate transfer of adenosine triphosphate (ATP). Covalent phosphorylation of such amino acid induces protein conformational change [1]. Immobilizing such amino acid derivative onto surface can be used to probe specific details such as molecular conformational changes and energy transfer involved in phosphorylation. Another interesting amino acid and closely related to Tyrosine is DOPA. DOPA has a big role in mussel adhesive proteins [2, 3] and the possibility of the cross-linking process on surfaces is interesting to study. It can also serve as an electroactive ligand for indirect determination of aluminum in biological samples [4]. This molecule in the future can be used as affinity sensing molecule for coordination of Al^{3+} existing in the body [5].

A way to study these amino acids on the surface is by chemically linking them to a thiol and making use of the self-assembly technique to immobilize them on the surface. Previous studies on self-assembled monolayers (SAMs) involving aromatic thiols [6–8] serve as significant references in characterizing the model surfaces under study. NEXAFS spectroscopy (otherwise known as XANES) is one tool used to extract chemical and structural information of organic films. Several studies have recently used NEXAFS to characterize amino acids and peptides [9–12].

In this work, both Tyrosine and DOPA are linked to 3-mercaptoproprionic acid through an amide bond. The resulting molecule namely Tyrosine-terminated Propanethiol (TPT) and DOPA-terminated Propanethiol (DOPA-PT) are adsorbed on gold surface through thiol chemistry. Chemical states and molecular orientation of the adsorbates are investigated by NEXAFS. The characterized surfaces will be subjected to biomolecular interaction studies using technique such as surface plasmon resonance (SPR). Electrochemical studies will also be employed to study relevant metallic ion interactions with the surfaces.

2. Experimental

2.1. *Sample preparation*

The TPT and DOPA-PT were synthesized at the Department of Chemistry, Linköping University. The related synthetic pathway is shown elsewhere [13]. The adsorbates were prepared from ethanol solutions with a concentration of 1 mM.

The gold substrates used were prepared by electron beam evaporation of 2000 Å thick Au at a rate of 10 Å/s onto clean single-crystal Si(100) wafers. Before evaporation of the gold film, the silicon wafers were first coated with a 20–25 Å thick Ti layer at a rate of 2 Å/s. The base pressure was always $<5 \times 10^{-9}$ Torr and the evaporation pressure, $<2 \times 10^{-8}$ Torr. The thin gold film has preferred (111) with grain size of 70–300 Å and with the outer parts of these grains showing extremely flat films [14]. The gold surfaces were cleaned in a 5 : 1 : 1 mixture of MilliQ water, 25% hydrogen peroxide, and 30% ammonia for 5 min at 80 °C and then thoroughly rinsed in MilliQ water.

The gold surfaces were incubated in the solutions for the duration of more than 24 h, rinsed in deionized water and then ultrasonicated in deionized water for 5 minutes. The deionized resistance of the deionized water is 18.2 MΩ-cm. It is followed by blow-drying of the surfaces with nitrogen gas and then immediately analyzed. The DOPA-PT multilayer sample was prepared by letting a droplet of high-concentration DOPA-PT dry on a prepared monolayer on gold surface, while letting a stream of gaseous nitrogen pass over the surface.

2.2. *NEXAFS*

The NEXAFS spectra were recorded at the synchrotron storage ring MAX II at MAX–Lab in Lund, Sweden using the D1011 bending magnet beamline. The beamline is equipped with a modified SX-700 monochromator [15]. The measurements were carried out at the C1s and O1s absorption edge in the partial electron yield mode with retarding voltage of −150 V and −300 V, respectively. Linear polarized synchrotron light with a polarization factor of ∼85% was used. The energy resolution was ∼0.5 eV. The incidence angle of the synchrotron light used was 90° (*E*-vector in surface plane) and 30° or 20° (*E*-vector near surface normal) to monitor the orientation of the adsorbates. The raw NEXAFS spectra were normalized to the incident photon flux by division through a spectrum of a sputtered clean gold sample.

3. Results and Discussion

A NEXAFS spectrum reveals information about the local bonding environment around specific atoms including the chemical states

*e-mail: rodpe@ifm.liu.se

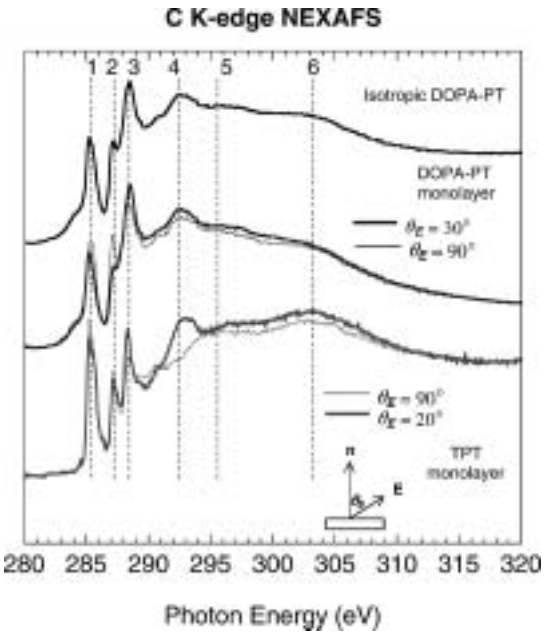

Fig. 1. C K-edge NEXAFS spectra of isotropic and monolayer DOPA-PT on gold and monolayer TPT on gold.

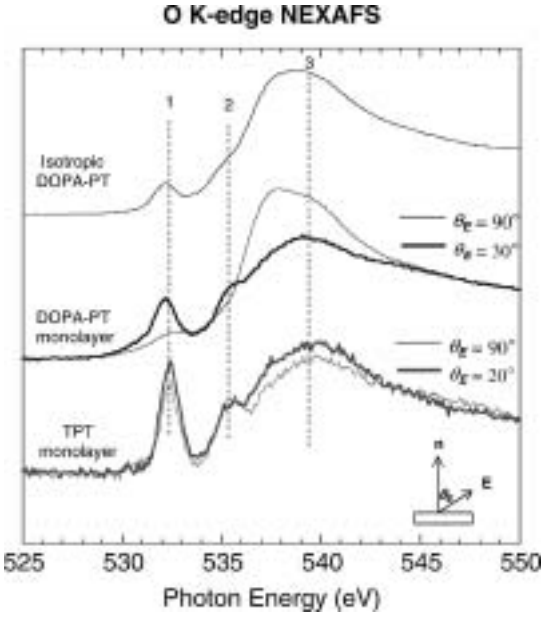

Fig. 2. O K-edge NEXAFS spectra of isotropic and monolayer DOPA-PT on gold and monolayer TPT on gold.

of these atoms. Determination of average orientation of the molecules can also be achieved from the polarization effects observed as intensity modulations of peaks in the spectra when X-ray incidence angles are varied. The C K-edge and O K-edge spectra of TPT and DOPA-PT on Au at selected X-ray incidence angles are shown in Figure 1 and 2, respectively. Summary of the assignments of the peaks are shown in Table I and II for C K-edge and O K-edge spectrum, respectively.

The C K-edge spectra (Fig. 1) for both DOPA-PT and TPT show three narrow peaks associated with bound resonances. The peak at about 285 eV (peak 1) is associated with the $\pi^*_{C=C}$ states of the aromatic ring. This peak can be split into two peaks upon close observation which is consistent with the phenylalanine and tyrosine amino acid, identified as a vibrational fine structure from the expected shifts of $1s \rightarrow \pi^*$ associated with different

Table I. *Excitation energies and assignments in C K-edge NEXAFS spectra of TPT and DOPA-PT adsorbed on gold.*

	Excitation Energy (eV)		
Peak number[a]	TPT/Au	DOPA-PT/Au	Assignment
1	285.2	285.2	$\pi^*_{C=C}$
2	287.2	287.2	$\pi^*_{C=C}(^bC1s \rightarrow \pi^*)$
3	288.3	288.4	$\pi^*_{C=O}$
4, 5	293.1, 295.2	292.6, 296.3	$\sigma^*_{C\text{-}C}$; $(\sigma^*_{C\text{-}N})$
6	303.3	302	$\sigma^*_{C=C}$; $(\sigma^*_{C=O})$

[a]Refer to Figure 1.
[b]C connected to OH.

Table II. *Excitation energies and assignments in O K-edge NEXAFS spectra of TPT and DOPA-PT adsorbed on gold.*

	Excitation Energy (eV)		
Peak number[a]	TPT/Au	DOPA-PT/Au	Assignment
1	532.2	532	$\pi^*_{C=O}$
2	535.5; (537)	535	$\sigma^*_{O\text{-}H}$, $(O1s \rightarrow \pi^*)$
3	540	540	$\sigma^*_{C\text{-}O}$

[a]Refer to Figure 2.

carbon sites around the ring [12]. The second band around 287 eV (peak 2) is assigned as the C1s(C-OH) $\rightarrow 1\pi^*$ transition. The assignment is consistent with Tyrosine related molecules [9, 12] and is similar to that found previously for phenols [16, 17] and hydroquinones [17]. The strong resonance about 288 eV (peak 3) arises primarily from the C 1s to π^* transition in carbonyl group present in the peptide bond. The peak position is consistent with the carbonyl C $1s \rightarrow \pi^*_{C=O}$ transition found for other molecular system such as nylon with amide motif [18], disulfide containing amide [19] and a cysteine-containing peptide tether [20]. Also at this energy, additional π^* states in the phenyl ring and Rydberg resonances in the alkyl carbon chain of the molecule contributes to the intensity [21]. Broad peaks related to shape resonances at about 293 eV (peak 4) show an excitation of C 1s electrons into σ^* (C-C) orbitals in the ring and short alkyl chain [22]. The peak at about 296 eV (peak 5) is also accounted to C-C σ^* convoluted with C-N σ^*. The broad peak at about 303 eV (peak 6) corresponds to C=C σ^* convoluted with C=O σ^* resonances.

Fingerprinting of the two closely related molecule can be based on the extent of the intensity difference between characteristic peaks. A close look at the bound resonances of C K-edge spectra shows difference in the intensity of the peaks between TPT and DOPA-PT. Apparent reduction in the intensity of the lines near 285 eV relative to the intensity of the carbonyl peak at 288 eV can be observed when DOPA-PT is compared with TPT. The reduction is due to the intensity redistribution, which is caused by hydroxyl group substitution. Similar observation between phenylalanine (Phe) and tyrosine (Tyr) innershell absorption spectra is seen. Apparent reduction in intensity of lines near 285.2 eV relative to the intensity of the carboxyl π^* peak is observed [12]. Also, the appearance of peak at 287 eV is seen for Tyr as compared with Phe [9, 12]. Similar trend applies also when TPT is compared with DOPA-PT. Increase in the intensity of peak 2 relative to peak 1 can be observed from DOPA-PT as compared to TPT. This is due to splitting of oscillator strength and transfer of intensity to the C1s(C-OH) $\rightarrow 1\pi^*$ peak. Increase in the intensity (or more pronounced peak) of C $1s \rightarrow \sigma^*_{C-C}$ around 292 eV is also observed on DOPA-PT (compared to TPT) due to the same

reason. Additional observation to DOPA-PT spectrum includes a weak feature at about 284 eV, which could be some small amount of contaminants.

The O K-edge spectrum in Figure 2 has peaks at about 532 eV, 535 eV and about 540 eV. Peak 1 is assigned to the O 1s $\rightarrow \pi^*_{C=O}$ transition in the carbonyl part of the peptide bond. The peak position is consistent with that of spectrum of Nylon having amide moiety [18]. The peak appearing as shoulder for DOPA-PT at about 535 eV is more intense for TPT. This peak is seen in the O 1s spectra of alcohols [23] and previously attributed to O 1s $\rightarrow \sigma^*_{O-H}$ transitions. A feature due to oxygen contribution of the delocalized C=C π^* around 537 eV can also be observed. This O 1s $\rightarrow \pi^*$ transition feature is supported by the Extended Huckle (EHMO) calculation results done by Francis and Hitchcock for phenols and hydroquinones [17]. The broad 540 eV peak is assigned to the σ^*(C-O) consistent with that of phenol and hydroquinone NEXAFS spectra [17].

Comparing the NEXAFS spectra acquired at different X-ray incidence angles, orientation of the molecules can be predicted based on the dependence of the intensity of the angle of light incidence. The intensity of NEXAFS resonance depends on the orientation of the polarization of light with respect to the molecular orbital that is probed [24]. The intensity is at its maximum if the direction of the electric field of radiation (E-vector) and the final state orbital is parallel with each other. Conversely, when E- vector is orthogonal to the direction of the final state orbital, the resonance is greatly attenuated. In the C K-edge spectrum for the two types of adsorbates, the aromatic π^* feature is slightly more intense at normal incidence than in grazing. The band associated with the 1s $\rightarrow \pi^*$ excitation at C atom bound to OH groups is also more intense from normal to grazing incidence. Bands assigned to C-C σ^* and C=C σ^* features are faintly more intense at grazing angle. This indicates that the molecules (particularly the aromatic molecules) on the average are oriented more "standing-up" than "lying-down". The increase in intensity of the band assigned to the C-O σ^*, which is associated with the hydroxyl groups attached to the ring, supports more the "standing up" orientation of the aromatic ring. The band at about 288 eV associated with primarily the C=O π^* feature is more intense at the grazing incidence than the normal incidence. This indicates that the peptide is positioned with the carbonyl groups almost parallel to the gold surface. This orientation is supported further by the increase in the intensity of the band assigned to the O 1s $\rightarrow \pi^*_{C=O}$ transition (see peak 1, Figure 2) at grazing incidence for TPT and more for DOPA-PT molecule.

The average tilt values of the molecule are obtained by quantitative analysis of the angular dependence of the NEXAFS resonance intensities. The calculations are based on the procedure developed by Stöhr [24]. This involves taking the area of the peak at normal and grazing photon incidence and calculating the relative ratio of the integrated intensity, I_{90}/I_{30} *(or* I_{90}/I_{20}*)*, where I_{90} is the intensity (area) of the π^* peak at normal photon incidence and I_{30} (or I_{20}) that at grazing incidence. The average tilt value is obtained from the vector-like orbital intensity ratio (I_{90}/I_{30} or I_{90}/I_{20}) as a function of the tilt angle of the π^* and σ^* orbital from the surface normal with the assumption that the polarization is ~0.85 [24]. From the small angular variation of the C=C 1π^* - intensity in the spectra, it is estimated that the ring plane of the aromatic ring for DOPA-PT exhibits a preferential orientation with an average tilt angle (α) of about 64° ± 2°. For TPT, it estimated to be about 60° ± 2° [25]. The estimations are very close to the approximation done by Lee, *et al.* [8] for tilt angle

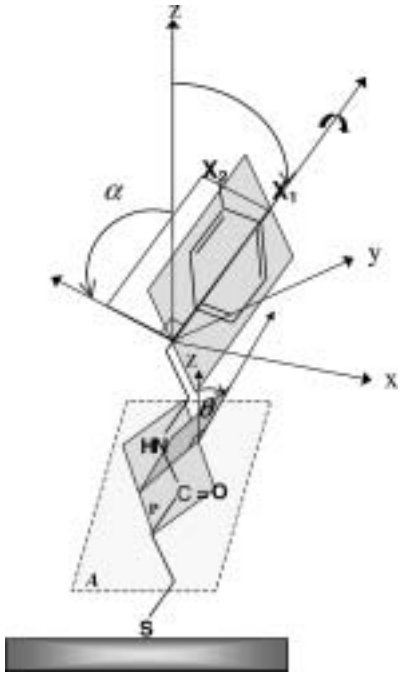

Fig. 3. Schematic structure representing the two molecules when adsorbed on gold showing angles extracted from NEXAFS used to characterize the monolayer's orientation. X_1 and X_2 represents the hydroxyl (-OH) functional groups. X_1 is only present in TPT while both X_1 and X_2 are present in DOPA-PT. The peptide plane (plane P) is assumed to be in/plane with the main molecular axis plane (plane A).

of phenyl-terminated SAMs having an even number of methylene units. The average tilt angle is close to the magic angle (55°) but larger than it. It indicates a certain degree of order (as supported by the XPS angle dependent measurement, ellipsometry and contact angle measurements) with a certain degree of disorder to be considered. The dichroism of the resonances associated with the $\pi^*_{C=C}$ states of the aromatic ring is rather small compared with dichroism of the π^* resonances for the thiol-derived aromatic SAMs on gold having average tilt angle of the aromatic chain of about 22° [26]. Also from the observed angular variation of intensity in the C K-edge NEXAFS spectrum, the tilt angle of the π^* orbital of C=O (in the peptide bond) for DOPA-PT is approximately 53° ± 2° relative to the normal of the surface. TPT has about 52° ± 2° [25] which is of the same tilt angle as that of DOPA-PT. A schematic orientation representing the two related adsorbates is shown in Figure 3. The angle, θ, is used to approximate the orientation of the main molecular axis. The C=O π^* orbital is perpendicular to the peptide (bond) plane and that the plane is assumed to be coplanar with the molecular axis of the molecule. Also, it is assumed that the amide has a trans conformation with adjacent CH chains. From the abovementioned fact and assumption, the main molecular axis of the DOPA-PT molecule is estimated to be tilting about 37° ± 2° relative to the surface normal and the molecular axis of TPT is estimated to be about 38° ± 2°. For comparison, it can be mentioned that for phenyl-terminated organic surfaces, a 46°- tilt angle of the methylene chain with respect to the surface normal has been reported [22].

4. Conclusion

Amino acid linked to short amidethiol has been studied in this work. Analogues such as TPT and DOPA-PT are adsorbed to

gold surfaces and their chemical states and molecular orientation is investigated by NEXAFS spectroscopy. The characteristic NEXAFS spectra of both TPT and DOPA-PT can be used as fingerprints of the two given amino acid derivatives. The two closely related molecule shows similar structural orientation when adsorbed on gold surface. Knowing the molecular orientation of such interesting derived biomolecules, future investigations and studies related to biosensing will be well executed and understood.

Acknowledgements

This project was supported by grants from the Swedish National Science Research Council (NFR), The Swedish Research Council (VR) and Carl Tryggers Foundation.

References

1. Johnson, L. N. and Barford, D., Ann. Rev. Biophys. Bio. **22**, 199 (1993).
2. Yu, M., Hwang, J. and Deming, T. J., J. Am. Chem. Soc. **121**, 5825 (1999).
3. Yu, M. and Deming, T., J. Macromolecules **31**, 4739 (1998).
4. Zhang, F., Bi, S., Li, H., Chen, Y. and Dai, L., Electroanalysis **13**, 1054 (2001).
5. Martell, A. E., Motekaitis, R. J. and Smith, R. M., Polyhedron **9**, 171 (1990).
6. Jung, H. H., Won, Y. D., Shin, S. and Kim, K., Langmuir **15**, 1147 (1999).
7. Ishida, T. *et al.*, J. Phys. Chem. B **103**, 1686 (1999).
8. Lee, S. *et al.*, Langmuir **17**, 7364 (2001).
9. Boese, J., Osanna, A., Jacobsen, C. and Kirz, J. J., Electron Spectrosc. Relat. Phenom. **85**, 9 (1997).
10. Nyberg, M. *et al.*, J. Chem. Phys. **112**, 5420 (2000).
11. Tanaka, M., Nakagawa, K., Koketsu, T., Agui, A. and Yokoya, A., J. Synchrotron. Radiat. **8**, 1009 (2001).
12. Kaznacheyev, K. *et al.*, J. Phys. Chem. A **106**, 3153 (2002).
13. Uvdal, K., Ekeroth, J., Konradsson, P. and Liedberg, B., J. Coll. Int. Sci. **260**, 361 (2003).
14. Uvdal, K., Bodö, P. and Liedberg, B., J. Coll. Int. Sci. **149**, 162 (1992).
15. Nyholm, R., Svensson, S., Nordgren, J. and Flodström, S. S., Nucl. Instrum. Meth. Phys. Res. Sect. A **246**, 267 (1986).
16. Solomon, J. L., Madix, R. J. and Stöhr, J., Surf. Sci. **255**, 12 (1991).
17. Francis, J. T. and Hitchcock, P., J. Phys. Chem. **96**, 6598 (1992).
18. Urquhart, S. G. and Ade, H., J. Phys. Chem. B **106**, 8531 (2002).
19. Vance, A. L., Langmuir **18**, 8123 (2002).
20. Baas, T., Gamble, L., Hauch, K. D., Castner, D. G. and Sasaki, T., Langmuir **18**, 4898 (2002).
21. Bagus, P. S. *et al.*, Chem. Phys. Lett. **248**, 129 (1996).
22. Wacker, D., Weiss, K., Kazmaier, U. and Wöll, Ch., Langmuir **13**, 6689 (1997).
23. Ishii, I. and Hitchcock, A. P., J. Electron Spectrosc. **87**, 830 (1987).
24. Stohr, J., "NEXAFS Spectroscopy", (Springer, Berlin, 1992).
25. Petoral, R. M. and Uvdal, K., J. Electron. Spectrosc. Relat. Phenom. **128**, 159 (2003).
26. Frey, S. *et al.*, Langmuir **17**, 2408 (2001).

Physica Scripta. Vol. T115, 855–858, 2005

An XAS Study of the Cation Binding Sites in the Purple Membrane of *Halobacterium Salinarum*

Francesc Sepulcre[1*], Maria Grazia Proietti[2], Maurizio Benfatto[3], Stefano Della Longa[3,4], Joaquin García[2] and Esteve Padrós[5]

[1]Departament d'Enginyeria Agroalimentària i Biotecnologia, Escola Superior d'Agricultura, Universitat Politècnica de Catalunya, Barcelona, Spain
[2]Instituto de Ciencia de los Materiales de Aragón-Dep. Física de la Materia Condensada, CSIC-Universidad de Zaragoza, Facultad de Ciencias, Zaragoza, Spain
[3]Lab. Nazionali di Frascati-INFN-PO Box 13-00044 Frascati, Italy
[4]Dip. Medicina Sperimentale, Univ. L'Aquila, via Vetoio-67100-L'Aquila, Italy
[5]Unitat de Biofísica, Departament de Bioquímica i Biologia Molecular, Facultat de Medicina, Universitat Autònoma de Barcelona, Barcelona, Spain

Received June 26, 2003; accepted November 4, 2003

PACS number: 87.15.−v

Abstract

X-ray absorption measurements were performed on Ca^{2+} and 5 Mn^{2+} regenerated purple membrane in order to obtain structural information about the cation environment. For the regenerated membrane with 5 Mn^{2+}, EXAFS analysis shows a first six-coordination sphere with two Mn-O distances (2.18 Å and 2.49 Å), whereas for the 5 Mn^{2+} regenerated bleached membrane the first shell is formed by 6 oxygen atoms at 2.17 Å. In the case of Ca^{2+}-substituted bacteriorhodopsin, *ab initio* calculations of the X-ray absorption cross section based on a full multiple scattering approach, with a best fit of the experimental data, show that the Ca^{2+} environment is composed by 6 oxygen atoms showing a distorted orthorhombic symmetry, while Ca^{2+} in water solution has a regular octahydrated first sphere of coordination. Our results provide strong direct evidence of the specific binding site of the metal cation in bacteriorhodopsin and are in good agreement with previous molecular models suggesting that there could be a high affinity cationic site in the proximity of the retinal pocket.

1. Introduction

Bacteriorhodpsin (BR) is a seven-helical transmembrane protein found in the purple membrane (PM) of *Halobacterium salinarum*. It has a retinal molecule covalently linked to Lys-216 through a protonated Schiff base. When it absorbs a photon, it undergoes a photochemical cycle during which the retinal configuration changes from *all-trans* to *13-cis*. This induces protein conformational changes that result in the translocation of a proton from the inside to the outside of the cell, returning both the retinal molecule and the protein to their initial states. In fact, bacteriorhodopsin converts the energy of light into an electrochemical proton gradient, which is used by the bacteria to produce ATP by ATP-synthases (for reviews see [1, 2]).

Native PM contains divalent cations (Ca^{2+} and Mg^{2+}) that are necessary to maintain the structure of the protein and its function [3]. Removal of these cations from the PM increases the apparent pK of the blue/purple transition from about 3.2 in water to 5.5. This change is reversible by addition of a variety of cations. The binding has been explained in terms of specific chemical binding to negatively charged groups (most probably carboxylic groups of the protein). Different affinity sites, 5 of high and medium affinity, and 5 of low affinity have been found, although their localization is not yet clear [4–6]. An alternative model suggested a non-specific binding to the Gouy-Chapman bilayer [7].

Several three-dimensional models of bacteriorhodopsin have been published [8–10], but so far none of them gives any evidence about the bound cations, perhaps because they are in part or completely lost upon crystallization. In contrast, all of these three-dimensional models show different Asp and Glu groups that in terms of geometry and bound distances are compatible with cation binding sites.

Due to the strict requirements of classical X-ray crystallography about sample preparation, and to its low sensitivity to the system dynamics, X-ray Absorption Spectroscopy (XAS) has become an important alternative and a complementary technique to obtain information about the cation environment because it allows the study of purple membrane in solution, i.e. in an environment which is much closer to its physiological state.

In this work we present two complementary analyses. In order to study the local environment of the high-affinity cation binding site of PM we have first measured XAS spectra, at the Ca K-edge, of deionised membrane regenerated with Ca^{2+}. In the second part we study the medium affinity binding sites, and the effect of the retinal in the maintenance of structure, by comparing XAS spectra of a deionised membrane regenerated with 5 Mn^{2+} per mol of protein (5 Mn/BR sample) with a deionised bleached membrane regenerated with 5 Mn^{2+} per mol of protein (5 Mn/BO sample).

2. Materials and Methods

Purple membrane was isolated from the *Halobacterium salinarum* strain S9, as described previously [11]. Cations were removed from purple membrane by an extensive dialysis in front of a cation-exchange Dowex AG-50W resin, and the regeneration was done at pH 5. Bleaching of the purple membrane was effected by its illumination in the presence of 1 M hydroxylamine and 4 M NaCl at room temperature with a 150 W lamp.

EXAFS of the Mn/BR samples were carried out at 230 K in fluorescence mode at the Mn K-edge, at the beam-line ID29 of the European Synchrotron Radiation Facility (ESRF). The final concentration of the protein was about 2–3 mM.

Measurements at the Ca K-edge were carried out at the beam line ID26 (ESRF) that is dedicated to the study of very dilute systems, requiring high photon flux ($>10^{13}$ ph/s). The samples were deposited on the sample holders and were kept overnight in a closed chamber in order to get a partially dried film by applying a mild vacuum. Monochromatic beam was obtained, in both cases, by means of a Si(111) double crystal, with an energy resolution $\Delta E/E = 1.4 \cdot 10^{-4}$. The fluorescence signal at the Ca and Mn K-edge, was detected by a multi-element Silicon-drift solid state detector. The absorption spectrum of Mn^{2+} and Ca^{2+} in water were also recorded as reference systems.

*e-mail: Francesc.Sepulcre@upc.es

In order to extract the structural/geometrical information on the Ca^{2+} first coordination shell that is contained in the fine structure just above the edge, we performed a quantitative analysis of the XANES spectrum using the MXAN code [12].

The EXAFS spectra at the Mn K-edge were analysed by a least-squares fit procedure, comparing the experimental spectrum with a theoretical signal generated by the FEFF8 code [13].

3. Results and Discussion

3.1. *The high affinity binding site*

Because the low S/N ratio of the Ca^{2+}-substituted BR sample, a standard EXAFS analysis is not relevant (i.e. the k-range experimental data for this samples is limited) and also because we attempt to make a quantitative geometrical characterization of the high-affinity binding site by comparing our experimental data with know X-ray structures. Therefore, in this case we focus our attention on the XANES region.

The XANES spectra of deionized PM after reconstitution with Ca^{2+} at a molar ratio of 1:1 (Ca^{2+} : BR), is shown in Fig. 1. It is the average of several scans taken during an overall integration time of about 12 hours, carried out moving the sample in the X-ray beam to avoid radiation damage. At this Ca concentration only the high affinity binding site should be filled. The experimental spectra of the Ca^{2+}-BR complex show a small shoulder at about 40 eV above the edge due, probably, to a multiple excitation.

Several studies have suggested that a divalent cation is located in the proximity of the retinal binding pocket [14–16] associated with Asp-85 and Asp-212. To test this hypothesis, we performed a fitting of the experimental data with a molecular model obtained from the optimized geometry described in [16] by selecting a sphere of radius 6 Å centred on the absorbing atom containing the side chains of Asp85 and Asp212, three water molecules and a part of the retinal chromophore. The starting cluster to be refined includes 6 oxygen atoms in a distorted octahedral-like configuration with Ca-O distances varying from 1.98 Å to 2.24 Å, corresponding to an average distance of 2.12 Å. The results of this analysis are shown in Fig. 1. The best fit of the experimental data, corresponds to a first coordination shell of 6 O atoms, in a quite distorted geometry, with a Ca-O average distance of 2.31 Å.

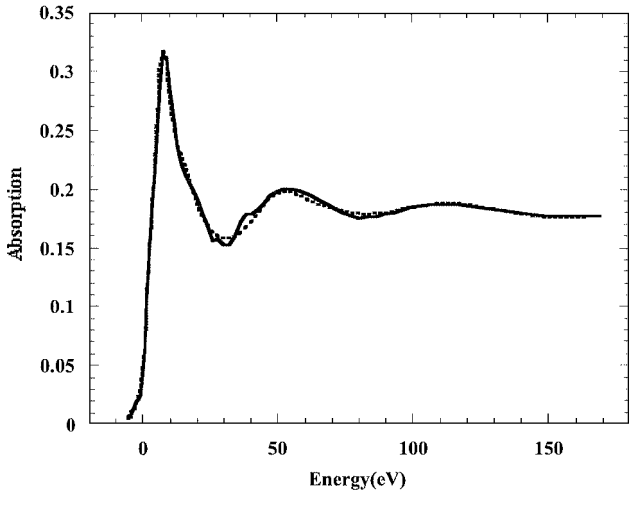

Fig. 1. Theory-vs-experiment best-fit results for Ca^{2+}-BR complex starting from Asp85-Asp212-3H_2O cluster. The O-C-O distances are correlated. The solid line correspond to the experimental data.

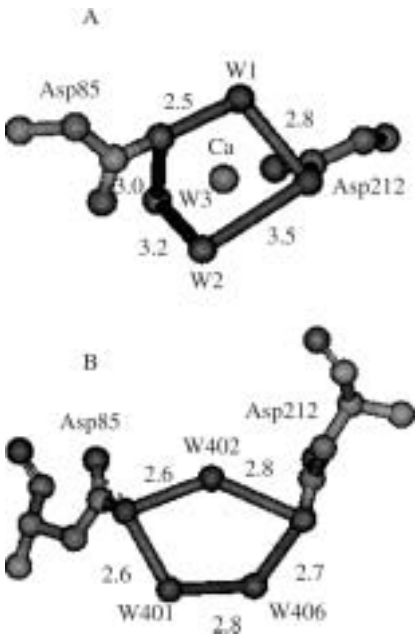

Fig. 2. A) Ca^{2+}-coordination in the vicinity of the Schiff base, corresponding to the best-fit for the Ca^{2+}-BR complex starting from the putative cluster described in [16]. B) X-ray crystallographic structure of the Schiff base region from PDB entry 1C3W [9]. The numbers are bond distances in Ångstroms.

It has to be noted that the refinement results show an increase of the average Ca-O distance, as expected due to the increased ionic radius of Ca in comparison with the Mg cation of the model [16]. The agreement between the experimental data and the fitting calculations is very good, suggesting that this internal cluster is a possible high-affinity binding site in the protein. Figure 2A shows a detailed view of the computed best fit to the Asp85-Asp212-3H_2O cluster. As it can be observed, the first sphere around the Ca^{2+} ion has a very distorted octahedral coordination formed by the O atoms of Asp212, one O atom of Asp85 and three water molecules.

The best fit curve for Ca^{2+} in water, obtained using the same starting atomic clusters as for the protein sample corresponds instead, to a regular square for the first hydration shell ($n = 8$) of the calcium atom at an average distance of 2.35 Å.

These results are consistent with our previous EXAFS work in which we found an octahedral geometry for the high-affinity Mn^{2+} binding site [17]. This similarity suggests that both cations (Mn^{2+} and Ca^{2+}) could bind to the same high-affinity binding site.

The crystallographic structures of bacteriorhodopsin have reported the location of internal water molecules near the Schiff base region, forming a pentagonal cluster [8–10]. As can be seen in Fig. 2, our results reproduce this pentagonal cluster remarkably well. The discrepancy in the O-O distances and angles between the crystallographic structures cited above and the cluster proposed in this work could be due to the fact that in the last refinement process of the crystallographic structures the Ca^{2+} cation is not included.

3.2. *The medium affinity binding sites and the effect of the retinal extraction*

ESR studies on the binding of the paramagnetic Mn^{2+} cation [4] have indicated that the apparent affinity constants for Ca^{2+} and Mn^{2+} to the deionised BR were almost identical. Therefore, and with the purpose to extrapolate the conclusions to the physiologically important cations (e.g. Ca^{2+}) we used in our experiments the same conditions used by these authors. The

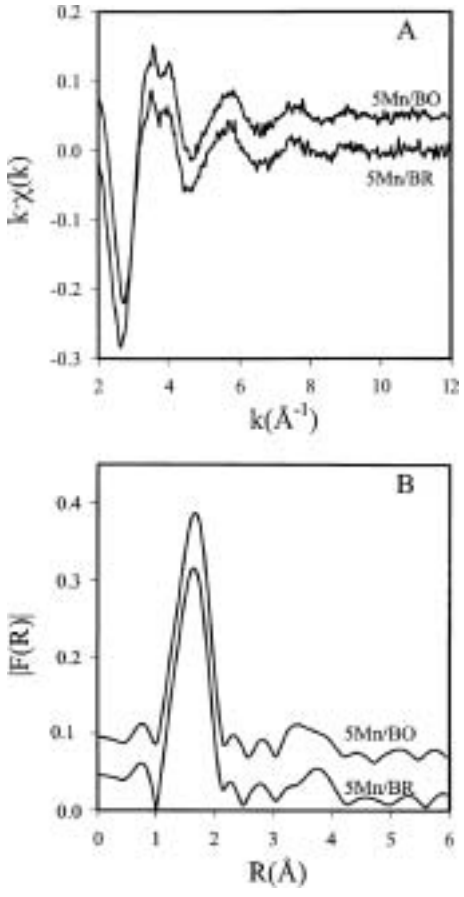

Fig. 3. A) EXAFS spectra of the 5 Mn/BR and 5 Mn/BO samples, taken at the Mn K-edge at 230 K. B) FT of the $k\cdot\chi(k)$ data, calculated in the range 2–12 Å with a Gaussian window.

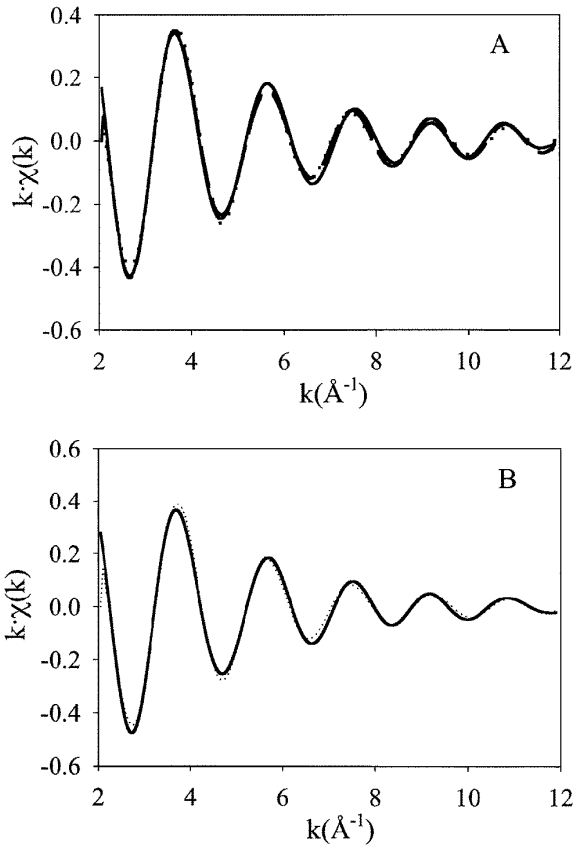

Fig. 4. (A) Single-shell best fit (dotted line), two-shells best fit (dashed line) and filtered experimental signal curve (solid line) for 5 Mn/BR. (B) Single-shell best fit (dotted line) and filtered experimental signal curve (solid line) for 5 Mn/BO.

relevance of these data is enhanced by the fact that they were obtained with different techniques [4, 5].

The raw EXAFS data of 5 Mn/BR, 5 Mn/BO and its Fourier transforms are shown in Figs. 3 and 4 respectively. The $\chi(k)$ signals of Mn^{2+} for both samples are quite close to each other. The FT of the spectra show a main peak centered at about 1.6 Å, and no appreciable contribution due to further shells is observed in any case. As we show in [17], if one of the high and/or medium affinity sites were located in the lipidic region, the Fourier transform of this spectra should show a second peak due to the next nearest neighbours, P and/or S atoms in the phospho- and sulpholipids. Therefore, cation binding is not taking place on the outer lipidic region of the membrane.

To obtain Mn^{2+}-O distances for the protein, we transformed back to k-space the first shell R-space contribution and performed a best fit procedure (Fig. 4) of the experimental data with theoretical phases and amplitudes calculated using the FEFF8 code [13]. The same theoretical signal was also used to fit the Mn^{2+} solution filtered spectrum. The results are reported in Table I. Coordination numbers, Debye-Waller factors, and interatomic distances were iterated. A distance of 2.17 ± 0.01 Å is obtained for Mn^{2+}-O in both the 5 Mn^{2+} regenerated and 5 Mn^{2+} bleached-regenerated membrane. The coordination numbers are equal to six, within the experimental error, for both samples. The Mn^{2+}-O distance found for the Mn solution sample is equal to 2.2 ± 0.01 Å, i.e. 0.03 Å longer than in the protein, demonstrating that in the protein samples the Mn^{2+} are located in the protein environment.

Further information obtained from the fit procedure was that, despite of the close similarity between the two protein samples, the best fit procedure result is different. In the case of the 5 Mn/BR data, the best fit is obtained when an extra Mn-O shell at 2.49 ± 0.02 Å is included. The fit corresponding to the sample in which the retinal has been eliminated (5 Mn/BO) only allows one distance at about 2.17 Å, suggesting that retinal extraction induces

Table I. *Best fit results for 5 Mn/BR, 5 Mn/BO and Mn^{2+} solution samples. The error on Mn-O distances are equal to 0.01 Å for the short Mn-O distance and equal to 0.02 Å for the longer Mn-O distance found for the 5 Mn/BR sample. Errors on Debye-Waller factor and coordination numbers are of about 20%.*

One shell	One shell	Two shell
5 Mn^{2+}/BR		
N1 (fix) = 6	N1 = 5.2	N1 = 5.6
R1 = 2.178 Å	R1 = 2.173 Å	R1 = 2.184 Å
$\sigma^2 = 0.004$	$\sigma^2 = 0.0012$	$\sigma^2 = 0.0136$
NR = $2.0 \cdot 10^{-3}$	NR = $2.0 \cdot 10^{-3}$	N2 = 1.36
		R1 = 2.490 Å
		$\sigma^2 = 0.002$
		NR = $1.6 \cdot 10^{-3}$
5 Mn^{2+}/BO		
N1 (fix) = 6	N1 (No fix) = 5.2	Not allowed
R1 = 2.173 Å	R1 = 2.172 Å	
$\sigma^2 = 0.003$	$\sigma^2 = 0.003$	
Mn^{2+} in water		
N1 (fix) = 6	N1 (No fix) = 5.7	
R1 = 2.200 Å	R1 = 2.200 Å	
$\sigma^2 = 0.005$	$\sigma^2 = 0.004$	

changes in the environment of Mn^{2+}. The loss of the heterogeneity of cation binding sites in the bleached sample suggest that the structural change produced in the protein by the retinal extraction affect the geometry of the cation binding sites. It is know that retinal extraction produces tertiary structural changes with only small alterations of the secondary structure. Therefore cations can help in the protein compactness, because the carboxylic groups that participate in cation binding are from different helices.

All these results are a strong evidence of the specific binding site of the metal cation to bacteriorhodopsin.

Acknowledgments

The authors gratefully acknowledge Beamline ID26 of ESRF for grating in-house research beamtime, and in particular Dr. A. Sole for the kind technical assistance and fuitful discussions during the experiments.

References

1. Haupts, U. *et al*., Ann. Rev. Biophys. Biomol. Struct. **28**, 367 (1999).
2. Lanyi, J. K., Biochemistry (Moscow) **66**, 1192 (2001).
3. Chang, C. H., Chen, J. G., Govindjee, R. and Ebrey, T. G., Proc. Natl. Acad. Sci. USA **82**, 396 (1985).
4. Duñach, M., Seigneuret, M., Rigaud, J. L. and Padrós, E., Biochemistry **26**, 1179 (1987).
5. Zhang, Y. N., Sweetman, L. L., Awad, E. S. and El-Sayed, M. A., Biophys. J. **61**, 1201 (1992).
6. Zhang, Y. N. *et al*., Proc. Natl. Acad. Sci. U.S.A. **90**, 1445 (1993).
7. Szundi, I. and Stoeckenius, W., Biophys. J. **61**, 1201 (1989).
8. Belrhali, H. P. *et al*., Structure **7**, 909 (1999).
9. Luecke, H., Schobert, B., Richter, H. T., Cartailler, J. P. and Lanyi, J. K., J. Mol. Biol. **291**, 899 (1999).
10. Luecke, H. *et al*., J. Mol. Biol. **300**, 1237 (2000).
11. Oesterhelt, D. and Stoeckenius, W., Methods. Enzymol. **31**, 667 (1974).
12. Benfatto, M. and Della Longa, S., J. Synchrotron Rad. **8**, 1087 (2001).
13. Ankudinov, A., Ravel, B., Rehr, J. J. and Conradson, S. D., Phys. Rev. B. **52**, 7565 (1998).
14. Jonas, R. and Ebrey, T. G., Proc. Natl. Acad. Sci. USA **88**, 149 (1991).
15. Tan, E. H. L., Govender, D. S. K. and Birge, R. R., J. Am. Chem. Soc. **118**, 2752 (1996).
16. Pardo, L. *et al*., Biophys. J. **75**, 777 (1998).
17. Sepulcre, F. *et al*., Biophys. J. **70**, 852 (1996).

Physica Scripta. Vol. T115, 859–861, 2005

Simulation of XANES Spectra for Protein-Bound Metal Centers: Analysis of Linear Dichroism Data

Peter Liebisch[1], Michael Haumann and Holger Dau

Freie Universität Berlin, Fachbereich Physik, Arnimallee 14, D-14195 Berlin, Germany

Received June 26, 2003; accepted December 17, 2003

Abstract

For protein-bound transition metals, the structure of the metal site (geometric arrangement of the nuclei) and the electronic structure (oxidations state and orbital occupancy) can be investigated by X-ray absorption spectroscopy. While the extended X-ray absorption fine-structure (EXAFS) is theoretically well understood and the advantages of EXAFS spectroscopy on protein-bound metal centers have been repeatedly demonstrated, quantitative analysis of the near-edge structure (XANES) is more demanding. However, by now XANES simulations, for which a number of codes are available, may be useful to understand geometric and electronic structure effects.

For a simplified model of the manganese complex in photosystem II we simulate polarization-dependent XANES spectra using the FEFF 8.2 code [Ankudinov *et al.*, Phys Rev. B **12** (1998).], which includes self-consistent muffin-tin potentials and polarization-dependent full multiple-scattering calculations. We derive a scheme to analyze the polarization dependence of XANES data that facilitates a treatment of partially uni-directionally oriented samples. Reasonably good agreement between simulations and experiments is obtained for the chosen model of the photosystem II manganese complex and its orientation with respect to the protein-carrying membrane.

1. Introduction

X-ray absorption spectroscopy is frequently applied to collect information on geometric and electronic structure of the catalytic centers in metallo-proteins [1, 2]. While the extended fine-structure (EXAFS) is readily analyzed by least-square fits to an analytical expression to yield coordination numbers, distances and disorder parameters, no closed expression exists for the description for the near-edge region (XANES). Nevertheless, application of modern *ab-initio* computer simulations can provide insight in ligand geometry (distances and angles) and the electronic structure [1, 3, 4]. Interestingly X-ray absorption spectra depend on the angle between the electric field vector of the polarized X-rays and the anisotropic sample, an effect that has been exploited in single-crystal studies and surface science.

For biological samples where single crystals are not available, as it is the case for many membrane proteins, a frequently viable approach involves the use of non-crystalline, but uni-directionally oriented samples where the metal complex has a preferential orientation with respect to the sample normal. Photosystem II (PSII) is a protein complex embedded in the thylakoid membrane of cyanobacteria and higher plants; it contains tetra-manganese complex [5]. PSII-containing membrane fragments can be deposited onto a plane surface by paint-dry techniques or centrifugation such that the membrane plane becomes oriented preferentially parallel to the plane of the substrate surface of the macroscopic sample (for references see [5] and [2]).

For such unidirectionally ordered samples with significant disorder (mosaic spread) we have developed an approach to analyze the single-scattering EXAFS on the basis of curved-wave theory quantitatively [6]. However, this approach is not applicable to XANES spectra. To demonstrate the potential of XANES analysis we show first attempts to understand experimental results from partially oriented samples by XANES simulations.

2. Materials and Methods

Simulations were performed using the *ab-initio* full-multiple scattering (FMS) code FEFF 8.2 [3]. The simulations are performed polarization-dependent using self-consistent potential calculations (SCF) in the muffin-tin approximation with 15% overlap between the muffin tins. The radius for the SCF and the FMS calculations was chosen large enough to include all atoms in the cluster.

3. Results

In general, the normalized X-ray absorption is directly proportional to the matrix element of the transition from initial to the final state as given by Fermi's Golden Rule. For a given polarization, $\vec{\boldsymbol{\epsilon}}$, the absorption is therefore given as $\mu \sim |\vec{\boldsymbol{\epsilon}} \cdot \langle f\,|\vec{\boldsymbol{r}}|\,i\rangle|^2$ (p. 279 of [7]). Performing the quadrature after component-wise expansion of the vectorial expression yields

$$\mu(\vec{\boldsymbol{\epsilon}}) = \epsilon_x^2\mu_{xx} + \epsilon_y^2\mu_{yy} + \epsilon_z^2\mu_{zz} + 2\epsilon_x\epsilon_y\mu_{xy} + 2\,\epsilon_y\epsilon_z\mu_{yz} + 2\epsilon_z\epsilon_x\mu_{zx}. \quad (1)$$

Thus, $\mu(\vec{\boldsymbol{\epsilon}})$ is described by a second rank tensor with six independent parameters [8] which can be visualized as an absorption ellipsoid. Therefore with six independent simulations for different polarization directions an equation system can be set up and which provides the tensor components. Writing Eq. (1) as quadratic form

$$\mathbf{1} = \vec{\boldsymbol{\epsilon}}^T\mathbf{A}\vec{\boldsymbol{\epsilon}} \quad (2)$$

allows the calculation of Eigenvectors and Eigenvalues of the coefficient matrix, which to the principal axes of the absorption ellipsoid and the inverse square root of their length. We denote the principal-axes unit vectors (Eigenvectors of $\mathbf{A}$) as $\vec{\boldsymbol{v}}_1$, $\vec{\boldsymbol{v}}_2$ and $\vec{\boldsymbol{v}}_3$ and the corresponding Eigenvalues as D_1, D_2 and D_3. Then the length of each principal axis is given by: $L_i = 1/\sqrt{D_i} = \sqrt{\mu_i}$; $i = 1, 2, 3$.

Thus we can write for the X-ray absorption in the molecule system

$$\mu(E, \vec{\boldsymbol{\epsilon}}) = \sum_{i=1}^{3} \mu_i(\vec{\boldsymbol{v}}_i \cdot \vec{\boldsymbol{\epsilon}}_i)^2 = \sum_{i=1}^{3} \mu_i \cos^2 \Theta_{v_i,\epsilon_i} \quad (3)$$

For each principle axis unit vector, the absorption is proportional to the squared cosine of $\Theta_{v,\epsilon}$ rendering each term analogous to the cosine term in Eq. (2) of Dittmer and Dau [6]. In continuation of the analogy, we introduce Θ_i, the angles between the principle-axis unit vectors and the membrane normal ($\vec{\boldsymbol{N}}$), as well as Θ_E, the

[1] peter.liebisch@physik.fu-berlin.de

angle between the electric field vector and the membrane normal. Following the rationale given in [6], we finally arrive at the result

$$\mu(E, \Theta_E) = \frac{1}{3}\sum_{i=1}^{3}\mu_i + \frac{1}{6}\,(3\cos^2\Theta_E - 1)\,I_{ord}\sum_{i=1}^{3}\mu_i(3\cos^2\Theta_i - 1) \qquad (4)$$

with the order parameter, I_{ord}, which has been defined in [6] (Eq. 8) as an integral over the properly normalized distribution function of the membrane normals, $P(\alpha)$, according to:

$$I_{ord} = 2\pi^2\int_0^{\pi/2}(3\cos^2(\alpha) - 1)P(\alpha)\sin(\alpha)\,\mathrm{d}\alpha. \qquad (5)$$

The I_{ord}-value of 1 is obtained for perfect orientation, and I_{ord} is zero for an isotropic distribution.

As an example we discuss polarization-dependent simulations for the simple mixed-valent di-μ-oxo-bridged manganese dimer shown in Fig. 1. The native tetra-manganese complex of PSII may consist of two binuclear units both being similar to the complex shown in Fig. 1.

In Fig. 2 we show spectra of layered PSII membranes for angles between the X-ray electric field vector and the sample normal of 15°, 35°, 55° and 75°. Here, the edge position of the 75° spectrum is shifted by 0.7 eV to higher energies compared to the 15° spectrum; the magnitude of the pre-edge peak is maximal in the 75° spectrum and minimal for 15°.

In the simulations we use a highly simplified structural model for the water-oxidizing complex of PSII. The native manganese complex seems to consist of two di-μ-oxo bridged Mn_2-units [5]. Linear Dichroism EXAFS analysis shows that the Mn-Mn vector is at an angle of about 70° to the membrane normal and that the di-μ-oxo plane is rather parallel than perpendicular to the membrane plane [1, 2, 5, 9]. XANES analysis suggests a $Mn(III)_2Mn(IV)_2$ complex in the dark-stable S_1-state [1, 2, 5]. Here we use a single Mn(III)-(μ-O)$_2$-Mn(IV) unit assuming that the native complex consists of two such units. The oxidation state of the manganese atoms is incorporated in two ways: (1) as formal oxidation state by substitution of water ligands by (negative) hydroxyl ligands and (2) by means of the bonding distances that are typical for the respective oxidation states.

The specrta calculated separately for Mn(III) and Mn(IV) for different polarization angles are shown in Fig. 3 whereas Fig. 4 shows the average spectrum. Firstly we can state that the polarization-dependent changes in the experimental spectra are reproduced. Secondly we note, that the modeling of the oxidation states works quite well since an upshift of the edge position by about 3–4 eV is known to be typical for an oxidation state change of +1 (see [1]). However, the polarization dependence is largely overestimated by the simulations. For the following reasons this is to be anticipated: (1) the actual XAS samples are not perfectly oriented but partially disordered; (2) in the Mn_4-complex of the PSII the $Mn_2(\mu\text{-O})_2$ planes are certainly not both perfectly parallel to the membrane plane; and (3) only partial orientation exists (partially uni-directionally oriented samples).

The latter argument necessitates angle averaging. This can be performed if the absorption ellipsoid is known at each energy. Figure 5 shows the absorption ellipsoids for selected X-ray energies where μ corresponds to the square of the length of the radius vector for a given orientation (also indicated by the surface color).

Applying the result of Eq. (4) to the absorption ellipsoids calculated for each energy point we can calculate XANES spectra corresponding to a distinct degree of orientation ($I_{ord} = 0.45$) and

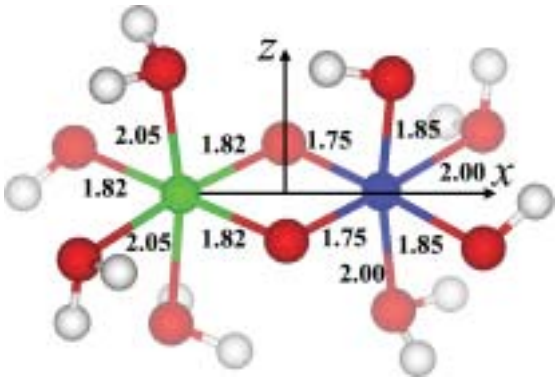

Fig. 1. Structure of a hypothetical di-μ-oxo-bridged manganese complex. Red spheres stand for oxygen atoms, white spheres for hydrogen, the green sphere for Mn(III), and the blue one for Mn(IV). The numbers indicate the bond length in Å. The axes indicate the orientation of the coordinate system selected for the simulations: The x-axis points along the Mn-Mn vector, the y-axis connects the two bridging oxygens and the z-axis is perpendicular to the $Mn_2(\mu\text{-O})_2$-plane.

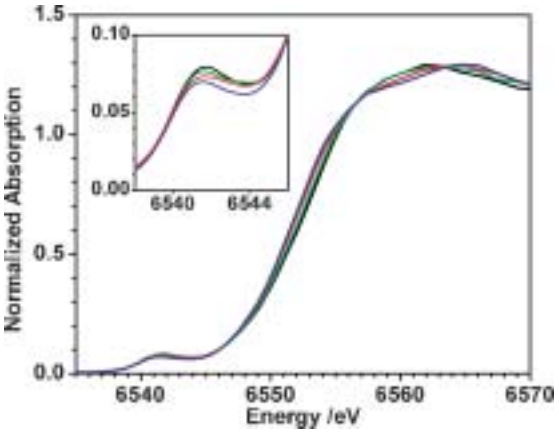

Fig. 2. XANES spectra of the PSII manganese complex measured at excitation angles of $\Theta_E = 15°$ (blue line), 35° (red line), 55° (green line) and 75° (black line) on partially oriented PSII membrane particles. The inset shows the pre-edge region on an expanded scale. Sample preparation and data collection as described in [9, 10].

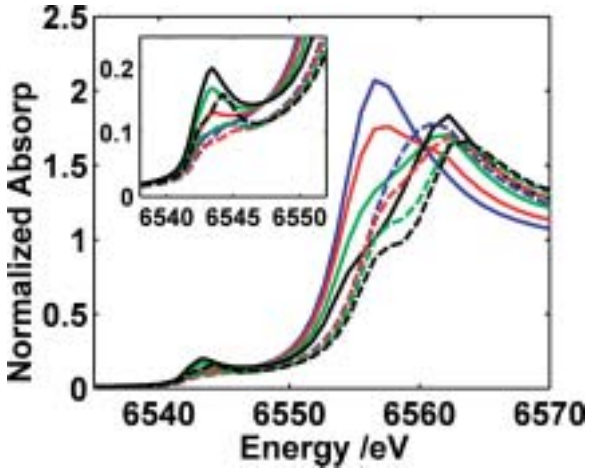

Fig. 3. Simulated polarization dependence of the XANES for the Mn(III) (solid lines) and Mn(IV) (dashed lines) in the dimer structure of Fig. 1. The polarization vector was chosen in the x-z-plane at angles with the z-axis of $\Theta_E = 15°$ (blue line), 35° (red line), 55° (green line) and 75° (black line).

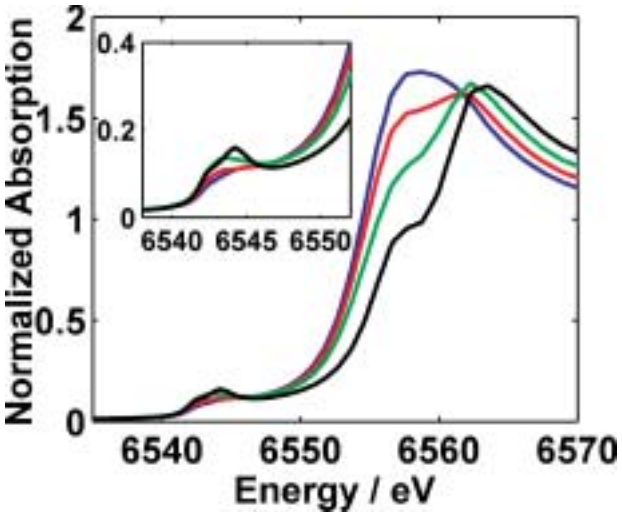

Fig. 4. XANES spectra obtained by averaging of the corresponding Mn(III) and Mn(IV) spectra of Fig. 3. $\Theta_E = 15^\circ$ (blue line), 35° (red line), 55° (green line) and 75° (black line).

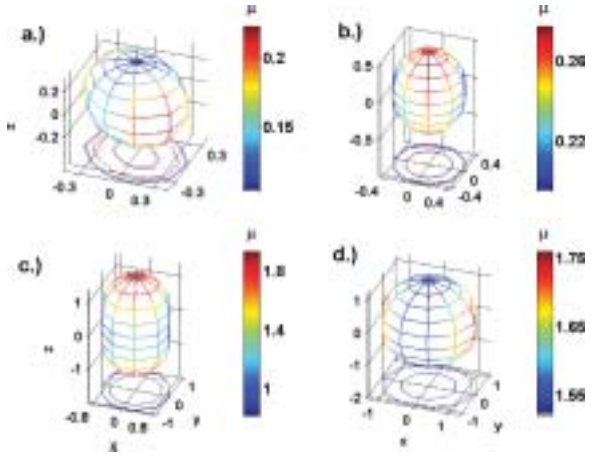

Fig. 5. Shape of the absorption ellipsoids for different energies for the Mn(IV) atom in the model structure: a.) 6544 eV, b.) 6550 eV, c.) 6555 eV and d.) 6560 eV. The axes are chosen to lie as indicated in Fig. 1, the length of a vector pointing from the origin to the ellipsoid surface at a direction $\vec{\boldsymbol{\epsilon}}$ is given by $\sqrt{\mu(\vec{\boldsymbol{\epsilon}})}$. The normalized absorption μ is also indicated by the surface color.

a distinct orientation of the molecular system with respect to the membrane normal. The spectra shown in Fig. 6 were calculated assuming that the $Mn_2(\mu\text{-}O)_2$ plane lies in the membrane plane.

We observe a polarization dependence which not only qualitatively reflects the experimental results but also is of approximately correct magnitude with respect to the edge-shift and the angle-dependence of the pre-edge magnitude. Furthermore, in the range of the shape resonance a cross-over point is found that is similar to the one in the experimental data. The second crossing is missing in the simulation which is most probably due to the grossly simplified model.

Figure 7 shows the simulated spectra under the assumption that the $Mn_2(\mu\text{-}O)_2$ plane is perpendicular to the membrane plane. Obviously, the results are not in agreement with the experiment.

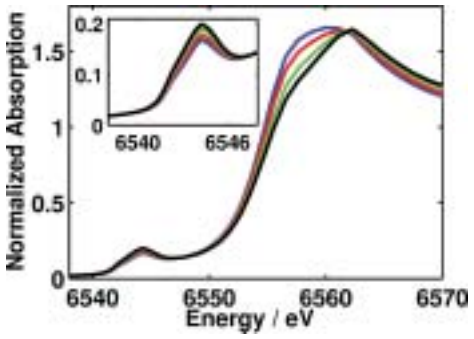

Fig. 6. Spectra resulting from angle averaging under the assumption that the $Mn_2(\mu\text{-}O)_2$-plane lies in the membrane plane ($\vec{z} \parallel \vec{N}$). Blue line, $\Theta_E = 15^\circ$; red line, $\Theta_E = 35^\circ$; green line, $\Theta_E = 55^\circ$, black line $\Theta_E = 75^\circ$.

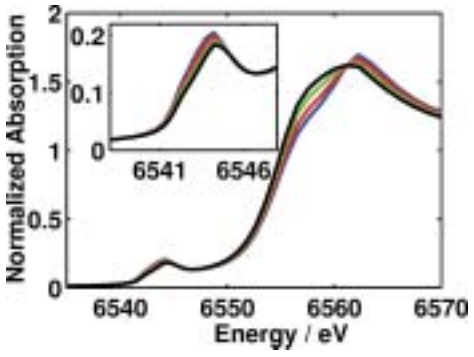

Fig. 7. Spectra resulting from angle averaging under the assumption that the $Mn_2(\mu\text{-}O)_2$-plane is perpendicular to the membrane plane ($\vec{z} \perp \vec{N}$) (same color code as in Fig. 6).

We feel that the simulation of the linear dichroism (LD) in the XANES represents a promising new approach. In the future the LD-XANES analysis may complement the LD-EXAFS analysis.

Acknowledgments

Financial support from the Deutsche Forschungsgemeinschaft (SFB 498, project C6 and C8) and from the Bundesministerium für Bildung und Forschung (grant 05/KS1KEA-6) is gratefully acknowledged. We thank Dr. T. Neisius (ESRF, Grenoble, beamline ID26) and Dr. W. Meyer-Klauke (DESY, Hamburg, EMBL outstation) for their excellent support.

References

1. Dau, H., Liebisch, P. and Haumann, M., Anal. Bioanal. Chem. (2003), in press.
2. Dau, H. and Haumann, M., J. Syncrotron. Rad. **10**, 76 (2003).
3. Ankudinov, A. L., Ravel, B., Rehr, J. J. and Conradson, S. D., Phys. Rev. **B12**, 7565 (1998).
4. Natoli, C. R., Benfatto, M., Della-Longa, S. and Hatada, K., J. Syncrotron. Rad. **10**, 26 (2003).
5. Dau, H., Iuzzolino, L. and Dittmer, J., Biochim. Biophys. Acta. **1503**, 24 (2001).
6. Dittmer, J. and Dau, H., J. Phys. Chem. **B102**, 8196 (1998).
7. Stöhr, J., "NEXAFS spectroscopy", Springer Series in Surface Sciences, (Springer Verlag, Berlin 1992).
8. Brouder, C., J. Phys. Cond. Mat. **2**, 701 (1990).
9. Schiller, H., *et al.*, Biochemistry **37**, 7340 (1998).
10. Iuzzolino, L., Dittmer, J., Dörner, W., Meyer-Klaucke, W. and Dau, H., Biochemistry **37**, 17112 (1998).

Physica Scripta. Vol. T115, 862–863, 2005

Investigation of the Local Structure of Fe(II) Bleomycin and Peplomycins using Theoretical Analysis of XANES

G. Smolentsev[1], A. V. Soldatov[1*], E. Wasinger[2], E. Solomon[2], K. Hodgson[2,3] and B. Hedman[2,3]

[1]Department of Physics, Rostov State University, 5, Sorge street, 344090 Rostov-on-Don, Russia
[2]Department of Chemistry, Stanford University, Stanford, California 94305, USA
[3]Stanford Synchrotron Radiation Laboratory, Stanford University, Stanford, California 94305, USA

Received June 26, 2003; accepted October 14, 2003

PACS number: 78.70.Dm

Abstract

The active site geometry of Fe(II)-bleomycin, peplomycin and its derivatives have been studied on the basis of theoretical multiple scattering simulations of the Fe K-edge X-ray absorption near edge structure. Comparisons of the experimental and theoretical spectra calculated for the different models of Fe(II)-bleomycin reveal serious distortions of the ligands nearest to Fe. This includes the presence of one ligand with a very short bond length as well as angular distortions. Reconstruction of the nearest environment of the Fe during perturbation of axial ligand was investigated for peplomycin. It was found that replacement of carbamoyl group of the mannose with solvent molecule led to a small increase of average radius (0.03 Å) of the first atomic shell around Fe ion and elongation of the shortest bond length (0.10 Å).

1. Introduction

Investigation of the non-heme active site structure of bleomycin (Blm) and its variations during ligand substitution is a key step to understand the antibiotic activity of this complex and its ability to degrade DNA with site specificity. At present there are no high-resolution crystal structure data of bleomycin or its analogues such as peplomycin. Current insight into the Fe-ligand geometry is based on NMR or optical spectroscopic data as well as on molecular dynamic results. A description of recent results in this field can be found in [1, 2]. The secondary amine of β-aminoalanine (Ala), pyrimidine (Pyr) and imidazole (Imid) rings and amine nitrogen of β-hydroxyhistidine (His) are found to be the equatorial ligands to the metal centers in all bleomycins studied to date. Nevertheless, the axial ligation of the metal center still remains unclear. Different models with the primary amine of Ala and either carbamoyl substituent of mannose (Man) or solvent molecule occupying axial positions have been proposed. Moreover, some models represent opposite chiralities of the metal center. XANES spectroscopy is a sensitive probe of metal arrangement in bio-molecules and we have applied it to clarify axial ligands and geometry in bleomycin.

2. Method of calculation

The method of XANES simulations is based on a full multiple scattering scheme in the framework of the muffin-tin approximation. It was described in detail in [3]. A cluster of 54 atoms for Blm and peplomycin (Pep) and 51 nearest to Fe atoms for iso-peplomycin (Iso-Pep) have been chosen using the criterion of spectrum convergence as a function of cluster size. The molecular muffin-tin potential was obtained by a self-consistent-field scattering waves technique within the local density approximation. To take into account the broadening of the experimental spectrum according to the core hole lifetime, the finite mean free path of the photoelectron and the experimental resolution, the theoretical spectra were convoluted with a Lorentzian function. We have used the value of 1.25 eV for the core hole bandwidth, an energy dependent function from [4] representing all inelastic processes, and a value of 1.4 eV for experimental resolution.

Within the limit of small variations of structural parameters (less than 0.15 Å if the parameter is a distance) a simple approximation to interpolate a spectrum as a function of these parameters can be used:

$$I(E, p_1 + \delta p_1, p_2 + \delta p_2, \ldots, p_n + \delta p_n) = I(E, p_1, p_2, \ldots, p_n) + \sum_{i=1}^{n} \frac{\partial I}{\partial p_i}(E)\delta p_i,$$

where

$$\frac{\partial I}{\partial p_i}(E) = \frac{I(E, p_1, p_2, \ldots, p_i + \Delta p, \ldots, p_n) - I(E, p_1, p_2, \ldots, p_n)}{\Delta p}.$$

Such an approach allows a significant reduction in computational time during the geometry optimization using a standard fitting technique (only $n + 1$ multiple scattering calculations are needed, where n is a number of parameters). Tests of approximation accuracy were performed but they are out of the scope of this paper.

3. Results and discussion

Calculations of the Fe K-edge XANES of bleomycin were performed for 7 models generated using the molecular dynamic technique [1]. All variants of axial ligation with the primary amine of Ala and different second ligands (nitrogen or oxygen of carbamoyl group of the mannose or oxygen of the solvent molecule) were tested. Models 1, 2, 5 and 6 involve only endogenous ligands. In models 1 and 5 the second axial position is occupied by the carbamoyl oxygen, while models 2 and 6 include the nitrogen of the same group. Pairs 1,5 and 2,6 represent opposite chiralities of the metal center. Models 3 and 7 were derived from models 1 and 5 respectively by substituting the carbamoyl with a solvent molecule. In these models the sugar moiety is located near the solvent molecule. In model 4 the Fe ligation is the same as that in model 7, but the sugar moiety is close to the primary amine of Ala. A more detailed description of the models can be found in [1].

*e-mail: Soldatov@rsu.ru

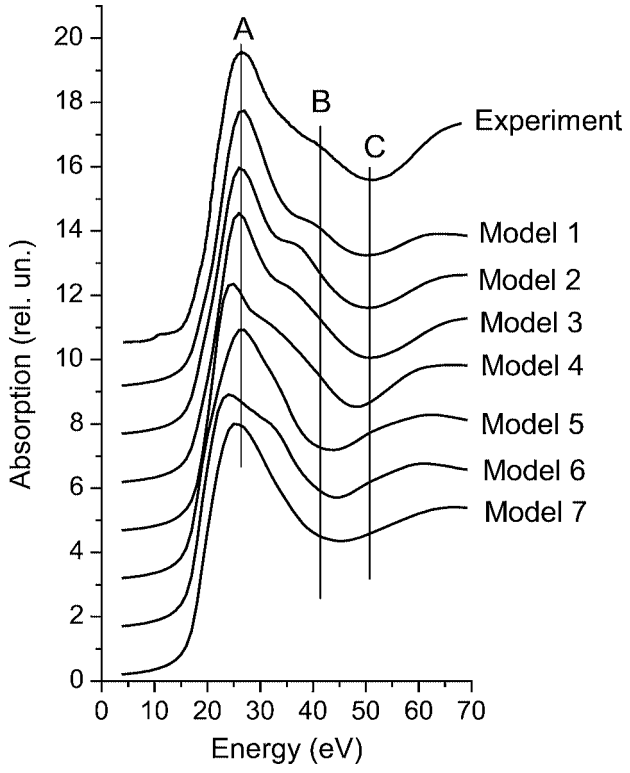

Fig. 1. Experimental and theoretical Fe K-edge XANES of bleomycin. Calculations for 7 models from [1] are presented.

A comparison of theoretical spectra with experimental spectrum in fig. 1 shows that models 1, 2, 3 and 4 correctly predict the relative energy separation between maximum A and minimum C, while this energy separation is very small for models 5–7. The shapes of spectra 1, 2 and 3 between features A and C are very similar, but the position of shoulder B depends on the model. The best agreement between the experimental and theoretical spectra is achieved for model 1 with the mannose oxygen in the second axial position. Therefore this model is the most realistic among the seven models considered. The key parameters that distinguish this model from models 2 and 3 are angular distortions of the six ligands nearest to Fe. For example primary amine of Ala-Fe-Imid angle is 67° for model 1 and 98° and 105° for models 2 and 3 respectively. Also, angles between the second axial ligand and ligands in the equatorial plain significantly different.

Subsequent simulations were performed to address the structural origin of geometry reconstruction found upon perturbation of one of the axial ligands. Active sites of Blm and Pep are expected to be very similar, because the bithiazole tail, which solely distinguishes Blm from Pep, does not participate in Fe ligation. This also correlates with the results of an EXAFS analysis [5]. In contrast, in the case of Iso-Pep, perturbation of one of the axial ligands, namely replacement of mannose carbamoyl with the 2-hydroxy group, modifies the ligand arrangement. It was shown using EXAFS and pre-edge data analysis [5], that this complex remains six-coordinate, therefore the oxygen from a solvent water molecule was proposed as a second axial ligand. This type of coordination corresponds to model 3 above. Nevertheless differences between the experimental spectra of Pep and Iso-Pep are not so severe as the differences between theoretical spectra from models 1 and 3. Experimentally, there is only an overall shift of the experimental spectra and a small increase of main peak intensity, while theoretical spectra are distinguished from each other mostly by the energy of peak B.

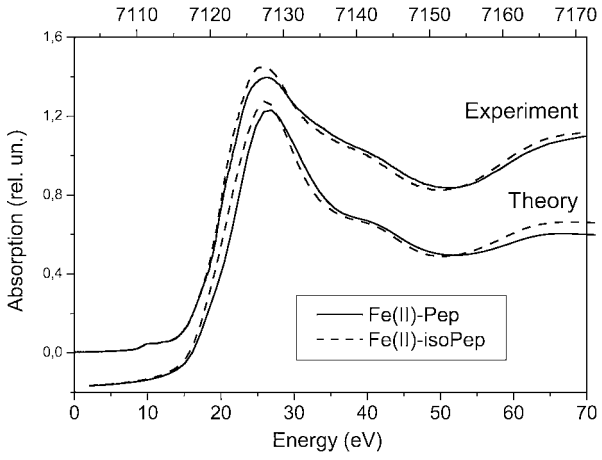

Fig. 2. Experimental and theoretical Fe K-edge XANES of peplomycin and iso-peplomycin. Calculations for model A of iso-peplomycin are presented.

Table I. *Fe-ligand bond lengths (in Å) for Fe(II)-Pep, Blm and two models of Iso-Pep.*

Ligand	Fe(II)-Pep (Blm)	Iso-Fe(II)-Pep Model A	Iso-Fe(II)-Pep Model B
Pyrimidine	2.02	1.99	2.05
Imidazole	2.06	2.07	2.09
Amide (hydroxyhistedine)	1.89	2.07	1.97
Secondary amine (aminoalanine)	2.13	2.14	2.15
Axial N (mannose)	2.03	2.05	2.06
Axial N (aminoalanine)	2.05	2.07	2.09
Average 1 shell distance	2.03	2.06	2.07

Thus, we conclude that axial ligand perturbation does not produce angular distortions of the octahedron of ligands nearest to Fe. Therefore a further refinement of the geometry was performed by optimizing the Fe-ligand bond lengths while all ligand-Fe-ligand angles remained fixed.

The results of these simulations are presented in fig. 2. Fe-ligand bond lengths are summarized in tab. I. The model of Fe(II)-Pep corresponds to model 1 reported in [1], but all Fe-ligand distances were expanded to 0.03 Å. Theoretical spectra of Iso-Pep, calculated for the models with the nearest equatorial nitrogen from Imid and amide of His are very similar (Models A and B in Table I). It is impossible to choose the best fit from these two models on the basis of XANES analysis alone. Nevertheless, the nearest ligand was assigned as Imid on the basis of results from optical spectroscopy [2]. Therefore model A of Iso-Pep is the most realistic.

Acknowledgment

We thank Prof. T. Lehmann (Instituto Venezolano de Investigaciones Cientificas (IVIC), Venezuela) for sharing with us her structural data on Fe(II)-Blm and for useful discussions.

References

1. Lehmann, T. E., J. Biol. Inorg. Chem. **7**, 305 (2002).
2. Loeb, K. E., Zaleski, J. M., Hess, C. D., Hecht, S. M. and Solomon, E. I., J. Am. Chem. Soc. **120**, 1249 (1998).
3. Della Longa, S., Soldatov, A., Pompa, A. and Bianconi, A., Comp. Materials Sci. **4**, 199 (1995).
4. Muller, J. E., Jepsen, O. and Wilkins, J. W., Solid State Commun. **42**, 365 (1982).
5. Wasinger, E. C., Zaleski, K. L., Hedman, B., Hodgson, K. O. and Solomon, E. I., J. Biol. Inorg. Chem. **7**, 157 (2002).

Physica Scripta. Vol. T115, 864–866, 2005

An Enhanced Electronic State in ZnTPP Induced by Interaction with Solvation: A Multiple-Scattering Calculation of X-ray Absorption Near-Edge Spectra

Tao Liu[1,2] and Lin X. Chen[1]

[1]Chemistry Division, Argonne National Laboratory, Argonne, Illinois 60439, U.S.A.
[2]Synchrotron Radiation Laboratory, Institute of High Energy Physics, Chinese Academy of Sciences, Beijing, 100039, P.R. China

Received June 26, 2003; accepted in revised form November 4, 2003

PACS number: 3320Rm

Abstract

Metalloporphyrins (MP) are important for a wide variety of biological processes and photosynthesis and have been intensively investigated by X-ray absorption spectroscopy. The typical metal K-edge XANES spectra of the square-planar MTPP show a very sharp peak on the rising edge of the main absorption peak, which was assigned to $1s \rightarrow 4p_z$ electronic transition. We carried out a series of multiple-scattering calculations of porphyrin molecules and found that this peak can be greatly enhanced due to the π-π stacking of phenyl rings below and above the porphyrin plane. Density of state calculations confirmed that the emergence of this electronic state is due to the interaction of the $4p_z$ orbital of the metal with π orbitals of an aromatic solvent molecule with its plane parallel with the macrocycle. This XANES feature of metalloporphyrins can be used to investigate the solvent-solute interactions with presumed non-ligating solvent.

Metalloporphyrins (MP) are analogs of heme and chlorophylls that play critical roles in photosynthesis because of their intense absorption in the visible and UV regions which allows them to perform light harvesting as well as light energy conversion. Meanwhile, MP are also capable of ligating with a variety of small molecules as axial ligands, such as oxygen, which are vital in oxygen transportation of red blood cells [1, 2]. The basic unit of MP consists of a porphyrin macrocycle in an essentially planar structure, but a variety of nonplanar conformations could be induced by the metal ions in the center as well as by the peripheral substituted groups. Such a flexibility in the structure is believed to be important for its various applications, e.g., as nanoscale molecular devices [3] or selective oxidative catalysts [4]. Therefore, it is important to use XAFS technique to investigate MP structures in solvated or ligated states, the conformations of the macrocycles in catalytic reactions. X-ray absorption near-edge structure (XANES) can probe the local structures and electronic properties, regardless of the sample crystallinity. The recent development of computational methods, such as FEFF using multiple-scattering (MS) theory allows us to investigate the XANES features of MP as well as their correlation with the density of states in more quantitative ways [5–7]. Therefore, the solvent solute interactions that may affect electronic states can be analyzed.

Room temperature XANES spectra of zinc tetraphenyl-porphyrin (ZnTPP) and its copper analog, CuTPP in tolune and pyridine solutions were measured at a wiggler beamline (11ID-D) of Basic Energy Science Synchrotron Research Center, Advanced Photon Source at Argonne National Laboratory, with a Si-220 double crystal in the monochromator. All the spectra were collected in fluorescence mode using a nine element solid state detector (Canberra).

ZnTPP and CuTPP remain unligated in toluene (the inset of Fig. 1), the XANES spectra of both exhibit a sharp peak at the rising edge of absorption (peak A), as shown in Fig. 1,

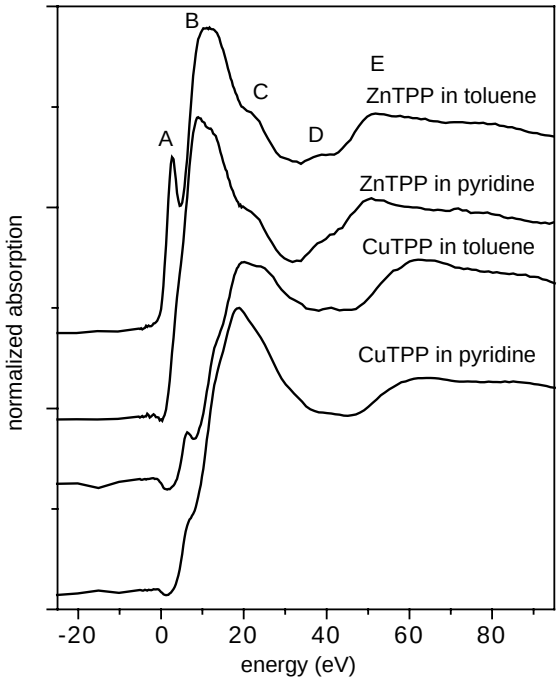

Fig. 1. XANES spectra of ZnTPP and CuTPP solutions in toluene and in pyridine.

which is assigned to the 1s to $4p_z$ transition of transition metals [8]. However, in ligating solvents, pyridine or piperidine, this peak is attenuated significantly due to the axial ligation of solvent molecules with the metal, forming a penta-coordinated square-pyramidal or a hexa-coordinated octahedral geometry. Consequently, the $4p_z$ orbital of the transition metal is less empty and delocalized due to the ligation [9].

A series of XANES and l-density of state ($l = \mathrm{s, p, d, \ldots}$, -DOS) calculations were carried out using FEFF8 programs (version 8.10) [5], a real-space full multiple-scattering approach using a self-consistent potential. The whole molecule around the central Zn atom was included to construct the self-consistent field (SCF) potential. XANES spectra were calculated using the Hedin-Lundqvist self-energy with an energy dispersion of -0.1 eV to account for the core hole lifetime and the instrumental broadening effects. Full multiple scattering (FMS) calculations were used for all calculations. The muffin-tin radii were overlapped up to 1.3 to reduce the effects of discontinuities between adjacent regions. The Debye-Waller factors were set to zero because of their negligible influence on the XANES spectra.

Figure 2 shows MS calculations for a single molecule of ZnTPP with increasing number of neighboring atoms around Zn defined by the MS radii used in the calculation. Each cluster

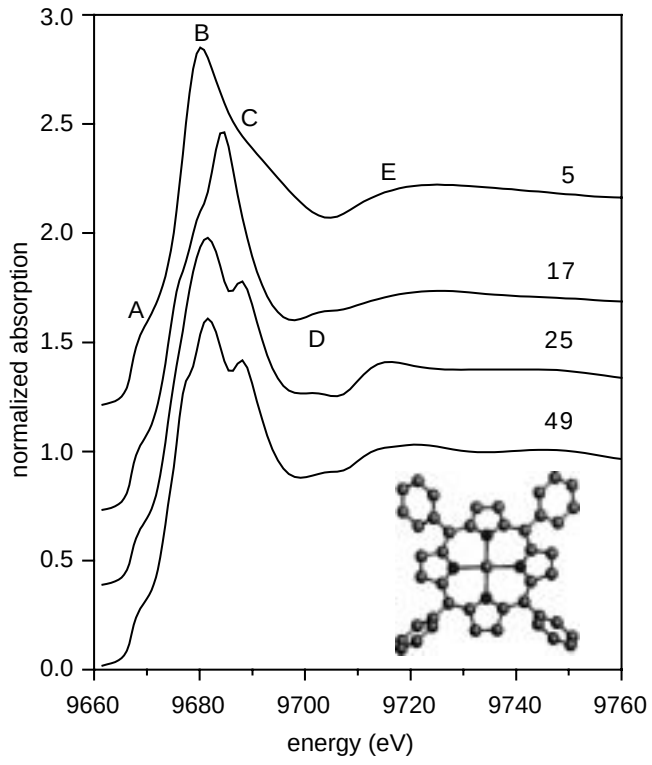

Fig. 2. MS calculations for clusters built by gradually increasing the size of the molecular around the central Zn atom; 5: ZnN_4; 17: ZnN_4C_{12}; 25: ZnN_4C_{20}; 49: ZnN_4C_{44}, the inset shows ZnTPP molecule.

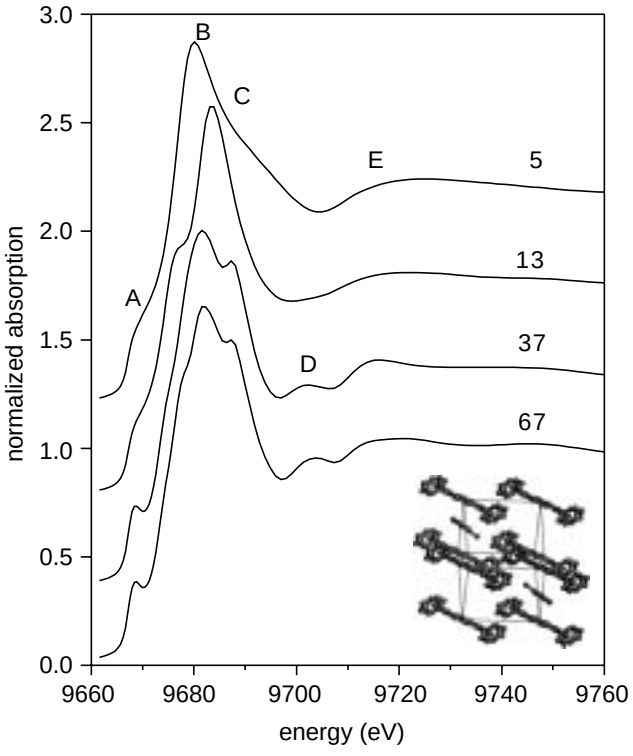

Fig. 3. MS calculations for clusters built by gradually increasing the cluster size around the central Zn atom; 5: ZnN_4; 17: ZnN_4C_{12}; 37: ZnN_4C_{22}; 67: ZnN_4C_{42}, the inset shows the triclinic crystal ZnTPP of toluene solvate.

was constructed from the ZnTPP crystal structure with solvated toluene molecules [9]. Zn-N_4 cluster displays main features A, B and E. While the calculations extend to more neighboring atoms, peak B splits into B and C, and peak D emerged. Apparently distant neighbors are responsible for the evolution of the spectra. Compared with the experimental results, the main features of B, C, D and E are produced. However, the separation of B and C is not distinct and peak A is less distinct than observed experimentally for the ZnTPP in toluene solution. One possibility of this distinction is due to the insufficient accuracy of the self-consistent field potentials [5].

In a parallel calculation that included the solvated toluene molecule (Fig. 3), the toluene molecules above and below the ZnTPP plane were included for clusters larger than 13 atoms. The two phenyl rings above and below the ZnTPP plane form a close packed cluster so that the π-π interactions of ZnTPP with the two phenyl-rings result in an enhancement of peak A.

To further demonstrate this, clusters were built by stacking two phenyl-rings above and below the ZnTPP plane and changing the spacing of the rings to the ZnTPP plane. As is clearly shown in Fig. 4, peak A develops and becomes more pronounced as the distance to the ZnTPP is reduced, meanwhile, peak B is shifted to higher energy. Figure 5 shows that the p-DOS spectra of the excited state has a new electronic state developing right above the Fermi level as the phenyl-rings approach to ZnTPP.

For comparison, MS calculations on ZnTPP·$(H_2O)_2$, crystals (tetragonal, I4/m) [10] and ZnTPC(Py) crystals (triclinc P-1, benzene solvate) [11] were also performed, but no enhancement of peak A was observed in the XANES spectra as expected [8]. In both cases, Zn forms σ-bond instead of nonbonding π-π interaction with the solvent molecules. Zn forms chemical bonds with two oxygens as axial ligands in the former case and one nitrogen in the latter. Such a σ-bonding is much stronger due to

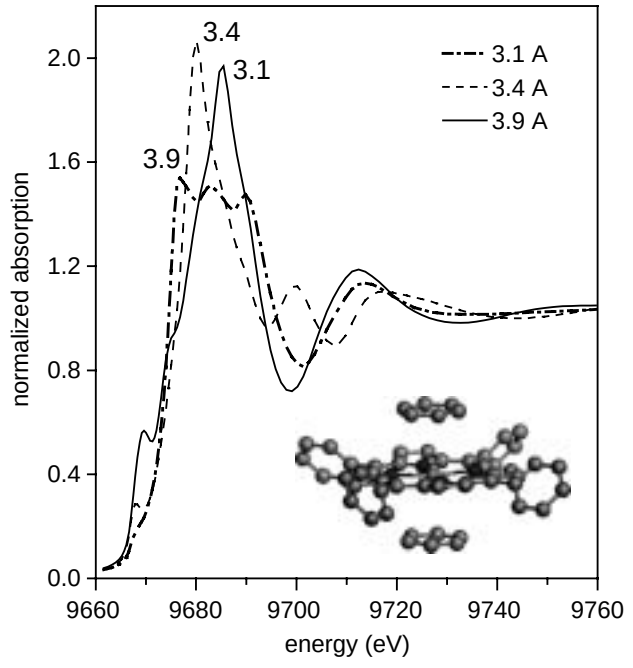

Fig. 4. XANES calculations of clusters built by placing two benzene above and below the ZnTPP plane (inset) and changing the spacing of benzene relative to the ZnTPP plane.

strong overlap between the Zn orbital in the z-direction with the solvent lone pair electrons, and is fundamentally different from the much weaker nonbonding π-π interaction where only slight electron density transfer between two parallel aromatic rings is expected.

The enhancement of the new excited electronic states is closely related to the multi-scattering paths due to atoms in

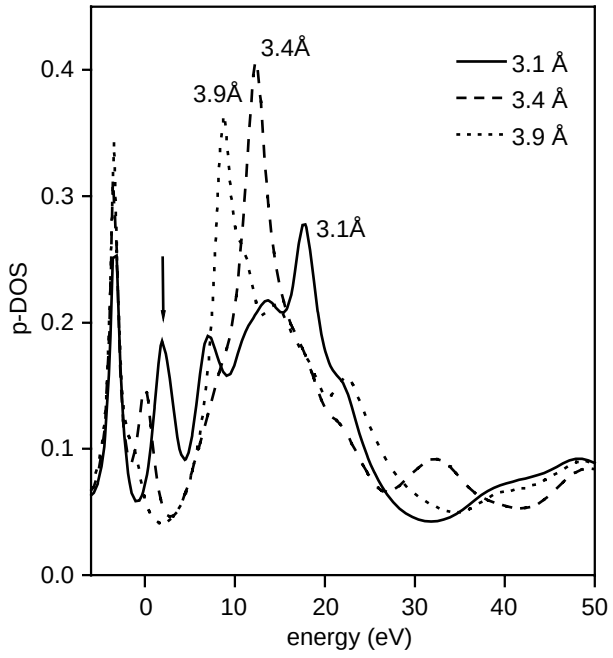

Fig. 5. p-DOS calculations of clusters built by placing two benzene above and below the ZnTPP plane (inset) and changing the spacing of benzene relative to the ZnTPP plane.

a solvent molecule simultaneously brought in the vicinity of the macrocycle, producing resonance from the interference between several scattering paths. Stacking of two phenyl rings above and below the porphyrin plane can form a close packed molecular cage. As reported previously [12], the main multiple scattering resonances in the XANES of $Fe(CN)_6$ complexes are associated with shape resonances within CN ligands. An excited photoelectron of low kinetic energy (10–30 eV) emitted by the central Fe atom can be "trapped" in virtual bound states built up of repeated scatterings from the C and N atoms of a CN group. This can produce a resonance and enhance the back-scattering amplitude of the ligand shell as a whole at these energies. This is reflected in the absorption cross section in a way which depends on the geometrical arrangement of the CN groups around the Fe atom. The same statement holds for our case. The confinement of the molecular multiple-scattering cage formed by rigid small molecules, can produce very intensive "shape resonances". In view of the molecular orbital theory, this enhanced electronic state in the MTPP can be associated with the π-π interactions exerted by p_z orbitals of the metal and the carbon atoms of the phenyl rings.

In conclusion a series of multiple-scattering calculations for XANES spectra from ZnTPP demonstrate that a peak at the rising edge of main absorption is greatly enhanced by the stacking of phenyl rings below and above the ZnTPP plane. This enhancement is associated with the shape resonant effect of the molecular cage. DOS calculations indicate that it arises likely from π-π interactions exerted by p_z orbitals of the metal and the carbon atoms of the phenyl rings. These XANES features of ZnTPP or CuTPP can be used to identify the solvation states in non-ligating solution.

Acknowledgements

This work is supported by the Division of Chemical Sciences, Office of Basic Energy Sciences, U.S. Department of Energy under contracts W-31-109-Eng-38. We are grateful to Prof. J. J. Rehr and Prof. A. L. Ankudinov for their useful discussions in terms of the FEEF calculations. We also appreciate the support from the staff at BESSRC, Advanced Photon Source, Argonne National Laboratory.

References

1. Barbara, P. F., Meyer, T. J. and Ratner, M. A., J. Phys. Chem. **100**, 13148 (1996).
2. Ochiai, E. I., "Bioinorganic Chemistry", (Boston: Allyn and Bacon, Inc. 1977), 85.
3. O'Neil, M. P. *et al.*, Science **257**, 63 (1992).
4. Van Veen, J. A. R. and Van Baar, J. F., Rev. Inorg. Chem. **4**, 293 (1982).
5. Ankudinov, A. L., Ravel, B., Rehr, J. J. and Conradson, S. D., Phys. Rev. B **58**, 7565 (1998).
6. Rehr, J. J. and Albers, R. C., Rev. Mod. Phys. **72**, 621 (2000).
7. Ankudinov, A. L., Rehr, J. J. and Bare Simon, R., Chem. Phys. Lett. **316**, 495 (2000).
8. Smith, T. A., Penner-Hahn, J. E., Berdin, M. A., Doniach, S. and Hodgson, K. O., J. Am. Chem. Soc. **107**, 5945 (1985).
9. Scheidt, W. R., Kastner, M. E. and Hatano, K., Inorg. Chem. **17**, 706 (1978).
10. Fleischer, E. B., Miller, C. K. and Webb, L. E., J. Am. Chem. Soc. **86**, 2342 (1964).
11. Spaulding, L. D., Andrew, L. C. and Williams, J. B., J. Am. Chem. Soc. **99**, 6918 (1977).
12. Bianconi, A., Dell'Ariccia, M., Durham, P. J. and Pendry, J. B., Phys. Rev. B**26**, 6502 (1982).

Physica Scripta. Vol. T115, 867–869, 2005

Biological XAFS at the BioCAT Undulator Beamline 18ID at the APS

R. A. Barrea[1,*], R. Fischetti[1,4], S. Stepanov[1,4], G. Rosenbaum[2], E. Kondrashkina[1], G. B. Bunker[1], E. Black[1], K. Zhang[1], D. Gore[1], R. Heurich[1], M. Vukonich[1], C. Karanfil[1], A. J. Kropf[3], S. Wang[1] and T. C. Irving[1]

[1]The Biophysics Collaborative Access Team (BioCAT), Dept of Biological Chemical, and Physical Sciences, Illinois Institute of Technology, Chicago, IL, 60616, USA
[2]SER-CAT, University of Georgia, USA
[3]CMT Division, Argonne National Laboratory, USA
[4]Present address: GMCA-CAT, Biology Division, Argonne National Laboratory, USA

Received June 26, 2003; accepted in revised form November 4, 2003

PACS number: 07.85.Qe

Abstract

The Biophysics Collaborative Access Team (BioCAT) undulator beam line at the Advanced Photon Source, Argonne, IL is a user facility devoted to the study of partially ordered and disordered biological materials by X-ray scattering, diffraction and absorption spectroscopy. Two sagital focussing, double-crystal (Si(111) and Si(400)) monochromators and a 1 m mirror provide monochromatic, horizontally and vertically focussed X-ray beams in the range of 4–35 keV. The small focal spots produced by this optics are well matched to novel XAFS detectors developed by BioCAT: a multilayer analyzer array and Bent Laue crystal based analyzers. Fast on-the-fly scans (∼5 s/scan) have been implemented to take full advantage of the high X-ray flux at the Advanced Photon Source. Such fast scans not only allow high throughput but also reduces radiation damage to labile biological samples. A closed–cycle displex cryostat is routinely used for low temperature XAS measurements. For continuous flow and time resolved XAS experiments, a dual syringe stopped-flow system has been implemented.

1. Introduction

The Biophysics Collaborative Access Team (BioCAT) undulator beam line, 18ID, at the Advanced Photon Source, Argonne, IL, is a high performance instrument designed for and dedicated to the study of partially ordered and disordered biological materials. X-ray Absorption Spectroscopy experiments include studies of dilute metalloprotein solutions (with a special emphasis on small volumes and time resolved XAS studies), oriented films, and oriented single crystals. High flux delivered into a small spot size is required for many practical time-resolved XAFS experiments and high throughput modes that employ flow systems. To this end, the beam line was designed to deliver doubly focused undulator beam, scannable over a wide energy range while maintaining a fixed position on the sample. The beamline has been operating since 1997 as an open facility to all researchers on the basis of peer reviewed research proposals. Here we describe the beamline optics, EXAFS specific instrumentation and performance. Representative experimental results of low temperature, room temperature flow experiments and time-resolved experiments are presented.

2. Beamline Optics

APS undulator "A" [1] provides a source of very intense monochromatic radiation in the 3.2–14 keV range (first harmonic) and 9.6–42 keV (third harmonic). The undulator gap may be scanned at rates of ca. 1 mm/sec under beamline control, permitting very fast scans over a typical XAS range of ca. 1 keV in 10 seconds. The undulator gap can also be tapered to deliver a smooth energy range on the order of 1 keV but with a significant loss in peak intensity. A differential pump separates the beamline vacuum structure from the storage ring permitting windowless operation so that experiments near the calcium edge at 4 keV are practical. Two independent double-crystal monochromator assemblies [2] cover the energy range of BioCAT interest. The two monochromators have identical mechanisms, but monochromator #1 has Si (111) crystals to cover an energy range from 3.4 keV to 14.6 keV, while those in monochromator #2 have a (400) orientation for energies from 7.9 keV up to 33.8 keV. Both monochromators have a cryo-cooled first crystal [3] and sagittal focusing second crystal assemblies for horizontal focusing of the beam. Horizontal focal spot sizes with a FWHM of 120–150 μm are typical for the energy range of 4.0–10.0 keV. An ULE glass-ceramic mirror (Rocketdyne Corporation) is used for harmonic rejection and it can be either used flat or eliptically bent to allow vertical focusing independently of any horizontal focusing. The mirror surface is divided into three lanes: bare ULE, Pd coated, and Pt coated to cover the full energy range of the beamline. When focused at the center of the experimental table the beam profile has been observed to be as small as 40 μm (FWHM). Additional details of the beamline optics can be found elsewhere [4].

3. Control software

The beamline control software is based on the Experimental Physics and Industrial Control System (EPICS) which is a distributed system using VME-based electronics with crate controllers running the proprietary real-time UNIX-like operating system VxWorks (Wind River Systems). To take full advantage of the high X-ray flux at the Advanced Photon Source and to reduce radiation damage to labile biological samples, two types of fast on-the-fly scans have been implemented: a "generic" fast scan and "energy" fast scan. With the generic scan we can scan any servo or stepper motor at the beamline while recording the output into the Joerger VCS16 scaler, with 16 inputs. The scan may use one of three different algorithms but all of them have the same lower limit to the time resolution of ∼150 ms/point. As a result, the typical generic scan time is ∼15–60 seconds. These scanning protocols have been very useful in beamline diagnosis and alignment and have found use in various experimental protocols. The fast energy scan is implemented for both the beamline monochromators. This scan makes use of a Struck 7201 multichannel scaler, with 32 inputs and 4k memory arrays per each input, which simultaneously record the monochromator encoder outputs and

*e-mail: barrea@bio.aps.anl.gov

the X-ray intensities. The minimum time per point for this scan is ∼1 ms and the total scan time is typically 1–10 s. We have also included the synchronous motion of monochromator and the beamline undulator into the energy scans so that the energy of the two devices can be changed simultaneously. Finally, all the energy and generic scans provide for two or three dimensional scans with stepwise motion of the second and the third motors respectively retaining continuous scanning in the first dimension.

For positional feedback, we have implemented an in-vacuum beam position monitor (BPM) developed by SBC-CAT [5]. This BPM is linear over a range of a few millimeters with a resolution of less than 2 μm. Using this BPM and a feed-forward approach to adjust the beam angle, we have been able to maintain constant exit height to ±25 μm over an XAS scan. In addition, a variable offset in the equations of motion of the monochromator conditions has been used to minimize energy-dependent beam position changes.

To maintain peak X-ray beam intensity during energy scans we have installed an analog feedback system consisting of: 1) a piezo-electric actuator, mounted to adjust the tilt angle of the second crystal relative to the first crystal 2) a lock-in amplifier (Stanford Research Systems model SR830 DSP), and 3) a custom-designed analog electronic feedback control unit. A small amplitude sine wave of frequency, f, is fed to the piezo actuator to impose a periodic variation on the beam intensity. When the two crystals are misaligned, the lock-in amplifier detects this intensity signal with signal strength proportional to the slope of the rocking curve. With the proper choice of phase angle, the sign of this correction signal will indicate the direction to drive the piezo in order to recover peak intensity. The correction signal is fed into an integrator, the output of which is summed with the dither sine wave and a manually adjustable offset, and then transmitted to the piezo amplifier. Amplitude of about 20% of the FWHM of the rocking curve is sufficient to drive the second crystal to the peak. The feedback system is capable maintaining a lock on the peak intensity for energy changes at a rate of 200 eV/s, allowing monochromator scans of 1000 eV in 5 seconds without losing intensity.

4. Experimental Equipment

Transmission ionization chambers modified from the CHESS design (Advanced Design Consultants, Lansing NY) are available for incident flux and transmission measurement. There are 4 current amplifiers (Keithley model 428), which are interfaced through the RS232 ports on the beamline workstations. For fluorescence detection there are fluorescence ionization chambers and large area plastic scintillator/photomultiplier tubes that can operate in either pulse counting or integrating modes in conjunction with a two dimensionally focused Soller slit assembly designed for the point-focused beam. Highly dilute systems require the capabilities of the multilayer analyzer [6, 7] and a bent Laue crystal based analyzer [8] for experiments at the Cd K edge, Mo K edge and Zn K edge.

XAS measurements on biological samples are conventionally performed at low temperature to reduce the radiation damage caused by the production of free radicals, and also to reduce the damping effect of temperature in the EXAFS oscillations. A low vibration, closed–cycle displex cryostat permits such experiments at temperatures down to 10 K. A Lakeshore Model 330 controller allows regulation of the Displex temperature under EPICS control.

In some cases it is desirable to measure the samples in solution at room temperature to characterize the dynamic changes in structure that bridge the static endpoints provided by crystallography and to avoid the artifacts that can be introduced by freezing. Furthermore, flow systems can reduce the duty cycle for a given measurement providing faster throughput of samples that will permit more elaborate types of experiments to be designed and executed than is possible with conventional approaches. For continuous and stopped-flow XAS experiments, a dual syringe stopped-flow system [9] has been implemented at BioCAT. The stop flow chamber can be cooled to temperatures as low as 233 K to lengthen the lifetime of a reaction. A portable UV-Vis spectrometer (Ocean Optics model 2000) is integrated into the stopped flow device through optical fiber and lenses allowing optical spectra to be collected simultaneously with an XAS measurement.

5. Results and discussion

The combination of the doubly focused beam and the efficient detectors available at BioCAT allow the study of dilute samples (ca. 1 mM). A typical scan time is 20–60 seconds with ca. 50 scans typically required to obtain good statistics, thus, a total time of 20–60 minutes suffices to complete an XAFS spectrum for each sample with either frozen samples or using the continuous flow system. Low temperature XAS experiments use the Displex

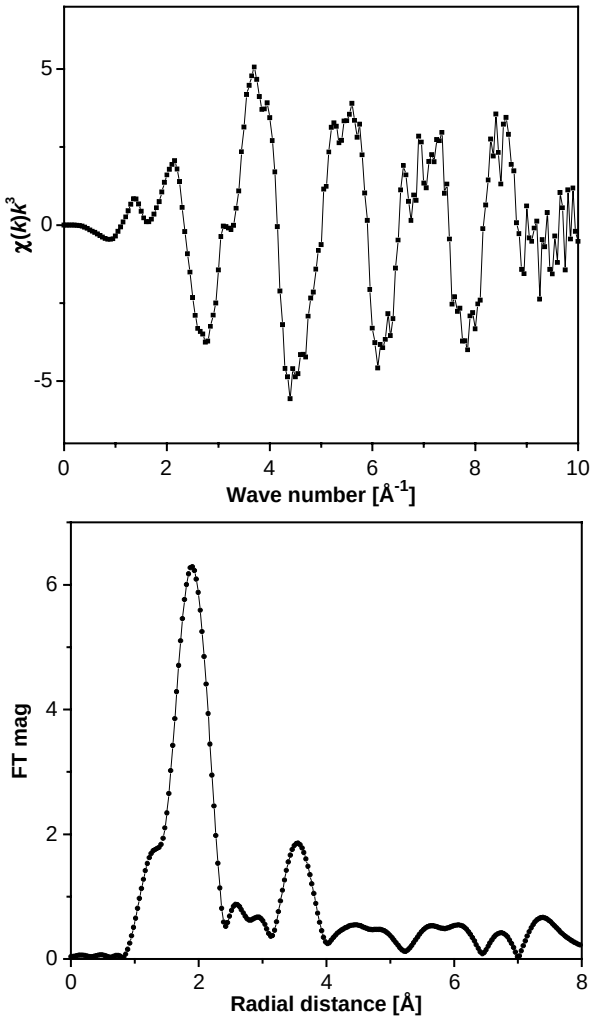

Fig. 1. EXAFS signal of a ∼1 mM Ca sample measured at 30 K with the multilayer analyzer (courtesy of Prof. C. Carmeli- Tel Aviv University).

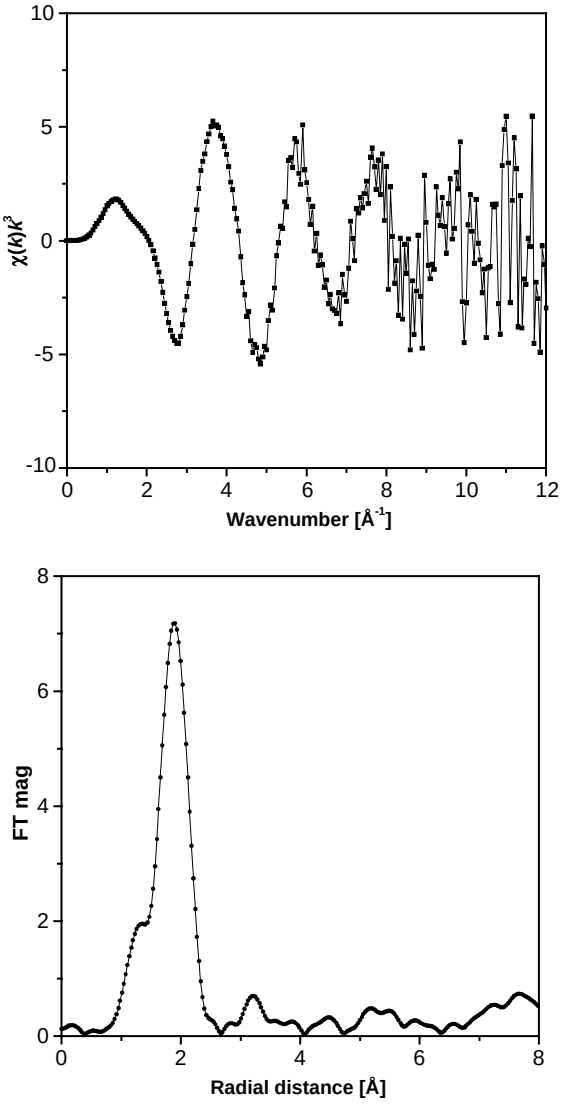

Fig. 2. EXAFS signal of a ∼1 mM Npl4 Zinc Finger protein measured at 40 K with the Zn Bent Laue analyzer (courtesy of Prof. T. Stemmler – Wayne State University).

cryostat and an aluminum sample holder, which can contain up to 5 sample cells. The multilayer analyzer or bent Laue analyzer, as appropriate, is mounted on one side of the cryostat exit windows, while the other window is used for sample exchange. The cryostat itself is mounted on an x-y stage that allows the user to raster scan the sample in two dimensions during the experiment. Depending on the particular case, each sample spot is exposed to the beam from 20 s to 120 s maximum and then a new spot is selected for subsequent scans. More than 200 spots may be measured in a single cell in our standard sample holders. This feature has been demonstrated to be very useful when working with samples that are sensitive to radiation damage. Figures 1 and 2 show EXAFS signal of a ∼1 mM Ca sample measured at 30 K measured with the multilayer analyzer (courtesy Prof. C. Carmeli-Tel Aviv University), and Zn protein samples at low temperature (35 K) measured with the Laue analyzer (courtesy Prof. T. Stemmler – Wayne State University).

The stop-flow system has also proved to be a versatile instrument for both time-resolved XANES studies [10] and continuous flow experiments. The Multilayer analyzer is currently being upgraded from 2 to 18 detection channels to increase maximum count rate. The Laue analyzer detector is also being upgraded to increase solid angle acceptance. Enhancements continue to improve overall beamline performance.

Acknowledgment

Use of the Advanced Photon Source was supported by the U.S. Department of Energy, Basic Energy Science, Office of Energy Research, under Contract No. W-31-109-Eng-38. BioCAT is a NIH-supported Research Center, RR08630.

References

1. Lai, B., Khounsary, A., Savoy, R., Moog, L. and Gluskin, E. (1993) Argonne Nat. Lab. ANL/APS TB-3.
2. Rosenbaum, G. *et al*., (2003) (submitted).
3. Ivanov, I. G. *et al.*, "Synchrotron Radiation Instrumentation: Eleventh US National Conference", (edited P. Pianetta *et al.*) pp. 271–275, (American Institute of Physics 2000).
4. Fischetti, R. *et al.*, The BioCAT Undulator Beamline 18ID: A Facility for Biological Non-Crystalline Diffraction and X-ray Absorption Spectroscopy at the Advanced Photon Source, (2003) submitted to J. Synchrotron Rad.
5. Akire, R.W., Rosenbaum, G. and Evans, G., J. Synchrotron Rad. **7**, 61 (2000).
6. Zhang, K., Rosenbaum, G. and Bunker, G., J. Synchrotron Rad. **5**, 1227 (1998).
7. Zhang, Ke, Rosenbaum, G. and Bunker, G., J. Synchrotron Rad. **6**, 220 (1999).
8. Karanfil, C. *et al.*, "Synchrotron Radiation Instrumentation: Eleventh US National Conference", (P. Pianetta *et al.*, eds.), pp. 178–182, (American Institute of Physics 2000).
9. Zhang, K., Dong, J. and Auld, D. S., Physica B **208**, 719 (1995).
10. Kleifeld, O., Frenkel, A. and Sagi, I., Nature Struct. Biol. **10**, 98 (2003).

Physica Scripta. Vol. T115, 870–872, 2005

Methodological Study Using XAS of an Arsenic-Based Antileukemia Treatment

Emmanuel Curis[a,1], Ioannis Nicolis[a], Sylvain Bohic[b], Andrea Somogyi[b], Alexandre Simionovici[b] and Simone Bénazeth[a]

[a]Laboratoire de biomathématiques, Faculté de pharmacie, Université Paris V – 4, avenue de l'Observatoire – 75006 Paris, France
[b]ESRF, BP 220, 38043 Grenoble, France

Received June 26, 2003; accepted January 28, 2004

Abstract

Acute promyelocytic leukemias relapses are treated by solubilised arsenic trioxide. The elimination rate of arsenic during the treatment is crucial. One way of elimination is by incorporating arsenic metabolites in hair. Micro-XANES experiments were performed at the ESRF ID-22 beamline on transversal hair cuts from two patients. A special code (LASE) was developed in order to refine the analysis of such data and led us to conclude that arsenic oxidation degree was +III. Micro-XANES experiments were coupled with X-Ray fluorescence elemental maps of hair sections. Given the dilution of the samples, maps were collected on thick slices. Hence width effects became sensible and caused distortions of the final image. In order to refine the location of arsenic in hair, we developed models to handle these width effects. These models allowed us to conclude that arsenic was distributed at the periphery of hair. Statistical tests were developed to evaluate the relevance of the models.

Résumé

Les rechutes de leucémies promyélocytaires aiguës sont traitées avec du trioxyde d'arsenic solubilisé. Connaître la vitesse d'élimination de l'arsenic au cours du traitement est important. L'étude des cheveux, l'une des voies d'élimination des métabolites de l'arsenic, permet d'apporter des éléments de réponse à cette question.

Pour réaliser cette étude, nous avons effectué, sur la ligne ID22 de l'E. S. R. F., des expériences de micro-XANES sur des coupes transversales de cheveux provenant de deux patients. Nous avons développé dans notre logiciel d'analyse LASE des procédures automatiques qui permettent d'affiner nos analyses. Cela nous a permis de conclure à un degré d'oxydation +III pour l'arsenic inclus dans les cheveux. Ces études par micro-XANES ont été couplées à des cartographies élémentaires par fluorescence X des coupes de cheveux. Ces cartes ont dû être faites à partir de coupes épaisses, pour lesquelles les effets d'épaisseur introduisent des distortions dans l'image finale. Pour mieux interpréter ces cartes, nous avons développé des modèles qui prennent en compte ces effets. Ils sont inclus dans le logiciel LASE et permettent de conclure à une distribution homogène de l'arsenic en périphérie du cheveu. Enfin, nous avons développé des outils statistiques pour quantifier la qualité des modèles obtenus.

1. Introduction

En s'inspirant de remèdes traditionnels chinois, diverses équipes ont pu montrer que le trioxyde d'arsenic, As_2O_3, est efficace dans le traitement de la leucémie promyélocytaire [1–4]. La Pharmacie centrale des hôpitaux de Paris (PCH) a donc mis au point un traitement à partir de ce composé, solubilisé en milieu basique. Cependant, compte-tenu de la toxicité de l'arsenic, il est important de bien connaître le devenir de cet arsenic injecté dans l'organisme. Deux questions se posent alors : quelles transformations chimiques subit l'arsenic et par quelle voie peut-il être éliminé, d'une part ; d'autre part, à quelle vitesse cette élimination est-elle effectuée.

Parmi les diverses voies d'élimination des éléments exogènes qui peuvent être étudiées, les cheveux présentent l'avantage d'être facilement prélevables, sans gêne notable pour le patient (contrairement au sang, par exemple) et, du fait de leur pousse, permettent d'accéder en un seul prélèvement au suivi temporel des concentrations en ces éléments exogènes (contrairement aux urines, par exemple).

Le but de l'expérience est de suivre la concentration (relative) en arsenic et son évolution chimique L'intensité des raies de fluorescence X permet d'accéder à la composition élémentaire des éléments traces tandis que des informations sur l'environnement chimique d'un atome absorbeur donné peuvent être obtenues par une analyse des spectres XANES enregistrés en mesurant le rendement total de fluorescence X en fonction de l'énergie d'excitation. De plus, la brillance des sources de rayonnement synchrotron actuelles permet de travailler sur des échantillons très dilués, ce qui permet ainsi de travailler sur un seul cheveu, voire sur une coupe d'un seul cheveu. On peut donc ainsi remonter à l'information temporelle, en suivant l'évolution du spectre de fluorescence le long d'un cheveu, compte-tenu de la vitesse de pousse du cheveu.

2. Localisation de l'arsenic dans les cheveux

Des études préliminaires, effectuées sur la ligne D15 du L. U. R. E., ont permis de vérifier que l'on pouvait détecter, sur un seul point d'un seul cheveu, la présence d'arsenic provenant du traitement (les cheveux des témoins présentant un signal pour l'arsenic négligeable par rapport au signal mesuré pour les cheveux des patients ayant commencé le traitement [5, 6]). Nous avons pu procéder à une analyse plus fine des cheveux, en utilisant le faisceau intense de la ligne ID-22 de l'E. S. R. F. à Grenoble.

L'étude de la localisation longitudinale permet de suivre la quantité d'arsenic éliminé par le cheveux au cours du temps. Nous avons donc, pour les cheveux de deux patients, suivi cette concentration le long d'un cheveu avec un pas de 0,5 mm au L. U. R. E. et 35 µm à l'E. S. R. F. ; chaque point a été répété trois fois. Les spectres obtenus ont été traités avec le logiciel WAPI [7]. Lorsque l'on suit la concentration en arsenic le long de ces cheveux avec un pas aussi faible, on note une variation rapide de la concentration en arsenic. Cette variation est à relier au dossier clinique du patient : on retrouve, par exemple, le nombre de prises du patient (fig. 1).

Ces résultats suggèrent que l'arsenic est rapidement capté par le cheveu, puisque l'on retrouve dans le cheveu les variations dues à l'injection discontinue du médicament. Ils suggèrent aussi qu'il n'existe pas d'organe de stockage transitoire de l'arsenic, qui capterait l'arsenic circulant dans le sang pour ensuite le relarguer, pour la même raison ; en particulier, les transitions sont rapides y compris lorsque l'on quitte les plateaux, alors qu'un éventuel relargage s'accompagnerait d'une décroissance plus lente. Au vu de ces résultats, on peut se poser la question de la forme de l'arsenic captée par le cheveu : s'agit-il d'une forme métabolisée, de la forme médicamenteuse ou d'un mélange des deux ?

[1] emmanuel.curis@pharmacie.univ-paris5.fr

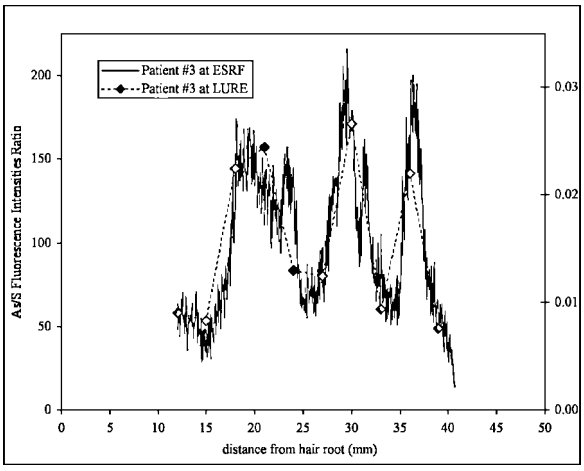

Fig. 1. «Évolution longitudinale du signal de fluorescence de l'arsenic le long d'un cheveu de malade, suivie au L. U. R. E. et à l'E. S. R. F.»

Pour savoir dans quelle partie du cheveu (de la périphérie vers le centre : cuticule, cortex, medulla – cette dernière parfois absente des cheveux humains) se trouvait l'arsenic, nous avons effectué des coupes fines de cheveu (épaisseur : 10 µm) à l'aide d'un cryomicrotome. Ces coupes ont été déposées sur un film en mylar, puis cartographiées sur la ligne ID-22 de l'E. S. R. F. Si les coupes des cheveux de patients avant le traitement, comme celles des témoins, ne présentent pas d'arsenic, comme l'on peut s'y attendre, les coupes effectuées au cours du traitement présentent, au contraire, une répartition très nette de l'arsenic dans le cheveu (fig. 2). Ces cartes suggèrent une répartition de l'arsenic plutôt en périphérie du cheveu ; cependant, elles présentent une nette asymétrie verticale. Compte-tenu de l'épaisseur, cette asymétrie peut très certainement provenir de la déformation de la carte, du fait de la géométrie de l'expérience, et n'est alors pas significative.

Pour valider cette hypothèse, nous avons construit dans notre logiciel d'analyse LASE (Logiciel d'analyse des spectres expérimentaux [8]) un modèle simple de l'expérience : nous avons dans un premier temps assimilé le cheveu à un cylindre, de symétrie radiale, l'arsenic étant disposé en périphérie. La concentration en arsenic en fonction de la localisation dans le cheveu est donc une fonction $f(x, y, z)$.

En pratique, le faisceau arrive avec un angle θ (45° idéalement) sur la coupe. Si l'on choisit le repère de sorte que la face d'entrée définisse les axes Ox et Oy, la normale à cette face (dans la direction de propagation du faisceau) l'axe Oz, alors les points de l'échantillon irradiés par le faisceau, supposé ponctuel et entrant en $(x_0, y_0, 0)$, sont sur la droite d'équation $(x, y, z) = (x_0, y_0, 0) +$

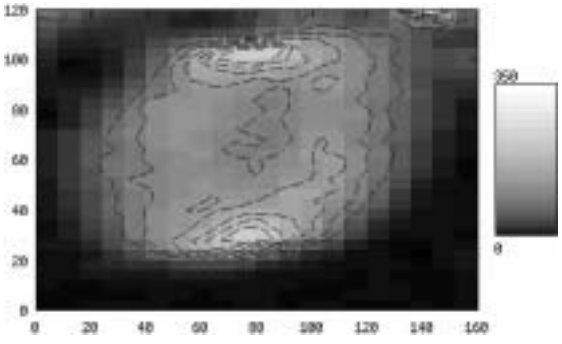

Fig. 2. «Répartition de l'arsenic dans une coupe transversale de cheveu, obtenue par micro-fluorescence X»

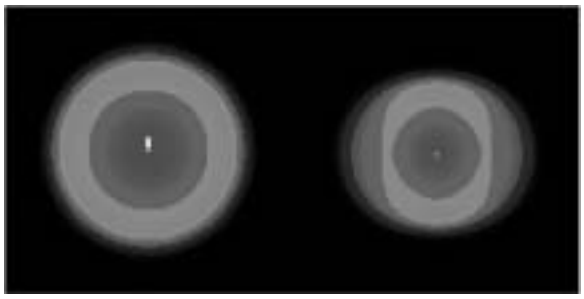

Fig. 3. «Modélisation des distorsions induites par l'épaisseur de la coupe de cheveu. À gauche, modèle de répartition idéale, symétrique, pour une coupe infiniment fine; à droite, distorsion de cette répartition lors de l'observation d'une coupe épaisse (10 µm).

$t\ (\cos\theta, 0, \sin\theta)$, avec t variant entre 0 (entrée du faisceau dans l'échantillon) et e, épaisseur de la coupe. Si l'on néglige la réabsorption par l'échantillon, le signal vu par le détecteur pour le point (x_0,y_0) de la carte finale est alors proportionnel à

$$F(x_0, y_0) = \int_0^e f(x_0 + t\cos\ \theta, y_0, t\sin\ \theta)\,\mathrm{d}t.$$

À partir de cette expression et du modèle de symétrie radiale avec localisation périphérique de l'arsenic, nous avons pu comparer la carte idéale (coupe infiniment fine, $F(x, y) = f(x, y, 0)$) et la carte attendue pour une coupe épaisse. Comme l'indique la fig. 3, on retrouve la déformation observée sur les coupes expérimentales. L'utilisation de ce modèle permet donc de valider l'hypothèse d'une localisation uniforme de l'arsenic en périphérie du cheveu[2]. Cette uniformité et la localisation spécifique sont en accord avec l'élimination de l'arsenic principalement sous une seule forme et mettant en jeu un seul mécanisme ; la localisation périphérique suggère que ce n'est pas directement dans le bulbe capillaire, mais plus loin, dans la zone de kératinisation ou de durcissement au niveau de la glande sébacée, qu'aurait lieu la capture de l'arsenic par le cheveu.

3. Nature chimique de l'arsenic inclus dans le cheveu

L'arsenic au degré d'oxydation +III peut être métabolisé dans l'organisme, ce qui s'accompagne d'une oxydation au degré +V. Les métabolites principaux du trioxyde d'arsenic sont l'acide arsénique et l'acide cacodylique (acide diméthylarsonique). Suivant l'étape à laquelle se fait la capture de l'arsenic par le cheveu, on peut s'attendre à trouver l'un ou l'autre de ces degrés d'oxydation dans le cheveu. Pour préciser ce degré d'oxydation, nous avons réalisé des expériences de micro-XANES au seuil K de l'arsenic, sur une coupe de cheveu contenant de l'arsenic, toujours sur la ligne ID-22 de l'E. S. R. F. Compte-tenu du résultat précédent, suggérant la présence d'une espèce majoritaire d'arsenic, nous avons travaillé sur l'ensemble de la coupe, de façon à avoir un signal suffisamment intense pour être utilisable.

Parallèllement, les spectres d'absorption au seuil K de l'arsenic ont été enregistrés, dans les mêmes conditions opératoires, pour plusieurs composés de référence : orpiment (As_2S_2 ; As^{III}), réalgar (As_2S_3 ; As^{III}), trioxyde d'arsenic (As_2O_3 ; As^{III}), arsénite de sodium ($NaAsO$; As^{III}), arséniate de sodium (NaH_2AsO_4 ; As^{V}),

[2] Quoiqu'il soit en théorie possible d'inverser l'expression pour retrouver la carte idéale à partir de la carte expérimentale, les essais que nous avons effectués montrent une très grande sensibilité au bruit qui rend difficilement exploitable la carte ainsi obtenue.

cacodylate de sodium ($NaAsO_2(CH_3)_2$; As^V), qui présentent les deux degrés d'oxydation attendus de l'arsenic dans l'organisme.

La comparaison des énergies de seuil mesurées sur ces références et sur le cheveu montre très nettement que l'arsenic dans le cheveu se trouve au degré d'oxydation +III. Rappelons par ailleurs que le spectre d'absorption au seuil K de l'arsenic de la solution injectable de médicament montre la présence d'arsenic III en solution [5].

L'analyse de ces spectres a nécessité le développement d'outils pour automatiser l'analyse. En effet, du fait de la dilution importante, il est nécessaire de répéter plusieurs fois la mesure. Cependant, pour réaliser la moyenne de ces spectres, il faut pouvoir contrôler leur superposition optimale. Nous avons donc développé d'une part un test permettant de savoir si la superposition était optimale, d'autre part des outils permettant de commencer le traitement de façon à obtenir cette optimalité. Une fois la moyenne réalisable, nous avons utilisé le modèle de propagation des erreurs que nous avons développé [9] au préalable pour réaliser le traitement. Le principe et les propriétés de ce test seront présentés dans un article dédié ; signalons juste que le critère de décision revient à une loi du khi-deux à $n - 1$ degrés de liberté. Si ce critère n'est pas satisfait, il n'est pas possible de faire les moyennes sans comprendre au préalable l'origine de la différence, pour y remédier ou pour inclure cette différence dans les incertitudes d'origine systématique.

Le plus souvent, le test précédent n'est pas satisfait à cause de décalages entre les spectres. En transmission, il suffit de corriger lors de l'élimination du fond continu pour obtenir des spectres superposables ; en fluorescence, la hauteur de seuil varie et une normalisation permet de s'affranchir de la difficulté. Il est cependant délicat de choisir manuellement les conditions de ces « corrections » pour obtenir un ensemble de spectres moyennables. C'est pourquoi nous avons intégré dans LASE les options permettant de réaliser cela : un spectre servant de référence, il est possible d'ôter le fond continu de, ou de normaliser, tous les autres spectres de la série de mesure en minimisant la distance (au sens des moindres carrés) entre la référence traitée et le résultat.

4. Conclusion & perspectives

Notre étude suggère que, lors de l'injection du traitement à base de trioxyde d'arsenic, l'arsenic est capté par le cheveu avant d'être métabolisé, puisqu'il reste au degré d'oxydation +III comme dans sa forme originelle. Cette captation se ferait rapidement, sans relargage puisque l'on retrouve le long du cheveu la structure temporelle des apports en arsenic. Elle se ferait sans doute après le bulbe folliculaire puisque l'on retrouve l'arsenic uniquement en périphérie du cheveu.

Pour mener à bien cette analyse, nous avons été amenés à développer divers outils d'analyse : modélisation des déformations induites par l'épaisseur sur la carte élémentaire obtenue par fluorescence des rayons X, test statistique pour contrôler l'homogénéité des spectres expérimentaux, automatisation des procédures de traitement des spectres pour palier au mieux l'inhomogénéité expérimentale révélée par les tests ci-dessus. Ces outils sont disponibles dans le logiciel d'analyse LASE qui peut être téléchargé librement [10].

Nous travaillons actuellement sur l'inclusion des effets d'épaisseur dans le modèle de cartographie, ainsi que sur la résolution du problème inverse (reconstruire l'image originale, en admettant une distribution homogène selon l'axe orthogonal à la coupe) malgré les problèmes de bruit. De plus, nous étudions l'amélioration du test de contrôle d'homogénéité, qui pour l'instant ne détecte pas certains types d'hétérogénéités.

Remerciements

Nous tenons à remercier Anne Héron, du Laboratoire de physiologie de la faculté de pharmacie de Paris V, qui a mis à notre disposition le cryomicrotome ; François Guyon, de la PCH, qui nous a fourni les échantillons de cheveux ; Virginie Lasserre, du laboratoire de biomathématiques, pour les discussions autour du test statistique développé.

References

1. Chen, G.-Q., *et al.*, Blood **89**, 3345 (1997).
2. Niu, C., *et al.*, Blood **94**, 3315 (1999).
3. Shen, Z.-X., *et al.*, Blood **89**, 3354 (1997).
4. Soignet, S. L., *et al.*, The New England J. Medicine **339**, 1341 (1998).
5. Nicolis, I., *et al.*, J. Synchrotron Radiation **8**, 984 (2001).
6. Nicolis, I., *et al.*, J. Trace Microprobe Techn. **20**, 565 (2002).
7. Wang, J. X., *et al.*, Note CEA -N-2756, 231-236 (1994).
8. Curis, Emmanuel, « Développement d'outils informatiques et statistiques pour l'analyse des spectres EXAFS – Application aux systèmes bioinorganiques », Thèse d'université, Orsay, (décembre 2000).
9. Curis, E. and Bénazeth, S., J. Synchrotron Radiation **7**, 262 (2000).
10. http://xlase.free.fr

Physica Scripta. Vol. T115, 873–876, 2005

First Observation of Natural Circular Dichroism for Biomolecules in Soft X-ray Region Studied with a Polarizing Undulator

Masahito Tanaka[1], Kazumichi Nakagawa[*1,2], Akane Agui[3], Kentaro Fujii[3] and Akinari Yokoya[3]

[1]Graduate School of Science and Technology, Kobe University, Tsurukabuto, Kobe 657-8501, Japan
[2]Faculty of Human Development, Kobe University, Tsurukabuto, Kobe 657-8501, Japan
[3]SPring-8, Japan Atomic Energy Research Institute, Mikaduki-cho, Sayo-gun, Hyogo 679-5148, Japan

Received June 26, 2003; accepted December 17, 2003

PACS number: 33.15.Ad.

Abstract

We measured natural circular dichroism (CD) for biomolecules in soft X-ray region for the first time. Natural linear dichroism (LD) for K(TiO)PO_4 (KTP) crystal was also measured at the K-edge energy of oxygen. Measurements of CD and LD spectra were performed at the soft X-ray undulator beamline BL23SU of SPring-8 in Japan. In this beamline, an APPLE-2 type variable undulator was installed as a light source. This undulator was operated under the phase modulation mode in which left and right circularly polarized light (LCPL and RCPL) was switched with about 0.1 Hz.

As a sample for CD measurement, we used sublimated film of L-, D- and DL-phenylalanine (Phe) and L- and D-serine (Ser) (thickness ∼300 nm) and measured CD (A_L−A_R) spectra in the nitrogen and the oxygen K-edge region, respectively. Here, A_L and A_R mean the abbreviation of absorption for LCPL and RCPL, respectively. For the Phe film, we observed a negative peak at about 407 eV for the L-Phe spectra. On the contrary, a positive peak for the D-Phe spectra and no spectral feature for the DL-Phe were observed. For the Ser film, we observed positive CD peaks at around 540 eV and 548 eV at the L-Ser spectra, on the contrary, negative peaks for the D-Ser. These results are the first CD spectra for biomolecules in the soft X-ray region.

We also used KTP crystal cut parallel to the plane (1,2,0) or (1,−2,0) as a sample of LD measurement and measured (A_L−A_R) spectra in the oxygen K-edge region and observed some peaks at about 530 eV. Since sign of these peaks were dependent on sample rotation angle in a plane perpendicular to the incident light, we concluded that these peaks are derived from linear anisotropy of crystal. Because of a weak linear polarization component of incident light, we could measure such LD spectra.

1. Introduction

Chirality is one of the characteristics of biomolecules such as amino acids and sugar; hence, they show natural circular dichroism (CD) which is a difference in the magnitude of absorption coefficient for left and right circularly polarized light (LCPL and RCPL). For a long time, CD in visible to ultraviolet region has been utilized to study structures of chiral molecules.

With the rapid advance of synchrotron radiation techniques such as undulators for circularly polarized radiation and a well-designed polarimeter and a retarder, natural circular dichroism measurements become possible in vacuum ultraviolet (VUV) to X-ray region. In the hard X-ray region, X-ray natural circular dichroism (XNCD) spectra of gyrotropic crystals have been measured by the group of J. Goulon [1–4] by a helical undulator, and by Y. Ueji [5] by a polarimeter and retarder made of diamond. Theoretical study of XNCD of gyrotropic crystal based on electric dipole (E1) – electric quadrupole (E2) interference have reported by Natoli [6]. In the 140 to 300 nm wavelength region, CD of gas phase [7] and aqueous solution [8] of organic molecules have been examined using a combination of synchrotron radiation and a photoelastic modulator. In the 180 ∼ 250 nm wavelength region, CD of amino acid film [9, 10] have been examined with modulation technique. In the VUV region higher than 9 eV, no result of CD measurement was reported to the best knowledge of the authors. In the soft X-ray region, pioneer work of CD measurement for metal complexes at Ti $L_{2,3}$ edges (around 460 eV) was reported by J. Goulon *et al*. [11]. However, no CD study has been reported for biomolecules in soft X-ray region as far as the authors know.

At the soft X-ray undulator beamline BL23SU [12–14] of SPring-8 in Japan, one can switch the LCPL and RCPL quickly (∼0.1 Hz) [15]. At this beamline, we have already measured X-ray absorption near edge structure (XANES) of amino acid sublimated films [16], as fundamental data of XNCD. In addition, a result of theoretical calculation of XNCD in the K-edge region of carbon, nitrogen and oxygen in amino acids were reported [17, 18], in which the electric dipole (E1) – magnetic dipole (M1) interference was suggested as a basic mechanism.

In this work, being encouraged by the theoretical calculation, we tried to measure CD spectra and natural linear dichroism (LD) spectra of amino acid films and KTP crystal in soft X-ray region. The reason of choosing amino acid for the present experiment is as follows: a) D-, L- and racemic samples are easily available. b) One can expect that the CD spectrum of D- and L-enantiomer sample should be the same magnitudes with the opposite sign each other. c) A racemic sample will be expected to show no CD. We selected phenylalanine (Phe) and serine (Ser) as samples for XNCD detection at the nitrogen and the oxygen K-edge region, respectively, because these amino acids show the strongest XNCD intensity in theoretical calculation [18]. We measured LD of a single crystal of KTP (potassium titanyl phosphate: $KTiOPO_4$), which was reported to show strong LD intensity and weak CD intensity in the hard X-ray region [3, 4].

2. Material and Experimental Method

2.1. *Sample Preparation*

Powder of D-, L-, DL-phenylalanine (D-Phe, L-Phe and DL-Phe), D- and L-Serine (D-Ser and L-Ser) were purchased from Wako Chemical Co. and KTP crystal (5 mm × 5 mm × 1 mm) cut parallel to the planes (1,2,0) and (1,–2,0) was purchased from Castech Co. The molecular structures of Phe and Ser were shown in Figure 1. These samples were used without further purification. Thin films of these amino acids were carefully prepared with vacuum sublimation technique [9, 10]. Powder of amino acid was put on a Kapton sheet, heated by a nichrome heater and evaporated at 370 ∼ 400 K onto an Au-coated BeCu substrate in vacuum

*corresponding author: Kazumichi Nakagawa, e-mail: nakagawa@kobe- u.ac.jp

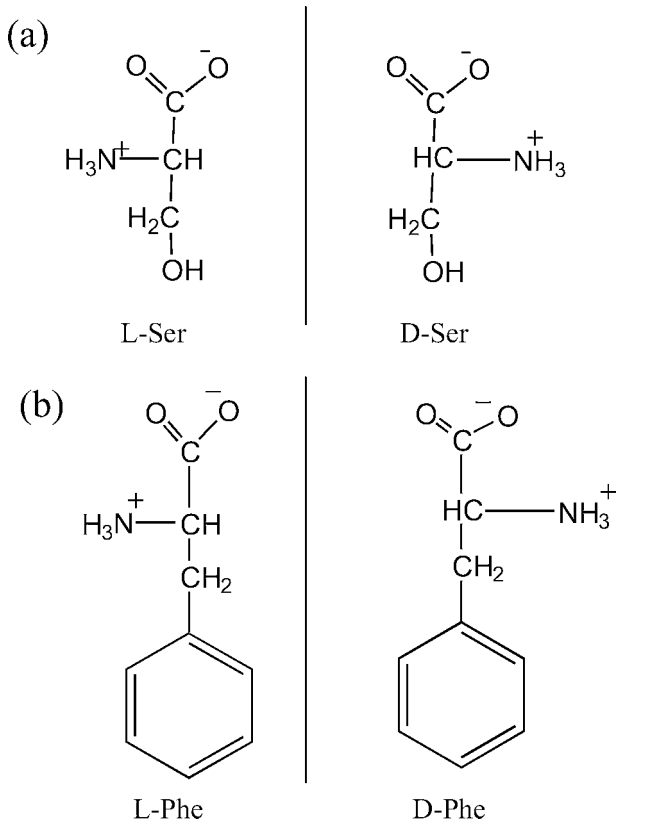

Fig. 1. Molecular structures of amino acids. (a): L- and D-Serine, (b): L- and D-phenylalanine.

($\sim 10^{-3}$ Pa). The thickness of each film was estimated to be about 300 nm by a quartz oscillator. Evaporated films were analysed by high performance liquid chromatography to confirm that thermal decomposition of samples during the vacuum sublimation did not occur. In the case of a KTP crystal, we sublimated thin carbon film ($\sim$5 nm) in order to eliminate charge up effects.

2.2. *XNCD measurement*

Measurements of XANES and XNCD spectra were carried out at Spring-8 BL23SU [12–15]. A double-array variable undulator of advanced planar polarized light emitter type (APPLE-2 type) was installed as a light source. This undulator was operated under the phase modulation mode in which LCPL and RCPL was switched with about 0.1 Hz [15]. In this work, LCPL is defined as the electric vector of circularly polarized light rotating counter-clockwise in a fixed plane by an observer looking at the light source.

Soft X-rays were monochromatized by a varied line-spacing monochromator [14]. The spectral width was set to less than 1 eV. The pressure of the sample chamber was lower than 10^{-6} Pa. All experiments were carried out at 300 K.

We measured the drain current from a sample (I) and that from the post focus mirror (I_0) by a picoammeter (Model TR8652, Advantest Co.) and obtained the quantity $A \equiv I/I_0$ which is proportional to the absorption coefficient. I_0 was measured to compensate the change in the electron beam current of the SPring-8 storage ring. We measured values of A as a function of photon energies and obtained XANES spectra. Denoting the value of A for LCPL as A_L and that for RCPL as A_R, we defined CD $\equiv A_L - A_R$, which is proportional to the real magnitude of the circular dichroism.

An orginal procedure of XNCD measurement was as follows; (1) determine the photon energy by grating rotation under the LCPL mode of the undulator, (2) measure the value of A_L, (3) switch the polarization to RCPL, (4) measure the value of A_R, (5) move to the next photon energy and measure the value of A_R, (6) switch the polarization to LCPL, (7) measure the value of A_L, and back to (1) to continue. In order to minimize the experimental time, we did not switch the polarization in step (5). In addition, in an attempt to obtain better statistics, we started step (1) under the LCPL mode, while in the next run we started from RCPL mode, and averaged those spectra. We measured four to eight XNCD spectra for each sample and averaged all spectra.

We moved the position of the soft X-ray spot on the amino acid sample at every XNCD measurement in order to avoid radiation damage. Since our evaporated films were uniform, we had a great advantage in normalizing the photocurrent intensity from different positions of a sample.

3. Result and Discussion

Figure 2-(a) shows a XANES spectrum of KTP crystal in the oxygen K-edge region and Figure 2-(b) shows $A_L - A_R$ spectra of KTP crystal with rotation angle $\theta = 0^\circ$, 45° and 90° in a plane perpendicular to the incident light. XANES of KTP crystal shows

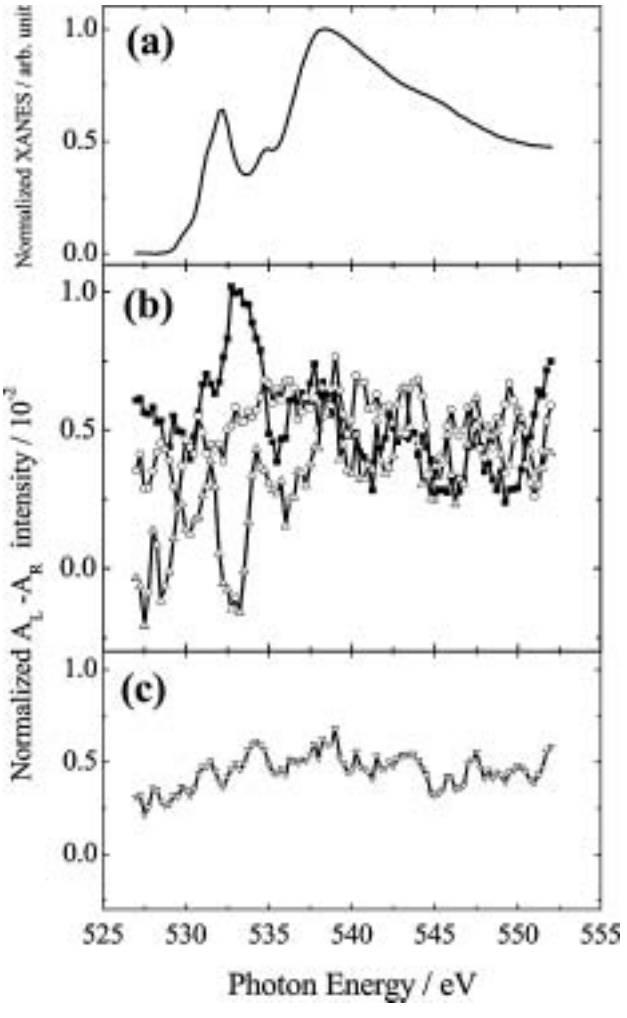

Fig. 2. (a) Normalized XANES spectrum of KTP crystal ($\theta = 0^\circ$) near the oxygen K-edge. (b) Normalized $A_L - A_R$ spectra of KTP crystal; closed square: $\theta = 0^\circ$, opened circle: $\theta = 45^\circ$ and opened triangle: $\theta = 90^\circ$. (c) Average of three $A_L - A_R$ spectra in Fig. 2-(b).

a strong peak at around 532 eV which is ascribed to the oxygen $1s \rightarrow \pi^*$ resonance. The $A_L - A_R$ spectrum at $\theta = 0^\circ$ shows a positive peak (∼0.5%) at around 533 eV. In the spectra at $\theta = 90^\circ$, this peak clearly reversed the sign to negative. At $\theta = 45^\circ$, this peak disappeared. In the higher energy region, we could not find any clear feature due to noisy signal. A similar angle dependence of the CD signals was reported by Goulon *et al*. [3, 4] in the hard X-ray region, near the Ti, K and P K-edge energy (∼4.98 keV, ∼3.61 keV and ∼2.15 keV). They ascribed the angle dependence to be due to LD. It is natural to conclude that our observation of the angle dependence can be ascribed to LD component of the soft X-ray absorption near the oxygen K-edge energy of the KTP crystal. Because of a weak linear polarization component of incident light, we could measure such LD spectra. Figure 2-(c) shows the average of three $A_L - A_R$ spectra. As seen from the figure, this average curve shows no features. This means that no CD component is found under the present signal to noise ratio. Detailed experiment of the angle dependence is now being planned.

Figure 3-(a) and -(b) show the XANES spectrum and the $A_L - A_R$ spectra of a Phe film near the nitrogen K-edge, respectively. The large peak at around 407 eV in XANES spectra was ascribed to the nitrogen $1s \rightarrow \sigma^*$ resonance. XANES of the Phe was similar to that of Gly [19], which is reasonable because Gly and Phe have the nitrogen atom at the same position (only in the amino group). Although the $A_L - A_R$ spectra of DL-Phe shows no feature, that of the L-Phe shows a negative peak at around 406 eV ($A_L - A_R$ intensity was about -0.2%), and that of the D-Phe shows positive peak and similar absolute intensity ($+0.2\%$). The molecular structures of the L-Phe and D-Phe are typically chiral. Because we observed the opposite sign and similar magnitude of $A_L - A_R$ intensity for L- and D-Phe, it is natural to conclude that we succeeded to observe the natural circular dichroism for biomolecules in the soft X-ray region for the first time. Reproducibility of these signals was sufficient to make this conclusion. The XNCD calculation for Phe by Li Yang [18] predicted some peaks within this energy region. Among them, the peak near the energy of 405 eV is in good agreement with our experimental results.

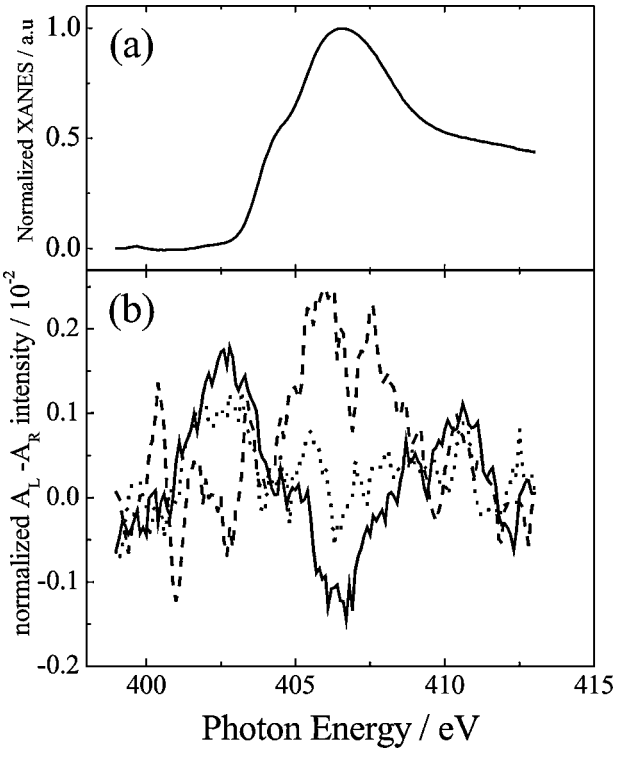

Fig. 3. (a) Normalized XANES spectrum of L-Phe film near the nitrogen K-edge. (b) Normalized $A_L - A_R$ spectra of Phe film; solid line: L-Phe, dashed line: D-Phe and dotted line: DL-Phe.

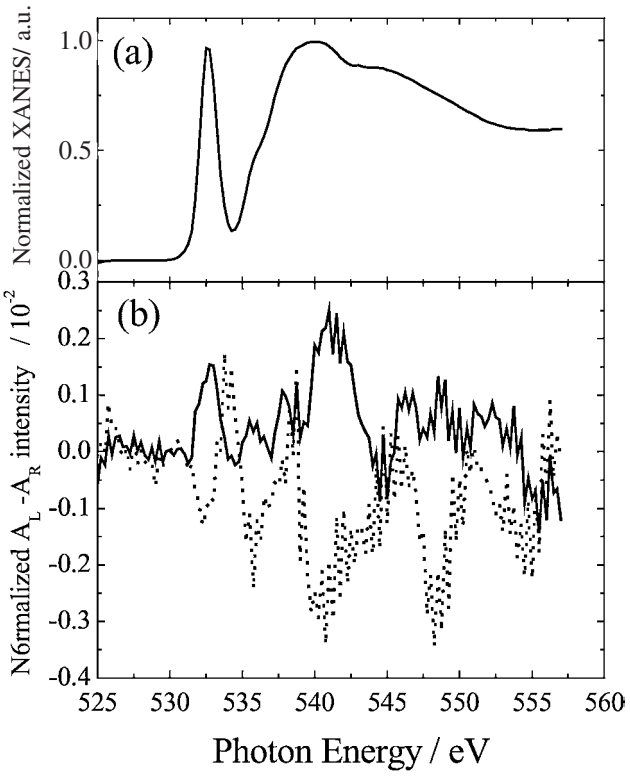

Fig. 4. (a) Normalized XANES spectrum of L-Ser film near the oxygen K-edge. (b) Normalized $A_L - A_R$ spectra of Ser film; solid line: L-Ser and dotted line: D-Ser.

Figure 4-(a) and -(b) show a XANES spectrum and $A_L - A_R$ spectra of Ser film near the oxygen K-edge, respectively. Details of Ser XANES were described in our recent paper [16]. As seen from Fig. 4-(b), at around 540 eV, positive and a negative peak was observed for L-Ser and D-Ser films of which $A_L - A_R$ intensities are about $\pm 0.2 \sim \pm 0.3\%$, respectively. This means that these peaks can also be ascribed to soft X-ray XNCD. In XANES spectrum (Fig. 4-(a)), the structure at around 540 eV was ascribed to the oxygen $1s \rightarrow \sigma^*$ resonance of the -OH group [16]. Thus, we concluded that this XNCD also originated from the -OH group. This result is good agreement with XNCD calculation [17]. In addition, we found small XNCD peaks at around 548 eV. According to the XANES peak assignment [16], this XNCD peak was considered to correspond to the $1s \rightarrow \sigma^*$ resonance of the $-COO^-$ group. However, in the theoretical calculation [17], such a XNCD peak was not predicted. The theoretical calculation [17] also predicted XNCD peaks within the region from 533 to 535 eV. In our experimental results, such XNCD peaks were sometimes found at around 532 eV. However, these peaks did not reproduce so well. Detailed experiment is necessary.

We succeeded to detect the XNCD of biomolecules besides of crystals in the soft X-ray region at the first time. More accurate and detailed experiment, for example, rotation angle dependence of XNCD spectra of KTP crystals, as well as improvement of the signal to noise ratio are now being planned.

Acknowledgement

This work was carried out at SPring-8 under the approval of the Japan Synchrotron Radiation Research Institute (JASRI) (2002A0123-NS1-np, 2002B0487-NS1-np and 2003A0380-NS1-np). Authors would like to thank deeply the machine group of JASRI and JAERI for their technical help and operating the beamline, especially Dr. Tomohiro Matsushita of JASRI for his adequate modification of the control programs for phase modulation and data acquisition.

References

1. Alanga, L., Peacock, R. D. and Stewart, B., Phys. Rev. Lett. **80**, 4799 (1998).
2. Goulon, J. *et al*., J. Chem. Phys. **108**, 6394 (1998).
3. Goulon, J. *et al*., J. Synchrotron Rad. **7**, 182 (2000).
4. Goulon, J. *et al*., Proc. SPIE **3773**, 316 (1999).
5. Ueji, Y., Okitsu, K., Sato, K. and Amemiya, Y., J. Jpn. Soc. Synchrotron Rad. Res. **13**, 48 (2000), (in Japanese).
6. Natoli, C. R. *et al*., Eur. Phys. J. B. **4**, 1 (1998).
7. Pulm, F., Schramm, J., Lagier, H. and Hormes, J., Enantiomer **3**, 315 (1998).
8. Matsuo, K., Matsushima, Y., Fukuyama, T., Senba, S. and Gekko, K., Chem. Lett. **2002**, 826 (2002).
9. Nakagawa, K. *et al*., "The role of radiation in the origin and evolution of life". (Edited by M. Akaboshi, N. Fujii and R. N. Gonzalez), (Kyoto University Press, Japan 2000), p. 353.
10. Tanaka, M., Kodama, Y. and Nakagawa, K., Enantiomer **7**, 185 (2002).
11. Goulon, J. *et al*., Jpn. J. Appl. Phys. **32 Suppl.** 284 (1993).
12. Yokoya, A. *et al*., J. Synchrotron Rad. **5**, 10 (1998).
13. Nakatani, T., Saitoh, Y., Teraoka, Y., Okane, T. and Yokoya, A., J. Synchrotron Rad. **5**, 536 (1998).
14. Saitoh, Y. *et al*., Nucl. Instr. Meth. Phys. Res. A **474**, 253 (2001).
15. Agui, A. *et al*., Rev. Sci. Instr. **72**, 3191 (2001).
16. Tanaka, M., Nakagawa, K., Koketsu, T., Agui, A. and Yokoya, A., J. Synchrotron Rad. **8**, 1009 (2001).
17. Plashkevych, O., Carravetta, V., Vahtras, O. and Ågren, H., Chem. Phys. **232**, 49 (1998).
18. Yang, Li, Plashkevych, O., Vahtras, O., Carravetta, V. and Ågren, H., J. Synchrotron Rad. **6**, 708 (1999).
19. Tanaka, M. *et al*., in preparation.

Physica Scripta. Vol. T115, 877–881, 2005

Polarization Dependent Grazing Incidence (GI) XAFS Measurements of Uranyl Cation Sorption onto Mineral Surfaces

Melissa A. Denecke[1], Dirk Bosbach, Kathy Dardenne, Patric Lindqvist-Reis, Jörg Rothe and Ri Zhu Yin

Forschungszentrum Karlsruhe, Institut für Nukleare Entsorgung, P.O. Box 3640, D-76021 Karlsruhe

Received June 26, 2003; accepted in revised form January 8, 2004

Abstract

Measurement of the polarization dependence of surface sensitive grazing incidence (GI) X-Ray absorption fine structure (XAFS) spectra at the U L3 edge is applied to identify reactive U(VI) sorption sites on various mineral surfaces. We use the known polarization dependence of the dioxouranium(VI) or 'uranyl' cation, $[O{=}U{=}O]^{2+}$, to experimentally determine its orientation when sorbed onto single crystal mineral surfaces (α-Al_2O_3, $CaCO_3$). The GIXAFS signal measured at different orientations of a U(VI) sorbed α-Al_2O_3 (11-20) wafer relative to the polarization vector of the incident synchrotron radiation, ε, indicates that the uranyl surface species exhibit a preferred surface orientation. Analysis of the EXAFS substantiates our previous findings, identifying the reactive sorption sites as AlO_6 octahedral edges on the surface. Initial results of uranyl sorbed onto freshly cleaved (10-14) surface of natural calcite indicate that uranyl cations sorb onto terrace step edges and not onto the surface plane or with an orientation of the $[O{=}U{=}O]^{2+}$ unit parallel to the (10-14) surface.

1. Introduction

In order to differentiate between specific sorption sites and to identify reactive sorption sites at specific crystallographic planes of minerals, we have begun polarized dependent GIXAFS investigations of uranyl loaded single crystal surfaces [1]. GIXAFS has been employed for many years to study single crystal surfaces in various fields of science [2]. We have introduced using the uranyl cation as a probe for polarized GIXAFS studies of cation mineral surface sorption. The uranyl cation, or other actinyl cations such as neptunyl and plutonyl cations, are excellent probes for such studies due to their linear structure. The linear $[O{=}U{=}O]^{2+}$ cation is structurally a long rod generally near 3.6 Å in length. When these units are oriented in a common direction, they exhibit remarkable differences in both their U L3 and L1 edge XAFS spectra, depending on their orientation relative to the polarization vector (ε) of the incident synchrotron beam [3]. By observing the polarization dependence of the GIXAFS U L3 edge signal of uranyl sorbed onto single crystal surfaces, their orientation can be deduced. From this, specific sorption sites can be identified.

Here we report polarization dependent U L3 edge GIXAFS results for uranyl sorbed onto the (11-20) surface of α-Al_2O_3 and onto the (10-14) surface of a natural calcite sample. Our previous investigation of uranyl sorbed onto the α-Al_2O_3 (11-20) surface showed that the octahedral edges (O_d-O_d-sites), with a O-O distance 2.61 Å , are the uranyl binding sites on the α-Al_2O_3 (11-20) surface. In that study, spectra recorded at only two relative angles between ε and the crystallographic c axis (ϕ) were available. To support the interpretation of those results, measurements of uranyl loaded α-Al_2O_3 (11-20) at defined ϕ angles are performed. The angles chosen are where ε is parallel and perpendicular to O_d-O_d-sites. In addition, measurements are made at angles where ε is parallel and perpendicular to the crystallographic c-axis. This is to probe two additional candidates for bidentate binding sites on the (11-20) surface; both are located at right angles to the c-axis. We consider bidentate sites because the polarization dependence previously observed [1] indicates uranyl to be bound in a bidentate fashion; a monodentate surface species would not be expected to exhibit any polarization dependence.

Uranyl sorption onto the cleavage plane of natural calcite is investigated to ascertain if preferential sorption occurs at either acute or obtuse angled terrace step edges, associated with the $[-441]_-$ and $[48\text{-}1]_-$ and with the $[-441]_+$ and $[48\text{-}1]_+$ steps, respectively. Investigations by other groups report a differential incorporation of uranyl cations between the two symmetrically non-equivalent vicinal surfaces associated with growth at these + and − steps during calcite single crystal growth [4]. The question remains if the step selective incorporation may result from a site-selective sorption.

2. Experimental

2.1. *Sample preparation*

Sorption sample preparation is carried out in Teflon® containers. A polished α-Al_2O_3 (11-20) wafer (three inches in diameter and 0.5 mm thick; TBL Kelpin, Neuhausen, Germany) is pre-cleaned with ethanol and in an ultrasound aqueous bath. The surface roughness is measured with AFM to be less than 1 nm. XPS studies of a smaller wafer surface of the same crystal cut before and after the cleaning process show that 6–7 at-% carbon remains on the cleaned wafer surface. The cleaning procedure quantitatively removed metals found on the uncleaned surface (Cu, Ni, Ca, Na, Mg, Zn). Laser fluorescence spectroscopy studies of the surface show that trace amounts of chromium are dispersed in the wafer bulk. Following equilibration in Milli-Q water overnight, the cleaned wafer is set to float atop 50 mL aqueous sorption solution for 26 h. The wafer is held on the sorption solution meniscus by the solution surface tension. The solution volumes and the pH and U content of the U perchlorate stock solution used to prepare the sorption solution are selected to yield $5.4 * 10^{-6}$ mol/L nat-U(VI), pH 5.4. The amount of U(VI) sorbed is quantified from analysis of samples prepared similarly using XFA and from autoradiographic measurement of an α-Al_2O_3 (11-20) wafer loaded with 233-U instead of nat-U. The wafer shows a homogeneous distribution of cations over the surface with ∼1 U atom/nm^2 loading. The sample is measured 4 weeks after preparation.

The calcite sample is prepared from a freshly cleaved crystal of natural origin (Creel, Chihuahua, Mexico). The cleaved (10-14) $CaCO_3$ surface is $2.5 \times 3.5\,cm^2$ with a calculated number of surface binding sites $= 4.4 * 10^9$ [5]. Sorption with U(VI) is performed by suspending the crystal from wooden toothpicks

[1] denecke@ine.fzk.de

attached to the backside of the crystal such that the freshly cleaved (10-14) surface is in contact with 20 mL aqueous $1.3 * 10^{-4}$ M U solution overnight. The $-\log H_c$ at the end of the contact time is measured to be 8.3. The calculated aqueous U speciation of the sorption solution is dominated by $UO_2(CO_3)_3^{4-}$ (87%) and $UO_2(CO_3)_2^{2-}$ (8%) [6].

The $UO_2(CO_3)_3^{4-}$ solution is prepared by diluting and mixing aliquots of aqueous $NaHCO_3$, Na_2CO_3 and UO_2^{2+} solutions to yield $[HCO_3^-]$, $[CO_3^{2-}]$ and $[UO_2^{2+}]$ concentrations of 45.5 mM, 45.5 mM and 9.09 mM, respectively. The measured $-\log H_c$ is 9.6.

2.2. *GIXAFS measurements*

The GIXAFS apparatus used is described in [1]. Uranium L3 edge GIXAFS measurements are performed at the X1 experimental station at the Hamburger Synchrotronstrahlungslabor (HASYLAB) using synchrotron light from the DORIS storage ring operating at 4.436 GeV with ring currents between 90 and 130 mA. Si(111) crystals are used in the double-crystal monochromator (DCM) in pseudo-channel cut mode. The energy of the beam is calibrated against the first derivative in the XANES spectrum of a Pt foil, defined as 11564.0 eV. The rocking curve is measured to give a FWHM of 1.5 mdeg. Samples are mounted in a circular, domed cell with two sets of double Kapton windows (for incident and reflected beam) located at right angles to one another and a window on top of the cell, perpendicular above the sample plane. The top window is for registering the fluorescent signal using a Canberra LEGe 5-element solid state detector, mounted above it. The incoming intensity is measured using 50 : 50 Ar : N_2 in the ionization chamber. A number of drops of Milli-Q water is placed in a circular trough inside of the domed sample cell in order to keep the samples moist during measurement. The calcite samples are held in place with carbon paste (Leit-C, Plano, Münster, Germany), the α-Al_2O_3 wafer by adhesive force exerted by a water drop placed between sample mount surface and the underside of the wafer.

The GIXAFS spectra of the U(VI) sorbed α-Al_2O_3 are measured with the sample surface oriented with respect to the impinging beam at an incident angle (θ_i) $\sim$ 90 mdeg below the observed angle of total external reflection. θ_i is determined from the measured vertical displacement of the reflected beam relative to the transmitted intensity. Spectra are recorded at four different orientations (see fig. 1). Because ε is at right angles to the incident beam, these angles are equivalent to ε being parallel and perpendicular to connecting O_d-O_d sites (32° and 122°), as well as parallel and perpendicular to the c-axis (0° and 90°). The calcite crystal is measured with θ_i set to a nominal angle of 100 mdeg. Two spectra are recorded with the sample oriented with the impinging beam at approximately 45° and 90° relative to the c-glide plane. This corresponds to ε being approximately parallel to the [-441] and [48-1] directions. The spectra are designated SO_0 and SO_270, respectively.

EXAFS, $\chi(k)$, are isolated from the raw, averaged data via standard procedures (background subtraction; normalization of the absorption to unity; conversion to wave vector, k, space; fitting k^2-weighted data with cubic spline functions to obtain the atomic background function, $\mu_0(E)$, for subsequent extraction of $\chi(k)$ [7]) using the WinXAS software [8]. Four or five scans for the α-Al_2O_3 samples and seven scans for the calcite samples are averaged in order to improve the signal to noise ratio of the measurements. The maximum of the most intense absorption feature in the individual spectra, the white line (WL) is used as the ionization energy (E_0), the origin for calculation of the $\chi(k)$-function and defining k. Spectra are analyzed using the feffit software [9] and phase/amplitude functions calculated with feff7 [10]. Theoretical fits are performed in R-space.

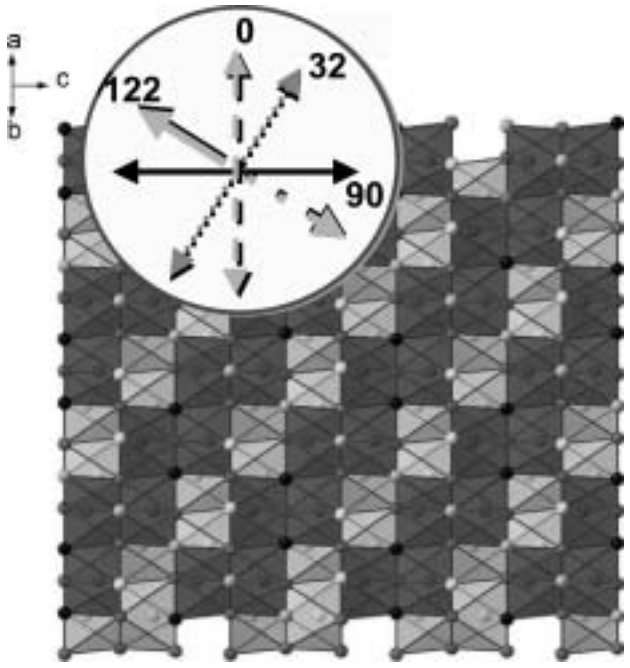

Fig. 1. View of the α-Al_2O_3 (11-20) surface normal to the crystallographic c-axis, intersecting the a,b-plane. Also shown is a cartoon of the wafer with lines depicting orientation for the spectra shown in fig. 2. Lines show orientation of the incident beam for the four measurements, numbers give angles between ε and the c-axis.

3. Results and discussion

3.1. *Uranyl sorbed α-Al_2O_3 (11-20)*

The k^2-weighted U L3 edge EXAFS and their corresponding Fourier transforms (FT) for uranyl sorbed α-Al_2O_3 (11–20) at the four different angles studied are shown in fig. 2. Because of the low loading of uranyl on the surface (1 cation/nm^2), the data quality is not good. There are subtle differences between spectra in the amplitude of the first two maxima and in the interference pattern between k 6.5 and 9 Å^{-1}. The data is fit to the EXAFS equation considering the polarization dependence of the EXAFS amplitude. This is done by introducing an effective coordination number (N_{eff}), which is related to the actual coordination number (N) by $N_{eff} = 1/2N(1 + 3\cos^2 \Theta)$ [3], where Θ is the angle between the bond axis and ε and N is, in this case, 2 and 5 for the axial (Oax) and equatorial (Oeq) oxygen coordination shells. The independent variables Θ(U=Oax) and Θ(U-Oeq) are included in the fit to describe the angle between ε and the $[O{=}U{=}O]^{2+}$ unit and between ε and the equatorial plane. The fit is performed on pairs of data sets simultaneously, i.e., the 122 and 32 spectra as one set and the 0 and 90 spectra as the other. The 90° relationship between the spectra in these pairs is defined in the fit. In this way, Θ(U-Oax) and Θ(U-Oeq) in the first spectrum are 90° from the corresponding values in the second spectrum of each pair. This procedure has the advantage that the number of parameters allowed to vary in the fit remains below the permitted degrees of freedom and the correlation between parameters is in all cases less than 60%. In contrast, for fits to individual data, the correlation between amplitude related variables N and Debye-Waller factors (σ^2) is estimated to be greater than 95%. Bond distances,

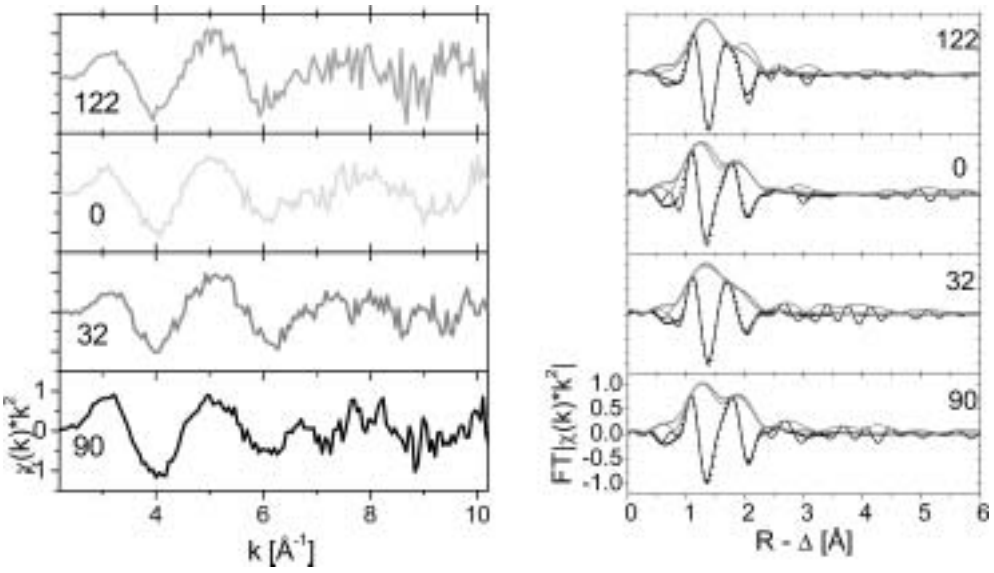

Fig. 2. U L3 EXAFS (left) and corresponding Fourier transforms (right) for the uranyl sorbed α-Al_2O_3 (11-20) sample measured at angles of the incident beam relative to the c-axis indicated (compare fig. 1). Fit results to the FT spectra are shown as triangle symbols.

Table I. *Metric parameters from fits to the U L3 EXAFS of the uranyl loaded α-Al_2O_3 (11–20) surface measured at angles indicated in fig. 1. The model for fits is described in the text.*

Spectrum	N_{eff} (Oax)	N_{eff} (Oeq)	R(Oax) [Å]	R(Oeq) [Å]	σ^2 (Oax) [Å^2]	σ^2 (Oeq) [Å^2]	Θ(U = Oax) [deg]	Θ(U = Oeq) [deg]
				First pair of data				
122	3.90	2.92	1.77	2.38	0.004	0.016	170	256
32	1.10	9.58					80	166
				Second pair of data				
0	2.64	5.47	1.74	2.42	0.005	0.013	42	129
90	2.36	7.03					132	219

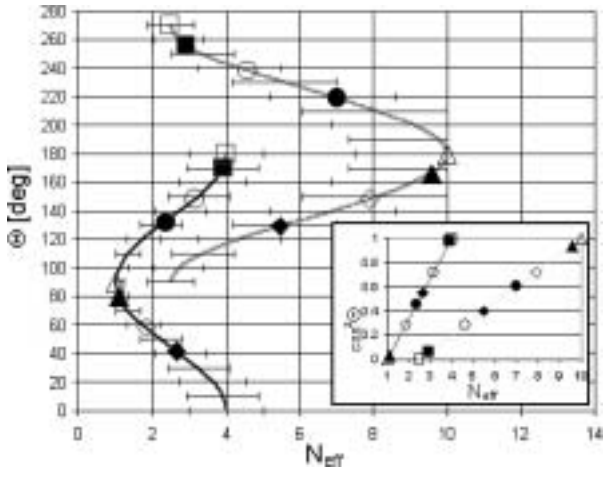

Fig. 3. Θ(U-Oax) (left) and Θ(U-Oeq) (right curve) as a function of N_{eff} for uranyl sorbed α-Al_2O_3 (11-20). Solid symbols are the values obtained from fits listed in Table 1 and open symbols theoretical values expected for binding to O_d-O_d surface site. Squares = 122; Triangles = 32; Diamonds = 0; Circles = 90. 25% error bars for N_{eff} are shown (values for N_{eff} for Oax below 1 and for Oeq above 10 are not defined). Corresponding values for N_{eff} versus $\cos^2\Theta$ are displayed in the insert.

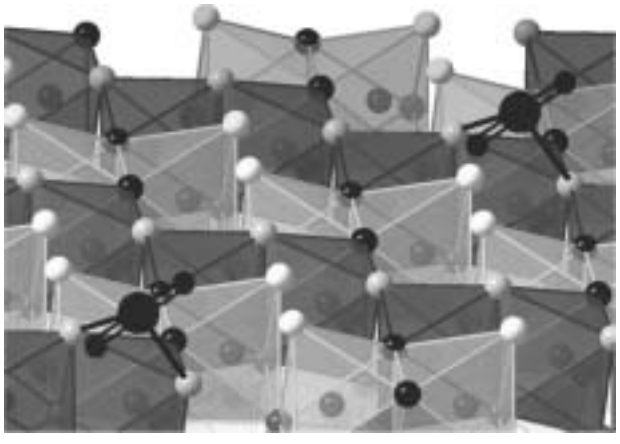

Fig. 4. Three dimensional cartoon of a single uranyl cation bound to an AlO_6 octrahedra edge on the α-Al_2O_3 (11-20) surface. The remaining equatorial ligands (three water molecules) have been omitted for clarity.

(R(U-Oax) and R(U-Oeq), and σ^2 are treated as global parameters for both spectra. The relative shift in ionization potential (ΔE_0) is held constant at −2.5 eV. The fit results are listed in Table I and depicted as triangular symbols in the FT spectra in Fig. 2. Fig. 3 compares the values for N_{eff} and the corresponding Θ(U-Oax) and Θ(U-Oeq) obtained from the fits with expected theoretical values for uranyl binding at the O_d-O_d sites.

EXAFS analysis corroborates our previous results [1] that uranyl cations sorbed onto the α-Al_2O_3 (11-20) surface are bound in a bidentate fashion through attachment of two Oeq in its equatorial plane to AlO_6 octrahedra edges (fig. 4). The Θ(U-Oax) and Θ(U-Oeq) obtained in the fits are all within 10–19° of values expected for binding at the O_d-O_d sites. ε is perpendicular

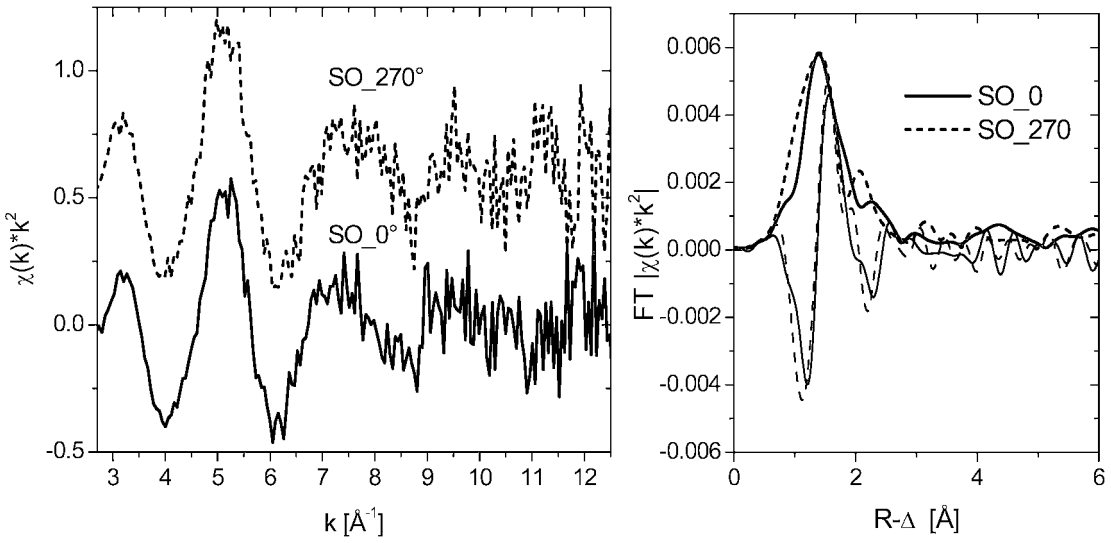

Fig. 5. U L3 EXAFS (left) and corresponding Fourier transforms (right) for the uranyl sorbed natural calcite (10-14) sample measured at angles with ε being approximately parallel to the $[-441]_-$ and $[48\text{-}1]_+$ directions (designated SO_0 and SO_270, respectively).

and parallel to O_d-O_d sites in the 122 and 32 spectra and we expect Θ(U-O*ax*) to be 180° (or 0) and 90°, respectively. The fit yields values 10° away. For the 0 and 90 spectra, ε is parallel and perpendicular to the c-axis. This translates to ε being 58° and 148° from expected values for $[O{=}U{=}O]^{2+}$ bound to O_d-O_d sites. The fit yields 42° and 132°, values only 16° smaller than expected for binding to AlO_6 octrahedra edges. If the other candidate binding sites situated at right angles to the c-axis were binding uranyl cations, Θ(U-O*ax*) values near 0° and 90° should be obtained; they are not. Although varied independently, the fit parameters obtained for Θ(U-O*eq*) are exactly 3° from the expected value of Θ(U-O*ax*) + 90° (the O*eq* plane is generally at a right angle to O*ax* atoms). This indicates that the linear uranyl units are parallel to the sample surface, otherwise a larger deviation of the fit values for Θ(U-O*eq*) from Θ(U-O*ax*) + 90° would be observed, i.e., the values obtained would be systematically shifted up or down from the curve Θ(U-O*eq*) as a function of N_{eff} in fig. 3. Also evident in fig. 3 is the relatively large deviation of the fit results for Θ(U-O*eq*) from the theoretical values for the 0 and 90 spectra. These are the spectra with largest Θ(U-O*eq*) deviation (19°) from that expected for binding to AlO_6 octrahedra edge. Possible explanations may have to do with poor quality of the data or relaxation/deviation of the surface atoms from their bulk crystalline terminated positions. More experiments are needed to determine the accuracy and precision of this particular technique.

3.2. *Uranyl sorbed calcite (10-14)*

The k^2-weighted U L3 edge EXAFS and their corresponding Fourier transforms (FT) for uranyl sorbed onto the natural calcite sample are depicted in fig. 5. Because the calculated aqueous U speciation of the alkaline uranyl solution used to prepare the sorption sample is dominated by $UO_2(CO_3)_3^{4-}$, we compare the EXAFS for the uranyl sorbed calcite with that for a $UO_2(CO_3)_3^{4-}$ reference solution shown in fig. 6. In order to correctly model the $UO_2(CO_3)_3^{4-}$ spectrum, multiple-scattering (MS) to the distal oxygen (*Odis*) along the U-C-*Odis* path must be included. Path analysis reveals this MS path to be responsible for the 'triplet' structure for k between 6.5 and 8.5 $Å^{-1}$. This oscillatory fingerprint of the $UO_2(CO_3)_3^{4-}$ EXAFS is missing in the EXAFS of the uranyl sorbed calcite in fig. 5. We conclude that the surface sorbed species does not reflect the majority solution species during sorption and is not simply a tricarbonato species. Studies of uranyl incorporated into calcite report loss or partial loss of three carbonato ligands [11], [4]. This seems also to be the case for the calcite sorbed species here.

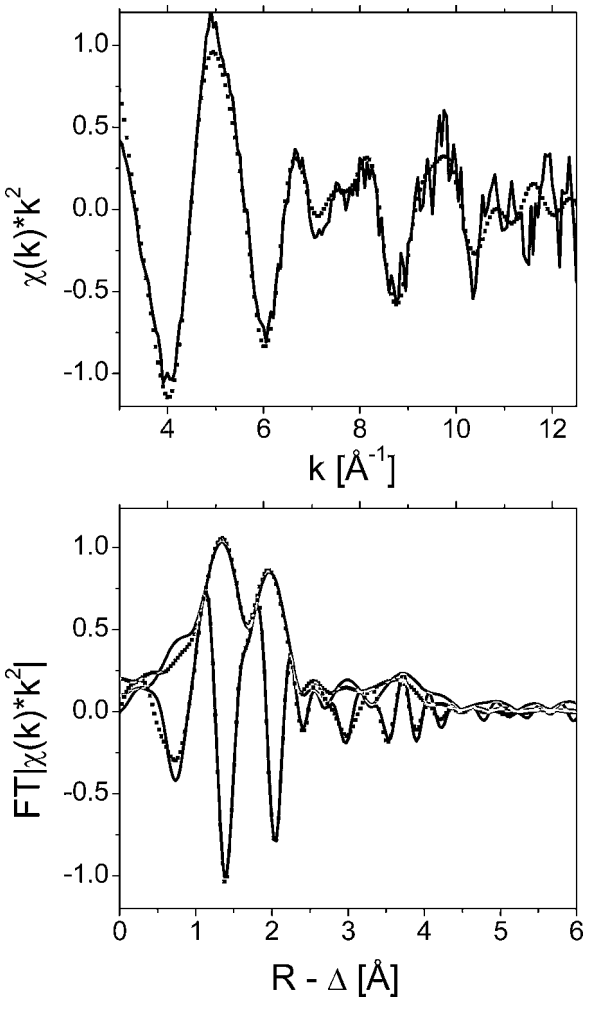

Fig. 6. U L3 EXAFS (top) and corresponding Fourier transforms (bottom) for an aqueous $UO_2(CO_3)_3^{4-}$ solution. Continuous lines are the experimental data; symbols represent a theoretical model of the data including multiple-scattering (U-O*ax*-U-O*ax* and U-C-O*dis*) paths.

Qualitative examination of the two spectra in fig. 5 provides the following information. The U-O*ax* shell in both spectra exhibits similar amplitudes. However, the U-O*eq* signal in the SO_0 spectrum is significantly different than in the SO_270 spectrum. There are two possible explanations for this apparent non-variance in Θ(U-O*ax*) with ε. Either the linear $[O{=}U{=}O]^{2+}$ units are perpendicular to ε or they are oriented at a small constant 'tilt' relative to ε in both the SO_0 and SO_270 spectra. That Θ(U-O*eq*) is observed to change with relative orientation of ε may infer that the coordination of U(VI) in its equatorial plane is significantly asymmetric. That uranyl appears to be oriented perpendicular (or at a constant tilt) to the (10-14) surface and that the equatorial coordination shows asymmetry in these measurements with the beam incident to [-441] and [48-1] directions may result from preferential sorption of uranyl cations onto one of the steps. These are preliminary, qualitative results. A more detailed analysis of these measurements and securing data recorded at additional angles is necessary before we are able to identify which step.

4. Conclusions

This method taking advantage of the GIXAFS polarization dependence for characterization of surface sorbed species offers great potential. Such molecular surface sorbed speciation at the mineral-water junction enables identification of reactive surface sites, differentiation between sorption reactions occurring at specific surface sites at different mineral crystallographic planes and verification of the presence of sorbed surfaces species proposed from bulk investigations. This information can, e.g., aid in predictive modeling of sorption reactions onto natural sorbents. This tool will be extended in the near future to polarization dependent Pu L3 edge GIXAFS studies of plutonyl cations sorbed onto mineral surfaces. It is also applicable to investigations of neptunyl sorption. Generally, the actinyl cations may become excellent probes for such molecular surface speciation studies due to their linear structure, which effects the large anisotropy of their XAFS signal utilized in this method.

References

1. Denecke, M. A., Dardenne, K., Lindqvist-Reis, P. and Rothe, J., Phys. Chem. Chem. Phys. **5**, 939 (2003).
2. See, e.g., Bargar, J. R., Towle, S. N., Brown, G. E. and Parks, G. A., Geochim. Cosmochim. Acta **60**, 3541 (1996) and Greaves, G. N., Adv. X-ray Anal. **34**, 13 (1991).
3. Hudson, E. A., Allen, P. G., Terminello, L. J., Denecke, M. A. and Reich, T., Phys. Rev. **B54**, 156 (1996).
4. Reeder, R. J., *et al.*, Geochim. Cosmochim. Acta **65**, 3491 (2001).
5. Surface site density for calcite is 5 sites/nm^2. Van Cappellen, P., Charlet, L., Stumm, W. and Wersin, P., Geochim. Cosmochim. Acta **57**, 3505 (1993). Moeller, P. and Sastri, C. S., Zeitschrift Physik. Chem. Neue Folge **89**, 80 (1974).
6. Speciation calculation performed with Phreeqc using the PSI-NAGRA Thermodynamic Database. Hummel, *et al*., (2002).
7. Koningsberger, D. E. and Prins, R., "X-ray Absorption: Principles, Applications, Techniques for EXAFS, SEXAFS and XANES", (Wiley Interscience, New York 1988).
8. Ressler, T., J. Physique IV **7**, C2-269 (1997).
9. Newville, M., Livins, P., Yacoby, Y., Rehr, J. J. and Stern, E. A., Phys. Rev. **B47**, 14126 (1993).
10. Rehr, J. J., Albers, R. C. and Zabinsky, S. I., Phys. Rev. Lett. **69**, 3397 (1992).
11. Kelly, S., *et al.*, Environ. Sci. Technol. **37**, 1284 (2003).

Physica Scripta. Vol. T115, 882–884, 2005

Tridimensional Imaging of Local Structure by X-Ray Absorption Spectroscopy

A. Di Cicco[1], A. Trapananti[1] and A. Filipponi[2]

[1]Istituto Nazionale di Fisica della Materia, INFN-LNF and Dipartimento di Fisica, Università di Camerino, Via Madonna delle Carceri, 62032 Camerino (MC), Italy
[2]INFM, Università dell'Aquila, Dip. di Fisica, via Vetoio 67010 Coppito, L' Aquila, Italy

Received June 26, 2003; accepted in revised form November 4, 2003

PACS numbers: 61.25.Mv, 61.10.Ht, 64.70.Dv, 61.20.Ja

Abstract

Current X-ray absorption spectroscopy (XAS) data-analysis of ordered and disordered systems is based on a peak decomposition of the n-body distribution functions. The limitation of this approach can be particularly severe for the purpose of modeling the local geometry in liquid and amorphous systems. We have developed a successful method for quantitative analysis of highly disordered structures using the Reverse Monte Carlo (RMC) refinement that can be applied simultaneously to diffraction and XAS data, allowing the construction of realistic tridimensional models. Here we present the results of the application of the method to gaseous Br_2 and to liquid Cu. The method incorporates all of the advances related to the application of advanced multiple-scattering (MS) codes and the n-body expansion for XAS data-analysis (GNXAS).

1. Introduction

Modern XAS (X-ray absorption spectroscopy) data-analysis is based on the structural refinement of the raw XAS data through accurate multiple-scattering (MS) calculations of the X-ray absorption cross-section. In particular, the GNXAS *ab-initio* data-analysis method for XAS data-analysis allows us to obtain fast and accurate simulations of the $\gamma^{(n)}$ MS XAS n-body signals, associated with the n-body distribution functions g_n describing the local structure around selected photoabsorbing atoms [1, 2]. The current strategy for the structural refinement requires modelling of the distribution functions as a superposition of distinct peaks associated with the neighboring atomic shells (first and further neighbors) for the pair distribution function g_2, with typical triangular atomic configurations (g_3), and so on [2, 3]. This approach is clearly appropriate for molecules or for ordered condensed matter, where the assumption about the existence of distinct g_2 and g_3 peaks at short distances is obviously fulfilled. In these systems, this "peak-fitting" method is a very fast and efficient tool, usually able to ensure a reliable reconstruction of the shape of the short-range distributions through a limited number of structural parameters defining suitable model functions.

In highly disordered substances, such as amorphous or liquid systems, short-range peaks of the n-body distribution functions are usually merged into a long-range tail and suitable constraints must be used in order to obtain meaningful structural results through XAS data [4]. The application of physical constraints into a still model-dependent peak-fitting approach has been shown to be very successful in describing the short-range pair distribution function of "simple" elemental melts ionic binary liquids and aqueous solutions (see ref. [4–9] and the review paper [10]). However, the extension of the peak-fitting approach to disordered multi-component systems is not a trivial task [11] and a reliable reconstruction of the shape of the higher-order distribution functions is practically impossible even in simple monatomic systems.

In view of the potential of the XAS technique in measuring the local structure in highly disordered systems through higher-order correlations, advances in XAS data interpretation are particularly important. In fact, knowledge of the pair distribution $g_2(r)$ does not allow us to obtain a unique tridimensional model of the local structure. The reconstruction of the local geometry in liquid systems needs additional improvements to current XAS data analysis schemes. A successful method for quantitative analysis of highly disordered structures is the Reverse Monte Carlo (RMC) refinement [11–13] that can be applied simultaneously to diffraction and XAS data, allowing the construction of a tridimensional model of the disordered system compatible with the observables under consideration. In particular, XAS data probe the local structure around photoabsorbing centers, while diffraction data provide the necessary medium and long-range constraints.

Application of the RMC method for XAS data-analysis was already suggested by Gurman and McGreevy [12] and preliminary applications to silver bromide and crystalline and amorphous silicon presented. The method was also applied for data-analysis of liquid GaSb and InSb [14]. We have now developed such a RMC method using state-of-the-art simulation techniques for calculating the XAS signal starting from ensembles of either molecular replicas or atoms in a box with cyclic boundary conditions. In the latter case, the RMC refinement is applied both to XAS experimental data and the $g(r)$ curve obtained by diffraction techniques.

2. Method

The RMC method [11, 13] is a variation of the standard Metropolis Monte Carlo procedure [15] whose aim is to produce a statistical ensemble of particles following the canonical distribution. In the original MMC technique the probability of finding a particular configuration of the ensemble of particles is proportional to $e^{\frac{-U}{KT}}$ where U is the total potential energy and T is the temperature. A weighted sampling procedure (Markov chain) allows to decrease the total energy U by moving the coordinates of the particles until it reaches and oscillates around an equilibrium value. In the RMC method, the role of the potential energy is played by the sum of the weighted squares of the difference between measured (A^E) and calculated (A^C) physical observables:

$$\chi^2 = \sum_{i=1}^{N} [A_i^E - A_i^C]^2 / \sigma_i^2. \quad (1)$$

As shown in the original papers [11, 16], the probability distribution is proportional to $e^{-\chi^2/2}$ and therefore $\chi^2/2$ in RMC equivalent to $\frac{U}{KT}$ of the original Monte Carlo.

In the present work, we have applied the method for the simultaneous RMC refinement of XAS and $g_2(r)$ data obtained by X-ray or neutron diffraction using the "state-of-the-art" multiple-scattering simulation techniques provided by GNXAS programs [1, 3].

For a single component system the structural XAS signal is related to the n-body distribution functions by:

$$\langle\chi(k)\rangle = \int_0^\infty \mathrm{d}r\ 4\pi r^2\rho\ g_2(r)\gamma^{(2)}(r,k) + \int \mathrm{d}r_1\ \mathrm{d}r_2\ \mathrm{d}\theta\ 8\pi^2 r_1^2 r_2^2 \times \sin(\theta)\rho^2 g_3(r_1,r_2,\theta)\gamma^{(3)}(r_1,r_2,\theta,k) + \cdots \quad \cdots \qquad (2)$$

where the short range nature of the n-body XAS $\gamma^{(n)}$ signals limits the integral in a region of linear dimensions of the order of few Å. The g_n functions are easily calculated using the atomic coordinates of the ensemble of atoms in the RMC box, and appropriate calculation strategies have been actually implemented to evaluate the XAS signal associated to the g_2 in a box of thousands of atoms. The main difference with the application described in ref. [12] is the use of sophisticated MS calculations within the n-body expansion and of the relationship given by Eq. (2) (a term $(g_2 - 1)$ instead of g_2 appears in the integral in ref. [12]).

These advances have been incorporated in a program (RMCXAS) interfaced with GNXAS [2, 3] and currently able to perform structural refinements of both molecular and condensed structures by using either an ensemble of replicas of the molecule or applying cyclic boundary conditions on a cubic box. The χ^2 function at each RMC step is simply given by:

$$\chi^2 = \sum_{i=1}^{N_{XAS}} [\chi^E(k_i) - \chi^C(k_i)]^2/\sigma_i^2 + \sum_{j=1}^{N_g} [g_2^E(r_j) - g_2^C(r_j)]^2/\sigma_j^2 \qquad (3)$$

where in the first term of the r.h.s. χ^C is calculated by the program starting from the actual atomic coordinates using Eq. (2) and the $\gamma^{(2)}$ signals given by GNXAS, χ^E is the raw XAS signal and σ_i^2 the noise function obtained from the experiment and evaluated by FITHEO (GNXAS program). In the second term, not used in molecular cases, g_2^C is the pair distribution associated with the atomic coordinates of the RMC box, g_2^E is a model pair distribution obtained by neutron/X-ray diffraction or molecular dynamics, and σ_j^2 is the variance associated with the pair distribution.

3. Results and Discussion

A first application to molecular bromine shows the main features of the RMC approach for the simpler diatomic structure and the validity of the structural results. The bond distribution of the Br_2 molecule has been investigated by XAS by several authors (see for example [17, 18] and ref. therein). Here we have used the Br K-edge experimental data measured at LURE, beamline D42, and published in ref. [17]. In previous works the data-analysis was performed using the standard Gaussian peak-fitting approach (average distance $R = 2.288$ Å and bond variance $\sigma^2 = 0.0019$ Å^2 for the XAS data under consideration, see [18] and ref. therein).

The RMC model used in this work is based on the calculated XAS signal associated with an ensemble of 500 Br_2 molecular replica. The starting configuration was chosen to mimic a Gaussian distribution with displaced values with respect to those found with the peak-fitting approach.

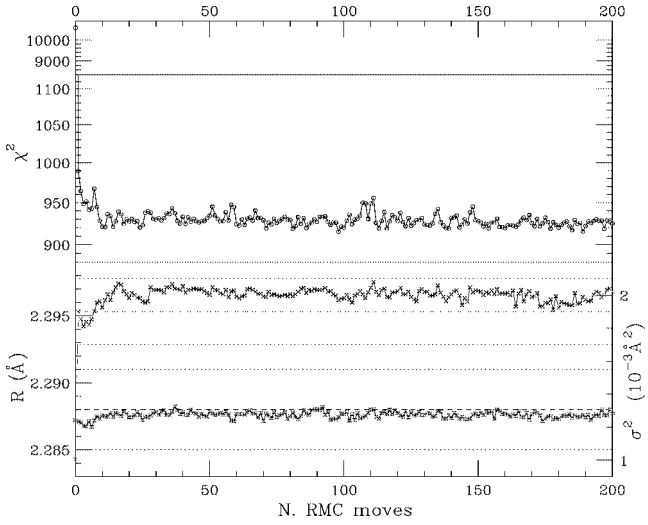

Fig. 1. Upper panel: trend of the χ^2 residual function for successive RMC moves. The χ^2 rapidly converges near to the expected value. Lower panel: average molecular distance R and distance variance σ^2 (upper curve) calculated for the set of RMC coordinates at each simulation step. Average distance and variance evaluated using the GNXAS peak-fitting procedure are shown as dashed lines (error bars indicated as dotted lines).

In Fig. 1, upper panel, we show the trend of the χ^2 residual function for successive moves of the 500 molecular replica of the Br_2 molecule, up to a total of 200 RMC moves. Each RMC move corresponds to 500 molecular distance moves (speed is about 1 s per RMC move on 500 MHz alpha CPU). The χ^2 is found to converge very rapidly near to the expected value (in the χ^2 distribution this is simply $E[\chi^2] = N$, where N is the number of data points). The average molecular distance R and distance variance σ^2, reached their equilibrium values after 10–20 RMC moves, as shown in the lower panel of Fig. 1. RMC average distance and variance are found to be in excellent agreement with those evaluated by using the GNXAS peak-fitting procedure in the Gaussian approximation on the same data set (dashed lines) and on more accurate experimental data [18]. In Fig. 2, upper panels we compare the raw $k\chi(k)$ XAS data with $k\chi(k)$ RMC simulations. In the corresponding lower panels we report the histograms of the radial distribution function $n(r)$, calculated starting from the RMC molecular configurations, Calculated $k\chi(k)$ signals and $n(r)$ before reaching equilibrium are shown in the left panels (initial configuration and those after 10, 20, 30, 40 steps). The results of the last 150 moves are reported in the right panels. In this case, $k\chi(k)$ simulations and residual (below) associated with successive RMC steps can not be distinguished. The different $n(r)$ corresponding to equilibrium configurations are shown with the average distribution (thick histogram) and compared with Gaussian distributions measured in previous works [18]. The results of the peak-fitting procedure and of the RMC refinement are clearly compatible confirming the validity of the approach.

In Fig. 3 we briefly report about the results of an RMC XAS data-analysis of liquid Cu measured at 1398 K (1-Cu) at the ESRF (BM29). The RMC simulation has been performed in a 864-atom cubic box of fixed density and considering both the XAS experimental data and the published $g_2(r)$ curve obtained by neutron diffraction (ND) [19] which acts as a constraint for the long-range behaviour (see Eq. (3)). The initial atomic configuration has been chosen to be compatible with the ND g_2. The RMC run needs more steps and longer times for equilibration,

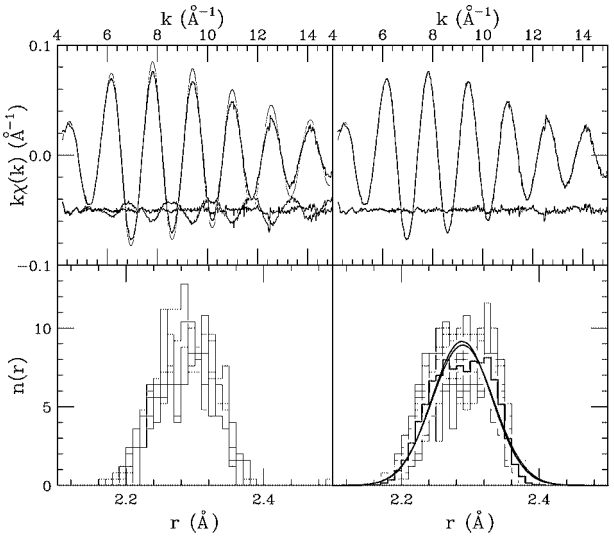

Fig. 2. Upper panels: on the left raw $k\chi(k)$ XAS data are compared with the first RMC simulations calculated before reaching equilibrium. Those corresponding to equilibrium configurations are shown on the right (16 simulations every 10 steps up to 200). Lower panels: on the left the histograms of the RMC radial distribution function $n(r)$ are shown for non-equilibrium configurations. On the right the different $n(r)$ corresponding to equilibrium configurations are compared with the average distribution (thick histogram) and with Gaussian distributions measured in previous works.

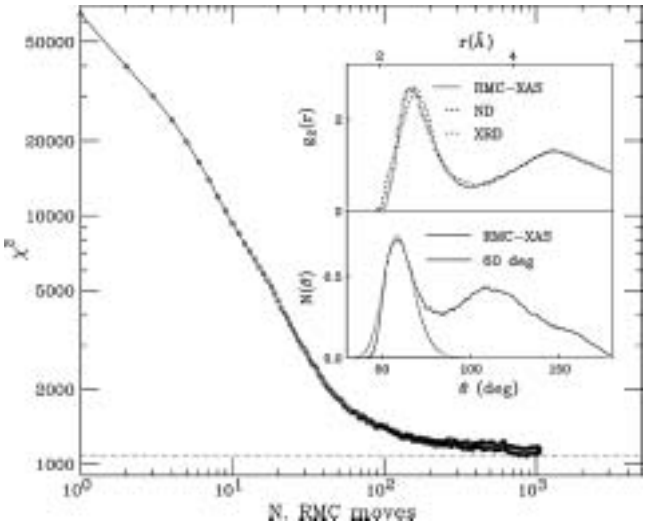

Fig. 3. Trend of the χ^2 residual function in liquid Cu at 1398 K. The inset (upper panel) shows the $g_2(r)$ associated with the RMC simulation and previous determinations using neutron (ND) and X-ray (XRD) diffraction. In the lower panel of the inset the full bond-angle $N(\theta)$ distribution resulting from the RMC simulation is compared with that of equilateral triangles.

that is reached after about 100–500 steps. The $g_2(r)$ obtained by the last 400 RMC steps reproduces almost exactly those given by ND [19] and XRD [20] above about 4 Å while the first-neighbour peak is narrower and shifted to shorter distances (see inset of Fig. 3, upper panel). The short-range shape of the RMC $g_2(r)$ is accurately reconstructed due to the unique sensitivity of the XAS signal. The RMC bond-angle distribution shown in the inset is calculated counting the number of triangular configurations per atom up to a selected limiting distance ($R_{cut} = 2.98$ Å).

The typical shape of the distribution contains a distinct peak around 60° associated with equilateral configurations and a second broad hump at about 110°. The 3-body contribution of the equilateral configuration is found to be very important to reproduce the XAS signal and the consequences on our understanding of the local structure of liquid Cu are discussed in detail elsewhere [22].

4. Conclusions

We have developed a new XAS data-analysis program based on the RMC approach that fully incorporates the advances contained in the GNXAS method. In particular, simultaneous refinement of raw XAS data and $g_2(r)$ curves is possible giving realistic reconstructions of the local structure compatible with both XAS and diffraction data. This is particularly important in disordered systems where the RMC model provides a tridimensional model compatible with the observables without the intrinsic limitations of the peak-fitting approach. The validity of the method has been put to a test on a simple molecular case (Br_2) where the results of a standard data-analysis have been reproduced. The application of this method to the study of the structure of liquid copper shows that realistic pair and triplet distribution functions can be measured and analysed by XAS.

References

1. Filipponi, A., Di Cicco, A. and Natoli, C. R., Phys. Rev. B **52**, 15122 (1995).
2. Filipponi, A. and Di Cicco, A., Phys. Rev. B **52**, 15135 (1995).
3. Filipponi, A. and Di Cicco, A., Task Quarterly **4**, 575 (2000).
4. Filipponi, A., J. Phys.: Condens. Matter **6**, 8415 (1994).
5. D'Angelo, P., Di Nola, A., D., Filipponi, A., Pavel, N. V. and Roccatano, D., J. Chem. Phys. **100**, 985 (1994).
6. Di Cicco, A. *et al*., J. Phys.: Condens. Matter **8**, 10779 (1996).
7. Di Cicco, A., Minicucci, M. and Filipponi, A., Phys. Rev. Lett. **78**, 460 (1997).
8. Filipponi, A., Di Cicco, A. and De Panfilis, S., Phys. Rev. Lett. **83**, 560 (1999).
9. D'Angelo, P. and Pavel, N. V., J. Chem. Phys. **111**, 5107 (1999).
10. Filipponi, A., J. Phys.: Condens. Matter **13**, R23 (2001).
11. Trapananti, A. and Di Cicco, A., Phys. Rev. B **70**, 014101 (2004).
12. McGreevy, R. L. and Pusztai, L., Mol. Sim. **1**, 359 (1988).
13. Gurman, S. J. and McGreevy, R. L., J. Phys.: Condens. Matter **2**, 9463 (1990).
14. McGreevy, R. L., J. Phys.: Condens. Matter **13**, R877 (2001).
15. Wang, Y., Lu, K. and Li, C., Phys. Rev. Lett. **79**, 3664 (1997).
16. Metropolis, N., Rosenbluth, A. W., Rosenbluth, M. N., Teller, A. H. and Teller, E., J. Phys. Chem. **21**, 1087 (1953).
17. McGreevy, R., Howe, M. A., Keen, D. and Clausen, K. N., in IOP conference series (1990), vol. 107, pp. 165–184.
18. D'Angelo, P., Di Cicco, A., Filipponi, A. and Pavel, N. V., Phys. Rev. A **47**, 2055 (1993).
19. Filipponi, A. and D'Angelo, P., J. Chem. Phys. **109**, 5356 (1998).
20. Eder, O. J., Erdpresser, E., Kunsch, B., Stiller, H. and Suda, M., J. Phys. F: Metal Phys. **10**, 183 (1990).
21. Waseda, Y., "The Structure of Non-Crystalline Materials" (McGraw-Hill, New York, 1980).
22. Di Cicco, A., Trapananti, A., Faggioni, S. and Filipponi, A., Phys. Rev. Lett. **91**, 135505 (2003).

Physica Scripta. Vol. T115, 885–887, 2005

Archeological Applications of XAFS: Prehistorical Paintings and Medieval Glasses

F. Farges[1,2], E. Chalmin[1,3], C. Vignaud[3], I. Pallot-Frossard[4], J. Susini[5], J. Bargar[6], G. E. Brown Jr[2,6] and M. Menu[3]

[1]Laboratoire des Géomatériaux, Université de Marne-La-Vallée, CNRS FRE 2455, 77454 Marne-La-Vallée cedex 2, France
[2]Department of Geological and Environmental Sciences, Stanford University, CA 94305-2115, USA
[3]Centre de Recherche et de Restauration des Musées de France (C2RMF-CNRS), Paris, France
[4]Laboratoire de Recherche des Musées de France (LRMH), Champs sur Marne, France
[5]European Synchrotron Radiation Facility (ESRF), Grenoble, France
[6]Stanford Synchrotron Radiation Laboratory, Menlo Park, CA 94025, USA

Received June 26, 2003; accepted November 11, 2003

PACS numbers: 61.10.Ht, 61.43.Fs, 02.70.Ns, 91.40.−k

Abstract

High-resolution manganese and iron K-edges XANES spectra were collected on several samples of archeological interest: prehistorical paintings and medieval glasses. XANES spectra were collected at the ID21 facility (ESRF, Grenoble, France) using a micro-beam device and at the 11-2 beamline (SSRL, Stanford, USA) using a submillimetric beam.

The medieval glasses studied are from gothic glass windows from Normandy (XIVth century). The aim of this study is to help understand the chemical durability of these materials, exposed to weathering since the XIVth century. They are used as analogues of weathered glasses used to dump metallic wastes. These glasses show surficial enrichment in manganese, due to its oxidation from II (glass) to III/IV (surface), which precipitates as amorphous oxy-hydroxides. Similarly, iron is oxidized on the surface and forms ferrihydrite-type aggregates.

The prehistorical paintings are from Lascaux and Ekain (Basque country). We choose in that study the black ones, rich in manganese to search for potential evidences of some "savoir-faire" that the Paleolithic men could have used to realize their paint in rock art, as shown earlier for Fe-bearing pigments. A large number of highly valuable samples, micrometric scaled, were extracted from these frescoes and show large variation in the mineralogical nature of the black pigments used, from an amorphous psilomelane-type to a well-crystallized pyrolusite. Correlation with the crystals morphology helps understanding the know-how of these early artists.

1. Introduction

Recently, a number of XAFS methods have been applied to archeology to help characterize highly valuable artifacts of historical importance such as Medieval gems [1] and Roman glasses [2]. Other applications currently underway include the study of the corrosion of inks used by J. S. Bach (cf. Dahn and co-workers in Berlin, Germany), the corrosion of Celtic weapons (Janssens's group in Antwerp, Belgium), the determination of growth rate of desert varnish to help dating petroglyphs (Lytle's group at SSRL) or the sulfur speciation in old and modern woods (see Jalilehvand, this volume).

Archeological studies require some extensive, multi-disciplinary studies, as the number of samples can be high and highly valuable (so undestructive). Also μ-techniques are useful to scan the sample heterogeneities, which can help highly to provide more clues on origins, uses and goals of the artifacts probed. For instance, extensive corrosion studies of Celtic weapons require a thorough study of the pre-edge feature of Fe at its K edge. From the pre-edge feature, accurate mapping of the iron redox can be achieved, which evidence, in the case of these weapons, some very localized areas (microns) of less corroded metal. Such characteristics can be used as tracers for some past technologies, commercial exchanges, creative actions (composers) or even legends. Surprisingly, we observed that reference studies are missing to help archeologists to perform their characterization in a robust manner. For instance, few studies exist to accurately determine the redox state of Mn from the analysis of its pre-edge feature at the K-edge.

Similarly, manganese shows large variation in redox and speciation, due to the large number of possible redox states that Mn can adopt under ambient conditions (metal, II, III, IV, V, VI and VII). As a result, studies of artifacts in which manganese plays a key role (such as pigments) are essential to trace past technologies. However, extensive studies of the redox of manganese are lacking. They might be useful also for other domains such as geochemistry and material sciences. In this study, we present a XANES study of a large number of Mn-bearing mineral samples in which the pre-edge feature is understood under the light of *ab initio* calculations. The obtained results are applied to the study of black prehistorical paintings (in which manganese dominates) and in medieval glasses (in which manganese is diluted at the 1–2 wt.% level).

2. Experimental

Mn K-edge XANES spectra for model compounds and archeological artifacts (pigments and glasses) were collected under high resolution conditions (∼0.6 eV) at SSRL (Stanford, USA) using beamline 11-2, Si(220) double-crystal monochromator, 0.3 vertical height for the slits before and after the monochromator. The energy reproducibility of the monochromator is ∼0.05 eV. Pre-edge features were collected using 0.1 eV steps whereas the main edge crest were collected with 0.3 eV steps to 300 eV above the absorption edge. Self-absorption effects were taken into account as the archeological samples could not be optimally prepared. Then, the XANES spectra were collected in the fluorescence mode. Several model compounds were used to check the accuracy of these corrections (using the code FLUO [3] and transmission data). In parallel, micro-XANES spectra were collected in order to map at the micron scale the manganese speciation. A Si(111) monochromator and a Fresnel focusing device were used at the ID21 beamline at ESRF (Grenoble, France). Spectra were collected in the fluorescence mode using a pin-diode and, when necessary corrected for self-absorption.

[1]Corresponding author (e-mail: farges@univ-mlv.fr)

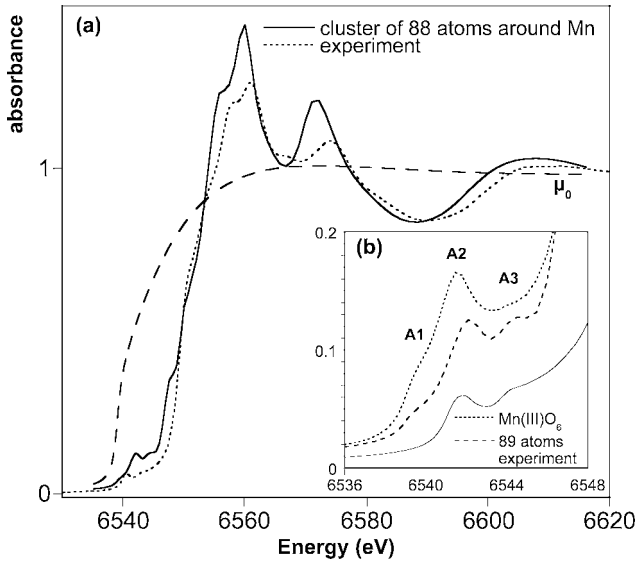

Fig. 1. (a) XANES and (b) pre-edge feature in manganite, (Mn(III)OOH): experimental (solid lines) versus *ab initio* calculations (FEFF, dotted lines), showing the importance of next-nearest manganese neighbors in the pre-edge feature (feature A3).

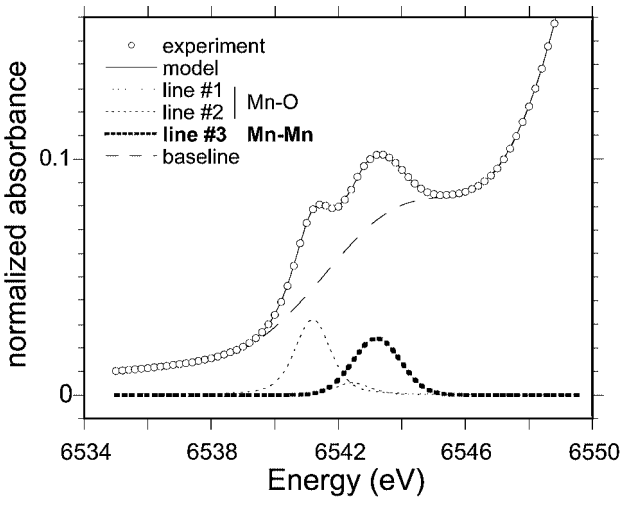

Fig. 2. Example of pre-edge model for Mn(IV), considering lines related to the Mz-O moiety and lines related to more distant Mn neighbors.

Mn-bearing model compounds include numerous oxides and silicates, natural or synthetic, well characterized and containing Mn(II,III,IV,V,VI,VII) in octahedral, square planar, cubic or tetrahedral geometry. The archeological artifacts include black pigments from the Lascaux cave (Dordogne, France – 18,000 years old) and medieval glasses (more or less weathered) from various gothic buildings (XIVth century BC) from Normandy (France) such as Ste Opportune du Bosc.

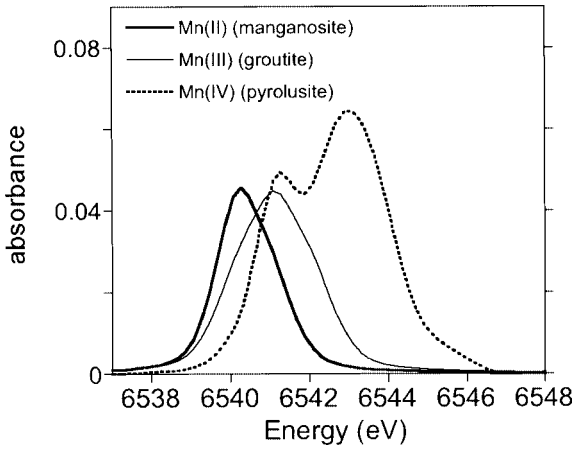

Fig. 3. Shift of the normalized pre-edge feature with Mn-redox, when transitions related to distant Mn are excluded.

3. Results

3.1. *Model compounds*

Figure 1a shows normalized, self-absorption corrected XANES spectra collected at the manganese K-edge in a typical model compound, namely Mn(III)OOH. Figure 1b shows its normalized pre-edge, obtained using a method described elsewhere [4]. The obtained pre-edge features for a given redox and geometry shows large variation among themselves, suggesting that the Mn-speciation is not the only contributor to the spectra. This is confirmed by *ab initio* calculations of the XANES (including the pre-edge feature assuming dipolar and quadrupolar transitions) performed using the FEFF8.28 package [5]. When the medium-range environment around manganese is included in the model, the pre-edge feature area increases, sometimes up to a factor 2. Multiplet calculations performed by F. de Groot on Mn(II,III,IV)O_6 clusters (*pers. comm.*) also confirm this observation: the calculated pre-edge with multiplets is, especially for Mn(IV), much smaller in area than that measured. A similar phenomenon was already observed for Fe-bearing oxides, for which the pre-edge features show transitions related to next-nearest Fe neighbors [6]. Based on these observations, we could find a strategy to consider only the transitions in the pre-edge feature related to the Mn-speciation (redox and geometry). In order to achieve this, we modelled the pre-edge with pseudo-Voigt lines with a fixed width and Gaussian percentage (1.3 and 45%, respectively). Only the first lines (2 for Mn(II) and Mn(III) and 3 for Mn(IV)) were taken into account (see Fig. 2) to derive robust redox and geometric information. As for Fe [4], the pre-edge information must be calculated based on the pre-edge centroid (weighted by the respective area of each line) versus its integrated area. When taken into account, the Mn pre-edge centroid shifts nearly linearly with redox (Fig. 3) and follows *ab initio* predictions.

3.2. *Prehistorical paintings*

Mn K-edge XANES spectra were normalized following the same protocol as the one for the model compounds. The samples were previously characterized using a wide combination of other methods, such as imaging (TEM and SEM, transmission and scanning electron microscopies, respectively), diffraction (electronic) and chemistry (EDXS and PIXE, energy dispersive and particule induced X-ray spectroscopy/emission, respectively). PIXE information was used to provide chemical information required for self-absorption corrections. For instance, two pigments from the "Great Black Bull" (GLAS65) and the "bichrome horse" (GLAS66) from the Painted Gallery (Fig. 4) show large differences in manganese speciation related to the

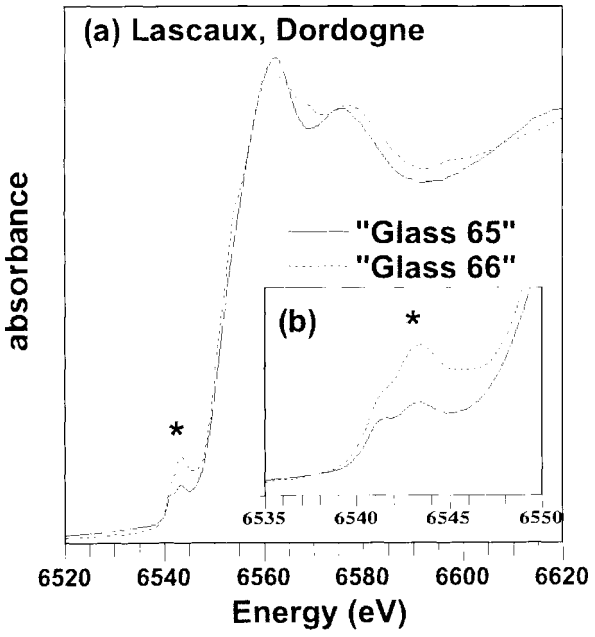

Fig. 4. Mn K-edge XANES spectra for 2 Lascaux pigments from the "Great Black Bull" (GLAS65) and the "bichrome horse" (GLAS66) from the Painted Gallery, showing changes in the XANES (a) and in the pre-edge feature (b) related to the presence of romanechite and pyrolusite.

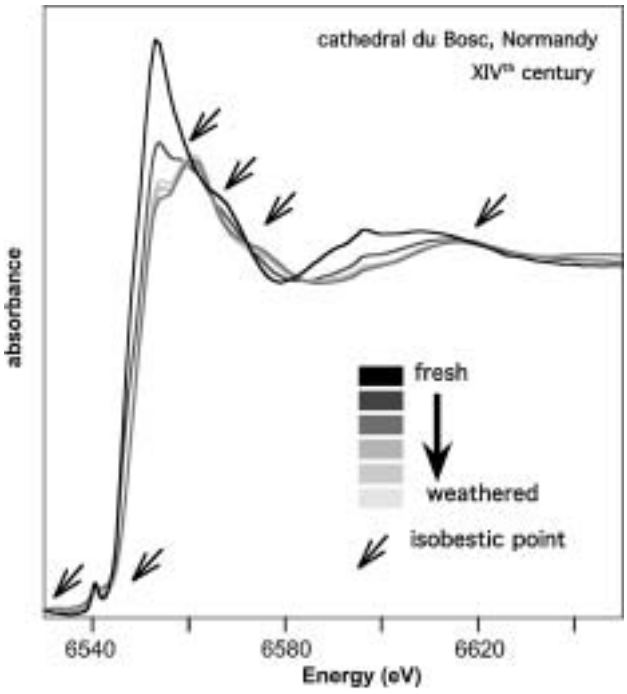

Fig. 5. XANES Profile at the Mn K-edge as a function of the glass thickness for a medieval glass window exposed to progressive weathering (from dark – "fresh" glass to light "weathered"). The data shows an oxidation of manganese from II to IV, which resulted in precipitation of manganese oxi-hydroxides at the origin of the darkening of the building. Isobestic points shows the number of knots in that data set of 6 spectra, suggesting that 2 end members can be extracted by inversion as suggested by PCA analysis.

presence of romanechite and pyrolusite. However, neither the XANES nor the morphological studies performed for these samples evidence the presence of any heating that would have modified the texture of these pigments prior to the painting [7]. 2D mapping experiments of the manganese K-edge XANES were carried out and are still under reduction to determine if some other paintings were manufactured from primary Mn-ore or from heat-treated ores.

3.3. *Medieval glasses*

Several medieval glasses were examined to study the weathering of the glass windows. Since the XIVth century, these glasses suffered from corrosion, especially the ones exposed to the outside (corrosion from water, pollution, seasonal changes etc.). Some samples were recovered from the building and show a progressive corrosion, as a function of their exposition to weather. Manganese K-edge spectra (Fig. 5) show a progressive shift of the Mn K-edge from the "fresh", unweathered glass (protected) to the highly corroded areas of the glass. In the fresh glass, manganese is divalent (as in most glasses) and in a "silicate"-type environment. When weathered, manganese oxidizes to +IV and forms environments close to these for manganese oxi-hydroxides (this promotes a surficial enrichment in manganese). A Principal Component Analysis of these spectra reveals that 2 end members can be extracted by inversion. These pure end-members (fully fresh and fully weathered) confirm these trends. This explains why the inside luminosity of medieval building is affected by the precipitation of these complex manganese hydroxides. Similar observations were made at the iron K-edge, where ferrihydrite-type materials precipitated in the corroded zones.

4. Conclusions

The availability of optimized sources, providing high-resolution, low noise and focusing techniques makes it an unique tool to study highly valuable samples from archaeologists. However, more methods (to diagnose reliably redox and speciation) are needed to help the archaeologists to accurately interpret their data. The main information that synchrotrons can provide is less matter/beam interaction (as compared to proton or electronic sources), drastic improvements in beam source, optics and detection. If "standard" laboratory methods are still required to first investigate these samples, X-ray absorption methods provide important information on redox and environments that can be used to source an origin or a technology. In some other cases (such as for medieval glasses presented here), archeological artefacts provide an interesting outlook on how materials can be preserved or react to ageing. This information is also important for curators to conserve their artefacts or for physicists and chemists to better understand material durability (for nuclear wastes for instance).

References

1. Reiche, I. *et al.*, Am. Mineral. **86**, 519 (2001).
2. Quartieri, S. *et al.*, Eur. J. Min. **14**, 749 (2002).
3. Haskel, D. (1999) www.aps.anl.gov/xfd/people/haskel.
4. Wilke, M. *et al.*, Am. Mineral. **65**, 713 (2001).
5. Ankudinov, A. L. *et al.*, Phys. Rev. B **58**, 7565 (1998).
6. Drager, G. *et al.*, Phys. Stat. Sol. B **146**, 287 (1984).
7. Chalmin, E. *et al.*, Appl. Phys. A **79**, 187 (2004).

Physica Scripta. Vol. T115, 888–890, 2005

EXAFS, XANES and *In-Situ* SR-XRD Characterization of Biogenic Manganese Oxides Produced in Sea Water

J. R. Bargar[1], S. M. Webb[1*] and B. M. Tebo[2]

[1]Stanford Synchrotron Radiation Laboratory, Menlo Park, CA, 94025, USA
[2]Scripps Institute of Oceanography, University of San Diego, La Jolla, CA 92093, USA

Received June 26, 2003; accepted in revised form November 4, 2003

PACS number: 61.10.−i

Abstract

Natural manganese oxide nanoparticles and grain coatings are ubiquitous in the environment and profoundly impact the quality of sediments via their ability to degrade and sequester contaminants. These oxides are believed to form dominantly via oxidation of Mn(II) by marine and freshwater bacteria and have extremely high sorptive capacities for heavy metals. We have used XANES, EXAFS, and synchrotron (SR)-XRD techniques to study biogenic manganese oxides produced by spores of the marine *Bacillus* sp., strain SG-1 in sea water as a function of reaction time under fully *in-situ* conditions. The primary biogenic product is a nanocrystalline solid with an oxidation state and layered phyllomanganate local structure similar to that in δ-MnO_2. XRD data show the biooxides to have a phyllomanganate 10 Å basal plane spacing, suggesting the interlayer is hydrated and contains calcium. Fits to EXAFS spectra suggest the octahedral layers of the biooxides to be relatively flat (out-of-plane bend $<10^{\circ}$) and to have relatively low octahedral layer Mn site vacancies (12 to 14%). These results suggest that aqueous Ca^{2+} is inserted into the biogenic oxide structure after completion of the enzymatic oxidation process. The biooxides observed in this study may be the most abundant manganese oxide phase suspended in the oxic and sub-oxic zones of the oceanic water column.

1. Introduction

Bacterially generated Mn oxides are ubiquitous in natural waters as reactive nanoparticles and grain coatings and have profound impacts on contaminant degradation, nutrient cycling, and carbon cycling in the environment. They have high sorptive capacities for metal ions, can degrade toxic organic contaminants, including aromatic hydrocarbons, and oxidize a variety of inorganics, e.g., Cr(III), Co(II), and hydrogen sulfide. Sequestration of dissolved heavy metals during Mn oxide biogenesis is believed to be a key mechanism for attenuation of contaminants in polluted waters. The most important pathway for environmental Mn oxidation is believed to be catalytic oxidation of Mn(II) by freshwater and marine bacteria [1–3]. Understanding the chemical mechanism(s) by which this process occurs is therefore crucial to understanding the cycling of essential and toxic trace constituents in the environment. In spite of their importance, relatively little is known about the mechanisms and products of bacterial Mn oxide biogenesis.

Our overarching goals are to define the mechanisms of bacterial Mn(II) oxidation and the structures, compositions, and reactivity of the resulting biooxides. In addition, manganese oxides are important reactive components of the oceanic water column, and we seek their identities and properties. We have previously investigated the products of bacterial Mn(II) oxidation in 50 mM NaCl solutions [4–6]. This work indicated that the primary biogenic oxidation product is a poorly crystalline phyllomanganate oxide with local structure and oxidation state similar to δ-MnO_2. We extend this work here to investigate how these reactions proceed in sea water (SW), which contains relatively high concentrations of dissolved magnesium (60 mM) and calcium (10 mM). Both solutes can react with manganese to form tunnel-structured manganese oxides such as todorokite. We seek to investigate whether such phases are created during bacterial Mn(II) oxidation, and to discern the implications for bacterial Mn(II) oxidation mechanisms.

2. Methods

SG-1 spores were incubated in 10 µM Mn(II) (added as $MnCl_2{\cdot}4H_2O$) in filtered (0.2 µm pore diameter) sea water (SW) obtained from the Scripps Pier. Experiments were started by adding approximately 1.3×10^{10} spores to each incubation vessel resulting in 2.2×10^6 spores $\cdot$ mL^{-1}. The sampling times for the experiment ranged from 6 to 80 hours. For each time point the entire sample was harvested by settling and centrifugation (4 °C). Samples were stored at −20 °C in about 10 mL of their original medium until analysis.

Mn K-edge XAS spectra were collected at room temperature from wet homogeneous spore-biooxide samples in rigid thermoplastic sample holders at SSRL beamline 4-3, which was equipped with a Si(220) monochromator and harmonic rejection mirror set at a 9 keV cut-off energy. Data were collected in transmission geometry to eliminate spectral distortion from self absorption, which is unavoidable and substantial in fluorescence data. Spectra were background subtracted and splined using the SIXPack software [7]. Linear combination fitting and EXAFS fitting were also performed with SIXPack. Energy was allowed to float by up to 0.15 eV during fits. In comparison, the energy difference between birnessite and δ-MnO_2 is about 0.4 eV. Model compound spectra were fit as unknowns, the results of which were fit with a linear regression to obtain the following:1-sigma error estimates: +/−1.7% for Mn(II), +/−2.6% for Mn(III) oxides, and +/− 2.9% for Mn(IV) oxides. These estimates are substantially larger than the ESDs obtained from individual fits (which typically had values of ∼0.5%). Phase and amplitude files for the EXAFS fitting were created with FEFF7 [8]. Mn EXAFS were fit using a model based on a layered phyllomanganate structure [6], which follows the concept used previously by Ressler *et al.* [9] and explicitly accounts for splitting of the Mn-O and Mn-Mn distances in the structure due to Jahn-Teller distortions, angular deviations from planar sheets (particularly important with Mn-Mn multiple scattering), aqueous and spore-bound Mn(II), Mn bound to the surfaces of Mn oxides, and vacancies present in the manganese octahedral layer. This model has been tested on relevant model spectra (birnessite, δ-MnO_2, and

*e-mail: bargar@ssrl.slac.stanford.edu

todorokite) and found to fit the EXAFS up to $R + \mathrm{SR} \sim 5.5$ Å for samples with good data up to k of 15 Å^{-1}.

X-ray diffraction intensity data were collected on wet solids in transmission geometry using the two-circle diffractometer on SSRL beamline 2-1 using a Bicron NaI detector equipped with Soller slits. The incident X-ray beam was tuned to 10 keV ($\lambda = 1.24$ Å) to improve beam penetration in to the wet samples and to provide Q-space access up to about 15 Å^{-1}. Wet sample slurries were placed in an aluminum sample cell with lexan windows. The diffractometer was calibrated with LaB_6 and has a 0.04° 2θ fwhm resolution. Data were collected in Q-space 0.004 Å^{-1}intervals in dose mode of 10,000 counts per point. Several scans were added together to improve signal to noise ratios for interesting regions.

3. Results and Discussion

Results from linear combination fits to Mn K-edge XANES spectra are summarized in Figure 1. Only Mn(II) (intracellular Mn(II) in clean spores) and δ-MnO_2 spectra were required to fit all sample spectra. Mn(III)-bearing phyllomanganates (birnessite, todorokite) were attempted as components in fits, but the amplitude of these components floated to zero during fitting. In addition, the edge intensity maximum (*i.e.*, the "white line") occurs at the same energy as obtained in δ-MnO_2. These observations suggest that the manganese local structure is similar to that in δ-MnO_2 (*i.e.*, a defected phyllomangante structure [10]) with an oxidation state close to Mn(IV). The proportion of δ-MnO_2 in the samples reaches 100% within 80 hours of reaction. This apparent oxidation rate is faster than obtained in 50 mM NaCl solution [4, 6]. The faster rate can be attributed to the presence of Ca^{2+}, which enhances the activity of the manganese-oxidizing enzyme [4].

The XRD intensity data for the 12 and 80 hour samples is shown in Figure 2. Prominent in the pattern are a 10.0 Å basal plane (001) reflection and a 5 Å (002) reflection. The presence of these reflections suggests the oxide to be a phyllomanganate, while the broad peaks indicate a very small particle size in the c stacking direction [11]. A basal plane spacing of 10.0 Å has previously been reported for a calcium-substituted phyllomanganate (*i.e.*, "Ca buserite") [12], for which Ca^{2+} was bound at interlayer sites.

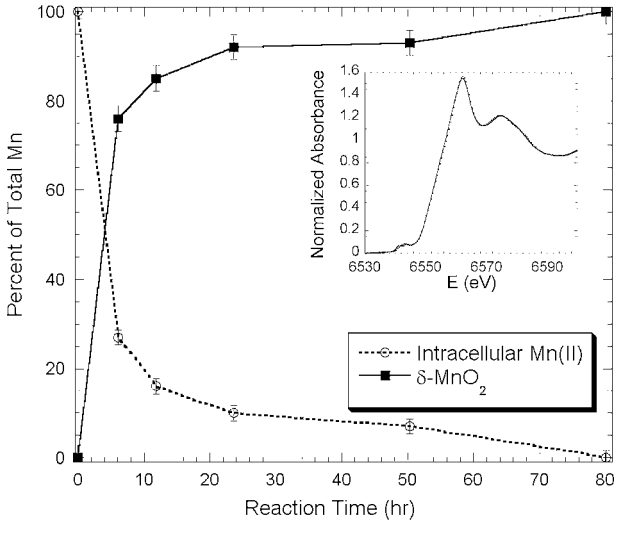

Fig. 1. Mn K-edge XANES fit results for spore-biooxide samples. Inset gives fit (solid line) to the 80 hr sample spectrum (dotted line).

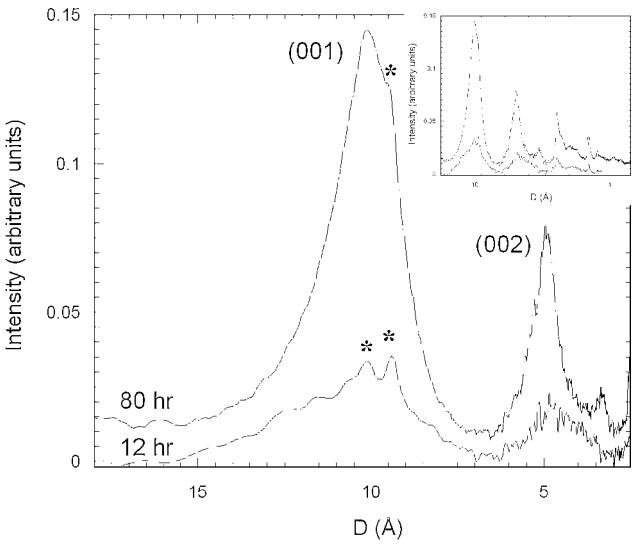

Fig. 2. X-ray diffraction intensity data for the 12 hr (bottom) and 80 hr (top) spore-biooxide samples. Inset gives the entire data range. *This peak/shoulder is from an unidentified trace compound in the spores.

Table I. *Summary of model parameters from the Mn K-edge EXAFS fitting results for the 6 and 80 hr spore-Mn(II) incubation samples. * Describes the fraction of the total Mn sites in the manganese octahedral layer that are unoccupied. † Describes the out-of-plane bend of the manganese octahedral layer in the direction parallel to the a axis. ‡ Describes the out-of-plane bend of the manganese octahedral layer in the direction parallel to the b axis.*

Sample	Vacancies (%)*	Out-of-plane bend angle (a-axis)†	Out-of-plane bend angle (b-axis)‡
6 hr	14	5°	0°
80 hr	12	10°	0°
todorokite	40	6°	19°
δ-MnO_2	23	0°	0°
birnessite	23	15°	0°

Biogenic mangese oxides prepared in the absence of dissolved Ca(II) (*i.e.*, in 50 mM NaCl solutions [4, 6]) did not exhibit any 10 Å basal plane reflections. The correlation between the 10 Å basal plane reflection in the sample XRD patterns and the presence of calcium suggests that the 10 Å stacking structure of the biooxide prepared in SW is controlled by incorporation of Ca^{2+} at interlayer sites.

Major details of the EXAFS fits to the 6 and 80 hour samples are summarized in Table I and fits are shown in Figure 3. We focus our discussion here on parameters specific to the linear multiple scattering Mn-Mn-Mn path in the manganese octahedral sheet, which has an effective scattering distance of about 5.5 Å. The amplitude of the linear multiple scattering feature is sensitive to bending of the manganese octahedral layer (*i.e.*, non-linear Mn-Mn-Mn angles) and to manganese site vacancies, both of which reduce multiple scattering intensity [9]. Fit-derived parameters for out-of-plane bend and manganese layer site vacancies are therefore a sensitive metric for comparing structures to one another and to triclinic birnessite, a phyllomanganate, and todorokite, a 3 × 3 tunnel-structure tektomanganate [11]. Todorokite has apparently high out-of-plane bend and relatively large vacancies due to the fact that it does not have continuous

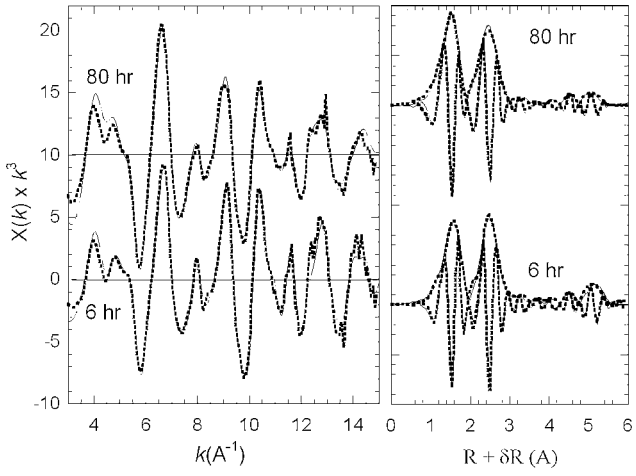

Fig. 3. EXAFS spectra and Fourier transforms (magnitude and imaginary component) (dotted lines) and fits (solid lines) to the 6 and 80 hour samples.

manganese octahedral layers. We refer the reader to Ressler *et al.* [9] for a detailed discussion of this model concept.

A summary of these fitted EXAFS parameters for the samples is provided in Table I. The octahedral layers in the biooxides (out-of-plane angles of 0° to 10°) less rumpled than in birnessite (0° to 15°) or todorokite (6° to 19°). The biooxides have a lower concentration of layer vacancies (12–14%) than δ-MnO_2, birnessite, or todorokite (23–40%). Vacancy values have a strong inverse correlation to particle size (*i.e.*, edge vacancies) for very small particle sizes. Thus a lower apparent vacancy concentration suggests larger particle sizes in addition to highly occupied layer structures.

4. Conclusions

Manganese biooxides are rapidly produced in sea water by reaction of Mn(II) with spores of the marine *Bacillus* sp., strain SG-1. XANES and EXAFS spectra and XRD intensity data indicate that the primary biogenic oxides are finely particulate phyllomanganates having a 10 Å basal plane spacing. Comparison of the present results to previously reported lattice constants for calcium-substituted phyllomanganates and to XRD data reported for biooxides produced in the absence of dissolved Ca^{2+} suggests that Ca^{2+} binds in the interlayers of the 10 Å biooxides. No other solid phase is identified in the samples over the time scale examined. EXAFS fits indicate that the biooxides have relatively high manganese octahedral layer site occupancies in comparison to other phyllomangantes (birnessite and δ-MnO_2) and only moderate out-of-plane bending of the octahedral layer.

Bacterial oxidation of Mn(II) by SG-1 spores generally does not require net consumption of calcium relative to Mn(II) and calcium is therefore not required to be present in the biooxides. SG-1 spores readily oxidize Mn(II) in calcium-free solutions to produce poorly crystalline δ-MnO_2-like biooxides with no basal plane reflections [4, 13]. Therefore, it is interesting that the primary biogenic product identified in the present study appears to contain calcium. This observation implies that calcium is acquired by the biooxide structure after completion of the enzymatic oxidation process.

Bacillus sp., strain SG-1 is a marine bacterium and a good general model for microbial manganese oxidizers. It is therefore likely that the 10 Å biooxide observed in this study could be one of the most abundant manganese oxides in the oceanic water column.

Acknowledgement

We would like to thank Apurva Mehta and Jeff Post for their many helpful discussions and advice. Portions of this research were carried out at the Stanford Synchrotron Radiation Laboratory, a national user facility operated by Stanford University on behalf of the U.S. Department of Energy, Office of Basic Energy Sciences. The SSRL Structural Molecular Biology Program is supported by the Department of Energy, Office of Biological and Environmental Research, and by the National Institutes of Health, National Center for Research Resources, Biomedical Technology Program. This work was supported by NSF grants to BMT/JRB (EAR-9725845 and CHE-0089208) and BMT (MCB-9808915).

References

1. Tebo, B. M., Nealson, K. H., Emerson, S. and Jacobs, L., Limnol. Oceanogr. **29**, 1247 (1984).
2. Tebo, B. M., Deep-Sea Res. **38**, S883 (1991).
3. Marble, J. C., Corley, T. L., Conklin, M. H. and Fuller, C. C., "Environmental factors affecting oxidation of manganese in Pinal Creek, Arizona," in Water-Resour. Invest. Rep. 99-4018A, (edited by D. W. Morganwalp and H. T. Buxton), (US Geological Survey, West Trenton, NJ, 1999), pp. 173–183.
4. Tebo, B. M., Bargar, J. R. and Webb, S. M., "Bacterial Manganese Oxide Mineral formation," Invited talk presented at the 223rd ACS National Meeting, April 7–11, 2002, Orlando, FL, (2002).
5. Bargar, J. R., Tebo, B. M. and Villinski, J. E., Geochim. Cosmochim. Acta **64**, 2737 (2000).
6. Webb, S. M., Bargar, J. R. and Tebo, B. M., "Synchrotron-Based Studies of Manganese Oxide Biomineralization.," in Eos Trans. AGU, 83(47) Suppliement of the Fall Meeting, December 6–10, 2002. (American Geophysical Union, San Francisco, 2002), Vol. 83(47), pp. V51A–1227.
7. Webb, S. M., "SIXPACK: a graphical user interface for XAS analysis using IFEFFIT," Physica Scripta, (in press).
8. Rehr, J. J., Zabinsky, S. I. and Albers, R. C., Phys. Rev. Lett. **69**, 3397 (1992).
9. Ressler, T., Brock, S. L., Wong, J. and Suib, S. L., J. Phys. Chem. B **103**, 6407 (1999).
10. Villalobos, M., Bargar, J. and Sposito, G., "Characterization of the Manganese Oxide Produced by Pseudomonas putida strain MnB1," Geochim. Cosmochim. Acta, **67**, 2649 (2003).
11. Burns, R. G. and Burns, V. M., "Manganese oxides," in "Marine Minerals", (edited by R. G. Burns), (Mineralogical Society of America, 1979), pp. 1–46.
12. Kuma, K. *et al*., Mineral. Magn. **58**, 425 (1994).
13. Tebo, B. M. *et al*., "Bacterially Mediated Mineral Formation: Insights into Manganese(II) Oxidation from Molecular Genetic and Biochemical Studies. Reviews in Mineralogy Volume 35," in Geomicrobiology: Interactions Between Microbes anbd Minerals, (edited by J. F. Banfield and K. H. Nealson), (Mineralogical Society of America, Washington, D.C., 1997), pp. 448.

Physica Scripta. Vol. T115, 891–893, 2005

Investigating Actinide Molecular Adducts from Absorption Edge Spectroscopy

C. Den Auwer[1*], S. D. Conradson[2], P. Guilbaud[1], P. Moisy[1], J. Mustre de Leon[3] and E. Simoni[4]

[1]CEA Marcoule DEN, 30207 Bagnols-sur-Cèze Cedex, France
[2]Los Alamos Nat. Lab., MST Division, Los Alamos, NM 87545, USA
[3]CINVESTAV Merida, Merida AP73 cordemex, CP 97310, Mexico
[4]Université Paris Sud, IPN, 91405 Orsay Cedex, France

Received June 26, 2003; accepted in revised form November 4, 2003

PACS number: 87.64.Fb

Abstract

Although Absorption Edge Spectroscopy has been widely applied to the speciation of actinide elements, specifically at the L_{III} edge, understanding and interpretation of actinide edge spectra are not complete. In that sense, semi-quantitative analysis is scarce. In this paper, different aspects of edge simulation are presented, including semi-quantitative approaches. Comparison is made between various actinyl (U, Np) aquo or hydroxy compounds. An excursion into transition metal osmium chemistry allows us to compare the structurally related osmyl and uranyl hydroxides. The edge shape and characteristic features are discussed within the multiple scattering picture and the role of the first coordination sphere as well as contributions from the water solvent are described.

1. Introduction

X-ray Absorption Near Edge Spectroscopy has long been used in a phenomenological approach as a fingerprint of the absorbing atom polyhedron geometry and electronic state. This approach is particularly useful to gather structural information when EXAFS data are not possible to collect. In some cases, the edge spectrum can also be informative about the spin density or central atom formal or effective charge. Many works have aimed at simulating and better understanding the edge features, especially in the case where the absorbing atom is a transition metal. Both phenomenological and *ab initio* approaches have been used in order to identify the edge features.

It is well beyond the scope of this paper to detail all the work that has been achieved in this area and in the present paper the authors intend to focus on the analysis of the absorption edge of actinide cations within actinyl molecular adducts. Because most of the early actinide cations (except Th) with oxidation states higher than IV form the actinyl AnO_2^{n+} ($n = 1, 2$) transdioxo entity, they are of technological and environmental importance [1]. Furthermore, the ubiquity of the uranyl cation in the geosphere, because of its remarkable stability, makes it one of the most extensively investigated cations within the actinide family. The major characteristic of actinyl cations is the occurrence of quasi linear O-An-O units with a short An-O multiple bond ranging from 1.7 to 1.9 Å in length, depending on the cation. This characteristic is also specific to the actinide family as only one analogue (the osmyl cation OsO_2^{2+}) is stable in the d block [2]. This is a good evidence of this specific type of bonding which involves significant participation of the 5f and 6d orbitals in the valence orbitals of the AnO_2^{n+} unit [3–6].

According to the selection rules associated with the dipolar transition of the absorption process, several final states can be probed in the case of actinides. Going from high to low energy (or from low to high primary quantum number of the initial state), L_I ($2s^27p^0 - 2s^27p^1$ transition at c.a. 21760 eV for U) or L_{III} edges ($2p^66d^0 - 2p^56d^1$ transition at c.a. 16730 eV for U) are particularly informative about the geometrical arrangement of the coordination sphere because of strong multiple scattering features [7, 8]; the M_{III} edge ($3p^66d^0 - 3p^56d^1$ transition at c.a. 4300 eV for U) shows the same features as the L_{III} edge with a reduced core hole life time broadening; $M_{IV,V}$ or $O_{IV,V}$ edges ($3,5d^{10}5f^n - 3,5d^95f^{n+1}$ transition at c.a. 3700 eV and 100 eV for U) allow one to probe directly the 5f states of the cation [9, 10]. In the search for a better understanding of the bonding properties of the actinyl cation with its ligands, a complementary analysis of the various absorption edges is needed, assuming that the technical experimental conditions related to actinide studies are met.

2. Experimental

Part of the experimental conditions related to either sample preparation or data acquisition have already been reported in the literature and will be referenced in the course of the article. For the osmium samples OsO_4(aq) (0.16 M) was prepared from solid OsO_4 (Acros Inc.) in KOH (1.6 M) solution. $OsO_2(OH)_4K_2$ was prepared from the above solution with addition of 0.5 ml of ethanol. A pink-red precipitate appeared readily. RAMAN spectra (not shown) were recorded for sample characterization. Os XANES spectra were recorded at the LURE facility (DCI ring) on the D44 experimental station using a double crystal Si(111) monochromator (calibration at the L_{III} edge of W). Spectra were recorded in transmission mode with air filled ion chambers.

XANES simulations were performed with versions .1 and .2 of the Feff8 code [11, 12]. All the simulations were performed with similar parameters using self consistentcy, full multiple scattering or path expansion (XANES 6 0.07 0.5; SCF x 0 30 0.05 10; FMS y 0; FOLP 0 1.15; UNFREEZEF; EXCHANGE 0 0 1) where x is the cluster size taken into account in the SCF loop and y is the cluster size taken into account in the FMS procedure. Clusters used for simulation were $UO_2(O)_4$ for solid state uranyl hydroxide; $OsO_2(O)_4$ for solid state osmyl hydroxide; $[OsO_4]_5$ for osmium tetra oxide in aqueous solution from crystallographic data [13]; $NpO_2(O)_4$ and $NpO_2(OH)_4$ for neptunyl hydroxide in aqueous solution in a 20 Å water box from molecular dynamics simulation.

Molecular dynamics simulations of neptunyl hydroxide in aqueous solution (AMBER6) have been carried out from the starting NpO_2O_4 cluster (fixed geometry). Optimization of the

*e-mail: christophe.denauwer@cea.fr

hydrogen atoms to complete the Np coordination sphere as well as the water molecules in a 20 Å box has been carried out. Note that for the Feff simulations, only one snapshot of the molecular dynamics simulation has been considered.

3. The edge spectrum as a fingerprint of the actinyl polyhedron

At the starting point of this investigation we have noticed the structural similarities between the uranyl cation and the osmyl cation (both at formal oxidation state VI) in their solid state hydroxide form. Both compounds exhibit two short axial M-O bonds in agreement with the "yl" structure and larger equatorial M-L bonds. In the case of $UO_2(OH)_2$ (Schoepite) and $OsO_2(OH)_4K_2$, 4 oxygen atoms are present in the equatorial plane (distorted in the case of Schoepite [14]). The EXAFS data fitting has given the following structural parameters : uranyl 2 O @ 1.76 Å, 2 O @ 2.31 Å, 2 O @ 2.47 Å in agreement with the literature [15]; osmyl 2 O @ 1.75 Å, 4 O @ 2.02 Å. It is now well known that all the actinyl adducts exhibit a characteristic high energy shoulder at the L_{III} edge (at c.a. 15 eV above the white line, depending on the distances [16]). This shoulder as been identified using multiple scattering theory as the sum of multiple scattering paths within the linear transdioxo unit O-An-O. Figure 1 compares the experimental absorption edges of solid state $UO_2(OH)_2$ [17] and $OsO_2(OH)_4K_2$ with the corresponding simulated spectra. The difference in intensity and sharpness between the two white lines A and A′ can be attributed to two factors : the core hole life time difference between uranium (7.4 eV [18]) and osmium (5.2 eV [18]) plus the localization effect of the 6d (uranium) or 5d (osmium) states. From a path expansion analysis, feature B (and B′) has been attributed to the transdioxo unit O-Os-O, and feature C to the triangular Os-O_{ax}-O_{eq} paths (which is 8 time degenerated within the square planar geometry around Os). The agreement between the experiment and the simulation is better in the case of uranyl than of osmyl. This is not yet fully understood. The difficulty might arise from the high symmetry of the osmyl coordination that leads to numerous scattering paths with only slight differences in scattering length (4-leg paths O-Os-O = 3.5 Å; 3-leg paths Os-O_{ax}-O_{eq} = 3.2 Å).

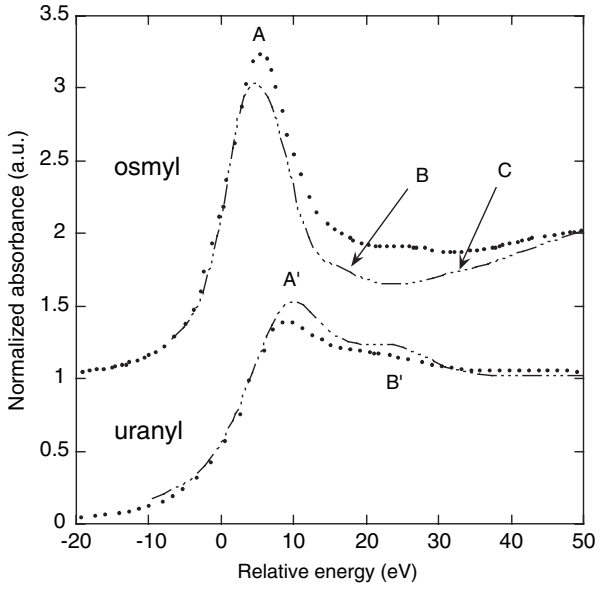

Fig. 1. Experimental (● ● ●) and simulated (—● ● ●—) (feff8.2, $x = y = 2.6$ Å) L_{III} edges of solid state $UO_2(OH)_2$ (uranyl) and $OsO_2(OH)_4K_2$ (osmyl). The experimental and simulated spectra have been shifted in energy with respect to their inflexion point value.

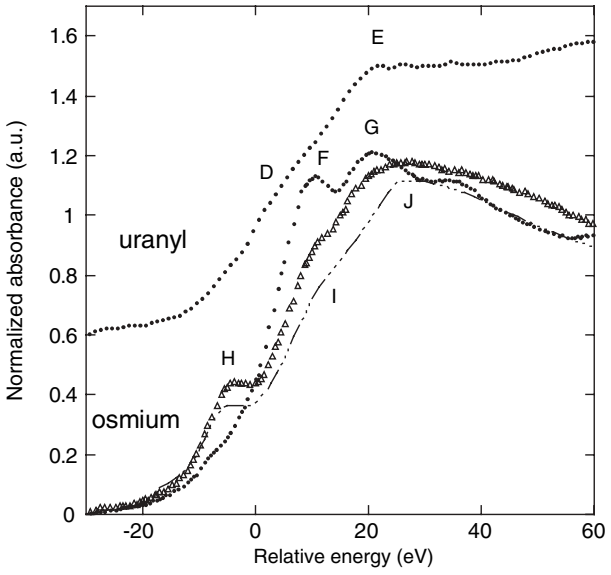

Fig. 2. Experimental L_I edges of OsO_4 in aqeous solution (ΔΔΔ), solid state $OsO_2(OH)_4K_2$ (● ● ●) and $UO_2(NO_3)_2.6H_2$ (● ● ●). Comparison is made with the simulation of OsO_4 (—● ● ●—) (feff8.2, $x = y = 3.5$ Å). The experimental and simulated spectra have been shifted in energy with respect to their inflexion point value.

At the L_I edge (see Fig. 2) the white line intensity is dramatically reduced. In the case of solid state uranyl nitrate, features D and E have been attributed respectively to the scattering contributions from the axial oxygens and from the equatorial oxygens [8]. For osmyl hydroxide, the absorption edge exhibits much sharper features F and G. To date, the simulation of this edge within a path expansion formalism has failed and features F and G have not been described. At the oxidation state VIII, osmium tetra oxide in aqueous solution is a slightly distorted tetrahedron by comparison with the solid state structure [13] (Raman spectra and EXAFS fitting have confirmed the structural similarity) with Os-O distances around 1.71 Å. The L_I edge of OsO_4 in aqueous solution exhibits the well known pre-edge feature attributed within the molecular orbital picture to a transition to the allowed hybridized 5d-6p manifold [19]. Within the multiple scattering picture, feature H (Fig. 2) can be built from constructive 3-leg (triangular Os-O-O′) and 4-leg (Os-O-Os-O) scattering paths (10 paths) within the tetrahedron, and feature I can be identified as arising from 3-leg paths (9 paths) including the oxygen atoms of vicinal tetrahedrons. With this procedure, a total of 27 paths is needed to reproduce the full multiple scattering calculation.

In aqueous solution, simulation of the actinyl absorption edge using a simple model cluster often lacks the influence of the solvent molecules. Similar to the osmyl coordination sphere in the solid state, the neptunyl(VI) polyhedron in basic aqueous medium [20] is composed of 2 axial oxygens at 1.82 Å and 4 O at 2.21 Å [21]. Comparison between Figures 1 and 3 shows that the position of the high energy shoulder B depends on the cluster geometry [16]. The intensity of white line A is poorly reproduced in the simulation when only 7 atoms are considered in the cluster ($x = y = 2.5$ Å) : $NpO_2(O)_4$. In order to position the hydrogen atoms around each oxygen of the 4 OH ligands as well as water molecules to mimic the solvent medium, a molecular dynamics calculation has been carried out, starting

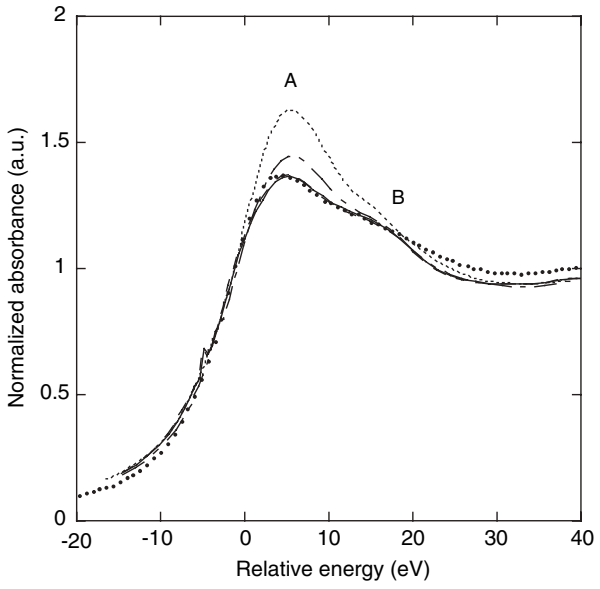

Fig. 3. Experimental (• • •) L_{III} edge of neptunyl hydroxide in aqueous solution compared to the simulation (feff8.1) of *i*) the $NpO_2(O)4$ cluster (· · · · · · · ·) ($x = y = 2.5$ Å); *ii*) the $NpO_2(O)_4$ cluster within a water box of 20 Å (— – —) ($x = y = 3.4$ Å); *iii*) the $NpO_2(OH)_4$ cluster within a water box of 20 Å (— —) ($x = 3.4$, $y = 2.5$ Å) and *iv*) the $NpO_2(OH)_4$ cluster within a water box of 20 Å (———) ($x = y = 3.4$ Å).

from $NpO_2(O)_4$. In a first step a better simulation of the edge was obtained when only the water solvent molecules were added around the 7 atom $NpO_2(O)_4$ moiety, up to 20 Å ($x = y = 3.4$ Å). This suggests an improvement in the potential calculation due to continuity around the atoms included in the SCF loop. In a second step the 4 hydrogen atoms of the 4 hydroxy ligands were also included as a second coordination sphere. Definite satisfactory agreement between the experiment and the edge simulation was then achieved ($x = y = 3.4$ Å). The same result was obtained with the above cluster and only the $NpO_2(O)_4$ moiety included in the FMS routine ($x = 3.4$, $y = 2.5$ Å). This confirms the influence of the cluster size in the calculation of the potentials. Furthermore it suggests that the hydrogen atoms of the 4 OH ligands play no or a negligible role in the scattering process.

4. Conclusion

Within the multiple scattering picture, L_{III} edges of the actinyl adducts have been satisfactorily simulated. Consideration of the 5d transition metal series shows that the structurally related osmyl hydroxide compound exhibits a significantly different L_{III} edge. This is attributed to slight structural differences between osmyl and uranyl hydroxide, and differences in core hole life time and localization of the 5d *versus* 6d states. From the bipyramidal osmyl hydroxide to the tetrahedral osmium tetra oxide, the L_I pre-edge feature can be used as a fingerprint of the polyhedron geometry. In addition to the well known molecular interpretation of the pre-edge transition, it has been simulated within the multiple scattering picture.

As suggested by the simulation of neptunyl hydroxide in aqueous solution, inclusion of second coordination sphere atoms as well as solvent molecules is essential in order to obtain reliable potentials. Thus, inclusion of a tridimensional network around the $OsO_2(O)_4$ moiety should improve the simulation of the osmyl hydroxide compound. Finally, quantum chemical calculations are being carried out on both uranyl and osmyl hydroxide in order to compare the valence orbital properties and in particular the 5d and 6d states.

Acknowledgments

This research was mainly carried out at the Laboratoire d'Utilisation du Rayonnement Electromagnétique (Orsay, France) a national user facility operated by CEA/CNRS/MR and the Stanford Synchrotron Radiation Laboratory (Stanford, USA), a national user facility operated by Stanford University on behalf of the U.S. Department of Energy, Office of Basic Energy Sciences. This work has been financially supported by CEA/DEN, PRACTIS (France) and by DOE OBES Division of Chemical Sciences under Contract W-7405 (USA).

References

1. Hennig, C. *et al*., J. Synchrotron Rad. **8**, 695 (2001).
2. Kaltsoyannis, N. and Scott, P., "The f elements", (Oxford Science Publisher, Zeneca 1999).
3. Hay, P. J., Martin, R. L. and Schreckenbach, G., J. Phys. Chem. A **104**, 6259 (2000).
4. Pyykkö, P., Laakkonen, L. J. and Tatsumi, K., Inorg. Chem. **28**, 1801 (1989).
5. Pepper, M. and Bursten. B., Chem. Rev. **91**, 719 (1991).
6. Denning, R. G., "Structure and Bonding", (Springer Verlag, Germany 1992), Vol. 79, 217.
7. Hudson, E. A., Rehr, J. J. and Bucher, J. J., Phys. Rev. B **52**, 13815 (1995).
8. Hudson, E. A., Allen, P. G., Terminello, L. J., Denecke, M. A. and Reich, T., Phys. Rev. B **54**, 156 (1996).
9. Den Auwer, C. *et al*., C. R. Acad. Sci. Paris, Série IIc **3**, 327 (2000).
10. Petiau, J. *et al*., Phys. Rev. B **34**, 7350 (1986).
11. Rehr, J. J. and Albers, R. C., Rev. Mod. Phys. **72**, 621 (2000).
12. Rehr, J. J. and Ankudinov, A. L., J. Elect. Spect. Related Phenom. **114–116**, 1115 (2001).
13. Krebs, B. and Hasse, K.-D., Acta Cryst. B **32**, 1334 (1976).
14. Taylor, J. C., Acta Cryst. B **27**, 1088 (1971).
15. Allen, P. G. *et al*., Radiochim. Acta **75**, 47 (1996).
16. Denecke, M. A., Proc. Workshop on Speciation, Techniques and facilities for Radioactive Materials at Sunchrotron Light Sources, OECD – NEA, 4–6 October, Grenoble, France (1998).
17. Jollivet, P., Den Auwer, C. and Simoni, E., J. Nucl. Mater. **301**, 142 (2002).
18. Kraus, M. O. and Oliver, J. H., J. Phys. Chem. Ref. Data **8**, 329 (1979).
19. Shadle, S. E., Hedman, B., Hodgson, K. O. and Solomon, E. I., J. Am. Chem. Soc. **117**, 2259 (1995).
20. Keogh, D. W., Clark, D. L. and Conradson, S. D., private communication.
21. Williams, C. W. *et al*., J. Am. Chem. Soc. **123**, 4346 (2001).

Physica Scripta. Vol. T115, 894–896, 2005

Combined XANES and EXAFS Study on the Bonding of Methyl Mercury to Thiol Groups in Soil and Aquatic Organic Matter

U. Skyllberg[1*], J. Qian[1,2] and W. Frech[2]

[1]Dept. of Forest Ecology, Swedish University of Agricultural Science, S-901 83 Umeå, Sweden
[2]Dept. of Chemistry, Umeå University, S-901 83 Umeå, Sweden

Received June 26, 2003; accepted December 17, 2003

PACS number: 6110 Ht

Abstract

We combined X-ray absorption near edge spectroscopy (XANES) and extended X-ray absorption fine structure (EXAFS) spectroscopy to determine the coordination chemistry of methyl mercury (CH_3Hg) in natural organic matter from an organic soil (OS), potentially soluble organic matter extracted from the soil (PSOS) and in a humic stream draining the soil (SOS). The sum of concentrations of highly reduced organic S groups (Org-S_{RED}), such as thiol (RSH), sulfide (RSR) and disulphide (RSSR) was 39, 42 and 47% of total S in SOS, PSOS and OS, respectively. No traces of inorganic sulfides were detected. Hg L_{III}-edge EXAFS analysis were determined on samples added CH_3Hg to yield CH_3Hg/Org-S_{RED} ratios in the range 0.01–1.62. At low ratios Hg was associated to one C atom (the methyl-group) at an average distance of 2.03 ± 0.02 Å and to one S atom at an average distance of 2.34 ± 0.03 Å, in the first coordination shell. At higher CH_3Hg/Org-S_{RED} ratios RSH groups were saturated and O and/or N atoms gradually took part in the bonding. Based on the assumption that RSH is the only S group accounting for the very strong complexation of CH_3Hg, approximately 17% of total organic S consisted of RSH groups in the organic soil, 14% in potentially soluble organic matter extracted from soil and 9% in aquatic organic matter.

1. Introduction

Mercury released into the atmosphere by combustion of fossil fuels may be long-range transported as $Hg^0(g)$. After oxidation to Hg^{2+}, mercury is deposited and partly transformed to methyl mercury (CH_3Hg) in wetlands and soils [1]. Subsequent accumulation of the highly bioavailable methyl mercury in organisms (e.g. fish) is a severe environmental problem in regions dominated by forest and wetlands [2, 3]. In order to understand mechanisms behind the formation and decomposition of methyl mercury, as well as how it is transported and made available for organisms in soils and waters, detailed information about the coordination chemistry of mercury and methyl mercury in natural organic matter (NOM) is crucial. We combined sulfur K-edge X-ray Absorption Near Edge Spectroscopy (K-XANES) and mercury L_{III}-edge Extended X-ray Absorption Fine Structure (L_{III}-EXAFS) spectroscopy in order to determine the coordination chemistry of methyl mercury in stream and soil NOM. Sulfur XANES was used to quantify the concentration of reduced sulfur groups (Org-S_{RED}). The same samples were added CH_3Hg to collect Hg EXAFS at varying Org-S_{RED}/CH_3Hg ratios.

2. Material and methods

2.1. *Organic soil and stream samples*

Organic samples were collected along a 2 m long "hydrological transect" situated in a 50 ha forested catchment at Svartberget Research Station, Vindeln, N Sweden. An organic peat soil (OS), potentially soluble organic substances from the organic soil (PSOS) and organic substances collected in a stream (SOS, stream organic substances) located 2 m away from the sampling point of the organic soil were sampled. pH in soil solution was 3.7 and in the stream 4.5. A soil sample was also collected from a fen peat (FP) of a sub-alpine environment, but within 5 km from the Atlantic Ocean, at Ifjord in northern Norway. This soil had a pH of 5.7 and a relatively high concentration of total sulfur (2.0%), as compared to samples from the hydrological transect. Soil samples were freeze-dried and homogenized by a tungsten carbide ball mill. Potentially soluble organic substances were gently extracted from OS and FP samples at pH 6 using a metal-chelating resin, and were thereafter flocculated by a minimal concentration of $Al(NO_3)_3$ [4]. Stream organics (19 mg organic C per liter) were collected from the Kallkällebäcken stream at Svartberget during spring flood (mid-May) when water moved through the organic soil close to the stream. A total of 48% of the organic carbon in the stream water was collected after flocculation by $Al(NO_3)_3$. Excess $Al(NO_3)_3$, and other salts, was removed by equilibrating the flocculate for 30 min in three portions of 100 ml distilled water. The SOS sample was freeze-dried and homogenized. XANES was determined on freeze-dried samples. Prior to the EXAFS study methyl mercury hydroxide, dissolved in a minimum of double-distilled water, was added to yield molar CH_3Hg/Org-S_{RED} ratios of 0.01–1.62 in the OS sample, 0.01–1.41 in PSOS, 0.01–1.19 in SOS and 0.30 in the FPOS sample. High-viscosity suspensions were mixed continuously for 7 days to reach equilibrium. OS, PSOS and SOS samples were freeze-dried and pellets were prepared 1–2 hours before each EXAFS experiment. For FPOS a newly prepared moist sample was used for EXAFS determination. Thiol (Amberlite GT73, Rohm and Haas) and carboxyl (Bio-Rex 70) resins added CH_3HgOH corresponding to 0.3 and 0.1% saturation of functional groups, were together with cinnabar (HgS-red, Merck) used as model compounds for EXAFS studies.

2.2. *XANES data collection and analysis*

Sulfur K-edge XANES data were collected on beamline X-19A at the National Synchrotron Light Source (NSLS) at Brookhaven National Laboratory (Upton, NY). Preparation and mounting of freeze-dried soil and stream organic samples is described in [4]. The energy was calibrated at 2482.5 eV with sodium sulfate. The energy drift between samples was corrected for by setting the energy of the sulfate peak to 10.0 eV above that of elemental S (2472.5 eV) [5]. All spectra were recorded in fluorescence mode using a Stern-Heald ionization detector filled with He gas [6]. The monochromator was detuned 70% at the S K-edge in order to reduce fluorescence induced by high-order harmonics.

Each XANES spectrum, representing an average of 3 to 12 scans, was deconvoluted into pseudo-components using a least-square fitting procedure. A series of Gaussian peaks was used to represent the s → p transitions and two arctangent step functions

*e-mail: ulf.skyllberg@sek.slu.se

were used to represent the transition of ejected photoelectrons to the continuum. The energy position of the s → p peaks and their peak areas are used to identify the oxidation states of S and their percentage of total S, after correcting for the change in absorption cross section area with increasing oxidation state. For further details on the fitting procedure see [7]. Electronic oxidations states were calculated for quantified XANES peaks using the linear relationship between the white line energy maximum and electronic oxidation state, derived from S compounds with identical formal and electronic oxidations states [5, 7].

2.3. *EXAFS data collection and analysis*

EXAFS data for the FPOS were collected at the bending-magnet beam line (X11A) at the National Synchrotron Light Source, Brookhaven National Laboratory (NSLS, Upton, NY, USA). EXAFS data for all other samples were collected at the undulator beam line ID26 at the European Synchrotron Radiation Facility (ESRF, Grenoble, France). At NSLS we mounted a moist sample in a 1.5 mm-thick polycarbonate holder with Kapton-tape (CHR-Furon) windows. The Si(111) double-crystal monochromator was detuned by 10%. The detector was a Stern-Heald fluorescence ion chamber filled with Kr gas. The monochromator energy was calibrated by selenium (K-edge, 12658 eV). At ESRF freeze-dried samples were mounted without any tape windows. A Cr-coated Si mirror allowed removing the high-energy harmonics from the incident X-ray beam. A cryogenically cooled fixed-exit double-crystal monochromator with Si(111) was used. The fluorescence signal was detected with a silicon photodiode and a Ga filter was installed between the sample and the detector to reduce the scattering radiation. The monochromator energy was calibrated at the Hg L_{III}-edge (12284 eV) using HgO (s).

An EXAFS spectrum represents the merged results of 4 to 10 scans. Details about data reduction and procedures used for fitting of the EXAFS spectra are found in [8]. Theoretical EXAFS scattering curves and parameters for first shell Hg−S, Hg−O and Hg−C bonding were generated by the FEFF-7 computer program [9]. Theoretical structural parameters for Hg−S, Hg−O and Hg−C bonds in organo-mercury compounds [10] were used as input for FEFF calculations. The accuracy of these was confirmed by fits of cinnabar (red HgS) compared with its theoretical structure and by model compounds with C−Hg−S coordination in thiol resin and with C−Hg−O coordination in carboxyl resin.

3. Results

Figure 1 shows the S XANES spectrum for the fen peat soil. In the raw data spectrum, two large peaks appear: the left one is represented by reduced sulfur and the right peak represents oxidized sulfur. The two peaks with highest oxidation states (electronic oxidation state 5.0 and 6.0) represent sulfonates and sulfate-esters, respectively. The peak designated Org-S_{RED} has an electronic oxidation state of 0.2 and represents sulfur functionalities of importance for trace metal binding. This peak represents the sum of organic poly- and disulfides (RSSR), organic sulfides (RSR) and thiols (RSH). In the OS, PSOS and SOS samples 47, 42 and 39% of total S was represented by Org-S_{RED}. The FP and FPOS samples contained 64 and 27% Org-S_{RED} of total S. No traces of inorganic S species (e.g. FeS, FeS_2) were detected in any of the samples. This means that total S (S_{TOT}) in these samples is a measure of total organic S.

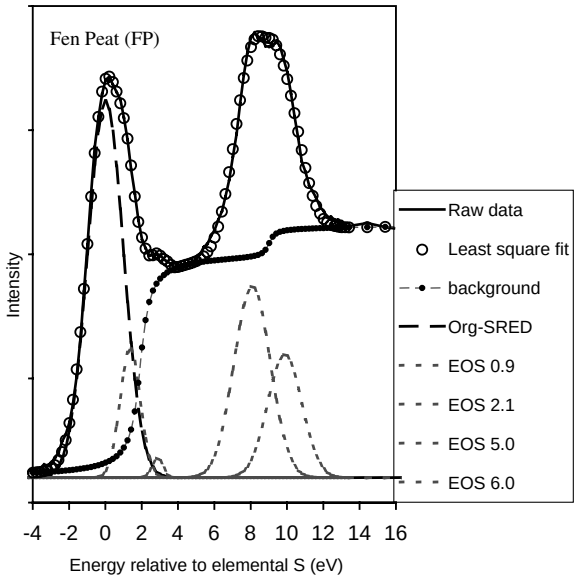

Fig. 1. Sulfur K-edge XANES spectrum for the FP sample. The *x*-axis is normalized to the K edge of elemental S (2 472 eV). Six Gaussian distribution peaks were found to be significant in the fit of the raw data. Electronic oxidation states (EOS) are given for each peak. The peak representing reduced organic S (Org-S_{RED}) has an EOS of 0.2 and made up 64% of total S in this sample.

In Fig. 2 Fourier-transformed Hg-EXAFS spectra for the FPOS sample and the OS (soil), PSOS and SOS (stream) samples are illustrated together with EXAFS spectra for two model compounds. The two peaks of the thiol (RSH) resin reflect a C−Hg bond (within the methyl mercury molecule) at 1.6 Å (corresponding to a bond length of 2.03 ± 0.02 Å) and an Hg−S bond at 2.0 Å (corresponding to a bond length of 2.34 ± 0.03 Å). A similar RSF for the FPOS suggests that CH_3Hg forms a

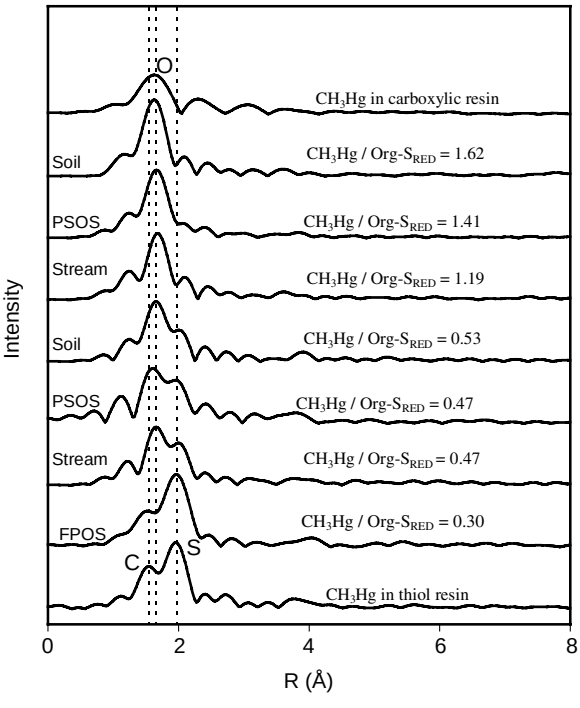

Fig. 2. Stacked, Fourier transformed EXAFS spectra for OS, PSOS, SOS and FPOS samples added methyl mercury to give different CH_3Hg/Org-S_{RED} molar ratios. As references spectra for a carboxyl resin (top) and a thiol resin (bottom), both added methyl mercury, are given. Spectra were not corrected for phase shift.

Table I. *Concentrations of methyl mercury, added to OS, PSOS and SOS samples used in EXAFS experiments, total organic S and reduced organic S determined by S XANES. Coordination numbers (CN) for S and O/N ligands determined after fitting CH_3Hg EXAFS data and calculated concentrations of RSH functionalities using equation (1).*

Sample	$[CH_3Hg]$	Org-S_{TOT}	Org-S_{RED}	CN_S	$CN_{O/N}$	[RSH] eq. (1)	[RSH]/Org-S_{TOT}	[RSH]/Org-S_{RED}
	-------- mmol kg^{-1} ----------					mmol kg^{-1}		
OS (0.53)	31	128	59	0.83	0.54	19	0.15	0.33
OS (1.08)	64	128	59	0.66	0.88	27	0.21	0.46
OS (1.62)	96	128	59	0.27	1.18	18	0.14	0.31
$OS_{average}$							0.17 ± 0.04	0.37 ± 0.08
PSOS (0.47)	32	162	69	0.65	0.56	17	0.11	0.26
PSOS (0.95)	65	162	69	0.53	0.72	28	0.17	0.40
PSOS (1.41)	97	162	69	0.30	1.10	21	0.13	0.30
$PSOS_{average}$							0.14 ± 0.03	0.32 ± 0.07
SOS (0.47)	23	131	50	0.85	0.60	13	0.10	0.27
SOS (1.19)	59	131	50	0.24	1.09	11	0.08	0.22
$SOS_{average}$							0.09 ± 0.01	0.24 ± 0.04

monovalent bond with RS^- groups in this sample. Above a certain CH_3Hg/Org-S_{RED} ratio, also oxygen (and possibly nitrogen, which cannot be separated from oxygen by EXAFS) functional groups take part in the bonding, due to a saturation of RSH groups. This is illustrated by a decrease of the shoulder at 2.0 Å, while the peak at 1.6 Å is broadened and slightly shifted to 1.7 Å for the OS, PSOS and SOS samples with CH_3Hg/Org-S_{RED} ratios of 0.47 to 0.53. For these samples the RSF represents a mixture of Hg−S and Hg−O/N bonds. In the samples with a CH_3Hg/Org-S_{RED} molar ratio of 1.19–1.62 the binding to O/N completely overrules the contribution from Hg−S and the RSF of these samples is quite similar to the RSF of methyl mercury bound to the carboxyl resin. The peak at 1.7 Å represents a mixture of C−Hg and Hg−O bonds, the latter having a bond length of 2.09 ± 0.01 Å. Exact coordination numbers and bond lengths were determined by fitting of EXAFS data in *k*-space (not shown here). All fits are reported in [8], and some CN's are given in table I.

Based on the assumption that methyl mercury forms monodentate bonds to RSH groups, thus not involving other S functionalities, and that all RSH groups will be saturated before any O/N sites become involved in the binding, EXAFS data could be used to calculate the concentration of RSH functional groups in OS, PSOS and SOC samples. For this purpose we used equation (1):

$$[RSH] = CN_S/(CN_S + CN_{O/N}) \times [CH_3Hg]. \quad (1)$$

CN_S and $CN_{O/N}$ are coordination numbers of sulfur and oxygen/nitrogen atoms in the first coordination shell and [ ] denote concentrations in mol kg^{-1}. Only samples added CH_3Hg exceeding the capacity of RSH were be used in the calculation of [RSH].

In table I calculated concentrations of RSH are related to concentrations of S_{TOT} and org-S_{RED} determined by XANES. It can be concluded that RSH contributed to less than 22% of total (in this case also organic) S and less than 38% of reduced organic S. An interesting observation is that the concentration of RSH seems to be highest in the soil, intermediate in potentially soluble organic matter from the soil and lowest in the stream. It should be noted that even if the pH at which EXAFS data were collected (3.8–4.0) was 6 orders of magnitude below the pKa of RSH, the concentration of protonated RSH groups still would be very small at the point O/N sites will be involved in the complexation of CH_3Hg. This is explained by the fact that the log k_1 for the binding of CH_3Hg to O/N sites is at least 8–9 orders of magnitude less than for RSH [4].

4. Conclusions

1) Only thiol groups (RSH) seems to be involved in the bonding of methyl mercury in oxidized soils and humic streams. Oxygen and nitrogen functionalities are involved only after saturation of RSH sites.
2) Between 24 and 37% of reduced organic S (likely representing the sum of RSH, RSSH, RSR and RSSR), as determined by S XANES, was represented by thiol groups (RSH) an organic soil, extracted organic substances from the soil and organic substances in the humic stream draining the soil.

Acknowledgment

Funding was provided by the Swedish Natural Science Research Council, Centre of Environmental Research, Umeå, Sweden and European Synchrotron Radiation Facility (exp. ME-64).

References

1. St. Louis, V. L., *et al*., Can. J. Fish. Aquat. Sci. **51**, 1065 (1994).
2. Hurley, J. P., *et al*., Environ. Sci. Technol. **29**, 1867 (1995).
3. Zillioux, E. J., Porcella, D. B. and Benoit, J. M., Environ. Toxicol. Chem. **12**, 2245 (1993).
4. Skyllberg, U., Qian, J., Frech, W., Xia, K. and Bleam, W. F., Biogeochem. In Press. (2003).
5. Waldo, G. S., Carlson, R. M. K., Moldowan, J. M., Peters, K. E. and Penner-Hahn, J. E., Geochim. Cosmochim. Acta. **55**, 801 (1991).
6. Lytle, F. W., *et al*., Nucl. Instr. Meth. Phys. Res. **226**, 542 (1984).
7. Xia, K., *et al*., Soil Sci. Soc. Am. J. **62**, 1240 (1998).
8. Qian, J., *et al*., Geochim. Cosmochim. Acta **66**, 3873 (2002).
9. Rehr, J. J., Booth, C. H., Bridges, F. and Zabinsky, S. I., Phys. Rev. B **49**, 12347 (1994).
10. Holloway, C. E. and Melnik, M., J. Organometal. Chem. **495**, 1 (1995).

Physica Scripta. Vol. T115, 897–900, 2005

XAFS Study on the Trace Amounts of Ytterbium Ions Incorporated in Calcium Carbonate Crystal

H. Tsuno[1*], H. Kagi[2], Y. Takahashi[3], T. Akagi[4] and M. Nomura[5]

[1]Institute for Environmental Management Technology, National Institute of Advanced Industrial Science and Technology (AIST), AIST Tsukuba West, Tsukuba 305-8569, Japan
[2]Graduate School of Science, The University of Tokyo, Tokyo 113-0033, Japan
[3]Graduate School of Science, Hiroshima University, Hiroshima 739-8526, Japan
[4]Faculty of Agriculture, Tokyo University of Agriculture and Technology, Tokyo 183-8509, Japan
[5]Photon Factory, Institute of Materials Structure Science, KEK, Tsukuba 305-0801, Japan

Received June 26, 2003; accepted in revised form November 4, 2003

PACS numbers: 61.10.Ht, 91.65.Nd

Abstract

We measured XAFS spectra of trace amount of ytterbium (Yb) incorporated in calcite, a stable phase of calcium carbonate. Calcium carbonate was precipitated from a mixed solution of $CaCl_2$ aq and $NaHCO_3$ aq with a given amount of $YbCl_3$. Concentrations of Yb were 5 μmol kg^{-1} in the starting solutions and Yb/Ca molar ratio in the precipitated calcium carbonate was 1.2×10^{-3}. Ytterbium L_{III}-edge XAFS spectra were collected in the fluorescence mode at the beamline BL-12C of the KEK-PF. Analysis of the XAFS results indicated, (1) Approximately 15% Yb ion existed as divalent ions in the calcite. (2) Yb^{3+}, major Yb species in the calcite, is located at the Ca^{2+} site in the calcite. The local structure around Yb^{3+} is significantly different from that of Ca^{2+}. The coordination number of Ca^{2+} in the crystal structure of calcite is 6 and Ca-O distance is 2.36 Å. In contrast, the nearest Yb-O coordination for Yb-doped calcite is split into two shells, the nearest 4 oxygen atoms and the second nearest 2 oxygen atoms, and their Yb-O distances are 2.24 Å and 2.77 Å, respectively. It was shown that localized structural relaxation occurred around Yb^{3+} which has smaller ionic radius than Ca^{2+}.

1. Introduction

Exploring the detailed chemical mechanism of dissolution and crystallization of calcium carbonate ($CaCO_3$) is one of the crucial issues in understanding the global cycling of CO_2 on the earth surface. Trace amount of rare earth elements (REEs) induces significant effects on the crystal growth and dissolution of calcium carbonate [1–4]. The substantial increase in the solubility of $CaCO_3$ [1, 2], the stabilization of the vaterite (labile phase of $CaCO_3$) [2, 4] and the inhibition of calcite growth [3] were caused by the addition of trace amount of lanthanum into the aqueous system. Furthermore, enrichment of REEs in calcium carbonate was shown by several studies [5, 6]. Very little is known about the uptake mechanism of REEs in calcium carbonate and their chemical state. X-ray absorption fine structure (XAFS) is practically the only method for the structural characterization of trace elements in solid materials [7]. XAFS in a fluorescence mode offers the advantage of element-discrimination and potentially high sensitivity to trace elements. In the present work, we investigated the chemical species of ytterbium incorporated in calcite and the local structure around it using X-ray absorption near-edge structure (XANES) and Extended X-ray absorption fine structure (EXAFS) techniques.

2. Experimental procedure

2.1. *Precipitation procedure*

Yb-doped calcium carbonate was prepared from a mixture of calcium chloride and sodium hydrogen carbonate solutions (30 mmol kg^{-1}, respectively) containing a given amount (5 μmol kg^{-1}) of ytterbium chloride. The experiments were conducted in a closed system in a surface-silanized glass vessel at 30°C. The starting solution was transferred into the vessel and immediately sealed with a silicone rubber stopper in which a pH electrode was embedded [2]. The amount of precipitate and ion activity products (IAP $= \gamma\ Ca^{2+}\ [Ca^{2+}] \times \gamma CO_3{}^{2-}\ [CO_3{}^{2-}]$) were calculated from the initial concentrations of all the chemical species in the system and pH at each sampling time after a previously reported method [1, 2]. The pH of solution changed from 7.8 at the beginning of reaction to 6.4 at the end of reaction. After standing for 1 day, the precipitate was filtered with a membrane filter with a pore size of 0.45 μm (Millipore® HAWP 024 00), rinsed with milli-Q water and dried at 110°C. Powder X-ray diffraction pattern indicated that the sample obtained was composed of calcite exclusively. The concentrations of Yb in the precipitates were determined by an inductively coupled plasma atomic emission spectrometer (ICPS-7000, Shimadzu Inc.). The concentrations of Yb in the synthesized calcite samples were about 1.1×10^{-3} in Yb/Ca molar ratio. $Yb(OH)_3$, $NaYb(CO_3)_2 \cdot n(H_2O)$, Yb_2O_3, $Yb_2(CO_3)_3 \cdot n(H_2O)$ powders and 5 mmol kg^{-1} $YbCl_3$ solution were used as standard materials of XANES measurements.

2.2. *XAFS spectroscopy*

XAFS spectra were collected in the fluorescence mode at the beamline BL-12C of the Photon Factory, High Energy Accelerator Research Organization (KEK-PF) in Tsukuba, Japan [8]. The KEK-PF storage ring was operated at 2.5 GeV with a maximum current of 450 mA. An Si(111) double-crystal monochromator was used to produce a monochromatic X-ray beam, with one crystal detuned for reduction of harmonics and the beam was focused into an area smaller than 1 square mm by a bent cylindrical mirror [8]. The Yb L_{III} (8947 eV) absorptions of samples were measured by the fluorescence yield (Yb Lα: 7.4 keV) using a 19 elements pure Ge solid-state detector with energy resolution sufficient to separate Yb signals from elastic scattering and fluorescence of other elements [9, 10]. The energy region around Yb-Lα fluorescence was selected by single-channel analyzers

*e-mail: h.tsuno@aist.go.jp

(SCA). The monochromator was calibrated at 8947 eV (Yb L_{III} absorption edge) using ytterbium oxide powder. XAFS spectra of solid samples were measured at approximately 20 K. The incident X-ray intensity (I_0) was monitored by an ion chamber which was filled with nitrogen gas. The X-ray absorption (μ) is expressed as $\mu = I_f/I_0$, where I_f is the intensity of fluorescence X-ray and μ is plotted against incident X-ray energy. Multiple scans (typically 3–5 times) were carried out for each sample and then averaged. The averaged XAFS spectra were converted to k space. The atomic contribution to the absorption coefficient (μ_0) was regarded as the smooth background in the EXAFS region of the each averaged XAFS spectra by a cubic spline method. $\chi(k)$ was extracted as usual and Fourier transformed into r-space. Determination of average interatomic distance, coordination number, and Debye-Waller factor for the isolated shell about an absorber in an unknown material were made by least-square fitting of the Fourier-filtered $\chi(k)$ function. Analyses of the EXAFS spectra were performed with the PC program, REX2000 (Rigaku Co.), which uses theoretical phase functions and amplitudes from McKale's table [11]. The interatomic distances and coordination numbers were given by fitting with errors of respectively ±0.02 Å and ±15–20%, assuming that systematic errors have been minimized in the experiment and data analysis. XANES spectra were also deconvoluted by REX2000 (Rigaku Co.).

3. Results and discussion

3.1. *XANES: Spontaneously induced reduction of trivalent ytterbium in calcite*

XANES spectra of the calcite and Yb-bearing standard materials had a significant white line around 8948 eV, which was assigned to electron transition 2p→5d6s of Yb^{3+} [12, 13]. The XANES spectrum of Yb in calcite is shown in Fig. 1. A discernible shoulder (A) is observed in the lower energy side of the main white line (B). This shoulder was not observed on XANES spectra of Yb-bearing materials. We attempted to fit the main peak at 8948 eV and the shoulder by a couple of a Gaussian function for white line and an arctangent function for continuum absorption, respectively. The deconvoluted components of XANES spectrum of Yb in calcite are shown in Fig. 1. A small peak (A) was resolved from the spectrum of calcite. Resultant peak position, peak height and FWHM of Gaussian curve for Peak A are 8940.2 eV, 0.14 a.u. (arbitrary unit) and 6.1 eV, and those for Peak B are 8948.6 eV, 0.88 a.u. and 6.1 eV, respectively. The position of Peak A was at lower energy by 8 eV than that of Peak B and is close to that of the absorption of Yb^{2+} [12–15]. Thus, we attributed peak A to Yb^{2+}. These results indicate that significant proportion of ytterbium existed as divalent ions in the calcite structure. Tanaka *et al.* suggested that the ratio of areas of peak A and B indicates directly the relative amounts of Yb^{2+} and Yb^{3+} [13]. Based on the report, we calculated that the 14–17% of Yb exists as Yb^{2+} in calcite. Thermodynamic calculation indicates that the $[Yb^{2+}]/[Yb^{3+}]$ ratio in the starting solution is smaller than 10^{-31}. In the starting solutions, trivalent ytterbium was predominant and divalent ion was negligible. This suggests that a part of Yb was reduced at some stage of calcium carbonate formation.

Yb^{3+} substitutes in the six-fold coordination for the Ca^{2+} site in calcite as mentioned in the following section. The ionic radii of Ca^{2+}, Yb^{3+} and Yb^{2+} in the six-fold coordination are 1.00, 0.868 and 1.02 Å, respectively [16]. The ionic radius of Yb^{2+} is quite close to that of Ca^{2+}. It is expected that Yb^{2+} can substitute at the calcium site of calcite with higher stability (affinity) than Yb^{3+} without significant mismatches in ionic radius as well as the ionic valence. For the stabilization of Yb^{2+} in the calcite structure, it is possible that some defects such as oxygen vacancy in the crystal structure of calcite can compensate the formation of Yb^{2+} in the oxidative condition. Further information of this result is described in Tsuno *et al.* 2003 [17].

3.2. *EXAFS: The local structure of Yb^{3+} incorporated in calcite*

The extended X-ray absorption fine structure (EXAFS) spectra of Yb in calcite can be attributed to Yb^{3+}, the major species in calcite, although we showed the presence of Yb^{2+} in calcite on the previous section. We regarded the structural information of Yb for EXAFS analysis as Yb^{3+}. The k^3-weighted $\chi(k)$ EXAFS of Yb incorporated in calcite is shown in Fig. 2. The spectrum collected at 20 K showed better S/N ratio than that taken at Room temperature, thus, it was used for detailed analysis. We adopted the spectrum at 20 K for the EXAFS analysis. Fig. 3

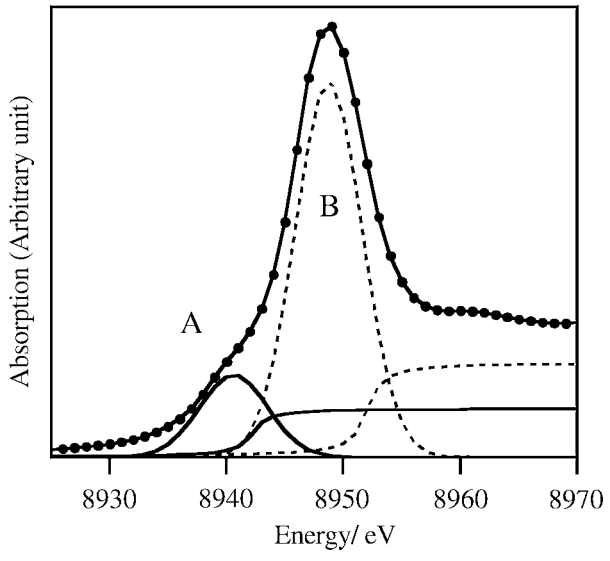

Fig. 1. Yb L_{III} edge normalized XANES and the deconvoluted spectra of Yb incorporated in calcite. A: Yb^{2+}, B: Yb^{3+}.

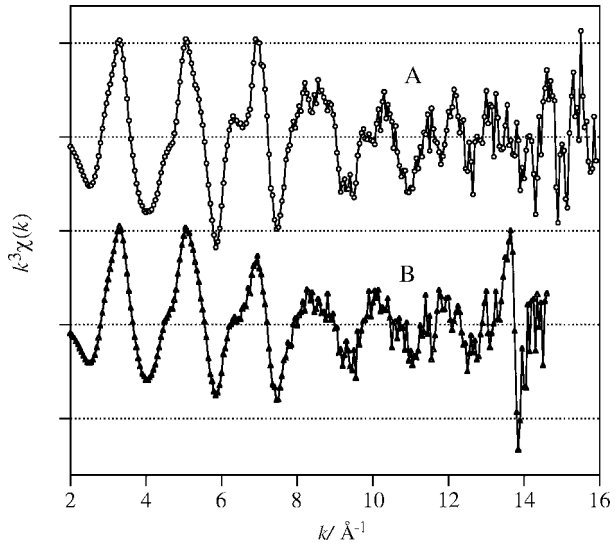

Fig. 2. The k^3-weighted $\chi(k)$ spectra for Yb incorporated in calcite. A: collected at 20 K, B: at room temperature.

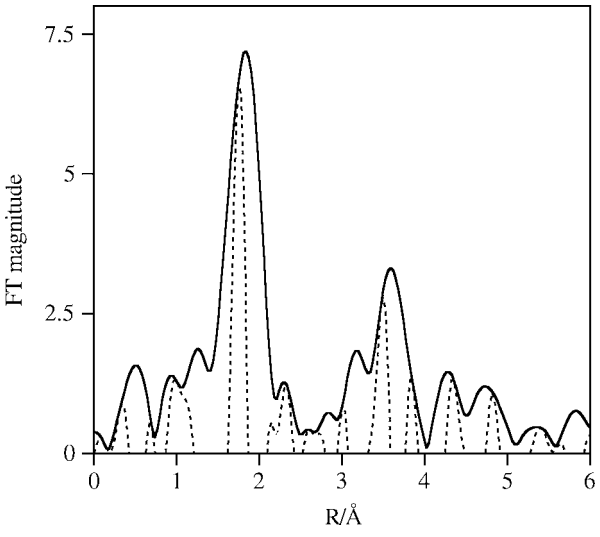

Fig. 3. Fourier transform of k^3-weighted Yb L_{III} EXAFS of Yb in $CaCO_3$ (no phase shift correction). Solid line: Radial structure function; Dashed line: imaginary part of FT.

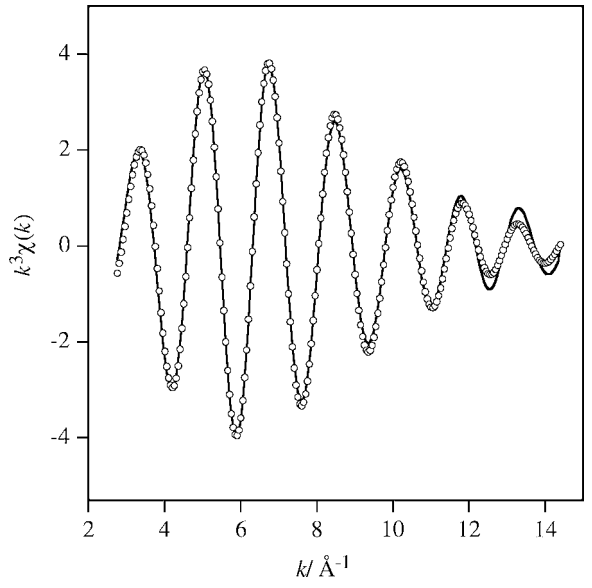

Fig. 4. Fit to the back Fourier transform of the first peak of k^3-weighted Yb L_{III} FT-EXAFS data shown in Fig. 3 performed in the range 1.5–2.1 Å. Open circle: experimental; Solid line: fitting.

shows Fourier transform of k^3-weighted $\chi(k)$ EXAFS of Yb-doped calcite (without phase-shift correction). A peak of radial structure function at about 1.8 Å is attributed to the nearest Yb-O interaction by assuming that Yb^{3+} occupies the Ca^{2+} site in calcite. The rough fitting for the back Fourier transform of the first peak in Fig. 3 brought the coordination number (N) as 4 and the larger residue of the fitting. It is an unreasonable value for Yb^{3+} coordination in calcite structure. Thus, we assumed that the first O-shell for Yb in calcite was splitting to near two shells. Fig. 4 shows the back Fourier transform of the first peak of k^3-weighted Yb L_{III} FT data between 1.5–2.1 Å shown in Fig. 3. The best fitting result indicates that there are 4 O atoms at 2.24 Å and 2 O atoms at 2.77 Å. The nearest Yb-O distance (2.24 Å) is comparative to the calculated Yb-O distance from the sixfold ionic radii of Yb^{3+} from Shanonn 1976 [16]. The nearest Yb-O distance (2.24 Å) in calcite is smaller than Ca-O distance (2.360 Å) of pure calcite [18]. Although the coordination number of Ca^{2+} for calcite is 6, all the

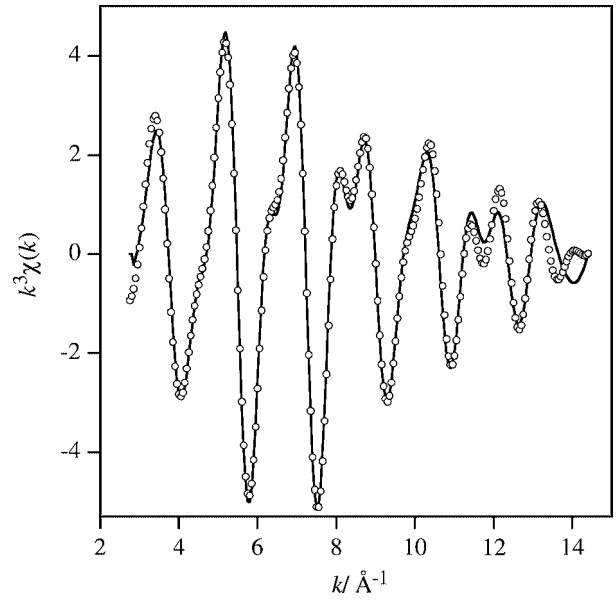

Fig. 5. The k^3-weighted Yb L_{III} edge EXAFS data, $\chi(k)$, for the calcite sample and the best-fit multishell model as a function of wave vector k. The data were fit with parameters described Table I. Open circle: experimental; Solid line: fitting.

six oxygen atoms could not be located in the same nearest shell to occupy Yb^{3+} at Ca^{2+} site in calcite. Thus, 4 oxygen atoms are located at the nearest shell with an Yb-O distance of 2.24 Å, while 2 oxygen atoms are pushed away from the nearest shell to a little far position. It was shown that the localized structural relaxation occurred around Yb^{3+} which has smaller ionic radius than Ca^{2+}.

Elzinga *et al*. showed that the nearest Yb-O shell in their Yb-doped calcite samples has coordination number of 7.5 and Yb-O distance 2.24 Å by EXAFS analysis [19]. Their fitting results had reasonable Yb-O distance but considerably large coordination number at Ca site in calcite structure. Thus, they fixed coordination number of 6 as chemical reasonable number from a comparison of the observed Yb-O distance with values predicted from sixfold and sevenfold ionic radii from Shanonn [16]. In contrast, our results are derived directly from EXAFS analysis and the distortion of YbO_6 octahedron was detected from the analysis.

For the Ca site of the calcite structure, the shells have the six nearest oxygen atoms at 2.360 Å, the nearest carbon atoms at 3.213 Å, the second nearest oxygen atoms at 3.459 Å, and calcium atoms at 4.048 Å and they have ideal coordination numbers (N) of 6 [18]. The mean Yb-O distance in calcite was 2.42 Å from the present experimental results. This mean value of Yb-O distance agrees with the size of the Ca^{2+} site in calcite. According to calcite structure, the coordination numbers of shells beyond the first oxygen group were fixed as 6 during refinement to reduce the

Table I. *Multishell best-fit parameters for Yb L_{III} EXAFS incorporated in calcite. N: coordination number; R: radial distance; σ: Debye-Waller factor.*

Shell	N	R(Å)	σ(Å)
Yb-O	4.1	2.24	0.066
Yb-O	1.9	2.77	0.119
Yb-C	6*	3.25	0.064
Yb-O	6*	3.34	0.110
Yb-Ca	6*	4.04	0.088

*Parameter fixed during refinement to reduce the number of fit parameters.

number of fit parameter. The k^3-weighted Yb L_{III} edge EXAFS data, $\chi(k)$, for the calcite sample and the best-fit multishell model were shown in Fig. 5. The results were well fit with the observation values. Best-fit parameters for Yb^{3+} incorporated in calcite are shown in Table I. The EXAFS fitting results support that Yb occupied the Ca sites in calcite as was expected.

Acknowledgement

The XAFS experiments were performed under the approval of the Photon Factory Program Advisory Committee (99G075 and 2001G122). This research was supported by Nissan Science Foundation and by a Grant-in-Aid (11304040, 13554018) from the Ministry of Education, Science, Sports and Culture. This study has been financially supported in part by the Research Fellowships of the Japan Society for the Promotion of Science for Young Scientists to H. T.

References

1. Akagi, T. and Kono, Y., Aquat. Geochem. **1**, 231 (1995).
2. Tsuno, H., Kagi, H. and Akagi, T., Bull. Chem. Soc. Jpn. **74**, 479 (2001).
3. Kamiya, N., Kagi, H., Notsu, K., Tsuno, H. and Akagi, T., Chem. Lett. **2002**, 890 (2002).
4. Tsuno, H., Kagi, H. and Akagi, T., Chem. Lett. **2002**, 960 (2002).
5. Terakado, Y. and Masuda, A., Chem. Geol. **69**, 103 (1988).
6. Zhong, S. and Mucci, A., Geochim. Cosmochim. Acta **59**, 443 (1995).
7. Brown Jr., G. E., Calas, G., Waychunas, G. A. and Patiau, J., "Reviews in mineralogy, Volume 18: Spectroscopic methods in mineralogy and geology". (edited by Hawthorne, F. C.) (Mineralogical Society of America, 1988), p. 431.
8. Nomura, M. and Koyama, A., KEK Report **95–15**, 1 (1996).
9. Nomura, M., KEK Report **98–4**, 1 (1998).
10. Nomura, M., J. of Synchrotron Radiat. **5**, 851 (1998).
11. Mckale, A. G., Veal, B. W., Paulikas, A. P., Chan, S. K. and Knapp, G. S., J. Am. Chem, Soc. **110**, 3763 (1988).
12. Hatwar, T. K. *et al*., Solid State Commun. **34**, 617 (1980).
13. Tanaka, T., Hanada, T., Yoshida, S., Baba, T. and Ono, Y., Jpn. J. Appl. Phys. **32**, 481 (1993).
14. Rao, C. N. R. *et al*., Chem. Phys. Lett. **76**, 413 (1980).
15. Baba, T. *et al*., J. Chem. Soc., Faraday Trans. **89**, 3177 (1993).
16. Shannon, R. D., Acta Crystallogr. **A32**, 751 (1976).
17. Tsuno, H., Kagi, H., Takahashi, Y., Akagi, T. and Nomura, M., Chem. Lett. **32**, 500 (2003).
18. Effenberger, H., Mereiter, K. and Zemann, J., Z. Kristallogr. **156**, 233 (1981).
19. Elzinga, E. J. *et al*., Geochim. Cosmochim. Acta **66**, 2875 (2002).

Physica Scripta. Vol. 115, 901–904, 2005

A Preliminary Study on the Speciation of Inorganic and Organic Tin Compounds Using XAFS

N. Sakakibara[1], Y. Takahashi[1], Y. Yamaguchi[2] and M. Nomura[3]

[1]Graduate School of Science, Hiroshima University, Hiroshima 739-8526, Japan
[2]Environment and Energy Department, National Maritime Research Institute, Mitaka, Tokyo 181-0004, Japan
[3]Photon Factory, Institute of Materials Structure Science, KEK, Tsukuba 305-0801, Japan

Received June 26, 2003; accepted November 26, 2003

PACS number: 61.10.Ht

Abstract

It is well known that organotin compounds such as tributyltin (TBT) and triphenyltin (TPT) leached from ship's antifouling paints cause disrupting endocrine called "imposex" in some species of marine snails. In this paper, XANES and EXAFS spectra for some Sn species including TBT and TPT were measured. Tin L_I-edge (4.464 keV) and L_{III}-edge (3.928 keV) XAFS were recorded in fluorescence mode using a Lytle detector at BL-9A, KEK-PF, Japan. In the beam line, all paths including I_0 ion chamber and a sample cell were purged with He, which enabled us to measure XAFS at soft X-ray region even for liquid samples like TBT. The XANES and EXAFS spectra of Sn metal, $SnCl_2$, SnO_2, TBT, and TPT showed that we can distinguish these species by this technique. This shows that XAFS can be a powerful tool for the speciation of Sn. Since XAFS is a non-destructive method, it can exclude the alteration of Sn compounds during pretreatment of conventional chromatographic analyses. It was also suggested that the difference in the features of XANES is more distinct at the L_I-edge than at the L_{III}-edge, whereas the detection limit is lower for the L_{III}-edge. The XANES spectrum at the L_{III}-edge was obtained even for the sample containing only 50 ppm of Sn as TBT in ethanol. Although the sensitivity may be insufficient for the Sn in seawater, the method can be applied to the speciation of Sn enriched in some biological samples or used in antifouling paints.

1. Introduction

It is well known that organotin compounds such as tributyltin (TBT) and triphenyltin (TPT) used in ship's antifouling paints and fishing nets have been used since 1960's in the world [1]. TBT and TPT leached from the antifouling paints have caused disrupting endocrine called 'imposex' in some species of marine snails [2]. Imposex is the imposition of male sexual characteristics on female snails and has caused a decrease in the population of neogastropod species. Their use in antifouling paints and fishing nets has produced toxic effects on non-target aquatic species (especially mollusks), and they are among the most toxic contaminants released into the aquatic environment by human activities [3–5].

Speciation of their organotin compounds has been of great interest due to their species-dependent toxicity and their widespread application as biocides [6]. In recent years, chromatography techniques such as gas chromatography (GC) or liquid chromatography (LC) have been widely used for analysis of organotin compounds [7–8]. These analytical methods essentially need many pretreatment procedures, such as extraction, purification, and derivatization.

In this work, we investigated whether XAFS would be effective for the speciation of inorganic and organic tin compounds using XAFS as a non-destructive method. The XAFS spectra of Sn in organotin compounds, such as TBT and TPT, were measured for the first time in this work. By XAFS because we do not need any pretreatments, any alteration of Sn compounds during the analysis can be excluded. In order to measure Sn-L edge XAFS, we used BL-9A at Photon Factory, KEK, specially designed to measure XAFS in the soft X-ray region (>2.2 keV) using fluorescence mode. The beamline is equipped with a double mirror to remove the harmonics, which is essential in the soft X-ray region. It is also possible to purge all paths with He including an I_0 ion chamber and a sample cell.

2. Samples and experimental procedures

Three inorganic Sn compounds, (Sn metal, $SnCl_2 \cdot 2H_2O$, and SnO_2,) and two organic Sn materials, (TBT (tributyltin chloride, $[CH_3(CH_2)_3]_3SnCl$) and TPT (triphenyltin chloride, $[C_6H_5]_3SnCl$)), were employed as reference materials for XAFS for Sn speciation. The Sn metal was about 100 μm in thickness. $SnCl_2 \cdot 2H_2O$ and SnO_2 were diluted to 5 wt% by BN and pressed into a pellet. These pellets were sealed by 4 μm polypropylene (Prolene®) bags. TBT and TPT were diluted by 5 wt% by ethanol and sealed by a polyethylene bag. A sample containing TBT and TPT at a known ratio was also measured. An antifouling paint was also employed for an example of the application of the XAFS technique to actual environmental materials.

XANES and EXAFS spectra for all samples were measured at beamline BL-9A at the Photon Factory, KEK, in Tsukuba, Japan [9]. The storage ring operating conditions were 2.5 GeV electron energy and 450–300 mA electron current. The beam size used in this study was smaller than $1 \times 0.5\,mm^2$ at the sample position. Tin L_I-edge (4.464 keV) and L_{III}-edge (3.928 keV) XANES and EXAFS spectra were recorded at room temperature in a fluorescence mode. A Si(111) monochromator was used and the beam was focused by a pair of bent conical mirrors coated with Rh. The samples were placed at a 45 degrees angle to the incident focused X-ray beam and the Lytle detector. To suppress the absorption of X-rays by air, all the paths including an I_0 ion chamber and a sample cell were purged with He. A pair of flat double mirrors was inserted in order to reduce the higher order reflections. The energy resolution ($\Delta E/E$) is 2×10^{-4} at 9 keV. A detailed layout of the beamline has already been reported [10–11]. For all experiments, SnO_2 was used as an energy reference material, where we set the energy of the white line peak of SnO_2 at 4.464 keV and 3.928 keV for L_I-edge and L_{III}-edge, respectively. The X-ray absorption (μ) defined as $\mu = I_F/I_0$ (I_F: fluorescence X-ray intensity; I_0: incident X-ray intensity) was plotted against incident X-ray energy.

XANES spectra for L_I-edge and L_{III}-edge were recorded with a 0.25 eV step (1 second for 1 point). The scanned energy range for L_I-edge XANES was from 4.42 to 4.54 keV, and from 3.91 to 3.97 keV for the L_{III}-edge. More than two scans were measured

and averaged. After removal of a linear preedge, the spectra were normalized by defining the average absorption between 4.526 and 4.564 keV equal to one for the L_I-edge and absorption between 4.038 and 4.135 keV for the L_{III}-edge.

Tin L_I-edge and L_{III}-edge EXAFS spectra were recorded in the energy range between 4.20 and 5.00 keV. Background corrections to extract the EXAFS functions $\chi(k)$ were made using a program, WinXAS version 2.1 [12]. The k^3-weighted $\chi(k)$ functions were Fourier transformed from k space ($2.90\,\text{Å}^{-1} < k < 6.70\,\text{Å}^{-1}$ and $3.190\,\text{Å}^{-1} < k < 7.461\,\text{Å}^{-1}$ for L_I-edge and L_{III}-edge, respectively) into R space to obtain a radial structural function (RSF).

3. Results and Discussion

The Sn L_I-edge XANES spectra of the reference materials and antifouling paint are shown in Fig. 1. The absorption peak occurs at 4.465 keV for Sn-metal and occurs at 4.470 keV for $SnCl_2$ and SnO_2 (Fig. 1). The XANES spectrum of TBT exhibits a single strong sharp peak at 4.466 keV and a small shoulder around 4.474 keV. The XANES spectrum of TPT exhibited a doublet feature, where the white line peak is less symmetric compared to that of TBT. The spectrum of the antifouling paint is not completely identical, but considerably similar to that of TBT, suggesting that TBT is contained in the antifouling paint. This result shows that L_I-edge XANES can be used as a fingerprint to distinguish organotin compounds (TBT and TPT) and inorganic Sn species.

Figure 2 shows Sn L_{III}-edge XANES spectra of the reference materials and the antifouling paint. The featureless L_{III}-edge XANES spectrum of Sn-metal may be caused by strong self-absorption due to the low X-ray energy of the L_{III}-edge relative to that of the L_I-edge. The spectra of other inorganic references, $SnCl_2$ and SnO_2, have two characteristic peaks (3.929 keV and 3.939 keV). The spectra of organotin compounds, TBT and TPT, have a large peak (around 3.932 keV) and a smaller peak (around 3.937 keV). The spectrum of the antifouling paint is similar to TBT, which confirms that TBT is contained in the antifouling paint. It is well known that TBT is soluble in ethanol. Chemical species which is extracted by ethanol from the antifouling paint shows a similar spectrum, suggesting that TBT was extracted in the ethanol (Fig. 2).

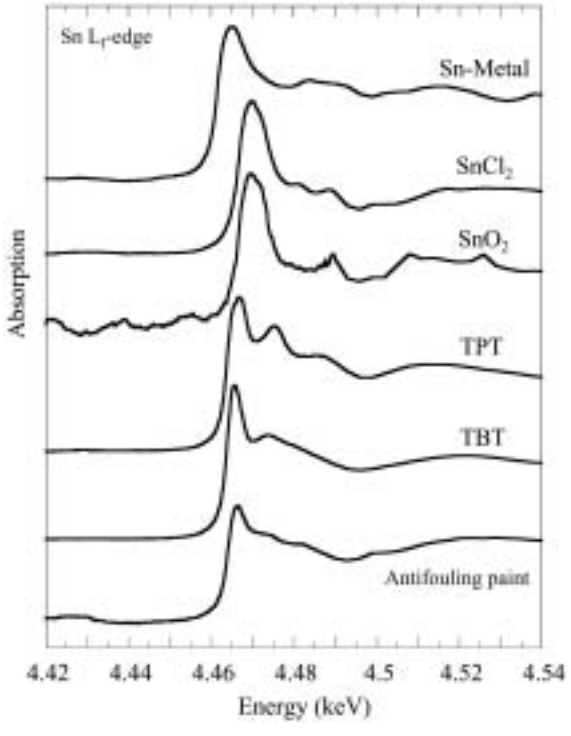

Fig. 1. XANES spectra at Sn L_I-edge for Sn-metal, $SnCl_2$, SnO_2, TBT, TPT, and antifouling paint.

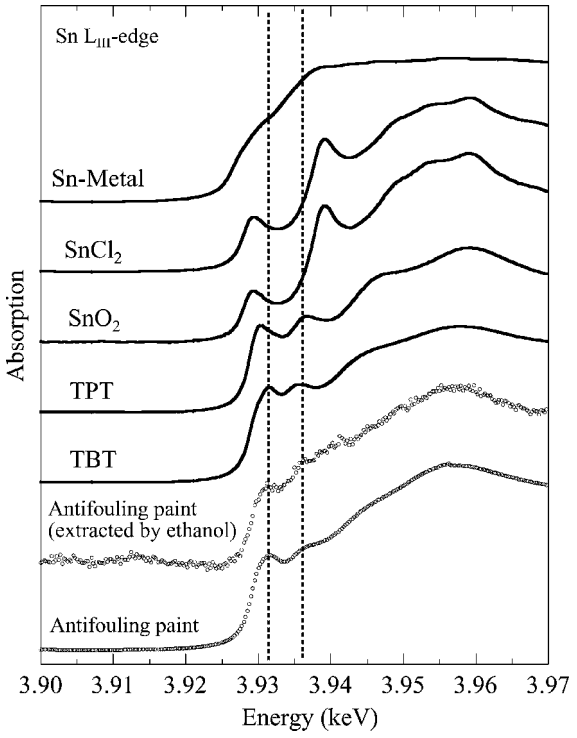

Fig. 2. XANES spectra at Sn L_{III}-edge for Sn-metal, $SnCl_2$, SnO_2, TBT, TPT, and antifouling paint.

The detection limit was estimated using various concentrations of TBT in ethanol sealed by a polyethylene bag. The L_{III}-edge XANES spectra for a solution containing 500 and 50 ppm Sn as TBT were collected 4 times and averaged to reduce random error. As shown in Fig. 3, the spectra of 50 and 500 ppm Sn solution were similar to that of 5 wt% Sn solution (5.0×10^4 ppm). The similarity indicates that the self absorption is not serious for the sample containing 5 wt% of Sn. XANES spectrum for 50 ppm Sn solution cannot be obtained for Sn L_I-edge. These facts suggest that L_{III}-edge is better than L_I-edge from the viewpoint of detection limit. Although the sensitivity may be insufficient for Sn in seawater (0.023–0.061 $\mu g/dm^3$) [13], some sediments containing a relatively large amount of Sn (10–20 ppm) and biological samples accumulating Sn could be detected by fluorescence XAFS.

Deconvolution of a spectrum of a mixture (TBT : TPT = 1 : 1; molar ratio) was preformed based on the normalized XANES spectra of TBT and TPT (Fig. 4). To utilize the energy shift of the white line, the fitting energy region was confined to a region between 3.917 and 3.940 keV. The mixing ratio estimated by the deconvolution (TBT: 49.2%) is similar to the mixture ratio (TBT: 49.0%). This result confirms that the Sn species in the sample can be estimated from XANES spectra if a few organotin compounds coexist in the sample. No spectral change was observed during repeated measurements for L_I-edge and L_{III}-edge XANES, showing that organotin compounds such as TBT and TPT were not altered during X-ray irradiation. These results

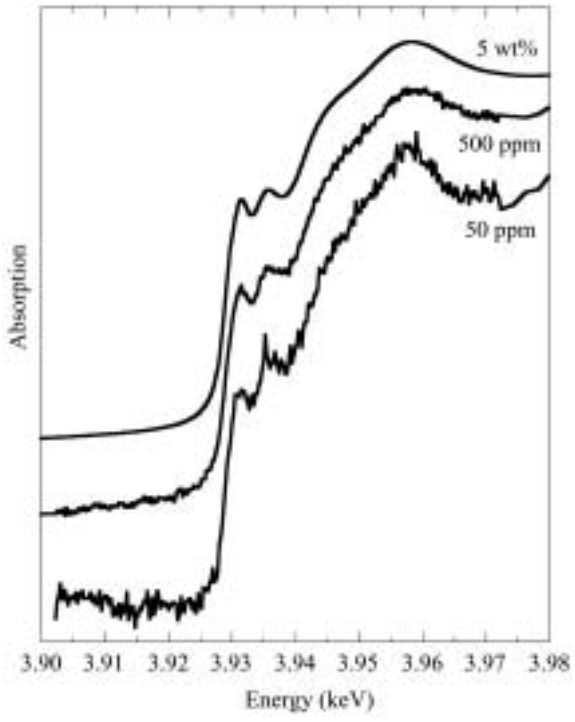

Fig. 3. Sn L_{III}-edge XANES spectra for Sn ethanol solutions containing 5 wt%, 500 ppm, and 50 ppm Sn as TBT in polyethylene bags.

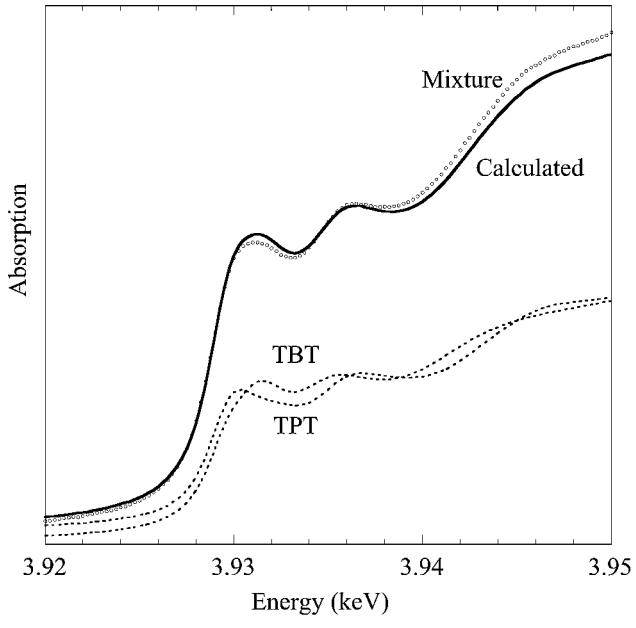

Fig. 4. Deconvolution of Sn L_{III}-edge XANES spectrum of the mixture (TBT : TPT = 49 : 51) and the spectra of 5 wt% TBT and TPT. The solid curve was obtained from a simulation based on the XANES spectra of TBT and TPT.

indicate that a spectroscopic method like XAFS is a powerful tool as a non-destructive method for speciation of tin compounds in the environment.

The radial structural functions (RSF) obtained by absolute values of Fourier transforms of k^3-weighted EXAFS functions for L_I-edge and L_{III}-edge are shown in Fig. 5. The phase shift of RSF was not corrected, since we use RSF as another fingerprint of the Sn species. It is difficult to distinguish $SnCl_2$, SnO_2, TBT, and TPT only from RSF, probably due to the small differences among

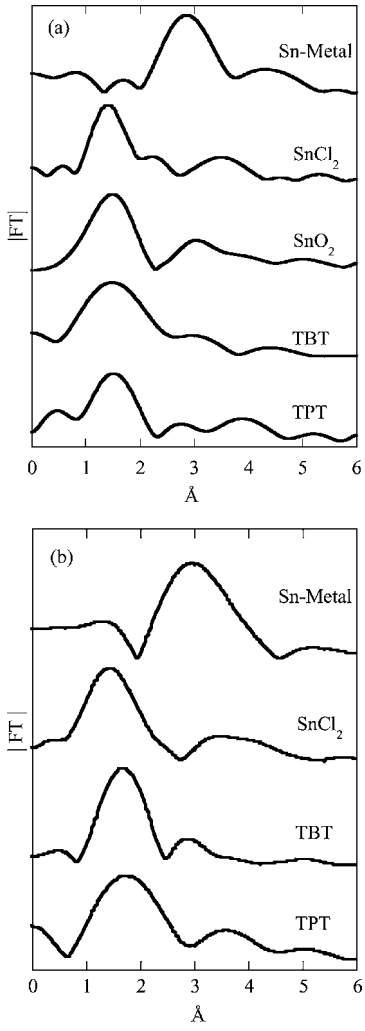

Fig. 5. Radial structural functions (phase shift is not corrected) obtained from EXAFS at (a) Sn L_I-edge and (b) Sn L_{III}-edge.

bond length of Sn to the neighboring atoms in these materials. In addition, the K-edge of Ca (4.038 keV) which is widely distributed in the environment may interfere with the EXAFS of Sn L_{III}-edge (3.928 keV), since the fluorescence by Ca K-edge may inhibit to measure the high energy region of Sn L_{III}-edge EXAFS. These facts suggest that XANES is probably better for Sn speciation in environment if we use Sn L-edge XAFS.

4. Conclusion

This study shows that XAFS, especially XANES, can be a powerful method for the speciation of Sn compounds in the environment. XAFS method dose not require complicated pretreatments like extraction, purification, and derivatization, which are essential in conventional chromatographic analyses. This is a great advantage of XAFS which enables us to exclude the alteration of Sn compounds in the sample during the analysis and pretreatments. Based on the detection limit of the Sn L-edge XAFS technique (ca. 50 ppm), it is thought that the application of the fluorescence XAFS to sediments, biological samples, and antifouling paints that contain a large amount of Sn is possible. Direct observation using XAFS will also be helpful for checking the alteration of organotin compounds during the pretreatment procedures in the conventional analyses.

Acknowledgement

This work has been financially supported by the Global Environmental Research Fund provided from the Ministry of the Environment awarded to Y.T. XANES experiments were performed with the approvals of KEK (Proposal No. 2002G244).

References

1. Horiguchi, T., Shiraishi, H., Shimizu, M. and Morita, M., J. Mar. Biol. Ass. U.K. **74**, 651 (1994).
2. Horiguchi, T., *et al*., Sci. Total Environ. **214**, 65 (1998).
3. Maguire, R. J., Appl. Organomet. Chem. **1**, 475 (1987).
4. Trass, T. P., Stab, J. A., Kramer, P. R. G., Cofino, W. P. and Aldenberg, T., Environ. Sci. Technol. **30**, 1227 (1996).
5. Ruiz, J. M., Bachelet, G., Caumette, P. and Donard, O. F. X., Environ. Pollut. **93**, 195 (1996).
6. Fent, K., Crit. Rev. Toxicol. **26**, 1 (1996).
7. Abalos, M. *et al*., J. Chromatography A **788**, 1 (1997).
8. Tao, H., Bunseki Kagaku **46**, 239 (1997) (in Japanese).
9. Nomura, M. and Koyama, A., KEK Report 95-15 (1996).
10. Nomura, M. and Koyama, A., J. Synch. Rad. **6**, 182 (1999).
11. Nomura, M. and Koyama, A., Nucl. Instrum. Meth. Phys. Res. **A 467–468**, 733 (2001).
12. Ressler, T., J. Synchrotron Rad. **5**, 118 (1998).
13. Harino, H., Fukushima, M., Kawai, S. and Megumi, K., Appl. Organomet. Chem. **12**, 819 (1998).

Physica Scripta. Vol. T115, 905–906, 2005

Hydration Effect on Structural Parameter of Chromium Loaded in Silica

Yu-Ling Wei[1*], Hsi-Chih Wang[1], Yaw-Wen Yang[2] and Jyh-Fu Lee[2]

[1]Department of Environmental Science, Tunghai University, Taichung City, 407 Taiwan
[2]National Synchrotron Radiation Research Center, Hsinchu, 300 Taiwan

Received June 26, 2003; accepted in reivsed form November 4, 2003

PACS number: 89.60−K

Abstract

This study used CrO_3-loaded silica as an example to illustrate how the hydration of the samples could affect the structural parameters of an environmental sample. Our results showed that as the moisture content in samples increased, the amplitude of the EXAFS increased, while the oscillation frequency of the EXAFS was virtually unchanged. The hydration of Cr(VI) enhanced the first-shell coordination number (Cr−O); the Debye-Waller factor was also changed. The first-shell coordination number was 4.55 for CrO_3-loaded silica slurry and 2.67 for the dry CrO_3-loaded silica. The Debye-Waller factor (σ^2) was 0.0036 for the slurry and 0.0014 for the dry one. In addition, hydration caused a considerable change in the pre-edge height and the white band of the XANES spectra of Cr(VI).

1. Introduction

Cr(III) is a necessary micronutrient for human, and Cr(VI) is carcinogenic [1]. In nature environment, chromium mainly exists in $Fe(CrO_2)_2$ [1]. Chromium element, Cr_2O_3, CrO_3, H_2CrO_4, chromate and dichromate salts have extensive application in industries of paint, alloy, electroplating, etc. Environmental pollution/contamination by chromium may eventually result in searing to plant, and neurosis, cancer, dermatosis to human [2].

Extended X-ray absorption fine structure (EXAFS) has been used to investigate the molecular environment of target element. This technique is applicable to the study between metal ions and water molecules [3]. The reaction between oxides and water molecules includes hydroxylation, hydration, chemisorption, and charge transfer [4]. Due to the higher charge/radius ratio of metal ions, metal ions were apt to form hydration shell in water [5]. In addition, metal ions in water might cause polarization of water molecules and this resulted in discrete hydration shell [6]. This polarization tended to increase the strength of hydrogen bonding, but reduce the O-H bonding strength of water molecules [6].

The objective of this study was to investigate the effect of hydration on structural parameter of chromium loaded in silica. This research was such designed that the results might be used to explain why both XANES and EXAFS fittings for samples dried at 105 °C were usually unsatisfactory.

2. Experiment

Amount of 62.95 gram CrO_3 of 99.99% purity from Aldrich corporation was end-to-end mixed with 500 gram silica in de-ionized water in a sealed PE bottle for 2 days at 30 rev/min. Part of mixture was then rigorously dried at 105 °C in an oven for 20 days to attain a considerably dry chromium(VI)-loaded silica powder, termed as "dry sample" in this study. The other part of the mixture was only partly dried at 105 °C for 3 days, and this sample was termed as "moistured sample". These samples along with the reference compounds (i.e., CrO_3 and Cr_2O_3) were recorded for their X-ray absorption spectra (XAS) on the wiggler C (BL-17C) beamline at the National Synchrotron Radiation Research Center (NSRRC) in Taiwan. The XAS spectra of "dry" and "moisturized" samples and the references were all recorded in transmission mode at room temperature. The wiggler C beamline had an eletron storage of 1.5 GeV, a current of 120–200 mA, and the scanning span of the monochromator was 4–15 keV. All data were analyzed with WinXAS 2.0 software [7].

3. Results and Discussion

Figure 1 shows the difference between the normalized XANES spectra for the "dry" and "moisturized" samples. Cr(VI) pre-edge spectrum is characterized by an intense peak due to the transition of Cr 1s core electrons to its 3d orbital. This arises from the lack of a center of inversion symmetry in the CrO_4 tetrahedral structure [8, 9]. The area of this peak in the normalized Cr XANES spectrum was demonstrated to be proportional to the Cr(VI)/Cr ratio [9]. Figure 1 indicates that the "moisturized sample" has a higher pre-edge peak than the "dry sample" with the peak intensity ratio of 1.2/1.0, while the corresponding peak area ratio is 1.1/1.0. The "moisturized sample" has slightly greater photon energy of about +1.0 eV energy shift at the normalized absorption of 0.5. This may be explained as the formation of hydrogen bonding between CrO_3 and the hydration because the formation of hydrogen bonding might cause the oxygen in the first coordinated shell to pull electron farther away from Cr, and this would shift the edge jump to higher photon energy. The XANES spectrum of the "moisturized sample" is also characterized with

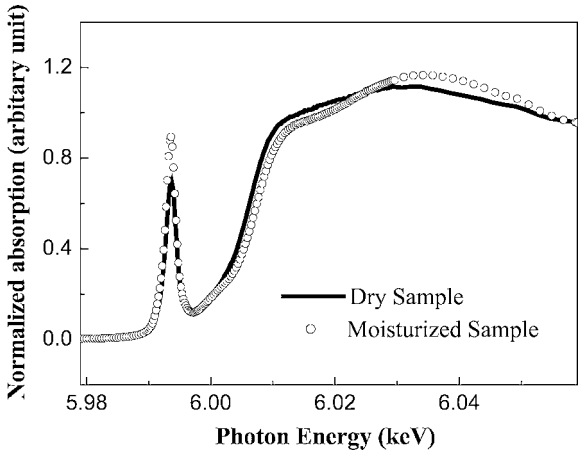

Fig. 1. XANES spectra of dry CrO_3-loaded silica and moisturized CrO_3-loaded silica.

*e-mail: yulin@mail.thu.edu.tw

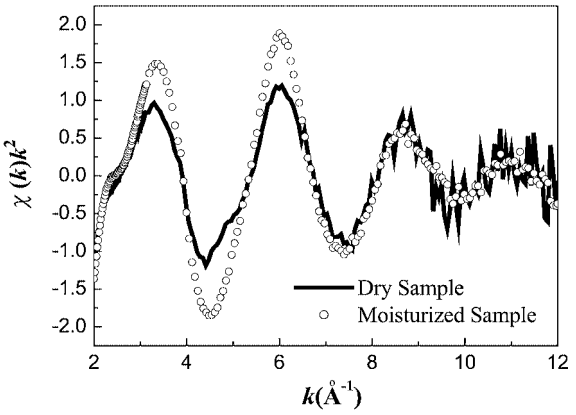

Fig. 2. EXAFS spectra of dry CrO_3-loaded silica and moisturized CrO_3-loaded silica.

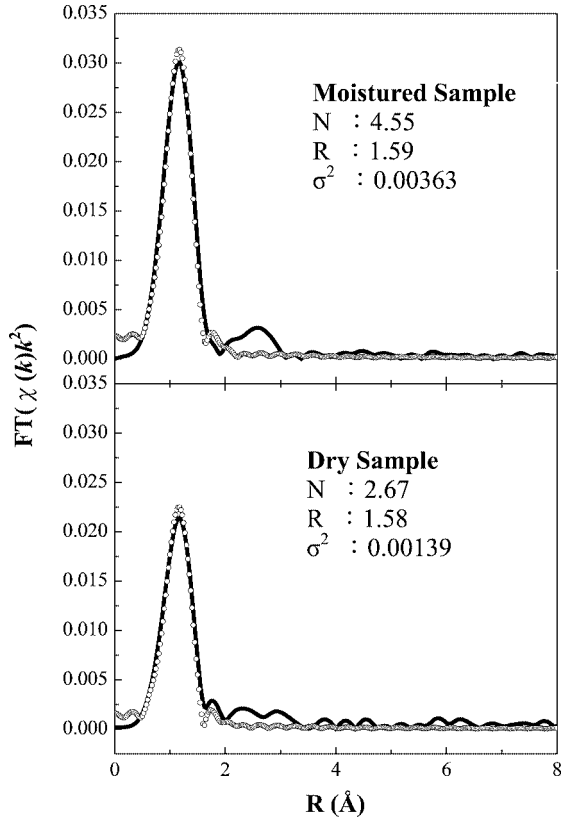

Fig. 3. Fourier transforms fitted for structural parameters of dry CrO_3-loaded silica and moisturized CrO_3-loaded silica.

a greater white line intensity than the "dry sample", that indicates a lower electron density in Cr d orbital.

Figure 2 shows the EXAFS spectra for the "moisturized" and "dry" samples in k space. The EXAFS spectrum of the "moisturized sample" was associated with higher amplitude in the k range of 2–6 $(Å)^{-1}$. However, the frequency of the EXAFS is not changed from dry sample to moisturized sample. Structural results deriving from EXAFS fitting using CrO_3 feff file are shown in each compartment of Figure 3. The coordination number (N) of the first Cr−O shell of the "moisturized sample" is much greater than that of the "dry sample" (i.e., 4.55 vs. 2.67). Therefore we suggest that water molecules might have moved to a position that was close enough to contribute to the coordination number of the first Cr−O shell. The results of the Debye-waller factor (σ^2) also support this suggestion; the "moisturized sample" is characterized with a much greater σ^2 value than the "dry sample": 0.00363 vs. 0.00139.

4. Conclusion

1. The content of moisture in Cr(VI)-loaded silica considerably affected the Cr XAS spectrum.
2. Cr(VI)-loaded silica with greater moisture content was characterized with greater preedge peak height, but the peak area did not seem to be affected by the moisture content.
3. Both the white line intensity in the normalized XANES spectrum and the amplitude of the EXAFS spectrum were enhanced with greater moisture content in Cr(VI)-loaded silica.
4. Both coordination number and Debye-Waller factor of the first coordination shell increased with greaterer moisture content in Cr(VI)-loaded silica. This suggested that water molecules might have moved to a position that was close enough to affect the first-shell molecular environment.

Acknowledgement

We thank the staff at NSRRC for their assistance during the experimentation.

References

1. Kotas, J. and Stasticka, Z., Environmental Pollution **107**, 263 (2000).
2. Gad, C. S., Sci. Tot. Environ. **86**, 149 (1989).
3. Munoz-Paez, A., Diaz, S. and Martin-Zamora, M. E., Physica B **208&209**, 395 (1995).
4. Blesa, M. A. *et al.*, Coordination Chem. Rev. **196**, 31 (2000).
5. Richens, D. T., "The Chemistry of Aqua Ions," (Wiley, Chichester, U.K. 1997).
6. Lindqvist-Reis, P., "Structure of Solvated Metal Ions," Doctoral Thesis, Department of Chemistry, Stockholm, Sweden (2000).
7. Ressler, T., J. Synchrotron Radiat. **5**, 118 (1998).
8. Sutton, S. R. *et al.*, Geochim. Cosmochim. Acta **57**, 461 (1993).
9. Bajt, S. *et al.*, Anal. Chem. **65**, 1800 (1993).

Physica Scripta. Vol. T115, 907–908, 2005

Effect of Water on XAS Spectrum of $Cu(NO_3)_2$ Reference

Nicky Cheng[1], Yu-Ling Wei[1*], Yaw-Wen Yang[2] and Jyh-Fu Lee[2]

[1]Department of Environmental Science, Tunghai University, Taichung City, 407 Taiwan
[2]National Synchrotron Radiation Research Center, Hsinchu, 300 Taiwan

Received June 26, 2003; accepted in revised form November 4, 2003

PACS number: 89.60−K

Abstract

To successfully fit the copper XANES and EXAFS spectra of a copper-containing sample, it is usually desirable to record the XAS spectra of various copper compounds. Nevertheless, $Cu(NO_3)_2$ reference is very hygroscopic, and the fitting results can be misleading if $Cu(NO_3)_2$ containing different amounts of H_2O is used as reference.

This study investigated the effect of water on the XAS spectrum of $Cu(NO_3)_2$ reference. The results, for the first shell (Cu–O), indicated that drier reference $Cu(NO_3)_2$ would have less coordination number. The interatomic distance was 1.95 Å that was independent of the moisture content in $Cu(NO_3)_2$ reference, and there was a slight variation in the Debye-Waller factor for the $Cu(NO_3)_2$ containing different moisture content. For the XANES spectra, it was found that the photon energy for the edge jump could be reduced by as great as 3–4 eV if $Cu(NO_3)_2$ was moisturized. This might have been due to the hydration effect on Cu^{2+}. The white line showed that there was more empty d orbital for the copper in the moisturized $Cu(NO_3)_2$ than for the drier one.

1. Introduction

Although copper is a necessary micronutrient to human, excessive intake of copper through inhalation, ingestion, and skin and eye contact may cause damage to mucous membrane and the upper respiratory tract [1, 2]. Pneumonia, vomiting, and poisoning phenomena can occur, too [1, 2]. In addition, it can cause pathological changes in central nervous system, liver, and kidney [1, 2]. The main man-made sources of copper contaminant include copper smelting, copper mining, metal rinsing, alloy manufacturing, electroplating, pesticide application, waste incineration, and electronics manufacturing [1]. In Taiwan, some heavily polluted areas were investigated and estimated to contain copper contaminant up to the level of more than 10% in weight. To develop an effective method to remedy copper contaminant in soils, solid wastes, and inorganic sludge, it is important to attain the information on copper speciation and molecular environment around copper in the Cu-containing matrices prior to and after remediation/treatment. This information is critical because based on which one can predict the effectiveness of the developed remediation/treatment technology. It is important especially when the long-term stability of the remedied/treated copper contaminant is concerned.

Copper nitrate is one of the frequently used reference compounds for the fitting of Cu XANES and EXAFS spectra. Nevertheless, it is very hygroscopic with solubility of 381/100 by weight in water [3]. This would incur great difficulty in using it as a reference compound. A previous study indicated that mixing of $Cu(NO_3)_2$ into silica and kaolin with de-ionized water, followed by drying at 105 °C for 3 days, resulted in the formation of $Cu(OH)_2$ via the hydroxylation of Cu^{2+} [4]. The Cu XANES fitting performance was not satisfactory [4]. Therefore, the objective of this study was to investigate the effect of hygroscopes of $Cu(NO_3)_2$ on the XAS spectrum of $Cu(NO_3)_2$.

2. Experimental

$Cu(NO_3)_2$ of G. R. grade from Riedel-de-Haën was used for this study. Two $Cu(NO_3)_2$ samples were prepared as follows for XAS measurement. The first $Cu(NO_3)_2$ sample that is termed "dry $Cu(NO_3)_2$" was prepared by grinding the $Cu(NO_3)_2$ chemical, and subsequent drying of the ground $Cu(NO_3)_2$ at 105 °C in an oven till constant weight. The "dry $Cu(NO_3)_2$" was then stored in a desiccator and ready for XAS measurement. The hygroscopic $Cu(NO_3)_2$ was prepared by adding one drop of de-ionized water into suitable amount of $Cu(NO_3)_2$ powder to simulate the hygroscopic phenomena of $Cu(NO_3)_2$ during the sample preparation just before copper XAS measurement. The hygroscopic $Cu(NO_3)_2$ was in a dense slurry form. Besides, $Cu(OH)_2$ of high purity from Riedel-de Haën was also recorded for its XAS spectra.

XAS spectra were all recorded on the wiggler C (BL-17C) beamline at the National Synchrotron Radiation Research Center (NSRRC) in Taiwan. The storage energy was 1.5 GeV, the electric current was 120–220 mA, and the energy spanning 4–15 keV for the monochromator. The edge jump for Cu is 8979 eV. All XAS spectra were recorded in transmittance mode at room temperature. Data reduction was carried out using WinXAS 2.0 [5].

3. Results and Discussion

Figure 1 shows the overplotting of the normalized Cu XANES spectra of "dry $Cu(NO_3)_2$", "hygroscopic $Cu(NO_3)_2$", and $Cu(OH)_2$ compound. It indicated that the photon energy of edge jump of the XANES spectrum of hygroscopic $Cu(NO_3)_2$ is about 3–4 eV less than that of "dry $Cu(NO_3)_2$". In fact, the photon energy for edge jump of the "hygroscopic $Cu(NO_3)_2$", was quite close to that of $Cu(OH)_2$. This is explained by the fact that

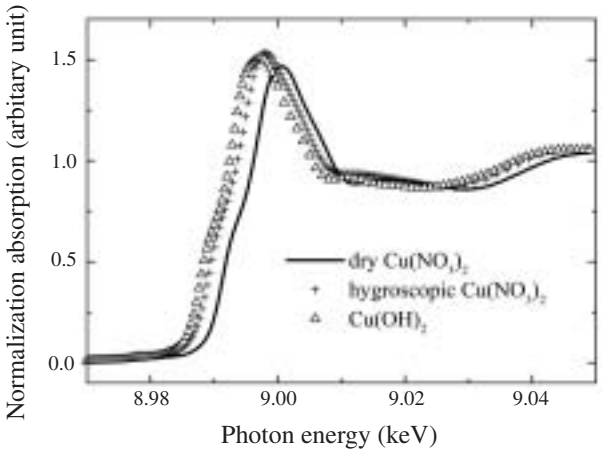

Fig. 1. XANES spectra for dry $Cu(NO_3)_2$, hygroscopic $Cu(NO_3)_2$, and $Cu(OH)_2$.

*e-mail: yulin@mail.thu.edu.tw

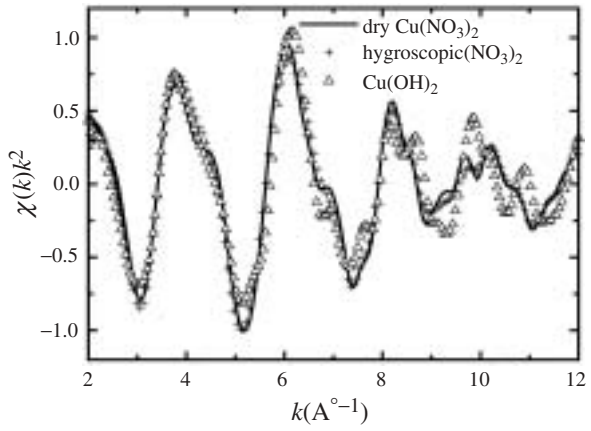

Fig. 2. EXAFS spectra for dry $Cu(NO_3)_2$, hygroscopic $Cu(NO_3)_2$, and $Cu(OH)_2$.

hygroscopic $Cu(NO_3)_2$ would decompose to form Cu^{2+} and $2NO_3^-$. The Cu^{2+} was then hydroxylated into $Cu(OH)_2$ [4]. The white line intensity of XANES spectra for "dry $Cu(NO_3)_2$" and "hygroscopic $Cu(NO_3)_2$" is also different from each other; the hygroscopic one is characterized with higher white line. In other words, the electron density in d orbital was less for the hygroscopic $Cu(NO_3)_2$. This was the reason why XANES fitting of samples involved $Cu(NO_3)_2$ reference was poor in our previous study [4].

Figure 2 presents the overplotting of the k^2-weighed EXAFS in k space for dry $Cu(NO_3)_2$, hygroscopic $Cu(NO_3)_2$, and $Cu(OH)_2$. It shows that there is some slight difference in EXAFS amplitude among these three spectra; while the oscillation frequency is virtually the same for these spectra. One may suggested that molecular environment around copper is only slightly different among dry $Cu(NO_3)_2$, hygroscopic $Cu(NO_3)_2$, and $Cu(OH)_2$. This suggestion will be further supported by the results obtained by comparing the structural parameters among them.

Figure 3 shows the overplotting of Fourier transform of the EXAFS spectra. Not much difference is observed among these spectra. Table I presents the coordination number (N), interatomic distance (R), and Debye-Waller factor (σ^2) of the first shell for dry $Cu(NO_3)_2$ and hygroscopic $Cu(NO_3)_2$ and Figure 4 shows the fitting of EXAFS spectra for dry $Cu(NO_3)_2$ and hygroscopic $Cu(NO_3)_2$. All data of structural parameters indicate that dry $Cu(NO_3)_2$ and hygroscopic $Cu(NO_3)_2$ have quite similar molecular environment, although the electronic state of copper is considerably different between them.

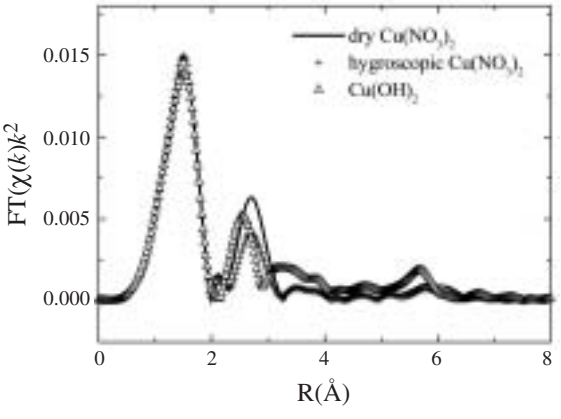

Fig. 3. Fourier transforms of EXAFS spectra for dry $Cu(NO_3)_2$, hygroscopic $Cu(NO_3)_2$, and $Cu(OH)_2$.

Table I. *Structural results based on the EXAFS fitting for dry $Cu(NO_3)_2$ and hygroscopic $Cu(NO_3)_2$.*

Sample	N	R (Å)	σ^2 (Å)^2
Dry $Cu(NO_3)_2$[a]	3.75	1.95	0.00388
Hygroscopic $Cu(NO_3)_2$[a]	3.94	1.95	0.00378

[a]Use $Cu(NO_3)_2$ feff for Fourier spectra fitting.

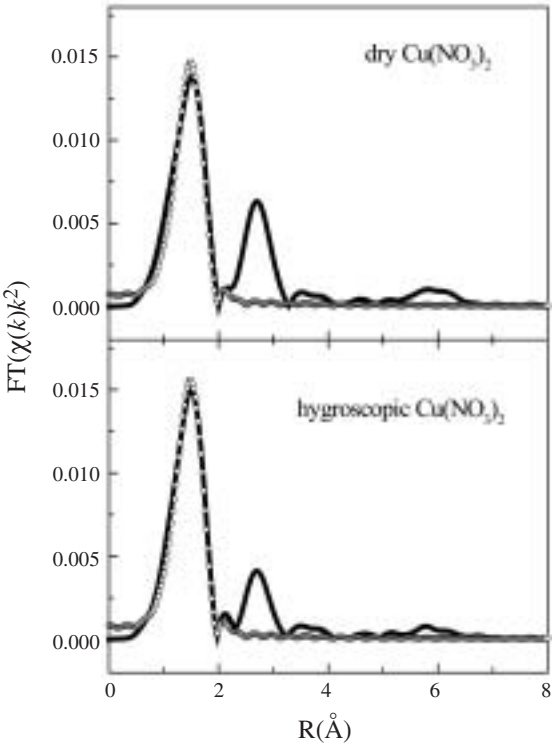

Fig. 4. Fitting of EXAFS spectra for dry $Cu(NO_3)_2$ and hygroscopic $Cu(NO_3)_2$.

4. Conclusion

1. Hydroxylation of hygroscopic $Cu(NO_3)_2$ resulted in partial formation of $Cu(OH)_2$.
2. Water molecules involved in hydroxylation of hygroscopic $Cu(NO_3)_2$ caused a considerable change in copper electronic state, as indicated by the shift of edge jump and the change of white line intensity. This would incur a poor fitting in copper XANES spectra for samples.
3. Molecular environment surrounding copper was virtually similar between dry and hygroscopic $Cu(NO_3)_2$.

Acknowledgment

We thank the staffs at NSRRC, Mr. Ming-Jan Hu, Mr Wei-Shun Liang, and Mr. Hsi-Chih Wang for their assistance in the experiment.

References

1. Merian, E., "Metals and their Compounds in the Environment," (New York, 1991), p. 893–908.
2. Windhilz, M., Budavari, S., Stroumtsos, L. Y. and Fertig, M. N., "The Merck Index," (Merck & Co., Inc., USA, 9th ed., 1976), p. 325.
3. Perry, R. H. and Clinton, C. H., "Chemical Engineers' Handbook," (McGraw Hill Book Company, 5th ed., 1973), p. 3–12.
4. Wei, Y. L., Yang, Y. W. and Cheng, N., Environ. Sci. Technol. **35**, 416 (2001).
5. Ressler, T., J. Synchrotron Radiat. **5**, 118 (1998).

Physica Scripta. Vol. T115, 909–911, 2005

Effect of Thermal Stabilization on Lead Speciation in Silica Leached with H_2SO_4/HNO_3

Ming-Jan Hu[1], Yu-Ling Wei[1*], Hui-Chin Huang[1], Yaw-Wen Yang[2] and Jyh-Fu Lee[2]

[1]Department of Environmental Science, Tunghai University, Taichung City, 407 Taiwan
[2]National Synchrotron Radiation Research Center, Hsinchu, 300 Taiwan

Received June 26, 2003; accepted in revised form December 15, 2003

PACS number: 89.60−K

Abstract

This study investigated thermally stabilized lead-contaminated silica at 300–900 °C, and the heated samples were leached with combined acid (H_2SO_4 + HNO_3, precursors of acid rain). The leached residues were studied with X-ray absorption spectroscopy (XAS) technique to determine the lead speciation therein. The results indicated that after heating at 300 °C, the main lead speciation in the leached residue was $PbSO_4$ (43%), and PbO and Pb_3O_4 constituted another 53%. For the samples heated at 700 °C and 900 °C, the main lead speciation in the leached residue was PbO (about 77% of the total lead in both leached residues), and $PbSO_4$ only accounted for 22–23% in the residues. No $Pb(NO_3)_2$ was detected in the residues due to its high solubility.

1. Introduction

Lead is a neurotoxin. Chronic intoxication of lead compounds results in body weight loss, poor health, anemia, gastrointestinal distress, and arthralgia [1]. Acute intoxication of lead causes anorexia, vomiting, etc. [1]. Lead level greater than 0.05 mg/L in blood can cause permanent damage to intelligence [1].

The main source of lead contaminant/pollutant in Taiwan has been associated with lead battery manufacturing. Lead compounds were frequently found in atmosphere, waste water stream, and soil nearby the manufacturing plant. In USA soils, lead was frequently found in the US superfund sites [2].

Thermal treatment of heavy metal-containing soils and solid wastes offers an effective alternative for soil remediation and solid waste treatment [3–6].

2. Experimental

The Pb^{2+}-doped silica powder (40,000 mg Pb/kg silica) was prepared by mixing a pre-calculated lead nitrate powder of G. R. grade (Riedel-de Haën) in de-ionized water with pre-weighed silica powder and subsequent drying of the slurry-like mixture at 105 °C for 3 days. Even dispersal of Pb onto the surface of silica powder was achieved by continuous mixing in a rotating mixer (ca. 30 rotations/min) for ten days. The dry Pb^{2+}-doped silica powder was then thermally treated at 300, 700, and 900 °C for four hours in a fixed-bed reactor that was made of stainless steel cylinder. The reactor was electrically heated to the pre-set temperatures before feeding in the dry Pb^{2+}-doped silica powder.

The effect of thermal stabilization on lead leaching was tested by acid leaching of the heated dry Pb^{2+}-doped silica powder. Combined acid of H_2SO_4 and HNO_3 (60 : 40 in weight) in de-ionized water having a pH 5.00 ± 0.05 was used to test the extent of Pb leaching from the heated samples. This test was carried out according to Method S101.60A issued by the Environmental Protection Administration (EPA) of Republic of China. It should be noted that both H_2SO_4 and HNO_3 are main precursors of acid rain. The Pb^{2+}-containing leachates collected from the leaching test were digested according to Method 3010 formulated by USEPA [7]. The concentration of Pb^{2+} in the digested leachates was measured with a flame atomic absorption spectrometer (FAAS). A stock solution from Merck Company containing 1000 mg Pb^{2+} per liter solution was diluted to various extents to prepare the calibration curves. Each curve spanned at least five different Pb concentrations. The lowest correlation coefficient (r^2) was required to be greater than 0.995 for all curves. Five replicate measurements of each diluted stock solution were carried out and the calibration curve was prepared prior to the measurement of a batch of samples. The method detection limit (MDL) was determined to be 0.54 mg Pb/kg silica. The Pb quality control (QC) standard solution was routinely measured to check the stability of the calibration curve. One check of the calibration curve by the standard solution was performed for every 20 unknown samples measured. The X-ray absorption spectroscopic (XAS) spectra were recorded on the wiggler C (BL-17C) beamline at the National Synchrotron Radiation Research Center (NSRRC) located in Hsinchu, Taiwan, Republic of China. The storage energy was 1.5 GeV, the beam current was 120–200 mA, and the energies of the monochromator photon beams are in the range of 4–15 keV. X-ray absorption spectra at the Pb-L^{III} edge (13055 eV) were collected at room temperature in transmission mode for the reference compounds and fluorescence mode for the acid-extracted residues of the thermally treated Pb-containing samples. Data reduction was carried out using WinXAS software [8]. This software is capable to perform species quantification for a multicomponent mixture based on their fingerprint in the XANES region [8]. The species quantification was achieved by simulating the experimental XANES spectrum through a least-squares procedure to refine the sum of a set of reference spectra [8]. Reference compounds that do not seem to exist in the sample often result in negative partial concentration or unreasonable energy shift [8].

3. Results and Discussion

Figure 1 shows the results of lead leaching from the samples heated at 300, 700, and 900 °C. It indicates that thermal treatment at higher temperature reduced lead leaching percentage more effectively (i.e., 5% at 900 °C vs. 26% at 300 °C).

Figure 2 presents the XANES spectra (left column) and their first derivatives (right column) for reference compounds

*e-mail: horix@ms17.hinet.net

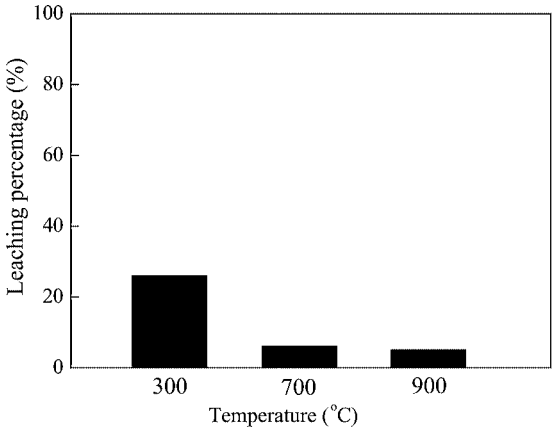

Fig. 1. Leaching percentage of lead from lead-containing samples thermally treated at 300, 700, and 900 °C.

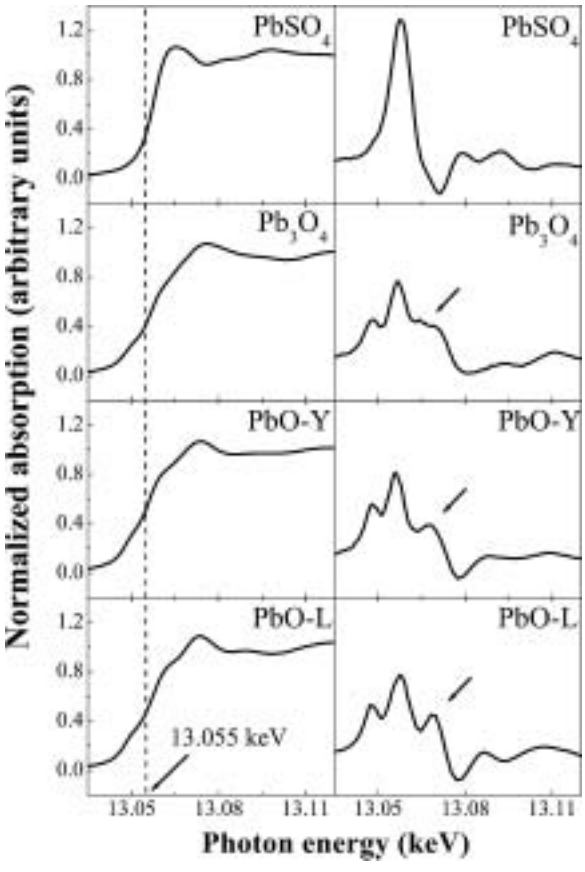

Fig. 2. XANES spectra (left column) and their first derivatives (right column) for the reference compounds.

$PbSO_4$, Pb_3O_4, PbO-yellow, and PbO-litharge. There are distinct differences among the spectra except between that for PbO-yellow and PbO-litharge. Only minor differences are observed between the XANES spectra for both PbO. The white line height for PbO-litharge reference is slightly higher than that for PbO-yellow.

Figure 3 presents the XANES spectra (right side) and their respective first derivatives (left side) for the acid-extracted residues of the thermally stabilized samples. The first derivative of the 300 °C-heated sample residue (see bottom right compartment of Fig. 3) is more similar to that of $PbSO_4$ reference compound (see top compartment of Fig. 2) than that of the 700 °C and 900 °C-heated sample residues. XANES fitting results indicate that the main lead species in the residue of the 300 °C-heated

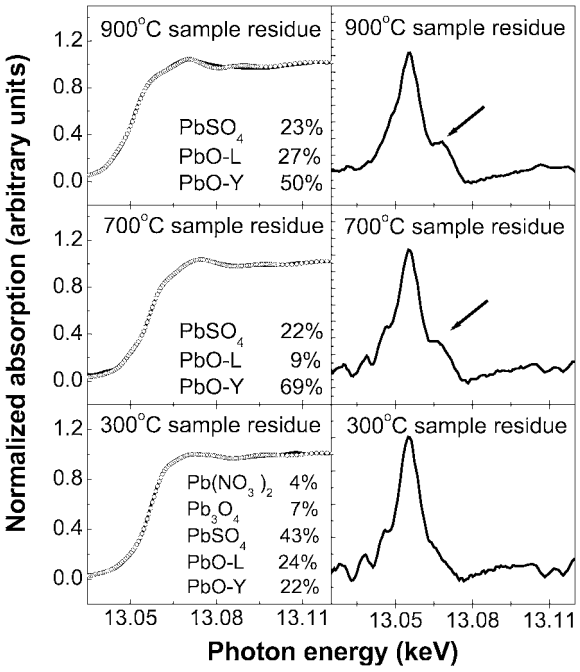

Fig. 3. XANES fitting (left column) and their first derivatives (right column) for the acid-extracted residues of the heated samples.

sample is $PbSO_4$; while that in the residues of the 700 °C- and 900 °C-heated samples is lead oxide (i.e., mostly the PbO-yellow). $PbSO_4$ content in the acid-extracted residues of the heated samples decreases with the thermal treatment temperature (i.e. 43% for 300 °C sample residue, 22–23% for 700–900 °C sample residues). This is reasonable because $PbSO_4$ may decompose into PbO and SO_2/SO_3. As to the lead oxide, thermal treatment at higher temperature followed by the combined-acid leaching resulted in greater transformation of PbO-yellow into PbO-litharge. Furthermore, $Pb(NO_3)_2$ was detected only in the extracted residue of 300 °C sample because it decomposes into PbO at about 500 °C.

Figure 4 depicts the fitting of the corresponding Fourier transforms of EXAFS and the resulted structural information is shown in Table I. The EXAFS spectra were k^2-weighed and were Fourier-transformed in the "k" range of 2.5–10.4. The first peak

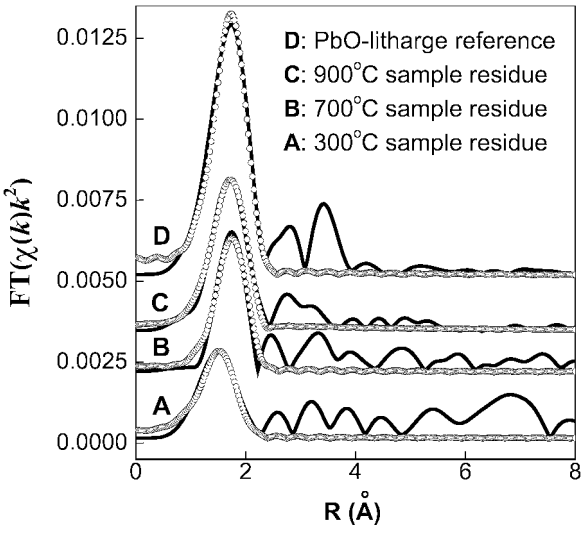

Fig. 4. Fitting of EXAFS spectra for the acid-extracted residues of the heated samples and for PbO-litharge reference compound.

Table I. *Structural results based on the EXAFS fitting for the acid-extracted residues of the heated samples.*

	$Pb(NO_3)_2$-doped SiO_2	
sample	N type at R (Å)	σ^2 (Å)^2
300 °C sample residue[a]	1.00 Pb-O at 2.18	0.004
700 °C sample residue[a]	1.45 Pb-O at 2.27	0.002
900 °C sample residue[a]	3.39 Pb-O at 2.24	0.013
PbO-L reference compound[a]	4.00 Pb-O at 2.29	0.006

[a]: fitted by PbO-L feff1.

(covering the range of: 0.4–2.26 Å) of the Fourier-transformed EXAFS spectra was fitted with PbO-litharge feff1 file to obtain the structure parameters of coordination number (N), Pb−O interatomic distance, and the Debye-Waller factor (σ^2) for the first shell. The first-shell coordination number is 1.00 for the 300 °C sample residue, 1.45 for the 700 °C one, and 3.39 for the 900 °C sample residue. This suggests that greater sintering reaction might occur in the 900 °C sample than the 700 °C one. The Debye-Waller factor (σ^2) is also greater for the 900 °C sample residue due to the greater extent of sintering reaction.

4. Conclusions

1. Effectiveness of thermal stabilization of Pb^{2+}-doped silica increased with greater treating temperature. Less Pb^{2+} was acid-leached from the sample thermally treated at higher temperatures.
2. Lead compounds in the acid-leached residues of the thermally treated samples tended to transform from $PbSO_4 + Pb(NO_3)_2$ into PbO-yellow and PbO-litharge. The content of PbO-litharge increases with higher thermal treatment temperature.
3. Both the results of the coordination number and Debye-Waller factor suggest that treatment at 900 °C resulted in greater sintering reaction than that at 700 °C.

Acknowledgment

We thank the staffs of NSRRC of Taiwan for their assistance in the experiment.

References

1. Green, V. A., Wise, G. W. and Callenbach, J. C., "Lead Poisoning," (1978).
2. Reed, B. E. and Moore, R., Proc. 26th Mid-Atlantic Industrial Waste Conference, USA, 425 (1994).
3. Lee, H. T., Proc. Fluidized-Bed Incineration Technol. Conference, Taiwan, 51 (1992).
4. Wei, Y. L., Lu, M. S. and Hu, S. H., Proc. Twenty-Sixth Mid-Atlantic Industrial Waste Conference, USA, 135 (1994).
5. Wei, Y. L., J. Environ. Sci. Health **A 32**, 2613 (1997).
6. Wei, Y. L. and Huang, Y. L. J., Environ. Quality, March–April issue, 343 (1998).
7. U.S. EPA. SW-846 Method 3010A, (1992).
8. Ressler, T., J. Synchrotron Radiat. **5**, 118 (1998).

Physica Scripta. Vol. T115, 912–914, 2005

Linking Monte-Carlo Simulation and Target Transformation Factor Analysis: A Novel Tool for the EXAFS Analysis of Mixtures

A. Rossberg* and A. Scheinost

Institute of Radiochemistry, Forschungszentrum Rossendorf, D-01314 Dresden, Germany
The Rossendorf Beamline, ESRF, F-38043 Grenoble, France

Received June 26, 2003; accepted June 28, 2004

PACS number: 6110HT

Abstract

Aqueous metal complexes are important chemical species in the geosphere, since they often determine the mobility of metals in the environment. While EXAFS spectroscopy is the method of choice to determine the structure of such species in environmental matrices, it often fails when several complexes coexist. In this case, all present complexes contribute to the EXAFS signal, and the deconvolution into single contributions is difficult. We have developed a new algorithm to determine the spectral contributions of the single in mixtures of species, based on a combination of Monte-Carlo Simulation and Target Transformation Factor Analysis (MCTFA). This novel approach requires solely the structure of the interacting ligand as input data, enabling the determination of complexes even in "messy" environmental samples.

1. Introduction

Many attempts have been made in the past to determine structure, chemical behavior and relative distribution of aqueous metal complexes at a given set of geochemical conditions (defined by pH; Eh; concentrations of aqueous ions, solids, gasses; temperature; etc.). EXFAS spectroscopy is one of the most versatile and powerful techniques to determine the often low concentrations in the presence of complex backgrounds typical for geochemical settings. However, if more than one metal complex exists, then the EXAFS signal is the superposition of the contributions of the backscattering atoms of all metal complexes, and only average structural parameter (i.e. radial distances, coordination numbers) can be obtained. In case the EXAFS spectra of isolated complexes can be measured, one can derive the identity and quantity of the complexes in mixtures by Target Transformation Factor Analysis (TFA) and/or Linear Combination Fits (LCF) [1, 2]. Especially for uranyl-organo-complexes, however, species may remain undetected because they cannot be prepared (and measured) as pure species. Under these conditions, the EXAFS spectra of the pure metal complexes may be obtained by Iterative Target Transformation Factor Analysis (ITFA) [3–6]. Starting point for ITFA is a series of EXAFS spectra measured in dependence of one ore more physicochemical parameters, which influence the speciation (relative concentration distribution of species) of the metal complexes. Although ITFA does not depend on EXAFS spectra of pure species, it still depends on speciation data, which may often be provided by thermodynamic data bases and models. If even the data of the relative species distribution are missing, however, ITFA must fail. Therefore, we propose another approach, where only the structure of the metal-binding ligand is required. Our approach varies the position of the metal in relation to the ligand by Monte-Carlo Simulation (MC). For each structural configuration, the theoretical EXAFS spectrum is then calculated and submitted as target test vector to TFA. We have tested this approach using a series of uranyl acetate complexes at varying pH.

2. Experimental

Eight samples were prepared in the pH range 0.10–4.48 at an ionic strength of 1.2 mol/L. For all samples [U(VI)] was 0.05 mol/L and the acetic acid concentration [ac] was 1 mol/L except for the sample at pH 4.48, where [U(VI)] = 0.025 mol/L and [ac] = 0.5 M. The U L_{III}-edge EXAFS spectra of the pH series were measured at the Rossendorf Beamline (ROBL) at the ESRF (Grenoble, France) in transmission mode at room temperature. Crystallographic data of sodium tris(acetato)dioxouranate [7] were used to create the ligand structure for the MCTFA and to calculate the theoretical phase and amplitude functions for EXAFS data analysis (FEFF6).

3. Monte-Carlo Simulation Target Transformation Factor Analysis (MCTFA)

MCTFA combines the advantages of modeling and statistics. The MC simulation allows to model the three dimensional structure of the complexes by using the experimental XAS spectra and the structure of the interacting ligand as constraints [8–10]. TFA allows to check whether the resulting EXAFS spectrum of the calculated complex is a component of the series of measured EXAFS spectra [1, 3, 11].

In the following capital bold letters are matrixes, small bold letters are vectors, and italic letters are scalars. Starting point of TFA is the calculation of the abstract (abs) factor solution for the abstract reproduction of the data matrix $\mathbf{D}_{(r,c)} = \mathbf{R}_{\mathbf{abs}(r,c)}\mathbf{C}_{\mathbf{abs}(c,c)}$ ($\mathbf{D}$ accumulates the c EXAFS spectra of complex mixtures at r measuring points, $\mathbf{R}_{\mathbf{abs}}$ and $\mathbf{C}_{\mathbf{abs}}$ contains eigenvectors) by using Eigenanalysis. The orthogonal factor solution consists of c eigenvectors. Only n (n – number of main components) eigenvectors are necessary to reproduce $\mathbf{D}$. In the second step of TFA, n is determined using the eigenvalues in $\mathbf{\Lambda}$ and the indicator function *IND* [11]. After the factor compression the dimension of $\mathbf{R}_{\mathbf{abs}}$ is (r, n) and that of $\mathbf{C}_{\mathbf{abs}}$ is (n, c). In the third step a EXAFS spectrum is subjected as a test vector $\mathbf{x}_{\mathbf{test}}$ and gives a predicted (pred) vector $\mathbf{x}_{\mathbf{pred}} = \mathbf{R}_{\mathbf{abs}}\,\mathbf{\Lambda}^{-1}\mathbf{R}'_{\mathbf{abs}}\mathbf{x}_{\mathbf{test}}$ ($'$ stands for transponse). The spectrum $\mathbf{x}_{\mathbf{test}}$ is a component of the spectra of the complex mixtures if it is in agreement with the predicted spectrum $\mathbf{x}_{\mathbf{pred}}$. The spectrum $\mathbf{x}_{\mathbf{test}}$ we calculated using MC technique.

The steps of the whole algorithm are as follows: (1) Fit of a spectrum of the series to determine Debye-Waller factors σ_i for the ligand atoms and the energy shift ΔE_0 (2) Eigenanalysis of the EXAFS spectra of mixtures, factor compression. (3) Set up a cube and insert the ligand molecule. (4) Put the metal atom at a random

*e-mail: rossberg@esrf.fr

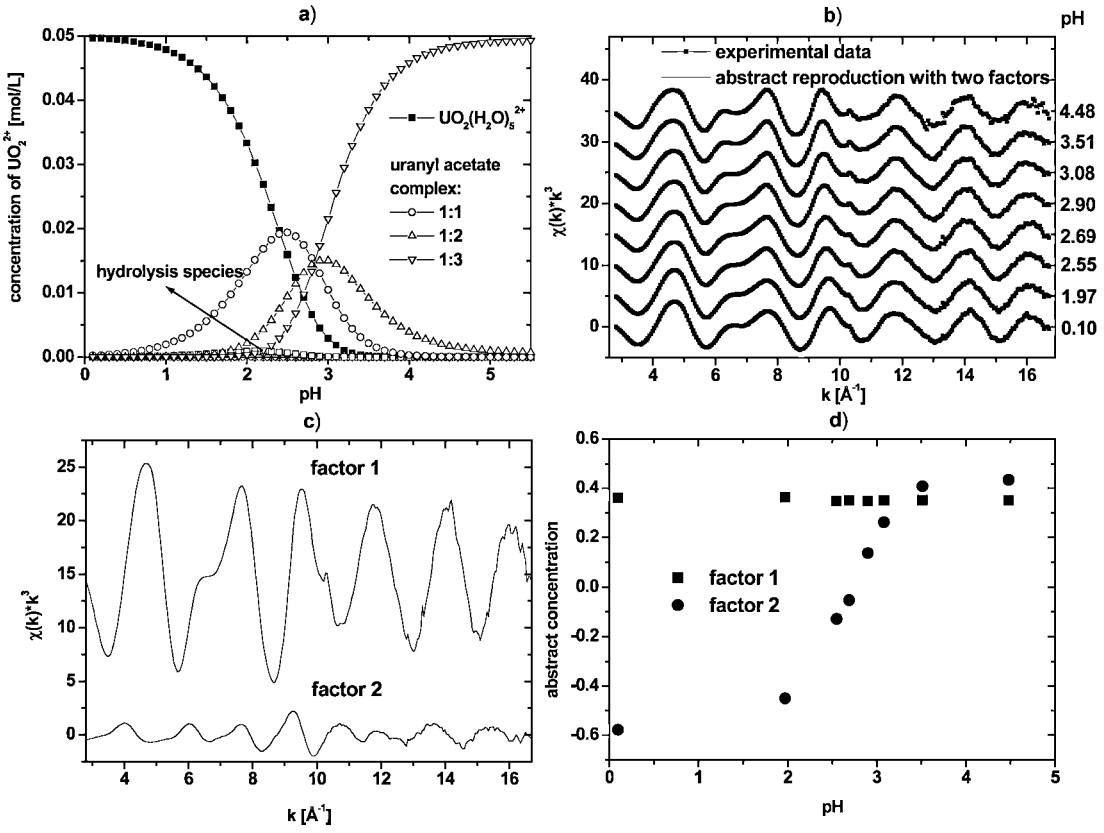

Fig. 1. (a) Speciation for [U(VI)] = 0.05 mol/L, [ac] = 1.0 mol/L, I = 1 mol/L (complex stability constants from [12]); (b) (c) content of data matrix **D** and their abstract reproduction using abstract spectra $\mathbf{R_{abs}}$ and (d) abstract concentrations $\mathbf{C_{abs}}$.

position in the cube. (5) Calculate the distances R_i between metal atom and the ligand atoms. (6) Calculate the theoretical EXAFS spectrum $\mathbf{x_{test}}$ using σ_i, R_i, and ΔE_0. (7) Calculate $\mathbf{x_{pred}}$ using the TFA procedure. (8) Determine χ^2 between $\mathbf{x_{test}}$ and $\mathbf{x_{pred}}$ and normalize χ^2 to the variance $\mathbf{x'_{pred}}\ \mathbf{x_{pred}}$, save the best normalized χ^2. (9) Go to step 4 and repeat m times. (10) Put the metal atom at the position of the lowest normalized χ^2, divide edge length of the cube by a factor, shift the center of the cube to the position of the metal atom, go to step 4 if the edge length of the cube is greater than the expected uncertainty in atomic distances otherwise stop. (11) The metal atom has reached the optimum position towards the ligand.

The algorithm has two advantages: (1) The TFA identifies also the spectrum of the pure complex $\mathbf{x_{test}}$ as a component of the spectral mixtures, therefore the algorithm is sensitive to the pure metal complexes. (2) Only the metal atom is moved during the MC simulation, which drastically reduces the computing time in relation to methods which move the whole ligand. This is especially important when large ligands are investigated.

4. Results and discussion

In the pH interval 0.10-4.48, the U(VI)/ac system contains four complexes (Fig. 1a).

Our previous study using ITFA [3, 5] has shown that only two spectroscopic components (i.e. factors, Fig. 1 b–d) are required to reproduce all spectra: the spectra of uranyl hydrate ($UO_2(H_2O)^{2+}$) and of the 1 : 3 U(VI)/ac complex, while the 1 : 1 and the 1 : 2 complexes can be reconstructed from them (Fig. 2).

From a structural point of view, these two spectroscopic units correspond to uranyl coordinated to a water molecule and uranyl

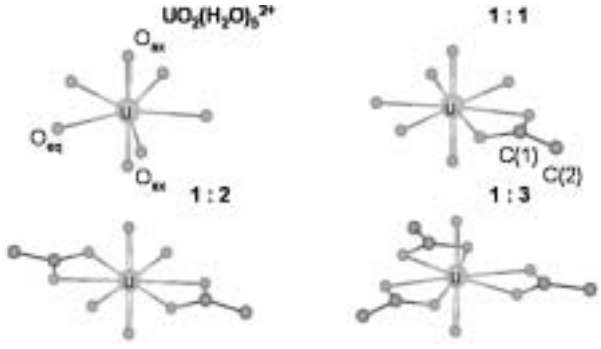

Fig. 2. Structures of uranyl hydrate and the U(VI)/ac complexes.

Table I. *EXAFS Structural parameters for the 1 : 3 U(VI)/ac complex (top) and MCTFA result (bottom; bold – determined, * constrains).*

	Atom	R	N	$\sigma^2 * 10^3$
1 : 3 U(VI)/ac complex	O_{ax}	1.78	2	1.4
	O_{eq}	2.47	6.0	8.5
	C_1	2.87	3.1	3.8
	C_2	4.39	3.1	3.8
U(VI)-carboxylate (MCTFA)	O_{ax}	1.78*	2*	1.7*
	O_{eq}	**2.46**	4*	9.5*
	C_1	**2.84**	2*	4.0*
	C_2	**4.34**	2*	4.0*

R – atomic distance [Å], N – coordination number, σ^2 – Debye-Waller factor [Å^2].

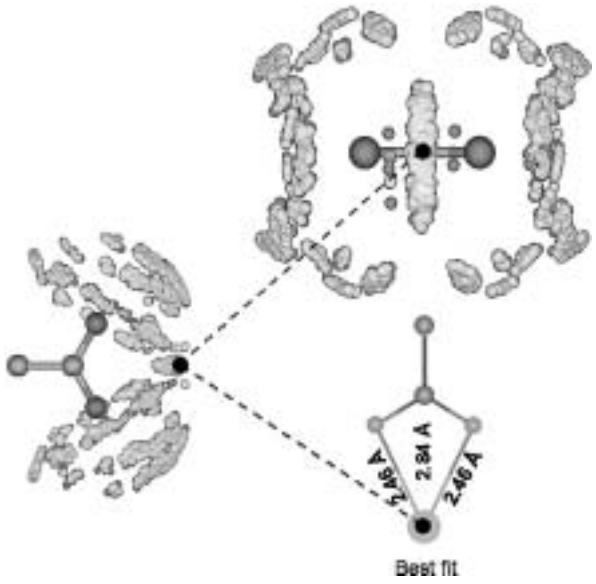

Fig. 3. MCTFA result. Brighter balls indicate U positions with the highest likelihood (best fits), darker balls indicate positions resulting in poorer fits. Structural data for the optimum position (black dot) are given in Table I.

coordinated to a carboxylic group in a bidentate arrangement. For all complexes only the number of this two structural units vary and the short-range structure as determined by EXAFS remains invariable (Table I). Note that this result was obtained by ITFA [3, 5]. In the following we demonstrate, that we can achieve the same uranyl-carboxylate structure by MCTFA, even when we use a much smaller pH range of 0.10–2.69, which does not include the pure end-member spectrum, and with a more restricted chi-range of 2.9–12.3 $Å^{-1}$, representing the typically poorer data quality of environmental samples. For the calculation of the theoretical EXAFS spectrum, we used the distance U-O_{ax}, σ^2 of O_{ax} and O_{eq}, and ΔE_0 determined from the spectrum at pH 2.69. Furthermore, we kept the distances of the two axial oxygen atoms constant, and accounted for the twofold degenerated 4-legged multiple scattering path of the uranyl chain in our calculation. Using these constraints, we achieved the structure of the uranyl-carboxylate unit in 110.000 iterations. The resulting U-O_{eq} distances are identical to those found by conventional EXAFS data analysis of the 1 : 3 U(VI)/ac complex considering an error of 0.02 Å (Table I, Fig. 3). Thus, we are confident that MCTFA may be successfully applied to solve the local structures of a wide range of complexes based solely on the ligand structure, which is often known. Thus, the newly developed method could be extremely useful to decipher the structure of metal complexes in environmental samples where a wide range of organic ligands, from simple organic acids to large biopolymers may be present.

Acknowledgement

We thank Tobias Reich for the preparation of the U(VI)/acetic acid samples and for fruitful discussions during the ITFA investigation.

References

1. Wasserman, S. R., J. Phys. IV France **7**, C2 (1997).
2. Scheinost, A. C., Kretzschmar, R., Pfister, S. and Roberts, D. R., Environmental Sci. Technol. **36**, 5021 (2002).
3. Roßberg, A., Doctoral Thesis, Technical University Dresden, (Dresden 2002).
4. Roßberg, A., Reich, T. and Bernhard, G., Analytical Bioanalytical Chem., online publication 6/17/2003 (2003).
5. Reich, T. and Roßberg, A., Physica Scripta this issue (2003).
6. Scheinost, A. C., *et al*., Physica Scripta this issue (2003).
7. Templeton, D. H., Zalkin, A., Ruben, H. and Templeton, L. K., Act. Cryst. **C41**, 1439 (1985).
8. McGreevy, R. L., J. Phys.: Condens. Matter **13**, 877 (2001).
9. Winterer, M., J. Appl. Phys. **88**, 5635 (2000).
10. Benefatto, M., Congiu-Castellano, A., Daniele, A. and Della Longa, S., J. Synchr. Rad. **8**, 267 (2001).
11. Malinowski, E. R., "Factor Analysis in Chemistry" (John Wiley & Sons, New York 1991).
12. Ahrland, S., Acta Chem. Scand. **5**, 199 (1951).

Physica Scripta. Vol. T115, 915–917, 2005

Ca-UO_2-CO_3 Complexation – Implications for Bioremediation of U(VI)

S. D. Kelly[1*], K. M. Kemner[1], S. C. Brooks[2], J. K. Fredrickson[3], S. L. Carroll[2], D. W. Kennedy[3], J. M. Zachara[3], A. E. Plymale[3] and S. Fendorf[4]

[1]Environmental Research Division, Argonne National Laboratory, 9700 South. Cass Ave, Argonne, IL, USA
[2]Oak Ridge National Laboratory, Oak Ridge, TN, USA
[3]Pacific Northwest National Laboratory, Richland, WA, USA
[4]Stanford University, Stanford, CA, USA

Received June 26, 2003; accepted January 8, 2004

PACS numbers: 01.30.Cc, 61.10.Ht, 82.30.Nr

Abstract

An attractive remediation strategy for the removal of highly soluble U(VI) from groundwater is microbial reduction of soluble U(VI) to U(IV) as insoluble uraninite. The feasibility of this remediation strategy depends on the rate and extent of microbial reduction of U(VI) in the presence of ions commonly found in groundwater that can form complexes with uranyl. Recently, Ca in solutions with U(VI) has been shown to inhibit microbial reduction of U(VI). Indirect evidence supports the formation of a Ca-UO_2-CO_3 complex that may be responsible for the limited microbial reduction of U(VI) in the presence of Ca, but direct evidence for the formation of a Ca-UO_2-CO_3 complex is needed for verification. X-ray absorption fine-structure measurements of solutions containing 50 μM U(VI) and 30 mM bicarbonate, with and without 5 mM Ca, were made to determine whether a Ca-UO_2-CO_3 complex was present. These results are discussed.

1. Introduction

Activities associated with the mining and processing of U ores have resulted in vast areas of environmental contamination. Current remediation strategies are based on the removal of soluble U(VI) from the aqueous phase by reducing it to insoluble U(IV) in the form of a uranium oxide precipitate, uraninite. The formation of the insoluble uraninite should minimize the transport of U from contaminated areas. Previous studies have shown that dissimilatory metal-reducing bacteria (DMRB) couple the oxidation of organic matter or of H_2 to the reduction of oxidized metals including U(VI). The feasibility of this remediation strategy depends on the rate and extent of microbial reduction of U(VI) in the presence of ions commonly found in groundwater that can form complexes with U(VI).

Factors that enhance or inhibit bacterial U(VI) reduction are not well understood. Recently, Ca in solutions with U(VI) has been shown to inhibit microbial reduction of U(VI) [1]. Indirect evidence of for a Ca-UO_2-CO_3 solution complex in solution has been demonstrated [2, 3]. Such complexes have been largely overlooked, because most equilibrium speciation models predict the dominant uranyl species in calcareous groundwater to be uranyl carbonates. These species may be responsible for the limited microbial reduction of U(VI). Direct evidence for the formation of a Ca-UO_2-CO_3 complex is needed to help clarify the cause of the limited microbial reduction of U(VI) in calcareous groundwater.

X-ray absorption fine-structure (XAFS) measurements of solutions containing environmentally relevant concentrations of U(VI) (50 μM), bicarbonate (30 mM), and acetate (5 mM) with and without Ca (5 mM) have been made to determine the presence of a Ca-UO_2-CO_3 complex. Our previous study [1] briefly reported results for a similar +Ca solution (with no added acetate) as supporting evidence for the formation of a Ca-UO_2-CO_3 complex. A more thorough analysis of the EXAFS data from two samples that differ only in the presence or absence of Ca is presented here.

2. Experimental Methods

The solution samples were prepared under anoxic conditions. Both solution samples contain 50 μM U(VI), 30 mM HCO_3, and 5 mM acetate. One sample (+Ca) also contains 5 mM $CaCl_2$ while the other sample (−Ca) did not. The U concentration in these samples of 50 μM are similar to the level of U contamination at the NABIR Field Research Center site, Oak Ridge National Laboratory, TN, USA, but are very dilute for EXAFS measurements. For our 3 mm thick sample the change in the absorption coefficient at the U L_3-edge is approximately 2×10^{-4}. This edge step is approximately two orders of magnitude smaller than a standard edge step for a fluorescence measurement. Uranium L_3-edge EXAFS measurements were made at the MR-CAT insertion device (10-ID) beamline [4] at the Advance Photon Source. The insertion device was tapered to reduce the variation in the X-ray intensity (to less than 15%) through the scanned energy range. A Si(111) double crystal monochromator was used to select the X-ray energy. A Rh mirror was used to remove X-rays with higher harmonic energies. The measurements were made in fluorescence mode by using a 13 element solid-state detector (Canaberra with XIA electronics). The incident X-ray intensity was monitored using a nitrogen filled ion chamber. The intensity of the nonfocused beam of approximately 1 mm square at the U L_3-edge is approximately 5×10^{13} photons/s. The integration time for each data point of approximately 12 s resulted in approximately one EXAFS scan per hour. The +Ca sample was scanned 3 times while the −Ca sample was scanned 10 times. The data were processed by using standard procedures and with UWXAFS [5] software package. The averaged $\chi(k)$ data are shown in Figure 1. Theoretical models were constructed with the program FEFF7 [6] and the crystallographic atomic positions of andersonite [7]. Automatic overlap of the muffin tin potentials was used in the FEFF7 calculation as previously reported [8].

*e-mail: skelly@anl.gov

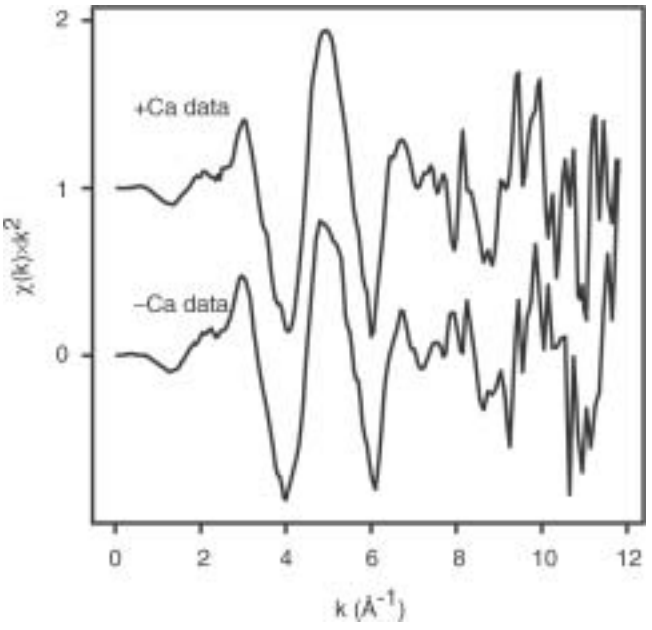

Fig. 1. Averaged $\chi(k) \cdot k^2$ data from the +Ca (2.7 to 10 $Å^{-1}$) and −Ca (2.7 to 9 $Å^{-1}$) samples.

3. EXAFS Data Analysis

Speciation calculations based on formation constants for a proposed Ca-UO_2-CO_3 complex indicated that this complex will be the major (∼98.4%) component in our +Ca sample [1]. The U(VI) is in the form of a uranyl tricarbonate species with an unknown number of Ca atoms, presumably bound to the distant oxygen atoms of the carbonate groups. A ball-and-stick model of this species is shown in Fig. 2. This figure shows the equatorial oxygen (Oeq) atoms in the plane of the page with the axial oxygen (Oax) atoms above and below the uranium atom. The model for this structure contains 4 shells of atoms. The coordination numbers in the model for the uranyl-tricarbonate species are held to the expected values based on the speciation calculations. These coordination numbers are 2 Oax, 6 Oeq, 3 C, and 3 Odist (distant oxygen atoms of the carbonate groups) as shown in Fig. 2.

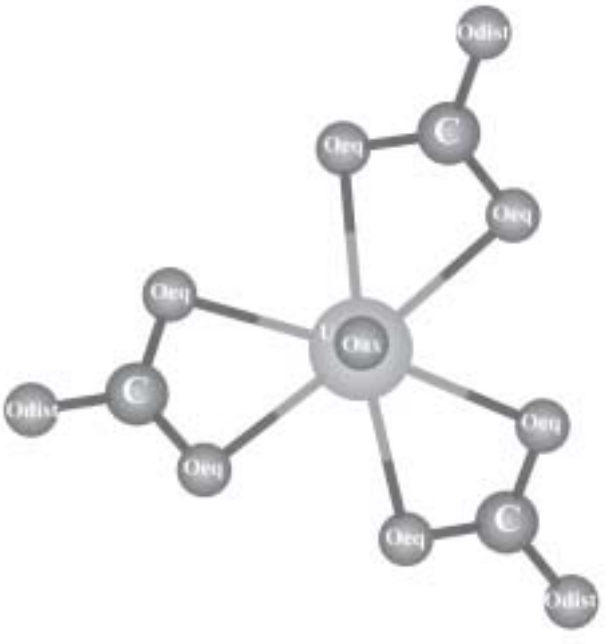

Fig. 2. Ball and Stick figure of $(UO_2)(CO_3)_3$ species. The uranyl moiety (UO_2^{2+}) is made up of the U atom bound with two axial oxygen (Oax) atoms that are located above and below the U atom.

Important U-Oax1-U-Oax2 and U-C-Odist multiple scattering (MS) paths that must be included in the model. The EXAFS variables for these MS paths can be approximately parameterized in terms of the single scattering (SS) path containing the end atoms. For a linear group of three atoms, U-C-Odist, the σ^2-value of the SS path U-Odist has been set equal to the σ^2-value of the MS paths. This is exactly true if the atoms are linear and becomes an approximation as they deviate slightly from linearity. The σ^2-values for the U-Oax1-U-Oax2 MS paths are parameterized as described elsewhere [8]. Based on other Ca-UO_2-CO_3 systems, the U-Ca distance is expected to be about 3.8 to 4.1 Å. This path was added to model our +Ca data. Table I lists the paths included in the model and the EXAFS parameterizations.

Both data sets (+Ca and −Ca) were fit simultaneously by using a k-weight values of 1, 2, and 3 in the Fourier transform. Initially all N, Δr and σ^2 values were constrained to the same values for both data sets. This initial model failed to reproduce both data sets simultaneously. The other extreme, allowing all N, Δr and σ^2 values to vary independently also failed because of our limited data ranges. The minimum freedom needed to describe the data accurately was determined to have equal N and Δr values for both data sets and variable σ^2 values (See Table I).

Table I. *EXAFS parameters for the simultaneous fits to +Ca and −Ca data sets. One S_0^2 value and one ΔE value were also determined in the fit. The two data sets have 6 common variables ($\Delta Roax$, $\Delta Roeq$, ΔRc, $\Delta Rodist$, ΔE, and S_0^2). The −Ca data set has 4 (σ^2oax-, σ^2oeq-, σ^2c-, and $\sigma^2odist-$) independent variables, while the +Ca data set has 7 (σ^2oax+, σ^2oeq+, σ^2c+, $\sigma^2odist+$, $Nca+$ $\Delta Rca+$, and σ^2ca+) independent variables. Therefore, the −Ca and +Ca data sets have averages of 7 and 10 variables, respectively. The −Ca and +Ca data sets have 14 and 16 independent points, respectively. The M.S. path U-C-Odist has a degeneracy of twice the S.S. path U-Odist because there are two equivalent M.S. paths (U-Odist-C and U-C-Odist).*

Path	Model	N	ΔR	σ^2
U-Oax	+Ca	2	$\Delta Roax$	σ^2oax+
	−Ca			σ^2oax-
U-Oeq	+Ca	6	$\Delta Roeq$	σ^2oeq+
	−Ca			σ^2oeq-
U-C	+Ca	3	ΔRc	σ^2c+
	−Ca			σ^2c-
U-Oax1-U-Oax1	+Ca	2	$2 \cdot \Delta Roax$	$4 \cdot \sigma^2oax+$
	−Ca			$4 \cdot \sigma^2oax-$
U-Oax1-Oax2	+Ca	2	$2 \cdot \Delta Roax$	$2 \cdot \sigma^2oax+$
	−Ca			$2 \cdot \sigma^2oax-$
U-Oax1-U-Oax2	+Ca	2	$2 \cdot \Delta Roax$	$2 \cdot \sigma^2oax+$
	−Ca			$2 \cdot \sigma^2oax-$
U-Ca	+Ca	$Nca+$	$\Delta Rca+$	σ^2ca+
U-Odist	+Ca	3	$\Delta Rodist$	$\sigma^2odist+$
	−Ca			$\sigma^2odist-$
U-C-Odist	+Ca	6	$\Delta Rodist$	$\sigma^2odist+$
	−Ca			$\sigma^2odist-$
U-C-Odist-C	+Ca	3	$\Delta Rodist$	$\sigma^2odist+$
	−Ca			$\sigma^2odist-$

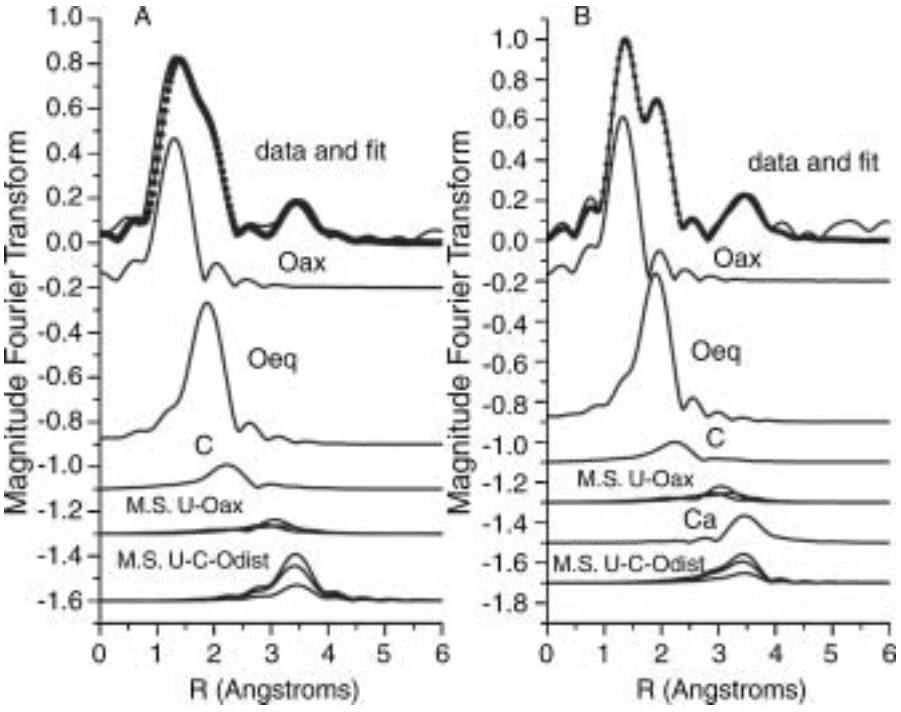

Fig. 3. The magnitude of the Fourier transform of the −Ca (A) and +Ca (B) data and the model using a *k*-weight of 2. The top of each panel shows the data (line) and the fit (symbols). Beneath the data and fit are the individual contributions to the model from each path. The fit range is 1 to 4 Å.

Table II. *Best-fit values from the simultaneous fit of +Ca and −Ca data. Values without uncertainties were not determined in the fit to the data. The best-fit value for S_0^2 is 0.83 ± 0.10 and ΔE is 5.3 ± 0.8 eV for all paths of both data sets.*

Path	Data Set	*N*	*R* (Å)	σ^2 ($\times 10^{-3}$ Å^2)
U-Oax	+Ca	2	1.82 ± 0.01	0 ± 1
	−Ca			1 ± 1
U-Oeq	+Ca	6	2.45 ± 0.01	5 ± 1
	−Ca			7 ± 2
U-C	+Ca	3	2.88 ± 0.03	12 ± 6
	−Ca			10 ± 8
U-Oax1-U-Oax1	+Ca	2	3.64 ± 0.01	0 ± 1
	−Ca			5 ± 5
U-Oax1-Oax2	+Ca	2	3.64 ± 0.01	0 ± 1
	−Ca			3 ± 3
U-Oax1-U-Oax2	+Ca	2	3.64 ± 0.01	0 ± 1
	−Ca			3 ± 3
U-Ca	+Ca	1.4 ± 1.2	4.02 ± 0.03	0 ± 1
U-Odist	+Ca	3	4.11 ± 0.02	8 ± 10
	−Ca			3 ± 3
U-C-Odist	+Ca	6	4.11 ± 0.02	8 ± 10
	−Ca			3 ± 3
U-C-Odist-C	+Ca	3	4.11 ± 0.02	8 ± 10
	−Ca			3 ± 3

Figure 3 shows the Fourier transform of the data and the best-fit models. Under the data and model in the Figure 3 is shown the individual contribution from each path included in the models, illustrating the importance of the MS paths and the overlap of the Odist paths with the Ca path. The best-fit values for all the paths included in the models are listed in Table II.

4. Conclusions

The best-fit value for the number of Ca atoms for the +Ca sample is 1.4 ± 1.2 indicating the presence of a Ca-UO_2-CO_3 complex in this sample. All the other parameters including the σ^2 values and Δr values, are within the uncertainties of previously reported values. Simultaneously fitting the +Ca and −Ca data was necessary to distinguish between the contribution from the Ca atom, the distant oxygen (Odist), and the MS paths (U-C-Odist) of the carbonate groups. Direct evidence of the Ca-UO_2-CO_3 complex and its role in bioreduction of U(VI) in calcareous ground waters like those found at the FRC must be considered in developing a feasible bioremediation strategy.

Acknowledgment

Use of the Advanced Photon Source and MRCAT was supported by the U.S. Department of Energy, Office of Science, Office of Basic Energy Sciences, under Contract No. W-31-109-ENG-38. The work was supported by the U.S. Department of Energy, Office of Science, Office of Biological and Environmental Research, Natural and Accelerated Bioremediation Program.

References

1. Brooks, S. C., *et al.*, Environ. Sci. Technol. **37**, 1850 (2003).
2. Kalmykov, S. N. and Choppin, G. R., Radiochim. Acta **88**, 603 (2000).
3. Bernhard, G., Geipel, G., Brendler, V. and Nitsche, H., Radiochim. Acta **74**, 87 (1996).
4. Segre, C. U., *et al.*, Synchrotron Radiation Instrumentation: Eleventh U.S. Conference **CP521**, 419 (2000).
5. Stern, E. A., Newville, M., Ravel, B., Yacoby, Y. and Haskel, D., Physica B **208 & 209**, 117 (1995).
6. Zabinsky, S. I., Rehr, J. J., Ankudinov, A., Albers, R. C. and Eller, M. J., Phys. Rev. B **52**, 2995 (1995).
7. Coda, A., Della Giusta, A. and Tazzoli, V., Acta Cryst. **B37**, 1496 (1981).
8. Hudson, E. A., Rehr, J. J. and Bucher, J. J., Phys. Rev. B **52**, 13815 (1995).

Physica Scripta. Vol. T115, 918–920, 2005

Iron and Manganese Minerals from South African Ironstone Deposits

A. Roy[1], G. R. Byerly [2], D. R. Lowe[3], M. W. Walsh[4] and C. Bianchetti

J. Bennett Johnston Sr. Center for Advanced Microstructures and Devices, Louisiana State University, Baton Rouge, LA 70806, USA

Received June 26, 2003; accepted in revised form July 22, 2003

PACS numbers: 87.64Gb, 89.60k

Abstract

Ironstone deposits are common in the Barberton Mountain Land of South Africa. They are composed of fine-grained goethite with significant amounts of several manganese oxide phases. Fossil bacteria in these rocks are often preserved within the iron and manganese oxide phases, and bacteria may have played a significant role in the formation of the deposits. Manganese minerals, in particular lithiophorite ($(LiAl_2(Mn_2^{+IV}Mn^{+III})O_6(OH)_6)$ and todorokite ($(Ca, Na, K)_x(Mn^{+IV}Mn^{+III})_6O_{12} \cdot 3.5H_2O)$), have been identified by X-ray diffractometry.

These rocks have now been studied by X-ray absorption fine structure spectroscopy. X-ray absorption near edge structure (XANES) spectroscopy showed that the oxidation state of both iron and manganese in these rocks is high. Least squares modeling of the X-ray absorption near edge structure (XANES) spectra shows that most of the manganese is present in the oxidation states +III and +IV, with no detectable manganese as +II. Similarly for iron, only +III oxidation state could be identified in most rocks. Extended X-ray absorption fine structure (EXAFS) studies confirm that both edge-sharing (lithiophorite, todorokite) and corner-sharing octahedra (todorokite) are present and constrains the proportions of these two minerals. Bacteria stabilized the higher oxidation states of iron and manganese during precipitation, acting as an important component of the mineralization.

1. Introduction

Bodies of ironstone deposits are common in the Barberton Mountains of South Africa. These deposits have been interpreted as products of Archean (3.5–3.2 Ga) sea-floor hydrothermal vents. Some of the present authors (Lowe and Byelry [1]) have recently reinterpreted them as modern subaerial deposits. Along with the geological arguments indicating very little deformation for such old rocks, one of the evidence in favor of modern origin of these deposits is the common occurrence of the mineral goethite. Goethite has low thermal stability, easily transforming to hematite at 80 °C–100 °C [2]. In addition to goethite, several manganese minerals are also present in these ironstone deposits.

Analysis of rock specimens from these locations by optical and electron microscopy showed that the iron and manganese minerals were probably of bacterial origin (Figs. 1, 2, and 3). The filamentous structure in Fig. 1 is typical of that reported by many researchers from bacterial deposits [3]. The radial acicular grains are composed or iron. Fig. 2 shows an optical thin section of the same rock. The translucent regions are the tubes whereas the dark opaque regions are filled with manganese minerals. Electron probe micro-analysis of the needles in Fig. 3 indicated them to be todorokite ($(Ca, Na, K)_x(Mn^{+IV}Mn^{+III})_6O_{12} \cdot 3.5H_2O$). Along with todorokite, lithiophorite($LiAl_2(Mn_2^{+IV}Mn^{+III})O_6(OH)_6$) was also identified in the rocks by X-ray diffractometry. Manganese minerals are typically very fine grained, poorly crystalline, and intimately mixed with other phases to such a degree that identification is difficult. In addition, none of the techniques used so far to characterize these rocks identify the oxidation state of either iron or manganese.

Resolution of the ambiguity in the oxidation states and the type of iron and manganese minerals should provide us with important information about the nature of biological oxidation of iron and manganese. This paper reports the results of the X-ray absorption fine structure (XAFS) studies.

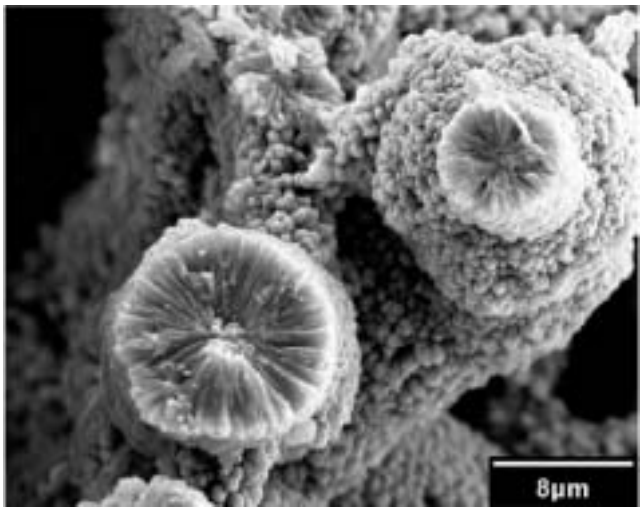

Fig. 1. Scanning electron micrograph of an ironstone showing evidence of bacterial precipitation of goethite.

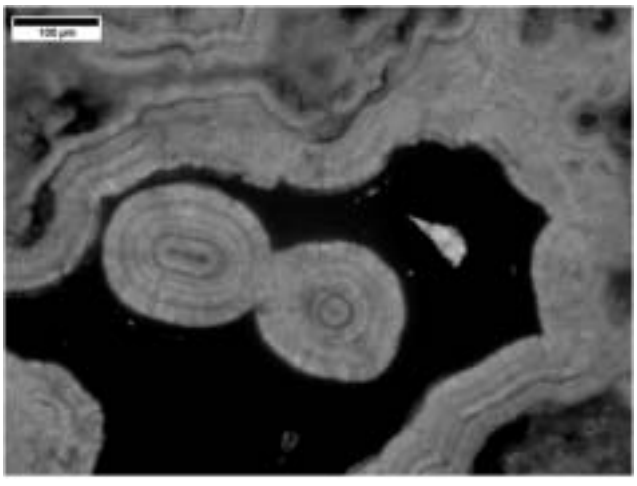

Fig. 2. Optical photomicrograph of a thin section (30 μm thickness) of the same rock as in Fig. 1.

[1]email: reroy@lsu.edu

[2]Department of Geology and Geophysics, Louisiana State University, Baton Rouge, LA 70803, USA.

[3]Department of Geological and Environmental Sciences, Stanford University, Stanford, CA 94305, USA.

[4]Department of Agronomy, Louisiana State University, Baton Rouge, LA 70803, USA.

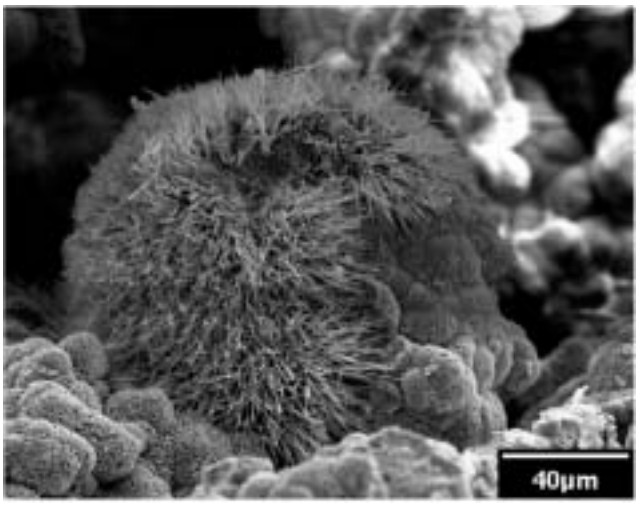

Fig. 3. Needle-like todorokite crystals.

2. Experimental Procedure

2.1. *Sample Locations*

The rocks studied in this investigation were obtained from three locations of the Barberton Mountain Land in South Africa and the details are provided in Table I.

2.2. *X-Ray Absorption Spectroscopy*

Manganese and iron K edge spectra were obtained at the J. Bennett Johnston Sr. Center for Advanced Microstructures and Devices (CAMD), Baton Rouge, Louisiana, USA. The synchrotron ring operates at 1.3 GeV with the ring current typically between 120 and 50 mA. The measurements were made at the Double Crystal Monochromator (DCM) beam line with Ge 220 crystals. The concentration of the elements was such that data could be collected in transmission for iron but both fluorescence and transmission modes had to be used for manganese. The experiments were conducted in air. XANES spectra for manganese and iron were collected from ca. 150 eV below the edge to up to 20 eV below the edge in 3 eV steps; from −20 eV to 60 eV above the edge in 0.3 eV steps; and 60 eV above the edge to 300 eV above the edge in 3 eV steps. For manganese EXAFS, the range over which data could be collected was limited by the iron K edge at 7112 eV. Thus only several hundred eV of data could be collected. The steps were 3 eV below the edge and 2 eV above the edge up to 7112 eV. The data were reduced with WinXAS [4], Athena, and Artemis.

3. Results and Discussion

Fig. 4 shows the iron XANES spectra of some selected ironstones along with those of some standard iron minerals. A synthetic ferrous oxide (from Alfa Aesar) XANES spectrum is also included

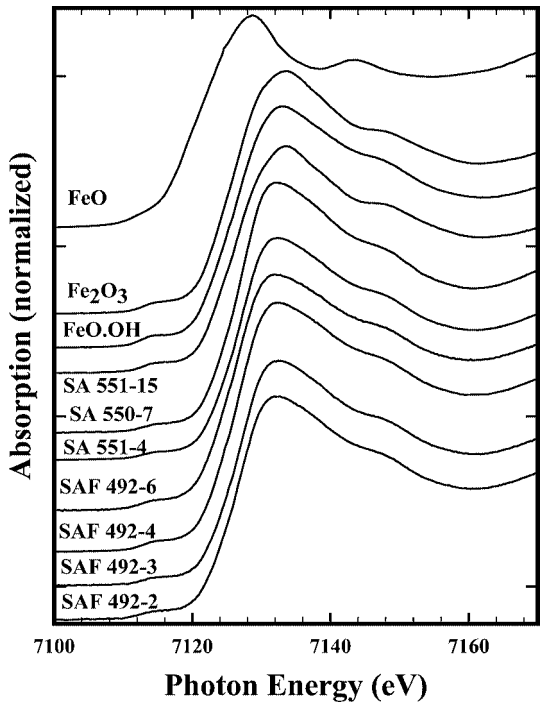

Fig. 4. Iron K edge XANES spectra from standard minerals and ironstones.

to show that no ferrous iron is present in any of these rocks. The locations of the pre-edge peak (7112.58 eV vs. 7113.22 eV), the edge (7126.42 eV vs. 7126.96 eV), the white line maxima (7133.07 eV vs. 7133.5 eV), and the minor peak (7145.65 eV vs. 7146.28 eV) beyond the white line are different for goethite and hematite. A comparison of the XANES spectra of the standard minerals with those of the ironstones shows that SA 551-15 (see Table I) contains hematite whereas the rest contains goethite. For example, least squares analysis of the spectrum SAF 492-2 indicates that 90% of it is goethite.

Fig. 5 shows the manganese K edge EXAFS spectra of some representative minerals from the ironstone deposits. The pseudo-radial distribution functions show three main peaks up to the distance of 3.5 Å. These are due to Mn-O, Mn-Mn_e and Mn-Mn_c shells [5], where the e and c subscripts stand for edge sharing and corner sharing configurations, respectively. SAF-492-2 does not have any corner sharing octahedra, indicating that it has edge sharing octahedra only and, thus, it is a layered structure. X-ray diffractometry previously identified lithiophorite, a mineral with a layered structure, in this specimen and thus confirms the structure determination by EXAFS. SA 550-7, has a strong Mn-Mn_c shell, suggesting a high degree of corner-sharing. X-ray diffractometry identified todorokite in this specimen, and the EXAFS data confirms the presence of a corner-sharing MnOx mineral in this specimen. The ratio of the peak heights of the shells Mn-Mn_e and Mn-Mn_c relates to the degree of corner-sharing in a

Table I. *Sample locations and descriptions.*

	Western Location	Central Location	Eastern Location
Latitude	25°55.749′ S	25°55.612′ S	25°54.384′ S
Longitude	30°50.178′ E	30°54.904′ E	31°01.076′ E
Elevation	Approximately 5,100 feet above sea level	Approximately 5,200 feet above sea level	Approximately 5,400 feet above sea level
Sample number	SAF 492-X SA 552-X	SA 550-X	SA 551-X
Minerals identified	Goethite, kaolinite, lithiophorite, todorokite	Mostly goethite	Goethite and hematite

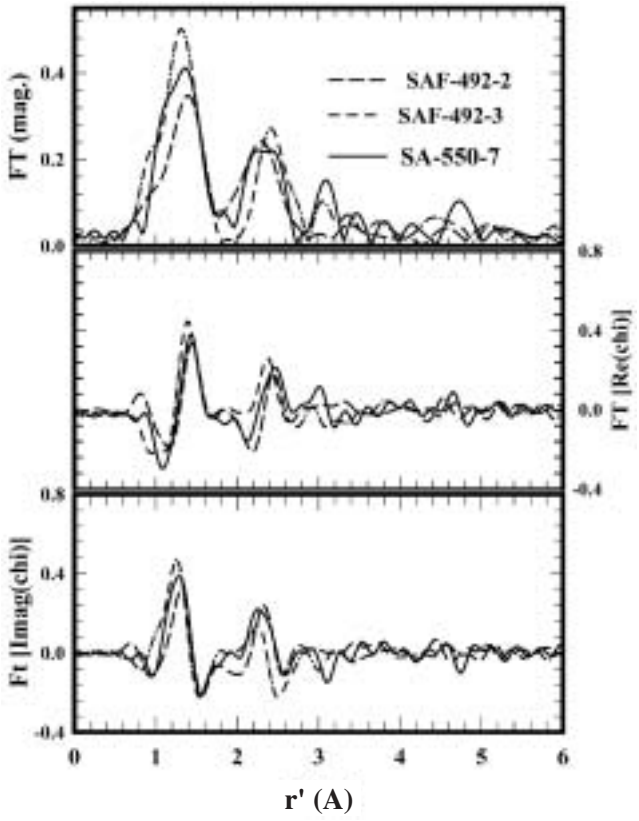

Fig. 5. Manganese K edge EXAFS spectra from some selected ironstones.

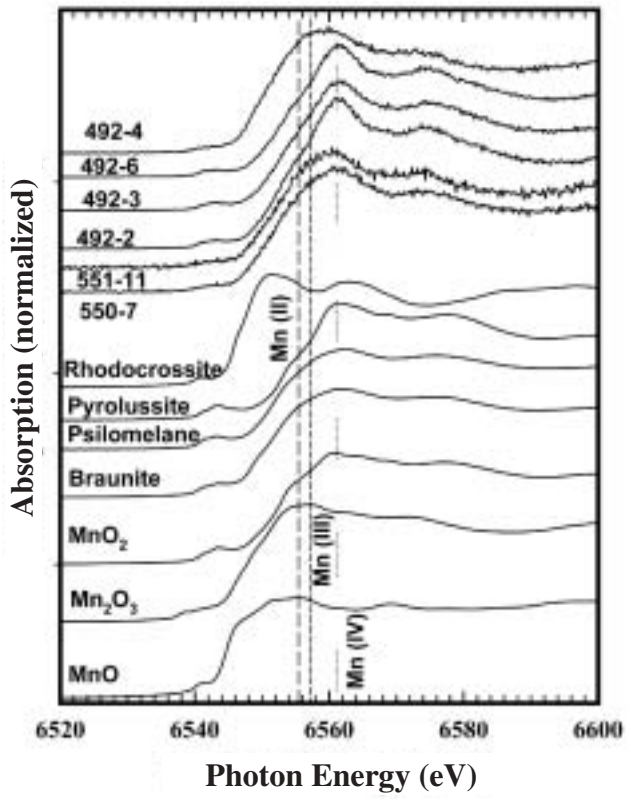

Fig. 6. Manganese K edge XANES spectra of some standard minerals and ironstones.

MnOx mineral [5]. This ratio is different in each of the specimens shown in the figure. If it is assumed that this ratio is constant in one mineral, then SAF492-3 could be a mixture of the minerals lithiophorite and todorokite.

Fig. 6 shows the manganese K edge XANES spectra of some of the representative minerals, along with those of some MnOx minerals and synthetic standards. The formal oxidation state of the manganese in these minerals ranges from +II to +IV, and the coordination from six to four. Least-squares modeling of the X-ray absorption near edge structure (XANES) spectra shows that most of the manganese is present in oxidation states +III and +IV, with no detectable manganese as +II.

X-ray absorption fine structure (XAFS) studies show that the oxidation state of iron and manganese in these rocks is high. They are +III for iron and +III and +IV for manganese. Iron and manganese oxidizing bacteria are common in nature. Such bacteria precipitated these minerals or their pre-cursors. Ehrlich [3] has proposed a manganese cycle in nature where the initial precipitate of bacterial oxidation is an amorphous MnO_2 which diagenetically alters to more crystalline varieties of minerals such as todorokite and lithiophorite. Hematite may also be a product of diagenetic alterations. Observations of thin sections of these rocks (Fig. 1) under the optical microscope indicated that the iron oxides formed first, with the voids later filled by the manganese minerals. The bacteria thus acted sequentially, depositing the iron oxides first followed by the manganese oxides.

4. Conclusions

The oxidation state of the iron and manganese minerals is high in the ironstones from the Barberton Mountain Land of South Africa. The present manganese minerals are probably diagenetic alteration products of initial amorphous MnO_2.

References

1. Lowe, D. R. and Byerly, G. R., Geology in press (2003).
2. Yapp, C., Ann. Rev. Earth Pl Sc **29**, 165 (2001).
3. Ehrlich, H. L., "Geomicrobiology" (Marcel Dekker, Inc., New York, 1996) p. 389.
4. Ressler, T., J. Synchrotron Radiat. **5**, 118 (1998).
5. Manceau, A. and Combes, J. M., Phys. Chem. Miner. **15**, 283 (1988).

Physica Scripta. Vol. T115, 921–922, 2005

In Situ Speciation of Nickel in Hydrous Melts Exposed to Extreme Conditions

M. Muñoz[1*], H. Bureau[2], V. Malavergne[1], B. Ménez[3], M. Wilke[4], C. Schmidt[5], A. Simionovici[6,7], A. Somogyi[6] and F. Farges[1,8]

[1]Laboratoire des Géomatériaux, CNRS FRE 2455, Université de Marne-La-Vallée, France
[2]Laboratoire Pierre-Süe, CEA, Saclay, France
[3]Laboratoire de Géosciences Marines, IPG, Paris, France
[4]Institut fuer Geowissenschaften, Potsdam Universitaet, Germany
[5]GeoForschungsZentrum Potsdam, Germany
[6]ESRF, Grenoble, France
[7]Laboratoire des Sciences de la Terre, ENS, Lyon, France
[8]Department of Geological and Environmental Sciences, Stanford University, USA

Received June 26, 2003; accepted November 4, 2003

PACS numbers: 61.10.Ht, 91.35.Gf, 91.65.Nd

Abstract

In situ high-temperature and high-pressure XAFS experiments were performed at the Ni K-edge, at the ID22 μ-beamline of the ESRF (Grenoble, France). The experimental setup consists of an externally heated "Bassett-modified" hydrothermal diamond-anvil cell. The sample chamber is loaded with a water-saturated haplorhyolitic glass: $(NaAlSi_3O_8)_{47}(KAlSi_3O_8)_{21}(SiO_2)_{32}$, together with an aqueous $NiCl_2$-solution (0.35 M) and an air bubble. The experiment is carried out to a temperature (T) of 780 °C, and the corresponding hydrostatic pressure (P) is calculated to be around 520 MPa, based on the equation of state of water. μ-XANES spectra are then collected *in situ* in the silicate melt and in the aqueous phase. Spectroscopic data are first interpreted in terms of speciation. At the experimental P-T conditions, nickel is essentially four-coordinated in the hydrous melt, whereas its coordination is 5 in the glass. Moreover, based on the theoretical description of the absorption edge, the XANES spectra are used to derive the "fluid/melt" partitioning coefficient for nickel (0.22 ± 0.05), as well as the density of the hydrated melt ($0.9 \pm 0.5\,g/cm^3$).

1. Introduction

Structural and thermodynamical properties of hydrous silicate melts are of major interest for understanding fundamental geological processes related to explosive volcanic eruptions. Particularly, information concerning trace element speciation, and "fluid/melt" partitioning behavior, is required for understanding the transport properties as well as the geochemical processes controlling the formation of deep Earth magmas. Also, information concerning the density of hydrous silicate melts is required to better understand the dynamic properties related to the ascension of "highly-hydrated" magmas. One way to obtain such information is to perform *in situ* experiments using a hydrothermal diamond-anvil cell. That method is particularly adapted for the study of hydrous silicate melts [1], and can typically reach temperatures to 1000 °C and pressures to 1–2 GPa.

2. Experimental

In situ high-temperature and high-pressure experiments are performed using a "Bassett-modified" hydrothermal diamond-anvil cell (HDAC). The sample chamber is loaded with a water-saturated glass of haplorhyolitic chemical composition: $(NaAlSi_3O_8)_{47}(KAlSi_3O_8)_{21}(SiO_2)_{32}$. Then, an aqueous $NiCl_2$-solution (0.35 M) is added with an air bubble in the sample chamber (see Fig. 1, left). The H_2O "liquid/vapor" homogenization temperature, measured before and after the heating run, is 295 ± 10 °C. Consequently, at the experimental temperature (i.e., 780 °C), the pressure is calculated to be around 520 MPa, based on the equation of state of water [2]. At the melt state, the silicate phase forms hydrated, and nearly-spherical "globules" in equilibrium with the aqueous phase [1, 3] (see Fig. 1, right).

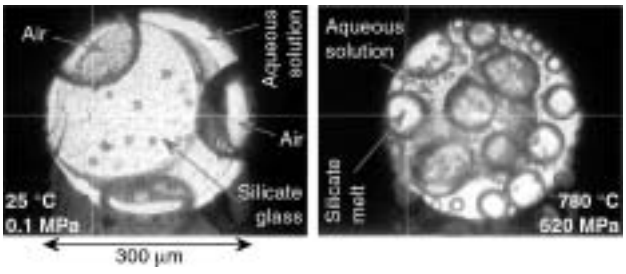

Fig. 1. Haplorhyolitic melt in an aqueous $NiCl_2$-solution (0.35 M), exposed to high temperature and high pressure.

During the experiment, μ-XANES spectra are collected at the Ni K-edge in fluorescence mode (ID22 beamline, ESRF, France); an optical monitoring of the sample being systematically performed before and after data acquisition. We used Si(111) double crystals monochromator, and Kirckpatrick-Baez focusing mirrors, so that the spatial resolution of the incident X-ray beam was 3×5 µm. Also, XANES spectra were collected using 0.1 eV steps in the pre-edge region and 0.5 eV steps in the main edge crest region.

3. Results and Discussion

The normalized Ni K-edge XANES spectra collected for the hydrated melt and the quenched glass are first interpreted in terms of nickel speciation. *Ab initio* calculations were performed using the FEFF 8.28 package assuming the crystal structure of NiO (6-coordinated Ni) and $NiCr_2O_4$ (4-coordiated Ni); the XANES spectra being calculated using Hedin-Lundqvist potentials and default values for all options.

Based on experimental [4] and theoretical approaches, the absorption edge XANES spectra as well as the position of the first "EXAFS" oscillation (gray line), traduce essentially the presence of NiO_4 moieties in the hydrous silicate melt

*e-mail: munoz@oreka.com

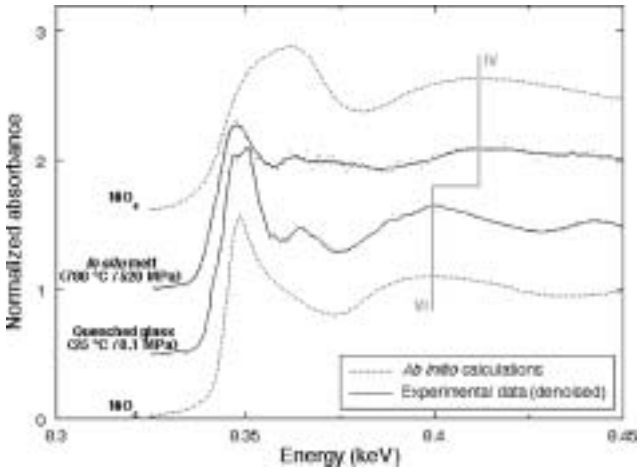

Fig. 2. Comparison between the Ni K-edge theoretical XANES spectra for NiO_4 and NiO_6 clusters, and the experimental spectra collected *in situ* for the hydrated silicate melt and for the quenched glass.

(see Fig. 2). This important result shows that quenched glasses are not appropriate images of their corresponding melts. Also, the coordination numbers of nickel in hydrous melts as well as in anhydrous melts [5] are similar, suggesting that water does not highly affect the local structural environment of nickel under *in situ* conditions.

The sample density (ρ) as well as the mass fraction of nickel (x_{Ni}) are then extracted from the μ-XANES spectra (edge jumps uncorrected) using the following equation [6]:

$$\alpha.\Delta\mu = \rho.x_{\mathrm{Ni}}.\Delta(\mu/\rho)_{\mathrm{Ni}} \quad (1)$$

in which $\Delta(\mu/\rho)_{\mathrm{Ni}}$ is the variation of the mass absorption coefficient before and after the edge, $\Delta\mu$ is the experimental edge jump at the Ni K-edge (modeled using an arctangent; see Fig. 3), and α is an "attenuation factor" due to the experimental setup. More precisely, this attenuation factor traduces the thickness of the sample, but also the non-linearity of the absorption coefficient due to the absorption of the X-ray beam by the diamonds, as well as the fluorescence detection at the rear of the HDAC.

In order to determine x_{Ni} and ρ under *in situ* conditions for the aqueous phase and the silicate phase, respectively, the attenuation factors are previously determined, based on the edge jumps of the different XANES spectra collected under ambient conditions:

- Concerning the aqueous phase, the nickel content and the density are well known before the experiment.
- Concerning the silicate phase, the density of the hydrous quenched glass can be estimated around $2.2\,\mathrm{g/cm^3}$ (see [7]). Also, the nickel content is determined after the experiment, using μ-PIXE (Particule Induced X-ray Emission) mapping (see [3]). Analyses were performed using the nuclear microprobe facility of LPS (CEA, Saclay, France).

Consequently, the "fluid/melt" partitioning coefficient obtained for nickel is 0.22 ± 0.05. Despite its important compatible character (i.e., crystal vs. melt; e.g., [8]), this result suggests a non-negligible mobilization of nickel by the aqueous fluid during the ascension of magmas.

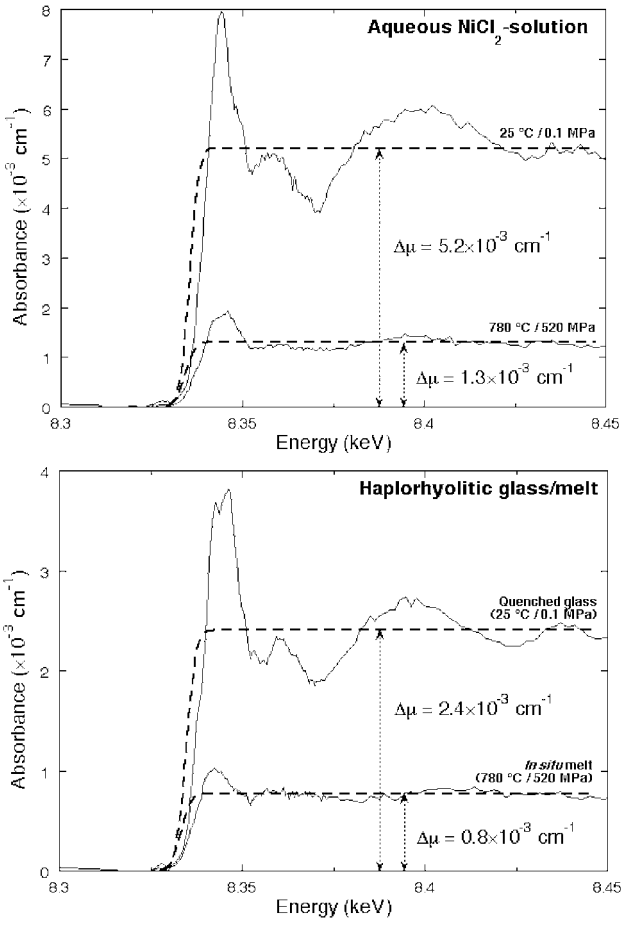

Fig. 3. μ-XANES spectra collected at the Ni K-edge for the aqueous $NiCl_2$-solution (up), and the haplorhyolitic phase (down), exposed to *in situ* (high-temperature/high-pressure) and ambient conditions.

Also, the density of the hydrous haplorhyolitic melt at 780 °C and 520 MPa is estimated to be $0.9 \pm 0.5\,\mathrm{g/cm^3}$, suggesting a particularly important proportion of water in the melt structure. This study represents the first attempt to measure a hydrous melt density well above the glass transition temperature, involving a major contribution to a better understanding of the structural and macroscopic properties of highly-hydrated magmas in conditions prior to explosive eruptions.

References

1. Shen, A. H. and Keppler, H., Nature **385**, 710 (1997).
2. Haar, L., Gallagher, J. S. and Kell, G. S., "NBS/NRC steam tables: thermodynamic and transport properties for vapor and liquid states of water in SI units" (Hemisphere publishing corp., New York 1984), p. 320.
3. Bureau, H. *et al.*, Nucl. Instr. Meth. Phys. Res. B. **210**, 434 (2003).
4. Farges, F., Brown Jr., G. E., Petit, P.-E. and Muñoz, M., Geochim. Cosmochim Acta **65**, 1665 (2001).
5. Muñoz, M., "Comportement d'éléments formateurs et modificateurs de réseau dans des magmas hydratés" (PhD thesis, Université de Marne-La-Vallée, France 2003), p. 247.
6. Teo, B. K., "EXAFS: Basic Principles and Data Analysis (9th ed.)" (Springer-Verlag, Berlin 1986), p. 349.
7. Ochs, F. A. and Lange, R. A., Science **283**, 1314 (1999).
8. Takahashi, E., Geochim. Cosmochim. Acta **42**, 1829 (1978).

Physica Scripta. Vol. T115, 923–924, 2005

Reverse Monte Carlo Simulations of EXAFS Spectra: Application to the Sorption of Gold on Iron Oxy-Hydroxides

M. Winterer[1] and F. Farges[2,3]

[1]Thin Films Division, Institute of Materials Science, Darmstadt University of Technology, 64287 Darmstadt, Germany
[2] Laboratoire des Géomatériaux, Université de Marne la Vallée and CNRS FRE 2455, 77454 Marne la Vallée cedex 2, France
[3]Department of Geological and Environmental Sciences, Stanford University, Stanford, CA 94305-2115, USA

Received June 26, 2003; accepted February 6, 2004

PACS numbers: 61.10.Ht, 02.70.Uu, 68.43.Fg, 89.60.−k, 83.80.Nb, 91.65.Rg

Abstract

The sorption of Au at the goethite-water interface is studied. In order to better understand sorption models for cations on mineral surfaces, reverse Monte-Carlo (RMC) simulations [1] were used to analyse EXAFS spectra. A starting model is constructed based on the (110) mineral surface separated by a layer of water molecules. Some of metal cations at the mineral-water interface are replaced by absorbed gold cations. All atomic positions are allowed to vary on both the mineral surface and in the water layer during the RMC simulations. Partial pair distribution functions and corresponding EXAFS spectra are computed and refined by a Metropolis algorithm. The final RMC model matches most EXAFS features (including short- and medium-range environments). The usual EXAFS parameters (coordination number, coordination distance and Debye-Waller factor and higher moments) are retrieved from the partial pair distribution functions by moment analysis. In case of Au at the the goethite-water interface four Au-O coordinations are found at an average distance of 1.99 Å with a second moment of 0.0013 Å^2. Two iron next-nearest neighbors show a broad distribution between 3.2 and 3.8 Å with an average coordination distance of 3.49 Å, a coordination number of 3 and a second moment of 0.013 Å^2. The results of the RMC simulations are compared with results of conventional EXAFS analysis methods.

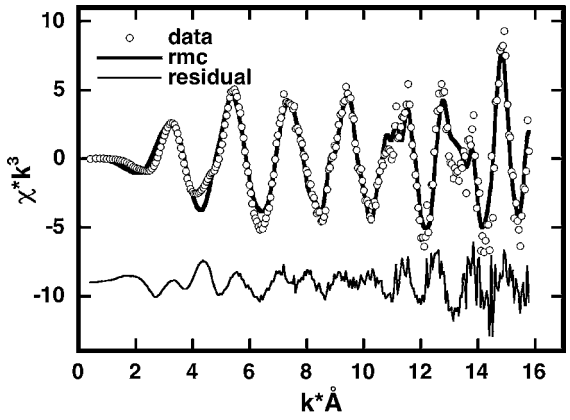

Fig. 1. EXAFS spectrum for Au sorbed on goethite surface at pH = 7 analyzed by RMC.

1. Introduction

Sorption of heavy metals onto finely divided minerals (such as clays or iron oxy-hydroxides) is an essential process in environmental geochemistry [2]. Toxic metals can then be fixed and locally concentrated because of sorption phenomena. This is also the case for strategic metals such as gold, which can be pre-concentrated on iron oxy-hydroxides, especially onto soils in tropical countries. X-ray absorption fine structure experiments are conducted to understand the sorption of gold onto iron oxy-hydroxides better, specifically, the speciation and connectivity of the gold moieties with the mineral surface [3]. Usually, the information for nearest neighbors is relatively easy to obtain, whereas for next-nearest neighbors it is much more difficult to extract, because of static disorder effects and overlapping signals. Here, simulations are required to analyze the experimental information, such as that provided by molecular dynamics or Reverse Monte Carlo (RMC) methods. In this study, we present the first application of a RMC simulation of an EXAFS spectrum applied to environmental sciences.

2. Experimental Methods

The EXAFS spectrum was chosen from a set of one hundred collected for various iron oxy-hydroxides [3] onto which trivalent gold was sorbed from an aqueous chlorine solution at various pH, Au/Cl molalities, conditions and mineral surfaces (bohemite, ferrihydrite and goethite). The goethite sample studied here is representative of the others in terms of the EXAFS signal: goethite was equilibrated at pH 7 with a gold chlorine solution (0.1 M [Cl] and 9.5 10^{-4} M [Au]). The gold concentration is 1.4 wt% corresponding to 0.09 μmol/m^2.

Au L_{III} edge EXAFS spectra were collected at 77 K using a 13-element solid state Ge detector available on beamline 4-3 at SSRL (Stanford, USA) (see fig. 1). We used Si (220) double-crystal monochromators with slits and a vertical aperture of 1 mm. The energy resolution is mostly limited due to a core hole lifetime of ∼8 eV. Scans were collected with 0.5 eV steps in the XANES and 0.05 Å^{-1} in the EXAFS region to 16 Å^{-1}. Photo-reduction was monitored by observing the drastic change in the XANES due to the formation of metallic gold induced by the beam. Gold photo-reduction was found to be less than 10% after averaging 10 scans (due to a rather quick data collection at low temperature). This is confirmed by a wavelet study of this spectrum [4], which established the lack of gold next-nearest atoms in the medium range environment of gold. Multiple-scattering events (related to the presence of square planar Au(III)O_4 moieties) are observed to interfere with the single-scattering contributions arising from iron next-nearest neighbors. However, this interference is significant only for the low k-range of the EXAFS signal (below 5 Å^{-1}) but this feature will be anyway considered in the RMC model.

The "rmcxas" package [1] was used to analyze the unfiltered EXAFS spectrum by RMC. The (110) surface of goethite was selected as model because it absorbs 90% of the gold. The initial configuration was constructed using a double (110) goethite surface, separated by a layer of water (randomized) (see fig. 2). Some Fe atoms at the mineral/water interface were replaced by

[1]Corresponding author: Markus Winterer, present address: Nanoparticle Process Technology, Department of Engineering Sciences, University Duisburg-Essen, 47057 Duisburg, Germany (email: markus.winterer@uni-duisburg.de).

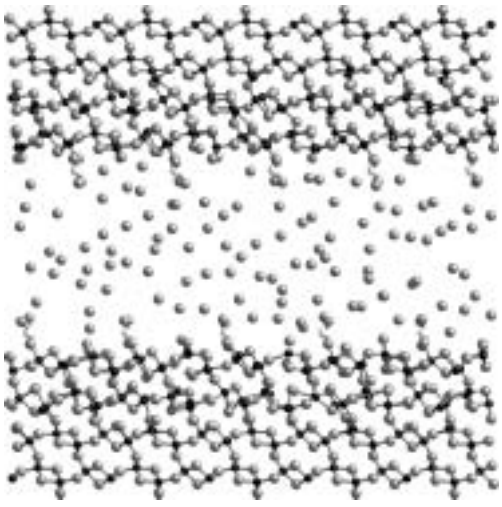

Fig. 2. RMC model of the goethite/water interface after refinement (Au: white, Fe: black, O: grey).

Au. Protons were neglected because they do not contribute to the EXAFS spectra. The simulation box is 54.6 × 30.1 × 54.1 Å large and contains 5680 atoms, including 20 Au atoms. During each RMC cycle, all atomic positions were allowed to vary up to 0.05 Å on both the (110) surfaces (10 Å deep into goethite) and in the water layer. After 260 cycles, the calculated model (using feff8 standards) matches all EXAFS features between 1 and 10 Å (the range of the pair distribution function). Most of the residual signal can clearly be attributed to multiple-scattering events within the AuO_4 polyhedra (details are provided in [4]).

3. Results and Discussion

A conventional EXAFS analysis of the EXAFS spectra was conducted assuming 4 shells:

- two for oxygen nearest neighbors: single- (SS) and multiple scattering (MS) of order 3 and 4, centered near 1.99 and 3.1 Å, respectively (3.9(3) atoms),
- two for iron next-nearest neighbors (SS), centered near 3.1 and 3.3 Å (total 2.0(5) atoms), respectively (attempts to model with an unique shell failed).

The RMC simulation results are consistent with this conventional analysis but significant additional information can be obtained in the medium range environment (see fig. 3):

- 3.5(7) O atoms located at 1.99 Å for the first neighbors with $\sigma^2 = 0.0013(12)$ Å^2,
- 2.0(4) next-nearest Fe atoms, centered near 3.49(3) Å with $\sigma^2 = 0.013(4)$ Å^2.

The agreement for the first neighbors is excellent. However, a significant underestimation (−0.3 Å) of the Au-Fe distances is observed for the conventional model, probably due to disorder effects in the complex medium range environment around Au at the mineral/water interface. Even more importantly, RMC results suggest that there is a broad distribution of Au-Fe distances (between 3.2 and 3.7 Å). This would mean that the shortest Au-Fe distance obtained by conventional methods is significantly affected by MS contributions arising from first neighbors (despite this contribution was also modeled using a separate shell during the whole refinement). This is again in agreement with a wavelet analysis of such spectrum [4], which evidenced a strong interference between both signals but could only be quantified

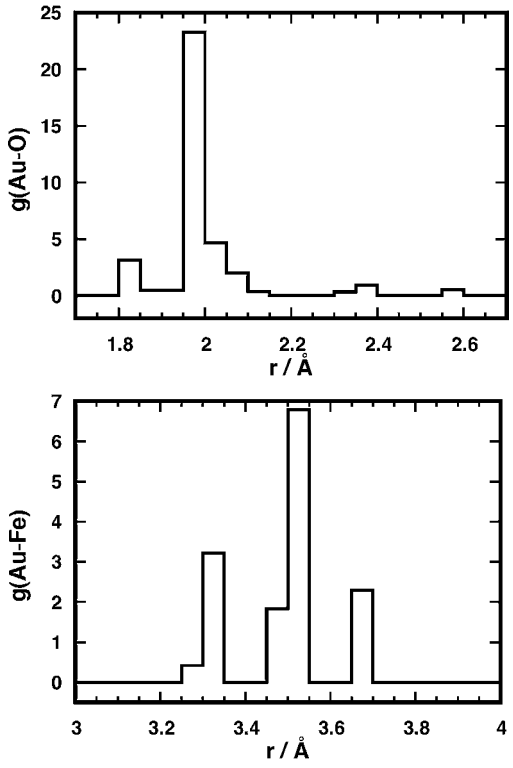

Fig. 3. Partial pair distribution functions for Au-O (top) and Au-Fe (bottom) as obtained by RMC analysis.

by the RMC discussed here. The RMC simulation also suggests that significant Au-O pairs (SS) interfere with Au-Fe pairs (SS) in the 3–3.5 Å range and these distant Au-O pairs were most likely modeled as Au-Fe pairs in the conventional EXAFS least-square model. From these RMC results, a dramatic change in the Au-O-Fe angles can be deduced (+20–40°), which affects the AuO_4-FeO_6 connectivity model (less edge-shared polyhedra as compared to when conventional EXAFS models are undertaken).

In conclusion, RMC simulations open new perspectives in environmental sciences, as they are based on a physical 3D models for sorption reproducing the experimental EXAFS information. Despite of the intrinsic limitations of RMC methods, structural information in the medium range environment probed by EXAFS can be quantitatively derived. Overlapping signals for cations and anions in the medium range structure of Au are evident. Also, the presence of a broad distribution of cation-cation distances is observed which cannot be detected by conventional EXAFS analyses. As a result of these disorder effects, the average cation-cation distances are underestimated by ca. 10%, which change drastically the models for the inter-polyhedral connectivity. This is of major importance for the analysis of EXAFS spectroscopy because it reveals methods to extract information on medium-range structures probed by EXAFS in complex materials. One important future development of the RMC analysis of EXAFS spectra is the computation of higher order distribution functions to include MS signals.

References

1. Winterer, M. *et al.*, J. Appl. Cryst. **35**, 434 (2002).
2. Fenter, P., Rivers, M., Sturchio, N. and Sutton, S., Rev. Mineralogy **49**, (2002).
3. Berrodier, I., Farges, F., Benedetti, M., Winterer, M., Brown, G. E., Jr. and Deveughèle, M., Geochim. Cosmochim. Acta (submitted, 2003).
4. Muñoz, M., Farges, F. and Argoul, P. (this volume).

Physica Scripta. Vol. T115, 925–927, 2005

XAFS Study of Local Structure with Picometer Accuracy: $Th_{1-x}U_xO_2$ and $Th_{1-x}Pu_xO_2$ Solid Solutions

J. Purans[1,2,*], G. Heisbourg[1], N. Dacheux[1], Ph. Moisy[3] and S. Hubert[1]

[1]Institut de Physique Nucléaire, Université Paris Sud, 91406-Orsay, France
[2]Dipartimento di Fisica dell'Università di Trento, 38050 Povo, Italy
[3]CEA-Marcoule-30207 Bagnols/Cèze Cedex, France

Received June 26, 2003; accepted in revised form November 4, 2003

PACS numbers: 61.10.Ht; 78.70.Dm

Abstract

XAFS spectroscopy using synchrotron radiation is an extremely suitable technique to study local atomic and electronic structure of mixed $Th_{1-x}U_xO_2$ and $Th_{1-x}Pu_xO_2$ oxides. Despite of XAFS technique overall success, a *pico-meter* barrier (10^{-2} Å) exists in XAFS data analysis. Here we present the dependence of the mixed oxide structure on composition, probed by XAFS with *picometer accuracy*. Complimentary XAFS spectra were measured at the Th, U, and Pu L-edges. We found that opposite to the lattice parameter obtained by XRD, the distances given by XAFS for the first and second shells do not follow completely neither Vegard's law nor the virtual crystal approximation (VCA). The Th-O, U-O and Pu-O distances obtained vary slightly upon dilution. These values are close to the ones expected from Vegard's law but are always smaller than the ones expected in VCA. The U-U(Th) and Th-Th(U) distances vary strongly upon dilution and the values are close to the ones expected from the VCA model but are always smaller than the ones expected by the Vegard law. The average lattice parameter calculated from XAFS data agrees well with a random distribution of metal (Th, U, Pu) and with one calculated from XRD data. With this complementary XAFS data on the local structure around two selected metal ions it is then possible to give a better view on the mixed oxides structure, the distribution of the two metal ions and local distortions in such medium crystal structure studied by XRD.

1. Introduction

In the last decade, there has been a renewal of interest in studying the feasibility of thorium based fuel reactors as a potential advanced fuel for Generation IV nuclear energy systems that can be operated to relatively high burn-ups, and producing less minor actinides than uranium based fuel [1, 2]. Solid solutions of uranium and thorium oxide are being developed as fuel for the thermal breeding reactors and high temperature gas cooled reactors.

The lattice constant of $Th_{1-x}U_xO_2$ and $Th_{1-x}Pu_xO_2$ solid solutions changes linearly with x in the whole region, a feature commonly referred to as Vegard's law [3, 4]. Such behaviour does not exclude a bimodal distribution of nearest-neighbour (NN) distances in the solid solutions as diffraction methods do not provide sufficient information on the local structure in disordered crystals [5]. It is somewhat surprising that the XAFS analysis well developed for solid solutions [6] has not yet been extensively exploited in the study of actinide dioxide solid solutions ($Th_{1-x}U_xO_2$, $U_{1-x}Pu_xO_2$, etc.).

2. Experimental details and data analysis

A series of solid solutions of $Th_{1-x}U_xO_2$ ($x = 0.0$, 0.11, 0.24, 0.37, 0.49, 0.65, 0.81, 0.91, 1) and $Th_{1-x}Pu_xO_2$ ($x = 0.0$, 0.13, 0.32, 0.66, 1.0) were prepared respectively in IPN (Orsay, France) and at CEA (Valhro, France) according the previously described procedure [2]. All the samples were characterized by using XRD. The lattice constant of $Th_{1-x}U_xO_2$ and $Th_{1-x}Pu_xO_2$ solid solutions changes linearly with x in the whole region in a good agreement with the literature data [2–4].

The XAFS measurements of $Th_{1-x}U_xO_2$ and of $Pu_{1-x}U_xO_2$ were performed on the D44 (XAS4) "hot" beam line of the LURE DCI synchrotron radiation facility (Orsay, France). A standard transmission scheme with a Ge (400) double crystal monochromator and two ion chambers containing argon gas was used. The powders of $Th_{1-x}U_xO_2$ and of $Th_{1-x}Pu_xO_2$ solid solutions were finely ground and mechanically mixed with cellulose powder. The adjusted thickness of the samples permits us to reach a value for the absorption jumps between 0.2 to 0.8 depending on the composition of the solid solutions.

The XAFS were treated using the "EDA" software package following the standard procedure [7]. The experimental XAFS spectra $\chi(k)k^2$ were Fourier transformed (FT) with a Kaiser-Bessel window in the 0–15 $Å^{-1}$ range. In all the FT's of the experimental spectra (Fig. 1) there are two main peaks located at 1.9 Å and 3.8 Å with a smaller pre peak at 3.2 Å, and lower peaks from 4.5 to 6 Å.

We have analysed the Th, U and Pu L_3-edge XAFS of the solid solutions to determine the change bond lengths in the first and second coordination shells as a function of solid solutions composition. Representative FT of the Th L_3-edge XAFS are shown in Fig. 1. As a general feature, the first peaks in the Th, U

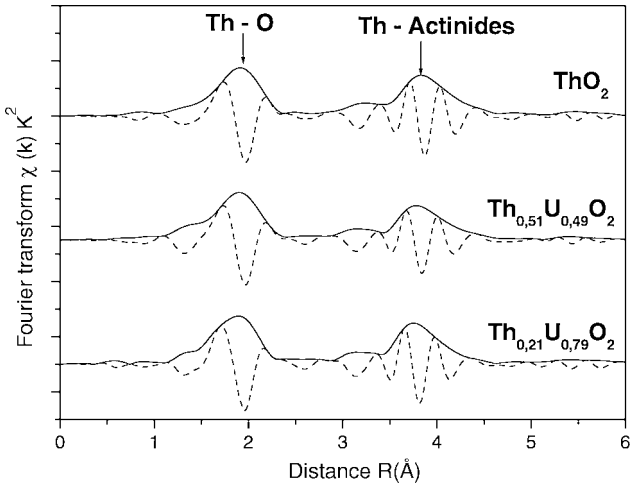

Fig. 1. Fourier Transforms of the experimental XAFS $\chi(k)k^2$ (Th L_3-edge) of ThO_2, $Th_{0,51}U_{0,49}O_2$ and $Th_{0,21}U_{0,79}O_2$.

*E-mail: purans@science.unitn.it

and Pu FT of the solid solutions are sharp and show a small, but significant and gradual shift to those in the respective standards (ThO_2 and UO_2). The second peak is also sharp and shows a more visible gradual shift from one end member to the other.

The single-shell XAFS spectra were fitted using single-scattering curved-wave formalism with picometer accuracy [8]. The XAFS data were analyzed using two different approaches: the phases and amplitudes were either calculated or obtained experimentally from a crystalline reference. Theoretical backscattering amplitudes and phases were calculated by the FEFF8 code using different clusters that mimic the possible environment of the An^{4+} ions in solid solutions, respectively [9].

3. Results and discussion

The interpretation of the XAFS spectra in $Th_{1-x}U_xO_2$ and $Th_{1-x}Pu_xO_2$ solid solutions is analogous to the pure oxides (see XAFS analysis of ThO_2, UO_2 and PuO_2 in ref. [10–13]) due to the very small differences in the scattering amplitude and phase shift functions of thorium, uranium and plutonium atoms: here the visible differences are only caused by the change of the lattice constant with the composition and by the very small differences in the scattering amplitude and phase shift functions of thorium and uranium (plutonium). The first effect is responsible for the shift in the energy position of the features of the FT while the second one for the small decrease of the second peak amplitude of the FT. We estimate that at room temperature the thermal broadening (Debye Waller factor) contributes $\sigma_2 = 0.005\,\text{Å}^2$ to the DW factor in the Th-O and U-O near-neighbour distribution.

3.1. *First-neighbor environment*

From the XAFS fitting data in the first coordination shell we conclude that the distances $R_{\text{U-O}}$, $R_{\text{Th-O}}$ and $R_{\text{Pu-O}}$ vary linearly upon dilution in the solid solutions (Figs. 2 and 3). The values ($R_{\text{Th-O}}$, $R_{\text{U-O}}$ and $R_{\text{Pu-O}}$) are closer to the ones expected from Vegard's law (Pauling model – the partial molar volume of each constituent is independent of concentration) than to the ones expected from the VCA. We estimate an uncertainty of 0.003 Å

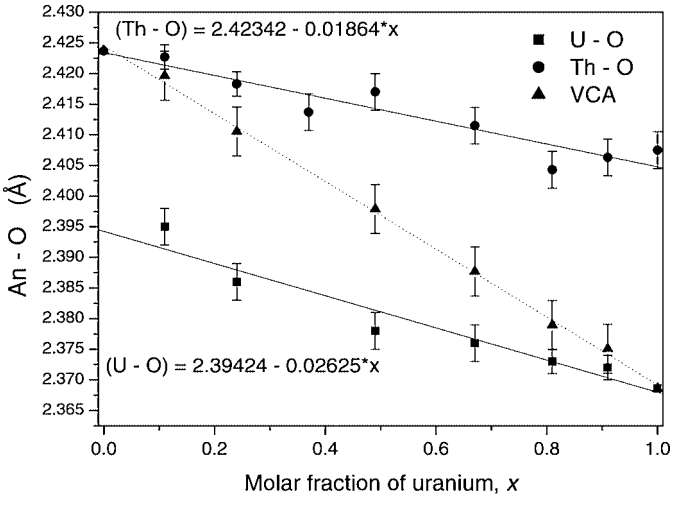

Fig. 2. Variation of the interatomic distances Th-O (● upper line) and U-O (■ bottom line) with the composition $Th_{1-x}U_xO_2$. The variation of crystal lattice parameter ($a/2$) follows Vegard's law (middle dotted line – XRD data). The average weighted distances (▲) calculated from the distances Th-O (●) and U-O (■) are also shown.

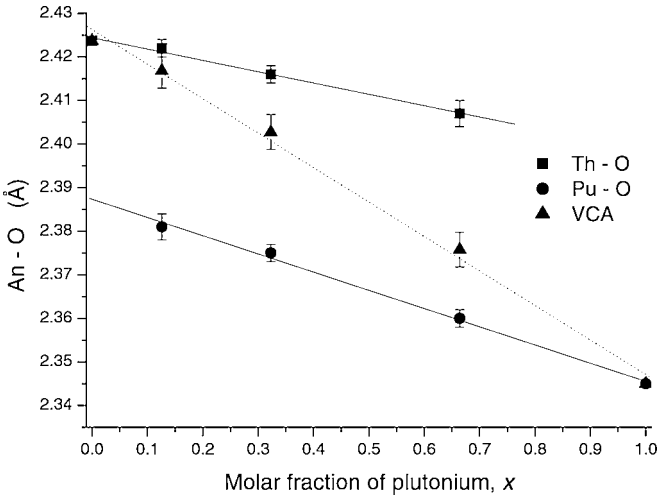

Fig. 3. Variation of the interatomic distances Th-O (■ upper line) and Pu-O (● bottom line) with the composition $Th_{1-x}Pu_xO_2$. The variation of crystal lattice parameter ($a/2$) follows the Vegard law (middle solid line – XRD data). The average weighted distances (▲) calculated from the distances Th-O (■) and Pu-O (●) are also shown.

in the near-neighbour distances, corresponding to a factor of 2 increase in the reliability of-fit parameter from a minimum value, expected in the dilute alloys (10 mol%) where the error is ∼0.005 Å. The total decrease in $R_{\text{Th-O}}$ in $Th_{1-x}U_xO_2$ from pure ThO_2 to pure UO_2 (linear interpolation to 0 mol% Th in UO_2) is 0.019 ± 0.003 Å, or ∼35% of the difference between $R_{\text{Th-O}}$ and $R_{\text{U-O}}$ in the end-point compounds (impurity limit). At the same time the increase in $R_{\text{U-O}}$ from pure UO_2 to the impurity limit of U in ThO_2 is 0.026 ± 0.003 Å, or ∼47% of the difference between $R_{\text{Th-O}}$ and $R_{\text{U-O}}$ in the end-point compounds. For comparison in $Th_{1-x}Pu_xO_2$ from pure ThO_2 to pure PuO_2 (linear interpolation to 0 mol% Th in PuO_2) is 0.025 ± 0.003 Å, or ∼32% of the difference between $R_{\text{Th-O}}$ and $R_{\text{Pu-O}}$ in the end-point compounds which is in good agreement with the value (35%) obtained for $Th_{1-x}U_xO_2$. So the local compressibility of [ThO_8] cluster is characteristic in these two solid solutions. At the same time the increase in $R_{\text{Pu-O}}$ from pure PuO_2 to the impurity limit of Pu in ThO_2 is 0.0425 ± 0.005 Å, or ∼54% of the difference between $R_{\text{Th-O}}$ and $R_{\text{Pu-O}}$ in the end-point compounds which is the highest "compressibility" observed.

3.2. *Second-neighbour environment*

On the contrary to the first shell, the U-U(Th) and Th-Th(U) distances vary strongly upon dilution and the values are close to the ones expected from the VCA model but are always smaller than the ones expected by the Vegard law. We estimate an uncertainty of 0.005 Å in the second-neighbour distances, corresponding to a factor of 2 increase in the reliability-of-fit parameter from a minimum value, expected in the dilute alloys (10 mol%) where the error is ∼0.005 Å. The total decrease in $R_{\text{Th-U(Th)}}$ from pure ThO_2 to pure UO_2 (linear interpolation to 0 mol% Th in UO_2) is 0.067 ± 0.003 Å, or ∼71% of the difference between $R_{\text{Th-Th}}$ and $R_{\text{U-U}}$ in the end point compounds. At the same time the increase in $R_{\text{U-Th(U)}}$ from pure UO_2 to pure ThO_2 (linear interpolation to 0 mol% U in ThO_2) is 0.080 ± 0.003 Å, or ∼86% of the difference between $R_{\text{Th-Th}}$ and $R_{\text{U-U}}$ in the end point compounds. The total decrease in $R_{\text{Th-Pu(Th)}}$ from pure ThO_2 to pure PuO_2 (linear interpolation to 0 mol% Th in PuO_2) is 0.105 ± 0.010 Å, or ∼84% of the difference between $R_{\text{Th-Th}}$ and $R_{\text{Pu-Pu}}$ in the end point

compounds. At the same time the increase in $R_{\text{Pu-Th(Pu)}}$ from pure PuO_2 to pure ThO_2 is 0.105 ± 0.010 Å, or ∼84% of the difference between $R_{\text{Th-Th}}$ and $R_{\text{Pu-Pu}}$ in the end point compounds.

References

1. Herring, J. S., MacDonald, P. E., Weaver, K. D. and Kullberg, C., Nucl. Eng. Design **203**, 65 (2001).
2. Fourest, B., Vincent, T., Lagarde, G., Hubert, S. and Baudoin, P., J. Nucl. Mater. **282**, 180 (2000).
3. Cohen, I. and Berman, R. M., J. Nucl. Mater. **18**, 77 (1966); and Bakker, K., Cordfunke, E. H. P., Konings, R. J. M. and Schram, R. P. C., J. Nucl. Mater. **250**, 1 (1997).
4. Freshley, M. D. and Mattys, H. M., General Electric Report HW-76559, 11.6 (1962).
5. Trope, M. F. and Garboczi, E. J., Phys. Rev. B **42**, 8405 (1990); Cai, Y. and Trope, M. F., Phys. Rev. B **46**, 15872 (1992).
6. Mikkelsen, Jr., J. C. and Boyce, J. B., Phys. Rev. B **15**, 7130 (1983).
7. Kuzmin, A., Physica B **208&209**, 175 (1995); J. Physique IV (France) **7**, C2-213 (1997).
8. Dalba, G., Fornasini, P., Grisenti, R. and Purans, J., Phys. Rev. Lett. **82**, 4240 (1999).
9. Rehr, J. J., Mustre de Leon, J., Zabinsky, S. I. and Albers, R. C., J. Am. Chem. Soc. **113**, 5135 (1991); Mustre de Leon, J., Rehr, J. J., Zabinsky, S. I. and Albers, R. C., Phys. Rev. B **44**, 4146 (1991).
10. Barrett, N. T., Greaves, G. N., Willis, B. T. M., Antonini, G. M. and Thornley, F. R., J. Phys. C: Solid State Phys. **21**, L791 (1988).
11. Wu, Z. and Farges, F., Physica B **266**, 282 (1999).
12. Begg, B. D. *et al.*, J. Nucl. Mater. **278**, 212 (2000).
13. Richmann, M. K., Redd, D. T., Kropf, A. J., Aase, S. B. and Lewis, M. L., J. Nucl. Mater. **297**, 303 (2001).

Physica Scripta. Vol. T115, 928–930, 2005

XAFS and Molecular Dynamics Study of Natural Minerals, Analogues of Ceramics for Nuclear Waste Storage

M. Harfouche[1,*], F. Farges[1,2], J. P. Crocombette[3] and A. M. Flank[4]

[1]Laboratoire des Géomatériaux, Université de Marne-La-Vallée, CNRS FRE 2455, 77454 Marne-La-Vallée cedex 2, France
[2]Department of Geological and Environmental Sciences, Stanford University, CA 94305-2115, USA
[3]Commissariat à l'Energie Atomique (CEA/Saclay), CEREM, 91191 Gif sur Yvette, France
[4]Laboratoire pour l'Utilisation du Rayonnement Electromagnétique, Bât 209D - B.P. 34 - 91898 Orsay Cedex, France

Received June 26, 2003; accepted in revised form November 10, 2003

PACS numbers: 61.10.Ht, 89.60.−k, 61.82.Ms, 61.72.Bb, 83.80.Nb

Abstract

Natural actinides (U and Th) are harmful for the crystalline structure of natural minerals, due to their irradiation. Natural minerals can then become amorphous to X-ray diffraction ("metamict") after being irradiated throughout a long period of time (10^8 years). Then, they are used as natural analogues of ceramics for nuclear waste storage. XAFS studies were performed in zircon, monazite and titanite to understand the effect of radiation damage on the local structure around Th, U, Zr and P and compared to available molecular dynamics (MD) simulations. In zircon, a local expansion around actinides (when substituting for Zr) is found. The radial expansion is a function of the metamictisation degree: up to ∼4 Å in crystalline zircon and larger in the metamict counterparts. *Ab-initio* calculations (FEFF7) were performed around Zr (∼23 000 sites) and around U (1000 to 3000 sites) in various crystalline and alpha-decay damaged zircon MD simulations. The calculated averaged EXAFS spectra confirms this expansion, which validates the use of the potentials used in the simulations as well as the alpha decay damage model considered in these MD simulations. Tetravalent actinides were found to be 8-coordinated in the undamaged structure, whereas their coordination drops to 7 in the damaged structures. In contrast to zircon, no local expansion around actinides in monazite was detected, despite some polymerization around P is measured (related to radiation damage). Finally, in some phases (such as titanite), actinides are found as oxyde-type clusters (ThO_2, UO_2). Consequently, actinides do not "systematically" substitute for major actions in these structure, in contrast to the common belief in mineralogy.

1. Introduction

Natural minerals may model long-term radiation effects by receiving very small amounts of radiation during hundreds of million years [1]. These mineral analogues offer a possibility to study the real effect of "*in-situ*" damage on the structure of ceramics receiving strong amounts of radiation. In the hope of identifying an adequate matrix to contain high activity nuclear wastes, a broad range of minerals of different structure is studied by XAFS methods (experimental and *ab-initio* XANES and EXAFS methods) and molecular dynamics. We studied the structural environment of several analogues such as zircon, monazite, zirconolite and titanite and compared experimental information to these reconstructed from molecular dynamics to (1) better understand the influence of radiation damage on crystals, (2) help validate the models used in molecular dynamics to simulate radiation damage and (3) provide accurate information on the way disorder effects influence the short-, and medium range environment probed by XAFS methods in these highly disordered materials.

*Corresponding author, e-mail: farges@univ-mlv.fr

2. Experimental Methods

A set of natural minerals that suffered radiation damage were investigated, including zircon ($ZrSiO_4$), monazite ($CePO_4$), zirconolite ($CaZrTi_2O_7$) and titanite ($CaTiSiO_5$). We have selected various samples of these minerals that contain significant amounts of natural actinides (Th and U from 0.01 to 30 wt.%). These samples (suffering severe radiation damage) are coming from various localities throughout the world (Sri Lanka, Madagascar, Brazil, South Africa, Canada etc.). They were thoroughly characterized using various methods (X-ray diffraction, electron microprobe, etc.) to differentiate between samples that suffered only from radiation damage to that suffered subsequent weathering. XAFS spectra for major elements were collected at the Si K- (zircon), P K- (monazite), Zr K- (zircon) and $L_{III/II}$-edges (zircon) to help validate the structure of these materials simulated by molecular dynamics. Then, XAFS spectra were collected for minor to trace amounts of actinides (L_{III}-edges of Th and U) to understand the effect of radiation damage on the local structure of the remaining actinides. XAFS spectra for soft X-ray energies were collected at the SA32 spectrometer (Super-Aco, Orsay, France) using a Ge(111) monochromator. We used total electron-yield detection to collect the spectra. Hard X-ray XAFS spectra (Zr K-edges and Th/U L_{III}-edges) were collected at SSRL (Stanford, USA) on beamline 11-2, using a Si(220) double-crystal monochromator. We used a Stern-Heald type fluorescence detector (filled with Xe) with Sr filters to filter the elastic scattering. EXAFS spectra were collected with 0.05 $Å^{-1}$ steps. Molecular dynamics simulations were performed for the zircon structure only, assuming several levels of radiation damage (recoil of 4 and 5 keV, respectively) with various U contents (1 atom, 4% and 12% of Zr atoms replaced by U). Simulations were performed using periodic conditions assuming 139,964 atoms. Details on the calculations (potentials etc.) are given elsewhere [2]. *Ab-initio* EXAFS calculations were undertaken using the FEFF7 code [3] at the Zr K-, and U L_{III}-edges on thousands of clusters provided by molecular dynamics and averaged to compare with the experiment.

3. Results and Discussion

The Zr $L_{II/III}$-edge XANES spectra of metamict zircon show a shift in the first EXAFS oscillation (Fig. 1) as compared to crystalline zircon. This confirms that Zr undergo a $8 \rightarrow 7$ coordination change with increasing radiation damage. Fourier Transforms of the Zr K-edge EXAFS spectra and their models (Fig. 2) show that the Zr-O average interatomic distance

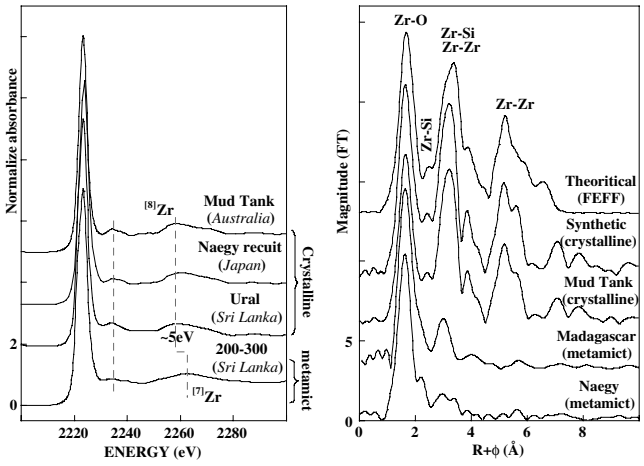

Fig. 1. Zr L_{III}-edge XANES (left) and FT's of Zr K-edge EXAFS (right; with k^3-weighting, $k = 1.5$–$13.5\,\text{Å}^{-1}$ and Kaiser-Bessel window) for crystalline and metamict zircons.

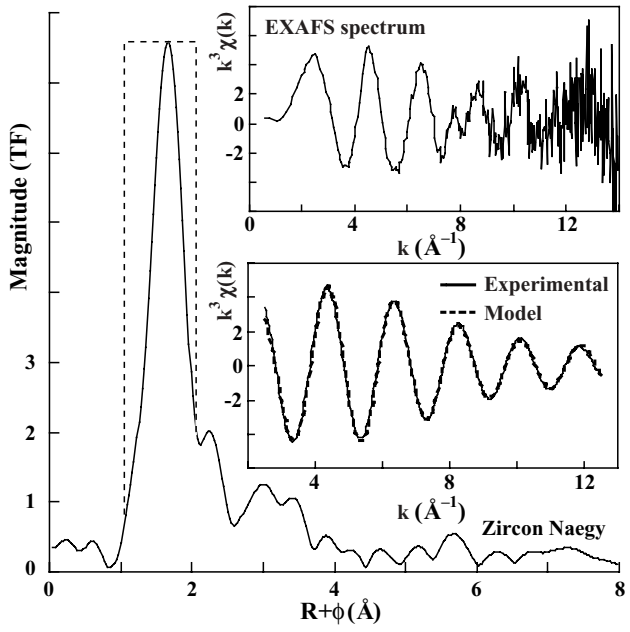

Fig. 2. Fourier transform of the EXAFS spectrum (inset, top) collected at Zr K-edge in a metamict zircon and the data modelling (inset, bottom).

decreases from 2.20 to 2.15 Å with increasing radiation damage, in agreement with [4]. The structure obtained from the MD simulations of the damaged regions in zircon is in agreement with the experiment for metamict zircons. In the damaged region, zirconium is surrounded, on the average, by 6.9 atoms at 2.14 Å (first neighbors are widely distributed from 2.0 to 2.4 Å). The average Zr K-edge *ab-initio* EXAFS was computed (using FEFF 7) from the MD simulation around Zr. The cumulant expansion model of that FEFF7 spectrum resulted in ∼7 atoms at 2.14 Å, suggesting that disorder effects were properly taken into acccount in the EXAFS models for the natural zircon samples.

In addition, next nearest neighbors are observed around Zr in the EXAFS spectra for natural metamict minerals. These contributions can be modeled as (edge-shared) Si second neighbors near 3.10 Å and more distant (despite relatively noisy) Zr-Si contributions (near 3.73 Å). The EXAFS modelisations based on MD simulations for Zr in damaged zircon confirm the presence of Zr-Si contributions (at 3.15 Å) and Zr-Zr contributions near 3.75 Å. The overall good agreement for the EXAFS models computed for the natural samples and the MD-simulations suggests that the MD models are representative of naturally occuring radiation damage. This agreement also confirm that disorder effects in the model of the experimental EXAFS for the next-nearest neighbors were properly taken into account (using cumulant expansion theory).

Analysis of the P K-edge EXAFS spectra in monazites suggests that the P-P pairs near 2.5 Å increases significantly in magnitude with radiation damage. Then, some polymerization of the PO_4 tetrahedra occurs as a consequence of increasing radiation damage. In contrast, any large structural reorganization due to radiation damage is observed around the other major elements such as Th.

Concerning minor, to trace amounts of actinides (Th and U) in natural minerals, we studied first the insertion of these cations in the crystalline minerals before studying the radiation damaged ones (Fig. 3). In crystalline minerals, the analysis of the EXAFS spectra suggests that Th and U are 8-coordinated with Th-O and U-O at 2.41(2) and 2.38(2) Å. Therefore, these cations keep their preferred coordination environment, even if the main site they occupy (e.g., the Zr site in zircon) is not fully adapted (in size and in redox) to these actinides sizes. However, the analysis of the EXAFS for the medium range structure around minor amounts of Th and U (0.05–0.2 wt.%) in zircon shows the presence of relatively longer (Th,U)-Zr bonds (3.7 Å) as compared to the ones in the original zircon (3.6 Å). This suggests the presence of a structurally «expanded» region up to 4 Å from the central actinide. This expansion is due to the insertion of a larger actinide in the site of a smaller Zr (see model on Fig. 4). However, in the 4–5.5 Å range around the central actinide, a relatively «contracted» region is observed, based on the measured EXAFS distances compared to the ones in the original zircon structure. Above 5.5 Å, the undistorted original structure of the host mineral is observed (Fig. 4). These regions around actinides were also observed in the MD simulations, validating then our EXAFS interpretations. These results also help us understanding the point defects that are created in the zircon structure when minor actinides replaces major zirconium atoms

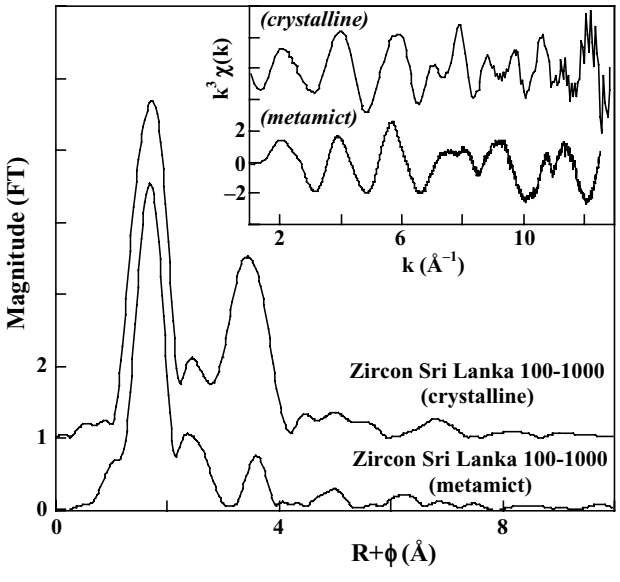

Fig. 3. FT's of the U L_{III}-edge EXAFS (inset) spectra for zircons: crystalline (top) and damaged (bottom).

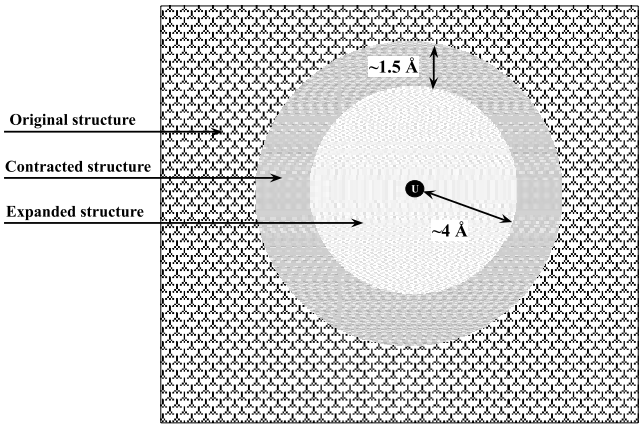

Fig. 4. Schematic representation of the local structure around actinides in crystalline zircon, as observed from EXAFS experiments and MD simulations.

(see Fig. 4). The influence of radiation damage on the local structure around these actinides was measured using Th/U-L_{III} EXAFS spectroscopy and compared to MD simulations (considering a 4 and 5 keV cascade). The agreement between the experimental information and the MD simulations was also excellent, suggesting that the MD methods reproduce faithfully natural radiation damage. We have found, in addition, that in both experiment and MD simulation, tetravalent actinides (Th and U) are 7-coordinated (EXAFS-derived Th-O and U-O distanced averaging anharmonically at 2.37 and 2.35 Å). To our knowledge, this is the first time that such a coordination environment is reported for tetravalent actinides.

In some other phases (titanite for instance), we observed that actinides do not replace a major cation in the structure but are present as actinide oxide-type clusters (ThO_2, UO_2; see Fig. 5). We think that subsequent heat treatment can be at the origin of migration of the actinides from its host matrix (as substituted) to some oxide-type cluster.

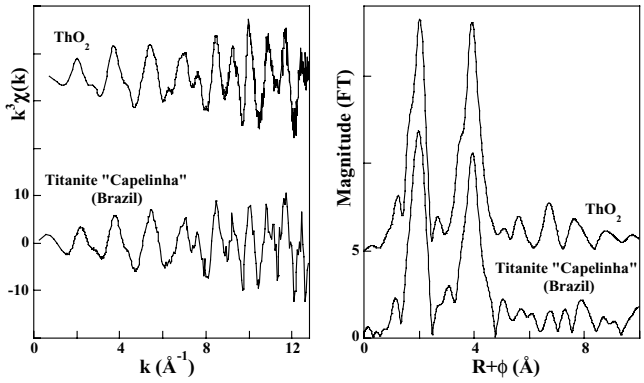

Fig. 5. EXAFS spectra collected at Th L_{III}-edge in a titanite sample from Brazil compared to ThO_2 and their Fourier transform.

4. Conclusions

Combination of XAFS and molecular dynamics of radiation damage in minerals analogues of ceramics for nuclear waste suggests that MD simulates adequately radiation damage, consistent with the observation of very old (10^8 years) metamict minerals. Also, important and unique information about the complex structure of the metamict state was extracted as well as on the sites of actinide in minerals that are geochemically important phases for dating or tracing major geologic events (such as volcanology). Finally, a better understanding on the way disorder affects EXAFS spectra is obtained.

References

1. Weber, W. J., Turcotte, R. P. and Roberts, F. P., Radiation Waste Mgmt. **2**, 295 (1982).
2. Crocombette, J. P. and Ghaleb, D., J. Nucl. Mater. **257**, 282 (1998).
3. Ankudinov, A. L., Ravel, B., Rehr, J. J. and Conradson, S. D., Phys. Rev. B **58**, 7565 (1998).
4. Farges, F., Phys. Chem. Miner. **20**, 504 (1994).

Physica Scripta. Vol. T115, 931–932, 2005

XAFS Studies on Vitrified Industrial Waste

F. Pinakidou[(a)], M. Katsikini[(a)], E. C. Paloura*[(a)], P. Kavouras[(a)], Ph. Komninou[(a)], Th. Karakostas[(a)] and A. Erko[(b)]

[(a)]Aristotle University of Thessaloniki, Department of Physics, GR 54124 Thessaloniki, Greece
[(b)]BESSY GmbH, Albert Einstein Str. 15, D12489, Berlin, Germany

Received June 26, 2003; accepted in revised form January 7, 2004

PACS numbers: 61.10.Ht, 61.43.Fs

Abstract

The oxidation state and local environment of Fe atoms in a series of vitrified lead-rich industrial wastes, as a function of the ash content, is studied using EXAFS and NEXAFS measurements at the Fe-K edge. The Fe-K EXAFS results reveal that the Fe-O distance and the coordination number in the 1st nearest neighbour shell decrease with increasing ash content in the vitrified product. Information on the iron's valence state and the role of Pb^{2+} ions in the glass matrix is drawn from the characteristics of the pre-edge features and the position of the absorption edge in the NEXAFS spectra.

1. Introduction

The solidification and stabilization of lead oxide-contaminated ash, which is a toxic industrial waste, is a process that allows for its safe disposal. The aim of this work is to determine the local environment of the Fe atoms (whose structural role depends on its oxidation state and the PbO concentration) in the glass matrix of lead-rich industrial wastes, using XAFS spectroscopies. The NEXAFS spectra of transition metals have a weak pre-edge peak (about 10 eV below the absorption edge), which is assigned to $1s \rightarrow 3d$ transitions. The intensity and energy position of this peak, as well as the energy position of the absorption edge, are sensitive to the oxidation state [1] and bonding geometry of the Fe atom [2]. Therefore, conclusions can be drawn on the oxidation state and bonding geometry of the Fe ion.

2. Experimental Details

The under study samples were produced with an incineration process that involves co-melting of lead contaminated ash (it consists mainly of iron oxides and $PbO \cdot PbBr_2$), with the appropriate quantities of vitrifying (SiO_2) and flux (Na_2O) agents at high temperatures (1400 °C), followed by fast cooling in order to form vitrified materials [3]. The under study vitrified products contain various concentrations of fly ash (ranging from 10% to 60%) and a SiO_2/Na_2O ratio equal to 2.33. A crystalline (powder) iron oxide, hematite α-Fe_2O_3 was also studied as a reference samples. The EXAFS and NEXAFS measurements were conducted at room temperature, using the KMC2 double-crystal monochromator of the electron storage ring BESSY-II in Berlin. The NEXAFS and EXAFS spectra were recorded at the Fe-K-edge, using a fluorescence yield detector (Si-PIN photodiode). The NEXAFS spectra were recorded in the energy range 7035–7150 eV, at an angle of incidence $\theta = 45°$.

3. Results and Discussion

The characteristics of the NEXAFS spectra were determined via fitting using a sigmoidal (Boltzman function) to simulate transitions to the continuum [4] and a Lorentzian to fit the pre-edge peak. Prior to fitting, the spectra were normalized for the transmission function of the monochromator, using the signal from an ionization chamber positioned in front of the sample, and were subjected to background subtraction and normalization to the atomic limit.

In the Fe-K-edge NEXAFS spectra, the intensity of pre-edge peak increases with increasing ash content (Fig. 1). It has been reported that the position of the pre-edge peak is a measure of the $Fe^{+3}/\Sigma Fe$ ratio [1] while its intensity, which is inversely proportional to the coordination number of the absorbing atom [2], is greater in non-centrosymmetric complexes (due to the large electric allowed dipole component from 3d-4p mixing) than in centrosymmetric complexes (where the $1s \rightarrow 3d$ transition has an electric quadripole nature). Therefore, the observed increase in the intensity of the pre-edge peaks indicates that the local environment around the Fe ion is becoming less symmetric as the ash content increases, i.e. the Fe atom tends to occupy tetrahedral sites. In addition to that the position of the pre-edge peak is independent of the ash content, indicating that, the $Fe^{+3}/\Sigma Fe$ ratio remains constant despite the changes in the concentration of the fly ash. Given that only Fe^{+3} ions can occupy both tetrahedral and octahedral sites in the glass matrix, the alteration in the

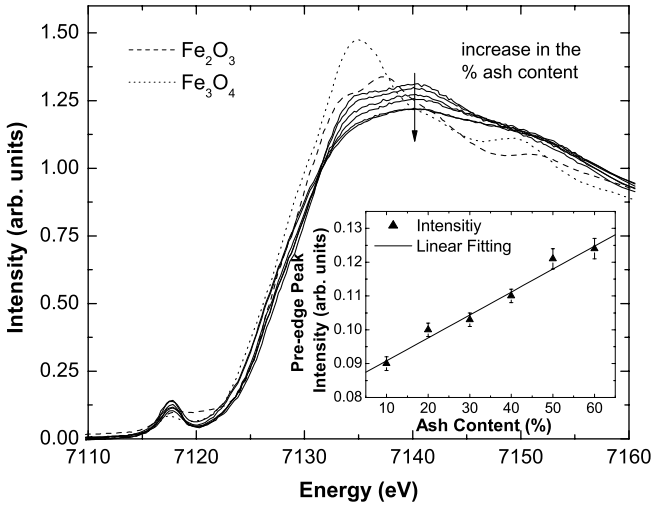

Fig. 1. NEXAFS Fe-K edge spectra of the under study samples. The dependence of the intensity of the pre-edge peak on the ash content is depicted in the inset of the graph.

*e-mail: paloura@auth.gr

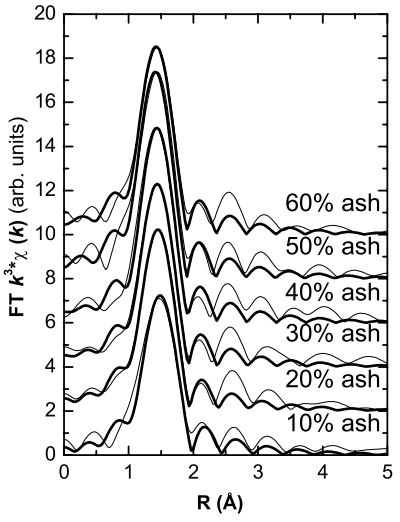

Fig. 2. The Fourier transforms (FT) of the $k^3\chi(k)$ spectra. The raw data and the fitting are shown in thin and thick solid lines, respectively.

local environment around the Fe atom (verified by both EXAFS and NEXAFS analysis) can be assigned only to Fe^{+3} ions. The energy position of the absorption edge (E_{abs}), in all the under study samples, is insensitive to the ash content and appears at energies higher than that in α-Fe_2O_3 and Fe_3O_4 (7126.2 and 7124.6 eV). This violet shift of the E_{abs} can be attributed to structural differences (distortion) in the Fe-O polyhedrons, due to the polarizability of the Pb-O bond, which in turn depends on the PbO concentration [5], [6].

The EXAFS spectra were normalized for the transmission function of the monochromator and subjected to subtraction of the atomic absorption using the AUTOBK [7] program. After their correction for self-absorption effects [8] and for energy shifts induced by the monochromator, the spectra were fitted using the FEFFIT [7] program. The model for the fitting was constructed using he FEFF8.0 program. The raw and fitted Fourier transforms of the k^3-weighted $\chi(k)$ spectra (calculated in the k-range 2.9–9.7 $Å^{-1}$) at the Fe-K-edge, are shown in Fig. 2. The Fe-K edge spectra were fitted using one shell and assuming the hematite (Fe_2O_3) model (octahedral structure). The fitting parameters were the bond length, the coordination number and the value of the Debye-Waller factor while the amplitude ($S_O{}^2$) was kept fixed to the value 0.85.

The EXAFS analysis reveals that as the ash content incorporated into the glass matrix increases, both the coordination number and the Fe-O distance decrease from 5.1 to 3.9 and 1.94 Å to 1.88 Å, respectively (Table I). These two distances are characteristic of octahedral and tetrahedral coordination and indicate the preferential occupation of tetrahedral sites by the Fe atoms, as the ash content increases.

The structural role of iron depends on its oxidation state; Fe^{3+} can form intermediate oxides, while Fe^{2+} acts as a glass modifier. Mossbauer spectroscopy measurements conducted in the under study samples [9] revealed that all glasses contain both Fe^{+2} and Fe^{+3} ions, and that Fe^{+2} ions occupy only octahedral sites, while the Fe^{+3} ions occupy both tetrahedral and octahedral sites. Furthermore, the Fe^{+2}/Fe^{+3} ratio remained constant in all vitrified products, i.e. it did not vary with the increase in the ash content. Therefore, the change in the environment around the Fe atom can be attributed to the different structural role of the Pb^{+2}, that strongly depends on the concentration of PbO and increases with the increase of the ash content.

Table I. *EXAFS results; R_1, N_1 and DW_1 correspond to the coordination number, interatomic distance and Debye-Waller factors in the 1st nn shell, respectively.*

Sample name	N_1 (±10%)	R_1 (Å) (±0.01)	DW_1 (Å^2)
10 ash%	5.1	1.94	7.3
20 ash%	4.5	1.92	5.6
30 ash%	4.1	1.89	4.5
40 ash%	4	1.88	3.2
50 ash%	4.3	1.88	4.7
60 ash%	3.9	1.88	4.2

4. Conclusions

A series of vitrified lead-rich solid industrial wastes has been studied by XAFS spectroscopy, in order to determine the effect of different ash concentrations in the formation of the glass matrix. The NEXAFS analysis reveals that the $Fe^{+3}/\Sigma Fe$ ratio is not affected by the increase in the ash concentration. Furthermore, the local environment around the Fe atom tends to become less ordered as the ash concentration increases. This is also affirmed by the EXAFS analysis where the Fe-O distance and the coordination number in the 1st nearest neighbour shell decrease, indicating that the environment around the Fe atom changes from octahedral to tetrahedral. Because the ratio Fe^{+2}/Fe^{+3} is constant, this change can be attributed to the presence of Pb^{+2} ions whose structural role into the glass matrix is different when the concentration of PbO increases. The different structural role of the Pb atom and the strong polarization of the Pb-O bond, can account for the violet shift of the absorption edge in the NEXAFS spectra.

References

1. Bajt, S. *et al.*, Geochim. Cosmochim. Acta **58**, 5217 (1994).
2. Westre, T. *et al.*, I. J. Am. Chem. Soc. **117**, 1309 (1995).
3. Kavouras, P. *et al.*, Waste Management **23**, 361 (2003).
4. Stöhr, J., "NEXAFS Spectroscopy" (Springer-Verlag, Berlin, 1992) p. 114.
5. Schultz-Munzenberg, C. *et al.*, J. Non- Cryst. Solids **238**, 83 (1998).
6. Fayon, F. *et al.*, J. Non- Cryst. Solids **232**/**234**, 403 (1998).
7. Mustre de Leon, J., Rehr, J. J., Zabinsky, S. I. and Albers, R. C., Phys. Rev. **B 44**, 4146 (1991).
8. Tröger, L. *et al.*, Phys. Rev. **B 46**, 3283 (1992).
9. Kalogirou, O., Private communication.

Physica Scripta. Vol. T115, 933–935, 2005

Monitoring Trace Amounts of Lead and Arsenic Adsorption by X-ray Absorption Fine Structure Combined with Fluorescence Spectrometry

Yasuo Izumi[1,*], Fumitaka Kiyotaki[1], Taketoshi Minato[1], Dilshad Masih[1] and Yoshimi Seida[2]

[1]Interdisciplinary Graduate School of Science and Engineering, Tokyo Institute of Technology, 4259 Nagatsuta, Midori-ku, Yokohama 226-8502, Japan
[2]Institute of Research and Innovation, 1201 Takada, Kashiwa 277-0861, Japan

Received June 26, 2003; accepted in revised form November 25, 2003

PACS number: 61.10.Ht

Abstract

X-ray absorption fine structure combined with fluorescence spectrometry was used for the speciation of trace amounts of lead and arsenic adsorbed. The Pb^{2+} species were effectively adsorbed on a layered material $Mg_6Fe_2(OH)_{16}(CO_3)\cdot 3H_2O$ from 100 ppb–1.0 ppm test aqueous solutions. A eutectic mixture of $PbCO_3$ and $Pb(OH)_2$ coagulated in the case of a 1.0 ppm Pb^{2+} solution, and in contrast, the major species was ion-exchanged Pb^{2+} in the case of the adsorption from the 100 ppb aqueous solution. The arsenic species were effectively adsorbed on intercalated Fe-montmorillonite from 50 ppb–16 ppm test aqueous solutions. In this concentration range, As^{3+} in the solution was oxidized upon adsorption. The adsorbed structure was suggested to be $[As^{V}(OH)_2(\mu\text{-}OFe)_2]$ both in the cases of adsorption of As^{3+} and As^{5+}.

1. Introduction

Speciation of toxic elements, such as Cr^{6+}, Cu^{2+}, Zn^{2+}, As^{3+}, Cd^{2+}, Hg^{2+}, and Pb^{2+} in the environment is important to the understanding of their effects to human health and to investigate the removal and reuse methods. XAFS gives direct information for the speciation of non-crystalline site. Higher-energy-resolution XAFS spectra are desirable for precise speciation. To improve energy resolution, the fluorescence X-rays emitted from a toxic element in the sample were analyzed by a high-energy-resolution Rowland-type spectrometer. This method is free from the problems associated with photon-counting losses (SSD) or spectral broadening effects at higher photon energies (Pb K-edge) [1].

Basic polyhydroxide compound of layered structure $Mg_6Fe_2(OH)_{16}(CO_3)\cdot 3H_2O$ (**1**) was found to be effective for lead(II) adsorption, especially when the flow rate of lead test solution was high [1]. Layered material was also good for arsenic (arsenite, arsenate) adsorption, especially in the case that iron material was intercalated between the layers of montmorillonite.

2. Experimental Section

2.1. *Samples*

Standard lead(II) compounds were used as received and diluted to 5.0 wt% of Pb by mixing with boron nitride. An ion-exchanged standard sample was prepared from lead(II) nitrate aqueous solutions on NaY zeolite (JRC-Z-Y4.8, $Na_{58}Al_{58}Si_{134}O_{384}\cdot 240H_2O$). The cation exchange ratio was 85.5%. An adsorbent **1** was synthesized by adding NaOH to the aqueous solution of $MgCl_2$ and $FeCl_3$ [1]. The specific BET surface area was 110 $m^2\,g^{-1}$. The interlayer spacing was 7.79 Å based on X-ray diffraction (XRD) measurements. A 1.0 ppm or 100 ppb lead(II) nitrate solution was adsorbed at a flow rate (space velocity) of 50 min^{-1} on adsorbent **1**.

Standard As^{III} and As^{V} compounds were used as received and diluted to 2.0 wt% of As by mixing with boron nitride. An adsorbent was prepared by the following procedure. 8.14 ml of a 0.43 M $Fe(NO_3)_3$ solution and 9.33 ml of a 0.75 M NaOH solution were mixed and left undisturbed in the dark at 290 K for 24 h. 0.5 wt% of Na-montmorillonite (Kunipia F, $Na_{1.5}Ca_{0.096}Al_{5.1}Mg_{1.0}Fe_{0.33}Si_{12}O_{27.6}(OH)_{6.4}$) was suspended in distilled water and the reaction mixture was added. The resultant powder obtained was dried for 72 h at 313 K. The Fe loading was 15.3 wt%. The sample is denoted as Fe-montmorillonite. 20 ml of 1–16 ppm solutions of $As^{III}{}_2O_3$ or $KH_2As^{V}O_4$ was adsorbed on 50 mg of Fe-montmorillonite in a 30-ml tube at 290 K for 12 h. 500 mg of Fe-montmorillonite was packed and 50–200 ppb solutions of $As^{III}{}_2O_3$ were flowed at a rate of between 1.4–2.1 ml min^{-1}. All the samples were pressed into 20 mm-diameter disks for X-ray measurements.

2.2. *X-ray Emission and Absorption Measurements*

The X-ray measurements utilizing a fluorescence spectrometer were performed on the Undulator Beamline 10XU of SPring-8 (Sayo). The storage ring energy was 8.0 GeV and the ring current was 100–50 mA. A Si(111) double crystal monochromator and a Rh-coated double mirror set were used. All the measurements were performed at 290 K. The X-ray fluorescence from the sample was analyzed by a Rowland-type spectrometer ($R = 220$ mm) equipped with a Johansson-type Ge(555) crystal (50×50 mm^2, Crismatec) and a scintillation counter (Oken). The energy resolution was 1.1 eV at the Cu $K\alpha_1$ emission (8 keV) including the contribution of the beamline [2] and 0.3 eV at the V $K\alpha_1$ emission (5 keV) based on the peak width of emission and the pre-edge absorption peaks [3].

The Pb $L\alpha_1$ emission spectrum was measured for Pb^{2+} adsorbed on compound **1** (Pb 0.12–1.0 wt%) and reference Pb compounds with the excitation energy set at 13064.3 eV. The fluorescence spectrometer was tuned to the center of the Pb $L\alpha_1$ peak and the Pb L_3-edge XAFS spectrum was measured. The Undulator gap and the piezoelement were optimized to maximize the X-ray beam flux at each data point.

The As $K\alpha_1$ emission spectrum was measured for arsenic adsorbed on the Fe-montmorillonite (As 0.13–0.48 wt%) and reference As compounds with the excitation energy set at 11885.0 eV. The fluorescence spectrometer was tuned to the center of the As $K\alpha_1$ peak and the As K-edge XAFS spectrum was measured. Measurements for standard As samples and a part of As adsorbed onto Fe-montmorillonites were carried out in transmission mode to evaluate the energy resolution and signal-to-background ratio of the spectra obtained in each mode.

*e-mail: yizumi@chemenv.titech.ac.jp

2.3. *XAFS Data Analysis*

Background subtraction of the raw XANES spectrum was performed by using a Victoreen parameter. The subtraction was not necessary in the case of XANES utilizing the fluorescence spectrometer. A smooth spline function was calculated in the postedge region, and then the spectrum was normalized. An EXAFS curve fitting analysis was performed using empirical phase-shift and amplitude parameters for the Pb-O and As-O bonds extracted from the EXAFS spectra of PbO_2 and $K[AsO_2(OH)_2]$ and theoretical phase-shift and amplitude parameters of the As•••Fe bond generated using the *ab-initio* calculation code FEFF 8.2 [4] for the coordinates of $AsFeO_4$ crystal [5].

3. Results and Discussion

3.1. *Pb Lα_1 Emission and L$_3$-edge Absorption Spectra*

The Pb Lα_1 emission peak appeared at 10551.5 eV for 0.12 wt% Pb adsorbed on compound **1** from a 100 ppb Pb^{2+} solution. The full width at a half maximum (FWHM) obtained by the peak fit using a pseudo-Voigt function was 11.7 eV. The core-hole lifetime width of Pb L_3 is 5.81 eV and the energy resolution of spectrometer was evaluated to be 10.1 eV, including the contribution of the beamline.

Normalized Pb L_3-edge XANES spectra are depicted in Figure 1. The rising edge for standard Pb^{II} inorganic compounds shifted by 2.8–4.3 eV toward higher energy compared to 13040.6 eV for Pb^0. The rising edge for lead (0.12–1.0 wt%) adsorbed on compound **1** appeared within the range 13042.9–13044.2 eV (a–c), demonstrating that the adsorbed lead state was II. The rising edge and maximum point energies for the spectrum for 1.0 wt% Pb on compound **1** (13044.2 and 13056.3 eV, respectively; Figure 1a) prepared from 1.0 ppm test solution resembled only that for $2PbCO_3{\cdot}Pb(OH)_2$ (13044.0 and 13055.5 eV, respectively; g).

The samples of 0.30 and 0.12 wt% Pb on compound **1** were both prepared from 100 ppb Pb^{2+} solution, and the two spectra (b) and (c) resembled each other. Based on the rising edge and the maximum point energies, these two spectra (13043.0 ± 0.1 eV and 13054.3 ± 0.7 eV, respectively) resembled only that for PbY (13043.4 and 13054.4 eV, respectively; d).

The comparison of post-edge peak at 13094–13097 eV and the unresolved shoulder peak at 13049 eV supported above assignments of lead species in Figure 1a–c. Most of the Pb^{2+} coagulated as a eutectic mixture of $PbCO_3$ and $Pb(OH)_2$ on compound **1** in the case from a 1.0 ppm solution. The hydroxyl groups should be derived from the buffering effect of basic surface of compound **1**. The formation of pure $PbCO_3$ by the reaction with intercalated/dissolved carbonate or pure $Pb_6O_4(OH)_4$ by the reaction with surface hydroxyl groups should be negligible. In contrast, in the case of the 100 ppb solution, the major lead phase was ion-exchanged Pb^{2+} via the surface reaction $-OH + Pb^{2+} \rightarrow -OPb^+ + H^+$. A shoulder peak at 13049 eV (Figure 1b and c) suggests a minor contribution from a coagulated eutectic mixture of $PbCO_3$ and $Pb(OH)_2$ on compound **1**. Pb L_3-edge EXAFS was measured for the sample of Figure 1a. The Pb-O bond was found at 2.4 Å and the coordination number (N) was ≈3 [6].

3.2. *As Kα_1 Emission and K-edge Absorption Spectra*

The As Kα_1 emission peak appeared at 10544.7 eV for 0.48 wt% As adsorbed on Fe-montmorillonite from a 16 ppm test solution of As^{5+}. The FWHM obtained by the peak fit using a pseudo-Voigt function was 5.72 eV. The total core-hole lifetime width for As Kα_1 is 3.08 eV and the energy resolution of the spectrometer was evaluated to be 4.8 eV, including the contribution of beamline. Note that this value will be an overestimation in the case that As^{5+} and As^{3+} co-exist as adsorbed in the sample. The corresponding value of energy resolution was estimated to be 1.3 eV for an arsenic metal sample.

Normalized arsenic K-edge XANES spectra are depicted in Figure 2. The maximum point energy above the edge shifts from 11867.1 for the arsenic metal (a) to 11868.5 for $As^{III}{}_2O_3$ (b) then to 11872.1 eV for $K[As^{V}O_2(OH)_2]$ (c). The maximum point energy for (d)–(g) was similar to the case of (c). The spectrum pattern of the arsenic adsorbed from the 16 ppm arsenate solution (d) closely resembled that of $K[AsO_2(OH)_2]$. Unexpectedly, spectra (e)–(g) for the samples prepared from the arsenite solution were more similar to (c) than they were to (b). Hence, in the case

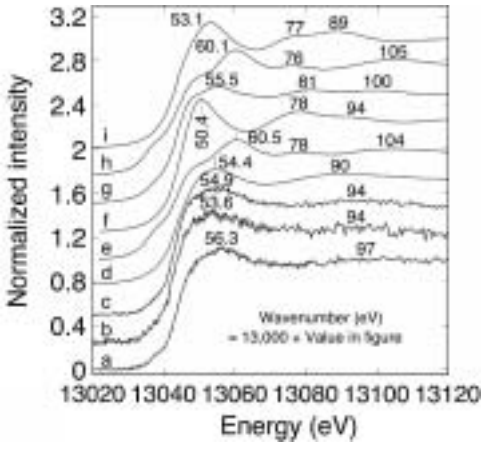

Fig. 1. Normalized Pb L_3-edge XANES spectra for Pb^{2+} on (1) measured utilizing a secondary fluorescence spectrometer (a–c). The Pb content was 1.0 wt% adsorbed from 1.0 ppm Pb^{2+} solution (a) and Pb 0.30 (b) and 0.12 wt% (c) from 100 ppb solution. Reference XANES spectra for PbY zeolite (d), PbO (e), $Pb(NO_3)_2$ (f), $2PbCO_3{\cdot}Pb(OH)_2$ (g), $Pb_6O_4(OH)_4$ (h), and $PbCO_3$ (i). (d)–(i) were measured in the conventional transmission mode.

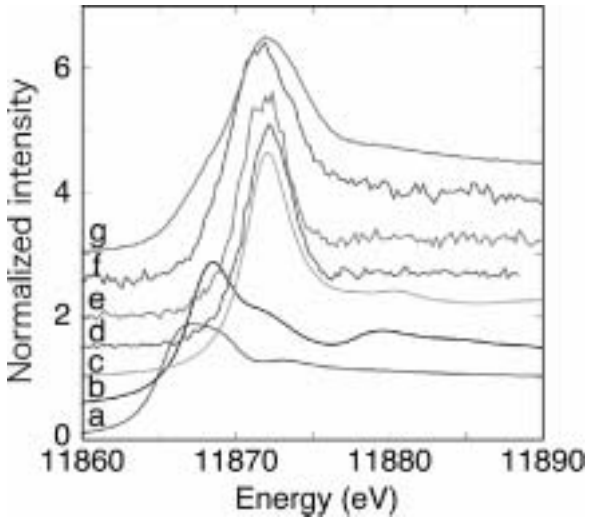

Fig. 2. As K-edge XANES spectra measured at 290 K for As metal (a), As_2O_3 (b), KH_2AsO_4 (c), and As adsorbed (d–g) on Fe-montmorillonite (Fe 15.3 wt%) from test solutions of 16 ppm of KH_2AsO_4 (d), 16 ppm of As_2O_3 (e), 200 ppb of As_2O_3 (f), and 50 ppb of As_2O_3 (g). Spectra (a)–(c) and (g) were measured in transmission mode and (d)–(f) were measured in fluorescence mode utilizing a secondary fluorescence spectrometer.

of the arsenic adsorbed from arsenite solutions in the range of 50 ppb–16 ppm, most of the As^{3+} was oxidized to As^{5+} upon adsorption. A minor peak for adsorbed As^{III} appeared as a shoulder feature at 11868.8–11869.8 eV in (e) and (f). Arsenic K-edge EXAFS was measured for arsenic adsorbed from 200 ppb–16 ppm on Fe-montmorillonite. The As-O and As•••Fe distances were 1.68 Å ($N \approx 3$) and 3.22–3.25 Å ($N \approx 2$), respectively. Also based on the crystallographic structure of FeO(OH) where $[FeO_6]$ octahedral are connected at the edge, the mechanism of oxidative adsorption of As may be formulated as equation **1**. $[AsO_2(OH)_2]^-$ was also suggested for spectrum d adsorbed from arsenate [9–11].

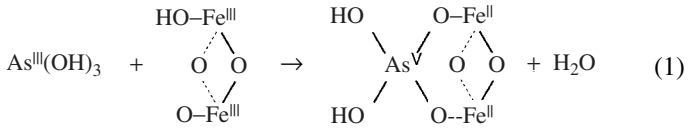

(1)

4. Conclusions

X-ray absorption fine structure combined with fluorescence spectrometry was successfully applied to trace amounts of lead and arsenic adsorbed from aqueous solutions containing 50 ppb–16 ppm of lead or arsenic. Based on Pb L_3-edge XANES, it was found that a eutectic mixture of $PbCO_3$ and $Pb(OH)_2$ coagulated in the case of the 1.0 ppm Pb^{2+} solution, whereas the major species was ion-exchanged Pb^{2+} in the case of adsorption from 100 ppb Pb^{2+} solution. Both arsenate and arsenite species were adsorbed on Fe-montmorillonite (Fe 15.3 wt%) from 50 ppb– 16 ppm solutions containing of As. In this concentration range, As^{3+} in solution was oxidized to As^{5+} upon adsorption. Because the As^{3+} is more toxic [8, 9], Fe-montmorillonite effectively trapped trace amounts of As^{3+} in solution and detoxified it.

Acknowledgments

This work was supported by a grant from the Grant-in-Aid for Encouragement of Young Scientists from the Ministry of Education, Culture, Sports, Science, and Technology (1474 0401) to proceed research and a grant from Tokuyama Science Foundation for the travel and housing at Malmo.

References

1. Izumi, Y., Kiyotaki, F., Minato, T. and Seida, Y., Anal. Chem. **74**, 3819 (2002).
2. Izumi, Y., Kiyotaki, F., Nagamori, H. and Minato, T., J. Electron Spectrosc. Relat. Phenom. **119**, 193 (2001).
3. Izumi, Y. *et al.*, Chem. Lett. **31**, 1154 (2002).
4. Ankudinov, A. L., Ravel, B., Rehr, J. J. and Conradson, S. D., Phys. Rev. B **58**, 7565 (1998).
5. Cheetham, A. K. *et al.*, Nature **320**, 46 (1986).
6. Izumi, Y., Kiyotaki, F. and Seida, Y., J. Phys. Chem. B **106**, 1518 (2002).
7. Oyanagi, H. *et al.*, J. Synchrotron Rad. **7**, 89 (2000).
8. Nordstrom, D. K., Science **296**, 2143 (2002).
9. Farquhar, M. L., Charnock, J. M., Livens, F. R. and Vaughan, D. J., Environ. Sci. Technol. **36**, 1757 (2002).
10. Waychunas, G. A., Fuller, C. C., Rea, B. A. and Davis, J. A., Geochim. Cosmochim. Acta **60**, 1765 (1996).
11. Randall, S. R., Sherman, D. M. and Ragnarsdottir, K. V., Geochim. Cosmochim. Acta **65**, 1015 (2001).

Physica Scripta. Vol. T115, 936–939, 2005

Determination of the Ce(IV)/Ce(III) Ratio by XANES in Soil Horizons and its Comparison with the Degree of Ce Anomaly

Y. Takahashi[1,2,*], K. Yuita[3], N. Kihou[3], H. Shimizu[1,2] and M. Nomura[4]

[1]Graduate School of Science, Hiroshima University, Hiroshima 739-8526, Japan
[2]Laboratory for Multiple Isotope Research for Astro- and Geochemical Evolution (MIRAGE), Hiroshima University, Hiroshima 739-8526, Japan
[3]National Institute for Agro-Environmental Sciences (NIAES), Tsukuba, Ibaraki 305-8604, Japan
[4]Photon Factory, Institute of Materials Structure Science, KEK, Tsukuba 305-0801, Japan

Received June 26, 2003; accepted in revised form November 4, 2003

PACS number: 61.10.Ht

Abstract

We have applied fluorescence XANES for the study of the oxidation state of Ce in natural solid materials. High sensitivity and high energy resolution of 19-element semiconductor detection system enables us to obtain XANES spectra of trace Ce in natural samples. In this study, we report an application of the method to soil horizons, where presence of Ce(IV) was found in the depth between 0.60 and 1.50 m in the soil horizon presumably due to the oxic condition in the layer compared with the shallower regions. The fact is consistent with the preferential enrichment of Ce in the soil relative to other REE (rare earth elements), which is called as the positive Ce anomaly in the REE patterns (REE pattern: relative abundances of REE in samples against reference materials such as chondrite, shale, etc). There is a correlation between the abundances of Ce(IV) and Mn(IV), suggesting that the oxidation of Ce by Mn(IV) oxides is responsible for the relative enrichment of Ce among REE. If we assume that Ce(IV) has been mainly produced by water-rock interaction, the Ce(IV)/Ce(III) ratio coupled with Ce abundance data suggests that considerable amount of REE is incorporated into the soil during its formation from primary minerals.

1. Introduction

Cerium is an important element in geochemistry to elucidate redox environment and chemical processes during formation of natural samples [1]. This is primarily due to the preferential enrichment or depletion of Ce relative to other REE often observed in natural samples. The anomalous behavior of Ce is called as the Ce anomaly which is a useful index in REE pattern (= relative abundances of rare earth elements (REE) normalized by proper materials such as chondrite or shale that represents the bulk compositions of the earth). An example of the (positive) Ce anomaly in REE pattern is found in a soil sample at 1.42 m depth as shown in Fig. 1. Usually, REE patterns become smooth curves, which reflects similar chemical characteristics among REEs. However, the anomalous value of Ce is often recognized in the REE pattern. This phenomenon has been considered to occur by chemical reactions including Ce(IV) during the formation processes of the sample, because other REE (except for Eu) behaves exclusively as trivalent ion in natural systems. However, few studies have identified the Ce(IV) species by direct physico-chemical methods due to the low sensitivity for the speciation study of Ce in natural samples. Recently, we have applied XANES for the determination of the Ce(IV)/Ce(III) ratio in natural samples such as ferromanganese nodules [2], weathered granites [3], cherts [3], zircons [4], and apatite fossils [5]. In this study, we have applied the method to a soil-water system using a well-controlled experimental paddy field in NIAES (National Institute for Agro-Environmental Sciences) in Tsukuba, Japan. In the paddy field, soil water samples at different depths can be extracted to determine concentration of dissolved REE that can be compared with the abundance in the soil. In the field, we can assume that the soil water comes from overlying horizon, since water flow in the field is usually downward. This enables us to simplify the input and output of the REE in the soil horizons.

2. Samples and experimental procedures

The experimental paddy field (size: 10 m × 50 m) in NIAES is located in Tsukuba, Japan, which was particularly designed to study the migration of trace elements in paddy soils [6]. The site of the paddy field consists of fine-textured Gray Lowland Soil. The parent material of the soil layer is mainly tephra (fine volcanoclastic materials) which deposited in late Pleistocence. The layer at the depth between 0 and 0.60 m is alluvial soil dressed in 1974. The Kanto Loam layer (late Pleistocene) is at the depth between 0.60 and 1.30 m, while a transitional zone is located between 1.30 and 1.70 m depth. The deeper layer (>1.70 m) is Joso Clay layer and sandy sediment of the Ryugasaki Formation (late Pleistocene). The paddy field is flooded from May to September. Porous ceramic cups are placed at the depths of 0.20, 0.50, 1.0, 1.5, 2.0 and 2.5 m to collect soil water and the cups are connected to vacuum pumps.

Cerium L_{III}-edge XANES spectra were measured at BL-12C line at the Photon Factory (Tsukuba, Japan) using a 19-element Ge detector [7], with which we can obtain XANES spectra of trace amount of Ce in soil samples (Ce: 20–60 ppm). Some spectra were taken by a similar method at BL01B1 at SPring-8, Japan [8]. Relative energy to peak top of white line of Ce(III) species (e.g., Ce(III)-oxalate; Fig. 3) at 5726 eV was used to show XANES spectra in this study. Manganese and Fe K-edge XANES were also measured by a similar method. REE abundances in soil and water samples were measured by ICP-MS as described in Takahashi *et al.* (2002) [9].

3. Results

REE patterns in the soil samples examined in this study are shown in Figs. 1a and 1b. Each sample is named by the average depth indicated in the brackets in Fig. 1. The soil horizon name is also shown in Fig. 1. It is observed that the Ce anomaly is not

*E-mail: takahasi@geol.sci.hiroshima-u.ac.jp

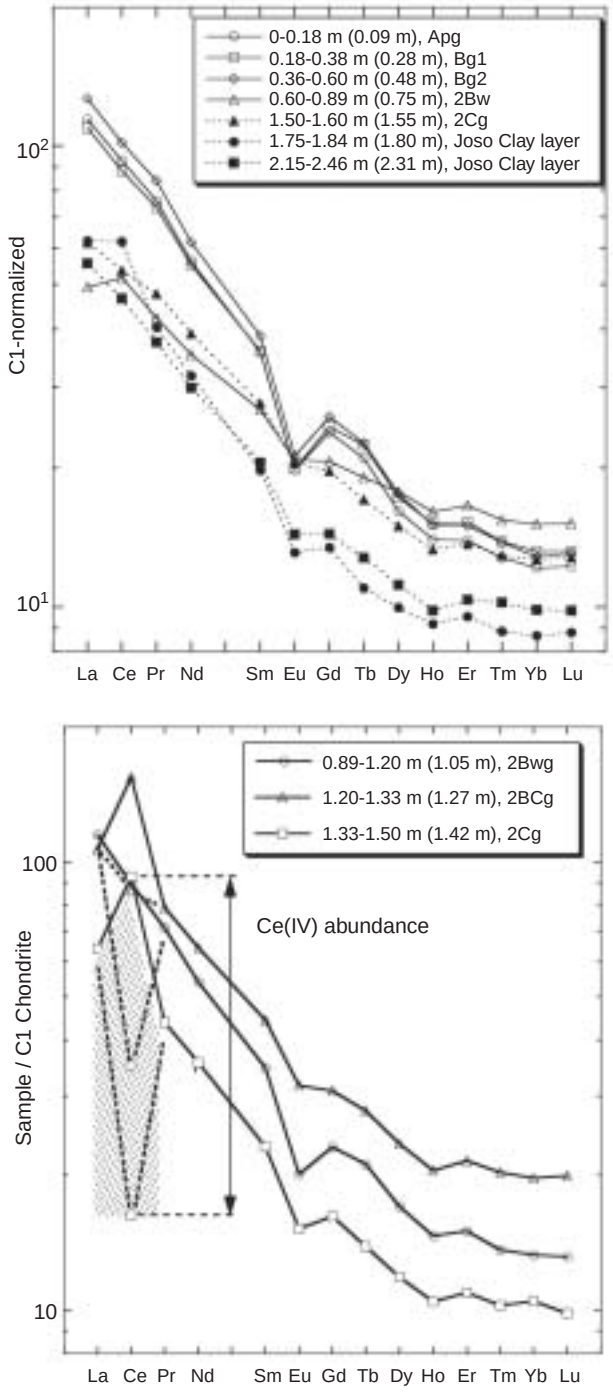

Fig. 1. (a) REE patterns of soil samples at various depths in the experimental paddy field in NIAES. REE abundances of C1 chondrite [15] were employed for the normalization. Soil horizon name (e.g., Apg) is also indicated in the figure. (b) REE patterns of soil samples at 1.05, 1.27 and 1.42 m depths with Ce(III) abundances (dotted curves) based on the Ce(IV)/Ce(III) ratio determined by XANES.

found in the horizon above 1.20 m depth except for the 0.75 m sample of the horizon 2Bw (Fig. 1). Actually, only the horizon at 0.75 m depth (2Bw) is not gleyed, rather oxic horizon, which is consistent with the appearance of the positive Ce anomaly in the horizon. The redox condition is rather anoxic ($Eh < 0$ mV) above 0.30 m during the flooded period in the paddy field due to the high content of organic carbon, while lower layer containing less amount of organic carbon is more oxic compared with the overlying region [8, 9]. This shows that the fractionation of Ce from other REE does not occur in these horizons above 0.30 m, since these horizons are not very oxic to produce Ce(IV). Between

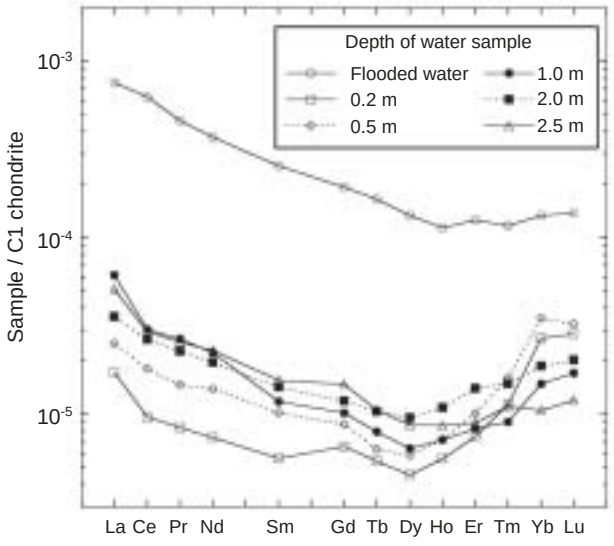

Fig. 2. REE patterns of soil waters at various depths in the experimental paddy field in NIAES. Europium abundances could not be determined due to large abundances of Ba in water samples, since the signal of BaO interferes with Eu in ICP-MS measurements.

1.20 and 1.84 m depth except for the 1.55 m sample, distinct positive Ce anomalies are observed. REE abundance in soil water samples recovered during flooded period (August, 2001) are much lower than those in flooded water, showing that reactions with soil particles undergo to determine REE abundance in soil waters (Fig. 2). Water samples at 0.20 m, 1.0 m, and 2.5 m depths show slightly negative Ce anomalies, while flooded water does not show the Ce anomaly. This suggests that the preferential removal of dissolved Ce from other REE in the soil horizons occurs in the depth due to the formation of Ce(IV) species.

It has been difficult so far to elucidate more information about Ce and REE migration only from REE patterns. Based on the Ce(IV)/Ce(III) ratio determined by XANES, we can extract more information about REE behavior. XANES spectra of Ce(III) reference materials can be well simulated by a pair of an arctangent function and a Lorentzian function whose centroid is shown at 0 eV as relative energy in Fig. 3 [5]. Cerium(IV) can be simulated similarly by three pairs of an arctangent function and a Lorentzian function. The centroid of the three Lorentzians are at 3 eV, 11 eV, and −6 eV, though the third one is subtle peak. Some XANES spectra of Ce in the soil samples are shown in Fig. 3, where XANES spectra of soil samples can be deconvoluted by those of Ce(III) and Ce(IV) reference materials. Cerium(IV) percentages obtained from the deconvolution are shown in Fig. 3.

4. Discussion

In the soil samples at shallow region (0.09 m, 0.28 m, and 0.48 m depths samples), XANES results show that Ce(III) is predominant, which is consistent with the speculation suggested by REE patterns. In the deeper region, considerable amount of Ce has been oxidized to Ce(IV) during water-rock interaction. Iron and Mn abundances, major constituents in soil, increase with depth in the soil horizons and show maximum at 1.27 m [8], which seems to be correlated with the degree of the positive Ce anomaly. This suggests that formation of Ce(IV) in soil can be related to the oxidation of Ce(III) by MnO_2 phase and possibly by Fe_2O_3 phase

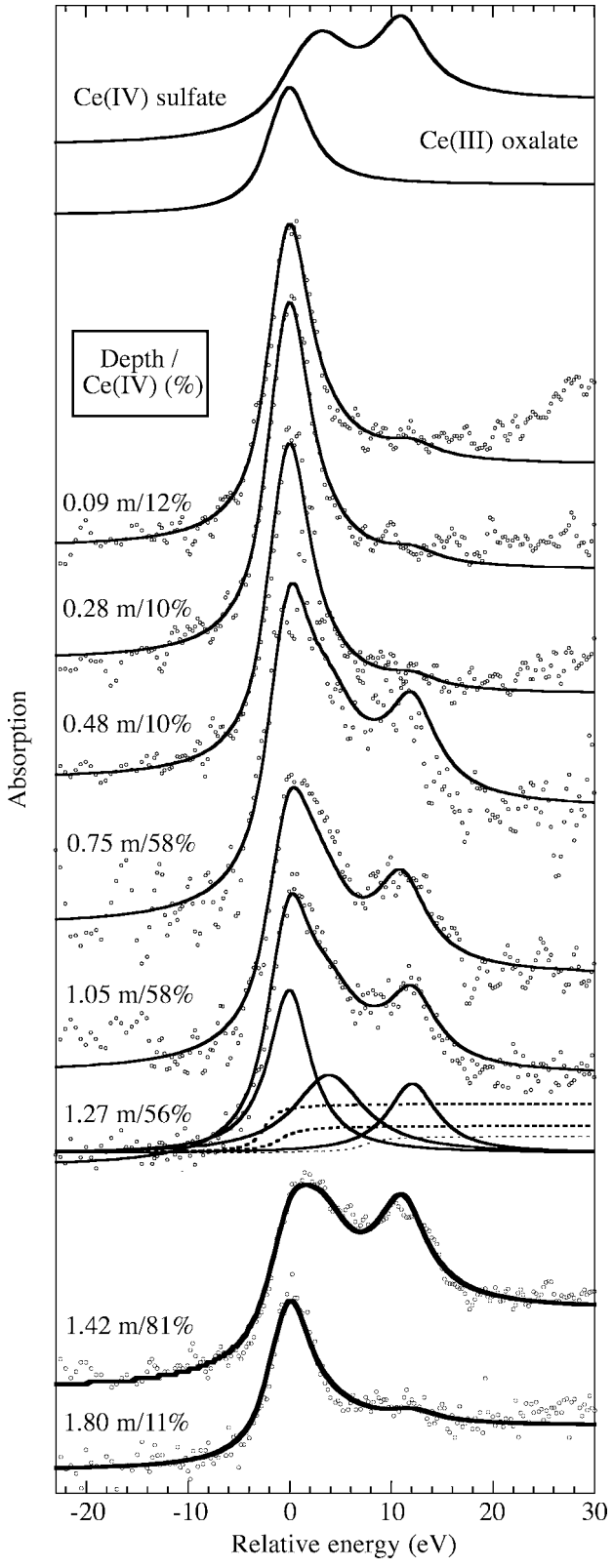

Fig. 3. Cerium L_{III}-edge XANES spectra of the soil samples with those of Ce(III) oxalate and Ce(IV) sulfate shown as reference materials.

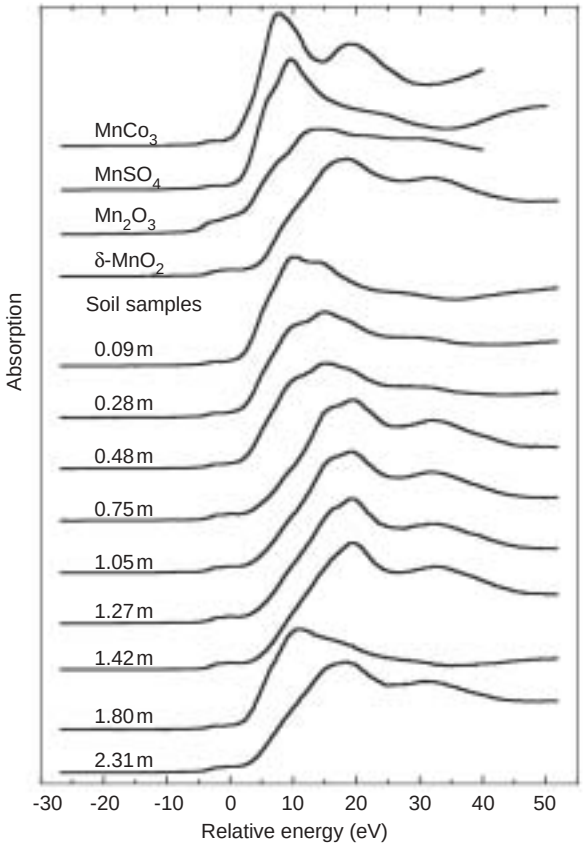

Fig. 4. Manganese K-edge XANES spectra of the soil samples with those of Mn reference materials.

as implied in various studies (e.g., Kawabe *et al.* [14]). In order to support the speculation, oxidation states of Fe and Mn were also studied by XANES. Iron K-edge XANES spectra of all samples examined in this study show similar spectra to ferrihydrite (spectra are not shown), showing that there is not strong correlation with Ce(IV) and Fe(III) (hydr)oxide abundances. On the other hand, the absorption edge of Mn shifts to higher energy with an increase in depth between 0 and 1.50 m depth (Fig. 4). This shows that Mn in the soil horizon takes higher oxidation states in the deeper horizons up to 1.50 m depth. The spectra of the samples at depth between 0.60 and 1.50 m are similar to that of δ-MnO_2, showing that δ-MnO_2 is main Mn phase in the horizon. This coincides with the fact that the amount of Ce(IV) is larger at the depth between 0.60 and 1.50 m. The lower horizon (1.80 m depth) is very reductive, since the horizon is at the top of the Joso Clay layer where ground water table exists during the non-flooded period. This is also reflected in the XANES spectra, that is, the 1.80 m depth sample contains lower abundance of Ce(IV), while Mn K-edge spectrum of the sample shifts to lower energy, showing that Mn(IV) oxides is not included in the horizon. These results suggest that the oxidation of Ce by Mn(IV) oxides is a main mechanism to produce Ce(IV) in the soil horizon. The oxidation of Ce(III) by δ-MnO_2 in natural aquifer has also been indicated in the case of ferromanganese nodules where Ce is completely oxidized by the oxidative sorption on δ-MnO_2 in marine environment [2]. Although it has been suggested that the oxidation of Ce(III) is also caused by iron (hydr)oxides [14], present results show that the oxidation by Mn oxides are more plausible mechanism to produce Ce(IV) in the soil horizon.

It has been suggested that Ce(IV) is produced by Mn(IV) oxides during water-rock interaction. Normally, the Ce anomaly is not found in igneous rocks due to the low content of Ce(IV) in magma [1, 2, 12, 13]. Therefore, it is expected that Ce(III) is predominant species in primary rocks before being subject to weathering to produce soil. This indicates that the presence of Ce(IV) provides the evidence of influence of water-rock interaction on the formation of the soil. Based on the Ce(IV)/Ce(III) ratios, Ce(III) abundances in soil samples showing

the positive Ce anomalies (1.05, 1.27, and 1.42 m depths samples) are plotted in the REE patterns (dotted curves in Fig. 1b). The REE patterns using Ce(III) abundances show negative Ce anomalies. As written above, such negative Ce anomalies cannot be produced during igneous rock formation processes. Tetravalent Ce fraction must be accreted to the soil as a consequence of water-rock interaction accompanied with the oxidation of Ce(III). For example, a fraction of Ce indicated as an arrow in Fig. 1b must have been added to the 1.42 m depth sample by water-rock interaction. Cerium(III) abundance estimated from the Ce(IV)/Ce(III) ratio is regarded to be closer to the Ce abundance originally retained in the primary rocks before subject to water-rock interaction to produce the soil sample. This means that at least shaded area in the Fig. 1b has been accreted to the soil during water-rock interaction, since original REE pattern is unlikely to exhibit any Ce anomalies (Fig. 1b). This suggests that considerable amount of REE has been incorporated into the soil during water-rock interaction. If the Ce(IV)/Ce(III) ratio is not available, it is not possible to discuss such a meaning of REE abundances in soils. For example, one may think that REE abundances of soil have been produced only as a result of removal of REE from primary rocks. However, this is not the case for the samples studied in this work based on the estimation by REE patterns coupled with the Ce(IV)/Ce(III) ratio. The Ce(IV)/Ce(III) ratio coupled with the degree of Ce anomaly shows that most of Ce has been incorporated into the soil during the formation process of soil from primary rocks.

Acknowledgement

This work has been financially supported by a grant-in-aid for scientific research from the Ministry of Education, Science, Sports and Culture of Japan that is awarded to Y. T. and H. S. XANES experiments were performed with the approvals' of KEK (Proposal No. 2000G267) and JASRI (Proposal No. 2001B0393-NX-np).

References

1. Henderson, P., "Rare Earth Element Geochemistry," (Elsevier, Amsterdam 1984).
2. Takahashi, Y., Shimizu, H., Usui, A., Kagi, H. and Nomura, M., Geochim. Cosmochim. Acta **64**, 2929 (2000).
3. Takahashi, Y. *et al.*, Earth Planet Sci. Lett. **182**, 201 (2000).
4. Takahashi, Y., Sakashima, T. and Shimizu, H., Geophys. Res. Lett. **30**, 1137 (2003).
5. Takahashi, Y., Sakami, H. and Nomura, M., Anal. Chim. Acta **468**, 345 (2002).
6. Yuita, K., Noda, T., Kihou, N., Hashimoto, N. and Kawamitsu, K., Jpn. J. Soil Sci. Plant Nutr. **73**, 57 (2002).
7. Nomura, M. and Koyama, A., KEK Report 95-15 (1996).
8. Takahashi, Y. *et al.*, Environ. Sci. Technol. **38**, 1038 (2004).
9. Yuita, K., personal communication.
10. Uruga, T. *et al.*, J. Synchrotron Rad. **6**, 143 (1999).
11. Takahashi, Y. *et al.*, Chem. Geol. **184**, 311 (2002).
12. Shreiber, H. D., Lauer, H. V. and Thanyasiri, T., Geochim. Cosmochim. Acta **44**, 1599 (1980).
13. Hinton, R. W. and Upton, B. G. J., Geochim. Cosmochim. Acta **55**, 3287 (1991).
14. Kawabe, I., Ohta, A., Ishii, S., Tokumura, M. and Miyauchi, K., Geochem. J. **33**, 167 (1999).
15. Anders, E. and Grevesse, N., Geochim. Cosmochim. Acta **57**, 197 (1989).

Physica Scripta. Vol. T115, 940–942, 2005

XRF and XAFS Analysis of Electrophoretically Isolated Nondenatured Proteins

K. M. Kemner[1,*], S. D. Kelly[1], E. J. O'Loughlin[1], T. Khare[1], L. A. Moe[2], B. G. Fox[2], M. I. Donnelly[1], Y. Londer[1], M. Schiffer[1] and C. S. Giometti[1]

[1]Argonne National Laboratory, 9700 South Cass Avenue, Argonne, IL 60439, USA
[2]Department of Biochemistry, 433 Babcock Drive, University of Wisconsin, Madison, WI 53706, USA

Received June 26, 2003; accepted in revised form February 11, 2004

PACS numbers: 82.39, 87.64.−t, 87.59.Ci, 87.64.Fb

Abstract

Microbial metal reduction is relevant for developing bioremediation strategies for contaminated sites containing toxic metal compounds, but the molecular mechanisms involved and the regulation of those mechanisms are poorly understood. Metal reduction capability is microbe specific, yet the involvement of metalloproteins in the transport of electrons from electron donor molecules to electron acceptor molecules (i.e., to the metals to be reduced) is common to all metal-reducing organisms. A thorough understanding of the mechanisms involved in metal reduction by microbes, with a focus on their metalloproteins, will provide valuable information about the metal reduction capability of the organisms and could provide general insight into the mechanisms of metalloprotein expression and regulation in other microbial systems as well. We are developing methods for the efficient separation, detection, and quantification of metalloproteins. Electrophoretic methods for protein separation have been combined with X-ray fluorescence mapping and XAFS to determine the abundance and local chemical environment of iron within a cytochrome.

1. Introduction

Microbial metalloproteins mediate critical processes such as metal reduction, tolerance to radiation, and degradation of organic contaminants. Elucidating the involvement of metalloproteins in biochemical networks is crucial to the development of bioremediation strategies for waste sites containing toxic organic and metal compounds, because currently the molecular mechanisms involved in microbial metal reduction and the regulation of those processes are only partially understood. To elucidate metalloprotein expression within whole cells and microbial communities, we have begun developing new technologies and strategies to enable coupling of X-ray fluorescence (XRF) imaging, XRF elemental analysis, and XAFS with electrophoretic methods.

2. Metalloproteins

Metalloproteins have been estimated to represent one-third of the proteins synthesized by biological systems. As the name suggests, these proteins include a metal atom or atoms in their three-dimensional structures. Typically, one or more relatively small metal atoms are associated with a much larger protein molecule. Metalloproteins participate in many of the essential reactions of metabolism and energy production, including reactions with potential bioremediation applications such as reduction of toxic metals and radionuclides and degradation of hazardous organic contaminants. In respiratory energy production, metalloproteins pass electrons down a controlled thermodynamic gradient to a final electron acceptor by altering the valence states of the metals. In the absence of oxygen, organisms can produce metalloproteins essential for the reduction of available metal ions, including contaminant metals found in soils, sediments, and aquatic systems. The metalloproteins that mediate these respiratory electron transfers are primarily cytochromes that carry Fe atoms coordinated in porphyrin rings. Other metals, notably Cu and Mn, also participate in such processes. For example, the terminal step of oxygen-dependent respiration involves cytochrome c oxidase, an enzyme containing Cu and Fe.

Beyond metal reduction, metalloproteins from various organisms also catalyze the oxidation of chelating agents (thereby halting dispersal of heavy metals and radionuclides mobilized by them) and the degradation of organic pollutants. Metalloproteins are also undoubtedly involved in microbial processes controlling the fixation and general cycling of carbon.

Current methods for identifying and characterizing new metalloproteins in complex mixtures are slow and laborious. Isotopic labeling of proteins with specific metal tags enables detection only of metalloproteins containing that specific metal (e.g., Fe). *In situ* labeling with radiolabeled metals can be problematic if the cell's uptake and metabolism of the radiolabeled molecules are inefficient. Staining methods for detection of metalloproteins, such as the heme stains, also allow for the detection of only one type of metalloprotein. The sensitivity of these specialized stains is also limited, necessitating the use of relatively large amounts of proteins (often over 100 μg of pure protein) for detection. New methods must be developed, therefore, to achieve high-throughput, global discovery and characterization of individual metalloproteins of different types in the complex mixtures of proteins produced by organisms.

3. Electrophoretic Separation of Proteins under Nondenaturing Conditions

The global detection and characterization of metalloproteins requires, in addition to the detection and characterization methods provided by XRF and XAFS, a method for separating complex mixtures into distinct protein components. Although many metalloproteins retain their metal moieties under denaturing conditions, we hypothesize that separation under nondenaturing conditions will preserve even the protein-metal interactions that might be disrupted by denaturation.

Separation of native proteins (i.e., nondenatured functional proteins with minimally disrupted protein structure) by one-dimensional (1-D) gel electrophoresis in cellulose acetate, starch, or polyacrylamide has been used effectively to characterize

*Corresponding author. e-mail: kemner@anl.gov

hundreds of enzyme activities and isozyme polymorphisms [1, 2]. Such 1-D separations of nondenatured proteins can be achieved by using 1-D zone electrophoresis or isoelectric focusing in starch or polyacrylamide. For zone electrophoresis, buffer and gel conditions are selected to optimize differences in the mass-to-charge ratio of the sample proteins. Selection of the ionic strength and pH of the running and sample buffers influences the charge separation, while selection of the separation matrix concentration, which influences the final pore size of the gel, affects the mass separation. Separation by isoelectric focusing, in contrast, depends only on differences in the net charges of the proteins, independent of their masses.

A 2-D separation based on two independent parameters, analogous to the separation by isoelectric point and size used in denaturing 2-D electrophoresis (2DE), would obviously overcome co-migration of proteins and dramatically increase the number of distinct proteins detectable. We recently developed such a method for the 2-D separation of proteins under nondenaturing conditions and applied the method to the analysis of proteins from the metal-reducing microbe *Shewanella oneidensis* [3].

4. Detection of Metalloproteins in Polyacrylamide Gel Strips

Although the XRF technique is a very powerful probe for identifying a variety of elements in a microbial system, the information provided is only the average for all of the free metal ions and the metalloproteins at the point of interaction with the X-ray beam. To investigate the interaction between a metal and one of the specific proteins expressed by the microbe, the size of the X-ray probe must be comparable to or smaller than the dimensions of the spatially resolved protein of interest. For the 1-D and 2-D gel systems discussed here, 0.1- to 1.0-mm X-ray beams are required to analyze the resolved protein bands in the polyacrylamide gels. Production of high-intensity X-ray beams of this size with an undulator X-ray source has been accomplished simply with the use of apertures the size of the desired spot.

In a preliminary experiment, a sample containing 0.5 μg of cytochrome c was resolved by using isoelectric focusing in immobilized pH gradient (IPG) strips. The portion of the gel containing the protein was cut out and mounted on a sample holder compatible with existing mounting devices at the Materials Research Collaborative Access Team (MRCAT) insertion device beamline at the Advanced Photon Source (APS) [4]. With a single-element solid-state XRF detector, a strong Fe Kα fluorescence signal was easily detected after less than 10 s of irradiation with a 10.5-keV X-ray beam. This result demonstrated that the necessary sensitivity exists for detection of the metal atoms in metalloproteins resolved in gels. In a subsequent experiment, various amounts of catalase (20, 100, and 200 μg) were resolved by isoelectric focusing on replicate IPG strips. One strip was stained for protein, and the others were then "imaged" in 1-D by XRF by translating the strip through the X-ray beam. Normalized integrated intensity of the Fe Kα fluorescence at the protein location on the strip is plotted versus the mass of metalloprotein applied to the IPG strips in Fig. 1. Results of linear regression analysis of these data conservatively indicate a 4 μg detector, 20-s integration time, and 10-keV X-ray probe energy. Realistic improvements to the experimental setup for better detection sensitivity include (1) measurement near resonance for Fe fluorescence detection (factor of ∼2), (2) use of all 13 elements of the solid-state detector at the MRCAT beamline (factor of 3.6), and (3) increased data collection time from 20 s to 600 s

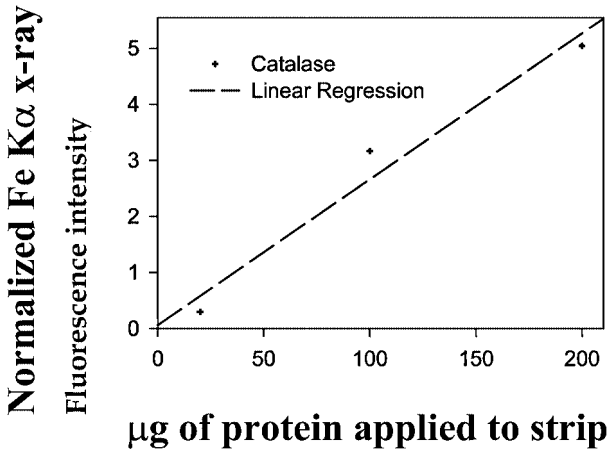

Fig. 1. Normalized integrated Fe Kα fluorescence intensity at the protein location on the IPG strip versus the mass of metalloprotein applied.

(factor of 30). These improvements would result in increased elemental detection sensitivity of >200-fold for a metalloprotein similar to catalase. This translates to sensitivity of better than 20 ng for metalloproteins with concentrations of Fe similar to that of catalase.

We evaluated this technique for investigating samples from microbial cultures. Specifically, we compared the reproducibility and accuracy of XRF elemental mapping for identifying the presence of cytochrome c7 (a triheme Fe-centered metalloprotein) overexpressed by an *Escherichia coli* culture (100 μg of total protein). In addition, 50 and 100 μg of purified cytochrome c7 (as calibration standards) and 200 μg of material from an *E. coli* control culture (i.e., not overexpressing cytochrome c7) were also measured. XRF measurements of the spatial distribution of the Fe Kα fluorescent intensity on a 1-D gel were performed at the MRCAT [4] beamline. A 10.5-keV X-ray beam (0.77mm × 1.0 mm) was used as a probe, and the fluorescent X-ray intensity was monitored with three elements of a multielement solid-state detector. Measurements were made on all samples at room temperature and at atmospheric pressures. Results for the relative intensities of the Fe Kα fluorescence radiation relative to the position on the gel are shown in Fig. 2. These results clearly illustrate (1) correlated elevations in Fe Kα fluorescence intensity for the cytochrome c7 standard and the *E. coli* overexpressing cytochrome c7 (at ∼59,000 μm, marked "A" on the strip),

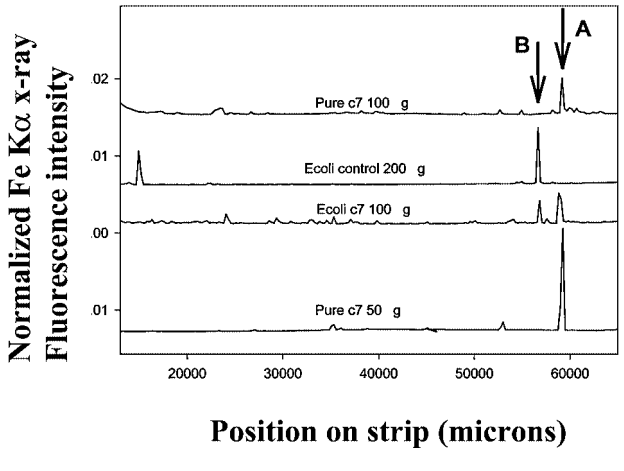

Fig. 2. Relative Fe Kα X-ray fluorescence intensities for cytochrome c7 standards and *E. coli* cell lysates relative to their positions on 1-D IPG gels.

(2) reproducibility (i.e., collocation of the Fe peak at ~59,000 μm, marked "A" on the gel strip, for two replicate samples), and (3) the presence of additional, reproducible Fe fluorescence radiation in both the overexpressed cytochrome c7 and control *E. coli* samples (at ~57,000 μm, marked "B" on the gel strip). These results clearly demonstrate that this approach enables identification of overexpressed metalloproteins in cultures. Observation of Fe peak at ~57,000 μm in both types of *E. coli* samples further demonstrates that this technique does not necessarily require a metalloprotein to be overexpressed in order to be detected.

5. XAFS Analysis of Proteins Separated on Nondenaturing Gels

In many instances, although identification of the presence of metalloproteins is extremely valuable, additional information concerning the structure and function of the metal center of the metalloprotein is desirable. The atoms that coordinate the metals of a protein alter their chemistry. For example, in cytochromes, Fe is bound by four equatorial nitrogen atoms from the porphyrin ring, plus axial ligands from the protein or the solvent. In some cases, a sulfur atom provides the axial ligand. XAFS spectroscopy can be an extremely valuable tool for probing the local chemical and structural environment of the metal within metalloproteins. To investigate the possibility of coupling the XAFS technique to procedures discussed above, we have made Fe XAFS measurements on a catalase protein after isoelectric focusing on polyacrylamide on a plastic backing (IPG strip). XAFS data were collected at room temperature in the fluorescence mode with an ion chamber in the Stern-Heald geometry [5, 6] by using a Lytle detector with an Mn filter. Linearity tests [7] indicated less than 0.5% nonlinearity in the experimental setup for a 50% attenuation of the incident radiation. Incident and transmitted X-ray intensities were monitored with ionization chambers with 100% free-flowing nitrogen gas at atmospheric pressures. Results of the fitting of the data ($\Delta k = 2.5$–$8.0\,\text{Å}^{-1}$, $\Delta r = 1$–$3\,\text{Å}$, 7 floating variables, and 2 degrees of freedom) to theoretical standards generated with the FEFF program [8] are shown in Fig. 3. Results from fitting analysis of these data indicate an average of 4 N/O and 1 N/O (at 1.98 Å and 2.05 Å, respectively) and 8 carbons (at 3.05 Å), plus additional carbons and multiple-scattering effects (at 3.2–3.4 Å), contributing to the local environment of the Fe. These results are consistent with previous XAFS studies of other purified and concentrated catalase proteins [9–11].

For future work, a low-temperature sample holder will be designed to reduce radiation effects that might alter the proteins being measured with XAFS. To increase the sensitivity of the XAFS technique to lower concentrations of metalloproteins, future XAFS measurements will also be made with a 13-element solid-state fluorescence detector.

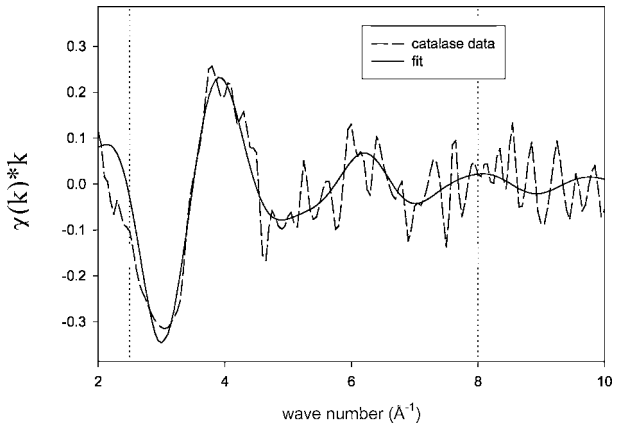

Fig. 3. Theoretical fitting (dashed line) of XAFS chi data (solid line) from catalase spatially isolated on an IPG strip.

6. Summary

In summary, we have described the results of the development of new approaches to identify and characterize metalloproteins. Specifically, we have described the integration of XRF mapping, XRF elemental analysis, and XAFS with electrophoretic methods. Further development of these integrated techniques to enable high-throughput analysis of frozen samples (to reduce the effects of radiation damage) holds great promise for the investigation of proteomic expression in a wide variety of biological systems.

Acknowledgments

Support for this work was provided by the U.S. Department of Energy Office of Science (DOE-SC), Office of Biological and Environmental Research, NABIR Pprogram. Support for the MRCAT and the APS is provided by the DOE-SC Office of Basic Energy Sciences under contract W-31-109-Eng-38. NSF MCB 9733734 to B.G.F.

References

1. Manchenko, G. P., "Handbook of Detection of Enzymes on Electrophoretic Gels," (CRC Press, Boca Raton, 1994).
2. Roth, G. M., "Electrophoresis of Enzymes," (Springer Verlag, Berlin, 1994).
3. Giometti, C. S., *et al.*, Proteomics **3**, 777 (2003).
4. Segre, C. U., *et al.*, "Synchrotron Radiation Instrumentation: Eleventh US National Conference," (Edited by P. Pianetta) (American Institute of Physics, City, 2000), p. 419.
5. Stern, E. A. and Heald, S. M., "Basic principles and applications of EXAFS, Handbook of Synchrotron Radiation," (North Holland, City, 1983).
6. Stern, E. A. and Heald, S. M., Rev. Sci. Instrum. **50**, 1579 (1979).
7. Kemner, K. M., Kropf, A. J. and Bunker, B. A., Rev. Sci. Instrum. **65**, 3667 (1994).
8. Zabinski, S. I., *et al.*, Phys. Rev. B **52**, 2995 (1995).
9. Berman, H. M., *et al.*, "The Protein Data Bank. Nucleic Acids Research," 235 (2000).
10. Brava, J., *et al.*, "Structure 3," 491 (1995).
11. Fita, I. and Rossmann, M. G., Proc. Nat. Acad. Sci. **A82**, 1604 (1985).

Physica Scripta. Vol. T115, 943–945, 2005

Direct Speciation of Lead, Zinc and Antimony in Fly Ash from Waste Treatment Facilities by XAFS spectroscopy

M. Takaoka[1,*], T. Yamamoto[2], T. Tanaka[3], N. Takeda[1], K. Oshita[1] and T. Uruga[4]

[1]Department of Urban & Environmental Engineering, Kyoto University, Kyoto, 606-8501, Japan
[2]Chemical Resources Laboratory, Tokyo Institute of Technology, Yokohama, 226-8503, Japan
[3]Department of Molecular Engineering, Kyoto University, Kyoto, 606-8501, Japan
[4]Japan Synchrotron Radiation Research Institute, Hyogo, 679-5198, Japan

Received June 26, 2003; accepted in revised form February 6, 2004

PACS numbers: 61.10.Ht, 89.60.Ec

Abstract

It is important to understand the chemical states of heavy metals in solid waste from municipal incinerator (MSWI) fly ash as both the toxicity and behavior in the environment of heavy metals differ with their chemical states. In this study, direct speciation of lead, antimony and zinc in MSWI fly ash was conducted by XAFS spectroscopy. Three kinds of fly ash from continuous stoker-type MSWIs and a kind of fly ash from an ash melting plant (AMP) were investigated. XAFS measurements were carried out on beam line BL01B1 at SPring-8. The lead, zinc and antimony spectra were collected in fluorescence detection mode at room temperature with a Si (111) or Si (311) monochromator. According to Pb LIII-edge XANES spectra, lead was estimated to be predominantly $PbCl_2$ in MSWI fly ashes and PbO in AMP fly ash. Zinc was estimated to be speciated predominantly as $ZnCl_2$ in MSWI fly ashes and a mixture of $2ZnCO_3{\cdot}Zn(OH)_2$, ZnO and ZnS in AMP fly ash. Antimony K-edge XANES spectra indicated that Sb is five-valent in all the fly ashes.

1. Introduction

In Japan, about 50 million tons of municipal solid waste (MSW) is generated every year and more than 75% of MSW is incinerated. The MSW incineration (MSWI) is an excellent technology from the viewpoint of weight and volume reduction of MSW and public sanitation. However, about 5 million tons of bottom ash and 1.2 million tons of fly ash are generated every year during this treatment. MSWI fly ash has recently attracted much attention because of its amount of heavy metals with low boiling point and the presence of trace organic contaminants such as dioxins.

It is important to understand the chemical state of heavy metals in MSWI fly ash on its recycling and detoxification because the toxicity and behavior of metal contaminants in the environment depend on their chemical state. Determining the chemical state of heavy metals in MSWI fly ash is required to prevent the pollution of soils and aquifers near disposal sites.

Determining the chemical speciation of heavy metals at low concentration levels in MSWI fly ash is impossible with physical techniques available in the laboratory, such as XPS or XRD [1, 2]. Chemical fractionation with solvents has been used [3, 4], but these methods are destructive and the initial chemical state may change during the sequential extraction. X-ray absorption fine structure (XAFS) spectroscopy enables quantitative metal speciation to be performed in diluted and chemically complex systems and, therefore, represents a method of choice to study fly ash.

*e-mail: takaoka@epsehost.env.kyoto-u.ac.jp

2. Materials and Methods

2.1. *Samples*

Fly ash 1 and 3 were sampled from the electrostatic precipitators of two different continuous stoker-type MSWIs. Fly ash 2 was sampled from the bag filter, which is a dust collector, in a continuous stoker-type MSWI. Fly ash 4 was sampled from the bag filter in an ash melting plant (AMP). Fly ash 2 and 4 contain a lot of calcium compounds because calcium hydroxide is injected before the bag filter for acid gas removal.

The fly ash samples were dried at 105 °C overnight for chemical analysis, but not for XAFS measurements.

For chemical analysis, 100 mg powder was digested for 60 minutes in an acid mixture of 5 ml HNO_3 (15.8 M), 2 ml HCl (11.4 M) and 3 ml HF (27.7 M) using a microwave oven (MDS-2000: CEM corp.) [5]. Then, the acidic solution was neutralized by 18 ml boric acid and set in the microwave oven for 5 minutes. Finally the heavy metals in the filtered solution were analyzed by inductively coupled plasma atomic emission spectroscopy (ICP-AES) (Shimadzu, ICPS-8000).

As target elements, lead and antimony were selected from the viewpoint of their toxicity and zinc was selected from the viewpoint of its recycling. The following compounds were selected as reference materials for XAFS analysis on the basis of the likely chemical form of heavy metals in fly ash.

Zinc compounds: Zn, ZnO, ZnS, $2ZnCO_3{\cdot}3Zn(OH)_2$ (basic zinc carbonate), $ZnSO_4$ and $ZnCl_2$; Antimony compounds: Sb, Sb_2O_3, Sb_2O_5 and SbOCl; Lead compounds: Pb, PbO, $PbCO_3$, $PbCl_2$, PbS, $PbSO_4$ and PbO_2. These materials were provided by Wako Pure Chemical industries, Soekawa Chemicals, and Nacalai Tesque. The specification of the fly ashes and their content in target elements are presented in Table I.

2.2. *XAFS Measurements*

Zn-K, Sb-K, and Pb-LIII edge XANES experiments were carried out on beamline 01B1 at SPring-8 (Hyogo, Japan), which operates at a ring energy of 8 GeV and a stored current from 60 to 100 mA. The main optics is the standard SPring-8 bending magnet system, which contains two mirrors and a fixed-exit double crystal monochromator. The Zn-K and Pb-LIII edge XANES spectra were measured with a Si (111) two-crystal monochromator, and Sb-K edge XANES spectra with a Si (311) two-crystal monochromator. Higher harmonics were reduced by reflection on the two mirrors. XANES spectra of reference materials and fly ash samples were recorded in transmission mode using ionization chambers and in fluorescent mode using a Lytle

Table I. *The specification of fly ash and the content of target elements.*

Sample	Fly Ash 1	Fly Ash 2	Fly Ash 3	Fly Ash 4
Processed materials	MSW	MSW	MSW	Ash
Operation	Continuous	Continuous	Continuous	Continuous
Furnace type	Stoker	Stoker	Stoker	melting furnace
Dust collector	ESP	BF	ESP	BF
Acid gas removal	Wet scruber	Lime injection	Wet scruber	Lime injection
Pb (mg/kg)	11000	6100	8000	10000
Zn (mg/kg)	24000	26000	18000	32000
Sb (mg/kg)	1800	1200	1400	940

detector, respectively. Sample absorbance was measured every 0.3 or 0.5 eV. The energy was calibrated by setting the pre-edge peak of a Cu foil at 8980.3 eV.

Data reduction was performed using the analysis program developed by Tanaka [6] at the Kyoto University Data Processing Center. The normalization procedure has been reported previously [6]. Pattern fitting analysis of XANES spectra was conducted using the commercial REX2000 software (Rigaku co Ltd), assuming that the unknown spectra were linear combinations of the reference spectra in our library [7]. Within the validity of this assumption, the precision on the percentage of species in the powdered samples is estimated to about 2%.

3. Results and Discussion

3.1. *Chemical State of Lead*

Figure 1 shows the Pb-LIII edge XANES spectra of the four fly ash samples and reference materials. The XANES spectra for the MSWI fly ashes 1–3 have a similar shape, in contrast to the AMP fly ash 4. Upon comparing the unknown XANES spectra to the set of known spectra, lead was estimated to be predominantly speciated as $PbCl_2$ in MSWI fly ash 1–3 and as PbO in the melting plant fly ash 4.

Two pattern fitting analyses were performed, differing in the exclusion, or not, of lead sulfide. Although the presence of sulfate

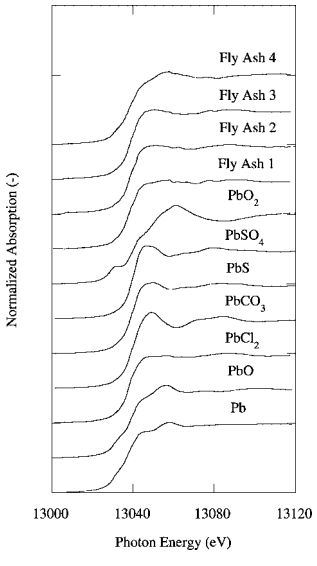

Fig. 1. Pb-LIII edge XANES spectra of four fly ash samples and reference materials.

Table II. *The results of pattern fitting analysis for XANES spectra.*

	MSWI fly ash 1		MSWI fly ash 2		MSWI fly ash 3		AMP fly ash 4	
Pb compounds								
$PbCl_2$	87		57	73	47	62	28	
PbO	13		8	7	5	5	59	
PbS			35		41			
$PbCO_3$				20	8	34		
PbO_2							13	
R	0.8		0.8	0.9	0.8	0.9	0.9	
Zn compounds								
$ZnCl_2$	75	40	66		61			4
ZnO	25	15					34	30
ZnS			34		39		27	
$2ZnCO_3{\cdot}3Zn(OH)_2$							39	13
$ZnFe_2O_4$		24						53
$ZnAl_2O_4$		22						
R	4.3	2.4	4.8		4.7		4.8	3.5

R: residual value $R = \frac{\sum(XANES_{Measured} - XANES_{Calculated})^2}{\sum(XANES_{Measured})^2} \times 100$.

on the surface of fly ash has been reported in the literature from XPS and XANES analysis [1, 8], $PbSO_4$ is not considered to be present in these fly ashes by XANES spectra. Therefore it is assumed that PbS is a possible species. Results reported in Table II show that $PbCl_2$ accounts for ~47 to 87% of Pb in the three MSWI fly ashes. This species is consistent with the high concentration of HCl in the flue gas of MSWI. MSWI fly ash 2 and 3 possibly contain PbS as the second most abundant Pb species. When PbS was excluded from the spectral fit, $PbCO_3$ made up ~20–34% of total Pb. In the AMP fly ash 4, ~59% and ~28% of total Pb was found to be speciated as PbO and $PbCl_2$, respectively. The low values of the residual parameter (*R*) indicate that satisfactory fits of model predictions to experimental data were obtained for all sample spectra.

The chemical states of lead in fly ash were not influenced by the dust collector type or acid gas removal method. Although the flue gas before acid gas removal in AMP was rich in HCl, PbO is the dominant species in the AMP sample. Therefore, Pb speciation is determined by other parameters, such as the furnace temperature and/or the initial chemical state in waste fed into the furnace and particles carried over from the furnace.

3.2. *Chemical State of Zinc*

Figure 2 shows Zn-K edge XANES spectra of the four fly ash samples and reference materials. MSWI fly ash 2 and 3 have similar spectra, and MSWI fly ash 1 a slightly different one. The spectrum of AMP fly ash 4 has a distinct shape and peak position from the three other spectra. Comparison with reference spectra suggests that Zn exists primarily as a Zn chloride phase in MSWI fly ash 1–3. The spectral features at 9667 eV and 9672 eV correspond in position to those of $ZnFe_2O_4$ and $ZnAl_2O_4$. Consistent with these observations, the assumption of 40 to 75% $ZnCl_2$ yielded optimal fits to these spectra with R values of 2.4 to 4.8.The inferred minor species are ZnS in MSWI fly ash 2 and 3, and ZnO and Zn-spinel in MSWI fly ash 1. Adding $ZnFe_2O_4$ and $ZnAl_2O_4$ as component species to the spectral fit of MSWI fly ash 1 reduced the fraction of $ZnCl_2$ from 74% to 40%. The likely presence of oxygenated Zn species is consistent with Jakob *et al.*'s results [9], which reported the presence of zinc and silica or

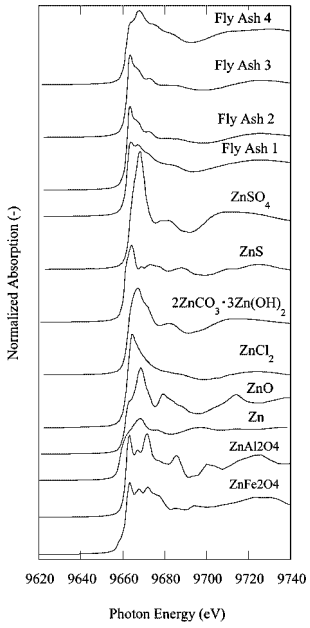

Fig. 2. Zn-K edge XANES spectra of four fly ash samples and reference materials.

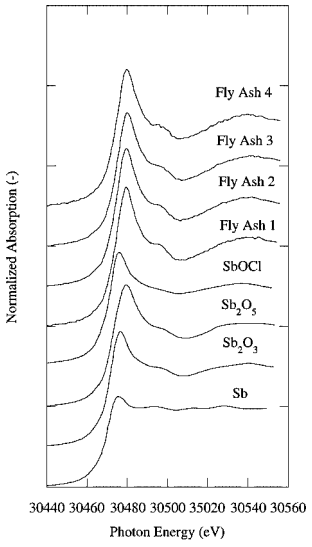

Fig. 3. Sb-K edge XANES spectra of four fly ash samples and reference materials.

aluminum double oxides in ash samples using XRD. In the AMP fly ash 4 sample, two phase compositions gave statistically similar results. One in which Zn is present as a mixture of ZnO, ZnS and $2ZnCO_3{\cdot}3Zn(OH)_2$ in similar proportions, and another consisting of a mixture of $ZnFe_2O_4$ (53%), ZnO (30%), $2ZnCO_3{\cdot}3Zn(OH)_2$ (13%), and $ZnCl_2$ (4%). In this sample, the amount of$ZnCl_2$ is very small, if present at all. These results were in agreement with leaching tests which showed that water soluble fraction of Zn in this ash was about 0.2%. The fact that the reconstructions of Pb spectra were better than those of Zn spectra (R-values were lower for the first set of spectra), partly results from the featureless shape of Pb spectra (i.e., they carry less structural and chemical information and, hence, are easier to simulate).

In conclusion, the chemical states of Zn and Pb in the MSWI fly ashes present similarities. Pb and Zn are essentially in the form of chloride and oxide in the first ash, and in the form of chloride and sulfide and the second and third ashes. This result suggests that the nature of the metal species is determined by the thermo-chemical conditions in the stoker.

3.3. *Chemical State of Antimony*

Figure 3 shows the Sb-K edge XANES spectra of the four fly ash samples and reference materials. The samples XANES spectra have almost the same shape, which suggests that they contain the same Sb species. The position of the peak maximum is at 30480 eV like in Sb_2O_5, and 30476 eV higher than in Sb_2O_3. Therefore, Sb is five-valent in the ash samples. This interpretation is confirmed by the height of the normalized white line, which equals1.60 in Sb_2O_3, 1.68 in Sb_2O_5, and 1.66 to 1.73 in the ashes.

Consequently, the oxidation state, and possibly the chemical form as well, of antimony in fly ash does not vary with the furnace type, waste fed into the furnace and particles carried over from the furnace, the dust collector type and the method used for acid gas removal. Although it has been predicted from thermodynamics that antimony is speciated as Sb_2O_3 or SbO_2 in MSWI fly ash [10, 11], we found here that Sb is five-valent with Sb_2O_5 being a possible species.

4. Conclusion

1) Lead and zinc are predominantly present as metal chloride in the MSWI fly ashes 1–3.
2) The second most abundant species are lead and zinc oxide in MSWI fly ash1, and metal sulfide in MSWI fly ashes 2 and 3. This indicates that the behavior of lead is similar to that of zinc and vice versa.
3) In AMP fly ash 4, metal chlorides are less abundant and the Zn and Pb speciation are dominated by oxide, and possible hydroxide or carbonated (Zn), forms.
4) Overall, these results indicate that the chemical forms of lead and zinc in fly ash is independent from type of the dust collector, the method of acid gas removal, and HCl concentration in flue gas.
5) Antimony is five-valent in all samples. Its speciation is thought to be unique and identical to Sb_2O_5. In a similar manner as Zn and Pb, Sb speciation is constant and independent from the burning or dust collection process.

Acknowledgement

The synchrotron radiation experiments were performed at the SPring-8 facility following the approval of the Japan Synchrotron Radiation Research Institute (JASRI) (Proposal No. 2000B0309-NX-np and 2001A0367-CX-np).The authors warmly thank Mr. Takehiko Murakami, Mr. Kazuo Yasui and Mr. Toshiyuki Kawai for their assistance during the measurement.

References

1. Takaoka, M., Kuramoto, Y., Takeda, N. and Fujiwara, T., Haikibutsugakkishi Ronbusyu **12**, 102 (2001) (in Japanese).
2. Takaoka, M., Takeda, N. and Miura, S., Wat. Sci. Tech. **36**, 275 (1997).
3. Tessier, A., Campbell, P. G. C. and Bisson, M., Anal. Chem. **51**, 844 (1979).
4. Takaoka, M., Kuramoto, Y., Takeda, N. and Fujiwara, T., JSCE, **VII-20**, 901 (2001) (in Japanese).
5. Takaoka, M., Nakatsuka, D., Takeda, N. and Fujiwara, T., Haikibutsugakkishi Ronbusyu **11**, 333 (2000) (in Japanese).
6. Tanaka T., *et al.*, J. Chem. Soc. Farad. Trans. **84**, 2987 (1988).
7. Yoshida, T., *et al.*, Physica B: Condens. Matter **208–209**, 581 (1995).
8. Kawai, J. *et al.*, Spectrochim. Acta Part B **58**, 635 (2003).
9. Jakob, A., Stucki, S. and Kuhn, P., Environ. Sci. Technol. **29**, 2429 (1995).
10. Watanabe, N., Inoue, S. and Ito, H., J. Mater. Cycles Waste Manag. **1**, 38 (1999).
11. Urabe, T., Seisogiho **20**, 100 (1995) (in Japanese).

Physica Scripta. Vol. T115, 946–948, 2005

Chemical States of Trace Heavy Metals in Sewage Sludge by XAFS Spectroscopy

M. Nagoshi*, T. Kawano, S. Fujiwara(1), T. Miura(1), S. Udagawa(1), K. Nakahara(1), M. Takaoka(2) and T. Uruga(3)

Steel Research Laboratory, JFE Steel Corporation, 1-1, Minamiwatarida, Kawasaki 210-0855, Japan
(1)Engineering Research Center, JFE Engineering Corporation, 1-1, Minamiwatarida, Kawasaki 210-0855, Japan
(2)Dept. of Environmental Engineering, Kyoto University, Sakyo-ku, Kyoto 606-8501, Japan
(3)SPring-8, JASRI, Kouto, Mikazuki-cho, Sayo-gun, Hyogo 679-5198, Japan

Received June 26, 2004; accepted in revised form June 10, 2004

PACS numbers: 61.10.Ht, 89.60.−k

Abstract

The chemical states of Cu, Zn, and As in sewage sludge have been investigated by X-ray absorption fine structure (XAFS) spectroscopy. XAFS spectra show that Cu and Zn of 150 ppm–200 ppm form sulfides of 2+, and As of less than 250 ppb exists as 3+ in the sludge under anaerobic state. The *in-situ* XAFS measurements reveal that under aerobic states, Zn sulfide is partially dissolved and As is partially oxidized to 5+ although Cu maintains sulfide form. The stability of these compounds in the sewage sludge is discussed.

1. Introduction

The chemical forms of heavy metals, such as Cu and Zn, in sewage depend on the sewage treatment process including condensation and aerobic treatments. The condensed heavy metals in sewage sludge potentially prevented us to apply the sludge to beneficial use, although their concentrations are very low. Chemical states of the heavy metals are very important information for developing highly safe and reliable techniques of removing or stabilizing the heavy metals. Sequential extraction method by Stover *et al.* [1] has been used for estimating the chemical forms of heavy metals in sewage sludge. However, this technique is an indirect method in which compounds of heavy metals would be chemically destructed.

X-ray fluorescence X-ray absorption fine structure (XAFS) technique has been applied to investigating the chemical states of trace elements in environmental matters, such as contaminated soil [2], contaminated water [3], and fly ash [4]. We have adopted X-ray fluorescence XAFS to heavy metals in sewage sludge in order to determine their chemical states directly [5, 6]. In this paper, K-edge XAFS spectra of Cu, Zn, and As in condensed sewage sludge measured under anaerobic and aerobic conditions are presented. The chemical states of these elements in the sewage sludge are discussed in terms of the stability of these elements. The results for Cu and Zn are compared with published data obtained by a sequential extraction technique.

2. Experimental

Secondary sludge (excess sludge or waste activated sludge) was collected after the anaerobic treatment from a typical sewage treatment plant in a city area of Japan. The sludge was condensed up to solid concentration of about 5%. The concentrations of Cu, Zn, and As are about 160 ppm, 200 ppm, and <250 ppb, respectively, in the condensed sludge.

XAFS measurements were carried out on the station BL01B1 with a two-crystal Si(111) monochromator at SPring-8 (Hyogo, Japan). The K-edge XAFS spectra were measured for Cu, Zn, and As in the X-ray fluorescence mode using a Ge 19-elements solid-state detector. Spectra for reference compounds and dilute solutions (about 100 ppm) of Cu and Zn were measured in the transmission mode and the X-ray fluorescence mode, respectively.

For the XAFS measurements under anaerobic conditions, the sludge was put into bags made of Mylar film and shielded from air. In order to put the sludge under aerobic state, the sludge was being aerated in a home-maid cell during XAFS measurements. The cell was made of acrylic plates and has Mylar windows for incident and reflected X-rays. The redox potential (E) of the sludge was measured using an ORP meter (Central Chemical Co.) just before and after each measurement. Typical redox potentials were about −100 mV and 400 mV for the sludge under anaerobic and aerobic conditions, respectively.

3. Results and discussion

Figure 1 ∼ Figure 4 show Cu-K, Zn-K, and As-K edge X-ray fluorescence XAFS spectra for sewage sludge measured under anaerobic conditions (spectrum (a)) and aerobic conditions (spectrum (b)). Spectra for several reference specimens are also shown in each figure. The Cu-K edge X-ray absorption near edge structure (XANES) spectra for the sludge under anaerobic and aerobic conditions are indistinguishable and similar to that for

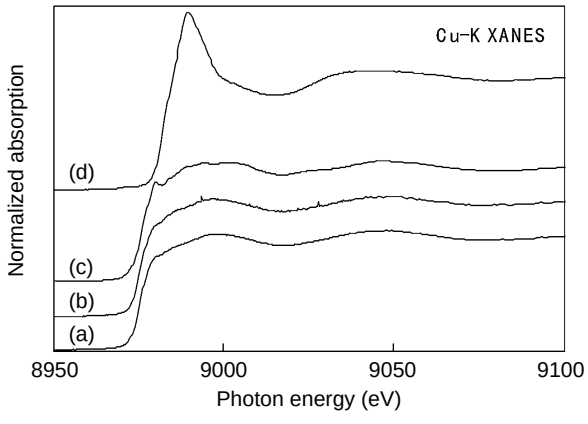

Fig. 1. Cu-K XANES spectra for excess sludge under (a) anaerobic and (b) aerobic conditions. The spectra for (c) CuS and (d) dissolved Cu (2+) in water are also presented.

*e-mail: m-nagoshi@jfe-steel.co.jp

CuS as shown in Fig. 1. The extended X-ray absorption fine structure (EXAFS) spectra for the sludge in both conditions were almost identical to that for CuS. These results show that almost all Cu atoms in the sludge form sulfide with the Cu valence of 2+ and the sulfide is stable against aerobic treatment.

The Zn-K edge XANES spectrum for the sludge in anaerobic state is close to that for ZnS (Fig. 2), which shows that Zn in the sludge mainly forms sulfide. However the amplitude of the EXAFS oscillation for the sludge is weaker than that for ZnS as shown in Fig. 3. Fine structures which are seen at about 3.5, 5, 6.5, and 8.5 $Å^{-1}$ in the spectrum for ZnS are smeared out in the spectrum for the sludge. These characteristics suggest that Zn sulfide forms small clusters and / or is structurally deformed in the sludge under anaerobic conditions. The Zn-K XAFS spectra for the sludge under aerobic conditions (spectra (b) in Fig. 2 and Fig. 3) were well reproduced by synthesizing the spectra for the sludge under anaerobic conditions and Zn (II) ions in water (spectra (d) in Fig. 2 and Fig. 3). This result shows that Zn sulfide in the sludge is partially dissolved by the aerobic treatment. It was estimated by the curve fitting method for the XANES spectrum that about 70% of Zn atoms in sulfide are dissolved under aerobic conditions in this study.

The As-K edge XANES spectra which are applicable to the identification of the chemical state of As are successfully recorded for As of less than 250 ppb in the sewage sludge as shown in Fig. 4.

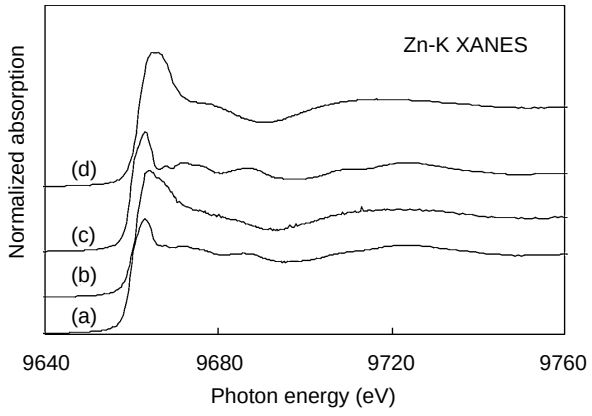

Fig. 2. Zn-K XANES spectra for excess sludge under (a) anaerobic and (b) aerobic conditions. The spectra for (c) ZnS and (d) dissolved Zn (2+) in water are also presented.

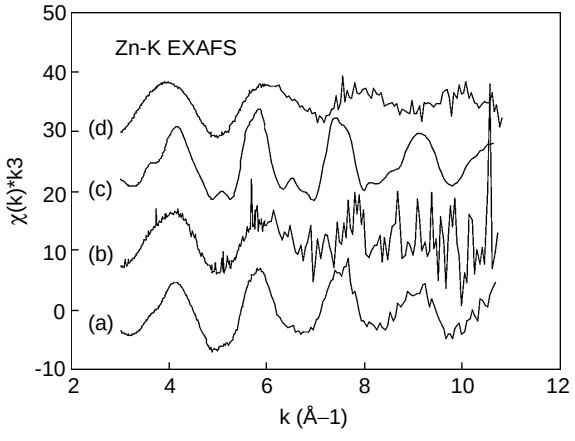

Fig. 3. k^3-weighted Zn-K EXAFS spectra for excess sludge under (a) anaerobic and (b) aerobic conditions. The spectra for (a) ZnS and (d) dissolved Zn (2+) in water are compared.

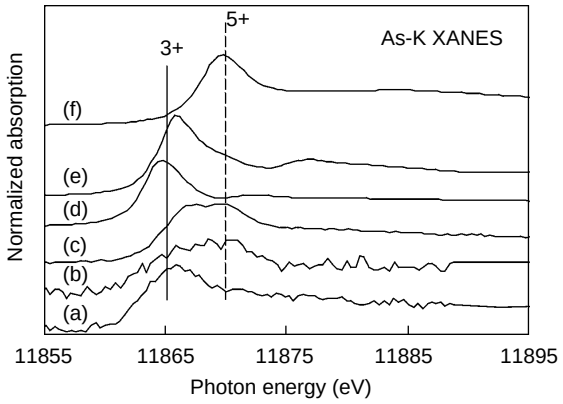

Fig. 4. As-K XANES spectra for excess sludge under (a) anaerobic and (b) aerobic conditions. The spectrum for (c) dried sludge is also shown as well as those for (d) As_2S_3, (e) As_2O_3 and (f) As_2O_5.

The main peak in the spectrum for the sludge under anaerobic state is located at a photon-energy corresponding to As of 3+. The spectral intensity at about 11870 eV where a peak of As of 5+ appears to increase under aerobic condition. This demonstrates that As of 3+ is partially oxidized to 5+ by the aerobic treatment.

In Fig. 4, the spectrum for a sludge dehydrated at 105 °C for 24 hr is also shown (spectrum (c)). A peak corresponding to As of 5+ appears in the spectrum for the dried sludge, which means that As of 3+ in the wet sludge is oxidized by the dehydration treatment. This result demonstrates that accurate information on the chemical state of sludge can be obtained from non-destructive analysis for wet sludge.

The stability of metal sulfides is well known. An E – pH (Pourbaix) diagram for the metal-sulfide system shows that the sulfides are dissolved when pH decreases or the redox potential (E) increases. The diagram also shows that copper (II) sulfide is more stable than zinc (II) sulfide. The pH value of the sludge was hardly changed by aerobic treatment. The dissolution of Zn sulfide, when the sludge is aerated, is explained by the transition from reduction to oxidation atmosphere.

The chemical forms of Cu and Zn in sewage sludge collected from several plants in Japan were estimated by a sequential extraction method [7]. The results averaged for excess sludge showed that about 50% of Cu and about 10% of Zn were classified as "sulfide precipitates". More than 70% of Zn was classified as "carbonate precipitates" and "organically bound" materials. These are significantly different from our XAFS results, although comparison of the results between different plants should be carefully done. As mentioned above, Zn sulfide is less stable than Cu sulfide in the same condition. The sequential extraction method classifies the chemical form of elements by searching whether substances are soluble in specific solvents or not [1]. The results of the method would be useful in controlling the stability of chemical substances. In the present case for Zn, the method would have estimated the fraction of sulfide to be only 10% due to the poor stability of Zn sulfide. The relatively high stability of Cu sulfide certainly provided higher fraction of sulfide. The sequential extraction technique will become more useful when complemented with chemical states obtained by XAFS analysis.

4. Conclusions

The chemical states of trace heavy metals, Cu, Zn, and As in the actual sewage sludge under anaerobic condition are clarified by X-ray fluorescence XAFS. *In-situ* measurements reveal the changes

of chemical states of Zn and As and the relatively high stability of Cu sulfide under aerobic condition. These results can be obtained only by non-destructive XAFS analysis. The differences between the identified chemical states of Cu and Zn in this study and those estimated by the sequential extraction method are explained by the stability of their sulfides.

Acknowledgements

The XAFS experiments were carried out at the SPring-8 with the approval of the Japan Synchrotron Radiation Research Institute (JASRI) (Proposal No. 2002A0239-NX-np and 2002B0290-NX-np).

References

1. Stover, R. C. *et al*., J.WPCF **47**, 2165 (1976).
2. Szulczewski, M. D., Helmke, P. A. and Blean, W. F., Environ. Sci. Technol. **31**, 2954 (1997).
3. Manceau, A. and Gallup, D. L., Environ. Sci. Technol. **31**, 968 (1997).
4. Nagoshi, M. *et al.*, "SPring-8 User Experiment Report (2000B), No.6", (JASRI, Hyogo, 2002), p. 16.
5. Nagoshi, M. *et al.*, "SPring-8 User Experiment Report (2002A), No.9", (JASRI, Hyogo, 2002), p. 6.
6. Nagoshi, M. *et al.*, "SPring-8 User Experiment Report (2003A), No.10", (JASRI, Hyogo, 2003), in press.
7. Morita, H. and Tsuboi, H., Water Sci. Technol. **42**, 159 (2000).

Physica Scripta. Vol. T115, 949–952, 2005

Determination of Uranyl Incorporation into Biogenic Manganese Oxides Using X-ray Absorption Spectroscopy and Scattering

S. M. Webb[1*], J. R. Bargar[1] and B. M. Tebo[2]

[1]Stanford Synchrotron Radiation Laboratory, Menlo Park, CA, 94025, USA
[2]Scripps Institute of Oceanography, University of San Diego, La Jolla, CA, 92093, USA

Received June 26, 2003; accepted November 4, 2003

PACS number: 61.10.−i

Abstract

Uranium is a toxic and radioactive contaminant in many settings, such as groundwaters and sediments. In oxidizing environments, uranyl (U(VI)) is thermodynamically the most stable oxidation state. Sorption or incorporation of U(VI) into reactive mineral phases are processes of major importance because they retard its transport. Biogenic manganese oxides are an important source of reactive mineral surfaces in the environment and may be potentially enhanced in bioremediation cases to improve natural attenuation. Experiments were performed in which U(VI) at various concentrations was present during manganese oxide biogenesis. At all concentrations there was strong uptake of U onto the oxides. Synchrotron based x-ray studies were carried out to determine the manner in which uranyl is incorporated into the oxide and how this incorporation affects the resulting manganese oxide structure and mineralogy. The EXAFS experiments show that uranyl does not appear to substitute into the lattice of the oxides, and is rather present as a strong surface complex. However, the presence of U(VI) on the Mn-oxide layers modifies the lattice constants and coherence lengths of the oxides. These results suggest a complex mechanism in which U transport is retarded by sorption and the surface area of the sorbent is increased.

1. Introduction

Uranium ore mining, processing, and manufacturing have contributed to groundwater contamination in numerous locations in the United States [1]. Uranium contamination is transported in groundwater primarily as the dissolved uranyl ion (U(VI)) which can intercept water supplies. Manganese oxide surfaces have been shown to have large capacities for heavy metal ion uptake [2–4]. In some groundwater environments, it has been shown that transuranic elements associate with manganese oxides preferentially over other mineral surfaces, including iron oxides [5]. Much of the manganese oxides found in the natural environment is considered to be of biologic origin [6–8]. Many diverse bacteria have been shown to rapidly catalyze the oxidation of the Mn(II) to Mn(III,IV) [9]. Biogenic rates of oxidation have been shown to be up to five orders of magnitude greater than abiotic rates under the same conditions [6, 8]. Thus, understanding the molecular mechanisms that are involved in the binding of uranyl to biogenic manganese oxide surfaces is critically important. This work uses x-ray techniques such as x-ray absorption spectroscopy and x-ray diffraction to examine how uranyl attaches to biogenic manganese oxides that form in the presence of the uranyl contamination and how this incorporation affects the structure of the biogenic manganese oxide.

2. Methods

Manganese oxide samples were prepared using spores of the marine bacterium *Bacillus sp.* g strain SG-1 to catalyze the oxidation of Mn(II) to Mn(IV) [10]. Spores were added to flasks containing 400 mL of incubation solutions to a final spore concentration of 10^8 spores per mL. The incubation solution contained 10 mM HEPES to maintain the pH at 7.5 and 10 mM Mn(II)-triflate. Additions of Mn-triflate and U(VI)-triflate were added daily to maintain metal concentrations as the oxidation progressed. Triflate was used as the counter-ion for all metal additions in order to minimize ternary complexation of uranyl by ions such as nitrate or chloride [11]. Carbonate was not excluded from the solutions to so as to simulate natural conditions. Uranyl concentrations in the flasks ranged in concentrations from 50 nM to 100 μM to span a large range of adsorption conditions (Table I). Incubations progressed for two weeks on a shaker platform after which the supernatants were drawn off and the manganese suspensions concentrated into a pellet by centrifugation.

All EXAFS and XRD measurements were performed on wet bioxides to prevent oxidation state and structural changes that can be driven by sample dehydration. Mn-K and U-L_{III}-edge XAS spectra were collected at SSRL beamline 4-3 with a Si(220) monochromator and, in the case of Mn, a harmonic rejection mirror with a cut-off energy set at 9 keV. Samples were collected in transmission geometry if possible, or in fluorescence mode for dilute samples. Fluorescence data were collected using either a 13-element Ge array detector or a Kr-gas-filled Lytle-type ionization chamber detector equipped with Sr x-ray filters. All spectra were background subtracted and splined using the SIXPack software [12]. Linear combination fitting and EXAFS fitting were also performed with SIXPack. O_{ax} and O_{eq} shells for U were fit initially and then subtracted from the raw data to create second-shell residual spectra. This allows a more sensitive fit of the second-shell contributions in the sample spectra without the interference of the O shells. Phase and amplitude files for the EXAFS fitting were created with FEFF7 [13, 14]. Since the Debye-Waller factors (σ) correlated highly with coordination numbers (CN), σs for some shells were each fixed at their average values. The U=O_{ax}=U=O_{ax} transdioxo multiple scattering path [15] was included in all fits. Mn EXAFS were fit using a model based on a layered phyllomanganate structure, loosely based on that of Ressler, *et al.* [16]. This model also accounts for splitting of the Mn-O and Mn-Mn distances in the structure due to Jahn-Teller distortions, angular deviations from planar sheets (particularly important with Mn-Mn multiple scattering), aqueous Mn(II), surface bound Mn species, and vacancies present in the Mn-layer lattice. Full details of the model are provided elsewhere [17]. This model has been tested on relevant model spectra (birnessite, δ-MnO_2) and found to fit the EXAFS up to $R \sim 5.5$ Å for samples with good data up to k of 15 $Å^{-1}$.

*e-mail: samwebb@slac.stanford.edu

X-ray diffraction intensity data were collected on wet solids in transmission geometry using the two-circle diffractometer on SSRL beamline 2-1 using a Bicron NaI detector equipped with Soller slits to examine the crystallinity and phases present in the biogenic Mn-oxide samples. The incident x-ray beam was tuned to 10 keV ($\lambda = 1.24$ Å) to improve beam penetration in to the wet samples and to provide Q-space access up to about 12 $Å^{-1}$. Wet sample slurries were placed in a custom sample cell between two lexan windows. The diffractometer was calibrated with LaB_6 and has a 0.04° 2θ fwhm resolution. Data were collected in Q-space in 0.004 $Å^{-1}$ intervals in dose mode of 10,000 counts per point. Several scans were added together to improve signal to noise ratios for interesting regions.

3. Results and Discussion

Incubation samples with large concentrations of U(VI) in the solution (>4 μM) visually appeared to inhibit manganese oxide formation. This was apparent by the decrease in amount of biogenic product in the centrifuged slurry at the end of the incubation experiment. The extreme case occurred in the highest U(VI) sample (100 μM) in which no manganese oxidation occurred.

Mn K edge EXAFS spectra change substantially as the amount of U(VI) in the sample increase, indicating that the local structure around Mn changes significantly as shown in Figure 1. At the highest U(VI) concentration, the spectra are similar to those for todorokite, a 3 × 3 tunnel structure tecktomangantate. Tunnel structures can be fit using the phyllomanganate EXAFS layer model (Figure 1). Doing so produces apparently high dihedral angles in the manganese octahedral plane and an abnormally high percentage of vacancies, which can be used to distinguish todorokite from true phyllomanganates. Table I shows the summary of major fitted EXAFS parameters for the sample series, including a metal-free biogenic manganese oxide and todorokite. The fit derived parameters for the samples progresses from those typical of well-defined layer structures at low metal concentrations, to value indicating a highly bent or pseudo-tunnel structure at high U(VI) concentrations. The transition from a layer to tunnel-like structure begins to occur at U(VI) concentrations around 4 μM and appears to be complete at 20 μM.

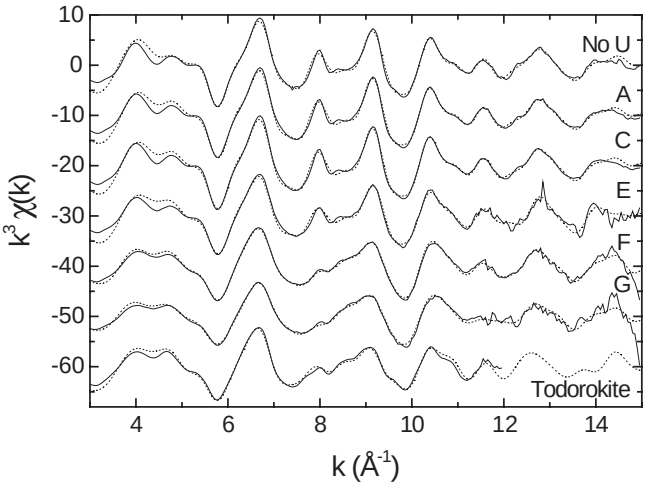

Fig. 1. Mn K-edge EXAFS for selected incubation samples and todorokite standard. Data are represented by solid lines, EXAFS fits by dotted lines. Note the change in diagnostic features around $k \sim 8$ $Å^{-1}$.

Table I. *Summary of model parameters from the Mn K-edge EXAFS fitting results for each of the uranyl-manganese oxide incubations. *Describes the fraction of the total Mn sites in the octahedral layer that are unoccupied. Large numbers of edge sites due to small particles will also affect this parameter. †Describes the out-of-plane bend of the manganese octahedral layer in the direction parallel to the a-axis. ‡Describes the out-of-plane bend of the manganese octahedral layer in the direction parallel to the b-axis.*

Sample	U(VI) added	Vacancies (%)*	Angle (a-axis)†	Angle (b-axis)‡
No metal	N/A	32	0	0
A	50 nM	30	1	0
B	100 nM	30	1	0
C	500 nM	28	1	0
D	1 μM	26	1	0
E	4 μM	60	6	0
F	10 μM	56	12	7
G	20 μM	65	5	20
Todorokite	N/A	40	6	19

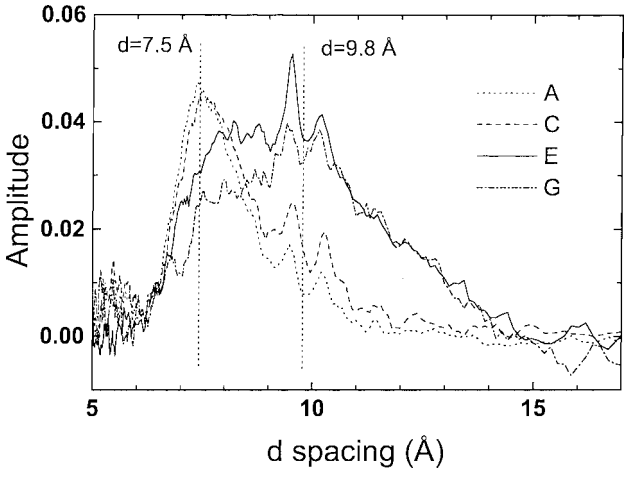

Fig. 2. X-ray diffraction data for the 001 basal plane reflections for the uranyl incubation samples.

XRD (Figure 2) shows that at low U(VI) concentrations, the XRD structure of the metal incubated oxides is dominated by a 7.5 Å phyllomanganate basal plan relection typical of birnessite-like phases and very similar to that of biooxides formed in the absence of U(VI). The breadth and low intensity of the peaks indicates very small particle size as well as structural disorder. The two sharp peaks at 9.4 and 10.1 Å are due to diffraction from the spores. As the concentration of U(VI) in the incubation increases, the intensity of the phyllomanganate basal plan reflection decreases. At the same time, a new broad peak at 9.8 Å is observed, indicating a phase with differing long-range structure, possible similar to todorokite. The change from 7.5 to 9.8 Å phases occurs at sample E, which is the same region in which EXAFS indicated significant changes in the Mn local structure were occurring.

U-L_{III}-edge EXAFS (Figure 3) of the incubation samples is dominated by the strong presence of equatorial and axial oxygens. Sample C and G were used as components for linear combination fits to spectra from samples D–F. Samples A and B have the same structure as C, but are significantly noisier due to the trace concentration of U in the sample. EXAFS fitting analysis of the residuals from the second shell of sample C shows contributions

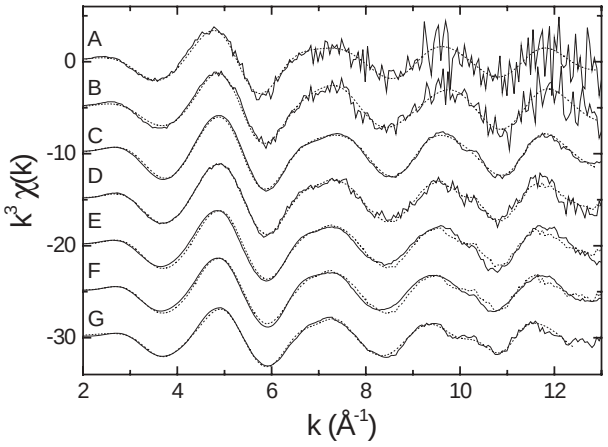

Fig. 3. U L-edge EXAFS for incubation samples. Data are represented by the solid lines, fits by the dotted lines. Samples A, B, C and G were fit in a shell-by-shell EXAFS fit, whereas samples D, E, and F were fitted as linear combinations of C and G.

Table II. *Fitting results of major parameters in shell-by-shell fitting of U L-edge EXAFS.*

Sample	Shell	N	R	σ^2
C	U-C	0.81	2.84	0.0041
	U-Mn	0.73	3.30	0.0130
G	U-C	1.43	2.88	0.0041
	U-Mn	0.31	3.81	0.0050
	U-Mn	0.28	4.29	0.0050
	U-O	1.31	4.01	0.0050

from C and Mn shells, suggesting a uranyl-carbonate ternary surface complex to the manganese oxide surface. The U-Mn distance of 3.30 Å is suggestive of a bidentate surface complex. Analysis of sample G is far more complex. The residual EXAFS shows strong oscillations past k of 12 $Å^{-1}$, suggesting the presence of more than just surface complexation, with the presence of strongly scattering metal shells. This sample is best fit with U-Mn shells at 3.81 and 4.29 Å and a U-O shell at 4.01 Å. These results are summarized in Table II.

The measurements all show that at increasing U(VI) concentrations, not only does the mechanism of U(VI) uptake on the biogenic oxide change, but the structure of the oxide itself changes as well. All three of these techniques show that the onset of the transitions occurring in the manganese oxide structure and U(VI) complexation take place at the same uranyl concentrations. At low uranyl concentrations, the results show that the dominant form of manganese oxide is poorly ordered, turbostratic layer manganate structure. Uranyl is adsorbed onto the oxide surfaces as a ternary carbonate complex, coordinated to the oxide surfaces in a bidentate fashion.

At high concentrations, the presence of U(VI) affects the manganese structure. The EXAFS model applied gives rise to larger apparent vacancies and increases in the dihedral angles along the a-b plane. This increase in angle has the effect of reducing the importance of Mn-Mn multiple scattering paths. The results are also strikingly like that of the 3 × 3 tunnel structure of todorokite. Additionally, the oxides 001 basal plane reflections of the XRD data move from 7.5 toward 9.8 Å. These items suggest a transformation of the manganese oxide to a pseudo-tunnel structure similar to todorokite. Since the XRD suggests that the altered biogenic oxides are still very poorly ordered, it is unlikely that the uranyl incorporated oxide is a typical 3 × 3 tunnel structure. These results suggest that the structure is more likely a 3 × n, where the distance between layers is consistent at 3 octahedra (9.8 Å), and the horizontal spacing is considered nearly random. The U(VI)-carbonate complex may stabilize the formation of these structures. The lack of bidentate U-Mn binding suggests that the mechanism of U incorporation into the structure is different at these high loadings as well. Further work is still required to develop a definitive model. However, the presence of a pseudo-todorokite manganese phase and the presence of strongly scattering Mn neighbors in the U EXAFS suggests that U is located in the tunnels of the manganese oxide.

4. Conclusions

At low U(VI) : Mn rations, uranyl is associated with biogenic manganese oxide surfaces as a ternary carbonate complex. At higher uranyl concentrations, the manganese oxides become strongly distorted and exhibit spectral characteristics suggesting the existence of tunnel structures. Uranyl appears to be structurally incorporated in the tunnels of these biooxides. This bonding mechanism, were it to occur in the environment, implies that manganese oxides may be suitable materials for long-term *in situ* stabilization of U(VI). Other work has shown that elevated concentrations of other metals, such as Co and Cu can also lead to todorokite-like tunnel structures [18]. Thus the concentrations of dissolved Ca and Mg may be major controls on the existence and reactivity of tunnel-structure biooxides in the environment.

Acknowledgement

The authors would like to thank Greg Dick and Anna Obraztsova for providing preparations of the SG-1 spores and Apurva Mehta and Jeff Post for their many helpful discussions and advice. Portions of this research were carried out at the Stanford Synchrotron Radiation Laboratory, a national user facility operated by Stanford University on behalf of the U.S. Department of Energy, Office of Basic Energy Sciences. The SSRL Structural Molecular Biology Program is supported by the Department of Energy, Office of Biological and Environmental Research, and by the National Institutes of Health, National Center for Research Resources, Biomedical Technology Program. Support for this work provided by a grant from the NSF-CRAEMS program (CHE-0089208).

References

1. Macaskie, L. E., "The application of biotechnology to the treatment of wastes produced from the nuclear-fuel cycle – biodegradation and bioaccumulation as a means of treating radionuclide-containing streams," Crit. Rev. Biotechnol. **11**, 41–112 (1991).
2. Murray, J. W., "The interaction of metal ions at the manganese dioxide-solution interface," Geochim. Cosmochim. Acgta **39**, 505–519 (1975).
3. Manceau, A., Gorshkov, A. I. and Drits, V. A., "Structural chemistry of Mn, Fe, Co, and Ni in manganese hydrous oxides: Part II. Information from EXAFS spectroscopy and electron and X-ray diffraction," American Mineralogist **77**, 1144–1157 (1992).
4. Nelson, Y. M., Lion, L. W., Shuler, M. L. and Ghiorse, W. C., "Lead binding to metal oxide and organic phases of natural aquatic biofilms," Limnology **44**, 1715–1729 (1999).
5. Duff, M. C. *et al*., "Mineral associations and average oxidation states of sorbed Pu on tuff," Environ. Sci. Technol. **33**, 2163–2169 (1999).
6. Tebo, B. M., "Manganese(II) oxidation in the suboxic zone of the Black Sea," Deep-Sea Research **38** (Suppl. 2), S883–S905 (1991).
7. Wehrli, B., Friedl, G. and Manceau, A., "Reaction rates and products of manganese oxidation at the sediment-water interface," in *Aquatic Chemistry: Interfacial and Interspecies Processes*, edited by C. P. Huang, C. R. O'Melia, and J. J. Morgan (Am. Chem. Soc., Washington, DC, 1995), Vol. 244, pp. 111–134.

8. Nealson, K. H., Tebo, B. M. and Rosson, R. A., "Occurrence and mechanisms of microbial oxidation of manganese," Advances in Applied Microbiology **33**, 279–318 (1988).
9. Tebo, B. M. *et al*., "Bacterially Mediated Mineral Formation: Insights into Manganese(II) Oxidation from Molecular Genetic and Biochemical Studies. Reviews in Mineralogy Volume 35," in *Geomicrobiology: Interactions Between Microbes and Minerals*, edited by J. F. Banfield and K. H. Nealson (Mineralogical Society of America, Washington, D.C., 1997), pp. 448.
10. Francis, C. and Tebo, B., "Enzymatic Manganese(II) oxidation by metabolically dormant spores of diverse Bacillus species," Appl. Environ. Microbiol. **68** (2), 874–880 (2002).
11. Bargar, J. R., Fuller, C. C. and Davis, J. A., "U(VI)-anion ternart complex formation on hematite," Abstr. Pap. Amer. Chem. Soc. **223**, 120–GEOC (2002).
12. Webb, S. M., "SIXPack: A graphical user interface for XAS analysis using IFEFFIT presented by Samuel Webb," Phys Scripta, this volume (2003).
13. Zabinsky, S. I. *et al*., Phys. Rev. B **52**, 2995 (1995).
14. Ankudinov, A. L., Ravel, B., Rehr, J. J. and Conradson, S. D., Phys. Rev. B **58**, 7565 (1998).
15. Hudson, E. A. *et al*., Phys. Rev. B **54**, 165 (1996).
16. Ressler, T., Brock, S. L., Wong, J. and Suib, S. L., J. Phys. Chem. B **103**, 6407 (1999).
17. Webb, S. M., Bargar, J. R. and Tebo, B. M., "EXAFS study of the formation of biogenic manganese oxides by the marine organism *Bacillus sp.* SG-1," (in review).
18. Webb, S. M., Bargar, J. R. and Tebo, B. M., "Structure of cobalt(II) entrained biogenic manganese oxides by EXAFS," (in prep).

Physica Scripta. Vol. T115, 953–956, 2005

Determination of Chemical Speciation by XAFS

F. Tannazi and G. Bunker*

CSRRI/BCPS/Physics, Illinois Institute of Technology, Chicago, IL 60616, USA

Received June 26, 2003; accepted in revised form June 28, 2004

PACS number: 82.80Ej

Abstract

Chemical speciation of toxic elements in the environment is an active area of research. In a physical (i.e. chemically inert) mixture of compounds, the X-ray absorption spectra in transmission mode or fluorescence mode at low concentration and high dispersion are linear combinations of the spectra of the constituents. As long as the linearity conditions are met, and the relevant constituents are known, linear fitting procedures can then be used directly to determine the composition. However, physical effects such as large particle sizes and aggregation can cause the breakdown of the linearity condition, resulting in systematic errors and incorrect conclusions. Here we present a simple and robust procedure for determination of molecular speciation by XAFS using a Linear Programming (LP) algorithm with constraints (positively and normalization), and errors introduced by particle size effects and other problems on the speciation results are discussed.

1. Introduction

Many samples studied by XAFS comprise a mixture of chemical forms, particularly environmental samples [1–3]. The interpretation of such spectra using conventional XAFS data analysis methods is not straightforward, and having an appropriate model which directly determines the speciation of the sample is very desirable. To our knowledge, all direct speciation methods used to date are based on the linearity assumption, i.e. the spectra consist of a weighted linear combination of the spectra of the sample's constituents. The validity of the linearity assumption depends on experimental conditions that may or may not be satisfied. Successful deconvolution of the spectra depends on how distinct (orthogonal) are the spectra of the various species, and one needs to have a sufficiently large and appropriate set of basis functions (standard spectra) to describe the data.

The validity of the linearity criterion depends on whether the particle sizes of the various species in the sample are much less than about one "absorption length" – otherwise the spectra will be distorted to some extent, in a nonlinear manner. In environmental samples measured *in situ* the particle size distribution is not controlled (being an intrinsic property of the sample), and the X-ray absorption lengths are strongly energy dependent, so that the particle size often may be comparable to or greater than natural particle sizes. Often one successfully apply linear methods to the speciation problem, but one also may readily encounter the limits of such approaches.

This paper presents a robust approach to applying the linear programming (LP) method to decompose the XAFS data into its constituent spectra within the linear approximation. This method has been applied to the soil core samples, environmental samples, and also calibrated with synthetic mixtures of specific materials. Experiments were performed on undulator beamlines ID–10 (MR-CAT) and ID-18 (BioCAT) at Advanced Photon Source. Initial measurements were made at Zn K-edge because Zn was the highest concentration element of interest. In an effort to obtain a sufficiently complete set of the basis functions, we tested several compounds, and also for calibration of the methods we tested synthetic mixtures of these compounds both in fluorescence and transmission modes.

The outline of this paper is as follows: Section 2 is devoted to a brief description of Linear Programming Method. Section 3 presents the results of the LP fitting and discussion about them. Section 4 addresses the particular and important problem of the Particle Size Effects and finally, conclusions are given in section 5.

2. Linear Programming Method

LP [4, 5] is a constrained minimization technique that in general allows one to find the global maximum or minimum of any linear function of multiple variables subject to a set of constraints that are defined by linear inequalities. One of the advantages of the LP that makes it especially useful for our task is the fact that "nonnegativity" is the usual constraint on any variable x_i, that represents the tangible amount of the some physical quantity. For example, in our case the physical quantity that can not be negative is the fraction of the ith compound α_i.

In the linear approximation the XAFS $\mu(E)$ data can be expressed as:

$$\mu_{\text{Sample}}(E) = \sum_i \alpha_i * \mu_{\text{i, Standard}}(E) \tag{1}$$

with two constraints:

$$\sum_{\text{i}} \alpha_i = 1 \quad \text{and} \quad \alpha_i \geq 0 \tag{2}$$

where the index i identifies the particular standard, and α_i is the fraction of the metal atoms in the sample that are found within species i. The first constraint implies that these coefficients are actually the fractions of the constituent species in the sample and their sum should be equal to one. Evidently the weights α_i cannot be negative (second constraint).

The starting point for any direct method is the fact that any spectrum consisting of N data points can be presented as a N-dimensional vector. In this work the term spectrum will be used to refer to the experimental data and vector to denote the mathematical representation of the spectrum. The term basis functions will refer to the set of all spectra of the standards. Also all of the XAFS spectra that are presented in this work are normalized to unit edge step and interpolated onto a uniform energy grid.

The mathematical representation of the linearity assumption for the $\chi(k)$ data which are multiplied by k^W is:

$$K^W * \chi_{\text{Sample}}(K) = \sum_i \alpha_i * K^W * \chi_{i,\text{Standard}}(K) \tag{3}$$

with the same constraints as eq (2). W is a weighting factor and in this example the data were un weighted ($W = 0$). We found that the result of the LP fitting for $\chi(k)$ data is much more accurate than

*email: bunker@iit.edu

the $\mu(E)$ data, presumably because the orthogonality conditions are met better for the $\chi(k)$ data compared to the $\mu(E)$ data. This is not necessarily always the case however.

The basic goal of LP is very simple: for n independent variables $x_1, \ldots x_n$, we want to minimize the *objective function* f:

$$f = c_1x_1 + c_2x_2 + \cdots + c_nx_n \tag{4}$$

subject to the m linear inequality constraints;

$$\begin{aligned} m_{11}x_1 \quad &+m_{12}x_2 + \cdots + m_{1n}x_n \geq b_1, \\ m_{21}x_1 \quad &+m_{22}x_2 + \cdots + m_{2n}x_n \geq b_2, \\ &\vdots \\ m_{m1}x_1 \quad &+m_{m2}x_2 + \cdots + m_{mn}x_n \geq b_m. \end{aligned} \tag{5}$$

It is more convenient to handle LP problems simply by setting up the vectors and matrix that represent the appropriate coefficient of the linear function that appears. The model problem then will be:

$$\text{Min}\{\boldsymbol{C} \cdot X | \mathbf{M} \cdot \boldsymbol{X} \geq \boldsymbol{B}\} \tag{6}$$

where $\boldsymbol{C}$ is an n-dimensional vector, $\mathbf{M}$ is an $m \times n$ matrix and $\boldsymbol{B}$ is an m-dimensional vector.

In the speciation problem, our goal, according to eq (1), is to minimize the following expression:

$$\left| \mu_{\text{sample}}(E) - \sum_i \alpha_i * \mu_{i,\,\text{standard}}(E) \right|. \tag{7}$$

We use the vector $\boldsymbol{S}$ to represent the spectrum μ_{sample} sampled on a specific grid, and the basis functions $\boldsymbol{b}$, or vectors $\boldsymbol{b}$, refer to the spectrum $\mu_{i,\,\text{standard}}$. Then the minimization of the expression (7) will be:

$$\text{Min}\left\{ \left| S - \sum_i \alpha_i * b_i \right| \right\} \tag{8}$$

subject to the constraint $\sum_i \alpha_i = 1$. Since the absolute value of the deviation between the data and the fit is minimized, rather than its square, this approach is less sensitive to outliers (and more robust) than least squares minimization. In the LP problem all of the coefficients are non-negative so additional positivity constraints on the coefficients are unnecessary. At this stage, if we have interpolated the $\mu(E)$ onto m energy points, then instead of having one objective function in the conventional LP model, we have $2m$ objective functions with one constraint, so a change in perspective is needed. It appears at first glance that the LP problem is of the wrong structure, but the approach we have taken is to reframe the problem.

The vector that is sought consists of the unknown weight coefficients, and also new variables that describe upper and lower bounds on the difference between the data and the linear combination at each point. Solving the problem in this form, consists of adding the auxiliary variables in the problem (i.e. the residuals) and taking the $2m$ objective functions as constraints. If we define an m-dimensional vector Y as:

$$\left| S - \sum_i \alpha_i * b_i \right| = \boldsymbol{Y}. \tag{9}$$

That implies:

$$-y_j \leq s_j - \sum_i \alpha_i * b_i \leq y_j, \qquad j = 1, \ldots, m \text{ and } i = 1, \ldots, n \tag{10}$$

where m is the number of energy points and n is the number of standards, and if we write them in the LP inequality model, the right hand inequalities can be written in this form:

$$y_j + \sum_i \alpha_i * b_i \geq s_j \tag{11}$$

and the left hand inequalities will be:

$$y_j - \sum_i \alpha_i * b_i \geq -s_j. \tag{12}$$

Writing the constraint: $\sum_i \alpha_i = 1$ in the LP form, we will have the conditions:

$$\sum_i \alpha_i \geq 1 \quad \text{and} \quad -\sum_i \alpha_i \geq -1. \tag{13}$$

Then we can show the constraints equations; eq (11), eq (12) and eq (13) in a matrix representation in the form of: $\mathbf{M} \cdot \boldsymbol{X} \geq \boldsymbol{B}$, eq (6):

$$\begin{bmatrix} 1 & 0 & 0 & 0 & \ldots & 0 & b_{11} & b_{21} & \ldots & b_{n1} \\ 0 & 1 & 0 & 0 & \ldots & 0 & \ldots & \ldots & \ldots & \ldots \\ 0 & 0 & 1 & 0 & \ldots & 0 & \ldots & \ldots & \ldots & \ldots \\ 0 & 0 & 0 & 1 & \ldots & 0 & \ldots & \ldots & \ldots & \ldots \\ \ldots & \ldots & \ldots & \ldots & \ldots & \ldots & \ldots & \ldots & \ldots & \ldots \\ 0 & 0 & 0 & 0 & \ldots & 1 & b_{1m} & b_{2m} & \ldots & b_{nm} \\ 1 & 0 & 0 & 0 & \ldots & 0 & -b_{11} & -b_{21} & \ldots & -b_{n1} \\ 0 & 1 & 0 & 0 & \ldots & 0 & \ldots & \ldots & \ldots & \ldots \\ 0 & 0 & 1 & 0 & \ldots & 0 & \ldots & \ldots & \ldots & \ldots \\ 0 & 0 & 0 & 1 & \ldots & 0 & \ldots & \ldots & \ldots & \ldots \\ \ldots & \ldots & \ldots & \ldots & \ldots & \ldots & \ldots & \ldots & \ldots & \ldots \\ 0 & 0 & 0 & 0 & \ldots & 1 & -b_{1m} & -b_{2m} & \ldots & -b_{nm} \\ 0 & \ldots & \ldots & \ldots & \ldots & 0 & 1 & 1 & \ldots & 1 \\ 0 & \ldots & \ldots & \ldots & \ldots & 0 & -1 & -1 & \ldots & -1 \end{bmatrix} \times \begin{bmatrix} y_1 \\ y_2 \\ y_3 \\ y_4 \\ \ldots \\ y_m \\ \alpha_1 \\ \alpha_2 \\ \ldots \\ \alpha_n \end{bmatrix} \geq \begin{bmatrix} s_1 \\ s_2 \\ s_3 \\ s_4 \\ \ldots \\ s_m \\ -s_1 \\ -s_2 \\ -s_3 \\ -s_4 \\ \ldots \\ -s_m \\ 1 \\ -1 \end{bmatrix} \tag{14}$$

where $\mathbf{M}$ is a $(2m + 2) \times (m + n)$ matrix, and as mentioned before, m is the number of the energy points, n is the number of basis functions. The data matrix $\boldsymbol{X}$ is an $(m + n)$ column matrix and evidently the matrix $\boldsymbol{B}$ is a $(2m + 2)$ column matrix. Our interests are primarily in the last n components of the matrix $\boldsymbol{X}$, which are the unknown coefficients α_i that we are seeking. The other (y) values are the residual errors, which are useful for quantifying errors through comparison with the measured or estimated noise distribution in the data. Error estimates can alternatively be obtained through a Monte Carlo type approach by generating an ensemble of spectra with random noise that corresponds to the error distribution, and then statistically describing the distribution of parameter values returned by repeated runs of the LP procedure.

The matrix representation of the objective function, $\boldsymbol{C} \cdot \boldsymbol{X}$, which is minimized in this program is:

$$\begin{bmatrix} 1 & 1 & 1 & 1 & \ldots & 1 & 0 & 0 & \ldots & 0 \end{bmatrix} \times \begin{bmatrix} y_1 \\ y_2 \\ y_3 \\ y_4 \\ \cdots \\ y_m \\ \alpha_1 \\ \alpha_2 \\ \cdots \\ \alpha_n \end{bmatrix}. \tag{15}$$

$\boldsymbol{C}$ is an $m + n$ row matrix whose first m components are equal to one and whose last n components are zero. That means the function that will be minimized in this program is the sum of the auxiliary variables or residuals, $\text{Min}\{y_1 + y_2 + \cdots + y_m\}$, which is in agreement with our first attempt to minimize expression (7).

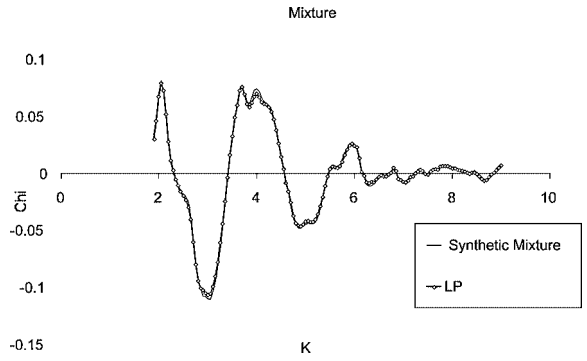

Fig. 1. LP fit to Synthetic mixture of four Zn compounds (see text). Experimental Data (solid line) and LP fit (symbols).

We have implemented this LP method in the *Mathematica* language. The result of fitting using this program for analytical mixtures was excellent. For experimental mixtures, although the accuracy of fitting results was very good, small discrepancies were observed which are mostly due to the quality of the samples and noise. Example of LP fitting for EXAFS and XAFS spectra are shown in the next section.

3. Results and Discussion

The LP method has been applied to several synthetic mixtures of Zn compounds. The standards which have been used to make these mixture samples are: ZnS, $ZnSO_4$, ZnO, $Zn(OH)_2$ and $ZnFe_2O_4$. Fig. 1 shows the result of LP fitting with the $\chi(k)$ spectra of a mixture of just four compounds; $ZnSO_4$, ZnS, ZnO and $ZnFe_2O_4$. The program was run with five basis functions one of which was an unnecessary basis function corresponding to the standard $Zn(OH)_2$ that was not present in the mixture. The results correctly indicated that the fraction was zero. The result of the decomposition of the unknown mixture was:

$$9\%ZnSO_4 + 40\%ZnS + 31\%ZnO + 20\%ZnFe_2O_4.$$

Our original goal of developing LP was to solve the speciation problem as applied to soil core samples from the Depue Wild Life Management Area in Illinois. The results of LP fitting for XAFS/XANES and EXAFS spectra are presented in Fig. 2 and Fig. 3. The LP program is very flexible in choosing which parts of the spectra we are trying to fit. For XAFS, choosing the first 30% of the m energy points is enough and for the EXAFS part 70% of the last m energy points is proper. The orthogonality of the basis functions differs in XANES and EXAFS regimes. LP fits for core samples included basis spectra of Zn sulfide, Zn oxide, Zn sulfate, Zn carbonate, Zn nitrate, Zn adsorbed to Montmorillonite (aged 6 months), and Zn adsorbed to HFO (aged 6 months) indicate predominantly Zn carbonate and Zn sulfate coordination.

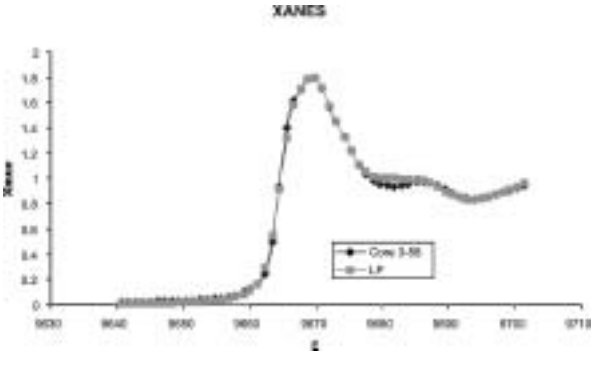

Fig. 2. XANES LP fit to experimental soil sample 3-58.

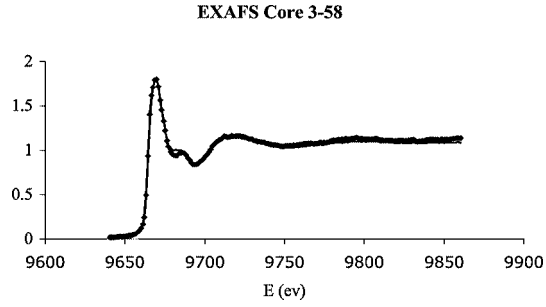

Fig. 3. XAFS LP fit to experimental soil sample 3-58.

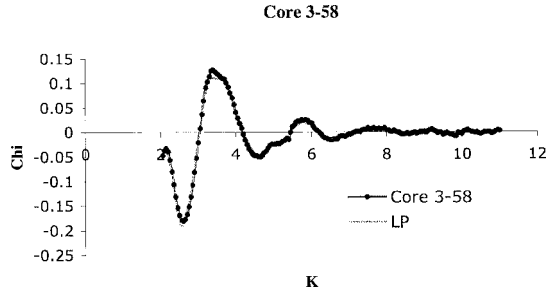

Fig. 4. EXAFS LP fit to experimental soil sample 3-58 chi data.

Fig. 4 shows the result of the LP fitting for the same soil core sample but for $\chi(k)$ data. As it was mentioned before, results of fitting to $\chi(k)$ data are much more reliable than fits to the $\mu(E)$ data, presumably because the $\chi(k)$ basis spectra are much more orthogonal than the $\mu(E)$ spectra. However, in some special cases the differences between spectra could be more distinct in the near-edge region, and in those cases, fitting to $\mu(E)$ would be preferred.

The imperfections in LP fitting for the soil core samples can be the result of any of the following reasons: insufficient basis set, similarity (nonorthogonality) between the XAFS spectra of the different standards, differences between the XAFS spectra of the synthetic standards which have been made in the laboratories and what is present in the natural sample, and particle size effects.

Speciation using linear approximation works well when the sample consists of a small number of known discrete components that are accurately represented in the library of basis functions. There are a number of complicating factors that must be considered, however, some obvious, and others less so:

1) The basis set must be sufficient to completely represent all the constituents of the samples. A large basis set is good, but only if it includes the correct basis functions for the sample. Omission of a needed basis function will cause systematic errors in the parameter values. A larger basis set is not necessarily better if it does not include the right functions.
2) Instrumental energy shifts between spectra of the standards must be carefully corrected, especially when fitting $\mu(E)$ data. EXAFS data are less sensitive to small energy shifts. Similarly, the energy resolution must be the same when near edge data are included in the fits.
3) The spectra that make up the basis set must reflect the material as it is found within the sample. For example, the standard spectra must be measured at the same temperature as the

sample. To some extent temperature effects can be addressed by including into the basis set spectra measured at different temperatures, but the strong similarity (and therefore non orthogonality) between basis functions can cause numerical instabilities, depending on the algorithm used.

Performing measurements of sample and standards at multiple temperatures could significantly improve the speciation results, because although the basis functions would change with temperature, their proportions generally would not.

4) Basis functions must correspond to well defined compounds. In some amorphous materials, the spectra may depend on time as the sample ages. Ignoring this effect can introduce significant errors.
5) Nonlinear relationships between the measured spectra and the compositions of the sample naturally occur in fluorescence, as described in the next section, and can cause serious systematic errors by effectively distorting the basis functions. We are exploring methods to correct for these effects.

4. Particle Size Effects

The physical characteristics of complex media can have a strong effect on the detected fluorescence spectra, which can undermine the reliability of speciation studies by XAFS.

Particle size effects [6, 7] can influence the apparent concentrations and therefore the speciation results.

In the simplest case of a slab of material with thickness x, it is easily shown that the fluorescence that is emitted from the sample is proportional to:

$$\left(\frac{\mu_s(E)}{\sin\theta}\right)\left(\frac{1-\exp(-\alpha x)}{\alpha}\right); \qquad \alpha = \left[\frac{\mu_t(E)}{\sin\theta} + \frac{\mu_t(E_f)}{\sin\varphi}\right] \quad (16)$$

where $\mu_s(E)$ and $\mu_t(E)$ are respectively the absorption coefficients of the element of interest and the total sample matrix, E and E_f are the energies of the incident and fluorescence X-ray photons, and θ and φ are the angles of incidence and exit radiations relative to the sample surface. The measured spectra are linear if $\alpha x \ll 1$, or if $\mu_s(E) \ll \mu_t(E)$, but in general the measured spectrum depends nonlinearly on $\mu_s(E)$.

Nonlinearity problems arise when the sample consists of concentrated species with particle sizes that are not small compared to one absorption length. In this case the penetration depth into the particles has an energy dependence that derives from the absorption coefficient of the element of interest, making the interpretation of the results much more complicated. Figure 5 simulates how the measured XAFS spectrum of MnO would vary as the size of the particles increases. The absorption length above the edge in MnO is only about 5 micrometers. Each spectrum is divided by the thickness to more clearly show the nonlinearity.

The detected fluorescence can be easily calculated from the equation above for various film thicknesses (here the incident and exit angles are taken as 45 degrees to the surface). The results are shown in figure 5 for thicknesses 0.125, .25, 0.5, 1.0, 2.0, 4.0 and 8.0 μm. It is evident that the spectra are reduced in magnitude and the spectra are also distorted in a nonlinear manner. These distortions are certain to cause systematic errors in the derived speciation results unless the particle sizes are much smaller than one absorption length.

In the environmental XAFS literature these potential problems appear to have been often ignored. In such samples the investigator has very little control over particle size, and when making *in situ* measurements one wishes to study the samples as they are, without further grinding.

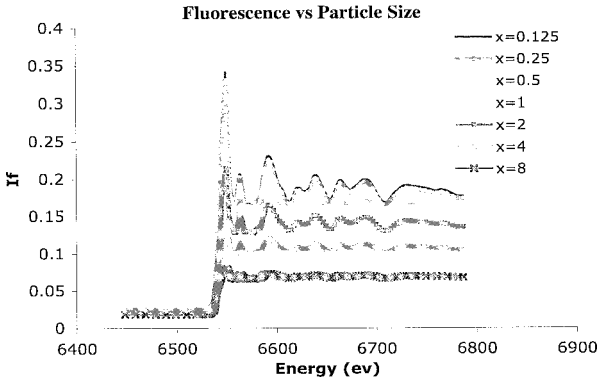

Fig. 5. Fluorescence spectrum vs particle size for MnO. Data simulated using equation 16. Each spectra is scaled by the thickness x, which its unit is micron.

The difficulties associated with particle size effects in *in situ* studies have a potential solution through use of resonant X-ray inelastic scattering. This technique in effect provides EXAFS spectra of a low energy edge while measuring at high energies. Experimentally one allows an intense high energy beam to penetrate the sample, while energy-analyzing with appropriate crystal optics the elastically scattered X-rays. Since the incident and scattered X-rays are both at high energies, particle size effects are irrelevant. The disadvantage of this technique is that it is relatively insensitive, but it should be suitable on appropriate undulator beamlines at third generation sources.

5. Conclusions

We have implemented a simple and robust approach to fitting compositions of experimental XAFS data in the linear superposition approximation by using Linear Programming methods. This approach has the benefits of directly locating the global minimum subject to positivity and normalization constraints. It also allows the experimenters to easily impose additional arbitrary linear constraints or bounds on the parameters. Some of the pitfalls and possible solutions associated with speciation by XAFS are discussed.

Acknowledgment

We would like to thank Peyman Meshkat for helpful remarks. Support was provided by the Illinois Waste Management and Research Center and the State of Illinois Higher Education Cooperative Agreement (HECA). BioCAT is supported by National Institutes of Health (NIH) RR08630. MRCAT is funded by the member institutions and the U.S. Department of Energy (DOE), Basic Energy Sciences (BES), under Contract No. DE-FG02-00ER45811. Use of the Advanced Photon Source was supported by the DOE, under Contract No. W-31-109-ENG-38.

References

1. Manceau, A. *et al.*, Env. Sci. Technol. **30**, 1540 (1996).
2. Webb, S. M., Leppard, G. G. and Gaillard, J.-F., Environ. Sci. Technol. **34**, 1926 (2000).
3. Morin, G. *et al.*, Am. Mineral. **84**, 420 (1999).
4. Press, W. H., Teukolsky, S. A., Vetterling, W. T. and Flannery, B. P., "Numerical Recipes in Fortran," second edition, (Cambridge University Press 1992).
5. Best, M. J. and Ritter, K., "Linear Programming," (Prentice-Hall Inc., Englewood Cliffs New Jersey 07632) 1985.
6. Heald, S. M., "Design of An EXAFS Experiment," in "X-ray Absorption", (Koningsberger, D. C. and Prins, R., eds.), (Wiley and Sons, New York, ch. 1 1988).
7. Bunker, G., "Basic Techniques in EXAFS: particle size effects," (1988), http://ixs.iit.edu/

Physica Scripta. Vol. T115, 957–959, 2005

Iron in Silicate Glasses: a Systematic Analysis of Pre-Edge, XANES and EXAFS Features

F. Farges[1,2,*], S. Rossano[1], Y. Lefrère[3], M. Wilke[4] and G. E. Brown Jr.[2,5]

[1]Laboratoire des Géomatériaux, Université de Marne-La-Vallée, CNRS FRE 2455, 77454 Marne-La-Vallée cedex 2, France
[2]Department of Geological and Environmental Sciences, Stanford University, CA 94305-2115, USA
[3]Saint Gobain Recherche, Aubervilliers, France
[4]Institut fuer Geowissenschaften, Universität Postdam, Potsdam, Germany
[5]Stanford Synchrotron Radiation Laboratory, Menlo Park, CA 94025, USA

Received June 26, 2003; accepted in revised form November 26, 2003

PACS numbers: 61.10.Ht, 61.43.Fs, 02.70.Ns, 91.40.−k

Abstract

A large number (67) of silicate glasses containing variable amounts of iron oxide were studied by high-resolution XANES spectroscopy at the Fe K-edge to determine an accurate method to derive redox information from pre-edge features. The glass compositions studied mimic geological magmas, ranging from basaltic to rhyolitic, dry and hydrous, with variable quench rates. The studied glasses also include more chemically simple calco-sodic silicate glass compositions. The Fe contents range from 30 wt.% to less than 2000 ppm. For most of the series of composition studied, the pre-edge information varies linearly with redox, even under high-resolution conditions. The average coordination of Fe(II) is often similar to its Fe(III) counterpart except in highly polymerized glasses because of the strong influence exerted by the tetrahedral framework on iron's sites. Natural volcanic glasses (from various volcanoes around the world) show similar variations. The average coordination of Fe(II) is often comprised between 4.5 and 5. Fe(III) shows larger variations in coordination (4 to 6, depending on composition). Bond valence models are proposed to predict the average coordination of Fe based on composition. Molecular dynamics simulations (Born-Mayer-Huggins potentials) were carried out on some compositions to estimate the magnitude of disorder effects (both static and thermal) in the XAFS analysis. XANES calculations (based on the MD simulations and FEFF 8.2) show large variations in the local structures around Fe. Also, 5-coordinated Fe(III) is found to be an important moiety in ferrisilicate glasses. For Fe(II), discrepancies between glass and melt are larger and are related to its greater structural relaxation at T_g. Also, a strong destructive interference between network formers and modifiers explain the relatively weak intensity of the next-nearest neighbors contributions in the experimental spectra.

1. Introduction

Iron affects significantly silicate melt and glass properties such as viscosity [1]. High resolution pre-edge and XANES features can help to further understand the origins of these dependences, provided systematic studies of glasses are undertaken at a given composition but variable oxygen fugacity conditions. If past studies demonstrated the presence of 5-coordinated sites around Fe(II) [2, 3] and the presence of a continuum of sites around Fe(II) [4], the exact effect of oxygen fugacity on the speciation of iron remain poorly understood, mostly because of the need to investigate a large experimental set of samples, which requires a significant amount of high-quality beamtime (i.e., under high resolution). In this study, we present a pre-edge, XANES and EXAFS study of iron in silicate glasses, in which the speciation if iron and the effects of disorder on XAFS spectra are understood in the light of molecular dynamics simulations.

2. Experimental

We studied a set of 67 silicate glasses containing variable amounts of network formers (such as Si and Al), network modifiers (Na, Ca, K), thus providing a large range of composition and polymerization degree encountered in silicate glasses of geochemical and industrial interest. For each composition, 3 to 7 glasses were equilibrated under variable oxygen fugacity to stabilize a specific Fe(II)/Fe(III) ratio. Fe K-edge XANES spectra were collected using the 11-2 beamline at SSRL (Stanford, USA) using Si(220) monochromators and reduced slit heights (0.3 mm) to achieve 0.6 eV experimental resolution. The monochromator energy calibration stability was ±0.05 eV. XAFS spectra were collected in the fluorescence mode, using a Stern-Heald type detector, a 3 μm Mn filter, Ag Soller slits and Xe absorbing gas. In the pre-edge region, energies were scanned with 0.1 eV steps, whereas 0.3 eV steps were used for the main edge crest region. Molecular dynamics calculations were undertaken following a similar procedure to the one described in [5]. *Ab-initio* XANES/EXAFS calculations were undertaken using the FEFF8.28 package [6] using default conditions, which included HL potentials, dipolar/quadrupolar transitions, self-consistency and full-multiple scattering formalism.

3. Pre-edge results

Fig. 1 shows typical XANES and their pre-edges collected for a series of sodo-calcic silicate glasses ("CNF1") containing 1 wt.% Fe and equilibrated at 7 different oxygen fugacities. The Fe(II)/Fe(III) ratio (as determined from wet chemical analyses) varies from 0.95 to 0.11 in this series of samples. When plotted in a diagram previously established for Fe(II)-, and Fe(III)-bearing model compounds (see [7] for details), the pre-edge information for these glasses (i.e., the centroid of the pre-edge doublet versus its integrated area) plots linearly as a function of the Fe(II)/Fe(III) ratio of the glasses (Fig. 1c). A Principal Component Analysis (see [8] for details) for each series of glasses suggested that two spectral end-members contribute to the XANES spectra (see also Fig. 1b). By inversion of the experimental XANES data set, we can estimate the XANES spectra for these end members as it was difficult to obtain experimentally CNF glasses containing only Fe(II) (respectively Fe(III)). The pre-edge information for these calculated end-members suggests that the average symmetry/coordination for the theoretical Fe(II) end member is similar (within errors) to that for its Fe(III) counterpart (CN ∼ 5.1 and 4.6 ± 0.3, respectively). This

*Corresponding author (e-mail: farges@univ-mlv.fr)

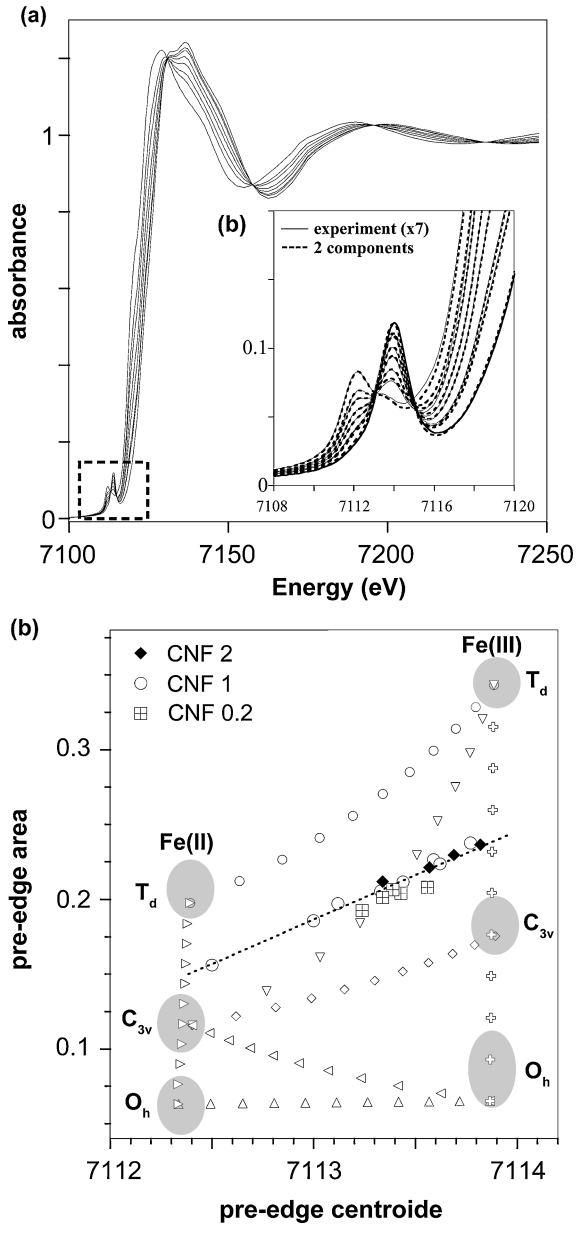

Fig. 1. Left: (a) Example of high-resolution Fe-K edge XANES spectra collected in the CNF1 series of sodo-calcic silicate glasses (1 wt.% Fe) and equilirated at 7 oxygen fugacities. (b) Zoom of the pre-edge feature, reconstructed using 2 components in the principle component analysis. Right: pre-edge information for 3 CNF glass series, which differ by their Fe content (2, 1 and 0.2 wt.%).

is consistent with the linear variation of the pre-edge information with redox (Fig. 1c). Most of the other series of glasses studied in this work show the same trends: under high resolution, Fe(II) and Fe(III) have similar symmetry in the end-member components (hence, a number of neighbor $= 5 \pm 0.5$).

4. MD simulations

Molecular dynamics (MD) simulations were performed for the two end-members of the CNF1 series (labelled CNFe2+ and CNFe3+) (see [4] and [5] for details). In each simulation, 10 atoms among 3800 are iron (either ferrous or ferric depending on the simulation considered). In each MD model, one site around Fe converged to a 3-coordinated site that was disgarded (as this coordination has never been observed experimentally around Fe(II) or Fe(III)). A bond valence analysis (see [9] and [5] for details) was conducted around each of the validated Fe atoms (i.e., in the 4-, and 5-coordination) to understand their connectivity to the main "glass/melt" structure. We could rationale most of the medium range environment around each iron atoms using a bond valence sums ($\sum$bv) around connecting oxygens:

Na-bearing glass : **Ca-bearing glass :**

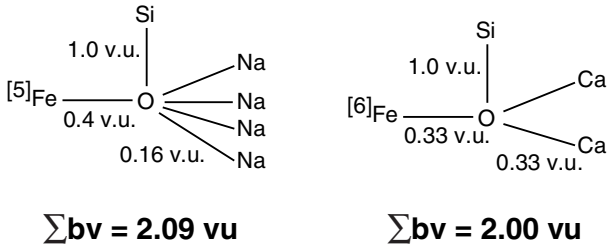

$\sum$bv = 2.09 vu **$\sum$bv = 2.00 vu**

"Half-way" configurations are possible in Na- and Ca-bearing compositions, with 1 Ca and 2 Na around the connecting oxygen. Around each oxygen connecting Fe to the tetrahedral framework (mostly Si atoms), the bond valence sums are close to 2, the value required for Pauling's second rule to be verified. These models suggest that Na and Ca are occupying the same structural position in Fe-bearing silicate glasses/melts (i.e., network modifiers). A systematic analysis of bond valence sums was conducted for each atom in the simulations (O but also Si, Na, Ca and Fe). On the average, most atoms are well bonded in terms of Pauling's second rule, suggesting that the simulations are structurally plausible. The MD-derived average Fe(III) coordination (4.3) is in excellent agreement with the experiment (4.6(3)). In contrast, Fe(II) shows a significant discrepancy (4.2 in the MD-"melt" vs. 5.1(3) in the glass) that is related to the much larger structural relaxation that occur at the glass transition temperature (Tg $\sim$ 950 K) around Fe(II) (a network modifier) than around Fe(III) (a network former; see [2]). Also, significant amounts of 5-coordinated Fe(III) can be observed (instead of 6-coordinated Fe(III) as often reported in previous studies). If confirmed experimentally, this is the first report of 5-coordinated moieties around Fe(III) in silicate glasses. As a result, we extracted the local structure to 10 Å around each Fe atom in the CNFe2+ and CNFe3+ simulations. We, then, conducted XANES and EXAFS *ab initio* calculations for each of these clusters.

5. FEFF models

Ab-initio XANES and EXAFS spectra were calculated using FEFF8.28 [6] for each iron site in each simulation. The calculated Fe K-edge XANES for CNFe2+ and CNFe3+ (Fig. 2a,b) show large variation of the spectrum profile from one cluster to another due to various local structure around Fe(II) and Fe(III). The agreement between the average XANES around Fe(III) and the experiment is better than for Fe(II), which is related to the coordination change around Fe(II) at Tg (see [2]). The EXAFS for the CNFe2+ simulation (Fig. 2c) shows large contributions arising from network formers (mostly Si) in the FT near 3 Å (see top curve). But these contributions suffer large phase cancellation (see curve "6 Å" on Fig. 2b) from network modifiers (Ca and Na). This suggests that important disorder effects occur in the medium range environment of Fe(II) in that model. Such analysis helps to better understand how disorder effects contribute to the XAFS spectra in disordered materials. In contrast, phase cancellation are less important around Fe(III) (Fig. 2d). Finally, the average

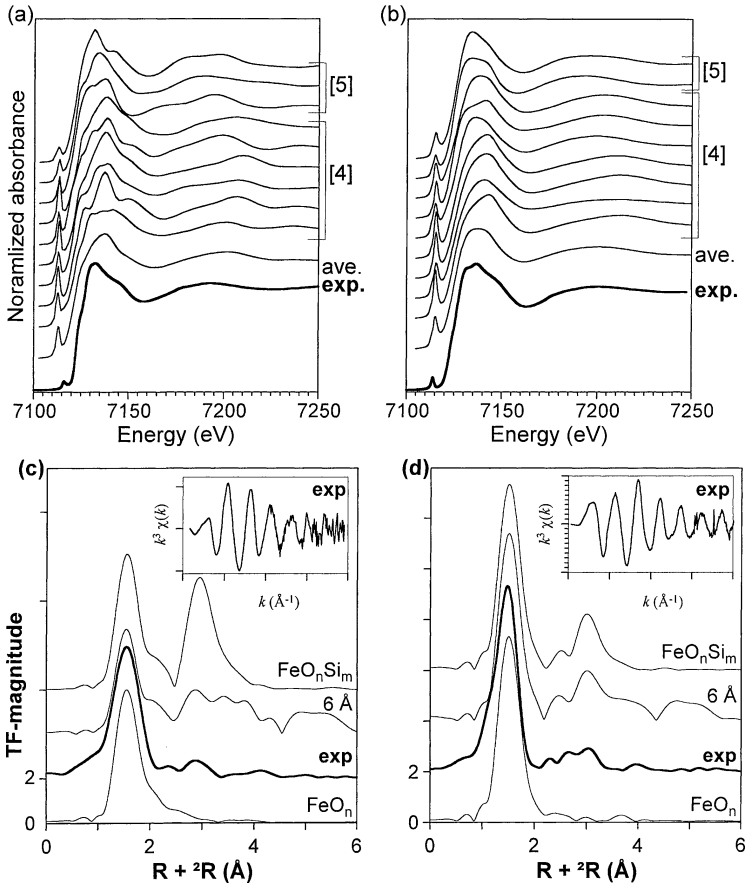

Fig. 2. FEFF 8.28 XANES (a,b) and EXAFS (c,d) calculated spectra based on the molecular dynamics models of the end-members of the CNF 1 composition: CNFe2+ (a,c) and CNFe2+ (b,d) respectively. Note the large variations in the XANES for CNFe2+ and CNFe3+ (for both model, the 10th cluster was omitted because of its unusal 3-coordination). On Figs. 2c/d, the cluster for "FeO_n" ($n = 4$ or 5) was calculated using a radial cut-off distance of 2.2 Å around the central Fe's. For the "FeO_nSi_m" cluster ($n = 4$, 5 and $m = 1$–4), a radial cut-off distance of 3.5 Å was used and, in addition, all network modifiers were excluded from the list of next-nearest neighbors. For the "6 Å" cluster, all next-rearest atoms up to 6 Å around the central atom were taken into account. Note also strong destructive interference for CNFe2+ due to network modifiers in the 3–4 Å range around Fe(II).

spectra calculated using FEFF for CNFe2+ and CNFe3+ MD models are comparable to the experiment (also obtained by inversion, see above) in the short-range environment (below 3 Å on the FT) but differs more in the medium-range environment (>3 Å). This is related to the poor modelling of thermal disorder by FEFF, which enhance artificially distant Fe-Si/Ca/Na pairs.

6. Conclusions

The Fe K pre-edge information for silicate glasses shows that the average coordination environment for Fe(II) and Fe(III) are close to each other and centred around a CN of 4.7 (±0.5). Molecular dynamics simulations confirm these findings and suggest that Fe(III) may occupy a significant amount of 5-coordinated sites in ferrisilicate glasses/melts. Bond valence analysis suggests that all atoms are usually well bonded, which means that they occupy plausible positions in the simulations. Then, *ab initio* XANES and calculations were undertaken (using FEFF8.28) and compared to the experiment (calculated by inversion of the data set). As the agreement is fair with experiment (it cannot be accurate because it compares a glassy to a melt state), the MD model provides interesting information of the effect of disorder in the next-nearest environment of Fe. According to MD simulations, the relatively weak Fe(II)-Si interactions observed in the EXAFS region is due mostly to a strong phase cancellation between constructive contributions arising from network forming Si and destructive contributions arising from network modifiers. This explains why the contribution arising from next-nearest neighbors are always relatively weak in the Fe K-edge EXAFS for silicate glasses (even around a network former like Fe(III)).

References

1. Mysen, B. O., Earth-Sci. Rev. **27**, 281 (1990).
2. Brown Jr. G. E. *et al.*, "Reviews in Mineralogy", **32** (The Mineral Soc. of America, Washington, 1995), p. 317.
3. Rossano, S. *et al.*, Phys. Chem. Min. **26**, 530 (1990).
4. Rossano, S. *et al.*, Europhys. Lett. **49**, 597 (2000).
5. Rossano, S. *et al.*, J. Non-Crystal. Sol. **304**, 167 (2002).
6. Ankudinov, A. L. *et al.*, Phys. Rev. B **58**, 7565 (1998).
7. Wilke, M. *et al.*, Am. Mineral. **65**, 713 (2001).
8. Wasserman, S. R., J. de Phys. IV (Coll.) **7-C2**, 203 (1997).
9. Farges, F. *et al.*, Geochim. Cosmochim. Acta **555**, 1564 (1991).

Physica Scripta. Vol. T115, 960–962, 2005

Copper and Silver Alloys under Extreme Conditions

A. Trapananti[1*], A. Di Cicco[1,2], E. Principi[1], S. De Panfilis[3] and A. Filipponi[4]

[1]INFM and Dipartimento di Fisica, Università di Camerino, I-62032 Camerino (MC) Italy
[2]INFN, Laboratori Naziouali di Frascati, I-00044 Frascati (Roma), Italy
[3]European Synchrotron Radiation Facility, B.P. 220, F-38043 Grenoble, France
[4]INFM and Dipartimento di Fisica, Università dell'Aquila, I-67010 Coppito (AQ), Italy

Received June 26, 2003; accepted January 27, 2004

PACS numbers: 61.10.Ht, 61.25.Mv, 61.50.Ks, 81.30.Hd

Abstract

We report about XAS (X-ray absorption spectroscopy) and ESXD (energy scanning X-ray diffraction) experiments on molten Cu_xSn_{1-x} and Ag_xPd_{1-x} and Cu_xPd_{1-x} alloys under high-pressure/high-temperature conditions for selected concentration. Recent advances in the analysis of XAS spectra of molten or disordered binary systems in the framework of the GNXAS method are discussed and their application to determine partial pair distribution functions in Cu6Sn5 is shown. The resulting distributions are compared with published X-ray diffraction data. Results about the disorder-order transition in $Ag_{0.5}Pd_{0.5}$ and $Cu_{0.6}Pd_{0.4}$ fcc random alloys are briefly discussed.

1. Introduction

Binary noble-metal alloys form an heterogeneous class of materials with different structural and electronic properties and a great variety in their phase diagrams corresponding to differences in the solubility of individual components. The Cu_xSn_{1-x} melts are known to crystallize in many distinct solid phases for different temperatures and concentrations [1]. On the other hand, several fcc binary alloys crystallize into various kind of ordered phases around the equiatomic composition upon decreasing temperature [2]. In particular the $Cu_{0.6}Pd_{0.4}$ alloy undergoes a peculiar transition ($T_c = 866$ K) toward an ordered β-phase having the B2(CsCl)-type structure [1] with a complete change in the lattice type instead of a simple atomic rearrangement in the original fcc lattice (as for $L1_0$(CuAu)-type, $L1_1$(CuPt)-type, and $L1_2$(Cu_3Au)-type structures). On the other hand, Ag_xPd_{1-x} alloys are known to form solid solutions for any concentration [1]. Very recently first-principles predictions of yet-unobserved structures in the Ag-Pd phase diagram have been reported [3]. According to these calculations, equiatomic $Ag_{0.5}Pd_{0.5}$ has a stable $L1_1$(CuPt)-type structure, below a critical transition temperature $T_c = 320$ K. The occurrence of such a structure has never been observed experimentally in binary materials other than Cu-Pt.

Despite the large interest of silver and copper alloys both for basic physics and for applications (ranging from medicine to electronics and electrical engineering), the structure of these systems has been poorly investigated, especially in the molten state and as far as the local order is concerned. In addition, the phase diagram of these alloys under high pressure conditions remains an almost unexplored domain (with some notable exceptions [4, 5]). Since pioneering studies by X-ray and neutron diffraction [6, 7], very few investigations have been performed to determine the short range arrangement around each atomic component.

In this context, the application of X-ray absorption spectroscopy (XAS) can play a fundamental role. The fine structure modulations (XAFS) of the X-ray absorption cross-section above the atomic absorption edges in condensed matter, are known to provide accurate information about the short range order around selected elements. Advances in data analysis scheme allowed us to obtain a reliable analysis of X-ray absorption spectra of molten and disordered systems [8, 9]. These methods have been recently extended, in order to make feasible the analysis of binary mixtures as binary alloys [10].

In this work we report about some recent experiments on copper and silver alloys studied in different regions of the (P,T) phase diagram, for selected concentrations. Cu_xSn_{1-x} alloys have been measured at 1073 K in their liquid phase for different concentrations. Solid $Ag_{0.5}Pd_{0.5}$ and $Cu_{0.6}Pd_{0.4}$ alloys have been investigated in a wide pressure and temperature region. Recent advances in the treatment of XAFS data of binary disordered system, are briefly discussed and the results of their application to the analysis of the Cu6Sn5 alloy are shown. The paper is organized as follows. Section 2 contains some experimental details about sample preparation, X-ray absorption and diffraction measurements. In sections 3 and 4 we report and discuss some results on different alloys. Section 5 contains concluding remarks.

2. Experimental

The experiments were performed mainly at the BM29 X-ray absorption spectroscopy beamline of the ESRF (European Synchrotron Radiation Facility). XAFS data on Cu-Sn alloys at Cu K-edge were collected at the LURE-D42 beamline. At the BM29 beamline, the conventional X-ray absorption transmission setup was complemented by a recently developed multi-channel detector collimator for the collection of high resolution energy-scanning X-ray powder diffraction patterns [11]. This setup supports different scanning and detection modes and allows us to switch between X-ray absorption spectroscopy, X-ray absorption temperature scans and energy scanning X-ray diffraction measurements [12]. High temperature measurements were performed using an high vacuum special furnace (L'Aquila-Camerino oven) designed to collect XAS and XRD spectra at high temperatures [13]. High pressure-high temperature conditions were obtained placing the samples in boron/epoxy bi-conical gaskets loaded inside a "Paris-Edinburgh" type large-volume press [14].

Cu_xSn_{1-x} alloys were produced mixing high purity CuO and SnO oxides powders, in the appropriate weight ratios, to obtain $x = 0.2$, 0.4, 0.55, 0.6, and 0.8 concentrations. These mixtures were finely ground, mixed with inert graphite powder (1 : 10 weight ratio) and then pressed into pellets (thickness $\simeq$1 mm). The alloys were produced *in-situ* by heating the pellets in

*Corresponding author. E-mail: angela.trapananti@unicam.it

high vacuum up to 1400 K. Copper and tin oxides decompose around 900 K forming metallic particles which alloy completely in the phase diagram region above the liquidus curve. X-ray diffraction measurements showed that the final samples were a dispersion of alloy particles, with a narrow spreading around the average concentration. Samples for high-pressure/high-temperature measurements were prepared mixing high purity Ag/Pd and CuO/Pd powders in suitable weight ratio for each concentration. The mixture was dispersed in an inert composite α-Al_2O_3/MgO (1 : 3) matrix in the appropriate ratio (1 : 12), then pelleted and melted in a graphite crucible under high vacuum conditions. After an accurate structural characterization by a laboratory angle-dispersive X-ray powder diffractometer, the final pellets were crushed into a fine powder and then pressed again into a 1.6 mm^3 cylinder. Each cylinder was directly placed into a graphite cylindrical oven and eventually loaded in a 7 mm boron/epoxy gasket, completed with the electrical feedthroughs for the sample heating. Temperature was monitored by inserting a Pt 10% Rh/Pt thermocouple through the gasket, while pressure was measured using the energy-scanning X-ray diffraction patterns and the MgO [15] and $MgAl_2O_4$ [16] equations of state.

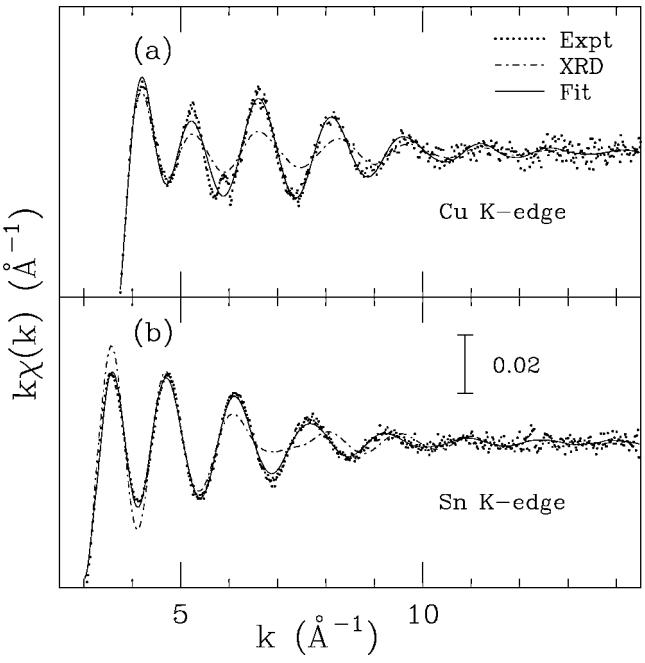

Fig. 1. Best-fit Cu (a) and Sn (b) K-edge XAFS signals compared with experimental data on molten Cu6Sn5 at 1073 K. Signals calculated from XRD partial distribution functions are also reported (dotdashed lines).

3. Local structure of molten alloys: Cu-Sn

Thermodynamical and structural properties of liquid Cu-Sn alloys have been extensively studied [17, 18]. The partial structure factors of molten Cu6Sn5 alloys have been determined by isotopic substitution neutron diffraction [6] and by X-ray scattering methods [7] assuming that the $S_{\alpha\beta}(k)$ were concentration independent. For this reason, we have chosen the Cu6Sn5 alloy to put to a test a new procedure for the refinement of the short-range structure of liquid binary mixtures from XAFS measurements. A valid method to combine XAFS data with the information provided by complementary techniques, like scattering experiments or molecular simulations, has been proposed by [19] and applied to the study of many different single component systems (see [9] for a review). In this framework the short-range peak of the partial distribution function is refined constraining the $g(r)$ and the corresponding $S(k)$ to keep their long-distance behavior, namely:

$$\lim_{r\to\infty} g(r) = 1, \tag{1}$$

$$\lim_{k\to 0}\left[1 + 4\pi\rho\int_0^\infty r^2[g(r)-1]\frac{\sin(kr)}{kr}\,\mathrm{d}r\right] = \frac{\rho K_T}{\beta} \tag{2}$$

where K_T is the isothermal compressibility and $\beta = (k_B T)^{-1}$. The same procedure has been successfully applied to two components charged liquids (e.g. molten salts [20]). In fact, requiring the charge screening in the Coulomb fluid, equation (2) still holds for each $S_{\alpha\beta}(k)$ separately (apart from a constant) [21]. It follows that each partial $g_{\alpha\beta}(r)$ can be refined independently from the others extending the constraints originally derived for mono-atomic systems.

In the general case, the isothermal compressibility is related to the $k \to 0$ limit by a more complicated equation [21], involving non-linear combinations of the $S_{\alpha\beta}(k)$. The derivation of physical constraints on the $g_{\alpha\beta}(r)$ is not straightforward. We have developed a new procedure which exploits the three long-wavelength limits of the Bhatia-Thornton $S_{NN}(k)$, $S_{Nc}(k)$ and $S_{cc}(k)$ structure factors [17], also related to isothermal compressibility. Full details on this method and its implementation in the framework of the GNXAS data analysis scheme are described elsewhere [10]. Here we report a simultaneous refinement of both Cu and Sn K-edges XAFS measurements on liquid Cu6Sn5 assuming the set of partial $g(r)$'s derived from X-ray scattering [7] as a starting model.

In Fig. 1, best-fit Cu and Sn K-edge calculated signals are compared with experimental data collected at 1073 K and signals calculated from the XRD partial distribution functions. The main frequency and amplitude of the signal, roughly associated with the first shell distance and coordination number are well reproduced. Reconstructed partial pair distribution functions are compared in Fig. 2 with XRD models.

The $g_{\mathrm{CuSn}}(r)$ first peak is slightly higher but qualitatively similar to that found by XRD. On the other hand, $g_{\mathrm{CuCu}}(r)$ and $g_{\mathrm{SnSn}}(r)$ distributions differ from the original model, especially on the short-distances side, to which XAFS is exceptionally sensitive. The rise of the $g_{\mathrm{CuCu}}(r)$ peak is steeper and the most probable Cu-Cu bondlength slightly shorter than from XRD. Similarly the first maximum and the foot of the $g_{\mathrm{SnSn}}(r)$ distribution are shifted of about 0.1 Å toward the low r side, indicating that the Sn-Sn bondlength and also the corresponding closest approach distance are shorter than from XRD. In order to follow the changes of the partial distributions functions with composition we are currently applying the same refinement to data collected for each concentration.

4. Metal alloys under high-pressure and high-temperature

The Ag_xPd_{1-x} alloy, with $x = 0.5$ nominal concentration, has been investigated in the 298-1650 K temperature range for pressures up to 5.6 GPa. High quality XAFS spectra at Ag and Pd K-edges and X-ray diffraction patterns have been collected. The subtle changes associated with an order-disorder transition, like variation of the bond variances affecting XAFS signals and intensity of Bragg peaks have not been observed upon increasing temperature. Therefore the occurrence of an ordered L_1 structure

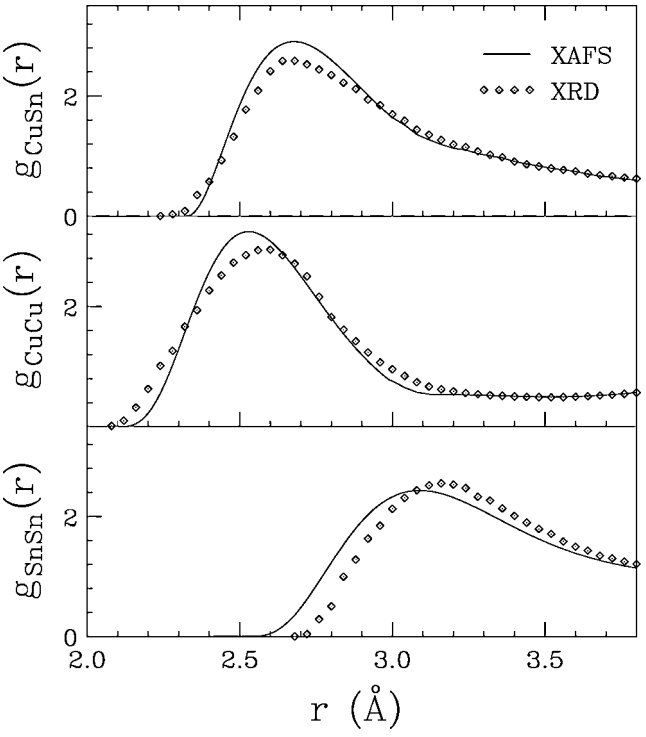

Fig. 2. Partial pair distribution functions reconstructed by XAFS compared with published XRD results [7] for liquid Cu6Sn5.

below $T_c = 320\,\mathrm{K}$, predicted by first-principles calculations, is not confirmed by the present work.

Since regular arrangements of atoms on lattice sites usually give higher packing densities than random arrangements, the application of pressure should make the ordered state favorable and then shift T_c toward higher temperatures, making easier its experimental detection. In Fig. 3 we report a series of XAFS spectra collected at room temperature for different pressures. Besides the slight frequency decrease (indicated by dashed lines), related to an obvious contraction of the first-neighbor bondlength as a function of pressure, we do not observe any evidence of changes in the short-range structure induced by pressurization. Similarly, no evidence of phase transitions has been found for increasing temperature in the whole range of pressures.

A similar investigation has been performed for the $Cu_{0.6}Pd_{0.4}$ alloy for which the presence of an order-disorder transition is well known. In this case a clear transition between the ordered B2(CsCl)-type structure and a disordered fcc structure has been observed by fixed energy X-ray absorption temperature scans, even under high pressure conditions.

5. Conclusions

In conclusion, we have developed new experimental and theoretical tools for a complete structural characterization of solid and molten binary alloys under extreme thermodynamical conditions. Cu- and Ag-based alloys have been investigated through a combination of complementary techniques like X-ray absorption spectroscopy, X-ray diffraction and fixed-energy X-ray absorption temperature scans. New procedures to prepare

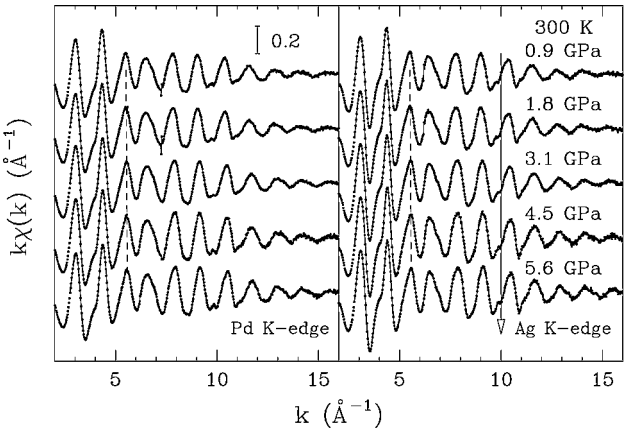

Fig. 3. Experimental XAFS signals at Pd (left panel) and Ag (right panel) K-edge of $Ag_{0.5}Pd_{0.5}$ alloy collected at RT for different pressures.

alloy samples for experiments under high-pressure and high-temperature conditions have been developed. A new methodology for the analysis of the X-ray absorption spectra of molten and disordered binary mixtures has been shown to give reliable results in a prototypical system like Cu6Sn5. Some short-distance details of the liquid Cu6Sn5 partial pair distribution functions, as the rise of the $g_{CuCu}(r)$ peak and the position of the foot and the first maximum of the $g_{SnSn}(r)$ have been refined respect to the XRD results, exploiting the unique sensitivity of the XAFS signal to short-range correlations. Temperature and pressure induced order-disorder transitions have been investigated. Evidence of the existence of an ordered phase in the $Ag_{0.5}Pd_{0.5}$ fcc random alloy has not been obtained in the present work.

References

1. Hansen, M., editor, "Constitution of binary alloys", (McGraw-Hill, New York, 1958).
2. Pearson, W. B., editor, "A Handbook of lattice spacings and structures of metals and alloys", (Pergamon press, New York, 1958).
3. Müller, S. and Zunger, A., Phys. Rev. Lett. **87**, 165502 (2001).
4. Iwasaki, H. and Kaneko, A., Jpn. J. Appl. Phys. **17**, 2041 (1978).
5. Ichikawa, M., Iwasaki, H. and Endo, S., Jpn. J. Appl. Phys. **20**, 623 (1981).
6. Enderby, J. E., North, D. M. and Egelstaff, P. A., Phil. Mag. **14**, 961 (1966).
7. North, D. M. and Wagner, C. N. J., Phys. Chem. Liq. **2**, 87 (1970).
8. Filipponi, A. and Di Cicco, A., Phys. Rev. B **52**, 15135 (1995).
9. Filipponi, A., J. Phys.: Condens. Matter **13**, R23 (2001).
10. Trapananti, A. and Di Cicco, A., Phys. Rev. B **70**, 014101 (2004).
11. Filipponi, A. *et al*., Rev. Sci. Instrum. **74**, 2654 (2003).
12. Filipponi, A. *et al*., Rev. Sci. Instr. **71**, 2422 (2000).
13. Filipponi, A. and Di Cicco, A., Nucl. Inst. Methods Phys. Res. B **93**, 302 (1994).
14. Besson, J. M. *et al*., Physica B **180 & 181**, 907 (1992).
15. Martinez-Garcia, D. *et al*., High Pressure Res. **18**, 339 (2000).
16. Kruger, M. B., Nguyen, J. H., Caldwell, W. and Jeanloz, R., Phys. Rev. B **56** (1997).
17. Bhatia, A. B. and Thornton, D. E., Phys. Rev. B **2**, 3004 (1970).
18. Turner, R., Crozier, E. D. and Cochran, J. F., J. Phys. C: Solid State Phys. **6**, 3359 (1973).
19. Filipponi, A., J. Phys.: Condens. Matter **6**, 8415 (1994).
20. Di Cicco, A., Minicucci, M. and Filipponi, A., Phys. Rev. Lett. **78**, 460 (1997).
21. March, N. H. and Tosi, M. P., "Atomic Dynamics in Liquids", (Dover, New York, 1991).

Physica Scripta. Vol. T115, 963–965, 2005

In Situ Investigations of Thin Film Formation by Reactive Sputtering

K. Bruder, P. Keil, D. Lützenkirchen-Hecht* and R. Frahm

Institut für Materialwissenschaften und Fachbereich Physik, Bergische Universität Wuppertal, Gaußstr. 20, D-42097 Wuppertal, Germany

Received June 26, 2003; accepted October 16, 2003

PACS numbers: 61.10.Ht, 61.10.Kw, 68.47.Gh, 81.15.Cd

Abstract

Surface sensitive, grazing incidence reflection mode X-ray absorption spectra were conducted in order to study the reactive sputtering processes in situ. The spectra were measured in the Quick-scanning EXAFS (QEXAFS) mode, so that, beginning from the initial stages of thin film formation, all the growth processes can be followed with a time resolution of about 30 s. The experiments were performed in a small sputter chamber with a magnetron source. In the present study, the growth of amorphous Ta-oxide films is studied.

1. Introduction

Thin film growth by magnetron sputtering usually involves the bombardment of the target material with accelerated ions, the evaporation of the target material into the gas phase and its deposition on the substrate. If a reactive gas species such as oxygen is present in the gas phase, a chemical reaction with the evaporated material can occur, leading to the deposition of a chemical compound, the surface and volume microstructure of which depends strongly on the details of the preparation procedures, like the working pressure and the gas composition, the nature of the substrate and its temperature etc (see, e.g. [1–4]). In the present study, we investigated the structure of reactively sputtered Ta_2O_5-films on float glass substrates in situ. Surface sensitive, grazing incidence reflection mode X-ray absorption spectra were measured using the Quick-scanning EXAFS (QEXAFS)-technique with a time resolution of about 25 s. Previous ex situ reflection mode EXAFS studies have shown that stochiometric amorphous thin films with very smooth surfaces can be prepared by reactive sputtering from a tantalum metal target in a pure O_2-atmosphere [5]. The sputter chambers for in situ investigations with X-rays that have been previously published in the literature usually consist of large vacuum chambers which require complex diffractometers for the experiments [6–8]. In this paper we will report on the first grazing incidence EXAFS experiments of reactively sputtered Ta_2O_5 thin films which were prepared and investigated in situ in a miniaturized high vacuum chamber with a magnetron source which can be mounted on a rather small reflectometer stage. Ta-oxide has potential applications in microelectronic devices, e.g. for the use as capacitor material in dynamic random access memories [9] or as gate insulator in metal-oxide-semiconductor field effect transistors [10].

2. Experimental

The experiments presented here were performed at the bending magnet station RÖMO II [11] at the DORIS III storage ring at HASYLAB (Hamburg, Germany). A double-crystal monochromator with two flat Si(111) crystals was used. Time resolved reflectivity data were collected at room temperature in the vicinity of the Ta L_3-edge (9.881 keV) for various glancing angles in the vicinity of the critical angle of total reflection ($\Theta_C \approx 0.25^\circ$). The incident, monochromatic X-ray beam was collimated to a size of about 255 µm × 10 mm (vertical × horizontal) by a slit system. Incident and reflected intensities were measured by means of nitrogen and argon filled ionization chambers, respectively. A second slit system in front of the second ionization chamber suppresses the intensity of non specularly reflected X-rays and shields this detector from the direct beam. All components of the reflectometer, i.e. the sample position, the angle of the detector arm and the slit system can be adjusted by stepper motors. Simultaneously with each EXAFS scan, a Ta-metal foil was measured in transmission between the second and third ionization chamber in order to calibrate the energy scale of the monochromator. Time resolved spectra were recorded in the quick-scanning EXAFS mode, in which the monochromator is moved continuously from smaller to higher energies and the spectrum is measured on the fly [11]. Typical reflection mode scans with a scan range of about 0.4 keV took about 25 s and consist of ca. 800 data points each of which was measured in about 0.016 s.

3. In situ cell design

Fig. 1 shows the sputter chamber on the reflectometer. It mainly consists of a glass cylinder with a diameter of ca. 10 cm with two large area Kapton windows for the incoming and the reflected beam. The used glass substrate (approx. 10 mm width and 20 mm length) is placed on a resistive heater in which a tungsten filament is embedded. The heater is remote controlled by a computer and enables temperatures up to 300 °C. The glass cylinder is placed on a stainless steel vessel with flanges for the sputter gas inlet, electrical feedthroughs for the measurement of the substrate temperature and the electrical resistivity of the sample and a pumping connection to a turbo-molecular pump. The top flange of the vacuum chamber accommodates the magnetron source with a tantalum metal target of approx. 60 mm diameter. The base pressure of the chamber is below $1 * 10^{-5}$ mbar. We used Argon with a small amount of O_2 as sputter gas. The films were sputtered at a pressure of about $3.44 * 10^{-3}$ mbar and a current of about 20 mA.

4. Results and Discussion

In Fig. 2, raw reflection mode EXAFS data are presented for a glancing angle $\Theta = 0.22^\circ$. It should be noted that no data processing or reduction such as smoothing or averaging was applied to the experimental data points. Every second spectrum is displayed, i.e. subsequent spectra in the graph correspond to a time interval of ca. one minute. The decrease in reflectivity at about

*e-mail: dirklh@uni-wuppertal.de

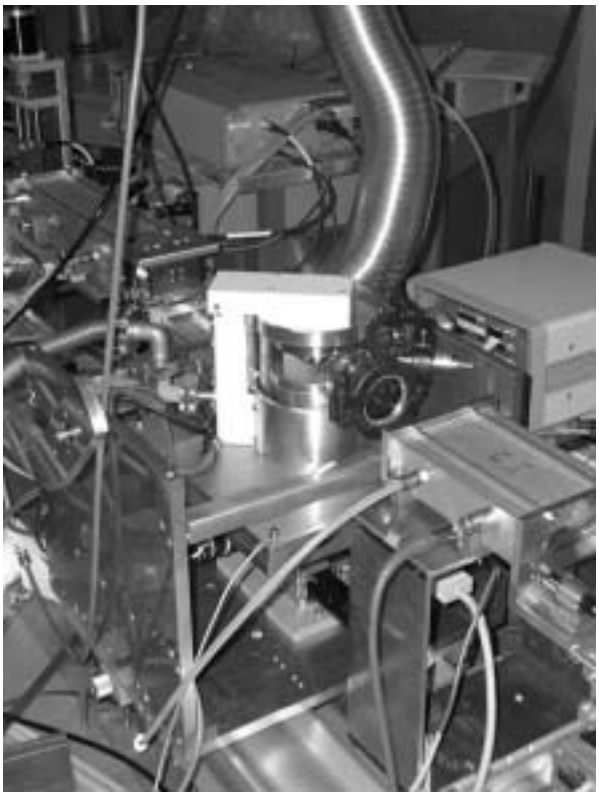

Fig. 1. Photo of the in situ sputter chamber on the reflectometer at the RÖMO II beamline at HASYLAB.

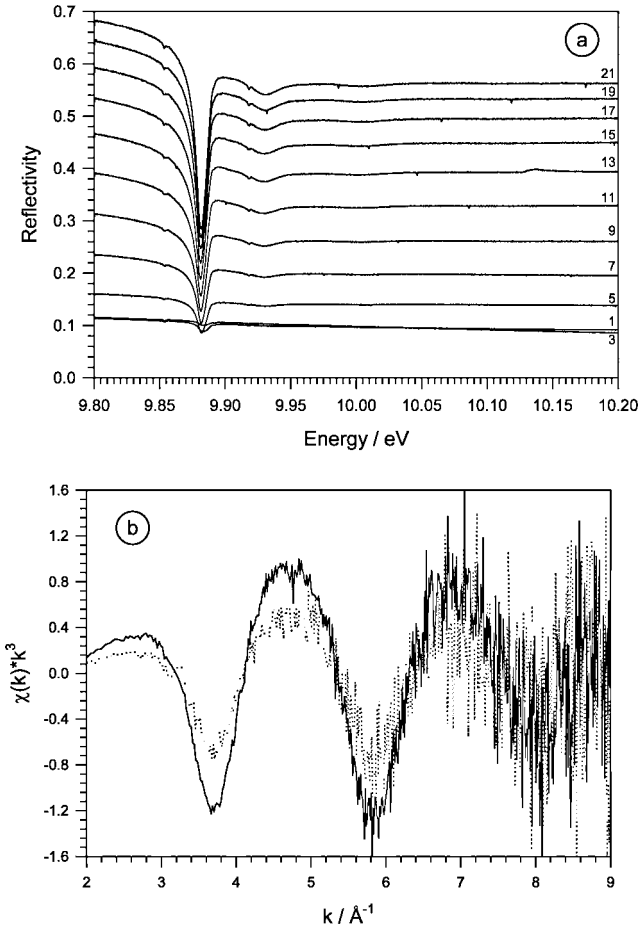

Fig. 2. (a) In situ reflection mode ($\theta = 0.22^\circ$) Ta L_3-edge spectra of the amorphous Ta-oxide layers during reactive sputter deposition at room temperature. Each spectrum was measured in about 25 s, every second spectrum is displayed. (b) k^3-weighted reflection mode fine structure of a single spectrum. The full and the dotted line correspond to sputtering times of about 700 s and 100 s, respectively.

9.89 keV belongs to the Ta L_3-edge. Obviously, the reflectivity of the sample increases with the sputtering time and thus with the oxide film thickness. This effect can easily be understood because the critical angle of total reflection for the bare glass substrate is about $\Theta_C \approx 0.18^\circ$ only, while that of Ta-oxide is about $\approx 0.25^\circ$. Working slightly below the critical angle of total reflection of Ta-oxide results in a high reflectivity of the deposited Ta-oxide layer and an increase of the X-ray reflectivity during the sputtering process accordingly. As can be seen in Fig. 2(a), the experimental data quality is high enough to resolve the weak EXAFS oscillations belonging to the amorphous sample even for films of some few nanometers thickness only.

For the further data processing, a smooth background $R_0(E)$ was subtracted from the reflectivity above the edge and the normalized reflectivity fine structure $\chi(E)$ was calculated according to:

$$\chi(E) = \frac{R(E) - R_0(E)}{R_0(E)}.$$

Subsequently, the energy scale was converted into a photoelectron wave number scale. Examples for the obtained reflectivity fine structures are presented in Fig. 2(b) for two different sputtering times. Obviously, even for only 100 s of sputtering, a pronounced fine structure belonging to the grown Ta-oxide film could be measured.

These fine structures were subjected to a Fourier-transform. As can be seen in Fig. 3, the intensity of the first peak at about 1.5 Å radial distance – which belongs to the first Ta-O-coordination of the oxide film – increases as a function of the sputter time, while its radial distance remains constant. This can be seen in more

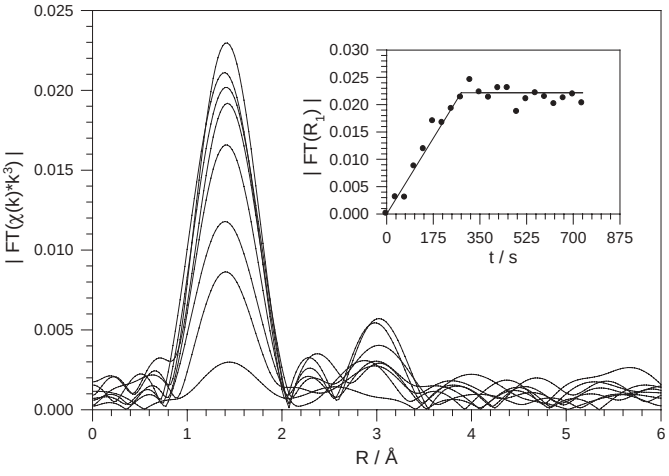

Fig. 3. Magnitude of the Fourier-transforms of the fine structure oscillations extracted from the reflection mode spectra presented in Fig. 2. In the insert, the increase of the peak at about 1.5 Å radial distance (R_1) belonging to the first Ta-O coordination of the growing oxide film is shown as a function of time. 60 s sputter time correspond to about 1.23 nm film thickness. (The data are not phase shift corrected. The k-range for the Fourier transformation is $2\,\text{Å}^{-1} \leq k \leq 9\,\text{Å}^{-1}$).

detail in the insert of Fig. 3, where the intensity of this peak is plotted as a function of sputtering time. According to the detailed analysis of specular reflectivity measurements (Θ-2Θ-scans) with

fixed photon energy, the film thickness was about 15 nm ± 0.2 nm, i.e. the deposition rate is about 1.23 nm/minute. Up to about 300 s sputtering time corresponding to a film thickness of about 6.2 nm, a linear increase of the peak intensity was found, while it is approximately constant for larger sputtering times. Therefore the evolution of the structure of the Ta-oxide film can be followed in situ as a function of time. From the presented data we can conclude that the near range order structure of the amorphous Ta_2O_5 thin films is already developed at very low coverages of the glass substrate. Since the penetration depth of the X-rays into the Ta-oxide film is about 10 nm for the used grazing angle, the constant value observed for the magnitude of the first coordination in the Fourier-transform can not simply be related to the situation that the film thickness equals the penetration depth. A similar behaviour has been observed for sputtered copper films in the past [12]. These experiments were interpreted by the presence of small clusters with a high degree of static disorder [12], which is also given for the amorphous Ta_2O_5-films under investigation in the present study. Therefore it is very likely that such effects are also responsible for the observed thickness dependence of the reflectivity fine structure.

Acknowledgements

We like to thank U. Haake for his help at the beamline during the experiments. We gratefully acknowledge the financial support by HASYLAB and the MWF Nordrhein-Westfalen.

References

1. Thornton, J. A., Vac. Sci. Technol. **11**, 666 (1974), Ann. Rev. Mater. Sci. **7**, 239 (1977).
2. Yoon, K. H., Choi, J.-W. and Lee, D.-H., Thin Solid Films **302**, 116 (1997).
3. Pakala, M. and Lin, R. Y., Suf. Coat. Technol. **81**, 233 (1996).
4. Hotovy, I., Huran, J., Janik, J. and Kobzev, A. P., Vacuum **51**, 157 (1998).
5. Lützenkirchen-Hecht, D. and Frahm, R., J. Synchrotron Rad. **8**, 478 (2001).
6. Payne, A. P., Clemens, B. M. and Brennan, S., Rev. Sci. Instrum. **63**, 1147 (1992).
7. H. You, H., Huang, K. G. and Kampwirth, R. T., Physica **B 221**, 77 (1996).
8. Zheng, J. Q., *et al*., J. Vac. Sci. Technol. **A 9**, 128 (1991).
9. McKinley, K. A. and Sandler, N. P., Thin Solid Films **290/291**, 440 (1996).
10. Matsui, M., *et al*., Jpn. Appl. Phys. **29**, 62 (1990).
11. Frahm, R., Rev. Sci. Instr. **60**, 2515 (1989).
12. Frahm, R., Barbee, T. W. and Warburton, W., Phys. Rev. **B44**, 2822 (1991).

Physica Scripta. Vol. T115, 966–969, 2005

The Electronic Structures of Crystalline and Aqueous Solutions of NaBr and $NaBrO_3$ Using *In-situ* Na K and Br L edge X-ray Absorption Spectroscopy

S. Matsuo[1], P. Nachimuthu[2,3], D. W. Lindle[2], R. C. C. Perera[3] and H. Wakita[1,4*]

[1]Advanced Materials Institute, Fukuoka University 8-19-1 Nanakuma, Jonan-ku, Fukuoka 814-0180, Japan
[2]Department of Chemistry, University of Nevada, Las Vegas 4505 Maryland Parkway, Box 454003, Las Vegas, NV 89154, U.S.A.
[3]Center for X-ray Optics, Lawrence Berkeley National Laboratory 1 Cyclotron Road, Berkeley, CA 94720, U.S.A.
[4]Department of Chemistry, Fukuoka University 8-19-1 Nanakuma, Jonan-ku, Fukuoka 814-0180, Japan

Received June 26, 2003; accepted November 4, 2003

PACS numbers: 71.15.Mb, 71.20.Dg, 78.70.Dm

Abstract

The electronic structures of crystalline and aqueous solutions of NaBr and $NaBrO_3$ were studied using *in-situ* Na K and Br L edge X-ray absorption spectra measured under ambient conditions. Analyses of Na K-edge X-ray absorption spectra show that NaBr and $NaBrO_3$ strongly dissociate in aqueous solution and form Na^+ hydration structures, $[Na(H_2O)_n]^+$ ($n = 0$–6). However, the size of the anions significantly affects the formation of the Na^+ hydration structures in aqueous solutions. The ligand field potential (10 Dq) observed in the Br L-edge X-ray absorption spectra allows in determining their dependence not only on the coordination structure between the Br and the first near neighbor but also the second near neighbor in crystalline state, and, the hydration structure and the counter cations in aqueous solutions. DV-Xα molecular-orbital calculations predict that the transitions in the Br L-edge NEXAFS occur from Br 2p to the unoccupied states containing mainly 4d orbitals of Br for both crystalline and aqueous solution. However, 5s and 5p of Br and 3p of Na in addition to the 4d orbitals of neighbor Br for crystalline NaBr and 5s and 5p of Br, 2p of O and 1s of H for aqueous NaBr also contribute to the unoccupied states.

1. Introduction

Many bromine containing compounds have been widely used in a variety of applications such as water purification, agriculture, cars, healthcare, photography, and most importantly as flame-retardants, and recent investigations have shown they persist in the environment [1–3]. Most of these bromine compounds are carcinogenic and toxic [2]. Recent *in-situ* X-ray absorption spectroscopic studies show that the inorganic chlorine compounds rapidly transform to less volatile organic compounds with chlorinated phenolic and aliphatic groups as the principal Cl forms during the humidification of plant material and, thus play a critical role in the cycling of Cl and of several major and trace elements in the environment and may influence human health [4]. Accordingly, the bromine compounds also have opportunities flowing out in the environment, and have possibilities to subsequently change to harmful substances in part of them since these compounds used for commercial applications. Thus, understanding the local electronic structures and the chemical states of the basic bromine compounds in aqueous solution in comparison with corresponding crystalline compounds is extremely important not only in environmental science but for solution chemistry as well.

The availability of synchrotron-radiation sources for X-ray-absorption spectroscopy has made near-edge X-ray-absorption fine structure (NEXAFS) and extended X-ray-absorption fine structure (EXAFS) powerful tools for detailed understanding of electronic and structural properties of materials lacking long-range order, such as catalysts, inorganic materials, minerals, glasses, organometallic complexes, and biological samples like enzymes [5–8]. A new experimental setup for materials requiring *in-situ* X-ray absorption spectral measurements under ambient conditions in the 400–2000 eV photon-energy region using both transmission and total-fluorescence-yield detection techniques has been developed. It's utility has been demonstrated by studying the optically switchable amorphous metal thin films (Mg-*TM*, where *TM* = Ti, Mn, Co, and Ni) under reaction conditions by the exposure of hydrogen, Na, Mg, Al, Br, Sr and Si compounds in crystalline state and in aqueous solutions etc. [9–11].

As a representative example, we present the structural and electronic properties of crystalline and aqueous solutions of NaBr and $NaBrO_3$ obtained from the analyses of the Na K-edge EXAFS and theoretical simulations of Br L-edge NEXAFS using DV-Xα molecular-orbital calculations in comparison with measured *in-situ* X-ray absorption spectra under ambient conditions.

2. Experimental section

Crystalline compounds (NaBr and $NaBrO_3$) were purchased from Aldrich Chemical Co. (Milwaukee, WI) and used for the measurements. The 0.1 M aqueous solutions were freshly made with de-ionized water. The X-ray absorption measurements were conducted at Beamline 6.3.1 at the Advanced Light Source (ALS), Lawrence Berkeley National Laboratory [12]. During the measurements, the ALS operated at 1.9 GeV between 200 mA and 400 mA. The total-fluorescence-yield was detected using a Hamamatsu GaAsP photodiode (G1127-02). The aqueous solutions were placed in a 6 mm diameter tube containing a 1.5–2 mm wide slit. The surface of the solution at the slit in the tube was exposed to the X-ray beam and fluorescent photons were collected from the solution by the detector (90° to the X-ray beam). For crystalline compounds, very thin layer of the sample was prepared on a conducting carbon tape and the measurements were performed at gracing incidence to minimize the self-absorption effects in the measured absorption spectra. Details of the experimental setup are given elsewhere [10]. The photon energy was calibrated using the first inflection points of the Na K and Al K edge X-ray absorption spectra of crystalline NaBr and Al metal, respectively. All the spectra were normalized to the absorption-edge jumps [6].

*Corresponding author. e-mail: wakita@fukuoka-u.ac.jp

The Na K-edge EXAFS were analyzed using WinXAS (2.1) [13]. The theoretical phase shifts and scattering amplitudes for the crystalline NaBr and $NaBrO_3$ were derived from the crystallographic data using the FEFF (6.01) codes [14]. The structure of $[Na(H_2O)_6]^+$ reported previously based on the solution X-ray diffraction studies was used for the aqueous solutions [15]. The curve fittings were performed in k space between $\sim 2.8\,Å^{-1}$ and $7.1\,Å^{-1}$ using multi-shells for crystalline and single-shell (Na-OH_2) for aqueous solutions.

The DV-Xα molecular-orbital calculations [16] were performed for Br L_3-edge NEXAFS for the crystalline and aqueous solution of NaBr as a representative example using a half-occupied core-level (Slater's transition state [17]) and an expanded basis set. For crystalline NaBr, a model consisting of 14 Na and 13 Br atoms with Br atom at the center based on the crystallographic data was used for the calculations [18]. For 0.1 M aqueous NaBr, the calculations performed previously based on a model with one Br atom surrounded by six water molecules were used for comparison [11]. In the DV-Xα calculations, Na and Br atoms were given the charges of $+1$ and -1, respectively. The resulting model was embedded into a Madelung potential field consisting of 702-point charges for the influence of electrostatic energy of the clusters. The unoccupied orbitals included in the calculations are 3p, 3d, 4s, and 4p of Na, and, 4d, 5s, 5p and 5d of Br. The outermost orbitals, 4p of Na and 5d of Br, were included in the calculations to suppress the numerical error for the rest of the orbitals, but they were excluded when evaluating the partial density-of-states (PDOS). The electron transition probabilities (ETP) were evaluated from the dipole matrix element between a core state and unoccupied molecular states [19, 20]. The ETP were convoluted using Gaussians with FWHM of 1.5 eV and 2.5 eV for NaBr clusters and hydrated Br^- ion models, respectively. An appropriate arctangent function was included in the simulated spectra to describe the absorption continuum.

3. Results and discussion

The Na K-edge EXAFS spectra for crystalline and aqueous solutions of NaBr and $NaBrO_3$ are shown in Fig. 1. The features

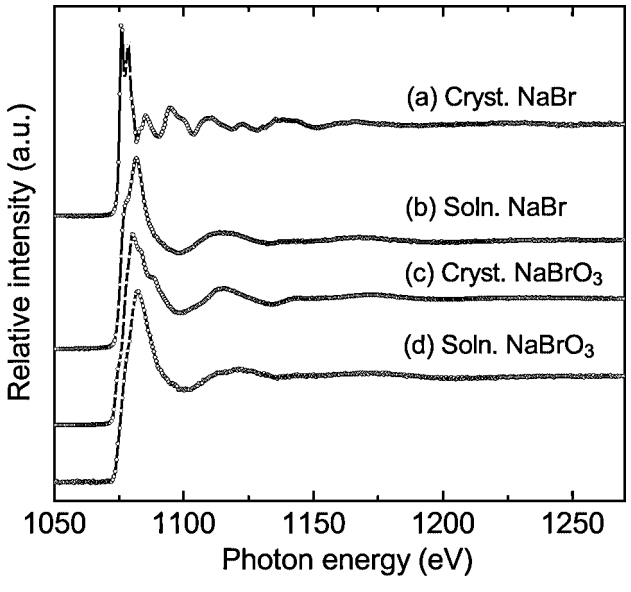

Fig. 1. The Na K-edge EXAFS for (a) crystalline NaBr, (b) 0.1 M aqueous NaBr, (c) crystalline $NaBrO_3$ and (d) 0.1 M aqueous $NaBrO_3$.

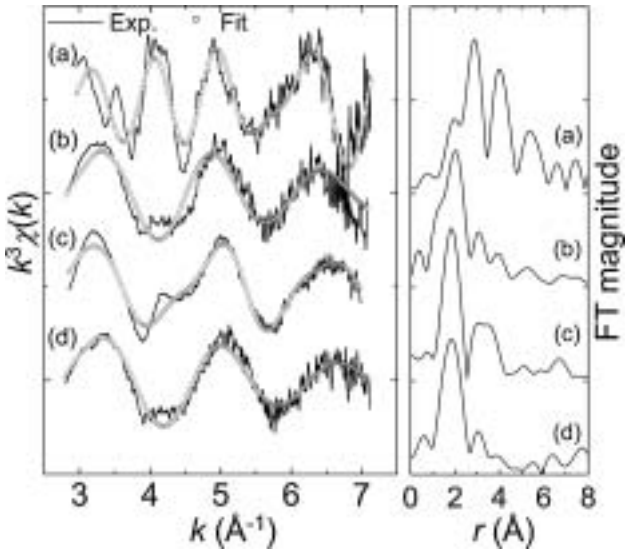

Fig. 2. The Na K-edge k^3-weighted EXAFS (left panel) and the corresponding Fourier-transformed radial distribution functions (right panel) for (a) crystalline NaBr, (b) 0.1 M aqueous NaBr, (c) crystalline $NaBrO_3$ and (d) 0.1 M aqueous $NaBrO_3$.

in the NEXAFS region for the crystalline NaBr are in good agreement with those reported previously by Murata *et al.* [21]. Further, the fine structures in the post-edge region are prominent in the spectrum for the crystalline NaBr unlike for the aqueous solution, where these features became broad suggesting the lack of long-range order in solution. The k^3-weighted Na K-edge EXAFS spectra and the corresponding Fourier-transformed radial distribution functions (RDFs) for crystalline and aqueous solutions of NaBr and $NaBrO_3$ are shown in Fig. 2. The changes in the profiles in both k^3-weigthed EXAFS and RDFs between crystalline and the corresponding aqueous solution reflect the effect of dissolution of NaBr and $NaBrO_3$ in water resulting from the disassociation of Na-Br/Na-BrO_3 bonds and the formation of Na^+ hydration structures, $[Na(H_2O)_n]^+$ ($n =$ 0–6). The coordination number (N), inter-atomic distance (r) and the disorder parameter (σ^2) derived from the analyses of Na K-edge EXAFS are given in Table I. For crystalline NaBr and $NaBrO_3$, the inter-atomic distances derived from the EXAFS fits with fixed coordination number of Na^+ to 6 are comparable to

Table I. *The coordination number (N), inter-atomic distance (r) and the disorder parameter (σ^2), derived from the analyses of Na K-edge EXAFS for the crystalline and 0.1 M aqueous solutions of NaBr and $NaBrO_3$.*

Sample	Shell	N	r/Å	σ^2/Å^2
Cryst. Na-Br	NaBr	6.0[a]	2.94[b]	1.6×10^{-2}[d]
	Na-Na	12.0[a]	4.27[b]	2.1×10^{-2}[d]
Soln. NaBr	Na-O	5.1[c]	2.38[b]	1.9×10^{-2}[d]
Cryst. $NaBrO_3$	Na-O	3.0[a]	2.32[b]	5.5×10^{-3}[d]
	Na-O	3.0[a]	2.59[b]	1.7×10^{-2}[d]
	Na-Br	3.0[a]	3.37[b]	2.8×10^{-4}[d]
	Na-Br	3.0[a]	3.60[b]	6.5×10^{-5}[d]
Soln. $NaBrO_3$	Na-O	4.4[c]	2.29[b]	1.8×10^{-2}[d]

[a]Fixed values. [b]Errors are all within $\pm 1.0 \times 10^{-4}$. [c]Errors are all within $\pm 6.4 \times 10^{-4}$. [d]Errors are all within $\pm 1.0 \times 10^{-5}$.

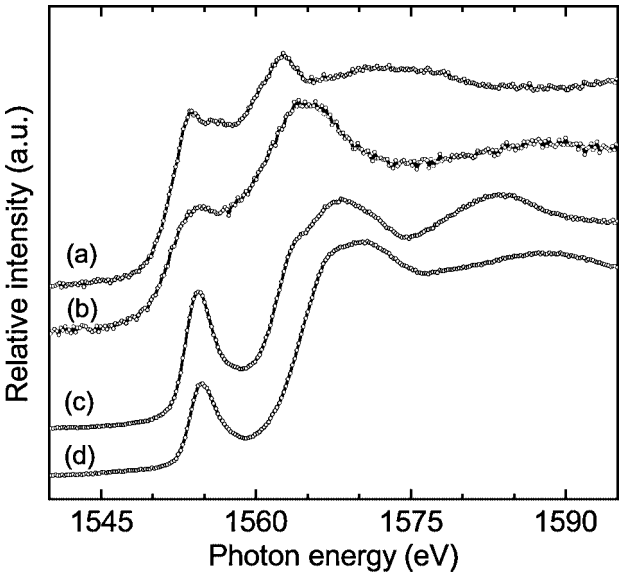

Fig. 3. The Br L_3-edge NEXAFS for (a) crystalline NaBr, (b) 0.1 M aqueous NaBr, (c) crystalline $NaBrO_3$ and (d) 0.1 M aqueous $NaBrO_3$.

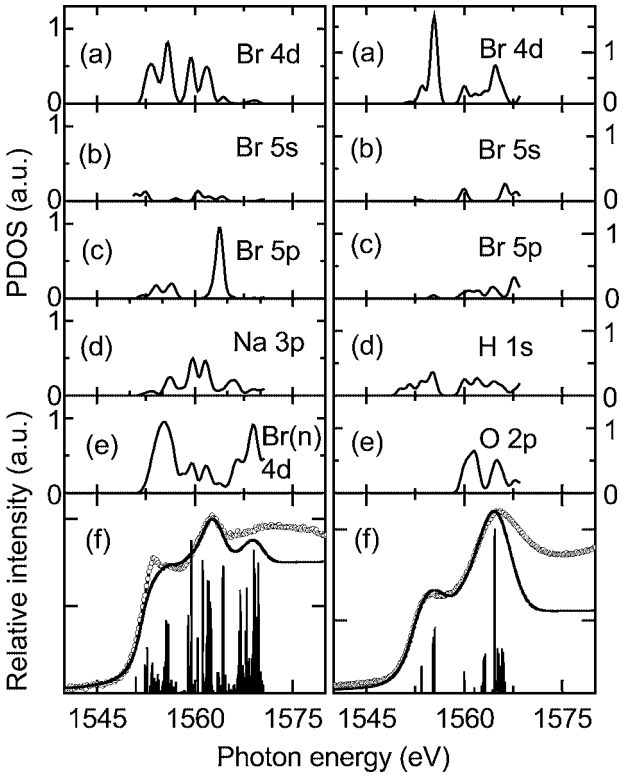

Fig. 4. Partial density of states (PDOS) (a–e), and the electron transition probabilities (ETP) (f) obtained from the DV-Xα molecular-orbital calculation using NaBr clusters and hydrated Br models in the energy range, 1540 eV to 1580 eV, for the crystalline (left panel) and aqueous solution (right panel) of NaBr, respectively. The convoluted ETP using Gaussians (FWHM of 1.5 eV and 2.5 eV for NaBr clusters and hydrated Br^- ion models, respectively) and appropriate arctangent functions (solid line) are compared with the experimental spectra (circle) for crystalline (left panel) and aqueous solution (right panel) of NaBr. Br(n) indicates neighbor Br.

those reported previously [18, 22]. The coordination numbers of Na^+ and the inter-atomic distances of Na-O are ∼5.1 and 2.38 Å for aqueous NaBr, and, ∼4.4 and 2.29 Å for aqueous $NaBrO_3$, respectively. The uncertainty of the hydration structures of Na^+ ions causes a decrease in the coordination numbers of Na^+ in the aqueous solutions of NaBr and $NaBrO_3$ compared to the corresponding crystalline compounds as suggested by the first-principles molecular dynamics simulations and solution X-ray diffraction studies [15, 23, 24]. However, the difference in the coordination numbers of Na^+ and the inter-atomic distances of Na-O between the aqueous solutions of NaBr and $NaBrO_3$ suggests the size of the anions, Br^- and $[BrO_3]^-$, plays an important role in the formation of the Na^+ hydration structures.

Bromine L_3-edge NEXAFS for the crystalline and aqueous solutions of NaBr and $NaBrO_3$ are shown in Fig. 3. The spectra show relatively two broad bands. In NaBr and $NaBrO_3$, Br is situated in cubic symmetry. Hence the unoccupied 4d orbitals of Br split into lower energy t_{2g} and higher energy e_g states by the ligand-field potential. Thus, the two bands observed in the Br L_3-edge NEXAFS are assigned to the excitation of $2p_{3/2}$ core electrons into the t_{2g} and e_g states of the unoccupied 4d orbitals. Consequently, the energy separation between t_{2g} and e_g states [$10\,Dq = E(e_g) - E(t_{2g})$] is directly related to the ligand-field potential which in turn depends on the inter-atomic distances between Br and the first near neighbor in crystalline compounds and the hydration in aqueous solutions as shown previously [11, 25]. The values of 10 Dq for the crystalline and aqueous solution of NaBr are ∼9.0 eV and ∼ 10.5 eV, respectively. Unlike NaBr, the 10 Dq value of ∼14 eV is found for both crystalline and aqueous solution of $NaBrO_3$. This is in turn ∼2 eV larger than the value reported for $KBrO_3$ (∼12 eV) [11]. These results suggest the dissociation of NaBr and $NaBrO_3$ into Na^+, Br^- and $[BrO_3]^-$ in aqueous solutions. However, $[BrO_3]^-$ ions are stable in aqueous solution and do not dissociate further. The change in the 10 Dq values between $NaBrO_3$ and $KBrO_3$ gives evidence that the ligand field potential depends not only on the coordination structure between the Br and the first near neighbor but also the second near neighbor in crystalline state, and, the hydration structure and the counter cations in aqueous solutions. This is also in accordance with the Na K-edge EXAFS results that suggest the size of the anions significantly affects the formation of the cation hydration structures in aqueous solutions.

The PDOS (a–e) and the electron transition probabilities (ETP) (f, bars) obtained from the DV-Xα molecular-orbital calculation using NaBr clusters and hydrated Br models in the energy range, 1540 eV to 1580 eV, are given in Fig. 4 for the crystalline (left panel) and aqueous solution (right panel) of NaBr, respectively. The simulated curves (f, solid line) along with the experimental (f, circle) spectra are also included in Fig. 4. It can be seen that the simulated spectra are in good agreement with the experimental spectra for both crystalline and aqueous solution of NaBr. Further, the ETP suggest that the transitions occur from Br 2p to the unoccupied states containing mainly 4d orbitals of Br for both crystalline and aqueous solution. However, 5s and 5p of Br and 3p of Na in addition to the 4d orbitals of neighbor Br for crystalline NaBr and 5s and 5p of Br, 2p of O and 1s of H for aqueous solution of NaBr also contribute to the unoccupied states as shown in PDOS.

4. Conclusions

Analyses of the Na K-edge EXAFS show the disassociation of Na-Br/Na-BrO_3 bonds in aqueous solution and the formation of Na^+ hydration structures, $[Na(H_2O)_n]^+$ ($n = 0$–6). However, the size of the anions significantly affects the formation of the Na^+ hydration structures in aqueous solutions. The Br L-edge NEXAFS also shows that NaBr and $NaBrO_3$ dissociate in aqueous solutions, however, $[BrO_3]^-$ ions do not dissociate

further. The ligand field potential obtained from Br L_3-edge NEXAFS indicates that it depends not only on the coordination structure between the Br and the first near neighbor but also the second near neighbor in crystalline state, and, the hydration structure and the counter cations in aqueous solutions. DV-Xα molecular-orbital calculations predict that the transitions in the Br L-edge NEXAFS occur from Br 2p to the unoccupied states containing mainly 4d orbitals of Br for both crystalline and aqueous solution. However, 5s and 5p of Br and 3p of Na in addition to the 4d orbitals of neighbor Br for crystalline NaBr and 5s and 5p of Br, 2p of O and 1s of H for aqueous NaBr also contribute to the unoccupied states.

Acknowledgments

This work was jointly supported by the Advanced Material Institute, Fukuoka University, Japan, the Nevada NSF EPSCoR RING-TRUE program under Award No. EPS-9977809, the Nevada DOE EPSCoR State-National Laboratory Partnership program under Award No. DE-FG02-01ER45898, and the Director, Office of Basic Energy Sciences, Division of Materials Science of the U.S. DOE under Contract No. DE-AC03-76SF00098.

References

1. de Boer, J., Wester, P. G., Klammer, H. J. C., Lewis, W. E. and Boon, J. P., Nature **394**, 28 (1998), and references therein.
2. Shiao, Y.-H. *et al.*, Cancer Lett. **187**, 207 (2002), and references therein.
3. Tittlemier, S. A., Fisk, A. T., Hobson, K. A. and Norstrom, R. J., Environ. Pollut. **116**, 85 (2002), and references therein.
4. Myneni, S. C. B., Science **295**, 1039 (2002).
5. Harada, M., Okada, T. and Watanabe, I., J. Phys. Chem. B **106**, 34 (2002).
6. Stöhr, J., "NEXAFS Spectroscopy" (Springer, Berlin, 1992).
7. Chen, J. G., Surf. Sci. Rep. **30**, 5 (1997).
8. de Groot, F., Chem. Rev. **101**, 1779 (2001), and references therein.
9. Farangis, B. *et al.*, Phys. Rev. B **67** (2003), Art. No. 085106.
10. Nachimuthu, P. *et al.*, J. Alloy. Compd. (2003), in press.
11. Matsuo, S., Nachimuthu, P., Lindle, D. W., Wakita, H. and Perera, R. C. C., J. Phys. Chem. A (2003), submitted.
12. Underwood, J. H. and Gullikson, E. M., J. Electron Spectrosc. Relat. Phenom. **92**, 265 (1998).
13. Ressler, T., J. Synchrotron Rad. **5**, 118 (1998).
14. Zabinsky, S. I., Rehr, J. J., Ankudinov, A., Albers, R. C. and Eller, M. J., Phys. Rev. B **52**, 2995 (1995).
15. Ohtaki, H. and Radnai, T., Chem. Rev. **93**, 1157 (1993), and references therein.
16. Adachi, H., Tshukada, M. and Satoko, C., J. Phys. Soc. Jpn. **45**, 875 (1978).
17. Slater, J. C., "Quantum Theory of Molecules and Solids" (McGraw-Hill, New York, 1974).
18. Ott, H., Z. Kristallogr. **63**, 209 (1923).
19. Taniguchi, K. and Henke, B. L., J. Chem. Phys. **64**, 3021 (1976).
20. Matsuo, S. and Wakita, H., Struct. Chem. **14**, 69 (2003).
21. Murata, T., Matsukawa, T. and Naoé, S., Physica B **158**, 610 (1989).
22. Templeton, D. H. and Templeton, L. K., Acta Crystallogr. A **41**, 133 (1985).
23. White, J. A., Schwegler, E., Galli, G. and Gygi, F., J. Chem. Phys. **113**, 1668 (2000).
24. Rempe, S. B. and Pratt, L. R., Fluid Phase Equilib. **183–184**, 121 (2001).
25. Sette, F., Sinkovic, B., Ma, Y. J. and Chen, C. T., Phys. Rev. B **39**, 11125 (1989).

Physica Scripta. Vol. T115, 970–973, 2005

FAME: A New Beamline for X-Ray Absorption Investigations of Very-Diluted Systems of Environmental, Material and Biological Interests

O. Proux[1*], X. Biquard[2], E. Lahera[1], J.-J. Menthonnex[1], A. Prat[3], O. Ulrich[2], Y. Soldo[4], P. Trévisson[5], G. Kapoujyan[5], G. Perroux[5], P. Taunier[3], D. Grand[5], P. Jeantet[5], M. Deleglise[5], J-P. Roux[5] and J-L. Hazemann[3]

[1]Laboratoire de Géophysique Interne et Tectonophysique, UMR CNRS/Université Joseph Fourier, 1381, rue de la Piscine, Domaine Universitaire, F-38400 Saint-Martin-D'Hères, France
[2]CEA/Grenoble, DRFMC/SP2M/NRS, 17 avenue des Martyrs, F-38054 Grenoble Cedex 9
[3]Laboratoire de Cristallographie, CNRS, 25 avenue des Martyrs, BP 166, F-38042 Grenoble cedex 9, France
[4]Laboratoire d'Electrochimie et de Physico-chimie des Matériaux et des Interfaces, UMR 5631 CNRS/INPG/UJF, 1130 rue de la Piscine, Domaine Universitaire, BP 75, F-38402 St. Martin d'Hères, France
[5]Service Etudes et Réalisation d'Appareillages Scientifiques, CNRS, 25 avenue des Martyrs, BP 166, F-38042 Grenoble cedex 9, France

Received June 26, 2003; accepted in revised form November 21, 2003

PACS numbers: 61.10.Ht, 07.85.Qe, 41.50.+h

Abstract

FAME is the French Absorption spectroscopy beamline in Material and Environmental sciences at the ESRF (France), operational since September 2002. Technically speaking, the source is a 0.85 T bending magnet and the main optical element is a two-crystals monochromator using either Si(111) or Si(220) monocrystals so that the available energy ranges from 4 to 40 keV. The first crystal is liquid nitrogen cooled in order to avoid a thermal bump and thus preserve the energy resolution. The second crystal is dynamically bent during the energy scan in order to focus the beam in the horizontal plane. Two bendable mirrors are located before and after the monochromator, for beam-collimation (to optimize the energy resolution) and vertical focalization, respectively. During scans, the beam on the sample is kept constant in position and size (around $150 \times 200\,\mu m^2$, V × H). The high flux on the sample combined with the sensitivity of our 30-elements fluorescence detector allow to decrease the detection limit down to 10 ppm or around less than a monolayer. Moreover, quick-EXAFS acquisition is operational: the acquisition time may be reduced down to 30 s.

1. Introduction

FAME is the French Absorption spectroscopy beamline in Material and Environmental sciences at the ESRF (France), in operation since September 2002. This beamline is one of the four french Collaborating Research Group (CRG) beamlines.

The possibility of determining the local structure of elements at very low concentration is one of the most important and appealing features of X-ray Absorption Spectroscopy. This technique gathers a large and growing community of users comprising environmentalists, electrochemists, biologists, material and catalysis scientists. That is why it was decided to provide this community with a dedicated beamline, thus extending available beamtime for absorption experiments. The XAS-station of CRG-IF was then transferred to the CRG-FAME beamline and a new optical line was designed and built. The project was supported by a number of laboratories from the Centre National de la Recherche Scientifique (CNRS), the Commissariat à l'Energie Atomique (CEA) and the Universities of Grenoble and Lyon. Given the high implication of regional laboratories, a partial financing from "Région Rhone-Alpes" has been moreover obtained. 50 to 60% of the beam time will be dedicated to environmental and earth science studies, the remainder will be used for material, chemical and biological applications. We give herein a brief description of the beamline, the various optical elements and the experimental apparatus. More technical details and pictures can be found on the FAME website [1].

2. General features

The FAME beamline is located on a 0.85 T bending magnet (BM) of the ESRF storage ring working at 6 GeV. The beamline design has been optimized in order to accept the 2 mrad horizontal and 0.3 mrad vertical divergences delivered by the BM, *i.e.* its full fan. The magnification ratio (source to monochromator distance *vs* monochromator to sample distance) has been chosen to be 3 to maximize the monochromator transmission. The flux on the sample is maximized when the beam is horizontally focused bending the 2nd crystal of the monochromator [2].

The basic optical design of FAME is shown in Fig. 1. The main optical element is the monochromator, located between two grazing-incidence mirrors. Due to the Rhodium coating of the mirrors, such a configuration is suitable for studies at energies lower than 22 keV. The beamline can also operate in a mirror-free configuration, extending the energy limit close to the BM cutoff. The photon energies available on FAME range then from 4 to 40 keV: all the elements with atomic number higher than 20 (Calcium) can be studied either at the K or L or both edges.

In order to define the size and the optic axis of the beam, two pairs of vertical and horizontal micrometric slits are located at 23.5 m (slits 1) and 30.5 m (slits 2) from the source. To decorrelate the beamline from possible variations in direction or position of the X-ray source, water-cooled tungsten carbide slits are located before our optical elements. The distance between these slits was taken as large as possible in order to precisely define the beam. Other slits are located after the first mirror (slits 3) and after the monochromator (slits 4), to remove the scattered beams induced by the optical elements.

FAME was designed in order to have the maximum flux on the sample, especially at low energies. Only two Be windows are on the beam path, a first 500 μm Be window between the storage ring and the beamline and a second one at the end of the beamline, just before the sample. The vacuum device was conceived using differential pumping between the different elements, in order to have a smooth transition between the $1 \sim 2 \cdot 10^{-9}$ mbar range

*Corresponding author: proux@grenoble.cnrs.fr

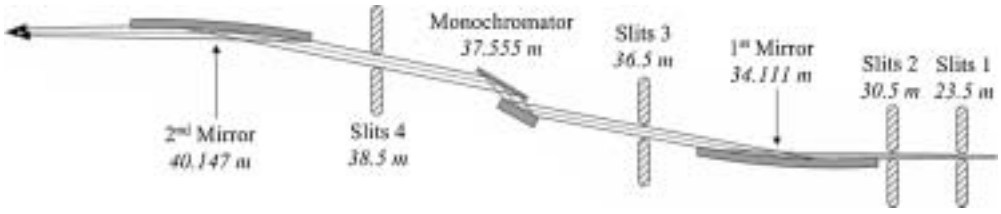

Fig. 1. Schematic diagram of the CRG-FAME beamline optic elements (side view). The distances from the BM source of the various elements are indicated (the sample is located at 50.065 m).

achieved in the mirrors chambers (ionic pumps) and the $2 \sim 5 \cdot 10^{-8}$ mbar range achieved in the monochromator (turbo pump linked to a cryo-pumping effect).

3. Optical elements

3.1. *First mirror*

The first optic component installed on FAME is a horizontal bendable mirror that deflects the beam vertically, manufactured by IRELEC (France). The mirror is a monocrystalline Silicium ingot with a 50 nm Rhodium coating (manufactured by SAGEM – REOSC S.A., France). Transverse and longitudinal inclinations of the mirror use goniometric cradles. They are completely separated from height and bender adjustment: all the movements are then uncorrelated. The mirror can be bended using a single jack bender (symmetric bending) and its position (height, incidence and tilt angles) can be adjusted independently from the vacuum vessel. The white beam incidence angle on the mirror can vary in the 3–7 mrad range. The cutoff energy ranges then from 9 to 22 keV.

The main functions of the 1st mirror are the following:

- collimation of the incident beam to adapt its vertical divergence to the 1st crystal of the monochromator, in order to optimize the energy resolution of the monochromator,
- reduction of the high energy harmonics' intensity,
- reduction of the heat load on the monochromator.

Optical tests were performed in the ESRF metrology laboratory with a Long Trace Profiler [3] and a PROMAP 512 apparatus, in order to check the radius of curvature, the slope error, profiles and shape errors and the rugosity. The obtained values are gathered in table I. With respect to the large size of the polished surface, the measured slope errors and roughness are really good.

The cooling device of the mirror has been designed in order to limit as much as possible the transmission of vibrations coming from the beamline to the reflecting surface. For this, the cooling apparatus is linked to the cooled part of the mirror *via* a liquid metallic alloy. The vibrations induced by the cold water circulation are then damped by the liquid alloy. Moreover, the cooling water temperature is continuously adjusted in order to obtain a 2 °C gradient of temperature for the water between the entrance and the exit of the mirror chamber. The slope error of the mirror is then as low as possible.

Table I. *Mirrors main characteristics.*

Mirrors characteristics	1st mirror	2nd mirror
optical and geometrical Lengths (mm)	*1150*–1350	*1250*–1450
optical and geometrical Widths (mm)	*80*–110	*80*–110
Thickness (mm)	54	35
minimum Bending Radius (km)	38	10
maximum Bending Radius (km)	3.4	1.0
mean and central rms slope error (μrad)	*2.4*–1.8	*3.0*–2.5
mean rms roughness (Å)	1.4 ± 0.3	2.6 ± 1.0

Table II. *Monochromator main characteristics.*

Monochromator characteristics	wanted	obtained
axis angular resolution	1/10000°	1/40000°
maximum angular deviation of the axis during rotation	5 μrad on 5° range	5 μrad on 40° range
2nd crystal translation precision	0.1 μm	0.1 μm
monochromator translation	65 ± 0.05 mm	100 ± 0.001 mm
maximum angular deviation of the monochromator during translation	5 μrad on 65 mm translation	5 μrad on 100 mm translation

3.2. *Monochromator*

A two-crystals monochromator is located after the first collimating mirror. Its design and construction were performed by our team. The main numerical characteristics are gathered in table II. The obtained characteristics, as checked by metrology at the ESRF [4], are always better than expected. Two kinds of monocrystals are available, Si(111) and Si(220), well adapted in the energy ranges 4–25 keV and 5–40 keV, respectively. Moreover, the monochromator can be used in two configurations: variable exit (pseudo-channelcut mode) and fixed exit (constant vertical position of the beam after the monochromator).

The first crystal is liquid nitrogen cooled at around 110 K to avoid thermal bump. At this temperature, the thermal conductivity of silicon is maximum and its thermal expansion is almost zero. The high heat load of the incoming beam (300 W at the maximum, in the mirror-free configuration) is removed using flexible copper wires, avoiding vibrations. The second crystal is dynamically curved (from 1 m to ∞) during XAFS energy scans in order to keep the beam focused on the sample in the horizontal plane [5]. The horizontal FWHM size of the spot is always below 300 μm, even at low energies (small radius of curvature of the 2nd crystal). Figure 2 shows an example of a focused beam shape obtained at 7 keV.

The axis of the monochromator is equipped with a RON905 encoder (resolution: 1/1000°), linked to an interpolator box (1/800). The theoretical resolution is then 1/80000° while the measured resolution is 1/40000° (Tab. II). The axis brushless motor is equipped with a McLennan PM600 motor controller.

The monochromator can work in two configurations: in the step-by-step mode (classical EXAFS) and in the continuous one (quick EXAFS). In both cases, the angle movement during the energy scan operates simultaneously with the adjustments

1) of the 2nd crystal curvature,
2) of the parallelism between the two crystals, allowing to remain at the maximum of the 2nd crystal's rocking curve,
3) of the EXAFS table height (see § 4).

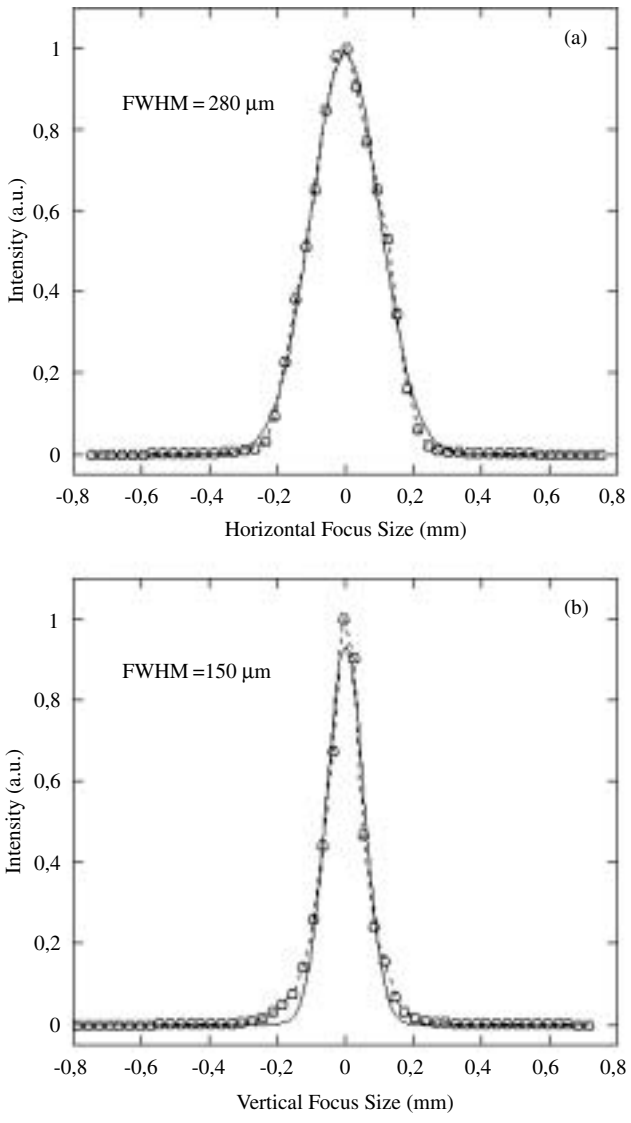

Fig. 2. Focused beam shapes in the horizontal (a) and vertical (b) planes, measured (open circles and dashed line) and superimposed Gaussian fit (solid line). The measurements have been performed at 7 keV using Si(111) monochromator crystals, with a 7 mrad incidence angles for the mirrors and using the entire vertical and horizontal divergences.

3.3. *Second mirror*

The 2nd mirror is located in the monochromatic part of the beamline. Its objectives are to eliminate the remaining harmonics and mainly to focus the beam in the vertical plane on the sample. The reflective angle is always equal to the one of the 1st mirror, in order to obtain a perfect horizontal beam after it. Compared to the 1st mirror, the 2nd one is longer and thinner (Tab. I), in order to reach smaller radius of curvature. Moreover, this high length allows us to keep its height fixed during an energy scan even if the output height of the monochromator varies (variable exit mode). The position of the beam on the mirror can then slightly change without being close to the edges.

The vertical size of the beam on the sample can then be adjusted between 100 to 500 µm (example Fig. 2.b), with respect to the kind of studied samples (mainly with respect to their homogeneity).

4. Experiment apparatus

The X-ray Absorption Spectroscopy (XAS) apparatus on FAME is composed of the previously existing elements on the IF beamline XAS station. The position of the experimental table (height, transversal translation and rotation) can be controlled so that the beam position on the sample remains constant. The height position (precision about 1 µm) is dynamically adjusted during an EXAFS scan, allowing the beam position on the sample to remain constant.

The sample is located on a "goniometric head" sample holder. Different movements are motorized: transverse and vertical translations, rotation (360°) and goniometric cradles (±7°). Different classical environment can be mounted on the goniometric head: 1) basic vacuum chamber (for low energy experiment), 2) liquid nitrogen and 3) liquid helium cryostats.

Moreover, the experimental environment can be easily adapted to the users' need and can accept several apparatus elaborated in other laboratories. This is especially suitable for *in situ* studies, electrochemistry cells [6], catalysis ovens in gaseous atmosphere [7], high temperature and high pressure cells [8, 9]...

Three kinds of detectors are used on FAME. The transmitted signals are measured with Si diodes collecting the beam scattered by kapton foils. The fluorescence measurements are performed using a 30-elements solid germanium Canberra energy-resolved detector. This detector is very well adapted for studies on highly diluted samples or thin films. For a 125 and 500 ns shaping time, its energy resolution is about 300 and 250 eV and the maximum allowed count rate by element is about 100 000 and 30 000 counts/s, respectively. Finally, an electron detector (analysis temperature from 77 to 300 K) working with helium atmosphere (Conversion Electron mode) is also well suitable for thin films studies.

5. Perspectives and conclusion

We have described the new CRG-FAME XAS beamline in operation at the ESRF (France) since september 2002. The main optic element is a two-crystals monochromator equipped with two kinds of monocrystals, Si(111) and Si(220). The available energy ranges from 4 to 40 keV. The first crystal is liquid nitrogen cooled in order to avoid thermal bump and thus to preserve the energy resolution. The second crystal is dynamically bended during the energy scan in order to focus the beam in the horizontal plane. Two bendable mirrors are located before and after the monochromator, for beam-collimation (optimisation of the energy resolution) and to obtain a vertical focus. The size (around $250 \times 150\,\mu m^2$) and the position of the beam on the sample is then kept constant during scans. The high flux on the sample combined with the sensitivity of the fluorescence detector allow to decrease the detection limit down to 10 ppm and the acquisition time of a spectrum to around 30 s (QEXAFS mode). A micro-focalisation apparatus (Kirkpatrick-Baez) will allow to decrease the size of the beam, $20 \times 20\,\mu m^2$ with full flux, $1 \times 1\,\mu m^2$ with slits. Preliminary micro-XAS experiments have been performed: construction of the optic elements will be achieved this year.

Acknowledgements

The authors wish to acknowledge the help of the ESRF technical staff and support groups and in particular Alonso Garcia C. and Patrunau V. (handling), Vassalli J. P. and Villermet P. (monochromator crystals realisation), Rommevaux A. (mirrors metrology), Van Der Kleij H. P. (monochromator metrology), the alignment group, especially Levet N. and Lefevre C. and all the people from the CRG liaison, Dettona E., Kaprolat A., Bombana J., Kilvington I., Glueckert M., Rigolet M. and Clément V. Thanks are also given to all the users who helped us for the beamline commissioning.

References

1. http://www.esrf.fr/UsersAndScience/Experiments/CRG/BM30B/
2. Hrdy, J., Rev. Sci. Instrum. **65**, 2147 (1994).
3. Hignette, O. and Rommevaux, A., Proc. SPIE **2856**, 314 (1996).
4. For more technical details see the webpage of the Precision Engineering Laboratory: http://www.esrf.fr/UsersAndScience/Experiments/TBS/MechanicsService/PELab/
5. Hazemann, J. L., Nayouf, K. and de Bergevin, F., Nucl. Instr. Meth. B **97**, 547 (1995).
6. Soldo, Y. *et al.*, Electroch. Acta **47**, 3081 (2002).
7. Geantet, C. *et al.*, Catalysis Lett., **73**, 95 (2001).
8. Pokrovski, G. S. *et al.*, Geochim. Cosmochim. Acta **66**, 3453 (2002), **66**, 4203 (2002).
9. Simonet, V. *et al.*, J. Chem. Phys. **116**, 2997 (2002).

Physica Scripta. Vol. T115, 974–976, 2005

Recent Advances and New Applications of Time-Resolved X-ray Absorption Spectroscopy

R. Frahm*, M. Richwin and D. Lützenkirchen-Hecht

Institut für Materialwissenschaften und Fachbereich Physik, Bergische Universität Wuppertal, Gaußstr. 20, 42097 Wuppertal, Germany

Received June 26, 2003; accepted November 4, 2003

PACS Ref: 07.85.Qe, 61.10.Ht, 68.35.-p, 68.55.-a

Abstract

The time-resolved X-ray absorption spectroscopy (QEXAFS) yields structural information about e.g. fast chemical decomposition reactions, thin film deposition, solid-state reactions, and phase transformations. Here we describe a new experimental set-up for QEXAFS experiments enabling the acquisition of full EXAFS spectra with a scan range of up to about 3 keV and a repetition rate of typically 10 Hz. Depending on photon flux and sample quality, repetition rates of up to 40 Hz can be used. The new monochromator design employs a fixed-exit channel cut crystal and a cam driven tilt table for rapid angular oscillations. The detection of fluorescence radiation or surface sensitive techniques can be applied. The new monochromator in combination with refractive X-ray lenses for beam focusing also allows XANES-microtomography in a reasonable time frame.

1. Introduction

Approximately 15 min are necessary to measure both the X-ray absorption near edge structure (XANES) and the extended X-ray absorption fine structure (EXAFS) in bulk materials with high accuracy using standard scanning monochromators. The continuous Quick scanning EXAFS (QEXAFS) technique [1, 2], however, allows measurements in seconds and can be applied especially for *in situ* experiments in condensed matter physics, chemistry and materials science. Processes studied cover e.g. catalytic reactions [3], thin film deposition [4], surfaces [5] and metal dissolution [6, 7]. However, the speed range of the normally used stepper motors limit the data collection times for one spectrum to about 1 s [8], however, even several edges can be accessed subsequently. Many QEXAFS beamlines are in standard operation worldwide at bending magnet and insertion device sources. An optimized crystal bender was developed to cope with the high heat loads from high power synchrotron radiation sources [9]. Using a synchronously moving undulator, even dilute biological samples can be investigated [10]. Faster measurements are feasible by combining fast data acquisition [11] with the Piezo-QEXAFS method [12], where tilt tables actuated by piezo-stages mounted below the monochromator crystals are used to change the Bragg angle in an oscillatory manner. This allows XANES scans at the Cu K-edge with a time resolution of down to 4.5 ms [11]. This technique allows investigating e.g. solid-state transformations in the millisecond range [13]. Even dilute samples can be investigated by detection of the fluorescence radiation [14] or total electron yield. Also wide scan ranges of typically 500 eV at 10 keV photon energy are accessible with a time resolution of down to 50 ms [15]. Such monochromators can make excellent use of third generation synchrotron sources as the attainable time resolution directly depends on the available photon flux.

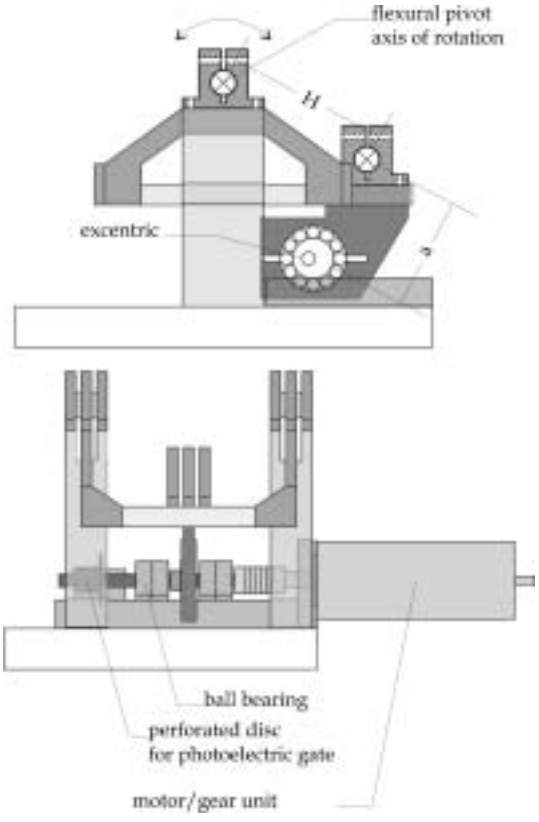

Fig. 1. Construction of the driving system of the monochromator: View from the front (top) and in the beam direction (bottom). See text for details.

2. New setup for wide energy ranges

In this paper we present a new experimental setup for QEXAFS experiments. The monochromator design employs a channel cut crystal mounted on a cam driven tilt table for rapid angular oscillations [16]. The general setup is shown in Fig. 1.

The excentricity of the disk mounted on the rotating shaft and the lengths H and a of the lever arms determine the accessible angular range. For the experiments $H = 79.4$ mm and $a = 55.5$ mm were used. Different disks can be mounted to change the angular range; in our case an excentricity of e.g. 1.4 mm relates to 1.01° amplitude in Bragg angle. The oscillating movement is approximately sinusoidal around the selected central Bragg angle.

3. Experimental results

Fig. 2 shows QEXAFS spectra of a Cu metal foil at different rotation frequencies of the drive shaft. Each rotation corresponds to two spectra, one up and one down in energy. Thus the scan times range from 50 ms at 10 Hz oscillation frequency to 12.5 ms

*e-mail: frahm@uni-wuppertal.de

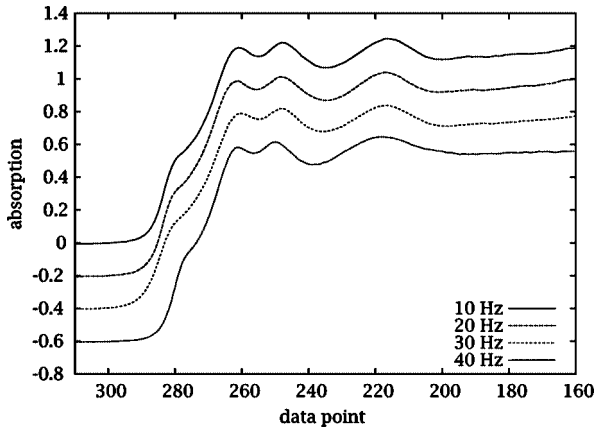

Fig. 2. QEXAFS spectra of a Cu metal foil at different oscillation frequencies. Scan times range from 50 ms (10 Hz) to 12.5 ms (40 Hz). Data were collected at the undulator beamline 1-ID at the APS (spectra vertically shifted).

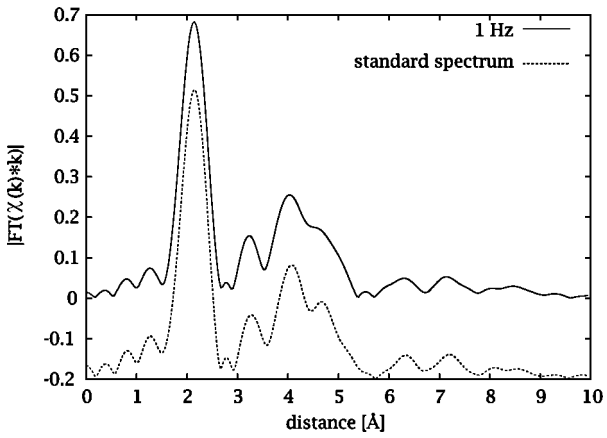

Fig. 4. Magnitude of the Fourier-transform of a fast Ni spectrum in comparison to the result of a standard measurement (vertically shifted).

at 40 Hz. A Si(111) crystal and a small excentricity resulting in a small angular range were selected to cover the Cu XANES range. The maximum frequency for stable operation of the whole setup amounted to about 40 Hz. Data were collected at the undulator beamline 1-ID at the APS. To avoid thermal effects in the first monochromator crystal due to the high heat load of the insertion device the first monochromator crystal was cryogenically cooled using liquid nitrogen.

An extended energy range of 700 eV at the K-edge of a Ni-foil measured with a larger excentricity is shown in Fig. 3, its Fourier transform in Fig. 4. The results agree with the standard data collection mode.

An EXAFS spectrum of a typical catalyst material composed from a mixture of CuO and ZnO is shown in Fig. 5. The scan range amounts to 1800 eV covering both Cu and Zn K-edges; the operation frequency was 10 Hz. The single scan shown was collected in 50 ms. Also displayed is a Cu reference foil measured *simultaneously* using the transmitted beam after the sample. This is an important possibility of the QEXAFS method which allows determining even small edge shifts during chemical reactions unambiguously.

In the case of large energy ranges, however, the beam offset changes significantly by the rotation of a simple channel cut crystal. Such beam movement is not acceptable for certain experiments. Thus for improved performance of the monochromator system, a fixed-exit channel cut crystal is available. In this case the two reflecting planes have a special shape [17, 18] to maintain a fixed exit height. A Si(311) crystal based on this principle is shown in Fig. 6. First tests demonstrated the basic operation of the principle; however, this crystal is optimized for work at high energies.

Especially in the fields of materials and environmental sciences much interest is in imaging the two or three dimensional

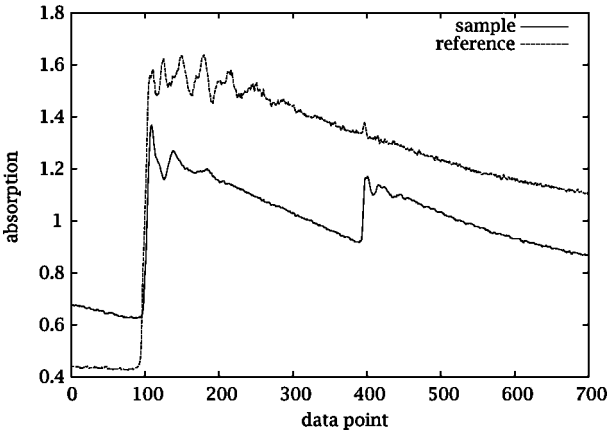

Fig. 5. EXAFS spectra of CuO/ZnO catalyst material and a Cu-foil measured simultaneously as reference at 10 Hz oscillation frequency.

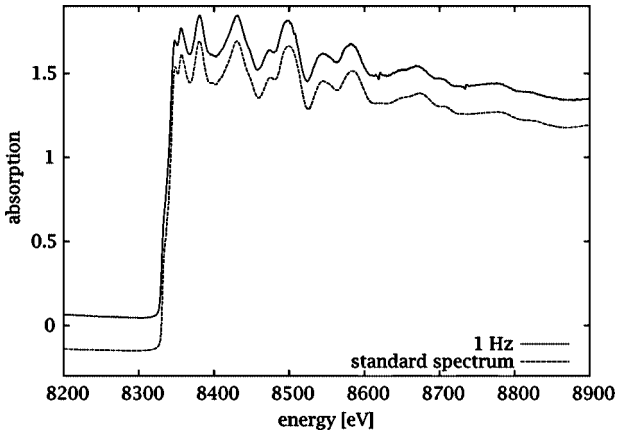

Fig. 3. Single EXAFS spectrum of Ni-metal foil at room temperature in the oscillatory mode in comparison with a standard measurement (vertically shifted).

Fig. 6. Channel cut Si(311) crystal for a fixed exit beam. Total length 100 mm, reflecting surfaces 45 mm.

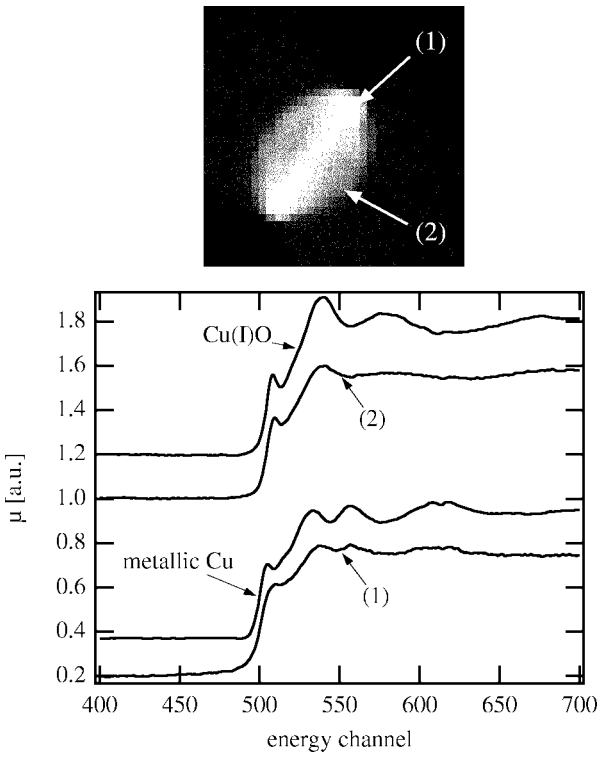

Fig. 7. Top: Absorption of the Cu(I)O/Cu sample described in the text. The size of the cross section shown is $170 \times 170\,\mu m^2$, the pixel size $5 \times 5\,\mu m^2$. Bottom: Reconstructed Cu K-edge spectra of the sample at the two positions labelled (1) and (2) in comparison to reference materials (spectra vertically shifted).

distribution of elements and their valance states with μm resolution. For a detailed analysis the knowledge of the XANES spectra or even EXAFS spectra at each position in three dimensions is necessary. Such investigations involve a multiplicity of scans, and conventional scanning is impractical. To cover 0.25 mm^2 with 5 μm resolution in just two dimensions requires 10.000 spectra, which results in several days of necessary beam time using conventional XAFS beamlines. If one uses an oscillating monochromator at reasonable 10 Hz operation frequency, the scan time reduces to about 8 min. Thus fast monochromators make such data collection feasible – even for the more demanding XAFS 3D-tomography. Such experiments were performed at the ESRF (bending magnet beamline) and the APS, exploiting here the highly intense beam from an X-ray undulator. Focusing was performed by X-ray lenses [19] yielding a micro beam size of about $6 \times 2\,\mu m^2$. The sample was translated and rotated to obtain a sufficiently large number of projections for the 3D reconstruction of the sample. At each position several fast XANES scans were collected, which makes it possible to determine the spatial distribution of valence and atomic short range order on the μm-scale, as shown in Fig. 7. Here a small tip made from a Cu foil covered with Cu(I)O was reconstructed. The Cu K-edge spectra shown in Fig. 7 were reconstructed for the two locations pointed out in the cross section of the sample. Further results of a real catalyst are given in [20].

4. Conclusions

The new cam driven monochromator system shows an excellent performance, long time stability and allows scanning large energy ranges up to several keV. Thus several edges can be covered in one spectrum. The accessible time resolution of currently 12.5 ms is sufficient for a wide range of scientific applications. Using cryogenic cooling, the silicon crystal optics is capable of receiving the full heat load from third generation undulator sources. The monochromator is a portable device that can easily be installed on almost any white beam experimental station. The new possibility to perform XAFS-microtomography investigations is very promising especially for materials science. By operating beamlines at special insertion devices generating circularly polarized light (see e.g. [21]) one can use QEXAFS even for investigations of magnetic processes in technologically important materials [22, 23].

Acknowledgment

The authors thank the staff members of the ESRF (BM5) and the APS (1-ID) for the excellent support. Use of the Advanced Photon Source was supported by the U.S. Department of Energy, Office of Science, Office of Basic Energy Science, under Contract No. W-31-109-ENG-38. This project was funded by the MWF Nordrhein-Westfalen. The preparation of figures by B. Griesebock and C. G. Schroer is highly appreciated.

References

1. Frahm, R., Nucl. Instr. Meth. Phys. Res. A **270**, 578 (1988).
2. Frahm, R., Rev. Sci. Instr. **60**, 2515 (1989).
3. Clausen, B. S., Topsøe, H. and Frahm, R., Adv. Catalysis **42**, 315 (1998).
4. Frahm, R., Barbee Jr., T. W. and Warburton, W., Phys. Rev. B **44**, 2822 (1991).
5. Hecht, D., Frahm, R. and Strehblow, H.-H., J. Phys. Chem. **100**, 10831 (1996).
6. Lützenkirchen-Hecht, D. and Frahm, R., J. Synchrotron Rad. **6**, 591 (1999).
7. Lützenkirchen-Hecht, D. and Frahm, R., J. Phys. Chem. B **105**, 9988 (2001).
8. Joe Wong, Fröba, M. and Frahm, R., Physica B **208&209**, 249 (1995).
9. Zaeper, R., Richwin, M., Lützenkirchen-Hecht, D. and Frahm, R., Rev. Sci. Instr. **73**, 1564 (2002).
10. Solé, V. A., Gauthier, C., Goulon, J. and Natali, F., J. Synchrotron Rad. **6**, 174 (1999).
11. Bornebusch, H., Clausen, B. S., Steffensen, G., Lützenkirchen-Hecht, D. and Frahm, R., J. Synchrotron Rad. **6**, 209 (1999).
12. Richwin, M., Zaeper, R., Lützenkirchen-Hecht, D. and Frahm, R., J. Synchrotron Rad. **8**, 354 (2001).
13. Grunwaldt, J.-D. *et al*., J. Phys. Chem. B **105**, 5161 (2001).
14. Lützenkirchen-Hecht, D., Grundmann, S. and Frahm, R., J. Synchrotron Rad. **8**, 6 (2001).
15. Richwin, M., Zaeper, R., Lützenkirchen-Hecht, D. and Frahm, R., Rev. Sci. Instr. **73**, 1668 (2002).
16. Richwin, M., Dissertation (in German), Universität Wuppertal, (Shaker Verlag, Aachen, ISBN 3-8322-1455- 0, 2003).
17. Spieker, P., Ando, M. and Kamiya, N., Nucl. Instr. Meth. **222**, 196 (1984).
18. Oestreich, S., Kaulich, B. and Susini, J., Rev. Sci. Instr. **70**, 1921 (1999).
19. Lengeler, B. *et al*., J. Synchrotron Rad. **6**, 1153 (1999).
20. Schroer, C.G. *et al*., Appl. Phys. Lett. **82**, 3360 (2003).
21. Frahm, R., Wollmann, R., Hammer, H. and Lützenkirchen-Hecht, D., J. Synchrotron Rad. **6**, 172 (1999).
22. Schütz, G. *et al*., Rev. Sci. Instr. **60**, 1661 (1989).
23. Knülle, M., Fischer, P., Frahm, R., Schütz, G. and Stähler, S., J. Appl. Phys. **73**, 5347 (1993).

Physica Scripta. Vol. T115, 977–979, 2005

The Dispersive X-ray Absorption Spectroscopy beamline at LNLS

Hélio C. N. Tolentino[a], Julio C. Cezar[a,b], Noêmia Watanabe[a], Cínthia Piamonteze[a,b], Narcizo M. Souza-Neto[a,b], Edilson Tamura[a], Aline Y. Ramos[a,c] and Regis Neueschwander[a]

[a]LNLS Laboratório Nacional de Luz Síncrotron, CP6192, 13084-971 Campinas, SP, Brazil
[b]IFGW, Universidade Estadual de Campinas CP6165, 13083-970 Campinas, SP, Brazil
[c]LMCP Laboratoire de Minéralogie – Cristallographie, UMR 7590 CNRS, Paris, France

Received June 26, 2003; accepted November 4, 2003

PACS numbers: 07.85.Qe, 61.10.Ht, 61.10.Eq

Abstract

The present paper describes the concept of the Dispersive X-ray Absorption Spectroscopy beamline at the Brazilian Synchrotron Light Laboratory. The present performance and some of the very first experiments are reported. Emphasis is put on experiments related to electrochemical reactions and resonant reflectivity on magnetic thin films and multilayers.

1. Introduction

We describe here the concept and present performance of the Dispersive X-ray Absorption Spectroscopy (DXAS) beamline at LNLS (Brazilian Synchrotron Light Laboratory). The specificity of this beamline is that it allows collecting absorption data simultaneously over an extended range of photon energies without any mechanical motion [1, 2]. This characteristic is specially suited for measurements requiring good accuracy and high stability, for instance in XANES and XMCD experiments [3, 4]. We present in this paper some very first commissioning results and preliminary experiments related to electrochemical insertion of metals into polymers and resonant reflectivity on magnetic thin films and multilayers.

2. The conceptual design and optics

The concept of a dispersive XAS beamline is based on a curved crystal monochromator that selects a bandwidth of a few hundred eV from the white synchrotron light source and focuses it at the sample position. The incident angle varies continuously along the crystal, providing a continuous change of the energy of the Bragg-reflected photons. The bending mechanism of the curved crystal monochromator has been developed at LNLS and its technical details will be published elsewhere. All rotations (Bragg, tilt and yaw angles) are accomplished by high precision Huber goniometers. The radius of curvature is imposed by two independent momenta on crystal extremities without changing the position of the central part. There is also a mechanism for twist correction and for cooling the crystal. Everything works inside a high vacuum chamber. The two independent momenta allow reducing significantly the spherical aberrations. The whole bandwidth is focused in the horizontal plane down to 150 μm. The vertical focusing is provided by an 800 mm-long Rh coated mirror, working at a grazing angle of 4 mrad. Its bending mechanism allows vertical beam collimation or focusing to about 500 μm at the sample position. This leads to the possibility of working with very small samples, like small single crystals or samples inside a high pressure cell.

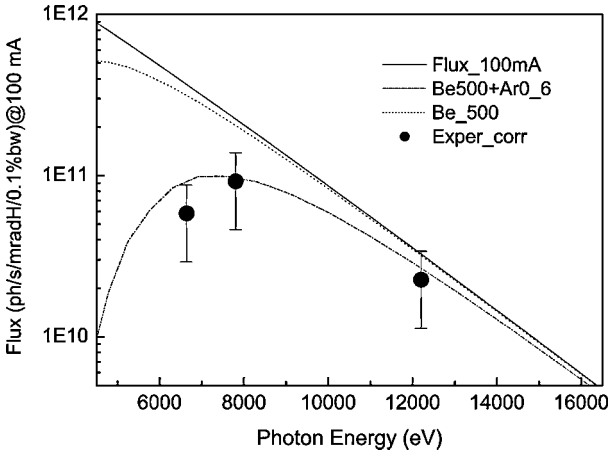

Fig. 1. Calculated photon flux at the DXAS/LNLS beamline. The continuous line represents the emitted flux from the bending magnet; the dotted line the flux attenuated by four 125 μm Be-windows, and the dashed-dot line the flux attenuated by the Be-windows and the 0.6 m-beam path in the air. Experimental points were measured with a photodiode at the focus point.

A curved Si(111) crystal monochromator selects radiation from a bending magnet source in the X-ray range from 4 keV up to 14 keV. The calculated flux throughput from LNLS storage ring working at 1.37 GeV and 100 mA is shown in figure 1. The measurements, after a total of 500 μm (4 × 125 μm) Be-windows and 0.6 m beam path in the air, have been performed with a photodiode at the focus point and are in good agreement with calculations. The beam path in the air can be reduced to a very small value and, for the range of interest, one can recover practically all emitted photons from the source, as shown by the curve that takes into account just the Be-windows. Taking advantage of this flux, time resolved experiments can be performed with a typical resolution of 100 ms. The acquisition of a spectrum that, in sequential mode, normally takes 20 to 40 minutes can be accomplished in less than one second in dispersive mode.

The detection handles the high flux conditions with a modified CCD camera. The cryogenically cooled CCD camera system has a front-illuminated, scientific grade 1, MPP CCD of 1340 × 1300 pixels, each pixel has $20 \times 20\,\mu m^2$ for a total image area of $26.8 \times 26.0\,mm^2$. A GdOS phosphor screen, optimized for 8 keV X-rays, receives the incoming beam at an angle of 20° and converts the X-ray to visible light. A set of lenses guides the light to the CCD detector with a demagnification factor of 1.75, so that the real pixel at the phosphor screen is $35 \times 35\,\mu m^2$. In fact, the resolution measured in the dispersion direction has been about 2.5 to 3 times that pixel, i.e. 100 μm, limited by the phosphor screen. To improve this resolution, which turns out to be the limiting factor, we have to work out the phosphor screen with a thinner deposited film.

*e-mail: helio@lnls.br

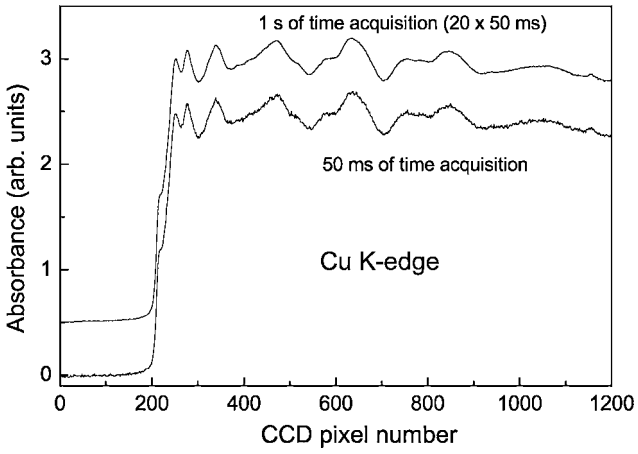

Fig. 2. Cu K edge spectrum at the DXAS beamline.

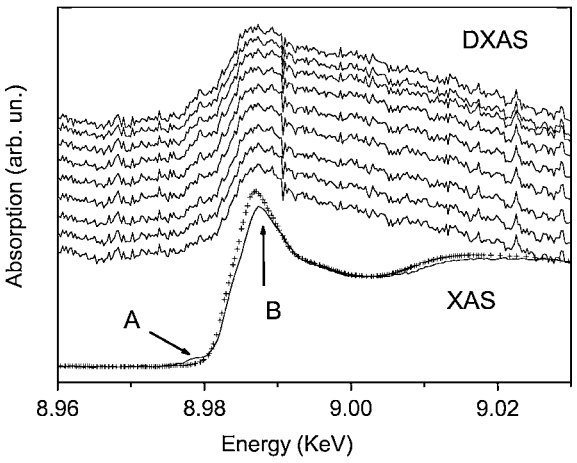

Fig. 3. In situ reaction at the Cu K edge spectrum followed at the DXAS beamline (bottom) and initial and final state measured using a step-by-step XAS scheme.

The energy-direction correlation coming out from the monochromator is transformed into an energy-position correlation along one direction of the two-dimensional CCD detector. The pixels of the CCD detector are integrated along the other direction to produce the XAS spectrum. There is no mechanical motion during the acquisition of a full spectrum. Spectra with a good signal/noise ratio can be collected with a typical time resolution of 50 ms. To improve the signal/noise ratio, 20 frames compose a full spectrum with 1 s of total acquisition time (Fig. 2).

3. Preliminary results

3.1. *Electrochemical cell for in situ study of metal insertion into polymers*

One of the most appealing applications of the dispersive XAS set-up is to follow in detail the many steps in a chemical reaction. Special attention is dedicated to the development of electrochemical cells to study the metal insertion into polymers and to the growth of small nanometric particles [5]. The aim is to understand the very first steps in the nucleation mechanism and to study the different phases of the reaction [6, 7]. In the particular case of copper insertion into polypyrrole, very different results have been presented in the literature, concerning the first steps of metal-polymer interaction. Some authors propose that the copper insertion is conducted by means of a Cu+1-PPy complex [7], while others suggest that this step is described by the formation of the $[\text{-}\,[(C_4H_2N)_3CH_3(CH_2)_{11}OSO_3\text{-}]yCu + 2]n$ $(y = 4)$ complex [6]. The chemical interaction between the metal and the polymer as well as the metal crystalline structure and the chemical bond at the surface are crucial issues related to small particles of magnetic and catalyst materials. First test experiments have been performed at the Cu K edge using a transmission cell [8]. The inclusion of Cu atoms into polypyrrole films has been followed (Fig. 3). The results are promising: the A feature in the spectrum, which is related to an increase of the local distortion of Cu site, is clearly seen to evolve in the very first steps of the reaction.

3.2. *Resonant scattering on magnetic thin films*

Resonant scattering of polarized X-rays from magnetic materials represents a powerful tool to investigate interesting magnetic phenomena, because magnetic effects are strongly enhanced [9, 10] when the photon energy is swept across an absorption edge. Resonant scattering from films and multilayers have been largely used in the soft X-ray range [11, 12]. However, it is worth noting that, in the hard X-ray domain, very few experiments were attempted in the past [13], and none is implemented at present, in spite of the great advantage arising from the possibility of working under a variety of extreme conditions.

A prototype experiment was performed in a multilayer structure formed by the alternate deposition of 1 nm of Co and 0.2 nm of Gd, repeated 40 times. Both the Co 1s (7709 eV) and the Gd 2p (7243 eV) resonances are accessible. Co is present in large amounts (about 40 nm) and carries a high magnetic moment compared to the reduced amount of Gd (about 30 atomic layers) combined with its low magnetic moment, at room temperature. On the other hand, the dichroism effect on the Co K-edge is much smaller than for Gd L_3 edge. Around the Gd L_3 edge, we measured the scattered intensity as a function of angle and photon energy. The critical angle for total external reflection as well as the Kiessig fringes related to the multilayer structure could be clearly identified. Around the Co K edge, we selected the radiation emitted about 0.3 mrad above the orbit and we disposed of an elliptically polarized beam with about 50% circular polarization rate. By applying a magnetic field parallel or antiparallel to the beam propagation axis we obtained the asymmetry ratio (or dichroism spectrum). The superior stability of the dispersive set up allowed us to collect dichroism spectra at a given angle and over a given energy range with a noise of the order of 0.03%.

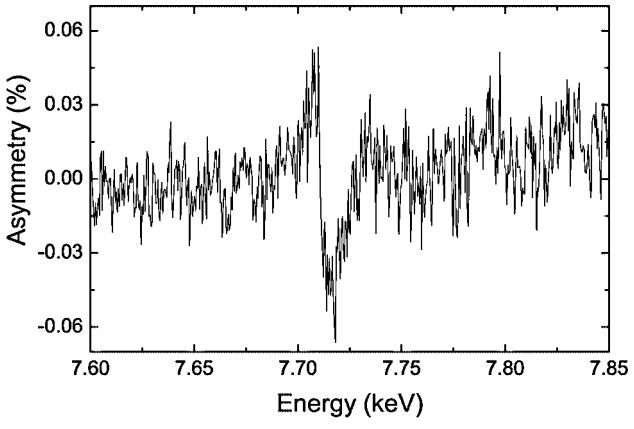

Fig. 4. The asymmetry ratio at the Co K edge for the Gd/Co multilayer system. The dichroic signal was obtained by collecting 128 spectra of about 30 s each. The applied magnetic field was 1 kOe at room temperature.

The measurement obtained at the Co K edge shows that a magnetic signal as low as 0.05% could be easily identified after one hour of acquisition time (Fig. 4).

Acknowledgements

We wish to thank FAPESP for the grants of J. C. Cezar and C. Piamonteze and CAPES for the grant of N. M. Souza-Neto. This work is supported by LNLS.

References

1. Dartyge, E. *et al*., Nucl. Instrum. Meth. A**246**, 452 (1986).
2. Tolentino, H., Dartyge, E., Fontaine, A. and Tourillon, G., J. Appl. Cryst **21**, 15 (1988).
3. Fontaine, A. *et al*., Rev. Sci. Instrum. **63**, 960 (1992).
4. Baudelet, F. *et al*., J. Synchrotron Rad. **5**, 992 (1998).
5. Alves, M. C. M., Watanabe, N., Ramos, A. Y. and Tolentino, H. C. N., J. Synchrotron Rad. **8**, 517 (2001).
6. Watanabe, N., Moraes, J. and Alves, M. C. M., J. Phys. Chem. B **106**, 11102 (2002).
7. Liu, Y. C. and Hwang, B. J., Thin Solid Films **339**, 233 (1999).
8. Kisner, A., Internal Report at LNLS, (2003).
9. Gibbs, D. *et al.*, Phys. Rev. Lett. **61**, 1241 (1988); Hannon, J. P., *et al.*, Phys. Rev. Lett. **61**, 1245 (1988).
10. Isaacs, E. D. *et al.*, Phys. Rev. Lett. **62**, 1671 (1989).
11. Kao, C. C. *et al*., Phys. Rev. Lett. **65**, 373 (1990).
12. Sacchi, M. *et al*., Phys. Rev. Lett. **81**, 1521 (1998).
13. Dartyge, E., Fontaine, A., Tourillon, G., Cortes, R. and Jucha, A., Phys. Lett. **113A**, 384 (1986).

Physica Scripta. Vol. T115, 980–983, 2005

SAMBA a New Beamline at SOLEIL for X-Ray Absorption Spectroscopy in the 4–40 keV Energy Range

S. Belin[1,*], V. Briois[1], A. Traverse[1], M. Idir[2], T. Moreno[2] and M. Ribbens[3]

[1]LURE-CNRS, Université Paris-Sud, BP 34, 91898 Orsay Cedex, France
[2]Optic Group of SOLEIL, Synchrotron SOLEIL, L'Orme des Merisiers, St Aubin, Gif-sur-Yvette, France
[3]Design office of SOLEIL, Synchrotron SOLEIL, L'Orme des Merisiers, St Aubin, Gif-sur-Yvette, France

Received June 26, 2003; accepted November 4, 2003

PACS number: 87.64.Gb

Abstract

The design of a new beamline dedicated to X-ray Absorption Spectroscopy (XAS) at the french synchrotron radiation laboratory SOLEIL is under development. This beamline dedicated to large and varied scientific communities from physics to chemistry and biology will be characterised by a lot of techniques combined to XAS, such as X-ray Diffraction, Differential Scanning Calorimetry, Raman Spectroscopy and UV-Visible Spectroscopy. The design of the SAMBA optics will be optimised in order to be very versatile, to cover the 4–40 keV energy range with a high photon flux and a good energy resolution. Measurements of the absorption coefficients will be done either in the step by step mode or in a quick mode. The beamline should be in operation in 2006. This paper summarizes its technical characteristics and calculated performances. Typically the performance would be at 10 keV around 10^{12} ph/s in a $200 \times 200\,\mu m^2$ beam spot.

1. Introduction

SOLEIL is a third-generation synchrotron source which will deliver its first photons in 2006 for the users community. The energy of the beam in the storage ring is 2.75 GeV with a current of 0.5 A. On this source, the Scientific Advisory Comittee has recommended a beamline dedicated to X-Ray Absorption Spectroscopy (XAS) for a wide range of samples. The specificity of SAMBA (Spectroscopy Applied to Materials Based on Absorption) will be to offer the possibility to combine XAS with other techniques of characterisation such as X-ray Diffraction, Differential Scanning Calorimetry, Raman Spectroscopy and UV-Visible Spectroscopy. The spectral range 4–40 keV is covered. A wide range of applications will be concerned in chemistry, catalysis, environmental sciences, biology, solid state physics... The main X-ray optics are a first collimating mirror, a sagittal focusing double-crystal monochromator and a second focusing mirror in the vertical direction at the sample position. The horizontal angular acceptance of SAMBA is about 6.25 mrad. We give herein a first description of the beamline.

2. Source characteristics

The beamline is designed to be used from 4 to 40 keV and it will be located on the bending magnet D09-1, whose characteristics are given in Table I. The magnetic field is 1.7 T ($Ec = 8.65$ keV). These parameters are those used for the optical simulations.

3. Beamline optics

The principle of the optics of the beamline is given Figure 1. It is very similar to that of H10 (LURE) [1], FAME [2] or GILDA (ESRF) [3]. To reduce the divergence of the beam from a bending magnet, a mirror M1 is set between the source and the monochromator to provide vertical collimation of the beam. This parabolic bendable mirror allows to reject the harmonics according to the incident angle θ_M of the beam. It is made of silicon coated with a layer of about 50 nm of Pd. We have represented on Figure 2 the reflectivity of the mirror M1 versus the energy for different θ_M.

Table I. *Characteristics of the bending magnet exit where SAMBA is located.*

Bending magnet	σ_x(μm)	σ_z(μm)	σ_x'(μrad)	σ_z'(μrad)
exit 1°	60.1	24.9	134.8	2.1

To collect the maximum of photons this mirror is located near the source at 14 m. The characteristics of the different optics of SAMBA are listed in Table II. The dimensions of the M1 mirror are $120 \times 1300\,mm^2$ and it will be water-cooled.

The thermal charges on the different optical elements have been evaluated considering that the horizontal acceptance is 6.25 mrad. They are gathered in Table III and they will require a water cooling system.

The monochromatization system (DCM) is described in the next section.

A second parabolic mirror M2 at 19.5 m is then used to provide vertical focusing of the beam at the sample position. M1, DCM and M2 are sitting on a same girder of about 5 m long, to simplify the alignment of the beamline.

4. Monochromatization system

Several reasons led us to propose two monochromators to satisfy the permanent access to the 4-40 keV energy range, the sagittal focusing and the Quick-EXAFS acquisition mode.

First, in contrast to flat crystals monochromator, the energy range 4–40 keV can not be permanently covered by a commercial monochromator containing two pairs of sagittal focusing crystals (Si(111) and Si(220) or Si(311)). Second, although both acquisition modes (EXAFS step by step and Quick-EXAFS) pose no technical problem, it appears that the fast scanning mode is not straightforward for implementing if the beam is sagitally focused. Indeed this involves that dynamic sagittal focusing is operating during the fast acquisition (typically less than 1 min) of EXAFS data. Furthermore, even if the bender of the sagittal focusing crystal can be used in flat position, its mechanic is bulky and heavy leading to incompatibility with a frequent Quick-EXAFS working mode. So, we have chosen to dedicate DCM1 to sagittal focusing in the energy range 4–20 keV, and DCM2 to

*e-mail: stephanie.belin@lure.u-psud.fr

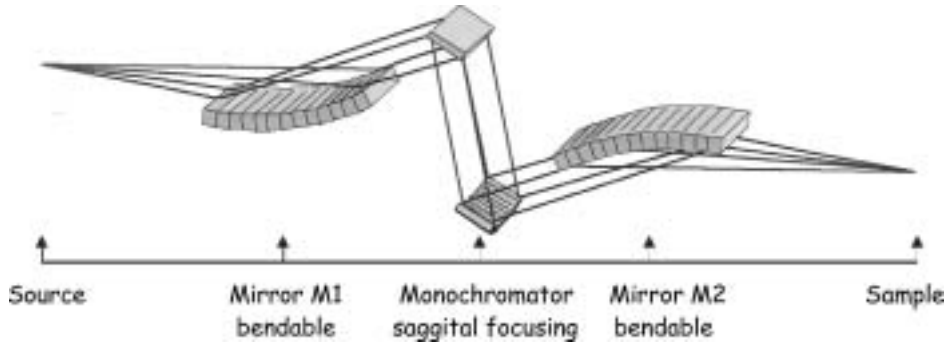

Fig. 1. Principle of the optics of the beamline.

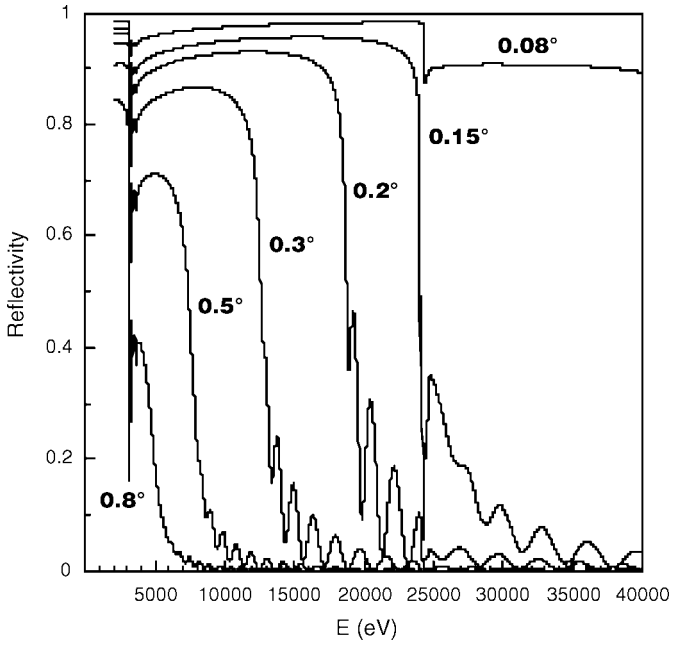

Fig. 2. Reflectivity of mirror M1 coated with Pd versus the photon energy for different incident angles θ_M.

Table II. *Beamline characteristics. The positions of the optics are given from the source.*

Element	Position (mm)	θ (°)	φ (°)	Element	Dimensions (mm)
Diaphragm D_1	12000	90	—	—	$80\times12\,mm^2$
Filter F_1	13000	90	0	Be 200 µm	—
Collimating Mirror M_1 (Parabole)	14000	0–0.6	0	Pd 500 Å	$88\times1200\times50\,mm^3$
Flat focusing Sagittal DCM_1	16000	5–40 5–40	0 180	Si111 and Si220	$100\times60\times30\,mm^3$ $100\times60\times30\,mm^3$
Flat DCM_2	18000	5–40 5–40	0 180	Si220	$100\times60\times30\,mm^3$ $100\times60\times30\,mm^3$
Focusing Mirror M_2 (Parabole)	19500	0–0.6	180	Pd 500 Å	$85\times1200\times50\,mm^3$
Sample for XAS	30000	90	—	—	—
Sample for SEXAFS	35000	90	—	—	—

Table III. *Thermal charges on the optics of SAMBA for 6.25 mrad horizontal acceptance.*

Element	transmitted P (W)	absorbed P (W)	∂P_{ABS} (W/mm^2)
Filter Be 200 µm	374.0	89.2	
Mirror M1 $\theta_M = 0.57°$	61.9	308.6	∼0.007
Crystal Si111 (23.29°) E = 5 keV	∼0.012	61.8	∼0.03
Filter Be 200 µm	373.5	93.6	
Mirror M1 $\theta_M = 0.1°$	130.8	16.0	∼0.001
Crystal Si220 (5.293°) E = 35 keV	∼0.005	118.1	∼0.23

The calculations are made considering perfect optical surfaces in the spectral range 0.1 to 100 keV.

Quick-EXAFS and step by step acquisition mode in the domain 5 to 40 keV without focusing. Both DCM will be installed in series on the girder of 5 m length. Note that the energy ranges correspond to standard incident Bragg angles between 5 and 40° for a monochromator equipped with Si(111) and Si(220) crystals. A first one, located 16 m from the source, DCM1, equipped with a first water-cooled Si(111) crystal permits horizontal focusing in the 4–20 keV energy range. A second monochromator, DCM2, located after DCM1 at 18 m from the source, will be dedicated to Quick-EXAFS and step by step acquisition mode in the domain 5 to 40 keV without focusing. It will be equipped with flat Si(220) crystals and the first one will also be water-cooled.

5. Choice of SAMBA geometry

The choice of SAMBA geometry arises from the study of the optical calculations realised by the optic group of SOLEIL. Four main requirements have been considered: the bending radii of the mirrors M1 and M2 versus the incident angle, the bending radius of the second crystal of DCM1 versus the Bragg angle, the beam size at the sample position versus the energy and the photon flux at the sample position versus energy. The results are plotted for the three considered geometries. The 3 : 1 notation means that the distance between the source and the monochromator is three times longer than the distance between the monochromator and the sample, this latter being fixed to 1.

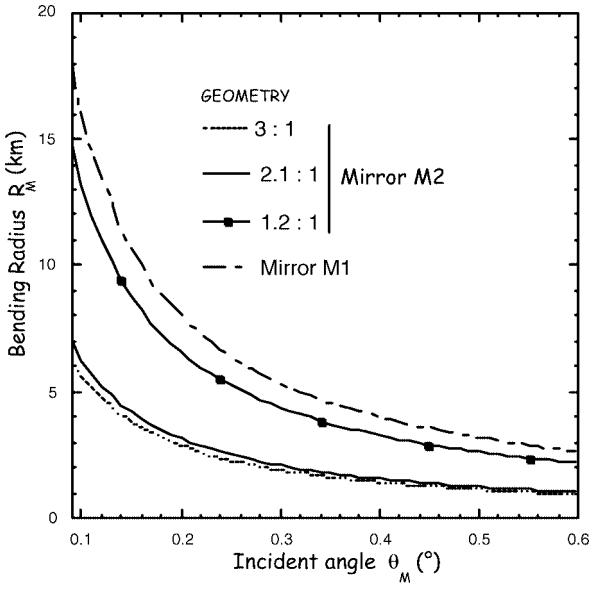

Fig. 3. Variation of the bending radius R_M of mirror M1 versus the incident angle θ_M.

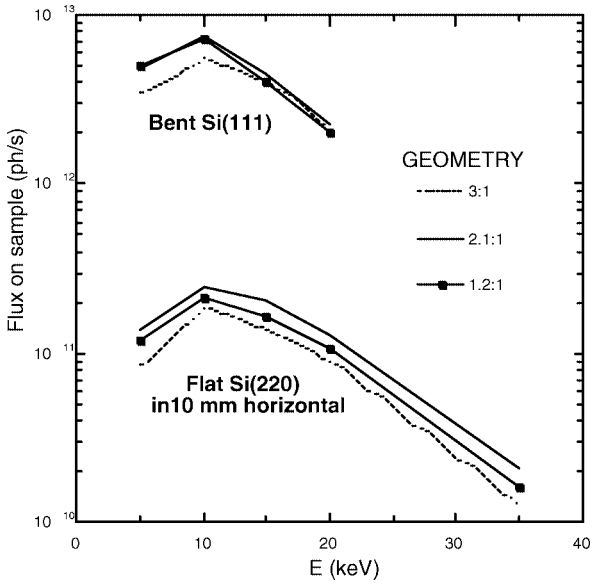

Fig. 5. Variation of the flux of photons at the sample position (30 m) as function of the incident energy.

5.1. *Bending radii*

The bending radii R_M of the mirrors M1 and M2 are presented in Figure 3 versus the incident angle. Note that 1 km is admitted as the smallest bending radius achieved with common bender without breakage or damage. Figure 3 shows that for M1 R_M is in all cases superior to 1 km whereas for M2, the 1.2 : 1 geometry is the only suitable one.

In the same way, we have reported in Figure 4 the variation of the bending radius R_S for the second crystal of the double crystal Si(111) monochromator DCM1 as function of the Bragg angle. As R_S must be larger than 1 m to avoid breakage, the 1.2 : 1 geometry is favourable if we want to reach a Bragg angle as small as 5°.

5.2. *Flux and size of the beam*

The calculated photon flux and beam size at the sample position are reported in Figures 5 and 6, respectively. The 1.2 : 1 geometry

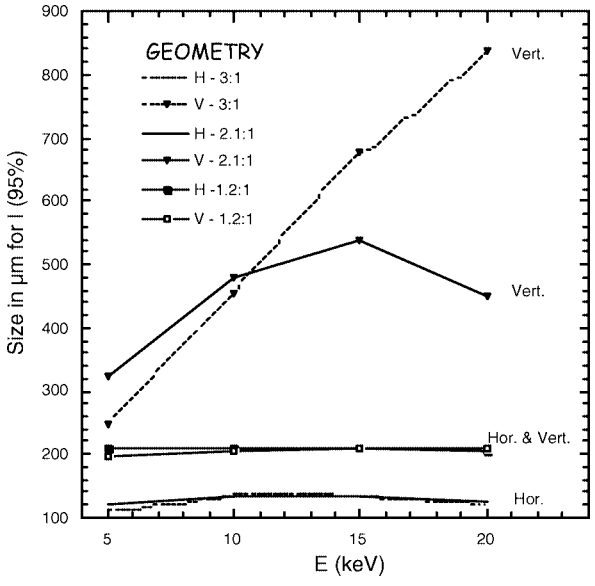

Fig. 6. Variation of the beam size at the sample position (30 m) versus the incident energy.

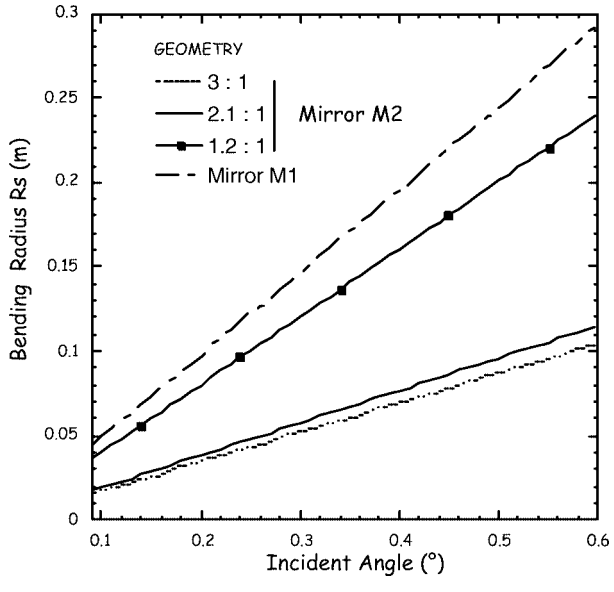

Fig. 4. Variation of the bending radius R_S of the second crystal of MDC1 equipped with Si(111) crystals versus the Bragg angle.

presents a higher photon flux than the 3 : 1 one. This geometry permits also to have a nearly symmetric and homogeneous size of the beam in the range 5 to 20 keV at the sample location (cf Figure 6). It is an interesting advantage in terms of distribution of the photon flux and also for combining complementary techniques with XAS.

6. Performances of SAMBA

The performances of SAMBA in terms of spot size, photon flux and energy resolution in the 1.2 : 1 geometry are summarized in Table IV. All these calculations were performed with slope error $\varepsilon_y = 0.3''(1.5\,\mu\text{rad})$ and $\varepsilon_x = 1''$ RMS (5 µrad) for the mirror M1 and M2 and with 3 Å roughness. Note that the spectral resolution is good. At 5 keV the spectral resolution is 0.6 eV, *i.e.* close to the Darwin resolution. At 35 keV the resolution close to 3.4 eV is better by a factor of 3.6 compared to the intrinsic spectral

Table IV. *Performances of SAMBA in the 1.2 : 1 geometry with 6.25 mrad of horizontal acceptance and with sagittal focusing for Si(111) and without focusing for Si(220).*

Energy (keV)		Flux (ph/s)	ΔE(eV)	Size	Bending Radius (mm)	θ Bragg (deg.)
5	Si 111	5×10^{12}	0.59	$210.5 \times 195.3\,\mu m^2$	5905.9	23.296
	Si 220	1.7×10^{12}	0.27	142 mm × 195 μm	—	40.225
10	Si 111	7.2×10^{12}	1.2	$208.3 \times 206.8\,\mu m^2$	2953	11.405
	Si 220	3×10^{12}	0.59	142 mm × 197.4 μm	—	18.838
15	Si 111	4.1×10^{12}	1.9	$207.4 \times 210.4\,\mu m^2$	1968.6	7.575
	Si 220	2.3×10^{12}	0.9	142 mm × 197 μm	—	12.431
20	Si 111	2×10^{12}	2.7	$206 \times 207.2\,\mu m^2$	1476.5	5.674
	Si 220	1.5×10^{12}	1.38	142 mm × 198.4 μm	—	9.291
35	Si 220	2.3×10^{12}	3.35	142 mm × 196.4 μm	—	5.293

broadening of K absorption edges of heavy elements (e.g. 12.3 eV at the Cs K edge (36 keV)) [4].

A comparison of SAMBA performances in focusing mode with other beamlines like FAME [2] or GILDA [3] (ESRF) shows that the implantation of the optics near the source is determinant to compete with these beamlines in terms of photons flux.

7. Beamline equipment

All the detection techniques will be available, transmission, total electron yield and emitted fluorescence.

Combined XAS experiments with other complementary techniques of characterisation of materials: X-ray Diffraction (XRD), Differential Scanning Calorimetry, Raman Spectroscopy and UV-Visible Spectroscopy will be proposed on SAMBA. Some of these combinations have already been implemented on the D44 station at LURE. They are fully described on a separate invited paper of the conference [5]. These combined techniques will be transferred to the new beamline SAMBA and they should take great benefit from the access to a third generation source, in particular for their use in time-resolved experiments.

Many ancillary devices like cryostats (He_{liq} and N_{2liq}), furnaces, goniometer, Paris-Edinburgh cells, thermostated liquid cells, many sample-holders . . . can also be used.

A second experimental hutch will be located at 35 m of the source in order to make surface EXAFS experiments.

References

1. Beamline website: http://www.lure.u-psud.fr/Experiences/DCI/h10/h10.htm.
2. Beamline website: http://www.esrf.fr/exp_facilities/BM8/handbook/control.html.
3. Beamline website: http://www.esrf.fr/exp_facilities/BM30B/BM30Bb-en.html.
4. Krause, M. O. and Oliver, J. H., J. Phys. Chem. Ref. Data **8**, 329 (1979).
5. Briois, V. *et al*., Physica Scripta, this conference.

Physica Scripta. Vol. T115, 984–985, 2005

X-Ray Absorption and De-Excitation Processes of Krypton Clusters Studied by the XAFS-PEPICO Synchronous Measurements

K. Nagaya[1], A. Mori[1], H. Murakami[1], M. Yao[1], Y. Ohmasa[1], H. Kajikawa[1], K. Kobayashi[1], Y. Kajihara[1], A. Chiba[1], Y. Nishikawa[1], M. Ishii[2], Y. Fujii[3] and E. Hayata[3]

[1]Department of Physics, Graduate School of Science, Kyoto University, Kyoto 606-8502, Japan
[2]SPring-8/JASRI, Mikazuki, Sayo, Hyogo 679-5148, Japan
[3]Department of Physics, Faculty of Science, Kyoto University, Kyoto 606-8502, Japan

Received June 26, 2003; accepted November 4, 2003

PACS numbers: 36.40.Mr, 36.40.Qv, 61.10.Ht

Abstract

XAFS-PEPICO synchronous measurement has been applied to free neutral krypton clusters to study the X-ray absorption and de-excitation processes of clusters. The PEPICO measurements for krypton atom reveal that the highly charged daughter ions of Kr^{z+} ($z = 3$–11) are generated as a result of the de-excitation process. As the cluster size increases, the Kr^+, Kr_2^+ and Kr_3^+ daughter ion, which is hardly observed in the atomic spectra, shows remarkable increase. The PIY spectrum of Kr^+, which is distinct from those of highly charged ions, is similar to the XAFS spectrum of solid krypton.

1. Introduction

The X-ray absorption fine structure (XAFS) is a potentially useful method to study the structure of the cluster. However, it is difficult to measure the XAFS of free clusters in the hard X-ray region mainly for two major reasons. First, the atomic density in the cluster beam is extremely low to apply the usual XAFS measurement. Secondly the X-ray absorption cross section decreases with increasing photon energy. However, by utilizing the intense X-ray source of the third generation synchrotron, it would be possible to study the XAFS of rarefied systems, such as cluster, in the hard X-ray region.

Recently, we have developed a method for the XAFS-PEPICO synchronous measurements and applied it to Se cluster beam [1]. The XAFS spectra taken in the total ion yield (TIY) were measured simultaneously with the PEPICO measurement, from which the information on the de-excitation process can be derived. Our study has shown that the size-selective structural analysis of free clusters has been carried out by utilizing the information on the de-excitation process of clusters.

In the present study, the XAFS-PEPICO synchronous method is applied to krypton clusters to study their X-ray absorption and de-excitation process. Krypton may serve as a standard sample because de-excitation processes for atomic krypton have been well studied.

2. Experimental

Figure 1 is a photograph of the newly developed cluster beam apparatus for XAFS measurement. The apparatus is composed of an expansion chamber and an analyzing chamber, which were separated from each other by a conical skimmer with an aperture of 1 mm. Each of the chambers was evacuated by a turbo molecular pump. Typical operating pressure was 1.0–3.0×10^{-3} Torr in the expansion chamber, and 4.0×10^{-6}–1.0×10^{-5} Torr in the analyzing chamber.

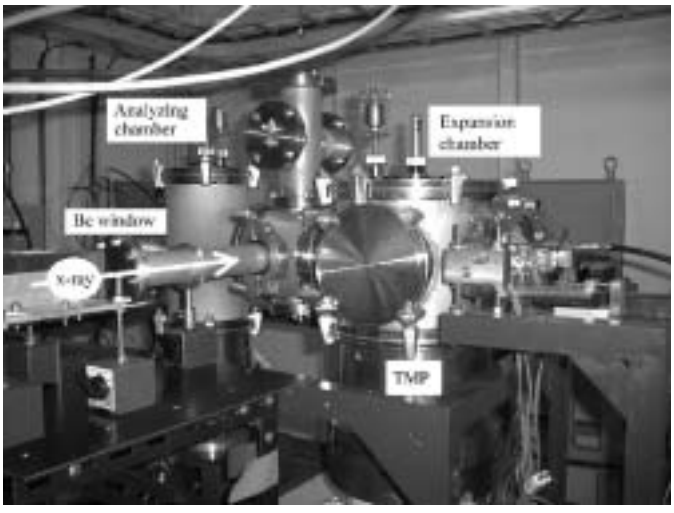

Fig. 1. Photograph of the cluster beam apparatus for XAFS measurement.

The cluster apparatus was placed in a high-brilliance XAFS station BL10XU at SPring8, where the X-ray emitted from the undulator was monochromized by a double crystal Si(111) monochromator [3]. Higher harmonics and back-ground radiation from the undulator were minimized by a double flat mirror with a variable critical energy. An ionization chamber filled with N_2 gas was used as a monitor of photon number. The photon flux of the X-ray was about 5.4×10^{12} photons/s during our measurement. After passage through an ionization chamber, the X-ray beam was led into the cluster beam apparatus through a beryllium window.

A neutral cluster beam was produced by a supersonic jet expansion method in the expansion chamber. In the cluster source, an alumina cylindrical nozzle of 0.08 mm in inner diameter was attached to the top of a cryostat, and cooled by liquid nitrogen. In the present study, both the temperature, T_0, and the stagnation pressure, p_0, of the krypton vapour were adjusted to control the cluster size distribution.

In the analyzing chamber, the cluster beam was intersected with the X-ray at right angles in the horizontal plane, then the ions and electrons were emitted. The photoions produced by absorbing an X-ray photon were extracted upward by a constant electric field to a modified Wiley-McLaren time-of-flight mass spectrometer [4] and detected by a channeltron, while the photoelectrons were extracted downward and immediately detected by another channeltron.

The XAFS spectrum for the mixed cluster beam was taken in the Total Ion Yield (TIY) mode. The TIY was obtained by counting

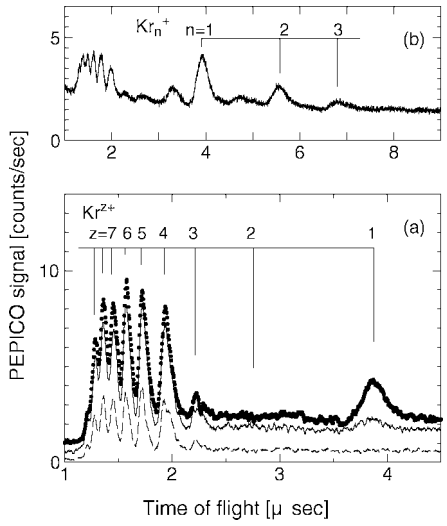

Fig. 2. PEPICO spectra for krypton clusters taken at photon energy of 14.5 keV. (a) PEPICO spectra with several p_0. The dashed line, solid line and dot correspond to $p_0 = 1, 3$, and 5 bar, respectively. T_0 was 302 K for all three spectra. (b) PEPICO spectrum for $T_0 = 150$ K and $p_0 = 4$ bar.

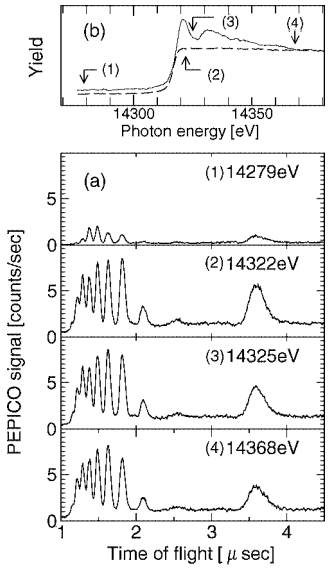

Fig. 3. (a) Typical PEPICO spectra measured at four energy points. (b) TIY spectrum of krypton atom (dashed line) and partial ion yield spectrum of Kr^{1+} (solid line).

the pulses due to the ion signals. For the PEPICO measurement, the photoelectron signal delivers the start pulse and the photoion signal delivers the stop pulse to a time-to-amplitude-converter, and the difference of the time-of-flight between the electron and ion was accumulated as a histogram in a multi-channel-analyzer. In the XAFS-PEPICO synchronous measurements, the PEPICO spectrum was recorded simultaneously at each photon energy where the TIY was measured [2].

3. Results

In fig. 2, the PEPICO spectra for krypton clusters taken at photon energy of 14.5 keV are shown as a function of the time of flight of the photoions. Fig. 2(a) shows the PEPICO spectra with the stagnation pressure p_0 of 1, 3, and 5 bar. The temperature T_0 was 302 K for all three spectra. The PEPICO spectrum taken under the condition of $T_0 = 302$ K and $p_0 = 1$ bar shows several prominent peaks in the time range between 1.0 and 2.5 μs which correspond to the highly charged daughter ions of Kr^{z+} with $z = 3$ to 12. Because no cluster has been observed for $T_0 = 302$ K and $p_0 = 1$ bar, these highly charged ions are produced by X-ray absorption of krypton atoms. The present distribution of the daughter ions stemming from atomic krypton agree well with the results of Krause [5], who measured the distribution of the daughter ions from krypton atom at a photon energy of 17.45 keV.

The krypton clusters have been generated by applying the pressure to the cluster source. As shown in fig. 2(a), Kr^{1+} ion appears with the increase of p_0. The peak width of Kr^{1+} is greater than that of higher charged daughter ions, suggesting that Kr^{1+} ions is produced by the coulomb explosion of multiply charged cluster ions. Cooling the nozzle promotes additional clustering. Fig. 2(b) shows a PEPICO spectrum for $T_0 = 150$ K and $p_0 = 4$ bar. The appearance of additional peaks at 5.7 μs (Kr_2^+) and 6.9 μs (Kr_3^+) indicates that the de-excitation process of clusters has been changed with the growth of cluster size.

In the present study, the PEPICO spectra have been measured simultaneously with the TIY spectrum at 140 energy points. Fig. 3(a) shows typical PEPICO spectra measured at four energy points. The energies are shown in the fig. 3(b) by arrows together with the TIY spectrum of krypton atom (dashed line) and partial ion yield spectrum of Kr^{1+} (solid line). As the photon energy increases, the intensity of the PEPICO increases abruptly at the absorption edge. For highly charged ions (Ke^{z+}: $z = 3$–10) the energy dependences of PEPICO peak intensity resemble the TIY spectrum of the atomic beam. However, the PIY of Kr^{1+} is distinct in energy dependence from those of highly charged ions. The PIY of Kr^{1+} looks like the XAFS spectrum of solid krypton [6]. These results are understood by the fact that the higher charged ions stem from krypton atoms and the Kr^{1+} stem from clusters. The likeness between the PIY of Kr^{1+} and the XAFS of solid krypton may be a result of the evolution of the electronic states in krypton clusters from the atom to the solid.

4. Summary

XAFS-PEPICO synchronous measurement has been applied to free neutral krypton clusters. The PEPICO spectra show a remarkable difference between krypton atom and krypton cluster. The energy dependence of PIY for Kr^{1+} is distinct from those of highly changed ions. The results suggest a difference of de-excitation processes between atomic krypton and krypton clusters.

Acknowledgements

The author thanks Dr. H. Tanida (JASRI) for supporting the experiment at SPring-8. The author is grateful to Mr. Y. Nakagawa for collaboration at the early stage of this work.

References

1. Nagaya, K. *et al*., Phys. Rev. Lett. **89**, 243401 (2002).
2. Nagaya, K., J. Phys. Soc. Jpn. **72**, 501 (2003).
3. Oyanagi, H. *et al*., J. Synchrotron Rad. **6**, 155 (1999).
4. Wiley, W. C. and McLaren, I. H., Rev. Sci. Instrum. **26**, 1150 (1955).
5. Krause, M. and Carlson, T., Phys. Rev. **158**, 18 (1967).
6. Kutzler, F. W. *et al*., Solid State Commun. **46**, 803 (1983).

Physica Scripta. Vol. T115, 986–988, 2005

Self-Absorption Correction Strategy for Fluorescence-Yield Soft X-ray Near Edge Spectra

R. Carboni[1], S. Giovannini, G. Antonioli[2] and F. Boscherini

INFM and Physics Department, University of Bologna viale C. Berti Pichat 6/2, 40127 Bologna, Italy

Received June 26, 2003; accepted in revised form November 4, 2003

PACS number: 61.10.Ht

Abstract

It is well known that fluorescence-yield X-ray absorption measurements of thick concentrated samples can exhibit severe spectral distortions due to the "self-absorption" effect. While reliable corrections for this effect have been described for the EXAFS region an accepted procedure does not exist for the XANES region, in which the distortions are more severe. This problem is of particular relevance in the soft X-ray region in which transmission measurements are usually impossible. We describe a procedure for the correction of XANES spectra for self-absorption spectral distortions which is based on the scaling of the experimental spectrum to tabulated cross-sections. We apply the method to polarization-dependent O K-edge measurements in cubic NiO, in which no intrinsic polarization dependence is expected. The procedure is able to reduce by a factor of 3 the self-absorption distortions.

1. Introduction

The most common experimental set-up for X-ray absorption spectroscopy (XAS) is the transmission geometry. Fluorescence detection is principally used in experiments with hard X-rays since its use in the soft X-ray range is hampered by the extremely low values of the fluorescence yield (10^{-2}–10^{-3}). With the availability of high brilliance third generation synchrotron radiation sources new opportunities exist for the application of fluorescence yield XAS (FY-XAS). Areas of interest for the application of soft X-ray FY-XAS in this context are, among others, the study of dopants, impurities and defects, of insulating materials, of samples inserted in magnetic fields; compared to electron yield (EY) detection, FY is more bulk sensitive and therefore better suited when structural information from the bulk of the sample is sought.

The photon energy dependence of the fluorescence intensity from dilute samples and thin layers is directly proportional to the absorption coefficient of the excited element [1]. For thick, concentrated samples, however, FY-XAS measurements can exhibit severe spectral distortions due to the 'self-absorption' effect [2–7]. This problem is of particular relevance in the soft X-ray region in which transmission measurements are virtually impossible.

The expression for the fluorescence photons flux $I_f(E)$, in the limit of an infinitely thick sample and small detection solid angle is [1]:

$$I_f(E) = I_0(E)\frac{\Omega}{4\pi}\varepsilon_f \frac{\mu_A(E)}{[\mu_A(E)+\mu_M(E)]+\mu_{tot}(E_f)\frac{\sin\phi}{\sin\theta}} \qquad (1)$$

where ϕ and θ are the angles between the sample surface and the impinging and the fluorescence beams, respectively; $\mu_A(E)$, $\mu_M(E)$, $\mu_{tot}(E_f)$ are the absorption coefficients of the absorber atom (A) and of the matrix (M) at the incidence energy E and the total absorption coefficient at the fluorescence energy E_f; $I_0(E)$, $\Omega/4\pi$ and ε_f are the incidence flux intensity, the solid angle covered by the detector and the fluorescence yield of atom A, respectively.

As can be seen from Eq. (1), when the condition $\mu_M(E) \gg \mu_A(E)$ is not verified (i.e. for concentrated samples) the number of fluorescence photons is not proportional to the absorption coefficient of the absorber atom $\mu_A(E)$: the presence of $\mu_A(E)$ in the denominator induces a distortion of the XAS signal. These distortions depend on the angular configuration as expressed by the term $\sin\phi/\sin\theta$. When the incidence angle is near 90° the dominant term in the denominator of Eq. (1) is the last one and the spectral distortions are minimized and can often be neglected. On the contrary, near grazing incidence the first term in the denominator becomes dominant and the spectra can be severely distorted.

It is possible to obtain an estimate of the magnitude of the self-absorption effect by evaluating the ratio between $\mu_A(E)$ and the sum of the last two terms in the denominator of Eq. (1).

$$R = \frac{\mu_A(E)}{\mu_M(E)+\mu_{tot}(E_f)\frac{\sin\phi}{\sin\theta}}. \qquad (2)$$

When R is greater or equal to 1 distortions are significant while they are negligible when R is close to zero. It is possible to reduce spectral distortions by using a normal incidence geometry but this method cannot be a general solution, since it makes it impossible to exploit or to study the polarization dependence of the XAS signal.

The distortions of the EXAFS spectral region have been recently described, together with appropriate corrections, by Tröger *et al.* [5] and by Pfalzer *et al.* [6]. The latter paper extended the correction of the self-absorption effect to the case in which the solid angle subtended by the detector is not negligible. While reliable self-absorption corrections have been described for the EXAFS region a complete correction procedure has not been published for the XANES region, despite the fact that the effect is well-known and its physical origin understood [4]. In the XANES region modulations in the XAS signal are greater than in the EXAFS one and therefore self-absorption distortions are more severe. Obtaining distortion-free XANES spectra appears particularly important in view of recent advances in quantitative interpretation [8]. In this paper we describe a strategy for the correction of self-absorption distortions in the XANES regions which is based on the scaling of the spectra to tabulated cross sections and apply it to the O K-edge XANES of NiO. A related method applicable to EY-XAS measurements has been recently described [9, 10]; in this case, however, it was necessary to keep the electron mean free path as a free parameter, since its value can be uncertain up to a factor of 3.

[1] roberta.carboni@bo.infm.it

[2] INFM and Physics Department, University of Parma, Parco Area delle Scienze 7/A, 43100 Parma, Italy.

2. Experimental Data

We carried out O K-edge XANES measurements of a NiO sample with its surface oriented parallel to the (100) lattice planes. The choice of NiO is motivated by its cubic structure: no intrinsic variation of the XANES signal is expected as a function of the angle between the impinging beam and the sample crystallographic orientation [11].

Measurements were made at the BEAR beamline [12] of the ELETTRA facility in Trieste, Italy. The resolution and flux were $\sim$200 meV and $5 \cdot 10^{10}$ ph/s, respectively, and the spot size was 20 by 200 μm. The NiO crystal was mounted in an ultrahigh vacuum chamber on a rotatable sample holder, biased +1000 V with respect to ground to avoid photoelectrons reaching the fluorescence detector. A signal proportional to the incident photon flux was obtained by measuring the photocurrent from a high transmission gold grid. A Si photodiode operated in the current mode was used for fluorescence detection; the photodiode area was 100 mm^2 and it was placed at a distance of 20 mm from the sample; typical photodiode currents were of the order of 10 pA.

We took FY-XANES spectra for two angles of the impinging beam ($\phi = 20^\circ, 70^\circ$) to observe the importance of self-absorption effect at the two extreme configurations, grazing incidence and normal incidence. The energy of the incidence X-rays was scanned between 520 eV and 570 eV. We normalized the FY raw spectra with $I_0(E)$ obtained from the gold grid, and from each spectrum we subtracted a linear pre-edge background.

The XANES data are reported in Fig. 1. While the two spectra are similar there are significant differences in the relative intensities of the peaks, the grazing incidence spectrum exhibiting an overall damping. The relative difference in the peak-to-valley ratio (taken respectively at 539 and 542 eV) between the two spectra is 39%. For the experimental conditions used the value of R defined in Eq. (2) is 0.72 for $\phi = 20^\circ$ while for $\phi = 70^\circ$ it is 0.25.

3. Correction Procedure

We now describe a procedure to correct the XANES spectra from self-absorption effects based on scaling the experimental spectrum to tabulated cross sections [13]. As a first step we describe a procedure which is applicable in the case of small solid angle of detection; subsequently this approximation is relaxed.

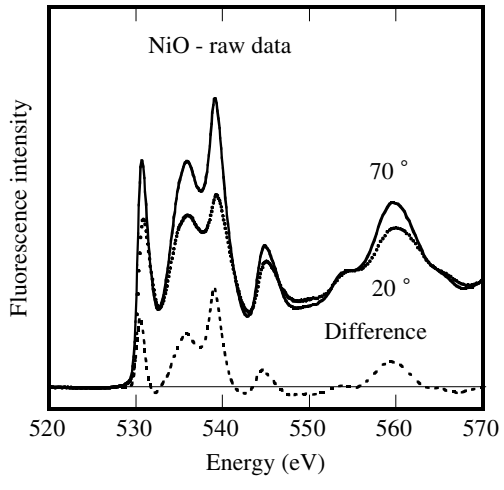

Fig. 1. Raw O K-edge XANES spectra of the NiO sample at 20°(dots) and 70°(continuous line) incidence angles and their difference (dashed line).

The method is valid provided: *i*) the composition and density of the sample are known, *ii*) the sample is much thicker than the photon absorption length and *iii*) the sample has a flat surface.

We define the normalized fluorescence intensity as $Y(E)$:

$$Y(E) = \frac{I_f(E)}{I_0(E)\varepsilon_f \Omega/4\pi}. \tag{3}$$

$Y(E)$ ranges from 0 to 1 and is equal to the fluorescence intensity per unit relative solid angle, fluorescence yield and incident flux. In terms of $Y(E)$ the absorption coefficient of the excited atom is:

$$\mu_A(E) = \frac{Y(E)}{1 - Y(E)} \left[\mu_M(E) + \mu_{tot}(E_f) \frac{\sin\phi}{\sin\theta} \right]. \tag{4}$$

If the quantities appearing in the denominator of Eq. (3) were reliably known it would be straightforward to calculate the corrected spectrum using Eq. (4). However, the precise determination of the solid angle is difficult and, especially in the soft X-ray range in which ionisation chambers are not commonly used, the quantitative measurement of the incident flux $I_0(E)$ is not available. The proposed method consists in bringing the experimental data $I_f(E)$ to the absolute scale of $Y(E)$ by multiplying by a factor β defined as:

$$\beta = \frac{1}{J} \frac{\mu_A^{At}(E)}{\mu_A^{At}(E) + \mu_M^{At}(E) + (\mu_A^{At}(E_f) + \mu_M^{At}(E_f))\sin\phi/\sin\theta}. \tag{5}$$

The symbols have their usual meaning and the superscript At indicates that tabulated atomic cross-sections at an energy just above the edge are used [13]; J is the experimental discontinuity in the fluorescence data which is estimated by extrapolating to the absorption edge energy the pre-edge and post-edge signals. The quantity $\beta \times I_f(E)$ is substituted for $Y(E)$ in Eq. (4) and the corrected spectrum is thus calculated.

When the solid angle covered by the detector is not small the geometrical factor in Eq. (1) and following cannot be simply defined as $\sin\phi/\sin\theta$; in this case the factor β, has a different value for each element of solid angle $d\Omega$ covered by the detector. In Fig. 2 the experimental geometry is illustrated. The incidence angle ϕ is constant in any particular measurement while the angle formed by the fluorescence beam with respect the sample surface varies across the detector. Defining the y axis as the normal to the sample surface and the plane xz as the sample surface, τ is the angle between the z axis and the exit beam, and θ is the angle between the x axis and the fluorescence beam. The solid angle element is $d\Omega = \sin\tau\, d\tau\, d\theta$. In this configuration the angle ξ of the fluorescence beam with respect the sample surface is not simply equal to θ except for $\tau = \pi/2$. ξ is important because it determines the length of the path the fluorescence X-rays must traverse through the sample and hence the magnitude of the self-absorption correction. For our experimental setup we obtained $\xi(\tau, \theta)$:

$$\xi(\tau, \theta) = \frac{\pi}{2} - \arccos(\sin\tau \sin\theta) \tag{6}$$

with τ ranging from $\tau_{min} = 76^\circ$ to $\tau_{max} = 104^\circ$ and θ from $\theta_{min} = 6^\circ$ to $\theta_{max} = 34^\circ$. To obtain the total correction factor the following integral must be calculated:

$$\beta(E, \phi) = \frac{1}{\Omega} \int_{\theta_{min}}^{\theta_{max}} \int_{\tau_{min}}^{\tau_{max}} \frac{\mu_A(E)}{\mu_T(E) + \mu_T(E_f)\frac{\sin\phi}{\sin\tau\sin\theta}} \, d\tau\, d\theta. \tag{7}$$

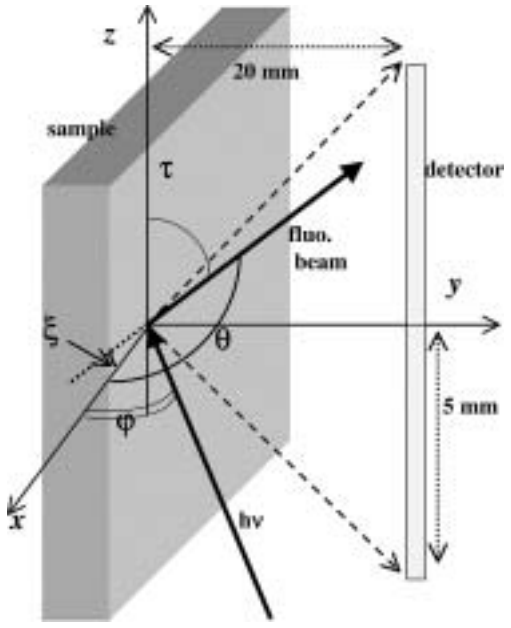

Fig. 2. Experimental geometry.

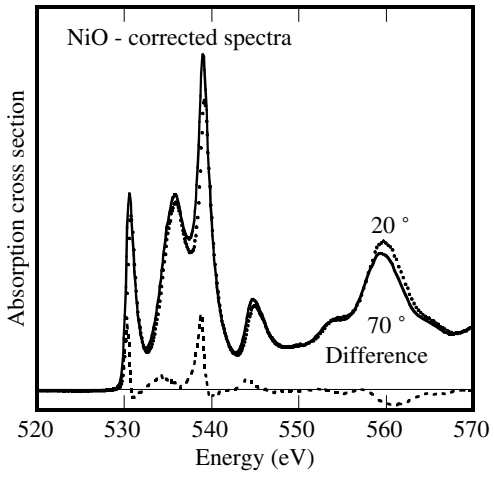

Fig. 3. Corrected O K-edge XANES spectra of the NiO sample at 20°(dots) and 70°(continuous line) incidence angles and their difference (dashed line).

It must be pointed out that the proposed method relies on the accuracy of atomic cross-sections and depends critically on the determination of the experimental discontinuity J.

The above described procedure was applied to the NiO XANES spectra and the result is shown in Fig. 3. As can be seen the differences between the two spectra are significantly reduced, as expected for a cubic structure. In fact, the relative difference in the peak-to-valley ratio is now 12%, a reduction by a factor of 3 with respect to the uncorrected data.

Acknowledgments

We are grateful to the staff of the BEAR beamline, N. Mahne, A. Giglia, M. Pedio and S. Nannarone for their assistance during the measurements and to A. Costa (University of Bologna) and A. Bazzini (University of Parma) for expert technical assistance. Work supported in part by INFM PURS-FLUX project.

References

1. Lee, P. A., Citrin, P. H., Eisenberger, P. and Kincaid, M., Rev. Mod. Phys. **53**, 769 (1981).
2. Goulon, J., Goulon-Ginet, C., Cortes, R. and Dubois, J. M., J. Phys. **43**, 539 (1982).
3. Tan, Z. J., Budnick, I. and Heald, S. M., Rev. Sci. Instrum. **60**, 1021 (1989).
4. Pompa, M., Flank, A.-M., Delaunay, R., Bianconi, A. and Lagarde, P., Physica B **208&209**, 143 (1995).
5. Tröger, L. *et al*., Phys. Rev. B **46**, 3283 (1992).
6. Pfalzer, P. *et al*., Phys. Rev. B **60**, 9335 (1999).
7. Eisebitt, S., Böske, T., Rubensson, J.-E. and Eberhardt, W., Phys. Rev. B **47**, 14103 (1993).
8. Della Longa, S., A. Arcovito, A., Girasole, M., Hazemann, J. L. and Benfatto, M., Phys. Rev. Lett. **87**, 155501 (2001) .
9. Nakajima, R., Stöhr, J. and Idzerda, Y. U., Phys. Rev. B **59**, 6421 (1999).
10. Gota, S., Gautier-Soyer, M. and Sacchi, M., Phys. Rev. B **62**, 4187 (2000).
11. Brouder, C., Ruiz López, M. F., Pettifer, R. F., Benfatto, M. and Natoli, C. R., Phys. Rev. B **39**, 1488 (1989); Brouder, C., J. Phys.: Condens. Matter **2**, 701 (1990).
12. Naletto, G., Pelizzo, M.-G., Tondello, G., Nannarone, S. and Giglia, A., SPIE Proc. **4145**, 105 (2001).
13. Yeh, J. and Lindau, I., At. Data Nucl. Data Tables **32**, 1 (1985).

Physica Scripta. Vol. T115, 989–991, 2005

XANES Mn K Edge in $NaNbO_3$ Based Ceramics Doped with Mn and Bi Ions

A. Wolska[1,2*], A. Molak[3], K. Lawniczak-Jablonska[2], J. Kachniarz[2], E. Piskorska[2], I. Demchenko[2], I. Gruszka[3] and D. W. Lindle[1]

[1]Department of Chemistry, University of Nevada, Las Vegas, NV 89154, USA
[2]Institute of Physics, Polish Academy of Sciences, Al. Lotników 32/46, 02-668 Warsaw, Poland
[3]Institute of Physics, University of Silesia, ul. Uniwersytecka 4, 40-007 Katowice, Poland

Received June 26, 2003; accepted June 23, 2004

PACS number: 78.70.Dm

Abstract

Sodium niobate based ceramics doped with Mn atoms have been sintered from oxides. The Bi co-dopants were introduced to increase the solubility limit for Mn atoms. Two series of samples were heated at lowered air pressure to produce oxygen nonstoichiometry. X-ray Absorption Near Edge Structure (XANES) spectra at Mn K-edge were measured for samples with and without Bi co-dopants. Theoretical XANES spectra were calculated using the Real Space Multiple Scattering method (FEFF 8 code). The simulation showed that ceramics samples have Pbcm symmetry and all of them have Mn atoms located in a Nb sublattice.

1. Introduction

Sodium niobate ($NaNbO_3$) is scientifically attractive because of its use as a base compound for forming solid solutions that have a combination of electrical and mechanical properties which have been shown to be promising for applications in high-temperature piezoelectric devices and, when ferroelectric properties are induced, acoustic transducers operating in the microwave range [1, 2].

Sodium niobate has a relatively susceptible structure which exhibits a sequence of six phase transformations, with seven possible existing stable phases. The room-temperature phase (called P) is an antiferroelectric phase with symmetry Pbcm [3, 4]. It has been shown that such factors as an induced external electric field [5], variation of pressure [6, 7, 8] or introducing dopant ions such as K, Ag, Ba in the sodium sublattice or Ta, Mn in the niobium sublattice can change internal stresses or electric fields thus affecting the stability of the phases. As a result, shifts in temperatures of the phase transitions and even appearance of new phases have been reported [8, 9, 10, 11].

In this work we investigated the effect of doping the sodium niobate based compound with Mn. There have been conflicting reports about the Mn position in the $NaNbO_3$ crystal lattice. EPR spectra analysis has shown that Mn^{2+} ions replaced Na^{1+} ions [12, 13], Mn_{Na}. On the other hand, recent XPS experiment suggest that Mn ions replace Nb^{5+} ions [14], Mn_{Nb}. However, it should be pointed out that from a stress-strain consideration or from point chemistry rules both the Mn_{Na} and Mn_{Nb} positions are just as probable [7, 8]. This is because the Mn ion can exist in several ionic states Mn^{2+}, Mn^{3+}, Mn^{4+} or may form covalent bonding. The solubility limit for Mn ions in a sodium niobate lattice was found not to exceed one atomic percent [14].

As a result of thermodynamic circumstances at sintering, we expect a certain concentration of oxygen vacancies (V_O). Moreover, by inducing oxygen non-stoichiometry or by co-doping with other ions, electrical stability can be reached. In this work we used bismuth ions to fulfil this stability condition. This is a reasonable choice due to the stability of the Bi^{3+} state and because the crystal radii in 8th fold co-ordination are comparable, meaning negligible strains are created when a sodium atom is replaced [7, 8, 15, 16]. However, there are still questions as to the real or dominant position of Mn ions in the sodium niobate structure.

With the aid of theoretical calculations, XANES (X-ray absorption near edge structure) is a good choice to investigate local structure. The atomic selectivity of this technique and its sensitivity to the geometrical arrangement of atoms around the absorbing atoms can help identify the specific position of atoms in the crystal lattice.

2. Experimental

2.1. *Sample preparation*

A $(Na_{1-x}Bi_x)(Mn_yNb_{1-y})O_3$ ceramic series was prepared by dry sintering, using a two-stage synthesis process [17, 18] where we used the following ratios of x to y : 0.06 : 0.04, 0.24 : 0.16. As a first step, the $(Na_{1-x})(Mn_yNb_{1-y})O_3$ precursor phase was produced from Na_2CO_3 (Sigma, purity ≥99%), Nb_2O_5 (Aldrich, purity ≥99.9%) and MnO (Aldrich, purity≥99%) powders in stoichiometric proportions. The powders were ball mill mixed for 12 hours, pressed lightly and then calcined at 1223 K for 3 hours. The second step consisted of crushing the precursor phase and mixing it with bismuth oxide, Bi_2O_3 (Sigma, purity ≥99%). Five percent more bismuth oxide was added to compensate for evaporation expected during sintering. The mixtures were then milled for 6 hours and calcined at 1173 K for 2 hours. Finally, after 3 hours of milling, the powders were pressed at 25 MPa into pellets ($\varphi = 1$ cm) and sintered in air at 1423 K for 2 hours.

A reference sample doped with Mn ($x = 0$, $y = 0.06$) was also made.

The "A" series samples were cut from these pellets and then placed in a vacuum oven. The "B" and "D" series were additionally treated to change their oxygen stoichiometry [13].

Series "B" samples were heated at 670 K for one hour in a vacuum of 10^{-2} Torr. The heating temperature was chosen ($\ll$1130 K) to prevent bismuth oxide from escaping the ceramic. These samples were expected to exhibit an oxygen deficiency.

The "D" Series were reduced during one hour at 720 K in a vacuum of 10^{-3} Torr. The chamber was then filled with air at ambient pressure and room temperature and then heated at 680 K for 30 minutes. This procedure should allow oxygen ions to be reintroduced into the ceramic crystal lattice and diminish the

*e-mail: awolska@lbl.gov

Table I. *Contents of Bi and Mn atoms (in x and y units) calculated from EPMA results. Differences between nominal and measured concentration of atoms are a consequence of bismuth oxides being highly evaporative below the temperature which is necessary for effective sintering.*

nominal concentration	name of the sample	Na $(1-x)$	Bi (x)	Mn (y)	Nb $(1-y)$
$NaMn_{0.04}Nb_{0.96}O_3$	Bi0Mn4A	1.00	—	0.02	0.98
$Na_{0.94}Bi_{0.06}Mn_{0.04}Nb_{0.96}O_3$	Bi6Mn4A	0.88	0.12	0.05	0.95
$Na_{0.76}Bi_{0.24}Mn_{0.16}Nb_{0.84}O_3$	Bi24Mn6A	0.91	0.09	0.06	0.94

oxygen nonstoichiometry. Therefore, these samples are expected to show similar properties to the "A" series.

2.2. *XANES and EPMA*

XANES measurements were performed at HASYLAB, Hamburg, on station A1. Mn K-edge absorption spectra were measured at room temperature using the 4-crystal monochromator in fluorescence detection mode, with an energy resolution of 0.5 eV at 10 keV. The solid samples were mounted on the sample holder using carbon tape.

In addition to the experimental XANES measurements, theoretical XANES spectra were calculated by using the real space full multiple scattering FEFF8 code [19]. The atomic coordinates used in this code were generated by ATOM3.0beta7 using crystallographic parameters from ref. [5], and clusters of 10 Å radii. Full multiple scattering calculations were performed for clusters containing 87 atoms. A 5.7 eV shift towards lower energy was applied to each calculated spectrum to allow comparison to the experimental spectra.

The composition of the "A" series samples (Tab. I) was determined by a Cameca Electron Probe MicroAnalyser (EPMA), model SX50 using a Si : Li detector, at a fixed electron beam energy of 20 keV.

3. Results and discussion

3.1. *"A" Series – samples obtained from sintering*

Theoretical calculations for Pbcm structure at the Mn K-edge were made for two cases, for a Mn atom replacing a Nb absorbing atom (Mn_{Nb}) and for a Mn atom replacing a Na absorbing atom (Mn_{Na}). Results show that XANES spectra are clearly different for both cases, see lower part of Fig. 1. The experimental spectra with Bi co-doping are quite similar to the theoretical spectrum calculated at the Mn_{Nb} K-edge, but are completely different than the K-Mn_{Na} results. This suggests that for both the Bi6-Mn4A and the Bi24-Bi16A samples, Mn atoms are located in a Nb sublattice. Further calculations made by replacing one of the Na atoms in the second shell with a Bi atom did not reveal a significant difference in the theoretical K-Mn_{Nb} XANES spectrum which is in agreement with our predictions.

Relative to the other samples, an XANES spectrum of the Bi0-Mn4A sample without Bi co-doping shows differences in the relative energy position of the absorption edge and for the intensity of the observed peaks (Fig. 1). Neither the theoretical K-Mn_{Na} spectrum nor the sums of various weights of K-Mn_{Na} and K-Mn_{Nb} spectra converges to the experimental spectrum. However, the theoretical K-Mn_{Nb} spectrum seems to be a closer match to the experimental data than the others, and allows us to draw the conclusion that Mn ions are not located in the sodium sublattice but in the nobium sublattice.

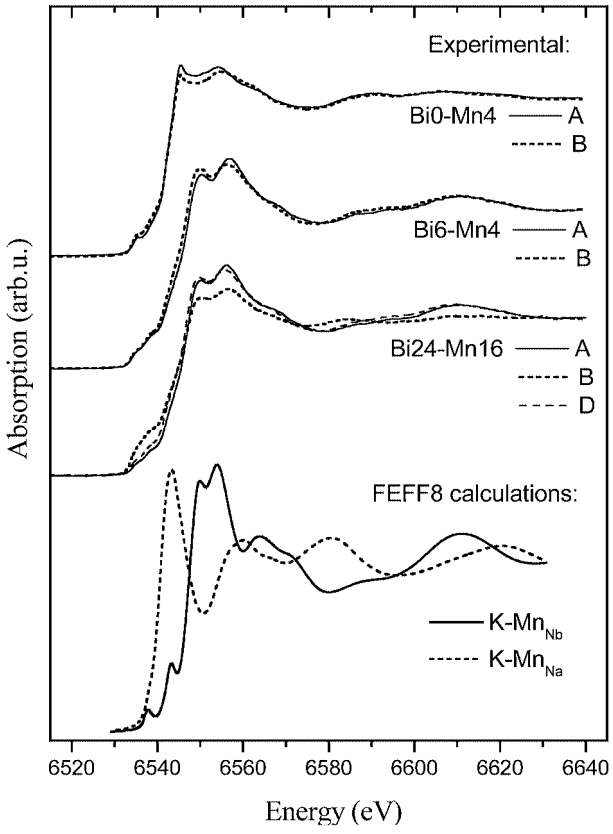

Fig. 1. Mn K-edge spectra calculated for a Mn absorbing atom located in Nb and Na sublattices and measured for samples with and without Bi co-doping (see text for details).

The first sub-shell consists of six oxygen atoms surrounding a Mn atom. Therefore, we expect the spectral shape of the K-Mn absorption edge to be very sensitive to oxygen atom vacancies and for any changes in their geometrical arrangement. Simulations made for Mn-O5 clusters located in the Pbcm structure confirm this assumption. The oxygen vacancy and rearrangement of one of the remaining oxygen atoms causes significant changes in the calculated spectrum. This indicates that oxygen non-stoichiometry and formation of Mn-O5 clusters are a possible cause of the observed differences between the measured and calculated spectra.

It can be concluded that all three ceramic samples (Bi0-Mn4A, Bi6-Mn4A, Bi24-Mn16A) have Pbcm symmetry and all of them have Mn atoms located in a Nb sublattice. However, in the case of Bi0-Mn4A, the crystal structure seems to be deformed because of oxygen defects which provide a charge compensation of Mn presence in the Nb sublattice. For the Bi6-Mn4A and Bi24-Mn16A ceramics, Bi atoms located in a Na sublattice appears to help the charge compensation that stabilizes the crystal structure.

3.2. *"B" series – samples with reduced oxygen content*

For the "B" series samples we expected an increased concentration of oxygen vacancies. This means that the absorption spectra of the "B" series samples should differ from their "A" series prototypes.

However, only the Bi24-Mn16B sample agrees with this prediction (Fig. 1). One can deduce that a significant amount of oxygen vacancies was created during the reduction process and the oxygen reduction procedure was effective. Furthermore, the

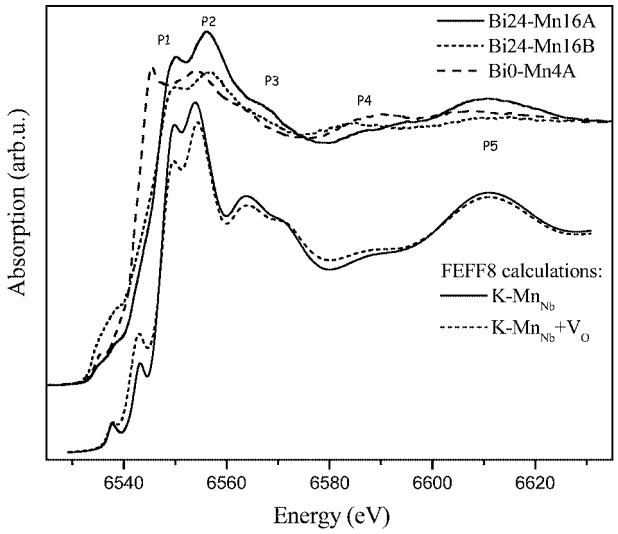

Fig. 2. Experimental Mn K-edge spectra for Bi24-Mn16A, Bi24-Mn16B and Bi0-Mn4A samples in comparison with theoretical calculations for a Mn absorbing atom located in an Nb sublattice (Mn-O6) and for a sublattice with one oxygen vacancy (Mn-O5).

similarity of the Bi24-Mn16A and Bi24-Mn16D spectra indicates that the process is reversible as was expected.

In Fig. 2 we show experimental XANES spectra for the Bi24-Mn16A and Bi24-Mn16B samples and theoretical spectra of an undefected K-Mn_{Nb} cluster and a theoretical spectrum of the same K-Mn_{Nb} cluster with one oxygen atom removed from the first shell without moving other atoms in the cluster. The changes in corresponding peak intensities are shifting in the same directions for all peaks from P1 to P5 which seems to indicate that oxygen vacancies are responsible for the noticed effect and the oxygen reduction procedure in the "B" series was effective.

As compared to the spectrum of Bi24-Mn16A, the tendencies for peaks P2 to P5 for Bi0-Mn4A are the same. This seems to confirm the importance of the role that oxygen defects play in deformation of the structure of the Bi0-Mn4A sample.

The lack of essential differences between the Bi0-Mn4A and Bi0-Mn4B spectra (Fig. 1) suggests that the amount of existing Mn-O5 clusters was close to the saturation level and the heating process used in making the samples may have caused only a slight change in defect concentration.

The Bi6-Mn4A and Bi6-Mn4B spectra are also similar. It seems that undefected Mn-O6 octahedra dominate the structure. It is also probable that the oxygen vacancies are located around Nb atoms forming Nb-O5 clusters and therefore are not visible from a K-Mn edge perspective. However, it is unclear why the amount of defected Mn-O5 clusters did not increase as in the case of the Bi24-Mn16B sample. We can only speculate that this is connected with the exceeded amount of Bi atoms with respect to Mn atoms in the Bi6-Mn4 sample (see Table I). Apparently, the role that Bi atoms play in the stabilization of the crystal structure is larger than expected.

4. Conclusions

XANES measurements, FEFF8 calculations and their analysis lead to the following conclusions:

1. For $(Na^{1+}Bi^{3+})(Mn^{k+}Nb^{5+})O_{3-z}$ ceramics, Mn atoms are located in a Nb sublattice.
2. Co-doped Bi ions help stabilize the crystal structure of the investigated samples.
3. In ceramics with only Mn dopants their presence seems to be compensated by a high amount of oxygen defects.

Acknowledgment

We would like to thank Dr. E. Welter for assistance in measurements at HASYLAB.

This work was partially supported by the State Committee for Scientific Research (Republic of Poland) Grant No. SPUB-M/DESY/P-03/ DZ-213/2000 and by the IHP-Contract HPRI-CT-1999-00040/2001-00140 of the European Commission.

We also acknowledge support from Nevada NSF EPSCoR under grant EPS-0318825.

References

1. Raevski, I. P., Prosandeev, S. A., Bogatin, A. S., Malitskaya, M. A. and Jastrabik, L., J. Appl. Phys. **93**, 4130 (2003).
2. Simon, A. and Ravez, J., Ferroelectrics **240**, 335 (2000).
3. Darlington, C. N. W. and Knight, K. S., Physica **B266**, 368 (1999).
4. Sakowski-Cowley, A. C., Lukaszewicz, K. and Megaw, H. D., Acta Cryst. **B25**, 851 (1969).
5. Zhelnova, O. A., Fesenko, O. E. and Smotrakov, V. G., Sov. Phys.-Solid State **28**, 144 (1986).
6. Pisarski, M., Acta Phys. Polon. **A57**, 413 (1980).
7. Molak, A., J. Phys.: Cond. Matter **9**, 11263 (1997).
8. Molak, A., J. Phys.: Cond. Matter **13**, 9561 (2001).
9. Rezhnitchenko, L. A. *et al*., Inorg. Mater. **33**, 1277 (1997).
10. Reznitchenko, L. A., Geguzina, G. A. and Dergunova, N. V., Inorg. Mater. **34**, 167 (1998).
11. Khemakhem, H., Simon, A., Von Der Muhll, R. and Ravez, J., J. Phys.: Cond. Matter **12**, 5951 (2000).
12. Bykov, I. P., Gejfman, I. N., Deigen, M. D. and Krulikovskii, B. K., Sov. Phys.-Solid State **20**, 109 (1978).
13. Molak, A., Solid State Commun. **62**, 413 (1987).
14. Kubacki, J., Molak, A. and Talik, E., J. Alloys Comp. **328**, 156 (2001).
15. Shannon, R. D., Acta Cryst. **A32**, 751 (1972).
16. Lemanov, V. V., Ferroelectrics **226**, 133 (1999).
17. Singh, G., Tiwari, V. S. and Wadhawan, V. K., Solid State Commun. **118**, 407 (2001).
18. Khim, A. S., Wang, J. and Junmin, X., J. Alloys Comp. **311**, 181 (2000).
19. Ankudinov, A. L., Ravel, B., Rehr, J. J. and Conradson, S. D., Phys. Rev. **B58**, 7565 (1998).

Physica Scripta. Vol. T115, 992–994, 2005

XAFS at Ritsumeikan SR Center

K. Handa[1*], K. Ozutsumi[2] and K. Kojima[2]

[1]Synchrotron Radiation Center, Ritusmeikan University
[2]Faculty of Science and Engineering, Ritsumeikan University, 1-1-1 Nojihigashi, Kusatsu, Shiga 525-8577, Japan

Received June 26, 2003; accepted January 30, 2004

PACS numbers: 07.85.Nc, 07.85.Qe, 78.70.Dm

Abstract

We have constructed an ultra soft X-ray absorption spectroscopy beamline at BL-2 and an XAFS spectrometer at BL-4 using a compact superconducting radiation source of the Ritsumeikan University. BL-2 is composed from an Au coated pre-focusing mirror and a concave diffraction grating with 1200 groves/mm and provides VUV absorption spectra by total electron yield method in the energy range 50–250 eV. BL-2 covers the K-edge absorption energies of elements from lithium to boron in the periodic table. BL-4 is composed of a double crystal monochromator with a working range from 15 to 75 deg and Si(220), Ge(220) and InSb(111) crystals. It covers the energy range of 1700–10500 eV, which corresponds to the K-edge absorption energies of elements from silicon to zinc.

1. Introduction

The X-ray absorption fine structure method is now widely used for structure and electronic state determination of many substances since synchrotron radiation has come to be used for XAFS measurements. Soft X-ray XAFS with K-edge absorption of light elements brings very profitable information in various fields and XAFS stations using soft X-ray have been constructed and developed in many SR facilities.

In 1996, a compact superconducting ring, AURORA, was installed at Ritsumeikan University [1]. Ultra Soft X-ray Absorption Spectroscopy beamline (BL-2) and XAFS beamline (BL-4) were constructed and have been used for research and education [2]. This paper reviews the outlines and measurement results of several standard samples at BL-2 and BL-4.

2. Outline of XAFS beamlines

2.1. *Storage Ring*

AURORA is a superconducting weak-focusing single-body magnet ring. The electron beam that is injected by a race-track-type microtron is boosted up to 575 MeV, and the field strength of the magnet is 3.8 T. The initial stored beam current is 300 mA [3]. As a result, the electron beam radius is 0.5 m and the critical energy of radiation is 844 eV. The electron beam size is 1.3 mm in horizontal and 0.14 mm in vertical direction. AURORA provides intense VUV light and soft X-rays as depicted in Figure 1, and it is very suitable for investigations in VUV and soft X-ray regions.

2.2. *Ultra Soft X-ray Absorption Spectroscopy beamline (BL-2)*

BL-2 is an instrument for ultra soft X-ray absorption spectroscopy in the energy range 50–250 eV, which corresponds to the K-edge energy range from lithium to oxygen in the periodic table. The beamline consists of an Au coated pre-focusing mirror and a concave diffraction grating (1200 groves/mm). The grating, an entrance slit and an exit slit are mounted on a Rowland circle. Absorption spectrum is measured by a total electron yield method that collects electrons emitted from samples with a channeltron detector (Murata Celatron EMT-6081B) or an electron multiplier (Hamamatsu R595).

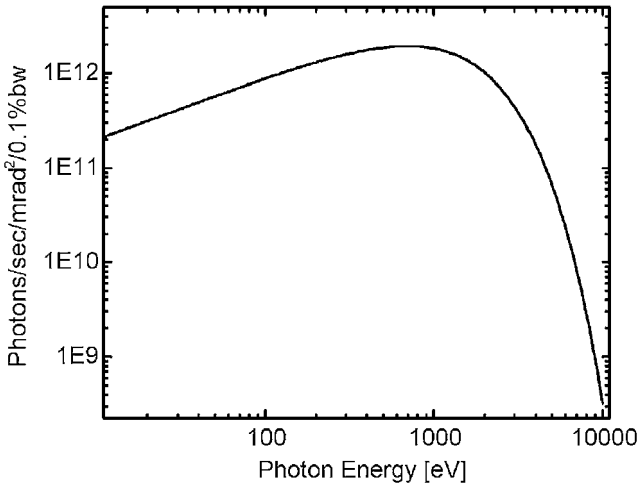

Fig. 1. Spectrum of the radiation emitted from the storage ring, AURORA, at Ritsumeikan SR Center.

The energy resolution is 10000 in $E/\mathrm{d}E$ and the photon flux is 5×10^{10} photons/s at 200 eV. Unfortunately, as shown in Figure 2, it is not possible to neglect the contamination of carbon compounds on grating and X-ray mirror because of the effects of long-time use and contamination of second order harmonics in the region from 50 to 100 eV. However, data with enough quality can be obtained by using energy spectroscopic detectors as channeltrons.

2.3. *XAFS spectrometer (BL-4)*

BL-4 consists of a slit, a double-crystal monochromator (Toyama, Golovchenko type) and detectors [4, 5]. The mechanical movement of the monochromator is in a range from 75° to 15°. The detectors are three ionization chambers (55 mm, 150 mm and 310 mm in length, OKEN), two scintillation counters (SC-50, Rigaku), high purity Ge SSD (Canberra), and Electron multiplier (Hamamatsu). The energy resolution is at least more than 10000 in $E/\mathrm{d}E$ by using Si(220) double crystal and photon flux passing through a 2 mm × 9 mm aperture is 1×10^{10} photons/s at 2400 eV by using InSb (111), as shown in Figure 2. The values, normalized to 1 mm^2, are a few orders of magnitude smaller than those of BL7C at the Photon Factory [6]. However, the quality of XAFS spectra is often degraded by contamination of higher-order harmonics. As shown in Figure 1, the steep decrease of

*e-mail: handa@se.ritsaumei.ac.jp

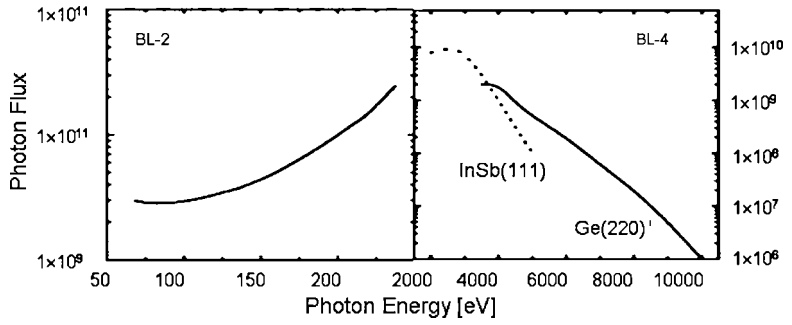

Fig. 2. Photon Flux.

X-ray intensity above 9–10 keV is characteristic of the X-ray spectrum emitted from AURORA. Even for measurements in soft X-ray regions using InSb(111) monochromator, the amount of the second-order harmonics must be negligible small because of the reflection intensity by InSb(222) is related with $(f_{In}-f_{Sb})^2$ for the crystal structure for InSb [7, 8]. Thus, users of this XAFS spectrometer need not to be serious about the contamination of higher-order harmonics. By using Si(220), Ge(220) and InSb(111) crystals, the XAFS spectrometer covers the K-edge absorption energies of elements from silicon to zinc, and the L_{III}-edge from Rb to W.

3. Standard Measurements at BL-2 and BL-4

Figure 3 shows a Li K-edge XANES spectrum of lithium halides, and Figure 4 shows a B K-edge XANES spectrum

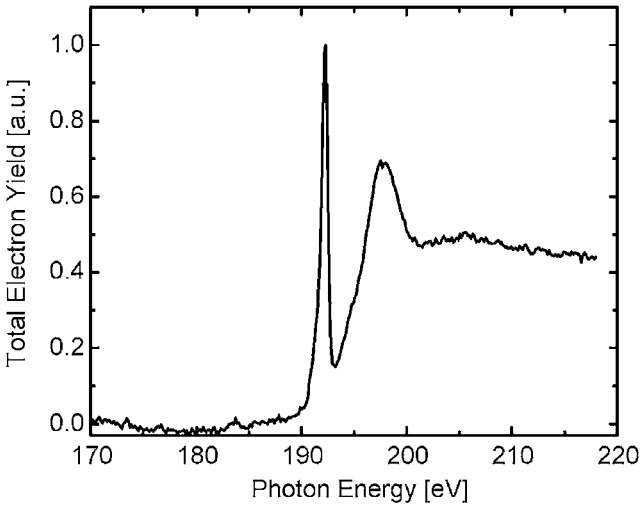

Fig. 4. B K-edge XANES spectrum of B_2O_3 crystal by TEY method at BL-2.

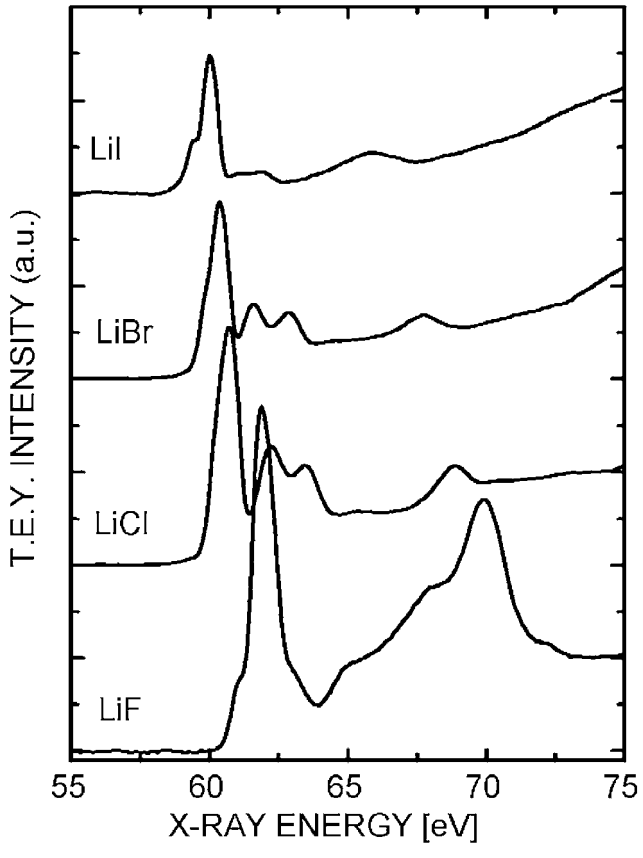

Fig. 3. Li K-edge XANES spectrum of lithium halides by TEY method at BL-2.

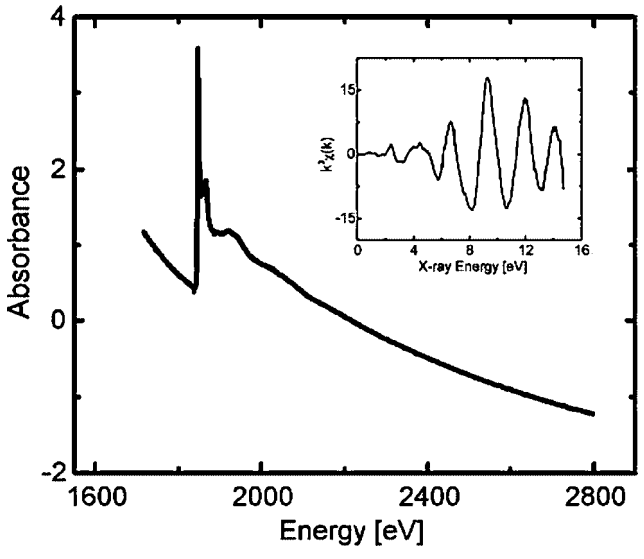

Fig. 5. Si K-edge EXAFS oscillation spectrum of Leucite $K[AlSi_2O_6]$ by transmission mode at BL-4.

of crystalline B_2O_3 powder using BL-2. The measurements were done by TEY method with EM as a detector. These data are in good agreement with the results at the other facilities [9].

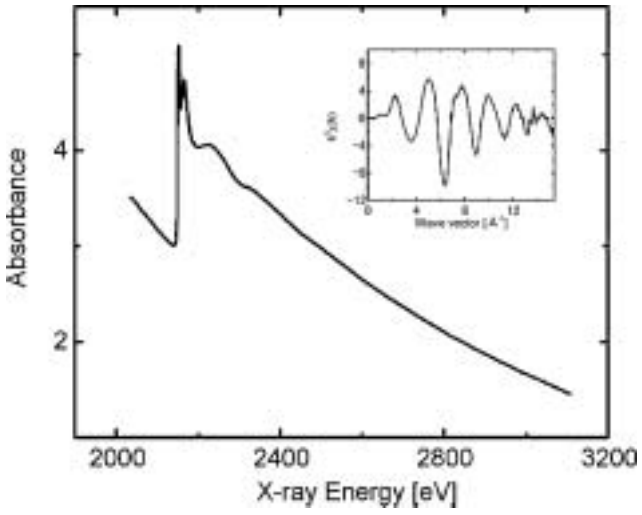

Fig. 6. P K-edge EXAFS oscillation spectrum of triethyl phosphate solution by transmission mode at BL-4.

At BL-4, it is possible to measure K-edges of light elements such as Si, P, and S under atmospheric pressure, and can therefore be applied to solution samples. Figures 5 and 6 depict a Si K-edge EXAFS oscillation of Leucite ($K[AlSi_2O_6]$), and a P K-edge EXAFS spectrum of triethyl phosphate (TEP) by transmission mode at BL-4. These spectru show that high quality data can be obtained at a compact ring.

References

1. Iwasaki, H. *et al*., J. Synchrotron Rad. **5**, 1162 (1998).
2. Tsuji, Y. *et al*., Adv. X-ray Anal. Japan **29**, 23 (1998).
3. Yamamoto, Y. *et al*., Nucl. Instrum. Meth. **A467**/**468**, 921 (2001).
4. Golovchenko, J. A. *et al*., Rev. Sci. Instrum. **52**, 509 (1981).
5. Murata, T. *et al*., J. Phys. (France) 47, Suppl. **C8**, 135 (1986).
6. Nomura, M. *et al*., KEK Report 91-1, National Laboratory for High Energy Physics, Tsukuba, Japan (1991).
7. Handa, K. and Ozutsumi, K., Phys. Chem. Glasses **44**, 171 (2003).
8. Handa, K. and Ozutsumi, K., Rev. Sci. Instrum. **75**, 111 (2004).
9. Fleet, M. E. and Muthupari, S. J., Non-Cryst. Solids **255**, 233 (1999).

Physica Scripta. Vol. T115, 995–997, 2005

Sub-Millimeter Synchrotron X-ray Focusing by Crystal Bender

Y. Yoneda, N. Matsumoto, Y. Furukawa[1)] and T. Ishikawa[2)]

JAERI/SPring-8, Kouto, Mikazuki-cho, Sayo-gun, Hyogo 679-5148, Japan
[1)]JASRI/SPring-8, Kouto, Mikazuki-cho, Sayo-gun, Hyogo 679-5198, Japan
[2)]RIKEN/SPring-8, Kouto, Mikazuki-cho, Sayo-gun, Hyogo 679-5148, Japan

Received June 26, 2003; accepted November 4, 2003

PACS numbers: 41.50.+h, 41.60.Ap, 07.85.−m, 07.85.Qe

Abstract

Sagittal focusing is known as one of the most efficient focusing methods for synchrotron X-rays which increases the photon density at the sample position. Results are reported on the performance of a fixed height exit bender with an unribbed silicon (311) crystal. The fixed height exit was achieved by using a 4-point bending mechanism. This bending mechanism is designed for the SPring-8 standard double crystal monochromater (DCM) of bending-magnet beamlines. By using unribbed crystal, the focused beam size was kept at 0.5 mm in the energy range from 35–60 keV. A dynamical sagittal-focusing test was performed around Dy K-edge (53.787 keV). The results underline that 0.5-mm-focus size and beam position are kept during scanning energies; that is, the XAFS measurement can be performed with a sample size = 1 mm.

1. Introduction

The method to focus monochromatic X-rays without losing energy resolution is important for XAFS experiments in order to get higher photon flux. The tunability of photon energy is essentially important especially in the case of X-ray spectroscopy. A sagittally focusing double-crytal monochromator (DCM) was developed by Sparks *et al*. [1, 2] and it is now used in some bending-magnet (BM) beamlines at SPring-8 [3, 4] and many beamlines at other facilities [5, 6, 7]. Higher energy X-rays above 100 keV are easily available from bending magnets of SPring-8. Therefore, the sagittally focusing for a wide energy range (5–150 keV) is preferable. Merits of sagittal focusing by crystal bender compared with focusing by a mirror or lens are wide energy range especially in the higher region, wide horizontal acceptance, smaller size of optical element, and so on.

At SPring-8, it has been three years since crystal benders for sagittal focusing were installed in a standard DCM [8]. The SPring-8 bender consists of a four-point bending mechanism. At first, we used a series of crystal slabs joined by thin hinges, cut parallel to the bending rods. This bender achieved a fixed-exit sagittal focusing for a wide X-ray energy range in adjustable-inclined geometry by only one pair of crystals. Symmetric 311 reflections and inclined 111, 511 and 733 reflections enabled us to focus.

However, the sagittal focus size was sometimes far larger than what the bender users desired. The width of the focused beam is limited by the polygonal nature of the bent crystal. The smallest horizontal size of the focused beam is 3 mm, which is the size corresponding to that of one crystal segment. We tried to solve the problem by using flat crystal instead of the slotted crystal. However, focusing with flat crystals is limited by the anticlastic bending caused by the non-zero Poisson coefficient since the Bragg planes between the first and second crystals lose their parallelism. One proposed solution involves minimizing the anticlastic curvature by using an unribbed rectangular crystal manufactured so that the length to width aspect ratio of the crystal has a particular value and insuring that the modeled boundary conditions are met in the final design. Since synchrotron X-rays test with Si(111) crystal at NSLS [2] confirmed that good sagittal focusing was obtained, the same design crystal was manufactured with Si(311).

Here we report the results of sagittal focusing test using the SPring-8 bending mechanism. The slotted bent crystal is replaced with an Si(311) unslotted (unribbed) crystal. A reasonably good focusing size of 0.5 mm was achieved from 35 keV to 60 keV. Moreover, a dynamic sagittal-focusing (fixed-height exit fixed size focusing with changing energies) is required for XAFS measurements. A dynamic sagittal test was also performed by measuring the Dy-K edge XAFS spectrum.

2. Crystal design

As Kushnir *et al*. have shown [9, 10], the anticlastic curvature can be minimized for a rectangular crystal with "clamped" or "biltin" boundary conditions if the length to width ratio (γ) of the crystal is 1.42. The test crystal used in this study was manufactured from 98 mm × 90 mm × 2 mm float zone silicon. After final etching, the ratio (γ) of the crystal is 1.435, as shown in Fig. 1.

3. Experimental

The focusing test was carried out at BL14B1 of SPring-8, which is a bending-magnet beam-line dedicated to JAERI equipped with

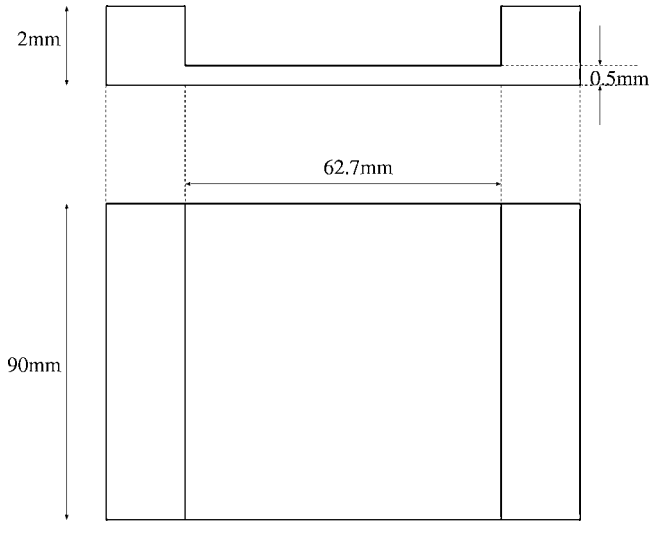

Fig. 1. Schematic diagram of the Si(311) test crystal used in this study. The crystal is machined out of a single Si(111) cylinder 100 mm in diameter by 100 mm thick to leave final rectangular Si(311) crystal dimension of 62.7 mm × 90 mm × 0.5 mm with thick supports.

a SPring-8 standard double-crystal monochromator. The fixed-exit bender was mounted on the second crystal stage of the monochromator. A pair of (311) Si crystals were used both for the first and second crystals. As for the first crystal, an indirect cooled flat plate was used instead of the standard SPring-8 direct fin-cooled crystal. The electron beam current during the test was around 100 mA.

The monochromator was located 36.5 m ($F_1 = 36.5$ m) from the source, where the horizontal beam size of the beam on the first crystal was 50 mm. To observe the focusing properties, beam images were recorded for different bending radii on Polaroid films (type 55) placed at a point 48.5 m from the source, where samples are usually put. Thus, the monochromator-focus point distance, F_2, was 16.5 m. These distances give a focusing ratio ($M = F_2/F_1$) of approximately 1/3. At the optimal bend in radius for each energy, intensity profiles were measured by scanning a 0.5 mm wide slit both horizontally and vertically. The horizontal scan showed the focusing property, whereas the vertical scan gave the beam height fluctuation. A series of tests gave us the optimal radius at each energy. We used the radius data for dynamic sagittal focusing [11], for which an absorption spectrum around the Dy K-edge was demonstrated.

4. Results and discussion

The beam images at the sample position for several values of the bending radius, R, are reproduced in Fig. 2 at 38 keV with 311 reflection. The crystal had $R = 8.0$ m when it was mounted on the bender. The horizontal beam size was 47 mm at the screen position for the maximum bent radius. At optimal focusing ($R = 4$ m), the horizontal sizes of the beam approached 0.5 mm, being larger than the theoretical value (0.2 mm).

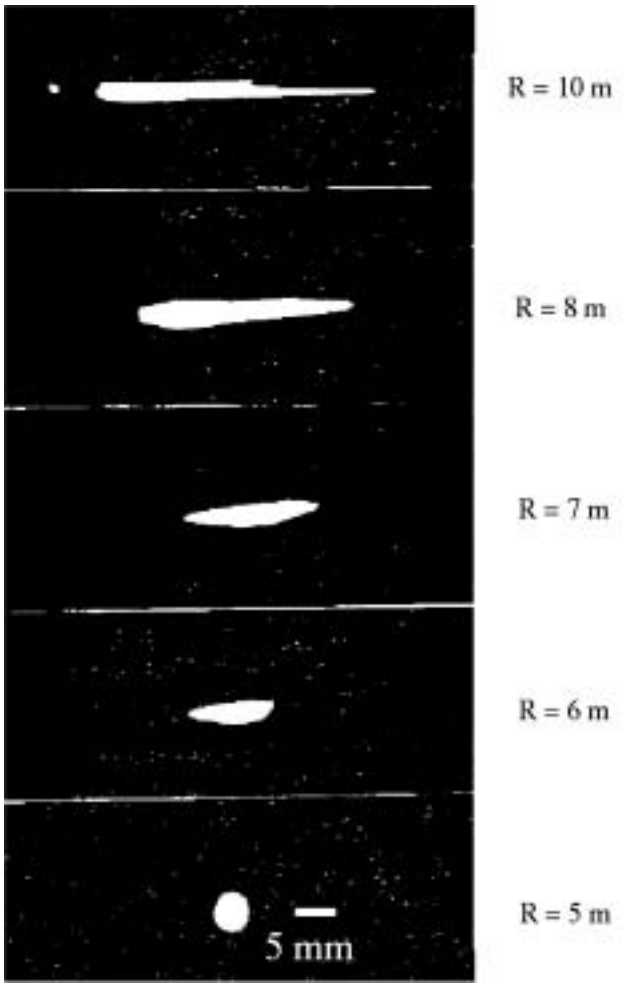

Fig. 2. Beam profiles obtained with the sagitally focusing crystal monochromator at 30 keV. The X-ray beam was focused by decreasing bending radius R.

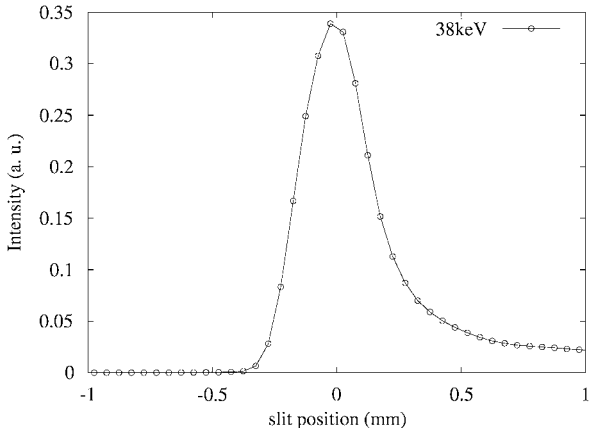

Fig. 3. Horizontal beam profile measured by moving a 500 μm slit on a sample stage, across the focused beam.

Figure 3 shows a spatial intensity profile measured at 38 keV by scanning a slit horizontally at the 3:1 focus position for the bent ($R = 4$ m) crystal. The slit used had 0.5-mm-width and was made of tungsten carbide. The measured increase of the flux density at the focal point was 70 times more than that of the flattened crystal, which is a little less than the ideal value due to the smaller diffraction efficiency of the bent crystal.

Energy resolution was measured with near-edge absorption data runs on the Dy K-edge at 53.787 keV in Dy foil, using the setup shown in Fig. 4(a). The 0.5-mm-focused incident X-rays were introduced through a 1.0 mm pin-hole slit. XAFS measurement was performed by dynamic sagittal focus mode, which means that the bending radius is optimized at every measurement energy from 53.6 keV to 54.2 keV. In Fig. 4(b)

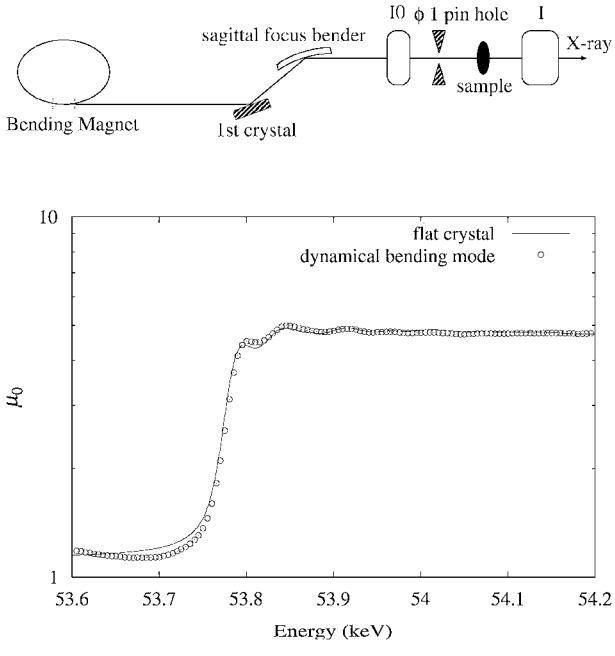

Fig. 4. (a) Experimental setup for XAFS measurement with sub-millimeter focusing beam. (b) Near-edge absorption spectra of Dy foil, registered in a dynamically focusing mode (circles) and with a flat crystal (line).

we compare the near-edge spectrum of Dy foil registered in the dynamically focusing mode on BL14B1 with a normal flat crystal on BL01B1 that is specialized for XAFS measurements at SPring-8 [12]. The two spectra are identical so we conclude that the energy resolution is not affected by sagittal focusing, nor are any distortions introduced.

Sub-millimeter synchrotron X-ray focusing was successfully achieved in the energy range from 38 keV to 57 keV by combining the unslotted crystal and SPring-8 standard bend mechanisms. In this performance test, changing the radius of curvature from 4 to 8 m dose not cause any significant change in the beam intensity.

5. Summary

Sagittal focusing was tested by using unslotted crystal that is designed for the SPring-8 standard benders. The flux density of the focusing X-ray beam was increased by 70 times compared with that using flat-flat double crystals. The dynamic sagittal focusing test was successfully performed with 1.0 mm pin-hole slit. This assures that XAFS measurements with millimeter-size samples are achievable by using the SPring-8 standard bender and the unslotted crystal.

Acknowledgments

This work was supported by Hyogo Science and Technology Association.

References

1. Sparks, Jr. C. J., Borie, B. S. and Hastings, J. B., Nucl. Instrum. Meth. **172**, 237 (1980).
2. Sparks, Jr. C. J., Borrie, B. S. and Hastings, J. B., Nucl. Instrum. Meth. **195**, 73 (1982).
3. Yoneda, Y., Matsumoto, N., Furukawa, Y. and Ishikawa, T., J. Synchrotron Rad. **8**, 18 (2001).
4. Yoneda, Y., Matsumoto, N., Furukawa, Y. and Ishikawa, T., Nucl. Instrum. Meth. A **467–468**, 370 (2001).
5. Pascarelli, S. *et al*., J. Synchrotron Rad. **3**, 147 (1996).
6. Matsushita, T., Ishikawa, T. and Oyanagi, H., Nucl. Instrum. Meth. A **246**, 377 (1986).
7. Koyama, A. *et al*., Rev. Sci. Instrum. **63**, 916 (1991).
8. Yabashi, M. *et al*., SPIE **3773**, 2 (1999).
9. Kushnir, V. I., Quitana, J. P. and Geogopoulos, P., Nucl. Instrum. Meth. A **328**, 588 (1993).
10. Kushnir, V. I., Quitana, J. P. and Rosenbaum, G., Nucl. Instrum. Meth. A **362**, 592 (1995).
11. Lamble, G. M. and Heald, S. M., Rev. Sci. Instrum. **63**, 880 (1992).
12. Uruga, T. *et al*., SPIE **3773**, 2 (1999).

Physica Scripta. Vol. T115, 998–1000, 2005

A Bent Silicon Crystal in the Laue Geometry to Resolve Actinide X-Ray Fluorescence for X-Ray Absorption Spectroscopy

A. J. Kropf†, J. A. Fortner[1], R. J. Finch[1], J. C. Cunnane[1] and C. Karanfil[2]

[1]Chemical Engineering Division, Argonne National Laboratory, Argonne, IL 60439, USA
[2]Illinois Institute of Technology, Chicago, IL 60616, USA

Received June 26, 2003; accepted in revised form December 17, 2003

PACS numbers: 61.10.Ht, 28.41.Kw

Abstract

A highly strained, curved silicon crystal in the Laue geometry has been used as a large area X-ray fluorescence analyzer for X-ray absorption spectroscopy. The analyzer is able to resolve the Lα fluorescence lines for neighboring actinide elements. A large gain in the signal-to-background ratio has been achieved for low levels of Mo, Np, and Pu in a UO_2 matrix. We have determined the chemical state of these elements in approved testing materials of uranium oxide spent nuclear fuel. Due to inelastic scattering from the predominant uranium, the concentration of Np measured, 0.6(2) mg Np/gram U, may be approaching the sensitivity limits for quantitative structural spectroscopy measurements.

1. Introduction

The primary limitation to using X-ray absorption fine-structure (XAFS) spectroscopy for many interesting environmental and biological problems is the presence of a high level of background radiation from a variety of sources, such as elements with lower energy absorption edges, radioactive elements, or scattered radiation from other beam interactions with the sample. We have demonstrated the effectiveness of a bent silicon wafer curved to a logarithmic spiral in the Laue geometry (bent Laue analyzer or BLA) to resolve neighboring actinide Lα lines and to measure the XAFS spectra of as low as 0.6 mg Np/gram U. In the process of making these measurements, we have found that inelastic scattering attributable to the uranium may pose an ultimate limit to quantitative XAS measurements on Np.

The design concept of the BLA has been discussed previously [1, 2]. The essential property of such an analyzer is that bending the crystal to a logarithmic spiral solves the mismatch between the narrow acceptance angle of a perfect crystal and the large divergence of fluorescence from the sample [1, 3, 4]. Except for the case in which the asymmetry angle is equal to the Bragg angle and the logarithmic spiral becomes a cylinder, the correct form is difficult to produce accurately with dynamical bending [1]. Therefore, we have used a fixed bender form, a CNC-milled aluminum block, over which the silicon wafer was bent. The instrument used for this experiment, with the exception of the silicon wafer, is described elsewhere [5].

2. Experiment

Measuring the L-edge fluorescence XAFS in mixed actinide samples is a challenging problem. For the samples we report here, excellent energy resolution is required, as the Lα_1 fluorescence lines for U, Np, and Pu are separated only by ca. 350 eV; the Lα_2 lines are separated by less than 150 eV from neighboring Lα_1 lines. We have used the BLA to study an approved testing material (ATM) of spent uranium oxide nuclear fuel that is primarily uranium(IV) oxide. This sample also contains small quantities of fission products [6–9]. We have also studied oxidized alteration phases that formed on the surface of this ATM during aqueous corrosion testing [6]. The matrix in the alteration phases is predominantly uranium(VI) oxide [8], easily distinguishing these particles from the unaltered spent fuel. We did not observe Np incorporated into the alteration phases, with an estimated sensitivity of better than 0.3 mg Np/gram U [8].

All measurements reported here were carried out on the MR-CAT undulator beamline, 10-ID, at the Advanced Photon Source (APS), Argonne National Laboratory. A cryogenically cooled Si(111) double-crystal monochromator was used to select the incident energy. An uncoated ULE glass mirror was used to reject higher-order harmonic content of the beam, so as not to rely upon the focusing mirrors for this critical function [10]. Kirkpatrick-Baez mirrors, positioned downstream of the harmonic rejection mirror, provided a focused beam smaller than 10 μm × 10 μm from an incident beam of ca. 250 μm × 250 μm (about 5% of the total incident beam).

The 140 μm Si wafer used for the BLA had a ⟨100⟩ surface normal and the ⟨111⟩ planes were used as the diffracting planes, resulting in a 35.3° asymmetry angle. The active area was a 30 mm × 120 mm rectangular window cut into the bender form to allow the X-rays to pass through to the detector. Direct X-rays were rejected by 70 mm long stainless-steel Soller slits, spaced at 1° intervals (about 3.6 mm apart at the analyzer center). Two NaI scintillation detectors were used to detect X-rays. The highest energy resolutions achieved for the analyzer were 71 eV and 79 eV (FWHM) at the positions of the two detectors, at the uranium Lα_1 fluorescence line (13615 eV).

3. Results and Discussion

3.1. *X-Ray Absorption Spectra*

Figure 1a shows a scan of the intensity vs. energy for the ATM sample as the incident energy is held fixed both below and above the Pu L_3 edge while the analyzer angle is scanned. Strontium Kα fluorescence is visible in both scans. The U Lα_1 fluorescence line is suppressed slightly by self-absorption as well as detector saturation. The Np Lα fluorescence is not visible on this scan due to the noise level. Figure 1b shows the fluorescence spectrum with the incident energy above and below the Mo K edge. The analyzer position and slits were optimized for Mo Kα radiation; as a consequence, the analyzer is clearly not aligned properly for the U Lα lines on the far left of the scan. Five fluorescence peaks are identified as the uranium Lβ lines, while the Mo Kα line appears, fortuitously, between two uranium Lβ lines. The resolution of this detector gives us unprecedented sensitivity to such minor constituents.

†email: kropf@cmt.anl.gov

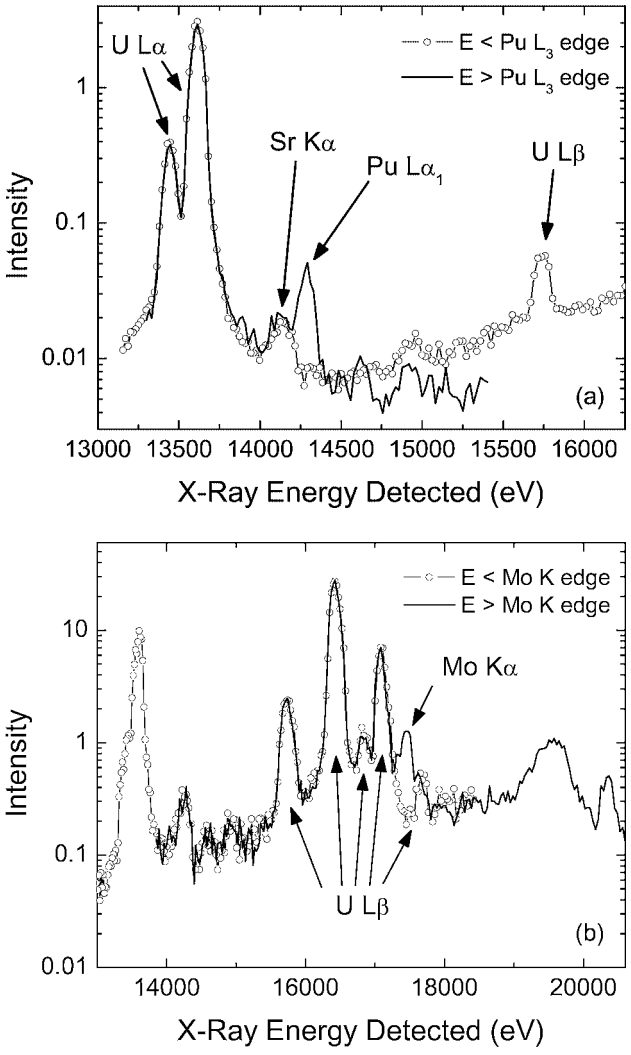

Fig. 1. Bent Laue analyzer angle scans with ATM sample. (a) Incident X-ray energy above and below the Pu L_3 edge, optimal tune for Pu Lα_1. (b) Incident X-ray energy above and below the Mo K edge, optimal tune for Mo Kα.

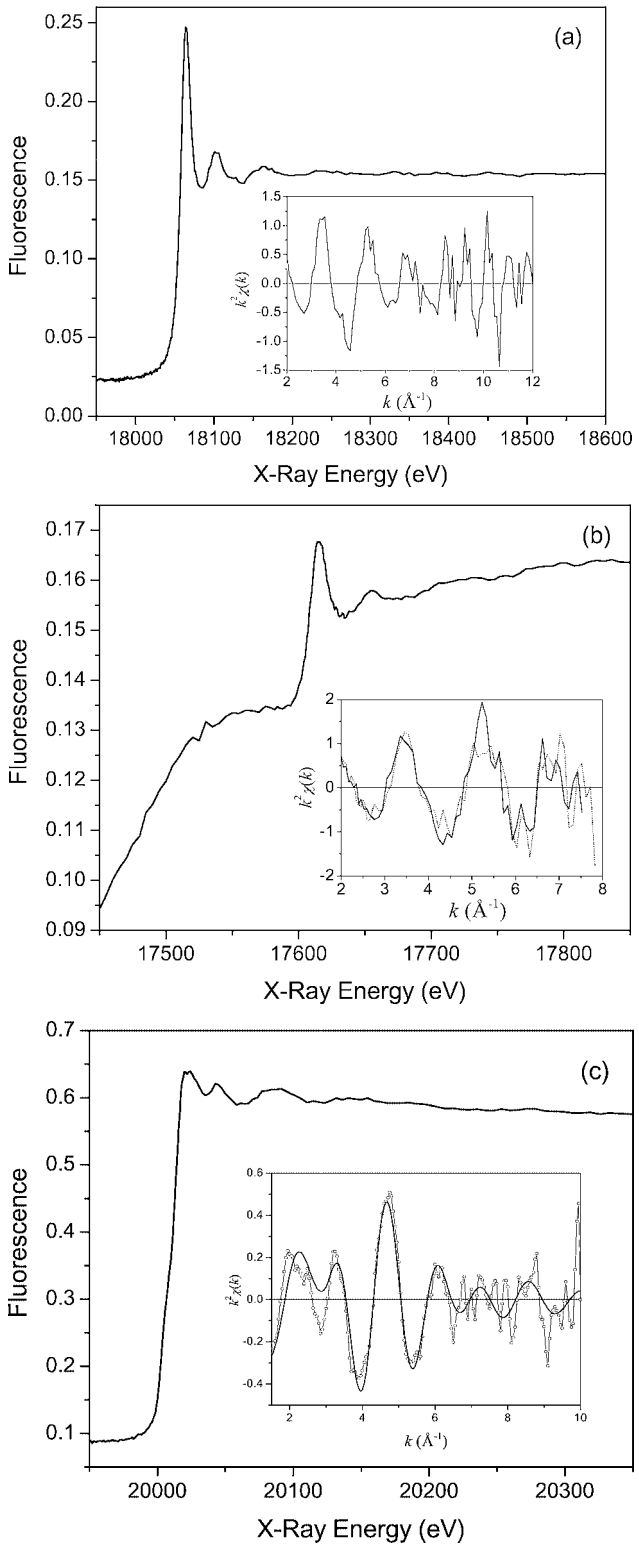

Fig. 2. X-ray absorption spectra of ATM sample using the BLA. (a) Pu L_3 edge and $\chi(k)$ data (inset). (b) Np L_3 edge and $\chi(k)$ data from the two detectors (inset), and (c) Mo K edge data with $\chi(k)$, dotted line and fit (inset).

Figure 2 shows the absorption spectra for Pu, Np, and Mo in the ATM sample. Plutonium, with the highest concentration (8.3 mg Pu/gram U [9]), gives the best signal. The $\chi(k)$ data clearly identifies the Pu in a PuO_2-like phase [11]. Fitting using methods similar to ref. [11] results in $R_{\text{Pu-O}} = 2.33(1)$ Å and $R_{\text{Pu-Ac}} = 3.86(2)$ Å, where Ac stands for Pu or U, which have similar backscattering amplitudes and phase shifts. This is quite similar to bulk PuO_2 from [11]: crystallographic structure fm-3m, $R_{\text{Pu-O}} = 2.344$ Å and $R_{\text{Pu-Pu}} = 3.833$ Å. Far more likely than the existence of a separate PuO_2 phase, is the incorporation of the Pu into the UO_2 matrix (also fm-3m).

The Mo is present in a lower concentration (3.0 mg Mo/gram U [9]) and the Fourier transform reveals some Mo-O ($R = 2.14(5)$ Å) and a larger number of Mo-metal ($R = 2.61(4)$ Å) scattering paths, indicating that the Mo is present in both oxide and metallic forms. Analysis of this spectrum is continuing as the Mo-metal Debye-Waller factor is large and may be contributing to an unusually short distance. At this point it is not possible to distinguish between two different phases or a phase containing both oxygen and metal bonds.

The Np is present in an even smaller amount: 0.4 mg Np/gram U calculated by Guenther *et al.* [9], or 0.6(2) mg Np/gram U as measured from the fluorescence spectra. The background on which the Np L_3-edge spectrum rides is comprised of the uranium fluorescence that makes it through to the detector and an unexpected contribution from inelastic scattering attributable to the uranium, to be discussed below. At 1 part in 1700, the Np signal to background ratio is 0.15, barely large enough to measure a usable EXAFS signal. The data shown are summed from 24 hours of data acquisition. Clearly much better counting statistics are needed to truly reveal the Np coordination environment. Nevertheless, from comparing the XANES to published spectra it seems reasonable to assign to the Np a +4

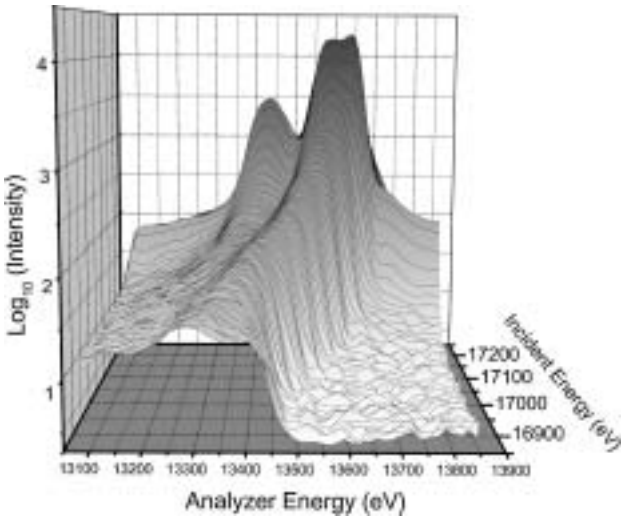

Fig. 3. X-ray fluorescence and inelastic scattering. Log_{10}(intensity) vs. incident energy and analyzer energy.

oxidation state [12]. The $\chi(k)$ data for the two detectors (inset, Fig. 2b) is also suggestive of Np in a UO_2-like phase given the similarity to the PuO_2 and UO_2 spectra ($R_{\text{Np-O}} = 2.34(3)$ Å and some evidence for $R_{\text{Np-Ac}} = 3.85(4)$ Å). Higher quality data to $12\,\text{Å}^{-1}$ would make this a much more convincing argument. If these data are corroborated by further evidence, the Np is also likely dispersed in the UO_2 on the U sites.

While the resolution of the analyzer is quite good, and the Np and U Lα peaks are well-resolved, the Np fluorescence at 13944 eV still sits on a background of uranium fluorescence. The tail of the uranium fluorescence distribution, at the position of the Np Lα_1 peak, is down by a factor of ca. 300 from scans (not shown) in which the uranium peak has not saturated the detector and self-absorption has been minimized. A higher resolution analyzer could potentially lower the background level and improve the sensitivity to Np.

3.2. *Inelastic scattering*

Figure 3 shows the X-ray intensity vs. the incident X-ray energy and the analyzer (output) energy. The two largest peaks are the uranium Lα_1 and Lα_2 fluorescence lines. One can clearly see the long tails to these peaks when the incident energy is *below* the U L_3 absorption edge threshold, where these U core levels are not excited. This is not due to an impure incident energy spectrum. Moreover, since the outgoing photon energy is different than the uranium fluorescence energies, these X-rays are not due to fluorescence decay. In fact, the energy of these background photons corresponds to the energy of the incident photons minus the uranium $M_{4,5}$ edge energies. As the incident energy approaches the U L_3 edge, the inelastic scattering appears to be resonantly enhanced, until it merges with the uranium Lα fluorescence line. As an aside, with an analyzer of high enough resolution, one could measure the uranium M edge spectra using high-energy X-rays by scanning the analyzer energy or by fixing the analyzer energy and scanning the incident energy.

Inelastic scattering could prove to be a fundamental limit for sensitivity to Np in a uranium matrix, or in similar systems, as it creates a background that cannot be discriminated against by any method, since the photons are, in fact, at the same energy as the photons of interest. With a higher resolution detector, the background level could be reduced, since fewer photons would be within the detector bandwidth. On the other hand, a smaller bandwidth means that the M edge structure would not be convoluted with a low resolution analyzer. Therefore, the M edge white line or EXAFS oscillations could contaminate the Np edge data. Figure 2b shows the uranium inelastic scattering that appears at lower energy than the Np L_3 edge. The onset energy of this feature can be altered by adjusting the angle of the analyzer. This property combined with the width of the inelastic scattering feature unambiguously distinguishes it from the Np fluorescence.

4. Conclusions

The bent Laue analyzer has exhibited promising results for a very difficult system. In fact, the high background rejection observed could recommend this type of detector for other applications. A bent Laue analyzer with a peak-to-valley ratio of better than 500 : 1 extends the useful spectroscopy limits by as much as a factor of 50 times compared to current state-of-the-art multielement germanium detectors, when used for mixed actinides. With a higher resolution analyzer (thinner crystal) and slightly more efficient Soller slits, it is likely that an additional factor of 3 in sensitivity could be achieved. However, given the interference of inelastic scattering, it is difficult to envision taking useful EXAFS spectra at concentrations lower than 0.05 mg Np/gram U.

Acknowledgments

Portions of this work were funded by the U.S. Department of Energy (USDOE), Office of Civilian Radioactive Waste Management, Yucca Mountain Program, and by the Nuclear Energy Research Initiative, USDOE Office of Nuclear Energy. Use of the Advanced Photon Source was supported by the U.S. Department of Energy, Office of Science, Office of Basic Energy Sciences, under Contract No. W-31-109-Eng-38. Work performed at MR-CAT is supported, in part, by funding from the Department of Energy under grant number DEFG0200ER45811.

The submitted manuscript has been created by the University of Chicago as Operator of Argonne National Laboratory (Argonne) under Contract No. W-31-109-ENG-38 with the U.S. Department of Energy. The U.S. Government retains for itself, and others acting on its behalf, a paid-up, nonexclusive, irrevocable worldwide license in said article to reproduce, prepare derivative works, distribute copies to the public, and perform publicly and display publicly, by or on behalf of the Government.

References

1. Zhong, Z. *et al.*, Synchrotron Rad. **6**, 212 (1999).
2. Karanfil, C. *et al.*, CP521, Synchrotron Radiation Instrumentation: SRI99: 11th U.S. National Conference, P. Pianetta *et al.*, eds., 178 (American Institute of Physics, New York, 2000).
3. Sakayanagi, Y., Jap. J. Appl. Phys. **21**, L225 (1982).
4. Wittry, D. B., Chang, W. Z. and Li, R. Y., J. Appl. Phys. **74**, 3534 (1993).
5. Kropf, A. J. *et al.*, Rev. Sci. Inst., submitted.
6. Finn, P. A., Tsai, Y. and C. Cunnane, J. C., Mat. Res. Soc. Symp. Proc. **713**, 607 (2003).
7. Finch, R. J., Buck, E. C., Finn, P. A. and Bates, J. K., Mat. Res. Soc. Symp. Proc. **556**, 431 (1999).
8. Fortner, J. A., Finch, R. J., Kropf, A. J. and Cunnane, J. C., Nucl. Tech., to be published.
9. Guenther, R. J. *et al.*, "Characterization of Spent Fuel Approved Testing Material – ATM-103", PNL-5109-103, Pacific Northwest Laboratory, Richland, WA (1988).
10. Segre, C. U. *et al.*, CP521, Synchrotron Radiation Instrumentation: SRI99: 11th U.S. National Conference, P. Pianetta *et al.*, eds., 419 (American Institute of Physics, New York, 2000).
11. Richmann, M. K., Reed, D. T., Kropf, A. J., Aase, S. B. and Lewis, M. A., J. Nucl. Mater. **279**, 303 (2001).
12. Soderholm, L., Antonio, M. R., Williams, C. and Wasserman, S. R., Anal. Chem. **71**, 4622 (1999).

Physica Scripta. Vol. T115, 1001–1003, 2005

The INE-Beamline for Actinide Research at ANKA

Melissa A. Denecke[1*], Jörg Rothe[1], Kathy Dardenne[1], Hubert Blank[2] and Josef Hormes[2]

[1]Forschungszentrum Karlsruhe, Institut für Nukleare Entsorgung, P.O. Box 3640, D-76021 Karlruhe
[2]Universität Bonn, Physikalisches Institut, Nußallee 12, D-53115 Bonn

Received June 26, 2003; accepted November 4, 2003

Abstract

The Institut für Nukleare Entsorgung (INE) at the Forschungszentrum Karlsruhe is presently constructing and will commission and operate an X-ray spectroscopy beamline dedicated to actinide research at the new synchrotron source ANKA. One great advantage of the INE-Beamline is that on-site, in situ actinide research is possible for studying, e.g., solid-water interface chemical reactions, which are not possible at other facilities. The design is for a multi-purpose beamline, i.e., a number of methods (XAFS, surface sensitive and spatial resolved techniques) are possible on one and the same sample. Planned is a safe and flexible containment concept for activities up to 10^6 times the limit of exemption. The design will allow spectroscopic investigations using photon energies from the K edge of S (2477 eV) to the Rh K-edge (23220 eV). The optics include collimating and focusing mirrors for a sub-mm beam dimension at the sample position. A later upgrade is planned to install auxiliary μ-focusing optics (e.g., a single bounce elliptical monocapillary or planar compound refractive lenses). The monochromator at the INE-Beamline is a Lemonnier type double-crystal X-ray monochromator (DCM), built at the Universität Bonn, Physikalisches Institut. The pressure inside the small diameter (380 mm) vacuum housing is $\sim 10^{-6}$ mbar, allowing fast changes of crystals, avoiding long pumping times. Multi-layer mirrors can be used in the DCM for wide band-pass experiments, e.g., for X-ray fluorescence analysis measurements. Installation of beamline components has been completed in October 2003. Operation begin is targeted for 2004.

1. Introduction

The Institut für Nukleare Entsorgung (INE) is designing, constructing and will commission and operate an X-ray spectroscopy beamline dedicated to actinide research at ANKA. There is a deficit of synchrotron facilities, where the infrastructure, safety equipment and expertise are available for performing research on radioactive samples. The INE-Beamline will help meet the growing demand for these investigations. One great advantage of the INE-Beamline is that the ANKA facility and INE's active laboratories are both located at the Forschungszentrum Karlsruhe. This not only minimizes hazards and simplifies administrative obligations associated with transporting radioactive samples to and from a controlled area laboratory and the synchrotron but also optimizes sample preparation and can allow for investigations of dynamic systems within a time-frame of hours. Samples can be prepared, characterized and analyzed using the spectroscopic, microscopic and structural methods available in INE before being investigated using synchrotron based methods at the INE-Beamline within a short time. The samples are also retrievable, so that sample characterization in INE laboratories shortly following the experiments at the beamline is possible.

2. The ANKA Light Source and the INE Beamline

The ANKA storage ring is operated at 2.5 GeV with a characteristic energy of 6.0 keV and presently with a beam current of ∼200 mA. The ring is refilled twice a day. The beam lifetime ranges from 15 to 30 h. The overview of the ANKA light source with the accelerator components and the beamlines installed in the $60 \times 60\,m^2$ experimental hall is depicted Fig. 1. The INE-Beamline is located at the bending magnet port designated 3.2–5 at the east side of the building. The envelope of the radiation protection hutch and the control cabin with integrated lock room bordering the experimental section of the radiation protection hutch is shown in Fig. 1.

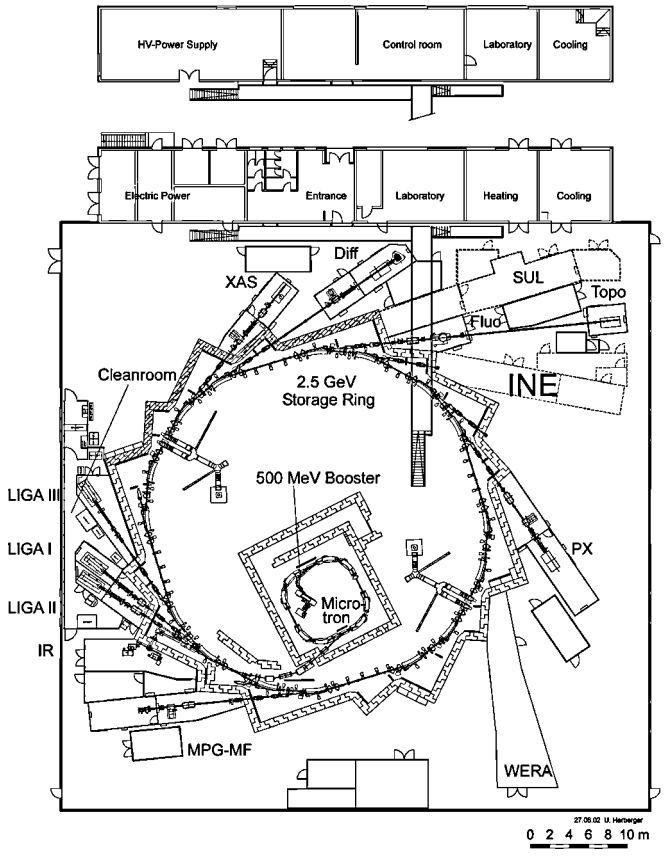

Fig. 1. Overview of the ANKA light source with the main accelerator and the beamlines installed in the $60 \times 60\,m^2$ hall. The location of the INE-Beamline (port 3.2–5) is indicated on the right.

3. INE-Beamline design and X-ray spectroscopic methods available for actinide speciation

The research and development at INE is largely aimed at safety assessment of proposed deep geological repositories for high-level, heat producing nuclear waste disposal. To ensure valid performance safety assessment, a molecular understanding of processes determinant in the fate of radionuclides, notably the actinides, is essential. A major portion of research at INE is concerned with

*e-mail: melissa@ine.fzk.de

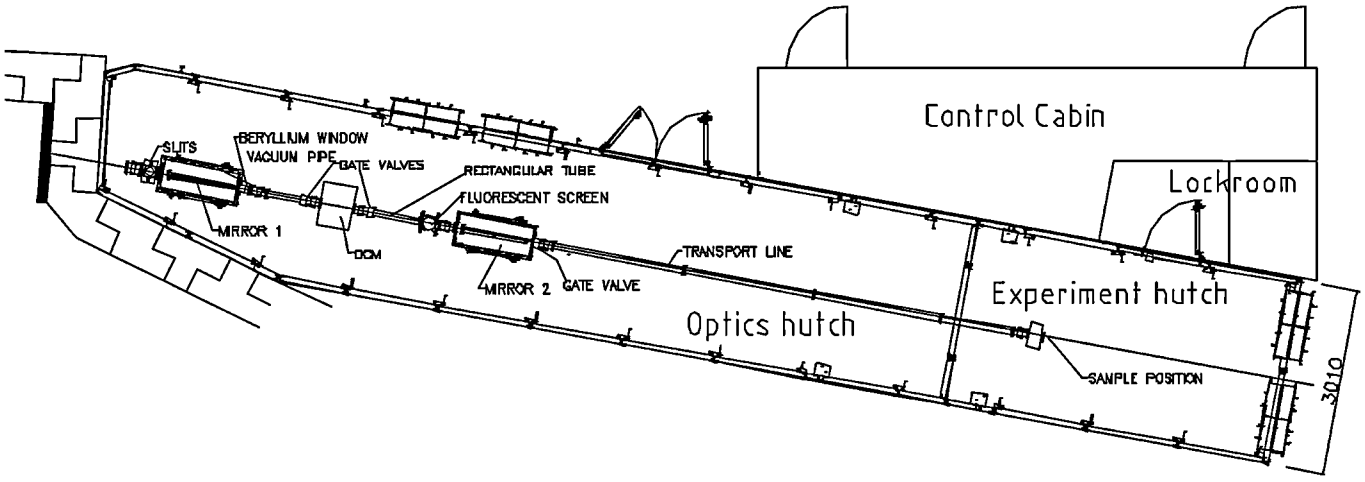

Fig. 2. INE-Beamline design layout. The beamshutter between optics and experiment hutch is not shown.

actinide speciation, including coordination and redox chemistry of actinides, determination and characterization of actinide cations sorbed onto surfaces (e.g., at the mineral-water interface), investigation of actinide containing precipitates, colloids and secondary phases, as well as glass and spent fuel corrosion. Because actinide speciation associated with nuclear disposal concerns is manifold, the INE-Beamline design is for a multi-purpose experimental station, i.e., a number of methods are possible on one and the same sample. The methods available are standard, surface sensitive and spatially resolved methods. The standard X-ray methods X-ray absorption fine structure (XAFS) and X-ray fluorescence (XRF) are available and it is possible to combine XAFS with X-ray diffraction (XRD). Because many reactions of actinides in the hydro- and geospheres are at interfaces and junctions, emphasis at the INE-Beamline is being placed on surface sensitive techniques based on grazing incidence (GI) geometry such as GI-XAFS, X-ray reflectivity and total external reflection X-ray fluorescence analysis (TXRF). In addition, a micro-focus option will be available after a planned future upgrade to offer spatially resolved measurements. This will allow chemical state imaging (μ-XAFS), elemental mapping (μ-XRF) and, to a limited extent, identification and distribution mapping of phases (μ-XRD).

Investigation of samples with activities up to 10^6 times the limit of exemption will be possible. The necessary infrastructure and safety equipment is available for active experiments. For example, the experimental section of the radiation hutch is equipped with a special ventilation/filter system, specially sealed chicanes, easily decontaminated surfaces and a personnel lock room with a hand-foot monitor for entry and exit. During the experiments, the samples themselves are contained within two levels of containment. The first is typically a sealed sample cuvette, vial or plastic bag. The second containment generally is a mechanically stable box or cylinder having sealed windows for beam entrance, transmitted beam and fluorescent beam, into which a sample or a number of samples on a sample changing stage are mounted. The windows are made of low-Z material, e.g., Kapton® or polycarbonate. A special protocol for working with radioactive samples at the INE-Beamline exists and must be adhered to. A portion of annual beamtime will be available at the INE-Beamline via the standard ANKA proposal procedure. Experiments are also possible through cooperation with INE. The INE-Beamline is also a pooled facility in the European ACTINET Network of Excellence.

3.1. *Optics*

The layout of the INE-Beamline design is given in Fig. 2. The design will allow spectroscopic investigations using photon energies from the K edge of S (2472 eV) to the Rh K-edge (23220 eV). The optics include Rh-coated collimating and focusing mirrors for a sub-mm beam dimension at the sample position. The synchrotron radiation beam is vertically collimated through the cylindrical mirror (M1) prior to entering the double-crystal monochromator (DCM). Upstream from the DCM, the beam is focused horizontally and vertically through a toroidal mirror (M2). A later upgrade is planned to make auxiliary μ-focusing optics available within the experimental hutch, e.g., a single bounce elliptical monocapillary or planar compound refractive lenses. These have the advantage for working with radioactive samples within their an air-tight containment barrier in that the focal length can be a number of centimeters.

3.2. *Monochromator*

The monochromator at the INE-Beamline is a Lemonnier type DCM. It is already built and accessory components are being installed at the Universität Bonn, Physikalisches Institut. The pressure inside the vacuum housing is $\sim 10^{-6}$ mbar and the vacuum housing only 380 mm in diameter, allowing fast changes of crystals, without long pumping times. Four pairs of crystals are available, Si(111), Si(311), Ge(220) and Ge(422). The DCM can also accommodate multi-layer mirrors for wide energy band-pass experiments, e.g., for XRF analysis measurements requiring high flux.

3.3. *Experimental station*

The optical tabletop in the experimental hutch is $1.2 \times 3\,\mathrm{m}^2$ breadboard, large enough to accommodate most any experimental set-up. Three ionization chambers (HASYLAB Design) and a LE-Ge five element fluorescence detector (Canberra) are available for recording XAFS spectra in transmission and fluorescence mode. The grazing incidence equipment consists of two goniometer cradles with a common center of rotation, a z-stage and a rotation stage (HUBER Diffraktion-stechnik GmbH). The first goniometer

cradle is for adjusting the relative incident angle (θi) of the impinging beam onto the sample surface. The other cradle is at right angles to θi and is used to adjust the sample surface to be plane-parallel with the storage ring orbit if necessary. The goniometer cradles are mounted on z-stage (vertical) for sample height adjustment. An additional motor for rotating around the sample surface normal is provided in order to change the sample surface orientation relative to the synchrotron beam polarization vector (ε) during polarization dependent measurements. The GI-equipment has been successfully employed at both HASYLAB (Beamline X1) [1] and ANKA (XAS-Beamline). A position sensitive detector array will be used for combined XAFS-XRD measurements.

4. Target dates

The front-end was installed in 2002. Radiation hutches were built in March 2003. The control cabin and media were installed in June/July 2003. The installation of the beamline optic components has been completed in October 2003. Commissioning of the INE-Beamline and first pilot experiments have begun in 2004. The INE-Beamline will be operational in 2005.

Reference

1. Denecke, M. A., Dardenne, K., Lindqvist-Reis, P. and Rothe, J., Phys. Chem. Chem. Phys. **5**, 939 (2003).

Physica Scripta. Vol. T115, 1004–1006, 2005

Ge Pixel Array Detector for high Throughput X-Ray Absorption Spectroscopy: Performance and Unconventional Applications

H. Oyanagi[1*], C. Fonne[2], D. Gutknecht[2], P. Dressler[2], R. Henck[2], M-O. Lampert[2], S. Ogawa[3], K. Kasai[4], A. Fukano[1] and S. Mohamed[1]

[1]National Institute of Advanced Industrial Science and Technology, 1-1-1 Umezono, Tsukuba 305-8568, Japan
[2]EURISYS MESURES, 1 Chemindela Roserate Lingolshem, 67834 Tanneries Cedex, France
[3]Ogawa Consulting Engineer's Office, 217 Famile Villa Gotennban Hihashitanaka, 1417-2 Gotennba, Shizuoka 417-0026, Japan
[4]NE Software Co. Ltd., 9-3 Wakaba, Kakizaki-cho, Inashiki-gun, Ibaraki 300-1249, Japan

Received June 26, 2003; accepted November 13, 2003

PACS numbers: 78.70.En, 61.10.Ht, 87.64.Fb

Abstract

For high throughput and energy-resolution florescence X-ray absorption spectroscopy (XAS), a novel Ge pixel array detector (PAD) with 100 segments has been developed. Two sets of PAD having different thickness values, *i.e.*, 10 mm (#1) and 7.5 mm (#2), were constructed and installed at Spring-8 (BL10XU) and Photon Factory (BL13B). Using a monolithic approach, a nearly perfect packing fraction (>88%) and commission rate (99%) were achieved, resulting in a significant improvement over a previous Ge multi-element detector. In the present PAD design, each segment is square-shaped having an active area of 22 mm^2. The average energy resolution at 5.9 keV was 220 eV (6 μs shaping time) and 240 eV (0.5 μs) in a high throughput mode. High efficiency X-ray detection over a wide energy range (5–60 keV) was confirmed. The present electronics-limited throughput maximum is 100 kcps per channel or 10 MHz in total. We will describe unconventional applications in fluorescence XAS demonstrating the capability of PAD. The recent *in-situ* XAS study under laser light required a small amount of specimen (less than 10^{-3} g).

1. Introduction

For X-ray absorption spectroscopy applications in dilute systems, a fluorescence detection technique [1] is used to overcome limitations in sensitivity. The bulk sensitivity limit in fluorescence XAS depends on both the flux of incident X-ray beam and detector performance, *i.e.*, energy resolution, efficiency and throughput. Rapid and sensitive measurements of surface XAS became feasible using a dense-packed solid state detector array [2]. For surface studies where the typical density of adsorbed atoms is in the order of $10^{14}/cm^2$, a grazing-incidence geometry can provide a means of surface-sensitive measurement. Moreover, fluorescence yield can be used in XAS applications to photo-induced phases using thin films or fine powders, solving a problem of mismatch between X-ray probe and visible photo penetration depth [3]. A large number of segmented X-ray detectors can control the systematic (nonstatistical) error by eliminating channels that suffer from strong scattering. A segmented X-ray detector is needed to minimize statistical and nonstatistical error.

The effective throughput of a solid state detector (SSD) can be increased by assembling detector elements with a close packing geometry. Various types of multi-element SSD arrays have been designed for this purpose [4–6]. A monolithic approach should be adopted in order to further improve the packing density beyond the present limit. Note that modern high energy photon sources (6–8 GeV) require detector efficiency over a wide range in energy (5–60 keV). This energy range is hardly covered by a silicon drift diode detector which has a superior performance in count rate and energy resolution [7]. To meet newly emerged requirements, a novel Ge pixel array detector (PAD) was designed and built. In this report, we describe basic specifications and performance of the first 100 segment Ge PAD.

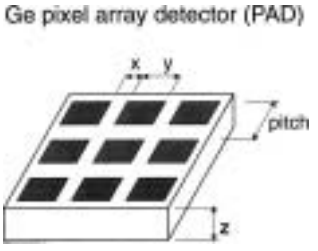

Fig. 1. Schematic of Ge pixel array detector and dimensional parameters, *i.e.*, pitch, pixel length, interpixel length and thickness.

2. Specifications of the PAD

The schematic arrangement of Ge PAD is shown in Fig. 1 where a part of the 10 × 10 array is shown. Two types of Ge PAD were fabricated. The two PADs have the same pixel length (y) and pitch (p) dimensions but different thicknesses (z), *i.e.*, the first PAD (PAD #1) has $z = 10$ mm while the second one (PAD #2) has $z = 7.5$ mm. PAD #1 with thicker z was designed for use with a higher energy storage ring (8 GeV *vs* 2.5 GeV) while PAD #2 was aimed at minimizing the incomplete charge collection event. One component of the electronic noise of the PAD is proportional to the input capacitance at the FET, which is a sum of the detector and FET capacitance (∼0.9 pF). Thus the strategy to maximize the energy resolution was to minimize the total capacitance as a function of p, x and z as much as possible. The fluorescence signal taken over a cone-like limited solid angle away from the scattering plane gives the lowest scattering intensity. From geometrical consideration, we have first determined the pitch p as 5 mm. However, the pixel-to-pixel capacitance increases sharply as a function of x below 300 microns and x was compromised. The pixel-to-ground capacitance also increases with thickness z.

3. Performance

The Ge pixel array is attached to contact pins and cooled by liquid nitrogen. Each output is fed into a separate analog preamplifier board. The transistor reset preamplifier was developed for the following reason. In resistor feedback preamplifiers, the need for large feedback resistances (>10^9 ohms) to reduce the noise induced by the resistor imposes a limit on counting rate.

*e-mail: h.oyanagi@aist.go.jp

Pulsed-light feedback has drawbacks such as slow diffusion in the input FET of the charge generated by the infrared flash upon preamplifier reset.

The PSC 741-N preamplifier consists of two components; an input circuit contained in the cryostat and cooled to a temperature slightly higher than 77 K, including the field-effect transistor, the reset transistor and the feedback capacitor. An external part contains a main board which processes the input pulses. To evaluate the performance, the analog-digital "hybrid" CAMAC module was developed. Each double width module accommodates linear amplifier circuits, SCA and histogram memory for eight channels. Totally thirteen CAMAC modules were built and accommodated into two CAMAC powered crates.

The performance of the detector was evaluated by the measurement of energy resolution, throughput and quality of fluorescence spectra for some dilute samples. The test was performed at the 27-pole wiggler beam line BL13B at the Photon Factory. An unfocused X-ray beam from a directly cooled Si(111) double-crystal monochromator was used. The energy resolution was determined for each channel from the full width at half maximum (FWHM) of the Mn K_α peak (5.9 keV) using a standard source (^{55}Fe). The best energy resolution was 215 eV at a low count rate using a shaping time of 6 μs as shown in Fig. 2. A slight degradation of energy resolution might be due to insufficient cooling efficiency and/or cross talks between the channels. The average energy resolution evaluated from FWHM values of Mn K_α peak (5.9 keV) was 235 eV with $z = 10$ mm (PAD #1). The average FWHM value for $z = 7.5$ mm (PAD #2) degraded to 245 eV due to the increase of pixel-to-ground capacitance.

Amplifier dead time degrades the throughput due to the pulse pile-up. We evaluated the amplifier throughput for each channel from the nonlinearity of the detector output rate as a function of input beam intensity evaluated from the incident beam flux i_0. Figure 3 shows a throughput curve (open circles) for the Cu K_α peak as a function of i_0 which was obtained by the single-channel analyzer output for a shaping time of 0.5 ms. Linearity of i_0 in this energy range is established by a simultaneous measurement of the beam intensity using a calibrated ionization chamber.

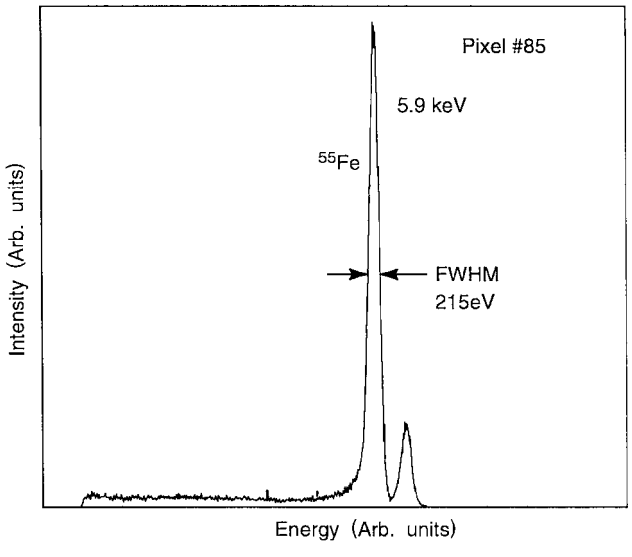

Fig. 2. MCA output (phase height distribution) for the Ge pixel array detector for ^{55}Fe (5.9 keV) using 6 μs shaping time.

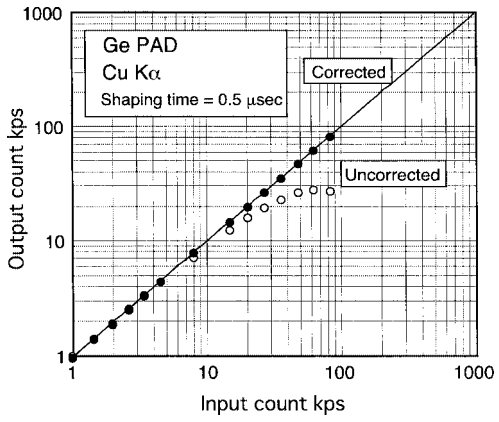

Fig. 3. Throughput curve for the Ge pixel array detector using Cu Kα (8.07 keV) and 0.5 μs shaping time.

The "hybrid" electronics output starts to deviate from a linear function for $i_0 > 10$ kcps. This shows that even with a fast shaping time (0.5 μs), it is required to correct the nonlinearity caused by the detector dead time effect. The fit seems to be valid for $i_0 < 100$ kcps above which the corrected curve does not give a good fit. After a dead time correction on a computer, a linear response is obtained below a count rate of 100 kcps. The total maximum count rate is thus evaluated to be maximum *ca.* 10 MHz. The present maximum throughput is limited by both analog (amplifier dead time) and digital (SCA and memory) circuits. If a digital signal processor (DSP) is used, the total throughput can be upgraded to 50 MHz [8]. Recent progress in DSP technology has made the maximum count rate 800 kcps per channel [9]. Combined with such a rapid data acquisition system, the potential of Ge PAD as a high throughput detector (*ca.* 100 MHz) would be fully utilized. In Fig. 4, Fe K-XANES spectra measured for fine powder specimen under photo-excitation (PIP), high temperature phase (HTP), and low temperature phase (LTP) of a typical spin-crossover complex $[FeII(2\text{-pic})_3]Cl_2EtOH$ (2-pic = 2-aminomethyl-pyridine) are compared. The spectral variation is consistent with the FeN_6 octahedron which expands by 0.2 Å upon photo-induced spin transition from $S = 0$ to $S = 2$ states. It was demonstrated that Ge PAD can provide high-quality excited state XAS spectra in fluorescence mode, solving an intrinsic mismatch problem between hard X-ray and visible photons.

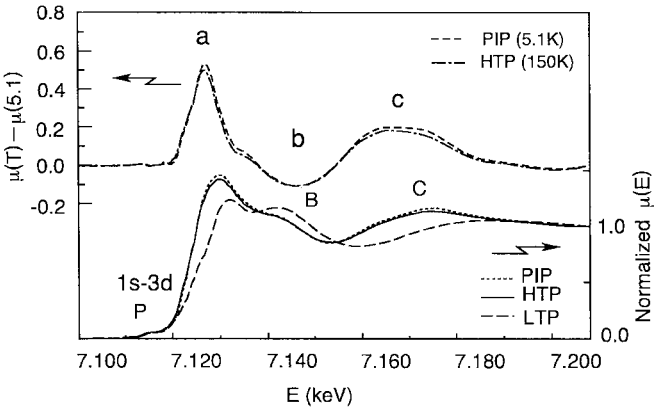

Fig. 4. Fe K-edge XANES spectra for $[Fe(2\text{-pic})_3]Cl_2EtOH$. The dotted line, dashed line and solid lines indicate the specra for high-temperature phase (HTP), low-temperature phase (LTP) and photo-induced phase (PIP).

4. Conclusions

A monolithic Ge 100 pixel array detector was developed. High performance in packing density, energy resolution and throughput was confirmed. 99% of pixels were found to be working. High efficiency over a wide energy range (5–60 keV) was demonstrated. Combined with laser excitation, XAS using Ge PAD provides new opportunities as a local probe of excited or photo-converted states.

References

1. Jaklevic, J. *et al*., Solid State Commun. **23**, 679 (1977).
2. Oyanagi, H., Shioda, R., Kuwahara, Y. and Haga, K., J. Synchrotron Rad. **2**, 99 (1995).
3. Kolobov, A., Oyanagi, O. and Tanaka, K., Phys. Rev. Lett. **87**, 14502 (2001).
4. Cramer, S. P., Tench, O., Yocum, M. and George, G. N., Nucl. Inst. Meth. **A266**, 586 (1988).
5. Oyanagi, H., Martini, M. and Saito, M., Nucl. Inst. Meth. **A403**, 58 (1998).
6. Farrow, R. *et al*., Proc. 8th Int. Conf. X-ray Absorption Fine Structure, (Berlin, 1994).
7. Gauthier, C. *et al*., Proc. 9th Int. Conf. X-ray Absorption Fine Structure, (Grenoble, 1996).
8. Warburton, W. *et al*., Proc. 9th Int. Conf. X-ray Absorption Fine Structure, (Grenoble, 1996).
9. Cheung, K.-C., private commun.; Cernik, R. J. *et al*., "Synchrotron Radiation Detector Roadmap" Ver. 1.6.
10. Oyanagi, H., Proc. 19th Int. Conf. X-ray and Inner-Shell Processes, Rome, Jun. 24–28, (2002).

Physica Scripta. Vol. T115, 1007–1010, 2005

ATHENA and ARTEMIS: Interactive Graphical Data Analysis using IFEFFIT

B. Ravel[1] and M. Newville[2]

[1]Naval Research Laboratory, Washington, DC 20375, USA
[2]The University of Chicago, Chicago, IL 60637, USA

Received June 26, 2003; accepted November 4, 2003

PACS numbers: 61.10.Ht, 07.05.−t, 07.05.Kf

Abstract

We introduce a new software package for analysis of XAS data. This package is based on the IFEFFIT library of analytical and numerical algorithms and uses the perl/Tk graphics toolkit. The two main components are ATHENA, a program for XAS data processing, and ARTEMIS, a program for EXAFS data analysis using theoretical standards from FEFF. These programs provide high quality analytical capabilities in a manner that is accessible to novices yet powerful enough to meet the demands of an expert. The programs run on all major platforms and are freely available under the terms of a free software license.

1. Software package

In this article we introduce a new software package for interactive, graphically-driven analysis of X-ray Absorption Spectroscopy (XAS) data. The two programs described here in detail are ATHENA, a program for XAS data processing, and ARTEMIS, a program for analysis of extended X-ray absorption fine-structure spectroscopy (EXAFS) data using theoretical standards computed [1] by FEFF. Both programs are based on the analytical algorithms of the IFEFFIT library [2] and both programs are written in the Perl programming language [3] and use the perl/Tk graphical toolkit [4] for all graphical interactions.

We recognize that users of XAS beamlines and practitioners of the spectroscopy require software that meets a broad range of analytic, programmatic, and social goals, which we describe below. In later sections we describe the main features of the two programs and discuss the relationship of free source code for data analysis software with the scientific method. Finally, we explain how to obtain these programs.

Here are our goals in this project:

High-quality analytic algorithms
ATHENA and ARTEMIS use the programmers interface to IFEFFIT, as described in reference [2]. Thus both programs have complete access to all the features of IFEFFIT, including all the capabilities of the programs AUTOBK [5] and FEFFIT [6]. In this article, any analytic feature ascribed to ATHENA or ARTEMIS is actually performed by IFEFFIT and the result is used via IFEFFIT's programming interface.

Highly usable GUI
The perl/Tk toolkit provides a full-featured, forms-based environment for interacting with and processing data. Plotting of data is handled using the PGPLOT plotting library [7].

Useful to novices, powerful for experts
Those already familiar with analysis of XAS data should find ATHENA and ARTEMIS quite easy to begin using. Novices to absorption spectroscopy find that a usable GUI combined with excellent analytic algorithms considerably lowers the barrier of beginning work in their new field. For the expert, ATHENA and ARTEMIS offer sophisticated options which allow the user to the most from measured data.

Free of cost, free source code
IFEFFIT, ATHENA, and ARTEMIS are available on the web for free download. Thus high-quality XAS analysis is available even to students and to researchers in developing countries. The availability of source code for data analysis software is very important philosophically. Because the code is licensed under very liberal terms, users are free to examine the code, understand its algorithms, modify the code to better suit their research needs, and share the codes with their colleagues.

Portability
ATHENA and ARTEMIS work on most common computer platforms including Microsoft Windows, Macintosh OSX, Linux, Solaris, and other common unixes. This is possible because all of the tools which they rely upon, IFEFFIT, Perl, perl/Tk, and PGPLOT, themselves operate on all these platforms. Additionally both programs save data to project files which are easily transferable between users, even those working on different platforms.

2. Features of ATHENA

ATHENA addresses all aspects of data processing including conversion of raw data to $\mu(E)$ data, background subtraction, Fourier transforming, and plotting. As such it is useful for data visualization at the beamline as well as for processing of data in preparation for data analysis. The normal view of the ATHENA window is shown in Fig. 1.

Data conversion from beamline format is handled in a flexible manner that allows conversion of column data from transmission, fluorescence, or electron yield experiments into $\mu(E)$ data. The conversion utility allows for on-the-fly summation of data from a multi-element detector. Alternately, each column of multi-element data can be imported as individual data groups for later inspection and summation. ATHENA also supports data preprocessing capabilities, including automated deglitching, alignment, truncation, and constraint of analysis parameters as a data file is imported.

Background subtraction is performed using the AUTOBK algorithm [5] which determines an empirical background spline based on a distinction between data and background in terms of Fourier components. Edge step normalization of the data is determined by a linear pre-edge subtraction and regression of a quadratic polynomial beyond the edge. Alternately, the data may be normalized by comparison to the isolated atomic background

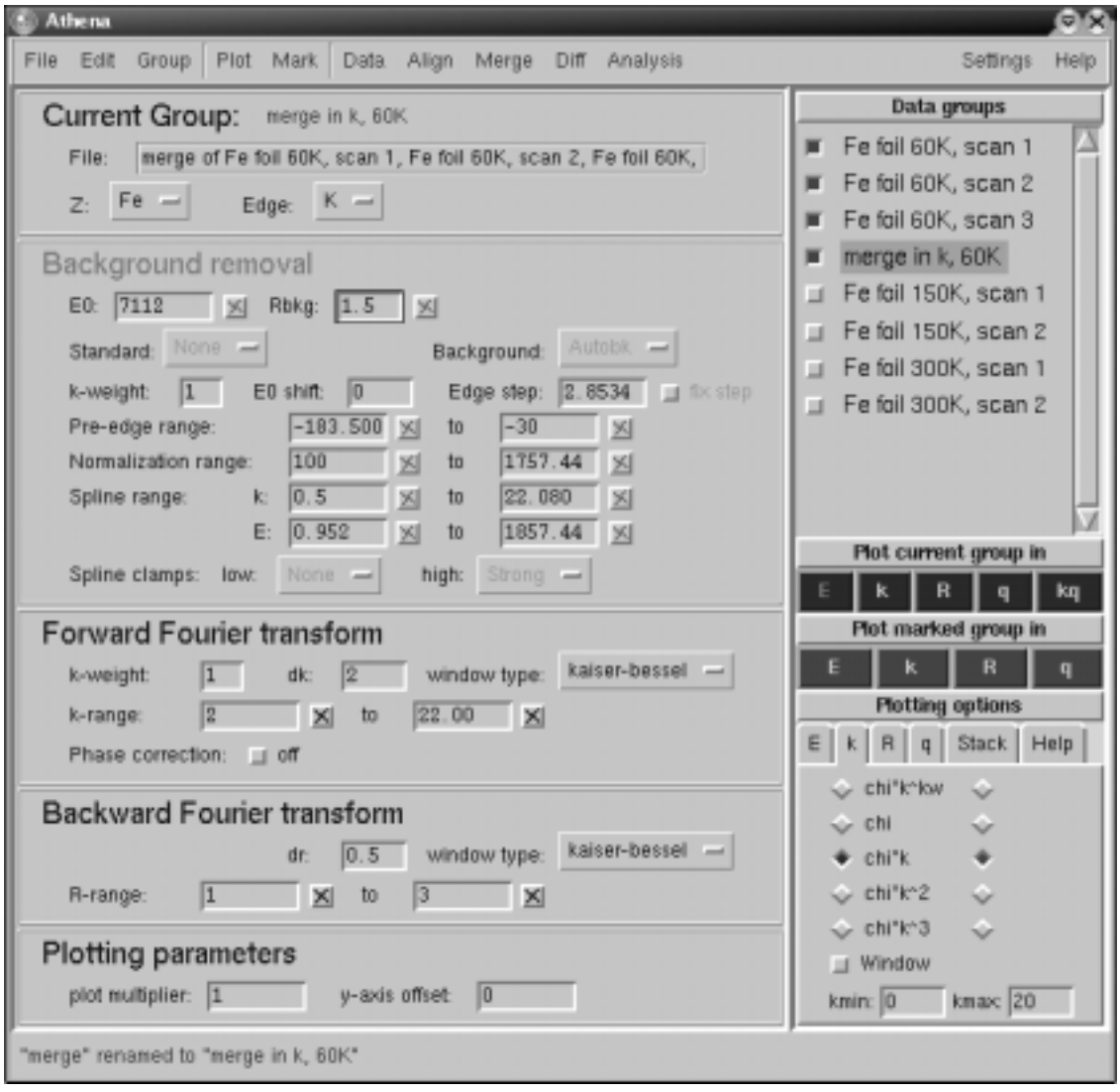

Fig. 1. ATHENA with several data scans imported. The list of imported scans is shown in the upper right corner. The left portion of the window displays the background removal and Fourier transform parameters for the selected data group, which is the one highlighted in the list. Parameters for configuring plots are set in the tabs in the lower right corner of the window.

computed using the Cromer–Liberman calculations [8]. This second normalization method is particularly attractive for XANES studies where consistency of normalization is very important. For comparison to XANES data, ATHENA can also import and display FEFF8 calculations [9].

One powerful feature of ATHENA is that processing and displaying many data sets simultaneously is as simple as for a single data set. In Fig. 1, the upper row of buttons labeled with the letters E, k, R, and q are for plotting single data sets in energy, k-space, R-space, or back-transformed k-space, respectively. The lower row of buttons will plot multiple data sets. ATHENA always keeps track of whether any parameters have been changed and will automatically perform background removals and Fourier transforms as needed. Background removal and Fourier transforming parameters can be adjusted for each data set individually or flexibly constrained between data sets.

Along with the basic chores of background removal and Fourier transforming, ATHENA provides a number of other features for data processing and analysis of XAS spectra. Some of the most significant are

1. Edge energy calibration.
2. Alignment in energy of spectra.
3. Deglitching, i.e. removal of spurious data points from $\mu(E)$ spectra, by an automated procedure or by manual selection of spurious points.
4. Merging of multiple data sets is energy or in k-space and computation of standard deviation spectra.
5. Log-ratio/phase-difference analysis [10] of back-transformed spectra.
6. Fitting of analytic functions (arctangents, Lorentzians, Gaussians) to near-edge spectra.

Features which are currently planned for and being implemented in ATHENA include principle component analysis, analysis of near edge spectra by linear combination of standard spectra, self-absorption corrections for fluorescence data, and dead-time corrections.

3. Features of ARTEMIS

ARTEMIS works within the framework of FEFF's multiple scattering path expansion [1, 11]. This means that the data is described as a summation of one or more scattering paths as computed by FEFF. For each path, the XAFS equation much be evaluated. This means that values of the parametric terms in the EXAFS equation – N, S_0^2, E_0, ΔR, and σ^2 – must be specified for each path

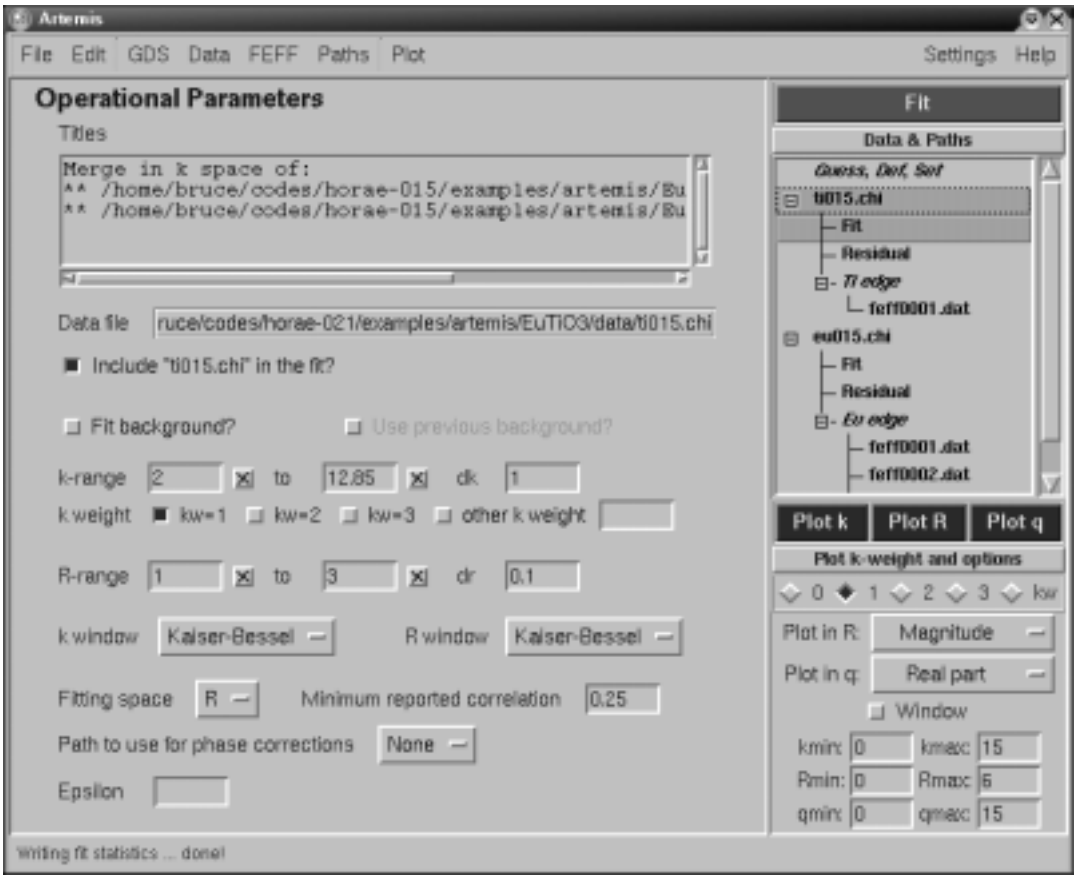

Fig. 2. ARTEMIS with data and FEFF calculations imported for a multiple-edge fit to $EuTiO_3$. The view displayed, shows how fitting ranges and Fourier transform parameters are set for the Ti edge portion of the fit. Parameters for configuring plots are set in the lower right corner of the window.

included in the fit. The path expansion and how it is parameterized and used in a fit is described elsewhere [6, 12]. As discussed in those references, EXAFS analysis can be quite subtle and complicated. By providing a graphical, forms-based mechanism for handling the many bookkeeping chores imposed by FEFF and IFEFFIT, ARTEMIS makes basic analysis chores simple and very sophisticated analysis problems tractable.

Shown in Fig. 2 is the ARTEMIS window in its data view. Other views (not shown) allow the user to set fitting parameters, to manage FEFF calculations, or to manage individual FEFF paths and the math expressions used to evaluate the terms in the EXAFS equation.

While ARTEMIS certainly is well-suited to simple, first-shell analysis of single data sets, it provides many advanced features, including

1. Multiple data set refinements.
2. Refinement using multiple *k*-weightings for any data set.
3. Use of multiple FEFF calculations in a single fit.
4. Co-refinement of a background spline to reveal correlations between the spline and the fitting parameters.
5. Arbitrary constraints between and restraints on parameters.
6. Error analysis, including uncertainties in and correlations between parameters.
7. Convenient plotting of the data, the fit, and any number of the individual paths used in the fit.

4. Free source code and the scientific method

Full disclosure of experimental procedures and results is one of the cardinal rules of the scientific method. We, as scientists, cannot and should not except results which cannot be reproduced by independent investigators. Consequently, we are obligated to explain enough detail of sample preparation, experimental procedure, theoretical background, and interpretation of the data that any reader with adequate background and inclination can fully reproduce a result. Most journals would refuse to consider publication of an article that hides details behind a veil of secrecy.

We believe that full disclosure is essential to science and to the dialogue between scientists, and that full disclosure applies to the software that is used in data analysis. In this day, most scientific disciplines depend on computer technology for many aspects of data collection and analysis. In particular, XAS is heavily dependent on computerized control for its data collection and on computer algorithms such as the Fast Fourier Transform [13] and general non-linear modeling algorithms [14] for its analysis.

It is essential that any reader of a scientific publication who has the necessary background and inclination be able to scrutinize the details of the codes used for the analysis. This requires that source code be freely available.

Freely available source code allows independent scrutiny of the procedures used and also allows scientists to modify and improve these procedures for their own needs. By using an Open Souce Software [15] license, such modifications can be dissemenated to the community either by the original authors or those making the modifications. In this way, new ideas and algorithms can build on and improve earlier work in an open and peer-reviewed manner to enrich the entire scientific community.

5. Resources

A project page for IFEFFIT exists at SourceForge.net, http://sourceforge.net/projects/ifeffit/. The source code for IFEFFIT can

be found at http://cars.uchicago.edu/ifeffit. You will also find IFEFFIT installer packages for Windows which also include ATHENA, ARTEMIS and a few other programs. ATHENA and ARTEMIS have their own web page, http://feff.phys. washington. edu/~ravel/software/exafs/. ATHENA and ARTEMIS as well as IFEFFIT are actively being developed and improved.

Acknowledgments

We would like to thank S. Kelly and everyone on the IFEFFIT mailing list for their enthusiasm and support for this project. Versions 0.8.020 of ATHENA and 0.6.005 of ARTEMIS are discussed in this paper.

References

1. Zabinsky, S. I., Rehr, J. J., Ankudinov, A., Albers, R. C. and Eller, M. J., Phys. Rev. B **52**, 2995 (1995).
2. Newville, M., J. Synchrotron Radiat. **8**, 322 (2001).
3. Wall, L., Christiansen, T. and Schwartz, R. L., "Programming Perl," (O'Reilly and Associates, Inc., Cambridge, second edition, 1996).
4. Lidie, S. and Walsh, N., "Mastering Perl/Tk," (O'Reilly and Associates, Inc., Cambridge, first edition, 2002).
5. Newville, M., Līviņš, P., Yacoby, Y., Rehr, J. J. and Stern, E. A., Phys. Rev. B **47**, 14126 (1993).
6. Newville, M. *et al*., Physica B **208&209**, 154 (1995).
7. Pearson, J., PGPLOT Graphic Library version 5.2.0, http://www.astro. caltech.edu/~tjp/pgplot/, 1997.
8. Cromer, D. T. and Liberman, D., J. Chem. Phys. **53**, 1891 (1970).
9. Ankudinov, A. L., Ravel, B., Rehr, J. J. and Conradson, S. D., Phys. Rev. B **58**, 7565 (1998).
10. Bunker, G., Nuc. Inst. Meth. **207**, 437 (1983).
11. Rehr, J. J. and Albers, R. C., Phys. Rev. B **41**, 8139 (1990).
12. Ravel, B., "EXAFS Analysis Using FEFF and FEFFIT," Lecture notes for a data analysis workshop of the same name available at http://feff.phys. washington. edu/~ravel/course/, 2000.
13. Brigham, E. O., "The Fast Fourier Transform," (Prentice-Hall, Englewood Cliffs, NJ, 1974).
14. Marquardt, D., SIAM J. Appl. Math. **11**, 431 (1963).
15. The Open Source Initiative, http://www.opensource.org/.

Physica Scripta. Vol. T115, 1011–1014, 2005

SIXPack: a Graphical User Interface for XAS Analysis Using IFEFFIT

S. M. Webb*

Stanford Synchrotron Radiation Laboratory, Menlo Park, CA, 94025, USA

Received June 26, 2003; accepted November 4, 2003

PACS number: 07.05.Kf

Abstract

SIXPack (Sam's Interface for XAS analysis Package), a graphical user interface that allows users simple manipulation and analysis of data, is presented. The modules of SIXPack allow users to: (1) load, calibrate, and average raw data files; (2) perform background subtractions; (3) perform principal component analysis and target transforms; (4) perform least squares fitting of data to standards and functions; (5) perform EXAFS fitting to FEFF phase and amplitude files; (6) create single scattering FEFF phase and amplitude files using a periodic table interface. Novel features of the program allow for the fitted correction of XANES spectra due to self-absorption effects in unknown matrices, which is particularly useful for analysis of geochemical and environmental systems. The core of the XAS analysis routine uses IFEFFIT. SIXPack is developed in Python, is installable across many operating systems and platforms, and is freely available with an Open Source license.

1. Introduction

As synchrotron facilities are inspiring new applications for XAS experiments, they are also reaching broader user bases than in the past. Many of these users are new to the methodology and physics of XAS analyses and bring highly complex materials requiring sophisticated data analysis techniques. This has led to the need for simple data analysis packages that are easy to use for beginners, yet powerful enough to tackle complex problems for advanced users.

IFEFFIT is a well-tested, reliable, interactive scriptable library of EXAFS algorithms [1]. An additional strong quality of IFEFFIT is that is can used easily from high level scripting languages, such as Python. In this fashion, easy to use graphical user interfaces (GUIs) can be built to aide in the analysis of XAS data. SIXPack (Sam's Interface for XAS analysis Package) is a GUI that is designed with this in mind, utilizing IFEFFIT as it analysis "kernel" and supplemented with many other routines for data input and other analysis.

SIXPack has been developed for use initially with the environmental and geochemical fields in mind, but has been shown to be useful in a wide range of XAS applications. SIXPack was written in the Python scripting language [2] and is distributed primarily as a Windows application. In addition, the source code may be compiled on Linux, UNIX and Apple platforms. The application and source code is available online as part of the IFEFFIT installation [3] or stand-alone [4]. HTML documentation is also available online [4].

2. Program Description

SIXPack is divided into six modules with each GUI performing a specific task in the data reduction process.

2.1. *SamView Module*

The SamView module is used to import raw data into the program and perform tasks such as averaging, energy calibration, and dead-time corrections. The module auto-recognizes the header of many raw file formats including SSRL, NSLS, and some ALS and APS beamlines. If the format is not recognized, it will revert to a generic ASCII file reader. The GUI provides an easy way to screen data files and eliminate problem channels and perform most pre-processing procedures.

2.2. *Background Subtraction Module*

The background subtraction module performs unit step edge normalization of XANES edges and the extraction of EXAFS from averaged data. The EXAFS $\chi(k)$ is isolated using the IFEFFIT-AUTOBK algorithms. A data editor also exists in this module to assist in deglitching data. The pre-edge region can be modeled as a gaussian tail to eliminate the effects of scattering leakage from energy dispersive detectors. A background subtraction parameter set optimized for a given sample can be applied easily across all loaded data sets to efficiently maintain consistent background removal over a large range of data allowing simple batch processing of data. Options also include saving normalized derivative spectra, in addition to $\mu(E)$, $\chi(k)$, and RDF.

2.3. *Principal Component Analysis Module*

The PCA module performs statistical analyses on a set of spectra to determine the number of "significant" or principal components required to describe the variation in the data. A number of criteria can be used to determine the proper number of principal components. Several of these criteria, including both visual and statistical methods, are provided in the module. The most robust, using the IND function of Malinowski, reaches a minimum at number of principal components [5].

The PCA result can then be used with a target transformation. The target transformation projects the spectrum from a reference compound onto the vector space defined by the components. If the target vector lies with this component space, then this reference compound is likely to be present in the dataset. A linear least-squares approach can then be used to determine the fractional amount of each reference compound in the unknown. The quality of the target transform is given by three parameters: χ^2, r-value, and SPOIL value [6]. The SPOIL value for an excellent target typically ranges from 0 to 1.5, good from 1.5 to 3, fair from 3 to 4.5, poor from 4.5 to 6, and unacceptable for values greater than 6 [7]. To assist in screening reference compounds, a library of compounds can be created from which the module will transform each one and report the outcomes in a table.

*e-mail: samwebb@slac.stanford.edu

2.4. *Least Squares Fitting Module*

Fitting experimental EXAFS data to calculate bond distances and coordination numbers becomes increasingly difficult in systems that are comprised of more than only a few components. In the natural environment, few elements will exist as pure phases due to chemical and physical inhomogeneities in samples such as soil fractions and sediment cores. Thus it becomes important to be able to examine the sample composition as a linear combination of standard components. This is accomplished through the linear least-squares fitting module of SIXPack.

The fitting module of SIXPack allows the user to fit data to any number of reference compounds and/or functional forms, including linear and quadratic forms, exponential and logarithmic forms, arctangents and error functions, and peak functions. Variables in the functional forms may be floated or kept constant. Constraints on the proportions of reference compounds, such as non-negativity and sum-to-one, may also be applied. The fitting routine is generic, requiring only a two-column ASCII file as input, and may be applied to data sets other than XAS, such as X-ray diffraction or UV-Vis spectroscopy.

A novel feature of the module is a parameterized correction for self-absorption (SA) effects in XANES spectra. This option applies a correction factor derived from the mathematics expressing the SA in the sample to the data. Assuming an infinitely thick sample at 45-degree incidence/45-degree detection (bisecting geometry), the XAS fluorescence measurement simplifies to

$$I_f/I_0 = \mu_s(E)/(\mu_s(E) + \mu_m) \tag{1}$$

where $\mu_s(E)$ is the rapidly changing absorption coefficient of the sample (*i.e.* the XANES or EXAFS) due to the element of interest and μ_m is the slowly varying absorption coefficient from other elements in the matrix. Since the desired quantity is the unimpacted absorption coefficient, $\mu_s(E)$, we can solve for this term knowing the measured value of I_f/I_0 (represented by R) giving

$$\mu_s(E) = fR\mu_m/(1 - fR) \tag{2}$$

where f is a scaling factor that accounts for normalization to a unit step-height. In environmental or natural samples, the absorption coefficient of the matrix is largely unknown. Thus in order to apply a correction, we can fit the data to an expression parameterized by two variables that characterize the net effect of the artifact – μ_m and the scaling factor f. These parameters modify the fluorescence data of the sample, where large values of either parameter imply no effect to the sample. An iterative process fits these SA variables to the former fit, followed by a new fit to the SA corrected data. After several iterations, the two fits will converge if a correction factor is needed. An example of this procedure is given in section 3.

2.5. *FEFF Single Scattering Interface Module*

SIXPack contains a module to interactively create single-scattering FEFF phase and amplitude files. This provides a quick way to test scattering paths without building large complex FEFF models. The GUI consists of an easy to use clickable periodic table from which the scattering and absorbing elements are chosen. The user may control several of the standard FEFF parameters, and chooses a distance and geometry of the complex. The module is compatible with FEFF versions 6 through 8 [8, 9].

2.6. *FEFF EXAFS Fitting Module*

The IFEFFIT core engine provides a quick, robust fitting procedure for EXAFS. The SIXPack GUI gives a simple form interface where the model is built in the traditional FEFFIT manner of terms and variables. Several templates are provided to assist the beginner in constructing simple shell-by-shell models. Due to the unconstrained nature of IFEFFIT variable definitions, complex mathematical relationships can be constructed between fitted variables and EXAFS parameters. This leads to the ability to build models of complexity that are limited only by the users

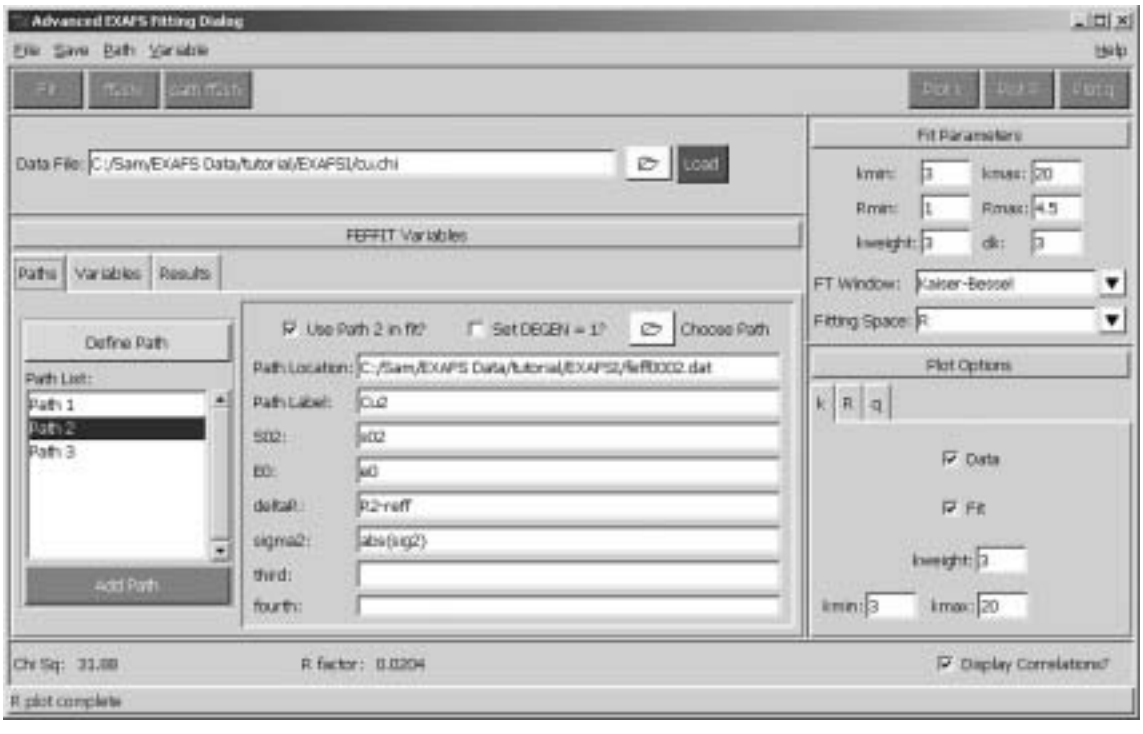

Fig. 1. Screenshot of the paths setup page of the EXAFS fitting module in SIXPack.

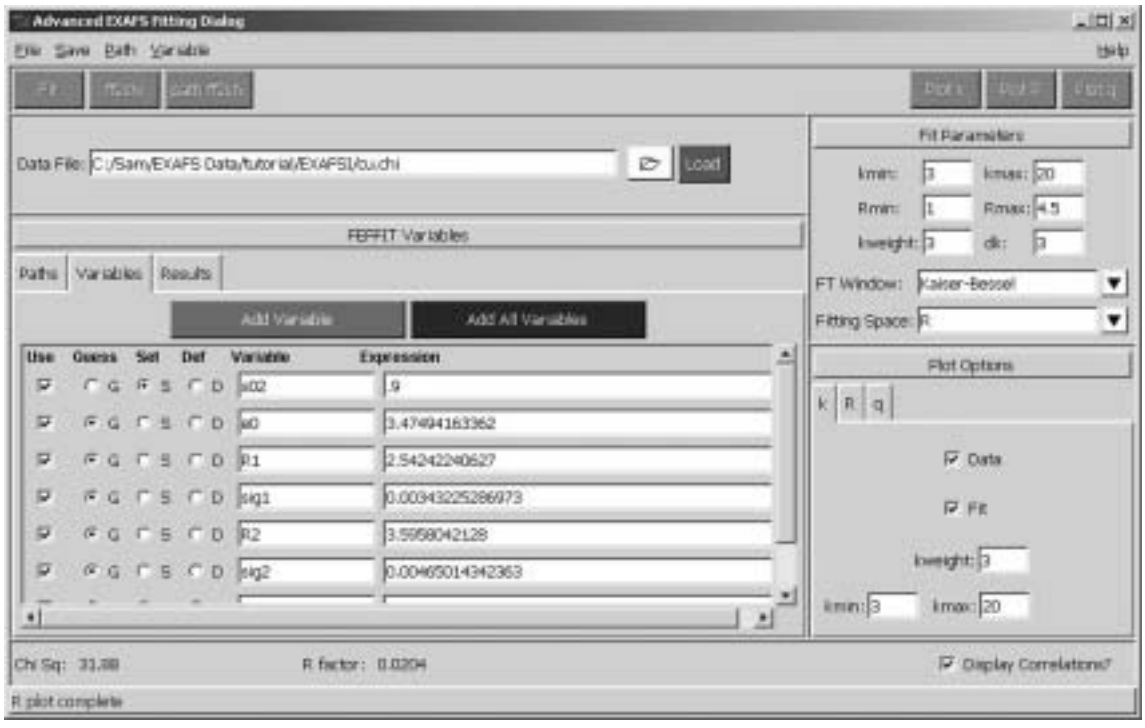

Fig. 2. Screenshot of the variables setup page of the EXAFS fitting module in SIXPack.

imagination. For example, models can include features such as fitting fractional components in the EXAFS, using bond angles as fitted parameters, and interpolating between FEFF paths. The fitting schemes can be saved for later use and altered manually using any text editor. Examples of the EXAFS fitting routine are given in the next section.

3. Examples

3.1. *EXAFS Fitting Example*

The EXAFS fitting module of SIXPack is displayed with the path setup page in Figure 1 and the variable setup page in Figure 2 to illustrate the GUI. The example shown is for sample data collected from Cu metal. The example fit is a simple model incorporating the first three coordination shells of Cu with 3 single-scattering paths. The $S_0{}^2$ parameter is set to a value of 0.9, path coordination numbers are obtained from FEFF, and all other EXAFS parameters are fitted. The resultant fit and data, as a screenshot from SIXPack, are shown in Figure 3.

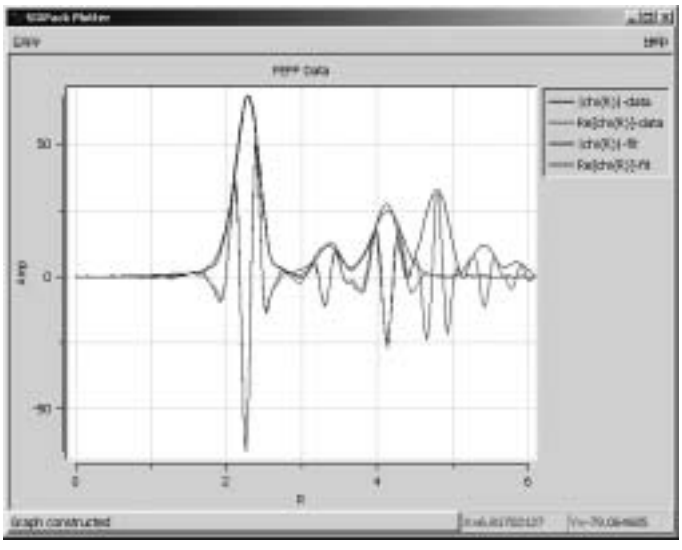

Fig. 3. Screenshot of sample data from Cu metal and its EXAFS fit in SIXPack.

3.2. *Least Squares Fitting with Self-Absorption Correction*

This example illustrates the self-absorption (SA) correction in SIXPack. A sample of a homogeneous biogenic manganese oxide was collected in both fluorescence and transmission geometries at BL 4-3 at SSRL using a harmonic rejection mirror set to a 9 keV cut-off energy. The transmission data can be fitted as a combination of Mn(II) ($MnCl_2$ in aqueous solution) and Mn(IV) (δ-MnO_2) reference compounds measured in transmission. These results are presented in Table I and Figure 4a. The same fit can be performed with the fluorescence data, resulting in a significantly different solution (Table I and Figure 4b). The impact of SA in the fluorescence data is observed by a distortion of the pre-edge, white line, and other features making the pre-edge transition appear larger and the white-line maximum smaller than observed in the transmission geometry. This artifact in the data, when fitted, results in the major component (Mn(IV)) being damped and appear to be less important to the overall fit. When the SA correction is used after approximately 10 iterations, an improved fit results from the fluorescence data with results that agree closely to the transmission fit (Table I and Figure 4c).

4. Conclusions

SIXPack is free software available online [4] and still in the early stages of development. Most basic forms of XAS and general fitting analyses are supported at this time, with many future improvements on the way. Comments and questions from users are encouraged.

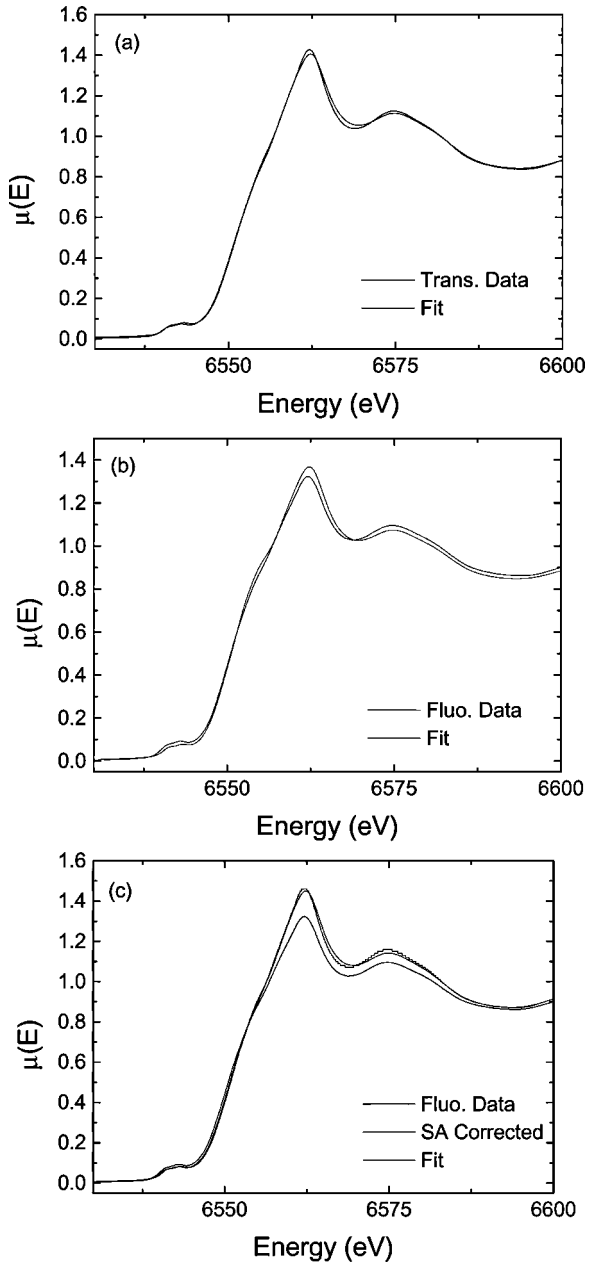

Fig. 4. Fit qualities of biogenic manganese oxide to transmission reference compounds. (a) Fit of transmission sample data. (b) Fit of fluorescence sample data. (c) Fit of self-absorption corrected fluorescence data.

Table I. *Fitting results of manganese reference compounds to a biogenic manganese oxide. Results illustrate the effects of fluorescence self-absorption on linear combination fits and the ability to correct for the effect.*

Fit Type	% as δ-MnO_2	% as $MnCl_2$ (aq)
Transmission	0.88	0.09
Fluorescence	0.77	0.18
SA Corrected Fluo	0.89	0.10

Acknowledgement

I would like to thank Matt Newville for all of his effort in writing and supporting IFEFFIT, without which, SIXPack would have never started. I would also like to thank Bruce Ravel for providing much of the inspiration and look and feel of many portions of the GUIs of SIXPack. Finally, many thanks go out to the users who have provided constant input and feedback into the direction of development of SIXPack.

References

1. Newville, M., "IFEFFIT: interactive XAFS analysis and FEFF fitting," J. Synchrotron Rad. **8**, 332–324 (2001).
2. van Rossum, G., "Python Documentation and Website," (http://www.python.org/, 1995).
3. Newville, M., "IFEFFIT Web Page and Online Documentation," (http://cars9.uchicago.edu/ifeffit/, 2000).
4. Webb, S. M., "SIXPack Webpage and Online Documentation," (http://www-ssrl.slac.stanford.edu/∼swebb/sixpack.htm, 2002).
5. Malinowski, E. R., "Determination of the number of factors and the experimental error in a data matrix," Anal. Chem. **49**, 612–617 (1977).
6. Malinowski, E. R., "Theory of error for target factor analysis with applications to mass spectrometry and numclear magnetic resonance spectrometry," Anal. Chim. Acta **103**, 359–354 (1978).
7. Manceau, A., Marcus, M. A. and Tamura, N., "Quantitative speciation of heavy metals in soils and sediments by synchrotron X-ray techniques," in *Applications of Synchrotron Radiation in Low-Temperature Geochemistry and Environmental Science*, edited by P. A. Fenter, M. L. Rivers, N. C. Sturchio and S. R. Sutton (Mineralogical Society of America, Washington, DC, 2002), Vol. 49, pp. 341–428.
8. Zabinsky, S. I. *et al.*, "Multiple-scattering calculations of X-ray absorption spectra," Physical Review B **52** (4), 2995–3009 (1995).
9. Ankudinov, A. L., Ravel, B., Rehr, J. J. and Conradson, S. D., "Real space multiple scattering calculation of XANES," Phys. Rev. B **58**, 7565 (1998).

Physica Scripta. Vol. T115, 1015–1016, 2005

Determination of Chemical Valence States in Dilute Samples Using a Combination of Fluorescence Ion Chamber and PIN Photon Diode

Y. N. Xie*, J. Zhang, J. Liu, T. Liu, T. D. Hu and Z. Y. Wu

Beijing Synchrotron Radiation Facility, Institute of High Energy Physics, Chinese Academy of Science, Beijing 100039, P.R.China

Received June 26, 2003; accepted March 30, 2004

PACS numbers: 07.85.Qe; 07.60.Rd

Abstract

Determination of chemical valence state is an important aspect for X-ray absorption spectroscopy (XAS) application. In this work a simple detecting system was developed for measuring the chemical states and recording X-ray absorption spectra of dilute samples. The new device consists of two parts: a Lytle-type ion chamber and a PIN photon diode detector, which are set side by side. The sample and the standard were placed in front of the two detectors respectively. The unfocused incident X-ray beam with certain size, hits on both the sample and the standard. The Lytle-type ion chamber detects the fluorescence signal from the sample while the PIN photon diode records the transmitted signal from the standard separately and simultaneously. Comparing the two spectra, the energy shift of the sample can be calibrated relative to a selected standard. This method is suitable for measuring high quality XANES spectra of low concentration samples at the 2nd generation synchrotron radiation sources exploiting either bending magnets or wigglers with large horizontal divergence.

1. Introduction

X-ray absorption spectroscopy (XAS), including X-ray absorption near-edge structure (XANES) and extended X-ray absorption fine structure (EXAFS) is a valuable tool for studying the local structural environment around an element in varied materials. Furthermore, electronic properties and valence state of the element can be obtained [1].

In the case of low-concentration samples, fluorescence XAS is the preferred technique. In a conventional fluorescence experiment, the incident beam of monochromatic X-rays is monitored by a semitransparent ionization chamber (I_0), and the flux of X-rays fluorescence through the sample is collected by a Lytle-type ionization chamber (I). The X-ray absorption coefficient $\mu(E)$ of the sample is given by $\mu_x = I_0/I$. However, The energy shifts are often unpredictable due to several effects, such as thermal loading of the monochromator crystals, the mechanical error of the monochromator, and orbit shifts etc. [2]. These give errors in valence state analysis and electronic structure simulation. Therefore, a precise *in situ* energy calibration method is needed for X-ray absorption spectroscopy.

In general, the energy monitor comprises three parts: (1) X-rays scattered elastically out of the incident beam (I_0), (2) XAS transmission standard, typically a thin metal or oxide foil, and (3) a detector with a monotonic response over the energy range of the experiment [2]. However the techniques are not suitable for measuring low concentration samples XAS.

Here, we developed a new XAS experimental system, which can collect the data of the standard and the sample simultaneously. Comparing the two spectra, the energy shift of the sample can be calibrated relative to a selected standard, and the chemical state changes of elements in dilute samples can be determined precisely.

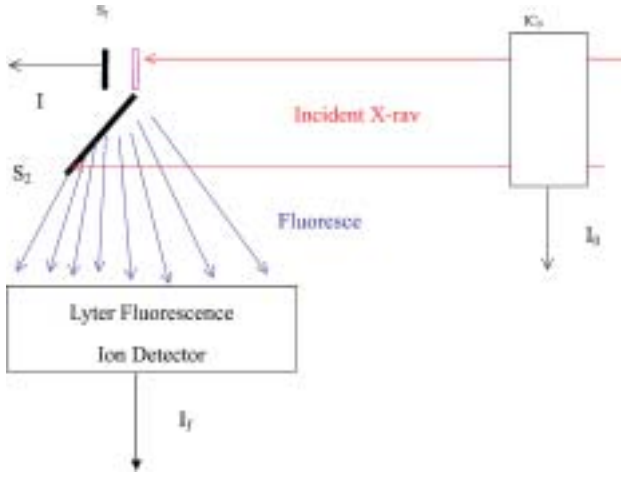

Fig. 1. Configuration of the experimental system.

The solution is free from machine instabilities in the fluorescence detection mode, and is available at 2nd generation synchrotron radiation sources which exploit either bending magnets or wigglers with large horizontal divergence.

2. Structure of the experimental system

The basic configuration of the measurement systems is illustrated in Fig. 1. Using a photodiode, one detects the transmitted signal (I_s) from the standard sample, while a Lytle-type ion chamber detects the fluorescence signal (I_f) from the real sample. Because of the small size and high sensitivity of the photodiode, the transmission detector uses just a part of the incident beam. Therefore the two detectors can be set side by side. The intensity of the incident beam (I_0) is measured by the front ion chamber. The X-ray absorption coefficient $\mu(E)$ of the standard is given by $\mu_x = \ln(I_s/I_0)$, and that of the sample is given by $\mu_x = I_f/I_0$. Comparing the two results, the X-ray absorption edge energy can be calibrated relative to a selected standard. Further, the valence state of the element can be determined precisely. A picture of the detector system is shown in Fig. 2.

3. Experimental set-up

3.1. *Sample preparation*

Saccharomyces Cerevisiae biomass (supplied by Beijing Five Star Brewery Company) was pulverized after lyophilization. 1000 μg Cr/ml of potassium dichromate was added into the lyophilized biomass. The chromium-yeast biomass was homogenized before lyophilization. The chromium compounds and lyophilized yeast powders were homogenized in an agate mortar,

*e-mail: Y.N. Xie xieyn@sun.ihep.ac.cn

Fig. 2. Picture of the detector.

fixed between two self-adhesive Scotch Tapes (3M) and then held on plastic sample holders.

3.2. *XANES set-up*

The XANES spectra at the Cr K edge were collected on the EXAFS station at 4WIB beamline of Beijing Synchrotron Radiation Facility (BSRF). The storage ring was operated at 2.2 GeV with a beam current of 100 mA. The monochromator is a Si(111) double crystal monochromator. By detuning the crystals of the monochromator high order harmonics were rejected. In this geometry, The XANES spectra of standard compound were collected using PIN diodes in transmission mode, while the sample was measured by a Lytle fluorescence ionized chamber with a vanadium filter. The signals from the two detectors were collected simultaneously.

4. Discussion

In order to test the performance of the system, we put standard compounds $K_2Cr_2O_7$ and Cr_2O_3 in front of the Lytle-type ion chamber and the PIN photodiodes, respectively. The unfocused incident X-ray beam with certain size, hit on both samples. The fluorescence signal is obtained from $K_2Cr_2O_7$ while the transmitted signal is from Cr_2O_3 separately and simultaneously. The results are shown in Fig. 3, according to the features of the two references [3, 4], Cr(VI) and Cr(III) can be clearly identified.

Another example demonstrating the advantage of this detector is measuring the valence state of chromium in saccharomyces Cerevisiae. Cr-yest-biomass is in fluorescence mode, while standard Cr_2O_3 is in transmission mode. Fig. 4 depicts the XANES at the Cr K-edge from the sample, along with standard Cr_2O_3. It is immediately apparent that the XANES spectra at the Cr K-edge of the sample is similar to that of standard Cr_2O_3, and different from the spectrum of the standard of $K_2Cr_2O_7$, revealing that the sample has become trivalent, rather than primitive hexavalent. The result can be interpreted as reduction of Cr(VI) to Cr(III) during the process of sample preparation, indicating that yeast can strongly reduce Cr(VI) to Cr(III), which has been used in the bio-sorption of Cr(VI) from environment [5].

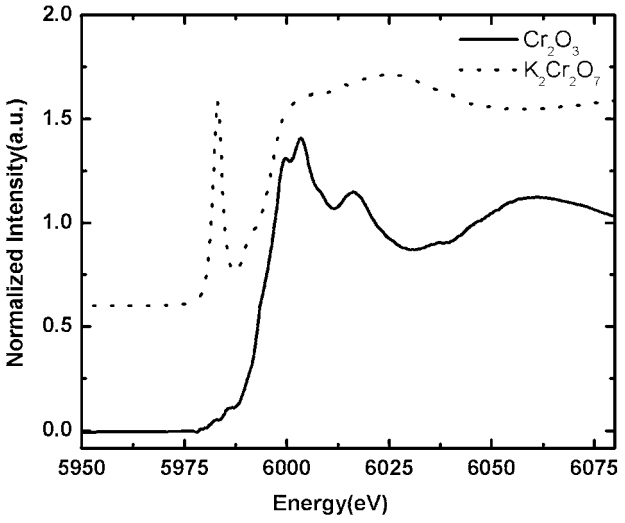

Fig. 3. XANES spectra at Cr K-edge of $K_2Cr_2O_7$ and Cr_2O_3.

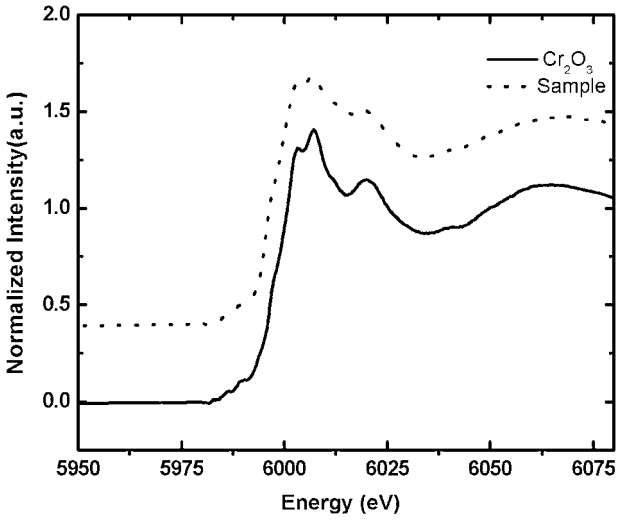

Fig. 4. XANES spectra at the Cr K-edge of yeast sample, standard compound Cr_2O_3.

5. Summary

A new XAS detection system in unfocused incident X-ray beam with large horizontal divergence, has been developed. PIN diodes detector and Lytle-type fluorescence detector simultaneously collect spectra of the standard in transmission and a low concentration sample in fluorescence mode. Comparing the two spectra, the energy shift of the sample can be calibrated relative to a selected standard. Also application to chromium valence state change in Saccharomyces Cerevisiae shows that this technique can be a promising means of characterizing the electronic and local structure of dilute systems.

References

1. Bianconi, A., in "X-ray Absorption: Principles, Applications, Techniques of EXAFS, SEXAFS, XANES," (Edited by Prins, R. and Koningsberger, D.), (Wiley, New York, 1988).
2. Cross, J. O. and Frenkel, A. I., Rev. Sci. Instrum. **70**, 38 (1999).
3. Szulczewski, M. D., Helmke, P. A. and Bleam, W. F., Environ. Sci. Technol. **31**, 2954 (1997).
4. Huggins, F. E., Najih, M. and Huffman, G. P., Fuel **78**, 233 (1999).
5. Omar, N. B., Merroun, M. L., Gonzalez-Munoz, M. T. and Arias, J. M., J. Appl. Bacteriol. **81**, 283 (1996).

Physica Scripta. Vol. T115, 1017–1018, 2005

Customization of an In-House XAFS Spectrometer for Sulfur Measurement

T. Taguchi[1*], K. Shinoda[2] and K. Tohji[2]

[1]XRD-division, Rigaku Corporation, 3-9-12 Matsubara-cho, Akishima-shi, Tokyo 196-8666, Japan
[2]Graduate School of Environmental Studies, TOHOKU University, 01 Aza-Aoba, Aramaki, Aoba-ku, Sendai-shi, Miyagi 980-8579, Japan

Received June 26, 2003; accepted in revised form January 28, 2004

PACS number: 0785Nc

Abstract

In-house XAFS spectrometers suitable for routine experiments are getting fairly popular today. One of the problems of such apparatus is the capability to study low atomic number materials. In general, elements with atomic number 20 (i.e. Ca) and below is difficult to measure because absorption of air becomes large. In this energy region, very important elements for environmental studies, such as S and P are involved. Either an evacuated or a He-filled X-ray path is required for getting enough photons in the low energy region. Since most in-house XAFS spectrometers apply Rowland Circle configuration, the spectrometer shows fairly complicated movement during energy scan. Varying the distance between the X-ray source and the bent crystal requires bellows for evacuating the X-ray path or substituting by He, but it restricts the spectrometer scanning range, especially on the low angle side. However, the low angle range (i.e. 30 to 60 degree) is most commonly used and X-rays are efficiently collected in this range. We have customized a commercial XAFS spectrometer to be capable for energies as low as 2 keV for sulfur measurement without sacrificing its scanning range.

1. Introduction

XAFS spectrometry is a powerful tool to characterize various materials. An in-house XAFS spectrometer can be used whenever a researcher wants data. That is quite important for interactive innovativeness and this is an advantage to the synchrotron facilities despite of the weakness of photon numbers available. An in-house XAFS apparatus is normally used in air environment, which determines the energy limit of the lower side. Below 5 keV, or lower than Ti K-edge (4,966 eV), the data acquisition becomes harder and harder when the atomic number of the target element decreases by one unit at the time. For instance, the number of photons available for K K-edge (3,607 eV) measurement is 1/8 of what is available for Ca K-edge (4,038 eV) measurement with the same optics under air. Evacuating the X-ray path or replacing air by He can significantly increase the number of photons available by magnitude of 1 or 2. From our experience, He path makes Ca K-edge measurement fairly easy, but K K-edge is still difficult. Thus the low energy limit for the in-house XAFS spectrometer is set for Ti under air and Ca with He path attachment.

In order to measure much lighter elements, such as Al (K-edge; 1,559 eV) or Si (K-edge; 1,838 eV), more effort needs to be spent. In this energy range, even 10 mm air absorbs more than half of the photons. Therefore both sample and detector must be put in vacuum in addition to the evacuation of the X-ray path. Among the light elements (atomic number less than 20), sulfur is quite important for environmental study. We have customized a commercial XAFS spectrometer [1, 2, 3] for sulfur measurement.

2. Design consideration

The most important factor for XAFS experiment is the number of photons available. Especially in the soft X-ray region, it becomes more important. In order to increase the X-ray intensity we considered the X-ray cover, the beryllium window and monochromator crystal.

The XAFS spectrometer we chose was designed for the air ambient and there is neither He path attachment nor vacuum path attachment. Then we had to design from the beginning. The choices were to design

i. Helium or vacuum path attachment
ii. Vacuum chamber
iii. Helium chamber

The first choice seems easy, but as the spectrometer moves in very complicated manner, it is difficult to design the path. Moreover the path restricts the scan range, especially the lower angle, and it reduces the number of elements, which can be measured with a single monochromator crystal. The second and third choices look almost the same. Putting the whole spectrometer in a large chamber sounds serious, but the design is not difficult apart from one point, the connection of inside and outside. Since the X-ray generator applies high voltage, evacuation by a rotary pump causes discharges. Helium ambient leads to the same problem as well. Therefore at least high-tension cables must be exposed to air that is a very good insulator. Figure 1 is a schematic drawing of the spectrometer chamber. The cover consists of two airtight chambers. One is the spectrometer chamber and the other is the sample chamber. In order to overcome the discharge problem, rubber bellows are attached between the X-ray generator and spectrometer chamber so that the high-tension terminal is exposed to the air ambient. Making this chamber evacuative, enormous strength against air pressure is needed. We finally decided making

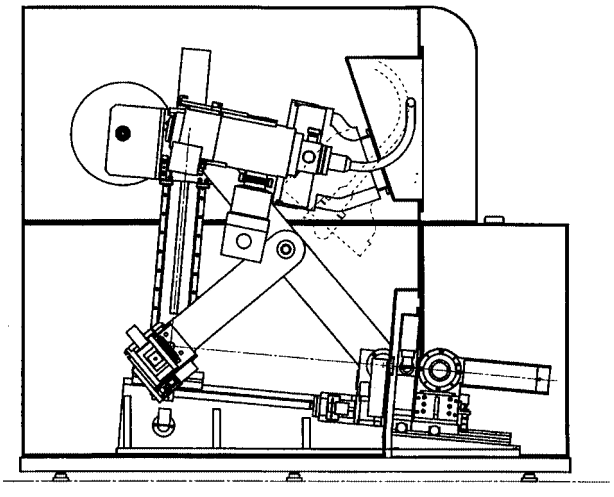

Fig. 1. Schematic diagram of the in-house spectrometer and helium chamber.

*e-mail: takey@rigaku.co.jp

this a helium chamber. The spectrometer chamber and the sample chamber can be filled by helium gas independently. The advantage of using a helium chamber other than its ease of building is that it is possible to examine liquid samples.

The absorption and scattering by air is the main cause of X-ray attenuation, but the secondary cause for the photon loss is due to the X-ray generator. Accelerated electrons hit a metal target in vacuum and produce X-rays. These X-rays are taken out through a beryllium window. Normally the thickness of this beryllium window is 0.4 mm. More than 90% of the X-ray photons are absorbed at 2,500 eV. Even the manufacturer's option of a beryllium window for soft X-rays has a thickness of 0.2 mm and absorbs 3/4 at the same energy. The thickness of the beryllium window is determined by considering the damage caused by the scattering electrons inside of the tube. Because the X-ray tube used for XAFS measurement does not apply as high tube voltage as ordinary X-ray diffraction applies, the energy of the scattered electrons is low. We have worked out the beryllium thickness and the electron energy, and then decided to use beryllium of thickness 0.05 mm, or 50 microns. The 50 microns beryllium transmits more than 70% of the X-rays at 2,500 eV.

For in-house XAFS spectrometer, either silicon or germanium single crystal is used as monochromator crystal. It is bent (Johan type) and shaved (Johansson type) in certain manners. According to Knapp [4], the energy resolution ΔE of the linear spectrometer can be expressed as

$$\Delta E = \frac{E^3(2d)^2}{8RC^2}\left[(W_s + W_f)^2 + \left(\frac{h^2}{8R}\right)^2 + \left(\frac{CE^2 \ln 2}{kd}\right)^2\right]^{1/2}.$$

C is a constant (12.398 keV · Å), d is the lattice constant, R is the Rowland circle radius, h is the height of the X-ray source and the receiving slit, W_s and W_f are the width of those respectively and the absorption coefficient of the crystal is approximated as $\mu = K/E^3$. At a smaller d, the energy resolution becomes better, but the number of photons decreases. As our spectrometer scan range is 30 to 90 degrees in 2θ, the d value must be in the range of $d = 3.65$ to 9.98 Å. Even Ge(111) ($d = 3.265$ Å) does not satisfy this. Possible choices are InSb(111) ($d = 3.74$ Å), EDDT(020) ($d = 4.404$ Å) and Beryl(1010) ($d = 7.985$ Å). We chose Beryl for the preliminary test since it has the largest d value among the three crystal and therefore it is expected to provide the maximum number of photons.

3. Experiment and Results

The X-ray intensity is monitored before and during the He replacement. A large amount of He is flowed in order to force out the air inside the chamber. When the X-ray intensity becomes saturated, regulator bulb is closed and Helium is flowed at constant rate, which is 30 l/min. The gain is measured at a few energy points and compared to the calculated value. At 7,000 eV (near the Fe K-edge), the measured gain was 2.5 and the calculated gain was 2.9. The measured gain was 90 and the calculated was 200 at 4,000 eV (Ca K-edge). The reason for the low gain is presumably due to improper replacement of the air. The gain was calculated again with some residual air along the X-ray path. Figure 2 shows a fit with the assumption that 90 mm air remained at the X-ray path for the energy region from 3,900 to 4,100 eV.

At energies below 3 keV, it was impossible to monitor X-rays in the air ambient. Using Beryl(1010) Johansson crystal, more than 100,000 photons/s are obtained at 2,400 eV with energy resolution

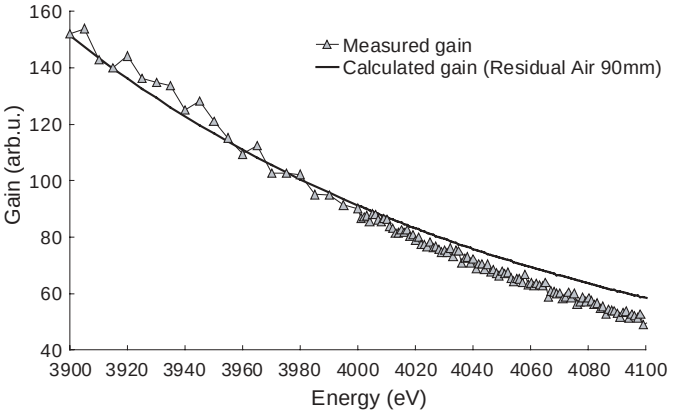

Fig. 2. Measured gain and calculated fit.

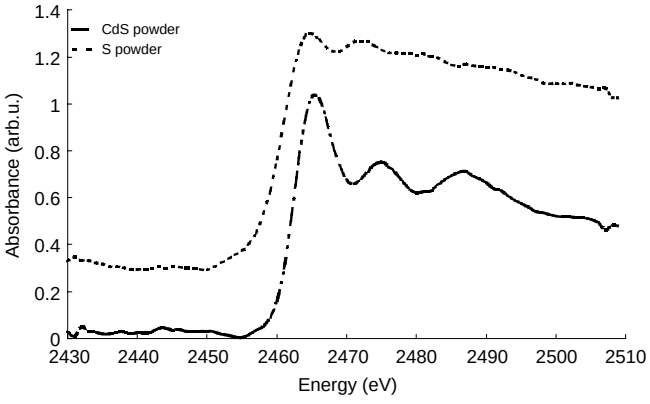

Fig. 3. XANES measurement of S and CdS.

better than 1 eV. Figure 3 shows sulfur powder and CdS XANES spectra measured with this spectrometer. At this energy range, the sample chamber needs to be replaced by helium, as well as the spectrometer chamber. Therefore a vacuum tight gas flow type proportional counter was used for the experiment since an ordinary detector caused discharge and counted no X-rays.

4. Conclusion

The soft X-ray capability (as low as to the S K-edge) of an in-house XAFS spectrometer is demonstrated. Sulfur in oil is turned to sulfur oxide (SOx), discharged to air and causes severe pollution. In addition, sulfur poisoning of catalysts has been a big problem for a long time and receives attention again since it plays an important role for the fuel cell development. Thus it is important study the chemical state of sulfur in materials, and it helps the effective removal of sulfur. Furthermore, many atoms' absorption edges (not only K, but also L and M) are at energies below 3.5 keV [5] and extent to much lower energy expands the usage of the in-house XAFS spectrometer.

References

1. Taguchi, T. *et al*., J. Synchrotron Rad. **8**, 363 (2001).
2. Taguchi, T., "Analytical Sciences 2001", Vol. 17 Supplement, (2001), i139–i141.
3. Taguchi, T., Harada, J., Tohji, K. and Shinoda, K., Adv. X-ray Anal. **45**, 397 (2002).
4. Knapp, G. S., "Laboratory EXAFS Facilities 1980", (Stern, E. A. ed.) (AIP, New York, 1980) 8.
5. Ohta, T., "X-ray Absorption Spectrometry -XAFS and its application-", IPC (2002), 115–127.

Physica Scripta. Vol. T115, 1019–1021, 2005

The Electronic and Optical Properties of Dendrimer-capped CdS Quantum Dots: A UV-vis and X-ray spectroscopy study

P. Zhang and T. K. Sham*

Department of Chemistry, University of Western Ontario, London, ON, N6A 5B7, Canada

Received June 26, 2003; accepted November 4, 2003

PACS numbers: 73.22.−f; 78.67.Hc

Abstract

The electronic and optical properties of a series of PAMAM-dendrimer capped CdS quantum dots (QDs) have been investigated with UV-vis absorption (UV-abs), photoluminescence (PL), X-ray absorption near-edge structure (XANES) and X-ray excited optical luminescence (XEOL) techniques. The size-dependent electronic behavior of the QDs was observed in both the UV-abs and XANES (S K-edge) spectroscopy. Findings from the PL and XEOL studies provide complementary information to the UV- and X-ray absorption results and shed further light on the stability of the CdS QDs upon aging.

1. Introduction

It has been well recognized that the electronic properties of semiconductor quantum dots (QDs) are very sensitive to their local structure such as doping, capping and surface defects [1]. More recently, it became apparent that the wet-chemical synthetic method for QDs can be use to tune these properties by simply varying the experimental conditions. In this contribution, we show that by varying the concentration of the capping molecules, PAMAM dendrimer, the electronic and optical properties of the CdS QDs can be modified. The properties of the QDs thus prepared were examined by UV-vis absorption, photoluminescence (PL), X-ray excited optical luminescence (XEOL) and X-ray absorption fine structure (XAFS). The QDs investigated are generation 4 PAMAM-OH dendrimer-capped CdS with a dendrimer : CdS ratio of 1 : 24, 1 : 12 and 1 : 6.

2. Experimental

The details of the synthetic procedure have been reported elsewhere [2]. In addition, the 1 : 12 CdS QDs synthesized within a few days (henceforth denoted "as-prepared") and after six months (henceforth denoted "aged") were also studied to address the effect of aging on the properties of the QDs. The UV-vis spectra were obtained with standard instrumentation. X-ray studies were conducted at the double crystal monochromator (DCM) beam line of the Canadian Synchrotron Radiation Facility (CSRF) at the Synchrotron Radiation Center (SRC), University of Wisconsin-Madison. In the X-ray near edge structure (XANES) study, total electron yield (TEY) and X-ray fluorescence yield (FLY) were recorded simultaneously using specimen current and a multi-channel- plate detector, respectively. X-ray excited optical luminescence (XEOL) was recorded using a JY H-100 monochromator that is equipped with a Hamamatsu 943-02 photomultiplier (PMT).

3. Results and Discussion

Fig. 1(a) shows the UV-vis absorption spectra of a series of dendrimer capped CdS QDs synthesized by increasing the dendrimer/CdS ratio, i.e. 1 : 24, 1 : 12 and 1 : 6. In general, it is believed that the less the capping molecules, the bigger the QDs in that decreasing the amount of capping molecules (e.g. from 1 : 6 to 1 : 24) would facilitate the growth of the CdS [3]. The UV-vis absorption spectra of the 1 : 24, 1 : 12 and 1 : 6 CdS QD samples (increasing dendrimer to CdS ratio) clearly exhibit this trend. As seen in Fig. 1, the exciton peak that is closely related to the QD size slightly shifts to higher energy region when going from the 1 : 24 (340 nm) to 1 : 12 (332 nm) and then to the 1 : 6 sample (330 nm). According to a widely used empirical size-exciton energy relationship, the size of these QDs should be in the range of 1–3 nm [4]. The photoluminescence (PL) spectra shown in Fig. 1(b) are consistent with the observation of the UV-vis (absorption) spectra. The luminescence band of the 1 : 6 sample exhibits a blue shift in the PL relative to the 1 : 12 and the 1 : 24 sample. Furthermore, the PL band becomes considerably sharper in going from 1 : 24 to 1 : 12 and to 1 : 6, indicating that with increasing dendrimer/CdS ratio, the size of the QDs become mores uniform [5].

The local structure and the electronic behavior of the QDs were studied by S K-edge XANES as shown in Fig. 2. A couple of observations are noteworthy. First, the QDs synthesized using a larger dendrimers/CdS rato, particularly the 1 : 6 ratio, exhibit a large contribution of oxide that is most likely a sulfate species since the peak position matches that of $CaSO_4$. Second, the edge jump corresponding to the S^{2-} species shows a noticeable blue shift for the 1 : 6 sample (Fig. 2 inset).

As the UV-vis spectroscopy result indicates, the QDs with a larger dendrimers/CdS ratio are smaller. The XANES results support this notion in that the QDs with higher dendrimer/CdS

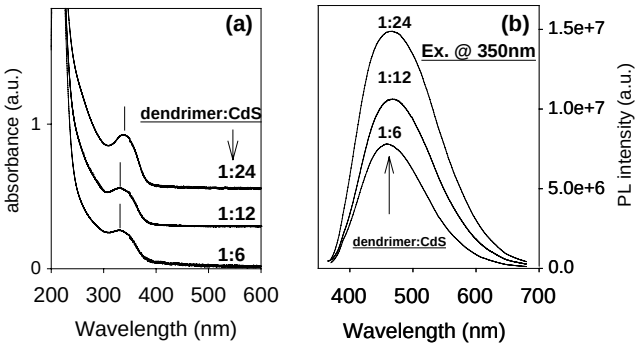

Fig. 1. UV-vis absorption and photoluminescence spectra of size-varied dendrimer-stabilized CdS QDs.

*Corresponding author's email address: sham@uwo.ca

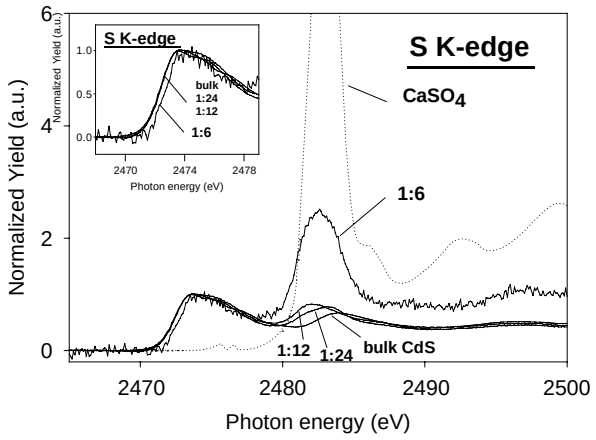

Fig. 2. S K-edge X-ray absorption near edge structure (XANES) of the CdS QDs and bulk CdS, $CaSO_4$ references.

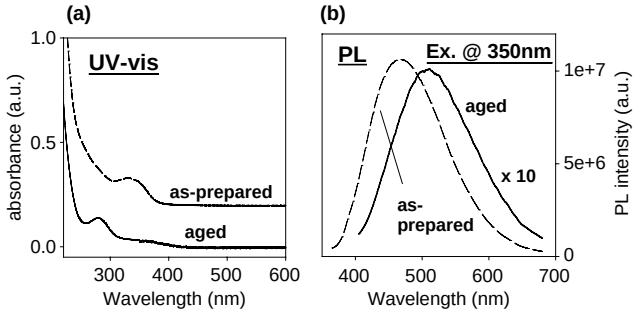

Fig. 3. UV-vis absorption spectra (a) and photoluminescence spectra (b) of a CdS QDs sample (1 : 12) measured within a few days (as-prepared) and after six months (aged).

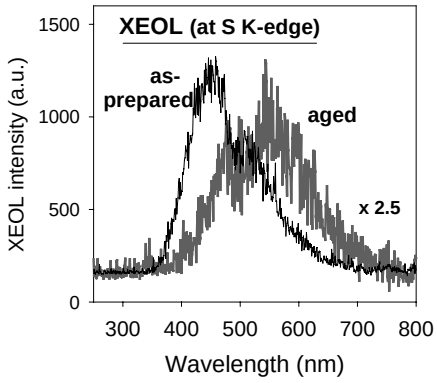

Fig. 4. X-ray excited optical luminescence (XEOL) spectra of the as-prepared and aged CdS QD sample (1 : 12) excited at S K-edge.

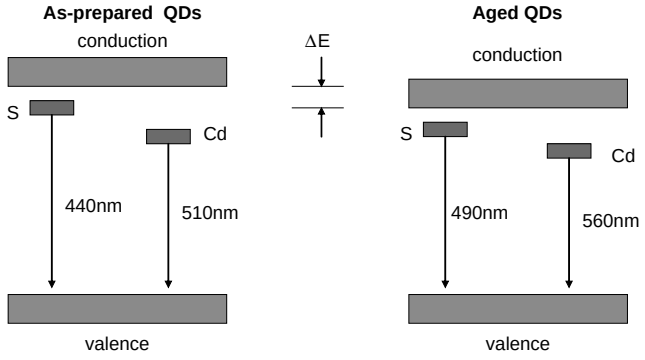

Fig. 5. A schematic illustration of the defect-involved luminescence mechanism of the as-prepared and aged dendrimer-capped CdS NPs.

ratio (1 : 6) display a more pronounced blue shift, which corresponds to a smaller size in terms of the quantum size effect. Moreover, a smaller QD has a larger contribution from the surface atoms, thus a more intense surface signal (surface sulfur oxidized to sulfate) is expected in the XANES. This explains the observation of a more intense sulfate peak in the XANES in that the higher the dendrimer to CdS ratio, the more intense the sulfate peak.

In a related study of the stability of the CdS QDs in the ambient, we selected the 1 : 12 sample with which UV-vis absorption and the PL spectra were collected a few days after (as-prepared) and six months after (aged). The results are shown in Fig. 3 where the absorption and PL spectra of the two samples show a dramatic difference. The absorption spectrum of the as-prepared sample exhibits an exciton band at ca. 332 nm whereas two bands were detected in the aged sample, one at ca. 370 nm and one at ca. 290 nm. Let us concentrate at the 370 nm band (the short wavelength band did not result in emission). According to classic quantum confinement theory [4], the first exciton peak determines the size of the NPs- the more blue/red-shifted the first exciton peak, the smaller/larger the QDs. The energy position of the first exciton peak shifts from 332 nm to 370 nm upon aging (a ∼40 nm shift). This clearly indicates an increase of the QDs size upon aging. The PL results are consistent with the absorption. In Fig. 3(b), the PL spectrum of the aged QDs clearly exhibits a red shift (∼50 nm) relative to the as-prepared sample. It is not too surprising since the PAMAM dendrimer interacts weakly with CdS relative to other capping molecules such as thiol [6], thus it cannot efficiently prevent the QDs from further aggregation upon aging. Another interesting observation is that the PL intensity decreases by a factor of 10 upon aging. This will be discussed below together with the XEOL results.

The X-ray excited optical luminescence (XEOL) excited at the S K-edge is shown in Fig. 4. As expected, the aged sample exhibits red-shifted (∼50 nm) XEOL bands relative to the as-prepared sample and the luminescence intensity of the aged QDs decreases (∼3 times) relative to the as-prepared sample. An inspection of the spectral shape reveals that both spectra exhibit two luminescence bands – bands at ca. 440 nm and 510 nm for the as-prepared sample and bands at ca. 490 nm and 560 nm for the aged sample.

Interestingly, the shorter-wavelength peak for the as-prepared sample is more intense than the other whereas in the aged sample, the longer-wavelength peak is more intense. It has been reported that in CdS QDs there are mainly two types of defects-related band-edge luminescence (i.e. radiation decay from defects near the conduction band to valence band) [7] – a short-wavelength emission attributed to S-related defect and a longer-wavelength emission attributed to Cd-related defect [8]. The two short-wavelength bands (440 nm for the as-prepared and 490 nm for the aged) observed in Fig. 4 reasonably match the reported S-defect emission (∼440 nm) and the longer-wavelength bands (510 nm, 560 nm) basically match the reported Cd-defect emission (∼580 nm) [8]. A schematic illustration of the attribution of these bands is shown in Fig. 5. It can be seen that from the as-prepared NPs to the aged sample, there is a band gap narrowing of ∼50 nm, or 0.2–0.3 eV. It indicates that after the six month, the NP size increases considerably, which is normal for the weakly capped NPs. Both Fig. 3 and Fig. 4 indicate that the aging also results in a decrease of the luminescence intensity of both S and

Cd-related emissions; moreover, the efficiency of the S-defect-related emission undergoes a more pronounced decrease.

4. Summary

We have reported the XEOL of dendrimer capped CdS quantum dots prepared under different conditions as well as the effect of aging. We found that in general, the higher the dendrimer to CdS ratio, the smaller the size as revealed from the optical studies. We also reported a dramatic change in the optical behaviour of these QDs upon aging. The detailed mechanism for the luminescence behavior of the CdS QDs upon aging remains unclear at the present. One possible reason is the change of the local environment of the S- and Cd-related defects in that in the S K-edge XANES (not shown), the aged CdS QDs exhibit a more intense sulfate resonance peak than the as-prepared QDs. Further experiments such as S and Cd K-edge EXAFS will provide new clues for the phenomenon.

Acknowledgement

We thank CSRF staff Drs. A. Jürgensen, Y.-F. Hu and K. H. Tan for their assistance in the measurements at CSRF. Research at UWO is supported by NSERC. SRC is supported by the US NSF grant #DMR-00-84402. The awards of an Ontario Graduate Scholarship and the R.R. Lumsden Scholarship to PZ are acknowledged.

References

1. Fendler, J. H., "Nanoparticles and Nanostructured Films, Preparation, Characterization and Application" (Wiley-VCH, Weinheim, 1998).
2. Zhang, P., Naftel, S. J. and Sham, T. K., J. Appl. Phys. **90**, 2755 (2001).
3. Templeton, A. C., Wuelfing, M. P. and Murray, R. W., Acc. Chem. Res. **33**, 27 (2000).
4. Steigerwald, M. L. and Brus, L. E., Acc. Chem. Res. **23**, 183 (1990).
5. Yu, W. W. and Peng, X., Angew. Chem. Int. Ed. **41**, 2368 (2002).
6. Zhang, P. and Sham, T. K., Appl. Phys. Lett. **81**, 736 (2002).
7. Wang, Y., "Advances in Photochemistry", (Edited by D. C. Neckers, D. H. Volman and G. Bunau) (John Wiley & Sons, 1995), v. **19**, pp. 179.
8. Wang, Y. and Herron, N., J. Phys. Chem. **92**, 4988 (1988).

Physica Scripta. Vol. T115, 1022–1025, 2005

Chemical Phase Separation in Zr Silicate Alloys: *an EXAFS Study Distinguishing Between Phase Separation with, and without XRD Detectable Crystallization*

G. B. Rayner, G. Lucovsky* and D. Kang

Department of Physics, Campus Box 8202, NC State University, Raleigh, NC 27695-8202, USA

Received June 26, 2003; accepted November 4, 2003

PACS numbers: 77.55.+f, 78.30.−j, 78.70.Dm, 79.60.−i

Abstract

Chemical phase separation at processing temperatures is an important issue for integration of Zr and Hf silicates alloys into advanced CMOS devices. Chemical phase separation into ZrO_2 and SiO_2 has been detected by different spectroscopic techniques, including Fourier transform infra red, X-ray photoelectron, and X-ray absorption spectroscopy, as well as X-ray diffraction and high resolution transmission electron microscopy imaging. Comparisons between these techniques for Zr silicates identify an unambiguous approach to distinguishing between chemical phase separation with different degrees of micro- and nano-crystallinity. This is important since all modes of chemical separation degrade the dielectric properties required for high-K applications.

1. Introduction

One of the more significant limitations for the integration of transition metal silicate alloys such as $(ZrO_2)_x(SiO_2)_{1-x}$ and $(HfO_2)_x(SiO_2)_{1-x}$ as gate dielectrics into advanced Si devices is a chemical phase separation of these pseudo-binary alloys into SiO_2 and transition metal oxides, $Zr(Hf)O_2$ for Z(Hf) silicate alloys [1–3]. Studies of phase separation are important for device processing, since it results in significant decreases in effective dielectric constants, reducing the gate capacitance required for aggressive device scaling. This separation occurs in the same regime of temperatures as that required for integration of deposited dielectrics into device fabrication protocols [4, 5]. For example, chemical phase separation occurs in the 1000 °C temperature range required for dopant activation in conventional processing of source, drain, and polycrystalline gate electrodes in field effect transistors. It is therefore important to identify spectroscopic approaches that not only identify chemical phase separation accompanied by crystallization detectable by conventional diffraction techniques such as XRD, but also to detect chemical phase separation that occurs with amorphous, or nano-crystalline phases too small for detection by conventional diffraction methods.

2. Experimental Procedures

Zr silicate films 10 to 100 nm thick were deposited onto Si(100) substrates at 300 °C by a remote plasma process described in detail elsewhere [2]. The Zr : Si ratio in the deposited films was determined by the relative flow rates of the respective Zr and Si source gases. The alloy composition of the bulk films, reported as the Zr : Si : O ratio, was determined by Rutherford backscattering spectrometry (RBS). RBS results indicated that the $(ZrO_2)_x(SiO_2)_{1-x}$ alloy films were homogeneous, and fully-oxidized with an uncertainty in composition, $\delta x = \pm 0.03$ [1, 2]. These results were used to calibrate on-line AES results where a linear dependence was demonstrated between the ratio of the derivative spectrum peak-to-peak heights for Zr_{MVV} and O_{KVV} features and alloy composition as determined by RBS. Films were annealed *ex-situ* in an inert Ar ambient for one minute utilizing an AG minipulse 310 rapid thermal annealing (RTA) apparatus with an uncertainty in annealing temperature of ±15 °C.

FTIR absorption measurements, in the mid-IR (4000–400 cm^{-1}) and far-IR (700–50 cm^{-1}), were performed utilizing a Nicolet Magna-FTIR 750 spectrometer. XRD measurements were made using a Bruker X-ray diffractometer with a beryllium area detector centered at 2θ positions of 25° and 50°. XPS measurements of O 1s, C 1s, Zr 3d, and Si 2p core levels were made using a Riber LAS-3000 spectrometer with non-monochromatic Mg Kα radiation (1253.6 eV) and a pass energy of 20 eV. EXAFS and NEXAS measurements were made at the National Synchrotron Light Source (NSLS) at Brookhaven National Laboratory [6]. Absorption spectra for the O K_1 edge NEXAFS were recorded by measuring the photon energy dependence of primary photoelectron yield, and absorption data for the EXAFS and NEXAS studies using the Zr K_1 edge were obtained by monitoring X-ray fluorescence.

3. Experimental Results and Data Analysis

Figures 1(a) and (b) illustrate changes in FTIR spectra following the 900°C RTA. In films with 25% or less ZrO_2, chemical phase separation is detected as a reduction of absorption in a 970 cm^{-1} shoulder associated with terminal Si-O groups produced by network disruption. In films with more than 50%, ZrO_2, the changes are greater, and the emergence of SiO_2 like spectral features after the 900 °C anneal establishes the separation. This approach does not identify the morphology of the separated ZrO_2 phase.

Figures 2(a) and (b) are differentiated XPS spectra for the O 1s core level feature in as-deposited films and for films that have been annealed at 900 °C in Ar for one minute. The asymmetric line shapes in the as-deposited films are a manifestation of systematic changes in O-atom bonding coordination, which has been shown to change systematically from two (2) in SiO_2, to three (3) at the chemically-ordered silicate composition of $x = 0.5$ ($ZrSiO_4$), and then increase to four (4) in ZrO_2 [2]. The differentiated spectra for different samples which span the 50% concentration range, are markedly different, and clearly identify the emergence of two distinct spectral features at core level binding energies close to those of the end-member elemental oxides, SiO_2 and ZrO_2.

*e-mail: lucovsky@unity.ncsu.edu

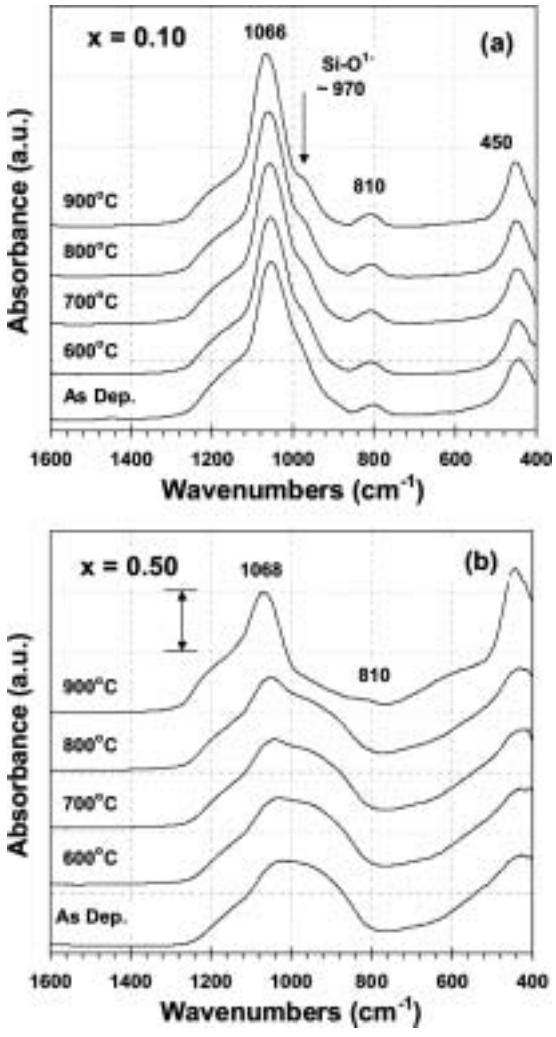

Fig. 1. FTIR spectral of Zr silicates alloys, 0.10 (top) and 0.5 (bottom) as function of temperature. Chemical phase separation is evident at 900 °C.

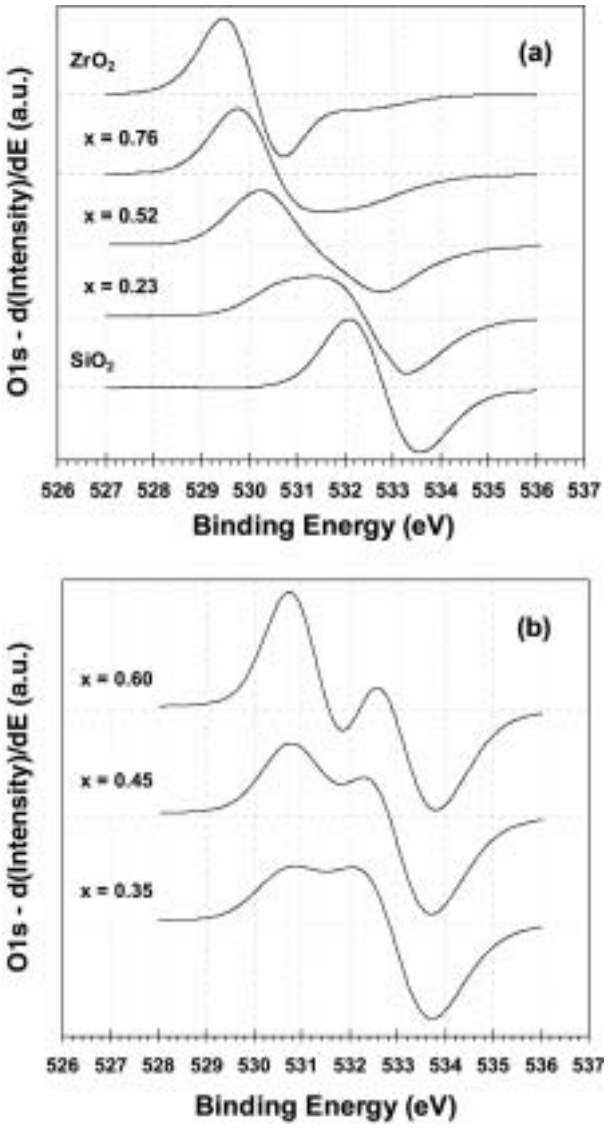

Fig. 2. Differentiated XPS spectra for the O 1s core level feature in as-deposited films and for films that have been annealed at 900 °C in Ar for one minute.

Finally, Figs. 3(a) and (b), and 4(a) and (b) compare respectively XRD and Fourier transformed EXAFS spectra for alloys Zr silicates with approximately 25% and 50% ZrO_2, including as-deposited and 900 °C annealed samples. The XRD spectra in Figs. 3(a) and (b) indicate the evolution of the X-ray scattering from as-deposited samples to those annealed at 900 °C. For the 25% alloy there is no evidence for the emergence of features at two-theta (2θ) values for any of the crystalline phases of ZrO_2. However, comparisons with SiO_2 XRDs confirm features associated with the alloy structure. These are more pronounced in the 50% alloy as a broad feature between about 26 and 34 degrees. In addition, the 50% alloy displays tetragonal crystalline features at 2θ values of ~28, 33 and 51 degrees.

Figures 4(a) and (b) indicate radial distributions functions obtained form Fourier transformed EXAFS spectra for 25% and 55% ZrO_2 alloys for as-deposited films and films annealed at 900 °C for one minute in Ar. The as-deposited films each show a feature associated with nearest-neighbor Zr-O bonding. The distance scale in the film has not been renormalized, and the real space spacing of this feature is ~0.22 nm. After annealing the RDFs show important qualitative and quantitative differences. A second shell feature in Fig. 4(a) assigned to Zr-Zr second neighbor distances emerges in the 25% ZrO_2 alloy, and its peak amplitude is about 40% of that of the Zr-O feature. In addition, there are also indications of third and fourth neighbor shells, but these are barely detectable above the background noise. In fact, the occurrence of stronger third and fourth shell features in the 55% sample helped to isolate these peaks. The RDF for the 55% ZrO_2 alloy is markedly different. The second shell, Zr-Zr feature is almost equal in magnitude to the Zr-O feature, and the third and fourth features are well above the background noise level. Based on these RDFs, the 50% alloy shows more long range order than the 25% alloy, and combined with the XRD results, the 55% alloy includes a tetragonal crystalline ZrO_2 phase after the 900 °C, anneal, but differences in long range order between the as-deposited and annealed 25% ZrO_2 alloy are too small for XRD detection.

A study of high resolution transmission electron micrographs clarifies this last point. The micrographs are included in Ref. [2]. The micrograph for the 25% alloy after 900 °C annealing displays dark and light patterns in the bright field image. The dark regions assigned to ZrO_2 on the basis of relative atomic masses, are approximately 3–5 nm in size, and are encapsulated by lighter regions assigned to the SiO_2 majority phase. This interpretation is consistent with the interpretation of FTIR and XPS data in Figs. 1 and 2. There is some evidence of crystalline organization in dark regions that are more than 5 nm distant from the Si substrate.

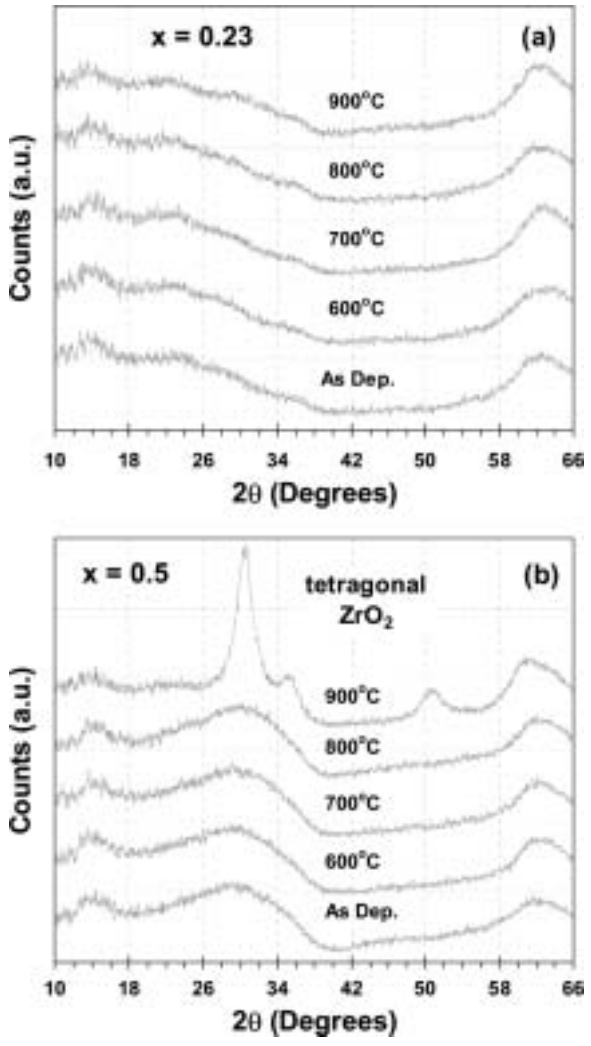

Fig. 3. XRD spectra for alloys Zr silicates with (a) 23% and (b) 50% ZrO_2 as-deposited through 900 °C annealing.

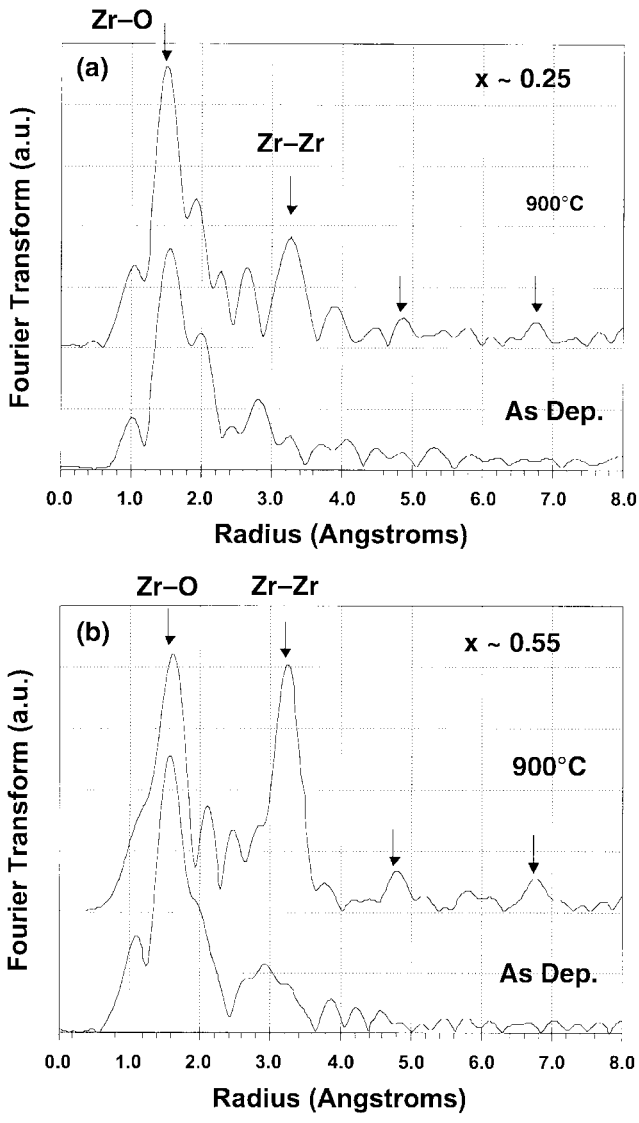

Fig. 4. Fourier transformed EXAFS spectra for alloys Zr silicates with (a) 25% and (b) 55% ZrO_2 as-deposited and after 900 °C annealing.

Combining the HRTEM and EXAFS, these regions are interpreted as being comprised of highly defective nano-crystals. In contrast, the HRTEM image for the 50% ZrO_2 alloy shows lattice planes indicative of micro-crystalline ZrO_2 that are again more distant that 3–5 nm from the Si-substrate. The 3–5 nm region devoid of micro- or nano-crystallite Si is assumed to occur because of compressive stress in the near interface region.

Studies of the O and Zr K_1 (1s) edges in Zr silicate alloys also show evidence for chemical phase separation after 900 °C annealing. These results are presented in Refs [7] and [8], and are complementary to the measurements discussed above. For example changes in the O K_1 edges in alloys with more than 50% ZrO_2 clearly indicate a crystalline ZrO_2 phase. In contrast, changes in the Zr K_1 edges indicate a change from Si to Zr second neighbors to a give Zr atom, i.e., phase separation, but with no direct evidence for crystallinity.

4. Summary

Zr silicate alloys films were prepared by remote plasma-enhanced chemical vapor deposition and compositions were obtained by RBS and AES. For Zr silicates with x between ~0.1 and 0.75, there are abrupt changes in the FTIR spectra between 400 cm^{-1} and 1100 cm^{-1} after rapid thermal annealing (RTA) for one minute in Ar at 900 °C, that indicate a chemical phase separation into SiO_2 and ZrO_2, but do not provide any information related to the crystallinity of the ZrO_2 product. Following the 900 °C RTA, changes in the O 1s XPS core level energies, and core level line shapes, and differentiated XPS signals as a function of alloy composition give unambiguous spectroscopic evidence for changes in O-atom bonding characteristic of 2-fold coordinated O-atoms in SiO_2, and continuous changing to 4-fold coordinated O in ZrO_2, but do not provide information relative to crystallinity. However, changes in the amplitudes of second-coordination shell Zr-Zr features compared to first-shell Zr-O features in Zr K_1 EXAFS RDFs before and after the RTA confirm differences in crystallite size as a function of alloy composition. Combined with HRTEM micrographs, these RDF differences are consistent with the grain sizes of ZrO_2 precipitates increasing from ~3 nm for 25% ZrO_2 alloys to >10 nm for 50% ZrO_2 alloys. XRD studies of silicate films with 25% ZrO_2 have shown relatively small changes in *amorphous-like* diffraction patterns after the 900 °C RTA, while alloys with 50% ZrO_2 indicate a tetragonal ZrO_2 phase after the anneal. Similar results have also been reported for Hf silicates, where the separation of homogeneous alloys can occur at temperatures approaching 1000 °C in SiO_2-rich alloy compositions [2].

In conclusion, combining FTIR and derivative XPS, with EXAFS RDFs, XRD and HRTEM imagining provides an

unambiguous and effective way to study chemical phase separation with *different degrees of crystallization*. This is of importance for semiconductor device processing since chemical phase separation at 900 °C in SiO_2-rich Zr and at 1000 °C in SiO_2-rich Hf silicates undetectable by XRD, can reduce gate dielectric capacitance, and therefore also reduce the current drive in FETs. Recently, SiO_2-rich Zr and Hf silicates with less than 40% $Zr(Hf)O_2$ have been shown to display reduced direct tunneling relative to their end member oxides [9]. If high-temperature processing produces a chemical phase separation with formation of nano-crystalline precipitates not detectable by XRD in these alloys, this will require the complementary characterizations for detection of chemical phase separation identified above: FTIR, XPS and EXAFS. Other issues yet to be resolved include properties of nitrided silicates, and defects at Si and poly-crystalline interfaces that give asymmetric behavior in N-/P-MOSFETs devices.

Acknowledgements

This research is support by the ONR, SRC, and NSF.

References

1. Rayner, G. B., Therrien, Jr., R. and Lucovsky, G., MRS Symp. Proc. **611**, c13.1 (2001).
2. Rayner, G. B., Kang, Jr., D., Zhang, Y. and Lucovsky, G., J. Vac. Sci. Technol. B **20**, 1748 (2002).
3. Maria, J. P. *et al*., J. Appl. Phys. **90**, 3476 (2001).
4. Wilk, G. D., Wallace, R. M. and Anthony, J. M., J. Appl. Phys. **87**, 484 (2001).
5. Wilk, G. D., Wallace, R. W. and Anthony, J. M., J. Appl. Phys. **89**, 5243 (2001).
6. Lucovsky, G. *et al*., Appl. Phys. Lett. **79**, 1775 (2001).
7. Rayner, G. B., Kang, Jr., H. and Lucovsky, G., J. Vac. Sci. Technol. B **21**, 1783 (2003).
8. Lucovsky, G. *et al*., J. Vac. Soc. Technol. B **20**, 1739 (2002).
9. Lucovsky, G., in "Extended Abstracts of Ultra-Thin Dielectric Workshop", (Izu-Atagawa, Japan, January 2003).

Physica Scripta. Vol. T115, 1026–1028, 2005

Tomographic X-Ray Absorption Spectroscopy

C. G. Schroer[a),1], M. Kuhlmann[1], T. F. Günzler[1], B. Lengeler[1], M. Richwin[2], B. Griesebock[2], D. Lützenkirchen-Hecht[2], R. Frahm[2], A. Mashayekhi[3], D. R. Haeffner[3], E. Ziegler[4], J.-D. Grunwaldt[5], and A. Baiker[5]

[1]II. Physikalisches Institut, Aachen University, D-52056 Aachen, Germany
[2]Institute of Materials Science and Department of Physics, Bergische Universität Wuppertal, Gaussstr. 20, D-42097 Wuppertal, Germany
[3]Argonne National Laboratory, Advanced Photon Source, Bld. 431, Argonne, IL 60439-4856, USA
[4]European Synchrotron Radiation Facility ESRF, BP 220, F-38043 Grenoble, France
[5]Swiss Federal Institute of Technology, ETH Hönggerberg, Institute for Chemical and Bioengineering, CH-8093 Zürich, Switzerland

Received June 26, 2003; accepted November 4, 2003

PACS numbers: 61.10.Ht, 41.50+4, 42.30.Wb

Abstract

Hard X-ray absorption spectroscopy is combined with scanning microtomography to reconstruct full near edge spectra of an elemental species at each point on an arbitrary virtual section through a sample. These spectra reveal the local concentration of different chemical compounds of the absorbing element inside the sample and give insight into the oxidation state and the local projected free density of states. The method is implemented by combining a quick scanning monochromator and data acquisition system with a scanning microprobe setup based on refractive X-ray lenses. The full XANES spectra reconstructed at each point of the tomographic slice allow one to detect slight variations in concentration of the chemical compounds, such as Cu and $Cu(I)_2O$.

X-ray absorption spectra reveal the local chemical environment of an element of interest. Its near edge spectra (XANES) can be used as a finger print for different chemical compounds, allowing one to determine their concentrations in a mixture. In many fields of science inhomogeneous samples are encountered, such as for example in physical chemistry (catalysts), materials science, biology, geology, and environmental science. In these samples, the composition of different chemical compounds can vary strongly as a function of position. A spatially averaged analysis often fails to reveal the information needed to understand the local chemical processes.

XANES microanalysis allows one to locally analyze inhomogeneous samples, provided the sample is thin enough in order to avoid averaging along the microbeam. This often requires difficult sample preparation that in addition is prone to change the chemical composition. One of the main strength of hard X-rays is their large penetration depth in matter that allows one to probe the volume of a specimen. In this article we have combined near edge spectroscopy with scanning microtomography to obtain full spectral information on an arbitrary virtual slice through an inhomogenious bulk sample. The method is illustrated for a sample taken from catalysis. Except for possible radiation damage, the method is non-destructive. A detailed description of the method is given in [1]. A complementary method, using full field imaging at different energies, is given in [2–4].

The experimental setup for this technique is shown in Fig. 1 and combines a fast scanning monochromator and data acquisition system developed at the University of Wuppertal [5–8] with a scanning microprobe setup based on beryllium parabolic refractive X-ray lenses [9, 10]. The hard X-rays from a synchrotron radiation source are monochromatized by a channel cut Si (111) double crystal monochromator and focused onto the sample position using a beryllium parabolic refractive lens. The

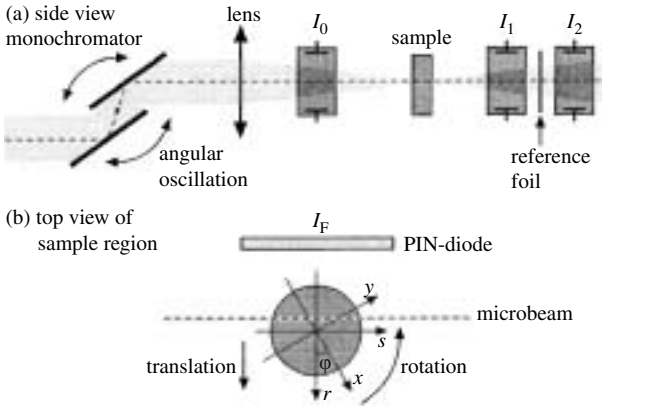

Fig. 1. (a) Side view of the setup for absorption spectroscopy tomography. (b) Top view of the sample region. The sample fixed coordinates (x, y) are rotated with respect to (r, s) by the angle ϕ. Both coordinate systems are translated with the sample. r denotes the position of the microbeam. The z coordinate perpendicular the slice is the same in both coordinate systems. Reprinted with permission from [1]. Copyright 2003, American Institute of Physics.

resulting pencil beam has a lateral dimension in the micrometer range. As shown in Fig. 1(a), three ionization chambers measure the flux I_0 incident on the sample, I_1 transmitted by the sample, and I_2 transmitted by a reference foil, respectively. Simultaneously, a PIN-diode measures the fluorescence radiation I_F emitted by the sample (see Fig. 1(b)).

An absorption spectroscopy tomogram is recorded by scanning the sample through the microbeam in a two dimensional scan in r and ϕ as shown in Fig. 1(b). The translational scan in r corresponds to a single tomographic projection. After recording a projection, the sample is rotated in ϕ by an integer fraction of 360° and the next projection is recorded. This procedure is repeated until the sample has completed a full rotation. At each position of the scan, a full absorption spectrum is recorded. In order to record the full tomogram in a reasonable time, the time to record an absorption spectrum at a single position in the scan must be of the order of one second or shorter. This is possible with a QEXAFS monochromator and fast data acquisition system [5–8]. In the present experiment, the system recorded 10 full absorption spectra per second with 10^4 data points each, measuring simultaneously the signals I_0 through I_F described above.

The main advantage of this scanning technique is that it yields full absorption spectra at each point (r, ϕ) in the sinogram, both in absorption and fluorescence (cf. Fig. 2). In addition, all spectra are calibrated in energy. The method was first tested at the bending magnet beamline BM5 of the European Synchrotron Radiation

a)Electronic mail: schroer@xray-lens.de

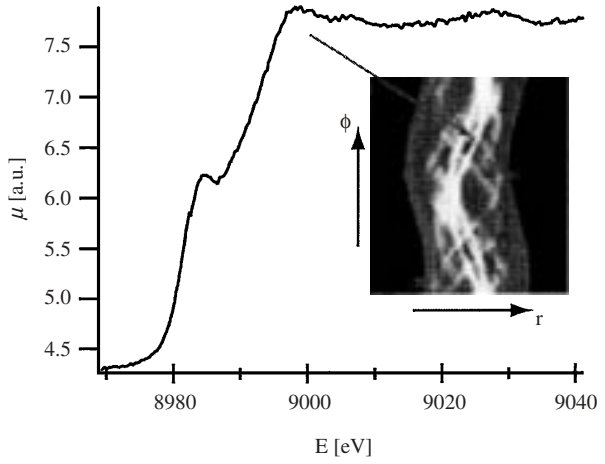

Fig. 2. (Color) XANES spectrum obtained at a single position (r, ϕ) in the tomographic scan. The position corresponds to the coordinates (r, ϕ) pointed to by the arrow in the inset that shows the absorption coefficient μ (at fixed energy $E = 9000\,\text{eV}$) as a function of r and ϕ, the so-called sinogram.

Facility (ESRF) in Grenoble, France. Although the feasibility of the method could be demonstrated at this beamline, recording larger tomograms requires the brilliance of a third generation insertion device. The experiments shown here were made at the undulator beamline 1-ID of the Advanced Photon Source (APS) in Argonne, Illinois. The sample is composed of a 30% CuO/ZnO catalyst that was twice reduced and re-oxidized by 4% H_2/He and 2% O_2/He at 200 °C–300 °C. After a final reduction the as grown Cu-particles on ZnO were re-oxidized at room temperature. The aim of the experiment was to analyze their structure and oxidation state in the volume. XANES tomograms were recorded both at the copper and zinc K-edge. At the copper K-edge, 101 projections with 90 translational steps of 10 μm each were recorded over 360°. The spectra recorded during the acquisition time of 1s at a given position are calibrated in energy using the spectra of the reference foil and summed up into a single spectrum. This is done for both the transmission and fluorescence channel. The negative logarithm of the transmission data yields the integral of the attenuation coefficient along the microbeam for each energy E.

Fig. 2 (inset) shows the transmission data at fixed energy for a full set of r and ϕ. This set constitutes the input data for transmission tomography. At each position (r, ϕ), a full XANES spectrum is available, a representative example of which is shown in Fig. 2.

Tomographic reconstruction yields the attenuation coefficient μ at each location (x, y) on the virtual slice. The attenuation coefficients below and above the K-edge of copper are depicted in Fig. 3(a) and (b), respectively. Fig. 3(c) shows the reconstructed spectra at the locations marked in Fig. 3(b) together with the reference spectra for metallic Cu, $Cu(I)_2O$, and Cu(II)O. At each location on the slice the reconstructed spectra can be fitted by these reference spectra (plus a constant stemming from other elements inside the sample). Two exemplary fits are shown as the red dashed curves in Fig. 3(c). In this way, the distribution of different copper compounds and of other elements (constant spectrum) can be obtained. The resulting distributions are shown in Fig. 3 of reference [1]. The quality of the fits to the spectra excludes significant concentrations of other compounds that have not a priori been taken into account. Copper is mainly contained in the present sample in metallic or monovalent osidation state. Slight variations in the relative concentrations of these constituents lead

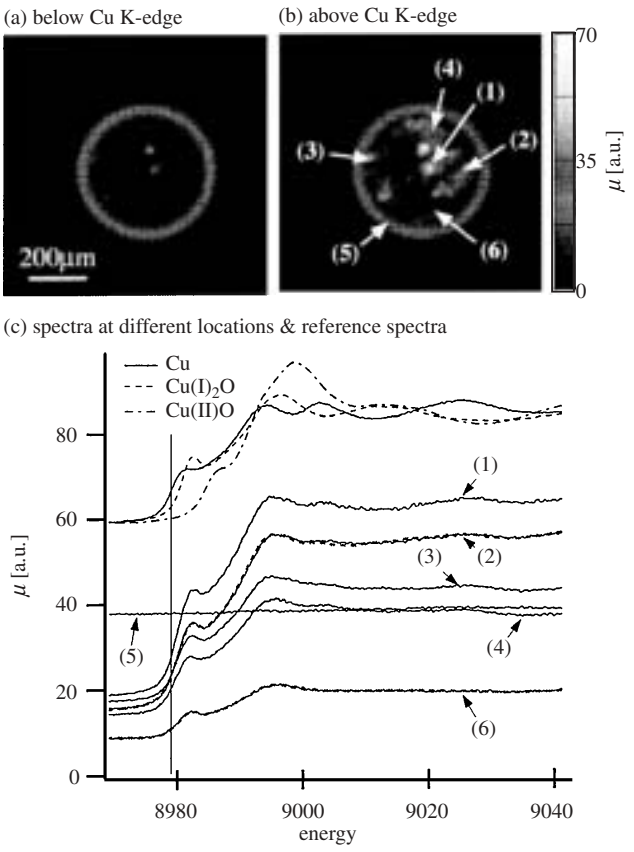

Fig. 3. (Color) reconstructed tomogram of a capillary filled with a CuO/ZnO catalyst (a) below ($E = 8970\,\text{eV}$) and (b) above the Cu K-edge ($E = 8995\,\text{eV}$). (c) Reconstructed XANES spectra at different locations marked in (b) and (offset) reference spectra of metallic Cu, $Cu(I)_2O$, and Cu(II)O. The dashed red curves in (c) represent two fits using the reference spectra. Reprinted with permission from [1]. Copyright 2003, American Institute of Physics.

to small changes in the near edge spectra. Faithful reconstruction of the relative concentrations requires full spectra, analyzing the residuals of the fits. For a detailed discussion see [1].

For more dilute samples, such as biological specimens, the fluorescence signal can be reconstructed. For fluorescence data the tomographic model is more complicated as self-attenuation effects need to be taken into account [11].

In the general case, absorption spectra of neighboring elements may overlap to produce a more complicated spectrum. This is the case for some of the spectra in the XANES tomogram recorded of the same sample at the zinc K-edge. Here, the Zn near edge spectra lie on top of the extended absorption fine structure of copper. Fig. 4 shows two spectra at locations marked by (1) and (2) in the reconstructed slice (lower right corner of Fig. 4). Spectrum (1) that is reconstructed at a location with high Cu concentration shows a slowly varying oscillation of Cu EXAFS being superimposed on the Zn XANES spectrum. Special care needs to be taken to separate these spectra from each other. Spectrum (2), on the other hand, comes from a pixel in the sample that contains only a small amount of Cu. For this pixel, a contribution of the Cu EXAFS to the spectrum is negligible.

The spatial resolution of the method is ultimately limited by the smallest spot size obtainable with hard X-ray optics [12–14]. The QEXAFS monochromator can be adjusted to cover the full EXAFS energy range [8]. In combination with achromatic X-ray optics, such as a Kirkpatrick-Baez total reflection mirror system [13, 15], the method can be extended to reconstruct full EXAFS spectra at each location on the reconstructed slice.

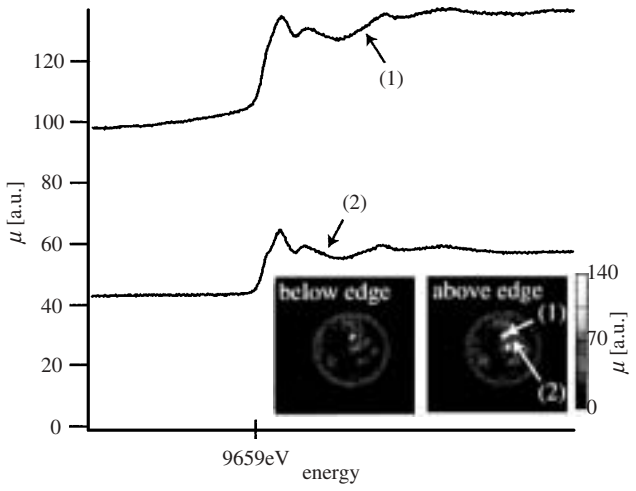

Fig. 4. (Color) XANES spectra (Zn K-edge) reconstructed at the locations marked by (1) and (2) in the tomographic slice shown in the inset. The tomographic reconstructions in the lower right corner show the absorption coefficient below and above the K-edge of Zn. Other than from Zn, the total attenuation in both spectra has contributions from Cu and other elements.

Acknowledgments

We thank Jean-Yves Massonnat for his excellent support during the experiment at beamline BM5 of the ESRF. Use of the Advanced Photon Source was supported by the U.S. Department of Energy, Office of Science, Office of Basic Energy Science, under Contract No. W-31-109-ENG-38.

References

1. Schroer, C. G. *et al*., Appl. Phys. Lett. **82**, 3360 (2003).
2. Bonse, U. *et al*., Nucl. Instrum. Meth. A **246**, 644 (1986).
3. Kinney, J. *et al*., Rev. Sci. Instrum. **59**, 196 (1988).
4. Rau, C., Somogyi, A., Bytchkov, A. and Simionovici, A., in (U. Bonse, ed.), "Developments in X-Ray Tomography III", vol. 4503 of Proc. of SPIE, pp. 249–255 (2002).
5. Lützenkirchen-Hecht, D., Grundmann, S. and Frahm, R., J. Synchrotron Rad. **8**, 6 (2001).
6. Richwin, M., Zaeper, R., Lützenkirchen-Hecht, D. and Frahm, R., J. Synchrotron Rad. **8**, 354 (2001).
7. Grunwaldt, J.-D. *et al*., J. Phys. Chem. B **105**, 5161 (2001).
8. Richwin, M., Zaeper, R., Lützenkirchen-Hecht, D. and Frahm, R., Rev. Sci. Instrum. **73**, 1668 (2002).
9. Lengeler, B. *et al*., J. Synchrotron Rad. **9**, 119 (2002).
10. Schroer, C. G. *et al*., in (D. C. Mancini, ed.), "Design and Microfabrication of Novel X-Ray Optics," vol. 4783 of Proc. of SPIE, pp. 10–18 (SPIE, Bellingham, 2002).
11. Schroer, C. G., Appl. Phys. Lett. **79**, 1912 (2001).
12. Yun, W. *et al*., Rev. Sci. Instrum. **70**, 2238 (1999).
13. Hignette, O. *et al*., in (I. McNulty, ed.), "X-Ray Micro- and Nano-Focusing: Applications and Techniques II", vol. 4499 of Proc. of SPIE, pp. 105–116 (2001).
14. Schroer, C. G. *et al*., Appl. Phys. Lett. **82**, 1485 (2003).
15. Kirkpatrick, P. and Baez, A., J. Opt. Soc. Am. **38**, 766 (1948).

Physica Scripta. Vol. T115, 1029–1031, 2005

Implementing Sub-ns Time Resolution into Magnetic X-Ray Microscopies

A. Puzic[1], H. Stoll[1], P. Fischer*[1], B. v. Waeyenberge[1], J. Raabe[2], G. Denbeaux[3], T. Haug[2], D. Weiss[2] and G. Schütz[1]

[1]Max-Planck-Institute for Metals Research, Heisenbergstrasse 3, 70569 Stuttgart, Germany
[2]University of Regensburg, Universitätsstrasse 31, 93040 Regensburg, Germany
[3]Center for X-ray Optics, LBNL, 1 Cyclotron Road, Berkeley CA 94720, USA

Received June 26, 2003; accepted December 4, 2003

PACS numbers: 07.85 Tt, 75.25+z, 75.75.+a

Abstract

X-ray microscopies using polarized X-rays allow for imaging magnetic microstructures down to a 20 nm lateral resolution with chemical sensitivity. Utilizing the pulsed time structure of synchrotron radiation a sub-ns time resolution can be implemented by performing stroboscopic pump-and-probe experiments. The temporal evolution of the magnetization in a 50 nm thin circular permalloy element with a diameter of 2 μm could be imaged with magnetic transmission X-ray microscopy. The magnetic pump pulse to the sample was generated electronically with a rise time of less than 100 ps up to 150 Oe by a microcoil. The probe pulse is the flash of the circularly polarized X-ray beam with a pulse width of about 70 ps at a frequency of 3 MHz. Images were recorded at varying delay times between pump and probe pulse up to 2000 ps. Fast detection schemes utilizing avalanche photo diodes are capable to pick individual bunches from the storage ring.

1. Introduction

The magnetism of systems with reduced dimensionality, as e.g. magnetic thin layers, multilayered films and laterally nanopatterned elements are subject to intensive experimental and theoretical studies. Magnetic thin film systems being composed of a large variety of elements to tailor a distinct functionality are key materials in current magnetic storage and sensor technologies. Laterally patterned magnetic elements in the sub-μm range can be prepared by adapting sophisticated techniques like e.g. e-beam lithographies which originally have been developed in semiconductor physics. Since the macroscopic behavior and the functionality of magnetic devices can be traced back to the magnetic microstructure, imaging magnetic domains on a nanometer scale is an outstanding challenge. In addition to the spatial imaging of static magnetic domain structures, where a huge variety of powerful techniques is available, recording the spin dynamics on a sub-second time scale is currently attracting rapidly increasing scientific interest. Precessional motion, the origin of damping and relaxation mechanisms, domain wall movements and coherent spin rotation and ultrafast switching processes are current scientific issues [1, 2, 3, 4, 5], which are being considered as new fast switching schemes in future magnetic storage and sensor technologies.

X-ray magnetic circular dichroism (XMCD) in core-level absorption, which detects basically the dependence of the X-ray absorption coefficient of circularly polarized radiation on the magnetization in a ferromagnetic species in the vicinity of an absorption edge, has become a powerful tool to investigate the magnetism of solids, surfaces and thin films. The magnetic contrast, which at the spin-orbit coupled $L_{2,3}$ edges in transition metals yields values up to 50% allows the combination of XMCD with imaging techniques to resolve the magnetic structure laterally. The first attempt reported in literature utilized a photoemission electron microscope (PEEM) [6].

Instead, magnetic transmission X-ray microscopy (MTXM) uses a high-resolution transmission X-ray microscope and the first results with a full-field microscope have been obtained at BESSY I in Berlin at the $L_{3,2}$ edges of Fe [7]. Currently, the full-field MTXM at the Advanced Light Source in Berkeley CA, where the presented data have been taken, has a lateral resolution down to 25 nm provided by Fresnel zone plates used as optical elements. Spin dynamics can be imaged with a stroboscopically pump and probe experiment where the magnetization is excited by short field pulses (pump) generated e.g. by small microcoils and probed by short (<70 ps) X-ray flashes of the synchtrotron source delayed with respect to the pump probe to obtain time spectra of the local laterally distributed magnetization.

In the following we describe the experimental setup for the pump-and-probe scheme and report on the observation of sub-ns magnetization dynamics in nanopatterned circular elements.

2. Experimental Details

The probe pulses are set by the time structure of the synchrotron. For the experiments described here the ALS was operating in the so-called two bunch mode, i.e. two electron bunches with a width of 70 ps are circulating in the storage ring at a frequency of about 3 MHz, i.e. the two bunches are separated in time by 328 ns and each of them contains a current up to 30 mA. In the corresponding multibunch mode some hundred bunches with each having a current up to 1–2 mA separated in time by only 2 ns are stored in the ring up to 8 h. Since the relaxation time of magnetization in small elements is of the order of tens of ns, the two-bunch mode operation is suited to study fast spin dynamics.

The pump pulses, i.e. fast magnetic field pulses exerted on the sample are generated by electronic pulses with a rise time less than 100 ps at a repetition rate matching the 3 MHz rate of the synchrotron. They are triggered by an ECL pulse given by the orbital clock of the storage ring and exhibit a time jitter of about 15 ps. Fed into a microcoil located adjacent to the magnetic element to be studied, these pulses provide a magnetic field pulse with its direction perpendicular the sample's surface. In order to study the temporal evolution of the magnetization the pump pulses are delayed relative to the probe pulse by a variable delay line in the range of −1000 ps and +3000 ps, whereby 0 ps defines the

*e-mail: peter.fischer@mf.mpg.de

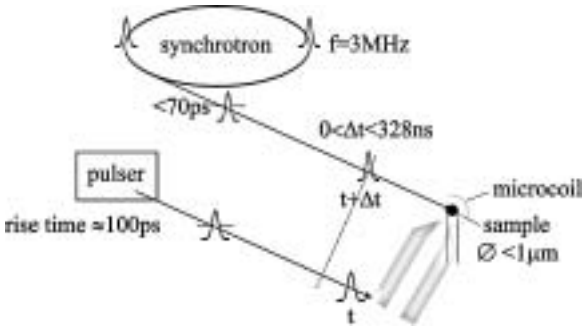

Fig. 1. Experimental setup for stroboscopic imaging with a pump-and-probe scheme at the ALS running in two-bunch mode.

coincidence of the pump and the probe pulse at the location of the sample's surface. An ultrafast photo diode (rise time 35 ps) and a fast avalanche photo diode (APD) (rise time 100 ps) situated close to the sample allow for accurate zeroing the delay time and in-situ monitoring of both pump and probe signals during the measurements. A schematic of the experimental setup is shown in Fig. 1.

The sample was a 50 nm thin and 2 μm diameter circular element of permalloy ($Ni_{81}Fe_{19}$). It has been prepared by e-beam lithography onto a 100 nm thin Si_3N_4 membrane with a transmission of 80% at a photon energy around 700 eV. Surrounding the sample a small 1 μm thin Cu microcoil with an inner diameter of 4 μm is prepared onto the same membrane. Fig. 2 shows a SEM image of the circular dot and the surrounding microcoil structure.

The relaxed, i.e. the static magnetization configuration in the circular microelement exhibits a vortex structure. The closed flux magnetization is described by the vorticity of the element, while in addition a singularity in the center with a pronounced out of plane magnetization is formed which could either point up or down (polarity). In Fig. 3 the schematic configuration of the magnetization in the circular element is displayed. Switching the magnetization of the element can reverse both the vorticity and polarity independently from each other [8].

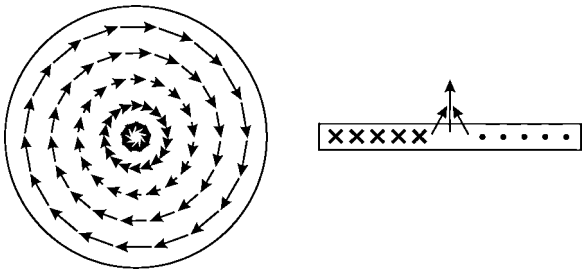

Fig. 3. Scheme of the relaxed static micromagnetic structure in a circular dot.

3. Results and Discussion

The temporal development of the magnetization is described by the Landau-Lifshitz equation $\frac{d\vec{J}_S}{dt} = \gamma[\vec{J}_S \times \vec{H}_{eff}] - \frac{\alpha}{J_S}[\vec{J}_S \times \vec{J}_S]$, accounting for both the precession of the magnetization in an external magnetic field $\boldsymbol{H}_{eff}$ with γ being the gyromagnetic ratio and the relaxation and damping of the system with α being a damping constant depending on the local geometry, anisotropy and morphology. So far a complete microscopic understanding of relaxation processes is lacking.

In Fig. 4 MTXM results with a circular PY element with diameter 2 μm are displayed. The sample is viewed at normal incidence to the photon beam and thus the static in-plane domain structure does not contribute to the magnetic contrast. The size of the vortec in the center is of the order of exchange lengths, which in permalloy amount to less than 10 nm and can thus be not resolved with MTXM. The field pulse applied normal to the sample plane creates a time-dependent z-component of the magnetization that can be recorded. Interesting features can be observed. The in plane magnetization of the elements performs a coherent switching that occurs on a time scale of less than 1 ns, since the white contrast seen observed at a delay time of 180 ps has reversed into a dark contrast at 980 ps. The inner part, i.e. the vortex of the element seems to be decoupled from that motion, since the white spot in the center remains up to 980 ps and is flipped rapidly at 1380 ps. A more complex temporal behaviour of the magnetization in the center is indicated by a shadowed dark region observed up to 380 ps. Since the applied magneticfield pulse has a duration of

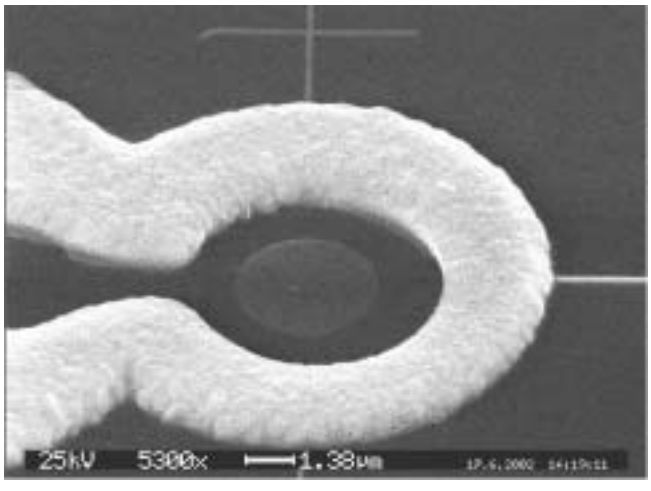

Fig. 2. Scanning electron microscopy of the sample studied. The circular dot and the surrounding microcoil are prepared by e-beam lithography onto a 100 nm Si_3N_4 membrane.

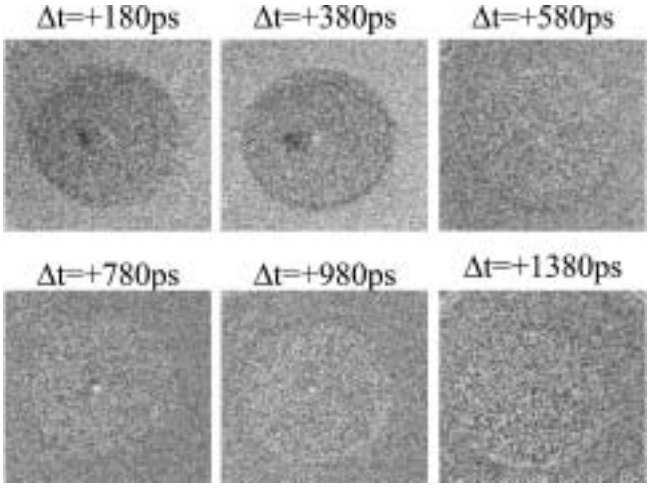

Fig. 4. Magnetic X-ray microscopy images of the temporal evolution of the magnetization in a circular dot at various delay times between pump and probe pulse.

500 ps this might be responsible for the observed feature where locally in-plane components of the magnetization could feel a torque due to the non static field pulse and are thus deviated from their symmetric position.

4. Outlook

Magnetic soft X-ray transmission microscopy allows the element-specific imaging of the magnetic domain structure of thin, multicomponent and nanostructured ferromagnetic systems. The inherent pulsed time structure of synchrotrons allows for the study of spin dynamics on a sub-ns scale with a stroboscopically pump-and-probe measurement.

Acknowledgment

This work has been partly funded by DFG grant no. FI 542/3-1,2.

References

1. Acremann, Y., *et al.*, Science **290**, 492 (2000).
2. Hiebert, W. K., *et al.*, J. Appl. Phys. **92**, 392 (2002).
3. Gerrits, T., van den Berg, H. A. M., Hohlfeld, J., Bär, L. and Rasing, T., Nature **418**, 511 (2002).
4. Park, J. P., *et al.*, Phys. Rev. B **67**, 020403(R) (2003).
5. Wachowiak, A., Science **298**, 578 (2002).
6. Stohr, J., *et al.*, Science **259**, 658 (1993).
7. Fischer, P., *et al.*, Z. Phys. B. Con. Mat. **101**, 313 (1996).
8. Höllinger, R., Killinger, A. and Krey, U., J. Magn. Magn. Mater. **261**, 178 (2003).

Physica Scripta. Vol. T115, 1032–1034, 2005

A Study of Transition Metal K Absorption Pre-Edges by Resonant Inelastic X-Ray Scattering (RIXS)

P. Glatzel*[1,2], U. Bergmann[3], F. M. F. de Groot[1], Bert M. Weckhuysen[1] and S. P. Cramer[2,3]

[1]Department of Inorganic Chemistry and Catalysis, Utrecht University, 3584 CA Utrecht, The Netherlands
[2]Department of Applied Science, University of California, Davis, California 95616, USA
[3]Physical Biosciences Division, Lawrence Berkeley National Laboratory, Berkeley, California 94720, USA

Received June 26, 2003; accepted January 30, 2004

PACS numbers: 78.70.Ck, 78.70.Dm, 78.70.En, 71.70.−d, 71.70.Ch, 71.15.−m

Abstract

The K absorption pre-edge structure arises from excitations into the lowest unoccupied states that are partly formed by metal 3d orbitals. The pre-edge energy position, intensity and spectral shape can give valuable insight into the metal site symmetry and electronic configuration. The excited electronic states that form the absorption pre-edge subsequently decay radiatively. This fluorescence decay can be recorded using a crystal spectrometer that has a similar energy bandwidth as the incident beam. Plotting the fluorescence intensity versus incoming and outgoing energy yields three-dimensional plots that offer numerous possibilities for further analysis. In this paper we show that resonant inelastic X-ray scattering (RIXS) considerably facilitates separation of the K pre-edge structure from the strong dipole allowed transitions at higher incident energies. Previously unobserved spectral features could be revealed. The spectra along the energy transfer axis contain information on the electronic structure that is complementary to K-edge absorption spectroscopy.

1. Introduction

The electronic states that form an absorption spectrum are resonantly excited states that subsequently decay. The released energy can be carried either by an electron that is excited into the continuum (resonant Auger effect) or by a photon (resonant X-ray scattering or RXS). A review of the resonant Auger effect was published by Armen [1]. A large body of work already exists on resonant X-ray scattering that was reviewed comprehensively by Gel'mukhanov and Ågren as well as Kotani and Shin [2]. We will focus in this article on resonant inelastic X-ray scattering (RIXS) at the transition metal K absorption pre-edges where only few studies have been done up until now.

2. The RIXS plane

After resonant excitation of a 1s electron, the subsequent radiative decay with the highest probability is a 2p to 1s (Kα) transition. The 3p to 1s (Kβ) transitions are about a factor 8 weaker [3]. An expression for the RIXS spectrum $F(\Omega, \omega)$, where Ω and ω are, respectively, the incident and emitted photon energy, can be derived from the differential cross section that describes the inelastic X-ray scattering process [2]. It is giving by

$$F(\Omega,\omega) = \sum_f \left| \sum_i \frac{\langle f|T_2|i\rangle\langle i|T_1|g\rangle}{E_g - E_i + \Omega - i\frac{\Gamma_K}{2}} \right|^2 * \frac{\Gamma_L/2\pi}{(E_g - E_f + \Omega - \omega)^2 + \frac{\Gamma_L^2}{4}}. \quad (1)$$

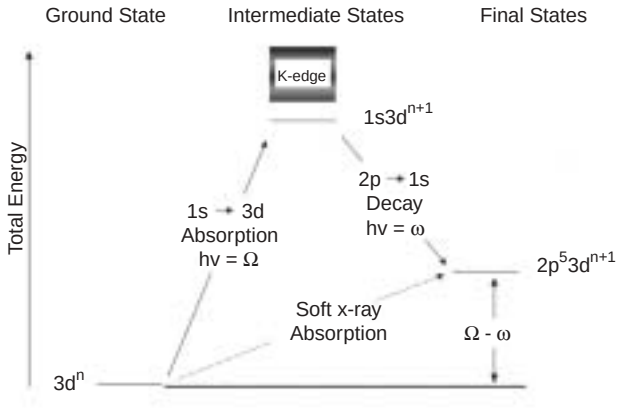

Fig. 1. Energy scheme for 1s2p RIXS in a transition metal ion. The vertical axis indicates the total energy of the electron configuration. For simplicity, atomic configurations are used and only 1s to 3d excitations are shown.

The intermediate state $|i\rangle$ is reached from the ground state $|g\rangle$ via a transition operator T_1. In a simplified picture using atomic configurations we can write $|g\rangle = 3d^n$ and $|i\rangle = 1s3d^{n+1}$, *i.e.* a 1s electron is resonantly excited into a 3d orbital (Figure 1). The intermediate states $|i\rangle$ in RIXS spectroscopy are the final states in conventional absorption spectroscopy. The spherical (SO_3) symmetry of the atomic 3d orbitals branches to the lower symmetry at the metal site. T_1 identifies with the quadrupole transition operator if the scattering atom is in centrosymmetric coordination (*e.g.* O_h symmetry). If the symmetry is reduced, *e.g.* to square pyramidal (C_{4v}) or tetrahedral (T_d), T_1 obtains some dipole contribution. In this case, the crystal field split 3d orbitals partly belong to the same irreducible representation of the point group as the metal 4p orbitals. The states can therefore mix and transitions from 1s to the 3d4p mixed states are dipole allowed [4]. The ratio of the dipole to the quadrupole contribution can be determined in single crystalline samples by analyzing the angular dependence of the absorption coefficient using linear polarized light [5] or by studying anomalous diffraction [6].

The final states are reached via a 2p or 3p to 1s dipole transition. The electron configurations of the RIXS final states are identical to the soft X-ray L-edge ($2p^53d^{n+1}$) and M-edge ($3p^53d^{n+1}$) absorption final states. However, the RIXS process is described by two transition matrix elements (cf. Equation (1)) that are connected coherently while an absorption spectrum arises from one transition (cf. Figure 1). Thus, the intensities in the fine structure of the spectra resulting from spin-orbit and electron-electron interactions as well as crystal field splittings might differ between K pre-edge RIXS and soft X-ray absorption.

*current address: European Synchrotron Radiation Facility, 38000 grenoble, France; e-mail: glatzel@esrf.fr

The incident energy Ω as well as the emitted energy ω are varied in a RIXS experiment. The recorded intensity is proportional to $F(\Omega, \omega)$ and is thus plotted versus a two-dimensional grid. The overall spectra are best displayed in contour plots. In order to assign the total energy of an electronic state to the axes of the contour plots we will use the energy transfer or final state energy $\Omega - \omega$ as opposed to the emitted energy ω (Figure 1). The energy transfer axis relates to the excitation energy in L- and M-edge absorption spectroscopy, respectively. The lifetime broadenings Γ_K for the intermediate states and $\Gamma_f (f = \mathrm{L}, \mathrm{M})$ for the final states then apply in the Ω and $\Omega - \omega$ direction, respectively. Scans with constant emission energy (CEE) represent diagonal cuts through the $(\Omega, \Omega - \omega)$ RIXS plane. They are usually plotted versus the incident energy axis and then exhibit a line sharpening effect when compared to an absorption scan [7, 8].

The instrumental broadenings stretch in the diagonal (incident beam) and vertical (emitted beam) direction in the $(\Omega, \Omega - \omega)$ plane. Resonant 1s excitations into localized orbitals with a discrete energy occur along a diagonal line if we neglect many-electron transitions. Spectral features off of this diagonal line towards larger energy transfer are due to electron-electron interactions in the final state between the unpaired p-electron and the valence shell. Continuum excitations or excitations into delocalized final states with a broad energy band can be viewed as an infinite number of resonant excitations infinitely close to each other. In the $(\Omega, \Omega - \omega)$ plane they thus appear as a diagonal streak [9].

3. Experiment

The spectra were recorded at the BioCAT beamlime 18 ID at the Advanced Photon source. The total incident flux in the first harmonic of the undulator radiation was on the order of 10^{12} to 10^{13} photons/s depending on the incident energy monochromator crystal. For incident energies below 8 keV a cryogenically cooled Si(111) double crystal monochromator was employed. Above 8 keV (Ni K-edge) the Si(400) Bragg reflection was used. The fluorescence spectrometer features up to 8 analyzer crystal [10]. The following Bragg reflections were used: Ge(331) for V Kα, Ge(333) for Mn Kα, Ge(620) for Fe Kβ and Si(620) for Ni Kα. The total data acquisition time to record one RIXS plane was 2–4 hours. Careful radiation damage studies were performed for each sample. Radiation sensitive samples were measured in a He-flow cryostat in an exchange gas surrounding. The RIXS plane was constructed by recording CEE scans (2–30 seconds each in 'on-the-fly' mode) for different emission energies. The beam position on the sample was changed with every scan and the spectra were corrected for variations in sample concentrations.

4. Results

A series of Ni coordination complexes shows the pre-edge shift with Ni oxidation state (Figure 2). While the K pre-edge yields identical spectra for Ni(II) high-spin and low-spin we can clearly identify the different Ni species in the energy transfer direction. The 1s2p RIXS plane for NiF_2 ($3d^8$ in O_h symmetry) shows one K pre-edge resonance and a pronounced asymmetry towards the energy transfer direction due to (2p,3d) multiplet interactions. The high energy shoulder in the energy transfer direction has been used as a diagnostic of high-spin Ni(II) [11]. The K pre-edge is nearly invisible in the conventional absorption scan of the Ni(III)

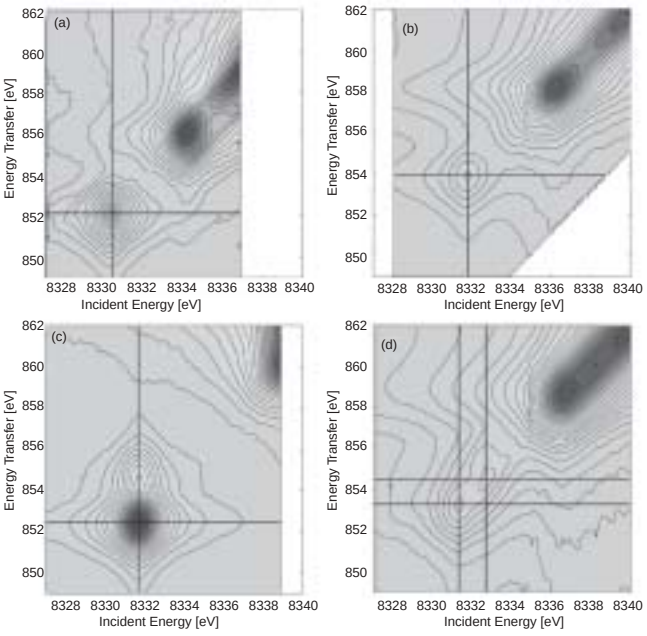

Fig. 2. $2p_{3/2}$ final states in the 1s2p RIXS contour plots for Ni coordination complexes: (a) Ni(I) in $[PhTt^{tBu}]NiCO$, Ni(II) (b) low-spin (ls) in $(Ph_4As)_2Ni(S_2C_2(CF_3)_2)_2$, Ni(II) (c) high-spin (hs) in NiF_2 and (d) Ni(III) low-spin in $[Ni(\eta^4\text{-DEMAMPA-DCB})]^-$. The vertical (constant incident energy) and horizontal (constant final state energy) lines indicate the lowest 1s to 3d resonances.

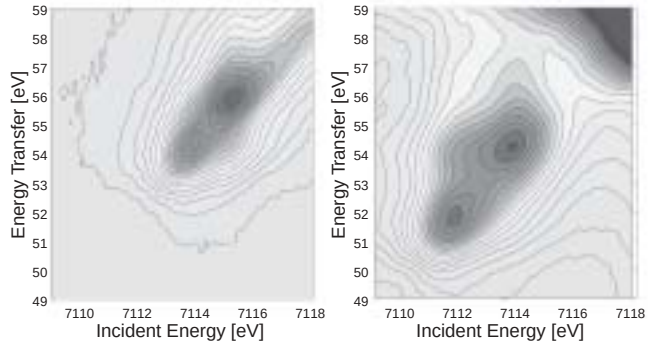

Fig. 3. 1s3p RIXS planes of Fe_2O_3 (left) and $Fe_{0.05}Mg_{0.95}O$ (right).

complex. Using the RIXS technique we can clearly resolve two strong resonances [12].

The 1s3p RIXS planes in Fe(II) ($Fe_{0.05}Mg_{0.95}O$) and Fe(III) (α-Fe_2O_3) in octahedral geometry show the pre-edge shift with oxidation state that we already observed for Ni. This is well documented in the literature (Figure 3) [13]. The crystal field splitting separates the two peaks for Fe(III) in Fe_2O_3 with $^5T_{2g}$ and ^5E_g symmetry. A theoretical analysis of the multiplet structure yields three 1s to 3d resonances for Fe(II) in $Fe_{0.05}Mg_{0.95}O$ with $^4T_1$, $^4T_2$ and $^4T_1$ terms [14]. A pronounced asymmetry relative to the diagonal towards larger energy transfer can be observed for the $Fe_{0.05}Mg_{0.950}O$ complex. This indicates strong (3p,3d) final state interactions. The RIXS spectra indicate that the center resonance with $^4T_2$ symmetry exhibits the strong final state interactions.

For a detailed analysis of the pre-edge features it is necessary to subtract the background due to the K main edge. We developed a procedure that fits horizontal cuts through the RIXS plane at constant energy transfer to Voigt line profiles [15]. The fit yields a background plane that can be subtracted from the experimental RIXS plane. An example is shown for MnO in Figure 4 where we also show ligand field multiplet calculations that reproduce

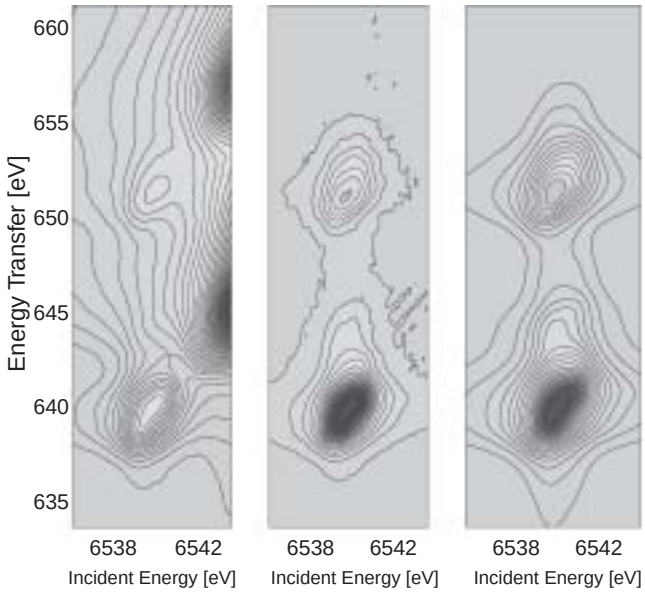

Fig. 4. 1s2p RIXS plane of MnO before (left) and after (center) subtraction of the K main edge together with ligand field multiplet calculations (10 Dq = 1.1 eV). The applied lifetime broadenings are $\Gamma_K = 1.1$ eV and $\Gamma_L = 0.5$ eV for the intermediate and final state, respectively, as well as 1.0 eV and 0.8 eV for the instrumental lifetime broadenings of the incident and the emitted X-rays. The features at 640 eV and 652 eV are the $2p_{3/2}$ and $2p_{1/2}$ final states, respectively.

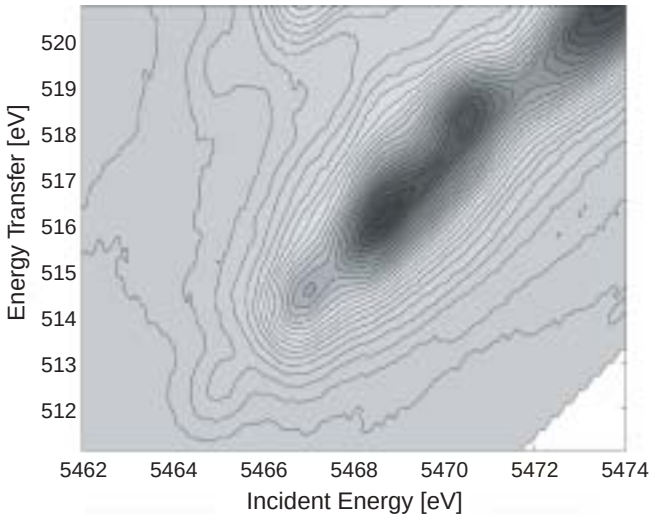

Fig. 5. $2p_{3/2}$ final states in the 1s2p RIXS plane of VF_4.

the experimental spectral shape after edge subtraction. The MnO $1s2p_{3/2}$ RIXS spectra can be fitted to two 1s resonances that are separated by the crystal field splitting similar to Fe_2O_3. This is consistent with 1s to 3d ligand field multiplet calculations for high-spin Mn(II) in O_h symmetry and thus indicates that quadrupole transitions contribute to the pre-edge intensity. The $2p_{3/2}$ final states exhibit a shoulder on the high energy transfer side that also appears in soft X-ray L-edge spectroscopy for high-spin Mn(II) compounds [16].

The K pre-edge of VF_4 presents a nice example for the interplay between crystal field and multiplet splittings. Both have approximately the same magnitude and result in four almost equally separated pre-edge structures (Figure 5) [17]. The two strong resonances at high incident energies appear to be further split. This could be indicative of the Jahn-Teller splitting in the t_{2g} orbitals.

5. Summary

RIXS spectroscopy enables to separate the K pre-edge from the main edge with a considerably higher accuracy than in conventional absorption spectroscopy. Previously unobserved spectral feature could be resolved. The energy transfer spectra contain information on the electronic structure that is complementary to the K pre-edge. Ligand field multiplet calculations can simulate the spectral features.

Acknowledgement

This work was supported by the National Institutes of Health Grants GM-44380 and the DOE Office of Biological and Environmental Research. Use of the Advanced Photon Source was supported by the U.S. Department of Energy, Basic Energy Sciences, Office of Science, under contract No. W-31-109-ENG-38. BioCAT is a National Institutes of Health-supported Research Center RR-08630.

References

1. Armen, G. B., Aksela, H., Åberg, T. and Aksela, S., J. Phys. B-At. Mol. Opt. Phys. **33**, R49 (2000).
2. Gel'mukhanov, F. and Ågren, H., Phys. Rep.-Rev. Sec. Phys. Lett. **312**, 91 (1999); Kotani, A. and Shin, S., Rev. Mod. Phys. **73**, 203 (2001).
3. Kortright, J. B. and Thompson, A. C., "X-ray Data Booklet". (Edited by Thompson, A. C. and Vaughan, D.) (Lawrence Berkeley National Laboratory, Berkeley 2001).
4. Griffith, J. S., "The theory of transition-metal ions". (University Press, Cambridge Eng. 1964).
5. Bocharov, S., Kirchner, T., Drager, G., Sipr, O. and Simunek, A., Phys. Rev. B **6304** art. no.-045104 (2001), Uozumi, T. *et al.*, Europhys. Lett. **18**, 85 (1992).
6. Finkelstein, K. D., Shen, Q. and Shastri, S., Phys. Rev. Lett. **69**, 1612 (1992).
7. de Groot, F. M. F., Krisch, M. H. and Vogel, J., Phys. Rev. B **66** art. no.-195112 (2002).
8. Carra, P., Fabrizio, M. and Thole, B. T., Phys. Rev. Lett. **74**, 3700 (1995).
9. Glatzel, P. and Bergmann, U., submitted to Coordin. Chem. Rev. in press (available on the web).
10. Bergmann, U. and Cramer, S. P., SPIE Proc. **3448**, 198 (1998).
11. Wang, H. X. *et al.*, J. Am. Chem. Soc. **122**, 10544 (2000).
12. Glatzel, P. *et al.*, J. Am. Chem. Soc. **124**, 9668 (2002).
13. Wilke, M., Farges, F., Petit, P. E., Brown, G. E. and Martin, F., Am. Miner. **86**, 714 (2001).
14. Westre, T. E. *et al.*, J. Am. Chem. Soc. **119**, 6297 (1997).
15. Glatzel, P. *et al.*, submitted to J. Am. Chem. Soc. **126**, 9946 (2004).
16. Cramer, S. P. *et al.*, **113**, 7937 (1991).
17. Solomonik, V. G. and Pogrebnaya, T. P., Russ. J. Inorg. Chem. **46**, 1851 (2001).

Physica Scripta. Vol. T115, 1035–1037, 2005

Direct Observation of Magnetic Depth Profile with a Depth-Resolved X-Ray Magnetic Dichroism Technique

K. Amemiya[1], S. Kitagawa[1], T. Yokoyama[2], D. Matsumura[1], H. Abe[1], H. Watanabe[2] and T. Ohta[1*]

[1]Department of Chemistry, Graduate School of Science, The University of Tokyo, Hongo, Bunkyo-ku, Tokyo 113-0033, Japan
[2]Institute for Molecular Science, Myodaiji-cho, Okazaki, Aichi 444-8585, Japan

Received June 26, 2003; accepted April 16, 2004

PACS numbers: 87.64.Ni, 61.10.Ht, 75.70.−i

Abstract

We have established a high-precision depth-resolved X-ray magnetic circular dichroism (XMCD) technique, in which the probing depth of the partial electron yield XMCD spectra is controlled by changing the detection angle of the emitted electrons. The data quality has been significantly improved by using an imaging-type microchannel plate detector. We applied this new technique to Fe ultrathin films grown on Cu(100), and directly confirmed that the surface two layers of the 7 ML Fe film are ferromagnetically coupled, while the inner layers are in the spin density wave (SDW) state at 130 K. Then we separately extracted the XMCD spectra for the surface ferromagnetic (FM) and inner SDW layers. It was indicated that the SDW magnitude is almost the same as the magnetic moment of the surface FM layers, and that the orbital moment of the surface layers is larger than that of the SDW ones. Moreover, the extracted spectrum for the SDW layers exhibited a bulk-like feature, while the surface spectrum was similar to that from the 2 ML film, in which no bulk component should be included.

1. Introduction

Although the magnetic depth profile of ultrathin films has attracted much interest, it has been investigated mainly by measuring the total magnetization as a function of film thickness. Such a technique is not always reliable, since it is based on the assumption that the magnetic properties at surface, interface, and inner layers are unchanged regardless of the film thickness. Therefore, some attempts have been made to clarify the magnetic depth profile without changing the film thickness. Magnetization induced second harmonic generation (MSHG) [1–3] is one of the most powerful methods to investigate surface magnetism, since it is intrinsically surface sensitive. However, no magnetic information on the inner layers can be obtained. Spin-polarized appearance potential spectroscopy (SP-APS) also gives depth-resolved information [4, 5]. The interpretation of the spectrum is unclear, however, so that no quantitative information is deduced from the data.

Recently, X-ray magnetic circular dichroism (XMCD) measurements with depth resolution were achieved by utilizing the X-ray standing wave method [6]. This technique is quite effective, since the spin and orbital magnetic moments can be quantitatively determined from an XMCD spectrum by using the well-known sum rules [7, 8]. However, the samples which can be investigated with this technique are restricted, because a multilayer interference structure is necessary under the ultrathin film sample in order to generate standing waves. Moreover, the precise sample rotation as well as a high-quality multilayer structure is necessary to achieve high depth resolution. Recently, we have developed a much simpler depth-resolved XMCD technique, in which the probing depth is controlled by changing the electron detection angles determined by a slit placed in front of a microchannel plate (MCP) detector [9]. This novel technique allows us to investigate any thin film sample without modification in the sample preparation process. It takes a long data accumulation time, however, because one has to record the XMCD spectrum at each detection angle.

In the present study, we have significantly improved the depth-resolved XMCD technique by using an imaging type MCP detector. All the spectra with various probing depths are recorded simultaneously, so that the data accumulation time was drastically reduced with much higher data quality. We applied this technique to ultrathin Fe films grown on Cu(100), which exhibit peculiar magnetic structures [1, 4, 10–16].

2. Experiments

Experimental layouts for the previous [9] and present depth-resolved XMCD experiments are schematically depicted in Fig. 1. In the previous setup, we put a slit in front of the MCP detector to restrict the electron acceptance angle, and translated the sample to change the detection angle. Therefore, it was necessary to record the XMCD spectrum at each detection angle, θ_d, keeping various conditions such as sample cleanliness and photon energy scale unchanged during a series of measurements. Moreover, some complicated manipulation for the sample or detector is required if one wants to obtain both grazing and normal incidence XMCD spectra in order to investigate the magnetic anisotropy. In contrast, in the present setup, the emitted electrons are simultaneously collected at various θ_d, with a system consisting of a MCP, phosphor screen, and CCD camera. Moreover, we only have to rotate the sample in order to change the X-ray incidence angle. It should be emphasized that uniformity of detection efficiency over the whole detector is *not* necessary, because one can normalize the

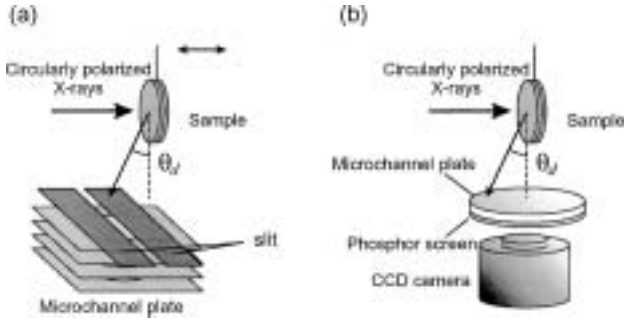

Fig. 1. Schematic layout for depth-resolved XMCD measurements with (a) a slit and (b) an imaging type detector.

*e-mail: ohta@chem.s.u-tokyo.ac.jp

obtained spectrum at each θ_d by using the absorption coefficients at the pre- and post-edge energies.

We adopted the partial electron yield mode with a retarding voltage of –500 V to enhance surface sensitivity. Accordingly, Fe LMM Auger electrons are mainly collected. Note here that the photoelectron and Auger electron diffraction effects are negligible, because the kinetic energy range for the collected electrons is so wide. The diffraction effects are further diminished by averaging over the azimuthal angles of the emitted electrons. Since the probing depth, λ_e, is not expected to be proportional to $\sin\theta_d$ in the case of partial electron yield detection mainly due to the inelastic scattering process, λ_e was experimentally determined for each θ_d by measuring the Fe-L edge jump as function of film thickness [9]. The estimated λ_e varies from 7.5 to 19.4 Å by changing θ_d in the range of 0–30° from the surface parallel direction.

All the experiments were performed in an ultrahigh-vacuum chamber placed at the soft X-ray station, BL-7A, in the Photon Factory [17]. Circularly polarized X-rays (circular polarization factor, $P_c \sim 0.85$) were obtained by collecting light emitted downward (-0.4 mrad) the orbit plane of the storage ring. The sample was magnetized by a current pulse through a yoke coil, and then the coil was retracted out during the measurements. A Cu(100) single crystal was cleaned by repeated cycles of Ar^+ bombardment (1.5 kV) and annealing to ~900 K. Fe was deposited at room temperature by electron bombardment heating of an iron rod, and the film thickness was monitored by *in situ* RHEED (reflection high-energy electron diffraction).

3. Results and discussion

Before describing the presents, let us summarize the earlier works concerning the ultrathin Fe/Cu(100) films [1, 4, 10–16]. As for the thermally deposited Fe films grown at room temperature, it has been believed that the Fe film exhibits ferromagnetic (FM) coupling below 4 ML (region I) and above 12 ML (region III), while it consists of the two-layer thick surface FM layers and inner antiferromagnetic ones in the case of 5–11 ML (region II). Recently, Qian *et al.* studied the magneto-optical Kerr effect (MOKE) as a function of film thickness and claimed that the inner layers of region II are in spin density wave (SDW) state with wave number $q = 2\pi/2.7d$ [16]. Here, d denotes the interlayer distance of the film. The ordering temperature for the inner layers in region II was reported to be ~200 K [11, 16].

Figure 2 shows Fe L-edge XMCD spectra for a 7 ML Fe film taken with various electron detection angles, θ_d. Since the film is known to have perpendicular magnetic anisotropy, all the spectra were taken at normal X-ray incidence. It is clearly seen that

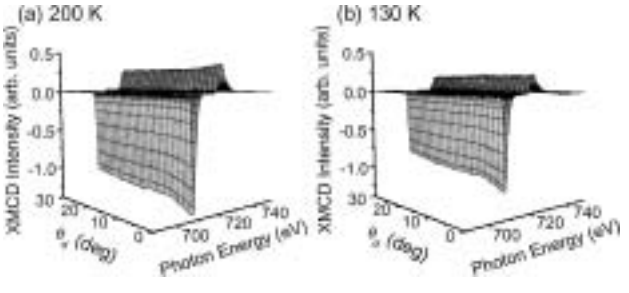

Fig. 2. Fe L-edge XMCD spectra for a 7 ML Fe film grown on Cu(100) taken with various electron detection angles, θ_d.

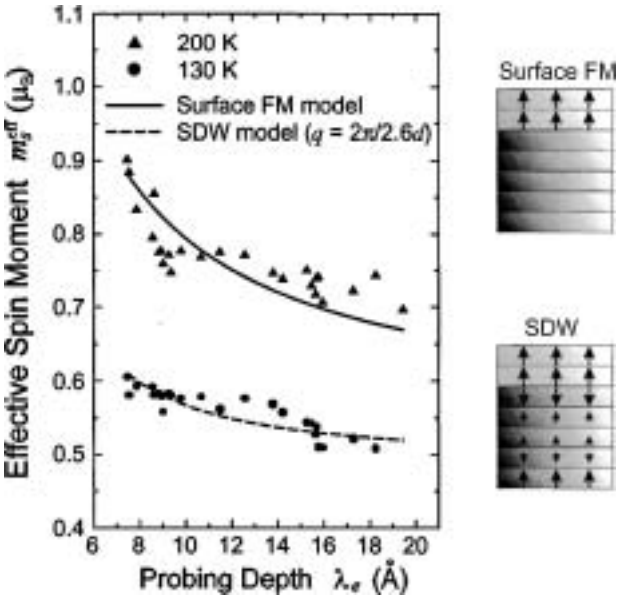

Fig. 3. Effective spin moment, $m_s^{\rm eff}$, as a function of probing depth, λ_e, together with the simulated curves assuming two-layer thick surface FM layers with the nonmagnetic inner layers (surface FM model) and the same with SDW inner layers with $q = 2\pi/2.6d$ (SDW model).

the XMCD intensity is reduced as θ_d increases both at 130 and 200 K. We can thus directly conclude that the magnetic moment is localized around the surface. Note here that the XMCD signals taken at 130 K were significantly smaller than those recorded at 200 K, suggesting some magnetic structure in the inner layers.

In order to further investigate the magnetic depth profile, effective spin magnetic moment, $m_s^{\rm eff} = m_s + 7m_T$, was estimated by applying the sum rules [7, 8] for each XMCD spectrum. The estimated moments are plotted in Fig. 3 as a function of λ_e, together with the simulated curves for the magnetic structures illustrated in the figure. In this simulation, we assumed an exponential decay for the emitted electrons, and neglected the self-absorption effect of the incident X-rays. The probing depth dependence at 200 K is well reproduced by the surface FM model, which consists of the two-layer thick surface FM layers and nonmagnetic inner layers. The reduction of the XMCD signals at 130 K can be explained by assuming that the inner layers are in the SDW state, where the first layer of the SDW state (third layer from the surface) is antiferromagnetically coupled with the surface FM layers. This behavior is in reasonable agreement with previous studies [11, 16] which indicated that the ordering temperature for the inner layers in ~200 K. We performed curve fitting analyses to determine the SDW wavenumber, yielding $q = 2\pi/2.6d$, which agrees well with our previous experiments [9] and the MOKE result [16].

Next, the layer-resolved spectra at 130 K were extracted in a similar manner described elsewhere [9]. We repeated the extraction procedure by changing q around $2\pi/2.6d$, finding again that $q = 2\pi/2.6d$ gives the smallest difference between the obtained data and simulation. The extracted XMCD spectra are depicted in Fig. 4. The XMCD spectrum for the first layer of the SDW has an opposite sign to that for the surface FM layers, this confirming the above-mentioned antiferromagnetic FM/SDW interface coupling. Moreover, it is suggested that the SDW amplitude is as large as the magnetic moment of the surface FM layers. Furthermore, we should note that the XMCD spectrum for the SDW layers has a small but significant structure just above

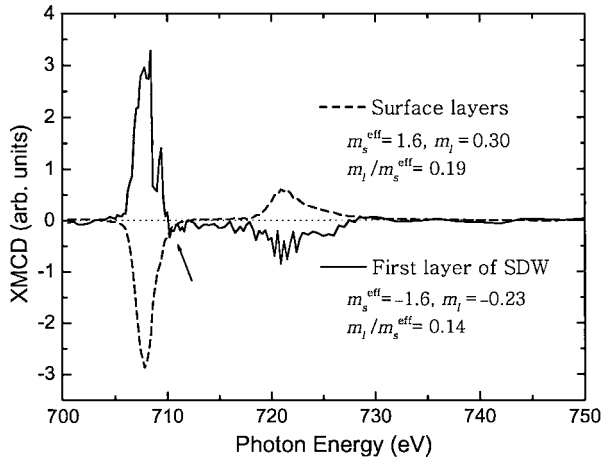

Fig. 4. Extracted Fe L-edge XMCD spectra for the surface FM (dashed line) and inner SDW (solid line) layers of the 7 ML film at 130 K. For the SDW layers, only the spectrum for the first layer (third layer from the surface) is given. A small structure above the L_{III} peak is indicated by an arrow in the XMCD spectrum for the SDW layers. The obtained effective spin moment (m_s^{eff}) and orbital one (m_l) are also indicated in the μ_B unit, together with their ratio.

the L_{III} peak with an opposite sign to the L_{III} peak (indicated by an arrow), while no such structure is found in the surface FM spectrum. Similar difference was reported for 2 and 40 ML Fe films grown on Pd(100) [18], where the opposite sign peak is observed only for the 40 ML film. They interpreted this as the difference in the diffuse magnetic moment [19] related to the empty s final states. No matter whether their interpretation is correct or not, the opposite sign peak can be attributed to a bulk-like feature, because the 2 ML spectrum should not include any bulk component. In fact, the opposite sign peak also appears in the bulk Fe spectrum [20]. We have thus succeeded in extracting the surface and bulk-like XMCD spectra separately from the single element film.

Finally we estimated the magnetic moments for the surface and inner layers by using the sum rules [7, 8] (see Fig. 4). The estimated magnetic moment of the surface FM layers is almost the same as that of the inner SDW ones, indicating again that the SDW amplitude is comparable to the magnetization of the surface FM layers. Moreover, the orbital moment of the surface layers is larger than that of the inner ones, which directly suggests the enhancement of the surface orbital moment.

4. Conclusions

We have significantly improved the depth-resolved XMCD technique by using an imaging type MCP detector. All the spectra with various probing depths are recorded simultaneously, so that the data accumulation time was drastically reduced with much higher data quality. We applied this technique to the Fe/Cu(100) films, and confirmed that the surface two layers of the 7 ML film are ferromagnetically coupled, while the inner layers are in the SDW state at 130. It was clearly indicated that the extracted XMCD spectrum for the surface FM layers is similar to the typical ultrathin film spectrum, while that for the inner layers has a bulk-like feature. The quantitative analyses suggested that the SDW amplitude is almost the same as the magnetization of the surface FM layers ($m_s^{eff} = 1.6\mu_B$), and that the orbital moment of the surface layers ($m_l = 0.30\mu_B$) might be larger than that of the SDW ones ($m_l = 0.23\mu_B$).

Acknowledgment

The present work has been performed under the approval of the Photon Factory Program Advisory Committee (PF-PAC No. 2001S2-003, 2001G013). The authors are grateful for the financial support of the Grant-in-Aid for Scientific Research (No. 13740390, 10304059, 12440193, 14204069) and the 21st Century COE Program from the Ministry of Education, Culture, Sports, Science and Technology.

References

1. Straub, M., Vollmer, R. and Kirschner, J., Phys. Rev. Lett. **77**, 743 (1996).
2. Reif, J., Zink, J. C., Schneider, C. M. and Kirschner, J., Phys. Rev. Lett. **67**, 2878 (1991).
3. Reif, J., Rau, C. and Matthias, E., Phys. Rev. Lett. **71**, 1931 (1993).
4. Detzel, Th., Vonbank, M., Donath, M. and Dose, V., J. Magn. Magn. Mater. **147**, L1 (1995).
5. Rangelov, G., Kang, H. D., Reinmuth, J. and Donath, M., Phys. Rev. B **61**, 549 (2000).
6. Kim, S. K. and Kortright, J. B., Phys. Rev. Lett. **86**, 1347 (2001).
7. Thole, B. T., Carra, P., Sette, F. and van der Laan, G., Phys. Rev. Lett. **68**, 1943 (1992).
8. Carra, P., Thole, B. T., Altarelli, M. and Wang, X., Phys. Rev. Lett. **70**, 694 (1993).
9. Amemiya, K., Kitagawa, S., Matsumura, A., Yokoyama, T. and Ohta, T., J. Physics: Cond. Matter **15**, S561 (2003).
10. Thomassen, J., May, F., Feldmann, B., Wuttig, M. and Ibach, H., Phys. Rev. Lett **69**, 3831 (1992).
11. Li, D., Freitag, M., Pearson, J., Qiu, Z. Q. and Bader, S. D., Phys. Rev. Lett. **72**, 3112 (1994).
12. Dunn, J. H., Arvanitis, D. and Mårtensson, N., Phys. Rev. B **54**, R11157 (1996).
13. Ellerbrock, R. D., Fuest, A., Schatz, A., Keune, W. and Brand, R. A., Phys. Rev. Lett. **74**, 3053 (1995).
14. Schmitz, D., Charton, C., Scholl, A., Carbone, C. and Eberhardt, W., Phys. Rev. B **59**, 4327 (1999).
15. Popescu, V., Ebert, H., Szunyogh, L., Weinberger, P. and Donath, M., Phys. Rev. B **61**, 15241 (2000).
16. Qian, D., Jin, X. F., Barthel, J., Klaua, M. and Kirschner, J., Phys. Rev. Lett. **87**, 227204 (2001).
17. Amemiya, K., Kondoh, H., Yokoyama, T. and Ohta, T., J. Electron Spectrosc. Relat. Phenom. **124**, 151 (2002).
18. LeCann, X., Boeglin, C., Carrière, B. and Hricovini, K., Phys. Rev. B **54**, 373 (1996).
19. O'Brien, W. L. and Tonner, B. P., Phys. Rev. B **50**, 12672 (1994).
20. Chen, C. T., *et al.*, Phys. Rev. Lett. **75**, 152 (1995).

Physica Scripta. Vol. T115, 1038–1040, 2005

Quantitative Zinc Speciation in Soil with XAFS Spectroscopy: Evaluation of Iterative Transformation Factor Analysis

A. C. Scheinost[1,2 *], A. Rossberg[1], M. Marcus[3], S. Pfister[2] and R. Kretzschmar[2]

[1]Institute of Radiochemistry, Forschungszentrum Rossendorf, D-01314 Dresden, Germany
[2]Institute of Terrestrial Ecology, ETH Zurich, CH-8952 Schlieren, Switzerland
[3]Advanced Light Source, Berkeley Lab, Berkeley, CA 94720, U.S.A.

Received June 26, 2003; accepted November 10, 2003

Abstract

We employed a combination of selective sequential extractions and bulk XAFS spectroscopy, and extracted spectral XAFS components and their concentrations by iterative transformation factor analysis (ITFA), in order to determine the Zn speciation in a smelter-contaminated, acidic soil. We compared the speciation by ITFA with one we performed earlier using principal component analysis and linear combination fit. ITFA identified 4 different species, two different franklinite-type phases (Zn-Fe spinels), sphalerite (Zn sulfide) and Zn oxalate, the latter forming as a precipitate during chemical extraction with oxalate solution. The second spinel-type phase could be extracted with the help of ITFA, although no appropriate reference sample was available. Spinel 1 and 2 have Zn-O distances of 1.96 and 1.99 Å, and Zn-Fe distances of 3.53 and 3.48 Å, respectively. The results from ITFA gave much better fits of experimental spectra and are better in line with elemental mapping and XAFS microspectroscopy. The major advantage of investigating XAFS data with ITFA is the possibility to derive all species even when part of the references are not available.

1. Introduction

Speciation of metals in contaminated soils is a prerequisite for predicting the environmental risks and to develop efficient and cost-effective remediation measures. While XAFS is the method of choice for providing molecular information on chemical forms, several coexisting species can be resolved only by the additional help of micro-spectroscopies, chemical and physical separation methods, and statistical methods [1–6]. Recently we have employed a combination of selective sequential extractions followed by XAFS spectroscopy, and have identified the spectral contributions by principal component analysis, target transforms and linear combination fits [7]. Another statistical method, ITFA, has been applied recently to derive the structure of two coexisting aqueous U(VI)-protocatechuic acid complexes [8]. This approach has the advantage that reference spectra of pure species can be substituted for by knowledge of the relative distribution of species in mixtures. That is, if the concentrations of at least some of the species are known from speciation modeling (or any other source like complementary spectroscopies), the spectra of the pure species can be calculated even when only spectra of species mixtures are available. The intention of the present paper was to investigate, whether this approach can be applied to decipher metal speciation in soils. As a model case, we investigated the Zn K-edge XAFS spectra collected from selective sequential extraction residuals of a contaminated soil [7].

2. Experimental

A topsoil sample was collected near the former zinc smelter in Palmerton, Pennsylvania [6]. This sample was ground, and subjected to increasingly aggressive extraction procedures [9]. After each of 6 extraction step, the removed zinc concentration was determined by atomic absorption spectrometry, and an XAFS spectrum was collected (fluorescence mode with Lytle detector at beamline X-11A, NSLS) [7]. The resulting 7 spectra (untreated soil sample and sample after each of 6 extraction steps) were investigated by ITFA [8, 10]. First, abstract Eigenvectors were derived from the set of XAFS spectra by principal component analysis. These Eigenvectors were used to estimate the number of species present (see below). Second, a Varimax rotation was applied to get qualitative concentrations of the factors. Third, additional information was used to derive real concentrations and real factors (i.e. the XAFS spectra of the pure species and their relative contributions) by iterative target transform.

3. Results and Discussion

Figure 1 (top) shows the first four Eigenvectors derived from XAFS spectra of the soil samples before and after 6 extraction steps. The amplitudes decline from vector 1 to 4. While vectors 1 to 3 still contain information similar to XAFS oscillations, vector 4 contains experimental noise only. Thus, the Eigenvectors suggest the presence of three species in all samples. From our previous investigations we knew that franklinite, sphalerite and zinc oxalate are the major Zn species of these samples [6, 7]. Therefore, by adding the spectra of these species to those of the soil samples, we would have expected to observe again three significant Eigenvectors only. However, Figure 1 (bottom) shows a fourth significant Eigenvector. Since we know the relative concentrations of three species in three of the spectra (the 3 reference spectra), we can now calculate the relative concentrations of all four species in the 10 samples by iterative target transform (Fig. 2). Finally, the real factors, i.e., the XAFS spectra of all four species, were derived (Fig. 3). Factor 2 is identical to the franklinite reference sample, factor 3 to the sphalerite sample, and factor 1 to the Zn oxalate reference. Factor 4 represents the fourth, unknown species. The spectral features (Fig. 3) and the fit results (Table I) suggest that factor 4 represents a second franklinite phase, which is distinguished from the franklinite reference by a larger Zn-O distance and a smaller Zn-Fe distance. The larger Zn-O distance may be due to Zn in both tetrahedral and octahedral coordination, which is not untypical for spinel structures. Furthermore, the difference in Zn-Fe distances may indicate different elemental composition, e.g. varying fractions of Zn, Fe and Mn in the structure.

In spite of their structural differences, the dissolution behavior of franklinite 1 and 2 is similar (Fig. 4). In the untreated soil sample, about 80% of the total zinc is in the two franklinite phases. During step 5, which is an oxalate solution step intended to dissolve weakly crystalline Fe oxides, a substantial amount of

*E-mail: scheinost@esrf.fr; Address: ESRF, B.P. 220, F-38043 Grenoble, France.

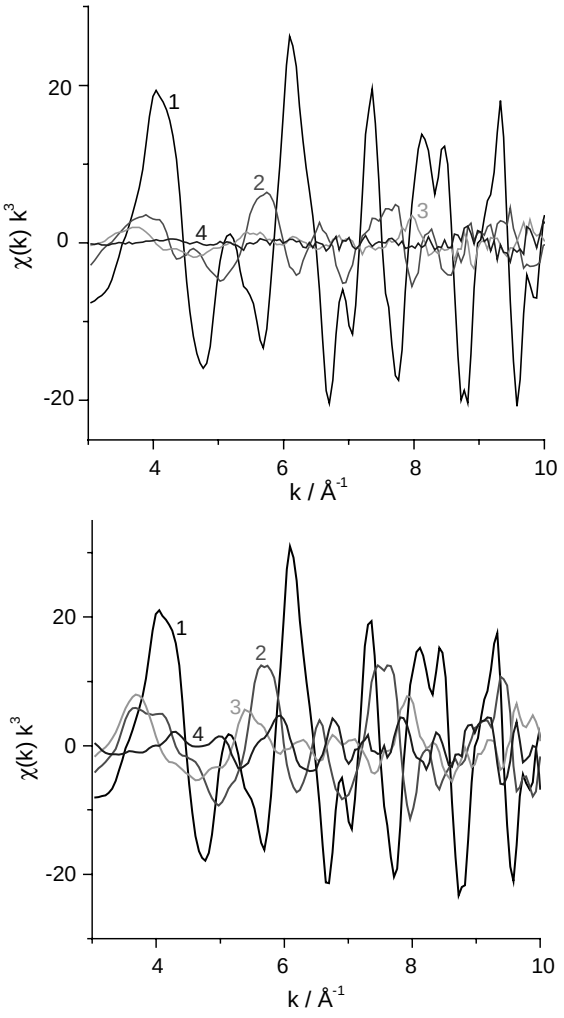

Fig. 1. First 4 Eigenvectors of XAFS spectra of the 7 soil samples (top), and of the XAFS spectra of 7 soils samples plus franklinite, sphalerite and Zn oxalate (bottom).

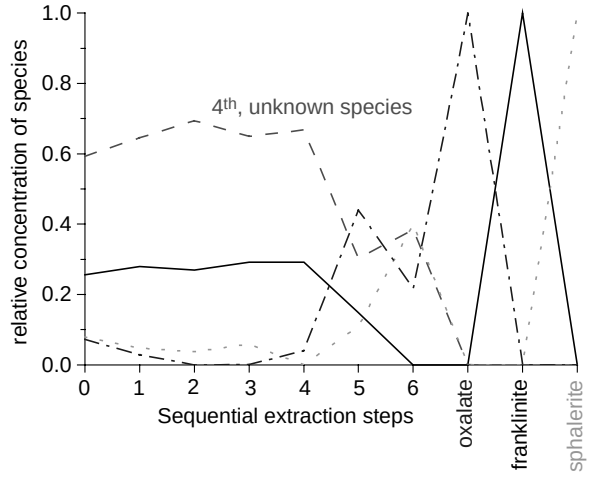

Fig. 2. Relative concentrations of the four species determined by ITFA.

Table I. *XAFS fit results of factors 2 and 4.*

	CN O	R [Å]	σ^2 [Å^2]	CN Fe	R [Å]	σ^2 [Å^2]	ΔE_0 [Å]	χ^2_{res} %
Factor 2	3.5	1.96	0.002	13.0	3.53	0.007	1.0	9.8
Factor 4	5.4	1.99	0.010	11.9	3.48	0.008	1.3	10.7
Franklinite XRD	4.0	1.99		12.0	3.50			

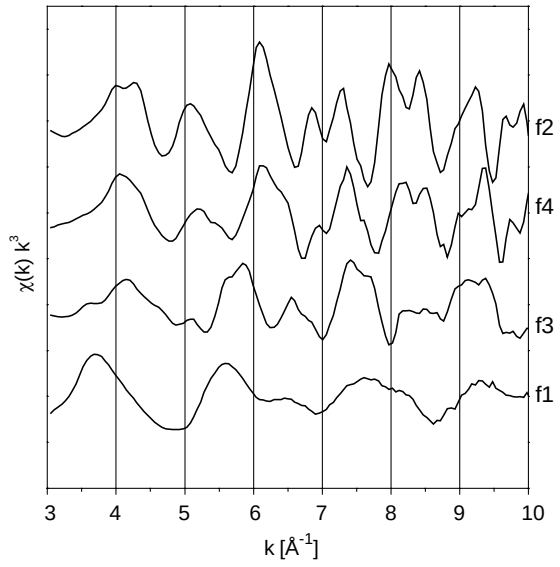

Fig. 3. Real spectral factors derived by ITFA, corresponding to the experimental XAFS spectra of franklinite (f2), sphalerite (f3) and Zn oxalate (f1). Factor 4 corresponds to the XAFS spectrum of the previously undetected species, a franklinite-like mineral.

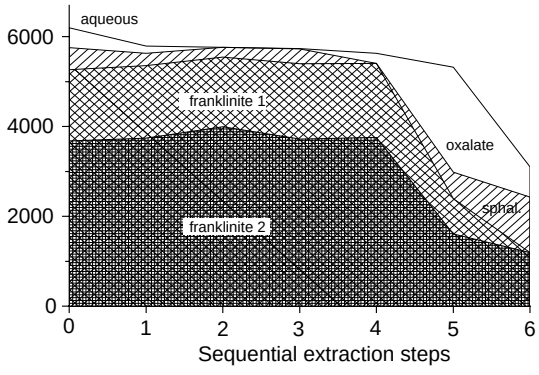

Fig. 4. Absolute species distribution (cumulative) of the untreated soil sample (step 0) and after each of the selective sequential extraction steps (1 to 6).

both franklinite phases is dissolved, but most of the dissolved Zn re-precipitates as Zn oxalate. The larger part of this Zn oxalate, and a smaller part of franklinite dissolves during step 6, a step intended to dissolve crystalline Fe oxides. None of these steps dissolves a significant amount of sphalerite, which hosts about 10% of total Zn (in the untreated sample). This is much less than the 30% derived by linear combination fits [7]. An amount of 10% is more consistent with the observations by XAFS microspectroscopy [6]. Furthermore, the reconstruction of the experimental spectra has significantly improved, giving another indication that the ITFA approach is superior to the approach employing principal component analysis, target transform and linear combination fits.

The problem of properly identifying aqueous and exchangeably sorbed Zn cations is evident from the fact, that ITFA assigns about 10% of Zn oxalate to the untreated soil sample. Step 1 employing a 1M NH_4NO_3 solution, removed 7% of Zn indicating that this amount is aqueous Zn^{2+} and/or Zn bound to cation exchange sites instead. The single O shell of aqueous Zn is a spectral feature also present in Zn oxalate, therefore making the discrimination by ITFA impossible.

In conclusion, we believe that ITFA has a great potential to improve the interpretation of XAFS of complex mixtures, since this statistical method depends less on a complete spectral database.

References

1. La Force, M. J. and Fendorf, S., Soil Sci. Soc. Am. J. **64**, 1608 (2000).
2. Ostergren, J. D., Brown, G. E., Jr., Parks, G. A. and Tingle, T. N., Environ. Sci. Technol. **33**, 1627 (1999).
3. Manceau, A. *et al*., Environ. Sci. Technol. **30**, 1540 (1996).
4. Manceau, A. *et al*., Am. J. Sci. **300**, 289 (2000).
5. Roberts, D. R., Scheinost, A. C. and Sparks, D. L., In "Geochemical and Hydrological Reactivity of Heavy Metals in Soils" (Selim, H. M., Kingery, W. L., Eds), (CRC Press: Boca Raton, 2003), pp. 187–227.
6. Roberts, D. R., Scheinost, A. C. and Sparks, D. L., Environ. Sci. Technol. **36**, 1742 (2002).
7. Scheinost, A. C., Kretzschmar, R., Pfister, S. and Roberts, D. R., Environ. Sci. Technol. **36**, 5021 (2002).
8. Rossberg, A., Reich, T. and Bernhard, G., Analytical Bioanalytical Chem. **376**, 631 (2003).
9. Zeien, H. and Brümmer, G. W., Mitt. Dtsch. Bodenkundl. Ges. **59**, 505 (1989).
10. Malinowski, E. R., "Factor Analysis in Chemistry" (John Wiley: New York, 1991).

Physica Scripta. Vol. T115, 1041–1043, 2005

X-Ray Natural Linear Dichroism (XNLD) Applied to the Determination of Relaxations Around Transition Metal Impurities in α-Al_2O_3

E. Gaudry[1], A. Kiratisin[1], Ph. Sainctavit[1], Ch. Brouder[1], F. Mauri[1], A. Ramos[1], A. Rogalev[2] and J. Goulon[2]

[1]Laboratoire de Minéralogie-Cristallographie, UMR 7590, Université Pierre et Marie Curie, case 115, 4 place Jussieu F-75252 Paris Cedex 05, France
[2]European Synchrotron Radiation Facility, BP 220, F-38043 Grenoble Cedex, France

Received June 26, 2003; accepted November 4, 2003

PACS numbers: 6110Ht, 6172Bb, 7870Dm

Abstract

The local environments around substitutional Cr^{3+} or Fe^{3+} ions in doped α-Al_2O_3 have been studied experimentally by dichroic X-ray absorption at the Cr and Fe K-edges in single crystals. A reliable method has been applied to remove diffraction peaks. This paper shows that the dichroic EXAFS analysis leads to the precise determination of the environment around impurity ions in α-Al_2O_3. The Cr or Fe coordination shell in doped α-Al_2O_3 is similar to the one of Cr in α-Cr_2O_3 or of Fe in α-Fe_2O_3. Aluminum or oxygen atoms at a farther distance are weakly affected by the presence of the impurity.

1. Introduction

Impurities in insulators modify the properties of the host crystal. Improvement in voltage holdoff capability can be obtained by doping plain alumina [1]. Laser light emission relies on the excited states of transition elements (Cr^{3+} for the first laser crystal) or rare earth (Eu^{3+}) in α-Al_2O_3 [2]. The color of allochromatic minerals results from minor impurities. Colorless corundum (α-Al_2O_3) becomes red ruby (α-$Al_2O_3:Cr^{3+}$) when few Cr^{3+} ions substitute for Al^{3+} ions. When few Fe^{3+} ions substitutes for Al^{3+} ions, α-$Al_2O_3:Fe^{3+}$ is yellow [3, 4]. Therefore, impurities play an essential role in the macroscopic properties of materials, in particular concerning the color or the dielectric behavior. The determination of the local structure around impurities is essential as a first step to understand the specific macroscopic properties of these materials.

The crystal structure of α-Al_2O_3 belongs to the space group $R\bar{3}2/c$ or D^6_{3d}, thus making it a uniaxial birefringent material [5]. The rhombohedral unit cell contains two Al_2O_3 formula. Aluminum ions are linked to six oxygen ions in a distorted octahedron. The six oxygen atoms are gathered into two groups of three atoms to comply with the C_3 symmetry. These two groups lie at two different distances from the central atom. The farther three oxygen atoms (O_2 type) compose the face shared by two joined octahedra. The nearest three oxygen atoms (O_1 type) are an edge shared by two joined octahedra. The ionic radius of the paramagnetic impurities is larger than the ionic radius of aluminum atoms ($r_{Cr^{3+}} = 0.615$ Å, $r_{Fe^{3+}} = 0.645$ Å and $r_{Al^{3+}} = 0.535$ Å in an octahedral site [6]). Since the Al-O bond in corundum is known to be ionocovalent [7], the relaxation is not exclusively geometric. The determination of the two precise metal oxygen bond lengths in the coordination shell is not obvious. X-ray absorption spectroscopy (XAS), in particular EXAFS, is a remarkable technique to probe the structural environment around a particular ion. However, the experimental determination of the distortion around transition metal impurities in α-Al_2O_3 powders is difficult to obtain from isotropic EXAFS spectra, since the differences between two fits of the experimental signal performed using either one averaged metal-oxygen distance or two different metal-oxygen distances leads to little improvement of the fit. Therefore, the analysis of the dichroic signal is needed to determine precisely the environment around impurities in corundum. This is done by using single crystals. Nevertheless, recording EXAFS on a single crystal is difficult due to the presence of diffraction peaks that strongly distort the experimental information [8]. We used a powerful method to remove diffraction peaks [14].

Our goal is to determine precisely the local environment around Cr^{3+} and Fe^{3+} in doped α-Al_2O_3. In the first part of this article, we show what kind of information is possible to reach using dichroic EXAFS. The dichroic EXAFS measurements, the process to remove diffraction peaks and the dichroic analysis of the spectra are described in the second part. Results are discussed and compared with *ab initio* energy minimization in the third part.

2. Dichroic EXAFS

Since the crystal structure belongs to the space group $R\bar{3}2/c$, the absorption cross section σ depends on the angle θ between the C_3 axis ([111] direction in the rhombohedral lattice) and the polarization $\hat{\epsilon}$ of X-rays [9] by $\sigma(\theta) = \sigma_0 + \sigma_1 \cos(2\theta)$. The isotropic cross section, analogous to the one of a powder, is given by $\sigma_0 - \frac{\sigma_1}{3}$. The dichroic cross section, given by the difference between $\sigma_{C_3 \| \hat{\epsilon}}$ and $\sigma_{C_3 \perp \hat{\epsilon}}$ is equal to $2\sigma_1$.

Since the six Al-O distances in the first coordination shell of α-Al_2O_3 are gathered into two groups lying at two different distances from the aluminum atom, and EPR measurements suggest that the chromium site in α-$Al_2O_3:Cr^{3+}$ is trigonal [10], we expect to determine the two metal-oxygen distances in the first coordination shell of the Cr and Fe impurities. In order to do that, the analysis of the dichroic EXAFS signal is essential. This is best seen in Fig. 1 where the calculated isotropic and dichroic EXAFS signals using the `feff8` code [11] have been represented for three different chromium environments described in the following and labeled cluster 1, cluster 2 and cluster 3. The three clusters contain 7 atoms (1 chromium atom and 6 oxygen atoms). The geometry in cluster 1 is given by *ab initio* density functional calculations [12]. It is built with three oxygen neighbors at 1.95 Å making an angle of 62.8 degrees with the C_3 axis and a further three at 2.00 Å with an angle of 48.4 degrees. In cluster 2, the chromium-oxygen bond angles are the same as for the preceding cluster and the bond distances for the six oxygen are set to the averaged value 1.975 Å. In cluster 3, the chromium atom is at the center of a pure oxygen octahedron (1.975 Å for the Cr-O bond lengths) and the dichroic EXAFS signal is zero (at least in the electric dipole approximation). One sees that dichroic EXAFS signals are much more sensitive to differences between chromium-oxygen bonds in the coordination shell than the isotropic signals. This proves that inequivalences

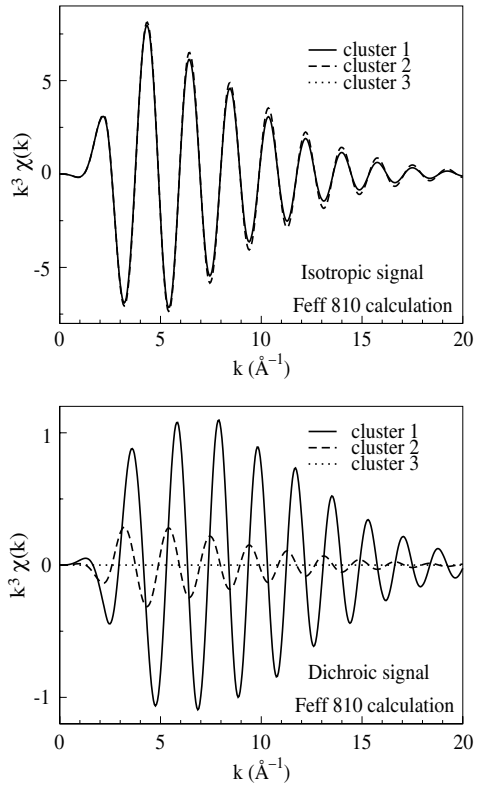

Fig. 1. Calculated isotropic (top) and dichroic (bottom) EXAFS signal of CrO_6 clusters. These clusters are made of 7 atoms (1 chromium atom and 6 oxygen atoms). Cluster 1 is given by density functional calculations (three oxygen atoms at 1.95 Å making an angle of 62.85 degrees with the C_3 axis and three other at 2.00 Å with the angle 48.36 degrees). In cluster 2, the Cr-O bond angles are the same as in cluster 1 and the bond distances for the six oxygen atoms are set to the averaged value 1.975 Å. Cluster 3 is a perfect octahedral cluster (1.975 Å for the Cr-O bond lengths).

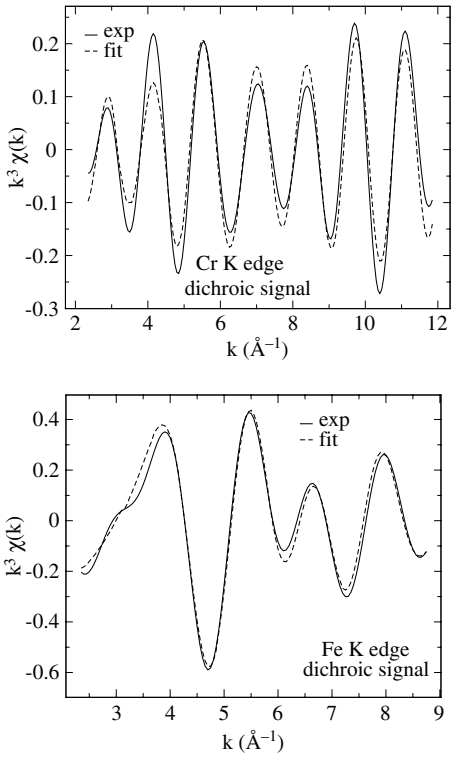

Fig. 2. Dichroic Fourier back-transformed experimental data $k^3\chi(k)$ (full line) and fit (dashed line) for Cr in α-$Al_2O_3:Cr^{3+}$ (top) and for Fe in α-Al_2O_3:Fe-Ti (bottom).

between oxygen atoms can reliably been addressed only through the EXAFS analysis of the dichroic signal.

3. Experimental details and results

Two types of single crystals synthesized by the Verneuil process are studied. They are a ruby ($Al_2O_3:Cr^{3+}$) containing 10000 ($\pm$500) wt ppm of chromium and a sapphire (Al_2O_3:Fe,Ti) containing 1500 ($\pm$50) wt ppm of iron and 750 ($\pm$30) wt ppm of titanium. The crystals are cut so that the C_3 axis is parallel to the surface. The chromium K-edge in α-Al_2O_3 and the iron K-edge in α-Al_2O_3:Fe-Ti have been measured on the ID12A beam line (European Synchrotron Radiation Facility, France) dedicated to polarization dependent spectroscopies [13]. In doing XAFS measurements of impurities in single crystals, one is faced with the problem of very intense diffraction peaks. These arise from either diffracted rays striking a fluorescence detector or from the occurrence of diffraction inside the crystal [8]. These diffraction rays may drag on and have devastating effects on the whole absorption spectrum, preventing any unambiguous EXAFS analysis [8]. A special technique called the rotating sample technique, proposed by J. Goulon, is applied to register the absorption spectra. This method, well described in [14] and [12], is used together with the filtering algorithm of [15] to obtain simultaneously both the isotropic absorption coefficient and the dichroic signal.

A standard procedure [16] is used to obtain the dichroic EXAFS signal $\chi_{dic}(k)$. Then, $\chi_{dic}(k)$ is analysed as a Fourier series of plane wavelets. The summation is over j shells and the signal for each shell is related to the back-scattering function $F_j(k)$, the total phase function $\Phi_{ij}(k)$, the electron mean free path $\lambda_j(k)$, the number N'_j, the bond distances r_j and the Debye-Waller factor σ_j:

$$\chi_{dic}(k) = -\frac{1}{k}\sum_j \frac{N'_j}{r_j^2} F_j(k) e^{-2\sigma_j^2 k^2} e^{-\frac{2r_j}{\lambda_j(k)}} \sin(2kr_j + \Phi_{ij}(k)) \quad (1)$$

where

$$N'_j = 3N_j\left[\frac{1}{N_j}\sum_i (\hat{\epsilon}_\parallel \cdot \hat{r}_j^i)^2 - \frac{1}{N_j}\sum_i (\hat{\epsilon}_\perp \cdot \hat{r}_j^i)^2\right] \quad (2)$$

with i runs over the jth shell.

Equation (1) is similar to the one of an isotropic signal except that the number N'_j is no longer a positive integer representing a number of atoms. In C_3 symmetry, the shell of neighbors are clustered in groups of three atoms, for which the angle θ_j between the bond $\hat{r}_j$ and the C_3 axis is constant. For such a shell, $N'_j = \frac{3}{2}(3\cos^2\theta_j - 1)$.

The dichroic Fourier back-transformed data $k^3\chi_{dic}(k)$ for Cr in α-$Al_2O_3:Cr^{3+}$ and for Fe in α-Al_2O_3:Fe-Ti are shown in Fig. 2. These experimental signals are fitted and results are displayed on Fig. 3.

4. Discussion and conclusion

Our ultimate purpose is the determination of the precise environment of a paramagnetic impurity present in a crystal of corundum. We found that the Cr-O distances in α-Al_2O_3 are 1.92 Å and 2.01 Å. The mean Cr-O distance (1.97 Å) is then in good agreement with the EXAFS measurements of Kizler *et al.* [17] (1.96 Å), and with optical measurements of Langer [18] (1.96 Å). For iron in α-Al_2O_3, we found that the two metal oxygen

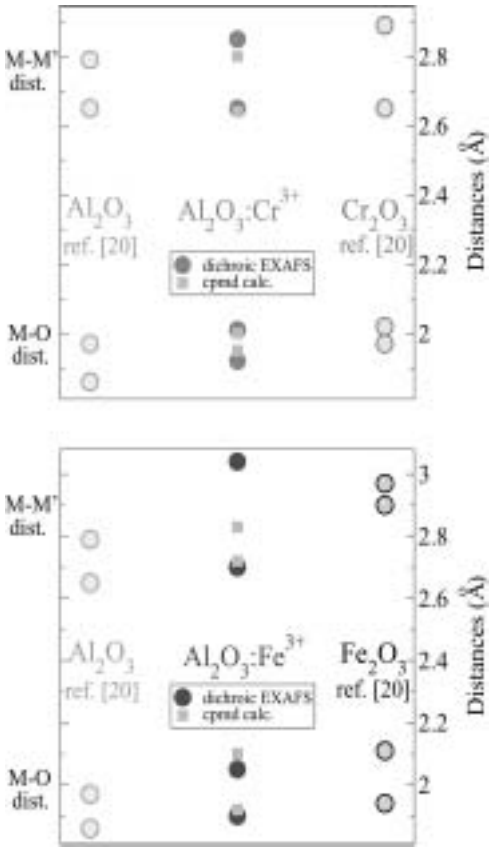

Fig. 3. Local environment around Cr in α-$Al_2O_3:Cr^{3+}$ (top) and around Fe in α-Al_2O_3 : Fe-Ti (bottom) from dichroic EXAFS (full circles) and *ab initio* calculations (squares). The results are compared with the structures of the Al_2O_3, Cr_2O_3 and Fe_2O_3 oxides (empty circles).

distances are 1.90 Å and 2.05 Å. It is then possible to have a description of the asymmetry of the impurity site by evaluating the parameter $\tau = 200\frac{d_{M-O_2}-d_{M-O_1}}{d_{M-O_2}+d_{M-O_1}}$ where d_{M-O_2} (resp. d_{M-O_1}) is the larger (resp. shorter) metal-oxygen distance in doped α-Al_2O_3. Despite similar Cr-O and Fe-O distances, the chromium and the iron site in doped α-Al_2O_3 are quite different ($\tau(Cr^{3+})$ = 4.58 and $\tau(Fe^{3+})$ = 7.59). In addition to the determination of the first neighbors distances, the analysis of the dichroic signal leads to the determination of the rather large second neighbors distances with a good reliability for α-$Al_2O_3:Cr^{3+}$. Indeed, the distribution of aluminum atoms in α-Al_2O_3 is strongly anisotropic and so yield a large contribution to the dichroic EXAFS signal. We found 2.65 Å and 2.85 Å for Cr-Al distances in α-$Al_2O_3:Cr^{3+}$. In the case of α-$Al_2O_3:Fe^{3+}$, the weak concentration of iron leads to a signal more difficult to analyze. We found 2.70 Å and 3.04 Å for Fe-Al distances in α-$Al_2O_3:Fe^{3+}$.

These bond lengths are in good agreement with results from *ab initio* energy minimization. Concerning metal-oxygen distances, they are 1.95 Å and 2.00 Å (Cr-O) and 1.92 Å and 2.10 Å (Fe-O). Concerning metal-aluminum distances, the are 2.64 Å and 2.80 Å (Cr-Al) and 2.72 Å and 2.83 Å (Fe-Al). The calculation permits us to have further structural information, in particular to know if the impurity ion is displaced, in respect to the position of the aluminum atom in α-Al_2O_3. Again, the result is different for the chromium or the iron impurity. The chromium atom is almost at the aluminum site, the oxygen atoms of its coordination shell move to accommodate for the larger ionic radius. Iron is repelled by the nearest aluminum neighbor along the C_3 axis. Its oxygen coordination shell is strongly relaxed, and further neighbors remain almost non displaced. That is in line with some previous EPR measurements where Fe is said to be moved by 0.04 Å ± 0.02 Å on the C_3 axis farther from the nearest aluminum neighbors [19].

It is possible now to picture the environment around the paramagnetic impurity in α-Al_2O_3. The local environment around the chromium ion in ruby is nearly the same as that in α-Cr_2O_3 [20]. The Cr-O bond lengths in ruby are closer to Cr-O bond lengths in α-Cr_2O_3 rather than to Al-O bond length in α-Al_2O_3 (see Fig. 3). However, Cr-Al (edge) distances are closer to Al-Al bond lengths in α-Al_2O_3 than to Cr-Cr bond lengths in α-Cr_2O_3. The case of iron in corundum is not exactly the same as that of chromium. The Fe-O bond lengths in blue sapphire are closer to the Fe-O bond lengths in α-Fe_2O_3 rather than to Al-O bond lengths in α-Al_2O_3. In both cases, the relaxation is local and does not affect atoms far from the chromium ion, within an error of about 1%.

Acknowledgments

We are glad to thank Françoise Vilain and Christophe Gauthier for their skillful help during preliminary experiments at LURE (Orsay) and ESRF (Grenoble). Ruby and blue kindly provided by Bruno Boizot and Georges Calas, who are at the origin of this piece of work. One of us (AK) thanks Thailand government for financial support during her PhD thesis. Computing time was partially supplied by the "Institut du Développement et des Ressources en Informatique Scientifique". This is IPGP contribution number 2913.

References

1. Miller, H. C., Physica C **104**, 183 (1981).
2. Verdozzi, C., *et al*., Phys. Rev. Lett. **80**, 5615 (1998).
3. Burns, R. G., "Mineralogical Applications of Cristal Field Theory," (Cambridge University Press, 1993).
4. Nassau, K., "The Physics and Chemistry of Color," (Wiley Interscience, 1983).
5. Nye, J. F., "Physical properties of crystals," (Clarendon Press, Oxford, 1957).
6. Shannon, R. D., Acta. Cryst. **A32**, 751 (1976).
7. Ching, W. Y. and Xu, Y. N., J. Am. Ceram. Soc. **77**, 404 (1994).
8. Emura, S., Maeda, H., Kuroda, Y. and Murata, T., Jpn. J. Appl. Phys. **32**, 734 (1993).
9. Brouder, Ch., J. Phys.: Condens. Matter **2**, 701 (1990).
10. Boizot, B., PhD thesis, Université Paris VI (1996).
11. Ankudinov, A. L., Ravel, B., Rehr, J. J. and Conradson, S. D., Phys. Rev. B **58**, 7565 (1998).
12. Gaudry, E., *et al*., Phys. Rev. B **67**, 094108 (2003).
13. Goulon, J., *et al*., J. Synchrotron Rad. **5**, 232 (1998).
14. Goulon, J., *et al*., SPIE Proceedings **3773**, 316 (1999).
15. Brouder, Ch., *et al*., In ICDIM proceedings, Johannesbourg 2, 89 (2000).
16. Teo, B. K., "EXAFS: basic principles and data analysis," (Springer Verlag, 1985).
17. Kizler, P., He, J., Clarke, D. R. and Kenway, P. R., J. Am. Ceram. Soc. **79**, 3 (1996).
18. Langer, K., Z. Kristallogr. **216**, 87 (2001).
19. Wen-Chen, Z., Physica B **245**, 119 (1998).
20. Pearson, W. B., Structure Reports, International Union of Crystallography **27** (1962).

Physica Scripta. Vol. T115, 1044–1046, 2005

Sub-Nanosecond Time Resolved XAFS of Laser Excited Thin Ge Films

E. A. Stern[1,*], D. L. Brewe[2], K. M. Beck[3], S. M. Heald[4] and Y. Feng[5]

[1]Department of Physics, Box 351560, University of Washington, Seattle, WA 98115, USA
[2]Pacific Northwest Consortium-Collaborative Access Team, Sector 20. Advanced Photon Source, Argonne National Laboratory, Argonne, IL 60439, USA; Department of Physics, University of Washington, Seattle, WA 98115, USA
[3]Pacific Northwest National Laboratory, P.O. Box 999, M/S K8-88, Richland, WA 99352, USA
[4]Pacific Northwest Consortium-Collaborative Access Team, Sector 20. Advanced Photon Source, Argonne National Laboratory, Argonne, IL 60439; Pacific Northwest National Laboratory, Richland, WA 99352, USA
[5]Department of Physics, Box 351560, University of Washington, Seattle, WA 98115, USA

Received June 26, 2003; accepted November 4, 2003

PACS numbers: 61.10.Ht, 61.80.Ba, 61.82.Fk

Abstract

A facility at PNC-CAT in the Advanced Photon Source measures with sub-nanosecond time resolution both XAFS and diffraction on femtosecond laser-excited samples. XAFS measures with relatively high efficiency the time for the laser excitation to couple to the lattice, the sample temperature after reaching thermal equilibrium, any ablation of the sample with time, and, in many cases can distinguish between the amorphous and crystalline states. Preliminary measurements on 200 nm thick polycrystal Ge films indicate that the time for transferring the laser excitation to thermal heating of the lattice is less than 2 nanoseconds when the initial temperature is 560 K.

1. Introduction

Understanding the kinetics of how excitations of a sample by 200 femtosecond (fs) laser pulses regain a new thermal equilibrium state is a fundamental materials science question that is only in its infancy. The melting of Ge by this means is particularly interesting because of its complex behavior. For example, the density of the liquid is greater (by 4.7%) and has a larger number of nearest neighbors (6 vs. 4). Previous investigations have probed the melting kinetics with Bragg diffraction, which is insensitive to changes after long-range order disappears. X-ray Absorption Fine Structure (XAFS) spectroscopy, however, does not require long-range order, and can therefore monitor local structural changes from the solid to the disordered liquid phase.

We have developed time-resolved XAFS capability on the subnanosecond time-scale that can extend over microsecond time periods for investigating the excitation kinetics of samples using a Ti-sapphire laser producing 4 μJ pulses of 250 femtosecond duration and 800 nm wavelength. The apparatus performs pump-probe experiments with a laser pump and an X-ray probe. The laser fires pulses at the APS P0 clock rate (∼272 kHz), collecting data from a given X-ray pulse each time around the ring, which is about two orders of magnitude faster than other laser systems used in similar time-resolution XAFS experiments. This allows the collection of data at a rate similar to that of typical non-time-resolved experiments. Diffraction measurements can also be made concurrently with the same time resolution, though we present only XAFS measurements in this paper.

The PNC-CAT insertion device (ID) beamline at sector 20 of the Advanced Photon Source (APS) employing Undulator A [1] was used in this experiment. The X-ray source in the 1 + 22 bunch mode used for the measurements has 23 bunches spaced by an interval of 1/24th of the ring circumference, which is 3.683 microseconds/24 = 153.4 ns. There is a larger interval of 307 ns between the 23rd bunch and the first bunch that follows for the next cycle around the ring. The width of the X-ray pulse is the same width of the electron bunch. All bunches have the same time width of about 50 ps because they have the same charge with a current of about 4.5 mA. The pulse used was one with neighbors 153.4 ns on either side. In the top-off mode used in this experiment the pulse with the lowest charge is injected every two minutes with electrons to bring it back to its maximum charge. In this manner the average ring current is maintained essentially constant but a given pulse is increased about 10% every 46 minutes. A schematic of the timing electronics associated with the laser and X-ray beams is shown in Fig. 1.

2. Experiment

The requirements of the Ge sample we measured are: (a) the X-rays should just probe that portion of the Ge that is excited by the laser, and (b) the excitations should remain in the probed

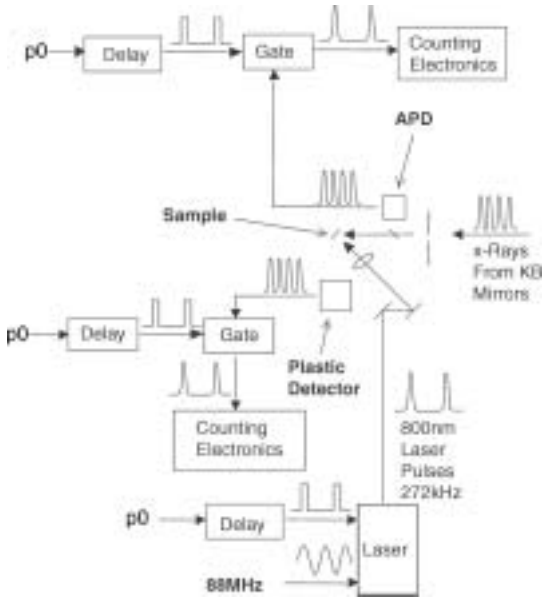

Fig. 1. Schematic of the timing electronics associated with the laser and X-ray beams. The P0 pulse is synchronized to the period of the APS ring period and is used to synchronize the laser pulse to a given X-ray pulse with a variable delay between the two. For a fixed time delay a standard XAFS scan is performed and this is repeated with steps in the time delay. The avalanche photodiode (APD) detects the I_0 of the X-ray pulse and the plastic detector detects the fluorescence signal from the sample induced by that same X-ray pulse.

*Email: stern@phys.washington.edu

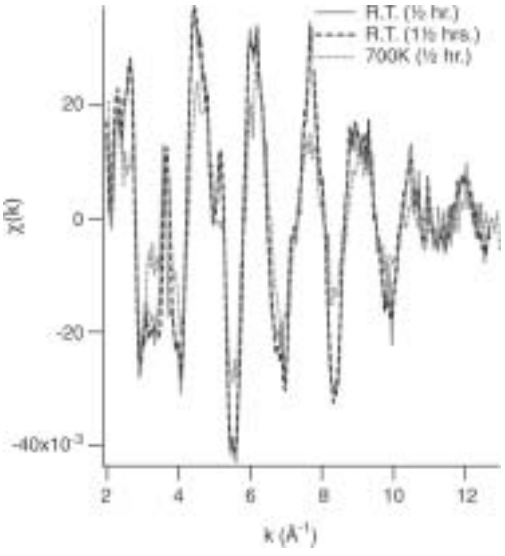

Fig. 2. EXAFS spectra measured from the $\Delta\mu x = 0.02$ thick Ge film after the indicated integration times for two different sample temperatures.

Fig. 3. A 2D scan of $\Delta\mu x$ of the sample with the focused X-ray beam. The dark area is about 50 μm in horizontal width and has about half the thickness of the surrounding region due to an accumulated ablation of the sample at a higher laser intensity than used in the measurements reported here.

region. These requirements were satisfied by a thin 200 nm thick Ge film (equal to the laser absorption length) evaporated on a (100) Si wafer covered on one face by a thermally grown 200 nm SiO_x film. During the evaporation the wafer was kept at 200 °C. After cooling to room temperature the wafer was treated with an anisotropic etch on the unoxidized face opposite from the one with the thin Ge film. The wafer was etched through to the oxide film forming a square pyramidal hole in the Si with the large opening in the unoxidized face and a small one 80 μm square in contact with the oxide film. The SiO_x film with its Ge film sample was thus freed from the Si backing in this 80 μm square, isolated from the Si wafer, and freely supported.

Figure 2 shows the EXAFS spectra obtained from a 10 μm focus X-ray beam on the 200 nm thick ($\Delta\mu x = 0.02$) polycrystal Ge film at room temperature (RT) and one heated to 700 K by the partially unfocused laser in a He environment to prevent oxidation. The temperature of the film was measured by determining the vibration amplitude of the Ge-Ge bond by EXAFS. The increased vibrations cause the amplitude of the EXAFS oscillations to decrease with increasing wavenumber k as seen for the 700 K plot. The high quality of the data is illustrated by comparing the average of 3 RT scans with one of them. The fully focused laser beam of 50 μm diameter gives an unattenuated energy per pulse of 200 mJ/cm^2 and produces a periodic time dependence in the temperature of the sample with the 3.68 μs period of the APS ring. At this power density the sample is ablated and to prevent this the power density was attenuated to 10 mJ/cm^2. Increasing the laser pulse energy density to more than 20 mJ/cm^2 caused ablation of the sample. The thickness of the Ge sample was chosen so that the laser would fully penetrate and excite it. Since the penetration depth of the X-rays is about 50 times that of the laser light the thin film assures that the X-rays sample a uniformly excited sample.

By measuring the XAFS signal one can determine, in addition to the Ge-Ge bond vibration amplitude, other features of the sample directly. Its thickness can be determined by the edge step in absorption or fluorescence signal allowing the determination of any ablation of the sample as shown in Fig. 3. Since the laser initially excites only the electrons in the sample, the time dependence of the transfer of this excitation to the lattice can be directly monitored by XAFS. Finally, the near-edge portion of the XAFS (the XANES) contains electronic information about the material and, for example, is sensitive to the shielding between the core hole and photoelectron that can be modified by the laser pulse in a semiconductor since the excited carrier density can be initially that of a metal. In addition, the excitation of the electron-hole carriers introduces a change in the absorption distribution at the edge which may be visible during the lifetime of the excited carriers. Moreover, the shape of the XANES can distinguish between the crystalline and amorphous state because its high-energy side has a shoulder in the crystal not present in the amorphous state (Fig. 4). XAFS can monitor the time dependence of these phenomena in the crystalline, amorphous and liquid state. Good XAFS spectra at a given delay time between the laser pump and the X-ray probe were accumulated in about 15–30 minutes. Careful tests were made that verified that both the 50 μm laser pump and 10 μm X-ray probe were overlapping and centered on the same point of the sample.

Figure 5 shows the magnitude of the Fourier transforms of the XAFS signal as a function of nominal time delay (t) between the

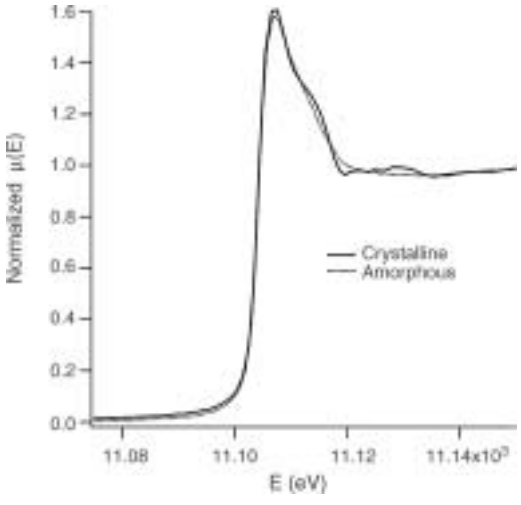

Fig. 4. The XANES of the Ge sample showing the difference between the initial amorphous state and the laser annealed polycrystal state employed in the measurements reported here.

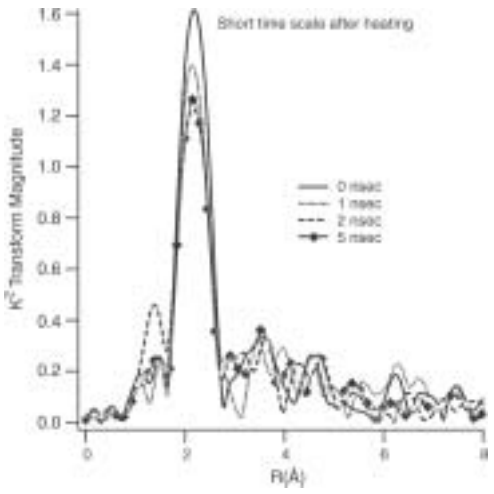

Fig. 5. The fourier transform magnitude of the EXAFS of the sample as a function of the nominal delay time between the laser and the X-ray pulses. The zero has not been carefully calibrated and could be off by 1 ns but the time differences are precise to 0.2 ns. The decrease of the magnitude indicates that the sample lattice has been heated to a new equilibrium temperature from 560 K to 740 K by the 200 fs laser pulse in less than 2 ns.

laser and X-ray pulses. The time delay differences are precise to 0.2 ns but the zero calibration may be off as much as about 1 ns. Note that the sample is hot enough at all times so that the thermal disorder is large enough so as to obscure all shells beyond the first shell. The temperature at nominal zero is 560 K. The magnitude of the first shell is the same as that found for times several ns before $t = 0$, indicating that the nominal zero in time is probably somewhat earlier than the true one. However, there is a definite heating at $t = 1$ ns and further heating at $t = 2$ ns as shown by the decreases in the height of the first shell. For the later time of 5 ns no further significant heating is apparent corresponding to a maximum temperature of 740 K. Measurements at longer delay times show that after the rapid heating the sample monotonically cools during the 3.6 µs between pulses to 560 K. Further measurements with a finer time difference are required to obtain a more accurate determination of the details of the rapid increase of the vibrations of the Ge-Ge bond induced by the laser excitation, but our present data indicates that it occurs in less than 2 ns.

3. Discussion

Since the direct gap is 1.1 eV in Ge, the 1.5 eV photons from a laser pulse initially couple most strongly to the valence electrons exciting them into the conduction band producing about 0.04 electron-hole pairs per Ge atom in the region irradiated by the laser. This electron-hole (e-p) cloud is confined between the SiO_x and He interfaces by the larger band gap of the oxide and the larger work function at the Ge/He interface and does not escape from the irradiated region with its much smaller thickness than laser beam diameter. The question to be answered is how and how fast the excitation equilibrates. Other measurement techniques have been employed to this question but ours is the first to apply XAFS. XAFS by measuring the Ge-Ge bond vibration amplitude can directly determine when the lattice has reached its thermal equilibrium, in contrast to the many other techniques applied to the problem.

We will discuss here only the one other technique that directly measured an aspect of the Ge-Ge bond, namely, the Raman effect [2]. Single crystals of Ge were employed as samples. Pump and variably delayed probe pulses were derived from a synchronously pumped R590 dye laser. The pulse duration was 4 ps, and both beams were focused to 50 µm diameter on the sample surface. The anti-stokes lines for the LO and TO phonon were monitored and the excitation of these modes decayed in the same time of 8 ps at RT. In this case neither the e-p cloud nor the phonons were confined in the irradiated region, but were free to propagate into the interior of the sample. An estimate of the time for excited phonons to escape from the probed region of 200 nm, using an average phonon speed for Ge of 5000 m/s, is 40 ps, not too different from the measured decay time. In addition, a simple calculation shows that the e-p cloud will escape from the probed region in times less than the resolution of the experiment. Assuming a conservative estimate of the average excitation energy of the electrons and holes above the gap of 0.1 eV the velocity of such particles is about 1.8×10^5 m/s and their escape time is about 1 ps, less than the laser pulse width. Thus the majority of the excited e-p pairs have escaped before the TO/LO excited phonons have decayed, further questioning whether the measured decay time of the phonons is significantly distorted by the escaping e-p pairs. By measuring changes in reflectivity on Ge films with pump-probe fast laser experiments [3] it has been determined that the e-p cloud has lifetimes of about 70 ps when it is confined within the probed region, so only a small fraction of the e-p pairs interacted with the probed sample in the Raman experiment. Moreover, the Raman measurement only addresses the lifetime of the TO/LO modes and does not assure that after their de-excitation the lattice is fully equilibrated. Thus, the measurement does not respond to most of the e-p pairs and does not track how the e-p pairs transfer their full energy to the TO/LO modes nor to the lattice. Our XAFS experiment, with the better than 0.1 ns time resolution we hope to attain, has the potential to determine the time for the e-p cloud to fully reach thermal equlibrium in the Ge sample.

4. Summary and Conclusion

XAFS can monitor many of the parameters of thin films. These are its temperature, its thickness, its local structure, and in many cases its structural phase. With self-supported thin films, sub-nanosecond time resolution, and femtosecond laser pulses at the period of the APS ring the kinetics of the transfer of the initial excitation to a thermal equilibrium condition can be followed by 30 minute XAFS scans on the PNC-CAT facility. Preliminary measurements with such a facility at PNC-CAT indicate that thermal equilibrium occurs for a 200 nm Ge film in a time scale less than 2 ns after excitation when the sample is initially at 560 K.

Acknowledgement

PNC-CAT facilities and research at these facilities is supported by the US DOE Office of Science grant no. DE-FG03-97ER45628. Use of the Advanced Photon Source was supported by the U.S. Department of Energy, Office of Science, Office of Basic Energy Sciences, under Contract No. W-31-109-ENG-38. Additional support was provided by Battelle-Pacific Northwest National Laboratory's (PNNL) Laboratory Directed Research Directorate (LDRD).

References

1. Heald, S. M. *et al.*, J. Synchrotron. Rad. **6**, 347 (1999); Heald, S. M. *et al.*, J. Synchrotron Rad. **8**, 342 (2001).
2. Young, J. F., Wan, K. and van Driel, H. M., Solid State Electron. **31**, 455 (1988).
3. Downer, M. C. and Shank, C. V., Phys. Rev. Lett. **56**, 761 (1986).

Physica Scripta. Vol. T115, 1047–1049, 2005

An X-ray Microspectroscopy Study of Hemochromatosis Liver and Diabetic Mice Kidney Tissues: Preliminary Observations

T. K. Sham[a*], P.-S. G. Kim[a], H. Ngo[a], S. Chakrabati[b] and P. C. Adams[b,c]

Departments of Chemistry[a], Pathology[b] and Medicine[c], University of Western Ontario, London, Canada, N6A 5B7

Received June 26, 2003; accepted November 21, 2003

PACS numbers: 78.70 Dm, 68.37.Yz

Abstract

We report preliminary observations of tissue images and micro-XAFS using X-ray microscopy techniques. Tissue specimens from hemocromatosis liver and knockout mice kidney were the subjects of the investigation. The X-ray microprobe experiments were conducted with a micro beam from an undulator beamline equipped with a set of K-B mirrors. Micro-beam XAFS studies at selected pixels of interest from the metal images were conducted. These techniques, together with optical and IR imaging provide a powerful tool for tissue analysis using synchrotron radiation. Preliminary Fe and Cu K-edge XAFS results from these experiments are reported and discussed.

1. Introduction

The X-ray micro beam technology at the insertion device beamlines of third generation light sources has evolved to become a powerful tool for microanalysis. The use of zone plate and KB mirrors optics can now provide routinely X-ray beams with sub-micron and micron spatial resolution, respectively, allowing for the collection of element images, which in turn can be used to facilitate micro-XANES and micro-XAFS analysis of hot spots or spots of interest, pixel by pixel. In this paper, we report preliminary results of a study of human hemochromatosis liver and mice kidney tissues at the Fe and Cu K-edge, respectively. We find that it is entirely feasible to use an X-ray micro-beam for the analysis of tissues.

Hemochromatosis is a disease in which the body absorbs excessive iron from the diet. Excess iron in the liver eventually leads to cirrhosis of the liver and hepatocellular carcinoma. It is the most common genetic disease in Canada (1 in 327 documented in a large population screening in London, Ontario, Canada) [1, 2]. Hemochromatosis is an autosomal recessive condition in which a defective gene has been inherited from each parent. Over 90% of patients have a mutated HFE gene. The exact role of the HFE protein in the pathogenesis of hemochromatosis is not completely understood [3]. It is useful to have chemical information about the distribution and chemical identity of Fe in liver tissues. We will present preliminary Fe K-edge micro-XAFS results of normal and hemochromatosis tissues.

In another tissue analysis, we are interested in testing a hypothesis in which it is thought that diabetes induced renal damage is mediated by the alternation of metallothionein (MT) and transition metal, especially Cu, in the kidney. The strategy is to investigate kidney tissues of transgenic mice with MT over-expression, MT knockout (KO) and wild type (WT) mice. Some Cu K-edge results for the knockout and the wild type (normal) mice tissues will be presented.

2. Experimental

Human biopsy liver tissues are obtained from Dr. Adam's clinic. Three specimens were examined in this study, a hemochromotosis liver tissue showing cirrhosis (henceforth labeled A4), a hemochromatosis liver cancer tissue (henceforth labeled A7) and a normal liver tissue (henceforth labeled B6). These tissues were prepared as thin slices of 10 microns on a substrate by standard procedures and were protected with a thin layer (∼5 micron) of paraffin. Both silicon wafer and high purity fused silica glass slides have been used as substrates, which show no detectable Fe and Cu impurities. The optical images (not shown) of the normal liver tissue (B6), the cirrhosis tissue (A4) and the cancer tissue (A7) show that the normal tissue is very uniform while the hemochromatosis cirrhosis tissue exhibits clusters of heavy iron accumulation. However, in the cancer tissue, the iron accumulation becomes less apparent. In another study, mice kidney tissues were from a KO and a WT mouse. There was no apparent difference in the morphology between the two tissues in their optical image.

The experiments were conducted at the microprobe station of the Pacific Northwest Consortium – Collaborative Access Team (PNC - CAT) ID line at the Advanced Photon Source (APS), Argonne National Laboratory [4]. APS operates at 7 GeV with an injection current of 100 mA (often in a top-off mode). The photon beam from the undulator was monchromatized with a cryogenically cooled Si (111) double crystal monochromator and

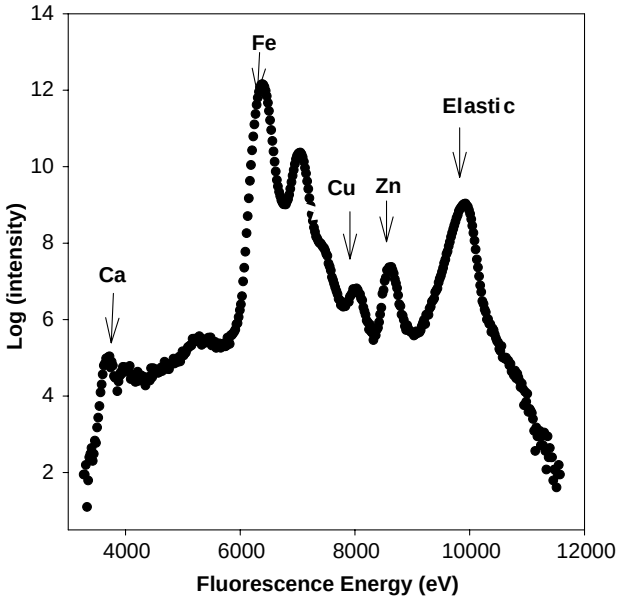

Fig. 1. Cu K-edge micro XAFS at a hot spot of the KO mouse kidney tissue compared with Zn K-edge XAFS of Zn metallothionein.

*e-mail: tsham@uwo.ca

focused with a set of KB mirror at the specimen with a spot of ∼5 micron (horizontal) × 7 micron (vertical). Specimens were placed at the sample holder at ∼45° with respect to the beam and to a liquid nitrogen-cooled, 13-element Ge solid-state detector. The sample holder can be scanned in x and y direction in micron steps with sub-micron precision.

The beam size was optimized and calibrated with a thin Pt wire prior to the mounting of the specimen by adjusting the horizontal and vertical KB mirrors. The specimen was then placed on the holder and at the focal point of a high-resolution video camera so that the position of the X-ray beam can be tracked optically. The monochromator was tuned to energies above the Fe K-edge in the liver study and the Fe K α fluorescence X-rays were monitored with the 13-element detector. Fig. 1 shows the fluorescence spectra of the A4 sample at an excitation-energy of 9.8 keV. It is apparent form Fig. 1 that there is a significant amount of Fe while Ca, Cu and Zn are also noticeable.

Element maps of metals of interest were then obtained by setting an energy window to collect fluorescence photons characteristic of Fe, Ca, Cu and Zn while scanning a region of the specimen (typically several hundreds of microns) pixel by pixel. Micro XAFS was then obtained at selected spots of interest from the element map.

3. Results and Discussion

A comparison of the Fe K-edge XAFS for the two hot spots in two different areas of the A4 specimen is shown in Fig. 2. The two XAFS in Fig. 2 exhibit a slightly different pattern as can be seen in the near edge region (inset). A Fourier transform of the EXAFS of the two hot spots are shown in Fig. 3, which shows a slightly different Fe-ligand bond length (by 0.1 Å) in the first shell. It must be noted that although this analysis is semi-quantitative at best with data collected from a limited number of scans, it does show that the local environment of Fe at these two hot spots is different. This result suggests that the technique is chemically sensitive and feasible for hemochromatosis Fe analysis. Similar maps and XAFS have also been obtained for the B6 and the A7 liver specimens. A comparison of the Fe K-edge XAFS (normalized) from two or more selected spots from each specimen indicates

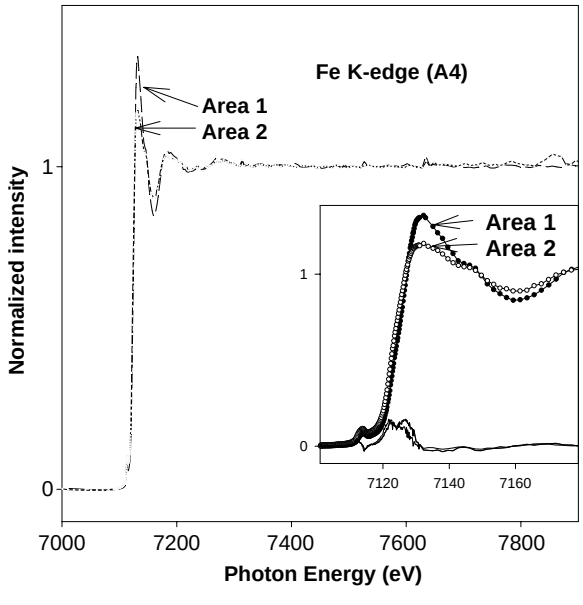

Fig. 2. Comparison of the XANES region of Fig. 6 with that of ferritin.

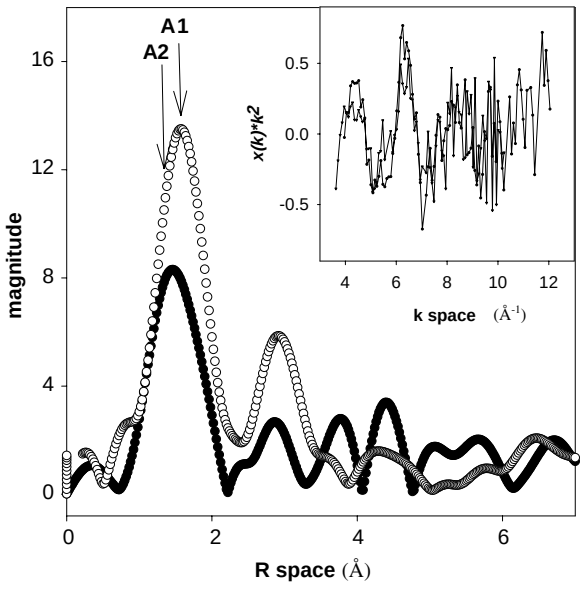

Fig. 3. Comparison of the Fe XAFS of a A4 hot spot with two standards: human ferritin and trans-ferrin (in diluted solution).

that there are excessive amount of Fe in A4 (largest edge jump), the cirrhosis specimen, relative to the normal tissue and that Fe in the cancer tissue (A7) is reduced considerably (by a factor of 10 judging by the relative edge jump) relative to A4, consistent with the optical images.

Fig. 4 shows the micro XAFS of Fe in a spot of A4 together with two standards: Ferritin (human) and Holo-tranferrin (human). It appears that the Fe XAFS in the hemichromatosis liver resembles that of ferritin, not a surprising result. Close examination of the Fe K-edge XANES of various spots of the specimens reveals some differences, which are shown in Fig. 5. The intensity of the 1s to p transition at the edge appears to decrease in the A4 specimen, which contains excessive Fe in the hot spots.

Finally, we also want to report a preliminary observation of Cu in the kidney specimens of the knockout and the wild type mice. There is a hypothesis that in the KO mice, the Cu is expected to be metallothionein and its concentration is expected to be smaller than that in the WT mice. Fig. 6 shows a typical Cu K-edge XAFS spectrum compared with that of a Zn metallothionein (Cu metallothionein is not very stable) [5]. It is expected that if Cu is in the metallothionein environment, its EXFAS may resemble that

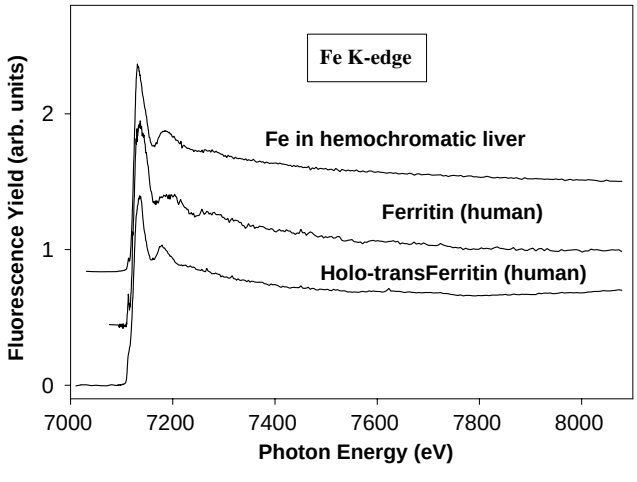

Fig. 4. Fourier transform of the EXAFS (inset) for the two hot spots shown in Fig. 2.

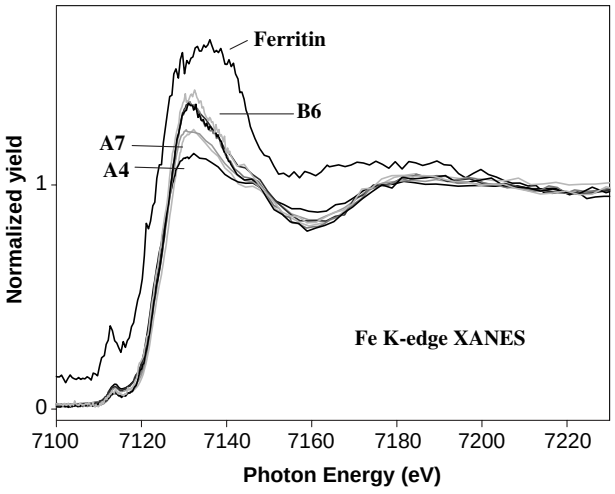

Fig. 5. Fe K-edge XAFS for the two hot spots. The XANES region and the corresponding first derivative are shown in the inset.

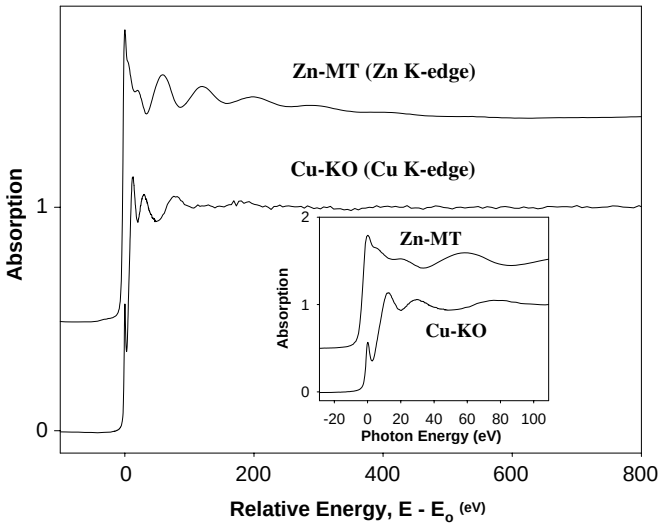

Fig. 6. X-ray fluorescence from metallic elements in the tissue excited with 9.8 keV photon.

of the Zn metallothionein. It is interesting then to find that Cu in these tissues exhibits XAFS very different from that of Zn metallothionein, suggesting a change in coordination. Further studies are needed. In addition, we also find that there is noticeably more Cu in the KO kidney than in the WT, while they both show the same XAFS, in contrast to the conventional wisdom.

4. Summary and Conclusion

We have reported some preliminary results of the microanalysis of metals in hemochromatosis liver and mice kidney tissues using a micro X-ray beam. The results clearly show that the microbeam technique can indeed be applied to yield useful information about the distribution and local environment of metal of interest in these tissues. This preliminary study allows us to embark on a systematic study of these tissues using X-ray microbeams.

Acknowledgement

The PNC-CAT at APS, Argonne National Laboratory is supported by the U.S. Department of Energy, Basic Energy Sciences, Office of Basic Science under contract Nos. W-31-109-Eng-38(APS). The PNC-CAT is also supported by an NSERC (Canada) MFA grant. We are indebted to Steve Heald and Robert Gordon for their technical assistance. Research at the University of Western Ontario (TKS) is supported by NSERC (Canada).

References

1. Adams, P. C., Can. Med. Assoc. J. **159**, 156 (1998).
2. Adams, P. C. *et al.*, Hepatology **31**, 1160 (2000).
3. Griffiths, W. and Cox, T., Human Molecular Genetics **9**, 2377 (2000).
4. Heald, S. *et al.*, J. Synchrotron Rad. **8**, 342 (2001).
5. Jiang, D.-T., Heald, S. M., Sham, T. K. and Stillman, M. J., J. Amer. Chem. Soc. **116**, 11004 (1994).

Physica Scripta. Vol. T115, 1050–1052, 2005

Light-Modulated XAFS Spectroscopy for Photo-Induced Structural Changes

K. Okamoto[1], K. Kohdate[1], K. Nagai[1], J. Miyawaki[1], H. Kondoh[1], T. Yokoyama[2], A. Nojima[1] and T. Ohta[1*]

[1]Department of Chemistry, School of Science, the University of Tokyo, Tokyo, 113-0033, Japan
[2]Institute for Molecular Science, Okazaki, 444-8585, Japan

Received June 26, 2003; accepted November 3, 2003

Abstract

The light-modulation method was applied to XAFS spectroscopy as a useful tool for the electronic and structural studies of light-excited states. Visible light for electronic excitation was modulated by an optical chopper and concomitant change in the X-ray absorbance was extracted by a lock-in amplifier. It is essential to reduce noises arising from several sources, especially those generated by the X-ray monochromator. Light-induced changes were measured successfully by the present approach with high S/N ratios for the Fe and Co K-edge XANES and EXAFS spectra of spin transition compounds. It is also possible to construct the pure EXAFS $k^3\chi(k)$ for the light-induced state from the light-modulated EXAFS difference spectrum. Detailed experiments including the signal amplitude and phase shift information revealed that the two components with different rate constants can be discriminated by changing the modulation frequency. The light-modulated XAFS method is found to be applicable to the systems with the excited-state ratio less than several percents. It has the following advantages; (1) simple experimental set-up, which requires only a visible-light source, an optical chopper, a lock-in amplifier, and a conventional XAFS beamline, and (2) free from the ground-state components because the light-induced absorbance difference is directly detected.

1. Introduction

Structural and electronic changes upon photoexcitation have attracted much attention and various methods have been developed to study the subject. X-ray absorption fine structure (XAFS) spectroscopy is one of the most useful tools to obtain direct information on local structures and electronic properties, especially for the materials without long-range ordering. However, it is much behind other methods for the study of short-lived photoexcited states.

There are two serious inherent problems in application of XAFS spectroscopy to photoexcited states. One is a large difference between visible light and X-rays in their absorption coefficients, and another is that the X-ray absorption edge energy is almost the same for ground and photoexcited states. By these reasons, conventional XAFS measurements of short-lived photoexcited species under continuous light irradiation often give a spectrum that is hardly distinguishable from the ground state, and extraction of information of the photoexcited state is very difficult. Several techniques have been developed for the studies of photoexcited states [1–6], which allows a 14-ns time resolution at the fastest. They are indeed powerful, but very elaborate and time consuming even with highly developed techniques and facilities. Further, the contribution of the remaining ground state species cannot be avoided.

The photo-modulation method, or the phase-sensitive detection method, is one of the popular methods to detect small spectral changes [7]. It is widely used in UV and visible spectroscopies, in which light is modulated periodically, making the signal follow the modulation to be detected by a lock-in amplifier, and only the synchronising component being extracted. It enables to detect weak signals hidden in a strong background without any subtraction of spectra. The purpose of the present study is to apply the photo-modulation method to XAFS spectroscopy as one of the useful tools for the study of photo-induced metastable states. It was performed by modulating the visible excitation light and detecting the concomitant X-ray absorbance change. We call this method the 'light-modulation' method hereafter to distinguish the pumping visible light from the probing X-rays.

2. Experimental

Experimental set-up for the fluorescent X-ray yield mode is shown in Fig. 1. Transmission experiments can also be performed with a similar set-up. Visible light was modulated using an optical chopper and introduced onto a sample through a PET window of the cryostat, together with incident X-rays I_0. The fluorescent X-rays were detected by a Lytle detector [8], whose intensity would be modulated in accordance with the change in the X-ray absorbance caused by modulated-light irradiation. Fluorescent X-ray signals, I_f, were divided into two after pre-amplifying with a picoammeter, one as the normal I_f and another for extraction and amplification of the modulating component, using a lock-in amplifier. Finally, I_0, I_f, and the output signal of the lock-in amplifier, I_{mod}, were collected with a counter/timer.

Because of the large difference between the absorption coefficients of X-rays and visible light, the light-modulated XAFS signal intensity becomes very small. Thus, much effort was paid

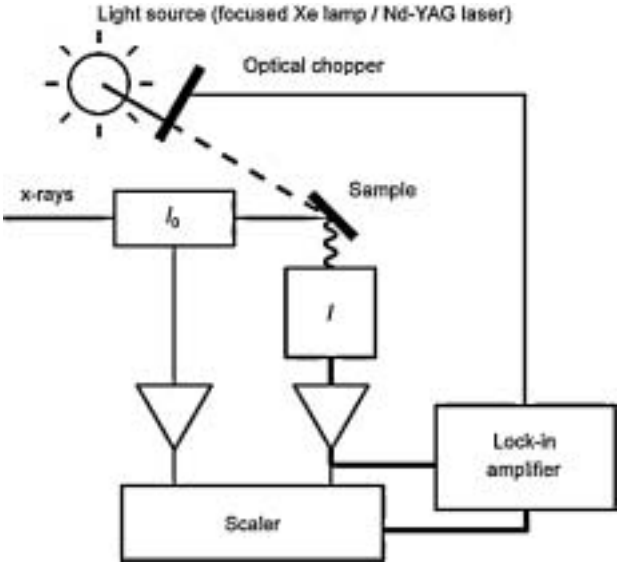

Fig. 1. Set-up for the light-modulated XAFS measurement.

*e-mail: ohta@chem.s.u-tokyo.ac.jp

to keep the noise level as low as possible. The Lytle detector was set in a soundproof box on a heavy base with vibration insulators made of silicone rubber and connected to the picoammeter with a low-noise cable to avoid vibration and electric noises, respectively. It was also essential to avoid signal fluctuations at each step of energy scanning caused by the monochromator. For this purpose, the signal counter was controlled by an external timer circuit to wait until the signal became stable. This elongated the measurement time, but improved the spectrum quality dramatically.

Light-induced spin transition compounds, $[Fe(pic)_3Cl_2]\cdot C_2H_5OH$ [9, 10], **1**, and $K_{0.4}Co_{1.3}[Fe(CN)_6]\cdot 4.2H_2O$ [11, 12], **2** were prepared according to the literatures. They both show spin transitions from low-spin (LS) to high-spin (HS) states at Fe and Co ions, respectively, which is induced by heat or light at low temperatures and accompanied by large changes of local geometric and electronic structures. Though the relaxation details have not been fully clarified yet, one of the Co-W analogue of **2** shows a first-order relaxation at X-ray-induced spin transition [13], while **1** shows a very complicated relaxation behaviour due to strong intermolecular interactions and the decay constant was estimated to be of seconds or subseconds at the applied temperatures [14, 15]. The samples were used as powders dispersed on Scotch tapes. Fe and Co K-edge XAFS experiments were carried out at Beamlines 9A [16] and 12C [17] in KEK-PF, using double-crystal Si(111) monochromators detuned by ~40%. The incident and transmitted X-rays were detected by ion chambers filled with N_2 and the fluorescent X-rays by a Lytle detector filled with Ar. Two types of the Lytle detectors, conventional and fast ones [8, 18], were used in the experiments. Data acquisition times were 2 s and 8 s for the conventional XANES and EXAFS measurement, respectively, and 20 s for the light-modulated spectra at the longest.

3. Results and discussion

Figure 2(a) shows the Fe K-edge XANES spectra of **1** at 30 K with and without white-light irradiation by a Xe lamp. Continuous light irradiation gave a similar spectrum (Fig. 2(a), solid line) to that of the pure HS phase at 300 K. It is reproduced as a linear combination of pure HS and LS spectra measured at 300 K and 30 K, respectively [9, 10], with the HS ratio of 0.88, assuming that the temperature dependence of XANES is negligible. Figure 2(b) shows the spectrum obtained by the light-modulation method. It is in good agreement with the difference spectra in Fig. 2(a), together with the EXAFS difference spectra in Fig. 3(a). Nd-laser irradiation at 532 nm gave an identical result. It was revealed that the light-modulated XAFS spectrum is detectable using our experimental set-up not only for the XANES but also for the EXAFS regions where only a small change is expected.

Figure 3(b) shows the EXAFS $k^3\chi(k)$ spectrum of the purely light-induced phase constructed from the difference spectrum in Fig. 3(a) using the HS/LS ratio obtained from the absorption difference at 7121 eV. It is roughly in good agreement up to $k \sim 6\,\text{Å}^{-1}$ with the HS spectrum at room temperature, indicating the structural similarity of the light-induced and high-temperature phases of **1**. Although the quantitative measurements should be achieved in the future, present result is very encouraging.

Figures 4(a) and (b) show the frequency dependence of the light-modulated XANES difference spectra $\Delta I_f/I_0$ at 30 K and 60 K, respectively. The signal intensity decreases monotonically upon faster modulation at 30 K, while at 60 K it is the strongest at

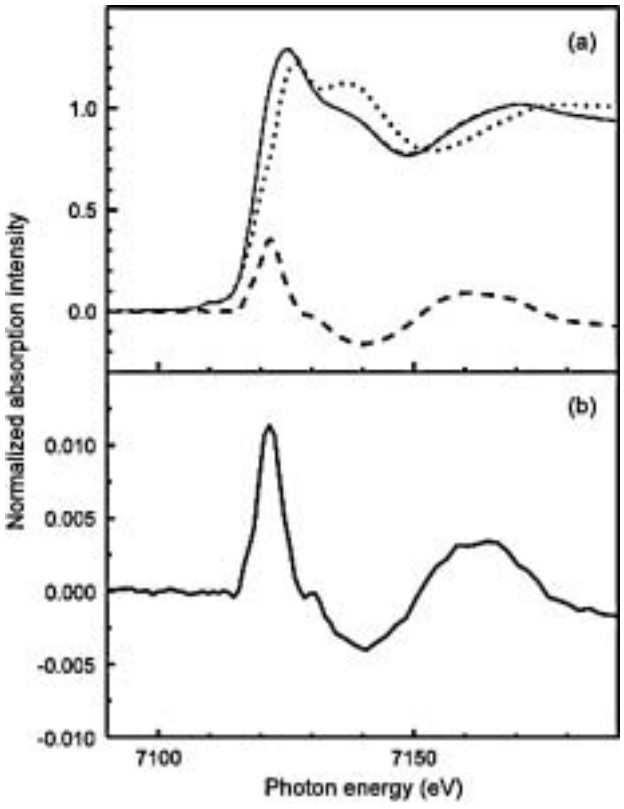

Fig. 2. Fe-K XANES spectra of **1** at 30 K (a) with and without Xe-lamp irradiation at 30 K (solid and dotted lines), and their difference (dashed line). (b) Fe-K XANES difference spectrum obtained by the light-modulated XAFS method with a modulation frequency of 10 Hz.

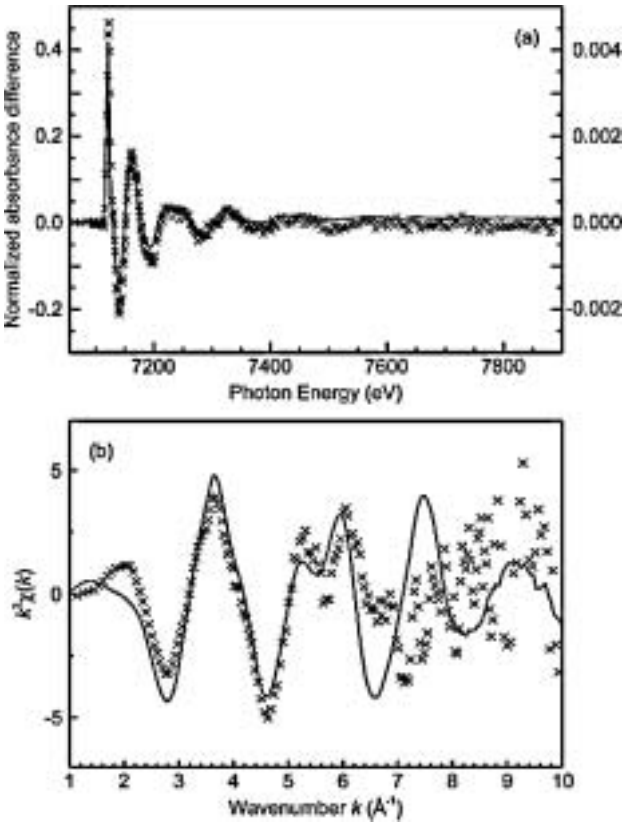

Fig. 3. (a) Fe-K EXAFS difference spectra of **1** at 30 K obtained by subtraction (solid line, left axis) and by the light-modulation method with a modulation frequency of 10 Hz (cross symbols, right axis). (b) Fe-K EXAFS $k^3\chi(k)$ of the room-temperature HS state (solid line) and EXAFS spectrum of the purely light-induced state at 30 K constructed from the light-modulated EXAFS spectrum in (a) (cross symbols).

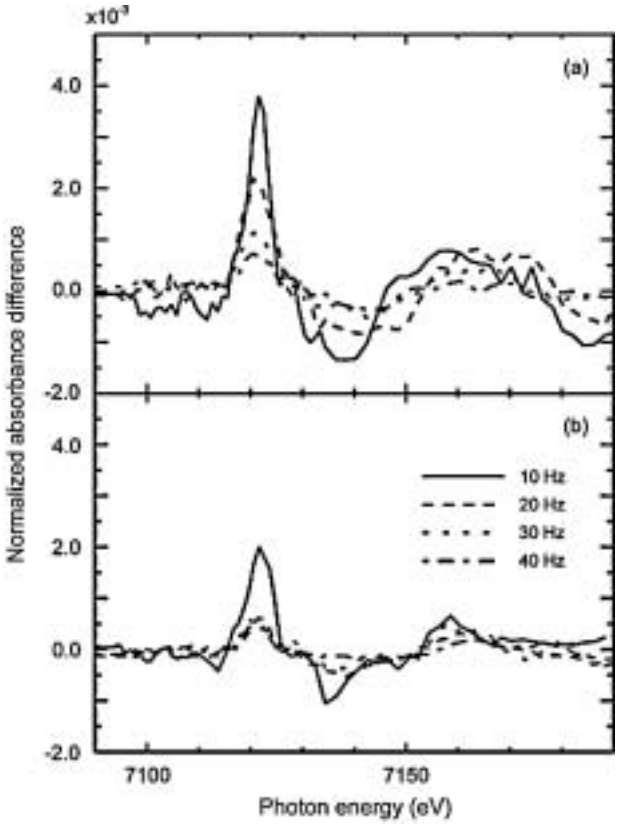

Fig. 4. Modulation-frequency dependence of Fe-K XANES spectra of **1** (a) at 30 K and (b) at 60 K. The fast-type Lytle detector was used with a phase shift of 180°.

10 Hz, becomes weaker at 20 Hz, and stays the same at higher modulation frequencies. The behaviour at 30 K is understood simply as a consequence of relatively slow relaxation to follow fast light modulation. On the other hand, thermally-induced transition is not negligible at 60 K, which results in a drastic decrease of the signal at 10 Hz. The temperature might also affect the photo-excited state and change the probability to transfer to the high spin state. This causes a different behaviour at higher frequencies from that at 30 K. It should be emphasized that the dependence of the modulation frequency enables us to discriminate the contributions with different time scales, light- and thermally-induced transitions in the present case. This is one of the advantages of the light-modulated XAFS method.

The detection limit of the light-modulation XAFS method would be the order of 10 ppm change of the edge jump, which corresponds the 10 μV change in a 1 V signal, as investigated using a prussian blue analogue, **2**. Spectrum subtraction gave an inaccurate result for such a small change, while the light-modulation method gave the same shape as that was expected from the temperature dependence of the XANES spectra of **2**. This demonstrates the superiority of the light-modulation method to the conventional subtraction method. The limiting factors are the high noise level in the experimental hall and the finite response rate of the ion-chamber detectors. However, we believe that the further development of the detectors would solve these problems, although noises coming from the X-ray beam itself cannot be avoided.

4. Conclusions

Present study demonstrates the applicability of the light-modulated XAFS spectroscopy as a method to study short-lived photoexcited states. Using two spin-transition compounds, changes caused by light-irradiation were detected successfully for both XANES and EXAFS, as a consequence of elimination of various noises. The modulation frequency change enables to study the relaxation process and to distinguish two components with different relaxation rates. The light-modulation XAFS method has the following advantages; (1) simple experimental set-up, which requires only a visible-light source, an optical chopper, a lock-in amplifier, and a conventional XAFS beamline, and (2) free from the ground-state components because the light-induced absorbance difference is directly detected. Although the current performance is enough for qualitative studies, more technical improvement is required for quantitative discussions such as the relaxation kinetics and detailed EXAFS analysis of light-induced structural changes.

Acknowledgements

The authors are grateful to Dr S. Emura (Osaka University) and Professor I. Watanabe (Osaka Women University) for fruitful discussions. Experimental support from Professor M. Nomura, Drs T. Obina and A. Koyama (KEK-PF), and Drs T. Uruga and H. Tanida (JASRI/SPring-8) are highly appreciated. The authors also thank Professors K. Hashimoto (The University of Tokyo) and O. Sato (KAST) for sample preparations, and Professor H. Okamoto (IMS) and Dr M. Suzuki (JASRI/SPring-8) for their help in instrumentation. The present work was performed under the approvals of the Photon Factory Program Advisory Committee (2000P019, 2001G319). One of the authors (K. O.) also appreciates the JSPS Research Fellowships for Young Scientists.

References

1. Thiel, D. J., Lîvinš, P., Stern, E. A. and Lewis, A., Nature **362**, 40 (1993).
2. Chance, M. R. *et al.*, Rev. Sci. Instrum. **64**, 2035 (1993).
3. Dent, A. J., Top. Catal. **18**, 27 (2002).
4. Chen, L. X. *et al.*, J. Chem. Phys. B **103**, 3270 (1999).
5. Mills, D. M., Lewis, A., Harootunian, A., Huang, J. and Smith, B., Science **223**, 811 (1984).
6. Chen, L. X., J. Electron Spectrosc. Relat. Phenomena **119**, 161 (2001).
7. Lakowicz, J. R., in 'Principles of fluorescence spectroscopy' (Plenum Press, New York, 1983), p. 95.
8. Lytle, F. W. *et al.*, Nucl. Instrum. Meth. **226**, 542 (1984).
9. Sorai, M., Ensling, J. and Gütlich, P., Chem. Phys. **18**, 199 (1976).
10. Sorai, M., Ensling, J., Hasselbach, K. M. and Gütlich, P., Chem. Phys. **20**, 197 (1977).
11. Sato, O., Einaga, Y., Iyoda, T., Fujishima, A. and Hashimoto, K., J. Phys. Chem. B **101**, 3903 (1997).
12. Yokoyama, T., Ohta, T., Sato, O. and Hashimoto, K., Phys. Rev. **B58**, 8257 (1998).
13. Yokoyama, T., Okamoto, K., Ohta, T., Ohkoshi, S. and Hashimoto, K., Phys. Rev. **B65**, 64438 (2002).
14. Romstedt, H., Hauser, A. and Spiering, H., J. Phys. Chem. Solids **59**, 265 (1998).
15. Ogawa, Y., *et al.*, Phys. Rev. Lett. **84**, 3181 (2000).
16. Nomura, M. and Koyama, A., J. Synchrotron Rad. **6**, 182 (1999).
17. Nomura, M. and Koyama, A., KEK Report **89**, 16 (1989).
18. Suzuki, M., Kawamura, N., Lytle, F. W. and Ishikawa, T., J. Synchrotron Rad. **9**, 99 (2002).

Physica Scripta. Vol. T115, 1053–1055, 2005

Anomalous Fine Structure in X-Ray Resonant Diffuse Scattering from Multilayers

A. Michel‡, M. Jaouen, A. Debelle, G. Abadias, C. Jaouen and M. Gailhanou*

Laboratoire de Métallurgie Physique, UMR 6630 du CNRS, Université de Poitiers SP2MI
Bd Marie & Pierre Curie, Téléport 2, BP 30179, 86962 Futuroscope Chasseneuil Cedex, France
*Laboratoire pour l'Utilisation du Rayonnement Electromagnétique Bât 209 D, Centre Universitaire de Paris-Sud, BP 34, 91898 Orsay Cedex, France

Received June 26, 2003; accepted December 4, 2003

PACS numbers: 61.10.Kw, 61.10.Ht, 68.35.Ct, 68.65.+g

Abstract

X-ray reflection is a well-known method for structural studies of multilayers. By measuring the specular reflectivity, the thicknesses, electron densities and interface roughness can be determined. On the other hand, the off-specular or diffuse scattering carries information about the lateral morphology and roughness of the interface. In particular, correlations of the interface roughness give rise to Resonant Diffuse Scattering (RDS). In this paper, we will show that RDS can be combined with the anomalous effect in order to obtain interfacial chemical information. Additionally we describe an experimental procedure that allows us to record anomalous RDS spectra exhibiting fine structures analogous to those observed in the well-known DAFS spectroscopy. Diffraction from Ni/Mo multilayers grown by ion beam sputtering are used to illustrate the method.

1. Introduction

Nowadays, much interest is devoted to multilayer systems due to their unique physical properties that make them attractive for optical, mechanical or electronic (magnetic recording, semiconductor devices) applications. These properties depend strongly on the structure of the stacking and more specifically on the interface between constituents (roughness, intermixing, etc...). Among others, X-ray reflectivity is a useful method for characterizing multilayers because it is sensitive to the refractive index and thus to the electronic density variations across the interfaces. This sensitivity to electronic density is enhanced in off-specular or Diffuse Scattering (DS) reflectivity experiments. In particular, the existence of Bragg DS peaks (Resonant DS: RDS) is explained by conformal roughness [1], e.g. when interfaces are strongly correlated to each other. In this contribution we will show that it is feasible to combine RDS and the anomalous effect using an experimental procedure analogous to the now well-established DAFS (Diffraction Anomalous Fine Structure) spectroscopy [2]. Such a method allows us to extract interfacial structural information at the atomic scale.

2. Experimental

The present study is focussed on a $[Ni_{22}/Mo_{12}]_{40}$ multilayer deposited on a Si (001) substrate using a direct ion beam sputtering method (primary Ar beam energy: 300 eV) which has been previously described [3]. The bilayer period Λ is 7.14 nm and the total thickness is 285.7 nm. High angle X-ray diffraction and high resolution transmission electron microscopy both give evidence [4] of a strong crystalline texture within the constituent layers, with the fcc Ni (111) planes being parallel to the bcc Mo (110) ones. The experiments were carried out at the Laboratoire pour l'Utilisation du Rayonnement Electromagnétique (LURE) at Orsay on the DCI storage ring at the H10 beam line. Its optical characteristics are described in ref. [5]. The specular reflectivity scan recorded at 8.1 keV, shown in Fig. 1, confirms the overall good quality of the multilayer since at least 8 Bragg peaks are observable within the investigated angular range. Fig. 2 shows the rocking curve, or ω scan, around the fourth Bragg peak. In that case, a single specular peak is seen as well as Yoneda wings on each side of the diffuse scattering intensity. However, when the grazing angle slightly shifts from the Bragg condition, a peak is still observable on the $\omega - 2\theta$ scan (insert in Fig. 1, fixed offset angle $\omega - \theta = -0.66°$). Such a rather intense Bragg diffuse scattering (the intensity ratio at the Bragg peak is around 13%)

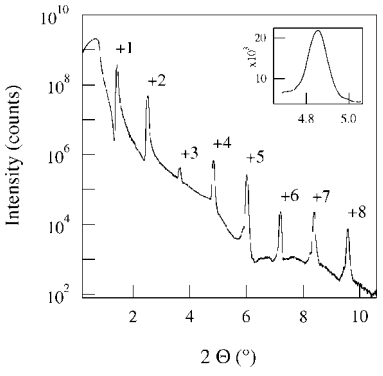

Fig. 1. Reflectivity profile for the $[Ni_{22}/Mo_{12}]_{40}$ multilayer sample recorded at 8.1 keV. Numbers indicate Bragg order. Insert: $\omega - 2\theta$ scan showing the RDS around the fourth Bragg order at the same photon energy (offset angle $\omega - \theta = -0.66°$).

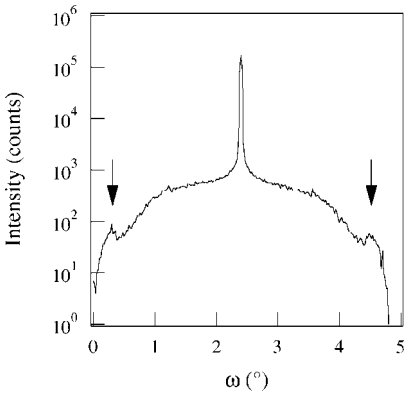

Fig. 2. Rocking curve (ω scan) around the fourth Bragg order of Fig. 1 at 8.2 keV. Arrows indicate the Yoneda wings.

‡ e-mail: Anny.S.Michel@univ-poitiers.fr

makes it possible to perform a DAFS-like experiment on RDS peaks. The presence of such RDS peaks attests the existence of a conformal roughness (lateral) within the multilayer since for small angles the variation of the q_z component of the scattering vector $\boldsymbol{q}$ is practically negligible so that an ω scan is equivalent to a q_x scan.

However one must take into account that the refractive index varies with the incident energy. Indeed, during a DAFS scan, one has to keep q and the angle $\psi = (\boldsymbol{q}, q_z)$ constant. It needs corrections for refraction that are given, according to the Snell-Descartes laws, by:

$$\cos(\omega) = \cos(\theta_c(\lambda))\cos(\omega_{int});$$
$$\cos(2\theta - \omega) = \cos(\theta_c(\lambda))\cos(2\theta_{int} - \omega_{int}) \quad (1)$$

where the index *int* is for angles internal to the sample, $\theta_c(\lambda)$ is the critical angle for total reflection determined from the specular reflectivity scan at the wavelength λ. These corrections have been included into the acquisition software procedures.

3. Data acquisition procedures

The raw RDS DAFS spectrum recorded at the Ni-K edge is shown in Fig. 3 where fine structures are clearly observed. However, the analysis needs to include the fluorescence effect, the contribution of which may become very important at low angles. The detector used to record these data is a Peltier cooled Si photodiode with an energy resolution which is rather poor (700 eV). Therefore each data point may include a fluorescent contribution that varies from point to point beyond the edge. The whole Multi Channel Analyzer (MCA) energy spectrum was recorded in the energy range 6–11 keV for each point of the incident energy and a fitting procedure was used to separate the different contributions to the spectrum. For each incident energy point, the MCA spectrum was fitted with Gaussian lines that account for the K_α and K_β fluorescent and elastic contributions (the ones of interest). During the fitting procedure the positions, intensities and widths of the K_α and elastic Gaussians are free to vary, while the position and intensity of the K_β line were fixed. Indeed the intensity ratio of the K_β and K_α lines can be calculated by taking into account the angle and energy dependant re-absorption of the fluorescence. A straightforward calculation gives:

$$\frac{I_\beta}{I_\alpha} = K\frac{\mu_E \sin(\varpi_e) + \mu_\alpha \sin(\varpi_i)}{\mu_E \sin(\varpi_e) + \mu_\beta \sin(\varpi_i)}\left[\frac{1 - e^{-\left(\frac{\mu_E}{\sin(\varpi_e)} + \frac{\mu_\beta}{\sin(\varpi_i)}\right)e_t}}{1 - e^{-\left(\frac{\mu_E}{\sin(\varpi_e)} + \frac{\mu_\alpha}{\sin(\varpi_i)}\right)e_t}}\right] \quad (2)$$

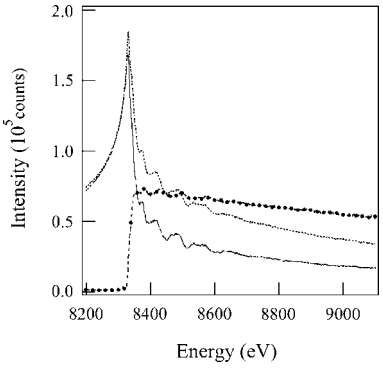

Fig. 3. Raw SCA DAFS (full line), pure elastic (dotted line) RDS DAFS and fluoresence (dashed line with diamonds) spectra at the Ni-K edge.

where $\varpi_i = \omega$ and $\varpi_e = 2\theta - \omega$ are the incident and exit angles, μ_E the absorption coefficient of the incident beam calculated according to the sample composition (μ_α is at E_{K_α}, μ_β at E_{K_β}), e_t its total thickness while K denotes the emission ratio K_β/K_α ($K = 0.1126$ for Ni). The pure elastic and fluorescence spectra retrieved using this fitting procedure are displayed in Fig. 3. This procedure works fairly well because the fluorescence is found to be nil below the Ni-K edge, while the elastic peak intensity is close to the intensity measured using a Single Channel Analyzer (SCA). It is obviously no longer the case beyond the edge since the SCA integrates a part of the fluorescence because of the too low energy resolution of the photodiode, whereas fitting the MCA gives good discrimination. Therefore the procedure proposed herein allows us to reconstruct a pure elastic DAFS spectrum which can be used to obtain the fine structure oscillations after making the necessary absorption correction.

4. Oscillatory component of the spectrum

The theory underlying RDS anomalous fine structure spectroscopy presented here is not yet established. However, the variation of q_z being very small for small angles, as a first approximation we can consider we are in specular reflectivity regime. In the kinematical limit, it has been shown [6] that the specular intensity scattered from Ni and Mo layers can be expressed as:

$$I(E) \propto |\rho_{Ni} f_{Ni}(E) - \rho_{Mo} f_{Mo}(E)|^2 \quad (3)$$

where ρ denotes the density and f the scattering factor for an atom. For the resonant Ni atoms, f_{Ni} can be split into a smooth and an oscillatory component:

$$f_{Ni}(E) = Z_{Ni} + f'_{Ni}(E) + i f''_{Ni}(E) + f''_{Ni}(E)\tilde{\chi}_{Ni}(E);$$
$$\tilde{\chi}_{Ni}(E) = \chi'_{Ni}(E) + i\chi''_{Ni}(E) \quad (4)$$

where Z is the atomic number, f' and f'' the real and imaginary parts of the bare atom anomalous corrections. $\chi(E)$ is the fine structure of interest of which the imaginary part is the EXAFS. Following Luo *et al.* [6], this oscillatory term can be expressed as:

$$\frac{I(E) - I_0(E)}{I_0(E)} = \frac{2\rho_{Ni} f''_{Ni}(E)\kappa_1}{\kappa_1^2 + \kappa_2^2}(\chi'_{Ni}(E) + \varepsilon\chi''_{Ni}(E)) \quad (5)$$

with $\kappa_1 = [\rho_{Ni}(Z_{Ni} + f'_{Ni}(E)) - \rho_{Mo}(Z_{Mo} + f'_{Mo}(E))$, $\kappa_2 = [(\rho_{Ni} f''_{Ni}(E)) + (\rho_{Mo} f''_{Mo}(E))]$ and $\varepsilon = \kappa_2/\kappa_1$. In Eq. (5), $I(E)$ is the measured intensity and $I_0(E)$ the smooth component of the intensity spectrum extracted from the experimental data using the method described in Ref. [7].

After normalization according to Eq. (5) and transformation in k-space, we obtain the oscillatory component $\chi(k) = (\chi'_{Ni}(k) + \varepsilon\chi''_{Ni}(k))$ of the RDS signal shown in Fig. 4. These results demonstrate that the oscillations above the edge are significant and representative of the absorption and scattering processes, even if this spectrum becomes noisy at high k values. It remains to isolate $\chi'_{Ni}(E)$ and $\chi''_{Ni}(E)$ that are related through Kramers-Kronig relations to obtain structural information using the EXAFS standard method for data analysis. Being out of the scope of the present contribution, these results will be presented in a forthcoming paper.

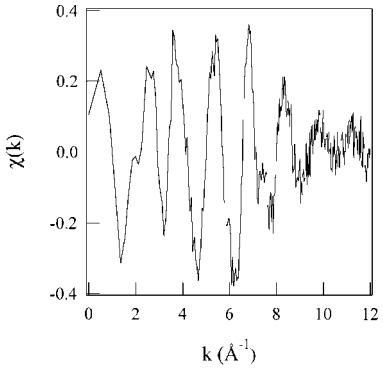

Fig. 4. Fine structure $\chi(k)$ of the elastic RDS DAFS spectrum of Fig. 3.

5. Conclusion

In this paper we have demonstrated that it is possible to perform DAFS-like experiments on Resonant Diffuse Scattering peaks. The feasibility of this new spectroscopy was illustrated with the example of a textured Ni/Mo multilayer sample. We have established a method for data acquisition that includes the reflectivity particularities of the off-specular diffraction. We also propose a method to remove the fluorescence using a fit of the whole detector spectrum at each point of the incident beam energy scan. It should be noted that such a method can be also used to obtain EXAFS spectra related to data recorded in the fluorescence mode.

References

1. Baumbach, T. and Mikulik, P., "X-ray and Neutron Reflectivity: Principles and Applications" (Springer-Verlag, Berlin, Heidelberg, New-York 1999), p. 234.
2. Sorensen, L. B., *et al.*, "Resonant Anomalous X-ray Scattering" (Elsevier Science, North-Holland, Amsterdam 1994), p. 389.
3. Abadias, G., *et al.*, Phys. Rev. B **65**, 212105 (2002).
4. Pacaud, J., *et al.*, "Polycristalline Metal and Magnetic Thin Films" (Materials Research Society, Pittsburgh 2001), p. G8.7. 1.
5. Gailhanou, M., *et al.*, Nucl. Inst. Meth. Phys. Res. A **467–468**, 745 (2001).
6. Luo, G. M., *et al.*, Phys. Rev. B **64**, 245404 (2001).
7. Proietti, M. G., *et al.*, Phys. Rev. B **59**, 5479 (1999).

Physica Scripta. Vol. T115, 1056–1058, 2005

Cadmium under High Pressure and High Temperature Conditions

M. Minicucci[1*], A. Trapananti[1], A. Di Cicco[1], S. De Panfilis[2] and G. Aquilanti[2]

[1]INFM and Dipartimento di Fisica, Università di Camerino, I-62032 Camerino (MC) Italy
[2]European Synchrotron Radiation Facility, B.P. 220, F-38043 Grenoble, France

Received June 26, 2003; accepted November 4, 2003

PACS numbers: 61.10.Ht, 61.25.Mv, 61.50.Ks, 81.30.Hd

Abstract

In this work liquid and solid cadmium has been investigated in a wide pressure and temperature range in order to provide new information about structure and transitions occurring in this metal. X-ray absorption, single-energy temperature scans and energy scanning X-ray diffraction data were collected in a 25–600 °C temperature and 0–5.8 GPa pressure range, exploiting the setup available at the ESRF-BM29 beam-line. Clear changes in the absorption spectra (measured at cadmium K-edge) and in the diffraction patterns, associated with the solid-liquid transition, allowed us to obtain an accurate measurement of the melting curve as a function of pressure. The structural data are compared with the few available calculations and X-ray scattering data on molten Cd at ambient pressure. High pressure data on liquid cadmium are reported for the first time and are essential to shed some light on the changes of the local structure induced by pressure.

1. Introduction

The divalent hexagonal closed packed (hcp) structured metal, cadmium, shows pressure dependences of several physical properties. Recently, it has been the subject of intense theoretical [1, 2, 3, 4] and experimental investigations [5, 6, 7, 8] mainly because it crystallizes in the hcp structure with an unusually large c/a axial ratio. This anomaly, common also to solid Zn, is usually related to the occurrence of an electronic topological transition (ETT) at high pressures and the existence of the ETT and its possible correlation with the observed anomalies is a debate still open. The structural change of this metal under pressure is itself of fundamental crystallographic interest. On the other hand, only a few measurements are available for what concerns the high-temperature behavior under pressure and even the melting curve. In the recent past, X-ray absorption spectroscopy (XAS) has been successfully used to investigate structural properties of liquid metals [9, 10] and in this context is able to give very accurate information. In particular the change in the shape of the XAS spectra at selected high-contrast energy points combined with energy scanning X-ray diffraction (ESXD), as a function of temperature at fixed pressure, is an excellent probe for locating phase transitions as shown by the recent extended use of single-energy X-ray absorption technique (SEXAD) [11]. This work presents experimental measurements of the melting curve, looking at the effect of pressure on the cadmium melting point. Moreover XAS data analysis results on solid and liquid cadmium are shown. First neighbor distance values and accurate reconstruction of pair distribution function of cadmium in its liquid phase as function of pressure are presented.

*Corresponding author. Fax +39 0737 402307; E-mail: marco.minicucci@unicam.it

2. Experimental

The experiments on solid and liquid cadmium were performed at the BM29 beam-line at the European Synchrotron Radiation Facility (Grenoble). Using an especially developed set-up [12], measurements were performed combining ESXD and XAS techniques for several temperatures up to the cadmium melting point at selected pressures. In particular, high resolution ESXD patterns were recorded by using a multi-channel detector collimator [13]. The conditions of high pressure (0.1–5.8 GPa) and high temperature have been obtained using a large volume Paris-Edinburgh (PE) press, having a 10 mm boron/epoxy toroidal gasket. The high toxicity of Cd metal together with the extreme experimental conditions of the measurements posed severe constraints. In fact the sample was prepared starting from micrometric powders of high-purity cadmium which were mixed with appropriate quantities of boron nitride and manipulated in a glove box under Ar atmosphere. Diffraction patterns of fine silicon powder mixed with the sample, were used as pressure markers. The powder obtained was pressed into a cylindrical shape of about 1.6 mm^3, insert into a graphite heater and then loaded in the toroidal gasket. The beamline was protected to avoid Cd contamination during the measurements, sealing the large volume PE press with a shield of kapton foil. The *in-situ* purification and characterization of the samples was preliminary performed increasing the temperature of the sample up to 500 °C and after comparing the XAS spectrum with a reference. The temperature was controlled by using a K type thermocouple inserted through the gasket.

3. Results and discussion

Low-noise K-edge XAS spectra of solid and liquid Cd were analyzed using multiple scattering (MS) calculations (GNXAS) [14, 15, 16]. Structural refinement is based on a fitting procedure that minimizes the difference between a model absorption signal and the experimental X-ray absorption raw data. Particular attention was paid to the modelling of the atomic background taking into account corrections associated with $[1s4p_{3/2}]$ and $[1s4p_{1/2}]$ double-electron excitation channels. The structural signal was calculated using an MS n-body expansion $\gamma^{(n)}$. In Fig. 1 we present the results of the fitting procedure of solid Cd at $T = 25$ °C and $P = 0.0$ GPa. Multiple-scattering two body $\gamma^{(2)}$ signals related to the first five neighbor shells around the Cd photoabsorbing site were calculated. The model and the experimental $k\chi(k)$ signals (lower part of figure) are in excellent agreement. The fitting procedure gives an average first-neighbor distance of 2.998 ± 0.005 Å in good agreement with the well known value for the lattice parameter $a = 2.97794$ Å at ambient pressure and $T = 25$ °C [17].

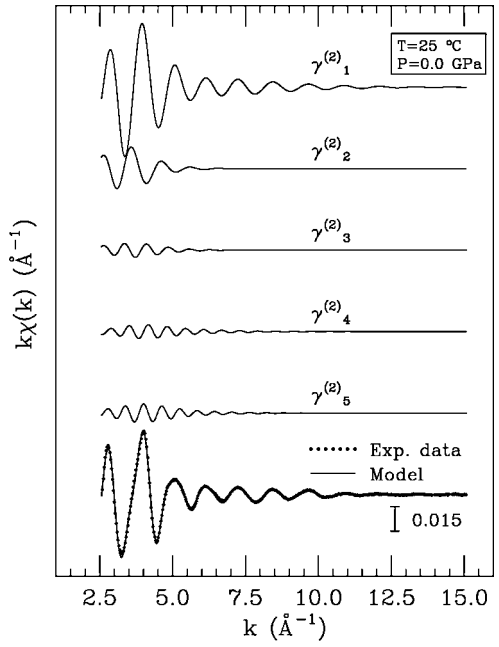

Fig. 1. Solid Cd EXAFS $k\chi(k)$ experimental data (Exp. data) at $T = 25\,^{\circ}$C and $P = 0.0$ GPa, compared with the best-fit multiple scattering $k\chi(k)$ signals. Individual two-body contributions associated with the first five neighbor shells are reported in the upper part of the figure, from top to bottom.

Our study has also been extended to the liquid phase of cadmium. The sensitivity of XAS to the local structure makes it possible to investigate the occurrence of phase transitions. In fact, we identified the solid-liquid phase transition of Cd, recording a series of precise measurements of the absorption coefficient at a single wavelength as a function of temperature at constant pressure, starting from 0.7 GPa up to 5.8 GPa. In Fig. 2 the single-energy scans performed at selected energy $E = 26.7145$ keV are shown. We chose this energy point because it appears more sensitive to the changes in the electronic density of unoccupied states occurring during the solid-liquid transition (see Fig. 3). The melting temperatures were determined looking at of the maximum

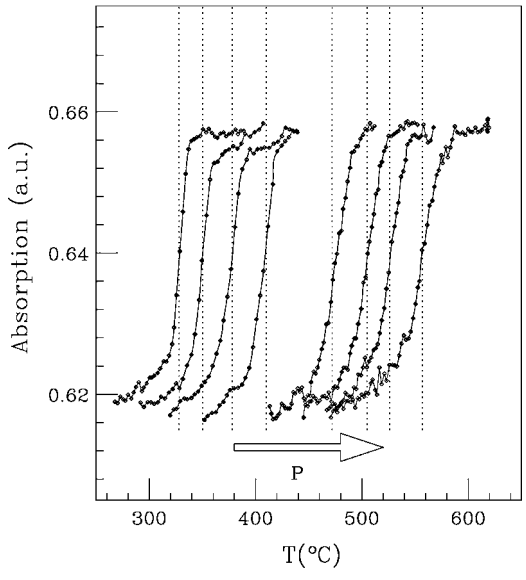

Fig. 2. Single-energy measurements as function of pressure. The pressure increases from left to right (0.7, 0.9, 1.3, 1.7, 3.0, 3.8, 4.6, 5.2 GPa respectively). The dotted lines define the temperatures of the melting-points.

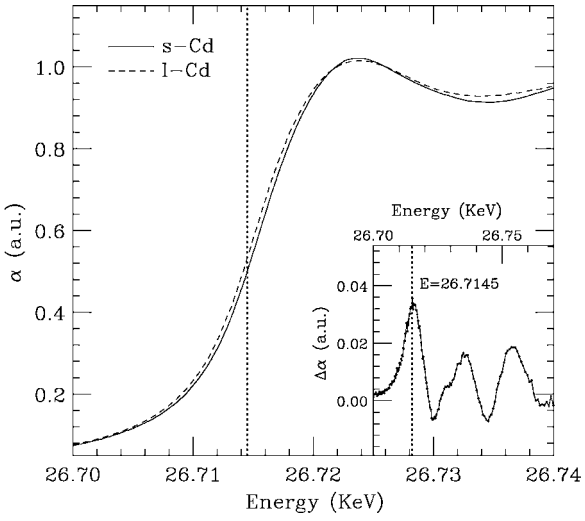

Fig. 3. XAS spectra of liquid (1-Cd) and solid cadmium (s-Cd) at $T = 440\,^{\circ}$C. In the inset we show the differences between the two spectra. We chose the SEXAD point $E = 26.7145$ keV as it corresponds to maximum variation of absorption during the solid-liquid phase transition.

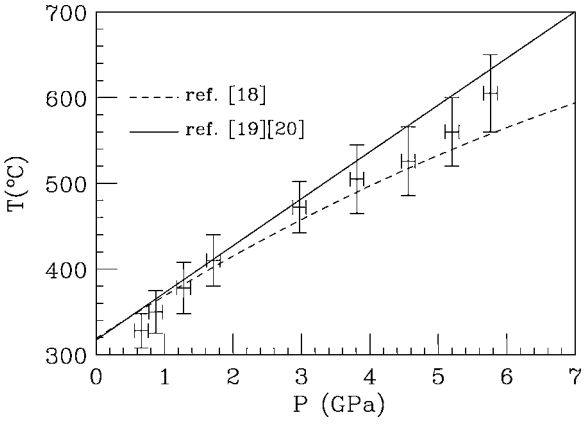

Fig. 4. Solid-liquid transition points determined by using SEXAD technique at constant pressures vs. melting curves previously determined [18, 19, 20].

of the derivative of SEXAD scans as a function of temperature and the results obtained are compared in Fig. 4 with previous data [18, 19, 20]. The results of our measurements lie in the region between the melting curves previously determined and are, substantially, in good agreement with existing determinations of the solid-liquid phase transition line. During the occurrence of the Cd liquid phase, we also recorded low-noise XAS spectra at the Cd K-edge. The XAS data analysis was performed following a scheme already applied in several molten systems [21, 22] using as a model an existing $g(r)$ previously determined [23] by XRD. The refinement of the short-range structure was carried out using an appropriate decomposition of the $g(r)$ model refining only the shape of the short-range peak. In fact, XAS technique is quite sensitive to the short-range distance but essentially blind to the long-range order. In Fig. 5, we report the refinement of $g(r)$ after the fitting procedure of the liquid Cd XAS spectrum at $T = 440\,^{\circ}$C and $P = 1.7$ GPa compared with the $g(r)$ model. In the inset we show the best fit of the liquid Cd at temperature and pressure cited above. The pair distribution function reconstructed after the refinement process, presents a shift toward larger distance of about 0.1 Å well outside our error bars. We found similar results from the data analysis of the whole set of liquid Cd XAS spectra at the various pressures.

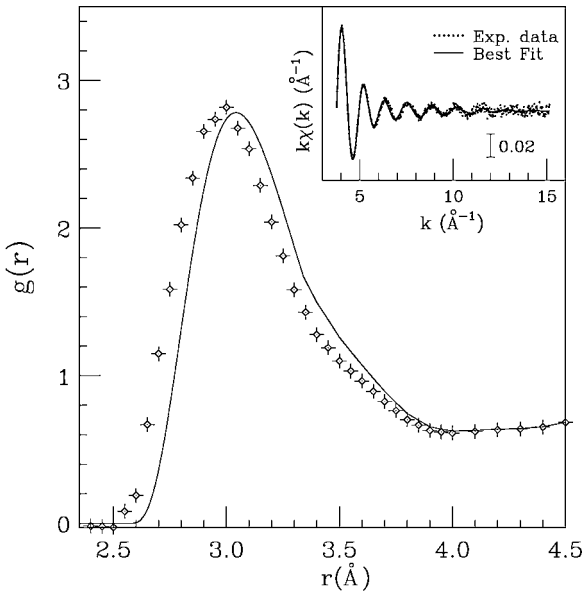

Fig. 5. Comparison between the pair distribution function of liquid Cd (solid line) at $T = 440\,^{\circ}\mathrm{C}$ and $P = 1.7\,\mathrm{GPa}$ determined by EXAFS and $g(r)$ from XRD (symbols) [23]. Inset: best fit (solid line) Cd K-edge EXAFS signal compared with experimental data of liquid Cd (dots).

4. Conclusions

Low-noise Cd K-edge EXAFS measurements of Cd in its solid and liquid phases were performed at BM29 beamline (ESRF). The cadmium melting curve was investigated using single-energy X-ray absorption temperature scan technique and X-ray diffraction, allowing to identify the melting temperatures at various fixed pressures. EXAFS data of solid Cd have been analyzed finding results in substantial agreement with previous diffraction studies. A detailed investigation of liquid Cd at various temperatures and pressures, has also been carried out using XAS technique. XAS data of liquid Cd have been analyzed using a pair distribution function derived from XRD measurements [23] as a starting point. The $g(r)$ obtained was compared with XRD results showing a shift of the foot of reconstructed $g(r)$ toward larger distances of about 0.1 Å. This result shows that XAS represent a powerful tool for investigating short-range structure, enhancing its complementarity with standard diffraction technique. Experiments were performed at the ESRF-BM29 beamline during allocated beamtime (HE-1407 project).

References

1. Novikov, D. L. *et al.*, Phys. Rev. B **59**, 4557 (1999).
2. Novikov, D. L., Freeman, A. J., Christensen, N. E., Svane, A. and Rodriguez, C. O., Phys. Rev. B **56**, 7206 (1997).
3. Lai, S. K., Wang Li and Tosi, M. P., Phys. Rev. A **42**, 7289 (1990).
4. Godwal, B. K., Meenakshi, S. and Rao, R. S., Phys. Rev. B **56**, 14871 (1997).
5. Godwal, B. K., Meenakshi, S., Rao, R. S. and Vijayakumar, V., J. Phys. Chem. Solids **59**, 747 (1998).
6. Takemura, K., Phys. Rev. B **56**, 5170 (1997).
7. Schulte O. and Holzapfel, W. B., Phys. Rev. B **53**, 569 (1996).
8. Schulte, O., Nikolaenko, A. and Holzapfel, W. B., High Pressure Res. **6**, 169 (1991).
9. Di Cicco, A., Aquilanti, G., Minicucci, M., Filipponi, A. and Rybicki, J., J. Phys.: Condens. Matter **11**, L43 (1999).
10. Filipponi, A., Di Cicco, A. and De Panfilis, S., Phys. Rev. Lett. **83**, 560 (1999).
11. Filipponi, A. *et al.*, J. Phys.: Condens. Matter **10**, 235 (1998).
12. Filipponi, A. *et al.*, Rev. Sci. Instr. **71**, 2422 (2000).
13. Filipponi, A. *et al.*, Rev. Sci. Instr. **74**, 2654 (2003).
14. Filipponi, A., Di Cicco, A. and Natoli, C. R., Phys. Rev. B **52**, 15122 (1995).
15. Filipponi, A. and Di Cicco, A., Phys. Rev. B **52**, 15135 (1995).
16. Di Cicco, A., Phys. Rev. B **53**, 6174 (1996).
17. "Landolt-Börnstein New Series," Group IV Vol. 6 (Berlin: Springer, 1987).
18. Kennedy, G. C. and Newton, R. C., "Solids under Pressure," (McGraw-Hill, New York, 1963).
19. Pistorius, C. W. F. T., High Temp.-High Pressures **7**, 451 (1975).
20. Millet, L. E., Thesis (Brigham Young Univ., Provo, Utah, 1968).
21. Filipponi, A., J. Phys.: Condens. Matter **6**, 8415 (1994).
22. Di Cicco, A. *et al.*, J. Phys.: Condens. Matter **8**, 10779 (1996).
23. Waseda, Y., "The Structure of Non-Crystalline Materials," (McGraw-Hill, New York, 1980).

Physica Scripta. Vol. T115, 1059–1061, 2005

Radial Distribution Function in Ionic Compounds at High Temperature and Pressure

E. Principi[1], M. Minicucci[1], S. De Panfilis[2] and A. Di Cicco[1]

[1]INFM, Università di Camerino, dip. di Fisica, via Madonna delle Carceri 62032, Camerino (MC), Italy
[2]ESRF Experimental Division – BM29, B.P. 220 38043 Grenoble Cedex, France

Received June 26, 2003; accepted November 4, 2003

PACS numbers: 61.10.Ht, 61.66.Dk, 61.20.Qg

Abstract

RbI and RbBr local atomic structure has been accurately investigated by using X-ray absorption spectroscopy (XAS) in a wide range of temperatures, covering the solid and the liquid phase. In the RbI case, the study has been extended also at high pressure up to 3.5 GPa. Rb, Br and I K-edge XAS spectra has been collected and analyzed using the GNXAS package. Multiple scattering and atomic background contributions have been taken into account, providing a very accurate determination of the first shell structural parameters. The experimental partial $g_{+-}(r)$ of the $RbBr_{1-x}I_x$ ionic alloy are also reported for the solid and the liquid phases, showing the characteristic bimodal distribution in pseudobinary alloys. These results can be very useful for testing the validity of theoretical ionic potentials employed in computer simulations.

1. Introduction

Structure and dynamics of alkali halides at high temperature have been widely studied using both theoretical and experimental means [1]. Standard experimental techniques which detect directly the structure factor $S(k)$, like neutron and X-ray scattering, have been successfully employed to investigate these systems. The radial distribution function $g_2(r)$ can be easily obtained from the $S(k)$ using the general relation

$$S(k) = 1 + \frac{4\pi\rho}{k}\int_0^\infty (g_2(r) - 1)\sin(kr)\,\mathrm{d}r. \quad (1)$$

Quite recently X-ray absorption spectroscopy (XAS) has offered a valid complement to the traditional diffraction techniques. Novel experimental devices [2] and data analysis procedures [3, 4] have been developed which have made possible to collect low noise XAS spectra of several liquid ionic compounds and to obtain very accurate structural information [5, 6, 7]. A relation similar to (1) holds for the EXAFS signal in the two body approximation

$$\chi(k) = \int_0^\infty 4\pi r^2 \rho g_2(r)\gamma^{(2)}(r,k)\,\mathrm{d}r, \quad (2)$$

where $\gamma^{(2)}(r,k)$ is the single scattering EXAFS signal, associated with the presence of a single atom at distance r from the photoabsorber, ρ is the number density [3, 4].

From (2) it follows that also $\chi(k)$ can be manipulated to reconstruct the radial distribution function $g_2(r)$. Therefore, in spite of several intrinsic differences in the nature of the $S(k)$ and the total EXAFS signal $\chi(k)$, both of them contain a similar structural information. However, the sensitivity of the XAS technique is limited only to few Å around the selected photoabsorber. In fact the amplitude of $\gamma^{(2)}(r,k)$ decreases exponentially to zero, due to the short photoelectrons mean free path. Nevertheless this is sufficient to define with excellent precision the first $g_2(r)$ peak. On the other hand the $S(k)$ contains a complete information about the short and long range order, but the structural details of the first shell are limited by the low values of k accessible in the standard diffraction experiments ($k_{max} \sim 8$ Å^{-1} for a Cu X-ray tube). Only very recently [8] the high real-space resolution measurements performed by means of synchrotron radiation, have made accessible the high k region up to 45 Å^{-1}.

These complementary characteristics suggest the possibility to combine EXAFS and XRD in the study of high disordered systems, like molten ionic compounds and alloys. In particular, EXAFS can be useful to increase the precision of $g(r)$ obtained in XRD experiments or produced by numerical simulations (MD, MC), refining their first peak. A simple but powerful method [3, 4] proposed by A. Filipponi and implemented in the GNXAS package [9, 10], makes this combination possible.

The need of employing the XAS technique becomes crucial especially in the investigation of more complex systems like the pseudobinary ionic alloys [11]. These salts are characterized by the presence of two different atomic species in the first coordination shell, which cause a bimodal bond length distribution behavior, not detectable by the standard diffraction techniques. Diffraction can provide only a weighted average of these distributions (Vegard's law), while EXAFS is able to discriminate between them and makes possible to reconstruct accurately the first peak of the two partial $g_{+-}(r)$. In the next sections we show an example of the advantages offered by the XAS technique in the investigation of the local order in ionic compounds and alloys. Reconstructed $g_{\text{Rb-Br}}(r)$ and $g_{\text{Rb-I}}(r)$ of solid and liquid RbBr, RbI and $RbBr_{1-x}I_x$ are presented, which are related to the first shell single scattering EXAFS signals.

2. Experimental and data analysis

The measurements have been realized at the European Synchrotron Radiation Facility (ESRF), at the BM29 XAS-ESXRD beamline [12]. The high purity samples have been finely grounded in a mortar, mixed in a C inert matrix and put into an high vacuum furnace [2] designed for high temperature XAS experiments. The $RbBr_{1-x}I_x$ alloys have been obtained by melting the two starting compounds into suitable quartz ampules under vacuum. The high pressure RbI experiment has been realized by means of a "Paris-Edinburgh" press. In the latter case, the samples have been mixed with a BN matrix and placed inside a 10 mm boron gasket. The XAS spectra have been collected both at the Rb K-edge and at the anions K-edge. The XRD set up [13] has allowed us to verify the melting of the samples and to detect the peaks position of the calibrant in the high pressure experiment. The data analysis has been performed using the GNXAS package, taking into account the contribution of the double electron excitations and the multiple scattering related to the triangular configurations

present in the cubic ionic lattices. Although the amplitude of the EXAFS signals is low in ionic compounds, the structural data obtained with the GNXAS analysis are particularly accurate, due to the double (and also triple) K-edge simultaneous fitting [11]. The fitting procedure of the XAS spectra, has been realized varying three structural parameters, namely, the first neighbor average distance (R), its variance (σ^2) and the skewness (β). Both in the solid and in the liquid case the first $g_{+-}(r)$ peak has been reconstructed using an asymmetric function dependent on the latter structural parameters, which express the probability of finding an atom at distance r from the photoabsorber:

$$p(r) = \frac{2}{\sigma|\beta|\Gamma(4\beta^{-2})}\left(\frac{4}{\beta^2}+\frac{2(r-R)}{\sigma\beta}\right)^{4\beta^{-2}-1} \cdot\exp\left[-\left(\frac{4}{\beta^2}+\frac{2(r-R)}{\sigma\beta}\right)\right], \quad (3)$$

where $\Gamma(x)$ is the Euler's Gamma function. In the liquid cases a "tail" [3] obtained by elaborating available numerical simulations [14, 15] has been added to the first peak.

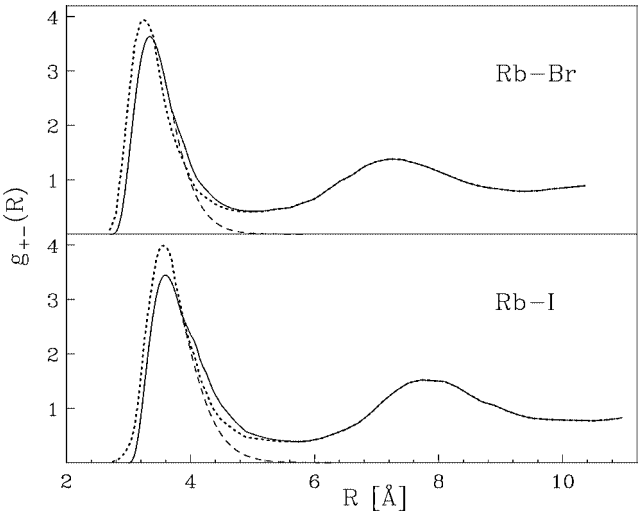

Fig. 2. Partial radial distribution of liquid RbBr ($T \sim 1000$ K) and RbI ($T \sim 950$ K) calculated respectively by MD [14] and MC [15] (dotted lines). EXAFS-refined curves are shown as solid lines. The first peaks calculated by GNXAS are drawn as dashed lines.

3. Solid and liquid RbBr, RbI and RbBrI

The first shell structural parameters in solid RbBr and RbI are shown in figure 1. Increasing the temperature, the first neighbor distance detected by EXAFS is found to be larger than the one obtained with XRD [16]. This is due to the positive orthogonal contribution of the thermal vibrations respect to the bonding direction, which are detectable only by EXAFS. Both the variance and the skewness increase monotonically with the temperature, indicating clearly that the thermal disorder and the asymmetry of the bond length distribution increase. Our data agree with previous low temperature [17] and room temperature [18] measurements. Moreover, in accord with the Lindemann criterion [19], the values of the thermal lattice vibrations just below the melting point ($T_m^{\mathrm{RbBr}} = 966$ K, $T_m^{\mathrm{RbI}} = 920$ K) are roughly 1/10 of the bond length.

In figure 2 the partial $g_{+-}(r)$ of RbBr and RbI are calculated respectively by Molecular Dynamics [14] and Monte Carlo [15] numerical methods. The EXAFS analysis allows us to refine the first shell peak of the $g_{+-}(r)$ (dashed lines) introducing the experimental structural parameters into the formula (3). It is evident that the simulations (dotted lines) overestimate the penetration of the first neighbors toward the central ion located at $R = 0$ Å. This points out the need of choosing more repulsive potentials in the simulations.

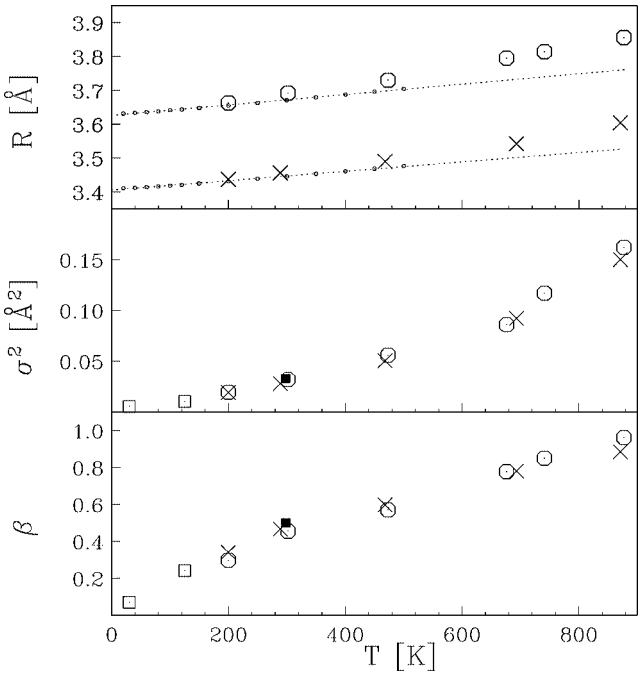

Fig. 1. Structural first shell parameters of solid RbBr (crosses) and RbI (circles) obtained from the EXAFS analysis. *Upper panel*: XRD data from [16] (small circles), fitted linearly (dotted lines). *Central and lower panel*: EXAFS data from [17] (empty squares), [18] (black squares).

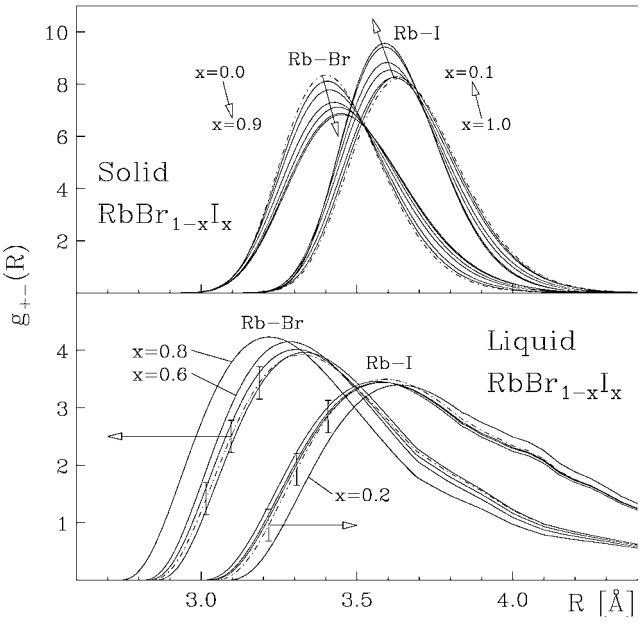

Fig. 3. Bimodal behavior of the first neighbor distance distribution in the $RbBr_{1-x}I_x$ alloy varying the concentration of I^- (equal to x) and Br^- (equal to $1-x$) anions. The dot-dashed lines indicate the RbBr ($x = 0$) and RbI ($x = 1$) compounds. The arrows indicate the trend of the $g_{\mathrm{Rb\text{-}Br}}(r)$ increasing x, and the trend of the $g_{\mathrm{Rb\text{-}I}}(r)$ increasing $1-x$. *Upper panel*: $x = 0.0, 0.1, 0.2, 0.4, 0.6, 0.8, 0.9, 1.0$. *Lower panel*: $x = 0.0, 0.2, 0.4, 0.6, 0.8, 1.0$; the error bars are applied to the $x = 0.0, 1.0$ cases.

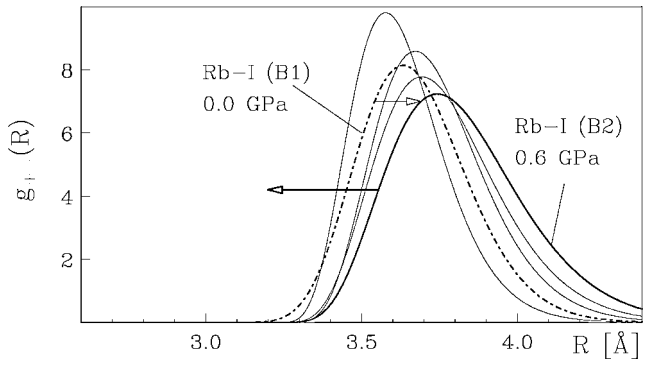

Fig. 4. RbI high pressure phase transition at room temperature. Dot-dashed line: $g_{\text{Rb-I}}(r)$ of RbI with the NaCl-type lattice (B1) at ambient pressure. Solid lines: $g_{\text{Rb-I}}(r)$ of RbI with the CsCl-type lattice (B2) at higher pressures (0.6, 1.5, 2.2, 3.5 GPa). The arrow indicate: the B1-B2 transition (right arrow), the B2 peak trend increasing the pressure (left arrow).

In figure 3 the two partial radial distributions $g_{+-}(r)$ of the $RbBr_{1-x}I_x$ alloy are shown at various concentrations x [11]. They clearly remain distinct varying the stoichiometry of the alloy (bimodal behavior) both in the solid (RT) and in the liquid phase. In the liquid case varying x both the $g_{+-}(r)$ distributions can be considered constant inside the experimental uncertainty (errors bars in figure 3). Nevertheless at the extreme concentrations, an evident shift in the $g_{+-}(r)$ positions is detectable. This effect suggest that the small Br^{-1} anions tend to approach the Rb^+ cations at (at $x = 0.8$), while the larger I^- anions behave in the opposite manner (at $x = 0.2$). This phenomenon, still not completely understood, could be caused by an effective charge screening [11]. In fact the high concentration of Br^- around the Rb^+ ions, can reduce the positive charge of the cations allowing the elongation of the Rb-I bonds. On the other hand, the high concentration of I^- at greater distances from the cations, could compress the Rb-Br distances. In the solid alloy the presence of the lattice constraints prevents this anomalous behavior at extreme concentrations preserving the homogeneous distribution of charge. Nevertheless the overall effect induced by the structural disorder on the lattice potential, is able to partially overcome the natural values of R and σ^2 (dot-dashed lines in figure 3). In fact a gradual increase of bond length and variance is present in $g_{\text{Rb-Br}}(r)$ increasing x. An opposite trend is followed by the $g_{\text{Rb-I}}(r)$ increasing $1 - x$. The intensity of this gradual evolution of the partial radial distributions, depends on the chemical characteristics of the bonds and on the lattice "rigidity" which define the topological rigidity parameter a^{**} [20, 21], with $a^{**} \sim 0.65$ in the $RbBr_{1-x}I_x$.

4. Solid RbI at high pressure

The well known RbI solid structural phase transition at low pressure $P_c = 0.4$ GPa [22, 23] is shown in figure 4, where the reconstructed $g_{\text{Rb-I}}(r)$ are calculated at the pressures of 0.0, 0.6, 1.5, 2.2, 3.5 GPa. The transition at P_c is detectable observing the change in shape and position of the first peak of the $g_{\text{Rb-I}}(r)$, due to the variation of the coordination number and the structural parameters (R, σ^2 and β) presented in table I. In fact upon the transition the lattice goes from the B1/NaCl-type structure (6 neighbors) to the B2/CsCl-type structure (8 neighbors), with a sudden increase of the number density ($\rho_{(0\,\text{GPa})} \simeq 0.020\,\text{atoms/Å}^3$, $\rho_{(0.6\,\text{GPa})} \simeq 0.023\,\text{atoms/Å}^3$) associated with an evident volume compression ($V_{(0.6\,\text{GPa})}/V_{(0\,\text{GPa})} \simeq 0.82$).

Table I. *First shell structural parameters in RbI upon pressurization at room temperature. N is the coordination number.*

pressure	N	R[Å]	σ^2 [Å^2]	β	phase
0.0 GPa	6	3.692(5)	0.033(1)	0.46(5)	B1
0.6 GPa	8	3.849(5)	0.054(1)	0.72(5)	B2
1.5 GPa	8	3.789(5)	0.044(1)	0.72(5)	B2
2.2 GPa	8	3.756(5)	0.035(1)	0.72(5)	B2
3.5 GPa	8	3.646(5)	0.025(1)	0.72(5)	B2

5. Conclusions

The XAS technique is a powerful tool to investigate the local order in high disordered matter. Here a method to reconstruct the $g_{+-}(r)$, starting from the EXAFS structural data has been proposed, which allows us to combine our results with the usual information provided by XRD or by theoretical simulations (MD, MC). Although a good understanding of structural disorder in solid ionic alloys has been reached during the last decade, further experimental and theoretical efforts have to be devoted to comprehend details and causes of the effects observed in liquid ionic alloys.

References

1. Rovere, M. and Tosi, M. P., Rep. Prog. Phys. **49**, 1001 (1986).
2. Filipponi, A. and Di Cicco, A., Nucl. Instr. & Meth. Phys. Res. B **93**, 302 (1994).
3. Filipponi, A., J. Phys.: Condens. Matter **6**, 8415 (1994).
4. Filipponi, A., J. Phys.: Condens. Matter **13**, R23 (2001).
5. Di Cicco, A. *et al.*, J. Phys.: Condens. Matter **8**, 10779 (1996).
6. Minicucci, M. and Di Cicco, A., Phys. Rev. B **56**, 11456 (1997).
7. Di Cicco, A., Taglienti, M., Minicucci, M. and Filipponi, A., Phys. Rev. B **62**, 12001 (2000).
8. Petkov, V. *et al.*, Phys. Rev. Lett. **83**, 4089 (1999).
9. Filipponi, A., Di Cicco, A. and Natoli, C. R., Phys. Rev. B **52**, 15122 (1995).
10. Filipponi, A. and Di Cicco, A., Phys. Rev. B **52**, 15135 (1995).
11. Di Cicco, A., Principi, E. and Filipponi, A., Phys. Rev. B **65**, 212106 (2002).
12. Filipponi, A. *et al.*, Rev. Sci. Instrum. **71**, 2422 (2000).
13. Filipponi, A. *et al.*, Rev. Sci. Instrum. **74**, 2654 (2003).
14. Copley, J. R. D. and Rahman, A., Phys. Rev. A **13**, 2276 (1976).
15. Baranyai, A., Ruff, I. and McGreevy, R. L., J. Phys. C: Solid State Phys. **19**, 453 (1986).
16. Pautamo, Y., Ann. Acad. Sci. Fennicae, Ser. A VI **129**, 45 (1963).
17. Frenkel, A. I. and Rehr, J. J., Phys. Rev. B **48**, 585 (1993).
18. Di Cicco, A., J. Phys. IV **7**, C2 (1997).
19. Lindemann, F., Z. Phys. **11**, 609 (1910).
20. Cai, Y. and Thorpe, M. F., Phys. Rev. B **46**, 15872 (1992).
21. Thorpe, M. F. and Garboczi, E. J., Phys. Rev. B **42**, 8405 (1990).
22. Cohen, A. J. and Gordon, R. G., Phys. Rev. B **12**, 3228 (1975).
23. Asaumi, K., Suzuki, T. and Mori, T., Phys. Rev. B **28**, 3529 (1983).

Physica Scripta. Vol. T115, 1062–1064, 2005

Real and Imaginary Parts of the Anisotropic Atomic Factor near the Fe K-Edge: Comparison Between two Theories and Experiment for Pyrite

J. Kokubun[1], K. Ishida[1], D. Cabaret[2], R. V. Vedrinskii[3], V. L. Kraizman[3], A. A. Novakovich[3], E. V. Krivitskii[3] and V. E. Dmitrienko[2,4*]

[1]Faculty of Science and Technology, Tokyo University of Science, Noda, Chiba 278-8510, Japan
[2]Laboratoire de Minéralogie et Cristallographie, Universités Paris VI et Paris VII, 4, place Jussieu, Paris Cedex 05, 75252, France
[3]Rostov State University, Rostov-Don, 344090 Russia
[4]A.V. Shubnikov Institute of Crystallography, Moscow, 119333, Russia

Received June 26, 2003; accepted November 19, 2003

PACS numbers: 61.10.Nz, 61.50.Ah, 61.10.−i, 71.90.+q

Abstract

The real and imaginary parts of the anisotropy of the iron atomic scattering factor are experimentally determined as functions of the X-ray energy near the iron K-edge in the FeS_2 (pyrite) crystal. The anisotropy is a result of a deformation of electronic states induced by local asymmetry of atomic environment of iron atoms in this cubic crystal and provides a quantitative measure of that deformation. Some Bragg reflections, otherwise forbidden by screw-axis or glide-plane symmetry operations, are caused by this anisotropy and their structure factors are proportional to the anisotropy. The energy spectra and azimuthal angle dependence of the anisotropy-induced "forbidden"' reflections is studied and the phase of the anisotropy is determined from an interference of the "forbidden" reflections with different multiple-wave reflections. The energy dependence of the real and imaginary parts of anisotropy is shown to be in good agreement with theoretical curves calculated within two different approaches (the full multiple scattering method employing cluster muffin-tin potential and the pseudopotential *ab initio* calculations). It is found that the anisotropy is much more sensitive to atomic environment and to the theoretical parameters than the average absorption coefficient.

1. Introduction

Only recently it was recognized that the resonant X-rays diffraction can be applied for rather sophisticated studies of magnetic and electronic structure of crystals [1, 2, 3, 4]. In most cases, the contribution of the magnetic and electronic structure effects are rather small in comparison with conventional X-ray scattering. However, this contribution is anisotropic and it is strongly enhanced in the resonant region near absorption edges of atoms, that is, it depends on frequency and polarizations of diffracting beams, on the anisotropy of atomic environment, and on the orientation of the magnetic and orbital moments. Owing to this anisotropy, one can use a very helpful tool to observe those small effects, the so-called "forbidden" reflections. Those reflections are forbidden due to some symmetry operations, like glide-planes and/or screw axes, but they can be excited just because of the anisotropy of X-ray suseptibility induced by magnetic ordering and/or by deformed electronic states of atoms.

The physical reason for these reflections is that the atomic scattering amplitudes (called usually the atomic scattering factors (ASF)) and the corresponding structure factors become tensor in XAFS regions. In other words, ASF depends on the polarizations and wave vectors of the initial and diffracted waves. Using different incident directions and different polarizations one can measure all the tensor components of the structure factors and obtain this way detailed information about the deformed electronic states and magnetic ordering.

In the absence of the magnetic ordering, the deformations of the electron wave functions are induced only by the asymmetrical configuration of neighboring atoms. The "forbidden" reflections of this type were first predicted and observed by Templeton and Templeton [5, 6] and a phenomenological theory of the resonant diffraction was developed in the dipole-dipole approximation [7, 8]. Since that time the "forbidden" reflections were observed in many crystals and several papers in this Proceedings are devoed to this phenomenon [9, 10].

However, similar to conventional reflections, the information available from "forbidden" reflections is restricted by the so-called *phase problem*: one can usually measure only intensity of a reflection whereas the information about its phase is lost. The phase is sensitive to the distortions of atomic wave functions and therefore it would be important to measure it. One method to do this is the interference between the "forbidden" reflections and the multiple-wave contribution from nonforbidden reflections. This interference appears for some orientations when the crystal is rotated around the reciprocal lattice vector of the "forbidden" reflection. The intensity of the "forbidden" reflection changes drastically in the region of the interference and depends on the relative phase of the "forbidden" and non-forbidden reflections. Supposing the phases of non-forbidden reflections known, one can measure this way the unknown phase of the "forbidden" reflection. Up to now there are only two works on the phase of the "forbidden" reflections: the preliminary studies of the phase of the anisotropy as a function of the X-ray energy near the iron absorption edge in FeS_2 [11] and the measurement of the phase of the 006 reflection in Ge for a fixed X-ray energy [12].

In this paper, a study of the real and imaginary parts of the Fe atomic factor in the pyrite, FeS_2, is presented. Section 2 describes the multiple-wave method used for the experimental solution of the phase problem. Then, in sections 3 and 4, different theoretical approaches are discussed and the comparison between theoretical and experimental spectra is presented in section 3.

2. Experimental

In the pyrite crystals, four equivalent Fe atoms are at positions with threefold symmetry $\bar{3}$ but the orientations of the corresponding threefold axes are different. Just this difference is responsible for

*dmitrien@ns.crys.ras.ru

the forbidden reflections and their structure factor is proprotional to the anisotropy $f_{||} - f_{\perp}$ where $f_{||}$ and $f_{\perp}$ are the eigenvalues of the tensor atomic factor f corresponding to directions parallel and perpendicular to the threefold axis.

Experimentally, one can probe only the reflection intensity for different polarizations of the incident and reflected beams. The intensity is proportional to the absolute value of the structure factors so that the phase is lost. In the case of the forbidden reflections, the structure factor F_H is proportional to the anisotropy of the atomic scattering factors of resonant atoms, and it would be very important to have access to the phase of the anisotropy.

The well known solution of this phase problem consists in exploring the interference between the reflection with unknown phase and a multiple-wave reflection with the known phase (see a survey in [13]). In the vicinity of the multiple-wave reflection, the intensity of the forbidden reflection contains a term proportional to $F_{\boldsymbol{H}} F^*_{\boldsymbol{H}-G} F^*_{\boldsymbol{G}}$ where $F_{\boldsymbol{G}}$ and $F_{\boldsymbol{H}-G}$ are the known structure factors of non-forbidden reflections $\boldsymbol{G}$ and $\boldsymbol{H} - G$. From the measured value of this term it is possible to calculate the phase of $F_{\boldsymbol{H}}$ and hence the real and imaginary part of $f_{||} - f_{\perp}$.

The theory of this effect was developed for FeS_2 in Ref. [15] where the best geometries for the observation were found. In the present work, the intensity of the 001, 003, and 011 forbidden reflection were measured at the Tsukuba Photon Factory and the real and imaginary parts of $f_{||} - f_{\perp}$ were found for the photon energies from 7105 to 7165 eV.

3. Muffin-tin (MT) calculations

The calculations of Fe K-edge anomalous atomic scattering factor (ASF) and intensities of the "forbidden" reflections for the FeS_2 crystal are performed by the one-electron multiple scattering Green's function method [14, 16]. The standard expression for the anomalous contribution into X-ray atomic scattering amplitude [24], determined in dipole-dipole approximation, is employed. The computer code was developed earlier at Rostov State University by A. A. Novakovich. A cluster muffintin (MT) approximation for the crystalline potential is used. The cluster MT potential is constructed by the same method which was successfully employed earlier for the XANES calculations [17, 18, 19, 20]. According to this method the atomic electron densities are calculated by the Herman-Skillman code [21] using the spin-independent local $X\alpha$-potential with the α-parameter determined by K. Shwartz [22].

The electron configurations of all the atoms, excluding the scattering one, are considered to be the same as those of free atoms. Taking into account that the scattering atom is excited at the intermediate stage of the anomalous X-ray scattering process we consider the electron configuration of this atom to contain 1s hole and additional screening 3d-shell charge. The incomplete screening model is used in the present calculations just as in the XANES calculations [17, 18, 19, 20], and the screening charge is assumed to be equal to 0.8 electrons. The atomic potentials used for the virtual photoelectron Green's function computations are considered to be spin independent and are determined through the free atom electron densities, calculated by the Hermann-Skillman code. A decreased value of the α parameter ($\alpha = 0.6$) is used for calculating these potentials [17, 18, 19, 20]. The MT zero level is chosen at -0.5 Ry relatively to the vacuum zero. As in the case of the XANES calculations, we consider the potential to be equal to MT-zero everywhere outside atomic spheres. The potential inside each atomic sphere is considered to be a sum of the corresponding free atom potential and a fixed energy shift ΔE, which is an adjusting parameter, determined so as to achieve the best agreement with the experiment. We consider the shifts to be acceptable if they do not exceed 0.5 Ry. The radii of the atomic MT spheres are chosen so as to exclude a discontinuity at the boundaries of the neighboring atomic spheres. In the case of the pyrite we obtain: $R_{Fe} = 1.263$ Å, $R_S = 1.11$ Å.

To include the processes of the photoelectron–hole pair decay, caused by many-electron effects, we calculate the Green's function for a complex valued energy parameter E. The imaginary part of E determining the energy-dependent width $\Gamma(E)$ of the electron-hole excitation state is a sum of the 1s hole width $\Gamma_h = 1$ eV [23] and the photoelectron one. The latter is considered to be equal to zero near the conduction band bottom and to increase rapidly with the photoelectron energy growth.

4. Full potential (FP) calculations

We performed the Full Potential (FP) calculations by using the method developed by Taillerfumier *et al*. [25, 26]. This method is a reciprocal-space scheme initially dedicated to the calculation of X-ray Absorption Near-Edge Structure at K or L edge. Since the theory is detailed in Ref. [25], only its main aspects are recalled here. The method uses norm-conserving Troullier-Martins [27] pseudopotentials. The pseudo-wave functions are expanded in a plane wave basis set. The scheme allows the reconstruction of the *all electron* wave functions by using the projector augmented wave method of Blöchl [28]. The method incorporates a recursive algorithm [29], that permits to transform an Hermitian matrix (here the pseudo-Hamiltonian) into a symmetric tridiagonal form, and to write the absorption cross section, σ, as a continued fraction [30]:

$$\sigma(\omega) = -4\pi\alpha\hbar\omega \times \mathcal{J}m \cfrac{\langle\tilde{\varphi}_{\boldsymbol{R}_0}|\tilde{\varphi}_{\boldsymbol{R}_0}\rangle}{a - E - \mathrm{i}\gamma - \cfrac{b}{a - E - \mathrm{i}\gamma - \cfrac{b}{a - E - \mathrm{i}\gamma - \cfrac{b}{\ddots}}}}. \quad (1)$$

In Eq. (1), α is the fine structure constant, $\hbar\omega$ is the photon energy of the incident beam, the energy E is equal to $\hbar\omega + E_i$ where E_i is the energy of the initial state (core state), and γ is a broadening parameter similar to $\Gamma/2$ used as above in the MT calculations. The $\{a_i\}$ and $\{b_i\}$ are two sets of real coefficients, corresponding to the diagonal and subdiagonal matrix elements of the pseudo-Hamiltonian in its tridiagonal representation, respectively. The pseudo-wave function $|\tilde{\varphi}_{\boldsymbol{R}_0}\rangle$ is non-zero only within a spherical core region (smaller than the usual muffin-tin sphere) centered on the absorbing atomic site $\boldsymbol{R}$. In the electric dipole approximation, $|\tilde{\varphi}_{\boldsymbol{R}_0}\rangle$ is defined by a sum over the ($\ell = 1$) components of the product of Blöchl's projector functions [28] and transition matrix elements between the initial core state and the *all electron* valence atomic wave functions:

$$|\tilde{\varphi}_{\boldsymbol{R}_0}\rangle = \sum_n \sum_m \sum_{,\pm} |\tilde{p}_{\boldsymbol{R}_{0,n,,m}}\rangle\langle\phi_{\boldsymbol{R}_{0,n,,m}}|\hat{\varepsilon}\cdot\boldsymbol{r}|\phi^c\rangle. \quad (2)$$

In Eq. (2), $\hat{\varepsilon}$ is the polarisation of the photon beam, and the sum over n is used if there is more than one Blöchl's projector function per angular momentum channel.

The FP method was used to calculate the imaginary part of the anomalous scattering factor, f'', since it is proportional

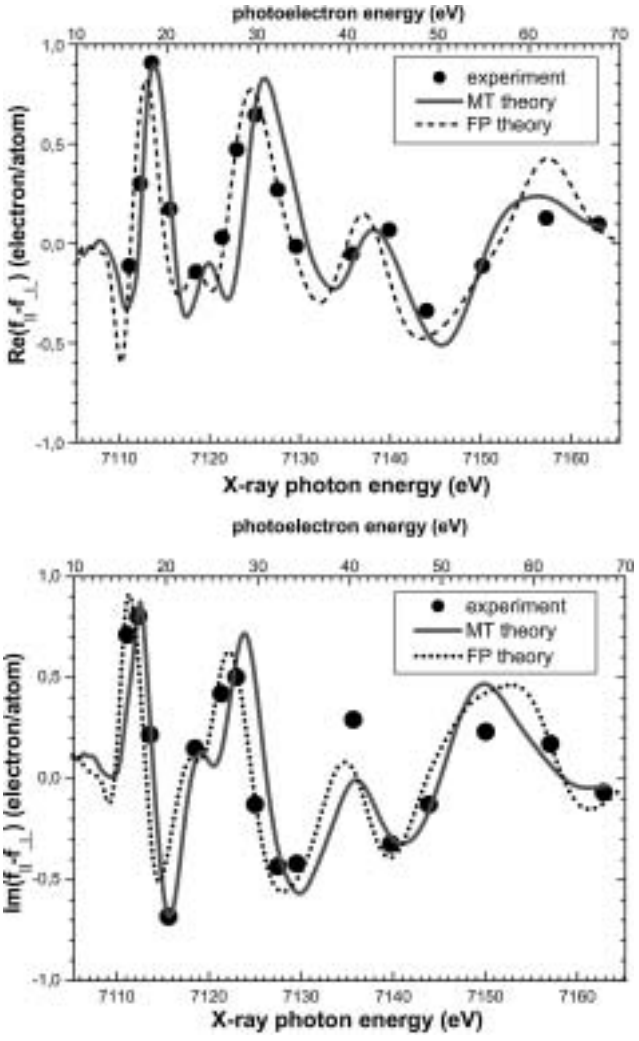

Fig. 1. Experimental (circles) values of the real (top) and imaginary (bottom) parts of the anisotropy $f_{||} - f_{\perp}$ of the iron atomic factor compared with the MT and FP calculated values as functions of the photon energy near the Fe K-edge.

to $\omega\sigma(\omega)$. Then the real part, f', was obtained by a Kramers-Kronig transform. The calculations were carried out on two kinds of cell, in order to investigate the influence of the core-hole effects onto the scattering factors: (*i*) the unit cell of pyrite, containing four FeS_2 entities, and (*ii*) a $2 \times 2 \times 2$ where one 1s electron was removed from the electronic configuration of only one of the 32 iron atoms. Since the calculations revealed that the electron-core-hole interaction has negligible effects on the f' and f'' spectra, all the FP calculated spectra described and presented below are the ground state calculations. The charge density was self-consistently calculated within the local density approximation using a 70 Ry cut-off energy for the plane wave expansion. Reciprocal space integrations were performed using $2 \times 2 \times 2$ and $8 \times 8 \times 8$ Monkhorst-Pack $\boldsymbol{k}$-point grids for the charge density and f'', respectively. We consider the (0, 0, 0) iron site as the $\boldsymbol{R}$ absorbing atom site. Thus the $f''_{||}$ and $f''_{\perp}$ components of f'' were obtained with $\hat{\varepsilon} \,||\, [111]$ and $\hat{\varepsilon} \perp [111]$, respectively. The continued fraction (Eq. (1)) was evaluated with $\gamma = 0.01$ Ry. More details about calculations may be found in [31].

5. Results and discussion

The measured values of the ASF anisotropy $f_{||} - f_{\perp}$ is shown in Fig. 1 together with the MT and FP calculated values. One can see that both theories provide rather good description of the experimental data. However the MT theory contains many fitting parameters whereas the unique free parameter of the FP calculations is the energy-dependent width at half maximum $\Gamma(E)$ of the Lorentzian function, that is used to convolute the f' and f'' spectra ($\Gamma(E)$ is the same both for the MT and FP calculations).

Acknowledgements

The work is partly supported by the grant INTAS 01-0822.

References

1. "Resonant Anomalous X-Ray Scattering. Theory and Applications", (Editors: G. Materlik, C. J. Sparks and K. Fischer) (North-Holland, Amsterdam, 1994).
2. Lovesey, S. W., Repts. Prog. Phys. **56**, 257 (1993).
3. Hodeau, J. L. *et al*., Chemical Reviews **101**, 1843 (2001).
4. Ishihara, S. and Maekawa, S., Repts. Prog. Phys. **65**, 561 (2002).
5. Templeton, D. H. and Templeton, L. K., Acta Crystallogr., Sect. A: Found. Crystallogr. **41**, 237 (1980).
6. Templeton, D. H. and Templeton, L. K., Acta Crystallogr., Sect. A: Found. Crystallogr. **41**, 133 (1985).
7. Dmitrienko, V. E., Acta Crystallogr., Sect. A: Found. Crystallogr. **39**, 29 (1983).
8. Dmitrienko, V. E., Acta Crystallogr., Sect. A: Found. Crystallogr. **40**, 89 (1984).
9. Ovchinnikova, E. N. *et al*., this Proceeding.
10. Collins, S. P. *et al*., this Proceeding.
11. Kokubun, J., Kuribayashi, M., Ishida, K. and Dmitrienko, V. E., Photon Factory Activity Rep. **15B**, 7 (1997).
12. Lee, T. L., Felici, R., Hirano, K., Cowie, B., Zegenhagen, J. and Colella, R., Phys. Rev. B **64**, 201316 (2001).
13. Weckert, E. and Hümmer, K., Acta Crystallogr., Sect. A: Cryst. Phys., Diffr., Theor. Gen. Crystallogr. **53**, 108 (1997).
14. Vedrinskii, R. V. and Novakovich, A. A., Fisika Metallov Materialovedenie **39**, 7 (1975).
15. Kokubun, J., Ishida, K. and Dmitrienko, V. E., J. Phys. Soc. Jpn. **67**, 1291 (1998).
16. Ashley, C. A. and Doniach, S., Phys. Rev. B **11**, 1279 (1975).
17. Poumellec, B. *et al*., Phys. Rev. B **58**, 6133 (1998).
18. Ravel, B., Stern, E. A., Vedrinskii, R. V. and Kraizman, V. L., Ferroelectrics **206–207**, 407 (1998).
19. Vedrinskii, R. V., Kraizman, V. L., Novakovich, A. A., Demekhin, Ph. V. and Urazhdin, S. V., J. Phys.: Condens. Matter **10**, 9561 (1998).
20. Vedrinskii, R. V. *et al*., Phys. Stat. Sol. b **226**, 203 (2001).
21. Herman, F. and Skillman, S., "Atomic Structure Calculation", (Englewood Cliffs, NJ, Prentice-Hall, 1963).
22. Schwarz, K., Phys. Rev. B **5**, 2466 (1972).
23. Keski-Rahkonen, O. and Krause, M. O., Atomic Data **14**, 139 (1974).
24. Berestetskii, V. B., Lifshits, E. M. and Pitaevskii, L. P., "Quantum Electrodynamics", (Nauka, Moscow, 1980).
25. Taillefumier, M., Cabaret, D., Flank, A.-M. and Mauri, F., Phys. Rev. B **66**, 195107 (2002).
26. Cabaret, D. *et al*., this Proceedings.
27. Troullier, N. and Martins, J. L., Phys. Rev. B **43**, 1993 (1991).
28. Blöchl, P. E., Phys. Rev. B **50**, 17953 (1994).
29. Lanczos, C., J. Res. National Bureau. Stand. **45**, 255 (1950). Lanczos, C., *ibid* **49**, 33 (1952).
30. Haydock, R., Heine, V. and Kelly, M. J., J. Phys. C: Solid State Phys. **5**, 2845 (1972). Haydock, R., Heine, V. and Kelly, M. J., *ibid* **8**, 2591 (1975). Haydock, R., Solid State Phys. **35**, 215 (1980).
31. Kokubun J. *et al*. Phys. Rev. B **69**, 245103 (2004).

Physica Scripta. Vol. T115, 1065–1067, 2005

Evidence for Two Mechanisms of Temperature-Dependent "Forbidden" Resonant Diffraction in ZnO

S. P. Collins[1,2*], D. Laundy[1], V. E. Dmitrienko[3], D. Mannix[4] and P. Thompson[4]

[1]Daresbury Laboratory, Warrington,WA4 4AD, UK
[2]Diamond Light Source Ltd, Rutherford Appleton Laboratory, Chilton, Didcot, Oxon, OX11 OQX, UK
[3]A.V. Shubnikov Institute of Crystallography, Moscow, 119333, Russia
[4]XMaS UK CRG, ESRF, BP 220, Grenoble Cédex, F-38043, France

Received June 26, 2003; accepted January 7, 2004

PACS numbers: 61.10.Nz, 61.50.Ah, 74.25.Kc, 61.10.−i, 63.20.−e, 71.90.+q

Abstract

The resonance spectrum of glide-plane forbidden X-ray diffraction have been measured for different temperatures in hexagonal ZnO near the zinc K-edge. This diffraction appears exclusively owing to anisotropy of the Zn atomic scattering factor induced either by thermal motion or by a temperature-independent dipole-quadrupole amplitude. The results provide the first evidence for a complex line shape in the spectrum of thermal motion induced scattering, and the first observation of a dramatic change in resonance spectrum with temperature.

The measurements are in excellent agreement with a phenomenological model, based on a combination of constant and a temperature-dependent amplitudes. This model has provided a means of extracting amplitude spectra of each component, and their relative phase. We find that the strongest spectral feature of the room-temperature resonance spectrum arises from a sudden phase change between the two resonant processes. These results are of great importance for better understanding of the temperature effect on the excited electronic states in crystals like hybridization of different orbitals, *etc.*

1. Introduction

Resonant X-ray diffraction at positions that are exactly forbidden by glide-plane or screw-axis selection rules have received a great deal of attention in recent years. Since such signals vanish in the case of a spherical (scalar) scattering response, the technique has played a key role in identifying orbital anisotropy in, for example, manganites and other strongly-correlated electron systems [1]. Most of these studies have exploited the coupling of the photon polarization to dipolar anisotropy (described by a second-rank tensor and represented geometrically by an ellipsoid) in order to reduce the symmetry of the scattering system. For many materials, however, the crystal symmetry is such that even dipolar anisotropy cancels in the calculation of structure factors, and the lowest-order residual scattering is described by third- or fourth-rank tensors. These effects have been observe experimentally [2–4], and attributed to (electric) dipole-quadruplole (E1E2) and pure quadrupole (E2E2) resonances, respectively.

Of special significance to this work is the series of studies of germanium [5–9], pioneered by Templeton & Templeton [2], who observed a sharp resonance just above the Ge K-edge, which was found to be consistent with the symmetry properties of a third-rank scattering tensor. Interpretation was given in terms of a mixed dipole-quadrupole resonance [2]. Recently, an alternative mechanism has been proposed [10], and observed in germanium [5, 7], whereby a third-rank scattering tensor arises from small thermal displacements from the nominal sites of high symmetry, coupled to local dipolar anisotropy. While the temperature-dependence of the resonant scattering in germanium does indeed show convincing evidence for two competing processes, i.e. a temperature-independent (TI) part, probably dominated by E1E2 events, and a Thermal Motion Induced (TMI) part, the spectra for each process are surprisingly similar, and there is very little temperature dependence in the spectral lineshape.

Since TMI scattering arises from the relative displacement of adjacent atoms, its strength depends crucially on the thermal population of optical phonon modes. The search for suitable materials in which to study this effect is therefore governed by the requirements for: (1) a suitable space-group, which includes glide-plane and/or screw-axis symmetry, (2) site symmetry such that forbidden reflections give no contribution from dipolar anisotropy, (3) an absorption edge resonance at a wavelength suitable for crystal diffraction, (4) a low-lying optical phonon mode, (5) a high quality single crystal sample. ZnO, which crystallizes with the wurtzite structure (space group $P6_3mc$, No. 186) and has an optical phonon mode of energy 12.4 meV at the Γ-point [11], satisfies the above requirements. Moreover, it is of considerable interest as a material for spintronics, and is commercially available as a substrate crystal.

2. Theoretical

The X-ray diffraction intensity for weak scattering can be written, for a fixed geometry, in terms of the electric field components of the incident ($\hat{\varepsilon}$) and scattered ($\hat{\varepsilon}'$) photon, and a Cartesian scattering matrix:

$$I \propto |\hat{\varepsilon}'^{*} F \hat{\varepsilon}|^2. \tag{1}$$

The matrix for TMI scattering is derived from the third-rank structure factor tensor by projecting onto the scattering vector [10]. For either atom type of the wurtzite structure (site symmetry $3m$), for the hhl (l = odd) glide-plane forbidden reflections, the resulting scattering matrix is of the form:

$$F(hhl) \propto h\langle u^2 \rangle \begin{pmatrix} 0 & 1 & 0 \\ 1 & 0 & 0 \\ 0 & 0 & 0 \end{pmatrix} \tag{2}$$

where the x, y and z axes are parallel to the crystal mirror-plane, glide-plane and 6-fold axis, respectively. $\langle u^2 \rangle$ is the mean square atomic displacement (we assume, for simplicity, that the only important displacement is of a Zn atom relative to all the neighboring atoms, and that the vibration is approximately isotropic). From Eq. (2) it is clear that the reflections of interest

*steve.collins@diamond.ac.uk

will be of the form *hhl*, with $l =$ odd and $h \neq 0$. One cannot infer that the scattering amplitude will simply scale with h, however, as a number of geometrical factors are introduced when transforming to the laboratory frame of reference. Similarly, the coordinate transformation leads to a complex characteristic dependence of the scattered intensity and polarization on the sample azimuthal angle. A more detailed description of the structure factor tensor and scattering matrix will be given in a subsequent communication, where the polarization and azimuthal intensity dependence will be discussed.

An important aspect of this work is that, for materials that crystallize with non-chiral space groups (which include both Ge and ZnO) the third-rank scattering tensors posses *precisely* the same elements, and are thus experimentally distinguishable only via their dependence on other physical variables, such as temperature.

3. Experimental

The experiments reported in this Letter were carried out on the XMaS UK CRG beamline at the European Synchrotron Radiation Facility. The bending-magnet beamline utilizes a Si 111 monochromator and a toroidal focusing mirror. The sample was a large ($10 \times 10 \times 1$ mm) plate, supplied by MaTecK GmbH, which was attached to a 50–800 K cryofurnace, mounted on the Eulerian cradle of a large multi-axis diffractometer. Photon polarization was perpendicular to the scattering plane. The absorption spectrum was measured from a thin ZnO powder, in order to apply absorption corrections to the diffraction data. Anisotropy in the absorption was assumed to be small.

One of the most severe complications with measurements of weak scattering with integer Miller indices is contamination by multiple scattering. Fortunately, the very high quality of the sample (the 004 rocking-curve width was below 0.02°) meant that the majority of such features were very sharp, and easily avoided by performing a modest azimuthal rotation. The azimuthal angles were kept close to zero (with 001 within the scattering plane) for most of the measurements, as this corresponded to the maximum calculated, and measured, resonant scattering intensity. Azimuthal scans were very limited in range, due to the crystal surface orientation, and will be the subject of a future study.

Resonant diffraction signals were observed at the 113 and 115 glide-plane-forbidden positions, with the 115 studied in some detail. No clear diffraction intensity was observed at the 003 position, which would require a structure-factor tensor of at least fourth rank. In stark contrast to the results from Ge, we find resonance spectra at high and low temperatures that are complex, extend over more than 30 eV in energy, and are completely different in line shape (Fig. 1). Weaker resonance features extend well beyond the absorption edge. The evolution of the resonance spectrum with temperature was determined from measurements at 18 temperatures, ranging from 59 to 800 K. The resulting dependence shows a remarkable array of features: at various photon energies, the intensities, with increasing temperature, are found to fall, to rise, to fall and rise, and to remain almost constant.

In the absence of a theoretical model for the resonant scattering, and in an attempt to separate the TI and TMI components, we have performed a least-squares fit of the measured intensities to a phenomenological two-process model [5], via the expression,

$$I(E) = \left| A(E)\,\mathrm{e}^{\mathrm{i}\phi(E)} + B(E)\coth\left(\frac{\hbar\omega_o}{2kT}\right)\right|^2 \mathrm{e}^{-2M} \qquad (3)$$

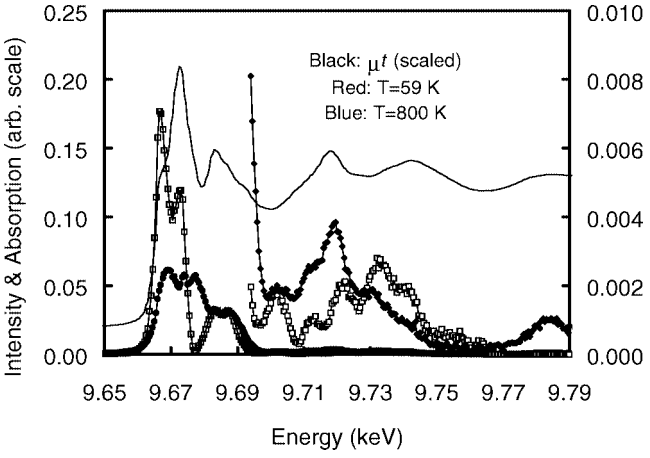

Fig. 1. The ZnO 115 resonance spectrum near the Zn K-edge. Red and blue solid lines correspond to temperatures of 59 and 800 K respectively. Total absorption is shown by the black line. The tails of the curves are shown in larger scale and correspond to the right axis.

where $A(E)$ and $B(E)$ represent energy-dependent (scalar) amplitudes for the TI and TMI scattering components, and $\phi(E)$ is the relative phase angle between the two components, which we assume to be independent of temperature. The factor $\langle u^2 \rangle$ scales with the thermal population of the optical phonon mode $\coth(\hbar\omega_o/2kT)$ if one assumes a simple model in which the phonon energy, $\hbar\omega_o$, is independent of the wavevector. The total scattering intensity is further modified by the Debye-Waller factor e^{-2M}, where M, which is a function of momentum transfer, temperature, atomic mass and characteristic (Debye) temperature, is discussed in detail by James [12]. For the present work, we take the average atomic mass $\overline{m} = 40.7$, and a Debye temperature of 370 K, determined from a crystal structure refinement study [13].

Eq. (3) was found to give a remarkably good fit to the data yielding three separate energy-dependent curves: the TI and TMI amplitudes, $A(E)$ and $B(E)$, and their relative phase, $\phi(E)$. These are shown in Fig. 2, in the form of their contributions to the resonant intensity at low temperature (58 K). The quality of the fit

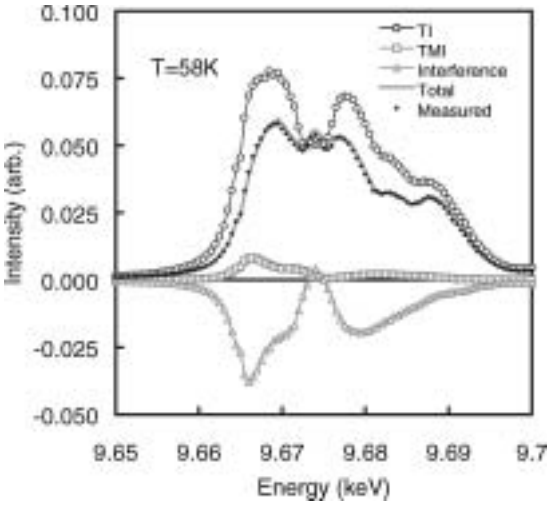

Fig. 2. The results of the least-squares fit to the model outlined in the text (Eq. (3)), shown in the form of intensity contributions (at $T = 58$ K) from thermal-motion-induced scattering (red line), temperature-independent scattering (blue line) and the interference term between these two resonant amplitudes (green line). The total fit is shown by the black line together with experimental points.

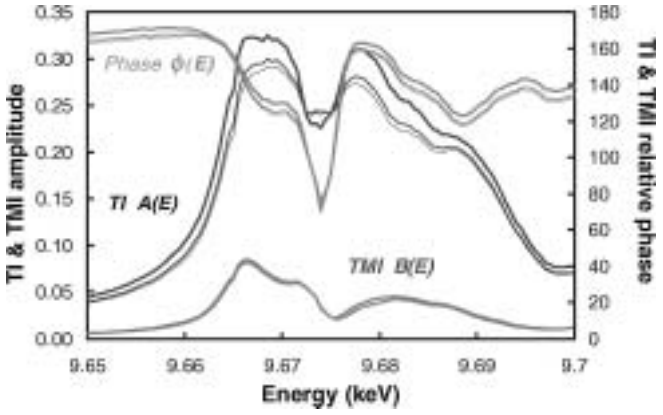

Fig. 3. The results of the least-squares fit to Eq. (3) for the TI and TMI amplitudes, $A(E)$ (blue lines) and $B(E)$ (red lines), and their relative phase, $\phi(E)$ (green lines). Different curves of the same color correspond to different phonon energies $\hbar\omega_o = 6.2$, 12.4, and 24.8 meV.

was found to be relatively insensitive to the value chosen for the optical phonon energy, $\hbar\omega_o$, giving an error interval ranging from 0 to 35 meV (Fig. 3). $A(E)$ and $\phi(E)$ depend very weakly on $\hbar\omega_o$ whereas $B(E)$ simply scales as $1/(\hbar\omega_o)$. While this effectively rules out the possibility of using the TMI scattering technique to extract precise phonon energies, it does, at least, suggest that the known dispersion in the low-lying optical mode [11], and the presence of high energy modes, should have only a modest effect on the above analysis, beyond an overall scaling of $B(E)$. Neglecting the Debye-Waller factor in Eq. (3) led to a significantly worse fit.

4. Results and discussion

The results from ZnO are interesting in several respects. First, they represent convincing evident for TMI scattering in a material other than Ge, suggesting that the phenomenon is more general than may have been inferred from previous work. Secondly, unlike Ge, we observe resonance spectra that are complex and change dramatically with temperature. The phenomenological model has proved extremely useful in establishing that the intensities can be understood very well with the assumptions that two processes are required, one of which has an amplitude that follows closely the population of the low-lying optical phonon mode, and that the phase between the two amplitudes is independent of temperature. Recently, a microscopic theoretical model was suggested for the spectrum and magnitude of TMI scattering [14].

The study of electronic systems in perturbed or excited states is one of the great challenges for the coming decades, towards which thermal-motion-induced scattering can play a small but significant role. The combination of experimental and theoretical studies of forbidden reflections should shed light on a number of important aspects of electronic structure, including hybridization, the evolution of electronic states with nuclear position, and the validity of the Born-Oppenheimer approximation. While recent theoretical work on Ge [9] supports the interpretation of the temperature-independent scattering component as arising from E1E2 processes, one cannot rule out a contribution from pure dipolar scattering, if one takes into account the variation in the scattering tensor with the relative displacement of the scattering centre from the nucleus. It is likely, however, that the limited extent of the 1s core level involved in the resonance will mean that this contribution is weak. Another possible interpretation of the temperature-independent scattering relates to the point-defect-induced anisotropy [15] Finally, it is interesting that the TI and TMI amplitudes for both Ge and ZnO are similar in magnitude, yet the physics of the two processes is very different. This could, of course, simply be coincidental.

Acknowledgements

This work is part of a program supported by INTAS grant 01-0822. The authors gratefully acknowledge EPSRC support of XMaS experiments.

References

1. Ishihara, S. and Maekawa, S., Rep. Prog. Phys. **65**, 561 (2002).
2. Templeton, D. H. and Templeton, L. K., Phys. Rev. B **49**, 14850 (1994).
3. Finkelstein, K. D., Shen, Q. and Shastri, S., Phys. Rev. Lett. **69**, 1612 (1992).
4. Kokubun, J., Nagano, T., Kuribayashi, M. and Ishida, K. J., Phys. Soc. Japan **67**, 3114 (1998).
5. Kokubun, J., Kanazawa, M., Ishida, K. and Dmitrienko, V. E., Phys. Rev. B **64**, 073203 (2001).
6. Lee, T. L. *et al.*, Phys. Rev. B **64**, 201316 (2001).
7. Kirfel, A., Grybos, J. and Dmitrienko, V. E., Phys. Rev. B **66**, 165202 (2002).
8. Detlefs, C., Physica **B345**, 45 (2004).
9. Elfimov, I. S., Skorikov, N. A., Anisimov, V. I. and Sawatzky, G. A., Phys. Rev. Lett. **88**, 015504 (2002).
10. Dmitrienko, V. E., Ovchinnikova, E. N. and Ishida, K., JETP Lett. **69**, 938 (1999).
11. Thoma, K., Dorner, B., Duesing, G. and Wegener, W., Solid State Commun. **15**, 1111 (1974).
12. James, R. W., "The Optical Principles of the Diffraction of X-rays", Ox Bow Press (Woodbridge, Connecticut): 219 (1964).
13. Abrahams, S. C. and Bernstein, J. L., Acta Cryst. B **25**, 1233 (1969).
14. Ovchinnikova, E. N., Oreshko, A. P., Joly, Y., Kirfel, A., Tolochko, B. P. and Dmitrienko, V. E., these proceedings.
15. Dmitrienko, V. E. and Ovchinnikova, E. N., Acta Cryst. A **56**, 340 (2000).

Physica Scripta. Vol. T115, 1068–1070, 2005

Melting of the Ge(111) Surface Probed by EELS

A. Di Cicco, B. Giovenali, R. Bernardini and E. Principi

Istituto Nazionale di Fisica della Materia, INFN-LNF and Dipartimento di Fisica, Università di Camerino, Via Madonna delle Carceri, 62032 Camerino (MC), Italy

Received June 26, 2003; accepted December 5, 2003

PACS numbers: 68.35.Rh, 64.60.−i, 73.20.−r, 79.20.Uv

Abstract

The Ge(111) surface exhibits a well-known structural transition at high temperature to a metallic phase. The transition is known to occur at about 1040 K and has been interpreted as due to the melting of the first surface layers. We have performed a new experiment with an improved high-temperature set-up which allows us to collect accurate Electron Energy Loss Spectroscopy data near the $M_{2,3}$ excitation edges. A probing depth of about 10 Å on collected EELS spectra was obtained tuning the electron gun at about 500 eV. The metalization of the surface has been clearly detected by the shift of the edge associated with the disappearance of the gap. EELS measurements, performed with a fine temperature step and under thermal equilibrium conditions, allowed us to obtain a new determination of the transition temperature which appears to be located at $T_c = 1010$ K with an accuracy of about 10 K.

1. Introduction

The Ge(111) surface exhibits a well-known structural transition at high temperature to a metallic phase [1–4]. The transition, involving the (1×1) surface reconstruction, is known to occur at about 1040 K, more than 160 K below the bulk melting temperature $T_m \sim 1210$ K [4, 5].

In previous works, different types of spectroscopies detected this transition and the current model for the high temperature phase is an incomplete surface melting involving the first Ge(111) bilayer [6, 7]. Experiments using low-energy electron diffraction (LEED) [1, 2], EELS at the $M_{4,5}$ threshold and near the elastic peak [4, 8], ellipsometry [9], surface X-ray diffraction [10], photoelectron diffraction [3], He atom scattering [11], and photoemission [12, 13] were performed confirming the metallic nature of the new phase occurring in a quite broad range of temperatures 970–1050 K. In spite of these efforts there is still some uncertainty about the temperature of the transition and about the number of layers involved for increasing temperature.

Stimulated by our previous experience in studying the structure of liquid and solid Ge at high temperature [14] by X-ray absorption spectroscopy (XAS) and by the sensitivity of this technique to structural and electronic phase transitions [15], we have performed an $M_{2,3}$-edge electron energy-loss spectroscopy (EELS) experiment aimed to improve our knowledge about the above-mentioned Ge(111) surface phase transition. In fact, the metalization induced by melting of bulk Ge can be easily detected and studied by the change of shape and shift of the edge position in Ge K-edge XAS spectra [14, 15]. These features can be also observed in surface-sensitive XAS-like techniques like EELS using standard laboratory systems. Moreover, a finer temperature step and a more precise calibration and measurement of the sample temperature have been achieved through the development of a new sample heating unit working under high vacuum conditions.

2. Experiment

The experiments were performed in a ultra-high vacuum (UHV) chamber equipped with a LEED system, a coaxial electron gun and cylindrical mirror analyzer (CMA). An ion gun (Ar) has been used for surface cleaning of a Ge(111) sample during proper annealing cycles. The surface was found to be clean according to the usual criteria of Auger electron spectroscopy (AES).

Special care was paid to the temperature control and heating elements. In Fig. 1 we show the design of the high-temperature

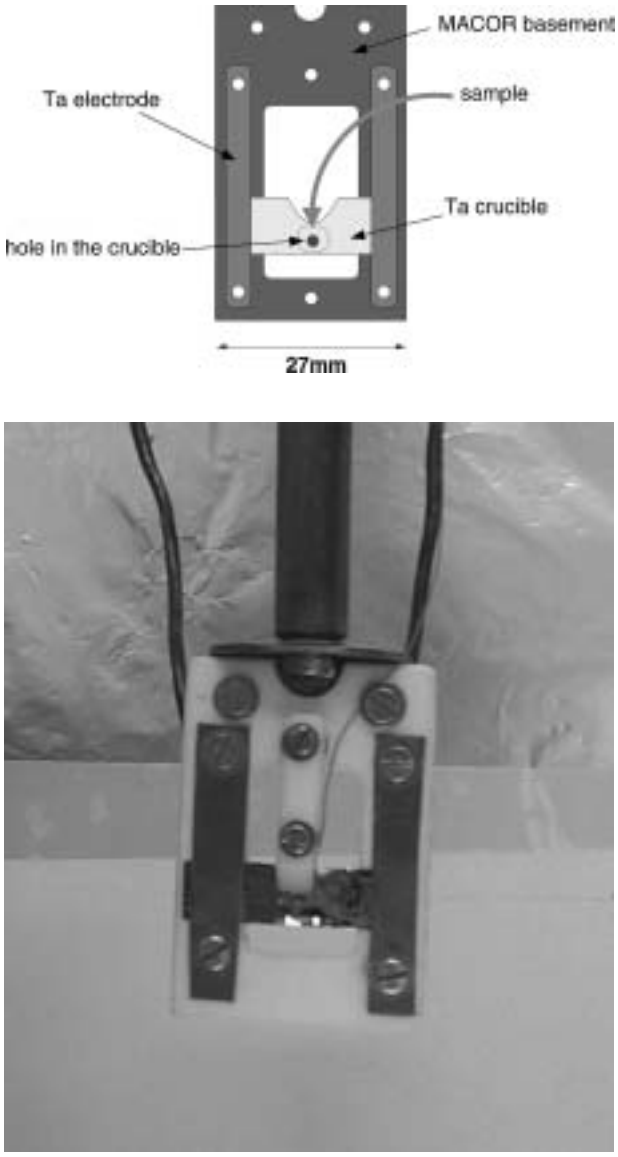

Fig. 1. Design of the high-temperature crucible for EELS measurements (top) and picture of the device (bottom) to be inserted into the ultra high-vacuum chamber.

crucible used for EELS measurements (top) and a picture of the device (bottom) developed for high temperature measurements into the UHV chamber. The heating element of the new device is a 5 μm thin Ta foil which is able to reach very high temperatures using typical currents of a few Amperes with typical voltages of 1–2 Volts. The geometry of the crucible-sample assembly is similar to the one developed for high-temperature XAS studies [16] and guarantees a precise temperature control and an excellent temperature homogeneity. The new device is made with UHV compatible components and allowed us to measure the temperatures with an accuracy better than 5 degrees using a K-type thermocouple placed between the Ta crucible and the sample. Direct contact between the reactive surface of the sample and the Inconel sheath of the thermocouple (Thermocoax, insulated, 0.25 mm diameter) was avoided using a thin boron nitride spacer. A ∼500 μm diameter hole allowed us to collect EELS, AES, and LEED signals from the Ge(111) surface. An important advantage of the present setup is that the presence of the metallic heating device allowed us to collect high-temperature data without using pulsed heating because of the low voltage applied to the crucible and the absence of current flow inside the sample. Clearly this allowed us to collect high-temperature EELS spectra under equilibrium thermal conditions.

The experimental results presented in this work are those related to the high-temperature $M_{2,3}$ EELS data that we collected using a fine temperature spacing near the phase transition temperature. The electron gun was tuned at 500 eV in order to have sufficient statistics, energy resolution and low background from secondary emission at the kinetic energy corresponding to the selected core level (binding energy of the M_3 level is $E_{M_3} \sim$ 120.8 eV). The inelastic mean free path of the electrons in the selected range of kinetic energies ($E_{kin} \sim$ 380 eV) is estimated to be about 10 Å in crystalline Ge (see ref. [17] and ref. therein). Therefore, the measured EELS signal is sensitive to the first 4–5 Ge(111) surface layers.

3. Results and Discussion

In Fig. 2 we report the EELS intensity as a function of temperature in the vicinity of the surface phase transition. EELS spectra have been measured in a range of about 60 eV accumulating 50 scans for each temperature to increase statistics. The intensity of the EELS spectra has been obtained in the usual way, using a polynomial function for the background in the pre-edge region and normalizing the $M_{2,3}$ electron loss above the M_3 and M_2 edges to unity ($E_{loss} \sim$ 150 eV). In this way EELS spectra can be directly compared on the scale of Fig. 2 where changes in the shape and position of the edges can be appreciated.

Looking at Fig. 2, we note that a change of shape and intensity of the EELS spectra occurs at about 1000 K and that a clear shift of the foot of the absorption edge (in the 114–118 eV region) is observed at about 1010 K. The change in the shape and relative intensity of the EELS spectra are also affected by the normalization procedures, that can introduce an uncertainty of the order of 1–2%. Of course, the energy shift near the edge can not influenced by normalization procedures and is a direct manifestation of a drastic change of the empty density of states near the Fermi Energy in the vicinity of the Ge(111) surface. This effect has been already observed in XAS spectra of bulk Ge upon melting [14, 15] and, more recently, in amorphous Ge under pressure [18].

The shift of the edge toward lower excitation energies is associated with the transition from a semiconductor to a metal phase. The energy gap disappears and new states near the Fermi level are available for the excited electrons, resulting in a shift of the order of 1 eV of the absorption and EELS edges. In the inset of Fig. 2 the shift of the EELS edge toward lower excitation energies is clearly visible.

The variation of the EELS intensity (ΔI) at fixed energy is reported in Fig. 3. The energy has been chosen in order to have the maximum contrast between a metallic and a non-metallic phase, i.e. on the rise of the M_3 edge ($E_{\text{loss}} \sim$117.4 eV, see dashed lines in the inset of Fig. 2). The trend reported in Fig. 3 is very clear showing a quite sharp transition occurring between 1010 and 1020 K. The intensity jump exceeds 5% of the total $M_{2,3}$ EELS signal, with a noise level of about 1%. This result shows that the Ge(111) surface undergoes a transition to a metallic phase beginning at about 1010 K. The width of the transition is about 10 K and involves several layers near the surface within the probing depth of the current experiment (about 10 Å). Above 1025 K, the EELS signal at fixed energy changes smoothly with temperature indicating that no further sharp transitions occur in the present temperature range.

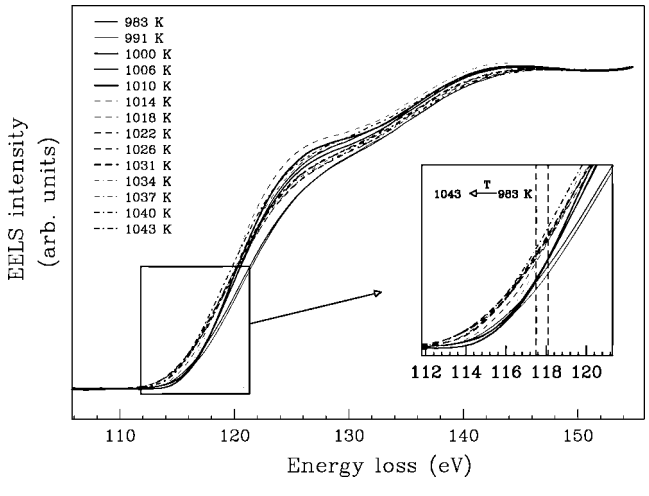

Fig. 2. EELS intensity as a function of temperature in the vicinity of the surface phase transition (983–1043 K, or 710–770 °C). EELS spectra are normalized to the measured intensity above the M_3 and M_2 edges ($E_{loss} \sim$150 eV). In the inset the shift of the EELS edge toward lower excitation energies is clearly visible.

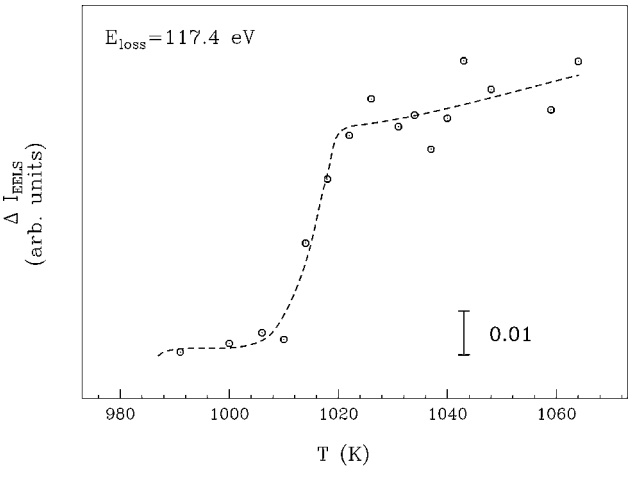

Fig. 3. Variation of the EELS intensity at fixed energy near the M_3 edge (E_{loss}= 117.4 eV). The surface phase transition is observed above 1010 K.

The present determination of the transition temperature is slightly lower than previously indicated (1040–1050 K). It has to be remarked that in previous works, temperature was measured with a pyrometer and sample was heated by direct application of a pulsed current. In these conditions the typical uncertainty for temperature was typically 20 K or worse. In some experiments (see ref. [9]) the transition was found to begin around 980 K. We believe that the present experiment represents probably the most clear observation of the surface phase transition and metalization of the Ge(111) under controlled conditions of temperature, and is likely to be one of the most accurate determinations of the transition temperature.

4. Conclusions

The metalization of the Ge(111) surface at high temperatures has been clearly detected by the shift of the EELS $M_{2,3}$ edges, associated with the disappearance of the gap. We developed a new UHV compatible high-temperature device suitable for EELS measurements with an accuracy of the temperature readout of about 5 K. The transition temperature was found to begin at about 1010 K with a typical width of 10 K. The probing depth of the electrons was about 10 Å.

This experiment shows that accurate EELS data collected using standard equipments can be successfully used to detect and study surface phase transitions. In particular, metalization of the surface can be clearly detected by the shift of the main edge. The accuracy in temperature measurements and fine temperature steps achieved in the present experiment suggest that the present experimental setup can be used for further studies of surface phase transitions. In particular, the energy dependence of the mean free path curve and the tunable energy could be used to study the progressive melting of inner layers.

Acknowledgments

The invaluable help of R. Gunnella and F. Bizzarri is gratefully acknowledged.

References

1. McRae, E. G. and Malic, R. A., Phys. Rev. Lett. **58**, 1437 (1987).
2. McRae, E. G. and Malic, R. A., Phys. Rev. B **38**, 13163 (1988).
3. Tran, T. T. *et al*., Phys. Rev. B **45**, 12106 (1992).
4. Modesti, S. *et al*., Phys. Rev. Lett. **73**, 1951 (1994).
5. Paolicelli, G. *et al*., J. Phys.: Condens. Matter **9**, 1959 (1997).
6. Tomagnini, O., Ercolessi, F., Iarlori, S., Di Tolla, F. D. and Tosatti, E., Phys. Rev. Lett. **76**, 1118 (1996).
7. Takeuchi, N., Selloni, A. and Tosatti, E., Phys. Rev. Lett. **72**, 2227 (1994).
8. Modesti, S. and Santoni, A., Solit State Commun. **72**, 315 (1989).
9. Abraham, M., Le Lay, G. and Hila, J., Phys. Rev. B **41**, 9828 (1990).
10. Mak, A. *et al*., Phys. Rev. Lett. **66**, 2002 (1991).
11. Meli, C. A., Greene, E. F., Lange, G. and Tonnies, J. P., Phys. Rev. Lett. **74**, 2054 (1995).
12. Santoni, A., Dhanak, V. R., Goldoni, A., Sancrotti, M. and Modesti, S., Europhys. Lett. **34**, 275 (1996).
13. Goldoni, A., Santoni, A., Sancrotti, M., Dhanak, V. R. and Modesti, S., Surface Sci. **382**, 336 (1997).
14. Filipponi, A. and Di Cicco, A., Phys. Rev. B **51**, 12322 (1995).
15. Filipponi, A. *et al*., J. Phys.: Condens. Matter **10**, 235 (1998).
16. Filipponi, A. and Di Cicco, A., Nucl. Inst. Meth. Phys. Res. B **93**, 302 (1994).
17. Powell, C. J. and Jablonski, A., J. Phys. Chem. Ref. Data **28**, 19 (1999).
18. Principi, E., Di Cicco, A., Decremps, F., Polian, A., De Panfilis, S. and Filipponi, A., Phys. Rev. B **69**, 201201 (2004).

Physica Scripta. Vol. T115, 1071–1073, 2005

Strong Participator Channels in the Non-Radiative Resonant Decay of B 1s Excitation in B_2O_3

A. B. Preobrajenski*[1,2], A. S. Vinogradov[2], E. Kleimenov[2,3], A. Knop-Gericke[3], S. A. Krasnikov[2,4], R. Szargan[4] and N. Mårtensson[1]

[1]MAX-lab, Lund University, S-22100 Lund, Sweden
[2]V.A. Fock Institute of Physics, St. Petersburg State University, 198504 St. Petersburg, Russia
[3]Fritz-Haber-Institut der Max-Planck-Gesellschaft, D-14195 Berlin, Germany
[4]Wilhelm-Ostwald-Institut für Physikalische und Theoretische Chemie, Universität Leipzig, D-04103, Leipzig, Germany

Received June 26, 2003; accepted in revised form June 10, 2004

PACS numbers: 31.70.Ks, 71.20.−b, 78.70.Dm, 79.60.−i

Abstract

We observe and analyze a considerable enhancement of photoelectron intensity of the valence band features in solid B_2O_3 upon tuning the photon energy across the B $1s \rightarrow \pi^*2p_z$ resonance. This enhancement is an evidence of the strong 2p electron correlations in pre-edge photoionization dynamics in boron oxide. Such strength of the correlation is unusual for a solid, whose valence band is composed of only s and p electrons. We assign these effects to the considerable spatial localization of the highest occupied and lowest unoccupied electronic states of boron oxide on the BO_3^{3-} quasi-molecular anion, as well as to the strong 2p electron coupling between them. Solid state effects in the electronic structure and B $1s \rightarrow \pi^*$ decay dynamics are found to be minor, while molecular effects of the BO_3^{3-} fragment are dominating.

1. Introduction

The vast majority of solid compounds may be naturally considered as being built of chemically stable molecular-like atomic groups, which can be called quasi-molecules. They represent an atom (cation) connected to several more electronegative neighbours by strong covalent bonding. Often these groups have isoelectronic and isostructural counterparts among free molecules. It depends mainly on the strength of chemical bonding between quasi-molecules to what extent the compound "remembers" its molecular origin. Sometimes (for example in III-V binary semiconductors) the interaction between such groups becomes as strong as inside them, the electronic states in the valence and conduction bands become quite delocalized, and a quasi-molecular approach to the description of electronic structure becomes probably meaningless. However for many classes of solid compounds this approach is very instructive and helpful in getting qualitative understanding of their electronic structure. It is also easy-to-use, since it implies comparative analysis of spectra instead of excessive theoretical calculations.

Such quasi-molecular perception of solid compounds may become helpful also in revealing the nature of their core excitations. Recently we reported on the essentially molecular nature of N $1s \rightarrow a_2''(\pi^*2p_z)$ and O $1s \rightarrow a_2''(\pi^*2p_z)$ core excitations in solid $M NO_3$ (M = Li, Na), which are determined mainly by the NO_3^- quasi-molecule [1, 2] (here a_2'' is the lowest unoccupied molecular orbital (MO) of the N π^*2p_z character in the notation of the D_{3h} symmetry group). This is quite understandable, because NO_3^- anions are well separated from each other, and the rather ionic cation-anion bonding is weaker than the covalent bonding inside NO_3^-. Our goal in the present study is to investigate the case of a solid compound with stronger chemical bonding between its quasi-molecules in order to test the prospects of such quasi-molecular approach to the description of electronic structure and core excitations in a more general situation. As a suitable example we consider boron oxide B_2O_3 being particularly interested in its planar BO_3 group. This group (which can be considered as quasi-molecular anion BO_3^{3-}) has almost ideal D_{3h} symmetry, being hence almost isostructural and isoelectronic with NO_3^- in $M NO_3$ and with the gas-phase molecule BF_3. BO_3 is generally accepted as the main building block of both low-pressure forms of B_2O_3: hexagonal crystalline [3] and amorphous (vitreous) [4]. Contrary to quasi-isolated NO_3^- anions in $M NO_3$, BO_3 units in B_2O_3 are linked via their oxygen atoms into chains in both conformations (although the inter-chain linkage in crystalline and vitreous forms is different).

In this paper we apply NEXAFS (near-edge X-ray absorption fine structure) spectroscopy and RAS (resonant Auger spectroscopy) at the B 1s edge in order to demonstrate that the formation and decay of the B $1s^{-1}a_2''(\pi^*2p_z)$ excitation in B_2O_3 has essentially quasi-molecular origin in spite of the partly covalent bonding between BO_3 units. Our data differ in part from the results reported recently by Muramatsu *et al.* [5], possibly because of another sample preparation procedure and/or lower spectral resolution used in Ref. [5]. We discuss our absorption and resonant electron emission spectra in terms of strong 2p-coupling between electrons in the highest occupied and promoted to the lowest unoccupied states of the BO_3 quasi-molecule.

2. Experiment

All spectra were measured at the D1011 beamline at MAX II storage ring in MAX-lab, Lund, Sweden, using a modified SX-700 plane grating monochromator and a high-resolution SES-200 electron energy analyzer. The photon energy resolution was set to 150 meV at the B 1s edge; the kinetic energy resolution was set to 150 meV. The NEXAFS spectra were measured in the total electron yield (TEY) mode with an MCP detector. Thin (20–25 nm) B_2O_3 layers were prepared *in situ* by thermal evaporation of thoroughly dehydrated B_2O_3 powder (Alfa Aesar) from a water-cooled effusion cell onto a polished copper plate pre-cleaned by Ar^+ sputtering. The temperature inside the cell was set to 850 °C in order to ensure reasonable deposition rates of 0.5–0.7 nm/min. The layers produced in this way were found free of contaminations and charging only weakly. All electron spectra presented below are corrected in energy for these charging effects using the position of the B 1s photoline in the second-order light, which were recorded in the same scan as the valence band spectra. We

*Corresponding author: Tel. +46-(0)46-2223629; e-mail: alexeip@maxlab.lu.se

suppose that the deposited B_2O_3 films were rather amorphous than polycrystalline. Thermal evaporation resulted in a small fraction of decomposed (oxygen-deficient) species. The contribution of the decomposed species into the off-resonance valence band spectra was below 7%, while it was vanishing into the on-resonance spectra. For a comparison and as a check of stoichiometry of the resulting films we measured at the same experimental conditions also the B 1s NEXAFS in ultrapure B_2O_3 and H_3BO_3 powders (Alfa Aesar).

3. Results and discussion

B 1s NEXAFS spectra of B_2O_3 thin film and reference B_2O_3 and H_3BO_3 are shown in Fig. 1. Note that the unusual dip at 195 eV in the spectra of powders is probably due to the sample charging. In accordance with previous studies [6] we assign the strong resonance A at 193.95 eV in the spectrum of B_2O_3 to the transitions of B 1s electrons to the unoccupied π^*2p_z molecular orbital (MO) of the $BO_3{}^{3-}$ anion. The broad feature B at 202.5 eV is caused by electron transitions into $\sigma^*2p_{x,y}$ MOs. The spectra of B_2O_3 and H_3BO_3 powders are practically identical in the energy position, relative intensities and shape of all features. This implies a rather weak influence of the inter-molecular covalent O-O bonding on the formation of both B $1s^{-1}\pi^*$ and $1s^{-1}\sigma^*$ core excitations, because in H_3BO_3 the BO_3 groups are connected via bridging hydrogen atoms [3]. While it is not very surprising in the case of strongly localized pre-edge π^* excitation, it is rather unexpected for the σ^* excitation, providing strong support for a quasi-molecular description of solid B_2O_3.

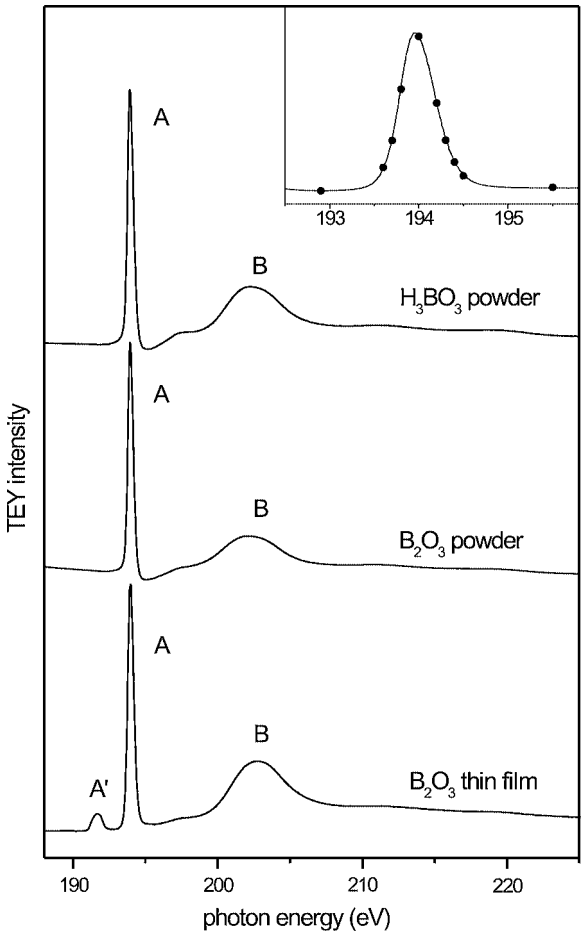

Fig. 1. B 1s NEXAFS spectra of the H_3BO_3 and B_2O_3 powder samples and of the B_2O_3 film prepared by thermal evaporation. Inset: B $1s \rightarrow \pi^*(2p_z)$ resonance measured from the B_2O_3 film; dots denote energies used for resonant excitation (Fig. 3).

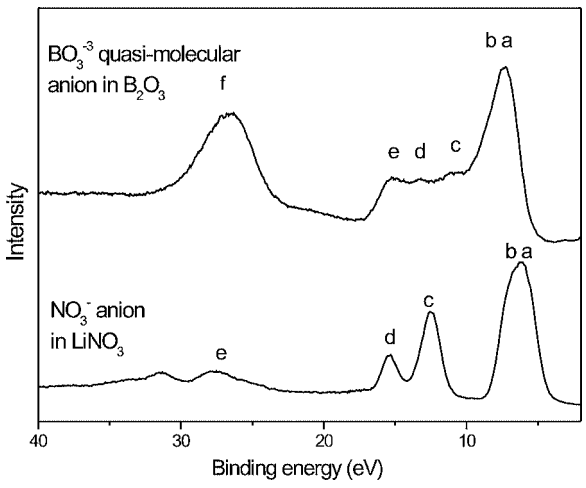

Fig. 2. Non-resonant photoelectron valence band spectra of solid B_2O_3 ($h\nu = 192.9$ eV) and $LiNO_3$ ($h\nu = 150.0$ eV).

In going from the spectra of reference powders to the spectrum of the deposited B_2O_3 film the spectral shape is generally preserved. It experiences only two minor changes: the charging-induced dip at 195 eV disappears and a decomposition-induced peak A′ at 191.7 eV arises. As discussed above, the fraction of decomposed species is small (below 7%) and does not influence further analysis. Close similarity between the overview spectra of the B_2O_3 film and the reference powder (not shown) provides evidence for stoichiometry of the investigated B_2O_3 layers.

Valence band structure of B_2O_3 was studied previously by photoemission and X-ray emission [5, 7, 8]. Fig. 2 shows photoemission valence band spectrum of our B_2O_3 film together with that of a $LiNO_3$ film measured for comparison in the same experimental conditions. In the spectrum of B_2O_3 feature a is commonly assigned to the non-bonding O 2p states, b-e is mainly due to the B 2p states with the contributions of O 2p into b, c and B 2s into e, and f is the O 2s photoline with an admixture of B 2p states. It should be noted that in all previous studies only three distinct features could be revealed in the upper valence band, while we definitely observed four features (a, c, d, e) at different photon energies, probably due to higher resolution and insignificant sample charging. Feature b is not resolved in the non-resonant spectra and can be found only by means of a systematic numerical analysis (not shown here). In Fig. 2 one can see significant similarities in the upper valence band structure of $LiNO_3$ and B_2O_3. The identification of the corresponding structures is also similar. Indeed, in analogy with $NaNO_3$ [1] we assign features a-b in the spectrum of $LiNO_3$ to the non-bonding O 2p states, c – to the mixture of N 2p, O 2p and O 2s states, d – to the mixture of O 2p, O 2s and N 2s states, e – to the mixture of O 2s and N 2p states. All these features have essentially quasi-molecular character and can be correctly described in terms of MOs of the NO_3^- anion [1, 2] Obvious similarities in the valence band structure between B_2O_3 and $LiNO_3$ allow us to assume that the valence band in B_2O_3 is also determined primarily by the electronic structure of the $BO_3{}^{3-}$ quasi-molecule, while the interaction between these units is much less significant. Another argument for the rather molecular character of the occupied electronic states in solid B_2O_3 is the close resemblance of the valence band spectra of B_2O_3

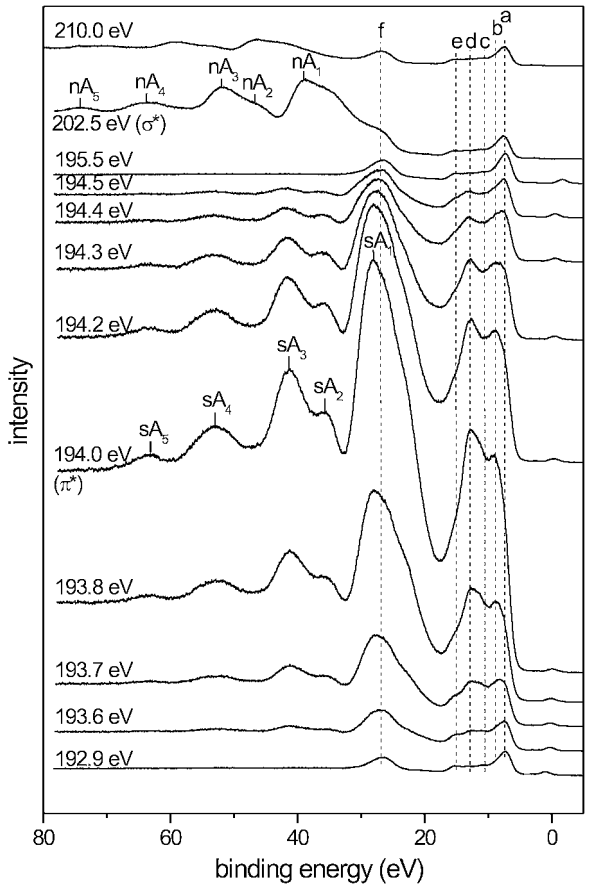

Fig. 3. Resonant Auger spectra of the valence band region of B_2O_3 measured with different photon energies across the B 1s absorption edge. The small peak close to 0 eV is due to the B 1s photoline in the second-order light.

and H_3BO_3 [8] and their B KVV Auger spectra [7] in spite of the essentially different bonding between BO_3 groups in these compounds.

The photon energy dependence of the B_2O_3 valence band spectra across the B 1s absorption edge is shown in Fig. 3. Most energies are chosen on the B $1s \rightarrow \pi^* 2p_z$ shape resonance (denoted by dots in the inset of Fig. 1). The spectra are normalized in intensity to the incident flux and are referred in energy to the Fermi level of the spectrometer. The on-resonance spectrum at 194.0 eV resembles that presented in Ref. [5], whereas off-resonant spectra look differently and resonant enhancement of the upper valence band features is much stronger in our spectra, probably due to considerably better resolution. Note also that the off-resonance spectra before and after the π^* peak (at 192.9 eV and 195.5 eV, respectively) are quite similar both in shape and intensity, which is not the case in Ref. [5].

Two types of spectral features can be clearly identified in the resonant Auger spectrum at 194.0 eV. The first type is due to resonant enhancement of the valence band signals a-f in course of the participator Auger (PA) process, while the second type of features (sA_1-sA_5) results from the spectator Auger (SA) process. In going from π^* to σ^* excitation (at 202.5 eV) PA features disappear completely, while SA features become practically identical with those of the normal Auger (NA) process being denoted nA_1-nA_5 in Fig. 3. All SA signals are shifted by 1.8 eV to higher kinetic energies relative to the corresponding NA ones (so-called spectator shift) due to the screening effect of the spectator electron. Besides that the SA features become narrower and experience changes in their relative intensities. Some additional contribution to the intensity of peak sA_1 may yield the PA enhancement of photoline f, though this effect is probably weak due to rather minor contribution of the B 2p states. The most interesting resonant effect, which can be seen in Fig. 3, is a drastic increase in intensity of the upper valence band signal (binding energy 4–19 eV) upon tuning photon energy across the B $1s \rightarrow \pi^* 2p_z$ resonance. Although a thorough analysis of this effect will be given elsewhere, several notes can be made now. First, the overall PA intensity enhancement in this spectral range (as computed after subtraction of a smooth monotonous background) is as great as by a factor of 27. Second, our numerical analysis (not shown) allows us to suggest that feature a, which is due to the non-bonding O 2p states, is enhanced at resonance just very weakly. Third, the strongest contribution to the overall enhancement gives feature d, which results primarily from the transitions into B 2p states. It should be noted that in ionic-molecular crystals $M NO_3$ (M = Li, Na) the situation with PA decay of the N $1s^{-1}\pi^*$ excitation is very similar [1, 2]. Since in $M NO_3$ it is determined exclusively by the quasi-isolated NO_3^- anion and not by the crystal, the situation should be similar in B_2O_3, where the PA decay of the B $1s^{-1}\pi^*$ excitation has to be determined by the BO_3 group despite the inter-molecular linkage.

The strength of the PA decay of the B $1s^{-1}\pi^*$ excitation observed in B_2O_3 is quite unusual for the solids with valence bands composed of only s and p electrons. Among other prominent examples of that kind one can mention the decay of the B $1s^{-1}\pi^*$ excitation in hexagonal BN [9] and already mentioned PA decay of the N $1s^{-1}\pi^*$ excitation in $M NO_3$ [1, 2]. In all these materials strong 2p electron correlations in pre-edge photoionization dynamics have been documented. These strong correlations result from the fact that the upper occupied and lower unoccupied electronic states in these solids are essentially localized on the corresponding quasi-molecular fragments and strongly coupled to each other. In general, our results for B_2O_3 show that the BO_3^{3-} fragment determines the electronic structure and the nature of formation and decay of the B $1s^{-1}\pi^*$ core excitation almost exclusively, in spite of the partly covalent bonding between BO_3 quasi-molecules.

Acknowledgements

This work was supported by the Russian Foundation for Basic Research (grant No. 01-03-32285), by the Deutsche Forschungsgemeinschaft (grant No. FOR 404), and by the Swedish Research Council and the Swedish Foundation for Strategic Research. A.S. Vinogradov gratefully acknowledges the financial support by the Wilhelm-Ostwald-Institut für Physikalische und Theoretische Chemie der Universität Leipzig. A.B. Preobrajenski acknowledges the support by the Swedish Foundation for International Cooperation in Research and Higher Education (STINT).

References

1. Preobrajenski, A. B. *et al.*, Phys. Rev. B **65**, 205116 (2002).
2. Preobrajenski, A. B. *et al.*, Chem. Phys. Lett. **368**, 125 (2003).
3. Wells, A. F., "Structural Inorganic Chemistry" (5th ed., Clarendon Press, Oxford 1984), p. 1066–1067.
4. Sakowski, J. and Herms, G., J. Non-Cryst. Solids **293–295**, 304 (2001) and references therein.
5. Muramatsu, Y. *et al.*, X-Ray Spectrom. **28**, 503 (1999).
6. Li, D., Bancroft, J. M. and Fleet, M. E., J. El. Spectr. Rel. Phenom. **79**, 71 (1996).
7. Joyner, D. J. and Hercules, D. M., J. Chem. Phys. **72**, 1095 (1980).
8. Postnikov, A. V. *et al.*, Phys. Rev. B **50**, 14849 (1994).
9. Shimada, H. *et al.*, J. El. Spectr. Rel. Phenom. **79**, 211 (1996).

Physica Scripta. Vol. T115, 1074–1076, 2005

Electronic Structure of FeF_2 and FeF_3 Studied by X-ray Absorption and Fluorescence Spectroscopy

S. A. Krasnikov*[1,2], A. S. Vinogradov[1], A. B. Preobrajenski[1,3], L. K. Gridneva[3], S. L. Molodtsov[1,4], C. Laubschat[4] and R. Szargan[2]

[1]V. A. Fock Institute of Physics, St. Petersburg State University, 198504 St. Petersburg, Russian Federation
[2]Wilhelm-Ostwald-Institut für Physikalische und Theoretische Chemie, Universität Leipzig, D-04103 Leipzig, Germany
[3]MAX-lab, University of Lund, P.O. Box 118, S-22100 Lund, Sweden
[4]Institut für Festkörperphysik, Technische Universität Dresden, D-01062 Dresden, Germany

Received June 26, 2003; accepted November 4, 2003

PACS numbers: 78.70.En, 78.70.Dm, 71.20.−b, 71.70.Ch

Abstract

High resolution investigations of polycrystalline FeF_2 and FeF_3 were performed by means of X-ray absorption and resonant X-ray fluorescence spectroscopy. The obtained F Kα fluorescence spectra of ionic FeF_2 and FeF_3 were analysed in comparison with the F Kα spectrum of the covalent anion TiF_6^{2-} in solid K_2TiF_6. The F Kα spectra of compounds under study consist of the main band accompanied by a low-energy shoulder. The latter can be associated with the valence subband of the Fe 3d – F 2p hybridized electron states. Strong high-energy shake-up satellites were observed in the F Kα spectra of these compounds when the excitation energy exceeds the F 1s ionisation threshold (∼690 eV). Information about local partial densities of states for FeF_2 was obtained from a comparative analysis of Fe L and F K X-ray fluorescence and valence-band photoemission spectra.

1. Introduction

Spectroscopic characterization of covalence bonding (hybridization) effects in the electronic structure of 3d transition metal (TM) compounds has a long history, but remains an issue of great fundamental interest. The hybridization between 3d electrons of the TM atom and *n*p electrons of the ligands is known to be responsible for the spatial delocalization of the 3d electron wave function. These effects can be studied by soft X-ray fluorescence (XF) spectroscopy, which is a site and symmetry selective and bulk sensitive tool, commonly used in investigations of electronic structure of matter. In contrast to electron spectroscopies, XF allows to easily probe insulators, since both the exciting and the analyzed particles (photons) are neutral. Nowadays XF becomes more and more popular due to the advent of high-brilliance synchrotron radiation (SR) sources (for review see, e.g., [1]). Tuning excitation energy across a particular absorption threshold may result in changes in XF spectra (resonant XF). In the case of TM compounds these changes provide information on the interplay between intra-atomic Coulomb interaction and interatomic hybridization [1].

The present work is aimed at investigating the hybridization-related features of the valence electron spectra of FeF_2, FeF_3 and K_2TiF_6 by means of resonant soft X-ray fluorescence and X-ray absorption spectroscopy (XAS). The electronic structure of TM fluorides, the most ionic of TM compounds, may provide important reference information for understanding the more complicated electronic structure of covalent TM compounds. We mainly focus on the F Kα and non-resonant Fe Lα fluorescence spectra examining the effect of the TM 3d – F 2p hybridization (resonant Fe $L_{2,3}$ fluorescence spectra will be presented elsewhere). The obtained F Kα spectra of ionic compounds FeF_2 and FeF_3 are analyzed in comparison with the F Kα spectrum of the covalent anion TiF_6^{2-} in solid K_2TiF_6. Furthermore, the F Kα spectra of solid ionic fluorides are particularly suitable for studying the effect of shake-up satellites on the lineshape of the emission spectra as a function of the exciting photon energy [2, 3]. Note that in all compounds under study the TM atom is coordinated in a similar way (octahedrally) to the fluorine atoms.

2. Experiment

The experiments were performed at the "bulk" branch of the undulator beamline I511 at the MAX II storage ring [4]. The powder samples (Alfa Aesar) were fixed on the carbon-tape strips attached to the sample holder. The modified SX 700 monochromator of this beamline was operated with a photon-energy resolution of 0.4 eV at the F K and the Fe $L_{2,3}$ edges. The soft X-ray absorption spectra were measured in the total electron yield mode and normalized to the incident photon flux. The X-ray fluorescence spectra were recorded using a high-resolution grazing-incidence X-ray spectrometer XES 300 with a resolution of 0.9 eV at the F K and the Fe $L_{2,3}$ edges. The optical axis of the X-ray spectrometer was set perpendicular to the beamline axis in the plane of polarization of the incident radiation in order to reduce the intensity of the elastically scattered peak. The angle between the sample normal and the spectrometer axis was 30°. The energy calibration of these spectra was done using the measured positions of the elastically scattered peak and the known position of the Fe Lα band for metallic Fe (705.0 eV [5]).

3. Results and discussion

A comparison between K_2TiF_6 and iron fluorides is quite natural, because the quasi-isolated covalent molecular anion TiF_6^{2-} (the main building block of K_2TiF_6) is almost isostructural with the FeF_6 octahedron. Fig. 1 shows high-resolution F 1s and Fe 2p X-ray absorption spectra of K_2TiF_6, FeF_3 and FeF_2. The F 1s absorption spectra of compounds under study can be divided in two spectral ranges, whose structural features are similar for all spectra. The first range consists of narrow resonance-like peaks a (a′) and b (or/and b′) located below the F 1s ionization threshold (∼690 eV) [6]. The second range is dominated by broader absorption bands c, d and e located slightly above the ionization threshold and significantly overlapping with each other. The crystal structure of all fluorides studied in the present work can be considered as three-dimensional arrays of interlinked (FeF_2 and FeF_3) or quasi-isolated (K_2TiF_6) MF_6 octahedra (M = Ti, Fe), which can be slightly (FeF_3) or strongly (FeF_2) distorted [7]. We suppose that not only in the ionic-molecular K_2TiF_6 crystal, but also in the rather ionic iron fluorides it is the MF_6 octahedra that determine the electronic structure, while the inter-octahedra

*Corresponding Author: Tel. +49-(0)341-9736457; Fax +49-(0)341-9736399; E-mail: krasnikov@rz.uni-leipzig.de

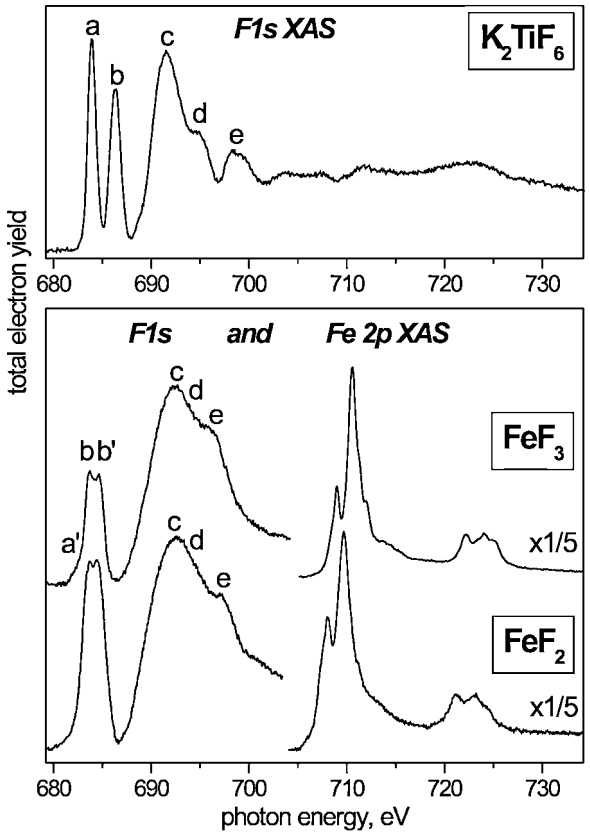

Fig. 1. X-ray absorption spectra of K_2TiF_6, FeF_3 and FeF_2.

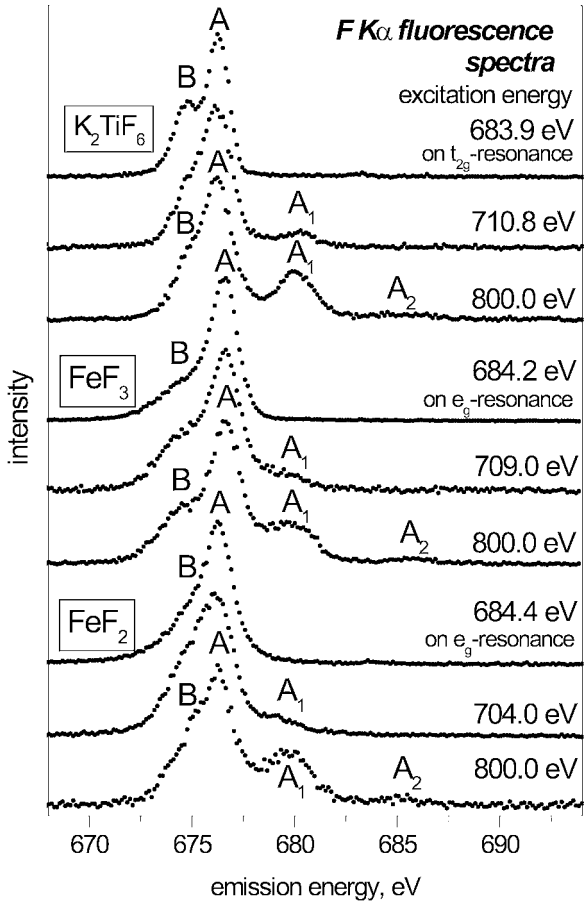

Fig. 2. F Kα X-ray fluorescence spectra of K_2TiF_6, FeF_3 and FeF_2 taken at the resonant and non-resonant excitation energies. The spectra are normalized to the same intensity of band A.

interaction is of less importance [6]. Covalent bonding between the 3d atom and the surrounding fluorine atoms can occur inside the octahedron due to mixing of the metal 3d, 4s,p and the fluorine 2p electron states. Indeed, the narrow resonance-like peaks a (a′) and b (b′) located below the F 1s ionization threshold in K_2TiF_6, FeF_3 and FeF_2 reflect the F 1s electron transitions into the empty t_{2g} and e_g electron states, which have hybridized F 2p – metal $3dt_{2g}$ and metal $3de_g$ origin, respectively [6, 8]. The following broad bands c-e located slightly above the F 1s threshold are caused by electron transitions into the unoccupied F 2p states which are hybridized with the metal 4s,p electron states. The similar shape of the Fe 2p absorption spectra of FeF_2 and FeF_3 results from the similar (octahedral) coordination of the Fe atom in these compounds [6, 8].

The effect of hybridization can also be demonstrated by comparison of the soft X-ray fluorescence spectra of K_2TiF_6, FeF_3 and FeF_2 excited by photons with resonant and non-resonant energies. As seen in Fig. 2 the F Kα spectra of the covalent molecular anion TiF_6^{2-} (in solid K_2TiF_6) and of the ionic compounds FeF_3 and FeF_2 are quite similar to each other revealing the main band A with a low-energy shoulder B. The energy position of A (676.2 eV for K_2TiF_6, 676.3 eV for FeF_2 and 676.6 eV for FeF_3) shows no appreciable change with the photon energy across the F 1s edge. In contrast to these spectra of the 3d TM compounds, the F Kα spectra of more ionic compounds KF and NaF are known to be dominated by only one main band that is located at the energy of band A [3, 9]. Indeed, the valence band of highly ionic fluorine compounds like KF and NaF is mainly of the F 2p character. Therefore, the corresponding fluorescence spectra consist of only one narrow band, which represents the dipole allowed transitions of the valence-band 2p electrons to the 1s core hole of the F^- anion. The energy position of this band reflects the energy separation between 1s and 2p levels of the F^- anion and undergoes no significant changes upon cation substitution. In iron fluorides the valence-band F 2p electron states can be divided into two partly overlapping bands. The energy position of the high-energy band A correlates well with the F Kα energy position in XF spectra of alkali fluorides and can be associated with the transitions from almost purely ionic F 2p states. On the other hand, the F Kα spectrum of the covalent molecular anion TiF_6^{2-} is very similar to that of iron fluorides. Thus, we associate shoulder B in the F Kα spectra of compounds under study with transitions from the valence subband of the metal (Fe, Ti) 3d – F 2p hybridized electron states. A similar hybridization related feature was observed in the O Kα emission spectra of TM oxides [10] and also in the S $L_{2,3}$ spectra of metal sulfides [11].

The XF spectra of K_2TiF_6, FeF_3 and FeF_2 vary differently at the energies of the t_{2g}- and the e_g-absorption resonances. The low-energy shoulder B in the spectrum of the covalent anion TiF_6^{2-} resonates appreciably as compared to the ionic iron fluorides and the energy separation between A and B is larger for K_2TiF_6 and FeF_3 (∼1.6 eV) than for FeF_2 (∼1.3 eV). The difference in the energy separation can originate from the fact that in the case of TiF_6^{2-} and FeF_3 the coordination octahedron is nearly perfect in contrast to the distorted octahedron in FeF_2. The higher intensity of the shoulder B in the resonant XF spectrum of TiF_6^{2-} comparing with that of the iron fluorides results from the stronger metal 3d – F 2p hybridization as well as the higher localization of the electron states in K_2TiF_6 than in FeF_3 and FeF_2.

At excitation energies about 15–20 eV higher than the F 1s ionization threshold high-energy shake-up satellites A_1 and A_2

begin to appear in the F Kα spectra of K_2TiF_6, FeF_3 and FeF_2 (Fig. 2). At energies of incident photons about 800 eV features A_1 and A_2 become quite intense. These shake-up satellites are due to the excitation process (initial-state satellites), since satellites caused by the emission process would have energies lower than the main bands. Shake-up satellites in the low-energy regime (i.e., only a few eV above the threshold) were observed first by Wassdahl *et al*. in resonant $L_{2,3}$ X-ray fluorescence from Cu and Zn metals [12]. Our observation of strong initial-state shake-up satellites in the F Kα spectra of all studied compounds confirms the validity of the sudden approximation for our systems even at low-energy excitations. This result follows the conclusion derived in Ref. [12] for Cu and Zn metals. The intensities of the shake-up satellites are known to rise with increasing excitation energy and to reach their maximum values for X-ray emission induced by high-energy electron or ion impact [9, 13]. To avoid distortion of the spectral shape for valence-band analysis the XF spectra should be excited with photon energies just slightly above the ionization threshold.

In Fig. 3 we compare the F Kα emission bands of FeF_2 and FeF_3 recorded at 684.4 eV (the resonance spectrum has been chosen in the case of FeF_2, because the shake-up satellite A_1 appears already at the excitation energy of 690 eV) and 697.5 eV, respectively, Fe Lα emission bands recorded at the excitation energy of 750.0 eV with the Fe $2p_{3/2}$ and F 1s absorption spectra of iron fluorides. The valence-band X-ray photoemission (XPS) spectrum of FeF_2 single crystal taken from Ref. [14] is shown by the dashed line. The XF and XAS spectra are aligned in the binding-energy scale using XPS binding energies of the core levels measured in the present study: E(Fe $2p_{3/2}$) = 712.1 eV, E(F 1s) = 684.9 eV for FeF_2 and E(Fe $2p_{3/2}$) = 714.5 eV, E(F 1s) = 685.0 eV for FeF_3.

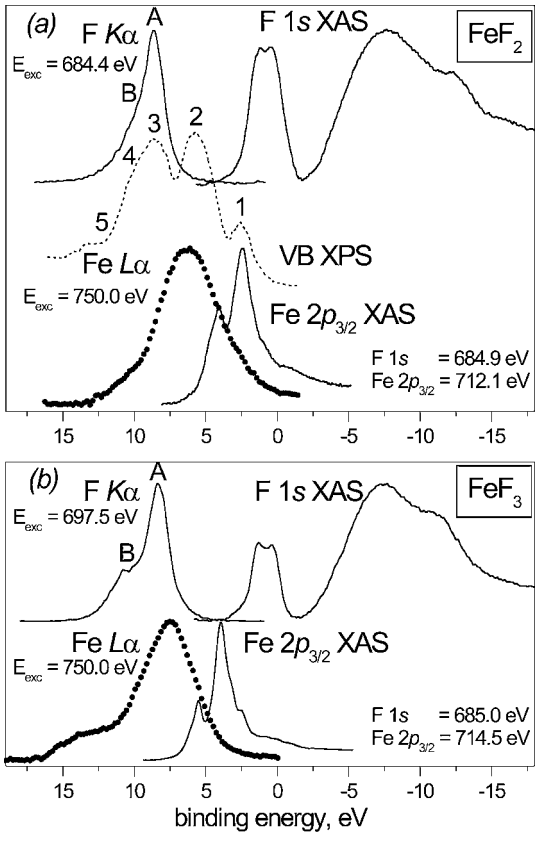

Fig. 3. Comparison of the Fe Lα-, F Kα-fluorescence and Fe $2p_{3/2}$-, F 1s-absorption of FeF_2 (a) and FeF_3 (b). Dashed line shows the valence-band photoemission spectrum of FeF_2 single crystal [14].

As seen in Fig. 3(a) the valence band of FeF_2 consists of three subbands: the upper subband (peak 2) is dominated by the Fe 3d electron states, the middle subband (peak 3) is dominated by the F 2p electron states, while the lower one (shoulder 4 and peak 5) is dominated by the F 2p electron states hybridized with the Fe 3d states (peak 1 is due to final-state multiplets [14]). The same valence-band structure can be derived from comparison of the XF and the XAS spectra for FeF_3 in Fig. 3(b). However, the relative energy positions of the subbands connected with the pure Fe 3d and F 2p electron states and with the hybridized Fe 3d – F 2p electron states differ a little for FeF_3 compared to that for FeF_2. The low-energy shoulder in the Fe Lα XF spectra of iron fluorides is caused also by the Fe 3d – F 2p hybridization.

The overall similarity of the corresponding XF (XAS) spectra of FeF_2 and FeF_3 reflects resembling structure of occupied (unoccupied) electron states for both fluorides. This similarity is surprising in the framework of different ionic-multiplet approaches because of quite different electronic configurations expected for Fe(II) and Fe(III) compounds in the initial, intermediate and final states. However, it can easily be understood within the framework of a quasi-molecular (FeF_6) approach to the electronic structure of FeF_2 and FeF_3. Indeed, if the electronic structure is determined mainly by the FeF_6 octahedra, while the way they are inter-linked is less critical, the spectra should look similar. An important point of this approach is the inclusion of the covalent mixing between the iron and fluorine valence electron states inside the FeF_6 quasi-molecule.

In conclusion, the X-ray fluorescence and the X-ray absorption measurements carried out for the iron fluorides FeF_3 and FeF_2 in comparison with the covalent molecular anion TiF_6^{2-} (in solid K_2TiF_6) demonstrate the significant role of the Fe 3d – F 2p hybridization (covalence bonding) in these ionic compounds. This hybridization effect is responsible for the double-band spectral shape of the F Kα and Fe Lα fluorescence spectra.

Acknowledgements

This work was supported by the RFBR (grant No. 01-03-32285), by the BMBF (grant No. 05SR8OL1-2) and by the DFG (grants No. FOR 404 and SFB463, TPB4). A. S. Vinogradov gratefully acknowledges the financial support by the Institut für Festkörperphysik der Technischen Universität Dresden and the Wilhelm-Ostwald-Institut für Physikalische und Theoretische Chemie der Universität Leipzig. A. B. Preobrajenski acknowledges the support by the Swedish Foundation for International Cooperation in Research and Higher Education (STINT).

References

1. Kotani, A. and Shin, S., Rev. Mod. Phys. **73**, 203 (2001).
2. Rubensson, J.-E., Eisebitt, S., Nicodemus, M., Boeske, T. and Eberhardt, W., Phys. Rev. B **50**, 9035 (1994).
3. Oura, M. *et al*., Phys. Rev. Lett. **90**, 173002 (2003).
4. Denecke, R. *et al*., J. Electron Spectrosc. Rel. Phenom. **101–103**, 971 (1999).
5. Bearden, J. A., Rev. Mod. Phys. **39**, 78 (1967).
6. Vinogradov, A. S. *et al*., submitted to Phys. Rev. B.
7. Wells, A., "Structural Inorganic Chemistry" (Clarendon, Oxford, UK, 1984).
8. Vinogradov, A. S. *et al*., BESSY Annual Report (2001), p. 137.
9. Mattson, R. A. and Ehlert, R. C., "Advances in X-ray Analysis" (Edited by G. R. Mallett, M. Fay and W. M. Mueller) (Plenum Press, New York, 1966), vol. 9, p. 471.
10. Fischer, D. W., Appl. Spectrosc. **25**, 263 (1971).
11. Szargan, R. and Meisel, A., Wiss. Zeitschrift der KMU, Math.-Nat. Reihe **20**, 41 (1971).
12. Wassdahl, N. *et al*., J., Phys. Rev. Lett. **64**, 2807 (1990).
13. Benka, O., Watson, R. L. and Kenefick, R. A., Phys. Rev. Lett. **47**, 1202 (1981).
14. Kowalczyk, S. P., Ley, L., McFeely, F. R. and Shirley, D. A., Phys. Rev. B **15**, 4997 (1977).

Physica Scripta. Vol. T115, 1077–1079, 2005

Sulfur K-Edge X-Ray Absorption Spectra for Dimethyl Sulfoxide in the Solvated Thallium(III), Indium(III), Gallium(III) and Aluminum(III) Ions

E. Damian[1], F. Jalilehvand[2], A. Abbasi[1], L. G. M. Pettersson[3] and M. Sandström[1,*]

[1]Department of Structural Chemistry, University of Stockholm, SE-106 91 Stockholm, Sweden
[2]Department of Chemistry, University of Calgary, Calgary, AB T2N 1N4, Canada
[3]Department of Physics, Alba Nova, Stockholm University, SE-106 91 Stockholm, Sweden

Received June 26, 2003; accepted November 4, 2003

PACS number: 6110Ht

Abstract

The sulfur K-edge X-ray absorption near edge spectra (XANES) of the hexakis(dimethyl sulfoxide) solvated trivalent group 13 ions, Al, Ga, In and Tl, in the solid state show larger splitting and different intensity distribution of the main sulfur 1s electronic excitations than for the uncoordinated dimethyl sulfoxide molecule. The transitions have been interpreted by density functional calculations, and the increased splitting is shown to be an effect of metal-oxygen orbital interactions in the bonds to the oxygen coordinated dimethyl sulfoxide ligand.

1. Introduction

The hexakis(dimethyl sulfoxide) solvates of the group 13 metal ions aluminium(III), gallium(III), indium(III) and thallium(III), were previously structurally characterized in the solid state as iodides or perchlorates by crystallography, EXAFS and vibrational spectroscopy (Table I) [1–3]. In the present study, sulfur K-edge XANES spectra are presented for dimethyl sulfoxide, free or as ligand to the group 13 metal ions. Dipole-allowed excitations of the sulfur 1s electron to unoccupied molecular orbitals with some p-character in bound states, dominate the absorption features in the near-edge region, and provide sensitive probes of the bonding because of the relatively narrow line widths and wide energy range. We found significant changes in the sulfur K-edge spectra of dimethyl sulfoxide even for coordination *via* the oxygen atom by the group 13 metal ions (Figure 1).

2. Experimental

Sulfur K-edge XANES spectra were recorded in fluorescence mode on beam line 6-2 of Stanford Synchrotron Radiation Laboratory (SSRL), under dedicated conditions (3 GeV and 75–100 mA). The beam path and sample were kept in helium of atmospheric pressure. A Lytle detector without filter and Soller slit was used for detection of the fluorescence signal from the sample. The X-ray energy was varied using a fully tuned Si(111) double monochromator with the energy scale calibrated by setting the lowest energy peak of sodium thiosulfate ($Na_2S_2O_3 \cdot 5H_2O$) to 2469.2 eV [4]. Higher order harmonics were rejected by means of a nickel-coated mirror. The instrumental broadening of the spectral features is about 0.5 eV. Finely ground metal salts, prepared as described elsewhere [2, 3], were dispersed as a thin layer on a sulfur-free Mylar adhesive tape. A cell with 5 μm sulfur-free polypropylene film windows was used for a 50 mM solution of DMSO in acetonitrile. The data were analyzed using the EXAFSPAK suite of computer programs [5], and normalized intensity spectra are presented in Figure 2.

Table I. *Bond lengths (Å), angles (°) and force constants (Ncm^{-1}) for $M(dmso)_6^{3+}$ complexes in the solid state (Refs. [2, 3]).*

Atom	Al(III)	Ga(III)	In(III)	Tl(III)	DMSO
M-O	1.894(4)	1.974(4)	2.145(3)	2.224(3)	
O-S	1.540(5)	1.539(5)	1.541(3)	1.544(4)	1.495(4)
M-O-S	127.1(3)	124.1(3)	123.1(2)	120.7(2)	
K(*M*O)	1.76	1.62	1.32	1.30	
K(OS)	4.60	4.17	4.27	4.28	5.06

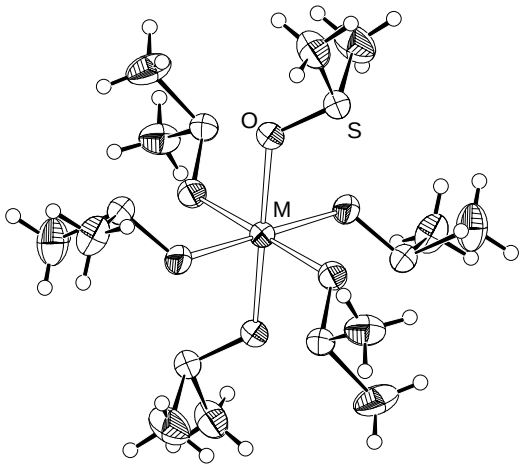

Fig. 1. The hexakis(dimethylsulfoxide)indium(III) ionic complex with six equivalent oxygen-coordinated DMSO ligands in the crystal structure of $[In(dmso)_6]I_3$ (295 K, 50% probability ellipsoids).

3. Computational details

Theoretical sulfur K-edge transitions were calculated for dimethyl sulfoxide molecules, free and with different types of simulated coordination (Table II), to assign the transitions observed in the experimental spectra. The computations were performed by means of the deMon StoBe density functional theory (DFT) program, using non-local gradient-corrected functionals throughout [6].

The overall spectrum was first generated by the transition potential DFT method [7], where the potential used to determine the excited states is by exciting half an electron from the 1s orbital. The differential relaxation effects on each excited state were computed separately by Kohn-Sham's excited state (ΔKS) DFT calculation method [8]. The relativistic effect was calculated to shift the ionization potential 7.4 eV for the sulfur K-edge, and was applied as an overall shift of the spectrum. Absolute energies corrected in this way in previous computations show satisfactory agreement with the experimental calibration used (see above) [8].

*e-mail: magnuss@struc.su.se

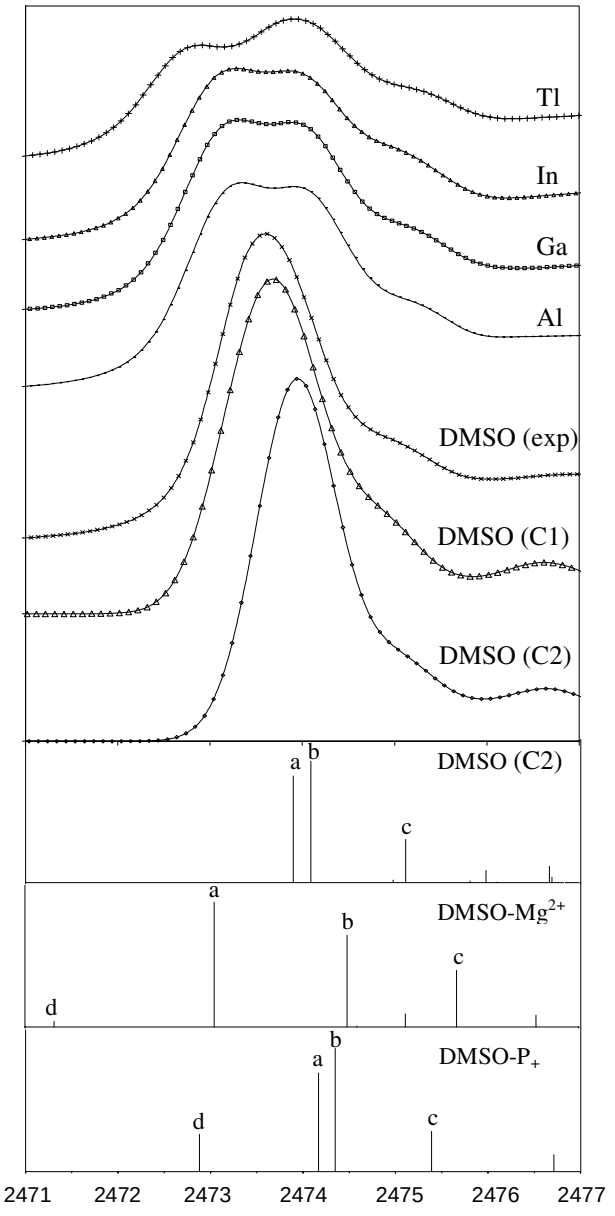

Fig. 2. Experimental sulfur K-edge XANES spectra (normalized intensities) of the hexakis(dimethyl sulfoxide)-M(III) solvates of the group 13 metal ions (from the top M = Tl, In, Ga and Al), and of 50 mM DMSO in acetonitrile. Below calculated spectra for free DMSO, C1 with the S-O distance 1.595 Å, and C2 with 1.495 Å (*cf*. Table II). The rows vertical bars represent the calculated energies and cross-sections for the X-ray induced excitations of the sulfur 1s electron for free DMSO (C2), for DMSO connected to an Mg^{2+} ion, and to a +1 point charge P_+, respectively.

Table II. *Interatomic distances (Å) and angles (°) used in the computation of spectra for free (C1 & C2) and coordinated (M) = Mg^{2+} or P_+) DMSO. P_+ represents a point charge +1.*

	Free	Coordinated
O-S	1.495 & 1.595	1.544
S-C	1.773	1.773
O-S-C	105.7	105.7
M-O	—	2.0
M-O-S	—	125

However, another calibration scheme with the thiosulfate peak set to 2472.02 eV, i.e. +2.8 eV, is also in use [9].

To simulate the interaction between a metal ion and a dimethyl sulfoxide ligand, we have computed the spectra of models with a point charge +1 (P_+) or an Mg^{2+} ion located at a possible coordination site relative to the oxygen atom of the DMSO molecule (Table II). In all calculations, C_s symmetry was assumed. For sulfur the iglo basis of Kutzelnigg was used in order to describe relaxation effects upon core-excitation [10]; this was extended with a very large, diffuse additional basis set for the evaluation of the spectra in a double-basis set approach. The basis sets used were for oxygen and carbon TZVP ((6311/311/1)), for hydrogen (311/1) and for the magnesium ion DZVP (6321/411*/1). The auxiliary bases (5,4;5,4) were introduced for sulfur and magnesium, (5,3;5,3) for oxygen and carbon, and (4,2;4,2) for hydrogen, where the nomenclature ((N_C(s), N_C(spd); N_{XC}(s), N_{XC}(spd)) indicates the number of s and spd-type functions that were used to fit and expand the Coulomb and exchange-correlation potentials, respectively.

4. Results and discussion

The sulfur K-edge XANES spectrum of dimethyl sulfoxide in solution shows an asymmetric peak at about 2473.5 eV with a shoulder at 2475 eV. These features are well explained by the three main calculated transitions (*a*, *b*, *c* in Fig. 2). By applying a Gaussian 1.0 eV broadening of the calculated features up to the computed ionisation potential, followed by a linear increase up to 8 eV over a 10 eV interval from the edge, the calculated curves C1 and C2 result, with a similar shape as the experimental (Figure 2). The calculated (gas phase) spectrum C2 is shifted 0.5 eV relative to the experimental solution spectrum. This shift may be caused by uncertainties in the calculated energy or the experimental calibration [4, 9]. Also, dipole-dipole interactions between the DMSO molecules in the acetonitrile solution may influence the shift, even though a large increase in the S–O bond length (0.1 Å, *cf*. Table II) would be needed to eliminate this shift (C1 in Fig. 2) .

The shapes of the excited state molecular orbitals (MO) show, for the strongest *b* transition (of A″ symmetry species in the C_s point group, *cf*. Fig. 3) excitation of the sulfur 1s electron to an antibonding MO of p character, and for the *a* and *c* transitions (of A′ symmetry) charge transfer from sulfur to the carbon and oxygen atoms.

The site symmetry of the crystalline $[M(dmso)_6]^{3+}$ solvates implies all six oxygen-bonded dimethyl sulfoxide ligands to be equivalent (Fig. 1). The sulfur K-edge XANES spectra for the Al, Ga and In solvates are similar with a slight increase in the splitting between the two main peaks from about 0.7 to 0.8 eV. For the Tl(III) solvate the split increases to 1.5 eV (Fig. 2). To simulate the effect on a coordinated DMSO ligand an Mg^{2+} ion was placed 2.0 Å from the oxygen atom in a similar position as the metal ions in the hexasolvates (Table II). The distance is chosen, based on previous DFT calculations [11], to give a reasonable balance between the electrostatic attraction and the Pauli repulsion effects between the orbitals in the M-O bond.

The Mg^{2+} ion shifts the transition *a* about 1.5 eV to lower energy, and increases its probability to slightly higher than that of *b* (Fig. 2). The orbital character of *a* becomes clearly antibonding with increased charge on the oxygen atom (Fig. 3). The *b* and *c* transitions increase only slightly in energy, and satisfactorily explain the features at 2474 and 2475.3 eV,

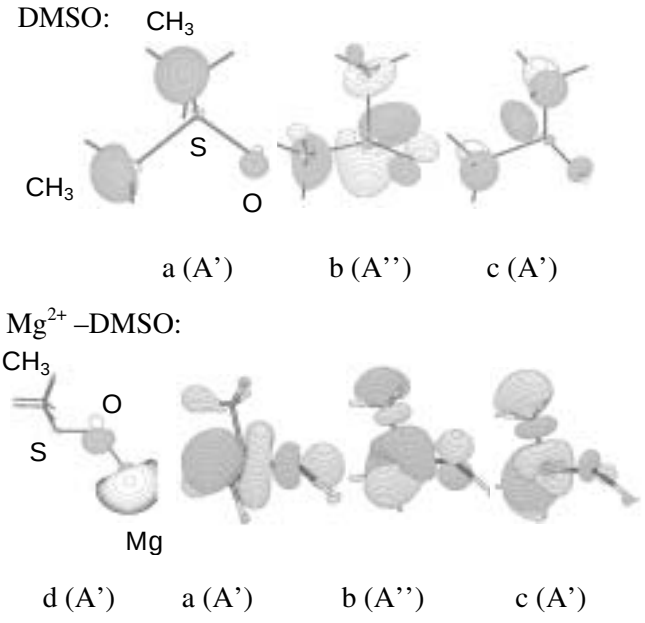

Fig. 3. Electron density contours for MO:s (different gray tones indicate different phase) corresponding to the one-particle excitations in Figure 2 of the sulfur 1s electron in: (top) free DMSO; (bottom) DMSO coordinated to an Mg^{2+} ion at a distance of 2.0 Å (*cf*. Table II).

respectively, which are found throughout the experimental spectra. A new weak transition (*d*) that appears at low energy (2471 eV), corresponds to charge transfer from sulfur to the magnesium ion, as shown by the orbital shapes in Figure 3.

To assess the importance of interatomic orbital interactions versus pure electrostatic effects the Mg^{2+} ion was replaced with a point charge (+1). The main effect is that the charge transfer transition *d* is less shifted but gains intensity, while the transitions *a*, *b* and *c* remain similar in energy and intensity to those in the free DMSO molecule (Figure 2). Thus, the orbital interactions induced by the M-O bond seem to cause the observed splitting in the spectra. The gradual increase in covalency from Al to In is only reflected in a small increase in the split between the main transitions, with the Tl(III) sulfur XANES spectrum clearly deviating from that trend. Thus, the large split in the Tl(III) spectrum indicates a substantial increase in the orbital interaction. Even though the Tl-O bond is the longest of the group 13 M-O bonds, it is the most covalent [3]. This is indicated by e.g. the trends of the vibrational force constants, the M-O-S angles and the S-O bond length (Table I). For the thallium(III) solvate the disorder parameters indicate vibronic mixing in the M-O bonds of the $5d_z^2$ and 6s orbitals, which are close in energy [2]. It seems probable that the isoelectronic hexakis(dimethyl sulfoxide) mercury(II) solvate, which is affected by vibronic mixing (or pseudo Jahn-Teller effect) to a higher extent [2], would show an even larger split in its sulfur spectrum (not studied yet).

5. Conclusions

The orbital interactions in the M-O bonds are the reason for the increase in the splitting observed between the main electronic transitions in the sulfur K-edge spectra of DMSO as oxygen coordinated ligand to a metal ion. The large splitting in the hexakis(dimethyl sulfoxide) thallium(III) solvate is probably connected to the close energy levels causing vibronic mixing between valence shell atomic orbitals in the Tl-O bonds.

Acknowledgements

The financial support by the Swedish Science Research Council and the allocation of beam-time and laboratory facilities by SRRL made this study possible. SSRL is operated by the Department of Energy, Office of Basic Energy Sciences. The SSRL Biotechnology Program is supported by the National Institutes of Health, National Center for Research Resources, Biomedical Technology Program, and by the Department of Energy, Office of Biological and Environmental Research.

References

1. Harrowfield, M. J., Skelton, B. W. and White, A. H., Aust. J. Chem. **43**, 759 (1990).
2. Ma, G. *et al*., Inorg. Chem. **40**, 6432 (2001).
3. Molla-Abbassi, A. *et al*., J. Chem. Soc., Dalton Trans. 1746 (2003).
4. Sekiyama, H., Kosugi, N., Kuroda, H. and Ohta, T., Bull. Chem. Soc. Jpn. **59**, 575 (1986).
5. George, G. N. and Pickering, I. J., EXAFSPAK; A Suite of Computer Programs for Analysis of X-ray Absorption Spectra, SSRL, Stanford University, CA., USA (1993).
6. deMon-KS StoBe version 1.0, Casida M. E. *et al*., deMon Software (2001).
7. Stöhr, J., NEXAFS spectroscopy, (Springer-Verlag, Berlin, Heidelberg 23, 1992).
8. Kolczewski, C. *et al*., J. Chem. Phys. **115**, 6426 (2001).
9. Hedman, B. *et al*., Nucl. Instr. Meth. **A246**, 797 (1986).
10. Kutzelnigg, W., Fleischer, U. and Schindler, M., "NMR-Basic Priniciples and Progress" (Springer Verlag, Heidelberg, 1990).
11. Pavlov, M., Siegbahn, P. E. M. and Sandström, M., J. Phys. Chem. **102**, 219 (1998).

Physica Scripta. Vol. T115, 1080–1083, 2005

Analysis of Ti Kα″ Spectra in X-ray Emission Spectroscopy

N. Shigeoka[1], H. Oohashi[1], T. Tochio[1], Y. Ito[1*], T. Mukoyama[2], A. M. Vlaicu[3], H. Yoshikawa[3] and S. Fukushima[3]

[1]Institute for Chemical Research, Kyoto University, Uji, Kyoto, 611-0011, Japan
[2]Kansai Gaidai University, 16-1 Nakamiyahigashino, Hirakata, Osaka 573-1001, Japan
[3]National Institute for Material Science, SPring-8, Mikazuki, Hyogo, 679-5198, Japan

Received June 26, 2003; accepted in revised form November 4, 2003

PACS numbers: 32.30.Rj, 32.80.Fb

Abstract

The Ti Kα″ satellite was investigated using a Johann-type spectrometer at the BL15XU undulator beam line, SPring-8. Ti Kα spectra were measured varying the excitation energy between 4996 eV and 10000 eV. The relative intensity of the Ti Kα″ satellite to that of the $K\alpha_{1,2}$ abruptly increases from 0% to 1.2% within 10 eV around 5010 eV. This indicates that shake-up process is likely to be concerned with creation of a 3p spectator hole which induces the Kα″ satellite. Onset energy of the satellite appearance experimentally determined is 5005 eV, and this value corresponds to the [1s3p] double ionization threshold energy in $Z + 1$ approximation. The experimental results of this work confirm that the origin of the Kα″ satellite is a 3p spectator hole as predicted by Scott theoretically.

1. Introduction

It is well-known that many satellite lines of X-ray emission spectra can be attributed to multi-electron excited states. For example, the $K\alpha_{3,4}$ satellite lines orginate from a $[1s2p] \rightarrow [2p^2]$ transition [2, 4]. Kα″ is the satellite which appears on the high energy side of the $K\alpha_1$ peak in elements having an atomic number of around 20. In 1936 Parratt measured the Kα″ spectra of all the $16 \leq Z \leq 23$ elements except argon changing the tube voltage [1]. He concluded that the origin of the Kα″ satellite was a KM → LM transition. But he did not specify what subshell contributes to the satellite. That may be because the energy distribution of the incident electron beam was widely spread. In 1986, half a century after Parratt's work, Scott theoretically predicted, using non-relativistic single configuration Hartree Fock calculation, that a 3p spectator hole is the origin of the Kα″ satellite [3].

On the other hand, the advent of the third generation synchrotron facilities provides us with intense well-tuned incident X-rays, very useful for investigations on evolutions of satellites associated with multi-electron excited states. Taking advantage of synchrotron radiation, some interesting work on evolution of satellites was made in the last decade. Fritsch *et al*. and Sternemann *et al*. investigated the evolution of the Cu $K\alpha_{3,4}$ satellite lines and that of the Ge Kβ‴ satellite lines respectively [4, 5]. Most recently, the dependence of the Cu $K\alpha_{1,2}$ profile on the excitation energy around 1s ionization threshold was studied by Galambosi *et al*. discussing the contribution of a 3d spectator hole [6]. This work is important not only because it elucidates the origin of the satellites but also because it provides us with information on how the probabilities of the shake processes depend on excitation energy.

Considering the situation described above, it seems significant to make investigations on the evolution of the Kα″ satellite in order to confirm experimentally that its origin is a 3p spectator hole as predicted by Scott. In the present work, the Ti Kα spectra were measured changing excitation energy from onset (a threshold for [1s3p] ionization) in the adiabatic to saturation in the sudden approximation limit. Our results indicate that the orgin of the Kα″ satellite is a [1s3p] double hole state produced by shake processes.

2. Experiment

The measurements were carried out at the BL15XU undulator beam line in SPring-8. To get monochromatic X-rays for excitation, a Si(111) double crystal monochromator with a bandpass of $\delta E/E \sim 10^{-4}$ was used, and the flux obtained was over 10^{12} photons/s. The sample was a pure Ti plate with a thickness of 1 mm.

The spectrometer employed was a Johann-type spectrometer whose Rowland circle radius was 750 mm. The signal was collected using a CCD detector of horizontally 1340 pixels × vertically 400 pixels (Roper Scientific Model LCX-400). A Be window with a thickness of 800 μm was placed in front of the CCD chip to cut visible lights and prevent the CCD chip from contact with air. The surface of the CCD chip tangentially touches the Rowland circle.

Besides measurements of the Ti Kα spectra, dark current was also measured every three hours. The exposure time for one frame was 10 seconds and 100 or 200 frames were acquired at each excitation energy while 100 frames were acquired for dark current. For each spectrum contribution of dark current was subtracted using corresponding dark current data.

A Johann-type spectrometer equipped with a position sensitive detector permits measuring data over the investigated energy range without scanning the 2θ angle formed by sample, analyzing crystal and detector. Si(220) crystal was used to analyze fluorescence X-rays with a detector of 26.8 mm length, which means the effective energy range of the detector is ∼75 eV at $2\theta = 91.42^\circ$ except for an inactive region at both ends of the CCD chip. With this effective energy range of the detector, the Ti $K\alpha_{1,2}$ and Kα″ spectra can be measured with one shot of the CCD at $2\theta = 91.42^\circ$ where the Ti $K\alpha_1$ (4508.4 eV) peak is located at the center of the effective energy range of the detector.

3. Data Analysis

Five Lorentzians were fitted to the measured Ti Kα spectra. Each Lorentzian corresponds to the $K\alpha_1$(diagram line), the $K\alpha_2$(diagram line), the $K\alpha_1$ satellite on the low-energy side of the $K\alpha_1$ peak, the $K\alpha_2$ satellite on the low-energy side of the $K\alpha_2$ peak, and the Kα″ satellite, respectively. Two satellites on the low-energy side of the $K\alpha_{1,2}$ peaks on copper were discussed by Deutsch *et al*. [7], Ito *et al*. [8], and Galambosi *et al*. [6] suggesting that they were the satellites originating from a

*Email address: yosi@elec.kuicr.kyoto-u.ac.jp

[1s3d] → [2p3d] transition. Both the position and the width of each fitting component were fixed and only its intensity scale factor was refined in the fit. Fixed values for Lorentzians except for that of the Kα″ satellite were determined by fitting four Lorentzians to the $K\alpha_{1,2}$ spectrum measured at an excitation energy of 4978 eV which is free from the effect due to the existence of the satellite caused by a [1s3p] double hole state or resonant Raman scattering. Fixed parameters of the satellite component were determined by fitting Lorentzians to the $K\alpha_{1,2}$ spectra at excitation energy of 6000 eV, where the satellite is well matured.

It was theoretically predicted that the Kα″ satellite distributes over not only the high energy side of $K\alpha_1$ but also between $K\alpha_1$ and $K\alpha_2$ [3]. However, it is difficult to fit Lorentzians to the latter component of the Kα″ satellite in the spectra because it is buried in the valley between $K\alpha_1$ and $K\alpha_2$. Full widths at half maximum of the Ti $K\alpha_{1,2}$ peaks in each spectrum were obtained by fitting two asymmetric Lorentzians to each experimental spectrum in order to clarify the contribution of the satellite to the whole $K\alpha_{1,2}$ spectra.

4. Results and Discussion

The results of the fitting done for the Ti $K\alpha_{1,2}$ spectra with excitation energies of 5005 eV, 5011 eV, 5018 eV and 6000 eV are shown in Fig. 1. The Lorentzian corresponding to the Kα″ satellite is drawn with a solid curve in the figure.

The dependence of the intensity of the satellite on the excitation energy obtained by the fitting is shown in Fig. 2. The relative

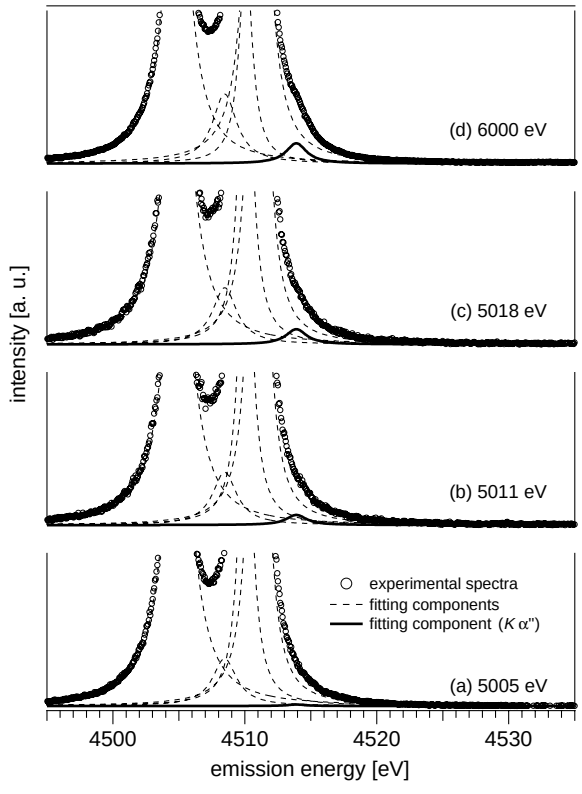

Fig. 1. Evolution of the Kα″ satellite (solid curve) with increasing excitation energy. The Kα″ satellite has no intensity in (a) where the excitation energy (5005 eV) is the threshold energy of the [1s3p] ionization. The intensity increases when excitation energy gets higher than the threshold (b, c). The evolution ceases when the excitation energy reaches around 5500 eV. The satellite in saturation is shown in (d).

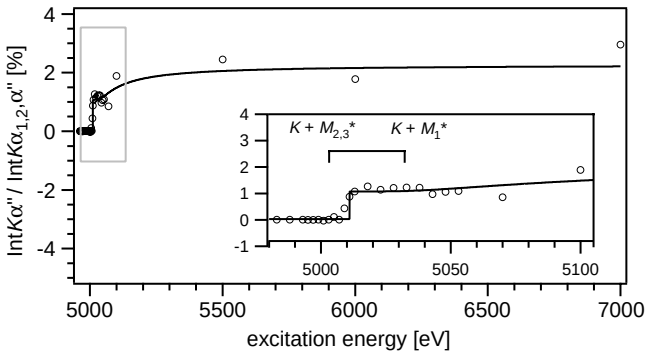

Fig. 2. The data shown as circles are the intensity of the Ti Kα″ satellite relative to that of the Kα lines as a function of excitation energy. The ionization threshold of $K + M_{2,3}^*$ and $K + M_1^*$ shown in the inset are estimated with $Z + 1$ approximation, where M_i^* means the binding energy of the M_i sub-shell of vanadium. The solid curve is the result of the fitting using Thomas model with a step function. Detailed explanations are in the text.

intensity of the Kα″ satellite to the whole $K\alpha_{1,2}$ intensity shows an abrupt jump from 0% to 1% within a range of 10 eV around 5010 eV as seen in Fig. 2. Although it stops increasing once around 5070 eV, it starts to increase again around 5100 eV and continue to increase until it almost saturates around 5500 eV. The relative intensity of the satellite is about 2.5% in saturation.

The solid curve in Fig. 2 is the result of fitting to the experimental data which was performed using the Thomas model [9, 10] with a step function. The Thomas model describes an excitation energy dependence of the shake-off probability and a step function describes that of the shake-up probability. The function fitted is expressed as

$$P(E) = P_{shake\text{-}up}(E) + P_{shake\text{-}off}(E)$$

where E is excitation energy. $P_{shake\text{-}up}$ is a step function defined as

$$P_{shake\text{-}up}(E) = \begin{cases} C & (E > E_{threshold}) \\ 0 & (E < E_{threshold}) \end{cases}$$

where C is a constant and $E_{threshold}$ is the onset energy of the satellite. P_{Thomas} is expressed as

$$P_{Thomas} = P_\infty \exp\left(-\frac{r^2 E_s^2}{15.32(E - E_{threshold})}\right),$$

where P_∞ is the saturated shake-off probability, r is the distance covered by an outgoing electron, E_s is the ionization threshold energy of a shaken electron. In our case the value of E_s was set to be 37.2 eV which corresponds to an ionization threshold energy of an $M_{2,3}$ electron determined by $Z + 1$ approximation. The other parameters were refined by the fitting and the following results were obtained: $C = 1.05 \pm 0.13$, $P_\infty = 1.19 \pm 0.19$, $r = 4.03\,\text{Å} \pm 1.05\,\text{Å}$ and $E_{threshold} = 5011.0\,\text{eV} \pm 0.14\,\text{eV}$.

The fitting result of $E_{threshold}$ shows an agreement with 5003.2 eV which is the [1s3p] ionization threshold energy obtained by $Z + 1$ approximation.

The probabilities of shake-up and shake-off processes by which an electron in the $M_i (i = 1, \ldots, 4)$ subshell is excited and ionized respectively were calculated in a manner described by Mukoyama and Ito [11]. The results are tabulated in Table I showing that the probabilities of $K + M_{2,3}$ double excitation (or ionization) due to the shake-up processes and the whole shake processes are $PM_{2,3(\text{shake-up})} = 2.71 \times 10^{-2}$ and $PM_{2,3(\text{shake})} = 6.55 \times 10^{-2}$, respectively.

Table I. *Probabilities of shake-up processes and shake-off processes involving an electron in M shell accompanying an ionization of an electron in K shell in Ti obtained by Dirac-Fock-Slater calculations. n stands for the principal quantum number of the orbital which a shaken M electron jumps into.*

	Initial shells			
Destinations	M_1	M_2	M_3	M_4
$n = 4$		6.508×10^{-3}	1.280×10^{-2}	3.085×10^{-2}
$n = 5$	7.032×10^{-4}	1.423×10^{-3}	2.811×10^{-3}	7.085×10^{-3}
$n = 6$	2.576×10^{-4}	5.628×10^{-4}	1.113×10^{-3}	2.934×10^{-3}
$n = 7$	1.243×10^{-4}	2.834×10^{-4}	5.608×10^{-4}	1.532×10^{-3}
$n = 8$	6.979×10^{-5}	1.636×10^{-4}	3.239×10^{-4}	9.103×10^{-4}
$n = 9$	4.317×10^{-5}	1.033×10^{-4}	2.045×10^{-4}	5.883×10^{-4}
$n = 10$	2.859×10^{-5}	6.946×10^{-5}	1.375×10^{-4}	4.035×10^{-4}
Total shake-up	1.227×10^{-3}	9.114×10^{-3}	1.795×10^{-2}	4.430×10^{-2}
Shake-off	6.662×10^{-3}	1.287×10^{-2}	2.551×10^{-2}	2.963×10^{-2}
Total	7.889×10^{-3}	2.198×10^{-2}	4.346×10^{-2}	7.393×10^{-2}

The ratio of the probability of the shake-up processes to that of the whole shake processes in the $K + M_{2,3}$ double excitation (or ionization) is

$$PM_{2,3(\text{shake-up})} : PM_{2,3(\text{shake})} \simeq 0.42 : 1$$

where $PM_{2,3(\text{shake-up})}$ means the sum of the probabilities of M_2 and M_3 shake-up processes accompanying a K shell ionization and $PM_{2,3(\text{shake})}$ is that of the whole shake processes. According to the results of the fitting in this work, the ratio of the contribution from the shake-up processes and that of the whole shake processes is approximately $1.05/(1.05 + 1.19) \simeq 0.47$. This indicates that the contribution of shake-up processes to the $K\alpha''$ satellite is much higher than that to the $K\alpha_{3,4}$ satellite which is less than one tenth of the shake-off processes.

The intensity distribution profiles of the $1s \rightarrow 2p$ diagram lines ($K\alpha_{1,2}$) and the $[1s3p] \rightarrow [2p3p]$ satellite emission were calculated using the code of GRASP [12] shown in Fig. 3. The $[1s3p] \rightarrow [2p3p]$ satellite spectra distributes over the high energy side of $K\alpha_1$ and between $K\alpha_1$ and $K\alpha_2$ similar to that in [3].

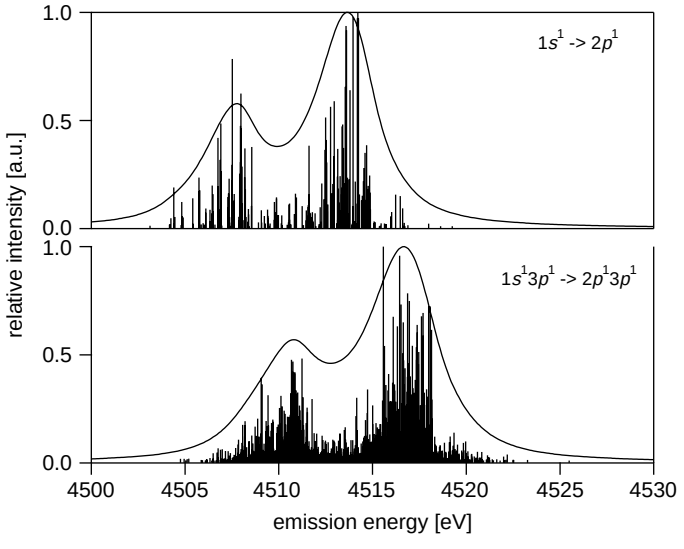

Fig. 3. Intensity distribution of $1s \rightarrow 2s$ transitions and $1s3p \rightarrow 2s3p$ transitions calculated using the code of GRASP. The results are shown as stick diagrams and as spectra obtained by a convolution with Lorentzians of 1.2 eV width. The intensity of each line is shown relative to the strongest one.

Table II. *Experimental and calculated values of the emission energies of the diagram lines and the satellite. Separation is the energy position of the emission line relative to that of $K\alpha_1$ line in both cases.*

Emission line	Energy (eV)	Separation (eV)
Experiment		
$K\alpha_1$	4510.8	
$K\alpha_2$	4505.0	−5.8
$K\alpha''$	4513.9	3.1
Calculation		
$K\alpha_1$	4513.7	
$K\alpha_2$	4507.8	−5.9
$K\alpha''$	4516.7	3.0

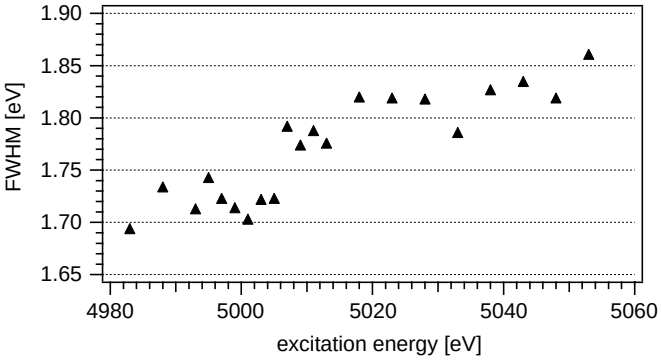

Fig. 4. Full width at half maximum of the Ti $K\alpha_1$ peak obtained by fitting an asymmetric Lorentzian to each peak in experimental data, respectively. Each data is shown as a function of excitation energy.

The peak positions of the diagram lines and satellite in the experimental and calculated spectra are compared with each other in Table II.

Full widths at half maximum of the $K\alpha_1$ peak obtained by fitting two asymmetric Lorentzians to each measured spectrum are shown in Fig. 4. As can be seen from the figure the width of the $K\alpha_1$ peak increases from ∼1.7 to ∼1.8 around an excitation energy of 5007 eV. It is obvious that the increase of the FWHM of the $K\alpha_1$ peak is ascribed to the appearance of the $K\alpha''$ satellite.

5. Conclusion

We investigated here the dependence of the intensity in the Ti $K\alpha''$ satellite on the excitation energy. The relative intensity of the satellite to the whole $K\alpha$ emission lines as a function of excitation energy jumps from 0% to 1.2% around 5005 eV, corresponding to the [1s3p] ionization threshold energy in $Z + 1$ approximation. It almost saturates around 5500 eV where its intensity is ∼2.5%.

Our results show that the origin of the $K\alpha''$ satellite is a 3p spectator hole as predicted by Scott. Judging from how the intensity of $K\alpha''$ increases, what creates a 3p spectator hole is considered to be shake-processes. Although the probability of the shake processes experimentally obtained (2.5%) is less than half of the theoretically calculated value (6.5%), this discrepancy may be lessened when we take it into consideration that one third of the satellite intensity is probably hidden between $K\alpha_1$ and $K\alpha_2$ in the measured spectra.

The dependence of the satellite intensity on the excitation energy was interpreted by combining Thomas model (for shake-off) with a step function (for shake-up). The results show that 47% of the Kα″ satellite is caused by shake-up processes. We also calculated the ratio of the probability of the [1s3p] shake-up processes to that of the whole shake processes in the sudden approximation and the result (42%) is close to the experimentally determined one (47%). The agreement between these values indicates that, for 3d transition elements, shake-up processes are more important in creating a 3p spectator hole accompanying an ionization of a 1s electron than in creating a 2p spectator hole accompanying an ionization of a 1s electron.

Acknowledgements

One of the authors (N. Shigeoka) would like to express his thanks to T. Shoji at the X-ray research laboratory, Rigaku Co., Ibaraki, Osaka for the preparation of analyzing curved crystals. This work has been performed at SPring-8 with the approval of the Independent Administrative Institution, National Institute for Material Science as Nanotechnology Support Project of the Ministry of Education, Culture, Sports, Science and Technology. (Proposal Nos. C02BL15XU-2009N & 2002B0438-NX-np/BL15XU).

References

1. Parratt, L. G., Phys. Rev. **49**, 502 (1936).
2. Kuhn, W. J. and Scott, B. L., Phys. Rev. A **34**, 1125 (1986).
3. Scott, B. L., Phys. Rev. A **34**, 4438 (1986).
4. Fritsch, M. *et al*., Phys. Rev. A **57**, 1686 (1998).
5. Sternemann, C., Kaprolat, A., Krisch, M. H. and Schulke, W., Phys. Rev. A **61**, 020501(R) (2000).
6. Galambosi, S. *et al*., Phys. Rev. A **67**, 022510 (2003).
7. Deutsch, M. *et al*., Phys. Rev. A **51**, 283 (1995).
8. Ito, Y. *et al*., in Proc. International Seminar on Photoionization in Atoms (ISPA), Kyoto University Press, 66 (2002).
9. Thomas, T. D., Phys. Rev. Lett. **52**, 417 (1984).
10. Thomas, T. D., J. Electron Spectrosc. Relat. Phenom. **40**, 259 (1986).
11. Mukoyama, T. and Ito, Y., Bull. Inst. Chem. Res., Kyoto Univ. **71**, 398 (1993).
12. Grant, I. P., McKenzie, B. J., Norrington, P. H., Mayers, D. F. and Pyper, N. C., Comput. Phys. Commun. **21**, 207 (1980).
13. Shigeoka, N. *et al.*, to be submitted.

Physica Scripta. Vol. T115, 1084–1087, 2005

[K+L] Double-Electron Transition in Fe

N. Shigeoka[1,*], H. Oohashi[1], T. Tochio[1], Y. Ito[1], T. Mukoyama[2], A. M. Vlaicu[3], H. Yoshikawa[3] and S. Fukushima[3]

[1]Institute for Chemical Research, Kyoto University, Uji, Kyoto, 611-0011 Japan
[2]Kansai Gaidai University, 16-1 Nakamiyahigashino, Hirakata, Osaka 573-1001 Japan
[3]National Institute for Material Science, SPring-8, Mikazuki, Hyogo, 679-5198, Japan

Received June 26, 2003; accepted November 4, 2003

PACS number: 32.30.Rj, 32.80.Fb

Abstract

Fe $K\alpha_{3,4}$ satellite spectra are investigated using a Johann-type spectrometer at the BL15XU undulator beam line, SPring-8. Intensity of the $K\alpha_{3,4}$ satellite relative to the $K\alpha_1$ emission line is found to increase asymptotically with excitation energy up to 9000 eV, and almost saturates at around 9500 eV. Satellite threshold energy is found to be 7882 eV ± 14 eV. This corresponds to the ionization energy of Fe $1s + 2p^*$, where * indicates that the value is from the $Z + 1$ approximation. The growth of satellite intensity with the excitation energy suggests that the 2p spectator holes are mainly created by shake-off in Fe, as suggested by Fritsch *et al.* [Phys. Rev. A **57**, 1686 (1998)] in a previous work on copper.

1. Introduction

Most studies into the contributions of shake processes in solids, vapors, etc. on X-ray absorption for elucidating electron correlations in atoms have been carried out by an Italian group, a Slovenian group, and a Japanese group *etc.* [1–10]. Extended shake-off saturation profiles are of special interest in X-ray absorption spectroscopy, as well as sharp multielectron photoexcitation features caused by resonance and shake-up [4, 5, 7, 10].

X-ray absorption of 3d transition metals has been examined in the K + L double photoabsorption energy region. However, no significant features attributable to multiple photoexcitation have been found in the spectra, and thus K + L edges in 3d elements have not been confirmed [3, 11]. This result could be explained by theoretical predictions of lower shake-up probabilities for K + L transitions [11], which predict that the transition edges observed in X-ray absorption spectra are due entirely to the shake-up process. That is, resonance and shake-up probabilities in the K + L transition of 3d elements are typically lower than detection accuracy so that pure long-range shake-off profiles in XAFS oscillations are difficult to obtain.

With the advent of third generation synchrotron radiation, experiments can be conducted on the threshold behavior of satellites, including the excitation dynamics of atoms. In particular, X-ray emission spectroscopy is suitable for studying satellites for electron correlation. The first detailed photoexcitation measurements were performed by Deslattes *et al.* [12], who examined multielectron vacancies in atomic argon using a combination of both emission and absorption spectroscopy. Deutsch and co-workers [13, 14] found pure shake-off behavior in the copper Kα X-ray satellite complex, and Sternemann *et al.* [15] measured the valence fluorescence satellite KM-$N_{2,3}$M transition of a solid germanium target. More recently Raboud *et al.* [16] measured the KL X-ray emission of argon induced by impact with monoenergetic photons to investigate the K + L double excitation from threshold to saturation.

The contributions of the 2s and 2p spectator transitions in 3d transition metals have only been investigated in copper. As investigation of lower Z 3d metals is needed to further understand multielectron excitation processes, spectator transitions in iron are investigated and presented.

2. Experiment

Measurements were carried out at the BL15XU undulator beam line, SPring-8, using a Johann-type spectrometer. A Si(111) double-crystal monochromator was used to generate a tuned X-ray excitation source, which has a bandpass of $\delta E/E \sim 10^{-4}$ and flux of over 10^{12}. A Johann geometry fluorescence spectrometer consisting of a 1.5-m-diameter Rowland circle on a horizontal plane and a curved Si(400) crystal was used to resolve fluorescence spectra. The spectrometer had a scanning range of 67° to 95°, and was evacuated to $\sim 10^{-3}$ torr using a scroll pump. A 20-μm-thick pure Fe foil was used as the sample. A NaI(Tl) scintillation counter was used to correct the signal and a N_2-gas-filled ionization chamber was used to monitor incident X-ray intensity in front of the target.

Two types of scan were used to investigate the excitation energy dependence of Fe $K\alpha_{3,4}$ spectra. First, the spectrometer was fixed in the Fe $K\alpha_{3,4}$ position ($2\theta \sim 91°$) and incident X-ray energy was scanned. X-rays were incident on the target at 75° to minimize the influence of fluctuations in incident beam spot position during the energy scan. From the first scan, a rough estimate of the $K\alpha_{3,4}$ satellite energy threshold was obtained, and energy values for the angle scan were determined. Several spectrometer angle scans were then conducted around $2\theta \sim 91°$, with excitation energy varied from 7850 eV to 10000 eV to trace variations in satellite spectra with excitation energy. During the angle scan, the incident angle of X-rays on the target was set to 45° to maximize fluorescence intensity at the detector.

3. Results and discussion

Results of the first scan around the threshold energy are shown in Figs. 1 and 2. The intensity of emissions at the Fe $K\alpha_{3,4}$ satellite complex energy can be seen to gradually increase as the excitation energy increases from around 8000 eV, and almost saturates at around 9500 eV, as shown in Fig. 1. Two lines are drawn in Fig. 2 to highlight the threshold of the satellites. Threshold values obtained from the $Z + 1$ approximation are shown in the inset [17]. Values of [1s2p] ionization threshold energy are in agreement with the experimental results. Calculations of shake-up and shake-off probabilities in K + L double electron transitions were performed in a manner similar to Mukoyama and Ito [18] using the Dirac-Fock-Slater method [19], with results listed in Table I.

*Email address: yosi@elec.kuicr.kyoto-u.ac.jp

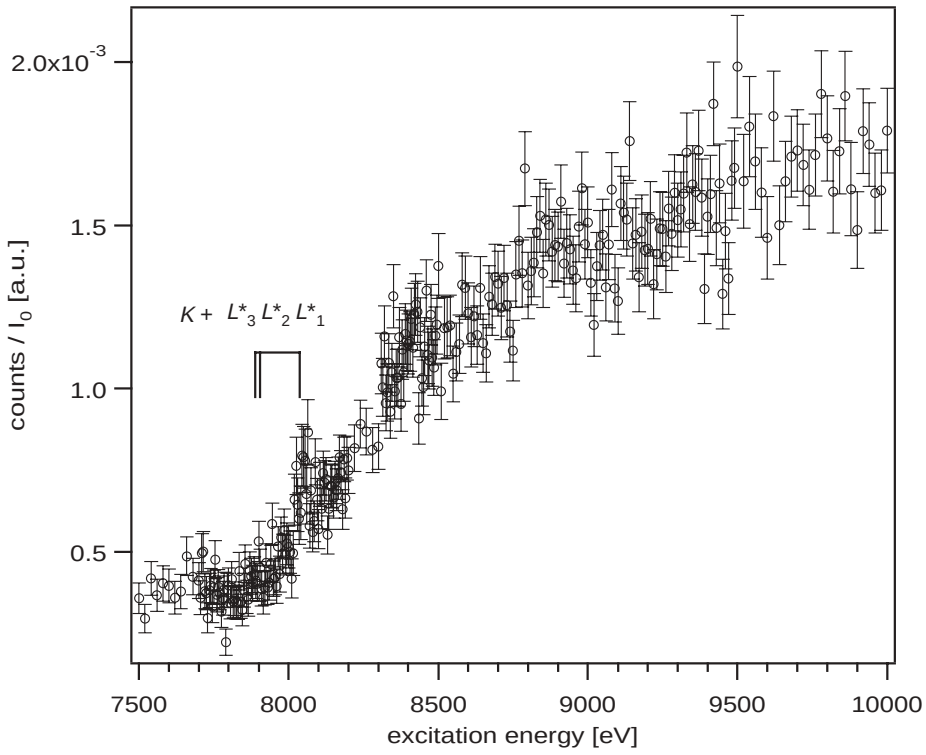

Fig. 1. Dependence of X-ray fluorescence emission intensity on excitation energy. Spectrometer 2θ was fixed at a position corresponding to the Fe K$\alpha_{3,4}$ emission. Excitation energy was scanned from 7500 eV to 10000 eV.

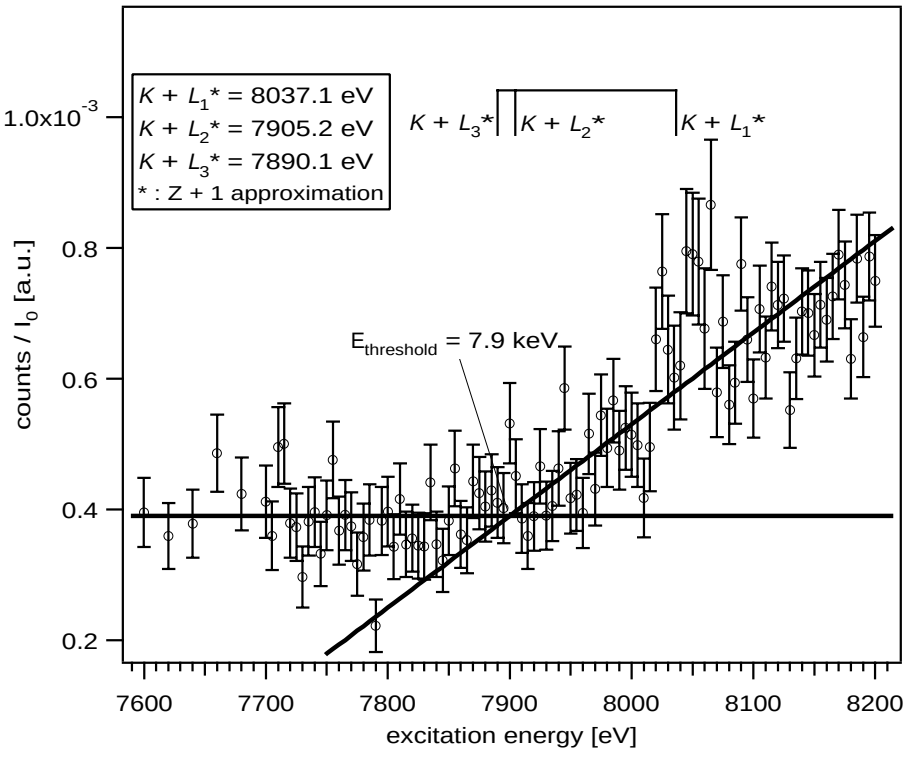

Fig. 2. Detailed plot of the data shown in Fig. 1 at around 7900 eV. Two lines have been drawn to highlight the threshold energy of satellite emissions. Values in the inset show the double hole creation threshold energies obtained by $Z + 1$ approximation. * indicate L sub-shell ionization energies in cobalt.

Moreover, a small intensity peak was clearly observed around the [1s2s] ionization threshold energy, possibly due to the appearance of a 2s hole. It is plausible that this peak is attributed to a resonance.

The observation of emissions influenced by 2s spectator holes is difficult compared to 2p holes because 2s spectator holes disappear faster than 2p holes through strong 2s2p Coster-Kronig transitions. Therefore contributions from [1s2s] shake processes may be observed as a part of satellite emissions with 2p spectator holes. If a 2s spectator hole is created and left around the small intensity peak in Fig. 2, the shape of the satellite complex may change due to the spectator hole itself. However, no clear evidence

Table I. *Probabilities of shake-up and shake-off involving L shells accompanied by K shell ionization in Fe using Dirac-Fock-Slater calculations. The $n = l$ column ($4 \leq l \leq 10$) shows the probability of shake-up to each $n = l$ shell.*

	Initial shells		
Destinations	L_1	L_2	L_3
$n = 4$		6.720×10^{-5}	1.323×10^{-4}
$n = 5$	1.300×10^{-5}	1.829×10^{-5}	3.645×10^{-5}
$n = 6$	4.990×10^{-6}	7.745×10^{-6}	1.549×10^{-5}
$n = 7$	2.448×10^{-6}	4.014×10^{-6}	8.040×10^{-6}
$n = 8$	1.382×10^{-6}	2.350×10^{-6}	4.711×10^{-6}
$n = 9$	8.567×10^{-7}	1.494×10^{-6}	2.998×10^{-6}
$n = 10$	5.675×10^{-7}	1.009×10^{-6}	2.025×10^{-6}
total shake-up	2.324×10^{-5}	1.021×10^{-4}	2.020×10^{-4}
shake-off	1.225×10^{-3}	1.975×10^{-3}	3.909×10^{-3}
total	1.248×10^{-3}	2.077×10^{-3}	4.111×10^{-3}

of contributions from 2s spectator holes could be confirmed within the accuracy of our experimental data.

Integrated intensity of the $K\alpha_{3,4}$ satellite complex is shown in Fig. 3 relative to the total $K\alpha_{1,2,3,4}$ emissions. Four reference data are also shown for comparison. The relative intensity of satellite complex can be seen to increase from 7900 eV and almost saturate at around 9500 eV. The data indicated by diamonds are experimental results from a conventional Fe X-ray tube measured using the same spectrometer as in the present work and an X-ray tube excitation voltage of 30 kV. The data indicated by triangles were measured using a double-crystal spectrometer. The target was pure Fe metal and a Rh X-ray tube with an excitation voltage of 40 kV was used. These values are in good agreement with the present 10000 eV experimental results, in which the satellites are almost fully developed. Data indicated by circles are calculated values of [1s2p] shake-off probability during K-shell ionization using the sudden approximation [20], and the circle with cross indicates the sum of calculated probabilities of [1s2s] and [1s2p] shake-off. The theoretical values, especially the latter, are in good agreement with the experimental results at an excitation energy of 10000 eV.

A small intensity peak is observed at an excitation energy of 8040 eV in Fig. 3 as well as in Fig. 2. This may be due to [1s2s] double electron excitation.

The solid line is the result of fitting the Thomas model [21] to the experimental data. In this model, the probability of creating a spectator hole via shake-off two-step-one (knockout of a second electron by the departing photoelectron) process is given by

$$P_{Thomas}(E_{ex}) = P_\infty \exp\left(\frac{-mr^2E_s^2}{2\hbar^2E_{ex}}\right),$$

where P_∞ is the probability at saturation, m is the mass of an electron, r is the distance covered by the photoelectron during the excitation process, and E_{ex} is the energy which is needed to excite a second electron. Replacing m and $\hbar$ with numerical values gives

$$P_{Thomas}(E) = P_\infty \exp\left(-\frac{r^2E_s^2}{15.32(E - E_{threshold})}\right).$$

During the fitting, E_s was fixed at 783.1 eV, P_∞ was fixed at 0.738% and other parameters were left free. The fixed E_s value was calculated from the weighted average of $L_{2,3}$ sub-shell binding energies of cobalt, obtained from the $Z + 1$ approximation. P_∞ was taken from the experimental value of the Fe X-ray tube (diamond in Fig. 3) that was measured using the same spectrometer as that in this work, but with an

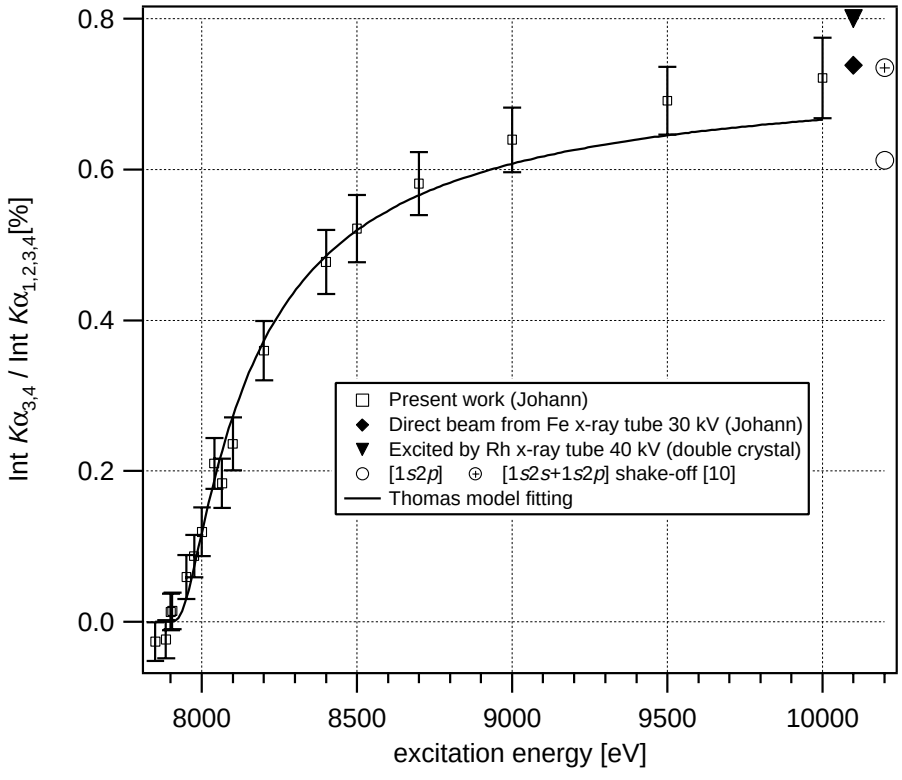

Fig. 3. Integrated intensity of $K\alpha_{3,4}$ satellite complex relative to total $K\alpha_{1,2,3,4}$ emissions. Squares with error bars show experimental data from the present work. Triangle, diamond, circle and circle with cross indicate experimental and theoretical reference values, as given by the legend. The solid line shows the results fitting to the Thomas model.

excitation voltage of 30 kV at which the satellite is expected to be saturated. Results of the fitting were: $r = 0.074\,\text{Å} \pm 0.003\,\text{Å}$ and $E_{threshold} = 7881.6\,\text{eV} \pm 14.2\,\text{eV}$. The threshold energy of these fitting results is in good agreement with the [1s2p] excitation threshold energy from the $Z + 1$ approximation. The origin of the Fe $K\alpha_{3,4}$ satellites may be 2p spectator holes created by [1s2p] shake-off.

Less agreement between the fitting results and experimental values of excitation probability occurs for $E > 9000\,\text{eV}$, with the fitting function dropping below the experimental values. This may suggest that contribution of 2p spectator holes created by combination of matured [1s2s] shake-off and 2s2p Coster-Kronig transitions.

A shake-off process seems to dominate 2p spectator hole creation processes because the integrated intensity of satellite complex exhibits monotonic increase. The theoretical values listed in Table I also suggest that 2p vacancies in L shells are mainly created by the shake-off process.

4. Conclusion

The experimental evolution of Fe $K\alpha_{3,4}$ satellite complex from threshold to saturation was presented. The threshold energy of satellite complex was found to be around 7890 eV, matching the [1s2p] ionization threshold energy given by the $Z + 1$ approximation. The origin of Fe $K\alpha_{3,4}$ satellites seems to be spectator holes in the 2p levels (L_2 or L_3 shell).

The integrated intensity of Fe $K\alpha_{3,4}$ satellite complex exhibited a simple increase from threshold, indicating that a shake-off process is the origin of 2p spectator holes.

A small intensity peak was observed at around 8040 eV, corresponding to $K + L_1$ ionization threshold energy. The shape of this peak did not match shake-off or shake-up, but appeared to be a sharp resonance. The 2s hole also seems to appear around the same energy, but no clear change in the satellite was observed within the measurement accuracy. Strong 2s2p Coster-Kronig transitions may fill 2s holes quickly, with contributions from [1s2s] shake-off observed as satellite emissions with 2p spectator holes.

The conclusion is supported by the good agreement between the relative intensities at an excitation energy of 10000 eV and theoretical [1s2s + 1s2p] shake-off probabilities.

The experimental data in the saturated region agree well with theoretical values from the sudden approximation [20], but there are few models that can reproduce the evolution of this kind of shake-off satellite. The Thomas model of shake-off probabilities [21] agrees to some extent with our experimental data, and also with copper [13, 14] and argon [16] data, but the model still has room for improvement [14]. Therefore, a new model that describes the evolution of shake-off probability on a solid theoretical grounding is required in this field of investigation.

Further experimental work is also needed to push theoretical developments. Copper, argon and iron have now been measured, with further experiments on other 3d transition elements, rare gases and higher-Z elements needed to allow more detailed discussion in this field.

Acknowledgements

One of the authors (N. Shigeoka) would like to express his thanks to T. Shoji at the X-ray research laboratory, Rigaku Co., Takatsuki, Osaka for the preparation of curved analyzing crystals. This work was conducted at SPring-8 with the approval of the Independent Administrative Institution National Institute for Material Science as a Nanotechnology Support Project of the Ministry of Education, Culture, Sports, Science and Technology. (Proposal Nos. C02BL15XU-2009N & 2002B0438-NX-np/BL15XU).

References

1. Dángelo, P., Di Cicco, A., Filipponi, A. and Pavel, N. V., Phys. Rev. A **47**, 2055 (1993).
2. Filipponi, A. and Di Cicco, A., Phys. Rev. A **52**, 1072 (1995).
3. Kodre, A., *et al.*, Phys. Rev. A **45**, 4682 (1992).
4. Gomilšek, J., Kodre, A., Arčon, I., Loireau-Lozac'h, A. M. and Bénazeth, S., Phys. Rev. A **59**, 3078 (1999).
5. Gomilšek, J., Kodre, A., Arčon, I. and Preseren, R., Phys. Rev. A **64**, 022508 (2001).
6. Ito, Y., *et al.*, Phys. Rev. A **46**, 6083 (1992).
7. Ito, Y., *et al.*, Phys. Rev. A **51**, 303 (1995).
8. Mukoyama, T. and Ito, Y., Nucl. Instrum. Meth. Phys. Res. B **87**, 26 (1994).
9. Deutsch, M. and Hart, M., Phys. Rev. Lett. **57**, 1566 (1986).
10. Schaphorst, S. J., *et al.*, Phys. Rev. A **47**, 1953 (1993).
11. Ito, Y., *et al.*, Jpn. J. Appl. Phys. **32**, Suppl. 32 (1993).
12. Deslattes, R. D., LaVilla, R. E., Cowan, P. L. and Henins, A., Phys. Rev. A **27**, 923 (1983).
13. Deutsch, M., Gang, O., Hämäläinen, K. and Kao, C. C., Phys. Rev. Lett. **76**, 2424 (1996).
14. Fritsch, M., *et al.*, Phys. Rev. A **57**, 1686 (1998).
15. Sternemann, C., Kaprolat, A., Krisch, M. H. and Schülke, W., Phys. Rev. A **61**, 020501(R) (2000).
16. Reboud, P.-A., *et al.*, Phys. Rev. A **65**, 062503 (2002).
17. Bearden, J. and Burr, A., Rev. Mod. Phys. **39**, 125 (1967).
18. Mukoyama, T. and Ito, Y., Bull. Inst. Chem. Res., Kyoto Univ. **71**, 398 (1993).
19. Liberman, D. A., Cromer, D. T. and Waber, J. T., Comput. Phys. Commun. **2**, 107 (1971).
20. Mukoyama, T. and Taniguchi, K., Phys. Rev. A **36**, 693 (1987).
21. Thomas, T. D., Phys. Rev. Lett. **52**, 417 (1984).

Physica Scripta. Vol. T115, 1088–1090, 2005

Reversed Monte Carlo Simulation to XAFS Spectra of Liquid GeO_2 Polymorphs

Zhonghua Wu[1*], Kunquan Lu[2], Chenxi Li[2], Wei Wang[2], Xiaojuan Niu[2], T. Uruga[3] and M. Nomura[4]

[1]Beijing Synchrotron Radiation Lab, Institute of High Energy Physics, Chinese Academy of Sciences, P.O. Box 918, Bin 2-7, Beijing 100039, P.R. China
[2]Center for Condensed Matter Physics & Institute of Physics, Chinese Academy of Sciences, Beijing 100080, P.R. China
[3]Spring-8, The Institute of Physical and Chemical Research, Wako, Saitama, 351-01, Japan
[4]High Energy Accelerator Research Organization, Institute of Materials Structure Science, Oho 1-1, Tsukuba 305-0801, Japan

Received June 26, 2003; accepted October 14, 2003

PACS numbers: 61.20.Ja, 61.10.Ht, 61.20.Qg

Abstract

X-ray absorption fine structure (XAFS) spectra of Ge-K edge of liquid GeO_2 polymorphs (quartz-type and rutile-type GeO_2) at temperature 1126 °C were collected at Beijing Synchrotron Radiation Facility (BSRF) and Spring-8. Reversed Monte Carlo (RMC) method was used to simulate the XAFS spectra with k^2-weight. More than 200 independent configurations were used to do statistic analysis. There are 3.7 oxygen atoms surrounding Ge with Ge-O bond length of 1.74 Å for rutile-type GeO_2 melt, and 3.6 oxygen atoms surrounding Ge with Ge-O bond length of 1.75 Å for quartz-type GeO_2 melt. The long-range order was completely destroyed and partial short-range and intermediate-range order were kept in the two kinds of liquid GeO_2 (at 1126 °C). Because partial Ge-O bonds were broken, the local atomic structures of liquid GeO_2 were reconstructed. Besides the four-folded Ge-O coordination, three-folded and five-folded coordinations were also found. The liquid structures of the two GeO_2 polymorphs are similar but not the same. The averaged Ge-O-Ge and O-Ge-O coordination triangles are larger in $QGeO_2$ melt than in $RGeO_2$ melt.

1. Introduction

GeO_2, as an analog of SiO_2, was widely used to study the structures and properties of glasses, liquid and minerals. Crystal structure, density and modulus, thermal expansivity, volume-temperature relationship, pressure-induced phase-transform, heat capacity, multielectron excitation, as well as amorphization were respectively, reported [1–7]. Many theoretical calculations including molecular dynamics simulation [8, 9] were also performed. Whereas a reverse Monte Carlo simulation for the liquid structures of GeO_2 polymorphs has never been found.

Germanium dioxide has two types of stable structure, one is the α-quartz-type GeO_2 with four oxygen atoms surrounding the germanium atom in $P3_221$ ($z = 3$) space group [10], another is the rutile-type GeO_2 with six oxygen atoms surrounding the germanium atom in $P4_2/mnm$ space group [11]. In this paper, (α-quartz-type GeO_2 and rutile-type GeO_2 are, respectively, abbreviated to $QGeO_2$ and $RGeO_2$. $RGeO_2$ was reported to have a melting point at 1086 °C, while $QGeO_2$ was reported to have a melting point at 1115 °C. We are interested in whether the melts structure is correlative with the crystalline structure of the counterpart or not. As the two GeO_2 crystalline phases ($QGeO_2$ and $RGeO_2$) are heated to same temperature above their melting points, are there the same structures of the melts?

High-temperature extended X-ray-absorption fine-structure [12] (EXAFS) technique and Reverse Monte Carlo [13] (RMC) simulation were used to get the structural information of the melts. We believe that this study could offer new opportunities for both fundamental research and technological applications.

*Email: Wuzh@mail.ihep.ac.cn

2. Experimental

In order to avoid the impurities in samples, $QGeO_2$ single crystal was chosen as the starting material. By grinding the single crystal, $QGeO_2$ powder was obtained fined than 400 mesh (about 10 μm). Partial $QGeO_2$ powder was mixed with 0.5% of Li_2CO_3. The mixture was compressed into a tablet of ϕ10 and heated at 950 °C for 20 hours. Repeatedly the procedure until the mixture has been completely transformed into $RGeO_2$ as confirmed by X-ray diffraction, then $RGeO_2$ powder was obtained by grinding the mixture fined than 400 mesh. A rhodium foil with rough surface was used as the sample holder. $QGeO_2$ and $RGeO_2$ powders were, respectively, directly smeared on the rhodium foil and put into a high-temperature furnace used for EXAFS measurement. EXAFS spectra were collected with fluorescence mode at Beijing Synchrotron Radiation Facility (BSRF) in China and Spring 8 Facility in Japan. The samples were positioned in 45 degree corresponding to the X-ray beam and the entrance of the Lytle fluorescence detector. A Gallium foil was used as the filter to decrease the unnecessary background. An aluminium foil with thickness of 10 μm was positioned between the furnace and the filter to prevent the detector from thermal radiation. More than three independent EXAFS scans of Ge-K absorption were carried out. A Si(311) monochromator was used to monochromize the incident X-ray at Spring 8 and the storage ring was run at 8 GeV with 300 mA current. A Si(111) monochromator was used at BSRF with storage ring running at 2.2 GeV and 100 mA. An ion chamber installed in front of the sample was optimum filled the mixture of Ar and N_2 gases to record the incident X-ray intensity. The energy resolution ($\Delta E/E$) is about 2×10^{-4}.

3. Data analysis

EXAFS spectra of Ge K-absorption were, respectively, recorded at 1126 °C for $QGeO_2$ and $RGeO_2$. Figure 1 shows the X-ray-absorption near-edge structure (XANES) spectra of $RGeO_2$ and $QGeO_2$. The EXAFS signals were extracted by a careful background removal using the derivate method [14]. The measured EXAFS signal is the sum of contributions from all atomic pairs α-β, where α is the central atom and β is the backscattering atom. If we define the partial radial distribution function as:

$$g_{\alpha\beta}(r) = \frac{n_\beta(r)}{4\pi r^2 \Delta r \rho_\beta}. \quad (1)$$

Here, $n_\beta(r)$ is the number of atom β at a distance between r and $r + \Delta r$ from a central atom α. ρ_β is the average number-density of atom β in the studied sample. Then, the EXAFS formula at atom

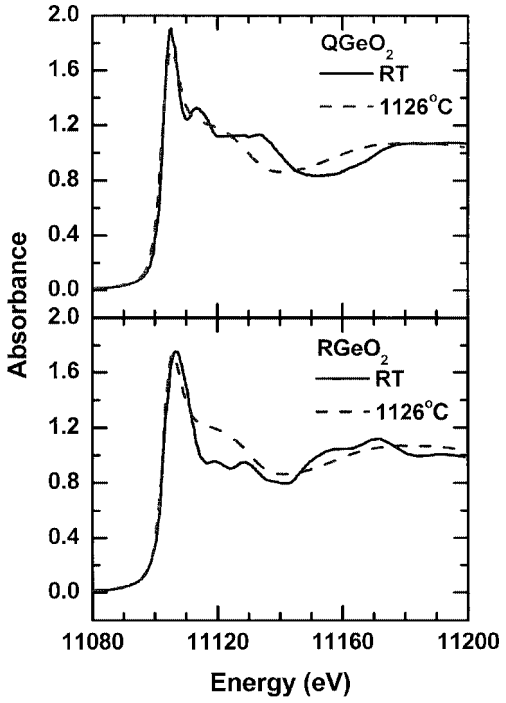

Fig. 1. X-ray-absorption near-edge spectra of Ge in $QGeO_2$ and $RGeO_2$.

α absorption-edge can be written as [13]:

$$\chi_\alpha(k) = \sum_\beta 4\pi\rho_\beta \int_0^\infty r^2(g_{\alpha\beta}(r) - 1)\chi_{\alpha\beta}(k, r)\,\mathrm{d}r. \quad (2)$$

Here, $\chi_{\alpha\beta}(k, r)$ is the EXAFS contribution of the single atomic pair (α, β) at distance r. The single atom-pair EXAFS function $\chi_{\alpha\beta}(k, r)$ was calculated with the FEFF program [15], its amplitude and phase shift were revised by using the experimental ones extracted from the bulk GeO_2 at room temperature. The systemic error of experiment in the measured EXAFS functions was largely compensated. Model-independent RMC method was used to simulate the experimental XAFS function $\chi_\alpha(k)$.

In RMC simulation, the crystal structures with 1944 atoms of room temperature GeO_2 was chosen as the initial configurations. The only constraint condition is the total number density ρ, which was fixed at 0.06056 $Å^{-3}$ for $RGeO_2$ and $QGeO_2$ melts according to the previous report [1, 2].

The k-region was chosen from 3.0 to 12.0 $Å^{-1}$ with spacing of 0.1 $Å^{-1}$. The r-region was chosen below 7.0 Å with spacing of 0.1 Å. Different step sizes were tested in the simulation, a best one of 0.2 Å was used to get the best simulation and avoid the local minimum. Figure 2 shows the experimental EXAFS curves and the RMC simulation ones for $RGeO_2$ (lower) and $QGeO_2$ (upper).

After the system reach the equilibrium, more than 200 independent configurations were randomly taken out. Average structural information can be counted from these configurations. There are about 3.7 oxygen atoms surrounding the central Ge atoms with Ge-O bond length of 1.74 Å in $RGeO_2$ melt, and 3.6 oxygen atoms at 1.75 Å in $QGeO_2$ melt. Ge-O pair distribution functions were obtained from these configurations as shown in Fig. 3.

4. Discussion

The XANES spectra of solids and melts are compared in Fig. 1. They are obviously different between solids and melts. The spectral characteristics of melts are closer to crystalline $QGeO_2$

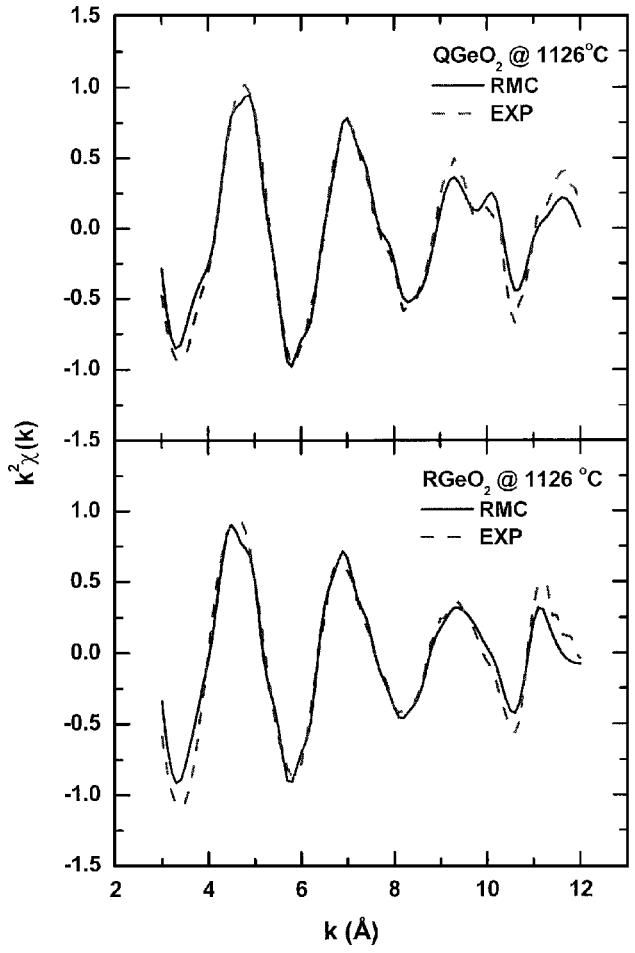

Fig. 2. Ge K-absorption XAFS spectra of $QGeO_2$ and $RGeO_2$ at 1126 °C. Solid lines are the RMC simulation curves. Dot lines are the XAFS experimental curves.

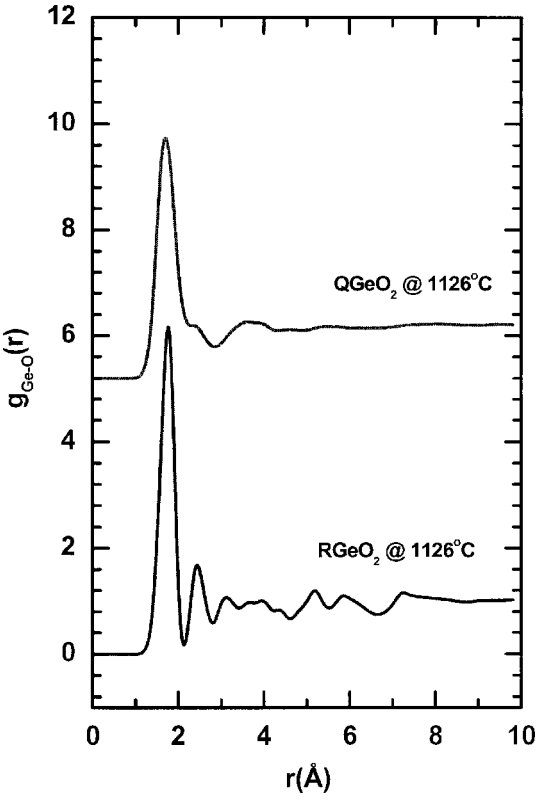

Fig. 3. Ge-O pair distribution functions in $QGeO_2$ and $RGeO_2$ melts at 1126 °C.

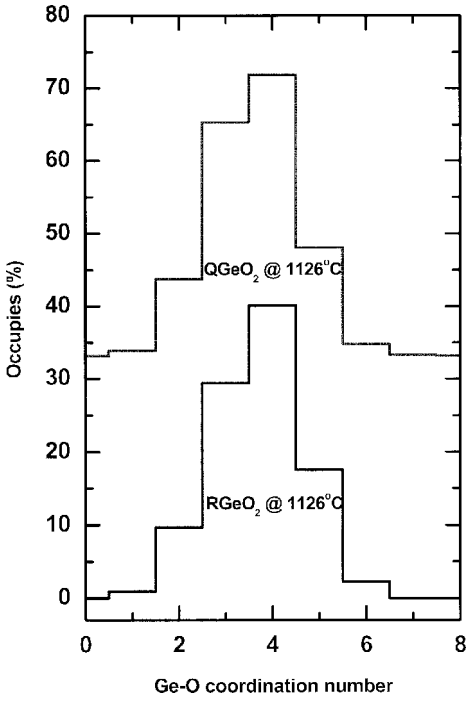

Fig. 4. Ge-O coordination number distribution in $QGeO_2$ and $RGeO_2$ melts at 1126 °C.

than $RGeO_2$ in local atomic structure. There is no change in the absorption jump that demonstrates that the samples keep the uniform thickness as they were heated from room temperature to high temperature (1126 °C).

Excellent RMC simulations to the experimental XAFS spectra are shown in Fig. 2. Figure 3 compares the Ge-O pair distribution functions $g_{\text{Ge-O}}(r)$ for $QGeO_2$ (upper) and $RGeO_2$ (lower). The room-temperature samples have an obvious long-range order distribution. The first peak of $g_{\text{Ge-O}}(r)$ defines the local atomic contributions. The near-neighbor bond length and coordination number can be obtained by directly counting the 200 independent atomic configurations with a maximum atom-pair distance restricted to 2.1 Å.

It can be seen that the two melts have similar structural parameters. Roughly, their structures are more similar to $QGeO_2$ instead of $RGeO_2$. In the RMC simulation, the atom number density is lower in melts than solids and the ratio of Ge and O atom numbers was kept at 1 : 2. Although the local structures are of shrinkage, the averaged volumes of melts are still larger than the corresponding solids.

The possibilities of coordination number for Ge-O bonds are shown in Fig. 4. The coordination number distribution is wider in melts than solids. The most probable coordination number is close to the averaged coordination number. For crystalline $QGeO_2$ and the two melts, the most probable Ge-O coordination number is 4. For solid $RGeO_2$, the most probable Ge-O coordination numbers is 6. The coordination distributions of the two melts are quite similar.

Other atom-pairs information can also be counted from these independent configurations. Generally speaking, they have similar coordination numbers and bond lengths. Two kinds of coordination triangle can be found from the two melts. One is the Ge-O-Ge triangle. Another is the O-Ge-O triangle. The average Ge-O-Ge and O-Ge-O angles are bigger in $QGeO_2$ melt than $RGeO_2$ melt. This is the statistic difference between the two GeO_2 melts.

5. Conclusion

The local atomic structures of the two GeO_2 melts at 1126 °C are similar to that of the crystalline $QGeO_2$, the most probable atomic configuration around Ge is Ge-O tetrahedron with Ge-O bond lengths of 1.74 Å. The long-range orders in melts were completely destroyed. There are two kinds of coordination triangles existing in these samples. Statistically, the Ge-O-Ge and O-Ge-O and O-Ge-O coordination triangles are bigger in $QGeO_2$ melt than $RGeO_2$ melt.

References

1. Dingwell, D. B., Knoche, R. and Webb, S. L., Phys. Chem. Minerals **19**, 445 (1993).
2. Holzapfel, C., Courtial, P., Dingwell, D. B., Chakraborty, S. and Palme, H., Chem. Geol. **174**, 33 (2001).
3. Ohtaka, O. *et al*., J. Synchrotron Rad. **8**, 791 (2001).
4. Itie, J. P. *et al*., Phys. Rev. Lett. **63**, 398 (1989).
5. Durben, D. J. and Wolf, G. H., Phys. Rev. B **43**, 2355 (1991).
6. Jorgensen, J. D., J. Appl. Phys. **49**, 5473 (1978).
7. Formoso, V. *et al*., Phys. Rev. B **61**, 187 (2000).
8. Tsuchiya, T., Yamanaka, T. and Matsui, M., Phys. Chem. Minerals **25**, 94 (1998).
9. Wefing, S., J. Non-Cryst. Solids **244**, 89 (1999).
10. Yamanaka, T. and Ogata, K., J. Appl. Cryst. **24**, 111 (1991).
11. Bolzan, A. A., Fong, C., Kennedy, B. J. and Howard, C. J., Acta Crystallographica B **39** (1983).
12. Sayers, D. E. and Bunker, B. A., "X-ray Absorption: Principles, Applications and Techniques of EXAFS, SEXAFS, and XANES", (edited by D. C. Koningsberger and R. Prins), (Wiley, New York, 1998).
13. Gurman, S. J. and McGreevy, R. L., J. Phys.: Condens. Matter **2**, 9463 (1990).
14. Hu, T. D., Xie, Y. N., Jin, Y. L. and Liu, T., J. Phys.: Condens. Matter **9**, 5507 (1997).
15. Rehr, J. J., Mustre de Leon, J., Zabinsky, S. I. and Albers, R. C., J. Am. Chem. Soc. **113**, 5135 (1991).

Physica Scripta. Vol. T115, 1091–1093, 2005

Keldysh's Green Function Approach to the Radiation Field Screening in MARPE and XAFS

Hiroko Arai* and Takashi Fujikawa

Graduate School for Science, Chiba University, Yayoi-cho 1-33, Inage, Chiba 263-8522, Japan

Received June 26, 2003; accepted October 16, 2003

Abstract

We study the radiation field screening in MARPE and XAFS in the non-relativistic Keldysh Green's function theory. So far these terms have rarely been investigated, however they are crucial to analyse resonant effects in XPS and XAFS. In this work we demonstrate the importance of the dynamical screening to discuss these resonant effects. We find that the resonant term in XAFS is written in terms of X-ray absorption factor $f(\omega)$ and related factor $\tilde{f}(\omega)$.

1. Introduction

EXAFS analyses of the backscattering amplitude identify the backscattering atomic species. It is, however, quite difficult to distinguish Mn from Fe or Co from the EXAFS analyses, because their backscattering amplitudes $f(\pi)$'s are quite similar.

Recent experimental developments of multi-atom resonant photoemission (MARPE) permit direct determination of near-neighbour atomic identities [1, 2]. So far much efforts has been paid to observe MARPE: Some have failed to observe them [3]. Theoretical approach based on scattering theory has been proposed by Garcia de Abajo *et al*. [4]. The present authors have used an alternative more sophisticated approach based on Keldysh Green's function theory [5]. Further refinement to include radiation field screening is also proposed [6]. These works have explicitly shown the structure factor of MARPE transition operator, which reflects the local symmetry around an X-ray absorbing atom. Despite these successful results, the MARPE intensities are too small compared with the experimental ones, since the dynamical screening has been neglected.

In this work we point out the importance of the polarization part W_p (dynamical screening part) of the screened Coulomb interaction to analyse MARPE by using skeleton expansion of Keldysh Green's function. This term also plays an important role in other resonant phenomena such as intra-atomic resonant photoemission spectra and in the discussion of the white line intensity in XAFS spectra.

2. MARPE

XPS intensity measuring photoelectrons with momentum $\boldsymbol{p}$ excited by photon energy ω near resonance is given by use of the skeleton expansion of Keldysh Green's function theory [5, 6]

$$I(\boldsymbol{p},\omega) \propto \sum_n |\langle f_{\boldsymbol{p}}^- |\Delta| g_n\rangle + \mathrm{i}\langle f_{\boldsymbol{p}}^- |X(\omega)| g_n\rangle + \mathrm{i}\langle f_{\boldsymbol{p}}^- |Z(\omega)| g_n\rangle|^2 \delta[\varepsilon_p + E_n(N-1) - \omega - E_0(N)] \quad (1)$$

where the particle Dyson orbital f_p and the hole Dyson orbital g_n are define by ($x = (\boldsymbol{r}, \sigma)$)

$$f_p(x) = \langle 0, N|\psi(x)|p, N+1\rangle,$$
$$g_n(x) = \langle n, N-1|\psi(x)|0, N\rangle. \quad (2)$$

The function $f_{\boldsymbol{p}}^-$ is a damping photoelectron wave under the influence of the optical potential. The first term of eq. (1) describes the normal photoemission processes. The second and the third terms describe the resonant processes. The latter includes contribution from the radiation field screening. Operators $X(\omega)$ and $Z(\omega)$ defined in ref. [5, 6] is written in terms of screened Coulomb interaction $W(\omega)$, $W(\omega) = v + v\pi(\omega)v$. We study the effect of the polarization part $W_p = v\pi v$ in detail. We notice that the reducible polarization propagator π is related to the irreducible polarization P, $\pi = P + PWP$. In this work we use an approximation $\pi \sim P_0$, where P_0 is the lowest order skeleton expansion of P

$$P_0(x, x'; \omega) = \sum_{mq} \left(\frac{f_q(x) f_q^*(x') g_m(x') g_m^*(x)}{\omega + \varepsilon_m - \varepsilon_q + \mathrm{i}\eta} - \frac{f_q(x') f_q^*(x) g_m(x) g_m^*(x')}{\omega - \varepsilon_m + \varepsilon_q - \mathrm{i}\eta} \right), \quad (3)$$

where $\varepsilon_m = E_0(N) - E_m(N-1)$, $\varepsilon_q = E_q(N+1) - E_0(N)$. In the analyses of MARPE the second term in eq. (1) can be neglected as discussed in ref. [6]. The polarization part in the element $\mathrm{i}\langle f_{\boldsymbol{p}}^- |Z(\omega)| g_n\rangle$ is given by neglecting the terms with large energy denominator

$$\langle f_{\boldsymbol{p}}^- g_j |W_p(\omega)| g_n f_s\rangle \sim \langle f_{\boldsymbol{p}}^- g_j |v P_0 v| g_n f_s\rangle \sim \sum_{mq} \frac{\langle f_{\boldsymbol{p}}^- g_m |g_n f_q\rangle \langle g_j f_q |f_s g_m\rangle}{\omega + \varepsilon_m - \varepsilon_q + \mathrm{i}\eta}. \quad (4)$$

To specify the problem, let us consider O1s MARPE in MnO, where ω is close to Mn 2p threshold. In this case g_m and g_j are approximated by Mn 2p core functions multiplied by intrinsic amplitudes, and g_n O 1s, f_s and f_q Mn 3d, and ε_m corresponds to the threshold of Mn 2p core excitation $\varepsilon_m \sim -I_d$. We stress the importance of the skeleton expansion; in the denominator we have exact ionization energy $-\varepsilon_m$ instead of orbital energy in the Hartree-Fock approximation. Since the incident X-ray energy ω is close to the Mn 2p threshold ($\omega \sim -\varepsilon_m$), eq. (4) has a large contribution near the core excitation energy. So far the influence of W_p has been neglected. However, this plays an important role in particular near the resonant energy.

*Electronic address: hiroko@graduate.chiba-u.jp

By using the procedure discussed in the next section, we can rewrite the inter-atomic resonant photoemission intensity

$$I(\boldsymbol{p},\omega) \propto \sum_n \left| \langle f_p^- |\Delta| g_n\rangle + \sum_{sj} \frac{\langle f_p^- g_j | g_n f_s\rangle \langle f_s|\Delta|g_j\rangle}{\omega+\varepsilon_j-\varepsilon_s+\mathrm{i}\Gamma} \times \left(1+\frac{\gamma}{\omega+\varepsilon_j+\mathrm{i}\Gamma}\right)\right|^2 \times \delta[\varepsilon_p + E_n(N-1) - \omega - E_0(N)] \tag{5}$$

where γ can be related to the deep core X-ray absorption factor f_d defined by eq. (16).

To study the influence of W_p on MARPE intensity, we calculate O1s MARPE for some MnO model clusters. Since the MARPE amplitude is proportional to r^{-3} (r is Mn-O distance), it is sufficient to consider only the nearest-neighbour Mn atoms. We should also note that O1s MARPE of this system is sensitive to the surface, because the O 1s photoelectron kinetic energy is ∼100 eV so that the photoelectron mean free path is quite small. Figure 1 shows the calculated MARPE for "MnO(001) surface model", where Mn atom along the $+z$ direction is lost and is in lower than octahedral symmetry keeping the Mn-O distance at 2.23 Å. Photoelectrons are detected along the surface normal. The MARPE without W_p is compared with that including W_p; the former gives weak MARPE whose relative intensity to the main photoemission band is about 1%. In contrast to this result the latter including the dynamical polarization gives a prominent peak comparable with the experimental one (∼12%), and still shows Fano like asymmetric shape. In this case we have used the parameter $\gamma = -1$ eV.

A different model studied here is a "distortion model" where two Mn atoms along the z axis have longer distance (+5%) than four Mn atoms in the xy plane. This model also gives rise to MARPE, however, it is much weaker (∼2%) than the "surface model". We again find an important contribution of the polarization part W_p to the MARPE intensity.

3. Resonant effect in XAFS

We have obtained the X-ray absorption intensity of photon energy ω by taking the radiation field screening into account [6]

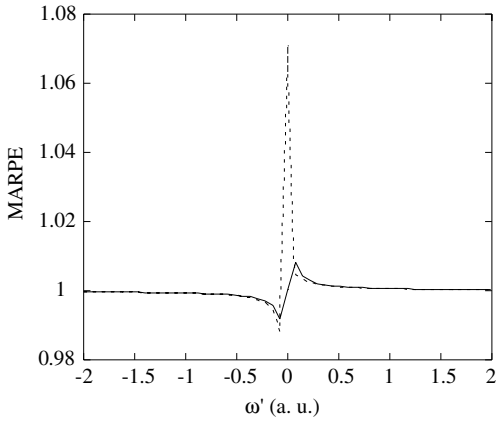

Fig. 1. Calculated O1s MARPE function of MnO (001) surface. We set the energy 0 at the resonant energy (Mn 2p threshold). Solid line shows the result without W_p and the dashed line with W_p.

$$I(\omega) \sim 2\pi \times \sum_{np}\left|\langle f_p|\Delta|g_n\rangle + \sum_{mq}\frac{\langle f_p g_m|W(\omega)|g_n f_q\rangle\langle f_q|\Delta|g_m\rangle}{\omega+\varepsilon_m-\varepsilon_q+\mathrm{i}\eta}\right|^2 \times\delta(\omega+\varepsilon_n-\varepsilon_p). \tag{6}$$

The second term can describe the resonant effect and is rewritten below. In the approximation $W \sim v$, we have

$$\sum_{mq}\frac{\langle f_p g_m|g_n f_q\rangle\langle f_q|\Delta|g_m\rangle}{\omega+\varepsilon_m-\varepsilon_q+\mathrm{i}\eta} \sim \sum_{\mathrm{d}q}\int \mathrm{d}x_1\,\mathrm{d}x_2\,\mathrm{d}x_3\; f_p^*(x_1)\phi_d^*(x_2)v(\boldsymbol{r}_1-\boldsymbol{r}_2)\phi_c(x_1) \times\Delta(x_3)\phi_d(x_3)g_{sc}(\boldsymbol{r}_2,\boldsymbol{r}_3;\omega+\varepsilon_d), \tag{7}$$

where the hole Dyson orbital $g_n(x)$ is approximated by $S_n^c\phi_c(x)$, whereas $g_n(x)$ is approximated by $S_m^d\phi_d(x)$: We only use one channel $S_n^c \sim \delta_{n0}, S_m^d \sim \delta_{m0}$ for simplicity, and g_{sc} is defined

$$g_{sc}(\boldsymbol{r}_2,\boldsymbol{r}_3;\omega+\varepsilon_d) \equiv \sum_q \frac{f_q(x_2)f_q^*(x_3)}{\omega+\varepsilon_d-\varepsilon_q+\mathrm{i}\eta}. \tag{8}$$

We thus reduce the problem to the calculation of the Green's function g_{sc}. In the lowest approximation we only consider the contribution from the X-ray absorber A, and neglect scattering terms, which yields

$$g_{sc}(\boldsymbol{r}_2,\boldsymbol{r}_3;\omega+\varepsilon_d) = \sum_L g_l(r_2,r_3;\omega+\varepsilon_d)Y_L^*(\hat{\boldsymbol{r}}_2)Y_L(\hat{\boldsymbol{r}}_3). \tag{9}$$

Substituting eq. (9) into eq. (7) we obtain

$$\text{eq. (7)} = \langle f_p|\lambda(\omega+\varepsilon_d)Y_{10}|\phi_c\rangle, \tag{10}$$

$$\lambda(\omega+\varepsilon_d;r_1) \equiv \sum_l \int \mathrm{d}r_2\,\mathrm{d}r_3\, r_2^2 r_3^3 R_{l_d}(r_2)R_{l_d}(r_3)\frac{r_<}{r_>^2} \times\frac{(2l_d+1)(2l+1)}{9}\langle l_d 0\, l0|1\rangle^2 g_l(r_2,r_3;\omega+\varepsilon_d), \tag{11}$$

where $r_< = \min(r_1,r_2)$, $r_> = \max(r_1,r_2)$, and R_{l_d} is the radial part of ϕ_d.

Next we consider the effects from W_p. By using the same approximation used above, we have

$$\sum_{mq}\frac{\langle f_p g_m|W_p(\omega)|g_n f_q\rangle\langle f_q|\Delta|g_m\rangle}{\omega+\varepsilon_m-\varepsilon_q+\mathrm{i}\eta} = \langle f_p|\lambda'(\omega+\varepsilon_d)Y_{10}|\phi_c\rangle \tag{12}$$

where λ' is the radial integral including λ, g_l and R_{l_d}. Finally we have the resonant X-ray absorption intensity summing up all terms considered above

$$I(\omega) = 2\pi\sum_{pc}|\langle f_p|\{r+\lambda(\omega+\varepsilon_d;r) + \lambda'(\omega+\varepsilon_d;r)\}Y_{10}(\hat{\boldsymbol{r}})|\phi_c\rangle|^2\delta(\omega+\varepsilon_n-\varepsilon_p). \tag{13}$$

The X-ray absorption factor f_d at the deep core ϕ_d is now defined by

$$\sum_{m_d}\langle\phi_d|\Delta^\dagger g_{sc}(\omega+\varepsilon_d)\Delta|\phi_d\rangle = -\tfrac{1}{2}f_d(\omega). \tag{14}$$

The resonant excitation operator λ is closely related to the deep core (ϕ_d) X-ray absorption factor f_d

$$\lambda(\omega+\varepsilon_d;r) = -\frac{2\pi}{3}\frac{1}{r^2}f_d(\omega). \tag{15}$$

In a similar way let us define $\tilde{f}_d$ by use of $\tilde{\Delta} = Y_{10}(\hat{\boldsymbol{r}})/r^2$

$$-\tfrac{1}{2}\tilde{f}_d(\omega) = \sum_{m_d}\langle\phi_d|\Delta^\dagger g_{sc}(\omega+\varepsilon_d)\tilde{\Delta}|\phi_d\rangle. \tag{16}$$

We thus obtain an interesting relation between $\lambda'(\omega+\varepsilon_d;r)$ and f_d and $\tilde{f}_d$,

$$\lambda'(\omega+\varepsilon_d;r) = \left(\frac{2\pi}{3}\right)^2 \frac{1}{r^2} f_d(\omega)\tilde{f}_d(\omega). \tag{17}$$

We thus have the X-ray absorption intensity near the resonant threshold in terms of Green's function g_{sc}

$$I(\omega) \sim -2\mathrm{Im}\sum_c \langle\phi_c|\Delta'(\omega+\varepsilon_d)^\dagger g_{sc}(\omega+\varepsilon_d)\Delta'(\omega+\varepsilon_d)|\phi_c\rangle,$$

$$\Delta'(\omega+\varepsilon_d) = \{r+\lambda(\omega+\varepsilon_d;r)+\lambda'(\omega+\varepsilon_d;r)\}Y_{10}(\hat{\boldsymbol{r}}), \tag{18}$$

where the sum over c means the sum over m_c. The resonant contribution from shallow core X-ray absorption near deep core threshold was first discussed in ref. [7]. We frequently use the $L_{2\,3}$ white line intensity to discuss the 3d hole population. From the above discussion 3d X-ray absorption intensity shows additional resonant behaviour near the 2p threshold, which makes the white-line analyses difficult and complicated.

4. Conclusion

We study the influence of the polarization part W_p of the screened Coulomb interaction $W(\omega)$ on MARPE and XAFS. We successfully relate the resonant term to the X-ray absorption factor f_d from the deep core ϕ_d, which has been used in the analyses of the resonant X-ray scattering. We should note that W_p also plays an important role in the other resonant phenomena accompanied by core excitations.

References

1. Kay, A., *et al*., Science **281**, 679 (1998).
2. Kay, A. W., *et al*., Phys. Rev. B **63**, 115119 (2001).
3. Nordlumb, D., *et al*., Phys. Rev. B **63**, 121402(R) (2001).
4. de Abajo, F. J. G., Van Hove, M. A. and Fadley, C. S., Phys. Rev. B **63**, 75404 (2001).
5. Fujikawa, T. and Arai, H., J. Electron. Spectrosc. **123**, 19 (2002).
6. Fujikawa, T. and Arai, H., Chem. Phys. Lett. **368**, 147 (2003).
7. Fujikawa, T., J. Synchrotron Rad. **8**, 76 (2001).

Physica Scripta. Vol. T115, 1094–1096, 2005

Lifetime-Broadening-Removed XANES Spectroscopy by High-Resolution Resonant Inelastic X-Ray Scattering

H. Hayashi[1,*], R. Takeda[1], Y. Udagawa[1], T. Nakamura[2,**], H. Miyagawa[2,***], H. Shoji[2,****], S. Nanao[2] and N. Kawamura[3]

[1]IMRAM, Tohoku University, 2-1-1 Katahira, Sendai 980-8577, Japan
[2]Intitute of Industrial Science, University of Tokyo, Komaba, Meguro, Tokyo 153-8505, Japan
[3]JASRI, Mikazuki, Hyogo 679-5198, Japan

Received June 26, 2003; accepted November 4, 2003

PACS numbers: 78.70.En, 61.10.Ht

Abstract

Resonant inelastic X-ray scattering (RIXS) is uniquely related to X-ray absorption oscillator strength distribution by Kramers-Heisenberg equation via lifetime widths of the states involved. By using RIXS spectra of CuO it is shown that XANES, where the lifetime broadening (LB) of the 1s core-hole is removed and that of the 2p hole determines the resolution, can be analytically deduced from RIXS profiles. Furthermore, it is demonstrated that numerical procedures can eliminate also the remaining 2p broadening, providing LB-free XANES.

1. Introduction

X-ray absorption near edge structure (XANES) provides one of the most useful tools for studying the density of the electronic states around selected atomic species. XANES features are, however, often smeared out because of the natural lifetime width of the core holes. In order to overcome this fundamental limitation, high-resolution fluorescence excitation (HRFE) spectroscopy has been proposed to obtain lifetime-broadening-removed (LBR) XANES spectra [1], where highly monochromatic incident X-ray energy is scanned across an absorption edge while monitoring the characteristic fluorescent X-rays with better resolution than the lifetime width. However, later it was suggested that, rigorously speaking, HRFE spectra can not be viewed as genuine LBR-XANES [2–4]. In addition, this technique is limited to atomic species where suitable high-resolution crystal analyzers are available for the characteristic lines [1, 3].

An alternative method of obtaining LBR-XANES by the use of resonant inelastic X-ray scattering (RIXS) has been theoretically suggested by Tulkki and Åberg [5] even before the proposition of the HRFE spectroscopy. Intense monochromatic X-rays recently available at third generation of synchrotron radiation facilities have made it possible to experimentally substantiate the observation of LBR-XANES from RIXS spectra [6]. In this work using CuO data it is demonstrated that 1s lifetime-broadening-removed (LBR) and 1s as well as 2p lifetime-broadening-removed or lifetime-broadening-free (LBF) XANES can be deduced from experimental RIXS spectra.

2. Experimental

The experiments were carried out at the BL47XU beamline at SPring-8. The experimental details were described elsewhere [6]. In short, incident X-rays (flux= $\sim 10^{14}$ photons/s; spectral width = 0.9 eV at 8 keV) were horizontally focused by a cylindrically-bent mirror and irradiated onto the sample, with an ion chamber monitoring the beam intensity. The scattered radiation was analyzed with a spherically-bent ϕ 75 mm Si(444) crystal having an 820 mm radius of curvature, and detected by a scintillation counter. To acquire 1s2p RIXS spectra, the incident energy remained fixed and the scattered photon energy was analyzed by moving the analyzer and the detector synchronously. In these measurements, the active area of the analyzer was limited to 40 mm in diameter, which resulted in the overall energy resolution (ΔE_{exp}) of 1.1 eV as determined by the FWHM of the elastic line. All data were taken on powder CuO at room temperature at a constant scattering angle of 80°.

For comparison, HRFE spectrum was derived from the intensity at Cu $K\alpha_1$ energy, 8047.8 eV, of each RIXS spectrum. Conventional XANES spectrum was obtained by monitoring the intensity of total fluorescence by a pin-photo diode while excitation energy is scanned.

3. Results and Discussion

3.1. *RIXS spectra of CuO*

Figure 1 shows excitation energy dependence of RIXS spectra of CuO. Spectral shape and intensity change with excitation energy significantly. Excitation with X-ray energies well above

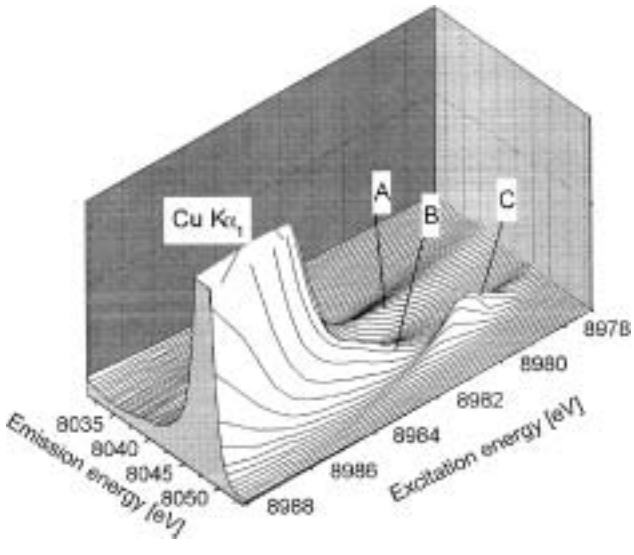

Fig. 1. Excitation energy dependence of resonant inelastic X-ray scattering (RIXS) spectra of CuO as a function of excitation energy and emission energy.

*e-mail: hayashi@tagen.tohoku.ac.jp
**Present address: JASRI, Mikazuki, Hyogo 679-5198, Japan
***Present address: Faculty of Engineering, Kagawa University, Hayashi-Cho, Takamatsu 761-0396, Japan
****Present address: Semiconductor Energy Laboratory Co., Ltd. Hase 398, Atsugi, Kanagawa, 243-0036, Japan

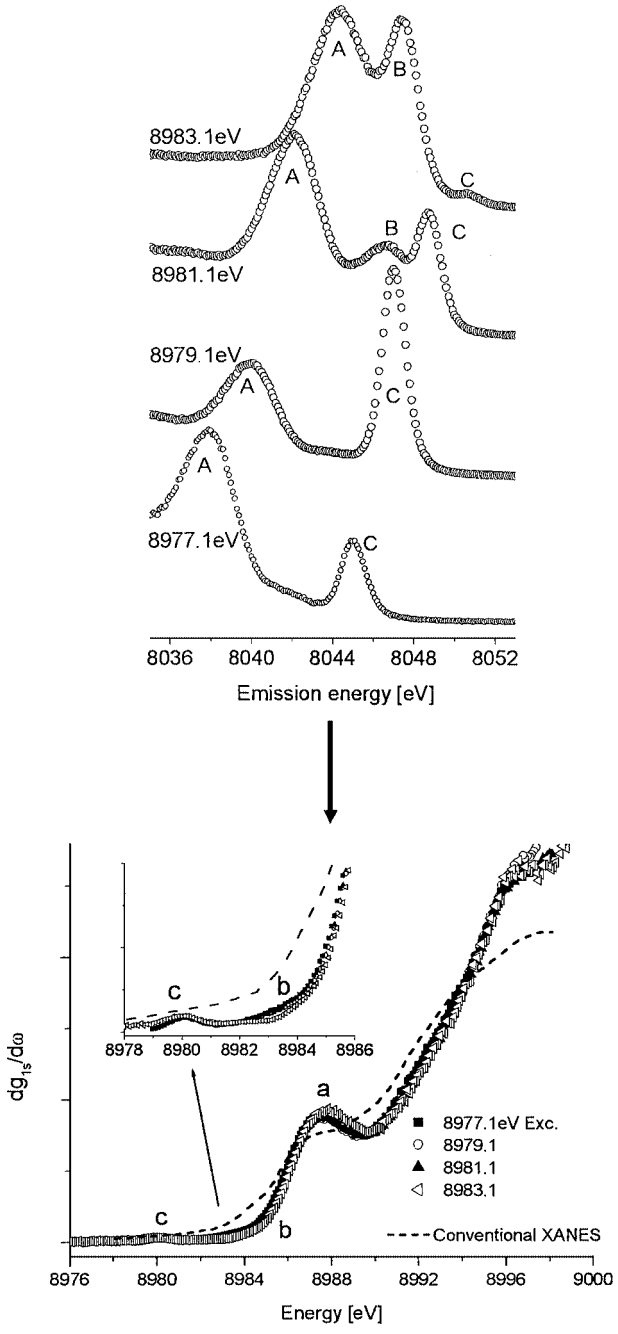

Fig. 2. Selected RIXS spectra of CuO (upper panel) and LBR-XANES profiles analytically calculated from them (lower panel). Conventional XANES is also shown in the lower panel for comparison.

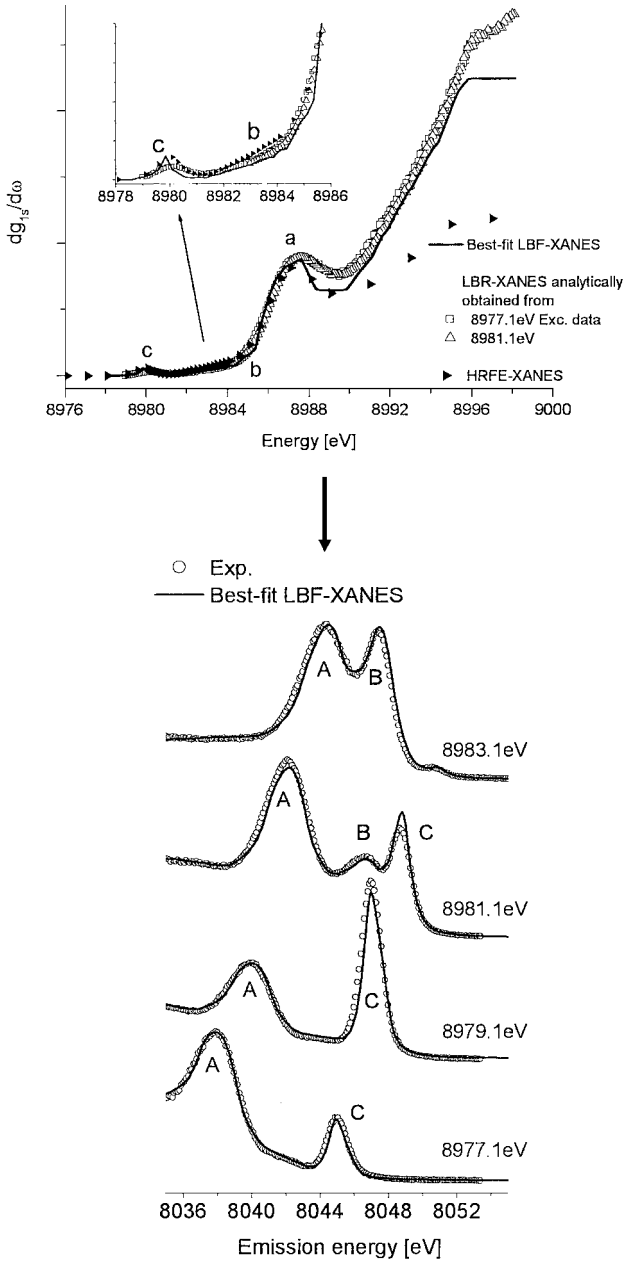

Fig. 3. Upper panel: the best-fit LBF-XANES ($dg_{1s}/d\omega$) as well as LBR-XANES spectra analytically obtained from RIXS by 8977.1 eV and 8981.1 eV excitation. Also shown is the HRFE spectrum. Lower panel: comparisons of the observed RIXS spectra and calculated ones by the use of best-fit ($dg_{1s}/d\omega$) model.

the K-absorption edge energy (∼8986 eV) yields a single band at 8047.8 eV, which is the well-known Cu Kα_1 fluorescence line (In Fig. 1 the Kα_1 peak is out of the scale). As the excitation energy lowered below the K-edge, the main feature corresponding to the Kα_1 (denoted A) is shifted down with its width broadened. By lowering the excitation energy to ∼8983 eV, a new branch, labeled B, appears, which can be seen as a distinct peak in Figs. 2 and 3. Another feature labeled C is prominent at the excitation energy below 8983 eV. As the excitation energy further lowered, the peak energy of A continues to shift to lower energy, preserving the energy loss (E_{loss}) of 939 eV. At the same time, the scattering intensities decrease monotonously. In contrast to the consecutive changes with excitation energy observed for A, the branch B is only observable within a small range of excitation energy, from ∼8981 to ∼8984 eV. Furthermore, the E_{loss} of the branch B varies with the excitation energy. On the other hand, E_{loss} for C remains constant (932 eV) and is independent of the excitation energy, as is the branch A. As the excitation energy is tuned to ∼8980 eV, which is the transition energy from 1s to the vacant 3d [7], the band C is the strongest with the band width much narrower than the normal Kα_1 fluorescence. These excitation energy dependencies of RIXS spectral features have been already reported [6, 8].

3.2. *Analytical deduction of LBR-XANES*

The differential cross section of 1s2p RIXS process can be deduced from the well-known Kramers-Heisenberg equation as follows [5]:

$$\frac{d\sigma(\omega_1)}{d\omega_2} \propto \int \frac{(\omega_2/\omega_1)(\Omega_{1s}+\omega)(dg_{1s}/d\omega)}{((\Omega_{1s}+\omega-\omega_1)^2+\Gamma_{1s}^2/4\hbar^2)((\omega_{2p}+\omega_2+\omega-\omega_1)^2+\Gamma_{2p}^2/4\hbar^2)}\,d\omega. \quad (1)$$

Here $\hbar\omega_1$ and $\hbar\omega_2$ are incident and scattered photon energies, $\hbar\omega$ refers to the kinetic energies of the excited electron or binding energy of the bound electron in the intermediate state, and Γ_{1s} and Γ_{2p} are the widths of the 1s and 2p levels, the energies of which are represented by $\hbar\Omega_{1s}$ and $\hbar\Omega_{2p}$. The $\mathrm{d}g_{1s}/\mathrm{d}\omega$ is the oscillator strength distribution for K-absorption, which is in general a superposition of discrete and continuous features.

Under the approximation that $\Gamma_{2p}/2\hbar \ll 1$, Eq. (1) can be transformed to a more transparent form [6] by using the Kα-emission condition $\hbar\omega_{K\alpha} = \hbar(\Omega_{1s} - \Omega_{2p}) = 8047.8\,\mathrm{eV}$ and employing the absorption energy $\omega_{abs} = \Omega_{1s} + \omega = \omega_{K\alpha} + \omega_1 - \omega_2$.

$$\frac{\mathrm{d}\sigma(\omega_1)}{\mathrm{d}\omega_2} \propto \frac{(\omega_2/\omega_1)\omega_{abs}(\mathrm{d}g_{1s}/\mathrm{d}\omega_{abs})}{(\omega_{K\alpha} - \omega_2)^2 + \Gamma_{1s}^2/4\hbar^2}. \tag{2}$$

This equation means that the cross section of 1s2p RIXS is, apart from the factor $(\omega_2/\omega_1) \times \omega_{abs}$, proportional to $\mathrm{d}g_{1s}/\mathrm{d}\omega_{abs}$ multiplied by a Lorentzian centered at $\omega_{K\alpha}$. Hence it is possible to calculate $\mathrm{d}g_{1s}/\mathrm{d}\omega$ analytically from the experimental RIXS spectra directly, or vice versa. Under the approximation employed here, $\mathrm{d}g_{1s}/\mathrm{d}\omega$ derived from RIXS by Eq. (2) is free from lifetime-broadening by Γ_{1s} and the width is determined only by ΔE_{exp} and Γ_{2p}.

In the upper panel of Fig. 2 the RIXS spectra of CuO excited at several excitation energies are shown. In the lower panel shown are LBR-XANES profiles of CuO analytically derived from the RIXS spectra by the use of Eq. (2). The inset shows 1s→3d transition region below the absorption edge in an expanded scale. It is rather striking that, in spite of significant differences in RIXS spectra employed, LBR-XANES derived by Eq. (2) almost overlaps with each other. Although not shown for clarity of the figure, a use of RIXS spectra at other excitation energies produces almost the same results as long as the excitation energy is below about 8984 eV.

In the lower panel of Fig. 2 conventional XANES is also shown. It is clear from the comparison that features in LBR-XANES are much more distinct than those in conventional XANES. This endorses that line-broadening by Γ_{1s}, which often hampers detailed analysis of conventional XANES, is removed in LBR-XANES derived from RIXS.

3.3. *Lifetime-broadening-free XANES by simulation*

In the derivation of Eq. (2) it has been assumed that Γ_{2p} is zero. Since the quality of the present RIXS data allows us to examine the profiles in detail numerically, attempted next is to derive $\mathrm{d}g_{1s}/\mathrm{d}\omega$ by numerical simulation based on Eq. (1) without such an assumption. The $\mathrm{d}g_{1s}/\mathrm{d}\omega$ profiles obtained from this procedure correspond to lifetime-broadening-*free* (LBF) XANES. Detailed procedures are described elsewhere [6].

In the upper panel of Fig. 3 a $\mathrm{d}g_{1s}/\mathrm{d}\omega$ model that reproduces observed RIXS spectra best is shown. Also shown are LBR-XANES profiles obtained in the previous section together with the HRFE spectra. It is evident that $\mathrm{d}g_{1s}/\mathrm{d}\omega$ obtained here shows much more distinct features than those obtained in the previous section and the HRFE spectra, demonstrating that the core-hole lifetimes of 2p as well as 1s are removed. Well above the absorption edge the HRFE spectra show significant deviation from LBR-XANES, the reason of which we believe is in the re-absorption effects. In the present method, since both the incident energy and the scattering energy are below the absorption edge, absorption is relatively weak and changes only slightly with excitation energy.

In the lower panel of Fig. 3 calculated RIXS profiles from the best-fit $\mathrm{d}g_{1s}/\mathrm{d}\omega$ model are compared with some of the experimental RIXS spectra. It is evident that the observed RIXS spectra, which vary enormously with excitation energy, almost exactly coincide with the corresponding ones generated by the *single* $\mathrm{d}g_{1s}/\mathrm{d}\omega$ model.

Roughly speaking, there are the following relations between $\mathrm{d}g_{1s}/\mathrm{d}\omega$ features and RIXS peaks. First, the main RIXS feature, which is indicated by A in Figs. 1–3, is essentially determined by the profile of the prominent features in XANES indicated by a in Figs. 2 and 3. The shape of the low-energy tail of the features a, indicated by b, determines the RIXS feature B. The discrete 1s→3d band c at 8980 eV is responsible to the prominent feature C in the RIXS spectra. From these observations it is confirmed that complicated behavior of the RIXS spectra, found in Figs. 1–3, can be explained qualitatively as the reflection of the LBF-XANES profile.

Many exciting applications of the present LBR-or LBF-XANES spectroscopy, e.g., the in-situ determination of the catalysts or batteries during reactions, could be envisaged.

Acknowledgment

This experiment was carried out at the SPring-8 under the proposal No. R02A47XU-0033N.

References

1. Hämäläinen, K., Siddons, D. P., Hastings, J. B. and Berman, L. E., Phys. Rev. Lett. **67**, 2850 (1991).
2. Carra, P., Fabrizio, M. and Thole, B. T., Phys. Rev. Lett. **74**, 3700 (1995).
3. Loeffen, P. W., *et al*., Phys. Rev. B **54**, 14877 (1996).
4. Kotani, A. and Shin, S., Rev. Mod. Phys. **73**, 203 (2001).
5. Tulkki, J. and Åberg, T., J. Phys. B **15**, L435 (1982).
6. Hayashi, H., *et al*., Phys. Rev. B **68**, 45122 (2003).
7. Kosugi, N., Kondoh, H., Tajima, H. and Kuroda, H., Chem. Phys. **135**, 149 (1989).
8. Hayashi, H., Udagawa, Y., Caliebe, W. A. and Kao, C.-C., Phys. Rev. B **66**, 33105 (2002).

Physica Scripta. Vol. T115, 1097–1098, 2005

A Multi-Crystal Spectrometer with a Two-Dimensional Position-Sensitive Detector for X-ray Fluorescence Spectroscopy

H. Hayashi, M. Kawata, R. Takeda and Y. Udagawa*

IMRAM, Tohoku University, 2-1-1 Katahira, Aoba-ku, Sendai 980-8577, Japan

Received June 26, 2003; accepted November 4, 2003

PACS numbers: 78.70.En, 61.10.Ht

Abstract

A newly designed multi-crystal X-ray spectrometer equipped with a two dimensional position sensitive proportional counter is described. The spectrometer employs five cylindrically bent rectangular Ge(4 4 0) crystals with $35 \times 100\,\mathrm{mm}^2$ in size, whose radius of curvature is 550 mm. Diffracted X-rays from each crystal are horizontally dispersed and vertically focused onto different portions of the detector, and spectra are constructed by adding data from five crystals. Resonant Kβ emission spectra of Mn compounds obtained with this spectrometer are presented.

1. Introduction

Resonant and near resonant X-ray fluorescence spectra, obtained by exciting around the absorption edge, varies significantly with excitation energy and contain invaluable information about the electronically excited states. What is essential to the resonant X-ray fluorescence experiments is a high-resolution spectrometer to analyze emitted radiation together with highly monochromatized intense exciting X-rays. Because the emission intensity sharply decreases with decrease in excitation energy from the absorption edge, the analyzer has to be also highly efficient. To achieve this goal, several attempts have been made so far. For example, Bergman *et al.* [1] have developed a *focusing-type* spectrometer having 8 spherically bent crystals. In this work, a *dispersive-type* spectrometer with 5 cylindrically bent crystals combined with a position sensitive detector, which has evolved from our previous design [2], is described. A large acceptance angle, high experimental resolution, and wide energy range make this spectrometer particularly suited for studies of resonant fluorescence spectroscopy.

2. A multi-crystal spectrometer with a two-dimensional position-sensitive detector

Fig. 1 shows the principle of a spectrometer employing a cylindrically bent crystal. The diffraction plane is illustrated as a hatched area. The X-rays from the sample point are horizontally dispersed according to their energies. On the other hand, vertically dispersed components are focused on a point along the central axis of the cylinder shown in Fig. 1. The distance from the diffracted point can be expressed as $f = R/\sin\theta_B$, where the θ_B and R are the Bragg angle and the radius of curvature of the crystal, respectively. Thus by placing a position-sensitive detector at the focus area, a wide spectrum can be obtained simultaneously.

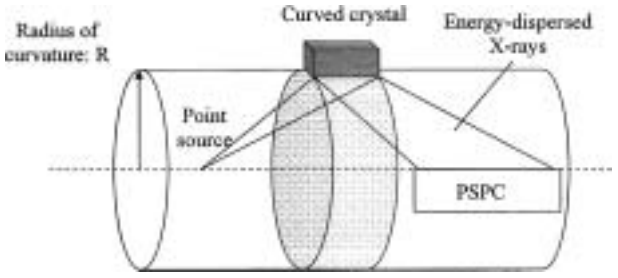

Fig. 1. The principle of a spectrometer employing a cylindrically bent crystal.

In this dispersive-type setting the energy resolution of the spectrometer ($\Delta E/E$) can be described by the following equation,

$$\Delta E/E = \cot\theta_B\,\Delta\theta, \tag{1}$$

where $\Delta\theta$ is the angular divergence, and is estimated from

$$\Delta\theta \simeq (d+s)/f. \tag{2}$$

Here d and s mean the horizontal beam size on the sample and the spatial resolution of the detector [3]. It should be noted that, unlike for the focusing modes [4], $\Delta\theta$ in the dispersive optics is independent of $\cot\theta_B$. Hence the dispersive-type optics can cover a wider energy range by one kind of crystal plane than the focusing-type optics, without severely deteriorating the resolution. This makes it possible to extend the atomic species to be investigated.

Fig. 2 illustrates a schematic geometry of the present spectrometer. Scattered radiation from the sample was analyzed with five cylindrically bent rectangular Ge(440) crystals with $35 \times 100\,\mathrm{mm}^2$ in size whose radius of curvature (R) is 550 mm. They are aligned with different tilt angles to focus images on different places of the detector. The crystals were held on a plate, which can be moved in horizontal direction to change the Bragg angles (θ_B). Analyzed X-rays are detected with a 2-dimensional position sensitive proportional counter (Hi-STAR, Bruker AXS) which is filled with Xe gas and equipped with 2D multiwire grid for readout.

Resultant 2D images, five horizontally-dispersed patterns, are converted to 1D spectrum by adding them after energy calibration.

3. Resonant Kβ emission measurements of MnO

To demonstrate the performance of the spectrometer, Kβ emission spectra of several Mn compounds were measured at various excitation energies across the Mn K-edge. In these experiments the overall energy resolution, estimated from FWHM of elastic lines, was about 1.4 eV. Owing to largely increased detection solid angle, the required data acquisition period is from only a few

*e-mail: udagawa@tagen.tohoku.ac.jp

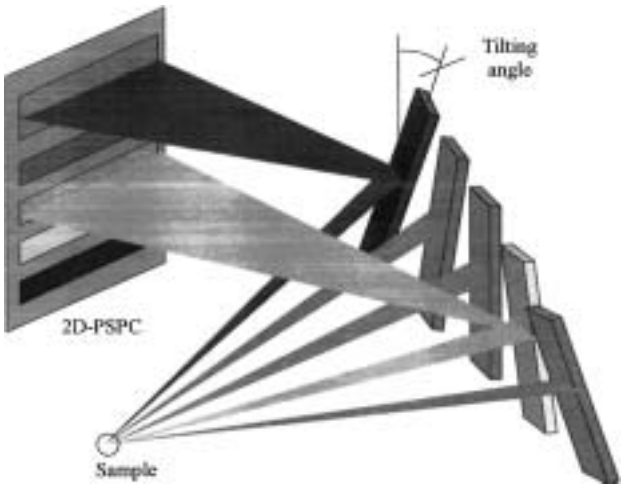

Fig. 2. A Schmatic diagram of dispersive-type 5-crystal spectrometer with a 2-dimensional position-sensitive detector.

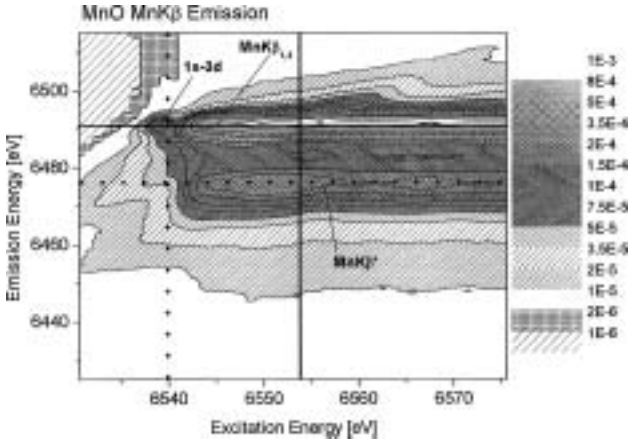

Fig. 3. A contour map of KB emission intensities of MnO as a function of both the excitation and emission energies.

minutes (resonant) to an hour (non-resonant) for each emission spectrum. Such short data acquisition period opens up a new possibility of X-ray emission spectroscopy; instead of a series of one-dimensional spectra, two-dimensional mapping is now possible. The results on MnO are shown in Fig. 3 as a contour plot, where the abscissa and the ordinate are excitation and emission energies; 46 spectra taken at different excitation energies are complied to make this map.

Traversing the contour plot parallel to the ordinate yields a usual emission spectrum obtained by exciting the X-ray energy as indicated at the abscissa. For example, by 6554 eV excitation, which is indicated by a vertical solid line, an emission spectrum with two prominent peaks corresponding to $K\beta_{1,3}$ and $K\beta'$ at 6491 and 6476 eV is obtained. Similarly, excitation at 6540 eV, indicated by a vertical dot, yields an asymmetric peak at 6491 eV. On the other hand, by traversing the contour plot along a horizontal line, one obtains excitation spectra for constant final state energy. The spectrum along the horizontal solid line in the figure will show strong 3d resonance, while another one along the horizontal dot will not exhibit 3d resonance.

Spin – dependent X-ray absorption of Mn compounds has been studied by Hämäläinen *et al.* [5]. They observed that XANES obtained by monitoring the $K\beta_{1,3}$ band is different from the one by $K\beta'$; in particular 3d resonance is observed only in the former. The observation is exactly what is obtained along the two horizontal lines in Fig. 3.

Of particular importance is the existence of structures that stretch diagonally in the plot. These correspond to resonant inelastic (Raman) scattering spectra, and from the analysis of these structures it is possible to deduce lifetime-broadening-removed or lifetime-broadening-free XANES spectra [6].

In summary, by a spectrometer combining 5 cylindrically bent dispersing crystals with position sensitive proportional counter, it is possible to obtain high-resolution emission spectra within a reasonable period of time. It opens up a new possibility of resonant X-ray emission spectroscopy.

Acknowledgments

The experiments were carried out at the SPring-8 under the proposals of No. 2002B0475-NX-np and No. R03A47XU-0017N.

References

1. Bergmann, U. and Cramer, S. P., SPIE Proc. **3448**, 198 (1998).
2. Hayashi, H., Udagawa, Y., Gillet, J.-M., Caliebe, W. A. and Kao, C.-C., in: "Chemical Applications of Synchrotron Radiation" (World Scientific, Singapore 2002), p. 850.
3. Hayakawa, S. *et al.*, Spectrochimica Acta B **54**, 171 (1999).
4. Wittry, D. B. and Sun, S., J. Appl. Phys. **67**, 1633 (1990).
5. Hämäläinen, K., Kao, C.-C., Hastings, J. B., Siddons, D. P. and Berman, L. E., Phys. Rev. B **46**, 14274 (1992).
6. Hayashi, H. *et al.*, Phys. Rev. B **68**, 45122 (2003). Proceedings of this conference.

Physica Scripta. Vol. T115, 1099–1101, 2005

ELNES Analysis for Silicon, Silicon Oxide and Their Interface

Hironobu Matsumoto[1*], Shin-ichi Nagamatsu[2], Masatoshi Nakazawa[3] and Takashi Fujikawa[1]

[1]Grad. School for Sci., Chiba Univ., Yagoi-cho, 1-33, Inage, Chiba, 263-8522, Japan
[2]Center for Frontier Electronics and Photonics Chiba Univ. Yahoi-cho, 1-33, Inage, Chiba 263-8522, Japan
[3]Hitachi, Ltd. Device Development Center, Shinmachi, 6-16-3, Ome, Tokyo, 198-8512, Japan

Received June 26, 2003; accepted October 16, 2003

PACS numbers: 79.20.Uv, 79.20.Ap

Abstract

We have measured and analyzed Si L_{23}-edge electron energy loss near edge structure (ELNES) spectra for silicon, silicon oxide and their interface. ELNES spectra have been recorded by a combination of high resolution electron energy loss spectroscopy and an installed slit built in a 300 keV transmission electron microscope. The projected slit allows us to have signals about each 0.7 nm width area of the specimen. These spectra change site by site from Si to SiO_2. With the aid of multiple scattering calculations, we have discussed the local structure near the interface.

1. Introduction

Si and SiO_2 are among the most important materials and are widely studied becasue of their fundamental and industrial importance. To obtain local structural and electric information, Si L_{23}-edge ELNES spectra have been measured by several authors [1, 2]. In particular much effort has been paid to study Si-SiO_2 interface structures. Si 2p core level angle-resolved photoemission was studied with some simple models based on the statistical cross-linking between Si and SiO_2 [3]. Si-SiO_2 bonds length in the interface region are estimated by an analysis for O K-edge EXELFS [4], and it was concluded that the interface bond length is slightly larger than that of SiO_2.

ELNES and XANES are commonly used to investigate short range structures and electronic states. Both of them mainly originate from the electric dipole transition from a selected core orbital to unoccupied states [5, 6]. The structures of ionization edges reflect the density of states with some excitonic contribution from the core hole that is created in this inelastic scattering process. In low energy ionization edge regions such as Si L_{23}, EELS is suited for investigating at high energy resolution.

Si L_{23}-edge EELS spectra for Si wafer covered with SiO_2 are successfully measured in a narrow domain with a width of each 0.7 nm on the sample. These spectra change site by site from Si to SiO_2.

In this study, we report full multiple calculations of Si L_{23}-edge ELNES for Si, SiO_2 Si-SiO_2 and their interfaces. We also discuss the theoretical results for Si and SiO_2 near the interface.

2. Experiment

(100)-oriented silicon wafer covered with thermally grown silicon oxide and SiN_x are studied in this work. A sample was prepared by a sliced specimen, 60 nm thick. EELS measurements were carried out by using high resolution electron energy loss spectroscopy built in a 300 keV TEM. In the TEM is installed a slit which allows having a signal on a region 0.7 nm times 27 nm at the position of the sample. This system has been developed as a useful tool to study a narrow region so we can distinct Si, SiO_2 and their interface spectra.

3. Theory

In the ELNES region, scattering from surrounding atoms are strong enough that the multiple scattering renormalization is crucial. The full multiple scattering ELNES formula used in this article is developed by one of the authors [5, 6] and obtained in the closed form as a typical XANES formula.

$$I(\boldsymbol{p}', \boldsymbol{p}) = -4\pi \mathrm{Im}[i^{\ell_1-\ell} t^A_{\ell_1} \mathrm{e}^{\mathrm{i}(\delta^A_{\ell_1}+\delta^A_{\ell})} \times \langle c|u^{\dagger}|L_1\rangle [(1-X)^{-1}]^{AA}_{L_1,L} \langle L|u|c\rangle] \quad (1)$$

where $u = u(\boldsymbol{p}', \boldsymbol{p})$ is one electron inelastic amplitude from $\boldsymbol{p}$ to $\boldsymbol{p}'$ and one electron state $|L\rangle = |R_{\ell}(r)Y_L(\hat{\boldsymbol{r}})\rangle$ is a partial wave of an EXAFS electron with angular momentum $L = (\ell, m)$. $(1-X)^{-1}$ represents a renormalized infinite order multiple scattering term, where the matrix $X^{\alpha\beta}$ can be written as

$$X^{\alpha\beta}_{L_1,L_2} = t^{\alpha}_{\ell_1}(k) G_{L_1,L_2}(kR_{\alpha} - kR_{\beta})(1-\delta_{\alpha\beta}) \quad (2)$$

where t^{α} and $G_{LL'}$ represent the T-matrix at site α and the Green function in an angular momentum representation. This matrix element describes a physical process where a photoelectron wave propagates from site β with angular momentum $L_2 = (\ell_2, m_2)$ to site α and is scattered off with angular momentum $L_1 = (\ell_1, m_1)$. The t-matrix reflects the electronic structure whereas G reflects the geometric structure. Thus ELNES spectra can give us useful information on electronic and geometric structures around the excited atom.

4. Results and Discussion

4.1. *Si and SiO₂*

We first consider the Si L_{23}-edge ELNES for Si and SiO_2. Figures 1(a) and 1(e) show a comparison between the experimental and theoretical Si L_{23}-edge ELNES spectra for SiO_2 and Si. To calculate these spectra, we use clusters with diamond structure for Si and crystalline quartz structure for SiO_2. These clusters have atoms up to 8 Å around an excited Si atom. To calculate the phase shift for SiO_2, electronic structures of Si and O atoms were referred to the density functional results [7].

The structure of theoretical ELNES spectra for Si is in good agreement with the experimental data in both the shape and the loss intensity.

In the case of Si L_{23}-edge ELNES for SiO_2, the agreement between the experimental and the theoretical spectra is good for

*Electronic address: matumoto@graduate.chiba-u.jp

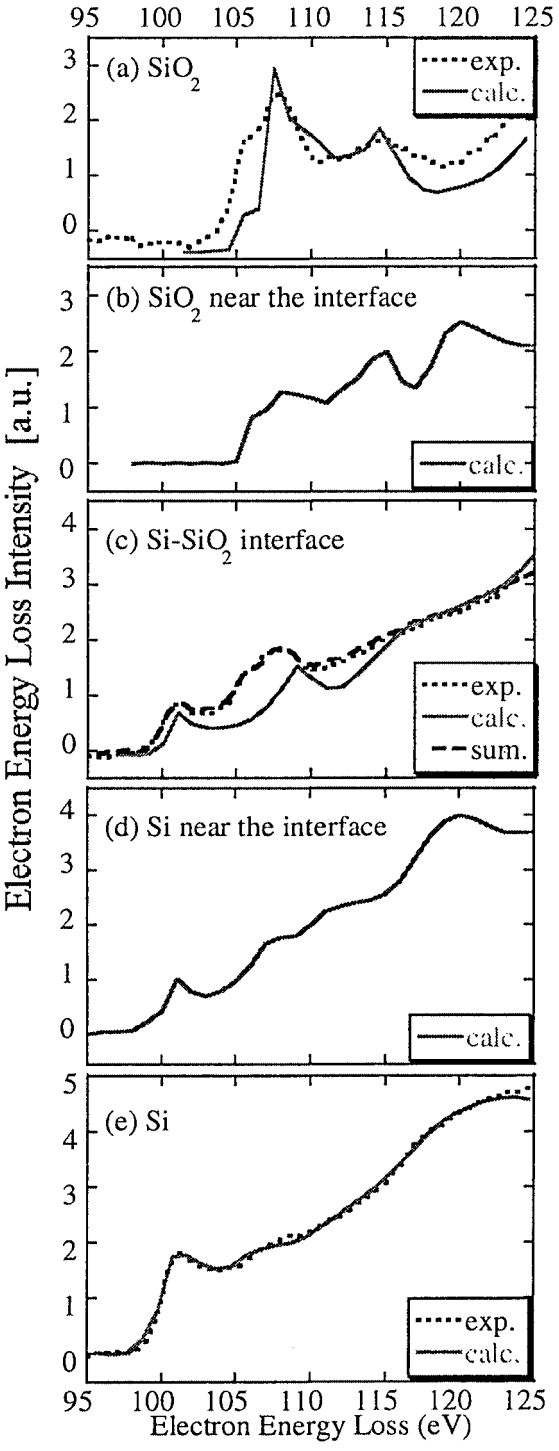

Fig. 1. Observed Si L_{23}-ELNES spectra (dotted lines) for SiO_2 (a) and Si (e) compared with the calculated ones (solid lines). The observed ELNES for the Si-SiO_2 interface is shown in (c), where we also show the weighted sum of observed spectrum (dashed line) for Si and SiO_2, compared with the calculated result at the interface. The ELNES spectra (b) show the calculated one for SiO_2 and (d) is for Si near the interface. The interface model is shown in Fig. 2.

the peak positions, however little worse in loss intensity. We have sharp peaks in the calculated results at 108 eV and 114 eV.

4.2. *Si-SiO_2 interface*

In this paper, we consider a abrupt interface model to calculate ELNES spectra for interface Si atoms. The interface geometry used in this model is shown in Fig. 2 where the interface Si atom is labeled (c). This model is obtained by joining a bulk truncated Si(111) lattice to pure SiO_2, with all the dangling bonds from

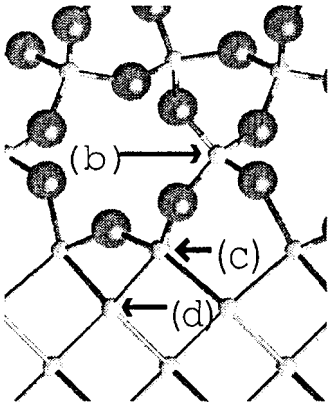

Fig. 2. A model of a Si-SiO_2 interface viewed from the side. Results of calculations for Si atom labeled (b), (c) and (d) correspond to the spectra in Figs. 1(b), 1(c) and 1(d) respectively. This model is obtained by joining a Si lattice, terminated by Si atoms with two back bonds each and two dangling bonds, to a pure SiO_2 lattice. Here each interface Si atom is with suboxide bonds.

both sides stitched together [3]. Below the terminating Si lattice, we assume each interface Si atom has two back bonds and two dangling bonds protruding to the other side of the interface. Then we join these protruded dangling bonds to O of SiO_2.

In Fig. 1(c), the observed ELNES for Si atoms in the interface region is compared with the weighted sum spectrum of these for Si and SiO_2 (*sum*-spectrum) and also with the calculated one for the interface. The observed interface spectrum reflects EELS passing through the window of the 0.7 nm width slit near the interface. We can see that the observed interface spectrum and the *sum*-spectrum show same structure. Hence we can conclude that the interface ELNES has information about the interface region and consists of linear combination spectra of Si and SiO_2.

The calculated Si L_{23}-edge ELNES for site (c) has two peaks. We found that one peak at 101 eV also observed in Si, as shown in Fig. 1(e), and an other at 108 eV.

4.3. *Near the interface*

Figures 1(b) and 1(d) show theoretical Si L_{23}-edge ELNES spectra for SiO_2 (*near*-SiO_2) and Si (*near*-Si) near the interface respectively. The corresponding excited Si atoms for *near*-Si and *near*-SiO_2 are represented in fig. 2, labeled (b) and (d) respectively.

The result for *near*-SiO_2 has similar structure as that of bulk spectra for SiO_2 and has small and broader peak at 108 eV and exhibits a additional peak at 115 eV.

The calculated result for *near*-Si has similar structure as that of bulk spectra for Si. The *near*-Si spectrum exhibits a smaller peak at 101 eV, compared with the observed Si spectrum in Fig. 1(e).

5. Concluding Remarks

Si L_{23}-edge ELNES spectra for Si, SiO_2 and their interface were measured by high resolution EELS spectroscopy. In order to investigate their detailed features, we have used full multiple scattering theory of ELNES for Si, SiO_2 and their abrupt interface. We assumed that their structures were diamond-Si, α-quartz and their abrupt interface model respectively. The calculated Si spectrum is good agreement with the experimental one. The calculation result for SiO_2 agrees for the peak positions. The observed interface ELNES spectrum has the structures of both the observed Si and SiO_2. Therefore, the interface region

spectrum consists of a linear combination of Si and SiO_2 spectra. In fact, the *sum* spectra agree with experimental interface ELNES.

We also calculated Si L_{23}-edge ELNES for the Si-SiO_2 interface and the neighbors in an abrupt interface model. The essence of this model is an abrupt transition from Si to SiO_2, with the dangling bonds from the two sides of the interface plane stitched together. The calculated spectrum for Si-SiO_2 interface has two peaks in the ELNES region, one is at 101 eV and the other is at 108 eV, and the feature of both observed Si and SiO_2 spectra as the observed interface region spectrum has the character of both Si and SiO_2. The calculated results for *near*-Si and *near*-SiO_2 spectra show similar structures to observed Si and SiO_2 ones respectively.

Acknowledgments

We would like to thank Yoshifumi Ogawa for supplying the experimental data.

References

1. Sifullah, M. S. M., Boothroyd, C. B., Botton, G. A. and Humphreys, C. J., Electron Microscopy **96**, 123 (1996).
2. Garvieand, L. A. J. and Buseck, P. R., Am. Miner. **84**, 946 (1999).
3. Luh, D. A., Miller, T. and Ching, T. C., Phys. Rev. Lett. **79**, 3014 (1997).
4. Yuan, Z. W., Csillag, S., Tafreshi, M. A. and Colliex, C., Ultramicroscopy **59**, 149 (1995).
5. Fujikawa, T., J. Phys. Soc. Jpn. **62**, 2155 (1993).
6. Fujikawa, T., "Handbook of Thin Film Materials" (edited by Nalwa, H. S.), (Academic Press 2002), Vol. 2, p. 415.
7. Ankudinov, A. L., Ravel, B., Rehr, J. J. and Conradson, S. D., Phys. Rev. B**58**, 7565 (1998).

Physica Scripta. Vol. 115, 1087–1099, 2005

Author Index

Invited and plenary

Abela R. 102
Amemiya K. 88
Ankudinov A. L. 24
Attenkofer K. 93
Baberschke K. 49
Belin S. 38
Benfatto M. 28
Bostick B. C. 80
Bouamrane F. 38
Bressler C. 102
Briois V. 38
Brouder Ch. 54
Brown G. E. 80
Calas G. 80
Carra P. 54
Carrier X. 38
Catalano J. G. 80
Che M. 38
Chen L. X. 93
Chergui M. 102
D'Angelo P. 28
Della Longa S. 28
Dent A. J. 72
Diaz-Moreno S. 72
Doyle C. S. 80
Evans J. 72
Farges F. 80
Fiddy S. G. 72
Fieber-Erdmann M. 45
Fujikawa T. 35
Gawelda W. 102
Goulon J. 54
Goulon-Ginet C. 54
Grolimund D. 102
Holub-Krappe E. 45
Ishii M. 97
Iwasawa Y. 59
Jaouen N. 54
Jennings G. 93
Johnson S. L. 102
Jubin C. 38
Juillot F. 80
Julve M. 38
Jyoti B. 72
Kaiser M. 102
Kendelewicz T. 80
Kondoh H. 88
Krafft J. M. 38
Krappe H. J. 45
Lescouëzec R. 38
Liu T. 93
Lucas H. 38
Marri I. 54
Morin G. 80
Nagasaka M. 88
Nakai I. 88
Nakao A. 97
Nambu A. 88
Newton M. A. 72
Nomura M. 59
Ohta T. 88
Pulcinelli S. H. 38
Rehr J. J. 24, 31
Ressler T. 66
Revill K. 80
Rogalev A. 54
Rossner H. H. 45
Saes M. 102
Santilli C. V. 38
Shaw G. B. 93
Shimada T. 88
Shirley E. L. 31
Soininen J. A. 31
Spormann A. M. 80
Suzuki A. 59
Tarnovsky A. N. 102
Templeton A. S. 80
Timpe O. 66
Tokumoto M. S. 38
Trainor T. P. 80
Uchihashi T. 97
van Bokhoven J. A. 76
Verdaguer M. 38
Villain F. 38
Wienold J. 66
Wilhelm F. 54
Yokoyama T. 88

Theory fundamental aspects

Aksela H. 119, 229
Aksela S. 119, 229
Ankudinov A. L. 162, 212
Argoul P. 221
Arčon I. 218, 235
Asakura K. 113
Avakyan L. 168, 215
Babanov Yu. A. 197, 237
Babanov Yu. 194
Baberschke K. 194
Bausk N. V. 115
Beccara S. a. 143
Benfatto M. 134, 152
Berrah N. 119
Binsted N. 155
Bollmann J. 188
Booth C. H. 202
Bridges F. 202
Brouder Ch. 191
Bugaev L. 168, 215
Bunker G. 175, 226
Cabaret D. 131, 191
Chen D. 140

Chukalina M. 232
Cibin G. 172
Crozier E. D. 197
Dalba G. 143, 149
D'Angelo P. 152
Dedkov Yu. 194
Dimakis N. 175, 226
Diop D. 143
Dmitrienko V. E. 252
Drahokoupil J. 179
Ebert H. 110
Edwards A. B. 155
Erenburg S. B. 115
Evans J. 155
Farges F. 168, 215, 221
Flank A. M. 165
Fonine M. 194
Fornasini P. 143, 149
Frahm R. 246
Fujikawa T. 185
Fujiwara A. 113
Funke H. 197, 232, 237
Gabrelian B. V. 162, 212
Gaudry E. 131, 191
Gomilšek J. P. 218, 235
Gordon R. A. 197
Goulon J. 191
Grisenti R. 143
Guentherodt G. 194
Harada I. 113
Hatada K. 134, 152
Hayakawa K. 152
Heinäsmäki S. 119
Hermann K. 128
Hiyama M. 136
Hribar M. 235
Hu T. D. 223
Huttula M. 229
Idzerda Y. U. 194
Joly Y. 252
Kamensky Yu. I. 237
Keil P. 246
Kirfel A. 252
Kiryanov S. 194
Knack S. 188
Kochur A. G. 125
Kodre A. 218, 235
Kolczewski C. 128
Kosugi N. 136
Kotani A. 113, 122
Koteski V. 188
Krüger P. 146
Kukk E. 119, 229
Kunicke M. 237
Kuzmin A. 149
Küger P. 122
Latokha Ya. 168, 215
Lavrentyev A. A. 162, 212
Lee J. M. 200
Li S. J. 223
Liu T. 223
Longa S. D. 152
Lützenkirchen-Hecht D. 246
Machek P. 179
Mahnke H.-E. 188
Marcelli A. 172, 223
Mauri F. 131, 191
Mazalov L. N. 115
Mihelič A. 218, 235
Miyanaga T. 185, 197
Molodtsov S. 194
Monti F. 149
Mottana A. 172
Muñoz M. 221
Nakai I. 240
Natoli C. R. 134, 146, 152, 223
Newville M. 159
Nikiforov Ya. I. 162, 212
Nikkinen J. 119
Nitta K. 185
Ogasawara H. 113
Okada K. 182
Oreshko A. P. 252
Ovchinnikova E. N. 252
Oyanagi H. 107, 140
Ozawa T. 205
Paris E. 223
Park H.-M. 240
Parlebas J. C. 122
Petrini D. 125
Prado R. J. 165
Purans J. 143
Rehr J. J. 162, 207, 212, 243
Reich T. 197
Rocca F. 143, 149
Rogalev A. 191
Romashev L. 194
Rossberg A. 232
Ruediger U. 194
Rusakova E. 168, 215
Ryazhkin A. V. 197
Sainctavit P. 131
Sainctavit Ph. 191
Sankari R. 229
Sanson A. 143, 149
Shirley E. L. 207, 243
Shulman R. S. 115
Sidorenko A. 194
Šimůnek A. 179
Sipr O. 149
Šipr O. 110, 179
Soininen J. A. 207, 243
Sokolenko A. 168, 215
Sun Z. 140, 249
Taguchi M. 122
Taguchi T. 205
Taillefumier M. 131
Tanaka K. 107
Tayagaki T. 107
Tolochko B. P. 252
Torgov V. G. 115
Us T. V. 115
Ventura G. D. 172
Vyalikh D. 194

Weber J. 188
Wei S. 140, 249
Weller M. T. 155
Welter E. 188
Wende H. 194
Wu Z. Y. 223
Wu Z. 172
Xie Y. N. 223
Yang D.-S. 200, 240
Yashiro H. 205
Zhang J. 223
Zhong W. 140

Materials

Abrahams I. 318
Abreu N. P. 418
Adamchuk V. K. 510
Adya A. K. 294
Agarwal A. 534
Akai T. 408
Akatsuka H. 294, 297
Akinaga H. 431
Ali R. 372
Aline Ramos Y. 428
Anpo M. 467
Arachi Y. 577
Artioli G. 271
Arčon I. 329, 415, 448
Asai T. 577
Asanuma T. 504
Assefa Z. 302
Auwer C. D. 342
Avendaño E. 464
Azens A. 464
Bacewicz R. 318
Bando K. K. 412
Bardelli F. 457
Bart J.-M. 342
Batchelor D. 356
Baudelet F. 346, 556
Baudelet F. 556
Bausk N. V. 439
Belin S. 346
Benfatto M. 308, 424
Besse J.-P. 288
Bian Q. 421
Binsted N. 281
Bitter J. H. 278
Blasco J. 471
Boscherini F. 308, 356, 424
Bouessay I. 326
Bourgeois S. 531
Bourgeon N. 346
Bradley J. 261
Bratina G. 329
Brennan S. 261
Bridges F. 264
Briois V. 288, 291, 516
Brown Jr. G. E. 405
Budnik P. S. 492, 495
Cachia J.-N. 342
Calas G. 525
Cao D. 264
Carboni R. 308, 356, 424
Cepek C. 308
Cezar J. C. 418
Chaker J. 516
Chang C. H. 564
Chaumont D. 291
Chen D. 399
Chen W. 399, 562
Ciatto G. 356
Cipriani C. 387
Congeduti A. 556
Cormier L. 316, 525
Couzinet B. 339
Crozier E. D. 492, 495
Dahmouche K. 516
Dalba G. 271
Dapiaggi M. 271
Datchi F. 381
D'Acapito F. 356
d'Acapito F. 384
de Groot F. M. F. 278
de Jong K. P. 278
De Panfilis S. 381, 387
De Salvador D. 356
Decremps F. 381
Deki S. 477
Dekkers M. 489
Delaunay R. 483
Della Longa S. 424
Deschanels X. 342
Deshpande A. P. 570
Di Cicco A. 381, 474
Diop D. 359
Doi Y. 513
Dominguez G. 261
Doriguetto A. C. 378
Dorofeev S. G. 365
Dreyfus C. 339
Dubiel M. 445
Ehrt D. 445
Eiras J. A. 378
Emura S. 442, 507, 577
Erenburg S. B. 439
Farges F. 405
Fedoseenko S. I. 510
Feitosa C. A. C. 486
Filipponi A. 381
Fillaux C. 339
Fjellvåg H. 281
Flank A.-M. 316, 320, 531
Fleet M. E. 323
Fons P. 523
Fornasini P. 271
Frahm R. 390, 559
Franzó G. 384
Freeouf J. L. 335
Fujita R. 294
Funakawa M. 480
García J. 471
Garnovskii A. D. 362

Giefers H. 538
Giglia A. 308, 424
Gille P. 255
Giovannini S. 308, 424
Giuli G. 387
Gloter A. 489
Golacki Z. 541
Gomilšek J. P. 329
Gordon R. A. 492, 495
Graham G. 261
Granado E. 428
Granqvist C. G. 464
Grenouillet L. 356
Grisenti R. 271
Gullikson E. M. 501
Guyomard D. 346
Guziewicz E. 541
Guziewicz M. 541
Haake U. 559
Haas H. 369
Hague C. F. 483
Haire R. G. 302
Hanada Y. 285
Handa K. 314, 433, 477
Harami T. 314
Hashimoto H. 285
Helio C. N. Tolentino 428
Hennig C. 352
Hernandes A. C. 486
Herrero-Martín J. 471
Higashi K. 567
Hinatsu Y. 513
Hirosawa I. 567
Honma T. 294, 567
Hu F. Y. 545
Ibanez A. 486
Ide J. 314, 433
Ikeda S. 359
Ilver L. 541
Imamura M. 412
Intissar M. 288
Isambert A. 489
Ishimura T. 375
Itié J. P. 339
Itié J.-P. 525
Ivanovic N. 369
Iwadate Y. 297
Iwanami Y. 332
Iwata K. 523
Jaouen N. 483
Jiang D. T. 492
Jiang Z. 421
Jiménez-Villacorta F. 450, 454
Jin Z. 520
Johnson C. S. 274
Joshi S. K. 570, 573
Journel L. 483
Judeinstein P. 516
Jürgensen A. 548
Jupille J. 320, 531
Kadono K. 504
Kageyama H. 504
Kaindl G. 510
Kajinami A. 294, 477
Kalendarev R. 556
Kanazawa Y. 467
Kaneko F. 520
Kanski J. 541
Kanuma T. 294
Kappler J.-P. 483
Kawano T. 480
Khouchaf L. 552
Kida K. 467
Kikas A. 396
Kim B. H. 393, 498
Kim D. C. 498
Kim J. S. 393, 498, 564
Kim K. Y. 564
Kim M. G. 393, 498
Kim P.-S. G. 545
Kita K. 459
Kitagawa T. 504
Kobayashi H. 577
Kobayashi K. 480
Kodre A. 329, 448
Kojima K. 314
Koningsberger D. C. 278
Kooser K. 396
Kopalko K. 541
Koteski V. 369
Koto K. 375
Kozanecka A. 318
Krappe H.-E. 369
Krasnikov S. A. 510
Kraus W. 352
Kravtsova A. N. 323
Krill G. 483
Krok F. 318
Kropf A. J. 274
Kubozono Y. 507
Kulkarni V. D. 442
Kumashiro R. 442
Kupsch A. 255
Kurosawa N. 314
Kuzmin A. 464, 556
Lagarde P. 316, 320, 531
Laubschat C. 510
Lebedev A. I. 365
Lee H. J. 393
Leroux F. 288
Letard I. 489
Li C. 399, 562
Linnen R. L. 405
Liu X. 323
Longa S. D. 308
Lopes L. P. 378
Lopez C. 342
Lu K. 399, 562
Lucovsky G. 335
Luening K. 261
Lützenkirchen-Hecht D. 390, 559
Maehara K. 567
Mahne N. 308, 424
Mahnke H.-E. 369

Maia L. J. Q. 486
Maignan A. 498
Majérus O. 525
Malič Kosec B. 448
Mariette H. 356
Mariot J.-M. 483
Martinson I. 396
Mascarenhas Y. P. 378
Mastelaro V. R. 378, 486
Matsubara K. 523
Matsubayashi N. 412
Matsuo J. 504
Matsuura H. 294, 297
Mazalov L. N. 439
Mehta L. K. 570
Meneghini C. 457
Menguy N. 489
Metson J. B. 312
Meyer D. C. 255
Michalowicz A. 326, 378, 486
Miyanaga T. 359, 459
Mizuguchi M. 431
Mizumaki M. 513
Mobilio S. 356, 384, 457
Molodtsov S. L. 510
Mori H. 567
Mori M. 372
Moriga T. 312
Moscovici J. 326
Motohashi H. 306
Mullens J. 415
Muñoz-Marít A. 450
Munsch P. 556
Murai K.-i. 267
Murakami S. 285
Muramatsu Y. 501
Murata T. 520
Nagoshi M. 480
Nakabayashi I. 267, 312
Nakagawa K. 520
Nakahara K. 523
Nakano H. 402
Nakata Y. 577
Nakatsuka A. 372
Namita H. 408
Nannarone S. 308, 424
Nelis D. 415
Neuville D. R. 316
Neves P. P. 378
Niki S. 523
Nikiforov A. I. 439
Nikitenko S. G. 365
Niklasson G. A. 464
Niu X. 399, 562
Nomura M. 332, 408
Nonaka T. 402
Numako C. 375
Nõmmiste E. 396
Ofuchi H. 431
Ohuchi K. 375
Okabayashi J. 431
Okado H. 567
Okamoto Y. 297, 302, 306
Okube M. 372, 375
Okuda C. 402
Okudera H. 372
Ono K. 431
Oshima M. 431
Ota H. 408
Ouvrard G. 346
Ozutsumi K. 314, 433
Paris E. 387
Park Y. W. 393, 498
Pasquini L. 424
Paufler P. 255
Pedio M. 308, 424
Perera R. C. C. 501
Peuget S. 342
Pianetta P. 261
Piilonen P. C. 405
Pirog I. V. 462
Polian A. 339, 381
Porsch F. 538
Prado R. J. 320, 531, 552
Pratesi G. 387
Preobrajenski A. B. 510
Prieto C. 450, 454
Principi E. 381, 474
Priolkar K. R. 442
Priolo F. 384
Prokert F. 352
Puddephatt R. J. 552
Pulcinelli S. H. 291, 516
Purans J. 464, 556
Raevskaya S. I. 462
Raevskii I. P. 462
Raquel 428
Raveau B. 498
Ray S. 457
Razumovskaya O. N. 462
Reck G. 352
Reich T. 352
Rizzato A. P. 291
Rocca F. 271
Rogalev A. 483
Rougier A. 326
Rueff J.-P. 483
Ruus R. 396
Rybicki J. 474
Saar A. 396
Sadowski J. 541
Sainctavit Ph. 489
Sánchez M. C. 471
Sakai A. 372
Sakamoto T. 297, 312
Saki R. 312
Sanson A. 271
Santilli C. V. 291, 516
Sarma D. D. 457
Sarode P. R. 442
Sato K. 359, 480
Scalese S. 384
Schell N. 352
Schlom D. G. 335

Schmerber G. 483
Schütz A. 445
Seki T. 504
Seno Y. 402
Sham T. K. 545
Shilkina L. A. 462
Shimada A. 302
Shimada H. 412
Shimizugawa Y. 504
Shimoyama I. 520
Shiozaki T. 480
Shirai K. 507
Shiwaku H. 302, 306
Shrivastava B. D. 573
Signorini L. 424
Sivkov V. N. 510
Sluchinskaya I. A. 365
Snead C. 261
Soldatov A. V. 323
Souza A. 428
Štangar U. L. 329
Stange M. 281
Stuerga D. 291
Subías G. 471
Sugihara T. 349
Sun Z. 399
Suzuki S. 302, 306
Suzuki Y. 459
Takahara S. 528
Takakura H. 433
Takasu H. 523
Takeda Y. 431
Takeuchi T. 504
Tanabe T. 435, 528
Tanaka M. 520, 577
Tanaka T. 412
Tatsumi T. 349
Terrasi A. 384
Thackeray M. M. 274
Tiano W. 271
Tolentino H. C. N. 418
Toyoda N. 504
Toyoyoshi R. 297
Trapananti A. 474
Traverse A. 450, 454
Tsuji J. 285
Tuilier M. H. 552
Twaróg A. 318
Ukyo Y. 402
Umesaki N. 294, 314, 433, 567
Uraev A. I. 362
Uruga T. 399, 459, 504, 513, 562
Valet J.-P. 489
Van Bael M. K. 415
van Dillen A. J. 278
Van Poucke L. C. 415
van Well A. A. 390
Van Werde K. 415
Vaughey J. T. 274
Verstraete J. 552
Vila M. 450, 454
Vinogradov A. S. 510
Vishnoi A. N. 534
Vlasenko V. G. 362, 462
Vuk A. Š. 329
Vyalikh D. V. 510
Wada H. 332
Wagemaker M. 390
Watanabe I. 459
Watanabe S. 294, 297
Wei S. 399, 421, 562
Weller M. T. 281
Westphal A. 261
Whitten J. L. 335
Wilhelm F. 483
Witjens L. C. 278
Witkowska A. 474
Wortmann G. 538
Wróbel W. 318
Wu Z. 387, 399, 562
Xie Z. 421
Yaita T. 302, 306
Yakimov A. I. 439
Yamada A. 523
Yamada M. 431
Yamaguchi S. 408
Yamamoto K. 314
Yamanaka T. 267
Yamashita H. 467
Yan W. 399, 421, 562
Yang X. C. 445
Yashima M. 372, 375
Yin S. 421
Yokoi H. 285
Yokoyama T. 583
Yoshiasa A. 267, 372, 375
Yoshida H. 435, 528
Yoshida T. 435, 528
Yoshii K. 513
Yoshitake H. 349
Zhang J. 421
Zhang Y. 335
Zhong W. 399

Magnetism

Agui A. 611
Aguirre-Tostada F. S. 620
Alonso J. A. 648
Amemiya K. 583
Ankudinov A. L. 600, 651
Arrio M.-A. 626
Baberschke K. 586, 600, 638, 651
Balbashev A. M. 654
Benea D. 586
Bian Q. 658
Blasco J. 594, 603, 641
Brice-Profeta S. 626
Bridges F. 629
Bushart S. 629
Casais M. T. 648
Chambers S. A. 597
Champion G. 635
Chen O. 658

Downward L. 629
Droopad R. 620
Droubay T. 597
Dvorak J. 623
Ebert H. 586
Favre-Nicolin E. 589
Fujikawa T. 632, 645
Fujioka H. 614
Fukumura T. 614
Gallagher K. 606
Garcia J. 603
García J. 594, 641
Gatteschi D. 635
Gleitsmann T. 638
Hasegawa T. 614
Heald S. M. 597
Herrera-Gomez A. 620
Hodeau J. L. 603
Idzerda Y. U. 623
Inaba Y. 580
Ishimatsu N. 580, 591
Isohama Y. 580
Isshiki M. 591
Jaouen N. 600
Jin Z. W. 614
Kappler J.-P. 635
Karapetrova E. 620
Kawamura N. 580, 591, 611, 616
Kawasaki M. 614
Kitagawa S. 583
Koinuma H. 614
Komatsu Y. 591
Leandersson M. 654
Letard I. 626, 635
Lev L. L. 654
Li Z. 600, 638
Lindau I. 654
Lograsso T. A. 600
Lussier A. 623
Martínez-Lopes M. J. 648
Maruko R. 632
Maruyama H. 580, 591
Massa N. E. 648
Matsumoto Y. 614
Matsumura D. 583
Matsushita T. 611
Mikheeva M. N. 654
Minár J. 586
Miyagawa H. 580, 616
Miyanaga T. 632, 645
Mizumaki M. 611
Muraoka H. 580
Nagamatsu S. 632, 645
Nakamura N. 580
Nakatani T. 611
Neumeier J. 629
Nylen H. 654
Ofuchi H. 614
Ogale S. B. 623
Ohta T. 583
Okamoto K. 645
Okazaki T. 632
Oshima M. 614
Piamonteze C. 648
Pianetta P. 620
Poulopoulos P. 600
Proietti M. G. 603
Ramos A. Y. 589, 648
Ranno L. 589
Ravel B. 606
Rehr J. J. 600, 651
Renevier H. 603
Rogalev A. 600
Rüttinger S. 638
Sakisaka Y. 632
Sánchez M. C. 594, 603, 641
Scherz A. 586, 600, 638
Schlagel D. L. 600
Schlom D. 620
Shimatsu T. 580
Shinde S. R. 623
Smolentsev G. 609
Soldatov A. V. 609
Sonobe Y. 580
Sorg C. 586, 600, 638
Souza-Neto N. M. 589
Subías G. 594, 603, 641
Suzuki M. 580, 616
Tolentino H. C. N. 589, 648
Tronc E. 626
Tsetlin M. B. 654
Venkatesan T. 623
Voronina E. V. 645
Wei S. 658
Wende H. 586, 600, 638, 651
Wilhelm F. 600
Woicik J. C. 620
Xie G. 658
Yang H. 658
Yin S. 658
Yu Z. 620
Zhang J. 658
Zhou L. 629
Zschack P. 620

Catalysis nano

Abbas M. I. 759
Abbas M. 717
Abe M. 685, 834
Afanasiev P. 724
Aghasyan M. 790
Ainai T. 765
Anpo M. 691
Arčon I. 753, 810
Asakura K. 781, 822
Babonneau D. 837
Baiker A. 769, 819, 831
Bando K. K. 787, 807, 825, 828
Bando K.-K. 822
Beale A. M. 678
Bell A. T. 688
Belyakova O. A. 705
Benfield R. E. 699

Bertino M. F. 776
Bertoni G. 695
Bian C. R. 781
Blum F. 776
Bönnemann H. 671, 773
Borgatti F. 695
Botti S. 717, 759
Brandès S. 681
Brendebach B. 773
Brennan S. 714
Brinkmann R. 773
Brunsch S. 729
Bucher S. 773
Bunker B. A. 776
Cabaret D. 681
Calvin S. 744
Carpenter E. E. 744
Cepek C. 695
Chattopadhyay S. 709
Chaudret B. 699
Chen D. 675, 733, 784
Chen X. 802
Chen Y. 675
Chen Z. 802
Choi S. H. 688
Chun W.-J. 781, 822
Ciardi R. 759
Colón G. 736
Corriu R. 681
David G. 681
Davoli I. 717
Denecke M. A. 769
Dong B. Z. 661
Doomes E. E. 790
Doudna C. M. 776
Dubiel M. 729
Dubois G. 681
Endruschat U. 671
Erades L. 699
Fan J. 733
Fan L. 709
Ferreira J. A. M. 727
Filin A. 703
Floreano L. 695
Fonda E. 837
Frahm R. 831
Frankel S. C. 721
Frenkel A. I. 721
Fujikawa T. 685, 756
Fukuda K. 756
Geantet C. 724
Giglia A. 695
Giovanelli L. 695
Giovannini S. 695
Gotter R. 695
Göttlicher J. 769
Goulon J. 681
Goulon-Ginet C. 681
Grandjean D. 699
Granwaldt 769
Griesebock B. 831
Grunwaldt J.-D. 769, 819, 831
Guilard R. 681
Guo L. 802
Hachiya H. 807
Hahn A. H. P. 794
Hannemann S. 769
Harris V. G. 744
Hattori T. 813
Hattori Y. 685
Hayes T. M. 703
He B. 784
Hidalgo M. C. 736
Homma T. 714
Hormes J. 671, 773, 790
Hoshino H. 765
Hu T. 784
Hu Y. 675
Huang W. 703
Ibrahim K. 717, 759
Ichihashi Y. 828
Ichikuni N. 756, 807, 825
Iijima S. 685
Imamura M. 724, 787, 828
Ismagilov Z. R. 740
Iwasawa Y. 834
Jaouen N. 681
Jentoft F. C. 794
Jentoft R. E. 794
Jiang J. C. 790
Jiang Y. 733
Jiang Z. 841
Joly Y. 681
Kanaoka K. 749
Kaneko K. 685
Kanezaki E. 749
Kanoh H. 685
Kashino S. 705
Kasuya D. 685
Kato K. 816
Kaučič V. 753, 810
Kawai T. 822
Kawano M. 667
Kelly S. D. 709
Kida K. 691
Kiener C. 819
Kochubey D. I. 736, 740
Kodre A. 753, 810
Köhl G. 671
Kojima I. 784
Konishi T. 685
Kriventsov V. V. 736, 740
Kubo N. 714
Kubota T. 667, 822
Kubozono Y. 705
Kumar Ch. S. S. R. 790
Lahiri D. 776
Lee Y.-K. 822
Li W. B. 749
Liu T. 721, 784
Liu W. 733
Lu P. 781
Luening K. 714
Lützenkirchen-Hecht D. 831

Magnano E. 695
Mahne N. 695
Maisonnat A. 699
Maksimov Yu. V. 736
Mangold S. 769
Marcelli A. 759
Marin G. B. 798
Matsubayashi N. 724, 787, 828
Matsui T. 822, 828
Matsumoto N. 765
Miyanaga T. 765
Modrow H. 671, 773, 790
Morgante A. 695
Moriga T. 749
Morrison S. A. 744
Mörtel R. 671
Murai K.-I. 749
Murakami Y. 749
Murayama H. 825
Nagabhushana K. S. 773
Nagai Y. 664
Nagamatsu S.-I. 756
Nakabayashi I. 749
Nannarone S. 695
Navio J. A. 736
Nayral C. 699
Nemudry A. P. 740
Nicholson D. G. 678
Niwa M. 816
Nonaka T. 664
Nonoyama S. 813
Novak Tušar N. 753, 810
Ohkubo T. 685
Ohnishi S. 781
Ohshiro S. 691
Okamoto Y. 667, 822
Okumura K. 816
Orihara M. 749
Orlanducci S. 717
Oyama T. S. 822
Pailloux F. 837
Palina N. 790
Palkar V. R. 709
Palshin V. 790
Pedio M. 695
Peng C. 703
Persans P. D. 703
Pianetta P. 714
Podyacheva Yu. O. 740
Poelman H. 798
Ramos A. Y. 727
Ressler T. 794
Reyniers M.-F. 798
Richwin M. 831
Riedel C. J. 744
Ristić A. 753, 810
Rogalev A. 681
Roger De Gryse 798
Rong L. X. 661
Ryder J. A. 688
Sakai H. 685, 834
Sancrotti M. 695
Sankar G. 678
Sato K. 724, 787, 828
Sato S. 822
Schüth F. 819
Segre C. U. 709
Sessa V. 717
Sheng B. 733
Shimada H. 724, 787
Shimazu S. 756, 807, 825
Shishido T. 762
Silversmit G. 798
Singh A. 714
Slovokhotov Yu. L. 705
Soulantica K. 699
Spiller E. 695
Stroud R. M. 744
Suda A. 664
Sun M. 802
Suzuki A. 834
Suzuki S. 781
Suzuki Y. 765
Takehira K. 762
Tanaka S. 749
Tanaka T. 664, 762, 828
Tanida H. 816
Teixeira S. R. 837
Terranova M. L. 717
Terry J. 776
Tittsworth R. 790
Tokuhiro A. 776
Tolentino H. C. N. 727
Toshima N. 781
Traverse A. 837
Tsodikov M. V. 736
Uematsu T. 756, 807, 825
Uruga T. 816
van Beek W. 678
van Bokhoven J. A. 798
van der Eerden A. 798
Wang Y. 762
Watanabe N. 727
Watari N. 781
Wei S. 675, 733, 784, 841
Wei Z. 841
Wilhelm F. 681
Wood B. R. 688
Wu Z. Y. 661, 717, 759
Wu Z. 802
Xie Y. 784
Xie Z. 784
Yamaguchi A. 834
Yamamoto T. 664
Yamashita H. 691
Yan W. 733
Yang X. C. 729
Yazawa Y. 813
Yokota S. 816
Yokoyama M. 834
Yoshida H. 813
Yoshimoto R. 816
Yoshimura Y. 822, 828
Yoshizawa K. 691

Yuasa M. 834
Yudasaka M. 685
Zhang J. 661, 802
Zhang Q. 762
Zhang X. 675, 733, 784, 841
Zhong J. 717
Zou S. 675, 841

Biology

Agui A. 873
Barra M. 847
Barrea R. A. 867
Bénazeth S. 870
Benfatto M. 855
Black E. 867
Bohic S. 870
Bunker G. B. 867
Chen L. X. 864
Curis E. 870
Dau H. 844, 847, 859
Fischetti R. 867
Fujii K. 873
García J. 855
Gore D. 867
Grazia Proietti M. 855
Haumann M. 844, 847, 859
Hedman B. 862
Heurich R. 867
Hodgson K. 862
Irving T. C. 867
Karanfil C. 867
Kondrashkina E. 867
Kropf A. J. 867
Lee J.-F. 905, 907, 909
Liebisch P. 844, 847, 859
Liu T. 864
Longa S. D. 855
Müller C. 847
Nakagawa K. 873
Nicolis I. 870
Padrós E. 855
Petoral Jr. R. M. 851
Rosenbaum G. 867
Sepulcre F. 855
Simionovici A. 870
Smolentsev G. 862
Soldatov A. V. 862
Solomon E. 862
Somogyi A. 870
Stepanov S. 867
Tanaka M. 873
Uvdal K. 851
Vukonich M. 867
Wang S. 867
Wasinger E. 862
Yokoya A. 873
Zhang K. 867

Environmental

Akagi T. 897
Auwer C. D. 891
Bargar J. R. 888, 949
Bargar J. 885
Bianchetti C. 918
Bosbach D. 877
Brooks S. C. 915
Brown Jr G. E. 885, 957
Bunker G. 953
Bureau H. 921
Byerly G. R. 918
Carroll S. L. 915
Chalmin E. 885
Cheng N. 907
Conradson S. D. 891
Crocombette J. P. 928
Dacheux N. 925
Dardenne K. 877
Denecke M. A. 877
Di Cicco A. 882
Donnelly M. I. 940
Erko A. 931
Farges F. 885, 921, 923, 928, 957
Fendorf S. 915
Filipponi A. 882
Flank A. M. 928
Fox B. G. 940
Frech W. 894
Fredrickson J. K. 915
Fujiwara S. 946
Giometti C. S. 940
Guilbaud P. 891
Harfouche M. 928
Heisbourg G. 925
Hu M.-J. 909
Huang H.-C. 909
Hubert S. 925
Izumi Y. 933
Kagi H. 897
Karakostas Th. 931
Katsikini M. 931
Kavouras P. 931
Kawano T. 946
Kelly S. D. 915, 940
Kemner K. M. 915, 940
Kennedy D. W. 915
Khare T. 940
Kihou N. 936
Kiyotaki F. 933
Komninou Ph. 931
Lefrère Y. 957
Lindqvist-Reis P. 877
Londer Y. 940
Lowe D. R. 918
Malavergne V. 921
Masih D. 933
Menu M. 885
Minato T. 933
Miura T. 946
Moe L. A. 940
Moisy P. 891
Moisy Ph. 925
Muñoz M. 921
Mustre de Leon J. 891

Ménez B. 921
Nagoshi M. 946
Nakahara K. 946
Nomura M. 897, 901, 936
O'Loughlin E. J. 940
Oshita K. 943
Pallot-Frossard I. 885
Paloura E. C. 931
Pinakidou F. 931
Plymale A. E. 915
Purans J. 925
Qian J. 894
Rossano S. 957
Rossberg A. 912
Rothe J. 877
Roy A. 918
Sakakibara N. 901
Scheinost A. 912
Schiffer M. 940
Schmidt C. 921
Seida Y. 933
Shimizu H. 936
Simionovici A. 921
Simoni E. 891
Skyllberg U. 894
Somogyi A. 921
Susini J. 885
Takahashi Y. 897, 901, 936
Takaoka M. 943, 946
Takeda N. 943
Tanaka T. 943
Tannazi F. 953
Tebo B. M. 885, 949
Trapananti A. 882
Tsuno H. 897
Udagawa S. 946
Uruga T. 943, 946
Vignaud C. 885
Walsh M. W. 918
Wang H.-C. 905
Webb S. M. 888, 949
Wei Y.-L. 905, 907, 909
Wilke M. 921, 957
Winterer M. 923
Yamaguchi Y. 901
Yamamoto T. 943
Yang Y.-W. 905, 907, 909
Yin R. Z. 877
Yuita K. 936
Zachara J. M. 915

Instrumentation

Antonioli G. 986
Belin S. 980
Biquard X. 970
Blank H. 1001
Boscherini F. 986
Briois V. 980
Bruder K. 963
Carboni R. 986
Cezar J. C. 977
Chiba A. 984
Cunnane J. C. 998
Dardenne K. 1001
De Panfilis S. 960
Deleglise M. 970
Demchenko I. 989
Denecke M. A. 1001
Di Cicco A. 960
Dressler P. 1004
Filipponi A. 960
Finch R. J. 998
Fonne C. 1004
Fortner J. A. 998
Frahm R. 963, 974
Fujii Y. 984
Fukano A. 1004
Furukawa Y. 995
Giovannini S. 986
Grand D. 970
Gruszka I. 989
Gutknecht D. 1004
Handa K. 992
Hayata E. 984
Hazemann J.-L. 970
Henck R. 1004
Hormes J. 1001
Hu T. D. 1015
Idir M. 980
Ishii M. 984
Ishikawa T. 995
Jeantet P. 970
Kachniarz J. 989
Kajihara Y. 984
Kajikawa H. 984
Kapoujyan G. 970
Karanfil C. 998
Kasai K. 1004
Keil P. 963
Kobayashi K. 984
Kojima K. 992
Kropf A. J. 998
Lahera E. 970
Lampert M.-O. 1004
Lawniczak-Jablonska K. 989
Lindle D. W. 966, 989
Liu J. 1015
Liu T. 1015
Lützenkirchen-Hecht D. 963
Lützenkirchen-Hecht D. 974
Matsumoto N. 995
Matsuo S. 966
Menthonnex J.-J. 970
Mohamed S. 1004
Molak A. 989
Moreno T. 980
Mori A. 984
Murakami H. 984
Nachimuthu P. 966
Nagaya K. 984
Neueschwander R. 977
Newville M. 1007
Nishikawa Y. 984

Ogawa S. 1004
Ohmasa Y. 984
Oyanagi H. 1004
Ozutsumi K. 992
Perera R. C. C. 966
Perroux G. 970
Piamonteze C. 977
Piskorska E. 989
Prat A. 970
Principi E. 960
Proux O. 970
Ramos A. Y. 977
Ravel B. 1007
Ribbens M. 980
Richwin M. 974
Rothe J. 1001
Roux J-P. 970
Shinoda K. 1017
Soldo Y. 970
Souza-Neto N. M. 977
Taguchi T. 1017
Tamura E. 977
Taunier P. 970
Tohji K. 1017
Tolentino H. C. N. 977
Trapananti A. 960
Traverse A. 980
Trévisson P. 970
Ulrich O. 970
Wakita H. 966
Watanabe N. 977
Webb S. M. 1011
Wolska A. 989
Wu Z. Y. 1015
Xie Y. N. 1015
Yao M. 984
Yoneda Y. 995
Zhang J. 1015

Emerging techniques

Abadias G. 1053
Abe H. 1035
Adams P. C. 1047
Amemiya K. 1035
Aquilanti G. 1056
Baiker A. 1026
Beck K. M. 1044
Bergmann U. 1032
Brewe D. L. 1044
Brouder Ch. 1041
Cabaret D. 1062
Chakrabati S. 1047
Cramer S. P. 1032
Debelle A. 1053
de Groot F. M. F. 1032
Denbeaux G. 1029
De Panfilis S. 1056, 1059
Di Cicco A. 1056, 1059
Dmitrienko V. E. 1062
Feng Y. 1044
Fischer P. 1029
Frahm R. 1026
Gailhanou M. 1053
Gaudry E. 1041
Glatzel P. 1032
Goulon J. 1041
Griesebock B. 1026
Grunwaldt J.-D. 1026
Günzler T. F. 1026
Haeffner D. R. 1026
Haug T. 1029
Heald S. M. 1044
Ishida K. 1062
Jaouen C. 1053
Jaouen M. 1053
Kang D. 1022
Kim P.-S. G. 1047
Kiratisin A. 1041
Kitagawa S. 1035
Kohdate K. 1050
Kokubun J. 1062
Kondoh H. 1050
Kraizman V. L. 1062
Kretzschmar R. 1038
Krivitskii E. V. 1062
Kuhlmann M. 1026
Lengeler B. 1026
Lucovsky G. 1022
Lützenkirchen-Hecht D. 1026
Marcus M. 1038
Mashayekhi A. 1026
Matsumura D. 1035
Mauri F. 1041
Michel A. 1053
Minicucci M. 1056, 1059
Miyawaki J. 1050
Nagai K. 1050
Ngo H. 1047
Nojima A. 1050
Novakovich A. A. 1062
Ohta T. 1035, 1050
Okamoto K. 1050
Pfister S. 1038
Principi E. 1059
Puzic A. 1029
Raabe J. 1029
Ramos A. 1041
Rayner G. B. 1022
Richwin M. 1026
Rogalev A. 1041
Rossberg A. 1038
Sainctavit Ph. 1041
Scheinost A. C. 1038
Schroer C. G. 1026
Schütz G. 1029
Sham T. K. 1019, 1047
Stern E. A. 1044
Stoll H. 1029
Trapananti A. 1056
Vedrinskii R. V. 1062
Waeyenberge B. v. 1029
Watanabe H. 1035
Weckhuysen B. M. 1032

Weiss D. 1029
Yokoyama T. 1035, 1050
Zhang P. 1019
Ziegler E. 1026

Related phenomena

Arai H. 1091
Bernardini R. 1068
Collins S. P. 1065
Damian E. 1077
Di Cicco A. 1068
Dmitrienko V. E. 1065
Fujikawa T. 1091, 1099
Fukushima S. 1080, 1084
Giovenali B. 1068
Gridneva L. K. 1074
Hayashi H. 1094, 1097
Ito Y. 1080, 1084
Jalilehvand F. 1077
Kawamura N. 1094
Kawata M. 1097
Kleimenov E. 1071
Knop-Gericke A. 1071
Krasnikov S. A. 1071, 1074
Laubschat C. 1074
Laundy D. 1065
Li C. 1088
Lu K. 1088
Mannix D. 1065
Mårtensson N. 1071
Matsumoto H. 1099
Miyagawa H. 1094
Molla-Abbassi A. 1077
Molodtsov S. L. 1074
Mukoyama T. 1080, 1084
Nagamatsu S.-i. 1099
Nakamura T. 1094
Nakazawa M. 1099
Nanao S. 1094
Niu X. 1088
Nomura M. 1088
Oohashi H. 1080, 1084
Pettersson L. G. M. 1077
Preobrajenski A. B. 1071, 1074
Principi E. 1068
Sandström M. 1077
Shigeoka N. 1080, 1084
Shoji H. 1094
Szargan R. 1071, 1074
Takeda R. 1094, 1097
Thompson P. 1065
Tochio T. 1080, 1084
Udagawa Y. 1094, 1097
Uruga T. 1088
Vinogradov A. S. 1071, 1074
Vlaicu A. M. 1080, 1084
Wang W. 1088
Wu Z. 1088
Yoshikawa H. 1080, 1084